Synthesis of substituted 4-azaisoindoles — New tacrine analogues

Henri Bekolo and Gilbert Kirsch

Abstract: The regioselective Friedländer reaction of 3-amino-4-cyanopyrroles with a series of cyclic ketones has enabled the first reported synthesis of substituted 4-azaisoindoles. Structurally, this new class of compounds stands for the first reported 4-azaisoindole tacrine analogues. A reaction mechanism for the formation of the reported 4-azaisoindoles is proposed.

Key words: 4-azaisoindoles, tacrine, Friedländer reaction, pyrroles, mechanism.

Résumé : La réaction de Friedländer des 3-amino-4-cyanopyrroles avec une série de cétones cycliques a permis la synthèse d'une nouvelle famille de composés: les 4-azaisoindoles substituées. Ces nouveaux composés sont de nouveaux analogues de la tacrine soit les 4-azaisoindoles analogues de la tacrine dont nous proposons aussi le mécanisme de formation.

Mots-clés : 4-azaisoindoles, tacrine, réaction de Friedländer, pyrroles, mécanisme.

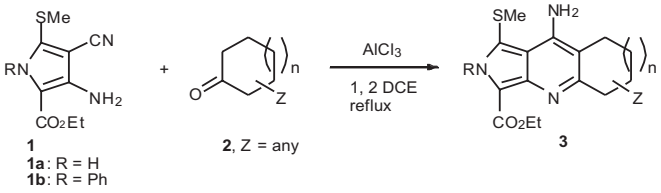
Introduction

We have previously developed an efficient synthesis of 3-amino-4-cyanopyrrole derivatives (1–3) and have set out to investigate their reactivity. Herein we give a preliminary account of our investigations, since pyrroles **1a** (1) and **1b** (3) have proven to be good synthons for the preparation of substituted 4-azaisoindoles **3** (Scheme 1).

While the derivatives of 4-azaindole have been extensively synthesized (4), the synthesis of the derivatives of the isomeric 4-azaisoindole seems to have been neglected despite their possible potential as bioactive molecules. A related example is the potent antitumor agent camptothecin, whose B and C rings system is a reduced tautomeric form of 4-azaisoindole (5). This lack of interest in the synthesis of 4-azaisoindoles stems from the current research endeavour aimed at developing a potent side effect free anti-Alzheimers's disease drug based on a tacrine analogue lead compound. Many research groups have been synthesizing and screening various kinds of heterocyclic system tacrine analogues for biological activities, but none has ever reported a synthesis nor a biological evaluation of 4-azaisoindole tacrine analogues, or any other "pyrrolo" tacrines (6–14), i.e., tacrine analogues having a pyrrole ring in place of the benzene ring of tacrine **4** (Fig. 1).

Tacrine was the first drug approved in the USA for the palliative treatment of Alzheimer's disease. However, its severe side effects, such as hepatotoxicity and gastrointestinal upset, represent an important drawback. Despite these limitations, tacrine appears as an important reference (9). So, a great synthetic and pharmacological research effort has been undertaken to design a tacrine analogue, which would be a more potent and side effect free drug.

Scheme 1. Friedländer synthesis of **3** from **1** and **2**.



Results and discussion

We have prepared 4-azaisoindole tacrine analogues **3a**–**3q** (Tables 1–8) in which, as in the previously reported analogues, the cyclohexane-fused ring (**3b**, **3h**) has been contracted (**3a**), enlarged (**3c**, **3d**), and replaced by functionalized cyclohexane rings (**3e**, **3f**, **3g**, **3l**, **3m**, **3n**, and **3p**) (14), a nitrogen-containing six-membered heterocyclic ring (**3j**) (14), and unlike the previously reported analogues, replaced by a pyran (**3q**) and a thiopyran ring (**3i**).

In most cases the Friedländer cyclizations (9) (Scheme 1) were complete within 2 h, yielding the 4-azaisoindoles **3** in good to quantitative yields, which is noteworthy as the primary amino group of **1** is expected to be weakly nucleophilic (15) and the "pyridine ring" might form at either substituent ortho to the primary amino group.

The α tetralone-type ketones **2e**, **2f**, **2n**, and **2o** were slow to react and required higher reagent–reactant concentrations. Considering the mechanistic pathway 2 (Scheme 2) that we have postulated, this slowness is probably the result of the

Received 28 August 2006. Accepted 20 November 2006. Published on the NRC Research Press Web site at http://canjchem.nrc.ca on 5 January 2007.

H. Bekolo[1] and G. Kirsch. Laboratoire d'Ingénierie Moléculaire et Biochimie Pharmacologique – 1, Boulevard Arago, 57078 Metz, France.

[1]Corresponding author (e-mail: hbekolo@hotmail.com).

 doi:10.1139/V06-180 © 2007 NRC Canada

Fig 1. Tacrine **4**.

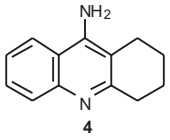
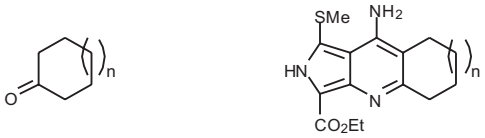


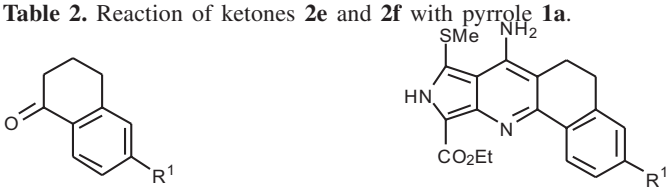
Table 1. Reaction of ketones **2a–2d** with pyrrole **1a**.



Ketone	Time (h)	Product	Yield (%)[a]
2a: n = 0	1	**3a**: n = 0	81
2b: n = 1	1	**3b**: n = 1	92
2c: n = 2	2	**3c**: n = 2	80
2d: n = 3	2	**3d**: n = 3	100

[a]Isolated yields.

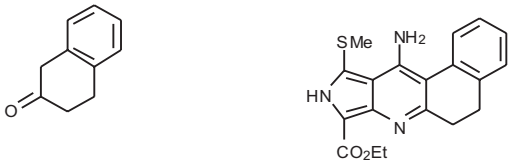
Table 2. Reaction of ketones **2e** and **2f** with pyrrole **1a**.



Ketone	Time (h)	Product	Yield (%)[a,b]
2e: R^1 = H	8	**3e**: R^1 = H	50
2f: R^1 = OMe	15	**3f**: R^1 = OMe	55

[a]Isolated yields.
[b]1,2 DCE (5 mL) was used.

Table 3. Reaction of ketone **2g** with pyrrole **1a**.



Ketone	Time (h)	Product	Yield (%)[a]
2g	2	**3g**	73

[a]Isolated yield.

reduced electrophilicity of the corresponding aluminium chloride coordinated carbonyls **5** whose α aromatic rings act by mesomeric effects as electron suppliers to the developing positive charge induced at the benzylic position by $AlCl_3$, thus slowing the enamine formation steps. As can be seen in Tables 2 and 7, the formations of azaisoindoles **3e** and **3f** assembled from **1a**, and **3n** and **3o** assembled from **1b**, required longer reaction times than those of **3b** and **3h**, respectively.

In the case of the formation of **3e** and **3f**, many unidentified by-products were detected, which would account for the modest obtained isolated yields of 50% and 55%, respectively.

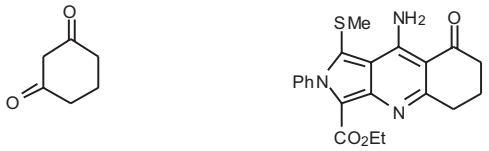
Table 4. Reaction of ketones **2b–2j** with pyrrole **1b**.



Ketone	Time (h)	Product	Yield (%)[a]
2b: X = CH_2	1	**3h**: X = CH_2	76
2i: X = S	1	**3i**: X = S	77
2j: X = N-Ts	2	**3j**: X = N-Ts	70

[a]Isolated yields.

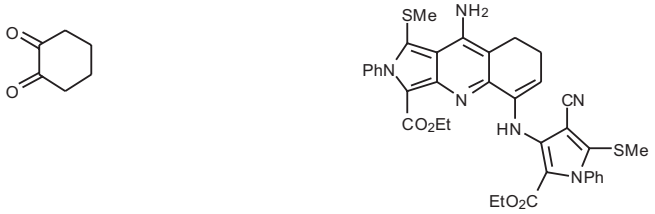
Table 5. Reaction of ketone **2l** with pyrrole **1b**.



Ketone	Time (h)	Product	Yield (%)[a]
2l	2	**3l**	80

[a]Isolated yields.

Table 6. Reaction of ketone **2m** with pyrrole **1b**.



Ketone	Time (h)	Product	Yield (%)[a]
2m	2	**3m**	25

[a]Isolated yields.

Table 7. Reaction of ketones **2n–2p** with pyrrole **1b**.



Ketone	Time (h)	Product	Yield (%)[a,b]
2n: X = O	15	**3n**: X = O	67
2o: X = NH	24	**3o**: X = NH	5
2p: X = N-SO_2Ph	2	**3p**: X = N-SO_2Ph	40

[a]Isolated yield.
[b]1,2 DCE (5 mL) was used.

In line with our reasoning, ketone **2o**, whose α pyrrole ring has a greater electron supplying ability than the furan ring of **2n**, reacted poorly with **1b** even after 24 h of reflux

© 2007 NRC Canada

Scheme 2. Possible mechanistic pathways for the Friedländer cyclization of α tetralone-type ketones.

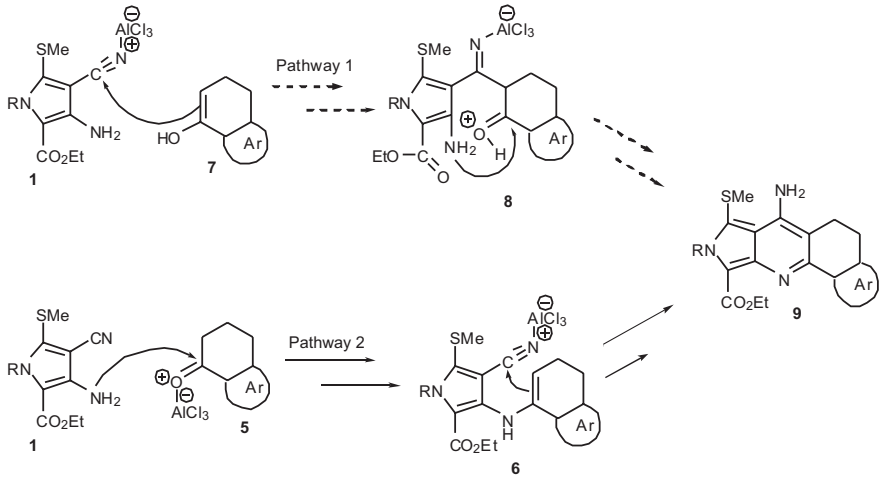
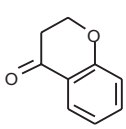
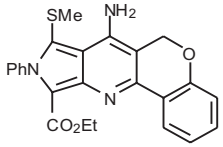


Table 8. Reaction of ketone **2q** with pyrrole **1b**.





Ketone	Time (h)	Product	Yield (%)[a]
2q	2	**3q**	86

[a]Isolated yield.

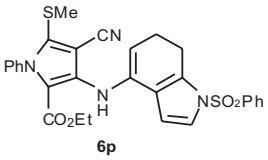
to yield traces (5%) of the corresponding azaisoindole **3o** along with the remaining starting materials **1b** and **2o**. A prolonged reaction time (5 days) resulted in recovering **1b** and **2o**; the expected product **3o** was not detected under these reaction conditions.

To gain further insight into the mechanistic pathway 2, we made the pyrrole ring of **2o** electron-deficient by protecting its NH group as the benzenesulfonylamide **2p**, which, as expected, reacted with **1b** within 2 h, more rapidly than did **2o**. All these facts have supported our proposed mechanistic pathway 2 for the formation of the 4-azaisoindoles of type **9**, and we have made it general for the formation of compounds **3**.

The 4-azaisoindole **3p** was isolated in only 40% yield. This is propably due to the slow intramolecular cyclization of the presumed enamine intermediate **6p** (Fig. 2), whose benzenesulfonyl group raises the energy barrier for the cyclization. Therefore, the uncyclized enamine **6p** might have enough time to undergo competing side reactions. A similar reasoning would account for the low isolated yield (25%) obtained in the case of **3m**; the CO group α to the corresponding enamine intermediate (**6m**) double bond would compare to the benzenesulfonyl group in **6p**. For similar reasons, the "pyridine ring" nitrogen atom might have prevented the possible further intramolecular cyclization of **3m** by raising the energy barrier for cyclization.

The good reactivity of the α tetralone-type ketone **2q** may then be surprising. We believe that the presumed corresponding enamine intermediate might have formed from **2q**

Fig 2. The likely intermediates **6p** and **6m**.



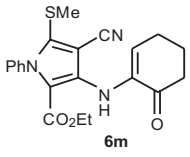
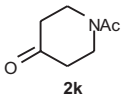
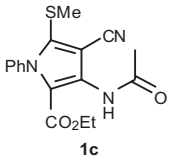


Fig 3. Ketone **2k** and pyrrole **1c**.





coordinated to $AlCl_3$ on both oxygen atoms. The aluminium chloride coordinated pyran ring oxygen would have made the carbonyl group somewhat more electrophilic by an electron-withdrawing inductive effect. The subsequent intramolecular enamine cyclization would have occured within an enamine species whose pyran ring oxygen was free of $AlCl_3$. This presumed positive electronic effect was probably less beneficial to the reactivity of ketone **2f** whose *p*-methoxy group oxygen is relatively far from the carbonyl group.

The mixture of **1b**, $AlCl_3$, and *N*-acetyl-4-piperidone (**2k**) (Fig. 3) was insoluble in refluxing 1,2 dichloroethane (1,2 DCE) and had to be heated for 24 h for complete consumption of pyrrole **1b**. We postulated that the amide functionality (Lewis base) part of piperidone **2k** was sufficiently basic to coordinate to $AlCl_3$ (Lewis acid) to form an insoluble complex, which plagued the reaction and led to the acylation of pyrrole **1b** as we isolated pyrrole **1c** (Fig. 3) as the major product (25%) among numerous by-products we could not separate. Not surprisingly, the basic 1-methyl-4-piperidone and 2,2,6,6-tetramethyl-4-piperidone that we attempted to react with **1b** and $AlCl_3$ in refluxing 1,2 DCE formed insoluble mixtures from which we could isolate what seemed to be degradation products from the ^{1}H NMR of the material we obtained after flash chromatography. We then prepared the less basic *N*-tosyl-4-piperidone (**2j**), which refluxed in a

© 2007 NRC Canada

homogeneous reaction mixture to provide **3j** cleanly in 70% isolated yield within 2 h.

In our effort to improve the yield (5%) of **3o**, the reaction was run in nitrobenzene as solvent at a higher temperature (130 °C) for 1 h, and we isolated some undentified material besides the remaining pyrrole **1b** and ketone **2o**. The use of extra pure H_2SO_4 as the catalyst, instead of $AlCl_3$, in refluxing 1,2 DCE led to complete consumption of **1b** and **2o** and the formation of a presumed new product, whose structure could not be determined by ^{1}H NMR. The acid catalyst, *p*-toluenesulfonic, did not help effect the desired transformation; **1b** and **2o** were recovered after 6 h of reflux in 1,2 DCE.

Attempts to improve the reactivity of 1-methyl-4-piperidone were made. Thus, acetic acid was used as cosolvent. It was believed that its presumed in situ protonated amino group would not coordinate to $AlCl_3$. Unfortunately, the expected cyclization did not proceed under these conditions as **1b** and the piperidone were recovered essentially after a 3 h reflux in CH_3CO_2H–1,2 DCE (1.5:8.5). The mixture of 1-methyl-4-piperidone, **1b,** and $AlCl_3$ in nitrobenzene as solvent at 110 °C resulted in complete disappearance of both reactants within 1 h, and no product was detected by TLC analysis. The use of polyphosphoric acid, instead of $AlCl_3$, in refluxing 1,2 DCE for 3 h was not helpful; only the two reactants were detected in the crude mixture by TLC analysis.

Conclusion

In summary, the standard Friedländer cyclization has enabled the first reported preparation of substituted 4-azaisoindoles and the first reported 4-azaisoindole tacrine analogues that we plan to have tested for biological evaluation.

Experimental

General

Melting points were determined on a Stuart Scientific SMP 3 capillary melting apparatus and were uncorrected. ^{1}H and ^{13}C spectra were recorded on a Brucker AC250 spectrometer using $CHCl_3$ as internal standard. The chemical shifts (δ) are reported in ppm. Commercially available ketones and $AlCl_3$ were used as purchased. Ketones **2j** (16) and **2p** were prepared using standard procedures. Pyrroles **1a** (1) and **1b** (3) were prepared as previously reported. For indications on the preparation of **1b**, please see the following.

Typical procedure for the preparation of 4-azaisoindoles 3

A mixture of pyrrole **1** (0.62 mmol), ketone **2** (3.1 mmol), and $AlCl_3$ (anhyd. granules, 99%, 3.1 mmol) in distilled 1,2 DCE (10 mL) was placed in an oil bath held at 115–120 °C for 2 h. After cooling to RT, a solution of aq. NaOH (pH 14) – THF (1:2, 15 mL) was added. The mixture was stirred for 15 min. Solvents were removed under reduced pressure. To the residue, CH_2Cl_2 (15 mL) and aq. NaOH (20 mL, pH 14) were added. The layers were separated and the aqueous layer was extracted with CH_2Cl_2 (3 × 15 mL). The combined extracts were dried ($MgSO_4$) and concentrated. Purification by flash chromatography (FC) on silica gel (MeOH–CH_2Cl_2, 6:94) afforded **3**.

8-Amino-1-methylsulfanyl-2,5,6,7-tetrahydro-2,4-diaza-s-indacene-3-carboxylic acid ethyl ester (3a)

Yield 81%; yellow crystals; mp 170 °C. ^{1}H NMR ($CDCl_3$) δ: 6.51 (br s, 2H, NH_2), 4.35 (q, *J* = 7.12 Hz, 2H), 2.99 (t, *J* = 7.62, 2H), 2.75 (t, *J* = 7.32 Hz, 2H), 2.48 (s, 3H), 2.25–2.05 (m, 2H), 1.35 (t, *J* = 7.01 Hz, 3H). ^{13}C NMR ($CDCl_3$) δ: 149.2, 138.4, 114.2, 111.3, 110.8, 59.6, 32.0, 26.5, 22.6, 20.5, 13.9. HRMS calcd. for $C_{14}O_2N_3H_{17}S$ $[MH]^+$: 292.111 42; found: 292.1116.

*9-Amino-1-methylsulfanyl-5,6,7,8-tetrahydro-2**H**-pyrrolo[3,4-**b**]quinoline-3-carboxylic acid ethyl ester (3b)*

Yield 92%; yellow crystals; mp 195 °C. ^{1}H NMR ($CDCl_3$) δ: 4.36 (q, *J* = 7.12 Hz, 2H), 2.80–2.60 (m, 2H), 2.44 (s, 5H), 1.95–1.75 (m, 4H), 1.37 (t, *J* = 7.01 Hz, 3H). ^{13}C NMR ($CDCl_3$) δ: 164.9, 151.6, 144.0, 136.3, 127.7, 114.0, 110.6, 104.5, 59.5, 28.7, 21.9, 21.4, 21.3, 20.4, 14.7. HRMS calcd. for $C_{15}O_2N_3H_{19}S$ $[MH]^+$: 306.127 07; found: 306.1271.

*10-Amino-1-methylsulfanyl-2,5,6,7,8,9-hexahydro-2,4-diaza-cyclohepta[**f**]indene-3-carboxylic acid ethyl ester (3c)*

Yield 80%; yellow crystals; mp 185 °C. ^{1}H NMR ($CDCl_3$) δ: 6.84 (br s, 2H, NH_2), 4.37 (q, *J* = 7.12 Hz, 2H), 2.95–2.80 (m, 2H), 2.75–2.60 (m, 2H), 2.47 (s, 3H), 1.83 (m, 2H), 1.71 (m, 2H), 1.59 (m, 2H), 1.38 (t, *J* = 7.01 Hz, 3H). ^{13}C NMR ($CDCl_3$) δ: 164.9, 150.9, 150.6, 135.6, 127.5, 114.3, 111.0, 109.7, 59.5, 35.7, 31.5, 26.5, 25.8, 24.4, 20.6, 14.7. HRMS calcd. for $C_{16}O_2N_3H_{21}S$ $[MH]^+$: 320.142 72; found: 320.1427.

8-Amino-6-methylsulfanyl-2,5-diaza-tricyclo[7.6.0.0^{3,7}]-pentadeca-1,3,6,8-tetraene-4-carboxylic acid ethyl ester (3d)

Yield quant; yellow crystals; mp 205 °C. ^{1}H NMR ($CDCl_3$) δ: 6.69 (br s, 2H, NH_2), 4.38 (q, *J* = 7.12 Hz, 2H), 2.85 (t, *J* = 6.10 Hz, 2H), 2.70 (t, *J* = 6.40 Hz, 2H), 2.49 (s, 3H), 1.79 (m, 2H), 1.68 (m, 2H), 1.49 (m, 2H), 1.43–1.25 (m, 5H). ^{13}C NMR ($CDCl_3$) δ: 165.0, 151.1, 148.0, 136.4, 127.7, 114.3, 110.9, 106.8, 59.4, 33.0, 30.6, 27.8, 25.9, 25.7, 23.0, 20.4, 14.7. HRMS calcd. for $C_{17}O_2N_3H_{23}S$ $[MH]^+$: 334.158 37; found: 334.1583.

*7-Amino-8-methylsulfanyl-5,9-dihydro-6**H**-benzo[**h**]pyrrolo[3,4-b]quinoline-10-carboxylic acid ethyl ester (3e)*

The reaction was carried out in 1,2 DCE (5 mL). FC (MeOH–CH_2Cl_2, 3:97). Yield 50%; yellow crystals; mp 185 °C. ^{1}H NMR ($CDCl_3$) δ: 7.75 (m, 1H), 7.45–7.25 (m, 3H), 6.77 (br s, 2H, NH_2), 4.41 (q, *J* = 7.12 Hz, 2H), 2.96 (t, *J* = 7.31 Hz, 2H), 2.76 (t, *J* = 6.97 Hz, 2H), 2.49 (s, 3H), 1.42 (t, *J* = 7.31 Hz, 3H). ^{13}C NMR ($CDCl_3$) δ: 138.5, 130.6, 128.6, 127.4, 122.7, 114.7, 111.2, 104.8, 59.7, 29.6, 27.8, 20.7, 20.2, 14.7. HRMS calcd. for $C_{19}O_2N_3H_{19}S$ $[MH]^+$: 354.127 07; found: 354.1271.

© 2007 NRC Canada

7-Amino-3-methoxy-8-methylsulfanyl-5,9-dihydro-6H-benzo[h]pyrrolo[3,4-b]quinoline-10-carboxylic acid ethyl ester (3f)

The reaction was carried out in 1,2 DCE (5 mL). FC (MeOH–CH_2Cl_2, 3:97). Yield 55%; reddish crystals; mp 184 °C. ^{1}H NMR ($CDCl_3$) δ: 7.70 (d, J = 7.92 Hz, 1H), 6.95–6.80 (m, 2H), 6.65 (br s, 2H, NH_2), 4.42 (q, J = 7.12 Hz, 2H), 3.85 (s, 3H), 2.95 (t, J = 7.01 Hz, 2H), 2.73 (t, J = 7.01 Hz, 2H), 2.50 (s, 3H), 1.43 (t, J = 7.02 Hz, 3H). ^{13}C NMR ($CDCl_3$) δ: 161.4, 150.6, 140.7, 136.5, 124.1, 121.0, 114.4, 113.8, 112.7, 110.7, 103.6, 59.5, 55.3, 28.1, 20.5, 20.0, 14.7. HRMS calcd. for $C_{20}O_3N_3H_{21}S$ $[MH]^+$: 384.137 64; found: 384.1377.

11-Amino-10-methylsulfanyl-5,9-dihydro-6H-7,9-diaza-cyclopenta[b]phenanthrene-8-carboxylic acid ethyl ester (3g)

$AlCl_3$ (4 equiv.) and ketone (2 equiv.) were used. Yield 73%; greenish crystals; mp 190 °C. ^{1}H NMR ($CDCl_3$) δ: 7.81 (d, J = 7.95 Hz, 1H), 7.36–7.04 (m, 3H), 6.86 (br s, 2H, NH_2), 4.38 (q, J = 7.12 Hz, 2H), 3.05–2.70 (m, 4H), 2.50 (s, 3H), 1.36 (t, J = 7.01 Hz, 3H). ^{13}C NMR ($CDCl_3$) δ: 137.0, 131.3, 128.3, 126.9, 126.4, 124.0, 114.5, 112.0, 105.2, 59.8, 28.2, 20.5, 14.5. HRMS calcd. for $C_{19}O_2N_3H_{19}S$ $[MH]^+$: 354.127 07; found: 354.1271.

9-Amino-1-methylsulfanyl-2-phenyl-5,6,7,8-tetrahydro-2H-pyrrolo[3,4-b]quinoline-3-carboxylic acid ethyl ester (3h)

The reaction mixture refluxed for 1 h. Yield 76%; yellow crystals; mp 100 °C. ^{1}H NMR ($CDCl_3$) δ: 7.55–7.40 (m, 3H), 7.35–7.20 (m, 2H), 4.15 (q, J = 7.12 Hz, 2H), 3.00 (t, J = 5.8 Hz, 2H), 2.53 (t, J = 6.10 Hz, 2H), 2.08 (s, 3H), 1.98–1.75 (m, 4H), 1.08 (t, J = 7.01 Hz, 3H). ^{13}C NMR ($CDCl_3$) δ: 159.0, 154.7, 151.8, 136.4, 131.9, 129.8, 128.7, 127.6, 110.1, 109.4, 108.7, 61.1, 29.4, 22.9, 21.5, 20.9, 20.8, 13.7. HRMS calcd. for $C_{21}O_2N_3H_{23}S$ $[MH]^+$: 382.158 37; found: 382.1585.

9-Amino-1-methylsulfanyl-2-phenyl-2,5,6,8-tetrahydro-7-thia-2,4-diaza-cyclopenta[b]naphthalene-3-carboxylic acid ethyl ester (3i)

Yield 77%; yellow crystals; mp 105 °C. ^{1}H NMR ($CDCl_3$) δ: 7.52 (m, 3H), 7.26 (m, 2H), 5.86 (br s, 2H, NH_2), 4.14 (q, J = 6.72 Hz, 2H), 3.65 (s, 2H), 3.32 (t, J = 6.10 Hz, 2H), 2.97 (t, J = 6.41 Hz, 2H), 2.12 (s, 3H), 0.84 (t, J = 6.40 Hz, 3H). ^{13}C NMR ($CDCl_3$) δ: 159.6, 159.3, 144.4, 141.3, 138.6, 128.2, 127.8, 127.7, 119.8, 115.5, 112.0, 105.6, 59.9, 35.3, 25.2, 22.5, 21.4, 13.7. HRMS calcd. for $C_{20}O_2N_3H_{21}S$ $[MH]^+$: 400.1148; found: 400.1148.

9-Amino-1-methylsulfanyl-2-phenyl-7-(toluene-4-sulfonyl)-5,6,7,8-tetrahydro-2H-2,4,7,-triaza-cyclopenta[b]naphthalene-3-carboxylic acid ethyl ester (3j)

After refluxing, CH_2Cl_2 (15 mL) and aq. NaOH (pH 14, 15 mL) were added, respectively. The two layers were separated. The aqueous layer was extracted with CH_2Cl_2 (2 × 15 mL). The combined organic layers were dried ($MgSO_4$) and concentrated. FC (MeOH–CH_2Cl_2, 3:97). Yield 70%; yellow crystals; mp 162 °C. ^{1}H NMR ($CDCl_3$) δ: 7.74 (d, J = 8.52 Hz, 2H), 7.60–7.40 (m, 3H), 7.35–7.05 (m, 4H), 5.90 (br s, 2H, NH_2), 4.21 (s, 2H), 4.12 (q, J = 7.32 Hz, 2H), 3.43 (t, J = 5.80 Hz, 2H), 3.15 (t, J = 5.80 Hz, 2H), 2.39 (s, 3H), 2.06 (s, 3H), 0.90 (t, J = 7.32 Hz, 3H). ^{13}C NMR ($CDCl_3$) δ: 159.6, 156.2, 144.4, 143.7, 142.1, 138.7, 133.2, 129.7, 128.8, 128.3, 127.9, 127.6, 119.4, 116.0, 111.6, 102.0, 60.0, 43.6, 43.2, 33.7, 21.5, 13.8. HRMS calcd. for $C_{27}O_4N_4H_{28}S_2$ $[MH]^+$: 537.162 47; found: 537.1624.

8-Tetrahydro-2H-pyrrolo[3,4-b]quinoline-3-carboxylic acid ethyl ester (3l)

FC (MeOH–CH_2Cl_2, 1:99). Yield 80%; white crystals; mp 164 °C. ^{1}H NMR ($CDCl_3$) δ: 7.60–7.35 (m, 3H), 7.24–7.14 (m, 2H), 7.09 (br s, 2H, NH_2), 3.98 (q, J = 7.31 Hz, 2H), 2.55 (t, J = 6.10 Hz, 2H), 2.47–2.25 (m, 5H), 2.20–2.00 (m, 2H), 0.89 (t, J = 7.31 Hz, 3H). ^{13}C NMR ($CDCl_3$) δ: 198.2, 160.4, 159.1, 137.6, 130.5, 129.5, 128.8, 104.0, 60.8, 36.4, 29.3, 21.6, 18.4, 13.4. HRMS calcd. for $C_{21}O_3N_3H_{21}S$ $[MH]^+$: 396.137 64; found: 396.1376.

9-Amino-5-(4-cyano-5-ethoxycarbonyl-2-methylsulfanyl-1-phenyl-1H-pyrrol-3-ylamino)-1-methylsulfanyl-2-phenyl-7,8-dihydro-2H-pyrrolo[3,4-b]quinoline-3-carboxylic acid ethyl ester (3m)

FC (100% CH_2Cl_2). Yield 25%; viscous yellow oil. ^{1}H NMR ($CDCl_3$) δ: 7.45 (br s, 1H, NH), 7.60–7.35 (m, 6H), 7.25–7.10 (m, 4H), 6.54 (t, J = 4.57 Hz, 1H), 5.06 (br s, 2H, NH_2), 4.10–3.90 (m, 4H), 2.59 (t, J = 6.40 Hz, 2H), 2.39 (s, 3H), 2.32 (s, 3H), 2.20–2.00 (m, 2H), 1.10–0.80 (m, 6H). ^{13}C NMR ($CDCl_3$) δ: 194.8, 159.6, 145.7, 139.5, 138.0, 134.5, 128.8, 128.7, 128.4, 128.3, 127.9, 127.8, 126.3, 60.0, 59.4, 37.4, 24.2, 23.0, 18.5, 17.9, 13.6, 13.5, 12.8.

6-Amino-7-methylsulfanyl-8-phenyl-5,8-dihydro-4H-3-oxa-8,10-diaza-dicyclopenta[a,g]naphthalene-9-carboxylic acid ethyl ester (3n)

The reaction was carried out in 1,2 DCE (5 mL). FC (MeOH–CH_2Cl_2, 3:97). Yield 67%; yellow crystals; mp 180 °C. ^{1}H NMR ($CDCl_3$) δ: 7.85–7.64 (m, 3H), 7.58 (d, J = 1.82 Hz, 1H), 7.55–7.40 (m, 2H), 7.25 (d, J = 1.82 Hz, 1H), 5.90 (br s, 2H, NH_2), 4.44 (q, J = 7.12 Hz, 2H), 3.35–3.00 (m, 4H), 2.32 (s, 3H), 1.48 (t, J = 7.01 Hz, 3H). ^{13}C NMR ($CDCl_3$) δ: 160.2, 156.3, 152.9, 143.8, 142.5, 141.9, 138.8, 128.6, 128.3, 128.0, 121.2, 119.7, 116.4, 112.6, 107.7, 103.1, 60.0, 21.6, 21.3, 14.0. HRMS calcd. for $C_{23}O_3N_3H_{21}S$ $[MH]^+$: 420.137 64; found: 420.1375.

6-Amino-7-methylsulfanyl-8-phenyl-3,4,5,8-tetrahydro-3,8,10-triaza-dicyclopenta[a,g]naphthalene-9-carboxylic acid ethyl ester (3o)

The reaction was carried out in 1,2 DCE (5 mL). FC (MeOH–CH_2Cl_2, 1.5:98.5). Yield 5%, white crystals. ^{1}H NMR ($CDCl_3$) δ: 8.52 (br s, 1H, NH), 7.55–7.40 (m, 4H), 7.30–7.15 (m, 2H), 6.67 (d, J = 1.85 Hz, 1H), 3.96 (q, J = 7.12 Hz, 2H), 2.75 (t, J = 6.10 Hz, 2H), 2.50 (t, J = 6.10 Hz, 2H), 2.40 (s, 3H), 0.93 (t, J = 7.01 Hz, 3H). ^{13}C NMR δ: 167.2, 159.3, 138.6, 138.0, 129.0, 128.9, 128.6, 128.5, 128.0, 127.9, 119.1, 114.5, 105.5, 59.8, 37.8, 29.6, 23.9, 23.5, 22.6, 18.4, 13.7.

6-Amino-3-benzenesulfonyl-7-methylsulfanyl-8-phenyl-3,4,5,8-tetrahydro-3,8,10-triaza-dicyclopenta[a,g]naphthalene-9-carboxylic acid ethyl ester (3p)

The reaction was carried out in 1,2 DCE (5 mL). After refluxing, the same work-up is used as for **3j**. FC (cyclohexane–

© 2007 NRC Canada

CH_2Cl_2, 2:8). Yield 40%; white crystals; mp 185 °C. ^{1}H NMR ($CDCl_3$) δ: 7.87 (d, *J* = 7.32 Hz, 2H), 7.75–7.40 (m, 6H), 7.29 (d, *J* = 3.65 Hz, 1Hz), 7.25–7.10 (m, 2H), 6.80 (d, *J* = 3.67 Hz, 1H), 3.92 (q, *J* = 7.12 Hz, 2H), 2.50–2.35 (m, 5H), 0.85 (t, *J* = 7.01 Hz, 3H). ^{13}C NMR ($CDCl_3$) δ: 194.2, 166.0, 159.0, 138.8, 138.5, 137.9, 134.5, 134.3, 129.6, 129.1, 128.8, 128.7, 128.5, 127.8, 127.0, 126.9, 124.6, 122.3, 114.1, 109.0, 60.0, 37.3, 28.9, 22.6, 13.6.

7-Amino-8-methylsulfanyl-9-phenyl-6H,9H-5-oxa-9,11-diaza-cyclopenta[b]phenanthrene-10-carboxylic acid ethyl ester (3q)

FC (MeOH–CH_2Cl_2, 3:97). Yield 86%; yellow crystals; mp 215 °C. ^{1}H NMR ($CDCl_3$) δ: 8.44 (d, *J* = 7.92 Hz, 1H), 7.60–7.45 (m, 3H), 7.40–7.20 (m, 3H), 7.10 (t, *J* = 7.62 Hz, 1H), 6.96 (d, *J* = 8.52 Hz, 1H), 5.72 (br s, 2H, NH_2), 5.20 (s, 2H), 4.28 (q, *J* = 7.12 Hz, 2H), 2.11 (s, 3H), 1.33 (t, *J* = 7.01 Hz, 3H). ^{13}C NMR ($CDCl_3$) δ: 160.2, 156.6, 142.7, 138.5, 131.1, 128.9, 128.5, 128.0, 125.8, 122.0, 120.3, 116.6, 112.4, 102.0, 63.6, 60.2, 21.6, 14.1. HRMS calcd. for $C_{24}O_3N_3H_{21}S$ $[MH]^+$: 432.137 64; found: 432.1377.

1-Benzenesulfonyl-1,5,6,7-tetrahydro-indol-4-one (2p)

To a solution of **2o** (0.3 g, 2.2 mmol, 1 equiv.) in 1,2 DCE (1 mL) was added benzenesulfonyl chloride (1.6 g, 8.8 mmol, 4 equiv.), Et_3N (1.8 g, 17.6 mmol, 8 equiv.) in 1,2 DCE (2 mL). The mixture was placed in an oil bath held at 93 °C for 1 h. HCl 1N (3 mL) and CH_2Cl_2 (10 mL) were added. The 2 layers were separated and the aqueous layer was extracted with CH_2Cl_2 (2 × 5 mL). The combined organic layers were dried ($MgSO_4$) and concentrated. Purification by FC (cyclohexane–CH_2Cl_2, 1:99) afforded **2p**. Yield 73%; beige solid; mp 122 °C. ^{1}H NMR ($CDCl_3$) δ: 7.85 (d, *J* = 7.92 Hz, 2H), 7.75–7.45 (m, 3H), 7.23 (d, *J* = 3.05 Hz, 1H), 6.60 (d, *J* = 3.05 Hz, 1H), 2.95 (t, *J* = 6.10 Hz, 2H), 2.39 (t, *J* = 6.40 Hz, 2H), 2.07 (m, 2H). ^{13}C NMR ($CDCl_3$) δ: 194.1, 143.6, 138.0, 134.5, 129.7, 126.9, 124.7, 122.2, 108.2, 37.2, 23.1, 22.7.

3-Amino-4-cyano-5-methylsulfanyl-1-phenyl-1H-pyrrole-2-carboxylic acid ethyl ester (1b)

This compound, fully described in ref. 3, was made according to the methodology we developed in ref. 2 for the preparation of compound 3 (see ref.2, Scheme 3) therein. The ketene phenylaminomethylthioacetal (see ref. 2, Table 3, entry e) was used. The mixture was refluxed in acetone for 5 days. Yield 70%; white crystals; mp 147–149 °C. ^{1}H NMR ($CDCl_3$) δ: 7.17–7.50 (m, 5H), 5.06 (br s, 2H, NH_2), 4.01 (q, *J* = 7.20 Hz, 2H), 2.40 (s, 3H), 0.94 (t, *J* = 7.20 Hz, 3H).

Acknowledgments

HB thanks Professor G. Kirsch for providing us with space and chemicals and graduate student David Thomae for helpful discussions.

References

1. G.L. Sommen, A. Comel, and G. Kirsch. Synth. Commun. **35**, 693 (2005).
2. G.L. Sommen, A. Comel, and G. Kirsch. Tetrahedron, **59**, 1557 (2003).
3. G.L. Sommen. Ph.D. Thesis, Département de Chimie, Université de Metz, Metz, France. 2003.
4. S. Cacchi, G. Fabrizi, and L.M. Parisi. J. Comb. Chem. **7**, 510 (2005).
5. Z. Zhang, K. Tanabe, H. Hatta, and S. Nishimoto. Org. Biomol. Chem. **3**, 1905 (2005).
6. K. Ninomiya, M. Sugano, A. Tobe, T. Morikana, T. Bessho, and H. Harada. Eur. Patent EP 0-427-636-A2, 15 May 1991.
7. P.R. Carlier, D.-M. Du, Y. Han, J. Liu, and Y.-P. Pang. Bioorg. Med. Chem. Lett. **9**, 2335 (1999).
8. P. Camps, R.E. Achab, J. Morral, D. Munoz-Torrero, A. Badia, J.E. Banos, N.M. Vivas, X. Barril, M. Orozco, and F.J. Luque. J. Med. Chem. **43**, 4657 (2000).
9. J.L. Marco, C. Rios, A.G. Garcia, M. Villarroya, M.C. Carreiras, C. Martins, A. Euleuterio, M. Orozco, and F.J. Luque. Bioorg. Med. Chem. **12**, 2199 (2004).
10. M. Rosini, V. Andrisano, M. Bartolini, M.L. Bolognesi, P. Hrelia, A. Minarini, A. Tarozzi, and C. Melchiorre. J. Med. Chem. **48**, 360 (2005).
11. A. Cappelli, A. Galleli, M. Manini, M. Anzini, L. Mennuni, F. Makovec, M.C. Menziani, S. Alcaro, F. Ortuso, and S. Vomero. J. Med. Chem. **48**, 3564 (2005).
12. E.J. Hennessy and S.L. Buchwald. J. Org. Chem. **70**, 7371 (2005).
13. M.I. Rodriguez-Franco, M.I. Fernandez-Bachiller, C. Perez, B. Hernandez-Ledesma, and B. Bartolome. J. Med. Chem. **49**, 459 (2006).
14. M.T. McKenna, G.R. Proctor, L.C. Young, and A.L. Harvey. J. Med. Chem. **40**, 3516 (1997).
15. R.A. Crochet, J.T. Boatright, C.D. Blanton, C.T. Wie, and W.E. Hochholzer. J. Heterocycl. Chem. **11**, 143 (1974).
16. T.A. Engler and J. Wanner. J. Org. Chem. **65**, 2444 (2000).

© 2007 NRC Canada

The efficient and chemoselective MoO_3-catalyzed oxidation of sulfides to sulfoxides and sulfones with H_2O_2

Mohammad Mehdi Khodaei, Kiumars Bahrami, and Mohammad Khedri

Abstract: Hydrogen peroxide together with MoO_3 as catalyst can efficiently and chemoselectivity oxidize sulfides to sulfoxides and sulfones in the presence of other oxidized functional groups in ethanol at 50 °C in short reaction times.

Key words: oxidation, sulfides, sulfoxides, sulfones, H_2O_2–MoO_3 system.

Résumé : En opérant dans l'éthanol à 50 °C pour de courtes périodes, le peroxyde d'hydrogène en présence de MoO_3 comme catalyseur peut oxyder d'une façon efficace et chimiosélective les sulfures en sulfoxydes et en sulfones, en présence d'autres groupes fonctionnels oxydés.

Mots-clés : oxydation, sulfures, sulfoxydes, sulfones, système H_2O_2–MoO_3.

[Traduit par la Rédaction]

Introduction

Sulfoxides are important intermediates in organic chemistry because of their application in fundamental research and other extended usage (1–7). As the sulfoxides are important for carbon–carbon bond formation and functional group transformation, the search for new methods for the selective oxidation of sulfides to sulfoxides continues despite the existence of a number of methods available for this transformation. Selective oxidation of sulfides to sulfoxides and sulfones with the same reagent system under adjusted reaction conditions is an important process in synthetic organic chemistry and only a few reports are available in the literature (8–13).

Aqueous hydrogen peroxide is an attractive oxidant because it is cheap, safely stored and handled, environmentally friendly, contains effective oxygen, and produces only water as a byproduct, which is easy to deal with after reactions. There are many reports on oxidation reactions of sulfides carried out by a combination of H_2O_2 and a catalyst that often increase the efficiency of the oxidant, and therefore the presence of the catalyst as an activator in the reaction can be necessary (14–26).

Results and discussion

In continuation of our research on the oxidation of organic compounds (27–29), we report here our efforts in developing new catalytic procedures for the oxidation of sulfides to sulfoxides and sulfones using aqueous hydrogen peroxide catalyzed by MoO_3 (Scheme 1).

A range of sulfides, dialkyl, diaryl, alkyl, aryl, and cyclic sulfides were subjected to the developed reaction procedure to afford sulfoxides with high chemoselectivity and excellent yields. The procedure proved to be compatible with other functional groups and to work under neutral conditions. Hydrogen peroxide was used as a 30% solution in water.

We carried out our initial studies with dibenzyl sulfide to find optimal reaction conditions. After studying various amounts of catalyst, we found that 0.05 equiv. of the catalyst was the best choice. Ethanol was selected as the best solvent as lower catalytic activity was observed with other solvents such as chloroform, dichloromethane, acetonitrile, and water. The optimum amount of H_2O_2 (30%) in this system was found to be 1.3 mmol; when higher amounts of oxidant was employed, a significant increase in the sulfone was observed. For dibenzyl sulfide, a separate experiment showed that the presence of the catalyst is necessary, since oxidation with H_2O_2 alone occurs rather slowly. Looking at the results reported in Table 1, it is readily seen that the reaction is very efficient, affording excellent yields of sulfoxides, generally around 95%, with a reaction time as short as 9 min. The selectivity with respect to the formation of sulfone is also high.

The chemoselectivity of sulfoxidation of sulfides containing a double bond was examined. As shown in Table 1, entry 13, high chemoselectivity was found as the sulfoxide was obtained in high yield without any detectable epoxidation of the double bond. Further selectivity of the proposed method was investigated and the results are indicated in Scheme 2. As can be seen, sulfides were selectively converted to

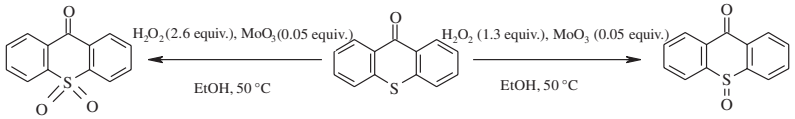
Received 20 September 2006. Accepted 17 November 2006. Published on the NRC Research Press Web site at http://canjchem.nrc.ca on 6 January 2007.

M.M. Khodaei,[1] K. Bahrami, and M. Khedri. Department of Chemistry, Faculty of Science, Razi University, Kermanshah 67149, Iran.

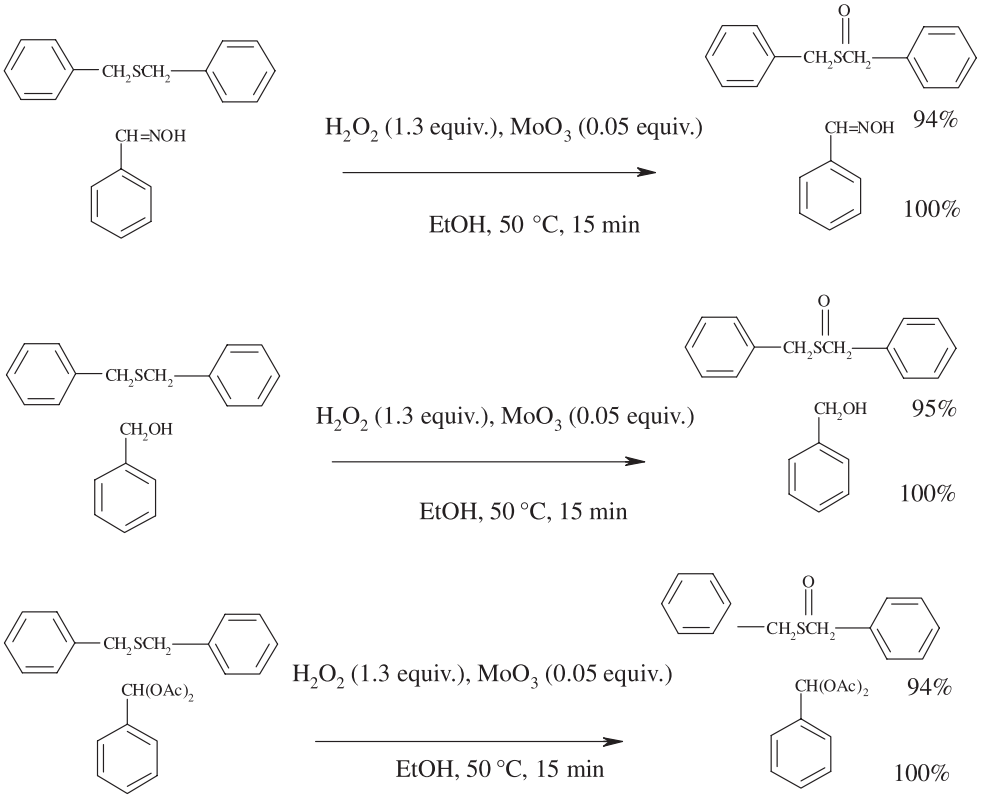
[1]Corresponding author (e-mail: mmkhoda@razi.ac.ir).

 doi:10.1139/V06-177 © 2007 NRC Canada

Scheme 1.



Scheme 2.



sulfoxides, while the oxime, acylal, and alcohol remained untouched under the same reaction conditions.

For the synthesis of sulfones several experiments were carried out with a 2.0:1 H_2O_2–substrate molar ratio to check whether sulfone could be efficiently obtained by using just a stoichiometric amount of oxidant and also whether in this case the high chemoselectivity found in the synthesis of sulfoxides could be observed. It was found that with 2.6 equiv. of oxidant a very efficient synthesis of sulfones is possible using higher concentrations of catalyst and longer reaction times than those used for the synthesis of sulfoxides. In all cases sulfones were isolated in almost quantitative yields. Sulfones were also obtained without any detectable formation of the corresponding epoxides (Table 2, entry 24). The results of the synthesis of sulfoxides from sulfides in different reaction conditions are listed in Table 3, which shows that our conditions were more effective than some others with respect to the yield and to the time of the reaction.

In conclusion, this catalytic system efficiently promoted the oxidation of sulfides to sulfoxides and sulfones. The method is simple, mild, and inexpensive. A further advantage of this method is its chemoselectivity in the presence of other oxidized functional groups.

Experimental

General experimental procedure for the preparation of sulfoxides

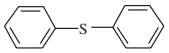
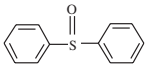
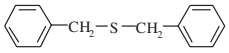
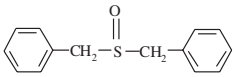
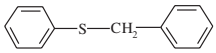
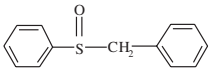
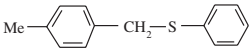
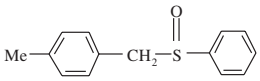
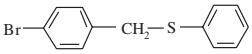
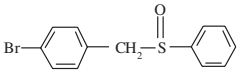
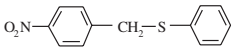
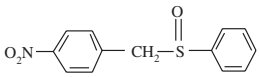
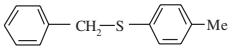
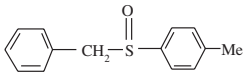
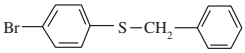
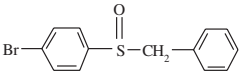
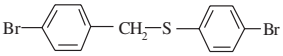
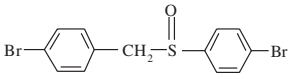
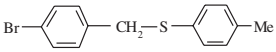
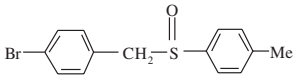
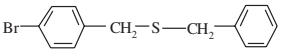
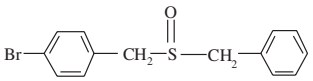
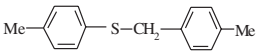
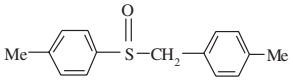
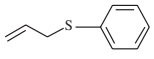
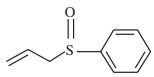
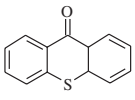
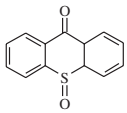
In a round-bottomed flask, H_2O_2 30% (0.15 mL, 1.34 mmol) was added to a mixture of sulfide (1 mmol) and MoO_3 (0.05 mmol, 0.007 g) in EtOH (2 mL). This mixture was stirred at 50 °C for the appropriate time according to Table 1. The progress of the reaction was followed by TLC. After completion of the reaction, H_2O (15 mL) was added to the reaction mixture and filtered. The solid residue was recrystallized from ethanol to obtain the pure product in 95%–98% yields.

General experimental procedure for the preparation of sulfones

To a mixtuure of sulfide (1 mmol) and MoO_3 (0.05 mmol, 0.007 g) in EtOH (2 mL), 30% aq. H_2O_2 (0.3 mL, 2.67 mmol) was added and the mixture was refluxed for 8–30 min (Table 2). The progress of the reaction was followed by TLC. After completion of the reaction, H_2O (15 mL) was added to the reaction mixture and filtered. The solid residue was recrystallized from ethanol to obtain the pure product in 92%–98% yields.

© 2007 NRC Canada

Table 1. Oxidation of sulfides to sulfoxides using an H_2O_2–MoO_3 system in ethanol.

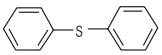
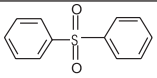
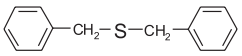
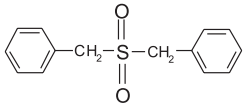
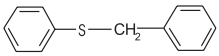
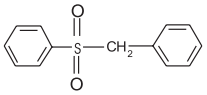
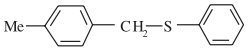
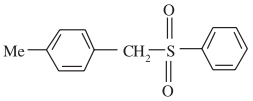
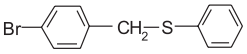
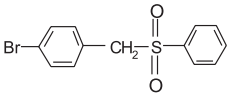
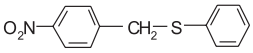
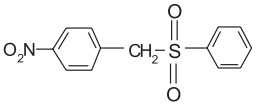
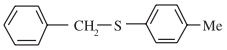
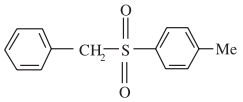
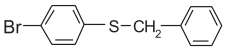
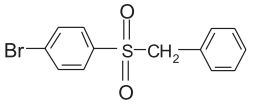
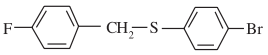
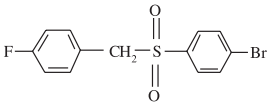
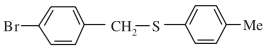
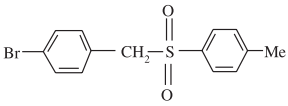
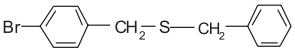
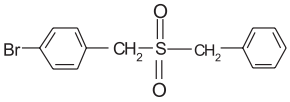
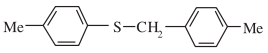
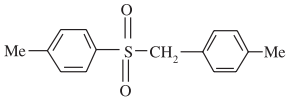
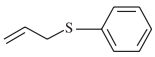
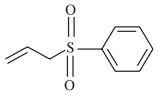
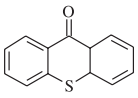
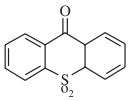
Entry	Substrate	Time (min)	Yield (%)[a]	Product
1		12	98	
2		14	96	
3		15	97	
4		9	97	
5		11	96	
6		17	95	
7		16	97	
8		14	96	
9		18	97	
10		12	97	
11		16	96	
12		13	98	
13		15	94	
14		40	98	

Note: All products were identified by comparison of their physical and spectral data with those reported in the literature.

[a]Isolated yields.

© 2007 NRC Canada

Table 2. Oxidation of sulfides to sulfones using an H_2O_2–MoO_3 system in ethanol.

Entry	Substrate	Time (min)	Yield (%)[a]	Product
1		40	97	
2		43	97	
3		40	98	
4		41	98	
5		50	98	
6		48	97	
7		43	98	
8		51	98	
9		50	97	
10		51	97	
11		46	97	
12		48	98	
13		45	94	
14		65	98	

Note: All products were identified by comparison of their physical and spectral data with those reported in the literature.

[a]Isolated yields.

© 2007 NRC Canada

Table 3. Comparison of the effects of different conditions for diphenylsulfoxide preparation from diphenylsulfide.

Entry	Conditions	Yield (%)	Time (min)	Ref.
1	MoO_3 (0.05 mmol), H_2O_2 (1.34 mmol), 50 °C, EtOH	98	12	
2	$PMo_{11}VO_{40}H_3Py$ (0.01mol), H_2O_2 (2 equiv.), RT, CH_3CN	95	120	30
3	Mn (III) Schiff-base complex (0.03 mmol), H_2O_2 (4 equiv.), RT, CH_3COOH	91	35	24
4	MoO_2Cl_2 (1.5 mol%), H_2O_2 (1.05 equiv.), RT, CH_3COCH_3–H_2O (1.5:1.0)	89	20	31
5[a]	TEMPO (0.01 mmol), Cu (II) complex (0.005 mmol), H_2O_2 (2 equiv.), 20 °C, CH_3CN	99	270	25
6[a]	$(Bu_4N)_3[PMo_{12}O_{40}]$ (0.01 mmol) – FAp (1 g), H_2O_2 (1.05 equiv.), 4 °C, solvent-free	85	4320	32
7	SeO_2 (1 equiv.), H_2O_2 (1 equiv.), RT, MeOH	90	10	26

[a]The sulfide was methyl phenyl sulfide.

Spectroscopic data

Compound **4** (Table 1) mp 97–99 °C. IR (KBr, cm^{-1}) ν_{max}: 1027. ^1H NMR (500 MHz, $CDCl_3$) δ_H: 7.50–7.41 (m, 5H), 7.08 (d, J = 7.7 Hz, 2H), 6.90 (d, J = 7.7 Hz, 2H), 4.08 (d, J = 12.6 Hz, 1H), 3.97 (d, J = 12.6 Hz, 1H), 2.35 (s, 3H).

Compound **8** (Table 1) mp 139 to 140 °C. IR (KBr, cm^{-1}) ν_{max}: 1067, 1034. ^1H NMR (500 MHz, $CDCl_3$) δ_H: 7.58 (d, J = 8.3 Hz, 2H), 7.32–7.27 (m, 3H, Ph), 7.24 (d, J = 8.3 Hz, 2H), 7.02 (d, J = 8.3 Hz, 2H), 4.10 (d, J = 12.5 Hz, 1H), 4.00 (d, J = 12.5 Hz, 1H).

Compound **4** (Table 2) mp 150–152 °C. IR (KBr, cm^{-1}) ν_{max}: 1137, 1298. ^1H NMR (500 MHz, $CDCl_3$) δ_H: 7.70–7.67 (m, 2H), 7.62 (t, J = 7.5 Hz, 1H), 7.48 (t, J = 7.5 Hz, 2H), 7.10 (d, J = 7.9 Hz, 2H), 7.00 (d, J = 7.9 Hz, 2H), 4.30 (s, 2H), 2.36 (s, 3H).

Compound **8** (Table 2) mp 156–158 °C. IR (KBr, cm^{-1}) ν_{max}: 1305, 1140, 1080. ^1H NMR (500 MHz, $CDCl_3$) δ_H: 7.60 (d, J = 8.5 Hz, 2H), 7.48 (d, J = 8.5 Hz, 2H), 7.37–7.30 (m, 3H), 7.10 (d, J = 7.2 Hz, 2H), 4.32 (s, 2H).

Acknowledgments

We are thankful to the Razi University Research Council for partial support of this work.

References

1. M. Hudlicky. Oxidation in organic chemistry. ACS Monograph Ser. 186. American Chemical Society, Washington, DC. 1990. p. 252.
2. J. Drabowski, P. Kielbasinski, and M. Mikolajczyk. Synthesis of Sulfoxides. John Wiley and Sons, New York. 1994.
3. S. Pati and Z. Rappoport. The synthesis of sulphones, sulphoxides, and cyclic sulphides. John Wiley and Sons, New York. 1994.
4. R.S. Varma, R.K. Saini, and H.M. Meshram. Tetrahedron Lett. **38**, 6525 (1997).
5. G.W. Gokel, H.M. Gerdes, and D.M. Dishong. J. Org. Chem. **45**, 3634 (1980).
6. W. Adam and L. Hadjiarapoglou. Tetrahedron Lett. **33**, 469 (1992).
7. Y. Ishii, H. Tanaka, and Y. Nishiyama. Chem. Lett. 1 (1994).
8. C.G. Venier, T.G. Squires, Y.-Y. Chen, G.P. Hussmann, J.C. Shei, and B.F. Smith. J. Org. Chem. **47**, 3773 (1982).
9. A. McKillop and J.A. Tarbin. Tetrahedron Lett. **24**, 1505 (1983).
10. R.P. Greenhalgh. Synlett, 235 (1992).
11. S. Yamazaki. Bull. Chem. Soc. Jpn. **69**, 2955 (1996).
12. R.S. Varma, R.K. Saini, and H.M. Meshram. Tetrahedron Lett. **38**, 6525 (1997).
13. B.M. Choudary, B. Bharathi, C.V. Reddy, and M.L. Kantam. J. Chem. Soc. Perkin Trans. 1, 2069 (2002).
14. D. Bethell, P.C.B. Page, and H. Vahedi. J. Org. Chem. **65**, 6756 (2000).
15. K. Yazu, T. Furuya, K. Miki, and K. Ukegawa. Chem. Lett. **32**, 920 (2003).
16. M. Matteucci, G. Bhalay, and M. Braley. Org. Lett. **5**, 235 (2003).
17. B. Yadollahi. Chem. Lett. **32**, 1066 (2003).
18. E. Baciocchi, M. Francesca Gerini, and A. Lapi. J. Org. Chem. **69**, 3586 (2004).
19. Y.-C. Jeong, S. Choi, Y.D. Hwang, and K.-H. Ahn. Tetrahedron Lett. **45**, 9249 (2004).
20. S. Velusamy, A. V. Kumar, R. Saini, and T. Punniyamurthy. Tetrahedron Lett. **46**, 3819 (2005).
21. K. Kaczorowska, Z. Kolarska, M. Katarzyna, and P. Kowalski. Tetrahedron, **61**, 8315 (2005).
22. K. Bahrami. Tetrahedron Lett. **47**, 2009 (2006).
23. J.R. Lindsay Smith, J. Murray, P.H. Walton, and T.R. Lowdon. Tetrahedron Lett. **47**, 2005 (2006).
24. F. Hossienpoor and H. Golchoubian. Tetrahedron Lett. **47**, 5195 (2006).
25. S. Velusamy, A.V. Kumar, R. Saini, and T. Punniyamurthy. Tetrahedron Lett. **46**, 3819 (2005).
26. J. Drabowicz and M. Mikolajczyk. Synthesis, 758 (1978).
27. M.M. Khodaei, P. Salehi, and M. Goodarzi. Synth. Commun. **31**, 1253 (2001).
28. P. Salehi, M.M. Khodaei, and M. Goodarzi. Synth. Commun. **32**, 1259 (2002).
29. P. Salehi, M.M. Khodaei, and M. Goodarzi. Russ. J. Org. Chem. 392 (2002).
30. G.P. Romanelli, P.G. Vazquez, and P. Tundo. Synlett, 75 (2005).
31. K. Jeyakumar and D.K. Chand. Tetrahedron Lett. **47**, 4573 (2006).
32. Y. Sasaki, K. Ushimarou, K. Iteya, H. Nakayama, S. Yamaguchi, and J. Ichihara. Tetrahedron Lett. **45**, 9513 (2004).

© 2007 NRC Canada

Electron-donating methoxyl group position effect on properties of diarylethene derivatives having a pyrazole unit

Tianshe Yang, Shouzhi Pu, Bing Chen, Jingkun Xu

Abstract: New types of asymmetrical photochromic diarylethene derivatives having a pyrazole unit, namely 1-[1,3,5-trimethyl-1-pyrazol-4-yl],2-[2-methyl-5-(4-methoxylphenyl)-1-thien-3-yl]perfluorocyclopentene (**1a**), 1-[1,3,5-trimethylpyrazol-4-yl],2-[2-methyl-5-(3-methoxylphenyl)-1-thien-3-yl] perfluorocyclopentene (**2a**), 1-[1,3,5-trimethyl-pyrazol-4-yl],2-[2-methyl-5-(2-methoxylphenyl)-1-thien-3-yl]perfluorocyclopentene (**3a**), and 1-[1,3,5-trimethyl-pyrazol-4-yl],2-[2-methyl-5-phenyl-1-thien-3-yl]perfluorocyclopentene (**4a**), were synthesized. Their optical and electrochemical properties, such as photochromism, photochromic cyclization–cycloreversion kinetics, and fluorescence and electrochemical properties were investigated in detail. The results show that all of these compounds have good photochromism, high cycloreversion quantum yield, and relatively strong fluorescence. Their cyclization–cycloreversion processes were determined to be zeroth to first order reactions. The oxidations of diarylethenes **1a**–**4a** were initiated at 0.73, 1.11, 0.79, and 1.03 V, respectively. Furthermore, introduction of the electron-donating methoxyl group at different positions of the terminal phenyl ring was found to strongly influence these optical and electrochemical properties.

Key words: photochromism, diarylethene, electron-donating group, optical and electrochemical properties.

Résumé : On a effectué la synthèse de nouveaux types de dérivés diaryléthènes asymétriques et photochomiques comportant une unité pyrazole, soit le 1-[1,3,5-triméthyl-1-pyrazol-4-yl]-2-[2-méthyl-5-(4-méthoxyphényl)-1-thién-3-yl]perfluorocyclopentène (**1a**), le 1-[1,3,5-triméthyl-1-pyrazol-4-yl]-2-[2-méthyl-5-(3-méthoxyphényl)-1-thién-3-yl]perfluorocyclopentène (**2a**), le 1-[1,3,5-triméthyl-1-pyrazol-4-yl]-2-[2-méthyl-5-(2-méthoxyphényl)-1-thién-3-yl]perfluorocyclopentène (**3a**) et le 1-[1,3,5-triméthyl-1-pyrazol-4-yl]-2-[2-méthyl-5-phényl-1-thién-3-yl]perfluorocyclopentène (**4a**). Les propriétés optiques et électrochimiques, telle la photochromie, la cinétique de la cyclisation/cycloréversion photochromique, la fluorescence et les propriétés électrochimiques ont toutes été étudiées en détail. Les résultats montrent que tous ces composés ont une bonne photochromie, un rendement quantique de cycloréversion élevé et une fluorescence relativement forte. On a déterminé que le processus des réactions cyclisation/cycloréversion est d'ordre zéro/un. Les oxydations des diaryléthènes **1a**–**4a** sont respectivement initiées à 0,73, 1,11, 0,79 et 1,03 V. De plus, on a observé que l'introduction du groupe méthoxy électrodonneur dans différentes positions du noyau benzénique terminal influence fortement les propriétés optiques et électrochimiques examinées plus haut.

Mots-clés : photochromie, diaryléthène, groupe électrodonneur, propriétés optiques et électrochimiques.

[Traduit par la Rédaction]

Introduction

Photochromic compounds have attracted considerable attention because of their potential application in photonic devices such as optical memories, photo-switches, and full-color displays (1–3). For practical application in optoelectronic devices, photochromic compounds should have good thermal stability at room temperature and high sensitivity. In addition, it is required to further develop thermally irreversible photochromic compounds whose photogenerated colored isomers are very stable and never return to the initial colorless isomers in the dark (4). Recently, several thermally irreversible photochromic compounds, such as furylfulgides, phenoxynaphthacene-quinones, and diarylethenes have been developed (5). Of these compounds, diarylethene derivatives are the most promising candidates for these applications because of their excellent thermal stability in both isomers, fatigue-resistant character, rapid response, and high reactivity in the solid state (6, 7).

To date, a large number of results concerning the synthesis and photochromic properties of diarylethenes with heterocyclic aryl rings have been reported. Among diarylethene derivatives synthesized to date, most are composed of thiophene or benzothiophene hetero-aryl groups (6–13). These compounds are known to exhibit excellent thermal

Received 12 October 2006. Accepted 29 November 2006. Published on the NRC Research Press Web site at http://canjchem.nrc.ca on 10 January 2007.

S. Pu.[1] Jiangxi Key Lab of Organic Chemistry, Jiangxi Science and Technology Normal University, Nanchang 330013, China; School of Chemistry & Chemical Engineering, Jiangsu Teachers University of Technology, Changzhou 213001, P.R. China.
T. Yang, B. Chen, and J. Xu. Jiangxi Key Lab of Organic Chemistry, Jiangxi Science and Technology Normal University, Nanchang 330013, P.R. China.

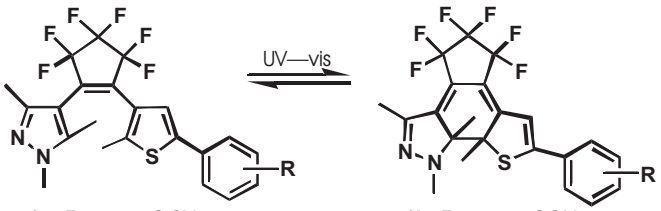
[1]Corresponding author (e-mail: pushouzhi@tsinghua.org.cn).

 doi:10.1139/V06-182 © 2007 NRC Canada

stability of both isomers and fatigue-resistant characteristics (6). In particular, diarylethenes with thiophene ring systems bearing terminal phenyl groups have been of considerable interest because the end group can be substituted by an electron-donating or -withdrawing group. These groups can inevitably influence the optoelectronic properties of corresponding diarylethenes (14). Besides diarylethene derivatives with thiophene or benzothiophene moieties, other hetero-aryl moieties, such as thiazole, (15–17), pyrrole (18), indole (19, 20), indene (21), benzofuran (22), crysothiophene (23) have also been reported. The photochromic performance of each kind of diarylethene derivative is strongly dependent on the aryl moieties. For example, diarylethenes with indole rings exhibit strong fluorescence (19), whereas those with pyrrole rings are thermally unstable and return to open-ring isomers even in the dark (22). When the aryl groups have low aromatic stabilization energy, the derivatives undergo thermally irreversible photochromic reactions (21). Pyrazole is an attractive aryl unit because of its low aromatic stabilization energy and the structure is similar to isothiazole and so is expected to undergo thermally irreversible photochromic reactions. Until now, photochromic hybrid diarylethene derivatives with pyrazole and thiophene moieties have not been reported, with the exception of one letter published by us (24).

For this paper, one of our research goals was to develop a new class of diarylethene derivatives that show good photochromic behavior. We also want to discuss the effect of electron-donating methoxyl group position on the optical and electrochemical properties of diarylethenes. Therefore, we have synthesized four asymmetrical diarylethene derivatives bearing a pyrazole unit and a thiophene moiety with methoxyl group at the para, meta, and ortho positions of terminal phenyl group, i. e. 1-[1,3,5-trimethyl-1-pyrazol-4-yl], 2-[2-methyl-5-(4-methoxylphenyl)-1-thien-3-yl]perfluorocyclopentene (**1a**), 1-[1,3,5- trimethylpyrazol-4-yl],2-[2-methyl-5-(3-methoxylphenyl)-1-thien-3-yl]perfluorocyclopentene (**2a**), 1-[1,3,5-trimethyl-pyrazol-4-yl],2-[2-methyl-5-(2-methoxylphenyl)-1-thien-3-yl]perfluorocyclopentene (**3a**), 1-[1,3,5-trimethyl-pyrazol-4-yl],2-[2-methyl-5-phenyl-1-thien-3-yl] perfluorocyclopentene (**4a**). The photochromism of diarylethenes **1a**–**4a**, which are discussed in this study, is shown in Scheme 1.

Scheme 1. Photochromism of diarylethenes **1a**–**4a.**



1a: R = *para*-OCH_3 **1b:** R = *para*-OCH_3
2a: R = *meta*-OCH_3 **2b:** R = *meta*-OCH_3
3a: R = *ortho*-OCH_3 **3b:** R = *ortho*-OCH_3
4a: R = H **4b:** R = H

Experimental

General methods

All solvents were purified by distillation before usage. NMR spectra were recorded on a Bruker AV400 (400 MHz) spectrometer using $CDCl_3$ as solvent and tetramethylsilane as an internal standard. IR spectra were recorded on a Bruker Vertex-70 spectrometer and mass spectra were measured with an Agilent MS Trap VL spectrometer. The absorption spectra were measured using an Agilent 8453 UV–vis spectrometer. Photo-irradiation was carried out using an SHG-200 UV lamp, a CX-21 UV fluorescence analysis cabinet, and a BMH-250 visible lamp. Light of appropriate wavelengths was isolated by different light filters. Fluorescence spectra were measured using a Hitachi F-4500 spectrophotometer. Electrochemical examinations were performed in a one-compartment cell using a Model 263 potentiostat–galvanostat (EG&G Princeton Applied Research) under computer control at RT. Platinum electrodes (diameter 0.5 mm) served as working electrode and counter electrode. Platinum wire was used as a quasireference electrode. It was calibrated using the ferrocene (Fc – Fc+) redox couple that has a formal potential, $E_{1/2}$, of +0.35 V vs. platinum wire. The typical electrolyte was acetonitrile (5.0 mL), which contained $LiClO_4$ (0.10 mol/L) and diarylethene (4.0×10^{-3} mol/L). All solutions were deaerated by a dry argon stream and maintained at a slight argon overpressure during electrochemical experiments.

Synthesis

The four diarylethenes **1a**–**4a** were prepared by the method shown in Scheme 2, and experimental details are given in the following.

Synthesis of 3,5-dibromo-2-methylthiophene (5)

To a stirred solution of 2-methylthiophene (24.0 g, 244.8 mmol) in acetic acid (100 mL) at 0 °C was slowly added a Br_2–acetic acid solution (*v*/*v*, 29:40). The reaction mixture was stirred overnight at this temperature. The reaction was stopped by the addition of water. The mixture was neutralized by Na_2CO_3 and extracted with ether. The ether extract was dried, filtrated, and concentrated. The residue was purified by distillation in vacuo. Compound **2** was obtained as a colorless oil, 50.7 g in 81.2% yield. ^{1}H NMR (400 MHz, $CDCl_3$, TMS) δ: 2.94 (s, 3H), 7.61 (s, 1H).

Synthesis of 3-bromo-2-methyl-5-thienylboronic acid (6)

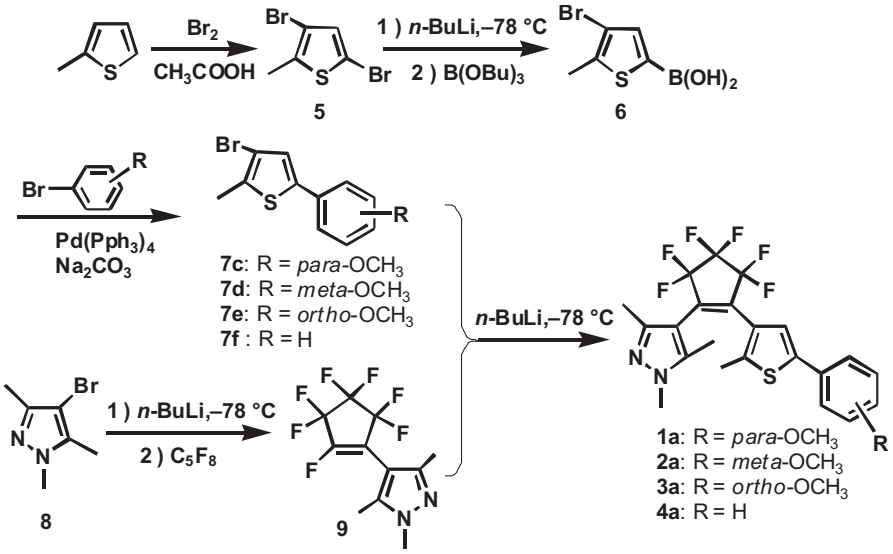
To a stirred solution of **2** (16.3 g, 63.7 mmol) in dry ether (150 mL) was added a 1.6 mol/L *n*-BuLi–hexane solution (40.6 mL, 65.0 mmol) at –78 °C under nitrogen atmosphere. Stirring continued for 30 min, and boric acid tri-butyl ester (18.8 mL) was quickly added to the reaction mixture. After increasing the temperature to RT, the reaction was stopped by the addition of 4% HCl (10 mL). The mixture was extracted with 4% NaOH (100 mL), and the aq. NaOH solution was neutralized by 10% HCl. The residue was washed, filtrated, and dried. The product **3** was obtained as yellowish solid, 12.0 g in 85.5% yield. ^{1}H NMR (400 MHz, $CDCl_3$, TMS) δ: 2.51 (s, 3H), 4.59 (s, 2H), 7.33 (s, 1H).

3-Bromo-2-methyl-5-(4-methoxylphenyl)thiophene (7c)

Compound **7c** was prepared by reacting compound **6** (5.0 g, 22.6 mmol) with 4-bromoanisole (4.23 g, 22.6 mmol) in the presence of $Pd(PPh_3)_4$ (0.8 g) and Na_2CO_3 (6.40 g, 60 mmol) in tetrahydrofuran (THF) (80 mL containing 10% water) for 15 h at 70 °C. Compound **7c** was purified by col-

© 2007 NRC Canada

Scheme 2. Synthetic route for diarylethenes **1a**–**4a**.



umn chromatography on SiO_2 using hexane as the eluent and obtained as baby-yellow solid in 78.3% yield. ^{1}H NMR (400 MHz, $CDCl_3$) δ: 2.40 (s, 3H, -CH_3), 3.83 (s, 3H, -CH_3), 6.89–6.91 (d, 2H, *J* = 8.8 Hz, phenyl-H), 6.99 (s, 1H, thienyl-H), 7.42–7.44 (d, 2H, *J* = 8.8 Hz, phenyl-H).

3-Bromo-2-methyl-5-(3-methoxylphenyl)thiophene (7d)

Compound **7d** was prepared by a method similar to that used for **7c** and obtained as a buff solid in 75.3% yield. ^{1}H NMR (400 MHz, $CDCl_3$) δ: 2.41 (s, 3H), 3.83 (s, 3H), 6.82–6.84 (d, 1H, *J* = 8.0 Hz, phenyl-H), 7.03 (s, 1H, thienyl-H), 7.08–7.10 (t, 2H, *J* = 4.0 Hz, phenyl-H), 7.25–7.29 (t, 1H, *J* = 8.0 Hz, phenyl-H).

3-Bromo-2-methyl-5-(2-methoxylphenyl)thiophene (7e)

Compound **7e** was prepared by a method similar to that used for **7c** and obtained as a buff solid in 70.2% yield. ^{1}H NMR (400 MHz, $CDCl_3$) δ: 2.41 (s, 3H, -CH_3), 3.91 (s, 3H, -CH_3), 6.95–6.99 (m, 2H, *J* = 7.6 Hz, phenyl-H), 7.27 (s, 1H, thienyl-H), 7.30 (s, 1H, phenyl-H), 7.53–7.55 (d, 1H, *J* = 8.0 Hz, phenyl-H).

3-Bromo-2-methyl-5-phenylthiophene (7f)

Compound **7f** was prepared by a method similar to that used for **7c** and obtained as a buff solid in 70.0% yield. ^{1}H NMR (400 MHz, $CDCl_3$) δ: 2.28 (s, 3H, -CH_3), 6.84 (s, 1H, phenyl-H), 7.12 (s, 1H, thienyl-H), 7.33–7.35 (d, 2H, *J* = 8.0 Hz, phenyl-H), 7.56–7.58 (d, 2H, *J* = 8.0 Hz, phenyl-H).

1-(1,3,5-Trimethylpyrazole)perfluorocyclopentene (9)

To a stirred solution of 4-bromo-1,3,5-trimethylpyrazole (**8**) (2.84 g, 15 mmol) in 50 mL of THF was added dropwise a 1.6 mol/L *n*-BuLi solution (9.4 mL, 15 mmol) at –78 °C under argon atmosphere. Stirring was continued for 30 min at the low temperature. Perfluorocyclopentene (2.04 mL, 15 mmol) was added to the reaction mixture at –78 °C, the mixture was stirred for another 1 h at this temperature, and then the reaction temperature was increased spontaneously to RT. The reaction was stopped by the addition of water. The mixture was extracted with ether and washed with aq. HCl (1 mol/L) and water, respectively. The organic layer was dried over $MgSO_4$, filtrated, and evaporated. The crude product was purified by column chromatography on SiO_2 using petroleum ether – acetic ether (4:1) as the eluent to give 2.98 g of compound **9** as a yellow oil in 65.8% yield. ^{1}H NMR (400 MHz, $CDCl_3$) δ: 2.20 (s, 3H, -CH_3), 2.22 (s, 3H, -CH_3), 3.77 (s, 3H, -NCH_3). ^{19}F NMR (400 MHz, $CDCl_3$) δ: –107.61 (2F), –118.36 (2F), –129.22 (1F), –130.51 (2F).

1-[1,3,5-Trimethyl-1-pyrazol-4-yl],2-[2-methyl-5-(4-methoxylphenyl)-1-thien-3-yl]perfluorocyclopentene (1a)

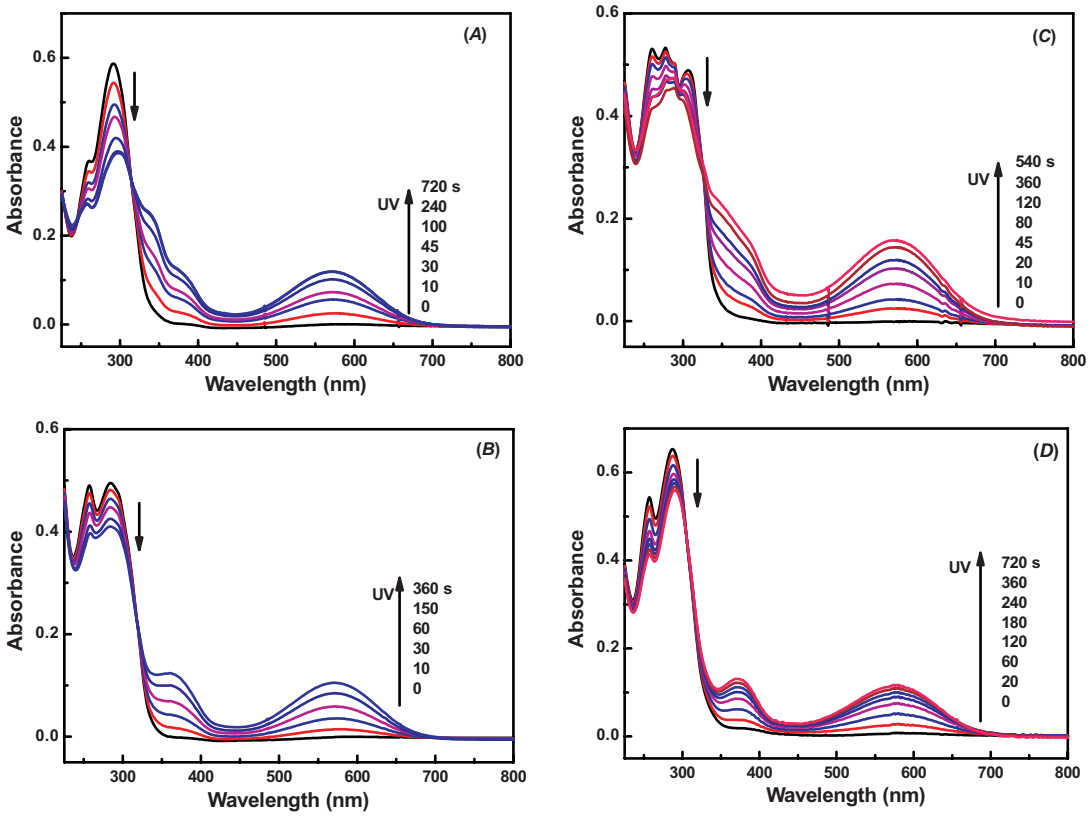
To stirred anhyd. THF (30 mL) containing **7c** (0.568 g, 1.66 mmol) was added dropwise a 1.6 mol/L *n*-BuLi solution (1.05 mL) at –78 °C under argon atmosphere. After the mixture was stirred for 30 min at –78 °C, compound **9** (0.5 g, 1.66 mmol), dissolved in anhyd. THF solvent, was added quickly. The reaction mixture was continuously stirred at –78 °C for 2 h, and the reaction was allowed to slowly warm to RT. The reaction was quenched by the addition of water. The product was extracted with ether, dried with $MgSO_4$, and concentrated in vacuo. The crude product was purified by column chromatography (petroleum ether – acetic ether, 4:1) to afford 0.35 g of diarylethene **1a** as yellow solid in 45.0% yield. ^{1}H NMR (400 MHz, $CDCl_3$) δ: 1.94 (s, 3H, -CH_3), 1.97 (s, 3H, -CH_3), 2.03 (s, 3H, -CH_3), 3.70 (s, 3H, -OCH_3), 3.84 (s, 3H, -NCH_3), 6.90–6.92 (d, 2H, *J* = 8.4 Hz, phenyl-H), 7.13 (s, 1H, thiophene-H), 7.44–7.47 (d, 2H, *J* = 8.4 Hz, phenyl-H). ^{13}C NMR (400 MHz, $CDCl_3$) δ: 10.54, 12.86, 14.30, 36.27, 55.40, 106.29, 114.38, 121.43, 122.87, 125.72, 126.23, 139.17, 139.63, 141.92, 146.46 159.48. IR (KBr, cm^{-1}) ν: 800, 821 (benzene 1,4-substituted), 1124 (-CF_2), 1255 (C-N, st), 1341, 1477, 1550 (thiophenene bond), 1611 (benzene skeleton), 2841 (-OCH_3), 2927, 2960 (-CH_3). ^{19}F NMR (400 MHz, $CDCl_3$) δ: –109.43 (2F), –110.52 (2F), –132.58 (2F). MS *m*/*z* (M^+): 487.2 (+H), 509.2 (+Na)

1-[1,3,5-Trimethyl-1-pyrazol-4-yl],2-[2-methyl-5-(3-methoxylphenyl)-1-thien-3-yl]perfluorocyclopentene (2a)

Diarylethene **2a** was prepared by a method similar to that

© 2007 NRC Canada

Fig. 1. Absorption spectral changes of diarylethenes **1**–**4** in hexane solution at RT (2.0×10^{-5} mol/L): (*A*) **1**, (*B*) **2**, (*C*) **3**, and (*D*) **4**.



used for **1a** and obtained as a solid in 38.0% yield. ^{1}H NMR (400 MHz, $CDCl_3$) δ: 1.96 (s, 3H, -CH_3), 1.97 (s, 3H, -CH_3), 2.03 (s, 3H, -CH_3), 3.70 (s, 3H, -OCH_3), 3.86 (s, 3H, -NCH_3), 6.84–6.86 (d, 1H, *J* = 8.0 Hz, phenyl-H), 7.05 (s, 1H, thiophene-H), 7.11–7.13 (d, 1H, *J* = 7.6 Hz, phenyl-H), 7.24 (s, 1H, phenyl-H), 7.28–7.32 (t, 1H, *J* = 8.0 Hz, phenyl-H). ^{13}C NMR (400 MHz, $CDCl_3$) δ: 10.01, 12.33, 13.98, 35.67, 54.85, 105.73, 110.92, 112.71, 117.67, 122.27, 125.29, 129.54, 134.17, 138.10, 138.65, 140.17, 141.32, 145.92, 159.54. IR (KBr, cm^{-1}) ν: 687, 770, 799, 882 (benzene 1,3-substituted), 1121 (-CF_2), 1271 (C-N, st), 1336,1434 (thiophenene bond), 1602 (benzene skeleton), 2841 (-OCH_3), 2948, 2966 (-CH_3, st). ^{19}F NMR (400 MHz, $CDCl_3$) δ: –109.45 (2F), –110.51 (2F), –132.58 (2F). MS *m*/*z* (M^+): 487.2 (+H), 509.1 (+Na).

1-[1,3,5-Trimethyl-1-pyrazol-4-yl],2-[2-methyl-5-(2-methoxylphenyl)-1-thien-3-yl]perfluorocyclopentene (3a)

Diarylethene **3a** was prepared by a method similar to that used for **1a** and obtained as solid in 41.2% yield. ^{1}H NMR (400 MHz, $CDCl_3$) δ: 1.96 (s, 3H, -CH_3), 1.97 (s, 3H, -CH_3), 2.04 (s, 3H, -CH_3), 3.69 (s, 3H,, -OCH_3), 3.92 (s, 3H, -NCH_3), 6.96–7.02 (dd, 2H, *J* = 8.0 Hz, phenyl-H), 7.27–7.29 (d, 1H, *J* = 8.0 Hz, phenyl-H), 7.42 (s, 1H, thiophene-H), 7.57–7.59 (dd, 1H, *J* = 7.6 Hz, phenyl-H). ^{13}C NMR (400 MHz, $CDCl_3$) δ: 10.49, 12.86, 14.21, 36.25, 55.53, 106.36, 111.69, 113.90, 121.01, 122.36, 124.59, 124.84, 127.86, 128.73, 137.05, 139.19, 140.96, 146.48, 146.95, 155.49. IR (KBr, cm^{-1}) ν: 751 (benzene 1,2-substituted), 1127 (-CF_2), 1274 (C-N, st), 1341, 1438 (thiophenene bond), 1635 (benzene skelteton), 2839 (-OCH_3), 2942 (-CH_3). ^{19}F NMR (400 MHz, $CDCl_3$) δ: –109.46 (2F), –110.51 (2F), –132.57 (2F). MS *m*/*z* (M^+): 487.2 (+H), 509.2 (+Na), 467.2 (-F).

1-[1,3,5-Trimethyl-1-pyrazol-4-yl],2-[2-methyl-5-phenyl-1-thien-3-yl]perfluorocyclopentene (4a)

Diarylethene **4a** was prepared by a method similar to that used for **1a** and obtained as solid in 44.1% yield. ^{1}H NMR (400 MHz, $CDCl_3$) δ: 1.96 (s, 3H, -CH_3), 1.97 (s, 3H, -CH_3), 2.03 (s, 3H, -CH_3), 3.84 (s, 3H, -NCH_3), 7.26 (s, 1H, thiophene-H), 7.30–7.32 (d, 1H, *J* = 7.6 Hz, phenyl-H), 7.37–7.40 (d, 2H, *J* = 7.6 Hz, phenyl-H), 7.52–7.54 (d, 2H, *J* = 7.6 Hz, phenyl-H). ^{13}C NMR (400 MHz, $CDCl_3$) δ: 10.54, 12.87, 14.51, 36.29, 106.25, 122.55, 125.60, 125.85, 127.85, 129.00, 133.37, 139.17, 140.61, 142.00, 146.45. IR (KBr, cm^{-1}) ν: 689, 756, 894 (benzene 1-substituted), 1124 (-CF_2), 1277 (C-N, st), 1341, 1443 (thiophenene bond), 1626 (benzene skeleton), 2928, 2960 (-CH_3). ^{19}F NMR (400 MHz, $CDCl_3$) δ: –109.45 (2F), –110.52 (2F), –132.58 (2F). MS *m*/*z* (M^+): 457.2 (+H), 479.2 (+Na), 437.3 (-F), (M^-) 413.4 (-3CH_3).

Results and discussion

Photochromism of diarylethenes 1–4

In hexane solution, the photochromic reactivity of diarylethenes **1**–**4** was examined. Figure 1 shows their absorption spectral changes induced by UV light at RT (2.0×10^{-5} mol/L). Compounds **1a**–**4a** exhibited good photochromic properties and can be toggled between their colorless open-ring isomers (**1a**–**4a**) and colored closed-ring isomers (**1b**–

© 2007 NRC Canada

Table 1. Absorption spectral properties of diarylethenes **1–4** in hexane at 2.0×10^{-5} mol/L.

Compound	$\lambda_{o,max}$ (nm)[a], ε (L mol^{-1} cm^{-1})	$\lambda_{c,max}$ (nm)[b], ε (L mol^{-1} cm^{-1})	Φ[c] $\Phi_{o\text{-}c}$	Φ[c] $\Phi_{c\text{-}o}$
1	291, 2.9×10^4	573, 1.0×10^4	0.47	0.57
2	284, 2.5×10^4	573, 7.9×10^3	0.45	0.53
3	278, 2.7×10^4	573, 1.1×10^4	0.43	0.46
4	287, 3.2×10^4	575, 8.8×10^3	0.27	0.40

[a]Absorption maxima of open-ring forms.
[b]Absorption maxima of closed-ring forms.
[c]Quantum yields of cyclization reaction, $\Phi_{o\text{-}c}$, and cycloreversion reaction, $\Phi_{c\text{-}o}$, respectively.

4b) by alternating irradiation with UV and visible light, as monitored using UV–vis absorption and ^{1}H NMR spectroscopy. Upon irradiation with 313 nm light, absorption bands in the visible region appear and the solutions turns blue as a result of the cyclization reactions to produce **1b–4b** (Fig. 1 and Table 1). In the photostationary state, the content of the closed-ring isomer can be easily analyzed with ^{1}H NMR spectroscopy by comparing the relative intensities of thiophene proton signals. According to this method, ^{1}H NMR spectroscopic studies performed on $CDCl_3$ (1.0×10^{-3} mol/L) solutions of **1a–4a** reveal that the contents of the closed-ring isomers (**1b–4b**) in photostationary states are 67% for **1b**, 69% for **2b**, 68% for **3b**, and 69% for **4b**, respectively. All the solutions of **1b–4b** can be decolorized by irradiating them with visible light of wavelengths greater than 500 nm to induce the cycloreversion reactions and reproduce **1a–4a**. The coloration–decoloration cycles of the four compounds could be repeated more than 20 times and a clear isosbestic point was observed at 315, 318, 327, and 309 nm for diarylethenes **1**, **2**, **3**, and **4**, respectively. The absorption spectral properties of the four compounds are summarized in Table 1. The quantum yields were determined by comparing the reaction yields of diarylethenes **1–4** in hexane against 1,2-bis(2-methyl-5-phenyl-3-thienyl)perfluorocyclopentene in hexane (25), and the results are also shown in Table 1. These data suggest that the maximum absorption wavelengths of closed-ring forms and the molar absorption coefficients of both open- and closed-ring forms of the four diarylethene compounds are not evidently different. However, the maximum wavelengths of open-ring forms and their cyclization–cycloreversion quantum yields are relatively remarkable. Among diarylethenes **1–4**, the quantum yields of cyclization and cycloreversion reactions of the *para*-methoxyl substituted derivative (**1**) are the greatest ($\Phi_{O\text{-}C}$ = 0.47, $\Phi_{C\text{-}O}$ = 0.57), while those of the the non-methoxyl substituent derivative (**4**) are the smallest ($\Phi_{O\text{-}C}$ = 0.27, $\Phi_{C\text{-}O}$ = 0.40). The values of the other two compounds are between those of diarylethenes **1** and **4**. As shown in Table 1, all cyclization–cycloreversion quanta of diarylethene derivatives with methoxyl group substituent (**1a–3a**) are much higher than that of the diarylethene with no methoxyl group (**4a**). The results indicate that the cyclization–cycloreversion quantum yield could be effectively increased when the electron-donating methoxyl group was introduced into the benzene rings. In addition for diarylethenes **1–4**, the values of their cycloreversion quantum yields are much higher than those of cyclization quantum yields (Table 1). This is an interesting characteristic of diarylethene derivatives having a pyrazole unit and is a significant difference between the diarylethenes reported here and other diarylethenes reported to date.

The property of fatigue resistance, i.e., the number of times photocyclization and ring-opening reaction cycles can be repeated without loss of performance, was examined at RT according to ref. 18. The hexane solution of compound **1** was irradiated alternatively with UV light (313 nm) and visible light (510 nm). The irradiation time was long enough for coloration to reach the photostationary state and for the color to be completely bleached. The absorbance of the open-ring form remained almost constant even after 200 coloration–decoloration cycles and a clear isosbestic point was observed at 315 nm after 200 cycles. Compounds **2–4** showed similar properties to that of **1**. The results suggested that the diarylethene derivatives bearing heterocyclic pyrazole ring show excellent fatigue resistance.

Photochromic cyclization–cycloreversion kinetics of diarylethenes 1–4

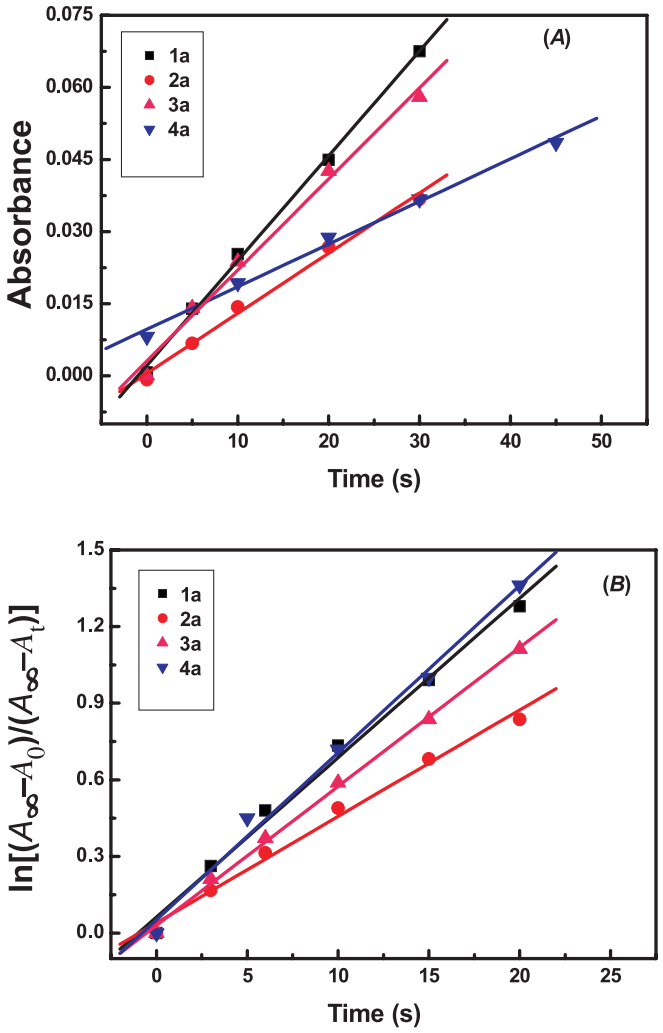
The photochromic cyclization and cycloreversion kinetics of diarylethenes **1–4** in hexane were investigated by irradiation by UV–vis (313 nm, from open to closed form) or visible light ($\lambda > 500$ nm, closed to open form), as shown in Fig. 2. The concentration of all solutions was 2.0×10^{-5} mol/L. All absorption data were collected at the maximum wavelength of every solution, i.e., at the maximum optical density. As shown in Fig. 2*a*, the cyclization kinetics of diarylethenes **1–4** in hexane show that the photochromic cyclization reaction follows zeroth-order kinetics; the relationships between absorbance and exposure time (A vs. t) show good linearity (linear correction factors >0.99) upon irradiation with UV light (313 nm) in all solutions. The slopes of the A vs. t lines gave the zeroth order rate constant, $k_{o\text{-}c}$. According to this method, all the k values for the cyclization process ($k_{o\text{-}c}$) of diarylethes **1–4** can be readily obtained in hexane and are 2.18×10^{-3}, 1.25×10^{-3}, 1.89×10^{-3}, and 0.89×10^{-3} mol/L s^{-1}, respectively. Similarly, the cycloreversion kinetic curves shown in Fig. 2*b* can be plotted according to eq. [1] (26),

$$[1] \qquad kt = \ln\left[\frac{A_\infty - A_0}{A_\infty - A_t}\right]$$

where k is the first-order rate constant, A_0, A_∞, and A_t are the observed absorption data measured at the beginning, at the end, and at time t of the reaction, respectively. The data in Fig. 2*b* represent a perfect linear fit, indicating that the

© 2007 NRC Canada

Fig. 2. The cyclization–cycloreversion kinetics of diarylethenes **1–4** in hexane (2.0×10^{-5} mol/L): (*A*) Cyclization kinetics upon irradiation with light (λ = 254 nm), (*B*) Cycloreversion kinetics, upon irradiation with visible light (λ > 510 nm).

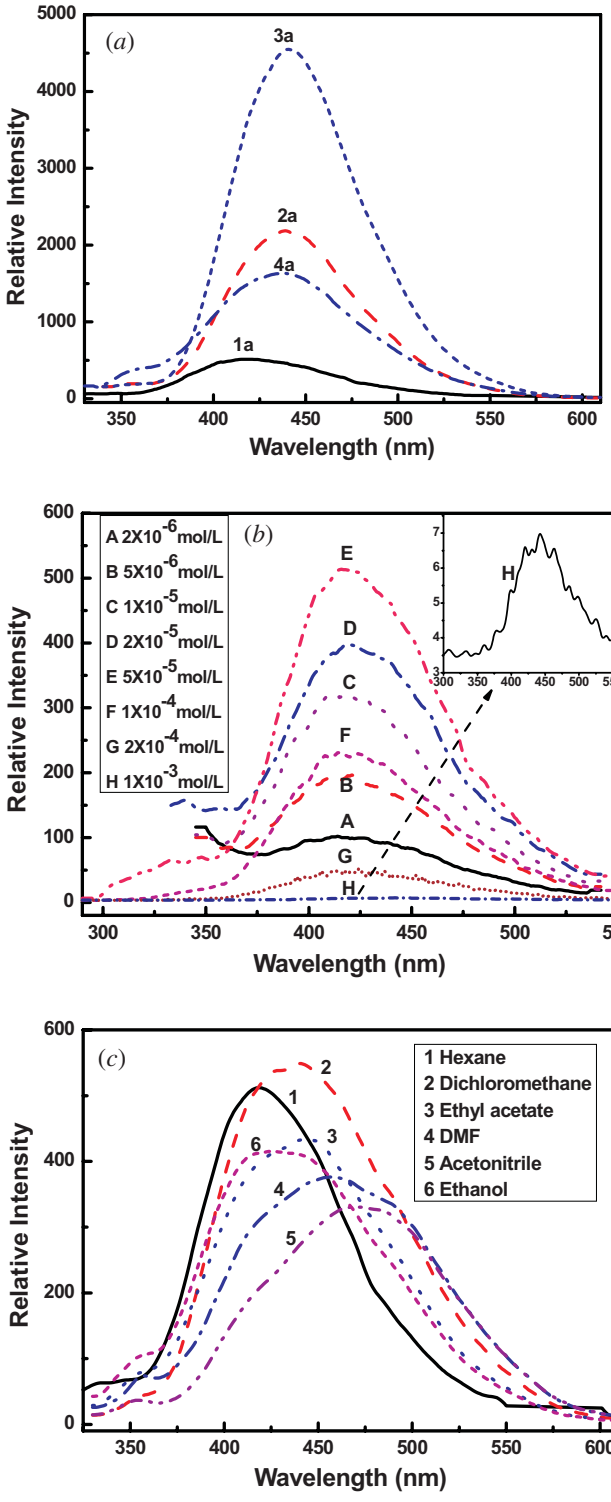


photochromic cycloreversion process follows first-order reaction kinetics. From Fig. 2*b*, the rate constant k of the cycloreversion process ($k_{c\text{-}o}$) of diarylethenes **1–4** in hexane were calculated to be 6.25×10^{-2}, 4.17×10^{-2}, 5.44×10^{-2}, and 6.55×10^{-2} mol/L s^{-1}, respectively. Of the four compounds, the $k_{o\text{-}c}$ of diarylethene **4** in hexane is the smallest, while its $k_{c\text{-}o}$ is the greatest in hexane. The result showed that the methoxyl group can effectively accelerate the photochromic cyclization reaction and suppress the cycloreversion reaction.

Fluorescence of diarylethenes 1–4

The fluorescence spectra of diarylethenes **1a–4a** (5.0×10^{-5} mol/L) in hexane at RT are illustrated in Fig. 3*a*. All exhibited good fluorescence at different wavelengths in hexane solution, when excited by their respective excitation wavelength. From Fig. 3*a*, we can clearly see that the hexane solutions containing diarylethenes **1a–4a** showed relatively strong fluorescence at 416, 438, 441, and 439 nm when excited at 280, 317, 315, and 320 nm, respectively.

Fig. 3. (*a*) Fluorescence spectra of diarylethenes **1a–4a** in hexane solution (5.0×10^{-5} mol/L) at RT, excited at 280, 317, 315, and 320 nm, respectively. (*b*) Fluorescence spectra of diarylethene **1a** in various concentrations in hexane at RT, monitored at 280 nm (*c*) Fluorescence spectra of diarylethene **1a** in different solutions at RT, monitored at 320 nm.



© 2007 NRC Canada

Table 2. Fluorescence spectral properties of diarylethenes **1a**–**4a** at various concentrations in hexane at RT.

	$\lambda_{em, max}$ (nm), (fluorescence intensity)			
Concn. (mol/L)	**1a**	**2a**	**3a**	**4a**
2×10^{-6}	414 (102)	438 (219)	440 (699)	422 (273)
5×10^{-6}	418 (193)	438 (484)	441 (1529)	420 (519)
1×10^{-5}	412 (320)	436 (816)	441 (2573)	423 (791)
2×10^{-5}	420 (394)	440 (1323)	441 (3394)	423 (1172)
5×10^{-5}	416 (514)	438 (2180)	441 (4366)	422 (1064)
1×10^{-4}	421 (228)	439 (2005)	442 (2637)	421 (573)
2×10^{-4}	421 (48)	443 (1084)	442 (641)	—[a]
1×10^{-3}	442 (7)	445 (24)	446 (29)	425 (10)

[a]No fluorescence peak.

The fluorescence maxima of the four compounds were observed to be between 416 and 441 nm, indicating that the effect on the fluorescence peak of the electron-donating methoxyl group and its position was relatively significant. On the other hand, the fluorescence intensities of diarylethenes **1a**–**4a** changed dramatically with the substituent position. The fluorescence intensities increased rapidly from the *para*-substituted **1a** to the *ortho*-substituted **3a** derivatives. The value of non-methoxyl-substituted diarylethene **4a** is located between those of the *para*-methoxyl-substituted **1a** and the *meta*-methoxly-substituted **2a** derivatives. Among the four compounds, the relative fluorescence intensity of the *ortho*-substituted derivative is the strongest, and that of the *para*-substituted derivative is the weakest. The result is exactly contrary to that reported in our previous paper (27). In that paper, the electro-withdrawing fluorine substituent position did not significantly affect the fluorescence peak of dithienylethene, but had a remarkable effect on the fluorescence intensity; the fluorescence intensity of the *ortho*-substituted derivative was the weakest, and that of the *para*-substituted derivative was the strongest. The possible reasons are due to the electro-donating nature of the methoxyl substituent of the terminal phenyl group and that the pyrazole ring can also possibly affect the fluorescence properties of the three diarylethenes. Upon irradiation with 313 nm light, their fluorescence intensity decreased, along with the photochromism, from open-ring form to closed-ring form, suggesting that all of the closed-ring forms of these four diarylethenes showed no fluorescence or that their fluorescence was very weak. These results are consistent with those of most reported diarylethenes (28–31).

The concentration dependence of fluorescence spectra of **1a** was measured in hexane solution at RT, shown in Fig. 3*b*. With the concentration increased from 2.0×10^{-6} to 5.0×10^{-5} mol/L, the maximum emission occurred almost at 416 nm when excited at 280 nm, and the relative fluorescence intensity increased dramatically. However, when the concentration was increased further from 5.0×10^{-5} to 1.0×10^{-3} mol/L, the maximum emission appeared redshifted from 416 to 442 nm, and the relative fluorescence intensity decreased remarkably. The hexane solution showed very weak fluorescence when the concentration was increased to 1.0×10^{-3} mol/L. This self-quench phenomenon perhaps resulted from the formation of excimers and (or) exciplexes in high concentration solutions so that a deactivation effect could occur during the excited state lifetime (32). Moreover, the concentration effect on the fluorescence spectra of diarylethenes **2a**–**4a** were also measured, and the results are summarized in Table 2. As shown in Table 2, compounds **2a**–**4a** showed similar fluorescent properties as **1a**, depending on the concentration employed. At high concentration, e.g., 1.0×10^{-3} mol/L, the fluorescence peak of each diarylethene was obviously redshifted comparing to other concentrations. For all four compounds, the relative fluorescence intensity showed a remarkable initial increase with subsequent dramatic decrease with increasing concentration. The greatest and the smallest values were obtained at 5.0×10^{-5} and 1.0×10^{-3} mol/L, respectively. The systematic redshift at high concentrations and the relatively remarkable fluorescence intensity decrease with increased concentration demonstrated that molecular aggregation and fluorescence quench may occur at higher concentration (31, 33).

The effects of the solvent on the fluorescence spectra of diarylethenes **1a**–**4a** were also investigated. Figure 3*c* shows the fluorescence spectra of **1a** (5.0×10^{-5} mol/L) in different solvents at RT. As shown in Fig. 3*c*, when excited at 320 nm, the fluorescence peaks of diarylethene **1a** were observed at 418, 440, 443, 456, 470, and 426 nm in hexane, dichloromethane, ethyl acetate, DMF, acetonitrile, and ethanol, respectively. The solvent effect on the fluorescence of diarylethenes **2a**–**4a** was also measured, and the fluorescence properties of these four diarylethenes in various solvents at RT are summarized in Table 3.

From these data, one can readily see that the fluorescence spectra depended remarkably on the polarity of solvent. The maximum fluorescence peaks of the four compounds appeared to be redshifted as the polarity of the solvent increased, except for ethanol for which the contrary occurred. The reason may be possibly attributed to its specific solvent–solute interaction such as hydrogen bonding with the fluorine atoms of the diarylethenes. In addition, the solvent effect on the relative fluorescence intensity showed relatively complex and irregular changes (Table 3). Under the same experimental conditions, the fluorescence intensities in ethanol are the strongest, except for diarylethene **1a**, for which the strongest intensity appeared in dichloromethane.

Electrochemistry of diarylethenes 1–4

It is reported that the ring-opening and -closing transformation of some diarylethenes can be initiated not only by

© 2007 NRC Canada

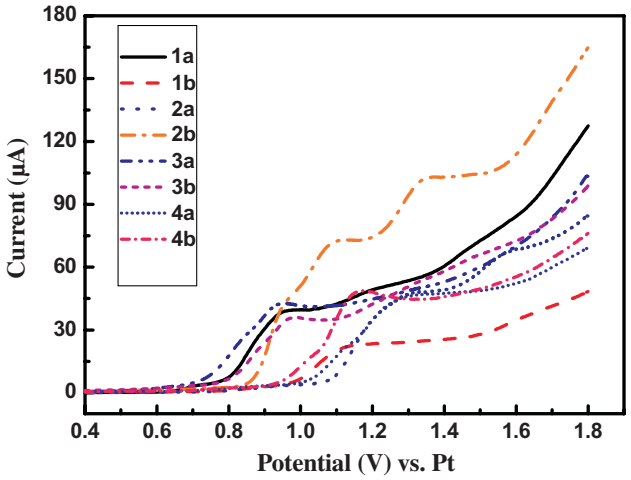
Table 3. Fluorescence properties of diarylethenes **1a**–**4a** in different solvents at 5.0×10^{-5} mol/L.

	$\lambda_{em,\ max}$ (nm), (fluorescence intensity)[a]			
Solvent	**1a**	**2a**	**3a**	**4a**
Hexane	416 (514)	438 (2180)	441 (4366)	439 (1630)
Dichloromethane	440 (549)	450 (2739)	452 (6354)	451 (2003)
Ethyl acetate	443 (433)	452 (2196)	452 (5560)	—[b]
DMF	456 (376)	460 (2225)	460 (5376)	461 (1531)
Acetonitrile	470 (330)	460 (2130)	463 (5629)	462 (1601)
Ethanol	426 (415)	449 (2833)	451 (7032)	448 (2176)

[a]Fluorescent maxima monitored at 320, 330, 333, and 320 nm for **1a**, **2a**, **3a**, and **4a**, respectively.
[b]No spectrum peaks.

UV or visible light irradiation but also by electrochemical or chemical, i.e., electrochromic, oxidation (34–36). The electrochemical properties of diarylethenes can be potentially applied to molecular scale electronic switches. Electrochemical examinations by the linear sweep method under the same experimental conditions using diarylethenes **1**–**4** were performed, and the results are shown in Fig. 4. As shown in Fig. 4, *para*-methoxyl and *ortho*-methoxyl substituted diarylethenes (**1** and **3**) showed similar electrochemical behavior. The oxidation onsets of **1a**, **1b**, **3a**, and **3b** initiated at 0.79, 1.00, 0.73, and 0.78 V, respectively. Both of the oxidation onsets of the open-ring forms of compounds **1** and **3** are lower than those of the corresponding closed-ring forms. This indicates that the electron-donating effect of the methoxyl group is more significant in the open-ring form. However, the oxidation onsets of compounds **2** and **4** were opposite to those of compounds **1** and **3**; the oxidation onsets of **2a**, **2b**, **4a**, and **4b** were 1.11, 0.87, 1.03, and 0.94 V, respectively. The oxidation onsets of the open-ring forms are higher than those of the closed-ring forms. This implies that the electron-donating effect of the methoxyl group or hydrogen atom is more significant in the closed-ring form of compounds **2** or **4**, respectively. Moreover, the differences between the open- and closed-ring forms of diarylethenes **1**–**4** (ΔV_{a-b}) were 0.21 for **1**, 0.24 for **2**, 0.05 for **3**, and 0.09 for **4**, respectively. At the same applied potential, the current density of **2b** was higher than that of **2a**, which is exactly opposite to the characterisitcs of **1a** and **1b**. The electronic current of compounds **3** and **4** at the same applied potential intersected. From the previous description together with Fig. 4, a reasonable conclusion can be drawn that the substitution of the electron-donating methoxyl group has a great effect on **1**–**3**. For ortho or meta position substitution of the methoxyl group, the oxidation potential onset showed a remarkable difference with ΔV_{a-b} greater than 0.2 V for **1** and **2**. On the other hand, when substituted at the ortho position, the electron-donating effect together with its steric effect plays a main role, which made the oxidation potential onsets of **3a** and **3b** similar to each other (ΔV_{a-b} = 0.05 V). A similar result was observed when the *ortho*-methoxyl group was substituted by a hydrogen atom (**4a** and **4b**, ΔV_{a-b} = 0.09 V). In addition, three oxidation processes can be readily observed during the anodic oxidation of **2a** and **2b**, while only two oxidation processes can be observed during anodic oxidation of the other three compounds. The three oxidation processes may involve the oxidation of a pyrazole ring, a thiophene ring, together with the benzene ring of compound

Fig. 4. The anodic polarization curves of diarylethenes **1**–**4**.



2. However, the substitution of the methoxyl group, or hydrogen atom, at the para and ortho position made the oxidation process of benzene unclear for **1a**, **1b**, **3a**, **3b**, **4a**, and **4b**. All these electrochemical results indicated that the substitution of the methoxyl group on the benzene and pyrazole units had great effect on both the open- and closed-ring forms of the three diarylethene derivatives. A detailed explanation requires further investigation.

Conclusions

Four new asymmetrical diarylethenes bearing a pyrazole unit were synthesized for the investigation of their optical and electrochemical properties. The effect of different substitution positions on the optical and electrochemical performances of diarylethenes was investigated. The results suggested that the optical and electrochemical properties of these diarylethene derivatives, such as photochromic properties, fluorescence, and their electrochemical characteristics, were significantly dependent on the effect of the electron-donating methoxyl substituent position and the pyrazole unit. The reason may be attributed to the different electron-donating effects when the methoxyl group was substituted on the different positions of the terminal benzene ring and the different aromatic stabilization energy of pyrazole unit from that of thiophene unit. All the diarylethenes reported in this study exhibited good photochromism and strong fluorescence. Significantly, their cycloreversion quantum yields are much higher than those of their cyclization quantum yields.

© 2007 NRC Canada

The results are very useful for the design of efficient photoactive and diarylethene compounds with excellent characteristics.

Acknowledgements

This work was supported by the Project of National Natural Science Foundation of China (grant No. 20564001), the Natural Science Foundation of Jiangxi, China (grant No.050017), the Science Funds of the Education Office of Jiangxi, China (grant No. [2005] 140), and the Projects of Fundamental Study & Applied Fundamental Study Funds of Jiangsu Teachers University of Technology.

References

1. H. Dürr and H. Bouas-Laurent. Photochromism molecules and System. Elsevier, Amsterdam. 1990.
2. M. Irie. Photo-reactive materials for ultrahigh-density optical memory. Elsevier, Amsterdam. 1994.
3. K. Higashiguchi, K. Matsuda, N. Tanifuji, and M. Irie. J. Am. Chem. Soc. **127**, 8922 (2005).
4. T. Kaieda, S. Kobatake, H. Miyasaka, M. Murakami, N. Iwai, Y. Nagata, A. Itaya, and M. Irie. J. Am. Chem. Soc. **124**, 2015 (2002).
5. S. Kobatake, K. Shibata, K. Uchida, and M. Irie. J. Am. Chem. Soc. **122**, 12135 (2000).
6. M. Irie. Chem. Rev. **100**, 1685 (2000).
7. H. Tian and S.J. Yang. Chem. Soc. Rev. **33**, 85 (2004).
8. Y. Chen and D.X. Zeng. J. Org. Chem. **69**, 5037 (2004).
9. K. Morimitsu, S. Kobatake, and M. Irie. Tetrahedron Lett. **45**, 1155 (2004).
10. K. Matsuda and M. Irie. J. Photochem. Photobiol. C, 5 169 (2004).
11. T.B. Norsten and N.R. Branda. Adv. Mater. **13**, 347 (2001).
12. T. Yamaguchi and M. Irie. J. Photochem. Photobiol. A, **178**, 162 (2006).
13. Y. Moriyama, K. Matsuda, N. Tanifuji, S. Irie, and M. Irie. Org. Lett. **7**, 3315 (2005).
14. S.Z. Pu, T.S. Yang, J.K. Xu, L. Shen, G.Z. Li, Q. Xiao, and B. Chen. Tetrahedron, **61**, 6623 (2005).
15. K. Uchida, T. Ishikawa, M. Takeshita, and M. Irie. Tetrahedron, **54**, 6627 (1998).
16. S. Takami and M. Irie. Tetrahedron, **60**, 6155 (2004).
17. S. Takami, S. Kobatake, T. Kawai, and M. Irie. Chem. Lett. **32**, 892 (2003).
18. K. Uchida, T. Matsuoka, K. Sayo, M. Iwamoto, S. Hayashi, and M. Irie. Chem. Lett. **28**, 835 (1999).
19. K. Yagi and M. Irie. Bull. Chem. Soc. Jpn. **76**, 1625 (2003).
20. M. Irie. Supramol. Sci. **3**, 87 (1996).
21. T. Yamaguchi and M. Irie. Tetrahedron Lett. **47**, 1267 (2006).
22. T. Yamaguchi and M. Irie. J. Org. Chem. **70**, 10323 (2005).
23. T. Yamaguchi, Y. Fujita, H. Nakazumi, S. Kobatake, and M. Irie. Tetrahedron, **60**, 9863 (2004).
24. S.Z. Pu, T.S. Yang, J.K Xu, and B. Chen. Tetrahedron Lett. **47**, 6473 (2006).
25. M. Irie, T. Lifka, S. Kobatake, and N. Kato. J. Am. Chem. Soc. **122**, 4871 (2000).
26. J. Sworakowski, K. Janus, and S. Nešpůrek. Adv. Colloid Interface Sci. **116**, 97 (2005).
27. S.Z. Pu, T.S. Yang, G.Z. Li, J.K. Xu, and B. Chen. Tetrahedron Lett. **47**, 3167 (2006).
28. K. Uchida, T. Matsuoka, S. Kobatake, T. Yamaguchi, and M. Irie. Tetrahedron, **57**, 4559 (2001).
29. H. Tian, B.Z. Chen, H. Tu, and K. M len. Adv. Mater. **14**, 918 (2002).
30. B.Z. Chen, M.Z. Wang, Y.Q. Wu, and H. Tian. Chem. Commun. (Cambridge), 1060 (2002).
31. S.Z. Pu, J.K. Xu, L. Shen, Q. Xiao, T.S. Yang, and G. Liu. Tetrahedron Lett. **46**, 871 (2005).
32. B. Valeur. Molecular fluorescence: Principles and applications. Wiley-VCH, Weinheim, Germany. 2001.
33. T. Fukaminato, T. Kawai, S. Kobatake, and M. Irie. J. Phys. Chem. B, **107**, 8372 (2003).
34. A. Peters and N.R. Branda. J. Am. Chem. Soc. **125**, 3404 (2003).
35. M.S. Kim, H. Maruyama, T. Kawai, and M. Irie. Chem. Mater. **15**, 4539 (2003).
36. X.H. Zhou, F.S. Zhang, P. Yuan, F. Sun, S.Z. Pu, F.Q. Zhao, and C.H. Tung. Chem. Lett. **33**, 1006 (2004).

© 2007 NRC Canada

Regioselective synthesis of novel *N*-aminotriazolophanes

Madhukar S. Chande, Pravin A. Barve, Rahul R. Khanwelkar, Shailesh S. Athalye, and Deepak S. Venkataraman

Abstract: Bis-[4-amino-l,2,4-triazoles] were prepared by fusion of dibasic acids and thiosemicarbazide by condensation of aromatic acid hydrazides with hydrazine hydrate and carbon disulphide. Regioselective alkylation of these bis-[4-amino-1,2,4-triazoles] with 1,ω-dihaloalkanes in the presence of potassium hydroxide in aqueous methanol afforded novel *N*-aminotriazolophanes. The stereochemistry and antibacterial activity of these *N*-aminotriazolophanes were studied. In the case of the triazolophanes **5h**, **8d**, and **8f**, both N-NH_2 groups were observed trans to each other, whereas for case of other triazolophanes both N-NH_2 groups were observed cis to each other.

Key words: 4-amino-l,2,4-triazole, 1,ω-dihaloalkane, S-alkylation, regioselective, *N*-aminotriazolophanes.

Résumé : On a préparé des bis[4-amino-l,2,4-triazoles] par fusion d'acides dibasiques et de thiosemicarbazide, par condensation d'hydrazides d'acides aromatiques avec de l'hydrate d'hydrazine et du sulfure de carbone. L'alkylation régiosélective de ces bis-[4-amino-1,2,4-triazoles] avec des 1,ω-dihalogénoalcanes en présence d'hydroxyde de potassium, en solution dans le méthanol, fournit de nouveaux *N*-aminotriazolophanes. On a étudié la stéréochimie et l'activité antibactérienne de des *N*-aminotriazolophanes. Dans les cas des triazolophanes **5h**, **8d** et **8f**, on a observé que les deux groupes N–NH_2 sont trans l'un par rapport à l'autre alors que dans les autres cas les deux groupes N–NH_2 sont cis.

Mots-clés : 4-amino-l,2,4-triazole, 1,ω-dihalogénoalcane, S-alkylation, régiosélective, *N*-aminotriazolophanes.

[Traduit par la Rédaction]

Introduction

Crown compounds have generated considerable interest during the last three decades because of their ability to form stable complexes with variety of metal and organic cations and anions (1). They also have wide application in phase transfer catalysis (2). In recent years various structural changes have been made to the basic "crown ether" structure to enhance the selective activity of the ligands (3). These changes involve the insertion of aromatic and (or) heterocyclic ring systems into the macrocycles. The incorporation of a heterocyclic subunit provides rigidity to the macrocycle and assists in increasing the stability of complexes formed with both metals and organic cations (3). The development of crown compounds, especially macrocyclic compounds containing a heterocyclic subunit, has gained importance because of their wide range of applications. Many reviews and monographs have been published that highlight their synthesis and application in synthetic organic chemistry as phase transfer catalysts and in analytical chemistry as ligands for complexation (2, 4).

Received 19 April 2006. Accepted 8 November 2006. Published on the NRC Research Press Web site at http://canjchem.nrc.ca on 23 January 2007.

M.S. Chande,[1] P.A. Barve, R.R. Khanwelkar, S.S. Athalye, and D.S. Venkataraman. Department of Chemistry, The Institute of Science, 15, Madam Cama Road, Mumbai 400 032, India.

[1]Corresponding author (e-mail: chandems@vsnl.com).

In recent years, attention has been increasingly paid to the synthesis of bisheterocyclic compounds, which exhibit various biological activities (5) including antibacterial, antifungicidal, tuberculostatic, and plant growth regulative properties. Bisheterocyclic compounds displayed much better antibacterial activity than heterocyclic compounds (6). Various 1,2,4-triazoles are found to be associated with diverse pharmacological activities such as antiasthmatic (7), antiviral (ribavirin) (8), antifungal (fluconazole) (9), antimicrobial (10), antibacterial (11), insecticidal (12, 11*c*), amoebicidal (13), hypnotic (14), cytotoxic (15), and hypotensive (16) activities. This moiety was also found in potent agonist and antagonist receptor ligands (17) in HIV-1 protease inhibitors (18) and in thrombin inhibitors (19). Along with these significant pharmaceutical uses, 1,2,4-triazole derivatives are effectively used in polymers, dyestuff, photographic chemicals, and agricultural chemicals (20).

We have previously reported on the regioselective synthesis of novel oxadiazolophanes (21) and *N*-aminotriazolophanes (22). In continuation of this ongoing program in the synthesis of novel macrocyclic ligands (21, 22), their computational studies (21*b*), and their application as phase transfer catalysts (PTC) (22*c*), we now report a facile regioselective synthesis of novel *N*-aminotriazolophanes.

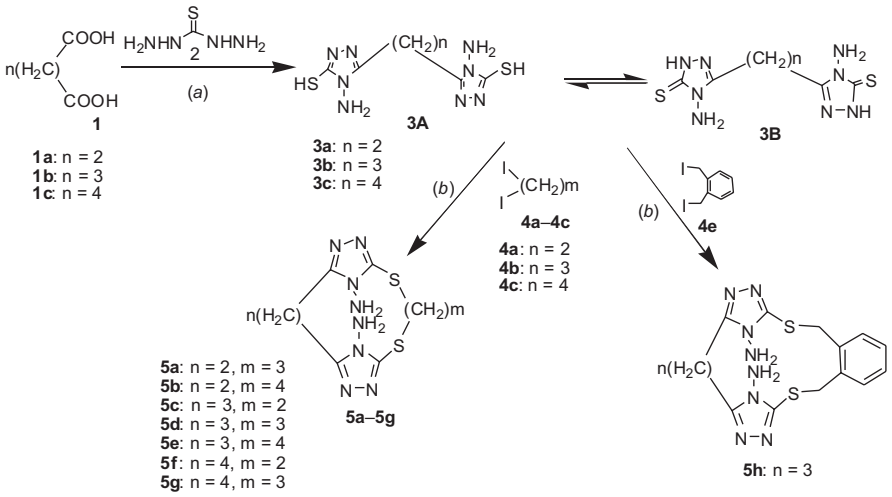
Results and discussion

Synthesis

The present work describes the versatile synthetic strategy for the regioselective synthesis of novel *N*-aminotriazolophanes

 doi:10.1139/V06-181 © 2007 NRC Canada

Scheme 1. Synthesis of *N*-aminotriazolophanes **5**. Reagents and conditions: (*a*) 170 °C, (*b*) KOH, aq. MeOH (80%), 80 °C.



that have been specially designed to study their stereochemistry.

Aminotriazole derivatives are well-known to be biologically active (23); e.g., 3-amino-1,2,4-triazole (amitrole) is known for its biological (24) and herbicidal (25) activities. 4-Amino-1,2,4-triazoles are potentially good corrosion inhibitors (26). Bisheterocyclic compounds prepared using 4-amino-1,2,4-triazoles derivatives exhibit significant biological activity (27, 5*f*). Hence, we decided to incorporate 4-amino-1,2,4-triazole as a basic unit in heterophane to further enhance heterophane's biological activity.

The obtained heterophanes (*N*-aminotriazolophanes) would be similar to lariat ether (28) with N-NH_2 groups as side arms. The study of the stereochemistry of these compounds is of interest because the two N-NH_2 groups would be either cis or trans to each other depending on the alkyl chain joining the two heterocyclic units and the thermodynamic stability of the molecule. This would in effect influence the properties of macrocycles such as cavity size.

There are many methods found in the literature for the synthesis of 3,5-disubstituted-4-amino-1,2,4-triazoles (29), but none of them concerns the synthesis of heterophanes. Bis-*N*-aminotriazoles **3a**–**3c** (30) were prepared in high yield by direct fusion of aliphatic diacids **1a**–**1c** with thiocarbohydrazine **2** (Scheme 1). The compound **3**, containing thioamido groups, has an amphoteric nature and can exist in tautomeric forms **3A** and **3B**. On alkylation of **3** with 1,ω-dihaloalkane, multiple products could form depending on the reaction condition.

The reaction of compounds **3a**–**3c** with diiodoalkanes **4a**–**4e** in aq. methanol (80%) in the presence of potassium hydroxide as base gave only products **5a**–**5h** regioselectively in good yield (Scheme 1, Table 1). The intramolecular alkylation, which regioselectively occurs at sulfur, is mainly due to the template formation, which is due to the presence of the hexadentate potassium ions where the two ligands are water molecules (31). The reaction was carried out in a large excess of solvent to ensure intramolecular cyclisation (high dilution condition). Reaction of compound **3** with dibromomethane was unsuccessful, perhaps because of the inability of the methyl group to link the two terminal thiol sulphur atoms.

The elucidation of the structures of **5a**–**5h** was accomplished on the basis of their spectral data and elemental analysis (Table 1). For example, the reaction of **3b** with 1,2 diiodoethane **4a** resulted in the formation of the desired *N*-aminotriazolophane **5c**, which was confirmed on the basis of NMR spectra. The ^{1}H NMR spectrum of the compound showed a triplet at δ: 3.37 for the S-CH_2 group in the ethane chain. The absence of a peak for C=S in the ^{13}C NMR spectrum confirmed the regioselectivity of S-alkylation. It showed a signal for S-CH_2 carbon at 29.6 ppm. From the above data, compound **5c** was identified as 1^4,5^4-diamino-6,9-dithia-1,5(3,5)-di-(1,2,4-triazola)cyclononaphane (32). The other *N*-aminotriazolophanes **5a**–**5h** were similarly synthesized and characterized.

To improve the solubility of the triazolophanes it was thought to incorporate a phenyl nucleus into the structure, which would also help in complexation or phase transfer catalyst (PTC) activity. Hence, the scope of the previous reaction was extended to the synthesis of benztriazolophane **8** (Scheme 2). Bistriazole **7** (33) was synthesized using the Reid and Heindel method [34] by the condensation of isophthalic acid dihydrazide **6** with hydrazine hydrate, carbon disulphide, and potassium hydroxide in methanol in high yield.

The reaction of **7** with **4a**–**4f** in aq. methanol (80%) in the presence of potassium hydroxide as a base gave the desired benztriazolophanes **8a**–**8f** regioselectively in moderate yield (Scheme 2, Table 1). The structure of the product was confirmed on the basis of spectral data and elemental analysis (Table 1). For example, the reaction of **7** with 1,2-diiodoethane **4a** resulted in the formation of the desired aminotriazolophane **8a**, which was confirmed on the basis of NMR spectra. The ^{1}H NMR spectrum of the compound showed a triplet at δ: 2.89 for the S-CH_2 group of the ethane chain. The absence of a peak for C=S in the ^{13}C NMR spectrum confirmed the regioselectivity of S-alkylation. It showed signals for S-CH_2 carbons at 27.9 and 30.0 ppm.

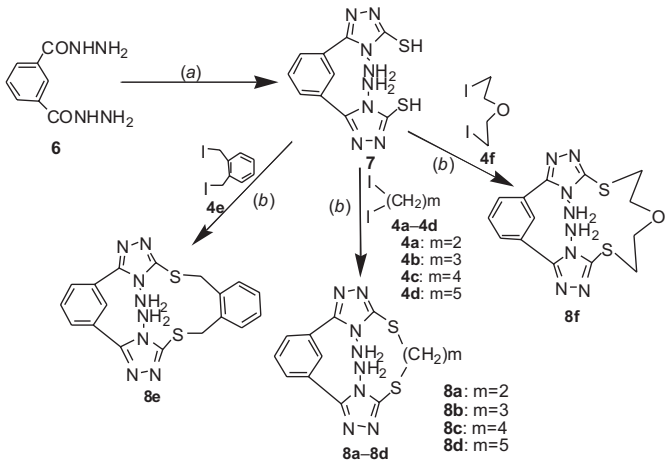
We have discussed in detail the regioselective N-alkylation (22*c*) and S-alkylation (21, 22*a*, 22*b*) for the synthesis of aminotriazolophanes. It was thought worthwhile to use O-alkylation for the synthesis of heterophane with an amino side arm. Hence, in continuation of this work on

© 2007 NRC Canada

Table 1. Preparation and analytical data of compounds.

Compound	Yield (%)	MP (°C)	Formulae	Found (required) (%)			
				C	H	N	S
3a	82	220	$C_6H_{10}N_8S_2$	—	—	—	—
3b	72	203	$C_7H_{12}N_8S_2$	—	—	—	—
3c	74	221	$C_8H_{14}N_8S_2$	—	—	—	—
5a	42	208	$C_9H_{14}N_8S_2$	36.23 (36.01)	4.73 (4.60)	37.55 (37.43)	21.49 (21.28)
5b	44	197	$C_{10}H_{16}N_8S_2$	38.44 (38.23)	5.16 (5.01)	35.87 (35.75)	20.53 (20.32)
5c	38	216	$C_9H_{14}N_8S_2$	36.23 (36.02)	4.73 (4.52)	37.55 (37.32)	21.49 (21.38)
5d	45	204	$C_{10}H_{16}N_8S_2$	38.44 (38.23)	5.16 (5.01)	35.87 (35.62)	20.53 (20.40)
5e	32	197	$C_{11}H_{18}N_8S_2$	40.47 (40.35)	5.56 (5.45)	34.33 (34.31)	19.65 (19.42)
5f	43	112	$C_{11}H_{18}N_8S_2$	40.47 (40.34)	5.56 (5.46)	34.33 (34.20)	19.65 (19.43)
5g	47	122	$C_{10}H_{16}N_8S_2$	38.44 (38.32)	5.16 (5.03)	35.87 (35.75)	20.53 (20.32)
5h	35	141	$C_{15}H_{18}N_8S_2$	48.11 (48.00)	4.84 (4.72)	29.92 (29.80)	17.13 (17.02)
7	82	>250	$C_{10}H_{14}N_8S_2$	39.22 (39.01)	3.27 (3.05)	36.60 (36.38)	20.91 (20.80)
8a	25	175	$C_{12}H_{12}N_8S_2$	43.37 (43.25)	3.61 (3.50)	33.74 (33.61)	19.28 (19.05)
8b	30	245	$C_{13}H_{14}N_8S_2$	45.09 (44.90)	4.05 (3.87)	32.37 (32.13)	18.49 (18.35)
8c	33	210	$C_{14}H_{16}N_8S_2$	46.67 (46.44)	4.44 (4.23)	31.11 (31.00)	17.78 (17.55)
8d	35	>250	$C_{15}H_{18}N_8S_2$	48.13 (48.01)	4.81 (4.58)	29.95 (29.72)	17.11 (17.00)
8e	47	235	$C_{18}H_{20}N_8S_2$	52.94 (52.71)	3.92 (3.78)	27.45 (27.31)	15.69 (15.46)
8f	44	>250	$C_{14}H_{20}N_8S_2O$	44.68 (44.55)	4.26 (4.12)	29.79 (29.56)	17.02 (16.80)
10	80	192	$C_8H_8N_4SO$	46.15 (46.02)	3.85 (3.72)	26.93 (26.72)	15.38 (15.15)
11	65	205	$C_{19}H_{20}N_8S_2O_2$	49.57 (49.46)	5.22 (5.10)	24.35 (24.23)	13.91 (13.78)
12a	35	>250	$C_{22}H_{24}N_8S_2O_2$	52.23 (52.11)	4.84 (4.60)	22.58 (22.36)	12.90 (12.66)
12b	36	220	$C_{23}H_{26}N_8S_2O_3$	52.08 (52.00)	5.66 (5.43)	21.13 (21.01)	12.08 (11.92)
14	80	>250	$C_8H_8N_4SO$	46.15 (46.01)	3.85 (3.62)	26.93 (26.70)	15.38 (15.24)
15	65	228	$C_{21}H_{24}N_8S_2O_2$	51.64 (51.51)	5.74 (5.62)	24.35 (24.23)	13.11 (13.00)
16	28	>250	$C_{26}H_{32}N_8S_2O_2$	56.52 (56.39)	5.78 (5.55)	20.29 (20.15)	11.59 (11.38)

Scheme 2. Synthesis of benztriazolophanes **8.** Reagents and conditions: (*a*) CS_2, $(NH_2)_2{\cdot}H_2O$, KOH, MeOH, 0–5 °C, (*b*) KOH, aq. MeOH (80%), 80 °C.



benztriazolophanes, salicylic acid hydrazide **9** was reacted with hydrazine hydrate, carbon disulphide, and potassium hydroxide in methanol to give compound **10** in high yield (Scheme 3). When **10** was reacted with 1,3-dibromopropane in methanolic potassium hydroxide, compound **11** was afforded regioselectively in good yield (Scheme 3, Table 1). The benztriazolophanes **12a** and **12b** were synthesized regioselectively as the only products in moderate yield by reacting **11** with dihaloalkanes in aq. methanol (80%) containing potassium hydroxide (Scheme 3, Table 1). The structure of the product was confirmed on the basis of spectral data and elemental analysis (Table 1). For example, reaction of **11** with 1,3-dibromopropane resulted in the formation of the desired compound **12a**, which was confirmed on the basis of NMR spectra. The ^{1}H NMR spectrum of the compound showed a triplet at δ: 3.66 for the S-CH_2 group of the propane chain and a triplet at δ: 4.08 for the O-CH_2 group of the propane chain. An M^+ peak at *m*/*z* 496 in the mass spectrum confirmed the formation of **12a**.

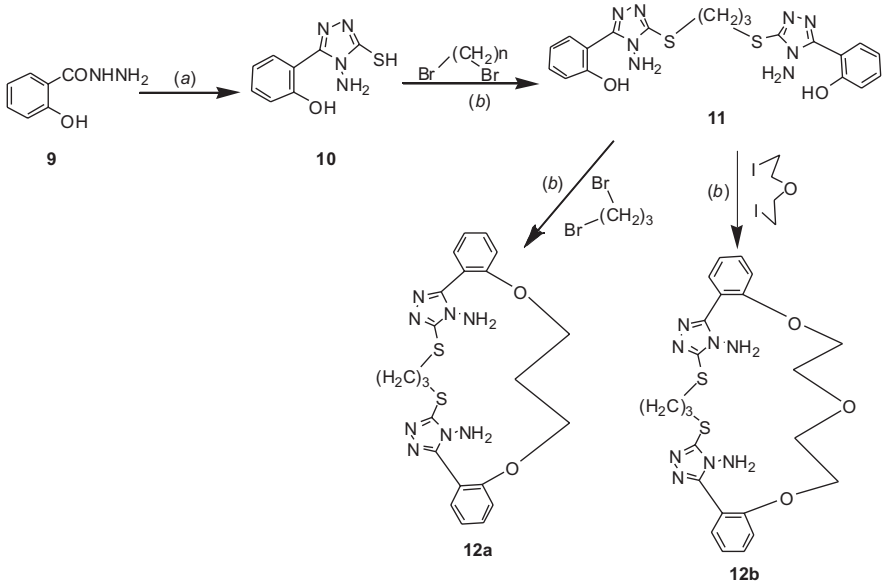
Similar reaction conditions were used to prepare compound **16** from *p*-hydroxy benzoic acid hydrazide **13**. When **13** was reacted with hydrazine hydrate, carbon disulphide, and potassium hydroxide in methanol, compound **14** was obtained in high yield. Compound **14** was reacted with 1,5-dibromopentane to afford **15** in moderate yield (Scheme 4, Table 1). Compound **15** was then reacted with 1,5-dibromopentane in methanolic potassium hydroxide to afford **16** in low yield (Scheme 4, Table 1).

Stereochemistry

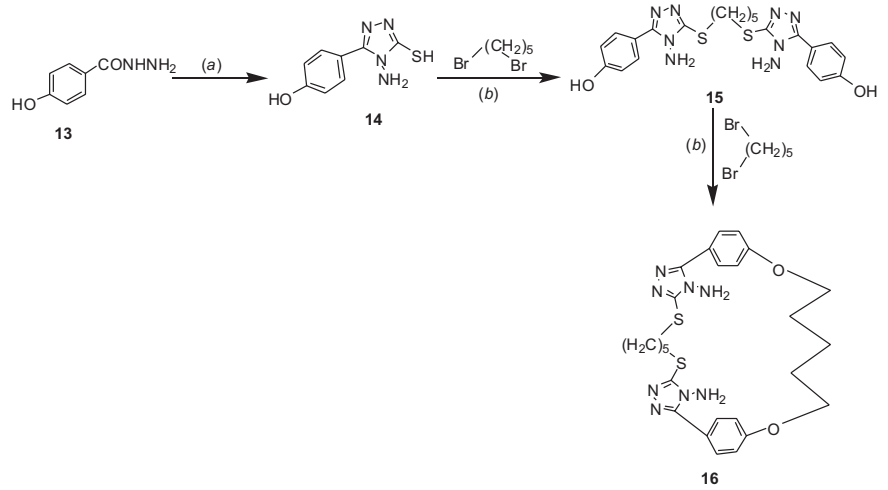
The stereochemistry of these *N*-aminotriazolophanes was studied using ^{1}H NMR spectral analysis and molecular modeling studies (35). It was observed that in compounds **5a**–**5g**,

© 2007 NRC Canada

Scheme 3. Synthesis of *N*-aminotriazolophanes **12.** Reagents and conditions: (*a*) CS_2, $(NH_2)_2{\cdot}H_2O$, KOH, MeOH, 0–5 °C, (*b*) KOH, aq. MeOH (80%), 80 °C.



Scheme 4. Synthesis of *N*-aminotriazolophanes **16.** Reagents and conditions: (*a*) CS_2, $(NH_2)_2{\cdot}H_2O$, KOH, MeOH, 0–5 °C, (*b*) KOH, aq. MeOH (80%), 80 °C.



8a–**8c**, and **8e** both N-NH_2 groups appeared as a single peak in the ^{1}H NMR, indicating that both N-NH_2 groups are cis to each other. This was also supported by the molecular modeling study. For compounds **5h**, **8d**, and **8f** (Fig. 1), two different peaks were observed for the N-NH_2 groups, indicating the presence of these groups in different magnetic environments. This showed that both N-NH_2 groups are trans to each other. The molecular model of **5h**, **8d**, and **8f** (Fig.1) showed that one of the NH_2 groups was hydrogen bonded to lone pairs of the ring nitrogen atoms, thus changing the magnetic environment.

Conclusion

In this paper, we have reported on a versatile and convenient route for the synthesis of novel *N*-aminotriazolophanes from aliphatic and aromatic acid hydrazides. For compounds **5h**, **8d**, and **8f**, both N-NH_2 groups are observed in different magnetic environments.

Experimental

General procedure for the synthesis of bis-(4-amino-5-mercapto-1,2,4-triazol-3yl)alkanes (3a–3c)

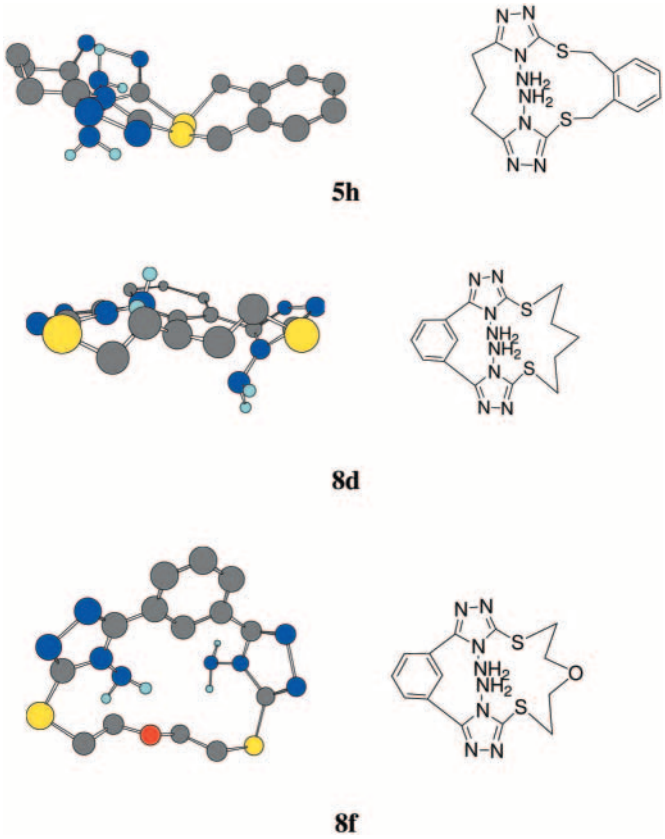
Compounds **3a**–**3c** were synthesized using a method from the literature [31].

General procedure for the synthesis of 5a–5h, 8a–8f, 11, 12a-12c, 15, and 16

Compounds **3a**–**3c**, **7**, **10**, **11**, **14**, and **15** (for the synthesis of **5a**–**5h, 8a**–**8f, 11, 12a**–**12b, 15** and **16**, respectively) (0.01 mol) were dissolved in aq. methanol (methanol–water, 80:20, 200 mL) containing potassium hydroxide (0.02 mol). A solution of 1,ω-dihaloalkane (0.01 mol) in methanol was

© 2007 NRC Canada

Fig. 1. Stereochemistry of *N*-aminotriazolophanes.



added dropwise for 1 h. This reaction mixture was then refluxed with stirring on a magnetic stirrer for 8 h. On cooling to 10–15 °C, solid separated out. The obtained solid was then filtered, washed with cold water, and recrystallized from aq. dimethyl formamide (DMF).

$1^4,4^4$-Diamino-5,9-dithia-1,4(3,5)-di(1,2,4-triazola)cyclononaphane (5a)

^{1}H NMR (500 MHz, DMSO-d_6) δ: 2.04 (p, 2H, CH_2), 3.21 (s, 4H, 2 × CH_2), 3.33 (t, 4H, 2 × S-CH_2), 5.95 (s, 4H, 2 × NH_2, D_2O exchangeable). ^{13}C NMR could not be scanned because of poor solubility.

$1^4,4^4$-Diamino-5,10-dithia-1,4(3,5)-di(1,2,4-triazola)cyclodecaphane (5b)

^{1}H NMR (500 MHz, DMSO-d_6) δ: 1.78 (p, 4H, 2 × CH_2), 3.12 (s, 4H, 2 × CH_2), 3.33 (t, 4H, 2 × S-CH_2), 5.95 (s, 4H, 2 × NH_2, D_2O exchangeable). ^{13}C NMR (500 MHz, DMSO-d_6, ppm) δ: 21.0, 28.1 (4 × CH_2), 30.3 (2 × S-CH_2), 151.2 (2 × S-C=N), 155.3 (2 × C=N).

$1^4,5^4$-Diamino-6,9-dithia-1,5(3,5)-di(1,2,4-triazola)cyclononaphane (5c)

^{1}H NMR (500 MHz, DMSO-d_6) δ: 2.38 (p, 2H, CH_2), 2.78 (t, 4H, 2 × CH_2), 3.37 (t, 4H, 2 × S-CH_2), 5.14 (s, 4H, 2 × NH_2, D_2O exchangeable). ^{13}C NMR (500 MHz, DMSO-d_6, ppm) δ: 22.1, 24.5, 29.7, (5 × CH_2), 148.7 (2 × S-C=N), 156.8 (2 × C=N).

$1^4,5^4$-Diamino-6,10-dithia-1,5(3,5)-di(1,2,4-triazola)cyclodecaphane (5d)

^{1}H NMR (500 MHz, DMSO-d_6) δ: 1.75 (p, 2H, CH_2), 2.05 (p, 2H, CH_2), 2.75 (t, 4H, 2 × CH_2), 3.11 (t, 4H, 2 × S-CH_2), 5.87 (s, 4H, 2 × NH_2, D_2O exchangeable). ^{13}C NMR could not be scanned because of poor solubility.

$1^4,5^4$-Diamino-6,11-dithia-1,5(3,5)-di(1,2,4-triazola)cycloundecaphane (5e)

^{1}H NMR (500 MHz, DMSO-d_6) δ: 1.74 (m, 4H, 2 × CH_2), 2.03 (p, 2H, CH_2), 2.70 (t, 4H, 2 × CH_2), 3.07 (t, 4H, 2 × S-CH_2), 5.80 (s, 4H, 2 × NH_2, D_2O exchangeable). ^{13}C NMR could not be scanned because of poor solubility.

$1^4,6^4$-Diamino-7,10-dithia-1,6(3,5)-di(1,2,4-triazola)cyclodecaphane (5f)

^{1}H NMR (500 MHz, DMSO-d_6) δ: 1.88 (m, 4H, 2 × CH_2), 2.51 (m, 4H, 2 × CH_2), 2.89 (t, 4H, 2 × S-CH_2), 5.75 (s, 4H, 2 × NH_2, D_2O exchangeable). ^{13}C NMR could not be scanned because of poor solubility.

$1^4,6^4$-Diamino-7,11-dithia-1,6(3,5)-di(1,2,4-triazola)cycloundecaphane (5g)

^{1}H NMR (500 MHz, DMSO-d_6) δ: 1.70 (m, 4H, 2 × CH_2), 2.02 (p, 2H, CH_2), 2.69 (m, 4H, 2 × CH_2), 3.33 (t, 4H, 2 × S-CH_2), 5.85 (s, 4H, 2 × NH_2, D_2O exchangeable). ^{13}C NMR could not be scanned because of poor solubility.

$1^4,5^4$-Diamino-8(1,2)-benzena-6,10-dithia-1,5(3,5)-di(1,2,4-triazola)cyclodecaphane (5h)

^{1}H NMR (500 MHz, DMSO-d_6) δ: 2.02 (p, 2H, CH_2), 2.70 (t, 4H, 2 × CH_2), 4.45 (s, 4H, 2 × S-CH_2), 5.81(s, 2H, NH_2, D_2O exchangeable), 5.85(s, 2H, NH_2, D_2O exchangeable), 7.16–7.33 (d, 4H, aromatic H). ^{13}C NMR (500 MHz, DMSO-d_6, ppm) δ: 22.1, 24.0, 33.5 (5 × CH_2), 126.9, 130.8, 135.5 (aromatic C), 152.8 (2 × S-C=N), 160.7 (2 × C=N).

$1^4,3^4$-Diamino-2(1,3)-benzena-4,7-dithia-1,3(3,5)-di(1,2,4-triazola)cycloheptaphane (8a)

^{1}H NMR (300 MHz, DMSO-d_6) δ: 2.89 (s, 4H, 2 × S-CH_2), 5.03 (s, 4H, 2 × NH_2, D_2O exchangeable), 6.84–7.56 (m, 4H, aromatic H). ^{13}C NMR (300 MHz, DMSO-d_6, ppm) δ: 30.0 (2 × S-CH_2), 127.1, 128.7, 130.1, 131.2 (aromatic C), 144.4 (2 × S-C=N), 153.7 (2 × C=N).

$1^4,3^4$-Diamino-2(1,3)-benzena-4,8-dithia-1,3(3,5)-di(1,2,4-triazola)cycloctaphane (8b)

^{1}H NMR (300 MHz, DMSO-d_6) δ: 1.96 (p, 2H, CH_2), 3.86 (t, 4H, 2 × S-CH_2), 5.51 (s, 4H, 2 × N-NH_2, D_2O exchangeable), 7.63 – 8.57 (m, 4H, aromatic H). MS (DI) *m/z*: 346 (M^+), 322, 304, 284, 243, 202, 129, 102, 91, 76, 59.

$1^4,3^4$-Diamino-2(1,3)-benzena-4,9-dithia-1,3(3,5)-di(1,2,4-triazola)cyclononaphane (8c)

^{1}H NMR (500 MHz, DMSO-d_6) δ: 1.06 (m, 4H, 2 × CH_2), 3.86 (t, 4H, 2 × S-CH_2), 6.18 (s, 4H, 2 × NH_2, D_2O exchangeable), 7.62 – 8.54 (m, 4H, aromatic H). ^{13}C NMR (500 MHz, DMSO-d_6, ppm) δ: 28.3 (2 × CH_2), 30.6, 30.7 (2 × S-CH_2), 127.1 – 134.3 (aromatic C), 141.3 (2 × S-C=N), 153.8 (2 × C=N). MS (DI) *m/z*: 360 (M^+), 330, 298, 256, 202, 171, 156, 143, 129, 102, 91, 77.

© 2007 NRC Canada

1^4,3^4-Diamino-2(1,3)-benzena-4,10-dithia-1,3(3,5)-di(1,2,4-triazola)cyclodecaphane (8d)

^{1}H NMR (300 MHz, DMSO-d_6) δ: 1.29 (m, 2H, CH_2), 1.69 (m, 4H, 2 × CH_2), 3.13 (t, 4H, 2 × S-CH_2), 6.11 (s, 4H, 2 × NH_2, D_2O exchangeable), 7.38- 7.81 (m, 4H, aromatic H). MS (DI) *m/z*: 374 (M^+), 358, 324, 304, 182, 144, 128, 102, 91, 80, 77.

1^4,3^4-Diamino-2(1,3)-6(1,2)-dibenzena-4,8-dithia-1,3(3,5)-di(1,2,4-triazola)cyclooctaphane (8e)

^{1}H NMR (500 MHz, DMSO-d_6) δ: 4.69 (t, 4H, 2 × S-CH_2), 6.21 (d, 4H, 2 × NH_2, D_2O exchangeable), 7.31- 8.61 (m, 8H, aromatic H). ^{13}C NMR (500 MHz, DMSO-d_6, ppm) δ: 32.6 (2 × S-CH_2), 127.1, 128.1, 128.8, 130.6, 131.2, 132.1, 135.6 (aromatic C), 147.5 (2 × S-C=N), 159.2 (2 × C=N). MS (DI) *m/z*: 408 (M^+), 322, 304, 288, 250, 220, 216, 192, 180, 128, 102, 90, 76.

1^4,3^4-Diamino-2(1,3)-benzena-7-oxa-4,10-dithia-1,3(3,5)-di(1,2,4-triazola)cyclodecaphane (8f)

^{1}H NMR (500 MHz, DMSO-d_6) δ: 3.08 (t, 2H, S-CH_2), 3.54 (t, 2H, O-CH_2), 5.90 (s, 2H, NH_2, D_2O exchangeable), 5.94 (s, 2H, NH_2, D_2O exchangeable), 7.40- 8.55 (m, 4H, aromatic H). ^{13}C NMR (500 MHz, DMSO-d_6, ppm) δ: 31.2 (2 × S-CH_2), 69.2, 70.7 (O-CH_2), 127.6, 129.3, 129.6, 131.3 (aromatic C), 154.1 (2 × S-C=N), 163.2 (2 × C=N). MS (DI) *m/z*: 376 (M^+), 299, 267, 223, 208, 170, 128, 102, 91, 76, 66.

1,3-Di-[4-amino-5(2′-hydroxyphenyl)-1,2,4-triazol-3-yl]mercapto propane (11)

^{1}H NMR (500 MHz, DMSO-d_6) δ: 2.22 (p, 2H, CH_2), 3.37 (t, 4H, 2 × S-CH_2) 6.06 (s, 4H, 2 × NH_2, D_2O exchangeable), 6.97–7.93 (m, 8H, aromatic H), 11.11 (s, 2H, 2 × OH, D_2O exchangeable). ^{13}C NMR (500 MHz, DMSO-d_6, ppm) δ: 29.5 (CH_2), 30.2 (2 × S-CH_2), 113.2, 116.9, 119.6, 129.7, 131.9, 156.2 (aromatic C), 153.9 (2 × S-C=N), 154.0 (2 × C=N).

1^4,9^4-Diamino-2,8(1,2)-dibenzena-3,7-dioxa-10,14-dithia-1(3,5)9(5,3)-di(1,2,4-triazola)cyclotetradecaphane (12a)

^{1}H NMR (500 MHz, DMSO-d_6) δ: 0.73 (p, 2H, CH_2), 1.12 (p, 2H, CH_2), 3.66 (t, 4H, 2 × S-CH_2), 4.08 (t, 4H, 2 × O-CH_2), 5.17 (s, 4H, 2 × NH_2, D_2O exchangeable), 6.87 – 7.45 (m, 8 H, aromatic H). MS (DI) *m/z*: 496 (M^+), 480, 443, 405, 318, 209, 167, 91, 84, 77.

1^4,9^4-Diamino-2,8(1,2)-dibenzena-3,7-dioxa-10,14-dithia-1(3,5)9(5,3)-di(1,2,4-triazola)cyclotetradecaphane (12b)

^{1}H NMR (500 MHz, DMSO-d_6) δ: 1.12 (p, 2H, CH_2), 3.66 (t, 4H, 2 × S-CH_2), 4.03 (t, 8H, 4 × O-CH_2), 5.62 (s, 4H, 2 × NH_2, D_2O exchangeable), 7.03–7.46(m, 8 H, aromatic H).

1,5-Di-[4-amino-5-(2′-hydroxyphenyl)-1,2,4-triazol-3-yl]mercapto pentane (15)

^{1}H NMR (500 MHz, DMSO-d_6) δ: 1.56 (p, 2H, CH_2), 1.75 (p, 4H, 2 × CH_2), 3.16 (t, 4H, 2 × S-CH_2), 6.01 (s, 4H, 2 × NH_2, D_2O exchangeable), 6.86–7.80 (dd, 8 H, aromatic H), 9.89 (s, 2H, 2 × OH, D_2O exchangeable). ^{13}C NMR (500 MHz, DMSO-d_6, ppm) 27.1, 28.6 (3 × CH_2), 30.9 (2 × S-CH_2), 115.2, 117.7, 129.4, 138.7 (aromatic C), 152.7 (2 × S-C=N), 154.0 (2 × C=N).

1^4,11^4-Diamino-2,10(1,4)-dibenzena-3,9-dioxa-12,18-dithia-1(3,5)11(5,3)-di(1,2,4-triazola)cyclooctadecaphane (16)

^{1}H NMR (500 MHz, DMSO-d_6) δ: 1.20 (p, 2H, CH_2), 1.43 (p, 2H, CH_2), 1.53 (p, 4H, 2 × CH_2), 3.12 (t, 4H, 2 × S-CH_2), 4.00 (t, 4H, 2 × O-CH_2), 6.00 (s, 4H, 2 × NH_2, D_2O exchangeable), 6.82–7.88 (dd, 8 H, aromatic H). MS (DI) *m/z*: 552 (M^+), 536, 520, 489, 446, 412, 396, 292, 239, 198, 137, 101, 91, 77.

General procedure for the synthesis of 7

Isophthalic acid dihydrazide **6** (0.01 mol) was dissolved in ethanol (20 mL) in the presence of potassium hydroxide (0.02 mol) and cooled to 5 °C. To this cold solution was added carbon disulphide (0.02 mol) under stirring. The potassium dithiacarbamate salt precipitated out and was filtered, washed with petroleum ether, and dried. This salt was fused with hydrazine hydrate (99%, 0.022 mol) at 90 °C for 4 h. The reaction mixture was poured onto cold water and filtered to remove traces of inorganic material. The filtrate was then treated with dilute hydrochloric acid until the pH of the solution became neutral. The obtained white product was then filtered, washed with cold water, and recrystallized from aq. DMF.

1,3-Bis-(4′-amino-5′-mercapto-1,2,4-triazol-3-yl)benzene (7)

^{1}H NMR (500 MHz, DMSO-d_6) δ: 5.72 (s, 4H, 2 × NH_2, D_2O exchangeable), 7.65- 8.41 (m, 4H, aromatic H), 13.98 (s, 2H, 2 × NH, D_2O exchangeable). ^{13}C NMR (500 MHz, DMSO-d_6, ppm) δ: 126.1, 127.4, 128.6, 129.8 (aromatic C), 148.8 (2 × C=N), 167.1 (2 × C=S).

General procedure for the synthesis of 10 and 14

Salicylic acid hydrazide **9** and *p*-hydroxy benzoic acid hydrazide **13** (for **10** and **14,** respectively) (0.01 mole) were dissolved in ethanol (20 mL) in the presence of potassium hydroxide (0.02 mole) and cooled to 5 °C. To this cold solution was added carbon disulphide (0.01 mole) under stirring. The potassium dithiacarbamate salt precipitated out and was filtered, washed with petroleum ether, and dried. This salt was fused with hydrazine hydrate (99%, 0.011 mole) at 90 °C for 4 h. The reaction mixture was then poured onto cold water and filtered to remove traces of inorganic material. The filtrate was treated with dilute hydrochloric acid until the pH of the solution became neutral. The obtained white product was then filtered, washed with cold water, and recrystallized from aq. DMF.

4-Amino-5(2′-hydroxyphenyl)-3-meracpto-1,2,4-triazole (10)

^{1}H NMR (500 MHz, DMSO-d_6) δ: 5.63 (s, 4H, 2 × NH_2, D_2O exchangeable) 6.92–7.44 (m, 4H, aromatic H), 10.37 (s, 1H, OH, D_2O exchangeable), 13.896 (s, 1H, S=C-NH, D_2O exchangeable). ^{13}C NMR (500 MHz, DMSO-d_6, ppm) 113.1, 116.2, 119.0, 130.9, 132.9, 156.1 (aromatic C), 149.2 (2 × C=N), 165.1 (2 × C=S).

© 2007 NRC Canada

4-Amino-5(4′-hydroxyphenyl)-3-meracpto-1,2,4-triazole (14)

^{1}H NMR (300 MHz, DMSO-d_6) δ: 5.73 (s, 4H 2 × N-NH_2, D_2O exchangeable), 6.85, 7.84 (dd, 4H, aromatic H), 10.02 (s, 1H, OH, D_2O exchangeable), 13.76 (s, 1H, S=C-NH, D_2O exchangeable). ^{13}C NMR (300 MHz, DMSO-d_6, ppm) 115.3, 116.5, 129.7, 159.4 (aromatic C), 149.6 (2 × C=N), 166.4 (2 × C=S).

Acknowledgement

The help rendered by the Regional Sophisticated Instrumentation Centres (RSIC), the Indian Istitute of Technology (IIT), and the Tata Institute of Fundamental Research (TIFR), the Department of Chemistry, University of Pune, and the Department of Chemistry, Institute of Science, Mumbai, are gratefully acknowledged. We also thank "Lady Tata memorial trust" for their financial support.

References

1. (*a*) E. Graf and J.M. Lehn. Helv. Chim. Acta, **64**, 1040 (1981); (*b*) B. Dietrich, M.W. Hosseini, J.M. Lehn, and R.B. Session. Helv. Chim. Acta, **66**, 1262 (1983); (*c*) M.W. Hosseini, J.M. Lehn, and M.P. Mertes. Helv. Chim. Acta, **66**, 2444 (1983); (*d*) A. Kumar, S. Mageswaran, and I.O. Sutherland. Tetrahedron, **42**, 3291 (1986); (*e*) J.S. Bradshaw and R.M. Izatt. Acc. Chem. Res. **30**, 338 (1997).
2. (*a*) G.R. Newkome, J.G. Traynham, and G.R. Baker. *In* Crown ethers and cryptands in compendium of heterocyclic compounds. Vol. 5. *Edited by* A.R. Katritzky. Pergamon Press, London, U.K. 1984. p. 763; (*b*) Phase transfer catalysis, fundamentals, applications and industrial perspective. *Edited by* C.M. Stark, C. Liotta, and M. Halpern. Chapman and Hall, New York. 1994.
3. J.S. Bradshaw, R.M. Izzat, A.V. Bordunov, C.Y. Zhu, and J.K. Hathaway. *In* Comprehensive supramolecular chemistry. Vol. 1. *Edited by* G.W. Gokel. Pergamon Press, New York. 1996. p. 35.
4. C.J. Pedersen. J. Am. Chem. Soc. **89**, 2495 (1970).
5. (*a*) H. Singh, L.D.S. Yadav, and B.K. Bhattacharya. J. Indian Chem. Soc. **56**, 1013 (1979); (*b*) N.C. Desai. Indian J. Chem. Sect. B, **32**, 343 (1993); (*c*) X.M. Feng, R. Chen, X.C. Liu, and Z.Y. Zhang. Chin. J. Appl. Chem. **8**, 28 (1991); (*d*) P.S. Upadhyay, R.N. Vansdadia, and A.J. Baxi. Indian J. Chem. Sect. B, **29**, 793 (1990); (*e*) J. Mohan, G.S.R. Anjaneyula, S. Sudhir, and D.R. Arora. J. Indian Chem. Soc. **66**, 330 (1989); (*f*) M.M. Ghorab, Sh. A.M. El-Sharief, Y.A. Ammar, and Sh. I. Mohamed. Farmaco, **55**, 354 (2000).
6. Z.Y. Zhang, X.L. Chen, L. Wei, and Z.L. Ma. Chem. Res. Chin. Univ. **7**, 129 (1991).
7. Y. Naito, F. Akahoshi, S. Takeda, T. Okada, M. Kajii, H. Nishimura, M. Sugiura, C. Fukaya, and Y. Kagitani. J. Med. Chem. **39**, 3019 (1996).
8. (*a*) A.S. Narang and R. Vince. J. Med. Chem. **20**, 1684 (1977); (*b*) E. De Clercq. J. Clin. Virol. **30**, 115 (2004).
9. (*a*) X. Collin, A. Sauleau, and J. Coulon. Bioorg. Med. Chem. Lett. **13**, 2601 (2003); (*b*) B.S. Holla and B. Kalluraya. Indian J. Chem. Sect. B, **27**, 683 (1988); (*c*) S. Giri, H. Singh, L.D.S. Yadav, and R.K. Khare. J. Indian Chem. Soc. **55**, 168 (1978).
10. M. Kidwai, P. Sapra, P. Misra, R.K. Saxena, and M. Singh. Bioorg. Med. Chem. **9**, 217 (2001).
11. (*a*) T. George, D.V. Mehta, R. Tahilramani, J. David, and P.K. Talwalker. J. Med. Chem. **14**, 335 (1971); (*b*) S. Papakonstantinou-Garoufalias, N. Pouli, P. Marakos, and A. Chytyroglou-Ladas. Farmaco, **57**, 973 (2002); (*c*) A.K. Sengupta and H.K. Misra. J. Indian Chem. Soc. **58,** 508 (1981).
12. M.M. Ghorab, S.G. Abdel- Hamide, M.S.A. El-Gaby, and S.M. El- Sayed. Acta Pharm. **49**, 1 (1999).
13. C.S. Andotra and S.K. Sharma. Proc. Natl. Acad. Sci. India Sect. A, **58**, 215 (1988).
14. J.B. Hester, A.D. Rudzik, and B.V. Kamdar. J. Med. Chem. **14**, 1078 (1977).
15. N.G.N. Milton. Neurotoxicology, **22**, 767 (2001).
16. (*a*) G. Burell, J.M. Evans, M.S. Hadley, F. Hicks, and G. Stemp. Bioorg. Med. Chem. Lett. **4**, 1285 (1994); (*b*) M.M. Ghorab, S.G. Abdel-Hamide, G.M. Ali, El Sayed, and H. Shaurub. Pestic. Sci. **48**, 31 (1996); (*c*) M.K. Mody, A.R. Prasad, T. Ramalingham, and P.B. Suttur. J. Indian Chem. Soc. **59**, 769 (1982).
17. (*a*) J.H. Wadsworth, S.M. Jenkins, B.S. Orlek, F. Cassidy, M.S.G. Clark, F. Brown, G.J. Riley, D. Graves, J. Hawkins, and C.B. Naylor. J. Med. Chem. **35**, 1280 (1992); (*b*) S.M. Jenkins, H. Wadsworth, S. Bromidge, B.S. Orlek, P.A. Wyman, G.J. Riley, and J. Hawkins. J. Med. Chem. **35**, 2392 (1992); (*c*) C. Chen, R. Dagnino, C.Q. Huang, J.R. McCarthy, D.E. Grigoriadis. Bioorg. Med. Chem. Lett. **11**, 3165 (2001); (*d*) B. Neumann-Schultz, L. Unger, K. Blumbach, D. Starck, D. Schoebel, and H. Treiber. International Patent WO-2000-0042038, 20 August 2000.
18. S.K. Thompson, A.M. Eppley, J.S. Frazee, M.G. Darcy, R.T. Lum, T.A. Tomaszeck, L.A. Ivanoff, J.F. Morris, E.J. Sternberg, D.M. Lambert, A.V. Fernandez, S.R. Patteway, T.D. Meek, B.W. Metcalf, and J.G. Gleason. Bioorg. Med. Chem. Lett. **4**, 2441 (1994).
19. J.V. Duncia, J.B. Santella, C.A. Higley, M.K. VanAtten, P.C. Weber, R.S. Alexander, C.A. Kettner, J.R. Pruitt, A.Y. Liauw, M.L. Quan, R.M. Knabb, and R.R. Wexler. Bioorg. Med. Chem. Lett. **8**, 775 (1998).
20. K.T. Potts. Chem. Rev. **61**, 87 (1961).
21. (*a*) M.S. Chande, A.A. Godbole, and C. Sajithkumar. Heteroat. Chem. **14**, 273 (2003); (*b*) M.S. Chande, A.A. Godbole, E. Coutinho, and P. Desai. Indian J. Chem. Sect. B, **42**, 397 (2002).
22. (*a*) M.S. Chande and S.S. Athalye. Synth. Commun. **29**, 1711 (1999); (*b*) M.S. Chande, and S.S. Athalye. Synth. Commun. **30**, 1667 (2000); (*c*) M.S. Chande, S.S. Athalye, and A.A. Godbole. Indian J. Chem. Sect. B, **43**, 670 (2004); (*d*) M.S. Chande, M.H. Uchil, and P.A. Barve. Heteroat. Chem. **17**, 329 (2006).
23. A.R. Katritzky, B.V. Rogovoy, V.Y. Vvedensky, K. Kovalenko, P.J. Steel, V.I. Markov, and B. Forood. Synthesis, **6**, 897 (2001).
24. (*a*) L. Ventura, J.A. Perez-Gonzales, and D. Ramon. FEMS Microbiol. Lett. **149**, 207 (1997); (*b*) G. Stemp and G. Burrell. Eur. Patent Appl. EP399834, 28 November 1990; (*c*) J.W. Clitherow. Eur. Patent Appl. EP367484, 9 May 1990.
25. (*a*) K. Wermann, M. Hartmann, and H.J. Bauer. Z. Chem. **24**, 120 (1984); (*b*) M. Hartmann, H.J. Bauer, and K. Wermann. Polym. Bull. 195 (1985); (*c*) J.L. Hilton. J. Agric. Food Chem. **17**, 182 (1969); (*c*) S.A. Lang and B.L. Walworth. US. Patent 4-169-838, 2 October 1979.
26. (*a*) B. Mernari, H. Elattari, M. Traisnel, F. Bentiss, and M. Lagrenee. Corros. Sci. **40**, 391 (1998); (*b*) F. Bentiss, M. Lagrenee, M. Traisnel, and J.C. Hornez. Corros. Sci. **41**, 789 (1999).

© 2007 NRC Canada

27. (*a*) B.S. Holla, B.M. Veerendra, K. Shivananda, and N.S. Kumari. Indian J. Chem. Sect. B, **43**, 2010 (2003); (*b*) B.S. Holla and R. Gonsalves. Boll. Chem. Farm. **137**, 467 (1998); (*c*) B.S. Holla, R. Gonsalves, and S. Shenoy. Farmaco, **53**, 574 (1998).
28. G.W. Gokel, D.M. Dishang, and C.J. Dimond. J. Chem. Soc. Chem. Commun. 1053 (1980).
29. (*a*) E. Muller and L. Herrdegen. J. Prackt. Chem. **102**, 113 (1921); (*b*) F. Dallacker. Monatsh. Chem. **91**, 294 (1960); (*c*) W.W. Zajact, J.F. Siuda, M.J. Nolan, and T.M. Santossusso. J. Org. Chem. **36**, 3539 (1971); (*d*) M.O. Abdel-Rahman, M.A.M. Kira, and N. Tolba. Tetrahedron Lett. **9**, 3871 (1968); (*e*) R.A. Bowie, M.D. Gardner, D.G. Neilson, K.M. Watson, S. Mahmood, V.J. Ridd. J. Chem. Soc. Perkin Trans. 1, 2395 (1972); (*f*) J.F. Geldard and F.J. Lions. J. Org. Chem. **30**, 318 (1965); (*g*) K. Matsukawa, J. Setsune, K. Takagi, and T. Kitao. Dyes Pigm. **3**, 307 (1982); (*h*) F. Bentiss, M. Lagrenee, M. Traisnel, B. Mernari, and H. Elattari. J. Heterocycl. Chem. **36**, 149 (1999); (*i*) F. Bentiss, M. Lagrenee, and D. Barbry. Tetrahedron Lett. **41**, 1539 (2000).
30. P.-F. Xu, X.-W. Sun, L.-M. Zhang, and Z.-Y. Zhang. J. Chem. Res. Synop. **2**, 170 (1999).
31. (*a*) D.H. Busch. Rec. Chem. Prog. **25**, 107 (1965); (*b*) D.H. Busch and L.H. Lindoy. Preparative inorganic reactions. Vol. 6. *Edited by* W.L. Jolly. Wiley-Interscience, New York. 1971.
32. For nomenclature please see: (*a*) W.H. Powell. Pure Appl. Chem. **70**, 1513 (1998); (*b*) H.A. Favre, D. Hellwinkel, W.H. Powel, and H.A. Smith. Pure Appl. Chem. **74**, 809 (2002).
33. A. Dubey, S. Kumar, and K. Naresh. Indian J. Heterocycl. Chem. **3**, 277 (1994).
34. J.R. Reid and N.D. Heindel. J. Heterocycl. Chem. **13**, 925 (1976).
35. CS Chem 3D Pro [computer program]. Version 5. CambridgeSoft, Cambridge, Mass. 1999.

© 2007 NRC Canada

Asymmetric synthesis, crystal structure, and antidepressant activity of 2-aryl-3-alkyl-5-methyl-2-morpholinol hydrochlorides

Gao Cao, Ai-Xi Hu, and Xin-Rong Xiao

Abstract: 2-Aryl-3-alkyl-5-methyl-2-morpholinols were synthesized from the reactions of chiral 2-aminopropan-1-ol with 2-bromo-1-phenylpropan-1-one, 2-bromo-1-(3-chlorophenyl)propan-1-one, 1-(4-(benzyloxy)phenyl)-2-bromopropan-1-one, 2-bromo-1-(6-methoxy- naphthalen-2-yl)propan-1-one, and 1-(4-(benzyloxy)phenyl)pentan-1-one in *N*-methyl-2-pyrrolidone (NMP), respectively. The 2-aryl-3-alkyl-5-methyl-2-morpholinols were reacted with hydrogen chloride to give the hydrochloride salts with yields of 56%–77%. The structures of the products were proven by means of their ^{1}H NMR, IR, and MS spectroscopic data. The stereochemical properties of representative products were established unambiguously by the X-ray single crystal analysis. The antidepressant activities of the title compounds were assayed by the mouse forced swimming test (FST). The FST results confirm the antidepressant properties of our products.

Key words: morpholinol hydrochloride, hemiacetal, chiral synthesis, X-ray diffraction, absolute configuration, antidepressant activity.

Résumé : Opérant dans la *N*-méthylpyrrolid-2-one (NMP), on a réalisé la synthèse de 2-aryl-3-alkyl-5-méthylmorpholin-2-ols par les réactions du 2-aminopropan-1-ol avec respectivement de la 2-bromo-1-phénylpropan-2-one, de la 2-bromo-1-(3-chlorophényl)propan-1-one, de la 1-[4-(benzyloxy)phényl]-2-bromopropan-2-one, de la 2-bromo-1-(6-méthoxynaphtalén-2-yl)propan-1-one et de la 1-[4-(benzyloxy)phényl]pentan-1-one. Les réactions des 2-aryl-3-alkyl-5-méthylmorpholin-2-ols avec de l'acide chlorhydrique conduit à la formation des chlorhydrates avec des rendements allant de 56 % à 77 %. On a confirmé l'identité des structures des produits à l'aide de données de résonance magnétique nucléaire du ^{1}H, de spectroscopie IR et de spectrométrie de masse. Les propriétés stéréochimiques de produits représentatifs ont été établies sans ambiguïté à l'aide de la diffraction de rayons X par des cristaux uniques. On a évalué les propriétés antidépressives des composés mentionnés dans le titre en les administrant à des souris impliquées dans un test où elles sont forcées de nager. Les résultats de ces études permettent de confirmer les propriétés antidépressives de ces produits.

Mots-clés : chlorhydrates de morpholinols, hémiacétal, synthèse chirale, diffraction des rayons X, configuration absolue, activité antidépressive.

[Traduit par la Rédaction]

Introduction

2-Aryl-2-morpholinol derivatives have been utilized extensively by chemists because of their pharmaceutical importance in drug design and extensive application in organic synthesis. The biological utility of 2-aryl-2-morpholinol derivatives is wide-ranging, including analeptic, antioxidant, hypocholesterolemic, anorectic, adrenergic blocking, and antifungal properties, and they are especially widely described for their antidepressant activities. 2-Aryl-2-morpholinol derivatives also have been used to treat human diseases such as tardive dyskinesia, minimal brain dysfunction, obesity, migraine, sexual dysfunction, chronic fatigue, restless legs syndrome, Parkinson's disease (1–9).

Research on phenylmorpholinols has led to the discovery of (3,5-difluorophenyl)morpholinol, a novel antidepressant agent and selective inhibitor of norepinephrine uptake, which is active in animal behavioral models that respond to effective clinical antidepressant drugs (10). The racemate compound 2-(3-chlorophenyl)-3,5,5-trimethyl-2-morpholinol has been synthesized and the (+) and (–) enantiomers of the racemate have been subsequently separated via chromatography (11, 12) or dynamic kinetic resolutions (13–15). This product is useful in prophylaxis or therapy, especially as a stimulant and antidepressant for the central nervous system. Musso (16) designed and synthesized a chiral hapten for radioimmunoassay of the antidepressant (2*S*,3*S*,5*R*)-2-(3,5-difluorophenyl)-3,5-dimethyl-2-morpholinol hydrochloride. However, the problem of the synthesis of 2-aryl-2-morpholinol derivatives is that the preparation requires a

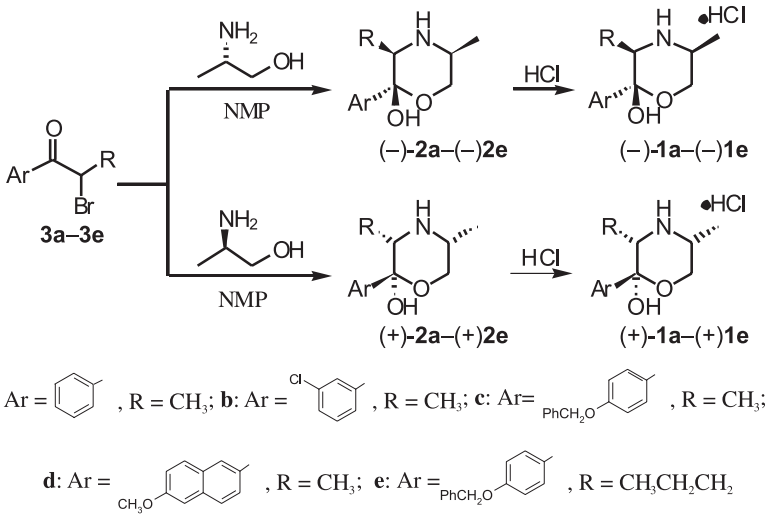
Received 4 October 2006. Accepted 1 December 2006. Published on the NRC Research Press Web site at http://canjchem.nrc.ca on 26 January 2007.

G. Cao. The School of Chemical and Energy Engineering, South China University of Technology, Guangzhou, P. R. China.
A.-X. Hu.[1] The School of Chemical and Energy Engineering, South China University of Technology, Guangzhou, P. R. China; College of Chemistry and Chemical Engineering, Hunan University, P. R. China.
X.-R. Xiao. College of Chemistry and Chemical Engineering, Hunan University, Changsha, P. R. China.

[1]Corresponding author (e-mail: axhu0731@yahoo.com.cn).

 doi:10.1139/V06-184 © 2007 NRC Canada

Scheme 1. Synthesis of 2-aryl-3-alkyl-5-methyl-2-morpholinol hydrochlorides.



long reaction time and that the solvent is volatile and poisonous (17–20).

By structural modification of the drug, it is possible to obtain new compounds with comparable activity and lower toxicity. On the other hand, enantiomers of the same drug can have different pharmacodynamic and pharmacokinetic properties. Today, most new drugs and those under development consist of a single optically active isomer. The current trend in drug markets is a rapid increase in the sales of chiral drugs. Chiral drugs represent close to 40% of all drug sales worldwide in 2001 (21). Therefore, the synthesis of chiral 2-aryl-3-alkyl-5-methyl-2-morpholinol hydrochlorides was undertaken.

In this study, we report the synthesis of novel chiral 2-aryl-3-alkyl-5-methyl-2-morpholinols **2a**–**2e** and their hydrochloride salts **1a**–**1e** by the reactions of chiral 2-aminopropan-1-ol with α-bromo-aromatic ketones **3a**–**3e** in *N*-methyl-2-pyrrolidone (NMP) and their antidepressant activities. The synthesis of the title compounds was shown in Scheme 1.

Results and discussion[2]

Synthesis of optically active 2-aryl-3-alkyl-5-methyl-2-morpholinol hydrochlorides

The optical rotations of 2-aryl-3-alkyl-5-methyl-2-morpholinol hydrochlorides by the reactions of (*S*)-2-aminopropan-1-ol and (*R*)-2-aminopropan-1-ol with α-bromo-aromatic ketones are levorotatory and dextrotatory, respectively. The detailed data are tabulated in Table 1.

2-Aryl-3-alkyl-5-methyl-2-morpholinol hydrochlorides synthesized from opposite configuration 2-aminopropan-1-ol have the analogous melting points and the analogous numerical value, but the optical rotation is in the opposite direction. 2-Aryl-3-alkyl-5-methyl-2-morpholinol hydrochlorides synthesized from contrary configuration 2-aminopropan-1-ols should be a pair of enantiomers.

When 2-amino-2-methyl-1-propanol reacted with chiral α-ketotriflate, the enantiopure hydroxylbupropion products conformationally locked at (2*S*,3*S*) or (2*R*,3*R*). The (2*R*,3*S*) or (2*S*,3*R*) isomer was not observed (22). In our products, the ^{1}H NMR spectra show only one double singlet at δ: 0.90–1.10 for the 3-CH_3 group of the morpholine ring, which shows that the synthesized compounds are single enantiomers. If the products are diastereomeric [(2*R*,3*R*,5*S*)-**1a** to (2*R*,3*R*,5*S*)-**1e** and (2*R*,3*S*,5*S*)-**1a** to (2*R*,3*S*,5*S*)-**1e**] or [(2*S*,3*S*,5*R*)-**1a** to (2*S*,3*S*,5*R*)-**1e** and (2*S*,3*R*,5*R*)-**1a** to (2*S*,3*R*,5*R*)-**1e**], the methyl group at the axial position should be in the downfield position because the deshielding effect is stronger than at the equatorial position. So, the 3-CH_3 group of the morpholine ring should have two double singlets in the ^{1}H NMR spectrum.

Single crystal investigation of the representative products

The structure and stereochemical properties of (2*S*,3*S*,5*R*)-3,5-dimethyl-2-(3-chlorophenyl)-2-morpholinol hydrochloride and (2*R*,3*R*,5*S*)-3,5-dimethyl-2-(6-methoxy-2-naphthyl)-2-morpholinol hydrochloride were investigated by X-ray diffraction. Colorless crystals suitable for X-ray diffraction analysis were grown by slow evaporation of the mixture of ethanol and ether (1:1 *v*/*v*). X-ray data were collected on a Bruker AXS SMART 1000 CCD diffractometer equipped with graphite monochromated Mo K_α radiation (λ = 0.710 73 Å). The data set was recorded at RT in ω–ϕ scan mode. Preliminary orientation matrices were obtained from the first frames using SMART (23). The data were empirically corrected for absorption and other effects using

[2] Supplementary data for this article are available on the journal Web site (http://canjchem.nrc.ca) or may be purchased from the Depository of Unpublished Data, Document Delivery, CISTI, National Research Council Canada, Ottawa, ON K1A 0R6, Canada. DUD 5120. For more information on obtaining material refer to http://cisti-icist.nrc-cnrc.gc.ca/irm/unpub_e.shtml. CCDC 292641 and 292642 contain the crystallographic data for this manuscript. These data can be obtained, free of charge, via http://www.ccdc.cam.ac.uk/conts/retrieving.html (Or from the Cambridge Crystallographic Data Centre, 12 Union Road, Cambridge CB2 1EZ, UK; fax +44 1223 336033; or deposit@ccdc.cam.ac.uk).

© 2007 NRC Canada

Table 1. 2-Aryl-3-alkyl-5-methyl-2-morpholinol hydrochlorides.

			(+)-**1a** to (+)-**1e**			(–)-**1a** to (–)-**1e**		
	Ar	R	mp (°C)	$[\alpha]^{20}_D$ (°)[a]	yield (%)[b]	mp (°C)	$[\alpha]^{20}_D$ (°)[a]	yield (%)[b]
a	C_6H_5	Me	178–180	+30.8	59.6	176–178	–32.8	56.0
b	3-Cl-C_6H_4	Me	203 to 204	+40.6	59.6	200 to 201	–44.6	56.2
c	4-$PhCH_2O$-C_6H_4	Me	161–163	+10.8	77.0	159–162	–11.5	63.4
d	6-MeO-$C_{10}H_6$	Me	182–184	+13.7	69.4	181–183	–13.6	64.9
e	4-$PhCH_2O$-C_6H_4	n-Pr	169–171	+5.6	60.4	169–171	–5.2	60.8

[a]Solvent was EtOH, concn. = 1.0.
[b]Yields are based on the starting **3a**–**3e**.

Table 2. Crystallographic data and structure refinement for (+)-**1b** and (–)-**1d**.

Compound	(+)-**1b**	(–)-**1d**
CCDC No.	292641	292642
Empirical formula	$C_{12}H_{17}NO_2Cl_2$	$C_{17}H_{22}NO_3Cl$
Formula mass	278.17	323.81
Colour, habit	Colourless, block	Colourless, block
Crystal dimensions (mm^3)	0.26 × 0.22 × 0.20	0.50 × 0.38 × 0.18
Crystal system	Orthorhombic	Orthorhombic
Space group	$P2_12_12$	$P2_12_12_1$
Z	4	4
a (Å)	8.718(2)	7.1093(4)
b (Å)	20.264(6)	7.6947(5)
c (Å)	7.882(2)	29.8868(19)
Collection ranges	$-10 \le h \le 9$, $-23 \le k \le 25$, $-9 \le l \le 9$	$-8 \le h \le 9$, $-9 \le k \le 7$, $-24 \le l \le 38$
T (K)	294(2)	292(2)
V ($Å^3$)	1392.5(6)	1634.93(17)
Calculated density (g/cm^3)	1.327	1.316
Mo K_α radiation (Å)	0.710 73	0.710 73
Absorption correction	Multiscan	Multiscan
F(000)	584	688
θ Range for data collection (°)	2.77–25.09	2.65–26.71
Measured reflections	7875	8797
Independent reflections	2836 (R_{int} = 0.0293)	3562 (R_{int} = 0.0185)
Data, restraints, parameters	2836, 0, 168	3562, 0, 203
Goodness-of-fit on F^2	1.029	1.055
Final R indices [$I > 2\sigma(I)$]	$R1$ = 0.0350, $wR2$ = 0.0724	$R1$ = 0.0544, $wR2$ = 0.0964
R indices (all data)	$R1$ = 0.0541, $wR2$ = 0.0808	R1 = 0.0408, $wR2$ = 0.1092
Absolute structure parameter	–0.02(6)	0.07(8)
Largest diff. peak and hole (e $Å^{-3}$)	0.185 and –0.253	0.350 and –0.170

SADABS (24). The structure was solved by direct methods and refined by the full-matrix least-squares methods on F^2 with the program SHELXTL-97 (25). H atoms were positioned at geometrically possible positions and refined using the riding model with U_{eq} set equal to the U_{eq} of the parent atom multiplied by 1.2 (or 1.5 for the methyl groups). O–H and N–H of (+)-**1b** were freely refined. Further details of data collection and structure refinement are given in Table 2.

Absolute configuration of the representative compounds

According to the molecular structure of (–)-**1d** with atom labeling (Fig. 1), the naphthalene ring C(7)–C(16) is essentially planar with a mean deviation of 0.0242(3) Å. The morpholine ring is a distorted chair somewhat flattened at C(2) and sharpened at C(5), and the dihedral angles between the C(3)–C(2)–O(1) and C(1)–C(5)–N(1) planes and the N(1)–C(3)–O(1)–C(1) plane are 45.9(2)° and 52.4(2)°, respectively. The 3-methyl group and the 5-methyl group make dihedral angles of 39.8(3)° and 38.4(3)° with respect to the C(2)–C(3)–N(1) and C(1)–C(5)–N(1) planes; the 2-hydroxy group and the 2-(6-methoxy-2-naphthyl) group make dihedral angles of 38.9(2)° and 31.0(3)° with respect to the C(3)–C(2)–O(1) plane, respectively. The 3- and 5-methyl groups and the 2-hydroxy group are on the same side of the morpholine ring, but the 2-(6-methoxy-2-naphthyl) group is on the reverse side. The chiral carbon atoms of (–)-**1d**, C(2) and C(3) are (*R*)-configuration, and C(5) is (*S*)-configuration. The absolute configuration of (–)-**1d** is (2*R*,3*R*,5*S*).

© 2007 NRC Canada

Fig. 1. The ORTEP (26) plot of the X-ray crystal structure of compound (–)-**1d** with 30% probability displacement ellipsoids.

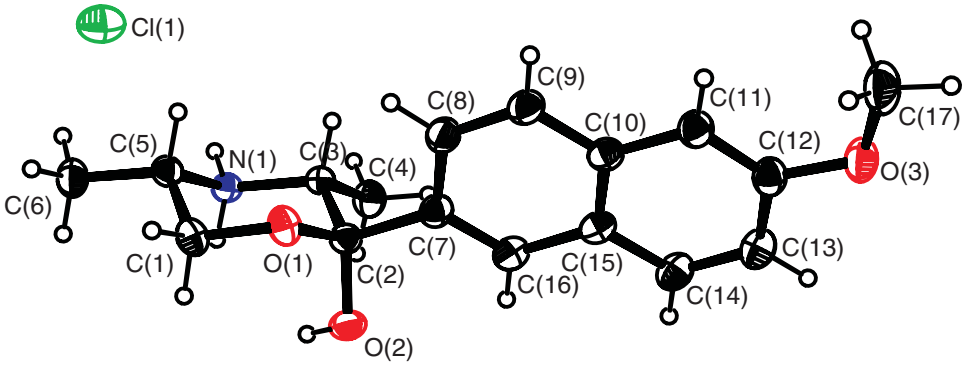
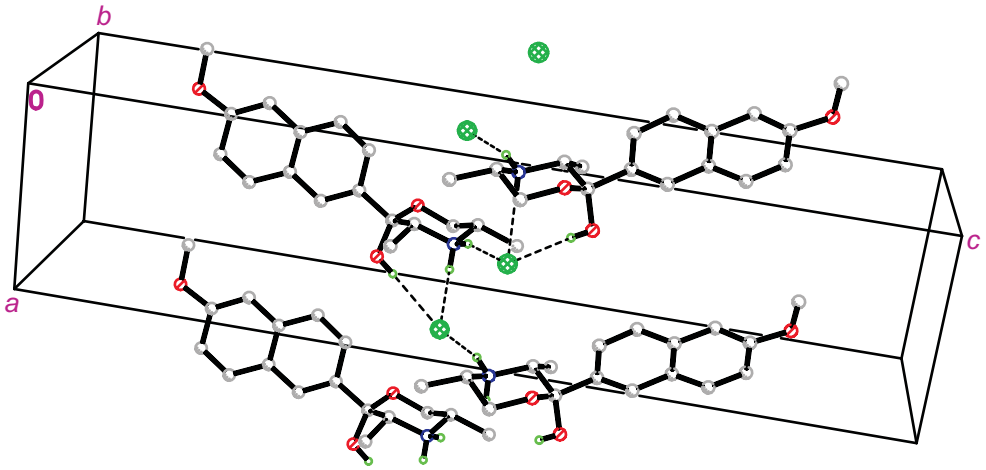


Fig. 2. The crystal packing of (–)-**1d**. For the sake of clarity, H atoms bonded to C atoms have been omitted. Hydrogen bonds have been shown as dashed lines.



The data obtained from the NMR spectral analysis and X-ray investigation are in good agreement, giving evidence of similar conformational behavior in the crystal and in solution. In addition, the structure exhibits intermolecular hydrogen bonds of type N–H–Cl and O–H–Cl. The hydrogen bonds are N(1)–H(1C)–Cl(1)^{i} (2.27 Å, 162.1°) with symmetry codes x–1/2, 1/2–y, –z and N(1)–H(1D)–Cl(1)^{ii} (2.23 Å, 173.6°) and O(2)–H(2)–Cl(1)^{ii} (2.51 Å, 176.7°) with symmetry codes x–1, y–1, z. (Fig. 2).

The molecular structure of (–)-**1d** in crystal is stabilized by the intermolecular hydrogen bonds and the intermolecular electrostatic interactions between the positively charged atom N^+ and Cl^-; the chlorine atom is set apart from the hydroxyl oxygen atom (on the reverse side of the morpholine ring), and the hydroxyl oxygen atom of (–)-**1d** does not itself form a hydrogen bond with the chlorine atom. The structure of (+)-**1b** with atom numbering is shown in Fig. 3 (27).

Compared with (–)-**1d**, the chlorine atom of (+)-**1b** is closer to the hydroxyl oxygen atom and this is probably caused by the 2-Ar substitutes. Atom O(1) in the hydroxyl group acts as a hydrogen-bond donor via H(1) to atom Cl(2) forming the hydrogen bond O(1)–H(1)–Cl(2) (2.29 Å, 166°). Atom N(1) of the morpholine ring acts as a hydrogen-bond donor via H(1C) and H(1D) to two of the other chlorine atoms of the molecule forming the hydrogen bonds N(1)–H(1C)–Cl(2)^{i} (2.27 Å, 173.1°) and N(1)–H(1D)–Cl(2)^{ii} (2.34 Å, 151°) (Fig. 4).

Our synthesis of **1a**–**1e** produced a chair model of a six-membered ring, and the configuration is stable when the aryl and alkyl groups are at an equatorial position. Thus, the two formed chiral carbon atoms C(2) and C(3) in our products maintain "*Z*" shape and not "*E*" shape. The configuration of the products is determined by the chirality of 2-aminopropan-1-ol. The products were (2*R*,3*R*,5*S*)-**1a** to (2*R*,3*R*,5*S*)-**1e**, namely (–)-**1a** to (–)-**1e** when (*S*)-2-aminopropan-1-ol was used. The products were (2*S*,3*S*,5*R*)-**1a** to (2*S*,3*S*,5*R*)-**1e**, namely (+)-**1a** to (+)-**1e**) when (*R*)-2-aminopropan-1-ol was used. (Fig. 5).

When R was an H atom, we did not obtain 2-aryl-5-methyl-2-morpholinol hydrochloride products by the same procedure. α-Bromo-1-aromatic ethanones, such as 2-bromo-1-(4-methoxyphenyl)ethanone, 1-(4-(benzylo-xy) phenyl)-2-bromoethanone, or 2-bromo-1-(6-methoxynaphthalen-2-yl)ethanone, reacted with chiral 2-aminopropan-1-ol during the HCl acidification process initially obtaining a solid, which absorbed water from the environment to form a stagnant oil. The ^{1}H NMR spectra did not indicate cyclic (morpholine) structure, and the IR spectra showed a carbonyl group absorption band of the hydrochloride salt. The hemiketals with R = H are likely to exhibit ring-opening in aq. HCl.

© 2007 NRC Canada

Fig. 3. The ORTEP plot of the X-ray crystal structure of compound (+)-**1b.**

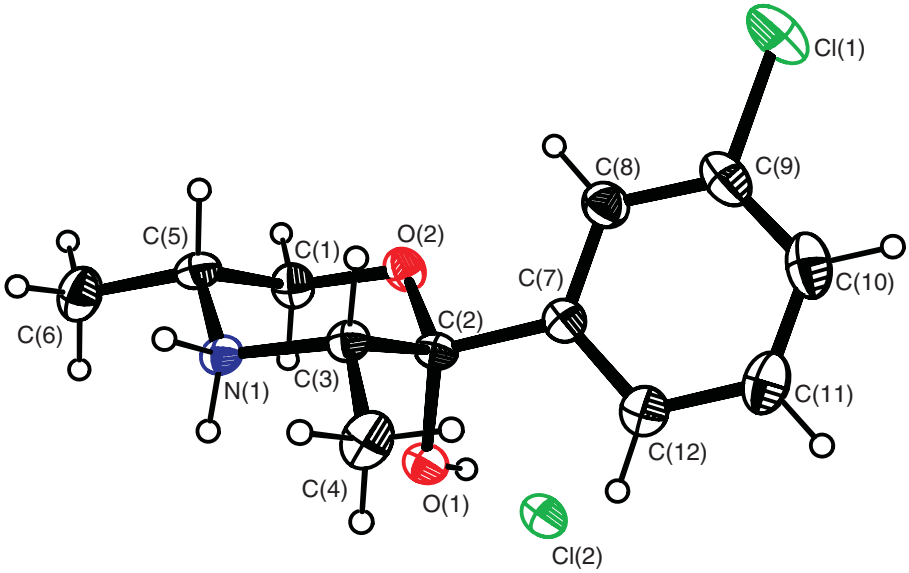
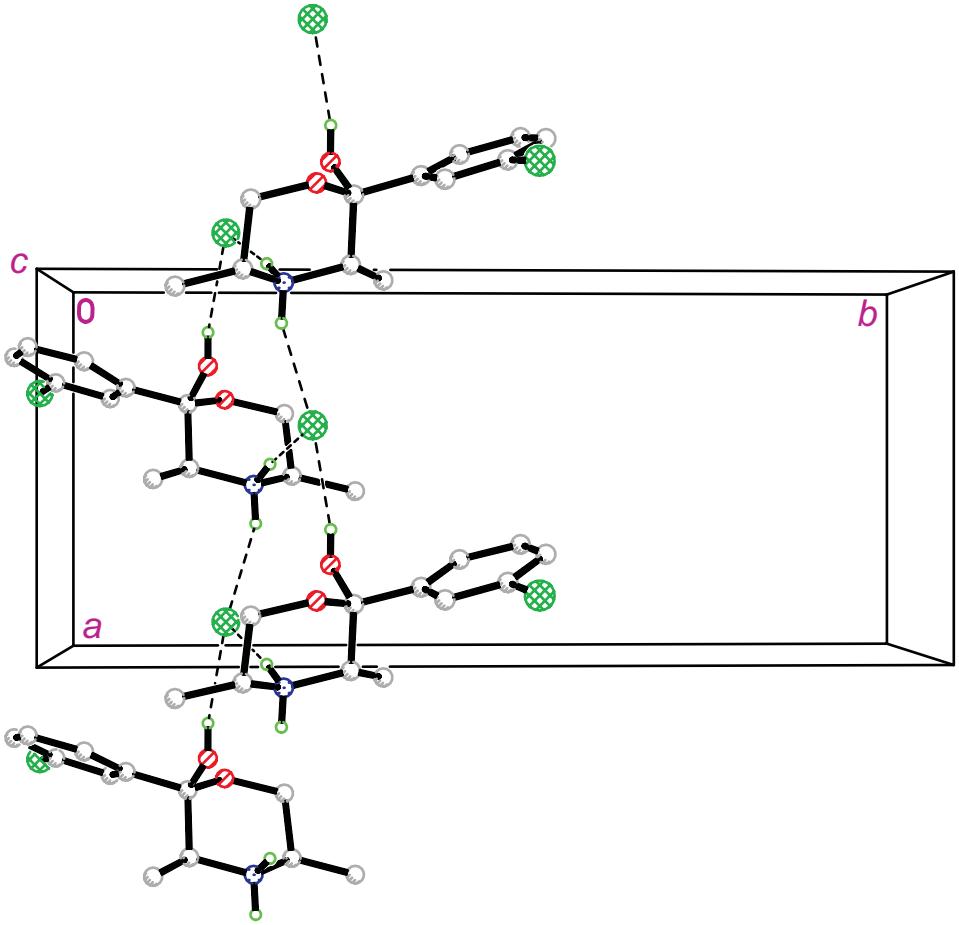


Fig. 4. Autostereogram of the crystal structure of (+)-**1b** with hydrogen bonds.

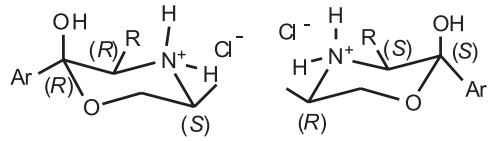


Antidepressant activities of 2-Aryl-3-alkyl-5-methyl-2-morpholinols hydrochloride

Clinical depression is one of the most complex human diseases. It has an unequivocally strong hereditary component and affects about 15% of the population at some point during their lives. The present study was undertaken to investigate the effect of 2-aryl-3-alkyl-5-methyl-2-morpholinols hydrochloride on depression in the mouse

© 2007 NRC Canada

Fig. 5. Absolute configuration of the title compound.



(2*R*,3*R*,5*S*)-(–)-**1a** to (2*R*,3*R*,5*S*)-(–)-**1e** (2*S*,3*S*,5*R*)-(+)-**1a** to (2*S*,3*S*,5*R*)-(+)-**1e**

forced swimming test (FST), an animal model of depression that is widely used to predict the antidepressant action of drugs in humans (28).

Male KM mice (the KM mouse strain is one of the outbred strains of mice introduced from Swiss mice to Kunming City, Yunnan Province, China) weighing 20–30 g were used in this study. The animals were housed in plastic cages under standard light (light on from 0700 to 2100 hours) and temperature (22 ± 1 °C) conditions for at least three days before experimentation with free access to standard laboratory food and tap water. Compounds **1d** and **1e** were chosen as title compounds and were suspended in a CMC solution (1%) with a concentration of 4 mg/mL in a dose volume of 0.1 mL per 10 g body weight in mice. Behavioral observations took place between 0800 and 1500 and each animal was used only once. A standard antidepressant drug amitriptyline was employed to standardize the animal models of depression and to compare the antidepressant efficacy of the title compounds.

Thirty minutes after intraperitoneal (IP) injection of the drugs, the mice were individually placed in a vertical glass cylinder (height of 25 cm, diameter of 12 cm) containing water (depth of 15 cm at 22 °C) and forced to swim. After an initial 2 min period of vigorous activity, each animal assumed a typical immobile posture. A mouse was considered to be immobile when it remained floating in the water without struggling, making only minimum movements of its limbs necessary to keep its head above water. The total duration of immobility was recorded during the next 4 min of a total 6 min test. The changes in immobility duration were studied after administering drugs in separate groups of animals. (Table 3).

According to the results in Table 3, the title compounds showed potent antidepressant activity, where the title compounds (+)-**1d** and (+)-**1e** show better activity than (–)-**1d** and (–)-**1e**, which shows that the configuration of (2*S*,3*S*,5*R*) compounds have greater antidepressant activity than the (2*R*,3*R*,5*S*) configuration.

Following the test, animals were allowed to dry and returned to their home cage. Adverse drug reactions were not observed in the 24 h period after the FST test. These results confirm the antidepressant properties of our products, suggesting the possible use of this drug in depressive patients that may be resistant to classical antidepressant therapy.

Conclusions

In summary, we report herein a rapid and efficient synthesis of some novel 2-aryl-3-alkyl-5- methyl-2-morpholinol hydrochlorides by the reaction of chiral 2-aminopropan-1-ol with α-bromo-aromatic ketones in NMP. Advantages of this approach include short reaction time, ease of operation, and excellent overall yields. The title compounds exhibited potent antidepressant activity in the FST test.

Table 3. Effects of target compounds on the time in mice forced swimming test.

Treatment	No. of mice	IP dose (mg/kg)	Immobility[a]
CMC (1%)	10	—	138.0±21.7
Amitriptyline	8	20	18.5±4.4[b]
(–)-**1d**	8	40	40.3±10.3[b]
(+)-**1d**	8	40	8.4±6.8[b]
(–)-**1e**	8	40	62.1±13.7
(+)-**1e**	8	40	24.8±7.3

[a]Results are expressed as mean ± S.E.M.
[b]$P < 0.05$ *vs.* CMC (1%).

Materials and methods

Instrumentation

All melting points were measured on an X-4 electrothermal digital melting point apparatus and were uncorrected. ^{1}H NMR spectra were recorded on a Varian Inova-400 instrument with TMS as internal standard operating at 399.970 MHz. IR spectra were recorded on Avatar 360FT infrared spectrometer, using KBr discs. ESI-MS measurements were recorded on a Finngan LCQ LC-MS spectrometer. Optical rotations were measured on a WZZ-3 polarimeter. TLC analysis was carried out on glass plates, kept in iodine, using silica gel. X-ray data were collected on a Bruker AXS Smart 1000 CCD diffractometer.

General experimental procedure for the preparation of α-bromo-aromatic ketones

α-Aromatic ketone (0.1 mol) was dissolved in anhydrous ethanol (200 mL) and the mixture was stirred and heated to reflux. Cupric bromide (0.2 mol) was added to the reaction mixture in batches and the course of the reaction was followed by TLC analysis. After the reaction finished, the mixture was filtered and concentrated in vacuo. The resulting residue was taken up in dichloromethane, washed with 10% hydrochloric acid, washed with water until neutral, dried over anhydrous sodium sulfate, and concentrated in vacuo to give racemic α-bromo-aromatic ketones **3a**–**3e** (29).

Preparation of 2-aryl-3-alkyl-5-methyl-2-morpholinols hydrochloride

The general experimental procedure was as follows. α-Bromo-aromatic ketones **3a**–**3e** (0.01 mol) were added to a solution of (*S*)-2-aminopropan-1-ol (0.04 mol) in NMP (10 mL), and stirred for 1 h at RT. When no trace of starting material remained (by TLC analysis), an excess of water (30 mL) was added to the mixture, then extracted with diethyl ether (30 mL). The aqueous layer was extracted further with diethyl ether (15 mL) three times. The organic extracts were combined, washed (10 mL water), and dried by anhydrous sodium sulfate. After filtering, the filtrate was stirred in an ice bath, the pH adjusted to acidity by passing anhyd. HCl through it slowly, yielding a white crystalline substance, which was filtered and washed with acetone, and dried to give (–)-**1a** to (–)-**1e**. Compounds (+)-**1a** to (+)-**1e**) were synthesized using (*R*)-2-aminopropan-1-ol by the same pro-

© 2007 NRC Canada

cedure. Selected characterization data of the products follows.

(2*R*,3*R*,5*S*)-3,5-Dimethyl-2-phenyl-2-morpholinol hydrochloride (–)-1a

^{1}H NMR (CD_3SOCD_3, 400 MHz) δ: 0.94 (d, *J* = 6.4 Hz, 3H, CH_3), 1.22 (d, *J* = 6.4 Hz, 3H, CH_3), 3.28–3.50 (br m, 2H, morpholine ring 3,5-H), 3.79–3.93 (m, 2H, morpholine ring 6-H), 7.36–7.54 (m, 6H, C_6H_5, OH), 8.75, 10.34 (2 × bs, 2H, NH, HCl). IR (KBr, cm^{-1}) ν: 3244, 3037, 2937, 2787, 2738, 2681, 2532, 2438, 1560, 1452, 1388, 1350, 1261, 1178, 1138, 1090, 1057, 1001, 764, 702. ESI-MS *m*/*z*: 209 (M^+ + 2 – HCl), 208 (M^+ + 1 – HCl), 190 (M^+ + 1 – HCl – H_2O).

(2*R*,3*R*,5*S*)-3,5-Dimethyl-2-(3-chlorophenyl)-2-morpholinol hydrochloride (–)-1b

^{1}H NMR (CD_3SOCD_3, 400 MHz) δ: 0.98 (d, *J* = 6.4 Hz, 3H, CH_3), 1.24 (d, *J* = 6.4 Hz, 3H, CH_3), 3.36–3.56 (br m, 2H, morpholine ring 3,5-H), 3.81–3.94 (m, 2H, morpholine ring 6-H), 7.45–7.59 (m, 4H, C_6H_4), 7.89 (s, 1H, OH), 8.78, 10.39 (2 × bs, 2H, NH, HCl). IR (KBr, cm^{-1}) ν: 3211, 2976, 2947, 2898, 2790, 2681, 2551, 2515, 2459, 1572, 1450, 1373, 1250, 1184, 1142, 1093, 1059, 997, 906, 800, 708. ESI-MS *m*/*z*: 244 (M^+ + 2 – HCl), 243 (M^+ + 1 – HCl), 242 (M^+ – HCl), 226 (M^+ + 2 – HCl – H_2O), 224 (M^+ – HCl – H_2O).

(2*R*,3*R*,5*S*)-3,5-Dimethyl-2-(4-benzyloxyphenyl)-2-morpholinol hydrochloride (–)-1c

^{1}H NMR (CD_3SOCD_3, 400 MHz) δ: 0.95 (d, *J* = 6.4 Hz, 3H, CH_3), 1.20 (d, *J* = 6.4 Hz, 3H, CH_3), 3.26–3.49 (br m, 2H, morpholine ring 3,5-H), 3.78–3.91 (m, 2H, morpholine ring 6-H), 5.10 (s, 2H, OCH_2), 7.01–7.45 (m, 10H, C_6H_4, C_6H_5, OH), 8.71, 10.20 (2 × bs, 2H, NH, HCl). IR (KBr, cm^{-1}) ν: 3286, 2941, 2792, 2679, 2553, 2455, 1604, 1510, 1456, 1387, 1240, 1173, 1057, 1005, 831, 41, 698. ESI-MS *m*/*z*: 315 (M^+ + 2 – HCl), 314 (M^+ + 1 – HCl), 296 (M^+ + 1 – HCl – H_2O).

(2*R*,3*R*,5*S*)-3,5-Dimethyl-2-(6-methoxy-2-naphthyl)-2-morpholinol hydrochloride (–)-1d

^{1}H NMR (CD_3SOCD_3, 400 MHz) δ: 0.97 (d, *J* = 6.4 Hz, 3H, CH_3), 1.23 (d, *J* = 6.4 Hz, 3H, CH_3), 3.57 (br m, 2H, morpholine ring 3,5-H), 3.87 (s, 3H, OCH_3), 3.92–3.97 (m, 2H, morpholine ring 6-H), 7.16–8.05 (m, 7H, $C_{10}H_6$, OH), 8.81, 10.17 (2 × bs, 2H, NH, HCl). IR (KBr, cm^{-1}) ν: 3404, 2951, 2893, 2800, 2740, 2682, 2596, 2490, 1610, 1485, 1387, 1269, 1198, 1063, 1001, 854. ESI-MS *m*/*z*: 289 (M^+ +2 – HCl), 288 (M^+ + 1 – HCl), 270 (M^+ + 1 – HCl – H_2O).

(2*R*,3*R*,5*S*)-3-Propyl-5-methyl-2-(4-benzyloxyphenyl)-2-morpholinol hydrochloride (–)-1e

^{1}H NMR (CD_3SOCD_3, 400 MHz) δ: 0.57–1.38 (m, 10H, CH_3, $CH_2CH_2CH_3$), 3.21–3.53 (br m, 2H, morpholine ring3,5-H), 3.75–3.91 (m, 2H, morpholine ring 6-H), 5.11 (s, 2H, OCH_2), 7.01–7.45 (m, 10H, C_6H_4, C_6H_5, OH), 8.78, 9.67 (2 × bs, 2H, NH, HCl). IR (KBr, cm^{-1}) ν: 3198, 2968, 1630, 1565, 1508, 1455, 1330, 1254, 1080, 1010. ESI-MS *m*/*z*: 342 (M^+ + 1 – HCl).

(2*S*,3*S*,5*R*)-3,5-Dimethyl-2-phenyl-2-morpholinol hydrochloride (+)-1a

^{1}H NMR (CD_3SOCD_3, 400MHz) δ: 0.96 (d, *J* = 6.4 Hz, 3H, CH_3), 1.23 (d, *J* = 6.4 Hz, 3H, CH_3), 3.54–3.60 (br m, H, morpholine ring3, 5-H), 3.83–3.97 (m, 2H, morpholine ring 6-H), 7.41–7.56 (m, 5H, C_6H_5), 8.02 (s, 1H, OH), 8.75, 10.17 (2 × bs, 2H, NH, HCl). IR (KBr, cm^{-1}) ν: 3244, 3037, 2936, 2787, 2738, 2681, 2532, 1560, 1541, 1452, 1388, 1350, 1261, 1092, 1057, 1001, 764, 702. ESI-MS *m*/*z*: 209 (M^+ + 2 – HCl), 208 (M^+ + 1 – HCl), 190 (M^+ + 1 – HCl – H_2O).

(2*S*,3*S*,5*R*)-3,5-Dimethyl-2-(3-chlorophenyl)-2-morpholinol hydrochloride (+)-1b

^{1}H NMR (CD_3SOCD_3 + D_2O, 400MHz) δ: 0.97 (d, *J* = 6.4 Hz, 3H, CH_3), 1.23 (d, *J* = 6.4 Hz, 3H, CH_3), 3.40–3.60 (br m, 2H, morpholine ring 3, 5-H), 3.85–3.95 (m, 2H, morpholine ring 6-H), 7.47–7.58 (m, 4H, C_6H_4), 7.890 (s, 1H, OH), 8.78, 10.39 (2 × bs, 2H, NH, HCl). IR (KBr, cm^{-1}) ν: 3209, 2942, 2790, 2458, 1572, 1551, 1454, 1254, 1201, 1145, 1090, 1002. ESI-MS *m*/*z*: 244 (M^+ + 2 – HCl), 243 (M^+ + 1 – HCl), 242 (M^+ – HCl), 226 (M^+ + 2 – HCl – H_2O), 224 (M^+ – HCl – H_2O).

(2*S*,3*S*,5*R*)-3,5-Dimethyl-2-(4-benzyloxyphenyl)-2-morpholinol hydrochloride (+)-1c

^{1}H NMR (CD_3SOCD_3, 400MHz) δ: 0.96 (d, *J* = 6.4 Hz, 3H, CH_3), 1.22 (d, *J* = 6.4 Hz, 3H, CH_3), 3.29–3.51 (br m, 2H, morpholine ring 3, 5-H), 3.79–3.93 (m, 2H, morpholine ring 6-H), 5.12 (s, H, OCH_2), 7.03–7.47 (m, 10H, C_6H_4, C_6H_5, OH), 8.70, 10.01 (2 × bs, 2H, NH, HCl). IR (KBr, cm^{-1}) ν: 3286, 2941, 2792, 2679, 2455, 1604, 1575, 1508, 1456, 1387, 1240, 1173, 1057, 1005, 831, 741, 698. ESI-MS *m*/*z*: 315 (M^+ + 2 – HCl), 314 (M^+ + 1 – HCl), 296 (M^+ + 1 – HCl – H_2O).

(2*S*,3*S*,5*R*)-3,5-Dimethyl-2-(6-methoxy-2-naphthyl)-2-morpholinol hydrochloride (+)-1d

^{1}H NMR (CD_3SOCD_3, 400MHz) δ: 1.00 (d, *J* = 6.4 Hz, 3H, CH_3), 1.26 (d, *J* = 6.4 Hz, 3H, CH_3), 3.59–3.65 (br m, 2H, morpholine ring 3, 5-H), 3.88 (s, 3H, OCH_3), 3.88–4.03 (m, 2H, morpholine ring 6-H), 7.19–8.03 (m, 6H, $C_{10}H_6$), 8.03 (s,1H, OH), 8.81, 10.29 (2 × bs, 2H, NH, HCl). IR (KBr, cm^{-1}) ν: 3401, 2951, 2893, 2800, 2740, 2682, 2596, 2490, 1610, 1485, 1387, 1269, 1198, 1063, 1001, 854. ESI-MS *m*/*z*: 289 (M^+ + 2 – HCl), 288 (M^+ + 1 – HCl), 270 (M^+ + 1 – HCl – H_2O).

(2*S*,3*S*,5*R*)-3-Propyl-5-methyl-2-(4-benzyloxyphenyl)-2-morpholinol hydrochloride (+)-1e

^{1}H NMR (CD_3SOCD_3, 400MHz) δ: 0.81 (t, *J* = 6.8Hz, 3H, 5-CH_3), 1.16–1.33 (m, 5H, CH_2CH_3), 1.84–1.89 (m, 2H, CH_2), 3.23–3.96 (br m, 4H, morpholine ring 3,5-H, 6-H), 5.25 (s, 2H, OCH_2), 7.02–7.48 (m, 9H, C_6H_4, C_6H_5), 8.06 (s, 1H, OH). IR (KBr, cm^{-1}) ν: 3164, 2956, 2798, 1613, 1587, 1513, 1467, 1402, 1312, 1249, 1098, 1011. ESI-MS *m*/*z*: 342 (M^+ + 1 – HCl).

Acknowledgement

This research was performed with the support of the Spe-

© 2007 NRC Canada

cialized Research Fund for the Doctoral Program of Higher Education (SRFDP) (No. 20040532002). We also gratefully acknowledge the financial support of the Hunan Provincial Science and Technology Project of China (No. 04SK3053–3).

References

1. J. Bartroli, E. Turmo, M. Alguero, E. Boncompte, M.L. Vericat, J. Garcia-Rafanell, and J. Forn. J. Med. Chem. **38**, 3918 (1995).
2. T. Mancilla, L.S. Zamudio-Rivera, H.I. Beltrán, L. Carrillo, and N. Farfán. Synthetic Communications, **35**, 357 (2005).
3. A.X. Hu, H.Y. Wu, K. Chen, L.T. Yang, and B. Zhou. Chin. J. Appl. Chem. **22**, 343 (2005).
4. J.E. Matthews and D.L. Musso. PCT Int. Appl. WO 2001-026641, 19 April 2001.
5. A. Feriani, G. Gaviraghi, G. Toson, B. Valsecchi, P. Caldirola, M. Ravasi, L. Merlini, C. Redaelli, E. Grana, and F. Zonta. Farmaco, **47**, 3 (1992).
6. J.C. Barland. PCT Int. Appl. WO 2005-053700, 16 June 2005.
7. P.F. Morgan, D.L. Musso, and J.J. Partridge. US Patent Appl. 2003064988, 3 April 2003.
8. M.C. Chrysselis, E.A. Rekka, and P.N. Kourounakis. J. Med. Chem. **43**, 609 (2000).
9. L.K. James, L.M. David, G.E. Boswell, E.S. Francis, and R.C. Barrett. J. Med. Chem. **39**, 347 (1996).
10. J.L. Kelley, D.L. Musso, and G.E. Boswell. US Patent 5-104-870, 14 April 1992.
11. J.A. Asche, J.A. Johnston, S.M. Learned-Coughlin, and A. Bye. US Patent Appl. 2003032643, 13 February 2003.
12. P. Adam, O. Ludemann-Hombourger, E. Ndzie, D.S. Ross, M. Schaeffer, and C. Suteu. PCT Int. Appl. WO 2005-040140, 6 May 2005.
13. J.J. Partridge. PCT Int. Appl. WO 2005-042503, 12 May 2005.
14. M.A. Harris and A. Negus. PCT Int. Appl. WO 2005-040141, 6 May 2005.
15. J.J. Partridge. PCT Int. Appl. WO 2005-044809, 19 May 2005.
16. D.L. Musso and J.L. Kelley. Tetrahedron: Asymmetry, **6**, 841 (1995).
17. J.L. Kelley, D.L. Musso, G.E. Boswell, and B.R. Cooper. Eur. Patent Appl. EP 0426416, 8 May 1991.
18. F. Berrée, A. Debache, Y. Marsac, B. Collet, P.G. Bleiz, and B. Carboni. Tetrahedron, **62**, 4027 (2006).
19. F. Berrée, A. Debache, Y. Marsac, and B. Carboni. Tetrahedron Lett. **42**, 3591 (2001).
20. A.A. Asselin and L.G. Humber. U. S. Patent 4-044-131, 23 August 1977.
21. H. Caner, E. Groner, L. Levy, and I. Agranat. Drug Discovery Today, **9**, 105 (2004).
22. Q.K. Fang, Z. Han, P. Grover, D. Kessler, C.H. Senanayake, and S.A. Wald. Tetrahedron: Asymmetry, **11**, 3659 (2000).
23. SMART [computer program]. Bruker AXS Inc., Madison, Wisconsin, USA. 2001.
24. G.M. Sheldrick. SADABS [computer program]. University of Göttingen, Göttingen, Germany. 1996.
25. SHELXTL [computer program]. Bruker AXS Inc., Madison, Wisconsin, USA. 1997.
26. L.J. Farrugia. J. Appl. Cryst. **30**, 565 (1997).
27. A.X. Hu, G. Cao, X.R. Xiao, and H.Y. Wu. Acta Crystallogr. Sect. E: Struct. Rep. Online, **62**, o1584 (2006).
28. R.D. Porsolt, M. Le-Pichon, and M. Jalfre. Nature (London), **266**, 730 (1977).
29. A.X. Hu, P. Chen, Z. Yang, X.Y. Wu, and K. Chen. Chin. J. Med. Chem. **12**, 340 (2002).

© 2007 NRC Canada

Cadmium chloride-catalyzed regioselective opening of oxiranes with aromatic amines — An improved protocol for the synthesis of 2-amino alcohols

S. Ramesh Kumar and P. Leelavathi

Abstract: Epoxides undergo rapid $CdCl_2$-catalyzed ring-opening reaction with aromatic amines in mild reaction conditions (room temperature), affording the corresponding 2-amino alcohols with high regioselectivity.

Key words: epoxides, aromatic amines, cadmium chloride, 2-amino alcohols.

Résumé : Sous l'influence d'une catalyse par le $CdCl_2$, les époxydes réagissent avec les amines aromatiques dans des conditions douces (température ambiante) et subissent une rapide réaction d'ouverture de cycle qui conduit à la formation des 2-aminoalcools correspondants avec une régiosélectivité élevée.

Mots-clés : époxydes, amines aromatiques, chlorure de cadmium, 2-aminoalcools.

[Traduit par la Rédaction]

Introduction

The aminolysis of epoxides is a classical route to β-amino alcohols, which are versatile intermediates with major functional groups for the synthesis of various biologically active natural and synthetic products (1). A straightforward synthetic approach for the preparation of β-amino alcohols involves heating an epoxide with an excess of an amine at an elevated temperature. However, this preparation suffers from disadvantages such as high temperature or prolonged reaction times. A variety of activators have been reported, such as metal perchlorates, halides, triflates (2), and ionic liquids (3). Many of these methods involve the use of expensive reagents, and occasionally, give undesirable side reactions or low yields of the desired products (4). Therefore, there is a demand for a new and efficient method for this transformation in more convenient and general conditions. Cadmium chloride is known in the literature as a mild and efficient catalyst for various organic transformations (5).

Results and discussion

As part of our ongoing program in developing new synthetic methods (6), we wish to report our results on regioselective ring opening of various oxiranes with aromatic amines, using a catalytic amount (20 mol%) of $CdCl_2$ in mild reaction conditions.

In a typical experiment, a dichloromethane solution of equimolar amounts of styrene oxide (**1**) and aniline (**2**) was stirred in the presence of $CdCl_2$ at room temperature to obtain the corresponding 2-amino alcohol (**3**) in 93% yield. The reaction was complete within 2 h, the ring opening took place in a regioselective manner, preferentially at the benzylic position. Likewise, styrene oxide and various substituted anilines afforded the 2-amino alcohol (Table 1, entries **a**–**d**).

Similarly, glycidyl phenyl ether and aliphatic alkyl oxiranes reacted smoothly with aryl amines to afford the corresponding 2-amino alcohols in very good yields (Table 1, entries **e**–**l**). The epoxide opening took place in a regioselective manner, preferentially at the unsubstituted oxirane carbon atom, to afford the product (**4**), as shown in Scheme1. Furthermore, cyclohexene oxide reacted smoothly with substituted aromatic amines to afford the corresponding β-amino alcohols (**5**) in excellent yields (Table 1, entries **m**–**p**), as shown in Scheme 2. The *trans* stereochemistry of **5** was deduced from the coupling constants of the ring protons at δ 3.10 (1H, ddd, J = 4.2, 9.5, 11.0 Hz) for HC–O and at δ 3.30 for HC–N (1H, ddd, J = 4.0, 10.0, 10.0 Hz).

All the products were characterized by ^{1}H NMR, IR, and MS. The method applied does not require anhydrous solvents, exclusion of moisture, or stringent reaction conditions. The reactions were clean and highly regioselective, affording high product yields in a reaction time of 2–4 h. The scope and the generality of this process are illustrated

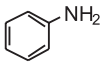
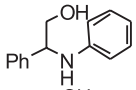
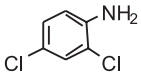
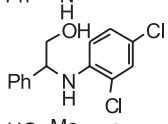
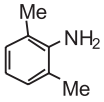
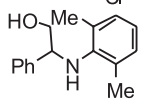
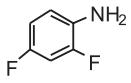
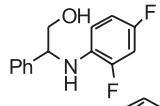
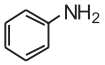
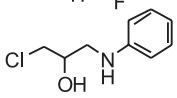
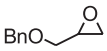
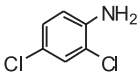
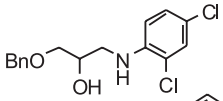
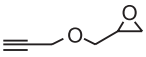
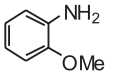
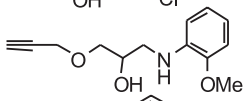
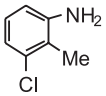
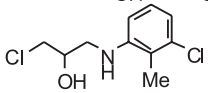
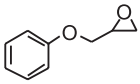
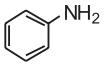
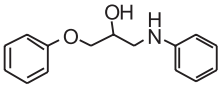
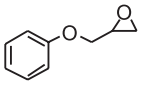
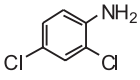
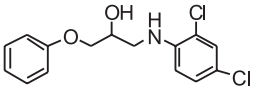
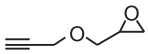
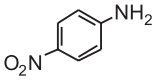
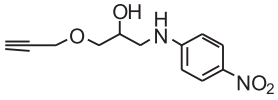
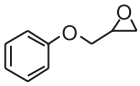
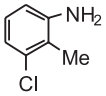
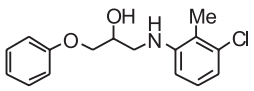
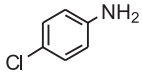
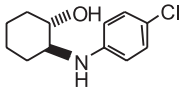
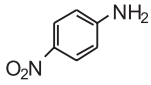
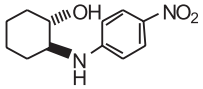
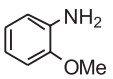
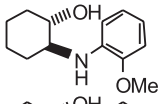
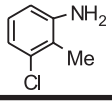
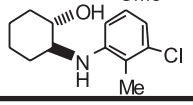
Received 21 September 2006. Accepted 16 November 2006. Published on the NRC Research Press Web site at http://canjchem.nrc.ca on 26 January 2007.

S.R. Kumar and P. Leelavathi.[1] Department of Chemistry, College for Women, Koti, Osmania University, Hyderabad 500 095, India.

[1]Corresponding author (e-mail: rameshteja_2001@yahoo.co.in).

 doi:10.1139/V06-186 © 2007 NRC Canada

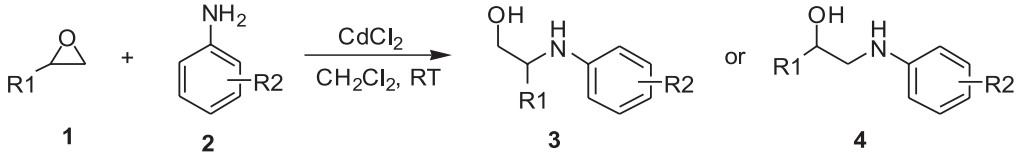
Table 1. $CdCl_2$-catalyzed ring-opening epoxides with aromatic amines.

Entry	Oxirane	Aniline	β-Amino alcohol	Reaction time (h)	Yield (%)[a]	Reference
a				2.0	93	3*a*
b				2.5	90	2*k*
c				2.5	91	2*k*, 3*a*
d				2.0	88	3*a*
e				3.5	84	2*i*, 2*m*, 2*n*
f				4.0	82	
g				3.5	83	
h				4.0	81	
i				2.5	89	2*m*, 3*a*
j				3.0	91	
k				3.0	86	
l				3.5	85	
m				3.0	86	2*f*, 2*g*
n				3.0	85	2*a*, 2*o*
o				3.0	91	2*a*, 2*f*, 2*l*, 2*p*
p				2.5	88	

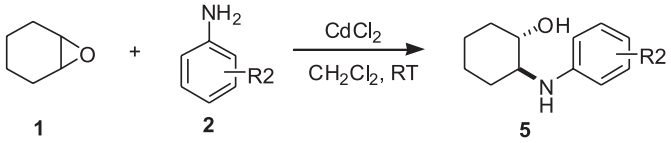
[a] Isolated and unoptimized yields.

© 2007 NRC Canada

Scheme 1.



Scheme 2.



with respect to various epoxides and different substituted amines. The advantage of $CdCl_2$ is its simplicity in handling and the easy workup procedure for the isolation of products.

Experimental section

General methods

All physical and spectroscopic data of the products were compared with those reported in the literature. IR spectra were recorded on a PerkinElmer FT-IR 240-c spectrophotometer. ^{1}H NMR spectra of $CDCl_3$ solutions with TMS as internal standard were recorded on a Gemini-200 spectrometer. Melting points were recorded on a Buchi R-535 apparatus. Mass spectra were recorded on a Finnigan MAT 1020 spectrometer at 70 eV.

General procedure

To a mixture of epoxide **1** (2 mmol) and aniline **2** (2 mmol) in dichloromethane (10 mL) was added $CdCl_2$ (73 mg, 0.4 mmol). The resulting mixture was stirred at room temperature for a specified period (see Table 1); the progress of the reaction was monitored by TLC. After the complete conversion of the starting material, the reaction mixture was diluted with dichloromethane (30 mL). The mixture was washed with water followed by brine solution. The organic layer was dried over Na_2SO_4 and concentrated under reduced pressure to obtain the crude product, which was purified by column chromatography (silica gel 60–120 mesh; ethyl acetate : petroleum ether).

Spectral data for all the compounds

2-Phenyl-2-phenylaminoethanol (3a)

Colourless liquid. IR (neat) ν: 3461, 3397, 3055, 3026, 2926, 2873, 1602, 1503, 1452, 1431, 1354, 1317, 1268, 1180, 1125, 1067, 1028, 926, 872, 752 cm^{-1}. ^{1}H NMR (200 MHz, $CDCl_3$) δ: 3.68 (dd, *J* = 6.5, 11.0 Hz, 1H), 3.89 (dd, *J* = 4.0, 11.0 Hz, 1H), 4.42 (dd, *J* = 6.5, 11.0 Hz, 1H), 6.49 (d, *J* = 7.0 Hz, 2H), 6.63 (t, *J* = 7.0 Hz, 1H), 7.04 (t, *J* = 7.0 Hz, 2H), 7.20–7.35 (m, 5H). EI-MS *m*/*z* (%): 213 (12, M$^+$), 182 (100), 104 (27), 77 (31), 51 (22).

2-(2,4-Dichlorophenylamino)-2-phenylethanol (3b)

Brown coloured syrup. IR (neat) ν: 3404, 3064, 2933, 2859, 1594, 1505, 1453, 1397, 1321, 1265, 1157, 1126, 1099, 1067, 1043, 936, 866, 839, 802, 749 cm^{-1}. ^{1}H NMR (200 MHz, $CDCl_3$) δ: 3.75–3.85 (m, 1H), 4.40–4.50 (m, 1H), 4.94 (t, *J* = 7.0 Hz, 1H), 6.36 (d, *J* = 8.5 Hz, 1H), 6.88 (dd, *J* = 4.0, 8.5 Hz, 1H), 7.26–7.40 (m, 6H). EI-MS *m*/*z* (%): 285 (10, M$^+$), 156 (25), 125 (100), 103 (20), 91 (85), 77 (15), 63 (18), 57 (20), 51 (20), 43 (26).

2-(2,6-Dimethylphenylamino)-2-phenylethanol (3c)

Colourless oil. IR (neat) ν: 3429, 3371, 3069, 2946, 2837, 1606, 1531, 1442, 1382, 1310, 1271, 1124, 1058, 981, 875, 812, 752 cm^{-1}. ^{1}H NMR (200 MHz, $CDCl_3$) δ: 1.70 (br s, OH, 1H), 3.60–3.70 (m, 1H), 3.88 (s, 3H), 3.90–3.95 (m, 1H), 4.48 (t, *J* = 7.0 Hz, 1H), 4.95 (br s, NH, 1H), 6.30 (d, *J* = 7.5 Hz, 1H), 6.52–6.65 (m, 2H), 6.72 (d, *J* = 7.5 Hz, 1H), 7.25–7.40 (m, 5H). EI-MS *m*/*z* (%): 242 (12, M$^+$), 212 (100), 196 (21), 141 (10), 120 (31), 91 (15), 77 (18), 65 (12), 51 (10).

2-(2,4-Difluorophenylamino)-2-phenylethanol (3d)

Brownish oil. IR (neat) ν: 3412, 3326, 3068, 2942, 2851, 1605, 1554, 1436, 1372, 1251, 1128, 1049, 1018, 936, 847, 752 cm^{-1}. ^{1}H NMR (200 MHz, $CDCl_3$) δ: 1.75 (br s, OH, 1H), 3.70 (dd, *J* = 6.0, 10.5 Hz, 1H), 3.91 (dd, *J* = 4.0, 11.0 Hz, 1H), 4.95 (t, *J* = 6.5 Hz, 1H), 6.18 (d, *J* = 6.5 Hz, 1H), 6.65–6.80 (m, 1H), 7.25–7.40 (m, 6H). EI-MS *m*/*z* (%): 249 (10, M$^+$), 218 (70), 156 (18), 125 (100), 103 (31), 91 (95), 77 (35), 61 (42), 57(70), 43 (55).

1-Chloro-3-phenylaminopropan-2-ol (3e)

Light coloured solid; mp 38–39 °C. IR (KBr) ν: 3404, 3396, 3062, 2952, 2836, 1602, 1583, 1505, 1456, 1404, 1318, 1259, 1247, 1213, 1169, 1102, 1090, 912, 847, 753 cm^{-1}. ^{1}H NMR (200 MHz, $CDCl_3$) δ: 2.85 (br s, 1H), 3.18–3.41 (m, 2H), 3.60–3.70 (m, 2H), 3.98–4.10 (m, 1H), 6.55–6.65 (m, 3H), 7.10–7.20 (m, 2H). EI-MS *m*/*z* (%): 185 (15, M$^+$), 168 (26), 106 (100), 77 (43), 51 (22).

1-Benzyloxy-3-(2,4-dichlorophenyl)aminopropan-2-ol (3f)

Colourless oil. IR (neat) ν: 3414, 3071, 2924, 2855, 1596, 1508, 1454, 1396, 1320, 1269, 1156, 1096, 1048, 869, 842, 753 cm^{-1}. ^{1}H NMR (200 MHz, $CDCl_3$) δ: 2.50 (d, *J* = 6.5 Hz, 1H), 3.18–3.45 (m, 2H), 3.65–3.75 (m, 2H), 4.05–4.15 (m, 1H), 4.60 (br s, 1H), 6.60 (d, *J* = 7.5 Hz, 1H), 7.18 (d, *J* = 7.5 Hz, 1H), 7.26 (s, 1H). EI-MS *m*/*z* (%): 312 (10, M$^+$), 253 (10), 178 (80), 174 (100), 111 (12), 79 (13), 57 (14), 43 (87).

3-(2-Methoxyphenyl)-1-(propargyloxy)aminopropan-2-ol (3g)

Light coloured solid; mp 41–42 °C. IR (KBr) ν: 3406, 3389, 3067, 2936, 2839, 1602, 1513, 1458, 1434, 1344, 1295, 1251, 1223, 1177, 1132, 1102, 1026, 908, 843, 743 cm^{-1}. ^{1}H NMR (200 MHz, $CDCl_3$) δ: 3.18 (t, *J* = 6.5 Hz, 1H), 3.30 (d, *J* = 6.5 Hz, 1H), 3.58 (d, *J* = 6.5 Hz, 1H), 3.80 (s, 3H), 3.98 (d, *J* = 6.5 Hz, 1H), 6.58–6.82 (m,

© 2007 NRC Canada

4H). EI-MS *m/z* (%): 235 (28, M^+), 136 (100), 121 (57), 77 (23), 65 (15), 51 (12).

1-Chloro-3-(3-chloro-2-methylphenyl)aminopropan-2-ol (3h)

Brown coloured syrup. IR (neat) ν: 3403, 3386, 3072, 2941, 2837, 1605, 1518, 1461, 1404, 1346, 1286, 1231, 1203, 1172, 1134, 1108, 1031, 917, 846, 748 cm^{-1}. ^1H NMR (200 MHz, $CDCl_3$) δ: 2.28 (s, 3H), 2.45 (br s, 1H), 3.25 (q, *J* = 6.5 Hz, 1H), 3.42 (dd, *J* = 4.0, 9.5 Hz, 1H), 3.65–3.75 (m, 2H), 4.00 (br s, 1H), 4.15 (br s, 1H), 6.53 (d, *J* = 7.0 Hz, 1H), 6.80 (d, *J* = 7.0 Hz, 1H), 7.05 (t, *J* = 7.0 Hz, 1H). EI-MS *m/z* (%): 234 (10, M^+), 232 (15), 156 (41), 154 (100), 125 (15), 117 (10), 89 (20), 77 (12), 51 (10), 43 (12).

1-Phenoxy-3-phenylaminopropan-2-ol (3i)

Colourless oil. IR (neat) ν: 3408, 3391, 3056, 2926, 2872, 1602, 1562, 1517, 1491, 1362, 1243, 1123, 1039, 947, 861, 742 cm^{-1}. ^1H NMR (200 MHz, $CDCl_3$) δ: 3.15 (dd, *J* = 7.5, 12.0 Hz, 1H), 3.36 (dd, *J* = 4.5, 12.0 Hz, 1H), 3.50–3.60 (m, 2H), 4.02–4.35 (m, 1H), 6.55–6.70 (m, 3H), 7.15–7.35 (m, 7H). EI-MS *m/z* (%):243 (18, M^+), 150 (23), 137 (32), 106 (100), 93 (14), 77 (41), 75 (16), 51 (31).

3-(2,4-Dichlorophenyl)-1-(phenoxy)aminopropan-2-ol (3j)

Colourless oil. IR (neat) ν: 3397, 3061, 3047, 2961, 2851, 1631, 1604, 1501, 1487, 1432, 1342, 1213, 1143, 1019, 951, 841, 748 cm^{-1}. ^1H NMR (200 MHz, $CDCl_3$) δ: 3.18 (dd, *J* = 6.0, 11.0 Hz, 1H), 3.32 (dd, *J* = 4.0, 11.0 Hz, 1H), 3.52–3.63 (m, 2H), 4.05–4.30 (m, 1H), 6.65 (d, *J* = 7.0 Hz, 1H), 7.10 (d, *J* = 7.0 Hz, 1H), 7.30 (s, 1H). EI-MS *m/z* (%): 312 (18, M^+), 275 (10), 219 (23), 175 (18), 163 (12), 146 (31), 134 (21), 109 (100), 90 (24), 74 (36), 49 (21).

3-(4-Nitrophenyl)-1-(propargyloxy)aminopropan-2-ol (3k)

Colourless solid; mp 73–75 °C. IR (KBr) ν: 3409, 3378, 3063, 2951, 2841, 1605, 1509, 1432, 1361, 1302, 1278, 1141, 1109, 1023, 972, 873, 804, 753 cm^{-1}. ^1H NMR (200 MHz, $CDCl_3$) δ: 3.12 (dd, *J* = 5.0, 10.5 Hz, 1H), 3.30 (dd, *J* = 5.0, 10.5 Hz, 1H), 3.50–3.60 (m, 2H), 3.88 (s, 3H), 3.93–3.98 (m, 1H), 6.32 (d, *J* = 7.0 Hz, 1H), 6.50–6.60 (m, 2H), 6.75 (d, *J* = 7.0 Hz, 1H), 7.30–7.45 (m, 5H). EI-MS *m/z* (%): 250 (22, M^+), 242 (10), 180 (26), 136 (31), 107 (100), 93 (19), 76 (48), 51(21).

3-(3-Chloro-2-methylphenyl)-1-(phenoxy)aminopropan-2-ol (3l)

Light yellow oil. IR (neat) ν: 3403, 3371, 3065, 2943, 2849, 1636, 1606, 1541, 1508, 1431, 1362, 1308, 1256, 1137, 1046, 1012, 937, 851, 749 cm^{-1}. ^1H NMR (200 MHz, $CDCl_3$) δ: 2.37 (s, 3H), 3.18 (dd, *J* = 5.5, 10.5 Hz, 1H), 3.32 (dd, *J* = 5.5, 10.5 Hz, 1H), 3.45–3.58 (m, 2H), 3.90–3.97 (m, 1H), 6.20 (d, *J* = 7.0 Hz, 1H), 6.70–6.85 (m, 1H), 7.30–7.40 (m, 6H). EI-MS *m/z* (%): 291 (21, M^+), 256 (18), 154 (21), 137 (100), 119 (56), 104 (11), 93 (15), 77 (25), 61 (412), 57(37), 43 (51).

1*-trans-*2-(4-Chlorophenylamino)cyclohexanol (3m)

White solid; mp. 61–62 °C. IR (KBr) ν: 3394, 3276, 3081, 2961, 2846, 1739, 1608, 1526, 1452, 1381, 1232, 1112, 1073, 952, 847, 753 cm^{-1}. ^1H NMR (200 MHz, $CDCl_3$) δ: 0.98–1.08 (m, 1H), 1.28–1.41 (m, 3H), 1.70–1.85 (m, 2H), 2.08–2.20 (m, 2H), 2.90 (br s, NH), 3.10 (ddd, *J* = 4.2, 9.5, 11.0 Hz, 1H), 3.30 (ddd, *J* = 4.0, 10.0, 10.0 Hz, 1H), 6.68–6.78 (m, 3H), 7.10–7.20 (m, 2H). EI-MS *m/z* (%): 227 (30, M^+), 191 (25), 167 (51), 114 (19), 96 (21), 77 (100), 56 (31), 52 (37), 45 (23).

1*-trans-*2-(4-Nitrophenylamino)cyclohexanol (3n)

Brown solid; mp 71–72 °C. IR (KBr) ν: 3394, 2928, 2856, 1740, 1622, 1582, 1528, 1453, 1347, 1262, 1133, 1067, 949, 854, 815, 792, 735 cm^{-1}. ^1H NMR (200 MHz, $CDCl_3$) δ: 0.80–0.95 (m, 1H), 1.22–1.45 (m, 3H), 1.70–1.85 (m, 2H), 2.08–2.20 (m, 2H), 3.20 (ddd, *J* = 4.2, 9.5, 11.0 Hz, 1H), 3.40 (ddd, *J* = 4.0, 10.0, 11.0 Hz, 1H), 3.80 (br s, 1H), 6.95 (d, *J* = 7.5 Hz, 1H), 7.30 (t, *J* = 7.5 Hz, 1H), 7.55 (t, *J* = 7.5 Hz, 1H). EI-MS *m/z* (%): 237 (79, M^+), 221(26), 194 (10), 178 (96), 152 (32), 139 (15), 121 (18), 118 (40), 106 (14), 92 (51), 65 (63), 57 (66), 41 (100).

1*-trans-*2-(2-Methoxyphenylamino)cyclohexanol (3o)

White solid; mp 56–57 °C. IR (KBr) ν: 3380, 3063, 3000, 2933, 2858, 1601, 1511, 1457, 1431, 1401, 1343, 1302, 1224, 1177, 1141, 1118, 1068, 1030, 936, 903, 850, 804, 799, 738 cm^{-1}. ^1H NMR (200 MHz, $CDCl_3$) δ: 0.98–1.18 (m, 1H), 1.25–1.41 (m, 3H), 1.70–1.80 (m, 2H), 2.05–2.20 (m, 2H), 2.75 (br s, NH), 3.10 (ddd, *J* = 4.1, 9.2, 11.0 Hz, 1H), 3.40 (ddd, *J* = 4.1, 9.2, 11.0 Hz, 1H), 3.85 (s, 3H), 6.60–6.85 (m, 4H). EI-MS *m/z* (%): 221 (90, M^+), 164 (12), 162 (100), 150 (15), 136 (26), 123 (90), 108 (84), 106 (11), 80 (81), 65 (11), 53 (31).

1*-trans-*2-(2-Chloro-3-methylphenylamino)cyclohexanol (3p)

Light coloured solid; mp 49–50 °C. IR (KBr) ν: 3408, 3374, 3061, 2935, 2861, 1603, 1585, 1506, 1456, 1429, 1389, 1346, 1312, 1267, 1214, 1163, 1131, 1097, 1059, 946, 913, 854, 763, 748 cm^{-1}. ^1H NMR (200 MHz, $CDCl_3$) δ: 0.94–1.15 (m, 1H), 1.23–1.40 (m, 3H), 1.68–1.79 (m, 2H), 2.02–2.20 (m, 2H), 2.40 (s, 3H), 2.85 (br s, NH), 3.15 (ddd, *J* = 4.3, 9.6, 11.0 Hz, 1H), 3.38 (ddd, *J* = 4.3, 9.6, 11.0 Hz, 1H), 6.50 (d, *J* = 6.5 Hz, 1H), 6.75 (d, *J* = 6.5 Hz, 1H), 7.05 (t, *J* = 6.5 Hz, 1H). EI-MS *m/z* (%): 241 (30, M^+), 204 (12), 189 (10), 127 (100), 114 (56), 90 (39), 75 (31), 65 (11), 51 (32).

References

1. (*a*) T. Kino, H. Halanaka, M. Hashimoto, M. Nishiyama, T. Goto, M. Okuhara, M. Kohsaka, H. Aoki, and H. Imanaka. J. Antibiot. **40**, 1249 (1987); (*b*) D.S. Bose and A.V. Narsaiah. Bioorg Med. Chem. **3**, 627 (2005); (*c*) E.J. Corey and X-M. Cheng. The logic of chemical synthesis. John Wiley, New York. 1989; (*d*) P.W. Erhardt, C.M. Woo, W.G. Anderson, and R.J. Gorczynski. J. Med. Chem. **25**, 1408 (1982); (*f*) A.V. Narsaiah. Synth. Commun. 1897 (2006).
2. (*a*) M. Curini, F. Epifano, M.C. Marcotullio, and O. Rosati. Eur. J. Org. Chem. 4149 (2001); (*b*) L.D. Pachon, P. Gamez, J.J.M. Van Bessel, and J. Reedijk. Tetrahedron Lett. **44**, 6025 (2003); (*c*) M.M. Khodaei, A.R. Khosropour, and K. Ghozati. Tetrahedron Lett. **45**, 3525 (2004); (*d*) T. Ollevier and G. Lavie- Compin. Tetrahedron Lett. **45**, 49 (2004); (*e*) Y. Yamamoto, N. Asao, M. Meguro, N. Tsukade, H. Nemoto, N. Adayari, J.G. Wilson, and H. Nakamura. J. Chem. Soc., Chem.

© 2007 NRC Canada

Commun. 1201 (1993); (*f*) A.K. Chakraborthi and A. Kondaskar. Tetrahedron Lett. **44**, 8315 (2003); (*g*) N.R. Swamy, G. Kondaji, and K. Nagaiah. Synth. Commun. **32**, 2307 (2002); (*h*) L.R. Reddy, M.A. Reddy, N. Bhanumathi, and K.R. Rao. New J. Chem. **25**, 221 (2001); (*i*) A.K. Chakraborti and A. Kondaskar. Tetrahedron Lett. **44**, 8315 (2003); (*j*) E. Rafiee, S. Tangestaninejad, M.H. Habibi, and V. Mirkhani. Synth. Commun. **36**, 3673 (2004); (*k*) A. McCluskey, S.K. Leitch, J. Garner, C.E. Caden, T.A. Hill, L.R. Odell, and S.G. Stewart. Tetrahedron Lett. **46**, 8229 (2005); (*l*) R.I. Kuteshy, S. Singh, N. Khan, S.H.R. Abdi, E. Suresh, and R.V. Jasra. Eur. J. Org. Chem. 1303 (2006); (*m*) A.K. Chakraborti, S. Rudrawar, and A. Kondaskar. Eur. J. Org. Chem. 3597 (2004). (*n*) A. Kamal, R. Ramu, M.A. Azar, and G.B.R. Khanna. Tetrahedron Lett. **46**, 2675 (2005); (*o*) G. Sekar and V.K.J. Singh. Org. Chem. **64**, 287 (1999); (*p*) F. Carrée, R. Gil, and J. Collin. Org. Lett. **7**, 1023 (2005); (*q*) J.S. Yadav, A.R. Reddy, A.V. Narsaiah, and B.V.S. Reddy. J. Mol. Catal. A, **261**, 207 (2006).

3. (*a*) J.S. Yadav, B.V.S. Reddy, A.K. Basak, and A.V. Narsaiah. Tetrahedron Lett. **44**, 1047 (2003); (*b*) J.S. Yadav, B.V.S. Reddy, K. Sadashiv, K. Harikishan, and A.V. Narsaiah. J. Mol. Catal. A, **220**, 153 (2004).
4. (*a*) J.K. Whitesel and S.W. Felman. J. Org. Chem. **45**, 755 (1980); (*b*) J. Yamada, Y. Yomoto, and Y. Yamamoto. Tetrahedron Lett. **30**, 4255 (1989).
5. A.V. Narsaiah and K. Nagaiah. Synthesis, 1253 (2004).
6. S. Ramesh Kumar and P. Leelavathi. J. Mol. Catal A, **240**, 99 (2005).

© 2007 NRC Canada

Copper-mediated N-arylation of electron-deficient pyrroles and indoles

Henri Bekolo[1]

Abstract: We have found that it is possible to N-arylate electron-deficient pyrroles and indoles having no carbonyl group α to the nitrogen ring in good to excellent yields under the Chan and Lam conditions using *N*-Ethyldiisopropylamine (DIEA) base as a substitute for triethylamine (TEA) and pyridine.

Key words: cupric acetate, arylboronic acid, N-arylation, pyrroles, indoles.

Résumé : Nous avons trouvé qu'il est possible de faire la N-arylation des pyrroles et des indoles pauvres en électrons ne possèdant pas de groupement carbonyle en position α de l'atome d'azote du noyau pyrrolique, avec de bons rendements, dans les conditions de Chan et Lam en remplaçant la triéthylamine (TEA) et la pyridine par la *N*-éthyldiisopropylamine (DIEA).

Mots-clés : acétate cuprique, acide arylboronique, N-arylation, pyrroles, indoles.

Introduction

The C–N bond forming reaction using stoichiometric (1–8) or catalytic (9–14) amounts of copper salt, a boronic acid, a nucleophile, and a base is a fast growing methodology that was pioneered by Chan and co-workers in its stoichiometric version (1, 2). Although various substrates have been efficiently N-arylated (15), the reaction outcome is somewhat unpredictable (8). To account for the successful N-arylation of electron-deficient pyrroles and indoles, it has been hypothesized that the presence of a carbonyl group α to the pyrrole ring nitrogen promotes the reaction and is, in part, a key to a successful reaction (5,6). Herein, we report good to excellent N-arylation yields of some commercially available electron-deficient pyrroles (Table 1, **1** and **2**) and indoles (Table 2, **5** and **6**) having no carbonyl group α to the pyrrole ring nitrogen.

Chan and Lam conditions for N-arylation of NH-containing heterocycles include a nucleophile, stoichiometric anhyd. $Cu(OAc)_2$, a boronic acid, and pyridine or Et_3N as a base in dichloromethane (DCM) at RT. Examples in the literature include the N-arylation of azoles (2), purines (3, 4), 2-pyridones and 3-pyridazinones (5). Closely related to this work is the N-arylation of indoles and pyrroles. Pyrrole itself has been N-arylated using catalytic copper salt in 89% yield (9), whereas, under stoichiometric $Cu(OAc)_2$ conditions, Lam et al. (2) and Srirangam and co-workers (6) reported less than 3% and 0% yields, respectively. In Lam et al. (2), indole itself was also reported to have been N-arylated in less than 3% yield.

Received 16 August 2006. Accepted 7 December 2007. Published on the NRC Research Press Web site at http://canjchem.nrc.ca on 26 January 2007.

H. Bekolo. Laboratoire d'Ingénierie Moléculaire et Biochimie Pharmacologique – 1, Boulevard Arago, 57078 Metz, France.

[1]Corresponding author (e-mail: hbekolo@hotmail.com).

Considering the successful N-arylation of amides, imides, sulfonamides, and ureas (1), Mederski et al. (5) hypothesized that the presence of a carbonyl group at the C-2 position of pyrrole and indole derivatives activates the heterocyclic ring nitrogen, thereby contributing to the positive outcome of the N-arylation process. They demonstrated the concept by N-arylation of the electron-deficient ethyl pyrrole-2-carboxylate in 50% yield and of a series of 2-carboxyindoles in 21% to 50% yields.

Under similar conditions, excellent N-arylation yields of electron-deficient pyrroles were reported by Srirangam and co-workers (6). However, these remarkable yields were restricted to pyrroles having a carbonyl group at either the 2 or the 5 position. Ethyl pyrrole-3-glyoxalate, the only reported example of stoichiometric copper-mediated N-arylation of an electron-deficient pyrrole lacking a carbonyl group α to the ring nitrogen, exhibited very poor reactivity, yielding traces of expected products in three runs out of four and with only 25% of the expected product. According to the authors, the excellent yields with α-deactivated pyrroles "might in part be attributed to the chelation of carbonyl oxygen to the pyrrole nitrogen-Cu complex".

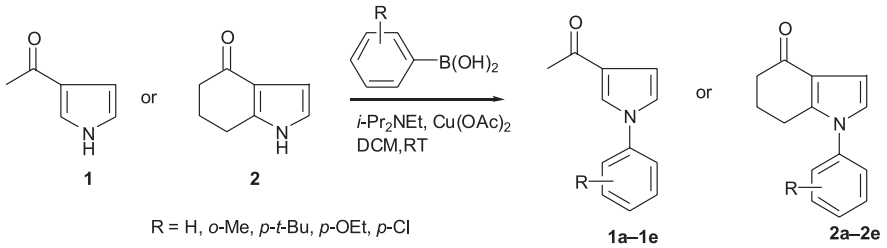
Although reasonable, the above hypothesis suggests the necessity of having a carbonyl group α to the pyrrole ring nitrogen to achieve synthetically useful yields of stoichiometric copper-mediated N-arylation of electron-deficient pyrroles and indoles. This prompted us to investigate the reactivity of electron-deficient pyrroles **1** and **2**, similar to ethyl pyrrole-3-glyoxalate, and indoles **5** and **6**.

Results and discussion

To our knowledge, DIEA has not been reported in experimental screenings as an optimal base in the Cu-mediated arylation of heteroatoms with arylboronic acids. DIEA was tested in the synthesis of the *N*-arylpyrrole **1a** (Table 1), which we isolated in 70% yield. TEA and pyridine did not

 doi:10.1139/V06-187 © 2007 NRC Canada

Table 1. $Cu(OAc)_2$-mediated N-arylation of **1** and **2** with $ArB(OH)_2$.



Product	Time (days)	Product yield (%)[a]	Recovered pyrrole **1** (%)[a]	Product[b]	Product yield (%)[a]	Time (days)
1a R = H	3	70	12	**2a** R = H	70	9
	3	25[c]	45			
	3	0[d]	69			
1b R = *o*-Me	5	70	0	**2b** R = *o*-Me	70	7
1c R = *p*-*t*-Bu	5	56	18	**2c** R = *p*-*t*-Bu	60[e]	14
1d R = *p*-OEt	14	50	23	**2d** R = *p*-OEt	60	14
1e R = *p*-Cl	5	47	38	**2e** R = *p*-Cl	43	6

[a]Isolated yields.
[b]Run on the 0.5 mmol scale in DMF. For **2b**, DCM (2 mL) was used; for **2e**, DCM was used.
[c]Et_3N was used instead of DIEA.
[d]Pyridine was used instead of DIEA.
[e]The reaction is cleaner in DCM.

efficiently promote the formation of **1a**. With this result, we decided to test the nonnucleophilic base DIEA with a range of *N*-arylpyrroles (Table 1). The expected products were isolated, along with the remaining starting pyrroles, phenolic by-products (up to 19%) that were already observed by Lam et al. (2), and symmetrical biaryls (up to 16%) that were also reported as side products by Lam et al. (14). These biaryls, characterized as dimers from arylboronic acids, most likely arose from the well-established $Cu(OAc)_2$-mediated oxidative dimerization of arylboronic acids (16).

Trisubstituted pyrrole **3** and tetrasubstituted pyrrole **4** (Fig. 1) were reacted with phenylboronic acid under our standard reaction conditions and found to be poor coupling partners. The reaction mixture with pyrrole **3** turned intensely red over time. After a 10-day reaction, 20% of the starting pyrrole **3** was recovered and 7% of the expected product **3a** (Fig. 1) was isolated (17), along with unidentified reddish by-products. Based on TLC analysis, pyrrole **4** did not react at all, even after a longer reaction time of 14 days.

The dramatic difference in reactivity between pyrroles **1** and **3** or **2** and **4** with phenylboronic acid may be accounted for by the methyl group steric hindrance at the α positions of **3** and **4** as copper-catalyzed coupling reactions are well-known to be extremely sensitive to steric effects in the nitrogen nucleophile. Pyrrole itself was reacted with phenylboronic acid in the dark for three days. The expected *N*-phenylpyrrole was isolated in 4% yield (9). We did not have an electron-rich pyrrole to test.

In this work, $Cu(OAc)_2$ is suspected to oxidize pyrrole anions as dark reddish unidentified by-products formed throughout the preparation of *N*-arylpyrroles. This hypothesis is supported by the fact that $Cu(OAc)_2$ is known to oxidize lithium enolates at temperatures as low as –78 °C (18).

To the best of our knowledge, there has been no report on the N-arylation under the Chan and Lam conditions of electron-deficient indoles having no carbonyl group at the C-2 position. Under the Chan and Lam conditions using DIEA, we have found that 3-acetylindole **5** and 5-nitroindole **6** lacking C-2 carbonyl groups undergo efficient N-arylations (Table 2).

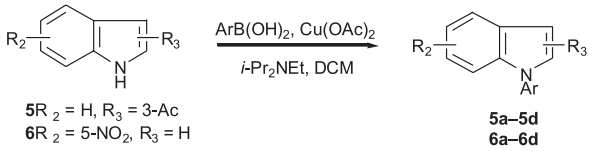
When reacted with phenylboronic acid in the presence of DIEA, Et_3N, and pyridine, 3-acetylindole **5** exhibited similar reactivity as 3-acetylpyrrole **1**. That is, the use of DIEA as a base for the preparation of *N*-arylindole **5a** led to the isolation of **5a** in high yield (85%) after a two-day reaction (Table 2), whereas, the use of Et_3N for the same reaction resulted in low isolated yield of **5a** (35%) even after a longer reaction time of four days. The use of pyridine resulted in no formation of the expected product **5a**, as with a base-free reaction. For the most part, the balance of the material was likely the remaining 3-acetylindole **5**, as judged by TLC analysis. The use of DIEA was then extended to the synthesis of other *N*-arylindoles (Table 2), and we were pleased to find that the reactions proceeded uneventfully in high isolated yields. The 3-acetylindole series afforded higher product yields. Low yield (45%) of the expected product was observed for the synthesis of *N*-arylindole **6d**, in the case of which a thick mixture formed within 2 h under our standard reaction conditions that had to be diluted with an additional 3 mL of DCM. Extending the reaction time from 6 to 10 days did not improve the yield.

The modest reactivity of 4-chlorophenylboronic acid in both pyrrole and indole series reflects the known coupling partners dependency of the Cu–$ArB(OH)_2$ N-arylation reactions (1,8).

The electron-rich 5-methoxyindole was allowed to react with phenylboronic acid to assess its reactivity under our re-

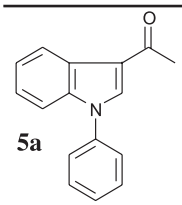
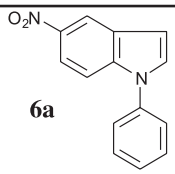
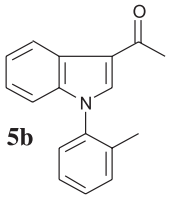
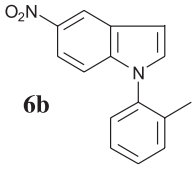
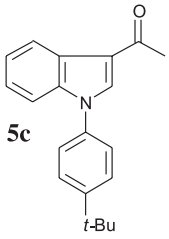
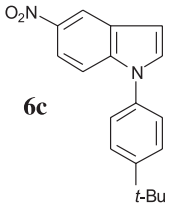
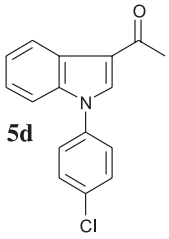
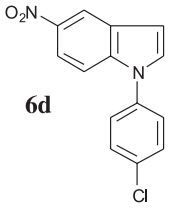
© 2007 NRC Canada

Table 2. $Cu(OAc)_2$–$ArB(OH)_2$ N-arylation of indoles **5** and **6**.



5R_2 = H, R_3 = 3-Ac
6R_2 = 5-NO_2, R_3 = H

5a–5d
6a–6d

N-arylindole	Yield (%)[a]	Time (days)	N-arylindole	Yield (%)[a]	Time (days)
 **5a**	100[b]	5	 **6a**	83	4
	85	2			
	35[c]	4			
	0[d]	2			
 **5b**	99	4	 **6b**	90	7
 **5c**	94	10	 **6c**	75[e]	10
 **5d**	65	8	 **6d**	45[e,f]	6

[a]Isolated yields.
[b]DMF was used instead of DCM.
[c]TEA was used instead of DIEA
[d]Pyridine was used instead of DIEA
[e]DCM (5 mL) was used for 1 mmol of **6**.
[f]The starting material **6** was recovered in 30% yield.

action conditions. After reacting for a week, the expected 5-methoxy-1-phenylindole was obtained in 7% isolated yield. The starting 5-methoxyindole was recovered in 70% yield. Under the same reaction conditions, the parent indole gave *N*-phenylindole (19) in 16% isolated yield, which is noteworthy. Indole was recovered in 76%.

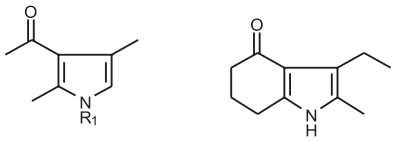
This efficient room temperature N-arylation of 3-acetylindole and 5-nitroindole complements the N-arylation methodologies for existing indoles that rely on the use of aryl halides as coupling partners at high temperature (19–34) and those that rely on the use of aryl bismuths (35) or arylboronic acids (5) as coupling partners at room temperature.

Conclusion

In conclusion, the reactivity of pyrroles **1** and **2**, indoles **5** and **6**, demonstrates that it is possible to achieve synthetically useful N-arylation yields of electron-deficient pyrroles and indoles having no carbonyl group α to the pyrrole ring nitrogen, under the Chan and Lam conditions using DIEA as a base.

© 2007 NRC Canada

Fig. 1. Pyrroles **3**, **3a**, and **4**.



3 R_1 = H
3a R_1 = Ph

4

Experimental

Chemicals were purchased from commercial sources and used as received. The ^{1}H and ^{13}C NMR spectra were recorded on an AC Brucker 250 MHz spectrometer using $CDCl_3$ as solvent. The chemical shifts (δ) are reported in ppm. Melting points were determined on a Stuart Scientific SMP 3 capillary melting point apparatus and are uncorrected.

Typical procedure

In a sealed (glass cap and parafilm) oven-dried 25 mL flask, a mixture of pyrrole or indole (1.0 mmol), $ArB(OH)_2$ (2.5 mmol), anhyd. $Cu(OAc)_2$ (2.5 mmol), DIEA (99%, 2.5 mmol) in dry DCM (2 mL) was stirred at RT for the indicated time. DCM was removed under reduced pressure. Water (10 mL) and $HCCl_3$ (10 mL) were added. The aqueous layer was extracted with $HCCl_3$ (2 × 10 mL). The concentrated organic layer was purified by flash chromatography (FC) on silica gel.

Please see ref. 19 for analytical data on **6a** (FC: DCM–cyclohexane, 3:7).

Pyrrole 1a

FC: DCM–cyclohexane 1:1. Pale yellow oil. ^{1}H NMR δ: 7.66 (t-like, 1H, *J* = 1.84 Hz), 7.55–7.20 (m, 5H), 7.04 (m, 1H), 6.81–6.71 (m, 1H), 2.46 (s, 3H). ^{13}C NMR δ: 193.2, 139.4, 130.0, 129.1, 127.4, 120.7, 6.9.

Pyrrole 2a

FC: DCM 100%. Beige solid, mp 95 to 96 °C. ^{1}H NMR δ: 7.60–7.2 (m, 5H), 6.80 (d, 1H, *J* = 3.05 Hz), 6.69 (d, 1H, *J* = 3.05 Hz), 2.77 (t, 2H, *J* = 6.10 Hz), 2.51 (t, 2H, *J* = 6.40 Hz), 2.20–2.00 (m, 2H). ^{13}C NMR δ: 194.5, 143.3, 138.5, 129.3, 127.6, 124.6, 124.7, 123.0, 106.2, 37.6, 23.8, 22.9.

Pyrrole 1b

FC: DCM 100%. ^{1}H NMR δ: 7.40–7.10 (m, 5H), 6.73 (s-like, 2H), 2.43 (s, 3H), 2.19 (s, 3H). ^{13}C NMR δ: 193.4, 139.1, 131.1, 128.5, 128.4, 126.6, 126.5, 126.2, 123.7, 113.4, 109.2, 27.0, 17.5.

Pyrrole 2b

FC: DCM 100%. ^{1}H NMR δ: 7.40–7.10 (m, 4H), 6.70 (d, 1H, *J* = 3.05 Hz), 6.62 (d, 1H, *J* = 3.05 Hz), 2.70–2.30 (m, 4H), 2.20–2.00 (m, 5H). ^{13}C NMR δ: 194.4, 144.2, 137.3, 135.2, 130.9, 128.9, 127.3, 126.7, 120.7, 105.6, 37.7, 23.7, 21.9, 17.1.

Pyrrole 1c

FC: DCM 100%. ^{1}H NMR δ: 7.63 (m, 1H), 7.45 (d, 2H, *J* = 8.55 Hz), 7.30 (d, 2H, *J* = 9.15 Hz), 7.00 (m, 1H), 6.74 (m, 1H), 2.44 (s, 3H), 1.37 (s, 9H). ^{13}C NMR δ: 193.4, 150.1, 137.1, 127.3, 126.5, 126.0, 124.1, 121.2, 120.6, 114.8, 110.4, 34.4, 31.2, 27.1.

Pyrrole 2c

FC: DCM 100%. ^{1}H NMR δ: 7.49 (d, 2H, *J* = 8.55 Hz), 7.24 (d, 2H, *J* = 8.52 Hz), 6.78 (d, 1H, *J* = 3.05 Hz), 6.67 (d, 1H, *J* = 3.05 Hz), 2.77 (t, 2H, *J* = 6.10 Hz), 2.51 (t, *J* = 6.4 Hz), 2.17–2.00 (m, 2H), 1.36 (s, 9H). ^{13}C NMR δ: 194.5, 150.8, 143.4, 135.9, 126.8, 124.7, 123.8, 123.1, 106.1, 37.5, 34.6, 31.5, 23.9, 22.5.

Pyrrole 1d

FC: DCM 100%. ^{1}H NMR δ: 7.55 (m, 1H), 7.25 (m, 2H), 6.90 (m, 3H), 6.70 (m, 1H), 3.97 (q, 2H, *J* = 4.87 Hz), 2.41 (s, 3H), 1.40 (t, 3H, *J* = 4.85 Hz). ^{13}C NMR δ: 193.3, 157.8, 132.8, 127.0, 122.4, 115.1, 110.1, 63.7, 27.0, 14.6.

Pyrrole 2d

FC: DCM 100%. ^{1}H NMR δ: 7.20 (d-like, 2H, *J* = 7.02 Hz), 6.98 (d-like, 2H, *J* = 6.71 Hz), 6.74 (d, 1H, *J* = 3.05 Hz), 6.65 (d, 1H, *J* = 3.05 Hz), 4.06 (q, 2H, *J* = 6.72 Hz), 2.71 (t, 2H, *J* = 6.10 Hz), 2.50 (t, 2H, *J* = 5.50 Hz), 2.20–2.05 (m, 2H), 1.45 (t, 3H, *J* = 6.72 Hz). ^{13}C NMR δ: 194.6, 158.4, 143.7, 131.4, 126.1, 121.3, 115.0, 105.9, 63.8, 37.7, 23.6, 22.8, 14.8.

Pyrrole 1e

FC: DCM 100%. ^{1}H NMR δ: 7.61 (m, 1H), 7.50–7.25 (m, 4H), 6.99 (m, 1H), 6.75 (m, 1H), 2.44 (s, 3H). ^{13}C NMR δ: 193.4, 138.2, 132.5, 129.8, 127.8, 123.8, 122.1, 121.1, 110.9, 27.1.

Pyrrole 2e

FC: DCM 100%. ^{1}H NMR δ: 7.55–7.40 (m, 2H), 7.32–7.20 (m, 2H), 6.77 (d, 1H, *J* = 3.05 Hz), 6.70 (d, 1H, *J* = 3.65 Hz), 2.75 (t, 2H, *J* = 6.10 Hz), 2.52 (t, 2H, *J* = 6.40 Hz), 2.20–2.05 (m, 2H). ^{13}C NMR δ: 194.4, 143.0, 137.0, 133.5, 129.5, 125.0, 122.8, 121.9, 106.6, 37.6, 23.8, 22.8.

Indole 5a

FC: DCM 100%. Beige solid, mp 145 °C. ^{1}H NMR δ: 8.52–8.45 (m, 1H), 7.93 (s, 1H), 7.65–7.42 (m, 6H), 7.40–7.20 (m, 2H), 2.56 (s, 3H). ^{13}C NMR δ: 193.2, 138.2, 136.8, 134.6, 129.8, 129.7, 127.9, 126.4, 124.8, 124.7, 123.8, 122.9, 122.6, 118.4, 110.7, 27.5.

Indole 5b

FC: DCM 100%. Yellow solid, mp 117 to 118 °C. ^{1}H NMR δ: 8.50–8.40 (m, 1H), 7.81 (s, 1H), 7.55–7.15 (m, 6H), 7.02 (d, 1H, *J* = 7.30 Hz), 2.56 (s, 3H), 2.08 (s, 3H). ^{13}C NMR δ: 193.2, 137.8, 136.7, 135.5, 135.1, 131.3, 129.1, 127.8, 127.0, 125.6, 123.6, 122.7, 122.4, 110.7, 27.5, 17.3.

Indole 6b

FC: cyclohexane–DCM 6:4. ^{1}H NMR δ: 8.65 (d, 1H, *J* = 1.83 Hz), 8.10–8.00 (m, 1H), 7.50–7.20 (m, 5H), 7.04 (d,

© 2007 NRC Canada

1H, J = 9.15 Hz), 6.85 (d, 1H, J = 3.05 Hz), 2.04 (s, 3H). ^{13}C NMR δ: 141.8, 139.5, 136.8, 135.4, 131.8, 131.3, 129.0, 127.7, 127.0, 118.0, 117.6, 110.3, 104.7, 17.3.

Indole 5c

FC: DCM–cyclohexane 2:8 then 1:1. ^{1}H NMR δ: 8.49 (d, 1H, J = 7.25 Hz), 7.93 (s, 1H), 7.65–7.20 (m, 7H), 2.58 (s, 3H), 1.46 (s, 9H). ^{13}C NMR δ: 193.4, 151.3, 137.2, 135.7, 134.9, 126.8, 124.5, 123.8, 123.0, 122.7, 118.4, 115.0, 111.0, 34.8, 27.6, 26.9.

Indole 6c

FC: DCM–cyclohexane 2:8. ^{1}H NMR δ: 8.63 (d, 1H, J = 2.25 Hz), 8.20–8.00 (m, 1H), 7.70–7.30 (m, 6H), 6.83 (d, 1H, J = 3.50 Hz), 1.40 (s, 9H). ^{13}C NMR δ: 131.4, 126.8, 124.2, 118.2, 117.7, 110.6, 105.3, 31.3.

Indole 5d

FC: DCM–cyclohexane 1:1. ^{1}H NMR δ: 8.50–8.40 (m, 1H), 7.89 (s, 1H), 7.60–7.20 (m, 7H), 2.60 (s, 3H). ^{13}C NMR δ: 134.3, 130.1, 126.1, 124.1, 123.2, 122.9, 110.6, 27.7.

Indole 6d

FC: DCM–cyclohexane 2:8. ^{1}H NMR δ: 8.63 (m, 1H), 8.20–8.05 (m, 1H), 7.60–7.35 (m, 6H), 6.87 (d, 1H, J = 3.00 Hz). ^{13}C NMR δ: 131.0, 130.2, 125.9, 118.3, 118.1, 110.3, 106.0.

5-Methoxy-1-phenylindole

FC: DCM–cyclohexane 3:7. ^{1}H NMR δ: 7.58–7.43 (m, 5H), 7.40–7.28 (m, 2H), 7.16 (d, 1H, J = 2.5 Hz), 6.94–6.84 (dd, 1H, J = 10 Hz, J = 2.5 Hz), 6.65–6.55 (m, 1H), 3.90 (s, 3H). ^{13}C NMR δ: 154.6, 140.0, 131.1, 129.8, 129.7, 128.4, 126.3, 124.1, 123.3, 118.9, 112.5, 111.4, 103.3, 102.7, 55.9.

Acknowledgments

HB thanks Professor G. Kirsch for providing space and chemicals. The financial support from Le Ministère de la Recherche-France for this work is acknowledged.

References

1. D.M.T. Chan, K.L. Monaco, R.P. Wan, and M.P. Winters. Tetrahedron Lett. **39**, 2933 (1998).
2. P.Y.S. Lam, C.G. Clark, S. Saubern, J. Adams, M.P. Winters, D.M.T. Chan, and A. Combs. Tetrahedron Lett. **39**, 2941 (1998).
3. A.K. Bakkestuen and L-L. Gundersen. Tetrahedron Lett. **44**, 3359 (2003).
4. Q. Dai, C. Ran, and R.G. Harvey. Tetrahedron, **62**, 1764 (2006).
5. W.W.K.R. Mederski, M. Lefort, M. Germann, and D. Kux. Tetrahedron, **55**, 12757 (1999).
6. S. Yu, J. Saenz, and J.K. Srirangam. J. Org. Chem. **67**, 1699 (2002).
7. P.Y.S. Lam, D. Bonne, G. Vincent, C.G. Clark, and A.P. Combs. Tetrahedron Lett. **44**, 1691 (2003).
8. D.J. Cundy and S.S. Forsyth. Tetrahedron Lett. **39**, 7979 (1998).
9. T.D. Quach and R.A. Batey. Org. Lett. **5**, 4397 (2003).
10. J.J. Strousse, M. Jeselnik, F. Tapaha, C.B. Jonsson, W.B. Parker, and J.B. Arterburn. Tetrahedron Lett. **46**, 5699 (2005).
11. J.P. Collman and M. Zhong. Org. Lett. **2**, 1233 (2000).
12. J.P. Collman, M. Zhong, L. Zeng, and S. Costanzo. J. Org. Chem. **66**, 1528 (2001).
13. J.P. Collman, M. Zhong, C. Zhang, and S. Costanzo. J. Org. Chem. **66**, 7892 (2001).
14. P.Y.S. Lam, G. Vincent, C.G. Clark, S. Deudon, and P.K. Jadhav. Tetrahedron Lett. **42**, 3415 (2001).
15. D.M.T. Chan and P.Y.S. Lam. *In* Boronic acids in organic synthesis and chemical biology. *Edited by* D.G. Hall. Wiley-VCH, Weinheim, Germany. 2005. p. 205.
16. A.S. Demir, O. Reis, and M. Emrullahoglu. J. Org. Chem. **68**, 10130 (2003).
17. A.S. Demir, I.M. Akhmedov, and Ö. Sesenoglu. Tetrahedron, **58**, 9793 (2002).
18. T. Kawabata, T. Minami, and T. Hiyama. J. Org. Chem. **57**, 1864 (1992).
19. J.C. Antilla, A. Klapars, and S.L. Buchwald. J. Am. Chem. Soc. **124**, 11684 (2002).
20. J. Lindley. Tetrahedron, **40**, 1433 (1984).
21. M.A. Khan and J.B. Polya. J. Chem. Soc. C, **85** (1970).
22. C.A. Harbert, J.J. Plattner, W.M. Welch, A. Weissman, and B.K. Koe. J. Med. Chem. **23**, 635 (1980).
23. H. Lexy and T. Kauffmann. Chem. Ber. **113**, 2755 (1980).
24. P.C. Unangst, D.T. Connor, S.R. Stabler, and R.J. Weikert. J. Heterocycl. Chem. **24**, 811 (1987).
25. Y. Kato, M.M. Conn, and J. Rebek, Jr. J. Am. Chem. Soc. **116**, 3279 (1994).
26. Y. Murakami, T. Watanabe, T. Hagiwara, Y. Akiyama, and H. Ishii. Chem. Pharm. Bull. **43**, 1281 (1995).
27. G. Mann, J.F. Hartwig, M.S. Driver, and C. Fernandez-Rivas. J. Chem. Soc. **120**, 827 (1998).
28. J.F. Hartwig, M. Kawatsura, S.I. Hauck, K.H. Shaughnessy, and L.M. Alcazar-Roman. J. Org. Chem. **64**, 5575 (1999).
29. D.W. Old, M.C. Harris, and S.L. Buchwald. Org. Lett. **2**, 1403 (2000).
30. M. Watanabe, M. Nishiyama, T. Yamamoto, and Y. Koie. Tetrahedron Lett. **41**, 481 (2000).
31. G.A. Grasa, M.S. Viciu, J. Huang, and S.P. Nolan. J. Org. Chem. **66**, 7729 (2001).
32. W.J. Smith, III and J.S. Sawyer. Tetrahedron Lett. **37**, 299 (1996).
33. S. Maiorana, C. Baldoli, P. Del Buttero, M. DI Ciolo, and A. Papagni. Synthesis, **735** (1998).
34. W.J. Smith, III and J.S. Sawyer. Heterocycles, **51**, 157 (1999).
35. D.H.R. Bartona, J.-P. Fineta, and J. Khamsia. Tetrahedron Lett. **29**, 1115 (1988).

© 2007 NRC Canada

Structures and energetics of CO_2–Ar_n clusters (n = 1–21) based on a non-rigid potential model

M. Böyükata, E. Borges, J.C. Belchior, and J.P. Braga

Abstract: Energetics and possible stable structures of CO_2–Ar_n (n = 1–21) clusters are investigated by performing molecular-dynamics simulations. The pairwise-additive approximation is tested to construct the potential energy function for describing the non-rigid particle interactions in the system. A potential model by Pariseau et al. (*Journal of Chemical Physics*, Vol. 42, p. 2335, 1965) is used for the internal motion of the CO_2 molecule and the Billing form potential (*Chemical Physics*, Vol. 185, p. 199, 1994) is used for all other pair interactions. The stable configurations are determined for the ground state of CO_2–Ar_n clusters, and the growing pattern process of the clusters is determined via rearrangement collisions. Ar atoms tend to surround the CO_2 molecule, and the clusters prefer to form three-dimensional compact structures. Obtained structures and energetics are in quantitative agreement with previous results (*Journal of Chemical Physics*, Vol. 109, p. 1343, 1998) that have used split–repulsion and ab initio potentials in which the molecule was treated as rigid.

Key words: argon, CO_2, cluster, potential energy function, molecular dynamics.

Résumé : Faisant appel à des simulations de dynamique moléculaire, on a étudié les énergies et les structures stables possibles d'agrégats de CO_2–Ar_n (n = 1–21). On a évalué une approximation additive par paire pour construire la fonction d'énergie potentielle qui permettrait de décrire les interactions de particules non-rigides dans le système. On a utilisé un modèle de potentiel proposé par Pariseau et al. (*Journal of Chemical Physics*, numéro 42, p. 2335, 1965) pour le mouvement interne des molécules de CO_2 et la forme de potentiel de Billing (*Chemical Physics*, numéro 185, p. 199, 1994) pour toutes les autres paires d'interactions. On a déterminé les configurations stables pour l'état fondamental des agrégats de CO_2–Ar_n et le processus du patron de croissance des agrégats a été déterminé par le biais de collisions de réarrangement. Les atomes d'argon tendent à entourer les molécules de CO_2 et les agrégats forment de préférence des structures compactes tridimensionnelles. Les structures qui ont été calculées et leurs niveaux d'énergie sont en accord quantitatif avec les résultats rapportés antérieurement (*Journal of Chemical Physics,* numéro 109, p. 1343, 1998) sur la base d'une répulsion divisée et de potentiels ab initio dans lesquels la molécule était traitée comme rigide.

Mots-clés : argon, CO_2, agrégat, fonction d'énergie potentielle, dynamique moléculaire.

[Traduit par la Rédaction]

Introduction

There has been considerable interest in the study of atomic and molecular clusters because of their potential application in the development of new type of materials (nanoparticles) (1–3). However, one of the main problems in the field of cluster science is describing the geometries of intermediate systems. In general, it is difficult to find any global minimum structure for molecular clusters. Even for simpler pair potentials, the number of local minima on the potential energy hyper-surface grows exponentially with increasing cluster size.

Received 12 September 2006. Accepted 3 November 2006. Published on the NRC Research Press Web site at http://canjchem.nrc.ca on 9 February 2007.

M. Böyükata,[1] E. Borges, J.C. Belchior,[2] and J.P. Braga. Departamento de Química – ICEx, Universidade Federal de Minas Gerais, Pampulha, (31.270–901) Belo Horizonte, MG, Brazil.

[1]Present address: Department of Physics, Bozok University, 66100, Yozgat, Turkey.
[2]Corresponding author (e-mail: jadson@ufmg.br).

Efficient methods have been used to study complex systems. For example, genetic algorithms (GA) have been applied to calculate the lowest energy for a specified potential energy function (PEF) (4, 5). Accurate results compared with ab initio data have shown that the approach can be used with some confidence (5, 6). Other methods such as basin hopping (BH) (7–9) have been widely used for determining global minima, such as using three empirical potentials for describing Si_n clusters (10). Goedecker has also suggested minima hopping (MH) as an alternative search method for complex molecular systems (11). Similarly, simulated annealing (SA) has also been employed to investigate closed-shell systems (12). Additionally, other strategies can be proposed as complementary tools for determining global minima of hypersurfaces as efficiently as possible.

Particularly for pure atomic and alloy systems, there are useful cluster studies, involving rare-gas atoms bound to a chromophore (e.g., HF and HCl) (13–16) for investigating solvation phenomena at the microscopic level (17, 18). The interactions of CO (17) and CO_2 (18) with rare-gas atoms have also received considerable attention because of their atmospheric importance (18). For example, extensive experimental studies of the CO_2–Ar system (19–25) and IR spectra

 doi:10.1139/V06-178 © 2007 NRC Canada

for the CO_2–Ar_2 trimer (26), as primitive model calculations for larger clusters, have been undertaken, along with theoretical investigations (27–33). Accordingly, several intermolecular potentials have been proposed for describing the interaction between CO_2 and Ar atoms (29–32). Similarly, empirical models, based on pairwise-additive approximation, have been used to construct the PEF for studying CO_2–Ar_n. To study CO_2–Ar_n clusters, Severson (18) used three different PEFs, proposed by Hutson et al. (34), Marshall et al. (35), and Bohac et al. (36), modified form of Hough and Howard (37, 38) for describing the molecule–argon (CO_2–Ar) interaction, together with interatomic Aziz potential for Ar–Ar (39). Using these pairwise-additive PEFs, the minimum-energy structures have been found, and rigid-body diffusion Monte Carlo simulations have been carried out for the ground vibrational states of these clusters. The PEFs for studying the CO_2–Ar interaction were fitted against accurate spectroscopic data (34) or calculated using a high level of ab initio methods (29, 35). However, they assumed the rigid body approximation for treating the internal motion of the system.

Similar to ref. 18, other investigations have been performed to find the minimum-energy structures for CO_2–Ar_n clusters with pairwise-additive potentials and also for a rigid molecular case. For example, Sperhac et al. (26) used a pairwise-additive potential proposed by Hough and Howard (37, 38) to describe CO_2 and Aziz potential for clusters up to 17 atoms. These kinds of studies showed that clusters provide a critical testing ground for theories, and a challenge exists to formulate theoretical models of particle bonding for even large-size ranges, which is a demanding task for computational analysis. However, this work may not be enough for modeling and exploring the potential energy surface for CO_2–Ar_n clusters because of the variety of resulting geometries and energetically different results, especially concerning CO_2 as a rigid molecule.

In the present work, the stable structures and energetics of CO_2–Ar_n complexes (n = 1–21) are analyzed by using molecular dynamics (MD) simulation. In addition, a suitable PEF is constructed by allowing the internal motion of CO_2.

The stable configurations of molecular-bonded clusters are determined for the non-rigid ground state of CO_2 in linear structure. This work intends to analyze the applicability of this newly constructed PEF to the cluster formation. The growing pattern of the clusters is investigated via rearrangement collision approaches similar to the studies of ref. 40 that have been efficiently used for structure analysis of metallic (40–42) and rare-gas (43) clusters. The latter works showed that the calculation procedure is efficient to study rare-gas clusters, and hence, the method is also used in the present study of CO_2Ar_n clusters.

Finally, the results of cluster structures and energetics will be compared with previous studies.

Potential-energy function and computational background

Potential energy function

The classical Hamilton's equations were solved to generate the motions of the particles. The Hamiltonian is as follows:

$$[1] \qquad H = \sum_{i=1}^{n} \frac{P_i^2}{2m_i} + V$$

where the first term corresponds to the kinetic energy of the system, P and m are the moment and the mass of the particles, respectively, and V is the potential of the whole system, describing the interaction. The interaction for the described molecule–argon complexes is usually assumed to be pairwise additive for the studies on argon clusters containing a monoatomic, diatomic, or tetraatomic impurities (17, 18). As previously mentioned, there are several potentials for describing the interaction for this particular system (27, 29, 34, 35). However, all of them assumed CO_2 as rigid. In the present study, the PEF for the CO_2–Ar_n clusters is proposed to be the sum of three terms for three different pair interactions. Each term describes a different interaction in the system to keep all particles within non-rigid conditions. The total potential energy of the system is written as

$$[2] \qquad V = V_{CO_2} + \sum_{l=1}^{n} V_{C-Ar_l} + \sum_{k=1}^{2}\sum_{l=1}^{n} V_{O_k-Ar_l} + \sum_{i\neq j}^{n} V_{Ar_i-Ar_j}$$

where i, j, and l specify the argon atoms up to n. The first term, describing the internal potential of CO_2, was based on spectroscopic and molecular beam scattering data (44). In this work, a Taylor series expansion of fourth-order was used for the internal coordinates. Therefore, the CO_2 potential can be written as

$$\begin{aligned}[3] \qquad V_{CO_2} = {} & f_{11}(r_1^2 + r_2^2) + f_{12}r_1r_2 + f_{\alpha\alpha}\theta^2 + f_{111}(r_1^3 + r_2^3) \\ & + f_{112}(r_1^2r_2 + r_1r_2^2) + f_{1\alpha\alpha}(r_1 + r_2)\theta^2 \\ & + f_{1111}(r_1^4 + r_2^4) + f_{1112}(r_1^3r_2 + r_1r_2^3) \\ & + f_{1122}\, r_1^2r_2^2 + f_{11\alpha\alpha}(r_1^2 + r_2^2)\theta^2 \\ & + f_{1\alpha\alpha}(r_1 + r_2)\theta^2 + f_{\alpha\alpha\alpha\alpha}\theta^4\end{aligned}$$

where r_1, r_2, and θ describe the molecular internal coordinates, and the coefficients (f) are the force constants (values in atomic units; f_{11} = 0.5148, f_{12} = 0.0814, $f_{\alpha\alpha}$ = 0.0901, f_{111} = –0.6498, f_{112} = –0.0515, $f_{1\alpha\alpha}$ = –0.0747, f_{1111} = –0.4652, f_{1112} = –0.0429, f_{1122} = –0.1066, $f_{1\alpha\alpha2}$ = 0.5139, $f_{11\alpha\alpha}$ = 0.2281, and $f_{\alpha\alpha\alpha\alpha}$ = –0.014) (44). The second, third, and fourth terms in eq. [2] are Buckingham form (BF) for C–Ar, O–Ar, and Ar–Ar pair interactions, respectively (17). This two-body BF is written according to

$$[4] \qquad V_{pair} = \frac{6\varepsilon e^{\lambda(1-r/r_e)}}{\lambda - 6} - \frac{\lambda\varepsilon}{\lambda - 6}\left(\frac{r_e}{r}\right)^6$$

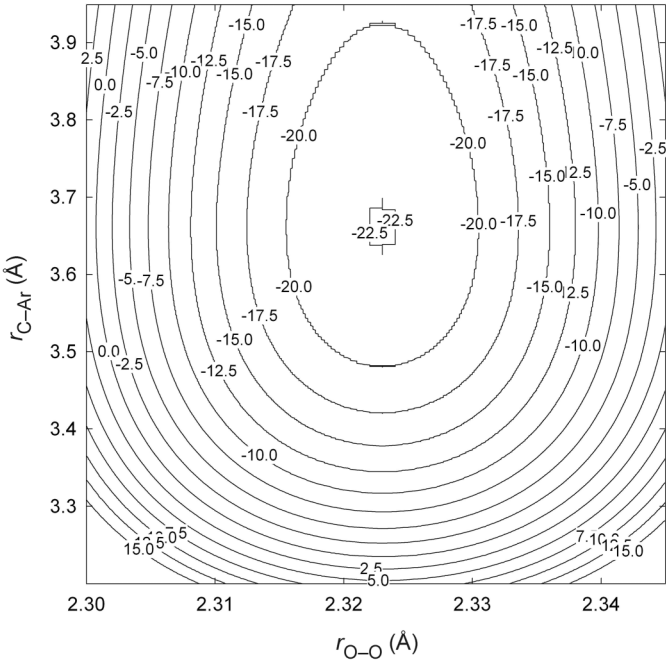
The pairwise-potential parameters are ϵ = 9.29 meV, r_e = 3.813 Å for C–Ar, ϵ = 7.8 meV, r_e = 3.6 Å for O–Ar, and ε = 12.34 meV, r_e = 3.757 Å for Ar–Ar. ε and r_e are the potential well-depth ($V(r_e) = -\varepsilon$) and equilibrium distance, respectively (17). The intramolecular potential parameters are ε = 10.5 eV and r_e = 1.162 Å for C–O (44). This type of additive potential (BF) was employed by Sevryuk and Billing, who have successfully studied argon–carbonmonoxide complexes for $Ar_n(CO)Ar_n$ clusters (see ref. 17).

Particularly for the Ar–Ar interaction, Aziz and Lennard–Jones (LJ) potential models have been widely used in the lit-

© 2007 NRC Canada

erature and are quantitative for describing Ar clusters (39, 45, 46). In our analysis, these potentials were also used to make a comparison with BF potential results. The LJ potential has advantages, such as permitting the investigation of relatively long-time phenomena, and it reliably describes static and dynamic properties. Our result for the CO_2–Ar structure is a T-shaped configuration, and this result is in good agreement with the global minimum calculated in refs. 18 and 33. However, the results with Aziz potential for larger structures are not as good as expected even though they accurately describe pure argon and Hg–Ar interactions (47). The three Ar–Ar potential energy functions are compared in the discussion part of the latter work. The BF potential is more efficient for describing non-rigid CO_2–Ar_n clusters. In Fig. 1, the contour graph of the PEF is given for the CO_2–Ar system. The potential-energy well corresponds to the T-shaped geometry. It shows that the closest distance between argon and carbon atoms is 3.68 Å in the stable geometry. The minimum-energy value of the CO_2–Ar interaction is –0.0225 eV, which is the "well-depth" of the contour at the distance of 2.323 Å between oxygen atoms in the molecule.

Fig. 1. Contour graph of the PEF used for CO_2–Ar system (energy value is 10^{-3} eV and SR, ab initio, and 3A values are taken from ref. 18).



Computational methodology

Although well-established methods, such as GA, BH, MH, and SA, are efficient ways to determine, in principle, global minima, the rearrangement collision approach based on MD can also be used as an alternative strategy to deal with complex global minimum calculations (41). The method is based on the Ergodic theorem, in which the main hypothesis lies at the foundation of classical statistical mechanics (48). It implies that the trajectory uniformly covers the energetically allowed regions of all classical phase space for a specified total energy (48). This approach has been recently tested for studying LJ-type potential for determining energetics and structures of iron clusters (Fe_n, n is up to 36). The results were compared with quantum mechanical calculations, and their growing pattern was analyzed (41). In the particular case of the CO_2–Ar_n system, the calculations were performed taking into account that to cover the phase space, the total energy had to be high enough to evaluate all the possible minima in the hypersurface. To avoid premature convergence to a local minimum, the whole phase space was searched with enough energy to go to a lower minimum in a similar way to that of the SA method (12).

In the present analysis, the potential energy of the system at $T = 0$ is equal to the target CO_2–Ar_{n-1} atom cluster energy. This energy changes along the motion of the projectile atom towards the target. Therefore, the potential energy value varies and a new value can be determined, depending on the final configuration of the new structure. In this building-up procedure, the colliding atom was sent from a relatively large distance to the target cluster. Formation of the new cluster is related to the translation (collision–kinetic) energy of the new projectile atom. If it is not low enough to keep all particles of the system in the potential well (i.e., the total energy is negative), new cluster formation is not possible. Time-dependent positions and momenta of the particles were described in Cartesian coordinates. The Runge–Kutta of the fifth- and sixth-order algorithm was used as the numerical integration of the classical coupled equations of motion. In the present study, all trajectories were checked to produce energy conservations of the order of 10^{-10} during the integration. The initial kinetic energies (from the collision energy of the projectile atom) are distributed amongst the kinetic energies of all particles in the system after the interaction starts. Moreover, the collision–interaction occurs around the fixed center of mass of the system. The maximum time of each simulation is 3.0×10^6 steps (one time step is 4.0×10^{-17} s). This process is repeated for five different random orientations of the initial configuration.

First, the CO_2 molecule is prepared as a target in an equilibrium linear structure, which is assumed to be the initial condition for the simulations. Through this collision in fusion regime, the CO_2–Ar cluster is constructed. In any collision process, there are three main regimes (fusion, scattering, and fragmentation), depending on the collision energy and impact parameter b (40). To avoid fragmentation, all collisions are realized with low collision energies, low enough to keep all particles together. Additionally, collision sites on the target cluster surface are also effective for these regimes. When the colliding atom, for example, hits the target cluster on any open site, a new structure can be easily constructed. In this study, the orientation space of the target clusters is represented by Euler angles (49) to reduce the effects of the specific target sites of cluster positions.

Upon relaxation, the cluster can be rearranged, and the most stable structure is determined through following each trajectory set and by checking the potential energy of the system at 200 steps up to the end of 3 million steps. The next generated configuration that has the energy nearest the minima in each trajectory set is kept, and after 5×10^4 relaxation steps, it is minimized by removing kinetic energy to find the corresponding structure. This means that, in total, 7.5 million points are searched in the phase space to find the

© 2007 NRC Canada

most stable geometry of each cluster. At the end of the kinetic energy minimization procedure, the Hamiltonian only depends on the potential energy (internal energy) of the system, i.e., the total energy E is equal to the potential energy value of eq. [2] because the kinetic energy is zero. After determining the new cluster, it is used as a seed for a new collision, and these processes are repeated to find a new larger cluster. As previously mentioned, this type of approach has been applied to other clusters (40–43). In this work, we will also discuss an efficient methodology to determine the possible growing mechanism of CO_2–Ar_n (up to $n = 21$) through the structural analysis of this particular system.

Results and discussion

The structural properties and the size-dependent characteristics of carbondioxide–argon complexes are investigated. The minimum-energy structures of CO_2–Ar_n were found by a rearrangement collision (e.g., Ar + CO_2–Ar_{n-1} → CO_2–Ar_n) to realize a building-up process. For all analyses, the colliding Ar atom comes from an asymptotic region. The new CO_2–Ar_n structure was searched in the phase space trajectory during the relaxation time to select its closest-packed coordinates. This selection was repeated five times for five different trajectory spaces of various random-collision sites. It was enough to cover the whole phase space because more searches did not provide any new lower-energy structures. After finding these coordinates, the system was taken into energy-minimization processes. By removing kinetic energy at 100 time steps, the minimum-energy structures were found.

The determined geometries of minimum-energy structures of CO_2–Ar_n ($n \leq 21$) are presented in Figs. 2 and 3. The use of Buckingham form PEF (17) (for C–Ar, O–Ar, and Ar–Ar pair interactions) with the internal potential, suggested by Pariseau et al. (44) for a non-rigid CO_2, in eq. [2] provides all possible minimum-energy structures for the intra- and intermolecular motion of the Ar and CO_2 molecule. Broadly speaking, our results of the structural-growing pattern agree well with the split-repulsion (SR) and ab initio results, particularly with the ab initio (for $n = 6$ and 14) data (18).

Although the probability-distribution functions calculated in ref. 18 are based on quantum mechanics, these calculations can be taken as reference data and should provide insights into classical analysis. As shown in Fig. 2, CO_2–Ar is in a T-shaped structure, which corresponds to an energy of 0.023 eV. The equilibrium distance between Ar and C is 3.66 Å, and this is in fair agreement with the probability-distribution functions for CO_2–Ar in ref. 18, which are almost 3.50, 3.51, and 3.56 Å for 3A, SR, and ab initio PEFs, respectively. Clearly, our result is closer to the ab initio calculation even using a totally different potential model, and hence, it seems that this much simpler potential model is suitable to classically describe CO_2–Ar clusters with particular attention, considering the molecule as non-rigid. Further analysis involving adding another Ar atom to the cluster produces the same trends compared with the structure calculated with those potentials from ref. 18. For CO_2–Ar_2, the distances between the argons and the molecule are also the same. The triangular arrangement of the three argon atoms, with two of them under the equatorial positions, was found, which is in fair agreement with SR and ab initio data; how-

Fig. 2. Optimized minimum-energy geometries of CO_2–Ar_n for n = 1–12.

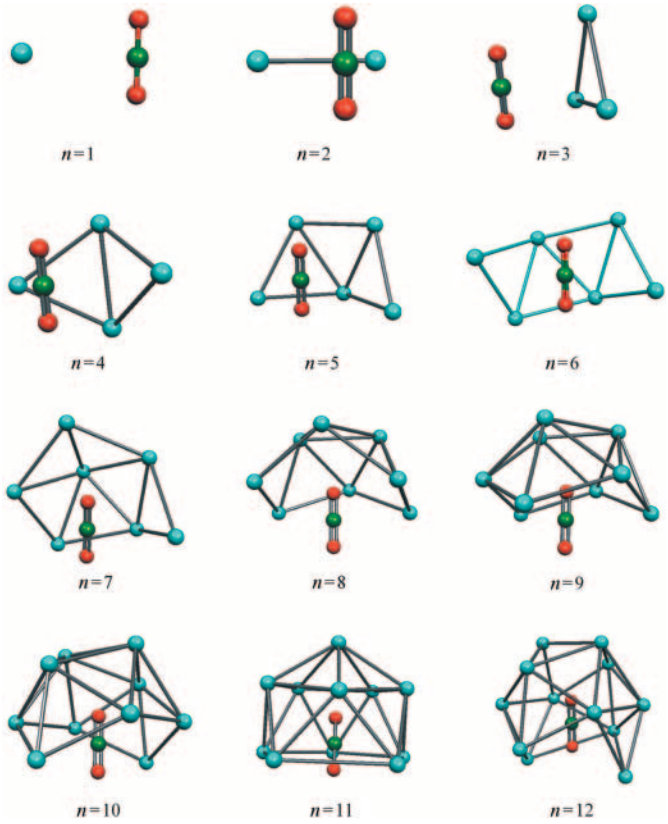
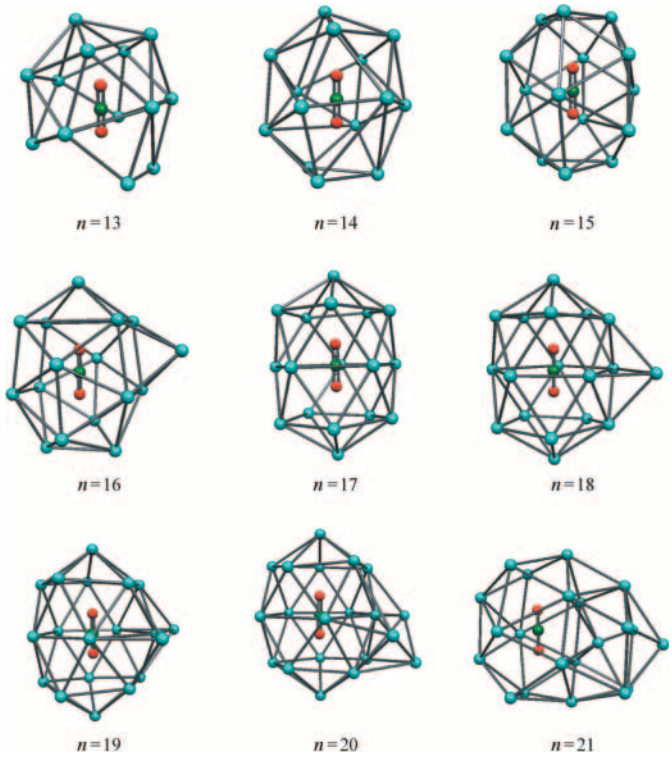


Fig. 3. Optimized minimum-energy geometries of CO_2–Ar_n for n = 13–21.



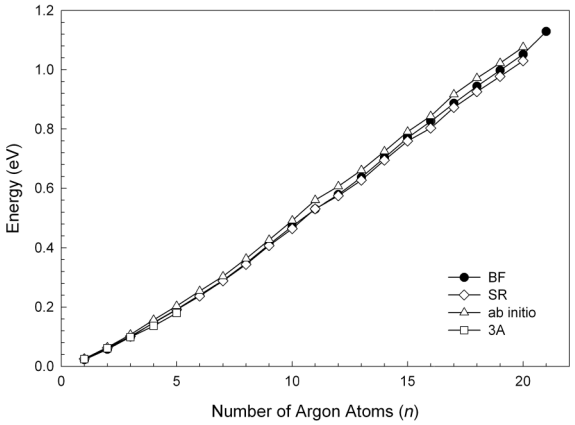
© 2007 NRC Canada

ever, it is slightly closer to the ab initio result. We calculated displacements of argon atoms from the molecule (3.7 and 3.9 Å), and it is again closer to the ab initio result. In the probability-distribution functions for CO_2–Ar_3, Severson (18) found two peaks at 3.6 and 4.25 Å for the ab initio PEFs, 3.5 and 4.35 Å for the SR potential, and only one peak at 3.5 Å using the 3A potential model. Our results also produce two values that can be correlated to the peaks observed in ref. 18. The first one can be considered quantitative, while the second result is assumed qualitative. In the latter case, one observes an equatorial position of Ar atoms surrounding carbon atoms within the same distance. Particularly for n = 4, a distorted tetrahedral geometry is found, with the molecule inserted along one edge of the tetrahedron and the Ar atoms at the vertices of that edge pushed apart and starting to make a lattice for the CO_2. In the minimum-energy structure of CO_2–Ar_5, the three Ar atoms are in near equatorial positions. We observed up to n = 6 minimum geometries in which the structures are within the growing pattern of constructing equatorial regions of the molecule (see Fig. 2). In ref. 18, SR structures for up to n = 5 and ab initio structures for up to n = 6 are very similar to our calculations. However, with the SR potential, Ar atoms start to cover polar sites of the molecule in a different manner for the stable CO_2–Ar_6 structure.

Seven argon atoms interacting with the CO_2 molecule have produced a five-atom ring and started to form a covered shape around one of the oxygens (Fig. 2). Thus, this is the first size where the argon atoms rearrange to start to cover the molecule, and this may provide an efficient growing mechanism. In this geometry, the molecule is slightly oriented towards the argon atoms. The growing mechanism continues to cover the molecule by increasing the number of argons to n = 8. The Ar_9 structure (Fig. 2) consists of a six-membered chair-configuration ring of Ar atoms topped by three more Ar atoms arranged in a triangular shape, and this result is closer to the SR structure rather than the ab initio result. When the number of argons becomes 10, almost half of the molecule and one of the oxygen atoms are totally closed. CO_2–Ar_{11} has two five-atom rings, one of them is around the bond length of C–O, and the other one is over the other covered oxygen with one argon on the top. For n = 10 and 11, the obtained structures are closer to the SR and ab initio results from ref. 18. In the case of Ar_{12}, one can observe that all of the argon atoms almost cover the molecule and there is an open site one of the oxygens. Our result with the same number of surrounding Ar atoms is in line with the corresponding structure in ref. 18, but in a different orientation.

For n = 13, the clusters continue to get closed-shell structures as illustrated in Fig. 3. The first completed solvation shell is found in the minimum-energy structure of CO_2–Ar_{14}. With SR and ab initio PEFs, the first closed-shell geometry was also obtained at the same size, but the structures are totally different (18); however, our result is much closer to the ab initio structure. To keep the lattice of the shell covering, the molecule–argon clusters rechange the forms of argon rings in the n = 14–17 region. For 15 Ar atoms, there is a larger complete solvation shell. This geometry is in good agreement with ref. 18 with particular attention paid to package formation, i.e., both produce the same qualitative cage

Fig. 4. Total energy values for CO_2–Ar_n (n = 1–20). SR, ab initio, and 3A values were taken from ref. 18.



structure surrounding the CO_2 molecule. For 16 Ar atoms surrounding the CO_2 molecule, the minimum-energy structure represents an argon addition outside a different inner solvation shell of 15 Ar atoms in the previous structure. In our observations, the stable structure prefers to grow by adding an atom to the open sites in the equatorial parts of CO_2–Ar_{15}, while the structure in ref. 18 grows in the polar side position.

For the minimum-energy structure of CO_2–Ar_{17} cluster, our result is in fair agreement with three intermolecular potentials in refs. 18 and 26. Therefore, one can state that such a geometry may be expected because the atoms form a closed symmetric shell structure, as also observed for other cases (n = 13 and n = 19). Hence, it seems that for a linear three-atomic molecule surrounded by rare gas atoms such as Ar, one can produce this type of geometry, i.e., it may be a "key" size or structure for comparison. Accordingly, considering that CO_2–Ar_{17} can be taken as a reference structure, one can use it to analyze other atomic-potential models to describe the Ar atom interactions surrounding the CO_2. For example, we consider the analysis taking the most common pair-potential model for Ar atoms, e.g., Aziz and LJ potentials. Obviously, in our particular studies, the BF potential produces better results to describe pair-additive approximation. For n = 18, the minimum-energy structure is in the shape of the argon-added shell structure of CO_2–Ar_{17} as shown in Fig. 3. For both CO_2–Ar_{17}, and CO_2–Ar_{18} clusters, one can verify an agreement with previously calculated geometries (18). CO_2–Ar_{19} and CO_2–Ar_{20} consist of an inner shell of 17 argon atoms. Similarly, in ref. 18, it was reported that for n = 18–20, the minimum-energy structures calculated from both the SR (34) and ab initio (35) PEFs consist of an inner shell of 17 argon atoms, with the remaining argon atoms outside of this shell. However, CO_2–Ar_{21} has an inner shell of 15 argon atoms. Severson also concluded that for CO_2–Ar_n clusters with $n \geq 18$, each of these was found to have an inner shell of either 15 or 17 argon atoms (18). In our analysis, further calculations were performed (n = 21), and similar trends have been observed.

Energy values are compared in Table 1. Clearly, our results are closer to those calculated by using the ab initio potential (18). The energies calculated using two potential models (LJ and Aziz) to describe argon interaction are also shown. In this particular analysis, eq. [2] is modified to con-

© 2007 NRC Canada

Table 1. Energies (eV) of CO_2–Ar_n (n = 1–5) structures.

	This work			Ref. 18		
n	BF	LJ	Aziz	SR	Ab initio	3A[a]
1	–0.023	–0.023	–0.023	–0.025	–0.026	–0.024
2	–0.056	–0.055	–0.057	–0.063	–0.064	–0.061
3	–0.099	–0.093	–0.093	–0.101	–0.108	–0.098
4	–0.148	–0.137	–0.143	–0.146	–0.157	–0.136
5	–0.192	–0.178	–0.164	–0.191	–0.204	–0.179

[a]See ref. 26.

sider these two potentials. As can be observed from Table 1, for adding up to 2 argon atoms, there are energy modifications in our calculations, and our results are underestimated in comparison with all energies from ref. 18. When compared with the ab initio results, our analysis shows that the pairwise-interaction potential modeled by Sevryuk and Billing (17) produces an almost-quantitative agreement. With respect to the 3A potential energies, Aziz for n = 2 and LJ for n = 4 and 5 are considered better than the BF potential results for describing Ar–Ar pair interaction. However, it seems that they are not valid, in general, for describing Ar_n interactions in these particular systems for $n \geq 3$. For example, the error analysis, with respect to the recent study with ab initio PEF (18), shows that the BF potential gives closer energy values than the LJ and Aziz potentials for all sizes. Moreover, our BF results for n = 3–5 are in better agreement with the ab initio data than the 3A potential. When the energy values are compared with SR results, the BF potential is the best PEF for n = 3, 4, and 5. On the other hand, the energy results are different with respect to the rigid body potential results for larger structures. Above n = 4, neither energetic nor structural similarities were observed using the Aziz potential even though the structural properties with the BF and LJ potentials are well converged. To calculate their energies with the Aziz and LJ potentials, we used the generated structures with the BF function. The energy values generated with both of them are far from the others. It means that although these potentials describe Ar_n clusters well, the obtained structures are not in equilibrium geometries, and the Aziz potential creates an absolutely different growing pattern in which argon atoms prefer to come together rather than surround the molecule. Moreover, the results show that the Aziz and LJ potential models generate different geometries compared with previous results, e.g., the ab initio calculations.

Table 2 shows the energy differences between CO_2–Ar_{17} and CO_2–Ar_1, $\Delta E = E(17) - E(1)$, for the potentials used in this work, and their corresponding relative errors are compared with respect to the ab initio and SR energy values. The BF potential result is similar to those obtained by other potentials (18). Moreover, it is the closest one to the ab initio PEF with 3.0% (better than LJ and SR), and when it is compared with SR, the relative error is 2.0%, as shown in the Table 2. Although the LJ potential can generate similar structures, energetically it does not produce reasonable values with respect to the rigid body potentials. Our results show that the BF function is useful for describing pair interactions in all sizes for both structural and energetic analyses. As shown in Fig. 4, the total energy of the stable structures

Table 2. Energy differences ($\Delta E = E(17) - E(1)$) and percentage errors with respect to the ab initio and SR potential values.

	This work		Ref. 18	
	BF	LJ	SR	Ab initio
ΔE (eV)	0.864	0.769	0.847	0.891
Error (1) (%)[a]	3.0	13.6	4.9	—
Error (2) (%)[b]	2.0	9.2	—	5.2

[a]With respect to the ab initio potential.
[b]With respect to the SR potential.

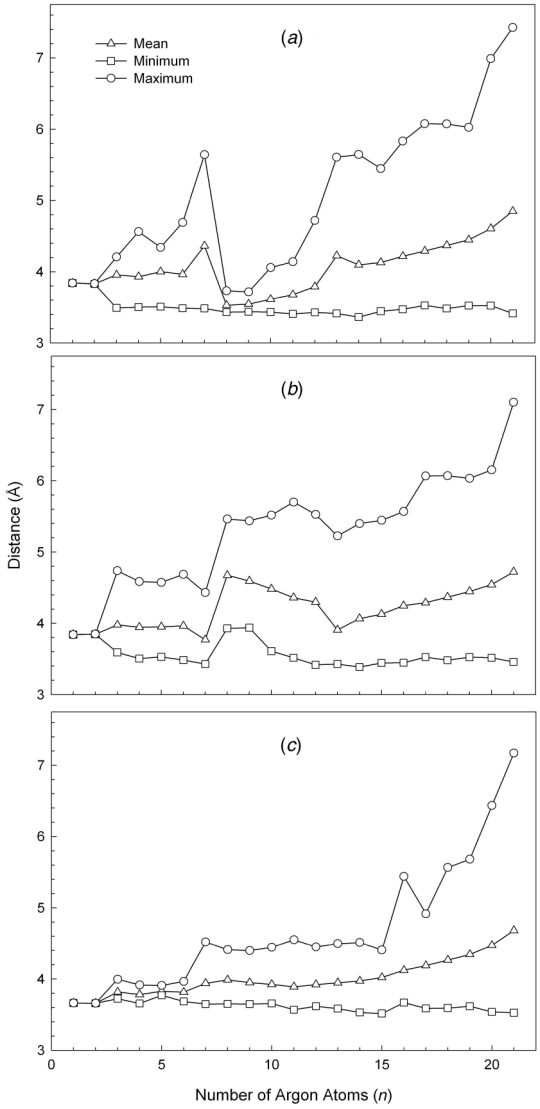
calculated with the BF potential is in better agreement with the ab initio and SR energies. Therefore, it seems that for the particular case of a CO_2 molecule surrounded by argon atoms, the BF potential function describes the cluster system well, at least up to n = 21. The interatomic distances are given in Fig. 5. We will also discuss their structural properties.

The ab intio results are assumed to be correct for the purpose of comparison with our classical calculations. Clearly, it seems that, considering the vibrational modes for the molecule, this produces more significant results for small clusters. This should be expected because the relaxation energy is more pronounced when only a few Ar atoms surround the molecule and can affect the cluster system when another Ar atom is added. For higher n's, one observes that the internal-energy relaxation does not affect the cluster structure formed. Therefore, for a higher order, one expects better agreement between our results and those shown in ref. 18, and this can be seen in Figs. 4 and 6. Accordingly, this particular analysis shows that for small clusters, the vibrational and rotational motions should be taken into account for more precise results. Thus, this type of study can be important to the growing mechanism of molecular clusters. Although the structures are similar, one can see that there is a large difference when the internal motion of the molecule is taken into account, and this can certainly affect the growing process. For example, for CO_2–Ar_2 to CO_2–Ar_5, our cluster energies with BF are almost 9% higher than those calculated considering the CO_2 as rigid with the ab initio PEF. For these particular sizes, the mean percentage error values for BF with respect to SR and 3A potentials are less than 6%. However, as the number of atoms surrounding the molecule increases, one observes no effect at all, and this should be expected because the relaxation can be more efficient with the availability of more degrees of freedom.

As in the atomic cluster case, one can determine the second-difference energy, and this can produce possible magic numbers for molecular clusters such as the system un-

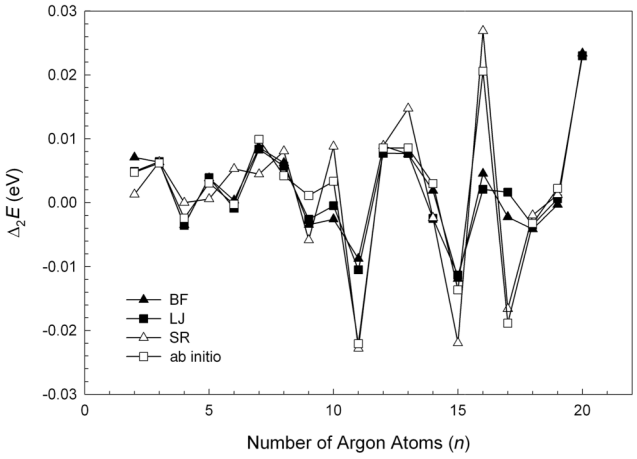
© 2007 NRC Canada

Fig. 5. Pair distances of argon atoms from CO_2 for (*a*) Ar–O1, (*b*) Ar–O2, and (*c*) Ar–C.



der analysis. Second-finite differences of the total energy are presented in Fig. 6 in which the values are calculated as $\Delta_2E = E_{n+1} + E_{n-1} - 2E_n$. This analysis gives information about the energetically relative stability of the geometries. The main trends of our results agree with the ab initio results. However, SR and BF potentials have different behaviors for the particular case of $3 \leq n \leq 9$. Through the peaks in the graph, several exceptionally stable structures are identified. In this work and for these small complexes, the structures CO_2–Ar_5, CO_2–Ar_7, CO_2–Ar_{12}, and CO_2–Ar_{16} are identified as being energetically more stable. The corresponding stable geometries for ab initio PEF are n = 3, 5, 7, 10, 11, and 16 and for the SR potential are n = 3, 6, 8, 10, 12, and 16. We can also see that CO_2–Ar_4, CO_2–Ar_6, CO_2–Ar_9, CO_2–Ar_{11}, and CO_2–Ar_{15} are the energetically less stable structures for the BF potential. On the other hand, n = 4, 6, 9, 11, 15, and 17 for the ab initio and n = 4, 7, 9, 11, 15, and 17 for the SR potential are relatively less stable clusters. Clearly, our results follow the same trends as previous studies (18).

Fig. 6. Second finite difference of the total energy for the obtained minimum-energy clusters (SR and ab initio values are taken from ref. 18).



Particularly for n = 14, the results of ref. 18 showed two structures, and we have also found two structures. One of these structures has a global minimum that is lower than the one found in ref. 18. From n = 14, the higher cluster order in our calculations differs from those in ref. 18 because of the differences in the growing process. Actually, the difference between higher structures arises because CO_2 is considered as non-rigid, and from small structures to large ones this will affect the growing process. For example, by comparing our n = 11 and n = 12 with those in ref. 18, one can observe that the cage formation is slightly twisted and this affects the next atom added to the cage. To analyze this point, the distances between the CO_2 molecule and the Ar atoms was calculated. Figure 5 illustrates the displacements of argon atoms from molecular atoms as a function of the number of surrounding atoms (n) in the optimized structures of the clusters up to CO_2–Ar_{21}. This type of analysis can help to determine the growing pattern. In this case, the system is described by BF potential. Maximum, minimum, and mean distances from first oxygen (Ar–O1), second oxygen (Ar–O2), and carbon (Ar–C) are monitored to demonstrate the close packing of the clusters during the growing process. In the case of CO_2–Ar, the distance between the argon atom and each of the oxygens is 3.84 Å, and this produces a T-shaped configuration. For the CO_2–Ar_2 structure, it is also approximately the same value. The growing process, in principle, can be separated into three regimes, namely, small (n up to 6), medium (n up to 15), and large (n up to 21). For the first regime, argon atoms fill the favorable equatorial sites of the molecule, and hence, for n = 1–6, one observes that the effects of the oxygens on the growing pattern are almost the same. For example, argon atoms prefer to locate in equal distances. However, in the medium-size case, argon atoms start to grow around one of the oxygen atoms (here, it is the O2 atom), and the displacement lines for O1 and O2 are absolutely different. Particularly for n = 7, the maximum distance of the argon atom from O2 is 4.43 Å, and it is shorter than the case for n = 6 (4.69 Å). However, the distance from the other oxygen atom (O1) is 5.64 Å in CO_2–Ar_7. Minimum distances for Ar–O1 vary between 3.84 Å (n = 1), and the lowest value of 3.36 Å (n = 11). For n = 7

© 2007 NRC Canada

and 9, the minimum Ar–O2 distances are 3.43 and 3.94 Å, respectively. In the second regime, argon atoms construct a closed-shell lattice covering one of the oxygen atoms, O2. For n = 7–9, the minimum distances from O2 increase, i.e., the lattice becomes larger around this oxygen. It continues to cover the molecule by adding atoms in the shell towards the oxygen O1.

Increasing the number of atoms leads to a closed-packing system. Especially for Ar–C distances, the internal atoms of the clusters come closer to the molecule, as shown in Fig. 5. The minimum distance of an atom from C is the shifted position of the closest argon atom around the center of CO_2. When the number of argons becomes 15, the closest argon is at a distance of 3.51 Å. However, for n = 7–15, the maximum displacement from the C atom is almost the same (see Fig. 5), and at n = 15, it reaches the lowest value (4.41 Å) in this regime. The different structural reorientations cause sudden increases and fluctuations in the maximum pair distances. For n = 14–18, all the structures are in different orientations even though they are in closed-shells. For example, the addition of an atom to CO_2–Ar_{15} leads to a new reorientation. The minimum and maximum pair distances increase suddenly for Ar–C displacements. The transformation to the spherical form of CO_2–Ar_{17} from CO_2–Ar_{16} decreases the distances. In the CO_2–Ar_{17} structure, argons are in symmetric locations with respect to the molecule, and the minimum and maximum distances between the argon and oxygen atoms are 3.53 and 6.07 Å, respectively. These values are 3.59 and 4.92 Å, respectively, for Ar–C distances. For more than 17 argon atoms, it turns back to an expected growing pattern based on the geometry of the CO_2–Ar_{17} cluster. For higher orders, i.e., n = 18–21, the mean displacements slightly increase. This corresponds to a growing process that seems to be concentrated only on the Ar–Ar potential interaction. For n > 18, it has also been found in ref. 18 that there is a small contribution from the CO_2 interaction, and this does not affect the growing process at all with respect to the molecule.

Summary and conclusion

To predict the structures of CO_2–Ar_n clusters, the primary non-rigid dynamics of the Ar + CO_2–Ar_{n-1} → CO_2–Ar_n collision process has been investigated in detail by means of classical MD analysis. The collision energy of the projectile atom and the orientation of the target cluster produced different trajectories. For all interactions, the energy transfers are obtained in the fusion regime of atom–cluster collision phenomena. The pairwise-additive PEF considered here gives a good structural and energetical agreement with previous available results (18). The potential used in this work (eq. [2]) gives an opportunity for considering the non-rigid molecular case. We obtained similar geometries and comparable energy values of the well depth at the minimum-energy T-shaped structure with the non-rigid pair-additive case. The minimum-energy structures produce similar features for the initial completed first solvation shell for n = 14. The largest value of n, for which all argon atoms are found in the inner solvation shell, is 17. Owing to these good agreements, we believe that the PEF and MD techniques may be used for investigating the effects of internal motion of CO_2 and any other thermodynamic properties, such as melting and fragmentation, for Ar_nCO_2 clusters.

The present study has also shown that the BF potential can also be considered as a model for understanding the growing mechanisms with a suitable construction of the PEF used. In addition, we have described the particle interactions in the system with pair-additive approaches, and the results agree well with previous studies (18). Accordingly, it can be concluded that these studies produced a comprehensive analysis of the dominant effects on cluster-growing phenomena. Finally, we have demonstrated that clusters of atom–molecule complexes can be obtained through one-atom collisions with the stable structures of smaller clusters. The rearrangement collision procedure used in this work provides an efficient tool for generating possible candidates for the ground-state and higher-energy structures of these types of clusters.

Acknowledgements

This work was supported by Conselho Nacional de Desenvolvimento Científico e Tecnológico (CNPq), Coordenação de Aperfeiçoamento de Pessoal de Nível Superior (CAPES), and Fundação de Amparo à Pesquisa do Estado de Minas Gerais (FAPEMIG) in Brazil and partially funded by the Research Fund of Erciyes University (FBA.06.07) in Turkey. The Programa de Apoio a Núcleos de Excelência (PRONEX)-FAPEMIG (EDT 2403/03) is also gratefully acknowledged. One of the authors (MB) would like to thank CNPq for a postdoctoral research grant. MB is also grateful to M.W. Severson for providing some data from his previous study.

References

1. E.R. Bernstein. Atomic and molecular clusters. Elsevier, Amsterdam. 1990.
2. G. Cardini, V. Schettino, and M.L. Klein. J. Chem. Phys. **90**, 4441 (1989).
3. A. Bonnamy, R. Georges, A. Benidar, J. Boissoles, A. Canosa, and B.R. Rowe. J. Chem. Phys. **118**, 3612 (2003).
4. G. Rossi, R. Ferrando, A. Rapallo, A. Fortunelli, B.C. Curley, L.D Lloyd, and R.L. Johnston. J. Chem. Phys. **122**, 194309 (2005).
5. B. Hartke. J. Phys. Chem. **97**, 9973 (1993).
6. A. Tomasulo and M.V. Ramakrishna. J. Chem. Phys. **105**, 10449 (1996).
7. D. Wales and J. Doye. J. Phys. Chem. A, **101**, 5111 (1997).
8. J. Doye and D. Wales. Phys. Rev. Lett. **80**, 1357 (1998).
9. J. Doye, D. Wales and M. Miller. J. Chem. Phys. **10**9 8143 (1998).
10. S. Yoo and X. Zeng. J. Chem. Phys. **119**, 1442 (2003).
11. S. Goedecker. J. Chem. Phys. **120**, 9911 (2004).
12. M.D. de Andrade, K.C. Mundim, and L.A.C. Malbouisson. Int. J. Quantum Chem. **103**, 493 (2005).
13. A. Sarsa, Z. Bačić, J.W. Moskowitz, and K.E. Schmidt. Phys. Rev. Lett. **88**, 123401 (2002).
14. D.T. Anderson, S. Davis, and D.J. Nesbitt. J. Chem. Phys. **107**, 1115 (1997).
15. S. Liu, Z. Bačić, and J.M. Moskowitz. J. Chem. Phys. **100**, 7166 (1994).

© 2007 NRC Canada

16. P. Niyaz, Z. Bačić, J.M. Moskowitz, and K.E. Schmidt. Chem. Phys. Lett. **252**, 23 (1996).
17. M.B. Sevryuk and G.D. Billing. Chem. Phys. **185**, 199 (1994).
18. M.W. Severson. J. Chem. Phys. **109**, 1343 (1998).
19. J.M. Steed, T.A. Dixon, and W.Klemperer. J. Chem. Phys. **70**, 4095 (1979).
20. S.W. Sharpe, R. Sheeks, C. Wittig, and R.A. Beaudet. Chem. Phys. Lett. **151**, 267 (1988).
21. S.W. Sharpe, D. Reifschneider, C. Wittig, and R.A. Beaudet. J. Chem. Phys. **94**, 233 (1991).
22. R.W. Randall, M.A. Walsh, and B.J. Howard. Faraday Discuss. Chem. Soc. **85**, 13 (1988).
23. G.T. Fraser, A.S. Pine, and R.D. Suenram. J. Chem. Phys. **88**, 6157 (1988).
24. E.J. Bohac, M.D. Marshall, and R.E. Miller. J. Chem. Phys. **97**, 4890 (1992).
25. E.J. Bohac, M.D. Marshall, and R.E. Miller. J. Chem. Phys. **97**, 4901 (1992).
26. J.M. Sperhac, M.J. Weida, and D.J. Nesbitt. J. Chem. Phys. **104**, 2202 (1996).
27. J.C. Belchior, J.P. Braga, and N.H.T. Lemes. Can. J. Chem. **79**, 211 (2001)
28. F. Thibault, B. Calil, J. Buldyreva, M. Chrysos, J.-M. Hartmann, and J.-P. Bouanich. Phys. Chem. Chem. Phys. **3**, 3924 (2001).
29. A.J. Misquitta, R. Bukowski, and K. Szalewicz. J. Chem. Phys. **112**, 5308 (2000).
30. C.F. Roche, A. Ernesti, J.M. Hutson, and A.S. Dickinson. J. Chem. Phys. **104**, 2156 (1996).
31. M.A. ter Horst and C.J. Jameson. J. Chem. Phys. **105**, 6787 (1996).
32. C.F. Roche, A.S. Dickinson, A. Ernesti, and J.M. Hutson. J. Chem. Phys. **107**, 1824 (1997).
33. T.R.Horn, R.B. Gerber, and M.A. Ratner. J. Phys. Chem. **97**, 3151 (1993).
34. J.M. Hutson, A. Ernesti, M.A. Law, C.F. Roche, and R.J. Wheatley. J. Chem. Phys. **105**, 9130 (1996).
35. P.J. Marshall, M.M. Szczesniak, J. Sadlej, G. Chalasinski, M.A. ter Horst, and C.J. Jameson. J. Chem. Phys. **104**, 6569 (1996).
36. E.J. Bohac, M.D. Marshall, and R.E. Miller. J. Chem. Phys. **97**, 4890 (1992).
37. A.M. Hough and B.J. Howard. J. Chem. Soc., Faraday Trans. 2, **83**, 173 (1987).
38. A.M. Hough and B.J. Howard. J. Chem. Soc., Faraday Trans. 2, **83**, 191 (1987).
39. R.A. Aziz. J. Chem. Phys. **99**, 4518 (1993).
40. J. Rogan, R. Ramírez, A.H. Romero, and M. Kiwi. Eur. Phys. J. D, **28**, 219 (2004).
41. M. Böyükata, E. Borges, J.C. Belchior, and J.P. Braga. J. Alloys Compd. **403**, 349 (2005).
42. M. Böyükata. Physica E, **33**, 182 (2006).
43. I.A. Solov'yov, A.V. Solov'yov, W. Greiner, A. Koshelev, and A. Shutovich. Phys. Rev. Lett. **90**, 053401 (2003).
44. M.A. Pariseau, E. Suzuki, and J. Overend. J.Chem. Phys. **42**, 2335 (1965).
45. F. Calvo and E. Yurtsever. Phys. Rev. B, **70**, 045423 (2004).
46. K. Nishio, J. Koga, T. Yamaguchi, and F. Yonezawa. Phys. Rev. B, **69**, 214201 (2004).
47. J. Zúñiga, A. Bastida, A. Requena, N. Halberstadt, and J.A. Beswick. J. Chem. Phys. **98**, 1007 (1993)
48. L. Boltzmann. Lectures on gas theory. Dover Publications, New York. 1995.
49. R.M. Lynden-Bell and A.J. Stone. Molec. Sim. **3**, 271 (1989).

© 2007 NRC Canada

Heterogeneities in sol–gel-derived paramagnetics-doped forsterites and willemites — Electron microprobe analysis and stretched-exponential ^{29}Si MAS NMR spin–lattice relaxation studies

J. Stephen Hartman, Arjun Narayanan, Suzie S. Rigby, David R. Sliwinski, Norman M. Halden, and Alex D. Bain

Abstract: We report the synthesis and analysis of sol–gel-derived samples of forsterite (Mg_2SiO_4) and willemite (Zn_2SiO_4), doped with paramagnetic Cu^{2+}, Ni^{2+}, and Co^{2+}, at a range of dopant concentrations. Electron probe microanalysis and backscattered electron imaging show the presence of major micrometre-scale heterogeneities in the distribution of paramagnetic centres. Despite the inhomogeneities, the ^{29}Si NMR spin–lattice relaxation behaviour is well-behaved and is consistent with the stretched-exponential expression $M_z(t) = M_z(\infty)\{1 - a \exp[-(t/T')^n]\}$. The exponent n is 0.5 within the experimental error in some samples. This value is consistent with relaxation by immobile isolated paramagnetic impurities with negligible ^{29}Si spin diffusion from the impurity centres, but careful curve fitting confirms that n is significantly larger than 0.5 in other samples. Relaxation efficiency is highly dependent on the dopant ion and its concentration. Although the purely empirical stretched-exponential function does not provide a unique physical picture, it is noteworthy that it is sufficiently robust to describe spin–lattice relaxation even in highly inhomogeneous systems. Spin–lattice relaxation is a useful probe of paramagnetics-doped solid samples, but NMR does not provide information on homogeneity. Careful sample characterization on the micrometre scale is highly desirable, as a complement to NMR studies.

Key words: MAS NMR, spin–lattice relaxation, ^{29}Si, forsterite, willemite, stretched-exponential relaxation, sol–gel, minor-component heterogeneity, backscattered electron analysis.

Résumé : On rapporte la synthèse et l'analyse d'échantillons dérivés de sol–gels de forsterite (Mg_2SiO_4) et willémite (Zn_2SiO_4) dopés avec des quantités diverses des ions paramagnétiques Cu^{2+}, Ni^{2+} et Co^{2+}. Une microanalyse avec une sonde électronique et l'obtention d'images électroniques avec rétrodiffusion montrent la présence d'importantes hétérogénéités à l'échelle du micrométre dans la distribution des centres paramagnétiques. Malgré les inhomogénéités, le comportement de relaxation spin–réseau du spectre RMN du ^{29}Si se comporte normalement et il est en accord avec l'expression exponentielle étendue $M_z(t) = M_z(\infty)\{1 - a \exp[-(t/T')^n]\}$. Aux erreurs expérimentales près, l'exposant n est égal à 0,5 dans certains échantillons. Cette valeur est en accord avec une relaxation par des impuretés paramagnétiques isolées immobiles avec une diffusion négligeable du spin ^{29}Si à partir des centres d'impureté; toutefois, des ajustements soignés des courbes indiquent toutefois que la valeur de n est largement supérieure à 0,5 dans d'autres échantillons. L'efficacité de la relaxation dépend fortement de l'ion dopant et de sa concentration. Même si la fonction exponentielle étendue qui est strictement empirique ne fournit pas une image physique unique, il est bon de noter qu'elle est suffisamment robuste pour décrire la relaxation spin–réseau même dans des systèmes hautement inhomogènes. La relaxation spin–réseau est un outil utile d'examen des échantillons solides dopés avec des produits paramagnétiques, mais la RMN ne fournit pas d'information sur l'homogénéité. Une caractérisation judicieuse de l'échantillon à l'échelle du micrométre est un complément très désirable aux études de RMN.

Mots-clés : RMN à l'angle magique de spin, relaxation spin–réseau, ^{29}Si, willémite, exponentielle de relaxation étendue, sol–gel, hétérogénéité du composant mineur, analyse électronique avec rétrodiffusion.

[Traduit par la Rédaction]

Received 19 June 2006. Accepted 1 November 2006. Published on the NRC Research Press Web site at http://canjchem.nrc.ca on 7 February 2007.

J.S. Hartman,[1] **A. Narayanan, S.S. Rigby, and D.R. Sliwinski.** Department of Chemistry, Brock University, St. Catharines, ON L2S 3A1, Canada.
N.M. Halden. Department of Geological Sciences, University of Manitoba, Winnipeg, MB R3T 2N2, Canada.
A.D. Bain. Department of Chemistry, McMaster University, Hamilton, ON L8S 4M1, Canada.

[1]Corresponding author (e-mail: shartman@brocku.ca).

 doi:10.1139/V06-183 © 2007 NRC Canada

Introduction

Forsterite (Mg_2SiO_4) and willemite (Zn_2SiO_4) are relatively simple nesosilicates (i.e., no Si–O–Si bridging, also called orthosilicates, or Q° silicates) (1, 2). Both readily undergo isomorphous replacement of the octahedral Mg^{2+}, or tetrahedral Zn^{2+}, by doubly charged paramagnetic transition-metal 2+ ions and can be readily synthesized by sol–gel (3) as well as classical (4) procedures. Because of this, they appeared to be well suited to serve as model systems for ^{29}Si NMR relaxation behaviour of natural silicate minerals with their trace amounts of various paramagnetic ions. Forsterite has been extensively studied by a variety of NMR techniques involving all possible magnetic nuclei (5–8). We report here our sol–gel synthesis, electron microprobe analysis, and ^{29}Si NMR spin–lattice relaxation studies of paramagnetics-doped synthetic forsterites and willemites.

Since the pioneering work of Lippmaa and coworkers in 1980 (9), high-resolution solid-state ^{29}Si NMR with magic angle spinning (MAS) (10, 11) has become an important tool in mineralogy (12–14) and materials science (15). It soon became evident that different samples of the same natural silicate mineral can give widely differing ^{29}Si NMR resolution and sensitivity (16–20). The variations are primarily due to the effects of dilute paramagnetic impurities, normally transition-metal cations replacing diamagnetic cations. Different samples of the same mineral typically have different impurities, present in different concentrations, and even trace amounts of paramagnetic impurities can have profound effects on both spin–lattice and spin–spin relaxation. Even before the advent of MAS, it was recognized that paramagnetic impurities facilitate ^{29}Si spin–lattice relaxation in solids (21).

The presence of randomly distributed paramagnetic centres creates a hierarchy of magnetic nuclei, differing only in their distance from a paramagnetic site. The nearer the ^{29}Si atoms are to the paramagnetic site, the more readily they relax (a T_1 effect) but also the broader the signals become (a T_2 effect (22), which can be supplemented by further broadening arising from magnetic susceptibility (23)). "In ordered systems, the sites are all the same and relax in random order, leading to an exponentially decaying signal. Paradoxically, in disordered systems the sites relax in a hierarchical order because disorder makes the sites different." (24). The NMR signal of a sample with fixed paramagnetic impurities is inherently a composite signal arising from many different local regions, each with its own peak width and its own spin–lattice relaxation time. Iwamiya and Gerstein (25) were apparently the first to recognize that the ^{29}Si spin–lattice relaxation in some zeolites was not exponential. We first reported stretched-exponential ^{29}Si spin–lattice relaxation in doped silicate minerals in 1991 (26) and have explored the phenomenon in other systems (27–29).

Spin–lattice relaxation by fixed paramagnetic impurities occurs via the electron–nuclear dipolar interaction, which has an inverse sixth-power distance dependence. This problem is usually treated by assigning "spheres of influence" to the paramagnetic impurities, each of which causes relaxation of the nuclei that lie within its sphere. Tse and Hartmann (30) considered the case of relaxation by paramagnetic impurities in the absence of spin diffusion and derived the following expression for stretched-exponential relaxation, with $n = 1/2$:

$$[1] \qquad M_z(t) = M_z(\infty)[1 - a \exp[-(t/T')^n]\}$$

In this equation, $M_z(t)$ is the z magnetization at time t, a is a parameter that reflects the z magnetization at time zero, and T' is the time constant for the recovery. If $n = 1$, then the recovery is exponential and T' becomes the normal spin–lattice relaxation time, T_1.

Following synthesis by well-established sol–gel methods, our brightly coloured doped samples appeared to be homogeneous by optical microscopy, but electron microprobe studies unexpectedly revealed a high degree of heterogeneity in the dopant ion distribution on the micrometre scale. Thus, our samples, being heterogeneous, cannot serve as model homogeneously doped systems. However, minor-component inhomogeneity turns out to be a common, and often overlooked, feature of naturally occurring minerals, as well as synthetic samples (31–34). This work emphasizes the desirability of element-specific electron microprobe analysis in the study of sol–gel-derived samples, especially those involving dopant ions, before drawing conclusions from solid-state NMR studies.

Experimental section

Preparation of materials

Two different modifications of sol–gel preparation methods (3), referred to as methods A and B, were used in preparing the paramagnetics-doped mineral samples listed in Tables 1 and 2. Both synthetic methods give colourless undoped forsterite and willemite but coloured paramagnetics-doped materials: Cu^{2+} (blue), Ni^{2+} (green), and Co^{2+} (pink forsterites but blue willemites, consistent with the change in Co^{2+}-site coordination from octahedral in forsterite to tetrahedral in willemite (35)). Additional approaches to doped forsterite samples were attempted, based on the methods of Kido et al. (36) and Selvaraj et al. (37), but with less success. Attempts to obtain materials doped with Mn^{2+} and Fe^{2+} using similar methods led to complications because of oxidation of the transition-metal ion. We are confident that the +2 oxidation state is retained for the Ni, Cu, and Co dopants on the basis of (*i*) the colours of the samples, and (*ii*) the fact that the +2 oxidation state is the most stable state for all of these metal ions, with weak-field ligands such as oxides (35).

Method A

Based on the approach to the synthesis of undoped forsterite developed by Kazakos et al. (38), this method was used to prepare paramagnetics-doped forsterites and willemites. For forsterites, $Mg(NO_3)_2{\cdot}6H_2O$ (Aldrich, USA) and the desired molar proportion of the transition-metal nitrate $Cu(NO_3)_2{\cdot}5H_2O$, $Ni(NO_3)_2{\cdot}6H_2O$, or $Co(NO_3)_2{\cdot}6H_2O$ (all from Aldrich, USA) were weighed into a Teflon beaker and dissolved with stirring in 95% ethanol, followed by pipetting in the stoichiometric quantity of tetraethylorthosilicate (TEOS; Aldrich, USA) while stirring. Solvents were removed between 60 °C and 80 °C in a water bath, whereupon gelation occurred. The clear, coloured gels were dried at 110 °C in air, followed by heating for 2 h at 400 °C in a

© 2007 NRC Canada

Table 1. Spin–lattice relaxation data for paramagnetics-doped forsterites.

		4.7 T			11.7 T	
Dopant ion (M^{2+})	% Doping[a]	T'^{b}(s)	n^{c}	FWHM[d] (Hz)	T'^{b}(s)	n^{c}
—	0	2200 ± 650	0.61 ± 0.3	12		
Ni	0.22	24 ± 4	0.5 ± 0.1	17	39 ± 3	0.42 ± 0.05
Ni	1.2	0.27 ± 0.01	0.59 ± 0.02	21	0.65 ± 0.02	0.67 ± 0.02
Ni	2.2	0.07 ± 0.004	0.56 ± 0.04	24	0.16 ± 0.01	0.64 ± 0.02
Ni	3.1	0.13 ± 0.011	0.6 ± 0.04	26	0.32 ± 0.01	0.6 ± 0.02
Ni	3.8	0.035 ± 0.001	0.69 ± 0.09		0.042 ± 0.002	0.61 ± 0.03
Ni	4.8	0.022 ± 0.002	0.61 ± 0.04	51		
Ni	5.2	0.031 ± 0.001	0.73 ± 0.02	49	0.04 ± 0.006	0.6 ± 0.1
Ni	5.4	0.028 ± 0.001	0.68 ± 0.03	68	0.047 ± 0.002	0.64 ± 0.03
Ni	5.6	0.033 ± 0.001	0.7 ± 0.02	70	0.055 ± 0.002	0.64 ± 0.03
Ni	6.6	0.105 ± 0.003	0.51 ± 0.2	71	0.26 ± 0.03	0.7 ± 0.1
Ni	9.1	0.012 ± 0.004	0.7 ± 0.2	89	0.019 ± 0.002	0.64 ± 0.06
Cu	0.09	100 ± 5	0.54 ± 0.02	14	199 ± 11	0.5 ± 0.03
Cu	0.19	34 ± 2	0.5 ± 0.02	26	64 ± 12	0.4 ± 0.1
Cu	0.33	7.4 ± 3	0.4 ± 0.1	29	13 ± 1	0.53 ± 0.02
Cu	0.46	3.7 ± 0.2	0.5 ± 0.02	34	7.6 ± 0.4	0.53 ± 0.03
Cu	0.54	3.9 ± 0.07	0.5 ± 0.1	31	7.0 ± 0.2	0.56 ± 0.01
Cu	1.2	0.69 ± 0.07	0.5 ± 0.02	26	1.6 ± 0.06	0.57 ± 0.02
Cu	1.6	0.61 ± 0.11	0.5 ± 0.1	28	1.2 ± 0.01	0.5 ± 0.04
Cu	3.4	0.28 ± 0.03	0.5 ± 0.03	36	0.6 ± 0.03	0.57 ± 0.03
Cu	3.6	0.16 ± 0.01	0.5 ± 0.04	43	0.29 ± 0.09	0.4 ± 0.09
Cu	9.3	0.028 ± 0.01	0.42 ± 0.16			
Co	0.03	284 ± 140	0.3 ± 0.2	46	870 ± 190	0.9 ± 0.2
Co	1.15	60 ± 7	0.7 ± 0.1	244		
Co	2.9	14 ± 7	0.9 ± 0.5	388		
Co	5.7	3.44	0.79			

[a]% Mg^{2+} that has been replaced by dopant ions, as determined by DCP analysis on the bulk sample. The dopant ions are not homogeneously distributed; see text and Fig. 2.
[b]Time constant in the stretched exponential expression (eq. [1]).
[c]Exponent in the stretched exponential expression (eq. [1]).
[d]Peak width, as full-width at half-maximum.

tube furnace in platinum-lined combustion boats, followed by firing overnight at 1050 °C. Similar procedures, using $Zn(NO_3)_2{\cdot}6H_2O$ instead of $Mg(NO_3)_2{\cdot}6H_2O$, were carried out to prepare paramagnetics-doped willemites.

Method B

Based on the work of Rehspringer et al. (39), this method was used to prepare further paramagnetics-doped forsterites. Magnesium ethoxide (Johnson Matthey Electronics, London, UK) and the transition-metal alkoxide ($Cu(OEt)_2$, Johnson Matthey Electronics, London, UK) or transition-metal acetylacetonate ($Cu(acac)_2$, $Ni(acac)_2$, or $Co(acac)_2$, all from Gelest Inc., PA, USA) were dissolved in dry methanol and glacial acetic acid in a Teflon beaker, and an alcoholic solution of TEOS was added with stirring. Typically, to prepare forsterite with 3% of its Mg replaced by Ni, 2.42 g (0.0212 mol) of $Mg(OEt)_2$ and 0.163 g (6.3×10^{-4} mol) of $Ni(acac)_2$ were added to a Teflon beaker, then 30 mL of dry methanol were added, followed by 5 mL of glacial acetic acid, under continuous stirring. After 5 min, a clear green solution was obtained. 2.43 mL (0.0109 mol) of TEOS was then pipetted into the beaker, followed by 3 mL of distilled water. Heating the solution between 60 and 80 °C for 2.5 h under continuous stirring to remove excess solvent led to the formation of a clear green gel, which was dried at 110 °C in air, then fired overnight at 1050 °C. Some samples were further heated at 1200 °C for up to a week, but this gave negligible change in their NMR behaviour.

Characterization of materials

Powder-pattern X-ray diffraction analysis was carried out on a Picker X-ray diffractometer with Cu Kα radiation (λ = 1.5418 Å), scanning at 1° per minute at a chart speed of 1 inch per minute. Mineral phases were identified by their *d* spacings. Alternatively, a Phillips PW1710 Automated Powder Diffractometer System instrument was used, with a dedicated IBM PC computer system using the Fein–Marquardt PDSM–Micro Powder Diffraction Search Match program. The analyses showed the desired mineral (forsterite or willemite) as the only major component, with typically up to a few percent of a single minor component: periclase (MgO) or enstatite ($MgSiO_3$) in forsterites, or zincite (ZnO) in some willemite samples. All of these are consistent with slight deviations from the desired stoichiometry of the reaction mixture. No attempt was made to quantify the amount of minor components.

The synthetic forsterites and willemites were analyzed for Ni, Cu, and Co by direct current plasma atomic emission (DCP) spectroscopy (40), using a Beckmann Spectra Scan DCP optical emission spectrophotometer. Background scans for each analyte were performed on standard solutions.

© 2007 NRC Canada

Table 2. Spin–lattice relaxation data for paramagnetics-doped willemites.

		4.7 T			11.7 T	
Dopant ion(M^{2+})	% Doping[a]	T'[b](s)	n[c]	FWHM[d] (Hz)	T'[b](s)	n[c]
—	0	4300 ± 2250	0.6 ± 0.2	10		
Ni	0.48	890 ± 80	0.7 ± 0.06	61		
Ni	0.76			363		
Ni	2.9	240	0.7	406		
Ni	5.8			439		
Cu	0.09	1100 ± 160	0.6 ± 0.09	26		
Cu	0.43	326 ± 16	0.6 ± 0.1	61		
Cu	1.08	70 ± 14	0.4 ± 0.1	82	97 ± 40	0.4 ± 0.2
Cu	1.95	25 ± 4	0.6 ± 0.1	112		
Cu	17.5	2.7	0.71	237		
Co	0.26	44 ± 20	0.5 ± 0.13	24	94 ± 7	0.6 ± 0.06
Co	0.91	1.1 ± 0.05	0.7 ± 0.03	48	1.6 ± 0.1	0.6 ± 0.04
Co	2.27	0.22 ± 0.01	0.78 ± 0.06	112	0.38 ± 0.01	0.8 ± 0.03
Co	4.64	0.1 ± 0.006	0.9 ± 0.08	182		
Co	6.92	0.09 ± 0.03	0.7 ± 0.3	231	0.1 ± 0.04	0.5 ± 0.2

[a]% Zn^{2+} that has been replaced by dopant ions, as determined by DCP analysis on the bulk sample. The dopant ions are not homogeneously distributed; see text and Fig. 3.
[b]Time constant in the stretched exponential expression (eq. [1]).
[c]Exponent in the stretched exponential expression (eq. [1]).
[d]Peak width, as full-width at half-maximum.

Wavelengths used were 312.598 nm for Cu, 340.512 nm for Co, and 231.604 nm for Ni. Forsterite samples were dissolved in a 1:8:2 mixture of nitric, hydrofluoric, and perchloric acids, and the solutions were diluted with 1% nitric acid. The undoped mineral, forsterite or willemite, was dissolved and added to the standard solutions used in the calibration to match the matrices of the sample solutions.

Electron microprobe studies (41) of selected samples were carried out using backscattered electrons (BSE) and point analysis on a CAMECA SX100 instrument in wavelength-dispersive mode. Small amounts of each sample were mounted in epoxy resin, care being taken to separate as many grains as possible. The very fine-grained nature of the samples resulted in the development of a few large aggregations consisting of a number of crystals. Within individual aggregations, the grain size of the willemite and forsterite crystals typically ranged from 10 to 50 μm; some grains and fragments were as large as 100 μm. The samples were gently polished and carbon coated. The willemite samples took a better polish, while the forsterite samples had a tendency to form a more "spongy" or rough surface. Beam conditions were established at 20 kV and 20 nA for Co, Ni, Cu, and Zn analysis, and 15 kV and 20 nA for Si and Mg. A beam diameter of 1 μm was used for point analysis. Well-characterized forsterite, willemite, and cuprite mineral standards were used to calibrate Mg, Si, Cu, and Zn, and a compound Co and Ni silicate standard was used for Co and Ni.

NMR instrumentation and methods

^{29}Si MAS NMR spectra were obtained on Bruker AC-200 and AM-500 spectrometers at magnetic fields of 4.7 T (frequency of 39.76 MHz) and 11.7 Tesla (frequency of 99.32 MHz), respectively. At 4.7 T, a home-built MAS probe of the Andrew–Beams type was used with a spinning speed of about 3 kHz. Typical spectra were obtained with 8 K data points and spectral widths of 10–50 kHz. Spectra at 11.7 T were obtained using a Doty 5 mm MAS probe with spinning speeds of 3 and 8 kHz. The 90°-pulse widths on the Bruker AC-200 and AM-500 instruments were typically 15–25 and 5.5 μs, respectively.

The saturation-recovery method (saturating comb – τ – 90°) (22) was used for the determination of spin–lattice relaxation behaviour. For the faster-relaxing samples, a train of 50–100 very closely spaced 1–5 μs pulses was used. The delays between pulses should not all be the same; we used various schemes and found that a repeating sequence of three different delay times in the ratio of 10:9:8 gave effective nulling of the magnetization. To adequately determine the exponent n as well as the time constant T' of eq. [1], data sets of 15 to 20 τ values were obtained.

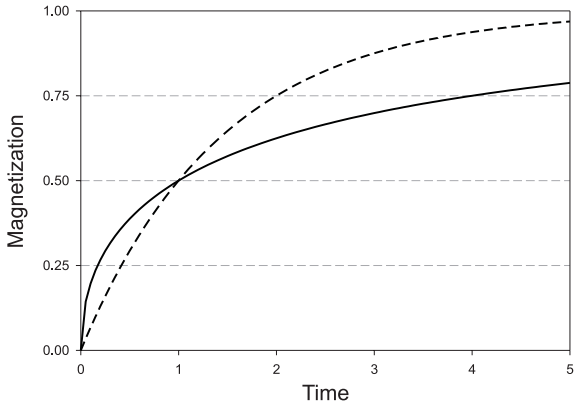
The closely spaced saturating comb of 90° pulses of the saturation-recovery method damaged the capacitors of our home-built 4.7 T MAS probe, so the inversion-recovery method (180° – τ – 90° – fixed delay) was used on this instrument for the fastest-relaxing samples. However, systematic errors can arise if the fixed delay between repetitions of the inversion-recovery pulse sequence is inadequate (22), and the "long-tailed" nature of the stretched-exponential decay curve (Fig. 1) exacerbates this problem. Conservative fixed delays of $100 \times T'$ (rather than the $5 \times T_1$ that is adequate for greater than 99% magnetization recovery when relaxation is exponential) were chosen to ensure equilibration. Inversion-recovery and saturation-recovery methods were both employed for some samples, and excellent agreement between them was obtained, provided that inversion-recovery fixed delays of at least $100 \times T'$ were used. However, the inversion-recovery method is impractical with slow-relaxing samples, especially when relaxation is stretched-exponential.

Data analysis

The time constant T' and the exponent n, indicating the degree of stretch of the stretched-exponential decay function, were obtained by fitting the data to the four-parameter

© 2007 NRC Canada

Fig. 1. Recovery of magnetization, following saturation, for a normal exponential (dashed line) and stretched exponential with $n = 0.5$ (solid line). Both recoveries have half-lives of 1 time unit.



stretched exponential function, where $M_z(\tau)$ is the macroscopic z magnetization at a time τ after a perturbing radio frequency pulse. Note that T', the time constant for nonexponential relaxation, differs from T_1, the time constant for exponential relaxation, unless the exponent n is equal to 1. The fits were carried out as described previously (28, 29), using commercially available software (Deltagraph Professional, Deltapoint Inc., Monterey, CA) as well as the program STRETCHR, developed by one of us (ADB), and were generally quite good despite the complication of allowing n to vary between 0.5 and 1 (29). The standard errors obtained from the fit are reported in Tables 1 and 2 along with the T' and n values. The 95% confidence intervals are usually 2–3 times the standard errors for both T' and n (29). We have shown (29) that the exponent n and the time constant T' are best determined if the τ values are chosen preferentially in the optimal regions 0, 0.2 T', 2.5 T', and 10 T'. With 15 to 20 τ values in each run, the optimal regions were well represented.

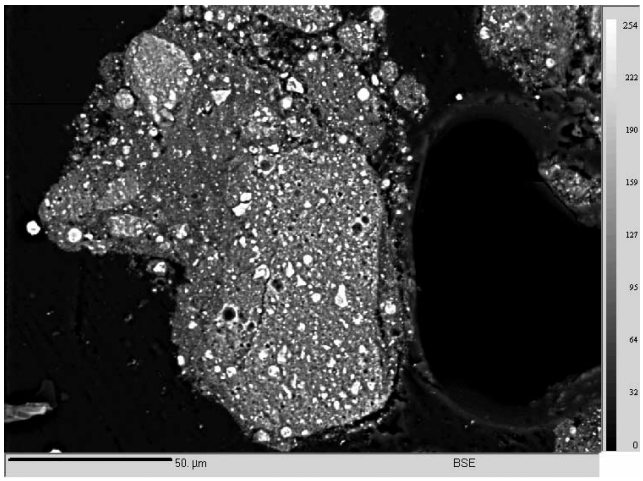
Results

Characterization of samples

Comparison of DCP analyses of the dopant concentrations with those calculated from the stoichiometry of the sol–gel synthesis starting mixtures showed that incorporation of copper was 10% to 20% less than expected, apparently because of volatilization during heating. Loss of copper was confirmed by the appearance of a green colour in the quartz tube of the tube furnace after heating at 1050 °C. In contrast, DCP analysis showed that the concentrations of Co and Ni in forsterites prepared by method B are normally 10% to 20% higher than expected from the starting material composition, consistent with some loss of silicon during the synthesis. A possible mechanism for the loss of silicon is through the exchange of ethoxy groups of TEOS with methoxy groups of methanol, which would give a more volatile silicon alkoxide. Similar problems have been reported when tetramethylorthosilicate (TMOS) was used as a sol–gel silicate precursor (42).

Optical microscopy at a magnification of 180 indicated that our initially prepared paramagnetics-doped samples were homogeneous. However, later electron microprobe

Fig. 2. Backscattered electron (BSE) image of a sol–gel synthesized nickel-doped forsterite sample in which 6.7% of the Mg is replaced by Ni, as determined by direct current plasma atomic emission (DCP) spectroscopy. The brightness scale corresponds to the level of Ni concentration, with the bright spots representing high Ni concentration.



studies, using backscattered electrons (BSE), on a selection of the willemite and forsterite samples showed that all of them are heterogeneous to varying extents on the micrometre scale. Figures 2 and 3 show BSE images of nickel-doped forsterite and willemite samples. Because the backscattering effectiveness of the transition-metal ions is much greater than that of Mg^{2+}, the BSE image gives a picture of the distribution of the paramagnetic ions. The mottled and zoned BSE patterns, on a scale of a few micrometres, show that the paramagnetic ions are inhomogeneously distributed. The mottled and zoned patterns of heavy element distribution have been confirmed by X-ray mapping and point analysis of these samples. Samples prepared by methods A and B were similarly heterogeneous.

The willemites show considerable variation in grey level in their backscattered electron images, corresponding to significant spatial variations in composition. The main variation observed is in the Zn/Si ratio. Light regions, typically rimming 20 µm grains, have a Zn/Si atomic ratio of about 1.8; darker (interior) regions have a ratio of about 1.2. In addition to the significant grey level variation within grains, there was also some variation between grains. Analysis of a number of bright grains showed that they consisted of ZnO, consistent with the powder pattern X-ray diffraction analysis. In the willemite of Table 2 and Fig. 3, where the overall Ni^{2+} content is nominally 5.8%, we get values of 0.52, 0.74, 0.53, and 0.64 atomic% Ni. This confirms that much of the Ni^{2+} has not been incorporated into the willemite lattice, consistent with its having partitioned into a minor component.

It was more difficult to get good electron microprobe analyses on the forsterite samples. Individual grains were relatively soft, so their surface did not polish well. However, significant grey level variations were observed, indicating chemical heterogeneity. In cases where multiple analyses were done on single grains, the most notable feature was the variation in the Mg/Si ratio. For example, the sample with a

© 2007 NRC Canada

Fig. 3. (*a*) Backscattered electron (BSE) image of a sol–gel synthesized nickel-doped willemite sample in which 5.8% of the Mg is replaced by Ni, as determined by direct current plasma atomic emission (DCP) spectroscopy, showing considerable variation in Ni concentration. (*b*) Enlargement of a portion of the image shown in (*a*), showing three distinct zones differing greatly in Ni concentration, the outer margin of the crystal being especially rich in Ni.

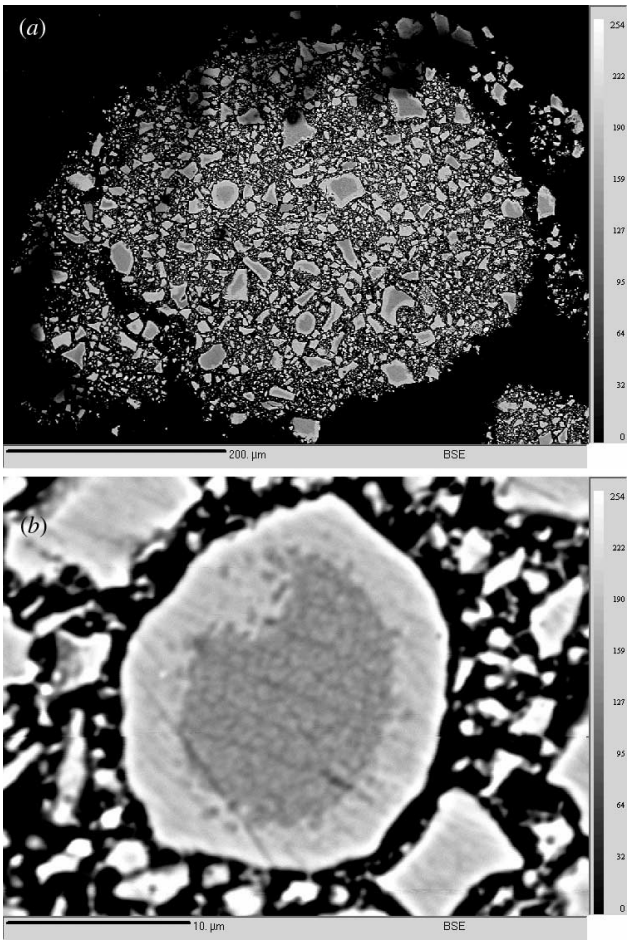
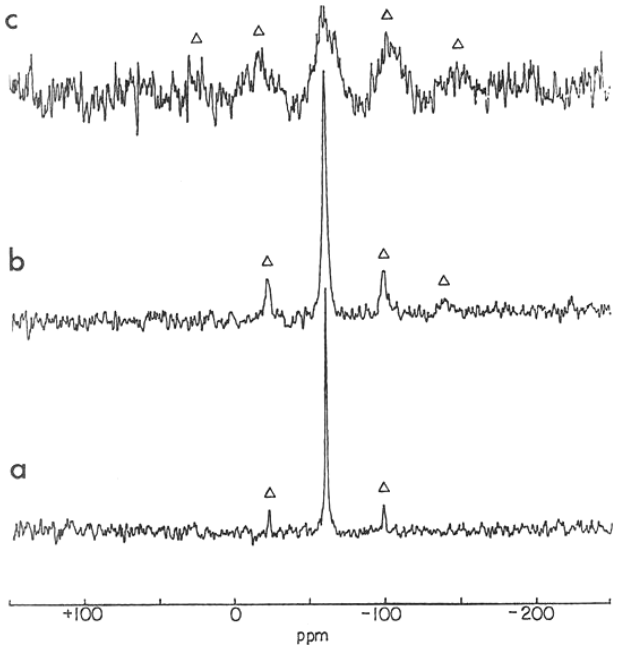


Fig. 4. 9.4 T (79.46 MHz) ^{29}Si MAS NMR spectra of Co^{2+}-doped forsterite at concentrations of (*a*) 0.018, (*b*) 0.87, and (*c*) 4.4 mol% (Co^{2+}/Mg^{2+}), from an early study of paramagnetics-doped forsterite in this laboratory.[2] Peaks marked with Δ are spinning sidebands.



nominal concentration of 0.09 atomic% Cu^{2+} showed a Cu content of 0.01 atomic% by microprobe analysis; Mg/Si ratios at the same spots varied from 1.4 to 2.05, and other paramagnetic species were not detected. In the sample with a nominal Co content of 5.7 atomic%, electron microprobe analyses detected 0.58 and 0.62 atomic% and a Mg/Si ratio of 1.97 and 1.64, respectively. Other samples gave much better agreement between electron microprobe analysis results and the values expected from sample composition. As with the willemite samples, this variation suggests that in some samples, only a fraction of the paramagnetic ion is incorporated into the forsterite lattice.

NMR studies

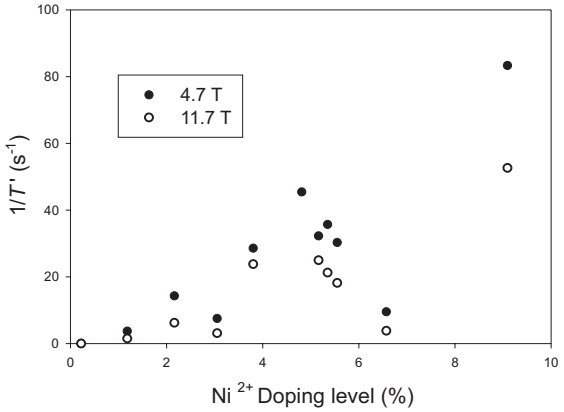
The single sharp ^{29}Si MAS NMR peaks of forsterite (–61.7 ppm from TMS; lit. –61.9 ppm) (43, 44) and willemite (–70.7 ppm) are consistent with the single silicon environment in each mineral and the lack of bridging oxygens (1). Increasing the concentration of the paramagnetic ion increases the number and relative intensity of the spinning sidebands and broadens the peaks, in the usual fashion (Fig. 4, Tables 1 and 2) (19, 45, 46), but does not appreciably change the chemical shift. The paramagnetic ions broaden the signal to different extents: $Ni^{2+} < Cu^{2+} << Co^{2+}$ for forsterites but $Co^{2+} < Cu^{2+} << Ni^{2+}$ for willemites, for similar concentrations of the transition-metal ions. Nuclear relaxation in paramagnetic systems can be complex and is affected by a number of factors related to the electronic states of a transition-metal ion (47, 48), which we have not investigated in the present work.

Tables 1 and 2 give the spin–lattice relaxation data for the paramagnetic-ion-doped forsterites and willemites at magnetic field strengths of 4.7 and 11.7 T. All samples exhibit stretched-exponential spin–lattice relaxation behaviour, with the exponent *n* being within experimental error of the theoretically expected (30, 49, 50) 0.5 in some cases (e.g., the Cu^{2+}-doped forsterites), but appreciably larger in other cases, with *n* values typically in the range of 0.6 and 0.7 (e.g., the Ni^{2+}-doped forsterites). Because of instrument time limitations, few relaxation studies were carried out on the slow-relaxing Ni^{2+}-doped willemites. Undoped synthetic forsterite and willemite relax extremely inefficiently, confirming that relaxation in our paramagnetics-doped samples is dominated by the dopant. Within each series, there is the expected trend to faster relaxation with increasing dopant concentration, but with a large amount of scatter (Fig. 5), consistent with widely varying incorporation of the para-

[2] R.L. (Millard) Flemming. B.Sc. thesis, Brock University, St. Catharines, ON. 1985.

© 2007 NRC Canada

Fig. 5. Stretched-exponential relaxation rate ($1/T'$), measured at two magnetic fields: 4.7 T and 11.7 T, as a function of Ni^{2+}-doping level in forsterites, as determined by direct current plasma atomic emission (DCP) spectroscopy on the bulk sample. The scatter is consistent with widely varying incorporation of Ni^{2+} into the forsterite lattice.



magnetic ion into the crystal lattice. The paramagnetic ions differ greatly in their ^{29}Si relaxation efficiency at equivalent concentrations, in the order of $Ni^{2+} > Cu^{2+} >> Co^{2+}$ for forsterites (Table 1) but $Co^{2+} >> Cu^{2+} > Ni^{2+}$ for willemites (Table 2). In the forsterites, Ni^{2+} gives the sharpest ^{29}Si signal and also the most efficient relaxation; whereas, it gives the broadest ^{29}Si signal and is the least effective in promoting spin–lattice relaxation in the willemites. This is consistent with the zoning seen in the willemite of Fig. 3.

The additional parameter makes it inherently more difficult to fit the stretched-exponential curve with variable n than the simple exponential ($n = 1$) curve (29), and errors are large in the determination of the exponent n. Moreover, in the fit, there is a high correlation between the parameters T' and n (29, 51). However, it is clear that at both magnetic fields, the Ni^{2+}-doped forsterites consistently have $n > 0.5$, while the Cu^{2+}-doped forsterites have n within experimental error of 0.5, the value expected for relaxation by randomly distributed paramagnetic impurities in the absence of spin diffusion (30, 49, 52). The Co^{2+}-doped forsterites probably have $n > 0.5$, but there are large uncertainties. The Cu^{2+}- and Co^{2+}-doped willemites have exponents approximately equal to, and greater than, 0.5, respectively.

Spin–lattice relaxation is less efficient at 11.7 T than at 4.7 T (Fig. 5), as expected from spectral-density considerations (22). There is also the possibility that there might be some residual spin diffusion effect when the stretched exponent is greater than 0.5. In that case, because of the larger Curie moment at higher magnetic field, the barrier radius to spin diffusion would increase, thus increasing the efficiency of nuclear relaxation. There was no apparent increase in spin–lattice relaxation efficiency when samples were stationary rather than spinning or (at 11.7 T) when spinning at 3 kHz rather than 8 kHz. Magic-angle spinning can suppress spin diffusion (53) and its contribution to spin–lattice relaxation. The absence of a spinning-rate dependence in this work supports our proposal that spin diffusion has a negligible effect on spin–lattice relaxation in our systems.

Discussion

Sample inhomogeneity

Our samples are intriguingly complex on the micrometre scale, but this is not evident from their NMR spectra. Attaining sample homogeneity from multicomponent sol–gel systems is difficult because the different components can hydrolyse at very different rates, and often more than a single phase is obtained (54, 55). The existence of a second phase in many of our samples, as described in the experimental section, allows partitioning of the transition-metal ion between major and minor phases: forsterite and MgO, forsterite and enstatite ($MgSiO_3$), or willemite and ZnO. This allows the transition-metal ion concentration in the major forsterite or willemite phase to differ greatly from that calculated from the overall sample composition. Partitioning preferentially into the minor phase, or along grain boundaries (as is evident in Fig. 3*b*), would deplete its concentration in the major phase and diminish its effectiveness in promoting spin–lattice relaxation.

We have found NMR evidence for such partitioning in a related study in which both forsterite and enstatite are present as major phases. Ni^{2+} doping, whether at a level of 0.2% or 5% replacement of Mg^{2+}, causes ^{29}Si in enstatite to relax faster than ^{29}Si in forsterite by a factor of ~4; whereas, Cu^{2+} doping at the same levels causes ^{29}Si in forsterite to relax more efficiently than ^{29}Si in enstatite. Clearly Ni^{2+} partitions into enstatite, while Cu^{2+} prefers forsterite. Such partitioning also occurs in natural mineral assemblages. Thus, Fe^{3+} partitions into kyanite in preference to quartz, making ^{29}Si spin–lattice relaxation far more efficient for the kyanite than for the quartz phase (27).

However minor-component inhomogeneity is not limited to systems containing more than one phase. Although it has often been assumed that minor impurities within a single phase are homogeneously distributed, it is possible to generate oscillatory zoning in synthetic single crystals (34). Trace element variation is also a feature of many natural minerals (31) and is most commonly seen in the form of oscillatory banding. Microbeam analytical techniques are necessary to detect micrometre-scale mineral zoning (32, 33). In natural systems, such variations are thought to be the product of differential diffusion of the various components that make up the phase, and similar processes may be in operation during the synthesis of our samples. Minor and trace elements can also accumulate along mineral cleavages, fractures, and grain boundaries (56).

Other complexities can arise in paramagnetics-doped systems. For example, if clusters of paramagnetic ions form, each cluster could simulate a single paramagnetic centre, with the result that there are fewer such centres, and relaxation should be less efficient. From such reasoning, Sen and Stebbins have concluded that clustering of Nd^{3+} ions must be occurring in SiO_2 glass (57).

Trends in ^{29}Si spin–lattice relaxation among samples

The much greater effectiveness of Ni^{2+} on spin–lattice relaxation in forsterite than in willemite is of interest. Ni^{2+} should be capable of substitution into the distorted octahedral Mg^{2+} sites in forsterite and into the tetrahedral Zn^{2+} site in willemite, and both octahedral and tetrahedral Ni^{2+} have

© 2007 NRC Canada

two unpaired electrons. We cannot exclude major differences in electron T_1 in the two very different Ni^{2+} environments, which would affect the likelihood of nuclear spin flips. Also, we cannot exclude clustering of the paramagnetic ion in willemite, as proposed by Sen and Stebbins for clustering of Nd^{3+} in SiO_2 glass (57). However, the great broadening of the ^{29}Si NMR signal by Ni^{2+} in willemites is consistent with the very inhomogeneous distribution of Ni^{2+}, with a high concentration at the grain boundaries, as shown in Fig. 3*b*. This should give rise to a large anisotropy in bulk magnetic susceptibility and large paramagnetics-induced line broadening (58, 59) but should be poor at relaxing the ^{29}Si. Essentially little Ni^{2+} is incorporated in these samples because we find that their T' values are similar to the value of the undoped willemite (Table 2).

Although forsterite has a relatively simple structure compared with many silicates, it does have two crystallographically nonequivalent sites for the M^{2+} ions (1). It has been shown that Ni, Co, and Zn prefer to go into the smaller M1 site, while Mn prefers to go into the M2 site (1). Moreover, several workers have found that the Mg^{2+}–M^{2+} distribution in natural and synthetic olivines (of which forsterite is the Mg end member) is not random as previously assumed, but is dependent upon temperature, oxygen fugacity, and composition (60, 61). Such complicating factors would be important in highly homogeneous monophasic samples; however, given the micrometre-scale inhomogeneity of our samples, we can neglect them here.

Alternative approaches to describing nonexponential relaxation

Nonexponential spin–lattice relaxation is often observed for ^{29}Si and other rare-spin nuclei in solids. ^{29}Si relaxation has been dealt with by either a stretched-exponential (27–29, 62, 63) or a power law (57, 64, 65) approach, with the latter having the feature that the power law exponent is directly proportional to the fractal dimension of the material (64). Nonexponential spin–lattice relaxation of other nuclei has also been handled by the stretched-exponential (66, 67) and power-law (68, 69) expressions. The two are not mutually exclusive, but the power law is valid only in the early stages of the relaxation process, before the "spheres of influence" of individual paramagnetic centres begin to overlap. A modified model has been developed, in which the relaxation behaviour is expressed as an error function (51). These authors discuss the relative merits of the different models of nonexponential relaxation and emphasize that all of them are approximations with their own strong and weak points.

Another possible approach is via multiple exponentials (70, 71). Istratov and Vyvenko discuss the complications arising when there are several exponents with similar time constants (70). The stretched exponential, although not discussed by these authors, could be considered as a limiting case of this, with a very large number of individual components. However, Istratov and Vyvenko conclude that the use of multiple exponents with similar time constants is inherently an "ill-posed problem"; there seems to be no advantage over the stretched-exponential approach.

Exponents intermediate between 0.5 and 1, such as we report here (Tables 1 and 2), have been observed in a number of earlier studies (28, 29, 64, 72, 73). Yesinowski and Baker (66), in studying ^{13}C spin–lattice relaxation in diamond formed by chemical vapour deposition, have concluded that electron–electron dipolar interactions, causing mutual electron–electron spin flips that will affect nearby nuclei, can be responsible for increasing the value of the exponent n. They also found that n diminished and the T' value increased as the spin rate increased, indicating that spin diffusion was not fully quenched despite the low natural abundance of ^{13}C. We detected no dependence of ^{29}Si spin–lattice relaxation effectiveness on spin rate, consistent with the results of Hayashi et al. in some of their mineral systems (74–76), indicating that spin diffusion among ^{29}Si atoms, which would be decreased by MAS, is ineffective. However Hayashi did find a dependence on spin rate in some systems (77). In ^{29}Si-enriched materials spin diffusion does appear to be effective because relaxation is exponential rather than stretched-exponential (78).

Some caveats

This work illustrates the following concerns that apply to many NMR studies of solids and need to be more widely recognized.

(1) Both natural and synthetic minerals can be inhomogeneous on the micrometre scale, and often have features such as banding of minor components, even when only one phase is present. Electron microprobe methods have great value in detecting such features.

(2) Spin–lattice relaxation in solids is often nonexponential, and this possibility should always be considered. Various models exist to deal with nonexponential spin–lattice relaxation, and one of the most generally applicable is the stretched-exponential model. The inability to obtain a good null for any value of the variable delay time, following the 180° inversion pulse in an inversion-recovery experiment, indicates a hierarchy of relaxation environments. The faster-relaxing broad signal recovers more quickly while the slower-relaxing sharp signal is still inverted so that, at the closest approach to a null, an inverted sharp peak is superimposed on a broad peak with positive intensity. Such a pattern is often observed in inversion-recovery NMR experiments on solids (e.g., see Fig. 7 in ref. 73 and Fig. 6 in ref. 79) and indicates that relaxation is not exponential and that a T' rather than a T_1 value should be determined.

(3) T_1 calculation software normally assumes exponential relaxation and readily generates "pseudo-T_1" values even when relaxation is nonexponential. We find that these are often within a factor of 2 of the actual T' values, so they can give at least an order-of-magnitude estimate of relaxation efficiency. However, such values can be misleading and are not adequate for quantitative work.

(4) When relaxation is nonexponential, the inversion-recovery sequence (fixed delay – 180° – τ – 90° – AQ) (80, 81) should not be used because of the very long "tail" of the recovery curve. Unless relaxation is very fast, no feasible value of fixed delay is likely to be long enough to ensure full recovery of the magnetization. This is illustrated by Fig. 1. A fixed delay that would be adequate for exponential relaxation will not allow the detection of whole populations of nuclei far from a

© 2007 NRC Canada

paramagnetic centre, which relax very slowly, leading to a reported relaxation time based mainly on the faster-relaxing regions of the sample. The saturation-recovery sequence (saturating comb – τ – 90° – AQ) eliminates this problem because it does not require equilibrium magnetization to be established, and it should be used instead. However, the use of peak height to determine signal intensity can introduce error, since peak widths differ in different local regions. Peak area rather than peak height can be determined, or sufficient line broadening can be applied so that the height advantage of the inherently sharp components becomes negligible.

(5) Letting n in eq. [1] vary rather than fixing it at 0.5 improves the fit in many systems in which relaxation is stretched-exponential, but the physical significance of fractional n values larger than 0.5 is not clear. It must be kept in mind that all of the models for nonexponential relaxation involve approximations (51, 70).

Conclusions

Preparing synthetic paramagnetics-doped minerals to avoid the complexities associated with natural minerals may merely replace one set of complexities by yet another, since the dopant ions themselves do not readily become homogeneously distributed. The stretched-exponential expression does provide a useful empirical description of spin–lattice relaxation caused by immobile paramagnetic impurities in solids even if the distribution of the paramagnetics is highly inhomogeneous. NMR alone gives little indication of the degree of inhomogeneity in such samples, and it is desirable to determine sample homogeneity on the micrometre scale by a microbeam analytical technique such as BSE before drawing structural conclusions from NMR studies.

The trends in spin–lattice relaxation with paramagnetic-ion concentration in our doped forsterites and willemites are as expected, while the striking dependence on the specific paramagnetic ion merits further study.

Acknowledgements

We thank Professor Barbara L. Sherriff (University of Manitoba) for helpful discussions; Professor Roberta L. Flemming (University of Western Ontario), Mitzi Siefried, and the late Professor Frans P. Koffyberg for their assistance in developing mineral-synthesis methods; Professors Uwe Brand and Ian D. Brindle for assistance with the DCP analysis; Tim Jones (Brock University), Brian Sayer (McMaster University), and Neil Ball (University of Manitoba) for assistance with the instrumentation; the Ministry of Colleges and Universities of the Province of Ontario, for the award of an Ontario Graduate Scholarship (to DRS); the Natural Sciences and Engineering Research Council of Canada (NSERC) for financial support and for a Summer Undergraduate Award (to SSR); and the referees for helpful comments.

References

1. W.A. Deer, R.A. Howie, and J. Zussman. Rock forming minerals. 2nd ed. John Wiley, New York. 1989.
2. C. Klein and C.S. Hurlbut. Manual of mineralogy. 21st ed. John Wiley, New York. 1999.
3. C.J. Brinker and G. Scherer. Sol–gel Science. The Physics and chemistry of sol–gel processing. Academic Press, Boston. 1990.
4. J.S. Hartman and R.L. Millard. Phys. Chem. Miner. **17**, 1 (1990).
5. S.E. Ashbrook, A.J. Berry, and S. Wimperis. Am. Mineral. **84**, 1191 (1999).
6. G. Kunath-Fandrei, L. Kelbauskas, D. Doring, H. Rager, and C. Jager. Phys. Chem. Miner. **26**, 55 (1998).
7. B. Winkler, P. Blaha, and K. Schwarz. Am. Mineral. **81**, 545 (1996).
8. K.P. Such and G. Lehmann. Chem. Phys. Lett. **143**, 463 (1988).
9. E. Lippmaa, M. Magi, A. Samoson, G. Engelhardt, and A.R. Grimmer. J. Am. Chem. Soc. **102**, 4889 (1980).
10. G. Engelhardt and D. Michel. High resolution solid state NMR of silicates and zeolites, John Wiley, Chichester. 1987.
11. C.A. Fyfe. Solid-state NMR for chemists. C.F.C. Press, Guelph, ON. 1983.
12. R.J. Kirkpatrick. Rev. Mineral. **18**, 341 (1988).
13. J.F. Stebbins and I. Farnan. Science (Washington, D.C.), **245**, 257 (1989).
14. J.F. Stebbins. MRS Bull. **17**, 45 (1992).
15. H. Eckert. Prog. Nucl. Magn. Reson. Spectrosc. **24**, 159 (1992).
16. P.F. Barron, R.L. Frost, and J.O. Skjemstad. J. Chem. Soc., Chem. Commun. 581 (1983).
17. P.F. Barron, P. Slade, and R.L. Frost. J. Phys. Chem. **89**, 3305 (1985).
18. T. Watanabe, H. Shimizu, A. Msuda, and H. Saito. Chem. Lett. 1293 (1983).
19. B.L. Sherriff and J.S. Hartman. Can. Mineral, **23**, 205 (1985).
20. K.J.D. MacKenzie and M.E. Smith. Multinuclear solid-state nuclear magnetic resonance of inorganic materials. Pergamon Materials Series, Oxford. 2002.
21. R.K. Harris and B.E. Mann. NMR and the periodic table. Academic Press, London. 1978.
22. E. Fukushima and S.B.W. Roeder. Experimental pulse NMR. A nuts and bolts approach. Addison-Wesley, Don Mills, ON. 1981.
23. A. Nayeem and J.P. Yesinowski. J. Chem. Phys. **89**, 4600 (1989).
24. W. Siebrand and T.A. Wildman. Int. Rev. Phys. Chem. **5**, 251 (1986).
25. J.H. Iwamiya and B.C. Gerstein. Zeolites **6**, 181 (1986).
26. J.S. Hartman, D.R. Sliwinski, and E.A. Cherniak. Abstracts of the 32nd experimental NMR conference, St. Louis. 1991. Poster 134.
27. J.S. Hartman and B.L. Sherriff. J. Phys. Chem. **95**, 7575 (1991).
28. J.S. Hartman, A. Narayanan, and Y.-X. Wang, J. Am. Chem. Soc. **116**, 4019 (1994).
29. A. Narayanan, J.S. Hartman, and A.D. Bain. J. Magn. Reson. **112A**, 58 (1995).
30. D. Tse and S.R. Hartmann. Phys. Rev. Lett. **21**, 511 (1968).
31. D.R. Veblen, J.F. Banfield, G.D. Guthrie, P.J. Heaney, E.S. Ilton, K.J.T. Livi, and E.A. Smelik. Science (Washington, D.C.), **260**, 1465 (1993).
32. N.M. Halden, F.C. Hawthorne, J.L. Campbell, W.J. Teedale, J.A. Maxwell, and D. Higuchi. Can. Mineral, **31**, 637 (1993).
33. N.M. Halden, W.J. Teedale, and J.L. Campbell. Can. Mineral, **33**, 961 (1995).
34. A. Putnis, L. Fernandez-Diaz, and M. Prieto. Nature (London), 358, 743 (1992).
35. F.A. Cotton, G. Wilkinson, C.A. Murillo, and M. Bochmann.

© 2007 NRC Canada

Advanced inorganic chemistry. 6th ed. John Wiley and Sons. New York. 1999. Chap. 17.
36. H. Kido, S. Komarneni, and R. Roy. J. Am. Ceram. Soc. **74**, 422 (1991).
37. U. Selvaraj, S. Komarneni, and R. Roy. J. Am. Ceram. Soc. **73**, 3663 (1990).
38. A. Kazakos, S. Komarneni, and R. Roy. Mater. Lett. 9, 405 (1990).
39. J.L. Rehspringer. *In* Ultrastructure processing of advanced ceramics. *Edited by* J.D. Mackenzie and D.R. Ulrich. Wiley-Interscience, New York. 1988.
40. P.J. Potts. A handbook of silicate rock analysis. Blackie, Glasgow. (1987).
41. S.B.J. Reed. Electron probe microanalysis. 2nd ed. Cambridge University Press, Cambridge. 1993.
42. K.E. Yeager and J.M. Burlitch. Chem. Mat. **3**, 387 (1991).
43. M. Magi, E. Lippmaa, A. Samoson, G. Engelhardt, and A.R. Grimmer. J. Phys. Chem. **88**, 1518 (1984).
44. K.A. Smith, R.J. Kirkpatrick, E. Oldfield, and D.M. Henderson. Am. Mineral. 68, 1206 (1983).
45. A.R. Grimmer, F. von Lampe, M. Magi, and E. Lippmaa. Z. Chem. 22, 343 (1983).
46. E. Oldfield, R.A. Kinsey, K.A. Smith, J.A. Nichols, and R.J. Kirkpatrick. J. Magn. Reson. **51**, 325 (1983).
47. A. Abragam and B. Bleaney. Electron paramagnetic resonance of transition ions. Dover Publications, New York. 1978.
48. R.S. Drago. Physical methods for chemists. 2nd ed. Saunders College Publishers, Fort Worth. 1992. Sections 12–9 to 12–11.
49. P.M. Henrichs, M.L. Cofield, R.H. Young, and J.M. Hewitt. J. Magn. Reson. **58**, 85 (1984).
50. I.J. Lowe and D. Tse. Phys. Rev. **166**, 279 (1968).
51. A. Labouriau, Y.W. Kim, and W.L. Earl. Phys. Rev. B, **54**, 9952 (1996).
52. W.E. Blumberg. Phys. Rev. **119**, 79 (1960).
53. T.T.P. Cheung. Phys. Rev. B, **23**, 1004 (1981).
54. N. Re. J. Non-Cryst. Solids, **142**, 1 (1992).
55. M. Henry, J.P. Jolivet, and J. Livage. Struct. Bond. **77**, 153 (1992).
56. N.M. Halden, J.L. Campbell, and W.J. Teedale. Can. Mineral. **33**, 293 (1995).
57. S. Sen and J.F. Stebbins. J. Non-Crys. Solids, **188**, 54 (1995).
58. D.L. Vander Hart, W.L. Earl, and A.N. Garroway. J. Magn. Reson. **44**, 361 (1981).
59. M. Alla and E. Lippmaa. Chem. Phys. Lett. **87**, 30 (1982).
60. A.G. Nord, H. Annersten, and A. Filippidis. Am. Mineral. **67**, 1206 (1982).
61. H. Annersten, T. Ericsson, and A. Filippidis. Am. Mineral. **67**, 1212 (1982).
62. J.A. Chudek, G. Hunter, G.W. McQuire, C.H. Rochester, and T.F.S. Smith. J. Chem. Soc., Faraday Trans. **92**, 453 (1996).
63. M.H. Alaimo and J.E. Roberts. Solid State Nucl. Magn. Reson. **8**, 241 (1997).
64. F. Devreux, J.P. Boilot, F. Chaput, and B. Sapoval. Phys. Rev. Lett. **65**, 614 (1990).
65. S. Sen and J.F. Stebbins. Phys. Rev. B, **50**, 822 (1994).
66. D.B. Baker and J.P. Yesinowski. 37th Rocky Mountain conference on analytical chemistry, Denver. 1995. Paper 256.
67. I.P. Goudemond, J.M. Keartland, and M.J.R. Hoch. Bull. Magn. Reson. **17**, 236 (1995).
68. Z. Xu and J.F. Stebbins. Solid State Nucl. Magn. Reson. **5**, 103 (1995).
69. E.M. Kunoff, S.D. Goren, C. Korn, Z. Gavra, J.R. Johnson, and J.J. Reilly. Solid State Nucl. Magn. Reson. **3**, 23 (1994).
70. A.A. Istratov and O.F. Vyvenko. Rev. Sci. Instrum. **70**, 1233 (1999).
71. Y.-Y. Lin, N.-H. Ge, and L.-P. Hwang. J. Magn. Reson. **105A**, 65 (1993).
72. R.H. Lewis, R.A. Wind, and G.E. Maciel. J. Mater. Res. **8**, 649 (1993).
73. B. Sutter, R.E. Taylor, L.R. Hossner, and D.W. Ming. Soil Sci. Soc. Am. J. **66**, 455 (2002).
74. S. Hayashi, T. Ueda, K. Hayamizu, and E. Akiba. J. Phys. Chem. **96**, 10928 (1992).
75. S. Hayashhi. Solid State Nucl. Magn. Reson. **3**, 323 (1994).
76. S. Hayashi and E. Akiba. Solid State Nucl. Magn. Reson. **4**, 331 (1995).
77. S. Hayashi. Bull. Magn. Reson. **17**, 300 (1996).
78. R.J. Kirkpatrick, D. Howell, B.L. Phillips, X.-D. Cong, E. Ito, and A. Navrotsky. Am. Mineral. **76**, 673 (1991).
79. X. Xie, Z. Yang, R. Ren, and L.L. Shaw. Mater. Sci. Eng. A, **255**, 39 (1998).
80. R.L. Vold, J.S. Waugh, M.P. Klein, and D.E. Phelps. J. Chem. Phys. **48**, 3831 (1968).
81. P.B. Kingley. Concepts Magn. Reson. **11**, 243 (1999).

© 2007 NRC Canada

Towards the development of a covalently tethered MALDI system — A study of allyl-modified MALDI matrixes

Sanela Martic, John D. Brennan, Michael A. Brook, Suzanne Ackloo, and Noemi Nagy

Abstract: An emerging application of matrix-assisted laser desorption ionization (MALDI) mass spectrometry is the analysis of low molecular weight (LMW) compounds, often via coupled liquid chromatography – MALDI-MS methods. However, in many cases, the low molecular weight region of MALDI mass spectra is obscured by the presence of signals originating from the matrix, suggesting that the development of tethered MALDI matrixes may be required to optimize MS performance for such compounds. To gain insight into potential sites for covalent attachment of MALDI matrixes, we have systematically investigated the role played by a variety of functional group motifs in determining matrix efficiency for three common MALDI matrixes, as judged both by total signal intensity and background noise from matrix decomposition for a set of LMW compounds. A series of allyl derivatives of standard matrixes was prepared, and the efficiency of these materials in the MALDI experiment was measured. All modifications of established matrixes, e.g., 2,5-dihydroxybenzoic acid (DHB), α-cyano-4-hydroxycinnamic acid (CHCA), and caffeic acid (CA), or close analogues led to decreased absolute signal intensity and signal-to-background levels. Improved performance was generally observed with (*i*) the presence of a phenolic group (carboxylic acids were less effective) (*ii*) crystalline derivatives, and (*iii*) compounds that had high extinction coefficients at wavelengths near to that of the exciting laser (337 nm). The most interesting derivatives were the *O*-allyl ether (**15**) and *N*-allyl amide (**16**) of caffeic acid. These compounds did not facilitate signals from all four analytes tested. However, the observed spectra contained fewer signals from the matrix than from the parent compound CA. These compounds demonstrate that functionalization of MALDI matrixes, ultimately leading to tethered matrixes, is possible without jeopardizing signal intensity.

Key words: MALDI, protected matrix, phenol, caffeic acid, allyl ether.

Résumé : L'analyse de composés de faibles masses moléculaires (FMM) est une application émergente de la spectrométrie de masse à désorption-ionisation au laser assistée par la matrice (SM MALDI), souvent couplée à des méthodes de chromatographie liquide. Toutefois, la région des faibles masses moléculaires des SM MALDI est souvent obscurcie par la présence de signaux provenant de la matrice ce qui suggère l'intérêt de développer de matrices MALDI liées pour optimiser la performance de la SM de tels composés. Afin d'identifier des sites potentiels de liaison pour relier d'une façon covalente les matrices MALDI et en se basant sur l'intensité totale du signal et le bruit de fond provenant de la décomposition de la matrice pour un ensemble de composés de faible masse moléculaire, on a examiné systématiquement le rôle qui est joué par une variété de motifs de groupes dans la détermination de l'efficacité de la matrice de trois matrices MALDI usuelles. On a préparé une série de dérivés allyliques de matrices standards et on a mesuré l'efficacité de ces matériaux dans l'expérience MALDI. Les modifications aux matrices établies, telles celles de l'acide 2,5-dihydroxybenzoïque (ADHB), de l'acide α-cyano-4-hydroxycinnamique (ACHC) et de l'acide caféique (AC) ou de produits fortement apparentés ont toutes conduit à des diminutions absolues de l'intensité du signal et des niveaux de signal à bruit de fond. On a généralement observé une amélioration de la performance avec: (*i*) une présence de groupe phénolique quoique celle d'acides carboxyliques ait été moins efficace, (*ii*) des dérivés cristallins et (*iii*) des composés dont le coefficient d'extinction est élevé à des longueurs d'onde se rapprochant de celle (337 nm) du laser excitant. Les dérivés les plus intéressants sont les dérivés de l'acide caféique comportant un groupe éther *O*-allyle (**15**) ou un amide *N*-allyle (**16**). Ces composés n'ont pas facilité les signaux de chacun des quatre analytes examinés. Toutefois, les spectres observés comportaient moins de signaux provenant de la matrice que celui de l'acide caféique fondamental. Ces composés démontrent qu'il est possible de fonctionnaliser des matrices MALDI, conduisant finalement à des matrices liées, sans mettre en péril l'intensité du signal.

Received 9 August 2006. Accepted 30 October 2006. Published on the NRC Research Press Web site at http://canjchem.nrc.ca on 9 February 2007.

S. Martic,[1] J.D. Brennan, and M.A. Brook.[2] Department of Chemistry, McMaster University, 1280 Main St. W., Hamilton, ON L8S 4M1, Canada.
S. Ackloo and N. Nagy. MDS-Sciex, 71 Four Valley Drive, Concord, ON L4K 4V8, Canada.

[1]Current address: Department of Chemistry, Queen's University, Kingston, ON K7L 3N6, Canada.
[2]Corresponding author (e-mail: mabrook@mcmaster.ca).

 doi:10.1139/V06-185 © 2007 NRC Canada

Mots-clés : désorption-ionisation au laser assistée par la matrice (MALDI), matrice protégée, phénol acide caféique, éther allylique.

[Traduit par la Rédaction]

Introduction

Since the development of matrix-assisted laser desorption ionization (MALDI) mass spectrometry in late 1980s (1), numerous advances have been made to expand its applicability and usability. Generally, MALDI is less demanding with respect to the purity of the sample than the electrospray ionization (ESI) technique. Other advantages such as reduction in signal suppression (2, 3), the presence of predominantly singly charged ions (i.e., relatively simple spectra), higher sensitivity, tolerance for salts and impurities (4, 5), and wide mass range (~300 kDa) make this method highly desirable for rapid and automated qualitative analysis.

Typically, UV–MALDI involves the use of an organic UV-absorbing molecule that co-crystallizes with the analyte, absorbs UV laser light, and effectively transfers energy to the analyte, and thus in turn leads to analyte desorption and ionization. MALDI has been successfully employed in the study of biomolecules (peptides, proteins, oligonucleotides, nucleic acids, carbohydrates, and so forth) and synthetic polymers. In general, a large molar excess of matrix:sample (from 100:1 to 1000 0:1) is used, since the matrix serves as the primary (and highly efficient) absorber of the UV laser radiation and breaks down rapidly, expanding into the gas phase (6).

Although the choice of matrix is generally a product of trial and error, several characteristics are generally considered to be necessary for good MALDI performance of the matrix. These include the following: efficient UV absorbance near the irradiation wavelength, crystallization of the matrix, and the presence of relevant chemical functionalities that act as a proton source. The organic molecules that are currently used as MALDI matrixes strongly absorb near 337 nm (emission wavelength of a nitrogen laser), undergo extensive crystallization, and are generally substituted phenols, carboxylic acids, and (or) amines, such as 2,5-dihydroxybenzoic acid (DHB) (**1**), α-cyano-4-hydroxycinnamic acid (CHCA) (**2**), caffeic acid (CA) (**3**), and so forth.

An emerging application of MALDI-MS is the analysis of low molecular weight (LMW) compounds (5, 7, 8, 9), either directly or via coupled liquid chromatography – MALDI-MS methods (5). However, a potential drawback of MALDI-MS is that the analysis of LMW species is difficult, since the clusters and multimers formed by the matrix can lead to LMW peaks that obscure those of the analyte (10, 11).

A number of different approaches have been developed to minimize the extent to which matrix-related interferences are present in the low molecular mass region of the spectrum. For example, in the case where it is convenient to use more analyte than matrix, it is possible to suppress matrix signals (8). However, analytes in normal applications are frequently available only in very low quantities, for example, from compound libraries; a matrix that generates obscuring signals in such cases in not practicable. In an alternative approach, interfacing of MALDI with tandem mass spectrometry (MS-MS) can allow selective detection of LMW compounds with minimal matrix background (5,7). However, this requires more specialized instrumentation, and thus, the method cannot be utilized with conventional MALDI-TOF MS systems. Alternatively, several materials that do not contain an organic matrix have been used as MALDI supports, including porous silicon (DIOS) (12, 13) and fine metal oxide inorganic particles, such as TiO_2 and ZnO (14). These newly developed methods use materials of high photoabsorptivity, low heat capacity, and large surface area. The methods produce minimal molecular fragmentation of analytes and can allow for great sensitivity. However, they exhibit limited capacity in terms of number of shots per spot. Thus, there is still a need for improved MALDI matrix materials, particularly for the analysis of compounds in the LMW region.

An alternative approach incorporates a photoactive matrix within a supporting film through either physical or covalent interactions. For example, Hutchens et al. have developed the surface-enhanced neat desorption (SEND) technique, in which energy-absorbing CHCA was covalently attached to the polymer by a photolabile ester linkage and was able to ionize covalently bound biomolecules as CHCA adducts (15). Alternatively, simply premixing the organic matrix, at various concentrations, with the silica precursor $Si(OEt)_4$ (TEOS), in the sol, leads to a photoactive film suitable for LMW compound analysis, which has been labeled sol–gel-assisted laser desorption ionization (SGALDI) (16, 17, 18). In yet another approach, a chemically modified silica gel, developed using an isocyanate spacer as a linker between the organic matrix and the preformed sol–gel, was successfully used as a MALDI support (19). The use of such silicas as MALDI supports can lead to the successful ionization and desorption of analytes; however, average signal intensity and therefore limits of detection are greatly compromised.

Given that there is a precedent both for covalent immobilization of matrix molecules to polymers (15) and for the use of silica as a support for MALDI (16–19), we are interested in exploring the development of sol–gel-based silica materials containing covalently bound matrix molecules as supports for MALDI-MS. To gain insight into potential sites for covalent attachment of MALDI matrixes, we have systematically investigated the role played by a variety of functional group motifs in determining matrix efficiency for three common MALDI matrixes, as judged both by total signal intensity and background noise from matrix oligomers for a set of LMW compounds. We report here the preparation of a series of derivatives of classical matrixes and analyze their ability to facilitate the MALDI experiment for a series of representative analytes.

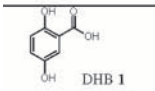
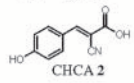
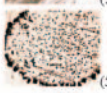
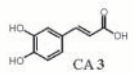
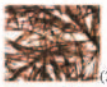
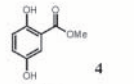
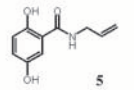
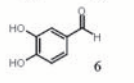
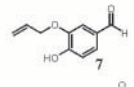
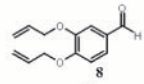
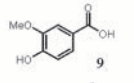
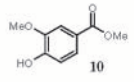
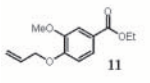
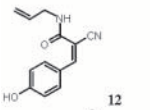
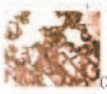
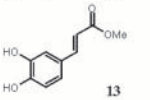
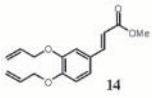
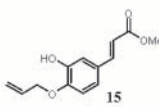
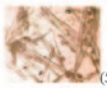
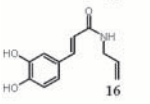
Results

Synthesis

The compounds examined as potential, new MALDI matrixes (Table 1) are derivatives of 2,5-dihydroxybenzoic acid (DHB) (**4**, **5**), related phenol aldehydes (**6**, **7**, **8**), acid derivatives (**9**, **10**, **11**), an α-cyano-4-hydroxycinnamic acid deriva-

© 2007 NRC Canada

Table 1. Synthesized organic matrixes.

Structure of the compound	λ_{max} (nm)	$\varepsilon_{@337nm}$[a] L mol^{-1}cm^{-1}	Optical micrographs[b] (magnification)[c]	MALDI signal to background[d] FLU 332	TMP 290	HP 375	glu-fib 1570
 DHB **1**	332	4139	 (20x)	(2)	3	3	4
 CHCA **2**	342	24467	 (5x)	400	600	300	150
 CA **3**	322	16023	 (20x)	120	50	90	120
 **4**	332	4347	 (5x)	None			
 **5**	324	4691	 (5x)	None			
 **6**	308	2738	 (20x)	None			
 **7**	310	2416	 A	None			
 **8**	304	1500	 A	None			
 **9**	292	1066	 (5x)	(2)	9[e]		
 **10**	292	1055	 A	0	9[e]	0	0
 **11**	294	1077	 A	0	14[e]	0	0
 **12**	326	8516	 (20x)	33	0	17	0
 **13**	324	8545	 (20x)	12	4	(2)	0
 **14**	300	2373	 (50x)	None			
 **15**	322	10222	 (50x)	12	20	30	0[f]
 **16**	318	9083	 (20x)	16	3	10	(2)

[a]UV characteristics measured at 0.120 nmol/L.
[b]Crystals from acetonitrile:water, containing 0.1% TFA (50:50 or 75:25 *v*/*v*).
[c]Crystalline, unless otherwise noted; A: amorphous solid.
[d]Breadboard MALDI-TOF Mass spectrometer (Research). (All MALDI-TOF MS spectra were obtained using 337 nm laser and 16 µJ laser intensity). As there is variability between spectra, these values represent the average integrated signal intensity of at least three spectra.
[e]This compound exhibited particularly inconsistent relative intensities among TMP, FLU, and HP.

tive (CHCA) (**12**), and caffeic acid (CA) derivatives (**13**, **14**, **15**, **16**), respectively. In general, all compounds were prepared using protecting group chemistry to allow the introduction of allyl groups in various forms and at various locations. Such groups are well established starting points for further elaboration to triethoxysilyl derivatives, based on hydrosilylation with $HSi(OEt)_3$, catalyzed by Karstedts Pt(0) catalyst, to create compounds such as those represented by **17**–**20**, which should permit the incorporation of these materials into sol–gel-derived T or TQ resins (20).[3] Although hydrosilylation is generally a very efficient reaction (Scheme 1), certain functional groups, particularly amines and aldehydes, can complex with the platinum catalyst or divert the reaction to undesired products. For example, it was not possible to silylate **8**, **12**, or **16** under a variety of conditions.

The starting compounds noted above are polyfunctional, usually containing both phenols and (or) carboxylic acids. Allyl groups were usually introduced in one of two complementary ways, using either Williamson etherification of phenols or amidation of carboxylic acids by the carbodiimide-catalyzed reaction of allylamine with the carboxylic acid (Scheme 1). During phenol etherification and subsequently for hydrosilylation experiments with triethoxysilane, it was generally necessary to protect carboxylic acids (20). We note that other chemical approaches can also be used to prepare silylated starting materials, including the modification of hydroxyphthalic anhydride with a common silane linker aminopropyltriethoxysilane (APTS) and the direct reaction of isocyanatopropyltriethoxysilane (IPTES) with 7-amino-4-methylcoumarin (Scheme 2). However, for the purposes of this study, it was sufficient to prepare allyl derivatives to allow for investigation of the roles of functional groups in supporting the MALDI process.

UV studies and crystal morphology

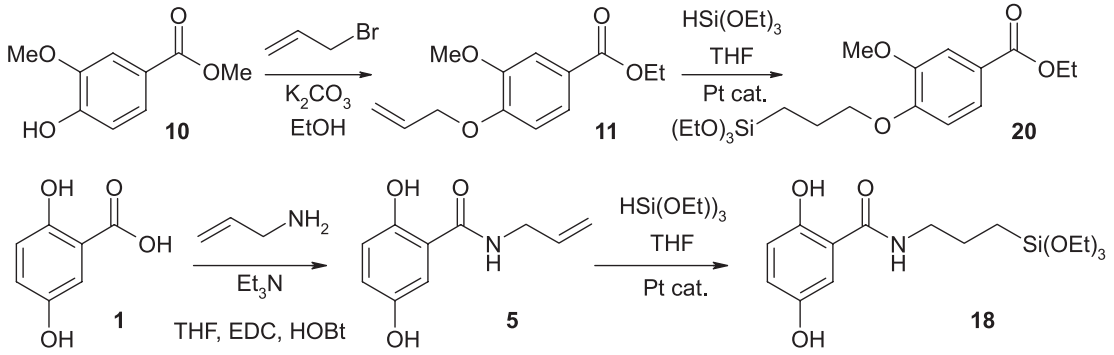
It has been reported that MALDI performance strongly correlates with both UV absorbance (21) and crystallinity (22, 23); however, some matrixes that lack crystal structure can perform well (24). The UV characteristics and representative optical micrographs of the parent compounds and allylated derivatives are collated in Table 1 (the synthetically modified matrix analogues were each (~20 mg) typically dissolved in 0.1% TFA:acetonitrile (1 mL; 50:50 *v*/*v* or 25:75 *v*/*v*) mixtures and were deposited on a MALDI support, such as a stainless steel plate, to give the micrographs shown). The solvent composition was varied for most matrixes to obtain optimal crystals (highest degree of crystallinity, without occluded solvent) that would lead to maximal signal intensities of the analytes. Multiple spots of these matrixes were used to generate average analyte intensities.

The nature of the functional groups greatly affected the UV molar extinction coefficients at the wavelength of the ni-

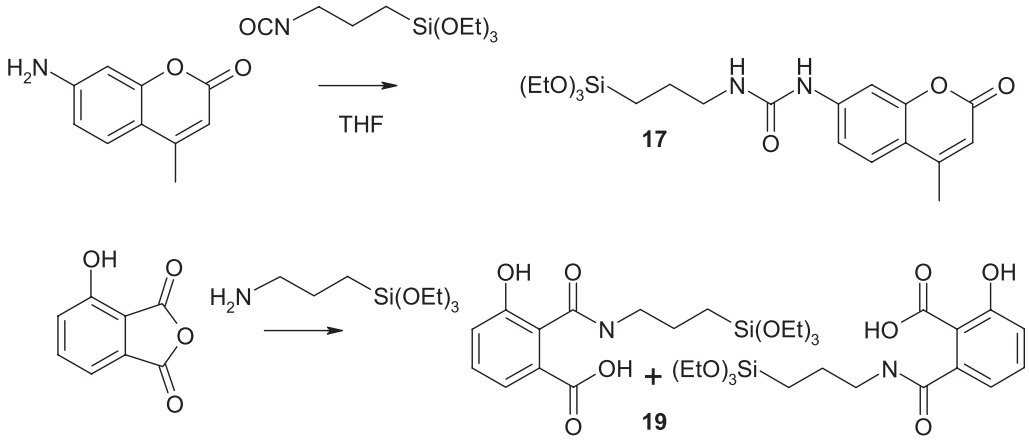
[3]T resins are derived from trifunctional silicon species, e.g., $RSi(OR')_3 + H_2O \rightarrow 3\ R'OH + RSi(O_{3/2})_n$, the latter is a T resin. Analogously, silica is a Q (quatrafunctional silicon species) resin: $Si(OR')_4 + H_2O \rightarrow 4\ R'OH + Si(O_{4/2})_n$. This nomenclature, commonly used for silicones, can also be used in combination (M, monofunctional; D, difunctional; T, trifunctional; and Q, quatrafunctional), for example, in TQ resins, see ref. 20.

© 2007 NRC Canada

Scheme 1. Sample synthetic schemes for allylation and the subsequent hydrosilylation.

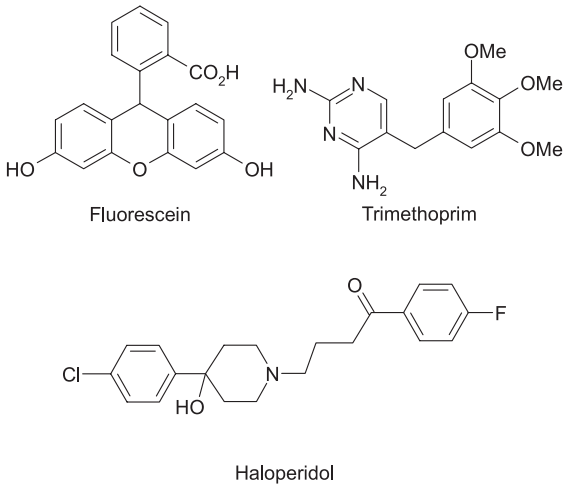


Scheme 2. Alternate approaches to the silylated matrixes.



trogen laser, 337 nm, typically used in the MALDI experiment. Notably, a laser change to 355 nm did not enhance the matrix performance in the samples studied, and therefore, the N_2 laser was the standard source used. Modifications of DHB did not significantly change the extinction coefficient (**4**, **5**), but derivatives of 3,4-dihydroxybenzoic acid (**6**–**11**), the CHCA derivative (**12**), and the CA derivatives (**13**–**16**) all had lower extinction coefficients. Therefore, the performance of these materials is expected to be less than that of the parent compounds.

Chart 1. Structures of fluorescein, trimethoprim, and haloperidol.



Effect of functional groups on MALDI efficiency

Four representative analytes were chosen for the study: haloperidol (HP, neutral, MW 375), trimethoprim (TMP, cationic, MW 290), fluorescein (FLU, anionic, MW 332) (see Chart 1), and the oligopeptide glu-fibrinopeptide (glu-fib, EGVNDNEEGFFSAR, MW 1570, a higher molecular weight, anionic, oligopeptide analyte). Preliminary experiments using conventional MALDI matrixes (DHB and CHCA) led to the following optimized conditions for MALDI experiments: 50:50 *v*/*v* acetonitrile : 0.1% trifluoroacetic acid (in water) solvent composition, 16 μJ laser intensity, 20 mg/mL matrix concentration, and 2.5 ng/μL analyte concentration. The same conditions were applied to the derivatized matrixes to study their efficiency solely as a function of chemical modification (i.e., a head-to-head comparison of the parent matrixes and their derivatives). The matrix performance under these conditions was judged solely on average signal intensity and matrix interference. We have also studied the effect of matrix:analyte ratio, where analyte concentrations used were 0.01 ng/μL, 0.04 ng/μL, 0.1 ng/μL, 1 ng/μL, and 2.5 ng/μL (20 mg/mL matrix concentration) to determine the detection limit of most matrixes. We found that most matrixes performed optimally when 1–2.5 ng/μL analyte concentration was used. In the second study, a laser intensity was varied in the range of 4–31 μJ. With the increase in laser power, the analyte signal increased, but this was accompanied by a significant increase in the overall matrix signal intensity, making the spectral in-

© 2007 NRC Canada

terpretation more complex. A laser intensity of 16 μJ led to adequate analyte signals with minimal matrix interference, and it was adopted as the optimized condition.

When MALDI-MS of glu-fib, trimethoprim, haloperidol, and fluorescein was performed using three standard matrix compounds, DHB **1**, CHCA **2**, and CA **3**, ionization of all four analytes was generally achieved (Table 1). The spectra were typically confounded by many peaks originating from the matrix (Fig. 1). However, it was interesting to note that the highest signal typically corresponded to the highest ϵ_{337nm} (CHCA > CA > DHB), which suggests that the facility for photoexcitation is a critical factor for the activation of the specific matrixes. These data provide a positive control for the remaining matrix compounds. Because these matrixes possess both phenols and an acid, it was unclear which of the functional groups plays the most important role in facilitating the ionization.

Two general classes of modifications were made on the original matrixes. In the first case, phenols remained uncapped, but carboxylic acids were replaced by aldehydes, esters, or amides. In the second case, phenols were capped, and free carboxylic acids were present. The results of the MALDI experiments obtained under identical conditions are shown in Table 1. Among the compounds studied, the best MALDI performance (for fluorescein, haloperidol, and TMP, but not glu-fib, Fig. 2), as judged by signal to background (S:B) ratios, was obtained using matrixes that possessed either one or two phenol groups, irrespective of the presence of an acid group, and a conjugated carbonyl group ion, e.g., allyl ether (**15**), and *N*-allylamide derivatives of CA (**16).** However, several compounds did not result in any analyte ionization. These could be divided into two classes: those with free phenols but protected carboxylic acids (**4**, **5**), and those with absorption wavelengths far from 337 nm (**7**, **8**, **14**). Note that two compounds (**10**, **11**) with λ_{max} far from 337 nm were still effective matrixes, but only for TMP.

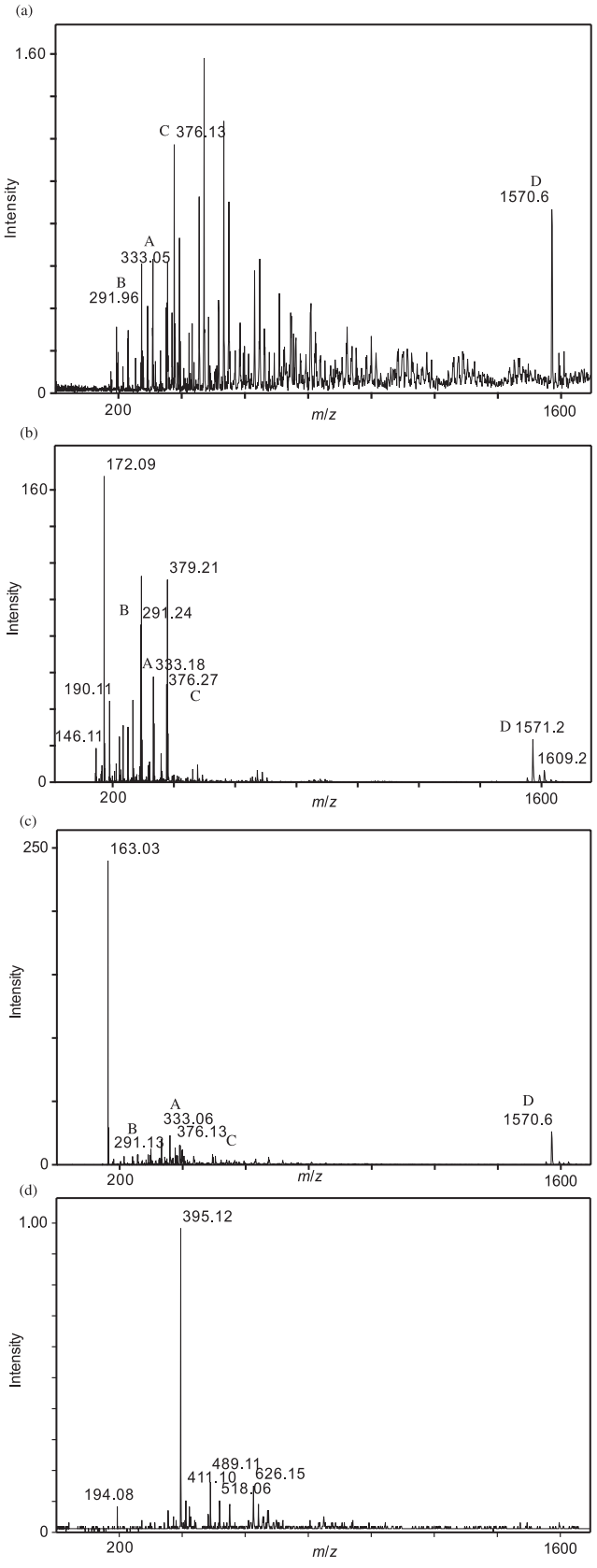
For those derivatized compounds that were effective matrixes, absolute ion intensities were far lower than with their parent compounds (Table 1). The efficiency of the matrix to promote analyte ionization is, thus, highly dependent on the nature of the available matrix functional groups. A significant suppression of matrix signals was observed with some matrixes. For example, the matrix noise correlated with DHB is almost 100 times higher than the matrix noise observed for its allylamide (**5**) derivative (Fig. 1*d*). Regrettably, the lower noise in these cases is not accompanied by higher signal:background levels (Table 1).

Discussion

Ionization mechanisms in MALDI are believed to involve chemical and (or) thermal ionization mechanisms, such as gas-phase photoionization, ion–molecule reactions, disproportionation, excited-state proton transfer, energy pooling, thermal ionization, and desorption of preformed ions (25).

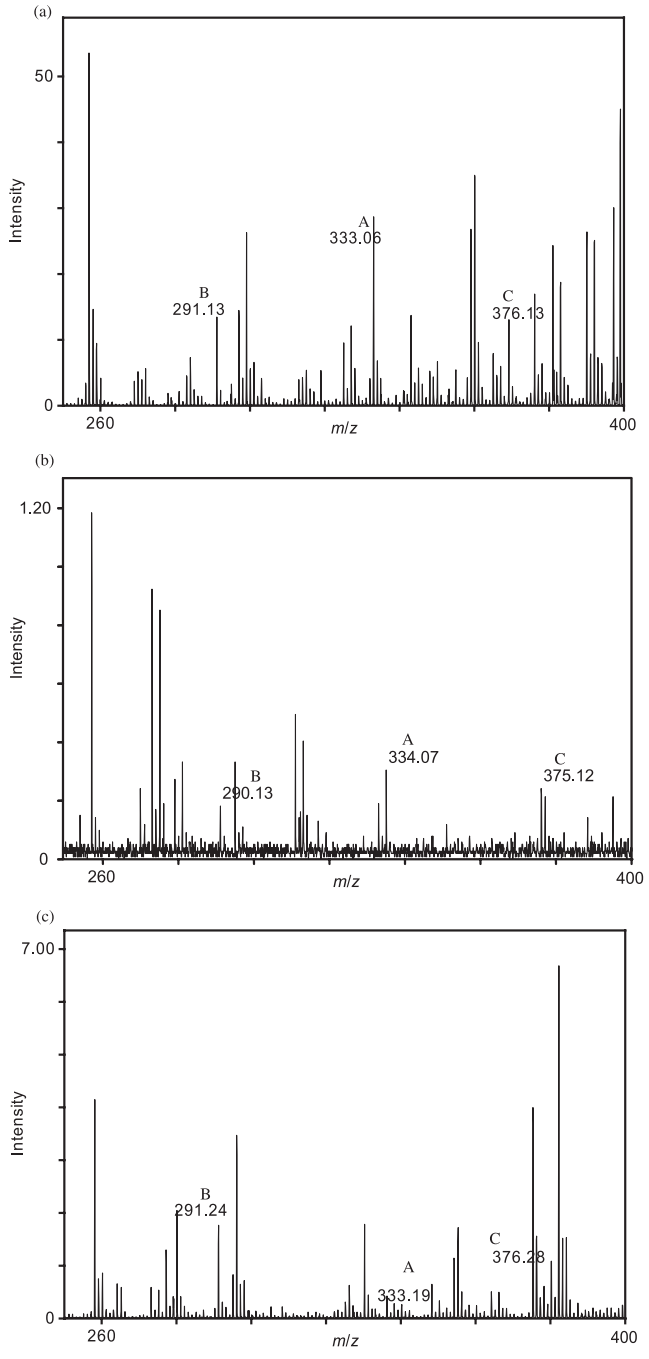
In the case of standard acidic matrixes, gas-phase proton transfer reactions between matrix ions and analyte are regarded as the main ionization pathway (21). MALDI spectra are generally populated with singly charged protonated, sodiated, or potassiated ions, as well as numerous matrix-related signals in the low mass region. Several studies, dem-

Fig. 1. MALDI-MS of fluorescein (A), trimethoprim (B), haloperidol (C), and glu-fib (D), using (*a*) DHB **1**, (*b*) CHCA **2**, (*c*) CA matrix **3**, and (*d*) **5**.



© 2007 NRC Canada

Fig. 2. MALDI-MS (MW 250–400 portion of the spectra) of fluorescein (A), trimethoprim (B), and haloperidol (C), using (*a*) CA matrix **3**, (*b*) **15**, and (*c*) **16**.



onstrating that the source of protons is a phenol rather than a carboxylic acid, have been published (26–29). It is certain that the acidic properties of the aromatic derivatives are strongly enhanced when molecules are laser-excited, and phenols are known to be more acidic in the gas phase than carboxylic acids (30).

Some authors found the derivatization of the phenolic groups to strongly degrade MALDI efficiency of the matrix, whereas others came to the opposite conclusion (31). It was further demonstrated that, with some free matrixes, exchangeable protons are not needed for ionization to take place. These results suggested that alternative mechanisms may be at play in the MALDI process. The explanation of what makes a material function as a matrix remains ambiguous. Irrespective of the specific mechanisms of ionization, factors including high UV-absorptivity at the wavelength of the laser, exchangeable protons, and, it has been argued, ease of crystallization and co-crystallization with analyte have been identified as key parameters affecting MALDI performance. These features have been examined in the series of allylated matrix analogues prepared, all of which led to significantly lower analyte signals than the standard matrixes DHB, CA, and CHCA, respectively.

It has been proposed that crystallization may be a key factor for effective MALDI matrixes (22). This contention is generally supported by the characteristics of the compounds prepared. Crystalline derivatives were in general more effective MALDI matrixes than amorphous compounds, e.g., **15** and **16**. However, this is not always true. For example, highly crystalline derivatives such as methyl 2,5-dihydroxybenzoate (**4**) failed to work as a matrix, while highly amorphous matrixes such as that derived from 3-methoxy-4-hydroxybenzoic acid (**9**) were effective at promoting selective TMP desorption and ionization, despite the absence of obvious crystals.

It was initially expected that compounds with a high extinction coefficient at 337 nm, the laser wavelength, would be highly effective matrixes. Indeed, compounds with absorption wavelengths far from 337 nm were not effective matrixes; however, many of the compounds with absorption maxima near this wavelength were also inactive as matrixes. Even compounds with relatively high extinction coefficients and λ_{max} close to 337 nm were not always effective, e.g., **13**. Thus, similar to the observations of Bashir et al. (26), UV absorption alone is not a sufficient criterion for selecting a useful matrix; two similarly absorbing molecules may perform completely differently.

It has been reported that an exchangeable phenolic or carboxylic acid proton is needed for proton transfer in the MALDI process (31). The synthesized compounds that acted as matrixes possessed at least one free phenol group (**9**–**13**, **15**, **16**). However, neither the presence of a phenol or a carboxylic acid is a guarantee of efficacy. For example, compounds **4** and **5**, both subtle, crystalline variations of DHB with similar λ_{max} and extinction coefficients, were not effective matrixes. By contrast, the most effective matrixes had free phenols and additionally were β-substituents of α,β-unsaturated carbonyl systems. These findings strongly suggest that such species should form a useful starting point for the preparation of silylated derivatives and ultimately covalently bound matrix systems.

The generally prepared protected matrixes exhibited different analyte selectivities from their non-modified parent compounds in addition to a significant attenuation of total signal and signal to background levels. The clearest demonstration of this is the comparison of compounds **13** and **15**. The latter exhibits a strong signal for HP and TMP, while the former only excited FLU effectively. In both cases, the matrixes lead to useful but selective signals. Utilization of these matrixes, therefore, needs to be accompanied by experiments to assess sensitivity to the analytes of interest.

© 2007 NRC Canada

Based on the objective to reduce LMW noise and to show efficacy across different analyte types, compounds **15** and **16** are of most interest. With respect to the key factors affecting matrix efficiency, a comparison of these compounds with their precursors CHCA **3** and **13** and the related derivative **14** is instructive. The order of efficacy based on the ability to enhance MALDI analyte signal intensity over background follows the order **3** » **15**, **16** > **13** » **14**. All compounds but **13** are crystalline; all have reasonably large extinction coefficients with λ_{max} values reasonably close to 337 nm, again except **14**. Compound **14** also has no free, acidic protons to be used for the proton transfer to analyte. It is not therefore surprising that **14** is an ineffective matrix.

The other compounds have, with the exception of **3**, which has a much higher extinction coefficient, very similar chemical and physical characteristics. The subtle differences are associated with the location and number of protecting groups. Free phenolic groups suffice to excite some of the analytes. The reduced signal to background ratio for **15** and **16**, when compared to **3**, is partially compensated for by the decrease in low molecular signals arising from the matrix (Fig. 2). An important finding is that the presence of the allyl group, key for the introduction of synthetic handles to permit binding to mineral oxide surfaces, reduces the efficacy of the MALDI matrix but does not destroy activity. This provides an opportunity to tether these materials to a variety of mineral oxide surfaces or to make mineral oxide films containing the matrix and use them as MALDI targets. Current work in this area is ongoing and shall be the subject of future reports.

Experimental

Chemicals

Allylamine, allyl bromide, 3-aminopropyltriethoxysilane (APTS), benzyl bromide, 3,5-dihydroxybenzaldehyde (**6**), 1-[3-(dimethylamino)propyl]-3-ethylcarbodiimide, 1-hydroxybenzotriazole hydrate, 3-hydroxyphthalic anhydride, 3-methoxy-4-hydroxybenzoic acid (**9**), (3-isocyanatopropyl)triethoxysilane, tetraethyl orthosilicate (TEOS, 99.999%), platinum (0)-1,3-divinyl-1,1,3,3-tetramethyldisiloxane in xylene ($Pt_2[CH_2{=}CHSiMe_2OSiMe_2CH{=}CH_2]4$ 2–3% Pt in xylene (Karstedt's catalyst)), triethylamine, and trifluoroacetic acid (99.8%) were obtained from Aldrich Chemical Company Inc. (Milwaukee, WI, USA). 2,5-Dihydroxybenzoic acid, α-cyano-4-hydroxycinnamic acid, coumarin, caffeic acid, triethoxysilane, sulfuric acid (98%), 3,4-dihydroxycinnamic acid, and 0.1 N HCl were obtained from Sigma-Aldrich (St. Louis, MO). Methanol, diethyl ether, ethyl acetate, dimethylformamide, dimethylsulfoxide, tetrahydrofuran, ethanol, potassium carbonate, dichloromethane, hexane, potassium hydroxide, sodium hydroxide, sodium chloride, magnesium sulfate, thionyl chloride, and pyridine were purchased from Caledon Laboratories, Ltd. (Georgetown, ON). Silica gel and sodium bicarbonate were purchased from EMD Chemicals Inc. (Darmstadt, Germany), while sodium carbonate was purchased from EM Science (Gibbstown, NJ), and 7-amino-4-methylcoumarin was purchased from INDOFINE Chemical Co. (Hillsborough, NJ).

Characterization

^1H and ^{13}C NMR were performed on either a Bruker AC-200 (200.13 MHz) or a Bruker AC-300 (300.13 MHz) spectrometer. Solid state ^{13}C NMR was performed on a Bruker AC-300 (at 300.13 MHz for ^{13}C) solid state spectrometer. Samples were dissolved in chloroform-*d* ($CDCl_3$), DMSO-d_6, or methanol-d_4 with chemical shifts (ppm, δ) reported relative to TMS as a reference. Coupling constants *J* were recorded in Hertz (Hz).

FTIR studies were recorded on a Bruker Equinox 55 spectrometer. Peaks were reported in wavenumbers (cm^{-1}), and the samples were run pure in their solid or liquid state.

Mass spectrometry to characterize the structures of the synthesized matrixes was performed using electron ionization (EI), chemical ionization (CI), liquid-chromatography mass spectrometry (LC–MS), or electrospray ionization (ESI) techniques.

Optical microscopy (Olympus BX41) was used to study crystal morphologies of the matrixes on MALDI plates.

UV-absorption measurements of solutions were made in 96 well plates using a Tecan SAFIRE platereader (monochromator based with XFLUOR software) with a wavelength resolution of 1 nm. All spectra were obtained at the ambient temperature and had appropriate background signals subtracted. In general, the products were characterized using ^1H and ^{13}C NMR, EI-MS, CI-MS, ESI-MS, UV, LC–MS, FTIR, and fluorescence.

Synthesis of the protected matrixes

Methyl 2,5-dihydroxybenzoate (4)

To 2,5-dihydroxybenzoic acid (1.154 g, 7.487 mmol), dissolved in methanol (5.28 mL), was added 98% H_2SO_4 (0.678 mL, 8.970 mmol). After the reaction mixture was refluxed at 65 °C for 29 h, the solution was extracted using diethyl ether. After the evaporation of the organic fractions and recrystallization from water, a white solid was obtained (yield: 0.488 g, 72%; mp 76 °C).

λ_{max} = 332 nm, ϵ_{337nm} = 4347.44 M^{-1} cm^{-1}, λ_{ex} = 340 nm, λ_{em} = 416 and 496 nm. FTIR (neat) ν (cm^{-1}): 3745, 3335, 1686, 1337, 1216. ^1H NMR (MeOH-d_4, 200 MHz) δ: 4.10 (3H, s), 7.04 (1H, dd, *J* = 3.7, 8.9 Hz), 7.18 (1H, d, *J* = 3.2, 8.9 Hz), 7.44 (1H, t, *J* = 3.4 Hz), 10.5 (1H, s, 2-OH). ^{13}C NMR (MeOH-d_4, 200 MHz) δ: 52.4, 114.7, 118.5, 121.1, 124.1, 147.8, 154.9, 155.6. CI^+-MS *m*/*z* (%): 168 [M^+] (73), 136 [M^+ – OH] (100), 108 (21), 80 (8). EI^+-MS *m*/*z* (%): 168 [M^+] (36), 136 [M^+ – OH] (100), 121 (44), 108 (32), 80 (13). ESI-MS *m*/*z*: 196 (13), 169 [M + H]$^+$(100), 155 (16), 83 (8). LC–MS: r_t = 9.45 min.

N-*Allyl 2,5-dihydroxybenzamide (5)*

To 2,5-dihydroxybenzoic acid (3.1004 g, 0.0201 mol), dissolved in dry tetrahydrofuran (160 mL), 1-[3-(dimethylamino)propyl]-3-ethylcarbodiimide (EDC) (4.307 g, 0.0221 mol, 1.1 equiv.), 1-hydroxybenzotriazole hydrate (HOBt) (2.723 g, 0.0201 mol, 1 equiv.), triethylamine (3.08 mL, 0.02211 mol, 1.1 equiv.), and DMAP (0.1608 g, 5%) were added. Previously dissolved allylamine (1.513 mL, 0.0201 mol, *d* = 0.76 g/mL) in THF was then added to the reaction flask. The mixture was stirred at room temperature overnight. Once the mixture was evaporated to dryness, the solid was dissolved in 0.1 N HCl and washed with ethyl acetate. Organic frac-

© 2007 NRC Canada

tions were washed with $NaHCO_3$, H_2O, NaCl, and brine and dried over $MgSO_4$. Column chromatography was performed with hexane : ethyl acetate (60:40 *v/v*) to remove residual allylamine and isolate the pure product as a white powder (yield: 1.0648 g, 34.3 %; mp 103 °C).

λ_{max} = 324 nm, ϵ_{337nm} = 4691.03 M^{-1} cm^{-1}, λ_{ex} = 340 nm, λ_{em} = 399, 441, 494 nm. FTIR (neat) ν (cm^{-1}): 3399, 3334, 1576, 1546, 1226, 993, 947. ^{1}H NMR (MeOH-d_4, 200 MHz) δ: 3.99 (2H, d, *J* = 5.2 Hz), 5.17 (1H, dd, *J* = 1.2, 10.3 Hz), 5.23 (1H, dd, *J* = 1.2, 17.2 Hz), 5.92 (1H, m, *J* = 5.2, 10.3, 19.4 Hz), 6.74 (1H, d, *J* = 8.8 Hz), 6.85 (1H, dd, *J* = 2.8, 8.8 Hz), 7.22 (1H, d, *J* = 2.8 Hz). ^{13}C NMR (MeOH-d_4, 200 MHz) δ: 42.8, 114.8, 116.2, 117.7, 118.9, 122.3, 135.5, 150.9, 153.5, 170.1. CI-MS *m/z* (%): 193 [M^+] (100), 175 (14), 164 (18), 136 (44), 108 (11). ESI-MS *m/z* (%): 306 [M + TFA]$^-$ (74), 238 [M + 45]$^-$ (97), 192 [M – H] (100), 138 (12), 112 (22). ESI-MS *m/z* (%): 194 [M + H]$^+$ (100), 65 (68), 216 [M + Na]$^+$ (12). CI-MS *m/z* (%): 193 (M^+). LC–MS: r_t= 8.18 min.

3-Allyloxy-4-hydroxybenzaldehyde + 4-allyloxy-3-hydroxybenzaldehyde (7); 3,4-diallyloxybenzaldehyde (8)

To 3,5-dihydroxybenzaldehyde (4.0234 g, 29.1 mmol), dissolved in 150 mL of absolute methanol, was added previously oven dried potassium carbonate (4.0273 g, 29.1 mmol). The mixture was heated to 50 °C, and allyl bromide (3.04 mL, 1.39 g/mL, 34.9 mmol) was added to the flask dropwise through a septum. The mixture was further heated to 60 °C and then refluxed overnight (16 h). After the solvent was evaporated, the brown liquid was dissolved in ethyl acetate and washed with 1 mol/L HCl until an acidic pH was obtained (pH = 6.2). After the separation and extraction with ethyl acetate, the organic fractions were washed with brine and dried with anhyd. $MgSO_4$. The organic solvent was evaporated, and the brown liquid was then separated using silica gel column chromatography with 3% methanol in dichloromethane as the solvent. Three different fractions were recovered: (*i*) monoallyloxy derivative (0.970 g, 24.5%; brown gel), (*ii*) diallyloxy derivative (0.8501 g, 21%; brown liquid), and (*iii*) mono/diallyloxy derivative mixture (yield: 1.8256 g, 45%; approximate mono/diallyloxy ratio in the mixture was 3.1:1 (from LC–MS intensity ratio)). Each fraction was separately characterized.

Monoallyl derivatives

λ_{max}= 322 nm, ϵ_{337nm} = 2411.54 M^{-1} cm^{-1}, λ_{ex} = 340 nm, λ_{em} = 395 and 433 nm. FTIR (neat) ν (cm^{-1}): 3420, 3090, 2980, 2860, 1681, 1548, 1508, 1271, 1125, 993. ^{1}H NMR ($CDCl_3$, 200 MHz) δ: 4.68 (2H, d, *J* = 5.4 Hz), 5.34 (1H, d, *J* = 19.5 Hz), 5.41 (1H, dd, *J* = 1.0, 17.3 Hz), 6.04 (1H, m), 6.94 (1H, d, *J* = 8.2 Hz), 7.38 (1H, dd, *J* = 1.8, 8.1 Hz), 7.48 (1H, d, *J* = 1.9 Hz), 9.80 (1H, s). ^{13}C NMR ($CDCl_3$, 200 MHz) δ: 69.9, 111.5, 114.4, 119.3, 124.5, 130.7, 131.9, 146.4, 150.9, 191.2. CI-MS *m/z* (%): 178.06 [M^+] (100), 149 (8), 137 (9). ESI-MS: 355 [2M – H]$^-$ (11), 291 [M + TFA]$^-$ (92), 177 [M – H]$^-$ (100), 136 (14). LC–MS: r_t = 15.11 min.

Diallyloxy derivative

λ_{max}= 304 nm; ϵ_{337nm} = 1500.00 M^{-1} cm^{-1}; λ_{ex}= 340 nm; λ_{em}= 394 and 434 nm. FTIR (neat) ν (cm^{-1}): 3050, 2931, 2750, 1695, 1684, 993. ^{1}H NMR (MeOH-d_4, 200 MHz) δ: 4.58 (2H, d, *J* = 4.8 Hz), 4.59 (2H, d, *J* = 5.1 Hz), 5.23 (1H, d, *J* = 1.5, 10.5 Hz), 5.28 (1H, d, *J* = 1.5, 10.4 Hz), 5.38 (1H, d, *J* = 1.5, 17.3 Hz), 5.47 (1H, d, *J* = 1.5, 17.4 Hz), 6.03 (1H, m, *J* = 5.2, 10.5 Hz), 6.04 (1H, m, *J* = 5.2, 18.3 Hz), 7.02 (1H, dd, *J* = 2.5, 8.2 Hz), 7.38 (1H, d, *J* = 2.0 Hz), 7.43 (1H, dd, *J* = 2.4, 8.2 Hz), 9.74 (1H, d, *J* = 2.5 Hz). ^{13}C NMR ($CDCl_3$, 200 MHz) δ: 69.8, 111.6, 112.4, 118.2, 118.4, 126.7, 130.2, 132.4, 132.7, 148.9, 153.9, 190.9. CI-MS *m/z* (%): 218 [M^+] (100), 177 (23), 149 (20), 121 (9). ESI-MS *m/z* (%): 363 (18), 331 [M + TFA]$^-$ (100), 249 (63), 217 [M – H]$^-$ (23), 176 (13). LC–MS: r_t = 17.0 min.

Methyl 4-hydroxy-3-methoxybenzoate (10)

After 3-methoxy-4-hydroxy benzoic acid (1.14 g, 6.7 mmol) was dissolved in methanol (50 mL) and cooled to 0 °C, thionyl chloride (2.44 mL, 33.8 mmol) was added dropwise through a rubber septum. The reaction mixture was stirred at room temperature for 20 h. The solvent was evaporated, and the mixture was extracted with diethyl ether, washed with sodium bicarbonate, water, sodium chloride, and brine. Organic fractions were evaporated to recover an ester as a white solid (yield: 0.974 g, 85.4%; mp. 59 °C).

λ_{max}= 292 nm, ϵ_{337nm} = 1054. 94 M^{-1} cm^{-1}, λ_{ex} = 340 nm, λ_{em} = 392 and 432 nm. FTIR (neat) ν (cm^{-1}): 3537, 3100, 3050, 2940, 1697, 1602, 1512, 1462, 1297, 1217, 1155, 777. ^{1}H NMR (MeOH-d_4, 200 MHz) δ: 3.84 (OCH_3, 3H), 3.88 (OCH_3, 3H), 6.82 (1H, d, *J* = 8.7 Hz), 7.51 (1H, s), 7.54 (1H, s). ^{13}C NMR (MeOH-d_4, 200 MHz) δ: 52.4, 56.4, 113.4, 115.9, 122.5, 124.9, 148.9, 152.8, 168.6. CI-MS *m/z* (%): 182 [M]$^+$ (85), 151 [M – OMe]$^+$ (100).

Ethyl 4-allyloxy-3-methoxybenzoate (11)

To a solution of 3-methoxy-4-hydroxy-ethyl benzoate (0.974 g, 5.35 mmol) in absolute ethanol (20 mL) was added previously oven dried potassium carbonate (0.739 g, 5.35 mmol). When the reaction mixture was heated to 50 °C, allyl bromide (0.539 g, 0.377 mL, 4.45 mmol) was added dropwise through a septum. The mixture was refluxed over night (16–18 h). After the solvent was evaporated, the brown liquid was dissolved in ethyl acetate and washed with 1 mol/L HCl until an acidic pH was obtained (pH = 6.2). After the separation of the organic fractions and extraction with ethyl acetate, the organic fractions were washed with brine and dried with anhyd. $MgSO_4$. The organic solvent was evaporated, and the brown liquid was then purified using silica gel column chromatography with hexane : ethyl acetate (60:40 *v/v*) mixture as the solvent. The yellow liquid was recovered in 42.5% yield (0.409 g).

λ_{max} = 294 nm, ϵ_{337nm} = 1076.60 M^{-1} cm^{-1}, λ_{ex} = 340 nm, λ_{em} = 392 and 433 nm. FTIR (neat) ν (cm^{-1}): 3084, 2981, 2930, 1708, 1599, 1511, 1267, 1214, 1018, 761. ^{1}H NMR (MeOH-d_4, 200 MHz) δ: 1.38 (3H, t, *J* = 7.2 Hz), 3.86 (OCH_3, 3H, s), 4.31 (2H, q, *J* = 7.2, 14.2 Hz), 4.62 (2H, d, *J* = 5.1 Hz), 5.26 (1H, d, *J* = 10.5 Hz), 5.41 (1H, dd, *J* = 1.4, 17.3 Hz), 6.05 (1H, m, *J* = 1.4, 16.7, 10.6 Hz), 6.96 (1H, d, *J* = 8.4 Hz), 7.54 (1H, d, *J* = 1.5 Hz), 7.60 (1H, q, *J* = 1.6, 8.4 Hz). ^{13}C NMR (MeOH-d_4, 200 MHz) δ: 14.6, 56.4, 61.9, 70.6, 113.4, 113.5, 118.1, 124.1, 124.6, 134.3, 150.5, 153.7, 167.9. CI-MS *m/z* (%): 237 [M^+] (100), 195 (28), 151 (9).

© 2007 NRC Canada

N-*Allyl-2-cyano-3-(4-hydoxy-phenyl)-acrylamide (12)*

To α-cyano-4-hydroxycinnamic acid (1.995 g, 0.0105 mol), dissolved in dry tetrahydrofuran (160 mL), 1-[3-(dimethylamino)propyl]-3-ethylcarbodiimide (EDC) (2.2238 g, 0.0116 mol, 1.1 equiv.), 1-hydroxybenzotriazole hydrate (HOBt) (1.418 g, 0.0105 mol, 1 equiv.), triethylamine (1.617 mL, 0.0116 mol, 1.1 equiv.), and DMAP (0.0997 g, 5%) were added. Previously dissolved allylamine (0.788 mL, 0.0105 mol) in THF (3 mL) was added to the reaction flask. The mixture was stirred at room temperature overnight. After evaporating to dryness, the solid was dissolved in 0.1 N HCl and washed with ethyl acetate. The organic fractions were washed with $NaHCO_3$, H_2O, NaCl, and brine and dried over $MgSO_4$. Column chromatography was performed with hexane : ethyl acetate (60:40 *v*/*v*) to remove residual allylamine and isolate the pure product as the yellow powder (yield: 1.737 g, 87 %; mp 255 °C).

λ_{max} = 326 nm, ϵ_{337nm} = 8511.54 M^{-1} cm^{-1}, λ_{ex} = 340 nm, λ_{em} = 434 nm. FTIR (neat) ν (cm^{-1}): 3327, 3190, 2970, 2218, 1649, 1568, 1538, 1053. ^{1}H NMR (MeOH-d_4, 200 MHz) δ: 3.96 (2H, d, *J* = 5.3 Hz), 5.15 (1H, dd, *J* = 1.2, 10.5 Hz), 5.22 (1H, dd, *J* = 1.3, 18.9 Hz), 5.88 (1H, m, *J* = 6.9, 10.2, 18.3 Hz), 6.90 (2H, d, *J* = 8.7 Hz), 7.88 (2H, d, *J* = 8.7 Hz), 8.10 (1H, s), 9.76 (1H, 4-OH, s). ^{13}C NMR (MeOH-d_4, 200 MHz) δ: 41.7, 99.2, 114.4, 114.9, 115.3, 122.8, 132.5, 133.0, 151.3, 161.6, 161.9. CI^+-MS *m*/*z* (%): 228 [M^+] (94), 221 [M-17] (37), 290 (17), 172 (48), 123 (28), 107 (100).

Methyl 3,4-dihydroxycinnamate (13)

To 3,4-dihydroxycinnamic acid (4.7096 g, 26 mmol) in methanol (150 mL) at 0 °C was added thionyl chloride (13.5 mL, 0.183 mol) dropwise over 30 min. After stirring the mixture for 24 h, the solvent was evaporated, and the white solid was isolated. From the acidic medium/diethyl ether workup, the organic layers were combined, and the solvent was evaporated. Further purification, using silica column chromatography, was performed with chloroform:methanol (9:1 *v*/*v*). The final white solid was obtained in the 85% yield, 4.001 g; mp 158 °C.

λ_{max} = 324 nm, ϵ_{337nm} = 8544.87 M^{-1} cm^{-1}, λ_{ex} = 340 nm, λ_{em} = 426 nm. FTIR (neat) ν (cm^{-1}): 3501, 3450, 3319, 3019, 1704, 1257, 1177. ^{1}H NMR (MeOH-d_4, 200 MHz) δ: 3.74 (3H, s), 6.25 (1H, d, *J* = 15.9 Hz), 6.77 (1H, d, *J* = 8.1 Hz), 6.93 (1H, d, *J* = 8.1 Hz), 7.02 (1H, s), 7.53 (1H, d, *J* = 15.9 Hz). ^{13}C NMR (MeOH-d_4, 200 MHz) δ: 52.0, 114.8, 115.1, 116.5, 122.9, 127.7, 146.9, 149.6, 156.5, 169.7. EI-MS *m*/*z* (%): 194 [M^+] (93), 163 (100), 145 (23), 134 (25), 117 (21). CI-MS *m*/*z* (%): 208 (18), 194 [M^+](24), 168 (55), 136 (100), 108 (22). ESI^+-MS *m*/*z* (%): 406 [2M + NH_4]$^+$ (23), 389 [2M + H]$^+$ (7), 221 (100), 194 [M + H]$^+$ (55). LC–MS: r_t= 15.18 min.

3,4-Diallyloxy-methyl cinnamate (14); 3-allyloxy-4-hydroxy-methyl cinnamate; 4-allyloxy-3-hydroxy-methyl cinnamate (15)

Anhydrous DMF (50 mL) was added to caffeic acid methyl ester (3.772 g, 0.0191 mol), sodium carbonate (3.314 g, 0.0385 mol), sodium iodide (1.005 g, 0.0064 mol), and allyl bromide (3.344 mL, 0.0401 mol). After the reaction was refluxed at 47 °C for 48 h, the solution was washed with aq. HCl and extracted with ethyl acetate. The combined organic fractions were evaporated to give a brown liquid that was separated using flash chromatography with a mixture of hexane: ethyl acetate (60:40 *v*/*v*). The monoallylated ester derivative was obtained as a white solid (yield: 0.6327 g, 17%). The diallyl derivative was isolated (yield: 0.4686 g, 12%) but was contaminated with the monoallyloxy species. The approximate mono/diallyloxy ratio in the mixture was 2.9:1 from LC–MS intensity ratio. The products were then recrystallized from hexane.

Monoallyl derivative

λ_{max} = 322 nm, ϵ_{337nm} = 10221.79 M^{-1} cm^{-1}, λ_{ex} = 340 nm, λ_{em} = 435 nm. ^{1}H NMR ($CDCl_3$, 200 MHz) δ: 3.78 (3H, s), 4.64 (2H, d, *J* = 5.0 Hz), 5.33 (1H, d, *J* = 10.6 Hz), 5.40 (1H, d, *J* = 17.4 Hz), 5.78 (1H, s, 3-OH), 6.01 (1H, m, *J* = 5.9, 10.5, 17.7 Hz), 6.28 (1H, d, *J* = 15.9 Hz), 6.83 (1H, d, *J* = 8.3 Hz), 6.99 (1H, d, *J* = 8.6 Hz), 7.10 (1H, s, *J* = 1.1 Hz), 7.58 (1H, d, *J* = 15.9 Hz). ^{13}C NMR ($CDCl_3$, 200 MHz) δ: 51.7, 69.9, 111.00, 113.4, 116.0, 118.0, 121.8, 128.3, 132.4, 144.8, 146.2, 147.6, 167.8. EI-MS *m*/*z* (%): 234 [M^+] (45), 203 (10), 193 (100), 165 (14), 133 (41). CI-MS *m*/*z* (%): 234 [M^+] (100), 203 (21), 193 (75), 165 (12), 174 (11). ESI^--MS *m*/*z* (%): 467 [2M – H]$^-$ (20), 233 [M – H]$^-$ (100), 191 (22). LC–MS: r_t= 17.03 min.

Diallyl peaks (from the mixture)

λ_{max} = 304 nm, ϵ_{337nm} = 1500.00 M^{-1} cm^{-1}, λ_{ex} = 340 nm, λ_{em} = 394 and 434 nm. FTIR (neat) ν (cm^{-1}): 3420, 2980, 2953, 1715, 1634, 1510, 1437, 1263, 1210, 1053. ^{1}H NMR ($CDCl_3$) δ: 3.78 (3H, s), 4.63 (4H, d, *J* = 5.1 Hz), 5.36 (2H, d, *J* = 12.0 Hz), 5.46, (2H, s), 6.05 (2H, m), 7.43 (1H, d, *J* = 10.1 Hz), 7.29 (1H, d, *J* = 7.5Hz), 7.67 (1H, s), 7.70 (1H, d, *J* = 9.1 Hz), 7.79 (1H, d, *J* = 10.5 Hz). ^{13}C NMR (MeOH-d_4, 200 MHz) δ: 51.7, 68.3, 69.9, 112.8, 113.5, 115.7, 118.1, 122.8, 128.9, 131.0, 133.2, 144.9, 146.2, 147.8, 167.9. EI-MS *m*/*z* (%): 274.12 [Di^+] (10), 234 [$Mono^+$] (48), 193 (100), 133 (41), 165 (13), 203 (12). ESI^--MS *m*/*z* (%): 307 (100), 192 (38), 387 (8). LC–MS: r_t= 15.33, 17.03 min.

N-*Allyl 3,4-dihydroxycinnamide (16)*

To 3,4-dihydroxycinnamic acid (3.8065 g, 0.0211 mol), dissolved in dry tetrahydrofuran (170 mL), 1-[3-(dimethylamino)propyl]-3-ethylcarbodiimide (EDC) (4.4555 g, 0.0232 mol, 1.1 equiv.), 1-hydroxybezotriazole hydrate (HOBt) (2.8512 g, 0.0211 mol, 1 equiv.), triethylamine (3.234 mL, 0.0232 mol, 1.1 equiv.), and DMAP (0.190 g, 5%) were added. Previously dissolved allylamine (1.2048 mL, 0.0211 mol) in THF (4 mL) was added to the reaction flask. The mixture was stirred at room temperature for 5 d. After evaporating to dryness, the solid was dissolved in 0.1 N HCl and washed with ethyl acetate. Organic fractions were washed with $NaHCO_3$, H_2O, NaCl, and brine and dried over $MgSO_4$. To the oily brown residue ethyl acetate was added, and a white precipitate was filtered off. The product was purified using mixed solvent-pair recrystallization (acetone:heptane) (yield: 2.001 g, 53 %; mp 182 °C).

λ_{max} = 318 nm, ϵ_{337nm} = 9083.33 M^{-1} cm^{-1}, λ_{ex} = 340 nm, λ_{em} = 438 nm. FTIR (neat) ν (cm^{-1}): 3340, 3320, 3200, 1649, 1581, 1540, 1234, 1182. ^{1}H NMR (MeOH-d_4,

© 2007 NRC Canada

200 MHz) δ: 3.87 (2H, dd, *J* = 1.3, 3.7 Hz), 5.08 (1H, dd, *J* = 1.3, 10.3 Hz), 5.18 (1H, d, *J* = 17.4 Hz), 5.82 (m, 1H, *J* = 1.4, 10.2, 17.8 Hz), 6.36 (1H, d, *J* = 15.7 Hz), 6.72 (1H, d, *J* = 8.2 Hz), 6.88 (1H, dd, *J* = 1.5, 8.2 Hz), 7.01 (1H, d, *J* = 1.6 Hz), 7.37 (1H, d, *J* = 15.6 Hz). ^{13}C NMR (MeOH-d_4, 200 MHz) δ: 42.8, 115.0, 116.3, 116.4, 118.1, 122.1, 128.2, 135.5, 142.5, 146.7, 148.8, 169.1. CI-MS *m/z* (%): 220 [M^+] (100), 163 (82), 153 (16), 136 (35). ESI-MS *m/z* (%): 439 [2M + H]$^+$ (62), 261 (6), 221 [M + H]$^+$ (100), 163 (5). LC–MS: r_t= 7.78 min.

Synthesis of silylated matrixes

(N-(3-Triethoxysilylpropyl)-N′-(7-(4-methylcoumarin)) urea (17)

7-Amino-4-methylcoumarin (AMC, 0.092 g, 0.522 mmol) was dissolved in dry THF (25 mL). After the mixture was stirred for 35 min at room temperature, (3-isocyanatopropyl)triethoxysilane (IPTES) (2.575 g, 0.999 g/mL, 10.4 mmol) was added, and the mixture was refluxed at 75 °C under nitrogen for 50 h. After the mixture was cooled to room temperature, the solvent was evaporated. The white powder was dissolved in dry dichloromethane (10 mL); hexane (20 mL) was added slowly to precipitate the product. After the mixture was allowed to sit for 3 days, the product was isolated as a white solid (yield: 0.0651 g, 71.1%; mp 198 °C) with suction filtration and washed with hexane (2 × 5 mL).

λ_{max} = 329 nm, ϵ = 22000 M^{-1} cm^{-1}, λ_{ex} = 334, λ_{em} = 390 nm. FTIR (neat) ν (cm^{-1}): 3480, 3320, 2974, 2940, 1677, 1539, 1073, 954, 773. ^{1}H NMR (MeOH-d_4, 200 MHz) δ: 0.67 (2H, m, *J* = 7.3 Hz), 1.24 (9H, t, *J*= 7.1 Hz), 1.57 (2H, m), 2.42 (3H, CH_3, s), 3.29 (2H, m), 3.72 (6H, q, *J* = 6.8 Hz), 6.18 (1H, s), 7.26 (1H, s), 7.55 (1H, d, *J* = 8.1 Hz), 7.61 (1H, d, *J* = 7.9 Hz). ESI$^+$-MS *m/z* (%): 713 (20), 670 (19), 423 [M + H]$^+$ (77), 248 (100). ESI$^-$-MS *m/z* (%): 535(29), 481 [M + 59]$^-$ (100), 421 [M – H]$^-$ (30). MALDI *m/z*: 883 [2M + K]$^+$, 445 [M + Na]$^+$, 423 [M + H]$^+$, 377 [M–OCH_2CH_3 + H]$^+$.

N-*(3-Triethoxypropylsilyl) 2,5-dihydroxybenzamide (18)*

To allyl 2,5-dihydroxybenzamide (0.0811 g, 0.419 mmol) dissolved in dry THF (5 mL) triethoxysilane (0.38 g, 0.433 mL, 2.52 mmol) and Karstedt's catalyst (3 drops) were added. The reaction mixture was stirred at room temperature for 21 h. The completion of the reaction was followed by ^{1}H NMR. After solvent evaporation and the removal of excess triethoxysilane under vacuum, a beige solid (yield: 0.077, 94.9 %; mp 270 °C) was obtained.

λ_{max} = 396 nm, λ_{ex} = 340 nm, λ_{em} = 446 and 495 nm. FTIR (neat) ν (cm^{-1}): 3420, 2962, 2930, 1547, 1491, 1037, 791. ^{1}H NMR ($CDCl_3$, 200 MHz) δ: 0.97 (2H, m, *J* = 7.4 Hz), 1.22 (9H, m, *J* = 7.0 Hz), 1.58 (2H, m, *J* = 7.7 Hz), 3.37 (2H, m, *J* = 6.2 Hz), 3.83 (6H, q, *J* = 7.0 Hz), 6.84 (1H, d, *J* = 8.9 Hz), 6.97 (1H, s), 7.06 (1H, d, *J* = 9.3 Hz). ESI-MS *m/z* (%): 422 (14), 396 [M + K]$^+$ (23), 382 (37), 333 [M–OCH_2CH_3 + Na] (12), 290.2 [M–2(OCH_2CH_3) + Na]$^+$ (19), 276 (59), 259 (55), 245 [M–3(OCH_2CH_3) + Na]$^+$ (32), 196 (100). CI-MS *m/z* (%): 499 (12), 438 (28), 393 (37), 332 (21), 227 (22), 196 (90), 136 (100). MALDI *m/z*: 771, 699, 654, 444, 430, 380 [M + Na]$^+$, 286.

6-Hydroxy-N-(3-aminopropyltriethoxysilyl)-phthalamic acid; 3-hydroxy-N-(3-aminopropyltriethoxysilyl)-phthalamic acid (19)

3-Hydroxyphthalic anhydride (0.1588 g, 0.90 mmol) was dissolved in DMSO (3 mL). 3-Aminopropyltriethoxysilane (0.217 mL, 0.213 g, 0.965 mmol) and anhyd. pyridine (0.217 mL, 0.213 g, 3.13 mmol) were added to the reaction mixture. After stirring for 39 h, the resulting green fluorescent mixture was further evaporated to remove any residual solvent. The yellow-green crystals were recovered as a mixture of isomers (yield: 0.317 g, 98%; mp 116 °C). The ^{1}H NMR, ^{13}C NMR, ^{29}Si NMR, UV, ESI-MS, and fluorescence were obtained for the product in solution. FTIR and ^{29}Si CPMAS were performed on the isolated solid.

λ_{max} = 347, λ_{ex} = 340 nm, λ_{em} = 516 nm. FTIR (neat) ν (cm^{-1}): 3200–2500, 2928, 1687, 1610, 1456, 1402, 1366, 1204, 735. ^{1}H NMR (DMSO-d_6, 200 MHz) δ: 7.17 (1H, q, *J* = 7.6, 7.8 Hz), 6.74 (1H, d, *J* = 7.9 Hz), 6.53 (1H, d, *J* = 7.1 Hz), 3.48 (6H, q, *J* = 6.9 Hz), 3.21 (2H, q, *J*= 6.9, 2.6 Hz), 1.65 (2H, m, *J* = 7.3 Hz), 1.06 (9H, t, *J* = 6.9 Hz), 0.61 (2H, m, *J* = 7.4 Hz). ^{1}H-^{1}H gradient COSY showed that methyl and methylene protons in the terminal ethoxy groups are coupled together, as were methylene protons in the propyl chain. ^{13}C NMR (DMSO-d_6, 200 MHz) δ: 18.7, 18.9, 22.8, 56.5, 58.1, 119.6, 120.3, 120.3, 129.3, 131.2, 156.2, 166.5, 167.9. ESI-MS$^-$ *m/z* (%): 384.4 [M – H]$^-$ (100), 356 (38), 328 (10), 300 (27). ^{29}Si CPMAS NMR (solid state, 300 MHz) δ: –67.53, –61.31, –53.37.

Ethyl 3-methoxy-4-(3-propyltriethoxysilyl)benzoate (20)

To ethyl 3-methoxy-4-allyloxybenzoate (0.3677 g, 1.65 mmol) in dry THF (10 mL) were added triethoxysilane (0.514 g, 0.604 mL, 3.3 mmol) and Karstedt's catalyst (three drops). The completion of reaction was ensured with ^{1}H NMR. After solvent evaporation, unreacted triethoxysilane was removed under high vacuum, and the brown liquid was purified by flash chromatography using hexane : ethyl acetate (30:70 *v/v*) mixture as the solvent. The pure brown liquid (yield: 84.6%, 0.311 g) was then characterized.

λ_{max} = 291 nm, λ_{ex} = 340 nm, λ_{em}= 437 nm. FTIR (neat) ν (cm^{-1}): 2975, 2950, 2910, 1712, 1600, 1512, 1270, 1073, 881, 790. ^{1}H NMR ($CDCl_3$, 200 MHz) δ: 0.75 (2H, t, *J* = 8.2 Hz), 1.21 (9H, t, *J* = 6.9 Hz), 1.38 (3H, t, *J* = 7.1 Hz), 1.98 (2H, m, *J* = 7.3, 8.5 Hz), 3.81 (6H, q, *J* = 6.9 Hz), 3.90 (3H, s, OMe), 4.05 (2H, t, *J* = 6.9 Hz), 4.34 (2H, q, *J* = 7.1 Hz), 6.87 (1H, d, *J* = 8.4 Hz), 7.53 (1H, d, *J* = 1.6 Hz), 7.65 (1H, q, *J* = 1.8, 8.4 Hz). CI-MS *m/z* (%): 373 (20), 358 (62), 239 (18), 249 (39), 205 (35), 197 (100), 163 (32). MALDI-TOF *m/z*: 401 [M + H]$^+$, 355 [M – 45], 315, 283, 253.

MALDI preparation

Four types of molecules were used for MALDI analysis to test the applicability of our system for various analytes, including small peptides and small organic molecules: Glu^1-fibrinopeptide B (32) (Glu-fib) (MW 1570), trimethoprim (TMP, MW 290), haloperidol (HP, MW 375), and fluorescein (FLU, MW 332). The final molarity of each analyte in water or in 0.1% TFA:acetonitrile was calculated to be Glu-fib (6.36 pmol/μL), TMP (34.48 pmol/μL), halo-

© 2007 NRC Canada

peridol (26.66 pmol/μL), and fluorescein (30.12 pmol/μL). The standard analyte solution was prepared at a 1:1:1:1 ratio (*v*/*v*) of Glu-fib, TMP, haloperidol, and fluorescein. 40 μL of the matrix solution (~20 mg/mL) was combined with 10 μL of a standard analyte mixture (final concentration after volume correction of each analyte was 2.5 ng/μL), and 1 μL aliquots of matrix–analyte mixture were applied to stainless-steel plates prior to MALDI analysis.

MALDI-TOF experiments

MALDI analysis was done using Breadboard MALDI-TOF mass spectrometer (research instrument provided by MDS Sciex), equipped with a 337 nm N_2 laser and a 20 kV acceleration voltage. Mass spectra were generated from the average of 300 laser shots, at 10 Hz laser rate, 210 mL/m focusing-gas flow, 90 mL/m cooling-gas flow, and 70% laser energy. The instrument was later made available as the proTOF™ 2000 MALDI O-TOF Mass Spectrometer (PerkinElmerSCIEX). The compounds **9**, **10**, and **11** were later tested, at which point only the proTOF™ instrument was accessible from the collaborating company. Average signals reported were obtained by guiding the laser from spot-to-spot within the same plate and the given values represent the average of at least three measurements per matrix derivative used. The experimental setup was used to obtain normalized signal intensities, and MALDI spectra presented herein are based on normalized data.

Conclusion

A series of allyl-protected compounds were prepared as potential MALDI matrixes. The MALDI response to four different analytes was much lower with all the synthesized compounds than with standard matrixes. Phenolic groups were generally beneficial, particularly when the UV-absorbing system was part of an α,β-unsaturated carbonyl system, because these functional groups facilitate charge transfer to analyte more effectively than carboxylic acids. The allyl derivatives (**15**, **16**) showed fewer matrix signals than the parent compound **3**.

The performance of silylated compounds in the MALDI experiment will form the basis of future reports and can be easily obtained from the allyl-protected compounds described herein. Ultimately, we shall report on the ability of a subset of these compounds, modified with hydrolysable silane groups, to serve as MALDI targets on their own or when processed into thin layers containing biomolecules.

Acknowledgements

We thank the Natural Sciences and Engineering Research Council of Canada (NSERC) and MDS-Sciex for financial support of this work. We also thank Dr. W. Davidson and Dr. T. Covey (Sciex) for helpful discussions and access to their research mass spectrometer.

References

1. M. Karas and F. Hillenkamp. Anal. Chem. **60**, 2299 (1988).
2. R. King, R. Bonfiglio, C. Fernandez-Metzler, C. Miller-Stein, and T. Olah. J. Am. Soc. Mass. Spectrom. **11**, 942 (2000).
3. B.K. Matuszewski, M.L. Constanzer, and C.M. Chavez-Eng. Anal. Chem. **70**, 882 (1998).
4. B. Zhang, C. McDonald, and L. Li. Anal. Chem. **76**, 992 (2004).
5. P. Kovarik, R.J. Hodgson, T.R. Covey, M.A. Brook, and J.D. Brennan. Anal. Chem. **77**, 3340 (2005).
6. L.F. Marvin, M.A. Roberts, and L.B. Fay. Clin. Chim. Acta, **337**, 11 (2003).
7. J. Gobey, M. Cole, J. Janiszewski, T. Covey, T. Chau, P. Kovarik, and J. Corr. Anal. Chem. **77**, 5643 (2005).
8. G. McCombie and R. Knochenmuss. Anal. Chem. **76**, 4990 (2004).
9. C. Pan, S. Xu, L. Hu, X. Su, J. Ou, H. Zou, Z. Guo, Y. Zhang, and B. Guo. J. Am. Soc. Mass. Spectrom. **16**, 883 (2005).
10. M. Karas, and R. Krüger Chem. Rev. **103**, 427 (2003).
11. J. Zhang, and R Zenobi. J. Mass Spectrom. **39**, 808 (2004).
12. E.P. Go, J.E. Prenni, J. Wei, A. Jones, S.C. Hall, E. Witkowska, Z. Shen, and G. Siuzdak. Anal. Chem. **75**, 2504 (2003).
13. J. Sunner, E. Dratz, and Y. Chen, Anal. Chem. **67**, 4335 (1995).
14. T. Kinumi, T. Saisu, M. Takayama, and H. Niwa. J. Mass. Spectrom. **35**, 417 (2000).
15. K.I. Voivodov, J. Ching, and T.W. Hutchens. Tetrahedron Lett. **37**, 5669 (1996).
16. J.L. Cohen and J.A. Cox. J. Sol–gel Sci. Tech. **28**, 15 (2003).
17. Y.-S. Lin, C.-H. Yang, and Y.-C. Chen. Rapid Commun. Mass Spectrom. **18**, 313 (2004).
18. Y.-S. Lin and Y.-C. Chen. Anal. Chem. **74**, 5793 (2002).
19. Q. Zhang, H. Zou, Z. Guo, Q. Zhang, X. Chen, and J. Ni. Rapid Commun. Mass Spectrom. **15**, 217 (2001).
20. M. Brook. Silicon in organic, organometallic, and polymer chemistry. Wiley, New York. 2000. Chap.12.
21. R. Zenobi and R. Knochenmuss. Mass. Spectrom. Rev. **17**, 337 (1998).
22. (*a*) Y. Dai, R.M. Whittal, and L. Li. Anal. Chem. **68**, 2494 (1996); (*b*) O. Vorm, P. Roepstorff, and M. Mann. Anal. Chem. **66**, 3281 (1994); (*c*) F.M.L. Amado, P. Domingues, M.G. Santana, A.J. Ferrer, and K.B. Tomer. Rapid Commun. Mass Spectrom. **11**, 1347 (1997).
24. K.I. Voivodov, J. Ching, and T.W. Hutchens. Tetrahedron Lett. **37**, 5669 (1996).
25. R. Zenobi and R. Knochenmuss. Mass Spectrom. Rev. **17**, 337 (1998).
26. S. Bashir, R. Mutter, and P.J. Derrick. Analyst, **128**, 1452 (2003).
27. M. Karas, U. Bahr and J.-R. Zeng. *In* Large ions: Their vaporization, detection, and structural analysis. *Edited by* T. Baer, C.Y. Ng, and I. Powis. Wiley, New York. 1996. Chap. 2.
28. M.E. Gimon, L.M. Preston, T.M. Solouki, A. White, and D.H. Russell. Org. Mass Spectrom. **27**, 827 (1992).
29. L.M. Preston, G.M. Kinsel, and D.H. Russell. J. Am. Soc. Mass Spectrom. **5**, 800 (1994).
30. (*a*) F.Y. Hassin and D. Marynick. J. Mol. Struct. **629**, 223 (2003); (*b*) J. Krause, M. Stoeckli, and P.U. Schlunegger. Rapid Commun. Mass Spectrom. **10**, 1927 (1996); (*c*) R. Notario. J. Mol. Struct. **556**, 245 (2000).
31. G. Grigorean, R.I. Carey, and I.J. Amster. Eur. J. Mass Spectrom. **2**, 139 (1996).
32. A.V. Loboda, S. Ackloo, and I.V. Chernushevich. Rapid Commun. Mass. Spectrom. **17**, 2508 (2003).

© 2007 NRC Canada

COMMUNICATION / COMMUNICATION

Heteropoly acid in ionic liquid — An efficient and recyclable system for one-pot three-component Mannich reaction

Meghana S. Rasalkar, Sachin V. Bhilare, Amol R. Deorukhkar, Nitin B. Darvatkar, and Manikrao M. Salunkhe

Abstract: This paper describes a one-pot three-component Mannich reaction, catalyzed by phosphotungstic acid ($H_3PW_{12}O_{40}$), a heteropoly acid in ionic liquid. The catalyst was found to be mild and efficient, and the protocol affords β-amino ketones in good yields under ambient conditions. Several ionic liquids and conventional organic solvents were employed for the reaction. The ionic liquid 1-butyl-3-methylimidazolium tetrafluoroborate ([bmim]BF_4) offered the best results in terms of yield of the products. It was observed that a homogeneous reaction medium proved beneficial for the yield of the reaction.

Key words: Mannich reaction, β-amino ketones, phosphotungstic acid, ionic liquid, recyclability.

Résumé : Dans ce travail on a réalisé une réaction de Mannich monotope à trois composants, catalysée par l'acide phosphotungstique ($H_3PW_{12}O_{40}$), un hétéropolyacide, dans un milieu ionique. On a trouvé que ce catalyseur est doux et efficace et que la méthode conduit à la formation de β-aminocétones avec de bons rendements, en opérant dans des conditions ambiantes. Pour réaliser cette réaction, on a utilisé plusieurs liquides ioniques ainsi que plusieurs solvants organiques conventionnels. Le liquide ionique du nom de tétrafluoroborate de 1-butyl-3-méthylimidazolium ([bmim]BF_4) est celui qui donne les meilleurs résultats en terme de rendement des produis. On a observé que le milieu réactionnel homogène s'avère utile pour le rendement de la réaction.

Mots-clés : réaction de Mannich, β-aminocétones, acide phosphotungstique, liquide ionique, possibilité de recycler.

[Traduit par la Rédaction]

Introduction

The Mannich reaction is very useful in the preparation of nitrogen-containing compounds (1–4). The reaction essentially proceeds via the condensation of an amine, an aldehyde, and a ketone to form β-amino carbonyl compounds. These compounds are very important biologically active molecules. Novel modifications of the Mannich reaction have been attempted by other researchers (5–10).[2] Some groups have reported the reaction of silyl enol ethers with imines in the presence of Lewis acids (11–13). Lanthanide triflates are quite attractive catalysts for Mannich reaction because of their high catalytic activity and low toxicity (14, 15). However, their high cost restricts their use. Other reports involve the use of HCl in H_2O–SDS and HBF_4 in organic solvent – H_2O systems (16, 17).

Recently, the research in the field of heterogeneous catalysis has experienced considerable growth. Heteropoly acids (HPAs) are polyoxometalate inorganic cage structures belonging to a promising class of solid acid catalysts. They may adopt the Keggin form (18) with the general formula $H_3MX_{12}O_{40}$, where M is the central atom and X is the heteroatom. Typically, M can be either phosphorous (P) or silicon (Si) and X can be tungsten (W) or molybdenum (Mo). HPAs have an enormous potential in catalyzing various types of synthetic organic transformations, which has not yet been fully realized. The low cost, availability, and environment-friendly nature make them suitable candidates for replacing

Received 13 September 2006. Accepted 20 November 2006. Published on the NRC Research Press Web site at http://canjchem.nrc.ca on 5 January 2007.

M.S. Rasalkar, S.V. Bhilare, A.R. Deorukhkar, N.B. Darvatkar, and M.M. Salunkhe.[1] Department of Chemistry, The Institute of Science, 15 Madam Cama Road, Mumbai 400 032, India.

[1]Corresponding author (e-mail: mmsalunkhe@hotmail.com).

[2]During the preparation of this manuscript, a one-pot three-component Mannich reaction, employing heteropoly acids in water, was reported; see ref. 10.

 doi:10.1139/V06-176 © 2007 NRC Canada

hazardous and expensive catalysts. HPAs are Brönsted acids, composed of heteropoly anions, with protons as the counter cations. They are more efficient than many conventional solid acid catalysts, such as mixed oxides, zeolites, and so forth. Some reactions, e.g., Friedel–Crafts acylation (19) and Fries rearrangement (20), are catalyzed by HPAs. The HPA catalysts are easily separated from the reaction mixture and recycled. The chemistry and general physical properties of these catalysts have been extensively discussed in a number of review articles (21, 22).

In the past decade, a new approach has been adopted for catalyst separation and recycling in catalytic reactions involving the use of room-temperature ionic liquids, especially those based upon 1-*n*-alkyl imidazolium cation. Ionic liquids, also called "the designer solvents", have been largely successful in replacing obnoxious organic solvents. Their high thermal stability and ability to solvate various substrates have made them highly useful in a variety of organic reactions (23, 24). Amongst other reports, an asymmetric version of the Mannich reaction, employing L-proline in ionic liquids, demonstrated by Barbas et al. (25) is worth mentioning (26–28). For the past few years, our group has been actively involved in exploring the field of ionic liquids (29–31) and has investigated various aspects of the different reactions using ionic liquid as solvents.

Realizing the growing significance of the use of heterogeneous solid acids as recyclable catalysts in organic synthesis, we describe here, for the first time, the use of a heteropoly acid in conjunction with an ionic liquid for a one-pot three-component Mannich reaction (Scheme 1). Our technique combines and maximizes the individual advantages of using heteropoly acids and ionic liquids in organic syntheses while satisfying the basic principles of green chemistry.

Results and discussion

Because it is more efficient to perform a direct Mannich reaction, which eliminates a separate step for imine preparation prior to the reaction, a one-pot reaction between benzaldehyde, *p*-anisidine, and acetone with heteropoly acid as the catalyst was carried out as a prototype. Initially, we chose a hydrophilic ionic liquid 1-butyl-3-methylimidazolium tetrafluoroborate ([bmim]BF_4) for the reaction. A simple procedure was used to carry out the Mannich reaction, wherein all the substrates, namely, an amine (1 mmol), HPA, an aldehyde (1 mmol), and a ketone (in excess) were mixed with the ionic liquid, respectively. To begin with, we decided to screen various heteropoly acids for the model reaction. We employed three different heteropoly acids, namely, phosphotungstic acid ($H_3PW_{12}O_{40}$) (PW_{12}), tungstosilicic acid ($H_4SiW_{12}O_{40}$) (SiW_{12}), and phosphomolybdic acid ($H_3PMo_{12}O_{40}$) (PMo_{12}) for the reaction. All the HPAs completely dissolved in the ionic liquid. 5 mol% of each of these HPAs were used. The reaction mixture was stirred at room temperature.

The reaction furnished the product 4-(4-methoxyphenylamino)-4-phenylbutan-2-one. However, it was observed that the substrates completely disappeared after 18 h only with PW_{12}. In case of other heteropoly acids, TLC showed the presence of *p*-anisidine even after prolonged reaction times.

Scheme 1. One-pot three-component Mannich reaction catalyzed by a heteropoly acid.

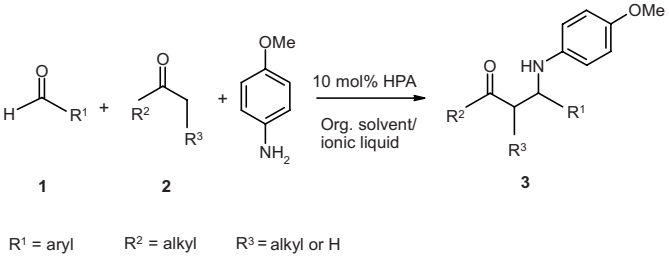


Table 1. Comparison of different heteropoly acids (HPAs) employed for Mannich reaction between *p*-anisidine, benzaldehyde, and acetone in [bmim]BF_4 at room temperature.

Heteropoly acid[a]	Time (h)	Yield[b] (%)
$H_3PW_{12}O_{40}$	18	70
$H_4SiW_{12}O_{40}$	18	61
$H_3PMo_{12}O_{40}$	18	45

[a]5 mol% of the HPA was used.
[b]Isolated yields.

These HPAs vary in their acidity, and hence, it was expected that this would affect the outcome of the reaction in terms of the yield. Studies have proven that PW_{12} is the strongest and most active heteropoly acid (32). It was observed that the yield of the reaction was directly related to the acid strength of the catalyst, as the yield for the various catalysts decreased in the order of $PW_{12} > SiW_{12} > PMo_{12}$. Hence, the best yield of the product of the reaction, i.e., 4-(4-methoxyphenylamino)-4-phenylbutan-2-one (70%), was obtained in 18 h with the strongest of the three heteropoly acids, i.e., phosphotungstic acid (PW_{12}). Considering PW_{12} as the superior heteropoly acid for the present study, we employed it in further investigations. The results are presented in Table 1.

The amount of catalyst was optimized to improve the yields. The yield was quite low (~40%) when phosphotungstic acid was used in low concentrations (1 mol%). Marked improvement in yields (88%) and reduced reaction times (12 h) were observed when the catalyst loading was increased to 10 mol%.

We carried out the reaction in various other hydrophilic as well as hydrophobic ionic liquids and conventional organic solvents to compare the outcome of the reaction in terms of the yield and the rate of the reaction. HPA dissolved in organic solvents like DMSO, DMF, and acetonitrile and hydrophilic ionic liquids, such as 1-butyl-3-methylimidazolium chloride ([bmim]Cl) and 1-methoxyethyl-3-methylimidazolium methanesulphonate ([moemim]OMs), to produce a homogenous system. However, HPA was insoluble in hydrophobic ionic liquids, such as 1-butyl-3-methylimidazolium hexafluorophosphate ([bmim]PF_6) and 1-hexyl-3-methylimidazolium tetrafluoroborate ([hmim]BF_4), and solvents like toluene. Better yields were obtained when the catalyst was soluble in the reaction medium compared with those obtained when the catalyst was insoluble in the reaction solvent. From these observations, it can be deduced that the solubility of the catalyst in the medium plays an important

© 2007 NRC Canada

Table 2. Phosphotungstic acid (PW_{12}) catalyzed Mannich reaction involving *p*-anisidine, benzaldehyde, and acetone in various solvents.

Entry	Solvent	Time (h)	Yield[a] (%)
1	[bmim]BF_4	12	88
2	[bmim]PF_6	12	62
3	[hmim]BF_4	12	64
4	[bmim]Cl	13	80
5	[moemim]OMs	15	80
6	DMSO	14	83
7	DMF	15	65
8	Acetonitrile	15	60
9	Toluene	15	51
10	Dichloromethane	15	55

Note: 10 mol% of PW_{12} was used.
[a]Isolated yields.

role in enhancing the outcome of the reaction and that a homogeneous system produces better yields.

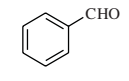
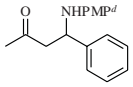
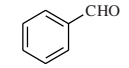
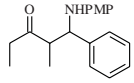
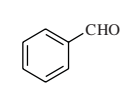
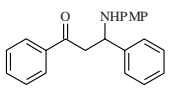
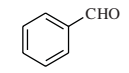
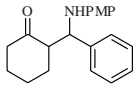
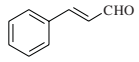
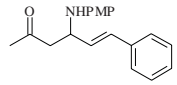
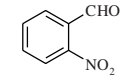
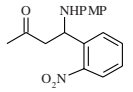
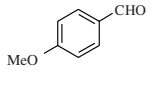
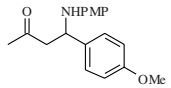
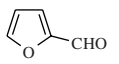
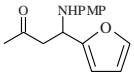
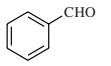
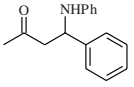
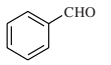
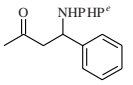
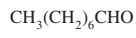
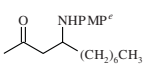
Amongst the various ionic liquids and organic solvents that were employed for the present study (see Table 2), the use of [bmim]BF_4 and DMSO resulted in good yields. The rate of the reaction was only slightly better in case of [bmim]BF_4 compared with DMSO. However, DMSO is highly obnoxious and has a detrimental effect on the environment. Hence, taking into account the various environmental constraints, [bmim]BF_4 was employed for further investigation.

Having ascertained the efficiency of the protocol for the model reaction between *p*-anisidine, acetone, and benzaldehyde, we next turned our attention to its synthetic utility in [bmim]BF_4 (Table 3). All the reactions were stirred for 24 h. At first, we decided to employ various aromatic aldehydes (**1**), keeping the ketone (**2**) and the amine moieties constant. Substituted benzaldehydes with electron-withdrawing or electron-donating groups (Table 3, entries 6 and 7) responded well to the reaction conditions, as the corresponding β-amino ketones (**3**) were obtained in 77% and 80% yield, respectively. A heteroaromatic aldehyde, namely, furfuraldehyde, was also chosen as a substrate, and it furnished the product in 72% yield (Table 3, entry 8). On the other hand, cinnamaldehyde, as an α,β-unsaturated aldehyde, gave comparatively lower yield (Table 3, entry 5).

Likewise, we altered the ketone moiety. Aliphatic ketones, such as 3-pentanone and cyclohexanone, and aromatic ketones, such as acetophenone, were selected. 3-Pentanone (Table 3, entry 2) gave better results than cyclohexanone (Table 3, entry 4). On the other hand, acetophenone (Table 3, entry 3) gave a moderate yield. Ketones were taken in excess to avert the formation of bis-Mannich product. Further, we chose two different amines, namely, aniline and *p*-amino phenol. The results were quite similar to those obtained with *p*-anisidine, albeit the yields were slightly lower. To examine the applicability of the protocol to aliphatic aldehydes, we decided to synthesize Mannich base taking *n*-octanal (Table 3, entry 11). However, the reaction yield was very low. The results are presented in Table 3.

The combination of the heteropoly acid and [bmim]BF_4 provides a homogeneous system for the reaction; hence, this prompted us to investigate the possibility of recycling the complete system of HPA and ionic liquid. The result was quite fruitful. The entire product could be isolated from the reaction mixture simply by ether extraction, and the system of the catalyst and the ionic liquid could be recovered and recharged with fresh substrates. We screened the system for two subsequent runs; the product was obtained in 83% and 75% yields, respectively.

Table 3. Synthesis of various β-amino ketones via the Mannich reaction, using phosphotungstic acid and employing different aldehydes, ketones, and amines in [bmim]BF_4.

Entry	Aldehyde **1**	Ketone **2**	Product[a] **3**	Yield[b] (%)
1				88
2				78[c]
3				65
4				73[c]
5				56
6				77
7				80
8				72
9				73
10				75
11				23

[a]Representative spectral data of some Mannich bases are given in the experimental section.
[b]Isolated yields.
[c]A *syn*:*anti* ratio of 42:58 for entry 2 and 35:65 for entry 4 was obtained and confirmed by ^{1}H NMR spectroscopic analysis of the crude product.
[d]PMP is *p*-methoxy phenyl.
[e]PHP is *p*-hydroxy phenyl.

Conclusion

We have demonstrated an efficient one-pot methodology

© 2007 NRC Canada

for the Mannich reaction using a combination of heteropoly acid and ionic liquid in the syntheses of β-amino carbonyl compounds. Both the catalyst and the ionic liquid could be easily recovered and recycled. The absence of undesirable side-products and ambient reaction conditions also enhanced the synthetic utility of the reaction.

Experimental

General procedure for Mannich reaction

To a mixture of the ionic liquid (2 mL) and phosphotungstic acid (0.1 mmol), an amine (1 mmol) and an aldehyde (1 mmol) were added. This was followed by the addition of a ketone (10 mmol). The resulting mixture was stirred at room temperature for 24 h. The progress of the reaction was monitored by TLC. The crude product was isolated by extracting the reaction mixture with diethyl ether (4 × 15 mL). The combined ether extractions were dried over Na_2SO_4, concentrated, and purified by CC to obtain the desired β-amino ketones, which were characterized by IR and ^{1}H NMR spectroscopy.

4-(4-methoxyphenylamino)-4-(phenyl)butan-2-one (Table 3, entry 1)

IR ν_{max} (cm^{-1}): 3385, 2899, 1710, 1515, 1033. ^{1}H NMR (300 MHz, $CDCl_3$) δ: 1.65 (s, 1H, N*H*), 2.17 (s, 3H), 3.31–3.59 (m, 2H), 3.68 (s, 3H), 4.91–4.94 (m, 1H), 6.51 (d, *J* = 8 Hz, 2H), 6.70 (d, *J* = 8 Hz, 2H), 7.33 (t, *J* = 6 Hz, 2H), 7.56 (t, *J* = 6 Hz, 1H), 7.9 (d, *J* = 6 Hz, 2H).

1-(4-methoxyphenylamino)-1-phenyl-2-methylpentan-3-one (Table 3, entry 2)

IR ν_{max} (cm^{-1}): 3394, 2939, 1705, 1518, 1251, 1035. ^{1}H NMR (300 MHz, $CDCl_3$) δ: 0.91 (t, *J* = 6 Hz, 3H, C*H*$_3$), 1.14 (d, *J* = 6 Hz, 3H, C*H*$_3$), 2.24 (q, *J* = 3 Hz, 2H, C*H*$_2$), 3.01–3.31 (m, 1H), 3.67 (s, 3H), 4.03 (s, 1H, N*H*), 4.21 (d, 1H, C*H*NH), 6.46 (d, *J* = 8 Hz, 2H), 6.67 (d, *J* = 8 Hz, 2H), 7.25–7.45 (m, 5H).

3-(4-methoxyphenylamino)-1,3-diphenyl-1-propanone (Table 3, entry 3)

IR ν_{max} (cm^{-1}): 3399, 2974, 1672, 1598, 1515, 1295, 1221, 1080, 1026. ^{1}H NMR (300 MHz, $CDCl_3$) δ: 3.41 (d, 2H), 3.65 (s, 3H), 4.93 (m, 1H), 6.48 (d, 2H), 6.51 (d, *J* = 8 Hz, 2H), 6.70 (d, *J* = 8 Hz, 2H), 7.01–7.24 (m, 3H), 7.21–7.38 (m, 5H).

General procedure for the recyclability of the system of the ionic liquid and heteropoly acids

The system containing the ionic liquid and the catalyst was regenerated from the total reaction mixture by consecutive extractions with diethyl ether, and then it was recharged with the amine, aldehyde, and ketone to carry out the next set of reactions. Then, a similar procedure as the previously mentioned was followed.

Acknowledgement

The authors gratefully acknowledge the financial support provided by the Department of Science and Technology, Government of India.

References

1. E.F. Kleinnmann. *In* Comprehensive organic synthesis. Vol. 2. *Edited by* B.M. Trost. Pergamon Press, New York. 1991. Chap. 4.
2. A. Cordova. Acc. Chem. Res. **37**, 102 (2004).
3. D.J. Hart and D.C. Ha. Chem. Rev. **89**, 1447 (1989).
4. S. Kobayashi and H. Ishitiani. Chem. Rev. **99**, 1069 (1999).
5. T. Ollevier and E. Nadeau. J. Org. Chem. **69**, 9292 (2004).
6. T. Mukaiyama. Org. React. **28**, 203 (1982).
7. T.K. Hollis and B.J. Bosnich. J. Am. Chem. Soc. **117**, 4570 (1995).
8. S.J. Danishefsky, S. Chackalamannil, P. Harrision, M. Silvestri, and P.J. Cole. J. Am. Chem. Soc. **107**, 2474 (1985).
9. M.M. Salter, J. Kobayashi, Y. Shimizu, and S. Kobayashi. Org. Lett. **8**, 3533 (2006).
10. N. Azizi, L. Torkiyan, and M. R. Saidi. Org. Lett. **8**, 2079 (2006).
11. I. Ojima, S. Inaba, and K. Yoshida. Tetrahedron Lett. **18**, 3646 (1977).
12. T.-P. Loh and L.-L. Wei. Tetrahedron Lett. **39**, 323 (1998).
13. K. Ishihara, M. Funahashi, N. Hanki, M. Miyata, and H.Yamamoto. Synlett, 963 (1994).
14. S. Kobayashi, M. Araki, H. Ishitani, S. Nagayama, and I. Hachiya. Synlett, 233 (1995).
15. S. Kobayashi, T. Busujima, and S. Nagayama. Synlett, 545 (1999).
16. T. Akiyama, K. Matsuda, and K. Fuchibe. Synlett, 322 (2005).
17. T. Akiyama, J. Takaya, and H. Kagoshima. Adv. Synth. Catal. **344**, 338 (2002).
18. T. Okuhara, N. Mizuno, and M. Misono. Adv. Catal. **41**, 113 (1996).
19. C. Castro, J. Primo, and A. Corma. J. Mol. Catal. A: Chem. **134**, 215 (1998).
20. E.F. Kozhevnikova, E.G. Derouane, and I.V. Kozhevnikova. Chem. Commun. 1178 (2002).
21. I.V. Kozhevnikova. Chem. Rev. **98**, 171 (1998).
22. N. Mizuno and M. Misono. Chem. Rev. **98**, 199 (1998).
23. J. Dupont, R.F. de Souza, and P.A.Z. Suarez. Chem. Rev. **102**, 3667 (2002).
24. S.-G. Lee, J.H. Park, J. Kang, and J.K. Lee. Chem. Commun. 1698 (2001).
25. N.S. Chowdari, D.B. Ramachary, and C.F. Barbas, III. Synlett, 1906 (2003).
26. G. Zhao, T. Jiang, H. Gao, B. Han, J. Hang, and D. Sun. Green Chem. **6**, 75 (2004).
27. X.-F. Yang, M. Wang, R.S. Varma, and C.-J. Li. J. Mol. Catal. A: Chem. **214**, 147 (2004).
28. S. Sahoo, T. Joseph, and S.B. Halligudi. J. Mol. Catal. A: Chem. **244**, 179 (2006).
29. M.C. Uzagare, Y.S. Sanghvi, and M.M. Salunkhe. Green Chem. **5**, 370 (2003).
30. R.T. Dere, R.R. Pal, P.S. Patil, and M.M. Salunkhe. Tetrahedron Lett. **44**, 5351 (2003).
31. M.S. Rasalkar, M.K. Potdar, and M.M. Salunkhe. J. Mol. Catal. B: Enzym. **27**, 267 (2004).
32. M. Ueno, H. Ishitani, and S. Kobayashi. Org. Lett. **4**, 3395 (2002).

© 2007 NRC Canada

Montmorillonite K-10 clay as reusable heterogeneous catalyst for the microwave-mediated solventless synthesis of phthalazinetetraones

Davood Habibi, Nosratollah Mahmoodi, and Omid Marvi

Abstract: Different phthalazino[2,3-b]phthalazine-5,7,12,14-tetraones were synthesized in a simple and environmentally benign method from the reaction of some phthalic anhydrides with semicarbazide or thiosemicarbazide using montmorillonite K-10 clay as solid heterogeneous acidic catalyst and microwaves under solvent-free conditions in good yields and short reaction times. The present method has many obvious advantages compared with those reported in the literature, including high efficiency, higher yield, operational simplicity, environmental benignity, and the possibility of recycling the solid clay. The solid clay catalyst used in the first cycle of the reactions was successfully recovered and reused in the second cycle, showing a gradual decrease in activity.

Key words: montmorillonite K-10 clay, microwave, solvent-free condition, phthalazinetetraones, semicarbazide, thiosemicarbazide.

Résumé : Faisant appel à une méthode simple et environnementalement bénigne, on a réalisé la synthèse de divers phtalazino[2,3-b]phtalazine-5,7,12,14-tétrones avec de bons rendements en faisant réagir des anhydrides phtaliques avec de la semicarbazide ou de la thiosemicarbazide, en présence d'argile de montmorillonite K-10 comme catalyseur acide solide et hétérogène, dans des conditions sans solvant, sous l'influence de microondes et des temps de réaction courts. Cette méthode présente des avantages évidents par comparaison avec celles rapportées dans la littérature, dont le fait qu'elle est environnementalement bénigne, sa grande efficacité, son rendement plus élevé, sa simplicité d'opération et la possibilité de recycler l'argile solide. De plus, de l'argile utilisée dans un premier cycle de réactions a été réutilisée avec succès dans un second cycle, ce qui démontre que la diminution de son activité n'est que graduelle.

Mots clés : argile de montmorillonite K-10, microonde, condition sans solvant, phtalazinetétrone, semicarbazide, thiosemicarbazide.

[Traduit par la Rédaction]

Introduction

In the past few decades, the synthesis of new heterocyclic compounds has been a subject of great interest because of their wide applicability. Heterocyclic compounds occur very widely in nature and are essential to life. Nitrogen-containing heterocyclic molecules constitute the largest portion of chemical entities and are part of many natural products, fine chemicals, and biologically active pharmaceuticals that are vital for enhancing quality of life (1).

Heterocyclic skeletons provide scaffolds on which pharmacophores can be arranged to yield potent and selective drugs (2). In this regard, the phthalazine scaffold has shown its potential as a useful structure for the generation of druglike libraries in the drug discovery process (3). Moreover, heterocyclic fused phthalazines have been found effective in the inhibition of p38 MAP kinase (4), the selective binding of the GABA receptor (5), as antianxiety drugs (6), as antitumor agents (7), and as high-affinity ligands to the $\alpha_2\delta$-1 subunit of the calcium channel (8). Despite their wide applicability among the various reported studies on fused nitrogen heterocycles (9), only a limited number of phthalazinetetraone derivatives have been synthesized (10). Cardia et al. (11) presented the most recent method for the synthesis of phthalazino[2,3-*b*]phthalazine-5,7,12,14-tetraone. Most of these procedures involve the use of corrosive reagents such as polyphosphoric and acetic acids and the reported yields are far from satisfactory. Therefore, the use of inexpensive and environmentally safe solid acids would extend the scope of these transformations. Recently, the use of solid acidic catalysts like clays, zeolites, and ion-exchange resins, has received much research interest in different areas of organic synthesis because of their environmental compatibility, reusability, greater selectivity, noncorrosiveness, low cost, and ease of handling.

In particular, the clay catalysts make the reaction process more convenient, economical, environmentally benign, and

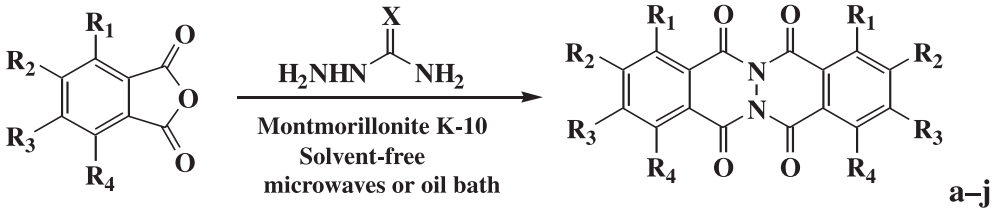
Received 6 November 2006. Accepted 13 December 2006. Published on the NRC Research Press Web site at http://canjchem.nrc.ca on 7 February 2007.

D. Habibi and O. Marvi.[1] Faculty of Chemistry, Bu-Ali Sina University, Hamedan, Iran.
N. Mahmoodi. Department of Chemistry, Faculty of Sciences, Guilan University, Rasht, Iran.

[1]Corresponding author (e-mail: marviomid@yahoo.com).

 doi:10.1139/V06-189 © 2007 NRC Canada

Scheme 1. Synthesis of phthalazino[2,3-b]phthalazine-5,7,12,14-tetraones on montmorillonite K-10 clay using microwave or oil bath.



a) X = O; $R_1 = R_2 = R_3 = R_4 = H$
b) X = O; $R_1 = R_2 = R_3 = R_4 = Cl$
c) X = O; $R_1 = NO_2$; $R_2 = R_3 = R_4 = H$
d) X = O; $R_2 = NO_2$; $R_1 = R_3 = R_4 = H$
e) X = O; $R_1 = F$; $R_2 = R_3 = R_4 = H$
f) X = S; $R_1 = R_2 = R_3 = R_4 = H$
g) X = S; $R_1 = R_2 = R_3 = R_4 = Cl$
h) X = S; $R_1 = NO_2$; $R_2 = R_3 = R_4 = H$
i) X = S; $R_2 = NO_2$; $R_1 = R_3 = R_4 = H$
j) X = S; $R_1 = F$; $R_2 = R_3 = R_4 = H$

act as both Bronsted and Lewis acids in their natural and ion-exchanged forms, enabling them to function as efficient catalysts for various transformations (12). Montmorillonite clays have been used as catalysts for a number of organic reactions and offer several advantages over classical acids: strong acidity, noncorrosive properties, recyclability, low cost, mild reaction conditions, high yields and selectivity, and the ease of setup and workup (13). Neat reactions, on the other hand, have their own practical problems such as overheating and charring of compounds because of ineffective dissipation of energy.

Also, in the last few years a growing interest has been shown in the use of microwave irradiation in organic synthesis (14). Microwave-assisted rapid organic reactions constitute an emerging technology that makes experimentally and industrially important organic syntheses more effective and more ecofriendly than conventional reactions (15). In addition, microwave-mediated solvent-free synthesis offers advantages for reducing hazardous explosions and the need to to remove solvents with high boiling points from the reaction mixtures. Moreover, coupling solventless synthesis with microwaves shows benefits of shorter reaction times, uniform heating, and higher yields (16, 17).

In continuation of our study on microwave-assisted reaction on solid surfaces (18, 19), herein we describe a convenient and simple method to synthesize some of the phthalazino[2,3-*b*]phthalazine-5,7,12,14-tetraones using montmorillonite clay K-10 as a heterogeneous acidic catalyst and microwave irradiation under solvent-free conditions. The solid montmorillonite clay was successfully recovered later and reused in subsequent reactions.

Results and discussion

Different substituted phthalic anhydrides and either semicarbazide or thiosemicarbazide reacted for 3–7 min under solvent-free conditions using microwave irradiation at 180 °C on montmorillonite K-10 clay (Scheme 1). Under classical heating conditions, the reactions were carried out at a similar temperature but for longer reaction times (40–70 min) and lower yields.

The polarity of the carbonyl group of semicarbazide is greater than its thiocarbonyl analog in thiosemicarbazide, so the $-NH_2$ group in thiosemicarbazide is a better nucleophile than the $-NH_2$ group in semicarbazide and hence will produce better yields. It seems that the nature of the substituents of phthalic anhydride has some effects on this reaction. It is of interest to note that the presence of electron-withdrawing groups like Cl and NO_2 gave high product yields and short reaction times compared with the unsubstituted phthalic anhydride. The use of the solid clay as an efficient heterogeneous acidic solid catalyst as well as microwave irradiation offer high product yields compared with conventional procedures. A comparison has been given in the general procedure section. Among the other advantages of our method is the recyclability of solid clay. The clay catalyst used in the first cycle was recovered by filtration, washed with methanol, and reused. Recyclability details of the clay have been explained in the footnote of Table 1. It is notable that all attempts to prepare the products in the absence of montmorillonite K-10 clay failed (despite 15 min irradiation at 180 °C). Therefore, the role of montmorillonite K-10 clay as a solid catalyst in this reaction is essential. Furthermore, the use of reusable solid acid makes this method quite simple, more convenient, and economically viable. Finally, in a second series of experiments the reactions were carried out under the conventional heating conditions using an oil bath at similar temperatures (170–180 °C, solvent-free) without microwave irradiation. It was observed that under classical heating the reactions gave the products with relatively lower yields and longer reaction times. Moreover, the reactions required continuous stirring to prevent charring. Comparison of the results clearly shows the preference of microwave irradiation over conventional heating. The results for the obtained products under both conditions are listed in Table 1.

Experimental

Melting points were measured on an Electrothermal 9100 apparatus. The IR spectra were obtained on a PerkinElmer FT IR GX instrument using KBr discs. The ^1H NMR and ^{13}C NMR spectra were recorded on a FT-NMR JEOL FX 90Q spectrometer using TMS as internal standard (δ given in ppm). Mass spectra were measured with a GCMS Agilent 5973N instrument. Elemental analyses were performed using a Heraeus CHN Rapid analyzer. Chemicals were purchased from the Sigma-Aldrich and Merck chemical companies and used without further purification. Montmorillonite K-10 clay

© 2007 NRC Canada

Table 1. The yields and reaction times of compounds **a**–**j**.

No.	Anhydride	Reagent	Compound[b]	Time (min)	Yield (%)[a] Fresh clay	Yield (%)[a] Recovered clay
1	Phthalic anhydride	Semicarbazide	**a**	7.0 (70)	61 (43)	54 (32)
2	Tetrachloro-phthalic anhydride	Semicarbazide	**b**	3.5 (45)	73 (56)	64 (38)
3	3-Nitro-phthalic anhydride	Semicarbazide	**c**	5.5 (60)	69 (52)	60 (35)
4	4-Nitro-phthalic anhydride	Semicarbazide	**d**	5.0 (55)	67 (48)	57 (34)
5	3-Fluoro-phthalic anhydride	Semicarbazide	**e**	6.0 (65)	65 (45)	58 (30)
6	Phthalic anhydride	Thiosemicabazide	**f**	5.0 (55)	67 (48)	61 (35)
7	Tetrachloro-phthalic anhydride	Thiosemicabazide	**g**	3.0 (40)	82 (61)	77 (43)
8	3-Nitro-phthalic anhydride	Thiosemicabazide	**h**	4.0 (50)	74 (53)	58 (34)
9	4-Nitro-phthalic anhydride	Thiosemicabazide	**i**	3.5 (45)	73 (55)	56 (39)
10	3-Fluoro-phthalic anhydride	Thiosemicabazide	**j**	4.0 (50)	70 (54)	64 (36)

Note: The results given in parentheses correspond to those reactions that were carried out under classical heating conditions (solvent-free, 170–180 °C, oil bath, without microwave irradiation).

[a]Isolated yields after recrystallization. The solid clay portion used in the first cycle was filtered off, washed with methanol (2 × 20 mL) under stirring for 1 h, and dried at 120 °C for 5 h under reduced pressure, to be reused in the subsequent reaction, which showed a gradual decrease in activity.

[b](**a**, **f**) Phthalazino[2,3-*b*]phthalazine-5,7,12,14-tetraone; (**b**, **g**) octachlorophthalazino[2,3-*b*]phthalazine-5,7,12,14-tetraone; (**c**, **h**) 1,11-dinitrophthalazino[2,3-*b*]phthalazine-5,7,12,14-tetraone; (**d**, **i**) 2,10-dinitro-phthalazino[2,3-*b*]phthalazine-5,7,12,14-tetraone; (**e**, **j**) 1,11-difluorophthalazino[2,3-*b*]phthalazine-5,7,12,14-tetraone.

was purchased from Fluka chemical company [surface area: 200 m^2/g; pH 2.5–3.5; chemical composition (average value): SiO_2 (73.0%), Al_2O_3 (14.0%), Fe_2O_3 (2.7%), CaO (0.2%), MgO (1.1%), Na_2O (0.6%), K_2O (1.9%)].

Typical procedure for microwave-mediated synthesis of phthalazino[2,3-b]phthalazine-5,7,12,14- tetraones

In a typical experiment, phthalic anhydride (2.2 mmol, 0.330 g), thiosemicarbazide (1 mmol, 0.091 g), and montmorillonite K-10 clay (1 g) were mixed in a mortar and the mixture was placed in a pyrex tube and introduced into a Synthewave 402® (Prolabo, France) single mode focused microwave reactor for 5 min at 180 °C (monitored temperature (20)) with continuous rotation. The reaction mixture was then allowed to cool to room temperature. The resulting product was extracted into dichloromethane (2 × 25 mL), filtered off, and the solvent was removed by rotary evaporation. The obtained product, phthalazino[2,3-*b*]phthalazine-5,7,12,14-tetraone (**f**), was very thoroughly washed with distilled water, dried in an oven, and recrystallized from acetic acid. Melting point 332–336 °C. Yield with the fresh K-10 clay, 67% and 0.195 g; yield with the recovered K-10 clay, 61% and 0.178 g (lit. values (11) mp 343 to 344 °C, yield 55%, reaction time 1.5 h using polyphosphoric acid). The solid clay portion was washed with methanol and dried at 120 °C under reduced pressure to be reused in the subsequent reactions, which showed a gradual decrease in activity (Table 1). With this procedure compounds, **a**–**j** were synthesized. The physical data (mp, IR, NMR, and MS) of known compounds **a** and **f** were found to be identical with those of authentic samples. Unknown compounds were characterized by mp, spectra (IR, NMR, and MS), and elemental analyses.

Phthalazino[2,3-b]phthalazine-5,7,12,14-tetraone (a, f)

Melting point 332–336 °C. IR (KBr, cm^{-1}) ν: 3092.7, 1853.5, 1792.6, 1763.5, 1686.4, 1597.4, 1471.3, 1258.7, 1109.8, 907.2. ^{1}H NMR (DMSO-d_6) δ: 7.81–7.98 (8H, m, Ar). ^{13}C NMR (DMSO-d_6) δ: 123.0, 129.3, 134.8, 168.9. MS *m/z*: 292 (M^+). Anal. calcd. for $C_{16}H_8N_2O_4$: C 65.76, H 2.76, N 9.58; found: C 65.12, H 2.60, N 9.48.

Octachlorophthalazino[2,3-b]phthalazine-5,7,12,14-tetraone (b, g)

Melting point 317–321 °C. IR (KBr, cm^{-1}) ν: 1846.7, 1835.4, 1775.7, 1757.76, 1373.9, 1299.3, 1233.8, 923.3. ^{13}C NMR (DMSO-d_6) δ: 170.24, 139.92, 135.46, 127.41. MS *m/z*: 568 (M^+). Anal. calcd. for $C_{16}Cl_8N_2O_4$: C 33.80, N 4.92; found: C 33.67, N 4.53.

1,11-Dinitrophthalazino[2,3-b]phthalazine-5,7,12,14-tetraone (c, h)

Melting point 271–274 °C. IR (KBr, cm^{-1}): 3172.9, 3026.24, 2922.0, 1669.9, 1603.3, 1578.1, 1560.8, 1491.6, 1336.5, 1298.2, 825.6. ^{1}H NMR (DMSO-d_6) δ: 7.92–8.63 (6H, m, Ar). ^{13}C NMR (DMSO-d_6) δ: 167.71, 167.43, 148.45, 136.85, 133.39, 132.70, 132.52, 129.61. MS *m/z*: 382 (M^+). Anal. calcd. for $C_{16}H_6N_4O_8$: C 50.26, H 1.57, N 14.56; found: C 50.14, H 1.38, N 14.33.

2,10-Dinitrophthalazino[2,3-b]phthalazine-5,7,12,14-tetraone (d, i)

Melting point 263–267 °C. IR (KBr, cm^{-1}) ν: 3106.3, 3006.5, 1641.8, 1626.7, 1598.7, 1539.9, 1466.6, 1355.1, 1188.4, 1061.3, 791.9. ^{1}H NMR (DMSO-d_6) δ: 8.36–8.94 (6H, m, Ar). ^{13}C NMR (DMSO-d_6) δ: 162.52, 162.43, 154.81, 137.78, 134.66, 133.19, 129.26, 122.34. MS *m/z*: 382 (M^+). Anal. calcd. for $C_{16}H_6N_4O_8$: C 50.26, H 1.57, N 14.56; found: C 50.09, H 1.29, N 14.25.

1,11-Difluorophthalazino[2,3-b]phthalazine-5,7,12,14-tetraone (e, j)

Melting point 298–302 °C. IR (KBr, cm^{-1}): 3021.9, 2921.0, 1671.2, 1603.1, 1577.8, 1560.2, 1491.3, 1336.6, 1299.7, 825.8. ^{1}H NMR (DMSO-d_6) δ: 7.82–8.27 (6H, m, Ar). ^{13}C NMR (DMSO-d_6) δ: 175.27, 163.66, 163.32, 163.08, 136.42, 136.27, 130.52. MS *m/z*: 328 (M^+). Anal. calcd. for

© 2007 NRC Canada

$C_{16}H_6F_2N_2O_4$: C 58.53, H 1.82, N 8.53; found: C 58.34, H 1.69, N 8.21.

Acknowledgement

Financial support from the Department of Chemistry, Faculty of Sciences, Bu-Ali Sina University, Hamedan, 6517838683, Iran is gratefully appreciated.

References

1. (*a*) Y. Ju and R.S. Varma. Tetrahedron Lett. **46**, 6011 (2005); (*b*) E.J. Noga, G.T. Barthalmus, and M.K. Mitchell. Cell Biol. Int. Rep. **10**, 239 (1986); (*c*) T. Kodama, M. Tamura, T. Oda, Y. Yamazaka, M. Nishikawa, S. Takemura, T. Doi, Y. Yoshinori, and M. Ohkuchi. U.S. Patent 6-498-169, 24 December 2002; (*d*) P. N. Craig. Comprehensive medicinal chemistry. *Edited by* C.J. Drayton. Pergamon Press, New York. 1991.
2. (*a*) V. Krchňák and M.W. Holladay. Chem. Rev. **102**, 61 (2002); (*b*) L.A. Thompson and J. A. Ellman. Chem. Rev. **96**, 555 (1996); (*c*) N.K. Terrett, M. Gardner, D.W. Gordon, R.J. Kobylecki, and J. Steele. Tetrahedron, **51**, 8135 (1995).
3. (*a*) M. Pal, V.R. Batchu, K. Parasuraman, and K.R. Yeleswarapu. J. Org. Chem. **68**, 6806 (2003); (*b*) N. Watanabe, Y. Kabasawa, Y. Takase, M. Matsukura, K. Miyazaki, H. Ishihara, K. Kodama, and H.J. Adachi. J. Med. Chem. **41**, 3367 (1998); (*c*) M. Napoletano, G. Norcini, F. Pellacini, F. Marchini, G. Morazzoni, F. Fattori, P. Ferlenga, and L. Pradella. Bioorg. Med. Chem. Lett. **12**, 5 (2002); (*d*) M. Van der Mey, A. Hatzelmann, I.J. Van der Laan, G.J. Sterk, U. Thibaut, and H.J. Timmerman. J. Med. Chem. **44**, 2511 (2001).
4. S. Mavel, I. Thery, and A. Gueiffier. Arch. Pharm. **335**, 7 (2002).
5. (*a*) R.W. Carling, K.W. Moore, L.J. Street, D. Wild, C. Isted, P.D. Leeson, S. Thomas, D. O'Connor, R.M. McKernan, K. Quirk, S.M. Cook, J.R. Atack, K.A. Wafford, S.A. Thompson, G.R. Dawson, Ferris, and J.L. Castro. J. Med. Chem. **47**, 1807 (2004); (*b*) L.J. Street, F. Sternfeld, R.A. Jelley, A.J. Reeve, R.W.Carling, K.W. Moore, R.M. McKernan, B. Sohal, S. Cook, A. Pike, G.R. Dawson, F.A. Bromidge, K.A. Wafford, G.R. Seabrook, S.A. Thompson, G. Marshall, G.V. Pillai, J.L. Castro, J.R. Atack, and A.M. MacLeod. J. Med. Chem. **47**, 3642 (2004).
6. Y. Imamura, A. Noda, T. Imamura, Y. Ono, T. Okawara, and H. Noda. Life Sci. **74**, 29 (2003).
7. J.S. Kim, H.-J. Lee, M.-E. Suh, H.-Y. Park Choo, S.K. Lee, H.J. Park, C. Kim, S.W. Park, and C.-O. Lee. Bioorg. Med. Chem. **14**, 3683 (2004).
8. A.D. Lebsack, J. Gunzner, B. Wang, R. Pracitto, H. Schaffhauser, A. Santini, J. Aiyar, R. Bezverkov, B. Munoz, W. Liu, and S. Venkatraman. Bioorg. Med. Chem. Lett. **14**, 2463 (2004).
9. (*a*) F. Gomez-Contreras and P.J. Navarro. Heterocycl. Chem. **16**, 1035 (1979); (*b*) S.C. Shin, K.H. Kang, and Y. Lee. Bull. Korean Chem. Soc. **11**, 22 (1990); (*c*) R.J. Kobilecky and A. Mckillop. Adv. Heterocycl. Chem. **19**, 215 (1976); (*d*) A.W. Murray and K.J. Vaughan. J. Chem. Soc. Chem. Commun. 1282 (1967); (*e*) F. Gomez-Contreras, M.L. Tamayo, P. Navarro, and M. Pardo. Tetrahedron, **34**, 3499 (1978); (*f*) H. Neunhoeffer. Comprehensive heterocyclic chemistry. Vol. 3. *Edited by* A.R. Katritzky and C.W. Rees. Pergamon Press, Oxford, Great Britain. 1984. p. 369; (*g*) H. Sieper, P. Tavs, and M. Liebigs. Ann. Chem. **704**, 161 (1967); (*h*) D.E. Davies, D.L.R. Reeves, and R.C. Storr. J. Chem. Soc. Chem. Commun. 808 (1980); (*i*) F. Willey, B. Andereas, and D. Tony. Heterocycles, **20**, 1271 (1983).
10. (*a*) T.J. Kealy. J. Am. Chem. Soc. **84**, 966 (1962); (*b*) D.B. Paul. Aust. J. Chem. **37**, 100 (1984); (*c*) H.D.K. Drew and H.H. Hatt. J. Chem. Soc. **26**, 16 (1937).
11. M.C. Cardia, S. Distinto, E. Maccioni, L. Bonsignore, and A. DeLogu. J. Heterocycl. Chem. **40,** 1011 (2003).
12. (*a*) J.H. Clark. Acc. Chem. Res. **35**, 791 (2002); (*b*) A. Cornelis and P. Laszlo. Synlett, 155 (1994).
13. (*a*) R.S. Varma. Tetrahedron, **58,** 1235 (2002); (*b*) T.S. Li and T.S. Jin. Chin. J. Org. Chem. **16**, 385 (1996); (*c*) M. Balogh and P. Laszlo. *In* Organic chemistry using clay. Spinger-Verlag, New York. 1993; (*d*) P. Laszlo. Science, **235**, 1473 (1987); (*e*) P. Laszlo. Pure Appl. Chem. **62**, 2027 (1990).
14. (*a*) R. Lauren, A. Leporterie, J. Dubac, J. Berlan, S. Lauverie, and F.M. Audhuy. J. Org. Chem. **57**, 7099 (1992); (*b*) S. Caddick. Tetrahedron, **51**, 10403 (1995); (*c*) P. Lidstrom, J. Tierney, B. Wathey, and J. Westman. Tetrahedron, **57**, 9225 (2001).
15. (*a*) A.K. Bose, M.S. Manhas, S.N. Ganguly, A.H. Sharma, and B.K. Banik. Synthesis, 1578 (2002); (*b*) A. Loupy, A. Petit, J. Hamelin, F. Texier-Boullet, P. Jacquault, and D. Mathe. Synthesis, 1213 (1998); (*c*) R.S. Varma. Green Chem. **1**, 43 (1999); (*d*) A. Loupy. Microwaves in organic synthesis. Wiley-VCH, Weinheim, Germany. 2002; (*e*) C.O. Kappe and A. Stadler. Microwaves in organic and medicinal chemistry. Wiley-VCH, Weinheim, Germany. 2005; (*f*) R.S. Varma. Clean Prod. Processes, **1**, 132 (1999); (*g*) J.P. Tierney and P. Lidstrom. Microwave assisted organic synthesis. Blackwell, Oxford, UK. 2005.
16. (*a*) G. Bram, A. Loupy, and D. Villemerin. Solid support and catalysed in organic chemistry. Ellis Horwood, London, UK. 1992; (*b*) D.C. Dittmer. Chem. Ind. 779 (1997); (*c*) S. Deshayes, L. Marion, A. Loupy, J.L. Luche, and A. Petit. Tetrahedron, **55**, 10851 (1999).
17. (*a*) M. Kidwai. Pure Appl. Chem. **73**, 147 (2001); (*b*) M. Kidwai, R. Venkataramanan, R.K. Garg, and K.R. Bhushan, J. Chem. Res. Synop. 586 (2000); (*c*) M. Kidwai, B. Dave, P. Misra, R.K. Saxena and M. Singh. Inorg. Chem. Commun. **3**, 465 (2000); (*d*) A. Boruah, M. Baruah, D. Prajapti, and J.S. Sandhu. Chem. Lett. 965 (1996).
18. D. Habibi and O. Marvi. Catal. Commun. **8**, 127 (2007).
19. (*a*) D. Habibi and O. Marvi. ARKIVOC Part (xiii) [online]. 8 (2006); (*b*) D. Habibi and O. Marvi. J. Serb. Chem. Soc. **70**(4), 579 (2005).
20. (*a*) R. Commarmot, R. Didenot, and J.F. Gardais. French Patent Priority No. FR19840003496, 27 Oct. 1986; (*b*) Fr. Prolabo. Patent 62241/D, 14669 Fr, 23 Dec. 1991.

© 2007 NRC Canada

Modular syntheses of oxazolinylamine ligands and characterization of group 10 metal complexes

Christine A. Caputo, Florentino d.S. Carneiro, Michael C. Jennings, and Nathan D. Jones

Abstract: The syntheses of aminoalkyloxazoline and pyrrolidinyloxazoline ligands, each of which bear a pair of chiral centres, by both known and new routes are reported. Variable temperature NMR studies show that the known stepwise syntheses of the pyrrolidinyl compounds are not complicated by epimerization; however, coordination of one of the aminoalkyl derivatives to Pt(II) under conditions of prolonged heating to 80 °C does give mixtures of diastereomeric *N*,*N*′-chelated complexes that result from inversion of the chiral centre associated with the aminoalkyl fragment. A new synthesis of pyrrolidinyloxazoline ligands that involves the Zn-catalyzed cyclization of Cbz-protected 2-cyanopyrrolidine and β-amino alcohols is also reported. This procedure offers the advantages of economy, shorter time, and fewer purification steps over the previously reported synthesis. In addition, the crystal structure of an enantiopure Pd(II) complex of an *N,N*′-chelated pyrrolidinyloxazoline is disclosed. This compound has a pseudo-C_2 axis of symmetry, which may make it suitable for asymmetric catalytic applications.

Key words: chiral ligands, ligand design, oxazolines, variable temperature NMR spectroscopy, asymmetric catalysis, coordination compounds, palladium, platinum

Résumé : Faisant appel à des méthodes connues et d'autres nouvelles, on a réalisé la synthèse de ligands aminoalkyloxazolines et pyrrolidinyloxazolines qui portent une paire de centres chiraux. Des études de RMN à température variable ont permis de montrer que la méthode synthèse connue par étape pour les composés pyrrolidinyles ne sont pas compliquées par l'épimérisation; toutefois, la coordination d'un des dérivés aminoalkyles du Pt(II), dans des conditions de chauffage prolongé à 80 °C, ne conduit pas à des mélanges de complexes *N,N*′-chélatés diastéréomères résultant de l'inversion du centre chiral associé au fragment aminoalkyle. On a aussi réalisé une nouvelle synthèse des ligands pyrrolidinyloxazolines qui implique une cyclisation catalysée par le zinc de β-amino-alcools sur la 2-cyanopyrrolidine portant un groupe protecteur Cbz. Par rapport aux méthodes antérieures, cette méthode présente l'avantage d'être plus économique, d'impliquer des temps de réaction plus courts et moins d'étapes de purification. De plus, on a déterminé la structure cristalline du complexe énantiopur du Pd(II) avec une pyrrolidinyloxazoline *N,N*′-chélatée. Ce produit présente un axe de symétrie pseudo-C_2 qui pourrait le rendre susceptible d'être utilisé dans des applications de catalyse asymétrique.

Mots clés : ligands chiraux, développement de ligands, oxazolines, spectroscopie RMN à température variable, catalyse asymétrique, composés de coordination, palladium, platine.

[Traduit par la Rédaction]

Introduction

Beginning in the late 1980s and continuing to the present day, the oxazoline (4,5-dihydrooxazole) ring has featured prominently as the chiral component of a broad range of ligands that have been used to great effect in asymmetric catalytic transformations (1, 2). In particular, the C_2-symmetric bis(oxazoline) class has seen widespread and very successful application, e.g., in cycloaddition, aldol, Michael, carbonylene, and related Lewis acid-catalyzed reactions (3). More recently, C_1-symmetric compounds bearing oxazoline rings that have been elaborated with aminoalkyl functional groups predominantly in the 2-position (e.g., Chart 1, **I**) (4) have come to the fore as an important subclass of ligands in their own right and as building blocks for more elaborate ligand systems (Chart 1, **II**–**IV**) (5–7). Less common variations bearing aminomethyl groups in the 4-position have also appeared (Chart 1, **XIV**) (8).

The advantages of the ligand family **I** have been documented in a recent report by Rajaram and Sigman (4): the compounds are conveniently made in a modular manner from readily available, optically pure starting materials, bear multiple independently variable stereocentres, and are amenable to further elaboration through manipulation of the amine (e.g., to give **II**–**IV**) (5–7, 9). We also point out that the presence of N*H* protons may have important ramifications for the use of these ligands in the asymmetric hydrogenation of C=O bonds. Variations on this theme have also included oxazolines incorporating pyrrolidine (**V**) (10), quinoline (**VI**) (11), aniline (**VII**, **XIII**) (12–14),

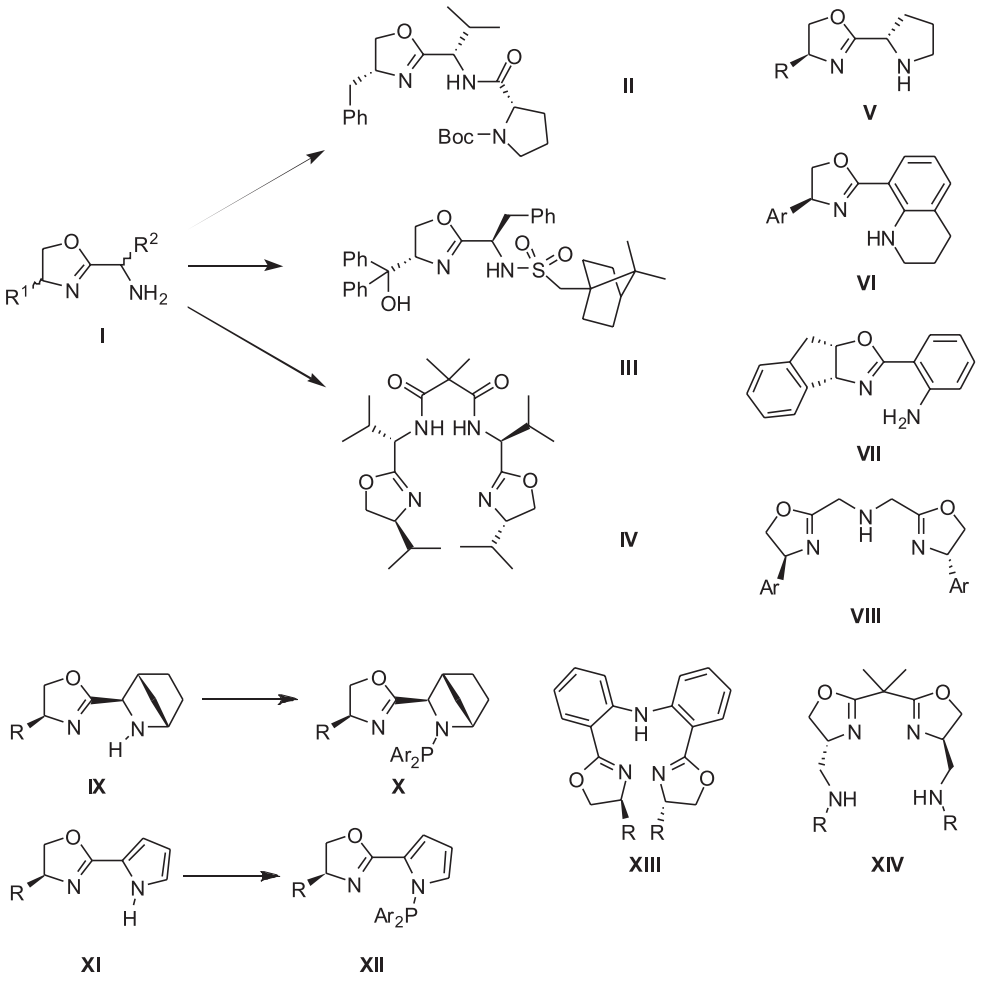
Received 4 October 2006. Published on the NRC Research Press Web site at http://canjchem.nrc.ca on 20 February 2007.

C.A. Caputo, F.d.S. Carneiro, M.C. Jennings, and N.D. Jones.[1] Department of Chemistry, The University of Western Ontario, London, ON N6A 5B7, Canada.

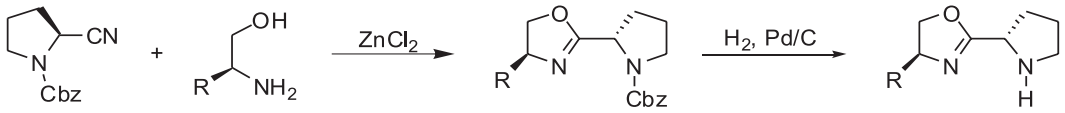
[1]Corresponding author (e-mail: njones26@uwo.ca).

 doi:10.1139/V06-188 © 2007 NRC Canada

Chart 1. Examples of oxazolinylamine ligands.



Scheme 1. General synthesis of pyrrolidinyloxazolines by the Zn-catalyzed cyclization of *N*-protected 2-cyanopyrrolidine and β-amino alcohols.



azabicyclo[2.2.1]heptane (**IX**) (15), pyrrole (**XI**) (16–18), and pyridine (not shown) ring systems (21).

To date, access to the pyrrolidinyloxazoline ligands **V** has been limited to a stepwise synthetic route outlined by McManus et al. (10). Herein, we propose an alternate approach that involves the Zn-catalyzed cyclization of Cbz-protected 2-cyanopyrrolidine and β-amino alcohols (Scheme 1). This new approach is quicker, more economical, and requires fewer purifications. It also puts the diversification step later in the synthesis, which allows expansion of ligand libraries more easily.

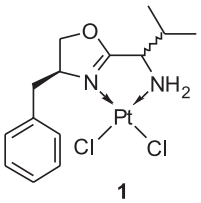
Ligands in classes **I** and **V** bear two stereocentres and are, in principle, susceptible to epimerization. Through careful stepwise synthesis, we show in this report that there is no epimerization of **V** either during ligand synthesis by the McManus route or during metal complexation. However, epimerization does occur during the coordination of a ligand of type **I** to Pt(II); two diastereomers of **1** (Chart 2) result from the reaction of the appropriate ligand and $PtCl_2(SMe_2)_2$ in boiling dichloroethane.

The compounds shown in Chart 1 have been used as ligands in asymmetric allylation (**II**, **XIII**) (5,13), alkylation (**IV**) (7,9), and crotylation (**XIII**) of aldehydes (13), Diels-Alder (**XI**) (16), hetero-Diels-Alder (**III**, **XI**) (6), and transfer hydrogenation (**V**, **VI VII**, **VIII** and **IX**) reactions (10–12,14,15); phosphine derivatives (**X**, **XII**) (19,20) have also been made and applied successfully in asymmetric hydrogenations.

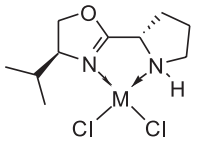
Catalysts for these reactions have typically been generated in situ. Therefore, well-characterized examples of *N,N′*-chelated oxazolinylamine metal complexes are rare. Those *N,N′*-chelated complexes that have been structurally characterized are for the most part confined to the pyridinyloxazolines (21) and to the adducts of **VII** (12) and **XI** (16). As part of our ongoing exploration of modularly-made chiral *N,N′*-chelating ligands, we also present in this work the synthesis and

© 2007 NRC Canada

Chart 2. Group 10 metal complexes of the oxazolinylamines reported in this work.



1



M = Pt (**2**), Pd (**3**)

characterization of group 10 metal complexes of ligands of type **I** and **V**, including an X-ray structural determination of a Pd(II) complex of **V** (Chart 2, **3**).

Experimental section

General considerations

Reagents were obtained from commercial sources and used as supplied unless otherwise indicated. These were of American Chemical Society (ACS) grade or finer. Solvents were dried and deoxygenated either by N_2 purge followed by passage through alumina columns (Innovative Technology or MBraun solvent purification systems) or by distillation under N_2 from the appropriate drying agent. All reactions were carried out under N_2 atmosphere using standard Schlenk techniques unless stated otherwise. Amino alcohols were prepared by the reduction of corresponding amino acids using a standard procedure (22). The metal complexes, *trans*-$PdCl_2(PhCN)_2$ and $PtCl_2(SMe_2)_2$, were prepared according to literature procedures (23, 24).

Thin-layer chromatography was performed using 250 μm silica gel glass plates with fluorescent indicator (254 nm, Rose Scientific, Edmonton, Alberta) and viewed by exposure to UV light and (or) immersion in a staining solution (ninhydrin, $KMnO_4$, or phosphomolybdic acid) followed by heating. Flash chromatography was performed using ACP ultra pure silica gel, 60 Å, 230–400 mesh (Silicycle, Québec, Quebec), using the eluent(s) specified. All solvent mixtures are reported as volume percentages.

^1H, $^{13}C\{^1H\}$, $^{19}F\{^1H\}$, correlated spectroscopy (COSY), and heteronuclear multiple quantum coherence (HMQC) NMR data were recorded on a 400 MHz Varian Mercury (400.085 MHz for ^1H, 100.602 MHz for ^{13}C, 376.458 MHz for ^{19}F) or a 400 MHz Varian Inova spectrometer (399.762 MHz for ^1H, 100.520 MHz for ^{13}C). Unless otherwise indicated, spectra were recorded at room temperature (RT) in a $CDCl_3$ solution using residual solvent proton (relative to external $SiMe_4$, δ 0.00) or solvent carbon (relative to external $SiMe_4$, δ 0.00) as an internal reference. Downfield shifts were taken as positive. Data for the ^1H NMR spectra are reported as follows: chemical shift (δ), multiplicity, integration, assignment, and coupling constant(s). All coupling constants are reported in Hertz (Hz) and the spin multiplicities are indicated as follows: singlet (s), triplet (t), quartet (q), multiplet (m), pseudo (p), and broad (br). Peaks due to the minor geometrical (*E* or *Z* isomer) when present in ^1H or ^{13}C spectra are denoted by *. Fractional values for the ^1H NMR integrations indicate the relative concentrations of *E* and *Z* isomers in solution.

High resolution mass spectrometry data were recorded using a Finnigan MAT 8200 instrument. IR spectra were recorded using a Bruker Vector 33 FT-IR spectrometer; samples were run either neat between KCl plates or prepared as KBr pellets. Data are reported in cm^{-1}; peak intensities are given as follows: strong (s), medium (m), weak (w), very (v).

Syntheses of oxazolinylamine ligands

1-{(4S)-4-Benzyl-4,5-dihydro-oxazol-2-yl}-(2S)-2-methyl-propylamine-carbamic acid ester 9H-fluoren-9-ylmethyl (4)

The title compound was made according to the method of Rajaram and Sigman (4). ^1H NMR (DMSO-d_6, 353 K) δ: 0.89 (pt, 6H, $CH(CH_3)_2$), 2.00 (m, 1H, $CH(CH_3)_2$), 2.70 (dd, 1H, $CHH'Ph$, $^2J_{HH}$ = 13.8, $^3J_{HH}$ = 6.8), 2.85 (dd, 1H, $CHH'Ph$, $^2J_{HH}$ = 13.6, $^3J_{HH}$ = 6.4), 3.93 (pt, 1H, ox $OCHH'$), 4.03 (pt, 1H, ox $OCHH'$), 4.23–4.36 (m, 5H, Fmoc C*H*, Fmoc CH_2, NHC*H*, ox NC*H*), 7.18 (m, 1H, Ph), 7.22–7.26 (m, 4H, Ph), 7.32 (m, 2H, Fmoc Ar), 7.39 (t, 2H, Fmoc Ar, $^3J_{HH}$ = 7.6), 7.72 (pt, 2H, Fmoc Ar), 7.87 (d, 2H, Fmoc Ar, $^3J_{HH}$ = 7.6). $^{13}C\{^1H\}$ NMR δ: 18.40, 19.15, 30.17, 41.15, 46.66, 54.81, 65.66, 66.53, 71.31, 120.07, 125.32, 125.36*, 126.09, 127.01, 127.61, 128.15, 129.25, 138.23, 140.69*, 143.76*, 143.85, 156.05, 165.55*. HRMS calcd. for $C_{29}H_{30}N_2O_3$: 454.2256; found: 454.2268.

1-{(4S)-4-Benzyl-4,5-dihydro-oxazol-2-yl}-(2S)-2-methyl-propylamine (5)

The synthesis by Rajaram and Sigman (4) was modified to use Et_2NH instead of piperidine. A 50 mL round-bottomed flask was charged with **4** (0.303 g, 0.662 mol) and MeOH (6 mL) was added to give a white suspension. Et_2NH (5 mL) was added over a period of 10 min at RT. The resulting pale beige solution was stirred for 30 min. The solution was concentrated in vacuo and the residue was purified by silica gel chromatography (MeOH–CH_2Cl2 10%–20%). The title compound was obtained as a beige oil. Yield 0.154 g (97%). ^1H NMR δ: 0.91 (d, 3H, $CH(CH_3)_2$, $^3J_{HH}$ = 6.8), 0.93 (d, 3H, $CH(CH_3)_2$, $^3J_{HH}$ = 6.8), 1.77 (br s, 2H, NH_2), 1.91 (m, 2H, $CH(CH_3)_2$, $^3J_{HH}$ = 6.8), 2.62 (dd, 1H, $CHH'Ph$, $^2J_{HH}$ = 13.6, $^3J_{HH}$ = 8.4), 3.06 (dd, 1H, $CHH'Ph$, $^2J_{HH}$ = 13.6, $^3J_{HH}$ = 5.2), 3.28 (d, 1H, NH_2CH, $^3J_{HH}$ = 5.2), 3.97 (dd, 1H, $OCHH'$, $^2J_{HH}$ = 8.8, $^3J_{HH}$ = 7.2), 4.16 (pt, 1H, $OCHH'$), 4.36 (m, 1H, NC*H*), 7.16–7.29 (m, 5H, Ph). $^{13}C\{^1H\}$ NMR δ: 17.79, 19.58, 32.38, 42.02, 55.77, 67.17, 72.10, 126.74, 128.75, 129.10, 129.17, 129.30, 129.49. HRMS calcd. for $C_{14}H_{21}N_2O$: 233.1660; found: 233.1648.

Syntheses of Fmoc- and Cbz-protected pyrrolidinyloxazolines

Compounds **7** and **9** were made according to modifications to the methods reported by McManus et al. (10), who developed them for the analogous Cbz-protected pyrrolidine derivatives **8** and **10**. Room temperature spectroscopic data for **8** and **10** matched those given in the literature. However, high-temperature NMR spectroscopic data were acquired by us to ensure that the reported splitting and broadening of peaks was in fact due to *E* and *Z* isomers arising from the amide and (or) carbamate (Cbz) bonds and not instead to the presence of diastereomers resulting from epimerization. This

© 2007 NRC Canada

determination was made based on the coalescence at high temperature of the isopropyl methyl peaks from a multiplet into two doublets of equal intensity and of the benzyl CH_2 multiplet into a sharp singlet. Both sets of data (low and high temperatures) are given for comparison.

Compounds **11** and **12** were prepared by deprotection of the Cbz group using Pd–C and H_2 gas as the hydrogen source. This differed from the procedure of McManus et al. (10), which used cyclohexene as the hydrogen source.

(2S)-Chlorocarbamoyl-pyrrolidine-1-carboxylic acid 9H-fluoren-9-ylmethyl ester (6)

Thionyl chloride (1.29 mL, 17.8 mmol) was added dropwise over a period of 2 min to a 100 mL round-bottomed flask charged with Fmoc-Pro-OH (3.38 g, 10.0 mmol) and dry toluene (30 mL). The mixture was heated to dissolve all solids and held at reflux for 2 h. The yellow solution was cooled to RT, then concentrated in vacuo to afford a yellow oil, which crystallized when stored at 5 °C. The product was used without further purification. IR (neat) ν: 1793 (s, C=O COCl), 1707 (s, C=O Fmoc).

(2S)-{(1S)-Hydroxylmethyl-2-methyl-propylcarbamoyl}-pyrrolidine-1-carboxylic acid 9H-fluoren-9-ylmethyl ester (7)

A solution of L-valinol (0.290 g, 2.40 mmol) and NEt_3 (0.390 mL, 2.80 mmol) in dry CH_2Cl_2 (5 mL) was added dropwise to a 100 mL Schlenk tube containing **6** (1.00 g, 2.80 mmol) and dry CH_2Cl_2 (30 mL) that had been cooled to 0 °C and flushed with N_2. The mixture was stirred at 0 °C for 20 min, warmed to RT, and stirred overnight. The mixture was concentrated to ~15 mL and washed with satd. aq. NH_4Cl (3 × 50 mL), H_2O (2 × 50 mL), and brine (50 mL). The organic layer was dried over $MgSO_4$ and concentrated in vacuo. The residue was purified by silica gel chromatography (MeOH–CH_2Cl_2 2%) to afford a nearly colourless oil. Yield 0.91 g (91%). ^{1}H NMR δ: 0.87 (d, 3H, CH(CH_3)$_2$, $^3J_{HH}$ = 6.8), 0.89 (d, 3H, CH(CH_3)$_2$, $^3J_{HH}$ = 6.8), 1.81–2.02 (m, 4H, CH(CH$_3$)$_2$, pyr NCH$_2$CH_2, pyr NCHCHH'), 2.16–2.30 (m, 1H, pyr NCHCHH′), 3.41–3.66 (m, 6H, pyr NCH_2, CONHCH, CH_2OH, OH), 4.21 (pt, 1H, Fmoc CH), 4.32–4.45 (m, 4H, Fmoc OCH_2, pyr NCH), 6.37* (br s, 0.3H, CONH), 6.83 (d, 0.7H, CONH, $^3J_{HH}$ = 6.8), 7.30 (pt, 2H, Fmoc Ar), 7.39 (pt, 2H, Fmoc Ar), 7.57 (d, 2H, Fmoc Ar, $^3J_{HH}$ = 7.6), 7.75 (d, 2H, Fmoc Ar, $^3J_{HH}$ = 7.2). ^{13}C{^{1}H} NMR δ: 18.79, 19.78, 24.86, 28.78*, 29.04, 47.33, 57.57, 61.01, 63.68, 68.00, 120.24, 125.21, 127.30, 128.00, 141.49, 143.91, 156.43, 172.56. HRMS calcd. for $C_{25}H_{31}N_2O_4$: 423.2292; found: 423.2278.

(2S)-{(1S)-Hydroxylmethyl-2-methyl-propylcarbamoyl}-pyrrolidine-1-carboxylic acid benzyl ester (8)

The title compound was made according to the procedure reported by McManus et al. (10). ^{1}H NMR (298 K) δ: 0.84 (pd, 3H, CH(CH_3)$_2$), 0.87 (d, 3H, CH(CH_3)$_2$, $^3J_{HH}$ = 7.2), 1.80 (m, 1H, CH(CH$_3$)$_2$), 1.91 (m, 2H, pyr NCH$_2$CH_2), 2.17 (br s, 1H, pyr NCHCHH′), 2.32 (br s, 1H, pyr NCHCHH'), 3.46–3.66 (m, 5H, CH_2OH, NHCH, pyr NCH_2), 4.35 (m, 1H, pyr NCH), 5.06–5.20 (m, 2H, Cbz OCH_2), 6.19 (s, 0.4H, CONH), 6.75 (s, 0.6H, CONH), 7.13–7.38 (m, 5H, Cbz Ar). ^{1}H NMR (353 K) δ: 0.84 (d, 3H, CH(CH_3)$_2$, $^3J_{HH}$ = 6.8), 0.88 (d, 3H, CH(CH_3)$_2$, $^3J_{HH}$ = 6.8), 1.81 (m, 1H, CH(CH$_3$)$_2$), 1.91 (m, 3H, pyr NCH$_2$CH_2, pyr NCHCHH′), 2.28 (br s, 1H, pyr NCHCHH'), 3.49–3.68 (m, 5H, CH_2OH, NHCH, pyr NCH_2), 4.35 (m, 1H, pyr NCH), 5.15 (s, 2H, Cbz OCH_2), 7.28–7.36 (m, 5H, Cbz Ar).

(2S)-2-{(4S)-4-Isopropyl-4,5-dihydro-oxazol-2-yl}-pyrrolidine-1-carboxylic acid 9H-fluoren-9-ylmethyl ester (9)

In a 100 mL Schlenk tube, a solution of **7** (0.384 g, 95.0 mmol) in dry CH_2Cl_2 (50 mL) was cooled to –78 °C. Diethylaminosulfur trifluoride (DAST) (0.137 mL, 1.05 mmol) was added dropwise over 5 min and the resultant pale yellow solution was stirred at –78 °C for 1 h, warmed to RT over ~3 h, and stirred overnight. The mixture was poured into satd. aq. $NaHCO_3$ (70 mL). The aqueous layer was discarded and the organic layer was washed with H_2O (2 × 50 mL). The aqueous layer was extracted with CH_2Cl_2 (2 × 50 mL). Combined organic layers were washed with brine (25 mL), dried over $MgSO_4$, and concentrated in vacuo. The residue was purified by silica gel chromatography (EtOAc–hexanes 30%–50%) to afford the title compound as an off-white foam. Yield 0.31 g (85%). ^{1}H NMR δ: 0.80 (d, 3H, CH(CH_3)$_2$, $^3J_{HH}$ = 6.8), 0.84 (d, 3H, CH(CH_3)$_2$, $^3J_{HH}$ = 6.8), 1.61 (m, 1H, CH(CH$_3$)$_2$), 1.91 (m, 3H, pyr NCH$_2$CH_2, pyr NCHCHH′), 2.17 (m, 1H, pyr NCHCHH'), 3.83 (pq, 1H, Fmoc CH), 3.93 (pt, 1H, ox OCHH′), 4.17 (pt, 1H, ox OCHH'), 4.25 (m, 2H, pyr NCH_2), 4.35 (m, 1H, ox NCH), 4.45 (br d, 1H, Fmoc OCH_2, $^3J_{HH}$ = 8.8), 7.33 (pt, 2H, Fmoc Ar), 7.41 (pt, 2H, Fmoc Ar), 7.65 (d, 2H, Fmoc Ar, $^3J_{HH}$ = 7.6), 7.86 (d, 2H, Fmoc Ar, $^3J_{HH}$ = 7.2). ^{13}C{^{1}H} NMR δ: 18.12, 19.60*, 22.93*, 22.95, 28.14, 28.28*, 30.13, 31.76*, 46.49*, 46.60, 46.61, 47.25*, 55.61*, 55.62, 59.51, 59.76*, 61.30, 61.40*, 66.44, 66.99*, 120.11, 125.16, 125.31*, 125.69, 127.14*, 127.67, 127.68*, 128.21*, 128.90, 140.61*, 140.74, 143.39, 143.78*, 143.93, 143.94* 153.96, 171.65, 172.02*. HRMS calcd. for $C_{25}H_{28}N_2O_3$: 404.2100; found: 404.2107.

(2S)-2-{(4S)-4-Isopropyl-4,5-dihydro-oxazol-2-yl}-pyrrolidine-1-carboxylic acid benzyl ester (10)

The title compound was made according to the procedure reported by McManus et al. (10). ^{1}H NMR (DMSO-d_6, 298 K) δ: 0.73 (d, 3H, CH(CH_3)$_2$, $^3J_{HH}$ = 6.8), 0.80 (m, 3H, CH(CH_3)$_2$), 1.53–1.58 (m, 0.6H, CH(CH$_3$)$_2$), 1.59–1.66 (m, 0.4H, CH(CH$_3$)$_2$), 1.81–1.90 (m, 3H, pyr NCH$_2$CH_2, pyr NCHCHH′), 2.10–2.20 (m, 1H, pyr NCHCHH'), 3.73–3.78 (m, 1.2H, pyr NCH_2), 3.84–3.87 (m, 0.8H, pyr NCH_2), 3.90 (pt, 0.6H, ox OCHH'), 3.98 (pt, 0.4H, ox OCHH'), 4.07 (pt, 0.6H, ox OCHH′), 4.16 (pt, 0.4H, ox OCHH′), 4.41 (dd, 0.4H, pyr NCH, $^3J_{HH}$ = 3.2, 8.8), 4.46 (dd, 0.6H, pyr NCH, $^3J_{HH}$ = 2.8, 8.0), 4.98–5.12 (m, 2H, Cbz OCH_2), 7.29–7.36 (m, 5H, Cbz Ar). ^{1}H NMR (DMSO-d_6, 393 K) δ: 0.79 (d, 3H, CH(CH_3)$_2$, $^3J_{HH}$ = 6.8), 0.83 (d, 3H, CH(CH_3)$_2$, $^3J_{HH}$ = 6.8), 1.61 (m, 1H, CH(CH$_3$)$_2$), 1.89 (m, 3H, pyr NCH$_2$CH_2, pyr NCHCHH′), 2.17 (m, 1H, pyr NCHCHH'), 3.83 (pq, 1H, pyr NCH_2), 3.81 (pq, 1H, ox NCH), 3.92 (pt, 1H, ox OCHH'), 4.14 (m, 2H, ox OCHH′), 4.48 (pd, 1H, pyr NCH), 5.08 (s, 2H, Cbz OCH_2), 7.29–7.35 (m, 5H, Cbz Ar).

Syntheses of (4*S*)-4-isopropyl-2-pyrrolidin-(2*S*)-2-yl-4,5-dihydrooxazole (11)

By deprotection of Fmoc

A 100 mL round-bottomed flask charged with **9** (0.310 g,

© 2007 NRC Canada

0.810 mmol) and MeOH (10 mL) was cooled to 0 °C before Et_2NH (5 mL) was added dropwise. The mixture was warmed to RT with stirring over 1.5 h. Volatiles were removed in vacuo. The residue was purified by silica gel chromatography (MeOH–CH_2Cl_2 4%–10%) to afford **9** as a nearly colourless oil. Yield 0.30 g (55%). Spectroscopic data were identical to those reported by McManus et al. (10).

By deprotection of Cbz

A solution of **10** (1.0 g, 3.16 mmol) in MeOH (30 mL) was added slowly to a 100 mL Schlenk tube containing Pd–C 10% *w/w* (0.30 g, 30 wt%.). The flask was purged with H_2 and was stirred under H_2 atmosphere at RT for 24 h. The suspension was filtered through a pad of Celite that was subsequently rinsed with MeOH (30 mL). The filtrate was concentrated in vacuo to give a pale yellow oil that was purified by silica gel chromatography (MeOH–CH_2Cl_2 5%) to afford **11** as a colourless oil. Yield 0.35 g (61%). Spectroscopic data were identical to those reported by McManus et al. (10).

Synthesis of (4S)-4-Benzyl-2-pyrrolidin-(2S)-2-yl-4,5-dihydrooxazole (12)

A solution of **18** (0.990 g, 2.70 mmol) in MeOH (40 mL) was deprotected according to the method described in the immediately preceding section. Yield 0.19 g (30%). Spectroscopic data matched those reported by McManus et al. (10).

Synthesis of cyanopyrrolidine derivatives

Our syntheses of **13** and **15** are modifications of those reported by Wallén et al. (25) for the analogous Boc-protected pyrrolidines **14** and **16**. The compounds were previously made by a different route by Cobb et al. (26, 27); they are now commercially available but are very expensive. To the best of our knowledge, only RT ^{1}H NMR characterization data have been reported in the open literature.

(2S)-2-Carbamoyl-pyrrolidine-1-carboxylic acid benzyl ester (13)

Ethyl chloroformate (3.99 mL, 41.7 mmol) was added dropwise to a cooled solution (–5 °C) of Cbz-Pro-OH (4.60 g, 18.5 mmol), NEt_3 (2.57 mL, 18.5 mmol), and THF (60 mL) in a 100 mL round-bottomed flask. The resulting slurry was stirred for 20 min at –5 °C and satd. aq. NH_4OH (5 mL) was then added dropwise. The solution was stirred at RT for 18 h. Volatiles were removed in vacuo and the residue was taken up in EtOAc (60 mL). The undissolved white precipitate was filtered off and rinsed with EtOAc (30 mL). The organic layer was dried over $MgSO_4$ and concentrated in vacuo to give an off-white amorphous solid, which was used without further purification. Yield 4.59 g (>99%). ^{1}H NMR δ: 1.87–1.99 (m, 2H, NCH_2CH_2), 2.16 (br s, 1H, NCHC*H*H′), 2.31 (br s, 1H, NCHCH*H′*), 3.44–3.54 (m, 2H, NCH_2), 4.28–4.35 (m, 1H, NC*H*), 5.10–5.18 (m, 2H, OCH_2Ar), 5.74* (br s, 0.5H, NH_2), 5.84 (br s, 0.5H, NH_2), 6.06* (br s, 0.5H, NH_2), 6.72 (br s, 0.5H, NH_2), 7.34 (m, 5H, Cbz Ar). ^{13}C{^{1}H} NMR δ: 23.39*, 24.28, 28.73, 30.97*, 46.78, 47.23*, 60.00, 60.38*, 67.04, 127.62, 127.87, 128.30, 136.20, 154.67*, 155.65, 174.63, 175.50*. HRMS calcd. for $C_{13}H_{16}N_2O_3$: 248.1161; found: 248.1169.

(2S)-2-Carbamoyl-pyrrolidine-1-carboxylic acid tert-butyl ester (14)

The title compound was made by the method of Wallén et al. (25). Yield >99%. ^{1}H NMR (DMSO-d_6, 353 K) δ: 1.39 (m, 9H, $O(CH_3)_3$), 1.72–1.87 (m, 3H, $NCH_2CH_2CH_2$, NCH_2CH_2CHH'), 2.07 (m, 1H, NCH_2CH_2CHH'), 3.28–3.40 (m, 2H, NCH_2) 4.03 (pdd, 1H, NC*H*CN). ^{13}C{^{1}H} NMR (DMSO-d_6) δ: 23.85, 24.54*, 28.68, 28.80*, 30.66*, 31.66, 46.06, 47.01, 47.22*, 59.99*, 60.20, 78.99, 79.08*, 154.00, 154.28*, 174.94*, 175.32. IR (neat) ν: 3406 (m, N-H), 1683 (s, CO amide), 1403 (m, C-N). HRMS calcd. for $C_{10}H_{18}O_3N_2$: 214.1317; found: 214.1312.

(2S)-2-Cyano-pyrrolidine-1-carboxylic acid benzyl ester (15)

A 250 mL round-bottomed flask was charged with **13** (4.37 g, 17.6 mmol) and dry THF (60 mL). The solution was cooled to 0 °C and NEt_3 (5.88 mL, 42.3 mmol) was added dropwise. Against a flow of N_2, trifluoroacetic anhydride (TFAA) (2.94 mL, 21.1 mmol) was added dropwise and the mixture was stirred for 1 h at 0 °C. The reaction was quenched by the addition of H_2O (25 mL) and all volatiles were removed in vacuo. The residue was taken up in CH_2Cl_2 (50 mL) and H_2O (20 mL) was added. The organic layer was washed with satd. aq. $NaHCO_3$ (20 mL) and brine (20 mL), dried over $MgSO_4$, and concentrated in vacuo. The resultant yellow oil was used without further purification. Yield 2.44 g (83%). ^{1}H NMR δ: 2.04–2.31 (m, 4H, NCH_2CH_2, $NCH_2CH_2CH_2$), 3.38–3.44 (m, 1H, NCH_2), 3.55–3.62 (m, 1H, NCH_2), 4.54–4.63 (m, 1H, NC*H*CN), 5.14–5.20 (m, 2H, OCH_2), 7.26–7.43 (m, 5H, Cbz Ar). ^{1}H NMR (333 K) δ: 2.01–2.30 (m, 4H, NCH_2CH_2), 3.42–3.48 (m, 1H, NCH_2), 3.56–3.61 (m, 1H, NCH_2), 4.58 (br s, 1H, NC*H*CN), 5.20 (s, 2H, OCH_2), 7.32–7.40 (m, 5H, Cbz Ar). ^{13}C{^{1}H} NMR δ: 23.68, 24.58*, 30.72*, 31.69, 45.86*, 86.26, 46.92, 47.45*, 67.57*, 67.75, 118.63*, 118.81, 128.08, 128.22, 128.50, 135.80*, 135.99, 153.54*, 154.24. HRMS calcd. for $C_{13}H_{14}N_2O_2$: 230.1055; found: 230.1061.

(2S)-2-Cyano-pyrrolidine-1-carboxylic acid tert-butyl ester (16)

The title compound was made using the method of Wallén et al. (25). Yield 82%. ^{1}H NMR δ: 1.46–1.50 (m, 9H, $C(CH_3)_3$), 2.01–2.24 (m, 4H, NCH_2CH_2, $NCH_2CH_2CH_2$), 3.30–3.39 (m, 1H, NC*H*H′), 3.42–3.55 (m, 1H, NCH*H′*), 4.42 (pdd, 0.5H, NC*H*), 4.55 (pd, 0.5H, NC*H*). ^{1}H NMR (DMSO-d_6, 353 K) δ: 1.46 (s, 9H, $C(CH_3)_3$), 1.94 (m, 2H, NCH_2CH_2), 2.12–2.25 (m, 2H, $NCH_2CH_2CH_2$), 3.34 (m, 2H, NCH_2), 4.60 (dd, 1H, NC*H*, $^3J_{HH}$ = 3.6, 8.0). ^{13}C{^{1}H} NMR δ: 24.13, 25.01*, 28.62, 30.88*, 31.71, 46.37, 46.67*, 47.41*, 47.55, 80.65, 120.53, 153.16, 153.83*. IR (neat, cm^{-1}) ν: 2980 (m, C-H), 2240 (vw, C≡N), 1701 (vs, C=O). HRMS calcd. for $C_{10}H_{16}O_2N_2$: 196.1212; found: 196.1213.

(2S)-2-Cyano-pyrrolidine·TFA salt (17)

Via an addition funnel, TFA (34 mL) was added dropwise over a period of 10 min to a 100 mL round-bottomed flask containing a cooled (0 °C) CH_2Cl_2 (124 mL) solution of **16** (2.44 g, 12.4 mmol). The solution was stirred for 2 h at 0 °C, then concentrated in vacuo to give an off-white oil. Et_2O (30 mL) was added slowly to produce a white crystalline solid. The slurry was filtered, and the solid rinsed with Et_2O (10 mL) before being dried under vacuum to obtain the

© 2007 NRC Canada

title compound as a white crystalline solid. Yield 1.10 g (56%), mp 92–94 °C. ^{1}H NMR (CD_3OD) δ: 2.07–2.33 (m, 3H, $NHCH_2CH_2$, $NHCHCHH'$), 2.43–2.52 (m, 1H, $NHCHCHH'$), 3.35–3.47 (m, 2H, $NHCH_2$), 4.68 (pt, 1H, NHCH), 4.92 (s, 1H, NH). $^{13}C\{^1H\}$ NMR δ: 23.15, 29.65, 45.14, 45.97, 116.53. $^{19}F\{^1H\}$ NMR δ: –77.37 (s). IR (neat) ν: 2261 (vw, C≡N), 1681 (vs, C=O). HRMS calcd. for $C_5H_9N_2$: 97.0766; found 97.0760; calcd. for $C_2F_3O_2^-$: 112.9850; found: 112.9683.

Syntheses of pyrrolidinyloxazolines via 2-cyanopyrrolidines

(2S)-2-{(4S)-4-Isopropyl-4,5-dihydro-oxazol-2-yl}-pyrrolidine-1-carboxylic acid benzyl ester (10)

A solution of **15** (1.55 g, 6.70 mmol) and L-valinol (1.08 g, 10.5 mmol) in chlorobenzene (120 mL) was added to a 250 mL round-bottomed flask containing $ZnCl_2$ (1.43 g, 10.5 mmol). The mixture was heated to reflux for 24 h. Solvent was removed in vacuo and the yellow residue was purified by silica gel chromatography (EtOAc–Hexanes 30%). The title compound was obtained as a yellow oil. Yield 1.82 g (85%). Spectroscopic data for this compound matched those reported by McManus et al. (10).

(2S)-2-{(4S)-Benzyl-4,5-dihydro-oxazol-2-yl}-pyrrolidine-1-carboxylic acid benzyl ester (18)

A similar procedure to that outlined earlier was carried out using **15** (0.605 g, 2.63 mmol), L-phenylalaninol (0.665 g, 4.40 mmol), and $ZnCl_2$ (0.599 g, 4.40 mmol) to obtain **18**. Yield 0.99 g (quant.). Spectroscopic data matched those reported by McManus et al. (10).

Syntheses of oxazolinylamine metal complexes

{1-((4S)-4-Benzyl-4,5-dihydro-oxazol-2-yl)-2-methylpropylamine}dichloroplatinum(II) (1)

A 100 mL round-bottomed flask was charged with $PtCl_2(SMe_2)_2$ (0.084 g, 0.215 mmol), **5** (0.050 g, 0.215 mmol), and 1,2-dichloroethane (20 mL). The mixture was heated to reflux and held for 7 h. After cooling to RT, stirring was continued overnight (18 h). Volatiles were removed in vacuo and Et_2O (10 mL) was added. The suspension was sonicated for 5 min to produce a dark yellow powder, which was filtered and rinsed with Et_2O (10 mL). The yellow solid (isolated as a mixture of diastereomeric metal complexes) was dried under vacuum. Yield 0.10 g (95%). ^{1}H NMR δ: 0.83 (d, 3H, $CH(CH_3)_2$, $^3J_{HH}$ = 6.8), 0.95 (d, 3H, $CH(CH_3)_2$, $^3J_{HH}$ = 6.8), 1.07* (d, 6H, $CH(CH_3)_2$, $^3J_{HH}$ = 6.8), 1.13* (d, 6H, $CH(CH_3)_2$, $^3J_{HH}$ = 6.8), 2.19 (m, 1H, $CH(CH_3)_2$), 2.34* (m, 1H, $CH(CH_3)_2$), 2.68* (dd, 1H, $^2J_{HH}$ = 13.2, $^3J_{HH}$ = 10.4, $CHH'Ph$), 3.01 (dd, 2H, $CHH'Ph$, $^2J_{HH}$ = 13.6, $^3J_{HH}$ = 8.4), 3.38 (dd, 1H, $CHH'Ph$, $^2J_{HH}$ = 13.6, $^3J_{HH}$ = 2.6), 3.73* (dd, 1H, $CHH'Ph$, $^2J_{HH}$ = 13.2, $^3J_{HH}$ = 2.4), 4.03 (dd, 1H, NH_2CH, $^3J_{HH}$ = 10.4, $^3J_{HH}$ = 5.2), 4.36–4.63 (m, 6H, NH_2CH*, NCH, NCH*, $OCHH'$, $OCHH'$*, $OCHH'$*), 4.78 (pt, 1H, OCH), 5.84 (t, 2H, NH_2), 5.98* (t, 2H, NH_2), 7.13–7.39 (m, 10H, Ph, Ph*). Anal. calcd. for $C_{14}H_{20}Cl_2N_2OPt$: C 33.74, H 4.05, N 5.62; found: C 33.99, H 4.18, N, 5.32. Crystals of the title compound suitable for X-ray diffraction analysis were grown by slow diffusion of iPr_2O into a concentrated solution of **1** in CH_2Cl_2.

Dichloro{(4S)-4-isopropyl-2-pyrrolidin-(2S)-2-yl-4,5-dihydro-oxazole}platinum(II) (2)

A 50 mL round-bottomed flask was charged with $PtCl_2(SMe_2)_2$ (0.227 g, 0.580 mmol), **11** (0.107 g, 0.580 mmol), and 1,2-dichloroethane (20 mL). The mixture was heated to reflux and held for 4 h. The suspension was filtered and rinsed with Et_2O (10 mL). The yellow solid was dried under vacuum. Yield 0.11 g (42%). ^{1}H NMR (DMSO-d_6) δ: 0.74 (d, 3H, $CH(CH_3)_2$, $^3J_{HH}$ = 6.8), 0.79 (d, 3H, $CH(CH_3)_2$, $^3J_{HH}$ = 6.8), 1.68 (m, 1H, $NHCH_2CHH'$), 1.91 (m, 1H, $NHCHCHH'$), 2.00 (m, 1H, $NHCH_2CHH'$), 2.17 (m, 1H, $NHCHCHH'$), 2.47 (m, 1H, $CH(CH_3)_2$), 2.99 (m, 1H, $NHCHH'$), 3.35 (m, 1H, $NHCHH'$), 4.01 (m, 1H, NHCH), 4.27 (pq, 1H, NCH), 4.63 (t, 1H, $OCHH'$, $^2J_{HH}$ = 9.2), 4.77 (m, 1H, $OCHH'$, $^2J_{HH}$ = 9.2, $^3J_{HH}$ = 4.4), 7.29 (q, 1H, NH, $^3J_{HH}$ = 4.8). Anal. calcd. for $C_{10}H_{18}Cl_2N_2OPt$: C 26.79, H 4.05, N 6.25; found: C 26.62, H 4.04, N 6.12.

Dichloro{(4S)-4-isopropyl-2-pyrrolidin-(2S)-2-yl-4,5-dihydro-oxazole}palladium(II) (3)

A solution of **11** (87.0 mg, 0.500 mmol) in CH_2Cl_2 (20 mL) was added to a 25 mL round-bottomed flask containing *trans*-$PdCl_2(PhCN)_2$ (19.2 mg, 0.500 mmol). The resultant orange solution was stirred for 3 h at RT. An orange precipitate began to form within the first 5 min of stirring. The solid was collected by filtration and rinsed with Et_2O (20 mL), then dried under vacuum. Yield 0.12 g (66%). ^{1}H NMR (DMSO-d_6) δ: 0.71 (pt, 6H, $CH(CH_3)_2$), 1.64 (m, 1H, $NHCH_2CHH'$), 1.82–1.92 (m, 2H, $NHCHCHH'$, $NHCH_2CHH'$), 2.07 (m, 1H, $NHCHCHH'$), 2.39 (m, 1H, $CH(CH_3)_2$), 2.84 (m, 1H, $NHCHH'$), 3.23 (m, 1H, $NHCHH'$), 3.86 (m, 1H, NCH), 4.16 (m, 1H, NHCH), 4.47 (pt, 1H, $OCHH'$), 4.60 (pq, 1H, $OCHH'$), 6.58 (m, 1H, NH). Anal. calcd. for $C_{10}H_{18}Cl_2N_2OPd$: C 33.40, H 5.05, N 7.79; found: C 33.66, H 5.25, N 7.48. Crystals of the title compound suitable for X-ray diffraction analysis were grown by slow diffusion of iPr_2O into a concentrated solution of **3** in CH_2Cl_2.

Crystallography

Crystal data for **3** were collected at low temperature (150 K) using a Nonius Kappa CCD area detector diffractometer running COLLECT software (Nonius BV, Delft, The Netherlands, 1997–2002). The unit cell parameters were calculated and refined from the full data set. Crystal cell refinement and data reduction were carried out using HKL2000 DENZO-SMN (Otwinowski and Minor 1997), and absorption correction was applied using HKL2000 DENZO-SMN (SCALEPACK). The SHELXTL PC V6.14 for Windows NT (Bruker AXS Inc., Madison, Wisconsin) suite of programs was used to solve the structure by direct methods. Subsequent Fourier difference syntheses allowed the remaining atoms to be located. All non-hydrogen atoms were refined with anisotropic thermal parameters. Hydrogen atom positions were calculated geometrically and were included as riding on their respective carbon atoms. The absolute structure parameter for **3** was 0.00 (5), which indicated that the correct diastereomer had been refined and that there

© 2007 NRC Canada

Table 1. Crystal data and refinement parameters for **3**.

Empirical formula	$C_{10}H_{18}Cl_2N_2OPd$
Formula weight (g mol^{-1})	359.56
Temperature (K)	150(2)
Wavelength (Å)	0.710 73
Crystal system	Monoclinic
Space group	$P2_1$
a (Å)	6.8508(3)
b (Å)	10.0099(5)
c (Å)	9.7236(4)
α, γ (°)	90
β (°)	100.676(2)
Volume	655.26(5)
Z	2
Density (calcd., g cm^{-3})	1.822
Absorption coefficient (mm^{-1})	1.805
F(000)	360
Crystal size (mm)	0.47 × 0.20 × 0.17
Range for data collection (°)	2.95 to 27.47
Index ranges	$-8 \le h \le 8$, $-11 \le k \le 12$, $-12 \le l \le 12$
Reflections collected	8168
Independent reflections (R_{int})	2781 (0.0460)
Absorption correction	Semi-empirical from equivalents
Maximum and minimum transmission	0.7430 and 0.4810
Refinement method	Full-matrix least-squares on F^2
Data, restraints, parameters	2781, 1, 146
Goodness-of-fit on F^2	1.119
Final R indices [$I > 2\sigma(I)$]	$R1$ = 0.0293, $wR2$ = 0.0723
R indices (all data)	$R1$ = 0.0317, $wR2$ = 0.0733
Absolute structure parameter	0.00(5)
Largest difference in peak and hole (e Å^{-3})	1.125 and –0.703

was no sign of racemic twinning. The crystal data and refinement parameters for **3** are listed in Table 1.[2]

Results and discussion

Aminomethyl-substituted ligands and complexes

The oxazolinylamine ligand **5** was made according to a minor modification of the method by Rajaram and Sigman (4) (Scheme 2). The reaction between Fmoc-protected L-valine and L-phenylalaninol using PPh_3–CCl_4 as the activator and diisopropylethylamine (DIPEA) as the base for both the initial amide bond formation and the subsequent ring closing to install the oxazoline gave the protected precursor **4**. Deprotection by diethylamine gave the desired ligand **5** in 54% overall yield.

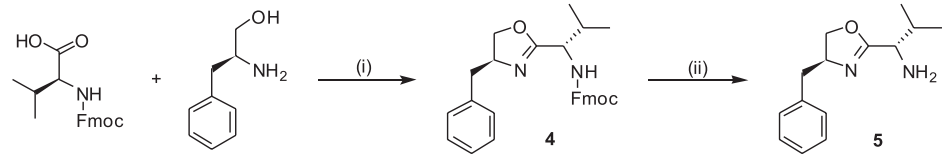
The Pt(II) complex **1** was made in 95% yield by the equimolar reaction of **5** and $PtCl_2(SMe_2)_2$ in a refluxing dichloroethane solution (Scheme 3). This yellow compound was soluble in moderately polar chlorinated organic solvents but insoluble in nonpolar solvents such as diethyl ether and hexanes.

The ^{1}H NMR spectrum of the free ligand **5** was consistent, as expected from previous work (4), with a single diastereomer (e.g., the isopropyl methyl peaks appeared as the expected two doublets at δ: 0.91, 0.93). However, the ^{1}H NMR spectrum of the corresponding Pt(II) complex **1** was dependent on the time allowed for the reaction between $PtCl_2(SMe_2)_2$ and **5**. It showed a "doubling" of all of the peaks (e.g., the isopropyl methyl peaks appeared as two pairs of doublets of almost equal intensity at δ: 0.83, 0.95 and 1.07, 1.13) when the reaction time was longer than 18 h; shorter reaction times gave simpler spectra in which doubling was greatly diminished. This phenomenon was consistent with the presence of a pair of diastereomeric metal complexes, which was confirmed by X-ray crystallography. Although the structure of **1** could not be refined sufficiently well for publication, the basic atom connectivity could be determined unequivocally. The unit cell contained equal

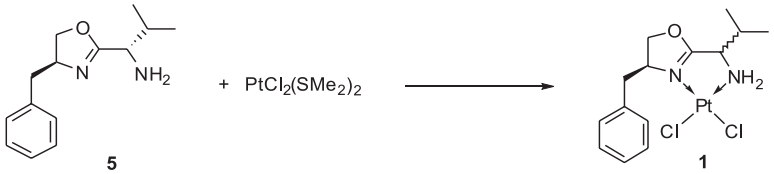
[2] Supplementary data for this article are available on the journal Web site (http://canjchem.nrc.ca) or may be purchased from the Depository of Unpublished Data, Document Delivery, CISTI, National Research Council Canada, Ottawa, ON K1A 0R6, Canada. DUD 5124. For more information on obtaining material refer to http://cisti-icist.nrc-cnrc.gc.ca/irm/unpub_e.shtml. CCDC 633044 contains the crystallographic data for this manuscript. These data can be obtained, free of charge, via http://www.ccdc.cam.ac.uk/conts/retrieving.html (Or from the Cambridge Crystallographic Data Centre, 12 Union Road, Cambridge CB2 1EZ, UK; fax +44 1223 336033; or deposit@ccdc.cam.ac.uk).

© 2007 NRC Canada

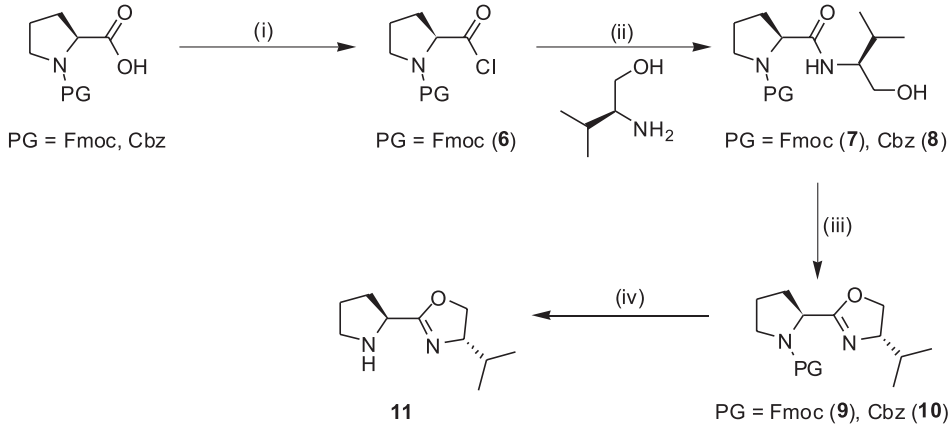
Scheme 2. Synthesis of the oxazolinylamine ligand **5** by the method of Rajaram and Sigman. (*i*) PPh_3–CCl_4–DIPEA; (*ii*) Et_2NH.



Scheme 3. Synthesis of **1**.



Scheme 4. Synthesis of pyrrolidinyloxazolines by the method of McManus et al. (*i*) $SOCl_2$, toluene, 5 h; (*ii*) NEt_3, CH_2Cl_2; (*iii*) NEt_3, DAST, CH_2Cl_2, –78 °C; (*iv*) PG = Fmoc: Et_2NH; PG = Cbz: H_2, 10% Pd–C, MeOH.



numbers of both the expected *S,S*-diastereomer and the unexpected *S,R*-diastereomer of **1**. This showed that the stereocentre associated with the aminoalkyl chain was susceptible to epimerization under the relatively harsh conditions used for the coordination reaction. ^{1}H NMR data indicated that the epimerization could be minimized (<10%) by simply reducing the reaction time to ~8 h. This result is important because catalysts incorporating ligands of this type have typically been generated in situ and have therefore generally not been well characterized; therefore, relationships drawn between the absolute configuration of the active catalyst and the observed *ee* in the product(s) of an asymmetric reaction are necessarily of limited validity. A solution of free ligand in dichloroethane was heated to reflux in the absence of metal for 24 h and, despite some decomposition, no epimerization was seen by ^{1}H NMR spectroscopy.

Pyrrolidine-substituted ligands

The pyrrolidinyloxazoline ligand **11** was made according to Scheme 4 (PG = Fmoc). This general method has been applied previously to the synthesis of **11** (and **12**, not shown) by McManus et al. (10), who instead used the Cbz-protecting group. These workers noted that the NMR spectra of their intermediates **8** and **10** were complicated by a doubling of many of the peaks but did not provide a rationale for this phenomenon.

It is well-known that the *E* and *Z* isomers of amide bonds can be seen by NMR spectroscopy at RT. These are ususally evidenced by a coalescence of some (if not all) peaks at high temperature because of rapid chemical exchange of *E* and *Z* isomers. Given our experience with **1** (vide supra), we were concerned that the doubling observed for all of the compounds **7**–**11** may have resulted not only from the presence of *E* and *Z* isomers but also from diastereomers arising at some stage during ligand synthesis. Presumably, epimerization of the pyrrolidine stereocentre could occur via the intermediate acid chloride **6** or, less likely, during the DAST-induced oxazoline ring-closing step to form **9** and **10**. It has been shown by Wipf and co-workers (28) that DAST is able to induce this cyclization with less than 1.5% racemization of sensitive substrates.

McManus et al. did not report high-temperature NMR data for their compounds. Therefore, we repeated the syntheses of the Cbz-protected compounds and examined both them and our Fmoc-protected species closely by variable temperature NMR spectroscopy. For the open chain compounds **7** and **8**, we concentrated on peaks due to the amide N*H* proton, and for the oxazolines **9** and **10**, on those due to the isopropyl methyl protons. Figure 1*a* shows the amide region of the ^{1}H NMR spectrum of **8** at RT and at 155 °C; Fig. 1*b* shows the isopropyl methyl region of the ^{1}H NMR spectrum of **10** at RT, and at 70 °C in DMSO-d_6 solution.

© 2007 NRC Canada

Scheme 5. Synthesis of pyrrolidinyloxazolines by Zn-catalyzed cyclization of 2-cyanopyrrolidine and β-amino alcohols. (*i*) EtOC(O)Cl, NEt_3; (*ii*) NH_4OH; (*iii*) TFAA, NEt_3; (*iv*) TFA; (*v*) amino alcohol, $ZnCl_2$, PhCl; (*vi*) H_2, Pd–C.

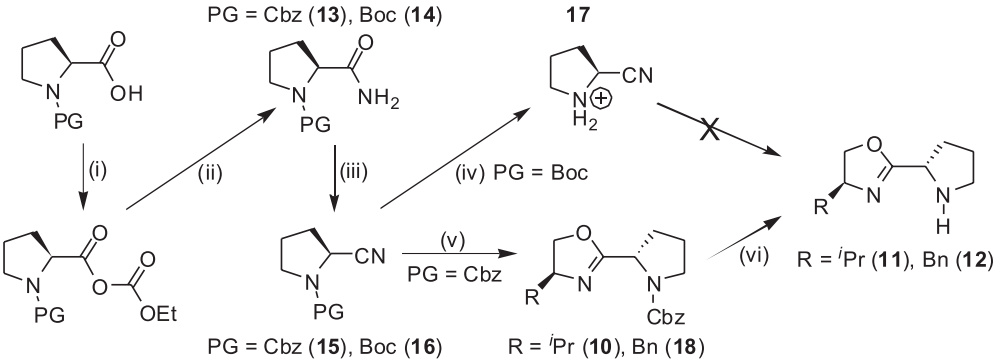
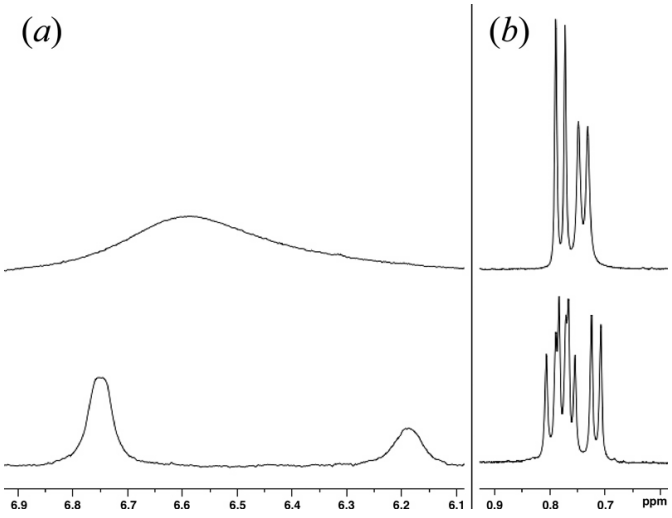


Fig. 1. (*a*) The δ 6.1–6.9 range of the ^{1}H NMR spectra of **8** at 155 °C (top) and at RT (bottom), and (*b*) the δ 0.6–0.9 range of the ^{1}H NMR spectra of **10** at 70 °C (top) and at RT (bottom) in DMSO-d_6 solution.



Coalescence of the peaks due to N*H* proton in **8** (from two broad singlets at δ: 6.18, 6.76 in the RT spectrum into a single broad peak at δ: 6.58 at 155 °C) and of those due to the isopropyl methyl protons in **10** (four doublets at δ: 0.73, 0.78, 0.79, 0.82 in the RT spectrum to two doublets at δ: 0.84, 0.88 at 70 °C) indicated that neither the acid chloride nor the DAST cyclization step were implicated in epimerization. The overall number, relative integrations, and splittings of the peaks in the high-temperature spectra were consistent with only a single diastereomer of the compound under study. These experiments implied that the likely cause of the doubling was not the presence of diastereomers but rather of *E* and *Z* isomers resulting from restricted rotation about the carbamate bond in **10** and the amide and (or) carbamate bond in **8**. The NMR spectra of our new Fmoc-protected analogues **7** and **9** were also complicated by the presence of *E* and *Z* isomers. These likewise simplified at high temperature.

Yields for the amide bond forming and cyclization steps in the Cbz- and Fmoc-protected pathways were not significantly different, being between 85% and 91%. However, differences arose in the final deprotection step. When PG = Cbz (Scheme 4), the deprotection was by hydrogenolysis; for PG = Fmoc, on the other hand, deprotection was achieved by treatment with base. These two routes gave isolated yields of 86% and 54%, respectively. The Fmoc deprotection was complicated by the decomposition of some of the intended product into an open chain peptide. The ^{1}H NMR spectra of the final products arising from the Cbz and Fmoc manifolds were identical and unequivocally consistent with the presence of only a single diastereomer.

We investigated an alternate approach to the pyrrolidinyloxazolines starting from protected (2*S*)-2-cyanopyrrolidines (Scheme 5, **15** and **16**), which were made using a modification to the syntheses presented by the groups of Wállen (25) and Ley (26, 27). Judicious choice of protecting group was essential. When PG = Boc, there was no reaction between the cyanopyrrolidine **16** and the amino alcohol; moreover, given the acidic conditions, a putative Boc-protected pyrrolidinyloxazoline would be difficult to deprotect without destruction of the oxazoline ring. Cleavage of Boc prior to oxazoline formation gave the TFA salt **17**, which in our hands could not be induced to react with the amino alcohol either in the presence or absence of $ZnCl_2$ and (or) base. The Fmoc protecting group was also problematic because its corresponding cyanopyrrolidine (not shown) decomposed under the reaction conditions. Finally, we found that treatment of Cbz-protected (2*S*)-2-cyanopyrrolidine **15** with amino alcohols in the presence of $ZnCl_2$ at elevated temperature cleanly gave the intended Cbz-protected pyrrolidinyloxazolines **10** and **18**, which were easily deprotected by hydrogenolysis to give the intended products **11** and **12**.

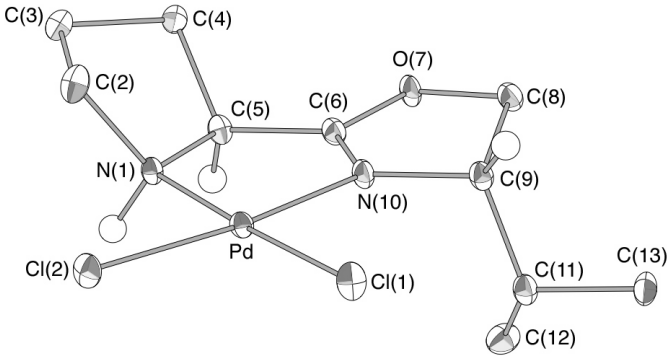
This route had distinct advantages over the route developed by McManus et al. First, the Cbz-protected 2-cyanopyrrolidine **15** could be made quickly and in high yield (a few hours in ~83% overall yield); second, the diversity-introducing step was placed later in the synthesis; third, the overall cost was reduced by elimination of the expensive DAST reagent; and finally, the number of required purification steps was reduced (there was no need for purification until after $ZnCl_2$-mediated oxazoline formation).

Metal complexes

The Pd(II) complex **3** was made in 66% yield by the equimolar reaction of *trans*-$PdCl_2(PhCN)_2$ and **11** in CH_2Cl_2 solution at RT. The analogous Pt(II) complex **2** was also

© 2007 NRC Canada

Fig. 2. ORTEP representation of the molecular structure of **3** (ellipsoids drawn at 50% probability). Except for those associated with chiral centres, H-atoms have been omitted for clarity. All of the chiral centres have the *S*-configuration.



made in 42% yield by equimolar reaction of $PtCl_2(SMe_2)_2$ and **11** in dichloroethane at 80 °C.

The molecular structure of **3** is represented as a thermal ellipsoid plot in Fig. 2; selected bond distances and angles appear in Table 2. As expected, the coordination geometry about the metal was essentially square planar. The N(1)–Pd–N(10) and Cl(1)–Pd–Cl(2) angles were approximately 81.8° and 93.1°, respectively. Although the Pd–N(10) (Pd–oxazoline) distance (2.008(4) Å) was shorter than the Pd–N(1) (Pd–pyrrolidine) distance (2.054(4) Å), the difference was not reflected in a corresponding trans influence for the chloride ligands: the Pd–Cl bond lengths were nearly identical and approximately 2.30 Å. The Pd–N(1) distance was in the range of those typically observed for Pd(II) complexes of pyrrolidines (2.05–2.11 Å). The mean plane of the oxazoline ring was very nearly coincident with the mean coordination plane containing the metal centre and its four ligated atoms; these two planes intersected at an angle of 7.98°. The pyrrolidine ring adopted an envelope configuration in which C(3) rested 0.639 Å from the mean plane defined by C(2), N(1), C(5), and C(4). This plane made an angle of 53.68° with the mean plane of the oxazoline ring.

The absolute configurations of C(9) and C(5) were both *S*, which was consistent with the expected configurations based on the L-proline and L-valinol starting materials; no epimerization occurred either during the ligand synthesis or on coordination to the metal. These configurations allowed the quadrant analysis typically applied to chiral C_2-symmetric complexes to be superimposed on this formally C_1-symmetric compound. In the orientation shown in Fig. 2, the steric bulk of the ligand occupied the top left and bottom right quadrants; the near 180° C(11)–N(10)–N(1)–C(2) torsion angle of 172.33°, together with the similar C(11)–C(9)–N(10) and C(2)–N(1)–N(10) angles (111.67° and 127.76°, respectively), further strengthened the pseudo-C_2-symmetric approach to thinking about this ligand.

The solid-state structure of **3** featured weak intermolecular N–H...Cl interactions of 3.33 Å that were only very slightly longer than the sum of the van der Waals radii of N and Cl (3.30 Å); the N–H–Cl angle was 156.15°. These interactions in the solid state point to the possibility that the N*H* groups of coordinated pyrrolidine (as well as of oxazolidine (29) and, presumably, related nitrogen heterocycles) are noninnocent and may participate in catalytic cycles (30).

Table 2. Selected bond distances, bond angles, and torsion angles for **3** with standard deviations in parentheses.

Bond distances (Å)	
Pd–N(10)	2.008(4)
Pd–Cl(2)	2.3000(12)
Pd–N(1)	2.054(4)
Pd–Cl(1)	2.3040(13)
Bond angles (°)	
N(10)–Pd–N(1)	81.84(17)
N(1)–Pd–Cl(2)	90.50(11)
N(1)–Pd–Cl(1)	176.39(12)
N(10)–Pd–Cl(2)	172.16(13)
N(10)–Pd–Cl(1)	94.57(13)
Cl(2)–Pd–Cl(1)	93.08(5)
Torsion angles (°)	
Cl(2)–Pd–N(1)–C(2)	58.7(3)
Pd–N(10)–C(9)–C(11)	69.0(6)

Conclusion

We have successfully characterized the first simple *N,N′*-chelated Pt and Pd complexes of oxazolinylamine ligands of type **I** and **V**. Our finding that type **I** ligands may epimerize upon metal complexation illustrates the importance of proper characterization of complexes prior to their use as catalysts. We also highlight the importance of including high-temperature NMR data in the characterization of the *N*-protected intermediates to these ligands as proof of stereochemical purity. We have applied a shorter and more cost effective route to the synthesis of pyrrolidinyloxazoline ligands via the $ZnCl_2$-mediated cyclization of Cbz-protected (2*S*)-2-cyanopyrrolidine with amino alcohols. This allows for quicker and easier access to this important class of chiral ligands. The application of ligands of type **I** and **V** in the asymmetric allylic oxidation of cyclic alkenes is currently under investigation.

Acknowledgments

We thank the Natural Sciences and Engineering Research Council of Canada (NSERC) and the University of Western Ontario for financial support of this work, and Professor Robert Hudson for useful discussions.

References

1. H.A. McManus and P.J. Guiry. Chem. Rev. **104**, 4151 (2004).
2. G. Helmchen and A. Pfaltz. Acc. Chem. Res. **3**, 336 (2000).
3. J.S. Johnson and D.A. Evans. Acc. Chem. Res. **33**, 325 (2000).
4. S. Rajaram and M.S. Sigman. Org. Lett. **4**, 3399 (2002).
5. J.-Y. Lee, J.J. Miller, S.S. Hamilton, and M.S. Sigman. Org. Lett. **7**, 1837 (2005).
6. S. Rajaram and M.S. Sigman. Org. Lett. **7**, 5473 (2005).
7. I.M. Pastor and H. Adolfsson. Tetrahedron Lett. **43**, 1743 (2002).
8. G.J. Rowlands and J.A. Griffith. Synthesis, **19**, 3446 (2005).

© 2007 NRC Canada

9. P. Västilä, I.M. Pastor, and H. Adolfsson. J. Org. Chem. **70**, 2921 (2005).
10. H.A. McManus, S.M. Barry, P.G. Andersson, and P.J. Guiry. Tetrahedron, **60**, 3405 (2004).
11. Y.-B. Zhou, F.-Y. Tang, H.-D. Xu, X.-Y. Wu, J.-A. Ma, and Q.-L. Zhou. Tetrahedron: Asymmetry, **13**, 469 (2002).
12. J.A. Cabeza, I. da Silva, I. del Rio, R.A. Gossage, D. Miguel, and M. Suárez. Dalton Trans. 2450 (2006).
13. H.A. McManus, P.G. Cozzi, and P.J. Guiry. Adv. Synth. Catal. **348**, 551 (2006).
14. Y. Jiang, Q. Jiang, and X. Zhang. J. Am. Chem. Soc. **120**, 3817 (1998).
15. A. Trifonova, K.E. Källström, and P.G. Andersson. Tetrahedron, **60**, 3393 (2004).
16. H. Brunner, F. Henning, and M. Zabel. Z. Anorg. Allg. Chem. **630**, 91 (2004).
17. H. Brunner, B. Nuber, and T. Tracht. Tetrahedron: Asymmetry, **9**, 3763 (1998).
18. H. Brunner and T. Tracht. Tetrahedron: Asymmetry, **9**, 3773 (1998).
19. A. Trifonova, J.S. Diesen, and P. G. Andersson. Chem Eur. J. **12**, 2318 (2006).
20. P.G. Cozzi, N. Zimmermann, R. Hilgraf, S. Schaffner, and A. Pfaltz. Adv. Synth. Catal. **343**, 450 (2001).
21. D.W. Dodd, H.E. Toews, F.d.S. Carneiro, M.C. Jennings, and N.D. Jones. Inorg. Chim. Acta, **359**, 2850 (2006).
22. M.J. McKennon and A.I. Meyers. J. Org. Chem. **58**, 3568 (1993).
23. F.R. Hartley. Organomet. Chem. Rev. A, 119 (1976).
24. J.D. Scott and R.J. Puddephatt. Organometallics, **2**, 1643 (1983).
25. E.A.A. Wallén, J.A.M. Christiaans, M.M. Forsberg, J.I. Venäläinen, P.T. Männistö, and J. Gynther. J. Med. Chem. **45**, 4581 (2002).
26. A.J.A. Cobb, D.M. Shaw, and S.V. Ley. Synlett, 558 (2004).
27. A.J.A. Cobb, D.M. Shaw, and S.V. Ley. Org. Biomol. Chem. **3**, 84 (2005).
28. A.J. Phillips, Y. Uto, P. Wipf, M.J. Reno, and D.R. Williams. Org. Lett. **2**, 1165 (2000).
29. S.A. Cardile, M.C. Jennings, and N.D. Jones. Dalton Trans. 4672 (2006).
30. C.A. Sandoval, T. Ohkuma, K. Muniz, and R. Noyori. J. Am. Chem. Soc. **125**, 13490 (2003).

© 2007 NRC Canada

Investigations of the mono- and dicycloaddition reactions of $[SNS][MF_6]$ (M = As, Sb) with the dinitriles $NCC(O)CN$ and $NCC(Cl)_2CN$ — Energetics and the preference for $[SNS]^+$ dicycloaddition products in solution and solid state

T. Stanley Cameron, Andreas Decken, Mary Gabriel, Carsten Knapp, and Jack Passmore

Abstract: The stepwise symmetry-allowed cycloaddition reactions of $[SNS]^+$ with the dinitriles NC–X–CN (X = CCl_2, CO) were investigated. The reaction of $[SNS]^+$ and dinitrile in 2:1 ratio yielded the dicycloaddition product quantitatively after 2 weeks (in situ ^{13}C NMR). At a 1:1 ratio, mixtures of mono- and dicycloaddition products were obtained that could not be completely separated from one another. The energetics of the reaction were estimated in the gas phase, in solution (SO_2 and CH_2Cl_2), and solid phases using DFT calculations (PBE0/6-311G*) and a "volume-based thermodynamics" approach for lattice enthalpies. Monocycloaddition products are stable in the gas phase and in solution with respect to disproportionation reactions, but in the solid state the disproportionation of 2 $[NC–X–(CNSNS)][AsF_6]$ into $[X(CNSNS)_2][AsF_6]_2$ and NC–X–CN is strongly favored because of the higher lattice enthalpy of the 1:2 salt. In the gas phase, the second cycloaddition is endothermic because of the charge repulsion of the two positive charges, but in the solid state the reaction is strongly favored because of the lattice enthalpy gain on the formation of the 1:2 ($[X(CNSNS)_2][AsF_6]_2$) from two 1:1 salts ($[NC–X–(CNSNS)][AsF_6]$ and $[SNS][MF_6]$). The crystal structures of the dicycloaddition products $[Cl_2C(CNSNS)_2][AsF_6]_2$ and $[OC(CNSNS)_2][AsF_6]_2$ and the monocycloaddition product $[Cl_2C(CNSNS)CN][AsF_6]$ were obtained. In $[Cl_2C(CNSNS)CN][AsF_6]$, the free nitrile groups interact with neighboring heterocycles further demonstrating that potential of free nitrile groups for introducing intermolecular interactions. $[OC(CNSNS)_2]^{2+}$ is a planar dication, which adopts the conformation with $S^{\delta+}\cdots O^{\delta-}$ contacts to optimize intramolecular electrostatic interactions.

Key words: crystal structure, sulfur–nitrogen, 1,3,2,4-dithiadiazolyium, nitriles, cycloaddition, DFT calculations, thermodynamics, energetics.

Résumé : On a étudié les réactions de cycloaddition permises par la symétrie du cation $[SCS]^+$ avec les dinitriles NC–X–CN (X = CCl_2, CO). La réaction du $[SCS]^+$ avec le dinitrile dans un rapport de 2:1 conduit, après deux semaines, à la formation quantitative du produit de cycloaddition, d'après le RMN du ^{13}C in situ. À un rapport de 1:1, fournit un mélange des produits de mono- et de dicycloaddition qu'il n'a pas été possible de séparer complètement. Faisant appel à des calculs de la théorie de la fonctionnelle de la densité (PBE0/6-311G*) et une approche thermodynamique basée sur le volume pour les enthalpies de réseau, on a évalué les énergies impliquées dans la réaction en phase gazeuse, en solution dans le SO_2 et le CH_2Cl_2 ainsi qu'en phases solides. Les produits de monocycloaddition sont stables en phase gazeuse et en solution par rapport aux réactions de disproportionation, mais à l'état solide la disproportionation de 2 $[NC–X–(CNSNS)][AsF_6]$ en $[X(CNSNS)_2][AsF_6]_2$ et NC–X–CN est fortement favorisée en raison de la grande enthalpie de réseau dans le sel 1:2. En phase gazeuse, la deuxième cycloaddition est endothermique en raison de la répulsion de charge des deux charges positives, mais à l'état solide la réaction est fortement favorisée en raison du gain en enthalpie de réseau lors de la formation du sel 1:2 ($[X(CNSNS)_2][AsF_6]_2$) à partir de deux sels 1:1 ($[NC–X–(CNSNS)][AsF_6]$ et $[SNS][MF_6]$). On a déterminé les structures cristallines des produits de dicycloaddition $[Cl_2C(CNSNS)_2][AsF_6]_2$ et $[OC(CNSNS)_2][AsF_6]$ et le produit de monocycloaddition $[Cl_2C(CNSNS)CN][AsF_6]$. Dans le $[Cl_2C(CNSNS)CN][AsF_6]$ les groupes nitriles libres interagissent avec les hétérocycles adjacents, et ce résultat met

Received 12 July 2006. Accepted 30 November 2006. Published on the NRC Research Press Web site at http://canjchem.nrc.ca on 20 February 2007.

T.S. Cameron. Department of Chemistry, Dalhousie University, Halifax, NS B3H 4J3, Canada.
A. Decken, M. Gabriel, C. Knapp, and J. Passmore.[1] Department of Chemistry, University of New Brunswick, Fredericton, NB E3B 6E2, Canada.

[1]Corresponding author (e-mail: passmore@unb.ca).

 doi:10.1139/V06-190 © 2007 NRC Canada

encore plus en évidence le potentiel qu'ont les groupes nitriles libres d'introduire des interactions intermoléculaires. Le $[OC(CNSNS)_2]$ est un dication planaire qui adopte la conformation impliquant des contacts $S^{\delta+}\cdots O^{\delta-}$ pour optimiser les interactions électrostatiques intramoléculaires.

Mots-clés : structure cristalline, soufre-azote, 1,3,2,4-dithiadiazolyium, nitriles, cycloaddition, calculs de la théorie de la fonctionnelle de densité, thermodynamique, énergies.

[Traduit par la Rédaction]

Introduction

The general utility of $[SNS]^+$ as a reagent (1) has been greatly enhanced by our recent convenient large-scale synthesis of the synthetically useful $[SNS][SbF_6]$ (2). The cycloaddition chemistry of this simple triatomic cation (1) with various unsaturated centers (e.g., C=C, C≡C, C≡N) has been extensively investigated (3). The reaction with nitriles yields 6π 1,3,2,4-dithiadiazolyium salts in essentially quantitative yields, and it represents the only general synthetic route to the derivatives of the [R–CNSNS] heterocyclic ring system (the 1,3,2,4-dithiadiazolyium salts with R = Me, Ph have also been prepared following a different approach (4)). The 6π 1,3,2,4-dithiadiazolyium cations can be readily reduced to the corresponding 7π radicals, which usually rearrange to the thermodynamically more stable 7π [R–CNSSN] isomers (3). Reactions with compounds containing two or more unsaturated centers (i.e., starting from di- and trinitriles) result in the corresponding stable multiradicals, whose physical properties and electronic structures are of interest.

So far, cycloaddition reactions of $[SNS]^+$ with multifunctional nitriles (e.g., NC–CN, *o*,*m*,*p*-$C_6H_4(CN)_2$) (5) resulted in the transformation of every nitrile group into a 1,3,2,4-dithiadiazolyium moiety (3). Attempts to isolate the intermediates, containing free nitrile groups, have been unsuccessful (3*c*). Only with $K[C(CN)_3]$ has the stepwise cycloaddition and the isolation of the intermediates been achieved (6). A free nitrile group could either (*i*) be used as means to link molecules in the solid state to modify the bulk properties (via –C≡N···S interactions), as has been demonstrated in the solid state structures of NC–C_6F_4–CN_2S_2 (7) and NC–CN_2S_2 (8); (*ii*) be a linker to a transition-metal center (via –C≡N···M coordination), or (*iii*) undergo another cycloaddition reaction to introduce a different functional group (e.g., –C≡N + "S_3^+" → –CNS_3^+ (9)). Thus, the stepwise cycloaddition of $[SNS]^+$ with multifunctional nitriles and the isolation of the intermediate monocycloaddition products is key to opening up new aspects of this area of chemistry. In this paper, we report the reactions of the dinitriles $NCC(Cl)_2CN$ and NCC(O)CN, respectively, with $[SNS]^+$ in a 1:2 ratio and attempts to isolate the monocycloaddition products from reactions using a 1:1 ratio. The underlying thermodynamics for all reactions are discussed, based on DFT calculations of species in the gas phase and in solution and including lattice enthalpies in the solid state.

Experimental

Preparative methods

All reactions were performed in glass vessels equipped with J. Young Teflon valves and a medium sintered glass frit. Techniques and apparatus have been described elsewhere (10).

FTIR spectra were recorded at 293 K on a Thermo Nicolet NEXUS 470 FTIR (resolution: 4 cm^{-1}) as nujol or fluorolube mulls between KBr discs. FTRaman spectra were recorded on a Bruker IFS66 FTIR equipped with a Bruker FRA106 FTRaman accessory, using a Nd-YAG laser (emission wavelength: 1064 nm; maximum laser power: 300 mW) in 5 mm Pyrex NMR tubes. Data were collected in the backscattering mode (180° excitation; resolution: 2.0 cm^{-1}). NMR spectra were recorded on a Varian 400 NMR spectrometer in 10 mm NMR tubes and were externally referenced to TMS (^{13}C) and H_3CNO_2 (^{14}N, ^{15}N). Elemental analyses were carried out by Galbraith Laboratories, Inc., Knoxville, TN, USA.

Sulfur dioxide (99.98%, Matheson) was stored over CaH_2, $CFCl_3$ (99.9%, Matheson) was stored over 3A molecular sieves, and CH_2Cl_2 (Aldrich) was refluxed over P_4O_{10}, and distilled. $NCC(Cl)_2CN$ (97%, Acros) was found to contain ~4% $NCC(Cl)_2CNH_2$ impurity and was purified by cooling to 0 °C and syringing out the dinitrile under an atmosphere of dry nitrogen. NCC(O)CN (11), $[SNS][AsF_6]$ (8), and $[SNS][SbF_6]$ (2) were prepared by the literature methods.

Synthesis of $[Cl_2C(CNSNS)_2][AsF_6]_2$

A mixture of $NCC(Cl)_2CN$ (1.38 g, 10.2 mmol) and $[SNS][AsF_6]$ (5.43 g, 19.8 mmol) was heated (60 °C) in 15 mL SO_2 with stirring for 2 weeks in a two-bulb apparatus with a condenser and a pressure-equalizing side arm (12).[2] Removal of the volatiles yielded a brown precipitate, which was washed with SO_2–$CFCl_3$ (1:1) until the extract became colourless (eight times). The solvent was removed via dynamic vacuum, leaving $[Cl_2C(CNSNS)_2][AsF_6]_2$ as a yellow powder-like, very sparingly soluble solid (4.86 g, 7.3 mmol, 74% isolated yield, based on $SNS[AsF_6]$).

[2] Precautions should be taken to avoid the explosion hazard when heating liquid SO_2 in a closed glass vessel (face shield, leather gloves, carefully built glass vessel). A reaction vessel with a water-cooled condenser and a pressure-equalizing side arm should be used to reduce the pressure in the apparatus.

© 2007 NRC Canada

Table 1. Crystal data and structure refinement.

Crystal	$[Cl_2C(CNSNS)_2][AsF_6]_2 \cdot 1/2\ SO_2$	$[Cl_2C(CNSNS)CN][AsF_6]$	$[OC(CNSNS)_2][SbF_6]_2$
Empirical formula	$C_3As_2Cl_2F_{12}N_4OS_{4.5}$	$C_3AsCl_2F_6N_3S_2$	$C_3F_{12}N_4OS_4Sb_2$
Formula weight	701.06	689.53	707.81
CCDC deposit no.	612110	612111	611958
Temperature (K)	253	296	193
Wavelength (Å)	0.71069 (Mo Kα)	1.54178 (Cu Kα)	0.71073 (Mo Kα)
Crystal size (mm^3)	0.22 × 0.15 × 0.15	0.21 × 0.14 × 0.06	0.40 × 0.15 × 0.075
Colour and habit	Colourless, block	Colourless, needle	Colourless, plate
Crystal system	Monoclinic	Orthorhombic	Triclinic
Space group	*C*2/*c*	$Pna2_1$	*P*1
a (Å)	20.457(4)	12.198(3)	6.4925(3)
b (Å)	12.985(4)	7.675(4)	7.4811(3)
c (Å)	15.245(3)	36.989(3)	9.3802(4)
α (°)	90	90	74.019(1)
β (°)	112.86(2)	90	81.785(1)
γ (°)	90	90	72.072(1)
Volume ($Å^3$)	3732(2)	3463(2)	415.89(3)
Z	8	12	1
$D_{calcd.}$ (mg/m^3)	2.496	2.313	2.826
Absorption coefficient (μ) (mm^{-1})	4.492	12.296	3.879
Reflections collected	3874	3264	8674
Independent reflections	3729 (R_{int} = 0.039)	2862	1887 (R_{int} = 0.0149)
Index range	$0 \le h \le 24$, $0 \le k \le 18$, $-20 \le l \le 19$	$0 \le h \le 13$, $0 \le k \le 8$, $-42 \le l \le 0$	$-8 \le h \le 8$, $-9 \le k \le 9$, $-12 \le l \le 12$
Data/parameters	976/202	979/266	1887/163
Goodness-of-fit on F^2	1.73	1.21	1.094
Final *R* indices [$I > 3\sigma(I)$]	R_1 = 0.0450, wR_2 = 0.0410	R_1 = 0.0670, wR_2 = 0.2370	R_1 = 0.0334, wR_2 = 0.0767
R indices (all data)	R_1 = 0.0453, wR_2 = 0.0410	R_1 = 0.0644, wR_2 = 0.2470	R_1 = 0.0362, wR_2 = 0.0785
Largest diff. peak and hole ($e/Å^{-3}$)	0.53 and –0.44	1.277 and –0.610	1.568 and –1.115

IR (KBr, nujol) (cm^{-1}): 1428 w, 1418 w, 1149 m, 1109 w, 969 m, 920 m, 883 m, 820 s, 800 s, 774 w, 680 s ($\nu_3\ AsF_6^-$), 588 m ($\nu_2\ AsF_6^-$), 498 w, 451 w. FTRaman: 1428 w, 1418 w, 1149 m, 1106 m, 967 w, 882 w, 826 s, 805 w, 774 w, 681 vs ($\nu_3\ AsF_6^-$), 587 vs ($\nu_2\ AsF_6^-$), 385 w, 371 m ($\nu_5\ AsF_6^-$), 346 m, 278 m, 229 m, 160 w, 138 m, 114 m. The actual spectra are given in the supplementary data.[3] ^{13}C NMR (100.6 MHz, SO_2, RT) δ: 72.0 ($[Cl_2\mathit{C}(CNSNS)_2]^{2+}$), 202.7 ($[Cl_2C(\mathit{C}NSNS)_2]^{2+}$). ^{14}N NMR (28.9 MHz, SO_2, RT) δ: –17 ($[Cl_2C(C\mathit{N}SNS)_2]^{2+}$), 30 ($[Cl_2C(CNS\mathit{N}S)_2]^{2+}$). ^{15}N NMR (28.9 MHz, SO_2, RT) δ: –31.6 ($[Cl_2C(C\mathit{N}SNS)_2]^{2+}$), 29.8 ($[Cl_2C(CNS\mathit{N}S)_2]^{2+}$). $C_3As_2Cl_2F_{12}N_4S_4$ calcd.: C 5.38, As 22.40, Cl 10.60, F 34.08, N 8.37, S 19.17; found: C 5.36, As 22.54, Cl 11.08, F 33.99, N 8.59, S 20.19%.[3]

$[Cl_2C(CNSNS)CN][AsF_6]$

A mixture of $NCC(Cl)_2CN$ (1.65 g, 12.2 mmol) and $[SNS][AsF_6]$ (2.27 g, 8.5 mmol) in 10 mL SO_2 was heated (60 °C) with stirring for 3 weeks in a two-bulb apparatus with a condenser and a pressure-equalizing side-arm (12).[2] Removal of the volatiles yielded a brown precipitate. Fresh SO_2 (8 g) and $CFCl_3$ (8 g) were condensed onto the brown solid, and the mixture was cooled to –70 °C, resulting in a brown solution over a yellow-brown precipitate. The solubles were decanted off, and the process was repeated until the filtrate was colourless (three times), leaving a yellow solid (shown to be a mixture of $[Cl_2C(CNSNS)_2][AsF_6]_2$ and $[Cl_2C(CNSNS)CN][AsF_6]_2$ by NMR). $Cl_2C(CNSNS)CN][AsF_6]_2$ could be only partly extracted from this mixture by washing with CH_2Cl_2. A few colourless crystals of the title compound were obtained from the yellow solid in a SO_2–$CFCl_3$ mixture by slow evaporation of the solvent (temperature gradient: 0–7 °C). Reactions using 1:1 stoichiometry gave similar results.

IR (KBr, nujol) (1300–430 cm^{-1}): 1261 w, 1230 w, 1150 w, 1085 m, 1009 m, 985 w, 960 s, 933 w, 903 s, 820 s, 807 s, 680 s ($\nu_3\ AsF_6^-$), 629 m, 583 m ($\nu_2\ AsF_6^-$), 566 m, 508 w, 470 w 449 s. FTRaman (2300–100 cm^{-1}): 2259 s (νC≡N), 1439 w, 1419 w, 1149 w, 958 w, 821 s, 806 m, 681 s ($\nu_3\ AsF_6^-$), 669 m, 586 s ($\nu_2\ AsF_6^-$), 484 w, 394 m, 371 m ($\nu_5\ AsF_6^-$), 336 w, 306 w, 284 w, 188 w, 168 m. The actual spectra are given in the supplementary data.[3]

[3] Supplementary data for this article, along with the crystallographic data, are available on the journal Web site (http://canjchem.nrc.ca) or may be purchased from the Depository of Unpublished Data, Document Delivery, CISTI, National Research Council Canada, Ottawa, ON K1A 0S2, Canada. DUD 5125. For more information on obtaining material, refer to http://cisti-icist.nrc-cnrc.gc.ca/irm/unpub_e.shtml. CCDC 611958, 612110, and 612111 contain the supplementary crystallographic data for this paper. These data can be obtained, free of charge, via www.ccdc.cam.ac.uk/conts/retrieving.html or from the Cambridge Crystallographic Data Centre, 12 Union Road, Cambridge CB2 1EZ, UK. (Fax: 44-1223-336033 or e-mail: deposit@ccdc.cam.ac.uk).

© 2007 NRC Canada

^{13}C NMR (100.6 MHz, SO_2, RT) δ: 60.0 ($[Cl_2C(CNSNS)CN]^+$), 111.2 ($[Cl_2C(CNSNS)CN]^+$), 203.4 ($[Cl_2C(CNSNS)CN]^+$). ^{14}N NMR (28.9 MHz, SO_2, RT) δ: –118 ($\nu_{1/2}$ = 580 Hz, $[Cl_2C(CNSNS)CN]^+$), –17 ($\nu_{1/2}$ = 1200 Hz, $[Cl_2C(CNSNS)CN]^+$), 30 ($\nu_{1/2}$ = 2600 Hz, $[Cl_2C(CNSNS)CN]^+$).

Synthesis of $[OC(CNSNS)_2][SbF_6]_2$

A mixture of NCC(O)CN (0.25 g, 3.1 mmol) and $[SNS][SbF_6]$ (1.96 g, 6.2 mmol) in 15 mL SO_2 was heated (60 °C) with stirring for 3 days in a two-bulb apparatus with a condenser and a pressure-equalizing side arm (12).[2] Removal of the volatiles yielded an orange precipitate, which was washed with SO_2–$CFCl_3$ (2:1). The solvent was removed via dynamic vacuum, leaving $[OC(CNSNS)_2][SbF_6]_2$ as a white powder-like insoluble solid (2.00 g, 2.8 mmol, 90% isolated yield, based on $SNS[AsF_6]$).

IR (KBr, nujol/fluorolube) (cm^{-1}): 1713 s (ν C=O), 1449 m, 1434 m, 1314 w, 1251 s, 1149 w, 1071 w, 956 s, 928 w, 885 w, 862 m, 796 s, 742 m, 731 s, 694 w, 668 vs (ν_3 SbF_6^-), 600 w, 587 m, 570 w (ν_2 SbF_6^-), 505 s, 492 w, 454 w, 433 s. The actual spectra are given in the supplementary data.[3] ^{13}C NMR (100.6 MHz, SO_2, RT) δ: 165.0 ($[OC(CNSNS)_2]^{2+}$), 194.0 ($[OC(CNSNS)_2]^{2+}$). ^{14}N NMR (28.9 MHz, SO_2, RT) δ: –17 ($[OC(CNSNS)_2]^{2+}$), 27 ($[OC(CNSNS)_2]^{2+}$).

The reaction of NCC(O)CN and $[SNS][SbF_6]$ in 1:1 ratio yielded a mixture of $[OC(CNSNS)_2]^{2+}$ and $[OC(CNSNS)CN]^+$, as identified by NMR. ^{13}C NMR (100.6 MHz, SO_2, RT) δ: 110.3 ($[OC(CNSNS)CN]^+$), 154.6 ($[OC(CNSNS)CN]^+$), 165.0 ($[OC(CNSNS)_2]^{2+}$), 194.0 ($[OC(CNSNS)_2]^{2+}$), 195.7 ($[OC(CNSNS)CN]^+$). ^{14}N NMR (28.9 MHz, SO_2, RT) δ: –120 ($\nu_{1/2}$ = 580 Hz, $[OC(CNSNS)CN]^+$), –20 ($\nu_{1/2}$ = 450 Hz, $[OC(CNSNS)_2]^{2+}$ and $[OC(CNSNS)CN]^+$), 27 ($\nu_{1/2}$ = 450 Hz, $[OC(CNSNS)_2]^{2+}$ and $[OC(CNSNS)CN]^+$).

Crystal structure determinations

Suitable single crystals, obtained from SO_2 solution, were coated with Paratone-N oil, mounted using a glass fibre, and frozen in the cold nitrogen stream of the goniometer. Data were collected on a Bruker AXS P4/Smart 1000 diffractometer (for $[OC(CNSNS)_2][SbF_6]_2$) or a Rigaku AFC5R diffractometer (for $[Cl_2C(CNSNS)CN][AsF_6]$ and $[Cl_2C(CNSNS)_2][AsF_6]_2$). The structures were solved by direct methods and refined by full-matrix least squares on F^2 (SHELXL) (13). The data were corrected for absorption. All figures illustrating structures were prepared using the program Diamond (14). Detailed crystal structure refinement data are given in Table 1.[3]

Quantum chemical calculations

All calculations have been carried out using the PBE0 DFT hybrid functional (15) with a 6-311G* basis set as implemented in Gaussian 03 (16). The free energies in solution were calculated using a polarization continuum model (PCM) with the integral equation formalism (IEF) (17). The following parameters were used to describe the solvent SO_2: dielectric constant (Eps) = 14.0, solvent radius (Rsolv) = 2.021 Å, molar volume (VMol) = 46.75 Å^3, numeral density (Rho) = 0.01288 Å^{-3}, and density = 1.37027 g/mL (18*a*).

Fig. 1. General scheme for the reaction of a dinitrile with $[SNS][MF_6]$.

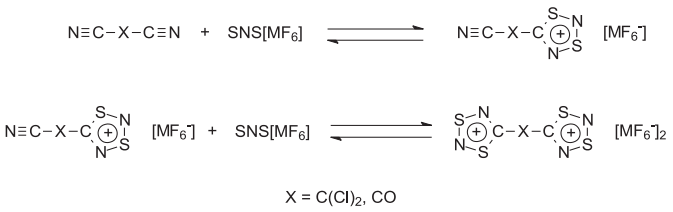
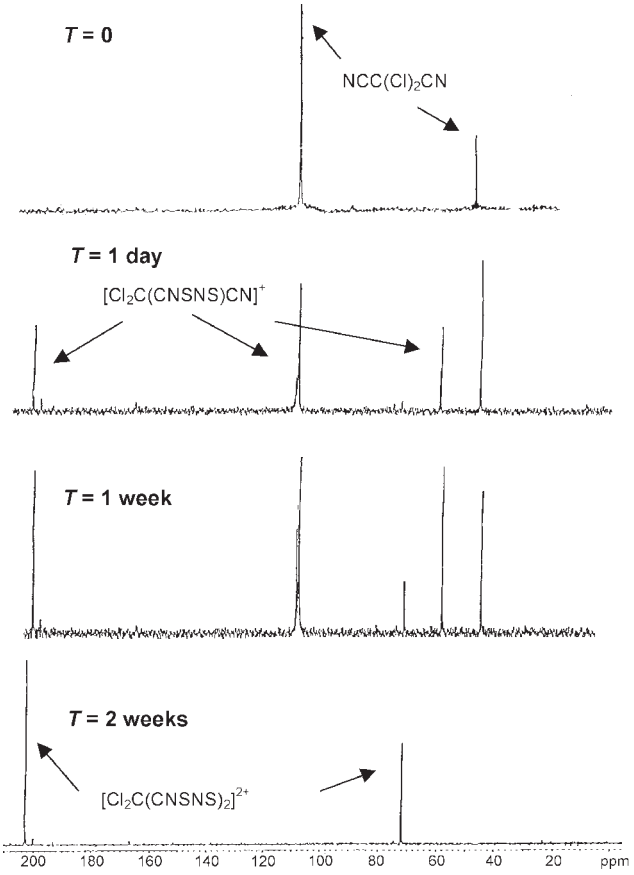


Fig. 2. In situ ^{13}C NMR spectra of the reaction of $NCC(Cl)_2CN$ with 2 $[SNS][AsF_6]$, followed over time.



Results and discussion

The reactions of the dinitriles NC–X–CN (X = CCl_2, CO) with $[SNS][MF_6]$, with 2:1 stoichiometry (SNS^+:dinitrile), in liquid sulfur dioxide gave the corresponding dicycloaddition products $[SNSNC–X–CNSNS]^{2+}$, as $[MF_6]^-$ salts in essentially quantitative yields. Reactions using 1:1 stoichiometries resulted in mixtures of the mono- and dicycloaddition products (Fig. 1).

To gain better insight, the reaction of $NCC(Cl)_2CN$ with $[SNS][AsF_6]$ in 1:2 ratio was followed in situ by ^{13}C NMR spectroscopy (Fig. 2). Immediately after the reaction had commenced, only starting materials were observed. After 1 day, peaks assigned to $[Cl_2C(CNSNS)CN]^+$ appeared, and after 1 week, the reaction mixture contained $[Cl_2C(CNSNS)CN]^+$ and $[Cl_2C(CNSNS)_2]^{2+}$. In reactions with two equivalents of $[SNS]^+$, peaks attributed to the intermediate mono-

© 2007 NRC Canada

Fig. 3. Structure of $[Cl_2C(CNSNS)_2]^{2+}$. Ellipsoids are drawn at the 50% probability level. Selected bond lengths (Å) and angles (°): C1—Cl1, 1.74(1); C1—Cl2, 1.78(1); C1—C2, 1.52(2); C1—C2, 1.53(2); N1—C2, 1.31(2); S1—N1 1.59(1); S1—N2 , 1.57(1); S2—N2, 1.57(1); S2—C2, 1.72(2); N3—C3, 1.32(2); S3—N3, 1.60(1); S3—N4, 1.59(1); S4—N4, 1.56(2); S4—C3, 1.71(1); C2–C1–C3, 109(1); dihedral angle between the two CNSNS rings 70.8(3).

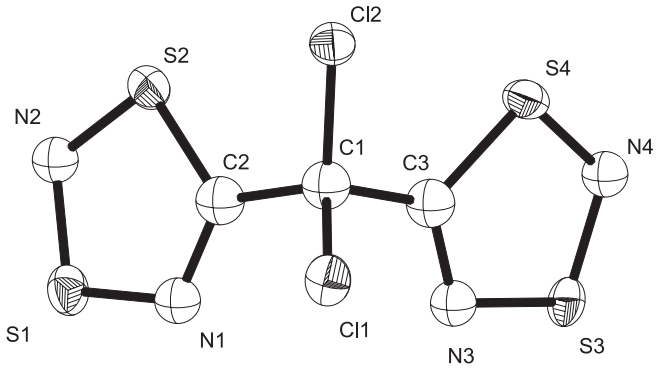
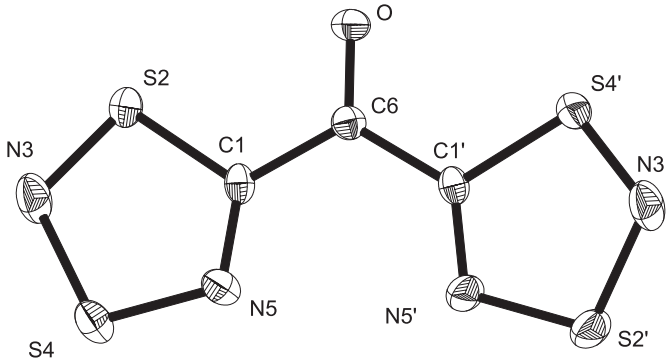


Fig. 4. Structure of $[OC(CNSNS)_2]^{2+}$. Ellipsoids are drawn at the 50% probability level. Selected bond lengths (Å) and angles (°): C6—O, 1.187(10); C1—C6, 1.503(19); C6—C1′, 1.50(2); C1—N5, 1.292(16); C1′—N5′, 1.30(2); S4—N5, 1.598(12); S2′—N5′, 1.596(9); N3—S4, 1.694(11); S2′—N3, 1.659(6); S2—N3, 1.561(5); N3—S4′, 1.476(10); C1—S2, 1.74(2); C1′—S,4′ 1.73(2); C1–C6–C1′, 104.7(10); dihedral angle between the two CNSNS rings, 18.4(3).



cyloaddition product disappeared after 2 weeks, leaving $[Cl_2C(CNSNS)_2]^{2+}$ as the clean product. Reactions with only one equivalent $[SNS]^+$ always result in a mixture of the mono- and the dicycloaddition product. In general, the dicycloaddition products are less soluble in liquid SO_2. Thus, the separation of the mono- from the dicycloaddition products was attempted by washing with different solvents (SO_2, CH_2Cl_2), but the complete separation of the products was not successful. Isolation of the small amount mono-cycloaddition product formed after 1 day was not attempted because of the necessary separation from an excess $[SNS]^+$ and does not present a feasible synthetic route to the monocycloaddition products.

X-ray crystal structures

The X-ray structures of the cations $[Cl_2C(CNSNS)_2]^{2+}$, $[OC(CNSNS)_2]^{2+}$, and $[Cl_2C(CN)(CNSNS)]^+$ are given in Figs. 3–5, and those of the $[MF_6]^-$ anions are included in the supplementary data.[3] The low quality of the structure determinations (high standard deviations) precludes a detailed discussion of the bond angles and distances; however, aver-

Fig. 5. Structure of $[Cl_2C(CN)(CNSNS)]^+$. Ellipsoids are drawn at the 50% probability level. Only one of the three crystallographically independent cations is shown with selected averaged bond lengths (Å) is shown: C6—N6, 1.16(6); C5—C6, 1.41(7); C5—Cl, 1.78(3); C4—C5, 1.50(4).

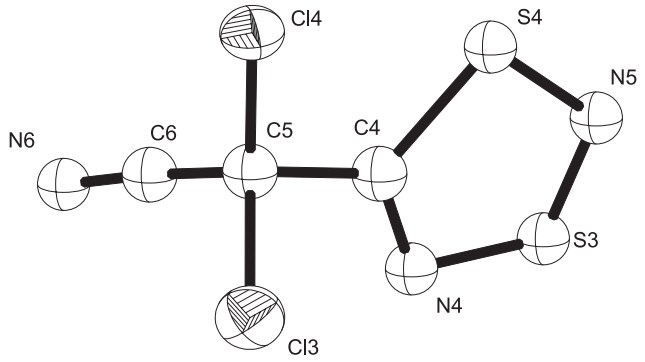
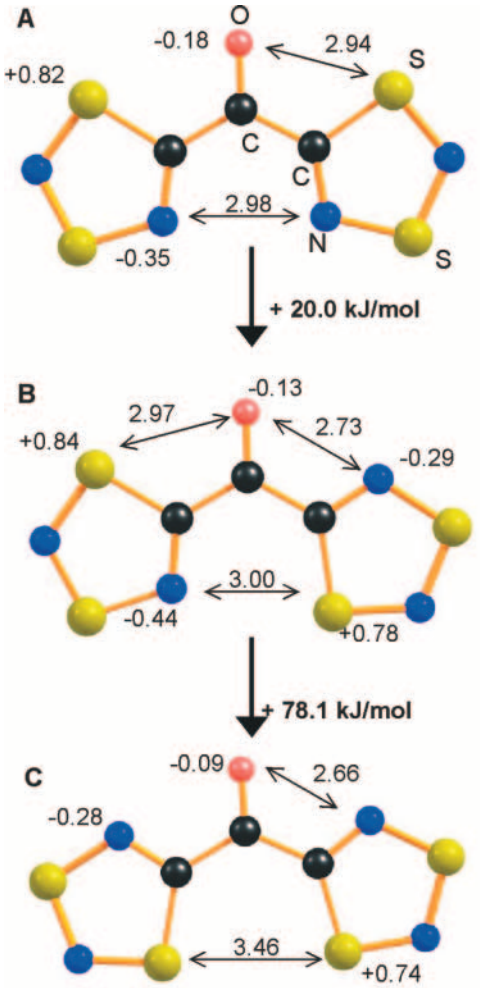


Fig. 6. Calculated (PBE0/6-311G*) geometries for the three rotational isomers of $[OC(CNSNS)_2]^{2+}$, including selected distances (Å) and Mulliken charges. Full computational details are given in the supplementary data.[3]



© 2007 NRC Canada

Fig. 7. $RCN^{\delta-}\cdots S^{\delta+}$ contacts in $[Cl_2C(CNSNS)CN][AsF_6]$ in the solid state. AsF_6^- anions are omitted for clarity. Symmetry transformations: ′ 0.5 + x, –0.5 – y, z; ″ –0.5 + x, 0.5 – y, z.

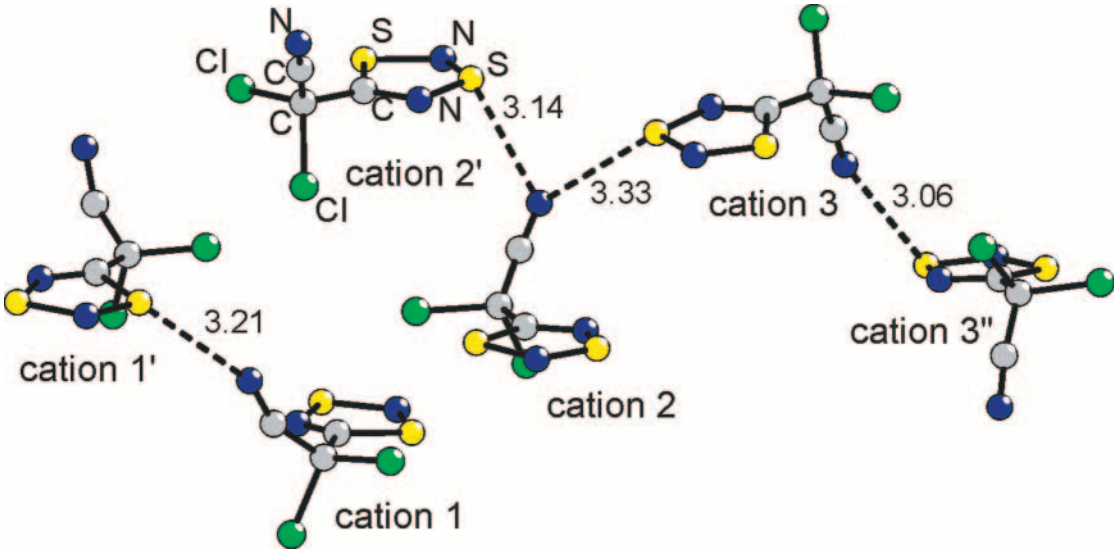


Table 2. Estimated reaction enthalpies and free energies.

Reaction	ΔH (g)	ΔH (s, $[AsF_6]^-$)	ΔG (SO_2)	ΔG (CH_2Cl_2)
NC–CN + $[SNS]^+ \rightarrow [NC–CNSNS]^+$	–80	–53	–49	–40
$[NC–CNSNS]^+ + [SNS]^+ \rightarrow {}^+[SNSNC–CNSNS]^+$	+162	–299	–34	–15
NC–C(O)–CN + $[SNS]^+ \rightarrow [NC–C(O)–CNSNS]^+$	–107	–62	–62	–54
$[NC–C(O)–CNSNS]^+ + [SNS]^+ \rightarrow {}^+[SNSNC–C(O)–CNSNS]^+$	+128	–321	–40	–22
NC–$C(Cl)_2$–CN + $[SNS]^+ \rightarrow [NC–C(Cl)_2–CNSNS]^+$	–112	+46[a]	–53	–43
$[NC–C(Cl)_2–CNSNS]^+ + [SNS]^+ \rightarrow {}^+[SNSNC–C(Cl)_2–CNSNS]^+$	+124	–341	–29	–10
Ph–CN + $[SNS]^+ \rightarrow [Ph–CNSNS]^+$	–177	–61	–66	–61
2 $[NC–CNSNS]^+ \rightarrow$ 2 NC–CN + 2 $[SNS]^+$	+160	+106	+98	—
2 $[NC–CNSNS]^+ \rightarrow {}^+[SNSNC–CNSNS]^+$ + NC–CN	+242	–246	+15	—
2 $[NC–C(O)–CNSNS]^+ \rightarrow$ 2 NC–C(O)–CN + 2 $[SNS]^+$	+214	+124	+124	—
2 $[NC–C(O)–CNSNS]^+ \rightarrow {}^+[SNSNC–C(O)–CNSNS]^+$ + NC–C(O)–CN	+236	–258	+22	—
2 $[NC–C(Cl)_2–CNSNS]^+ \rightarrow$ 2 NC–$C(Cl)_2$–CN + 2 $[SNS]^+$	+224	–92	+106	—
2 $[NC–C(Cl)_2–CNSNS]^+ \rightarrow {}^+[SNSNC–C(Cl)_2–CNSNS]^+$ + NC–$C(Cl)_2$–CN	+235	–388	+24	—

[a]Contains the heat of vaporization (estimated to be +54 kJ/mol, see supplementary data).[3]

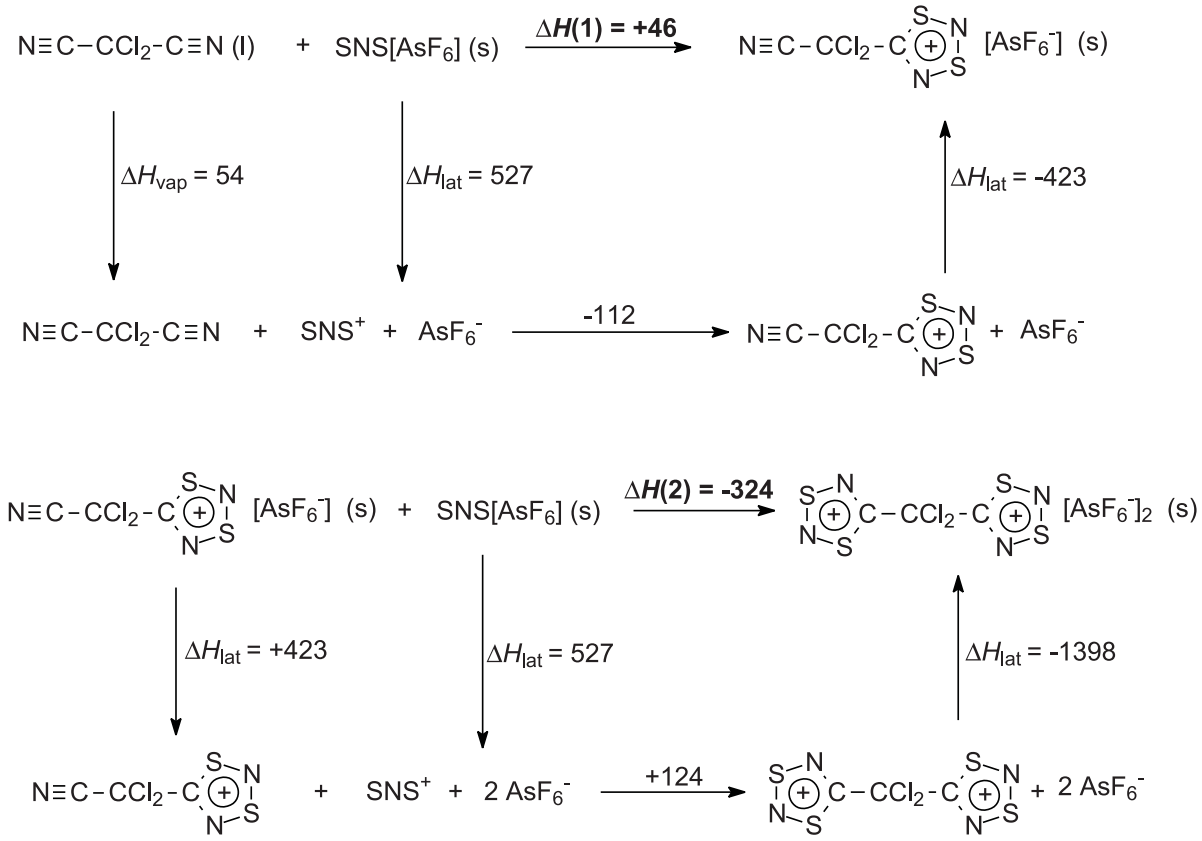
aged data for the chemically equivalent bonds agree with previously reported data for related $[R–CNSNS]^+$ cations (3, 5, 6). The structure of $[OC(CNSNS)_2][SbF_6]_2$ shows an interesting disorder of the entire cation, which is discussed in the supplementary data.[3] In the CCl_2 derivative, the $RCNSNS^+$ rings are connected via an sp^3 carbon center, resulting in an angle between the two CNSNS rings of 70.8(3)°, while in the CO compound, the rings are connected via an sp^2 carbon center, leading to an almost planar molecule (dihedral angle between the least-square planes of the two CNSNS rings 18.4(3)°) with the heterocyclic rings and the C=O group in one plane. The orientation of the rings with respect to each other is mainly governed by electrostatics. For $[OC(CNSNS)_2]^{2+}$, three rotational isomers A, B, and C are possibly depending on the orientation of the heterocyclic rings (the rotational isomers, including calculated charges, are given in Fig. 6). Calculations (PBE0/6-311G*) show that the experimental structure (Fig. 4) is also the calculated minimum structure A because of the attractive electrostatic $S^{\delta+}\cdots O^{\delta-}$ interactions. Rotating one ring in A by 180° gives B, which has one additional attractive $S^{\delta+}\cdots N^{\delta-}$ contact, but this is offset by the loss of one $S^{\delta+}\cdots O^{\delta-}$ contact and the additional repulsive $N^{\delta-}\cdots O^{\delta-}$ contact, resulting in an isomer 20 kJ/mol higher in energy. The third isomer C obtained by rotating both rings by 180° is even higher in energy because of the unfavorable electrostatics ($N^{\delta-}\cdots O^{\delta-}$ and $S^{\delta+}\cdots S^{\delta+}$).

Solid-state packing

In $[Cl_2C(CNSNS)_2][AsF_6]_2$, the dications are well separated from each other and surrounded by AsF_6^- anions. In contrast, in $[NCC(Cl)_2CNSNS][AsF_6]$, the cations show some interactions via $S^{\delta+}\cdots{}^{\delta}N{\equiv}C$ contacts between the nitrile groups and sulfur atoms of the neighboring cations (Fig. 7). This shows that the anticipated interactions between sulfur–nitrogen heterocycles can be created via free nitrile groups. Therefore, free nitrile groups are a promising and valuable tool in crystal engineering to introduce intermolecular inter-

© 2007 NRC Canada

Fig. 8. Born–Haber cycle for the first and the second cycloaddition reactions of $SNS[AsF_6]$ with $NCC(Cl)_2CN$. Energies are given in kJ/mol. Details are included with the supplementary data.[3]



actions between sulfur–nitrogen radicals in the solid state, as previously demonstrated by the characterization of the remarkable $NC–C_6F_4–CN_2S_2$ (6).

Energetics

The preference for the dicycloaddition products in reactions of dinitriles with $[SNS]^+$ in 1:1 ratio was puzzling. Previous explanations focused on kinetic factors (3*c*, 19) and suggested charges, atomic orbital coefficients, steric considerations, and possible transition states to account for this phenomenon but did not take any thermodynamic considerations into account. Therefore, the thermodynamics in the solid state, in SO_2 and CH_2Cl_2 solution, and in the gas phase were investigated to gain insight into the energetics of the cycloaddition reactions of $[SNS]^+$ with the dinitriles NC–CN, NC–C(O)–CN, and $NC–C(Cl)_2–CN$. All estimated values are compiled in Table 2. The lattice enthalpies were calculated using the "volume based thermodynamics" approach by Jenkins et al. (20), and full details are given in the supplementary data.[3] Figure 8 shows the Born–Haber cycle for the first and the second cycloaddition for the reaction of $[SNS][AsF_6]$ with $NCC(Cl)_2CN$ as an illustrative example. In the gas phase the first cycloaddition reaction is favorable by 112 kJ/mol, while the second cycloaddition, which transfers a second positive charge onto the molecule, is unfavorable by 124 kJ/mol. However, the situation is reversed in the solid state. Here, the first cycloaddition reaction is unfavorable essentially because the size of the cation ($[SNS]^+$ vs. $[Cl_2C(CNSNS)CN]^+$) is increased, and thus, lattice enthalpy of the salts is reduced. In contrast, the second cycloaddition is favorable because of the larger lattice enthalpy of the resulting 1:2 salt (dication and two monoanions) compared with the 1:1 salts (monocation and monoanion), which overcomes the unfavorable gas phase term. In general, multiple-charged ions are unstable in the gas phase with respect to dissociation into species with a smaller charge (21), but they can be stable as salts in the solid state because of the gain in lattice enthalpy (18). In SO_2 solution, the first and the second cycloaddition are favorable by –29 and –66 kJ/mol, respectively (–10 and –61 kJ/mol in CH_2Cl_2). The situation for other nitriles in all three phases is similar (Table 2); however, the nature (electron donating or withdrawing) and the size of the substituent or spacer groups, as well as different heats of vaporization, slightly change the values but not the general trend.

The thermodynamic preference for the dicycloaddition products becomes even clearer if the disproportionation of the monocycloaddition product into $[SNS]^+$ and the dinitrile (reaction 1) and into the dinitrile and the dicycloaddition product (reaction 2) are investigated (actual values are included in Table 2; Fig. 9 shows the situation for NC–CN as an illustrative example). In the gas phase, in SO_2, and CH_2Cl_2 solution, the monocycloaddition product is stable with respect to disproportionation in both directions, but in the solid state, the higher lattice enthalpy of the 1:2 salt relative to twice that of the 1:1 salt is greater than the gas phase term and makes the disproportionation into the dicycloaddtion product and the dinitrile favorable. Therefore, in the

© 2007 NRC Canada

Fig. 9. Relative energies (kJ/mol) for the disproportionation of $[NC–CNSNS]^+$.

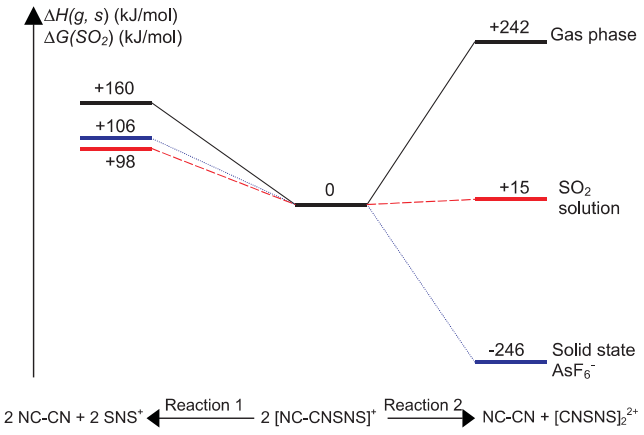
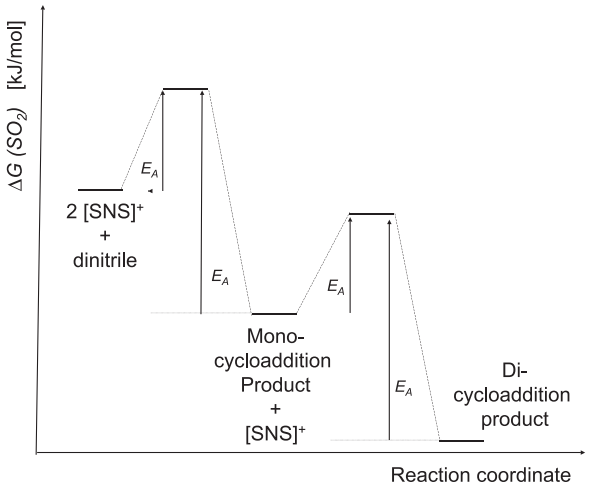


Fig. 10. Reaction coordinate for the stepwise reaction of a dinitrile with two equivalents of $[SNS]^+$ in SO_2 solution. See Table 2 for actual values.



solid state, the dicycloaddition product is the thermodynamic product in this type of reactions, and the lattice enthalpy gain in the second cycloaddition is the driving force.

However, the situation is much more complicated in reality. In addition to the idealized equilibria in solution and the solid state, experimental lattice enthalpies and solvation energies are reflected in the solubility, which plays an important role. $[SNS][MF_6]$ is soluble in SO_2 (the solubility has been determined to be 230 g/L in SO_2 (22)), while the monocycloaddition products are less soluble, and the dicycloaddition products are only sparingly soluble. Thus, the dicycloaddition product, once formed, precipitates out of solution and drives the equilibrium even further towards the dicycloaddition product.

In addition, kinetic effects also play a role. The activation energies for the first and the second symmetry-allowed cycloaddition are by definition smaller than the corresponding activation energies for the reverse cycloaddition reactions (Fig. 10). This implies that the proposed reverse cycloaddition reactions could also be significantly kinetically hindered. A reverse cycloaddition has been established in related sulfur–nitrogen systems (cf. $[S_3N_2]^{2+}$ (18*b*), $[(R_4C_2)_2S_2N]^+$ (23)), and a kinetic energy barrier for the reverse cycloaddition has been found experimentally in the later case. Our failure to prepare $[NC–CNSNS][MF_6]$ from reactions of an excess of NC–CN and $[SNS][MF_6]$ (5*a*) agrees with the underlying thermodynamics, the decreasing solubility of the dicycloaddition products, and the kinetically hindered and thermodynamically unfavorable reverse cycloaddition reaction.

The strategy to obtain the monocycloaddition products would be to use an $[SNS]^+$ salt of a very large anion to reduce the lattice enthalpy gain for the second step and also to increase the solubility in a solvent with a lower dielectric constant, and to use a lower reaction temperature. The recently published salt $[SNS][Al(OC(CF_3)_3)_4]$ (24), which is very soluble in CH_2Cl_2, is a good candidate and will be the subject of further investigations.[4]

Supplementary data

The supplementary data include the optimized geometries and total energies for all calculated molecules, structural parameters for the MF_6^- anions, disorder in the structure of $[OC(CNSNS)_2][SbF_6]_2$, vibrational spectra and calculated frequencies, details for the thermodynamic estimations, and calculated transition states.[4]

Acknowledgements

We thank the Natural Sciences and Engineering Research Council of Canada (NSERC) for funding (J.P.), the Alexander von Humboldt Foundation in Germany for providing a Feodor-Lynen Fellowship (C.K.), J. Mikko Rautiainen and Dr. Friedrich Grein for help with the DFT calculations, Aaron Mailman for discussions, and the referees for their helpful comments.

References

1. S. Parsons and J. Passmore. Acc. Chem. Res. **27**, 101 (1994), and refs. cited therein.
2. T.S. Cameron, A. Mailman, J. Passmore, and K.V. Shuvaev. Inorg. Chem. **44**, 6524 (2005).
3. Selected examples: (*a*) A.J. Banister, J.M. Rawson, W. Clegg, and S.L. Birkby. J. Chem. Soc., Dalton Trans. 1099 (1991); (*b*) A.J. Banister, I. Lavender, J.M. Rawson, W. Clegg, B.K. Tanner, and R.J. Whitehead. J. Chem. Soc., Dalton Trans. 1421 (1993); (*c*) S. Parsons, J. Passmore, and P.S. White. J. Chem. Soc., Dalton Trans. 1499 (1993); (*d*) A.J. Banister, I. Lavender, S.E. Lawrence, J.M. Rawson, and W. Clegg. J. Chem. Soc., Chem. Commun. 29 (1994); (*e*) J. Passmore and X. Sun. Inorg. Chem. **35**, 1313 (1996); (*f*) S. Brownridge, H. Du, S.A. Fairhurst, R.C. Haddon, H. Oberhammer, S. Parsons, J. Passmore, M.J. Schriver, L.H. Sutcliffe, and N.P.C. West-

[4] Indeed, the reaction of dichloro dicyano quinone with the more soluble $[SNS][Al(OC(CF_3)_3)_4]$ in SO_2 in 1:1 ratio only gave starting materials and the monocycloaddition product, indicating the accessibility of the monocycloaddition product using a large weakly coordinating anion and an equilibrium of educts and products in SO_2 solution. A. Mailman and J. Passmore, unpublished results.

© 2007 NRC Canada

wood. J. Chem. Soc., Dalton Trans. 3365 (2000); (*g*) H. Du, R.C. Haddon, I. Krossing, J. Passmore, J.M. Rawson, and M.J. Schriver. Chem. Commun. (Cambridge), 1836 (2002); (*h*) A. Decken, A. Mailman, S.M. Mattar, and J. Passmore. Chem. Commun. (Cambridge), 2366 (2005).

4. (*a*) A. Apblett and T. Chivers, J. Chem. Soc., Chem. Commun. 1889 (1987); (*b*) A. Apblett and T. Chivers. Can. J. Chem. **68**, 650 (1990).
5. (*a*) S. Parsons, J. Passmore, M.J. Schriver, and P.S. White. J. Chem. Soc., Chem. Commun. 369 (1991); (*b*) C. Aherne, A.J. Banister, A.W. Luke, J.M. Rawson, and R.J. Whitehead. J. Chem. Soc., Dalton Trans. 1277 (1992); (*c*) T.S. Cameron, M.T. Lemaire, J. Passmore, J.M. Rawson, K.V. Shuvaev, and L.K. Thompson. Inorg. Chem. **44**, 2576 (2005).
6. A.J. Banister, I. Lavender, J.M. Rawson, and W. Clegg. J. Chem. Soc., Dalton Trans. 859 (1992).
7. A.J. Banister, N. Bricklebank, I. Lavender, J.M. Rawson, C.I. Gregory, B.K. Tanner, W. Clegg, M.R.J. Elsegood, and F. Palacio. Angew. Chem. **108**, 2648 (1996); Angew. Chem., Int. Ed. Engl. **35**, 2533 (1996).
8. G. Antorrena, S. Brownridge, T.S. Cameron, F. Palacio, S. Parsons, J. Passmore, L.K. Thompson, and F. Zarlaida. Can J. Chem. **80**, 1568 (2002).
9. Selected recent examples: (*a*) G.D. Enright, J.R. Morton, J. Passmore, K.F. Preston, R.C. Thompson, and D.J. Wood. Chem. Commun. (Cambridge), 967 (1996); (*b*) T.S. Cameron, A. Decken, R.M. Kowalczyk, E.J.L. McInnes, J. Passmore, J.M. Rawson, K.V. Shuvaev, and L.K. Thompson. Chem. Commun. (Cambridge), 2277 (2006); (*c*) A. Decken, S.M. Mattar, J. Passmore, K.V. Shuvaev, and L.K. Thompson. Inorg. Chem. **45**, 3878 (2006).
10. (*a*) M. Murchie and J. Passmore. Inorg. Synth. **24**, 76 (1986); (*b*) M.P. Murchie, R. Kapoor, J. Passmore, G. Schatte, and T. Way. Inorg. Synth. **31**, 102 (1997).
11. E.G. Banucci. Macromol. Synth. **6**, 63 (1977).
12. R.W.H. Small, A.J. Banister, and Z.V. Hauptman. J. Chem. Soc., Dalton Trans. 1377 (1984).
13. G.M. Sheldrick. SHELX-97 Programs for crystal structure analysis [Computer program]. Release 97–2. Institut für Anorganische Chemie der Universität Göttingen, 1997.
14. Diamond 3.1d. Crystal Impact GBR [Computer program]. K. Bradenburg. Bonn, Germany.
15. (*a*) J.P. Perdew, K. Burke, and M. Ernzerhof. Phys. Rev. Lett. **77**, 3865 (1996); (*b*) J.P. Perdew, K. Burke, and M. Ernzerhof. Phys. Rev. Lett. **78**, 1396 (1997); (*c*) J.P. Perdew, M. Ernzerhof, and K. Burke. J. Chem. Phys. **105**, 9982 (1996); (*d*) C. Adamo and V. Barone. J. Chem. Phys. **110**, 6158 (1999).
16. M.J. Frisch, G.W. Trucks, H.B. Schlegel, G.E. Scuseria, M.A. Robb, J.R. Cheeseman, J.A. Montgomery, Jr., T. Vreven, K.N. Kudin, J.C. Burant, J.M. Millam, S.S. Iyengar, J. Tomasi, V. Barone, B. Mennucci, M. Cossi, G. Scalmani, N. Rega, G.A. Petersson, H. Nakatsuji, M. Hada, M. Ehara, K. Toyota, R. Fukuda, J. Hasegawa, M. Ishida, T. Nakajima, Y. Honda, O. Kitao, H. Nakai, M. Klene, X. Li, J.E. Knox, H.P. Hratchian, J.B. Cross, V. Bakken, C. Adamo, J. Jaramillo, R. Gomperts, R.E. Stratmann, O. Yazyev, A.J. Austin, R. Cammi, C. Pomelli, J.W. Ochterski, P.Y. Ayala, K. Morokuma, G.A. Voth, P. Salvador, J.J. Dannenberg, V.G. Zakrzewski, S. Dapprich, A.D. Daniels, M.C. Strain, O. Farkas, D.K. Malick, A.D. Rabuck, K. Raghavachari, J.B. Foresman, J.V. Ortiz, Q. Cui, A.G. Baboul, S. Clifford, J. Cioslowski, B.B. Stefanov, G. Liu, A. Liashenko, P. Piskorz, I. Komaromi, R.L. Martin, D.J. Fox, T. Keith, M.A. Al-Laham, C.Y. Peng, A. Nanayakkara, M. Challacombe, P.M.W. Gill, B. Johnson, W. Chen, M.W. Wong, C. Gonzalez, and J.A. Pople. Gaussian 03 [Computer program]. Revision b.05. Gaussian, Inc., Wallingford, CT. 2004.
17. (*a*) E. Cancès, B. Mennucci, and J. Tomasi. J. Chem. Phys. **107**, 3032 (1997); (*b*) M. Cossi, V. Barone, B. Mennucci, and J. Tomasi. Chem. Phys. Lett. **286**, 253 (1998).
18. (*a*) S. Brownridge, T.S. Cameron, H. Du, C. Knapp, R. Köppe, J. Passmore, J.M. Rautiainen, and H. Schnöckel. Inorg. Chem. **44**, 1660 (2005), and refs. cited therein. (*b*) W.V.F. Brooks, T.S. Cameron, S. Parsons, J. Passmore, and M.J. Schriver. Inorg. Chem. **33**, 6230 (1994).
19. S. Parsons, J. Passmore, M.J. Schriver, and X. Sun. J. Chem. Soc., Dalton Trans. 3342 (1991).
20. (*a*) H.D.B. Jenkins, H.K. Roobottom, J. Passmore, and L. Glasser. Inorg. Chem. **38**, 3609 (1999); (*b*) L. Glasser and H.D.B. Jenkins. Chem. Soc. Rev. 866 (2005), and refs. cited therein.
21. (*a*) M.K. Scheller, R.N. Compton, and L.S. Cederbaum. Science (Washington, D.C.), **270**, 1160 (1995); (*b*) D. Schröder and H. Schwarz. J. Phys. Chem. A **103**, 7385 (1999); (*c*) A. Dreuw and L.S. Cederbaum. Chem. Rev. **102**, 181 (2002).
22. G.K. MacLean. Ph.D. thesis, Department of Chemistry, University of New Brunswick, Fredericton, NB, Canada, 1984.
23. W.V.F. Brooks, S. Brownridge, J. Passmore, M.J. Schriver, and X. Sun. J. Chem. Soc., Dalton Trans. 1997 (1996).
24. C. Knapp, A. Mailman, G.B. Nikiforov, and J. Passmore. J. Fluorine Chem. **127**, 916 (2006).

© 2007 NRC Canada

Chemistry of the potassium, silver, and tetra(*n*-butyl)ammonium salts of sydnone *N*-oxide (Traube's anion)

Navamoney Arulsamy, D. Scott Bohle, and Inna Perepichka

Abstract: Traube's dianion, 4-methylcarboxysydnone-3-hydroxylate (2), and its monomethyl ester (**1**) are readily isolated as their di- and mono-potassium salts from the reaction of nitric oxide with dimethylmalonate and potassium methoxide in methanol. Metathesis reactions of **1** with silver nitrate and tetra(*n*-butyl)ammonium bromide yield the silver and tetra(*n*-butyl)ammonium salts of 4-methylcarboxysydnone-3-hydroxylate. In contrast to other known sydnone derivatives, the present sydnones are stable in both acidic and basic solutions. Single crystal X-ray diffraction data obtained for **2** and the silver salt (**3**) reveal planarity and delocalization of double bonds in the sydnone ring, indicating aromatic behavior. The tetra(*n*-butyl)ammonium salt (**4**) is soluble in a range of organic compounds. Cyclic voltammetric data measured for **4** in acetonitrile reveal an irreversible oxidation peak at +1.09 V vs. $Fc–Fc^+$ couple suggesting that the sydnone derivatives can be oxidized with an appropriate oxidizing agent. Differential scanning calorimetry data reveal thermal stability at ambient conditions and exothermic decomposition at high temperatures (>229 °C). The sydnone derivatives are characterized by two strong electronic absorptions in the UV region and rich vibrational (IR and Raman) spectra in the 1800–1500 cm^{-1} region. Density functional theory (B3LYP/6-311^{+++}G**) is applied to estimate the aromaticity of the sydnone ring and to assign the vibrational spectral data.

Key words: sydnone, trans-diazeniumdiolate, *N*-oxide.

Résumé : La réaction de l'oxyde nitrique avec le malonate de diméthyle et le méthylate de potassium en solution dans le méthanol permet d'obtenir facilement les sels di- et mono-potassiques du dianion de Traube, le 4-méthylcarboxysydnone-3-hydroxylate (**2**), ainsi que de son ester monométhylique (**1**). Les réactions de métathèse du composé **1** avec le nitrate d'argent et le bromure de tétra(*n*-butyl)ammonium conduit à la formation des sels d'argent et de tétra(*n*-butyl)ammonium du 4-méthylcarboxysydnone-3-hydroxylate. Par opposition à d'autres sydnones connues, les sydnones décrites dans ce travail sont stables tant en milieu acide qu'en milieu basique. Des données de diffraction des rayons X ont été obtenues pour le composé **2** et pour le sel d'argent (**3**); ils mettent en évidence que les doubles liaisons du noyau sydnone sont planes et délocalisées, ce qui indique un comportement aromatique. Le sel de tétra(*n*-butyl)ammonium du 4-méthylcarboxysydnone-3-hydroxylate est soluble dans une variété de composés organiques. Des mesures de voltampérométrie cycliques pour le composé **4**, mesurées dans l'acétonitrile, révèlent la présence d'un pic d'oxydation irréversible à 1,09 V par rapport au couple $Fc–Fc^+$, ce qui suggère que ces dérivés de la sydnone sont susceptibles d'être oxydés à l'aide d'un agent oxydant approprié. Les données de calorimétrie à balayage différentiel suggèrent que les composés sont thermiquement stables dans les conditions ambiantes et qu'ils donnent lieu à une décomposition exothermique à des températures supérieures à 229°C. Ces sydnones sont caractérisées par deux fortes bandes d'absorption dans la région UV et des spectres vibrationnels (IR et Raman) riches dans la région allant de 1500 à 1800 cm^{-1}. On a fait appel à la théorie de la fonctionnelle de la densité (B3LYP/6-311+++G**) pour évaluer l'aromaticité du cycle sydnone et pour attribuer les données du spectre de vibration.

Mots-clés : sydnone, trans-diazéniumdiolate, *N*-oxyde.

[Traduit par la Rédaction]

Introduction

The family of heterocyclic sydnones (1–4) and their closely related imines (5) have varied biological activities (6) and have been intensively investigated for their pharmaceutical properties (6, 7). Their general reaction characteristics include base instability and the ability to add a range of dipolarophiles to give new heterocycles (8). Based on their

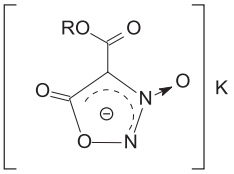
Received 8 September 2006. Accepted 20 December 2006. Published on the NRC Research Press Web site at http://canjchem.nrc.ca on 20 February 2007.

N. Arulsamy. Department of Chemistry, University of Wyoming, Laramie, WY 82071-3838, USA.
D.S. Bohle[1] and I. Perepichka. Department of Chemistry, McGill University, 801 Sherbrooke St. W., Montreal, QC H3A 2K6, Canada.

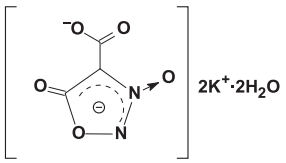
[1]Corresponding author (e-mail: scott.bohle@mcgill.ca).

 doi:10.1139/V07-001 © 2007 NRC Canada

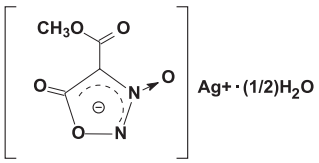
solid-state structures from X-ray crystallography (9–13) and the pattern in bond length alternation, sydnones are predicted to have little aromatic stabilization offered by the delocalized five-membered ring (10, 14).

[1] $HC(CO_2Me)_2^-$ —(2 NO; 2.5 atm; MeOH–MeOK)→  **1**

We recently discovered a new class of sydnone derivatives, their *N*-oxides or 3-hydroxy analogues (15). These new anions, first described but misformulated by Traube in 1895 (16), are readily prepared by adding two nitric oxides to dimethylmalonate (eq. [1], where 1 atm = 101.326 kPa). Purification by recrystallization from water returns as much as 31% of the monopotassium salt. Unlike their *N*-alkyl analogues, the *N*-oxo deriviatives are remarkably thermally stable, very soluble in water, and decompose only slowly in acid and not at all in base. As ligands they are compact and capable of multidentate coordination with a range of potential metals. As part of our effort to characterize these compounds and to more fully explore their chemistry, we sought to prepare salts that would be useful for cation metathesis and (or) would be soluble in solvents other than water. To this end we report herein (*i*) the isolation and characterization of the dipotassium salt of 4-carboxy-3-sydnone *N*-oxide **2**, (*ii*) the metathesis of the potassium in **1** for silver to give **3**, which is isolated as a hemihydrate and the metathesis of potassium with tetra(*n*-butylammonium) salt to give **4**, (*iii*) the determination of the solid-state structures of two of these solids by single crystal X-ray diffraction, and (*iv*) the comparison of the structures of two of these analogues with the theoretically calculated values as part of an effort to determine the degree of aromaticity in these rings. This new family of derivatives has already been extended by an elegant recent report of their preparation from lithiated terminal alkynes and nitric oxide (17).



2·2H$_2$O



3·(1/2)H$_2$O

Experimental

General procedures and analyses

Many of the instrumental and general procedures for preparation and characterization performed in our lab have been previously described (18, 19). Raman spectra were measured on a Kaiser Optics 5000 Raman microscope with excitation radiation of λ = 785 nm. The electrochemical behavior of tetra(*n*-butyl)ammonium salt **4** was studied by cyclic voltammetry (CV) at room temperature (RT) in anhydrous acetonitrile, using $Bu_4N^+PF_6^-$ as a supporting electrolyte (0.1 mol/L) under nitrogen (scan rates of 100–1000 mV s^{-1}). Experiments were performed with a BAS CV-50W electrochemical analyzer. Platinum wire, platinum disk, and Ag–$AgNO_3$ (in acetonitrile) were used as counter, working, and reference electrodes, respectively. The potential is given vs. ferrocene–ferrocenium (Fc/Fc+) couple, which was used as an internal reference.

Syntheses of new sydnone salts

Potassium 4-methylcarboxysydnone-3-hydroxylate (**1**) and sydnone-3-hydroxylate-4-carboxylate dihydrate (**2**·2H$_2$O) were obtained from the reaction of nitric oxide and dimethylmalonate in the presence of potassium methoxide (15). The dipotassium salt **2** is prepared by saponification of the crude reaction mixture of **1** in a boiling solution of KOH (1 mol/L) for 30 min during purification.

Silver 4-methylcarboxysydnone-*N*-oxide (3)

To a solution of **1** (0.218 g, 1.1 mmol) in water (5 mL) was added a solution of $AgNO_3$ (0.169 g, 1 mmol) in water (5 mL). The white precipitate formed was quickly redissolved by the addition of 3 drops of concd. NH_4OH. The clear solution was allowed to stand overnight in the dark and the black solid formed was filtered off. The colorless filtrate was allowed to evaporate slowly to ~3 mL in a dark room over a period of several days when colorless shiny crystals of **3**·(1/2)H$_2$O formed. The crystals were filtered, washed with cold water (2 mL), and dried in a vacuum oven at RT overnight. Yield: 0.245 g (89%) based on the amount of $AgNO_3$. UV λ_{max} (nm) in 0.1 mol/L aq. NH_4OH (ε (mol/L cm)$^{-1}$): 228 (12 476), 277 (9040). IR (cm^{-1}) ν: 3422w b, 3013w, 2960w, 1812w, 1742s, 1700s, 1649m, 1489m, 1464s, 1430m, 1387s, 1312w, 1208s, 1137s, 1038m, 953m, 808w, 772m, 657w. Anal. calcd. for $C_4H_4N_2O_{5.5}Ag$: C 17.46, H 1.47, N 10.19; found: C 17.32, H 1.12, N 9.96.

Tetra-*n*-butylammonium salt of Traube's anion, tetra(*n*-butyl)-4-methylcarboxysydnone *N*-oxide (4)

To a solution of **1** (0.720 g, 3.64 mmol) in 15 mL of water was added a saturated solution of tetra(*n*-butyl) ammonium bromide (1.41 g, 4.36 mmol) in 2 mL of water at RT. A white precipitate rapidly formed and after 30 min of stirring it was filtered and washed with a minimal amount of cold water. Recrystallization of this material from THF gave 1.20 g (82%) of **4**, mp 136 to 137 °C. UV (CH_3OH) λ_{max} (nm) (ε (mol/L cm)$^{-1}$): 228 (10 400), 276 (6200). IR (KBr, cm^{-1}) ν: 3003w, 2959s, 2873m, 1784w, 1746m, 1733s, 1700s, 1654m, 1506w, 1492w, 1483w, 1456w, 1449w, 1418w, 1382s, 1293w, 1207m, 1193m, 1137w, 1121m, 1024m, 946w, 923m, 880m, 802w, 773m, 760w, 741w, 666w, 649w, 407w. ^{1}H NMR (400 MHz, D_2O, ppm) δ: 0.95 (t, 12H, *J* = 7 Hz, *CH*$_3$-Bu), 1.37 (s ext, 8H, *J* = 7 Hz, *CH*$_2$-Bu), 1.66 (quint, 8H, *J* = 8 Hz, *CH*$_2$-Bu), 3.20 (t, 8H, *J* = 8 Hz, *CH*$_2$-Bu), 3.84 (s, 3H, *CH*$_3$-O). ^{13}C NMR (300 MHz, $CDCl_3$, ppm) δ: 13.9, 20.0, 24.2, 50.9, 59.0, 95.2, 160.1, 166.7. MS (ESI) *m*/*z* calcd. for $[N(C_4H_9)_4][C_4H_3N_2O_5]$: [M] 401; found $[N(C_4H_9)_4]^+$ 242 (100%), $[M + [N(C_4H_9)_4]]^+$ 643 (16%), $[M - [N(C_4H_9)_4]]^-$ 159 (100%), $[2M - [N(C_4H_9)_4]]^-$ 560 (95%). Elemental analysis calcd. for $C_{20}H_{39}N_3O_5$ (401 g/mol): C 59.82, H 9.79, N 10.47; found: C 59.90, H

© 2007 NRC Canada

Table 1. Crystal data and structure refinement for **2**·2H_2O and **3**·(1/2)H_2O.

Compound	**2**·2H_2O	**3**·(1/2)H_2O
Empirical formula	$C_3H_4K_2N_2O_7$	$C_8H_8Ag_2N_4O_{11}$
Formula weight	258.28	551.92
Space group	$P2_12_12_1$	C_2/c
a (Å)	5.6997(6)	15.303(2)
b (Å)	11.234(1)	9.289(1)
c (Å)	12.990(1)	10.797(2)
β (°)	90	113.18(2)
V (Å^3)	831.7(1)	1410.8(4)
Z	4	4
D_c (mg m^{-3})	2.063	2.598
Crystal size (mm^3)	0.80 × 0.38 × 0.32	0.36 × 0.24 × 0.20
Radiation (Å)	0.710 73	0.710 73
θ range (°)	2.40–24.98	2.90–24.99
T (K)	298	298
μ (mm^{-1})	1.156	2.850
F (000)	520	1064
Index ranges	$-1 \le h \le 6$, $-1 \le k \le 13$, $-1 \le l \le 15$	$-1 \le h \le 18$, $-11 \le k \le 1$, $-12 \le l \le 12$
Reflection collected	1238	1562
Independent reflections (R_{int})	1107 (0.0131)	1231 (0.0129)
Completeness of data (%)	98.2	98.7
Absorption coefficient (mm^{-1})	1.156	2.850
Max and min transmissions	0.2136 and 0.1816	0.3847 and 0.2579
Data, restraints, parameters	1107, 0, 127	1231, 0, 118
Goodness-of-fit on F^2	1.055	1.180
Final R indices [$I > 2(\sigma)$]	$R_1 = 0.0259$, $wR_2 = 0.0703$	$R_1 = 0.0256$, $wR_2 = 0.0625$
R indices (all data)	$R_1 = 0.0264$, $wR_2 = 0.0709$	$R_1 = 0.0268$, $wR_2 = 0.0631$
Absolute structure parameter	–0.01(6)	

9.75, N 10.49. Needles for single crystal X-ray diffraction were readily obtained from dichloromethane solutions, but unfortunately the crystals are highly mosaicked along their long axis and do not allow for a satisfactory refinement of the diffraction data.

X-ray crystallographic data

X-ray diffraction data for **2**·2H_2O, **3**·(1/2)H_2O, and **4** were collected on either a Bruker P4 or D8 diffractometer equipped with a molybdenum tube and a graphite monochromator at 25 °C. Table 1 contains diffraction data for **2**·2H_2O and **3**·(1/2)H_2O, whose structures have both been deposited with the CCDC under entries 171269 and 627294, respectively.[2] Unit-cell dimensions were determined from several accurately centered reflections in high 2θ angles using the program XSCANS (20). For the P4 data sets, 3 standard reflections measured after every 97 reflections exhibited no significant loss of intensity. The data were corrected for Lorentz polarization effects and absorption. The structure was solved by direct methods and refined by least-squares techniques on F^2 using the program SHELXTL (21, 22). In the dipotassium salt **2**, the identity of the ring atoms was confirmed by examining the refinement results for other possible structural isomers, e.g., in one case with an exocyclic nitro group. In all cases the resulting thermal parameters S_{gof} and the R values indicate that the best model is that shown in Fig. 4. Similar considerations were used in the structural elucidation for **1** (15) and spectroscopic confirmation of these structural assignments stems from the clear distinctions in the vibrational spectra for these isomers. As discussed later, the best structural agreement is for the *N*-oxide sydnone structures adopted here.

The dipotassium salt **2**·2H_2O crystallizes in the acentric orthorhombic space group $P2_12_12_1$ with four formula units. The refined Flack parameter of –0.01(6) indicates that the correct configuration is modeled in the solution. The ions and the water solvate are well ordered and are located on general positions. All non-hydrogen atoms were located in

[2] Supplementary data for this article are available on the journal Web site (http://canjchem.nrc.ca) or may be purchased from the Depository of Unpublished Data, Document Delivery, CISTI, National Research Council Canada, Ottawa, ON K1A 0R6, Canada. DUD 5126. For more information on obtaining material refer to http://cisti-icist.nrc-cnrc.gc.ca/irm/unpub_e.shtml. CCDC 171269 and 627294 contain the crystallographic data for this manuscript. These data can be obtained, free of charge, via http://www.ccdc.cam.ac.uk/conts/retrieving.html (Or from the Cambridge Crystallographic Data Centre, 12 Union Road, Cambridge CB2 1EZ, UK; fax +44 1223 336033; or deposit@ccdc.cam.ac.uk).

© 2007 NRC Canada

Table 2. Differential scanning calorimetry data for new sydnone *N*-oxides.

Compound	T_{onset} (°C)	T_{max} (°C)	ΔH (cal/g)	ΔH (kcal/mol)
2 $2K^+$	335.9	336.2	–416.9	–92.55
2 $2K^+ \cdot 2H_2O$	57.8	80.2	+79.35	+20.47
	318.9	330.7	–373.0	–96.23
3 $Ag^+ \cdot (1/2)H_2O$	194.6	199.6	+20.47	+5.65
	228.8	228.9	–125.0	–34.50
4 NBu_4^+	135.1	137.6	+31.10	+12.47
	273.5	302.3	–146.2	–58.63

the difference maps during successive cycles of least-squares calculations and were refined anisotropically. The H atoms were placed in calculated positions and refined isotropically by a riding model. Compound **3**·(1/2)H_2O crystallizes in the monoclinic space group *C*2/*c* with four formula units. The cation and anion are located on general positions and are well ordered. The oxygen atom of the water solvate is located on a two-fold axis of symmetry. All non-H atoms located in the difference maps during successive cycles of least-squares calculations and were refined anisotropically. The H atoms of the anion were placed in calculated positions and were refined isotropically. The H atom of the water was located and refined isotropically.

Computational details

We have studied the two anions $[MeO_2CCC(O)N(O) = NO]^-$ (in **2**) and $[O_2CCC(O)N(O) = NO]^{-2}$ (in **1, 3,** and **4**) as well as the neutral protonated derivative of **1**. In each case, the optimized structures were determined. Computations were carried out at the restricted Hartree–Fock (RHF) (23) and density functional theory (DFT). DFT calculations used the hybrid B3LYP functional (24) and triple zeta 6–311++G** basis sets (24, 25). Vibrational frequencies were calculated for all stationary points to define them as either minima or transition states. All of the described calculations were performed using Gaussian 98 (26).

Results

As part of our effort to explore this new approach to sydnone heterocyclic chemistry, we set out to prepare new salts with greater reactivity and (or) solubility. The salts described in this paper are easily purified by recrystallization, a common trait with these derivatives. With the exception of the photolabile silver salt **3**, the new Traube salts are all base stable and can be handled in the open as solutions or stored as solids without difficulty. The photolabile salt **3** becomes gray with age and should be stored cold and wrapped in foil to slow decomposition. Satisfactory elemental analyses of all new derivatives demonstrated their purity with their identity being unambiguously determined by the combination of spectroscopy and X-ray diffraction.

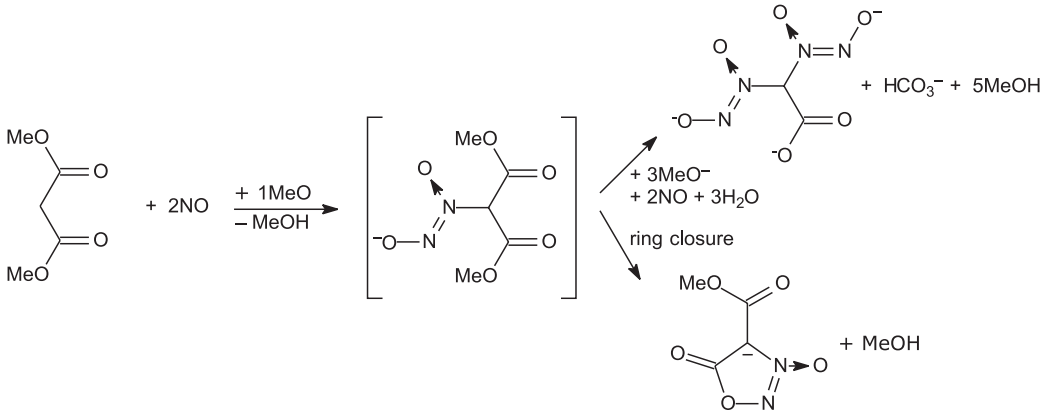
In addition to the sydnone **1**, neutral uncharged radical coupling products, $(MeO_2C)_2CH\text{-}CH(CO_2Me)_2$ and $(MeO_2C)_2CH\text{-}C(CO_2Me)_2\text{-}CH(CO_2Me)_2$, can be isolated in low and variable yields by dichloromethane extraction of the crude reaction precipitate (15). A bisdiazeniumdiolate, $[(O_2C)CH(N_2O_2)_2]^{3-}$, can also be isolated in 15% yield when the reaction is run at ambient temperatures and followed by an alkaline workup (15, 27). Both of these products represent the balance in rates of ring closure to give **1**, vs. one-electron oxidation to give the polymethylcarboxylate chains and second diazeniumdiolation to ultimately lead to the decarboxylated bisdiazeniumdiolation product from the intermediate in eq. [2], $[(MeO_2C)_2C(N_2O_2)]^{2-}$.

The silver and tetra(*n*-butyl)ammonium salts of the methylester of Traube's anion are readily isolated by treating aqueous solutions of **1** with the appropriate countercation. While the silver salt **3** has reduced solubility in many solvents, it retains sufficient solubility to be a useful reagent for halide metathesis reactions. The tetra(*n*-butyl)ammonium salt **4** is remarkably soluble in a wide range of organic solvents and is a useful reagent for sydnone synthesis.

Thermal and redox reactivity

The new sydnone *N*-oxide salts were characterized by DSC for thermal behavior and stability and the results are collected in Table 2. The hydrated salts **2** and **3** dehydrate

[2]



© 2007 NRC Canada

endothermically at ~60 and 195 °C, respectively, with further heating resulting in exothermic decomposition at 228 and 319 °C, respectively. The large exothermic release, their high density, and the pronounced stability of these salts suggest they may be useful candidates for solid state rocket propellants. The only reversible process found by DSC is a melting point for **4** at 135 °C with a relatively low endotherm.

In addition to their acid and base stability, seen later, the sydnone *N*-oxides are stable in air and can be stored in the open for prolonged periods with little change in composition or spectroscopic properties. The only significant redox behavior found by cyclic voltametry for **4** is an irreversible oxidation process at E_p = +1.09 V at 1000 mV s^{-1} (Fig. 1). Thus, strong oxidants are expected to react with these compounds and this reaction is currently being explored. No reduction processes were observed.

Fig. 1. Cyclic voltammogram for **4** in acetonitrile with *n*-Bu_4NPF_6 –CH_3CN at a scan rate of 1000 mV/s.

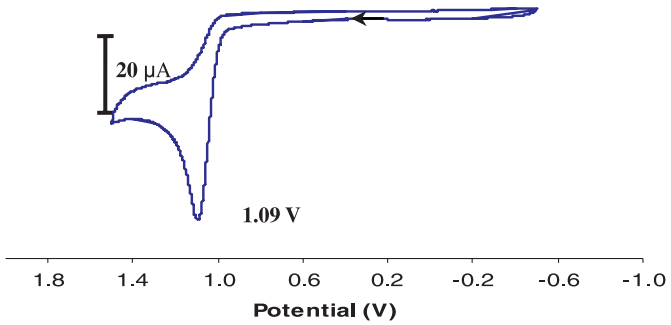


Table 3. UV-vis data for new sydnone *N*-oxides.

Compound	Solvent	λ_{max} (nm)	
1	Water	276	230
1	HCl (0.1 mol/L)	276	228
1	NaOH (1 mol/L)	277	227
2	Water	280	224
3	NH_4OH (0.1 mol/L)	277	228
4	Water	276	227
4	Tetrahydrofuran	277	—
4	Dichloromethane	282	—
4	Acetonitrile	280	232
4	Methanol	277	227
4	Dimethylformamide	280	—

Electronic spectroscopy

Unlike the *N*-alkyl and the *N*-aryl sydnones, which show a single absorption in the UV spectrum (λ = 290–325 nm, ε ~ 8000 $(mol/L)^{-1}$ cm^{-1}) the sydnone *N*-oxides exhibit two bands at higher energies. In aqueous solution the monomethylester of Traube's anion in **4** has two bands (λ = 228 nm, ε = 10 400 $(mol/L)^{-1}$ cm^{-1}, λ = 276 nm, ε = 6200 $(mol/L)^{-1}$ cm^{-1}) and for the dianion in **2** (λ = 224 nm, ε = 11 130 $(mol/L)^{-1}$ cm^{-1}, λ = 280 nm, ε = 8810 $(mol/L)^{-1}$ cm^{-1}) (15). The energy and intensities of both of these absorption bands are almost invariant with respect to pH, and in strong base or acid there are only minor changes in the spectrum of **2**. In contrast with these results are those for the cis diazeniumdiolates, which exhibit a single strongly solvatochromatically sensitive band at about 260 nm (28). Because of its extensive solubility, the spectrum of **4** has been measured in a variety of solvents and the energy and intensities of its bands are insensitive to either the solvent polarity or its hydrogen-bonding ability (Table 3). There is little evidence from UV–vis spectroscopy to suggest that the sydnone *N*-oxides interact strongly with common solvents.

Vibrational spectra

The highly polarized sydnone ring results in strong and characteristic IR spectra for its derivatives. In addition, the extensive delocalized bonding also means that they are highly polarizable with strong features in their Raman spectra. Both of the these predictions are experimentally borne out and vibrational spectroscopy is a useful tool for the characterization of sydnones. Moreover, these assignments, their interpretation, and the energies of these bands are highly diagnostic of the anion's electronic structure. Representative IR and Raman data for the key derivatives described in this paper are collected in Tables 4 and 5, respectively, with representative spectra for **2** juxtaposed in Fig. 2.

Prior discussions of the sydnone vibrational spectra have focused considerable attention on the band assigned to the exocyclic carbonyl stretch, ν(C=O), which typically has a range from 1718 to 1770 cm^{-1} (29, 30). The sydnone salts listed in Table 4 all have strong bands between 1738 and 1703 cm^{-1}, with a second strong band being assigned to the asymmetric carboxylate stretch, $\nu(CO_2)_{asym}$, occurring at slightly lower frequencies between 1700 and 1615 cm^{-1}. The number, energy, and intensities of these bands are not only cation dependent but hydration dependent. Many of these phenomena can be easily understood from the crystal structures discussed later, where carbonyl oxygen–cation interactions are observed for all species except **4**. For 3-phenyl- and 3-ethylsydnone, multiple peaks are also observed in this area and this has been attributed to a Fermi resonance (31). In Fig. 2, the possible splitting due to all of these effects can be seen by contrasting the IR and Raman spectra for the 1800–1700 cm^{-1} region. Whereas the Raman spectrum for anhyd. **2** has three bands, there are four IR active bands in this region. The calculated normal coordinates for the five strong IR active bands between 1500 and 1200 cm^{-1}, Tables S2 and S3, indicate that these framework modes are not as cation-sensitive and can be described as an asymmetric and symmetric ν(NNO), a ring-breathing mode and a symmetric carboxylate stretch combined with a ring-breathing mode.[2] The $\nu(NNO)_{asym}$ involves the exocyclic N–O, which has a large ν(NO) mode coupled to carboxylate stretch; it is observed as a weak band in the Raman spectrum between 1468 and 1459 cm^{-1} and is calculated for the disodium analog to be at 1468 cm^{-1} (Table S3).[2] The IR spectra of all salts contain strong bands in this region and in others as well. The $\nu(NNO)_{sym}$ band is calculated to be at 1386 cm^{-1} and corresponds with strong bands in the IR between 1387 and 1384 cm^{-1}, and between 1399 and 1387 cm^{-1} in the Raman spectrum. The symmetric ring-breathing mode is one of the strongest bands in the Raman spectrum with a range of 1351 to 1289 cm^{-1} and from 1343 to 1310 cm^{-1} in the IR. For the disodium complex it is calculated to be at 1368 cm^{-1}, which

© 2007 NRC Canada

Table 4. IR data for sydnone salts.

1 K^+	2964w	1812w	**1738s**	**1698s**	1512m	**1490s**	**1386s**	**1208s**	**1140s**	1047m	**956s**	806w	**773s**	683w	500m
				1654s		**1429s**	1324m			**1039s**	938m		**767**s	678w	
				1629s			**1310s**							659w	
2 $2K^+$			1769m	**1690s**		**1454s**	**1385s**	1245m	1150m	1039m	956m	**823s**	**796s**	681m	478w
			1734s	**1619s**			**1343s**	**1228s**		1011m	921m		**776s**	658m	
													758w		
													728w		
2 $2K^+ \cdot 2H_2O$	**3420s br**		1772m	**1615s**		1450m	1384m	**1229s**	1149m	1038m	**957s**	**822s**	**795s**	661m	525m
			1736s				1342m			1008w	922m		774m		
			1688s				1314m						726w		
3 $Ag^+ \cdot (1/2)H_2O$	3422w	1812w	**1742s**			1489m	**1387s**		**1137s**	1038m	953m	808w	772m	657w	
	3013w		**1700**s			**1464s**	1312w								
	2960w					**1430m**									
4 NBu_4^+	3003w		1784w	1654m	1506w	1492w	**1382s**	1293w	1193m	**1024**m	946w	**880m**	**773m**	666w	
	2959s		1746m			1483w		1207m	**1121m**		**923m**		741w	649w	
	2873m		**1733s**			1456w									
			1700s			1449w									
						1418w									

Note: Data is given in cm^{-1} as measured in KBr. Bands displayed in boldface are prominent common bands. Relative intensities are given using the following abbreviations: strong (s), medium (m), weak (w), broad (br).

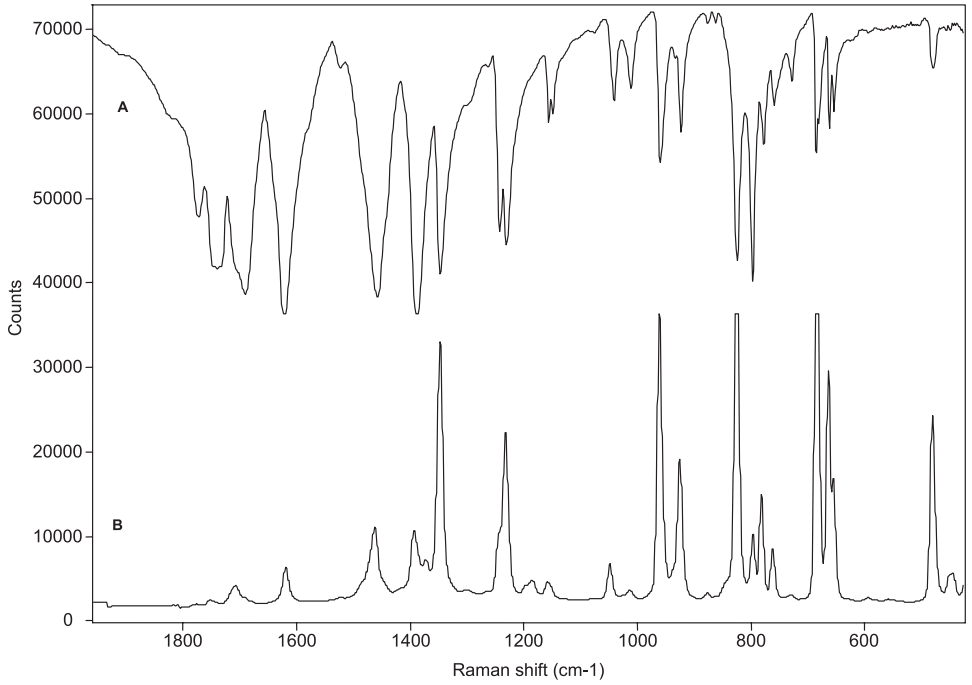
Table 5. Raman data for sydnone salts.

1 K^+	1739w	1654w	1467w	1399w	1210w	1143w	1041w	**958s**	**810s**	**776s**	**678s**	474m	343m	167w
	1701m		1404w	1339w				941s		732w	**658s**	405m	314w	138m
				1310s										**116s**
2 $2K^+$	1715w	1619w	1464w	1394w	1238m	1156w	1048w	**961s**	**831s**	762w	**684s**	485m	368w	122w
				1351s				922m			663m	446w	225m	
												412w		
3 $Ag^+ \cdot (1/2)H_2O$	1700w	1689m	1468w	1394w	**1289s**	1135w	1046w	952m	**811s**	780m	**680s**	484m	350w	178w
			1429w	**1313w**	1209w			931w		725w	**663w**	402w	330w	**126s**
													264w	
4 NBu_4^+	1736w	1659w	1459m	1387w	**1296s**	1153w	**1052m**	947w	897w	**798s**	**667s**	467m	389w	**155w**
	1704w			1328m	1206w	**1136m**	1034w	**924s**	881w	760m	648m	406w	356w	**106s**
								912m					333w	
													253s	

Note: Measured as a crystalline solid using 785 nm excitation radiation. Abbreviations are the same as in Table 4.

© 2007 NRC Canada

Fig. 2. Midrange IR A (top) and B (bottom) Raman spectra of **1**. IR measured as a KBr suspension and the Raman measured as a crystalline solid with 785 nm excitation.

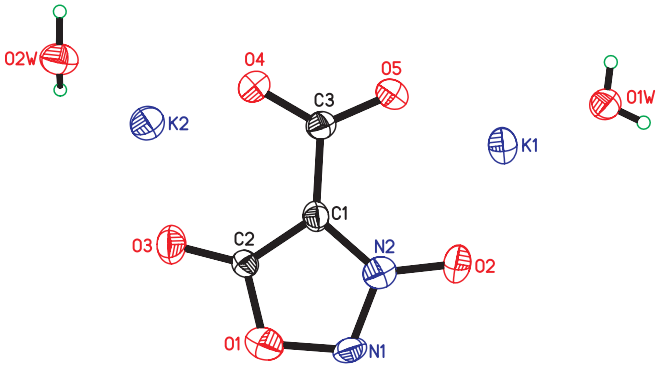


is only slightly higher than the observed values of 1351 and 1340 cm^{-1} for the Raman and IR spectra of **2**, respectively. The strong combined carboxylate stretch and ring-breathing mode, which is calculated to be at 1262 for the disodium analog of **2**, compares with the experimental values of 1238 and 1228 cm^{-1} for the dipotassium salt **2**. The final mode worth mentioning is the strong Raman active mode at 961 cm^{-1} in the spectrum of **2**, which corresponds well with a ring-breathing mode calculated to have an energy of 976 cm^{-1}. The normal coordinate for this band corresponds to an intracyclic N–O stretch that expands the ring. Taken together, these and other bands for the sydnones make vibrational spectroscopy an insightful method for their characterization.

Crystallographic studies of new sydnone *N*-oxide salts

Crystallography is an important method for the unambiguous characterization of the new salts described in this paper. Common characteristics of the anions is their rigid coplanarity and short exocyclic N–O and C–O bond lengths. Within the rings the bond length ranges are relatively small, 1.324(4)–1.405(3) Å for **1**, 1.334(3)–1.390(3) Å for **2**, and 1.314(4)–1.408(5) Å for **3**. Overall the monoanions in **1** and **3** are similar to one another with the dianion in **2** having a smaller range of intraring distances. The structure of **1** has already been communicated (15). Here we present and contrast the structural results for the dipotassium and silver salts with **1**. As mentioned in the experimental section, attempts to obtain diffraction grade crystals of the tetra(*n*-butyl)ammonium salt **4** have been hampered by the mosaicity of their needle morphology. Consistently, the crystals are heavily zoned along the principal axis of the needle, giving rise to a striated appearance, when viewed by crosspolarized optical microscopy, and broad Bragg peaks on the diffractometer.

Fig. 3. The asymmetric unit in the crystals of **2**·2H_2O. Thermal ellipsoids are drawn at the 50% probability level.



As a result, the diffraction data is of limited quality, with the setting in the most suitable space group, C_2, converging to a good refinement for the cation but to a badly disordered layer of anions. Thus, the best *R* for the more intense reflections is only ~8%, with the disorder in the anions limiting any meaningful interpretation of the metric parameters. These results will not be discussed further.

The dipotassium salt **2** crystallizes as a dihydrate, **2**·2H_2O, with the resulting structure consisting of strongly interacting potassium cations, sydnone-3-hydroxylate-4-carboxylate anions, and water solvates (Fig. 3). The exocylic C=O bond at 1.256(3) Å is slightly longer than a typical carbonyl double bond, 1.20 Å (32), because of its conjugation to the ring. The delocalization of the charges over the entire anion is also illustrated by its interaction with the cations. The carboxylato and exocyclic O atoms (O2, O3, O4, and O5) and a ring nitrogen atom (N1) are involved in ionic interaction with the K^+ ions.

© 2007 NRC Canada

Fig. 4. Coordination spheres of the two cations in **2**·2H_2O. H atoms are omitted and the thermal ellipsoids are drawn at the 50% probability level.

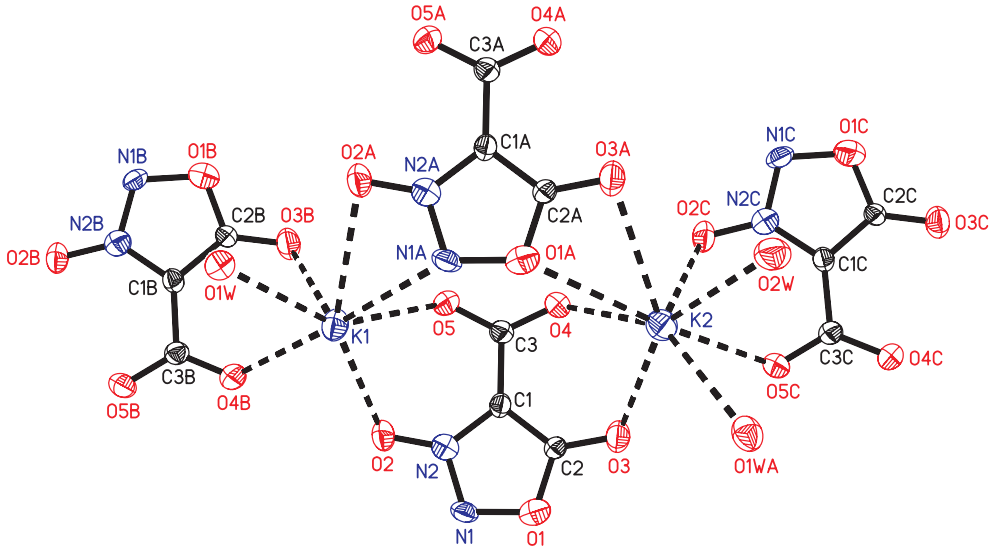
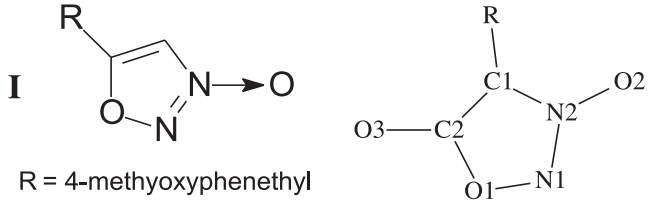


Table 6. Comparison of metric parameters for structurally characterized sydnones.

Bond[a]	*N*-Arylsydnones[b]	**1**[c] (K^+)	**2** ($2K^+$)	**3** (Ag^+)	**I**[d]
C1–N2	1.32–1.34	1.380(3)	1.377(3)	1.378(5)	1.381(3)
N1–N2	1.31–1.32	1.324(3)	1.342(3)	1.314(4)	1.295(3)
N2–O2	—	1.262(3)	1.257(3)	1.269(4)	1.270(2)
N1–O1	1.38–1.39	1.386(3)	1.390(3)	1.397(4)	1.386(3)
C1–C2	1.39–1.40	1.405(3)	1.384(4)	1.408(5)	1.329(3)
C2–O3	1.21–1.22	1.229(3)	1.256(3)	1.230(5)	—
C2–O1	1.39–1.42	1.367(3)	1.334(3)	1.373(5)	1.353(2)

Note: All values in Å.
[a]The numbering scheme is shown immediately following the footnotes.
[b]Range of values for nine structurally characterized *N*-alkylsydnones taken from ref. 41.
[c]Taken from ref. 15.
[d]Taken from ref. 17 and corresponds to the sydnone shown below.



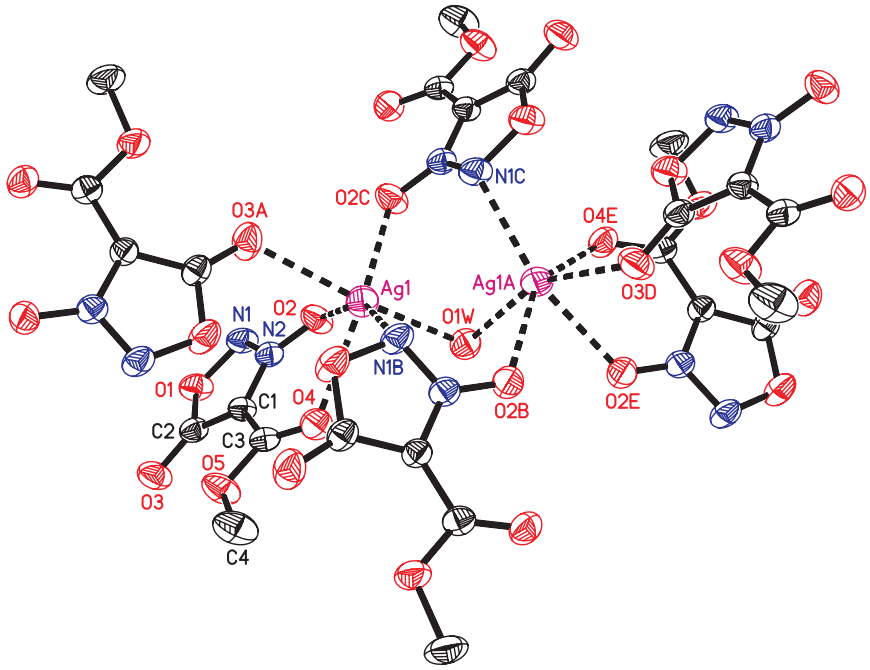
One of the cations (K1) is in a seven-coordinate geometry with two pairs of O atoms from two different anions, a diazeniumdiolate O atom, and an N atom of another anion along with a solvate O atom being the ligands. Cation K2 is in an eight-coordinate geometry also with two pairs of O atoms from two anions, a diazeniumdiolate N and O atoms of another anion, and two water solvate O atoms being the ligands. Two anions bridge the cations as shown in Fig. 4, and the remaining anions bind the cations in different coordination modes. The anion and the two water solvates bind two neighboring nonequivalent cations leading to a compact three-dimensional network. In addition, the two water solvates are also involved in hydrogen bonding with each other and both carboxylato oxygen atoms (Tables S4–S8).[2]

The structure of the silver salt **3**·(1/2)H_2O consists of strongly interacting silver cation, 4-methylcarboxysydnone-3-hydroxylate anion, and a half water solvate. The whole of the anion is planar, but the lengthening of the exocyclic C=O double bond and the ring N=N double bond (Table 6) is not as pronounced as for the respective bonds in **2**·2H_2O. The structure of the potassium salt of the anion has been previously characterized (15) and the features of the anions in both salts are nearly identical.

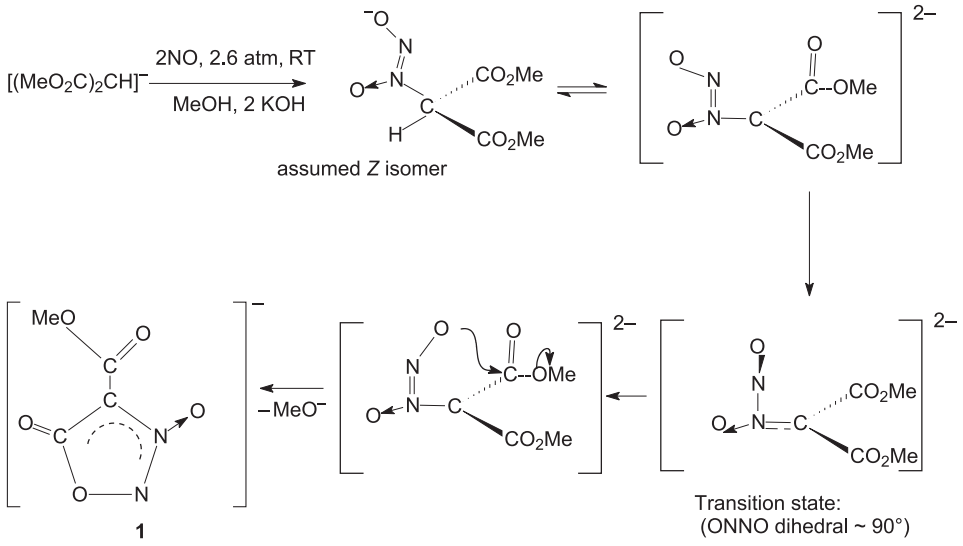
The anion coordinates through the exocyclic N–O and C=O oxygen atoms O2 and O3, the ring nitrogen atom N1, and the carboxylate oxygen atom O4 as shown in Fig. 5. The coordination sphere around the cation is a highly distorted octahedron with the silver being coordinated to four anions and a water solvate. Two of the anions and the water solvate act as bridges between two neighboring silver centers, which are separated by 3.412(5) Å. The solvate water oxygen atom and the exocyclic C=O oxygen atom belonging to neighbor-

© 2007 NRC Canada

Fig. 5. View of the 4-methylcarboxysydnone-3-hydroxylate anion and the silver cation in **3**·(1/2)H_2O. H atoms are not shown and the thermal ellipsoids are drawn at the 50% probability level.



Scheme 1. Proposed mechanism for the formation of sydnone *N*-oxides from the addition of NO to dimethylmalonate.



ing dimers interact with each other through hydrogen bonding with the associated O1W···O3 interatomic distance and the O1W-H1W···O3 bond angle being 2.903(4) Å and 157(7)°, respectively.

The key metric parameters for all three available sydnone *N*-oxides are contrasted with those for the *N*-arylsydnones in Table 6. A common feature in all three structures is the similarity of the core ring structure not only in the three *N*-oxide salts but also between the *N*-oxides and the *N*-arylsydnones. Remarkably, as reflected in the diffraction results, the bonding in the sydnone core in these compounds is not significantly affected by the substituents at either C1 or N2. Within the limits of interpretation imposed by the estimated standard deviations, the major change seen for the *N*-oxides is in the value of C2–O1, the intracyclic C–O bond, which is significantly shorter for the *N*-oxides. Comparing the dianion in **2** with the monoanions in **1** and **3**, there is a trend towards lengthening of the N–N and the exocyclic C–O bonds, while the C–C bond is slightly shorter.

Discussion

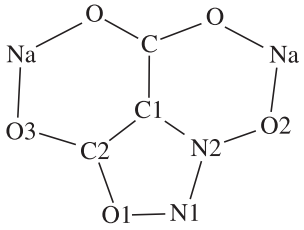
The surprisingly facile base-mediated reaction of nitric oxide and dimethylmalonate is one of the few that returns a product with a trans (*E*) arrangement of the ONNO framework (15, 33, 34). A common feature of these and other (35–37) exceptions is their ability to cyclize or ring-close to give a stable NNO-containing heterocyclic product; they also have available low energy transition states that allow for fac-

© 2007 NRC Canada

Table 7. Comparison of experimental and theoretically calculated (B3LYP/6311++G**) metric parameters for ground-state geometries of sydnone dianion and derivatives.

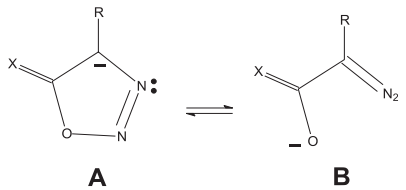
Bond	Observed in **2** ($2K^+$)	Dianion	Disodium salt[a]	Diprotonated (**C**)
C1-N2	1.377(3)	1.367 15	1.394 31	1.393 72
N1-N2	1.342(3)	1.333 53	1.300 52	1.308 73
N2–O2	1.257(3)	1.280 67	1.283 45	1.255 6
N1–O1	1.390(3)	1.412 13	1.388 57	1.420 45
C1–C2	1.384(4)	1.408 79	1.410 98	1.364 48
C2–O3	1.256(3)	1.235 88	1.238 96	1.255 6
C2–O1	1.334(3)	1.410 04	1.381 1	1.308 73

[a]Metric parameters are from the ground-state optimized structure corresponding to the water-free neutral disodium salt shown immediately following the footnote.



ile *Z* to *E* isomerization. In the case of NO addition to dimethylmalonate, we hypothesized that initial *Z* addition followed by deprotonation, isomerization, and finally ring-closing condensation would account for the observed product (Scheme 1) (15). We have recently made similar observations for the diazeniumdiolates derived from *i*-$PrNH_2$ (33, 34). An alternative mechanism with stepwise addition of nitric oxides has recently been theoretically evaluated (38) and we note that there remains considerable interest in the mechanistic details of these reactions (39, 40).

However the sydnone *N*-oxide products that result from these reactions are interesting and novel heterocycles in their own right, with the combination of the delocalized negative charge and the *N*-oxide group being particularly important features. Heterocycle *N*-oxides often display remarkably different chemistry from the original heterocycle. In this case, N-oxygenation allows for the isolation of the 1,2,3-oxadiazole heterocycle. Unsubstitued N3 sydnones are known as reactive intermediates that are difficult to isolate (2, 41). In general, this is believed to be due to the position of the equilibrium between the heterocycle **A** and its ring-opened valence tautomer, the diazoketone **B**. Thus, the instability may be due to the ease of elimination of nitrogen or nitrous oxide from the putative heterocycle **A** or **B**. We are aware of only a single prior report of a sydnone *N*-oxide related to **1**–**4** in the literature, but this corresponds to an unsaturated ring resulting from the addition of nitrosyl chloride to 2,5-dimethyl-2–4-hexadiene (37). Since our initial communication on the results in this area, this family of heterocycles has been expanded to include products from the addition of NO and terminal alkynes (17).



A **B**

During initial studies to elucidate the structure of **2**, the gas phase ground state structures and vibrational spectra of the dianion and its disodium salt were calculated with density function theory with triple zeta quality basis sets. In related calculations of other nitrogen oxide derived anions we have found this level of theory suitable for modelling their ground states, their dynamics, and their vibrational spectra (19). This level of theory has also recently been applied to the related sydnone *N*-oxides derived from terminal acetylenes and nitric oxide (38). As shown in Table 7, the difference between the ground state structures for the dipotassium salt **2** and the gas phase dianion are substantial. These differences are most likely the consequence of strong cation–anion interactions as the observed metric parameters are markedly closer to those calculated for the ground state of the anhydrous disodium salt shown in Tables 7 and 8.

The calculated vibrational frequencies and activities for the ground state of the anion of **1**, the dianion in **2**, and the disodium analog of **2** are listed in Tables S1–S3, respectively.[2] When contrasted with the experimental results in Tables 4 and 5 for the mono- and di-potassium salts, the sensitivity of the predicted vs. experimental bands to the cation identity is quite clear and it correlates with the trends seen for the various salts. In particular, the bands associated with the exocyclic ν(C=O), which has strong bands at 1738 cm^{-1} in the IR for **1**, is predicted to be at 1809 cm^{-1} in the gas phase. In contrast, the gas phase dianion has a pair of strong active IR bands calculated to be at 1714 and 1636 cm^{-1}, while in the anhydrous salt **2** these bands are shifted apart to 1734 and 1619 cm^{-1}. For the disodium analog of **2**, these bands are calculated to be at 1725 and 1635 cm^{-1}, which are surprisingly close to the gas phase values. Although the specific identity of the cation has a modest influence on their energy, incorporation of the material into a lattice will bring new anion–cation interactions, as seen in Fig. 5 for the silver salt **3**.

The unusual reactivity patterns of the these new sydnone *N*-oxides can also be understood in terms of the theoretical

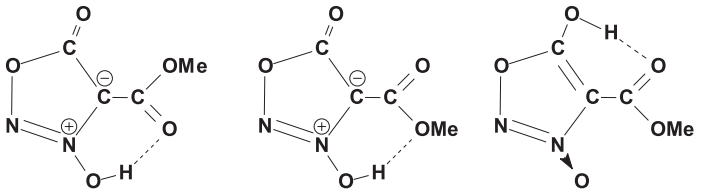
© 2007 NRC Canada

Table 8. Comparison of experimental and theoretically calculated (B3LYP/6-311++G**) metric parameters for ground-state geometries for sydnone monoanion and derivatives.

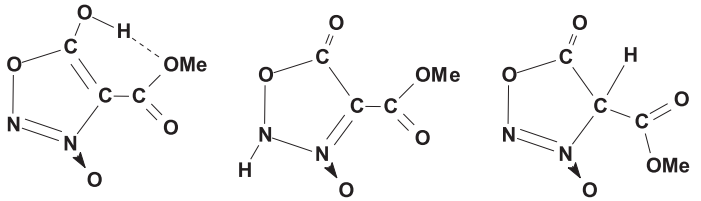
Bond	Observed in **1** (K^+)	Gas phase monoanion	Sodium salt	Monoprotonated (**C**)
C1–N2	1.380(3)	1.395 96	1.394 31	1.393 72
N1–N2	1.324(3)	1.325 58	1.300 52	1.308 73
N2–O2	1.262(3)	1.276 33	1.283 45	1.255 6
N1–O1	1.386(3)	1.409 71	1.388 57	1.420 45
C1–C2	1.405(3)	1.423 88	1.410 98	1.364 48
C2–O3	1.229(3)	1.227 69	1.238 96	1.255 6
C2–O1	1.367(3)	1.415 33	1.381 1	1.308 73

Note: See the numbering scheme shown in Table 6 for atom labels.

Scheme 2. Protonation sites and relative energies for the monoanion.



Structure	**C**	**D**	**E**
Rel. Energy (kcal mol^{-1})	0.0	5.66	5.40



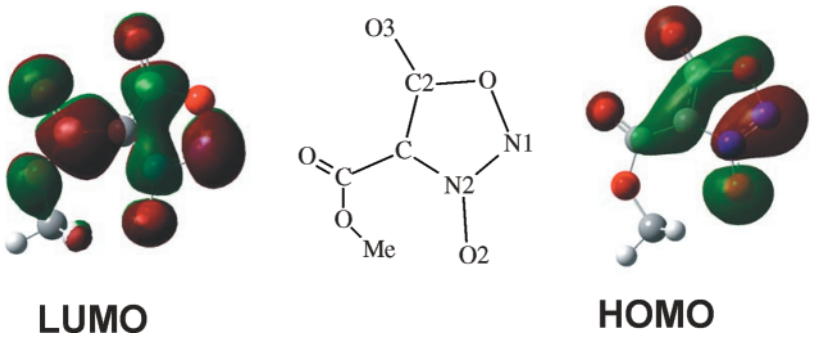
Structure	**F**	**G**	**H**
Rel.Energy (kcal mol^{-1})	8.77	10.12	18.97

density functional calculations. Not too surprisingly the base stability of **1** and **2** is in part due to their anionic charge, which provides some stabilization from nucleophilic attack. This effect would not be seen in the neutral *N*-alkyl and *N*-aryl sydnones, which are both more acid and base sensitive. To understand the profound acid sensitivity in these derivatives we have calculated and optimized the structures shown in Scheme 2, where the various possible protonation sites are shown and ranked by relative energy. With the exception of the highest energy isomers **G** and **H,** all of the isomers have internal H bonds between two oxygens. While strongly hydrogen-bonding solvents might disrupt these intramolecular bonds, the variation of energy would probably not be more than 1 or 2 kcal $mole^{-1}$ (1 cal = 4.184 J) and thus the relative stabilities of the isomers is most likely to be predicted by the gas phase results shown in Scheme 2. In prior calculations for diazenimdiolates we have found that the inclusion of solvent effects with continuum models does not alter the relative energies for related isomers (33). Metric parameters and vibrational frequencies for the optimized neutral structures **C–H** are in the Supplementary data tables, Part I.[2] The lowest energy structure corresponds to N–O protonation, **C**, with the highest energy site being the carbon protonated derivative **H**. Remarkably, N-protonation is predicted to be very unfavored, with **G** being almost 10 kcal mol^{-1} higher in energy than **C**. This follows the general trend for sydnones and diazeniumdiolates, which in general tend not to react or have detectable Lewis acid–base interactions with the nitrogen lone pair. The observation that there is a weak silver–nitrogen interaction in Fig. 5 suggests that new derivatives from the electrophilic addition to nitrogen may be accessible in this system. This reactivity theme will be taken up in subsequent papers.

The debate on the degree of aromaticity of sydnones and how to account for their electronic structures is both sustained and ambiguous (42, 43). Experimentally, these are clearly planar heterocycles with large dipole moments, typically greater than 6 D (2), and they are often termed mesoionic or mesomeric betaines (44). One of their characteristic features has been suggested by Simas et al. (43) to be that the "electrons and charges are delocalized over different regions separated by single bonds. Furthermore, the carbon-

© 2007 NRC Canada

Fig. 6. Frontier orbitals for the anion in **1**[$MeO_2CCC(O)N_2O$]$^-$, B3LYP//6–311++G**. Both are out of plane π orbitals.



substituted side chain is associated with the HOMO whereas the nitrogen substituent is associated with the LUMO". While these observations rationalize the observed high dipoles and the marked 1,3-dipolarophile reactivity of sydnones, they do not account for the bond length trends observed for *N*-alkyl sydnones in general or in the sydnone *N*-oxides described here. In particular, the C1–N2, N1–O1, and C2–O2 bonds in Table 6 are all shorter than the corresponding single bonds. The applicability of the Simas criteria quoted above for the sydnone *N*-oxides is also suspect, as an inspection of the frontier orbitals in Fig. 6 reveals. Although the HOMO does indeed have an overlapping interaction with its side chain, the LUMO is diffuse and not entirely localized to areas of "large positive π charge" with the two regions separated by "single bonds" as suggested for *N*-alkylsydnones.

Although aromaticity and its chemical consequences remain important themes of research, and there have been many important contributions to understanding its role in heterocycles (45, 46), important recently developed tools in understanding and gauging aromaticity in unusual compounds such as these sydnone *N*-oxides are the nuclear independent chemical shift (NICS) methods, as described by Schleyer and co-workers (47). It is widely expected that sydnones have low aromaticity with a recent text listing a value of 17% aromaticity with respect to benzene (48). However, when NICS methods are used to calculate ring currents for the anion in **1** and the dianion in **2**, we find that their respective NICS(0) and NICS(1) values are –9.5 and –5.19 for **1** and –10.1 and –5.9 for **2**. To determine the influence of ion pairing on these calculated NICS values we performed the computation with sodium cations included in the crystallographically determined potassium positions for **1** and **2**. For the monosodium salt corresponding to **1**, the NICS(0) and NICS(1) values are 9.5 and 7.1, while for the disodium salt of **2** these values are not much changed at 9.5 and 5.19. These small changes in NICS with inclusion of ion interactions are similat to those found for other alkalilmetal salts of the boralkanyl anions (49). The NICS values also contrast with those values for benzene of 8 and –10.2 (47) and those we calculate for 3,4-dimethylsydnone, –9.4 and –7.0. These same NICS methods calculate chemical shifts for the ring carbons in the monoanion in **1** to be 171.2 and 100.8 ppm and for the dianion of **2** to be 175.6 and 108.0 ppm. The experimental values are 171.0 and 98.5 ppm for **1** in $CDCl_3$ and 172.2 and 101.7 ppm for **2** in D_2O, so there is good agreement between theoretical predictions and experiment, in this case. Clearly, NICS methods suggest that there is significant aromaticity in these systems and the challenge is to unambiguously determine the chemical consequences of its presence.

Conclusion

The sydnone *N*-oxides form a new class (48) and new synthetic approach to heterocycles with a 1,2,3-oxodiazole core. In contrast with the known *N*-alkyl and *N*-aryl sydnones, the *N*-oxides share similar structures and spectroscopic properties but are markedly less reactive. These anions have a potentially rich coordination chemistry and in this paper the preparation and characterization of two new salts with silver, **3**, and $N(n\text{-}Bu)_4$, **4**, cations are described. Vibrational spectroscopy is a useful tool for their characterization as many of their bands are strongly IR and Raman active. Descriptions of the bonding in these derivatives remains a fundamental theoretical challenge with one of principal unsolved problems being how do we account for their stability in terms of a bonding description for the heterocycle. Initial theories to account for their relatively weak and diminished aromaticity suggests that other factors may be responsible for their stability, but NICS calculations suggest this may not be the case. Aromaticity is of course a concept initially rooted in our understanding of electron precise rings. Sydnones are dominated by electron-rich elements for which conventional descriptions of aromaticity may not be the most appropriate.

Acknowledgment

We gratefully acknowledge Natural Sciences and Engineering Research Council of Canada (NSERC) for support in the form of a discovery grant to DSB, the Canada Research Chairs and Canadian Funds for Innovation, and the Canadian Institues of Health Research (CIHR) for a Chemical Biology Fellowship to Dr. Inna Perepichka.

References

1. C.N. Kuo, S.P. Wang, M.Y. Yeh, and H.J. Tien. J. Chin. Chem. Soc. **39**, 641 (1992).
2. L.B. Clapp. *In* Comprehensive heterocyclic chemistry I. Vol. 4. *Edited by* A.R. Katrizky, C.W. Rees, and E.F.V. Scriven. Pergamon Press, London, UK. 1984. p. 365.
3. V.G. Yashunskii and L.E. Kholodov. Russ. Chem. Rev. **49**, 54 (1980).

© 2007 NRC Canada

4. F.H.C. Stewart. Chem. Rev. **64**, 129 (1964).
5. H. Hidaka, I. Matsumoto, J. Yoshizawa, S. Kotani. Eur. Patent EP0073345, 03 September 1983.
6. M. Boes and W. Fleischhacker. Pharm. Unserer Zeit, **13**, 51 (1984).
7. N. Grynberg, R. Gomes, T. Shinzato, A. Echevarria, and J. Miller. Anticancer Res. **12**, 1025 (1992).
8. K. Takagi, M. Shiro, S. Takeda, and N. Nakamura. J. Am. Chem. Soc. **114**, 8414 (1992).
9. J. Hasek, P.T. Beurskens, J. Obrda, S. Nespurek, H. Schenk, K. Goubitz, K. Huml, and J.D. Schagen. Coll. Czech. Chem. Commun. **50**, 1764 (1985).
10. R. Improta, F. Santoro, C. Barbier, F. Giordano, and G. Del Re. THEOCHEM, **433**, 291 (1998).
11. T.J. King, P.N. Preston, J.S. Suffolk, and K. Turnbull. J. Chem. Soc. Perkin Trans. 2, 1751 (1979).
12. V.A. Kozinskii, O.V. Zelenskaya, S. Bruckner, and L. Malpezzi. J. Heterocycl. Chem. **21**, 1889 (1984).
13. W.-F. Kuo, I.T. Lin, S.-W. Sun, and M.-Y. Yeh. J. Chin. Chem. Soc. **48**, 769 (2001).
14. J.M. Fan, Y. Wang, and C.H. Ueng. J. Phys. Chem. **97**, 8193 (1993).
15. N. Arulsamy and D.S. Bohle. Angew. Chem. Int. Ed. **41**, 2089 (2002).
16. W. Traube. Ber. Dtsch. Chem. Ges. **28**, 1785 (1895).
17. T. Sugihara, K. Kuwahara, A. Wakabayashi, H. Takao, H. Imagawa, and M. Nishizawa. Chem. Commun. (Cambridge), 216 (2004).
18. N. Arulsamy, D.S. Bohle, A.L. Korich, and K.R. Mondanaro. Tetahedron Lett. **44**, 4267 (2003).
19. N. Arulsamy and D.S. Bohle. J. Am. Chem. Soc. **123**, 10860 (2001).
20. XSCANS [computer program]. Version 2.31. Bruker AXS, Inc., Madison, Wis. 1993.
21. G.M. Sheldrick. University of Göttingen, Göttingen, Germany, 1997.
22. SHELXTL [computer program]. Version 5.10. Bruker AXS, Inc., Madison, Wis. 1997.
23. C.C. Roothaan. Rev. Mod. Phys. **23**, 69 (1951).
24. A.D. Becke. J. Chem. Phys. **98**, 5648 (1993).
25. C. Lee, W. Yang, and R.G. Parr. Phys. Rev. B, **37**, 785 (1988).
26. M.J. Frisch, G.W. Trucks, H.B. Schlegel, G.E. Scuseria, M.A. Robb, J.R. Cheeseman, V.G. Zakrzewski, J.A. Montgomery, R.E. Stratmann, J.C. Burant, S. Dapprich, J.M. Millam, A.D. Daniels, K.N. Kudin, M.C. Strain, O. Farkas, J. Tomasi, V. Barone, M. Cossi, R. Cammi, B. Mennucci, C. Pomelli, C. Adamo, S. Clifford, J. Ochterski, J.A. Petersson, P.Y. Ayala, Q. Cui, K. Morokuma, D.K. Malick, A.D. Rabuck, K. Raghavachari, J.B. Foresman, J. Cioslowski, J.V. Ortiz, B.B. Stefanov, G. Liu, A. Liashenko, P. Piskorz, I. Kamaromi, R. Gomperts, R.L. Martin, D.J. Fox, T. Keith, M.A. Al-Laham, C.Y. Peng, A. Nanayakkara, C. Gonzalez, M. Challacombe, P.M.W. Gill, B.G. Johnson, W. Chen, M.W. Wong, J.L. Andres, M. Head-Gordon, E.S. Replogle, and J.A. Pople. Gaussian [computer program]. Gaussian Inc., Pittsburgh, Penn. 1998.
27. N. Arulsamy and D.S. Bohle. Acta Crystallogr. Sect. E. **61**, m930 (2005).
28. L.K. Keefer, J. Flippen-Anderson, C. George, A.P. Shanklin, T.M. Dunams, D. Christodoulou, J.E. Saavedra, E.S. Sagan, and D.S. Bohle. Nitric Oxide, **5**, 377 (2001).
29. J.C. Earl, J.W. le Fevre, A.G. Pulford, and A. Walsh. J. Chem. Soc. 2207 (1951).
30. H.U. Daeniker and J. Druey. Helv. Chim. Acta, **40**, 918 (1957).
31. Y.G. Borod'ko and Y.K. Syrkin. Opt. Spektrosk. **11**, 261 (1961).
32. J. March. Advanced organic chemistry. 2nd ed. McGraw-Hill, New York. 1977. pp. 22–28.
33. Y.-N. Wang, D.S. Bohle, C.L. Bonifant, G.N. Chmurny, J.R. Collins, K.M. Davies, J.R. Deschamps, J.L. Flippen-Anderson, L.K. Keefer, J.R. Klose, J.E. Saavedra, D.J. Waterhouse, D. Parrish, and J. Ivanic. J. Am. Chem. Soc. **127**, 5388 (2005).
34. J.E. Saavedra, D.S. Bohle, K.N. Smith, C. George, J.R. Deschamps, D. Parrish, J. Ivanic, Y.-N. Wang, M.L. Citro, and L.K. Keefer. J. Am. Chem. Soc. **126**, 12880 (2004).
35. K.A. Ogloblin, N.V. Girbasova, and A.A. Potenkhin. Russ. J. Org. Chem. **9**, 2252 (1973).
36. S.F. Nelsen, M.F. Teasley, and M. Kaftory. J. Org. Chem. **53**, 5930 (1988).
37. A.B. Nelson. Diss. Abstr. Int. B, **38**, 1721 (1977).
38. Y. Wu, Y. Xue, D. Xie, and G. Yan. J. Org. Chem. **70**, 5045 (2005).
39. M.D. Lim, I.M. Lorkovic, and P.C. Ford. Inorg. Chem. **41**, 1026 (2002).
40. Y.-L. Zhao, M.D. Bartberger, K. Goto, K. Shimada, T. Kawashima, and K.N. Houk. J. Am. Chem. Soc. **127**, 7964 (2005).
41. T.L. Gilchrist and P.M. O'Neill. *In* Comprehensive heterocycle chemistry II. Vol. 5. *Edited by* A.R. Katrizky, C.W. Rees, and E.F.V. Scriven. Pergamon Press, London, UK. 1996. pp. 165–178.
42. A. Katritzky. Chem. Ind. (London), 521 (1955).
43. A.M. Simas, J. Miller, and P.F.A. Filho. Can. J. Chem. **76**, 869 (1998).
44. W.D. Ollis and C.A. Ramsden. Adv. Heterocycl. Chem. **19**, 1 (1976).
45. B.Y. Simkin, V.I. Minkin, and M.N. Glukhovtsev. Adv. Heterocycl. Chem. **56**, 303 (1991).
46. C.W. Bird. Tetrahedon, **41**, 1409 (1985).
47. Z. Chen, C.S. Wannere, C. Corminboeuf, R. Puchta, and P.v.R. Schleyer. Chem Rev. **105**, 3842 (2005).
48. A. Katritzky and A.F. Pozharskii. Handbook of heterocyclic chemistry. 2nd ed. Pergamon Press, Oxford, UK. 2000.
49. W. Loesslein, H. Pritzkow, P.v.R. Schleyer, L.R. Schmitz, and W. Siebert. Eur. J. Inorg. Chem. 1949 (2001).

© 2007 NRC Canada

Rhenium and manganese modified activated carbon as catalyst for methanol decomposition

T. Tsoncheva, S. Vankova, O. Bozhkov, and D. Mehandjiev

Abstract: Bicomponent manganese and rhenium modified activated carbon materials, prepared by different methods, are studied and compared with the corresponding monocomponent materials as catalysts in methanol decomposition to CO and hydrogen. The best catalytic activity and stability is observed for the sample obtained by simultaneous deposition of Mn and Re precursors. The complex character of the catalytic active centre, including manganese and rhenium irons in various oxidative states, is discussed. The determining role of the Mn(II) ions in the improvement of the catalytic properties is assumed.

Key words: rhenium, manganese, activated carbon, methanol decomposition.

Résumé : On a étudié divers matériaux à deux composés formés de charbon activé modifié par du manganèse et du rhénium qui ont été préparés par diverses méthodes et on a comparé ces propriétés à celles des matériaux correspondants à un composant aux fins de leur action comme catalyseurs pour la décomposition du méthanol en CO et en hydrogène. La stabilité et l'activité catalytique les plus élevées sont observées avec l'échantillon qui a été obtenu par le dépôt simultané des précurseurs Mn et Re. On discute du caractère complexe du centre d'activité catalytique, y compris les sels de manganèse et de rhénium des atomes de fer dans divers états d'oxydation. On fait l'hypothèse que les ions de Mn(II) jouent un rôle déterminant dans l'amélioration des propriétés catalytiques.

Mots-clés : rhénium, manganèse, charbon activé, décomposition du méthanol.

[Traduit par la Rédaction]

Introduction

Catalysis plays an important role in the development of clean energy conversion processes (1–3). The main interests include improving energy conversion efficiencies, minimizing emissions, and using "renewable" sources of clean energy (4–6). Among various possibilities in this regard, methanol decomposition to CO and hydrogen attracts considerable interest as an economically viable and sustainable energy conversion process (7–12). It has been reported that decomposed methanol could be a clean and effective fuel for a number of stationary and mobile installations such as vehicles, fuel cells, and gas turbines. The process is also important as a reversible chemical reaction that can be used for the storage of hydrogen. Finally, methanol decomposition is a highly endothermic reaction (ΔH° = +128 kJ/mol), which is why it is well-studied to recover waste heat and (or) to increase the heating value of methanol fuel in combustion engines. However, the wide usage of methanol decomposition for various applications requires the development of highly effective and low cost catalysts that work at lower temperatures with high stability. The main contemporary trends in this area address the development of catalysts with new designs and minimal noble metal loading. Recent progress points to the tailoring of nanoscale metal–metal oxide materials with regulated particle size and morphology (13–15). A possible method for the preparation and stabilization of such materials is by deposition on various porous supports (16, 17). Among the supports, activated carbon is a preferred carrier because of its well-developed porous structure, high specific surface area, a large number of different surface functional groups, and catalytic inertness (18, 19). On the other hand, bimetallic systems reveal additional ways to expand the family of catalysts (14, 16, 20, 21). Both metallic and nanosize effects could be a major sources of changes in the electronic structure of the active phase, producing catalytic properties.

Various materials, usually based on copper and noble metals, have been studied as suitable catalysts for methanol decomposition (7, 9, 10). However, the low catalytic stability and low selectivity due to methane formation were mentioned as the main problems for the former and the latter materials, respectively. At the same time, the data on the catalytic behaviour of manganese-based materials in methanol decomposition are rather insufficient (22–27). Its promotion effect on copper-based catalysts has been established (23, 24, 26). In our previous study, we demonstrated higher catalytic stability but lower activity, in comparison with their copper analogue, in methanol decomposition for manganese

Received 2 November 2006. Accepted 2 January 2007. Published on the NRC Research Press Web site at http://canjchem.nrc.ca on 20 February 2007.

T. Tsoncheva.[1] Institute of Organic Chemistry, Bulgarian Academy of Sciences, Acad. G. Bonched Str., bl. 9, 1113 Sofia, Bulgaria.
S. Vankova. Department of Chemistry, University of Sofia, 1000 Sofia, Bulgaria.
O. Bozhkov and D. Mehandjiev. Institute of General and Inorganic Chemistry, Bulgarian Academy of Sciences, Acad. G. Bonchev Str., bl.11, 1113 Sofia, Bulgaria.

[1]Corresponding author (e-mail: tsoncheva@orgchm.bas.bg).

 doi:10.1139/V07-004 © 2007 NRC Canada

Table 1. Samples composition, BET surface areas, and intrinsic rates of conversion at different temperatures for Re and (or) Mn supported on AC materials.

Sample	BET (m^2/g)	Chemical composition (wt%)		Intrinsic rate of conversion (mol g^{-1} h^{-1})[a]		
		Mn	Re	600 K	625 K	650 K
Re/AC	752	—	1.5	0.46	0.53	0.52
Mn/AC	448	5.1	—	0.23	0.47	1.17
ReMn(1:3)/AC-N	282	5.1	1.5	0.79	1.11	1.29
ReMn(1:3)/AC-R	269	5.1	1.5	0.23	0.61	1.01
ReMn(1:3)/AC-S	435	5.1	1.5	1.22	1.32	1.33
ReMn(1:1)/AC-S	406	2.5	2.5	1.09	1.18	1.64

[a]All values to be multiplied by 10^5

supported on activated carbon materials (27). Recently, we also found that Re additives have beneficial effects on catalytic stability of copper-activated carbon materials (28).

Here we focus our attention on the role of Re additives on the catalytic behaviour of manganese supported on activated carbon materials in methanol decomposition. We also attempt to elucidate the complex character of the active center of the catalyst.

Experimental

Materials

Activated carbon (commercial product derived from apricot pits) with specific surface area of 910 m^2/g and pore volume of 0.64 cm^3/g was used as a support (29). Three methods were applied for metal oxide deposition using a modified incipient wetness technique by spraying the support with the corresponding manganese and (or) rhenium precursor.

Method 1

Activated carbon (AC) (2.0 g) was treated with a solution of $Mn(NO_3)_2$ (7.8%). After drying at 383 K for 1 h, the samples were heated at 573 K for 6 h (heating rate was 0.6 K/min) in vacuum. The prepared material was denoted as Mn/AC. The obtained material was then treated with an aq. solution of NH_4ReO_4 (1%). The sample was dried at 383 K for 1 h and then treated at 573 K for 6 h (heating rate was 0.6 K/min). The sample was denoted as ReMn(1:3)/AC-N.

Method 2

AC (2.0 g) was treated with an aq. solution of NH_4ReO_4 (1%). The sample was dried at 383 K for 2 h and then treated at 573 K for 6 h (heating rate was 0.6 K/min). The prepared material was denoted as Re/AC. The material was then treated for 1 h with solution of $Mn(NO_3)_2$ (7.8%). After drying at 383 K for 1 h, the sample was heated at 573 K for 6 h (heating rate was 0.6 K/min) in vacuum. The obtained material was denoted by ReMn(1:3)/AC-R.

Method 3

AC (2.0 g) was treated with a mixture of aq. solutions of NH_4ReO_4 and $Mn(NO_3)_2$ (Re–Mn 1:3). After drying at 383 K for 1 h, the sample was heated at 573 K for 6 h (heating rate was 0.6 K/min) in vacuum. The obtained material was denoted by ReMn(1:3)/AC-S.

A material denoted by ReMn(1:1)/AC-S with an Re–Mn ratio of 1:1 was also obtained by method 3 and was used as a reference sample in the study.

Table 1 presents data for the phase composition and specific surface area for Re and Mn supported on activated carbon materials that were obtained by different sequence of metal oxides deposition.

Methods of investigation

Textural characteristics were determined by low-temperature (77.4 K) nitrogen physisorption. The specific surface area was estimated by the BET method. Mn content in the samples was determined by atomic absorption technique using a Pye Unicam SP90V instrument. Rhenium content in the samples was determined by vacuum thermal extraction followed by quantitative kinetic analysis, based on the catalytic activity of Re to the *N*,*N*-dimethyldithiooxamide (DMDTO) reduction with $SnCl_2$ in alkaline medium. An alkaline extraction of rhenium from the activated carbon, followed by the quantitative kinetic determination, was also done (30, 31). The magnetic measurements were performed with a Faraday type magnetic balance in the temperature range of 298–473 K. EPR spectra were done with a ERS 22Q spectrometer at 100–400 K. XP spectra were performed using an ESCALAB MkII (VG Scientific) instrument. X-ray diffraction powder patterns were obtained on a Philips APD-15 diffractometer equipped with Cu Kα radiation source and graphite monochromator.

Catalytic test

The catalytic experiments were carried out in a flow reactor with a methanol partial pressure of 1.57 kPa, WHSV (weight hourly space velocity) of 1.5 h^{-1}, and under thermoprogrammed conditions at a heating rate 2 K/min. Some experiments were also done under isothermal conditions at 650 K. The gas chromatographic analysis was performed online using a Porapak Q and molecular sieve columns. The results were calculated using the method of absolute calibration. A carbon-based material balance was done. Before the catalytic test, the samples were pretreated for an hour at 373 K in argon.

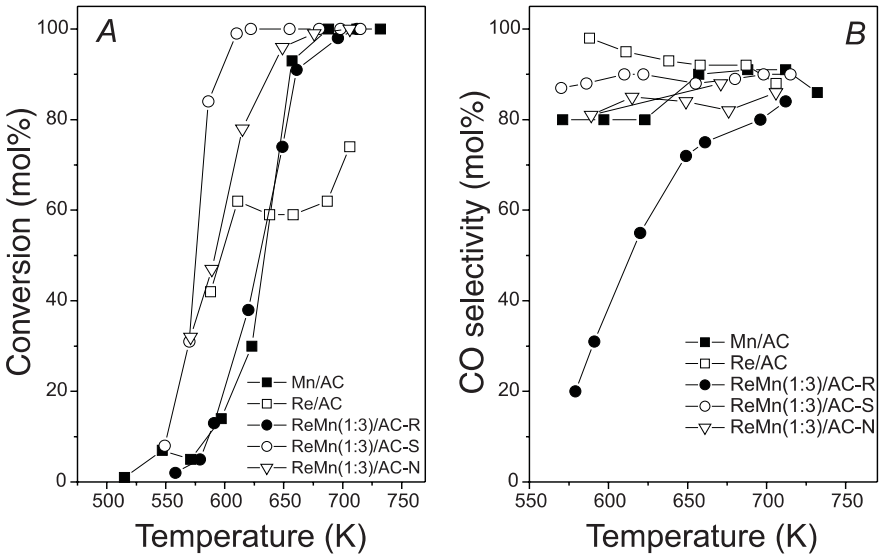
Results and discussion

Methanol decomposition on various manganese and rhenium modified materials

Figure 1 presents data on the catalytic activity (Fig. 1*A*)

© 2007 NRC Canada

Fig. 1. Methanol conversion (*A*) and CO selectivity (*B*) vs. temperature on various samples containing Mn and (or) Re.

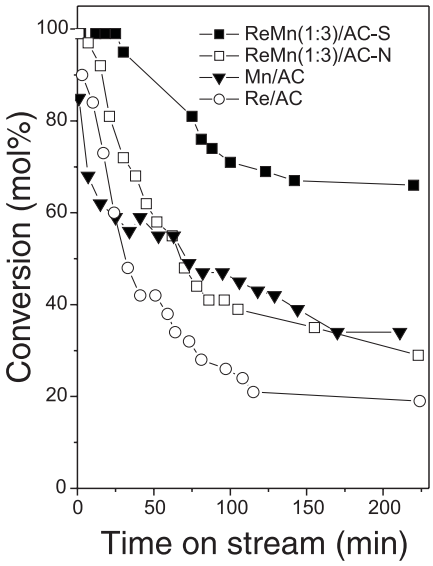


and CO selectivity (Fig. 1*B*) in methanol decomposition for various Re and (or) Mn supported on activated carbon material. Monocomponent Re- or Mn-modified samples exhibit catalytic activity above 550 and 600 K, respectively, CO being the main carbon-containing product. Methane is also registered as a by-product and its yield is higher for Mn/AC. At the same time, the catalytic behaviour of all bicomponent Re and Mn materials differs significantly from their monocomponent analogues and essentially depends on the order of metals deposition. The highest catalytic activity, combined with high selectivity to CO, is observed for the sample obtained by simultaneous deposition of Re and Mn. As a whole, the catalytic activity for both Re–Mn materials, prepared by consecutive deposition of various active components, is lower than ReMn(1:3)/AC-S and it is combined with significant differences in the CO selectivity depending on the order of their deposition (Fig. 1*B*). ReMn(1:3)/AC-S is also characterized by significantly higher catalytic stability under isothermal conditions in comparison with all other studied materials (Fig. 2). The catalytic behaviour of bicomponent samples depends also on the Re–Mn ratio and better catalytic activity above 570 K is achieved with ReMn(1:3)/AC-S than with ReMn(1:1)/AC-S (Fig. 3). The intrinsic rates of conversion for the studied materials at different temperatures are presented in Table 1. As can be seen, a well-defined and the most pronounced tendency for catalytic activity increase at lower temperature, in comparison with Re/AC and Mn/AC, is found only for ReMn(1:3)/AC-S.

Physicochemical characterization of manganese and rhenium modified materials

Despite the variations in the catalytic behaviour of the samples (Figs. 1–3, Table 1), their XRD patterns (not shown) show reflections of almost the same intensity, corresponding to a well-crystallized Mn_3O_4 phase. No reflections of rhenium or other manganese oxides are found. To clarify the catalytic effects described earlier, more precise magnetic measurements combined with EPR and XPS studies of the samples were also performed.

Fig. 2. Methanol conversion vs. time on stream at 650 K for selected samples containing Mn and (or) Re.



Magnetic measurements

Table 2 displays data for effective magnetic moments (μ_{eff}) and Weiss constants (Θ) for the Re–Mn materials obtained by the different preparation methods. Their calculated correlation constants (*R*) are similar and are characterized by high values (0.9923–0.9938), which indicates the preservation of the Curie–Weiss law. The experimental values of μ_{eff}, when compared with the corresponding theoretical ones for the separate ions (32, 33), could be evidence for the presence of Mn ions in different oxidative states. The higher negative values of Θ combined with high values of μ_{eff}, which are observed for ReMn(1:3)/AC-S, could be ascribed to the higher content of Mn(II) in this sample. On the other hand, the predominant presence of Mn ions in higher oxidative states, Mn(III) and Mn(IV), could be assumed for the samples formed by the consecutive deposition of rhenium and manganese. Moreover, based on the observed close val-

© 2007 NRC Canada

Table 2. Effective magnetic moments (μ_{eff}), Weiss constants (Θ), and possible calculated combinations of Mn ions for the studied samples.

			Possible combinations of Mn ions (%)					
Sample	μ_{eff} (BM)	Θ (K)	Mn(II)	Mn(IV)	Mn(III)	Mn(IV)	Mn(II)	Mn(III)
ReMn(1:3)/AC-N	4.40	–83	27	73	55	45	Not calcd.	
ReMn(1:3)/AC-R	4.58	–77	34	68	70	30	Not calcd.	
ReMn(1:3)/AC-S	5.66	–212	81	19	Not calcd.	65	35	
Mn/AC	5.46	–286	74	26	Not calcd.	56	44	

Fig. 3. Methanol conversion (empty circles) and CO selectivity (full circles) for samples with various Mn–Re ratios, obtained by simultaneous deposition of the precursors.

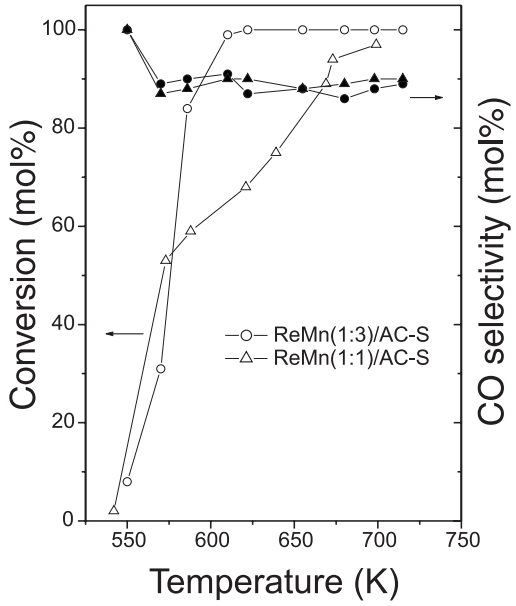
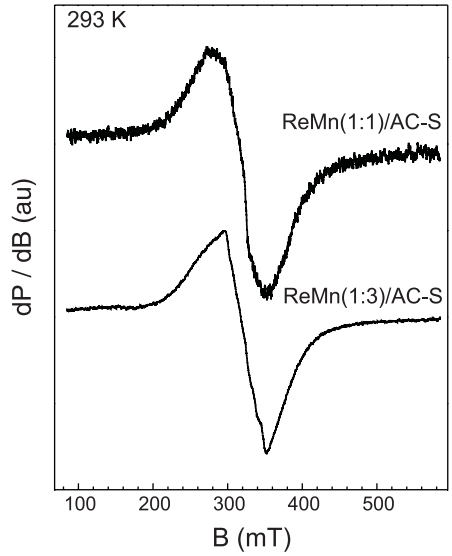


Fig. 4. EPR spectra of samples with various Re–Mn ratios obtained by simultaneous deposition of the precursors.



ues of μ_{eff} and Θ for these samples, less pronounced differences in the Mn ion states depending on the order of Mn and Re deposition could be assumed. The lower value of μ_{eff} observed for ReMn(1:1)/AC-S (μ_{eff} = 4.07 BM), compared with that for ReMn(1:3)/AC-S (μ_{eff} = 5.66 BM), could be an indication of a decrease in the Mn(II) ion content with an Re–Mn ratio increase.

EPR study

EPR measurements for the bicomponent samples with different Re–Mn ratios confirm the magnetic results for the presence of Mn(II) and of Mn(IV) ions, probably in interaction between themselves or with Re species. The room temperature EPR spectra (Fig. 4) show a broad unstructured resonance of about 70 mT in width, which could be ascribed to the predominant presence of antiferomagnetically connected Mn(II) and (or) Mn(IV) ions (34–36), the former being present in higher amounts in ReMn(1:3)/AC-S than in ReMn(1:1)/AC-S. A very broad and low signal with high value of *A*, constant of fine interaction, probably belonging to rhenium in an oxidative state lower than Re(VII) is detected for Re/AC (28). A very slight indication of a sextet in the EPR spectrum (g = 2.002 and *A* = 9.4 mT), typical of isolated Mn(II), is also observed for ReMn(1:3)/AC-S.

XPS measurements

Figure 5 presents $Mn2p_{3/2}$ (Fig. 5*A*) and Re4f (Fig. 5*B*) photoelectron lines for selected materials, prepared by different procedures. Data for binding energies (BEs) are collected in Table 3. The BE of the principal $Mn2p_{3/2}$ peak for both samples is ~642.2 eV, which may correspond mainly to MnO_2. However, according to the literature data (36) a complete and large overlapping of the $Mn2p_{3/2}$ peak position dominates between MnO_2 and Mn_2O_3 on the one hand and Mn_3O_4 and Mn_2O_3 on the other. Thus, determining the manganese oxidation state on the basis of only the $Mn2p_{3/2}$ peak position is difficult. The primary chemical state of Re in these samples features a doublet at 46.2 and 48.6 eV, which could be assigned to Re $4f_{7/2}$ and Re $4f_{5/2}$ spin-orbit components. According to ref. 37, the spectrum of pure Re_2O_7 also exhibits two less distinct lines at 46.9 and 49.3 eV. According to ref. 37 and the refs. cited therein, the BEs of Re $4f_{7/2}$ for the metal Re and Re(VI) ions differ signficantly and are 40.5 and 44.9 eV, respectively. It was also established that the BEs depend upon both the formal oxidative state and on the nearest neighbours of the Re atoms (38). At the same time, in some XPS studies on supported metal particles, the BEs were found to be particle size dependent, increasing by ~0.5 eV as the particle size decreased from 5 to 1 nm (39, 40). Here, the observed lower values of BEs for Re $4f_{7/2}$ compared with that of bulk Re_2O_7 may be explained by the different charging of the activated carbon support vs. the unsupported oxide. They could be also attributed to Re having

© 2007 NRC Canada

Fig. 5. XPS of ReMn(1–3)/AC-S and ReMn(1–3)/AC-R for (*A*) Mn2p and (*B*) Re4f photoelectron lines.

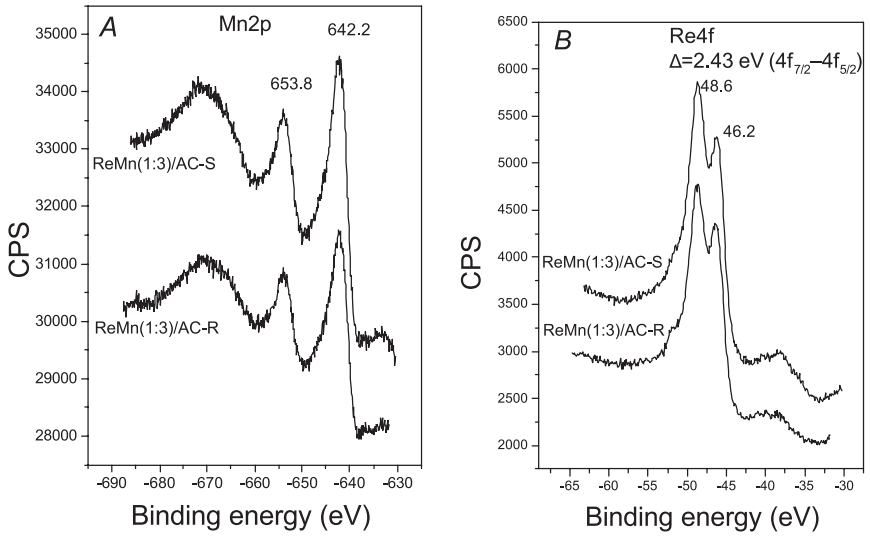


Table 3. Binding energies of C 1S, O 1S, Re 4f, and Mn 2p lines for selected Re–Mn supported on AC samples.

Sample	C1S (eV)	O1S (eV)	Re4f (eV)	Mn2p (eV)	Mn–Re ratio (%)
ReMn(1:3)/AC-S		530.5			
	285	532.6	46.2	642.2	1.867
		535.6	48.6		
ReMn(1:3)/AC-R		530.7			
	285	532.8	46.2	642.2	1.500
		536.3	48.6		

a slightly lower oxidative state than +7 because of the partial reduction of Re during the preparation of the samples (41). The existence of additional interactions between Re and Mn ions is also not excluded. The calculated atomic ratios for the samples show higher surface Mn content for the sample prepared by simultaneous metals deposition (Table 3). This could be due to the surface enrichment with Mn or smaller particles size in the case of ReMn(1:3)/AC-S, and it is an additional indication of the influence of Re on the manganese state.

Concluding remarks

Bicomponent Re and Mn supported on activated carbon materials exhibit good catalytic stability and high activity in methanol conversion to CO and hydrogen at lower temperatures compared with the corresponding monocomponent materials. The observed effects depend strongly on the procedures used to modify the activated carbon; e.g., loading of Re and Mn simultaneously produces a better sample. The combined magnetic, EPR, and XPS measurements for all studied Re–Mn materials show the presence of Mn and Re ions in various oxidative states, probably interacting between themselves. Based on the theoretical and experimentally obtained values of μ_{eff}, some calculations for the possible manganese ion combinations in the catalytic active centre for the studied materials were performed (Table 2). It can be seen that the sample with better catalytic activity and stability (ReMn(1:3)/AC-S) is characterized by a higher amount of Mn(II) combined in active centers with Mn(III) and (or) Mn(IV) ions. The assumption of the significant role of Mn(II) ions in methanol decomposition is in accordance with our previous study of monocomponent Mn/AC materials that were prepared from various manganese precursors (27). Their formation seems to be facilitated by the presence of rhenium ions, the effect being most pronounced when simultaneous loading of Re and Mn is applied. The influence of Re is not only due to the increase in manganese dispersion but also probably to additional electronic effects caused by the ability of rhenium to adopt a variety of oxidative states (see the earlier section on XPS measurements).

Acknowledgements

Thanks are due to Assistant Professor Dr. R. Stoyanova for EPR spectra and discussion. Thanks are also due to G. Tyuliev for XPS measurements.

References

1. J.J. Spivey. Catal. Today, 100 171 (2005).
2. R.T Anastas, L.B. Bartlett, M.M. Kirhhoff, and T.C.Williamson. Catal. Today, **55**, 11 (2000).
3. T.G. Kaufmann, A. Kaldor, G.F. Stundz, M.C. Kerby, and L.L. Ansell. Catal. Today, **62**, 77 (2000).
4. Catalysis in C1 chemistry. *Edited by* W. Keim. D. Reidel Publishing Co., Dordrecht, Holland. 1983.
5. J.M. Fox. Catal. Rev.-Sci. Eng. **35**, 169 (1993).

© 2007 NRC Canada

6. National Research Council. Catalysis looks to the future. National Academy Press, Washington, DC. 1992.
7. J. Agrell, B. Lindstroem, L.J Pettersson, and S. Jaras. Catalysis, **16**, 67 (2002).
8. Methanol production and use. *Edited by* W.H. Cheng and H.H. Kung. Marcel Dekker books, New York. 1994. chap. 1.
9. L.J. Pettersson and K. Sjöström. Combust. Sci. Technol. **80**, 265 (1991).
10. W.H. Cheng. Acc. Chem. Res. **32**, 685 (1999).
11. Y. Matsumura, K. Tanaka, N. Tode, T. Yazawa, and M. Haruta. J. Mol. Catal. A: Chem. **152**, 157 2000.
12. M.P. Kapoor and Y. Matsumura. J. Mol. Catal. A: Chem. **178**, 169 (2002).
13. H.H. Kung and M.C. Kung. Catal. Today, **9**7 219 (2004).
14. L. Guczi. Catal. Today, **101**, 53 (2005).
15. P. Suzdalev, V.N. Buravtsev, Y.V. Maksimov, A.A. Zharov, and V.K. Imshennik. J Nanopart. Res. **2**, 485 (2003).
16. A.Y Stakheev and L.M Kustov. Appl. Catal. A, **188**, 3 (1999).
17. A. Taguchi and F. Schüth. Microporous Mesoporous Mater. **77**, 1 (2005).
18. R. Schlögl. Handbook of heterogeneous catalysis. *Edited by* G. Ertl, H. Knözinger, and J. Weitkamp. Wiley-VCH, Weinheim, Germany. 1997. p. 138.
19. F. Rodriguez-Reinoso. Carbon. **36**, 159 (1998).
20. L. Guczi and I. Kiricsi. Appl. Catal. A, **186**, 375 (1999).
21. B. Coq and F. Figueras. J. Mol. Catal. A: Chem. **173**, 117 (2001).
22. R. Zhang, Y. Sun, and S. Peng. Stud. Surf. Sci. Catal. **130**, 2129 (2000).
23. W.H. Cheng. Appl. Catal. A, **130**, 13 (1995).
24. W.H. Cheng, C.Y. Shiau, T.H. Liu, H.L. Tung, J.F. Lu, and C.C. Hsu. Appl. Catal. A, **170**, 215 (1998).
25. D. Mehandjiev, S.Vankova, and T. Tsoncheva. Oxid. Commun. **25**, 441 (2002).
26. T. Tsoncheva, S. Vankova, and D. Mehandjiev. React. Kinet. Catal. Lett. **80**, 383 (2003).
27. S. Vankova, T. Tsoncheva, and D. Mehandjiev. Catal. Commun. **5**, 95 (2004).
28. T. Tsoncheva, S. Vankova, O. Bozhkov, and D. Mehandjiev. J. Mol. Catal. A: Chem. **225**, 245 (2005).
29. V. Minkova, M. Razvigorova, M. Goranova, L. Ljutzkanov, and G. Angelova. Fuel, **70**, 713 (1991).
30. O.D. Bozhkov and L.V. Borisova. J. Anal. Chem. **54**, 10531 (1999).
31. O.D. Bozhkov and L.V. Borisova. Anal. Commun. **33**, 133 (1996).
32. E.E. Mabbs and D.J. Machin. Magnesium and transition metal complexes. Chapman and Hall, London, UK. 1973. p. 152.
33. A. Earnshow. Introduction to magnetochemistry. Academic Press, London, UK. 1968.
34. K.A. Müller, W. Berlinger, K.W. Blazey, and J. Albers. Solid State Commun. **61**, 21 (1987).
35. R. Stoyanova, M. Gorova, and E. Zhecheva. J. Phys. Chem. Solids, **61**, 615 (2000).
36. C.D. Wagner, W.M. Riggs, L.E. Davis, and J.F. Moulder. Handbook of X-ray photoelectron spectroscopy. *Edited by* G.E. Muilenberg. PerkinElmer, Eden Prairie, Minn. 1979.
37. J. Okal, W. Tylus, and L. Kepinski. J. Catal. **22**5 498 (2004).
38. E.S. Shpiro, V.I. Avaev, G.V. Antoshin, M.A. Ryashentseva, and K.M. Minachev. J. Catal. **55**, 402 (1978).
39. T. Huizinga, H.F.J. Van 'T Blik, J.C Vis, and R. Prins. Surf. Sci. **135**, 580 (1983).
40. B.L. Mojet, J.T. Miller, D.E. Ramaker, and D.C. Koningsberger. J Catal. **186**, 373 (1999).
41. A. Cimino, B.A. De Angelis, D. Gazzoli, and M.Valigi. Z. Anorg. Allg. Chem. **460**, 86 (1980).

© 2007 NRC Canada

Biradical radiationless decay channel in adenine and its derivatives[1]

Marek Z. Zgierski, Serguei Patchkovskii, and Edward C. Lim

Abstract: Coupled-cluster calculations of increasing accuracy (approximate doubles: CC2; doubles: EOM-CCSD; connected triples: CR-EOM-CCSD(T)) for CIS-optimized potential energy profiles of adenine and its derivatives indicate that the ultrafast internal conversion of the optically excited $\pi\pi^*$ state occurs through a state switch to a biradical state, which intersects the ground state at a lower energy. The electronic nature of the biradical state is defined by an electronic configuration in which one unpaired electron occupies a π^* orbital confined to the five-membered ring. The second unpaired electron is localized very strongly on a p-type C2 atomic orbital of the six-membered ring. The biradical state minimum has a strongly puckered six-membered ring and a C2–H bond, which is twisted nearly perpendicular to the average ring plane. Consistent with the biradical-mediated internal conversion, the $\pi\pi^*$ state lifetime is extremely short in adenine and 9-methyladenine, which have barrierless crossing to the biradical state. The lifetime is slightly longer in *N*,*N*-dimethyladenine, which has a small barrier for the state switch. In 2-aminopurine the biradical state is found above the $\pi\pi^*$ state, preventing the biradical state switch and dramatically increasing the lifetime. These results, combined with an earlier work on pyrimidine bases, strongly suggest the importance of a direct decay of the doorway $\pi\pi^*$ state via a biradical state switch in the photophysics of DNA, even though the nature of the biradical state is somewhat different in purines and pyrimidines.

Key words: adenine, guanine, DNA damage, radiationless decay, biradical, ab initio, coupled clusted.

Résumé : Des calculs d'agrégats couplés de plus en plus précis (approximation de doubles : CC2 ; doubles : EOM-CCSD ; triples liés : CR-EOM-CCSD(T)) effectués sur des profils d'énergie potentielle optimisés au niveau CIS de l'adénine et de ses dérivés indiquent que la conversion interne ultra rapide de l'état optiquement excité $\pi\pi^*$ se produit par le biais par un changement d'état vers un état biradicalaire qui intercepte l'état fondamental à une énergie inférieure. La nature électronique de l'état biradicalaire est définie par une configuration électronique dans laquelle un électron non pairé occupe une orbitale π^* confinée dans un cycle à cinq chaînons. Le deuxième électron non pairé est très fortement localisé sur une orbitale atomique C2 de type p du cycle à six chaînons. Le minimum d'énergie de l'état biradicalaire comporte un noyau à six chaînons fortement plissé et une liaison C2–H qui est repliée d'une façon presque perpendiculaire par rapport à la position moyenne du cycle. En accord avec la conversion interne catalysée par un biradical, le temps de vie de l'état $\pi\pi^*$ est extrêmement court pour l'adénine et la 9-méthyladénine pour lesquels il existe un passage sans barrière vers l'état biradicalaire. Dans le cas de la 2-aminopurine, on a trouvé que l'état biradicalaire est à un niveau supérieur à celui de l'état $\pi\pi^*$ ce qui a comme effet d'empêcher le passage à l'état biradicalaire et d'augmenter d'une façon dramatique le temps de vie. Ces résultats, combinés à ceux obtenus antérieurement dans un travail sur les bases pyrimidines, suggèrent fortement l'importance d'une décroissance directe de l'état $\pi\pi^*$ initial par le biais d'un état biradicalaire dans la photophysique de l'ADN, même si la nature de l'état biradicalaire est quelque peu différente dans les purines et les pyrimidines.

Mots clés : adénine, guanine, dommage à l'ADN, décroissance sans rayonnement, biradical, ab initio, agrégat couplé.

[Traduit par la Rédaction]

Introduction

The high degree of photostability of DNA and RNA, despite strong adsorption by the natural bases (adenine, guanine, thymine, cytosine, and uracil) in the near UV region is one of the most enduring mysteries of photobiology (1). Radiationless decay of electronically excited states in oligonucleotides and native nucleic bases is complex, with multiple time constants required to describe the evolution of the excited state population (1, 2). The outcome of the decay is also highly sensitive to the local environment and secondary structure (3). Even decep-

Received 13 October 2006. Accepted 15 January 2007. Published on the NRC Research Press Web site at http://canjchem.nrc.ca/ on 27 February 2007.

M.Z. Zgierski[2] and S. Patchkovskii. National Research Council of Canada, 100 Sussex Drive, Ottawa, ON K1A 0R6, Canada.
E.C. Lim. Department of Chemistry and the Center for Laser and Optical Spectroscopy, The University of Akron, Akron, OH 44325-3601, USA.

[1]We are grateful to the Ohio Supercomputer Center for grants of computer time. ECL thanks the U.S. Department of Energy for the support of this work. ECL is the holder of the Goodyear Chair in Chemistry at The University of Akron.
[2]Corresponding author (e-mail: marek.zgierski@nrc.ca).

 doi: 10.1139/V07-006 © 2007 NRC Canada

tively simple DNA duplexes exhibit very complex photochemical behavior in solution (1) with up to four decay constants (4) and evidence of extensive nuclear dynamics in excited states (4).

Recent improvements in high-power pulsed lasers and molecular beam preparation techniques (5–7) allowed studies of photodynamics of isolated DNA bases in the gas phase. The observation of rapid radiationless decay for all natural nucleobases in the gas phase (8–10) indicated that photostability is a relatively simple intrinsic property of the bases, especially because the initial experiments were consistent with monoexponential excited state decay for most of the bases (10). Later experiments in transient multiphoton ionization (8–16) and time-resolved photoelectron spectroscopy (17–19) revealed the complex nature of the radiationless decay in isolated bases as well. For all natural DNA bases excited state decay is multiexponential (13, 17), indicating the presence of intermediate states and (or) multiple competing ionization channels. The excited state lifetimes are also highly sensitive to the excitation wavelength (9, 14, 17, 20) as would be expected for competing activated decay channels.

To further complicate matters, coinciding lifetimes of the excited states do not guarantee that the decay mechanisms are identical even in chemically closely-related species. For example, the measured exponential time constants in 9H-adenine and 9-methyl-adenine are essentially identical, an observation used to discount (12, 13) the $\pi\sigma^*$ decay channel (21, 22) in adenine. However, as revealed by time-resolved photoelectron spectra, the rapidly decaying component in adenine is largely attributable to the $\pi\sigma^*$ channel (18, 19). Moreover, experimental evidence also exists for hydrogen ejection (16, 23, 24), excited state proton transfer (11, 24), and long-lived optically active (25) and dark (10, 16, 26) states.

The abundance of available high-resolution gas phase data for the free bases and their analogs (20, 27–31) led to a recent explosion in theoretical investigations of radiationless decay. Many possible deactivation mechanisms were considered in DNA bases, including the proximity effect (32) (see ref. 1 for a recent overview) and a two-state process mediated by an $n\pi^*$ state (33). The classic aromatic biradical decay mechanism, extensively studied in ethylene and benzene (34–37), was first seen (38) but not initially recognized in thymine. This mechanism provides an efficient one-step decay pathway from the initially prepared $\pi\pi^*$ state to the ground state. It was extensively explored for pyrimidine bases (39–43) and used for a successful prediction of the lifetime for a pyrimidine base analog (6F-uracil) (41). Although the biradical mechanism appears to account for most of the decay in free pyrimidine bases at low excess energies, other mechanisms were also investigated and may become important at shorter wavelengths and in different environments. In particular, decay mediated by a dark $n_O\pi^*$ state was studied in cytosine (44) and uracil (45). Another classic decay mechanism, mediated by $\pi\sigma^*$ states dissociative along the X–H coordinate (46), was studied in uracil (47) although no experimental evidence for this pathway was found in the closely related thymine (16). Excited state proton transfer (40, 48–50), excitation transfer to a second stacked (51) or hydrogen-bonded (50, 52) base, and decay pathways involving accidental three-state crossings (53, 54) were also examined for pyrimidine bases. The latter process was claimed to be dominant in cytosine (53).

Perhaps unsurprisingly, electronically richer purine bases and their analogs present an even more complicated picture. Two optically active $\pi\pi^*$ states are known to be important (1). The stronger ^1L_a state involves partial charge transfer from the five- to six-membered ring. The more stable ^1L_b state involves an excitation localized on the six-membered ring. Additionally, one or more optically inactive $n\pi^*$ states and Rydberg states correlating to $\pi\sigma^*$ excitations localized on N–H (21, 22) or C–C (55) bonds are believed to be involved. Among the excited state relaxation mechanisms explored for guanine are excited state tautomerization (56, 57), tautomerism due to multiple minima in N–H bonds in excited state (57), proton (40, 49, 58), excitation (59) transfer to a hydrogen-bonded base, and proton transfer to the solvent (60). Dynamical surface-hopping calculations on guanine and analogs (61, 62) also reveal the importance of large-scale off-plane distortions of the six-membered ring (52, 58). Even more possibilities were examined for a simpler, more extensively studied adenine and its analogs (most importantly 2-aminopurine). The proposed mechanisms include twisting of the $-NH_2$ substituent (25, 63), decay mediated by the lowest $n\pi^*$ state (33, 64, 65), and $\pi\sigma^*$ states involving azine N–H (21, 22) and amino N–H (55) bonds. Other possibilities include excited state proton transfer (50, 66, 67), most likely mediated by protic solvents (66) although no evidence for such transfer was found in a recent condensed-phase experimental study (2). Opening of the five-membered ring of adenine leading to fragmentation was predicted to occur at higher energies (55). Deactivation through accidental triple-state crossings was also suggested to be important in adenine (54).

Despite the initial indications (68) of planar structures for the low-lying $\pi\pi^*$ excited states in adenine and suggestions that nonplanar structures may be biologically not relevant due to steric constraints in DNA (64), large-amplitude deviations from planarity are clearly involved in most low-energy deactivation pathways in purine bases (guanine (61, 62), adenine (31, 50, 55, 64, 65, 69–72)). In an attempt to quantify the role of nonplanar distortions in the excited state decay pathways in adenine and its analogs, several studies appeared in the last two years (31, 55, 64, 65, 70–72). Two of these investigations (31, 65) employ a DFT–MRCI technique, while no less than five publications (55, 64, 70–72) explore deactivation pathways at the CASPT2//CASSCF level.

Multiple competing deactivation pathways were identified in all studies (31, 55, 64, 65, 70–72). Discounting the biologically irrelevant pathway involving the N_9–H $\pi\sigma^*$ state, all studies agree that at low excess energies the most efficient mechanism proceeds through conical intersection(s) with the S_0 ground state reached by a large-amplitude out-of-plane twisting of the C_2–H fragment. The distortion is accompanied by disruption of the π-conjugation between the C_2 carbon and the rest of the π system. As a result, the lowest excited singlet state at these geometries is best described as a biradical formed by unpaired electrons localized respectively on the C_2 carbon atom and the five-membered ring of adenine (31, 55, 64, 65, 70–72). Because of negligible overlap between the unpaired electrons a nearby triplet state must also be present, opening possible pathways to intersystem crossing and long-lived dark states. The low-energy decay pathway in adenine is thus qualitatively similar to the biradical channel in pyrimidine bases.

The detailed electronic and nuclear dynamics leading to the biradical conical intersection is quite complicated and is sensitive to the assumptions and approximations made in the calculations. For instance, in ref. 65 the initially excited $\pi\pi^*$ ^1L_b state

© 2007 NRC Canada

converts barrierlessly to the $n\pi^*$ state, which then decays to the ground state through a conical intersection separated from it by a small barrier. The corresponding conical intersection is characterized by a large out-of-plane twist of the C_2–H bond. In refs. 55, 64, the initially excited $\pi\pi^*$ ^1L_a state decays barrierlessly to the ground state through a "CI_{32}" conical intersection identical to the intersection of ref. 65. The more stable ^1L_b $\pi\pi^*$ state can either cross (essentially barrierlessly) to the ^1L_a surface and decay through CI_{32} or convert to the $n\pi^*$ state and then decay through a "CI_{16}" intersection, separated from $n\pi^*$ by a barrier. The CI_{16} intersection is characterized by a large-amplitude out-of-plane twist of the C_6–NH_2 bond (55, 64). Both conical intersections are qualitatively similar to the main surface-hopping regions previously identified in the dynamical simulation of guanine radiationless decay (62). The excited state decay mechanism elaborated later in refs. 70–72 is qualitatively similar to that described in refs. 55, 64, 65. The electronic nature of the CI_{32} intersection is somewhat ambiguous and is characterized as a crossing between $n\pi^*$ and S_0 states by refs. 65, 70 and as a crossing between ^1L_a $\pi\pi^*$ and S_0 states by refs. 55, 64, 71, 72.

Despite the quantitative differences between the paths taken by the system to reach the CI_{32} intersection, the *existence* of the low-energy state crossing of this type appears to be the determining factor in the rapid decay of 9H-adenine (55, 64, 65, 70–72) and a significant excited-state lifetime found in 2-aminopurine (31, 72). Therefore, for a *qualitative* analysis and understanding of radiationless decay in purine bases, it appears to be reasonable to ignore the detailed dynamics leading to the biradical conical intersection CI_{32} and concentrate on the qualitative properties of the intersection itself.

In this respect, it is important to realize that despite exaggerated claims of the accuracy and rigor of computational results sometimes made (72) any prediction for a system of the complexity of adenine necessarily involves models and approximations. Due to the exorbitant computational cost, these approximations are not always easily controllable. As an example, consider the 0–0 transition energies for the lowest $n\pi^*$ and $\pi\pi^*$ states of adenine calculated in refs. 55, 64, 70–72 using very similar computational techniques and basis sets (Table 1). The calculated excitation origins for both states are scattered over 0.5 eV. More importantly, except for ref. 71, all calculations overestimate the relative stability of the $n\pi^*$ state by amounts likely to be significant in biological settings. Clearly, the judgment calls made by the authors in the construction of the CASSCF active spaces constitute a critical (and unavoidable) factor in these calculations. In fact, it is possible to argue that the results of ref. 71, while in worse numerical agreement with experiment, come from a more balanced model and are therefore the most appropriate for the discussion of inter-surface transitions.

Although CASPT2//CASSCF and related MRQDPT2 techniques are unquestionably the most accurate computational approaches currently available for studies of excited states in medium-sized molecules, such calculations remain extremely labor-intensive (see the Supplementary information of ref. 72 for an illustration). Therefore, it is important to examine whether the *qualitative* features of radiationless decay in adenine and its analogs can be reproduced by simpler and less onerous techniques.

In this work, we explore the radiationless decay of the doorway $\pi\pi^*$ state of adenine and its analogs, such as

Table 1. Published CASPT2//CASSCF energies (in eV) of the two lowest 0-0 transitions from the ground state of adenine, in comparison with experimental and coupled cluster results.

	$n\pi^*$	$\pi\pi^*$ (^1L_b)
Calcd. (55, 64)	4.48	4.69
Calcd. (70)	4.55	4.67
Calcd. (71)	5.01	5.05
Calcd. (72)	4.52	4.83
Expt. (20, 30)	4.47	4.48
CC2[a]	4.60	5.13
EOM-CCSD[a]	4.89	5.67
DELTA-CR-EOM-CCSD(T)[a,b]	4.21	4.98

[a]This work. All coupled cluster values are calculated using cc-pVDZ basis set at optimized CIS/cc-pVDZ geometries.
[b]DELTA-CR-EOM-CCSD(T) excitation energy, where the triples correction is applied to the excited state only. This value is expected (76) to provide better balance for singles-dominated excited states.

N,*N*-dimethyladenine and 2-aminopurine. According to ref. 13, methylation of the amino group increases the lifetime by a factor of $\sim$ 2, while transfer of this group to another position in the six-membered ring (from C6 to C2) stabilizes the $\pi\pi^*$ state allowing for a large emission quantum yield. We demonstrate that simple, black-box type coupled-cluster methods (approximate doubles: CC2; doubles: EOM-CCSD; connected triples: CR-EOM-CCSD(T)) are able to explain differences in lifetimes of the $\pi\pi^*$ states of these three molecules. The simplicity of use of the coupled-cluster techniques becomes essential in investigations of much larger fragments of the DNA chain, such as cytidine and its derivatives (73).

Methods

The cc-pVDZ basis set is used in all calculations presented in this paper. We use a simple configuration interaction singles (CIS) method to find partially optimized geometries and utilize these geometries to perform calculations of the energies of the excited electronic states with inclusion of electron correlations. To this end, a coupled cluster method with an approximate inclusion of double excitations (CC2 (74)) is applied to all four molecules. For adenine, the completely renormalized equation of motion coupled cluster (CR-EOM-CCSD(T)) method (75, 76) is used as an additional check. The multiconfigurational complete active space self-consistent field (CASSCF) technique is often the method of choice for similar investigations of small regions of potential energy surfaces. However, designing sufficiently large, consistent CASSCF active spaces becomes very time-consuming and laborious for regions where the H–C5–C4–H angle changes from nearly 0° (as in the initially populated $\pi\pi^*$ state) to almost 150° in the biradical state. CASSCF also tends to miscalculate the ordering of the $\pi\pi^*$ and $n\pi^*$ states (39, 42, 44), known to be sensitive to dynamical correlations involving low-lying σ orbitals (69). The coupled cluster method, on the other hand, provides consistent $\pi\pi^*$ and $n\pi^*$ results for the complete range of geometries explored and is therefore the method of choice for studying the problem. CIS calculations were performed with the use of Gaussian98 program (77), while the equation of motion coupled cluster dou-

© 2007 NRC Canada

bles calculations, extended to include completely renormalized perturbatively connected triples (CR-EOM-CCSD(T)) (75, 76), were done with the GAMESS program (78). Unless mentioned otherwise, type IID triples corrections were used. This type of approach has been shown to produce meaningful results as long as the contribution from multiply excited configurations does not change drastically on the explored potential energy surface of the excited state (41, 42).

The CC2 model has been previously demonstrated to provide reliable results for vertical excitations in π-electron systems, even with relatively small basis sets (74, 79, 80). The lack of diffuse functions in the cc-pVDZ basis in fact has a beneficial side effect of shifting the intruding Rydberg states to higher energies (80), simplifying analysis and interpretation of the results. At the same time, energies of the valence excitation are reproduced well (80), possibly with a small underestimation relative to the basis set limit (81).

It should be emphasized that the electronic ground states of DNA bases acquire significant multiconfigurational character away from the ground state equilibrium geometry and may be poorly approximated by a closed-shell Hartree–Fock solution. As a result (79, 82), calculated CC2 energies for distorted structures are at best qualitative estimates so that quantitative agreement with experiment should not be expected. This can be seen from the values of the D1 diagnostics (82) for the ground-state CC2 solutions. Values in the range 0.07–0.08 are found at the ground-state geometries, increasing somewhat to 0.07–0.09 for the CIS-optimized geometries of the first $\pi\pi^*$ excited state. Dramatic increases to 0.2–0.3 are found for the CIS-optimized biradical geometries, indicating that the calculated values are to be treated with extreme caution (82). At the same time, calculated excited states at all geometries are dominated by single excitations, with $r1$ amplitudes accounting for 88%–95% of all presently reported excited states.

The reduced excitation level (REL) diagnostic in EOM-CCSD calculations does not exceed 1.1 at all geometries presently studied, indicating the dominant single excitation character with respect to the lowest single-determinant solution. Excited states of this type are typically well-described by EOM-CCSD even when the ground state is no longer of a single-determinantal character. As an additional accuracy check, we calculated the ground-state energy of selected adenine and 2-aminopurine structures at the CR-CC(2,3) (83) level. This approach is explicitly constructed to provide accurate description of a subset of multiconfigurational states, specifically states of biradical type. Unfortunately, CR-CC(2,3) is currently available only for states defined by the CCSD cluster operator with a single-determinant reference (typically the ground state). As a result, meaningful exploration of excited state surfaces in not possible with this technique. At the optimized CIS biradical geometries of both adenine and 2-aminopurine (see later), absolute CR-CC(2,3) energies are just 25 mH (0.7 eV) below the corresponding CR-EOM-CCSD(T) IID results. The close agreement between the two approaches suggests that the approximate treatment of multiconfigurational wavefunctions in CR-EOM-CCSD(T) calculations is adequate for adenine and its analogs.

All CC2 calculations were performed using Turbomole (84) version 5.7, using resolution-of-the-identity CC2 implementation (85) with the standard (82) RI-optimized fitting basis sets. Transition moments (81) are calculated in the dipole gauge.

Adenine and 9-CH_3-adenine

CIS–cc-pVDZ geometry optimization places the minimum of the $\pi\pi^*$ doorway (L_b) state 0.119 eV (960 cm^{-1}) below the minimum of the $n\pi^*$ state. The $\pi\pi^*$ state minimum possesses planar six- and five-membered rings, and only the hydrogen atoms of the amino group are not in the plane of the rings. The out-of-plane deformation of the N3–C2–N1–C6 dihedral angle is the lowest frequency vibration in the $\pi\pi^*$ state with the unscaled frequency of just 114 cm^{-1}. On the other hand, the CIS-optimized $n\pi^*$ state has a strongly out-of-plane deformed six-membered ring and the N3–C2–N1–C6 dihedral angle is equal to $-36.36°$ with the C2 and N3 atoms displaced in the opposite directions from the plane. The N3–C2–N1–C6 dihedral angle deformation mode has the unscaled frequency of 338 cm^{-1}. The biradical state minimum, which was confirmed by vibrational analysis, occurs at the N3–C2–N1–C6 dihedral angle of $-58.74°$. The C2 hydrogen atom is twisted to be almost perpendicular to the average plane of the molecule with a C6–N1–C2–H dihedral angle of 83.1°. The CIS energy of the biradical state is only 0.061 eV below the minimum of the CIS $\pi\pi^*$ state. The structure of the minimum of the biradical state is similar to the calculated structure of the conical intersection between the L_a (64, 72) or $n\pi^*$ (65) and the ground state. The CIS energies of the $\pi\pi^*$, $n\pi^*$, and biradical states as functions of the N3–C2–N1–C6 dihedral angle, with all other parameters fully optimized for each state, are depicted in the left panel of Fig. 1. The structure of the biradical state is shown in Fig. 2. The singly occupied orbitals (SOMOs) in this state are illustrated in Fig. 3. The lower energy SOMO is dominated by the five-membered ring, while the higher energy SOMO is strongly localized on the C2 atom. The biradical state correlates at planar geometry to the ^1L_a $\pi\pi^*$ state. The CIS calculations place the minimum of the biradical state only 1.769 eV above the ground-state potential. Inclusion of a perturbative CIS(D) correlation correction (86, 87) decreases the gap to 0.21 eV.

The vertical excitation energies for the lowest $\pi\pi^*$ and $n\pi^*$ states obtained by CR-EOM-CCSD(T) calculations are 4.90 and 4.94 eV, respectively. This compares well with the recent CASPT2 calculations, which give the respective energies at 4.74 and 5.00 eV (70), 4.96 and 5.16 eV, (72), or 5.01 and 5.05 eV (71). The relative CIS and CC2 energies of the CIS minima of the the electronic excited states of adenine and of its 9-CH_3 derivative with respect to the minimum energy of the ground state are given in Table 2. The differences between the energy of the biradical state and the ground state at the biradical geometry are collected in Table 3. We can see that the difference between the CR-EOM-CCSD(T) energy of the biradical state and the CCSD energy of the ground state (the DELTA-CR-EOM-CCSD(T) approximation (76)) becomes negative, indicating crossing of the two surfaces before the minimum of the biradical state is reached. Except for the (uncorrelated) CIS approach, this gap is calculated consistently to be below 1 eV, indicating very efficient internal conversion to the ground state. Because the geometries of the biradical and ground states are very different, many soft modes will become efficient accepting modes in the radiationless decay process, not unlike the situation found for the superfast decay of the excited electronic state in butadiene (88). Methylation of the C9 atom changes the relative energies of the $\pi\pi^*$ and biradical states only marginally, shifting both excitations to the red and slightly closing the gap

© 2007 NRC Canada

Fig. 1. Energies of the low-lying states of adenine as functions of the C6–N1–C2–N3 dihedral angle for the CIS (left panel) and CC2, CCSD, and CCSD(T) (right panel) levels of calculations. EOM-CCSD (dashed, red lines) and CR-EOM-CCSD(T) (solid, black lines) energies in the right panel are shifted upward by 0.01 and 0.03 au, respectively, with respect to the CC2 (dotted, blue lines) energies. The squares, diamonds, and circles refer to the three different electronic states ($\pi\pi^*$, $n\pi^*$, and biradical). All energies are calculated at the optimized CIS–cc-pVDZ geometries along the C6–N1–C2–N3 minimum energy path.

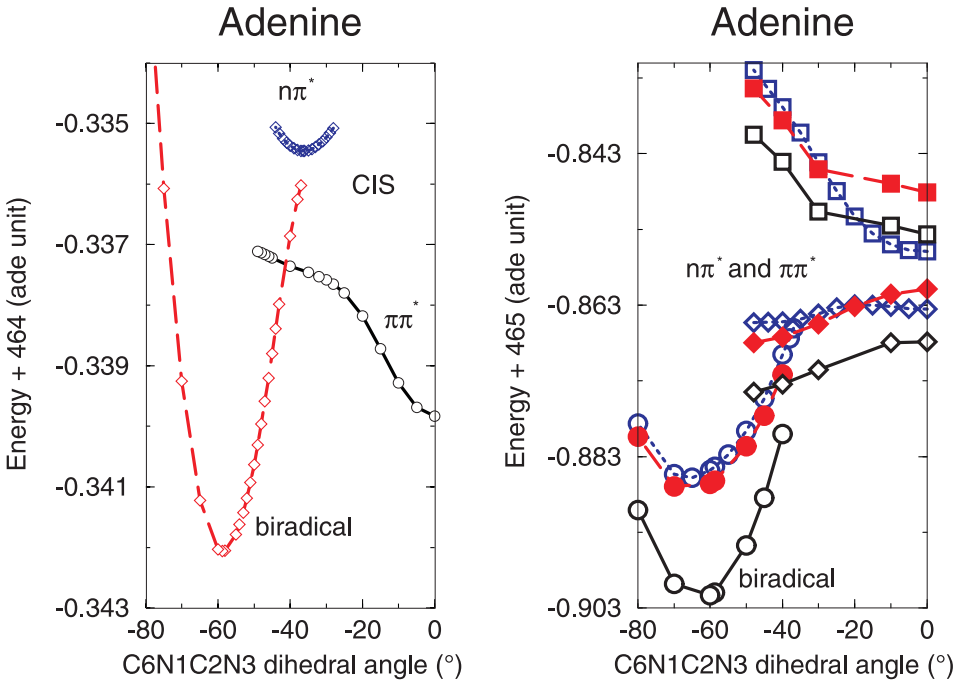
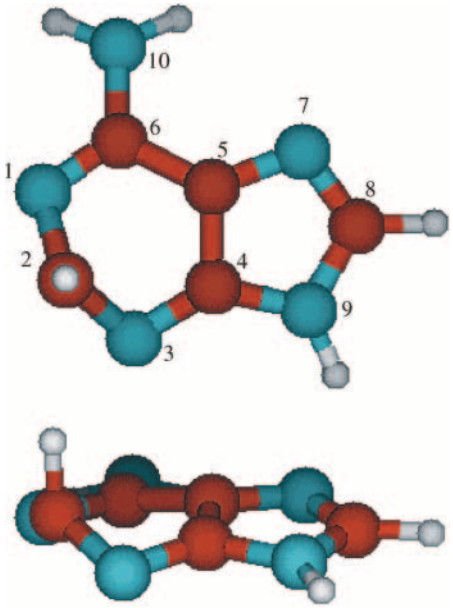


Fig. 2. Two different projection of the structure of the biradical state of adenine and the numbering of the atoms.



between the two minima. One could expect that such a minor change would lead to a negligible increase in the lifetime of the $\pi\pi^*$ state. Indeed, the excited-state lifetime of 9-methyladenine is only about 10% longer than that of adenine (13). The CIS minimum energy paths along the C6–N1–C2–H dihedral angle in adenine were used to calculate single-point energies of the $n\pi^*$, $\pi\pi^*$, and biradical states by CC2, EOM-CCSD, and CR-EOM-CCSD(T) correlated methods. The results are presented

Table 2. Energies (eV) of the minima of the excited state surfaces with respect to the singlet ground state minimum.

State	Adenine		9-CH_3-adenine		2-aminopurine	
	CIS	CC2	CIS	CC2	CIS	CC2
$\pi\pi^*$	6.078	5.126	6.023	4.931	5.536	4.318
$n\pi^*$	6.197	4.911			5.728	4.351
biradical	6.017	4.352	5.995	4.330	6.295	4.502

Table 3. Energy differences (eV) between the biradical state and the singlet ground state surface at the CIS-optimized biradical geometry.

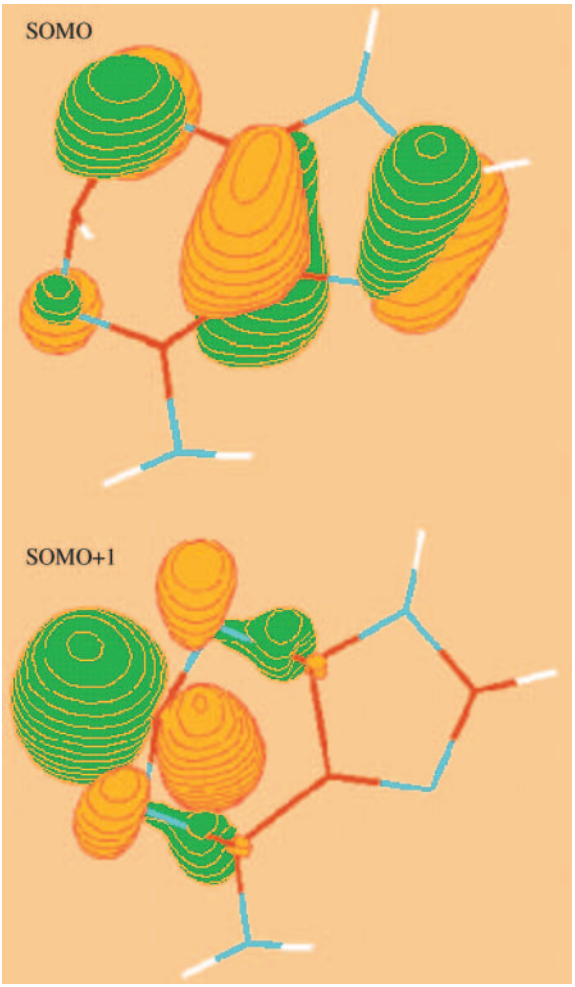
Level	Adenine	9-CH_3-adenine	2-aminopurine
CIS	1.769		2.972
CIS(D)	0.208	0.145	1.611
CC2	0.726	0.679	1.989
EOM-CCSD	0.782		2.104
CR-EOM-CCSD(T)[a]	−0.164		1.297

[a]DELTA-CR-EOM-CCSD(T) excitation energy, where the triples correction is applied to the excited state only. This value is expected (76) to provide better balance for singles-dominated excited states.

in the right panel of Fig. 1. Solid (black) lines refer to the highest level (CR-EOM-CCSD(T) calculations), dashed (red) lines refer to the EOM-CCSD results, while the dotted (blue) lines show the CC2 energies. Inclusion of electron correlation and multiple excitations strongly stabilizes the biradical state. Thus, at the CR-EOM-CCSD(T) level, the minimum of the biradical state is ∼ 1.3 eV below the original vertically excited $\pi\pi^*$ ^1L_b

© 2007 NRC Canada

Fig. 3. The two singly occupied molecular orbitals in the dominant electronic configuration of the biradical state of adenine from CIS–cc-pVDZ calculationS.



state. The corresponding values at the CCSD and CC2 levels are 1.1 and 0.8 eV, respectively. The nπ^* and $\pi\pi^*$ states are involved in a conical intersection around −30° and are strongly mixed in the vicinity. The nπ^* state is found 0.38 eV (CR-EOM-CCSD(T)), 0.34 eV (EOM-CCSD), or 0.21 eV (CC2) below the $\pi\pi^*$ state at the planar ring geometry.

Because the qualitative behaviour of the reaction paths at the CR-EOM-CCSD(T) level is similar to the (much cheaper) CC2 results, we have adopted the CC2//CIS level for the calculation of reaction paths in adenine derivatives. As can be seen in Fig. 2, the value of the HC–2N1–C6 dihedral angle is very different in the biradical state compared with that in the planar $\pi\pi^*$ ^1L_b state. Constrained CIS optimization of the lowest singlet state leads to a continuous minimum energy path connecting these two states (Fig. 4, left panel). The corresponding CIS reaction barrier along this path is only 0.135 eV. No barrier is found along the same path in single point CC2 calculations, which place the biradical state below the $\pi\pi^*$ state in the whole range of HC–2N1–C6 dihedral angle (Fig. 4, right panel). In this respect, it should be noted that while a constrained minimum energy path does not necessarily give a faithful representation of the reaction coordinate, the existence of a *barrierless* reaction path is sufficient to demonstrate the absence of an activation barrier. Thus, the initially populated $\pi\pi^*$ ^1L_b state should decay to the biradical state very rapidly in a barrierless fashion. The biradical state will, in turn, upon approaching the ground state potential energy surface, undergo fast internal conversion to the vibrationally hot ground electronic state. Subsequent vibrational cooling returns molecule to its initial condition before absorption of a photon. It should be emphasized that this radiationless decay mechanism is identical to the pathway previously discovered in guanine (62) and recently located in adenine and its derivatives (31, 55, 64, 65, 70–72).

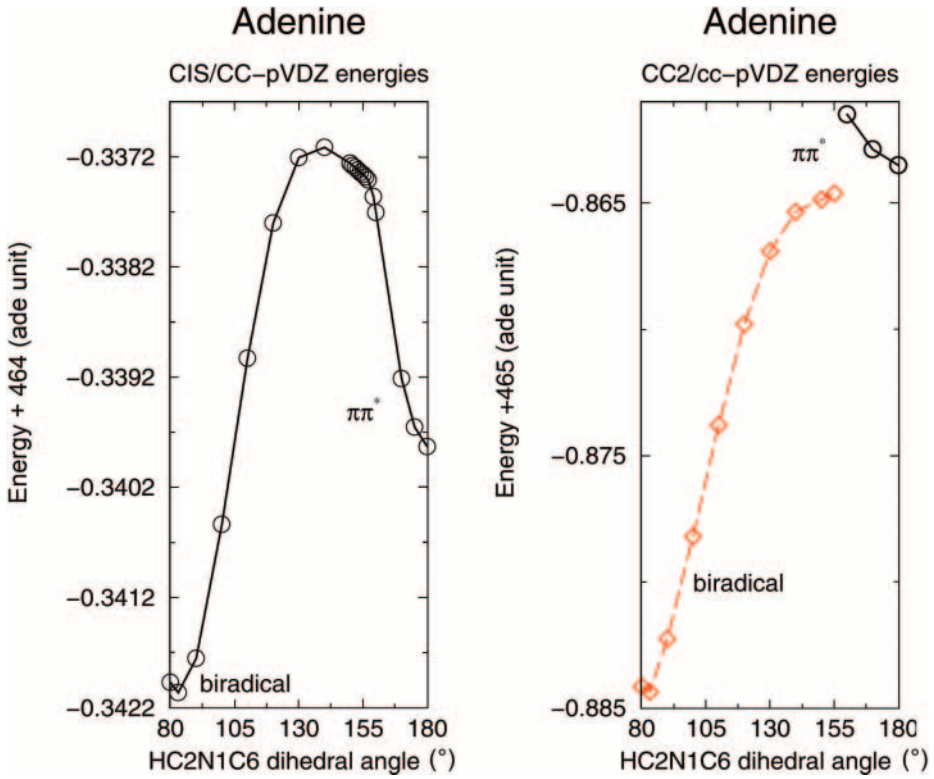
N,*N*-dimethyladenine

Experimentally, substitution of two methyl groups into the amino group of adenine extends the lifetime of the optically excited $\pi\pi^*$ state by a factor of 2–3 (13). If decay through the biradical state dominates in this adenine derivative as well, then the elongation of the lifetime of the initially prepared state would indicate either some destabilization of the biradical state or the introduction of a small energy barrier between the two states, or possibly both.

Figure 5 (top) depicts the optimized CIS structure of the biradical state minimum for *N*,*N*-dimethyladenine. This minimum was verified by force field calculations showing that all harmonic frequencies are real. Except for the two methyl groups, this structure is almost identical to the biradical state structure of adenine (Fig. 2). Figure 6 presents the results of the CIS (solid black lines for the $\pi\pi^*$ state and dashed red lines for the biradical state) and CC2 (solid maroon lines and dashed blue lines) calculations for the minimum energy paths along the C6–N1–C2–N3 dihedral angle on the energy surfaces of the $\pi\pi^*$ and biradical states. As in adenine, the vertically excited $\pi\pi^*$ (^1L_b) state relaxes to a geometry with a flat 6-membered ring, a slightly pyramidalized amino group, and the N10 atom displaced away from the ring plane. The CIS minimum of the biradical state is calculated to be 0.211 eV above the minimum of the $\pi\pi^*$ state. There is also a small pyramidalization of the amino group of the biradical state, however, the N10 (amino) atom remains in the same plane as the five-membered ring. The out-of-plane deformation is limited (as in the case of adenine) to the N3–C2–N1–C6 dihedral angle of −58.7° and to the H–C2–N1–C6 dihedral angle of 83.0°, both values being almost the same as in adenine. Single-point CC2 energies of the two states at optimized CIS geometries are shown by solid (maroon) lines for the $\pi\pi^*$ state with different degrees of amino group pyramidalization and the dashed (blue) line for the biradical state. The two minima on the CC2//CIS $\pi\pi^*$ state surface correspond to distinct conformations of the amino group with respect to the five-membered ring plane. In the lower Franck–Condon minimum the N10–C6–C5–N7 dihedral angle is 37.8°, while in the higher minimum at N3–C2–N1–C6 and N10–C6–C5–N7 it is 40° and 3.1°, respectively. At the CC2//CIS level of theory the biradical state lies ∼ 0.169 eV below the minimum of the $\pi\pi^*$ state. CIS(D) calculation places the minimum of the biradical state 0.56 eV below the minimum of the $\pi\pi^*$ state (similar calculation for adenine gives the value of 1.25 eV for the same energy difference). Thus, our calculations suggest that methylation of the amino group of adenine leads to a slight destabilization of the biradical state, even though it remains well below the minimum of the $\pi\pi^*$ state. At the same time a modest energy barrier develops between the two states along the mini-

© 2007 NRC Canada

Fig. 4. The energy of the lowest excited state of adenine as a function of the H–C2–N1–C6 dihedral angle at partially optimized CIS geometries. Left panel: the CIS energies; right panel: the CC2 energies.

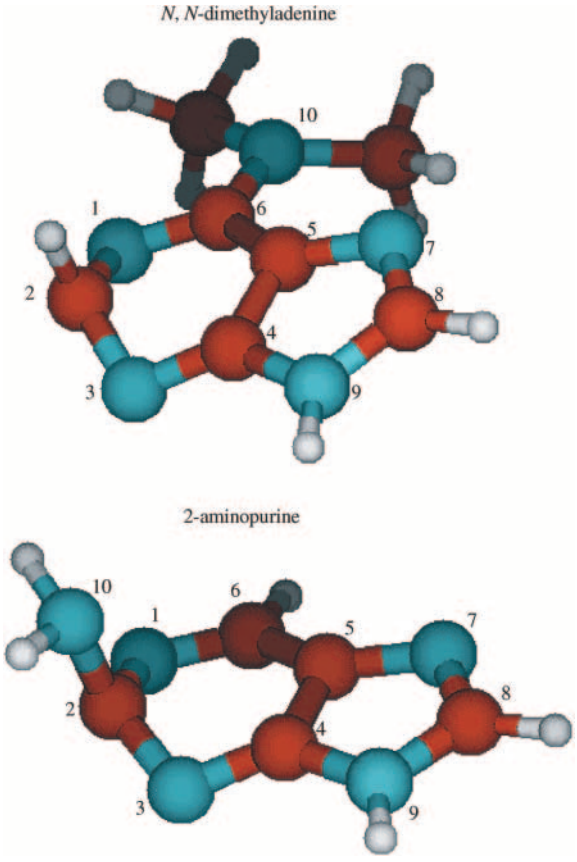


mum energy path corresponding to the increasing N3–C2–N1–C6 dihedral angle. Both effects should lead to a modest increase of the lifetime of the initially excited $\pi\pi^*$ state, as is observed experimentally (13). Note that a deeper minimum appears near the planar geometry on the $\pi\pi^*$ potential energy surface of *N*,*N*-dimethyladenine (Fig. 6) than in adenine. This should lead to a relatively long lifetime of a few low-lying vibronic levels of the $\pi\pi^*$ electronic manifold. Indeed, it is observed that below 125 K the quantum yield of fluorescence from the initially excited $\pi\pi^*$ state of *N*,*N*-dimethyladenine suddenly increases and that at 80 K the lifetime reaches 2 ns (89). This observation is in a qualitative agreement with our results.

2-Aminopurine

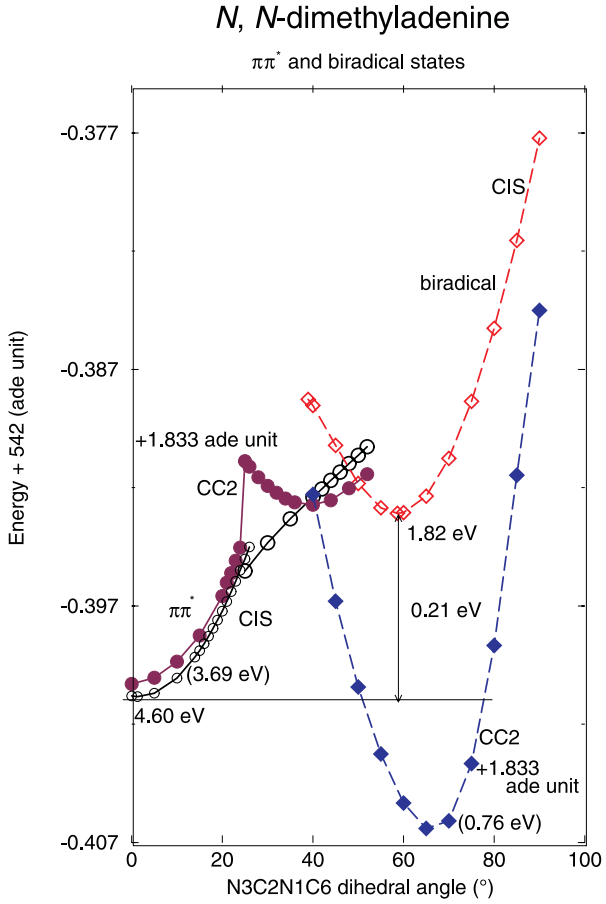
This isomer of adenine, in which the amino group is switched from the C6 atom to the C2 atom shows a long lifetime of the excited $\pi\pi^*$ state and a large fluorescence quantum yield (90). Obviously, replacement of the C2 hydrogen by an amino group closes a very effective internal conversion channel of the lowest $\pi\pi^*$ state. 2-Aminopurine (2AP) readily replaces adenine (6-aminopurine) in DNA forming pairs with thymine and also with cytosine (91). It is used extensively as an intrinsic fluorescence probe in DNA (92, 93). Broo (33), Rachofsky (69), and others (1) have argued that the vibronic coupling of the $\pi\pi^*$ (S_1) state with the close-lying $n\pi^*$ (S_2) state determines the efficiency of internal conversion in 2AP via the proximity effect (32, 94–96). This proposal is consistent with the dramatically longer lifetime of 2AP (13, 90) compared with adenine (with a smaller S_2-S_1 gap), and the dramatic increase in the fluorescence yield of 2AP with increasing solvent polarity (which increases the S_2-S_1 gap

Fig. 5. The CIS-optimized structure of the biradical states in (top) *N*,*N*-dimethyladenine and (bottom) 2-aminopurine.



© 2007 NRC Canada

Fig. 6. Energies of the $\pi\pi^*$ and biradical states of *N*,*N*-dimethyladenine as functions of the C6–N1-C2-N3 dihedral angle with all remaining parameters optimizes at the CIS–cc-pVDZ level. Solid (black) lines and open circles show CIS energies of the $\pi\pi^*$ state with the two opposite pyramidalizations of the dimethylamino group. Dashed (red) lines and diamonds give CIS energies of the biradical state. CC2 energies are shown by solid (maroon) lines and filled circles for the $\pi\pi^*$ state and by the dashed (blue) line and filled diamonds for the biradical state. All CC2 energies are shifted uniformly upward by 1.833 au. The numbers near the minima indicate the energy gap (in eV) relative to the singlet ground state surface at the same geometry.



by stabilizing the lowest $\pi\pi^*$ (^1L_a) state with respect to the $n\pi^*$ state (69). As originally found by Marian and co-workers (31) and later confirmed by more elaborate calculations (72), the biradical channel decay in 2AP becomes relatively unimportant at the same time. It is however important to confirm that our simple CC2//CIS calculations lead to the same outcome.

Figure 5 (bottom) depicts the CIS structure of the minimum of the biradical state for 2-aminopurine. Again, force field calculations show that all harmonic frequencies are real. The relative CIS and CC2 energies of the minima of the the electronic excited states of 2-aminopurine with respect to the minimum energy of the ground state are collected in Table 2. The CC2 results for vertical excitation energies are in good agreement with previous CIPSI and TDDFT calculations for this molecule (63) as well as with MCQDPT results (69). They also agree with the recent CASPT2//CASSCF calculations (72). The CC2//CIS energies of the minima of the $\pi\pi^*$, $n\pi^*$ and biradical states in 2-aminopurine are all within a range of 0.2 eV, with the minimum of the $\pi\pi^*$ found at the lowest energy. The differences between the energies of the biradical state and the ground state at the same geometrical configuration are given in Table 3. While the change in calculated relative stability of the $\pi\pi^*$ and $n\pi^*$ states is small in comparison to adenine, the location of the minima of the biradical states of the two molecules changes dramatically. Both CIS and CC2 methods predict the minimum of the biradical state above the minimum of the $\pi\pi^*$ state with an energy barrier between the two states along the reaction path defined by the N3–C2–N1–C6 dihedral angle. It appears that substitution of an electron-donating group on the C2 carbon atom destabilizes the p orbital on C2, which has to accommodate a localized unpaired electron in the biradical state. The energy gap between the minimum of the biradical state and the ground state potential energy surface is also much larger than 1 eV. Both of these factors would make the biradical channel inactive in the internal conversion process of the optically excited $\pi\pi^*$ state, at least at low excess photon energies. Given this conclusion, the interpretation of 2AP photophysics based on the proximity effect appears very reasonable. Figure 7 depicts the CIS and CC2 minimum energy paths along the N3–C2–N1–C6 dihedral angle in the $\pi\pi^*$ and biradical states of 2-aminopurine. Solid lines and circles refer to the $\pi\pi^*$ state while dashed line and diamonds refer to the biradical state. Again, as in *N*,*N*-dimethyladenine, there are two possible pyramidalization structures of the amino group in the $\pi\pi^*$ state. Since the minimum of the biradical state lies above any of the two minima of the lowest excited $\pi\pi^*$ state, the decay of the latter via the biradical state is switched off in 2-aminopurine. This justifies the long lifetime of the $\pi\pi^*$ S_1 state and thus, the high fluorescence quantum-yield observed in this molecule.

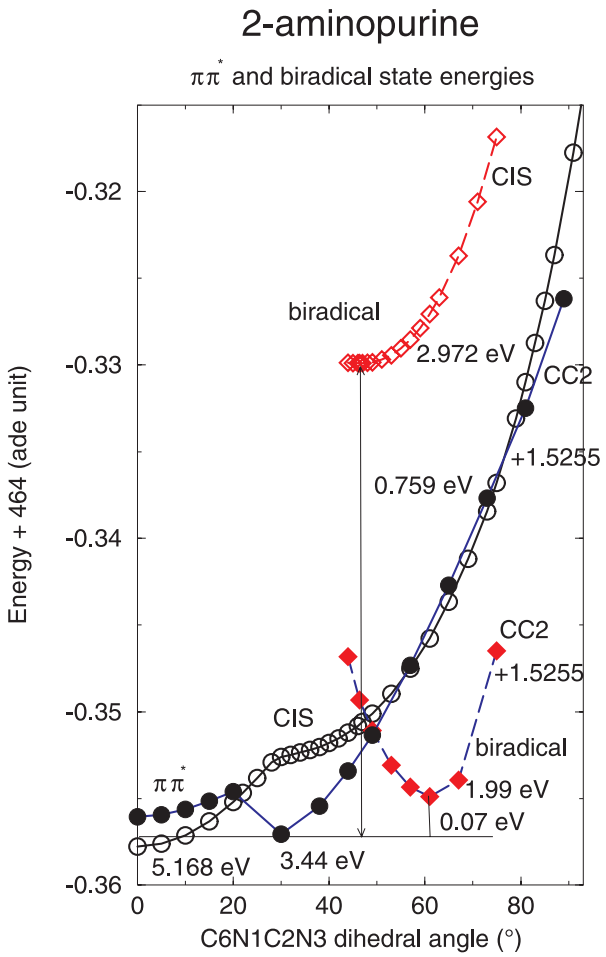
Summary and conclusions

The rate of radiationless decay of the optically prepared $\pi\pi^*$ state of adenine and its derivatives and isomers depends critically on the substituents. Methylation of the C6 amino group slows down the process almost threefold, while moving the amino group from the C6 to the C2 position produces a highly fluorescent isomer with a very slow internal conversion to the ground state. We have confirmed that the previously proposed direct decay of the $\pi\pi^*$ state through a switch to a biradical state and subsequent crossing the ground state potential energy surface satisfactorily explains the observed differences in lifetimes of the doorway state in adenine derivatives and isomers. Consistent with this mechanism, the excited-state lifetimes are very short in adenine and 9-methyladenine, which have barrierless crossing of the initially excited $\pi\pi^*$ state to the biradical state, slightly longer in *N*,*N*-dimethyladenine that has a small barrier for the state switch and very long in 2-aminopurine that has the biradical state above the $\pi\pi^*$ state, and thus the biradical channel is shut off.

All qualitative features of the biradical channel are well-reproduced at the simple, computationally inexpensive CC2//CIS technique. At this level, routine calculations are possible on much larger and more biologically relevant systems, such as base pairs, nucleotides, and short strands of DNA and RNA. The CC2 results are in a close agreement with much more elaborate CR-EOM-CCSD(T) and CASPT2 calculations.

© 2007 NRC Canada

Fig. 7. The energies of the $\pi\pi^*$ and biradical states of 2-aminopurine as functions of the C6–N1–C2–N3 dihedral angle. The solid CIS (black) and CC2//CIS (blue) lines show the energies of the lowest $\pi\pi^*$ state (^1L_a) with the two opposite pyramidalizations of the amino group. The dashed CIS (red) and CC2 (blue) lines show the energies of the biradical state. The CC2 energies are shifted uniformly upward by 1.5255 au. The numbers near the minima indicate the energy gap (in eV) to the ground state surface at this geometry.



The same conclusions apply also to another DNA purine base, guanine, in which the biradical state, with the NH_2 group positioned almost perpendicular to the average plane of the six-membered ring, plays a leading role in an ultrafast radiationless decay of the intitially excited $\pi\pi^*$ state.[3] The latter is characterized by a very shallow minimum with a negligible energy barrier for switching to the biradical state.

The mediating biradical state is somewhat similar in nature to the intermediate state present in pyrimidine bases (41, 42), where it is also very sensitive to chemical substitutions and thus strongly influences the internal conversion process of an initially prepared $\pi\pi^*$ state. The purine biradical state involves a strong ruffling of the six-membered ring and out-of-plane deformation of the C2 substituent with respect to the average ring plane. The biradical character of the intermediate state arises because of the separation of two initially paired π electrons, with one electron localized on a carbene-like p orbital of the C2 atom and the other electron confined to a π^* orbital in the five-membered ring. In pyrimidines, both unpaired electrons are localized on the neighboring p orbitals of C5 and C6 atoms. The similarity of the biradical state in adenine with those in pyrimidines is however not complete, since, in the former this state evolves from the higher planar L_a $\pi\pi^*$ state when the six-membered ring deformed, necessitating a state switch to access it. Our results for adenine are in accord with a series of recent papers (55, 64, 65, 70–72). Those for 2-aminopurine concur with the conclusions presented in ref. 31 as well as with ref. 72, which appeared after the completion of our work.

The biradical-mediated radiationless decay mechanism appears to be conserved by the molecular evolution of the DNA bases. We speculate that the mechanism confers evolutionary advantage by minimizing the probability of mutations among all competing pathways. Indeed, the biradical decay channel in cytosine, thymine, and uracil operates without disrupting hydrogen bonding in canonical DNA base pairs. In adenine, only one hydrogen bond is affected with all high-amplitude distortions confined to the (light) hydrogen atom at C2. At the same time, the hydrogen remains strongly covalently bonded, such that the base pairing is restored immediately upon the biradical state decay.

Very recent work in our laboratories has shown that cyclohexanyl guanosine, cyclopentanyl cytosine, and cyclopentanyl uracil, in which the twist of the C2–N bond in guanine and the C5–C6 bond in pyrimidine bases are strongly hindered by the presence of an exocyclic aliphatic ring, do not exhibit ultrashort (subpicosecond) excited-state lifetimes (Marek Z. Zgierski, Serguei Patchkovskii , Takashige Fujiwara, William G. Kofron, and Edward C. Lim. Manuscript in preparation.). The result provides strong support to the biradical decay mechanism presented in this paper.

[3] M.Z. Zgierski, S. Patchkovskii, and E.C. Lim. Biradical decay mechanism in guanine. Unpublished results. 2006.

References

1. C.E. Crespo-Hernández, B. Cohen, P.M. Hare, and B. Kohler. Chem. Rev. **104**, 1977 (2004).
2. C.E. Crespo-Hernández, B. Cohen, and B. Kohler. Nature, **436**, 1141 (2005).
3. Y. Xu and H. Sugiyama. Angew. Chem. Intl. Ed. **45**, 1354 (2006).
4. O.J.G. Somsen, L.B. Keukens, M. Niels de Keijzer, A. van Hoek, and H. van Amerongen. Chem. Phys. Chem. **6**, 1622 (2005).
5. D.M. Neumark. Ann. Rev. Phys. Chem. **52**, 255 (2001).
6. I. Fischer. Chem. Soc. Rev. **32**, 59 (2003).
7. A. Stolow. Ann. Rev. Phys. Chem. **54**, 89 (2003).
8. E. Nir, K. Kleinermanns, L. Grace, and M.S. de Vries. J. Phys. Chem. A, **105**, 5106 (2001).
9. D.C. Lührs, J. Viallon, and I. Fischer. Phys. Chem. Chem. Phys. **3**, 1827 (2001).
10. H. Kang, K.T. Lee, B. Jung, Y.J. Ko, and S.K. Kim. J. Am. Chem. Soc. **124**, 12958 (2002).
11. C. Plützer, I. Hünig, and K. Kleinermanns. Phys. Chem. Chem. Phys. **5**, 1158 (2003).
12. H. Kang, B. Jung, and S.K. Kim. J. Chem. Phys. **118**, 6717 (2003).
13. C. Canuel, M. Mons, F. Piuzzi, B. Tardivel, I. Dimicoli, and M. Elhanine. J. Chem. Phys. **122**, 074316 (2005).
14. T. Pancur, N.K. Schwalb, F. Renth, and F. Temps. Chem. Phys. **313**, 199 (2005).

© 2007 NRC Canada

15. E. Samoylova, H. Lippert, S. Ullrich, I.V. HertelâŁ, W. Radloff, and T. Schultz. J. Am. Chem. Soc. **127**, 1782 (2005).
16. M. Schneider, R. Maksimenka, F. Johannes Buback, T. Kitsopoulos, L.R. Lago, and I. Fischer. Phys. Chem. Chem. Phys. **8**, 3017 (2006).
17. S. Ullrich, T. Schultz, M.Z. Zgierski, and A. Stolow. Phys. Chem. Chem. Phys. **6**, 2796 (2004).
18. S. Ullrich, T. Schultz, M.Z. Zgierski, and A. Stolow. J. Am. Chem. Soc. **126**, 2262 (2004).
19. H. Satzger, D. Townsend, M.Z. Zgierski, S. Patchkovskii, S. Ullrich, and A. Stolow. Proc. Natl. Acad. Sci. USA. **103**, 10196 (2006).
20. N.J. Kim, G. Jeong, Y.S. Kim, J. Sung, S.K. Kim, and Y.D. Park. J. Chem. Phys. **113**, 10051 (2000).
21. A.L. Sobolewski, W. Domcke, C. Dedonder-Lardeux, and C. Jouvet. Phys. Chem. Chem. Phys. **4**, 1093 (2002).
22. A.L. Sobolewski and W. Domcke. Eur. Phys. J. D, **20**, 369 (2002).
23. M. Zierhut, W. Roth, and I. Fischer. Phys. Chem. Chem. Phys. **6**, 5178 (2004).
24. I. Hünig, C. Plützer, K.A. Seefeld, D. Löwenich, M. Nispel, and K. Kleinermanns. Chem. Phys. Chem. **5**, 1427 (2004).
25. J. Andreásson and A.H.B. Albinsson. J. Phys. Chem. B, **103**, 9782 (1999).
26. Y. He, C. Wu, and W. Kong. J. Phys. Chem. A, **107**, 5145 (2003).
27. W. Chin, M. Monsa, I. Dimicoli, F. Piuzzi, B. Tardivel, and M. Elhanine. Eur. Phys. J. D, **20**, 347 (2002).
28. E. Nir, C. Plützer, K. Kleinermanns, and M. de Vries. Eur. Phys. J. D, **20**, 317 (2002).
29. C. Plützer and K. Kleinermanns. Phys. Chem. Chem. Phys. **4**, 4877 (2002).
30. N.J. Kim, H. Kang, Y.D. Park, and S.K. Kim. Phys. Chem. Chem. Phys. **6**, 2802 (2004).
31. K.A. Seefeld, C. Plützer, D. Löwenich, T. Häber, R. Linder, K. Kleinermanns, J. Tatchen, and C.M. Marian. Phys. Chem. Chem. Phys. **7**, 3021 (2005).
32. E.C. Lim. J. Phys. Chem. **90**, 6770 (1986).
33. A. Broo. J. Phys. Chem. A, **102**, 526 (1998).
34. R.J. Buenker, V. Bonačić-Koutecký, and L. Pogliani. J. Chem. Phys. **73**, 1836 (1980)
35. S. Kato. J. Phys. Chem. **86**, 3045 (1988).
36. I.J. Palmer, I.N. Ragazos, F. Bernardi, M. Olivucci, and M.A. Robb. J. Am. Chem. Soc. **115**, 673 (1993).
37. A.L. Sobolewski, C. Woywod, and W. Domcke. J. Chem. Phys. **98**, 5627 (1993).
38. M.K. Shukla and P.C. Mishra. Chem. Phys. **240**, 319 (1999).
39. M. Merchań and L. Serrano-Andreś. J. Am. Chem. Soc. **125**, 8108 (2003).
40. A.L. Sobolewski and W. Domcke. Phys. Chem. Chem. Phys. **6**, 2763 (2004).
41. M.Z. Zgierski, S. Patchkovskii, T. Fujiwara, and E.C. Lim. J. Phys. Chem. A, **109**, 9384 (2005).
42. M.Z. Zgierski, S. Patchkovskii, and E.C. Lim. J. Chem. Phys. **123**, 081101 (2005).
43. T. Gustavsson, N. Sarkar, E. Lazzarotto, D. Markovitsi, V.B.R. Improta. J. Phys. Chem. B, **110**, 12843 (2006).
44. N. Ismail, L. Blancafort, M. Olivucci, B. Kohler, and M.A. Robb. J. Am. Chem. Soc. **124**, 6818 (2002).
45. S. Matsika. J. Phys. Chem. A, **108**, 7584 (2004).
46. A.L. Sobolewski and W. Domcke. Chem. Phys. **259**, 181 (2000).
47. C.M. Marian, F. Schneider, M. Kleinschmidt, and J. Tatchen. Eur. Phys. J. D, **20**, 357 (2002).
48. A.L. Sobolewski and W. Domcke. Chem. Phys. **294**, 73 (2003).
49. A.L. Sobolewski, W. Domcke, and C. Hättig. Proc. Natl. Acad. Sci. USA. **102**, 17903 (2005).
50. S. Perun, A.L. Sobolewski, and W. Domcke. J. Phys. Chem. A, **110**, 9031 (2006).
51. J.M. Jean and K.B. Hall. Proc. Natl. Acad. Sci. USA. **98**, 37 (2001).
52. M.K. Shukla and J. Leszczynski. J. Phys. Chem. A, **106**, 4709 (2002).
53. L. Blancafort and M.A. Robb. J. Phys. Chem. A, **108**, 10609 (2004).
54. S. Matsika. J. Phys. Chem. A, **109**, 7538 (2005).
55. S. Perun, A.L. Sobolewski, and W. Domcke. Chem. Phys. **313**, 107 (2005).
56. B. Mennucci, A. Toniolo, and J. Tomasi. J. Phys. Chem. A, **105**, 7126 (2001).
57. J. Černý, V. Špirko, M. Mons, P. Hobza, and D. Nachtigallová. Phys. Chem. Chem. Phys. **8**, 3059 (2006).
58. M.K. Shukla and J. Leszczynski. J. Phys. Chem. A, **109**, 7775 (2005).
59. M.K. Shukla and J. Leszczynski. Chem. Phys. Lett. **414**, 92 (2005).
60. H. Langer, N.L. Doltsinis, D. Marx. Chem. Phys. Chem. **6**, 1734 (2005).
61. H. Langer and N.L. Doltsinis. Phys. Chem. Chem. Phys. **5**, 4516 (2003).
62. H. Langer and N.L. Doltsinis. Phys. Chem. Chem. Phys. **6**, 2742 (2004).
63. B. Mennucci, A. Toniolo, and J. Tomasi. J. Phys. Chem. A, **105**, 4749 (2001).
64. S. Perun, A.L. Sobolewski, and W. Domcke. J. Am. Chem. Soc. **127**, 6257 (2005).
65. C.M. Marian. J. Chem. Phys. **122**, 104314 (2005).
66. L.M. Salter and G.M. Chaban. J. Phys. Chem. A, **106**, 4251 (2002).
67. R.-X. He, X.-H. Duan, and X.-Y. Li. Phys. Chem. Chem. Phys. **8**, 587 (2006).
68. S.K. Mishra, M.K. Shukla, and P.C. Mishra. Spectrochim. Acta A, **56**, 1355 (2000).
69. E.L. Rachofsky, J.B.A. Ross, M. Krauss, and R. Osman. J. Phys. Chem. A, **105**, 190 (2001).
70. H. Chen and S. Li. J. Phys. Chem. A, **109**, 8443 (2005).
71. L. Blancafort. J. Am. Chem. Soc. **128**, 210 (2006).
72. L. Serrano-Andrés, M. Merchán, and A.C. Borin. Proc. Natl. Acad. Sci. USA. **103**, 8691 (2006).
73. M.Z. Zgierski and S. Alavi. Chem. Phys. Lett. **426**, 398 (2006).
74. O. Christiansen, H. Koch, and P. Jłrgensen. Chem. Phys. Lett. **243**, 409 (1995).
75. P. Piecuch, S.A. Kucharski, K. Kowalski, and M. Musial. Comp. Phys. Comm. **149**, 71 (2002).
76. K. Kowalski and P. Piecuch. J. Chem. Phys. **120**, 1715 (2004).
77. M.J. Frisch, G.W. Trucks, H.B. Schlegel, G.E. Scuseria, M.A. Robb, J.R. Cheeseman, V.G. Zakrzewski, J.A. Montgomery, Jr., R.E. Stratmann, J.C. Burant, S. Dapprich, J.M. Millam, A.D. Daniels, K.N. Kudin, M.C. Strain, O. Farkas, J. Tomasi, V. Barone, M. Cossi, R. Cammi, B. Mennucci, C. Pomelli, C. Adamo, S. Clifford, J. Ochterski, G.A. Petersson, P.Y. Ayala, Q. Cui, K. Morokuma, N. Rega, P. Salvador, J.J. Dannenberg, D.K. Malick, A.D. Rabuck, K. Raghavachari, J.B. Foresman, J. Cioslowski, J.V. Ortiz, A.G. Baboul, B.B. Stefanov, G. Liu, A. Liashenko, P. Piskorz, I. Komaromi, R. Gomperts, R.L. Martin,

© 2007 NRC Canada

D.J. Fox, T. Keith, M.A. Al-Laham, C.Y. Peng, A. Nanayakkara, M. Challacombe, P.M.W. Gill, B. Johnson, W. Chen, M.W. Wong, J.L. Andres, C. Gonzalez, M. Head-Gordon, E.S. Replogle, and J.A. Pople. Gaussian 98, Gaussian 98, Revision A.11.3, Gaussian, Inc., Pittsburgh, Penn. 2002.
78. M.W. Schmidt, K.K. Baldridge, J.A. Boatz, S.T. Elbert, M.S. Gordon, J.J. Jensen, S. Koseki, N. Matsunaga, K.A. Nguyen, S. Su, T.L. Windus, M. Dupuis, and J.A. Montgomery. J. Comput. Chem. **14**, 1347 (1993).
79. O. Christiansen, J. Gauss, J.F. Stanton, and P. Jłrgensen. J. Chem. Phys. **111**, 525 (1999).
80. A. Öhrn and O. Christiansen. Phys. Chem. Chem. Phys. **3**, 730 (2001).
81. C. Hättig and A. Köhn. J. Chem. Phys. **117**, 6939 (2002).
82. F. Weigend, A. Köhn, and C. Hättig. J. Chem. Phys. **116**, 3175 (2002).
83. P. Piecuch and M. Włoch. J. Chem. Phys. **123**, 224105 (2005).
84. R. Ahlrichs, M. Bär, M. Häser, H. Hors, and C. Kölmel. Chem. Phys. Lett. **162**, 165 (1989).
85. C. Hättig and F. Weigend. J. Chem. Phys. **113**, 5154 (2000).
86. M. Head-Gordon, R.J. Rico, M. Oumi, and T.J. Lee. Chem. Phys. Lett. **219**, 21 (1994).
87. J.F. Stanton, J. Gauss, N. Ishikawa, and M. Head-Gordon. J. Chem. Phys. **103**, 4160 (1995).
88. F. Zerbetto and M.Z. Zgierski. J. Chem. Phys. **93**, 1235 (1990).
89. B. Albinsson. J. Am. Chem. Soc. **119**, 6369 (1997).
90. A. Holmén, B. Nordén, and B. Albinsson. J. Am. Chem. Soc. **119**, 3114 (1997).
91. L.W. McLaughlin, T. Leong, F. Benseler, and N. Piel. Nucl. Acid. Res. **16**, 5631 (1988).
92. P.-O. Lycksell, A. Gräslund, F. Claesens, L.W. McLaughlin, U. Larsson, and R. Riegler. Nucl. Acid. Res. **15**, 9011 (1987).
93. T.M. Nordlund, D. Xu, K.O. Evans, R. Riegler, A. Gräslund, and L.W. McLaughlin. Biochem. **28**, 9095 (1989).
94. W. Siebrand and M.Z. Zgierski. Chem. Phys. Lett. **72**, 411 (1980).
95. W. Siebrand and M.Z. Zgierski. J. Chem. Phys. **72**, 1641 (1980).
96. W. Siebrand and M.Z. Zgierski. J. Chem. Phys. **75**, 1230 (1981).

© 2007 NRC Canada

Aluminum pentafluorophenyl–amide complexes

Carsten Cornelissen, Gigi Chan, Jason D. Masuda, and Douglas W. Stephan

Abstract: The pentafluoroaryl amine $(C_6F_5)_2NH$ (**1**) reacts with $AlH_3{\cdot}NEtMe_2$ to give $[(C_6F_5)_2N]AlH_2{\cdot}NEtMe_2$ (**2**) and $[(C_6F_5)_2N]_2AlH{\cdot}NEtMe_2$ (**3**). The related fluorinated-aryl amine $(C_6F_5)(n\text{-}C_4H_9)NH$ (**4**) also reacts with $AlH_3{\cdot}NEtMe_2$ to give $[(C_6F_5)(n\text{-}C_4H_9)N]_3Al{\cdot}NEtMe_2$ (**5**). This latter compound undergoes ligand exchange with PMe_3 or *N*-methylimidazole to form $[(C_6F_5)(n\text{-}C_4H_9)N]_3Al{\cdot}PMe_3$ (**6**) and $[(C_6F_5)(n\text{-}C_4H_9)N]_3Al{\cdot}$(Me-imid) (**7**), respectively. The latter amine also reacts with $AlMe_3$, affording $[Me_2AlN(C_6F_5)(n\text{-}C_4H_9)]_2$ (**8**).

Key words: almunium, amides, pentafluorophenylamine.

Résumé : L'amine pentafluorée $(C_6F_5)_2NH$ (**1**) réagit avec le complexe $AlH_3{\cdot}NEtMe_2$ pour conduire à la formation du $[(C_6F_5)_2N]AlH_2{\cdot}NEtMe_2$ (**2**) et du $[(C_6F_5)_2N]_2AlH{\cdot}NEtMe_2$ (**3**). L'amine aromatique fluorée apparentée $(C_6F_5)(n\text{-}C_4H_9)NH$ (**4**) réagit aussi avec le complexe $AlH_3{\cdot}NEtMe_2$ pour conduire à la formation du $[(C_6F_5)(n\text{-}C_4H_9)N]_3Al{\cdot}NEtMe_2$ (**5**). Ce dernier produit subit une réaction d'échange de ligand avec le PMe_3 ou le *N*-méthylimidazole pour conduire à la formation du $[(C_6F_5)(n\text{-}C_4H_9)N]_3Al{\cdot}PMe_3$ (**6**) et du $[(C_6F_5)(n\text{-}C_4H_9)N]_3Al{\cdot}$(Me-imid) (**7**) respectivement. Cette dernière amine réagit aussi avec le $AlMe_3$ avec formation du $[Me_2AlN(C_6F_5)(n\text{-}C_4H_9)]_2$ (**8**).

Mots-clés : aluminium, amides, pentafluorophénylamine.

[Traduit par la Rédaction]

Introduction

Lewis acids play dominant roles as co-catalysts in olefin polymerization and as catalysts in a variety of reactions in organic chemistry. The borane $B(C_6F_5)_3$ has been studied in such applications (1, 2), and a number of studies have targeted structural modifications. For example, Marks and co-workers (3–9), as well as Piers and co-workers (1, 10–13), have developed elegant syntheses to both elaborate the substituents on B or to access *bis*-borane compounds. Related alanes have also been prepared and evaluated for a variety of applications in catalysis (14–16). Generally, fluoroarylalanes have been effective in these applications (17–23), although they have proved to be dangerous, as species such as $Al(C_6F_5)_3$ are known to be heat and shock sensitive. In an effort to develop new Al-based Lewis acids, we began an exploration of the Al–amide derivatives, incorporating pentafluoroaryl substitutents. In this paper, we describe the synthesis and structure of several such compounds. An initial attempt to apply these species to the activation of early metal-catalyst precursors is also briefly described.

Experimental section

General data

All preparations were done under an atmosphere of dry, O_2-free N_2, employing both Schlenk line techniques and an MBraun or Vacuum Atmospheres inert-atmosphere glovebox. Solvents were purified, employing a Grubbs-type solvent purification system, manufactured by Innovative Technologies. All organic reagents were purified by conventional methods. ^1H, $^{31}P\{^1H\}$, ^{19}F, and $^{13}C\{^1H\}$ NMR spectra were recorded on Bruker Avance-300 and -500 spectrometers. All spectra were recorded at 25 °C. Trace amounts of protonated solvents were used as a reference for ^1H NMR spectra, while the solvent was used as a reference for $^{13}C\{^1H\}$ spectra, and chemical shifts for ^1H and $^{13}C\{^1H\}$ spectra were reported relative to $SiMe_4$. $^{31}P\{^1H\}$ NMR spectra were referenced to external 85% H_3PO_4. IR spectra were recorded on a Bruker FTIR spectrometer. Combustion analyses were done in-house, employing a PerkinElmer CHN Analyzer. $(C_6F_5)_2NH$ (**1**) was purchased from Aldrich Chemical Co. $(C_6F_5)(n\text{-}C_4H_9)NH$ **(4)** was prepared following a literature procedure (24).

Synthesis of $[(C_6F_5)_2N]AlH_2{\cdot}EtMe_2$ (2)

A solution of $(C_6F_5)_2NH$ (0.524 g, 1.5 mmol) in toluene (10 mL) was added dropwise to a solution of $AlH_3{\cdot}NEtMe_2$ (3.0 mL, 1.5 mmol, 0.5 mol/L in toluene) at 25 °C. The reaction mixture was stirred overnight, and the solvent was removed in vacuo to yield 0.653 g (1.45 mmol, 97%) of a light yellow oil. ^1H NMR (CD_2Cl_2): 2.85 (q, $^3J_{HH}$ = 7 Hz, 2H, NCH_2Me), 2.48 (s, 6H, NMe_2), 1.18 (t, $^3J_{HH}$ = 7.3 Hz, 3H, NCH_2Me). ^1H NMR (CD_2Cl_2, –80 °C): 3.39 (br s, 2H, Al*H*), the resonance for Al*H* was not observed. $^{13}C\{^1H\}$ NMR (CD_2Cl_2): 144.9 (dm, $^1J_{FC}$ = 239 Hz, *o*-C_6F_5), 138.4 (dm, $^1J_{FC}$ = 246 Hz, *m*-C_6F_5), 138.0 (dm, $^1J_{FC}$ = 250 Hz, *m*-C_6F_5), 126.2 (m, C_6F_5), 54.4 (s, NCH_2Me), 44.5 (s, NMe_2), 8.6 (s, NCH_2Me). ^{19}F NMR (CD_2Cl_2): –149.2 (d, $^3J_{FF}$ = 23 Hz, *o*-C_6F_5), –164.7 (t, $^3J_{FF}$ = 23 Hz, *p*-C_6F_5), –165.5 (m, *m*-C_6F_5). Anal. calcd. for $C_{16}H_{13}AlF_{10}N_2$: C 42.68, H 2.91, N 6.22; found: C 42.46, H 2.56, N 6.13.

Received 13 November 2006. Accepted 6 December 2006. Published on the NRC Research Press Web site at http://canjchem.nrc.ca on 27 February 2007.

C. Cornelissen, G. Chan, J.D. Masuda, and D.W. Stephan.[1] Department of Chemistry & Biochemistry, University of Windsor, Windsor, ON N9B 3P4, Canada.

[1]Corresponding author (e-mail: stephan@uwindsor.ca).

 doi:10.1139/V07-003 © 2007 NRC Canada

Synthesis of $[(C_6F_5)_2N]_2AlH{\cdot}NEtMe_2$ (3)

$AlH_3{\cdot}NEtMe_2$ (5 mL, 2.5 mmol, 0.5 mol/L in toluene) was added dropwise to a vigorously stirring solution of $(C_6F_5)_2NH$ (2.618 g, 7.5 mmol) in toluene (5 mL) at 25 °C. After stirring overnight, the white product was collected on a frit, washed three times with pentane, and dried in vacuo. For a second fraction, the solvent was removed in vacuo, and the crude product **3** was recrystallized from pentane to yield 1.94 g (overall, 1.7 mmol, 68%) of a white solid. ^{1}H NMR (CD_2Cl_2): 2.98 (q, $^3J_{HH}$ = 7 Hz, 2H, NC*H*$_2$Me), 2.52 (s, 6H, NMe_2), 1.14 (t, $^3J_{HH}$ = 7 Hz, 3H, NCH_2*Me*), the resonance for Al*H* was not observed. ^{1}H NMR (CD_2Cl_2, –80 °C): 3.21 (br s, 1H, Al*H*). $^{13}C\{^1H\}$ NMR (CD_2Cl_2): 145.6 (dm, $^1J_{FC}$ = 246 Hz, *o*-C_6F_5), 139.0 (dt, $^1J_{FC}$ = 251 Hz, $^3J_{FC}$ = 13 Hz, *p*-C_6F_5), 138.0 (dm, $^1J_{FC}$ = 255 Hz, *m*-C_6F_5), 124.3 (m, *i*-C_6F_5), 53.0 (s, N*C*H$_2$Me), 43.0 (s, N*Me*$_2$), 6.7 (s, NCH_2*Me*). ^{19}F NMR (CD_2Cl_2): –147.6 (d, $^3J_{FF}$ = 20 Hz, *o*-C_6F_5), –161.7 (t, $^3J_{FF}$ = 21 Hz, *p*-C_6F_5), –164.7 (m, *m*-C_6F_5). Anal. calcd. for $C_{28}H_{12}AlF_{20}N_3$: C 42.18, H 1.52, N 5.27; found: C 41.66, H 1.56, N 5.73. Single crystals suitable for X-ray diffraction experiments were obtained by cooling a saturated pentane solution to –30 °C overnight.

Synthesis of $[(C_6F_5)(n\text{-}C_4H_9)N]_3Al{\cdot}NEtMe_2$ (5)

$AlH_3{\cdot}NEtMe_2$ (5 mL, 2.5 mmol, 0.5 mol/L in toluene) was added dropwise to a vigorously stirring solution of $(C_6F_5)(n\text{-}C_4H_9)NH$ (**4**) (1.794 g, 7.5 mmol) in toluene (5 mL) at 25 °C. After stirring overnight, the solvent was removed in vacuo. The crude product was recrystallized from pentane to yield 1.466 g (1.8 mmol, 72%) of a white solid. ^{1}H NMR (CD_2Cl_2): 3.18 (q, $^3J_{HH}$ = 7 Hz, 2H, NC*H*$_2$Me), 2.92 (m, 6H, NC*H*$_2$CH$_2$), 2.62 (s, 6H, N*Me*$_2$), 1.17 (t, $^3J_{HH}$ = 7 Hz, 3H, N*CH*$_2$Me), 1.04 (m, 6H, NCH_2CH_2), 0.92 (m, 6H, CH_2CH_2Me), 0.76 (m, 9H, CH_2CH_2*Me*). $^{13}C\{^1H\}$ NMR (CD_2Cl_2): 147.4 (dm, $^1J_{FC}$ = 235 Hz, *o*-C_6F_5), 138.2 (dm, $^1J_{FC}$ = 250 Hz, *m*-C_6F_5), 127.6 (m, *ipso*-C_6F_5), 52.1 (s, N*C*H$_2$Me), 51.5 (s, N*Me*$_2$), 43.4 (s, N*C*H$_2$CH$_2$), 32.9 (s, NCH$_2$*C*H$_2$), 20.5 (s, CH$_2$*C*H$_2$Me), 14.0 (s, CH$_2$*C*H$_2$*Me*), 5.3 (s, NCH_2*Me*), the resonances for *p*-C_6F_5 were masked by the *m*-C_6F_5 signal. ^{19}F NMR (CD_2Cl_2): –147.2 (d, $^3J_{FF}$ = 20 Hz, *o*-C_6F_5), –165.1 (t, $^3J_{FF}$ = 21 Hz, *p*-C_6F_5), –166.6 (m, *m*-C_6F_5). Anal. calcd. for $C_{34}H_{38}AlF_{15}N_4$: C 50.13, H 4.70, N 6.88; found: C 50.01, H 4.55, N 6.54. Single crystals suitable for X-ray diffraction experiments were grown from pentane.

Synthesis of $[(C_6F_5)(n\text{-}C_4H_9)N]_3Al{\cdot}PMe_3$ (6) and $[(C_6F_5)(n\text{-}C_4H_9)N]_3Al{\cdot}$(Me-imid) (7)

These compounds were prepared in a similar fashion, using the appropriate reagent; thus, only one preparation is detailed. PMe_3 (0.17 mL, 1.67 mmol) was added to a solution of **5** (545 mg, 0.67 mmol) in toluene (5 mL) and stirred overnight at 25 °C. The solvent was removed in vacuo, and the crude product was recrystallized from pentane to yield 145 mg (0.18 mmol, 27%) of a white microcrystalline solid **6**. ^{1}H NMR (C_7D_8): 3.05 (m, 6H, NC*H*$_2$), 1.06 (m, 12H, C*H*$_2$C*H*$_2$Me), 0.78, (t, $^3J_{HH}$ = 7 Hz, 9H, CH$_2$*Me*), 0.71 (d, $^2J_{PH}$ = 8 Hz, 9H, P*Me*$_3$). $^{13}C\{^1H\}$ NMR (C_7D_8): 146.0 (dm, $^1J_{FC}$ = 240 Hz, *o*-C_6F_5), 137.9 (dm, $^1J_{FC}$ = 252 Hz, *m*-C_6F_5), 136.8 (dm, $^1J_{FC}$ = 253 Hz, *p*-C_6F_5), 136.2 (m, *ipso*-C_6F_5), 49.7 (s, N*C*H$_2$), 33.3 (s, NCH$_2$*C*H$_2$), 20.2 (s, *C*H$_2$Me), 13.7 (s, CH$_2$*Me*), 10.7 (d, $^1J_{PC}$ = 23.2 Hz, P*Me*$_3$), *ipso*-C_6F_5 resonances was not detected. ^{19}F NMR (C_7D_8): –149.4 (d, $^3J_{FF}$ = 23 Hz, *o*-C_6F_5), –165.2 (m, *m*-C_6F_5, *p*-C_6F_5). $^{31}P\{^1H\}$ NMR (C_7D_8): –50.3 (s, *P*Me$_3$). Anal. calcd for $C_{33}H_{36}AlF_{15}N_3P$: C 48.48, H 4.44, N 5.14; found: C 48.22, H 4.21, N 5.01. Compound **7**: 162 mg, white solid (0.2 mmol, 100%). ^{1}H NMR (CD_2Cl_2): 8.00 (s, 1H, NC*H*N), 7.03 (s, 1H, NC*H*CHN), 7.00 (s, 1H, NCHC*H*N), 3.82 (s, 3H, N*Me*), 3.09 (m, 6H, NC*H*$_2$), 1.10 (m, 12H, C*H*$_2$C*H*$_2$Me), 0.76 (t, $^1J_{HH}$ = 7 Hz, 9H, CH$_2$*Me*). $^{13}C\{^1H\}$ NMR (CD_2Cl_2): 146.2 (d, $^1J_{CF}$ = 234 Hz, *o*-C_6F_5), 139.6 (s, N*C*HN), 138.0 (m, *m*-C_6F_5), 127,1 (s, NCH*C*HN), 122.4 (s, MeN*C*H), 49.6 (s, N*C*H$_2$), 35.6 (s, N*Me*), 33.7 (s, NCH$_2$*C*H$_2$), 20.5 (s, *C*H$_2$Me), 14.1 (s, CH$_2$*Me*), resonances for *p*-C_6F_5 and *ipso*-C_6F_5 were not detected. ^{19}F NMR (CD_2Cl_2): –150.4 (d, $^3J_{FF}$ = 20 Hz, *o*-C_6F_5), –167.5 (m, *m*-C_6F_5), –168.7 (m, *p*-C_6F_5). Anal. calcd. for $C_{34}H_{33}AlF_{15}N_5$: C 49.58, H 4.04, N 8.50; found: C 49.21, H 4.13, N 8.67.

Synthesis of $[Me_2AlN(C_6F_5)(n\text{-}C_4H_9)]_2$ (8)

A solution of $(C_6F_5)(n\text{-}C_4H_9)NH$ (1.436 g, 6 mmol) in toluene (6 mL) was added slowly to a solution of $AlMe_3$ (95 μL, 2 mmol) in toluene (3 mL) at –30 °C. The solution was allowed to warm to 25 °C overnight. After the solvent was reduced in vacuo to half of its volume, the solution was stored at –30 °C overnight to yield colourless crystals. The product was collected on a frit in dried in vacuo to yield 862 mg (1.5 mmol, 73%). ^{1}H NMR (C_6D_6): 3.18 (m, 4H, NC*H*$_2$), 1.23 (m, 4H, NCH$_2$C*H*$_2$), 0.97 (m, 4H, *CH*$_2$Me), 0.73 (t, $^3J_{HH}$ = 7 Hz, 6H, CH$_2$Me), –0.04 (m, 6H, $AlMe_2$), –0.73 (m, 6H, $AlMe_2$). $^{13}C\{^1H\}$ NMR (C_6D_6): 145.3 (dm, $^1J_{FC}$ = 244 Hz, *o*-C_6F_5), 139.6 (dm, $^1J_{FC}$ = 255 Hz, *p*-C_6F_5), 138.0 (dm, $^1J_{FC}$ = 257 Hz, *m*-C_6F_5), 122.9 (m, *ipso*-C_6F_5), 55.9 (s, N*C*H$_2$), 29.6 (s, NCH$_2$*C*H$_2$), 20.3 (s, *C*H$_2$Me), 13.7 (s, CH$_2$*Me*), –9.6 (br, Al*Me*$_2$), –10.5 (br, Al*Me*$_2$). ^{19}F NMR (C_6D_6): –140.3 (d, $^3J_{FF}$ = 23 Hz, *o*-C_6F_5), –155.2 (t, $^3J_{FF}$ = 23 Hz, *p*-C_6F_5), –161.9 (dd, $^3J_{FF}$ = 23 Hz, $^3J_{FF}$ = 23 Hz, *m*-C_6F_5). Anal. calcd for $C_{24}H_{30}Al_2F_{10}N_2$: C 48.82, H 5.12, N 4.74; found: C 48.61, H 5.11, N 4.65. Single crystals suitable for X-ray diffraction experiments were obtained by storing a concentrated pentane solution at –30 °C overnight.

X-ray data collection and reduction

Crystals were manipulated and mounted in capillaries in a glovebox, thus, maintaining a dry, O_2-free environment for each crystal. Diffraction experiments were performed on a Siemens SMART System CCD diffractometer. The data were collected in a hemisphere of data in 1329 frames with 10 s exposure times. The observed extinctions were consistent with the space groups in each case. The data sets were collected ($4.5° < 2\theta < 45–50.0°$). A measure of decay was obtained by recollecting the first 50 frames of each data set. The intensities of reflections within these frames showed no statistically significant change over the duration of the data collections. The data were processed using the SAINT and XPREP processing packages. An empirical absorption correction, based on redundant data, was applied to each data set. Subsequent solution and refinement was performed, using the SHELXTL solution package.

Structure solution and refinement

Non-hydrogen atomic-scattering factors were taken from

© 2007 NRC Canada

Table 1. Crystallographic data.

Crystal	**1**	**2**·C_6H_5Me	**4**	**8**
Empirical formula	$C_{12}HF_{10}N$	$C_{35}H_{20}AlF_{20}N_3$	$C_{34}H_{38}AlF_{15}N_4$	$C_{24}H_{30}Al_2F_{10}N_2$
Formula weight	349.14	889.52	814.66	590.46
Crystal system	Monoclinic	Triclinic	Monoclinic	Monolcinic
a (Å)	21.383(5)	12.3959(19)	23.36(3)	14.713(3)
b (Å)	5.9810(14)	12.7928(19)	8.902(10)	12.980(2)
c (Å)	4.5176(11)	13.306(2)	19.97(2)	15.085(3)
α (°)		104.584(2)		
β (°)	100.344(3)	106.602(2)	112.660(15)	98.488(2)
γ (°)		108.169(2)		
Volume (Å^3)	568.4(2)	1781.5(5)	3833(8)	2849.3(9)
Space group	*C*2	*P*1	$P2_1/c$	$P2_1/n$
$D_{calcd.}$ (g cm^{-3})	1.02	1.658	1.412	1.376
Z	1	2	4	4
Absorption coefficient (μ) (mm^{-1})	0.118	0.195	0.156	0.183
Reflections collected	2325	17357	35570	26972
Data $F_o^2 > 3\sigma(F_o^2)$	811	6274	6754	5013
Parameters	107	536	487	349
R_1[a]	0.0291	0.0539	0.0577	0.0557
wR_2[b]	0.0727	0.1112	0.1063	0.1272
Goodness-of-fit	0.729	0.997	0.998	1.019

[a]Data collected at 20 °C with Mo Kα radiation (λ = 0.71069 Å), $R_1 = \Sigma||F_o| - |F_c||/\Sigma|F_o|$.
[b]$wR_2 = [\Sigma w(F_o^2-F_c^2)^2/\Sigma(wF_c)^2]^{1/2}$.

the literature tabulations (25). The heavy-atom positions were determined, using direct methods, employing the SHELXTL direct methods routine. The remaining non-hydrogen atoms were located from successive difference Fourier map calculations. The refinements were carried out by using full-matrix least-squares techniques on *F*, minimizing the function $w(|F_o| - |F_c|)^2$, where the weight *w* is defined as $4F_o^2/2\sigma(F_o^2)$, and F_o and F_c are the observed and calculated structure factor amplitudes, respectively. In the final cycles of each refinement, all non-hydrogen atoms were assigned anisotropic temperature factors in the absence of disorder or insufficient data. In the latter cases, atoms were treated isotropically. H-atom positions were calculated and allowed to ride on the carbon to which they are bonded, assuming a C–H bond length of 0.95 Å. Hydrogen-atom temperature factors were fixed at 1.10 times the isotropic temperature factor of the C atom to which they are bonded. The H-atom contributions were calculated but not refined. The locations of the largest peaks in the final difference Fourier map calculation, as well as the magnitude of the residual electron densities in each case, were of no chemical significance. Additional details are provided in the supplementary data.[2] Crystallographic data for **1**, **2**, **4**, and **8** are given in Table 1.

Results and discussion

The pentafluoroaryl amine $(C_6F_5)_2NH$ (**1**) has not been frequently used as a ligand in main-group or tranisition-metal chemistry. In initiating work with this species, we were able to obtain X-ray quality crystals of **1** (Fig. 1). The reaction of this amine with AlH_3·$NEtMe_2$ in a 1:1 ratio affords a light-yellow oil **2** in 97% isolated yield. The ^{1}H NMR data were consistent with the presence of coordinated $NEtMe_2$, although resonances attributable to Al–H fragments were not observed at 25 °C. At –80 °C, a resonance appeared at 3.39 ppm, and it was attributed to two protons on Al. The ^{19}F NMR spectrum of **2** showed the resonances expected for the amide substituents. Based on these data and elemental analyses, compound **2** was formulated as $[(C_6F_5)_2N]AlH_2$·$NEtMe_2$ (Scheme 1).

Using 1:3 stoichiometry, the reaction of AlH_3·$NEtMe_2$ with $(C_6F_5)_2NH$ proceeds upon stirring at 25 °C for 12 h to afford the product **3** (Scheme 1). The product was recrystallized from pentane to yield a white crystalline material in 83% yield. For compound **3**, the ^{1}H NMR spectrum showed resonance attributable to coordinated $NEtMe_2$, although no resonances attributable to AlH were observed. Nonetheless, similar to **2**, cooling to –80 °C resulted in the observation of a ^{1}H NMR resonance at 3.21 ppm attributable to the single Al–H atom. The $^{13}C\{^1H\}$ NMR spectrum revealed the corresponding ^{13}C resonances, as well as signals arising from C_6F_5 rings. Similarly, the ^{19}F NMR data are consistent with the presence of the $(C_6F_5)_2N$ fragments. Suitable crystals were obtained from a pentane solution at

[2]Supplementary data for this article are available on the journal Web site (http://canjchem.nrc.ca) or may be purchased from the Depository of Unpublished Data, Document Delivery, CISTI, National Research Council Canada, Ottawa, ON K1A 0R6, Canada. DUD 5132. For more information on obtaining material, refer to http://cisti-icist.nrc-cnrc.gc.ca/irm/unpub_e.shtml. CCDC 633717 and 633720 contain the crystallographic data for this manuscript. These data can be obtained, free of charge, via http://www.ccdc.cam.ac.uk/conts/retrieving.html (or from the Cambridge Crystallographic Data Centre, 12 Union Road, Cambridge CB2 1EZ, UK; fax +44 1223 336033; or deposit@ccdc.cam.ac.uk).

© 2007 NRC Canada

Scheme 1.

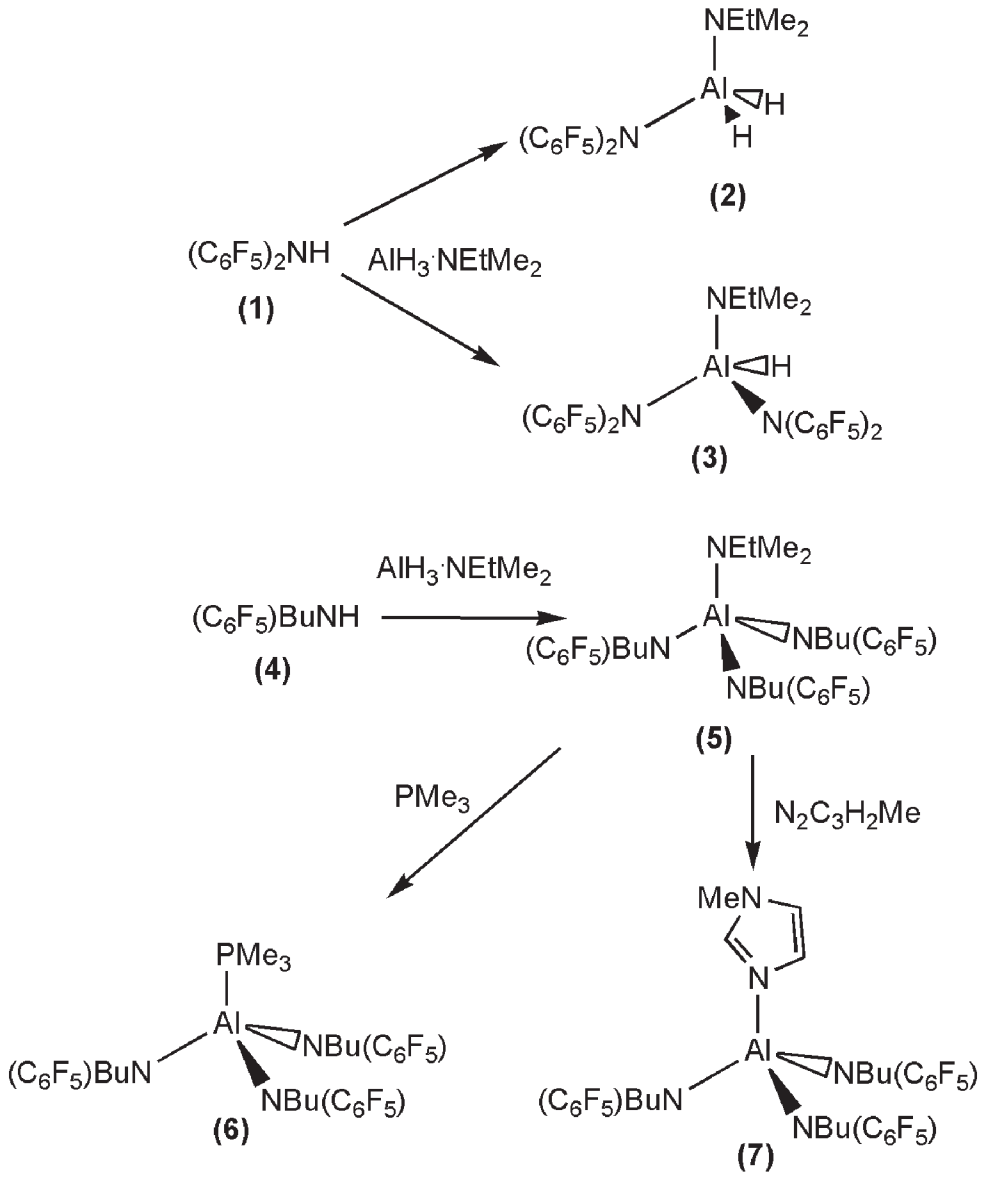
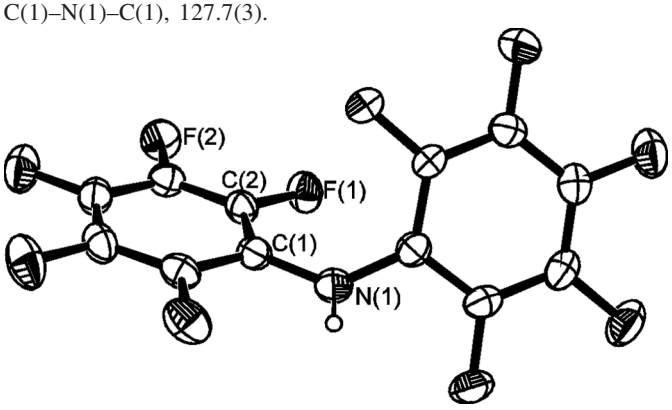


Fig. 1. ORTEP drawing of **1** (30% thermal ellipsoids are shown). Selected distances (Å) and angles (°): N(1)—C(1), 1.389(3); C(1)–N(1)–C(1), 127.7(3).

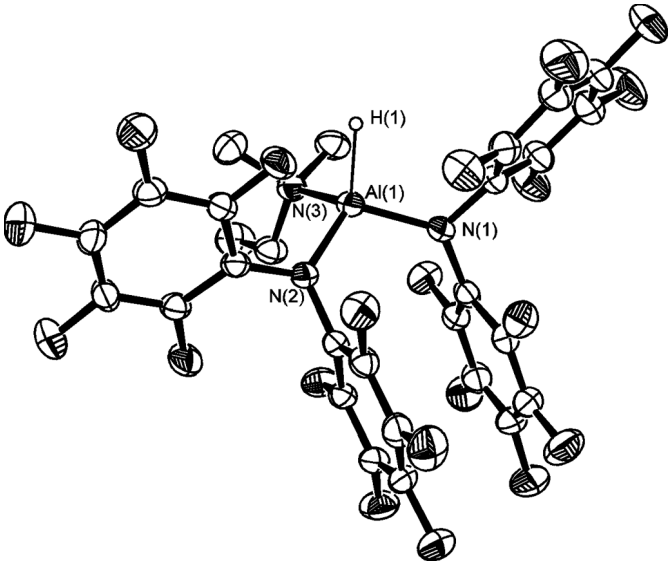


–30 °C, allowing the unambiguous determination of the nature of **3**, as $[(C_6F_5)_2N]_2AlH{\cdot}NEtMe_2$, by a single-crystal X-ray diffraction study (Fig. 2). The geometry about Al is pseudo-tetrahedral, with the amide Al—N distances averaging 1.855(3) Å. The coordinated tertiary amine gives rise to an Al—N distance of 2.006(3) Å. The resulting N–Al–N angles range from 105.48(12)° to 113.78(13)°. The Al-bound H atom was located and refined, giving rise to an Al–H distance of 1.62 Å. Similar Al—H distances have been reported for $(i\text{-}Pr_2C_6H_3N)C(Me)CHPPh_2(NC_6H_3\text{-}i\text{-}Pr_2)AlH_2$ (26). Adjacent arene rings on the two amide ligands are oriented in an approximately parallel offset π-stacking arrangement. The distance between these rings is 3.284 Å, while the angle between the planes is 2°.

The related fluorinated-aryl amine $(C_6F_5)(n\text{-}C_4H_9)NH$ (**4**) was prepared via a known method (24). Reactions of this less bulky and more basic amine with $AlH_3{\cdot}NEtMe_2$ in 1:1 and 2:1 ratios afforded unresolved mixtures of products.

© 2007 NRC Canada

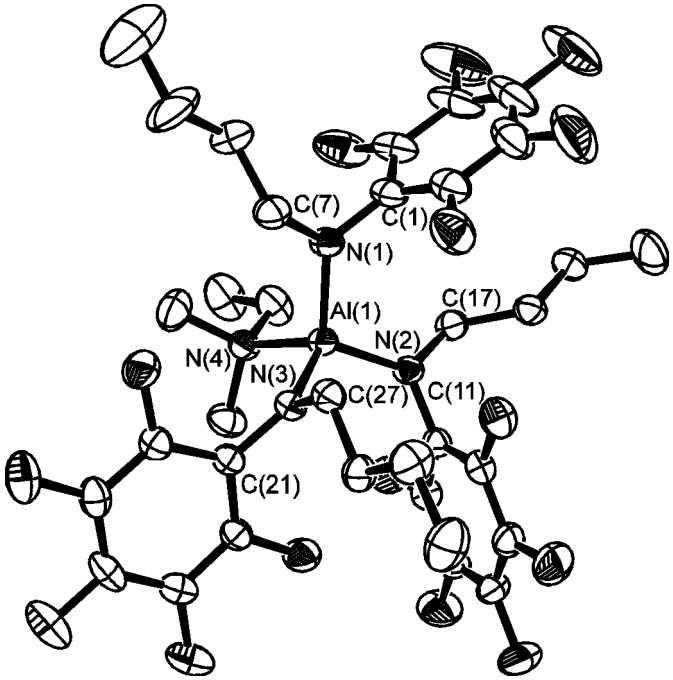
Fig. 2. ORTEP drawing of **2** (30% thermal ellipsoids are shown). All hydrogen atoms except the AlH are omitted for clarity. Selected distances (Å) and angles (°): Al(1)—N(1), 1.855(3); Al(1)—N(2), 1.856(3); Al(1)—N(3), 2.006(3); N(1)–Al(1)–N(2), 111.44(13); N(1)–Al(1)–N(3), 113.78(13); N(2)–Al(1)–N(3), 105.48(12).



However, the reaction of **4** in a 3:1 ratio with $AlH_3{\cdot}NEtMe_2$ proceeded to give a white solid **5** in 72% isolated yield. ^1H NMR data were consistent with a ratio of amide to coordinated $NEtMe_2$ of 3:1. $^{13}C\{^1H\}$ and ^{19}F NMR data also supported the formulation of **5** as $[(C_6F_5)(n\text{-}C_4H_9)N]_3Al{\cdot}NEtMe_2$ (Scheme 1). This view was subsequently confirmed via X-ray crystallography (Fig. 3). The Al center in **5** has a pseudo-tetrahedral geometry with Al—N distances for the amide ligands ranging from 1.827(3) Å to 1.838(4) Å. These distances are slightly shorter than those reported earlier for **3**, consistent with the increased basicity of the amide derived from **4**. The coordinated amine $NEtMe_2$ gave rise to an Al—N distance of 2.043(4) Å. Interestingly, this distance is significantly shorter than that seen in **4**, suggesting that although the Al in **5** has three amide ligands, the Al center is more accessible to the donor, presumably because of the lesser steric demands of the amide substituents.

Compound **5** reacts with other donors to afford the replacement of the coordinated amine. For example, the reaction with PMe_3 results in the formation of the white microcrystalline product **6**, albeit in a relatively low isolated yield of 27%. ^1H NMR confirms the displacement of the coordinated $NEtMe_2$ by PMe_3. In addition, the observation of a $^{31}P\{^1H\}$ NMR signal at –50.3 ppm is consistent with coordination to Al, and thus, the formulation of **6** as $[(C_6F_5)(n\text{-}C_4H_9)N]_3Al{\cdot}PMe_3$ (Scheme 1). In a similar fashion, the reaction of **5** with *N*-methylimidazole $MeN_2C_3H_3$ results in the displacement of the amine, affording the product $[(C_6F_5)(n\text{-}C_4H_9)N]_3Al{\cdot}$(Me-imid) (**7**) in quantitative yields (Scheme 1). NMR data supported this formulation, although repeated attempts to isolate X-ray quality crystals of **7** were unsuccessful. The dramatically higher yields of **7** than **6** are consistent with hard–soft donor considerations, as well as the lesser steric congestion provided by the imidazole N-atom donor.

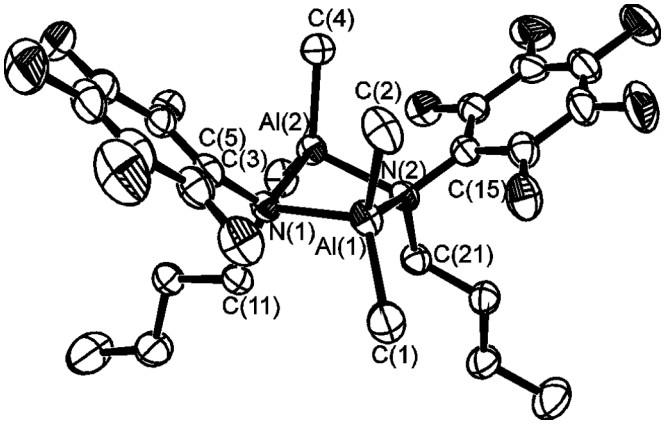
Fig. 3. ORTEP drawing of **4** (30% thermal ellipsoids are shown). Hydrogen atoms are omitted for clarity. Selected distances (Å) and angles (°): Al(1)—N(1), 1.838(4); Al(1)—N(2), 1.833(3); Al(1)—N(3), 1.827(3); Al(1)—N(4), 2.043(4); N(3)–Al(1)–N(2), 114.55(15); N(3)–Al(1)–N(1), 111.01(16); N(2)–Al(1)–N(1), 112.25(14); N(3)–Al(1)–N(4), 106.37(14); N(2)–Al(1)–N(4), 105.66(15); N(1)–Al(1)–N(4), 106.34(14).



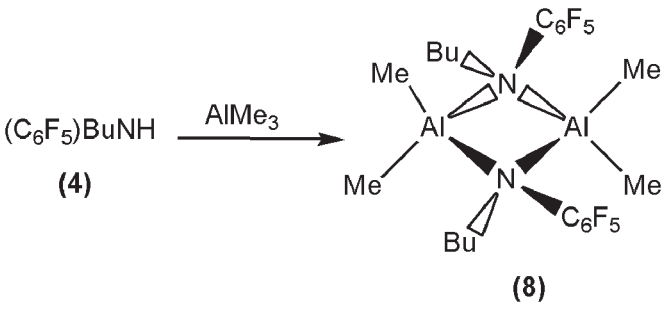
In contrast to the reactions with $AlH_3{\cdot}NEtMe_2$, the amine **4** reacts with $AlMe_3$ in a 1:1 ratio to form the colorless crystalline product **8** in 73% isolated yield. The ^1H NMR spectrum of **8** is consistent with replacement of one methyl group by an amide ligand. However, this spectrum also shows two resonances at –0.04 and –0.73 ppm, attributable to Al-bound methyl groups. This suggests molecular dissymmetry and the formulation of **8** as $[Me_2AlN(C_6F_5)(n\text{-}C_4H_9)]_2$ (Fig 4, Scheme 2). The $^{13}C\{^1H\}$ and ^{19}F NMR and elemental analysis data were also consistent with this formulation. Single crystals of **8**, suitable for X-ray diffraction experiments, were grown from a concentrated pentane solution at –30 °C. The X-ray data confirmed the dimeric formulation of **8**, in which the amido-N atoms bridge the two Al centers. The substituents on N are oriented such that the C_6F_5 rings are on *cis*. It is this feature that accounts for the inequivalent methyl groups on the Al atoms. The Al—N distances were found to range from 1.993(3) Å to 2.031(3) Å, significantly longer than the terminal Al–amide distances described earlier. The geometry and metric parameters are similar to those recently reported for a series of Al-dimers $[Me_2AlN(C_6F_nH_{5-n})H]_2$($n$ = 1, 2, 4, and 5) (27). The Al—C distances range from 1.947(4) to 1.959(3) Å, similar to those seen in the previously mentioned Al-dimers and in $[Me_2Al(NPt\text{-}Bu_3)]_2$ (28). The Al-centers are pseudo-tetrahedral, with C–Al–C′ and N–Al–N′ angles averaging 122.4(2)° and 86.8(1)°, respectively. In addition, the Al_2N_2

© 2007 NRC Canada

Fig. 4. ORTEP drawing of **8** (30% thermal ellipsoids are shown). Hydrogen atoms are omitted for clarity. Selected distances (Å) and angles (°): Al(1)—C(1), 1.947(4); Al(1)—C(2), 1.956(4); Al(1)—N(2), 1.993(3); Al(1)—N(1), 2.031(3); Al(1)—Al(2), 2.8280(14); Al(2)—C(4), 1.958(3); Al(2)—C(3), 1.959(3); Al(2)—N(1), 2.002(3); Al(2)—N(2), 2.030(3); C(1)–Al(1)–C(2), 123.70(18); C(1)–Al(1)–N(2), 112.08(15); C(2)–Al(1)–N(2), 109.36(14); C(1)–Al(1)–N(1), 111.89(14); C(2)–Al(1)–N(1), 106.70(15); N(2)–Al(1)–N(1), 86.87(10); C(4)–Al(2)–C(3), 121.04(18); C(4)–Al(2)–N(1), 110.78(14); C(3)–Al(2)–N(1), 113.11(14); C(4)–Al(2)–N(2), 107.39(14); C(3)–Al(2)–N(2), 112.50(14); N(1)–Al(2)–N(2), 86.65(10); Al(2)–N(1)–Al(1), 89.02(10); Al(1)–N(2)–Al(2), 89.33(10).



Scheme 2.



core is essentially planar, and thus, this results in an Al—Al′ separation of 2.8280(14) Å.

Summary

Several Al compounds incorporating hexafluorophenylamido-ligands have been prepared and characterized. The amides derived from the amines $(C_6F_5)_2NH$ and $(C_6F_5)(n\text{-}C_4H_9)NH$ react with $AlH_3.NEtMe_2$ to give the momeric Al products **2**, **3**, and **5**, with varying numbers of amido-substituents. The degree of substitution appears to be dominated by the steric demands of the amide subsitutents. Donor exchange is facile for **5**, readily affording **6** and **7**. The amine $(C_6F_5)(n\text{-}C_4H_9)NH$ also reacts with $AlMe_3$ to give the dimeric product **8**. These Al–amido species proved to be generally difficult to handle and demonstrated poor reactivity. We will continue to develop new main-group chemistry that will result in new activators for applications in olefin polymerization catalysts.

Acknowledgements

Financial support from the Natural Sciences and Engineering Research Council of Canada (NSERC) is gratefully acknowledged.

References

1. W.E. Piers and T. Chivers. Chem. Soc. Rev. **26**, 345, (1997).
2. G. Erker. Dalton Trans.1883, (2005).
3. Y.-X. Chen, M.V. Metz, L. Li, C.L. Stern, and T.J. Marks. J. Am. Chem. Soc. **120**, 6287, (1998).
4. Y.-X. Chen, C.L. Stern, S. Yang, and T.J. Marks. J. Am. Chem. Soc. **118**, 12451, (1996).
5. L. Li, C.L. Stern, and T.J. Marks. Organometallics, **19**, 3332, (2000).
6. T.J. Marks and Y.-X. Chen. US Patent 6-087-460, 2000.
7. T.J. Marks and Y.-X. Chen. US Patent 6-130-302, 2000.
8. T.J. Marks, L. Li, Y.-X. Chen, M.H. McAdon, and P.N. Nickias. PCT Int. Appl. WO 9906412, 1999.
9. M.V. Metz, D.J. Schwartz, C.L. Stern, T.J. Marks, and P.N. Nickias. Organometallics, **21**, 4159, (2002).
10. D.J.H. Emslie, W.E. Piers, and M. Parvez. Angew. Chem., Int. Ed. Engl. **42**, 1252, (2003).
11. I. Ghesner, W.E. Piers, M. Parvez, and R. McDonald. Organometallics, **23**, 3085, (2004).
12. R. Roesler, W.E. Piers, and M. Parvez. J. Organomet. Chem. **680**, 218, (2003).
13. P.E. Romero, W.E. Piers, S.A. Decker, D. Chau, T.K. Woo, and M. Parvez. Organometallics, **22**, 1266, (2003).
14. T. Ooi, and K. Maruoka. Sci. Synth. **7**, 225, (2004).
15. A.W. Langer, Jr. US Patent 4-096-092, 20 June 1978.
16. G.B. Smith, D.H. McDaniel, E. Biehl, and C.A. Hollingsworth. J. Am. Chem. Soc. **82**, 3560, (1960).
17. T. Belgardt, J. Storre, H.W. Roesky, M. Noltemeyer, and H.-G. Schmidt. Inorg. Chem. **34**, 3821, (1995).
18. J.S. Kim, L.M. Wojcinski, II, S. Liu, J.C. Sworen, and A. Sen. J. Am. Chem. Soc. **122**, 5668, (2000).
19. W.R. Mariott, L.O. Gustafson, and E.Y.-X. Chen. Organometallics, **25**, 3721, (2006).
20. D. Chakraborty, and E.Y.X. Chen. Inorg. Chem. Commun. **5**, 698, (2002).
21. A. Rodriguez-Delgado, and E.Y.-X. Chen. Inorg. Chim. Acta, **357**, 3911, (2004).
22. J. Klosin, G.R. Roof, E.Y.-X. Chen, and K.A. Abboud. Organometallics, **19**, 4684, (2000).
23. W.R. Mariott, L.M. Hayden, and E.Y.-X. Chen. ACS Symp. Ser. **857**, 101, (2003).
24. V.E. Platonov, A. Haas, M. Schelvis, M. Lieb, K.V. Dvornikova, O.I. Osina, T.V. Rybalova, and Y.V. Gatilov. J. Fluorine Chem. **114**, 55, (2002).
25. D.T. Cromer, and J.T. Waber. Int. Tables X-ray Crystallogr. **4**, 71, (1974).
26. J.D. Masuda, D.M. Walsh, P. Wei, and D.W. Stephan. Organometallics, **23**, 1819, (2004).
27. P. Shukla, A.H. Cowley, J.N. Jones, J.C. Gordon, and B.L. Scott. Dalton Trans.1019, (2005).
28. C.M. Ong, P. McKarns, and D.W. Stephan. Organometallics, **18**, 4197, (1999).

© 2007 NRC Canada

The reactivity of an anionic gallium *N*-heterocyclic carbene analogue with a solution stable digermene

Paul A. Rupar, Michael C. Jennings, and Kim M. Baines

Abstract: The reaction of the anionic gallium(I) *N*-heterocyclic carbene (NHC) analogue **3** with the solution stable digermene **5** results in the formation of the gallium NHC – germylene complex **8**. The gallium NHC – germylene complex **8** was derivatized with CH_3I and $(CH_3)_3SiCl$.

Key words: digermene, carbene analogue, germylene, gallium(I).

Résumé : Le composé **3**, un analogue du carbène *N*-hétérocyclique (CNH) anionique du gallium(I), réagit avec une solution stable de digermène **5** pour conduire à la formation du complexe CNH du gallium – germylène, **8**. On a préparé les dérivés de ce complexe avec le CH_3I et le $(CH_3)_3SiCl$.

Mots-clés : digermène, analogue de carbène, germylène, gallium(I).

[Traduit par la Rédaction]

Introduction

There is a growing interest in the chemistry of low-valent gallium compounds because of their inherently interesting structure and bonding and their potential utility in the synthesis of novel transition-metal and main-group species (1). Although many stable gallium(I) compounds have been reported, the synthesis of the negatively charged gallium *N*-heterocyclic carbene $KGa\{N(Ar)CH\}_2$ (Ar = 2,6-diisopropylphenyl) (**3**) was particularly significant, since it can be synthesized reliably in high yield, and thus, it is a readily accessible reagent for the synthesis of new gallium-containing compounds (2). For many years, we have been interested in the reactions of digermenes, with a focus on cycloaddition reactions and the formation of small ring systems (3). The lack of synthetic methods for small rings, containing both gallium and germanium (4), and the accessibility of **3** prompted us to examine its reaction with digermenes, as a potential method for the synthesis of a three-membered ring containing both gallium and germanium.

Recently, the reaction between **3**·tmeda (tmeda = tetramethylethylenediamine) and two digermenes ($R_2Ge{=}GeR_2$, R = $CH(SiMe_3)_2$ (**1a**) and R = 2,4,6-triisopropylphenyl (**2a**)) has been reported (5). Complex **4** was isolated from the reaction of **3**·tmeda with digermene **1a** (see Scheme 1). Digermene **1a** readily dissociates to germylene **1b** in solution, and thus, the formation of the anionic complex **4** is most likely because of the direct reaction of **3**·tmeda with the germylene **1b**. No reaction was observed between digermene **2a** and **3**·tmeda. Unlike digermene **1a**, digermene **2a** does not readily dissociate in solution at room temperature (6), providing a plausible explanation for the difference in reactivity between the two digermenes.

We now report on the reaction between gallium(I) **3** and the digermene, tetramesityldigermene (**5a**), which does not dissociate in solution,[2] and we will compare our results to those of the previous study (5).

Results and discussion

The addition of two equivalents of **3** to a yellow THF solution of **5a** initially results in the formation of a dark-red solution, which rapidly changes colour to orange (Scheme 2). After the removal of the solvent, analysis of the product mixture by ^{1}H NMR spectroscopy revealed the presence of a new compound **8** and hexamesitylcyclotrigermane (**6**) in a 9:1 ratio. The ^{1}H NMR spectrum of compound **8** revealed that it contained a $\{N(Ar)CH\}_2$ ligand and two equivalent mesityl groups. Compound **8** was purified by successive washes with hexanes. Crystals of **8** were grown from toluene at –30 °C and unambiguously identified by X-ray crystallography as the anionic, donor-stabilized germylene (Scheme 2).

Compound **8** crystallized as a symmetrical dimer, half of which is shown in Fig. 1. The structural metrics of **8** are similar to those previously reported for **4** (5). The unsolvated potassium is directly associated with the germanium with a bond length of 3.3987(15) Å. Furthermore, the potassium

Received 4 January 2007. Accepted 7 January 2007. Published on the NRC Research Press Web site at http://canjchem.nrc.ca on 27 February 2007.

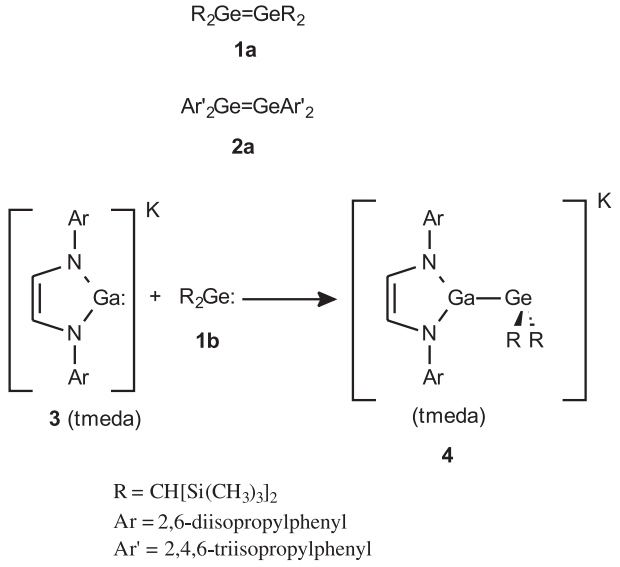
P.A. Rupar, M.C. Jennings, and K.M. Baines.[1] Department of Chemistry, The University of Western Ontario, London, ON N6A 5B7, Canada.

[1]Corresponding author (e-mail: kbaines2@uwo.ca).

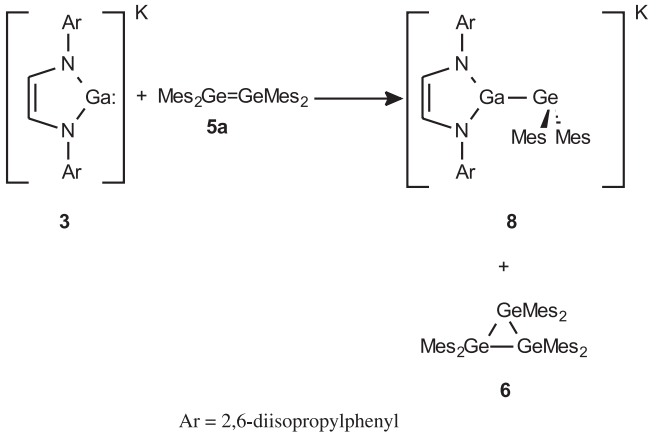
[2]The addition of 2,3-dimethylbutadiene, a well-known and efficient trap for germylenes, to a THF solution of tetramesityldigermene does not yield any 1,1-dimesityl-3,4-dimethylgermacyclopent-3-ene (K.L. Hurni, P.A. Rupar, and K.M. Baines, unpublished results).

 doi:10.1139/V07-002 © 2007 NRC Canada

Scheme 1.

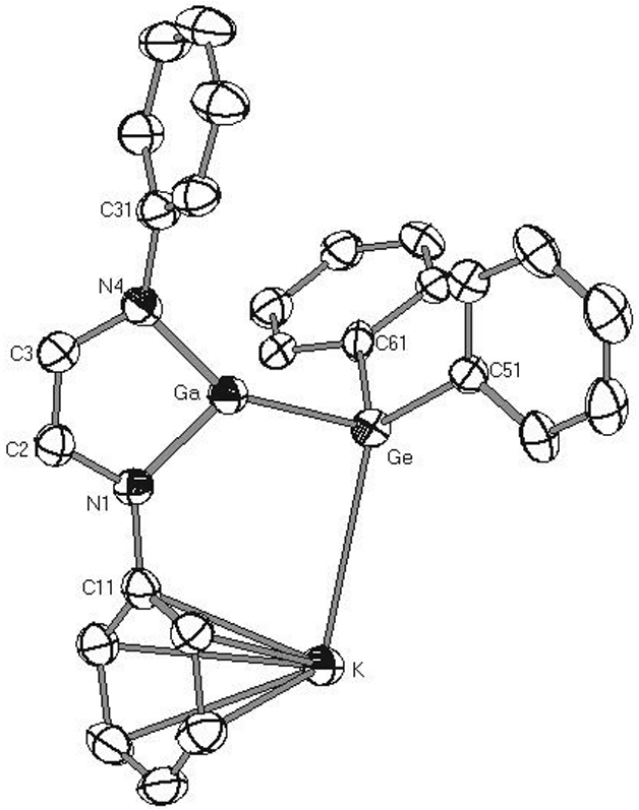


Scheme 2.



bridges between the aromatic diisopropylphenyl group of one molecule and the aromatic ring of the mesityl group of a second molecule (not shown in Fig. 1). The metrics of the $\{N(Ar)CH\}_2$ backbone are typical of those found in other gallium NHC complexes, i.e, the N—Ga bond length (average is 1.886 Å) is significantly shorter, and the N–Ga–N bond angle is larger (85.8(2)°), compared with the uncomplexed anionic gallium NHC (approximately 2.01 Å and 82°, respectively). The Ga—Ge bond length in **8** is 2.4600(8) Å, which is typical of other gallium–germanium single bonds,[3] but shorter than that found in **4**. The longer Ga—Ge bond length in **4** (2.5396(8) Å) was attributed to the increased steric congestion around the germanium centre (5). The geometry about the germanium in **8** is pyramidal, and the Ga–Ge–Mes bond angles are more acute (99.01(16) Å and 102.85(15) Å) than expected, given the steric bulk. Also, the K–Ge–C51–C61 fragment is close to planar (sum of the angles is 355.5°). These features are consistent with the previous report, suggesting that the germanium centre can be described as sp^2-hybridized with the gallium donating

Fig. 1. Thermal ellipsoid plot (50% probability surface) of **8**. Isopropyl groups, methyl groups, and hydrogens have been omitted for clarity. Selected bond lengths (Å): Ge—Ga = 2.4600(8), Ge—K = 3.3987(15), Ge—C(51) = 2.021(6), Ge—C(61) = 2.030(6), Ga—N(1) = 1.887(5), Ga—N(4) = 1.884(5), N(1)—C(2) = 1.392(7), N(4)—C(3) = 1.378(7), C(2)—C(3) = 1.323(7), N(1)—C(31) = 1.439(7), N(4)—C(11) = 1.4306(7); and angles (°): Ga–Ge–C(51) = 99.01(16), Ga–Ge–C(61) = 102.85(15), Ga–Ge–K = 90.02(3), C(51)–Ge–K = 119.28(17), C(61)–Ge–K = 126.97(16), C(51)–Ge–C(61) = 109.2(2), N(1)–Ga–N(4) = 85.8(2), Ge–Ga–N(4) = 149.47(15), Ge–Ga–N(1) = 123.88(14), Ga–N(4)–C(3) = 110.1(4), Ga–N(1)–C(2) = 110.7(4), N(4)–C(3)–C(2) = 116.9(6), N(1)–C(2)–C(3) = 116.5(6), Ga–N(1)–C(11) = 129.7(4), Ga–N(4)–C(31) = 129.6(4).



into the empty p orbital on the germanium (5), as in a base-stabilized germylene.

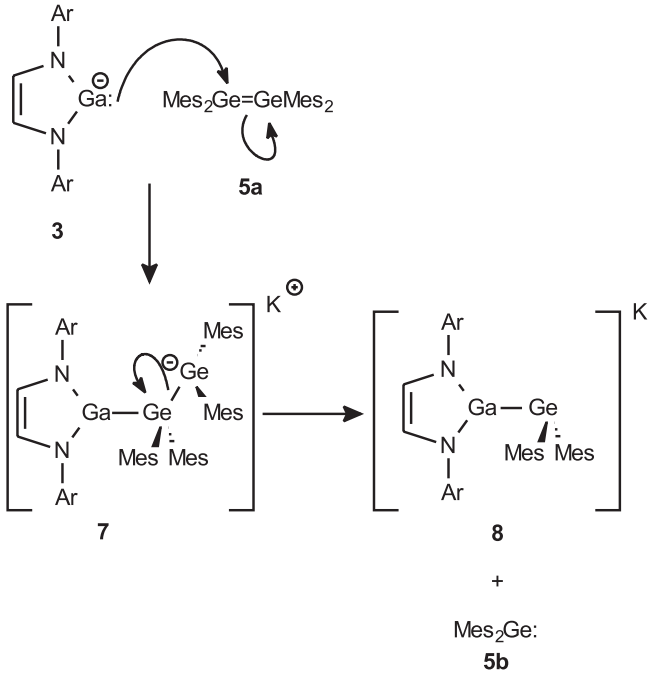
Unlike digermene **1a**, digermene **5a** does not dissociate to the corresponding germylene in solution. Thus, we do not believe that the major pathway to compound **8** is by the direct reaction of the germylene with the gallium NHC **3**. We propose that the addition of **3** to digermene **5a** initially yields the germyl potassium **7**, which then eliminates the transient dimesitylgermylene **5b** (Scheme 3).

Germylene **5b** can then dimerize to give **5a** (7), react with a molecule of **3** to form **8**, or insert into the double bond of **5a**, resulting in the formation of cyclotrigermane **6** (Scheme 4) (8). Because digermene **5a** is generated by the photolysis of cyclotrigermane **6**, the observation of the cyclotrigermane in the product mixture may also be attributed to incomplete photolysis. However, careful examination of the ^{1}H NMR

[3] A survey of the Cambridge Crystallographic Database revealed a Ga—Ge single-bond length average of 2.46 Å.

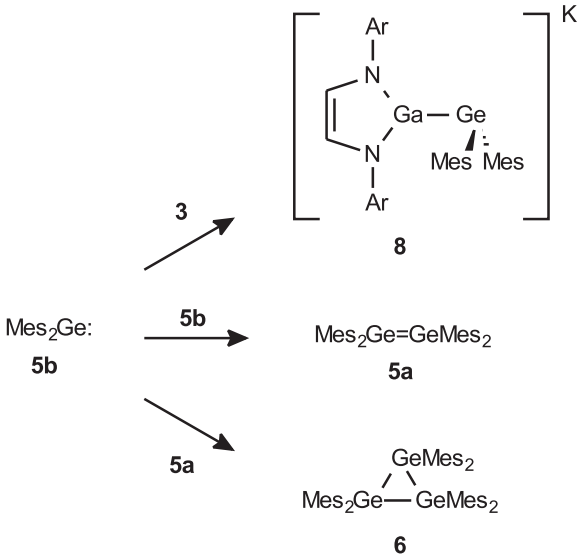
© 2007 NRC Canada

Scheme 3.



Ar = 2,6-diisopropylphenyl

Scheme 4.

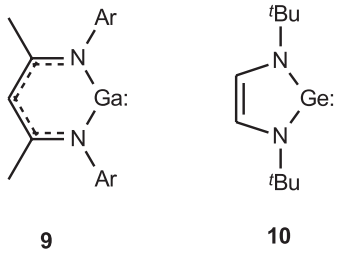


Ar = 2,6-diisopropylphenyl

spectrum of the solution of **5a** prior to the addition of **3** revealed the complete absence of cyclotrigermane **6**. Thus, the amount of cyclotrigermane present must be less than 5% (the assumed lower detection limit of the NMR experiment). This is much less than the 10% generated during the reaction of **5a** with **3.**

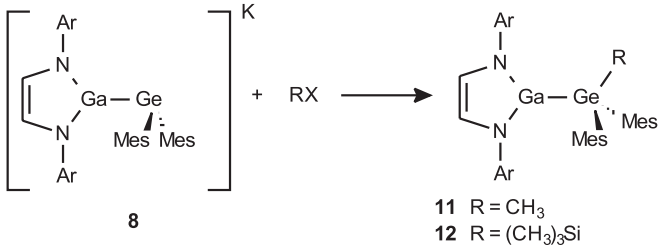
A similar mechanism has been proposed to explain the results of the addition of Grignard reagents to tetramesityldigermene **5a** (9). The nucleophilic addition of RMgX to the digermene resulted in the formation of a germyl Grignard reagent, which underwent subsequent elimination of MesMgX to give a germylene. Our results show that direct addition of **3** to digermenes is possible, and the reaction of **3** with a digermene does not require prior dissociation to a germylene.

Chart 1.



Ar = 2,6-diisopropylphenyl

Scheme 5.



RX = CH_3I
or
$(CH_3)_3SiCl$

Ar = 2,6-diisopropylphenyl

We have also investigated the reactivity of two additional NHC analogues towards **5a**. The neutral gallium(I) HC[MeC(2,6-*i*-$Pr_2C_6H_3$)N]$_2$Ga (**9**) (10) and the germanium NHC analogue Ge{N(*t*-Bu)C(H)}$_2$ (**10**) (11) (Chart 1) were added to a solution of digermene **5a**. However, in both cases, no reaction was observed, likely because of the decreased nucleophilicity of these compounds.

Salt-elimination reactions of 8

To explore the reactivity of **8**, both CH_3I and $(CH_3)_3SiCl$ were added to the new complex (Scheme 5). The addition of CH_3I to a solution of **8** dissolved in THF resulted in the instantaneous formation of a white precipitate. Analysis of the reaction mixture by ^{1}H NMR spectroscopy revealed the quantitative conversion of **8** to a new species **11**. The product was unambiguously identified by mass spectrometry and NMR spectroscopy. The EI mass spectrum of **11** revealed the highest-mass ion at *m/z* 772, with the expected isotopic distribution corresponding to the molecular ion of methylated **8**. The ^{1}H–^{13}C gHMBC spectrum of **11** showed a correlation between the signal at 0.77 ppm in the ^{1}H dimension, assigned to the Ge–CH_3 group, and the signal at 136.20 ppm in the ^{13}C dimension, assigned to the *ipso*-mesityl carbon. All signals in the ^{1}H and ^{13}C NMR spectra of **11** were entirely consistent with the proposed structure.

© 2007 NRC Canada

The addition of $(CH_3)_3SiCl$ to a THF solution of **8** resulted in the rapid change in colour of the solution from orange to yellow. NMR spectroscopic analysis (^1H, ^{13}C, and ^{29}Si) of the solid, isolated after solvent removal, was consistent with the formation of the trimethylsilyl adduct of **8**. Yellow crystals of **12** were grown from a solution of toluene and acetonitrile at –30 °C and analyzed by X-ray diffraction. Compound **12** crystallizes with two distinct molecules in the asymmetric unit. Although chemically identical, they differ structurally by the orientation of the mesityl substituents and the length of the gallium–germanium bond. The difference in the Ga—Ge bond length (2.4082(9) Å vs. 2.4312(10) Å) is most likely because of the increased steric demands caused by the rotation of one of the mesityl substituents. Only one of the molecules from the unit cell is presented in Fig. 2.

The structure of **12** is similar to that of **8** except the potassium has been replaced with $(CH_3)_3Si$. The metrics of the *N*-heterocyclic backbone are essentially unchanged from **8**. The geometry about the germanium is now a distorted tetrahedron. The Ga–Ge–*ipso*-C angles have increased from 99.01(16)° and 102.85(15)° in **8** to 103.31(12)° and 113.63(11)° in **12**. Interestingly, the Ga—Ge bond length has decreased from 2.4600(8) Å in **8** to 2.4312(10) Å in **12** despite the added steric bulk of the $(CH_3)_3Si$ group. In the initial report on the synthesis of **4**, the orbital contribution from germanium to the gallium–germanium bond was described as being mostly p in character because of the lack of change in hybridization (5). We believe that in the $(CH_3)_3Si$ adduct **1**, the orbital contribution from germanium is more sp^3 in character, resulting in a contraction of the gallium–germanium bond.

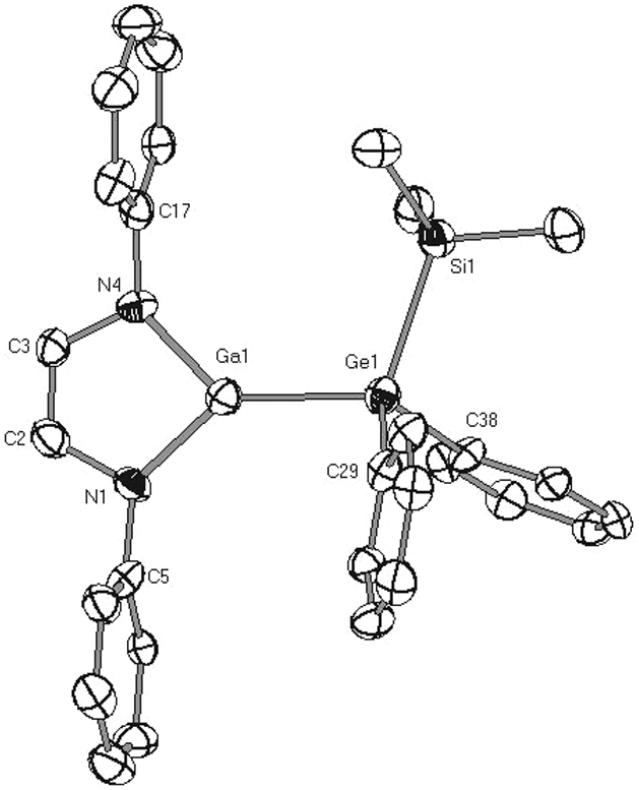
Conclusions

In summary, the addition of the gallium NHC analogue **3** to the solution stable digermene **5a** resulted in the formation of complex **8**. The molecular structure of **8** was determined and found to be similar to the previously reported gallium NHC complex **4** (5). The formation of **8** from **5a** demonstrates that the gallium NHC analogue **3** is able to add directly to digermenes and cause subsequent cleavage of the germanium–germanium bond. Dissociation of digermenes into germylenes is not a prerequisite for a reaction to occur with **3**. The gallium(I) compound **9** and the germanium NHC analogue **10** have both been found to be unreactive towards digermene **5a**, presumably because they are less nucleophilic than **3**.

Finally, the anionic complex **8** was derivatized with CH_3I and $(CH_3)_3SiCl$, forming compounds **11** and **12**, respectively. The molecular structure of the $(CH_3)_3Si$ adduct **12** was determined and the Ga—Ge bond length decreased, compared with the parent compound **8**. This is consistent with the bonding model proposed for gallium NHC base-stabilized germylenes (5).

We are continuing our research on the synthesis of gallium–germanium ring systems. Other methods are now being explored, including salt eliminations. We will report on our subsequent findings in due course.

Fig. 2. Thermal ellipsoid plot (50% probability surface) of **12**. Isopropyl groups, methyl groups, and hydrogens have been omitted for clarity. Selected bond lengths (Å): Ge(1)—Ga(1) = 2.4311(10), Ge(1)—Si(1) = 2.4162(19), Ge(1)—C(29) = 2.011(3), Ge(1)—C(38) = 2.026(3), Ga(1)—N(1) = 1.881(5), Ga(1)—N(4) = 1.862(4), N(1)—C(2) = 1.389(7), N(4)—C(3) = 1.392(7), C(2)—C(3) = 1.335(8), N(1)—C(5) = 1.428(5), N(4)—C(17) = 1.437(5); and angles (°): Ga(1)–Ge(1)–Si(1) = 107.65(5), Ga(1)–Ge(1)–C(29) = 103.31(12), Ga(1)–Ge(1)–C(38) = 113.63(11), Si(1)–Ge(1)–C(29) = 125.33(13), Si(1)–Ge(1)–C(38) = 99.15(13), C(29)–Ge(1)–C(38) = 108.13(16), Ge(1)–Ga(1)–N(1) = 137.68(15), Ge(1)–Ga(1)–N(4) = 134.19(17), Ga(1)–N(1)–C(2) = 108.4(4), Ga(1)–N(4)–C(3) = 109.1(4), N(1)–Ga–N(4) = 88.1(2), N(1)–C(2)–C(3) = 117.3(6), N(4)–C(3)–C(2) = 117.0(6), Ga(1)–N(1)–C(5) = 131.3(4), Ga(1)–N(4)–C(17) = 130.5(4).



Experimental

All manipulations were carried out under a dry N_2 environment at room temperature in a glovebox. Solvents were dried by passing through an alumina column and were subsequently degassed. $KGa\{N(Ar)CH\}_2$ was synthesized following the literature procedure (2). All other chemicals were purchased from commercial sources and used without further purification. NMR chemical shifts are reported in ppm with coupling constants in hertz. All spectra were acquired using C_6D_6 as the solvent. ^1H NMR spectra were referenced to residual C_6D_5H (7.15 ppm). ^{13}C spectra were referenced to the ^{13}C central transition (128.0 ppm) of C_6D_6. ^{13}C signals were unambiguously assigned using ^1H–^{13}C gHSQC and ^1H–^{13}C gHMBC spectroscopy. ^{29}Si chemical shifts were obtained using ^1H–^{29}Si gHMBC spectroscopy and refer-

© 2007 NRC Canada

enced externally to $(CH_3)_4Si$ (0.0 ppm). The purity of all compounds was determined by ^1H NMR spectroscopy (see supplementary data).[4] Melting points were determined under a N_2 atmosphere and are uncorrected.

Preparation of $KMes_2GeGa\{[N(Ar)CH]_2\}$ (8)

To a yellow solution of Mes_4Ge_2 (**5a**) (0.161 mmol, from the photolysis of 100 mg of Mes_6Ge_3 (**6**)) dissolved in THF (5 mL) was added a red THF (2 mL) solution of $KGa\{N(Ar)CH\}_2$ (**3**) (0.32 mmol, 0.16 g) to give a dark red solution. After 5 min, the colour of the solution changed to orange. The solvent was removed under vacuum, yielding an orange residue. The residue was taken up in hexanes, and a centrifuge was used to remove the suspended salts. The yellow precipitate was collected and washed with hexanes repeatedly. Compound **8** was collected, as a yellow powder, in 60% yield (0.15 g, 0.19 mmol); mp 98 °C dec. ^1H NMR: 1.02 (d, $^3J_{HH}$ = 6 Hz, 12 H, *i*-Pr CH_3), 1.23 (d, $^3J_{HH}$ = 6 Hz, 12 H, *i*-Pr CH_3), 2.15 (s, 6 H, *p*-Mes–CH_3), 2.21 (s, 12 H, *o*-Mes–CH_3), 3.58 (sept, $^3J_{HH}$ = 7 Hz, 4 H, *i*-Pr CH), 6.30 (s, 2 H, C_2H_2), 6.67 (s, 4 H, *m*-Mes–H), 7.01 (s, 6 H, *m*,*p*-Ar–H). $^{13}C\{^1H\}$NMR: 20.96 (*p*-Mes–CH_3), 24.40 (*i*-Pr–CH_3), 25.56 (*i*-Pr–CH_3), 27.04 (*o*-Mes–CH_3), 28.30 (*i*-Pr–CH), 121.40 (C_2H_2), 122.86 (*m*-Ar–CH), 124.86 (*p*-Ar–CH), 128.28 (*m*-Mes–CH), 134.36 (*p*-Mes–C), 143.14 (*o*-Mes–C), 147.02 (*o*-Ar–C), 148.47 (*i*-Ar–C), 150.83 (*i*-Mes–C). ESIMS (negative ion) *m*/*z* (%): 376 ($[\{N(Ar)CH\}_2]^-$, 100).

Preparation of $MeMes_2GeGa\{[N(Ar)CH]_2\}$ (11)

Excess methyl iodide (0.1 mL) was added to an orange THF (5 mL) solution of **8** (0.16 mmol, 130 mg). A white precipitate formed instantly, and the solution turned yellow. The solvent was removed under vacuum, and the residue was extracted with hexanes. The suspended salts were removed by centrifugation, yielding a yellow hexanes solution. The solvent was removed under vacuum to give **11**, as a yellow powder, in a yield of 97% (0.12 g, 0.155 mmol). ^1H NMR: 0.77 (s, 3 H, CH_3–Ge), 1.13 (d, $^3J_{HH}$ = 7 Hz, 12 H, *i*-Pr CH_3), 1.26 (d, 12 H, $^3J_{HH}$ = 6 Hz, *i*-Pr CH_3), 2.02 (s, 6 H, *p*-Mes–CH_3), 2.15 (s, 12 H, *o*-Mes–CH_3), 3.57 (sept, 4 H, $^3J_{HH}$ = 7 Hz, *i*-Pr CH), 6.32 (s, 2 H, C_2H_2), 6.57 (s, 4 H, *m*-Mes–H), 7.13–7.20 (m, 6 H, *m*,*p*-Ar–H). $^{13}C\{^1H\}$NMR: 5.35 (Ge–Me), 20.84 (*p*-Mes–CH_3), 23.84 ($CH(CH_3)_2$), 24.58 (*o*-Mes–CH_3), 25.98 ($CH(CH_3)_2$), 28.68 ($CH(CH_3)_2$), 121.94 (C_2H_2), 123.30 (*m*-Ar–CH), 125.96 (*p*-Ar–CH), 129.54 (*m*-Mes–CH), 136.20 (*i*-Mes–C), 138.22 (*p*-Mes–C), 142.22 (*o*-Mes–C), 145.63 (*o*-Ar–C), 145.70 (*i*-Ar–*C*); EIMS *m*/*z* (%): 772 ($[M]^+$, 50), 564 ($[M^+$ – GeMesMe], 70), 445 ($[Ga\{N(Ar)CH\}_2]^+$, 30), 327 ($[GeMes_2Me]^+$, 100). HR-EIMS: calcd. for $C_{45}H_{61}{}^{69}Ga^{74}GeN_2$ 772.331; found: 772.328.

Preparation of $(CH_3)_3SiMes_2GeGa\{[N(Ar)CH]_2\}$ (12)

Excess $(CH_3)_3SiCl$ (50 µL, 0.39 mmol) was added to an orange THF solution (2 mL) of **8** (100 mg, 0.12 mmol). The colour of the solution immediately turned yellow, and the solution was stirred for 5 min. The solvent was removed under vacuum, yielding a yellow residue. The residue was taken up in hexanes (5 mL), and the suspended solids were removed by centrifugation. The hexanes were removed under vacuum, leaving behind a yellow-orange residue of essentially pure **12** with a yield of 67% (0.07 g, 0.08 mmol); mp 190–192 °C. ^1H NMR: –0.01 (s, 9 H, $Si(CH_3)_3$), 1.14 (d, $^3J_{HH}$ = 7 Hz, 12 H, *i*-Pr CH_3), 1.27 (d, $^3J_{HH}$ = 7 Hz, 12 H, *i*-Pr CH_3), 2.05 (s, 6 H, *p*-Mes–CH_3), 2.08 (s, 12 H, *o*-Mes–CH_3), 3.53 (sept, $^3J_{HH}$ = 7 Hz, 2 H, *i*-Pr–CH), 6.31 (s, 2 H, C_2H_2), 6.82 (s, 4 H, *m*-Mes–CH), 7.12–7.21 (m, 6 H, *m*,*p*-Ar–CH). $^{13}C\{^1H\}$NMR: 1.36, 14.34, 20.85, 23.37, 26.29, 26.52, 28.85, 122.58, 123.31, 125.88, 129.15, 136.58, 137.45, 142.37, 145.80, 146.42. ^{29}Si NMR: –2.3. EIMS *m*/*z* (%): 830 ($[M]^+$, 58), 564 ($[M^+ – (CH_3)_3SiGeMes$, 21), 445 ($[M^+ – (CH_3)_3SiGeMes_2]$, 43), 385 ($[(CH_3)_3SiGeMes_2]$, 100).

Crystal structure determinations[5]

Crystals of **8**·(2 toluene) were grown from a concentrated toluene solution. A flat, yellow needle was mounted on a glass fibre stored at –30 °C. Crystallographic parameters are given in Table 1. Data were collected at low temperature (–123 °C) on a Nonius Kappa-CCD area detector diffractometer with COLLECT (Nonius B.V., Delft, The Netherlands, 1999). The unit cell parameters were calculated and refined from the full data set. Crystal cell refinement and data reduction were carried out, using HKL2000 DENZO-SMN (12). The absorption correction was applied, using HKL2000 DENZO-SMN (SCALEPACK).

The SHELXTL/PC V6.14 for Windows NT (Bruker AXS, Madison, Wisconsin) suite of programs was used to solve the structure by direct methods. Subsequent difference Fourier syntheses allowed the remaining atoms to be located. The molecule was well ordered and consisted of two Ga–Ge moieties linked by a K atom. The K atom produced a dimer by forming an interaction with the two different aromatic rings. The toluene molecules of solvation were also well ordered. All of the non-hydrogen atoms were refined with anisotropic thermal parameters. The hydrogen-atom positions were calculated geometrically and were included as riding on their respective carbon atoms.

The largest-residue electron-density peak (0.756 e/Å^3) was associated with the Ga–Ge bond. Full-matrix least-squares refinement on F^2 gave R_1 = 7.09 for 2σ data and wR_2 = 18.17 for all data (GoF = 1.023).

Crystals of **12**·(2.5 toluene) were grown from a concentrated toluene–acetonitrile solution at –30 °C. Crystallographic parameters are given in Table 1. A yellow plate was mounted on a glass fibre. Data were collected at low temperature (–123 °C) on a Nonius Kappa-CCD area detector diffractometer with COLLECT (Nonius B.V., Delft, The Netherlands, 1999). The unit cell parameters were calculated and refined from the full data set. Crystal cell refinement

[4] Supplementary data for this article are available on the journal Web site (http://canjchem.nrc.ca) or may be purchased from the Depository of Unpublished Data, Document Delivery, CISTI, National Research Council Canada, Ottawa, ON K1A 0S2, Canada. DUD 5127. For more information on obtaining material, refer to http://cisti-icist.nrc-cnrc.gc.ca/irm/unpub_e.shtml.

[5] CCDC 632305 (**8**) and 632306 (**12**) contain the crystallographic data for this manuscript. These data can be obtained, free of charge, via http://www.ccdc.cam.ac.uk/conts/retrieving.html (Or from the Cambridge Crystallographic Data Centre, 12 Union Road, Cambridge CB2 1EZ, UK; fax +44 1223 336033; or deposit@ccdc.cam.ac.uk).

© 2007 NRC Canada

Table 1. Summary of the crystallographic data for compounds **8** and **12**.

Crystal	**8**·(2.0 toluene)	**12**·(2.5 toluene)
Empirical formula	$C_{116}H_{148}Ga_2Ge_2K_2N_4$	$C_{55.75}H_{77}GaGeN_2Si$
Formula weight	1961.20	945.59
Temperature (K)	150(2)	150(2)
Wavelength (Å)	0.71073	0.71073
Crystal sysem	Orthorhombic	Triclinic
Space group	*Pbca*	*P*1
a (Å)	33.7506(7)	12.1913(6)
b (Å)	24.7122(5)	19.5294(10)
c (Å)	12.7699(3)	22.1905(14)
α (°)	90	95.785(3)
β (°)	90	94.883(3)
γ (°)	90	95.664(3)
Volume (Å^3)	10650.8(4)	5206.6(5)
Z	4	4
Calculated density (mg/m^3)	1.223	1.206
Absorption coefficient (mm^{-1})	1.185	1.154
F(000)	4144	2010
Crystal size (mm^3)	0.88 × 0.13 × 0.03	0.55 × 0.43 × 0.04
θ range for data collection (°)	2.55–25.03	2.55–25.03
Reflections collected	78104	42115
Independent reflections	9398 [R_{int} = 0.140]	17669 [R_{int} = 0.109]
Completeness to θ = 25.03°	99.9%	96.0%
Absorption correction	Semi-empirical from equivalents	Semi-empirical from equivalents
Maximum and minimum transmission	0.9710 and 0.4236	0.9580 and 0.5694
Refinement method	Full-matrix least-squares on F^2	Full-matrix least-squares on F^2
Data/restraints/parameters	9398/8/559	17669/1/989
Goodness-of-fit F^2	1.033	0.950
Final *R* indices [$I > 2\sigma(I)$]	R_1 = 0.0687, wR_2 = 0.1451	R_1 = 0.0663, wR_2 = 0.1185
R indices (all data)	R_1 = 0.1515, wR_2 = 0.1729	R_1 = 0.1849, wR_2 = 0.1516
Largest diff. peak and hole (e Å^{-3})	0.756 and –0.573	0.745 and –0.649

and data reduction were carried out, using HKL2000 DENZO-SMN (12). The absorption correction was applied, using HKL2000 DENZO-SMN (SCALEPACK).

The SHELXTL/PC V6.14 for Windows NT (Bruker AXS, Madison, Wisconsin) suite of programs was used to solve the structure by direct methods. Subsequent difference Fourier syntheses allowed the remaining atoms to be located. There were two distinct molecules in the asymmetric unit. They are chemically identical but crystallographically different because of the orientation of the mesitylene groups. There were three toluene molecules of solvation, and one was located on a symmetry site and refined at 0.5 occupancy. All of the non-hydrogen atoms, except the 0.5 occupancy toluene molecule, were refined with anisotropic thermal parameters. The hydrogen-atom positions were calculated geometrically and were included as riding on their respective carbon atoms.

The largest-residue electron-density peak (0.745 e/Å^3) was associated with the 0.5 occupancy toluene molecule. Full-matrix least-squares refinement on F^2 gave R_1 = 6.63 for 2σ data and wR_2 = 15.16 for all data (GoF = 0.950).

The data were weak but no data were discarded in the final refinement. The 0.5 occupancy toluene was poorly defined, and it is the portion of the solution responsible for the Alert level A's or B's in the IUCR checkCIF program.

Acknowledgement

We thank the Natural Sciences and Engineering Research Council of Canada (NSERC) and the Ontario Photonics Consortium (OPC) for funding. We thank Doug Hairsine for acquiring mass spectrometric data and Dr. P. Ragogna and members of the Ragogna group for helpful discussions. We also thank Teck Cominco Ltd. (Vancouver, B.C.) for a generous gift of $GeCl_4$.

References

1. (*a*) W. Uhl. Naturwissenschaften, **91**, 305 (2004); (*b*) N.J. Hardman, A.D. Phillips, and P.P. Power. ACS Symp. Ser. **822**, 2 (2002); (*c*) R.J. Baker and C. Jones. Coord. Chem. Rev. **249**, 1856 (2005); (*d*) C. Gemel, T. Steinke, M. Cokoja, A. Kempter, and R.A. Fischer. Eur. J. Inorg. Chem. 4161 (2004).
2. R.J. Baker, R.D. Farley, C. Jones, M. Kloth, and D.M. Murphy. J. Chem. Soc., Dalton Trans. 3844 (2002).
3. (*a*) M.S. Samuel and K.M. Baines. J. Am. Chem. Soc. **125**, 12702 (2003); (*b*) N.J. Mosey, K.M. Baines, and T.K. Woo. J. Am. Chem. Soc. **124**, 13306 (2002); (*c*) S.E. Gottschling, A.J. Guivernau Jacobs, M.C. Jennings, and K.M. Baines. Silicon Chem. **1**, 1 (2002); (*d*) M. Sulkes, M.J. Fink, S.E. Gottschling, and K.M. Baines. Organometallics, **21,** 2438 (2002); (*e*) M.S. Samuel, M.C. Jennings, and K.M. Baines. J. Organomet. Chem. **636**, 130 (2001); (*f*) M.S. Samuel, M.C. Jennings, and

© 2007 NRC Canada

K.M. Baines. Organometallics, **20**, 590 (2001); (*g*) C.E. Dixon and K.M. Baines. Phosphorus, Sulfur Silicon Relat. Elem. **124**, 123 (1997); (*h*) C.E. Dixon, H.W. Liu, C.M. Vander Kant, and K.M. Baines. Organometallics, **15**, 5701 (1996) (*i*) K.M. Baines, J.A. Cooke, C.E. Dixon, H.W. Liu, and M.R. Netherton. Organometallics, **13**, 631 (1994).

4. A.F. Richards, M. Brynda, and P.P. Power. Organometallics, **23**, 4009 (2004).
5. S.P. Green, C. Jones, K.-A. Lippert, D.P. Mills, and A. Stasch. Inorg. Chem. **45**, 7242 (2006).
6. (*a*) M. Weidenbruch. J. Organomet. Chem. **646**, 39 (2002); (*b*) F. Meiners, W. Saak, and M. Weidenbruch. Z. Anorg. Allg. Chem. **628**, 2821 (2002); (*c*) T. Tsumuraya, S. Sato, and W. Ando. Organometallics, **9**, 2061 (1990); (*d*) H. Schäfer, W. Saak, and M. Weidenbruch. Organometallics, **18**, 3159 (1999).
7. (*a*) W. Ando, T. Tsumuraya, and A. Sekiguchi. Chem. Lett. 317 (1987); (*b*) W. Ando, H. Itoh, T. Tsumuraya, and H. Yoshida. Organometallics, **7**, 1880 (1988); (*c*) W. Ando, H. Itoh, and T. Tsumuraya. Organometallics, **8**, 2759 (1989); (*d*) N.P. Toltl, W.J. Leigh, G.M. Kollegger, W.G. Stibbs, and K.M. Baines. Organometallics, **15**, 3732 (1996); (*e*) W.J. Leigh and C.R. Harrington. J. Am. Chem. Soc. **127**, 5084 (2005).
8. T. Tsumuraya, Y. Kabe, and W. Ando. J. Organomet. Chem. **483**, 131 (1994).
9. (*a*) K.L. Fujdala, D.W.K. Gracey, E.F. Wong, and K.M. Baines. Can. J. Chem. **80**, 1387 (2002); (*b*) C.E. Dixon, M.R. Netherton, and K.M. Baines. J. Am. Chem. Soc. **120**, 10365 (1998).
10. N.J. Hardman, B. Eichler, and P.P. Power. J. Chem. Soc., Chem. Commun. 1991 (2000).
11. W.A. Hermann, M. Denk, J. Behm, W. Scherer, F. Klingan, H. Bock, B. Solouki, and M. Wagner. Angew. Chem., Int. Ed. Engl. **31**, 1485 (1992).
12. Z. Otwinowski and W. Minor. *In* Methods in enzymology. Vol. 276: Macromolecular crystallography, Part A. *Edited by* C.W. Carter, Jr. and R.M. Sweet. Academic Press, New York. 1997. p. 307.

© 2007 NRC Canada

COMMUNICATION / COMMUNICATION

Ruthenium(III) acetylacetonate [$Ru(acac)_3$] — An efficient recyclable catalyst for the acetylation of phenols, alcohols, and amines under neat conditions

Ravi Varala, Aayesha Nasreen, and Srinivas R. Adapa

Abstract: A catalytic amount of ruthenium(III) acetylacetonate (2 mol%) [$Ru(acac)_3$] enables solvent-free acetylation of phenols, alcohols, and amines at ambient temperature in good to excellent yields. Furthermore, the catalyst could be recovered and reused at least three times without a significant loss in yields.

Key words: acetylation, protecting groups, ruthenium(III) acetylacetonate, phenols, alcohols, amines.

Résumé : L'utilisation d'une quantité catalytique d'acétylacétonate de ruthénium(III) (2 mol %) [$Ru(acac)_3$] permet de réaliser l'acétylation, sans solvant, de phénols, d'alcools et d'amines à la température ambiante, avec des rendements allant de bons à excellents. De plus, il est possible de récupérer le catalyseur et de le réutiliser au moins trois fois sans diminution significative des rendements.

Mots-clés : acétylation, groupes protecteurs, acétylacétonate de ruthénium(III), phénols, alcools, amines.

[Traduit par la Rédaction]

Introduction

Acetylation of phenol, alcohol, and amine functionalities is one of the most frequently used transformations in organic synthesis (1). Among the various protecting groups used for the hydroxyl function, acetyl is the most common because it is easy to introduce, stable in acidic reaction conditions, and easily removable by mild alkaline hydrolysis. In general, this can be achieved by treating alcohols with acid anhydrides or acid chlorides in the presence of stoichiometric amounts of amine bases such as tertiary amines (2), 4-(dimethylamino)pyridine (DMAP), 4-(1-pyrrolidino)pyridine (PPY) (3), and Bu_3P (4). Acylation of alcohols can also be achieved under an acid-catalyzed condition by treating alcohols with acid anhydrides in presence of several protic acids (5) and by using various metal salts as Lewis acids (6).

Certain reported methodologies suffer from one or more of the following disadvantages (5, 6): (*i*) potential health hazard (DMAP is highly toxic (e.g., intravenous LD_{50} in the rat is 56 mg/kg), and Bu_3P is flammable (flash point is 37 °C)); (*ii*) difficult handling (Bu_3P undergoes aerial oxidation, and triflates are moisture sensitive); (*iii*) high cost of the catalysts (e.g., triflates); (*iv*) special efforts required to prepare the catalysts ($Bi(OTf)_3$, Nafion-H, yttria–zirconia, and $AlPW_{12}O_{40}$); (*v*) lack of atom economy (use of excess of acetylating agents); (*vi*) stringent reaction conditions and the requirement of prolonged reaction times; (*vii*) in many cases, the reported acylation methodologies are applicable to only alcohols and are not suitable for acid-sensitive substrates; and (*viii*) in addition, the metal triflates may involve competitive side reactions (e.g., dehydration and rearrangement) with acid-sensitive substrates because of the large negative $H_\circ$ value of TfOH. Furthermore, the use of large amounts of acylating agents and activators should be avoided to promote green chemistry and atom efficiency.

Despite a number of precedents, a catalytically efficient practical alternative that can be used under milder and cost-effective conditions for this very important transformation is highly desirable, and there is still scope for further improvement. Another promising approach to environment-friendly chemistry is to minimize or completely eliminate the use of harmful organic solvents in organic syntheses. This is because organic reactions run under solvent-free conditions are advantageous because of their enhanced selectivity, effi-

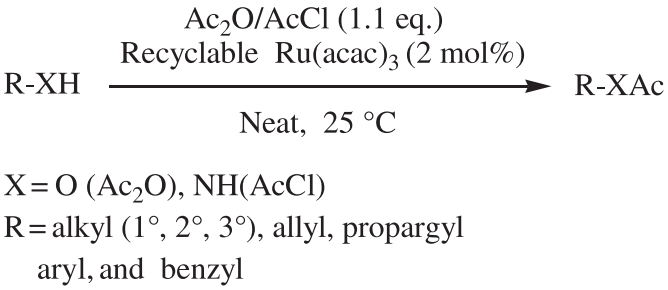
Received 16 September 2006. Accepted 07 December 2006. Published on the NRC Research Press Web site at http://canjchem.nrc.ca on 7 February 2007.

R. Varala,[1] A. Nasreen, and S.R. Adapa. Indian Institute of Chemical Technology, Hyderabad 500 007, India.

[1]Corresponding author (e-mail: rvarala_iict@yahoo.co.in).

 doi:10.1139/V06-191 © 2007 NRC Canada

Scheme 1.



ciency, ease of manipulation, cleaner product formation, and the avoidance of toxic or volatile solvents (7). Thus, a paradigm shift from using solvents toward solvent-free reactions not only simplifies organic synthesis but also improves process conditions for large-scale synthesis.[2]

Recently, we have reported [$Ru(acac)_3$] as an efficient Lewis acid (LA) catalyst for chemoselective tetrahydropyranylation (THP) of alcohols and phenols under solvent-free conditions (8).

Results and discussion

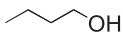
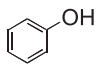
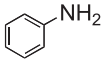
In a continuation of our recent efforts to develop new synthetic routes for carbon–carbon and carbon–heteroatom bond formation and heterocycles (9), we herein present our preliminary results using an efficient recyclable [$Ru(acac)_3$]-catalyzed solvent-free acetylation of hydroxy and amine functions (Scheme 1). The procedure, based on the Lewis acid catalytic activity of the [$Ru(acac)_3$], represents an environmentally benign alternative to current chemical processes that use water-intolerant Lewis acids.

Initially, we have screened a few available acetylacetonates, such as [$VO(acac)_2$], [$Pd(acac)_2$], [$Ru(acac)_3$], and [$Co(acac)_3$], for the model reaction between aniline (1 mmol) and acetyl chloride (1.1 mmol) under neat conditions at ambient temperature. Among the catalysts tested, [$Ru(acac)_3$] proved to be the most efficient LA catalyst in terms of yields and reaction time (the corresponding acetylated product was obtained in 5 min with quantitative isolated yield >99%). An optimum concentration of 2 mol% of [$Ru(acac)_3$] is sufficient to afford the acetylated product in an excellent yield. While optimizing the acylating agent, several features that deserved comment are shown in Table 1.

In case of alcohols and phenols (Table 1, entries 1 and 2), acetic anhydride was preferred over the corresponding acid chloride or acetic acid. It is significant to note that acetyl chloride was preferred over acetic anhydride with the acetylation reaction of amines (Table 1, entry 3). This is in complete contrast with the observations reported by Yadav et al. (6*c*). This clearly demonstrates that the acetylation reaction behaviour is completely dependent on the chosen catalyst. Acetylation of amines, using acetic acid at ambient temperature, with our catalyst did not give acetylated product.

The direct condensation of acetic acid with alcohols is generally avoided because the equilibrium between the substrates and the products require the elimination of water from the reaction mixture, using a dehydrant or azeotropically, to shift the equilibrium in favor of the product.

Table 1. Effect of acylating agent in [$Ru(acac)_3$]-catalyzed acetylation of phenols, alcohols, and amines.

Entry	Substrate	Acylating agent[a]	Time(h)	Yield (%)[b]
1		**A**	0.5	60
		B	0.5	82
		C	0.5	90
2		**A**	2.0	71
		B	2.0	78
		C	2.0	91
3		**A**	5 min	>99
		B	0.5	NR[c]
		C	0.5	62

[a] **A** = CH_3COCl; **B** = CH_3COOH; **C** = $(CH_3CO)_2O$.
[b] Isolated yields.
[c] NR = No reaction.

Table 2. Results of the recycling and reuse of [$Ru(acac)_3$] in the acetylation of aniline, as a model substrate.

Cycle	Yield (%)[a]
1	99
2	99
3	97
4	96

[a]Isolated yields with reused catalyst (recovered catalyst 99%, 99%, and 98% respectively).

Intrigued by the observations in hand, we have studied the scope and the generality of this process for a wide range of aromatic and aliphatic phenols, alcohols and amines.

One of the important features of the present developed protocol for the formation of acetylated products is that absolute anhydrous conditions are not required. The reactions are clean and devoid of unwanted products and gave the corresponding acetylated products in moderate to excellent yields. Very importantly, this protocol allowed us to adopt a simple work-up procedure by employing ether to dissolve the organic material not the catalyst, which could be easily removed by filtration. The recovered catalyst is oven dried at 60 °C for 2 h and then reused for the model reaction without significant loss of yield for at least three cycles (Table 2; Table 3, entry 27).

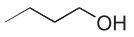
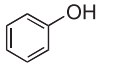
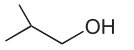
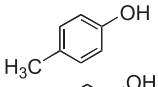
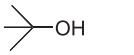
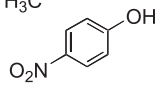
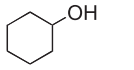
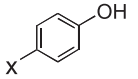
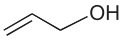
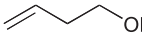
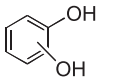
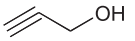
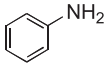
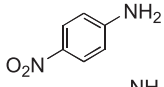
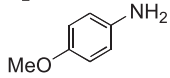
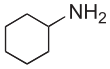
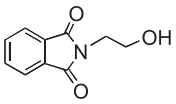
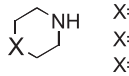
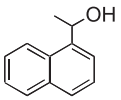
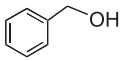
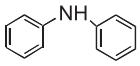
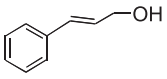
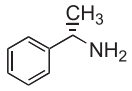
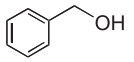
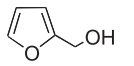
As evident from Table 3, the described methodology illustrates a fine acetylation procedure that has wide applicability, extending the scope to alkyl (1°, 2°, and 3°), allyl, propargylic, aryl, and benzylic alcohols (Table 3, entries 1–36).

Under optimized reaction conditions, secondary and tertiary alcohols do not experience any competitive dehydration (Table 3, entries 3, 4, and 12). Acid-sensitive functionalities, such as allylic and propargylic substrates (Table 3, entries 5–8 and 14), are tolerated, and no rearrangement took place for those substrates. Chiral alcohols and amines (Table 3, entries 9 and 36) were easily acetylated with complete retention of

[2] Exothermicity of a large-scale reaction should be controlled by maintaining the temperature and using an appropriate solvent, if necessary.

© 2007 NRC Canada

Table 3. Ruthenium(III) acetylacetonate-catalyzed acetylation of phenols, alcohols, and amines.

Entry	Substrate	Time (h)/ Acylating agent	Yield (%)[a]	Entry	Substrate	Time (h)/ Acylating agent	Yield (%)[a]
1		0.5/**C**	90	17		2.0/**C**	91
2		5.5/**C**	80	18		8.0/C	80
3		12/**C**	65	19		12/C	65
4		4.0/**C**	92	20 21 22		x =F x =Br x =Cl	3.0/C 2.5/C 4.0/C	95 90 87
5		10/**C**	89	23		15.0/C	62
6		8.0/**C**	78	24 25 26		o- = *m*-= *p*- =	12/C 8.0/C 6.5/C	72 85 88
7		6.5/**C**	87	27		5 min/A	99
8		5.0/**C**	91	28		1.0/A	85
9	(R)-Menthol	6.5/**C**	82	29		5.5/A	92
10	Geraniol	8.0/**C**	85	30		6/A	82
11		15/**C**	90	31 32 33		X=CH_2 X=O X=S	10 min/A 10 min/A 30 min/A	95 98 90
12		10/**C**	78	34	$(PhCH_2)_2NH$	18/A	78
13		5.0/**C**	90	35		24/A	65
14		7.5/**C**	72	36		8.0/A	88
15		6.0/**C**	88				
16		5.5/**C**	75				

[a] All isolated products were characterized by IR, ^{1}H NMR, and mass spectral analyses.

the optical purity. Steric factors played vital role in affecting acetylation (Table 3, entries 34 and 35), and the reaction completion took longer times with moderate yields.

Next, the scope of the present methodology was extended to other anhydrides and acid chlorides to test the efficacy of the catalyst, and the results are quite satisfactory. From Table 4, solid anhydrides, such as benzoic, maleic, succinic, and phthalic anhydrides, also reacted well in the acylation reaction with the model substrates chosen.

The present [Ru(acac)$_3$]-catalyzed acetylation may probably follow the mechanism depicted in Scheme 2: For alcohols and phenols, initially, electrophilic activation by [Ru(acac)$_3$] for possible coordination to both carbonyl oxygen atoms of the anhydride **2** to form a six-membered transition state, and then nucleophilic attack by the alcohol **1** to give the desired acetylated product **3**. For amines, [Ru(acac)$_3$] first activates the acyl halide **4** and then polarizes it on the nucleophilic amine **5** to form the corresponding acetylated product **6** and regenerates back.

The efficiency and generality of the present [Ru(acac)$_3$]-catalyzed protocol can be realized at a glance by comparing our results for the chosen model substrates with those of

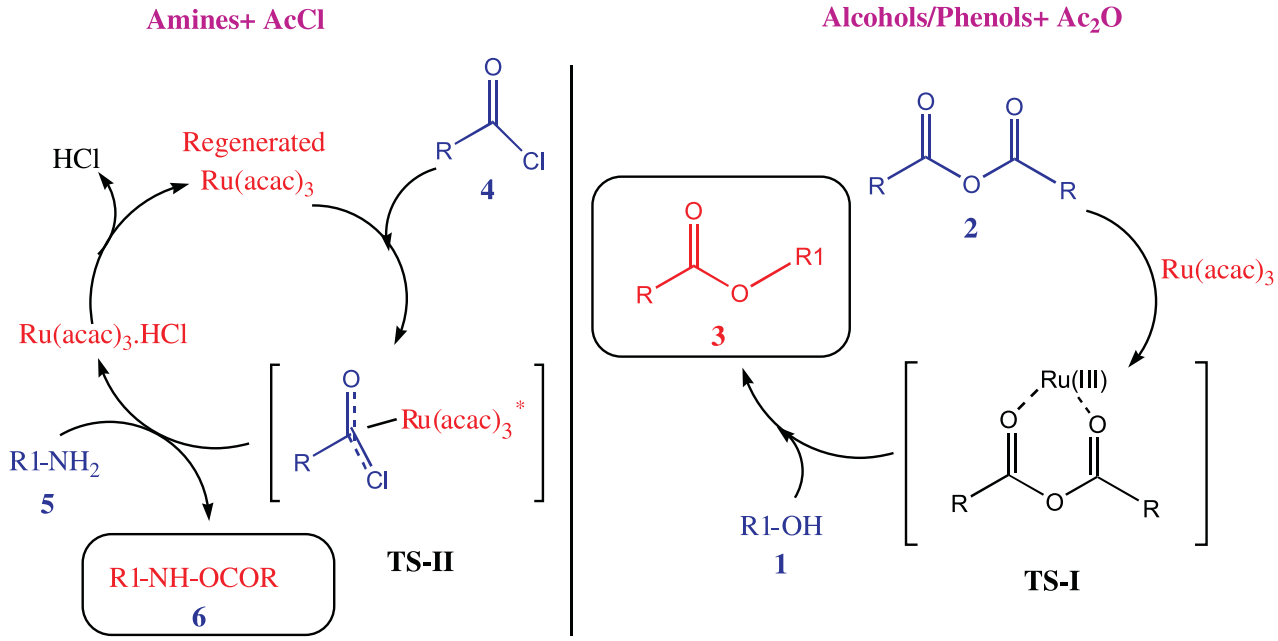
© 2007 NRC Canada

Table 4. Acylation of *n*-butanol, aniline, and piperidine with different anhydrides and acyl chlorides.

Entry	Substrate	Acylating agent	Conditions	Time	Yield (%)[a]
1	*n*-butanol	Benzoic anhydride	RT	3.0 h	90
		Maleic anhydride		3.0 h	80
		Succinic anhydride		3.0 h	82
		Phthalic anhydride		3.5 h	78
		Boc anhydride		1.0 h	92
		Propionic anhydride		1.0 h	95
		Butyric anhydride		1.0 h	98
2	2-Naphthol	Benzoic anhydride		3.5 h	88
		Succinic anhydride	RT	4.0 h	62
		Boc anhydride		2.5 h	85
3	Aniline	Benzoyl chloride	RT	20 min	95
		CH_2=CHCOCl		30 min	78
4	Piperidine	Benzoyl chloride	RT	10 min	92
		CH_2=CHCOCl		15 min	88

[a]Isolated yields.

Scheme 2. Proposed mechanism for the [Ru(acac)$_3$]-catalyzed acetylation of phenols, alcohols, and amines.



some recently developed procedures (as shown in Table 5). The reactions have been compared with respect to the reaction times, mol% of the catalyst used, and the yields.

Conclusion

In summary, we have developed a mild, efficient, and highly selective methodology for the acetylation of alcohols using [Ru(acac)$_3$] as LA catalyst (2 mol%). Notable features of the protocol are clean and simple solvent-free reaction conditions, non-aqueous workup, and the use of recyclable and environmentally benign catalyst. This work widens the scope of using transition-metal salts and complexes in organic synthesis because of the nontoxic nature of the catalyst. We believe that this protocol will be a valuable addition to acetylation-related modern synthetic methodologies.

Typical experimental procedure

The hydroxy or amine compound (Table 3, entries 1–36; 1.0 mmol), acylating agent (1.1 mmol), [Ru(acac)$_3$] (2 mol%) were placed, successively, in a flask under neat conditions at room temperature. After stirring, the reaction mixture was treated with Et_2O (2 × 5 mL), and the catalyst was removed by filtration. The filtrate extracts were concentrated under reduced pressure, and the crude product was then purified by silica-gel chromatography (hexane – ethyl acetate). All the obtained acylated products were characterized by IR,

© 2007 NRC Canada

Table 5. Comparison of the catalytic efficiency of $[Ru(acac)_3]$ with some recently reported catalysts.

Entry	Catalyst	mol%	AA[a]	Time (min)	Yield (%)[b]
For the reaction of aniline with an acylating agent					
1	**$[Ru(acac)_3]$ (neat)**	2	A	5	99
2	$AlPW_{12}O_{40}$ (neat)	0.5	C	1	96
3	I_2	10	C	105	77
4	$NbCl_5$	20	C	60	95
5	Zeolite	5	B	30	73
6	Fe^{+3}-Montmorillonite	20	B	180	98
7	$Gd(OTf)_3$–$[bmim][BF_4]$	0.2	C	120	96
For the reaction of *n*-butanol with an acylating agent					
1	**$[Ru(acac)_3]$ (neat)**	2	C	30	90
2	$CuSO_4 \cdot 5H_2O$ (neat)	10	C	1440	93
3	$Sn(tpp)(OTf)_2$	1	C	60	87
For the reaction of phenol with an acylating agent					
1	**$[Ru(acac)_3]$ (neat)**	2	C	120	91
2	$CuSO_4 \cdot 5H_2O$ (neat)	10	C	90	92
3	$H_{14}[NaP_5W_{30}O_{110}]$	0.1	C	60	95
4	$Gd(OTf)_3$–$[bmim][BF_4]$	0.2	C	120	88
5	I_2	10	C	30	90
6	K-10–DCM	100[c]	C	120	83

[a]Acylating agent.
[b]Isolated yields.
[c]mg/1 mmol.

^{1}H NMR spectroscopy, and mass spectrometry, and their structures are consistent with their published physical data (6).

Acknowledgments

We thank Dr. J.S. Yadav, Director, Indian Institute of chemical technology, and Council of Scientific Industrial Research (CSIR, India) for financial support. A. Nasreen thanks the Department of Sciene and Technology, New Delhi for sponsoring project (GAP-0128).

References

1. (*a*) T.W. Green and P.G.M. Wuts. Protective groups in organic chemistry. John Wiley & Sons, New York. 1991. pp. 150–160; (*b*) A.L. Pearson and W.J. Roush. Handbook of reagents for organic synthesis: activating agents and protecting groups. John Wiley & Sons, UK. 1999. pp. 9–16; (*c*) P.J. Kocienski. Protecting groups. Georg Thieme Verlag, Stuttgart. 1994. p. 23.
2. R.I. Zhdanov and S.M. Zhenodarova. Synthesis, 222 (1975).
3. (*a*) G. Hofle, W. Steglich, and H. Vorbruggen. Angew. Chem., Int. Ed. Engl. **17**, 569 (1978); (*b*) W. Steglich and G. Hofle. Angew. Chem., Int. Ed. Engl. **8**, 981 (1969); (*c*) E.F.V. Seriven. Chem. Soc. Rev. 12, 129 (1983).
4. E. Vedejs, N.S. Bennett, L.M. Conn, S.T. Diver, M. Gingras, S. Lin, P.A. Oliver, and M.J. Peterson. J. Org. Chem. **58**, 7286 (1993).
5. A.C. Cope and E.C. Herrick. Org. Synth. **IV**, 304 (1963).
6. For most recent reports, see: (*a*) K. Jeyakumar and D.K. Chand. J. Mol. Cat. A: Chemical, **255**, 275 (2006), see the list of catalysts cited therein; (*b*) A. Orita, C. Tanahashi, A. Kakuda, and J. Otera. J. Org. Chem. **66**, 8926 (2001); (*c*) V.K. Yadav and K.G. Babu. J. Org. Chem. **69**, 577 (2004).
7. For reviews on solvent-free organic synthesis, see: (*a*) G.W.V. Cave, L. Raston, and J.L. Scott. Chem. Commun. 2159 (2001); (*b*) K. Tanaka and F. Toda. Chem. Rev. **100**, 1025 (2000).
8. R. Varala and S.R. Adapa. Can. J. Chem. **84**, 1174 (2006).
9. (*a*) R. Varala, E. Ramu, and S.R. Adapa. Bull. Chem. Soc. Jpn. **79**, 140 (2006), and refs. cited therein; (*b*) R. Varala, E. Ramu, N. Sreelatha, and S.R. Adapa. Tetrahedron Lett. **47**, 877 (2006); (*c*) R. Varala, E. Ramu, and S.R. Adapa. Chin. J. Chem. **24**, 807 (2006); (*d*) R. Varala, E. Ramu, N. Sreelatha, and S.R. Adapa. Synlett, **7**, 1009 (2006); (*e*) R. Varala, N. Sreelatha, and S.R. Adapa. Synlett, **10**, 1549 (2006); (*f*) M.M. Alam, R. Varala, E. Ramu, and S.R. Adapa. Lett. Org. Chem. **3**, 187 (2006); (*g*) R. Varala, E. Ramu, and S.R. Adapa. Synthesis, **22**, 3825 (2006); (*h*) R. Varala, N. Sreelatha, and S.R. Adapa. J. Org. Chem. **71**, 8283 (2006); (*i*) R. Varala, N. Sreelatha, and S.R. Adapa. Bull. Korean Chem. Soc. **27**, 1079 (2006); (*j*) R. Varala, A. Nasreen, E. Ramu, and S.R. Adapa. Tetrahedron Lett. **48**, 69 (2007).

© 2007 NRC Canada

COMMUNICATION / COMMUNICATION

Fluoride detection based on fluorescence enhancement of thioureido naphthalene derivative

Sourav Chakraborty and Matthew A. Tarr

Abstract: A novel thioureido naphthalene derivative was synthesized and characterized. The compound proved itself as an effective fluoride sensor with respect to selectivity and sensitivity. In acetonitrile, the fluorescence intensity increased by 40-fold with the addition of 5 equiv. of fluoride. Fluorescence intensity did not substantially change with other halides, suggesting that the thioureido protons interact strongly with fluoride but not with other halides. The enhanced fluorescence is due to increased quantum efficiency of the fluoride complex.

Key words: fluoride sensing, thioureido compound, fluorescence.

Résumé : On a synthétisé et caractérisé un nouveau dérivé thiouréidonaphtalène. Le composé s'avère être efficace pour détecter l'ion fluorure tant par rapport à la sélectivité que qu'à la sensibilité. Dans l'acétonitrile, l'intensité de la fluorescence est multipliée par quarante lorsqu'on ajoute cinq équivalents de fluorure. L'intensité de la fluorescence ne subit pas de modification substantielle avec les autres halogénures, ce qui suggère que les protons thiouréido interagissent fortement avec l'ion fluorure mais pas avec les autres halogénures. L'augmentation de la fluorescence résulte d'une augmentation de l'efficacité quantique du complexe du fluorure.

Mots-clés : détection de l'ion fluorure, composé thiouréido, fluorescence.

[Traduit par la Rédaction]

Introduction

Anions play various important roles in biological and environmental processes in nature (1–6). Although considerable attention has been focused on the selective detection of anions using visible colorimetric sensors (7–19), less progress has been made with the more-powerful technique of fluorescence. Fluoride sensing is important, since fluoride plays crucial roles in dental caries (20) and other medical issues such as osteoporosis (21). Excess fluoride, however, causes fluorosis (22–25), a type of fluoride toxicity that is typically related to an increase in bone density. The important consequences of elevated and depleted fluoride concentration make effective fluoride sensing an important tool. Although a series of fluoride-sensor compounds have already been reported (7, 9, 12, 13, 15, 17, 18, 26–41) by several researchers, there remains a strong practical impetus to improve the detection at micromolar to submicromolar (29) levels. In addition, past research mainly focused on urea-based sensors (26–28, 30), while the whole new vista of novel thiourea-based sensors (12, 15, 35, 36, 40, 41) was largely unexplored.

Results and Discussion

We, therefore, synthesized and characterized 1,8-bis(phenylthioureido)naphthalene as a fluorescent probe for fluoride detection, as well as a chromogenic fluoride sensor. The structure of compound **1** was confirmed by ^{1}H and ^{13}C NMR and mass spectral analysis (Fig. 1).[2] In the presence of fluoride, this compound shows a new fluorescence peak (with λ_{max} = 447.5 nm), as shown in Fig. 2. Chloride, bromide, or iodide addition did not cause any change in the fluorescence intensity or shape.[2]

Received 19 October 2006. Accepted 25 January 2007. Published on the NRC Research Press Web site at http://canjchem.nrc.ca on 28 February 2007.

S. Chakraborty and M.A. Tarr.[1] Department of Chemistry, University of New Orleans, 2000 Lakeshore Drive, New Orleans, LA 70148, USA.

[1]Corresponding author (e-mail: mtarr@uno.edu).

[2]Supplementary data for this article are available on the journal Web site (http://canjchem.nrc.ca) or may be purchased from the Depository of Unpublished Data, Document Delivery, CISTI, National Research Council Canada, Ottawa, ON K1A 0S2, Canada. DUD 5137. For more information on obtaining material, refer to http://cisti-icist.nrc-cnrc.gc.ca/irm/unpub_e.shtml.

 doi:10.1139/V07-009 © 2007 NRC Canada

Compound 1.

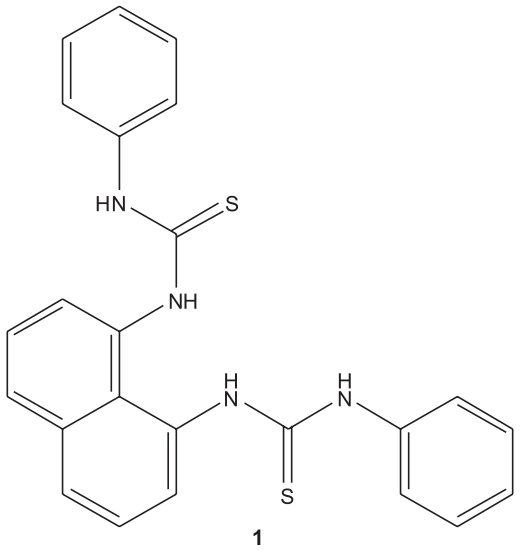
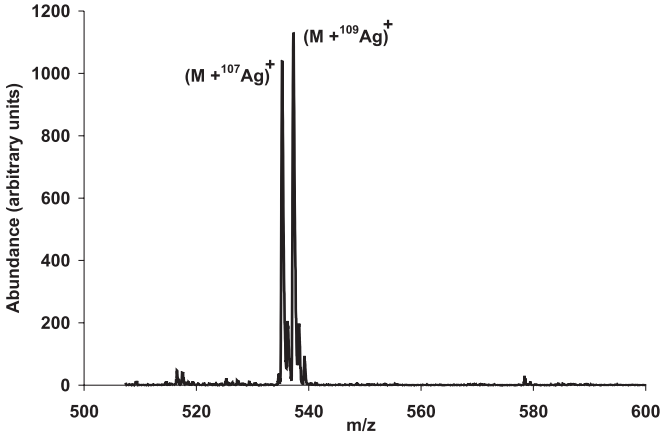


Fig 1. MALDI mass spectrum of 1,8-bis(phenylthioureido)naphthalene (Ag adduct). Mass of compound **1** is 428 amu.



A fluorescence response to acetate and dihydrogenphosphate has been observed, although the response to fluoride is substantially higher than that for these other anions. The fluorescence response to 9 equiv. of dihydrogenphosphate is approximately equal to that observed for 1 equiv. of fluoride. Similarly, 9 equiv. of acetate yielded a fluorescence signal that was approximately equal to the addition of 2 equiv. of fluoride.[2] Separate experiments showed that even in the presence of 1 mmol/L acetate or 1 mmol/L dihydrogenphosphate, compound **1** still showed enhanced fluorescence with the addition of 0.25 equiv. of fluoride. While some interfering signals may result from the presence of these anions, the response to fluoride is not inhibited by their presence.

A titration experiment (^{1}H NMR) showed substantial changes upon the addition of fluoride. The thioureido proton signal decreased rapidly and broadened with the addition of fluoride (Fig. 3). No significant changes in the aromatic proton signals were apparent. The observed changes in the thioureido ^{1}H NMR signal suggest strong H-bonding between thioureido protons and fluoride ions, with exchange on the NMR time scale. Because of its small size and high charge density, the fluoride ion had a much stronger interaction with the thioureido protons than the other halides, resulting in the selective fluorescence enhancement by fluoride.

Fig 2. Fluorescence spectra on the addition of fluoride to compound **1** in acetonitrile. Initial concentration of the compound is 50 μmol/L. Fluoride was added in 12.5 μmol/L increments. Excitation wavelength = 345 nm, emission maximum = 447.5 nm.

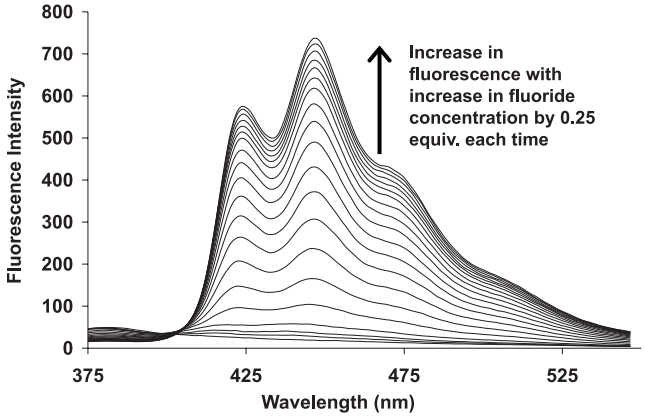
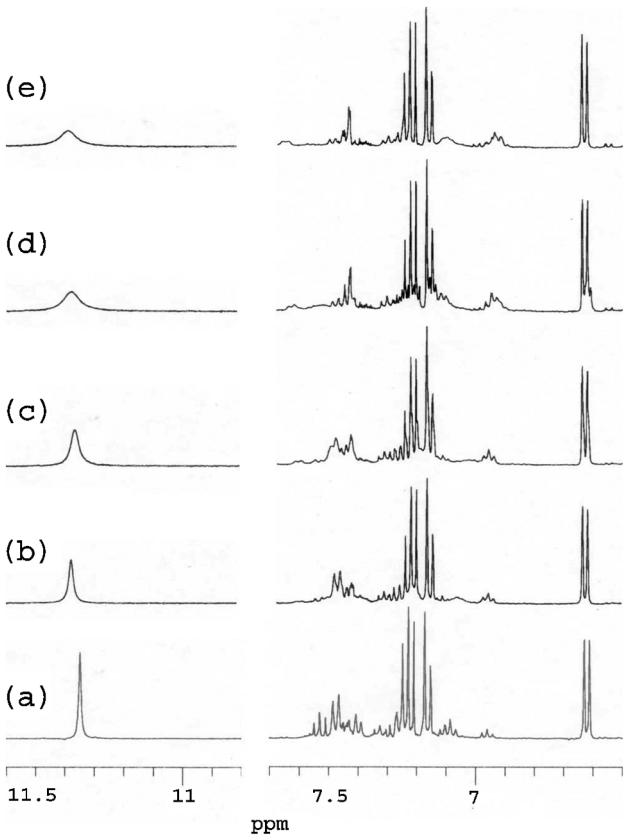


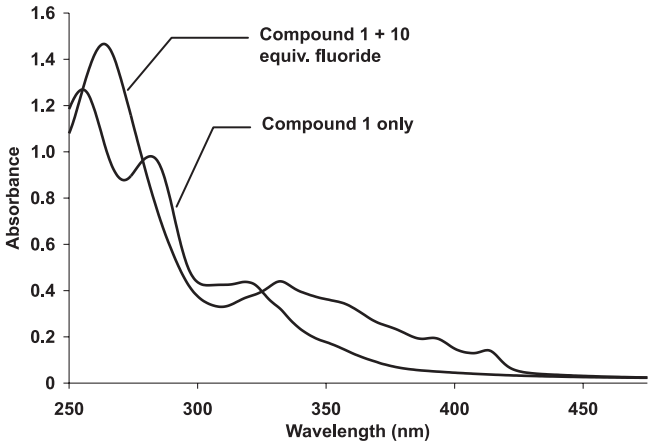
Fig 3. Partial ^{1}H NMR (400 MHz) of compound **1** (5 mmol/L) in DMSO-d_6 upon the addition of tetrabutylammonium fluoride: (*a*) 0 μmol/L, (*b*) 10 μmol/L, (*c*) 20 μmol/L, (*d*) 30 μmol/L, and (*e*) 40 μmol/L



Fluorescence intensity increased significantly with the addition of fluoride, while other halides showed little or no

© 2007 NRC Canada

Fig 4. Absorbance of compound **1** (50 μmol/L), before and after the addition of 500 μmol/L of fluoride.



change. An approximate 40-fold enhancement in fluorescence intensity at 447.5 nm was observed in the presence of 5 equiv. of fluoride (50 μmol/L compound **1**, 250 μmol/L F^-). Furthermore, the addition of only 0.25 equiv. of fluoride (12.5 μmol/L F^-) resulted in an approximate 1.5-fold increase in fluorescence intensity at 447.5 nm, indicating that detection limits in the low- to sub-micromolar range are possible. UV–vis absorbance spectra (Fig. 4) were acquired to determine if compound **1** can also behave as a chromogenic sensor. After the addition of 10 equiv. of tetrabutylammonium fluoride, a bathochromic shift in the absorbance spectrum was clearly observed. With the presence of fluoride, the absorbance extended into the visible region, indicating that the detection of fluoride could be carried out colorimetrically, perhaps even with the naked eye. However, superior detection limits exist using fluorescence methods.

The data in Fig. 4 indicate an approximate doubling in the absorbance at 345 nm upon the addition of excess fluoride. Fluorescence data (Fig. 2) illustrate an approximate 40-fold enhancement near saturation (the point where all compound **1** molecules are bound to fluoride). Since fluorescence at low concentration is proportional to absorbance, these data indicate that only a small portion of the fluorescence enhancement can be accounted for by the increased absorbance. Consequently, we can conclude that the fluoride complex has a larger quantum yield than the unbound **1**. Based on the absorbance and fluorescence data, the enhancement in quantum yield is estimated to be 20-fold. This observation agrees with previous reports that suggested improved planarity (28) and lack of relaxation via twisted conformations (42, 43), as possible mechanisms for enhanced fluorescence in ureido derivatives.

In summary, a novel thiourea-based sensor molecule, 1,8-bis(phenylthioureido)naphthalene, was synthesized and characterized. The compound showed fluorescent enhancement in the presence of fluoride. This response was selective for fluoride, with chloride, bromide, and iodide producing little or no response. The large enhancements in fluorescence (40-fold observed in this study) suggest that this molecule may provide improved analytical characteristics over previously described molecules, especially since many other studies have reported molecules that exhibit either fluorescence quenching in the presence of fluoride (14) or show only changes in absorbance (15, 26, 30, 31). Compound **1** may also be advantageous, since its fluoride complex can be excited in the visible region.

The potential practical applications of compound **1** appear to be versatile and include fiber optic and nanometric sensors for fluoride. Current work focuses on immobilizing compound **1** on a solid support such as a fiber optic or nanoparticles for the detection of fluoride in aqueous media.

Experimental section

All starting materials were purchased and used without further purification. ^1H and ^{13}C NMR were recorded on a 400 MHz spectrometer, operating at 9.4 T. NMR experiments were carried out in DMSO-d_6 with 0.05% (*v*/*v*) TMS. Mass spectra were acquired with a MALDI-TOF mass spectrometer. Fluorescence experiments were carried out in acetonitrile solution, with excitation wavelength of 345 nm and emission range of 375–550 nm with 7.5 nm slit widths. UV–vis absorbance experiments were carried out with quartz cuvettes (path length is 1 cm).

2.39 mmol of 1,8-diaminonaphthalene was dissolved in 20 mL of dry THF. Two drops of triethylamine was added, and this mixture was then added dropwise over 1 h to 32.5 mmol of phenylisothiocyanate, which was dissolved in 20 mL of THF. The system was kept in a nitrogen atmosphere. The mixture was stirred at room temperature for 24 h. The progress of the reaction was monitored by TLC (eluent: 4% acetonitrile in chloroform). The mixture of the compounds was purified by column chromatography (eluent: 4% acetonitrile in chloroform). The yield was approximately 20–22%.

Selected data for compound 1

Mp 135–137 °C dec. ^1H NMR (DMSO-d_6) δ 11.43 (s, 2H), 7.53 (d, J = 7.8 Hz, 2H), 7.46 (t, J = 7.8 Hz, 2H), 7.28 (t, J = 7.8 Hz, 4H), 7.21 (d, J = 7.9 Hz, 4H), 7.13 (t, J = 7.9 Hz, 2H), 6.67 (d, J = 7.8 Hz, 2H), two additional thioureido protons were not observed because of exchange. ^{13}C NMR (100 MHz, DMSO-d_6) δ 173.7 (q), 140.6 (q), 136.1 (q), 134.8 (q), 129.6 (2 × CH), 129.1 (CH), 122.6 (CH), 119.9 (CH), 119.0 (2 × CH), 116.9 (q), 105.4 (CH). MALDI-MS showed the silver adducts (^{107}Ag, ^{109}Ag) at m/z = 535, 537 amu, corresponding to the expected molar mass of 428 amu.

Acknowledgment

We extend our heartiest thanks to Dr. Vicki Colvin, Dr. James Tour, and Rice University for providing lab and office space following Hurricane Katrina. We also acknowledge the contributions of Dr. Alexander (Sandy) Yates, for MALDI-TOF experiments at Rice University, and Goutam Biswas, for his help in interpreting the NMR spectra. This project was supported by the Louisiana Board of Regents Health Excellence Fund (HEF(2001–06)-08).

References

1. F.P. Schmidtchen and M. Berger. Chem. Rev. **97**, 1609 (1997).

© 2007 NRC Canada

2. J.L. Sessler and J.M. Davis. Acc. Chem. Res. **34**, 989 (2001).
3. P.A. Gale. Coord. Chem. Rev. **240**, 1 (2003).
4. R. Martinez-Manez and F. Sancenon. Chem. Rev. **103**, 4419 (2003).
5. C. Suksai and T. Tuntulani. Chem. Soc. Rev. **32**, 192 (2003).
6. I.E. Stibor. Top Curr. Chem. 255 (2005).
7. C.B. Black, B. Andrioletti, A.C. Try, C. Ruiperez, and J.L. Sessler. J. Am. Chem. Soc. **121**, 10438 (1999).
8. P. Anzenbacher, K. Jursikova, and J.L. Sessler. J. Am. Chem. Soc. **122**, 9350 (2000).
9. H. Furuta, H. Maeda, and A. Osuka. J. Am. Chem. Soc. **123**, 6435 (2001).
10. H. Miyaji and J.L. Sessler. Angew. Chem., Int. Ed. **40**, 154 (2001).
11. S. Yamaguchi, S. Akiyama, and K. Tamao. J. Am. Chem. Soc. **123**, 11372 (2001).
12. D. Jimenez, R. Martinez-Manez, F. Sancenon, and J. Soto. Tetrahedron Lett. **43**, 2823 (2002).
13. P. Piatek and J. Jurczak. Chem. Commun. (Cambridge), 2450 (2002).
14. S.K. Kim and J. Yoon. Chem. Commun. (Cambridge), 770 (2002).
15. D.A. Jose, D.K. Kumar, B. Ganguly, and A. Das. Org. Lett. **6**, 3445 (2004).
16. D.E. Gomez, L. Fabbrizzi, M. Licchelli, and E. Monzani. Org. Biomol. Chem. **3**, 1495 (2005).
17. S. Xu, K. Chen, and H. Tian. J. Mater. Chem. **15**, 2676 (2005).
18. H.J. Kim, S.K. Kim, J.Y. Lee, and J.S. Kim. J. Org. Chem. **71**, 6611 (2006).
19. T. Gunnlaugsson, M. Glynn, G.M. Tocci, P.E. Kruger, and F.M. Pfeffer. Coord. Chem. Rev. **250**, 3094 (2006).
20. K.L. Kirk. Biochemistry of the halogens and inorganic halides. Plenum Press, New York. 1991.
21. M. Kleerkoper. Endocrinol. Metab. Clin. N. Am. **27**, 441 (1998).
22. J.A. Weatherhall. A handbook of experimental pharmacology. XX/1. Springer-Verlag, Berlin. 1969.
23. A. Wiseman. A handbook of experimental pharmacology. XX/2. Springer-Verlag, Berlin. 1970.
24. R.H. Dreishbuch. Handbook of poisoning. Lange Medical Publishers, Los Altos, CA. 1980.
25. S. Ayoob and A.K. Gupta. Crit. Rev. Env. Sci. Technol. **36**, 433 (2006).
26. E.J. Cho, J.W. Moon, S.W. Ko, J.Y. Lee, S.K. Kim, J. Yoon, and K.C. Nam. J. Am. Chem. Soc. **125**, 12376 (2003).
27. J.Y. Kwon, Y.J. Jang, S.K. Kim, K.-H. Lee, J.S. Kim, and J. Yoon. J. Org. Chem. **69**, 5155 (2004).
28. G. Xu and M.A. Tarr. Chem. Commun. (Cambridge), 1050 (2004).
29. I.H.A. Badr and M.E. Meyerhoff. J. Am. Chem. Soc. **127**, 5318 (2005).
30. E.J. Cho, B.J. Ryu, Y.J. Lee, and K.C. Nam. Org. Lett. **7**, 2607 (2005).
31. X. Peng, Y. Wu, J. Fan, M. Tian, and K. Han. J. Org. Chem. **70**, 10524 (2005).
32. D.H. Lee, J.H. Im, J.-H. Lee, and J.-I. Hong. Tetrahedron Lett. **43**, 9637 (2002).
33. Y.P. Zhao, C.C. Zhao, L.Z. Wu, L.P. Zhang, C.H. Tung, and Y.J. Pan. J. Org. Chem. **71**, 2143 (2006).
34. T. Ghosh, B.G. Maiya, and M.W. Wong. J. Phys. Chem. A, **108**, 11249 (2004).
35. T. Gunnlaugsson, A.P. Davis, J.E. O'Brien, and M. Glynn. Org. Biomol. Chem. **3**, 48 (2005).
36. F.M. Pfeffer, T. Gunnlaugsson, P. Jensen, and P.E. Kruger. Org. Lett. **7**, 5357 (2005).
37. E. Quinlan, S.E. Matthews, and T. Gunnlaugsson. Tetrahedron Lett. **47**, 9333 (2006).
38. X. Zhang, L. Guo, F.-Y. Wu, and Y.-B. Jiang. Org. Lett. **5**, 2667 (2003).
39. L. Nie, Z. Li, J. Han, X. Zhang, R. Yang, W.-X. Liu, F.-Y. Wu, J.-W. Xie, Y.-F. Zhao, and Y.-B. Jiang. J. Org. Chem. **69**, 6449 (2004).
40. S.-I. Sasaki, M. Mizuno, K. Naemura, and Y. Tobe. J. Org. Chem. **65**, 275 (2000).
41. Y. Tobe, S.-I. Sasaki, M. Mizuno, and K. Naemura. Chem. Lett. 835 (1998).
42. A. Morimoto, L. Biczok, T. Yatsuhashi, T. Shimada, S. Baba, H. Tachibana, D.A. Tryk, and H. Inoue. J. Phys. Chem. A, **106**, 10089 (2002).
43. T. Morozumi, T. Anada, and H. Nakamura. J. Phys. Chem. B, **105**, 2923 (2001).

© 2007 NRC Canada

Synthesis and enhanced neuroprotective activity of C60-based ebselen derivatives

Xu-Feng Liu, Wen-Chao Guan, and Weng-Shan Ke

Abstract: A C_{60}-based ebselen derivative 4 was synthesized through the cycloaddition of C_{60} with the azide (**3**) containing the ebselen component. It was obtained in a four-step synthesis starting from 2-(chloroseleno)benzoyl chloride and 2-(2-aminoethoxy)ethanol in 53% yield (based on consumed C_{60}). Its structure was characterized by ^{1}H NMR, ^{13}C NMR, IR, UV, and FAB-MS. To verify that the C_{60}-based ebselen derivative **4** had enhanced antioxidative and neuroprotective activity, the C_{60} derivative **5** and the ebselen derivative **6** were selected to treat cortical neuronal cells using the same procedures as with the C_{60}-based ebselen derivative **4**. The cellular viability of different derivative treatment groups was estimated by LDH leakage assay and MTT assay. At the same final concentration (30 μmol/L), the results showed that the antioxidative and protective potencies of the C_{60}-based ebselen derivative **4** (MTT (OD) 0.340 ± 0.035, LDH release (UL^{-1}) 4.80 ± 0.16) against H_2O_2-mediated neuronal injury have an advantage over those of C_{60} derivative **5** (MTT (OD) 0.297 ± 0.036, LDH release (UL^{-1}) 5.37 ± 0.31) and ebselen derivative **6** (MTT (OD) 0.267 ± 0.027, LDH release (UL^{-1}) 5.85 ± 0.26). Correspondingly, the GPX activity of **4** (1.62 U/μmol) was higher than that of **5** (0.77 U/μmol) and **6** (1.24 U/μmol). These findings demonstrate that the incorporation of two components with similar biological activity (C_{60} component and ebselen component) may be a desirable way of obtaining a new and more biologically effective C_{60}-based compound.

Key words: fullerene, ebselen derivative, azide, neuroprotective activity, cellular viability.

Résumé : On a réalisé la synthèse du dérivé **4** de l'ebsélène à base de C_{60} en procédant à la cycloaddition du C_{60} sur l'azide (**3**) qui contient une composante d'ebsélène qui a été obtenu en quatre étapes à partir du chlorure de 2-(chlorosélénо)benzoyle et de 2-(2-aminoéthoxy)éthanol, avec un rendement de 53% sur la base de la quantité de C_{60} utilisé. On a caractérisé sa structure par spectroscopies RMN du ^{1}H et du ^{13}C, par infrarouge, ultraviolet et spectrométrie de masse avec bombardement rapide. Dans le but de vérifier l'augmentation de l'activité antioxydante et neuroprotective du dérivé **4** de l'ebsélène à base de C_{60}, son activité a été comparé à celles du dérivé en C_{60} 5 et du dérivé de l'ebsélène **6** pour le traitement d'une cellule corticoneuronale, en utilisant les mêmes techniques. La viabilité cellulaire des groupes traités par divers dérivés a été évaluée par une combinaison de l'évaluation de l'émission de lactase déshydrogénase (LDH) et du clivage du bromure de 3-(4,5-diméthylthiazol-2-yl)-2,5-diphényltétrazolium (MTT). Les résultats montrent que, à la même concentration finale (30 μmol/L), les pouvoirs antioxydant et protecteur du dérivé **4** de l'ebsélène à base de C_{60}, (MTT (OD) 0,340 ± 0,035, émission de LDH (UL^{-1}) 4,80 ± 0,16) contre les dommages neuronaux provoqués par le H_2O_2 sont plus grands que ceux apportés par le dérivé en C_{60} (**5**), (MTT (OD) 0,297 ± 0,036, émission de LDH (UL^{-1}) 5,37 ± 0,31) et ceux apportés par le dérivé de l'ebsélène (**6**), (MTT (OD) 0,267 ± 0,027, émission de LDH (UL^{-1}) 5,85 ± 0,26). D'une façon correspondante, l'activité GPX du composé **4** (1,62 U/mmole) est supérieure à celles du composé **5** (0,77 U/mmole) et du composé **6** (1,24 U/mmole). Ces observations démontrent que l'incorporation de deux composants ayant des activités biologiques semblables (le composant en C_{60} et le composant de l'ebsélène) peut s'avérer être une façon désirable d'obtenir un composé à base de C_{60} qui soit biologiquement plus actif.

Mots-clés : fullerène, dérivé de l'ebsélène, azide, activité neuroprotective, viabilité cellulaire.

[Traduit par la Rédaction]

Introduction

Research in modern medical science (1) has suggested that free radicals are associated with a number of neurodegenerative diseases such as Parkinson's disease, Huntington's disease, and Alzheimer's dementia. Some reactive oxygen species (ROS), including superoxide ($O_2^{\cdot-}$) and hydroxyl (·OH) radicals and the nonradical molecules H_2O_2,

Received 16 September 2006. Accepted 2 February 2007. Published on the NRC Research Press Web site at http://canjchem.nrc.ca on 15 March 2007.

X.-F. Liu. Department of Chemistry, Huazhong University of Science & Technology, Wuhan 430074, P.R. China; Ministry of Education Key Laboratory for the Synthesis and Application of Organic Functional Molecules, Hubei University, Wuhan 430062, P.R.China.
W.-C. Guan.[1] Department of Chemistry, Huazhong University of Science & Technology, Wuhan 430074, P.R. China.
W.-S. Ke. College of Life Science, Hubei University, Wuhan 430062, P.R. China.

[1]Corresponding author (e-mail: wcguan04@yahoo.com.cn).

 doi:10.1139/V07-010 © 2007 NRC Canada

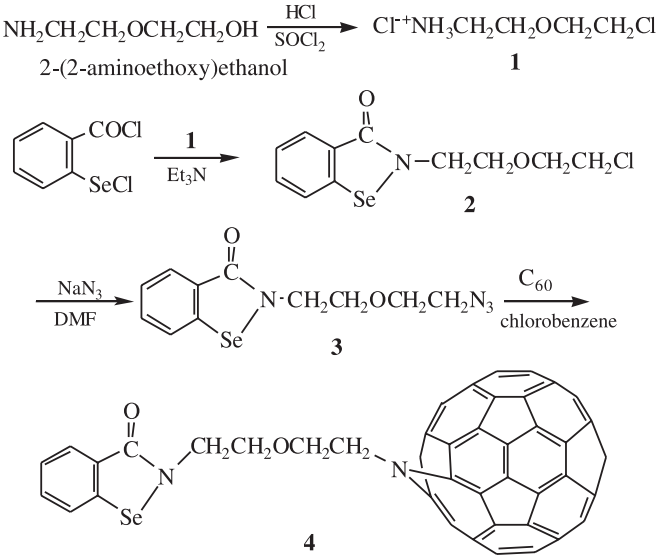
are believed to be major contributors to oxidative damage in neurodegenerative diseases. Reactive oxygen species produced during oxidative stress may cause various kinds of biological damage such as lipid peroxidation, protein oxidation and cross-linking, and lead to neuronal cell death (2). In light of a link between active oxygen species and neurodegenerative conditions, the development of chemopreventive agents with antioxidative activity is a recognized approach against neurological injury caused by ROS.

C_{60} fullerenes, owing to their electronic structure as an electron-poor polyolefine, are highly reactive with various organic radicals (3) and have drawn considerable attention in the area of antioxidant research. An electron paramagnetic resonance analysis has shown that C_{60} derivatives, such as carboxyfullerenes, fullerenols, and Hexa(sulfobutyl)fullerenes, have excellent capabilities to scavenge deleterious reactive oxygen species (4). In addition, neuroprotective effects of water-soluble C_{60} derivatives on oxidative injuries have also been extensively studied in several cell cultures and animal models of CNS damage. For example, carboxyfullerenes were confirmed to prevent apoptotic injury of cultured cortical neurons evoked by *N*-methyl-D-aspartate and β-amyloid peptide (5) and to inhibit iron-induced oxidative stress in rat brains (6). The same carboxyfullerenes were also reportedly able to inhibit cerebellar granule cell apoptosis (7) possibly via reducing the generation of ROS. Other fullerene derivatives, such as fullerenol, hexasulfobutylated C_{60} (FC4S), C_{60}(glucosamine)$_6$, have also been shown to possess neuroprotective potency related to their antioxidative property. Fullerenol was demonstrated to be a powerful scavenger for the free radicals induced by ischemia–reperfusion injury of the small intestine (8). Hexasulfobutylated C_{60} (FC4S) could be employed to be a free radical remover in biological systems (9). Recently, C_{60}(glucosamine)$_6$ has been found to prevent renal ischemia–reperfusion-induced apoptosis formation and superoxide generation (10). All these results demonstrate that fullerene and its derivatives possess an antioxidative activity and may be useful for neuroprotective agents in several acute or chonic neurodegenerative diseases.

On the other hand, ebselen and its analogues have been shown to possess glutathione (GSH) peroxidase-like activity and may act as an antioxidants and free radical scavengers (11). Recently, ebselen and its analogues were reported to have a neuroprotective effect against brain ischemic insults and glutamate-induced neurotoxicity (12). More recently, ebselen and its derivatives were demonstrated to have neuroprotective effects on laboratory rat spinal cord injuries (13). All the biological effects afforded by ebselen and its analogues are obviously related to their antioxidative properties and free radical scavenger activities.

In view of the described antioxidative and neuroprotective properties of C_{60} and ebselen derivatives, it is expected that the covalent attachment of a biologically active ebselen component to [60]fullerene may lead to the formation of a new C_{60}-based ebselen derivative possessing better antioxidative and neuroprotective properties than either of the parent C_{60} or ebselen. In this paper we report the synthesis of the new C_{60}-based ebselen derivative **4** by a cycloaddition reaction between C_{60} and ebselenyl azide, which contains a solubilizing ethyleneglycol chain. We also report on the neuroprotection of **4** against hydrogen peroxide induced neuronal insults in cortical cell cultures.

Scheme 1. Synthesis of the C_{60}-based ebselen derivative **4**.



Results and discussion

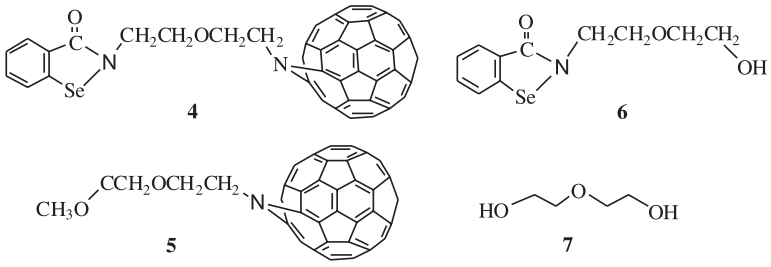
Synthesis and spectroscopic properties of C_{60}-based ebselen derivative 4

The preparation of the C_{60}-based ebselen derivatives **4** was carried out in four steps as depicted in Scheme 1. The chloride **1** was prepared by reacting 2-(2-aminoethoxy)ethanol and thionyl chloride ($SOCl_2$) under identical conditions to those used in ref. 14. The obtained chloride **1** was reacted with 2-(chloroseleno)benzoyl chloride, prepared in a four-step synthesis starting from anthanilic acid (15) in dry $CHCl_3$ in a molar ratio of 1.5:1 in presence of Et_3N. The reaction mixture was concentrated and purified by flash chomatography (silica gel, eluent 3:1 ethyl acetate – petroleum) to give the ebselen derivative **2** in 73% yield. Reaction (16) of ebselen derivative **2** with sodium azide (NaN_3) in a molar ratio of 1:3 in dry dimethylformamide (DMF) resulted in the desired azide **3** in 80% yield. Cycloaddition (17) of the azide **3** with C_{60} in an equimolar ratio in refluxing chlorobenzene under a nitrogen atmosphere gave the target compound **4** in a 53% yield (based on consumed C_{60}) after purification by flash chomatography eluting with toluene, followed by a toluene–$CHCl_3$ mixture (4:1).

The spectroscopic data for compound **4** are in agreement with the proposed structure. The ^{13}C NMR spectrum (150 MHz, $CDCl_3$) of compound **4** exhibits four aliphatic carbon peaks between 41.53 and 71.13 ppm and one carbonyl peak at 166.52 ppm. The peaks between 126.95 and 134.22 are assigned to the phenylene carbons of the ebselen moiety. There are 31 peaks between 133.51 and 147.90 ppm, and the signal at around 80.0 ppm corresponding to the bridgehead carbons is not observed. These data indicate that the C_{60} moiety of compound **4** has C_s symmetry with an annulene structure of monosubstituted C_{60} azafulleroid (17). In the ^1H NMR spectrum (600 MHz, $CDCl_3$) of compound **4**, two triplets (7.67, J = 7.3 Hz and 7.45, J = 7.3 Hz) and

© 2007 NRC Canada

Fig. 1. Compounds **4**, **5**, **6**, and **7** used in this study.



two doublets (8.05, J = 7.4 Hz and 7.87, J = 7.1 Hz) are attributed to phenyl protons. The resonances of methylene protons of the ethylene glycol chain are detected as four triplets (4.13, J = 6.3 Hz; 3.81, J = 6.3 Hz; 3.68, J = 6.7 Hz; 2.81, J = 6.7 Hz) that are similar to those of the starting azide with a small downfield shift due to the influence of the carbon sphere (17, 18). The IR spectrum of compound **4** shows characteristic bands of the fullerene moiety at 1430, 1035, and 528 cm^{-1} and an absorption of C=O at 1610 and 1567 cm^{-1}. The UV–vis spectrum of compound **4** displays typical absorptions due to the fullerene skeleton at 330, 268, and 258 nm, while the absorption at 420nm, characteristic of aziridinofullerenes, is absent, further confirming that compound **4** possesses an open annulene structure.

Cytotoxicity determination

The cytotoxicities of the C_{60}-based ebselen derivative **4**, the C_{60} derivative **5** (Fig. 1), and the ebselen derivative **6** (Fig. 1) in cortical neuronal cells were evaluated and determined based on their concentration-dependent effects on cell growth (MTT test) (Fig. 2*a*) and LDH leakage (Fig. 2*b*).

Results in Fig. 2*a* show that compound **5** in the concentration range of 0~50 μmol/L did not manifest cytotoxic effects. Compounds **4** and **6**, at concentrations ranging from 1 to 30 μmol/L, were able to slightly stimulate cell growth. However, when their concentrations were higher than 38 μmol/L, cell growth was significantly inhibited. In parallel with the results of the MTT test, cells treated with compound **4**, **5**, or **6** at concentrations of 1~30 μmol/L for 24 h did not show an obvious increase in LDH leakage (Fig. 2*b*). When cells were treated with compound **4** or **6** at concentrations higher than 38 μmol/L, a significant increase in LDH activity in the medium was observed. These cytotoxicity tests show that compounds **4**, **5**, and **6** at a concentration of up to 30 μmol/L have no toxic effect on cortical neurons. We thus decided to use 30 μmol/L in all subsequent experiments.

Effects of C_{60} derivative 5, ebselen derivative 6, and C_{60}-based ebselen derivative 4 on cellular viability and LDH release

To verify the enhanced neuroprotective activity of compound **4**, compounds **5**, **6**, and **7** (Fig. 1) were also used to treat cortical neuronal cells according to the same procedures as **4**.

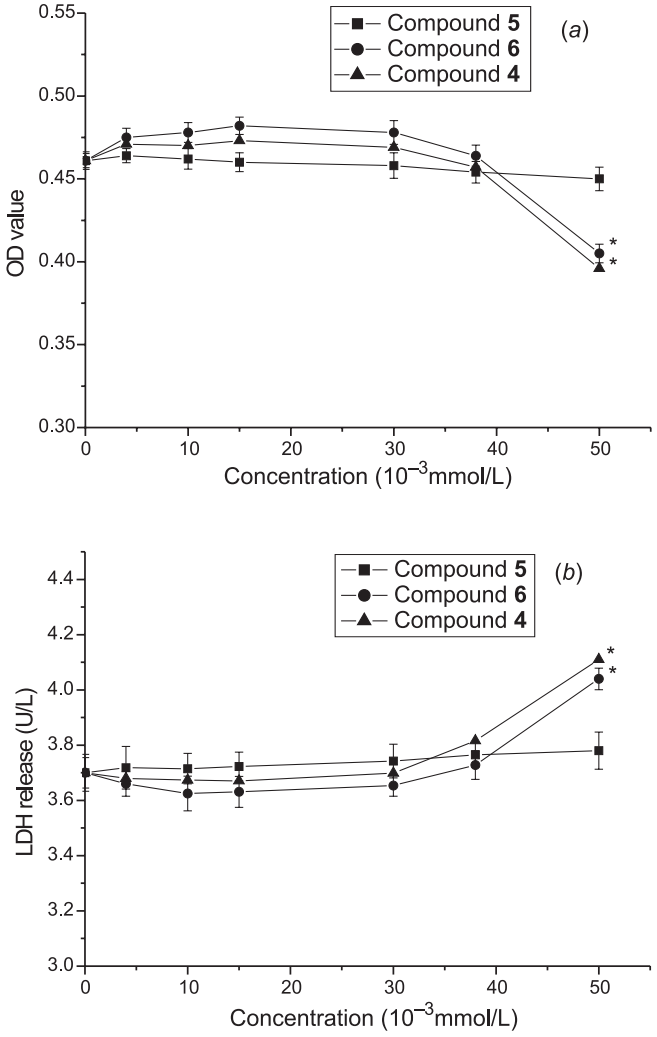
Cell viability and cell damage were estimated by MTT assay and LDH leakage assay, respectively. The measurement results of LDH release and MTT (OD) are shown in Fig. 3. Compared with the control group, the treatmeant of cortical culture with H_2O_2 (150 μmol/L) for 2 h caused a decrease of MTT (OD) from 0.463 ± 0.024 to 0.220 ± 0.016 ($P < 0.01$) and an increase of LDH content in the extracellular media from 3.69 ± 0.16 to 7.93 ± 0.20 ($P < 0.01$), indicating H_2O_2-induced neuronal injury. Compound **4**, **5**, or **6** alone at a concentration of 30 μmol/L did not cause obvious changes in the MTT (OD) value and LDH release (compared with control group) (Fig. 3). However, they were effectively able to attenuate the H_2O_2-mediated increase of LDH release and the decrease of the MTT (OD) value (Fig. 3). MTT (OD) was elevated from 0.220 ± 0.016 (H_2O_2 alone) to 0.297 ± 0.036 (**5**), 0.267 ± 0.027 (**6**), 0.340 ± 0.035 (**4**) ($P < 0.01$) (Fig. 3*a*), and LDH release was reduced from 7.93 ± 0.20 (H_2O_2 alone) to 5.37 ± 0.31 (**5**), 5.85 ± 0.26 (**6**), 4.80 ± 0.16 (**4**) ($P < 0.01$) (Fig. 3*b*). Furthermore, compound **7** alone (30 μmol/L) did not modify the MTT (OD) value and LDH release (compared with the control group), indicating that the linker ($CH_2CH_2OCH_2CH_2$) in compounds **4**, **5**, and **6** has no influence on their neuroprotective activities.

Cellular viability in compounds **4** + H_2O_2 group (MTT (OD) 0.340 ± 0.035) was higher than that of compound **5** + H_2O_2 group (0.297 ± 0.036) or compound **6** + H_2O_2 group (0.267 ± 0.027). The LDH release (4.80 ± 0.16 UL^{-1}) for **4** was consistently lower than that of compound **5** + H_2O_2 group (5.37 ± 0.31) or compound **6** + H_2O_2 group (5.85 ± 0.26). These results indicate that the antioxidative and protective potency of C_{60}-based ebselen derivative **4** against H_2O_2-mediated neuronal injury show an advantage over those of the C_{60} derivative **5** and the ebselen derivative **6**.

However, the neuroprotective potency of compound **4** was marginally higher than those of the parent compounds **5** and **6** by 10%–20%. This is plausibly explained by the fact that the antioxidant capabilities of fullerene derivatives are influenced by various complex factors. First, the antioxidative activities of fullerene derivatives derive from their scavenging action on active oxygen radicals (·OH, O_2^{-}·), and the scavenging mechanism may be due to the electron-poor polyolefine bonds of the C_{60} moiety, which are highly reactive toward the addtition of radicals. Thus, the integrity of the conjugated bonds in the C_{60} cage (addition number), the electronegativity of adduct groups, and the steric hindrance of adduct groups against the attack of free radicals would all influence the antioxidant capabilities of fullerene derivatives. Besides, characteristics of fullerene derivatives, such as their amphipathic nature, solubility, and aggregation, are also not negligible. Another important influencing factor could be the special molecular mechanism responsible for the

© 2007 NRC Canada

Fig. 2. Dose-dependent effects of compounds **4**, **5**, and **6** on the (*a*) neuronal cell growth (MTT test) and (*b*) LDH leakage. Values are mean ± SD of 4 experiments. *$P < 0.05$ compared with the control (one-way ANOVA with Newman–Keuls test).



neuroprotective effects produced by these compounds. Different mechanisms influence discrepancies in neuroprotective efficacy. In conclusion, the antioxidant capabilities of fullerene derivatives are ultimately determined by the combined effects of all the aforementioned factors.

GPX-like activity of compounds 4, 5, and 6

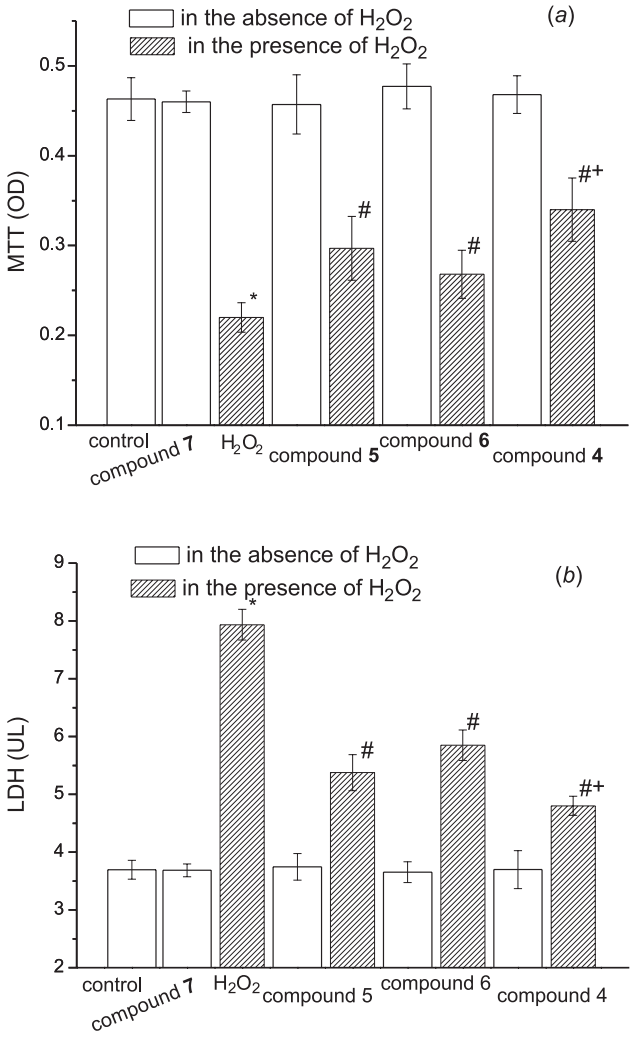
GPX activities were measured by a coupled enzymatic assay as described in a subsequent section, "Measurement of the GPX activity of compounds 4, 5, and 6". The decrease of NADPH absorption at 366 nm is a measure of GSH peroxidase activity (eqs. 1 and 2).

$$[1] \quad 2GSH + H_2O_2 \xrightarrow[\text{peroxidase}]{GSH} GSSG + 2H_2O$$

$$[2] \quad GSSG + NADPH + H^+ \xrightarrow[\text{reductase}]{GSH} 2GSH + NADP^+$$

The GPX-like activities of compounds **4**, **5**, or **6** in the catalyzed reduction of H_2O_2 are listed in Table 1. Experiments revealed that compounds **4**, **5**, and **6** all displayed

Fig. 3. (*a*) MTT (OD) of cortical neurons treated with compound **4**, **5**, **6**, or **7** in the presence or absence of H_2O_2. (*b*) LDH release of cortical neurons treated with compound **4**, **5**, **6**, or **7** in the presence or absence of H_2O_2. Values are mean ± SD of 8 experiments. Statistical comparisons were made using one-way ANOVA followed by a Newman–Keuls test as post hoc analysis. Differences were accepted as significant at $P < 0.05$ and $P < 0.01$, $P < 0.01$ (*) vs. control, $P < 0.01$ (#) vs. H_2O_2 group, $P < 0.05$ (+) vs. compound **5** with H_2O_2 or **6** with an H_2O_2 group.



GPX-like activities, and the catalytic action of compounds **4** and **6** was superior to that of ebselen. Furthermore, the GPX activity of compound **4** (1.62 U/μmol) was found to be higher than those of compounds **5** (0.77 U/μmol) and **6** (1.24 U/μmol).

Conclusions

The present work describes the synthesis of a C_{60}-based ebselen derivative that contains an ethyleneglycol chain between the fullerene and the biologically active ebselen component. The C_{60}-based ebselen derivative showed stronger neuroprotective potency than either of the parent C_{60} derivative or ebselen derivative alone. This enhanced neuroprotective potency can be reasonably attributed to both an

© 2007 NRC Canada

Table 1. The GPX activities of compounds **4**, **5**, and **6** (using hydrogen peroxide as the substrate in the presence of GSH).

GPX mimic	Ebselen (PZ51)	Compound **5**	Compound **6**	Compound **4**
Activity (U/μmol)	0.99 (19)	0.77	1.24	1.62

improvement of its free radical scavenging capabilities and an improvement of its GPX-like activities. From this encouraging result it can be concluded that through selecting appropriate antioxidative components and introducing them to [60]fullerenes, we can obtain a new C_{60}-based antioxidant with better antioxidative ability, and that this is also an effective strategy for designing and synthesizing C_{60}-based antioxidants.

Experimental

Reagents and instruments

C_{60} (99% purity) was prepared by the Institute of Fullerenes of Wuhan University. All solvents and reagents were dried using standard procedures prior to use. All other commercially available compounds were used as received. Melting points were determined with a Digital Melting Point Apparatus (WRS-IB). Column chromatography was performed on silica gel (200–300 mesh). IR spectra were obtained on a Spectrum One PerkinElmer spectrometer in pellets with KBr. UV spectra were recorded on PerkinElmer λ 17 instrument. ^{1}H and ^{13}C NMR spetra were recorded on a Varian INOVA 600NMR instrument in CDCl3 at 600 and 150 MHz. Mass spectra and high-resolution mass spectra were performed on a JMS XS05H instrument.

An 18-day old Wister rat fetus was provided by the Experimental Animal Center of Tongji Medical College, Huazhong University of Science & Technology (China). D-Hanks, trypsinase, and DMEM were purchased from Gibco Co. (USA). Fetal calf serum (FCS), cytarabine hydrochlride, sodium azide, and potassium phosphate were purchased from Tianjin Biochemical Factory (China). Poly-L-lysine, DMSO, MTT, NADPH, GSH, and GSH reductase were obtained from Sigma-Aldrich Chemical Co. (USA). An LDH assay kit was obtained from Beijing Chemical Kit Company (China). Spectrophotometric measurements were made using a Konton UV-922 spectrophotometer. The optical density of each well was measured at 550 nm using an enzyme-linked analyzer (Bio-Rad550, USA).

Chemistry

2-(2-Chloroethoxy)ethylamine hydrochloride (1)

According to the procedure described in ref. 14, diethylene glycolamine (1.89 g, 18 mmol) was converted into the chloride **1** (1.79 mg, 80%) as a white solid. IR (KBr, cm^{-1}) ν: 3050 (N-H), 2920 (C-H), 1210 (C-N), 1110 (C-O-C), 750 (C-Cl). ^{1}H NMR (600 MHz, DCl_3) δ: 7.60 (3H, b, NH_3^+), 4.08 (2H, t, J = 6.8 Hz, OCH_2), 3.62 (2H, t, J = 6.4 Hz, OCH_2), 3.49–3.53 (4H, m, $ClCH_2$, NCH_2).

2-(2-(2-Chloroethoxy)ethyl)benzo[d][1,2]selenazol-3(2H)-one (2)

To a solution of **1** (747.6 mg, 6 mmol) and triethylamine (1.2 g, 12 mmol) in dry chloroform (50 mL) was added dropwise a solution of 2-(chloroseleno)benzoyl chloride (1.02 g, 4 mmol) in dry chloroform (40 mL) at 5~10 °C under stirring. The mixture was slowly warmed to 40 °C and stirred for 10 h. The resultant mixture was cooled and washed with 5% $NaHCO_3$ (2 × 50 mL), a saturated aq. solution of NaCl (2 × 50 mL), and was then evaporated to dryness. The residue was chromatographed on silica gel and eluted with 3:1 ethyl acetate – petroleum to give the ebselen derivative **2** (889 mg, 73%) as a pale yellow solid. TLC R_f 0.56 (ethyl acetate – petroleum ether 3:1); mp 110.4–111.3 °C. IR (KBr, cm^{-1}) ν: 3050 (C-H_{Ar}), 615, 1570 (amide C=O), 1280 (amide C-N), 1174 (C-O-C), 760 (C-Cl). ^{1}H NMR (600 MHz, $CDCl_3$) δ: 8.03 (1H, d, J = 7.5 Hz, ArH), 7.88 (1H, d, J = 7.0 Hz, ArH), 7.65 (1H, t, J = 7.2 Hz, ArH), 7.42 (1H, t, J = 7.2 Hz, ArH), 4.08 (2H, t, J = 6.2 Hz, NCH_2), 3.65~3.62 (4H, m, CH_2OCH_2), 3.53 (2H, t, J = 7.0 Hz, $ClCH_2$). ^{13}C NMR (150 MHz, $CDCl_3$) δ: 166.52 (amide C=O), 134.35 (phenylene C), 132.58, 132.04, 129.22, 127.84, 127.0 5 (phenylene C), 70.16 (CH_2O), 69.12 (OCH_2), 43.52 (CH_2Cl), 40.22 (NCH_2).

2-(2-(2-Azidoethoxy)ethyl)benzo[d][1,2]selenazol-3(2H)-one (3)

To the obtained ebselen derivative **2** (762 mg, 2.5 mmol) dissolved in dry dimethylformamide (DMF) (80 mL) was added sodium azide (487.5 mg, 7.5 mmol). The mixture was warmed to 65 °C and stired for 12 h. The unreacted NaN_3 was removed by filtration, and DMF was distilled under reduced pressure. The yellow residue was washed with water, centrifuged, and then dried to constant weight at 80 °C in vacuo. The obtained yellow solid (622.4 mg, 80%) was used for the next reaction without further purification. Melting point ~130 °C decomp. IR (KBr, cm^{-1}) ν: 3055 (C-H_{Ar}), 2135 (N_3), 1620, 1573 (amide C=O), 1276 (amide C-N), 1170 (C-O-C). ^{1}H NMR (600 MHz, $CDCl_3$) δ: 8.02 (1H, d, J = 7.6 Hz, ArH), 7.86 (1H, d, J = 7.2 Hz, ArH), 7.67 (1H, t, J = 7.2 Hz, ArH), 7.41 (1H, t, J = 7.3 Hz, ArH), 4.06 (2H, t, J = 6.2 Hz, NCH_2), 3.65 (2H, t, J = 6.2 Hz, CH_2O), 3.50 (2H, t, J = 7.2 Hz, OCH_2), 1.92 (2H, t, J = 7.2 Hz, N_3CH_2). ^{13}C NMR (150 MHz, $CDCl_3$) δ: 166.50 (amide C=O), 134.37 (phenylene C), 132.56, 132.02, 129.20, 127.84, 127.03 (phenylene C), 70.20 (CH_2O), 69.35 (OCH_2), 48.26 (CH_2N_3), 40.12 (NCH_2).

Reaction of C_{60} with azide 3 to give 4

C_{60} (250 mg, 0.345 mmol) was dissolved in 200 mL of chlorobenzene. Under nitrogen atmosphere the solution was heated at reflux and the azide **3** (107.4 mg, 0.345 mmol) in chlorobenzene (6 mL) was added dropwise. Heating was then continued for 8 h. The solution was concentrated and the crude residue chromatographed on a column with silica gel to give 95 mg of C_{60} (elution with toluene) and 114.5 mg (53% based on consumed C_{60}) of the monoaddition product **4** as a brown black solid (elution with a toluene–$CHCl_3$ mixture 4:1). UV–vis ($CDCl_3$) λ (nm): 330, 268, 258, 213. IR (KBr, cm^{-1}) ν: 3045 (C-H_{Ar}), 1610, 1567 (amide C=O), 1430 (C_{60}), 1275 (amide C-N), 1184 (C-O-C), 1035 (C_{60}), 753 (C-Cl), 528 (C_{60}). ^{1}H NMR (600 MHz, $CDCl_3$) δ: 8.05 (1H, d,

© 2007 NRC Canada

J = 7.4 Hz, ArH), 7.87 (1H, d, *J* = 7.1 Hz, ArH), 7.67 (1H, t, *J* = 7.3 Hz, ArH), 7.45 (1H, t, *J* = 7.3 Hz, ArH), 4.13 (2H, t, *J* = 6.3 Hz, $CONCH_2$), 3.81 (2H, t, *J* = 6.3 Hz, CH_2O), 3.68 (2H, t, *J* = 6.7 Hz, OCH_2), 2.81 (2H, t, *J* = 6.7 Hz, NCH2). ^{13}C NMR (150 MHz, $CDCl_3$) δ: 166.52 (amide C=O), 147.90 (2), 147.05 (2), 145.12 (2), 144.76 (4), 144.65 (2), 144.58 (2), 144.39 (2), 144.36 (2), 144.20 (2), 143.89 (2), 143.75 (1), 143.58 (2), 143.47 (1), 143.43 (2), 143.26 (2), 143.13 (2), 142.93 (2), 142.82 (2), 142.70 (2), 142.58 (2), 142.55 (2), 140.74 (2), 140.64 (2), 139.11 (1), 138.39 (1), 137.92 (2), 137.41 (2), 137.37 (2), 136.01 (2), 135.60 (2), 134.22 (phenylene C), 133.51 (2) (31 C_{60} sp^2 carbons), 132.44, 132.14, 129.14, 127.76, 126.95 (6 phenylene carbons), 71.13 (CH_2O), 69.87 (OCH_2), 61.28, 41.53 (NCH2). MS (FAB, NBA) *m/z*: 1004 (M^+ + H), 735 ($C_{60}NH^+$).

Preparation of ebselen derivative 6

Following the procedure described in ref. 20, diethylene glycolamine (1.456 g, 13.86 mmol) was reacted with 2-(chloroseleno)benzoyl chloride gave ebselon derivative **1** (2.5 g, 63%) as white needles; mp 116.7–117.5 °C. IR (KBr, cm^{-1}) ν: 3630 (O-H), 3048 (C-H_{Ar}), 1610, 1573 (amide C=O), 1283 (amide C-N), 1170 (C-O-C). ^1H NMR (600 MHz, $CDCl_3$) δ: 8.00 (1H, d, *J* = 7.6 Hz, ArH), 7.86 (1H, d, *J* = 7.1 Hz, ArH), 7.63 (1H, t, *J* = 7.3 Hz, ArH), 7.43 (1H, t, *J* = 7.3 Hz, ArH), 4.92 (1H, s, OH), 4.10 (2H, t, *J* = 6.2 Hz, NCH_2), 3.77~3.64 (4H, m, CH_2OCH_2), 3.54 (2H, t, *J* = 6.2 Hz, CH_2OH). ^{13}C NMR (150 MHz, $CDCl_3$) δ: 166.55 (amide C=O), 134.33 (phenylene C), 132.54, 132.08, 129.20, 127.85, 127.00 (phenylene C), 72.26 (CH_2O), 69.23 (CH_2O), 61.52 (CH_2OH), 39.20 (NCH2).

Preparation of the C_{60} derivative 5

According to the procedure described in ref. 18, the reaction of l-azido-3,6-dioxoheptane (59.5 mg, 0.41 mmol) with fullerene (C_{60}) (300 mg, 0.42 mmol) gave the C_{60} derivative **5** (125.7 mg, 54% based on unrecovered C_{60}) as a purple solid. IR (KBr, cm^{-1}) ν: 2935, 1640, 1275, 1184 (C-O-C), 1030 (C_{60}), 528 (C_{60}). ^1H NMR (600 MHz, $CDCl_3$) δ: 4.01~3.94 (4H, m, OCH_2CH_2O), 3.76 (2H, t, *J* = 6.7 Hz, OCH_2), 3.52 (3H, s, OCH_3), 2.96 (2H, t, *J* = 6.7 Hz, NCH_2). ^{13}C NMR (150 MHz, $CDCl_3$) δ: 147.83 (2), 147.02 (2), 145.07 (2), 144.75 (2), 144.71 (2), 144.55 (2), 144.46 (2), 144.32 (2), 144.26 (2), 144.15 (2), 143.80 (2), 143.68 (1), 143.48 (2), 143.41(1), 143.36 (2), 143.16 (2), 143.05 (2), 142.87 (2), 142.72 (2), 142.58 (2), 142.53 (2), 140.83 (2), 140.68 (2), 139.18 (2), 138.41 (1), 137.91 (1), 137.64 (2), 137.21 (2), 137.17 (2), 136.17 (2), 135.67 (2), 133.57 (2) (32 C_{60} sp^2 carbons), 71.63 (CH_2O), 70.05, 69.63 (CH_3O), 60.13, 58.87 (CH_2N). MS (FAB, NBA) *m/z*: 838 (M^+ + H), 735 ($C_{60}NH^+$), 720 (C_{60}).

Biological activity

Primary cortical neuronal cultures

Primary cultures of rat cortical neurons were established using a modification of previous methods (21), which are briefly outlined here. Cortical tissue from an 18-day old Wistar rat fetus was dissociated and put in D-Hanks with trypsinase (0.125%) to be digested for 20 min at 37 °C. The trypsinase was removed and the dissociated neurons were washed with DMEM–FCS (10%), and filtrated through a 200-order stainless steel sieve. After centrifugation at 4000*g* for 10 min, the cells were gently resuspended in DMEM–FCS (10%). The cell suspensions were vaccinated to poly-L-lysine (0.01) coated 96-well plates at the density of 1×10^5 cells per well. All cells were incubated in a DMEM culture medium containing 10% FCS, penicillin (100 U/mL), and streptomycin 100 μg/mL) at 37 °C in a 95% air – 5% CO_2 humidified culture box. On the 3rd day of vaccination, cytarabine (the terminal concentration 10 μmol/L) was added to the culture medium to prevent proliferation of nonneuronal cells.

On the 10th day of culture the neural cells could be used for the experiment and were randomly divided into different groups: control group, H_2O_2-injured group, compound-treated groups in the absence of H_2O_2 (compound **4**, **5**, **6**, and **7**), and compound-treated groups in the presence of H_2O_2 (compound **4** + H_2O_2, **5** + H_2O_2, and **6** + H_2O_2).

Cytotoxicity assessment of compounds 4, 5, and 6

The cytotoxicity of compounds **4**, **5**, and **6** was measured using MTT assay and LDH leakage assay prior to investigating their neuroprotective effects on H_2O_2-damaged cortical neuronal cells. Cells were cultured at the density of 1×10^5 cells per well in a DMEM culture medium containing FCS (10%), penicillin (100 U/mL), and streptomycin (100 μg/mL). When cells were attached to the bottom of the culture plates, the culture medium was replaced by the fresh DMEM culture medium containing the compound (**4**, **5**, or **6**) at diverse final concentrations from 0 to 50 μmol/L. After 24 h of incubation, cell viability and LDH leakage were determined by the MTT assay and LDH leakage assay, respectively. The MTT assay is based on the ability of viable mitochondria to convert MTT, a soluble tetrazolium salt, into an insoluble formazan precipitate, which is dissolved in dimethyl sulfoxide and quantified by spectrophotometry (22). LDH leakage assay is based on the ability of the LDH released in the culture medium to transform NAD to NADH. The increase of NADH is quantified by spectrophotometry. The activity unit of LDH is defined as the amount of LDH that produces 1 μmol NADH per min from NAD^+. The activity is expressed in U/L of the extracellular medium.

Culture treatments

Compounds **4**, **5**, and **6** were dissolved in DMSO, diluted with sterile water to prepare their stock solutions (10 mmol/L), and maintained at 4 °C. At the time of the change in medium, stock solutions were further diluted and applied to the cultures.

Oxidative injury (23) of the group was induced by adding H_2O_2 (final concentration 150 μmol/L) to the serum-free DMEM culture medium containing DMSO (0.2%) supplement and incubating at 37 °C for 2 h. After that treatment, the culture medium was replaced with fresh serum-free DMEM and the cells were cultured continuously for 24 h in a culture box. For compound-treated groups in the absence of H_2O_2, the neuronal cells were cultured with serum-free DMEM containing compound **4**, **5**, **6**, or **7** (final concentration 30 μmol/L) at 37 °C for 24 h. For compound **4**, **5**, or **6** in H_2O_2-treated groups, cortical neuronal cultures were pretreated with compound **4**, **5**, or **6** (final concentration

© 2007 NRC Canada

30 μmol/L) for 2 h, followed by exposure to H_2O_2 (150 μmol/L) for another 2 h. Afterwards, the cell cultures received the same treatmeant as the H_2O_2-injured groups. Control cells were not subjected to H_2O_2 and the various compounds, but were cultured in a serum-free DMEM medium supplemented with DMSO (0.2%) for 24 h.

Measurement of cell activity (24)

Cell viability was determined by measuring the mitochondrial dehydrogenase activity (MDHA) using reduction of MTT. After the culture treatments described earlier, an MTT solution (final concentration 0.5 mg/mL) was added to each well, and the cells were cultured at 37 °C for 4 h. After removal of the medium, formazan crystals produced by MDHA in viable cells were dissolved with dimethyl sulfoxide (200 μL). The value of opical density of each well was measured at 550 nm using an enzyme-linked analyzer.

Determination of (LDH) release (25)

Cellular damage was evaluated by measuring the release of lactate dehydrogenase (LDH) into the culture medium. LDH content in the extracellular medium was determined using the LDH assay kit according to the kit instructions.

Measurement of the GPX activity of compounds 4, 5, and 6

GPX activities of compounds **4**, **5**, and **6** were measured according to the method of Wilson et al. (19). The test mixture contained EDTA (1 mmol/L), sodium azide (1 mmol/L), GSH (1 mmol/L), NADPH (0.25 mmol/L), GSH reductase (1 U), DMSO (0.2%), and the test compound (30 μmol/L) in potassium phosphate buffer (50 mmol/L, pH 7.4). The reaction was carried out at 37 °C and was initiated by the addition of hydroperoxide (0.5 mmol/L). The rate of NADPH oxidation was followed over a 3 min period by monitoring the decrease of NADPH UV absorption at 366 nm (ε 3.5 × 10^3 $mol^{-1}Lcm^{-1}$). The rate of nonenzymatic reaction was determined in a mixture without a test compound (blank). The net rate of enzymatic oxidation of NADPH was used to calculate enzyme activity (1 μmol of NADPH consumed per minute). The activity is expressed in U/μmol of enzyme mimic.

Acknowledgment

This work was supported by National Science Foundation of China (No. 20474020.)

References

1. C.E. Beyer, J.D. Steketee, and D. Saphire. Biochem. Pharmacol. **56**, 1265 (1998).
2. E.R. Stadtman and B.S. Berlett. Chem. Res. Toxicol. **10**, 485 (1997); T.M. Moore, P.L. Khimenko, and A.E. Taylor. Chin. J. Physiol. **9**, 65 (1996).
3. P.J. Krusic, E.Wasserman, P.N. Ketzer, J.R. Morton, and K.F. Preston. Science (Washington, D.C.), **254**, 1183 (1991).
4. F. Cheng, X.Yang, H. Zhu, J. Sun, and Y. Liu. J. Phys. Chem. Solids, **61**, 1145 (2000); Y.S. Zhu, D.Y. Sun, and G.Z. Liu. Chem. J. Chin. Univ. **17**, 1127 (1996); L.Y. Chiang, F.J. Lu, and J.T. Lin. J. Chem. Soc. Chem. Commun. 283 (1995); S.C. Chueh, M.K. Lai, M.S. Lee, L.Y. Chiang, T.I. Ho, and S.C. Chen. Transplant. Proc. **31**, 1976 (1999).
5. L.L. Dugan, D.M. Turetsky, C. Du, D. Lobner, M. Wheeler, C.R. Almli, C.K.-F. Shen, T.-Y. Luh, D.W. Choi, and T.S. Lin. Proc. Natl. Acad. Sci. USA. **94**, 9434 (1997); L.L. Dugan, J.K. Gabrielsen, S.P. Yu, T-S. Lin, and D.W. Choi. Neurobiology of Disease. **3**, 129 (1996).
6. A.M.Y. Lin, B.Y. Chyi, S.D. Wang, H.H.Yu, P.P. Kanakamma, T.Y. Luh, C.K. Chou, and L.T. Ho. J. Neurochem. **72**, 1634 (1999).
7. M. Bisaglia, B. Natalini, R. Pellicciari, E. Straface, W. Malorni, D.Monti, C. Franceschi, and G. Schettini. J. Neurochem. **74**, 1197 (2000).
8. H-Sh. Lai, W-J. Chen, and L-Y. Chiang. World J. Surg. **24**, 450 (2000).
9. Y.T. Lee, L.Y. Chiang, W.J. Chen, and H.C. Hsu. Proc. Soc. Exp. Biol. Med. **224**, 69 (2000); S.S. Huang, Sh.K. Tsai, Ch.L. Chin, L.Y. Chiang, H.M. Hsieh, and C.M. Teng. Free Radic. Biol. Med. **30**, 643 (2001).
10. Ch.T. Chien, Ch-F. Chen, Su-M. Hsu, L.Y. Chiang, and M-K. Lai. Fullerene Sci. Technol. **9**, 77 (2001).
11. A. Müller, E. Cadenas, P. Graf, and H. Sies. Biochem. Pharmacol. **33**, 3235 (1984); X.J. Ren, L. Yang, J. Liu, D. Su, D. You, Ch Liu, K. Zhang, and G. Luo. Arch. Biochem. Biophys. **387**, 250 (2001).
12. L.O. Porciuncula, J.B.T. Rocha, C.R. Boeck, D. Vendite, and D.O. Souza. Neurosci. Lett. **299**, 217 (2001); I.H. Graham, D.I. Masayasu, and H. Macrae. Free Radic. Biol. Med. **34**, 56 (2003).
13. M. Kalayci, O. Coskun, F. Cagavi, M. Kanter, F. Armutcu, and S. Gul. Neurochem. Res. **30** (3), 403 (2005).
14. J.W. Lown, A.V. Joshua, and L.W. McLaughlin. J. Med. Chem. **23**, 798 (1980).
15. T. Schewe. Gen. Pharmacol. **26**, 1153 (1995).
16. R. Adems, J. Press, and E. Deegan. Synth. Commun. **21**,675 (1991).
17. M. Prato, Q.C. Li, F. Wudl, and V. Lucchini. J. Am. Chem. Soc. **115**, 1148 (1993).
18. J. Craig, P.M. Saville, and J.W. White. J. Org. Chem. **59**, 3503 (1994).
19. S.R. Wilson, P.A. Sucker, R.C. Hung, and A. Spector. J. Am. Chem. Soc. **111**, 5936 (1989).
20. M. Osajda and J. Młochowski. Tetrahedron, **58**, 7531 (2002).
21. J.Y. Koh, and D.W. Chol. J. Neurosci. Methods, **7**, 357 (1987); M. Schena, D.Shalon, and R.W. Dais. Science (Washington, D.C.), **270**, 467 (1995).
22. M.C. Alley, A. Scudieco, M.L. Monks, M.J. Hursey, D.L. Czerwinski, B.J. Fine, J.G. Abbott, R.H. Mayo, and M.R. Shoemaker. Cancer Res. **48**, 589 (1988).
23. M.B. Hensen, S.E. Nilsen, and K. Berg. J. Immunol. Methods, **l19**, 203 (1998); M.Yoshizumi, T. Kogame, Y. Suzaki, and Y. Fuijita. Br. J. Pharmacol. 1**36**, 1023 (2002).
24. T.J. Mosmann. Immunol. Methods, **65**, 55 (1983); C. Behl, J.B. Davis, R. Lesley, and D. Schubert. Cell (Cambridge, Mass.), **77**, 817 (1994).
25. J.Y. Koh and D.W. Choi. J. Neurosci. Methods, **20**, 83 (1987); K.A. Hartnett, A.K. Stout, S. Rajdev, P.A. Rosenberg, I.J. Reynolds, and E.J. Aizenman. J. Neurochem. **68**, 1836 (1997).

© 2007 NRC Canada

Acyl transfer from carboxylate, carbonate, and thiocarbonate esters to enzymatic and nonenzymatic thiolates

Christian Gravel, Danielle Lapierre, Judith Labelle, and Jeffrey W. Keillor

Abstract: Transglutaminases (EC 2.3.2.13) (TGases) catalyze calcium-dependent acyl transfer reactions between peptide-bound glutamine residues as acyl donors and peptide-bound lysine residues as acyl acceptors, resulting in the formation of intermolecular ε-(γ-glutamyl)lysine crosslinks. The mechanistic details of its "ping-pong" transamidation reaction remain unknown. In particular, few studies have been published probing the nucleophilicity of TGase using acyl-donor substrates of varied electrophilicity. Herein we report the synthesis of activated esters of carbonates, carbamates, and thiocarbonates and their reactions with simple thiols, as a nonenzymatic point of reference, and with the catalytic cysteine residue of guinea pig liver TGase. Our kinetic results show that the simple substitution of a side chain methylene unit by oxygen or sulphur had a surprising effect on both substrate affinity and acylation reactivity. Furthermore, they provide unexpected insight into the importance of a side chain heteroatom for conferring affinity for tissue TGase as well as revealing an interesting class of irreversible inhibitors.

Key words: enzyme kinetics, enzyme inhibition, transglutaminase, acyl-transfer reactions, carbamate, thiocarbonate, carbonate.

Résumé : Les transglutaminases (EC 2.3.2.13) (TGases) catalysent, avec dépendance au calcium, le transfert d'un groupement acyle entre les résidus glutamine d'une première protéine et les résidus lysine d'une seconde protéine. Ceci résulte en la formation de réticulation intermoléculaire du type ε-(γ-glutamyl)lysine. Les détails mécanistiques de sa réaction de transamidation de type « ping-pong » restent inconnus. En particulier, peu d'études explorant la nucléophilie de la TGase à l'aide de substrats donneurs d'électrophilie variable ont été publiées. Dans cet article, nous rapportons la synthèse des esters activés des carbonates, carbamates et thiocarbonates ainsi que leurs réactions avec des thiols simples, comme point de référence non-enzymatique, et avec la cystéine catalytique de la TGase de foie de cobaye. Nos résultats cinétiques démontrent que la substitution simple d'un groupement méthylène par un oxygène ou par un soufre a un effet surprenant sur l'affinité de substrat ainsi que sur la réactivité d'acylation. De plus, ils permettent un aperçu inattendu de l'importance de la présence d'un hétéroatome dans la chaîne latérale pour conférer l'affinité pour la TGase tissulaire et révèlent une classe d'inhibiteurs irréversibles intéressants.

Mots-clés : cinétique enzymatique, inhibition d'enzyme, transglutaminase, transfert de groupement acyle, carbamate, thiocarbonate, carbonate.

Introduction

Transglutaminases (EC 2.3.2.13) (TGases) belong to a class of enzymes known as aminoacyltransferases that catalyze calcium-dependent acyl transfer reactions between peptide-bound glutamine residues as acyl donors and peptide-bound lysine residues as acyl acceptors, resulting in the formation of intermolecular ε-(γ-glutamyl)lysine crosslinks (1). TGases form a family of related enzymes found in plasma, tissues, and extracellular media in all vertebrates. One of the best known TGases is the well-characterized human plasma coagulation enzyme Factor XIIIa, activated by thrombin from its tetrameric zymogen during the coagulation process (2, 3). Other types of TGase known to date include the keratinocyte TGase (type I) (4), two epidermal TGases (types III and V), a TGase localized in the prostate (type IV) (5, 6), and the ubiquitous tissue TGase (type II), the focus of our research interest. Guinea pig liver tissue TGase (gTGase) was chosen as a model of the human enzyme for this work because it is 88% homologous (7) to the human tissue TGase (hTGase) and is readily purified in its recombinant His-tagged form (8). gTGase is a monomeric protein comprising 690 amino acids with a calculated molecular weight of 78.7 kDa. It is not glycosylated (1) although it possesses six potential *N*-glycosylation sites and contains 17 cysteine residues, none of which are comprised in disulfide bonds (9). One of these acts as the catalytic nucleophile, in a Cys-His-Asp triad reminiscent of that of the cysteine proteases. Comparison of the amino acid sequence of gTGase with those of the only TGases for which X-ray structures are

Received 18 December 2006. Accepted 5 February 2007. Published on the NRC Research Press Web site at http://canjchem.nrc.ca on 15 March 2007.

C. Gravel,[1] D. Lapierre,[1] J. Lavelle, and J. W. Keillor.[2] Département de chimie, Université de Montréal, CP 6128, Succursale centre-ville, Montréal, QC H3C 3J7, Canada.

[1]These authors contributed equally to this work.
[2]Corresponding author (e-mail: jw.keillor@umontreal.ca).

 doi:10.1139/V07-011 © 2007 NRC Canada

available — Factor XIIIa (10), human epidermal Tgase (eTGase) (11), human tissue TGase (hTGase) (12), and a fish tissue TGase (fTGase) (13) — indicates that the catalytic triad of gTGase would be composed of Cys-276, His-334, and Asp-358. The catalytic acyl-transfer reaction is known to proceed through a modified "ping-pong" mechanism (14) that is yet to be completely understood despite the involvement of TGase in critical processes such as the stabilization of extracellular matrices, formation of cross-linked cell envelopes, cell-matrix assembly, wound healing, and cellular adhesive processes (1). TGase has been implicated in important physiological disorders, such as amyloid protein aggregation leading to Alzheimer's disease (15), thrombosis, arteriosclerosis (16), autoimmune gluten intolerance (Celiac disease) (17, 18), cataract development (19), and Hb-Koln disease (2). TGase has also been implicated in neurodegenerative diseases related to an increase in transamidated (20) polyglutamine-containing peptide, leading to aggregation in neural tissues such as Huntington's disease (21). In the ping-pong mechanism, the acyl donor substrate undergoes nucleophilic attack by the active site thiolate, followed by the release of an equivalent of ammonia. The thiolester acyl enzyme intermediate thus obtained then undergoes a second nucleophilic attack by the acyl acceptor substrate, typically a primary amine, leading to the formation of a new isopeptidic compound and the regeneration of the free enzyme. These steps are facilitated by the presence of a general acid–base catalyst, His-334 (22). Water can also compete weakly as an acyl acceptor during the deacylation step, resulting in the net hydrolysis of the initial acyl-donor amide.

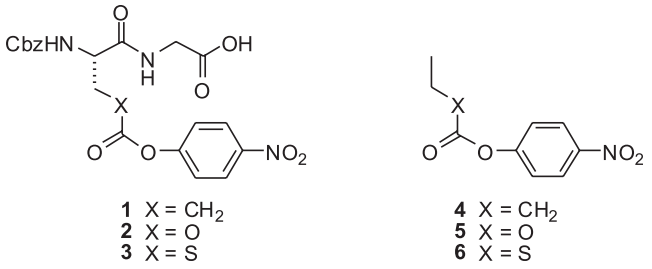
While a significant amount of data is available regarding the specificity and reactivity of various glutamine substrates (23, 24), far fewer studies have been published probing the nucleophilicity of TGase using acyl-donor substrates of varied electrophilicity. In addressing this paucity of data we carried out kinetic studies with nonenzymatic thiols to provide a point of reference. The thermal decomposition of such esters (25) and their susceptibility to nucleophilic attack by phenolate, secondary acyclic amines, and pyridines have been reported (26, 27, 28), but kinetic studies concerning the acylation of simple thiols by carboxylate-, carbonate-, carbamate-, and thiocarbamate-esters are also relatively few (29, 30). Herein we report on the reaction of the activated esters of carbonates, carbamates, and thiocarbonates with simple thiols and the catalytic cysteine residue of gTGase.

Results and discussion

Design and synthesis of acyl-donor reactants

Compounds **1**, **2**, and **3** (see Fig. 1) were designed to bear the essential structural elements required for recognition by TGase as an acyl-donor substrate, i.e., a hydrophobic, planar moiety on the *N*α of the glutamine residue, a central amino acid having L configuration (31), and at least two methylene units in its side chain (asparagine not being recognized as a substrate) (22, 32, 33). The C-terminal glycine residue is not absolutely required but improves binding by an order of magnitude probably by distancing the terminal negative charge from the carboxylate of the central amino acid (33). Compounds **4**, **5**, and **6** (Fig. 1) were chosen as simplified

Fig. 1. Acyl-donor reactants studied herein.



functional models because of their commercial availability or synthetic accessibility as well as their resemblance to the reactive side chains of **1**, **2**, and **3**. Although it may have been interesting to study the acylation TGase from *p*-nitrophenyl carbamates (e.g., X = NH in Fig. 1), we confirmed that these molecules undergo a rapid elimination reaction in water releasing *p*-nitrophenolate and generating the corresponding isocyanate (34, 35, 36, 37), making their kinetic study impossible.

Compound **1** was synthesized as described previously (22). Compounds **2** and **3** were synthesized according to the pathways shown in Schemes 1 and 2, respectively. These synthetic routes are both straightforward, consisting of an initial protection of the amino groups of either serine (for compound **2**) or cystine (for compound **3**) with benzyl chloroformate (Cbz–Cl), followed by peptide coupling using TBTU as a coupling agent and subsequent introduction of the *p*-nitrophenoxycarbonyl moiety. In the case of compound **3**, a reduction step was required prior to side chain functionalization. Finally, deprotection of the *tert*-butyl ester provided the desired compounds **2** and **3** in modest unoptimized yields (34% and 40% overall isolated yields, respectively) but in quantities sufficient for subsequent kinetic studies.

Compound **4** is commercially available (Sigma-Aldrich) and compounds **5** and **6** were obtained by following known protocols (38, 39) in which *p*-nitrophenolate reacts with ethyl chloroformate and ethyl thiochloroformate with yields of 77% and 94%, respectively (Scheme 3).

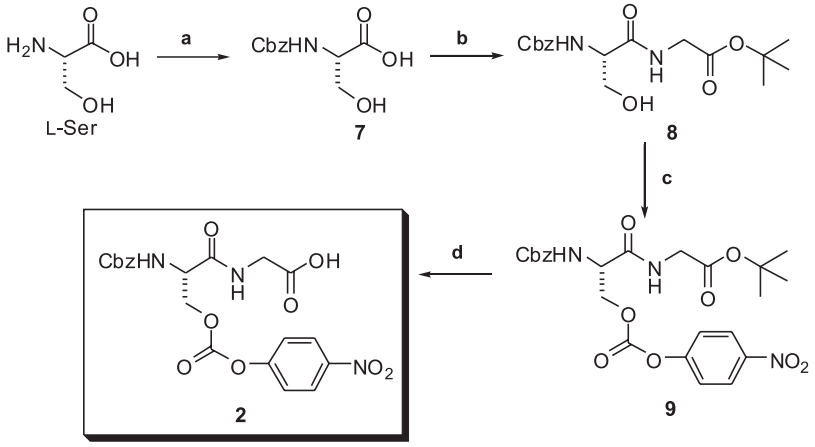
Nonenzymatic kinetics

The reactions of ester **4**, carbonate **5**, and thiocarbonate **6** with either ethanethiol or cysteamine were followed spectrophotometrically by monitoring the increase in absorbance at 410 nm due to released *p*-nitrophenol. Under pseudo first-order conditions with thiol concentrations over 10-fold higher than those of compounds **4**–**6**, reaction kinetics were found to be clean first-order over at least five half-lives, allowing the determination of pseudo first-order rate constants (k_{obs}) by fitting the absorbance data to a simple mono-exponential equation (see Experimental section). The variation of k_{obs} as a function of thiol concentration provided the second order rate constants (k_2) for each of the thiolysis reactions studied. Figure 2 shows a representative example.

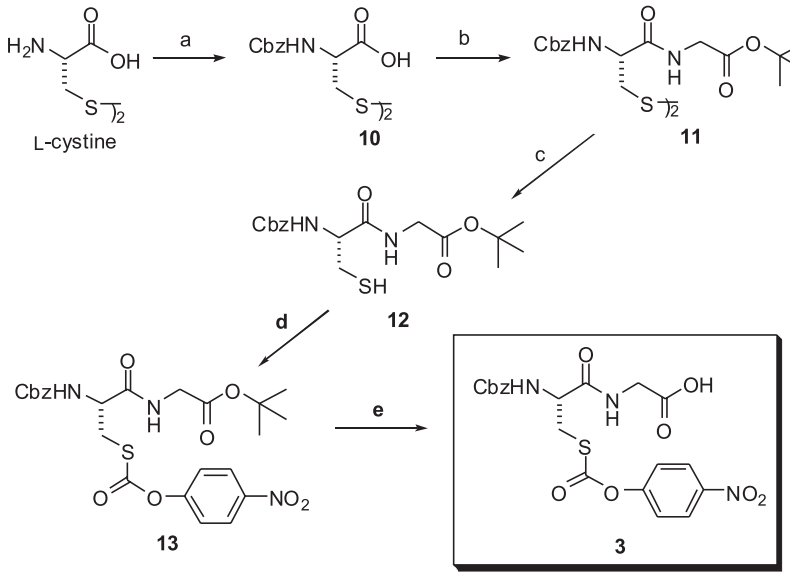
Second-order rate constants were thus obtained using either cysteamine or ethanethiol as nucleophiles at both pH 7 and 8. The results, shown in Table 1, demonstrate the greater reactivity of both thiols at higher pH, consistent with the thiolate being the active nucleophile. Also shown in bold in Table 1 are second-order rate constants normalized for the

© 2007 NRC Canada

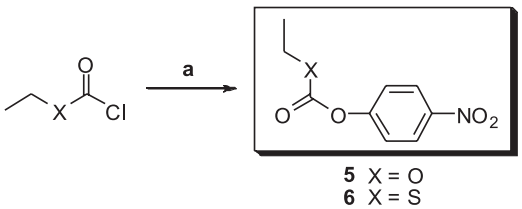
Scheme 1. Synthesis of *N*-benzyloxycarbonyl-*O*-(*p*-nitrophenyloxycarbonyl)-L-serinylglycine (**2**). (**a**) CbzCl, aq. $NaHCO_3$, RT, overnight, 58%; (**b**) GlyOtBu, TBTU, DIEA, ACN, RT, overnight, 94%; (**c**) pNPCOCl, Et_3N, ACN, 0 °C, 3 h, 63%; (**d**) TFA, CH_2Cl_2, 0 °C, 1 h, quantitative.



Scheme 2. Synthesis of *N*-benzyloxycarbonyl-*S*-(*p*-nitrophenyloxycarbonyl)-L-cysteinylglycine (**3**). (**a**) CbzCl, aq. $NaHCO_3$, RT, overnight, 99%; (**b**) GlyOtBu, TBTU, DIEA, ACN, RT, overnight, 60%; (**c**) $NaBH_4$, ethanol–$CHCl_3$, RT, 30 min, quantitative; (**d**) pNPCOCl, DIEA, $CHCl_3$, 0 °C, 15 min, 68%; (**e**) TFA, $CHCl_3$, 0 °C, 1 h, quantitative.



Scheme 3. Synthesis of ethyl *p*-nitrophenyl formate (**5**) and *S*-ethyl *p*-nitrophenyl thioformate (**6**). For compound (**5**), **a**: sodium *p*-nitrophenoxyde, acetonitrile, 0 °C, 30 min, 77%; for compound (**6**), **a**: *p*-nitrophenol, pyridine, CH_2Cl_2, 0 °C, 16 h, 94%.



5 X = O
6 X = S

fraction of thiolate present at each pH, based on literature values for the corresponding pK_a values (34, 35). This normalization generates similar values at each pH, within experimental error, for most of the compounds studied.

It is also clear from Table 1 that ester **4** reacts most rapidly with both thiols, followed by thiocarbonate **6** and (or) carbonate **5**. This trend in their relative reactivity most likely reflects their relative electrophilicity and a rate-limiting step involving nucleophilic attack by thiolate. In support of this supposition of relative electrophilicity, the ^{13}C chemical shifts of the side chain carbonyl groups of compounds **4**–**6**, indicative of their relative deshielding or electron density, are noted to be 172, 170, and 153 ppm, respectively, following the same general trend as their reactivity. The decreased electrophilicity of derivatives **5** and **6** compared with **4** suggests that resonance stabilization of the carbonyl group through electron donation from an adjacent heteroatom is more important than electron withdrawal through inductive effects.

It is also instructive to compare the relative reactivity of cysteamine and ethanethiol. It is evident from Table 1 that

© 2007 NRC Canada

Table 1. Second-order rate constants (k_2 (mol/L min)$^{-1}$) for the thiolysis of compounds **4**–**6** at 25 °C.

	Cysteamine pK_a = 8.35 and 10.49 (40)		Ethanethiol pK_a = 10.35 (41)	
Reactant	pH 7, f_{RS^-} = 0.043	pH 8, f_{RS^-} = 0.31	pH 7, f_{RS^-} = 4.5×10^{-4}	pH 8, f_{RS^-} = 4.5×10^{-3}
Ester **4**	4.65±0.07	30.4±0.9	0.057±0.004	0.66±0.06
	109±2	**98±3**	**130±9**	**160±16**
Carbonate **5**	1.89±0.03	11.1±0.4	0.035±0.007	0.19±0.01
	44.2±0.7	**36±2**	**78±16**	**42±2**
Thiocarbonate **6**	2.7±0.1	17.9±0.6	0.010±0.006	0.16±0.02
	63±2	**58±2**	**22±13**	**36±4**

Note: Values in boldface are normalized for the fraction of thiolate present at a given pH (f_{RS^-}). Reported experimental errors derive from linear regression of the first-order data.

Fig. 2. Determination of second order rate constants for the thiolysis of ester **4** (squares), carbonate **5** (triangles) and thiocarbonate **6** (circles) upon reaction with cysteamine (35 °C, pH = 7.0). Inset: typical mono-exponential reaction from which k_{obs} was measured.

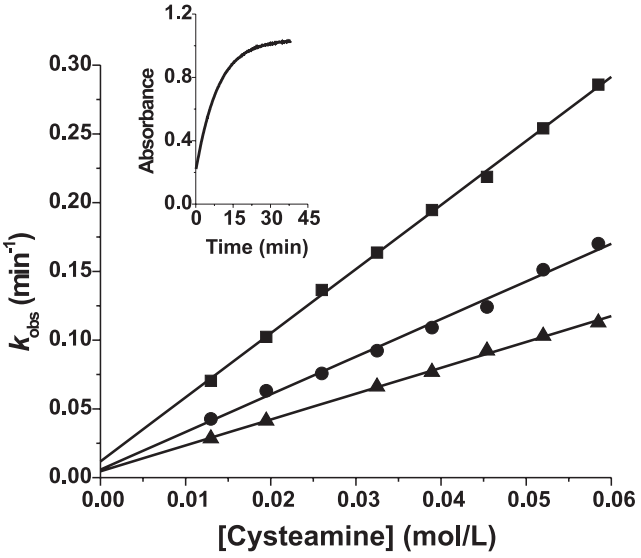
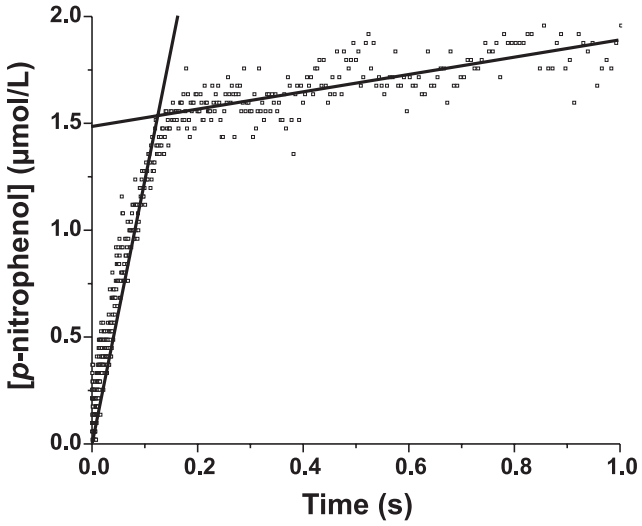


Fig. 3. Acylation of 2.2 μmol/L of gTGase by 198 μM of ester **1** at 25 °C and pH 7.0 (0.1 mol/L MOPS). (See Experimental for background correction.).



while the presence of a pendant ammonium group serves to decrease the pK_a of the thiol group of cysteamine, it does not further accelerate the reaction of the thiolate form significantly above that of ethanethiol. As has been noted previously, a pendant ammonium group can assist in the thiolysis of amides by acting as an intramolecular general acid protonating an amine leaving group (42). However, it has also been noted that this role is not required for a leaving group such as *p*-nitrophenolate (42, 43), also present in compounds **1**–**6**, whose departure does not require protonation.

Enzymatic kinetics

Compounds **1**–**3** were tested as substrates for recombinant gTGase and found to display similar kinetic behaviour during the first second of reaction. As shown in Fig. 3, rapid release of *p*-nitrophenol corresponding roughly to one equivalent of enzyme (0–0.1 s) was followed by slower turnover (0.1–1.0 s). The pre-steady state "burst" is consistent with the rapid acylation of gTGase by compounds **1**–**3**, leading to the corresponding acyl-enzyme featured in the ping-pong mechanism of Fig. 4. The initial rates of this burst phase were measured as a function of substrate concentration and fitted according to the hyperbolic Michaelis–Menten equation (see Experimental section) as shown in Fig. 5. The kinetic parameters obtained in this fashion are shown in Table 2.

At first glance, it is evident that the kinetic parameters measured for ester **1** and carbonate **2** are similar. Insofar as the K_M values reflect enzyme affinity for the substrate, it is not surprising that this parameter would be similar for the analogous compounds **1** and **2**. Moreover, the slight decrease in the acylation rate constant (k_{acyl}) on passing from the ester to the carbonate is to be expected for the reasons outlined earlier in the discussion of compounds **4** and **5**. Namely, the carbonate ester is presumably less electrophilic than the carboxylate ester as a result of resonance stabilization from the adjacent oxygen atom and therefore less susceptible to nucleophilic attack by the active site thiolate.

However, there is a reversal of this apparent trend on consideration of the kinetic parameters obtained for thiocarbonate **3**. The replacement of the γ-methylene unit of **1** by a sulfur atom in **3** leads to a ~20-fold decrease in the K_M and an increase in the value of k_{acyl}, suggesting a significant increase in affinity. The acylation rate constant itself increases by a factor of ~2.5, resulting in a combined ~50-fold increase in the efficiency of the enzymatic reaction (re-

© 2007 NRC Canada

Fig. 4. Ping-pong mechanism of TGase catalytic cycle.

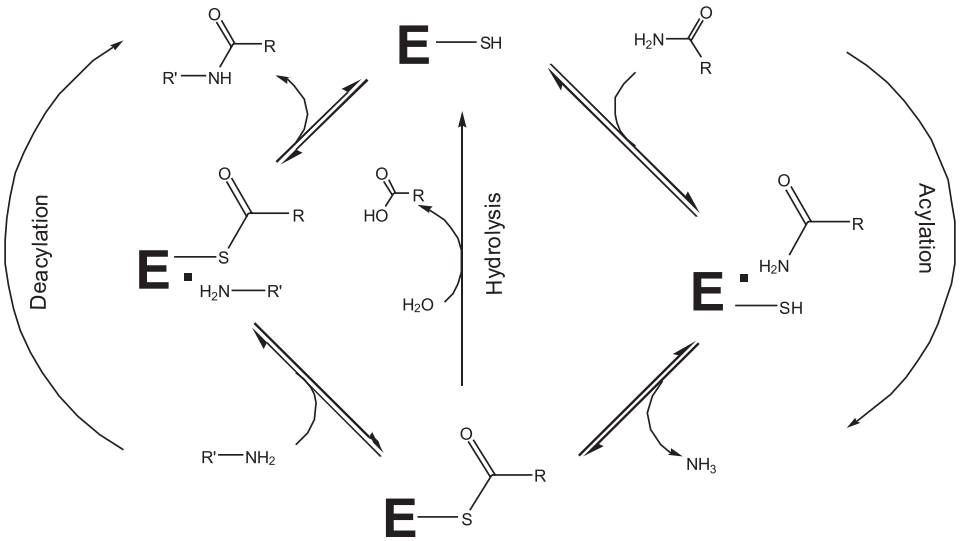


Fig. 5. Saturation kinetics of gTGase acylation by (*A*) ester **1** (squares), carbonate **2** (circles) and (*B*) thiocarbonate **3** (triangles). Each data point represents the average of 2–7 measurements. Lines through the data points were determined by non-linear regression to the hyperbolic Michaelis-Menten model (see Experimental).

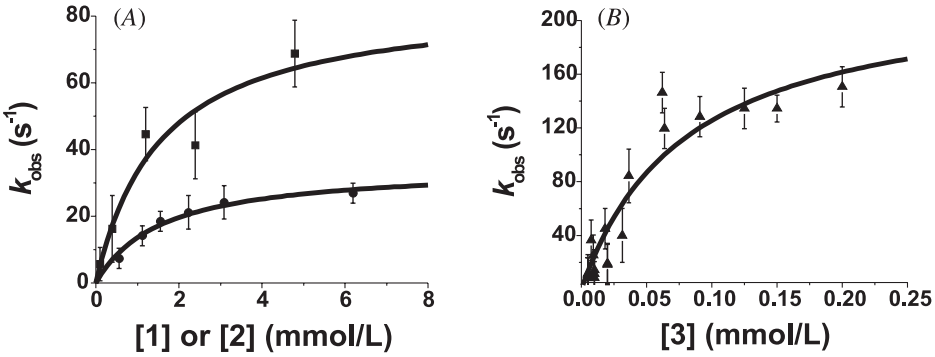


Table 2. Kinetic parameters determined for the acylation of gTGase by compounds **1**–**3** at 25 °C and pH 7.0 (0.1 mol/L MOPS).

Compound	K_M (mmol/L)	k_{acyl} (s^{-1})	k_{acyl}/K_M (mmol/L $s)^{-1}$
Ester **1**	1.5±0.8	85±15	57±40
Carbonate **2**	1.6±0.3	35±2	22±5
Thiocarbonate **3**	0.080±0.027	226±37	2800±1400

Note: Reported experimental errors are standard deviations from nonlinear regression of the data.

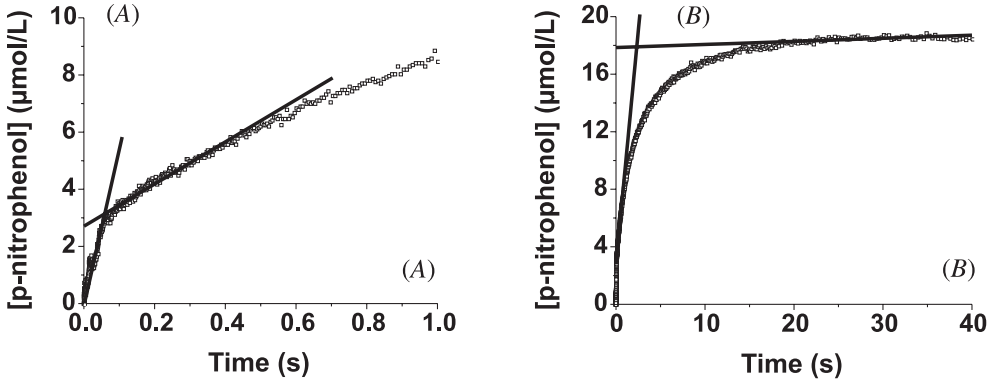
flected in k_{acyl}/K_M). These results go against expectations based on the reactivity of models **4**–**6** in solution. Based on the earlier discussion for thiocarbonate **6**, substrate analogue **3** was expected to be *less* reactive than ester **1** owing to its lower electrophilicity due to carbonyl-stabilizing resonance forms but *more* reactive than carbonate **2** because of the reduced resonance stabilization from carbon–sulfur orbital overlap. Clearly, other forces are at play in the enzymatic reactions of **1**–**3** that take place in a constrained, hydrophobic, and functionalized active site, compared with the model reactions of **4**–**6** that take place in free aqueous solvent.

Among these interactions are those that result in the activation of the bound substrate. Many enzymes that catalyze acyl-transfer reactions from amide groups, for example, are thought to twist the amide out of its normally planar geometry, thereby decreasing resonance stabilization and activating the carbonyl toward nucleophilic attack (43, 44). Such torsion may also be present in the Michaelis complexes formed upon binding compounds **1**–**3**. Further, one may suppose that the larger sulphur atom of thiocarbonate **3** would render it more susceptible to steric distortion, easily reducing carbon–sulphur orbital overlap and subsequently the importance of resonance stabilization. At the limit, the sulphur atom of thiocarbonate **3** would only exert an electron-withdrawing inductive effect, effectively making it a better acylating agent than the ester **1**.

Alternatively, the sulphur atom in the side chain of **3** may simply allow for better placement of the reactive carbonyl in

© 2007 NRC Canada

Fig. 6. Acylation of 2.0 μM of gTGase by 3.10 mM of carbonate **2** showing : **A**) initial burst and turnover; **B**) turnover and final loss of activity. (See Experimental.)



the enzyme active site. It is known that the active site of gTGase is located at the bottom of a relatively long and narrow well, allowing the enzyme to react with glutamine residues but not with asparagines (32). The introduction of a sulphur atom in the place of a methylene unit would subtly affect the bond lengths and bond angles of the side chain effectively increasing its length (45), more easily placing the acyl group within the trajectory of the active site nucleophile. Consistent with this hypothesis, we have noted that many of the irreversible glutamine-analogue gTGase inhibitors that we have synthesized in the past show greater efficiency with increasing side chain length (46, 47).

Finally, while our understanding of detailed interactions leading to substrate affinity is grossly limited by the lack of any ligand-bound crystal structure, our modelling of tissue Tgase (48) allows us to speculate why the enzyme shows increased affinity for the thiocarbonate **3**. It is known that two tryptophan residues (Trp-240 and Trp-331) and one histidine residue (His-300) form the walls of the tunnel leading the side chain to the active site. Sulphur, being a highly polarizable atom, may form favourable interactions with the faces of these aromatic residues leading to tighter binding (lower K_M), while positioning the carbonyl group to react more rapidly with the active-site thiol (higher k_{acyl}).

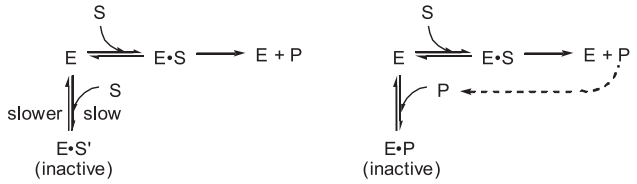
Inhibition kinetics

Upon closer examination of the stopped-flow traces obtained for the reaction of compounds **2** and **3** with gTGase, it was noted that over a longer time scale (up to 40 s) the slope of the "slow phase" levelled off in a nearly complete loss of activity (Fig. 6). This behaviour was not observed for ester **1**, where all of the ester substrate was consumed during the slow phase.

Knowing the final concentration of *p*-nitrophenol released prior to apparent inactivation by compounds **2** and **3** (Fig. 6*B*) allows us to estimate that the enzyme turns over ~7 times with carbonate **2** and ~4 times with thiocarbonate **3**. Apparently, all three compounds **1**–**3** initiate rapid acylation (burst phase), followed by the slower catalytic turnover of the respective acyl-enzyme (second phase). However in the case of carbonate **2** and thiocarbonate **3**, a competing event takes place that does not occur with ester **1**, leading to inhibition of the enzyme.

To characterize the inhibition, a competition experiment was carried out between ester **1** (used as the substrate) and thiocarbonate **3** (used as an inhibitor). This experiment revealed that the presence of **1** was able to temporarily protect the enzyme from inactivation by **3**, suggesting strongly that both compounds are bound in the same site. However even in the presence of ester **1**, the enzyme was still slowly inactivated by thiocarbonate **3** leading to a loss of about 50% of activity after 5 min when using 20 μmol/L of **1** (1 K_M) and 100 μmol/L of **3**. Interestingly, even after a long period (>30 min) of incubation with 100 μmol/L of thiocarbonate **3**, the addition of an aliquot of ester **1** revealed that some residual activity remained suggesting that the inactivation may be reversible. However, mass spectroscopy experiments confirmed that upon incubation with thiocarbonate **3**, the mass of gTGase increased by the expected mass of the acyl portion (see Experimental section).

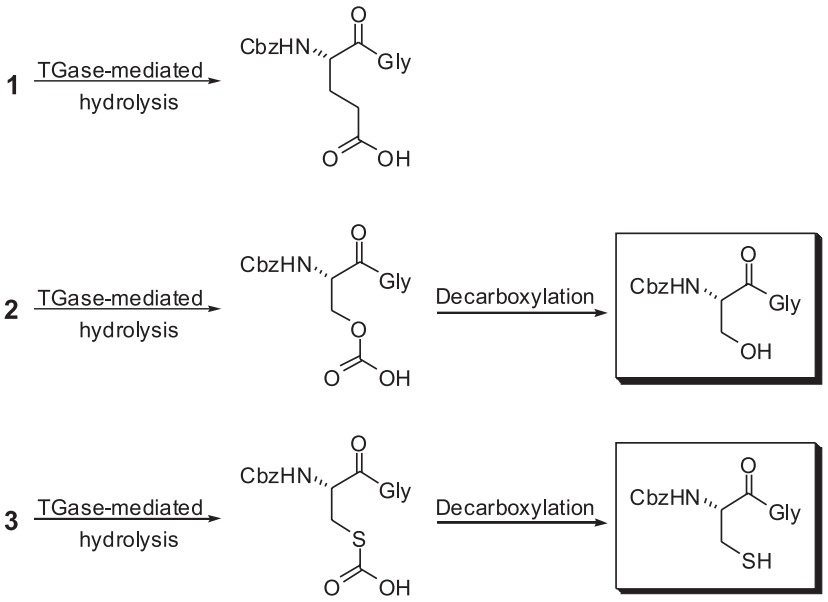
Scheme 4. Two hypotheses for observed time-dependent inactivation by carbonate **2** and thiocarbonate **3**. (***A***) Two alternate binding modes or binding sites and (***B***) product inhibition.



These observations led us to formulate two hypotheses regarding the inactivation mechanisms of carbonate **2** and thiocarbonate **3**. The first possibility is that both compounds **2** and **3** could have two different binding modes, one of which would lead to typical substrate-like behaviour resulting in normal turnover as for **1** (i.e., the second phase of the stopped-flow traces, Fig. 6*A*). However, an alternate binding mode for both **2** and **3** having a slow k_{on} and an even slower k_{off} would slowly lead to a tightly bound inactive form of the enzyme (see Scheme 4*A*). This binding mode could be related to the presence of a heteroatom on the side chain of **2** and **3** in the place of the methylene group of compound **1**. Examination of our tissue TGase model (48) shows that at least four gTGase residues (Trp-240, His-304, Tyr-518, and Asn-519) present a polarized hydrogen atom within <5 Å of the side chain heteroatom. The formation of a strong dipole–dipole interaction with the sulphur atom of **3**, or even a hydrogen bond with the oxygen atom of **2**, may provide the driving force for adopting an alternative tight binding mode within the active site that leads to inhibition.

© 2007 NRC Canada

Scheme 5. Difference in final product obtained after TGase-mediated hydrolysis of compounds **1**–**3** followed by subsequent decarboxylation for compounds **2** and **3**.



Alternatively, this different binding mode could very well be related to a different binding site, such as for example the GTP binding site, that is known to modulate the enzyme's activity through allosteric effects (12). Recently, Case and Stein (49) reported TGase inhibitors that bind either directly in this GTP binding site or in a site that regulates GTP binding. Their results also demonstrate the possibility of inhibition through the differential interaction of a given inhibitor with different conformational states of the enzyme. This further supports our hypothesis that our inhibitors may be bound by TGase at more than one site. Furthermore, putative binding at a different site could lead to acyl transfer to an adjacent nucleophile, which may explain the minor peak observed by mass spectrometry that corresponds to a doubly acylated enzyme (see Experimental section).

The second possibility is that the released product of the hydrolysis step could act as an inhibitor. Inhibition by this product would be time-dependent as its concentration increases during the catalytic turnover of its parent compound (see Scheme 4*B*). In potential support of this hypothesis, the reaction products formed after catalytic hydrolysis of **2** and **3** may undergo further spontaneous decarboxylation leading to the final products Cbz-Ser-Gly and Cbz-Cys-Gly, respectively. For example, a rate constant of 0.4 s^{-1} was recently measured under physiologically relevant reaction conditions for the decarboxylation of monoalkyl carbonate salt (50); presumably, the decarboxylation of a monoalkyl thiocarbonate would be even faster. These decarboxylation products would differ substantially from the reaction product of **1** (Scheme 5). This may explain why ester **1** showed no time-dependent inhibitory effect whatsoever.

To test this hypothesis, simple inactivation experiments were carried out in the presence of Cbz-Ser-Gly, the ultimate decarboxylated product deriving from the hydrolysis of compound **2**. No inhibition was observed, even in the presence of up to 10 mmol/L of Cbz-Ser-Gly. While this result does not strictly rule out the possibility that the hydrolysed substrate may act as an inhibitor prior to expected decarboxylation, it leads us to favour the differential binding mode hypothesis (Scheme 4*A*) as an explanation of the observed inhibition.

Conclusions

A series of gTGase substrate analogues was prepared in which the electrophilicity of the reactive carbonyl was varied by the presence of adjacent heteroatoms. Kinetic studies with model compounds provided a nonenzymatic reference for the expected rate dependence. However, the simple substitution of a side chain methylene unit by oxygen or sulphur had a surprising, counter-intuitive effect on both substrate affinity and acylation reactivity. This kinetic characterization served to illustrate the challenges associated with studying free-energy relationships in enzymatic reactions. It also provided unexpected insight into structural elements important for conferring affinity for tissue TGase as well as revealing an interesting class of irreversible inhibitors. Further work is underway to exploit these compounds as mechanistic probes and to explore their in vivo utility as inhibitors.

Materials and methods

Synthesis

General

All commercial reagents were used without further purification. Dichloromethane and tetrahydrofuran (THF) were dried using a GlassContour system (Irvine, California) column. Dry acetonitrile was bought from EM Science and used without distillation. *p*-Nitrophenyl butanoate (**4**) was purchased from Sigma-Aldrich and used without further purification. Melting points were uncorrected. Water was purified using a Millipore BioCell system.

© 2007 NRC Canada

Ethyl* p-*nitrophenyl carbonate (5)

To a suspension of sodium *p*-nitrophenolate (20 mmol) in 20 mL of anhydrous acetonitrile, a solution of ethyl chloroformate (29 mmol) in 10 mL of acetonitrile was added dropwise at 0 °C under nitrogen atmosphere. The mixture was stirred for 30 min at 0 °C and then for 3 h at room temperature (RT). Solvent was then evaporated under reduced pressure and the solid obtained was washed with dichloromethane to give 3.2 g (77%) of product as a white powder. R_f 0.74 (100% EtOAc), mp 67 to 68 °C. IR (KBr) ν: 3119, 2918, 1756, 1617, 1597, 1518, 1351, 1304, 1281. ^{1}H NMR (DMSO-d_6, 400 MHz, ppm) δ: 1.30 (3H, t, J = 7.1 Hz), 4.29 (2H, q, J = 7.1 Hz), 7.55 (2H, d, J = 9.2 Hz), 8.31 (2H, d, J = 9.2 Hz). ^{13}C NMR (DMSO-d_6, 100 MHz, ppm) δ: 14.77, 66.11, 123.50, 126.25, 145.97, 152.86, 156.17. HRMS calcd. for $C_9H_9NO_5$: 211.048 073; found: 211.048 034. Anal. calcd. for $C_9H_9NO_5$: C 51.19, H 4.30, N 6.63; found: C 51.21, H 4.50, N 6.37.

Ethyl* p-*nitrophenyl thiocarbonate (6)

To a suspension of *p*-nitrophenol (9 mmol) and pyridine (9 mmol) in 15 mL of anhydrous dichloromethane, a solution of ethyl thiochloroformate (9 mmol) in 4 mL of dichloromethane was added dropwise at 0 °C under nitrogen atmosphere. The mixture was stirred for 15 min at 0 °C and then left overnight at RT. The mixture was then extracted with 30 mL of distilled water and the organic layer was washed with 30 mL of NaOH (0.5 mol/L), 30 mL of satd. NaCl, and again with 30 mL of distilled water before being dried over $MgSO_4$ and passed through a silica gel plug using 100% $CHCl_3$ as eluant. Evaporation under reduced pressure provided 1.87 g (93.5%) of product as a white powder. R_f 0.58 (100% $CHCl_3$), mp 60 to 61 °C. IR (KBr) ν: 3084, 2973, 2936, 1708, 1621, 1590, 1532, 1490, 1347, 1098. ^{1}H NMR (DMSO-d_6, 300 MHz, ppm) δ: 1.30 (3H, t, J = 7.3 Hz), 2.97 (2H, q, J = 7.3 Hz), 7.53 (2H, d, J = 9.2 Hz), 8.30 (2H, d, J = 9.2 Hz). ^{13}C NMR (DMSO-d_6, 100 MHz, ppm) δ: 15.54, 26.32, 123.72, 126.33, 146.14, 155.98, 170.01. HRMS calcd. for $C_9H_9NO_4S$: 227.025 230; found: 227.024 816. Anal. calcd. for $C_9H_9NO_4S$: C 47.57, H 3.99, N 6.16, S 14.11; found: C 47.45, H 3.86, N 6.09, S 13.64.

N-*Benzyloxycarbonyl-*L*-serine (7)*

Sodium bicarbonate (6.3 mmol) was dissolved in 6 mL of distilled water and L-serine (0.95 mmol) was added to the solution. Once the solution was completely dissolved, benzyl chloroformate (0.63 mmol) was added dropwise at 0 °C and the mixture was stirred for 2 h at 0 °C and then overnight at RT. The aqueous phase was washed with Et_2O (4 × 5 mL) and then acidified to pH 1 with concd. HCl and extracted with EtOAc (4 × 10 mL). The combined organic layers were then washed with water, dried over $MgSO_4$, and concentrated to provide 88 mg (58%) of product as a white solid. R_f 0.054 (hexanes–EtOAc 70:30), mp 116 to 117 °C (lit. value (51) 117–119 °C). $[\alpha]_D^{20}$ +5.52° (c 1.81, HOAc) (lit. value (51) 5.8 ± 0.5° (c 2.7, HOAc)). IR (KBr) ν: 3443–2555, 3319, 3029, 2940, 1748, 1690, 1535, 1478, 1248, 1060. ^{1}H NMR (CD_3OD, 300 MHz, ppm) δ: 3.84 (1H, dd, J = 4.0 and 11.3 Hz), 3.90 (1H, dd, J = 4.9 and 11.4 Hz), 4.28 (1H, t, J = 4.4 Hz), 5.12 (2H, s), 7.29–7.39 (5H, m). ^{13}C NMR (CD_3OD, 75 MHz, ppm) δ: 56.71, 62.08, 66.71, 127.87, 128.46, 137.14, 157.60, 172.75. HRMS calc. for $C_{11}H_{13}NO_5$: 240.087 20; found: 240.088 53. Anal. calc. for $C_{11}H_{13}NO_5$: C 55.23, H 5.48, N 5.86; found: C 55.10, H 5.90, N 5.84.

N-*Benzyloxycarbonyl-*L*-serinylglycine* tert-*butyl ester (8)*

To a solution of *N*-Cbz-L-serine (**7**) (1.3 mmol) in 13 mL of anhydrous acetonitrile, diisopropylethylamine (DIEA) (5.2 mmol) was added dropwise at RT under nitrogen atmosphere, and the solution was left to stir for 5 min before glycine *tert*-butyl ester (2.6 mmol) was added. Once the solution was completely dissolved, TBTU (2.6 mmol) was added and the mixture was stirred overnight. A 50 mL aliquot of EtOAc was then added to the mixture and the organic phase was washed with saturated NaCl (2 × 15 mL), HCl (0.1 mol/L, 15 mL), 5% $NaHCO_3$ (15 mL), and again with satd. NaCl (15 mL) before being dried over $MgSO_4$, filtered, and concentrated in vacuo. The crude product was purified by flash chromatography on silica gel using 60:39:1 EtOAc–hexanes–HOAc as the eluant to provide 0.66 g (94%) of product as a white solid. R_f 0.33 (hexanes–EtOAc 30:70), mp 67–70 °C. $[\alpha]_D^{20}$ –7.71° (c 1.75, $CHCl_3$). IR (KBr) ν: 3379, 3094, 2982, 2894, 1737, 1690, 1659, 1554, 1520, 1466, 1456, 1339, 1062. ^{1}H NMR ($CDCl_3$, 300 MHz, ppm) δ: 1.47 (9H, s), 3.06 (1H, s), 3.70 (1H, dd, J = 11 and 5.4 Hz), 3.95 (2H, d, J = 5.5 Hz), 4.13 (1H, m), 4.28 (1H, m), 5.15 (2H, s), 7.30–7.42 (5H, m). ^{13}C NMR ($CDCl_3$, 75 MHz, ppm) δ: 28.37, 42.50, 63.26, 67.47, 82.79, 128.41, 128.52, 128.89, 136.57, 156.99, 169.58, 171.69. HRMS calcd. for $C_{17}H_{24}N_2O_6$: 353.171 26; found: 353.172 30. Anal. calcd. for $C_{17}H_{24}N_2O_6$: C 57.94, H 6.86, N 7.95; found: C 57.78, H 7.33, N 8.00.

N-*Benzyloxycarbonyl*-O-(p-*nitrophenoxycarbonyl*)-*L*-*serinylglycine* tert-*butyl ester (9)*

To a solution of *N*-Cbz-L-SerGly *tert*-butyl ester (**8**) (1.6 mmol) dissolved in 5 mL of anhydrous acetonitrile, pyridine (7.9 mmol) was added dropwise under nitrogen. The solution was stirred for a few minutes and was then placed in an ice bath. At 0 °C, *p*-nitrophenyl chloroformate (1.6 mmol) was then added and the bath removed while the mixture was stirred for 3 h. A 20 mL volume of EtOAc was added and the organic layer was washed with HCl (3 mmol/L, 3 × 10 mL), dried over $MgSO_4$, filtered, and concentrated in vacuo. The crude product was purified by flash chromatography on silica gel using 30:70 EtOAc–hexanes as the eluant. A 0.51 g (63%) quantity of the product was obtained as a white powder that could be recrystallized from CH_2Cl_2–hexanes. R_f 0.37 (hexanes–EtOAc 60:40), mp 52–54 °C. $[\alpha]_D^{20}$ +6.87° (c 1.50, $CHCl_3$). IR (KBr) ν: 3317, 3085, 2980, 2939, 1773, 1737, 1729, 1670, 1594, 1349, 1554, 1520, 1493, 1455, 1214, 1049. ^{1}H NMR ($CDCl_3$, 300 MHz, ppm) δ: 1.47 (9H, s), 3.96 (2H, s), 4.51 (1H, dd, J = 11.1 and 4.7 Hz), 4.65 (1H, dd, J = 11.0 and 5.3 Hz), 4.72 (1H, m), 5.17 (2H, d, J = 12.0 Hz), 5.79 (1H, s), 6.83 (1H, s), 7.27–7.37 (7H, m), 8.25 (2H, d, J = 9.1 Hz). ^{13}C NMR ($CDCl_3$, 75 MHz, ppm) δ: 28.45, 42.59, 53.90, 68.07, 68.66, 83.25, 122.26, 125.76, 128.65, 128.89, 129.08, 145.94, 152.60, 155.71, 156.55, 156.67, 168.55, 168.90. HRMS calcd. for $C_{24}H_{27}N_3O_{10}$: 518.177 49; found:

© 2007 NRC Canada

518.176 30. Anal. calcd for $C_{24}H_{27}N_3O_{10}$: C 55.70, H 5.26, N 8.12; found: C 55.03, H 5.33, N 8.04.

N-*Benzyloxycarbonyl*-O-*(*p-*nitrophenoxycarbonyl)-*L-*serinylglycine (2)

To a solution of *N*-Cbz-*O*-(*p*-nitrophenoxycarbonyl)-L-serinylglycine *tert*-butyl ester (**9**) (0.4 mmol) in 2.5 mL of anhydrous dichloromethane, 500 µL (6.5 mmol) of trifluoroacetic acid (TFA) was added dropwise at 0 °C under nitrogen atmosphere. The solution was stirred at 0 °C for 1 h and then an additional portion (300 µL, 4.0 mmol) of TFA was added and the solution was stirred for an additional 3 h while the solution was allowed to warm to RT. A final portion of 150 µL of TFA (2.0 mmol) was then added and the solution was stirred at RT for 1 h before the solvent was removed in vacuo to provide 0.165 g (92%) of product as a yellow solid. R_f 0.28 (99:1 EtOAc–HOAc), mp 59–61 °C. $[\alpha]_d^{20}$ +11.0° (c 0.96, $CHCl_3$). IR (KBr) ν: 3747–2633, 3086, 2968, 1772, 1740, 1734, 1640, 1595, 1351, 1526, 1493, 1455, 1279, 1049. ^{1}H NMR ($CDCl_3$, 300 MHz, ppm) δ: 4.12 (2H, d, $J \approx 17$ Hz), 4.50 (1H, dd, J = 4.5 (3.8) and 10.7 Hz), 4.60 (1H, dd, J = 6.5 (5.8) and 10.9 Hz), 4.82 (1H, m), 5.15 (2H, d, J = 11.8 Hz), 5.84 (1H, s), 7.10 (1H, s), 7.29–7.39 (7H, m), 8.26 (2H, d, J = 9.2 Hz). ^{13}C NMR ($CDCl_3$, 75 MHz, ppm) δ: 41.81, 53.80, 68.17, 68.63, 122.19, 125.72, 128.50, 128.93, 129.05, 135.91, 145.90, 152.69, 155.53, 157.07, 169.74, 172.68. HRMS calcd. for $C_{20}H_{19}N_3O_{10}$: 462.114 87; found: 462.116 50. Anal. calcd. for $C_{20}H_{19}N_3O_{10}$: C 52.06, H 4.15, N 9.11; found: C 50.33, H 4.20, N 8.41.

N-*Benzyloxycarbonyl*-L-*cystine (10)*

To 1.44 g (5.94 mmol) of L-cystine in 175 mL of water was added 5 g (60 mmol) of $NaHCO_3$ and the mixture was cooled to 0 °C. A 1.70 mL volume (13.0 mmol) of benzyl chloroformate was added dropwise and the biphasic solution was stirred vigorously overnight. After acidification to pH 3 using 6N HCl, the aqueous phase was extracted with 3 × 150 mL EtOAc and the extract was concentrated in vacuo to give 3.38 g (99%) of a clear oil. R_f 0.05 (50:50 EtOAc–hexanes). ^{1}H NMR (CD_3OD, 300 MHz, ppm) δ: 2.98 (1H, dd, J = 9.1 and 13.9 Hz), 3.25 (1H, dd, J = 4.3 and 13.9 Hz), 4.51 (1H, dd, J = 4.3 and 9.1 Hz), 5.07 (2H, s), 7.27 (5H, m). ^{13}C NMR (CD_3OD, 75 MHz, ppm) δ: 41.18, 54.71, 67.81, 128.84, 129.03, 129.51, 139.09, 158.54, 174.02.

N-*Benzyloxycarbonyl*-L-*cystinylglycine* tert-*butyl ester (11)*

A 3.38-g (6.6 mmol) portion of *N*-benzyloxycarbonyl-L-cystine (**10**) and 5.76 mL (33 mmol) of DIEA were dissolved in 120 mL of anhydrous acetonitrile. To this solution was added 2.76 g (17 mmol) of glycine *tert*-butyl ester hydrochloride and 6.36 g (20 mmol) of TBTU. The mixture was stirred overnight. The next day, 120 mL of EtOAc was added and the organic phase was washed with 3 × 120 mL satd. NaCl, 100 mL 1N NaOH, and 100 mL H_2O. After concentration in vacuo and purification by silica gel chromatography (15 cm × 2.5 cm, 33% EtOAc–toluene), 2.91g (60%) of a white solid was obtained. R_f 0.43 (50:50 EtOAc–hexanes). ^{1}H NMR ($CDCl_3$, 300 MHz, ppm) δ: 1.42 (9H, s), 2.87 (1H, dd, J = 11 and 15 Hz), 3.10 (1H, dd, J = 15 and 4 Hz), 3.77 (1H, dd, J = 18 and 5 Hz), 4.00 (1H, dd, J = 18 and 5 Hz), 5.10 (1H, m), 5.16 (2H, s), 5.8 (1H, d, J = 9 Hz), 7.31 (5H, m), 7.95 (1H, t, J = 5 Hz). ^{13}C NMR ($CDCl_3$, 75 MHz, ppm) δ: 27.90, 41.93, 46.04, 55.10, 67.15, 81.98, 127.50, 127.97, 128.37, 136.30, 156.87, 168.27, 170.02. HRMS calcd. for $C_{34}H_{46}N_4O_{10}S_2$ + H: 735.272 81; found: 735.272 07.

N-*Benzyloxycarbonyl*-L-*cysteinylglycine* tert-*butyl ester (12)*

A 100-mg (0.136 mmol) portion of *N*-benzyloxycarbonyl-L-cystinylglycine *tert*-butyl ester (**11**) and 100 mg (2.6 mmol) of sodium borohydride were dissolved in a mixture of 2 mL of ethanol and 2 mL of $CHCl_3$. The mixture was shaken for 30 min at RT. Then, 5 mL of $CHCl_3$ was added and the organic phase was washed with HCl (10 mL, 1 mol/L) and then concentrated in vacuo. If necessary, the product can then be purified by silica gel chromatography using 30:70 EtOAc–hexanes as eluant. To avoid oxidation, the last step was carried out immediately. R_f 0.50 (50:50 EtOAc–hexanes). ^{1}H NMR ($CDCl_3$, 300 MHz, ppm) δ: 1.17 (3H, s), 1.42 (1H, dd, J = 8.4 and 11.4 Hz), 2.58 (1H, ddd, J = 15.2, 11.4, and 6.6 Hz), 2.97 (1H, ddd, J = 15.2, 8.4, and 5.1 Hz), 3.87 (2H, d, J = 6.2 Hz), 4.50 (1H, m), 5.19 (2H, s), 6.04 (1H, d, J = 9.2 Hz), 7.11 (1H, t, J = 6.2 Hz), 7.61 (5H, m). ^{13}C NMR ($CDCl_3$, 75 MHz, ppm) δ: 27.91, 41.92, 46.14, 55.12, 67.02, 81.95, 127.80, 127.92, 128.74, 136.25, 156.92, 168.32, 170.06.

N-Benzyloxycarbonyl*-S-*(*p-*nitrophenyloxycarbonyl)-*L-*cysteinylglycine* tert-*butyl ester (13)

First, 110 mg (0.3 mmol) of *N*-benzyloxycarbonyl-L-cysteinylglycine *tert*-butyl ester (**12**) and 104 µL of DIEA were dissolved in 0.5 mL of $CHCl_3$ at 0 °C. Then, 60 mg (0.3 mmol) of *p*-nitrophenyl chloroformate dissolved in 0.5 mL of $CHCl_3$ was added at 0 °C and the mixture was shaken for 15 min. The mixture was then purified by silica gel chromatography using 1:2 EtOAc–hexanes. The product was obtained as 68 mg (68%) of a yellow solid. R_f 0.50 (1:1 EtOAc–hexanes). ^{1}H NMR ($CHCl_3$, 300 MHz, ppm) δ: 1.18 (3H, s), 3.19 (1H, dd, J = 6.4 and 13.5 Hz), 3.37 (1H, dd, J = 4.1 and 13.5 Hz), 3.88 (2H, d, J = 4.0 Hz), 4.70 (1H, dd, J = 4.1 and 6.4 Hz), 5.23 (1H, d, J = 13.2 Hz), 5.27 (1H, d, J = 13.2 Hz), 5.80 (1H, d), 6.95 (1H, t), 7.56 (2H, d, J = 10.5 Hz), 7.62 (5H, m), 8.58 (2H, d, J = 10.5). ^{13}C NMR ($CDCl_3$, 75 MHz, ppm) δ: 28.2, 28.5, 43.3, 53.2, 65.2, 122.2, 124.8, 127.2, 127.3, 127.8, 136.6, 145.1, 155.1, 155.4, 167.3, 168.0, 169.9.

N-*Benzyloxycarbonyl*-S-*(*p-*nitrophenyloxycarbonyl)-*L-*cysteinylglycine (3)

To 34 mg (64 µmol) of *N*-benzyloxycarbonyl-*S*-(*p*-nitrophenoxycarbonyl)-L-cysteinylglycine *tert*-butyl ester (**13**) dissolved in 2 mL of chloroform was added 500 µL (6.5 mmol) of TFA at 0 °C. The solution was stirred for 1 h and then evaporated in vacuo. The product thus obtained was used without further purification. R_f 0.12 (50:50 EtOAc–hexanes). ^{1}H NMR ($CHCl_3$, 400 MHz, ppm) δ: 3.10 (1H, dd, J = 6.3 and 13.6 Hz), 3.26 (1H, dd, J = 4.1 and 13.6 Hz), 4.05 (2H, d, J = 3.8 Hz), 4.82 (1H, dd, J = 4.1 and 6.3 Hz), 5.23 (1H, d, J = 13.1 Hz), 5.27 (1H, d, J = 13.1 Hz), 6.30 (1H, d, J = 8.1 Hz), 7.56 (2H, d, J = 10.5 Hz), 7.62 (5H, m), 7.87

© 2007 NRC Canada

(1H, t), 8.58 (2H, d, J = 10.5). ^{13}C NMR ($CDCl_3$, 75 MHz, ppm) δ: 28.0, 43.3, 53.2, 65.1, 122.2, 124.9, 127.2, 127.3, 127.8, 136.4, 145.0, 155.2, 155.4, 167.3, 168.0, 171.7. HRMS calcd, for $C_{20}H_{19}N_3O_9S$ + H: 478.091 48; found: 478.092 51.

TGase expression and purification

TGase was obtained according to a previously published procedure developed in the group (8). Enzyme activity was determined using the hydroxamate assay (52).

Pre-equilibrium kinetics

A buffer solution containing MOPS (110 mmol/L), $CaCl_2$ (3.3 mmol/L), and EDTA (55 mmol/L) was adjusted to pH 7.0. The enzymatic solution was prepared by dissolving approximately 1.5 mg of lyophilized gTGase in 6 mL of buffer solution. Protein concentration was measured using the D_C Protein Assay from BioRad (Mississauga, Ontario) and verified to be approximately 0.25 mg/mL in all cases. Stock substrate solutions were prepared by dissolving a known quantity of compound **1**, **2**, or **3** into dry, degassed acetonitrile. All pre-equilibrium kinetic data were collected using a SX.18MV stopped-flow reaction analyser from Applied Photophysics (London, UK). Measurements for the single mixing stopped-flow method were taken at an absorption wavelength of 410 nm. The injection syringes were of 2.5 mL volume for the enzyme solutions and of 0.25 mL volume for the substrate solution, ensuring a 1:10 mixing ratio resulting in final concentrations of 100 mnol for MOPS, 3 mmol/L for $CaCl_2$, 50 μmol/L for EDTA, and 10% acetonitrile. The optical path within the cell was 10 mm. The temperature was kept at 25 °C using an Isotemp 1016P bath from Fisher Scientific. All kinetic runs were corrected for background absorption from the buffer and substrate solutions. Pre-steady state and initial steady state rates were measured by linear regression over time ranges up to and from the obvious inflection point to give a linear correlation of at least R^2 = 0.99. Finally, all runs were corrected for nonenzymatic background hydrolysis by subtracting from each the final slope of the value obtained in the control experiments in which no TGase was used. Ensuing Michaelis–Menten plots were fit to the standard hyperbolic equation. All linear and nonlinear regression was performed using Microcal™ Origin® 6.0 software from Microcal Software, Inc.

Nonenzymatic hydrolysis kinetics

All measurements were made using a UV–vis Cary Varian 100 Bio spectrophotometer and disposable polystyrene cells. Final conditions in each cuvette were MOPS (0.1 mol/L, pH 7), μ = 0.2 mol/L (KCl) and a variable quantity of either ethanethiol or cysteamine, ranging from 10 to 60 mmol/L. Reactions were initiated by adding 50 μL of a DMF solution of acyl-transfer reactant to 950 μL of buffered thiol solution, resulting in an initial reactant concn. of 0.13 mmol/L. The release of *p*-nitrophenol was followed at 410 nm and absorbance data were fitted to a monoexponential equation ($Abs_t = Abs_\infty(1 - \exp[-k_{obs}t])$). The extinction coefficient for *p*-nitrophenolate at 25 °C and pH 7 was determined experimentally to be 8040 $(mol/L)^{-1}$ cm^{-1} (22). Correction for background hydrolysis was obtained by simultaneously running control experiments in absence of nucleophile in a second cell, while using the dual beam function of the instrument.

Mass spectroscopy

A solution of TGase (5 μmol/L), **3** (25 mmol/L), $CaCl_2$ (3 mmol/L), and EDTA (50 μmol/L) in Tris buffer (0.1 mol/L, pH = 7.0) was incubated for 15 min at 25 °C. Aliquots were withdrawn and injected on an Agilent HPLC-MS (1100 series, MSD TOF) equipped with a Poroshell 300SP-C8 column and running a 0.35 mL/min flow rate acetonitrile gradient (0 min, 20%; 6 min, 100%; 7 min, 100%; 7.2 min, 20%; 12 min, 20%). Protein was detected after 4.74 min and deconvolution showed a m/z ratio of 78 890 Da for the inhibitor-free sample of His-tagged enzyme. For the sample obtained after incubation in the presence of inhibitor, m/z ratios of 79 229 Da (major) and 79 568 Da (minor) were found, consistent with the expected mass increase due to addition of the acyl moiety of **3**.

Acknowledgments

This work was supported by the Natural Sciences and Engineering Research Council (NSERC) of Canada. CG and DL thank NSERC for postgraduate scholarships, and CG and JL thank the Fonds Québecois de Recherche sur la Nature et les Technologies (FQRNT) for postgraduate scholarships.

References

1. D. Aeschlimann and M. Paulsson. Thromb. Haemostasis, **71**, 402 (1994).
2. C.S. Greenberg, P.J. Birckbichler, and R.H. Rice. FASEB J. **5**, 3071 (1991).
3. N. Takahashi, Y. Takahashi, and F.W. Putnam. Proc. Natl. Acad. Sci. USA. **83**, 8019 (1986).
4. M.A. Philips, B.E. Stewart, Q. Qin, R. Chakravarty, E.E. Floyd, A.M. Jetten, and R.H. Rice. Proc. Natl. Acad. Sci. USA. **87**, 9333 (1990).
5. K.C. Ho, V.E. Quarmby, F.S. French, and E.M. Wilson. J. Biol. Chem. **267**, 12660 (1992).
6. S.-Y. Kim, I.-G. Kim, S.-I. Chung, and P.M. Steinert. J. Biol. Chem. **269**, 27979 (1994).
7. W. Dietrich, T. Ehnis, M. Bauer, P. Donner, U. Volta, E.O. Riecken, and D. Schupann. Nature Med. **3**, 797 (1997).
8. S.M.F.G. Gillet, R.A. Chica, J.W. Keillor, and J.N. Pelletier. Protein Expression Purif. **33**, 256 (2004).
9. K. Ikura, T. Nasu, H. Yokota, Y. Tsuchiya, R. Sasaki, and H. Chiba. Biochemistry, **27**, 2898 (1988).
10. A.N. Glazer and E.L. Smith. The Enzymes. Academic Press, New York. 1971.
11. H.-C. Kim, Z. Nemes, W.W. Idler, C.C. Hyde, P.M. Steinert, and B.J. Ahvazi. J. Struct. Biol. **135**, 73 (2001).
12. S. Liu, R.A. Cerione, and J. Clardy. Proc. Natl. Acad. Sc. USA. **99**, 2743 (2002).
13. K. Noguchi, K. Ishikawa, K.-I. Yokoyama, T. Ohtsuka, N. Nio, and E.-I. Suzuki. J. Biol. Chem. **276**, 12055 (2001).
14. J.E. Folk. J. Biol. Chem. **244**, 3707 (1969).
15. P.H. Jensen, E.S. Sorensen, T.E. Petersen, J. Gliemann, and L.K. Rasmussen. Biochem. J. **310**, 91 (1995).
16. W. Borth, V. Chang, P. Bishop, and P. Harpel. J. Biol. Chem. **268**, 18149 (1991).

© 2007 NRC Canada

17. O. Molberg, S.N. McAdam, R. Korner, H. Quarsten, C. Kristiansen, L. Madsen, L. Fugger, H. Scott, O. Noren, P. Roepstorff, K.E.A. Lundin, H. Sjostrom, and L.M. Sollid. Nature Med. **4**, 713 (1998)
18. S. Reif and A. Lerner. Autoimmun. Rev. **3**, 40 (2004).
19. P.J.T.A. Groenen, J.J. Grootjans, N.H. Lubsen, H. Bloemendal, and W.W. Jong. J. Biol. Chem. **269**, 831 (1994).
20. S. Igarashi, R. Koide, T. Shimohata, M. Yamada, Y. Hayashi, H. Takano, H. Date, M. Oyake, T. Sato, A. Sato, S. Egawa, T. Ikeuchi, H. Tanaka, I. Hozumi, I. Inuzuka, H. Takahashi, and S. Tsuji. Nat. Genet. **18**, 111 (1998).
21. A.J.L. Cooper, K.R. Sheu, J.R. Burke, O. Onodera, W.J. Strittmatter, A.D. Roses, and J.P. Blass. J. Neurochem. **69**, 431 (1997).
22. A. Leblanc, C. Gravel, J. Labelle, and J.W. Keillor. Biochemistry, **40**, 8335 (2001).
23. H. Sato, N. Yamada, N. Shimba, and Y. Takahara. Anal. Biochem. **281**, 68 (2000).
24. L. Shan, O. Molberg, I. Parrot, F. Hausch, F. Filiz, G.M. Gray, L.M. Sollid, and C. Khosla. Science (Washington, D.C.), **297**, 2275 (2002).
25. D.J. Verrinder, M.J. Hourigan, and J.M. Prokipcak. Can. J. Chem. **56**, 2582 (1978).
26. E.A. Castro, F. Ibanez, S. Lagos, M. Schick, and J.G. Santos. J. Org. Chem. **57**, 2691 (1992).
27. E.A. Castro, P. Pavez, and J.G. Santos. J. Org. Chem. **66**, 3129 (2001).
28. E.A. Castro, P. Pavez, and J.G. Santos. J. Org. Chem. **67**, 4494 (2002).
29. E.A. Castro, P. Pavez, and J.G. Santos. J. Org. Chem. **68**, 9034 (2003).
30. S.L. Shames and L.D. Byers. J. Am. Chem. Soc. **103**, 6170 (1981).
31. S.I. Chung, R.I. Shrager, and J.E. Folk. J. Biol. Chem. **245**, 6424 (1970).
32. T. Ohtsuka, M. Ota, N. Nio, and M. Motoki. Biosci. Biotechnol. Biochem. **64**, 2608 (2002).
33. J.E. Folk and S.I. Chung. Adv. Enzymol. Relat. Areas Mol. Biol. **38**, 109 (1973).
34. P. Adams and F.A. Baron. Chem. Rev. **65**, 567 (1965).
35. D.J. Woodcock. Chem. Comm. (London), 267 (1968).
36. A.F. Hegarty and L.N. Frost. Chem. Comm. 500 (1972).
37. A.F. Hegarty and L.N. Frost. J. Chem. Soc. Perkin Trans. 2, 1719 (1973).
38. M.I. El Seoud and O.A. El Seoud. J. Org. Chem. **46**, 2286 (1981).
39. S.M. Rahmathullah, J.E. Hall, B.C. Bender, D.R. McCurdy, R.R. Tidwell, and D.W. Boykin. J. Med. Chem. **42**, 3994 (1999).
40. W.P. Jencks and K. Salvesen. J. Am. Chem. Soc. **93**, 4433 (1971).
41. R.E. Benesch and R.J. J. Benesch. J. Am. Chem. Soc. **77**, 5877 (1955).
42. J.W. Keillor and R.S. Brown. J. Am. Chem. Soc. **114**, 7983 (1992).
43. K.I. Skorey and R.S. Brown. J. Am. Chem. Soc. **107**, 4070 (1985).
44. M. Morin, C. Rivard, and J.W. Keillor. Org. Biomol. Chem., **4**, 3790 (2006).
45. A. Planas and J.F. Kirsch. Biochemistry, **30**, 8268 (1991).
46. C. Marrano, P. de Macédo, P. Gagnon, D. Lapierre, and J.W. Keillor. Bioorg. Med. Chem. **9**, 3231 (2001).
47. C. Marrano, P. de Macédo, and J.W. Keillor. Bioorg. Med. Chem. **9**, 1923 (2001).
48. R.A. Chica, P. Gagnon, J.W. Keillor, and J.N. Pelletier. Protein Sci. **13**, 979 (2004).
49. A. Case and R.L. Stein. Biochemistry, **46**, 1106 (2007).
50. G. Papageorgiou, A. Barth, and J.E.T. Corrie. Photochem. Photobiol. Sci. **4**, 216 (2005).
51. Handbook of fine chemicals and laboratory equipment. Sigma-Aldrich Company, 2000–2001.
52. J.E. Folk, and S.I. Chung. Methods Enzymol. **113**, 358 (1985).

© 2007 NRC Canada

Comparison study of live cells by atomic force microscopy, confocal microscopy, and scanning electrochemical microscopy

Xiaocui Zhao, Nils O. Petersen, and Zhifeng Ding

Abstract: In this report, three kinds of scanning probe microscopy techniques, atomic force microscopy (AFM), confocal microscopy (CM), and scanning electrochemical microscopy (SECM), were used to study live cells in the physiological environment. Two model cell lines, CV-1 and COS-7, were studied. Time-lapse images were obtained with both contact and tapping mode AFM techniques. Cells were more easily scratched or moved by contact mode AFM than by tapping mode AFM. Detailed surface structures such as filamentous structures on the cell membrane can be obtained and easily discerned with tapping mode AFM. The toxicity of ferrocenemethanol (Fc) on live cells was studied by CM in reflection mode by recording the time-lapse images of controlled live cells and live cells with different Fc concentrations. No significant change in the morphology of cells was caused by Fc. Cells were imaged by SECM with Fc as the mediator at a biased potential of 0.35 V (vs. Ag/AgCl with a saturated KCl solution). Cells did not change visibly within 1 h, which indicated that SECM was a noninvasive technique and thus has a unique advantage for the study of soft cells, since the electrode scanned above the cells instead of in contact with them. Reactive oxygen species (ROS) generated by the cells were detected and images based on these chemical species were obtained. It is demonstrated that SECM can provide not only the topographical images but also the images related to the chemical or biochemical species released by the live cells.

Key words: live cells, atomic force microscopy, confocal microscopy, scanning electrochemical microscopy.

Résumé : Dans ce travail, on a utilisé trois techniques de microscopie avec sonde à balayage, la microscopie de force atomique (MFA), la microscopie confocale (MC) et la microscopie à balayage électrochimique (MBEC), pour étudier des cellules vivantes dans un environnement physiologique. Dans ces expériences, on a étudié deux lignées de cellules modèles, CV-1 et COS-7. On a obtenu des images par les techniques de MFA en modes de contact ainsi que de percussion. Les cellules peuvent être plus facilement rayées ou déplacées par le mode de contact de la MFA que par le mode de percussion de la MFA. En utilisant le mode de percussion de la MFA, on peut obtenir et facilement discerner des structures superficielles détaillées, telles des structures filamenteuses sur la membrane cellulaire. On a étudié la toxicité du ferrocèneméthanol (Fc) sur des cellules vivantes en faisant appel à la MC en mode de réflexion en enregistrant des images accélérées de cellules vivantes contrôlées et de cellules vivantes avec diverses concentrations de Fc. Le Fc n'a pas provoqué de changements dans la morphologie des cellules. On a obtenu des images de cellules à l'aide de la MBEC en présence de Fc à un potentiel polarisé de 0,35 V (vs. Ag/AgCl avec une solution saturée de KCl). Les cellules ne présentent pas de changements visibles après une heure, ce qui indique que la MBEC n'est pas une technique invasive et qu'elle présente un avantage unique pour l'étude des cellules molles puisque l'électrode effectue son balayage au-dessus des cellules plutôt que de les toucher. On a détecté que des espèces réactives à l'oxygène (EOR) sont générées par les cellules et on a obtenu des images sur la base de ces espèces chimiques. On a démontré que la MBEC peut non seulement fournir des images topographiques, mais aussi des images reliées aux espèces chimiques ou biochimiques qui sont générées par les cellules vivantes.

Mots-clés : cellules vivantes, microscopie de force atomique, microscopie confocale, microscopie à balayage électrochimique.

Introduction

The study of single live cells has received increasing attention recently. Among the many analytical methods, atomic force microscopy (AFM), confocal microscopy (CM), and scanning electrochemical microscopy (SECM) have become more and more important to study living cells under physiological conditions and can provide a lot of structural and related functional information (1–3). AFM can image the morphology of living cells because of its high

Received 25 October 2006. Accepted 24 January 2007. Published on the NRC Research Press Web site at http://canjchem.nrc.ca on 21 March 2007.

X. Zhao and Z. Ding.[1] Department of Chemistry, The University of Western Ontario, London, ON N6A 5B7, Canada.
N.O. Petersen.[2] National Institute for Nanotechnology, 11421 Saskatchewan Drive, Edmonton, AB T6G 2M9, Canada.

[1]Corresponding author (e-mail: zfding@uwo.ca).
[2]Corresponding author (e-mail: nils.petersen@nrc-cnrc.gc.ca).

 doi:10.1139/V07-007 © 2007 NRC Canada

spatial resolution. The other major application of AFM is real time monitoring of morphological changes of live cells in response to intracellular and extracellular stimuli (4–7). CM provides optical information for focal planes inside cells without the use of fluorescent probes. However, AFM and CM cannot provide the desired chemical and biochemical information in cell metabolism processes, such as redox species moving across cell membranes or cell respiration. In contrast, the electrochemical method is now widely used to directly determine species, such as reactive oxygen species (ROS) (8–18) or nitric oxide (19, 20), released from cells by using a well-positioned ultramicroelectrode (UME) or a chemically modified UME. There are a couple of reasons for this. First, the electrode at a biased potential close to living cells can monitor the immediate ROS flux from the cells by recording the corresponding current under physiological conditions without disturbing the biological mechanisms. Second, different types of ROS species can be identified by the amperometry method at different electrode potentials (18). Therefore, high selectivity can be obtained during the detection process. To position the electrode well and get images based on the detected chemical and biochemical information, the SECM technique has been developed (21). SECM involves the measurement of electrochemically active species with an UME when it is positioned above or moved across the cell surface. Since the electrochemical current is proportional to the concentration of a redox species in solution, any change in the chemical activities disturbs the electrochemical response of the electrode. This perturbation provides information on cellular functions and cellular topographies. More recently, SECM has become an important tool to study live cells because it can provide chemical or biochemical information about their metabolism (22–33). It has been used for measuring photosynthetic electron transport (22) and effects induced by cadmium (29) in single guard cells; for monitoring the oxygen consumption of single bovine embryos (23); for studying the toxicity of menadione on hepatocytes and detection of efflux of thiodione from isolated cells after menadione-induced oxidative stress (24); for imaging and real time detection of morphological changes of neuron cells before and after exposure to nerve growth factor (25); for high-resolution imaging of model neurons obtained with constant distance mode SECM (26); and for investigating the pathway of transmembrane charge transfer in nonmetastatic and metastatic human breast cells (27) and in bacteria (28). Our group has previously shown that SECM can be used to study the effect of Cd induced stress on single stomata in Brassica juncea (29). We found that plants treated with $CdCl_2$ (0.20 mmol/L) had lower stomatal density and larger stoma size compared with control plants, and that oxygen evolution above individual stomatal complexes in Cd-treated plants was lower than that from control plants.

In this report, time-lapse cell images were obtained with AFM, CM, and SECM. ROS profiles were mapped above COS-7 live cells, which are redox species released by living cells and include hydrogen peroxide, hydroxyl radicals, and superoxide anions. ROS are generated within the cells as by-products of biological oxidations and of cellular respiration (34). We demonstrated that SECM can provide not only topographical but also chemical information in contrast to AFM and CM.

Experimental section

Chemicals

Ferrocenemethanol (Fc, 97%, Sigma-Aldrich, Mississauga, Ontario) stock solution was prepared at a concentration of 0.90 mmol/L. Culture media, serum, antibiotics, and glutamine were purchased from Gibco (Invitrogen Canada Inc., Burlington, Ontario). Deionized water (Milli-Q, Millipore, Bedford, Massachusetts, 18.2 MΩ resistivity) was used to prepare all aqueous solutions.

Cell culture

CV-1 and COS-7 cells (American Type Culture Collection, ATCC, Manassas, Virginia) (35) were used in the experiments. Both CV-1 and COS-7 cells were cultured in Eagle Minimum Essential Medium (EMEM) (Gibco) with 10% fetal bovin serum (FBS) (Gibco), 100 U/mL penicillin G, and streptomycin (Gibco), 2 mmol/L glutamine (Gibco) at 37 °C in a humidified atmosphere with 5% CO_2. One day before each experiment, cells were subcultured onto a Petri dish with a transparent glass bottom (MatTek Corporation, Ashland, USA). Before AFM and CM experiments, the red growth media was replaced with transparent Opti-MEMI media (modified EMEM media without phenol red) (Gibco) with 10 mmol/L Hepes buffer solution (Gibco) to see the cells clearly under the inverted microscopy. For SECM experiments, Opti-MEMI medium was used as the medium with 0.45 mmol/L ferrocenemethanol.

Experimental setup

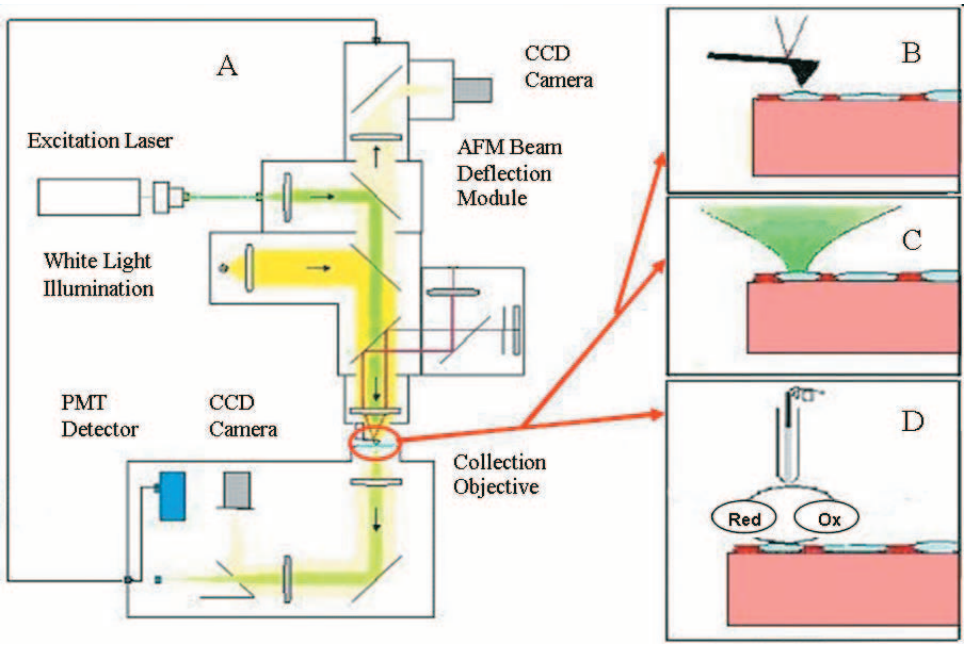
All AFM, CM, and SECM images were recorded by the same instrument, an Alpha-SNOM (WITec, Ulm, Germany), which uses a closed loop scanning system.

The experimental setup for AFM is shown in Figs. 1A and 1B. Both contact mode and tapping mode AFM were used to image cells in the culture media. Silicon nitride cantilevers with a spring constant of 0.20 N/m were used in the experiments for contact mode and tapping mode AFM imaging. In tapping mode AFM, the AC mode end cap was used, which constrained a piezo transducer to oscillate the cantilever at its mechanical resonance. The oscillation amplitude of the cantilever was used as a feedback signal to measure topographic variations of the sample. This resulted in a topography image. Another type of image, a phase image, was also recorded by monitoring the phase between excitation (the free cantilever oscillation) and cantilever motion. Before scanning, a resonance frequency was selected automatically by performing a frequency sweep in the desired range. A resonant frequency of about 26 kHz with amplitude of 0.20 V was obtained in the cell culture medium by applying a 0.20 V potential to a piezo transducer for cantilever oscillation. The resolution in the Z direction of AFM is 4 Å. The lateral resolution depends on the AFM tip used in the experiment. For example, if the tip radius of curvature is about 5 nm, the lateral resolution of AFM will be about 10 nm.

The experimental setup for CM is shown in Figs. 1A and 1C. Reflection confocal images were obtained using the same instrument with a 488 nm Argon laser (Coherent Inc., Santa Clara, California) as the light source. The illumination power of the laser was adjusted to about 2 mW. The laser

© 2007 NRC Canada

Fig. 1. Experimental setup for AFM (A and B), confocal microscopy (A and C), and SECM (A and D). (A) An illustrative scheme for Alpha-SNOM. (B) Enlargement of scanning probe part (a cantilever with AFM tip and scanning stage) for AFM. (C) Enlargement of scanning probe part (a 60× water immersion objective and scanning stage) for confocal microscopy. (D) Enlargement of scanning probe part (an electrode holder with a 2.0 µm Pt electrode and scanning stage) for SECM.



beam was fed into the CM with a 4 µm diameter optical fibre. The reflected light from the cells was collected by a multi-mode optical fibre with a diameter of 50 µm, which served as a pinhole for CM, and was then transmitted to a photomultiplier tube (PMT, Hamamatsu, Japan). Different optical density filters were used to attenuate the laser intensity and to keep minimal laser intensity on the cells to avoid unnecessary photobleaching. The reflective light intensity was kept under 1000 counts to prevent the photobleaching effect and enhance the sensitivity of CM. To obtain high-resolution images, we used a 60× water immersion objective lens (Nikon, Mississauga, Canada) with a numerical aperture of 1 and a long working distance of 2 mm. In every experiment, focal planes of cells were selected in the middle plane through the cells. The lateral resolution for CM is about 200 nm and the vertical resolution is about 500 nm.

The SECM instrument was modified from Alpha-SNOM by replacing the objective with an electrode holder and a custom-made Pt (2.0 µm diameter) electrode (29, 36) (Fig. 1, A and D). The electrochemical signal (current signal) was fed into one data acquisition channel of the Alpha-SNOM instrument. All the electrochemical experiments were performed with an electrochemical analyser (CH 832a, CH Instruments, Austin, Texas). The electrochemical system consisted of two electrodes. A 2.0 µm Pt was used as the working electrode and a Ag/AgCl electrode, with a saturated KCl solution, was used as both the reference and the counter electrode. In the experiments, the SECM electrode was brought closer to the cells and positioned at a desired height with a certain applied potential while the current was monitored. The probe approach curve (current vs. distance curve) was then plotted. At a fixed height, the working electrode was scanned in a plane with an applied potential by moving the scanning stage. Constant height SECM images can be obtained by recording current vs. lateral coordinates in the scanning plane. The scanning area can be repeatedly scanned because of the closed loop system. For SECM, the resolution is about 2 µm because a 2.0 µm diameter electrode is used in the experiment. The whole scanning process (the movement of scanning stage and the plot of image) was controlled by the WITec software adapted from CM mode.

Results and discussion

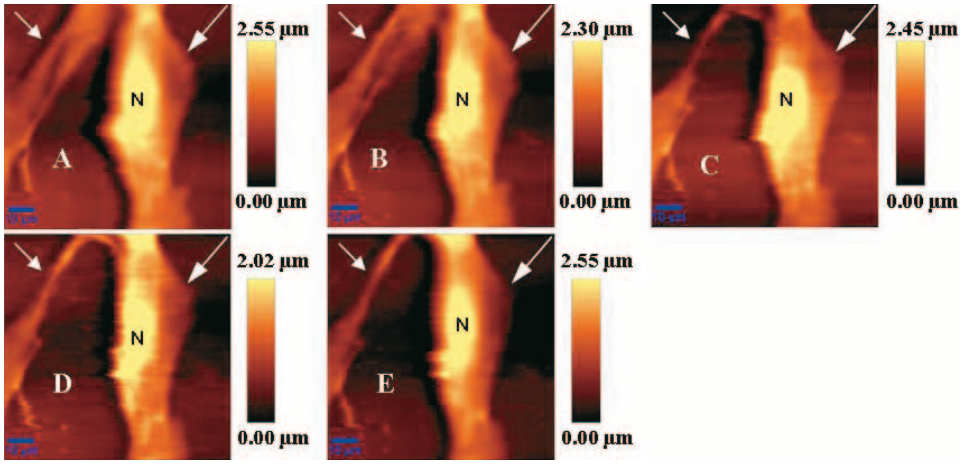
Contact mode and tapping mode AFM images of CV-1 live cells

Figure 2 shows time-lapse cell images taken within a 1 h period with contact mode AFM. The same scanning region was scanned repeatedly with the closed loop scanning system. In the image, a nucleus (labelled N) and two branches (labelled with arrows) were observed (Fig. 2A). As AFM scanning continued, the right branch (large arrow) became fuzzy (Fig. 2B), and cells began to shrink in size (Fig. 2C). The left branch (small arrow) became narrower and shrunk significantly, as can be seen from the connection between the branch and the nuclus (Fig. 2D). At the end, the left branch became a line and the height of this branch increased in the last scan (Fig. 2E) because of the injuries to the cell membranes that resulted in a rounding of the cell. The cell body became smaller and smaller. From the height level bars beside the topography images, we determined that the height of the cells changed from 2.02 µm to 2.55 µm. This evidence supported the fact that the cells were becoming rounded.

Using contact mode AFM, we can clearly see the cell membrane and nuclei (Fig. 2) under physiological conditions. However, cells were easily injured by the AFM tip because the tip was in physical contact with the cells (1). The spring constant of the cantilever used in the experiments was

© 2007 NRC Canada

Fig. 2. Time-lapse contact mode AFM images of CV-1 cells. Images were obtained (A) 20 min, (B) 30 min, (C) 40 min, (C) 50 min (D), and (E) 60 min after cells were taken out of the incubator. The scale bars in the images represent 10 μm. The scan rate is 1 s/line (256 lines/image). The acquisition time for every image is about 5 min. N, large arrow, and small arrow indicate the nucleus, right branch, and left branch, respectively.

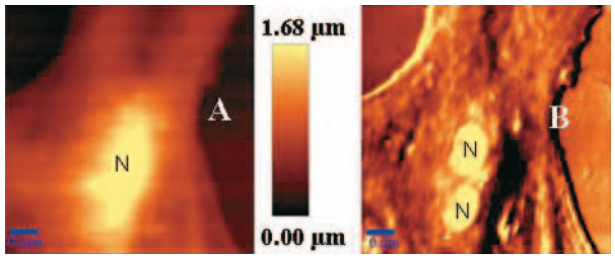


0.20 N/m. However, the average spring constant of cells is 0.0020 N/m (37, 38), which is one hundredth of that of our cantilever. When the tip scans over the soft cells, plasma membranes may be deformed or the tip might penetrate through the membrane (39). This may cause irreversible injury to the cell that eventually leads to cell death. The injured cell may become vulnerable and loosely attached to the substrate. You et al. (40) studied the disruptive effect of the cantilever tip on cell morphology using AV 12 and SK-N-SH cells, and they found that the extracellular matrix could be removed and the adhesion ability of cells could be degraded after several scans. In this way cells were injured, rounded up, and decreased in size (40). A less harmful imaging method should be used to image soft cells.

Tapping mode AFM, in which the tip is intermittently in contact with cells, was applied to image soft cells under physiological conditions. Both a topography image (Fig. 3A) and a phase image (Fig. 3B) were recorded. Two bright zones corresponding to the nucleus areas (N) surrounded by relatively flat membranes are shown (Fig. 3B). Long filamentous structures (bundles of stress fibers) or cytoskeleton elements, which were heterogeneous in distribution and organization over the cell membranes, can be easily seen (Fig. 3B). However, the filamentous structures of the cells were not detectable in topography images (Fig. 3A) because of the height of the cell (1.68 μm), which contributed to a large contrast between the high nucleus and flat membrane. The two nuclei cannot be distinguished either. Only one large nuclear area (N) can be seen in the topography image. The filamentous structures of the CV-1 cells were also imaged based on deflection signals and could not be revealed in images based on amplitude signals with tapping mode AFM (41). This phenomenon has been explained as resulting from the higher sensitivity of deflection signals to local stiffness of cells because the stiffness of cytoskeleton elements was higher than that of the plasma membrane of cells (41).

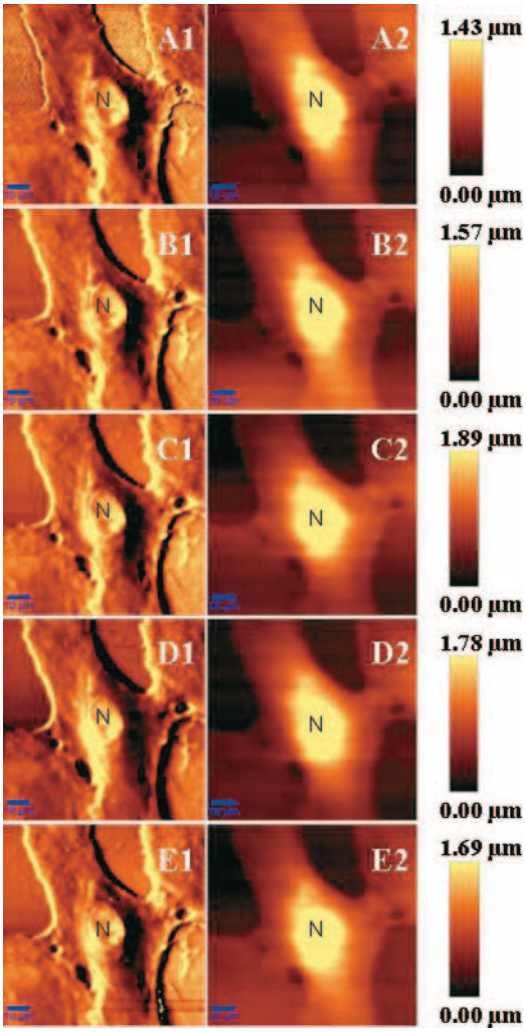
Time-lapse images of CV-1 cells were also recorded with tapping mode AFM. The same scanning region was repeatedly scanned with the closed loop scanning system. The images on the left side panels are phase images (Fig. 4, A1–E1). The images on the right side panels are topography images (Fig. 4, A2–E2) of the same areas. One nucleus (N) and the boundaries of three cells were obviously apparent in the phase images. As can be seen from Fig. 4, the images were almost the same except for a slight change in the cell–cell boundary within a 1 h scanning period. Cell–cell interaction was not disrupted and cells were not moved by the tip, in contrast to what happened in contact mode AFM. This is because in tapping mode AFM the tip was in contact with the cells only for a short time and then lifted up. Therefore, the lateral forces were drastically reduced and this mode was much more suitable for imaging live cells. It is important to note that the image A1 in Fig. 4 seemed obscure just after scanning over the nucleus. Cellular materials such as cellular debris, metabolic products, or cellular secretion, may be adsorbed at the apex of the scanning tip resulting in a slightly lower resolution (1). The vertical movements of cells also can be measured from the topography images (Fig. 4, A2–E2). The highest part of the cells was 1.43 μm in the first image (Fig. 4, A2). In the following scan, the cells moved up and the height was 1.57 μm (Fig. 4, B2). The cells continued to move up in the next two runs and the heights were 1.78 (Fig. 4, C2) and 1.89 μm (Fig. 4, D2), respectively. In the last scan, the cells moved down and the height of the cells

Fig. 3. Tapping mode AFM images of CV-1 cells, (A) topography image and (B) phase image. The lateral scale bars in the images represent 10 μm. The scan rate is 1 s/line (256 lines/image). The acquisition time for every image is about 5 min. N indicates the nucleus area.



© 2007 NRC Canada

Fig. 4. Time-lapse tapping mode AFM images of CV-1 cells. Images were obtained (A1) and (A2) 20 min, (B1) and (B2) 30min, (C1) and (C2) 40 min, (D1) and (D2) 50 min, and (E1) and (E2) 60 min after cells were taken from the incubator. The scale bars in the images represent 10 µm. The scan rate is 1 s/line (256 lines/ image). The acquisition time for every image is about 5 min. N indicates the nucleus area.



decreased to 1.69 µm (Fig. 4, E2). During the cell movement process, the total change in height was 0.31 µm. This submicro movement can be accurately detected by AFM. The advantages of AFM, i.e., spatial high resolution and high sensitivity, were again demonstrated here.

Reflection CM images of COS-7 cells

In our experiments, the external surface changes of unstained live cells within a 1 h period were visualized by CM in reflection mode. The same area was repeatedly imaged, using the closed loop scanning stage. As can be seen from Fig. 5, the membrane and nucleus of an individual COS-7 cell were clearly imaged. The morphology of the cell did not change dramatically. Small changes at the cell edge might be due to the slow movement of the cell. We can conclude that cells can survive and are still healthy under weak laser illumination.

The toxicity of ferrocenemethanol (a widely used redox mediator in electrochemistry) on live cells was studied with CM. After one image of a cell was recorded (Fig. 6A), a certain amount of ferrocenemethanol was added to the Petri dish and was well mixed with the culture medium by using a micropipette. Time-lapse images were recorded in the same region as for images without ferrocenemethanol. Images of cells were obtained with dosages of ferrocenemethanol at different concentrations ranging from 1 to 450 µmol/L. Figure 6 shows cell images using 450 µmol/L of ferrocenemethanol. As seen in the images, there was almost no change in the shape or size of cells indicating that ferrocenemethanol caused almost no morphology changes. To confirm this conclusion, cells were split among a dozen petri dishes with the same density. Half of these cells were used as control cells. The other half were cultured in the culture medium for one day and the culture medium was replaced with ferrocenemethanol at various concentrations. The cells were then incubated overnight. The number of cells was counted and the shapes of cells were observed under the 60× objective. The number of cells detected after ferrocenemethanol treatment was almost the same as the number of control cells. The shapes of cells treated with ferrocenemethanol were similar to those of the control cells.

One of the advantages of CM, using fluorescence as the detection signal, is the ability to take optical slices through a three dimensional specimen, e.g., cells or tissues, and produce an image containing information from each of the focal planes (3, 42). Without labelling, a single COS-7 cell was imaged at different focus planes using reflection CM. By putting these focus planes together, a three-dimensional image of the cell was obtained that contained all the information from all the focus planes of the cell. Normally, COS-7 cells are about 5 µm in height, while CV-1 cells are just 2 µm high. Some cell lines are even higher. For example, PC12 cells are about 7 µm in height (43). To acquire focal plane images from the top and bottom of the cell, a total depth of 7 µm was scanned in our experiments by recording 15 stack images with a 500 nm depth difference between two successive images. As seen in Fig. 7, different images from different focal planes of the cell were obtained. Image 1 of Fig. 7 is from the highest focal plane through the cell. The edge of the cell can be clearly seen and the nucleus is shown in the brightest region. In sequence, the objective was moved 500 nm down to obtain image 2 in Fig. 7 as the second highest focal plane through the cell. In this image, the size and shape of the cell was the same as that in image 1, but the nuclear region became less bright and more obvious. In the following runs, the nuclear region became darker and was easily discerned in the images. Finally, by putting all 15 images together, a three-dimensional image of the cell can be obtained (Fig. 7, image 16).

Cyclic voltammetry and SECM approach curve to live cells

Cyclic voltammetry (CV) was carried out using a 2.0 µm diameter Pt electrode as a working electrode and a Ag/AgCl electrode as both reference and counter electrode. A detailed fabrication of the ultramicroelectrodes (UME) (2.0 µm Pt) was described previously (29, 36). A solution of 0.90 mmol/L ferrocenemethanol was used to test the electro-

© 2007 NRC Canada

Fig. 5. Time-lapse images of COS-7 cells with confocal microscopy within 1 hour. Integration time, 0.005 s; Pixel, 256 56. Images were obtained (A) 11 min; (B) 20 min; (C) 29 min; (D) 38 min; (E) 54 min and (F) 61 min after cells were taken from the incubator. The scale bars in the images represent 9 µm. The acquisition time for every image is about 6 min.

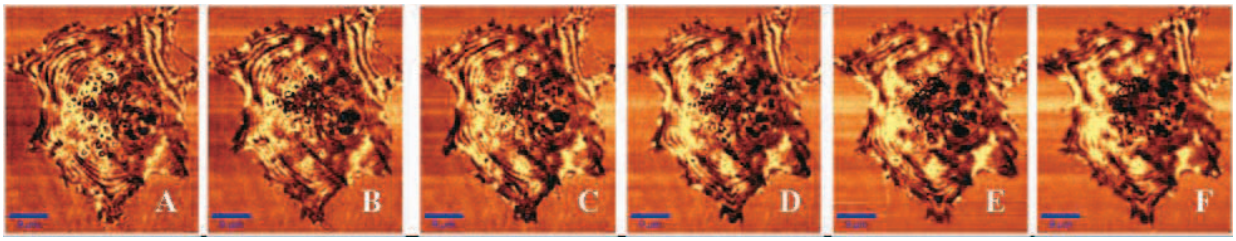


Fig. 6. Cell images of COS-7 cells with confocal microscopy (A) before adding ferrocenemethanol, (B) 9 min, (C) 17 min, (D) 32 min, and (E) 62 min after adding 450 µmol/L ferrocenemethanol. The scale bars in the images represent 8 µm. Integration time: 0.005 s; pixels: 256 × 256. The acquisition time for every image is about 6 min.

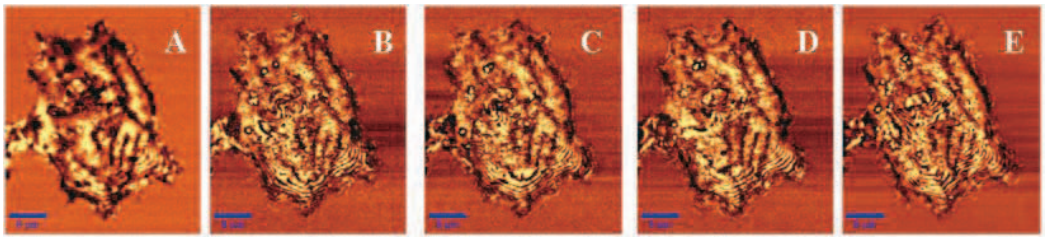
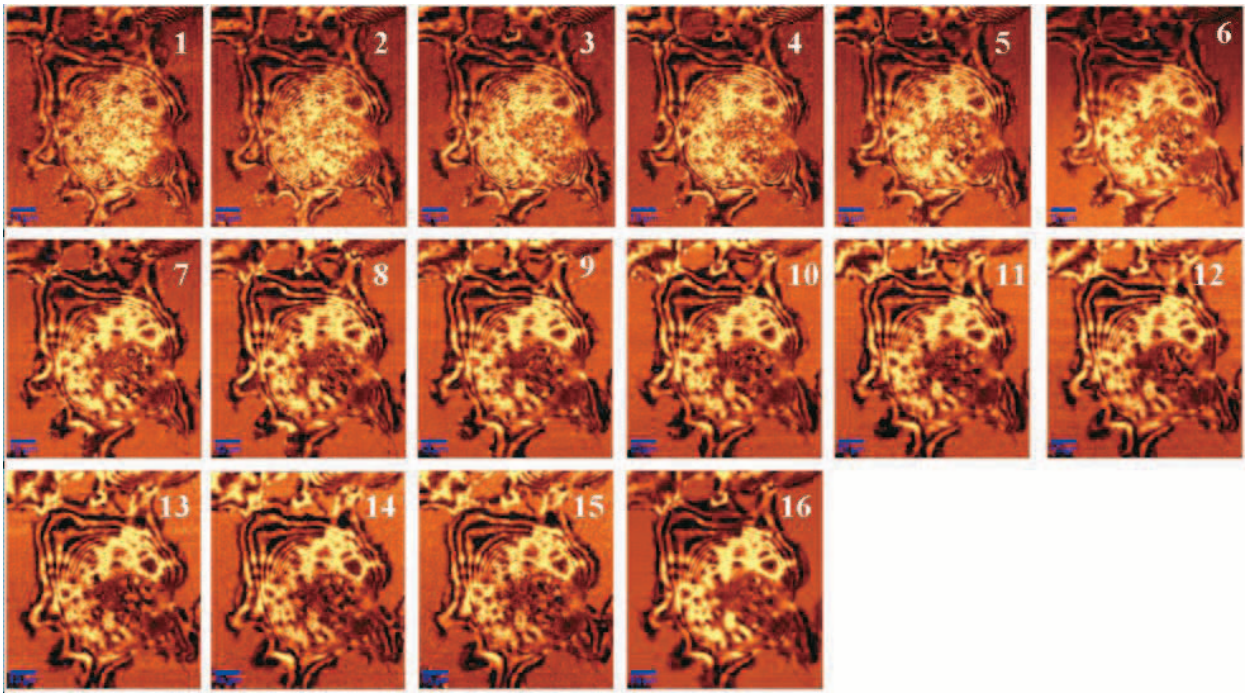


Fig. 7. Stack of 15 images (1–15) of COS-7 cells using confocal microscopy with a depth of 500 nm between consecutive images and a three-dimensional image (image 16) formed by overlapping 15 images (from image 1 to image 15) together. The scale bars in the images represent 10 µm. Integration time: 0.005 s; pixels: 128 × 128. The acquisition time for every image is about 1 min.



chemical behaviour of the electrode (Fig. 8A). A steady state current of 0.29 nA was obtained. The effective radius, a, (36) of the electrode can be calculated with this steady state current by using eq. [1],

$$[1] \qquad a = i_{T,\infty}/4nFDC^0$$

where $i_{T,\infty}$ is the steady state current of the electrode, n is the number of electrons transferred, F is Faraday constant, D, and C^0 are the diffusion coefficient and concentration of ferrocenemethanol. The diffusion coefficient used was 7.8×10^{-6} cm^2/s (44). The calculated value of the electrode radius was 1.1 µm, which was very close to the value of 1.0 µm in the specification that the manufacturer provided to us (Goodfellow Corporation, Devon, Pennsylvania).

After positioning the working electrode above the nucleus of one cell, the electrode with a biased potential of 0.35 V

© 2007 NRC Canada

Fig. 8. (A) Cyclic voltammogram (scan rate 0.01 V/s) and (B) probe approach curve to a cell nucleus in 0.90 mmol/L ferrocenemethanol solution with a 2.0 µm diameter electrode for RG = 5.

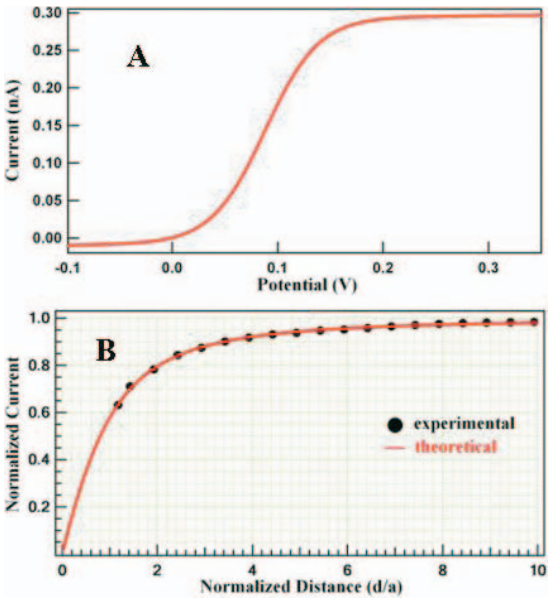
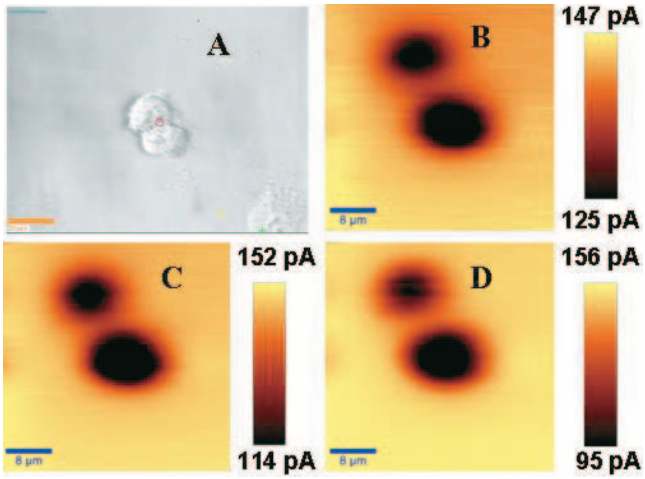
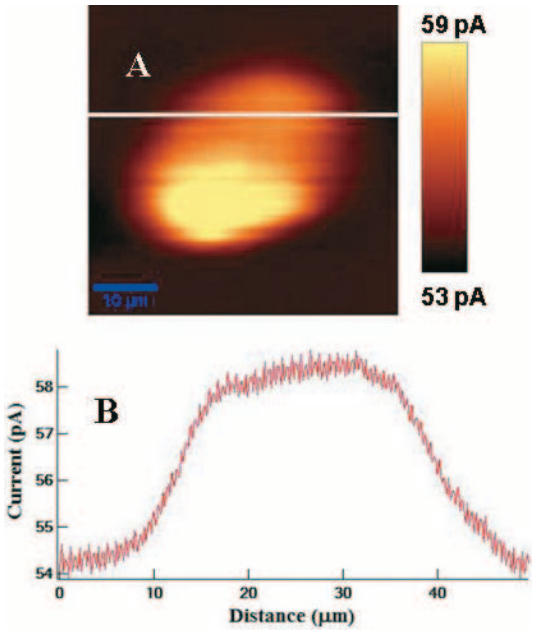


Fig. 9. (A) Optical picture of COS-7 cells subsequently imaged by SECM. Time-lapse SECM images (40 µm × 40 µm) of COS-7 cells after (B) 28 min, (C) 41 min, and (D) 54 min after cells were moved from an incubator with a 2.0 µm diameter electrode for RG = 5 at a biased potential of 0.35 V (vs. Ag/AgCl). Ferrocenemethanol concentration was 0.45 mmol/L. The distance between the electrode and the cell is about 2.0 µm (normalized current = 0.8). The scale bars in the images represent 8 µm. Integration time at each image pixel: 0.01 s; pixels: 256 × 256. The acquisition time for every image is about 12 min.



was slowly moved downward and the diffusion-limiting current of ferrocenemethanol oxidation was monitored. When the electrode was far from the cells, a constant current was obtained because of the hemispherical diffusion of ferrocenemethanol at a constant concentration of 0.90 mmol/L. The current decreased as the electrode was moved toward the cell because the hemispherical diffusion of ferrocenemethanol from solution to the electrode was partially blocked by the cell and so-called negative feedback was obtained. The electrode was stopped until the normalized current (the ratio of actual tip current, i_T, to the steady state current when the electrode is far away from the cell, $i_{T,\infty}$) was about 0.60. A theoretical probe approach curve (PAC) was plotted with the experimental one (Fig. 8B) (45), and the two matched very well. When the electrode was stopped at a normalized current of about 0.8 or 0.6, the distance between the electrode and cells was about 2.0 or 1.2 µm, which can be read from the theoretical PAC (36, 45).

Fig. 10. (A) SECM image at a biased potential of –0.80 V (vs. Ag/AgCl) with a 2.0 µm diameter electrode for RG = 5. The distance between the electrode and the cell is about 1.7 µm (normalized current = 0.75). The scale bars in the images represent 10 µm. Integration time at each image pixel: 0.01 s; pixels: 256×256. The acquisition time for every image is about 12 min. (B) Trace obtained by plotting a white horizontal line in image A.



Time-lapse SECM images

Cell topographies at different times were also recorded with SECM within a 1 h period using ferrocenemethanol (0.45 mmol/L) as the mediator. First, the cells of interest were located with the aid of an objective (Fig. 9A). The electrode was positioned above one cell and was moved toward the cell until the distance between the electrode and the cell nucleus was about 2.0 µm (normalized current = 0.8) with a biased potential of 0.35 V applied to the probe. With this biased potential, cells were scanned slowly (integration time at each image pixel is 0.01 s). The acquisition time for every image is about 12 min with 256 × 256 pixels. Since the cells blocked the ferrocenemethanol diffusing to the electrode, oxidization current decreased while the electrode was scanned over the cell and the negative feedback was obtained. Two cells were shown as two holes in the images.

© 2007 NRC Canada

Dark areas represented low current and bright areas corresponded to high current (Figs. 9B, 9C, and 9D). Nuclei (dark area) and part of the membranes (brown area) can be seen. Within 1 h the cell did not change because the tip scanned above the cells without touching them, which demonstrated that SECM was a noninvasive technique and had a unique advantage for study of soft cells.

Detection of ROS released by cells with SECM

At normal concentrations, ROS are essential to cells because of the important functions that they perform. However at elevated concentrations, ROS are harmful because they can damage key macromolecules, such as nucleic acids, proteins, and lipids, and ultimately cause cell death (34). Arbaults et al. (13) detected the immediate burst of ROS using amperometric detection with a platinized carbon fiber microelectrode by puncturing the cell cytoplasmic membrane with the microelectrode. Matsue's group also detected ROS release with electrochemical methods and the chemiluminescence method using phorbol myristate acetate (PMA) differentiated cells (14).

In our experiments, the working electrode was positioned about 1.7 μm (normalized current of 0.75) above the nucleus of the living COS-7 cells using oxygen as the mediator with a biased potential of –0.80 V, at which O_2 is reduced (eq. [2]).

$$[2] \qquad O_2 + 4e^- + 2H_2O \rightarrow 4OH^- \qquad \text{(eq. [2])}$$

At the same height, the electrode was scanned above the cell. A more negative feedback should be obtained if there were no species released by the living cells for the following two reasons (29): (*i*) cell respiration consumed O_2 and contributed to a lower concentration of O_2; (*ii*) the O_2 diffusion blockage also resulted in the decreased concentration of O_2. However, a positive feedback was observed and cells were shown as bumps instead of holes in the SECM image (Fig. 10A) as a result of increased current (Fig. 10B). ROS should have been generated by cells and diffused to the tip surface and reduced at the tip, which resulted in the increased current. ROS, such as superoxide ($O_2^{\cdot-}$), hydroxyl radicals ($OH^{\cdot-}$), and hydrogen peroxide are easier to reduce than oxygen. They were all reduced at the applied potential –0.80 V. The current observed represents the total concentrations of these species. Further study of this aspect is in progress in our lab. Note that Amatore's group (18) observed the ROS release from macrophages through the oxidation of these species. It also can be seen from image 10A and curve 10B that the current monitored above the cell nucleus is more positive than the current recorded above cell membranes. A higher concentration of ROS would contribute to a higher current. Two factors may contribute to this observation. First, as is well-known, the cell nucleus is higher than the cell membrane. Therefore, the distance between the electrode and cell nucleus is smaller than the distance between the electrode and cell membranes with the constant height SECM method. ROS are very active and if the electrode is not close enough to the cells some radicals such as hydroxyl or superoxide anion radicals can react with chemicals in the solution before diffusing to the surface of the electrode and will not be detected, giving a relatively low current. However when the electrode is closer to the cells, the ROS generated by cells can easily diffuse to the electrode and be monitored by the electrode. Another reason may be that the region near the nucleus of the cell may release more ROS than the membrane region.

Conclusions

We have used both contact and tapping mode AFM to image the topography of living cells. Nuclei and flat membranes can be readily identified by contact mode AFM under physiological conditions. However, cells were easily damaged or moved by the tip with time because the cells are a hundred times softer than the cantilever. Using nondestructive tapping mode AFM, high-resolution images were obtained. It was possible to image subcellular structures, e.g., filamentous structures and cytoskeletal structures. Cells were less damaged, but image clarity deteriorated with time as a result of debris on the cantilever tip from cellular material (1). The time-lapse images of living cells revealed that the tapping mode was more suitable for imaging live cells than contact mode. However, AFM provided only topographic information, not information about biochemical and biological reactions taken place in the cells (1).

With CM, the detailed structure and shape of cells were observed. There were few changes of cell shapes beyond slight movements of cell edges. Time-lapse images changed slightly as a result of water evaporation. Cell morphology changed very little with ferrocenemethanol treatment over several hours, indicating that ferrocenemethanol does not cause much change in cell morphology. Its use as a redox mediator in the subsequent SECM experiments may therefore be acceptable. One of the advantages of CM, the optical slicing of the cells, was demonstrated by scanning 15 images taken at different heights of the cell, with a 500 nm height difference between two adjacent focal planes. A three-dimensional image was reconstructed from the images obtained at these different focal planes.

Real time changes in cell morphology were imaged and monitored by constant height mode SECM with ferrocenemethanol as the mediator. The nucleus and membrane were visible when the tip was lowered until a normalized current of 0.8 was obtained. Cell morphology did not change with time because the tip was scanned above the cells without touching them. ROS generated by the cells were detected and images based on this chemical signal were obtained. The advantage of SECM, such as providing images based on chemical or biochemical information (detection of species released or consumed by the cells, respiration and photosynthesis, and transmembrane electron transfer) about cells was clearly demonstrated.

Acknowledgments

We appreciate the financial support for this research from Canadian Institute for Photonic Innovations (CIPI), the Natural Sciences and Engineering Research Council of Canada (NSERC), Ontario Photonics Consortium (OPC), Canada Foundation for Innovation (CFI), Ontario Innovation Trust (OIT), Premier Research Excellence Award (PREA), and the University of Western Ontario (UWO) Academic Development Fund (ADF) as well as a Start-up Fund. Our lab is part

© 2007 NRC Canada

of the Centre of Chemical Physics (CCP) and Western Institute of Nano Science (WINS) at UWO. Thanks to PhD student, Renkang Zhu, in our lab for providing the microelectrodes. We thank Dr. Ian Mitchell, Dr. Peter Norton, Dr. Karen Davenport, and Dr. Maxim Anikovskiy for fruitful discussions and their kind help with cell culturing. Technical assistance from John Vanstone, Jon Aukema, Sherrie McPhee, Mary Lou Hart, and Marty Scheiring is gratefully acknowledged.

References

1. H.X. You and L. Yu. Methods Cell Sci. **21**, 1 (1999).
2. T. Yasukawa, T. Kaya, and T. Matsue. Electroanalysis, **12**, 653 (2000).
3. P. Vesely and A. Boyde. J. Anat. **198**, 641 (2001).
4. D. Braunstein and A. Spudich. Biophys. J. **66**, 1717 (1994).
5. M. Fritz, M. Radmacher, and H.E. Gaub. Biophys. J. **66**, 1328 (1994).
6. R. Lal, B. Drake, D. Blumberg, D.R. Saner, P.K. Hansma, and S.C. Feinstein. Am. J. Physiol. **269**, C275 (1995).
7. A.E. Pelling, S. Sehati, E.B. Gralla, J.S. Valentine, and J.K. Gimzewski. Science (Washington, D.C.), **305**, 1147 (2004).
8. S.-C. Chang, N.P. Rodrigues, N. Zurgil, J.R. Henderson, F. Bedioui, C.J. McNeil, and M. Deutsch. Biochem. Biophys. Res. Commun. **327**, 979 (2005).
9. H.A. Hill, D.G. Tew, and N.J. Walton. FEBS Lett. **191**, 257 (1985).
10. S.-C. Chang, N. Pereira-Rodrigues, J.R. Henderson, A. Cole, F. Bedioui, and C.J. McNeil. Biosens. Bioelectron. **21**, 917 (2005).
11. S. Arbault, P. Pantano, N. Sojic, C. Amatore, M. Best-Belpomme, A. Sarasin, and M. Vuillaume. Carcinogenesis, **18**, 569 (1997).
12. S. Arbault, N. Sojic, D. Bruce, C. Amatore, A. Sarasin, and M. Vuillaume. Carcinogenesis, **25**, 509 (2004).
13. S. Arbault, P. Pantano, J.A. Jankowski, M. Vuillaume, and C. Amatore. Anal. Chem. **67**, 3382 (1995).
14. S. Kasai, H. Shiku, Y.-s. Torisawa, H. Noda, J. Yoshitake, T. Shiraishi, T. Yasukawa, T. Watanabe, T. Matsue, and T. Yoshimura. Anal. Chim. Acta, **549**, 14 (2005).
15. S. Mesaros, Z. Vankova, A. Mesarosova, P. Tomcik, and S. Grunfeld. Bioelectrochem. Bioenerg. **46**, 33 (1998).
16. Y. Isogai, T. Tsuyama, H. Osada, T. Iizuka, and K. Tanaka. FEBS Lett. **380**, 263 (1996).
17. A. Lachgar, N. Sojic, S. Arbault, D. Bruce, A. Sarasin, C. Amatore, B. Bizzini, D. Zagury, and M. Vuillaume. J. Virol. **73**, 1447 (1999).
18. C. Amatore, S. Arbault, C. Bouton, K. Coffi, J.-C. Drapier, H. Ghandour, and Y. Tong. Chem. Bio. Chem. **7**, 653 (2006).
19. S. Borgmann, I. Radtke, T. Erichsen, A. Bloechl, R. Heumann, and W. Schuhmann. Chem. Bio. Chem. **7**, 662 (2006).
20. S. Isik, M. Etienne, J. Oni, A. Bloechl, S. Reiter, and W. Schuhmann. Anal. Chem. **76**, 6389 (2004).
21. A.J. Bard. *In* Scanning electrochemical microscopy. *Edited by* A.J. Bard and M.V. Mirkin. Marcel Dekker, Inc., New York. 2001.
22. M. Tsionsky, Z.G. Cardon, A.J. Bard, and R.B. Jackson. Plant Physiol. **113**, 895 (1997).
23. H. Shiku, T. Shiraishi, H. Ohya, T. Matsue, H. Abe, H. Hoshi, and M. Kobayashi. Anal. Chem. **73**, 3751 (2001).
24. J. Mauzeroll, A.J. Bard, O. Owhadian, and T.J. Monks. Proc. Natl. Acad. Sci. USA, **101**, 17582 (2004).
25. J.M. Liebetrau, H.M. Miller, J.E. Baur, S.A. Takacs, V. Anupunpisit, P.A. Garris, and D.O. Wipf. Anal. Chem. **75**, 563 (2003).
26. R.T. Kurulugama, D.O. Wipf, S.A. Takacs, S. Pongmayteegul, P.A. Garris, and J.E. Baur. Anal. Chem. **77**, 1111 (2005).
27. B. Liu, S.A. Rotenberg, and M.V. Mirkin. Proc. Natl. Acad. Sci. USA, **97**, 9855 (2000).
28. C. Cai, B. Liu, M.V. Mirkin, H.A. Frank, and J.F. Rusling. Anal. Chem. **74**, 114 (2002).
29. R. Zhu, S.M. Macfie, and Z. Ding. J. Exp. Bot. **56**, 2831 (2005).
30. T. Yasukawa, T. Kaya, and T. Matsue. Anal. Chem. **71**, 4637 (1999).
31. M. Nishizawa, K. Takoh, and T. Matsue. Langmuir, **18**, 3645 (2002).
32. Y. Takii, K. Takoh, M. Nishizawa, and T. Matsue. Electrochim. Acta, **48**, 3381 (2003).
33. T. Kaya, M. Nishizawa, T. Yasukawa, M. Nishiguchi, T. Onouchi, and T. Matsue. Biotechnol. Bioeng. **76**, 391 (2001).
34. K. Pantopoulos, S. Mueller, A. Atzberger, W. Ansorge, W. Stremmel, and M.W. Hentze. J. Biol. Chem. **272**, 9802 (1997).
35. Y. Gluzman. Cell, **23,** 175 (1981).
36. R. Zhu and Z. Ding. Can. J. Chem. **83**, 1779 (2005).
37. A.L. Weisenhorn, M. Khorsandi, S. Kasas, V. Gotzos, and H.-J. Butt. Nanotechnology, **4**, 106 (1993).
38. J.H. Hoh and C.A. Schoenenberger. J. Cell Sci. **107**, 1105 (1994).
39. E. Henderson, P.G. Haydon, and D.S. Sakaguchi. Science (Washington, D.C.), **257**, 1944 (1992).
40. H.X. You, J.M. Lau, S. Zhang, and L. Yu. Ultramicroscopy, **82**, 297 (2000).
41. V. Vie, M.C. Giocondi, E. Lesniewska, E. Finot, J.P. Goudonnet, and C. Le Grimellec. Ultramicroscopy, **82**, 279 (2000).
42. G. Pellacani, A.M. Cesinaro, and S. Seidenari. J. Invest. Dermatol. **125**, 532 (2005).
43. Y. Takahashi, Y. Hirano, T. Yasukawa, H. Shiku, H. Yamada, and T. Matsue. Langmuir, **22**, 10299 (2006).
44. W.J. Miao, Z.F. Ding, and A.J. Bard. J. Phys. Chem. B, **106**, 1392 (2002).
45. Y. Shao and M.V. Mirkin. J. Phys. Chem. B, **102**, 9915 (1998).

© 2007 NRC Canada

Zirconium(IV) chloride-catalyzed synthesis of 1,5-benzodiazepine derivatives

K. Srinivasa Reddy, Ch. Venkateshwar Reddy, M. Mahesh, K. Rosi Reddy, P.V.K. Raju, and V.V. Narayana Reddy

Abstract: Zirconium tetrachloride efficiently catalyzes the cyclocondensation reaction of *o*-phenylenediamine and a ketone in refluxing 1,2-dichloroethane to afford the corresponding 2,3-dihydro-1*H*-1,5-benzodiazepine in high yield. The formation of specific regioisomers and their structural elucidation are reported for the first time.

Key words: zirconium tetrachloride, *o*-phenylenediamines, ketones, 1,5-benzodiazepines, ^{1}H NMR, regioisomers.

Résumé : Le tétrachlorure de zirconium catalyse d'une façon efficace la réaction de cyclocondensation de l'*o*-phénylènediamine avec les cétones, dans du 1,2-dichloroéthane au reflux, pour conduire à la formation des 2,3-dihydro-1*H*-1,5-benzodiazépines, avec un rendement élevé. On rapporte pour la première fois la formation de régioisomères spécifiques ainsi que l'élucidation de leurs structures.

Mots-clés : tétrachlorure de zirconium, *o*-phénylènediamines, cétones, 1,5-benzodiazépines, RMN du ^{1}H, régioisomères.

[Traduit par la Rédaction]

Introduction

Benzodiazepines are important pharmaceutical compounds that are frequently used as prescribed drugs for combating central nervous system (CNS)-related diseases mainly because of their anticonvulsant, hypnotic, and other properties (1, 2). They are also used as intermediates in the manufacture of commercially important cationic dyes for acrylic fibers (3) and also used as starting materials for the preparation of fused ring compounds such as triazolo- (4), oxadiazolo- (5), oxazino- (6), or furano-benzodiazepines (7). More interestingly, the related diazapines showed unusual and novel pharmacological activity as HIV-1 reverse transcriptase inhibitors, as evidenced by niverperin (8). Because of their versatile biological activity and commercial utility, the synthesis of these compounds has acquired greater attention in synthetic organic chemistry and led to the development of new synthetic strategies. Generally, these compounds are prepared by cyclocondensation of *o*-phenylenediamine with α,β-unsaturated carbonyl compounds (9), β-haloketones (10), or ketones, involving combinations of Lewis acids and transition-metal salts like BF_3-etherate (11), $NaBH_4$ (12), polyphosphoric acid or (SiO_2) (13), $MgO/POCl_3$ (14), $Yb(OTf)_3$ (15), and Al_2O_3/P_2O_5 under microwave conditions (16). However, many of these methods suffer from drawbacks, such as drastic reaction conditions, cumbersome workup procedures, low yields, and co-occurrence of several side reactions. Therefore, there is still a need to develop new catalytic methods for the synthesis of these biologically active compounds.

Recently, zirconium(IV) chloride has received considerable attention as an efficient Lewis acid catalyst for various organic transformations such as Biginelli's reaction (17), electrophilic amination of activated arenes (18), thioacetylation of acetals, (19) deoxygenation of heterocyclic-*N*-oxides (20), reduction of nitro-compounds (21), and conversion of carbonyl compounds to 1,3-oxathiolanes (22). To continue our interest in zirconium(IV) chloride as a catalyst for novel synthetic methodologies (17, 23), we envisaged its use and effect in the cyclocondensation of ketones with *o*-phenylenediamine.

Results and discussion

In this paper, we wish to present the results of a facile one-pot method for the synthesis of 1,5-benzodiazepines catalysed by $ZrCl_4$,and also to report, for the first time, the unequivocal structure elucidation of the regioisomers formed in this reaction. Typically, 5 mmols of *o*-phenylenediamine were reacted with 10 mmols of ketone in 1,2-dichloroethane under refluxing condition for 30–180 min (Scheme 1). The cyclocondensation is catalyzed by 10 mol% of $ZrCl_4$ to afford the corresponding 1,5-benzodiazepine derivatives in good to excellent yields. The effects of different solvents such as acetonitrile, tetrahydrofuran, ethanol, dichloromethane, and 1,2-dichloroethane on the yield of 1,5-benzodiazepine in presence of 10 mol% of catalyst was studied, and it was observed that 1,2-dichloroethane was the solvent of choice in terms of yield and reaction time. Regarding the optimum quantity of the catalyst, it was found that 10 mol% of $ZrCl_4$ is necessary to promote the reaction. However, no reaction was observed in the absence of the catalyst,

Received 20 September 2006. Accepted 22 February 2007. Published on the NRC Research Press Web site at http://canjchem.nrc.ca on 21 March 2007.

K.S. Reddy, Ch. V. Reddy, M. Mahesh, K.R. Reddy, P.V.K. Raju, and V.V.N. Reddy.[1] Organic Chemistry Division II, Indian Institute of Chemical Technology, Hyderabad 500007, India.

[1]Corresponding author (e-mail: vvnreddy1@rediffmail.com).

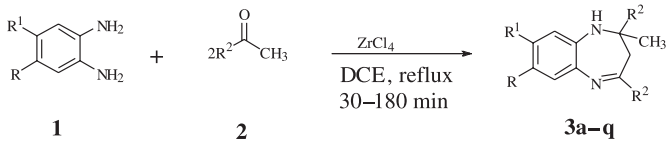
 © 2007 NRC Canada

Table 1. Zirconium(IV) chloride-catalyzed formation of 1,5-benzodiazepines.

Product[a]	R	R^1	R^2	Yield (%)[b]	Time (min)	Mp (°C)[b]
3a	H	H	C_6H_5	90	30	107–108
3b	H	H	4-(Me)–C_6H_4	96	60	88–89
3c	H	H	4-(Cl)–C_6H_4	94	55	133–135
3d	H	H	4-(Br)–C_6H_4	97	50	145–146
3e	H	H	4-(OMe)–C_6H_4	89	65	120–121
3f	H	H	4-(NO_2)–C_6H_4	92	60	132–133
3g	H	H	CH_3	96	30	119–120
3h	H	H	CH_2–CH–$(CH_3)_2$	88	90	117–118
3i	CH_3	CH_3	C_6H_5	92	45	118–120
3j	CH_3	CH_3	4-(NO_2)–C_6H_4	97	60	127–128
3k	CH_3	CH_3	4-(Cl)–C_6H_4	92	45	146–147
3l	CH_3	CH_3	4-(Me)–C_6H_4	95	60	120–122
3m	NO_2	H	C_6H_5	70	180	144–145
3n	NO_2	H	4-(Cl)–C_6H_4	72	180	173–174
3o	NO_2	H	4-(Br)–C_6H_4	80	180	160–162
3p	OCH_3	H	C_6H_5	85	150	120–121
3q	OCH_3	H	4-(Cl)–C_6H_4	85	150	115–118

[a]All products were characterized by ^{1}H NMR, IR, and mass spectroscopy.
[b]Isolated and unoptimized yields, and melting points are uncorrected.

Scheme 1.



1 **2** **3a–q**

even after prolonged reaction time (>18 h), under the present reaction conditions.

Optimizing the reaction conditions, we extended this procedure to a number of 1,5-bezodiazepine derivatives, using $ZrCl_4$ (10 mol%) in 1,2-dichloroethane at reflux temperature. The results summarized in Table 1 indicate the scope and generality of the reaction with respect to the examples described therein. As shown in Table 1, the reaction of acetone with *o*-phenylenediamine in the presence of $ZrCl_4$ afforded 2,2,4-trimethyl-2,3-dihydro-1*H*-benzodiazepine (Table 1, entry 7) in 96% yield. Acetophenone reacted with *o*-phenylenediamine under similar reaction conditions to yield 2-methyl-2,4-diphenyl-2,3-dihydro-1,5-bezodiazepine (Table 1, entry 1) in 90% yield. The cyclocondensation of *o*-phenylenediamine with *para*-substituted acetophenones and aliphatic ketones afforded the corresponding 1,5-benzodiazepine derivatives in good yields (88%–97%), indicating that the substitution on a ketone substrate has little effect on the yield (Table 1, **3a–i**). The cyclocondensation reaction may be proceeding via an intramolecular imine–enamine cyclization, promoted by $ZrCl_4$, as depicted in Scheme 2 (13). It may be presumed that the carbonyl group of the ketone coordinates with $ZrCl_4$, forming a complex **C** (17) for which we have no evidence, yet its formulation seems reasonable. The amine of *o*-phenylenediamine attacks the carbonyl group of the ketone, giving the intermediate dimine **A**. Then, 1,3-shift of the hydrogen attached to the methyl group occurs to form an isomeric enamine **B**, which on cyclization affords the seven-membered ring.

4-Substituted *o*-phenelenediamines were reacted with acetone, as well as acetophenone, to give the corresponding 1,5-benzodiazapine derivatives. Although the formation of 7- or 8-substituted 1,5-benzodiazepines from the corresponding 4-substituted *o*-phenylenediamines (e.g., 4-chloro, 4-nitro, 4-methyl, and 4-benzoyl) and acetone, acetophenone, or cyclohexanone was previously reported, the structure confirmation of the products has not been reported, and there exists ambiguity of the regioisomers (24). Similar to this is the case of the formation of a mixture of regioisomers in the ratio of 60:40, corresponding to 7- and 8- substituted 1,5-benzodiazapine derivatives obtained from 4-chloro and 4-benzoyl *o*-phenolenediamines and acetone (25). At this point, it is noteworthy to mention that the $ZrCl_4$-catalyzed reaction between 4-nitro, 4-methoxy *o*-phenylenediamine and the acetophenone derivative led to the formation of specific regioisomer in good yields (**3m–q**). The formation of regioisomers is in accordance with the mechanism (Scheme 2) proposed by Jung and co-workers (13), in which the intramolecular imine–enamine cyclization is favored by the presence of an electron-withdrawing group (NO_2) *para* to imine moiety, and *para* to enamine moiety in case of an electron-donating group (OCH_3). The intermediate formed in this reaction does not require the activation of amino-functionality, and as a result, the electronic nature of the substituent may not have significant effect on the yield; however, it affected the nature of cyclization, leading to the formation of specific regioisomers. We report detailed structural elucidation of the regioisomers (**3m–q**), using ^{1}H NMR spectroscopic data and the chemical shifts of the diagnostic protons along with the coupling constants, in Table 2 for the first time.

In 2-methyl-7-nitro-2,4-di(4′-chlorophenyl)-2,3-dihydro-1*H*-1,5-benz-odiazepine (**3n**, Fig. 1*a*), the *meta* coupled doublet at δ 8.18 ppm (J = 2.4 Hz) is assigned to a proton (6-H) *ortho* to the imine nitrogen of benzodiazepines, which is in the downfield region compared with the *ortho* coupled doublet at δ 6.76 ppm (9-H) (J = 9.0 Hz), which is *ortho* to the amine nitrogen. The *ortho* and *meta* coupled doublet of doublet at δ 7.89 ppm (J = 9.0 and 2.4 Hz) is assigned to 8-H.

© 2007 NRC Canada

Scheme 2.

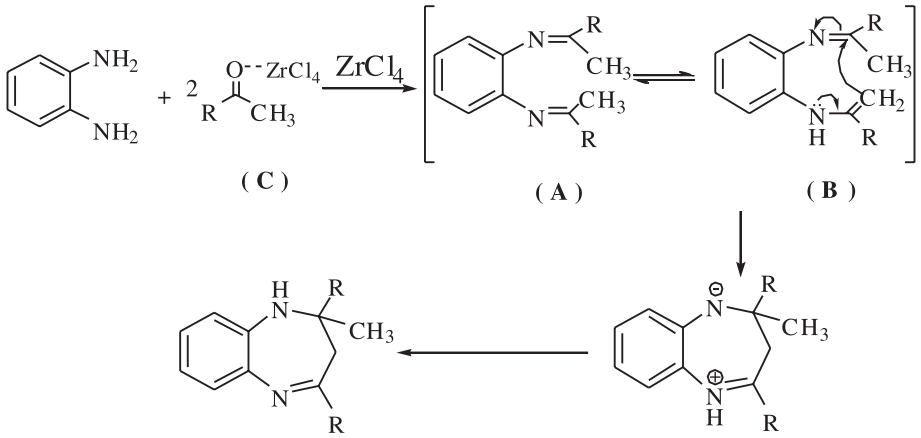


Table 2. Selected ^{1}H NMR chemical shifts of compounds **3m**, **3n**, **3o**, **3p**, **3q**, and **3r**.

Compound	$C_{6\text{-H}}$	$C_{8\text{-H/7-H}}$	$C_{9\text{-H}}$
3m	δ 8.24	δ 7.92	δ 6.76
	d (*J* = 2.5 Hz)	dd (*J* = 8.5 and 2.5 Hz)	d (*J* = 8.4 Hz)
3n	δ 8.18	δ 7.89	δ 6.76
	d (*J* = 2.4 Hz)	dd (*J* = 9.0 and 2.4 Hz)	d (*J* = 9.0 Hz)
3o	δ 8.26	δ 7.95	δ 6.81
	d (*J* = 2.4 Hz)	dd (*J* = 8.9 and 2.4 Hz)	d (*J* = 8.9 Hz)
3p	δ 7.19 d	δ 6.52	δ 6.28
	Merged[a]	dd (*J* = 8.7 and 2.2 Hz)	d (*J* = 2.2 Hz)
3q	δ 7.20 d	δ 6.54	δ 6.26
	Merged[a]	dd (*J* = 8.7 and 2.3 Hz)	d (*J* = 2.3 Hz)
3r (*N*-methyl)	δ 6.90	δ 6.68	δ 6.76
	d (*J* = 9.0 Hz)	dd (*J* = 9.0 and 3.0 Hz)	d (*J* = 3.0 Hz)

[a]Merged with the ab quartet of other aromatic protons.

The same analogy is applicable to 2-methyl-7-nitro-2,4-diphenyl-2,3-dihydro-1*H*-1,5-benzodiazepine (**3m**) and 2-methyl-7-nitro-2,4-di(4′-bromophenyl)-2,3-dihydro-1*H*-1,5-benzodiazepine (**3o**). However, in case of methoxy substituted benzodiazepines, namely 2-methyl-8-methoxy-2,4-diphenyl-2,3-dihydro-1*H*-1,5-benzodiazepine (**3p**) and 2-methyl-8-methoxy-2,4-di(4′-chlorophenyl)-2,3-dihydro-1*H*-1,5-benzodiazepine (**3q**) (Table 1), the *meta* coupled doublet (9-H) at δ 6.28 ppm (*J* = 2.2 Hz) is in the most shielded region, and the *ortho*-coupled proton (6-H) signal is merged with the other aromatic-proton signals in the region of δ 7.1–7.2 ppm. The doublet of doublet at δ 6.52 ppm (7-H) with a coupling constant of 8.7 and 2.2 Hz, respectively, is assigned to *ortho* and *meta* couplings of 6-H and 9-H protons. This clearly indicates that the shielded proton in this derivative is *ortho* to the amine nitrogen. Therefore, structure **3p** has been assigned for the methoxy-substituted benzodiazapine derivative (Fig. 1*b*). This is further confirmed by converting compound **3p** into its *N*-methyl derivative (1,2-dimethyl-2,4-diphenyl-2,3-dihydro-1*H*-1,5-benzodiazepin-8-yl methyl ether (**3r**)) using dimethyl sulfate under phase transfer catalysis (PTC) conditions (26). The ^{1}H NMR spectrum of the methylated compound **3r** (Fig. 1*b*) revealed the presence of a *meta*-coupled doublet at δ 6.76 ppm (*J* = 3.0 Hz), *ortho*-coupled doublet at δ 6.90 ppm (*J* = 9.0 Hz), and doublet of doublet at δ 6.68 ppm (*J* = 9.0 and 3.0 Hz) that are assigned to 9-H, 6-H, and 7-H, respectively.

To the best of our knowledge, 2-methyl-8-methoxy-2,4-di(4′-chlorophenyl)-2,3-dihydro-1*H*-1,5-benzodiazepine (**3q**) is reported for the first time, and the structures of the regioisomers have been unequivocally assigned, based on IR, NMR, and mass spectral data, and finally confirmed by X-ray crystallographic analysis.[2]

In conclusion, the results reveal that $ZrCl_4$ has proved to be an effective catalyst for the synthesis of 2,3-dihydro-1*H*-1,5-benzodiazepines. This protocol offers several advantages, such as selectivity, high yields, shorter reaction times, and simple workup procedure. Moreover, the interesting outcome of the present study is the isolation of the specific regioisomers **3m**–**q** in high yields, and their structures have been unequivocally characterized by spectroscopic data for the first time.

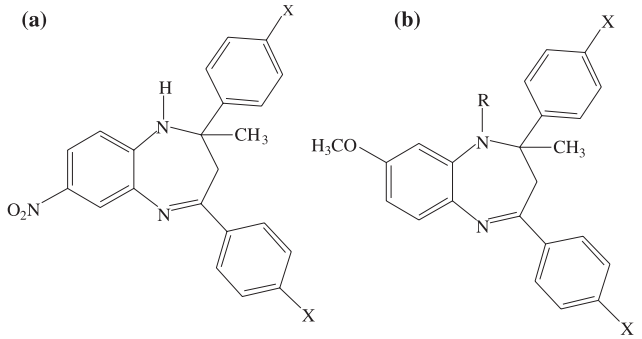
Experimental

NMR, spectra were recorded on Gemini 200, 300, and 400 MHz and Avance 600 spectrometers in $CDCl_3$, using TMS as internal standard. IR spectra were recorded on a

[2]G.Y.S.K. Swamy, K. Ravikumar, V.V.N. Reddy, and K.S. Reddy. Manuscript in preparation.

© 2007 NRC Canada

Fig. 1.



3m: X = H
3n: X = Cl
3o: X = Br

3p: R = X = H
3q: R = H, X = Cl
3r: R = CH_3, X = H

Nicolet 740 FTIR spectrometer, and Mass spectra were recorded on a VG Micro Mass 7070H. The melting points were determined in open glass capillaries on a Metler FP 51 melting point apparatus and are uncorrected. All reactions were carried out using reagent-grade solvents, and the reagents were purchased from local suppliers except $ZrCl_4$, which was purchased from Merck Limited, Mumbai.

General procedure for the $ZrCl_4$-catalyzed synthesis of 1,5-benzodiazepines (3)

A mixture, containing *o*-phenylenediamine (5 mmol), ketone (10 mmol), and $ZrCl_4$ (10 mol%) in 1,2-dichloroethane (15 mL), was refluxed for an appropriate period of time, as mentioned in Table 1. After completion of the reaction, as indicated by TLC, the reaction mixture was cooled to room temperature and washed with water (3 × 10 mL). The organic layer was dried over anhyd. Na_2SO_4, and the solvent was removed under reduced pressure. The crude mixture was purified by column chromatography on silica gel (100–200 mesh), using hexane – ethyl acetate (98:2) as an eluent to afford the pure products.

Spectroscopic data

*2-Methyl-7-nitro-2,4-diphenyl-2,3-dihydro-1*H-*1,5-benzodiazepine (3m)*

Yellow solid; mp 144–145 °C. IR (KBr) (cm^{-1}): 3300, 1651. ^{1}H NMR (200 MHz, $CDCl_3$) δ 1.80 (s, 3H, CH_3), 3.05–3.37 (dd, 2H, CH_2, *J* = 12.6 Hz), 4.40 (br s, 1H, NH, D_2O exchangeable), 6.76 (d, 1H, ArH, *J* = 8.4 Hz), 7.1–7.4 (m, 8H, ArH), 7.6 (d, 2H, ArH, *J* = 6.74 Hz), 7.92 (dd, 1H, ArH, *J* = 8.5 and 2.5 Hz), 8.24 (d, 1H, ArH, *J* = 2.50 Hz). ^{13}C NMR (75 MHz, $CDCl_3$) δ 30.7, 44.2, 69.0, 119.0, 122.3, 125.0, 127.0, 127.4, 128.1, 128.4, 130.0, 134.6, 139.4, 140.1, 144.4, 146.0, 167.2. MS–FAB *m/z* (%): 357 ($[M]^+$, 30), 345 (10), 282 (20), 241 (100), 194 (10), 130 (25), 119 (30), 78 (10), 57 (50). HR-ESIMS: ($[MH]^+$) *m/z* calcd. for $C_{22}H_{20}N_3O_2$: 358.1555; found: 358.1566.

*2-Methyl-7-nitro-2,4-di(4′-chlorophenyl)-2,3-dihydro-1*H-*1,5-benzodiazepine (3n)*

Yellow solid; mp 173–174 °C. IR (KBr) (cm^{-1}): 3500, 1600, 1550, 1300. ^{1}H NMR (200 MHz, $CDCl_3$) δ 1.73 (s, 3H, CH_3), 2.92–3.35 (dd, 2H, CH_2, *J* = 13.6 Hz), 4.43 (br s, 1H, NH, D_2O exchangeable), 6.76 (d, 1H, ArH, *J* = 9.0 Hz), 7.13 (d, 2H, ArH, *J* = 9.2 Hz), 7.18 (d, 2H, ArH, *J* = 8.0 Hz), 7.21 (d, 2H, ArH, *J* = 8.5 Hz), 7.41 (d, 2H, ArH, *J* = 8.2 Hz), 7.89 (dd, 1H, ArH, *J* = 9.0 and 2.4 Hz), 8.18(d, 1H, ArH, *J* = 2.4Hz). ^{13}C NMR (75 MHz, $CDCl_3$) δ 31.1, 43.9, 69.1, 119.2, 122.5, 126.7, 127.4, 128.3, 128.4, 128.6, 133.5, 134.7, 136.7, 137.6, 140.7, 143.9, 144.3, 165.7. MS–FAB *m/z* (%): 426 ($[M + H]^+$, 15), 391 (25), 274 (15), 154 (55), 136 (45), 107 (28), 91 (60), 77 (50), 57 (100). HR-ESIMS: ($[MNa]^+$) *m/z* calcd. for $C_{22}H_{18}N_3O_2Cl_2$: 448.0595; found: 448.0595.

*2-Methyl-7-nitro-2,4-di(4′-bromophenyl)-2,3-dihydro-1*H-*1,5-benzodiazepine (3o)*

Yellow solid; mp 160–162 °C. IR (KBr) (cm^{-1}): 3500, 1500, 1550, 1310. ^{1}H NMR (400 MHz, $CDCl_3$) δ 1.74 (s, 3H, CH_3), 2.94–3.35 (dd, 2H, CH_2, *J* = 13.6 Hz), 4.50 (br s, 1H, NH, D_2O exchangeable), 6.81 (d, 1H, ArH, *J* = 8.9 Hz), 7.2–7.43 (m, 8H, ArH), 7.95 (dd, 1H, ArH, *J* = 8.9 and 2.4 Hz), 8.26 (d, 1H, ArH, *J* = 2.4 Hz). ^{13}C NMR (150 MHz, $CDCl_3$) δ 31.0, 43.9, 69.2, 119.3, 121.7, 122.6, 125.2, 127.1, 127.3, 128.5, 131.5, 131.6, 134.8, 138.1, 140.8, 143.8, 144.8, 165.8. MS–FAB *m/z* (%): 516 ($[MH + 2]^+$, 80), 391 (45), 319 (40), 154 (100), 136 (85). HR-ESIMS: ($[MH]^+$) *m/z* calcd. for $C_{22}H_{18}N_3O_2Br_2$: 513.9765; found: 513.9780.

*2-Methyl-8-methoxy-2,4-diphenyl-2,3-dihydro-1*H-*1,5-benzodiazepine (3p)*

Yellow solid; mp 120–121 °C. IR (KBr) (cm^{-1}): 3350, 2950, 1620, 1490, 1250. ^{1}H NMR (300 MHz, $CDCl_3$) δ 1.74 (s, 3H, CH_3), 2.94–3.15 (dd, 2H, CH_2, *J* = 12.87 Hz), 3.54 (br s, 1H, NH, D_2O exchangeable), 3.80 (s, 3H, OCH_3), 6.28 (d, 1H, ArH, *J* = 2.2 Hz), 6.52 (dd, 1H, ArH, *J* = 8.7 and 2.2 Hz), 7.10–7.25 (m, 5H, ArH), 7.51 (m, 6H, ArH). ^{13}C NMR (75 MHz, $CDCl_3$) δ 30.1, 43.6, 55.4, 71.5, 105.6, 106.7, 125.4, 126.9, 127.0, 128.0, 128.3, 129.3, 130.8, 133.0, 139.5, 140.1, 147.7, 158.2, 165.1. MS–FAB *m/z* (%): 343 ($[M + H]^+$, 100), 224 (85), 209 (20), 154 (40), 136 (50). HR-ESIMS: ($[MH]^+$) *m/z* calcd. for $C_{23}H_{23}N_2O$: 343.1810; found: 343.1818.

*2-Methyl-8-methoxy-2,4-di(4′-chlorophenyl)-2,3-dihydro-1*H-*1,5-benzodiazepine (3q)*

Yellow solid; mp 115–118 °C. IR (KBr) (cm^{-1}): 3350, 3000, 1610, 1490, 1230. ^{1}H NMR (300 MHz, $CDCl_3$) δ 1.72 (s, 3H, CH_3), 2.85–3.11 (dd, 2H, CH_2, *J* = 13.7 Hz), 3.51(br s, 1H, NH, D_2O exchangeable), 3.80 (s, 3H, OCH_3), 6.26 (d, 1H, ArH, *J* = 2.3 Hz), 6.54 (dd, 1H, ArH, *J* = 8.7 and 2.3 Hz), 7.20 (m, 5H, ArH), 7.51 (d, 4H, ArH, *J* = 9.3 Hz). ^{13}C NMR (75 MHz, $CDCl_3$) δ 30.2, 43.3, 55.4, 71.1, 105.6, 107.0, 127.0, 128.0, 128.2, 128.3, 130.9, 132.7, 133.0, 135.6, 138.3, 139.0, 145.8, 158.4, 163.3. MS–FAB *m/z* (%): 411 ($[M + H]^+$, 100), 258 (85), 154 (45), 57 (30). HR-ESIMS: ($[MH]^+$) *m/z* calcd. for $C_{23}H_{21}N_2OCl_2$: 411.1030; found: 411.1029.

Acknowledgements

K.S.R. and K.R.R thank the Director of the Indian Institute of Chemical Technology (IICT) for financial support.

© 2007 NRC Canada

Ch.V.R. and M.M. thank the Council of Scientific and Industrial Research (CSIR), New Delhi, for the awards of fellowship.

References

1. (*a*) R.K. Smalley. *In* Comprehensive organic chemistry. Vol. 4. *Edited by* D. Barton and W.D Ollis. Pergamon, Oxford. 1979. p 600; (*b*) J.K. Landquist. *In* Comprehensive heterocyclic chemistry. Vol. 1. *Edited by* A.R. Katritzky and C.W. Rees. Pergamon, Oxford. 1984. p. 166.
2. L.O. Randall and B. Kappel. *In* Benzodiazepines. *Edited by* S. Garattini, E. Mussini, and L.O. Randall. Ravan Press, New York. 1973. p. 27, and refs. cited therein.
3. R.C. Harris and J.M. Straley. FR Patent 1537757, 30 August 1968.
4. M.C. Aversa, A. Feriazzo, P. Gianneho, and F.H. Kohnke. Synthesis, 230 (1986).
5. A. Chimirri, S. Grasso, R. Ottana, G. Romeo, and M. Zappala. J. Heterocycl. Chem. **27,** 371 (1990).
6. A.M. El-Sayed, H. Abdel-Ghany, and A.M.M. El-Saghier. Synth. Commun. **29**, 3561 (1999).
7. K.V.V.Reddy, P.S. Rao, and D.Ashok. Synth. Commun. **30**, 1825 (2000).
8. K.D. Hargrave, J.R. Proudfoot, K.G. Grozinger, E. Cullen, and S.R. Kapadia. J. Med. Chem. **34**, 2231 (1991).
9. P. Stahlofen and W. Reid. Chem. Ber. **90**, 815 (1957).
10. W. Reid and E. Torinus. Chem. Ber. **92**, 2902 (1959).
11. J.A.L. Herbert and H. Suschitzky. J. Chem. Soc., Perkin Trans. 1, 2657 (1974).
12. H.R. Morales, A. Bulbarela, and R. Contreras. Heterocycles, **24**, 135 (1986).
13. D.I. Jung, T.W. Choi, Y.Y. Kim, I.S. Kim, Y.M. Park, Y.G. Lee, and D.H. Jung. Synth. Commun. **29**, 1941 (1999).
14. M.S. Balkrishna and B.A. Kaboudin. Tetrahedron Lett. **42**, 1127 (2001).
15. M. Curini, F. Epifano, M.C. Marcotullio, and O. Rosati. Tetrahedron Lett. **42**, 3193 (2001).
16. B. Kaboudin and K. Navaee. Heterocycles, **55**, 1443 (2001).
17. Ch.V. Reddy, M. Mahesh, P.V.K. Raju, T.R. Babu, and V.V.N. Reddy. Tetrahedron Lett. **43**, 2657 (2002).
18. R. Lenarsic, M. Kocevar, and S. Polanc. J. Org. Chem. **64**, 2558 (1999).
19. (*a*) H. Firouzabadi, N. Iranpoor, and B. Karimi. Synlett, **3**, 319 (1999); (*b*) H. Firouzabadi, N. Iranpoor, and B. Karimi. Synlett, **3**, 321 (1999).
20. K.P. Chary, G.H. Mohan, and D.S. Iyengar. Chem. Lett. **12**, 1339 (1999).
21. K.P. Chary, S.R. Ram, and D.S. Iyengar. Synlett, **5**, 683 (2000).
22. B. Karimi and H. Seradj. Synlett, **6**, 805 (2000).
23. M. Mahesh, Ch.V. Reddy, K.S. Reddy, P.V.K. Raju, and V.V.N. Reddy. Synth. Commun. **34**, 4089 (2004).
24. (*a*) D.V. Jarikote, S.A. Siddiqui, R. Rajagopal, T. Daniel, R.J. Lahoti, and K.V. Srinivasan. Tetrahedron Lett. **44,** 1835 (2003); (*b*) J.S. Yadav, B.V.S. Reddy, S. Praveenkumar, K. Nagaiah, N. Lingaiah, and P.S. Saiprasad. Synthesis, 901 (2004); (*c*) J.S. Yadav, B.V.S. Reddy, S.P. Kumar, and K. Nagaiah. Synthesis, 480 (2005); (*d*) S.K. De, and R.A. Gibbs. Tetrahedron Lett. **46**, 1811 (2005); (*e*) R. Varala, R. Enugala, S. Nuvula, and S.R. Adapa. Synlett, 7 1009 (2006).
25. M. Pozarentzi, J. Stephanidou-Stephanatou, and C.A. Tsoleridis. Tetrahedron Lett. **43**, 1755 (2002).
26. Ch.V. Reddy, M. Mahesh, P.V.K. Raju, and V.V.N. Reddy. Synth. Commun. **32**, 2797 (2002).

© 2007 NRC Canada

Triazene derivatives of (1,*x*)-diazacycloalkanes. Part VIII. Synthesis and characterization of a series of 1,4-di[2-aryl-1-diazenyl]-2-methylpiperazines[1]

Naomi Hunter, Reid Tingley, Brad Peori, and Keith Vaughan

Abstract: A series of 1,4-di-[2-aryl-1-diazenyl]-2-methylpiperazines (**4a**–**n**) have been synthesized by the reaction of 2-methylpiperazine with 2 equiv. of the appropriate diazonium salt. The products have been characterized by IR and NMR spectroscopy, and the molecular composition has been verified by HR-EIMS, with accurate mass measurement of the molecular ion. The presence of a chiral centre at C_2 of the piperazine ring in the bistriazene **4** creates a multitude of diastereotopic protons in the methylene groups of the piperazine ring, as evidenced by the complexity of the NMR spectra, which nevertheless can be fully assigned in some cases, such as the tolyl- (**4h**) and phenyl- (**4j**) derivatives. These two compounds also show a discrimination between the two *N*-arydiazenyl groups, as evidenced by the doubling of several aromatic-carbon signals in the ^{13}C NMR spectra. The assignment of the proton and carbon signals in **4h** and **4j** has been aided by the use of 2D NMR spectroscopy. A DEPT spectrum of **4j** clearly discriminates the methylene carbons and also indicates the methine carbons of the piperazine ring. COSY spectra provide clear information about the interactions between diastereotopic protons; when these results are combined with the results of HSQC spectroscopy, the proton and carbon signals can be fully correlated, leading to an unequivocal assignment of the proton and carbon atoms of the piperazine ring. The HSQC spectrum of **4j** also gives a complete correlation of the aromatic-proton and -carbon signals. These results compare favorably with the previously reported assignments of proton and carbon signals for triazenes of type **1** and bistriazenes of type **3**.

Key words: triazene, bistriazene, piperazine, 2-methylpiperazine, diastereotopic protons, diazonium coupling, 2D NMR, COSY, DEPT, HSQC.

Résumé : On a effectué la synthèse d'une série de 1,4-di-[2-aryldiaz-2-ényl]-2-méthylpipérazines (**4 a**–**n**) en procédant à la réaction de la 2-méthylpipérazine avec deux équivalents du sel de diazonium approprié. On a caractérisé les produits par spectroscopies IR et RMN et on a vérifié la composition moléculaire par spectrométrie de masse à haute résolution, avec ionisation électronique et mesure précise de la masse de l'ion moléculaire. La présence d'un centre chiral au niveau du C_2 du noyau pipérazine du bistriazène **4** crée une multitude de protons diastéréotopes dans les groupes méthylènes du noyau pipérazine qui sont détectés dans le spectre RMN qu'on a toutefois pu complètement attribuer dans quelques cas, tel ceux des dérivés tolyle (**4h**) et phényle (**4j**). Ces deux composés montrent aussi une discrimination entre les deux groupes *N*-aryldiazényles qui est détectée par le dédoublage de plusieurs signaux de carbones aromatiques dans le spectre RMN du ^{13}C. L'attribution des signaux des protons et de plusieurs signaux de carbones dans les composés **4h** et **4j** a été rendue possible par l'utilisation de la spectroscopie RMN en 2D. Un spectre « DEPT » du composé **4j** permet de distinguer les carbones méthyléniques et permet aussi d'identifier les carbones méthines du noyau pipérazine. Les spectres « COSY » fournissent aussi des informations claires concernant les interactions entre les protons diastéréotopes; quand on combine ces résultats avec les résultats de la spectroscopie « HSQC », on peut établir une corrélation totale des protons et des atomes de carbone qui conduit à une attribution sans équivoque des protons et des atomes de carbone du noyau pipérazine. Le spectre « HSQC » du composé **4j** permet aussi d'avoir une corrélation complète des signaux des protons et des atomes de carbone. Ces résultats se comparent favorablement avec les attributions des signaux des protons et des atomes de carbone rapportés antérieurement pour les triazènes du type **1** et les bistriazènes du type **3**.

Mots-clés : triazène, bistriazène, pipérazine, 2-méthylpipérazine, protons diastéréomères, couplage de diazonium, RMN-2D, « COSY », « DEPT », « HSQC ».

[Traduit par la Rédaction]

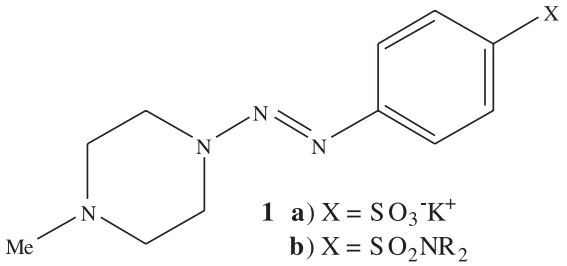
Received 19 September 2006. Accepted 30 January 2007. Published on the NRC Research Press Web site at http://canjchem.nrc.ca on 27 March 2007.

N. Hunter, R. Tingley, B. Peori, and K. Vaughan.[2] Department of Chemistry, Saint Mary's University, Halifax, NS B3M 3X6, Canada.

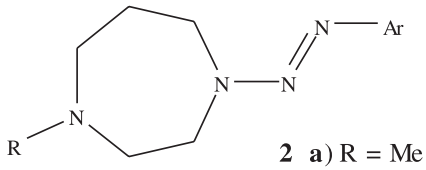
[1]For Part VII in this series, see Can. J. Chem. **84**, 1434 (2006).
[2]Corresponding author (e-mail: keith.vaughan@smu.ca).

 doi:10.1139/V07-013 © 2007 NRC Canada

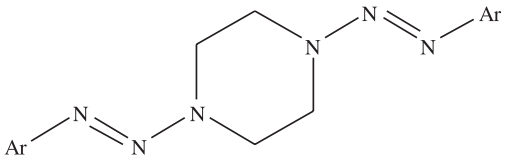
Chart 1.



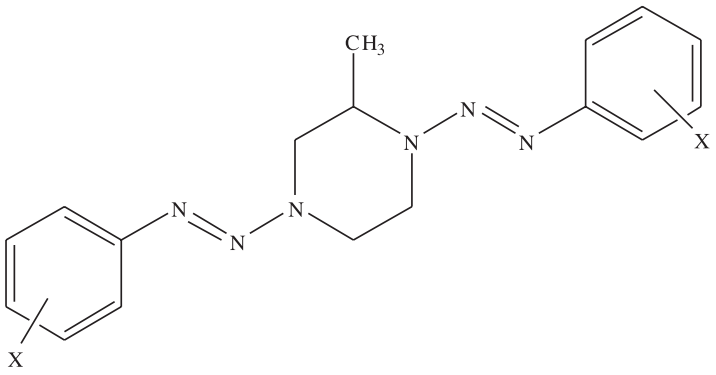
1 **a**) X = $SO_3^-K^+$
b) X = SO_2NR_2
c) X = NO_2



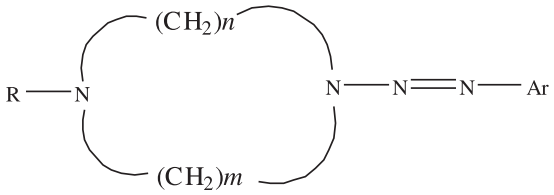
2 **a**) R = Me
b) R = Ar–N=N–



3



4 **a**) X = *p*-CN
b) X = *p*-NO_2
c) X = *p*-CO_2Me
d) X = *p*-CO_2Et
e) X = *p*-$COCH_3$
f) X = *p*-$CONH_2$
g) X = *p*-SO_2NH_2
h) X = *p*-CH_3
i) X = *p*-Br
j) X = H
k) X = *o*-CN
l) X = *o*-NO_2
m) X = *o*-Cl
n) 3-pyridyl



5

Introduction

In Part I of this series (1), the diazonium coupling reaction of 1-methylpiperazine was explored to synthesize the 4-methyl-1-(2-aryldiazen-1-yl-)piperazines (**1**) (see Chart 1). In the process of characterizing these triazenes by NMR spectroscopy, the chemical-shift parameters of the protons and carbons in the piperazine ring were clearly established and verified by some classical 2D NMR work. These data were used to advantage in characterizing the 4-methyl-1-[aryldiazenyl]-homopiperazines (**2a**), which have been described, along with the 1,4-di-(2-aryldiazen-1-yl)diazepanes (**2b**), in Part II of this series (2). The bistriazenes (**2b**) were obtained by the reaction of the homopiperazine with the diazonium salt in a 1:2 molar proportion. This bis(diazotization) strategy was subsequently explored with piperazine itself, and the synthesis of a series of 1,4-di-(2-aryldiazen-1-yl-)piperazines (**3**) was described in Part III of this series (3). The bistriazenes of type **3** were characterized by a range of spectroscopic techniques, and the data were compared with some previously published work (4), in which several of the bis(aryldiazenyl)piperazines had already been described.

The potential biological activity of triazene derivatives of piperazine has been studied by several groups. Butkus and co-workers investigated a series of aminoazobenzene sulfonic acids, such as **1a**, for their potential anti-inflammatory activity (5). A series of sulfonamides **1b** were

© 2007 NRC Canada

prepared by Lalezari and Afgahi (6) as potential anti-tumour agents, and the nitro derivatives **1c** and **3** (Ar = *p*-nitrophenyl) were prepared and investigated for their phytotoxic activity (7).

The work described in this paper is a logical extension of our previous study (3) of the synthesis of the symmetrical bistriazenes of series **3** to the unsymmetrical bistriazene series **4**, in which a methyl substituent is introduced at position 2 of the piperazine ring. In characterizing the series of bistriazenes (**3**), we observed that the eight protons of the piperazine ring occur as a single peak. The equivalence of all eight methylene protons in **3** is a little surprising in view of the potential for variation in chemical shift from either (*i*) axial vs. equatorial proton environment, (*ii*) *syn* or *anti* orientation of the *N*-aryldiazenyl groups, or (*iii*) a combination of both of these. We concluded that the dynamic effects in molecules of type **3** must be occurring faster than the NMR time-frame.

The introduction of asymmetry in the piperazine ring, as in structure **4**, might have some interesting consequences. In principle, the aryldiazenyl groups in **4** are in different environments; an interesting challenge is to see if high-field NMR can resolve these aryl groups. Furthermore, the C_2 carbon in **4** is a stereocenter, creating the situation where the methylene hydrogens at C_3, C_5, and C_6 become diastereotopic. Thus, the resolution and interpretation of the NMR spectra of the bistriazenes of type **4** have the potential of being an interesting and non-trivial exercise. These considerations prompted us to explore the effect of introducing a methyl substituent into the piperazine ring of the 1,4-bis(aryldiazenyl)piperazine system, and this paper reports the synthesis and characterization of a series of 1,4-di[2-aryl-1-diazenyl]-2-methylpiperazines (**4a**–**n**), with an in-depth analysis of the NMR spectra of these novel compounds.

Experimental

All reagents were reagent-grade materials, purchased from Sigma-Aldrich Canada Ltd., and were used without further purification. Melting points were determined on a Fisher–Johns melting-point apparatus and are uncorrected. IR spectra were obtained using Nujol mulls with a Bruker Vector 22 spectrometer. ^{1}H and ^{13}C NMR spectra were obtained using either Bruker 400 MHz and 500 MHz spectrometers at the Atlantic Region Magnetic Resonance Center (ARMRC) at Dalhousie University, Halifax, NS or the ANASAZI 60 MHz EFT spectrometer at Saint Mary's University. Chemical shifts were recorded in $CDCl_3$ or d_6-DMSO solutions at 20 °C (as specified), and are relative to TMS as internal standard. Accurate mass measurements were obtained on a CEC 21–110B mass spectrometer, operated at a mass resolution of 8000 (10% valley) by computer-controlled peak matching to appropriate PFK reference ions. Spectra were obtained using electron ionization at 70 V and a source temperature of 175 °C, with samples being introduced by means of a heatable quartz probe. The standard deviation of mass measurement is ±0.0008 amu, which is an average of 3.6 ppm over the mass range of 100 to 300 amu.

1,4-Di-[2-aryl-1-diazenyl]-2-methylpiperazines (4a–n)

General procedure

The aromatic primary amine (0.01 mol) was dissolved in 12 mL of 3 mol/L hydrochloric acid by heating, if necessary, and the resulting solution was cooled in an ice/salt bath to 0 °C. The solution was diazotized with a solution of sodium nitrite (0.76 g) in water (3 mL) while maintaining the temperature below 5 °C, and then stirred for a further 0.5 h in the cold. A solution of 2-methylpiperazine (0.5 g), dissolved in water (10 mL), was added slowly to the mixture. After stirring for a further 0.5 h, the mixture was further neutralized with saturated sodium carbonate solution, and then stirred until precipitation was deemed to be complete (1–3 h). The solid product was filtered under suction, dried, and recrystallized from an appropriate solvent to give compounds **4a**–**n**.

1,4-Di-[2-(p-cyanophenyl)-1-diazenyl]-2-methylpiperazine (4a)

Yield 46%; yellow prisms; from DMSO; mp 187–189 °C. IR (nujol, cm^{-1}) ν_{max}: 2221 (CN), 849 (OOP). ^{1}H NMR (60 MHz, $CDCl_3$) δ: 1.46 (3H, d, J = 6.7 Hz, methyl at C_2), 4.12 (6H, br m, ring CH_2's), 4.50 (1H, br m, CH at C_2), 7.52 (4H, d, J = 8.6 Hz, arom.), 7.64 (4H, d, J = 8.7 Hz, arom.). HR-MS *m/z*: calcd. for $C_{19}H_{18}N_8$: 358.1654; found: 358.1649 (EI).

1,4-Di-[2-(p-nitrophenyl)-1-diazenyl]-2-methylpiperazine (4b)

Yield 37%; red prisms; from DMSO; mp 200 °C. IR (nujol, cm^{-1}) ν_{max}: 1509 (NO_2), 1377 (NO_2), 849 (OOP). ^{1}H NMR (60 MHz, $CDCl_3$) δ: 1.49 (3H, d, J = 6.5 Hz, methyl at C_2), 4.16 (6H, m, ring CH_2's), 4.48 (1H, m, CH at C_2), 7.54 (4H, d, J = 8.8 Hz, arom.), 8.23 (4H, d, J = 9.1 Hz, arom.). HR-MS *m/z*: calcd. for $C_{17}H_{18}N_8O_4$: 398.1451; found: 398.1455 (EI).

Methyl 4-[2-(4-{2-[4-(methoxycarbonyl)phenyl]-1-diazenyl}-3-methylpiperazino)-1-diazenyl]benzoate (4c)

Yield 90%; pale-yellow needles; from ethanol; mp 146–148 °C. IR (nujol, cm^{-1}) ν_{max}: 1716 (C=O), 859 (OOP). ^{1}H NMR (500 MHz, $CDCl_3$) δ: 1.46 (3H, d, J = 6.5 Hz, methyl at C_2), 3.91 (6H, s, O–Me × 2), 4.05 (2H, br, H_b × 2), 4.12 (3H, br m, H_d, H_e, and H_f), 4.25 (1H, br, H_c), 4.61 (1H, m, CH at C_2, H_a), 7.50 (4H, dd, J = 3.5 and 8.5 Hz, arom.), 8.04 (4H, dd, J = 1.0 and 8.5 Hz, arom.). HR-MS *m/z*: calcd. for $C_{21}H_{24}N_6O_4$: 424.1859; found: 424.1849 (EI).

Ethyl 4-[2-(4-{2-[4-(ethoxycarbonyl)phenyl]-1-diazenyl}-3-methylpiperazino)-1-diazenyl]benzoate (4d)

yield 30%; yellow needles; from ethanol; mp 103–104 °C. IR (nujol, cm^{-1}) ν_{max}: 1704 (C=O), 857 (OOP). ^{1}H NMR (60 MHz, $CDCl_3$) δ: 1.39 (9H, m, methyl at C_2 + methyl protons of the ester groups), 4.07 (6H, m, ring CH_2's), 4.37 (5H, m, CH at C_2 + methylene protons of the ester groups), 7.49 (4H, d, J = 9 Hz, arom.), 8.06 (4H, d, J = 9 Hz, arom.). HR-MS *m/z*: calcd. for $C_{23}H_{28}N_6O_4$: 452.2172; found: 452.2169 (EI).

© 2007 NRC Canada

1,4-Di-[2-(p-acetylphenyl)-1-diazenyl]-2-methylpiperazine (4e)

Yield 26%; amorphous brown powder; from ethanol – ethyl acetate; mp 184 °C. IR (nujol, cm^{-1}) ν_{max}: 1672 (C=O), 846 (OOP). ^1H NMR (60 MHz, $CDCl_3$) δ: 1.41 (3H, d, J = 6.4 Hz, methyl at C_2), 2.53 (6H, s, acetyl Me), 4.04 (6H, m, ring CH_2's), 4.40 (1H, m, CH at C_2), 7.45 (4H, d, J = 8.5 Hz, arom.), 7.93 (4H, d, J = 8.7 Hz, arom.). HR-MS *m/z*: calcd. for $C_{21}H_{24}N_6O_2$: 358.1654; found: 358.1649 (EI).

1,4-Di-[2-(p-carboxamidophenyl)-1-diazenyl]-2-methylpiperazine (4f)

Yield 49%; yellow prisms; from ethanol–DMSO; mp 267–270 °C. IR (nujol, cm^{-1}) ν_{max}: 3383 (NH), 3191 (NH), 1653 (C=O), 856 (OOP). ^1H NMR (60 MHz, d_6-DMSO) δ: 1.34 (3H, d, J = 6.4 Hz, methyl at C_2), 4.10 (6H, br m, ring CH_2's), 4.57 (1H, br m, CH at C_2), 7.44 (4H, d, J = 8.3 Hz, arom.), 7.92 (4H, d, J = 8.5 Hz, arom.). HR-MS *m/z* (%): 247 ($[M - ArN_2]^+$, 1), 121 ($[Ar]^+$, 100), 105 ($[C_6H_4CHO]^+$, 12.5).

1,4-Di-[2-(p-sulfonamidophenyl)-1-diazenyl]-2-methylpiperazine (4g)

Yield 83%; brown prisms; from ethanol; mp 187–190 °C. IR (nujol, cm^{-1}) ν_{max}: 3336 (NH), 3227 (NH), 839 (OOP). ^1H NMR (60 MHz, d_6-DMSO) δ: 1.37 (3H, d, J = 6.4 Hz, methyl at C_2), 4.12 (6H, br, ring CH_2's), 4.60 (1H, br m, CH at C_2), 7.31 (4H, br, NH_2 × 2), 7.51 (4H, d, J = 8.7 Hz, arom.), 7.84 (4H, d, J = 8.6 Hz, arom.). HR-MS *m/z* (%): 283 ($[M - ArN_2]^+$, 13), 184 ($[ArN_2]^+$, 2), 157 ($[C_6H_4SO_2NH]^+$, 61), 77 ($[C_6H_5]^+$, 100).

1,4-Di-[2-(p-tolyl)-1-diazenyl]-2-methylpiperazine (4h)

Yield 55%; deep-pink prisms; from ethanol–water; mp 78–80 °C. IR (nujol, cm^{-1}) ν_{max}: 821 (OOP). ^1H NMR (500 MHz, $CDCl_3$) δ: 1.42 (3H, d, J = 6.7 Hz, methyl at C_2), 2.35 (6H, s, tolyl Me), 3.77 (1H, m, H_c), 3.92 (2H, d, J = 4.7 Hz, H_b), 3.96 (1H, m, H_f), 4.04 (1H, m, H_e), 4.13 (1H, m, H_d), 4.45 (1H, br m, H_a), 7.16 (4H, d, J = 8.1 Hz, arom.), 7.36 (4H, dd, J = 2.1 and 8.3 Hz, arom.). ^{13}C NMR (125.8 MHz, $CDCl_3$) δ: 15.95 (Me at C_2), 21.1 (tolyl Me), 42.3, 45.7, 53.6, 120.6/120.7, 129.5, 136.1/136.2, 147.9/148.1. HR-MS *m/z*: calcd. for $C_{19}H_{24}N_6$: 336.2062; found: 336.2071 (EI).

1,4-Di-[2-(p-bromophenyl)-1-diazenyl]-2-methylpiperazine (4i)

Yield 90%; small white prisms; from ethanol; mp 129–131 °C. IR (nujol, cm^{-1}) ν_{max}: 829 (OOP). ^1H NMR (500 MHz, $CDCl_3$) δ: 1.43 (3H, d, J = 6.5 Hz, methyl at C_2), 3.81 (1H, br m, H_c), 3.96 (2H, two overlapping broad singlets, H_b), 4.01 (1H, t, J = 5.3 Hz, H_f), 4.07 (1H, septet, J = 4.3 Hz, H_e), 4.17 (1H, br m, H_d), 4.51 (1H, br, CH at C_2), 7.34 (4H, dd, J = 3.5 and 8.5 Hz, arom.), 7.47 (4H, dd, J = 1.5 and 8.5 Hz, arom.). HR-MS *m/z*: calcd. for $C_{17}H_{18}N_6Br_2$: 463.9959; found: 463.9970 (EI).

1,4-Di-[2-(phenyl)-1-diazenyl]-2-methylpiperazine (4j)

Yield 84%; pale-yellow prisms; from hexanes; mp 54–57 °C. IR (nujol, cm^{-1}) ν_{max}: 762 and 691 (OOP). ^1H NMR (500 MHz, $CDCl_3$) δ: 1.44 (3H, d, J = 6.7 Hz, methyl at C_2), 3.81 (1H, m, H_c), 3.96 (2H, d, J = 4.5 Hz, H_b), 4.00 (1H, m, H_f), 4.08 (1H, m, H_e), 4.17 (1H, m, H_d), 4.51 (1H, br m, CH at C_2), 7.20 (2H, m, arom.), 7.36 (4H, t, J = 7.5 Hz, arom.), 7.46 (4H, d, J = 8.4 Hz, arom.). ^{13}C NMR (125.8 MHz, 323 K, $CDCl_3$) δ: 16.0 (Me at C_2), 42.5 (CH_2), 45.2 (CH_2), 53.0 (CH_2), 53.8 (CH), 120.9, 126.4/126.5, 128.9, 150.3/150.5. HR-MS *m/z*: calcd. for $C_{17}H_{20}N_6$: 308.1749; found: 308.1750 (EI).

1,4-Di-[2-(o-cyanophenyl)-1-diazenyl]-2-methylpiperazine (4k)

Yield 71%; pale-orange wafers; from ethanol; mp 130–131 °C. IR (nujol, cm^{-1}) ν_{max}: 2223 (CN), 767 and 722 (OOP). ^1H NMR (400 MHz, $CDCl_3$) δ: 1.50 (3H, br, methyl at C_2), 4.07 (2H, br, ring CH_2), 4.23 (4H, br m, ring CH_2's), 4.45 (1H, br m, CH at C_2), 7.23 (2H, t, J = 7.4 Hz, arom.), 7.53 (2H, t, J = 7.8 Hz), 7.60 (2H, t, J = 8.5 Hz, arom.), 7.64 (2H, d, J = 7.7 Hz, arom.). ^{13}C NMR (100.6 MHz, $CDCl_3$) δ: 16.0 (vbr, Me at C_2), 44.0, 50.0, 56.0, 108.1 (CN), 117.6/117.7, 125.9, 126.0, 133.2, 152.2, 152.5 (arom.). HR-MS *m/z*: calcd. for $C_{19}H_{18}N_8$: 358.1654; found: 358.1648 (EI).

1,4-Di-[2-(o-nitrophenyl)-1-diazenyl]-2-methylpiperazine (4l)

Yield 68%; yellow prisms; from ethanol, mp 99–100 °C. IR (nujol, cm^{-1}) ν_{max}: 1528 (NO_2), 1377 (NO_2), 854 (OOP). ^1H NMR (400 MHz, $CDCl_3$) δ: 1.44 (3H, br, methyl at C_2), 4.09 (6H, br m, ring CH_2's), 4.45 (1H, vbr, CH at C_2), 7.24–7.30 (2H, m, arom.), 7.49–7.54 (4H, m, arom.), 7.70–7.73 (2H, dd, J = 3.9 and 8.6 Hz, arom.). ^{13}C NMR (100.6 MHz, $CDCl_3$) δ: 16.0 (w, Me at C_2), 119.8/120.0, 123.9, 125.8/125.9, 132.3/132.4, 143.1/143.3, 145.2. HR-MS *m/z*: calcd. for $C_{17}H_{18}N_8O_4$: 398.1451; found: 398.1441 (EI).

1,4-Di-[2-(o-chlorophenyl)-1-diazenyl]-2-methylpiperazine (4m)

Yield 53%; yellow needles; from water, mp 87–88 °C. IR (nujol, cm^{-1}) ν_{max}: 721 (OOP). ^1H NMR (500 MHz, $CDCl_3$) δ: 1.46 (3H, d, J = 6.5 Hz, methyl at C_2), 3.91 (1H, br, H_b), 4.04 (2H, br, H_e and H_b'), 4.13 (2H, m, H_c and H_d), 4.28 (1H, br, H_f), 4.61 (1H, br, CH at C_2), 7.12 (2H, tt, J = 1.8 and 7.7 Hz, arom.), 7.23 (2H, tt, J = 1.8 and 7.7 Hz), 7.41 (2H, dd, J = 1.5 and 8.0 Hz, arom.), 7.45 (2H, dt, J = 1.5 and 8.1 Hz, arom.). ^{13}C NMR (125.77 MHz, $CDCl_3$) δ: 15.9 (w, Me at C_2), 118.7, 126.9/127.0, 127.13/127.15, 129.8/129.9, 130.2, 146.5/146.7. HR-MS *m/z*: calcd. for $C_{17}H_{18}N_6Cl_2$: 376.0970; found: 376.0982 (EI).

1,4-Di-[2-(3-pyridyl)-1-diazenyl]-2-methylpiperazine (4n)

Yield 57%; oil. IR (nujol, cm^{-1}) ν_{max}: 702 and 798 (OOP). ^1H NMR (60 MHz, $CDCl_3$) δ: 1.45 (3H, d, J = 6.5 Hz, methyl at C_2), 4.07 (6H, m, ring CH_2's), 4.50 (1H, m, CH at C_2), 7.2–7.5 (2H, m, arom.), 7.7–7.95 (2H, m, arom.), 8.43 (2H, dd, J = 1.6 and 4.7 Hz, arom.), 8.74 (2H, dd, J = 0.9 and 2.5 Hz, arom.).

Results and discussion

The target molecules, 1,4-di-[2-(3-aryl)-1-diazenyl]-2-methylpiperazine (**4a**–**n**), were synthesized by reacting 1 equiv. of 2-methylpiperazine with 2 equiv. of the appropri-

© 2007 NRC Canada

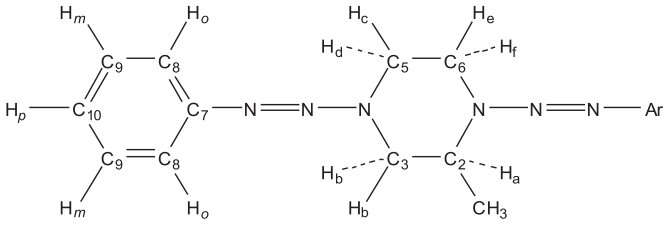
ate diazonium salt. The products are stable, crystalline solids, with the exception of the 3-pyridyl derivative (**4n**), which is an oil. The yields, which are variable in the range from poor (26%) to excellent (98%), depend on the nature and position of the aryl substituent. The yield is generally lower for electron-withdrawing substituents, but is higher if the substituent is in the *ortho* position, e.g., compare **4k** with **4a**. The products were first characterized by IR spectroscopy to confirm the presence of the aryl substituent, as indicated by the detection of bands from either carbonyl, nitrile, nitro, or NH groups, and the OOP bending vibration, characteristic of the substitution pattern. The molecular composition of each compound was established by HR-EI mass spectrometry with accurate mass measurement of the molecular ion, except for the cases of compounds **4f**, **4g**, and **4n**, which did not show molecular ions in the mass spectra. However, the mass spectrum of the amide **4f** contained peaks corresponding to fragments including the $[M - ArN_2]^+$ fragment at *m*/*z* 247. The analogous fragment is observed at *m*/*z* 283 in the mass spectrum of the sulfonamide **4g**.

Supporting evidence for the structures of the compounds **4a**–**n** was obtained from ^{1}H NMR analysis, which proved to be as complex and challenging as we could have expected. The aromatic protons give rise to the predictable pattern of an AA′BB′ system in the *p*-disubstituted benzenes (**4a**–**i**) or the complex pattern of an *o*-substituted benzene (**4k**–**m**), an unsubstituted benzene (**4j**), or a 3-pyridyl ring (**4n**). In most cases, the difference in the aryl groups, arising from the presence of the C_2 methyl substituents, is not detectable; the proton spectra give the appearance of indistinguishable aryl groups, and in many instances, the ^{13}C NMR spectra contain a single set of signals. However, several ^{13}C NMR spectra show doubling of many of the carbon signals, which we interpret as resolving the carbon signals of the two aryl groups. In the unsubstituted phenyl derivative (**4j**), two of the carbon signals are doubled, whereas in the *p*-tolyl compound (**4h**), three of the four carbon signals are doubled. In the *o*-cyanophenyl compound (**4k**), there is some doubling of the carbon signals, but in the *o*-nitrophenyl derivative, at least four of the six carbon signals are doubled. A similar observation is made in the ^{13}C NMR spectrum of the *o*-chlorophenyl analogue (**4m**).

The 2-methyl substituent on the piperazine ring consistently gives rise to a three-proton doublet in the range of 1.3–1.5 ppm, with a coupling constant of ~6.5 Hz, arising from the splitting by the adjacent CH proton at C_2, which itself is clearly observed in all spectra at 4.4–4.6 ppm, either as a complex multiplet or a broad hump. The resolution of the signals of the six methylene hydrogen atoms of the piperazine ring is variable, depending on the nature of the substituent in the phenyl ring. Those compounds with a strong electron-withdrawing group (**4a**–**g**, **4k**, **4l**, and **4n**) afford a proton spectrum with almost no resolution of the methylene protons, and these spectra show a broad six-proton multiplet at ~4.1 ppm. In compounds **4c** and **4m**, the methylene protons are partially resolved, whereas compounds **4h**, **4i**, and **4j** show complete resolution.

The ^{1}H NMR spectrum of the *p*-tolyl derivative **4h** also shows some details (for the key to the proton and carbon labels in this compound, see Fig. 1). The aromatic protons are clearly resolved. A six-proton singlet at 2.35 ppm is readily

Fig. 1. The key to the proton and carbon labels in **4h**.



assigned to the protons of the tolyl methyl groups. The doublet of the C_2 methyl is clearly resolved at 1.42 ppm, and H_a at C_2 is observed as a broad multiplet at 4.45 ppm. Four of the ring methylene hydrogens are observed as multiplets at 3.77, 3.96, 4.04, and 4.13 ppm. The remaining two methylene protons appear as two lines at 3.91 and 3.92 ppm. In the ^{13}C NMR spectrum of **4h**, the methyl carbon attached to C_2 is observed at 16.0 ppm, compared with the tolyl methyl carbon at 21.7 ppm. Three of the four carbons of the piperazine ring are observed at 42.3, 45.7, and 53.6 ppm. The assignment of these signals to specific protons and carbons of the piperazine ring is facilitated by 2D NMR.

The COSY spectrum of compound **4h** is reproduced in Fig. 2, which shows that the protons at 3.77 and 4.13 ppm are stongly coupled together, indicating that these protons are attached to the same carbon atom. Other proton–proton interactions are observed between 3.96 and 4.04 ppm, 3.96 with 3.77 ppm, and 4.45 with both 3.92 and 3.77 ppm. The final piece of the puzzle, with respect to the assignment of the protons in **4h**, is the HSQC spectrum shown in Fig. 3. First, the proton signal of H_a at 4.45 ppm correlates with the carbon signal at 53.6 ppm, which is assigned to C_2. Second, the 3.96 and 4.04 ppm proton signals, assigned to H_e and H_f, respectively, correlate with the carbon signal at 42.3 ppm, which we thereby assign to C_6. The H_c and H_d protons at 3.77 and 4.13 ppm, respectively, correlate with the C_5 carbon signal at 45.7 ppm. The final piece of information in Fig. 3 is a bonus, which is the correlation of the 3.91–3.92 ppm proton signals with a carbon signal at 53.0, which is very clear in the HSQC spectrum but was not picked out from the ^{13}C NMR spectrum of **4h**. This carbon signal must, therefore, be assigned to C_3, and the 3.91–3.92 signals are assigned to the H_b protons. Thus, a complete assignment of the proton and carbon signals of compound **4h** has been achieved.

Further evidence for these NMR correlations is provided by the series of NMR spectra obtained from the phenyl derivative **4j**. Figure 4 shows the ^{1}H NMR spectrum of **4j**. The details of resolution of the five aromatic protons of the phenyl ring are remarkable. The signals from the piperazine ring protons are equally impressive and very similar to those of the *p*-tolyl derivative (**4h**) in the range of 3.75–4.50 ppm. The H_c signal at 3.81 ppm has an apparent multiplicity of a septet, but in reality there are eight lines, i.e., a doublet of doublets of doublets, because of the coupling of the H_c proton to protons H_d, H_e, and H_f, with the two central lines overlapping. The signal of H_e at 4.08 ppm has a similar septet appearance; it is coupled to H_c, H_d, and H_f. Figure 5 shows stacked spectra of a VT NMR experiment in the range of 3.7–4.7 ppm for compound **4j**. The resolution of the piperazine ring protons disappears at low temperature, indi-

© 2007 NRC Canada

Fig. 2. COSY NMR spectrum of 1,4-di-[2-(*p*-tolyl)-1-diazenyl]-2-methylpiperazine (**4h**) in $CDCl_3$.

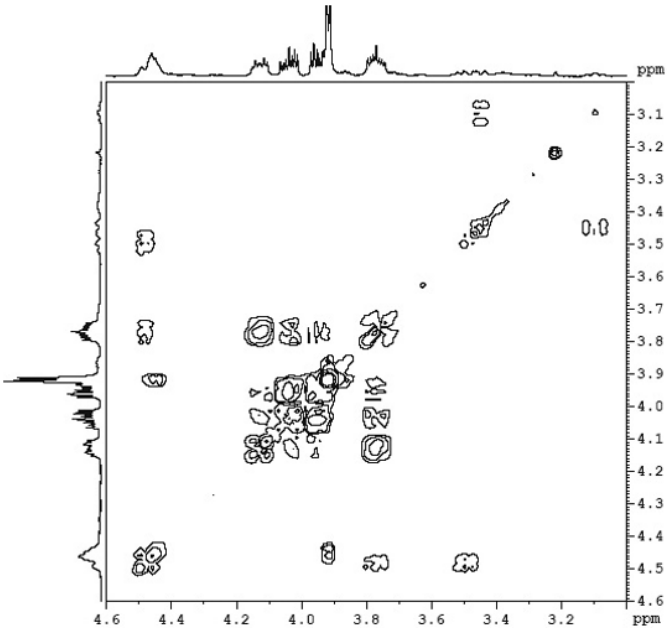


Fig. 3. HSQC NMR spectrum of 1,4-di-[2-(*p*-tolyl)-1-diazenyl]-2-methylpiperazine (**4h**) in $CDCl_3$.

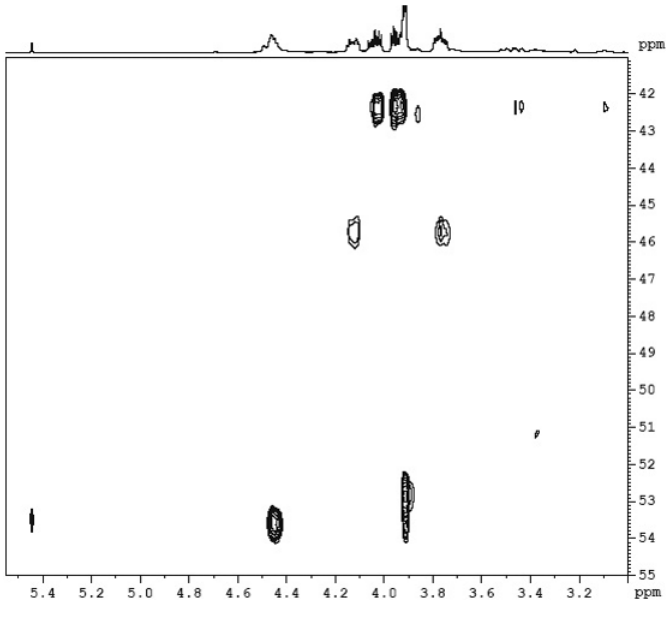
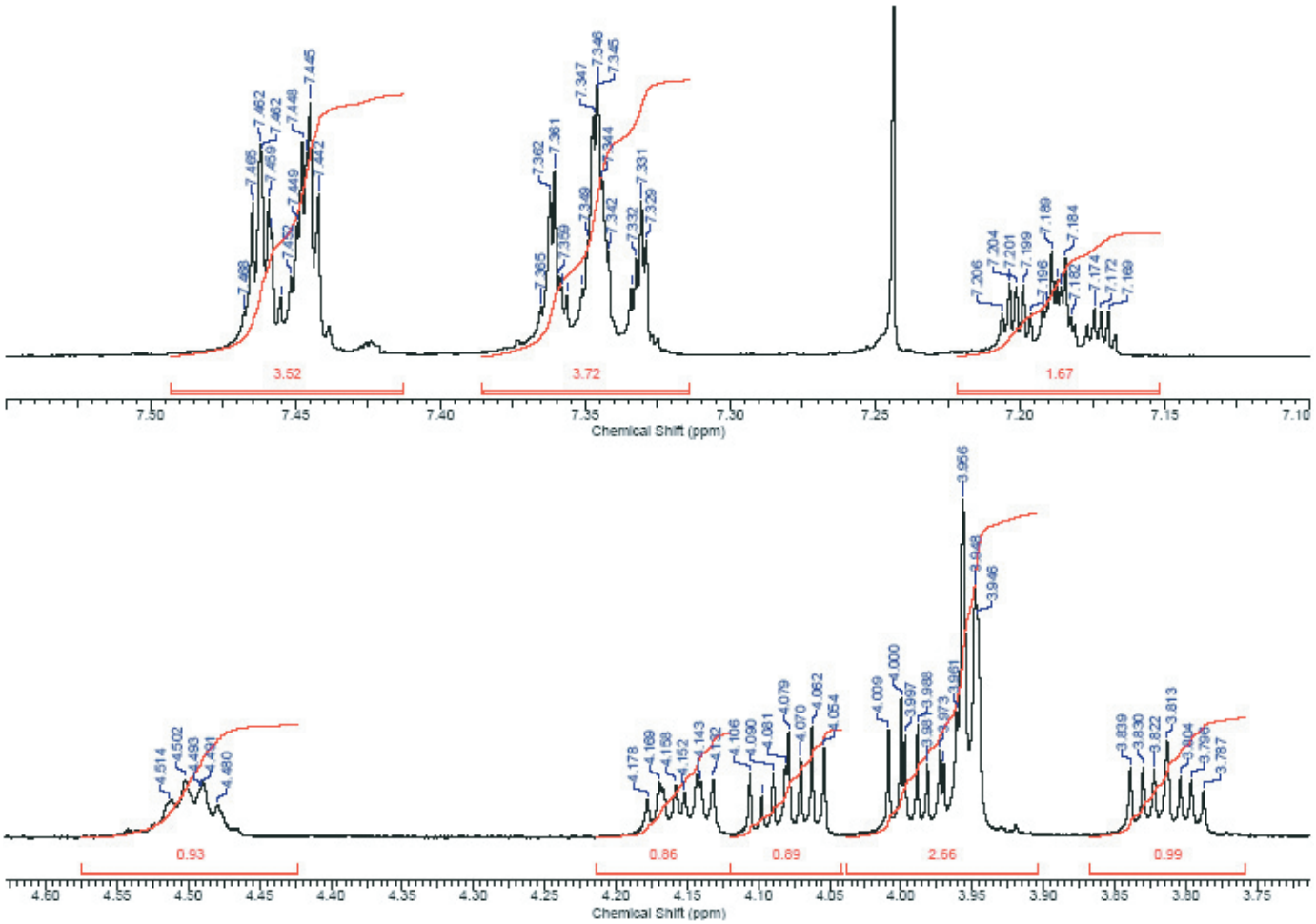


Fig. 4. ^1H NMR spectrum of 1,4-di-[2-(phenyl)-1-diazenyl]-2-methylpiperazine (**4j**) in $CDCl_3$ at 323 K.



© 2007 NRC Canada

Fig. 5. Stacked VT ^{1}H NMR spectra of 1,4-di-[2-(phenyl)-1-diazenyl]-2-methylpiperazine (**4j**) in $CDCl_3$.

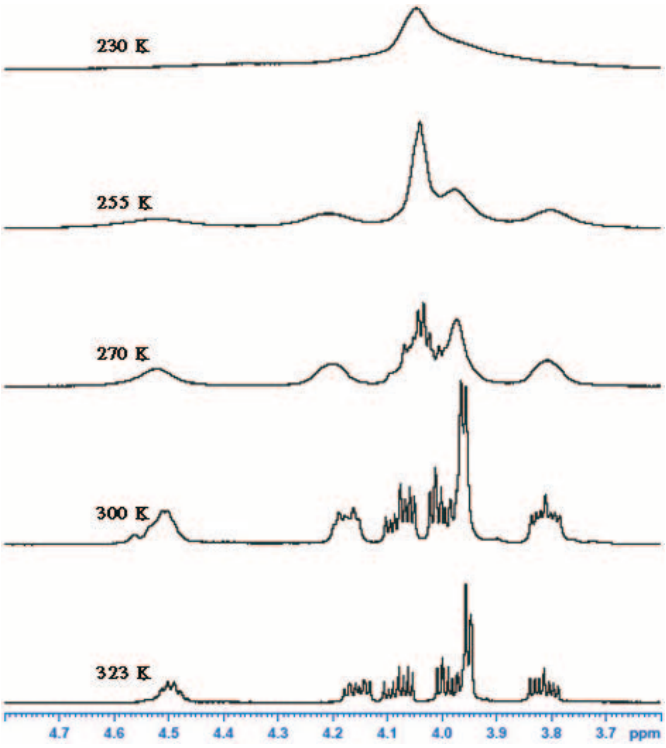


Fig. 6. HSQC NMR spectrum of 1,4-di-[2-(phenyl)-1-diazenyl]-2-methylpiperazine (**4j**) in $CDCl_3$ at 323 K.

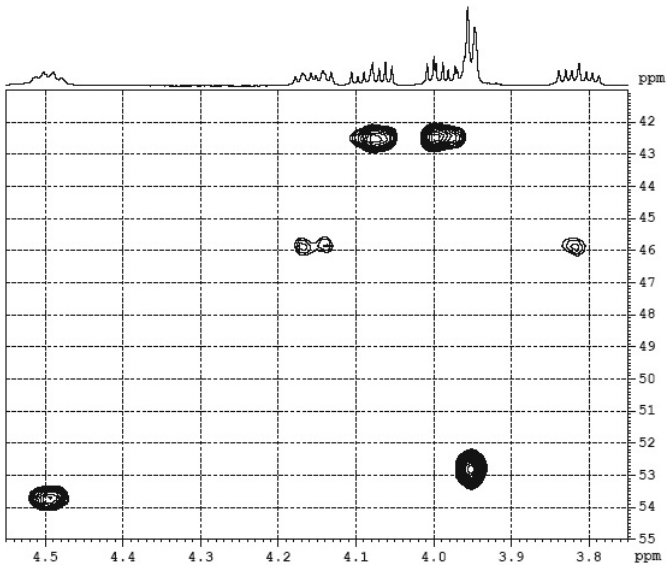
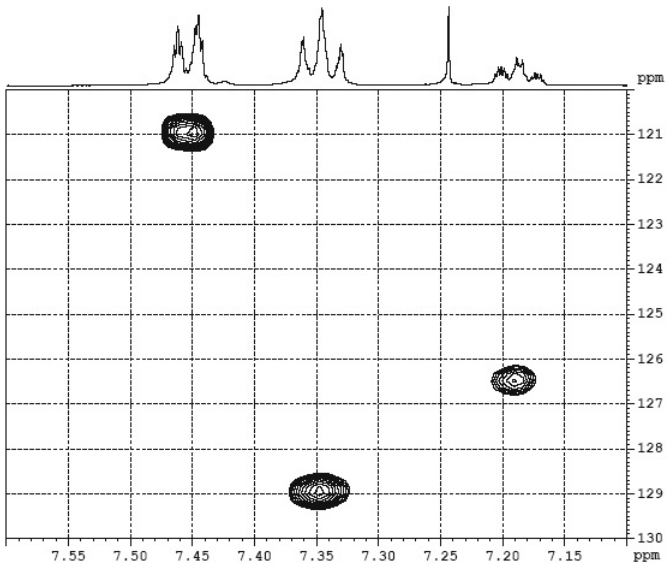


Fig. 7. The aromatic region of the HSQC NMR spectrum of 1,4-di-[2-(phenyl)-1-diazenyl]-2-methylpiperazine (**4j**) in $CDCl_3$ at 323 K.



cating that the various dynamic equilibria are occurring very quickly at ambient temperature. Moreover, it would appear that the broadening of the signals as the temperature is lowered is due to the freezing out of the conformational equilibria of the piperazine ring. The DEPT ^{13}C NMR spectrum of **4j** shows that the signal at 53.8 ppm is a methine carbon (C_2), and those at 42.5 and 53.0 ppm are methylene carbons. The HSQC spectrum of the piperazine ring proton region of **4j**, shown in Fig. 6, provides unequivocal assignment of the protons and carbon atoms in that compound. The 4.00 and 4.08 ppm signals are assigned to H_e and H_f, attached to the 42.5 ppm carbon (C_6), respectively. The 3.81 and 4.17 ppm signals are assigned to H_c and H_d, which are attached to the 45.9 ppm carbon (C_5), respectively, whereas the 4.51 ppm signal is assigned to the methine proton H_a, attached to C_2 (53.8 ppm). The remaining proton signal at 3.96 ppm is assigned to H_b, attached to C_3 (53.0 ppm). The final piece of the puzzle is the HSQC spectrum of the aromatic region of **4j** (Fig. 7), which shows the correlation between the aromatic proton signals and the carbon signals (Fig. 1). Based on the integration, the one-proton signal at 7.20 ppm is assigned to the *para* proton, H_p; the HSQC evidence shows that this proton is bonded to the 126.4 ppm carbon (C_{10}). The 7.36 ppm proton signal is a two-proton triplet, so this is assigned to the *meta* hydrogens, H_m, which correlates with the 128.9 ppm signal of C_9. The *ortho* hydrogens must, therefore, be assigned to the two-proton doublet at 7.46 ppm, which correlates with the 120.9 ppm carbon signal of C_8. This leaves the 150.3 ppm carbon signal to be assigned to the *ipso* carbon (C_7).

Finally, it is necessary to compare these results and conclusions with the previously observed and assigned NMR parameters for the triazenes of types **1** (1) and **3** (3). In the symmetrical bistriazenes of type **3**, the methylene groups of the piperazine ring give rise to a proton signal at ~4.1 ppm, which compares with the chemical shift assigned to the methylene protons in **4a**–**n** in the range of 3.8–4.1 ppm. The methylene carbon signals in **3** occur at ~46–47 ppm, compared with the observed signal at ~46 ppm, assigned to the C_5 carbon of compounds **4j** and **4h**. The analogous carbon in the piperazine ring of the compounds of type **1** occurs at ~47 ppm, and the analogous methylene protons of structure **1** give rise to proton signals at ~3.9 ppm. So, there is considerable agreement in the NMR parameters among these compounds, but the bottom line is the extraordinary degree of

© 2007 NRC Canada

complexity in the spectra of compounds of series **4** because of the introduction of a chiral centre at C_2.

Conclusion

This paper is part VIII in a series that describes the synthesis of a variety of triazenes and bistriazenes of the general classification, 1-aryldiazenyl-(1,*x*)-diazacycloalkanes, described by the general structure **5** (see Chart 1), where $m = 1$ or 2 and $n = 2–5$. Previously, we reported new triazenes derived from piperazine ($m = n = 2$) (1, 3), homopiperazine ($m = 2$, $n = 3$) (2), imidazolidine ($m = 1$, $n = 2$) (8), and hexahydropyrimidine ($m = 1$, $n = 3$) (9). The new piperazines of series **4** fit to the general structure **5**, where $m = 2$ and $n = 2$. Future work in this field of chemistry will endeavour to further extend the family of 1,4-di-(2-aryl-1-diazenyl)piperazines by preparing derivatives with multiple substituents in the piperazine ring.

Acknowledgements

The authors are grateful to the Natural Sciences and Engineering Research Council of Canada (NSERC) for a Discovery Grant to the principal author (KV) and an Undergraduate Summer Research Award (2004) to Naomi Hunter. We are grateful to the Faculty of Graduate Studies and Research at Saint Mary's University for a Summer Research Award (2004). We are also grateful to the Atlantic Region Magnetic Resonance Centre (ARMRC) at Dalhousie University for providing NMR spectra and to Dalhousie University for providing mass spectral data. In particular, we would like to thank Dr. Bob Berno for assistance with the interpretation of the NMR spectral data and Mr. Xiao Feng for assistance with mass spectra.

References

1. V.R. Little and K. Vaughan. Can. J. Chem. **82**, 1294 (2004)
2. S.L. Moser and K. Vaughan. Can. J. Chem. **82**, 1725 (2004)
3. V.R. Little, R. Tingley, and K. Vaughan. Can. J. Chem. **83**, 471 (2005)
4. E. Yamarates, A. Disli, and Y. Yildirir. Org. Prep. Proc. Int. **31**, 429 (1999)
5. M. Kąþemëkaitë, Z. Talaikytë, G. Niaura and E. Butkus. Molecules, **7**, 706 (2002)
6. I. Lalezari and F. Afgahi. J. Pharm. Sci. **64**, 698 (1975).
7. M. Mazza, G. Pagani, G. Calderara, and L. Vicarini. Farmaco Ed. Sc. **28**, 846 (1973).
8. J.F. Glister and K. Vaughan. J. Heterocycl. Chem. **43**, 217 (2006)
9. S.L. Moser, R. Church, M.B. Peori, and K. Vaughan. Can. J. Chem. **83**, 1071 (2005).

© 2007 NRC Canada

Silica-supported $ZnCl_2$ — A highly active and reusable heterogeneous catalyst for the one-pot synthesis of dihydropyrimidinones–thiones

Raman Gupta, Monika Gupta, Satya Paul, and Rajive Gupta

Abstract: A novel silica-supported zinc chloride catalyst was prepared and investigated for the Biginelli reaction. The key features of the catalyst include rapid reaction with 100% conversion of aldehyde, good catalyst recyclability, and high stability under the reaction conditions (passes hot filtration test successfully). A low catalyst loading (12 mol% of $ZnCl_2$) was required to achieve a quantitative reaction. Other catalysts such as SiO_2–$AlCl_2$, SiO_2–$AlCl_2$–$ZnCl_2$ were also prepared and their activity was compared with SiO_2–$ZnCl_2$ for the Biginelli reaction.

Key words: silica gel, zinc chloride, Biginelli compounds, heterogeneous catalysis, reusability.

Résumé : On a préparé un nouveau catalyseur de chlorure de zinc supporté par du gel de silice et on a étudié son utilité dans la réaction de Biginelli. Le catalyseur est caractérisé par une vitesse de réaction rapide avec une conversion de l'aldéhyde à 100%, une bonne facilité de récupération du catalyseur et une grande stabilité dans les conditions de la réaction puisqu'il passe avec succès le test de la filtration à chaud. La charge de catalyseur nécessaire pour obtenir une réaction quantitative est faible (12 moles% de $ZnCl_2$) est faible. On a aussi préparé d'autres catalyseurs, tel le SiO_2–$AlCl_2$, SiO_2–$AlCl_2$–$ZnCl_2$ et on a comparé leur activité avec celle du SiO_2–$ZnCl_2$ pour la réaction de Biginelli.

Mots-clés : gel de silice, chlorure de zinc, composés de Biginelli, catalyse hétérogène, possibilité de réutilisation.

[Traduit par la Rédaction]

Introduction

Green chemistry, the design of chemical products and processes that reduce or eliminate the use and generation of hazardous substances (1), is an overreaching approach that is applicable to all aspects of chemistry. From feedstock to solvents, synthesis, and processing, green chemistry actively seeks ways to produce materials in a way that is more benign to human health and the environment (2). The area of catalysis is sometimes referred to as a "fundamental pillar" of green chemistry (3).

The development of heterogeneous catalysts for fine chemical synthesis has become a major area of research recently, as the potential advantages of these materials (simplified recovery and reusability and the potential for incorporation in continuous reactors and microreactors) over homogeneous systems can make a major impact on the environmental performance of a synthesis (3, 4). The majority of these novel catalysts are based on silicas, primarily since silica displays many advantageous properties such as excellent stability (chemical and thermal), high surface area, good accessibility, and catalytic materials can be robustly anchored onto its surface to provide catalytic centres (5).

Received 13 October 2006. Accepted 23 February 2007. Published on the NRC Research Press Web site at http://canjchem.nrc.ca on 21 March 2007.

R. Gupta, M. Gupta, S. Paul,[1] R. Gupta. Department of Chemistry, University of Jammu, Jammu 180 006, India.

[1]Corresponding author (e-mail: paul7@rediffmail.com).

Zinc chloride, an inexpensive and easily available Lewis acid catalyst, has been widely used in organic synthesis. However, it suffers from the serious drawback of being highly hygroscopic in nature so that it always needs to be fused prior to use and requires highly anhydrous conditions; it also produces exogenous wastes. These issues make the work-up process cumbersome.

Pyrimidinones and their derivatives are medicinally important as calcium channel blockers and also are antiviral, antibacterial, antihypertensive, and α-1a-antagonists (6). The betzelladine alkaloids containing the dihydropyrimidine core unit are particularly notable, as they were recently found to be potent HIV gp-120-CD_4 inhibitors (7).

The Biginelli reaction, which was discovered more than a century ago (8), is one of the most important reactions in the synthesis of dihydropyrimidinones (DHPMs). The classical Biginelli reaction of an aldehyde, β-ketoester, and urea or thiourea requires strongly acidic conditions. Low to moderate yields are usually obtained, in particular when substituted aromatic or aliphatic aldehydes are employed. Recently, many methods for preparing DHPMs have been developed, and the Biginelli reaction has gained particular importance for ongoing research programs (9). However, many of these methods have drawbacks such as long reaction times, low product yields, harsh reaction conditions, the use of stiochiometric reagents, difficulties in work-up, the use of toxic and inflammable solvents, and incompatibility with other functional groups in the molecules. Therefore, there is a need to develop a heterogeneous catalyst for the synthesis of Biginelli compounds that is mild, reusable, eas-

 doi:10.1139/V07-018 © 2007 NRC Canada

ily separable, compatible with acid sensitive functional groups, and cost-effective.

Keeping in view the biological importance of Biginelli compounds and that of heterogeneous catalysis in academia and industry, we wish to report here the application of heterogeneous catalysis to the synthesis of Biginelli compounds using reusable silica-supported zinc chloride (12 mol% of Zn as determined by atomic absorption spectrophotometer). Recently, $ZnCl_2$ has been reported for the synthesis of Biginelli compounds (10).

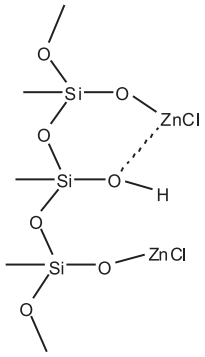
Results and discussion

Silica-supported zinc chloride was prepared by refluxing $ZnCl_2$ (3 g) with activated K100 silica gel (10 g) in sodium dried toluene for 10 h; at this temperature, some of the $ZnCl_2$ may react with the surface hydroxyl groups to create highly acidic species chemically bonded to the support. After separation of the catalyst by filtration under reduced pressure, it was dried at 110 °C for 12 h and stored in a desiccator. It could be used for several months. The proposed structure of the catalyst in which $ZnCl_2$ reacted with the surface hydroxyl groups of the silica gel is shown in Fig. 1. The other catalysts, SiO_2–$AlCl_2$ (11) (anhydr. $AlCl_3$ 3 g, SiO_2 10 g) and SiO_2–$AlCl_2$–$ZnCl_2$ ($AlCl_3$ 1.5 g, $ZnCl_2$ 1.5 g, SiO_2 10 g) were prepared by a similar procedure and stored in a desiccator. The stability of these catalysts was determined by thermogravimetric analysis (TGA). For SiO_2–$ZnCl_2$, the initial weight loss at 80 °C followed by 95-150 °C and 285-310 °C may be due to the loss of residual solvent and HCl, which may have formed during the reaction of $ZnCl_2$ with silica gel. Up to 310 °C, there is no possibility of loss of physiosorbed and chemisorbed $ZnCl_2$ from the surface of silica gel, so it is safe to carry out the reaction at 80 °C.

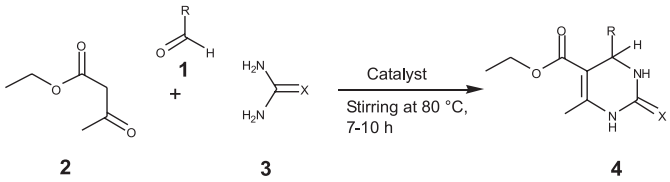
To optimize the reaction conditions, the reaction of 4-methoxybenzaldehyde, ethyl acetoacetate, and urea was selected as the model to examine the effects of catalyst (5–20 mol%), different solvents (methylene chloride, toluene, and acetonitrile), and reagents at different temperatures (RT, 50, 80, and 100 °C). The reactions were monitored by TLC and all yields reported in Tables 1 and 2 are isolated yields. The best conditions employ 0.12:1:1:1 mole ratios of catalyst (12 mol% of Zn, 0.2 g), 4-methoxybenzaldehyde, ethyl acetoacetate, and urea at 80 °C for 7 h using acetonitrile as the solvent.

Using optimized conditions, the reactions of various aromatic–heterocyclic aldehydes, ethyl acetoacetate, and urea or thiourea were investigated (Scheme 1). It was found that all the reactions proceeded smoothly to give the corresponding 3,4-dihydropyrimidin-2-(1*H*)-ones–thiones in high yields (Table 1). Cinnamaldehyde, which showed poor yield in the absence of catalyst and 81% yield in the presence of very expensive lanthanide triflate (12), gave the corresponding pyrimidinones–thiones **4g** and **4p** in 85% and 87% isolated yields. Both aromatic aldehydes bearing electron-donating groups such as 4-OMe (**4b**, 92%) and electron-withdrawing groups such as 4-NO_2 (**4d**, 91%) gave excellent yields. More importantly, 2-furfuraldehyde, which normally gives low yield of products (9*c*, 13) afforded the desired products in 86% (**4f**) and 82% (**4o**) yields in 8.5 and 8 h, respectively. 2-

Figure 1. Probable structure of covalently anchored silica-supported zinc chloride.



Scheme 1.



Chloro-3-formylquinolines gave low yield of products (**4i** 20%, **4r** 32%). The mildness of the procedure makes this procedure very selective as the chlorine atoms in **4h**, **4i**, **4q**, and **4r** remain unaffected under the reaction conditions. The results are summarized in Table 1, which clearly indicates the generality and scope of the reaction with respect to various aromatic, heterocyclic, and unsaturated aldehydes.

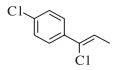
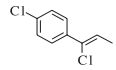
The activity of the catalyst SiO_2–$ZnCl_2$ was also compared with unsupported anhydr. $ZnCl_2$ (0.0408 g, 12 mol%), $AlCl_3$ (0.0399 g, 12 mol%), and other silica supported catalysts SiO_2–$AlCl_2$ (0.185 g, 12 mol% of Al) and SiO_2–$AlCl_2$–$ZnCl_2$ (0.2 g, 5.5 mol% of Zn, 7.5 mol% of Al) taking 4-methoxybenzaldehyde, ethyl acetoacetate, and urea to give 3,4-dihydropyrimidinone **4b** as the model reaction, using acetonitrile as solvent and 80 °C as the reaction temperature. The results are summarized in Table 2. Among all catalysts, SiO_2–$ZnCl_2$ was found to be the most active, stable, and reusable catalyst.

To verify whether the reaction was catalyzed by SiO_2-$ZnCl_2$ or by the silica gel used for preparing the catalyst, we carried out the reaction (in the case of product **4b**) using activated silica gel (0.2 g) under similar conditions as with SiO_2-$ZnCl_2$. It was found that **4b** was formed in 23% yield (based on ^{1}H NMR) in 7 h. This clearly indicates that the reaction was catalyzed by SiO_2-$ZnCl_2$.

When using a supported metal catalyst, two important issues need to be addressed to qualify this to be a purely heterogeneous catalyst. One is the possibility that some active metal migrates from the solid to the liquid phase and that this leached metal salt would become responsible for a significant part of the catalytic activity. To rule out the contribution of the homogeneous catalysis in the results shown in Table 1, the reaction of 4-methoxybenzaldehyde, ethyl acetoacetate, and urea was carried out in the presence of SiO_2–$ZnCl_2$ until the conversion was 30% (^{1}H NMR yield, after 1 h), and at that point the solid was filtered off at the

© 2007 NRC Canada

Table 1. Silica-supported zinc chloride catalyzed synthesis of 3,4-dihydropyrimidinones–thiones (**4a**–**4r**) at 80 °C using acetonitrile as solvent.

Compound	R	X	Time (h)	Yield (%)	mp, lit. mp
4a	C_6H_5	O	8.5	90	207 to 208, 209 to 210 (10)
4b	4-$MeOC_6H_4$	O	7	92	203 to 204, 201 to 202 (14)
4c	4-ClC_6H_4	O	7	87	215 to 216, 216 to 217 (10)
4d	4-$NO_2C_6H_4$	O	7.5	91	208 to 209, 211–213 (10)
4e	4-HO-3-$MeOC_6H_3$	O	9	92	232 to 233, 231 to 232 (14)
4f	2-Furfuryl	O	8.5	86	205 to 206, 208–210 (10)
4g	Ph-CH=CH	O	9	85	241 to 242, 245 to 246 (10)
4h[a]		O	8.5	70	159–161
4i[a]		O	10	20	>230, >265 (15)
4j	C_6H_5	S	8	83	193 to 194, 191–193 (16)
4k	4-$MeOC_6H_4$	S	8.5	88	151 to 152, 150–153 (16)
4l	4-ClC_6H_4	S	8.5	87	213 to 214, 207 to 208 (17)
4m	4-$NO_2C_6H_4$	S	8	88	205–207
4n	4-HO-3-$MeOC_6H_3$	S	10	83	149–151, 147–149 (18)
4o	2-Furfuryl	S	8	82	186–188, 183 (dec, 18)
4p	Ph-CH=CH	S	10.5	87	242 to 243, 243–245 (18)
4q[a]		S	9.2	72	165–167
4r[a]		S	10	32	217–219

[a]In case of compounds **4h**, **4i**, **4q**, and **4r** catalysts, 16 mol% was used.
[b]Yield refers to the isolated yield from three experimental runs.

Table 2. Effect of various catalysts in the synthesis of 3,4-dihydropyrimidinone (**4b**) from 4-methoxybenzaldehyde, ethyl acetoacetate, and urea at 80 °C using acetonitrile as solvent.

Catalyst	Time (h)	Yield (%)[a]
No catalyst	7	No reaction
$ZnCl_2$	7	55
$AlCl_3$	7	20
SiO_2–$ZnCl_2$	7	92
SiO_2–$AlCl_2$[b]	7	35
SiO_2–$ZnCl_2$–$AlCl_2$[b]	7	65

[a]Isolated yield of the purified products based on separation by column chromatography.
[b]Catalysts SiO_2–$AlCl_2$ and SiO_2–$ZnCl_2$–$AlCl_2$ were prepared by the similar procedure given in the experimental section for SiO_2–$ZnCl_2$.

reaction temperature. The liquid was then transferred to another flask and the reaction was continued for the remaining time, but no further significant formation of product was observed. This indicates that no active species was present in the supernatant and that the observed catalysis is purely heterogeneous. The second important point concerning heterogeneous catalysis is the deactivation and reusability of the catalyst. To test this, a series of 4 consecutive runs of the reaction of 4-methoxybenzaldehyde, ethyl acetoacetate, and urea with SiO_2–$ZnCl_2$ was carried out (1st use: 92% isolated yield after 7 h; 2nd use: 85% isolated yield after 8.5 h; 3rd use: 78% isolated yield after 12 h; 4th use: 67% isolated yield after 16 h). These results demonstrate that there is a decrease in the activity of the catalyst after every use. This may be due to either the deactivation of active centres resulting from complexation with both starting materials and products or microscopic changes in the structure of the catalyst. However, AAS analysis after the 4th use indicates that there is no change in the amount of Zn from the fresh to the 4th use of the catalyst.

Experimental

General

Silica gel (K100, 0.063–0.200 mm) was purchased from Merck (Germany) and anhydrous zinc chloride was purchased from Merck (India) and fused prior to use. All melting points were determined on a Perfit melting point apparatus and are uncorrected. ^{1}H NMR spectra were registered on a Bruker DPX-200 NMR spectrometer (200 MHz) in $CDCl_3$ – $CDCl_3$ + DMSO-d_6 using tetramethylsilane as internal standard. The IR spectra were recorded using KBr disc on PerkinElmer FTIR spectrophotometer. Mass spectral data were recorded on Jeol JMS D-300 mass spectrometer at 70 ev. Thermal analysis was carried out on DTG-60 Shimadzu thermal analyzer with heating rate of 10 °C/sec and the amount of metal content was determined on a double beam atomic absorption spectrophotometer GBC 932 AB (manufactured in Australia). The catalyst was stirred in dil. HCl for 10 h and the resulting filtrate was subjected to atomic absorption spectrophotometric analysis. Elemental analysis was carried out on Leco-CHNS-932 elemental analyzer manufactured by Leco corporation (USA).

Preparation of activated silica

K100 silica gel (10 g) was added to a round-bottomed

© 2007 NRC Canada

flask (250 mL) containing a 1:1 mixture of conc. HCl and distilled water (100 mL). The reaction mixture was refluxed in an oil bath for 24 h. On cooling, silica gel was filtered off and washed with excess distilled water until the washings were neutral. It was dried in an oven at 110 °C for 15 h.

General procedure for the preparation of silica-supported zinc chloride

To a mixture of anhydrous zinc chloride (3 g) and activated silica (10g, K100) in a round-bottomed flask (100 mL), sodium dried toluene (60 mL) was added and the reaction mixture was refluxed for 10 h. SiO_2–$ZnCl_2$ was obtained as a free-flowing powder after filteration under reduced pressure and dried at 110 °C for 12 h. It was stored in a desiccator and could be used for several months without loss of activity.

General procedure for the preparation of 3,4-dihydropyrimidinones–thiones

To a mixture of aldehyde **1** (2.5 mmol), ethyl acetoacetate **2** (2.5 mmol), and urea or thiourea **3** (2.5 mmol) in a round-bottomed flask (100 mL), acetonitrile (15 mL) was added. The reaction mixture was stirred at RT for 5 min and then the catalyst SiO_2–$ZnCl_2$ (200 mg, 12 mol% of Zn) was added and the stirring was continued at 80 °C in an oil bath for an appropriate time (Table 1). After completion of the reaction (monitored by TLC), the reaction mixture was filtered off. The product was obtained after removal of the solvent under reduced pressure and crystallization from EtOAc – petroleum ether. The residue was washed with acetonitrile followed by methylene chloride and dried at 110 °C for 5 h. It could be used further for carrying out the reaction.

The structures of the products were confirmed by IR, ^{1}H NMR, and mass spectral data, and comparison with authentic samples prepared according to the literature methods.

Spectral data of selected compounds

Ethyl 6-methyl-4-(4-methoxyphenyl)-3,4-dihydropyrimidin-2(1H)-one-5-carboxylate (4b)

IR (KBr, cm^{-1}) ν_{max}: 3390, 3243, 3106, 2958, 1706, 1651, 1278, 1088. ^{1}H NMR (DMSO-d_6) δ 1.01–1.20 (t, 3H, J = 7 Hz, CH_2CH_3), 2.30 (s, 3H, CH_3), 3.80 (s, 3H, OCH_3), 3.90–4.20 (q, 2H, J = 7 Hz, CH_2CH_3), 5.60 (s, 1H, C4-H), 6.80–6.90 (d, 2H, J = 7.2 Hz, ArH), 7.15–7.25 (d, 2H, J = 7.2 Hz, ArH), 7.65 (bs, 1H, NH), 9.17 (bs, 1H, NH). m/z: 290 (M^+).

Ethyl 6-methyl-4-(4-nitrophenyl)-3,4-dihydropyrimidin-2(1H)-one-5-carboxylate (4d)

IR (KBr, cm^{-1}) ν_{max}: 3449, 3258, 3184, 3015, 1686, 1648, 1582. ^{1}H NMR (DMSO-d_6) δ 1.05–1.20 (t, 3H, J = 7 Hz, CH_2CH_3), 2.35 (s, 3H, CH_3), 4.00– 4.20 (q, 2H, J = 7 Hz, CH_2CH_3), 5.45 (s, 1H, C4-H), 7.40– 7.60 (d, 2H, J = 7.2 Hz, ArH), 8.10– 8.25 (d, 2H, J = 7.2 Hz, ArH), 7.69 (bs, 1H, NH), 9.27 (bs, 1H, NH). m/z: 305 (M^+).

Ethyl 4-[2-chloro-2-(4-chlorophenyl)vinyl]-6-methyl-3,4-dihydropyrimidin-2(1H)-one-5-carboxylate (4h)

IR (KBr, cm^{-1}) ν_{max}: 3408, 3318, 3232, 2986, 1702, 1652, 1560, 1453. ^{1}H NMR ($CDCl_3$) δ 1.12–1.22 (t, 3H, J = 7 Hz, CH_2CH_3), 2.34 (s, 3H, CH_3), 4.10–4.23 (q, 2H, J = 7.1 Hz, CH_2CH_3), 5.43 (d, 1H, C4-H), 6.15 (d, 1H, CH=), 7.47 (d, 2H, ArH), 7.95 (d, 2H, ArH), 8.02 (bs, 1H, NH), 9.42 (bs, 1H, NH). m/z: 355 (M^+), 358 (M+2). Anal. calcd. for $C_{16}H_{16}Cl_2N_2O_3$: C 54.10, H 4.54, N 7.88; found: C 54.07, H 4.51, N 7.86.

Ethyl 4-(2-chloro-3-quinolinyl)-6-methyl-3,4-dihydropyrimidin-2(1H)-one-5-carboxylate (4i)

IR (KBr, cm^{-1}) ν_{max}: 3438, 3312, 3227, 2973, 1704, 1648, 1562, 1446. ^{1}H NMR (DMSO-d_6) δ 0.95–1.15 (t, 3H, J = 7.2 Hz, CH_2CH_3), 2.36 (s, 3H, CH_3), 3.95–4.15 (q, 2H, J = 7.2 Hz, CH_2CH_3), 5.70 (s, 1H, C4-H), 7.60–7.90 (m, 4H, ArH), 8.04 (s, 1H, ArH), 8.30 (bs, 1H, NH), 9.35 (bs, 1H, NH). m/z: 344 (M^+).

Ethyl 6-methyl-4-phenyl-3,4-dihydropyrimidin-2(1H)-thione-5-carboxylate (4j)

IR (KBr, cm^{-1}) ν_{max}: 3412, 3312, 3174, 3096, 2967, 1667, 1610, 1575. ^{1}H NMR (DMSO-d_6) δ 1.02–1.18 (t, 3H, J = 7.1 Hz, CH_2CH_3), 2.32 (s, 3H, CH_3), 4.02–4.21 (q, 2H, J = 7.1 Hz, CH_2CH_3), 5.50 (s, 1H, C4-H), 7.15–7.35 (m, 5H, ArH), 8.90 (bs, 1H, NH), 9.95 (bs, 1H, NH). m/z: 276 (M^+).

Ethyl 6-methyl-4-(4-nitrophenyl)-3,4-dihydropyrimidin-2(1H)-thione-5-carboxylate (4m)

IR (KBr, cm^{-1}) ν_{max}: 3429, 3218, 3142, 3018, 1693, 1558. ^{1}H NMR (DMSO-d_6) δ 1.10–1.22 (t, 3H, J = 7.2 Hz, CH_2CH_3), 2.38 (s, 3H, CH_3), 4.07–4.23 (q, 2H, J = 7.1 Hz, CH_2CH_3), 5.61 (s, 1H, C4-H), 7.43–7.64 (d, 2H, ArH), 8.14–8.30 (d, 2H, ArH), 8.3 (bs, 1H, NH), 9.63 (bs, 1H, NH). m/z: 321 (M^+). Anal. calcd. for $C_{14}H_{15}N_3O_4S$: C 52.32, H 4.70, N 13.07, S 9.97; found: C 52.29, H 4.68, N 13.05, S 9.94.

Ethyl 4-[2-chloro-2-(4-chlorophenyl)vinyl]-6-methyl-3,4-dihydropyrimidin-2(1H)-thione-5-carboxylate (4q)

IR (KBr, cm^{-1}) ν_{max}: 3422, 3311, 3218, 2996, 1658, 1556, 1445. ^{1}H NMR ($CDCl_3$) δ 1.08–1.17 (t, 3H, J = 7.1 Hz, CH_2CH_3), 2.39 (s, 3H, CH_3), 4.07–4.18 (q, 2H, J = 7.2 Hz, CH_2CH_3), 5.52 (d, 1H, C4-H), 6.21 (d, 1H, CH=), 7.54 (d, 2H, ArH), 8.04 (d, 2H, ArH), 8.22 (bs, 1H, NH), 9.53 (bs, 1H, NH). m/z: 371 (M^+), 374 (M + 2). Anal. calcd. for $C_{16}H_{16}Cl_2N_2O_2S$: C 51.76, H 4.34, N 7.54, S 8.63; found: C 51.73, H 4.31, N 7.52, S 8.59.

Ethyl 4-(2-chloro-3-quinolinyl)-6-methyl-3,4-dihydropyrimidin-2(1H)-thione-5-carboxylate (4r)

IR (KBr, cm^{-1}) ν_{max}: 3423, 3343, 3232, 2978, 1678, 1560, 1460. ^{1}H NMR (DMSO-d_6) δ 1.05–1.23 (t, 3H, J = 7.2 Hz, CH_2CH_3), 2.41 (s, 3H, CH_3), 3.98–4.21 (q, 2H, J = 7.0 Hz, CH_2CH_3), 5.73 (s, 1H, C4-H), 7.63–7.90 (m, 4H, ArH), 8.08 (s, 1H, ArH), 8.43 (bs, 1H, NH), 9.55 (bs, 1H, NH). m/z: 361 (M^+), 363 (M + 2). Anal. calcd. for $C_{17}H_{16}ClN_3O_2S$: C 56.42, H 4.45, N 11.61, S 8.86; found: C 56.39, H 4.41, N 11.60, S 8.84.

Conclusion

In conclusion, we have developed a mild, simple, cost-effective, and green procedure for the synthesis of dihydropyrimidinones using reusable SiO_2–$ZnCl_2$ under het-

© 2007 NRC Canada

erogeneous catalysis conditions. Moreover, the mild reaction conditions, high yield of products, ease of work-up, compatibility with various functional groups, and the ecologically clean procedure, will make the present method a useful and important addition to the current methodologies for the Biginelli synthesis.

Acknowledgement

One of the authors (MG) thanks the Council of Scientific and Industrial Research (CSIR), New Delhi, for awarding Senior Research Fellowship (SRF).

References

1. P.T. Anastas, L.G. Heine, and T.C. Williamson. Introduction to green chemical syntheses and processes. American Chemical Society, Washington, DC. 2000. Chap. 1.
2. R.L. Garrett. Pollution prevention, green chemistry, and the design of safer chemicals. *In* Designing safer chemicals: Green chemistry for pollution prevention. *Edited by* S.C. DeVito and R.L. Garrett. American Chemical Society, Washington, DC. 1996. Chap. 1.
3. P.T. Anastas, M.M. Kirchhoff, and T.C. Williamson. Appl. Catal. A, **221**, 3 (2001).
4. Handbook of green chemistry and technology. *Edited by* J. H. Clark and D.J. Macquarrie. Blackwell, Oxford, UK. 2002.
5. (*a*) E.B. Mubofu, J.H. Clark, and D.J. Macquarrie. Green Chem. **3**, 23 (2001); (*b*) S. Paul and J.H. Clark. Green Chem. **5**, 637 (2003); (*c*) C. Baleizao, A. Corma, H. Garcia, and A. Leyva. Chem. Commun. (Cambridge), 606 (2003).
6. (*a*) K.S. Atwal, G.C. Rovnyak, B.C. O'Reilly, and J. Schwartz. J. Org. Chem. **54**, 5898 (1989); (*b*) G.C. Rovnyak, S.D. Kimbal, B. Beyer, G. Cucinotta, J.D. Dimarco, J. Gougoutas, A. Hedberg, M. Malley, J.P. MaCarthy, R. Zhang, and S. Mereland. J. Med. Chem. **38**, 119 (1995); and refs. cited therein; (*c*) C.O. Kappe, W.M.F. Fabian, and M.A. Semons. Tetrahedron, **53**, 2803 (1997); (*d*) K.S. Atwal, B.N. Swanson, S.E. Unger, D.M. Floyd, S. Mereland, A. Hedberg, and B.C. O'Reilly. J. Med. Chem. **34**, 806 (1991).
7. L.E. Overman, M.H. Rabinowitz, and P.A. Renhowe. J. Am. Chem. Soc. **117**, 2657 (1995).
8. P. Biginelli. Gazz. Chem. Ital. **23**, 360 (1893).
9. (*a*) B.C. Ranu, A. Hajra, and U. Jana. J. Org. Chem. **65**, 6270 (2000); (*b*) R. Verala, M.M. Alam, and S.R. Adapa. Synlett, 67 (2003); (*c*) J. Lu, Y. Bai, L. Wang, B. Yang, and H. Ma. Tetrahedron Lett. **41**, 9075 (2000); (*d*) C.V. Reddy, M. Mahesh, P.V. Raju, T. Babu, and V.V. Reddy. Tetrahedron Lett. **43**, 2657 (2002); (*e*) M. Xia and Y. Wang. Tetrahedron Lett. **43**, 7703 (2002); (*f*) S.T. Jin, H.-X. Wang, C.-Y. Xing, X.-L. Li, and T.-S. Li. Synth. Commun. **34**, 3009 (2004); (*g*) R. Ghosh, S. Maiti, and A. Chakraborty. J. Mol. Catal. A: Chem. **217**, 47 (2004); (*h*) Y. Zhu, Y. Pan, and S. Huang. Synth. Commun. **34**, 3167 (2004); (*i*) S.K. De and R.A. Gibbs. Synthesis, 1748 (2005).
10. Q. Sun, Y.-Q. Wang, Z.-M. Ge, T.-M. Cheng, and R.-T. Li. Synthesis, 1047 (2004).
11. J.K. Shorrock, J.H. Clark, K. Wilson, and J. Chisem. Org. Process Res. Dev. **5**, 249 (2001).
12. Y. Ma, C. Qian, L. Wang, and M. Yang. J. Org. Chem. **65**, 3864 (2000).
13. A.S. Praskar, G.K. Dewkar, and A. Sudalai. Tetrahedron Lett. **44**, 3305 (2003).
14. J. Lu and Y. Bai. Synthesis, 466 (2002).
15. P. Shanmugam, G. Annie, and P.T. Perumal. J. Heterocycl. Chem. **40**, 879 (2003).
16. M. Zhang and Y.-Q. Li. Synth. Commun. **36**, 835 (2006).
17. A. Hegedus, Z. Hell, and H. Vigh. Synth. Commun. **36**, 129 (2006).
18. C. Liu, J. Wang, and Y. Li. J. Mol. Catal. A: Chem. **258**, 367 (2006).

© 2007 NRC Canada

1D and 2D NMR investigations of the micelle-formation process in 8-phenyloctanoate micelles

Josette M. Landry, D. Gerrard Marangoni, Michael D. Lumsden, and Robert Berno

Abstract: The micellization process of sodium 8-phenyloctanoate in a deuterated aqueous solution was studied, using ^{1}H NMR spectroscopy and two-dimensional (2D) nuclear Overhauser enhancement spectroscopy (NOESY). ^{1}H NMR spectra, acquired for the sodium 8-phenyloctanoate before and after the critical micelle concentration (CMC) value, showed that large chemical-shift changes were observed for both the aromatic proton peaks and the peaks for the methylene protons near the terminal phenyl group. The plots for the methylene protons near the headgroup do not show these large chemical-shift changes. These observations support the view that the terminal phenyl ring of the surfactant is primarily located in the micellar interior. The 2D NOESY experiments show significant cross-peaks, between the phenyl protons and the methylene protons of the surfactant, that substantiate the conclusions on those drawn from NMR aromatic solute induced shift (ASIS) experiments on the same and similar systems. All these observations are consistent with the Gruen model of the micelle and previous NMR NOESY experiments for other surfactant systems.

Key words: surfactants, micelles, NMR, NOESY.

Résumé : Faisant appel à la spectroscopie RMN du proton et à la spectroscopie RMN du proton bidimensionnelle avec effet Overhauser nucléaire (« NOESY »), on a étudié le processus de micellisation du 8-phényloctanoate de sodium dans une solution aqueuse deutérée; les données acquises pour le 8-phényloctanoate de sodium avant et après la valeur de la concentration micellaire critique (CMC) mettent en mettent en évidence l'apparition de changements importants dans les déplacements chimiques des pics des protons aromatiques ainsi que des pics des protons des groupes méthylènes proches des groupes phényles terminaux. Les courbes des protons des groupes méthylènes adjacents des groupes carboxyles ne présentent pas ce genre de changements importants de leurs déplacements chimiques. Ces observations sont en accord avec les vues selon lesquelles le noyau aromatique terminal d'un agent de surface est situé principalement dans la phase micellaire intérieure. Les expériences de « NOESY » bidimensionnelles montrent l'existence de croisements importants de pics entre les protons aromatiques du groupe phényle et les protons des groupes méthylènes de l'agent de surface, ce qui corrobore les conclusions qui avaient étaient déduites d'expériences de RMN sur le déplacement induit de solutés aromatiques sur les mêmes systèmes et d'autres apparentés. Toutes ces observations sont en accord avec le modèle de Gruen de la micelle et avec les expériences de RMN « NOESY » pour d'autres systèmes d'agents de surface.

Mots-clés : agents de surface, micelles, RMN, « NOESY ».

[Traduit par la Rédaction]

Introduction

Surfactant molecules contain a hydrophobic part (tail) and hydrophilic part (head). They are typically organic-based and have specific properties that make them useful for a wide variety of applications. A very important property is that they lower the surface tension of a solvent (1–4). They are also able to act as emulsion agents to bring immiscible phases together (5–8). Surfactant molecules will aggregate to form micelles above a certain concentration, referred to as the critical micelle concentration or CMC value. The CMC value is detected by plotting a physicochemical property like conductivity measurements, viscosity measurements, NMR chemical shift or relaxation rates, or surface tension measurements and observing the "break" or inflection point in the property vs. concentration plot.

It has been demonstrated in the past two decades that NMR studies of surfactant solutions can provide a wealth of information on the conformations of surfactant molecules (9, 10). ^{13}C NMR chemical shifts provide information on the conformations of the chains that are comprising the micelles (11–14). ^{13}C relaxation-rate measurements, as a function of the magnetic field strength, have demonstrated that the motions of the surfactant carbons near the headgroups tend to be more restricted, while those near the end of the alkyl chain are essentially isotropic (15–17). NMR ring-current shift measurements of phenyl groups, attached to surfactant

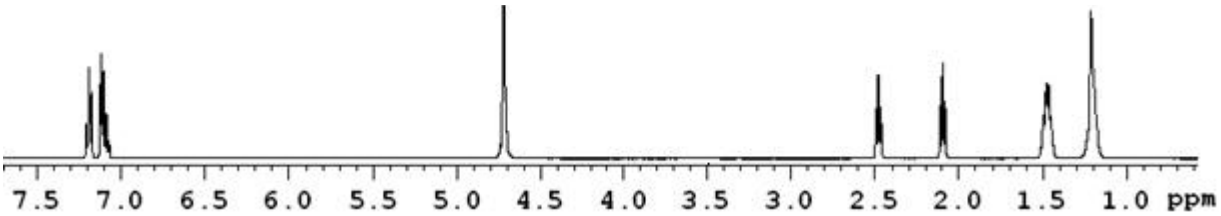
Received 23 October 2006. Accepted 19 January 2007. Published on the NRC Research Press Web site at http://canjchem.nrc.ca on 27 March 2007.

J.M. Landry and D.G. Marangoni.[1] Department of Chemistry, St. Francis Xavier University, P.O. Box 5000, Antigonish, NS B2G 2W5, Canada.
M.D. Lumsden and R. Berno. Atlantic Region Magnetic Resonance Centre (ARMRC), Dalhousie University, Halifax, NS B3H 4J3, Canada.

[1]Corresponding author (e-mail: gmarango@stfx.ca).

 doi:10.1139/V07-008 © 2007 NRC Canada

Fig. 1. Typical NMR spectrum for the sodium 8-phenyloctanoate system.



chains, have been used to examine the structure of phenyl-containing surfactants and the locations of aromatic and non-aromatic solubilizates in the interior of surfactant micelles (18–21).

Two-dimensional nuclear Overhauser enhancement spectroscopy (NOESY) provides significant information on the intra- and inter-molecular proximity of protons in a number of systems. NOESY experiments give spectra that correlate protons that are within a spatial proximity of 0.5 nm. It is extensively used in the determination of the conformations of nucleic acids, proteins, and membranes (22). In the case of micellar systems, the NOE cross-peaks are indicative of intra- and inter-molecular protons that are close enough in space to have dipolar interactions (23–25). It has been shown in the literature that these cross-peaks correlate extremely well with other experiments used to probe the structure of micelles and mixed micelles, such as luminescence probing and aromatic solute-induced shifts. NOESY experiments are preferable because of the noninvasive nature of the technique.

Surfactant molecules, containing an aromatic ring, can provide a convenient group that can be monitored for aromatic ring-current shifts. Gao et al. examined the micellization process of the sodium 10-phenyldecanoate system and found that large upfield shifts were observed for the aromatic protons and the methylene protons near the terminal phenyl group, while the shifts of protons, attached to the methylene protons near the headgroup, were very small (20). From this, it was proposed that the terminal phenyl group is, on average, located in the micellar interior. In this paper, we will examine the ^{1}H chemical shifts of the sodium 8-phenyldecanoate system, as a function of the surfactant concentration. The NMR ring-current effects will be used to determine the average location of the phenyl groups in the micelle interior. These ring-current shifts will be correlated with the results from the 2D NOESY NMR experiments. These techniques provide conclusive evidence of the average location of the aromatic groups in the micelle interior, and will be used to show that the aromatic rings do, indeed, sample the entire micelle interior.

Experimental

Sodium 8-phenyloctanoic acid (FW = 220.31 g/mol) was purchased from Lancaster (97% pure). A bulk solution of sodium 8-phenyloctanoate (0.1 mol/L) was made up by transferring the acid in D_2O and adding NaOD dropwise until it was completely dissolved. A slight excess of a base was used to prevent hydrolysis, which resulted in the appearance of turbidity in the NMR tube. The solution was sonicated, and the final pD was adjusted to a value between 10 and 11. D_2O was purchased from both Sigma-Aldrich and Norell and was 99.9% pure. Samples of different concentrations were made up in the NMR tubes directly by pipetting appropriate amounts of a stock surfactant solution and D_2O, respectively.

The 1D NMR spectra (^{1}H) for the ω-phenyloctanoate surfactant system were obtained on a Bruker AC-200 at St. Francis Xavier University, operating at 200.13 MHz, for protons and a Bruker AVANCE-500 at the Atlantic Region Magnetic Resonance Centre (ARMRC) at Dalhousie University. A typical ^{1}H spectrum for the ω-phenyloctanoate system is given in Fig. 1. The ^{1}H spectra were referenced to the HOD peak, which was assigned a value of $\delta = 4.71$ ppm. The 2D experiments (COSY and NOESY) were performed on the AVANCE-500 spectrometer at the ARMRC. The mixing times and the delay times for the NOESY experiments were estimated from the spin–lattice relaxation times of the surfactant, determined in separate experiments. In all cases, we used an acquisition delay of ~$3 \times T_1$ and a mixing time of ~$1 \times T_1$ to obtain the NOESY spectra. For the COSY experiments, the data were zero-filled once and multiplied by a sine-bell window in both dimensions prior to the 2D Fourier transform. In the gradient NOESY experiments, 128 transients of either 2 or 4 scans (8 scans in the water-suppression experiments) over 512 × 128 complex data points were acquired. All acquisitions were done in phase-sensitive mode, with and without the saturation of the water resonance at ~4.7 ppm. The data were zero-filled twice in t_1 and multiplied by a squared sine-bell function in both dimensions before the 2D Fourier transform.

Results and discussion

The proton resonances on the hydrocarbon chain were assigned using standard COSY techniques. The sodium ω-phenyloctanoate surfactant protons are numbered consecutively from the carboxylate group. ^{1}H NMR chemical shifts were determined as a function of the inverse surfactant concentration. The averaged CMC value for the sodium ω-phenyloctanote systems was found to be 0.055 ± 0.002 mol/L from the breaks in the ^{1}H chemical shifts vs. inverse surfactant concentration plot. The difference in the Gibbs energy of micellization between the sodium ω-phenyloctanoate and the sodium ω-phenyldecanoate surfactant yields a Gibbs energy of transfer, of the CH_2 group into the micelle, of –3.2 kJ/mole, which agrees with the Gibbs transfer energies/CH_2 for a number of conventional monomeric anionic and cationic surfactants (26). The aggregation number of the surfactant has been estimated from the ^{1}H chemical shifts as a function of the inverse surfactant concentrations, as we have done previously using

© 2007 NRC Canada

^{13}C chemical shifts (27). The average aggregation number from the ^{1}H chemical shifts was 25 ± 2, suggesting that these micelles are small and likely hydrated in the micelles palisade layer region. It should be noted that this value of 25 is virtually the same as that obtained by Gao et al. for the 10-carbon surfactant of the same family (20). The aggregation numbers, obtained from the application of a mass-action model to the ^{13}C chemical shifts, are likely to be smaller than those obtained from luminescence-probing experiments and light scattering, as has been discussed in the literature by Söderman and Guering (28). We will now turn our attention to discussing the locations of the phenyl groups inside the micelles, as deduced by ^{1}H NMR ring-current shift measurements.

^{1}H NMR chemical-shift differences for the sodium ω-phenyloctanoate resonances are presented in Figs. 2–4. In this paper, we define the chemical-shift difference as follows:

$$[1] \qquad \Delta\delta = \delta(\text{aq}) - \delta(\text{obs})$$

Hence, a low frequency shift is defined as having a positive value of Δδ. When we examine the plots of the observed chemical shifts for the 8-phenyloctanoate system, we clearly see that the protons on or near the terminal benzene ring undergo significant low-frequency shifts upon micelle formation (i.e., they are characterized by large, positive Δδ values). In Figs. 2–4, we also observe that these large low-frequency shifts, leading up to and at the CMC of the surfactant, are much larger than the observed ^{1}H chemical shifts for surfactant systems like sodium dodecylsulfate (SDS) or dodecyltrimethylammonium bromide (DTAB). In fact, the chemical-shift changes of the CH_2 protons near the terminal phenyl group upon micelle formation range between 0.25 and 0.40 ppm on the 200 MHz spectrometer, and are comparable to the observed Δδ values for some ^{13}C resonances upon micelle formation (27).

For protons, the chemical shifts are dominated by the diamagnetic-shielding term, which is primarily influenced by the reduction in the electron density around the ^{1}H nucleus because of the electronegativity of bonded atoms. The ring-current effect arises from the strong anisotropy in the magnetic susceptibility, attributed to the produced ring current when the applied field, perpendicular to the magnetic plane, induces the circulation of the π electrons around the ring. With a proton attached to the ring a deshielding occurs, whereas protons above and below the ring should experience an enhancement in the local shielding, and hence, a decreased chemical shift. The fact that we only observe decreased resonance frequencies for the ω-phenyloctanoate protons is consistent with the presence of a neighbouring-group effect from the aromatic rings. Our results for the ω-phenyloctanoate are in excellent agreement with the results of Gao et al. and Nagakawa et al. (29). We note that, on average, we observed large ring-current shifts for protons attached to C7, C8, C*m*, C*o*, and C*p* upon micellization, but small shifts were observed for the protons at C2 and C3. If the phenyl group was located, on average, near the micelle interior, we would expect to see significant shifts for the C7, C8, C*m*, C*o*, and C*p* protons, but small shifts for the protons near the micelle surface (the C2 and C3 protons). These observations are also consistent with the line-broadening of the

Fig. 2. Chemical shifts of the C*o* (◆), C*m,* (■), and C*p* (▲) protons of the sodium 8-phenyloctanoate system as a function of the inverse surfactant concentration.

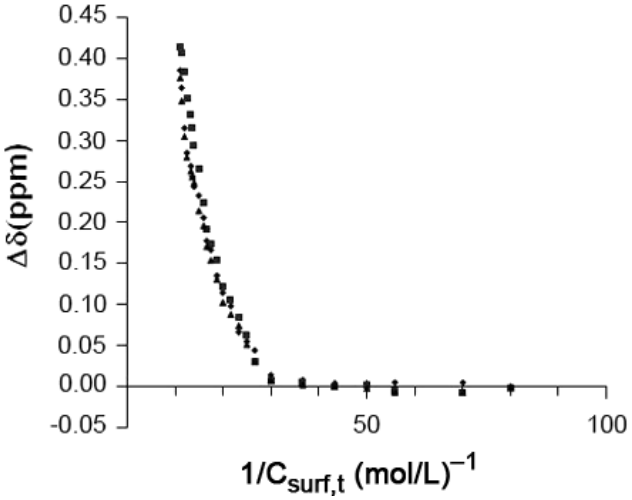


Fig. 3. Chemical shifts of the C7 (■) and C8 (▲) protons of the sodium 8-phenyloctanoate system as a function of the inverse surfactant concentration.

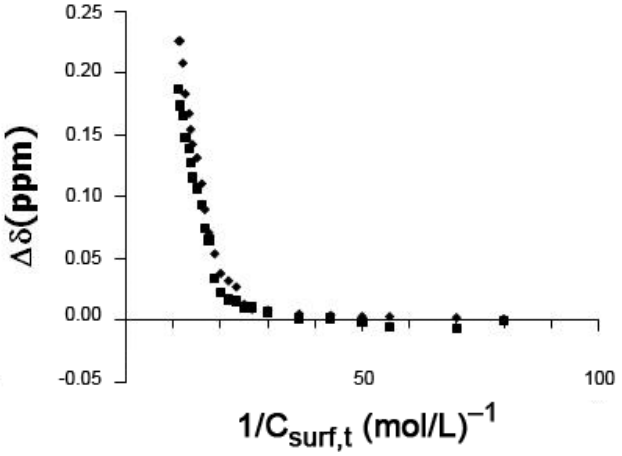
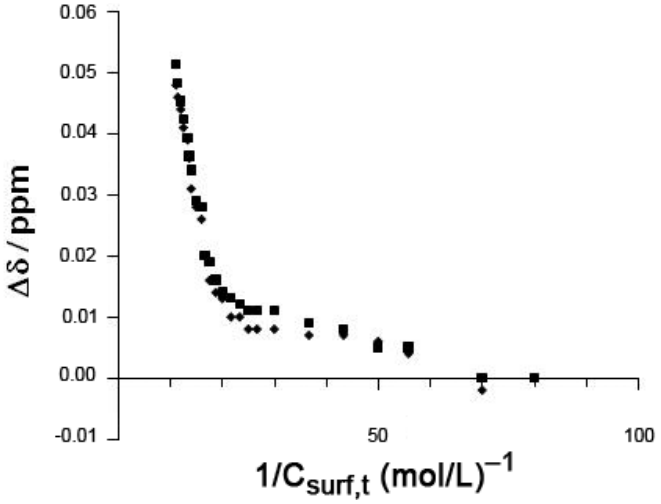
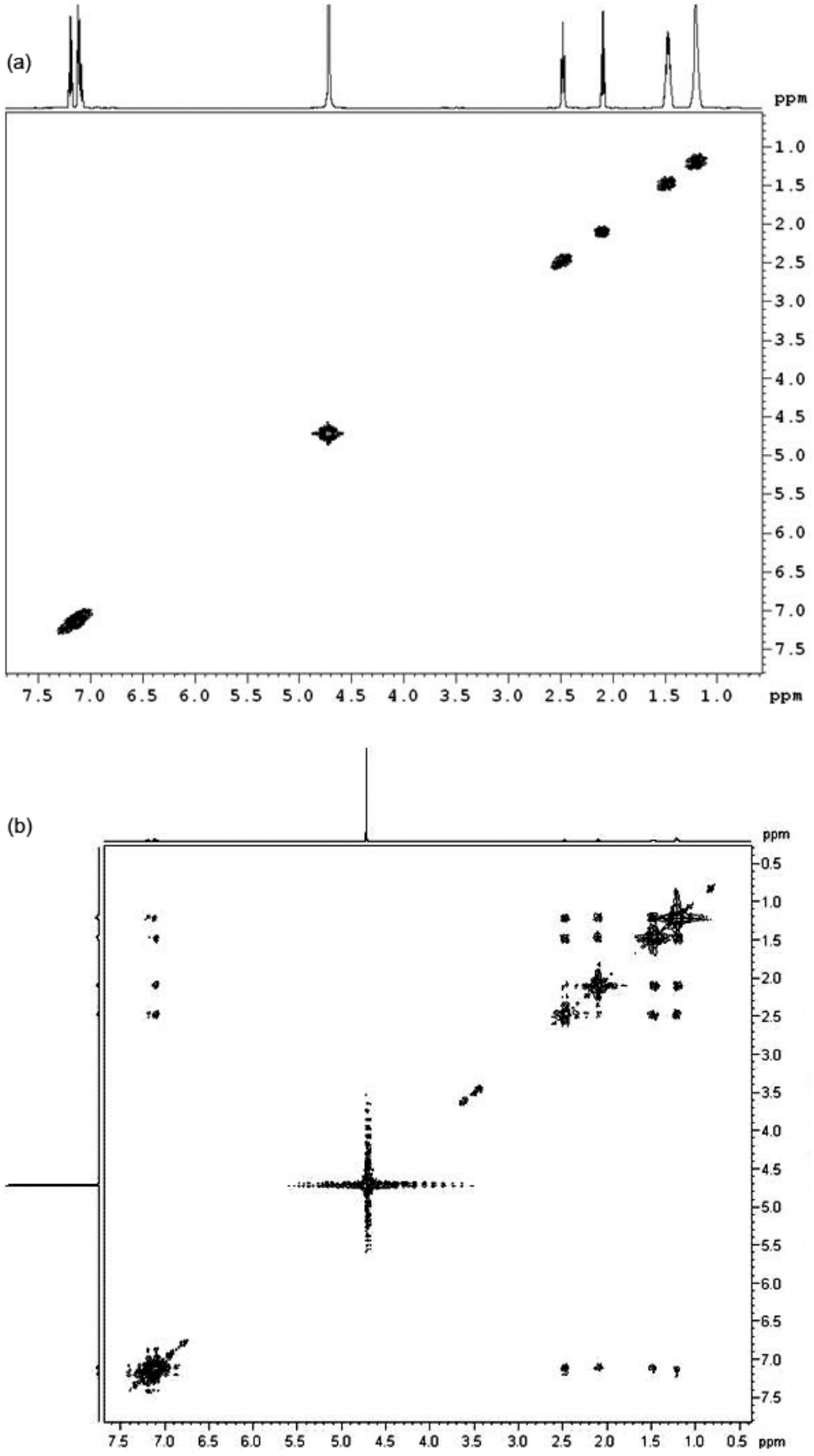


Fig. 4. Chemical shifts of the C2 (■) and C3 (▲) protons of the sodium 8-phenyloctanoate system as a function of the inverse surfactant concentration.



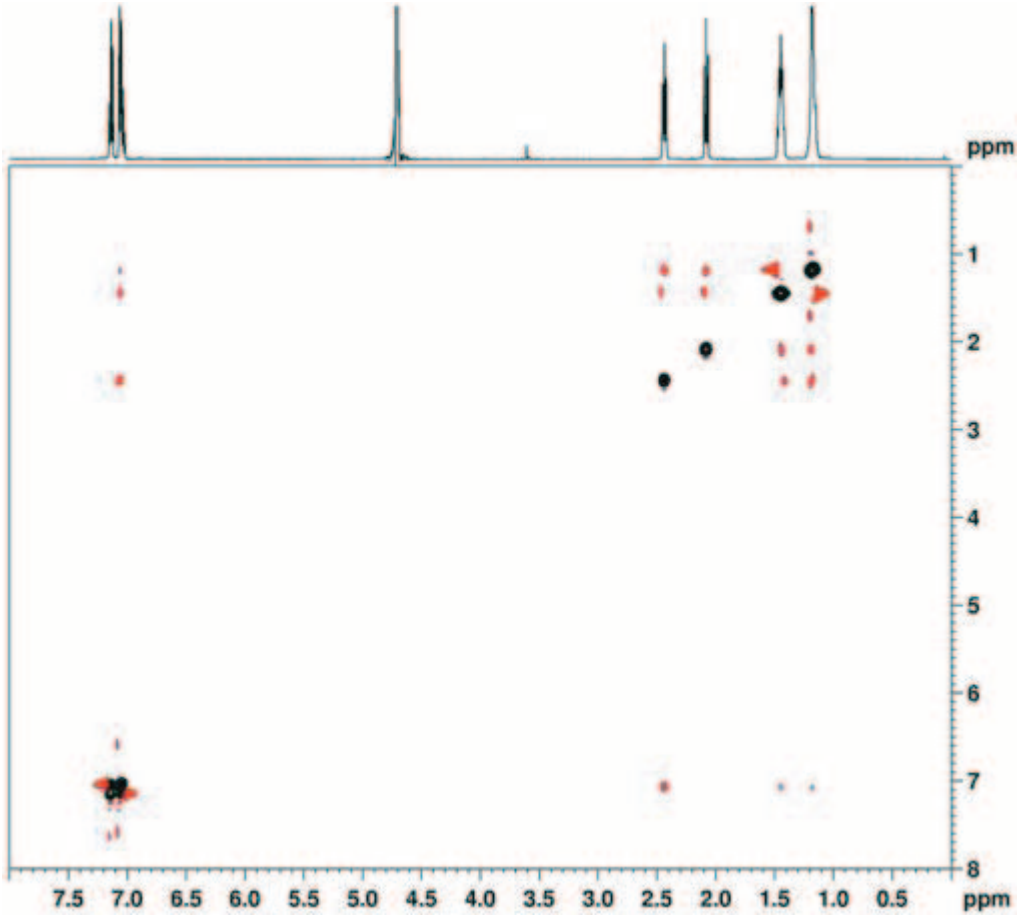
© 2007 NRC Canada

Fig. 5. The 2D NOESY spectrum of a sodium 8-phenyloctanoate system at (*a*) 0.015 mol/L, (*b*) 0.090 mol/L.



© 2007 NRC Canada

Fig. 6. The 2D NOESY spectrum of a 0.10 mol/L solution of sodium 8-phenyloctanoate system with suppression of the solvent peak around 4.7 ppm.



ω-phenyldecanoate proton resonances by $Mn^{2+}(D_2O)^{6+}$, observed by Stark et al. (30).

The use of aromatic ring-current induced shifts has been criticized in the literature (31). Hence, it is instructive to consider another NMR technique with which the spatial arrangements of the hydrocarbon chains can be deduced in a noninvasive manner. 2D NOESY experiments have been shown to provide excellent insights into the nature of the micelle-formation process, solubilization in mixed micelles, and the formation of polymer–surfactant complexes. In case of the ω-phenyloctanoate system, we have obtained the NOESY spectra for the surfactant in micellar form at two concentrations: one at ~2 × the CMC of the surfactant and one at ~1/3 of the CMC value of the surfactant (Fig. 5). In case of the spectrum at 0.090 mol/L (Fig. 5*a*), it is clear that significant cross-peaks, which indicate the proximity of the protons between the neighbouring surfactant molecules, occur in the NOESY experiments. These cross-peaks are completely absent in the spectrum at the lower (<CMC) concentration. The spectrum at the higher concentration exhibits cross-peaks, indicative of through-space dipole–dipole coupling between protons either on adjacent surfactant molecules or even on the same molecule. The cross-peaks indicate the spatial proximity of the protons on adjacent surfactant molecules or the protons on the same surfactant molecule within a distance of 5 Å (22). In fact, we observe substantial chain–proton correlations between the protons in the micelle headgroups region and protons on the end of the chain, which would indicate that the surfactant chain is certainly bent back towards the surface of the micelles, as has been discussed previously (20). Examining the phenyl resonances at around 7.1 to 7.2 ppm, we observe the existence of cross-peaks between the phenyl resonances and the remaining chain protons in the surfactant. Apparently, the correlation between the phenyl protons and the protons near the headgroups of the surfactant is quite significant, indicating that the benzene rings are capable of bending back and interacting with the protons near the surfactant headgroups. The picture that emerges from these NOESY experiments is that the phenyl groups are indeed not buried in the interior of the surfactant micelles, but there is a significant amount of chain motion and bending within the hydrocarbons core of the micelles, which is in excellent agreement with the results of both ^{13}C NMR relaxation-rate measurements (15–17) and ^{13}C NMR chemical-shift measurements (11–13).

We have also obtained the NOESY spectrum for the same system at a slightly higher concentration (0.10 mol/L) using a solvent-suppression technique known as excitation sculpting to remove the water peaks from the spectra. The spectrum is presented in Fig. 6. Clearly, the cross-peaks that existed at 0.090 mol/L do exist at the higher surfactant concentration (~2 × the CMC of the surfactant). In this case, we

© 2007 NRC Canada

again observe cross-peaks between the benzene protons (δ = 7.2 ppm) and all the surfactant chain protons. This is consistent with the phenyl rings being able to sample the entire micellar interior, and this is again in excellent agreement with the ASIS experiments of Gao et al. for benzene in SDS micelles (21). Gao et al. concluded that phenyl rings are distributed rather uniformly throughout the interior of ω-phenyldecanoate micelles. In our NOESY experiments, the cross-peak volume between the phenyl protons and the C7 and C8 appears to be larger than that of the phenyl protons with C2 and C3, which is in excellent agreement with ASIS experiments. Hence, these observations seem to support the notion that the phenyl rings are primarily located in the micellar core, but they do bend back towards the micellar surface, as predicted by the Gruen model (32).

Summary and conclusion

The ^{1}H NMR chemical shifts and the NOESY spectra for ω-phenyloctanoate have been determined for the concentration range above and below the CMC of the surfactant. The ^{1}H chemical differences after micelle formation are substantially larger for the protons near the benzene rings in the chain. These shifts are consistent with the phenyl rings, attached to the end of the surfactant chain, bending back towards the micellar surface, which agrees with the previous work of Gao et al. on the ω-phenyldecanoate system. The 2D NOESY spectra, obtained for the same system, seem to bear out the hypothesis that the benzene ring is not anchored in the micellar interior but is in rapid exchange throughout the micellar interior.

Acknowledgements

The financial support of the Natural Sciences and Engineering Research Council of Canada (NSERC) (research grant, D.G. Marangoni) and the St. Francis Xavier University Council for Research (Graduate Award, J.M. Landry) is greatly appreciated.

References

1. F.E. Friedli. Detergency of specialty surfactants. Vol. 98. Marcel Dekker, New York. 2001.
2. B. Widom, P. Bhimalapuram, and K. Koga. Phys. Chem. Chem. Phys. **5**, 3085 (2003).
3. R. Zana. Adv. Colloid Interface Sci. **57**, 1 (1995).
4. C. Chachaty. Prog. Nucl. Magn. Reson. Spectrosc. **19**, 183 (1987).
5. M.J. Rosen. Cosmet. Toiletries, **113**, 49 (1998).
6. D. Bais, A. Trevisan, L R. apasin, P. Partal, and C. Gallegos. J. Colloid Interface Sci. **290**, 546 (2005).
7. M. Monduzzi and S. Mele. J. Phys. Chem. **105**, 12579 (2001).
8. P. Wilde, A. Mackie, F. Husband, P. Gunning, and V. Morris. Adv. Colloid Interface Sci. **63**, 108 (2004).
9. O. Soderman, P. Stilbs, and W.S. Price. Concepts Magn. Reson. A, **23A**, 121 (2004).
10. O. Söderman and P. Stilbs. Prog. Nucl. Magn. Reson. Spectrosc. **26**, 445 (1994).
11. B. Persson, T. Drakenberg, and B. Lindman. J. Phys. Chem. **80**, 2124 (1976).
12. Z. Dega-Szafran, E. Dulewicz, and M. Szafran. Magn. Reson. Chem. **38**, 43 (2000).
13. S. Shimizu, P.A.R. Pires, H. Fish, T.K. Halstead, and O.A. El Seoud. Phys. Chem. Chem. Phys. **5**, 3489 (2003).
14. Z. Gao, R.E. Wasylishen, and J.C.T. Kwak. J. Phys. Chem. **94**, 773 (1990).
15. H. Wennerström, B. Lindman, O. Söderman, T. Drakenberg, and J. Rosenholm. J. Am. Chem. Soc. **101**, 6860 (1979).
16. M. Monduzzi, A. Ceglie, B. Lindman, and O. Söderman. J. Colloid Interface Sci. **136**, 113 (1990).
17. O. Söderman and P. Stilbs. Chem. Phys. Lipids, **41**, 117 (1986).
18. H.Z. Yuan, X.L. Tan, G.Z. Cheng, S. Zhao, L. Zhang, S.Z. Mao, J.Y. An, J.Y. Yu, and Y.R. Du. J. Phys. Chem. B, **107**, 3644 (2003).
19. Z. Gao, R.E. Wasylishen, and J.C.T. Kwak. Macromolecules, **22**, 2544 (1989).
20. Z. Gao, R.E. Wasylishen, and J.C.T. Kwak. J. Colloid Interface Sci. **137**, 137 (1990).
21. R.E. Wasylishen, J.C.T. Kwak, Z. Gao, E. Verpoorte, J.B. MacDonald, and R.M. Dickson. Can. J. Chem. **69**, 822 (1991).
22. K. Wüthrich. NMR of proteins and nucleic acids. Wiley-VCH, New York. 1986.
23. B.E. Hawrylak and D.G. Marangoni. Can. J. of Chem. **77**, 1241 (1999).
24. H. Yuan, L. Luo, L. Zhang, S. Zhao, S. Mao, J. Yu, L. Shen, and Y. Du. Colloid. Polym. Sci. **280**, 479 (2002).
25. S.Z. Mao and Y.R. Du. Acta Phys. Chim. Sin. **19**, 675 (2003).
26. R. Zana. Langmuir, **12**, 1208 (1996).
27. G.D. Boucher, A.C. MacDonald, B.E. Hawrylak, and D.G. Marangoni. Can. J. Chem. **76**, 1266 (1998).
28. O. Söderman and P. Guering. Colloid. Polym. Sci. **265**, 76 (1987).
29. T. Nakagawa, H. Inoue, H, Jizimoto, and K. Horiuchi. Kolloid Z. Z. Polym. **229**, 159 (1969).
30. R.E. Stark, R.W. Storrs, and M.L. Kasakevich. J. Phys. Chem. **89**, 272 (1985).
31. P. Stilbs. J. Colloid Interface Sci. **122**, 593 (1988).
32. D.W.R. Gruen. J. Phys. Chem. **89**, 146 (1985).

© 2007 NRC Canada

Asymmetric organocatalytic direct aldol reactions of cyclohexanone with aldehydes in brine

Wen-Ping Huang, Jia-Rong Chen, Xin-Yong Li, Yi-Ju Cao, and Wen-Jing Xiao

Abstract: Organocatalytic asymmetric direct aldol reactions in brine with high diastereo- and enantioselectivities, using a readily available bifunctional amide catalyst, were developed.

Key words: aldol reaction, organocatalyst, asymmetric catalysis, water.

Résumé : Opérant dans de la saumure et faisant appel à un amide bifonctionnel facilement disponible comme catalyseur organique, on a développé des réactions aldoliques directes et asymétriques qui se produisent avec des diastéréo- et énantiosélectivités élevées.

Mots-clés : réaction aldolique, catalyse organique, catalyse asymétrique, eau.

[Traduit par la Rédaction]

Introduction

Water, the essential medium for the construction of chemical bonds in life, was widely accepted as "a contaminant in organic synthesis". Unless water is used as a reactant, the use of water was usually avoided in reaction systems. Nevertheless, Breslow and co-workers investigated Diels–Alder reactions in water in 1980s, and it was found that water could remarkably increase the reaction rate and selectivities (1). Since then, there has been considerable efforts to develop organic reactions, using water as an additive or a solvent instead of conventional organic solvents, with respect to environmental concerns, safety, and cost (2, 3). In contrast, there have been relatively few investigations using brine as the reaction media (4), although the reaction efficiency in brine may be superior to that in water. Herein, we report organocatalytic direct aldol reactions of cyclohexanone with aldehydes in brine, using our bifunctional organocatalyst **4e**. The reactions afforded the desired products in high yields and in excellent diastereo- and enantioselectivities.

Organocatalysis, primarily because of the operational simplicity, the cheap catalyst, and the potential industrial applications, has received renewed attention and became the focus of intensive research endeavor (5). In 2000, almost three decades after the first report of enantioselective proline-catalyzed intramolecular aldol reaction presented by Eder et al. (6*a*) and Hajos and Parrish (6*b*), List and co-workers described fundamental work on proline-catalyzed asymmetric intermolecular aldol reactions of ketones and aldehydes (7). After that, there has been a large amount of research activities in this field (8), which has resulted in the development of asymmetric organocatalysis. Although water as an additive has a certain positive effect on organocatalytic aldol reactions (9), the use of a large amount of water or aqueous buffer as solvent has been found to be detrimental in some cases (10). Recently, studies by Mase and co-workers (11*a*), Hayashi and co-workers (11*b*, 11*c*), Dziedzic and co-workers (11*d*), and Wu and co-workers (11*e*) revealed the possibility to carry out enantioselective direct aldol reactions in water, along or together with organic solvents, by the design and use of new organocatalysts (Scheme 1). Part of our ongoing project aimed at developing readily available bifunctional organocatalysts of broad utility to chemical transformations and with industrial potential (8*j*, 9*d*). Thus, we were interested in applying our artificial bifunctional amine catalysts **3** and **4** to aldol reactions in brine.

Received 12 December 2006. Accepted 9 February 2007. Published on the NRC Research Press Web site at http://canjchem.nrc.ca on 27 March 2007.

W.-P. Huang. Key Laboratory of Pesticide and Chemical Biology, Ministry of Education, College of Chemistry, Central China Normal University, 152 Luoyu Road, Wuhan, Hubei 430079, China; Department of Chemistry, Xianning College, Xianning, Hubei 437000, China.
J.-R. Chen, X.-Y. Li, Y.-J. Cao, and W.-J. Xiao.[1] Key Laboratory of Pesticide and Chemical Biology, Ministry of Education, College of Chemistry, Central China Normal University, 152 Luoyu Road, Wuhan, Hubei 430079, China.

[1]Corresponding author (e-mail: wxiao@mail.ccnu.edu.cn).

Results and discussion

The efficiency of our bifunctional catalysts was first evaluated with the direct asymmetric aldol reaction in water. Reaction of 4-nitrobenzaldehyde with cyclohexanone was performed in the presence of 20 mol% of catalyst **3** and 20 mol% of acetic acid (HOAc) (co-catalyst) at room temperature in 1 mL of water, and the aldol product **7a** (Fig. 1) was afforded in 89% yield, with 88% enantiomeric excess (ee) and a diastereomeric ratio (dr) of 92:8 (Table 1, entry 1). Encouraged by this result, we further examined the catalytic efficiency of the chiral amides **4a–e** in the presence of various acid additives (12). Notably, all the reactions with bifunctional catalysts **3** and **4a–e** proceed smoothly with good diastereo- and enantioselectivities, and **4e** shows the best catalytic activity with HOAc as the co-catalyst (Table 1, entries 1–10). Lowering the temperature to 0 °C further im-

 doi:10.1139/V07-012 © 2007 NRC Canada

Scheme 1. Privileged organocatlaysts examined for aldol reaction in water.

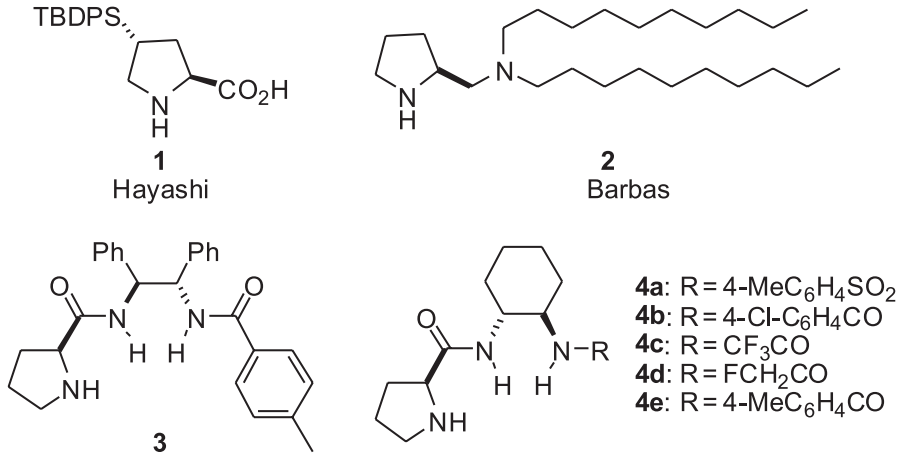
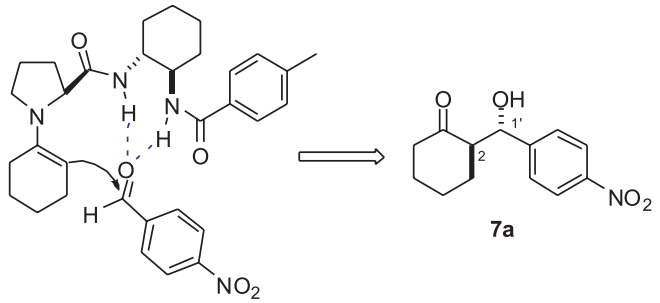


Fig. 1. Proposed transition state.

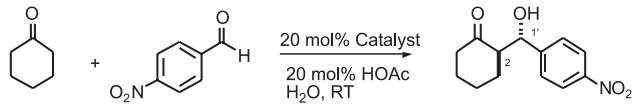


proves the dr from 89:11 to 92:8, although the product suffered a slight decrease of ee (Table 1, entry 11). The use of brine as solvent was remarkable in our catalytic system, and diasteroselectivity reached 95:5 (Table 1, entry 12). Therefore, brine was chosen as the solvent for further optimization. The chiral amide – acid combinations were also evaluated in different ratios, and the best ratio of catalyst **4e** to HOAc was 1:2 (Table 1, entries 12–15). The superior levels of asymmetric induction and efficiency, exhibited by the amide **4e** – HOAc in brine affording the aldol adduct **7a** in 92% yield with 93% ee and 95:5 dr, prompted us to select these catalytic conditions for further investigation (Table 1, entry 14).

Using these optimized conditions, reactions of cyclohexanone with various aldehydes, catalyzed by **4e** in brine, were then examined. As summarized in Table 2, the aromatic aldehydes **6a**–**i** reacted well with **5**, and the aldol adducts **7a**–**i** formed in high yields with high diastereo- and enantioselectivities (Table 2, entries 1 and 4–11). The only exception is the case of benzaldehyde, in which the ee was 83%, and the dr was 85:15 (Table 2, entry 12). Heteroaromatic aldehydes, such as **6k**, could also be successfully employed in this reaction with a lower yield of 43% (Table 2, entry 13). Notably, the reaction can still proceed well with little loss in selectivity even when the catalyst loading was reduced to 5 mol%, or only 2 equiv. of ketone was used (Table 2, entries 2 and 3).

The scope of this class of aldol reactions was also extended to a series of other ketone donors (Table 3). The reaction with the water-miscible ketone **6m** affords the aldol

Table 1. Screening of catalysts in the direct aldol reaction of cyclohexanone and p-nitrobenzaldehyde.

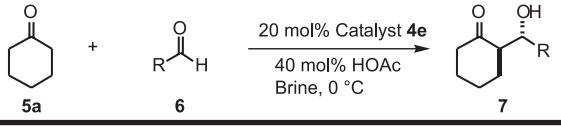


Entry	Catalyst	Additive	*t* (h)	Yield (%)[a]	*anti*:*syn*[b]	ee(%)[c]
1	**3**	HOAc	5	89	92:8	88
2	**4a**	HOAc	5	89	82:17	87
3	**4b**	HOAc	5	93	89:11	90
4	**4c**	HOAc	12	94	86:14	88
5	**4d**	HOAc	96	85	88:12	79
6	**4e**	HCl	72	8	78:12	76
7	**4e**	TsOH	72	25	84:16	86
8	**4e**	(+)-CSA[d]	12	89	93:7	77
9	**4e**	$PhCO_2H$	3	95	88:12	86
10	**4e**	HOAc	5	94	89:11	91
11[e]	**4e**	HOAc	5	81	92:8	89
12[e,f]	**4e**	HOAc	5	88	95:5	90
13[e,f]	**4e**	-	12	90	86:14	83
14[e,f]	**4e**	HOAc[g]	7	92	95:5	93
15[e,f]	**4e**	HOAc[h]	7	82	95:5	93

Note: Unless otherwise shown, the reaction was conducted with catalyst (0.1 mmol), additive (if used, 0.1 mmol), *p*-nitrobnezaldehyde (0.5 mmol) and cyclohexanone (2.5 mmol) in water (1.0 mL).
[a]Yield of the isolated product.
[b]Determined by ^{1}H NMR spectroscopy.
[c]Determined by chiral-phase HPLC analysis for *anti*-product.
[d]D-(+)-10-Camphorsulfonic acid.
[e]The reaction was peformed at 0 °C.
[f]Brine (1 mL) was used as solvent.
[g]40 mol% HOAc was used.
[h]80 mol% HOAc was used.

© 2007 NRC Canada

Table 2. Catalyst (**4e**–HOAc)-catalyzed direct aldol reactions of **5a** with aldehydes **6** in brine.



5a **6** **7**

Entry	R	Product	*t* (h)	Yield (%)[a]	*anti*:*syn*[b]	ee (%)[c]
1	4-NO_2-Ph-	**7a**	7	92	95:5	93
2[d]	4-NO_2-Ph-	**7a**	38	88	90:10	91
3[e]	4-NO_2-Ph-	**7a**	14	81	92:8	91
4	3-NO_2-Ph-	**7b**	12	91	96:4	96
5	2-NO_2-Ph-	**7c**	12	85	99:1	96
6	4-CN-Ph-	**7d**	12	86	91:9	91
7	4-Br-Ph-	**7e**	42	84	97:3	93
8	3-Br-Ph-	**7f**	23	76	94:6	90
9	4-Cl-Ph-	**7g**	42	80	95:5	92
10	2-Cl-Ph-	**7h**	19	82	99:1	91
11	2,4-Cl-Ph-	**7i**	19	88	99:1	94
12	Ph-	**7j**	43	72	85:15	83
13	2-furyl-	**7k**	72	43	89:11	86

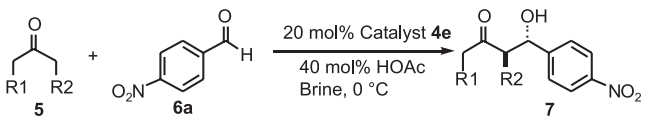
Note: The reaction was performed with **4e** (0.1 mmol), HOAc (0.2 mmol), aldehyde (0.5 mmol), and cyclohexanone (2.5 mmol) in brine at 0 °C for the indicated time.
[a]Yield of the isolated product.
[b]Determined by ^{1}H NMR spectroscopy.
[c]Determined by chiral-phase HPLC analysis for *anti*-product.
[d]5 mol% of the catalyst was used.
[e]2 equiv. of cyclohexanone was used.

adduct in good yield with high diastereo- and enantioselectivity, while moderate results were obtained with acetone as donor (Table 3, entries 1, 2). Significantly, the reaction preferentially occurred at the C3 position of butanone. To our surprise, although the reaction of cyclopentanone afforded the *syn*-diastrereomer as maojor product with 55% ee, the ee for the *anti*-adduct is still up to 92% (Table 3, entry 3).

Interestingly, the absolute configuration of the major aldol adduct **7a** was determined to be (2*R*,1*S*) by ^{1}H NMR spectroscopic analysis and comparison of HPLC retention time with literatures (11). Thus, we proposed that **4e**–HOAc catalyzed a *Si*-face of enamine attack on *Si*-face of the arylaldehyde. Notably, this result showed completely different transition-state model from the previously proposed L-proline-based aldol transition state (13) and recent Barbas and Hayashi's experiments (11). This unusual π-facial differentiation of enamine may be affected by the two-hydrogen-bond bearing chiral diaminocyclohexane backbone. Further studies on the mechanism are underway.

We have also found that this process is appropriate for gram-scale reactions, eventhough the catalyst loading is only 5 mol%, and water is 5500 mol%. The diastereo- and stereoselectivities are excellent (see eq. [1]). From a green-chemistry perspective, this is the real organocatalyzed aldol reaction in water (In Hayashi's catalytic system, 300 mol% water was used as solvent (11*b*)).

Table 3. Catalyst (**4e**–HOAc)-catalyzed direct aldol reactions of **5** with aldehydes **6a** in brine.

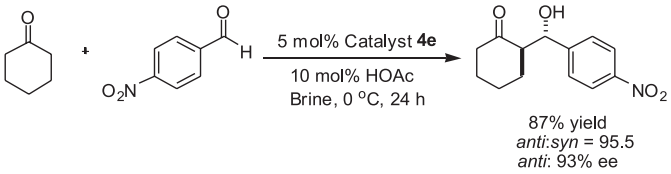


5 **6a** **7**

Entry	R1	R2	Product	*t* (h)	Yield (%)[a]	*anti*:*syn*[b]	ee (%)[c]
1[d]	H	H	**7l**	39	71	—	66
2[e]	H	Me	**7m**	72	55	97:3	93
3[f]	-$(CH_2)_2$-	—	**7n**	23	75	35:65	92

Note: The reaction was performed with **4e** (0.1 mmol), HOAc (0.2 mmol), aldehyde (0.5 mmol), and cyclohexanone (2.5 mmol) in brine at 0 °C for the indicated time.
[a]Yield of the isolated product.
[b]Determined by ^{1}H NMR spectroscopy.
[c]Determined by chiral-phase HPLC analysis for *anti*-product.
[d]10 equiv. of acetone was used.
[e]The aldol adduct, occured at the C1 position, was obtained with 19% yield.
[f]The ee of *syn*-product is 55%.

[1]



Experimental section

General methods

Unless otherwise noted, commercial reagents were used as received. Hexane and ethyl acetate, for flash column chromatography, were distilled before use. Flash column chromatography was performed using 200–300 mesh silica gel. ^{1}H NMR spectra were recorded on Varian Mercury 400 (400 MHz) spectrophotometers. Chemical shifts are reported in ppm from the solvent resonance, as the internal standard ($CDCl_3$: 7.26 ppm). Data are reported as follows: chemical shift, multiplicity (s = single, d = doublet, t = triplet, q = quartet, br = broad, and m = multiplet), coupling constants (Hz), and integration. ^{13}C NMR spectra were recorded on Varian Mercury 400 (100 MHz) spectrophotometers with complete proton decoupling ($CDCl_3$: 77.0 ppm). Chiral HPLC was performed on Agilent 1100 series with chiral columns (Chirapak AS, AD, OD, and OJ columns; Daicel Chemical Ind. Ltd.). Catalysts **3** and **4** were prepared by the previously described methods (8*j*).

Typical procedure for aldol reaction using the bifunctional catalyst 4e–HOAc in brine (Table 1, entry 14)

To a mixture of catalyst **4e** (33 mg, 0.10 mmol), cyclohexanone (0.26 mL, 2.5 mmol), and brine (1 mL), acetic acid (11.6 μL, 0.20 mmol) was added at 0 °C. The reac-

© 2007 NRC Canada

tion mixture was stirred for 10 min in a closed system, and then *p*-nitrobenzaldehyde (76 mg, 0.5 mmol) was added. The reaction mixture was stirred for 7 h, then the reaction was quenched by the addition of saturated ammonium chloride solution and extracted three times with ethyl acetate (3 mL). The mixture of combined organic phases was stirred over anhydr. $MgSO_4$, filtered, and concentrated to give pure aldol adduct **7a**, as white solid, through column chromatography on silica gel (hexane – ethyl acetate (3:1)). The enantiomeric excess (ee) of **7a** was determined by chiral-phase HPLC analysis.

2-[Hydroxy-(4-nitro-phenyl)-methyl]-cyclohexanone (7a)

Yield: 92%; *anti*:*syn* (95:5). *Anti*-diastereomer: ^{1}H NMR (400 MHz, $CDCl_3$, δ): 1.29–2.09 (m, 6H), 2.30–2.47 (m, 2H), 2.55–2.61 (m, 1H), 4.10 (s, 1H), 4.87 (d, *J* = 8.4 Hz, 1H), 7.48 (t, *J* = 8.0 Hz, 1H), 8.16 (d, *J* = 8.4 Hz, 2H). ^{13}C NMR (100 MHz, $CDCl_3$, δ): 24.5, 27.5, 30.6, 42.5, 57.0, 73.8, 123.4, 127.8, 147.4, 148.4, 214.6. HPLC (Chiralcel AD-H, Hexane–*i*-PrOH (95:5), 1.0 mL/min, 254 nm, 20 °C): t_R = 49.5 min (minor) and t_R = 67.6 min (major), ee = 93%. *Syn*-diastereomer: ^{1}H NMR (400 MHz, $CDCl_3$, δ): 1.50–2.13 (m, 6H), 2.39–2.50 (m, 2H), 2.61–2.65 (m, 1H), 3.20 (s, 1H), 5.48 (d, *J* = 2.0 Hz, 1H), 7.48 (d, *J* = 8.8 Hz, 2H), 8.20 (d, *J* = 8.8 Hz, 2H). ^{13}C NMR (100 MHz, $CDCl_3$, δ): 24.7, 25.9, 27.8, 42.6, 56.7, 70.1, 123.4, 126.6, 147.0, 149.1, 214.1. HPLC (Chiralcel AD-H, Hexane–*i*-PrOH (95:5), 1.0 mL/min, 254 nm, 20 °C): t_R = 35.2 min and t_R = 44.3 min.

2-[Hydroxy-(3-nitro-phenyl)-methyl]-cyclohexanone (7b)

Yield: 91%; *anti*:*syn* (96:4). *Anti*-diastereomer: ^{1}H NMR (400 MHz, $CDCl_3$, δ): 1.33–2.10 (m, 6H), 2.32–2.48 (m, 2H), 2.58–2.64 (m, 1H), 4.14 (s, 1H), 4.87 (d, *J* = 8.4 Hz, 1H), 7.50 (t, *J* = 8.0 Hz, 1H), 7.64 (t, *J* = 7.6 Hz, 1H), 8.12 (d, *J* = 7.6 Hz, 1H), 8.18 (d, J = 1.6 Hz, 1H). ^{13}C NMR (100 MHz, $CDCl_3$, δ): 24.5, 27.5, 30.6, 42.5, 57.0, 73.8, 121.9, 122.7, 129.2, 133.1, 143.2, 148.1, 214.7. HPLC (Chiralcel AD-H, Hexane–*i*-PrOH (95:5), 1.0 mL/min, 254 nm, 20 °C): t_R = 37.3 min (major) and t_R = 48.4 min (minor), ee = 96%. *Syn*-diastereomer: ^{1}H NMR (400 MHz, $CDCl_3$, δ): 1.48–2.10 (m, 6H), 2.33–2.46 (m, 2H), 2.62–2.66 (m, 1H), 3.27 (s, 1H), 5.44 (d, *J* = 2.0 Hz, 1H), 7.48 (t, *J* = 8.0 Hz, 1H), 7.64 (t, *J* = 7.6 Hz, 1H), 8.06 (t, *J* = 6.0 Hz, 1H); 8.15 (s, 1H). ^{13}C NMR (100 MHz, $CDCl_3$, δ): 24.6, 25.8, 27.7, 42.4, 56.6, 69.7, 120.8, 121.9, 129.0, 131.9, 143.9, 148.1, 214.0. HPLC (Chiralcel AD-H, Hexane–*i*-PrOH (95:5), 1.0 mL/min, 254 nm, 20 °C): t_R = 29.9 min and t_R = 32.6 min.

2-[Hydroxy-(2-nitro-phenyl)-methyl]-cyclohexanone (7c)

Yield: 85%; *anti*:*syn* (99:1). *Anti*-diastereomer: ^{1}H NMR (400 MHz, $CDCl_3$, δ): 1.51–1.78 (m, 6H), 2.25–2.40 (m, 2H), 2.69–2.75 (m, 1H), 4.04 (s, 1H), 5.39 (d, *J* = 7.2 Hz, 1H), 7.37 (t, *J* = 8.0 Hz, 1H), 7.57 (t, *J* = 7.6 Hz, 1H), 7.70 (d, *J* = 8.0 Hz, 1H), 7.76 (d, *J* = 8.0 Hz, 1H). ^{13}C NMR (100 MHz, $CDCl_3$, δ): 24.7, 27.6, 30.8, 42.5, 57.1, 69.3, 123.8, 128.2, 128.9, 132.9, 136.3, 148.6, 214.5. HPLC (Chiralcel OD-H, Hexane–*i*-PrOH (95:5), 1.0 mL/min, 254 nm, 20 °C): t_R = 37.6 min (major) and t_R = 45.9 min (minor), ee = 96%. *Syn*-diastereomer: ^{1}H NMR (400 MHz, $CDCl_3$, δ): 1.47–2.08 (m, 6H), 2.33–2.43 (m, 2H), 2.80–2.84 (m, 1H), 3.70 (s, 1H), 5.92 (d, *J* = 2.0 Hz, 1H), 7.38 (t, *J* = 8.4 Hz, 1H), 7.60 (t, *J* = 7.2 Hz, 1H), 7.80 (d, *J* = 7.6 Hz, 1H), 7.94 (d, *J* = 8.4 Hz, 1H). ^{13}C NMR (100 MHz, $CDCl_3$, δ): 24.7, 26.3, 27.2, 42.3, 54.8, 66.3, 124.5, 127.8, 129.5, 133.0, 137.1, 213.7. HPLC (Chiralcel OD-H, Hexane–*i*-PrOH (95:5), 1.0 mL/min, 254 nm, 20 °C): t_R = 24.7 min and t_R = 27.2 min.

2-[Hydroxy-(4-cyano-phenyl)-methyl]-cyclohexanone (7d)

Yield: 86%; *anti:syn* (91:9). *Anti*-diastereomer: ^{1}H NMR (400 MHz, $CDCl_3$, δ): 1.31–2.11 (m, 6H), 2.30–2.48 (m, 2H), 2.53–2.59 (m, 1H), 4.07 (s, 1H), 4.82 (d, *J* = 8.4 Hz, 1H), 7.43 (d, *J* = 8.4 Hz, 2H), 7.62 (d, *J* = 8.0 Hz, 2H). ^{13}C NMR (100 MHz, $CDCl_3$, δ): 24.6, 27.6, 30.6, 42.5, 57.0, 74.0, 111.5, 118.6, 127.7, 132.1, 146.3, 214.7. HPLC (Chiralcel OD-H, Hexane–*i*-PrOH (95:5), 1.0 mL/min, 220 nm, 20 °C): t_R = 47.6 min (minor) and t_R = 60.8 min (major), ee: 91%. *Syn*-diastereomer: ^{1}H NMR (400 MHz, $CDCl_3$, δ): 1.52–2.12 (m, 6H), 2.33–2.48 (m, 2H), 2.57–2.61 (m, 1H), 3.19 (s, 1H), 5.42 (s, 1H), 7.42 (d, *J* = 8.0 Hz, 2H), 7.62 (d, *J* = 8.4 Hz, 2H). ^{13}C NMR (100 MHz, $CDCl_3$, δ): 24.7, 25.8, 27.8, 42.5, 56.7, 70.1, 110.7, 118.8, 126.5, 132.0, 147.0, 214.1. HPLC (Chiralcel OD-H, Hexane–*i*-PrOH (95:5), 1.0 mL/min, 220 nm, 20 °C): t_R = 32.6 min and t_R = 40.1 min.

2-[Hydroxy-(4-bromo-phenyl)-methyl]-cyclohexanone (7e)

Yield: 84%; *anti:syn* (97:3). *Anti*-diastereomer: ^{1}H NMR (400 MHz, $CDCl_3$, δ): 1.24–2.08 (m, 6H), 2.28–2.37 (m, 2H), 2.43–2.57 (m, 1H), 3.40 (s, 1H), 4.73 (d, *J* = 8.4 Hz, 1H), 7.18 (d, *J* = 8.0 Hz, 2H), 7.45 (d, *J* = 8.4 Hz, 2H). ^{13}C NMR (100 MHz, $CDCl_3$, δ): 24.6, 27.6, 30.6, 42.5, 57.2, 74.0, 121.6, 128.6, 131.3, 140.0, 215.1. HPLC (Chiralcel OD-H, Hexane–*i*-PrOH (95:5), 1.0 mL/min, 220 nm, 20 °C): t_R = 24.0 min (minor) and t_R = 28.6 min (major), ee: 93%. *Syn*-diastereomer: ^{1}H NMR (400 MHz, $CDCl_3$, δ): 1.46–2.08 (m, 6H), 2.30–2.45 (m, 2H), 2.50–2.56 (m, 1H), 3.04 (s, 1H), 5.31 (d, *J* = 2.4 Hz, 1H), 7.12 (d, *J* = 8.4 Hz, 2H), 7.44 (d, *J* = 8.4 Hz, 2H). ^{13}C NMR (100 MHz, $CDCl_3$, δ): 24.7, 25.8, 27.8, 42.5, 56.9, 70.0, 120.6, 127.5, 131.1, 140.5, 214.4. HPLC (Chiralcel OD-H, Hexane–*i*-PrOH (95:5), 1.0 mL/min, 220 nm, 20 °C): t_R = 13.7 min and t_R = 16.9 min.

2-[Hydroxy-(3-bromo-phenyl)-methyl]-cyclohexanone (7f)

Yield: 76%; *anti:syn* (94:6). *Anti*-diastereomer: ^{1}H NMR (400 MHz, $CDCl_3$, δ): 1.35–2.31 (m, 6H), 2.11–2.49 (m, 2H), 2.54–2.60 (m, 1H), 4.04 (s, 1H), 4.74 (d, *J* = 8.8 Hz, 1H), 7.18–7.24 (m, 2H), 7.41–7.49 (m, 2H). ^{13}C NMR (100 MHz, $CDCl_3$, δ): 24.6, 27.6, 30.7, 42.6, 57.2, 74.1, 122.5, 125.7, 129.8, 129.9, 130.9, 143.3, 215.1. HPLC (Chiralcel OD-H, Hexane–*i*-PrOH (90:10), 0.5 mL/min, 220 nm, 20 °C): t_R = 18.1 min (major) and t_R = 23.5 min (minor), ee: 90%. *Syn*-diastereomer: HPLC (Chiralcel OD-H, Hexane–*i*-PrOH (90:10), 1.0 mL/min, 220 nm, 20 °C): t_R = 15.1 min and t_R = 16.6 min.

2-[Hydroxy-(4-chloro-phenyl)-methyl]-cyclohexanone (7g)

Yield: 80%; *anti*:*syn* (95:5). *Anti*-diastereomer: ^{1}H NMR

© 2007 NRC Canada

(400 MHz, $CDCl_3$, δ): 1.26–2.11 (m, 6H), 2.31–2.49 (m, 2H), 2.52–2.59 (m, 1H), 3.61 (s, 1H), 4.76 (d, J = 8.4 Hz, 1H), 7.25 (d, J = 8.4 Hz, 2H), 7.31 (d, J = 8.8 Hz, 2H). ^{13}C NMR (100 MHz, $CDCl_3$, δ): 24.6, 27.2, 30.7, 42.6, 57.3, 74.0, 128.3, 128.4, 133.5, 139.5, 215.2. HPLC (Chiralcel OD-H, Hexane–*i*-PrOH (95:5), 1.0 mL/min, 220 nm, 20 °C): t_R = 22.1 min (minor) and t_R = 26.0 min (major), ee: 92%. *Syn*-diastereomer: ^{1}H NMR (400 MHz, $CDCl_3$, δ): 1.49–2.09 (m, 6H), 2.32–2.46 (m, 2H), 2.53–2.57 (m, 1H), 2.92 (s, 1H), 5.34 (d, J = 2.0 Hz, 1H), 7.23 (d, J = 8.4 Hz, 2H), 7.30 (d, J = 8.4 Hz, 2H). ^{13}C NMR (100 MHz, $CDCl_3$, δ): 24.8, 25.9, 27.8, 42.6, 57.0, 70.0, 127.1, 128.2, 132.6, 140.0, 214.5. HPLC (Chiralcel OD-H, Hexane–*i*-PrOH (95:5), 1.0 mL/min, 220 nm, 20 °C): t_R = 13.5 min and t_R = 16.6 min.

2-[Hydroxy-(2-chloro-phenyl)-methyl]-cyclohexanone (7h)

Yield: 82%; *anti:syn* (99:1). *Anti*-diastereomer: ^{1}H NMR (400 MHz, $CDCl_3$, δ): 1.51–2.09 (m, 6H), 2.28–2.46 (m, 2H), 2.63–2.70 (m, 1H), 3.92 (s, 1H), 5.34 (d, J = 8.0 Hz, 1H), 7.19 (t, J = 7.6 Hz, 1H), 7.28 (d, J = 7.6 Hz, 1H), 7.31 (d, J = 8.0 Hz, 1H), 7.53 (d, J = 7.6 Hz, 1H). ^{13}C NMR (100 MHz, $CDCl_3$, δ): 24.8, 27.7, 30.3, 42.6, 57.5, 70.3, 127.1, 128.2, 128.6, 129.1, 132.8, 139.0, 215.1. HPLC (Chiralcel AD-H, Hexane–*i*-PrOH (95:5), 1.0 mL/min, 220 nm, 20 °C): t_R = 17.2 min (major) and t_R = 19.7 min (minor), ee: 91%. *Syn*-diastereomer: ^{1}H NMR (400 MHz, $CDCl_3$, δ): 1.49–2.10 (m, 6H), 2.35–2.48 (m, 2H), 2.78–2.83 (m, 1H), 3.16 (s, 1H), 5.71 (d, J = 1.2 Hz, 1H), 7.19 (t, J = 8.0 Hz, 1H), 7.27 (d, J = 4.4 Hz, 1H), 7.31 (d, J = 8.0 Hz, 1H), 7.56 (d, J = 8.0 Hz, 1H). ^{13}C NMR (100 MHz, $CDCl_3$, δ): 24.7, 25.8, 27.8, 42.5, 53.5, 67.5, 126.5, 128.1, 128.4, 129.1, 130.7, 138.6, 214.5. HPLC (Chiralcel AD-H, Hexane–*i*-PrOH (95:5), 1.0 mL/min, 220 nm, 20 °C): t_R = 9.0 min and t_R = 10.2 min.

2-[Hydroxy-(2,4-dichloro-phenyl)-methyl]-cyclohexanone (7i)

Yield: 88%; *anti:syn* (99:1). *Anti*-diastereomer: ^{1}H NMR (400 MHz, $CDCl_3$, δ): 1.53–2.11 (m, 6H), 2.33–2.48 (m, 2H), 2.61–2.64 (m, 1H), 4.09 (d, J = 4.0 Hz, 1H), 5.28 (d, J = 8.0 Hz, 1H), 7.27–7.35 (d, J = 8.0 Hz, 2H), 7.49 (d, J = 8.8 Hz, 1H). ^{13}C NMR (100 MHz, $CDCl_3$, δ): 24.8, 27.7, 30.3, 42.6, 57.5, 70.0, 127.5, 128.8, 129.2, 133.4, 133.7, 137.8, 215.0. HPLC (Chiralcel OD-H, Hexane–*i*-PrOH (90:10), 0.5 mL/min, 220 nm, 20 °C): t_R = 14.9 min (major) and t_R = 18.4 min (minor), ee: 94%. *Syn*-diastereomer: HPLC (Chiralcel OD-H, Hexane–*i*-PrOH (90:10), 0.5 mL/min, 220 nm, 20 °C): t_R = 10.8 min and t_R = 11.4 min.

2-(Hydroxy-phenyl-methyl)-cyclohexanone (7j)

Yield: 72%; *anti:syn* (85:15). *Anti*-diastereomer: ^{1}H NMR (400 MHz, $CDCl_3$, δ): 1.25–2.10 (m, 6H), 2.32–2.49 (m, 2H), 2.58–2.65 (m, 1H), 4.78 (d, J = 6.0 Hz, 1H), 7.29–7.36 (m, 5H). ^{13}C NMR (100 MHz, $CDCl_3$, δ): 24.7, 27.8, 30.8, 42.6, 57.4, 74.7, 127.0, 127.9, 128.3, 140.9, 215.5. HPLC (Chiralcel OD-H, Hexane–*i*-PrOH (90:10), 1.0 mL/min, 220 nm, 20 °C): t_R = 18.2 min (major) and t_R = 26.5 min (minor), ee: 83% *Syn*-diastereomer: ^{1}H NMR (400 MHz, $CDCl_3$, δ): 1.48–2.10 (m, 6H), 2.32–2.47 (m, 2H), 2.57–2.62 (m, 1H), 5.39 (d, J = 2.4 Hz, 1H), 7.23–7.35 (m, 5H). ^{13}C NMR (100 MHz, $CDCl_3$, δ): 24.8, 26.0, 27.9, 42.6, 57.1, 70.6, 125.7, 126.9, 128.1, 141.4, 214.8. HPLC (Chiralcel OD-H, Hexane–*i*-PrOH (90:10), 1.0 mL/min, 220 nm, 20 °C): t_R = 14.7 min and t_R = 16.2 min.

2-(Furan-2-yl-hydroxy-methyl)-cyclohexanone (7k)

Yield: 43%; *anti/syn* (89:11). *Anti*-diastereomer: ^{1}H NMR (400 MHz, $CDCl_3$, δ): 1.30–2.10 (m, 6H), 2.34–2.46 (m, 2H), 2.88–2.90 (m, 1H), 3.90 (d, J = 3.6 Hz, 1H), 4.81 (d, J = 8.4 Hz, 1H), 6.26 (d, J = 3.2 Hz, 1H), 6.30 (q, J = 2.8 Hz, 1H), 7.36 (d, J = 1.2 Hz, 1H). ^{13}C NMR (100 MHz, $CDCl_3$, δ): 24.6, 27.7, 30.5, 42.5, 54.8, 68.1, 107.9, 110.0, 142.2, 153.5, 214.9. HPLC (Chiralcel AD-H, Hexane–*i*-PrOH (95:5), 1.0 mL/min, 220 nm, 20 °C): t_R = 25.8 min (major) and t_R = 28.6 min (minor), ee: 86%. *Syn*-diastereomer: ^{1}H NMR (400 MHz, $CDCl_3$, δ): 1.61–2.10 (m, 6H), 2.34–2.45 (m, 2H), 2.78–2.82 (m, 1H), 3.11 (d, J = 4.8 Hz, 1H), 5.26 (t, J = 3.6 Hz, 1H), 6.26 (d, J = 2.8 Hz, 1H), 6.30 (q, J = 2.8 Hz, 1H), 7.33 (d, J = 1.6 Hz, 1H). ^{13}C NMR (100 MHz, $CDCl_3$, δ): 24.7, 27.2, 27.5, 42.4, 54.5, 66.5, 106.5, 110.2, 141.4, 154.6, 213.6. HPLC (Chiralcel AD-H, Hexane–*i*-PrOH (95:5), 1.0 mL/min, 220 nm, 20 °C): t_R = 17.8 min and t_R = 19.5 min.

4-Hydroxy-3-methyl-4-(4-nitro-phenyl)-butan-2-one (7m)

Yield: 55%; *anti/syn* (97:3). *Anti*-diastereomer: ^{1}H NMR (400 MHz, $CDCl_3$, δ): 1.01 (d, J = 7.6 Hz, 3H), 2.21 (s, 3H), 2.87–2.94 (m, 1H), 3.34 (d, J = 4.8 Hz, 1H), 4.87 (d, J = 8.0 Hz, 1H), 7.51 (d, J = 8.4 Hz, 2H), 8.21 (d, J = 8.8 Hz, 2H). ^{13}C NMR (100 MHz, $CDCl_3$, δ): 14.1, 29.7, 53.2, 75.4, 123.7, 127.5, 147.5, 149.3, 212.8. HPLC (Chiralcel AS-H, Hexane–*i*-PrOH (93:7), 1.0 mL/min, 254 nm, 20 °C): t_R = 51.1 min (major) and t_R = 75.9 min (minor). *Syn*-diastereomer: HPLC (Chiralcel AS-H, Hexane–*i*-PrOH (93:7), 1.0 mL/min, 254 nm, 20 °C): t_R = 47.6 min and t_R = 66.8 min.[2]

Conclusions

In summary, we have developed an organocatalytic asymmetric direct aldol reaction in brine with high diastereo- and enantioselectivities, using a readily available bifunctional amide catalyst. From a green-chemistry view, employing brine or water as the reaction medium is environment-friendly and safe, regardless of performing the reaction under truly aqueous conditions or not (14). Further studies that focus on the application of this catalyst system to other types of transformations are under investigation in our laboratory.

[2] Supplementary data for this article are available on the journal Web site (http://canjchem.nrc.ca) or may be purchased from the Depository of Unpublished Data, Document Delivery, CISTI, National Research Council Canada, Ottawa, ON K1A 0S2, Canada. DUD 5138. For more information on obtaining material, refer to http://cisti-icist.nrc-cnrc.gc.ca/irm/unpub_e.shtml.

© 2007 NRC Canada

Acknowledgement

We are grateful for the financial support from the National Natural Science Foundation of China (20672040), the National Basic Research Program of China (2004CCA00100), the program for New Century Excellent Talents in University (NCET-05–0672), and the Hubei Province Science Fund for Distinguished Young Scholar (2004ABBC011).

References

1. (*a*) D.C. Rideout and R. Breslow. J. Am. Chem. Soc. **102**, 7816 (1980); (*b*) R. Breslow, U. Maitra, and D.C. Rideout. Tetrahedron Lett. **24**, 1901 (1983); (*c*) R. Breslow and U. Maitra. Tetrahedron Lett. **25**, 1239 (1984); (*d*) R. Breslow. Acc. Chem. Res. **24**, 159 (1991); (*e*) R. Breslow. Acc. Chem. Res. **37**, 471 (2004).
2. (*a*) Organic synthesis in water. *Edited by* P.A. Grieco. Blackie Academic & Professional, London. 1998; (*b*) U.M. Lindstrom. Chem. Rev. **102**, 2751 (2002); (*c*) S. Kobayashi and K. Manabe. Acc. Chem. Res. **35**, 209 (2002), and refs. cited therein; (*d*) C.-J. Li. Chem. Rev. **105**, 3095 (2005); (*e*) C.-J. Li and L. Liang. Chem. Soc. Rev. **35**, 68 (2006), refs. cited therein.
3. D. Sinou. Adv. Synth. Catal. **344**, 221 (2002).
4. (*a*) N. Mase, K. Watanabe, H. Yoda, K. Takabe, F. Tanaka, and C.F. Barbas, III. J. Am. Chem. Soc. **128**, 4966 (2006); (*b*) P.M. Synowiec and B. Bunikowska. Ind. Eng. Chem. Res. **44**, 2273 (2005).
5. For recent reviews on asymmetric organocatalysis, see: (*a*) H. Gröger and J. Wilken. Angew. Chem. **113**, 545 (2001); Angew. Chem., Int. Ed. **40**, 529 (2001); (*b*) P.I. Dalko and L. Moisan. Angew. Chem. **113**, 3840 (2001); Angew. Chem., Int. Ed. **40**, 3726 (2001); (*c*) B. List. Tetrahedron **58**, 5573 (2002); (*d*) E.R. Jarvo and S.J. Miller. Tetrahedron, **58**, 2481 (2002); (*e*) S.T. Handy. Chem. Eur. J. **9**, 2938 (2003); (*f*) A. Berkssel and H. Gröger. Asymmetric organocatalysis. Wiley-VCH, Weinheim. 2005; (*g*) P.I. Dalko and L. Moisan. Angew. Chem. **116**, 5248 (2004); Angew. Chem., Int. Ed. **43**, 5138 (2004); (*h*) Y.Hayashi. J. Synth. Org. Chem. Jpn. **63**, 464 (2005); (*i*) J. Seayad and B. List. Org. Biomol. Chem. **3**, 719 (2005).
6. (*a*) U. Eder, G. Sauer, and R. Wiechert. Angew. Chem. **83**, 492 (1971); Angew. Chem., Int. Ed. Engl. **10**, 496 (1971); (*b*) Z. G. Hajos and D.R. Parrish. J. Org. Chem. **39**, 1615 (1974).
7. (*a*) B. List, R.A. Lerner, and C.F. Barbas, III. J. Am. Chem. Soc. **122**, 2395 (2000); (*b*) W. Notz and B. List. J. Am. Chem. Soc. **122**, 7386 (2000).
8. Representative examples include: (*a*) K. Sakthievel, W. Notz, T. Bui, and C.F. Barbas, III. J. Am. Chem. Soc. **123**, 5260 (2001); (*b*) B. List, P. Pojarliev, and C. Castello. Org. Lett. **3**, 573 (2001); (*c*) C. Pidathala, L. Hoang, N. Vignola, and B. List. Angew. Chem., Int. Ed. **42**, 2785 (2003); (*d*) A. Bøgevig, N. Kumaragurubaran, and K.A. Jørgensen. Chem. Commun. **6**, 620 (2002); (*e*) A.B. Northrup and D.W.C. MacMillan. J. Am. Chem. Soc. **124**, 6798 (2002); (*f*) A.B. Northrup, I.K. Mangion, F. Hettche, and D.W.C. MacMillan. Angew. Chem., Int. Ed. **43**, 2152 (2004); (*g*) Y. Sekiguchi, A. Sasaoka, A. Shimomoto, S. Fujioka, and H. Kotsuki. Synlett, **11**, 1655 (2003); (*h*) A.B. Northrup and D.W.C. MacMillan. Science (Washington, D.C.), **305**, 1752 (2004); (*i*) Z. Tang, F. Jiang, L.-T. Yu, L.-Z. Gong, A.-Q. Mi, Y.-Z. Jiang, and Y.-D. Wu. J. Am. Chem. Soc. **125**, 5262 (2003); (*j*) J.-R. Chen, H.-H. Lu, X.-Y. Li, L. Cheng, J. Wan, and W.-J. Xiao. Org. Lett. **7**, 4543 (2005); (*k*) Y.-J. Cao, H.-H. Lu, Y.–Y. Lai, L.–Q. Lu, and W.-J. Xiao. Synthesis, 3795 (2006); (*l*) A. Cordova, W. Notz, and C.F. Barbas, III. Chem. Commun. **6**, 3024 (2002); (*m*) Y.-S. Wu, Y. Chen, D.-S. Deng, and J. Cai. Synlett, 1627 (2005); (*n*) S.S. Chimni, D. Mahajan, and V.V. Suresh Babu. Tetrahedron Lett. **46**, 5617 (2005).
9. (*a*) Z. Tang, Z.-H. Yang, L.-F. Cun, L.-Z. Gong, A.-Q. Mi, and Y.-Z. Jiang. Org. Lett. **6**, 2285 (2004); (*b*) H. Torii, M. Nakadai, K. Ishihara, S. Saito, and H. Yamamoto. Angew. Chem., Int. Ed. **43**, 1983 (2004); (*c*) A.I. Nyberg, A. Usanp, and P.M. Pihko. Synlett, 1891 (2004); (*d*) D.-P. Li, Y.-C. Guo, Y. Ding, and W.-J. Xiao. Chem. Commun. 799 (2006); (*e*) J.-R. Chen, X.-Y. Li, X.-X. Xing, and W.-J. Xiao. J. Org. Chem. **71**, 8198 (2006); (*f*) Y.-J. Cao, Y.-Y. Lai, X. Wang, Y.-J. Li, and W.-J. Xiao. Tetrahedron Lett. **48**, 21 (2007).
10. (*a*) T. Darbre and M. Machuqueiro. Chem. Commun. **3**, 1090 (2003); (*b*) Y.-Y.Peng, Q.-P. Ding, Z. Li, P.-G. Wang, and J.-P. Cheng. Tetrahedron Lett. **44**, 3871 (2003); (*c*) Y.-S. Wu, W.-Y. Shao, C.-Q. Zheng, Z.-L. Huang, J. Cai, and Q.-Y. Deng. Helv. Chim. Acta, **87**, 1377 (2004).
11. (*a*) N. Mase; Y. Nakai, N. Ohara, H. Yoda, K. Takabe, F. Tanaka, and C.F. Barbas, III. J. Am. Chem. Soc. **128**, 734 (2006); (*b*) Y. Hayashi, T. Sumiya, J. Takahashi, H. Gotoh, T. Urushima, and M. Shoji. Angew. Chem., Int. Ed. **45**, 958 (2006); (*c*) Y. Hayashi, S. Aratake, T. Okano, J. Takahashi, T. Sumiya, and M. Shoji. Angew. Chem., Int. Ed. **45**, 5527 (2006); (*d*) P. Dziedzic, W. Zou, J. Hafren, and A. Cordova. Org. Biomol. Chem. **4**, 38 (2006); (*e*) Y. Wu, Y. Zhang, M. Yu, G. Zhao, and S. Wang. Org. Lett. **8**, 4417 (2006).
12. (*a*) B. List, P. Pojarliev, and H.J. Martin. Org. Lett. **3**, 2423 (2001); (*b*) J.M. Betancort, and C.F. Barbas, III. Org. Lett. **3**, 3737 (2001); (*c*) N. Mase, R. Thayumanavan, F. Tanaka, and C.F. Barbas, III. Org. Lett. **6**, 2527 (2004); (*d*) J.M. Betancort, K. Sakthivel, R. Thayumanavan, F. Tanaka, and C.F. Barbas, III. Synthesis, 1509 (2004); (*e*) A. Alexakis and O. Andrey. Org. Lett. **4**, 3611 (2002); (*f*) O. Andrey, A. Alexakis, and G. Bernardinelli. Org. Lett. **5**, 2559 (2003); (*g*) O. Andrey, A. Alexakis, A. Tomassini, and G. Bernardinelli. Adv. Synth. Catal. **346**, 1147 (2004); (*h*) N. Mase, F. Tanaka, and C.F. Barbas, III. Org. Lett. **5**, 4369 (2003); (*i*) F. Tanaka, R. Thayumanavan, N. Mase, and C.F. Barbas, III. Tetrahedron Lett. **45**, 325 (2004).
13. (*a*) S. Bahmanyar and K.N. Houk. J. Am. Chem. Soc. **123**, 12911 (2001); (*b*) L. Hoang, S. Bahmanyar, K.N. Houk, and B. List. J. Am. Chem. Soc. **125**, 16 (2003); (*c*) S. Bahmanyar, K.N. Houk, H.J. Martin, and B. List. J. Am. Chem. Soc. **125**, 2475 (2003); (*d*) F.R. Clemente, and K.N. Houk. J. Am. Chem. Soc. **127**, 11294 (2005).
14. (*a*) A.P. Brogan, T.J. Dickerson, and K.D. Janda. Angew. Chem., Int. Ed. **45**, 8100 (2006); (*b*) Y. Hayashi. Angew. Chem., Int. Ed. **45**, 8103 (2006).

© 2007 NRC Canada

Monte Carlo simulation study of the effects of acidity and LET on the primary free-radical and molecular yields of water radiolysis — Application to the Fricke dosimeter

Narongchai Autsavapromporn, Jintana Meesungnoen, Ianik Plante, and Jean-Paul Jay-Gerin

Abstract: Monte Carlo simulations are used to investigate the effects of acidity (pH) on the primary yields of various chemical species produced in the radiolysis of de-aerated aqueous sulfuric acid solutions over the range from neutral solution to 0.4 mol/L H_2SO_4. The effects of the quality of radiation, measured in terms of linear energy transfer (LET), have also been studied for LET varying from ~0.3 to 15 keV/μm at ambient temperature. Our results show that an increase in acidity ($1 < pH < 4$) leads to an increase in the yield $G_{e^-_{aq}+H\cdot}$ of the "reducing" free radicals (hydrated electron and H• atom) and a slight increase in $G_{\cdot OH}$ and $G_{H_2O_2}$, while there is a slight decrease in G_{H_2}. At $pH < 1$, •OH radicals react with HSO_4^- anions to form $SO_4^{\cdot-}$ radicals, resulting in a steep decrease in $G_{\cdot OH}$. By contrast, in the range of pH from ~4 to 7, the calculated yield values are independent of sulfuric acid concentration. In both neutral water and 0.4 mol/L H_2SO_4 (pH 0.46) solutions, the primary molecular yields increase upon increasing LET to ~15 keV/μm with a concomitant decrease in those of free radicals. As an exception, $G_{H\cdot}$ at first increases with LET, reaching a maximum near 6.5 keV/μm before decreasing steeply at higher LET. The results obtained are generally in good agreement with available experimental data over the whole acidity and LET ranges studied. Finally, as an application, we have simulated the radiation-induced oxidation of ferrous sulfate solutions in aerated aq. 0.4 mol/L H_2SO_4 (Fricke dosimeter) as a function of time up to ~50 s and addressed the effects of LET on the resulting ferric ion yield at 25 °C. The production of Fe^{3+} ions is highly sensitive to free-radical yields, especially H• atoms (via formation of $HO_2^{\bullet}$), resulting in a marked decline of $G(Fe^{3+})$ with increasing LET. The general trend of the observed variation of $G(Fe^{3+})$ with radiation quality is well reproduced by our computed Fe^{3+} ion yield values.

Key words: liquid water, acidic (H_2SO_4) aqueous solutions, radiolysis, free-radical and molecular yields, linear energy transfer (LET), Fricke dosimeter, Monte Carlo simulations.

Résumé : À l'aide de calculs de simulation Monte Carlo, nous avons étudié l'influence de l'acidité (pH) sur les rendements primaires des diverses espèces chimiques produites lors de la radiolyse de solutions aqueuses désaérées d'acide sulfurique dans la gamme de concentrations ~0–0.4 mol/L en H_2SO_4. L'influence de la qualité du rayonnement, décrite en termes de transfert d'énergie linéique (TEL), a aussi été étudiée pour des valeurs de TEL entre ~0,3 et 15 keV/μm à la température ambiante. Nos résultats montrent que, pour des irradiations avec des rayonnements de faible TEL, une augmentation en acidité ($1 < pH < 4$) conduit à une augmentation du rendement $G_{e^-_{aq}+H\cdot}$ de l'entité réductrice radicalaire (électron hydraté et atome H˙) et à un faible accroissement de $G_{\cdot OH}$ et $G_{H_2O_2}$, alors que G_{H_2} diminue légèrement. À $pH < 1$, les radicaux •OH réagissent avec les anions HSO_4^- pour former les radicaux $SO_4^{\cdot-}$, entraînant une diminution marquée de $G_{\cdot OH}$. En revanche, pour des pH entre ~4 et 7, les valeurs des rendements calculées sont indépendantes de la concentration en acide sulfurique. Autant pour l'eau liquide neutre que pour les solutions H_2SO_4 0,4 mol/L (pH 0,46), les rendements primaires moléculaires augmentent avec le TEL alors que ceux des espèces radicalaires diminuent de façon concomitante. Le cas de $G_{H\cdot}$ est singulier, puisqu'il augmente initialement avec le TEL, atteint un maximum à ~6,5 keV/μm, puis décroît rapidement à TEL plus élevé. Les résultats obtenus s'accordent bien avec les données expérimentales disponibles dans la littérature pour toute la gamme d'acidité et de TEL considérée. À titre d'application, nous avons enfin simulé l'oxydation radio-induite des ions ferreux en milieu H_2SO_4 0,4 mol/L aéré (dosimètre de Fricke) en fonction du temps jusqu'à ~50 s et étudié l'influence du TEL sur le rendement d'apparition des

Received 6 December 2006. Accepted 22 February 2007. Published on the NRC Research Press Web site at http://canjchem.nrc.ca on 24 April 2007.

This work is dedicated to the memory of Professor David A. Armstrong.

N. Autsavapromporn, J. Meesungnoen, I. Plante, and J.-P. Jay-Gerin.[1] Département de Médecine Nucléaire et de Radiobiologie, Faculté de Médecine et des Sciences de la Santé, Université de Sherbrooke, 3001, 12e Avenue Nord, Sherbrooke, QC J1H 5N4, Canada.

[1]Corresponding author (e-mail: jean-paul.jay-gerin@USherbrooke.ca).

 doi:10.1139/V07-021 © 2007 NRC Canada

ions ferriques à 25 °C. La production des ions Fe^{3+} est très sensible à la valeur des rendements radicalaires, en particulier les atomes H• (via la formation de HO_2•), résultant en une décroissance marquée de $G(Fe^{3+})$ lorsque le TEL augmente. L'allure générale de la variation expérimentale de $G(Fe^{3+})$ avec la qualité du rayonnement utilisé est bien reproduite par nos valeurs calculées des rendements d'ions Fe^{3+}.

Mots-clés : eau liquide, solutions aqueuses acides (H_2SO_4), radiolyse, rendements radicalaires et moléculaires, transfert d'énergie linéique (TEL), dosimètre de Fricke, simulations Monte Carlo.

Introduction

A large fraction of radiation chemistry has been concerned with studies of water and its solutions[2] mainly because of the unique importance of water, particularly in biological systems (living cells are composed of about 70%–85% water by weight) and also in various domains of nuclear science and technology, such as water-cooled nuclear power reactors (where water is used both as neutron moderator and as the heat transport medium). A good summary of the present status of aqueous radiation chemistry is given in refs. 1–4.

The radiolysis of pure liquid water (in the absence of oxygen) by low-LET (linear energy transfer or energy loss per unit track length, -dE/dx) radiation such as ^{60}Co γ-rays, fast electrons, or high-energy protons, can be described under ordinary irradiation conditions by the following *global* equation, written for an absorbed energy of 100 eV (1),

$$[1]\quad G_{-H_2O}H_2O \rightsquigarrow G_{e^-_{aq}}e^-_{aq} + G_{OH^-}OH^- + G_{H^+}H^+ + G_{H\cdot}H\cdot + G_{H_2}H_2 + G_{\cdot OH}\cdot OH + G_{H_2O_2}H_2O_2 + G_{HO_2\cdot/O_2\cdot^-}HO_2\cdot/O_2\cdot^- + \ldots$$

where the coefficients G_X are the so-called "primary" free-radical and molecular yields ("long-time" or "escape" yields) representing the numbers of the various radiolytic species X (e^-_{aq}, OH^-, H^+, H•, H_2, •OH, H_2O_2, HO_2•/O_2•$^-$, …) that remain throughout the bulk of the solution after spur expansion owing to diffusion.[3] At ambient temperature, this spur expansion is essentially complete on the microsecond time scale after the initial energy deposition. At this time, the species that have diffusively escaped from spur or track reactions become homogeneously distributed in the bulk of the solution and available to react with added solutes (treated as spatially homogeneous) at moderate concentrations. At this stage, G_{-H_2O} denotes the corresponding yield for net water decomposition. For ^{60}Co γ-radiation and neutral water at ambient temperature (LET ~0.3 keV/μm, pH 7), the values of the primary yields are (3),

$$[2]\quad \begin{array}{lll} G_{e^-_{aq}} = 2.50 & G_{H\cdot} = 0.56 & G_{H_2} = 0.45 \\ G_{\cdot OH} = 2.50 & G_{H_2O_2} = 0.70 & G_{HO_2\cdot/O_2\cdot^-} = 0.02 \\ G_{-H_2O} = 3.94 & & \end{array}$$

These values, including the contribution of hydroperoxyl/superoxide anion radicals (HO_2•/O_2•$^-$, pK_a = 4.8, is a minor radiolytic product and can be usually omitted in the case of low-LET radiation)[4] are connected by the equations:

$$[3]\quad G_{e^-_{aq}} + G_{OH^-} = G_{H^+}$$

$$[4]\quad G_{e^-_{aq}} + G_{H\cdot} + 2G_{H_2} = G_{\cdot OH} + 2G_{H_2O_2} + 3G_{HO_2\cdot/O_2\cdot^-}$$

$$G_{-H_2O} = G_{e^-_{aq}} + G_{H\cdot} + 2G_{H_2} - G_{HO_2\cdot/O_2\cdot^-} = G_{\cdot OH} + 2G_{H_2O_2} + 2G_{HO_2\cdot/O_2\cdot^-}$$

expressing the charge conservation (electroneutrality) and material balance of eq. [1], respectively.[5] Examination of the material balance eq. [4] normally serves as a stringent criterion for a consistent set of G values.

For ^{60}Co γ-irradiated 0.4 mol/L sulfuric acid aqueous solutions at room temperature (pH 0.46), representative values of the primary free-radical and molecular product yields are (e.g., see ref. 5):

$$[5]\quad \begin{array}{lll} G_{e^-_{aq}+H\cdot} = 3.66 & G_{H_2} = 0.40 & \\ G_{\cdot OH} = 2.84 & G_{H_2O_2} = 0.78 & \\ G_{HO_2\cdot/O_2\cdot^-} = 0.02 & G_{-H_2O} = 4.44 & \end{array}$$

In fact, radiolysis experiments concerning acidic solutions were carried out before those for neutral solutions [the most commonly used acid was H_2SO_4 in 0.4 mol/L aqueous solutions, although a few other acids such as HCl, $HClO_4$, and $(COOH)_2$ were also employed in radiation yield determina-

[2] In fact, experiments showing that water is decomposed by the action of dissolved radium salts were carried out shortly after Henri Becquerel's discovery of radioactivity (1896). One reviewer of this paper pointed out that Sir William Ramsay [J. Chem. Soc. Trans. **91**, 931 (1907)] was the first to systematically perform a series of complete experiments relating to the action of radium "emanation" on water. His article entitled, "The chemical action of the radium emanation. Part I. Action on distilled water", was published in 1907, precisely a century ago. A historical account of the radiation chemistry of water is given in ref. 1 and refs. cited therein.

[3] The symbol G with the formula of the species as subscript is used here to represent the "primary" yield of species X. Note that, following convention, the symbol G(X) with the formula of the product in parentheses denotes the experimental 100-eV yield of the "final" product X. Throughout this paper, values of G are expressed in units of molecules per 100 eV of absorbed energy; for conversion into SI units, 1 molec./100 eV ≈ 0.10364 μmol/J.

[4] The production of HO_2•/O_2•$^-$ is significant only in high-LET radiation tracks (e.g., see ref. 3).

[5] Equations [3] and [4] can readily be derived by writing that, at any time, the total (algebraic) charge of the transient species and stable products formed in the decomposition of water should be zero and the total number of H• atoms in the transients and products considered should be equal to twice the number of O atoms.

© 2007 NRC Canada

tions at low pH] for historical reasons related to the early development of the standard aerated ferrous sulfate (Fricke) dosimeter (6). One of the reasons that dictated the choice of sulfuric acid came from the fact that the dominant anion HSO_4^- was then considered to not intervene in the course of the radiolysis. The concentration of 0.4 mol/L H_2SO_4 was originally selected to provide the same mass absorption for X-rays in the dosimeter solution as in air (7). At such a high concentration of H_2SO_4, the H^+ ions very rapidly scavenge most, if not all, of the e_{aq}^- radicals in the spurs/tracks to form $H^\cdot$ atoms (5, 8–10):

$$[6] \qquad e_{aq}^- + H^+ \rightarrow H^\cdot$$

with a bimolecular rate constant $k_6 \approx 1.12 \times 10^{10}$ $(mol/L)^{-1}$ s^{-1} (value corrected to take into account the effects of ionic strength at this acid concentration; see later) (11–15). The total primary yield of the reducing radicals e_{aq}^- and $H^\cdot$ may then be represented by the sum $G_{e_{aq}^- + H^\cdot} = G_{e_{aq}^-} + G_{H^\cdot}$.

A great many experimental and theoretical studies have shown that the yields in the radiolysis of water and aqueous solutions are highly dependent on the distances separating the primary products from each other along the track of the ionizing radiation. The distribution of separations, commonly referred to as the "track structure" (e.g., see ref. 3), is largely determined by the geometry of the physical energy loss events, or in other words by the quality of the radiation. An often used specifier of beam quality is the LET. The most evident effect of increasing the LET of the radiation is to give lower free-radical and higher molecular primary yields (3, 16–20). This behavior is explained by the increased intervention of radical–radical reactions as the local concentration of radicals within the track increases. In fact, as the LET increases, the initially isolated "spherical" spurs change to a situation in which the spurs overlap to form continuous "cylindrical" tracks consisting of a "core" of intense ionization and electronic excitation surrounded by a region composed of the tracks of knocked-out secondary electrons (δ-rays) called the "penumbra" (21–23). This should permit fewer free radicals to escape combination and recombination reactions during the expansion of the tracks and, in turn, the formation of more molecular products.

One of the best studied systems in radiation chemistry is the aerated dilute solution of ferrous sulfate in aq. 0.4 mol/L H_2SO_4, which is referred to as the "Fricke dosimeter" after Hugo Fricke who first published accounts of its properties in 1927–1929 (6). The chemistry of this system is based on the oxidation of ferrous ions to ferric ions by the oxidizing species $HO_2^\cdot$ (bearing in mind the rapid conversion of e_{aq}^- and $H^\cdot$ to $HO_2^\cdot$ at low pH and in the presence of oxygen), $^\cdot OH$, and H_2O_2 that are produced in the radiolytic decomposition of water (see later) (2, 7, 16, 24). From this mechanism, the yield of Fe^{3+} ions can be expressed in terms of the primary free-radical and molecular yields, given earlier, by the following stoichiometric equation (2, 24):

$$[7] \qquad G(Fe^{3+}) = 3(G_{e_{aq}^- + H^\cdot} + G_{HO_2^\cdot}) + G_{^\cdot OH} + 2G_{H_2O_2}$$

This relationship, which has been confirmed by experiment, shows that the production of Fe^{3+} ions is highly sensitive to factors that alter the free-radical yields, especially the yield of $H^\cdot$ atoms. In particular, $G(Fe^{3+})$ depends on the type of the radiation used. Data by a number of different authors have shown that $G(Fe^{3+})$ steadily decreases with increasing LET, this dependence reflecting the lower yields of radicals that escape the high-LET track as compared with low-LET radiolysis (e.g., see refs. 7, 11, 16, and 25–33). The Fricke dosimeter is a widely used liquid chemical dosimeter because of the accuracy, reproducibility, and linearity of its response as a function of dose (with care, Fricke dosimetry is capable of 0.1% precision for ^{60}Co γ-rays and high-energy X-rays and electrons) (33). In fact, its well-established characteristics are a standard in radiation–chemical work for comparison of yields under various conditions, both for experimental observations and for theoretical calculations.

For years, it has repeatedly been underlined that the problem of the influence of pH on the primary free-radical and molecular yields of water radiolysis is not yet totally resolved, especially at extreme values of pH where a certain confusion still exists (5, 10, 31). To gain further insights into our understanding of the effects of varying acidity and LET in the radiation chemistry of water, in the present study we have performed Monte Carlo simulations of the radiolysis of aq. H_2SO_4 solutions (over the range from neutral solution to 0.4 mol/L H_2SO_4) to calculate the variations of $G_{e_{aq}^- + H^\cdot}$, $G_{^\cdot OH}$, G_{H_2}, and $G_{H_2O_2}$ with pH for different values of the LET varying from ~0.3 to 15 keV/μm. This is followed, as an application, by a Monte Carlo study of the radiolytic oxidation of Fe^{2+} to Fe^{3+} ions in the Fricke dosimeter as a function of time (up to ~50 s) to address the influence of the radiation quality on the ferric ion yield. The results in each case are tested against the available experimental data.

This paper deals only with results at 25 °C. The main features of our simulation approach are presented in the next section, followed by the results and their discussion. Conclusions are drawn in the final section.

Monte Carlo simulations

Monte Carlo simulation techniques are used to model the complex succession of events that are generated in liquid water and sulfuric acid aqueous solutions under irradiation. The detailed description and implementation of our Monte Carlo code IONLYS-IRT that simulates the nonhomogeneous distribution of reactive species initially produced by the energy deposition by the incident radiation and by all the secondary electrons that it has generated (i.e., the radiation track structure) and the subsequent chemical reactions of these species with each other and with available solutes has been given previously (see ref. 34 and the refs. therein). In brief, the IONLYS simulation program models, on an event by event basis, all of the events of the early physical ($<10^{-15}$ s) and physicochemical ($\sim 10^{-15}$–10^{-12} s) stages in the track development. The complex spatial distribution of reactants at the end of the physicochemical stage, which is provided as an output of the IONLYS program, is then used directly as the starting point for the subsequent nonhomogeneous chemical stage ($\sim 10^{-12}$–10^{-6} s). This third and final stage, during which the individual reactive species diffuse randomly and react with one another (or with the environment) until all spur or track processes are complete, is covered by our IRT program. This program employs the "independent reaction times" (IRT) method (35, 36), a computer efficient stochastic simulation technique that is used to

© 2007 NRC Canada

simulate reaction times without following the trajectories of the diffusing species. The IRT method relies on the approximation that the reaction time of each pair of reactants is independent of the presence of other reactants in the system. Within the framework of this approach, the competition between the reactions is simply described via a sorting out of the stochastically sampled reaction times of each potentially reactive pair. The IRT simulation technique also allows one (as is the case in this study) to include in a simple way pseudo first-order reactions of the radiolytic products with various scavengers that are homogeneously distributed in the medium. The ability of our IRT program to give accurate time-dependent chemical yields has been well validated by comparison with a full step-by-step Monte Carlo simulation, which does follow the reactant trajectories in detail (37).

To reproduce the effects of fast electron or ^{60}Co γ-radiolysis, we use short (~100 μm) segments of 300 MeV proton tracks, over which the LET value obtained in the simulations is nearly constant[6] and equal to ~0.3 keV/μm at 25 °C. The number of proton histories (~150) is chosen so as to ensure only small statistical fluctuations when calculating average yields while keeping acceptable computer time limits. We should note that the use of high-energy protons as primary particles was more appropriate here than that of electrons since we wanted to study track segments over which the LET is essentially constant. In fact, a proton that has the same LET as an electron must also have an energy ~2000 times larger, and consequently its LET is much less affected by a given series of energy depositions (11, 36).

The reaction scheme and reaction parameters, as well as the diffusion coefficients of reactive species used in our IRT program for the radiolysis of pure liquid water, are taken from Tables 1 and 2 of ref. 36. Only slight adjustments were made in some reaction rate constants and diffusion coefficients to take account of the latest data available from the literature.

Modeling the effects of acidity

To simulate the radiolysis of water under acidic conditions, we have used aqueous solutions of sulfuric acid of various concentrations in the range ~0–0.4 mol/L (i.e., at different pH values between ~7 to 0.46). As discussed earlier, much experimental and theoretical work has been done over many decades on the radiation chemistry of aq. H_2SO_4 solutions (especially, in 0.4 mol/L sulfuric acid), at least in part because of the fact that sulfuric acid was widely employed in the early development of the Fricke and other chemical dosimeters (custom then dictated its continued usage) (38). For aq. H_2SO_4 (a diprotic acid) we have:

$$[8] \qquad H_2SO_4 \underset{pK_{a1}}{\overset{H^+}{\rightleftarrows}} HSO_4^- \underset{pK_{a2}}{\overset{H^+}{\rightleftarrows}} SO_4^{2-}$$

Table 1. Reactions added to the pure water reaction scheme to simulate the radiolysis of de-aerated aq. H_2SO_4 solutions, at 25 °C.

Reaction	k ((mol/L)$^{-1}$ s^{-1})
$H^{\cdot} + SO_4^{\cdot-} \rightarrow HSO_4^-$	1.0×10^{10} [a]
$H^{\cdot} + S_2O_8^{2-} \rightarrow SO_4^{\cdot-} + HSO_4^-$	2.5×10^{7} [b]
$^{\cdot}OH + HSO_4^- \rightarrow H_2O + SO_4^{\cdot-}$	1.5×10^{5} [c]
$e_{aq}^- + S_2O_8^{2-} \rightarrow SO_4^{\cdot-} + SO_4^{2-}$	1.2×10^{10} [b]
$H_2O_2 + SO_4^{\cdot-} \rightarrow HO_2^{\cdot} + HSO_4^-$	1.2×10^{7} [d]
$OH^- + SO_4^{\cdot-} \rightarrow {}^{\cdot}OH + SO_4^{2-}$	8.3×10^{7} [d]
$SO_4^{\cdot-} + SO_4^{\cdot-} \rightarrow S_2O_8^{2-}$	4.4×10^{8} [d]

Note: The rate constants given here for the reactions between ions are at ionic strength equal to zero.
[a]Ref. 42.
[b]Ref. 14.
[c]Value used in this work (see text).
[d]Ref. 43.

with $pK_{a1} \approx -3$ and $pK_{a2} = 1.987$ at 25 °C (39, 40). Hence, H_2SO_4 is virtually completely dissociated when dissolved in water above pH ≈ 0, and the solution contains mainly H^+, HSO_4^-, and a certain amount of SO_4^{2-}.[7] The concentration of each species changes as the total acid concentration changes.

We summarize in the following the model assumptions and procedures we have used to carry out the Monte Carlo simulations of the radiolysis of aq. H_2SO_4 solutions with IONLYS-IRT (some of the details of our computational modeling have already been given in refs. 11 and 41). As noted before, the effects of the background concentrations of H^+ in solutions were added to the IRT program as pseudo first-order reactions. We also supplemented the pure water reaction scheme to include the reactions listed in Table 1, which account for the species present in irradiated sulfuric acid solutions. At high acidities, a certain proportion of the $^{\cdot}OH$ radicals react with hydrogen sulfate (or bisulfate) ions[8] to form the sulfate radical $SO_4^{\cdot-}$ according to (e.g., see refs. 14, 42, and 44–46):

$$[9] \qquad {}^{\cdot}OH + HSO_4^- \rightarrow H_2O + SO_4^{\cdot-}$$

The importance of $SO_4^{\cdot-}$ (or equivalently, its protonated form $HSO_4^{\cdot}$, although no pK_a value has been determined) as an intermediate in the radiolysis of aq. H_2SO_4 solutions at low pH has long been recognized. However, the value of the rate constant (k_9) for reaction [9] is not well established, and the data reported thus far in the literature span a range of about an order of magnitude ($1.3–15 \times 10^5$ (mol/L)$^{-1}$ s^{-1}) (14, 42, 44, 45). In view of such uncertainty, instead of choosing, somewhat arbitrarily, a particular value of k_9 among those already published, we have selected $k_9 = 1.5 \times 10^5$ (mol/L)$^{-1}$ s^{-1} in this study by adjusting this parameter so as to match, at low LET, the experimental (47–50) and simulated values of $G_{\cdot OH}$ in the region of pH < 1–2. Concomitantly, the $SO_4^{\cdot-}$ escape yields calculated using this value of k_9 are also found, in this acid range, to be less than the

[6] Such an analysis thus gives the track segment yields at a well-defined LET (e.g., see ref. 3).
[7] In this work, the dissociation of HSO_4^- is simply treated for the entire range of pH studied as a weak-acid problem in dilute aqueous solutions. Under these conditions, the concentrations of H^+ ($F + x$), HSO_4^- ($F - x$), and SO_4^{2-} (x) are readily determined, at equilibrium, by solving the quadratic equation, $K_{a2} = [H^+]\,[SO_4^{2-}]/[HSO_4^-] = (F + x)\,(x)/(F - x)$, where F and K_{a2} are the considered concentration of H_2SO_4 and its second acid dissociation constant ($K_{a2} = 10^{-pK_{a2}} \approx 0.0103$), respectively.
[8] Contrary to the hydrogen sulfate ion HSO_4^-, the sulfate ion, SO_4^{2-} has been reported to be unreactive toward $^{\cdot}OH$.

© 2007 NRC Canada

$G_{SO_4^{\bullet-}}$ values measured experimentally (42, 48, 50). This observation is consistent with the fact that there are two distinct formation processes of the $SO_4^{\bullet-}$ radical (for a review see ref. 51), the indirect process via $^{\bullet}OH$ radical attack on HSO_4^- according to reaction [9] (which we have considered) and the direct action of radiation on the sulfuric acid anions (which we have not considered in our simulations; see later). Unfortunately, a more quantitative comparison between modeling and experiment is difficult to offer at this stage, as the experimental discrimination between the two contributing components of $G_{SO_4^{\bullet-}}$ has not been clearly elucidated yet. The diffusion coefficients of HSO_4^-, $SO_4^{\bullet-}$, SO_4^{2-}, and $S_2O_8^{2-}$, employed in the Monte Carlo simulations are taken to be (in units of 10^{-9} m^2 s^{-1}) 1.385 (for both HSO_4^- and $SO_4^{\bullet-}$), 1.065, and 1.145, respectively (52).

In addition, we have introduced in the IRT program the effects due to the ionic strength of the solutions (e.g., see ref. 53) for reaction [6] and for the recombination of the proton with the hydroxyl ion (11, 34):

[10] $OH^- + H^+ \rightarrow H_2O$

as well as for all reactions between ions [except for the peculiar bimolecular self-recombination of hydrated electrons for which there is no evidence of any ionic strength effect (54)], including those given in Table 1. To relate rate constant and ionic strength of the solution, we used the following equation, obtained from the Brönsted–Bjerrum model of ionic reactions and the extended Debye–Hükel theory of ionic solutions (55, 56):

$$[11] \qquad \log\left(\frac{k}{k_o}\right) = 1.02\, Z_a Z_b \left(\frac{I^{1/2}}{1+I^{1/2}}\right) - 2bI$$

where k is the rate constant at ionic strength I, k_0 is the rate constant in the limit of zero ionic strength (i.e., at infinite dilution), Z_a and Z_b are the algebraic numbers of charges on the reactants (positive for cations and negative for anions), and b is a parameter taken as ($0.15\, Z_a Z_b$) in this study. I is defined as (57):

$$[12] \qquad I = \frac{1}{2}\sum_i Z_i^2 C_i$$

where Z_i is the charge number of the ith ion and C_i is its molar concentration. The sum extends over all ionic species present in the solution. According to eq. [11], the rate constant will increase, decrease, or remain the same with increasing ionic strength, depending on whether the reactants have the same sign, opposite signs, or whether one reactant is neutral. For example, in 0.4 mol/L H_2SO_4 solutions, the rate constants for reactions [6] and [10], corrected for these effects, are $k_6 \approx 1.12 \times 10^{10}$ $(mol/L)^{-1}$ s^{-1} (see earlier) and $k_{10} \approx 5.97 \times 10^{10}$ $(mol/L)^{-1}$ s^{-1} (instead of 2.11×10^{10} and 11.3×10^{10} $(mol/L)^{-1}$ s^{-1} in neutral water at 25 °C, respectively) (11–15, 36).

Finally, in our simulations the direct action of ionizing radiation on the sulfuric acid anions (mainly HSO_4^-) is neglected, which is a reasonably good approximation over the range of sulfuric acid concentration studied (up to ~0.4 mol/L). In fact, in 0.4 mol/L H_2SO_4 (pH 0.46), only about 3.5% of the total energy expended in the solution is initially absorbed by direct action on HSO_4^- (rather than on H_2O) (assuming that the energy absorbed by each component is proportional to its electron fraction) (58). However, at higher acid concentrations this effect can no longer be neglected (42, 48, 50, 59).

Modeling the effects of radiation quality (LET)

The influence of the quality of the radiation (or LET) on the yields of the radiolytic species produced in neutral water and in aq. 0.4 mol/L sulfuric acid solutions at 25 °C has been investigated by performing a series of simulations with protons of various initial energies and therefore various LET. In this study, we limit ourselves to the incident proton energy range ~300–2.1 MeV, corresponding to LET values between ~0.3 and 15 keV/μm (11, 60, 61).

As mentioned earlier, the calculations are performed by simulating short (~20–100 μm) proton track segments over which the energy and LET of the proton are well-defined and remain essentially constant. Typically, about 5000 to 35 000 reactive chemical species are generated in the chemical development of such simulated track segments (depending on the LET). Statistically, the kinetics of ~30–150 different proton tracks (depending on the proton energy) are usually simulated to obtain computed averages of chemical yields for comparison with experiment.

Simulations of the Fricke dosimeter

To stochastically model the chemistry of the ferrous–sulfate Fricke dosimeter, we have added to the IRT program the reactions of Fe^{2+} ions with the oxidizing species $HO_2^{\bullet}$, $^{\bullet}OH$, and H_2O_2 that are formed in the water of the irradiated solution under aerated conditions. The mechanism for the radiolytic oxidation of Fe^{2+} ions to Fe^{3+} is well-understood and the rate constants of the individual reactions taking place are known. The reaction scheme is as follows (2, 7, 14–16, 24, 36, 62–64):

[6] $e_{aq}^- + H^+ \rightarrow H^{\bullet}$
$k_6 \approx 1.12 \times 10^{10}$ $(mol/L)^{-1}$ s^{-1}
pK_a ($H^{\bullet}/e_{aq}^-$) = 9.59

[13] $H^{\bullet} + O_2 \rightarrow HO_2^{\bullet}$
$k_{13} = 2.1 \times 10^{10}$ $(mol/L)^{-1}$ s^{-1}

[14] $Fe^{2+} + {}^{\bullet}OH \rightarrow Fe^{3+} + OH^-$
$k_{14} = 3.4 \times 10^{8}$ $(mol/L)^{-1}$ s^{-1}

[15] $Fe^{2+} + HO_2^{\bullet} \rightarrow Fe^{3+} + HO_2^-$
$k_{15} = 7.9 \times 10^{5}$ $(mol/L)^{-1}$ s^{-1}

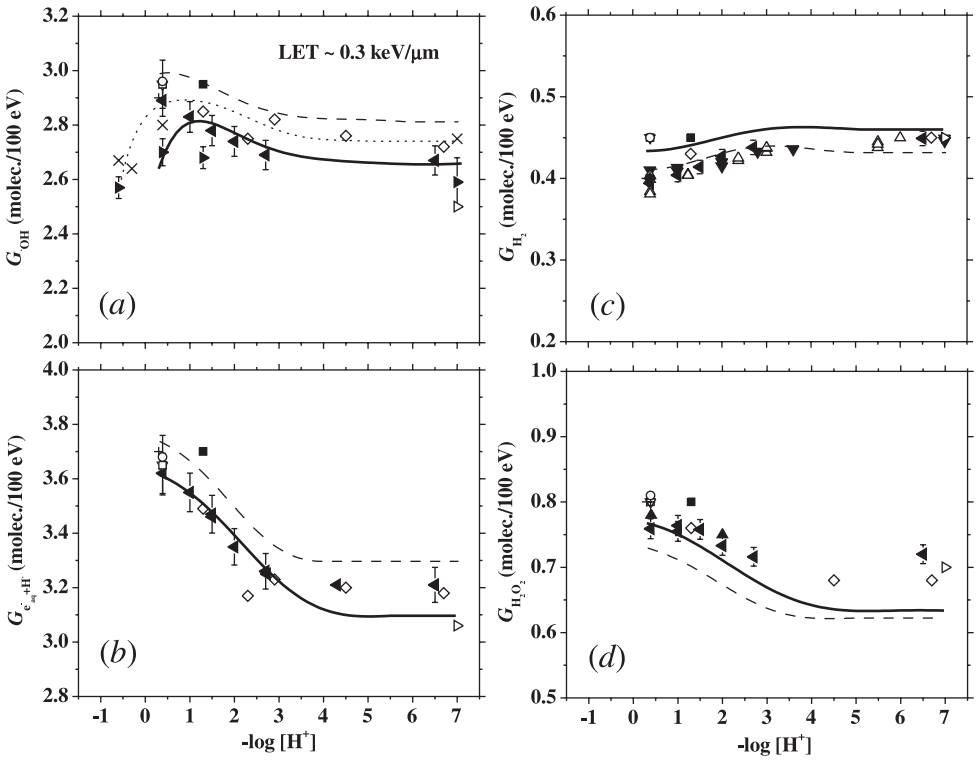
[16] $HO_2^- + H^+ \rightarrow H_2O_2$
$k_{16} \approx 2.66 \times 10^{10}$ $(mol/L)^{-1}$ s^{-1}
pK_a (H_2O_2/HO_2^-) = 11.62

[17] $Fe^{2+} + H_2O_2 \rightarrow Fe^{3+} + {}^{\bullet}OH + OH^-$
$k_{17} = 52$ $(mol/L)^{-1}$ s^{-1}

[10] $OH^- + H^+ \rightarrow H_2O$
$k_{10} \approx 5.97 \times 10^{10}$ $(mol/L)^{-1}$ s^{-1}
pK_a (H_2O/OH^-) = 13.999

© 2007 NRC Canada

Fig. 1. Variations of the primary free-radical and molecular yields (in molec./100 eV) of the radiolysis of de-aerated aq. H_2SO_4 solutions by 300 MeV incident protons (LET ~0.3 keV/μm) as a function of –log [H^+] over the sulfuric acid concentration range 0–0.4 mol/L at 25 °C. The solid and broken lines represent the results of our Monte Carlo simulations for (*a*) $G_{\cdot OH}$, (*b*) $G_{e^-_{aq}+H^\cdot}$, (*c*) G_{H_2}, and (*d*) $G_{H_2O_2}$, obtained at 10^{-6} and 10^{-7} s after the initial energy deposition, respectively. The calculations were performed with k_9 = 1.5×10^5 $(mol/L)^{-1}$ s^{-1} (see text); this value of k_9 was adjusted to match the experimental and simulated values of $G_{\cdot OH}$ in the region of pH < 1–2. This is shown in (*a*) where the curve of $G_{\cdot OH}$ vs. –log [H^+] calculated at 2.5×10^{-7} s is also presented for H_2SO_4 concentrations up to ~4 mol/L (dotted line), for the sake of comparison. Note that in solutions greater than 0.4 mol/L sulfuric acid, the measured $G_{\cdot OH}$ data were corrected to account for the direct action of radiation on HSO_4^- anions according to a procedure given in ref. 48 based on the formula $(G_{\cdot OH})^0 = G_{\cdot OH}/E_w$, where $(G_{\cdot OH})^0$ is the *G*-value for ·OH production that results from energy absorption by water and E_w denotes the electron fraction of water. Experimental data: ref. 3 (▷), refs. 8 and 69 (△), refs. 10 and 47 (◇), ref. 48 (▶), ref. 49 (◀), ref. 50 (×), refs. 66 and 67 (□), ref. 68 (○), ref. 70 (▼), ref. 71 (▽), ref. 72 (●), refs. 73 and 74 (+), ref. 75 (■), and ref. 76 (▲). For conversion of yield values into SI units, 1 molec./100 eV ≈ 0.10364 μmol/J.



As we can see, each H· atom forms a hydroperoxyl radical, and each of these radicals oxidizes three Fe^{2+} ions, one by reaction [15] and two by the reaction sequence [16], [17], and [14]. Each ·OH radical oxidizes one Fe^{2+} ion, and each molecule of H_2O_2 oxidizes two Fe^{2+} ions. Summing all sources of Fe^{3+} ions, the yield of ferric ions in an aerated solution $G(Fe^{3+})$ is related to the escape yields of the free radicals and molecular species of water radiolysis by eq. [7].

Note that the values of k_6, k_{10}, and k_{16} shown earlier and used in the simulations have been corrected using eqs. [11] and [12] for the effects due to the ionic strength in the case (under study here) of a solution made of 0.4 mol/L H_2SO_4 and 5 mmol/L $FeSO_4$. Note also that, as we have mentioned above, for solutions of 0.4 mol/L in H_2SO_4 there is a small amount of ·OH radicals that react with HSO_4^- to form $SO_4^{\cdot-}$ (reaction [9]). However, the overall ferric ion yield remains the same as given by eq. [7] since the sulfate radical reacts with Fe^{2+} in the same way as ·OH (24, 43):

[18] $SO_4^{\cdot-} + Fe^{2+} \rightarrow Fe^{3+} + SO_4^{2-}$

$k_{18} \approx 2.79 \times 10^8$ $(mol/L)^{-1}$ s^{-1}.

Under normal irradiation conditions, the radical concentrations are low compared with the background concentrations of acid, Fe^{2+} ions, and oxygen (~2.5×10^{-4} mol/L) in solution, and the reactions were treated in the IRT program as pseudo first-order (see earlier). In modeling the Fricke dosimeter, the slowest component of the kinetics of Fe^{3+} formation is due to the Fenton-type reaction [17] (65). For example, in the case of 5 mmol/L $FeSO_4$ solutions considered here, this reaction takes several seconds to go to completion, which increases signficantly the computer time usually chosen for modeling the radiolysis of water (typically ~1 μs). In this work, the time evolution of $G(Fe^{3+})$ has been followed until ~50 s.

Results and discussion

The effects of acidity on the primary free-radical and molecular yields

Figure 1 displays our calculated values of $G_{\cdot OH}$, $G_{e^-_{aq}+H^\cdot}$, G_{H_2}, and $G_{H_2O_2}$ for the radiolysis of air-free aqueous sulfuric acid solutions at 25 °C as a function of –log [H^+] in the range from neutral solution to 0.4 mol/L H_2SO_4, using 300 MeV

© 2007 NRC Canada

incident protons (LET ~0.3 keV/μm). Available experimental data (3, 8, 10, 47–50, 66–76) are also included for comparison. Our results show that an increase in acidity (1 < pH < 4) leads to an increase in $G_{e^-_{aq}+H^\cdot}$ and slight increases in $G_{^\cdot OH}$ and $G_{H_2O_2}$, while there is a slight decrease in G_{H_2}. At pH < 1, $G_{^\cdot OH}$ diminishes steeply. By contrast, in the range of pH from ~4 to 7, the calculated yield values are constant and independent of sulfuric acid concentration. As can be seen from Fig. 1, the computed primary yield values are generally in good agreement with the experimental values over the whole acidity range studied.

As the direct action of radiation on the sulfuric acid anions has been ignored in our simulations, the "initial" yields of the radiolytic species arising from the radiolysis of pure water can be regarded as essentially independent of the H_2SO_4 concentration. Hence, the variation of the yields of those species with acid concentration only results from the various chemical reactions that contribute to their formation or decay, while the spurs expand by diffusion. To gain further insight into the effects of acidity on $G_{^\cdot OH}$, $G_{e^-_{aq}+H^\cdot}$, G_{H_2}, and $G_{H_2O_2}$, it is thus of interest to examine the unfolding of those various reactions that lead to the different primary yields shown in Fig. 1. This can readily be done with our Monte Carlo simulations, which enable us to determine quantitatively the time dependence of each reaction. Table 2 summarizes the major spur/track reactions that are involved in the primary yields of water decomposition products. The importance of these reactions can be quantified by the yield variations ΔG that they cause over the time interval of nonhomogeneous track chemistry (~10^{-12}–10^{-6} s). Figures 2 and 3 compare, for pure neutral water and 0.4 mol/L H_2SO_4 (pH 0.46) aqueous solutions, respectively, the time profiles of the extents ΔG of each of these reactions, calculated from our simulations for low-LET radiolysis.

Table 2. Most important spur/track reactions inferred from our Monte Carlo simulations of the nonhomogeneous chemical stage in the low-LET radiolysis of de-aerated neutral liquid water and aqueous sulfuric acid solutions at 25 °C and in the time interval ~10^{-12}–10^{-6} s.

Symbol[a]	Reaction
[R1] (or [6])	$e^-_{aq} + H^+ \rightarrow H^\cdot$
[R2]	$e^-_{aq} + e^-_{aq}$ (+ 2 H_2O) $\rightarrow H_2 + 2\ OH^-$
[R3]	$e^-_{aq} + H^\cdot$ (+ H_2O) $\rightarrow H_2 + OH^-$
[R4]	$e^-_{aq} + H_2O_2 \rightarrow {}^\cdot OH + OH^-$
[R5]	$e^-_{aq} + {}^\cdot OH \rightarrow OH^-$
[R6]	${}^\cdot OH + OH^- \rightarrow O^{\cdot -} + H_2O$ $O^{\cdot -} + H_2O \rightarrow {}^\cdot OH + OH^-$
[R7]	${}^\cdot OH + H^\cdot \rightarrow H_2O$
[R8]	${}^\cdot OH + {}^\cdot OH \rightarrow H_2O_2$
[R9] (or [9])	${}^\cdot OH + HSO_4^- \rightarrow H_2O + SO_4^{\cdot -}$
[R10]	$H^\cdot + H^\cdot \rightarrow H_2$

[a]Reaction symbols used in the text.

The hydroxyl radical

The hydroxyl radical is the main oxidizing radical formed when aqueous sulfuric acid solutions are irradiated. As can be seen in Fig. 1*a*, our calculated values of $G_{^\cdot OH}$ are independent of pH over the range ~4–7, slightly increase at pH < 4 to reach a weakly pronounced maximum around pH 1, and then fall steeply as the pH is further reduced below 1. From Fig. 2*a*, it is seen that in neutral water ${}^\cdot OH$ is produced mainly by reaction [R4], whereas its decay is dominated by reactions [R8], [R5], [R7], and [R6] (in order of decreasing importance). In contrast, in 0.4 mol/L H_2SO_4 solutions (see Fig. 3*a*), the formation of ${}^\cdot OH$ due to reaction [R4] is decreased by almost 100% because of the occurrence of the very rapid reaction [6] of the H^+ ions, which at this acid concentration capture most, if not all, of the e^-_{aq} radicals in the spurs. For the same reason, the removal of ${}^\cdot OH$ due to reaction [R5] is also significantly decreased at low pH in favor of reaction [R7]. Finally, as discussed above, there is a decrease of ${}^\cdot OH$ caused by reaction [9].

The reducing free-radical species e^-_{aq} and $H^\cdot$

As shown in Fig. 1*b*, the effect of increasing –log [H^+] from ~0.4 to 7 is to reduce our calculated values of $G_{e^-_{aq}+H^\cdot}$ (= $G_{e^-_{aq}} + G_{H^\cdot}$) from ~3.7 to 3.1 molec./100 eV (that is by less than 20%), which is in good agreement with experiment. In the pH range ~4–7, $G_{e^-_{aq}+H^\cdot}$ is independent of acid concentration. From Figs. 2*b* and 2*c*, it is seen that in neutral water the decay of the e^-_{aq} yield up to ~10^{-6} s is mainly due to the reactions [R5] and [R1] (or [6]) of e^-_{aq} with ${}^\cdot OH$ radicals and H^+ ions. In 0.4 mol/L H_2SO_4 solutions, however, it clearly appears from Fig. 3*b* that reaction [R1] largely dominates the decay of e^-_{aq}, which is rapidly converted in the spurs into the hydrogen atom. This reaction occurs mostly at early times (<10^{-9} s).

As for the $H^\cdot$ atom, Figs. 2*c* and 3*c* show that in both neutral water and 0.4 mol/L sulfuric acid solutions reaction [R7] is responsible for most of its decay, while its production takes place mainly through the occurrence of reaction [R1].

Molecular hydrogen

As is well established, G_{H_2} slightly decreases with increasing acidity (8, 10, 47, 49, 59, 69, 70, 72–74; see also ref. 5). As one can see from Fig. 1*c*, our calculations reproduce such a decrease in G_{H_2} at pH < 4, in agreement with experiment. In the range of pH ~4–7, G_{H_2} is independent of acidity. The measured microsecond yield value, G_{H_2} = 0.45 molec./100 eV at pH 7, is also well reproduced by our simulations.

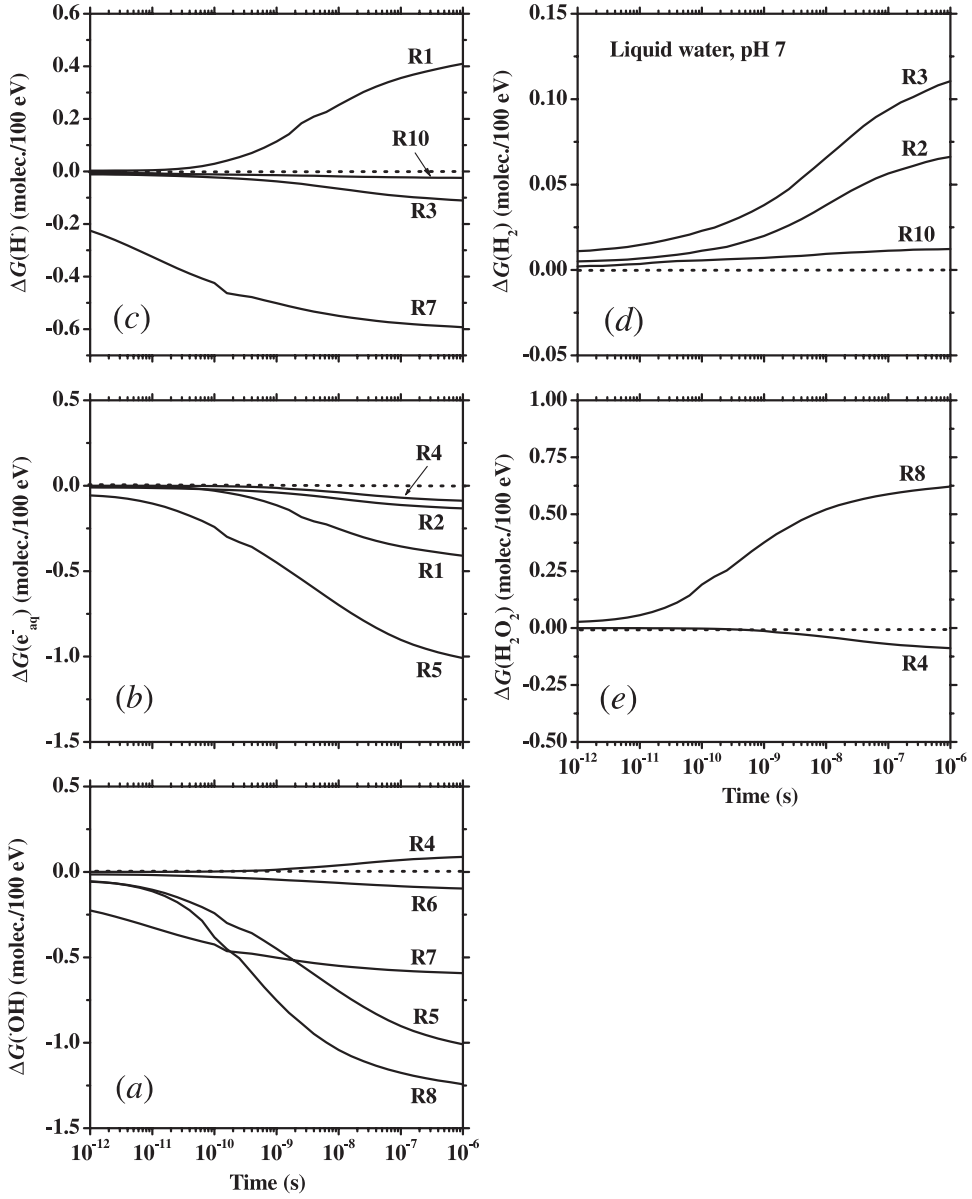
Figure 2*d* shows that in neutral water the production of H_2 is predominantly due to reactions [R3] and [R2] (in order of decreasing importance). By contrast, as the acidity increases reaction [R10] occurs to an increasing extent in the spurs. As it clearly appears from Fig. 3*d*, reactions [R2] and [R3] are only of minor importance in 0.4 mol/L H_2SO_4 solutions, and the production of H_2 under such acidic conditions can be almost entirely attributed to reaction [R10].

Hydrogen peroxide

As is shown in Fig. 1*d*, our calculated values of $G_{H_2O_2}$ remain unaffected by changes of pH in the range ~4–7 and increase as –log [H^+] is decreased from ~4 to 0.4, in good agreement with experiment. It has long been established from modeling and experimental studies that the main precursor of the molecular yield of H_2O_2 is ${}^\cdot OH$ through the spur reaction [R8] of ${}^\cdot OH$ with itself. The importance of this reaction is quantified in Figs. 2*e* and 3*e*. As can be seen, there is clear evidence that the combination reaction of ${}^\cdot OH$

© 2007 NRC Canada

Fig. 2. Time dependence of the extents ΔG (in molec./100 eV) of the main spur/intratrack reactions that are involved in the formation and decay of (*a*) $^{\cdot}OH$, (*b*) e^-_{aq}, (*c*) $H^{\cdot}$, (*d*) H_2, and (*e*) H_2O_2 (see text and Table 2), calculated from our Monte Carlo simulations of the radiolysis of de-aerated liquid water by ~300 MeV protons (LET ~0.3 keV/μm) at neutral pH, 25 °C, and in the interval 10^{-12}–10^{-6} s. Note that the initial yields of $^{\cdot}OH$, e^-_{aq}, $H^{\cdot}$, H_2, and H_2O_2, calculated at the end of the physicochemical stage, are ~5.43, 4.26, 0.97, 0.28, and 0.11 molec./100 eV, respectively.



radicals is the major source of primary hydrogen peroxide both in neutral water and in 0.4 mol/L H_2SO_4 solutions. Figure 2*e* also shows that in neutral water the decay of H_2O_2 is dominated by the back reaction [R4]. In contrast to this situation, in 0.4 mol/L H_2SO_4 solutions the removal of H_2O_2 due to the occurrence of reaction [R4] is decreased by almost 100%.

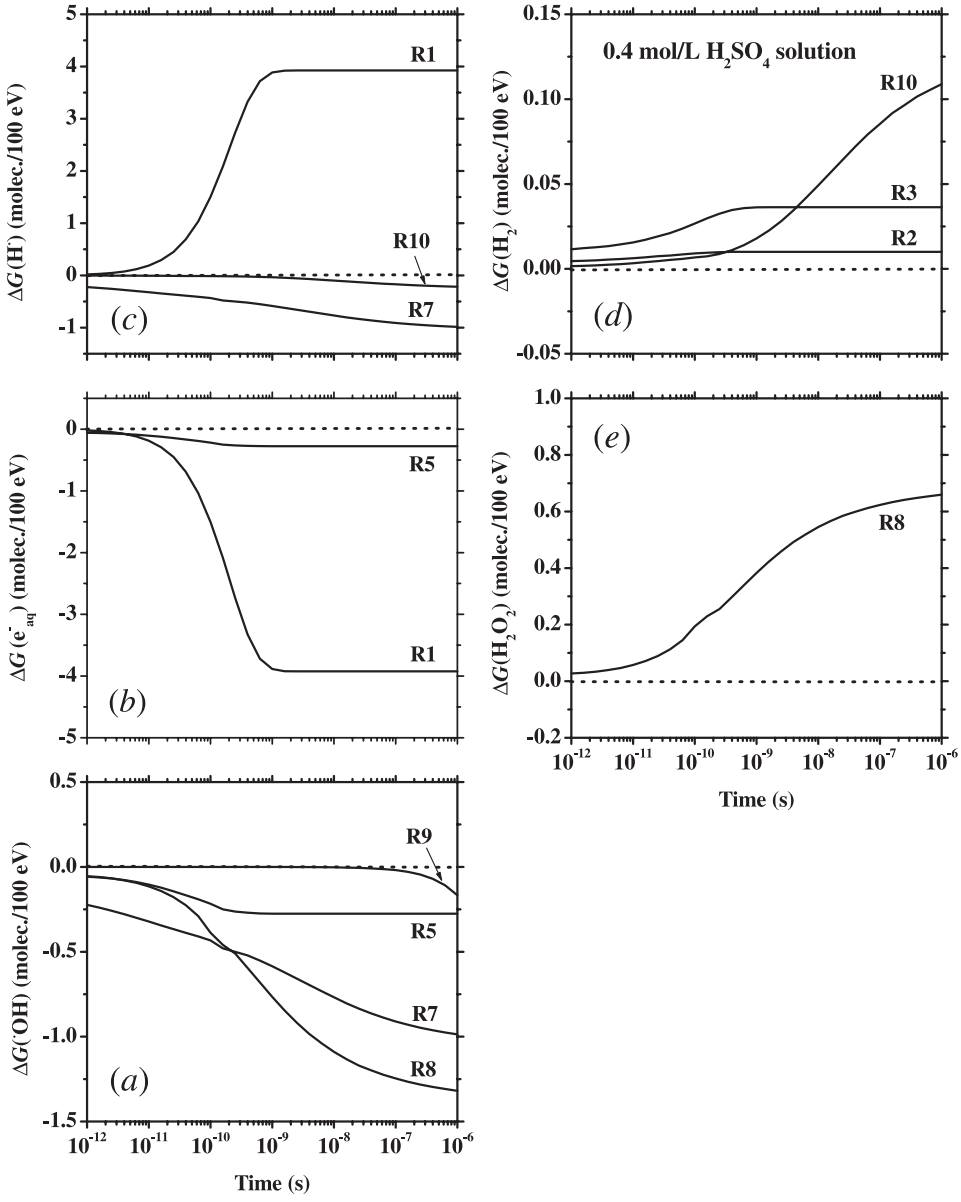
Proposed interpretation of the effects of acidity on the primary free-radical and molecular yields

As can be seen in Figs. 1*a*–1*d*, the values of the primary free-radical and molecular product yields do not change in the range ~4 < pH < 7. This can easily be explained if we consider, as mentioned earlier, that the main effects of acidity on the primary yields of the radiolysis of aqueous solutions at low pH are attributed to the presence of H^+ ions, which can rapidly scavenge hydrated electrons through reaction [6] (or [R1]). At pH 4 for example, one has a H^+ concentration of 10^{-4} mol/L and a scavenging power, defined as the product k_6 [H^+] (e.g., see ref. 20), of ~2.05×10^6 s^{-1}. Hence, the time scale over which reaction [6] occurs, measured by the reciprocal of the scavenging power, is ~5×10^{-7} s. Therefore, the addition of 10^{-4} mol/L H^+ ions will contribute only very little to the scavenging of e^-_{aq} in the spurs. Under such conditions, a change of pH from 7 to ~4 has, indeed, no effect on either radical or molecular primary yields.

At pH < 4, the concentration of H^+ ions is high enough to be able to convert the e^-_{aq} radicals in the spurs or tracks into $H^{\cdot}$ atoms, interfering to some extent with the back reactions

© 2007 NRC Canada

Fig. 3. Time dependence of the extents ΔG (in molec./100 eV) of the main spur/intratrack reactions that contribute to the formation and decay of (*a*) $^{\cdot}OH$, (*b*) e^-_{aq}, (*c*) $H^{\cdot}$, (*d*) H_2, and (*e*) H_2O_2 (see text and Table 2), calculated from our Monte Carlo simulations of the radiolysis of de-aerated 0.4 mol/L H_2SO_4 aqueous solutions by ~300 MeV protons (LET ~0.3 keV/μm) at 25 °C and in the interval 10^{-12}–10^{-6} s. The initial yields of $^{\cdot}OH$, e^-_{aq}, $H^{\cdot}$, H_2, and H_2O_2, calculated at the end of the physicochemical stage, are as in the legend of Fig. 2.



forming water (see Figs. 3*b* and 3*c*). According to Hayon (69, 77) and as clearly shown in Fig. 2*b* from our simulations, these electrons in neutral solution would have predominantly combined, in the absence of other electron-accepting solutes with which they could react, with $^{\cdot}OH$ to form water:

[R5] $\quad e^-_{aq} + {}^{\cdot}OH \rightarrow OH^-$

$$k_{R5} = 2.95 \times 10^{10}\ (\text{mol/L})^{-1}\ \text{s}^{-1} \quad (15)$$

The $H^{\cdot}$ atoms, on the contrary, react less efficiently than e^-_{aq} with $^{\cdot}OH$ in the spurs:

[R7] $\quad H^{\cdot} + {}^{\cdot}OH \rightarrow H_2O$

$$k_{R7} = 1.55 \times 10^{10}\ (\text{mol/L})^{-1}\ \text{s}^{-1} \quad (15)$$

This reduction in reactivity is also the result of $H^{\cdot}$ having a larger diffusion coefficient (7.0×10^{-9} m^2 s^{-1}) than e^-_{aq} (4.9×10^{-9} m^2 s^{-1}) (4, 15, 78). The effect of acid is thus to decrease in the spur time scale the importance of the back reaction [R5]. The conversion of e^-_{aq} to $H^{\cdot}$ in the spurs in acidic solution, and the subsequent "protection" of the $^{\cdot}OH$ radicals against the action of hydrated electrons (69, 77, 79) lead to the following consequences:

(*i*) Since the reducing free-radical entities are less reactive while the spurs expand, owing to the intervention of reaction [R7], $G_{e^-_{aq}+H^{\cdot}}$ increases on going from neutral to acidic solutions, as observed experimentally (Fig. 1*b*).

(*ii*) At low pH this mechanism tends to increase $G_{^{\cdot}OH}$. This is clearly seen in Fig. 1*a* where $G_{^{\cdot}OH}$ slightly increases at pH < 4.

© 2007 NRC Canada

(*iii*) Due to the dimerization of the ·OH radicals, $G_{H_2O_2}$ also increases with increasing acidity up to 0.4 mol/L H_2SO_4, in good agreement with experiment (Fig. 1*d*). At higher sulfuric acid concentrations, however, our simulations predict (data not shown) that $G_{H_2O_2}$ should diminish owing to the removal of ·OH radicals due to the increased intervention of reaction [9] (or [R9]) (see Fig. 1*a*). Unfortunately, there is at present no experimental or theoretical data available in the literature with which to compare our results.

(*iv*) The yield of molecular hydrogen is gradually lowered below pH 4 (Fig. 1*c*). This is explained by the fact that as the acidity progressively increases, the contribution of the self reaction of the H· atom:

$$[R10] \quad H^{\cdot} + H^{\cdot} \rightarrow H_2$$

$$k_{R10} = 5.03 \times 10^9 \text{ (mol/L)}^{-1} \text{ s}^{-1} \quad (15)$$

becomes more important. As can be seen in Fig. 3*d*, this reaction is the dominant chemical route for producing H_2 in 0.4 mol/L H_2SO_4 solutions. Under neutral conditions (see Fig. 2*d*), reaction [R10] is only of minor importance, and the production of H_2 can be almost entirely attributed to reaction [R3]:

$$[R3] \quad e^-_{aq} + H^{\cdot} (+ H_2O) \rightarrow H_2 + OH^-$$

$$k_{R3} = 2.5 \times 10^{10} \text{ (mol/L)}^{-1} \text{ s}^{-1} \quad (80)$$

and to a lesser extent reaction [R2]. Since reaction [R10] is less efficient than reaction [R3], conversion of the e^-_{aq} to H· atoms leads to a lowering of G_{H_2} at low pH.

(*v*) Finally, the yield of decomposition of water G_{-H_2O} increases as the pH decreases below ~4, in order of course, to maintain the material balance in eq. [4].

Overall, our present Monte Carlo calculations generally agree well with experiment (see Fig. 1). Results clearly show that the primary free-radical and molecular yields of the radiolysis of aqueous solutions are influenced by the addition of H^+ ions, especially at high sulfuric acid concentrations. However, in accord with a previous conclusion by Draganić and Draganić (10), there is no strong dependence of those yields on pH.

The effect of LET on the primary free-radical and molecular yields of the radiolysis of neutral liquid water and aq. 0.4 mol/L H_2SO_4 solutions

Figures 4 and 5 show the variations of our computed primary free-radical and molecular yields as a function of LET over the range ~0.3–15 keV/μm for de-aerated neutral liquid water and aq. 0.4 mol/L H_2SO_4 solutions, respectively, at 25 °C. For the sake of comparison, available experimental data for various radiation types and different authors (3, 8, 20, 48, 49, 66–76, 81–100) are also included in the figures. Overall, our computed results are in good agreement with the measured yields. In both neutral water and acidic solutions it is seen that, in general, the primary yields of molecular products increase with increasing LET at the expense of those of free radicals. These variations in radical and molecular yields reflect the effect of changing conditions on the extent of radical–radical reactions within spurs/tracks; as mentioned earlier, high LET favors high reaction rates for radicals within the dense columnar regions of tracks. We should notice, however, the peculiar behavior of $G_{H^{\cdot}}$ in neutral water. In fact, unlike the other radical yields our calculated $G_{H^{\cdot}}$ values exhibit a slight maximum near 6.5 keV/μm before decreasing at higher LET (Fig. 4*a*). The origin of this maximum was discussed in detail previously (101). In essence, this variation of $G_{H^{\cdot}}$ as a function of LET does not arise from a change in the initial yield of H· atoms (i.e., at the end of the physicochemical stage), which is nearly constant over the LET range studied, but rather from the various reactions that are involved in their production and decay in the time interval of nonhomogeneous spur/track chemistry (see Table 2). As one can see from Figs. 2*c* and 4*a*, our calculations, which confirm the results previously obtained by Meesungnoen et al. (101), show that the overall effect of LET on $G_{H^{\cdot}}$ is dominated by reaction [R1] (or [6]) up to the maximum of $G_{H^{\cdot}}$ at ~6.5 keV/μm and by reactions [R7], [R3], and [R10] (in order of decreasing importance) at higher LET.

Together with the yields obtained at 10^{-6} s (Figs. 4 and 5, solid lines), we also show our primary free-radical and molecular yield values calculated at 10^{-7} s after irradiation (Figs. 4 and 5, broken lines). Such a comparison is given as a means to estimate the sensitivity of our computed escape yields with regards to the uncertainty in assigning a value for the time (generally quoted ~10^{-6}–10^{-7} s in the literature) marking the end of the nonhomogeneous radiation chemical stage (that is, when the expanding spurs and tracks overlap, or equivalently, when the species are considered to be homogeneously distributed in the solution). As can be seen from Figs. 4 and 5, the differences found between these two sets of yield values at 10^{-6} and 10^{-7} s depend strongly on the particular species and LET. For low-LET radiation, these differences are of the order of a few percent only (but never exceed ~10%) suggesting that at ~10^{-7} s after the ionizing event, the intratrack reactions in fast electron or γ-radiolysis are already nearly complete. By contrast, there are considerably more reactions of species in high-LET tracks than in the spurs produced by fast electrons. In fact, the differences observed in yield values at 10^{-6} and 10^{-7} s become more important with increasing LET (e.g., they amount to ~30%–40% at ~15 keV/μm for the particular case of e^-_{aq} and ·OH, compared with ~3%–10% at ~0.3 keV/μm). These differences reflect the changes in the nature of the track structure; at high LET, the species will not escape as they diffuse along the axis of the cylindrical track and will continue to react among themselves to longer times (in the absence of solutes) (e.g., see refs. 102 and 103).

The material balance eq. [4] for reducing (e^-_{aq}, H· and H_2) and oxidizing (·OH, H_2O_2, and $HO_2^{\cdot}/O_2^{\cdot-}$) species is found to be satisfied throughout the range of LET studied for both neutral water and acidic solutions:

(*i*) For neutral water we have (at 10^{-6} s) for ^{60}Co γ radiation (LET ~ 0.3 keV/μm):

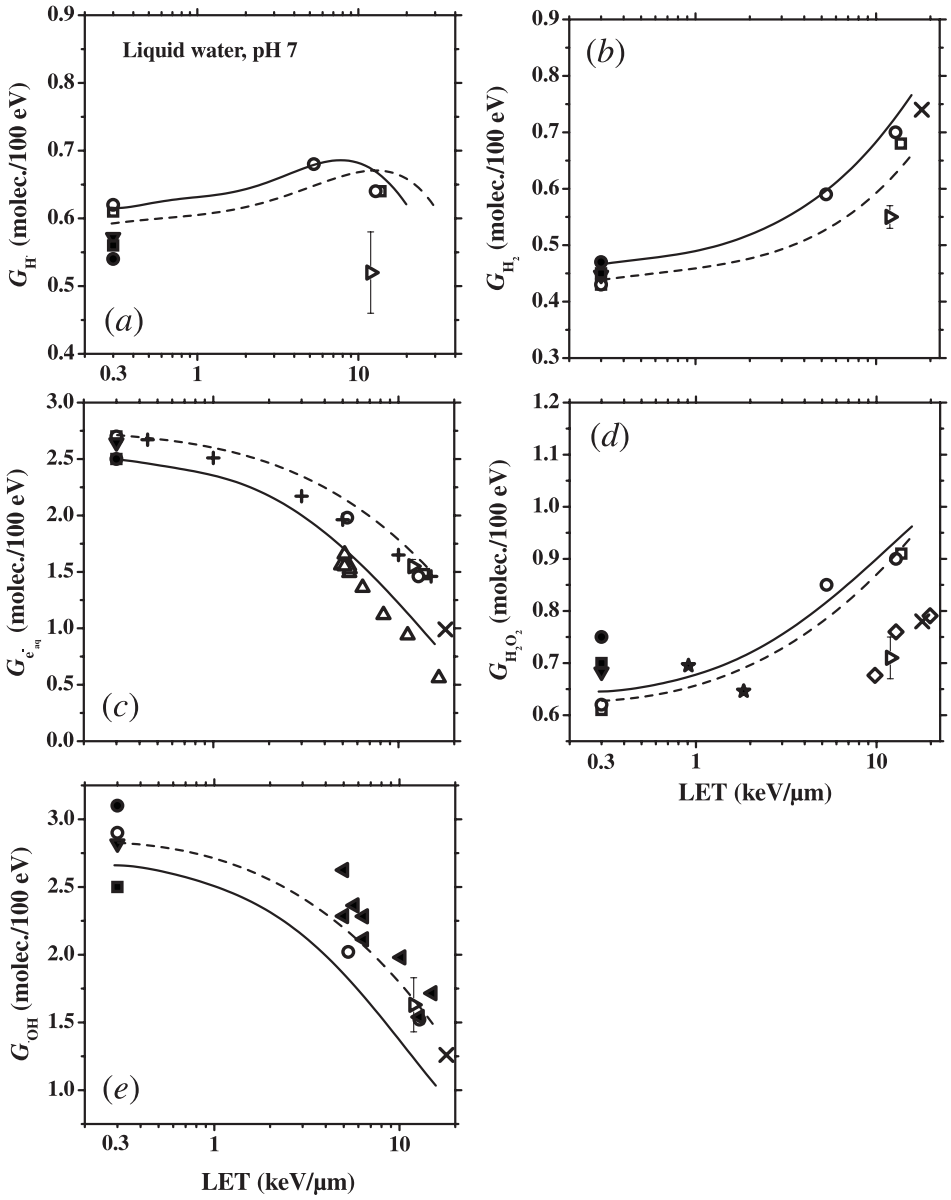
$$G_{red} = G_{e^-_{aq}} + G_{H^{\cdot}} + 2G_{H_2} = 4.05 \pm 0.04, \text{ and}$$

$$G_{ox} = G_{\cdot OH} + 2G_{H_2O_2} + 3G_{HO_2^{\cdot}/O_2^{\cdot-}} = 3.99 \pm 0.05$$

in good agreement with the experimental value of ~3.94 molec./100 eV given in eq. [2]; for a LET of ~12.8 keV/μm, our calculated primary yields are: G_{red} =

© 2007 NRC Canada

Fig. 4. Variations of the primary free-radical and molecular yields (in molec./100 eV) of the radiolysis of de-aerated neutral liquid water at 25 °C as a function of LET over the range ~0.3–15 keV/μm (up to ~20 keV/μm for the primary yield of H· atoms). The solid and broken curves represent the results of our Monte Carlo simulations for (*a*) $G_{H\cdot}$, (*b*) G_{H_2}, (*c*) $G_{e^-_{aq}}$, (*d*) $G_{H_2O_2}$, and (*e*) $G_{\cdot OH}$ at 10^{-6} and 10^{-7} s, respectively. Experimental data: ref. 3 (■), ref. 20 (data taken from the line marked "selected" in Fig. 7.7.1, which is a fit of experimental yields from different authors at various LET) (+), ref. 81 (▷), ref. 82 (▼), ref. 83 (□), ref. 84 (○), ref. 85 (△), ref. 86 (◀), ref. 87 (◇), ref. 88 (★), ref. 89 (×), and ref. 90 (●). LET values used here for the various types of radiation considered correspond to dose-average LET values, taken from ref. 60.



3.14 ± 0.04 and G_{ox} = 3.10 ± 0.03, which compare well with the values of ~3.09 and 3.05 molec./100 eV deduced for this LET from the room temperature yield data reported by Elliot et al. (15, 81), respectively.

(*ii*) For 0.4 mol/L H_2SO_4 solutions, we have similarly (at 10^{-6} s) for ^{60}Co γ radiation:

$G_{red} = G_{e^-_{aq}+H\cdot} + 2G_{H_2}$ = 4.47 ± 0.04, and

G_{ox} = 4.26 ± 0.07

in good accord with the experimental value of ~4.44 molec./100 eV given in eq. [5]; for a LET of ~13.7 keV/μm, we find G_{red} = 3.84 ± 0.03 and G_{ox} = 3.73 ± 0.04, which compare satisfactorily with the values of ~3.81 and ~3.98 molec./100 eV reported by Barr and Schuler (71) and Schuler and Allen (91) for 18 MeV deuterons, respectively.

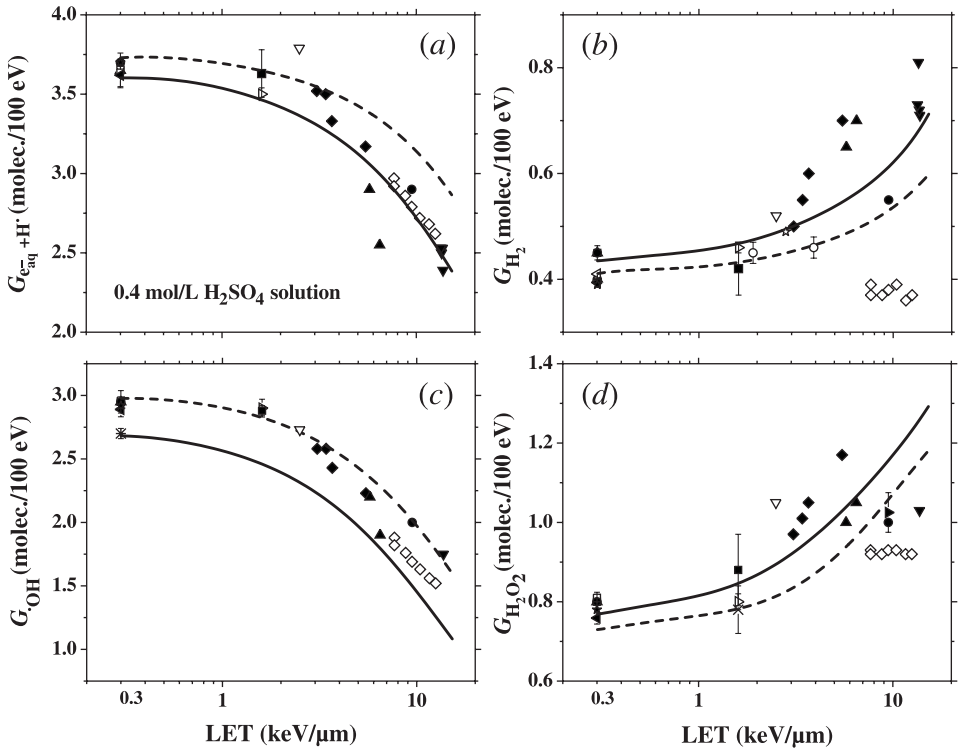
The effect of LET on the chemistry and the yield of the Fricke dosimeter

Kinetics of Fe^{3+} formation

As an application and also as a test of the reliability of our primary yields, Monte Carlo simulations were used to study

© 2007 NRC Canada

Fig. 5. Variations of the primary free-radical and molecular yields (in molec./100 eV) of the radiolysis of de-aerated 0.4 mol/L H_2SO_4 aq. solutions (pH 0.46) at 25 °C as a function of LET over the range ~0.3–15 keV/μm. The solid and broken curves represent the results of our Monte Carlo simulations for (*a*) $G_{e^-_{aq}+H^\cdot}$, (*b*) G_{H_2}, (*c*) $G_{\cdot OH}$, and (*d*) $G_{H_2O_2}$ at 10^{-6} and 10^{-7} s, respectively. Experimental data: refs. 8 and 69 (△), ref. 48 (✳), ref. 49 (◀), refs. 66 and 67 (▲), refs. 66, 68, and 92 (□), ref. 70 (◁), refs. 71 and 91 (▼), ref. 72 (○), refs. 73 and 74 (+), ref. 75 (in 0.05 mol/L H_2SO_4) (●), ref. 76 (★), ref. 93 (◆), ref. 94 (×), ref. 95 (▷), ref. 96 (▽), ref. 97 (◇), ref. 98 (■), ref. 99 (▶), and ref. 100 (☆). Dose-average LET values used here for the various radiations considered are taken from ref. 60.



the LET dependence of the oxidation of ferrous ions in the radiolysis of air-saturated solutions of 5 mmol/L $FeSO_4$ in aq. 0.4 mol/L H_2SO_4 (the ferrous-sulfate Fricke dosimeter).[9,10] As described earlier, the mechanism of this chemical system, well-understood in terms of oxidation of Fe^{2+} ions to Fe^{3+} by $H^\cdot$ atoms (via production of $HO_2^\cdot$), $^\cdot OH$ radicals, and H_2O_2, includes the sequence of reactions [6] and [13]–[17]. Figure 6 shows the kinetics of Fe^{3+} formation as obtained from our simulations for 300 MeV irradiating protons (LET ~ 0.3 keV/μm) at ambient temperature. As can be seen from this figure, $G(Fe^{3+})$ is time dependent as a result of the differences in the lifetimes of the reactions making up the radiolysis mechanism (2, 105, 106). The fastest reaction of Fe^{2+} ions is with $^\cdot OH$ radicals. It is completed on a microsecond time scale. The oxidation of Fe^{2+} by $HO_2^\cdot$ is slower and requires a few milliseconds for completion. The slowest component in the formation of Fe^{3+} is due to Fe^{2+} oxidation by H_2O_2 (both the molecular product yield and that formed by reaction [16]). This latter reaction takes place at times longer than ~0.1 s and is completed by about 30 s.

The accepted value of the ferric ion yield in the Fricke dosimeter, obtained for ^{60}Co γ-rays, high-energy X-rays, or fast electrons, is $G(Fe^{3+})$ = 15.6 ± 0.2 molec./100 eV (e.g., see refs. 7, 25, 28, and 107–110) at 25 °C. Under the same low-LET conditions, our computed value of $G(Fe^{3+})$ at ~50 s is found to be equal to ~15.7 molec./100 eV (Fig. 6), in very good agreement with the standard value.

Variation of G(Fe³⁺) with LET

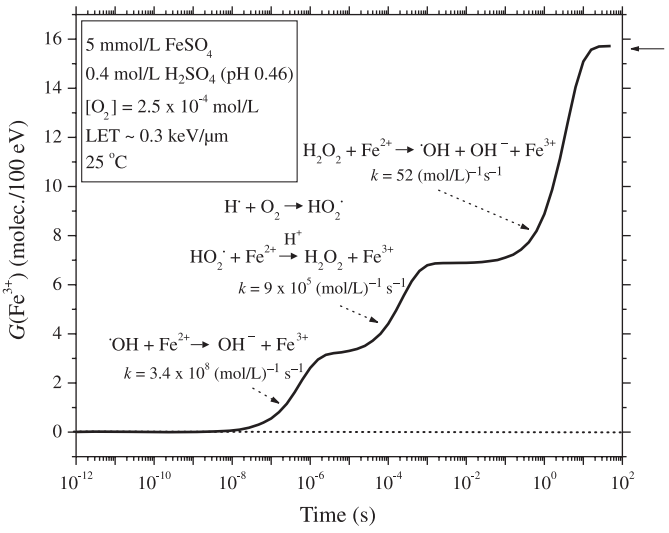
Figure 7 shows the values of $G(Fe^{3+})$ calculated from our Monte Carlo simulations of the radiolysis of aerated solutions of 5 mmol/L $FeSO_4$ in aq. 0.4 mol/L H_2SO_4 as a function of LET over the range ~0.3–15 keV/μm at 25 °C. It is seen that as the LET increases the yield diminishes. Our computed values are compared with experimental data of ferric ion yields vs. LET obtained by a number of different workers (26, 28, 33, 67, 72, 81, 91, 95, 108, 109, 111–123) using a variety of methods for radiations of different energies. Despite the relatively large uncertainties of the reported measurements, there is a good agreement between theory and experiment. Also shown in the figure are the curves of $G(Fe^{3+})$ vs. LET calculated at two different times chosen for the completion of spur/track processes (namely, 10^{-7} and 10^{-6} s after the energy deposition event) on the basis of the

[9] Note that the commonly used Fricke solution typically contains 1 mmol/L $FeSO_4$ and is saturated with air. The "super-Fricke" dosimeter, saturated with oxygen and containing 10 mmol/L ferrous sulfate, is seldom used. See ref. 30.

[10] A preliminary report of this work has been presented at the 48th Annual Meeting of the Japanese Society of Radiation Chemistry, Osaka, Japan, October 12–14, 2005. See ref. 104.

© 2007 NRC Canada

Fig. 6. Time evolution of $G(Fe^{3+})$ (in molec./100 eV) in the radiolysis of air-saturated solution of 5 mmol/L $FeSO_4$ in aq. 0.4 mol/L H_2SO_4 at 25 °C. The concentration of dissolved oxygen used in the calculations is ~2.5×10^{-4} mol/L. The solid line shows our simulated kinetics of Fe^{3+} ion formation. The arrow on the right of the figure shows the accepted value (15.6 molec./100 eV) of the yield of the Fricke dosimeter for ^{60}Co γ-rays and fast electrons.



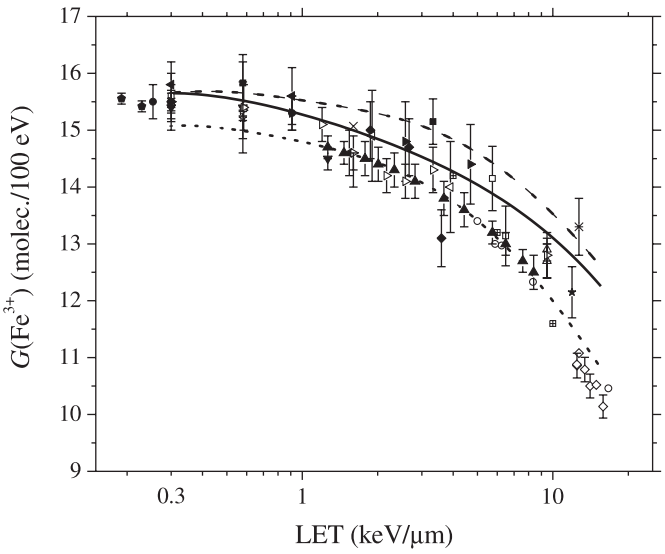
values of G(primary yields) using eq. [7]. As can be seen, the values of $G(Fe^{3+})$ obtained from our Monte Carlo simulations are found to lie between the two curves of the yields obtained from eq. [7] at 10^{-7} and 10^{-6} s, over the whole LET range considered.

This dependence of $G(Fe^{3+})$ on LET results from the fact that the production of ferric ions in the Fricke system is most sensitive to radical yields; indeed, according to eq. [7], the lower the yield of radicals which escape the radiation track, the lower the Fricke G-value. Since increasing LET has the effect of reducing the free-radical product yields from water (see Fig. 5), it follows that $G(Fe^{3+})$ also decreases as the LET increases.

Conclusions

In this study, we have used Monte Carlo simulations to investigate the influence of acidity (pH) on the primary yields of the various chemical species produced in the radiolysis of de-aerated aqueous sulfuric acid solutions over the range of H_2SO_4 concentrations ~0–0.4 mol/L. The effects of the quality of radiation, a measure of which is its LET, has also been studied for LET varying from ~0.3 to 15 keV/μm at ambient temperature. Our results show that an increase in acidity ($1 < pH < 4$) leads to an increase in the yields of the reducing radicals (e^-_{aq} and H· atom) and the oxidizing products (·OH radical and H_2O_2), while the yield of H_2 decreases. At $pH < 1$, ·OH radicals react with HSO_4^- anions to form $SO_4^{\cdot-}$ radicals, resulting in a marked decrease in $G_{\cdot OH}$. By contrast, at $pH > 4$, the yields are essentially independent of sulfuric acid concentration. In both neutral liquid water and 0.4 mol/L H_2SO_4 (pH ~ 0.46) solutions, the most evident effect of increasing LET is an increase in the primary yields of molecular products, accompanied by a corresponding decrease in those of free radicals. As an exception, $G_{H\cdot}$ at first increases vs. LET, then reaches a maximum near 6.5 keV/μm before decreasing steeply at higher LET. The results obtained are in generally good agreement with available experimental data over the whole acidity and LET ranges studied.

Fig. 7. Plot of the ferric ion yield $G(Fe^{3+})$ (in molec./100 eV) for aerated 0.4 mol/L H_2SO_4 aq. solution (Fricke dosimeter) at 25 °C against LET in the range ~0.3–15 keV/μm. The solid curve represents the values of $G(Fe^{3+})$ calculated from our Monte Carlo simulations. The broken and dotted lines correspond to the Fricke G-values calculated at 10^{-7} and 10^{-6} s, respectively, from eq. [7] based on G(primary products). Experimental data: ref. 26 (▲), ref. 28 (●), ref. 33 (⬟), ref. 67 (□), ref. 72 (◁), ref. 81(★), refs. 91, 108, and 121 (○), ref. 95 (×), refs. 109 and 122 (◀), ref. 111 (▼), ref. 112 (▽), ref. 113 (in 0.05 mol/L H_2SO_4) (▷), ref. 114 (in 0.05 mol/L H_2SO_4) (▶), ref. 115 [based on $G(Fe^{3+})$ = 15.6 molec./100 eV for ^{60}Co γ-rays] (■), ref. 116 (△), ref. 117 (◇), ref. 118 (in 0.05 mol/L H_2SO_4) (◆), ref. 119 (☆), ref. 120 (✳), and ref. 123 (⊞). Dose-average LET values used here for the various radiation types considered are taken from ref. 60. Note that, for X-rays, there are in certain cases insufficient experimental details for an estimate of the average energy of electrons resulting from photon absorption in the solution to be made. This results in some uncertainty in assigning an average LET value to the corresponding reported $G(Fe^{3+})$ results.



Finally, as an application, we have simulated the chemical development of the Fricke dosimeter (aerated solution of ferrous sulfate in aq. 0.4 mol/L H_2SO_4) as a function of time up to ~50 s and addressed the effects of LET on the resulting ferric ion yield at 25 °C. The production of Fe^{3+} ions is found to be highly sensitive to free-radical yields, especially H· atoms, and is strongly dependent on the quality of the radiation. Our calculated values of $G(Fe^{3+})$ agree very well with the experimental yields.

The good overall agreement between calculated and experimental yield values obtained for both neutral water and acidic solutions, as well as for the Fricke dosimeter, gives

© 2007 NRC Canada

strong support to the validity and consistency of the assumptions employed in this study.

Acknowledgments

One of the authors (NA) expresses his appreciation to Dr. Kashane Chalermwat, Dr. Nisa Chawapun, and Dr. Wisatre Kongcharoensuntorn for their support and continuous encouragement during the course of this study. JPJG thanks the Japan Society for the Promotion of Science for a 2005 JSPS Invitation Fellowship for Research in Japan, which allowed him to present preliminary results of this work as part of an invited talk at the 48th Annual Meeting of the Japanese Society of Radiation Chemistry, held in Osaka, Japan, on October 12–14, 2005. The financial assistance of the Natural Sciences and Engineering Research Council of Canada (under Grant No. 9020–04) is gratefully acknowledged.

References

1. C. Ferradini and J.-P. Jay-Gerin. Can. J. Chem. **77**, 1542 (1999).
2. J.W.T. Spinks and R.J. Woods. An introduction to radiation chemistry. 3rd ed. Wiley, New York. 1990. p. 243.
3. J.A. LaVerne. Radiat. Res. **153**, 487 (2000); *In* Charged particle and photon interactions with matter: chemical, physicochemical, and biological consequences with applications. *Edited by* A. Mozumder and Y. Hatano. Marcel Dekker, New York. 2004. p. 403.
4. G.V. Buxton. *In* Charged particle and photon interactions with matter: chemical, physicochemical, and biological consequences with applications. *Edited by* A. Mozumder and Y. Hatano. Marcel Dekker, New York. 2004. p. 331.
5. C. Ferradini and J.-P. Jay-Gerin. Res. Chem. Intermed. **26**, 549 (2000).
6. H. Fricke and S. Morse. Am. J. Roentgenol. Radium Ther. **18**, 430 (1927); Philos. Mag. 7th Ser. **7**, 129 (1929).
7. H. Fricke and E.J. Hart. *In* Radiation dosimetry. 2nd ed. Vol. II. *Edited by* F.H. Attix and W.C. Roesch. Academic Press, New York. 1966. p. 167.
8. E. Hayon. *In* Radiation chemistry of aqueous systems. *Edited by* G. Stein. The Weizmann Science Press of Israel, Jesuralem, Israel. 1968. p. 157.
9. G.V. Buxton. *In* Proceedings of the third international congress of radiation research. Cortina d'Ampezzo, Italy, June 26–July 2, 1966. *Edited by* G. Silini. North-Holland, Amsterdam. 1967. p. 235; Radiat. Res. Rev. **1**, 209 (1968).
10. I.G. Draganić and Z.D. Draganić. The radiation chemistry of water. Academic Press, New York. 1971. p. 123.
11. J. Meesungnoen, M. Benrahmoune, A. Filali-Mouhim, S. Mankhetkorn, and J.-P. Jay-Gerin. Radiat. Res. **155**, 269 (2001).
12. M.J. Bronskill, R.K. Wolff, and J.W. Hunt. J. Chem. Phys. **53**, 4201 (1970).
13. C.D. Jonah, J.R. Miller, and M.S. Matheson. J. Phys. Chem. **81**, 931 (1977).
14. G.V. Buxton, C.L. Greenstock, W.P. Helman, and A.B. Ross. J. Phys. Chem. Ref. Data, **17**, 513 (1988).
15. A.J. Elliot. Rate constants and *G*-values for the simulation of the radiolysis of light water over the range 0–300 °C. Report AECL-11073. Atomic Energy of Canada Ltd., Chalk River, Ontario. 1994; A.J. Elliot, D.C. Ouellette, and C.R. Stuart. The temperature dependence of the rate constants and yields for the simulation of the radiolysis of heavy water. Report AECL-11658. Atomic Energy of Canada Ltd., Chalk River, Ontario. 1996.
16. A.O. Allen. The radiation chemistry of water and aqueous solutions. D. Van Nostrand Co., Princeton, New Jersey. 1961. p. 49.
17. J. Pucheault. *In* Actions chimiques et biologiques des radiations. 5ème Sér. *Edited by* M. Haïssinsky. Masson, Paris, France. 1961. p. 31.
18. W.G. Burns and H.E. Sims. J. Chem. Soc., Faraday Trans. 1, **77**, 2803 (1981).
19. A. Appleby. Radiat. Phys. Chem. **34**, 121 (1989).
20. D.R. McCracken, K.T. Tsang, and P.J. Laughton. Aspects of the physics and chemistry of water radiolysis by fast neutrons and fast electrons in nuclear reactors. Report AECL-11895. Atomic Energy of Canada Ltd., Chalk River, Ontario. 1998.
21. J.L. Magee and A. Chatterjee. J. Phys. Chem. **84**, 3529 (1980).
22. C. Ferradini. J. Chim. Phys. **76**, 636 (1979).
23. A. Mozumder. Fundamentals of radiation chemistry. Academic Press, San Diego, California, USA. 1999. p. 41.
24. R.C. Das. Radiat. Res. Rev. **3**, 121 (1971).
25. R. Bensasson, A. Bernas, M. Bodard, L. Bouby, M. Cottin, M. Duflo, F. Kieffer, A. Koulkès, N. Leray, J. Pucheault, and C. Vermeil. *In* Tables of constants and numerical data. Vol. 13. *Edited by* M. Haïsinski and M. Magat. Pergamon, Oxford, UK. 1963.
26. ICRU Report 17. Radiation dosimetry: X rays generated at potentials of 5 to 150 kV. International Commission on Radiation Units and Measurements, Washington, DC. 1970.
27. A. Chatterjee and J.L. Magee. J. Phys. Chem. **84**, 3537 (1980).
28. ICRU Report 34. The dosimetry of pulsed radiation. International Commission on Radiation Units and Measurements, Bethesda, Maryland. 1982.
29. J.A. LaVerne and R.H. Schuler. J. Phys. Chem. **91**, 5770 (1987).
30. See ref. 2, p. 71.
31. Y. Tabata, Y. Ito, and S. Tagawa (*Editors*). CRC handbook of radiation chemistry. CRC Press, Boca Raton, Florida. 1991. pp. 321 and 571.
32. S.M. Pimblott and J.A. LaVerne. J. Phys. Chem. A, **106**, 9420 (2002).
33. N.V. Klassen, K.R. Shortt, J. Seuntjens, and C.K. Ross. Phys. Med. Biol. **44**, 1609 (1999).
34. J. Meesungnoen and J.-P. Jay-Gerin. J. Phys. Chem. A, **109**, 6406 (2005).
35. P. Clifford, N.J.B. Green, M.J. Oldfield, M.J. Pilling, and S.M. Pimblott. J. Chem. Soc. Faraday Trans. 1, **82**, 2673 (1986); S.M. Pimblott, M.J. Pilling, and N.J.B. Green. Radiat. Phys. Chem. **37**, 377 (1991); S.M. Pimblott and N.J.B. Green. Res. Chem. Kinet. **3**, 117 (1995).
36. Y. Frongillo, T. Goulet, M.-J. Fraser, V. Cobut, J.P. Patau, and J.-P. Jay-Gerin. Radiat. Phys. Chem. **51**, 245 (1998).
37. T. Goulet, M.-J. Fraser, Y. Frongillo, and J.-P. Jay-Gerin. Radiat. Phys. Chem. **51**, 85 (1998).
38. E.J. Hart. J. Chem. Educ. **34**, 586 (1957).
39. J.A. Dean. Handbook of organic chemistry. McGraw-Hill, New York. 1987. pp. 8–56.
40. J.-J. Max, C. Ménichelli, and C. Chapados. J. Phys. Chem. A, **104**, 2845 (2000); see also H. Chen and D.E. Irish. J. Phys. Chem. **75**, 2672 (1971).
41. J. Meesungnoen and J.-P. Jay-Gerin. Radiat. Res. **164**, 688 (2005).
42. P.-Y. Jiang, Y. Katsumura, R. Nagaishi, M. Domae, K. Ishikawa, K. Ishigure, and Y. Yoshida. J. Chem. Soc. Faraday Trans. **88**, 1653 (1992).

© 2007 NRC Canada

43. P. Neta, R.E. Huie, and A.B. Ross. J. Phys. Chem. Ref. Data, **17**, 1027 (1988).
44. C. Ferradini. *In* Actions chimiques et biologiques des radiations. 10ème Sér. *Edited by* M. Haïssinsky. Masson, Paris, France. 1966. p. 89.
45. Y. Tang, R.P. Thorn, R.L. Mauldin III, and P.H. Wine. J. Photochem. Photobiol. A, **44**, 243 (1988).
46. R.E. Huie and L.W. Sieck. *In* S-centered radicals. *Edited by* Z.B. Alfassi. Wiley, Chichester. NY. 1999. p. 63.
47. I.G. Draganić, M.T. Nenadović, and Z.D. Draganić, J. Phys. Chem. **73**, 2564 (1969).
48. R.W. Matthews, H.A. Mahlman, and T.J. Sworski. J. Phys. Chem. **76**, 1265 (1972); Radiat. Res. **39**, 534 (1969).
49. K. Sehested, E. Bjergbakke, and H. Fricke. Radiat. Res. **56**, 385 (1973); K. Sehested, H. Corfitzen, and H. Fricke. J. Phys. Chem. **74**, 211 (1970).
50. B. Lesigne, C. Ferradini, and J. Pucheault. J. Phys. Chem. **77**, 2156 (1973); J. Phys. Chem. **76**, 3676 (1972).
51. Y. Katsumura. *In* Radiation chemistry: Present status and future trends. *Edited by* C.D. Jonah and B.S.M. Rao. Elsevier, Amsterdam. 2001. p. 163.
52. D.R. Lide (*Editor*). CRC handbook of chemistry and physics. 84th ed. CRC Press, Boca Raton, Florida. 2003. pp. 5–96.
53. D.C. Harris. Exploring chemical analysis. 2nd ed. W.H. Freeman, New York. 2001. p. 233.
54. K.H. Schmidt and D.M. Bartels. Chem. Phys. **190**, 145 (1995).
55. E.A. Guggenheim. Philos. Mag. 7th Ser. **19**, 588 (1935); C.W. Davies. J. Chem. Soc. 2093 (1938); R.A. Robinson and R.H. Stokes. Electrolyte solutions: The measurement and interpretation of conductance, chemical potential and diffusion in solutions of simple electrolytes. 2nd ed. (revised). Butterworths Publications Ltd., London, UK. 1959. p. 223.
56. G. Czapski and H.A. Schwarz. J. Phys. Chem. **66**, 471 (1962).
57. T. Solomon. J. Chem. Educ. **78**, 1691 (2001).
58. E.R. Johnson and A.O. Allen. J. Am. Chem. Soc. **74**, 4147 (1952).
59. J.W. Boyle. Radiat. Res. **17**, 427 (1962); Radiat. Res. **17**, 450 (1962).
60. D.E. Watt. Quantities for dosimetry of ionizing radiations in liquid water. Taylor & Francis, London, UK. 1996. p. 82.
61. ICRU Report 49. Stopping powers and ranges for protons and alpha particles. International Commission on Radiation Units and Measurements, Bethesda, Maryland. 1993.
62. H. Shiraishi, G.R. Sunaryo, and K. Ishigure. J. Phys. Chem. **98**, 5164 (1994).
63. T. Lundström, H. Christensen, and K. Sehested. Radiat. Phys. Chem. **69**, 211 (2004).
64. See ref. 52, pp. 8–46.
65. B. Halliwell and J.M.C. Gutteridge. Free radicals in biology and medicine. 3rd ed. Oxford University Press, Oxford, UK. 1999. p. 36.
66. See ref. 16, p. 32.
67. M. Lefort. J. Chim. Phys. **54**, 782 (1957); Annu. Rev. Phys. Chem. **9**, 123 (1958); M. Cottin and M. Lefort. J. Chim. Phys. **53**, 267 (1956).
68. H.A. Mahlman and J.W. Boyle. J. Am. Chem. Soc. **80**, 773 (1958); H.A. Mahlman. J. Am. Chem. Soc. **81**, 3203 (1959).
69. E. Hayon. J. Phys. Chem. **65**, 1502 (1961); Trans. Faraday Soc. **61**, 734 (1965); J. Phys. Chem. **69**, 2628 (1965).
70. C.H. Cheek, V.J. Linnenbom, and J.W. Swinnerton. Radiat. Res. **19**, 636 (1963); Report of NRL Progress. US Naval Research Laboratory, Washington, DC. July 1962. p. 11.
71. N.F. Barr and R.H. Schuler. Radiat. Res. **7**, 302 (1957).
72. M.H. Back and N. Miller. Nature (London), **179**, 321 (1957).
73. C.J. Hochanadel and S.C. Lind. Annu. Rev. Phys. Chem. **7**, 83 (1956).
74. C. Ferradini and J. Pucheault. Biologie de l'action des rayonnements ionisants. Masson, Paris, France. 1983. p. 25; J. Pucheault and C. Ferradini. J. Chim. Phys. **54**, 659 (1957).
75. E. Collinson, F.S. Dainton, and J. Kroh. Proc. R. Soc. London Ser. A, **265**, 422 (1962).
76. T.J. Sworski. J. Am. Chem. Soc. **76**, 4687 (1954).
77. E. Hayon. J. Phys. Chem. **68**, 1242 (1964).
78. K.H. Schmidt, P. Han, and D.M. Bartels. J. Phys. Chem. **96**, 199 (1992).
79. M. Haïssinsky. J. Chim. Phys. **62**, 1141 (1965). *In* Actions chimiques et biologiques des radiations. 11ème Sér. *Edited by* M. Haïssinsky. Masson, Paris, France. 1967. p. 131.
80. B. Pastina and J.A. LaVerne. J. Phys. Chem. A, **105**, 9316 (2001).
81. A.J. Elliot, M.P. Chenier, D.C. Ouellette, and V.T. Koslowsky. J. Phys. Chem. **100**, 9014 (1996); The temperature dependence of *G*-values for aqueous solutions irradiated with a 23 MeV $^2H^+$ beam. Report AECL-10659. Atomic Energy of Canada Ltd., Chalk River, Ontario. 1992.
82. A.J. Elliot, M.P. Chenier, and D.C. Ouellette. J. Chem. Soc. Faraday Trans. **89**, 1193 (1993).
83. A. Appleby and H.A. Schwarz. J. Phys. Chem. **73**, 1937 (1969); H.A. Schwarz, J.M. Caffrey, Jr., and G. Scholes. J. Am. Chem. Soc. **81**, 1801 (1959).
84. R.H. Bisby, R.B. Cundall, H.E. Sims, and W.G. Burns. Faraday Discuss. Chem. Soc. **63**, 237 (1977).
85. C.A. Naleway, M.C. Sauer, Jr., C.D. Jonah, and K.H. Schmidt. Radiat. Res. **77**, 47 (1979); M.C. Sauer, Jr., K.H. Schmidt, E.J. Hart, C.A. Naleway, and C.D. Jonah. Radiat. Res. **70**, 91 (1977).
86. M.C. Sauer, Jr., C.D. Jonah, K.H. Schmidt, and C.A. Naleway. Radiat. Res. **93**, 40 (1983).
87. B. Pastina and J.A. LaVerne. J. Phys. Chem. A, **103**, 1592 (1999).
88. V. Wasselin-Trupin, G. Baldacchino, S. Bouffard, and B. Hickel. Radiat. Phys. Chem. **65**, 53 (2002).
89. H.E. Sims, C.B. Ashmore, P.K. Tait, and W.S. Walters. *In* Proceedings of Japan Atomic Industrial Forum, Inc. (JAIF). International conference on water chemistry in nuclear power plants. Kashiwazaki, Japan, October 13–16, 1998. p. 894; C.B. Ashmore, H.E. Sims, P.K. Tait, and W.S. Walters. The measurement of water radiolysis product yields at high temperature and pressure. Final report. Report AEAT-2223. UK Atomic Energy Authority. 1997–1998.
90. M.C. Kent and H.E. Sims. *In* Proceedings of the 6th international conference on water chemistry of nuclear reactor systems. British Nuclear Energy Society, London, UK. 1992. p. 153.
91. R.H. Schuler and A.O. Allen. J. Am. Chem. Soc. **79**, 1565 (1957).
92. A.O. Allen. Radiat. Res. Suppl. **4**, 54 (1964).
93. T.J. Hardwick. Discuss. Faraday Soc. **12**, 203 (1952); A.O. Allen. Radiat. Res. **1**, 85 (1954).
94. F.S. Dainton and H.C. Sutton. Trans. Faraday Soc. **49**, 1011 (1953).
95. K. Coatsworth, E. Collinson, and F.S. Dainton. Trans. Faraday Soc. **56**, 1008 (1960); F.S. Dainton. Radiat. Res. Suppl. **1**, 1 (1959).
96. J. Bednář and J. Teplý. Collect. Czech. Chem. Commun. **24**, 127 (1959); J. Bednář. Chem. Listy, **53**, 1083 (1959).
97. G.L. Kochanny, Jr., A. Timnick, C.J. Hochanadel, and C.D. Goodman. Radiat. Res. **19**, 462 (1963).

© 2007 NRC Canada

98. T. Balkas, F.S. Dainton, J.K. Dishman, and D. Smithies. Trans. Faraday Soc. **62**, 81 (1966).
99. G. Lemaire, C. Ferradini, and J. Pucheault. J. Phys. Chem. **76**, 1542 (1972); G. Lemaire and C. Ferradini. Radiochem. Radioanal. Lett. **5**, 175 (1970).
100. E.J. Hart. Annu. Rev. Phys. Chem. **5**, 139 (1954).
101. J. Meesungnoen, J.-P. Jay-Gerin, A. Filali-Mouhim, and S. Mankhetkorn. Chem. Phys. Lett. **335**, 458 (2001).
102. J.L. Magee and A. Chatterjee. *In* Radiation chemistry: principles and applications. *Edited by* Farhataziz and M.A.J. Rodgers. VCH Publishers, New York. 1987. p. 137.
103. J.A. LaVerne and H. Yoshida. J. Phys. Chem. **97**, 10720 (1993).
104. J.-P. Jay-Gerin, N. Autsavapromporn, and J. Meesungnoen. *In* Proceedings of the 48th annual meeting of the Japanese Society of Radiation Chemistry, Osaka, Japan, October 12–14, 2005. *Edited by* S. Tagawa. Osaka University, Osaka. 2005. p. 67.
105. J.P. Keene. Radiat. Res. **22**, 14 (1964).
106. M. Běgusová and S.M. Pimblott. Radiat. Prot. Dosim. **99**, 73 (2002).
107. C.J. Hochanadel and J.A. Ghormley. J. Chem. Phys. **21**, 880 (1953).
108. R.H. Schuler and A.O. Allen. J. Chem. Phys. **24**, 56 (1956).
109. W.K. Sinclair and R.J. Shalek. Radiology, **70**, 92 (1958).
110. See ref. 16, p. 13.
111. J.V. Davies, D. Greene, J.P. Keene, J. Law, and J.B. Massey. Phys. Med. Biol. **8**, 97 (1963).
112. D.M. Donaldson and N. Miller. J. Chim. Phys. **52**, 578 (1955).
113. A.O. Fregene. Radiat. Res. **31**, 256 (1967).
114. L.H. Gevantman and J.F. Pestaner. J. Chem. Phys. **31**, 1140 (1959).
115. T.J. Hardwick. Can. J. Chem. **30**, 17, 39 (1952).
116. E.J. Hart. Radiat. Res. **1**, 53 (1954); W.R. McDonell and E.J. Hart. J. Am. Chem. Soc. **76**, 2121 (1954).
117. E.J. Hart, W.J. Ramler, and S.R. Rocklin. Radiat. Res. **4**, 378 (1956); A.R. Anderson and E.J. Hart. Radiat. Res. **14**, 689 (1961).
118. J.L. Haybittle, R.D. Saunders, and A.J. Swallow. J. Chem. Phys. **25**, 1213 (1956).
119. M. Peisach and J. Steyn. Nature (London), **187**, 58 (1960).
120. M.C. Sauer, Jr., E.J. Hart, C.A. Naleway, C.D. Jonah, and K.H. Schmidt. J. Phys. Chem. **82**, 2246 (1978).
121. N.F. Barr and R.H. Schuler. J. Phys. Chem. **63**, 808 (1959).
122. R.J. Shalek, W.K. Sinclair, and J.C. Calkins. Radiat. Res. **16**, 344 (1962).
123. J.A. LaVerne and R.H. Schuler. J. Phys. Chem. **98**, 4043 (1994).

© 2007 NRC Canada

REVIEW / SYNTHÈSE

The natural bite angle — Seen from a ligand's point of view[1]

Olaf Kühl

Abstract: The natural bite angle concept is examined using *N*,*N*′-bisphosphino urea ligands as rigid scaffolds. The ligand has an upper limit of about 95° for the observed bite angle in chelate complexes, but prefers a much lower one. The ligand can be described as possessing downward flexibility. The dependence of the bite angle on the P—P distance within the ligand and the M—P bond length is illustrated. The metal tries to force the ligand into its own preferred structure, whereas the ligand wants to achieve a short P—P distance. A truly rigid ligand such as the *N*,*N*′-bisphosphino urea family is thus seen to clearly discriminate between metal atoms according to their individual assertiveness, using the P—P distance in the complex as a measure. Although the natural bite angle concept is valid and helpful in determining the possible bite-angle range for ligands before it is actually synthesised, its practical applicability seems to be limited to those cases where the flexibility range of the ligand allows for only one metal-preferred bite angle to be realized.

Key words: natural bite angle, ligand effects, ligand design.

Résumé : On a examiné le concept de l'angle naturel de prise en utilisant des ligands de *N*,*N*′-bisphosphinourées comme échafauds rigides. La limite supérieure pour l'angle de prise observé du ligand dans des chélates complexes, toutefois, sa préférence se situe à une valeur de beaucoup inférieure. On peut dire que le ligand possède une flexibilité descendante. On illustre la dépendance de l'angle de prise sur la distance P—P dans le ligand et sur la longueur de la liaison M—P. Le métal tend à forcer le ligand à prendre sa structure préférée alors que le ligand tend à raccourcir la distance P—P. Il apparaît donc que des ligands vraiment rigides, tels ceux de la famille de la *N*,*N*′-bisphosphinourée, peuvent faire une discrimination entre des atomes métalliques suivant leurs propres préférences en utilisant la distance P—P dans le complexe comme mesure. Même si le concept d'angle naturel de prise est valide et peut être utile dans la détermination des limites probables de l'angle de prise de ligands avant même qu'ils soient synthétisés, la limite de son domaine d'application semble limité aux cas où la limite de flexibilité du ligand ne permet de réaliser qu'un seul angle de prise d'un métal.

Mots-clés : angle de prise naturel, effets de ligand, mise au point de ligand.

[Traduit par la Rédaction]

Introduction

For decades, ligand design and engineering have been at the core of research into new and improved transition-metal complexes for homogeneous catalysis (1). Ligand design methods are only meaningful if the reaction mechanism, the required properties of the metal, the ligand and the substrate, as well as the influence of reaction conditions are thoroughly understood. Because there are rather narrow limits for the choice of metal, temperature, and pressure, and the substrates are largely dictated by the target product, the main focus for the improvement of catalysts is often on the ligand (1).

The ligand frequently carries such useful information as electronic (2) and steric properties (3), chirality (4), symmetry, and hemilability (5). Methods to determine the electronic and steric properties of the ligands, using IR and NMR spectroscopy, electrochemical methods, thermodynamical data and cone angles, as well as theoretical calculations, were devised (6). The best known of these techniques are the steric and electronic parameters defined by Tolman for monodentate ligands (2, 3) that were later adapted for chelating ligands (7). The Tolman electronic parameter (TEP) is defined as the A_1 band of the νCO stretching vibration observed in the IR spectra of $[Ni(CO)_3L]$. The TEP value can be calculated from any other series of transition-

Received 3 August 2006. Accepted 26 February 2007. Published on the NRC Research Press Web site at http://canjchem.nrc.ca on 18 April 2007.

O. Kühl. The Chemistry Department, The University of Alabama, Shelby Hall, Tuscaloosa, AL 35487, USA (e-mail: okuhl@bama.ua.edu).

[1]Dedicated to Professor Joachim Heinicke on the occasion of his 60th birthday, with my warmest congratulations and best wishes.

 doi:10.1139/V07-023 © 2007 NRC Canada

metal carbonyl complexes of phosphanes, and theoretical methods to calculate it are available (6). Arguably the best technique, but one that requires a large amount of experimental data, is the quantitative analysis of ligand effects (QALE), developed by Giering et al. (8–10).

The discovery that chelate ligands have beneficial properties that are not observed for monodentate ligands (4) led to the widespread use of chelate ligands in homogenous catalysis. This chelate effect had to be described in terms of electronic and (or) steric contributions. Rather obvious factors are increased complex stability with chelate coordination and the stronger influence of ligand chirality on the asymmetry of the catalyst, and thus the stereoselectivity of the reaction (4). The influence of the chelate ligand on the geometry of the metal, and therefore on crucial intermediates in the catalytic cycle, was discovered relatively late. The electronic influence of chelate ligands can be determined by calculating the TEP value using the Crabtree formula (7) or converting it from any other suitable carbonyl complex of the ligand (6).

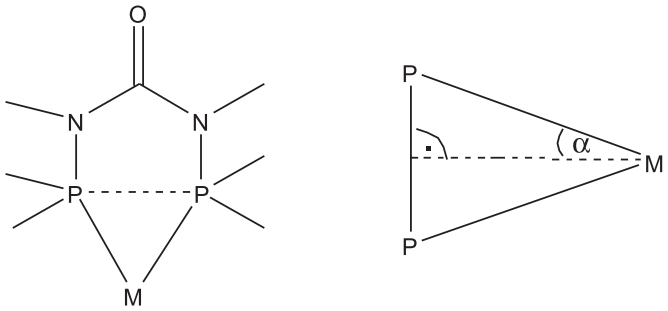
The steric properties of a chelate ligand are only insufficiently represented by the adjusted Tolman cone angle. Therefore, a new parameter, the natural bite angle (1, 11, 12), was introduced.

The natural bite angle

The natural bite angle is defined as the angle formed by the two donor atoms of the chelate ligand and the metal atom under the condition that the metal atom exerts no influence on the ligand (1, 11, 12). In the solid state, the donor atoms in the free ligand are often unfavorably orientated for metal coordination, and hence, crystal structure determinations are not often helpful in measuring the natural bite angle. Instead, it can be calculated using molecular mechanics (MM). The procedure is rather simple and involves orientating the two donor atoms of the ligand (phosphorus in our case) towards an imaginary metal atom, assigning a fixed metal-to-donor-atom bond length and no force to the P–M–P angle (12) (see Fig. 1). The force field is used to calculate the distance between the two donor atoms, and thus the P–M–P angle known as the natural bite angle.

In this definition, the natural bite angle of a ligand depends only on two parameters: the M—P bond length and the P—P distance. The P—P distance is calculated by the molecular mechanics (MM) program used, but the M—P bond length must be chosen. Therefore, it is crucial to standardize the M—P values to make natural bite angles comparable in the literature. This amounts to choosing a specific metal as the standard and means that if another metal rather than the standard one is chosen, the natural bite angle has to be adjusted to the individual M—P bond length. The natural bite angle was introduced into the literature by Casey (11) and further developed by van Leeuwen (1, 12), using rhodium (I) catalysts as models. Both authors used different default values for the standard Rh—P bond (230 and 231.5 pm, respectively). Small as the difference of 1.5 pm may seem, it nonetheless translates to a difference of 0.6° in the resulting natural bite angle. The comparability of the two datasets is, therefore, somewhat compromised.

Fig. 1. Illustration of the definition of the natural bite angle taking a bisphosphino urea ligand as an example.



$$\alpha = 0.5\ \text{P–M–P}$$

$$\text{P–M–P} = 2\ \sin^{-1}\ (\text{P—P} / 2\ \text{M—P})$$

This becomes more important if different catalyst metals are considered. The M—P bond length of 231.5 pm lies in the middle of the range for typical M—P bond lengths: Mo(0), 245 pm (13, 14); Rh(I), 231.5 pm (12); Cu(I), 226 pm (15); Pd(II)/Pt(II), 220 pm (14, 16); Ni(0), 218 pm (17, 18). The difference of 27 pm in the range of M—P bond lengths translates into a natural bite angle spread of 12°. A statistical analysis performed by Dierkes and van Leeuwen (12) on the chelate ligands $Ph_2P(CH_2)_2PPh_2$ and $Ph_2P(CH_2)_3PPh_2$ shows that indeed most structurally determined bite angles of their complexes fall within a 10° range. This can be interpreted as an unchanged P—P distance and a dependence of the bite angle on the M—P bond length. Therefore, it might be better to report the P—P distance rather than the bite angle, since the bite angle is significantly influenced by the M—P bond length, and thus the choice of metal, when by definition it ought to be independent of it.

However, the mean values of the observed bite angles are 87° and 91°, respectively, and thus very close to the metal-preferred values for octahedral and square-planar metal complexes that dominate the literature.

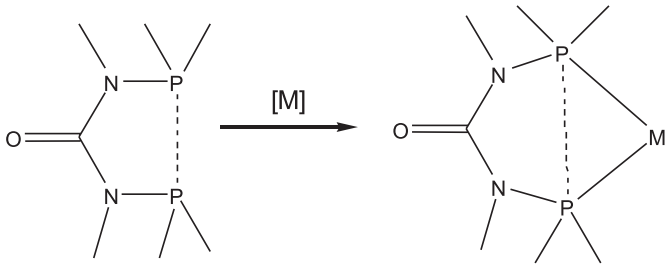
The mathematical relationship between the P—P distance, the M—P bond length, and the P–M–P angle (the observed bite angle) means that the metal can attain the preferred bite angle by the adjustment of the M—P bond length, i.e., if the natural bite angle of the ligand is too large for a chelate complex to be formed, the P–M–P angle can be reduced by increasing the M—P bond length. A weaker coordination of the metal is then offset by a chelate bonding mode. More importantly, the flexibility of the M—P bond length increases the flexibility range of the natural bite angle that is defined as a 3 kcal/mol deviation in energy from the natural bite angle value (11, 12).

The phosphino urea ligand system

An experimentally verified natural bite angle of a diphosphane ligand requires a method that measures the P—P distance in a conformation suitable to chelate bonding to a metal, but in the absence of such metal. This can easiest be done when the ligand crystallizes in such a conformation, and thus the P—P distance can be measured by X-ray crystal structure determination.

© 2007 NRC Canada

Fig. 2. The widening of the ligand mouth (P—P distance increase) upon chelate coordination of the bisphosphino urea ligands.



In addition, the ligand backbone should be truly rigid, meaning that the metal has to use considerable force to open the mouth of the ligand (see Fig. 2), thereby increasing the P—P distance and the bite angle. Only then can the influence of the metal be determined, and more importantly, which metals are more assertive. Rigidity does not mean that the P—P distance cannot be increased at all, but rather that the resistance of the ligand is high enough to be able to distinguish between metals of equal geometrical preferences.

Bisphosphino ureas (19) contain the NC(O)N backbone that is characterised by its planarity, its short N—C bonds (138–140 pm), and a rather rigid N–C–N angle (118–121°) (14, 16, 20–24). The phosphorus atoms would be coplanar with the NC(O)N unit; however, the repulsion of the phosphorus atom lone pairs (PALP) that point towards each other results in a noticeable dislocation of the phosphorus atoms from the common plane in the free ligand (see Fig. 3) (17, 24).

In all structurally determined bisphosphino ureas, the phosphorus atoms face each other with the PALP pointing towards each other or towards an imaginary metal atom (20–22). They are pre-orientated for metal coordination, and the P—P distance, determined from their crystal structures, can be taken to calculate their natural bite angles.

Chelate coordination to metals results in an unfavorable bond-lengths distribution with the urea backbone displaying short bond lengths (N—C is around 138–140 pm), and the metal giving rise to significantly longer M—P bond lengths (220–248 pm). Hence, to preserve the planarity of the ensuing metallacycle, the metal will have to force the ligand's mouth open, widening the N–C–N angle. However, the ligand effectively resists this, and instead, the metallacycle folds along the P—N vector (the line connecting the P and N atoms that are not bonded to each other), preserving the accustomed P—P distance even in the metal complex (16, 17, 24). Indeed, the value of the P—P distance in the metal complex can be taken as an indication of how assertive the metal is.

Flexibility of the ligand

The N–C–N unit in the bisphosphino urea backbone can be seen as a strong spring that causes the ligand to be very rigid as much as it prevents the P—P distance to increase largely. Indeed, the question of rigidity was identified early as a central issue in the understanding of the natural bite angle concept (1, 11, 12). As a measure of the flexibility of a chelate ligand, a bite angle range is calculated using molecular mechanics techniques encompassing all structures within 3 kcal/mol from the minimum (11). In many cases, that translates into a flexibility range of about 30–40° (12). That makes octahedral, square planar, tetrahedral, and even trigonal planar (trigonal bipyramidal) metal geometries easily accessible to the ligand. The observed bite angles for these flexible ligand systems will be metal-preferred rather than dependent on the natural bite angle of the ligand. Furthermore, there will be no effective discrimination between the ee and the ea coordination in trigonal-bipyramidal metal complexes (ee: equatorial–equatorial; ea: equatorial–axial). Consequently, no favorable product distribution in the rhodium-catalyzed hydroformylation of linear aldehydes can be expected, assuming that the bite angle of the ligand plays a central role in it.

Bisphosphino urea ligands were reacted with metal precursors, featuring metal-preferred bite angles ranging from 90° to 180°: 90° (octahedral) Cr(0), Mo(0), W(0) (13, 14, 20); 90° (square planar) Pd(II), Pt(II) (14, 16, 23); 90° (ea-trigonal bipyramidal) Fe(0) (20); 109.5° (tetrahedral) Ni(0) (17), Cu(I) (24); 120° (ee-trigonal bipyramidal) Fe(0) (20); and 180° (linear) Au(I) (14). With the exception of the trigonal bipyramidal geometry, all geometries have at least one structurally determined representative, enabling a detailed insight into the ligand preferences (see Fig. 4).

The experimentally determined P—P distances in the free bisphosphino urea ligands range from 280 to 308 pm (20–22) (see Fig. 5 and Table 1). These translate into uncommonly small natural bite angles (using 231.5 pm as the standard). If actually observed bite angles are considered, then it becomes soon apparent that any metal can force the mouth of these ligands open (see Fig. 2). In all metal complexes, the P—P distance is greater than that observed in the free ligand, ranging from 309.9 pm to 324.6 pm (see Table 2).

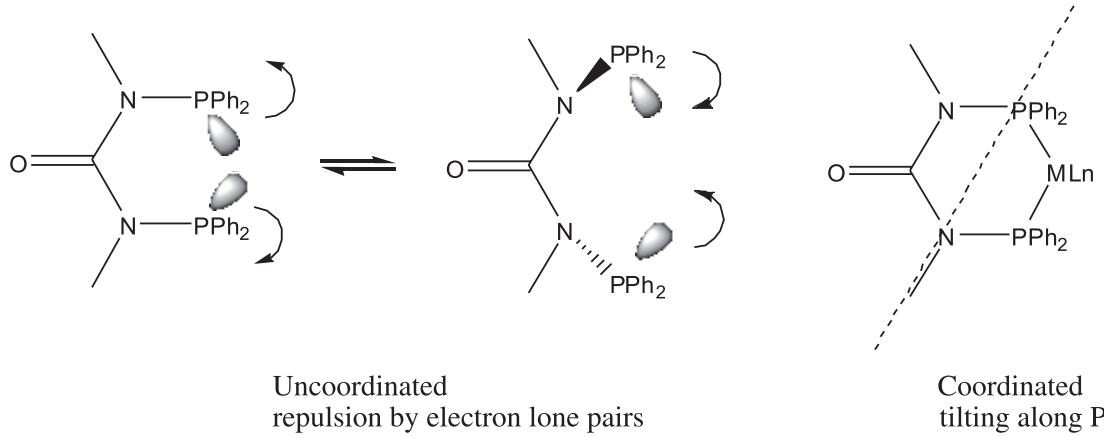
Geometry around the metal

From the observed bite angles ranging from 80.7° to 94.8°, the bisphosphino urea ligands only support metal-preferred bite angles of 90°. The exception is the copper(I) complex, which is distorted tetrahedral (24). However, for the copper(I) complex, the only evidence for chelation is in the solid state. In solution, the complex is labile, and the metallacycle opens as one of the phosphorus atoms dissociates from the copper atom. In fact, the compound displays dynamic behavior in solution even at low temperatures, probably via a fast dissociation–association mechanism (24). A similar Ni(0) complex, probably with a preferred tetrahedral geometry, shows similar dynamic behavior, although no crystal structure was reported (17).

If the preferred bite angle of the metal is further increased, the bisphosphino urea ligand will no longer act as a chelate ligand, but it will bridge two metal atoms in a κ^1 fashion. This is observed in the reactions of the ligand with $[Fe_2(CO)_9]$ (20) and [AuCl(tht)] (tht = tetrahydrothiophene) (14). Gold(I) complexes favor linear geometries with a P–Au–L angle of 180°, and it is no surprise that the rigid bisphosphino urea ligand will not accommodate such a large bite angle. Quite expectedly, it chooses to act as a bis-κ^1 ligand to two gold atoms instead.

© 2007 NRC Canada

Fig. 3. The structure of bisphosphino urea ligands in the free state (left) and in metal chelate complexes (right).



The case of the Fe(0) carbonyl complex is quite different as a trigonal-bipyramidal complex has two accessible bite angles: 120° for ee coordination and 90° for ea coordination. It is this choice for which the natural bite angle concept was developed using rhodium as the model atom.

From the previously mentioned arguments, it is understandable that the bisphosphino urea ligand will not occupy the ee sites, as the metal-preferred bite angle of 120° is certainly inaccessible for the rigid chelate ligand. However, the ea sites seem comparable to the situation in octahedral and square-planar complexes, where the metal-preferred bite angles are 90°. The answer can be found by carefully studying the reaction conditions employed. A suspension of $[Fe_2(CO)_9]$ in toluene was treated with $\{PhBu^tPN(Me)\}_2CO$ at room temperature. Under these conditions, the bisphosphino urea ligand can cleave the Fe—Fe bond but cannot displace a carbonyl ligand from the iron fragment. Heating would be needed for this reaction to occur. As a consequence, the two phosphorus atoms of the ligand react seperately with one $[Fe_2(CO)_9]$ molecule each until the iron complex is consumed. The question of suitable bite angles does not arise.

Another feature of bisphosphino urea ligands is clearly demonstrated by the reactions with the Ni(0) (17), Cu(I) (24), Fe(0) (20), and Au(I) (14) precursors. Despite their apparent steric crowdedness and their preference for nonbonding P—P contacts, they can evidently rotate freely around the P—N bond (see Fig. 6). Another interesting detail is supplied by the reaction between $\{PhBu^tPN(Me)\}_2CO$ and *cis*-$[W(CO)_4$(norbornadiene)] (20). The product is not the expected P,P′-chelate complex, but a P,O-chelate complex where the carbonyl oxygen atom is bound to the metal (see Fig. 7). Evidently, the steric congestion around the phosphorus atoms prevents the attack of the second phosphorus atom on tungsten, while the norbornadiene ligand is still bound to it in a κ^2 fashion (with one double bond) in the transition state. Instead, coordination of the less-crowded carbonyl group is preferred.

In the bisphosphino ureas, we find a rare case where the P—P distance in the free ligand can be determined from the crystal structure and proves to be smaller than the distance in any of their metal-chelate complexes. The very short P—P distances in the free ligand are far shorter than the sum of the van der Waals radii of phosphorus (25) and indicative of a positive interaction between the two phosphorus atoms. In principle, one of the phosphino groups can utilize its lone pair to act as a Lewis base towards the other phosphino group. This behavior is observed in related systems, resulting in a P—P bond and a five-membered ring system (6). This very short P—P distance has been identified as the cause why the natural bite angle of the free bisphosphino urea ligand could not be calculated by standard MM methods (17). In fact, the authors reported that the van der Waal's radius for phosphorus had to be significantly reduced to reproduce the natural bite angle of $\{Ph_2PN(Me)\}_2CO$.

Softness of the metal

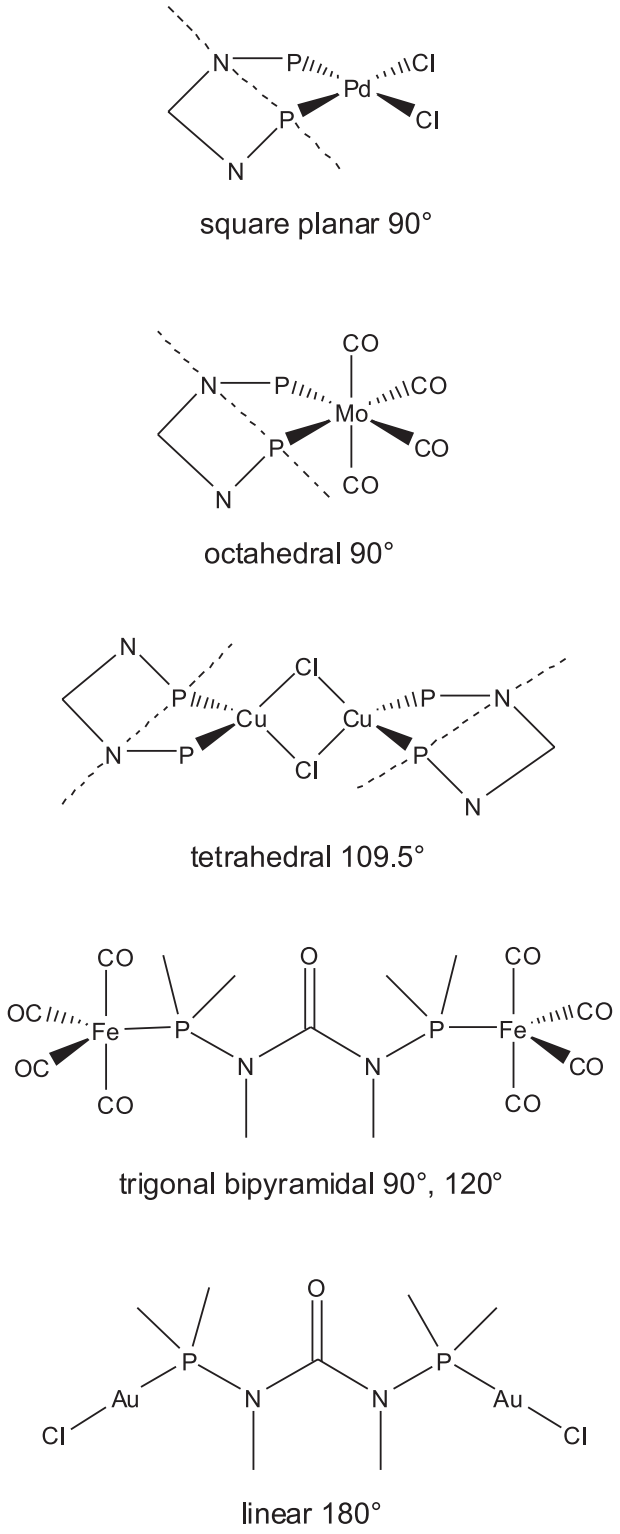
In the metal complexes, the ligand apparently wants to maintain the short P—P distance but is opposed by the interplay of the metal-preferred bite angle and the M—P bond length. The combination of their optimal values produces a P—P distance that exceeds that of the free ligand. The increase of the P—P distance in the metal complex compared with the free ligand can therefore be seen in terms of the influence or the assertiveness of the metal, since the metal forces the mouth of the ligand open.

Looking at the respective metal atoms and their accompanying preferred bite angles, a trend manifests itself. The greatest P—P distances are found for the 3d and 4d elements: copper, molybdenum, and palladium, whereas the P—P distances in complexes of the 5d element platinum approach the values for the free ligands (309.9, 312.2, and 314.0 pm, respectively). It seems that the ligand is determined to attain its resting position (the free ligand status quo) regardless of the preferences of the metal. With the "softer" 5d element platinum, it almost achieves its goal; however, with the somewhat "sturdier" 3d and 4d elements, it has to make significant concessions.

The case of copper is quite different. The preferred geometry of copper(I) is tetrahedral, and thus, the copper atom wants to realize a larger bite angle (109.5°). As it cannot increase the P—P distance far enough, it has to settle for a short M—P bond length, and indeed, the observed Cu—P bond length of 223.5 pm is at the bottom end of the observed bond length range for Cu(I)—P in chelate complexes (15).

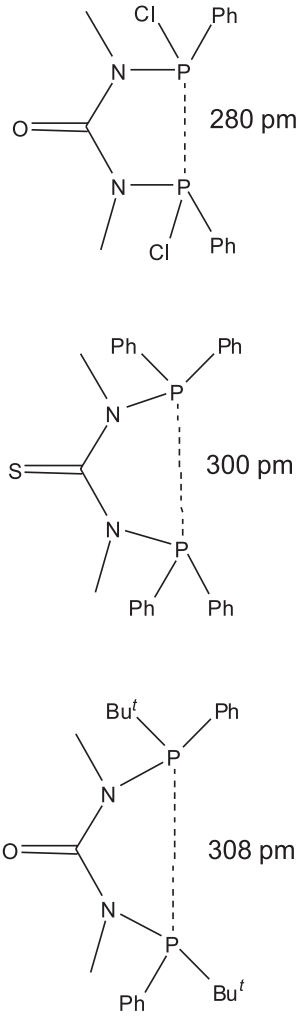
© 2007 NRC Canada

Fig. 4. The metal-coordination geometries observed in the complexes of bisphosphino urea ligands.



The copper complex is a special case in another context. The chelate bonding mode is only observed in the solid state and opens up in solution with accompanying Cu—P bond fissure. There is reason to believe that the stabilizing supramolecular π–π stacking interactions of the phenyl rings in the solid state are the cause for the feasibility of a distorted tetrahedral geometry around copper despite the two very acute bite angles of 93.2 (P–Cu–P) and 95.9° (Cl–Cu–Cl). The copper(I) complex effectively defines the upper limit of the bisphosphino urea ligand bite-angle range.

Fig. 5. The P—P distance in the free bisphosphino urea ligands. The resulting natural bite angles are 74.6°, 80.8°, and 83.4°, respectively (with 231.5 pm as standard M—P bond length).



Difficulties in molecular modelling (MM) calculations

The natural bite angle method will only fail when there are unforseen effects that significantly influence the P—P distance in the ligand. This is clearly the case for the bisphosphino urea ligands with exceptionally short P—P distances in the free ligands. These short P—P distances are due to attractive forces between the two phosphorus atoms that are not appreciated by the force fields of the standard MM programs. Consequently, erroneous P—P distances and natural bite angles are predicted by these programs in these cases (17).

The natural bite angle concept was based on a great deal of statistical evidence (12), and it may be beneficial to reflect on the validity of this evidence. By far, the majority of the chelate complexes of diphosphanes are either octahedral

© 2007 NRC Canada

Table 1. Selected bond lengths (pm) and angles (°) for structurally determined bisphosphino urea ligands.

Ligand	P—P distance (pm)	Standard bite angle (°)	N–C–N angle (°)	N—C bond length (pm)
$\{PhClPN(Me)\}_2CO$	280.6	74.6	117.0	138.2
$\{PhBu^tPN(Me)\}_2CO$	308	83.4	117.1	139.1
$\{Ph_2PN(Me)\}_2CS$	300	80.8	115.7	137.2

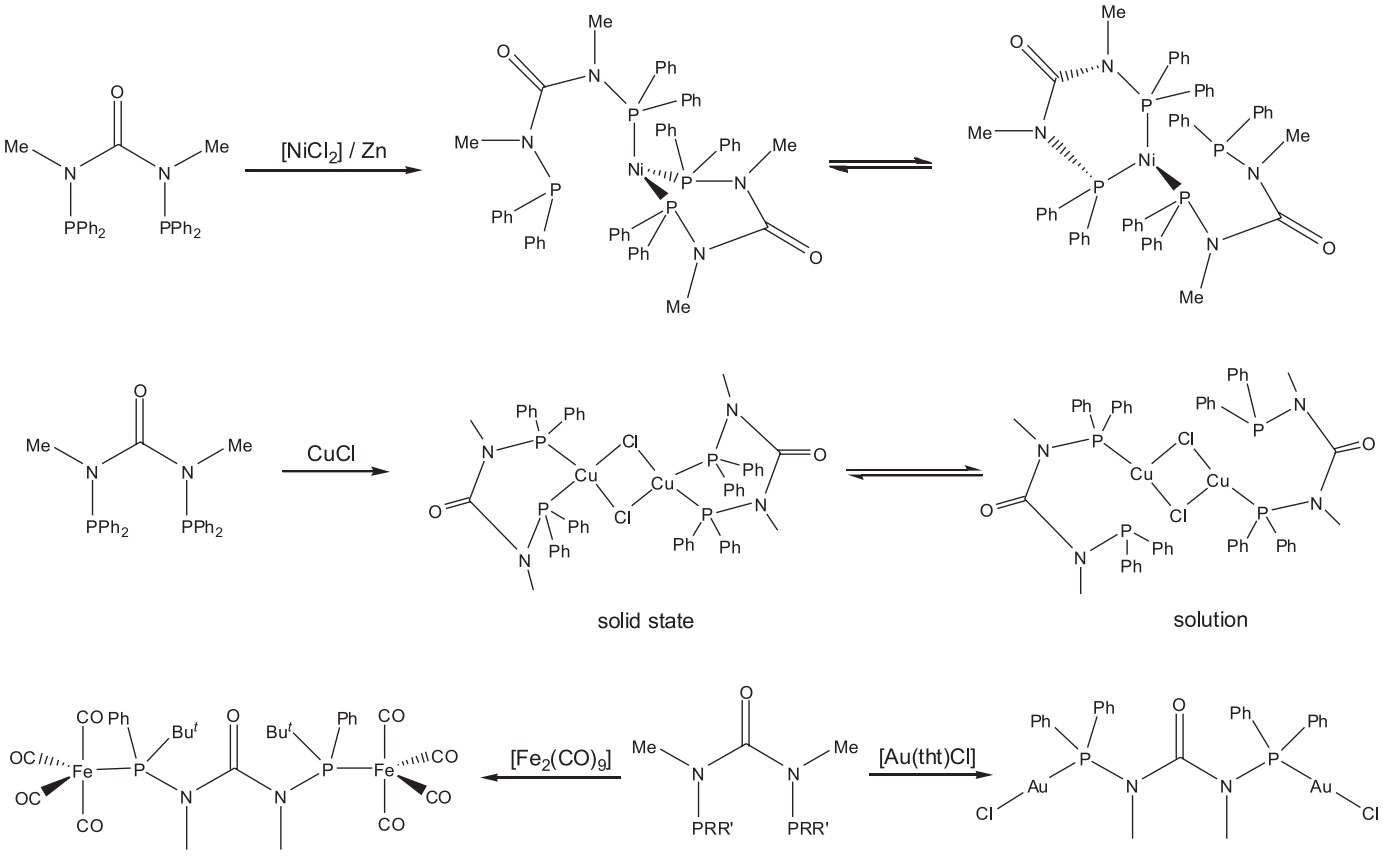
Note: The standard bite angle was determined with a M—P bond length of 231.5 pm.

Table 2. Selected bond lengths (pm) and angles (°) for structurally determined bisphosphino urea metal complexes.

Complex	M—P bond length (pm)	P—P distance (pm)	P–M–P angle (°)	N–C–N angle (°)	N—C bond length (pm)
$CuCl\{Ph_2PN(Me)\}_2CO$	223.5	324.6	93.2	120.1	139.3
$Mo(CO)_4PP'$	243.0	321.3	82.8	120.8	139.4
$Mo(CO)_4\{Ph_2PN(Me)\}_2CO$	248.3	321.6	80.7	118.6	139.5
$Pd(PP')Cl_2$	219.8	319.4	93.2	120.1	139.7
$PdCl_2\{Ph_2PN(Me)\}_2CO$	220.5	324.3	94.8	122.9	137.9
$PdCl_2\{Ph_2PN(Et)\}_2CO$	221.6	317.2	91.5	120.2	139.0
$PtCl_2\{Ph_2PN(Me)\}_2CO$	220.6	314.0	90.7	119.8	138.7
$PtCl_2\{Ph_2PN(Et)\}_2CO$	221.5	309.9	88.8	117.8	139.8
$PtCl_2\{Bu^tPhPN(Me)\}_2CO$	221.9	312.2	89.4	116.7	139.4

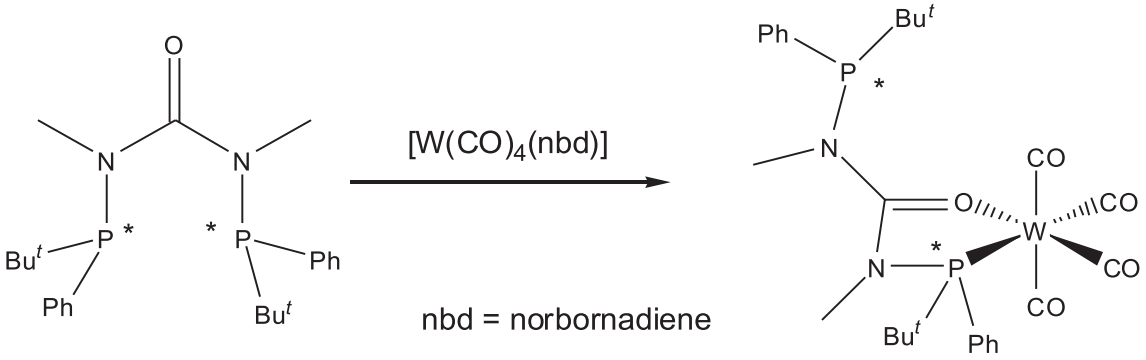
Note: $PP' = \{P(OC_6H_3Bu^t_2\text{-}2,4)_2N(Me)C(O)N(Me)PPh_2\}$.

Fig. 6. The rotational flexibility of bisphosphino urea ligands as seen in their metal complexes.



© 2007 NRC Canada

Fig. 7. The P,O-coordination mode of bisphosphino urea ligands.



or square-planar because most catalyst metals prefer square-planar geometries (Pt(II), Pd(II), Ir(I), Rh(I), and to some extent Ni(II)), whereas the popular group VI metals (W, Mo, and Cr) prefer an octahedral geometry. The most popular diphosphane ligands are 1,ω-diphosphino alkanes (12) that, with the exception of dppm (bis-diphenylphosphino methane), have natural bite angles in the vicinity of 90°. It is not surprising that a narrow distribution is observed when a perfect match between the natural bite angle of the ligand and the metal-preferred bite angle is its foundation.

However, the natural bite angle concept might target the wrong parameter altogether. The only relevant parameter wholly determined by the ligand is the P—P distance in the free ligand, whereas the M—P bond length and the bite angle are dependent on the choice of the metal. It would therefore be better if the P—P distances were calculated and reported rather than the bite angles that rely on the standardized M—P bond lengths and are only valid for one specific metal atom.

The definition of the natural bite angle calls for a dummy atom that pulls the two phosphorus atoms of the ligand into the same direction, but the M—P bond length (and choice of metal) is left to the individual researcher. That would mean that natural bite angles were not standardized and confusing, if not completely useless. On the other hand, standardization to a specific bond length (normally 231.5 pm for Rh(I)) generates a false sense of validity for the standardized natural bite angle if applied to other metal complexes. A plain P—P distance would at least recognize the need to convert the value to the metal presently under consideration but lacks the appeal of a simple, ready-to-use value.

Upward and downward flexibility

It is not enough to average all data found in the literature. Instead, the rigidity of the ligand backbone has to be taken into account. It can be expected that a flexible ligand will adapt to the metal geometry presented to it. That is plainly seen in the available statistical evidence. But what happens if the ligand backbone strongly resists the geometry offered by the metal? Three cases can be differentiated: total rigidity, upward flexibility, and downward flexibility. Bisphosphino urea ligands display downward flexibility, meaning that they have an upper limit (about 324 pm or 95°) and strive towards the resting state of the free ligand (about 300 pm or 80°). Upward flexibility describes the opposite situation, and total rigidity means that the ligand does not yield either way.

Good examples for upward flexibility are the complexes formed in the reaction between metallocene dichlorides (M = Ti, Zr) and 1,4-dichlorobutin-2 or 1,4-disubstituted butadiins-1,3 with magnesium as the reducing agent (see Fig. 8). In both cases, the preferred bite angle of the ligand is 180°, although the orientation of the ligand-based orbitals used for binding to the metal would suggest a somewhat smaller angle. The ligand has to bend to coordinate to the metal in chelate fashion. It is very surprising that it tolerates a bite angle as low as 97–101° (26–28). The bite angle has to be so low because of the large Cp–M–Cp angle of about 130° that leaves no more space for a larger bite angle. As the ligand would clearly prefer a larger bite angle if it could be accommodated by the metal, the system can be taken as an example of upward flexibility even in the absence of a structurally determined example. The alternative for the ligand is the formation of a cyclopropene-ring system with the other two carbon atoms pending as a side chain (28).

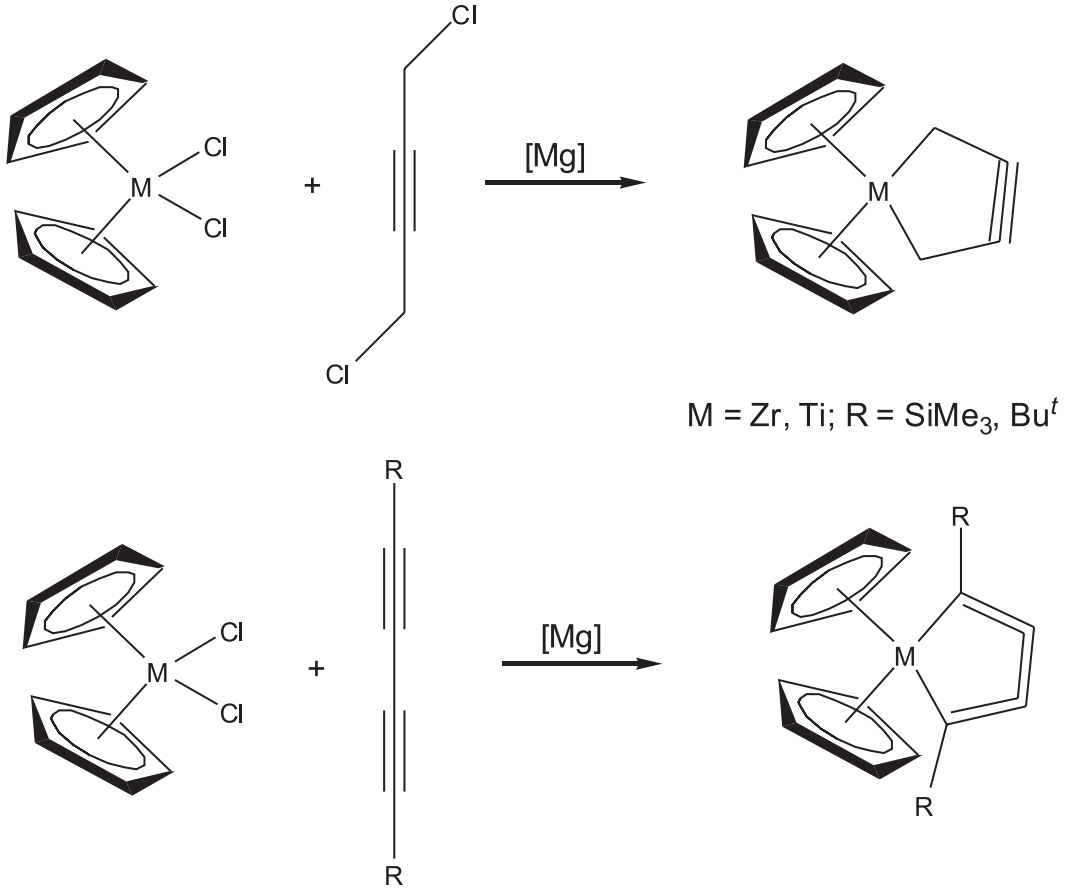
Upward and downward flexibilities only make sense when there is a definite aim to achieve. The most important discrimination is between the ea and ee coordination in trigonal bipyramidal complexes. This is seen as a decisive factor in the product distribution of hydroformylation reactions (29–31). A flexible ligand (typical range is 30–40°) will not be able to discriminate between a metal-preferred bite angle of 90° (ea) and 120° (ee). However, a downward flexible ligand of, e.g., 105° will only realize ea coordination, whereas an upward flexible ligand of, e.g., 105° will only realize ee coordination. MM calculations can normally settle this issue, as they can calculate the natural bite angle and the flexibility range. It is then easy to determine which metal-preferred bite angles lie within this range.

Conclusions

The natural bite angle concept is far more complex than what is suggested by the simple geometrical equation that defines it. First, the natural bite angle was defined for rhodium(I) complexes (11, 12), meaning that the natural bite angle has to be adjusted for the different M—P bond lengths when other metals are considered. Second, the effective flexibility range of the ligand has to be taken into account when the natural bite angle is used to discriminate between two different metal-preferred bite angles, and third, the tolerance

© 2007 NRC Canada

Fig. 8. Formation of the metallocene but-2-yne and metallocene buta-1,2,3-triene complexes.



of the metal towards distortions in its coordination sphere needs to be considered.

Considering the rather large flexibility range of most ligands (30–40°) (12), the range of the observed M—P bond lengths for a given metal, and the tolerance for distortions displayed by most metal centres, it can be expected that only a select minority of chelate ligands will completely discriminate between two different metal-preferred bite angles such as the ones observed in a trigonal-bipyramidal complex. The majority of chelate ligands will simply populate both accessible bite angles to different degrees. In cases where this is decisive for the product formed, a more or less favorable product distribution will be the result.

The importance for the bite angle concept in ligand design lies not in the absolute value of the P—P distance but in its flexibility range and its application to a specific M—P bond length range. The ideal case is a chelate ligand displaying an upward or downward flexibility that is suitable only for one and not the other of two possible metal-preferred bite angles.

References

1. P.W.N.M. van Leeuwen, P.C.J. Kamer, J.N.H. Reek, and P. Dierkes. Chem. Rev. **100**, 2741 (2000).
2. C.A. Tolman. Chem. Rev. **77**, 313 (1977).
3. C.A. Tolman. J. Am. Chem. Soc. **92**, 2953 (1970).
4. Ch. Elschenbroich and A. Salzer. Organometallchemie. 2nd ed. B.G. Teuber, Stuttgart. 1988.
5. P. Braunstein and F. Naud. Angew. Chem., Int. Ed. **40**, 680 (2001).
6. O. Kühl. Coord. Chem. Rev. **249**, 693 (2005).
7. D.R. Anton and R.H. Crabtree. Organometallics, **2**, 621 (1983).
8. A.L. Fernandez, M.P. Wilson, A. Prock, and W.P. Giering. Organometallics, **20**, 3429 (2001).
9. A.L. Fernandez, A. Prock, and W.P. Giering. J. Chem. Soc., Perkin Trans. 2, 1023 (2000).
10. M.R. Wilson, D.C. Woska, A. Prock, and W.P. Giering. Organometallics, **12**, 1742 (1993).
11. C.P. Casey and G.P. Whiteker. Isr. J. Chem. **30**, 299 (1990).
12. P. Dierkes and P.W.N.M. van Leeuwen. J. Chem. Soc., Dalton Trans. 1519 (1999).
13. O. Kühl. Dalton Trans. **949** (2003).
14. A.M.Z. Slawin, M. Wainwright, and J.D. Woollins. J. Chem. Soc., Dalton Trans. 2724 (2001).
15. A. Sterzik, E. Rys, S. Blaurock, and E. Hey-Hawkins. Polyhedron, **20**, 3007 (2001).
16. O. Kühl and S. Blaurock. Inorg. Chem. **43**, 6543 (2004).
17. O. Kühl and W. Langel. Inorg. Chem. Commun. **6**, 74 (2003).
18. O. Kühl, P.C. Junk, and E. Hey-Hawkins. Z. Anorg. Allg. Chem. **626**, 1591 (2000).
19. O. Kühl. Coord. Chem. Rev. **250**, 2867 (2006).
20. R. Vogt, P.G. Jones, A. Kolbe, and R. Schmutzler. Chem. Ber. **124**, 2705 (1991).
21. M. Gruber, R. Schmutzler, and D. Schomburg. Phosphorus, Sulfur, and Silicon, **80**, 205 (1993).
22. G. Bettermann, R. Schmutzler, S. Pohl, and U. Thewalt. Polyhedron, **6**, 1823 (1987).

© 2007 NRC Canada

23. P.G. Jones, R. Schmutzler, and R. Vogt. Acta Crystallogr. Sect. E: Struct. Rep. Online, **E58**, m476 (2002).
24. O. Kühl, S. Blaurock, and T. Carls. Inorg. Chem. **45**, 1723 (2006).
25. A. Hollemann and N. Wiberg. Lehrbuch der anorganischen chemie. 91st–100th ed. Walter de Gruyter, New York–Berlin. 1985.
26. N. Suzuki, N. Alhara, H. Takahara, T. Watanabe, M. Iwasaki, M. Saburi, D. Hashizume, and T. Chihara. J. Am. Chem. Soc. **126**, 60 (2004).
27. E.D. Jemmis, A.K. Phukan, and K.T. Giju. Organometallics, **21**, 2254 (2002).
28. P.-M. Pellny, F.G. Kirchbauer, V.V. Burlakov, W. Baumann, A. Sannenberg, and U. Rosenthal. J. Am. Chem. Soc. **121**, 8133 (1991).
29. L.A. Van der Veen, P.H. Keeven, G.C. Shoemaker, J.N.H. Reek, P.C.J. Kamer, P.W.N.M. Van Leeuwen, M. Lutz, and A.L. Spek. Organometallics, **19**, 872 (2000).
30. C.P. Casey, G.T. Whiteker, M.G. Melville, L.M. Petrovich, J.A. Gavney, and D.R. Powell. J. Am. Chem. Soc. **114**, 5535 (1992).
31. C.P. Casey, G.T. Whiteker, M.G. Melville, L.M. Petrovich, J.A. Gavney, and D.R. Powell. J. Am. Chem. Soc. **114**, 10680 (1992).

© 2007 NRC Canada

ERRATUM / ERRATUM

Carbonate radical anion — Thermochemistry

D.A. Armstrong, W.L. Waltz, and A. Rauk

Ref: Can. J. Chem. **84**, 1614–1619 (2006)

In the paper above on page 1616, Table 1 has errors in footnotes *b* and *d* in the last column [data for $\Delta_f H°$ (Rec.)]. Also, footnote *d* appeared in the incorrect row; it should have appeared in the first row for the species HCO_3^-. Table 1 is reproduced below with the corrections in boldface. Please note that because of the change in order of appearance, footnote *d* is now *c* and footnote *c* is now *d*.

Table 1. Values of electronic energies (EE in Hartrees), ZPEs, and $H° - H_0°$ (in kJ mol^{-1}), and S° (in J mol^{-1} K^{-1}) for carbonate radical and related species.

Species	EE[a]	ZPE	$H° - H_0°$	$S°$	$\Delta_f H°$ (Calc.)	$\Delta_f H°$ (Rec.)[b]
HCO_3^-	–264.159 33	68.5	11.8	266.4	–736.3	–743.9[c]
HNO_3	–280.576 02	69.4	11.7	265.9	–138.1	–135.0
$HCO_2^{\cdot}$	–188.851 80	41.8	10.8	244.7	–138.6	–127.0
$HCO_3^{\cdot}$	–264.022 56	66.4	12.0	273.0	–377.3	–364.9[d]
NO_3^-	–280.062 41	36.5	10.8	245.7	–315.3	–307.0
$NO_3^{\cdot}$	–279.917 68	27.8	13.0	245.7	67.5	73.7
$CO_3^{\cdot -}$	–263.514 91	31.4	12.0	257.8	–568.6	–564.8[d]
CH_3OH	–115.538 07	135.1	11.3	239.7	–201.8	–201.0
CH_4	–40.409 51	117.0	10.0	186.0	–73.8	–74.6
H_2	–1.165 7	26.6	8.68	130.3	—	0.0
H^+	0.0	0.0	6.20	108.8	—	1530.0

Note: $H° - H_0°$ and S° $\Delta_f G°$ at 298 K and 1 atm (1 atm = 101.326 kPa).
[a]CBS-RAD EEs (include ZPEs).
[b]**From ref. 29**.
[c]**See R.R. Squires. Int. J. Mass Spectrom. Ion Processes, 117, 565 (1992).**
[d]This study; see text.

Received 21 March 2007. Published on the NRC Research Press Web site at http://canjchem.nrc.ca on 31 March 2007.

D.A. Armstrong and A. Rauk.[1] Department of Chemistry, University of Saskatchewan, Saskatoon, SK S7N 5C9, Canada.
W.L. Waltz. Department of Chemistry, University of Calgary, Calgary, AB T2N 1N4, Canada.

[1]Corresponding author (e-mail: rauk@ucalgary.ca).

 doi:10.1139/V07-028 © 2007 NRC Canada

Interactions of platinum(II)-derivatized triplex-forming oligonucleotides with DNA[1]

Meghan A. Campbell, Tracey McGregor Mason, and Paul S. Miller

Abstract: Polypyrimidine oligonucleotides can bind to tracts of contiguous purines in double-stranded DNA to form triple-stranded complexes. The stability of the triplex is reduced significantly if the target purine tract is interrupted by a single pyrimidine. Previous studies have shown that incorporation of an N^4-aminoalkylcytosine into the triplex-forming oligonucleotide (TFO), opposite a single CG interruption, facilitates triplex formation. Examination of molecular models suggested that further modification of the amino group of the aminoalkyl arm might enable adduct formation with the N7 of the guanine of the CG interruption. To test this, we prepared 2′-deoxyribo-and 2′-*O*-methylribo-TFOs that contained cytosine (**C**), N^4-(2-aminoethyl)cytosine (**ae-C**), or diethylenetriamineplatinum(II) (**DPt-C**) or *cis*-aquodiammineplatinum(II) (**cPt-C**) derivatives of N^4-(2-aminoethyl)cytosine, positioned opposite a CG interruption of a polypurine tract found in the *pol* gene of HIV-1 proviral DNA. Although the **C**- and **ae-C**-derivatized deoxyribo-TFOs formed triplexes of modest stability and the **DPt-C**-modified TFO failed to form a triplex, the **C**- and **ae-C**-derivatized 2′-*O*-methylribo-TFOs formed remarkably stable triplexes (T_m = 57 °C). The **DPt-C**- and **cPt-C**-modified 2′-*O*-methylribo-TFOs also formed triplexes, although their stabilities were reduced (T_m = 33 °C), suggesting that the tethered platinum group may interfere sterically with TFO binding. Consistent with this hypothesis was the observation that triplex stability was restored (T_m = 57 °C) when the diethylenetriamineplatinum(II) group was tethered to the 5′-end of the 2′-*O*-methylribo-TFO via a 2-aminoethylcarbamate linkage. Taken together, these results suggest that 2′-*O*-methylribo-TFOs may be particularly useful in targeting purine tracts in DNA that have CG interruptions, and that further modification with platinum derivatives could lead to the design of TFOs that are capable of covalent binding to their target, thus increasing the effectiveness of the TFO.

Key words: triplex-forming oligonucleotide, TFO, cisplatin, interrupted polypurine tract.

Résumé : Les oligonucléotides de polypyrimidine peut se lier à des ensembles purines contiguës dans de l'ADN à double brin pour former des complexes à trois brins. La stabilité du complexe est réduite d'une façon significative si l'ensemble de purine cible est interrompue par une seule pyrimidine. Des études antérieures ont montré que l'incorporation d'une N^4-aminoalkylcytosine dans le l'oligonucléotide formant le triplex (OFT) vis-à-vis une seule interruption CG facilite la formation du triplex. L'examen de modèles moléculaires suggère qu'une autre modification du groupe amino de la chaîne aminoalkyle pourrait rendre possible une formation d'adduit avec le N7 de la guanine de l'interruption CG. Afin de vérifier cette hypothèse, on a préparé des 2′-désoxyribo- et 2′-*O*-méthylribo-OFT qui contenaient de la cytosine (**C**), N^4-(2-aminoéthyl)cytosine (**ae-C**) ou des dérivés du diéthylènetriamineplatine(II) (**DPt-C**) ou du *cis*-aquodiammineplatine(II) (**cPt-C**) à base de N^4-(2-aminoéthyl)cytosine qui ont été positionnés en face d'une interruption CG d'un ensemble de polypurines dans le gène *pol* de l'ADN du HIV-1 proviral. Même si désoxyribo-OFT modifié par la cytosine (**C**) et l'**ae-C** conduit à la formation de complexes ne présentant qu'une modeste stabilité et que le OFT modifié par le **DPt-C** ne conduit pas à la formation de triplex, le 2′-*O*-méthylribo-OFT modifié par **C** ou par **ae-C** conduit à la formation de triplex d'une stabilité remarquable (T_m = 57 °C). Les 2′-*O*-méthylribo-OFT modifiés par **DPt-C** et **cPt-C** forment aussi des triplex, même si leurs stabilités sont réduites (T_m = 33 °C), ce qui suggère que le groupe platine en laisse peut interférer stériquement avec la fixation du OFT. En accord avec cette hypothèse, on a observé que la stabilité du triplex est restaurée (T_m = 57 °C) lorsque le groupe diéthylènetriamineplatine(II) est mis en laisse à l'extrémité 5′ du 2′-*O*-méthylribo-OFT par le biais d'une liaison 2-aminoéthylcarbamate. L'ensemble de ces résultats suggère que les 2′-*O*-méthylribo-OFT sont particulièrement utiles pour cible des blocs de purine dans de l'ADN qui comportent des interruptions CG et que des modifications subséquentes avec des dérivés du platine pourraient conduire à la mise au point d'OFT capables de se lier d'une façon covalente à leur cible, ce qui aurait comme effet d'augmenter l'efficacité du OFT.

Mots-clés : oligonucléotide formant un triplex, OFT, cisplatine, ensemble de polypurine interrompu.

[Traduit par la Rédaction]

Received 27 December 2006. Accepted 13 February 2007. Published on the NRC Research Press Web site at canjchem.nrc.ca on 21 March 2007.

M.A. Campbell, T. McGregor Mason, and P.S. Miller.[2] Department of Biochemistry and Molecular Biology, Bloomberg School of Public Health, The Johns Hopkins University, 615 North Wolfe Street, Baltimore, MD 21025, USA.

[1]This article is part of a Special Issue dedicated to Professor Kelvin K. Ogilvie.

[2]Corresponding author (e-mail: pmiller@jhsph.edu).

 doi:10.1139/V07-016 © 2007 NRC Canada

Introduction

Oligonucleotides can be designed to target and bind to polypurine tracts in double-stranded DNA through the formation of triple-stranded complexes (1–8). The bases of these so called triplex-forming oligonucleotides (TFOs) contact the target purine bases through the major groove of DNA. Two types of binding motifs, the pyrimidine-purine-pyrimidine motif and the purine-purine-pyrimidine motif, have been identified. In the former motif, bases of an all-pyrimidine TFO, whose backbone polarity is parallel to that of the purine tract, form Hoogsteen-type hydrogen bonds with adenine and guanine bases in the target strand. In the latter motif, bases of an all-purine TFO, whose backbone polarity is antiparallel to that of the purine tract, form reversed Hoogsteen-type hydrogen bonds with the purines of the target strand. In addition to these two motifs, a "mixed" motif has been described, in which T and G residues of the TFO bind to A and G residues, respectively, of the purine tract.

Triplex formation requires a tract of contiguous purine bases in the target strand. It has been know for some time that interruption of the purine tract of the target by a single pyrimidine can greatly reduce the stability of the triplex or eliminate its formation altogether (9–14). There have been a number of attempts to design or identify base analogs that can be incorporated into TFOs to "recognize" pyrimidine interruptions, and thus stabilize the resulting triplex (14–36). These efforts have met with varying degrees of success. We have previously reported that N^4-(2-aminopropyl)- and N^4-(2-acetamidopropyl)-modified cytosines targeted to a CG interruption can stabilize triplex formation when incorporated into deoxyribopyrimidine TFOs (17). The results suggested that the amino or acetamido groups of these modified bases could make contacts across the major groove with the guanine of the CG interruption. Recently McLaughlin and coworkers (37, 38) synthesized a deoxyribothymidine TFO carrying a 5′- platinum-modified alkyl group and demonstrated that this TFO could covalently bind to its target via the formation of a guanine–platinum adduct adjacent to the TFO binding site. This observation, coupled with our own, suggested that the modification of the aminoalkyl arm of an internal N^4-(aminoalkyl)cytosine residue with a reactive platinum group might create a TFO that could bind covalently to the guanine base of the CG interruption.

This report describes the syntheses of deoxyribonucleoside TFOs derivatized with platinated N^4-(2-aminoethyl)cytosine residues and the characterization of their interactions with a short DNA duplex, whose purine tract contains a single CG interruption. Similarly modified 2′-*O*-methylribonucleoside TFOs were also prepared, and their binding interactions with the DNA duplex were characterized. Although the platinated TFOs proved to have inferior binding capabilities, the unmodified 2′-*O*-methylribonucleoside TFOs showed remarkably high affinities for the DNA target.

Results and discussion

DNA targets and TFOs

Figure 1 shows the two DNA targets used in this study. The **DNA-1** target, where Y is G and Z is C, is 17 base pairs in length and consists of an uninterrupted purine tract. The **DNA-2** target, where Y is C and Z is G, contains a single pyrimidine interruption at position 12 of the duplex. The sequence of this second duplex corresponds to nucleotides 4899–4915, found in the coding region of the pol-1 gene of HIV-1 proviral DNA.

Fig. 1. General structure of TFO and its DNA target; C = 5-methylcytosine.

```
5'-TTCTTCTTTTCXTTTCT   TFO
5'-AAGAAGAAAAGYAAAGA | DNA TARGET
3'-TTCTTCTTTTCZTTTCT |
```

Also shown in Fig. 1 is the general sequence of the TFO, whose bases consist of thymine and 5-methylcytosine residues. The polarity of the TFO is the same as that of the purine strand of the target duplex. Base X is either a cytosine or modified cytosine base. The sequences of the TFOs are shown in Table 1, and the structures of the modified bases at X are shown in Schemes 1 and 2. TFOs with two different types of backbones were investigated: those consisting of deoxyribonucleotides, series **1** TFOs, and those consisting of 2′-*O*-methylribonucleotides, series **2** and **3** TFOs. In these internally modified TFOs, base X is positioned opposite the CG interruption in the **DNA-2** target. An additional 2′-*O*-methylribo-TFO, **4**, was prepared, in which the diethylenetriamineplatinum(II) [Pt(dien)] group was positioned at the 5′-end of the oligonucleotide. This 5′-modified TFO contains a deoxycytidine residue at position X.

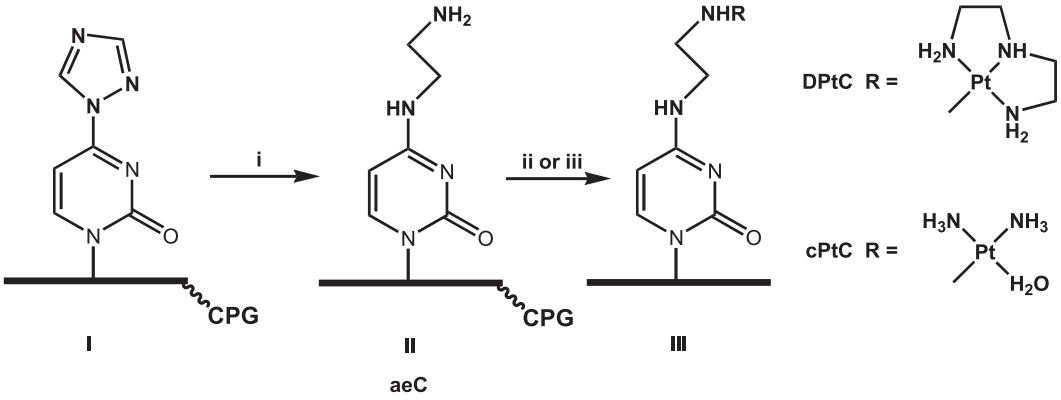
Syntheses of platinum-modified TFOs

The oligonucleotides were synthesized on controlled-pore glass supports by automated oligonucleotide chemistry, using either protected deoxyribonucleoside-3′-*O*-bis(diisopropylamino)-β-cyanoethylphosphoramidites or protected 2′-*O*-methylribonucleoside-3′-*O*-bis(diisopropylamino)-β-cyanoethylphosphoramidites. For TFOs **1** and **3**, deoxycytidine was placed at position X, whereas 2′-*O*-methylcytidine was placed at position X in TFO **2**. The internally modified TFOs in series **1** and **3** were prepared as shown in Scheme 1. These oligonucleotides were prepared with 4-triazole-deoxyuridine residue incorporated at position X (structure **I**). The support-bound, protected oligonucleotide was then converted to the N^4-(2-aminoethyl)-C derivative, **II**, by treating the support with ethylenediamine. The aminoethyl derivatized oligonucleotide was released from the support and deprotected by treatment with ammonium hydroxide. The oligonucleotide was then purified by strong anion exchange (SAX)-HPLC. The aminoethyl group was converted to the Pt(dien) or the *cis*-chlorodiammineplatinum(II) derivative, **III**, by reacting the oligomer with chlorodiethylenetriamineplatinum (II) chloride, [Pt(dien)Cl]Cl, or *cis*-diamminedichloroplatinum(II) dichloride (*cis*-DDP), respectively. The platinum-derivatized TFOs were purified by SAX-HPLC.

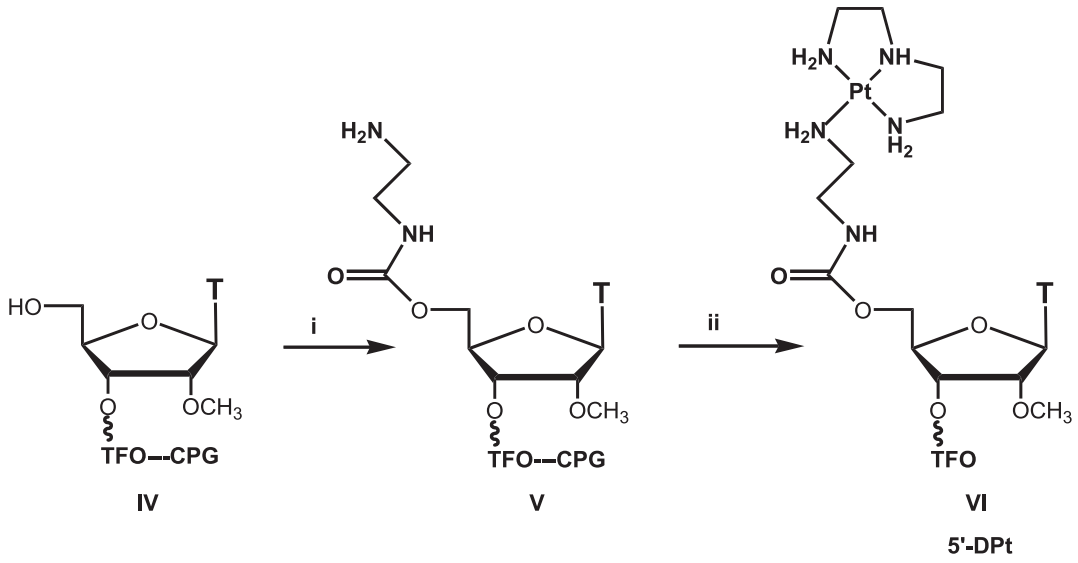
TFO **4**, which contains a 5′-Pt(dien) group, was prepared as shown in Scheme 2. The oligonucleotide was synthesized with deoxycytidine incorporated at position X, and the 5′-terminal dimethoxytrityl group was removed to give oligonucleotide **IV**. The support-bound, protected oligonucleotide was converted to its 5′-(2-aminoethyl)carbamate derivative, **V**, by sequential treatment with carbonyldiimidazole and ethylenediamine. The derivatized oligonucleotide was

© 2007 NRC Canada

Scheme 1. (*i*) Ethylenediamine, (*ii*) [Pt(dien)Cl]Cl, (*iii*) *cis*-DDP.



Scheme 2. (*i*) (*a*) Carbonyldimidazole, (*b*) ethylenediamine; (*ii*) [Pt(dien)Cl]Cl.



cleaved from the support and deprotected by treatment with ammonium hydroxide. Following purification by SAX-HPLC, the oligonucleotide was converted to the Pt(dien) derivative, **VI**, by reaction with [Pt(dien)Cl]Cl. Each of the oligonucleotides was characterized by MALDI-TOF mass spectrometry, as indicated in Table 1.

Triplex formation by deoxyribo-TFOs

The presence of a single pyrimidine interruption can adversely affect the stability of a triplex. This can be observed by comparing the thermal stability of the triplex formed between TFO **1** and **DNA-1**, which contains a contiguous purine tract, with that of the triplex formed between TFO **1** and **DNA-2**, which contains a CG interruption. As shown by the melting curves in Fig. 2, the **1/DNA-1** triplex displays a single transition, whose midpoint (T_m) is 63 °C, which corresponds to dissociation of all three strands. In contrast, the melting curve of the **1/DNA-2** triplex shows two transitions. The first transition at 34 °C corresponds to the dissociation of the TFO. The remaining duplex then melts at 63 °C, as signaled by the second transition. Although molecular models suggest that the cytosine at position X can be accommodated within the major groove of the triplex opposite the CG interruption, it seems unlikely that it forms any productive hydrogen-bond contacts with this base pair. The loss of hydrogen-bonding interactions could account for the 29 °C reduction in the stability of the triplex.

As shown in Table 2, replacement of the cytosine at X with N^4-(2-aminoethyl)cytosine, TFO **1-ae**, results in a small increase in the stability of the triplex formed with **DNA-2**. Molecular models suggest that the 2-aminoethyl arm of **1-ae** is too short to reach across the major groove and make contact with the guanine of the CG base pair of the target. However, the primary amino group of this arm would be expected to be protonated at pH 6.5. This protonation could reduce the overall charge repulsion between the phosphate backbone of the TFO and those of **DNA-2**, and thus help stabilize the triplex. Consistent with this hypothesis is the observation that the acetamido derivative of **1-ae**, which eliminates the positive charge of the 2-aminoethyl group, forms a triplex with **DNA-2**, whose T_m is approximately 2 °C less than that of the triplex formed by **1-ae**.[3]

Platinum(II) compounds, such as *cis*-DDP, react readily with the N7 of the guanines of the double-stranded DNA to

[3] P.S. Miller and co-workers. Unpublished results.

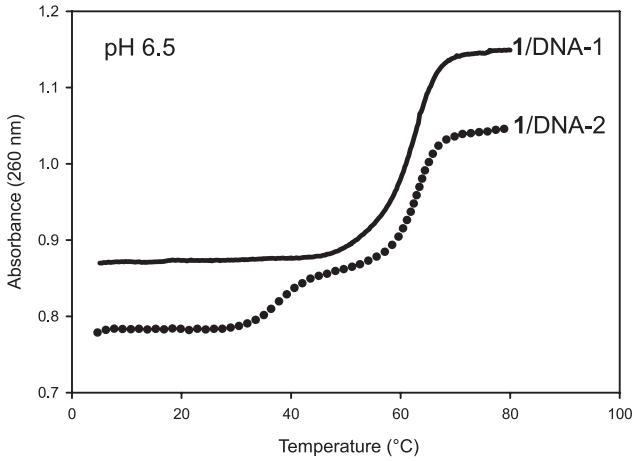
© 2007 NRC Canada

Table 1. Sequences of TFOs.

Oligonucleotide[a]	X[b]	*m/z* Calculated	*m/z* Observed
d-TTCTTCTTTTCXTTTCT			
1	d-C	5087.77	5099.36
1-ae	d-aeC	5131.84	5132.62
1-DPt	d-DPtC	5430.09	5426.70
mr-TTCTTCTTTTCXTTTCT			
2	mr-C	5597.77	5597.58
3	d-C	5567.77	5567.73
3-ae	d-aeC	5611.80	5611.08
3-DPt	d-DPt	5910.03	5910.81
3-cPt	d-cPtC	5840.89	5840.20
mr-5′-DPt-TTCTTCTTTTCXTTTCT			
4	d-C	5953.10	5952.87

[a]d, 2′-deoxyribo; mr, 2′-*O*-methylribo; and C, 5-methylcytosine.
[b]aeC, N^4-(2-aminoethyl)cytosine; DPtC, [Pt(dien)Cl] derivative of N^4-(2-aminoethyl)cytosine; and cPtC, *cis*-chlorodiammineplatinum derivative of N^4-(2-aminoethyl)cytosine.

Fig. 2. Thermal denaturation of triplexes formed by **1** and **DNA-1** (▬) or **1** and **DNA-2** (●●●). The experiments were carried out in a buffer, containing 100 mmol/L MOPS, pH 6.5, 100 mmol/L sodium acetate, and 2.5 mmol/L magnesium.



from intra- and interstrand platinum cross-links (39). Derivatization of the amino group of 2-aminoethyl arm of TFO **1-ae** with *cis*-DDP could position Pt near the guanine of the CG interruption, and thus enable covalent attachment of the TFO to the pyrimidine-rich strand of the DNA duplex. To determine if the guanine of an isolated CG interruption is accessible to platination, the triplex shown in Fig. 3 was prepared. This triplex is comprised of a 17-base pair duplex that consists of complementary strands of deoxyadenosine and thymidine residues. These AT base pairs are interrupted by a single internal CG base pair located 12 nucleotides in from the 5′-end of the deoxyadenosine strand. The TFO consists of thymidines and a single deoxycytidine, positioned opposite to the CG interruption. Triplex formation was confirmed by UV thermal denaturation analysis (data not shown). The 5′-end of the pyrimidine strand of the duplex was end labeled with ^{32}P-phosphate. The triplex was then incubated with [Pt(dien)Cl]Cl at 4 °C, which is 14 °C below the dissociation temperature of the TFO strand, and the products of the reaction were analyzed by denaturing polyacrylamide gel electrophoresis. As shown in Fig. 3, a new, slower migrating band appears in the gel, which corresponds to the N7-G platinum adduct of the labeled pyrimidine strand of the triplex. Thus, this experiment demonstrates that the N7-G of the CG interruption is accessible to platination through the major groove of the triplex.

Table 2. Triplex melting temperatures.

TFO	X[a]	Target	Y	Z	T_m °C[b]
1	d-C	DNA-1	G	C	63
1	d-C	DNA-2	C	G	34
1-ae	d-aeC	DNA-2	C	G	40
1-DPt	d-DPtC	DNA-2	C	G	<5
2	mr-C	DNA-1	G	C	78
2	mr-C	DNA-2	C	G	57
3	d-C	DNA-2	C	G	57
3-ae	d-aeC	DNA-2	C	G	54
3-DPt	d-DPtC	DNA-2	C	G	33
4	d-C	DNA-2	C	G	57

[a]d, 2′-deoxyribo; mr, 2′-*O*-methylribo; aeC, N^4-(2-aminoethyl)cytosine; and DPtC, [Pt(dien)Cl] derivative of N^4-(2-aminoethyl)cytosine.
[b]Melting temperatures were determined at pH 6.5 in a buffer, containing 100 mmol/L 3-(*N*-morpholino)propanesulfonic acid, 100 mmol/L sodium acetate, and 2.5 mmol/L magnesium acetate.

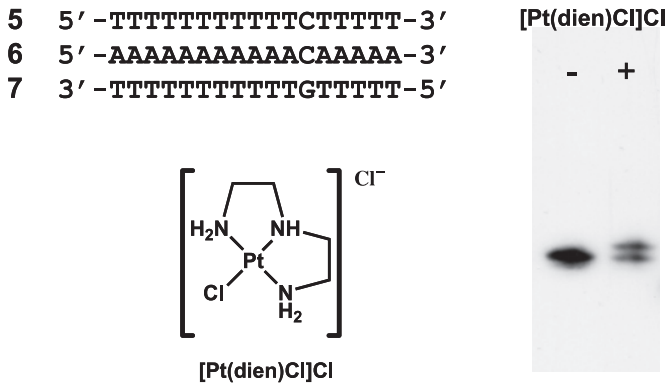
A nonreactive Pt(dien) derivative, **1-DPt**, was prepared to determine the effect of the platinum group on triplex formation. As shown in Table 2, this modified TFO was unable to form a triplex with **DNA-2** under conditions where stable triplex formation was observed with the 2-aminoethyl-derivatized TFO, **1-ae**. Triplex formation was also assayed under conditions where increasing concentrations of **1-DPt** were incubated with **DNA-2**. Under these conditions, the TFO was present in 2- to 10-fold excess over the target duplex. Triplex formation was monitored by nondenaturing polyacrylamide gel electrophoresis, and as shown in Fig. 4, no triplex could be detected, even in the presence of a 10-fold excess of **1-DPt**. These results suggest that although free [Pt(dien)Cl]Cl can react with the guanine of the CG interruption, when tethered to a TFO, this platinum(II) group may sterically interfere with formation of the triplex. The observation that the acetamido derivative of **1-ae**, a less bulky modification, can from a triplex, whose T_m is 38 °C (data not shown), is consistent with this conjecture.

Triplex formation by 2′-*O*-methylribo-TFOs

The triplexes, formed by the deoxyribo-TFOs **1** and **1-ae** and **DNA-2**, have rather low thermal stabilities. Previous work, from our laboratory and others, has shown that TFOs that are comprised of 2′-*O*-methylribonucleosides often form significantly more stable triplexes with double-stranded DNA targets than those formed by the corresponding deoxyribo-TFOs (40–45). The reasons for this increase are not entirely clear. 2′-*O*-Methylribonucleosides exclusively adopt a 3′-endo conformation, which would be expected to preorganize the TFO in an A-form conformation that is compatible with the final A-like conformation of the triplex. In addition, the somewhat hydrophobic 2′-*O*-methyl groups of the nucleosides may contribute to the stacking interactions along the backbone of the TFO when it is engaged in triplex

© 2007 NRC Canada

Fig. 3. Reaction of [Pt(dien)Cl]Cl with the triplex formed by oligonucleotides **5**, **6**, and [^{32}P]-**7**. The triplex was incubated in the presence or absence of [Pt(dien)Cl]Cl, and the reaction mixture was analyzed by denaturing polyacrylamide gel electrophoresis.



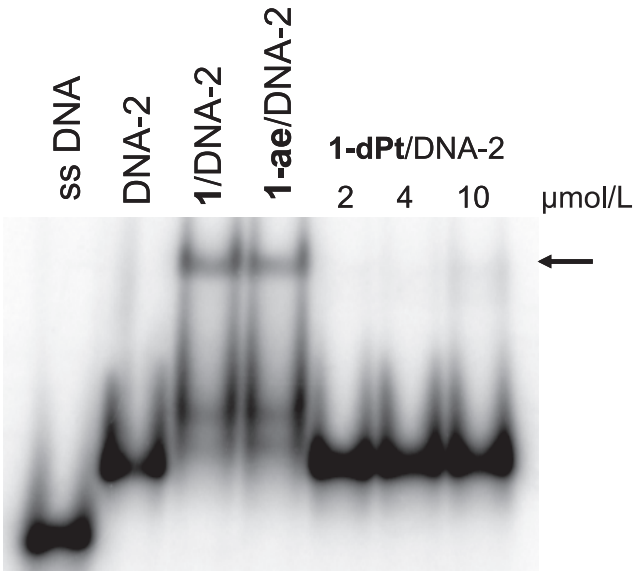
formation. Both of these factors may contribute to the overall triplex stability.

The 2′-*O*-methylribonucleotide analog of **1**, TFO **2**, was prepared, and its interactions with **DNA-1** and **DNA-2** were examined by thermal denaturation experiments. As shown in Table 2, the T_m of the triplex formed between TFO **2** and **DNA-1** is 15 °C higher than that of the corresponding triplex formed by TFO **1**. This result is consistent with the expectation that 2′-*O*-methylribo-TFOs form more stable triplexes than 2′-deoxyribo-TFOs. This increased stability carries over to the triplex formed between TFO **2** and the CG interrupted target **DNA-2**. Although the interruption decreases the stability as expected, this triplex still has a remarkably high T_m, 57 °C, which is 23 °C higher than that of the corresponding triplex formed by deoxyribo-TFO **1**. Interestingly, substitution of the 2′-*O*-methylcytidine at position X in **2** with deoxycytidine, TFO **3**, did not diminish the stability of the triplex. These results suggest that modification of TFOs with 2′-*O*-methylribonucleotides may be an effective way to address the problem of pyrimidine interruptions in triplex binding sites.

Like its deoxyribo counterpart, the N^4-(2-aminoethyl)cytosine derivative of TFO **3**, **3-ae**, formed a stable triplex with **DNA-2**, although in this case the modification reduced the T_m by 3 °C. Conversion to the Pt(dien) derivative, **3-DPt**, significantly reduced the T_m. Relocating the Pt(dien) group to the 5′-end of the TFO, as in TFO **4**, restored the T_m of the triplex to the same value as that of the triplex formed with unmodified TFO **3**. As was the case with the deoxyribo-TFO, this result is consistent with the idea that the somewhat bulky platinum group may sterically hinder the formation of the triplex.

Although derivatization with the platinum group reduced triplex stability, the T_m of the **3-DPt/DNA-2** triplex, 33 °C, is sufficiently high to determine if platinum can react with the guanine of the CG interruption of **DNA-2**. To test this, the *cis*-chlorodiammineplatinum(II) derivative of TFO **3**, **3-cPt**, was prepared. Gel electrophoresis studies, carried out under nondenaturing conditions, showed that **3-cPt** forms a triplex with **DNA-2** (see Fig. 5). When electrophoresis was carried out under denaturing conditions, little or no covalent adduct was observed, even after prolonged incubation at

Fig. 4. Interactions of DNA duplex **DNA-2** with TFOs **1**, **1-ae**, or **1-DPt**. A 1 μmol/L solution of [^{32}P]-**DNA-2** was incubated with 2 μmol/L TFO **1** or 2 μmol/L TFO **1-ae** or 2, 4, or 10 μmol/L TFO **1-DPt**, and the solutions were analyzed by nondenaturing polyacrylamide gel electrophoresis. The left two lanes of the gel contain labeled single-stranded DNA and [^{32}P]-**DNA-2**, respectively. The position of the triplex is indicated by the arrow.



20 °C (data not shown). This result suggests that if the platinum group resides in the vicinity of the CG guanine, it may not be positioned properly for productive reaction to occur. It may be possible to remedy this situation by changing the length of the linker. Alternatively, the platinum-modified linker could be relocated to the 5′-end of the TFO, where, in analogy to the results of Sharma and McLaughlin (37, 38), it could react with the guanines outside the TFO binding site.

Conclusion

Polypurine-rich tracts are found throughout the human genome, particularly in the promoter regions of genes. Such tracts are potential target sites for therapeutic or diagnostic TFOs. Frequently, these tracts contain single pyrimidine interruptions. The ability to form stable triplexes with such sites could significantly expand the range of sequences that can be targeted by TFOs. Our results suggest that 2′-*O*-methylribo-TFOs may be particularly useful in targeting sites that have CG interruptions. Further modification with platinum derivatives, compounds that have already been shown to be effective therapeutic agents, could lead to the design of TFOs that are capable of covalent binding to their target, thus increasing the effectiveness of the TFO.

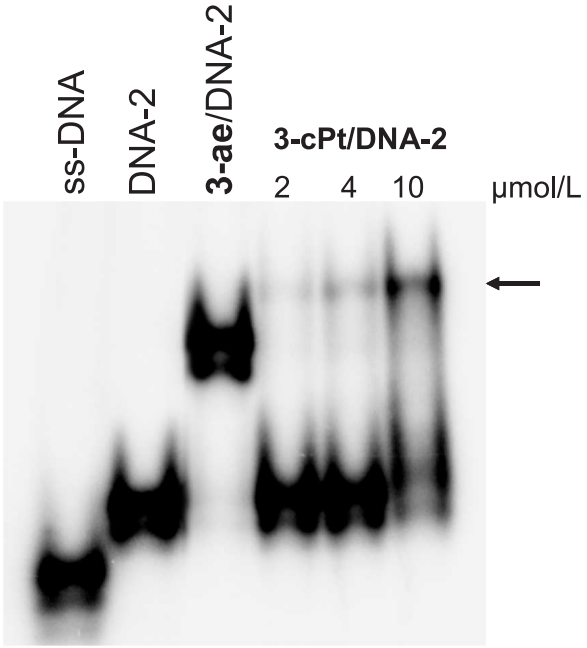
Experimental

Materials

Protected 2′-deoxy- and 2′-*O*-methylribonucleoside-3′-*O*-bis(diisopropylamino)-β-cyanoethylphosphoramidites and 2′-*O*-methyl-5-methyluridine-3′-*O*-bis(diisopropylamino)-β-cyanoethylphosphoramidite were purchased from Glen Research Inc., Sterling, VA. The base-protecting groups were

© 2007 NRC Canada

Fig. 5. Interactions of DNA duplex **DNA-2** with TFOs **3-ae** or **3-cPt**. A 1 μmol/L solution of [^{32}P]-**DNA-2** was incubated with 2 μmol/L TFO **3-ae** or 2, 4, or 10 μmol/L TFO **3-cPt**, and the solutions were analyzed by non-denaturing polyacrylamide gel electrophoresis. The left two lanes of the gel contain labeled single-stranded DNA and [^{32}P]-**DNA-2**, respectively. The position of the triplex is indicated by the arrow.



benzoyl (A,C) or isobutyryl (G). 5′ Nucleoside-derivatized controlled-pore glass supports, 4,5-dicyanoimidazole, 1-*H*-tetrazole or 5-ethylthiotetrazole, Cap Mix A, Cap Mix B, and oxidizing solution were also purchased from Glen Research Inc., Sterling, VA. 2′-*O*-Methyl-5-methyluridine-derivatized CPG was purchased form ChemGenes Corp., Ashland, MA. Phosphoramidite solutions were prepared using synthesis-grade acetonitrile (Fisher Scientific) that was dried and stored over calcium hydride. MALDI-TOF analysis was performed in the AB Mass Spectrometry/Proteomics Facility at The Johns Hopkins School of Medicine, with support from the National Center for Research Resources Shared Instrumentation, Grant 1S10-RR14702.

Synthesis of oligonucleotides

The oligonucleotides, whose sequences are shown in Fig. 1 and Table 1, were synthesized on an ABI DNA synthesizer (model 392 or 3400), using phosphoramidite chemistry and standard automated procedures. The phosphoramidite solutions were made to a concentration of 0.15 mol/L; 5-ethylthiotetrazole was used as the activating agent, and coupling times were 120 s for deoxyribonucleoside phosphoramidites and 450 s for 2′-*O*-methylribonucleoside phosphoramidites. The oligonucleotides were deprotected and removed from their supports by incubating the CPG in a solution containing 300 μL of concentrated ammonium hydroxide and 100 μL of 95% ethanol for 3.5 h at 55 °C. The supernatant from this reaction was evaporated and residue dissolved in 200 μL of 50% aq. acetonitrile. The oligonucleotides were purified by SAX-HPLC on a Dionex DNAPac PA 100-4 × 250 mm column (Dionex Corp., Sunnyvale, CA), using a 30 min linear gradient of 0 to 0.5 mol/L sodium chloride in a solution containing 100 mmol/L Tris, pH 7.8, and 10% acetonitrile at a flow rate of 1.0 mL/min. The oligonucleotide solutions were desalted on either a C-18 SEP PAK cartridge (Waters, Inc, Milford, MA) or a C-18 Clarity Tube (Phenomenex, Inc., Torrance, CA). The concentration of purified oligomers was determined from their UV absorbance at 260 nm, using calculated extinction coefficients based on nearest neighbor approximations (46). The compositions of the oligonucleotides were confirmed by MALDI-TOF mass spectrometry (see Table 1).

Preparation of 2-aminoethyl-modified TFOs

TFOs **1-ae** and **3-ae** were prepared by incubating the CPG support-bound, protected oligonucleotide with a 0.25 mol/L solution of ethylenediamine in dry pyridine for 30 min at room temperature. The CPG was then washed with dry acetonitrile, and the oligomers were deprotected and purified, as described above.

The 5′-(2-aminoethyl)carbamate derivative of **3** was prepared by incubating the detritylated CPG support-bound oligonucleotide with a 500 mmol/L solution of carbonyldiimidazole in dry acetonitrile for 4 h at room temperature. The CPG was washed with dry acetonitrile, dried under vacuum, and then incubated with a solution containing 750 mmol/L ethylenediamine and 350 mmol/L triethylamine in dry acetonitrile. The CPG was washed with dry acetonitrile, and the oligonucleotide was deprotected and purified, as described above.

Preparation of platinum-modified TFOs

Solutions of the platinum compounds were prepared as follows: [Pt(dien)Cl]Cl was prepared according to the method of Roat and Reedijk (47). A 1 mmol/L solution of this compound in water was prepared and stored in the dark at room temperature. A 5 mmol/L solution of *cis*-DDP (Sigma-Aldrich, Inc.) was incubated with 10 mmol/L silver nitrate overnight at 37 °C. The resulting precipitate was centrifuged, and the supernatant containing *cis*-diaminediaquoplatinum(II) dinitrate was stored in the dark at room temperature.

A 10 mmol/L solution of the aminoethyl-modified TFO in 500 μL of water was incubated with 100 μmol/L [Pt(dien)Cl]Cl or 100 μmol/L *cis*-diamminediaquoplatinum(II) dinitrate at 37 °C for 2–6 h. The platinated TFOs were purified by either SAX-HPLC or by HPLC on a 4.6 × 150 mm C-18 reversed-phase column, using a 30 min linear gradient of 0% to 52.5% methanol in 50 mmol/L Tris, pH 8.5, at a flow rate of 1.2 mL/min. The compositions of the platinum-modified TFOs were confirmed by MALDI-TOF mass spectrometry (see Table 1).

Reaction of a DNA triplex with [Pt(dien)Cl]Cl

The 5′-end of oligonucleotide **7** (see Fig. 3) was phosphorylated using polynucleotide kinase and γ-[^{32}P]-ATP, mixed with equivalent amounts of oligonucleotides **5** and **6**, and evaporated to dryness. The residue was dissolved in 28.2 μL of triplex buffer that contained 100 mmol/L 3-(*N*-morpholino)propanesulfonic acid (MOPS), pH 6.5, 100 mmol/L sodium acetate, and 2.5 mmol/L magnesium ac-

© 2007 NRC Canada

etate to a final concentration of 5.6 μmol/L of each strand. The solution was heated at 65 °C for 15 min, cooled slowly to room temperature, and incubated overnight at 4 °C. Aliquots (1.8 μL) of 10 mmol/L [Pt(dien)Cl]Cl or triplex buffer were added, and the solutions were incubated at 4 °C for 24 h. A 1 μL aliquot of each reaction mixture was denatured in 5 μL 90% formamide loading buffer and then electrophoresed on a 20% polyacrylamide gel run under denaturing conditions at 800 V. The gel was autoradiographed at –80 °C.

Thermal denaturation experiments

A solution of **DNA-1** or **DNA-2** and the TFO were prepared in 1 mL of triplex buffer, containing 100 mmol/L MOPS, pH 6.5, 100 mmol/L sodium acetate, and 2.5 mmol/L magnesium acetate such that the final concentration of each strand was 2 μmol/L. Each solution was heated to 90 °C for 10 min, allowed to cool slowly to room temperature, and stored overnight at 4 °C. The absorbance at 260 nm was monitored using a Cary 3E spectrophotometer, fitted with a thermoelectric cell holder at 0.25 °C intervals as the solution was heated from 5 °C to 80 °C at a rate of 0.4 °C/min. The melting temperature was determined by plotting the first derivative of the absorbance vs. temperature profile and is accurate to ±1 °C.

Interactions of TFOs with DNA as monitored by gel electrophoresis

The pyrimidine strand of **DNA-2** was phosphorylated, using polynucleotide kinase and γ-[^{32}P]-labeled ATP at a specific activity of 10 Ci/mmol. This labeled strand (50 pmol) was mixed with 50 pmol of its unlabeled complementary strand, and the solution was evaporated to dryness. The residue was dissolved in 35 μL of triplex buffer; the solution was heated to 90 °C for 10 min, and then slowly cooled to room temperature. Solutions containing 20, 40, or 100 pmol of the TFO were evaporated to dryness; the residues were each dissolved in 3 μL of triplex buffer; 7 μL aliquots of the labeled **DNA-2** were added, and the solutions were incubated overnight at 4 °C. A 2 μL aliquot of 50% glycerol was added to each sample, and the solutions loaded onto a 20% native polyacrylamide gel that was run at 100 V at 4 °C. The gel was dried and imaged using a Typhoon phosphorimager.

Reaction of 3-cPt with DNA-2

[^{32}P]-Labeled **DNA-2** (specific activity 100 Ci/mmol) was prepared as previously described. A solution containing 30 pmol of the labeled duplex was evaporated to dryness, and the residue was dissolved in 30 μL of triplex buffer. The duplex solution was heated to 90 °C for 10 min and cooled slowly to room temperature. Solutions containing 4, 10, or 20 pmol of **3-cPt** were evaporated to dryness; the residue was dissolved in 10 μL of the labeled duplex solution, and the reaction mixture was incubated at 20 °C for 24 or 72 h. Each reaction mixture was quenched with 10 μL of 90% formamide gel loading buffer. These samples were electrophoresed on a 20% denaturing polyacrylamide gel and run at 800 V. The gel was dried and imaged using a Typhoon phosphorimager.

Acknowledgements

The authors thank Dr. Terry Brown for the use of his phosphorimager. This research was supported by a grant form the National Institutes of Health, GM 057140 (PSM). TMM was supported by a Ruth L. Kirchstein National Research Service Award (CA108326).

References

1. I. Radhakrishnan and D.J. Patel. Biochemistry, **33**, 11405 (1994).
2. M.D. Frank-Kamenetskii and S.M. Mirkin. Annu. Rev. Biochem. **64**, 65 (1995).
3. J.S. Sun, T. Garestier, and C. Helene. Curr. Opin. Struct. Biol. **6**, 327 (1996).
4. K.R. Fox. Curr. Med. Chem. **7**, 17 (2000).
5. B.P. Casey and P.M. Glazer. Prog. Nuc. Acid Res. Mol. Biol. **67**, 163 (2001).
6. M.P. Knauert and P.M. Glazer. Hum. Mol. Genet. **10**, 2243 (2001).
7. K.M. Vasquez and P.M. Glazer. Q. Rev. Biophys. **35**, 89 (2002).
8. J.M. Kalish and P.M. Glazer. Ann. N. Y. Acad. Sci. **1058**, 151 (2005).
9. R.F. Macaya, D.E. Gilbert, S. Malek, J.S. Sinsheimer, and J. Feigon. Science (Washington, D.C.), **254**, 270 (1991).
10. J.S. Sun, J.L. Mergny, R. Lavery, T. Montenay-Garestier, and C. Helene. J. Biomol. Struct. Dyn. **9**, 411 (1991).
11. J.L. Mergny, J.S. Sun, M. Rougee, T. Montenay-Garestier, F. Barcelo, J. Chomilier, and C. Helene. Biochemistry, **30**, 9791 (1991).
12. R.W. Roberts and D.M. Crothers. Proc. Natl. Acad. Sci. U.S.A. **88**, 9397 (1991).
13. K. Yoon, C.A. Hobbs, J. Koch, M. Sardaro, R. Kutny, and A.L. Weis. Proc. Natl. Acad. Sci. U.S.A. **89**, 3840 (1992).
14. P.S. Miller and C.D. Cushman. Biochemistry, **32**, 2999 (1993).
15. L.L. Kiessling, L.C. Griffin, and P.B. Dervan. Biochemistry, **31**, 2829 (1992).
16. H.U. Stilz and P.B. Dervan. Biochemistry, **32**, 2177 (1993).
17. C.Y. Huang, C.D. Cushman, and P.S. Miller. J. Org. Chem. **58**, 5048 (1993).
18. S. Verma and P.S. Miller. Bioconjugate. Chem. **7**, 600 (1996).
19. C.Y. Huang, G. Bi, and P.S. Miller. Nucleic Acids Res. **24**, 2606 (1996).
20. S. Kukreti, J.S. Sun, T. Garestier, and C. Helene. Nucleic Acids Res. **25**, 4264 (1997).
21. D.M. Gowers and K.R. Fox. Nucleic Acids Res. **27**, 1569 (1999).
22. I. Prevot-Halter and C.J. Leumann. Bioorg. Med. Chem. Lett. **9**, 2657 (1999).
23. D. Loakes. Nucleic Acids Res. **29**, 2437 (2001).
24. D. Guianvarc'h, R. Benhida, J.L. Fourrey, R. Maurisse, and J.S. Sun. Chem. Commun. (Cambridge), 1814 (2001).
25. S.P. Parel, J. Marfurt, and C.J. Leumann. Nucleosides, Nucleotides and Nucleic Acids, **20**, 411 (2001).
26. S. Obika, Y. Hari, M. Sekiguchi, and T. Imanishi. Chem. Eur. J. **8**, 4796 (2002).
27. H. Torigoe, Y. Hari, S. Obika, and T. Imanishi. Nucleosides, Nucleotides and Nucleic Acids, **22**, 1571 (2003).
28. H. Torigoe, Y. Hari, S. Obika, and T. Imanishi. Nucleosides, Nucleotides and Nucleic Acids, **22**, 1097 (2003).
29. M. Jazouli, D. Guianvarc'h, K. Bougrin, M. Soufiaoui, P. Vierling, and R. Benhida. Nucleosides, Nucleotides and Nucleic Acids, **22**, 1277 (2003).

© 2007 NRC Canada

30. S. Buchini and C.J. Leumann. Nucleosides, Nucleotides and Nucleic Acids, **22**, 1199 (2003).
31. S.D. Osborne, V.E. Powers, D.A. Rusling, O. Lack, K.R. Fox, and T. Brown. Nucleic Acids Res. **32**, 4439 (2004).
32. S. Sasaki, Y. Taniguchi, R. Takahashi, Y. Senko, K. Kodama, F. Nagatsugi, and M. Maeda. J. Am. Chem. Soc. **126**, 516 (2004).
33. Y. Taniguchi, A. Nakamura, Y. Senko, K. Kodama, F. Nagatsugi, and S. Sasaki. Nucleosides, Nucleotides and Nucleic Acids, **24**, 823 (2005).
34. Y. Wang, D.A. Rusling, V.E. Powers, O. Lack, S.D. Osborne, K.R. Fox, and T. Brown. Biochemistry, **44**, 5884 (2005).
35. K.R. Fox and T. Brown. Q. Rev. Biophys. **38**, 311 (2005).
36. Y. Taniguchi, A. Nakamura, Y. Senko, F. Nagatsugi, and S. Sasaki. J. Org. Chem. **71**, 2115 (2006).
37. S.K. Sharma and L.W. McLaughlin. J. Am. Chem. Soc. **124**, 9658 (2002).
38. S.K. Sharma and L.W. McLaughlin. J. Inorg. Biochem. **98**, 1570 (2004).
39. D.M. Noll, T.M. Mason, and P.S. Miller. Chem. Rev. **106**, 277 (2006).
40. M. Shimizu, A. Konishi, Y. Shimada, H. Inoue, and E. Ohtsuka. FEBS Lett. **302**, 155 (1992).
41. M. Shimizu, T. Koizumi, H. Inoue, and E. Ohtsuka. Bioorg. Med. Chem. Lett. **4**, 1029 (1994).
42. S. Wang and E.T. Kool. Nucleic Acids Res. **23**, 1157 (1995).
43. S. Wang and E. Kool. Biochemistry, **34**, 4125 (1995).
44. K. Ushijima, T. Ishibashi, H. Yamakawa, S. Tsukahara, K. Takai, T. Maruyama, and H. Takaku. Biochemistry, **38**, 6570 (1999).
45. R.A. Cassidy, N. Puri, and P.S. Miller. Nucleic Acids Res. **13**, 4099 (2003).
46. J D. Puglisi and I. Tinoco, Jr. Methods Enzymol. **180**, 304 (1989).
47. R.M. Roat and J. Reedijk. J. Inorg. Biochem. **52**, 263 (1993).

© 2007 NRC Canada

An approach for the synthesis of duplexes containing N^3T-butyl-N^3T interstrand cross-links via a bisphosphoramidite strategy[1]

Christopher James Wilds, Ernest Palus, and Anne Marietta Noronha

Abstract: DNA duplexes containing an interstrand cross-link have been synthesized utilizing a bis-3′-*O*-phosphoramidite deoxythymidine dimer where the N^3 atoms are bridged by a butyl linker. With this approach sufficient quantities of high purity cross-linked duplexes are obtained that will enable various biochemical and structural studies to aid in research directed towards understanding the mechanism of interstrand cross-linked DNA repair. This methodology has advantages over a previously reported method to synthesize cross-linked DNA duplexes involving a monophosphoramidite of the same cross-linked thymidine dimer including circumventing the use of costly 5′-*O*-deoxyphosphoramidites in the assembly of the cross-linked duplex by solid-phase synthesis. This strategy can be employed to produce cross-linked duplexes in which the lesions are engineered to have a directly opposed (**1**–**1**) or staggered (**1**–**2** or **2**–**1**) orientations. Biophysical studies of duplexes containing this N^3T-butyl-N^3T cross-link in staggered **1**–**2** and **2**–**1** orientations reveal that both duplexes have a higher T_m than a non-cross-linked duplex suggesting that these linkages do not result in the destabilization of duplex DNA. Circular dichroism spectra of the **1**–**2** and **2**–**1** cross-linked duplexes exhibit minor differences from B-form structure, which correlates with molecular modeling studies.

Key words: chemically modified oligonucleotides, interstrand cross-link, DNA adduct, DNA repair.

Résumé : Faisant appel à un dimère bis-3-*O*-phosphoramidite de désoxythymidine dans lequel les atomes en N^3 sont attachés par un lien butyle, on a réalisé la synthèse de duplex d'ADN contenant une réticulation entre brins. Avec cette approche, il a été possible d'obtenir des quantités suffisantes de duplex réticulés de grande pureté qui permettront de réaliser diverses études biochimiques et structurales qui aideront dans les études orientées vers la compréhension du mécanisme de réparation de l'ADN réticulée entre les brins. Pour la synthèse de duplex d'ADN réticulés impliquant un monophosphoramidite du même dimère de thymidine réticulée, cette méthodologie présente plusieurs avantages par rapport à une méthode proposée antérieurement, dont celui d'éviter dans l'assemblage du duplex réticulé par la synthèse en phase solide l'utilisation des 5'-*O*-désoxyphosphoramidites de coût élevé. Cette stratégie peut être utilisée pour produire des duplex réticulés dans lesquels les lésions sont construites de façon à présenter des orientations qui soient opposées (**1**–**1**) ou décalées (**1**–**2** ou **2**–**1**). Les études biophysiques des duplex contenant la réticulation N^3T-butyl-N^3T dans les orientations décalées **1**–**2** et **2**–**1** révèlent que ce deux duplex présentent du T_m dont la valeur est supérieure à celle du duplex non réticulé, ce qui suggère que ces liaisons ne résultent pas d'une déstabilisation du duplex de l'ADN. Les spectres de dichroïsme circulaire des duplex réticulés en **1**–**2** et en **2**–**1** présentent des différences mineures par rapport à celui de la structure de forme B, ce qui est en bon accord avec les études de modélisation moléculaire.

Mots-clés : oligonucléotides modifiés chimiquement, réticulation entre les brins, adduit d'ADN, réparation d'ADN.

[Traduit par la Rédaction]

Introduction

The role that covalent DNA lesions play in cancer chemotherapy needs no introduction. Interstrand cross-links (ICL) exert their therapeutic effect on cancer cells by preventing DNA strand separation and normal mitosis and ultimately lead to apoptosis, thus halting the process of cell proliferation. However, the development of resistance to the effects of antitumor agents is often due to enhanced repair of interstrand cross-links (1–5). Although a number of repair pathways including homologous recombination and nucleotide excision repair have been implicated in cross-link repair in bacteria and mammalian cells (1), an understanding of the molecular mechanisms that are involved is lacking. Since development of resistance is one of the primary reasons for treatment failure, understanding how to alter the signaling of repair enzymes should allow chemotherapeutic agents to effectively stop the spread of cancer cells.

To correlate the structures of ICL and their repair, a number of groups have focused on methods to produce larger

Received 17 December 2006. Accepted 13 February 2007. Published on the NRC Research Press Web site at canjchem.nrc.ca on 27 March 2007.

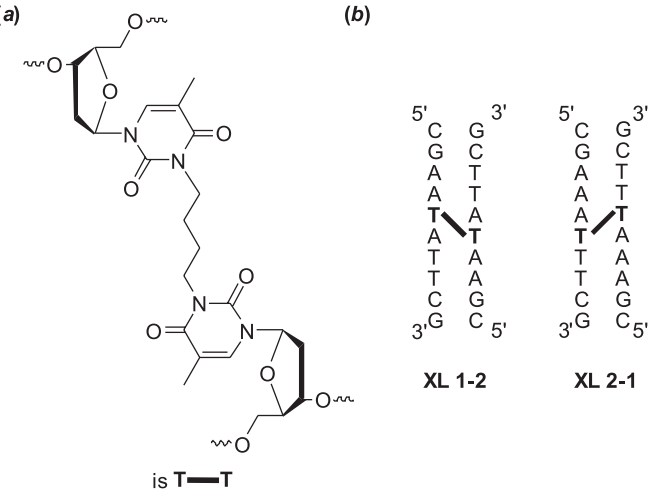
C.J. Wilds,[2] E. Palus, and A.M. Noronha. Department of Chemistry and Biochemistry, Concordia University, 7141 Sherbrooke St. West, Montréal, QC H4B 1R6, Canada.

[1]This article is part of a Special Issue dedicated to Professor Kelvin K. Ogilvie.

[2]Corresponding author (e-mail: cwilds@alcor.concordia.ca).

 doi:10.1139/V07-015 © 2007 NRC Canada

Fig. 1. (*a*) Structure of the N^3T-butyl-N^3T interstrand cross-link. (*b*) Sequences of the **XL 1–2** and **XL 2–1** cross-linked duplexes.



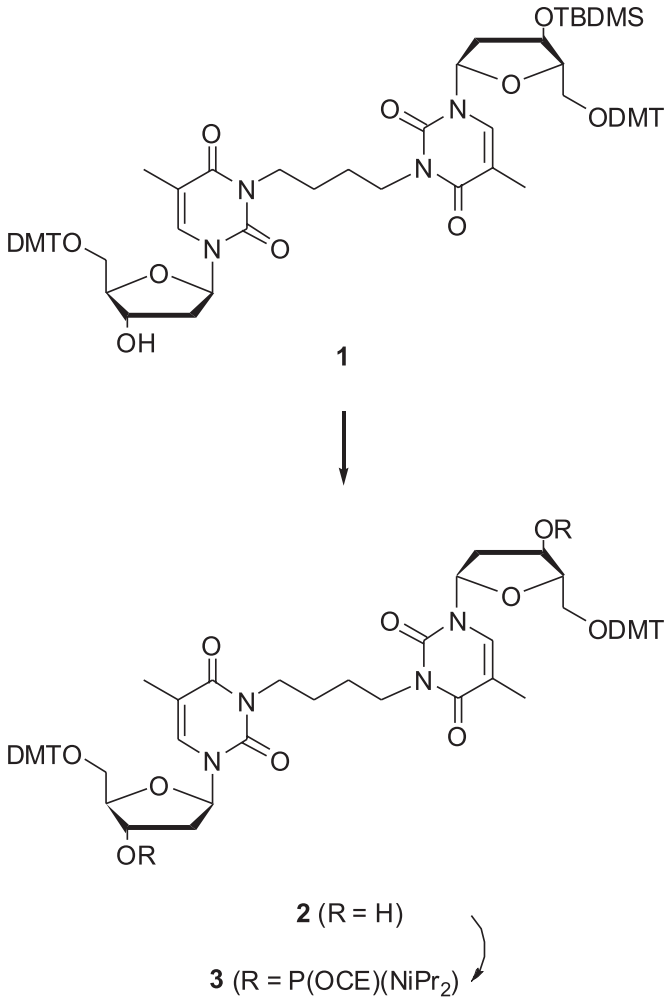
amounts of DNA duplexes containing well-defined lesions or mimics thereof. An attractive approach to produce cross-linked duplexes involves de novo synthesis of cross-linked phosphoramidites and solid-phase synthesis (6–11) over the more traditional route of treating duplex DNA with an excess of bifunctional alkylating agent to produce the ICL (12). The latter method not only suffers from poor yields, but in addition produces numerous monoalkylated and other side products that must be separated from the desired cross-linked product.

We recently described the synthesis and characterization of short DNA duplexes that contain directly opposed N^3T-alkyl-N^3T interstrand cross-links using a phosphoramidite reagent to introduce them in DNA by solid-phase oligonucleotide synthesis (13). This methodology has allowed the solid-phase syntheses of a number of cross-linked duplexes of well-defined structure that have been engineered to contain an ICL between a mismatched TT base-pair (13). In fact, this particular ICL is of considerable interest because it shares similarities to the interstrand cross-links produced by the reaction of duplex DNA with bifunctional alkylators such as bischloroethylnitrosourea, which forms a N^1G-ethyl-N^3C cross-link in sequences containing GC base pairs (14) or busulfan, which links the N^7 atoms of two deoxyguanosines with a butyl linker in duplex DNA (15).

Although thymine is not the major base alkylated by agents such as dimethylnitrosamine and *N*-methyl-*N*-nitrosourea (16), it is the most photochemically reactive base (17). Exposure to UV radiation in sunlight results in the formation of cis-syn pyrimidine photodimers, a cause of skin cancer (18, 19). Intercalation of psoralen at 5′-d(TA) sites followed by absorption of long wavelength UV irradiation results in [2 + 2] photocycloaddition at the 3,4 or 4′,5′ double bonds of psoralen and the 5,6 double bond of thymidine producing an interstrand cross-link (20, 21).

The use of bisphosphoramidites in oligonucleotide chemistry to produce branched oligonucleotide structures has been well studied and documented by many groups, especially those of Ogilvie and Damha (22–24). As part of our investigation on the synthesis and properties of interstrand cross-linked DNA we have developed a modified synthesis

Scheme 1. Chemical synthesis of bisphosphoramidite **3**.



of this N^3T-butyl-N^3T cross-link via a bisphosphoramidite strategy that allows for the production of larger amounts of material fairly easily. In this report we describe the syntheses of short DNA duplexes that contain N^3T-butyl-N^3T interstrand cross-links and discuss some of their physical properties.

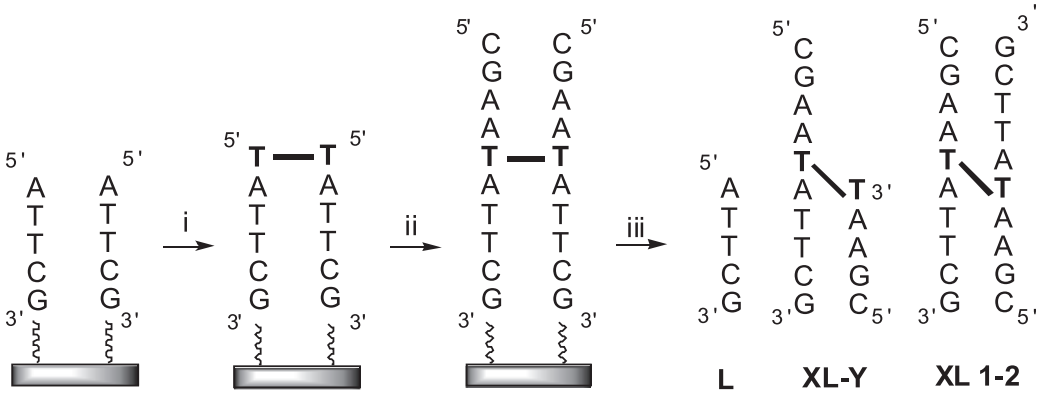
Results

Syntheses and characterization of cross-linked duplexes

The structure of the N^3T-butyl-N^3T interstrand cross-linked adduct and the cross-linked duplexes (**XL 1–2** and **XL 2–1**) are shown in Fig. 1. The cross-linked duplexes (**XL 1–2** and **XL 2–1**) are similar to sequences that contain a N^3T-ethyl-N^3T cross-link, which enables comparison of the effects of a two and four carbon linkage between the *N3* atoms of deoxythymidine in cross-linked DNA (25). The approach to construct these duplexes requires the synthesis of bisphosphoramidite **3** according to the methodology shown in Scheme 1. Starting from 1-{N^3-[5′-*O*-(dimethoxytrityl)-3′-*O*-(*tert*-butyldimethylsilyl)-2′-deoxythymidylyl]}-4-{N^3-[5′-*O*-dimethoxytrityl)-2′-deoxythymidylyl]}butane **1**, the synthesis of which was previously reported, the 3′-*O*-TBDMS group was removed with TBAF to form the symmetrical dimer **2** that was then phosphitylated to produce the cross-linked bisphosphoramidite **3** in good yield. The molecular

© 2007 NRC Canada

Scheme 2. Methodology to construct the cross-linked duplex **XL 1–2** via solid-phase synthesis. (*i*) Coupling of bisphosphoramidite **3**, (*ii*) chain extension with 3′-*O*-deoxyphosphoramidites, and (*iii*) cleavage from the solid support and deprotection using NH_4OH–ethanol (3:1).



weight obtained for this compound was in agreement with the expected value and the ^{31}P NMR spectra contained two peaks at 153.6 and 153.7 ppm, in the region diagnostic of a phosphoramidite.

The solid-phase synthetic strategy used to prepare the cross-linked duplexes is illustrated in Scheme 2 for the sequence **XL 1–2**. All syntheses were carried out on a 1 µmol scale with the first nucleoside attached via the 3′-OH group to a controlled pore glass (CPG) solid support with a loading of 64 µmol/g. Cross-linked duplex assembly begins with commercially available 3′-*O*-deoxyphosphoramidites. The N^3T-butyl-N^3T bisphosphoramidite **3** is coupled simultaneously to the 5′-ends of two oligonucleotide chains attached to the solid support. A chain extension around the 5′ ends of the cross-linked site with 3′-*O*-deoxyphosphoramidites completes the synthesis of the cross-linked duplex. Unlike our previous strategy to synthesize N^3T-alkyl-N^3T interstrand cross-linked DNA duplexes (13, 26), this strategy did not require removal of a TBDMS protecting group at one of the 3′ alcohol functionalities of the N^3T-butyl-N^3T dimer while the cross-linked dimer was still attached to the solid support. This was accomplished by removal of the support from the oligonucleotide synthesizer and treatment with TBAF solution (1 mol/L in THF) for 30 min, before being returned to the oligonucleotide synthesizer for chain extension to complete the synthesis of the cross-linked duplex. The current methodology overcomes problems previously encountered with the removal of the TBDMS group prior to extension of the final arm of the duplex, such as variable efficiency in the desilyation encountered in the synthesis of both N^4T-alkyl-N^4T and N^4C-alkyl-N^4C cross-linked duplexes (13, 27). Lower yields of cross-linked duplexes were observed with longer exposure times to TBAF, presumably due to cleavage of the oligonucleotide from the solid support (28). Another benefit of this methodology is that a lower concentration of bisphosphoramidite **3**, specifically 0.03 mol/L as opposed to 0.15 mol/L, is used in cross-linked oligonucleotide assembly. The lower concentration of bisphosphoramidite **3** in the coupling reaction to the oligonucleotide attached to the solid-support promotes the synthesis of branched molecules, such as the desired cross-linked product and **XL**-**Y** type failure sequences over linear counterparts such as **L** (see Scheme 2). The synthesis of longer cross-linked duplexes should not present any additional limitations to those that are also encountered in the synthesis of linear oligonucleotides. Finally, expensive 5′-*O*-deoxyphosphoramidites are not required for such syntheses, permitting correct polarity within the chains of the duplex but at a reduced cost.

The cross-linked oligomers were cleaved from the solid support and deprotected with a mixture of concentrated ammonium hydroxide – ethanol (3:1) at 55 °C for 4 h and analyzed by both strong anion exchange (SAX) HPLC and polyacrylamide gel electrophoresis (PAGE). The analysis of the crude and purified products for the synthesis of **XL 1–2** via PAGE is shown in Fig. 2. The crude deprotection products are shown in lane 2 with two major products visible having mobilities similar to a 16- and 20-mer. Purification of the cross-linked duplexes were performed by SAX HPLC using a sodium chloride gradient (0–0.5 mol/L) over 30 min in a buffer that contained 100 mmol/L Tris-HCl and 10% acetonitrile. The major side product in these syntheses was the deprotected form of **XL**-**Y**, which resulted from the coupling of only one phosphoramidite moiety to a linear CPG bound oligomer. The nucleoside composition of this side product was confirmed by nuclease digest followed by reversed-phase HPLC analysis. This is formed in favor over the linear uncoupled sequence (Scheme 2, designated **L**). The duplexes **XL 1–2** and **XL 2–1**, whose retention times are shown in Table 1, eluted as single peaks and were obtained in approximately 15% yield after desalting, compared with less than 10% by previously reported methods (13).

Duplexes **XL 1–2** and **XL 2–1** were digested with a combination of snake venom phosphodiesterase and calf intestinal phosphatase and analyzed by C-18 reversed phase HPLC. As shown in Table 1, each duplex was hydrolyzed to its component deoxynucleosides and the N^3T-butyl-N^3T dimer in ratios consistent with the composition of each particular duplex. In addition to this characterization, each duplex was analysed by MALDI TOF mass spectrometry. As shown in Table 1, the experimentally determined molecular weights were in agreement with calculated values.

Thermal denaturation (T_m) and circular dichroism (CD) studies

Results of UV thermal denaturation (T_m) experiments are shown in Fig. 3. Both duplexes **XL 1–2** and **XL 2–1** exhibit

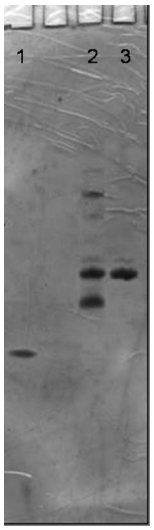
© 2007 NRC Canada

Table 1. Retention times, nucleoside ratios, and mass spectral data for cross-linked duplexes **XL 1–2** and **XL 2–1.**

Cross-linked duplexes	Retention time (min)[a]	Nucleoside composition	Nucleoside ratios		Mass	
			Expected	Observed	Expected	Observed
XL 1–2	23.487	dC	1.00	1.00	6105.18	6105.39
		dG	1.00	1.04		
		dT	1.00	0.98		
		dA	1.50	1.54		
		dT-dT	0.25	0.20		
XL 2–1	23.743	dC	1.00	1.00	6105.18	6105.54
		dG	1.00	1.00		
		dT	1.00	0.91		
		dA	1.50	1.50		
		dT-dT	0.25	0.20		

[a]Retention times (min) of cross-linked duplexes on SAX HPLC using a 0.0–0.5 mol/L linear gradient of sodium chloride over 30 min.

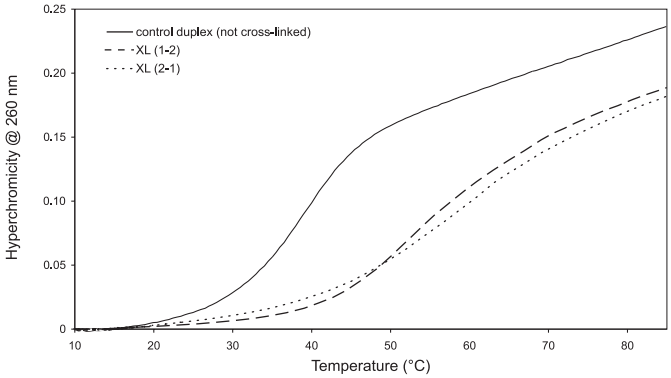
Fig. 2. Polyacrylamide gel electrophoresis (20%, PAGE) analysis of cross-linked duplex **XL 1–2**. (Lane 1) Control 10mer, (lane 2) crude cross-linked duplex **XL 1–2**, and (lane 3) SAX HPLC purified **XL 1–2**.



a sigmoidal denaturation profile with T_m values of 53 and 55 °C, respectively. In comparison, the non-cross-linked control duplex (5′-dCGAAATTTCG)$_2$ gave a T_m of 37 °C.

The circular dichroism (CD) spectra of these duplexes are shown in Fig. 4. All three duplexes exhibit features typical of a B-form duplex. In the case of cross-linked duplex **XL 2–1** the peaks have a higher amplitude, a characteristic of DNA duplex that contain uninterrupted AT-rich tracts that have increased intrastrand base stacking (19). Molecular models that have been geometry-optimized using an Amber force field for the **XL 1–2** and **XL 2–1** cross-linked duplexes, as well as their non-cross-linked counterparts, suggest that when the cross-link is in the **1–2** orientation there is a greater distortion induced in the duplex than in the **2–1** orientation (Fig. 5*b* and 5*d*). Molecular models generated using an Amber force field for non-cross-linked B-form duplexes have a distance of 2.9 Å between the *N3* atom of deoxythymidine and the N1 atom of deoxyadenosine when

Fig. 3. Hyperchromicity (A_{260}) vs. temperature profiles of non-cross-linked control duplex (5′-dCGAAATTTCG)$_2$ (solid line), cross-linked duplexes **XL 1–2** (broken line), and **XL 2–1** (dotted line). Solutions contained cross-linked duplex (2 μmol/L) and control duplexes (2.25 μmol/L) in sodium chloride (90 mmol/L), sodium phosphate (10 mmol/L), and ethylenediaminetetraacetate buffer (1 mmol/L) at pH 7.0 were heated at 0.5 °C/min.



base-paired. For the **XL 1–2** and **XL 2–1** cross-linked duplexes this distance increases to 4.1 and 4.2 Å, respectively. The distance in B-form DNA between the O4 atom of deoxythymidine and the N6 atom of deoxyadenosine is 2.9 Å. For the **XL 1–2** and **XL 2–1** cross-linked duplexes this distance increases to 5.4 and 3.0 Å, respectively, suggesting that in the latter case the two atoms are close enough to form a hydrogen bond. The cross-linked site of each AT base pair for the **XL 1–2** cross-link has the adenine bases displaced vertically along the helical axis. For the **XL 2–1** duplexes, the adenine bases exhibit some twist.

These results illustrate some differences from studies of cross-linked oligonucleotides containing a N^3T-ethyl-N^3T cross-link in **1–2** and **2–1** orientations. Both ethyl cross-linked duplexes were stabilized relative to the non-cross-linked duplex, however the **2–1** duplex was more stable by 24 °C, compared with 6 °C for the **1–2** duplex. The **2–1** and **1–2** N^3T-butyl-N^3T duplexes were both significantly stabilized relative to the non-cross-linked control by 18 and 16 °C, respectively. Although neither NMR or X-ray struc-

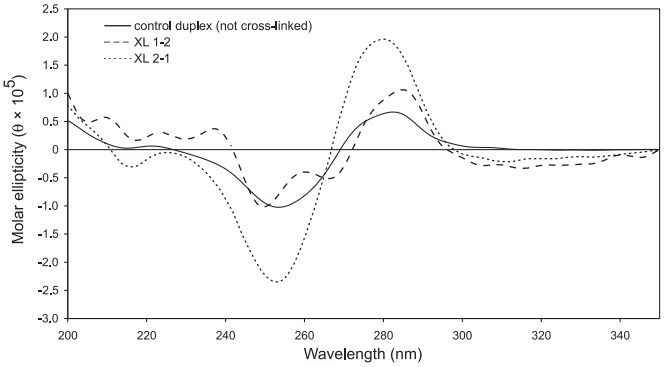
© 2007 NRC Canada

Table 2. Thermal denaturation of cross-linked duplexes **XL 1–2** and **XL 2–1** and the non-cross-linked control.

Duplex	T_m (°C)[a]
XL 1–2	53
XL 2–1	55
Control	37

[a]Experiments were carried out in buffer containing sodium chloride (90 mmol/L), sodium phosphate (10 mmol/L), and ethylenediaminetetraacetate buffer (1 mmol/L) at pH 7.0. The concentration of each duplex was ~2.25 μmol/L.

Fig. 4. Circular dichroism spectra of non-cross-linked control duplex (5′-dCGAAATTTCG)$_2$ (solid line), cross-linked duplexes **XL 1–2** (broken line), and **XL 2–1** (dotted line). Solutions contained cross-linked duplexes (2 μmol/L) and control duplex (2.25 μmol/L) in sodium chloride (90 mmol/L), sodium phosphate (10 mmol/L), and ethylenediaminetetraacetate buffer (1 mmol/L) at pH 7.0. Spectra were recorded at 10 °C.



tures are available for the **1–2** or **2–1** cross-links, the solution structure of an undecamer containing a mispair aligned N^3T-ethyl-N^3T interstrand cross-link suggest that it is well-accomodated between the minor and major grooves, maintaining interstrand stacking with flanking bases (30). In the case of mispair-aligned N^3T-butyl-N^3T undecamers, the solution structure showed a dramatic widening of the major groove and large propeller twisting for the mispair (31). Duplexes containing the N^3T-ethyl-N^3T cross-link in both **1–2** and **2–1** orientations with complementary 3′-overhanging ends were synthesized and their ability to undergo self-ligation with T4 DNA ligase was investigated (25). The **2–1** cross-linked N^3T-ethyl-N^3T duplex underwent rapid self-ligation, whereas no multimeric products were observed for the duplex **1–2** under identical conditions suggesting some structural deformation preventing multimerization of the **1–2** sequence. The similar thermal stability of both **XL 1–2** and **XL 2–1** N^3T-butyl-N^3T sequences, as opposed to the differing stability of the N^3T-ethyl-N^3T cross-links, may be due to the additional flexibility of the butyl vs. ethyl linkage between the bases allowing the former to be better accommodated into a B-form duplex in either orientation.

This current study provides a simplified means for the production of N^3T-alkyl-N^3T interstrand cross-links that may be synthesized with either **1–1**, **1–2**, or **2–1** staggered orientations. The differing properties of these cross-linked duplexes provides a means to synthesize molecules that cause differing levels of distortions within DNA that should allow for progress in the elucidation of repair pathways of interstrand cross-linked DNA.

Experimental section

General

Compound **1**, namely 1-{N^3-[5′-O-(dimethoxytrityl)-3′-*O*-(tert-butyldimethylsilyl)-2′-deoxythymidylyl]}-4-{N^3-[5′-*O*-(dimethoxytrityl)-2′-deoxythymidylyl]}butane was prepared as previously described (13). 5′-*O*-Dimethoxytrityldeoxyribonucleoside-3′-*O*-(β-cyanoethyl-*N*,*N*′-diisopropyl) phosphoramidites and protected deoxyribonucleoside-controlled pore glass (CPG) supports were purchased from Proligo, Inc. (Boulder, Colorado). All solid phase oligonucleotide syntheses were carried out with 500 Å pore size controlled pore glass solid support with a nucleoside loading of 64 μmol/g. All other chemicals and solvents were purchased from Sigma-Aldrich Chemical Company (Milwaukee, Wisconsin) and used as is. Strong anion exchange (SAX) HPLC was carried out using a Dionex DNA PAC PA-100 column (0.4 cm × 25 cm) purchased from Dionex Corp. (Sunnyvale, California) on a Waters Breeze HPLC system. Reversed phase HPLC was carried out using a Symmetry C-18 5 μm column (0.46 cm × 15 cm) purchased from Waters Inc. (Milford, Massachusetts). The columns were monitored at 260 nm for analytical runs or 290 nm for preparative runs. Denaturing polyacrylamide gel electrophoresis was carried out on 20 cm × 20 cm × 0.75 cm gels containing 20% acrylamide and 7 mol/L urea in TBE (89 mmol/L Tris, 89 mmol/L boric acid, and 0.2 mmol/L ethylenediaminetetraacetate buffered at pH 8.0). The running buffer was TBE. Oligonucleotides were detected by UV shadowing. MALDI-TOF mass spectra for oligonucleotides were conducted at the Johns Hopkins University Mass Spectrometry Facility using a Voyager DE-STR MALDI-TOF instrument. ESI mass spectra for small molecules were collected at the Department of Chemistry at McGill University using a Kratos MS25RFA mass spectrometer. NMR spectra of nucleosides were collected using a Varian INOVA 300 MHz NMR spectrometer.

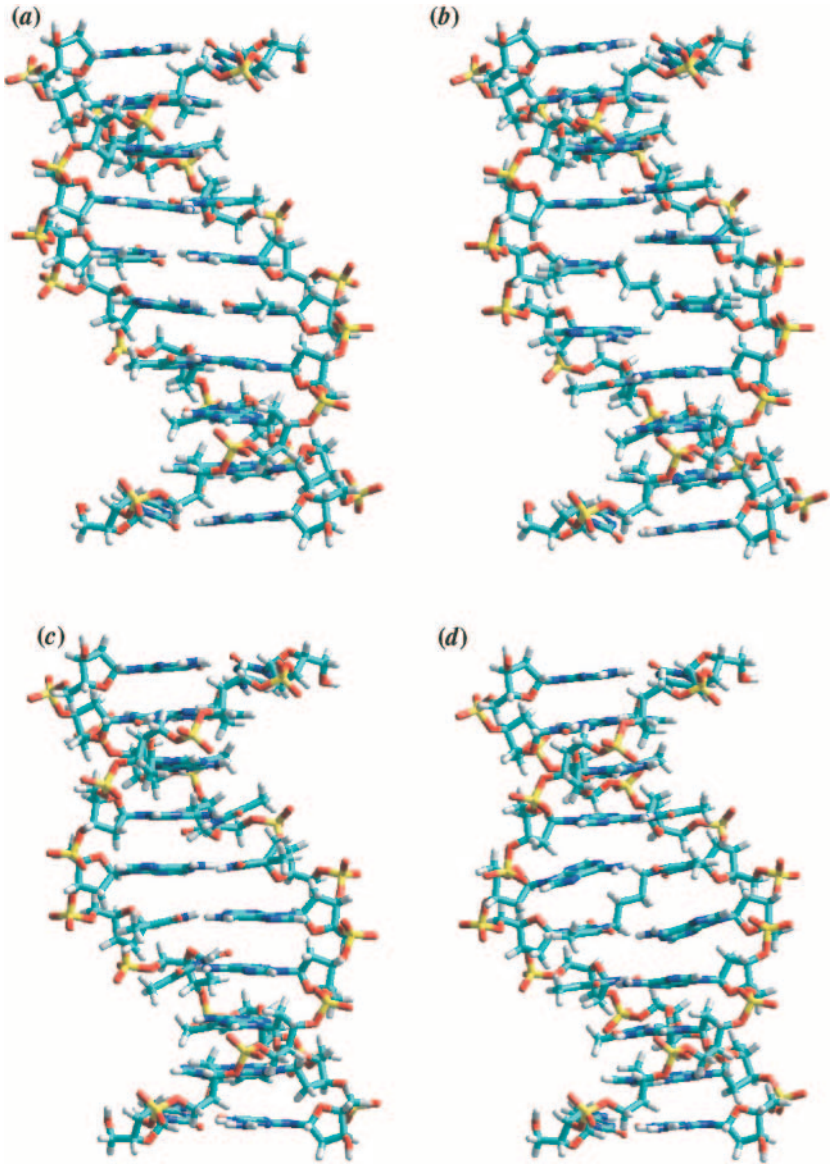
Chemical synthesis

1-{N^3-[5′-O-(Dimethoxytrityl)-2′-deoxythymidylyl]}-4-{N^3-[5′-O-(dimethoxytrityl)-2′-deoxy thymidylyl]} butane 2

To a stirred solution of nucleoside **1** (250 mg, 0.198 mmol) in tetrahydrofuran (1 mL) was added tetrabutylammonium fluoride (1 mol/L in THF, 0.219 mL, 0.219 mmol). The reaction was allowed to proceed at room temperature (RT) for 30 min. The solvent was removed in vacuo. The crude was taken up in dichloromethane (25 mL), extracted twice with sodium bicarbonate (3%, 25 mL), then dried over sodium sulfate. The crude was filtered, evaporated to dryness, and purified by flash column chromatography using a 4:1 ethyl acetate – hexanes solvent system to yield compound **2** as a colorless foam (215 mg, 95.2%). R_f (SiO_2) 0.175 (hexanes – ethyl acetate, 1:4). ^{1}H NMR (300 MHz, d_6-DMSO, ppm) δ: 1.50–1.54 (10H, -CH_2-CH_2- and C5-CH_3),

© 2007 NRC Canada

Fig. 5. Geometry-optimized molecular models of duplexes viewed from the major groove (*a*) (5′-dCGAATATTCG)$_2$, (*b*) **XL 1–2**, (*c*) (5′-dCGAAATTTCG)$_2$, and (*d*) **XL 2–1**.



2.19–2.37 (4 H, H2′ and H2″), 3.20–3.32 (4H, H5′ and H5″), 3.78 (12H, -OCH_3), 3.80–3.87 (4H, -CH_2-N^3-), 3.94–3.97 (2H, H4′), 4.34–4.41 (2H, H3′), 6.29 (2H, H1′), 6.92–7.45 (26 H, DMT), 7.62 (2H, H6). ESI-MS calcd.: 1142.5 [M + Na^+]; found: 1165.3.

1-{N^3-[5′-O-(Dimethoxytrityl)-3′-O-(β-cyanoethyl-N,N′-diisopropyl)phosphoramidite]}-2′-deoxythymidylyl]}-4-{N^3-[5′-O-(dimethoxytrityl)-2′-deoxythymidylyl-3′-O-(β-cyanoethyl-N,N′-diisopropyl)phosphoramidite]}butane 3

To a stirred solution of nucleoside **2** (200 mg, 0.175 mmol) in THF (0.8 mL) was added diisopropylethylamine (0.080 mg, 0.61 mmol) followed by *N*,*N*-diisopropylamino cyanoethyl phosphonamidic chloride (196 uL, 0.52 mmol). The reaction was stirred at RT for 2 h. Upon completion, the reaction was quenched by the addition of dichloromethane (25 mL) and the solution was extracted with sodium bicarbonate (3%, 25 mL). The organic layer was dried over sodium sulfate, filtered, and evaporated. The product, a colorless powder, was precipitated from hexanes (0.220 g, 81.5%). R_f (SiO_2) 0.76 (hexanes – ethyl acetate, 1:4). ^{31}P NMR (161.8 MHz, d_6-acetone, ppm) δ: 153.6, 153.7. ESI-MS calcd.: 1542.7 [M + Na^+]; found: 1565.2.

Oligonucleotide synthesis and purification

The cross-linked duplexes, whose sequences are shown in Fig. 1, were assembled using an Applied Biosystems Model 3400 synthesizer according to standard cyanoethyl-phosphoramidite chemistry protocols (6). Long chain alkylamine controlled pore glass (LCAA-CPG) was used as the solid support. The nucleoside phosphoramidites were diluted in anhydrous acetonitrile at a concentration of 0.15 mol/L for the 3′-phosphoramidites or 0.03 mol/L for the cross-linked bisphosphoramidite **3**. Assembly of the se-

© 2007 NRC Canada

quences was carried out as follows: (*a*) detritylation with 3% trichloroacetic acid in dichloromethane; (*b*) nucleoside phosphoramidite coupling time of 2 min for commercial phosphoramidites and 30 min for the cross-linked bisphosphoramidite; (*c*) capping with 1:1 *v*/*v* of acetic anhydride–2,6,lutidine–tetrahydrofuran 1:1:8 (*v*/*v*/*v*, solution A) and 1-methyl-1-*H*-imidazole–tetrahydrofuran 16:84 (*w*/*v*, solution B); (*d*) oxidation with 0.02 mol/L iodine in tetrahydrofuran–water–pyridine, 2.5:2:1. The 5′-terminal trityl groups were removed on the synthesizer. The oligomer-derivatized CPG was transferred from the reaction column to screw-capped microfuge tubes fitted with teflon lined caps and the protecting groups were removed by treatment with 1 mL of concentrated ammonium hydroxide – ethanol (3:1) for 4 h at 55 °C. The cross-linked duplexes were purified by SAX HPLC with a 30 mL linear gradient of sodium chloride in a buffer that contained 100 mmol/L Tris (pH 7.8) in 10% acetonitrile at a flow rate of 1.0 mL/min. The purified oligomers were then desalted using C-18 SEP PAK cartridges (Waters Inc.) as previously described (13).

Nuclease digestion and MALDI-TOF mass spectrometry

The cross-linked oligomers (0.2 A_{260} unit) were characterized by digestion with a combination of snake venom phosphodiesterase (0.28 unit) and calf intestinal phosphatase (5 units) in a buffer containing Tris (pH 8.1, 10 mmol/L) and magnesium chloride (2 mmol/L) as previously described (13). The resulting mixture of nucleosides was analyzed by reversed phase HPLC and the ratio of nucleosides determined. The results are given in Table 1. The molecular weights of each cross-linked oligomer were determined by MALDI-TOF mass spectrometry using an Applied Biosystems Voyager DE-STR and the results are shown in Table 1.

UV thermal denaturation studies

Molar extinction coefficients for the oligonucleotides and cross-linked duplexes were calculated from those of the mononucleotides and dinucleotides according to nearest-neighbour approximations (units = 10^4 $(mol/L\ cm)^{-1}$) (7). Non-cross-linked duplexes were prepared by mixing equimolar amounts of the interacting strands and lyophilizing the resulting mixture to dryness. The resulting pellet was then redissolved in sodium chloride (90 mmol/L), sodium phosphate (10 mmol/L), and EDTA buffer (1 mmol/L) at pH 7.0, to give a final concentration of 2.25 μmol/L in each strand. The cross-linked duplexes were dissolved in 1 mL of the described buffer to give a final concentration of 2 μmol/L. The solutions were then heated to 80 °C for 15 min on a sand bath, cooled slowly to RT, and stored at 4 °C overnight before measurements. Prior to the thermal run, samples were degassed by placing them in a Speed Vac concentrator for 2 min. Denaturation curves were acquired at 260 nm at a rate of heating of 0.5 °C/min. using a Varian CARY 300 spectrophotometer fitted with a 12-sample thermostated cell block and a temperature controller. The data were analysed in accordance with the convention of Puglisi and Tinoco and transferred to Microsoft Excel for analysis.

Circular dichroism (CD) spectroscopy

Circular dichroism spectra were obtained on a Jasco J-700 spectropolarimeter equipped with a NESLAB RTE-111 circulating bath. Samples were allowed to equilibrate for 5–10 min at 5 °C in sodium chloride (90 mmol/L), sodium phosphate (10 mmol/L), and EDTA (1 mmol/L) at pH 7.0 to a final concentration of 2 μmol/L in each strand for the cross-linked duplexes and 2.25 μmol/L for the control duplex. Each spectrum was an average of 5 scans. Spectra were collected at a rate of 100 nm/min with a bandwidth of 1 nm and sampling wavelength of 0.2 nm using fused quartz cells (Hellma, 165-QS). The CD spectra were recorded from 350 to 200 nm at 10 °C. The molar ellipticity was calculated from the equation $[\theta] = \theta/Cl$, where θ is the relative ellipticity (mdeg), C is the molar concentration of oligonucleotides (moles/L), and l is the path length of the cell (cm). The data were processed on a PC computer using Windows™-based software supplied by the manufacturer (Jasco, Inc.) and transferred into Microsoft Excel for presentation.

Molecular modeling studies

Molecular models of 10-bp duplexes (5′-dCGAATATTCG)$_2$ and (d-CGAAATTTCG)$_2$ as well as duplexes containing a N^3T-butyl-N^3T interstrand cross-link linking deoxythymidine at the underlined sites (d-CGAA$\underline{T}$ATTCG)$_2$ (**XL 1–2**) and (d-CGAAA$\underline{T}$TTCG)$_2$ (**XL 2–1**) were built using HyperChem molecular modeling software. All duplexes were geometry-optimized using the AMBER forcefield.

Acknowledgements

The authors are grateful for financial support of this project from the Natural Sciences and Engineering Research Council of Canada (NSERC), the Canada Foundation for Innovation (CFI), and the Canada Research Chair (CRC) program. We are also indebted to Ms. Margaret Wear and Dr. Paul Miller at Johns Hopkins University for MALDI-TOF analysis of oligonucleotides and Mr. Nadim Saade and Dr. Bruce Lennox at McGill University for ESI-MS analysis of nucleosides.

References

1. M.L. Dronkert and R. Kanaar. Mutat. Res. **486**, 217 (2001).
2. F. Ali-Osman, A. Rairkar, and P. Young. Cancer Biochem. Biophys. **14**, 231 (1995).
3. P.M. O'Connor and K.W. Kohn. Cancer Commun. **2**, 387 (1990).
4. Y. Kano and Y. Fujiwara. Mutat. Res. **81**, 365 (1981).
5. S. Fan, J.K. Chang, M.L. Smith, D. Duba, A.J. Fornace Jr., and P.M. O'Connor. Oncogene, **14**, 2127 (1997).
6. E.A. Harwood, P.B. Hopkins, and S.T. Sigurdsson. J. Org. Chem. **65**, 2959 (2000).
7. E.A. Harwood, S.T. Sigurdsson, N.B.F. Edfeldt, B.R. Reid, and P.B. Hopkins. J. Am. Chem. Soc. **121**, 5081 (1999).
8. P.A. Dooley, M. Zhang, G.A. Korbel, L.V. Nechev, C.M. Harris, M.P. Stone, and T.M. Harris. J. Am. Chem. Soc. **125**, 62 (2003).
9. P.A. Dooley, D. Tsarouhtsis, G.A. Korbel, L.V. Nechev, J. Shearer, I.S. Zegar, C.M. Harris, M.P. Stone, and T.M. Harris. J. Am. Chem. Soc. **123**, 1730 (2001).
10. L.V. Nechev, C.M. Harris, and T.M. Harris. Chem. Res. Toxicol. **13**, 421 (2000).

© 2007 NRC Canada

11. L.V. Nechev, I. Kozekov, C.M. Harris, and T.M Harris. Chem. Res. Toxicol. **14**, 1506. (2001).
12. J.O. Ojwang, D.A. Grueneberg, and E.L. Loechler. Cancer Res. **49**, 6529 (1989).
13. C.J. Wilds, A.M. Noronha, S. Robidoux, and P.S. Miller. J. Am. Chem. Soc. **126**, 9257 (2004).
14. P.L. Fischhaber, A.S. Gall, J.A. Duncan, and P.B. Hopkins. Cancer Res. **59**, 4363 (1999).
15. W.P. Tong and D.B. Ludlum. Biochim. Biophys. Acta, **608**, 174 (1980).
16. A.E. Pegg. Cancer Invest. **2**, 223, (1984).
17. C. Russmann, J. Stollhof, C. Weiss, R. Beigang, and M. Beato. Nucleic Acids Res. **26**, 3967 (1998).
18. J.V.P. Cadet. The photochemistry of nucleic acids. Wiley, New York. 1990.
19. J.E. Cleaver and E. Crowley. Front. Biosci. **7**, D1024 (2002).
20. J.E. Hearst. Annu. Rev. Biophys. Bioeng. **10**, 69 (1981).
21. J.E. Hearst. Chem. Res. Toxicol. **2**, 69 (1989).
22. M.J. Damha and K.K. Ogilvie. Biochemistry, **27**, 6403 (1988).
23. M.J. Damha, R.T. Pon, and K.K. Ogilvie. Tetrahedron Lett. **26**, 4839 (1985).
24. K.K. Ogilvie, M.J. Damha, N. Usman, and R.T. Pon. Pure Appl. Chem. **59**, 325 (1987).
25. C.J. Wilds, A.M. Noronha, S. Robidoux, and P.S. Miller. Nucleosides, Nucleotides and Nucleic Acids, **24**, 965 (2005).
26. D.M. Noll, A.M. Noronha, and P.S. Miller. J. Am. Chem. Soc. **123**, 3405 (2001).
27. A.M. Noronha, C.J. Wilds, and P.S. Miller. Biochemistry, **41**, 8605 (2002).
28. R.S. Braich and M.J. Damha. Bioconjugate Chem. **8**, 370 (1997).
29. J. Aymaan, M. Coll, C.A. Frederick, A.H.-J. Wang, and A. Rich. Nucleic Acids Res. **17**, 3229 (1989).
30. M. Webba da Silva, C.J. Wilds, A.M. Noronha, O.M. Colvin, P.S. Miller, and M.P. Gamcsik. Biochemistry, **43**, 12549 (2004).
31. M. Webba da Silva, R.G. Bierbryer, C.J. Wilds, A.M. Noronha, O.M. Colvin, P.S. Miller, and M.P. Gamcsik. Bioorg. Med. Chem. **13**, 4580 (2005).

© 2007 NRC Canada

Commercialization of automated RNA synthesis — Twenty years on[1]

Gerald Zon

Abstract: Following the introduction of the first successful automated DNA synthesizer by Applied Biosystems Inc. (ABI) in 1983, the company was in a position to consider the commercialization of additional chemistries to enable the automated synthesis of RNA oligonucleotides or other analogs. This retrospective account provides a personal view of how ABI collaborated with Professor Kelvin K. Ogilvie in 1986 to commercialize automated RNA synthesis, using the 2′-*O*-alkylsilyl-protected monomers that he pioneered. The influence of end-user scientific applications on this decision-making process is highlighted, together with the influence of such applications on subsequent commoditization of RNA. Hopefully, these perspectives will provide chemists with further appreciation of the sometime complex and unpredictable interplay between academically interesting chemistry and evolving scientific applications that influence commercialization, and vice versa.

Key words: RNA, synthesis, automated, 2′-*O*-alkylsilyl phosphoramidite, siRNA.

Résumé : À la suite de l'introduction avec succès du premier appareil de synthèse automatique de l'ADN par Applied Biosystems Inc, (ABI), en 1983, la compagnie était en excellente position pour faire la commercialisation des méthodes chimiques additionnelles nécessaires aux synthèses automatiques d'oligonucléotides de l'ARN et d'autres analogues. Cette revue rétrospective fournit une vue personnelle de la façon dont ABI a collaboré avec le professeur Kelvin K. Ogilvie en 1986 pour commercialiser des synthèses automatiques d'ARN à l'aide des monomères protégés par les groupes 2′-*O*-alkylsilyles qu'il avait développé. On met en évidence l'influence des applications scientifiques des usagers sur cette décision ainsi que l'influence de telles applications sur la commercialisation subséquente d'ARN. Il est à espérer que ces perspectives permettront aux chimistes de mieux comprendre les relations souvent complexes et imprévisibles entre de la chimie académiquement intéressante et les applications scientifiques en évolution qui influencent la commercialisation et vice versa.

Mots-clés : ARN, synthèse, automation, 2′-*O*-alkylsilyle phosphoramidite, siARN.

[Traduit par la Rédaction]

Introduction

After the long trip from Applied Biosystems Inc. (ABI) in Foster City, California, to Montréal, Quebec, my business colleague, Elaine Heron, and I were quite tired and glad to check-in to our hotel near McGill University late one night in November 1986. Just that week, I had moved from the National Institutes of Health (NIH) to join ABI, a fledgling biotechnology company, and so the excitement of meeting Professor Kelvin K. Ogilvie the next morning to discuss the possibility of commercializing automated RNA synthesis kept me awake. I had read Ogilvie's papers on the use of 2′-*O*-alkylsilyl nucleoside monomers for automated RNA assembly and looked forward to meeting him and discussing the use of these reagents with ABI's DNA synthesizer, an instrument that had been successfully introduced three years earlier. The context of this eventual milestone in the commercialization of RNA synthesis is the subject of this personalized account. The intent is to provide chemists with insights on how corporate "biotechnology tool" providers such as ABI must find a balance between introducing interesting new chemistry per se and supporting their customer's scientific applications. Many businesses seek the so-called "killer applications" for products, i.e., applications that are widely pursued by many customers. In the early 1980s, following the dawn of recombinant DNA techniques and molecular genetics, killer applications, such as DNA hybridization probes and DNA sequencing primers, were clearly evident. However, in 1986, the circumstances were quite different for synthetic RNA. Although there were a few biophysical or biochemical studies that needed synthetic RNA, there was no widely recognized killer application. ABI's inclination to commercialize automated RNA synthesis at that time was, therefore, predicated on the hope that scientists would find a killer application for synthetic RNA, if enabling technology was made available, hopefully sooner rather than later to avoid carrying an unprofitable product line. Although, important new uses for synthetic RNA, such as synthetic ribozymes and RNA aptamers, eventually did evolve, this did not occur until many years later. The hoped-

Received 31 October 2006. Accepted 19 January 2007. Published on the NRC Research Press Web site at canjchem.nrc.ca on 27 March 2007.

G. Zon. Advanced Research and Technology, Applied Biosystems, 850 Lincoln Centre Drive, Foster City, California 94404, USA. (e-mail: zonjn@appliedbiosystems.com).

[1]This article is part of a Special Issue dedicated to Professor Kelvin K. Ogilvie.

 doi:10.1139/V07-005 © 2007 NRC Canada

for killer application did not occur until relatively recently with the advent of RNA interference (RNAi) methodology, a discovery for which Andrew Z. Fire and Craig C. Mello were awarded the Nobel Prize in Physiology or Medicine in 2006. During the ensuing 20 years, various improvements in automated RNA synthesis yield, scale, and throughput have been reported by scientists and engineers at ABI, and elsewhere, some of whom are contributors to, or cited in this Special Issue to honor Professor Ogilvie. What follows is a brief retrospective on the beginnings of commercial automated synthesis of RNA.

The DNA prelude to RNA

During 1981, there were a number of independent circumstances that would ultimately converge some seven years later and lead to the commercialization of automated RNA synthesis by ABI in 1988. From a personal perspective, in 1981, I was using Vega Biotechnologies Inc. (VBI) peptide-synthesis equipment at NIH to manually synthesize a pool of mixed-base oligodeoxynucleotides by the phosphotriester method for use as degenerate hybridization probes by my colleagues. The months it took to make and purify just this one pool of probes was quite discouraging. It was, therefore, with real interest that I read Ogilvie's 1981 article in *Science* (1) entitled "Automated Synthesis of Gene Fragments", wherein a 14-mer was made in just 6.5 h! In addition to this stunning automation of DNA synthesis, I was quite familiar with trivalent organophosphorus chemistry and thought that the described use of methylchlorophosphite monomers offered not only the efficiencies that were described but also provided chemical flexibility for modified internucleotide linkages. Moreover, successful extension to RNA was indicated by the last sentence of this publication (1) that referred to a manuscript in preparation demonstrating that "this basic procedure also applies to the synthesis of RNA sequences". The co-authors of this publication (1) were at Bio Logicals Inc. (BLI), a Canadian company in Toronto. Detailed descriptions by Bender and Ogilvie of automated solid-phase synthesis of DNA and RNA, using blocked phosphodichloridites such as $MeOPCl_2$, were also published in 1981 in a patent application by BLI (2). In this methodology, the synthesis of RNA took advantage of extensive earlier work by Ogilvie and co-workers (3) on nucleoside monomers having 2′-blocking groups such as the *tert*-butyldimethylsilyl group. However, the initial focus was on DNA synthesis, as evident in a January 23, 1981 *New York Times* article (4), which reported that genes could be made by machine. A rapid, automated assembly of DNA had been demonstrated the previous day at the Chemists' Club in New York city by scientists from BLI and Ogilvie, who was a member of the firm's scientific advisory board.

Two other significant events, relating to DNA and RNA synthesis, also occurred during 1981. The first was the publication of a patent application (5), describing the work by Caruthers and Matteucci on inorganic (e.g., silica) solid-phase synthesis of DNA or RNA that featured the coupling of protected nucleoside 3′-methylphosphomonotetrazolide that was made in situ from the corresponding monochlorodite. Secondly, Beaucage and Caruthers (6) published a communication, describing deoxynucleoside 3′-phosphoramidites as a new class of key intermediates for DNA synthesis. The phosphoramidites had great utility because they were sufficiently stable for easy handling and prolonged storage, yet they were precursors for the virtually instantaneous and in situ generation of reactive phosphotetrazolides within a flow-through column of solid support. Consequently, it was possible to bypass the great instability of both phosphochloridites and phosphotetrazolides when in solution. 1981 was also the year in which ABI began operation. ABI started as a company that intended to commercialize protein sequencers, DNA synthesizers, and other automated systems, as the "picks and shovels for the biotechnology gold rush", to quote Sam Eletr, co-founder and first CEO. The first protein sequencers that were introduced later that year featured proprietary "zero-dead-volume" valves. Two years later, these same valves would also be beneficially utilized in ABI's DNA synthesizer to minimize wasted reagents and solvents, and thus offer more favorable economics. In 1983, the immediate goal was to use phosphoramidite chemistry to provide a fast and reliable "push button" DNA synthesis system. ABI's initial business strategy was to meet the great demand for synthetic DNA, for use as hybridization probes and sequencing primers, in recombinant DNA technology and academic research. This meant focusing ABI's resources on introducing a synthesizer that would initially provide DNA, but would still be compatible with future reagents for synthesizing other types of oligonucleotides, such as RNA or other modifications. However, as indicated later in this article, several scientifically driven market factors arose and needed to be evaluated. This caused ABI to focus on the automated synthesis of DNA-based oligonucleotide analogs before proceeding with RNA synthesis.

Chemistry options and applications

Although a number of companies, such as ABI, Beckman, Biosearch, BLI, Systec, and VBI, were offering automated systems for the synthesis of DNA in 1982–1983 (7), commercialization of automated RNA synthesis remained on the horizon. Instead, much attention was focused on improving the efficiency of DNA synthesis. For example, Adams and co-workers at Monsanto (8) reported outstanding results for the manual synthesis of a 51-mer, using sterically hindered (e.g., *N,N*-diisopropyl-)3′-phosphoramidites (6), in conjunction with a long-chain linker to controlled-pore glass vs. silica (5), and detritylation with protic acids vs. $ZnBr_2$ (5), and these modifications were soon being evaluated for automated synthesis. In addition, there were several issues related to coupling performance and controversial DNA quality, user preferences (e.g., faster time-to-DNA and "no thiophenol!"), and the question of whether to use *O*-methyl (6, 9, 10) or *O*-(β-cyanoethyl) (11) phosphate protection to settle. While these and other chemistry and engineering issues were being addressed at ABI to define and introduce its initial automated DNA synthesizer, the company was also contemplating what the next-generation chemistry would be. One potentially large market opportunity was the synthesis of sequence-specific inhibitors of gene expression. At ABI, the methylphosphonate (P–Me) class of DNA analogs, originally envisioned by Ts'o and Miller at The Johns Hopkins

© 2007 NRC Canada

University, was pursued by William Efcavitch, who prepared methylphosphonamidites for solid-phase synthesis. I agreed with this view of P–Me analogs and was keen on extending the scope of phosphoramidite chemistry to produce oligonucleotide analogs with modified phosphotriester (RO–P) or phosphorothioate (P–S) internucleotide linkages. These novel compounds would be more resistant to enzymatic degradation and suitable for use in antisense applications. Providing these novel chemistries and a larger-scale instrumentation for their synthesis thus became a large part of ABI's commercialization interests during 1983–1986. Finally, hydrogen phosphonate (H–phos) chemistry (12) for the synthesis of DNA or RNA (12*a*), and P–S or other analogs (12*b*), had to be carefully evaluated in view of the possibility that this alternative chain-assembly chemistry might provide significant advantages over phosphoramidite chemistry. The potential advantages of H–phos synthesis were widely touted by many leading nucleic acid chemists, who were contacted by ABI in 1986. However, such advantages did not materialize in extensive work at ABI or elsewhere. ABI, therefore, discounted H–phos chemistry, as a commercially viable, generally applicable alternative for chain-assembly, and focused attention on the use of phosphoramidite methodology for DNA and RNA synthesis.

While automated DNA synthesis was maturing, Ogilvie and his McGill group continued to refine their RNA synthesis protocols. Ogilvie's published work in this period indicated the benefits of transitioning from the initial phosphochloridite approach (13) to the adoption of *N,N*-diisopropyl phosphoramidite reagents (8–10). The sometimes controversial issue about potential 2′–3′ linkage rearrangement, using 2′-*O*-alkylsilyl vs. 2′-*O*-tetrahydropyranyl protection, and trade-offs regarding compatibility or not of these groups, respectively, during acid-catalyzed deprotection of the 5′-*O*-di(or mono)methoxytrityl moiety (11, 14), was also being resolved in favour of the 2′-*O*-alkylsilyl protecting groups.

A decision by ABI to launch automated RNA synthesis with 2′-alkylsilyl monomers

With all of the previously mentioned background information, our meeting with Ogilvie in November 1986 was aimed at the technical evaluation of the current status of RNA synthesis in his laboratory as a basis for possible commercialization by ABI. During the course of the discussion, I was pleasantly surprised and truly impressed by the progress that had been made by Richard T. Pon, who had recently finished his graduate studies, and by Nassim Usman and Masad J. Damha, who were in the midst of their graduate work. All of the major chemistry issues, particularly hypothetical linkage rearrangement, were discussed in detail and fully addressed. Moreover, Ogilvie shared with us his intent to synthesize, sequence, and functionally characterize a relatively long tRNA analog. We indicated the importance of this goal to ABI from the standpoint of providing the scientific community with compelling data for the quality of synthetic RNA. ABI had previously used analogous DNA-cloning and -sequencing results to ensure customers of the high quality of the synthetic DNA and address concerns of a few, who were skeptical of the quality of DNA that could be made so easily. By the end of the day, Elaine Heron and I were prepared to support a collaboration aimed at demonstrating that Ogilvie's monomers for RNA synthesis would be successful. That confidence was predicated in large part on our seeing Ogilvie's promising preliminary results, obtained with 2′-*O*-alkylsilyl-protected phosphoramidites using a BLI synthesizer, as were subsequently reported (14). We provided an ABI DNA synthesizer for his continuation of that work and to transition his chemistry to the widely used ABI instrument platform. This investment was a relatively low-risk proposition, given the progress already demonstrated, and subsequent work with this system led to the desired result: a landmark publication by Ogilvie and co-workers (15) in 1988 describing the synthesis, sequencing, and functional activity of a 77-mer $tRNA^{fmet}$ analog, prepared using 2′-*O*-alkylsilyl RNA phosphoramidites.

That year, ABI introduced automated RNA synthesis to its extensive base of DNA synthesis customers with the release of detailed protocols prepared by Alex Andrus (*ABI User Bulletin*, No. 47. April 18, 1988). At that time, 2′-*O*-alkylsilyl *N,N*-diisopropyl phosphoramidite monomers and solid supports were available from Peninsula Laboratories Inc. in Belmont, California, where they were commercialized by one of Ogilvie's former students, Taifeng Wu. As described elsewhere (16), follow-up work by ABI scientists and collaborators included the introduction of base-labile groups for fast deprotection of nucleobases, a reagent and protocol for improved desilylation, synthesis scale-up, use of polystyrene as a solid support, and the introduction of a new reagent for sulfurization that could be applied to RNA.

Postscript

Following these beginnings of commercial RNA synthesis, other academic and corporate researchers have continued to make significant contributions to the field. Particularly, noteworthy developments include the new 2′-*O*-triisopropylsilyloxymethyl (TOM) (17) and 2′-*O*-bis(2-acetoxyethoxy)methyl (ACE) (18) protecting groups, which have become well established. Other new 2′-protecting groups are also being developed, e.g., 2′-*O*-(*t*-butyl)dithiomethyl (DTM) (19), but their long-term popularity remains to be determined. On the other hand, RNA synthesis using Ogilvie's original 2′-*O*-*t*-butyldimethylsilyl protection is still widely employed by commercial suppliers (20) even though over 20 years have lapsed since its first use with phosphoramidite chemistry.

While these kinds of chemistry improvements were not surprising, it is probably true that very few, if any, persons anticipated two major changes related to automated RNA synthesis that were driven from the perspective of scientific applications, i.e., customer demand. First was the transition of customers from "make RNA" to "buy RNA", which also applied to DNA, and represents true commoditization of RNA and DNA. That shift, from customers making their own RNA or DNA to buying it from a commercial supplier or core lab, was enabled by the evolution of a service industry that used largely ABI, and eventually other, synthesizers to make and sell RNA or DNA to thousands of customers worldwide, on a daily basis, for a myriad of uses. Many types of biological applications in this marketplace require

© 2007 NRC Canada

only relatively small quantities of each sequence but need large numbers of different sequences relatively quickly and at a relatively low price. These requirements have been enabled by the development of small-scale, high-throughput synthesizers such as the MerMade-384 that can produce RNA or DNA in four 96-well plates (see www.Bioautomation.com). The second unanticipated change was the advent of RNAi methodology, which uses synthetic short-interfering RNA (siRNA) to very efficiently silence gene expression. This technology has provided the long-awaited killer application for RNA synthesis, and very large numbers of synthetic RNAs are now routinely produced. This widespread usage of synthetic siRNA is evidenced by 3261 citations in *Chem. Abstr.*, indexed to the search term siRNA, during the year 2005, of which 576 were also indexed to the search terms synthesis or synthetic. Remarkably, 157 (27%) of these reports are patents. The relatively huge demand for synthetic siRNA in RNAi applications has provided a compelling economic incentive for academic or corporate chemists to continue to develop faster, better, and cheaper methods for the preparation of siRNA, and chemically modified analogs thereof, for basic and applied research. One market survey estimated that in 2006 ~15 000 research labs would have performed RNAi studies with synthetic siRNA, having a market value of ~$100 million,[2] while another survey projects that the market value of siRNA technology will grow to ~$250 million in 2009.[3] Like past pursuit of antisense oligonucleotide therapeutics, which fueled the development of kilogram-scale DNA synthesis and purification, the current pursuit of therapeutic applications of siRNA and its analogs has refueled efforts to extend such manufacturing technology to similarly large quantities of RNA-based compounds.

Significant investments in siRNA therapeutics are also reflected in the October 30, 2006 announcement by Merck & Co. Inc. that it intends to acquire Sirna Therapeutics Inc. for $1.1 billion. It is truly exciting to imagine what may be written in 2016 in an article that could be entitled "Commercialization of automated RNA synthesis — Thirty years on".

Acknowledgements

I am very grateful to Vincent M. Powers, in the ABI Legal Department, for providing assistance with obtaining archived documents and Alex Andrus at Genentech for refreshing my memory of past events that are referred to here. Publications of marketing surveys were kindly provided by John R. O'Neill in ABI Library Services.

References

1. G. Alvarado-Urbina, G.M. Sathe, W.-C. Liu, M.F. Gillen, P.D. Duck, R. Bender, and K.K. Ogilvie. Science (Washington, D.C.), 214, 270.
2. R. Bender and K.K. Ogilvie. EP 40099 (A1), 1981.
3. K.K. Ogilvie, S.L. Beaucage, A.L. Schifman, N.Y. Theriault, and K.L. Sadana. Can. J. Chem. **56**, 2768 (1978).
4. H.M. Schmeck, Jr. The New York Times, 23 Jan. 1981.
5. M.H. Caruthers and M.D. Matteucci. EP 35719 (A2), 1981.
6. S.L. Beaucage and M.H. Caruthers. Tetrahedron Lett. **22**, 1859 (1981).
7. J.A. Smith. Am. Biotechnol. Lab. 15 (1983).
8. (*a*) S.P. Adams, K.S. Kavka, E.J. Wykes, S.B. Holder, and G.R. Galluppi. Abstracts of the 183 rd Meeting of the American Chemical Society, Las Vegas, NV, March 1982; (*b*) S.P. Adams, K.S. Kavka, E.J. Wykes, S.B. Holder, and G.R. Galluppi. J. Am. Chem. Soc. **105**, 661 (1983).
9. R.T. Pon, M.J. Damha, and K.K. Ogilvie. Nucleic Acids Res. **13**, 6447 (1985).
10. N. Usman, R.T. Pon, and K.K. Ogilvie. Tetrahedron Lett. **26**, 4567 (1985).
11. R. Kierzek, M.H. Caruthers, C.E. Longfellow, D. Swinton, D.H. Turner, and S.M. Frier. Biochemistry, **25**, 7840 (1986).
12. (*a*) P.J. Garegg, C. Henrichson, I. Lindh, T. Regberg, J. Stawinski, and R. Stroemberg. Bioact. Mol. **3**, 93 (1987); (*b*) B. Froehler. Tetrahedron Lett. **27**, 5575 (1986).
13. R.T. Pon and K.K. Ogilvie. Tetrahedron Lett. **25**, 713 (1984).
14. N. Usman, K.K. Ogilvie, M.-Y. Jiang, and R.J. Cedergren. J. Am. Chem. Soc. **109**, 7845 (1987).
15. K.K. Ogilvie, N. Usman, K. Nicoghosian, and R.J. Cedergren. Proc. Natl. Acad. Sci. USA, **85**, 5764 (1988).
16. (*a*) H. Vu and B.L. Hirschbein. Tetrahedron Lett. **32**, 3005 (1991); (*b*) P. Wright, D. Lloyd, W. Rapp, and A. Andrus. Tetrahedron Lett. **34**, 3373 (1993); (*c*) Brian Sproat, F. Colonna, B. Mullah, D. Tsou, A. Andrus, A. Hample, and R. Vinayak. Nucleosides and Nucleotides, **14**, 255 (1995).
17. R. Micura. Chem. Eur. J. 5, 2077 (1999).
18. S.A. Scaringe, F.E. Wincott, and M.H. Caruthers. J. Am. Chem. Soc. **120**, 11820 (1998).
19. A. Semenyuk, A. Foldesi, T. Johansson, C. Estmer-Nilsson, P. Blomgren, M. Brannvall, L. A. Kirsebom, and M. Kwiatkowski. J. Am. Chem. Soc. **128**, 12356 (2006).
20. B.S. Sproat. Methods in Mol. Biol. (Totowa, NJ, United States), **288**, 17 (2005).

[2] "RNAi 2004 Strategic Opportunities", January 2004, Select Biosciences, Crestland House, Acton, Sudbury, UK.
[3] "siRNA Technologies", August 2004, Front Line Strategic Market Reports, Navigant Consulting Inc., Chicago, Illinois.

© 2007 NRC Canada

Characterization of pH3DZ1 — An RNA-cleaving deoxyribozyme with optimal activity at pH 3[1]

Md. Monsur Ali, Srinivas A. Kandadai, and Yingfu Li

Abstract: We previously described a cis-acting RNA-cleaving deoxyribozyme known as pH3DZ1 that exhibits optimal catalytic activity at pH 3.0 (Zhongjie Liu, Shirley H. Mei, John D. Brennan, and Yingfu Li. J. Am. Chem. Soc. **125**, 7539 (2003)). This DNA catalyst was made of a 99-nucleotide (nt) catalytic domain covalently linked to a 23-nt DNA–RNA chimeric substrate containing a single ribonucleotide as the cleavage site. In the present work, we conducted an extensive sequence examination of this deoxyribozyme via nucleotide truncation and reselection experiments, with a goal to minimize its size and identify the nucleotides that are crucial to its catalytic function. A trans-acting deoxyribozyme that can process an external substrate was also successfully designed. Stretches of 30 and 17 nucleotides from the 5′ and 3′ ends of the trans catalyst, respectively, were found to be completely dispensable; in contrast, few nucleotides could be deleted internally without producing a detrimental effect. The reselection experiment led to the discovery of 7 and 5 absolutely conserved nucleotides located at the 5′ and 3′ ends of the minimized catalyst, respectively, separated by a 31-nt element in which 14 highly conserved nucleotides were scattered among 17 variable nucleotides. The shortened deoxyribozyme and the original catalyst showed a similar pH profile with the optimal activity at pH 3; however, the minimized deoxyribozyme still exhibited strong catalytic activity at pH 2.5, while the full-length catalyst was barely active at this pH. Finally, it was found that this deoxyribozyme generated two cleavage fragments, one with 2′,3′-cyclic phosphate and the other with 5′-OH.

Key words: DNA, deoxyribozyme, RNA cleavage, in vitro selection, catalysis.

Résumé : Dans un travail antérieur (Zhongjie Liu, Shirley H. Mei, John D. Brennan, and Yingfu Li. J. Am. Chem. Soc. **125**, 7539 (2003)), on a décrit un désoxyribozyme connu sous le nom de code pH3DZ1, qui est capable de cliver l'ARN, qui agit d'une façon cis et dont l'activité catalytique est optimale à un pH de 3,0; ce catalyseur d'ADN a été fait en liant le domaine catalytique 99-nucléotide (nt) à un substrat chimérique 23-nt ADN–ARN ne contenant qu'un seul ribonucléotide comme site de clivage. Dans le travail présenté maintenant, on a fait appel à des expériences de tronquage et de resélection pour effectuer un examen extensif de la séquence de ce désoxyribozyme dans le but de minimiser sa taille et d'identifier les nucléotides qui sont cruciaux à son fonctionnement catalytique. On a aussi développé avec succès un désoxyribozyme agissant de façon *trans* qui peut traiter un substrat extérieur. On a identifié des blocs respectivement de 30 et de 17 nucléotides des extrémités 5′ et 3′ du catalyseur trans dont on peut se dispenser complètement; par opposition à cette situation, il n'y a que peu de nucléotides internes qui peuvent être éliminés sans produire des effets néfastes. L'expérience de resélection a permis de découvrir des blocs de 7 et 5 nucléotides absolument nécessaires qui sont situés respectivement aux extrémités 5′ et 3′ du catalyseur minimisé et qui sont séparés par un élément de 31-nt dans lequel 14 des nucléotides à conserver sont éparpillés parmi les 17 nucléotides variables. Le désoxyribozyme raccourci et le catalyseur original présentent tous les deux des profiles de pH semblables, avec une activité optimale à un pH de 3; toutefois, le désoxyribozyme raccourci présentait encore une forte activité catalytique à un pH de 2,5 alors que le catalyseur global était pratiquement inactif à ce pH. Enfin, on a trouvé que ce désoxyribozyme génère deux fragments de clivage, un avec un phosphate 2′,3′,-cyclique et l'autre avec un 5′-OH.

Mots-clés : ADN, désoxyribozyme, clivage d'ARN, sélection in vitro, catalyse.

[Traduit par la Rédaction]

Introduction

Although DNA is best known as the material that stores the genetic information of all living organisms on earth, in recent years it has also been widely explored as a synthetic material in diverse applications ranging from the design of biosensors (1–6), to the construction of nanodevices (7–11), and to the creation of catalysts (12–18).

The first catalytic DNA was reported in 1994 (19), and since then hundreds of DNA sequences with catalytic abili-

Received 22 December 2006. Accepted 17 February 2007. Published on the NRC Research Press Web site at canjchem.nrc.ca on 4 April 2007.

M. Ali, S.A. Kandadai, and Y. Li.[2] Department of Biochemistry and Biomedical Sciences and Department of Chemistry, McMaster University, 1200 Main Street West, Hamilton, ON L8N 3Z5, Canada.

[1]This article is part of Special Issue dedicated to Professor Kelvin K. Ogilvie.

[2]Coresponding author (e-mail: liying@mcmaster.ca).

 doi:10.1139/V07-017 © 2007 NRC Canada

ties have been isolated from random-sequence DNA pools using a well-established laboratory technique known as "in vitro selection" (20, 21). Commonly known as deoxyribozymes and even simply DNAzymes, DNA catalysts have been obtained to catalyze diverse chemical reactions including cleavage and ligation of DNA or RNA (22–41), 5′-phosphorylation and 5′-adenylation of DNA (42–44), porphyrin metallation (45), and thymine dimer repair (46). From a theoretical perspective, DNA catalysts offer an important platform for the fundamental examination of inherent catalytic capabilities of nucleic acids. From a practical point of view, DNA catalysts have great potential to be exploited as desirable molecular tools for innovative chemical and biological applications.

Aiming to investigate the fundamental catalytic capability of DNA and to obtain DNA catalysts that can function under harsh chemical conditions, we recently carried out in vitro selection experiments to derive self-cleaving deoxyribozymes that were active in a highly acidic environment (34). The effort led to the isolation of several unusual DNA catalysts with optimal catalytic activity at a defined acidity that precisely reflected the pH value specifically set during the in vitro selection experiment (such as pH 3, 4, 5, or 6). The deoxyribozyme that was active at the most acidic condition was named pH3DZ1, which was derived under pH 3.0 as the constant solution acidity and expectedly exhibited the optimal activity at this pH (34).

The major goal of the present study was to conduct a comprehensive analysis of the sequence requirement of pH3DZ1 in an effort to minimize its size and identify the nucleotides that are most crucial to its catalytic function.

Results

Removal of the two primer-binding sequence elements from pH3DZ1

pH3DZ1 was originally isolated from a random-sequence DNA library by in vitro selection while the pH of the reaction mixture was maintained at 3.0 (34). The full-length pH3DZ1 is a 122-nucleotide (122-nt) cis-acting catalyst cleaving a covalently attached DNA–RNA chimeric substrate that has a single ribonucleotide as the cleavage site. It was shown previously that the last 15 nucleotides of pH3DZ1, which were used as the 3′ primer binding arm for a polymerase chain reaction (PCR) amplification during the in vitro selection, could be removed without affecting the catalyst activity (34). This shortened deoxyribozyme, named pH3DZ1S, was used as the reference sequence in this report (Fig. 1*A*).

For description convenience, we divide the sequence of pH3DZ1S into two sequence elements (Fig. 1*A*): a 23-nt "substrate" domain (Fig. 1*A*, numbered –1 to –23 in the 3′-5′ direction) and an 84-nt "catalyst" domain (numbered 1 to 84 in the 5′-3′ direction). It should be noted that the substrate domain contains three special nucleotides abbreviated as R, F, and Q. R denotes adenine ribonucleotide, the only ribonucleotide in the otherwise all-DNA sequence. F and Q denote a fluorescein-labeled thymine deoxyribonucleotide (fluorescein-dT) and a DABCYL-labeled thymine deoxyribonucleotide (DABCYL-dT), respectively. Such modifications were intended for the future exploration of pH3DZ1 as a potential biosensor because the catalytic activity is directly linked to the generation of a fluorescence signal.

The 15 nucleotides at the 5′-end of the catalyst domain within pH3DZ1S (Fig. 1*A*, G_1-A_{15}) were used as the 5′ primer-binding arm for the PCR amplification step during the original in vitro selection experiment. To assess whether this sequence element could be removed, we designed a shortened sequence EC1 (Fig. 1*B*). To compare the catalytic activity of EC1 to pH3DZ1S, we constructed radioactive cis-acting deoxyribozymes using the following procedure: the substrate S1 and the two catalysts were produced separately by automated DNA synthesis and purified by preparative denaturing (urea, 8 mol/L) polyacrylamide gel electrophoresis (denaturing PAGE); each catalyst was phosphorylated at the 5′-end using γ-^{32}P[ATP] and T4 polynucleotide kinase; each phosphorylated catalyst was joined to the substrate by DNA ligation with T4 DNA ligase in the presence of a template oligonucleotide (Fig. 1*C*; T1 for pH3DZ1S ligation; T2 for EC1 ligation) followed by purification by denaturing PAGE. This procedure produced the ^{32}P-labeled pH3DZ1S and EC1 with the ^{32}P-phosphodiester bond (Fig. 1*A*, indicated with "*") linking the substrate domain to the catalyst domain. Upon RNA cleavage, the 3′-cleavage fragment (Fig. 1*D*, designated as "clv") would be radioactive and can be detected by autoradiography.

The activities of pH3DZ1S and EC1 were assessed in a time-course study and the data are given in Fig. 1*D*. The two deoxyribozymes had almost identical time-course profiles. A small amount of cleavage (~2%) was observed after 1 min incubation; when the reaction time was progressively increased, the percentage of cleaved product was also increased; at 1000 min reaction time, about 50% of the cis-acting catalyst was cleaved. The data in Fig. 1*D* indicate that none of the 30 nucleotides located in the two primer-binding arms were recruited as the catalytically important nucleotides during in vitro selection. We term these residues as "dispensable nucleotides", which are shown as gray letters in Fig. 1*E* and subsequent figures.

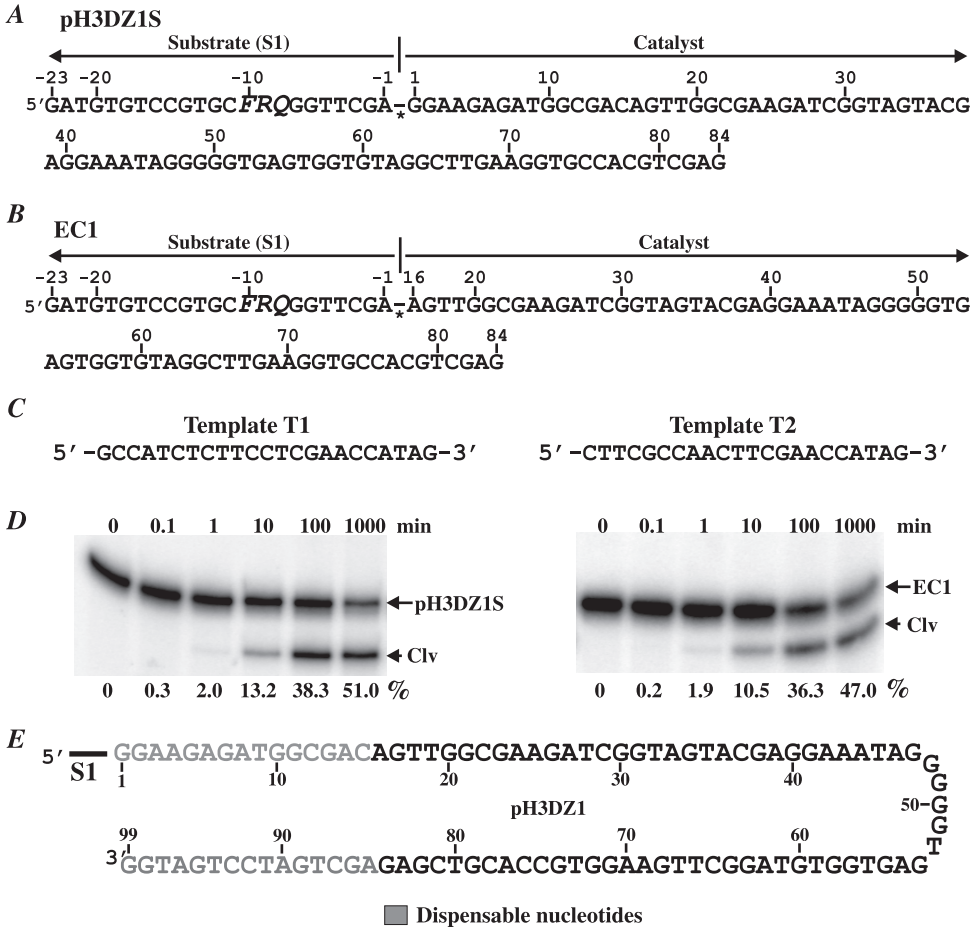
Engineering a trans-acting deoxyribozyme

Both pH3DZ1S and EC1 are cis-acting catalysts that cleave the substrate covalently attached to the catalyst. As described earlier, the process of making these cis-acting constructs was time-consuming and expensive. To expedite the sequence assessment process, we sought to derive a trans-acting (i.e., bimolecular) system where a deoxyribozyme can cleave a substrate provided as a separate molecule.

Almost all cis-acting RNA-cleaving deoxyribozymes derived by in vitro selection to perform catalysis under neutral conditions can be relatively easily converted into trans-acting deoxyribozymes because these deoxyribozymes typically use two Watson–Crick helical binding arms to recognize their substrates (47). pH3DZ1 was not expected to adopt the same strategy simply because the Watson–Crick base pairings would not apply to a DNA catalyst that functions in a highly acidic environment (because N1 of adenosine and N3 of cytosine are protonated at low pH (13)). Indeed, our attempts to identify Watson–Crick binding arms in pH3DZ1 were not successful (data not shown).

© 2007 NRC Canada

Fig. 1. Examination of the relevance of the original primer-binding sites to the catalytic activity of pH3DZ1. (*A*) The sequence of pH3DZ1S in which the 3′ primer-binding site of pH3DZ1 (5′ AGCTGATCCTGATGG3′) is deleted. This cis-acting catalyst is divided into two sequence elements, the substrate (S1) domain numbered –1 to –23 in the 3′-5′ direction and the catalyst domain numbered 1 to 84 in the 5′-3′ direction. F denotes fluorescein-deoxythymidine, R denotes riboadenosine, and Q denotes DABCYL-deoxythymidine. The symbol "*" indicates the ^{32}P-labeled phosphodiester linkage for the assay shown in (*D*). (*B*) The sequence of EC1 is a shortened version of pH3DZ1, where both of the original primer-binding sites are removed. (*C*) The sequences of T1 and T2 templates used for ligating S1 to the relevant catalyst in (*A*) and (*B*), respectively. (*D*) The cleavage activity of pH3DZ1S (image on left) and EC1 (image on right). The numbers above and below each image are the reaction time points (in minutes) and percentages of cleavage, respectively. "Clv" on the side of each image denotes the relevant cleavage product that can be detected by autoradiography. (E) The sequence of pH3DZ1 with dispensable nucleotides indicated in gray.



The finding that the constant 15-nt segment between G_1 and A_{15} is dispensable seems to suggest that we might be able to design a trans-acting catalyst simply by breaking pH3DZ1S into two separate molecules right at the substrate–catalyst junction. This manipulation indeed resulted in a fully functional bimolecular assembly made of ETA (84 nt) as the enzyme and S1 (23 nt) as the substrate (Fig. 2, panels *A* and *B*). Using the same time-course assay that was used for pH3DZ1S and EC1, we found that ETA exhibited a cleavage activity that was very similar to the two cis-acting deoxyribozymes (comparing Fig. 1*D* with Fig. 2*B*). It should be noted that the trans systems were assessed under the following single-turnover condition: S1 = 0.5 μmol/L and ETA= 25 μmol/L (S1–ETA 1:50).

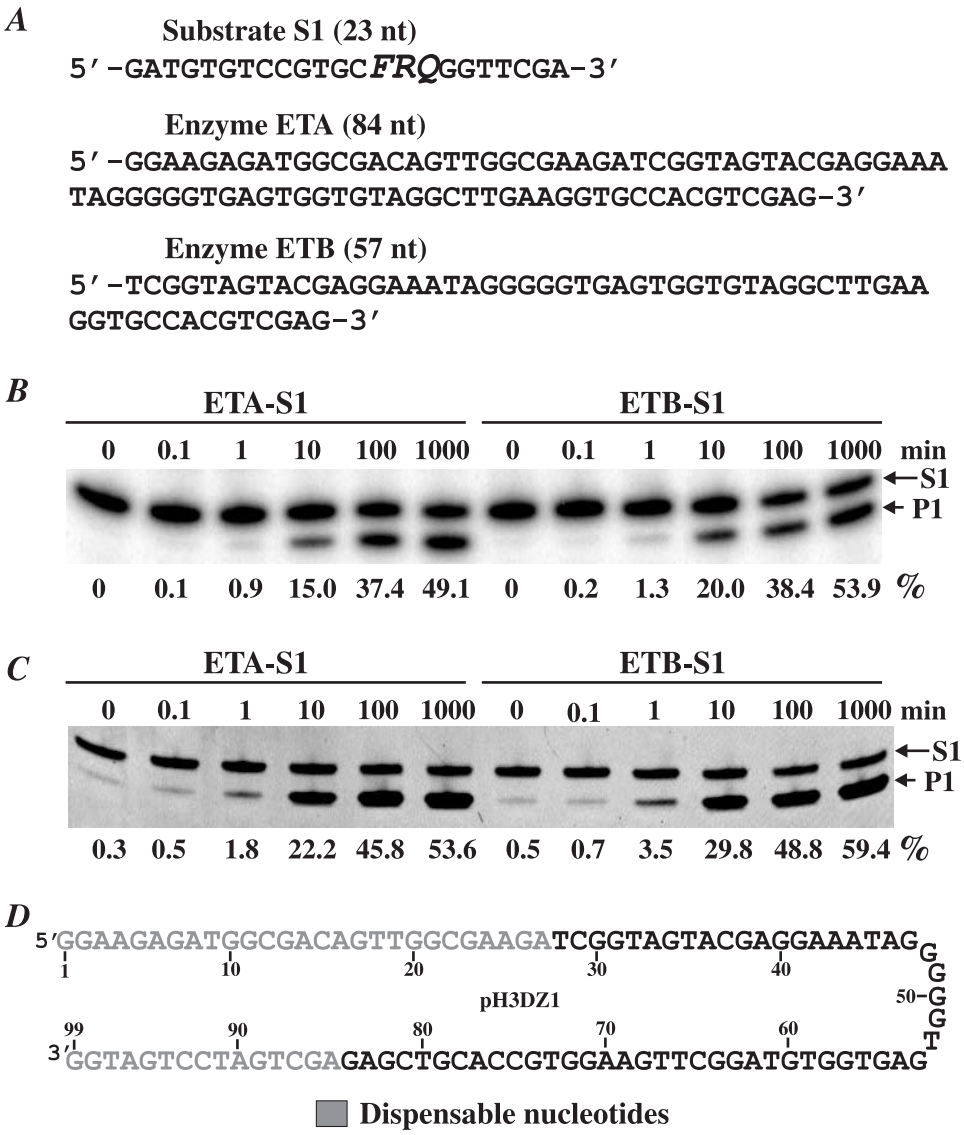
Interestingly, we further found that 27 nucleotides from the 5′-end of ETA could be completely removed; the resultant catalyst, named ETB (its sequence is given in Fig. 2*A*), was as active as ETA in processing S1 (Fig. 2*B*). Based on this observation, ETB was adopted as the reference deoxyribozyme for the subsequent sequence truncation experiments to be detailed in the next section.

Up to this point, the activity of the deoxyribozyme constructs was assessed using radioactive (via ^{32}P-label) deoxyribozyme–substrate constructs and autoradiography (phosphorimaging). Since the substrate sequence also contains the fluorescein label, the activity of the deoxyribozymes can also be followed with fluorescence imaging (fluorimaging) (35). Therefore, we also performed the fluorescence scan of the same time-course gel shown in Fig. 2*B* and the result is shown in Fig. 2*C*.

Because the substrate S1 also has a DABCYL quencher placed two nucleotides away from the fluorescein, the substrate would have a low level of fluorescence due to fluorescence quenching. The cleaved product P1, however, would

© 2007 NRC Canada

Fig. 2. Design of trans-acting deoxyribozymes. (*A*) The sequence of trans-acting deoxyribozyme systems. S1 is the external substrate for the two fully active trans-acting pH3DZ1 constructs denoted ETA (84 nt) and ETB (57 nt). ETB has the same sequence as ETA except that the 27 nucleotides located at the 5′ end of ETA are deleted. (*B*) and (*C*) The cleavage activity of ETA and ETB towards S1. The numbers above and below each image are the reaction time points (in minutes) and percentages of cleavage, respectively. S1 was labeled with 5′-^{32}P-phosphate. "P1" on the side of each image denotes the 5′-cleavage fragment that can be detected by phosphorimaging (*B*) and fluorimaging (*C*). The percent cleavage in (*B*) and (*C*) was calculated by eqs. [2] and [1] described in the text, respectively. (*D*) The sequence of pH3DZ1 with dispensable nucleotides indicated in gray.



produce an enhanced fluorescence. It was previously found that the cleavage of such substrates could generate an approximately 6-fold increase of fluorescence in the PAGE-based assay (48, 49). Indeed, we noticed that scanning the cleavage gel by fluorimaging provided much more sensitive visual results for low cleavage activity. Using the 1 min incubation of ETA-S1 as an example, in the phosphorimaging scan the cleavage product band was barely visible (Fig. 2*B*, lane 3), while in the fluorimaging scan the product band was much more evident (Fig. 2*C*, lane 3). Because of this observation, we chose to assess the cleavage activity of deoxyribozyme constructs by fluorimaging in the remaining experiments.

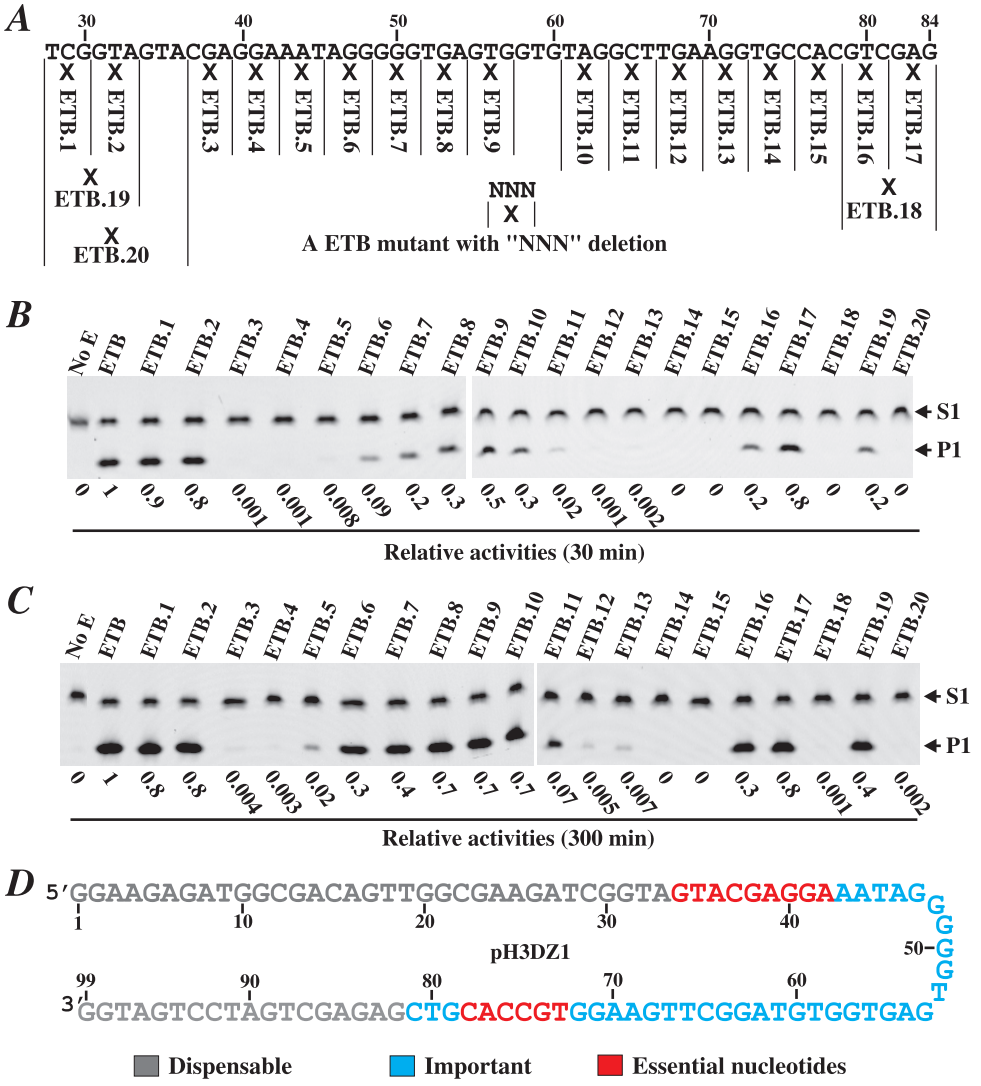
We calculated the cleavage percentages based on the fluorescence intensity for both ETA–S1 and ETB–S1 and compared the values to those derived by radioactivity assessment. The data are given in Fig. 2*C*. Since the cleavage product was about 6-fold more fluorescent than the substrate, we computed the cleavage percentage from fluorimaging using eq. [1],

$$[1] \quad \text{Percent cleavage} = 100\% \times (F_{\text{product}} / 6) / [F_{\text{substrate}} + (F_{\text{product}} / 6)]$$

where F_{product} and $F_{\text{substrate}}$ represent the fluorescence intensity of the cleaved product P1 and uncleaved substrate S1, respectively. In comparison, the cleavage percentage from phosphorimaging was calculated using eq. [2],

© 2007 NRC Canada

Fig. 3. Deletion mutants of deoxyribozyme ETB. (*A*) The sequence of ETB and its deletion mutants with specified nucleotides truncated. For example, ETB.13 is an ETB mutant with the deletion of $A_{70}G_{71}G_{72}$. Most of the ETB mutants carry a 3-nt deletion except for ETB.18 (6-nt deletion), ETB.19 (6-nt deletion), and ETB.20 (9-nt deletion). (*B*) and (*C*) The fluorimage of the cleavage activity of the truncated trans-acting mutants towards S1 at 30 min and 300 min, respectively. "S1" and "P1" on the side of each image denote the substrate and its 5′-cleavage fragment. The activity of each mutant deoxyribozyme is normalized in reference to ETB using eq. [2] described in the text. (*D*) The sequence of pH3DZ1 with component nucleotides categorized as "dispensable", "important", and "essential" according to the truncation data to this point.



[2] Percent cleavage = 100%

$$\times R_{product} / (R_{substrate} + R_{product})$$

where $R_{product}$ and $R_{substrate}$ are the radioactivity of the cleaved product and uncleaved substrate, respectively.

We found that the cleavage activities computed by both methods are largely in agreement with each other. For example, for the 10 and 100 min time points, 15.0% and 37.4% cleavage were observed for ETA–S1 by the phosphorimaging method, while 22.2% and 45.8% cleavage were registered by the fluorimaging method.

We briefly examined the turnover ability of the trans-acting ETB. When ETB (0.1 µmol/L) was mixed with S1 (10 µmol/L) under our standard reaction conditions, 1, 4, 9, and 17 turnovers were observed after the mixture was incubated for 0.5, 2, 4, and 8 h, respectively. This finding indicates that ETB is a "true" enzyme and is capable of ~2 turnovers per hour. The full kinetic characterization of trans-acting ETB will be the subject of a future investigation and the results will be reported elsewhere.

Finally, Fig. 2*D* provides an update on the nucleotide dispensability in the sequence of pH3DZ1 (comparing Figs. 1*E* and 2*D*).

Assessing truncation mutants of ETB

We next synthesized and assessed a series of truncation mutants of ETB by making sequential 3-nt deletions starting from T_{28} and ending at G_{84} (ETB.1 to ETB.17). Two 6-nt (ETB.18 and ETB.19) and one 9-nt (ETB.20) deletion mutants were also examined. Figure 3*A* illustrates the deletion

© 2007 NRC Canada

map. The cleavage activity of the examined mutants (revealed by fluorimaging) is provided in Figs. 3*B* and 3*C*. It should be noted that each deoxyribozyme was assessed in two reaction time points, a 30 min reaction (Fig. 3*B*, a time point designed to reveal mutants with a strong activity) and a 300 min incubation (Fig. 3*C*, to test for weakly active mutants). To provide a quantitative comparison of the activity of the mutant deoxyribozymes, we normalized the activity of each mutant against ETB using eq. [3],

$$[3] \quad \text{Relative activity} = \%\ \text{cleavage of a mutant} / \%\ \text{cleavage of ETB}$$

where % cleavage is calculated by eq. [1]. The calculated data are given at the bottom of the PAGE gels in Figs. 3*B* and 3*C*.

The results presented in Fig. 3 reveal some important information about the sequence requirements of pH3DZ1. First, two sequence elements, those between G_{34} and T_{45} and those between T_{67} and C_{78}, are extremely critical to the function of pH3DZ1, as the deletion of any 3 sequential nucleotides in these regions resulted in mutant deoxyribozymes that were either completely inactive (ETB.3, ETB.4, ETB.14, and ETB.15) or barely active (ETB.5, ETB.12, and ETB.13). Second, the sequence element covering T_{46}–T_{66} is highly important; truncation of any 3-nt element in this region produced mutant deoxyribozymes with either medium activity (ETB.7, ETB.8, ETB.9, and ETB.10) or severely reduced activity (ETB.6 and ET.11).

Moreover, the findings that ETB.16 (3-nt deletion), ETB.17 (3-nt deletion), and ETB.18 (6-nt deletion covering nucleotide deletions of both ETB.17 and ETB.18) were weakly active, strongly active, and completely inactive, respectively, point to the following: (*i*) the $G_{82}A_{83}G_{84}$ motif is dispensable, (*ii*) the $G_{79}T_{80}C_{81}$ motif plays an important role for catalysis, and (*iii*) more importantly, G_{79} is a critical residue. The last point in particular can be justified by comparing the reduced activity of ETB.16 (we speculate that the critical role of G_{79} in this mutant was fulfilled by G_{82}) and the loss of activity of ETB.18 (in which both G_{79} and G_{82} are absent).

Finally, comparing the activities of the four mutant deoxyribozymes with various nucleotides truncated from the 5′-end (i.e., ETB.1 and ETB.2 having two sequential 3-nt deletions; ETB.19 with a 6-nt truncation that covers both ETB.1 and ETB.2; and ETB.20 with three additional nucleotides removed beyond ETB.19) led to the following comments: (*i*) the $T_{28}C_{29}G_{30}$ sequence element is dispensable (revealed by the strong activity of ETB.1), (*ii*) only one of the two tandem GTA elements located near the 5′-end ($G_{31}T_{32}A_{33}$ and $G_{34}T_{35}A_{36}$) is required for the function of pH3DZ1 (revealed by the strong activity of ETB.2 and the loss of activity of ETB.20), and (*iii*) at least one nucleotide needs to be retained prior to $G_{34}T_{35}A_{36}$ for the full activity of the deoxyribozyme (revealed by the medium activity of ETB.19).

Figure 3*D* provides an updated summary of nucleotide requirements for the function of pH3DZ1 (where dispensable, important, and essential nucleotides are colored gray, light-blue, and red, respectively) after taking into consideration the sequence truncation results.

In vitro selection experiment to further identify the functionally essential nucleotides

The truncation experiments discussed earlier indicate that the minimized deoxyribozyme ETB.2 contains all of the catalytically important or essential nucleotides. To assess the importance of individual nucleotides within the shortened deoxyribozyme, we conducted a reselection experiment using a mutant deoxyribozyme library synthesized based on the sequence of ETB.2. The sequences of all DNA molecules used for reselection are shown in Fig. 4*A*. The library sequence is denoted L1 in which the nucleotides corresponding to G_{31}–G_{84} of the original pH3DZ1 were partially mutagenized (76% of the original nucleotide and 24% of the equal mixture of other three nucleotides at each relevant position, following a previous protocol (50)) during chemical synthesis of the library. However, new constant regions were added to this catalytic motif as primer binding arms for the purpose of avoiding the cross-contamination by the original pH3DZ1.

The reselection scheme is depicted in Fig. 4*B*, which is similar to that used for the original selection (34). Briefly, each selection cycle consists of eight steps. In step I, 87-nt DNA L1 is ligated to the 17-nt substrate S2. The ligated 104-nt DNA is purified by PAGE (step II) and then allowed to self-cleave in the selection–assay buffer (step III). The 89-nt cleavage fragment is isolated by PAGE (step IV) and amplified by PCR using primers P1 and P2 (step V). The resulting 105-bp PCR product is used as the template for second PCR using primers P2 and P3 for the introduction of a ribonucleotide linkage embedded in front of the L1 sequence (step VI). After treatment with NaOH to cleave the ribonucleotide linkage (step VII), the 87-nt cleavage fragment is purified by PAGE, phosphorylated at the 5′-end (step VIII), and used to initiate the next selection cycle.

We chose to use a relatively long reaction time (5 h) for the purpose of identifying catalytically essential nucleotides. The progress of the selection is shown in Fig. 4*C*. Although there was no detectable cleavage activity from the initial library (generation 0 or G0), 8% and 22% of the molecules in G1 and G2 were found to self-cleave, respectively. Surprisingly, the activity of G3 (12% cleavage) was lower than that of G2, and we attribute this abnormality to some unidentified experimental errors. By G4 and G5, the cleavage activity was observed to reach saturation at ~40%. Because of this, G5 was cloned and 31 clones were successfully sequenced.

Figure 5*A* lists the sequences of these deoxyribozyme mutants (the primer-binding arms are omitted for clarity) along with a variation index (V.I.) chart compiled according to a previously published protocol (51). Briefly, the V.I. value for each random position was derived as follows: the observed mutation rate at each position / 0.24 (the mutation rate of the starting library). A V.I. value of 0 indicates that the base of the given nucleotide is absolutely conserved in all of the sequenced clones. If the base of a given nucleotide is not specifically involved in catalysis, the V.I. value is expected to be close to 1. Bases with V.I. values significantly smaller

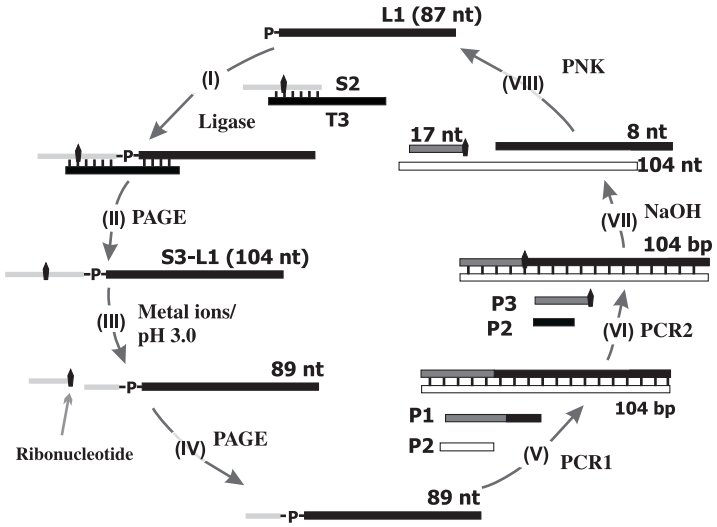
© 2007 NRC Canada

Fig. 4. Reselection of pH3DZ1 variants. (*A*) All the sequences used for reselection. L1 is the library where lower case letters indicate the primer-binding arms and the upper case letters indicate the partially randomized nucleotides. P1, P2, and P3 are forward, reverse, and ribo-terminated DNA primers for PCR, respectively. T3 is the template for the ligation of substrate S2 and L1. (*B*) Selection scheme. Each selection cycle consists of steps I–VIII. (I) 87-nt DNA L1 is ligated to 17-nt substrate S2. (II) Ligated 104-nt DNA is isolated by PAGE. (III) Purified 104-nt DNA is incubated with metal ions at pH 3 for RNA cleavage. (IV) The 89-nt cleavage fragment is isolated by PAGE. (V) The recovered 89-nt DNA is amplified by PCR using primers P1 and P2. (VI) 105-bp PCR product in (V) is further amplified by PCR using primers P2 and P3 to introduce a ribonucleotide linkage embedded in front of the L1 sequence. (VII) The resulting double-stranded DNAs are treated with NaOH to cleave the ribonucleotide linkage. (VIII) The cleavage fragments are phosphorylated at 5′ end and used to initiate the next round. (*C*) Reselection progress. Percentage of cleavage is plotted against selection rounds.

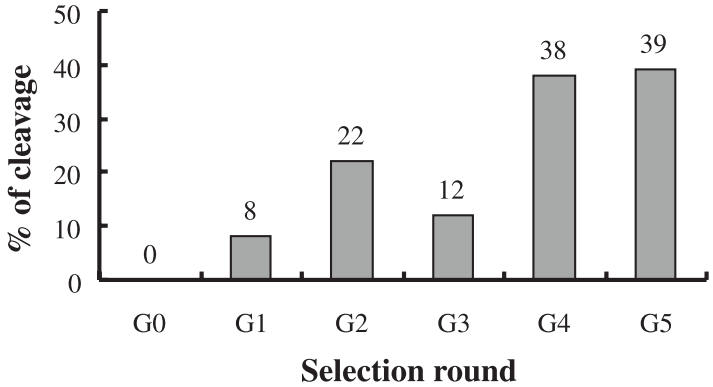
A

```
L1: 5′-gttcgacgaagatcgGTAGTACGAGGAAATAGGGGGTGAGTGGT
    GTAGGCTTGAAGGTGCCACGTCGAGgcttactcatgtgctagc-3′
S2: 5′-GATGTGTCCGTGCFRQG-3′
P1: 5′-ATCATAATGTATTCATGGTTCGACGAAGATCG-3′
P2: 5′-GCTAGCACATGAGTAAGC-3′
P3: 5′-ATCATAATGTATTCATGr-3′
T3: 5′-CGATCTTCGTCGAACCATATGACGGACACATC-3′
```

B



C

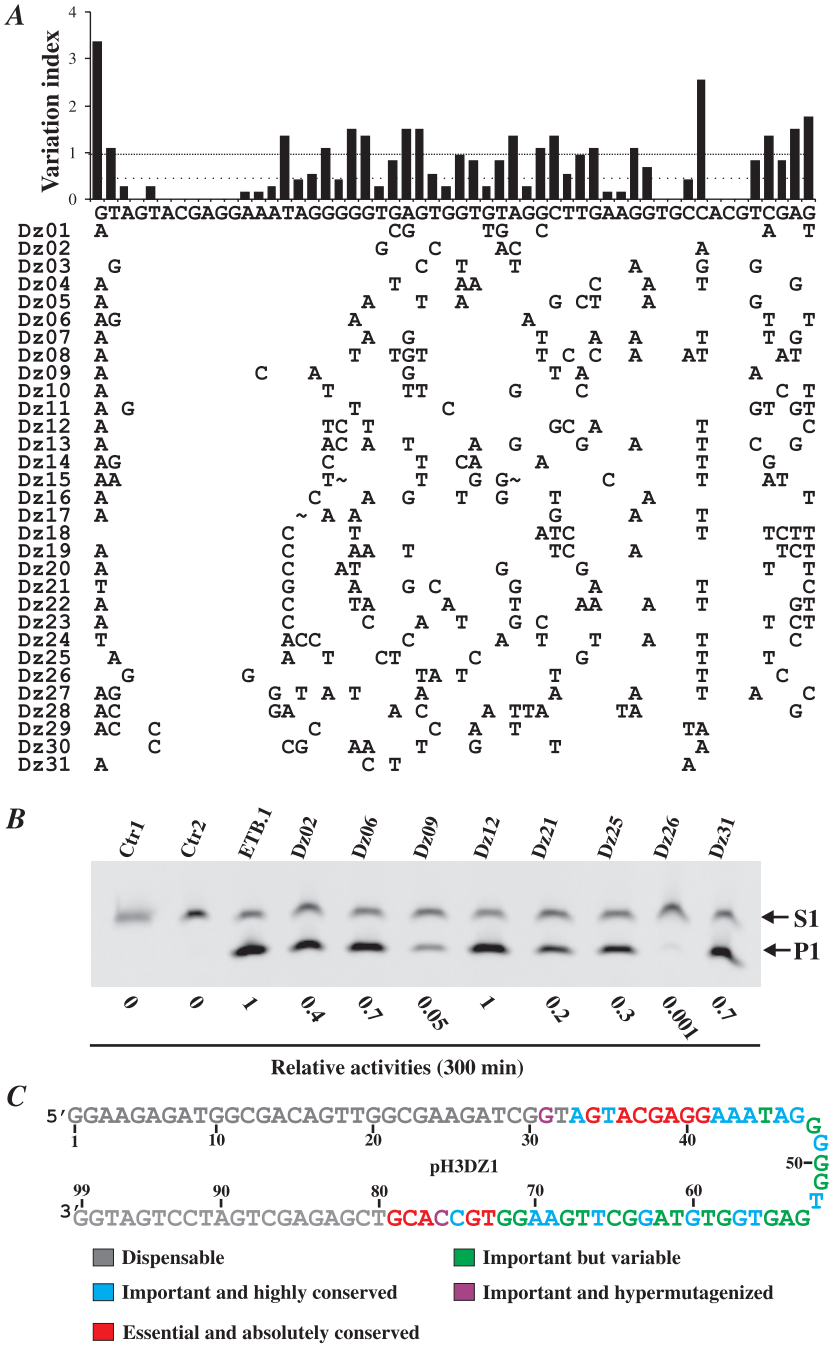


than 1 (such as 0.5 marked on the variation index chart) are taken as important residues for catalysis. V.I. values larger than 1 could mean that the base(s) observed in the selected mutants may offer a selective advantage over the original base (51).

The data in Fig. 5*A* reveal that 12 nucleotides within pH3DZ1 are absolutely conserved (red nucleotides in Fig. 5*C*) and they are G_{34}, A_{36}, C_{37}, G_{38}, A_{39}, G_{40}, G_{41}, T_{73}, G_{74}, A_{77}, C_{78}, and G_{79}. In addition, the following seventeen nucleotides are highly conserved (with V.I. values at 0.5 or smaller; Fig. 5*C*, light-blue nucleotides): A_{33}, T_{35}, A_{42}, A_{43}, A_{44}, A_{46}, G_{47}, G_{49}, T_{52}, T_{56}, G_{57}, G_{60}, G_{63}, T_{66}, A_{69}, A_{70}, and C_{75}. Two nucleotides, G_{31} and C_{76}, (Fig. 5*C*, purple nucleotides), exhibit V.I. values significantly larger than 1. Inter-

© 2007 NRC Canada

Fig. 5. Mutant deoxyribozymes isolated from reselection. (*A*) Sequence analysis of the terminal pool. The variation index (V.I.) was complied upon sequencing 31 clones from the G5 population. The V.I. was calculated by dividing the observed mutation rate at each position by 0.24 (the mutation rate of the starting library). The wild-type sequence is shown at the bottom of V.I. chart (the constant nucleotides are omitted for clarity). The two dotted lines indicate V.I. values of 1 and 0.5, respectively. The actual mutations in each deoxyribozyme (named Dz01–Dz31) are listed; the missing letters in each sequence indicate that no mutation was observed in those locations and "~" indicates a deletion at this location. (*B*) The fluorescent image of the cleavage activity of 8 deoxyribozymes randomly chosen from (*A*), where Ctr1 is the reaction mixture at 0 min and Ctr2 is the substrate only incubated in the reaction buffer without enzyme for the same time period as the test samples. (*C*) The sequence of pH3DZ1 with component nucleotides now categorized as "dispensable", "important but variable", "important and highly conserved", "important and hypermutagenized", and "essential and absolutely conserved" according to both the truncation and reselection data.

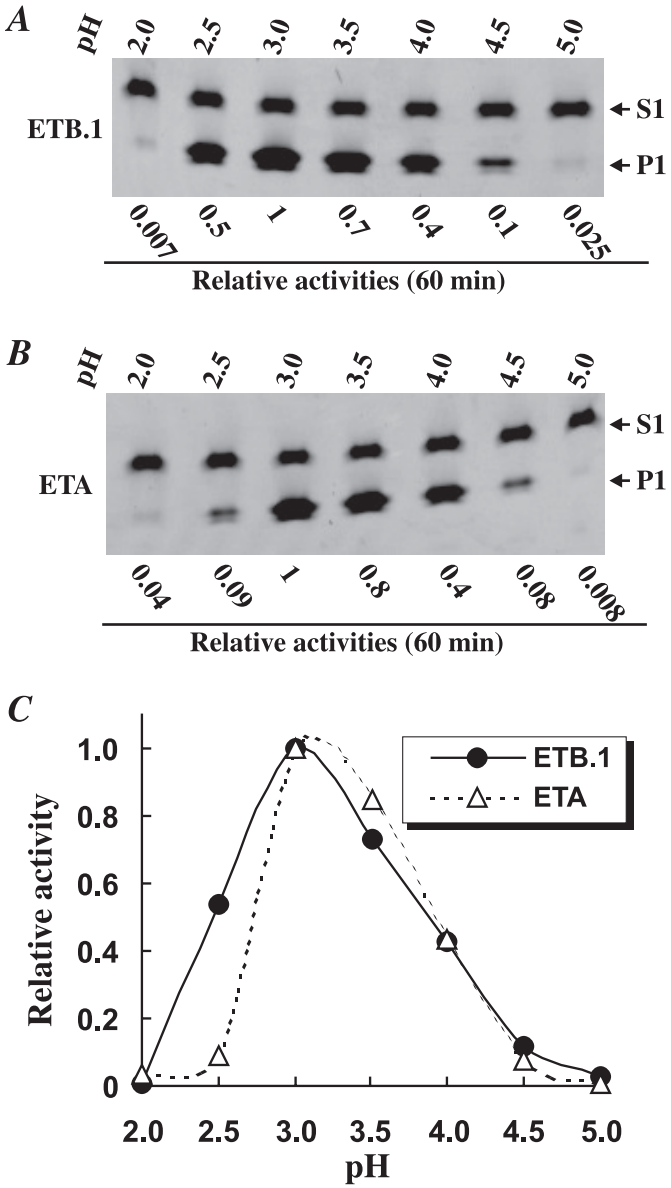


estingly, G_{31} was almost exclusively mutated to A while C_{76} predominately mutated to T (Fig. 5*A*).

The above observations are consistent with the sequence truncation data discussed earlier (see Fig. 3). For example, the absolutely conserved nucleotides fall precisely within the two crucial sequence elements between G_{34} and T_{45} and between T_{67} and C_{78}, identified through the examination of truncation mutants. Not surprisingly, the reselection experi-

© 2007 NRC Canada

Fig. 6. Comparison of pH profiles of full-size and truncated trans-acting pH3DZ1. (*A*) and (*B*) are pH-dependent cleavage activities of ETB.1 and ETA towards S1, respectively. S1 and ETB.1 or ETA were incubated under a given pH for 60 min and the cleavage products were analyzed by denaturing PAGE. "S1" and "P1" on the side of each image denote the substrate and its 5′-cleavage fragment, both of which can be detected by fluorimaging. The activity of each deoxyribozyme is normalized in reference to its activity at pH 3.0 following eq. [1] in the text. (*C*) The pH profile of ETB.1 and ETA. The relative activity of each deoxyribozyme is plotted against pH of the solution.



ment verifies the postulated essentiality of G_{79}. Likewise, the same experiment identified A_{33} as a highly conserved nucleotide, confirming our speculation that at least one nucleotide preceding G_{34} must be retained to maintain the full activity of the deoxyribozyme. Moreover, the finding that 14 nucleotides within the T_{46}–T_{66} sequence element are highly conserved substantiates the importance of this central element revealed by the truncation experiments presented in Fig. 3.

To demonstrate that the selected deoxyribozyme variants are catalytically active, we assessed the activity of the eight clones randomly chosen from the sequences listed in Fig. 5*A*. These mutant deoxyribozymes were chemically synthesized without the two primer-binding arms, incubated with the substrate S1 for 300 min (the duration time for reselection), analyzed by PAGE, which was scanned by fluorimaging (Fig. 5*B*). By normalizing the activities of these mutant deoxyribozymes against ETB.1, we found that three of these mutants (Dz06, Dz12, and Dz31) have a strong activity (with a relative activity between 0.7 and 1), three other mutants (Dz02, Dz21, and Dz25) have a medium activity (relative activity between 0.2 and 0.4), one mutant (Dz09) has a weak activity (relative activity of 0.05), and one mutant (Dz26) is barely active (relative activity of 0.001). The very weak activity of Dz26 could be rationalized by the mutational data as this mutant had two mutations occur to the extremely conserved nucleotides (i.e., A_{32} to G, A_{42} to G; their V.I. values are much smaller than 0.5); in contrast, the other more active mutants had maximally one such mutation.

Comparison of pH dependences of full-length and truncated *trans*-deoxyribozymes

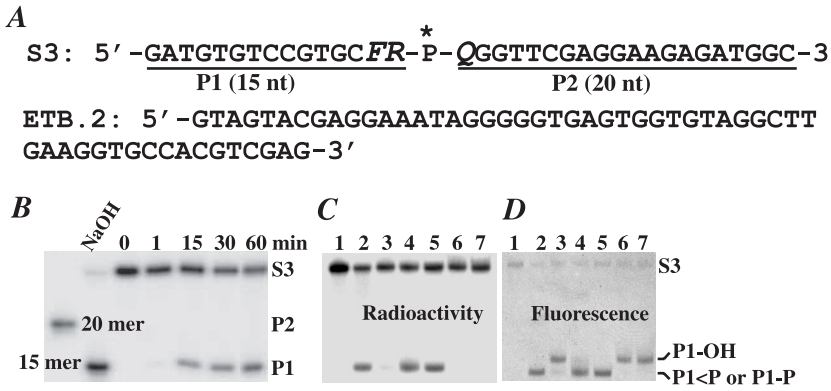
An experiment was carried out to compare pH profiles of the full-length *trans*-deoxyribozyme ETA and its shortened version ETB.1. Each deoxyribozyme was assessed for the cleavage activity towards S1 within 60 min under solution conditions with variable acidity, analyzed by denaturing PAGE, and scanned for fluorescence (Fig. 6; panel *A* for ETB.1; panel *B* for ETA). The activity of each deoxyribozyme at chosen pH points was normalized against their activity at pH 3.0, and the derived values (given under the PAGE gels in Figs. 6*A* and 6*B*) were then plotted in Fig. 6*C*. We found that the profile of ETA was almost identical to that of the cis-acting full-length pH3DZ1 (34). The pH dependences of ETA and ETB.1 were also quite similar: both deoxyribozymes had the highest activity at pH 3.0 and showed a progressive decrease in activity when the pH of the solution was raised from 3.0 to 5.0; both were almost inactive when the pH was increased to 5.0 or decreased to 2.0. However, there was one significant difference in that ETB.1 retained a substantial activity at pH 2.5, whereas ETA was only weakly active at this pH. The precise reasons for this deviation are not clear to us at the moment; however, we speculate that the 45 nucleotides removed from the 5′-end of ETA might contain nucleotides (or a sequence element) that exhibit inhibitory effects towards the function of the catalytic core at pH 2.5.

Characterization of cleavage products

To characterize the cleavage products produced by pH3DZ1, we followed a previously published protocol that utilizes a specially labeled substrate containing ^{32}P-labeled phosphodiester linkage at the cleavage site that permits the tracing of the transfer of the phosphorous atom from the substrate to the cleavage products (52). The substrate (denoted S3) was produced by ligating a matching 5′-^{32}P-labeled oligonucleotide to a relevant 3′-ribo-terminated

© 2007 NRC Canada

Fig. 7. Characterization of the products of pH3DZ1-mediated RNA-cleavage. (*A*) Sequences of substrate S3 with ^{32}P-labeled phosphodiester linkage (denoted by **P***) at the cleavage site and the trans-acting deoxyribozyme ETB.2. (*B*) Tracing phosphoester transfer. S3 was first incubated with ETB.2 for 0, l, 15, 30, and 60 min; the resultant reaction mixtures were then analyzed by 10% denaturing PAGE. Upon cleavage, S3 was converted into a visible (radioactive) 5′-cleavage fragment P1 (15 nt) and invisible (nonradioactive) 3′-cleavage fragment P2 (20 nt). The first lane shows 5′-^{32}P-labeled P2; the second lane shows the cleavage product produced when S3 was reacted with NaOH (0.25 mol/L) for 10 min at 90 °C. (*C*) and (*D*) Determination of the chemical nature of the phosphate at the end of P1 by enzymatic digestion. P1 was further found to contain a 2′,3′-cyclic phosphate terminus using T4 polynucleotide kinase (PNK), calf intestine alkaline phosphatase (CIAP), and 2′,3′-cyclic nucleotide 3′-phosphodiesterase (CNPase). Lane 1: S3 alone; lane 2: S3 incubated with ETB.2 for 60 min; lanes 3–7: S3 incubated with ETB.2 (60 min) followed by PNK (lane 3), CIAP (lane 4), CNPase (lane 5), first CNPase then PNK (lane 6), first CNPase then CIAP (lane 7). Each reaction mixture was analyzed on 10% denaturing PAGE. The images in (*C*) and (*D*) were taken from the same gel using phosphorimaging and fluoroimaging



oligonucleotide; this produced S3 with ^{32}P-labeled phosphodiester linkage right at the cleavage junction (Fig. 7, marked with "*"). When S3 was incubated with ETB.2 for various time points, only one cleavage product was observed on the autoradiograph (Fig. 7*B*). Since the visible cleavage fragment had the same gel mobility as the 15-nt DNA ladder (but not the 20-nt DNA ladder), we can conclude that the 5′-cleavage fragment (P1) acquired a terminal phosphate at the 3′-end, while the 3′-cleavage fragment (P2) had an unphosphorylated 5′-hydroxyl group.

We next examined whether the terminal phosphate of P1 was in the form of a 2′,3′-cyclic phosphate or a 2′- and (or) 3′-monophosphate through treatment of three protein enzymes: T4 polynucleotide kinase (T4 PNK, which has both 2′,3′-cyclic nucleotide 3′-phosphodiesterase activity and 2′- and 3′-phosphatase activity), calf intestine alkaline phosphatase (CIAP, which has 2′- and 3′-phosphatase activity but does not have 2′,3′-cyclic phosphodiesterase activity), and 2′,3′-cyclic nucleotide 3′-phosphodiesterase (CNPase, which has the ability to hydrolyze 2′,3′-cyclic phosphate solely to 2′-phosphate) (52). When the ETB.2–S3 reaction mixture (Fig. 7*C*, lane 2) was incubated with PNK (Fig. 7*C*, lane 3), P1 lost its radioactivity; when incubated with CIAP (Fig. 7*C*, lane 4), P1 retained its radioactivity. These two observations strongly suggest that P1 has a 2′,3′-cyclic phosphate. When the same reaction mixture was first treated with CNPase and then further treated with either CIAP (Fig. 7*C*, lane 6) or PNK (Fig. 7*C*, lane 7), the radioactivity of P1 was lost (note that the radioactivity of P1 remained unchanged when it was treated with CNPase alone; Fig. 7*C*, lane 5). The fluorescence scan of the same gel (Fig. 7*D*) further verified the loss of the terminal phosphate from P1 after the digestion with PNK (Fig. 7*C*, lane 3), CNPase–CIAP (Fig. 7*C*, lane 6), and CNPase–PNK (Fig. 7*C*, lane 7): the dephosphorylated P1 was expected to migrate relatively slower because of the loss of the negative charges associated with the phosphate group. From these analyses, we conclude that the cleavage of S3 by ETB.2 produces a 5′-cleavage fragment with a 2′,3′-cyclic phosphate and a 3′-cleavage fragment with a 5′-OH. It is interesting to note that the same products are found for all naturally occurring self-cleaving ribozymes and all man-made RNA-cleaving nucleic acid enzymes (47, 52).

Discussion

Most artificial nucleic acid enzymes (ribozymes and deoxyribozymes) were derived to perform catalysis at neutral pH. However, several ribozymes and deoxyribozymes that can catalyze chemical transformations in acidic environments have also been reported. These include a self-cleaving ribozyme (53), an RNA-cleaving deoxyribozyme (34, 50), and an RNA-ligating ribozyme (54, 55) that perform their catalytic functions at pH 4; an RNA-cleaving deoxyribozyme with optimal activity at pH 4.8 (34); an RNA-ligating ribozyme that operates at pH 5.8 (56); and an RNA-cleaving deoxyribozyme with best activity at pH 6 (34, 48). The existence of this array ribozymes and deoxyribozymes that are functional at low pH strongly indicates that the catalytic power of nucleic acids is not lost in acidic environments. Among these acidic nucleic acid enzymes, pH3DZ1 is the only catalyst that can still perform catalysis in a highly acidic environment at pH 3.

pH3DZ1 was originally isolated from a random-sequence DNA pool as a cis-acting deoxyribozyme to carry out the reaction of cleaving a covalently attached chimeric RNA–DNA substrate at a single RNA linkage in a highly acidic solution (pH 3.0) (34). In the present work, we have converted pH3DZ1 from a cis-acting catalyst into a trans-acting deoxyribozyme that is capable of cleaving an external substrate. Through comprehensive sequence truncations, we have reduced the size of the trans catalyst from 99 nt to 51 nt, with the removal of 30 and 18 residues from the 5′ and

© 2007 NRC Canada

3′ ends of the catalyst, respectively. Internal nucleotide truncation experiments showed that the minimized trans catalyst contains two essential short sequence elements flanking a larger central sequence motif. This central element appears to play important (but not essential) roles in the catalytic function of pH3DZ1, based on the observation that deleting as few as 3 nucleotides anywhere in this region severely reduced the activity of the trans catalyst.

A reselection experiment was subsequently performed, which led to the identification of 12 absolutely conserved, 17 highly conserved, and 2 hyper-mutated nucleotides. Not surprisingly, all absolutely conserved nucleotides are distributed in the two essential sequence elements, with 7 nt at the 5′ end of the minimized catalyst and 5 nt at the 3′ end. The reselection experiment also revealed that the central sequence element contained 14 of the 17 highly conserved nucleotides, which explains why each 3-nt deletion within this region caused significant reduction in the activity of the deoxyribozyme.

It is reasonable to speculate that many (if not all) of the absolutely conserved nucleotides at the two ends of the minimized catalyst are involved both in the construction of the catalytic site and in the catalyst–substrate recognition, and the substrate-binding and (or) catalytic roles rendered by these essential nucleotides also require the additional support provided by the nucleotides in the central sequence element. The precise structure of pH3DZ1 can only be revealed by high-resolution techniques including NMR and X-ray crystallography, which will be the subject of future experimentation.

Many RNA-cleaving deoxyribozymes that cleave a standard RNA substrate or an RNA–DNA chimeric substrate under neutral pH have been isolated from random-sequence DNA pools by in vitro selection experiments (19, 28–39, 41, 57–65). The optimized pH3DZ1 is different from the known neutral pH-functional RNA-cleaving deoxyribozymes such as 10–23 and 8–17 in the following aspects. First, neutral deoxyribozymes are relatively small in size. Both 10–23 and 8–17 are made of less than 30 nucleotides, roughly half of which were used as the catalytic core and the other half as two substrate-binding arms (30, 37). The minimized pH3DZ1 is about twice as large, requiring ~50 nucleotides for the full catalytic activity. Second, the neutral RNA-cleaving deoxyribozymes whose secondary structures have been characterized interact with their substrates through the formation of two short Watson–Crick helices. Because of extensive protonation at the N1 atom of adenosine and the N3 atom of cytosine (both of which are hydrogen-bonding sites in Watson–Crick base pairs) at pH 3, DNA is not expected to adopt Watson–Crick interactions in this highly acidic environment. We speculate that the lack of simple yet effective Watson–Crick interactions might be the key reason behind the increased size of pH3DZ1, because pH3DZ1 may require a large number of nucleotides for the formation of more complex tertiary structure.

The two unique properties associated with pH3DZ1, its optimal activity in highly acidic solutions and its synchronized catalysis-signaling capability, may offer an opportunity for creating unique molecular sensors for unconventional applications. It is conceivable that the in vitro selection approach could be utilized again to select low pH-functional allosteric deoxyribozymes from random-sequence pools with a built-in minimized pH3DZ1 sequence. Such molecular sensors might be useful for detecting organic molecules soluble only in highly acidic aqueous solutions, for monitoring chemical (or enzymatic) reactions that can only be carried out in acidic environment, or for analyzing biological samples under highly acidic conditions for the purpose of inactivating nucleases. We are currently testing these ideas and will report our findings in future publications.

Materials and methods

All the DNA oligonucleotides used in this study were synthesized by automated DNA–RNA synthesis (W.M. Keck Oligonucleotide Synthesis Facility, Yale University, New Haven, Connecticut, and Integrated DNA Technologies) following the standard phosphoramidite chemistry. The partially randomized DNA library used for reselection was synthesized using the following mixture of the four standard phosphoramidites (produced by manual mixing): 76% of the wild-type nucleotide and 8% of each of the remaining 3 nucleotides using a protocol described previously (50). Before use, DNA oligonucleotides were purified by 10% denaturing (8 mol/L urea) PAGE. The triisopropylsilyloxymethyl (TOM) group of the DNA–RNA chimeric substrate was removed following the previously reported method (35). Radioactive nucleotides ([γ-^{32}P]ATP and [α-^{32}P]dGTP) were purchased from GE Healthcare. T4 DNA ligase, T4 polynucleotide kinase (PNK), and deoxynucleoside 5′-triphosphates (dNTPs) were purchased from MBI Fermentas. All other chemical reagents were purchased from Sigma-Aldrich and used without further purification.

All catalytic assays and reselection experiments were conducted in the selection–assay buffer containing citric acid (50 mmol/L), NaCl (500 mmol/L), with the acidity of the solution adjusted to pH 3.0 at 25 °C. The 2× stop solution contained EDTA (80 mmol/L, pH 8.0, 25 °C), urea (16 mol/L), Tris (180 mmol/L), boric acid (180 mmol/L), sucrose (20% *w*/*v*), xylene cyanol (0.05%) and bromophenol blue (0.05%). The DNA phosphorylation and ligation reactions were performed according to the manufacturer protocols.

Assessing activity of cis-acting deoxyribozymes

For cleavage reactions involving cis-acting deoxyribozymes, the deoxyribozymes were first ligated with the 23-nt substrate (its sequence is given in Fig. 1*A*) following the previously reported protocol (35). The ligated construct was then purified by 10% PAGE. This deoxyribozyme (1 pmol in 2.5 μL H_2O) was heated at 90 °C for 30 s and then cooled to room temperature (RT) for 5 min. The cleavage reaction was started with the addition of 2.5 μL of 2× selection–assay buffer at RT. The final DNA concentration was set at ~0.2 μmol/L. An aliquot of the reaction mixture was withdrawn at 0.1, 1, 10, 100, and 1000 min and quenched with the 2 × stop solution. Cleavage products were analyzed by 10% denaturing PAGE and product yields were determined by quantitating product bands using Typhoon and ImageQuant software (Molecular Dynamics).

© 2007 NRC Canada

Assessing activity of trans-acting deoxyribozymes

For cleavage reactions involving trans-acting deoxyribozymes under single-turnover conditions, 2.5 pmol of each substrate (S1) was mixed with 75 pmol of a relevant deoxyribozyme (the volume was adjusted to 2.5 μL with double distilled water), heated to 90 °C for 30 s and cooled to RT for 5 min. Then, 2.5 μL of 2× selection–assay buffer was added to initiate the cleavage reaction at RT. After the time period as indicated in the relevant figures, the reaction was stopped by adding the 2× stop solution. The cleaved products were analyzed by 10% denaturing PAGE and the product yields were visualized using Typhoon 9200 and quantitated using ImageQuant software. It should be noted that Typhoon 9200 was used for both phosphorimage and fluorimage in this study.

Reselection of pH3DZ1 mutants

A partially randomized DNA library was used to carry out the reselection according to the previously reported protocol (35) with some variations (all the DNA sequences are listed in Fig. 4*A*). Briefly, 500 pmol of gel-purified library (L1) was phosphorylated at the 5′-end with 20 μCi of [γ-^{32}P]ATP and PNK and then ligated with the substrate S2. In the first round of reselection, 100 pmol of ligated DNA in 50 μL of water was heated at 90 °C for 30 s and cooled to RT for 5 min. After addition of 50 μL of the 2× selection–assay buffer and incubation for 5 h at RT, the reaction was quenched by EDTA (pH 8.0) to a final concentration of 30 mmol/L. The cleavage fragment was isolated by 10% denaturing PAGE, amplified by PCR, and then made into single-stranded DNA, all according to the previous protocol (35). Subsequent rounds of reselection were carried out in a similar way. The DNA population after the sixth round was cloned by TA cloning technique and the plasmids from ~30 clones were sequenced, again following the previously published protocol (35).

Determination of pH profiles

The RNA cleavage activity of trans-acting deoxyribozyme ETA and ETB.1 (sequences given in Figs. 2 and 3) was assessed in solutions with pH of 2.0, 2.5, 3.0, 3.5, 4.0, 4.5, and 5.0 (pH of each final mixture). The reaction mixture containing 2.5 pmol of substrate S1 (5′-^{32}P labeled) and 75 pmol of deoxyribozyme was heated to 90 °C for 30 s and cooled to RT for 5 min. The cleavage reaction was initiated with the addition of 2.5 μL of the 2× selection–assay buffer. After incubation at RT for 30 min, the reaction was stopped by adding the 2× stop solution. The products were analyzed by 10% denaturing PAGE. The bands were visualized by Typhoon 9200 and quantified by ImageQuant software.

Characterization of cleavage products

Preparation of substrate (S3)

Five hundred pmol of P2 was radiolabeled at the 5′-end with γ-^{32}P[ATP] and covalently ligated to P1 following the reported method (52). This ligated 35-nt substrate (sequence shown in Fig. 7) was purified by 10% denaturing PAGE.

Determination of cleavage products by enzymatic digestion

S3 (0.5 μmol/L) was allowed to cleave in the presence of ETB.2 (15 μmol/L, 60 μL reaction volume) for 1 h under the same selection–assay condition as described earlier. The cleaved products were isolated by ethanol precipitation (four times) and the pellet was resuspended in 24 μL of deionized water. One μL of this DNA solution was used for each enzymatic probing reaction that involved PNK, CIAP, CNPase, CNPase–PNK, and CNPase–CIAP, respectively. Both PNK- and CIAP-mediated reactions were carried out at 37 °C for 1 h in a 10 μL reaction mixture containing 10 units of either PNK or CIAP in a reaction buffer supplied by the manufacturer. The CNPase-mediated hydrolysis of 2′,3′-cyclic phosphate was conducted at 37 °C for 1 h in a 6 μL mixture containing ~5.0 units of CNPase, Tris–HCl (50 mmol/L, pH 7.5 at 25 °C), NaCl (50 mmol/L), DTT (1 mmol/L), and glycerol (10%). To this reaction mixture, PNK (or CIAP) buffer was added, followed by the addition of PNK (or CIAP); the final reaction volume reached 10 μL. Each mixture was incubated at 37 °C for another hour. Following the inactivation of the concerned enzyme at 90 °C for 2 min, the DNA fragments in the mixture were separated by 10% denaturing PAGE and analyzed using Typhoon 9200 and ImageQuant software.

Acknowledgement

This work was partially supported by research grants from Canadian Institutes for Health Research (CIHR), the Natural Sciences and Engineering Research Council of Canada (NSERC) through a network grant, SENTINEL (Canadian Network for the Development and Use of Bioactive Paper), the Canada Foundation for Innovation and the Ontario Innovation Trust. YL is a Canada Research Chair.

References

1. N.K. Navani and Y. Li. Curr. Opin. Chem. Biol. **10**, 272 (2006).
2. L. Murphy. Curr. Opin. Chem. Biol. **10**, 177 (2006).
3. S. Tombelli, M. Minunni, and M. Mascini. Biosens. Bioelectron. **20**, 2424 (2005).
4. N.L. Rosi and C.A. Mirkin. Chem. Rev. **105**, 1547 (2005).
5. M.M. Cheng, G. Cuda, Y.L. Bunimovich, M. Gaspari, J.R. Heath, H.D. Hill, C.A. Mirkin, A.J. Nijdam, R. Terracciano, T. Thundat, and M. Ferrari. Curr. Opin. Chem. Biol. **10**, 11 (2006).
6. E. Katz and I. Willner. Angew Chem. Int. Ed. **43**, 6042 (2004).
7. N.C. Seeman. Trends Biochem. Sci. **30**, 119 (2005).
8. N.C. Seeman. Nature (London), **421**, 427 (2003).
9. B. Yurke, A.J. Turberfield, A.P. Mills, Jr., F.C. Simmel, and J.L. Neumann. Nature (London), **406**, 605 (2000).
10. Y. Benenson, T. Paz-Elizur, R. Adar, E. Keinan, Z. Livneh, and E. Shapiro. Nature (London), **414**, 430 (2001).
11. H. Yan, X. Zhang, Z. Shen, and N.C. Seeman. Nature (London), **415**, 62 (2002).
12. J.C. Achenbach, W. Chiuman, R.P. Cruz, and Y. Li. Curr. Pharm. Biotechnol. **5**, 321 (2004).
13. G.F. Joyce. Annu. Rev. Biochem. **73**, 791 (2004).
14. D.S. Wilson and J.W. Szostak. Annu. Rev. Biochem. **68**, 611 (1999).

© 2007 NRC Canada

15. S.K. Silverman. Org. Biomol. Chem. **2**, 2701 (2004).
16. R. Fiammengo and A. Jaschke. Curr. Opin. Biotechnol. **16**, 614 (2005).
17. Y. Li and R.R. Breaker. Curr. Opin. Struct. Biol. **9**, 315 (1999).
18. A. Peracchi. ChemBioChem. **6**, 1316 (2005).
19. R.R. Breaker and G.F. Joyce. Chem. Biol. **1**, 223 (1994).
20. A.D. Ellington and J.W. Szostak. Nature (London), **346**, 818 (1990).
21. C. Tuerk and L. Gold. Science (Washington, D.C.), **249**, 505 (1990).
22. B. Cuenoud and J.W. Szostak. Nature (London), **375**, 611 (1995).
23. A. Sreedhara, Y. Li, and R.R. Breaker. J. Am. Chem. Soc. **126**, 3454 (2004).
24. A. Flynn-Charlebois, T.K. Prior, K.A. Hoadley, and S.K. Silverman. J. Am. Chem. Soc. **125**, 5346 (2003).
25. A. Flynn-Charlebois, Y. Wang, T.K. Prior, I. Rashid, K.A. Hoadley, R.L. Coppins, A.C. Wolf, and S.K. Silverman. J. Am. Chem. Soc. **125**, 2444 (2003).
26. W.E. Purtha, R.L. Coppins, M.K. Smalley, and S.K. Silverman. J. Am. Chem. Soc. **127**, 13124 (2005).
27. Y. Wang and S.K. Silverman. J. Am. Chem. Soc. **125**, 6880 (2003).
28. R.R. Breaker and G.F. Joyce. Chem. Biol. **2**, 655 (1995).
29. W. Chiuman and Y. Li. J. Mol. Biol. **357**, 748 (2006).
30. R.P. Cruz, J.B. Withers, and Y. Li. Chem. Biol. **11**, 57 (2004).
31. D. Faulhammer and M. Famulok. Angew Chem. Int. Ed. Engl. **35**, 2809 (1996).
32. A.R. Feldman and D. Sen. J. Mol. Biol. **313**, 283 (2001).
33. J. Li, W. Zheng, A.H. Kwon, and Y. Lu. Nucleic Acids Res. **28**, 481 (2000).
34. Z. Liu, S.H. Mei, J.D. Brennan, and Y. Li. J. Am. Chem. Soc. **125**, 7539 (2003).
35. S.H. Mei, Z. Liu, J.D. Brennan, and Y. Li. J. Am. Chem. Soc. **125**, 412 (2003).
36. P. Ordoukhanian and G.F. Joyce. J. Am. Chem. Soc. **124**, 12499 (2002).
37. S.W. Santoro and G.F. Joyce. Proc. Natl. Acad. Sci. USA. **94**, 4262 (1997).
38. S.W. Santoro, G.F. Joyce, K. Sakthivel, S. Gramatikova, and C.F. Barbas., III. J. Am. Chem. Soc. **122**, 2433 (2000).
39. K. Schlosser and Y. Li. Biochemistry, **43**, 9695 (2004).
40. L. Lermer, Y. Roupioz, R. Ting, and D.M. Perrin. J. Am. Chem. Soc. **124**, 9960 (2002).
41. W. Chiuman and Y. Li. Chem. Biol. **13**, 1061 (2006).
42. Y. Li and R.R. Breaker. Proc. Natl. Acad. Sci. USA. **96**, 2746 (1999).
43. Y. Li, Y. Liu, and R.R. Breaker. Biochemistry, **39**, 3106 (2000).
44. W. Wang, L.P. Billen, and Y. Li. Chem. Biol. **9**, 507 (2002).
45. Y. Li and D. Sen. Nat. Struct. Biol. **3**, 743 (1996).
46. D.J. Chinnapen and D. Sen. Proc. Natl. Acad. Sci. USA. **101**, 65 (2004).
47. S.K. Silverman. Nucleic Acids Res. **33**, 6151 (2005).
48. Y. Shen, J.D. Brennan, and Y. Li. Biochemistry, **44**, 12066 (2005).
49. Y. Shen, W. Chiuman, J.D. Brennan, and Y. Li. ChemBioChem. **7**, 1343 (2006).
50. S.A. Kandadai and Y. Li. Nucleic Acids Res. **33**, 7164 (2005).
51. J.C. Achenbach, G.A. Jeffries, S.A. McManus, L.P. Billen, and Y. Li. Biochemistry, **44**, 3765 (2005).
52. S.A. Kandadai, W. Chiuman, and Y. Li. Chem. Commun. (Cambridge), 2359 (2006).
53. V.K. Jayasena and L. Gold. Proc. Natl. Acad. Sci. USA. **94**, 10612 (1997).
54. Y. Miyamoto, N. Teramoto, Y. Imanishi, and Y. Ito. Biotechnol. Bioeng. **75**, 590 (2001).
55. Y. Miyamoto, N. Teramoto, Y. Imanishi, and Y. Ito. Biotechnol. Bioeng. **90**, 36 (2005).
56. H. Kuhne and G.F. Joyce. J. Mol. Evol. **57**, 292 (2003).
57. A. Roth and R.R. Breaker. Proc. Natl. Acad. Sci. USA. **95**, 6027 (1998).
58. K. Schlosser and Y. Li. J. Mol. Evol. **61**, 192 (2005).
59. K. Schlosser, J.C. Lam, and Y. Li. Nucleic Acids Res. **34**, 2445 (2006).
60. M.A. Carrigan, A. Ricardo, D.N. Ang, and S.A. Benner. Biochemistry, **43**, 11446 (2004).
61. C.R. Geyer and D. Sen. Chem. Biol. **4**, 579 (1997).
62. Y. Lu, J. Liu, J. Li, P.J. Bruesehoff, C.M. Pavot, and A.K. Brown. Biosens. Bioelectron. **18**, 529 (2003).
63. P.J. Bruesehoff, J. Li, A.J. Augustine, III, and Y. Lu. Comb. Chem. High Throughput Screening, **5**, 327 (2002).
64. D.M. Perrin, T. Garestier, and C. Helene. J. Am. Chem. Soc. **123**, 1556 (2001).
65. A.V. Sidorov, J.A. Grasby, and D.M. Williams. Nucleic Acids Res. **32**, 1591 (2004).

© 2007 NRC Canada

Ion-tagged synthesis of an oligoribonucleotide pentamer — The continuing versatility of TBDMS chemistry[1]

Robert A. Donga, Tak-Hang Chan, and Masad J. Damha

Abstract: An oligoribonucleotide has been synthesized in solution, using an ionic-liquid-based soluble tag at a scale several hundred times that of a standard solid-phase synthesis approach. Ogilvie's 2′-TBDMS strategy was adopted, and because of the resultant increase in lipophilicity, it allowed an easier purification of the growing oligomer compared with the previously observed for DNA, which does not require 2′ protection. The procedure is illustrated by the synthesis of the pentaribonucleotide sequence AGAUC, corresponding to a segment of the $tRNA^{fMet}$ from *E. coli.*

Key words: solution-phase RNA synthesis, ionic-liquid tag.

Résumé : Nous avons réalisé la synthèse d'un oligoribonucléotide en solution en utilisant un support soluble à base d'un liquide ionique dont la quantité correspond à plusieurs centaines de fois celle qui serait utilisée dans une approche basée sur une synthèse en phase solide normale. On a adopté la stratégie 2′-TBDMS d'Ogilvie et on a trouvé que, en raison de son caractère lipophile, la purification de l'oligomère croissant se fait beaucoup plus facilement que ce qui a été observé avec l'ADN qui ne requiert pas de protection en 2′. La méthode est illustrée par la synthèse de la séquence du pentaribonulcléotide AGAUC qui correspond à un segment de la $t\text{-}ARN^{fMet}$ du *E. coli*.

Mots-clés : synthèse d'ARN en solution, traceur ionique liquide.

[Traduit par la Rédaction]

Introduction

Since it was first introduced by Ogilvie and co-workers in 1974 (1), the *tert*-butyl dimethylsilyl (TBDMS) group has become the standard 2′-protecting group in both solid- and solution-phase oligomerizations of ribonucleotides (2). Along with the phosphoramidite approach (3) to ribonucleoside coupling, the TBDMS group remains one of the most widely used 2′-protecting groups for commercially available ribo-phosphoramidites. With the advent of RNAi and an increasing number of RNA-based therapeutics progressing toward clinical development (4), the TBDMS approach will continue to be an important resource as more commercially viable processes are developed for the large-scale synthesis of oligoribonucleotides.

However, the limitation in RNA chemistry, thus far, has been the cost-efficient preparation of oligomers at a sufficiently large scale. A solid-phase approach to large-scale DNA and RNA synthesis is expensive because of the cost of the solid supports and the need for a large excess of phosphoramidite compared with what is usually required in a solution-phase approach (5). A conventional solution-phase approach, where the 3′-terminal nucleoside is not linked to a support but simply protected at the 3′ position (and 2′ for RNA), is intrinsically arduous because of the necessity of chromatographic purification after each coupling cycle. An alternative approach, developed by Bonara et al. (6), uses a soluble polyethylene glycol tag for DNA solution-phase synthesis. In an effort to improve this strategy, which requires an energy-intensive cooling step during purification, and to adapt it to use in RNA, we have been exploring the utility of ionic liquids as soluble supports in oligonucleotide synthesis (7). Herein, we report the preparation of a pentaribonucleotide in solution, requiring only simple precipitations at ambient temperature for purification during the chain-extension cycles. The process retains the versatile TBDMS group as the 2′-protecting group. The pentaribonucleotide was prepared on a 1 g scale and was assembled in 32 h (an average of 8 h per coupling cycle).

Received 10 January 2007. Accepted 28 February 2007. Published on the NRC Research Press Web site at canjchem.nrc.ca on 18 April 2007.

R.A. Donga, T.-H. Chan, and M.J. Damha.[2] Department of Chemistry, McGill University, Montreal, QC H3A 2K6 Canada.

[1]This article is part of a Special Issue dedicated to Professor Kelvin K. Ogilvie.

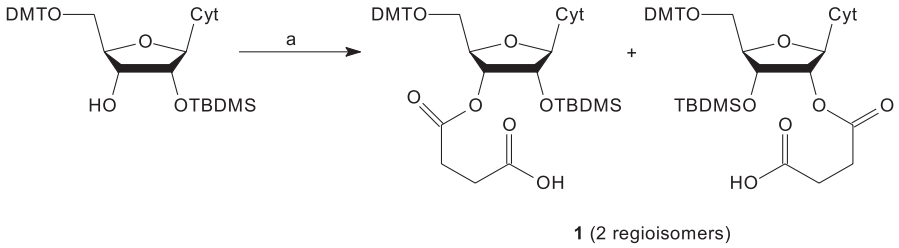
[2]Corresponding author (e-mail: masad.damha@mcgill.ca).

Discussion

The sequence of the selected pentaribonucleotide represents base positions 45 to 49 of an unpaired coil region of *N*-formyl methionine tRNA from *E. coli*. It was selected primarily because it contains all four common ribonucleosides. It is also a sequence that has been previously synthesized in solution by Damha using the phosphite triester approach (8), which required several weeks to achieve. The latter compound serves as a good reference standard for the pentaribonucleotide made by the process described here.

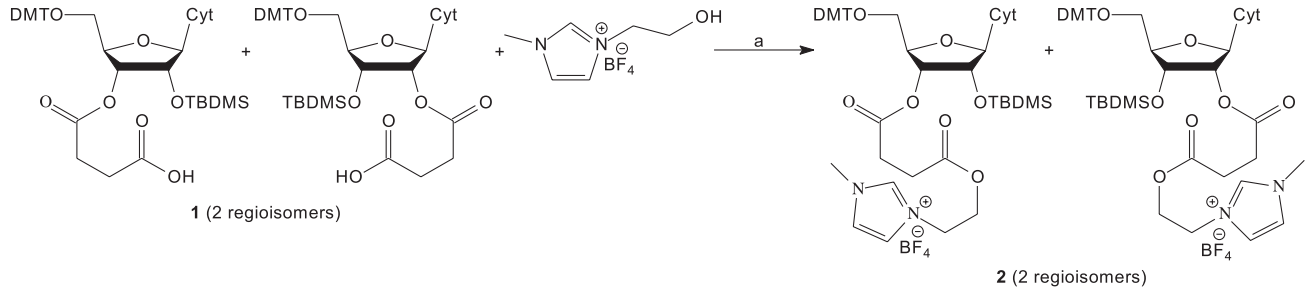
 doi:10.1139/V07-022 © 2007 NRC Canada

Scheme 1. Nucleoside succinylation.



a: Succinic anhydride, 4-dimethylaminopyridine, and anhydrous acetonitrile

Scheme 2. Coupling of ionic tag.



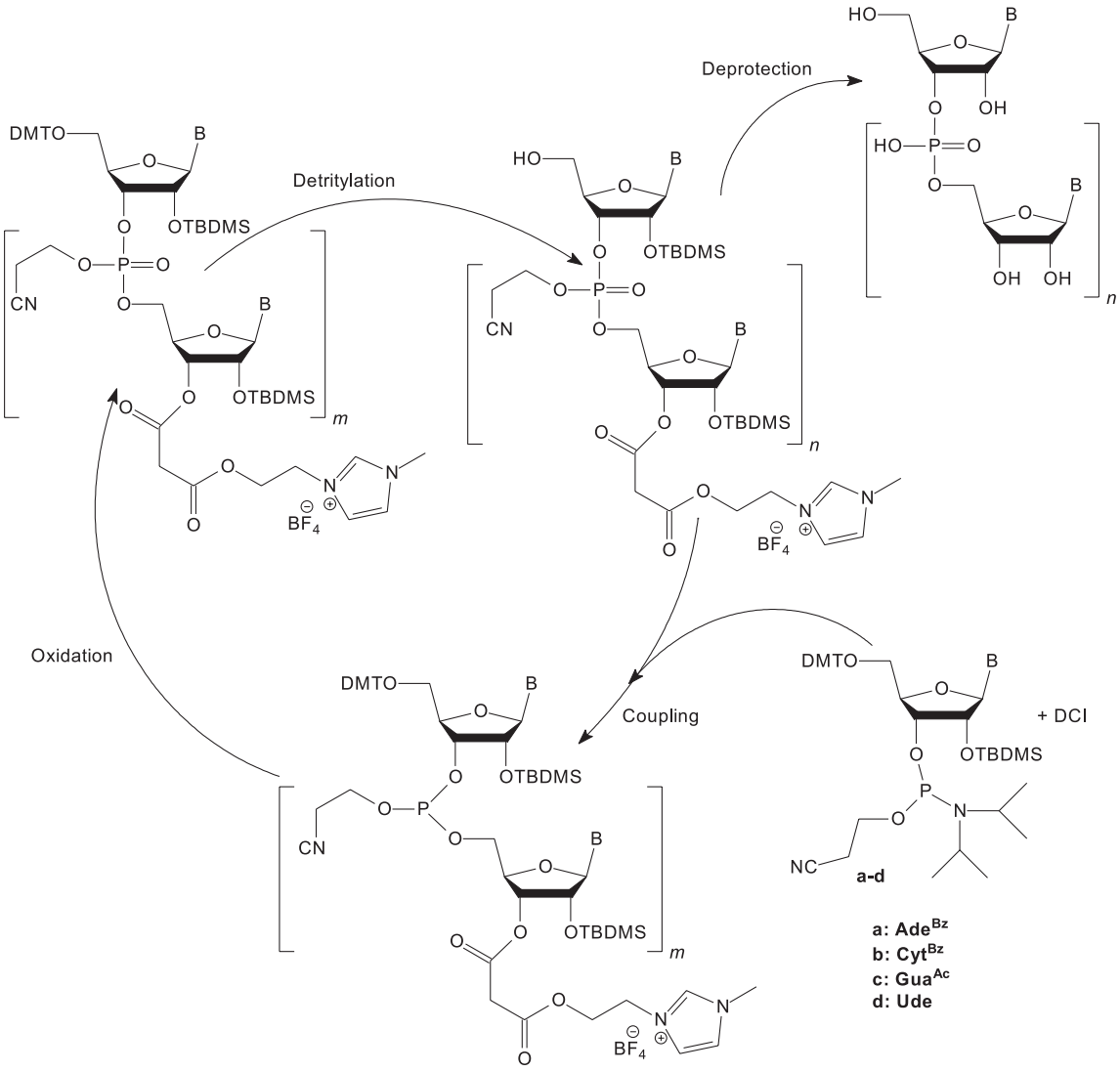
a: *O*-(benzotriazol-l-yl)-*N*,*N*,*N*',*N*'-tetramethyluronium tetrafluoroborate, triethylamine, and anhydrous acetonitrile

Synthesis began with the attachment of the 3′-cytidine to the ionic ethyl-methyl-imidazolium tag through a succinyl linker. Thus, *N*-benzoyl-2′-*tert*-butyldimethylsilyl-5′-dimethoxytrityl-cytidine was reacted with succinic anhydride in the presence of 4-dimethylaminopyridine (DMAP). The presence of the base, DMAP, caused the 2′-TBDMS protecting group to isomerize, yielding a statistical mixture of 2′-TBDMS- and 3′-TBDMS-protected cytidine with no alteration of the other protecting groups (Scheme 1). However, this isomerization is inconsequential, since the 2′/3′-silyl group and the 3′/2′-succinyl linker of this terminal nucleoside will be removed to release the required 2′- and 3′-OH groups during the final deprotection step of the desired full-length pentamer. In addition, it would be expected that the solubility properties of the two regioisomers, an important consideration for the purification steps, would be very similar. Succinylation at the free 3′- or 2′-hydroxyl group provided the 2′/3′-succinylated nucleoside along with some unreacted nucleoside. This crude mixture was then esterified with the free hydroxyl group of the ionic tag (Scheme 2). In our previous work (7), dicyclohexylcarbodiimide (DCC) was used as the condensing reagent, but long reaction times were required (3–7 d), and the yield of the desired succinate ester was only 65%–85%. An alternative coupling reagent, *O*-(benzotriazol-1-yl)-*N*,*N*,*N*′,*N*′-tetramethyluronium tetrafluoroborate (TBTU), proved to be more suitable for this reaction. In addition, its counterion, tetrafluoroborate, matched that of the ionic liquid employed as the tag. Thus, the succinylated nucleoside **1** and TBTU were first mixed in the solid state, followed by the addition of the ionic liquid [3-(2′-hydroxyethyl)-1-methylimidazolium tetrafluoroborate], triethylamine, and finally the solvent. The reaction was complete in less than 90 min, yielding the desired product **2** and a small amount of nucleoside dimer; the latter formed by the reaction of **2** with a small amount of 5′-DMT rC^{NBz} TBDMS that was carried forward from the succinylation step. At this point, a water–chloroform extraction was performed to remove any excess ionic liquid, the excess coupling reagent, and the resulting tetramethylurea by-product of the reaction, leaving a mixture of nucleoside dimer and the desired product **2**. The ion-tagged nucleoside **2** was easily separated from the dimer and any other remaining impurities by two simple precipitations. In our previous work on DNA oligomers (7), the preferred precipitation medium consisted of a mixture of ethyl acetate and diethyl ether. This yielded purer precipitates than diethyl ether alone by effectively solubilizing the undesired by-products while generating the desired tagged oligomer as a finely divided precipitate. However, when this media was used here, it was found that the nucleoside **2** was slightly soluble, resulting in a loss of the desired product and collapse of the precipitate into a slightly impure waxy solid. Therefore, the system was changed to neat diethyl ether as this was found to restore the desired properties of the precipitation medium with no appreciable loss of the tagged materials.

The synthesis cycle (Scheme 3) requires the removal of the DMT group at the 5′-terminus of the growing oligonucleotide chain. Generally, this is achieved by treatment with trifluoroacetic acid in dichloromethane. In our earlier work on DNA, this step was often problematic, especially for removing the DMT group from the nucleoside unit directly linked to the ionic tag. We ascribe the slower rate of DMT cleavage to the proximal imidazolium ion, which makes protonation of the O5′ rate limiting. A similar phenomenon is generally invoked to explain the slower rate of esterification of glycine (NH_3^+–CH_2–COOH), relative to propanoic acid under acidic conditions (9). Consistent with this notion, the rate of detritylation increases as the site of

© 2007 NRC Canada

Scheme 3. Oligoribonucleotide coupling cycle (illustrated as one regioisomer).



protonation is spatially removed from the positively charged ion tag (i.e., rate of detritylation of trimer > monomer; see later). Alternate detritylation methods employing Lewis acids, such as zinc bromide, were tested and found to be somewhat successful, but Lewis acids were more difficult to remove via precipitation. Thymine and cytosine, and to a greater extent adenine and guanine, are sensitive to acid-mediated depyrimidation/depurination (10), rendering the application of stronger acids troublesome in DNA synthesis. Because of the inductive effects of 2′-OH groups, RNA is not as prone to acid-mediated depurination; therefore, a stronger acid may be employed in the detritylation step. Thus, *p*-toluenesulphonic acid was selected as the detritylation reagent, as it was found that a single treatment was sufficient to achieve complete detritylation of the first nucleoside. Weaker acids, such as trifluoroacetic acid, required multiple treatments and longer reaction times to achieve the same result.

With the 5′ position of the 3′-nucleoside deblocked, the oligomerization cycle could begin (Scheme 3). The nucleoside **3** was mixed with 1.66 equiv. of ribouridine (2′-TBDMS-protected) 3′-cyanoethylphosphoramidite, using 4,5-dicyanoimidazole (DCI) as the activator (0.06 mol/L in anhyd. acetonitrile). After 2 h of stirring, excess *tert*-butanol (approximately 6 equiv.) was added to quench the excess phosphoramidite and to enhance the solubility of the resulting nucleoside 3′-(*tert*-butyl-2-cyanoethyl) phosphite triester by-product in the precipitation medium. The intermediate UpC dimer was isolated and purified by adding the reaction mixture dropwise to stirred diethyl ether. The resultant fine precipitate was filtered over celite and recovered from the filter by dissolving in acetone.

Once purified, the intermediate UpC phosphite triester was redissolved in anhydr. acetonitrile, and a capping step was performed using acetic anhydride and DMAP. In our DNA synthesis (7), oxidation of the intermediate phosphite triester to the phosphate was achieved using iodine as the oxidant. This procedure necessitated a difficult extraction to remove the generated salts but precluded the need for a capping step, since any unreacted oligomer would be removed with the aq. phase. The difficulty of the extraction (because of the formation of strong emulsions) outweighed the advan-

© 2007 NRC Canada

Table 1. Physical data.

Compound	Recovery (%)	Formula[a]	^{31}P NMR (ppm)	*m/z* (Calculated)	*m/z* (Experimental)
5-DMT rC Succ-IL (**2**)	73	$C_{53}H_{62}N_5O_{11}Si^+$	—	972.4	972.3
5-HO rC Succ-IL (**3**)	93	$C_{32}H_{44}N_5O_9Si^+$	—	670.3	670.2
5-DMT rUC Succ-IL (**4**)	93	$C_{71}H_{90}N_8O_{19}PSi_2^+$	—	1445.6	1446.0
5-HO rUC Succ-IL (**5**)	>100	$C_{50}H_{72}N_8O_{17}PSi_2^+$	0.082 to –0.513	1143.4	1143.5
5-DMT rAUC Succ-IL (**6**)	91	$C_{97}H_{123}N_{14}O_{26}P_2Si_3Na^{2+}$	—	1034.4	1034.5
5-HO rAUC Succ-IL (**7**)	>100	$C_{76}H_{105}N_{14}O_{24}P_2Si_3^+$	0.510 to –0.508	1743.6	1744.4
5-DMT rGAUC Succ-IL (**8**)	99	$C_{118}H_{154}N_{20}O_{34}P_3Si_4Na^{2+}$	—	1311.5	1311.7
5-HO rGAUC Succ-IL (**9**)	91	$C_{97}H_{136}N_{20}O_{32}P_3Si_4Na^{2+}$	0.637 to –0.466	1160.4	1161.0
5-DMT rAGAUC Succ-IL (**10**)	95	$C_{144}H_{187}N_{26}O_{41}P_4Si_5Na^{2+}$	—	1611.6	1611.8
5-HO rAGAUC Succ-IL (**11**)	96	$C_{123}H_{169}N_{26}O_{39}P_4Si_5Na^{2+}$	0.599 to –1.318	1460.5	1460.8

tage of the removal of the capping step, especially since the capping step overcomes the undesirable O6 extension sometimes observed for guanosine (11). Thus, in the present protocol for RNA, the capping step was reinstated, and the oxidation procedure was changed to employ a reagent that would not require extractions. *tert*-Butylhydroperoxide (6 mol/L) in decane was chosen and found to completely oxidize the phosphite triester in less than 15 min. A further advantage is that it could easily be removed, together with its by-product *tert*-butanol, since it was completely soluble in the precipitation medium. At this point, it was observed by mass spectroscopy that the original tetrafluoroborate counteranion of the tag had been exchanged for dicyanoimidazolide, an effect that was not observed in our previous work on DNA synthesis. Indeed, anion exchange occurred several times during the synthesis cycles, alternating between dicyanoimidazolide and *p*-toluenesulphonate, but this did not appear to adversely affect the solubility properties of the intermediate di (UpC), tri (ApUpC), tetra (GpApUpC), and pentanucleotides (ApGpApUpC), isolated during and after each coupling step (see later). It had been previously observed in other experiments (data not shown) that the solubility properties of these types of molecules were adversely affected when exchanges occurred for halides; thus, the identity of the counterion is of importance, since a change in solubility can have a dramatic impact on the quality and yield of the synthesis cycle. Therefore, this must be taken into account during the design of the oligomerization cycle such that if anion exchanges occur, the resulting ion-paired molecule maintains an acceptable level of solubility in the solvents used for synthesis and recovery, while also maintaining its insolubility in the precipitation medium.

Chain extension proceeded as previously outlined, but it was found that the yields exceeded 100% after the detritylation steps, as determined by the weight of the product (Table 1). This was due to the incomplete removal of *p*-toluenesulphonic acid, which subsequently interfered with the next coupling steps (e.g., premature detritylation following the next coupling step). Once this effect was realized, the detritylating reagent was substituted with the volatile trifluoroacetic acid, which could be more readily removed during the precipitation step or afterwards, by evaporation if necessary. Again, this approach necessitated two acid treatments per detritylation step, but no further premature detritylation was observed at the coupling stage, and precipitations alone were sufficient to remove the acid. Thus, while it has been found that weaker acids may be used for the detritylation step of the oligomerization cycle shortly after the initial nucleoside is deprotected, multiple treatments are still required so it would be advantageous to use stronger acids if their complete removal could be assured.

One of the advantages of solution-phase over solid-phase synthesis of oligomers is the capacity to directly monitor chain elongation by various means, including mass spectrometry (MS). Indeed, ion-tagged oligomers are especially amenable to this technique, since the molecules contain permanent positive charges. This means that ion-tagged molecules only need to have their solutions nebulized in an electrospray ionization (ESI) source to give very strong MS signals. Indeed, when using an octopole analyzer, short oligomers provided excellent results. Long oligomers quickly exceed the upper limits of the mass detector; however, in these cases multiple charging occurred more readily, pulling the analyte back into an observable window (Fig. 1). This is noticed by comparing the mass spectrum for longer oligomers to that of UpC (Fig. 2). For the dimer, the ion tag creates a high-energy barrier to protonation and likewise to formation of these adducts. As the chain length increases, the site of protonation is spatially removed from the positively charged ion tag, and adducts are readily observed. Using this technique, the identities of all post-detritylation compounds were confirmed by HR-ESIMS (Table 2).

Finally, the pentamer **11** was deprotected to the free nucleotide in parallel with a sample of the original sequence **8**, made by the original solution-phase approach (8). This consisted of treatment of 1–2 mg of each detritylated (but otherwise fully protected oligomer) with 1 mL of 40% (*v*/*v*) aq. methylamine and incubating at 60 °C for 20 min. The resultant solution was cooled to –78 °C and dried under vacuum. The resultant solid was treated with 300 µL of 1.5:0.75:1 (*v*/*v*/*v*) triethylamine trihydrofluoride – 1-methyl-2-pyrrolidinone – triethylamine solution and incubated for 90 min at 60 °C (12). The reaction mixture was then cooled to ambient temperature and 1 mL of anhyd. ethanol was added. The samples were mixed and cooled at –78 °C for 30 min, resulting in precipitates. The samples were then centrifuged at 14000 r/min at 4 °C for 30 min, and the supernatant was removed. The precipitates were washed

© 2007 NRC Canada

Fig. 1. Low resolution ESIMS of **9**.

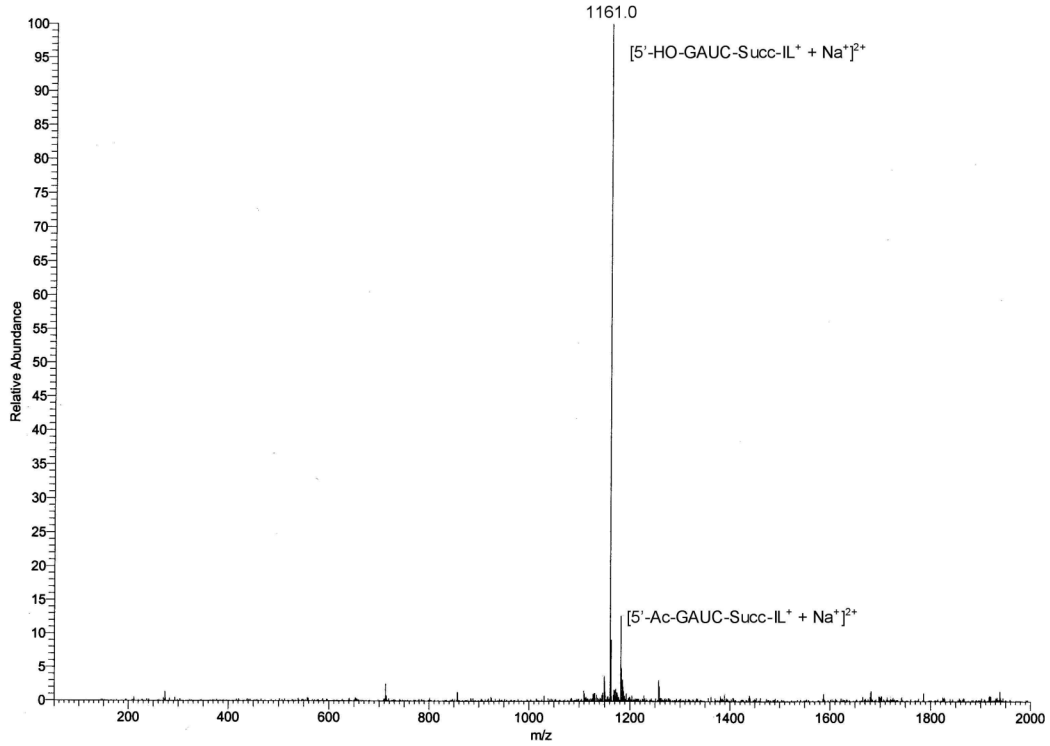
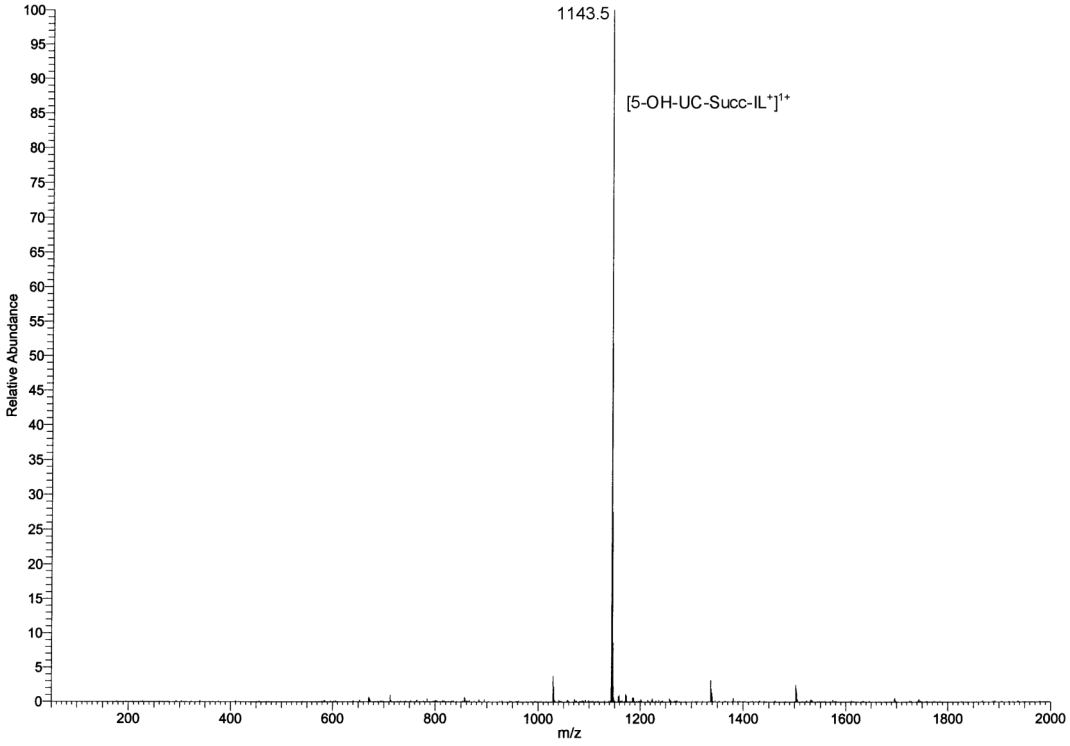


Fig. 2 Low resolution ESIMS of **3**.



with 200 μL of –78 °C ethanol, and then the residual solvent was removed under vacuum. The precipitates were dissolved in 1 mL of autoclaved, deionized water and loaded onto Waters® Sep-Pak™ C_{18} cartridges for desalting. The cartridges were rinsed with water, and then the desired products were eluted with 1:1:1 (*v*/*v*/*v*) water–methanol–acetonitrile. The solvent was removed under vacuum to yield the crude, deprotected AGAUC pentamers.

The identity and purity of the pentamers were assessed using a triethylammonium acetate ion-pairing reverse-phase

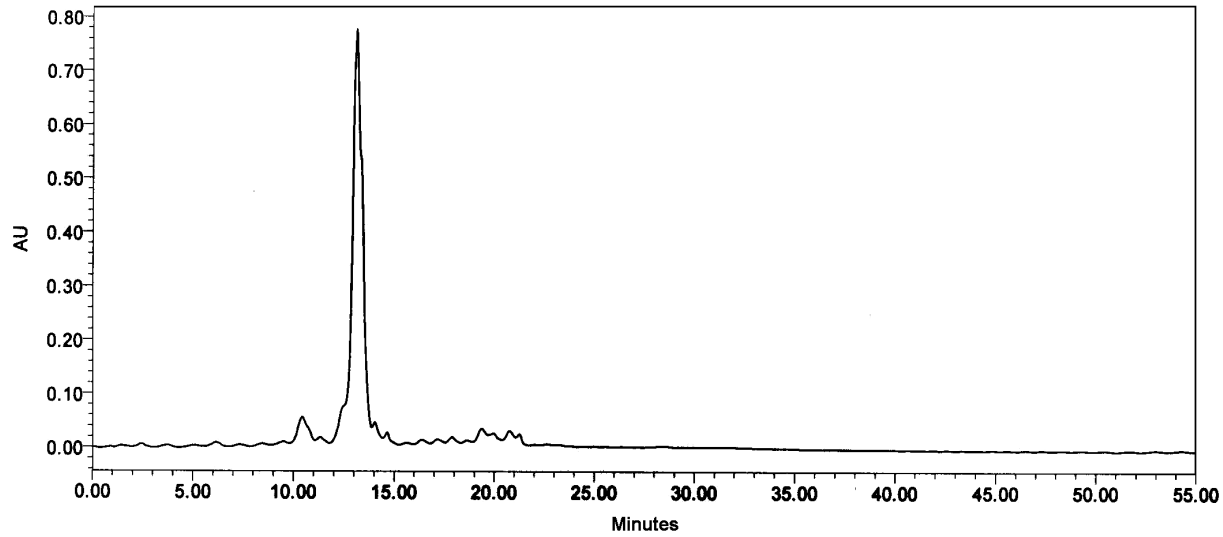
© 2007 NRC Canada

Table 2. HR-ESIMS data.

Compound	Formula[a]	*m/z* (Calculated)	*m/z* (Experimental)
5-HO rC Succ-IL (**3**)	$C_{32}H_{44}N_5O_9Si^{+1}$	670.29069	670.29028
5-HO rUC Succ-IL (**5**)	$C_{50}H_{73}N_8O_{17}Si_2P^{+2}$	572.21727	572.21795
5-HO rAUC Succ-IL (**7**)	$C_{76}H_{106}N_{14}O_{24}Si_3P_2^{+2}$	872.31268	872.31383
5-HO rGAUC Succ-IL (**9**)	$C_{97}H_{137}N_{20}O_{32}Si_4P_3^{+2}$	1149.39748	1149.39934
5-HO rAGAUC Succ-IL (**11**)	$C_{123}H_{171}N_{26}O_{39}Si_5P_4^{+3}$	966.66590	966.66546

[a]Excluding counterion.

Fig. 3. HPLC chromatogram of the co-injection of **11** and solution-phase synthesized standard.



HPLC analysis on a Phenomenex® Clarity™ semipreparatory-scale column. The samples were injected individually, and the major peaks in the chromatograms were collected and analyzed by low resolution ESIMS in the negative mode. The major ion found in both cases corresponded exactly to the expected mass of the fully deprotected AGAUC pentamers missing a single proton (1551 daltons). The two samples were also co-injected at a 1:1 ratio in the HPLC column and found to overlap perfectly (Fig. 3). As a final test to show that the deprotected compounds were identical, they were analyzed side by side, co-loaded on a 24% polyacrylamide gel, and electrophoresed (data not shown). In all cases, single bands with the same electrophoretic mobility were found, showing that indeed the synthesis using the ionic tag yielded, after deprotection, an identical compound to that of the standard solution-phase-derived molecule.

Conclusion

In summary, a functional method has been developed to rapidly synthesize oligoribonucleotides in solution and in excellent yields. The method utilizes simple precipitations as the sole purification method during chain elongation and is amenable to scales several hundred times that of a standard solid-phase synthesis. Although 5′-detritylation continues to pose a challenge, the presence of the lypophilic TBDMS group greatly enhances the solubility of the phosphoramidite monomers in the medium used for the precipitation-based purifications. Thus, the purification of RNA using this approach is superior to that of DNA, as observed in our previous work (7). We believe that the soluble ionic tag we have developed, in conjunction with Ogilvie's RNA method, enable the synthesis of short RNA oligomers as rapidly as DNA. We will further explore the limits of this method with target sequences corresponding to those of short interfering RNA (19–23 nucleotides).

Experimental

N-benzoyl-2′/3′-*tert*-butyldimethylsilyl-3′/2′-succinyl-5′-dimethoxytrityl-cytidine (1)

N-benzoyl-2′-*tert*-butyldimethylsilyl-5′-dimethoxytrityl-cytidine (1 g, 1.31 mmol) was mixed with succinic anhydride (0.39 g, 3.93 mmol) and 4-dimethylaminopyridine (0.16 g, 1.34 mmol), and the mixture was dissolved in 30 mL of dry acetonitrile. The reaction was stirred for 4 d at room temperature, and the progress was determined by TLC (9:1 dichloromethane–methanol), which showed the disappearance of the starting material and the appearance of two products (2′-3′ isomerization of the TBDMS-protecting group). The solvent was removed under vacuum, and the resulting solid was taken up in chloroform and extracted with water. The organic layer was dried with anhyd. sodium sulphate, filtered, and the solvent was removed under vacuum. The resulting crude product (1.1 g,

© 2007 NRC Canada

97%) was used without further purification. $C_{47}H_{54}N_3O_{11}Si^+$ (low resolution ESIMS) calculated: 864.3; found: 863.9.

N-benzoyl-2′/3′-*tert*-butyldimethylsilyl-3′/2′-(1-succinyl-4-[3-(2″-oxyethyl)-1″-methylimidazolium tetrafluoroborate])-5′-dimethoxytrityl-cytidine (2)

Compound **1** (1.1 g, 1.31 mmol) was mixed with TBTU (0.5 g, 1.58 mmol), 3-(2′-hydroxyethyl)-1-methylimidazolium tetrafluoroborate (0.34 g, 1.58 mmol) and triethylamine (0.4 mL, 2.62 mmol). The mixture was dissolved in 20 mL dry acetonitrile and stirred for 90 min. The solvent was then removed under vacuum, and the resulting oil was taken up in chloroform and extracted with water. The organic layer was dried over sodium sulphate. The solvent was removed under vacuum, and the resulting solid was dissolved in 5 mL of acetone. The solution was added dropwise to stirred diethyl ether, resulting in a finely divided precipitate. The precipitate was filtered off, rinsed with diethyl ether, taken up in acetone, and precipitated again. The solid was filtered off, rinsed, and collected from the filter by dissolution in acetone (1.01 g, 73%) and was used without further purification. $C_{53}H_{62}N_5O_{11}Si^+$ (low resolution ESIMS) calculated: 972.4; found: 972.3, tetrafluoroborate counterion by ESIMS.

N-benzoyl-2′/3′-*tert*-butyldimethylsilyl-3′/2′-(1-succinyl-4-[3-(2″-oxyethyl)-1″-methylimidazolium *p*-toluenesulphonate])-cytidine (3)

Compound **2** (0.69 g, 0.65 mmol) was dissolved in 10 mL of 0.1 mol/L *p*-toluenesulphonic acid solution in acetonitrile and stirred for 10 min. Methanol (5 mL) was added to quench the trityl cation, and the reaction mixture was added dropwise to stirred diethyl ether, resulting in a finely divided precipitate. The precipitate was filtered off, rinsed with diethyl ether, taken up in acetone, and precipitated again. The solid was filtered off, rinsed, and collected from the filter by dissolution in acetone (0.51 g, 93%) and was used without further purification. $C_{32}H_{44}N_5O_9Si^{+1}$ (HR-ESIMS) required: 670.29069; found: 670.29028, *p*-toluenesulphonate counterion by ESIMS.

5′-DMT-rU-(2′-TBDMS)-3′-5′-rC-(*N*-Bz)-2′/3′-TBDMS-Succ-IL (as dicyanoimidazolide salt) (4)

Compound **3** (0.44 g, 0.53 mmol) was mixed with 2-*tert*-butyldimethylsilyl-5-dimethoxytrityl-uridine-3-cyanoethyl-phosphoramidite (0.75 g, 0.88 mmol) and dicyanoimidazole (0.14 g, 1.2 mmol), and the mixture was dissolved in 20 mL of dry acetonitrile. The reaction mixture was stirred for 2 h, and then 0.5 mL of *tert*-butanol was added. The mixture was stirred a further 15 min and was then precipitated from diethyl ether as with previous compounds. The precipitate was isolated from the filter by dissolving in acetone and then removing the solvent under vacuum. The resulting solid was dissolved in 5 mL of dry acetonitrile and 250 μL each of a 17.5% (*v*/*v*) solution of acetic anhydride in anhyd. acetonitrile and saturated dimethylaminopyridine in 25% (*v*/*v*) anhyd. pyridine – acetonitrile. This reaction mixture was stirred for 10 min, and then 0.5 mL of 6 mol/L *tert*-butylhydroperoxide in decane was added. After a further 10 min of stirring, the reaction mixture was added dropwise to stirred diethyl ether, resulting in a finely divided precipitate. The precipitate was filtered off, rinsed with diethyl ether, and collected from the filter by dissolution in acetone (0.77 g, 93%) and was used without further purification. $C_{71}H_{90}N_8O_{19}PSi_2^+$ (low resolution ESIMS) calculated: 1445.6; found: 1446.0, dicyanoimidazolide counterion by ESIMS.

5′-HO-rU-(2′-TBDMS)-3′-5′-rC-(*N*-Bz)-2′/3′-TBDMS-Succ-IL (as *p*-toluenesulphonate salt) (5)

Compound **4** (0.77 g, 0.49 mmol) was dissolved in 10 mL of 0.1 mol/L *p*-toluenesulphonic acid solution in acetonitrile and stirred for 10 min. Methanol (5 mL) was added to quench the trityl cation, and the reaction mixture was added dropwise to stirred diethyl ether, resulting in a finely divided precipitate. The precipitate was filtered off, rinsed with diethyl ether, taken up in acetone, and precipitated again. The solid was filtered off, rinsed and collected from the filter by dissolution in acetone (0.68 g, 0.65 g theoretical yield, excess thought to be residual salts), dried under vacuum, and was used without further purification. ^{31}P NMR (ppm): 0.082 to –0.513. $C_{50}H_{73}N_8O_{17}Si_2P^{+2}$ (HR-ESIMS) required: 572.21727; found: 572.21795, *p*-toluenesulphonate counterion by ESIMS.

5′-DMT-rA-(*N*-Bz, 2′-TBDMS)-3′-5′-rU-(2′-TBDMS)-3′-5′-rC-(*N*-Bz)-2′/3′-TBDMS-Succ-IL (as dicyanoimidazolide salt) (6)

Compound **5** (0.60 g, 0.46 mmol) was mixed with *N*-benzoyl-2′-*tert*-butyldimethylsilyl-5′-dimethoxytrityl-adenosine (1.65 g, 1.67 mmol) and dicyanoimidazole (0.12 g, 1.0 mmol), and the mixture was dissolved in 10 mL of dry acetonitrile. Upon addition of solvent, the solution turned pale orange, indicating that the excess mass appreciated in the previous step was likely *p*-toluenesulphonic acid, causing some detritylation of the incoming phosphoramidite. The reaction was stirred for 1 h, and then 0.5 mL of *tert*-butanol was added. The mixture was stirred a further 15 min and was then precipitated from diethyl ether, as with previous compounds. The precipitate was isolated from the filter by dissolving in acetone and then removing the solvent under vacuum. The resulting solid was dissolved in 5 mL of dry acetonitrile and 250 μL each of a 17.5% (*v*/*v*) solution of acetic anhydride in anhyd. acetonitrile and saturated dimethylaminopyridine in 25% (*v*/*v*) anhyd. pyridine – acetonitrile. This reaction mixture was stirred for 10 min, and then 0.5 mL of 6 mol/L *tert*-butylhydroperoxide in decane was added. After a further 10 min of stirring, the reaction mixture was added dropwise to stirred diethyl ether, resulting in a finely divided precipitate. The precipitate was filtered off, rinsed with diethyl ether, collected from the filter by dissolution in acetone (0.89 g, 91%), and was used without further purification. $C_{97}H_{123}N_{14}O_{26}P_2Si_3Na^{2+}$ (low resolution ESIMS) calculated: 1034.4; found: 1034.5, dicyanoimidazolide counterion by ESIMS.

5′-HO-rA-(*N*-Bz, 2′-TBDMS)-3′-5′-rU-(2-TBDMS)-3′-5′-rC-(*N*-Bz)-2′/3′-TBDMS-Succ-IL (as *p*-toluenesulphonate salt) (7)

Compound **6** (0.89 g, 0.41 mmol) was dissolved in 5 mL of 0.1 mol/L *p*-toluenesulphonic acid solution in acetonitrile and stirred for 10 min. Methanol (1 mL) was added to quench the trityl cation, and the reaction mixture was added dropwise to stirred diethyl ether, resulting in a finely divided

© 2007 NRC Canada

precipitate. The precipitate was filtered off, rinsed with diethyl ether, dissolved off the filter with acetone, and dried under vacuum. TLC analysis indicated that detritylation was incomplete, so the solid was dissolved in a further 5 mL of 0.1 mol/L *p*-toluenesulphonic acid solution in acetonitrile and stirred for 10 min. Methanol (1 mL) was again added to quench the trityl cation, and the reaction mixture was precipitated as before. The precipitate was filtered off, rinsed with diethyl ether, and collected off the filter by dissolution in acetone. The solution was concentrated under reduced pressure to an approximate volume of 5 mL and was again precipitated from diethyl ether. The solid was filtered off, rinsed with diethyl ether and collected from the filter by dissolution in acetone (0.81 g, 0.79 g theoretical yield, excess thought to be residual salts), dried under vacuum, and was used without further purification. ^{31}P NMR (ppm): 0.510 to –0.508. $C_{76}H_{106}N_{14}O_{24}Si_3P_2^{+2}$ (HR-ESIMS) required: 872.31268; found: 872.31383, *p*-toluenesulphonate counterion by ESIMS.

5′-DMT-rG-(*N*-Ac, 2′-TBDMS)-3′-5′-rA-(*N*-Bz, 2′-TBDMS)-3′-5′-rU-(2′-TBDMS)-3′-5′-rC-(*N*-Bz)-2′/3′-TBDMS-Succ-IL (as *p*-toluenesulphonate salt) (8)

Compound **7** (0.71 g, 0.37 mmol) was mixed with *N*-acetyl-2′-*tert*-butyldimethylsilyl-5′-dimethoxytrityl-guanosine (0.72 g, 0.77 mmol) and dicyanoimidazole (0.10 g, 0.84 mmol), and the mixture was dissolved in 7 mL of dry acetonitrile. Upon addition of the solvent, the solution turned slightly orange, indicating that the excess mass appreciated in the previous step was likely *p*-toluenesulphonic acid, causing some detritylation of the incoming phosphoramidite. The reaction was stirred for 1 h, and then 0.5 mL of *tert*-butanol was added. The mixture was stirred a further 15 min and was then precipitated from diethyl ether, as with previous compounds. The precipitate was isolated from the filter by dissolving in acetone and then removing the solvent under vacuum. The resulting solid was dissolved in 5 mL of dry acetonitrile and 250 µL each of a 17.5% (*v*/*v*) solution of acetic anhydride in anhyd. acetonitrile and saturated dimethylaminopyridine in 25% (*v*/*v*) anhyd. pyridine – acetonitrile. This reaction mixture was stirred for 10 min, and then 0.5 mL of 6 mol/L *tert*-butylhydroperoxide in decane was added. After a further 10 min of stirring, the reaction mixture was added dropwise to stirred diethyl ether, resulting in a finely divided precipitate. The precipitate was filtered off, rinsed with diethyl ether and collected from the filter by dissolution in acetone (1.02 g, 99%), and was used without further purification. Low resolution MS indicated that no anion exchange occurred in this cycle (i.e., counterion remained *p*-toluenesulphonate). $C_{118}H_{154}N_{20}O_{34}P_3Si_4Na^{2+}$ (low resolution ESIMS) calculated: 1311.5; found: 1311.7, *p*-toluenesulphonate counterion by ESIMS.

5′-HO-rG-(*N*-Ac, 2′-TBDMS)-3′-5′-rA-(*N*-Bz, 2′-TBDMS)-3′-5′-rU-(2′-TBDMS)-3′-5′-rC-(*N*-Bz)-2′/3′-TBDMS-Succ-IL (as *p*-toluenesulphonate salt) (9)[3]

Compound 8 (1.02 g, 0.37 mmol) was dissolved in 5 mL of 3% (*v*/*v*) trifluoroacetic acid in acetonitrile (~0.4 mol/L) and stirred for 10 min. Acetone (1 mL) was added to facilitate precipitation, and the reaction mixture was added dropwise to stirred diethyl ether, resulting in a finely divided precipitate. The precipitate was filtered off, rinsed with diethyl ether, dissolved off the filter with acetone, and dried under vacuum. The solid was redissolved in trifluoroacetic acid solution and stirred for 10 min. Acetone (1 mL) was again added, and the reaction mixture was precipitated as before. The precipitate was filtered off, rinsed with diethyl ether, and collected off the filter by dissolution in acetone. The solution was concentrated under reduced pressure to an approximate volume of 10 mL and was again precipitated from diethyl ether. The solid was filtered off, rinsed with diethyl ether and collected from the filter by dissolution in acetone (0.82 g, 91%), dried under vacuum, and was used without further purification. ^{31}P NMR (ppm): 0.637 to –0.466. $C_{97}H_{137}N_{20}O_{32}Si_4P_3^{+2}$ (HR-ESIMS) required: 1149.39748; found: 1149.39934, *p*-toluenesulphonate counterion by ESIMS.

5′-DMT-rA-(*N*-Bz, 2′-TBDMS)-3′-5′-rG-(*N*-Ac, 2′-TBDMS)-3′-5′-rA-(*N*-Bz, 2′-TBDMS)-3′-5′-rU-(2-TBDMS)-3′-5′-rC-(*N*-Bz)-2′/3′-TBDMS-Succ-IL (as *p*-toluenesulphonate salt) (10)

Compound **9** (0.71 g, 0.29 mmol) was mixed with *N*-benzoyl-2-*tert*-butyldimethylsilyl-5′-dimethoxytrityl-adenosine (0.72 g, 0.77 mmol) and dicyanoimidazole (0.08 g, 0.65 mmol), and the mixture was dissolved in 7 mL of dry acetonitrile. No colour change was observed upon solvent addition this time. The reaction mixture was stirred for 2 h, and then 0.5 mL of *tert*-butanol was added. The mixture was stirred a further 15 min and was then precipitated from diethyl ether, as with previous compounds. The precipitate was isolated from the filter by dissolving in acetone and then removing the solvent under vacuum. The resulting solid was dissolved in 5 mL of dry acetonitrile and 250 µL each of a 17.5% (*v*/*v*) solution of acetic anhydride in anhyd. acetonitrile and saturated dimethylaminopyridine in 25% (*v*/*v*) anhyd. pyridine – acetonitrile. This reaction mixture was stirred for 10 min, and then 0.5 mL of 6 mol/L *tert*-butylhydroperoxide in decane was added. After a further 10 min of stirring, 1 mL of acetone was added, and the reaction mixture was added dropwise to stirred diethyl ether, resulting in a finely divided precipitate. The precipitate was filtered off, rinsed with diethyl ether and collected from the filter by dissolution in acetone (0.92 g, 95%), and was used without further purification. $C_{144}H_{187}N_{26}O_{41}P_4Si_5Na^{2+}$ (low resolution ESIMS) calculated: 1611.6; found: 1611.8, *p*-toluenesulphonate counterion by ESIMS.

5′-HO-rA-(*N*-Bz, 2′-TBDMS)-3′-5′-rG-(*N*-Ac, 2′-TBDMS)-3′-5′-rA-(*N*-Bz, 2′-TBDMS)-3′-5′-rU-(2′-TBDMS)-3′-5′-rC-(*N*-Bz)-2′/3′-TBDMS-Succ-IL (as *p*-toluenesulphonate salt) (11)

Compound **10** (0.92 g, 0.27 mmol) was dissolved in 5 mL of 3% (*v*/*v*) trifluoroacetic acid in acetonitrile (~0.4 mol/L) and stirred for 10 min. Acetone (1 mL) was added to facilitate precipitation, and the reaction mixture was added dropwise to stirred diethyl ether, resulting in a finely divided precipitate. The precipitate was filtered off, rinsed with di-

[3] Because of the residual *p*-toluenesulphonic acid observed carrying over in the previous two coupling cycles, it was decided that a volatile acid would be used for subsequent detritylations.

© 2007 NRC Canada

ethyl ether, dissolved off the filter with acetone, and dried under vacuum. The solid was redissolved in trifluoroacetic acid solution and stirred for 10 min. Acetone (1 mL) was again added, and the reaction mixture was precipitated as before. The precipitate was filtered off, rinsed with diethyl ether, and collected off the filter by dissolution in acetone. The solvent was removed under reduced pressure. TLC analysis indicated that detritylation was incomplete, so a third acid treatment was performed following exactly the same procedure as before. After precipitation and redissolution off the filter with acetone, the solution was concentrated under reduced pressure to an approximate volume of 10 mL and was again precipitated from diethyl ether. The solid was filtered off, rinsed with diethyl ether and collected from the filter by dissolution in acetone (0.81 g, 96%), and dried under vacuum. No further purification was performed. ^{31}P NMR (ppm): 0.599 to –1.318. $C_{123}H_{171}O_{39}N_{26}P_4Si_5^{+3}$ (HR-ESIMS) required: 966.66590; found: 966.66546, *p*-toluenesulphonate counterion by low resolution ESIMS.[4]

Acknowledgements

We acknowledge the financial support from the Natural Sciences and Engineering Research Council of Canada (NSERC) in the form of grants to M.J.D. and T.-H.C. This work was also supported by a scholarship award from the Chemical Biology Strategic Training Initiative of the Canadian Institutes of Health Research to R.A.D. We would like to acknowledge Alain Lesimple and Orval Mamer for the HR-ESIMS measurements.

References

1. K.K. Ogilvie, K.L. Sadana, E.A. Thompson, M.A. Quilliam, and J.B. Westmore. Tetrahedron Lett. 2861 (1974).
2. K.K. Ogilvie, N. Usman, K. Nicoghosian, and R.J. Cedergren. Proc. Natl. Acad. Sci. USA. **85**, 5764 (1988).
3. S.L. Beaucage and M.H. Caruthers. Tetrahedron Lett. **22**, 1859 (1981).
4. K.K. Jain. Mol. BioSyst. **2**, 523 (2006).
5. R.T. Pon, S. Yu, Z. Guo, R. Deshmukh, and Y.S. Sanghvi. J. Chem. Soc., Perkin Trans. 1, 2638 (2001).
6. G.M. Bonora, C.L. Scremin, F.P. Colonna, and A. Garbesi. Nucleic Acids Res. **18**, 3155 (1990).
7. R.A. Donga, M. Khaliq-Uz-Zaman Syed, T.-H. Chan, and M.J. Damha. J. Org. Chem. **71**, 7907 (2006).
8. M.J. Damha. Developments in the chemical synthesis of nucleic acids and their analogues. Ph.D. thesis, McGill University, Montreal. 1988.
9. A. Streiwieser, C.H. Heathcock, and E.M. Kosower. Introduction to organic chemistry. 4th ed. Macmillan Publishing Company, NY. 1992.
10. M. Roger and R.D. Hotchkiss. Proc. Natl. Acad. Sci. USA. **47**, 653 (1961).
11. R.T. Pon, M.J. Damha, and K.K. Ogilvie. Nucleic Acids Res. **13**, 6447 (1985).
12. L. Bellon and C. Workman. Deprotection of RNA. US Patent 6-054-576, 2000.

[4] Supplementary data for this article are available on the journal Web site (http://canjchem.nrc.ca) or may be purchased from the Depository of Unpublished Data, Document Delivery, CISTI, National Research Council Canada, Ottawa, ON K1A 0S2, Canada. DUD 5148. For more information on obtaining material, refer to http://cisti-icist.nrc-cnrc.gc.ca/irm/unpub_e.shtml.

© 2007 NRC Canada

Synthesis and structure of fluoroindole nucleosides[1]

Jelena Božilović, Jan W. Bats, and Joachim W. Engels

Abstract: Chemically modified bases are frequently used to stabilize nucleic acids, to study the driving forces for nucleic acid structure formation, and to tune DNA and RNA hybridization conditions. Nucleoside analogues are chemical means to investigate hydrogen bonds, base stacking, and solvation as the three predominant forces that are responsible for the stability of nucleic acids. To obtain deeper insight into the contributions of these interactions to RNA stability, we decided to synthesize some novel nucleic acid analogues where the nucleobases are replaced by fluoroindoles. Fluorinated indoles can be compared with fluorinated benzimidazoles to determine the role of nitrogen in five-membered ring systems. The synthesis of fluoroindole ribonucleosides as well as the X-ray crystal structures of all synthesized fluoroindole ribonucleosides are reported here. These compounds could also be building blocks for a variety of biologically active RNA analogues.

Key words: indoles, nucleosides, crystal structure, glycosilation, indole-synthesis.

Résumé : Des bases chimiquement modifiées sont souvent utilisées pour stabiliser les acides nucléiques, pour étudier la force motrice pour la formation de la structure d'acides nucléiques et pour ajuster les conditions d'hybridation de l'ADN et de l'ARN. Les analogues de nucléosides sont des méthodes chimiques d'étudier les liaisons hydrogènes, l'empilement des bases et la solvatation comme les trois forces prédominantes, responsables de la stabilité des acides nucléiques. Afin de mieux évaluer les contributions de ces interactions à la stabilité de l'ARN, on a effectuer la synthèse de nouveaux analogues de l'acide nucléique dans lesquels les nucléobases sont remplacées par de fluoroindoles. On peut comparer les fluoroindoles aux benzimidazoles fluorés pour déterminer le rôle de l'azote dans le système cyclique à cinq chaînons. On rapporte la synthèse des ribonucléosides de fluoroindoles ainsi que les structures déterminées par diffraction des rayons X de tous les ribonucléosides de fluoroindoles. Ces composés pourraient aussi être utilisés dans la synthèse d'une variété d'analogues de l'ARN biologiquement actifs.

Mots-clés : indoles, nucléosides, structure cristalline, glycosilation, synthèse de l'indole.

[Traduit par la Rédaction]

Introduction

A series of fluorobenzimidazole nucleosides has been synthesized earlier and we reported the stabilizing contribution of a C–F···H–C bond (1, 2). The inability of fluorine to compete with stronger hydrogen bond acceptors, such as oxygen and nitrogen, is due to its low polarizability and contracted lone pairs. The fluorobenzimidazole analogues investigated so far all show very similar properties. Indole structure is present in a variety of natural compounds, such as amino acids, alkaloids, etc. The position of fluorine as shown by the dipole moments (Fig. 1) has a greater influence on charge distribution for fluoroindoles than for fluorobenzimidazoles. Thus, we decided to synthesize and evaluate a similar pattern of substitution on fluoroindoles (Fig. 1). To the best of our knowledge, the ribofluoro–indole compounds have not been synthesized and evaluated, though some deoxy compounds have recently been under investigation. The thermodynamic and spectroscopic studies give no information on the fine structure and conformational dynamics of fluorobenzimidazole-containing RNA. Such information would be a valuable comparison to determine the influence of nitrogen in the five-membered ring. As the charge distribution and dipole moments between those two classes of compounds differ significantly, we also expected to observe differences in RNA oligonucleotide stability as a result of containing those building blocks. Here we report strategies for the synthesis (3) of fluoroindole building blocks and the X-ray crystal structures of all synthesized fluoroindole ribonucleosides.

Received 9 January 2007. Accepted 18 February 2007. Published on the NRC Research Press Web site at canjchem.nrc.ca on 18 April 2007.

J. Božlović, J.W. Bats, and J.W. Engels.[2] Institute for Organic Chemistry and Chemical Biology, Max-von-Laue-Str. 7, 60438 Frankfurt am Main, University of Frankfurt, Germany.

[1]This article is part of a Special Issue dedicated to Professor Kelvin K. Ogilvie.

[2]Corresponding author (e-mail: Joachim.Engels@chemie.uni-frankfurt.de).

Synthesis

The synthesis of fluoroindoles (which are not commercially available) was achieved very efficiently in a four-step procedure (4) as shown in Fig. 2. Methyl azidoacetate, an in-

 doi:10.1139/V07-020 © 2007 NRC Canada

Fig. 1. Synthesized fluoroindoles (4FBI, 5FBI, etc. are abbreviations for substituted fluorobenzimidazoles).

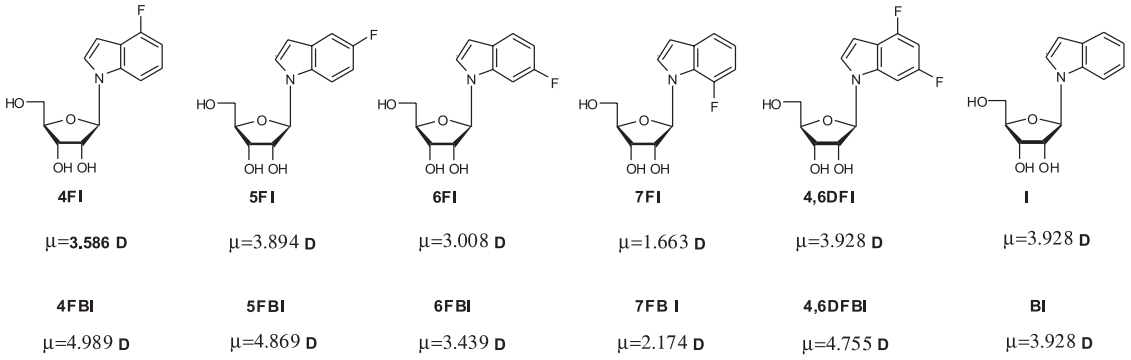
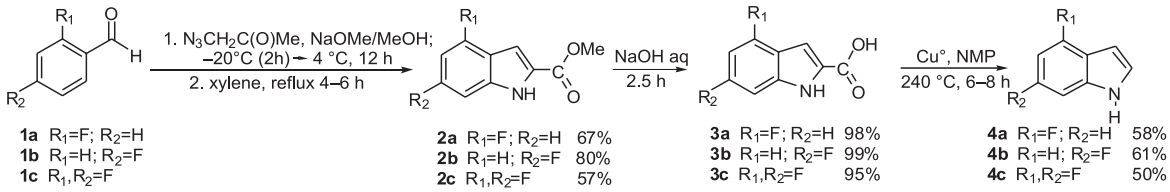


Fig. 2. Synthesis of fluoroindoles.



termediate in indole synthesis, was synthesized by a literature procedure (5). The prolonged reaction time and lower temperature improved the literature procedures (**2a**–**2c**). After hydrolysis of the methyl ester the decarboxylation followed, during which the main problem lies in the very high temperature at which the reaction occurs. Prolonging the reaction time does not lead to higher yields.

The direct synthesis of ribonucleosides was tried with 5-*O*-*tert*-butyldimethylsilyl-2,3-*O*-isopropylidene-α-D-ribofuranosyl chloride as the ribofuranosyl donor and a base for deprotonation of indole. Reaction conditions were varied: solvents (CH_3CN, THF, toluene), bases (NaH, TDA1–KOH), temperatures (RT to 70 °C), and reaction times (30 min to 19 h). When CH_3CN was used as a solvent and TDA1–KOH as a base, we obtained yields below 5% and separation of the obtained products was difficult to achieve (6). The Vorbrueggen method, though varying the time (2, 4, 8, and 12 h, reflux), gave no product. As can be seen, a variety of conditions and bases were tried but they did not result in a successful ribonucleoside synthesis.

As none of the direct glycosilations tried was successful, we decided to first synthesize the deoxy derivative and then the ribo derivative thereof, as shown in Fig 3. For glycosilation, we used the protected chlorodeoxyribose derivative (7). The deoxy derivative was obtained in very high yield. The key point is that the glycosilation reaction is very fast and that therefore only the β isomer is obtained (isomerization of the sugar **5** does not take place because of the fast reaction time). After deprotection, the 5′-OH is protected again with TBDPS-Cl and 3′-OH with MsCl. Deprotection of 5′-OH and elimination of OMs is accomplished in a one-step procedure. All yields reported are very good (more than 90%) except for the dihydroxilation with OsO_4 for which the yields vary from 45%–70% (based on **10a**–**10e**). However, the overall yields are between 27% and 46%. Despite the formally "long way" of synthesis, all procedures are worked out as routine and the overall yields are satisfactory.

Crystal structures of fluoroindoles

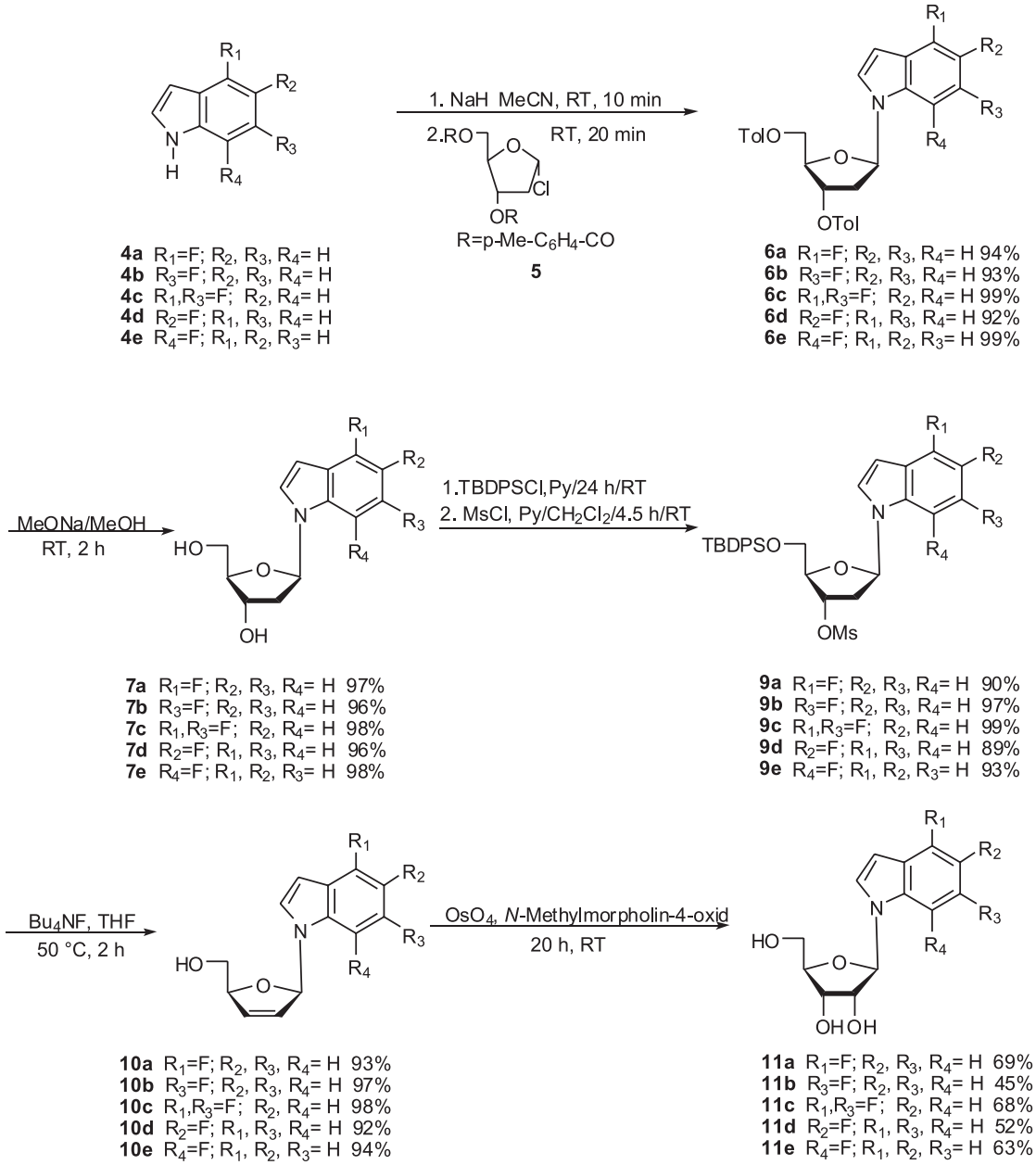
The crystal structures of 5FI, 6FI, and 4,6DFI are isomorphous and have the orthorhombic space group $P2_12_12_1$. The structures 4FI and 7FI are monoclinic with space groups $P2_1$ and $C2$, respectively. The five-membered furanose ring has a conformation between a *C*2-exo, *C*3-endo half chair, and a *C*3-endo envelope in four of the five compounds. A *C*2-endo, *C*3-exo half chair is found for 4FI. The fluoroindole groups are essentially planar and adopt anti orientations about the glycosyl bond. The O4′–C1′–N–C7 torsion angles are –99.8, –86.2, –79.8, –171.0, and –85.8 ° for 4FI, 5FI, 6FI, 7FI, and 4,6DFI, respectively. The outlying value for 7FI may result from an intramolecular C–H···F interaction between the 7-fluoro atom and the H2′ atom (distance F···H = 2.51 Å).

The crystal packings of all five structures show layers of molecules connected by intermolecular O–H···O hydrogen bonds. The packing in 4FI is shown in Fig. 4. Layers of molecules are found parallel to the [0 0 1] plane. Molecules within each layer are not only connected by hydrogen bonding between the hydroxyl groups but are also connected by weak C–H···O and C(furanose)–H···π(indole) interactions. There is no hydrogen bonding between neighboring layers. Instead, the indole groups of neighboring layers are connected by C(indole)–H···π(indole) contacts. The shortest H···C distance is 2.79 Å The 4-fluoro atom is of minor importance for the crystal stabilization. The shortest intermolecular H···F distance is 2.69 Å.

The crystal packing in 6FI is shown in Fig. 5. A similar packing is found in the isomorphous 5FI and 4,6DFI structures. Again, layers of molecules are found parallel to the [0 0 1] plane. Molecules within a layer are connected by three O–H···O hydrogen bonds, three weak intermolecular C–H···O contacts, and a weak intermolecular C(furanosyl)–H···π(indole) interaction. The fluoroindole units of neighboring layers show intermolecular C(indole)–H···F contacts

© 2007 NRC Canada

Fig. 3. Efficient synthesis of fluoroindole nucleosides.



with H···F distances of 2.40 Å and C–H–F angles of 155 °. There also is an additional C(indole)–H···π(indole) interaction with H···C distances of 2.71 and 2.72 Å.

In the isomorphous 5FI structure, a similar C(indole)–H···F contact occurs with a H···F distance of 2.46 Å and a C–H–F angle of 146 °. The isomorphism of the 5-fluoro and the 6-fluoro compounds may seem surprising but can easily be understood as a C(6)–F(6)···H(5)–C(5) contact occurring in 6FI and a related C(6)–H(6)···F(5)–C(5) contact in 5FI, with only the fluorine position reversed. A similar packing is also observed for 4,6DFI. Here, only the 6-fluoro atom is involved in an intermolecular C–H···F contact (H···F distance 2.39 Å, C–H–F angle 155 °), while the 4-fluoro atom is not involved in any short contacts.

A somewhat different packing pattern is found for 7FI. This structure contains bilayers of molecules parallel to the [0 0 1] plane. The molecules in each bilayer are connected by three intermolecular O–H···O hydrogen bonds, a weak intermolecular C(furanose)–H···π(indole) interaction, and an intermolecular C–H···F contact (H···F distance 2.30 Å, C–H–F angle 124 °). Neighboring bilayers are connected by C(indole)–H···π(indole) contacts only, with a shortest H···C distance of 2.84 Å.

Thus the conclusion of this work is that all five compounds form two-dimensional networks of hydrogen-bonded molecules. The indole units point away from the layers. The packing between the layers is governed by a competition of weak C–H···π and C–H···F interactions and thus depend on the substitution pattern of the fluorine containing indole units. Similar results were found for a series of fluorine-substituted 1-(β-D-ribofuranosyl)phenyls (8).

Unfortunately it is impossible to compare in depth the

© 2007 NRC Canada

Fig. 4. Crystal packing of 4-fluoro-1-(β-D-ribofuranosyl)indole.

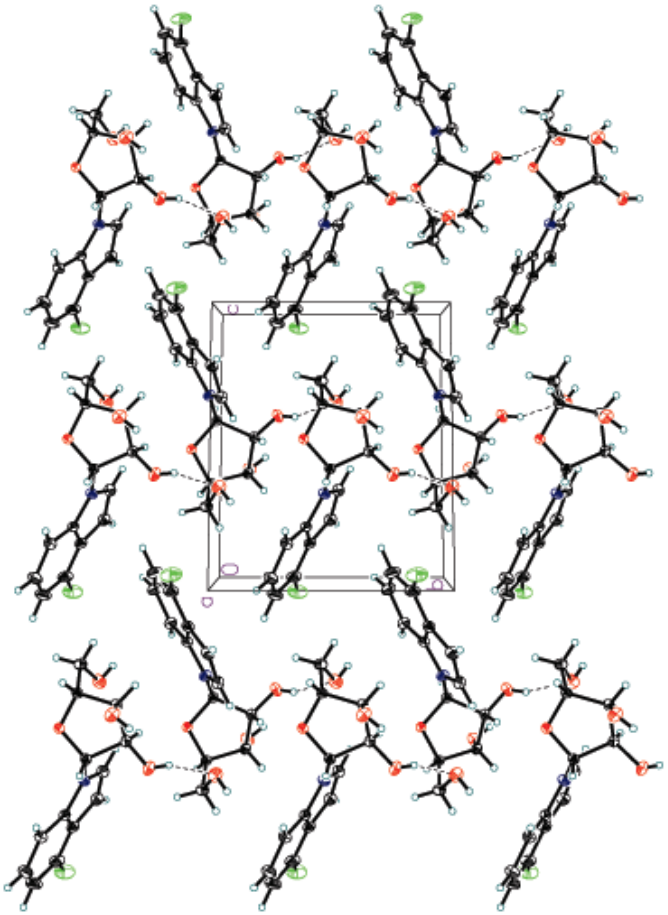
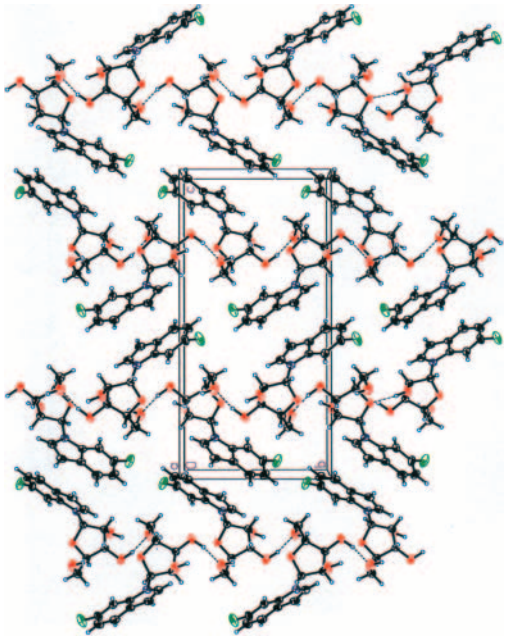


Fig. 5. Crystal packing of 6-fluoro-1-(β-D-ribofuranosyl)indole.



crystal structures of fluoroindoles and fluorobenzimidazoles because the only known crystal structure of fluorobenzimidazole is that of 1′,2′-dideoxy,3′,5′-dihydroxy-1′-(4-fluoro-6-methylbenzimidazole)-β-D-ribofuranose. There are, however, some similarities between fluoroindoles and this compound. Intermolecular C–H···F contacts also play a dominant role in the packing of the the crystal structure of 1′,2′-dideoxy,3′,5′-dihydroxy-1′-(4-fluoro-6-methylbenzimidazole)-β-D-ribofuranose (9). The molecules in this structure are connected into bilayers by O–H···O, O–H···N, C–H···O, and C–H···N hydrogen bonds. Neighboring bilayers are connected by three different C–H···F interactions with H···F distances between 2.51 and 2.59 Å.

Experimental section

Crystal structure analyses of 4FI, 5FI, 6FI, 7FI, and 4,6DFI

The compounds were crystallized from methanol or methanol–water. Single crystals were measured on a Siemens SMART 1K CCD diffractometer with Mo Kα radiation. Details of the measurements and the crystal data are given in Table 1. Empirical absorption corrections were made. Equivalent reflections, including Friedel opposites, were merged. The structures were determined by direct methods and refined by least-squares against all measured F^2 values. H atoms were either taken from a difference synthesis and refined or they were geometrically positioned and were constrained. Crystallographic data in cif format for the compounds 4FI, 5FI, 6FI, 7FI, and 4,6DFI can be found in the Supplementary Data.[3]

General

The anhydrous solvents, for example, methanol, acetonitrile, pyridine, CH_2Cl_2, and THF, were obtained from Fluka and used without further purification. Flash column chromatography was performed on (FC) silica gel (40–63 μm) from Merck, TLC on silica gel 60 F_{254} plates from Merck, NMR on a Bruker-AM250 and Bruker-AMX400 (^{1}H, ^{13}C, ^{19}F) spectrometers (δ in ppm, J in Hz), MS on a PerSeptive Biosystems MALDI-TOF spectrometer and Fisons VG platform II (ESI = electrospray-ionization).

General procedure for the preparation of methyl indole-2-carboxylates (8a–8c)

To a solution of MeONa (28.6 mL, 5.4 mol/L MeONa in MeOH) in MeOH (60ml) at –20 °C was added a solution of benzaldehyde (33 mmol) and methyl azidoacetate (135 mmol) in MeOH (34 mL) dropwise over 30 min. The mixture was stirred for 3 h at –20 °C and overnight at 4 °C. The heterogenous mixture was then poured over ice, allowed

[3] Supplementary data for this article are available on the journal Web site (http://canjchem.nrc.ca) or may be purchased from the Depository of Unpublished Data, Document Delivery, CISTI, National Research Council Canada, Ottawa, ON K1A 0R6, Canada. DUD 5154. For more information on obtaining material refer to http://cisti-icist.nrc-cnrc.gc.ca/irm/unpub_e.shtml. CCDC numbers 631201, 631202, 631203, 631204, and 631205 contain the crystallographic data for this manuscript. These data can be obtained, free of charge, via http://www.ccdc.cam.ac.uk/conts/retrieving.html (Or from the Cambridge Crystallographic Data Centre, 12 Union Road, Cambridge CB2 1EZ, UK; fax +44 1223 336033; or deposit@ccdc.cam.ac.uk).

© 2007 NRC Canada

Table 1. Crystal data for compounds 4FI, 5FI, 6FI, 7FI, and 4,6DFI.

Compound	4FI	5FI	6FI	7FI	4,6DFI
Empirical formula	$C_{13}H_{14}FNO_4$	$C_{13}H_{14}FNO_4$	$C_{13}H_{14}FNO_4$	$C_{13}H_{14}FNO_4$	$C_{13}H_{13}F_2NO_4$
Formula weight	267.25	267.25	267.25	267.25	285.24
T (K)	157(2)	158(2)	159(2)	166(2)	155(2)
Wavelenght (Å)	0.71073	0.71073	0.71073	0.71073	0.71073
Crystal system	Monoclinic	Orthorombic	Orthorhombic	Monoclinic	Orthorombic
Space group	$P2_1$	$P2_12_12_1$	$P2_12_12_1$	$C2$	$P2_12_12_1$
a (Å)	6.7842(16)	5.8582(8)	5.8244(11)	15.078(4)	5.7950(12)
b (Å)	8.512(2)	10.001(2)	10.0373(18)	4.6615(10)	10.143(3)
c (Å)	10.359(2)	20.029(3)	20.640(4)	17.765(6)	20.863(4)
β (°)	102.390(12)	90.00	90.00	109.610(12)	90.00
Volume (Å ^{3})	584.3(2)	1173.5(3)	1206.7(4)	1176.2(6)	1226.3(5)
Z	2	4	4	4	4
D_{calcd} (g cm^{-3})	1.519	1.513	1.471	1.509	1.545
Absorption coefficient (mm^{-1})	0.123	0.122	0.119	0.122	0.134
F (000)	280	560	560	560	592
Crystal size (mm)	0.6 × 0.6 × 0.11	0.55 × 0.1 × 0.08	0.6 × 0.15 × 0.03	0.9 × 0.36 × 0.03	0.7 × 0.09 ×x 0.05
Θ range for data collection (°)	2.0–32.7	2.0–30.8	2.0–27.4	2.4–31.0	2.0–29.9
Reflections collected	10 407	19 168	11 376	9 870	19 653
Independent reflections (R_{int})	2123 (0.018)	2036 (0.071)	1529 (0.223)	1934 (0.065)	1959 (0.068)
Observed reflections ($I > 2\sigma(I)$	2043	1458	990	1456	1543
Goodness-of-fit on F^2	1.13	1.04	1.18	0.97	1.08
Final R1 [$I > 2\sigma(I$]	0.029	0.045	0.074	0.040	0.040
w $R2$ (all data)	0.079	0.092	0.155	0.089	0.090

to warm to 5–10 °C, filtered, and the precipitate was washed with water. The solid was immediately dissolved in xylenes (100 mL) and the solution was washed with brine and dried over $MgSO_4$. The resulting solution was added dropwise to a flask of xylenes (200 mL) at reflux and the solution was held at reflux until TLC indicated the reaction was complete (3–6 h). The mixture was concentrated to dryness. The residue was purified by flash column chromatography (CH_2Cl_2).

Methyl-4-fluorindol-carboxylate (2a)

This compound was obtained from **1a** as a white solid in 66.7% yield. TLC (CH_2Cl_2). R_f 0.63. ^{1}H NMR (250 MHz, DMSO-d_6, ppm) δ: 12.29 (s, 1H, NH), 7.35 (m, 2H, 6H, 7H), 7.17 (s, 1H, 3H), 6.86 (m, 1H, 5H), 3.92 (s, 3H, OCH_3). ^{13}C NMR (62.9 MHz, DMSO-d_6) δ: 163.18 (C=O), 162.11 (C2), 159.38 (C6), 138.03 (C8), 128.55 (C9), 124. 36 (C7), 110.43 (C5), 108.75 (C3), 98.60 (C4), 52.47 (OCH_3). ESI-MS: 193.8 $[M + H]^+$.

Methyl-6-fluorindol-carboxylate (2b)

This compound was obtained from **1b** as a white solid in 80% yield. TLC (CH_2Cl_2). R_f 0.68. ^{1}H NMR (250 MHz, DMSO-d_6, ppm) δ: 11.99 (s, 1H, NH,), 7.69 (dd, 1H, J = 5.52 Hz, J = 8.82 Hz, 7H), 7.16 (m, 2H, 3H, 4H), 6.96 (m, 1H, 5H), 3.87 (s, 3H, OCH_3). ^{13}C NMR (62.9 MHz, DMSO-d_6, ppm) δ: 163.18 (C=O), 162.11 (C2), 159.38 (C6), 138.03 (C8), 128.55 (C9), 124. 36 (C7), 110.43 (C5), 108.75 (C3), 98.60 (C4), 52.47 (OCH_3). ^{19}F NMR (235.4 MHz, DMSO-d_6, ppm) δ: –117,22 (m, 1F, 6F). ESI-MS: 191.6 $[M + H]^+$.

Methyl-4,6-difluorindol-carboxylate (2c)

This compound was obtained from **1c** as a white solid in 73% yield. TLC (CH_2Cl_2). R_f 0.49. ^{1}H NMR (400 MHz, DMSO-d_6, ppm) δ: 12.36 (s, 1H, NH), 7.16 (m, 1H, 7H), 7.04 (m, 1H, 3H), 6.92 (ddd, 1H, J = 2.0 Hz, J' = 8.3 Hz, J'' = 8.3 Hz, 5H), 3.89 (s, 3H, OCH_3). ^{19}F NMR (235.4 MHz, DMSO-d_6, ppm) δ: –116.65 (m, 1F, 6F), –114.20 (m, 1F, 4F). ESI-MS: 209.6 $[M - H]^-$. EI anal. calcd.: C 56.88, H 3.34, N 6.63; found: C 57.04, H 3.41, N 6.48.

General procedure for the preparation of indole-2-carboxylic acids (9a–9c)

Methyl indole-2-carboxylates (21.6 mmol) were added to a solution of aq. 2 mol/L NaOH (350 mL). The mixture was stirred at reflux for 1–2 h. The solution was cooled and neutralized with concd. HCl. The resulting precipitate was collected by filtration, washed with water, and dried under vacuum to obtain indole-2-carboxylic acid.

4-Fluorindole-2-carboxylic acid (3a)

This compound was obtained from **2a** as a white solid in 98% yield. ^{1}H NMR (250 MHz, DMSO-d_6, ppm) δ: 12.09 (s, 1H, NH), 7.29–7.19 (m, 2H, 6H, 7H), 7.95 (m, 1H, 3H), 3.39 (bs, 1H, COOH). ^{19}F NMR (235.4 MHz, DMSO-d_6, ppm) δ: –120.77 (m, 1F, 4F). ESI-MS: 177.6 $[M - H]^-$.

6-Fluorindole-2-carboxylic acid (3b)

This compound was obtained from **2b** as a white solid in 99% yield. TLC (CH_2Cl_2–MeOH 95:5). R_f 0.33. ^{1}H NMR (250 MHz, DMSO-d_6, ppm) δ: 12.97 (bs, 1H, COOH), 11.80 (s, 1H, NH), 7.66 (dd, 1H, J = 8.8 Hz, J' = 5.5 Hz, 4H), 7.12 (m, 2H, 3H, 7H), 6.51 (ddd, 1H, J = 8.8 Hz, J' = 9.7 Hz, J'' = 2.5 Hz, 5H). ^{19}F NMR (235.4 MHz, DMSO-d_6, ppm) δ: –117.86 (m, 1F, 6F). ESI-MS: 179.2 $[M + H]^+$.

© 2007 NRC Canada

4,6-Difluorindole-2-carboxylic acid (3c)

This compound was obtained from **2c** as a white solid in 99% yield. ^{1}H NMR (400 MHz, DMSO-d_6, ppm) δ: 8.25 (bs, 1H, NH), 7.10 (s, 1H, 3H), 7.02 (dd, 1H, J = 9.4 Hz, J = 1.3 Hz, 7H), 6.91 (m, 1H, 5H), 3.42 (bs, 1H, COOH). ^{19}F NMR (235.4 MHz, DMSO-d_6, ppm) δ: –116.91 (m, 1F, 6F), –114.82 (m, 1F, 4F). ESI-MS: 197.9 $[M + H]^+$.

General procedure for the preparation of fluorinated indoles (4a–4c)

The indole-2-carboxylic acid (12.5 mmol), copper powder (50 mmol), and *N*-methylpyrrolidinon (200 mL) were heated at reflux. A continuous stream of argon bubbled slowly through the reaction mixture via a metal tube, while maintaining reflux for 6–12 h. The mixture was cooled, filtered through Celite, and the filter cake was washed with ether. The filtrate and ether were diluted with water (500 mL) and extracted four times with ether. The organic extract was washed with water and brine, dried with $MgSO_4$, and concentrated to dryness. The residue was purified by flash column chromatography (CH_2Cl_2).

4-Fluoroindole (4a)

This compound was obtained from **3a** as white crystals in 58% yield. TLC (*n*-hexan–EtOAc 85:15). R_f 0.40. ^{1}H NMR (400 MHz, $CDCl_3$, ppm) δ: 11.41 (bs 1H, NH), 7.39 (m, 1H, 2H), 7.23 (m, 1H, 7H), 7.05 (m, 1H, 6H), 6.76 (m, 1H, 5H), 6.49 (d, 1H, 3H). ESI-MS: 133.7 $[M - H]^-$. EI anal. calcd.: C 71.10, H 4.48, N 10.36; found: C 71.38, H 4.64, N 10.44.

6-Fluoroindole (4b)

This compound was obtained from **3b** as white crystals in 61% yield. TLC (*n*-hexan–EtOAc 85:15). R_f 0.38. ^{1}H NMR (400 MHz, $CDCl_3$, ppm) δ: 8.12 (bs 1H, NH), 7.59 (d, 1H, J = 3.3 Hz, 2H), 7.18 (dd, 1H, J = 8.7 Hz, J' = 5.6 Hz, 4H), 7.07 (dd, 1H, J = 2.2 Hz, J' = 10.2 Hz, 7H), 6.90 (ddd, 1H, J = 8.7 Hz, J' = 2.2 Hz, J'' = 10.1 Hz, 5H), 6.54 (d, 1H, J = 3.3 Hz, 3H). ^{19}F NMR (235.4 MHz, $CDCl_3$, ppm) δ: –121.83 (m, 1F, 6F). ESI-MS: 121.8 $[M + H]^+$. EI anal. calcd.: C 71.11, H 4.44, N 10.37; found: C 71.20, H 4.42, N 10.50.

4,6-Difluoroindole (4c)

This compound was obtained from **3c** as white crystals in 50% yield. TLC (*n*-hexan–EtOAc 85:15). R_f 0.43. ^{1}H NMR (400 MHz, DMSO-d_6, ppm) δ: 7.35 (d, 1H, J = 2.6 Hz, 2H), 7.04 (dd, 1H, J = 2.1 Hz, J' = 9.6 Hz, 7H), 6.77 (m, 1H, 5H), 6.45 (d, 1H, J = 2.0 Hz, 3H), 3.46 (bs, 1H, NH). ^{13}C NMR (100.6 MHz, DMSO-d_6, ppm) δ: 159.60 (C4), 157.22 (C6), 137.85 (C5), 126.67 (C8), 122.98 (C3), 116.78 (C9), 109.91 (C7), 97.32 (C2). ESI-MS: 152.2 $[M - H]^-$.

General procedure for the preparation of 1-[2′-desoxy-3′,5′-bis-*O*-(4-methylbenzoyl)-β-D-*erythro*-pentofuranosyl]-indoles (6a–6e)

To a solution of indole (6.2 mmol) in 80 mL of CH_3CN was added NaH (9.7 mmol) at room temperature (RT). The resulting solution was stirred at RT for 10 min. 3,5-Bis-*O*-(4-methylbenzoyl)-D-*erythro*-pentofuranosyl-α-chloride (7.4 mmol) was then added and stirring was continued for 20 min. The reaction was quenched by adding Dowex-80 and the resulting mixture was filtered and concentrated to dryness. The residue was purified by flash column chromatography (hexane–EtOAc 85:15).

1-[2′-Desoxy-3′,5′-bis-O-(4-methylbenzoyl)-β-D-erythro-pentofuranosyl]-4-fluoroindole (6a)

This compound was obtained from **4c** as a white foam in 94% yield. TLC (hexane–EtOAc 85:15). R_f 0.29. ^{1}H NMR (400 MHz, $CDCl_3$, ppm) δ: 7.95 (m, 4H, H_{Ar}), 7.45 (d, 1H, J = 3.4 Hz, 2H), 7.32–7.06 (m, 6H, H_{Ar}), 6.82 (m, 1H, 5H), 6.66 (d, 1H, J = 3.4 Hz, 3H), 6.45 (pt, 1H, J = 5.6 Hz, J' = 6.7 Hz, 1′H), 5.72 (m, 1H, 3′H), 4.76 (m, 2H, 5′H), 4.62 (m, 1H, 4′H), 2.89 (m, 1H, 2′H_β), 2.70 (m, 1H, 2′H_α), 2.47 (s, 3H, Ar-CH_3), 2.44 (s, 3H, Ar-CH_3). ^{19}F NMR (235.4 MHz, $CDCl_3$, ppm) δ: –121,79 (m, 1F, 4F). ESI-MS: 510.0 $[M + Na]^+$. EI anal. calc.: C 71.46, H 5.34, N 2.87; found: C 71.19, H 5.49, N 3.03.

1-[2′-Desoxy-3′,5′-bis-O-(4-methylbenzoyl)-β-D-erythro-pentofuranosyl]-6-fluoroindole (6b)

This compound was obtained from **4b** as a white foam in 94% yield. TLC (hexane–EtOAc 85:15). R_f 0.30. ^{1}H NMR (400 MHz, $CDCl_3$, ppm) δ: 8.05 (d, 2H, J = 8.2 Hz, *o*-Tol-H), 7.96 (d, 2H, J = 8.2 Hz, *o′*-Tol-H), 7.59 (d, 1H, J = 3.3 Hz, 2H), 7.37 (dd, 1H, J = 10.2 Hz, J' = 2.1 Hz, 7H), 7.30 (d, 2H, J = 8.0 Hz, *m*-Tol-H), 7.26 (d, 2H, J = 8.0 Hz, *m′*-Tol-H), 6.93 (ddd, 1H, J = 8.8 Hz, J' = 2.1 Hz, J'' = 10.1 Hz, 5H), 6.59 (d, 1H, J = 3.3 Hz, 3H), 6.41 (pt, 1H, $J_{1'H2'H\beta}$ = 6.0 Hz, $J_{1'H,\,2'H\alpha}$ = 7.2 Hz, 1′H), 5.74 (m, 1H, 3′H), 4.67 (m, 2H, 5′H), 4.61 (m, 1H, 4′H), 2.88 (m, 1H, 2′H_β), 2.69 (m, 1H, 2′H_α), 2.49 (s, 3H, Ar-CH_3), 2.45 (s, 3H, Ar-CH_3). ESI-MS: 488.8 $[M + H]^+$. EI anal. calcd.: C 71.46, H 5.34, N 2.87; found C 71.42, H 5.53, N 3.08.

1-[2′-Desoxy-3′,5′-bis-O-(4-methylbenzoyl)-β-D-erythro-pentofuranosyl]-4,6-difluoroindole (6c)

This compound was obtained from **4c** as a white foam in 99% yield. TLC (hexane–EtOAc 85:15). R_f 0.33. ^{1}H NMR (400 MHz, DMSO-d_6, ppm) δ: 8.00 (d, 2H, J = 8.2 Hz, *o*-Tol-H), 7.86 (d, 2H, J = 8.2 Hz, *o-′*Tol-H), 7.63 (d, 1H, J = 3.5 Hz, 2H), 7.53 (dd, 1H, J = 9.6 Hz, J' = 1.7 Hz, 7H), 7.50 (d, 2H, J = 1.6 Hz, *m*-Tol-H), 7.37 (d, 2H, J = 8.2 Hz, *m′*-Tol-H), (ddd, 1H, J = 1.7 Hz, J' = 9.4 Hz, J'' = 9.4 Hz, 5H), 6.59 (m, 2H, 1′H, 3H), 6.12 (m, 1H, 4′H), 4.55 (m, 2H, 3′H, 5′H), 2.94 (m, 1H, 2′H_β), 2.70 (m, 1H, 2′H_α), 2.41 (s, 3H, Ar-CH_3), 2.37 (s, 3H, Ar-CH_3). ^{19}F NMR (235.4 MHz, DMSO-d_6, ppm) δ: –119.00 (m, 1F, 6F), –118.01 (m, 1F, 4F). ESI-MS: 527.9 $[M + Na]^+$.

1-[2′-Desoxy-3′,5′-bis-O-(4-methylbenzoyl)-β-D-erythro-pentofuranosyl]-5-fluoroindole (6d)

This compound was obtained from **4c** as a white foam in 92% yield. TLC (hexane–EtOAc 85:15). R_f 0.35. ^{1}H NMR (400 MHz, $CDCl_3$, ppm) δ: 8.00 (d, 2H, J = 8.0 Hz, Tol-H), 7.91 (d, 2H, J = 8.0 Hz, Tol-H), 7.86 (m, 2H, H_{Ar}), 7.37 (m, 5H, H_{Ar}), 6.92 (ddd, 1H, J = 8.9 Hz, J = 11.0 Hz, J = 2.1 Hz, 6H), 6.59 (pt, 1H, $J_{1'H2'H\beta}$ = 6.1 Hz, $J_{1'H,2'H\alpha}$ = 6.8 Hz, 1′H), 6.53 (d, 1H, J = 3.1 Hz, 2H), 5.71 (m, 1H, 3′H), 4.61 (m, 1H, 4′H), 4.52 (m, 2H, 5′H), 2.95 (m, 1H, 2′H_β), 2.70 (m, 1H, 2′H_α), 2.46 (s, 3H, Ar-CH_3), 2.39 (s, 3H, Ar-CH_3). ^{19}F NMR (235.4 MHz, $CDCl_3$, ppm) δ: –124.11 (m, 1F, 5F). ESI-MS: 509.8 [M + Na]$^+$. EI anal. calcd.: C 71.45, H 5.38, N 2.87, found: C 71.22, H 5.50, N 2.65.

© 2007 NRC Canada

1-[2′-Desoxy-3′,5′-bis*-O-*(4-methylbenzoyl)*-β-*D*-erythro-*pentofuranosyl]-7-fluoroindole (6e)

This compound was obtained from **4b** as a white foam in 99% yield. TLC (hexane–EtOAc 85:15). R_f 0.39. ^{1}H NMR (400 MHz, DMSO-d_6, ppm) δ: 7.96 (m, 2H, H_{Ar}), 7.86 (m, 2H, H_{Ar}), 7.69 (d, 1H, J = 3.3 Hz, 2H), 7.43–7.30 (m, 5H, H_{Ar}), 7.04 (m, 2H, H_{Ar}), 6.70 (pt, 1H, $J_{1'H2'Hβ}$ = 6.6 Hz, $J_{1'H,2'Hα}$ = 7.6 Hz, 1′H), 6.63 (d, 1H, J = 3.3 Hz, 3H), 5.69 (m, 1H, 3′H), 4.57–4.46 (m, 3H, 5′H, 4′H), 2.96 (m, 1H, 2′$H_β$), 2.74 (m, 1H, 2′$H_α$), 2.37 (s, 3H, Ar-CH_3), 2.35 (s, 3H, Ar-CH_3). ^{19}F NMR (282.3 MHz, DMSO-d_6, ppm) δ: –132.04 (m, 1F, 7F). ESI-MS: 505.1 [M + NH_4]$^+$. EI anal. calcd: C 71.46, H 5.34, N 2.87; found: C 71.35, H 5.39, N 2.68.

General procedure for the preparation of 1-[2′-desoxy-β-D-*erythro*-pentofuranosyl]-indoles (7a–7e)

A mixture of 1-[2′-desoxy-3′,5′-bis-*O*-(4-methylbenzoyl)-β-D-*erythro*-pentofuranosyl]-indole (5.8 mmol) and 6.9 mL 5.4 mol/L MeONa in MeOH (37.2 mmol) in MeOH (200 mL) was stirred at RT for 2 h. The reaction was quenched by adding Dowex-80 and the resulting mixture was filtered and concentrated with silica gel to dryness. The residue was purified by flash column chromatography (hexane–EtOAc 1:2).

1-(2′-Desoxy*-β-*D*-erythro-*pentofuranosyl)-4-fluoroindole (7a)

This compound was obtained from **6a** as a white solid in 97% yield. TLC (CH_2Cl_2–MeOH 9:1). R_f 0.57. ^{1}H NMR (400 MHz, DMSO-d_6, ppm) δ: 7.64 (d, 1H, J = 3.4 Hz, 2H), 7.43 (d, 1H, J = 8.2 Hz, 7H), 7.12 (m, 1H, 6H), 6.83 (m, 1H, 5H), 6.57 (d, 1H, J = 3.4 Hz, 3H), 6.37 (pt, 1H, $J_{1'H,2'Hβ}$ = 6.2 Hz, $J_{1'H,2'Hα}$ = 7.6 Hz, 1′H), 5.29 (d, 1H, J = 4.1 Hz, 3′OH), 4.89 (t, 1H, J = 5.4 Hz, 5′OH), 4.35 (m, 1H, 3′H), 3.82 (m, 1H, 4′H), 3.53 (m, 2H, 5′H), 2.47 (m, 1H, 2′$H_β$), 2.41 (m, 1H, 2$H_α$). ^{13}C NMR (400 MHz, DMSO-d_6, ppm) δ: 138.28 (d, J = 44.8 Hz, C4), 125.92 (C2), 122.21 (C6), 119.15 (C_{Ar}), 117.05 (C_{Ar}), 106.96 (C7), 104.33 (C5), 99.13 (C3), 87.08 (C4′), 84.71 (C1′), 70.64 (C3′), 61.76 (C5′), 40.13 (C2′). ESI-MS: 252.0 [M + H]$^+$. EI anal. calcd.: C 62.14, H 5.62, N 5.57; found: C 62.33, H 5.80, N 5.35.

1-(2′-Desoxy*-β-*D*-erythro-pentofuranosyl)-6-fluoroindole (7b)

This compound was obtained from **6b** as a white solid in 96% yield. TLC (CH_2Cl_2–MeOH 9:1). R_f 0.57. ^{1}H NMR (400 MHz, DMSO-d_6, ppm) δ: 7.59 (d, 1H, J = 3.3 Hz, 2H), 7.52 (dd, 1H, J = 8.7 Hz, J' = 5.6 Hz, 4H), 7.47 (m, 1H, 7H), 6.90 (ddd, 1H, J = 8.7 Hz, J' = 2.2 Hz, J'' = 10.1 Hz, 5H), 6.51 (d, 1H, J = 3.3 Hz, 3H), 6.33 (pt, 1H, $J_{1'H,2'Hβ}$ = 6.4 Hz, $J_{1'H,2'Hα}$ = 7.2 Hz, 1′H), 5.26 (d, 1H, J = 4.2 Hz, 3′OH), 4.89 (t, 1H, J = 5.3 Hz, 5′OH), 4.35 (m, 1H, 3′H), 3.81 (m, 1H, 4′H), 3.53 (m, 2H, 5′H), 2.47 (m, 1H, 2′$H_β$), 2.21 (m, 1H, 2$H_α$). ^{19}F NMR (235.4 MHz, DMSO-d_6, ppm) δ: –120.84 (m, 1F, 6F). ESI-MS: 249.9 [M – H]$^-$.

1-(2′-Desoxy*-β-*D*-erythro-*pentofuranosyl)-4,6-difluoroindole (7c)

This compound was obtained from **6c** as a white solid in 98% yield. TLC (hexane–EtOAc 1:2). R_f 0.17. ^{1}H NMR (400 MHz, DMSO-d_6, ppm) δ: 7.56–7.29 (m, 12H, H_{Ar}), 6.86 (ddd, 1H, J = 1.9 Hz, J' = 10.3 Hz, J'' = 10.2 Hz, 5H), 6.47 (d, 1H, J = 3.4 Hz, 3H), 6.34 (pt, 1H, $J_{1'H,2'Hβ}$ = 6.4 Hz, $J_{1'H,2'Hα}$ = 6.5 Hz, 1′H), 5.35 (d, 1H, J = 4.6 Hz, 3′OH), 4.43 (m, 1H, 3′H), 3.89 (m, 1H, 4′H), 3.72 (m, 2H, 5′H), 2.49 (m, 1H, 2′$H_β$), 2.30 (m, 1H, 2′$H_α$), 2.05 (s, 9H, *t*-Bu). ^{13}C NMR (100.6 MHz, DMSO-d_6, ppm) δ: 155.7 (d, J = 50.6 Hz, C4), 154.8 (d, J = 62.2 Hz, C6), 141.5 (C8), 137.5 (C_{Ar}), 135.8 (C_{Ar}), 135.6 (C_{Ar}), 135.2 (C_{Ar}), 133.0 (C_{Ar}), 132.2 (C_{Ar}), 129.8 (C_{Ar}), 128.5 (C_{Ar}), 128.2 (C_{Ar}), 128.1 (C_{Ar}), 127.9 (C_{Ar}), 127.5 (C_{Ar}), 126.9 (C2), 111.2 (C9), 103.1 (C3), 95.7 (C5), 93.6 (C7), 83.5 (C1′), 83.3 (C4′), 65.3 (C3′), 64.2 (C5′), 36.0 (C2′), 25.73 (Si$C(CH_3)_3$), 20.5 (SiC(CH_3)$_3$). 19.5 (SiC(CH_3)$_3$), 14.5 (SiC(CH_3)$_3$). ESI-MS: 505.8 [M – H]$^-$.

1-(2′-Desoxy*-β-*D*-erythro-*pentofuranosyl)-5-fluoroindole (7d)

This compound was obtained from **6d** as a white foam in 96% yield. TLC (CH_2Cl_2–MeOH 9:1). R_f 0.56. ^{1}H NMR (400 MHz, DMSO-d_6, ppm) δ: 7.90 (d, 1H, J = 3.2 Hz, 2H), 7.71 (m, 1H, 7H), 7.35 (m, 1H, 4H), 7.03 (ddd, 1H, J = 8.7 Hz, J' = 2.1Hz, J = 10.2 Hz, 6H), 6.54 (d, 1H, J = 3.2 Hz, 3H), 6.40 (pt, 1H, $J_{1'H,2'Hβ}$ = 6.3 Hz, $J_{1'H,2'Hα}$ = 6.9 Hz, 1′H), 5.32 (d, 1H, J = 4.1 Hz, 3′OH), 4.92 (t, 1H, J = 5.2 Hz, 5′OH), 4.40 (m, 1H, 3′H), 3.86 (m, 1H, 4′H), 3.57 (m, 2H, 5′H), 2.57 (m, 1H, 2′$H_β$), 2.28 (m, 1H, 2$H_α$). ^{19}F NMR (282.3 MHz, DMSO-d_6, ppm) δ: –124.53 (m, 1F, 5F). ESI-MS: 249.8 [M – H]$^-$. EI anal. calcd: C 62.14, H 5.62, N 5.57; found: C 62.32, H 5.78, N 5.45.

1-(2′-Desoxy*-β-*D*-erythro-*pentofuranosyl)-7-fluoroindole (7e)

This compound was obtained from **6d** as a white foam in 98% yield. TLC (CH_2Cl_2–MeOH 9:1). R_f 0.63. ^{1}H NMR (300 MHz, DMSO-d_6, ppm) δ: 7.73 (d, 1H, J = 3.2 Hz, 2H), 7.40 (m, 1H, H_{Ar}), 6.97 (m, 2H, H_{Ar}), 6.51 (m, 2H, 3H, 1′H), 5.31 (d, 1H, J = 4.2 Hz, 3′OH), 4.85 (t, 1H, J = 5.6 Hz, 5′OH), 4.31 (m, 1H, 3′H), 3.72 (m, 1H, 4′H), 3.53 (m, 2H, 5′H), 2.40 (m, 1H, 2′$H_β$), 2.37 (m, 1H, 2$H_α$). ^{13}C NMR (300 MHz, DMSO-d_6, ppm) δ: 132.50 (d, J = 45.0 Hz, C7), 132.40 (C2), 126.42 (C_{Ar}), 123.05 (C_{Ar}), 122.93 (C_{Ar}), 119.97 (C_{Ar}), 119.80 (C_{Ar}), 116.80 (C_{Ar}), 87.10 (C4′), 86.07 (C1′), 70.71 (C3′), 61.83 (C5′), 60.47 (C2′). ^{19}F NMR (282.3 MHz, DMSO-d_6, ppm) δ: –132.23 (m, 1F, 7F). ESI-MS: 250.0 [M – H]$^-$.

General procedure for the preparation of 1-(2′-desoxy-5′-*O*-*tert*-buthyldiphenylsilyl-β-D-*erythro*-pentofuranosyl)-indoles (13a–13f)

To a solution of 1-[2′-desoxy-3′,5′-bis-*O*-(4-methylbenzoyl)-β-D-*erythro*-pentofuranosyl]-indole (3.75 mmol) in pyridine (20 mL) at 0 °C was added dropwise *tert*-butyldiphenylsilylchloride (4.3 mmol) in 30 min. The mixture was stirred at RT for 24 h and concentrated with silica gel to dryness. The residue was purified by flash column chromatography (hexane–EtOAc 4:1).

1-(2′-Desoxy-5′-*O*-*tert*-buthyldiphenylsilyl-β-D-*erythro*-pentofuranosyl)-4-fluoroindole (8a)

This compound was obtained from **7a** as a white solid in 87% yield. TLC (CH_2Cl_2–MeOH 99:1). R_f 0.51. ^{1}H NMR (400 MHz, DMSO-d_6 ppm) δ 7.59 (m, 4H, H_{Ar}), 7.52 (d, 1H, J = 3.4 Hz, 2H), 7.39 (m, 13H, H_{Ar}), 7.08 (m, 1H, 6H), 6.83 (m, 1H, 5H), 6.50 (d, 1H, J = 3.4 Hz, 3H), 6.41 (pt, 1H,

© 2007 NRC Canada

$J_{1'H,H\beta}$ = 6.6 Hz, $J_{1'H,H\alpha}$ = 7.9 Hz, 1′H), 5.40 (d, 1H, *J* = 4.5 Hz, 3′OH), 4.48 (m, 1H, 3H), 3.93 (m, 1H, 4′H), 3.72 (m, 2H, 5′H), 2.53 (m, 1H, 2′H_β), 2.32 (m, 1H, 2′H_α), 0.98 (s, 9H, *t*-Bu. ^{19}F-NMR (235.4 MHz, DMSO-d_6, ppm) δ –122.47 (m, 1F, 4F); ESI-MS: 490.2 $[M + H]^+$.

1-(2′-Desoxy-5′-*O-tert*-buthyldiphenylsilyl-β-D-*erythro*-pentofuranosyl)-6-fluorindole (8b)

This compound was obtained from **7b** as a white solid in 85% yield. TLC (*n*-hexan–EtOAc 4:1). R_f 0.20. ^{1}H NMR (250 MHz, $CDCl_3$, ppm) δ: 7.65–7.15 (m, 14H, H_{Ar}), 6.82 (ddd, 1H, *J* = 8.7 Hz, *J′* = 2.2 Hz, *J″* = 10.1 Hz, 5H), 6.43 (d, 1H, *J* = 3.2 Hz, 3H), 6.20 (pt, 1H, $J_{1'H,H\beta}$ = 6.3 Hz, $J_{1'H,H\alpha}$ = 7.3 Hz 1′H), 5.25 (d, 1H, *J* = 4.1 Hz, 3′OH), 4.65 (m, 1H, 3H), 3.97 (m, 1H, 4′H), 3.78 (m, 2H, 5′H), 2.57 (m, 1H, 2′H_β), 2.31 (m, 1H, 2′H_α), 1.02 (s, 9H, *t*-Bu). ^{19}F NMR (235.4 MHz, DMSO-d_6, ppm) δ: –120.74 (m, 1F, 6F). ESI-MS: 490.2 $[M + H]^+$.

1-(2′-Desoxy-5′-*O-tert*-buthyldiphenylsilyl-β-D-*erythro*-pentofuranosyl)-4,6-fluorindole (8c)

This compound was obtained from **7c** as a white solid in 88% yield. TLC (*n*-hexan–EtOAc 1:2). R_f 0.17. ^{1}H NMR (400 MHz, DMSO-d_6, ppm) δ: 7.56–7.29 (m, 12H, H_{Ar}), 6.86 (ddd, 1H, *J* = 1.9 Hz, *J′* = 10.3 Hz, *J″* = 10.2 Hz, 5H), 6.47 (d, 1H, *J* = 3.4 Hz, 3H), 6.34 (pt, 1H, $J_{1'H,2'H\beta}$ = 6.4Hz, $J_{1'H,2'H\alpha}$ = 6.5 Hz, 1′H), 5.35 (d, 1H, *J* = 4.6 Hz, 3′OH), 4.43 (m, 1H, 3′H), 3.89 (m, 1H, 4′H), 3.72 (m, 2H, 5′H), 2.49 (m, 1H, 2′H_β), 2.30 (m, 1H, 2′H_α), 2.05 (s, 9H, *t*-Bu). ^{13}C NMR (100.6 MHz, DMSO-d_6, ppm) δ: 155.7 (d, *J* = 50.6 Hz, C4), 154.8 (d, *J* = 62.2 Hz, C6), 141.5 (C8), 137.5 (C_{Ar}), 135.8 (C_{Ar}), 135.6 (C_{Ar}), 135.2 (C_{Ar}), 133.0 (C_{Ar}), 132.2 (C_{Ar}), 129.8 (C_{Ar}), 128.5 (C_{Ar}), 128.2 (C_{Ar}), 128.1 (C_{Ar}), 127.9 (C_{Ar}), 127.5 (C_{Ar}), 126.9 (C2), 111.2 (C9), 103.1 (C3), 95.7 (C5), 93.6 (C7), 83.5 (C1′), 83.3 (C4′), 65.3 (C3′), 64.2 (C5′), 36.0 (C2′), 25.73 (Si*C*$(CH_3)_3$), 20.5 (SiC(*C*$H_3)_3$). 19.5 (SiC(*C*$H_3)_3$), 14.5 (SiC(*C*$H_3)_3$). ESI-MS: 505.8 $[M - H]^-$.

1-(2′-Desoxy-5′-*O-tert*-buthyldiphenylsilyl-β-D-*erythro*-pentofuranosyl)-5-fluorindole (8d)

This compound was obtained from **7d** as a white solid in 86% yield. TLC (*n*-hexan–EtOAc 4:1). R_f 0.23. ^{1}H NMR (400 MHz, DMSO-d_6, ppm) δ: 8.62 (d, 1H, *J* = 3.1 Hz, 2H), 7.50 (m, 12H, H_{Ar}), 6.95 (ddd, 1H, *J* = 8.6 Hz, *J′* = 2.1 Hz, *J″* = 10.1 Hz, 6H), 6.45 (m, 2H, 2H, 1′H), 5.44 (d, 1H, *J* = 4.2 Hz, 3′OH), 4.53 (m, 1H, 3′H), 4.05 (m, 1H, 4′H), 3.85 (m, 2H, 5′H), 2.60 (m, 1H, 2′H_β), 2.38 (m, 1H, 2′H_α), 1,04 (s, 9H, *t*-Bu). ^{19}F NMR (283.3 MHz, DMSO-d_6, ppm) δ: –124.76 (m, 1F, 5F) ESI-MS: 489.1 $[M - H]^-$.

1-(2′-Desoxy-5′-*O-tert*-buthyldiphenylsilyl-β-D-*erythro*-pentofuranosyl)-7-fluorindole (8e)

This compound was obtained from **7e** as a white solid in 89% yield. TCL (*n*-hexan–EtOAc 4:1). R_f 0.36. ^{1}H NMR (400 MHz, DMSO-d_6, ppm) δ: 7.66 (m, 5H, H_{Ar}), 7.48–7.38 (m, 7H, H_{Ar}), 7.10–7.01 (m, 2H, H_{Ar}), 6.60 (pt, 1H, $J_{1'H,H\beta}$ = 6.3 Hz, $J_{1'H,H\alpha}$ = 7.1 Hz, 1′H), 6.55 (d, 1H, *J* = 3.1 Hz, 2H), 5.47 (d, 1H, *J* = 4.3 Hz, 3′OH), 4.50 (m, 1H, 3′H), 3.97 (m, 1H, 4′H), 3.77 (m, 2H, 5′H), 2.48 (m, 1H, 2′H_β), 2.39 (m, 1H, 2′H_α), 1.04 (s, 9H, *t*-Bu). ^{19}F NMR (282.3 MHz, DMSO-d_6, ppm) δ: –132.64 (m, 1F, 7F). ESI-MS: 490.2 $[M + H]^+$. EI anal. calcd.: C 71.13, H 6.59, N 2.86; found: C 70.84, H 6.83, N 2.67.

General procedure for the preparation of 1-(2′-desoxy-5′-*O-tert*-buthyldimethylsisyl-3′-*O*-mesyl-β-D-*erythro*-pentofuranosyl)-indoles (9a–9f)

To a solution of 1-(2′-desoxy-5′-*O-tert*-buthyldiphenylsilyl-β-D-*erythro*-pentofuranosyl)-indole (3.2 mmol) in mixture of CH_2Cl_2 and pyridine (4:1, 75 mL) at 0 °C was added MsCl (64 mmol) and stirred at RT over night. After the addition of MeOH (20 mL) and further stirring for 20 min, the mixture was concentrated to dryness and coevaporated with toluene. The residue was purified by flash column chromatography (hexane–EtOAc 4:1).

1-(2′-Desoxy-5′-*O-tert-*butyldimethylsisyl-3′-O-*mesyl*-β-D-erythro-*pentofuranosyl)-4-fluorindol (9a)

This compound was obtained from **8a** as a white foam in 90% yield. TLC (hexane–EtOAc 75:25). R_f 0.51. ^{1}H NMR (400 MHz, $CDCl_3$, ppm) δ: 7.74–7.12 (m, 13H, H_{Ar}), 6.82 (m, 1H, 5H), 6.59 (d, 1H, *J* = 3.3 Hz, 3H), 6.37 (pt, 1H, $J_{1'H,2'H\beta}$ = 8.6 Hz, $J_{1'H,2'H\alpha}$ = 5.5 Hz, 1′H), 5.52 (m, 1H, 3′H), 4.33 (m, 1H, 4′H), 3.88 (m, 2H, 5′H), 3.07 (s, 3H, SCH_3), 2.72 (m, 2H, 2′H), 1.12 (s, 9H, *t*-Bu). ^{19}F NMR: (235.4 MHz, $CDCl_3$, ppm) δ: –121.87 (m, 1F, 4F). ESI-MS: 568.3 $[M + H]^+$.

1-(2′-Desoxy-5′-*O-tert-*butyldimethylsilyl-3′-O-*mesyl*-β-D-erythro-*pentofuranosyl)-6-fluoroindole (9b).

This compound was obtained from **8b** as a white foam in 97% yield. TLC (hexane–EtOAc 4:1). R_f 0.30. ^{1}H NMR (400 MHz, DMSO-d_6, ppm) δ: 7.69–7.20 (m, 14H, H_{Ar}), 6.93 (ddd, 1H, *J* = 8.8 Hz, *J′* = 2.3 Hz, *J″* = 9.4 Hz, 5H), 6.32 (pt, 1H, $J_{1'H,2'H\beta}$ = 5.5 Hz, $J_{1'H,2'H\alpha}$ = 3.5 Hz, 1′H), 5.53 (m, 1H, 3′H), 4.34 (m, 1H, 4′H), 3.93 (dd, 1H, *J* = 11.4 Hz, *J′* = 3.2 Hz, 5′H_α), 3.84 (dd, 1H, *J* = 4.2 Hz, *J′* = 11.4 Hz, 5′H_β), 3.10 (s, 3H, SCH_3), 2.76 (m, 1H, 2′H_β), 2.47 (m, 1H, 2′Hα), 1.14 (s, 9H, *t*-Bu). ^{13}C NMR (100.6 MHz, DMSO-d_6, ppm) δ: 161.18 (C_{Ar}), 158.81 (C4), 136.42 (C_{Ar}), 135.58 (d, *J* = 10.6 Hz, C6), 132.48 (C_{Ar}), 129.97 (C8), 127.92 (C_{Ar}), 125.44 (C3), 124.38 (C_{Ar}), 121.69 (C9), 109.25 (C7), 96.75 (C2), 96.45 (C5), 84.87 (C1′), 83.90 (C3′), 80.27 (C4′), 76.68 (C5′), 63.38 (C2′), 38.44 (SCH_3), 26.92 (SiC(*C*$H_3)_3$), 19.24 (Si*C*$(CH_3)_3$). ESI-MS: 568.5 $[M + H]^+$.

1-(2′-Desoxy-5′-*O-tert-*butyldimethylsisyl-3′-O-*mesyl*-β-D-erythro-*pentofuranosyl)-4,6-fluorindole (9c)

This compound was obtained from **8c** as a white foam in 99% yield. TLC (*n*-hexan–EtOAc 85:15). R_f 0.16. ^{1}H NMR (400 MHz, DMSO-d_6, ppm) δ: 7.60–7.33 (m, 12H, H_{Ar}), 6.92 (m, 1H, 5H), 6.54 (d, 1H, *J* = 3.4 Hz, 3H), 6.45 (pt, 1H, $J_{1'H,2'H\beta}$ = 6.3 Hz, $J_{1'H,2'H\alpha}$ = 6.4 Hz, 1′H), 5.44 (m, 1H, 3′H), 4.26 (m, 1H, 4′H), 3.81 (m, 2H, 5′H), 3.30 (s, 9H, SCH_3), 2.85 (m, 1H, 2′H_β), 2.73 (m, 1H, 2′H_α), 0.99 (s, 9H, *t*-Bu). ^{19}F NMR (235.3 MHz, DMSO-d_6, ppm) δ: –119.02 (m, 1F, 6F), –117.84 (m, 1F, 4F). ESI-MS: 505.8 $[M + H]^+$. EI anal. calcd.: C 61.52, H 5.68, N 2.39; found: C 61.35, H 5.47, N 2.43.

1-(2′-Desoxy-5′-*O-tert-*butyldimethylsisyl-3′-O-*mesyl*-β-D-erythro-*pentofuranosyl)-5-fluorindole (9d)

This compound was obtained from **8d** as a white foam in 89% yield. Yield 2.89 g (89%). TLC (*n*-hexan–EtOAc 4:1).

© 2007 NRC Canada

R_f 0.20. ^{1}H NMR (300 MHz, $CDCl_3$, ppm) δ: 7.55 (m, 4H, H_{Ar}), 7.38–7.15 (m, 9H, H_{Ar}), 6.84 (m, 1H, 6H), 6.37 (d, 1H, J = 3.0 Hz, 3H), 6.24 (pt, 1H, $J_{1'H,2'H\beta}$ = 7.2 Hz, $J_{1'H,2'H\alpha}$ = 6.2 Hz, 1′H), 5.43 (m, 1H, 3′H), 4.23 (m, 1H, 4′H), 3.71 (m, 2H, 5′H), 2.98 (s, 3H, SCH_3), 2.61 (m, 2H, 2′H), 1.05 (s, 9H, *t*-Bu). ^{19}F NMR (282.3 MHz, $CDCl_3$, ppm) δ: –124.40 (m, 1F, 5F). ESI-MS: 567.9 $[M + H]^+$. EI anal. calcd.: C 63.47, H 6.04, N 2.47; found: C 63.36, H 6.20, N 2.39.

*1-(2′-Desoxy-5′-*O*-tert-buthyldimethylsisyl-3′-*O*-mesyl-β-D-erythro-pentofuranosyl)-7-fluorindole (9e)*

This compound was obtained from **8e** as a white foam in 93% yield. TLC (*n*-hexan–EtOAc 4:1). R_f = 0.36. ^{1}H NMR (400 MHz, DMSO-d_6, ppm) δ: 7.64–7.59 (m, 5H, H_{Ar}), 7.49–7.31 (m, 7H, H_{Ar}), 7.10–6.98 (m, 2H, H_{Ar}), 6.61 (pt, 1H, $J_{1'H,2'H\beta}$ = 7.1 Hz, $J_{1'H,2'H\alpha}$ = 6.6 Hz, 1′H), 6.53 (m, 1H, H_{Ar}), 5.46 (m, 1H, 3′H), 4.27 (m, 1H, 4′H), 3.74 (m, 2H, 5′H), 3.30 (s, 3H, SCH_3), 2.93 (m, 1H, 2′H_β), 2.81 (m, 1H, 2′Hα), 1.00 (s, 9H, *t*-Bu). ^{19}F NMR (282.3 MHz, DMSO-d_6, ppm) δ: –132.56 (m, 1F, 7F). ESI-MS: 567.9 $[M + H]^+$.

General procedure for the preparation of 1-(2′,3′-didesoxy-β-D-*glycero*-pent-2-enofuranosyl)indoles (10a–10e)

To a solution of compound 14 (2.8 mmol) in THF (50 mL) was added Bu_4NF (1 mol/L solution in THF, 10.4 mL). The mixture was stirred at 50 °C for 2 h (Ar atmosphere) and concentrated to dryness. The residue was purified by flash column chromatography (1st $CHCl_3$–MeOH 95:5; 2nd $CHCl_3$–MeOH 98:2).

1-(2′,3′-Didesoxy-β-D-glycero-pent-2-enofuranosyl)-4-fluoroindole (10a)

This compound was obtained from **9a** as a white solid in 93% yield. TLC ($CHCl_3$–MeOH 95:5). R_f 0.47. ^{1}H NMR (400 MHz, DMSO-d_6, ppm) δ: 7.75 (d, 1H, J = 4.0 Hz, 2H), 7.59 (d, 1H, J = 4.6 Hz, 1′H), 7.22 (m, 2H, 6H, 7H), 6.91 (m, 1H, 5H), 6.61 (d, 1H, J = 4.0 Hz, 3H), 6.55 (m, 1H, 3′H), 6.21 (m, 1H, 2′H), 4.93 (t, 1H, J = 5.7 Hz, 5′OH), 4.87 (m, 1H, 4′H), 3.67 (m, 2H, 5′H). ^{19}F NMR (282.3 MHz, DMSO-d_6, ppm) δ: –122.40 (m, 1F, 4F). ESI-MS: 233.8 $[M + H]^+$.

1-(2′,3′-Didesoxy-β-D-glycero-pent-2-enofuranosyl)-6-fluoroindole (10b)

This compound was obtained from **9b** as a white solid in 97% yield. TLC ($CHCl_3$–MeOH 95:5). R_f 0.51. ^{1}H NMR (400 MHz, DMSO-d_6, ppm) δ: 7.55 (m, 2H, 2H, 7H), 7.37 (d, 1H, J = 3.4 Hz, 1′H), 7.03 (m, 1H, 4H), 6.91 (ddd, 1H, J = 8.6 Hz, J' = 2.2 Hz, J'' = 9.9 Hz, 5H), 6.49 (m, 2H, 3H, 3′H), 6.13 (m, 1H, 2′H), 4.86 (t, 1H, J = 5.6 Hz, 5′OH), 4.78 (m, 1H, 4′H), 3.52 (m, 2H, 5′H). ^{19}F NMR (250.1 MHz, DMSO-d_6, ppm) δ: –120.88 (m, 1F, 6F). ESI-MS: 233.9 [M + H]+). EI anal. calcd.: C 66.94, H 5.19, N 6.01; found: C 66.85, H 5.34, N 6.12.

1-(2′,3′-Didesoxy-β-D-glycero-pent-2-enofuranosyl)-4,6-fluoroindole (10c)

This compound was obtained from **9c** as a white solid in 99% yield. TLC ($CHCl_3$–MeOH 95:5). R_f 0.52. ^{1}H NMR (400 MHz, DMSO-d_6, ppm) δ: 7.51 (dd, 1H, J = 1.8 Hz, 7H), 7.43 (d, 1H, J = 3.4 Hz, 2H), 7.03 (d, 1H, J = 1.3 Hz, 1′H), 6.89 (ddd, 1H, J = 1.8 Hz, J' = 10.3 Hz, J'' = 10.2 Hz, 5H), 6.56 (d, 1H, J = 3.4 Hz, 3H), 6.48 (m, 1H, 2′H), 6.13 (m, 1H, 2′H), 6.13 (m, 1H, 3′H), 4.87 (t, 1H, J = 5.4 Hz, 5′OH), 4.81 (m, 1H, 4′H), 3.51 (m, 2H, 5′H). ^{19}F NMR (235.4 DMSO-d_6, ppm) δ: –119.17 (m, 1F, 6F), –118.37 (m, 1F, 4F). ESI-MS: 251.9 $[M + H]^+$.

1-(2′,3′-Didesoxy-β-D-glycero-pent-2-enofuranosyl)-5-fluoroindole (10d)

This compound was obtained from **9d** as a white solid in 93% yield. TLC ($CHCl_3$–MeOH 95:5). R_f 0.46. ^{1}H NMR (400 MHz, DMSO-d_6, ppm) δ: 7.70 (m, 1H, 6H), 7.42 (d, 1H, J = 3.6 Hz, 1′H), 7.33 (m, 1H, 2H), 7.03 (m, 2H, 7H, 3′H), 6.52 (m, 2H, 4H, 2′H), 6.15 (d, 1H, J = 3.1 Hz, 3H), 4.86 (t, 1H, J = 5.4 Hz, 5′OH), 4.80 (m, 1H, 4′H), 3.55 (m, 2H, 5′H). ^{19}F NMR (282.3 MHz, DMSO-d_6, ppm) δ: –124.44 (m, 1F, 5F). ESI-MS: 233.7 $[M + H]^+$. EI anal. calcd.: C 66.94, H 5.19, N 6.01; found: C 66.80, H 5.49, N 5.83.

1-(2′,3′-Didesoxy-β-D-glycero-pent-2-enofuranosyl)-7-fluoroindole (10e)

This compound was obtained from **9e** as a white solid in 93% yield. TLC ($CHCl_3$–MeOH 95:5). R_f 0.51. ^{1}H NMR (400 MHz, DMSO-d_6, ppm) δ: 7.52 (m, 2H, 2H,6H), 7.40 (d, 1H, J = 3.4 Hz, 1′H), 7.03 (m, 1H, 4H), 6.91 (m, 1H, 5H), 6.50 (m, 2H, 3H,3′H), 6.13 (m, 1H, 2′H), 4.86 (t, 1H, J = 5.6 Hz, 5′OH), 4.78 (m, 1H, 4′H), 3.52 (m, 2H, 5′H). ^{19}F NMR (250.1 MHz, DMSO-d_6, ppm) δ: –120.88 (m, 1F, 6F). ESI-MS: 233.9 $[M + H]^+$. EI anal. calcd.: C 66.94, H 5.19, N 6.01; found: C 66.85, H 5.24, N 6.18.

General procedure for the preparation of 1′-desoxy-1′-(indolyl)-β-D-ribofuranose (16a–16f)

Compound 15 (4.4 mmol) and *N*-methyl-morpholine oxide (11.9 mmol) were dissolved in 50 mL of acetone–water (8:1) and OsO_4 (5.5 mL, 2.5% in 2-methyl-2-propanol) was added. The mixture was stirred at RT for 20 h, 10% $Na_2S_2O_4$ (15 mL) was then added and stirring was continued for 15 min. The mixture was treated with water (100 mL) and extraced with EtOAc (2 × 150 mL). The combined extracts were washed with brine, dried over $MgSO_4$, and concentrated to dryness. The residue was purified by flash column chromatography (hexane–EtOAc 1:2).

1′-Desoxy-1′-(4-fluoroindolyl)-β-D-ribofuranose (11a)

This compound was obtained from **10a** as white crystals in 69% yield. TLC (CH_2Cl_2–MeOH 95:5). R_f 0.21. ^{1}H NMR (400 MHz, DMSO-d_6, ppm) δ: 7.66 (d, 1H, J = 3.4 Hz, 2H), 7.42 (d, 1H, J = 8.3 Hz, 7H), 7.12 (m, 1H, 6H), 6.84 (m, 1H, 5H), 6.58 (d, 1H, J = 3.3 Hz, 3H), 5.88 (d, 1H, J = 6.1 Hz, 1′H), 5.34 (d, 1H, J = 5.4 Hz, 2′OH), 5.14 (s, 1H, 3′OH), 5.02 (t, 1H, J = 5.6 Hz, 5′OH), 4.26 (d, 1H, J = 5.0 Hz, 2′H), 4.08 (m, 1H, 3′H), 3.93 (m, 1H, 4′H), 3.61 (m, 2H, 5′H). ^{19}F NMR (250.4 MHz, DMSO-d_6, ppm) δ: –122.53 (m, 1F, 4F). ESI-MS: 265.7 $[M - H]^-$.

1′-Desoxy-1′-(6-fluoroindolyl)-β-D-ribofuranose (11b)

This compound was obtained from **10b** as white crystals in 45% yield. TLC (CH_2Cl_2–MeOH 95:5). R_f 0.21. ^{1}H NMR (250 MHz, DMSO-d_6, ppm) δ: 7.58 (d, 1H, J = 3.4 Hz, 2H), 7.53 (dd, 1H, J = 8.6 Hz, J' = 5.6 Hz, 4H), 7.46 (dd, 1H, J =

© 2007 NRC Canada

2.1 Hz, J' = 10.7 Hz, 7H), 6.91 (ddd, 1H, J = 8.6 Hz, J' = 2.1 Hz, J'' = 9.7 Hz, 5H), 6.51 (d, 1H, J = 3.4 Hz, 3H), 5.81 (d,1H, J = 6.1 Hz, 1′H), 5.30 (d, 1H, J = 6.7 Hz, 3′OH), 5.12 (d, 1H, J = 5.0 Hz, 2′OH), 5.03 (t, 1H, J = 5.3 Hz, 5′OH), 4.19 (m, 1H, 2′H), 4.08 (m, 1H, 3′H), 3.90 (m, 1H, 4′H), 3.61 (m, 2H, 5′H). ^{13}C NMR (62,9 MHz, DMSO-d_6, ppm) δ: 160.01 (C2), 135.70 (C4), 126. 58 (C7), 125.27 (C8), 121.38 (C6), 108.10 (C5), 102.16 (C9), 97.13 (C3), 89.04 (C1′), 84.88 (C4′), 73.90 (C2′), 70.21 (C3′), 61.42 (C5′), 124. 36 (C7), 110.43 (C5), 98.60 (C4), 52.47 (OCH_3). ^{19}F NMR (250.1 MHz, DMSO-d_6, ppm) δ: –120.95 (s, 1F, 6F). ESI-MS: 265.9 [M – H]$^-$. EI anal. calcd.: C 58.42, H 5.28, N 5.24; found: C 58.33, H 5.30, N 5.17.

1′-Desoxy-1′-(4,6-fluoroindolyl)-β-D-ribofuranose (11c)

This compound was obtained from **10c** as white crystals in 68% yield. TLC (hexane–EtOAc 1:2). R_f 0.15. ^{1}H NMR (400 MHz, DMSO-d_6, ppm) δ: 7.65 (d, 1H, J = 3.4 Hz, 2H), 7.41 (dd, 1H, J = 1.7 Hz, J' = 10.1 Hz, 7H), 6.88 (ddd, 1H, J = 2.0 Hz, J' = 10.3 Hz, J'' = 10.3 Hz, 5H), 6.58 (d, 1H, J = 6.6 Hz, 3H), 5.82 (d, 1H, J = 6.2 Hz, 1′H), 5.34 (d, 1H, J = 6.7 Hz, 2′OH), 5.14 (d, 1H, J = 4.9 Hz, 3′OH), 5.06 (t, 1H, J = 5.3 Hz, 5′OH), 4.23 (m, 1H, 2′H), 4.07 (m, 1H, 3′H), 3.94 (m, 1H, 4′H), 3.62 (m, 2H, 5′H). ^{19}F NMR (235.2 MHz, DMSO-d_6, ppm) δ: –118.17 (m, 1F, 6F), –119.13 (m, 1F, 4F). ESI-MS: 283.8 [M + H]$^+$.

1′-Desoxy-1′-(5-fluoroindolyl)-β-D-ribofuranose (11d)

This compound was obtained from **10c** as white crystals in 52% yield. TLC (hexane–EtOAc 1:2). R_f 0.21. ^{1}H NMR (400 MHz, DMSO-d_6, ppm) δ: 7.70 (d, 1H, J = 3.4 Hz, 2H), 7.40 (d, 1H, J = 8.1 Hz, 7H), 7.12 (m, 1H, 6H), 6.84 (m, 1H, 4H), 6.52 (d, 1H, J = 3.4 Hz, 3H), 5.78 (d, 1H, J = 6.2 Hz, 1′H), 5.30 (d, 1H, J = 5.4 Hz, 2′OH), 5.18 (s, 1H, 3′OH), 5.04 (t, 1H, J = 5.6 Hz, 5′OH), 4.36 (d, 1H, J = 5.0 Hz, 2′H), 4.09 (m, 1H, 3′H), 3.91 (m, 1H, 4′H), 3.62 (m, 2H, 5′H). ^{19}F NMR (250.4 MHz, DMSO-d_6, ppm) δ: –124.54 (m, 1F, 5F). ESI-MS: 265.7 [M – H]$^-$).

1′-Desoxy-1′-(7-fluoroindolyl)-β-D-ribofuranose (11e)

This compound was obtained from **10e** as white crystals in 48% yield. TLC (CH_2Cl_2–MeOH 95:5). R_f 0.22. ^{1}H NMR (400 MHz, DMSO-d_6, ppm) δ: 7.72 (d, 1H, J = 3.2 Hz, 2H), 7.40 (d, 1H, J = 8.3 Hz, 4H), 7.10 (m, 1H, 6H), 6.84 (m, 1H, 5H), 6.58 (d, 1H, J = 3.2 Hz, 3H), 5.88 (d, 1H, J = 6.1 Hz, 1′H), 5.32 (d, 1H, J = 5.4 Hz, 2′OH), 5.12 (s, 1H, 3′OH), 5.01 (t, 1H, J = 5.6 Hz, 5′OH), 4.26 (d, 1H, J = 5.0 Hz, 2′H), 4.08 (m, 1H, 3′H), 3.93 (m, 1H, 4′H), 3.61 (m, 2H, 5′H). ^{19}F NMR (250.4 MHz, DMSO-d_6, ppm) δ: –122.50 (m, 1F, 7F). ESI-MS: 265.9 [M – H]$^-$).

Acknowledgement

The authors acknowledge the financial support by the Deutsche Forschungsgemeinschaft, SFB 579.

References

1. J. Parsch and J.W. Engels. J. Am. Chem. Soc. **124**, 5664 (2002).
2. A. Živković and J.W. Engels. Nucleosides, nucleotides and nucleic acids, **24**, 1023 (2005).
3. J. Božilović and J.W. Engels. Collect. Symp. Ser., **7**, 385 (2005).
4. J.B. Blair, D. Kurrasch-Orbaugh, D. Marona-Lewicka, M.G. Cumbay, V.J. Watts, E.L. Barker, and D.E. Nichols. J. Med. Chem. **43**, 4701 (2000).
5. A.F. Flavia, R.A.R. da Rosa, and M.G. Nascimento. J. Braz. Chem. Soc. **14**, 11 (2003).
6. H. Rosemeyer and F. Seela. Helv. Chim. Acta, **71**, 1573 (1988).
7. V. Rolland, M. Kotera, and J. Lhomme. Synth. Comm. **27**, 3505 (1997).
8. J.W. Bats, J. Parsch, and J.W. Engels. Acta Crystallogr. Sect. C. **56**, 201 (2000).
9. B.M. O'Neil, J.E. Ratto, K.L. Good, D.C. Tahmassebi, S.A. Helquist, J.C. Morales, and E.T. Kool. J. Org. Chem. **67**, 5869 (2002).

© 2007 NRC Canada

High-quality oligo-RNA synthesis using the new 2′-*O*-TEM protecting group by selectively quenching the addition of *p*-tolyl vinyl sulphone to exocyclic amino functions[1]

Chuanzheng Zhou, Wimal Pathmasiri, Dmytro Honcharenko, Subhrangsu Chatterjee, Jharna Barman, and Jyoti Chattopadhyaya

Abstract: During the F^--promoted deprotection of the oligo–RNA, synthesized using our 2′-*O*-(4-tolylsulfonyl)ethoxymethyl (2′-*O*-TEM) group [Org. Biomol. Chem. **5**, 333 (2007)], *p*-tolyl vinyl sulphone (TVS) is formed as a by-product. The TVS formed has been shown to react with the exocyclic amino functions of adenosine (A), guanosine (G), and cytidine (C) of the fully deprotected oligo–RNA to give undesirable adducts, which are then purified by HPLC and unambiguously characterized by ^{1}H, ^{13}C Heteronuclear Multiple Bond Correlation (HMBC) NMR and mass spectroscopic analysis. The relative nucleophilic reactivities of the nucleobases toward TVS have been found to be the following: N^6–A > N^4–C > N^2–G > > N^3–U. This reactivity of TVS toward RNA nucleobases to give various Michael adducts could, however, be suppressed by using various amines as scavengers. Among all these amines, morpholine and piperidine are the most efficient scavenger for TVS, which gave highly pure oligo–RNA even in the crude form and can be used directly in RNA chemical biology studies.

Key words: RNA synthesis, RNA alkylation, *p*-tolyl vinyl sulphone, Michael addition.

Résumé : Au cours de la déprotection sous l'influence de l'ion fluorure de l'oligo–ARN synthétisé à l'aide de notre groupe protecteur 2′-*O*-(4-tolylsulfonyl)éthoxyméthyl (2′-*O*-TEM) [Org. Biomol. Chem. **5**, 333 (2007)], il y a formation de la *p*-tolyl vinyl sulfone (TVS) comme sous-produit. Il a été montré que la TVS réagit avec les fonctions aminées exocycliques de l'adénosine (A), de la guanosine (G) et de la cytidine (C) de l'oligo-ARN complètement déprotégé pour conduire à la formation de produits indésirables qui ont été purifiés et caractérisés sans ambiguïté par spectrométrie de masse et par corrélation des liaisons multiples hétéronucléaires (CLMH) des spectres RMN du ^{1}H et du ^{13}C. On a établi que les réactivités nucléophiles relatives des nucléobases vis-à-vis de la TVS sont dans l'ordre suivant: N^6–A > N^4–C > N^2–G > > N^3–U. En utilizant diverses amines comme pièges, il serait toutefois possible d'éliminer cette réactivité de la TVS vis-à-vis des nucléobases pour conduire à divers adduits de Michael. Parmi ces amines, la morpholine et la pipéridine sont les pièges les plus efficaces pour la TVS; leur utilization conduit, même dans le produit brut, à la formation d'oligo–ARN très pur qui peut être utilizé dans des études de chimie biologique de l'ARN

Mots-clés : synthèse d'ARN, alkylation d'ARN, *p*-tolyl vinyl sulfone, addition de Michael.

[Traduit par la Rédaction]

Introduction

The discovery of RNA interference (RNAi) (1) and especially the finding that small interfering RNA (siRNA) (2) can induce degradation of the target RNA have highlighted the need for facile chemical synthesis of oligo–RNA sequences (e.g., a synthetic 21 mer siRNA) (2) and have thereby stimulated work on the development of new methodology for the chemical synthesis of RNA (3–7). Recently, we have developed a new RNA synthesis strategy based on protecting 2′-OH with a 2-(4-tolylsulfonyl)ethoxymethyl (2′-*O*-TEM) (8) group and showed its successful use in the solid-phase synthesis of at least 12 different oligo–RNAs of varying sizes (14–38 mer long) and sequences (8). The main advantages of this 2′-*O*-TEM group based RNA synthesis strategy (8) are (*i*) the low coupling time (120s), (*ii*) high

Received 5 February 2007. Accepted 13 March 2007. Published on the NRC Research Press Web site at canjchem.nrc.ca on 27 April 2007.

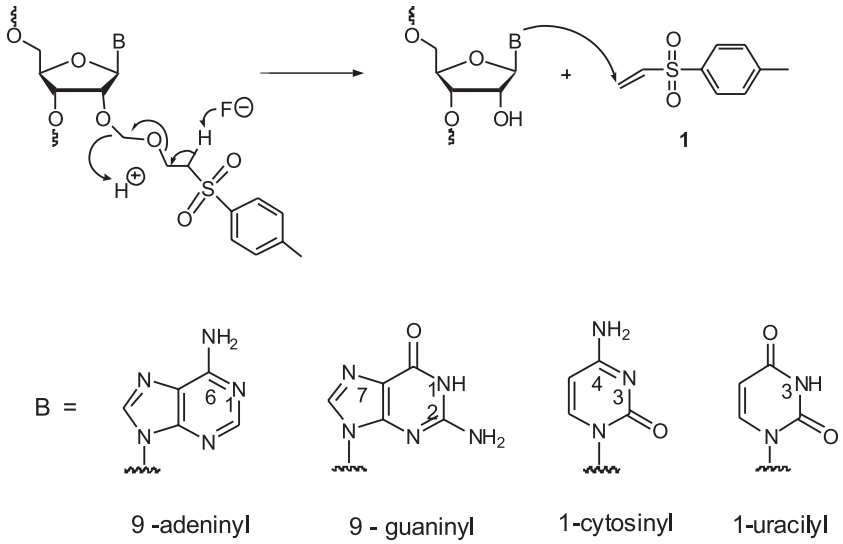
In honor of the career contributions of Professor Kelvin Kenneth Ogilvie and for his significant contributions in the field of nucleoside/nucleic acid chemistry and automated DNA and RNA synthesis.

C. Zhou, W. Pathmasiri, D. Honcharenko, S. Chatterjee, J. Barman, and J. Chattopadhyaya.[2] Department of Bioorganic Chemistry, Box 581, Biomedical Center, Uppsala University, S-751 23 Uppsala, Sweden.

[1]This article is part of a Special Issue dedicated to Professor Kelvin K. Ogilvie.
[2]Corresponding author (e-mail: jyoti@boc.uu.se).

 doi:10.1139/V07-025 © 2007 NRC Canada

Scheme 1. Mechanism of deprotection of the 2′-*O*-TEM group and the adduct formation with tolyl vinyl sulfone (**1**).



stepwise coupling yield (97%–99%), leading to (*iii*) the crude RNA, obtained after a simple deprotection step. The crude form RNA was sufficiently pure for chemical biology research without the need for any additional purification steps.

The 2′-*O*-TEM group is stable upon ammonia treatment and can be quickly cleaved by 1 mol/L tetrabutylammonium fluoride (TBAF) in THF through F^--promoted β elimination (Scheme 1). But the by-product *p*-tolyl vinyl sulphone (TVS) (**1**), which is generated during deprotection, attacks the nucleophilic sites of nucleobases of the oligo–RNA to form some undesirable side products that somewhat reduce the purity of the oligo–RNA. To obtain clean oligo–RNA at the end of the synthesis, we had earlier employed a mixture of 10% (*v*/*v*) *n*-propylamine and 1% (*v*/*v*) bis(2-mercaptoethyl)ether in 1 mol/L TBAF–THF as a scavenger for TVS during the deprotection of the 2′-*O*-TEM group. Clearly, we wanted to find other neutral alternative(s) to this scavenger because bis(2-mercaptoethyl)ether has a foul odour and it can also deactivate many enzymes, even in trace amounts (ppm).

Earlier work (8) has excluded N^3 of 1-uracilyl as a reactive centre for the side product formation. To this point, the potential nucleophilic sites have been known to be N^1 of 9-adeninyl (9, 10), N^7 and N^1 of 9-guaninyl (11, 12), and N^3 of 1-cytosinyl (13, 14). In this study, through isolation of the pure adducts formed with TVS and by identifying them unambiguously by MS and NMR, we have unexpectedly found that N^2 of 9-guaninyl, N^4 of 1-cytosinyl, and especially N^6 of 9-adeninyl are the reactive nucleophilic sites for adduct formation with TVS, and more powerful scavengers were therefore developed.

Results and discussion

Deprotection of the 2′-*O*-TEM group from dimeric RNAs

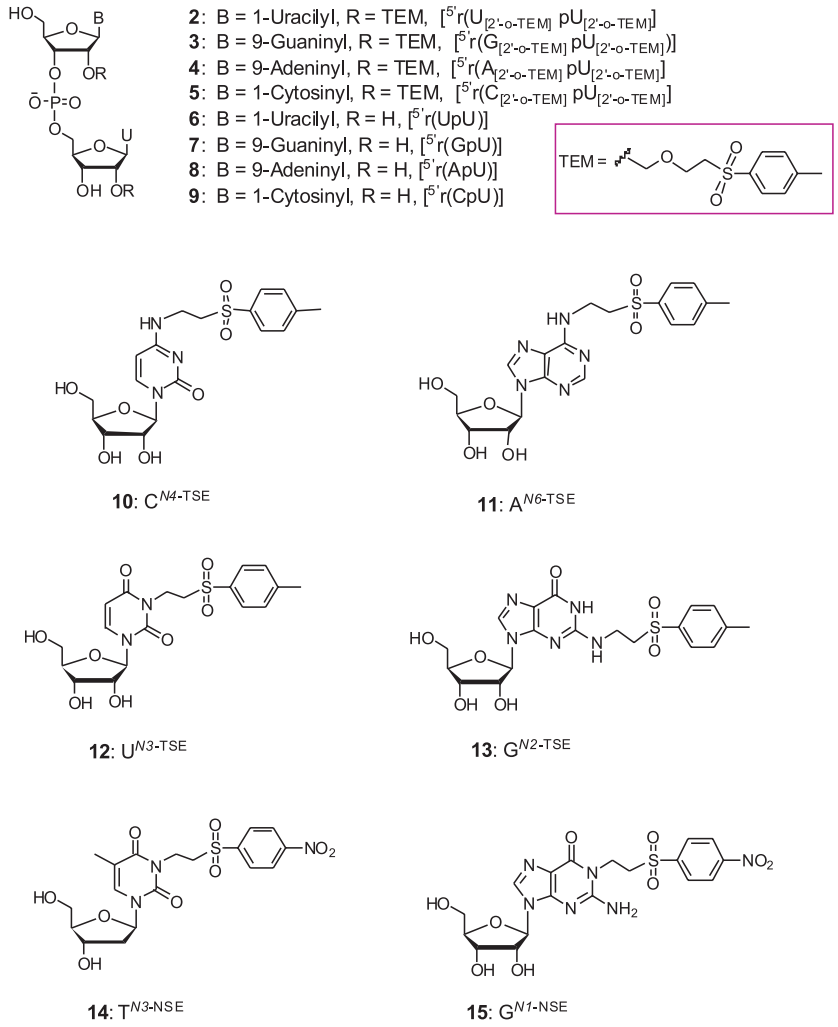
It was known (8) that when deprotecting with 1 mol/L TBAF–THF, pure poly-U can be easily obtained as the sole product, hence the lactam function of 1-uracilyl and the internucleotidic phosphate backbone are not amenable to adduct formation with TVS. We anticipated that the possible nucleobases that could potentially be involved in the adduct formation with TVS are 9-guaninyl, 9-adeninyl, and 1-cytosinyl moieties in oligo–RNA. Keeping this in mind, four dimeric ribonucleotides, $^{5'}r(U_{[2'\text{-}o\text{-TEM}]}\ pU_{[2'\text{-}o\text{-TEM}]})$ (**2**), $^{5'}r(G_{[2'\text{-}o\text{-TEM}]}\ pU_{[2'\text{-}o\text{-TEM}]})$ (**3**), $^{5'}r(A_{[2'\text{-}o\text{-TEM}]}\ pU_{[2'\text{-}o\text{-TEM}]})$ (**4**), $^{5'}r(C_{[2'\text{-}o\text{-TEM}]}\ pU_{[2'\text{-}o\text{-TEM}]})$ (**5**), (Scheme 2), were synthesized. They were treated with 1 mol/L TBAF–THF for 4 h at RT, then the reaction mixtures were analyzed by reverse phase HPLC (RP-HPLC). The RP-HPLC profiles are shown in Fig. 1.

As expected, $^{5'}r(U_{[2'\text{-}o\text{-TEM}]}\ pU_{[2'\text{-}o\text{-TEM}]})$ (**2**) upon treatment with 1 mol/L TBAF–THF gave a single product (Fig. 1*A*, R_T = 5.89 min), which proved to be the desired product $^{5'}r(UpU)$ (**6**) by MALDI-TOF MS (*m*/*z* calcd.: 551.10 $[MH]^+$; found: 551.11). Treatment of $^{5'}r(G_{[2'\text{-}o\text{-TEM}]}\ pU_{[2'\text{-}o\text{-TEM}]})$ (**3**) with 1 mol/L TBAF–THF also gave the desired product $^{5'}r(GpU)$ (**7**). (Fig. 1*B*, R_T = 6.56 min, *m*/*z* calcd.: 590.12 $[MH]^+$; found: 590.11). We therefore could safely exclude 1-uracilyl and 9-guaninyl aglycons as substrates for adduct formation with TVS.

The RP-HPLC analysis of the reaction of $^{5'}r(C_{[2'\text{-}o\text{-TEM}]}\ pU_{[2'\text{-}o\text{-TEM}]})$ (**5**) is shown in Fig. 1*C*. The product with R_T = 4.75 min was proved by MS to be the fully deprotected product $^{5'}r(CpU)$ (**9**) (*m*/*z* calcd.: 550.12 $[M]^-$; found: 550.12). However, the peak appearing at 18.43 min (Fig. 1*C*) was the major product, which was analyzed by MS (*m*/*z* found: 730.32 $[M]^-$). This suggested that this product was formed by the reaction of one molecule of PVS with $^{5'}r(CpU)$ (**9**). This major product was separated and its base composition was analyzed by digesting it with mixture of phosphodiesterase I and shrimp alkaline phosphatase (see experimental section). The digestion mixture was applied to RP-HPLC analysis. As shown in the Fig. 1*C* inset, the digestion gave two products. One appears at 4.06 min, corresponding to uridine. The second peak appears at 17.01 min. It was probably formed by the addition of TVS to cytidine and clearly needed further characterization (represented by **X** in Fig. 1*C*).

© 2007 NRC Canada

Scheme 2. **10**: N^4-(4-tolylsulfonylethyl)cytidine ($C^{N4\text{-}TSE}$); **11**: N^6-(4-tolylsulfonylethyl)adenosine ($A^{N6\text{-}TSE}$); **12**: N^3-(4-tolylsulfonylethyl)uridine ($U^{N3\text{-}TSE}$); **13**: N^2-(4-tolylsulfonylethyl)guanosine ($G^{N2\text{-}TSE}$); **14**: N^3-(4-nitrophenylsulfonylethyl)thymidine ($T^{N3\text{-}NSE}$); **15**: N^1-(4-nitrophenylsulfonylethyl)guanosine ($G^{N1\text{-}NSE}$).



Dimer $^{5'}r(A_{[2'\text{-}o\text{-}TEM]}\ pU_{[2'\text{-}o\text{-}TEM]})$ (**4**) was treated with 1 mol/L TBAF–THF and gave a very small amount of the desired product $^{5'}r(ApU)$ (**8**) (Fig. 1*D*, R_T = 8.54 min, *m*/*z* calcd.: 572.41[M]$^-$; found: 572.31). The predominant reaction product (*m*/*z* found: 754.34 [M]$^-$) appears at 21.00 min. Base composition analysis of this major product by enzymatic digestion, as described earlier, gave uridine (Fig. 1*D* inset, R_T = 3.95 min) and another product (Fig. 1*D*, represented by Y, R_T = 21.83 min). This result suggested that both the cytidine and adenosine were reactive toward adduct formation with TVS.

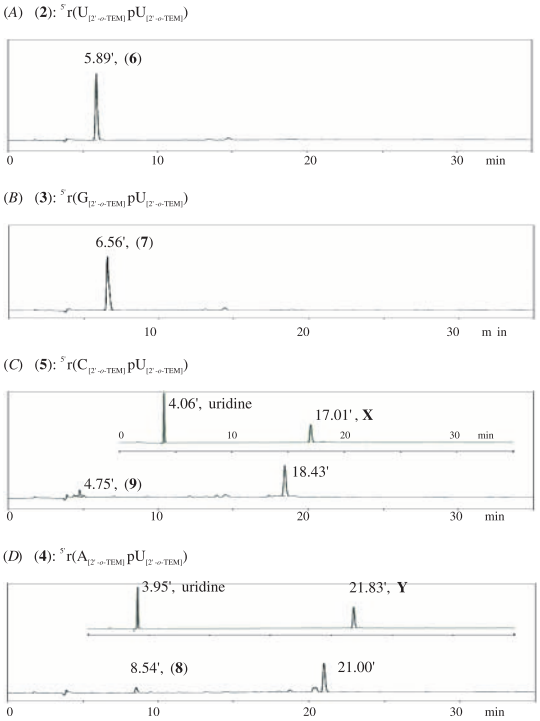
Characterization of TVS adducts with aglycones of RNA

To determine the chemical nature of the adducts (**X** and **Y** in the HPLC elution profile in Figs. 1*C* and 1*D*), either cytidine or adenosine was treated with 3 equiv. of TVS at RT in 1 mol/L TBAF–THF for 24 h. The major product of the reaction between cytidine and TVS was separated by silica gel chromatography. This compound showed $[MH]^+$ at *m*/*z* 426.17, which suggested that it was an unimolecular adduct of TVS and cytidine. The chemical shift of β-C ($\delta_{\beta\text{-}C}$, 34.69 ppm, see Fig. 2 and Table 1) (12) suggested that the TVS is attached to the N atom, and the potential site could be either N^4 or N^3 of cytidine. The assignment of the covalent binding site of TVS could easily be achieved by ^1H, ^{13}C Heteronuclear Multiple Bond Correlation (HMBC) NMR experiment (12). As shown in Fig. 2*A*, the β-H shows a strong cross peak with C4 (shown by red line) but no cross-correlation with the C2, which strongly supports the explanation that the TVS has been formed as an adduct to N^4 of cytidine to give N^4-(4-tolylsulfonylethyl)cytidine ($C^{N4\text{-}TSE}$, **10**).

The reaction between adenosine and TVS gave a major product with $[MH]^+$ at *m*/*z* 450.18, which also indicated that a unimolecular adduct had formed between TVS and adenosine. Two unambiguous NMR proofs were used to confirm that TVS is indeed covalently bonded to the N^6 of adenosine to give product N^6-(4-tolylsulfonylethyl)adenosine ($A^{N6\text{-}TSE}$, **11**): (*i*) in the ^1H,^{13}C HMBC spectrum (Fig. 2*B*), the HN^6 shows cross coupling with C5, C6, and β-C, and (*ii*) more direct proof is the fact that the HN^6 of adenosine shows a strong cross peak with β-H (Fig. S2.1) in the ^1H, ^1H

© 2007 NRC Canada

Fig. 1. RP-HPLC analysis of the reaction products upon treatment of compounds **2–5** with 1 mol/L TBAF–THF at RT for 4 h. The products (R_T = 18.43 min in *C* and R_T = 21.00 min in *B* were digested respectively by mixture of phosphodiesterase and alkaline phosphatase. HPLC analysis of the digestion reaction is shown in the inset. RP-HPLC conditions: 0′→10′→35′, A →A–B 9:1, *v*/*v*→A–B 2:8, RT, flow rate 1 mL/min. Buffer A: 0.1 mol/L TEAA in H_2O–CH_3CN (*v*/*v*, 95:5). Buffer B: 0.1 mol/L TEAA in H_2O–CH_3CN (*v*/*v* 50:50).



COSY NMR spectrum, thereby confirming that the N^6 of adenosine has undergone a conjugate Michael addition to TVS.[3]

Co-injection of compound **10** with **X** on RP-HPLC has also shown that they are the same compound. In the same way, **Y** was shown to be compound **11** (Fig. S5.1 and S5.2).[3]

It has been reported that thymidine and guanosine can react with with acrylonitrile or phenylvinyl sulfone in the presence of a base such as tetra-*n*-butylammonium hydroxide (12), TBAF–THF (15), or ammonia (16, 17). These α,β-unsaturated compounds were adducted to the N^3 of thymidine (12, 15–17) and the N^1 of guanosine (12), respectively. Here, we have also studied the reaction between uridine or guanosine with TVS in 1 mol/L TBAF–THF. As reported (12), TVS is adducted to the N^3 of uridine (NMR spectra shown in Figs. 2*C* and S3) to give the product N^3-(4-tolylsulfonylethyl)uridine ($U^{N3\text{-}TSE}$, **12**).[3] For guanosine, the predominant product was proved to be N^2-(4-tolylsulfonylethyl)guanosine ($G^{N2\text{-}TSE}$, **13**) in an unambiguous manner by NMR and not $G^{N1\text{-}TSE}$, as earlier believed (12). Thus, (*i*) the imino proton is present ($\delta_{N1\text{-}H}$ = 10.94 ppm, see Fig. S4.1) in the ^1H NMR spectrum of **13**; (*ii*) the $\delta_{\beta\text{-}C}$ and $\delta_{\beta\text{-}H}$ (see Table 1) in **13** are much different than in compound N^1-(4-nitrophenylsulfonylethyl)guanosine ($G^{N1\text{-}NSE}$, **15**, Scheme 2) (12); (*iii*) in the ^1H,^{13}C HMBC spectrum (Fig. 2*D*), β-*H* shows a strong cross peak with C2 but none with C5, C6, or C8 in **13**.[3]

The Michael addition between the α,β-unsaturated compound, such as acrylonitrile with DNA or RNA under different conditions, leads to cyanoethylation of nucleobases, which has been studied extensively. Because of the natural electronic structure of nucleobases (18), the cyanoethylation generally occurs at N^3 of uridine (19) and cytidine (9), N^1 of adenosine (9, 20), N^7, and N^1 of guanosine (9, 12). Though cyanoethylation at N^6 of adenosine (20) was also observed, it was in fact obtained by Dimroth rearrangement (21) of N^1 of cyanoethylated adenosine in the presence of a strong base such as aqueous sodium hydroxide. Alkylation of nucleosides with other reagents such as diazomethane and dimethyl sulfate also occurs at the ring nitrogen atom such as N^7 and N^1 of purine (10, 11) and N^3 of pyrimidine (11, 14).

The present unexpected findings may have important applications in directly alkylating exocyclic amines of nucleosides as probes to determine the structure and (or) function of a nucleic acid (22, 23). Many methods have been developed for the alkylation of exocyclic amino groups (24–26), but these methods (24–26) are multi-step reactions and are time-consuming and laborious. To our knowledge, no direct alkylation method has been developed until now. The present finding that TVS can indeed be added selectively to an exocyclic amino of cytidine, adenosine, and guanosine provides an easier way to the direct alkylation of exocyclic amino groups of nucleobases if they exist as a part of a non-hydrogen-bonded loop or hairpin structure in the RNA scaffolds. Moreover, the phenyl moiety of TVS is relatively easy to derivatize for fluorescence detection purposes. Alternatively, by attaching other functional groups to the phenyl moiety, such as some specific cross-linking agents, we can conveniently introduce various functional groups to the non-hydrogen-bonded exocyclic amino of the nucleobases to map the folding in the RNA scaffolds by estimating spatial proximities.

Relative nucleophilic reactivities of the exocyclic amino groups of RNA toward TVS

Earlier we showed that in dimeric RNAs neither uridine nor guanosine participates in the adduct formation with TVS. Subsequently we showed that all of the four monomeric ribonucleosides are found to react with TVS. This apparent contradiction may be explained by comparing the nucleophilic reactivities of different ribonucleoside aglycons in an oligo–RNA toward TVS. We therefore chose a tetrameric RNA, 5′r(UpApCpG) (**16**, Scheme 3), for a model study; 0.5 OD (12.5 μmol) of **16** was treated with 0, 1/4, 1/2, 1, 2, 4, and 20 equiv. of TVS, respectively, in 1 mol/L TBAF–THF (total reaction volume 40 μL) at RT for 24 h. The aliquots of the reactions were analyzed by RP-HPLC (Fig. 3). The maldi-tof MS spectra showed that each of the

[3] Supplementary data for this article are available on the journal Web site (http://canjchem.nrc.ca) or may be purchased from the Depository of Unpublished Data, Document Delivery, CISTI, National Research Council Canada, Ottawa, ON K1A 0R6, Canada. DUD 5155. For more information on obtaining material refer to http://cisti-icist.nrc-cnrc.gc.ca/irm/unpub_e.shtml.

© 2007 NRC Canada

Fig. 2. ^{1}H, ^{13}C HMBC NMR spectrum of compounds **10** (panel *A*, crosspeaks at δ 3.81), **11** (panel *B*, crosspeaks at δ 6.9), **12** (panel *C*, crosspeaks at δ 4.36), and **13** (panel *D*, crosspeaks at δ 3.51, 3.58).

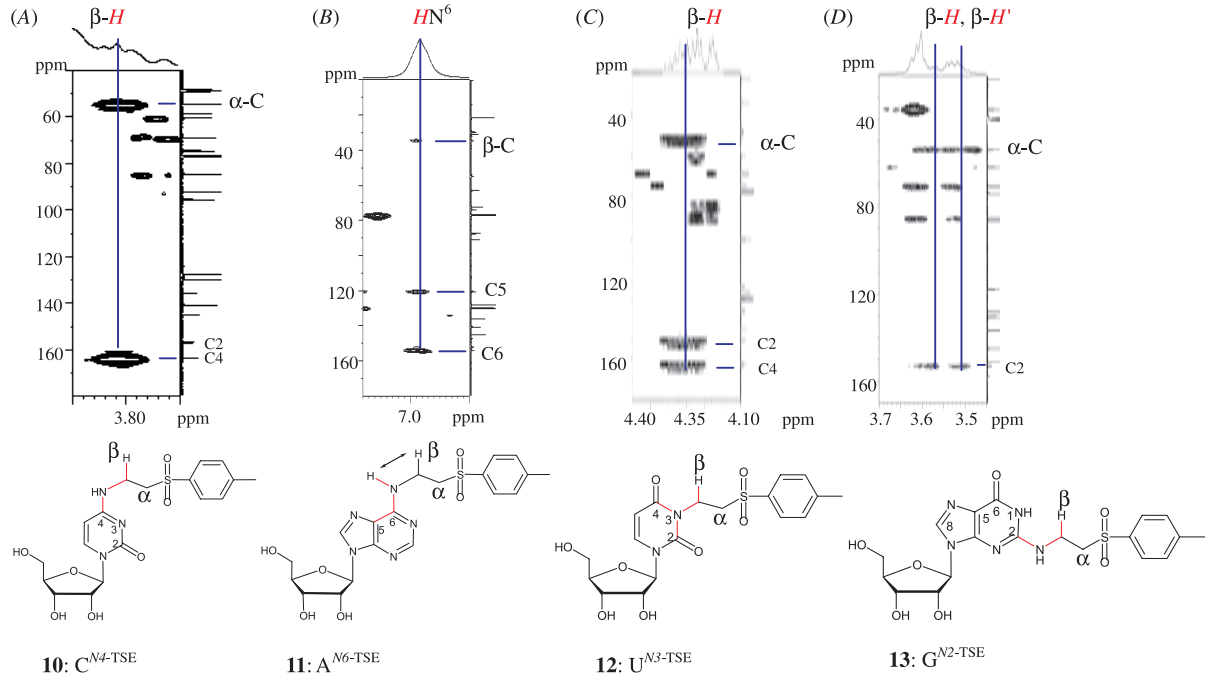


Table 1. Comparison of the chemical shifts of β-H and β-C of compounds **10**–**15**.

Compounds	$\delta_{\beta\text{-C}}$ (ppm)	$\delta_{\beta\text{-H}}$ (ppm)
10	34.69	3.80
11	34.65	3.89
12	34.95	4.25
13	35.66	3.61, 3.50
14[a]	34.60	4.12
15[a]	34.70	4.31

[a]The NMR data are taken from Mag and Engels (12).

three products **17** (*m/z* found: 1406.23 $[MH]^+$), **18** (*m/z* found: 1406.23 $[MH]^+$), and **19** (*m/z* found: 1406.26 $[MH]^+$) has only one molecule of TVS attached, thereby suggesting that the products **17**, **18**, and **19** are isomeric in nature. Furthermore, base composition analysis of these products by enzyme digestion showed that **17** is $^{5'}$r(UpApCpG$^{N2\text{-TSE}}$), **18** is $^{5'}$r(UpAp$C^{N4\text{-TSE}}$ pG), and **19** is $^{5'}$r(Up$A^{N6\text{-TSE}}$ pCpG) (see Fig. 4).

The yields of the three products in the reactions between $^{5'}$r(UpApCpG) (**16**) and different stoichiometries of TVS are listed in Table 2. In the presence of a limited amount of TVS, (1/4, 1/2 equiv.), only N^6 of adenosine was alkylated to give $^{5'}$r(Up$A^{N6\text{-TSE}}$ pCpG) (**19**). With the increase in concentration of TVS (1 or 2 equiv.), N^4 of cytidine was also alkylated to give $^{5'}$r(UpAp$C^{N4\text{-TSE}}$ pG) (**18**). By increasing the amount of TVS further to 20 equiv., a small amount of product by the alkylation of N^2 of guanosine was also observed to give $^{5'}$r(UpApCpG$^{N2\text{-TSE}}$) (**17**). This proves that the alkylation tendency of ribonucleotide by TVS in oligo–RNA in 1 mol/L TBAF–THF follows the sequence, N^6 – A > N^4 – C > N^2 – G > > N^3 – U. By controlling the concentration of TVS, selective alkylation of N^6 of adenosine, or both N^6 of adenosine and N^4 of cytidine, or all the exocyclic amino functions of ribonucleobases is possible. Since all the exocyclic amino functions participate in H-bond formation in the tertiary structure of nucleic acid, their selective alkylation by TVS gives the possibility of identifying those nucleobases that are not hydrogen bonded, and thus TVS can be used as a chemical probe for the structure and function of the nucleic acid.

Morpholine and piperidine as scavenger for TVS to avoid adduct formation

In the 2′-*O*-TEM group based solid-phase RNA synthesis (8), a mixture of 10% *n*-propylamine and 1% bis(2-mercaptoethyl) ether was used as the scavenger for TVS. Two disadvantages of employing bis(2-mercaptoethyl)ether as the deprotecting agent are its foul odour and its ability, in trace amounts, to possibly cause enzyme deactivatation in biological assays. In this study we wanted to use an appropriate amine as the sole scavenger to examine if the quality of the crude RNA could be further improved.

The Michael addition of amine to TVS (27–29) has shown that primary amines are notably less reactive than secondary amines because the former binds to two moles of solvent through H-bonds, compared with the latter that binds only to one mole of the solvent. It was also shown (27–29) that large differences in the basicity of amines has relatively little effect on the reactivity. Thus morpholine (pK_a = 8.4) is about one seventh as reactive as piperidine (pK_a = 11.1), but the former is > 100 times less basic. In our case, the ideal amine should have better nucleophilicity toward TVS than the exocyclic amino groups of the nucleobases of RNA, and at the same time the basicity of the amine cannot compromise any oligo–RNA chain cleavage. Keeping this in mind, several types of amines with very different pK_a values were se-

© 2007 NRC Canada

Scheme 3.

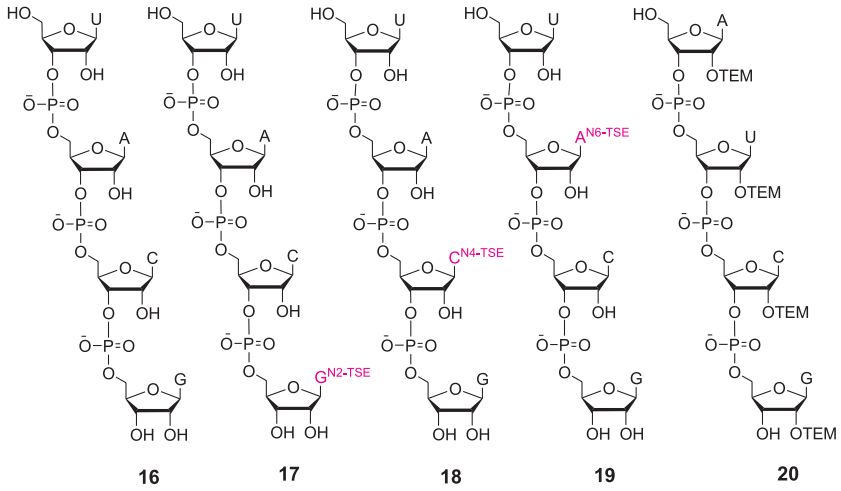
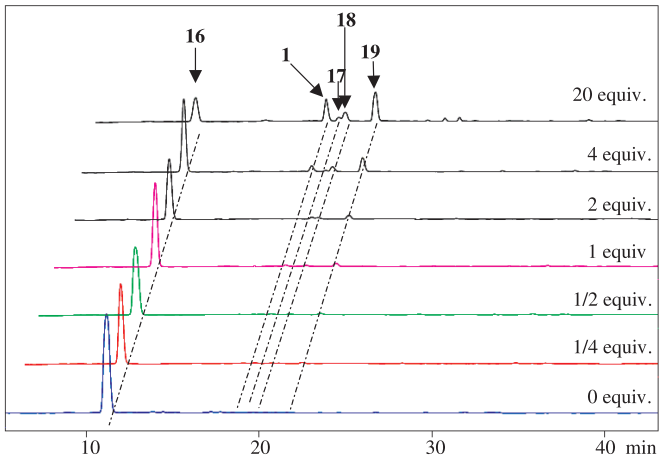


Fig. 3. RP-HPLC analysis of the reactions between $^{5'}$r(UpApCpG) (**16**) (0.5 OD, 12.5 µmol) with 0, 1/4, 1/2, 1, 2, 4, and 20 equiv. of TVS in 1 mol/L TBAF–THF at RT for 24 h. Each reaction has the same total volume of 40 µL. RP-HPLC conditions: 0′→10′→42′, A→A–B 9:1 →B, RT, flow rate 1 mL/min. Buffer A: 0.1 mol/L TEAA in H_2O–CH_3CN (*v*/*v*, 95:5). Buffer B: 0.1 mol/L TEAA in H_2O–CH_3CN (*v*/*v* 50:50).

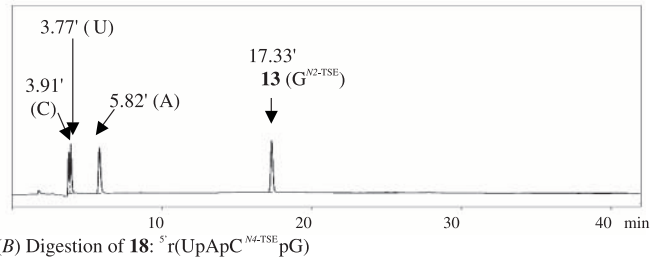


lected to test their abilities as scavengers of TVS in 1 mol/L TBAF–THF solution. The $^{5'}$r(A$_{[2'\text{-}o\text{-TEM}]}$ pU$_{[2'\text{-}o\text{-TEM}]}$ pC$_{[2'\text{-}o\text{-TEM}]}$ pG$_{[2'\text{-}o\text{-TEM}]}$ (**20**, Scheme 3) was used as the model compound and was treated with 1 mol/L TBAF–THF containing 10% (*v*/*v*) of different amines at RT for 24 h, and the reaction mixtures were analyzed by RP-HPLC (Fig. S7).[3] The percentage of chain cleavage product and side products formed through the reaction of TVS to oligo–RNA were obtained by integrating the HPLC profile (see Fig. S7) and they are given in Table 3.[3]

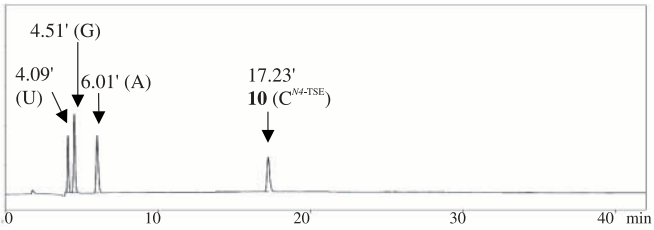
Table 3 shows that a primary or secondary amine, such as *n*-propylamine, piperidine, or morpholine, when used alone can scavenge TVS more efficiently than the standard deprotection condition (8) [a mixture of *n*-propylamine and bis(2-mercaptoethyl)ether] employed earlier for the deprotection of the 2′-*O*-TEM group. Among these amines, the morpholine and piperidine are especially attractive.

Fig. 4. The compounds **17**, **18**, and **19** were digested by a mixture of phosphodiesterase and alkaline phosphatase. The HPLC profiles of digestion mixture are shown in (*A*) **17**, (*B*) **18**, and (*C*) **19.** RP-HPLC conditions: 0′→10′→42′, A→A–B 9:1, *v*/*v* →B, RT, flow rate 1 mL/min. Buffer A: 0.1 mol/L TEAA in H_2O–CH_3CN (*v*/*v*, 95:5). Buffer B: 0.1 mol/L TEAA in H_2O–CH_3CN (*v*/*v* 50:50). Abbreviations are A = adenosine, G = guanosine, C = cytidine, U = uridine, $A^{N6\text{-TSE}}$ = N^6-(4-tolylsulfonylethyl)adenosine, $C^{N4\text{-TSE}}$ = N^4-(4-tolylsulfonylethyl)cytidine, $G^{N2\text{-TSE}}$ = N^2-(4-tolylsulfonylethyl)guanosine.

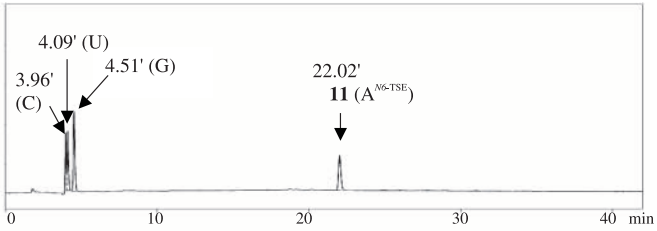
(*A*) Digestion of **17**: $^{5'}$r(UpApCpG$^{N2\text{-TSE}}$)



(*B*) Digestion of **18**: $^{5'}$r(UpApC$^{N4\text{-TSE}}$pG)



(*C*) Digestion of **19**: $^{5'}$r(UpA$^{N6\text{-TSE}}$pCpG)



© 2007 NRC Canada

Table 2. The yields (%) of three isomeric products **17**, **18**, and **19** in the reactions between $^{5'}$r(UpApCpG) (**16**) and different stoichiometries of TVS (**1**).

Stoichiometry of TVS (**1**)	$^{5'}$r(UpApCpG$^{N2\text{-}TSE}$) (**17**)	$^{5'}$r(UpApC$^{N4\text{-}TSE}$ pG) (**18**)	$^{5'}$r(UpA$^{N6\text{-}TSE}$ pCpG) (**19**)
0	0	0	0
1/4	0	0	1.4
1/2	0	0	1.5
1	0	1.0	3.4
2	0	1.9	5.1
4	0.8	5.3	15.1
20	4.5	13.2	42.0

Table 3. Deprotection[a] of **20** with 1 mol/L TBAF–THF containing different amines.

Amine[a]	pK_a[c]	Oligo–RNA chain cleavage (%)	TVS adduct with oligo–RNA (%)
Standard condition[b]	—	9.1	17.0
n-Propylamine	10.71	1.6	8.1
Piperidine	11.12	8.3	0
Morpholine	8.33	0	7.2

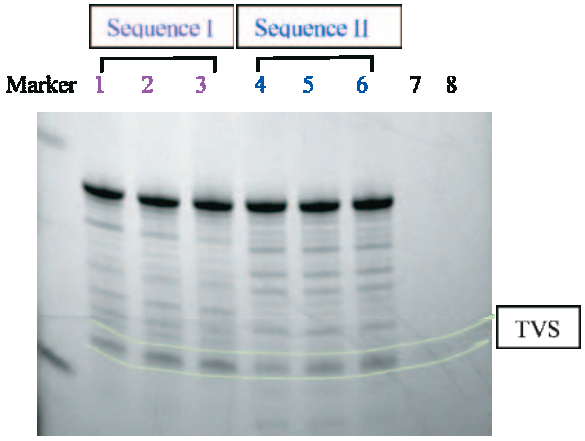
[a]Deprotection reagents: a solution of 10% (*v*/*v*) of each amine in 1 mol/L TBAF–THF, RT, 24 h.
[b]A mixture of 10% *n*-propylamine and 1% bis(2-mercaptoethyl)ether in 1 mol/L TBAF–THF (8).
[c]The pK_a values are taken from Perrin (30).

Morpholine, benefiting form its lower pK_a (8.4), does not cause any chain cleavage but allows the addition of TVS to oligo–RNA to some extent (7.2%) in 1 mol/L TBAF–THF solution. On the other hand, piperidine can completely quench the reaction between TVS and oligo–RNA, but it leads to a small amount (8.3%) of chain cleavage (Table 3).

To examine the potential of morpholine and piperidine as candidates as scavengers of the undesirable byproduct TVS, we have deprotected two 21-mer RNAs using 1 mol/L TBAF–THF, containing either a mixture of *n*-propylamine and bis(2-mercaptoethyl)ether (8), piperidine, or morpholine. Thus, two 21-mer RNAs were synthesized on a solid support with the 2′-*O*-TEM group using our published procedure (8) (sequence I: 5′-GAC GUA AAC GGC CUC AAG UUC; sequence II: 5′-ACU UGU GGC CGU UUA CGU CGC). After treatment with 25% NH_3–MeOH for 20 h at RT and then for 4 h at 40 °C, they were divided into three parts and incubated with (*a*) the standard deprotecting reagent (8) (1 mol/L TBAF–THF containing 10% *n*-propylamine and 1% bis(2-mercaptoethyl) ether), (*b*) 1 mol/L TBAF–THF containing 10% of piperidine, or (*c*) 1 mol/L TBAF–THF containing 10% of morpholine at RT for 20 h. After evaporation of the volatile materials, the products were first passed through a Sep-Pak® Plus (C18, reverse phase) (31) column to remove hydrophilic matter such as excess of F^-, and then NAP^{TM}-10 (Sephadex G25) column (32) to separate the smaller molecules from the larger ones on the basis of size (thus, the full-size oligo–RNA elutes from the truncated sequences and hydrophobic protecting group residues) to give the crude products, which are of high purity and can be used directly for various biological experiments. These crude products were analyzed by 20% denatured PAGE and gel picture obtained by UV–visualization (Fig. 5).

As shown in Fig. 5, all three deprotecting conditions give highly pure crude RNA. Use of morpholine or piperidine,

Fig. 5. 20% denatured PAGE picture of crude RNAs obtained from the deprotection of RNA sequence I (5′-GAC GUA AAC GGC CUC AAG UUC) and RNA sequence II (5′-ACU UGU GGC CGU UUA CGU CGC) with different 2′-*O*-TEM deprotecting conditions. The 2′-*O*-TEM group was deprotected with 1 mol/L TBAF–THF containing different scavengers at RT for 20 h. Lanes 1 and 4: 10% *n*-propylamine and 1% bis(2-mercaptoethyl)ether. Lanes 2 and 5: 10% piperidine. Lanes 3 and 6: 10% morphholine. Marker, upper band: xylene cyanol blue; bottom band: bromophenol blue. Gel picture obtained by UV–vis (254 nm) showing all UV absorbing compounds both nucleic acids (full product and n-1 failure sequences) as well as the cleaved protecting groups. Note that the noncharged TVS (**1**) (λ_{max} = 233 nm) also runs on the gel and is visible by 254 nm light shadowing if in high concentration (Fig. S8).[3] The bands between dashed lines correspond to TVS. Lanes 7 and 8 were run together as a control. Lane 7 product obtained by incubating compound TVS with 1 mol/L TBAF–TMF. Lane 8 product obtained by incubating compound TVS with 1 mol/L TBAF–TMF containing 10% morpholine.



© 2007 NRC Canada

however, gives only a very minor improvement of RNA purity (~84%) compared with that of the standard condition (8) (~82%) [a mixture of *n*-propylamine and bis(2-mercaptoethyl)ether], which is in contrast to the result obtained from the deprotection of the tetrameric RNA (**20**) (see Table 3) with the above three reagents.

Conclusion

In this study, we found that N^6 of adenosine, N^4 of cytidine, and N^2 of guanosine, just as N^3 of thymidine (12), can be alkylated by the α,β-unsaturated compound TVS in 1 mol/L TBAF–THF solution through Michael addition. In oligo–RNA, their nucleophilicities toward TVS are different: N^6 – A > N^4 – C > N^2 – G >> N^3 – U. Hence, by controlling the concentration of TVS, selective alkylation of these nucleophilic sites can be easily achieved. This discovery not only provides a new approach for the alkylation of non-hydrogen-bonded exocyclic amino groups of nucleobases in RNA, but also provides a new strategy for the potential application of the reagent TVS as a chemical probe for detecting the structure and (or) the function of nucleic acid. To avoid adduct formation and chain cleavage during deprotection of 2′-*O*-TEM group with 1 mol/L TBAF–THF, both morpholine and piperidine have been proved to be good scavengers of TVS, which can give high quality crude RNA, bypassing the practical problems of employing the mixture of *n*-propylamine and bis(2-mercaptoethyl)ether (8).

Experimental section

General experimental methods

Chromatographic separations were performed on Merck G60 silica gel. Thin layer chromatography (TLC) was performed on Merck pre-coated silica gel 60 F_{254} glass-backed plates. ^{1}H NMR spectra were recorded at 270.1 MHz and 500 MHz, respectively. ^{13}C NMR spectra were recorded at 67.9 MHz, 125.7 MHz, and 150.9 MHz, respectively. Chemical shifts are reported in ppm (δ scale). Reversed-phase (RP) HPLC: Kromasil 100, C18, 5μ, 100*4.6 mm. Flow 1 mL/min at RT, UV detector with detecting wavelength of 260 nm. Buffer A: 0.1 mol/L TEAA in H_2O–CH_3CN (95:5). Buffer B: 0.1 mol/L TEAA in H_2O–CH_3CN (50:50). Polyacrylamide gel electrophoresis (PAGE): 20% acrylamide (acrylamide/bisacrylamide 29:1), 7 mol/L urea, TBE buffer.

Oligoribonucleotide synthesis

Oligo–RNAs **2–5** and **20** were synthesized through our published procedure (8). After the completion of the automated solid-phase synthesis, the solid supports were treated with 25% NH_3–MeOH at RT overnight, filtered, and purified by HPLC. Oligo–RNA **14** was synthesized by a TBDMS approach according to reported procedure (33) and purified by HPLC. Their structural integrity were verified by MALDI-TOF MS: (**2**) calcd. 974.92 $[MH]^+$, found 975.29; (**3**) calcd. 1013.94 $[MH]^+$, found 1014.24; (**4**) calcd. 997.95 $[MH]^+$, found 998.25. (**5**) cal. 973.94 $[MH]^+$, found 974.29; (**20**) calcd. 2071.85 $[MH]^+$, found 2070.15; (**14**) calcd. 1224.21 $[MH]^+$, found 1224.19.

The 21-mer RNAs, sequence I and sequence II, were synthesized according to our published procedure (8). After completion of the synthesis, the solid supports were treated with 25% NH_3–MeOH at RT for 20 h and then at 40 °C for 4 h. After filtration, each sample was separated into three parts and the volatile materials were evaporated. The residues were co-evaporated with dry methanol twice and dried in vacuum. Then they were treated with 1 mol/L TBAF–THF (dried over 4 Å molecular sieves overnight) containing different scavengers at RT for 20 h. After evaporation of the volatile matter, the residues were diluted with double-distilled water and applied to a NAP-10 column (Amersham Pharmacia Biotech, Sweden). Loading volume is 1 mL and elution was done with 1.2 mL of double-distilled water. The collected fractions were subjected to Sep-Pak® Plus C18 cartridges (Waters) according to manufacturer instructions, to give the crude products. The crude RNAs were subjected to 20% denatured PAGE analysis without any purification step.

General procedure of reaction between ribonucleosides with *p*-tolyl vinyl sulphone (1)

Ribonucleoside (1 mmol) was dissolved in dry 1 mol/L TBAF–THF (5ml) and *p*-tolyl vinyl sulphone **1** (3 mmol for adenosine, cytidine, uridine and 1 mmol for guaonsine) was added. The reaction was stirred at RT for 24 h and analyzed by HPLC. Then the reaction mixture was evaporated to dryness. The residue was diluted with dichloromethane (DCM) and washed with satd. $NaHCO_3$ and dried over $MgSO_4$. The major product was obtained by short column chromatography.

N^4-(4-tolylsulfonylethyl) cytidine (10) ($C^{N4\text{-}TSE}$)

HPLC analysis of the reaction mixture showed that 38.6% of the cytidine was transformed into product **10** and 38.3% of the cytidine was unreacted. CC (DCM, MeOH from 2% to 10%). ^{1}H NMR (270 MHz, $CDCl_3$ + CD_3OD) δ: 2.45 (s, 3H, Ph*Me*), 3.46 (t, *J* = 5.8 Hz, 2H, SO_2CH_2), 3.75–3.96 (m, 4H, $SO_2CH_2CH_2$, 5′,5″-*H*), 4.09 (broad, 1H, 4′-*H*), 4.18 (broad, 2H, 2′3′-*H*), 5.69 (d, *J* = 1.5 Hz, 1H, 1′-*H*), 5.76 (d, *J* = 7.4 Hz, 1H, 5-*H*), 7.37 (d, *J* = 7.7 Hz, 2H, ph*H*), 7.77 (d, *J* = 8.3 Hz, 2H, ph*H*), 7.87 (d, *J* = 7.4 Hz, 1H, 6-*H*). ^{13}C NMR (67.9 MHz, $CDCl_3$ + CD_3OD) δ: 23.94 (Ph*Me*), 34.69 ($SO_2CH_2CH_2$) 54.79 ($SO_2CH_2CH_2$), 60.88 (5′-C), 69.31 (3′-C), 74.94 (2′-C), 84.88 (4′-C), 92.53 (1′-C), 95.81 (5-C), 127.98 (ph), 130.24 (ph), 136.10 (ph), 141.11 (C6), 145.47 (ph), 157.21 (2-C), 164,05 (C4). MALDI-TOF MS: calcd.: 426.13 $[MH]^+$; found: 426.17.

N^6-(4-tolylsulfonylethyl) adenosine (11) ($A^{N6\text{-}TSE}$)

HPLC analysis of the reaction mixture showed that 35.6% of the adenosine was transformed into product **11** and 56.8% of the adenosine was unreacted. CC (DCM, Acetone from 20% to 50%). ^{1}H NMR (270 MHz, $CDCl_3$ + CD_3OD) δ: 2.36 (s, 3H, Ph*Me*), 3.50 (t, 2H, SO_2CH_2), 3.69 (t, 1H, 5′-*H*), 3.84–4.01 (m, 3H, 5″-*H*, $SO_2CH_2CH_2$), 4.26 (broad, 1H, 4′-*H*), 4.44 (broad, 1H, 3′-*H*), 5.50 (broad, 1H, 2′-O*H*), 5.84 (d, *J* = 6.7 Hz, 1H, 1′-H), 6.62 (broad, 1H, 5′-O*H*), 6.97 (t, *J* = 6.1 Hz, 1H, N^6H), 7.25 (d, *J* = 7.9 Hz, 2H, ph*H*), 7.74 (d, *J* = 8.2 Hz, 2H, ph*H*), 7.90 (s, 1H, 8-*H*), 8.03 (s, 1H, 2-*H*). ^{13}C NMR (67.9 MHz, $CDCl_3$ + CD_3OD) δ: 21.60 (Ph*Me*), 34.65 ($SO_2CH_2CH_2$) 54.91 ($SO_2CH_2CH_2$), 62.99 (5′-C), 72.37 (3′-C), 74.01 (2′-C), 87.45 (4′-C), 90.86 (1′-

© 2007 NRC Canada

C), 120.46 (5-C), 127.90 (ph), 130.00 (ph), 135.95 (ph), 140.67 (8-C), 145.07 (ph), 147.49 (4-C), 152.06 (2-C), 154.08 (6-C). MALDI-TOF MS: calcd.: 450.14 $[MH]^+$; found: 450.19.

N^3-(4-tolylsulfonylethyl) uridine (12) ($U^{N3\text{-}TSE}$)

HPLC analysis of the reaction mixture showed that 57.2% of the uridine was transformed to product **12** and 34.1% of the uridine was unreacted. CC (DCM, MeOH from 5% to 7%). ^{1}H NMR (270 MHz, $CDCl_3$ + CD_3OD) δ: 2.39 (s, 3H, Ph*Me*), 3.42 (t, *J* = 7.0 Hz, 2H, SO_2CH_2), 3.76 (dd, *J* = 12.2 Hz, 2H, 5′,5″-*H*), 3.99 (d, *J* = 1.5 Hz, 1H, 4′-*H*), 4.10–4.21 (m, 4H, 2′, 3′, -*H*, $SO_2CH_2CH_2$), 5.65 (d, *J* = 8.1 Hz, 1H, 5-*H*), 5.72 (d, *J* = 2.3 Hz, 1H, 1-*H*), 7.32 (d, *J* = 7.8 Hz, 2H, ph*H*), 7.74 (d, *J* = 8.2 Hz, 2H, ph*H*), 7.85 (d, *J* = 8.1 Hz, 1H, 6-*H*). ^{13}C NMR (67.9 MHz, $CDCl_3$ + CD_3OD) δ: 23.88 (Ph*Me*), 34.95 ($SO_2CH_2CH_2$) 52.56 ($SO_2CH_2CH_2$), 60.95 (5′-C), 69.41 (3′-C), 74.73 (2′-C), 85.16 (4′-C), 91.13 (1′-C), 101.40 (5-C), 128.04 (ph), 130.11 (ph), 135.67 (ph), 139.81 (6-C), 145.36 (ph), 150.92 (2-C), 162.60 (4-C). MALDI-TOF MS: calcd.: 427.11 $[MH]^+$; found: 427.15.

N^2-(4-tolylsulfonylethyl) guanosine (13) ($G^{N2\text{-}TSE}$)

HPLC analysis of the reaction mixture showed that 50.3% of the guanosine was transformed to product **13** and 23.8% of the guanosine was unreacted. The product **13** was too polar to purify by silica gel column chromatography, hence preparative HPLC was used to purify a small amount of product **13** for NMR and MS analysis. ^{1}H NMR (270 MHz, DMSO-d_6) δ: 2.38 (s, 3H, Ph*Me*), 3.51–3.60 (m, 6H, SO_2CH_2, $SO_2CH_2CH_2$, 5′,5″-*H*), 3.99 (t, *J* = 1.5 Hz, 1H, 4′-*H*), 4.11 (t, 1H, 3′-*H*), 4.47 (t, *J* = 5.3 Hz, 1H, 2′-*H*), 5.68 (d, *J* = 5.8 Hz, 1H, 1′-*H*), 6.88 (br., 1H, N^2H), 7.42 (d, *J* = 7.9 Hz, 2H, ph*H*), 7.77 (d, *J* = 8.2 Hz, 2H, ph*H*), 7.93 (s, 1H, 8-*H*), 10.94 (br., 1H, N^1H). ^{13}C NMR (67.9 MHz, DMSO-d_6) δ: 21.64 (Ph*Me*), 34.95 ($SO_2CH_2CH_2$) 54.11 ($SO_2CH_2CH_2$), 62.11 (5′-C), 70.99 (3′-C), 74.27 (2′-C), 85.87 (4′-C), 87.21 (1′-C), 117.70 (5-C), 128.17 (ph), 130.43 (ph), 136.46 (8-C), 136.70 (ph), 144.96 (ph), 151.06 (4-C), 152.89 (2-C), 157.67 (6-C). MALDI-TOF MS: calcd.: 466.23 $[MH]^+$; found: 466.13.

Base composition analysis

Shrimp alkaline phosphatase and phosphodiesterase I (*Crotalus adamanteus* venom) were purchased from Amersham Pharmacia Biotech, Sweden. A reaction mixture containing 20 mmol/L Tris-HCl (pH 8.0), 10 mmol/L $MgCl_2$, shrimp alkaline phosphatase (0.5 unit), and phosphodiesterase I (*Crotalus adamanteus* venom) (0.4 unit) was added to oligoribonucleotide (0.1 OD unit at 260 nm) with a total reaction volume of 30 µL. The reaction mixture was incubated at 37 °C for 12 h and subjected to HPLC analysis directly.

Acknowledgements

Generous financial support from the Swedish Natural Science Research Council (Vetenskapsr et), the Swedish Foundation for Strategic Research (Stiftelsenf Strategisk Forskning), and the EU-FP6 funded RIGHT project (Project no. LSHB-CT-2004–005276) is gratefully acknowledged.

References

1. A. Fire, S. Xu, M.K. Montgomery, S.A. Kostas, S.E. Driver, and C.C. Mello, Nature (London), **391**, 808 (1998).
2. S.M. Elbashir, J. Harborth, W. Lendechel, A. Yalcin, K. Weber, and T. Tuschl. Nature (London), **411**, 494 (2001).
3. C.B. Reese. Org. Biomol. Chem. **3**, 3851 (2005).
4. S. Pitsch, P.A. Weiss, L. Jenny, A. Stutz, X. Wu, and H.C. Acta. Helv. Chim. Acta, **84**, 3773 (2001).
5. S.A. Caringe, F.E. Wincott, and M.H. Caruthers. J. Am. Chem. Soc. **120**, 11820 (1998).
6. A. Semenyuk, A. Foldesi, T. Johansson, C. Estmer-Nilsson, P. Blomgren, M. Brannvall, L.A. Kirsebom, and M. Kwiatkowski. J. Am. Chem. Soc. **128**, 12356 (2006).
7. T. Ohgi, Y. Masutomi, K. Ishiyama, H. Kitagawa, Y. Shiba, and J. Yano. Org. Lett. **7**, 3477 (2005).
8. C.Z. Zhou, D. Honcharenko, and J. Chattopadhyaya. Org. Biomol. Chem. **5**, 333 (2007).
9. J.J. Solomon, I.L. Cote, M. Wortman, K. Decker, and A. Segal. Chem. Biol. Interactions, **51**, 167 (1984).
10. J.W. Jones and R.K. Robins. J. Am. Chem. Soc. **85**, 193 (1963).
11. P.D. Lawley and P. Brookes. Biochem. J. 127 (1963).
12. M. Mag and J.W. Engels. Nucleic Acids Res. **16**, 3525 (1988).
13. P. Brookes, and P.D. Lawley. J. Chem. Soc. 1348 (1962).
14. R.L.C. Brimacombe, B.E. Griffin, J.A. Haines, W.J. Haslam, and C.B. Reese. Biochemistry, **4**, 2452 (1965).
15. K.K. Ogilvie and S.L. Beaucage. Nucleic Acids Res. **7**, 805 (1979).
16. T. Umemoto and T. Wada. Tetrahedron Lett. **46**, 4521 (2005).
17. D.C. Capaldi, H. Gaus, A.H. Krotz, J. Arnold, R.L. Carty, M.N. Moore, A.N. Scozzari, K. Lowery, D.L. Cole, and V.T. Ravikumar. Org. Process Res. Dev. 832 (2003).
18. B. J. Pullman. Chem. Soc. B, 1621 (1959).
19. J. Ofengand. Methods Enzymol. **20**, 162 (1971).
20. A. Segal, U. Mate, and J.J. Solomon. Chem. Biol. Interactions, **28**, 333 (1979).
21. J.D. Engel. Biochem. Biophys. Res. Comm. **64**, 581 (1975).
22. R. Micura, W. Pils, C. Höbartner, K. Grubmayr, M.O. Ebert, and B. Jaun. Nucleic Acids Res. **29**, 3997 (2001).
23. H.M. Kong, L.F. Lin, N. Porter, S. Stickel, D.P.J. Byrd, and R.J. Roberts. Nucleic Acids Res. **28**, 3216 (2000).
24. O. Gorchs, M. Mernandez, L. Garriga, E. Pedroso, A. Grandas, and J. Farras. Org. Lett. **4**, 1827 (2002).
25. C. Höbartner, C. Kreutz, E. Flecker, E. Ottenschlager, W. Pils, K. Grubmayr, and R. Micura. Monatsh. Chem. **134**, 851 (2003).
26. M. Beier, and W. Pfleiderer. Helv. Chim. Acta, **86**, 2533 (2003).
27. S.T. McDowell, C.J.M. Stirling. J. Chem. Soc. B, 343 (1967).
28. S.T. McDowell and C.J.M. Stirling. J. Chem. Soc. B, 348 (1967).
29. S.T. McDowell and C.J.M. Stirling. J. Chem. Soc. B, 351 (1967).
30. D.D. Perrin. Dissociation constants of organic bases in aqueous solution. Supplement. Butterworths, London, UK. 1972.
31. F. Wincott, A. DiRenzo, C. Shaffer, S. Grimm, D. Tracz, C. Workman, D. Sweedler, C. Gonzalez, S. Scaringe, and N. Usman. Nucleic Acids Res. **23**, 2677 (1995).
32. Handbook of gel filtration, principles and methods. *Edited by* Amersham Biosciences.
33. J. Milecki, E. Zamaratski, T.V. Maltseva, A. Földesi, R. Adamiak, and J. Chattopadhyaya. Tetrahedron Lett. **55**, 6603 (1999).

© 2007 NRC Canada

Hydrophilic modifications in peptide nucleic acid — Synthesis and properties of PNA possessing 5-hydroxymethyluracil and 5-hydroxymethylcytosine[1]

Robert H.E. Hudson, Yuhong Liu, and Filip Wojciechowski

Abstract: We have investigated the chemistry for the incorporation of C5-hydroxymethyl-uracil and -cytosine in peptide nucleic acid (PNA) and the subsequent effect of this modification on PNA hybridization behavior. Largely based on literature precedent, we prepared a peptide nucleic acid monomer, possessing 5-hydroxymethyuracil, which was compatible with Fmoc-based oligopeptide synthesis. An improved, large-scale synthesis of 5-hydroxymethylcytosine was developed, as a starting point for the synthesis of a monomer containing this nucleobase. In each case, the hydroxyl group was blocked as a *t*-butyldiphenylsilyl ether, and the exocyclic amino group of cytosine was additionally blocked with the benzoyl-group. The modified monomers were incorporated into isolated positions in the oligomer sequence using standard protocols. The modified oligomers showed that the 5-hydroxymethyl group is compatible with triplex and duplex formation.

Key words: peptide nucleic acid, hydroxymethyluracil, hydroxymethylcytosine, modified nucleobase, hybridization.

Résumé : On a étudié la chimie de l'incorporation d'un C5-hydroxyméthyl-uracile et d'une -cytosine dans un acide nucléique peptidique (ANP) ainsi que l'effet de cette modification sur le comportement d'hybridisation de l'ANP. En se basant principalement sur les précédents trouvés dans la littérature, on a préparé un acide nucléique peptidique monomère possédant un groupe 5-hydroxyméthyluracile qui était compatible avec une synthèse d'oligopeptide basée sur l'utilisation d'un groupe Fmoc. On a développé une synthèse à grande échelle améliorée de la 5-hydroxyméthylcytosine qui a été utilisée comme point de départ pour la synthèse d'un monomère contenant cette nucléobase. Dans chaque cas, le groupe hydroxyle a été bloqué par un éther *t*-butyldiphénylsilyle et on a de plus bloqué le groupe amino exocyclique de la cytosine à l'aide d'un groupe benzoyle. On a incorporé les monomères modifiés dans des positions isolées de la séquence de l'oligomère en faisant appel aux protocoles habituels. Les oligomères modifiés ont permis de montrer que le groupe 5-hydroxyméthyle est compatible avec la formation d'un triplex et d'un duplex.

Mots-clés : acide nucléique peptidique, hydroxyméthyluracile, hydroxyméthylcytosine, nucléobase modifiée, hybridisation.

[Traduit par la Rédaction]

Introduction

Ready access to synthetic oligonucleotides has enabled much of the tremendous progress witnessed in molecular biology, forensics, diagnostics, and related areas over the past couple of decades. Some applications of oligonucleotides, especially in hostile environments containing DNA or RNA degrading enzymes, require structural modifications to resist degradation. Out of endeavors to make robust oligonucleotide analogs, peptide nucleic acid (PNA) was born (1). PNA is an oligonucleotide mimic based on a polyamide repeat unit. It exhibits very tight and specific binding to complementary nucleic acids and continues to be of interest for both in vitro diagnostic applications and in vivo therapeutic use (2).

Although the original design of PNA "works" quite well (see Fig. 1), possessing excellent hybridization affinity and selectivity, often-cited limitations are its poor water solubility, poor ability to remain in solution and a tendency to be adsorbed onto surfaces, sequence-dependent aggregation, and a general difficulty in penetrating cellular membranes. These biophysical properties are related in various degrees to the non-ionic structure of PNA. Judicious chemical modifications can improve these biophysical properties while maintaining the highly desirable hybridization properties. For example, the aqueous solubility of PNA is improved by the attachment of a cationic amino acid, such as lysine, to one or both ends of the oligomer (3). Alternatively, introduction of charged (guanidinium) groups along the backbone structure improves the aqueous solubility and also facilitates cellular-membrane penetration (4). Another strategy to improve the solubility of PNA is to introduce hydrophilic nucleobase replacements (5).

The modular nature of PNA is particularly amenable to structural variation, and this has led to the synthesis of a wide variety of modified PNAs. We have chosen to investi-

Received 22 December 2006. Accepted 5 February 2007. Published on the NRC Research Press Web site at canjchem.nrc.ca on 5 May 2007.

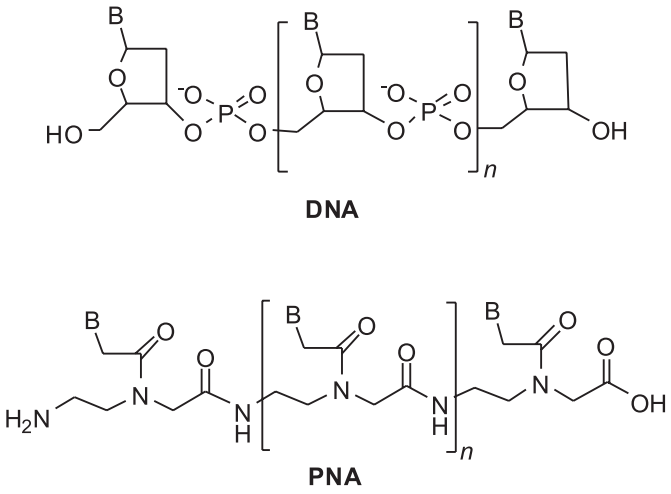
R.H.E. Hudson,[2] Y. Liu, and F. Wojciechowski. Department of Chemistry, The University of Western Ontario, London, ON N6A 5B7, Canada.

[1]This article is part of a Special Issue dedicated to Professor Kelvin K. Ogilvie.

[2]Corresponding author (e-mail: rhhudson@uwo.ca).

 doi:10.1139/V07-030 © 2007 NRC Canada

Fig. 1. Structures of DNA and PNA.



gate nucleobase modifications as a way to introduce additional functionality, which may be distributed throughout the PNA oligomer without changing the *N*-2-aminoethylglycine backbone structure. Our approach, as reported herein, was to make a conservative structural modification that added hydrophilic character, which was synthetically accessible and would be sterically tolerated in a duplex or triplex structure. The 5-hydroxymethyl modification of pyrimidines (Fig. 2) fulfilled these requirements.

The 5-hydroxymethyl modification constitutes a relatively minor structural change to the nucleobases, representing the replacement of a hydrogen on 5-methyluracil (thymine) or 5-methylcytosine by a hydroxyl. The resulting 5-substituent is placed in the major groove and is expected to be sterically well tolerated (6). Other advantages are that the chemistry is accessible and starts with inexpensive reagents, and substitution does not produce a new stereocenter and thereby avoids problems of enantiomeric purity in the product.

Experimental

General

All reagents and solvents were obtained from common commercial sources and used without further purification, unless indicated. Anhydrous solvents were prepared by passing the reagent-grade solvent through columns of activated alumina (Innovative Technologies). Chromatography was carried out using silica gel 60 (particle size 0.063–0.200 mm; Merck). TLC was carried out on plastic sheets, silica gel 60 F_{254}, layer thickness of 0.2 mm (Merck). NMR spectra were recorded on Mercury 400 (400.1 MHz for ^{1}H; 100.6 MHz for ^{13}C) and Inova 400 spectrometers. Chemical shift values, reported in ppm, were referenced by the spectrometer to the residual proton in the deuterated solvents used to record the spectra. Resonances, attributed to conformers due to restricted rotation around amide bonds (i.e., rotamers), are reported as major (ma) and minor (mi) in the ^{1}H and ^{13}C NMR spectra. Assignments are shown for selected resonances that have been unambiguously identified by the use of 2D NMR correlation experiments. Multiplicity of signals are indicated where appropriate (s: single, d: doublet, t: triplet, q: quartet, m: mulitplet, br: broad, v: very). Melting points were determined on a Gallenkamp melting-point apparatus and are reported uncorrected.

5-Hydroxymethyluracil (1)

The synthesis of 5-hmU followed our previously reported method (7). Specifically, triethylamine (42 mL, 300 mmol) was added to a suspension of uracil (22.4 g, 200 mmol) and paraformaldehyde (18.0 g, 600 mmol) in water (600 mL). The mixture turned into a clear solution after heating to 60 °C. The solution was stirred at 60 °C overnight after which time the water was removed under vacuum until the volume reached 60 mL. To this residue, 60 mL of ethanol (95%) was added, and the resultant solution was left to stand at room temperature for 30 min. Once a precipitate formed, the mixture was placed in the refrigerator at 4 °C for several hours, a white solid was collected by filtration, and was washed with cold ethanol. The filtrate was cooled to –20 °C, and a second crop of **1** was collected. Further crops were yielded by reducing the volume of the filtrate by one half and diluting with an equal volume of 95% ethanol, followed by cooling to –20 °C. White solid; 26.1 g (92%); mp (from ethanol) 360 °C dec (lit. 300 °C dec.) (13). TLC ($CHCl_3$–CH_3OH, 4:1): R_f 0.16. ^{1}H NMR (400.1 MHz, DMSO-d_6, ppm) δ: 11.04 (s, 1H, NH), 10.69 (d, J = 5.20 Hz, 1H, NH), 7.22 (d, J = 5.20 Hz, 1H, H6), 4.85 (t, J = 5.60 Hz, 1H, OH), 4.09 (d, J = 4.80 Hz, 2H, –CH_2–). ^{13}C NMR (100.6 MHz, DMSO-d_6, ppm) δ: 163.6, 151.2, 138.0, 112.6, 55.8. HR-MS (EI) calcd. for $C_5H_6O_3N_2$: 142.0378; found: 142.0376.

Ethyl(5-hydroxymethyluracil-1-yl)acetate (2)

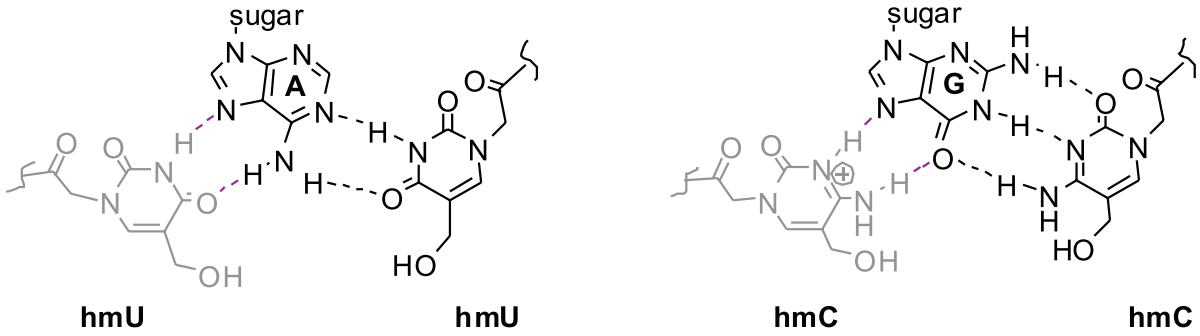
To a suspension of 5-hydroxymethyluracil (22.4 g, 158 mmol) and K_2CO_3 (21.8 g, 158 mmol) in DMF (475 mL) was added ethyl bromoacetate (98%, 28.3 g, 166 mmol). The reaction mixture was stirred overnight after which time the K_2CO_3 was removed by filtration, and the DMF was removed under vacuum, thus yielding a white solid. The solid was washed with H_2O (180 mL) by stirring the slurry for approximately 2 h. The first crop of **2** (21.4 g) was obtained by filtration and drying. Further crops were recovered from the filtrate by reducing its volume. White solid; 82% (29.5 g); mp 178–180 °C. TLC ($CHCl_3$ – CH_3OH, 4:1): R_f 0.46. ^{1}H NMR (400.1 MHz, DMSO-d_6, ppm) δ: 11.42 (s, NH), 7.53 (s, 1H, H6), 5.07 (t, J = 5.60 Hz, 1H, OH), 4.54 (s, 2H, –CH_2–), 4.13 (m, 4H, overlapping –OCH_2–), 1.21 (t, J = 7.20 Hz, 3H, –CH_3). ^{13}C NMR (100.6 MHz, DMSO-d_6, ppm) δ: 168.1, 163.0, 150.7, 141.7, 113.4, 61.2, 55.9, 48.8, 14.2. HR-MS (EI) calcd. for $C_9H_{12}O_5N_2$: 228.0746; found: 228.0748.

Ethyl[5-(*t*-butyldiphenylsilanyloxymethyl)uracil-1-yl]acetate (3)

To a solution of ethyl(5-hydroxymethyluracil-1-yl)acetate (5.01 g, 22 mmol) and imidazole (3.29 g, 48 mmol) in DMF (110 mL) was added *tert*-butyldiphenylchlorosilane (TBDPS-Cl, 98%, 6.64 g, 23.7 mmol) with stirring. The solution was stirred overnight after which time the reaction was stopped by adding 5% $NaHCO_3$ in H_2O (11 mL). The solvents were removed under vacuum to give a white solid.

© 2007 NRC Canada

Fig. 2. (*a*) Expected base-pairing of adenine (A, DNA strand) with 5-hydroxymethyluracil-containing PNA in duplex formation (black) and triplex formation (black and grey). (*b*) Expected base-pairing between guanine (G, DNA strand) with 5-hydroxymethylcytosine-containing PNA in duplex formation (black) and triplex formation (black and grey).



This material was dissolved in dichloromethane (250 mL), washed with H_2O (100 mL × 3), and the organic phase was separated and dried over sodium sulfate. The crude product was obtained after removing the dicholormethane by vacuum and was subsequently purified by trituration with hexanes to remove the silanol byproduct (TBDPS-OH; R_f 0.96; ethyl acetate–DCM, 1:2). The yield was 99% (10.2 g); mp 168–170 °C. TLC (ethyl acetate – DCM, 1:2): R_f 0.71. ^{1}H NMR (400.1 MHz, DMSO-d_6, ppm) δ: 11.52 (s, NH), 7.65–7.67 (m, 4H, Ar–H), 7.62 (s, 1H, C6–H), 7.43–7.48 (m, 6H, Ar–H), 4.59 (s, 2H, N–CH_2–), 4.36 (s, 2H, O–CH_2Ar), 4.16 (q, J = 7.20 Hz, 2H, O–CH_2–), 1.21 (t, J = 7.20 Hz, 3H, C–CH_3), 1.00 (s, 9H, SiC–CH_3). ^{13}C NMR (100.6 MHz, DMSO-d_6, ppm) δ: 168.3 (C7), 163.0 (C2), 150.8 (C1), 142.6 (C4), 135.2 (C13), 132.7 (C12), 130.0 (C15), 128.0 (C14), 112.0 (C3), 61.3 (C8) 58.9 (C5), 48.9 (C6), 26.7 (C11), 18.9 (C10), 14.1 (C9). HR-MS (EI) calcd. for $C_{25}H_{30}O_5N_2Si$: $[M + H]^+$, 467.2002; found: 467.1994.

[5-(*t*-butyldiphenylsilanyloxymethyl)uracil-1-yl]acetic acid (4)

To a solution of ethyl[5-(*t*-butyldiphenylsilanyloxymethyl)uracil-1-yl]acetate (10.6 g, 22.7 mmol) in THF (204 mL) and H_2O (22 mL) at 0 °C was added 2.5 mol/L NaOH (47 mL, 6 equiv.). The mixture was stirred at 0 °C for 20 min, then 1 mol/L HCl (170 mL) was added to stop the reaction. The aqueous phase was extracted with ethyl acetate four times (400 mL × 1, 100 mL × 3). The ethyl acetate phase was washed with H_2O (100 mL × 2) and then dried over sodium sulfate. The solvent was removed under vacuum to yield the title compound: white solid; 8.2 g, 96%; mp 169–170 °C. TLC (ethyl acetate – DCM, 1:2): R_f 0.71. ^{1}H NMR (400.1 MHz, DMSO-d_6, ppm) δ: 13.14 (br s, 1H, COOH), 11.47 (s, 1H, NH), 7.65–7.67 (m, 4H, Ar), 7.62 (s, 1H, C6–H), 7.41–7.50 (m, 6H, Ar), 4.49 (s, 2H, N–CH_2–), 4.35 (s, 2H, O–CH_2–), 1.00 (s, 9H, –CH_3). ^{13}C NMR (100.6 MHz, DMSO-d_6, ppm) δ: 169.8, 163.0, 150.9, 142.8, 135.2, 132.8, 130.0, 128.0, 111.8, 58.9, 48.8, 26.7, 18.9. MS (ESI) calcd. for $[C_{23}H_{26}O_5N_2Si + Na]^+$: 461.15; found: 461.1.

Methyl(*N*-(2-((9H-fluoren-9-yl)methoxy)carbonyl)aminoethylglycinate hydrochloride (5)

To a suspension of methyl 2-aminoethylglycinate dihydrochloride (6.0 g, 20.8 mmol) and Fmoc-*N*-hydroxysuccinimide (10.8 g, 1.1 equiv.) in dioxane (100 mL) was added aq. $NaHCO_3$ (3 equiv., 7.4 g/120 mL) with rapid stirring for 50 min. The reaction mixture was diluted with 400 mL H_2O, which produced an instant white precipitate that redissolved on the addition of DCM (350 mL). This aqueous phase was extracted with DCM (2 × 300 mL), and then the DCM phase was dried over sodium sulfate, acidified with Et_2O – HCl (5 mol/L), and cooled in the freezer overnight. The desired product was collected by filtration: white solid; 7.0 g, 61%; mp 110–113 °C. Further product can be obtained by reducing the volume of the filtrate. TLC (CH_3COOEt – CH_3OH, 95:5; visualized with UV and 0.3% ninhydrin (purple)): R_f 0.24. ^{1}H NMR (400.1 MHz, DMSO-d_6, ppm) δ: 9.44 (br s, 2H, H_2N^+), 7.90 (d, J = 7.20 Hz, 2H, Ar), 7.70 (d, J = 7.20 Hz, 2H, Ar), 7.58 (t, J = 5.60 Hz, CONH), 7.42 (t, J = 7.20 Hz, 2H, Ar), 7.33 (t, J = 7.60 Hz, 2H, Ar), 4.33 (d, J = 6.80 Hz, 2H, –CH_2–O), 4.23 (t, J = 6.80 Hz, 1H, Ar_2–CH–), 4.00 (s, 2H, N–CH_2–), 3.74 (s, 3H, O–CH_3), 3.33 (overlapping with water, –CH_2–CH_2–), 3.02 (t, J = 6.00 Hz, 1.8H, ma, –CH_2–CH_2–), 2.90 (mi, 0.2H). ^{13}C NMR (100.6 MHz, DMSO-d_6, ppm) δ: 167.1, 156.3, 143.9, 140.8, 127.7, 127.2, 125.3, 120.2, 65.7, 52.7, 46.7, 46.6, 46.5, 36.6. MS (EI) calcd. for $[C_{20}H_{22}O_4N_2HCl – HCl]^+$: 354.16; found: 354.1.

Byproducts identified as dibenzofulvene: R_f 0.96 (ethyl acetate – methanol, 95:5), and 2-oxo-3-*N*-(Fmoc)piperazine: R_f 0.42 ($CHCl_3$ – CH_3OH – CH_3COOH, 90:8:2). Mp 172–174 °C.

Methyl(2-(((9H-fluoren-9-yl)methoxy)carbonyl)aminoethyl)glycinate (6)

The hydrochloride salt of the title compound (3.0 g, 7.8 mmol) was suspended in dichloromethane (350 mL) and shaken against a saturated aq. $NaHCO_3$ solution (150 mL × 3) to liberate the free base. The phases were separated, and the combined aqueous phases were back-extracted with dichloromethane (100 mL × 3). The organic phase was dried over sodium sulfate, and the solvent was removed under vacuum to yield the free base as a white wax-like product: 2.70 g (99%); mp 76–78 °C. TLC (ethyl acetate – methanol, 95:5; visualized by UV and 0.3% ninhydrin (purple)): R_f 0.30. ^{1}H NMR (400.1 MHz, $CDCl_3$, ppm) δ: 7.76 (d, J = 7.60 Hz, 2H, Ar), 7.61 (d, J = 7.60 Hz, 2H, Ar), 7.40 (t, J = 7.60 Hz, 2H, Ar), 7.32 (t, J = 7.20 Hz, 2H, Ar), 5.36 (br, ma, CONH), 5.12 (br, mi, CONH), 4.40 (d, J = 7.20 Hz, 2H, –CH_2–O), 4.22 (t, J = 6.80 Hz, 1H, Ar_2–CH–), 3.73 (s, 3H,

© 2007 NRC Canada

O–CH_3), 3.42 (s, 2H, N–CH_2–C(O)), 3.27 (q, J = 5.60 Hz, ma, CONH–CH_2–), 3.17 (mi, CONH–CH_2–), 2.75 (t, J = 5.60 Hz, ma, –CH_2–N), 2.62 (mi, –CH_2–N). ^{13}C NMR (100.6 MHz, $CDCl_3$, ppm) δ: 173.1, 156.7, 144.2, 141.5, 127.8, 127.2, 125.2, 120.1, 40.8, 66.7, 52.0, 50.4, 48.8, 47.4. HR-MS (EI) calcd. for $C_{20}H_{22}O_4N_2$: 354.1580; found: 354.1581.

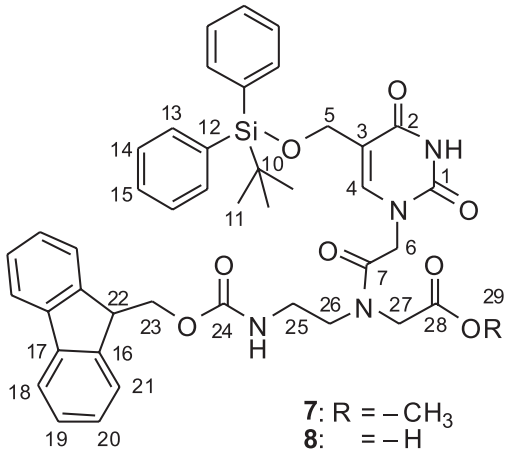
Fmoc hmU-OMe (7)

To a suspension of methyl(2-(((9H-fluoren-9-yl)methoxy)carbonyl)aminoethyl)glycinate (**6**) (1.61 g, 4.5 mmol) and the nucleobase acetic acid derivative **4** (3.18 g, 7.3 mmol) in DMF (45 mL) was added 1-ethyl-3-(3′-dimethylaminopropyl)carbodiimide hydrochloride (EDC, 1.39 g, 7.3 mmol) in two portions within 0.5 h. The mixture was stirred for 16 h at room temperature, and then the reaction mixture was diluted with dichloromethane (1000 mL). This solution was washed with 0.05 mol/L HCl (200 mL × 4), saturated $NaHCO_3$ (200 mL × 3), and H_2O (450 mL × 7), respectively. The organic layer was separated and dried over Na_2SO_4, and the solvent was removed under vacuum at room temperature. The crude product (white foam) was purified by gradient column chromatography (DCM, ethyl acetate, ethyl acetate – methanol (95:5), respectively) to yield the title compound as a white foam (Fig. 3): 3.10 g, 88% yield. TLC (ethyl acetate – methanol, 95:5; visualized by UV and 0.3% ninhydrin (purple)): R_f 0.63. ^{1}H NMR (400.1 MHz, $CDCl_3$, ppm) δ: 7.19–7.77 (m, overapping 19H, Ar), 6.06 (br t, ma, backbone NH) and 5.45 (br t, mi, backbone NH), 4.51–4.54 (br s, overlap H5 and its rotamer), 4.51–4.54 (br s, ma, H6) and 4.37–4.44 (overlap, mi, H6), 4.37–4.44 (overlap, H23 and its rotamer), 4.17–4.20 (m, H22), 4.17–4.20 (mi, H27) and 4.07 (s, ma, H27),[3] 3.74 (s, ma, H29) and 3.78 (s, mi, H29), 3.57 (br s, ma, 1.6 H, H26) and 2.88 (br s, mi, 0.4 H, H26), 3.45 (br m, ma, H25) and 3.38 (br m, mi, H25), 1.08 (s, ma, H11) and 1.09 (s, mi, H11). ^{13}C NMR (100.6 MHz, $CDCl_3$, ppm) δ: 170.1 (C28), 167.3 (C7), 162.7 (C2), 157.0 (C24), 151.2 (C1), 144.0 (C16), 141.4 (C17), 141.2 (C4), 135.7 (C13), 133.0 (C12), 130.0 (C15), 128.0 (C14), 127.8 (C19), 127.2 (C20), 125.2 (C21), 120.1 (C18), 114.2 (C3), 66.9 (C23), 59.1 (C5), 53.0 (r), 52.6 (C29), 50.5 (r), 49.0 (C27), 48.9 (C26), 48.6 (r), 48.5 (C6), 47.3 (C22), 39.2 (r), 39.6 (C25), 27.1 (C11), 19.4 (C10). HR-MS (ESI-TOF) calcd. for $[C_{43}H_{46}O_8N_4Si + Na]^+$: 797.2983; found: 797.3022.

Fmoc-hmU-OH (8)

The ester precursor to the PNA monomer acid (2.93 g, 3.78 mmol) was dissolved in THF (32 mL), and then H_2O (21 mL) was added to produce a turbid mixture. The mixture was cooled to 0 °C, and 2.5 mol/L NaOH (12 mL, 8 equiv.) was added. The mixture was stirred for 5 min at 0 °C during which time the mixture cleared to produce a homogeneous solution. The reaction was stopped by addition to a separatory funnel containing a mixture of ethyl acetate (400 mL) and 0.3 mol/L HCl (200 mL). The acidic aqueous phase was extracted by ethyl acetate (150 mL × 3). The ethyl acetate washes were combined (~850 mL), washed with H_2O (100 mL × 3), and dried over Na_2SO_4. The ethyl acetate was removed under vacuum at room temperature to yield an off-white (yellowish) foam (Fig. 3). The product was purified by column chromatography using a gradient of solvents (DCM; DCM–methanol (90:10), (85:15), and (78:22); respectively) to give the title compound as an off-white solid: 2.60 g, 90%; mp 216–21s7 °C. TLC ($CHCl_3$ – CH_3OH – CH_3COOH, 90:8:2; visualized with UV and 0.3% ninhydrin (grey)): R_f 0.08. ^{1}H NMR (400.1 MHz, DMSO-d_6, ppm) δ: 11.39 (br s, uracil NH) and 11.36 (br s, uracil NH), 7.29–7.88 (overlapping signals, 18H Ar, backbone NH), 4.75 (s, mi, 0.2H, H6) and 4.56 (s, ma, 1.8H, H6), 4.23–4.35 (m, overlap, 2H, H5) and (r, H23), 4.17–4.20 (m, overlap, H23, H22), 3.95 (s, 2H, H27),[3] 3.44 (br m, mi, H26) and 3.38 (br m, ma, H26), 3.36 (br m, mi, H25) and 3.16 (br m, ma, H25), 0.98 (s, 9H, H11). ^{13}C NMR (100.6 MHz, DMSO-d_6, ppm) δ: 171.5 (C28), 166.9 (C7), 163.0 (C2), 156.2 (C24), 150.9 (C1), 143.9 (C16), 143.3 (C4), 140.7 (C17), 135.2 (C13), 132.8 (C12), 129.9 (C15), 128.0 (C14), 127.6 (C19), 127.1 (C20), 125.3 (C21), 120.1 (C18), 111.4 (C3), 65.6 (C23), 58.9 (C5), 51.4 (r), 48.5 (C27), 48.1 (C6), 47.6 (r), 46.9 (C26), 46.7 (C22), 38.7 (r), 38.0 (C25), 26.7 (C11), 18.8 (C10). HR-MS (ESI-TOF) calcd. for $[C_{42}H_{44}O_8N_4Si + Na]^+$: 783.28261; found: 783.2841.

Fig. 3. Structure of the 5-hydroxymethyluracil (hmU) PNA monomer ester (R = –CH_3) and acid (R = –H), defining the arbitrary numbering system used in NMR signal assignments.



5-Hydroxymethylcytosine (9)

Triethylamine (16.5 mL, 118 mmol) was added to a suspension of cytosine (5.27 g, 47.4 mmol) and paraformaldehyde (3.28 g, 109 mmol) in water (140 mL). The mixture was stirred and heated under reflux for 72 h. After 24 h and 32 h of reaction, a second and third portion of paraformaldehyde (1.14 g, 38.0 mmol) and (0.57 g, 19.0 mmol) was added, respectively. After completion of the reaction, the volatile components (water and triethylamine) were removed under vacuum to give a dark-coloured residue (12.8 g), which represented greater than 100% theoretical yield. This residue was dissolved to produce a clear solution by heating with 35 mL of 95% ethanol and 18–24 mL H_2O, depending on solubility. The solution was left at room tem-

[3] Variable position (3.85 – 4.20 ppm), depending on the protonation state of the carboxylic acid.

© 2007 NRC Canada

perature for a short time during which a precipitate formed. Further precipitation was induced by cooling to 4 °C. The first crop of 5-hydroxymethylcytosine, 4.2 g (5-hmC, yellow solid, purity ≈ 90% (wt%), 7%–8% (wt%) cytosine, as determined by ^{1}H NMR spectroscopy) was collected by filtration and washed three times with 20 mL of 95% ethanol. This first crop represents 57% chemical yield of **9** from cytosine. Reduction in the volume of the filtrate gave subsequent crops of 5-hmC. The later crops contained proportionally more cytosine and other unidentified compounds. Nonetheless, these impure fractions of 5-hmC were suitable for further use. The total yield of 5-hmC calculated from all recovered fractions, based on determining the purity by ^{1}H NMR spectroscopy, was 85%. This experiment was repeated many times and proved to be reproducible. Mp 300 °C dec. TLC (*t*-butyl alcohol – methyl ethyl ketone – H_2O – NH_4OH, 4:3:2:1): R_f 0.32, compared with R_f 0.46 for cytosine. ^{1}H NMR (400.1 MHz, DMSO-d_6, ppm) δ: 10.60 (v br, ring NH), 7.28 (s, 1H, C6–H), 7.10 (br, NH_2), 6.54 (br, NH_2), 4.99 (v br, OH), 4.16 (s, 2H, O–CH_2–Ar). ^{13}C NMR (100.6 MHz, DMSO-d_6, ppm) δ: 165.6, 157.0, 140.8, 104.9, 57.1. HR-MS (EI) calcd. for $[C_5H_7O_2N_3 + H]^+$: 142.0616; found; 142.0620.

Ethyl(5-hydroxymethylcytosin-1-yl)acetate (10)

To a suspension of crude 5-hydroxymethylcytosine (**9**) (8.97 g, 68% (wt%), 43 mmol) and K_2CO_3 (5.97 g, 43.2 mmol) in dry DMF (140 mL), was added ethyl bromoacetate (5.6 mL, 98% pure, 47.5 mmol). The reaction mixture was stirred overnight, and a dark-coloured oil was obtained after removal of the K_2CO_3 by filtration through a pad of Celite and evaporation of DMF under vacuum. Ethyl acetate (120 mL) was added to triturate the residue, which was sonicated (often 1–2 h, sometimes up to 5 h), and then a brown solid was isolated by filtration. The solid crude product was washed with a small amount of ethyl acetate (50 mL × 3). All of the mass was accounted for in the crude material, which was found to contain the desired product (**10**, 60% (wt%)) along with the dialkylated byproduct (19% (wt%)), some unreacted starting material **9** (~20% (wt%); R_f 0.06; DCM – CH_3OH, 4:1), and small amounts of unidentified compounds, as estimated by examination of ^{1}H NMR spectra. The crude material was suitable for the next reaction. The title compound **10** could also be purified by solvent gradient silica-gel column chromatography (DCM; DCM – CH_3OH (90:10), (85:15), and (80:20); respectively). Mp 175–177 °C, as isolated from chromatography. TLC (DCM – CH_3OH, 4:1): R_f 0.25. ^{1}H NMR (399.8 MHz, DMSO-d_6, ppm) δ: 7.54 (s, 1H, C6–H), 7.33 (br s, NH_2), 6.62 (br s, NH_2), 5.11 (t, J = 5.20 Hz, OH), 4.45 (s, 2H, –CH_2–N), 4.17 (d, J = 5.20 Hz, 2H, O–CH_2–Ar), 4.11 (q, J = 7.20 Hz, 2H, O–CH_2–), 1.19 (t, J = 7.20 Hz, 3H, –CH_3). ^{13}C NMR (100.6 MHz, DMSO-d_6, ppm) δ: 168.8, 165.0, 155.7, 144.2, 105.7, 60.9, 57.1, 50.0, 14.1. HR-MS (EI) calcd. for $[C_9H_{13}O_4N_3]^+$: 227.0906; found: 227.0905.

Identified byproduct: *N*1,*N*4-bisalkylated nucleobase: ethyl(*N*4-(2-ethoxy-2-oxoethyl)-5-(hydroxymethylcytosin-1yl)acetate. TLC (DCM – CH_3OH, 4:1): R_f 0.52. ^{1}H NMR (400.1 MHz, DMSO-d_6, ppm) δ: 7.88 (s, 1H, C6–H), 5.44 (t, J = 5.2, –OH), 4.72 (s, 2H, N1–CH_2–), 4.32 (d, J = 5.3, 2H, O–CH_2–Ar), 4.29 (s, 2H, N4–CH_2–), 4.16 (q, J = 7.1, 4H, 2 × –CH_2–), 1.22 (t, J = 7.2, 6H, 2 × –CH_3). ^{13}C NMR (100.6 MHz, DMSO-d_6, ppm) δ: 185.2, 170.9, 167.9, 145.9, 144.6, 108.8, 61.6, 61.5, 56.1, 49.7, 49.0, 14.1.

Ethyl[5-(*t*-butyldiphenylsilanyloxymethyl)cytosin-1-yl]acetate (11)

Crude ethyl(5-hydroxymethylcytosin-1-yl)acetate (**10**), which contained 5-hmC, was used as the starting material for this transformation. As a byproduct, 5-(*t*-butyldiphenylsilanyloxymethyl)cytosine was obtained, which could be alkylated by ethyl bromoacetate to give the title compound, as a supplementary route to the following one.

As an example, a particularly impure sample was utilized. To a solution of crude ethyl(5-hydroxymethylcytosin-1-yl)acetate (**10**) (5.08 g, 48% (wt%), ~11 mmol) and imidazole (3.66 g, 54 mmol) in DMF (115 mL) was added TBDPS-Cl (8 mL, 27.0 mmol) with stirring. The solution was stirred overnight, and then a saturated solution of $NaHCO_3$ (10 mL) was added to stop the reaction. The DMF and H_2O were removed under vacuum to yield a dark-brown oil, which was dissolved in ethyl acetate (300 mL) and washed with H_2O (150 mL × 4). Unreacted starting materials (**9** and **10**), as well as dialkylated hmC, were removed by the aqueous washes. Compound **9** was recovered by back-extraction with ethyl acetate, the efficacy of which was monitored by TLC. The ethyl acetate phase was dried over Na_2SO_4, and the solvent was removed under vacuum to yield compound **9** along with silylated 5-hmC. The title compound **11** was isolated as a slightly orange solid, 40% yield, by flash column chromatography, using a gradient of solvents (hexane, ethyl acetate, and ethyl acetate – methanol (96:4) for **9**; ethyl acetate – methanol (75:25) for 5-(*t*-butyldiphenylsilanyloxymethyl)cytosine). Mp 183–185 °C, as isolated from chromatography. TLC (ethyl acetate – methanol, 95:5) R_f 0.18. ^{1}H NMR (400.1 MHz, $CDCl_3$, ppm) δ: 7.64 (d, J = 8.00 Hz, 4H, Ar), 7.38–7.48 (m, 6H, Ar), 6.48 (s, 1H, C6–H), 4.42 (s, 2H, SiO–CH_2–Ar), 4.31 (s, 2H, –CH_2–N), 4.19 (q, J = 6.40 Hz, 2H, –O–CH_2–), 1.26 (t, J = 6.40 Hz, 3H, –CH_3), 1.04 (s, 9H, SiC–CH_3). ^{13}C NMR (100.6 MHz, $CDCl_3$, ppm) δ: 143.6, 168.2, 166.0, 156.2, 135.8, 132.7, 130.3, 128.1, 105.0, 62.0, 61.4, 50.2, 27.0, 19.3, 14.3. HR-MS (EI) calcd. for $[C_{25}H_{31}O_4N_3Si + H]^+$: 466.2162; found: 466.2155.

Identified byproduct: 5-(*t*-butyldiphenylsilanyloxymethyl)cytosine; white solid. TLC (ethyl acetate – methanol, 95:5): R_f 0. ^{1}H NMR (400.1 MHz, DMSO-d_6, ppm) δ: 7.63 (d, J = 6.00 Hz, 4H, Ar), 7.42–7.50 (m, 6H, Ar), 7.10 (s, 1H, C6–H), 4.46 (s, 2H, SiO–CH_2–Ar), 1.00 (s, 9H, SiC–CH_3). MS (TOF-MS, ES$^+$) calcd. for $[C_{21}H_{25}O_2N_3Si + H]^+$: 380.1794; found: 380.1794.

Ethyl[4-benzoyl-5-(*t*-butyldiphenylsilanyloxymethyl)cytosin-1-yl]acetate (12)

To a solution of ethyl[5-(*t*-butyldiphenylsilanyloxymethyl)cytosin-1-yl]acetate (3.42 g, 7.3 mmol) in anhyd. pyridine (35 mL) was added benzoyl chloride (1 mL, 8.0 mmol) with stirring. The solution was stirred overnight, ethyl acetate (300 mL) was added, and the solution was washed with 1 mol/L HCl (200 mL × 2) to remove most of

© 2007 NRC Canada

the pyridine.[4] The ethyl acetate phase was subsequently washed with 0.02 mol/L HCl (200 mL × 3) and then water (200 mL × 3) to remove traces pyridine. The acidic aqueous phase was back-extracted by ethyl acetate (200 mL). The ethyl acetate phases were combined and dried over Na_2SO_4. The crude product had the appearance of an orange oil after removal of the solvent. Column chromatography (hexane, hexane–EtOAc (95:5) and (92:8) for **12**; EtOAc – CH_3OH (95:5) to recover **11**; R_f 0.04 (EtOAc – DCM, 1:6) was used to purify the crude material. White solid; 92% (4.16 g, after column-chromatography purification); mp 130–132 °C. TLC (EtOAc – DCM, 1:6): R_f 0.76. ^{1}H NMR (400.1 MHz, $CDCl_3$, ppm) δ: 13.19 (s, 1H, NH), 8.03 (d, J = 7.20 Hz, 2H, Ar), 7.63 (d, J = 6.40 Hz, 4H, Ar), 7.28–7.40 (m, 10H, Ar and C6–H), 4.70 (s, 2H, O–CH_2–Ar), 4.43 (s, 2H, N–CH_2–), 4.20 (q, J = 7.20 Hz, 2H, O–CH_2–), 1.24 (t, J = 7.20 Hz, 3H, –CH_3), 1.04 (s, 9H, –Si–CCH_3). ^{13}C NMR (100.6 MHz, $CDCl_3$, ppm) δ: 179.6, 167.2, 158.2, 148.5, 141.3, 136.8, 135.6, 133.0, 132.6, 130.2, 130.0, 128.2, 128.1, 115.2, 62.4, 59.4, 49.9, 27.0, 19.5, 14.3. HR-MS (EI) calcd. for $[C_{32}H_{35}O_5N_3Si]^+$: 569.2346; found: 569.2352.

[4-*N*-Benzoyl-5-(*t*-butyldiphenylsilanyloxymethyl)cytosin-1-yl]acetic acid (13)

To a solution of **12** (2.78 g, 4.88 mmol) in THF (55 mL) and H_2O (14 mL) at 4 °C was added 2.5 mol/L NaOH (16 mL, 8 equiv.). The mixture was stirred at 0 °C for 15 min, and the reaction was stopped by decanting into a separation funnel containing ethyl acetate (280 mL) and 0.25 mol/L HCl (190 mL) in which the reaction mixture was acidified, and **13** was obtained. The ethyl acetate phase was washed with H_2O (140 mL × 2). The aqueous phase was extracted with ethyl acetate (280 mL × 2). The ethyl acetate phases were combined and washed with H_2O (400 mL), dried over Na_2SO_4, and the solvent was removed under vacuum to yield the title compound as a white foam: 2.74 g (99% yield). TLC (ethyl acetate – DCM, 1:6; same eluent used for **12**): R_f 0. ^{1}H NMR (400.1 MHz, $CDCl_3$, ppm) δ: 8.06 (d, J = 7.20 Hz, 2H, Ar), 7.68 (m, 4H, Ar), 7.34–7.49 (m, 10H, Ar and C6–H), 4.73 (s, 2H, O–CH_2–Ar), 4.54 (s, 2H, –CH_2–N), 1.09 (s, 9H, SiC–CH_3). ^{13}C NMR (100.6 MHz, $CDCl_3$, ppm) δ: 177.7, 170.8, 158.7, 149.6, 142.8, 136.2, 135.7, 132.9, 132.8, 130.2, 129.8, 128.4, 128.1, 114.5, 59.6, 50.5, 27.1, 19.5. HR-MS (ESI-TOF, positive ion mode) calcd. for $[C_{30}H_{31}O_5N_3Si + H]^+$: 542.2111; found: 542.2091.

Fmoc hmC-OMe (14)

Compound **13** (3.83 g, 7.1 mmol) and hydroxybenzotriazole (HOBt, 1.03 g, 7.6 mmol) were dissolved in anhyd. DMF (39 mL). The solution was cooled to 0 °C. After adding *N*,*N*′-dicyclohexylcarbodiiimide (DCC, 1.58 g, 7.6 mmol) in one portion, the mixture was taken off the ice and stirred at room temperature for 1 h during which time a thick white precipitate of dicyclohexylurea (DCU) was formed. Methyl(2-(((9H-fluoren-9-yl)methoxy)carbonyl)aminoethyl)glycinate (2.52 g, 7.1 mmol) was added, and the mixture was stirred overnight. The precipitated DCU was filtered out by passing the solution through a pad of Celite. The filtrate was diluted with DCM (450 mL) and washed with acidic water twice (H_2O, 250 mL; 1 mol/L HCl, 6 mL) to remove the unreacted backbone submonomer, then washed with $NaHCO_3$ (satd. 250 mL × 2) and H_2O (300 mL × 3), respectively. All aqueous phases were back-extracted with DCM. The combined organic phases were dried over Na_2SO_4, and the solvent was removed under vacuum (RT). The crude product (yellow oil) was purified by column chromatography (hexane, hexane – ethyl acetate (80:20), (60:40), and (10:90) for the title compound, whereas ethyl acetate – methanol (98:2) and (95:5) was used to recover the backbone). White solid; 3.61 g, (58%); mp 125–126.5 °C (softens at 92 °C). TLC (ethyl acetate – methanol, 95:5; visualized with UV and 0.3% ninhydrin (green)): R_f 0.62. ^{1}H NMR (400.1 MHz, $CDCl_3$, ppm) δ: 13.26 (v br, NH), 8.13 (d, J = 7.20 Hz, 2H, H32), 7.29–7.74 (m, 22H, aromatic protons), 6.06 (br t, ma, backbone NH) and 5.48 (br t, J = 4.80 Hz, mi, backbone NH), 4.77 (s, 2H, H5), 4.64 (s, ma, H6) and 4.52 (s, mi, H6), 4.47 (d, J = 6.80 Hz, ma, H23) and 4.40 (d, J = 7.20 Hz, mi, H23), 4.22–4.25 (m, 1H, H22), 4.09 (s, ma, H27) and 4.22–4.25 (m, mi, H27), 3.73 (s, ma, H29) and 3.79 (mi H29), 3.73 (br, ma, H26) and 2.95 (br, mi H26), 3.46 (br, ma, H25) and 3.41 (br, mi H25), 1.15 (s, mi, H11) and 1.13 (s, ma, H11). ^{13}C NMR (100.6 MHz, $CDCl_3$, ppm) δ: 179.3 (C30), 169.9 (C28), 166.9 (C7), 158.5 (C2), 156.9 (C24), 148.5 (C1), 143.8 (C16), 142.8 (C4), 141.2 (C17), 136.7 (C31), 135.5 (C13), 133.0 (C12), 132.4 (C34), 130.0 (C15), 129.8 (C32), 128.1 (C33), 127.9 (C14), 127.7 (C19), 127.1 (C20), 125.1 (C21), 119.9 (C18), 114.2 (C3), 66.7 (C23), 59.3 (C5), 52.4 (ma, C29) and 52.9 (mi, C29), 48.9 (ma, C6) and 49.1 (mi, C6), 48.8 (ma, C27) and 50.3 (mi, C27), 48.7 (C26), 47.2 (C22), 39.0 (mi, C25) and 39.4 (ma, C25), 26.9 (C11), 19.3 (C10). HR-MS (ESI-TOF) calcd. for $[C_{50}H_{51}O_8N_5Si + Na]^+$: 900.3405; found: 900.3430.

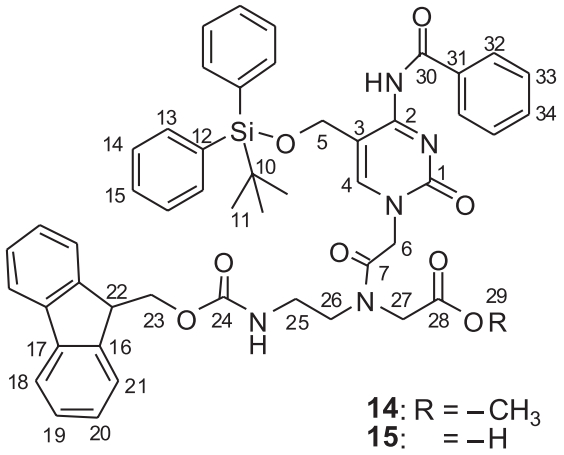
Fmoc-hmC-OH (15)

Compound **14** (3.40 g, 3.9 mmol) (Fig. 4) was dissolved in THF (42 mL) and H_2O (11 mL). The solution was cooled to 4 °C in an ice-bath, and then 2.5 mol/L NaOH (12.1 mL, 8 equiv.) was added. The solution was stirred for 5 min at 4 °C, and then the reaction was stopped by decanting it into a separation funnel containing ethyl acetate (500 mL) and acidified water (36 mL of 1 mol/L HCl and 200 mL of H_2O). The ethyl acetate phase was washed with H_2O (200 mL × 2). The aqueous phase was extracted with ethyl acetate (150 mL × 2). The organic phase was separated and dried over Na_2SO_4. The solvent was removed under vacuum (RT). The crude product (off-white solid, 3.7 g) was purified by flash column chromatography (hexane, hexane – ethyl acetate (50:50), ethyl acetate, and ethyl acetate – methanol (95:5), (80:20), and (75:25)). White solid; 2.95 g (90%); mp 186–187 °C, as isolated from chromatography (softens at 130 °C). TLC (EtOAc – CH_3OH, 95:5; visualized with UV and 0.3% ninhydrin (green)): R_f 0.04. ^{1}H NMR (400.1 MHz,

[4] Caution: care must be taken in the amount of HCl used, which should be calculated based on complete neutralization of pyridine; excess acid removed the *N*4-Bz group.

© 2007 NRC Canada

Fig. 4. Structure of the 5-hydroxymethylcytosine (hmC) PNA monomer ester (R = –CH_3) and acid (R = –H), defining the arbitrary numbering system used in NMR signal assignments.



DMSO-d_6, ppm) δ: 7.96 (d, J = 7.60 Hz, 2H, H32), 7.31–7.89 (22H, aromatic protons), 7.28–7.55 (overlap, 1H, backbone NH), 4.92 (s, mi, H6) and 4.72 (s, ma, H6), 4.60 (s, mi, H5) and 4.58 (s, ma, H5), 4.34 (d, J = 6.80 Hz, mi, H23) and 4.24 (d, J = 6.40 Hz, ma, H23), 4.19–4.20 (m, 1H, H22), 3.99–4.01 (br, depending on the state of protonation, 2H, H27), 3.47 (b, ma, H26) and 3.30 (br m, mi, H26), 3.39 (br m, ma, H25) and 3.17 (br m, mi, H25), 0.97 (s, 9H, H11). ^{13}C NMR (100.6 MHz, DMSO-d_6, ppm) δ: 172.1 (C30), 171.5 (C28), 167.3 (C7), 158.7 (C2), 156.6 (C24), 148.7 (C1), 146.3 (C4), 144.0 (C16), 140.8 (C17), 136.3 (C31), 135.3 (C13), 132.8 (C12), 132.5 (C34), 130.0 (C32), 129.3 (C15), 128.2 (C33), 128.0 (C14), 127.7 (C19), 127.2 (C20), 125.3 (C21), 120.1 (C18), 111.9 (C3), 65.7(C23), 59.2(C5), 51.1 (mi, C27) and 49.4 (ma, C27), 48.6 (C6), 47.7 (mi, C26) and 47.1 (ma, C26), 46.9 (C22), 38.2 (C25), 26.7 (C11), 18.9 (C10). HR-MS (ESI-TOF) calcd. for $[C_{49}H_{49}O_8N_5Si - H]^+$: 862.32722; found: 862.3262**.**

Synthesis of PNA oligomers

PNA oligomers were synthesized on a 5 μmol scale using the standard FastMoc module on an Applied Biosystems 433A synthesizer employing a NovaSyn TGR (Rink amide) resin. The hexameric PNA (**P1**) was synthesized using the Rink amide resin with a loading of 0.23 mmol/g. Oligomers (**P2**–**P5**) were prepared on a Rink amide resin preloaded with lysine (approximate loading: 0.065 mmol/g).

Resin cleavage and deprotection

To the resin bound oligomer (**P1**–**P5**) was added an ice-cold solution of TFA (950 μL) and triethylsilane (25 μL). The resin was agitated for 2 h. After filtration, TFA was removed with a stream of nitrogen, and the oligomer was precipitated, as a white solid, with cold diethyl ether (15 mL). Under these conditions, the TBDPS protecting group is also removed.

Oligomer **P4**, which contains an hmC residue, was additionally treated with concentrated aq. ammonia (1 mL, 55 °C for 12 h). The solution was dried under reduced pressure to give an off-white solid.

Oligomer purification

The crude, solid oligomers were dissolved in aq. TFA (0.1%), filtered, and purified by RP-HPLC, using a 250 mm × 4.6 mm, C18-bonded phase, 300 Å pore, and 5 μm particle-size column.

Characterization of PNAs

Mass spectral analysis of oligomers was performed at the UWO Biological Mass Spectrometry Laboratory. Electrospray ionization time-of-flight mass spectrometry (ESI-TOF MS) was performed with mass calibration provided by myoglobin (M^+ = 16951.49 Da, average mass) or histatin 5 (M^+ = 3036.33 Da, monoisotopic mass) (see Table 1).

Binding analysis

Poly(riboadenylic acid) (poly(rA)) was purchased from Sigma (Milwaukee, WI). Mixed sequence oligonucleotides were synthesized and purified by standard methods or purchased from the University Core DNA Services (Calgary, AB). Thermal denaturation of PNA:NA complexes (~2 μmol/L in nucleobases) was measured at 260 nm with a temperature ramp of 0.5 °C/min under ionic conditions (150 mmol/L NaCl, 10 mmol/L Na_2HPO_4, and 0.1 mmol/L EDTA at pH 7.0). A minimum of two independent samples were run many times, and the T_m was estimated by determining the maximum in the first derivative of the denaturation curve. The error associated with the T_m values is ±0.5 °C.

Results and discussion

The goal of this work was to achieve the synthesis of 5-hydroxymethyl-derivatized uracil and cytosine PNA monomers, incorporate these modified bases into PNA, and study their impact on hybridization. As a starting point, we were interested in a scalable and straightforward approach to the synthesis of the monomers. Key considerations were on the preparation of the 5-hydromethyluracil and -cytosine and subsequently the use of an appropriate protecting-group strategy for the hydroxyl functional group.

5-Hydroxymethyluracil-containing PNA

The synthesis of 5-hydroxymethyluracil monomer (hmU), suitable for Fmoc-based peptide chemistry, is outlined in Scheme 1. We took the approach of preparing the appropriate (pyrimidin-1-yl)acetic acid ester derivative, which would be condensed with the methyl[*N*-2-(Fmoc-amino)ethyl]glycinate "backbone" submonomer in a convergent fashion, which we have previously reported (8). The synthesis starts with the inexpensive uracil and a one-step hydroxymethylation. Despite the potential biological importance of 5-hydroxymethyluracil and nucleoside derivatives thereof (9–12),[5]

[5] 5-hmU is a component of bacteriophage DNA, as well, there exists hmU specific binding proteins. The DNA of the dinoflagellate *Gyrodinium cohnii* contains 5-hmU. Glycosylated hmU is found in *Typanosoma Brucei*, the causative organism of African sleeping sickness. 5hmU is caused by oxidative damage to DNA

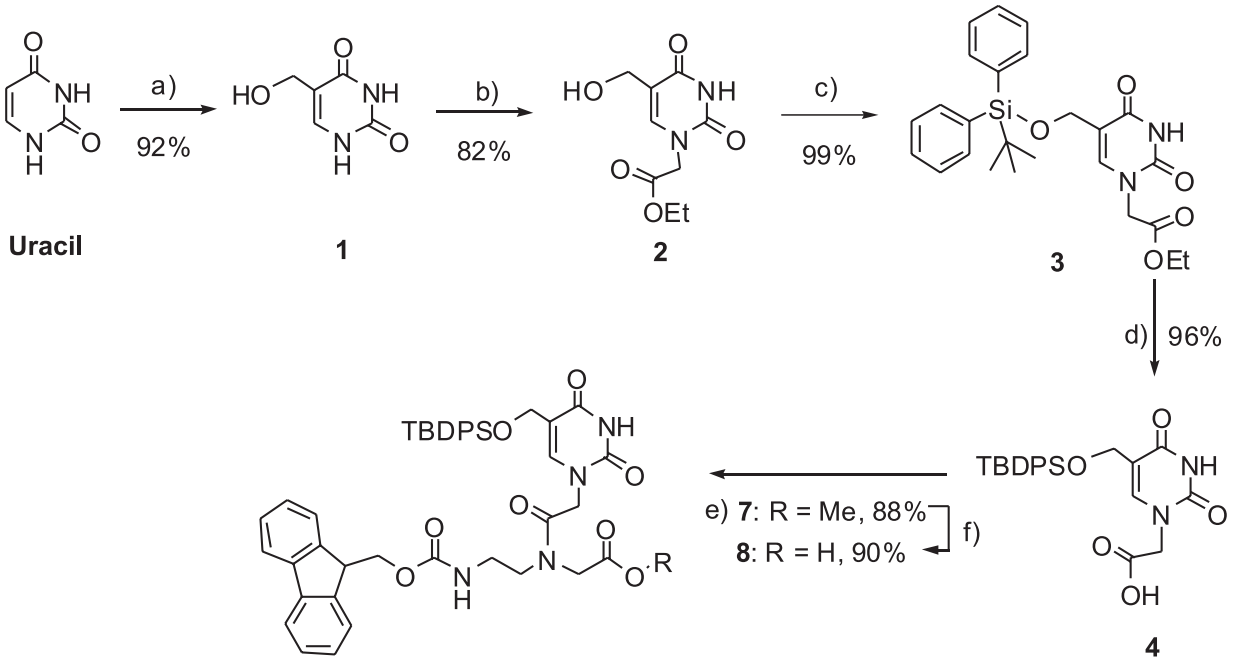
© 2007 NRC Canada

Table 1. Mass spectral characterization of PNA oligomers.

Oligomer	Sequence	Found	Calculated
P1	Ac-(hmU)T(hmU)T(hmU)T-Lys-NH_2	1832.50	1832.76
P2	H-Gly-GTA GAT CCC T-Lys-NH_2	2887.86	2887.80
P3	H-Gly-GTA GAT CTC T-Lys-NH_2	2902.78	2902.82
P4	H-Gly-GTA GAT C(hmC)C T-Lys- NH_2	2917.68	2917.83
P5	H-Gly-GTA GAT C(hmU)C T-Lys- NH_2	2918.93	2918.82

Note: Abbreviations in use: 5-hydroxymethyluracil (hmU), 5-hydroxymethylcytosine (hmC).

Scheme 1. Reagents and conditions: (*a*) $(HCHO)_n$, 0.5 mol/L Et_3N, 60 °C, 16 h; (*b*) $BrCH_2CO_2Et$, K_2CO_3, DMF, RT, 16 h; (*c*) TBDPS-Cl, imidazole, DMF, RT, 16 h; (*d*) 0.43 mol/L NaOH, 0 °C, 20 min; (*e*) methyl[*N*-2-(Fmoc-amino)ethyl]glycinate (**6**), EDC, DMF, RT, 16 h; (*f*) (*i*) 0.46 mol/L NaOH, 0 °C, 5 min; (*ii*) H^+.



there exist but a few synthetic routes to the modified nucleobase. Hydroxymethyluracil has been prepared by the reaction of uracil with paraformaldehyde in water, using an inorganic base (13, 14). However, we wished to avoid the potential problem of separating the nucleobase from inorganic salts and were inspired by the report of triethylamine-catalyzed hydroxymethylation of the deoxynucleoside (15). The reaction of paraformaldehyde with uracil in aq. NEt_3 (0.5 mol/L) proceeds smoothly overnight, and the product conveniently crystallizes from the reaction solvent.

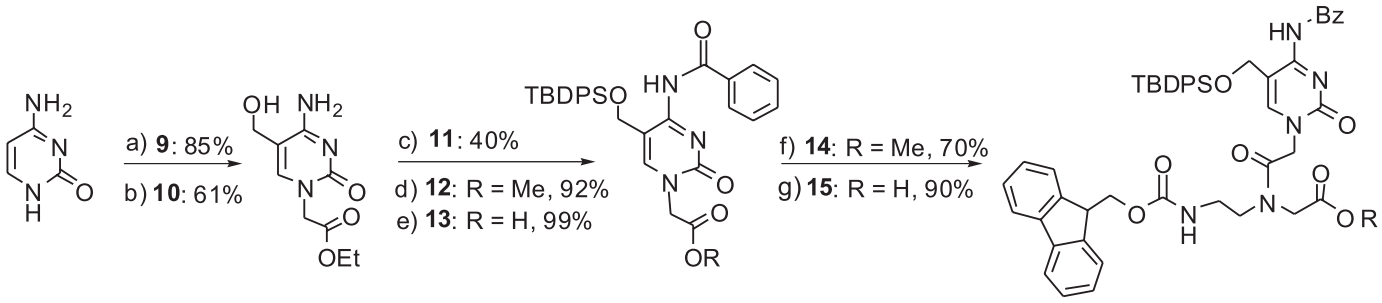
As with uracil, thymine, and related derivatives, we next proceeded to the alkylation of the nucleobase with ethyl bromoacetate in anhyd. DMF with K_2CO_3 (16), suspecting that we would achieve the desired chemoselectivity, based on the pKa differences between the 5-hydroxyl group and the lactam/imide groups of the heterocycle. We observed complete selectivity for N-alkylation and recovered the desired N1-derivative in good yield. The only byproduct that we were able to identify from this reaction was the *N*1,*N*3-bisalkylated nucleobase.

Next, we chose a silyl ether as the masking group for the 5-hydroxy functionality for ease of installation and removal as well as orthogonality to the Fmoc- group and the methyl ester of the backbone. Initially, we prepared the *t*-butyldimethylsilyl ether, but this proved not robust enough in model studies; thus, we turned to the *t*-butyldiphenylsilyl ether. This group was stable to alkyl ester hydrolysis (0.43 mol/L NaOH, THF – H_2O, 0 °C, >40 min), Fmoc-removal (30% piperidine in DMF, 40 min), and normal workup conditions (pH 1–12), yet was completely and rapidly removed by treatment with TFA. After settling on a hydroxyl-protecting group, standard transformations yielded the hmU monomer **8** with some noteworthy points. The condensation of the backbone submonomer **6** with the modified nucleobases **4** was mediated by the use of the carbodiimide reagent EDC without the use of additional base or additives. As well, the best yield and least elimination of the Fmoc-group were obtained when the acid component was used in excess (1.6 equiv.) relative to the backbone submonomer free base. In this instance, the isolated yields of **7** were reliably high (88%) with a minimal loss of the base-labile Fmoc-group (<4%).

The penultimate step, the saponification of the monomer ester (**7**), was also carefully done to avoid loss of the Fmoc-

© 2007 NRC Canada

Scheme 2. Reagents and conditions: (*a*) $(HCHO)_n$, 0.75 mol/L Et_3N, H_2O, 3 d, 95 °C; (*b*) K_2CO_3, DMF, $BrCH_2CO_2Et$, 24 h; (*c*) TBDPS-Cl, imidazole, DMF, 16 h; (*d*) BzCl, pyridine; (*e*) 0.46 mol/L NaOH, 15 min, 4 °C; (*f*) **6**, DCC, HOBT, DMF; (*g*) (*i*) 0.46 mol/L NaOH, 0 °C, 5 min; (*ii*) H^+.



group. The reaction conditions (8 equiv. of NaOH, 0.46 mol/L, 5 min) were optimized to give complete hydrolysis, while minimizing concomitant removal of the Fmoc-group. Nonetheless, some Fmoc- groups were lost (4%–8%), yet the final monomer was recovered in 90% yield from column chromatography. The optimized conditions for the condensation and hydrolysis reactions were then used for the synthesis of the hmC monomer **15**.

5-Hydroxymethylcytosine-containing PNA

Although 5-hydroxymethylcytosine has been known for some time in the context of a modified base found in the DNA of the *Escherichia coli* T-even bacteriophages (17) and in the nucleoside antibiotic mildiomycin (18), there has been no report of its synthesis from cytosine, via hydroxymethylation, until quite recently. Aside from isolation from these natural sources, early syntheses are based on multistep de novo heterocycle formation (19).

Our initial attempts to produce hmC under similar conditions of reaction to those used for the synthesis of hmU were unproductive. During this period of time, Abdel-Rahman and El Ashry reported a small-scale (1 mmol) hydroxymethylation of cytosine with paraformaldehyde in 0.5 N KOH solution under microwave irradiation (20). Our attempts to repeat this synthesis failed. However the report of the reaction of 2-deoxycytosine monophosphate with paraformaldehyde in the presence of 5 mol/L KOH (75 °C, 4 d) (12% yield) (21) motivated our further efforts on the direct hydroxymethylation of cytosine. Although the reaction of cytosine in aq. KOH with paraformaldehyde failed miserably, hmC was formed in good chemical yield (~85%) when triethylamine was employed along with higher reaction temperature and longer reaction time. We found that a molar excess of paraformaldehyde was necessary for the reaction to proceed in good chemical yields, but the addition must be made portion-wise during the course of the reaction. For instance, addition of greater than 3 equiv. of paraformaldehyde at the beginning of the reaction causes the formation of undesired and unidentified byproducts and made the recovery of hmC by recrystallization unfeasible. The reaction completely fails to give the desired product at 10 equiv. of paraformaldehyde. To overcome these problems, the amount of paraformaldehyde was carefully controlled and added in several portions during the reaction ($(HCHO)_n$ – cytosine (mol) 3.5:1), Scheme 2. The hmC is recovered from the reaction solution by crystallization. Although later crops are significantly contaminated with unreacted cytosine (up to approximately 20% (wt%)), they are still suitable for use in the next step.

The next necessary transformations are installation of nucleobase-protecting groups and alkylation. For cytosine, either of two routes may be used: N4-protection followed by N1-alkylation in the presence of either K_2CO_3 or NaH (22, 23); or the reverse, N1-alkylation in the presence of NaH and then protection of the exocyclic amino group (24). Both routes were attempted and gave identical yields; thus, the alkylation was simply performed in DMF with K_2CO_3, as was done with 5-hydroxymethyluracil.

Following alkylation, the nuclebase was protected, first by silylation of the hydroxyl group and then benzoylation of the exocyclic amino group. The silylation step gave a poor yield, likely by interference by the adjacent amino group, which could not be improved even by use of an excess TBDPS-Cl (2 equiv.). The remaining transformation to yield the hmC PNA monomer **15** proceeded without incident.

Synthesis and hybridization properties of PNA containing C5-hydroxymethylpyrimidines

The hmU and hmC PNA monomers were used for both automated and manual PNA-oligomer synthesis. Initially, standard conditions were employed (resin loading 0.23 mmol/g), and this was suitable for the incorporation of hmU in isolated positions (**P1**) by automated methods. However, upon attempts to prepare contiguously modified oligomers by manual methods, the synthesis failed after 5 or 6 residues. Although these oligomers were identified by mass spectrometry, they were inseparable, and further sequence elongation was not possible. Therefore, we turned to lower-loading resin (0.06 mmol/g), which did not resolve this problem. However, the lower-loading resin was subsequently used to prepare singly modified oligomers **P2**–**P4**, which allowed us to evaluate the effect of the hmU or hmC substitution for T or C, respectively.

The oligomers were examined for their ability to bind complementary nucleic acids (Table 2). The poly(hmU/T) hexamer was used for triplex formation with poly(rA), wherein two strands of PNA bind to the RNA strand, thus giving each complex a total of six modifications. Compared with the unmodified oligomer, there was a slight drop in T_m (–1.5 °C) per insert. Interestingly, the same modest T_m drop

© 2007 NRC Canada

Table 2. Summary of T_m values for complexes formed between PNA and complementary DNA or RNA.

Oligomer	Sequence	Complement	T_m (°C)	ΔT_m/mod[d] (°C)
P0	Ac-TTT TTT-K-NH_2[a]	poly(rA)	62.0	—
P1	Ac- (hmU)T(hmU)T(hmU)T-Lys-NH_2	poly(rA)	53.0	–1.5
P2	H-Gly-GTA GAT CCC T-Lys-NH_2	DNA[b]	50.7	—
P3	H-Gly-GTA GAT CTC T-Lys-NH	DNA[c]	47.3	—
P4	H-Gly-GTA GAT C(hmC)C T-Lys- NH_2	DNA[b]	49.3	–1.4
P5	H-Gly-GTA GAT C(hmU)C T-Lys- NH_2	DNA[c]	46.0	–1.3

[a]From ref. 7.
[b]Complementary deoxyoligonucleotide sequence: 5′-AGA GAT CTA C-3′.
[c]Complementary deoxyoligonucleotide sequence: 5′-AGG GAT CTA C-3′.
[d]ΔT_m/mod: the difference in the melting temperature of modified oligomer compared with the unmodified oligomer on a per-substitution basis.

was observed in the singly modified duplexes (**P4** and **P5**), regardless of the identity of the nucleobase. These investigations represent the first study of the effect of 5-hydroxymethylpyrimidines on complex stability in either DNA or analogs. Previous studies have focused on the glycosylated derivatives (25), wherein only the diaminoglycoside conjugate was stabilizing towards duplex formation (26, 27). Relevant studies to 5-hydroxymethylcytosine have been focused on the interaction between oligonucleotides bearing this modification and enzymes and have not included T_m measurements (28, 29).

In summary, we have described a convenient, large-scale synthesis of 5-hydroxymethylcytosine and 5-hydroxymethyluracil and the transformation of these modified nucleobases in monomers compatible with PNA synthesis. The modifications were placed in isolated positions in sequences capable of either triplex formation or duplex formation. Dense functionalization of PNA oligomers was not achieved, likely because of the hydrophobic/steric nature of the protected hmU and hmC monomers. A single modification had a small negative impact on the stability of the complex, independent of the particular nucleobase, and multiple substitutions had an additive effect. Overall, the substitution of a hmU or hmC for T or C, respectively, is tolerated in both the context of a duplex or a triplex, within the sequences examined. Further investigation on the optimization of the protecting-group strategy and oligomerization chemistry is needed to fully evaluate this modification and its impact on the biophysical properties of PNA.

Acknowledgements

The authors thank the Natural Sciences and Engineering Research Council of Canada (NSERC) and the Academic Development Fund at The University of Western Ontario for support of this work. Prof. G. Lajoie and Ms. Paula Pittock of the Biological Mass Spectrometry Laboratories (UWO) are thanked for their expert assistance with mass spectral characterization of the polyamides. Mr. Doug Hairsine, Department of Chemistry, is thanked for performing HR-MS of small molecules. Mr. David Dodd is acknowledged for performing polyacrylamide gel electrophoresis of PNA (data not shown).

References

1. P.E. Nielsen, M. Egholm, R.H. Berg, and O. Buchardt. Science (Washington, D.C.), **254**, 1497 (1991).
2. P.E. Nielsen, U. Koppelhus, and F. Beck. *In* Pseudo-peptides in drug discovery. *Edited by* P.E. Nielsen. Wiley-VCH, Weinheim, Germany. 2004. Chap. 4.
3. F. Beck. *In* Methods in molecular biology: Peptide nucleic acids, methods and protocols. Vol. 208. *Edited by* P.E. Nielsen. Humana Press Inc., Totowa, NJ, USA. 2002. Chap. 2.
4. P. Zhou, A. Dragulescu-Andrasi, B. Bhattacharya, H. O'Keefe, P. Vatta, J.J. Hyldig-Nielsen, and D.H. Ly. Bioorg. Med. Chem. Lett. **16**, 4931 (2006).
5. B.D. Gildea, S. Casey, J. MacNeil, H. Perry-O'Keefe, D. Sørensen, and J.M Coull. Tetrahedron Lett. **39**, 7255 (1998).
6. G.R. Revandkar and T.S. Rao. *In* Comprehensive natural products: DNA and aspects of molecular biology. Vol. 7. *Edited by* E.T. Kool. Elsevier Sciences Ltd., Oxford, UK. 2002. Chap. 2.
7. R.H.E. Hudson and F. Wojciechowski. Can. J. Chem. **83**, 1731 (2005).
8. R.H.E. Hudson, M. Goncharenko, A. Wallman, and F. Wojciechowski. Syn. Lett. **9**, 1442, (2005).
9. (*a*) G.G. Johnson and E.P. Geiduschek. Biochemistry, **16**, 1473 (1977); (*b*) J.R. Greene and E.P. Geiduschek. EMBO J. **4**, 1345 (1985).
10. P.M.M. Rae. Proc. Natl. Acad. Sci. U.S.A. **70**, 1141 (1973).
11. F. VanLeeuwen, M.C. Taylor, A. Mondragon, H. Moreau, W. Gibson, R. Kieft, and P. Borst. Proc. Natl. Acad. Sci. U.S.A. **95**, 2366, (1998).
12. M. Berger, J. Cadet, and J. Ulrich. Can. J. Chem. **63**, 6, (1985).
13. R.E. Cline, R.M. Fink, and K. Fink. J. Am. Chem. Soc. **81**, 2521 (1959).
14. U. Chiacchio, A. Corsaro, J. Mates, P. Merino, A. Piperno, A. Rescifina, G. Romeo, R. Giovanni, and T.T. Roberto. Tetrahedron, **59**, 4733, (2003).
15. C.J. LaFrancois, J. Fujimoto, and L.C. Sowers. Chem. Res. Toxicol. **11**, 75, (1998).
16. R.H.E. Hudson and J.M. Moszynski. Synlett, **18**, 2997, (2006).
17. G.R. Wyatt and S.S. Cohen. Nature (London), **170**, 1072, (1952).
18. S. Harada and T. Kishi. J. Antibiot. (Tokyo), **31**, 519, (1978).
19. T.L.V Ulbricht and C.C. Price. J. Am. Chem. Soc. **21**, 567, (1956), and refs. cited therein.
20. A.A.-H. Abdel-Rahman and E.-S.H. El Ashry. Synlett, **12**, 2043, (2002).
21. A.H. Alegria. Biochim. Biophys. Acta, **149**, 317, (1967).

© 2007 NRC Canada

22. K.L. Dueholm, M. Egholm, C. Behrens, L. Christensen, H.F. Hansen, T. Vulpius, K.H. Petersen, R.H. Berg, P.E. Nielsen, and O. Buchardt. J. Org. Chem. **59**, 5767, (1994).
23. Z. Timar, L. Kovacs, G. Kovacs, and Z. Schmel. J. Chem. Soc., Perkin Trans. 1, 19, (2000).
24. L. Christensen, H.F. Hansen, T. Koch, and P.E. Nielsen. Nucleic Acids Res. **26**, 2735, (1998).
25. No T_m data reported: J.J. Turner, N.J. Meeuwenoord, A. Rood, P. Borst, G.A. van der Marcel, and J.H. van Boom. Eur. J. Org. Chem. 3832, (2003).
26. J. Hunziker. Bioorg. Med. Chem. Lett. **9**, 201, (1999).
27. R. Tona, R. Bertolini, and J. Hunziker. Org. Lett. **2**, 1693, (2000).
28. S. Tardy-Planechaud, J. Fujimoto, S.S. Lin, and L.C. Sowers. Nucleic Acids Res. **25**, 553, (1997).
29. M. de Kort, P.C. de Visser, J. Kurzeck, N.J. Meeuwenoord, G.A. van der Marcel, W. Rüger, and J.H. van Boom. Eur. J. Org. Chem. 2075, (2001).

© 2007 NRC Canada

Kinetic characterization of a cis- and trans-acting M^{2+}-independent DNAzyme that depends on synthetic RNaseA-like functionality — Burst-phase kinetics from the coalescence of two active DNAzyme folds[1]

Richard Ting, Jason M. Thomas, and David M. Perrin

Abstract: This work describes the kinetics of the DNAzyme 9_{25}-11, a combinatorially selected, M^{2+}-independent ribophosphodiesterase that is covalently modified with both cationic amines and imidazoles. At 13 °C, cis- and trans-cleaving constructs of 9_{25}-11 demonstrate the highest rate constants reported to date for any M^{2+}-independent nucleic acid catalyst, investigated at physiological ionic strength and pH 7.5 (0.3 min^{-1} for self cleavage and 0.2 min^{-1} for intermolecular cleavage). In contrast to the cis-cleaving species, single-turnover experiments with the trans-cleaving species exhibit biphasic cleavage data, suggesting the presence of two conformations of the catalyst–substrate complex. Pulse–chase experiments demonstrate that both complexes lead to substrate cleavage. Under multiple-turnover conditions, the higher rate constant appears in a burst phase that decays to a slower steady state exhibiting a rate constant of 0.0077 min^{-1}, a value approximating that of the slow-cleaving phase seen in single-turnover experiments. Slow product release is excluded as the source of the burst phase. An integrated rate equation is derived to describe burst-phase kinetics based on the funneling of the initial population of fast-cleaving conformation into a steady-state population composed largely of the slow-cleaving conformation.

Key words: RNase mimics, DNAzymes, ribozymes, kinetics, RNA cleavage.

Résumé : Dans ce travail, on décrit la cinétique de la 9_{25},11-ADNzyme, une ribophosphodiestérase M^{2+}-indépendante qui a été sélectionnée d'une façon combinatoire et qui a été modifiée d'une façon covalente avec des amines cationiques ainsi que des imidazoles. À 13 °C, de tous les catalyseurs d'acide nucléique, l'entité 9_{25},11 de clivage cis- et trans- présente la constante de vitesse la plus élevée pour une activité M^{2+}-indépendante, à force ionique physiologique et à un pH de 7,5 (0,3 min^{-1} pour l'autoclivage et de 0,2 min^{-1} pour le clivage intermoléculaire). Par opposition à ce qui est observé avec des espèces à clivage cis-, des expériences à simple rotation avec des espèces à clivage trans- fournissent des données relatives à un clivage biphasique ce qui suggère la présence de deux conformations du complexe catalyseur substrat. Des expériences de recherche de pulsation démontrent que les deux complexes conduisent à un clivage du substrat. Dans des conditions impliquant plusieurs rotations, il semble que la constante de vitesse la plus élevée soit dans une phase explosive qui ralentit vers un état stationnaire plus lent dont la constante de vitesse est 0,0077 min^{-1}, une valeur qui se rapproche de celle de la phase lente du clivage observé dans les expériences à rotation unique. Une libération lente de produit est exclue comme source de la phase explosive. On a dérivé une équation de vitesse intégrée pour décrire la cinétique de la phase explosive; elle est basée sur une orientation de la population initiale de la conformation à clivage rapide dans une population d'état stationnaire formée en grande partie de la conformation à clivage lent.

Mots-clés : imitation de la RNase, ADNzymes, ribozymes, cinétique, clivage de l'ARN.

[Traduit par la Rédaction]

Introduction

The discovery of catalytic RNA, and combinatorial methods for the in vitro selection of unnatural nucleic acid catalysts (ribozymes and DNAzymes) (1), have intrigued chemists and biologists alike. Following the identification of any catalyst, be it re-engineered from a naturally occurring ribozyme or from a combinatorially selected species, conditions for characterization are often chosen to push the envelope of catalysis (e.g., a high k_{cat} or M^{2+}-independence), even if such conditions are not absolutely physiologically applicable. For instance, naturally occurring ribozymes and

Received 15 December 2006. Accepted 13 March 2007. Published on the NRC Research Press Web site at canjchem.nrc.ca on 10 May 2007.

R. Ting, J.M. Thomas, and D.M. Perrin.[2] The Department of Chemistry, University of British Columbia, 2036 Main Mall, Vancouver, BC V6T 1Z1, Canada.

[1]This article is part of a Special Issue dedicated to Professor Kelvin K. Ogilvie.

[2]Corresponding author (e-mail: dperrin@chem.ubc.ca).

 doi:10.1139/V07-037 © 2007 NRC Canada

their unnatural variants have been studied at high concentrations of di- and mono-valent metal cations (e.g., 10–400 mmol/L Mg^{2+}, or 800 mmol/L NH_4Cl and 100 mmol/L Mg^{2+}, or 4 mol/L LiCl) (2–7). In a similar vein, two combinatorially selected DNAzymes have been found to exhibit impressive k_{cat} values in the order of 10 min^{-1} in the presence of 10 mmol/L Mn^{2+} or 100 μmol/L Pb^{2+} (8, 9). Generally in these cases, the most important rate constant is taken to be that of chemistry, which is most readily identified under single-turnover conditions. Nevertheless, to fully evaluate a catalyst's potential, it should also be characterized under multiple-turnover conditions where very high values of k_{cat} may not be expressed because of the slow product release (e.g., HH16, RNaseP, VS) (5, 7, 10–12) that results from the conditions chosen to favor k_{cat}.

Our interest in catalytic nucleic acids involves synthetically incorporating protein-like functionalities to increase k_{cat} values for M^{2+}-independent RNA cleavage (13). The impetus for this comes from the fact that numerous investigations of naturally occurring ribozymes have addressed the question of M^{2+}-independence (2–4, 14–24). Furthermore, several combinatorial selections have identified DNAzymes that can operate without Mg^{2+}, thus underscoring a general interest in M^{2+}-independent activity (25–27). These studies identified self-cleaving species with k_{obs} values in the order of 10^{-3} min^{-1}. With few exceptions (6), when nucleic acid catalysts are evaluated under physiological ionic strength where M^{2+} is minimally present (e.g., 0.2 mmol/L Mg^{2+} and 150 mmol/L monovalent M^+), k_{cat} values for intermolecular cleavage are low and turnover remains quite elusive. In light of the fact that intracellular levels of M^{2+} (28–31) may limit the in vivo activity of such catalysts, recent reviews (32–34) have further highlighted the potential utility of M^{2+}-independent ribonucleases as research tools and therapeutics. Moreover, the importance of turnover with regards to therapeutic development has also been noted (35). At physiological pH and submolar concentrations of M^+ (absence of an M^{2+}, polyamine, or histamine) (36), turnover by an unmodified nucleic acid catalyst has yet to be observed.

Using the combinatorial selection methods developed early on (37–39), we and others have discovered DNAzymes with protein-like cationic amines and imidazoles that can cleave RNA in the absence of a M^{2+}, as does RNaseA (13, 40–43). We now seek to quantify the catalytic advantages that synthetically modified nucleosides may impart under conditions where unmodified nucleic acid catalysts have been found to be catalytically deficient. It is under these somewhat more stringent conditions that we may properly gauge the advantage that modified nucleotides will bring.

Recently, we reported on the general kinetic properties of the modified DNAzyme 9_{25}-11t, which catalyzed ribophosphodiester hydrolysis in the absence of an M^{2+} at 24 °C (k_{cat} of 0.03 min^{-1}) (13). Previous studies on M^{2+}-dependent ribozymes and DNAzymes employed conditions that deviate drastically from physiological, but enhance rate constants for cleavage. Herein, we identify conditions that favor a significantly higher k_{cat} value with respect to M^{2+}-independent RNA hydrolysis; in the case of 9_{25}-11, the change in conditions involves simply lowering the temperature from 24 °C to 13 °C, a temperature that deviates from most physiological applications. At 13 °C, the rate constants for both intramolecular cleavage, $k_{self\text{-}cleave}$, and single-turnover intermolecular cleavage, $k_{cat\ STR}$, increase by approximately an order of magnitude. These observations demonstrate the highest rate constants to date for any nucleic acid catalyst evaluated at submolar ionic strength and pH in the absence of M^{2+}.

In the case of intermolecular cleavage, the higher rate constant observed under single-turnover conditions is manifested in a burst phase that precedes a slow steady-state rate under multiple-turnover conditions. After excluding slow product release, we developed a fully integrated kinetic framework that involved dynamic partitioning of an active-catalyst conformation into a less active one to account for the observed burst phase. Fersht (44) and others (45) have discussed conformational partitioning and hysteretic behavior as explanations for a burst phase. To explain the observed burst phase, we developed an alternative model that differs from other hystereses (see later), and this model may apply to any catalyst displaying similar kinetic behavior, irrespective of its composition.

Materials and methods

Enzymes and chemicals

Enzymes, ^{32}P-labeled nucleotides, reagents, and buffers were purchased from commercial sources (NEB, Roche, Amersham-USB, PerkinElmer, and Fermentas). 5-aminoallyl-deoxyuridine, 8-histaminyl-deoxyadenosine phosphoramidites, and triphosphates were synthesized as previously described (40, 46).

Oligonucleotides

S1, 5′-GCGTGCC**rC**GTCTGTT-3′; 3D2, 5′-GCGTGCC**rC**-GTCTG-3′; 3A2, 5′-GCGTGCC**rC**GTCTGTTGG-3′; 5D2, 5′-GTGCC**rC**GTCTGTT-3′; S1-OMe, the non-cleavable substrate analogue containing a 2′-*O*-methyl cytosine ribonucleotide in place of the ribocytidine of S1; pre-$P_{5'}$, the chemical precursor to the 5′-cleavage product of S1, 5′-GCGTGCC**rC**p-3′ (where p is a 3′-phosphate); $P_{3'}$, the 3′-cleavage product of S1, 5′-GTCTGTT-3′; and the trans-cleaving catalyst 9_{25}-11t (where the letter "t" denotes trans-cleaving), 5′-CCAACAG**UUCUCAU**CCG**UAGUGAA**GGC-ACGC-3′ (where **U** = 5-aminoallyldeoxyuridine and **A** = 8-histaminyldeoxyadenosine) were synthesized using standard automated solid-phase methods. The cis-cleaving sequence, 9_{25}-11c (where the letter "c" denotes cis-cleaving), was synthesized using Sequenase 2.0, as previously described (40). All labeled and unlabeled oligonucleotides were purified by 7 mol/L urea (D-PAGE) gels, ethanol precipitated, desalted on a G-25 spin column, and stored in water at –20 °C prior to use. The 5′-cleavage product of S1 possessing a 2′,3′-cyclic phosphate, $P_{5'}$, was synthesized according to literature precedent (10, 13, 47) and verified by MALDI-TOF analysis: $[M - H]^-$ *m/z* (predicted): 2462.4; *m/z* (experimental): 2460.6.

Oligonucleotide labeling

Substrates S1, 3D2, 3A2, 5D2, S1-OMe, and the 5′-cleavage product, $P_{5'}$, were 5′ end labeled with T4 polynucleotide kinase lacking 3′-phosphatase activity (Fermentas).

© 2007 NRC Canada

Sequenase 2.0 was used to extend 3D2 against a complementary template by two nucleotides ([α-^{32}P] TTP) to give 3′-^{32}P labeled S1. To generate 3′-^{32}P labeled $P_{3'}$, 3′-^{32}P labeled S1 was treated with NaOH and then gel-purified to give 3′-^{32}P labeled $P_{3'}$.

Kinetic experiments

The procedures used are generally adapted from literature precedents (10, 11, 48, 49). Self-cleavage experiments were performed as previously described (50). Kinetic experiments with the trans-cleaving species, 9_{25}-11t, were performed under mineral oil in a Julabo F-10 temperature-controlled water bath. Substrate, catalyst, and chase solutions were buffered in CB200 (50 mmol/L Tris HCl pH 7.5, 1 mmol/L EDTA, and 200 mmol/L NaCl), unless specified otherwise, where CB200 refers to cleavage buffer with 200 mmol/L NaCl. Multiple independent data sets were collected for all experiments. Autoradiography data were generated using Molecular Dynamics phosphor screens and a Molecular Dynamics Typhoon 9200 phosphorimager and were quantified with ImageQuant v5.2. Volumes were corrected for background using ImageQuant v5.2 histogram peak correction. The kinetic constants reported in this text result from least-square fits of data using SigmaPlot 2001 v7.101. Errors associated with the constants are the standard errors generated from these fits.

Single-turnover (STR) kinetics, determination of $k_{obs\ STR}$

Cleavage reactions in trans were initiated by mixing equal volumes of 9_{25}-11t at increasing concentrations (5–1500 nmol/L) and trace radiochemical quantities of the labeled substrate S1 (<1 nmol/L) in CB200 (buffer) at 13 °C. Aliquots were removed at various time points, quenched with formamide solution, and resolved by 7 mol/L urea denaturing 20% 29:1 monomer/bis(polyacrylamide) gel electrophoresis (20% D-PAGE). First-order rate constants, $k_{obs\ STR}$, were obtained by fitting data to the single-exponential eq. [1]

$$[1] \qquad [P]_t = [P]_\infty(1 - e^{-k_{obs\ STR}t})$$

where $[P]_t$, and $[P]_\infty$ are the fractions of substrate cleaved at time t and at the end point, respectively. Rate constants for biphasic curves were obtained by fitting data to the following double-exponential equation

$$[2] \qquad [P]_t = [P_{fast}]_\infty(1 - e^{-k_{obs\ fast\ STR}t}) + [P_{slow}]_\infty(1 - e^{-k_{obs\ slow\ STR}t})$$

where the subscripts "fast" and "slow" identify the constants that describe fast and slow phases, respectively.

Determination of the maximum first-order rate constant ($k_{cat\ STR}$) and the catalyst concentration at which the rate is half-maximal ($K_{M\ STR}$) under single-turnover conditions

For each of the fast- and slow-cleaving phases, $k_{cat\ STR}$ and $K_{M\ STR}$ were determined by plotting $k_{obs\ STR}$ against total 9_{25}-11t concentration, $[E_t]$, using the hyperbolic equation

$$[3] \qquad k_{obs\ STR} = \frac{k_{cat\ STR}[E_t]}{K_{M\ STR}[E_t]}$$

Pulse–chase cleavage experiments to determine the dissociation rate constants for S1 ($k_{-1\ fast}$ and $k_{-1\ slow}$)

Pulse–chase cleavage experiments followed literature precedents (48, 49). The chase was initiated typically 3 min after the pulse by the addition of unlabeled S1 in CB200 in 50-fold excess over the catalyst. Data corrected for cleavage prior to the chase (49) were fit to eq. [2] to obtain the rate constants $k_{chase\ fast}$ and $k_{chase\ slow}$. The S1 dissociation rate constant, k_{-1}, was determined from k_{chase}, according to eq. [4] (49)

$$[4] \qquad k_{-1} = k_{chase} - k_{cat\ STR}$$

Pulse–chase native gel shift assays used for determining the dissociation rate constants for an S1 substrate analogue ($k_{-1\ fast\ S1\text{-}OMe}$ and $k_{-1\ fast\ S1\text{-}OMe}$)

Aliquots of 9_{25}-11t (0.5 μmol/L) and trace radiochemical quantities of 5′-^{32}P labeled S1-OMe were equilibrated in CB200 at 13 °C overnight. The chase was initiated by the addition of unlabeled S1 in 100-fold excess over the catalyst. The reactions were stopped by placing the tubes on ice and adding a 1/10 of the volume of ice-cold loading solution (70% sucrose, 0.01% bromophenol blue, and 0.01% xylene cyanol in CB200). In a 4 °C cold room, samples were loaded on a pre-cooled native gel run at 4 °C and 3 W (~50 mA) with CB200 as the running buffer under peristaltic circulation. The first-order dissociation rate constants, $k_{-1\ fast\ S1\text{-}OMe}$ and $k_{-1\ slow\ S1\text{-}OMe}$, were obtained by fitting biphasic data to the double-exponential equation

$$[5] \qquad f = f_o + f_{\infty\ fast}(1 - e^{-k_{-1\ fast\ SI\text{-}OME}t}) + f_{\infty\ slow}(1 - e^{-k_{-1\ slow\ SI\text{-}OME}t})$$

where $f_{\infty\ fast}$ and $f_{\infty\ slow}$ are the respective maximum fractions of bound substrate analogue that dissociates in the fast- or slow-dissociating phases, and f_o is the fraction of S1-OMe that was not bound to 9_{25}-11t at $t = 0$.

Native gel shift assays used for determining the dissociation rate constant of product oligonucleotides

Product-dissociation constants for 9_{25}-11t were measured as described earlier for $k_{-1\ S1\text{-}OMe}$, using 5′-^{32}P labeled $P_{5'}$ or 3′-^{32}P labeled $P_{3'}$. These experiments were carried out with each product in the absence or presence of the other at 50 μmol/L.

Multiple-turnover (MTR) kinetics using denaturing PAGE analysis

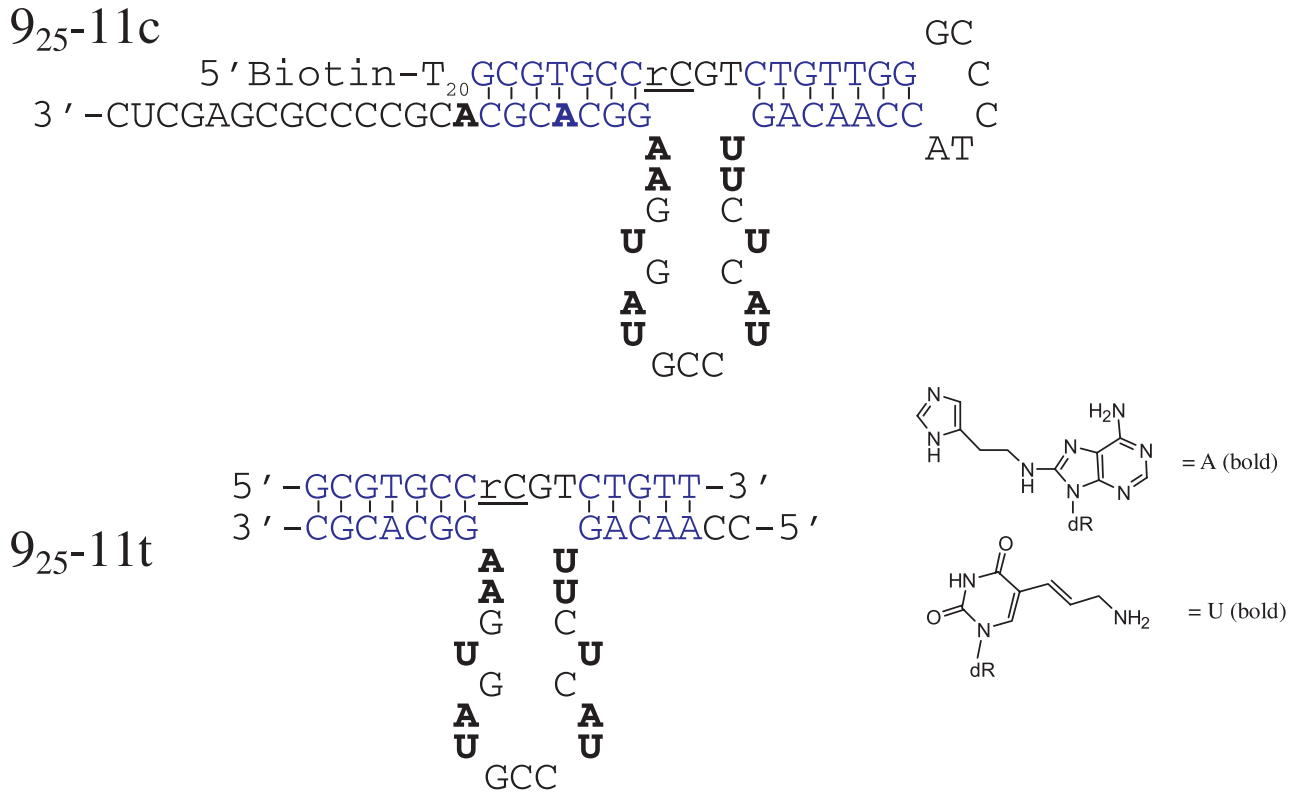
Multiple-turnover experiments were performed at a ratio of [S]/[E] ≥ 15 in CB200 at 13 °C. Cleavage was quantified according to protocols detailed for the single-turnover experiments. For steady-state analysis, multiple-turnover kinetic data following the burst phase were fit to the equation

$$[6] \qquad P = k_{obs\ MTR}\ t + P_o$$

where P_o is the amplitude of the burst phase. Values of $k_{obs\ MTR}$ obtained at different enzyme concentrations were

© 2007 NRC Canada

Figure 1. The sequences of 9_{25}-11c, prepared by templated enzymatic polymerization of synthetic monomer triphosphates, and 9_{25}-11t, synthetically prepared on the solid phase. Substrate S1 is shown hybridized to 9_{25}-11t. Emboldened **A** and **U** represent the modified nucleotides shown at right. The rC indicates the target ribophosphodiester bond. Predicted Watson–Crick pairs are indicated by a dash between blue-colored complementary bases.



plotted vs. total catalyst concentration, $[E_t]$, according to the following equation

[7] $$k_{\text{obs MTR}} = [E_t]\ k_{\text{cat steady state MTR}}$$

To obtain values for the burst-phase constants, multiple-turnover data were fit to the equation

[8] $$P = C(1 - e^{-k_{\text{burst}}t}) + k_{\text{obs MTR}}t$$

The initial rate of product formation was determined by linear regression of the cleavage data obtained at early time points (up to 12 min). A first-order rate constant was obtained by dividing the initial rate by the total catalyst concentration multiplied by the 0.35 fraction to reflect the fraction of the catalyst initially present in the fast-cleaving conformation as determined by the amplitudes for each phase (see Results and Discussion sections for the rationale of attributing this value).

Native PAGE analysis of multiple-turnover kinetics – An attempt to observe a product–catalyst complex

Multiple-turnover experiments were performed using 5′-^{32}P labeled S1 and 3′-^{32}P labeled S1. Reaction concentrations were 1 µmol/L for 9_{25}-11t and 10 or 15 µmol/L for the substrate, S1. Aliquots were removed and quenched in formamide loading solution (for D-PAGE) or added to 1/10 of the volume ice-cold native gel loading solution. Resolution by D-PAGE and native PAGE at 4 °C was performed as described earlier.

Error analysis

Variance from week to week was found to be as high as 30%, and up to 30% when the resynthesis of catalyst 9_{25}-11t is considered. Others have reported the same for unmodified ribozymes (7, 10, 48, 49). For the self-cleaving sequence 9_{25}-11c, errors from day to day were generally lower (~ 10%–20%), and variance seemed to depend on the freshness of both the Sequenase used to synthesize 9_{25}-11c and the dGTPα^{32}P used for internal labeling. To control for such error, all self-cleavage measurements were conducted on the same day for the six temperatures noted.

Attempts at ligation

Ligation reactions under single-turnover and external-equilibrium-shift conditions were performed at 13 °C as previously described (13).

Results

The unimolecularity of the enzymatically prepared self-cleaving species, 9_{25}-11c (where the letter "c" denotes cis-cleaving), allowed us to estimate a chemical-cleavage rate constant without having to entertain the complicating effects of enzyme–substrate association and dissociation. Once this was investigated, we turned our attention to catalysis in trans with 9_{25}-11t (where the letter "t" denotes trans-cleaving), a synthetic trans-cleaving derivative of 9_{25}-11c that was evaluated under single- and multiple-turnover conditions. Figure 1 shows the two synthetically modified nucleosides, the self-

© 2007 NRC Canada

Table 1 Comparison between rate constants obtained for 9_{25}-11c and 9_{25}-11t at 13 °C.

Observed rate constant at 13 °C	Substrate	Biphasic	Method of determination	Value
9_{25}-11c				
$k_{\text{self-cleave}}$	—	N	Single-turnover kinetics	0.28±0.02 min^{-1}
9_{25}-11t STR				
$k_{\text{cat fast STR}}$	S1	Y	Single-turnover kinetics	0.20±0.01 min^{-1}
$k_{\text{cat slow STR}}$	S1	Y	Single-turnover kinetics	0.0036±0.0001 min^{-1}
$K_{\text{M fast STR}}$	S1	Y	Single-turnover kinetics	170±30 nmol/L
$K_{\text{M slow STR}}$	S1	Y	Single-turnover kinetics	21±4 nmol/L
$k_{\text{chase fast}}$	S1	Y	Pulse–chase single-turnover kinetics	0.233 min^{-1}
$k_{\text{chase slow}}$	S1	Y	Pulse–chase single-turnover kinetics	0.0041 min^{-1}
$k_{-1\text{ fast}}$	S1	Y	Pulse–chase single-turnover kinetics	0.03 min^{-1}
$k_{-1\text{ slow}}$	S1	Y	Pulse–chase single-turnover kinetics	0.0005 min^{-1}
$k_{-1\text{ fast S1–OMe}}$	S1-OMe	Y	Pulse–chase/native PAGE	0.014±0.004 min^{-1}
$k_{-1\text{ slow S1–OMe}}$	S1-OMe	Y	Pulse–chase/native PAGE	0.0023±0.0005 min^{-1}
$k_{\text{cat 5D2 STR}}$	5D2	N	Single-turnover kinetics	0.038±0.002 min^{-1}
$K_{\text{M 5D2 STR}}$	5D2	N	Single-turnover kinetics	590±70 nmol/L
$k_{\text{chase 5D2}}$	5D2	N	Pulse–chase single-turnover kinetics	0.066±0.002 min^{-1}
$k_{-1\text{ 5D2}}$	5D2	N	Pulse–chase single-turnover kinetics	0.036 min^{-1}
$k_{\text{cat 3D2 STR}}$	3D2	N	Single-turnover kinetics	0.0069±0.0003 min^{-1}
$K_{\text{M 3D2 STR}}$	3D2	N	Single-turnover kinetics	121±16 nmol/L
Product-dissociation constants				
k_{-3} (see Fig. S7)[3]	3′ P	N	Native gel shift assay	0.19±0.02 min^{-1}
k_{-4} (see Fig. S7)[3]	5′ P	N	Native gel shift assay	0.75±0.02 min^{-1}
k_{-5} (see Fig. S7)[3]	5′ P	N	Native gel shift assay	0.8±0.1 min^{-1}
k_{-6} (see Fig. S7)[3]	3′ P	N	Native gel shift assay	0.31±0.08 min^{-1}
9_{25}-11t MTR				
$k_{\text{cat steady state MTR}}$	S1		Multiple-turnover kinetics	0.0077±0.0007 min^{-1}
$k_{\text{cat MTR 5D2}}$	5D2		Multiple-turnover kinetics	0.0193±0.0006 min^{-1}
$k_{\text{cat MTR 3D2}}$	3D2		Multiple-turnover kinetics	0.0041±0.0003 min^{-1}
$k_{\text{obs thermocycle MTR}}$	S1		Multiple-turnover kinetics	0.064±0.002 min^{-1}

cleaving species (9_{25}-11c), and the trans-cleaving species (9_{25}-11t) with its substrate S1. All rate constants measured at 13 °C are listed in Table 1. A full kinetic scheme that lists representative values from this table is given in the Supplementary data.[3]

The maximum rate constant for the self-cleavage of 9_{25}-11c ($k_{\text{obs STR}}$) is observed at ~13 °C

Previously, a value of 0.044 min^{-1} had been reported for $k_{\text{self-cleavage}}$ for 9_{25}-11c at 37 °C (40). As part of an initial study to see if varying several conditions (e.g., concentration of M^{2+}, buffer, ionic strength, temperature, and so forth) would cause an increase in the value of the observed self-cleavage rate constant, $k_{\text{self-cleave}}$, the kinetics of 9_{25}-11c was investigated as a function of temperature. Plots of the self-cleaved fraction vs. time at which it approached 70% cleavage at all temperatures, were monophasic, and fit to eq. [1] (Fig. 2A). Of the temperatures surveyed, the cleavage rate constant appears to be maximal at ~13 °C with a $k_{\text{self-cleave}}$ of 0.28 ± 0.02 min^{-1} (Fig. 2B). Although this rate constant varied linearly with sodium concentration between 20 and 200 mmol/L NaCl, no increase was observed at higher ionic strength (e.g., 0.2–1 mol/L NaCl). Furthermore, $[Mg^{2+}]$ up to 5 mmol/L had little effect (data not shown). As variation in the values of the self-cleavage rate constant could be as high as 20% from day to day, all self-cleavage reactions were performed on the same day using six different temperature baths to minimize error and ensure internal consistency.

To probe whether a folding step was rate-limiting at 13 °C (51, 52), pre-folding was attempted by preincubation of 9_{25}-11c under various conditions known to suppress cleavage activity followed by sudden restoration of permissive conditions (see Supplementary data) (52).[3] No conditions could be found to permit prefolding such that a faster cleav-

[3] Supplementary data for this article are available on the journal Web site (canjchem.nrc.ca) or may be purchased from the Depository of Unpublished Data, Document Delivery, CISTI, National Research Council Canada, Ottawa, ON K1A 0S2, Canada. DUD 5165. For more information on obtaining material, refer to http://cisti-icist.nrc-cnrc.gc.ca/irm/unpub_e.shtml.

© 2007 NRC Canada

Figure 2. (A) Time courses for the cleavage of the cis-cleaving sequence, 9_{25}-11c, at different temperatures in CB200 buffer. Radiochemical amounts of 9_{25}-11c were incubated in CB200 at (○) 8 °C, (▽) 13 °C, (△) 22 °C, and (□) 30 °C (4 °C and 45 °C are not shown). Data were fit to the single-exponential eq. [1]. R^2 were greater than 0.983; the mean R^2 value is 0.989. (B) Observed cleavage rates, $k_{\text{self-cleave}}$, obtained from single-exponential fits were plotted against temperature demonstrating an optimal rate constant, $k_{\text{self-cleave}}$, of 0.28 min^{-1} at 13 °C.

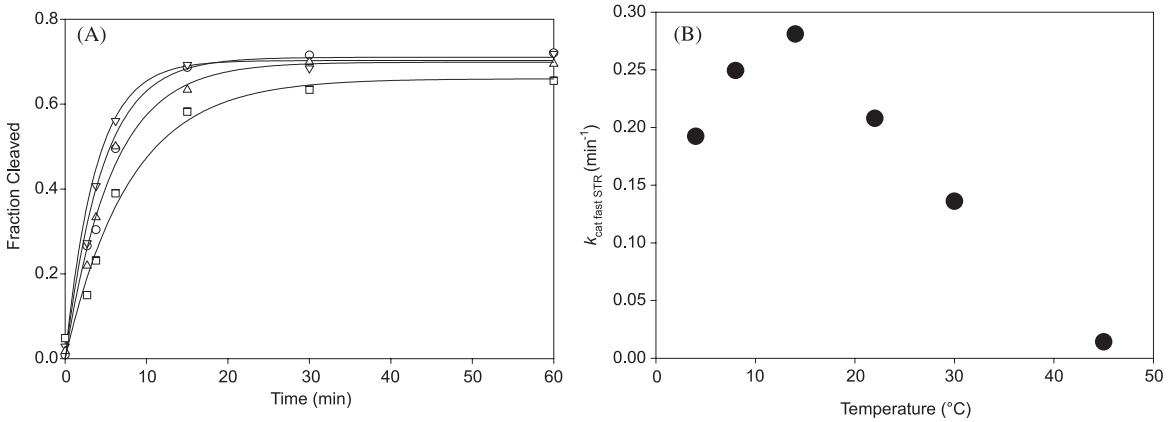
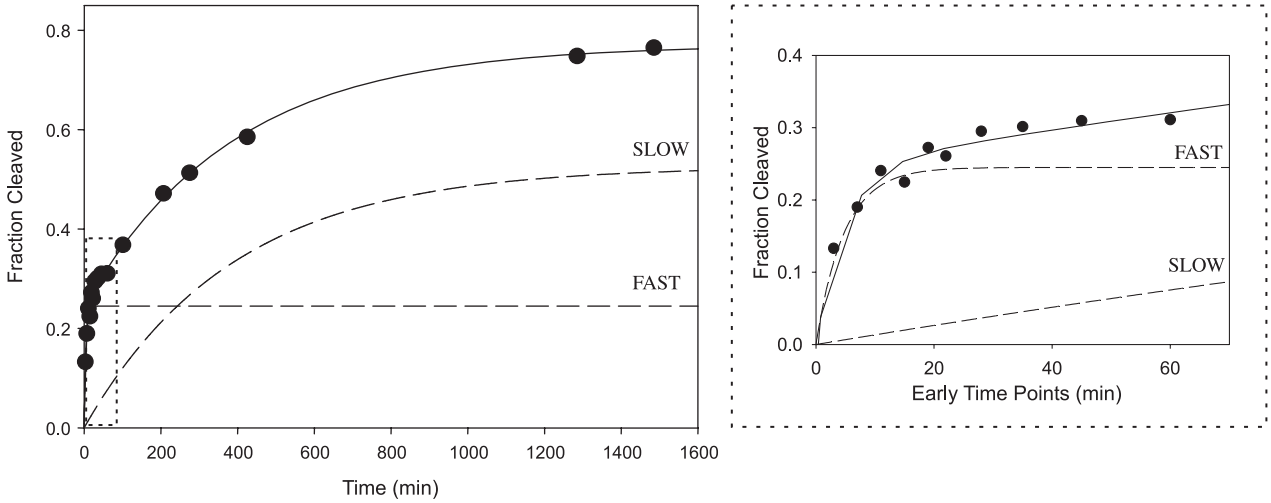


Figure 3. Single-turnover data for the cleavage substrate S1 by the trans-cleaving catalyst 9_{25}-11t at 13 °C in CB200. Dashed lines display theoretical S1 cleavage traces of the individual phases.[4]



age rate could be identified. Given the comparatively small size of the catalytic motif and the fact that neither sigmoidal nor lag-phase kinetics were observed, the chemical step for self-cleavage was assumed to be rate-limiting not folding.

Single-turnover cleavage of S1 by 9_{25}-11t at 13 °C displays biphasic kinetics

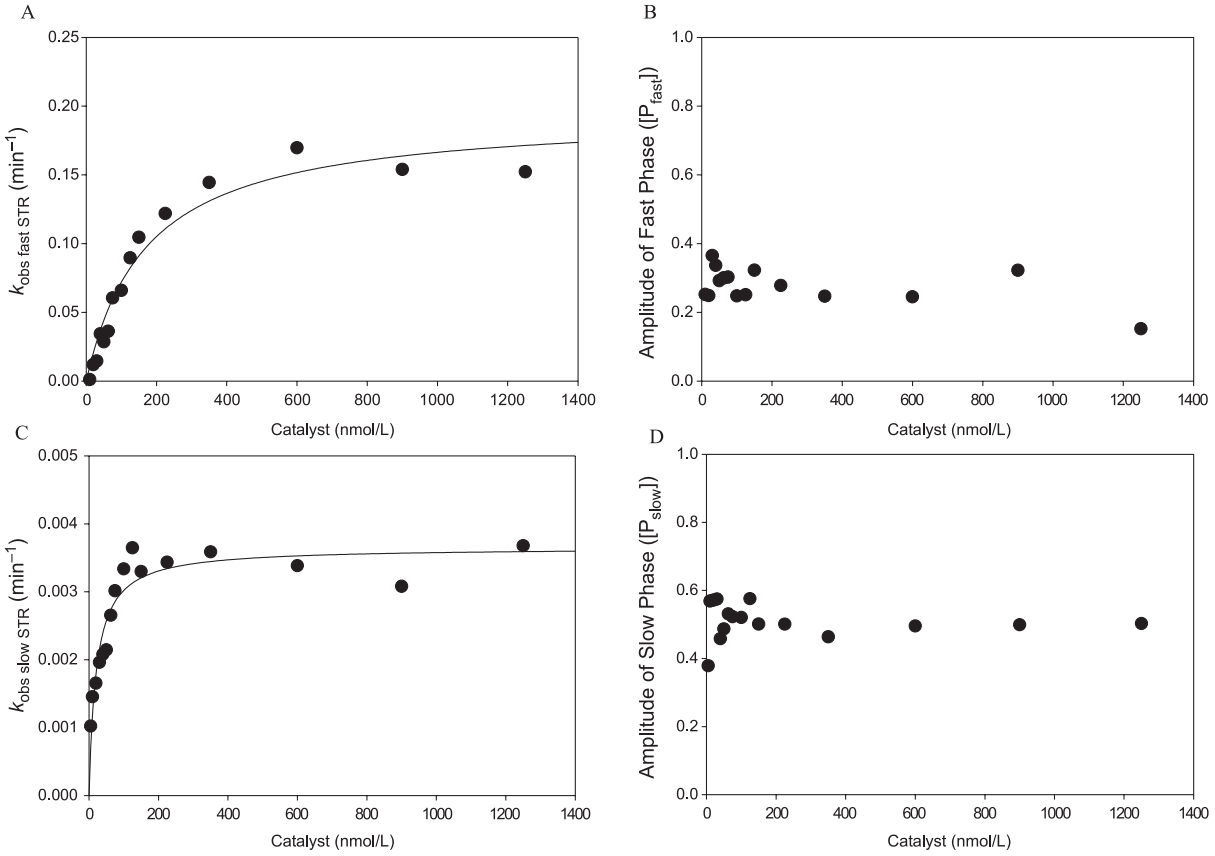
The rate constant for 9_{25}-11c self-cleavage provided a benchmark for evaluating intermolecular catalysis by the trans-cleaving construct, 9_{25}-11t. Trans-cleavage was initially examined under single-turnover conditions with S1 at 13 °C. These data could not be fit to a single-exponential function given by eq. [1]. Instead, data were fit to a double-exponential function given by eq. [2] (Fig. 3). For all catalyst concentrations, ~35% of the substrate is cleaved in the fast phase, while ~65% of the substrate is cleaved in the slow phase. Generally, percentages are normalized to the maximum amount of substrate cleaved (Figs. 4B and 4D).

For each phase, a value of $k_{\text{cat STR}}$ and a value of the pseudo-Michaelis constant, $K_{\text{M STR}}$, were obtained by fitting $k_{\text{obs fast STR}}$ or $k_{\text{obs slow STR}}$ to a hyperbolic plot against total catalyst concentration (eq. [3]). The values so determined for $K_{\text{M fast STR}}$ and $k_{\text{cat fast STR}}$ were 170 ± 30 nmol/L and 0.20± 0.01 min^{-1}, and for $K_{\text{M slow STR}}$ and $k_{\text{cat slow STR}}$, the values were 21 ± 4 nmol/L and 0.0036 ± 0.0001 min^{-1}, respectively (Figs. 4A and 4C). Based on these values, the ratio of k_{cat}

[4] Data were fit to the double-exponential eq. [2]. The cleavage reaction was performed with 900 nmol/L catalyst and <1 nmol/L substrate S1 in CB200 at 13 °C. Fitting data to the double-exponential eq. [2] gives 0.996 for R^2 at 13 °C (graph at right details the early-time points enclosed in the colored box). Fitting data to a single-exponential gives an R^2 value of 0.704. The observed rate constant for the fast-cleavage phase, $k_{\text{obs fast STR}}$, is 0.21 ± 0.02 min^{-1} (fast-phase amplitude is 25 ± 0.7%). The observed rate constant for the slow-cleavage phase, $k_{\text{obs slow STR}}$, is 0.0026 ± 0.0002 min^{-1} (slow-phase amplitude is 53 ± 1%).

© 2007 NRC Canada

Figure 4. Effect of 9_{25}-11t concentration on the fast- and slow-phase rate constants and phase amplitudes in single-turnover experiments at 13 °C in CB200. Observed rate constants at different catalyst concentrations, $k_{obs\ fast\ STR}$, were obtained by fitting substrate cleavage data to the double-exponential eq. [2]. The values $k_{obs\ fast\ STR}$ and $k_{obs\ slow\ STR}$ at various 9_{25}-11t concentrations were fit separately to eq. [3]. (A) Effect of 9_{25}-11t concentration on $k_{obs\ fast\ STR}$: the maximum first-order fast-rate constant, $k_{cat\ fast\ STR}$, is 0.20 ± 0.01 min^{-1}, and the catalyst concentration at which the reaction rate is half-maximum for the fast phase, $K_{M\ fast\ STR}$, is 170 ± 30 nmol/L (R^2 is 0.952). (B) Effect of 9_{25}-11t concentration on the fast-phase amplitude. The fraction of substrate cleaved through the fast-cleavage rate constant (not normalized for the extent of cleavage), $[P_{fast}]_\infty$, is 28%. (C) Effect of 9_{25}-11t concentration on $k_{obs\ slow\ STR}$ ($k_{cat\ slow\ STR}$ is 0.0036 ± 0.0001 min^{-1}, and $K_{M\ slow\ STR}$ is 21 ± 4 nmol/L, and R^2 is 0.892). (D) Effect of 9_{25}-11t concentration on the slow-phase amplitude.[5]



$_{STR}/K_{M\ STR}$ for the more active conformation is calculated to be ~1.2 × 10^6 $(mol/L)^{-1}$ min^{-1}. The observation of the fast phase suggests that a significant fraction of 9_{25}-11t displays a $k_{cat\ STR}$ value comparable to $k_{self\text{-}cleave}$ for 9_{25}-11c.

Investigating the nature of the biphase

The number of studies addressing either biphasic kinetics, catalytic heterogeneity, or both in catalytic RNA has become rather extensive (5, 7, 48, 52–54). However, fewer examples of such have been identified with DNAzymes. In addition, only a few studies have characterized synthetically modified DNAzymes (13, 40–43). For these reasons, elucidating the origin of the biphasic nature of 9_{25}-11t was pursued. Four reasonable explanations could account for the observed biphasic single-turnover kinetics: (*i*) the presence of synthetic impurities arising from the solid-phase synthesis of 9_{25}-11t, (*ii*) catalyst dimerization or aggregation (55, 56), (*iii*) the existence of a significant reverse reaction (ligation) rate (5), or (*iv*) the presence of kinetically inactive folds (48, 57).

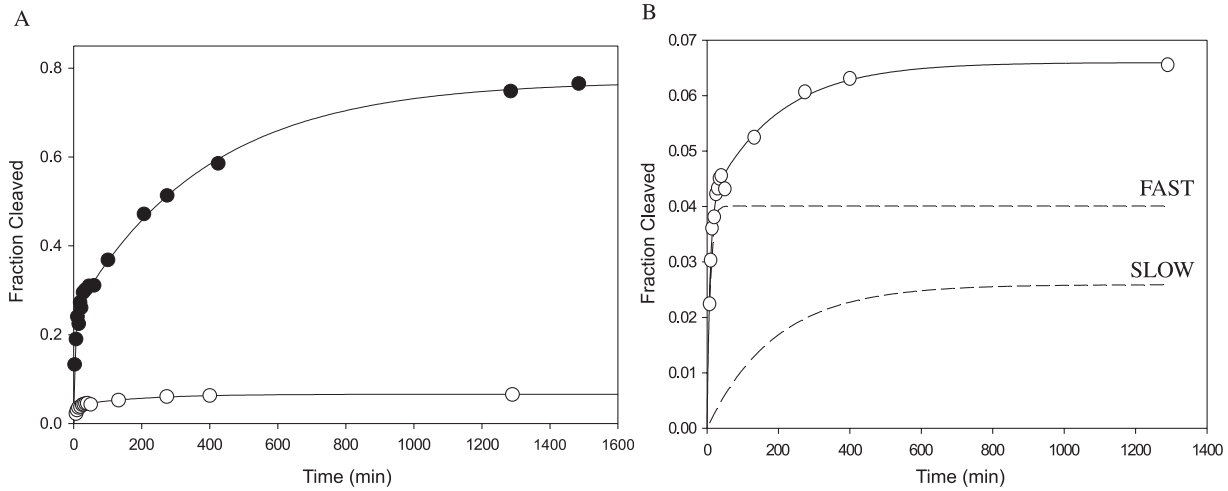
The presence of synthetic impurities is unlikely given the following observations: (*i*) two independent syntheses of 9_{25}-11t and at least three different purifications of each (six purifications in total) all resulted in functional catalysts that exhibited nearly identical biphasic kinetics at 13 °C, (*ii*) single-turnover kinetics at 24 °C were homogeneous and monophasic (13), suggesting that heterogeneity is not an intrinsic quality of the synthetic preparation, but rather dependent on low temperature, and (*iii*) single-turnover kinetics with alternate substrates 3D2 and 5D2 at 13 °C were monophasic (see Supplementary data, pp. S2–S3).[3]

Dimerization–aggregation has been seen in hammerhead variants (55, 56) and is certainly plausible for 9_{25}-11t, given its high degree of autocomplementarity that affords the pos-

[5] The average value of $[P_{slow}]_\infty$ is 52%. The relative invariance of $[P_{fast}]_\infty$ and $[P_{slow}]_\infty$ as a function of catalyst concentration suggests that these fractions are independent of the catalyst concentration. Catalyst concentrations ranged from 5 nmol/L to 1500 nmol/L.

© 2007 NRC Canada

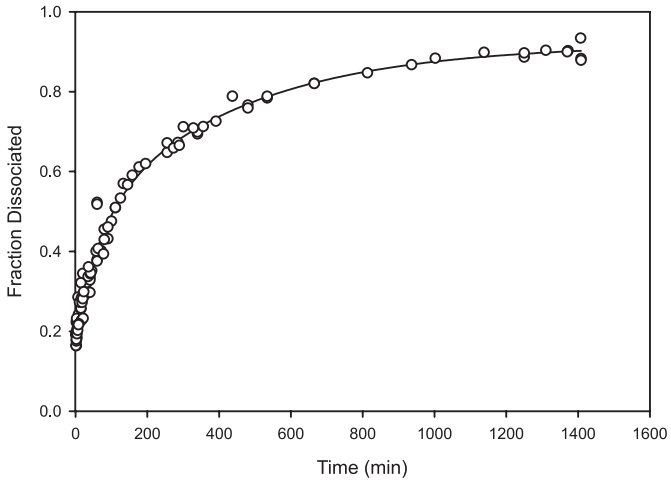
Figure 5. Determination of substrate-dissociation rate constants for substrate S1 by pulse–chase cleavage assay with 9_{25}-11t in CB200 13 °C. (A) 900 nmol/L Catalyst was incubated with <1 nmol/L S1 (●), or 112 nmol/L catalyst and <1 nmol/L S1 were challenged with 50 µmol/L of excess unlabeled S1 for 3 min (○).[6] (B) Rescaling the fraction-cleaved axis for the chased reaction clearly shows biphasic behavior. Dotted lines indicate the constituent curves for the fast and slow phases.



sibility that kinetically favored hairpins are in competition with thermodynamically favored dimers. That possibility was excluded based on (*i*) the absence of any observable high-molecular-weight aggregates in native gel retardation analysis of 9_{25}-11t, (*ii*) the invariance of the single-turnover amplitudes for each phase with catalyst concentration (Figs. 4B and 4D), and (*iii*) the observation that the multiple-turnover steady-state S1 cleavage rate increased linearly with increasing catalyst concentration over a range of 50 nmol/L to 1 µmol/L catalyst (see later). Finally, a significant reverse-reaction (ligation) rate could have explained biphasic kinetics, as has been described for the VS ribozyme (5). This was experimentally excluded for 9_{25}-11t; at 13 °C, no ligation could be detected.

Excluding the first three explanations, conformational heterogeneity was investigated as the origin of the biphase. This explanation was elaborated by Esteban et al., who employed pulse–chase kinetic assays under single-turnover conditions to demonstrate that biphasic kinetics, observed for the hairpin ribozyme, were due to the presence of one active and one essentially inactive catalyst–substrate conformation (48). Some important differences emerged between 9_{25}-11t and the hairpin ribozyme; in contrast to the monophasic curves obtained for the hairpin ribozyme (48) in pulse–chase experiments, the curves obtained for 9_{25}-11t remain distinctly biphasic (Fig. 5). This suggests that each of the two ES complexes can lead to substrate cleavage. Two first-order rate constants were observed in the pulse–chase experiment: $k_{\text{chase fast}} = 0.23\ \text{min}^{-1}$ and $k_{\text{chase slow}} = 0.0041\ \text{min}^{-1}$. Using eq. [4] and the respective values of $k_{\text{cat STR}}$, we calculated

Figure 6. Pulse–chase analysis by native gel electrophoresis to determine the first-order rate constant for the dissociation of the 2′-OMe substrate analogue (S1-OMe) from 9_{25}-11t at 13 °C in CB200.[7]



two values for substrate S1 dissociation constants: $k_{-1\ \text{fast}}$ is 0.03 min^{-1} and $k_{-1\ \text{slow}}$ is 0.0005 min^{-1} (Fig. 5).

To corroborate these dissociation constants, pulse–chase native gel shift assays were performed with a nonhydrolyzable substrate analog (S1-OMe). These data were also biphasic, and rate constants could be calculated from eq. [5] (Fig. 6): $k_{-1\ \text{fast S1-OMe}}$ was 0.014 ± 0.004 min^{-1} with an amplitude for the fast phase of 26 ± 7%, and $k_{-1\ \text{slow S1-OMe}}$ was

[6] Data for the unchased reaction were fit to eq. [2], giving 0.21 min^{-1} for $k_{\text{obs fast STR}}$ and 0.0026 min^{-1} for $k_{\text{obs slow STR}}$ (R^2 is 0.996). Data for the chased reaction were fit to eq. [2], giving 0.233 min^{-1} for $k_{\text{chase fast}}$ and 0.0041 min^{-1} for $k_{\text{chase slow}}$ (R^2 is 0.981). These values were treated according to eq. [4] to give the substrate dissociation rate constants, $k_{-1\ \text{fast}}$ and $k_{-1\ \text{slow}}$.

[7] A trace of 5′-^{32}P labeled S1-OMe was incubated with 9_{25}-11t (1 µmol/L) in CB200. The chase was commenced by the addition of an equal volume of 100 µmol/L unlabeled substrate in CB200. Aliquots were taken at various times, added to 1/10 of the volume of 70% sucrose (held in an ice bath) to halt further dissociation, and then quickly loaded onto 20% native PAGE gels run at 4 °C. The fraction of S1-OMe dissociated was plotted vs. time. The data were fit to a double-exponential eq. [5], which returned the following dissociation rate constants and phase amplitudes: $k_{-1\ \text{fast S1-OMe}} = 0.014 \pm 0.004\ \text{min}^{-1}$, $k_{-1\ \text{slow S1-OMe}} = 0.0023 \pm 0.0005\ \text{min}^{-1}$, amplitude fast = 27 ± 7%, and amplitude slow = 46 ± 6%.

© 2007 NRC Canada

0.0023 ± 0.0005 min^{-1} with a slow-phase amplitude of 46 ± 6%. Despite the structural difference imparted by the 2′-OMe substitution, these dissociation constants are consistent with those observed for substrate S1 in the kinetic pulse–chase experiments. Likewise, the amplitudes agree with those observed in single-turnover cleavage experiments.

Attempts to restore monophasic kinetics

In an attempt to simplify the study of 9_{25}-11t under conditions where $k_{cat\ STR}$ is optimal, we tried to find conditions that would not involve multiple conformations of the E or ES complex with different activities, as had been done for the group I intron ribozyme (52). Thus, 9_{25}-11t was subjected to various treatments (58) in the hope of attaining well-behaved kinetics (see Supplementary data, p. S4).[3] Despite numerous treatments, biphasic kinetics persisted under single-turnover conditions. Moreover, the relative amplitudes and $k_{cat\ STR}$ values of the two phases did not change significantly.

Monophasic kinetics were observed with substrates containing fewer bases at either the 5′ or the 3′ terminus (sequences are given in the Supplementary data)[3]: substrate 5D2 was truncated by two bases at the 5′ terminus, whereas substrate 3D2 was truncated by two bases at the 3′ terminus. Nevertheless, the values for $k_{cat\ STR}$ obtained with these substrates, $k_{cat\ 5D2\ STR}$ and $k_{cat\ 3D2\ STR}$, were both lower than the value of $k_{cat\ fast\ STR}$ observed with S1. The third substrate, 3A2, contained two additional complementary bases at the 3′ terminus and displayed biphasic kinetics that gave lower values for $k_{cat\ STR\ fast}$ and $k_{cat\ STR\ slow}$ as well as a reduced extent of cleavage (see Supplementary data, Figs. S1–S3).[3] Despite biphasic kinetics, substrate S1 was retained for continued investigation because the experimental value of $k_{cat\ fast\ STR}$ was higher than the values obtained with other substrates. As with other DNAzymes that give different and even biphasic kinetics when reconfigured to cleave alternative substrates (59), 9_{25}-11t appears to be especially sensitive to substrate length.

Multiple-turnover cleavage of S1 by 9_{25}-11t at 13 °C

Multiple-turnover experiments were conducted at 13 °C with a saturating concentration of substrate S1 and various catalyst concentrations. Substrate cleavage as a function of time was linear following a clearly evident burst phase at initial-time points (Fig. 7A–7C). When the steady-state multiple-turnover rate constant was plotted against enzyme concentration (see eqs. [6] and [7]), the value of $k_{cat\ steady\ state\ MTR}$ was found to be 0.0077 ± 0.0007 min^{-1} (Fig. 7D). This value is similar (within a factor of two) to that of $k_{cat\ slow\ STR}$ (0.0036 ± 0.0001 min^{-1}) observed in the single-turnover experiments with S1, suggesting that the steady-state phase represents turnover by a catalyst population that exists largely as the slow-cleaving conformation.

The initial rate of product formation at the outset of the burst phase was calculated by the method of initial rates (44), for which we made two assumptions: (*i*) the slow-cleaving conformation of the catalyst contributed negligibly to catalysis at early-time points and (*ii*) the initial rate of product formation in the burst phase reflected an effective catalyst concentration that was corrected to reflect the fraction of catalyst that is in the fast conformation in single-turnover experiments (i.e., 1 μmol/L × 0.35). By this analysis, the initial first-order rate constant was found to be 0.10 ± 0.03 min^{-1}, which is close (within a factor of two) to the value of the first-order rate constant ($k_{cat\ fast\ STR} = 0.2 \pm 0.01$ min^{-1}), extracted for the fast phase under the single-turnover conditions. It remained important to identify the basis for the slow steady-state rate. Since slow product release commonly explains burst-phase kinetics, and because that would certainly have been consistent with the reduction in temperature from 24 °C to 13 °C, we next investigated this possibility.

Slow product release does not account for the burst phase

To address slow product release, we attempted to measure the dissociation rate constants for both $P_{5'}$ and $P_{3'}$. The rate of product dissociation at 13 °C was too high to be effectively measured by native PAGE assays; more than 95% of the electrophoretically separable, radioactive complex had already dissociated within 0.5 min of the addition of the chase (data not shown). These results are qualitatively meaningful in that they show that the product-dissociation rate constants are much higher than either $k_{cat\ fast\ STR}$ or $k_{cat\ slow\ STR}$. Product inhibition was also evaluated under multiple-turnover conditions: addition of one or both products at 50 μmol/L prior to the addition of substrate S1 at 15 μmol/L produced no effect on the burst phase (data not shown), suggesting that the catalyst's affinity for product is also quite low.

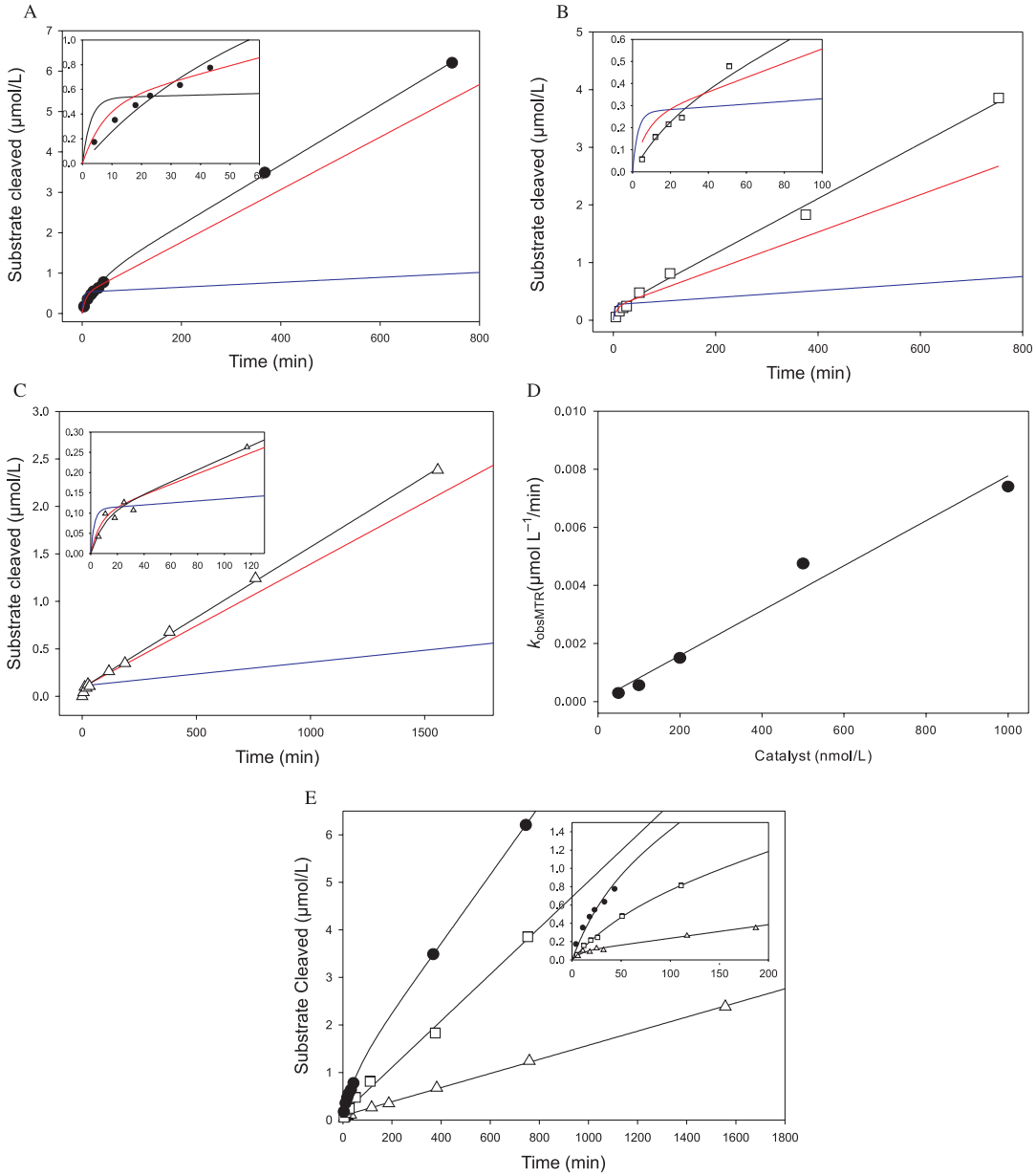
Although these experimental results suggest that product release is not rate-limiting, a *caveat* associated with the experimental basis of these experiments must be entertained: directly following cleavage, 9_{25}-11t might retain one or both products in a distinct complex that undergoes a slow conformational change before releasing product. By such reasoning, the free catalyst used in either experiment may not bind products, with the same affinity as a catalyst–product complex, on its descent from the transition state in a conformationally coupled step that could explain slow product release. If that were the case, any measurement of product- dissociation rate constants obtained by incubating free catalyst with product would provide misleading values. To further address this concern, we examined multiple-turnover kinetics by native PAGE in the hope of observing a trapped catalyst–product complex.

Native PAGE analysis of multiple-turnover provides additional evidence against slow product release

If the steady-state rate constant were to reflect slow product release rather than chemistry, then $k_{cat\ steady\ state\ MTR}$ would actually represent a product-dissociation constant. Consequently, the half-life for either the $EP_{5'}$ or the $EP_{3'}$ complex, would be ~90 min, and at least one of these complexes would be observable by native PAGE gel retardation experiments. Multiple-turnover reactions were initiated for varying times at 13 °C, stopped by placing on ice, and immediately analyzed by native PAGE at 4 °C. The experiment was performed for both 3′- and 5′-labeled S1 to investigate and ultimately exclude slow product release. While a steady-state level of ES complex was observed, no EP complex could be observed (3′ or 5′ product). Multiple-turnover cleav-

© 2007 NRC Canada

Figure 7. Multiple-turnover cleavage of substrate S1 by 9_{25}-11t at 13 °C in CB200. Cleavage reactions were peformed with varying concentrations of catalyst, 15 µmol/L unlabeled S1, and <1 nmol/L 5′-labeled S1 in CB200 at 13 °C. Cleavage was allowed to proceed until a maximum of 20% of the substrate was cleaved. (A) 1000 nmol/L Catalyst. (B) 500 nmol/L Catalyst. (C) 200 nmol/L Catalyst. Black traces are the result of fitting data to eq. [8]; red traces are predicted by eq. [17] for the model shown in Scheme 2B (using $k_{cat\ fast}$ = 0.2 min^{-1}, $k_{cat\ slow}$ = 0.0036 min^{-1}, $k_{-1\ fast}$ = 0.014 min^{-1}, $k_{-1\ slow}$ = 0.0023 min^{-1}, fraction$_{fast}$ = 0.35, fraction$_{slow}$ = 0.65, and $[ES_{fast}]_o = 0.35 \times [E_t]$); and blue traces are predicted by eq. [17] for the model shown in Scheme 2C (using $k_{cat\ fast}$ = 0.2 min^{-1}, $k_{cat\ slow}$ = 0, k_i = 0.37 min^{-1}, k_{-i} = 0.0036 min^{-1}, and $[ES_{fast}]_o = [E_t]$). (D) Determination of the first-order steady-state rate constant, $k_{cat\ steady\ state\ MTR}$, by linear-regression analysis of $k_{obs\ MTR}$ vs. 9_{25}-11t concentration (according to eq. [7]; $k_{cat\ steady\ state\ MTR}$ is 0.0077 ± 0.0007 min^{-1} and the intercept is 0.000 ± 0.0003 µmol/L min^{-1}; R^2 is 0.975). (E) Compiled multiple-turnover data at all catalyst concentrations clearly displaying the burst nature of the 9_{25}-11t system. (●) 1000 nmol/L; (□) 500, 200, and 100 nmol/L; (○) 50 nmol/L 9_{25}-11t.

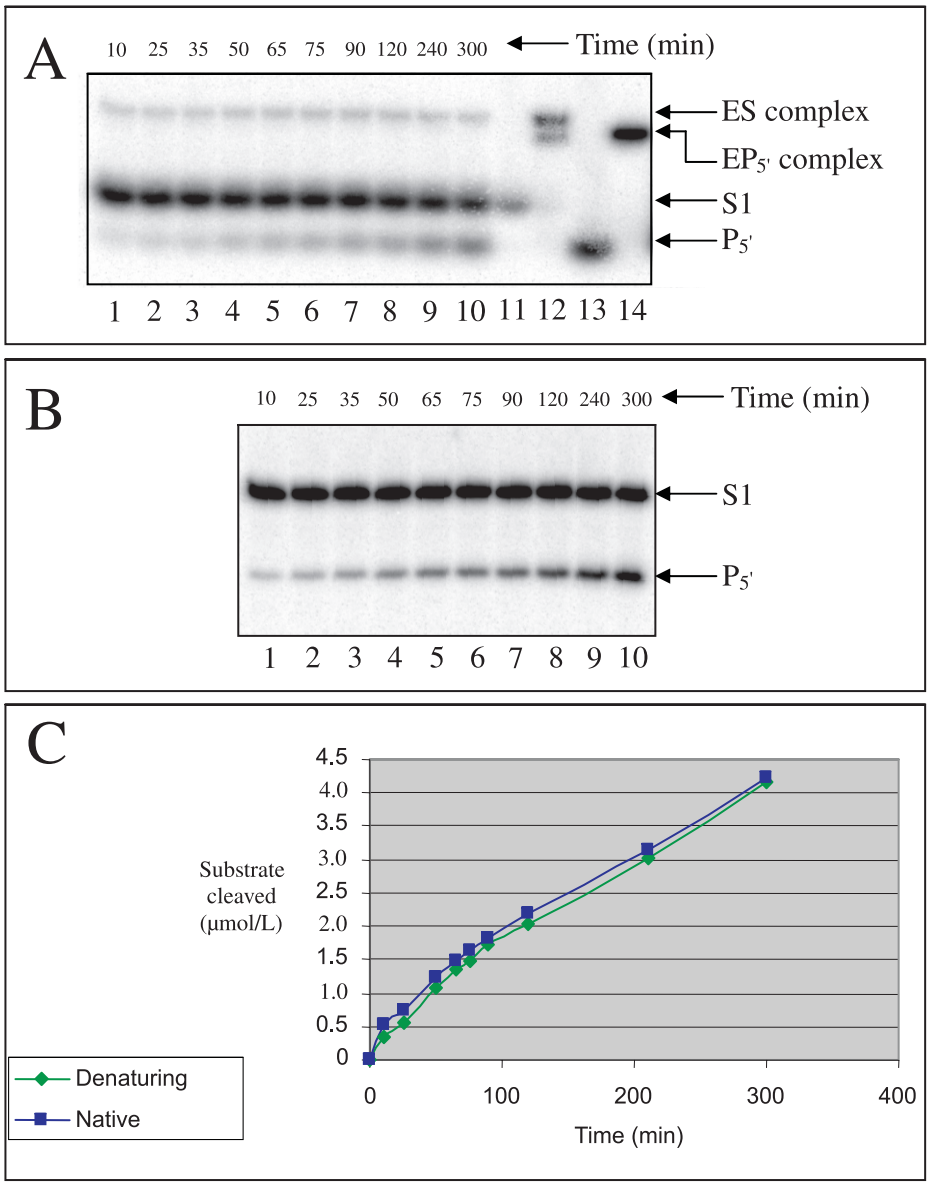


age of 5′-labeled S1, as observed by native PAGE, is shown in Fig. 8A. Aliquots from the same cleavage reaction were also analyzed by denaturing PAGE, shown in Fig. 8B. Plots of the appearance of product over time, as observed by native and denaturing PAGE, both showed a burst phase and overlap closely (see Fig. 8C), indicating that no product is retained in an $EP_{5'}$ complex. The same result was obtained with the 3′-labeled substrate (see Supplementary data, Fig. S5).[3]

To verify that this native PAGE multiple-turnover technique effectively detects slow product release at a rate comparable to the steady-state rate observed for 9_{25}-11t, this technique was applied to the hammerhead ribozyme (variant HH16), which indeed displayed burst-phase kinetics attributed to slow product release under multiple-turnover conditions (10, 11). Analysis of the HH16 multiple-turnover reaction by denaturing PAGE clearly demonstrated burst-

© 2007 NRC Canada

Figure 8. Native PAGE analysis of multiple-turnover cleavage of substrate S1 by 9_{25}-11t at 13 °C in CB200. (A) Lanes 1–10: time course for multiple-turnover reaction (1 µmol/L catalyst, 15 µmol/L S1, in CB200 at 13 °C) as observed by native PAGE at 4 °C. Control lanes reveal electrophoretic mobilities of: uncleaved S1 (lane 11), ES1 complex (lane 12) (some $EP_{5'}$ complex is also visible), $P_{5'}$ (lane 13), $EP_{5'}$ complex (lane 14). The reaction lanes show a small, steady-state amount of ES1, and no observable $EP_{5'}$. (B) The same time course (lanes 1–10) for the same reaction as in (A) run on a denaturing PAGE gel. (C) Plots of substrate cleaved vs. time for both the native and denaturing gels.[8]



phase kinetics, whereas analysis by native PAGE showed a completely linear appearance of free product over time ($k_{\text{steady state}} \approx 0.005$ min^{-1}) because of the retention of products in an $EP_{5'}$ complex (see Supplementary data, Fig. S6).[3]

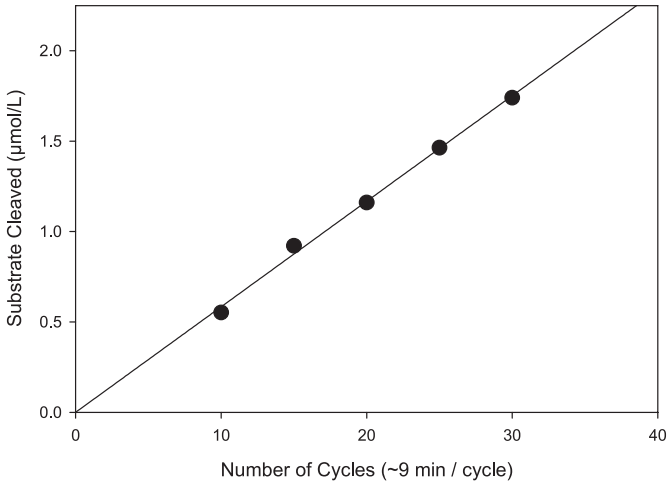
Temperature cycling enhances the rate of multiple turnover and demonstrates catalyst stability

Thermal cycling of the cleavage reaction was used to overcome the multiple-turnover limitations, associated with burst-phase kinetics, by taking advantage of both the optimum temperature for the single-turnover cleavage at 13 °C and the optimum temperature previously identified for steady-state multiple-turnover at 24 °C (13). By cycling the temperature (15 s at 13 °C, 7 min at 24 °C, and 15 s at 95 °C), we obtained an apparent first-order rate constant $k_{\text{obs thermocycle MTR}}$, of 0.064 ± 0.002 min^{-1} (Fig. 9). Notably, this rate constant is a composite that comprises all reaction steps during the temperature cycling. Although this value is only 30% of the fastest initial rate observed for 9_{25}-11t, it represents a 20-fold improvement over the steady-state multiple-turnover rate at 13 °C, and a modest improvement over the previously reported steady-state rate at 24 °C (13).

[8] Production of the unbound product, as observed in the native gel, matches the production observed by denaturing gel, indicating that the burst phase is not due to slow release of the 5′ product.

© 2007 NRC Canada

Figure 9. The effect of temperature cycling on the multiple-turnover rate of S1 substrate cleavage by 9_{25}-11t at 13 °C in CB200.[9]



The overall rate is increased, presumably by restoring the faster burst-phase rate with each thermal cycle. Qualitatively, this experiment also demonstrates that the synthetic modifications are thermally stable over a wide temperature range, underscoring the resilience of the catalyst and its chemical modifications.

Discussion

On the choice of conditions for characterization

Following the discovery of any catalyst, one is at liberty to choose meaningful conditions for characterization. As 9_{25}-11 is the first DNAzyme to present two synthetic functionalities that are characteristic of protein enzymes, we contend that it is important to report on conditions where k_{cat} values are increased substantially, even if those conditions deviate from physiological relevance. Following our initial report of self-cleavage at 37 °C (40), we have now found that 9_{25}-11c exhibits a substantially increased rate constant for self-cleavage, $k_{self\text{-}cleave}$ (~0.3 min^{-1}) at 13 °C. This value falls within an order of magnitude of a hypothetical upper limit for selecting DNAzymes using a biotin–avidin self-cleavage system (40), and is to date, the highest value reported for M^{2+}-independent and co-factor independent self-cleavage at pH 7.5 and physiological ionic strength seen in any nucleic acid catalyst (RNA or DNA).

We then questioned whether a value similar to $k_{self\text{-}cleave}$ could be observed with 9_{25}-11t at 13 °C under both single- and multiple-turnover conditions. It was important to examine this because the re-engineering of a self-cleaving species for catalytic turnover often leads to a significant reduction in the value of the observed cleavage rate constant. Within a somewhat complicated biphasic regime at 13 °C, we identified a cleavage rate constant, $k_{cat\ fast\ STR}$, in the engineered synthetic species 9_{25}-11t, which compares quite favorably with 9_{25}-11c, the enzymatically prepared self-cleaving progenitor. Identifying maximal rates in both cis- and trans-cleaving species examines the limitations of nucleic acid catalysts and suggests the potential advantages imparted by the inclusion of modified nucleotides in selection.

Summary of experimental findings

In general, biphasic kinetics under single-turnover conditions are common to ribozymes or DNAzymes; however, the reasons for that may be quite diverse. In developing a kinetic model, we first excluded catalyst missynthesis, aggregation, and ligation as origins of the biphasic kinetics. Thus, the most likely explanation was the presence of two or more DNAzyme folds. The characterization of biphasic single-turnover kinetics at 13 °C for 9_{25}-11t reveals that a minor fraction of the population of 9_{25}-11t displays an increased cleavage rate constant similar in value to that observed for 9_{25}-11c at 13 °C. Furthermore, we find that under multiple-turnover conditions at 13 °C, the elevated cleavage rate constant is expressed in a pre-steady-state burst phase.

With regard to developing a kinetic model for the cleavage of S1 by 9_{25}-11t at 13 °C, one of the most salient experimental observations is the persistence of biphasic kinetics in the pulse–chase single-turnover cleavage assay. This observation indicates that two conformations of the ES complex are formed, and that both can lead to substrate cleavage. It is this observation that clearly differentiates the kinetic model for 9_{25}-11t from that for the hairpin constructs previously described by Esteban et al. (48) (Scheme 1A) where pulse–chase single-turnover cleavage experiments exhibited monophasic behavior.

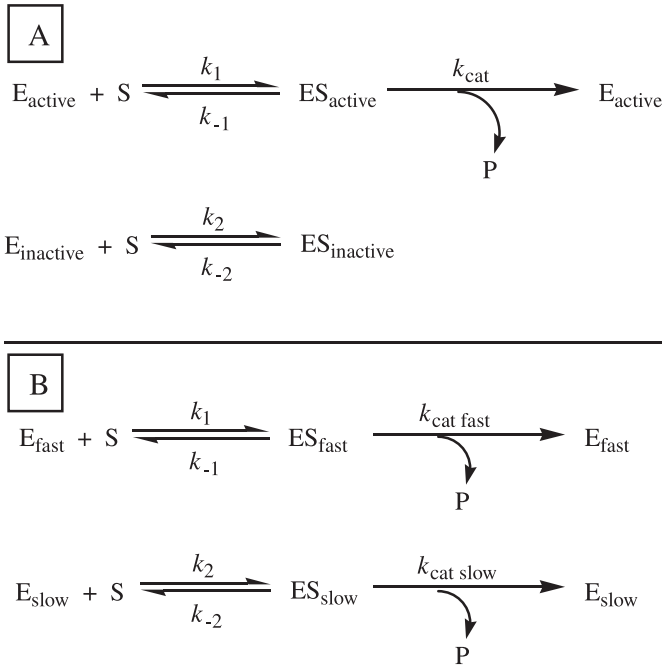
The fully elaborated kinetic model for cleavage of S1 by 9_{25}-11t at 13 °C must also explain the observation of burst-phase kinetics under multiple-turnover conditions. We first examined the most common ascription of burst-phase kinetics, namely, slow product release, which a priori would have been consistent with the reduction in temperature (25) that allowed for an apparent increase in $k_{cat\ STR}$. Pulse–chase native PAGE assays demonstrated that product-dissociation rates are too fast to be measured by this method. In addition, we added back one or both products at 50 µmol/L prior to the start of multiple-turnover assays and found no effect on the burst phase. Most conclusively, no catalyst–product complex could be observed by native PAGE analysis of multiple-turnover reactions using 5′- and 3′-^{32}P labeled substrates. Based on these results, slow product release was excluded as the source of the burst phase at 13 °C for 9_{25}-11t.

Irreversible chemical inactivation of the catalyst was also considered as an explanation for burst-phase kinetics. However, temperature cycling with excess S1 gave a higher turnover rate than could be achieved at any single temperature. This experiment suggests that the collapse of the initial burst-phase rate to the steady-state rate is not due to the permanent inactivation of the catalyst. Rather, it demonstrates that the faster initial rate can be restored, which suggests a

[9] 100 nmol/L Catalyst, 15 µmol/L unlabeled S1, and <1 nmol/L 5′-labeled S1 was incubated in buffer CB200 at 13 °C. The reaction was placed into a PCR temperature cycler programmed as follows: 13 °C for 15 s, 22 °C for 7 min, and 95 °C for 15 s. With temperature-ramping time included, the time for one cycle was ~9 min. Aliquots were removed for analysis after every five cycles. Data were fit to a linear equation: $k_{obs\ thermocycle\ MTR}$ is 0.58 ± 0.02 $cycle^{-1}$ or 0.064 ± 0.002 min^{-1} for the 9 min cycle (R^2 is 0.996). The linearity of the graph indicates that the catalyst is not deactivated upon heating. A control reaction done with only labeled substrate in CB200 showed a negligible amount of cleavage during the temperature program.

© 2007 NRC Canada

Scheme 1.



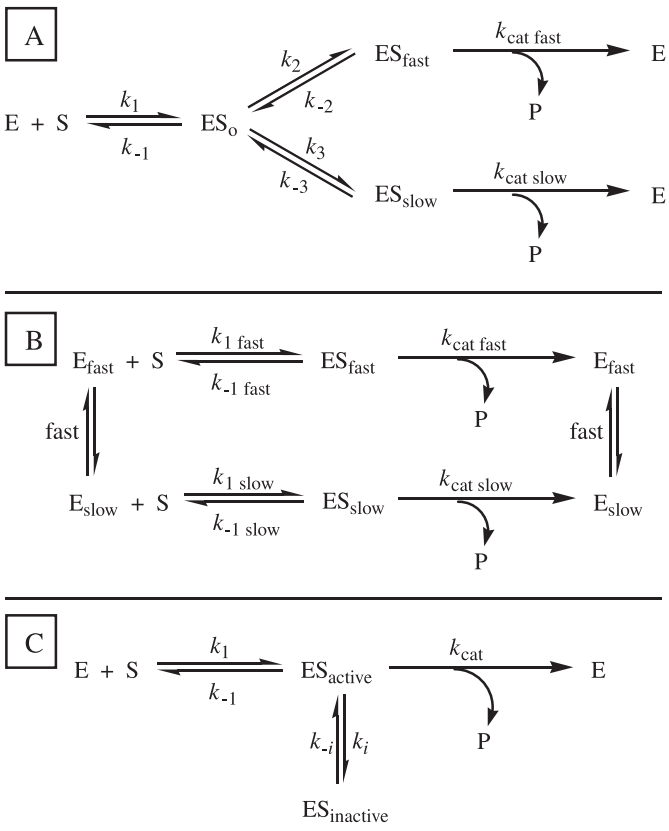
conformational partition as a source of the burst phase in the absence of slow product release. An alternative explanation for the burst phase must therefore be considered based on conformational partitioning (see later). At this point, the model shown in Scheme 1B can be excluded. Although it can explain biphasic pulse–chase kinetics, it does not predict burst-phase multiple-turnover kinetics in the absence of slow product release for the following reason: E_{fast} and E_{slow} (as well as ES_{fast} and ES_{slow}) cannot interconvert, so the ratio of ES_{fast} to ES_{slow} remains constant. The overall multiple-turnover rate is simply the sum of two independent linear rates.

Evaluation of kinetic models that are qualitatively consistent with the data

Three similar kinetic models that are qualitatively consistent with the data are shown in Scheme 2. Each can explain biphasic single-turnover and pulse–chase kinetics ($k_{fast} \neq k_{slow}$). Each model can also explain burst-phase kinetics under multiple-turnover conditions: because both the slow and inactive ES complexes cleave and (or) dissociate the substrate much more slowly than the more active ES complex, the concentration of the former increases (and the latter decreases) until a steady state is achieved.

The first model (scheme 2A) involves partitioning of unstructured free catalyst by competing association/folding pathways. In this model, the ratio of the association/folding rate constants (k_1) for each phase should reflect the observed partition ratio in single-turnover experiments. Using the constants $K_{M\ STR}$, k_{-1}, and $k_{cat\ STR}$, determined for the fast and slow phase experimentally, the apparent association constants, $k_{1\ fast}$ and $k_{1\ slow}$, are calculated to be 1.4×10^6 $(mol/L)^{-1}$ min^{-1} and 2.0×10^5 $(mol/L)^{-1}$ min^{-1}, respectively.

Scheme 2.



In contrast, the observed partition ratio in single-turnover experiments favors cleavage through the slow phase by a wide margin. Clearly, this model can be excluded because it is not quantitatively consistent with the data obtained from single-turnover experiments.

A closely related model (Scheme 2B) appears to be consistent with all of the kinetic data. This model presupposes the existence of preformed conformations of the fast- and slow-cleaving catalyst that equilibrate rapidly relative to the rate of substrate association. The consequences of this model parallel those of the previous model (Scheme 2A) with the exception that the observed single-turnover partition ratio can now be rationalized as the ratio of pseudo-first-order association rate constants in a Curtin–Hammett analysis (eq. [9]).

$$[9] \qquad \frac{[E_{fast}]k_{on\,fast}}{[E_{slow}]k_{on\,slow}} = \frac{[P_{fast}]_\infty}{[P_{slow}]_\infty}$$

According to this model, a small, fast-cleaving fraction (e.g., 5%) of the total free catalyst can bind the substrate at a significantly faster rate than the much more plentiful, slow-cleaving conformation to skew the partition observed under single-turnover conditions more in favor of the fast phase.[10]

[10]It should be noted that eq. [9] applies under single-turnover conditions whether or not the unbound catalyst conformations are equilibrating because the binding of trace substrate does not appreciably alter the unbound-catalyst populations. Under multiple-turnover conditions, eq. [9] only applies when the unbound-catalyst conformations are rapidly equilibrating, that is, where substrate association is described by a Curtin–Hammett-type regime.

© 2007 NRC Canada

Scheme 3.

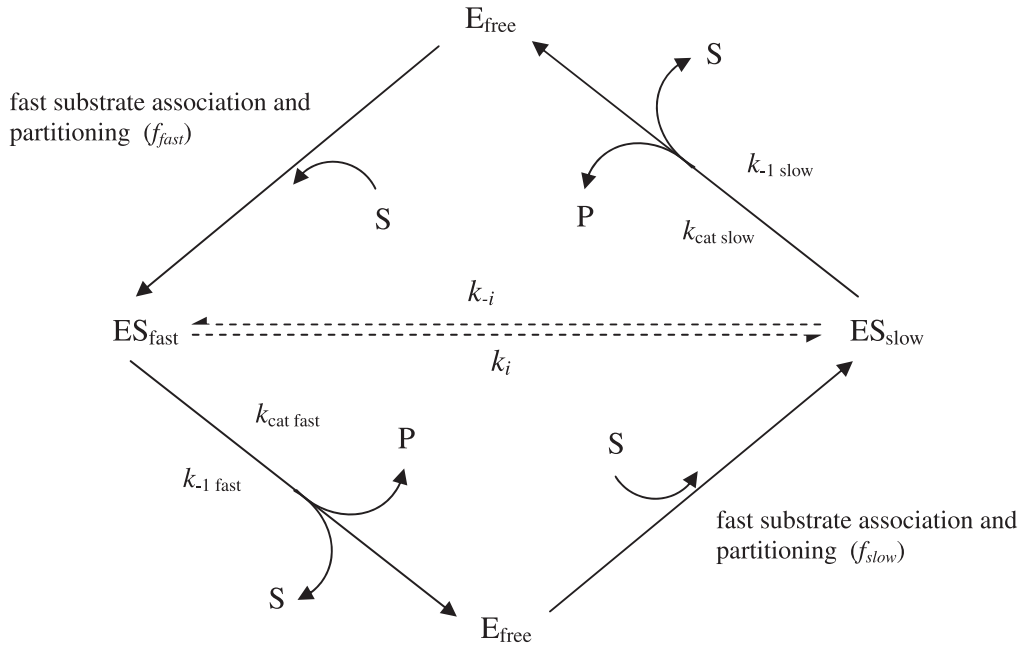


Table 2. Multiple-turnover rate constants for the cleavage reaction with noted concentrations of 9_{25}-11t and 15 μmol/L S1 in CB200 at 13 °C.

Data source	Burst amplitude (C) (μmol/L)	Burst decay (k_{burst}) (min^{-1})	Steady state ($k_{obs\ MTR}$) (μmol/L min^{-1})
1000 nmol/L 9_{25}-11t			
Experimental data	0.7±0.2	0.03±0.01	0.0074±0.0002
Scheme 2B simulation	0.47	0.14	0.0065
Scheme 2C simulation	0.53	0.37	0.0012
500 nmol/L 9_{25}-11t			
Experimental data	0.20±0.09	0.05±0.05	0.0048±0.0002
Scheme 2B simulation	0.23	0.14	0.0032
Scheme 2C simulation	0.27	0.37	0.00062
200 nmol/L 9_{25}-11t			
Experimental data	0.09±0.01	0.10±0.05	0.0015±0.0001
Scheme 2B simulation	0.093	0.14	0.0013
Scheme 2C simulation	0.11	0.37	0.00025

Note: Rate constants obtained by fitting multiple-turnover data (see Fig. 7) to eq. [8] are compared with rate constants predicted by simulation of kinetic models shown in Schemes 2B and 2C (see text for full description of simulations).

To test the validity of this model quantitatively, eqs. [10A–10C] were derived based on Scheme 3 to describe the time-dependent appearance of product (see Supplementary data, pp. S8–S9).[3] Scheme 3 describes the pathways for the interconversion of ES_{fast} and ES_{slow} via E_{Free}; the dotted lines connote an assumption that the substrate-bound forms do not readily interconvert.

$$[10A]\quad P(t) = (k_{cat\ slow STR}) - k_{cat\ fast STR}) \times \left(\frac{[k_{-i}[E_t] - (k_i + k_i)[ES_{fast}]_o]}{(k_{-i} + k_i)^2}\right)(1 - e^{-(k_{-1} + k_i)t}) + \left[k_{cat\ slow STR} + (k_{cat\ fast STR} - k_{cat\ slow STR}\left(\frac{k_{-i}}{k_{-i} + k_i}\right)\right][E_t]t$$

where

$$[10B]\quad k_i = (k_{cat\ fast\ STR} + k_{-1\ fast})f_{slow}$$

$$[10C]\quad k_{-i} = (k_{cat\ slow\ STR} + k_{-1\ slow})f_{fast}$$

Given the number of variables in eq. [10A], we were unable to obtain least-squares fits for multiple-turnover data. Instead, multiple-turnover simulations were performed by substituting rate constants determined from single-turnover and pulse–chase experiments into eqs. [10A–10C] (specifically $k_{cat\ fast\ STR}$ = 0.2 min^{-1}, $k_{cat\ slow\ STR}$ = 0.0036 min^{-1}, $k_{-1\ fast}$ = 0.014 min^{-1}, $k_{-1\ slow}$ = 0.0023 min^{-1}, $fraction_{fast}$ = 0.35, $fraction_{slow}$ = 0.65, $[ES_{fast}]_o = 0.35 \times [E_t]$). The simulations for this model closely resemble the experimental multiple-turnover data (see red-colored traces in Fig. 7).

Data from multiple-turnover experiments were also fit to eq. [8], allowing comparison of the experimental and simu-

© 2007 NRC Canada

lated values of the burst amplitude (C), the burst-decay constant (k_{burst}), and the steady-state rate constant ($k_{cat\ steady\ state\ MTR}$) (see Table 2). This simulation closely reproduced the experimental steady-state rate constant. However, with regards to the burst-phase constants, the agreement between simulation and experiment was within only an order of magnitude. Equation [10A] predicts that k_{burst} should be invariant with catalyst concentration. When the data were fit to eq. [8], k_{burst} was not well-determined, i.e., the values varied from 0.03 to 0.1 min^{-1} with no regular dependence on catalyst concentration (eq. [10A] predicts a value of 0.14 min^{-1} for all catalyst concentrations). The low level of substrate cleaved during the burst phase (especially at low catalyst concentrations) made quantitation by phosphorimaged autoradiography difficult, casting doubt on the accuracy of the burst-decay and amplitude constants obtained from fitting data to eq. [8].

Another closely related kinetic model, shown in Scheme 2C, involves partitioning between an active and an inactive ES complex following the initial formation of the active complex upon substrate binding. In this case, the normalized fraction of the substrate cleaved in the slow phase in single-turnover experiments is given by the following equation that is based on the two competing pathways for the decomposition of ES_{active}

$$[11] \quad f_{slow} = \frac{k_i}{k_i + k_{cat\ fast\ STR}}$$

where k_i is the rate constant as defined in Scheme 2C for the conversion of the ES_{active} into the $ES_{inactive}$. Using eq. [11] and the experimentally determined $k_{cat\ fast\ STR}$ and f_{slow} values, one can calculate the value of k_i to be 0.37 min^{-1}. In this model, the slow-cleaving phase would result from the slow isomerization of the inactive ES complex to the active one; therefore, k_{-i} is assumed to be equal to the measured value of $k_{cat\ slow\ STR}$ (0.0036 min^{-1}).

A multiple-turnover simulation was performed for this model as well (see Table 2 and blue traces in Fig. 7). In this case, eq. [10A] still applies where $k_{cat\ fast\ STR}$ = 0.2 min^{-1}, $k_{cat\ slow\ STR}$ = 0, and $[ES_{fast}]_o = [E_t]$, and eqs. [10B] and [10C] are replaced with the values k_i = 0.37 min^{-1} and k_{-i} = 0.0036 min^{-1}. As shown in Fig. 7 and Table 2, the steady-state rate is significantly underestimated by this model; the burst (exponential)-decay constant (k_{burst} is approximately equal to 0.37 min^{-1}, i.e., the sum of $k_{-i} + k_i$) is overestimated, more so by this model (Scheme 2C) than by the previous model (Scheme 2B). Thus, the model that seems to be most congruent with the data is that shown in Scheme 2B.

Concluding remarks: relevance to (*i*) other nucleic acid catalysts and (*ii*) kinetics of protein catalysts that exhibit burst-phase absent slow product release

(*i*) Whereas irregular kinetics have been characterized for group I intron, hairpin, and HDV ribozymes (48, 52, 54), these kinetics have not been thoroughly examined for DNAzymes. This study of the irregular kinetics of 9_{25}-11t may prove pertinent to DNAzymes and biocatalysts in general, and the discussion of possible kinetic models may prove useful to those confronted with biphasic kinetics. For instance, in contrast to initial reports on the 10–23 DNAzyme that described a catalytically perfect activity limited by chemistry and not product release (8), a recent report has now described biphasic kinetics under single-turnover conditions at 10 mmol/L Mg^{2+} for a 10–23 sequence that targeted an 18-nucleotide subsequence of the mRNA of the vanilloid receptor subtype (59). Although no explanation for this observation was provided, several factors may contribute to this observation, including target mRNA accessibility and folding. Biphasic kinetics and substrate-dependent k_{cat} values would limit the generality of reconfiguring a selected catalytic motif to cleave any given target sequence.

In this report, we have investigated some of the properties and limitations of this catalyst at lower temperature. Of note is a significantly higher rate constant for M^{2+}-independent RNA hydrolysis at 13 °C than the value that was initially reported for either of 9_{25}-11t or 9_{25}-11c at higher temperature (13, 40, 60). Although the enhanced cleavage rate displayed by 9_{25}-11c is expressed by a minor fraction of 9_{25}-11t, this finding extends the apparent rate enhancement for this modified DNAzyme by another order of magnitude over its unmodified counterparts selected under similar conditions (26, 27). The identification of a faster rate in case of 9_{25}-11c and 9_{25}-11t would also suggest that higher rate constants may be realized at physiological temperature in future selections, particularly if the low-temperature optimum is due to particular aspects of the initial selection.[11] This work should help focus efforts at using new chemistries and more stringent reselection conditions in the hope of overcoming the limitations of biphasic kinetics and a low-temperature optimum, thereby more fully exploiting the advantage provided by modified nucleotides.

(*ii*) With regards to protein catalysts, slow product release, accompanied by a conformational change is often found to explain burst-phase kinetics. This is the case for the ATP Sulfurylase-GTPase (61). In the context of an exonuclease-deficient mutant of T7 DNA polymerase, a burst phase was explained not entirely by product release but by conformational partitioning on the template DNA (62). Finally, two acyl–enzyme intermediates with different rate constants for product hydrolysis have been observed for a mutant β-lactamase to explain a burst phase (63). The phenomenon of a two different substrate-bound enzymes that interconvert slowly yet appreciably over the time period during which multiple turnover is measured has been termed "enzyme hysteresis" and has been reviewed in 1970 (45). In the model we present here to explain the observed burst for 9_{25}-11t, we do not need to invoke a slow partition between substrate-bound forms, but rather a fast interconversion between two conformations of the free catalyst that are locked into place by substrate binding. In that regard, for the case where two distinctly active

[11]This is a reasonable recollection of the ambient temperature in a drafty lab, in Paris during February when the first four rounds of selection were conducted: Feb 9, 15, 18, and 24 of the year 2000. By the fourth round, detectable activity appeared with little increase observed in generations 5–9.

© 2007 NRC Canada

and interconvertable conformations of the free catalyst can provide for burst-phase kinetics, to the best of our knowledge, there is no precedent for a formal treatment thereof. To that end, the equations developed herein not only fit the data accumulated for 9_{25}-11t, but may apply to any catalyst that exhibits biphasic kinetics under single-turnover conditions and burst-phase kinetics under multiple-turnover in the absence of slow product release.

Acknowledgments

D.M.P was awarded a Junior Career Scholar Award from the Michael Smith Foundation for Health Research in British Columbia, J.M.T and R.T. were supported by Natural Sciences and Enginnering Research Council of Canada (NSERC) and Gladys Estella Laird postgraduate fellowships, respectively. Operating and salary support was provided by UBC start-up funds, the Michael Smith Foundation for Health Research in British Columbia, and NSERC, and continued funding by the Canadian Institutes of Health Research (CIHR). The Canadian Foundation for Innovation (CFI) provided funding for major equipment. The authors declare no conflicts of interest.

The authors are grateful to Mr. Ben Clifford for advice on assembling a buffer-recirculation system for the native gels, Mr. Chris Hipolito for the synthesis of histaminyl-dATP, Dr. Leonard Lermer for the synthesis of 9_{25}-11t, and to Professor Michael C.L. Gerry and Professor Martin Tanner for helpful discussions regarding the mathematical description of the multiple-turnover data.

References

1. S.K. Silverman. Nucleic Acids Res. **33**, 6151 (2005).
2. J.B. Murray, A.A. Seyhan, N.G. Walter, J.M. Burke, and W.G. Scott. Chem. Biol. **5**, 587 (1998).
3. J.L. O'Rear, S. Wang, A.L. Feig, L. Beigelman, O.C. Uhlenbeck, and D. Herschlag. RNA, **7**, 537 (2001).
4. E.A. Curtis, and D.P. Bartel. RNA, **7**, 546 (2001).
5. R. Zamel, A. Poon, D. Jaikaran, A. Andersen, J. Olive, D. De Abreu, and R.A. Collins. Proc. Natl. Acad. Sci. USA, **101**, 1467 (2004).
6. M.D. Canny, F.M. Jucker, E. Kellogg, A. Khvorova, S.D. Jayasena, and A. Pardi. J. Am. Chem. Soc. **126**, 10848 (2004).
7. J.A. Beebe and C.A. Fierke. Biochemistry, **33**, 10294 (1994).
8. S.W. Santoro and G.F. Joyce. Biochemistry, **37**, 13330 (1998).
9. J. Li and Y. Lu. J. Am. Chem. Soc. **122**, 10466 (2000).
10. K.J. Hertel, D. Herschlag, and O.C. Uhlenbeck. Biochemistry, **33**, 3374 (1994).
11. M.J. Fedor and O.C. Uhlenbeck. Biochemistry, **31**, 12042 (1992).
12. A. Tallsjo and L.A. Kirsebom. Nucleic Acids Res. **21**, 51 (1993).
13. R. Ting, J.M. Thomas, L. Lermer, and D.M. Perrin. Nucleic Acids Res. **32**, 6660 (2004).
14. B.M. Chowrira, A. Berzal-Herranz, and J.M. Burke. Biochemistry, **32**, 1088 (1993).
15. D.J. Earnshaw and M.J. Gait. Nucleic Acids Res. **26**, 5551 (1998).
16. J.E. Olive and R.A. Collins. Biochemistry, **37**, 6476 (1998).
17. K. Stolze, S.C. Holmes, D.J. Earnshaw, M. Singh, D. Stetsenko, D. Williams, and M.J. Gait. Bioorg. Med. Chem. Lett. **11**, 3007 (2001).
18. R. Welz, C. Schmidt, and S. Müller. Biochem. Biophys. Res. Commun. **283**, 648 (2001).
19. T.S. Wadkins, I.-H. Shih, A.T. Perrotta, and M.D. Been. J. Mol. Biol. **305**, 1045 (2001).
20. A.T. Perrotta, I.-H. Shih, and M.D. Been. Science (Washington, D.C), **286**, 123 (1999).
21. R. Pinard, K.J. Hampel, J.E. Heckman, D. Lambert, P.A. Chan, F. Major, and J.M. Burke. EMBO J. **20**, 6434 (2001).
22. A. Luptak, A.R. Ferre-D'Amare, K. Zhou, K.W. Zilm, and J.A. Doudna. J. Am. Chem. Soc. **123**, 8447 (2001).
23. A.K. Oyelere, J.R. Kardon, and S.A. Strobel. Biochemistry, **41**, 3667 (2002).
24. D.S. Knitt and D. Herschlag. Biochemistry, **35**, 1560 (1996).
25. M.A. Carrigan, A. Ricardo, D.N. Ang, and S.A. Benner. Biochemistry, **43**, 11446 (2004).
26. D. Faulhammer and M. Famulok. J. Mol. Biol. **269**, 188 (1997).
27. C.R. Geyer and D. Sen. Chem. Biol. **4**, 579 (1997).
28. P.J. Mulquiney and P.W. Kuchel. NMR Biomed. **10**, 129 (1997).
29. E. Murphy, C.C. Freudenrich, L.A. Levy, R.E. London, and M. Lieberman. Proc. Natl. Acad. Sci. USA, **86**, 2981 (1989).
30. E. Murphy, C. Steenbergen, L.A. Levy, B. Raju, and R.E. London. J. Biol. Chem. **264**, 5622 (1989).
31. Y. Suzuki, H. Komatsu, T. Ikeda, N. Saito, S. Araki, D. Citterio, H. Hisamoto, Y. Kitamura, T. Kubota, J. Nakagawa, K. Oka, and K. Suzuki. Anal. Chem. **74**, 1423 (2002).
32. A. Peracchi. Rev. Med. Virol. **14**, 47 (2004).
33. L.-Q. Sun, M.J. Cairns, E.G. Saravolac, A. Baker, and W.L. Gerlach. Pharmacol. Rev. **52**, 325 (2000).
34. H.A. James and I. Gibson. Blood, **91**, 371 (1998).
35. R.E. Christoffersen and J.J. Marr. J. Med. Chem. **38**, 2023 (1995).
36. A. Roth and R.R. Breaker. Proc. Natl. Acad. Sci. USA, **95**, 6027 (1998).
37. C. Tuerk and L. Gold. Science (Washington, D.C.), **249**, 505 (1990).
38. A.D. Ellington and J.W. Szostak. Nature (London), **346**, 818 (1990).
39. R.R. Breaker and G.F. Joyce. Chem. Biol. **1**, 223 (1994).
40. D.M. Perrin, T. Garestier, and C. Helene. J. Am. Chem. Soc. **123**, 1556 (2001).
41. A.V. Sidorov, J.A. Grasby, and D.M. Williams. Nucleic Acids Res. **32**, 1591 (2004).
42. S.W. Santoro, G.F. Joyce, K. Sakthivel, S. Gramatikova, and C.F. Barbas. J. Am. Chem. Soc. **122**, 2433 (2000).
43. S.P. Zinnen, K. Domenico, M. Wilson, B.A. Dickinson, A. Beaudry, V. Mokler, A.T. Daniher, A. Burgin, and L. Beigelman. RNA, **8**, 214 (2002).
44. A. Fersht. Enzyme structure and mechanism. 2nd ed. W.H. Freeman & Co., New York. 1985. pp. 195–196.
45. C. Frieden. J. Biol. Chem. **245**, 5788 (1970).
46. L. Lermer, J. Hobbs, and D.M. Perrin. Nucleosides Nucleotides and Nucleic Acids, **21**, 651 (2002).
47. R. Naylor and P.T. Gilham. Biochemistry, **5**, 2722 (1966).
48. J.A. Esteban, A.R. Banderjee, and J.M. Burke. J. Biol. Chem. **272**, 13629 (1997).
49. I.-H. Shih and M.D. Been. Biochemistry, **39**, 9055 (2000).
50. J.M. Thomas, R. Ting, and D.M. Perrin. Org. Biomol. Chem. **2**, 307 (2004).
51. M.D. Been, A.T. Perrotta, and S.P. Rosenstein. Biochemistry, **31**, 11843 (1992).

© 2007 NRC Canada

52. R. Russell and D. Herschlag. J. Mol. Biol. **291**, 1155 (1999).
53. J.A. Esteban, N.G. Walter, G. Kotzorek, J.E. Heckman, and J.M. Burke. Proc. Natl. Acad. Sci. USA, **95**, 6091 (1998).
54. T.S. Brown, D.M. Chadalavada, and P.C. Bevilacqua. J. Mol. Biol. **341**, 695 (2004).
55. S.V. Amontov and K. Taira. J. Am. Chem. Soc. **118**, 1624 (1996).
56. T. Kuwabara, S.V. Amontov, M. Warashina, J. Ohkawa, and K. Taira. Nucleic Acids Res. **24**, 2302 (1996).
57. T.K. Stage-Zimmermann and O.C. Uhlenbeck. RNA, **4**, 875 (1998).
58. S.P. Rosenstein and M.D. Been. Biochemistry, **29**, 8011 (1990).
59. J. Kurreck, B. Bieber, R. Jahnel, and V.A. Erdmann. J. Biol. Chem. **277**, 7099 (2002).
60. L. Lermer, Y. Roupioz, R. Ting, and D.M. Perrin. J. Am. Chem. Soc. **124**, 9960 (2002).
61. S. Sukal and T.S. Leyh. Biochemistry, **40**, 15009 (2001).
62. S.S. Patel, I. Wong, and K.A. Johnson. Biochemistry, **30**, 511 (1991).
63. A. Dubus, S. Normark, M. Kania, and M.G.P. Page. Biochemistry, **33**, 8577 (1994).

© 2007 NRC Canada

TRIBUTE / HOMMAGE

From Public U to Private U

ABOUT THE AUTHOR

Kelvin K. Ogilvie, C.M., Ph.D., D.Sc., H.Col., F.C.I.C., was (1993-2003) president and vice-chancellor of Acadia University in Wolfville, Nova Scotia where he led the development and implementation of the acclaimed Acadia Advantage Program, which was recognized by, and incorporated into, the Permanent Collection of the Smithsonian Institute in Washington, DC in 1999. He is a leading expert in biotechnology, bioorganic chemistry, and genetic engineering. His scientific accomplishments include the development of the "Gene Machine", an automated process for the manufacture of DNA. He is the inventor of Ganciclovir, a drug used worldwide to fight infections that occur when one's immune system is weakened. Both of these achievements were recognized in 2000 as "Milestones of Canadian Chemistry in the 20th Century" by the Canadian Society of Chemistry. He also developed a general method for the chemical synthesis of large RNA molecules, demonstrated by the first total chemical synthesis of a functional Transfer RNA (tRNA) molecule, which is still the basis for RNA synthesis worldwide. He has also written and spoken extensively on the challenges facing Canada as a nation, the role of the "knowledge" economy, postsecondary education, and entrepreneurship.

Dr. Ogilvie became a faculty member in the Department of Chemistry at the University of Manitoba in 1968. He moved to McGill University in 1974 and in 1984 was appointed founding Director, Office of Biotechnology, and Canadian Pacific Professor of Biotechnology at McGill. In 1987, he moved to Acadia University to serve as Vice-President (Academic) and Professor of Chemistry.

Dr. Ogilvie has served on numerous national and international organizations, including the Atomic Energy Control Board, the National Biotechnology Advisory Committee, the National Advisory Board for Science and Technology, and the Canadian eBusiness Initiative. He has served as scientific advisor to numerous technology companies and as a consultant and expert witness for international pharmaceutical and biotechnology companies. He is a widely sought-after speaker, has a number of patents, and his 150 scientific publications have received more than 5000 citations. He recently completed a three-year term as the initial Chair of the Premier's Advisory Council on Innovation (Nova Scotia), is currently AIMS Senior Fellow for Postsecondary Education, a member of the Board of Genome Canada, the Board of Governors of Quest University, and the Scientific Advisory Board of NRC's Institute of Marine Bioscience.

Dr. Ogilvie was named a Steacie Fellow in 1992, was admitted to the Order of Canada in 1991, and received the Manning Principal Award as Canada's outstanding contributor to innovation in 1992. He was identified as "a Canadian Who Made a Difference" in the 1988 Maclean's Honour Roll, has received three honourary degrees, the Queen Elizabeth Golden Jubilee Medal, the Commemorative Medal of the 125th Anniversary of the Confederation of Canada, and appeared as a mystery guest on "Front Page Challenge" (1988). He has also received the Buck-

From Public U to Private U

À PROPOS DE L'AUTEUR

Kelvin K. Ogilvie, C.M., Ph.D., D.Sc., H.Col., MICC a été recteur et vice-chancelier de l'Université Acadia, à Wolfville (Nouvelle-Écosse), de 1993 à 2003, où il a dirigé l'élaboration et la mise en œuvre du programme Acadia Advantage - programme reconnu et prisé qui a été intégré à la Collection permanente du Smithsonian Institute de Washington D.C., en 1999. M. Ogilvie est une figure de proue de la biotechnologie, de la chimie bio-organique et du génie génétique. Parmi ses réalisations scientifiques figure la mise au point de la « machine à gènes », processus automatisé de fabrication d'ADN. Il a également inventé le ganciclovir, médicament utilisé d'un bout à l'autre de la planète pour combattre les infections chez les humains immunodéficients. En 2000, la Société canadienne de chimie a reconnu ces deux réalisations comme des « jalons de la chimie canadienne au XXe siècle ». M. Ogilvie a également mis au point une méthode générale de synthèse chimique de grandes molécules d'ARN, démontrée par la première synthèse chimique complète d'une molécule fonctionnelle d'ARN de transfert (ARNt), qui constitue encore aujourd'hui le fondement de la synthèse de l'ARN partout dans le monde. Il a également prononcé de nombreux discours et rédigé bon nombre d'articles sur les défis auxquels le Canada fait face en tant que pays, le rôle de l'économie du savoir, les études postsecondaires et l'entrepreneuriat.

M. Ogilvie est devenu professeur au Département de chimie de l'Université du Manitoba en 1968. Il s'est ensuite joint à l'Université McGill, en 1974. En 1984, il a été nommé directeur du Bureau de la biotechnologie et professeur titulaire de la chaire de biotechnologie du Canadien Pacifique à l'Université McGill. En 1987, il entre en fonction à l'Université Acadia à titre de vice-recteur (Affaires universitaires) et professeur de chimie.

M. Ogilvie a mis son expertise au service d'organismes nationaux et internationaux, y compris la Commission canadienne de sûreté nucléaire, le Comité consultatif national de la biotechnologie, le Conseil consultatif des sciences et de la technologie, et l'Initiative canadienne pour le commerce électronique. Il a également servi de conseiller scientifique auprès d'un grand nombre d'entreprises technologiques ainsi que d'expert-conseil et de témoin expert pour des sociétés pharmaceutiques et biotechnologiques internationales. M. Ogilvie est un conférencier très recherché. De plus, il est titulaire de nombreux brevets et auteur de 150 publications scientifiques qui ont fait l'objet de plus de 5 000 citations. Il a récemment terminé un mandat de trois ans à titre de premier président du Advisory Council on Innovation, qui exerce son rôle auprès du premier ministre de Nouvelle-Écosse. Il est actuellement agrégé supérieur de recherches en matière d'enseignement postsecondaire pour AIMS et membre du conseil de Génome Canada, du Conseil des gouverneurs de l'Université Quest et du Conseil scientifique consultatif de l'Institut des biosciences marines du CNRC.

M. Ogilvie a été nommé agrégé titulaire de la bourse Steacie en 1992, a été décoré de l'Ordre du Canada en 1991 et a reçu le prix Manning Principal en 1992 pour sa remarquable contribution à l'innovation au Canada. Il a été cité au tableau d'honneur du magazine Maclean's en 1988 comme Canadien « qui a su changer les choses ». Il est titulaire de

© 2007 NRC Canada

Whitney Medal of the ACS (1983). Dr. Ogilvie was named an Honourary Colonel in the Canadian Air Force and was an inaugural inductee into the Nova Scotia Discovery Centre Science and Technology Hall of Fame in 2002.

trois grades honorifiques, il a reçu la médaille du jubilé d'or de la Reine Élisabeth II et la médaille commémorative du 125e anniversaire de la Confédération du Canada, et il a même pris part à l'émission de télévision Front Page Challenge en tant qu'invité mystère (1988). En 1983, il a reçu la médaille Buck-Whitney de l'ACS. Enfin, M. Ogilvie a été nommé colonel honoraire à l'Aviation canadienne et est devenu un des premiers membres du Temple de la renommée pour la science et la technologie du Discovery Centre, en Nouvelle-Écosse, en 2002.

© 2007 NRC Canada

This special issue is dedicated to

Professor Kelvin Kenneth Ogilvie

to honour his outstanding contributions to Canadian chemistry

Associate Editors: Andrew Bennet and Masad Damha

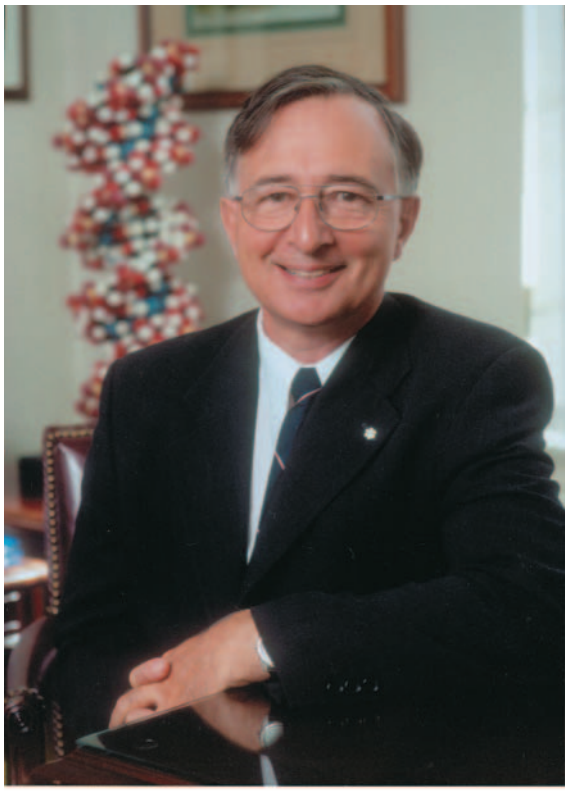
Le présent numéro est dédié à

Professor Kelvin Kenneth Ogilvie

pour sa contribution exceptionnelle à la chimie au Canada

Directeurs scientifiques associés : Andrew Bennet et Masad Damha

© 2007 NRC Canada



Professor Kelvin K. Ogilvie

© 2007 NRC Canada

Étude DFT des réactions de cycloaddition de type Diels–Alder sur le 4-aza-6-nitrobenzofuroxane

Sameh Ayadi et Manef Abderrabba

Résumé : Dans ce travail, nous avons étudié théoriquement les réactions de Diels–Alder à demande inverse d'électrons entre le 4-aza-6-nitrobenzofuroxane **1** et les diénophiles de type **3a**–**3c**. Nous avons discuté de point de vue thermodynamique et orbitalaire la possibilité et la stéréosélectivité de ces réactions. Les états de transition de la réaction entre le 4-aza-6-nitrobenzofuroxane **1** et les diénophiles de type **3a**–**3c** ont été déterminés.

Mots-clés : Diels–Alder à demande inverse d'électrons (DADEI), méthode DFT, 4-aza-6-nitrobenzofuroxane.

Abstract: The purpose of this work is a theoretical study of Diels–Alder reactions between the 4-aza-6-nitrobenzofuroxan **1** with a series of dienophiles **3a**–**3c**. From a thermodynamic and orbital point of view, we discuss the reactivity and the stereoselectivty of these reactions. Activation barriers in the Diels–Alder reactions of compound **1** with a series of dienophiles **3a**–**3c** have been calculated and discussed.

Key words: inverse electron demand Diels–Alder (IEDDA), DFT method, 4-aza-6-nitrobenzofuroxane.

Introduction

Le 4-aza-6-nitrobenzofuroxane **1** est un électrophile puissant (1) analogue à celui de 4,6-dinitrobenzofuroxane DNBF **2** qui était considéré comme la référence en chimie hétérocyclique dans les processus d'addition ou de substitution nucléophile (1–3). Plusieurs travaux de recherche ont montré que le 4,6-dinitrobenzofuroxane est capable de réagir comme diénophile ou hétérodiénophile dans des réactions de cycloaddition de type Diels–Alder (1, 4–7).

Nous avons trouvé intéressant d'effectuer une étude théorique sur la possibilité et la stéréosélectivité des réactions de Diels–Alder à demande inverse d'électrons entre le 4-aza-6-nitrobenzofuroxane **1** et les diénophiles de type **3a**–**3c** tels que l'éthénol **3a**, le vinylamine **3b** et l'éther de méthyle **3c** (fig. 1).

Dans chaque cas, nous avons vérifié que ces réactions sont sous le contrôle des orbitales frontières, comme la plupart des réactions de Diels–Alder (6). Nous avons par la suite étudié de point de vue thermodynamique et cinétique la possiblité et la régiosélectivité des réactions de Diels–Alder entre le 4-aza-6-nitrobenzofuroxane **1** et les diénophiles de type **3a**–**3c**.

Les méthodes de calcul

Cette étude a été réalisée en utilisant le programme GAUSSIAN 98 (8). Les calculs ont été effectués au niveau DFT avec les bases standard 3-21G*, 6-31G* et 6-31G**. Nous avons utilisé la fonctionnelle B3-LYP dans laquelle l'énergie d'échange est calculée par la méthode de Becke à trois paramètres, et la corrélation est calculée par la méthode de Lee, Yang et Paar (9, 10). En effet il a été récemment établi que cette DFT était actuellement la plus performante pour ce type de système (11).

Résultats et discussion

Étude thermodynamique

Nous avons réalisé une étude thermodynamique sur la possibilité et la régiosélectivité de la réaction entre le 4-aza-6-nitrobenzofuroxane **1** et les diénophiles de type **3a**–**3c**, tels que l'éthénol **3a**, le vinylamine **3b** et l'éther de méthyle **3c** (fig. 2). En utilisant la méthode de calcul DFT/B3-LYP avec les bases standard 6-31G*, 6-31G** et 3-21G*, nous avons déterminé dans les conditions standard (298,15 °K et 1 atm; 1 atm = 100,325 kPa) les variations d'énergie réactionnelle ΔE_r, les variations d'enthalpie libre réactionnelle ΔG_r, les variations d'enthalpie réactionnelle ΔH_r et le ZPE qui correspond aux réactions (I) et (II) (tableau 1).

Comme le montre le tableau 1, les variations d'enthalpie libre réactionnelle ΔG_r sont toutes négatives, par conséquent les réactions sont possibles et favorisées thermodynamiquement. De plus, nous avons remarqué que les valeurs de la variation d'enthalpie libre réactionnelle ΔG_r qui correspond aux réactions (I) sont toujours supérieures en valeur absolue aux valeurs de la variation d'enthalpie libre réactionnelle qui correspond aux réactions (II). Ce qui nous a permis de dire

Reçu le 20 décembre 2006. Accepté le 22 février 2007. Publié sur le site Web des Presses scientifiques du CNRC à revcanchim.cnrc.ca, le 24 avril 2007.

S. Ayadi[1] et M. Abderrabba. Unité de recherche Physico-chimie moléculaire, Institut préparatoire aux études scientifiques et techniques (IPEST), B.P. 51, 2070 la Marsa, Tunisie.

 doi:10.1139/V07-026 © 2007 CNRC Canada

Fig. 1.

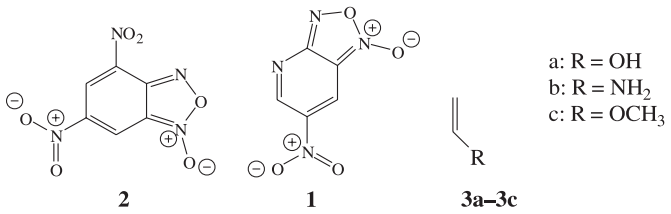
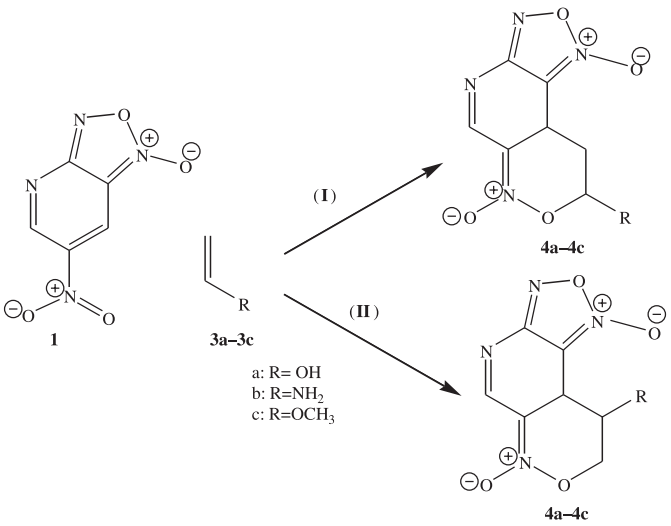


Fig. 2.



que les réactions (I) donnent toujours les produits majoritaires de la réaction.

Nous avons aussi remarqué que les valeurs de la variation de l'énergie ΔE_r qui correspond aux réactions (I) sont plus importantes que celles de la variation de l'énergie ΔE_r qui correspond aux réactions (II). Ce qui confirme de nouveau que les produits majoritaires de la réaction sont les régioisomères de type **4a**–**4c**.

Étude des orbitales frontières

En utilisant la méthode de calcul DFT/B3-LYP avec les bases standard 6-31G**, 6-31G* et 3-21G*, nous avons déterminé l'énergie de la LUMO et l'énergie de la HOMO de 4-aza-6-nitrobenzofuroxane **1** et l'énergie de la LUMO et la HOMO des diénophiles de type **3a**–**3c** (voir tableau 2).

Le diagramme orbitalaire des réactifs 4-aza-6-nitrobenzofuroxane **1** et l'éthénol **3a**, calculé au niveau DFT avec la fonctionnelle B3-LYP et la base standard 6–31G** est donné sur la figure 3.

Ce diagramme orbitalaire donne une bonne indication qualitative quant à la réactivité de notre système. L'interaction principale se produisant entre la LUMO de 4-aza-6-nitrobenzofuroxane **1** et la HOMO du diénophile (l'éthénol **3a**) démontre que notre système correspond bien à une réaction de Diels–Alder à demande inverse d'électrons (DADEI) (12–16). Dans le cas de l'interaction du 4-aza-6-nitrobenzofuroxane **1** avec le vinylamine **3b** et l'éther de méthyle **3c**, nous avons aussi trouvé une réaction de Diels–Alder à demande inverse d'électrons (DADEI), puisque l'interaction principale se produit entre la LUMO de l'hétérodiène de la molécule **1** et la HOMO de vinylamine **3b** et l'éther de méthyle **3c**. Comme le montre le tableau 2, la différence d'énergie HOMO–LUMO est plus petite dans le cas de la réaction du 4-aza-6-nitrobenzofuroxane **1** avec le vinylamine **3b** que dans le cas de la réaction de 4-aza-6-nitrobenzofuroxane **1** avec l'éthénol **3a** ou avec l'éther de méthyle **3c**; résultat attendu, car NH_2 est un meilleur donneur Π et un moins bon attracteur σ que OH, et la réaction devrait donc être plus facile.

L'examen des coefficients (2pz) des orbitales frontières au niveau DFT/B3-LYP de 4-aza-6-nitrobenzofuroxane **1** (fig. 4) montre que le coefficient de la LUMO de carbone C5 est toujours inférieur à celui du carbone C7, celui-ci paraît donc plus réactif. C'est-à-dire que l'addition d'une molécule de diénophile de type **3a**–**3c** sur le 4-aza-6-nitrobenzofuroxane **1** se fait en premier lieu sur le carbone C7.

Dans le but de déterminer la stéréoselectivité de la réaction entre le 4-aza-6-nitrobenzofuroxane **1** avec les diénophiles, tels que l'éthénol **3a**, le vinylamine **3b** et l'éther de méthyle **3c**, nous avons déterminé par la méthode DFT avec la fonctionnelle B3-LYP et les bases standards 6-31G**, 6-31G* et 3-21G* les coefficients (2pz) des orbitales frontières HOMO des diénophiles de type **3a**–**3c** et les coefficients (2pz) des LUMO du carbone C7 et de l'oxygène numéro 8 (O8) pour le 4-aza-6-nitrobenzofuroxane **1** (tableau 3).

L'examen des coefficients des orbitales frontières présentés sur la figure 5 montre que la réaction entre le 4-aza-6-

Tableau 1. Valeurs calculées (kcal·mol^{-1}) des variations d'énergie réactionnel ΔE_r, des variations d'enthalpie libre réactionnel ΔG_r, des variations d'enthalpie réactionnel ΔH_r et le ZPE.

	ΔE_r	ΔE_r + ZPE	ΔH_r	ΔG_r
DFT/B3-LYP avec la base standard (6-31G)**				
Les produits de la réaction (I)				
4a	–21,5	–21,5	14,6	–18,4
4b	–27,4	–27,4	19,4	–20,3
4c	–14,8	–14,9	21,7	–13,7
Les produits de la réaction (II)				
4′a	–18,8	–18,7	15,4	–15,5
4′b	–24,5	–24,5	12,3	–18,7
4′c	–12,1	–12,2	19,7	–10,4
DFT/B3-LYP avec la base standard (6-31G*)				
Les produits de la réaction (I)				
4a	–24,7	–24,6	12,7	–26,7
4b	–23,9	–23,9	13,8	–30,1
4c	–20,3	–21,3	15,1	–19,3
Les produits de la réaction (II)				
4′a	–213	–21,4	10,1	–24,6
4′b	–24,1	–24,2	19,3	–28,3
4′c	–17,3	–17,1	18,2	–17,1
DFT/B3-LYP avec la base standard (3-21G*)				
Les produits de la réaction (I)				
4a	–30,4	–31,3	16,7	–34,3
4b	–37,1	–37,2	19,3	–39,4
4c	–25,2	–25,1	13,2	–28,7
Les produits de la réaction (II)				
4′a	–28,7	–28,6	17,1	–30,1
4′b	–32,3	–31,2	22,3	–28,2
4′c	–24,1	–25,1	14,3	–19,3

© 2007 CNRC Canada

Tableau 2. L'énergie (eV) de la LUMO et l'énergie de la HOMO du 4-aza-6-nitrobenzofuroxan **1** et des dienophiles de type **3a–3c** (calculée avec la méthode DFT/B3-LYP)

	HOMO			LUMO		
	DFT/3-21G*	DFT/6-31G**	DFT/6-31G*	DFT/3-21G*	DFT/6-31G**	DFT/6-31G*
1	–11,2	–10,4	–8,9	–3,7	–3,1	–2,6
3a	–10,5	–9,5	–8,7	1,7	1,8	1,3
3b	–9,4	–8,8	–7,1	1,6	1,5	1,3
3c	–10,7	–9,5	–8,3	1,9	1,9	1,4

Fig. 3. Diagramme orbitalaire du 4-aza-6-nitrobenzofuroxan **1** et de l'éthénol **3a** (calculé avec la méthode DFT/6-31G**).

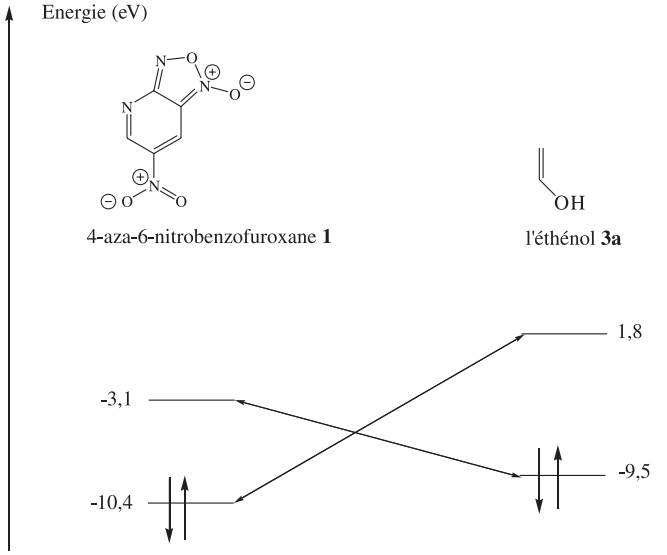
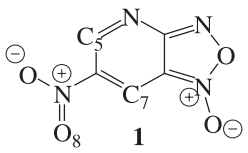


Fig. 4.



nitrobenzofuroxane **1** avec le vinylamine **3b** devrait être aussi plus stéréosélective que celle avec l'éthénol **3a**. Au niveau DFT/B3-LYP avec la base 3-21G*, les coefficients (2pz) de 4-aza-6-nitrobenzofuroxan deviennent respectivement 0,36 (C7) et 0,28 (O8), différence encore peu marquée. Au niveau DFT/B3-LYP avec la base 6-31G**, la différence est accentuée, favorisant la formation de la liaison (C7–C1) et la liaison (O8–C2) qui conduit à la formation du composé **4b**. Ce résultat est en accord avec le résultat trouvé par l'étude thermodynamique.

Calcul des états de transition

Dans le but d'étudier la régiosélectivité de la réaction entre le 4-aza-6-nitrobenzofuroxane **1** avec les diénophiles, tels que l'éthénol **3a**, le vinylamine **3b** et l'éther de méthyle **3c**, nous avons déterminé les états de transition pour la formation des composés de type **4a**–**4c** et **4′a**–**4′c** (fig. 2).

Les calculs théoriques montrent que la formation de régioisomère **4a** est favorisée par rapport au régioisomère **4′a**. En utilisant la méthode de calcul DFT/B3-LYP avec les bases standard 6-31G**, 6-31G* et 3-21G*, nous avons trouvé une grande énergie d'activation respectivement de 30,3; 36,4 et 32,5 kcal·mol^{-1} aux niveaux de calcul cités précédemment. Ces valeurs sont plus grandes que celles trouvées pour les états de transition conduisant à la formation des régioisomères **4a**; la formation du régioisomère **4′a** est improbable.

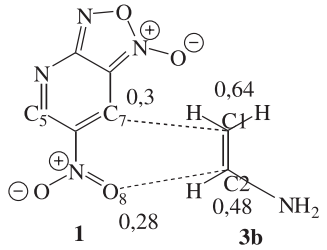
La comparaison des profils énergitiques des réactions conduisant respectivement aux régioisomères **4a** et **4′a** est donnée sur la figure 6.

Nous avons déterminé au niveau de calcul DFT/B3-LYP avec les bases standard 6-31G**, 6-31G* et 3-21G* les états de transition pour la formation des régioisomères **4b** et **4′b** ainsi que les états de transition pour la formation des régioisomères **4c** et **4′c** (tableau 4).

Tableau 3. L'énergie (eV) des coefficients des HOMO des dienophiles de type **3a–3c** et les coefficients des LUMO du 4-aza-6-nitrobenzofuroxane **1** (calculée avec la méthode DFT/B3-LYP).

	DFT/3-21G*	DFT/6-31G*	DFT/6-31G**
Coefficients des HOMO des diénophiles de type 3a–3c			
L'éthénol **3a**			
C1	0,65	0,49	0,47
C2	0,38	0,43	0,41
Vinylamine **3b**			
C1	0,64	0,46	0,42
C2	0,48	0,39	0,33
L'éther de methyle **3c**			
C1	0,51	0,52	0,53
C2	0,38	0,47	0,42
Coefficients des LUMO de 4-aza-6-nitrobenzofuroxan 1			
C7	0,36	0,28	0,34
O8	0,28	0,25	0,31

Fig. 5. Interactions orbitalaires entre les coefficients (2pz) de la LUMO du diène de la molécule **1** et les coeficients (2pz) de la HOMO du diénophile le vinylamine **3b** (valeurs calculées avec la méthode DFT/B3-LYP avec la base standard 3-21G*; eV).



© 2007 CNRC Canada

Fig. 6. Profil énergitique des réactions conduisant aux régioisomères **4a** et **4′a** en DFT/B3-LYP avec la base standard 6-31G** (énergies en kcal·mol^{-1}).

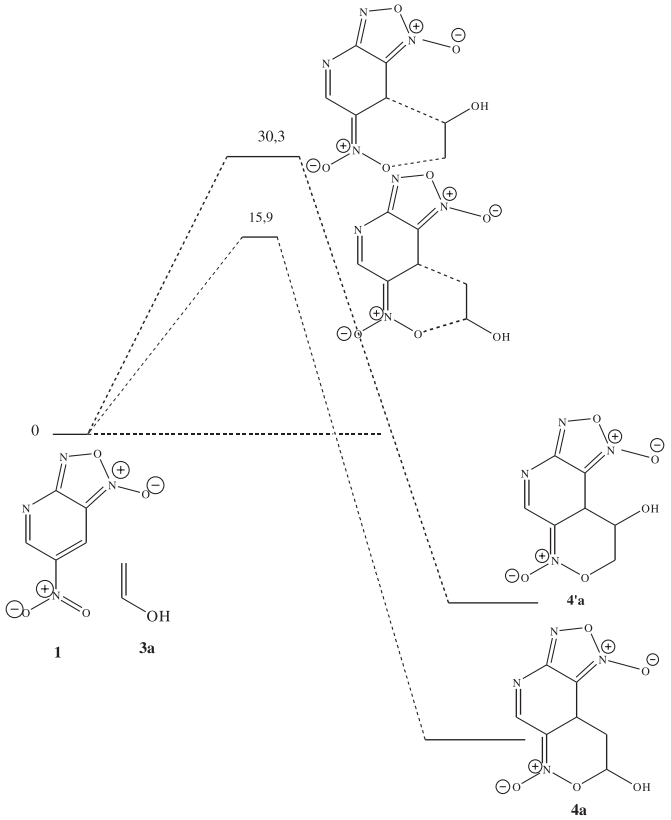


Tableau 4. Énergies relatives *E** (kcal·mol^{-1}) des états de transition par rapport aux énergies des réactifs (calculée avec la méthode DFT/B3-LYP).

	DFT/3-21G*	DFT/6-31G**	DFT/6-31G*
1			
3a			
3b			
3c			
4a (endo)	16,8	15,9	21,6
4a (exo)	17,1	16,3	22,3
4′a (endo)	32,5	30,3	36,4
4′a (exo)	33,7	30,7	35,2
4b (endo)	12,8	9,2	10,1
4b (exo)	31,2	10,3	10,8
4′b (endo)	28,3	27,1	31,1
4′b (exo)	29,7	27,6	31,8
4c (endo)		18,7	22,7
4c (exo)		19,4	22,9
4′c (endo)		32,3	38,1
4′c (exo)		33,7	36,7

Dans le cas de la réaction du 4-aza-6-nitrobenzofuroxane **1** avec le vinylamine **3b**, l'état de transition apparaît plus proche des réactifs que pour l'énol **3a**. Comme le montre le tableau 4, l'énergie d'activation pour la formation de régioisomères **4′b** et **4′c** est plus importante que l'énergie d'activation pour la formation de régioisomères **4b** et **4c**. Ce qui explique de nouveau que la formation des régioismères **4b** et **4c** est favorisée par rapport à la formation des régioisomères **4′b** et **4′c**.

Fig. 7. Géométrie des états de transition de la formation des composés **4a** endo.

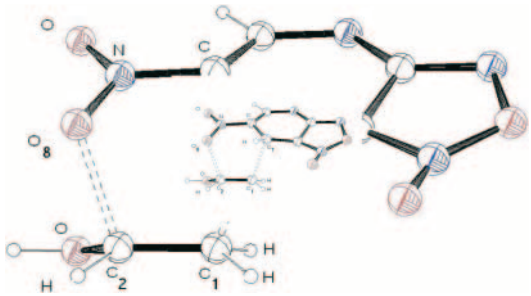


Tableau 5. Longueurs des liaisons en formation C–O et C–C dans l'état de transition pour la cycloaddition de la molécule **1** avec le diénophile **3a**–**3c** dans les approches endo (**4a)** et exo (**4a).**

	C–C	C–O	C–C	C–O
	(endo) **4a**		(exo) **4a**	
DFT/6-31G**	2,03	2,27	1,98	2,29
DFT/6-31G*	2,18	2,39	2,17	2,25
DFT/3-21G*	1,96	2,41	2,13	2,53
	(endo) **4b**		(exo) **4b**	
DFT/6-31G**	2,10	2,36	2,03	2,35
DFT/6-31G*	1,87	2,21	1,89	2,24
DFT/3-21G*	1,93	2,18	1,99	2,54
	(endo) **4c**		(exo) **4c**	
DFT/6-31G**	1,96	2,11	1,98	2,15
DFT/6-31G*	2,03	2,32	2,18	2,31
DFT/3-21G*	2,02	2,41	2,17	2,51

Dans le but de déterminer la stéréospécificité de la réaction entre le 4-aza-6-nitrobenzofuroxane **1** avec les diénophiles **3a**–**3c**, nous avons déterminé les états de transition correspondant à l'addition concertée conduisant au composé **4** dans les deux approches endo et exo. Les énergies correspondantes sont reportées dans le tableau 4.

Les résultats montrent que la forme endo est favorisée par rapport à la forme exo. La géométrie des états de transition de **4a** endo est présentée sur la figure 7.

Si on compare les longueurs des liaisons en formation, on constate que la liaison C–C est plus courte que la liaison C–O, l'état de transition est donc caractéristique d'un mécanisme concerté asynchrone (17–20), d'autant plus que la valeur finale de la longueur C–O est plus petite que celle de la longueur C–C. Ces distances sont assez proches de celles trouvées pour les Diels sans hétéroatomes (de 2,2 à 2,3 Å; 1 Å = 1 nm) (tableau 5) (11).

Conclusion

Nous avons réalisé une étude théorique sur la possibilité et la stéréosélectivité des réactions de Diels–Alder à demande inverse d'électrons entre le 4-aza-6-nitrobrnzo-

© 2007 CNRC Canada

furoxane et les diénophiles **3a**–**3c**, tels que l'éthénol **3a**, le vinylamine **3b** et l'éther de méthyle **3c**. Les résultats de calculs théoriques par la méthode DFT avec la fonctionnelle B3-LYP et les bases standards 6-31G**, 6-31G* et 3-21G* montrent que ces réactions sont possibles théoriquement et, par conséquent, elles sont favorisées thermodynamiquement. Ces résultats de calculs montrent aussi que les produits majoritaires de la réaction sont les régioisomères de type **4a**–**4c**. Les calculs des états de transition montrent que le produit cinétique de la réaction sont les régioisomères de type **4a**–**4c** et en plus les régioismères endo sont favorisées par rapport aux régioisomères exo.

En conclusion, les calculs sembleraient indiquer que l'addition de vinylamine **3b** sur le 4-aza-6-nitrobenzofuroxane **1** devrait être plus facile et plus stéréosélective que l'addition de l'éthénol **3a**, ce qui présente évidemment un grand intérêt pour les expérimentateurs.

Bibliographie

1. F. Terrier, M. Sebban, R. Goumont, J.C. Hallé, G. Moutiers, I. Cangelosi et E. Buncel. J. Org. Chem. **65**, 7391 (2000).
2. F. Terrier. Nucleophilic aromatic displacement. VCH. New York. 1991.
3. F. Terrier. Chem. Rev. **82**,77 (1982).
4. J.C. Hallé, D. Vichard, M.J. Pouet et F. Terrier. J. Org. Chem. **62**, 7178 (1997).
5. P. Sepulcri, J.C. Hallé, R. Goumont, D. Riou et F. Terrier. J. Org. Chem. **64**, 9254 (1999).
6. P. Sepulcri, R. Goumont, J.C. Hallé, D. Riou et F. Terrier. J. Chem. Soc. Perkin Trans. 2, 51 (2000).
7. D. Vichard, L.J. Aley et F. Terrier. Tetrahedron Lett. **42**, 7571 (2001).
8. M.J. Frisch, G.W. Trucks, H.B. Schlegel, G.E. Scuseria, M.A. Robb, J.R. Cheeseman, V.G. Zakrzewski, J.A. Montgomery, Jr., R.E. Stratmann, J.C. Burant, S. Dapprich, J.M. Millam, A.D. Daniels, K.N. Kudin, O. Farkas, J. Tomasi, V.Barone, M.Cossi, R. Cammi, B. Mennucci, C. Pomelli, C. Adamo, S. Clifford, J. Ochterski, G.A. Petersson, P.Y. Ayala, Q. Cui, K. Morokuma, P. Salvador, J.J. Dannenberg, D.K. Malick, A.D. Rabuck, K. Raghavachari, J.B. Foresman, J. Cioslowski, J.V. Ortiz, A.G. Baboul, B.B. Stefanov, G. Liu, A. Liashenko, P. Piskorz, I. Komaromi, R. Gomperts, R.L. Martin, D.J. Fox, T. Keith, M.A. Al-Laham, C.Y. Peng, A. Nanayakkara, M. Challacombe, P.M.W. Gill, B. Johnson, W.Chen, M.W. Wong, J.L. Andres, C. Gonzalez, M. Head-Gordon, E.S. Replogle et J.A. Pople. Gaussian 98. Revision A.11. Gaussian, Inc., Pittsburgh, Penn. 2001.
9. C. Lee, W. Yang et R.G. Parr. Phys. Rev. B, **37**, 785 (1988).
10. A.D. Becke. Phys. Rev. A. **38**, 3098 (1988).
11. E. Goldstein, B. Brett et K.N. Houk. J. Am. Chem. Soc. **118**, 6036 (1996).
12. W. Carruthers. Cycloadditions reactions in organic synthesis. Tetrahedron Organic Chemistry Series. Vol. 8. Pergamon, New York. 1990.
13. I.E. Marko et G.R. Evans. Tetrahedron Lett. **35**, 2767 (1994).
14. W.E. Bachmann et N.C. Deno. J. Am. Chem. Soc. **71**, 3062 (1949).
15. (*a*) J. Sauer. Bul. Soc. Chim. Belg. **101**, 521 (1992); (*b*) J. Sauer. 1,2,4,5-Tetrazines in comprehensive heterocyclic chemistry. 2e éd. *Sous la direction de* A.R. Katritzky, C.W. Rees et E.F.V. Scriven. Pergamon Press, New York. **6**, 901 (1996).
16. H. Waldmann. Synthesis, **6**, 535 (1994).
17. M.J.S. Dewar, S. Olivella et J.J.P Steward. J. Am. Chem. Soc, **108**, 5771 (1986).
18. M.J.S. Dewar. J. Am. Chem. Soc. **106**, 209 (1984).
19. F. Bernardi, A. Bottomi, M.J. Field, M.F. Guest, I.H. Hillier, M.A. Robb et A. Venturini. J. Am. Chem. Soc. **110**, 3050 (1988).
20. Y. Li et K.N. Houk. J. Am. Chem. Soc. **115**, 7478 (1993).

© 2007 CNRC Canada

N-Bromosuccinimide (NBS) — Selective and effective catalyst for trimethylsilylation of alcohols and phenols using hexamethyldisilazane and their regeneration under mild and neutral reaction conditions

Ardeshir Khazaei, Amin Rostami, Ayeh Raiatzadeh, and Marjan Mahboubifar

Abstract: Structurally diverse alcohols and phenols were trimethylsilylated in a clean and efficient reaction with hexamethyldisilazane (HMDS) based on the use of a catalytic amount of *N*-bromosuccinimide under both dichloromethane and solvent-free conditions at room temperature. Deprotection of trimethylsilyl ethers was also be achieved efficiently in the presence of a catalytic amount of NBS in methanol at ambient temperature.

Key words: N-bromosuccinimide, solvent-free, alcohols, phenols, hexamethyldisilazane, trimethylsilyl ether, catalyst, detrimethylsilylation.

Résumé : Opérant à la température ambiante, on a effectué d'une façon propre et efficace la triméthylsilylation d'alcools et de phénols de structures différentes par réaction avec de l'hexaméthyldisilazane (HMDS), dans du dichlorométhane ou sans solvant, en présence d'une quantité catalytique de *N*-bromosuccinimide (NBS). La déprotection des éthers triméthylsilyles peut aussi se faire d'une façon efficace en présence d'une quantité catalytique de NBS, dans le méthanol, à la température ambiante.

Mots clés : N-bromosuccinimide, sans solvant, alcools, phénols, hexaméthyldisilazane, éther triméthylsilyle, catalyseur, détriméthylsilylation.

[Traduit par la Rédaction]

Introduction

The protection of hydroxy groups through the formation of silyl ethers has been extensively utilized in organic synthesis (1). Silyl ethers are easily prepared, show resistance to oxidation, have good thermal stability and low viscosity, and are easily recoverable from their parent compounds. Moreover, numerous silylating methods can be utilized today; among them, trimethylsilylation is one of the most often used. Generally, the formation of trimethylsilyl ethers is carried out by the treatment of alcohols with trimethylsilyl chlorides or trimethylsilyl triflates in the presence of a base (2), Li_2S (3), and sometimes a nonionic super base catalyst (4). However, some of these methods frequently suffer from drawbacks such as a lack of reactivity or a difficulty removing amine salts derived from the reaction during the silylation reaction. HMDS is a stable, cheap, and commercially available compound that can be used for the preparation of trimethylsilyl ethers from hydroxy compounds, giving ammonia as the only by-product. Even though the handling of this reagent is easy, its main drawback is its poor silylating ability; forceful conditions and long reaction times are required (5). Therefore, for the activation of HMDS a variety of catalysts have been reported such as $(CH_3)_3SiCl$ (6), $ZnCl_2$ (7), zirconium sulfophenyl phosphonate (8), montmorillonite K-10 (9), I_2 (10), $LiClO_4$ (11), $H_3PW_{12}O_{40}$ (12), $Al(OTf)_3$ (13), $CuSO_4{\cdot}5H_2O$ (14), KBr (15), and $LiClO_4$–SiO_2 (16). Although these methods produce good results in many instances, few of these catalysts can do both protection and deprotection of alcohols and phenols as trimethylsilyl ethers. Therefore, there is still a demand to develop new mild methods for the trimethylsilylation of hydroxyl compounds and their regeneration in the presence of inexpensive and benchtop catalysts.

Similar to protection, deprotection of the trimethylsilyl ethers constitutes an important process in the synthetic chemistry of polyfunctional molecules, including the total synthesis of natural products. Although several methods

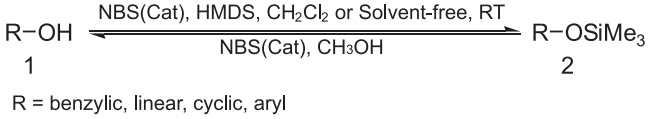
Received 1 January 2007. Accepted 21 March 2007. Published on the NRC Research Press Web site at canjchem.nrc.ca on 5 May 2007.

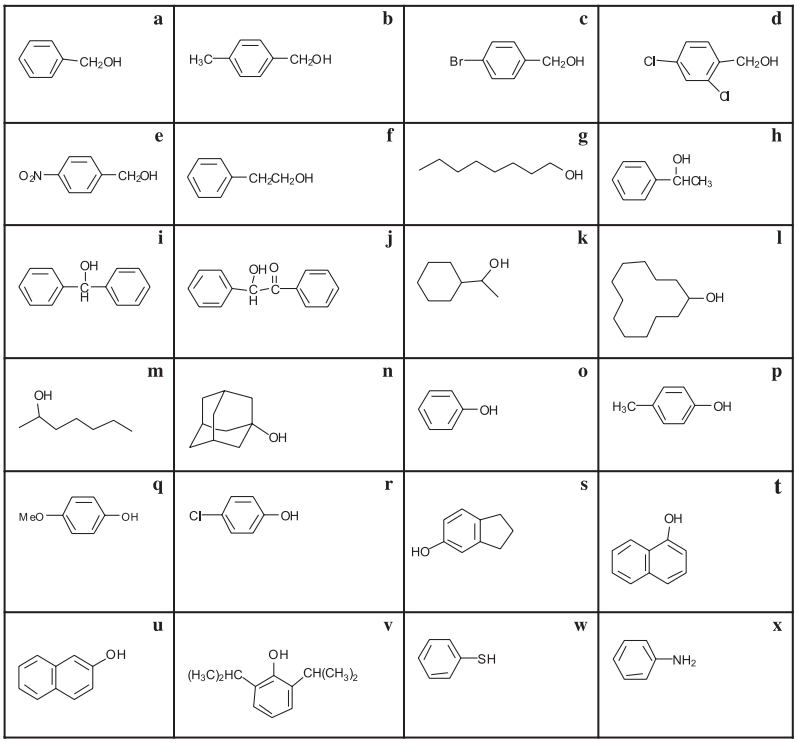
A. Khazaei[1], A. Raiatzadeh, and M. Mahboubifar. Faculty of Chemistry, Bu-Ali Sina University, Hamadan, Post Box No. 4119, Iran, 6517838683.
A. Rostami. Department of Chemistry, Faculty of Science, Kurdistan University, Sanandaj, Iran.

[1]Corresponding author (e-mail: khazaei_1326@yahoo.com or a_rostami372@yahoo.com).

 doi:10.1139/V07-029 © 2007 NRC Canada

Scheme 1.





Scheme 1

have been reported for the deprotection of trimethylsilyl ethers (17), the development of mild, efficient, ecofriendly, and selective reagents for the deprotection of trimethylsilyl ethers continues to be desirable.

Solvent-free reactions have attracted considerable attention in chemical processes for different reasons. They are valuable due to environmental safety, economic viewpoint, easy workup, high yields of the products, and (usually) fast reaction times (18). This is why we tried to develop a solvent-free version of this new reaction.

Results and discussion

In continuation of our interest in the application of *N*-halo compounds (19) in organic synthesis, we have found that NBS is an inexpensive commercially available reagent that has been used as an effective catalyst for the acetalization of carbonyl compounds (20*a*, 20*b*), the conversion of aldehydes to 1,1-diacetates (20*c*), and the acylation of alcohols (20*d*) under mild and nearly neutral reaction conditions.

In this present work, the catalytic application of NBS has been investigated as a selective reagent for the efficient trimethylsilylation of a wide range of alcohols and phenols under both solution and solvent-free conditions as well as the desilylation of the corresponding TMS ethers in methanol (Scheme 1).

We first examined the effect of different ratios of ROH–HMDS–catalyst. The 1:2:0.01 ratio for alcohols and phenols gave the best results and produced trimethylsilyl ethers in quantitative yields. As shown in Table 1, using a mixture of HMDS (2 mmol) and a catalytic amount of NBS (0.01 mmol), primary (alkyl and benzylic), secondary (hindered and unhindered), and tertiary alcohols and a variety of phenols (with electron-withdrawing and electron-releasing groups) were transformed into the corresponding trimethylsilyl ethers in good to high yield under both dichloromethane (I) and solvent-free (II) conditions at room temperature (RT). We observed that amines and thiols were not converted to the corresponding silyl ethers under these reaction conditions, even after prolonged reaction times.

Because of the nearly neutral nature of the reaction medium, no elimination by-products were observed at all. Subsequently, we discovered that the desilylation of the trimethylsilyl ethers can be carried out to obtain the corresponding alcohols and phenols in good to excellent yields by using the same catalyst in methanol at RT (Scheme 1 and Table 2).

We used this procedure for the selective trimethylsilylation of *n*-octanol (as a model for primary alcohols) or 2-pentanol (as a model for secondary alcohols) in the presence of 1-adamantanol (as a model for tertiary alcohols). The only observed products were *n*-octyl trimethylsilyl ether or 2-pentyl trimethylsilyl ether in 100% conversion (Scheme 2).

Similarly, in a binary mixture of 4-methoxyphenol and

© 2007 NRC Canada

Table 1. Trimethylsilylation of alcohols and phenols using HMDS catalyzed with NBS under both dichloromethane (I) and solvent-free (II) conditions at RT.

Entry	Substrate	Product[c]	Time (h)		Yield (%)[a]		Yield (%)[b]	
			I	II	I	II	I	II
1	**1a**	**2a**	2.10	1.10	90	100	84	95
2	**1b**	**2b**	2.35	1.00	93	100	85	95
3	**1c**	**2c**	2.35	0.84	95	100	91	96
4	**1d**	**2d**	2.30	1.00	95	100	89	93
5	**1e**	**2e**	1.46	1.50	95	95	89	90
6	**1f**	**2f**	1.00	0.50	85	100	80	96
7	**1g**	**2g**	2.10	1.50	81	100	78	94
8	**1h**	**2h**	0.75	1.50	90	80	87	77
9	**1i**	**2i**	5.11	5.00	95	90	90	86
10	**1j**	**2j**	8.00	8.00	83	80	79	74
11	**1k**	**2k**	12.00	10.00	95	80	91	76
12	**1l**	**2l**	6.00	5.00	94	100	90	95
13	**1m**	**2m**	2.50	5.00	80	100	74	93
14	**1n**	**2n**	48.00	30.00	95	100[d]	92	96[d]
15	**1o**	**2o**	0.75	0.50	96	100	91	95
16	**1p**	**2p**	2.00	0.75	90	100	85	93
17	**1q**	**2q**	0.50	0.58	90	100	83	95
18	**1r**	**2r**	2.10	0.84	99	100	95	95
19	**1s**	**2s**	2.21	1.00	97	100	91	95
20	**1t**	**2t**	3.00	1.50	99	90	93	85
21	**1u**	**2u**	2.30	1.00	85	100	80	92
22	**1v**	**2v**	5.00	5.50	30	100	23	94
23	**1w**	**2w**	15.00	15.00	0	0	0	0
24	**1x**	**2x**	15.00	15.00	0	0	0	0

[a]Conversion yields.
[b]Isolated yields.
[c]All products were characterized by comparison of their spectral data (^{1}H NMR and IR spectroscopy) with those of authentic samples.
[d]In this case the ratio of substrate–HMDS–NBS was 1:8:0.2.

Table 2. Deprotection of trimethylsilyl ethers in the presence of catalytic NBS (0.2 mmol) in methanol at RT.

Entry	Substrate	Product	Time (h)	Yield (%)[a]	Yield (%)[b]
1	**2a**	**1a**	1.17	100	94
2	**2b**	**1b**	1.00	100	95
3	**2c**	**1c**	0.84	100	95
4	**2d**	**1d**	0.84	100	96
5	**2e**	**1e**	1.33	80	76
6	**2f**	**1f**	2.50	100	94
7	**2g**	**1g**	4.00	90	83
8	**2h**	**1h**	2.00	100	96
9	**2i**	**1i**	6.00	30	23
10	**2j**	**1j**	14.00	100	95
11	**2k**	**1k**	8.00	100	93
12	**2l**	**1l**	3.50	100	95
13	**2m**	**1m**	5.00	100	94
14	**2n**	**1n**	24.00	100	96
15	**2o**	**1o**	0.42	95	89
16	**2p**	**1p**	0.75	95	89
17	**2q**	**1q**	0.42	100	94
18	**2r**	**1r**	0.84	100	95
19	**2s**	**1s**	1.00	95	90
20	**2t**	**1t**	1.00	95	91
21	**2u**	**1u**	0.84	100	95
22	**2v**	**1v**	5.00	100	95

[a]Conversion yields.
[b]Isolated yields.

2,6-diisopropylphenol (as a model for hindered phenol), 4-methoxyphenol was completely converted to the corresponding silyl ether, while 0% conversion was observed for 2,6-diisopropylphenol (Scheme 3).

To assess the catalytic activity of NBS for trimethylsilylation, we compared our results for the trimethylsilylation of 1-naphtol with the best of the well-known procedures from the literature (Table 3). The advantages and the characteristic aspects of the described method in this communication, in comparison with other previously reported catalysts, are the following: a variety of phenols (6, 10, 12) can be trimethylsilylated in good to high yields (11, 14) at RT (12, 14). In addition, the catalyst NBS is inexpensive, has no sensitivity to moisture (11), does not require a large amount of catalyst (11), and no special efforts are required for the reaction (14).

On the basis of the previously reported mechanism for the application of I_2 for the trimethylsilylation of alcohols (10) and the catalytic application of NBS for the protection of carbonyl and hydroxyl functional groups (18), one explanation for this process is that NBS may act as a source for the formation of Br^+, which polarizes the Si–N bond in HMDS to produce the reactive silylating agent (as a Lewis acid). Therefore, the mechanism shown in Scheme 4 is proposed.

Conclusion

In summary, we have shown that NBS is an efficient and selective catalyst for the protection of a variety of alcohols and phenols as TMS ethers using HMDS and their deprotection under very mild conditions. The product yields are good to high and the procedure is easy and clean. Therefore, this procedure could be utilized in transformations that need mild reaction conditions.

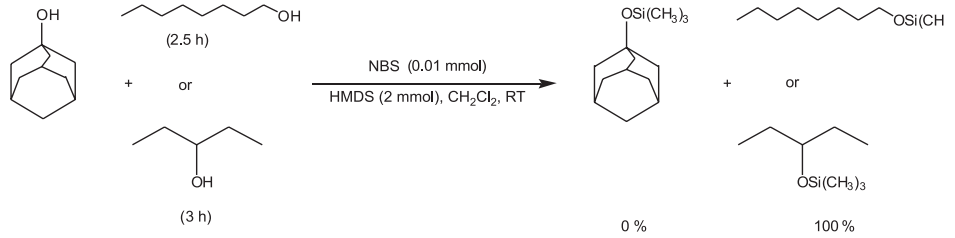
Experimental

General procedure for the trimethyisilylation of alcohols and phenols using HMDS catalyzed with NBS in solution

Alcohols or phenols (1 mmol) were added to a mixture of HMDS (2 mmol) and NBS (0.01 mmol) in CH_2Cl_2 (7 mL), and the mixture was then stirred at RT for the specified time (Table 1). The progress was monitored by TLC. After completion of the reaction, water (10 mL) was added to destroy the extra amounts of HMDS for alcohols and 5% aq. NaOH (10 mL) for phenols, then the organic layer was separated and dried over anhydr. Na_2SO_4. The solvent was evaporated, and *n*-hexane (20 mL) was added to the residual mixture. Insoluble catalyst was removed by filtration. Evaporation of the *n*-hexane under reduced pressure gave pure product without further purification.

© 2007 NRC Canada

Scheme 2.



Scheme 3.

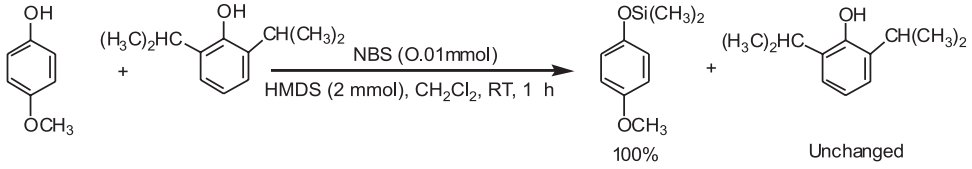
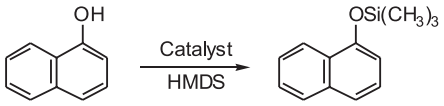
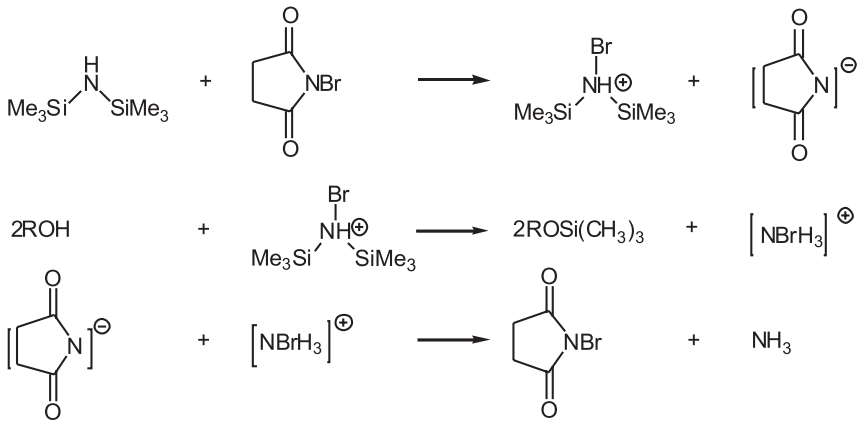


Table 3. Comparison of the activity of various catalysts in the trimethylsilylation of 1-naphtol with HMDS.



Entry	Catalyst	Conditions	HMDS–Cat	Time (h)	Yield (%)	Reference
1	NBS	Solvent-free, RT	2.0:0.01	1.50	85	This work
2	NBS	CH_2Cl_2, RT	2.0:0.01	3.00	93	This work
3	$CuSO_4{\cdot}5H_2O$	CH_3CN, reflux	0.7:0.10	38.00	50	14
4	$LiClO_4$	Solvent-free, RT	0.7:0.50	0.33	80	11
6	$H_3PW_{12}O_{40}$	Solvent-free, 55–60 °C	0.8:0.01	—	—	12
7	I_2	CH_2Cl_2, RT	0.8:0.01	—	—	10
8	$Si(CH_3)_3Cl$	Solvent-free, 125 °C	0.8:2 drops	—	—	6
9	Montmorillonite K-10	CH_2Cl_2, RT	—	—	92	9
10	KBr	CH_3CN, RT	0.7:0.10	0.13	85	15
11	$LiClO_4$-SiO_2	CH_2Cl_2, RT	0.7:0.10 g	2.00	90	16

Scheme 4.



© 2007 NRC Canada

General procedure for the trimethyisilylation of alcohols and phenols using HMDS catalyzed with NBS under solvent-free conditions

Alcohols or phenols (1 mmol) were added to a mixture of HMDS (2 mmol) and NBS (0.01 mmol), and the mixture was then stirred at RT for the specified time (see Table 1). The progress was monitored by TLC. After completion of the reaction, water (10 mL) was added to destroy the extra amounts of HMDS for alcohols and 5% aq. NaOH (10 mL) for phenols. The trimethylsilyl ethers were then extracted with *n*-hexane (20 × 2 mL), and the organic layer was dried over anhydr. Na_2SO_4. Evaporation of the *n*-hexane under reduced pressure gave pure product without further purification.

General procedure for the deprotection of trimethylsilyl ethers catalyzed with NBS

NBS (0.2 mmol) was added to a mixture of TMS ethers (1 mmol) in MeOH (3 mL), and the mixture was then stirred at RT for the specified time (Table 2). The progress of the reaction was monitored by TLC. On completion of the reaction, methanol was removed under reduced pressure and the product was purified through a short column of silica gel to obtain pure alcohol or phenol.

Acknowledgments

We are thankful to the Bu-Ali Sina University Research Councils for partial support of this work.

References

1. (*a*) G.V. Look, G. Simchen, and J. Heberle. Silylation agents. Fluka, Buchs, Switzerland. 1995; (*b*) T.W. Greene and P.G.M. Wuts. Protective groups in organic synthesis. 3rd ed. John Wiley, New York. 1999.
2. S.K. Chaudhary and O. Hernandez. Tetrahedron Lett. 99 (1979).
3. G.A. Olah, B.G.B. Gupta, S.C. Narang, and R. Malhotra. J. Org. Chem. **44**, 4272 (1979).
4. (*a*) B.A.D. Sa, D. McLeod, and J.G. Verkade. J. Org. Chem. **62**, 5057 (1997); (*b*) B.A.D. Sa and J.G. Verkade. J. Am. Chem. Soc. **118**, 2832 (1996).
5. C.A. Bruynes and T.K. Jurriens. J. Org. Chem. **47**, 3966 (1982).
6. (*a*) S.H. Langer, S. Connell, and J. Wender. J. Org. Chem. **23**, 50 (1958); (*b*) P. Gauttret, S. El-Ghammarti, A. Legrand, D. Coutrier, and B. Rigo. Synth. Commun. **26**, 7077 (1996).
7. H. Firouzabadi and B. Karimi. Synth. Commun. **23**, 1633 (1993).
8. M. Curini, F. Epifano, M.C. Marcotullio, O. Rosati, and U. Constantino. Synth. Commun. **29**, 541 (1999).
9. Z.H. Zhang, T.S. Li, F. Yang, and C.G. Fu. Synth. Commun. **28**, 3105 (1998).
10. B. Karimi and B. Golshani. J. Org. Chem. **65**, 7228 (2000).
11. N. Azizi and M.R. Saidi. Organometallics, **23**, 1457 (2004).
12. H. Firouzabadi, N. Iranpoor, K. Amani, and F. Nowrouzi. J. Chem. Soc. Perkin Trans. 1, 2601 (2002).
13. H. Firouzabadi, N. Iranpoor, S. Sobhani, and S. Ghassamipour. Synthesis, 595 (2005).
14. B. Akhlaghinia and S. Tavakoli. Synthesis, 775 (2005).
15. F. Shirini and M. Esmail. Synth. Commun. **36**, 1109 (2006).
16. N. Azizi, Y. Rozbeh, and M.R. Saidi. J. Organomet. Chem. **691**, 817 (2006).
17. (*a*) T.D. Nelson and R.D. Crouch. Synthesis, 1031 (1996) and refs. cited therein; (*b*) Lakoura and A. Akbari. Ind. J. Chem. Sect. B, **42**, 1165 (2003); (*c*) J.I. Levin, M.T. Du, and K. Park. Synth. Commun. **34**, 2773 (2004); (*d*) M.N. Bakola-Christianopoulou. J. Mol. Catal. **65**, 307 (1991); (*e*) D. Rotulosims and J. Prunet. Org. Lett. **4**, 4701 (2002); (*f*) Y.J. Wu, H. Huang, X. Shen, Q. Hu, C.-J. Tang, and L. Li. Org. Lett. **4**, 2141 (2002); (*g*) R. Gopinath and B.K. Patel. Org. Lett. **2**, 4177 (2000); (*h*) A. Vakalopoulos and H.M.R. Hoffmann. Org. Lett. **2**, 1447 (2000); (*i*) Z. Yu and J.G. Vercade. J. Org. Chem. **65**, 2065 (2000); (*j*) M.H. Habibi, S. Tangestaninejad, I. Mohammadpoor-baltork, V. Mirkhani, and B. Yadollahi. Tetrahedron Lett. **42**, 6771 (2001); (*k*) J.R. Hwu, M.L. Jain, F.-Y. Tasi, S.-C. Tasy, A. Balakumar, and G.H. Hakimelahi. J. Org. Chem. **65**, 5077 (2000); (*l*) R.D. Crouch, C.A. Romany, A.C. Kreshock, K.A. Menconi, and J.L. Zile. Tetrahedron Lett. **45**, 1279 (2004); (*m*) R.D. Crouch and A. Williams. Synth. Commun. **36**, 959 (2006).
18. F. Sieriz, C. Christine Thomassigny, and D. Lou. Curr. Org. Synth. **1**, 137 (2004).
19. (*a*) A. Khazaei, R.G. Vaghei, and M. Tajbakhsh. Tetrahedron Lett. **42**, 5099 (2001); (*b*) A. Khazaei, A. Aminimanesh, and A. Rostami. J. Chem. Res. Synop. 391 (2005); (*c*) A. Khazaei and A. Aminimanesh. Synthesis, 1739 (2004); (*d*) A. Khazaei, M.A. Zolfigol, and A. Rostami. Synthesis, 2959 (2004); (*e*) A. Khazaei, A. Rostami, Z. Tanbakochian, and Z. Zinati. J. Braz. Chem. Soc. **17**, 206 (2006); (*f*) A. Khazaei, A. Rostami, Z. Tanbakochian, and Z. Zinati. Catal. Commun. **7**, 214 (2006).
20. (*a*) B. Karimi, G.R. Ebrahimian, and H. Seradj. Org. Lett. **1**, 1737 (1999); (*b*) B. Karimi, H. Seradj, and G.R. Ebrahimian. Synlett. 1456 (1999); (*c*) B. Karimi and H. Seradj. Synlett. 641 (2000); (*d*) B. Karimi and H. Seradj. Synlett. 519 (2001).

© 2007 NRC Canada

Quinonoids from the barks of *Cratoxylum formosum* subsp. *pruniflorum*

Nawong Boonnak, Chatchanok Karalai, Suchada Chantrapromma, Chanita Ponglimanont, Akkharawit Kanjana-Opas, Kan Chantrapromma, and Hoong-Kun Fun

Abstract: A mixture of new bianthrones J (**1a** and **1b**) was isolated from the barks of *Cratoxylum formosum* subsp. *pruniflorum* together with six known quinonoids, namely bianthrone A_1 (**2**), vismones E (**3**) and D (**4**), 11-hydroxy-5-methoxy-2,2,9-trimethyl-2*H*-anthra[1,2-b]-pyran-7,12-dione (**5**), vismiaquinone (**6**), and 3-geranyloxy-6-methyl-1,8-dihydroxyanthraquinone (**7**). Their structures were assigned on the basis of spectroscopic methods. The antibacterial and cytotoxic activities of compounds **3** and **4** were also reported.

Key words: Cratoxylum formosum subsp. *pruniflorum*, bianthrone, vismone, anthraquinone, antibacterial activity, cytotoxicity.

Résumé : À partir de l'écorce de *Cratoxylum formosum* subsp. *pruniflorum* on a isolé de nouvelles bianthrones J (**1a** et **1b**) aux côtés de six quinonoïdes connues, soit la bianthrone A_1 (**2**), les vismones E (**3**) et D (**4**), la 11-hydroxy-5-méthoxy-2,2,9-triméthyl-2*H*-anthra[2,1-b]pyrane-7,12-dione (**5**), la vismiaquinone (**6**) et la 3-géranyloxy-6-méthyl-1,8-dihydroxyanthraquinone (**7**). On a attribué leurs structures sur la base de méthodes spectroscopiques. On a aussi déterminé les activités antibactériennes et cytotoxiques des composés **3** et **4**.

Mots-clés : Cratoxylum formosum subsp. *pruniflorum*, bianthrone, vismone; anthraquinone, activité antibactérienne, cytotoxicité.

[Traduit par la Rédaction]

Introduction

During the course of our investigation on the bioactive chemical components of plants belonging to the family Guttiferae, we have focused on *Cratoxylum formosum* subsp. *pruniflorum*, which is a shrub or small tree found widely in the northeastern part of Thailand. Decoction of the fresh or dried leaves from this plant has been used in traditional medicine as tonic, stomachic, and diuretic (1). This shrub produces various types of secondary metabolites including xanthones, triterpenoids, flavonoids, and anthraquinones (2–5). Some of these anthraquinones have been found to have cytotoxic and antiprotozoal activities (4, 6–7). We previously reported nine new xanthones and a new anthraquinone from the roots and barks of *C. formosum* subsp. *pruniflorum* (8). In continuation of our study, we describe herein the isolation and identification of a mixture of new bianthrones J (**1a** and **1b**) together with six known compounds (**2–7**). The antibacterial and cytotoxic activities of all the isolates were also evaluated.

Results and discussion

The crude CH_2Cl_2 and acetone extracts from the barks of *C. formosum* subsp. *pruniflorum* were fractionated by silica gel column chromatography to obtain a mixture of new bianthrones J (**1a** and **1b**) along with six known quinonoids (**2–7**).

A mixture of new bianthrones J (**1a** and **1b**) was obtained as a yellow-green powder. It showed a molecular ion peak at *m/z* 674.2864 $[M]^+$ in the HR EIMS (calcd. for *m/z* 674.2880), corresponding to a molecular formula $C_{42}H_{42}O_8$. Moreover, the bianthrones J also displayed a EIMS peak at *m/z* 338 $[M - 336]^+$ corresponding to the fragment ion of $C_{21}H_{22}O_4$, which was the same as that of 2-(3-methyl-1-butenyl)-1,8-dihydroxy-3-methoxy-6-methyl anthrone (9), a

Received 26 January 2007. Accepted 28 March 2007. Published on the NRC Research Press Web site at http://canjchem.nrc.ca on 5 May 2007.

N. Boonnak, C. Karalai,[1] S. Chantrapromma, and C. Ponglimanont. Department of Chemistry, Faculty of Science, Prince of Songkla University, Hat-Yai, Songkhla, 90112, Thailand.
A. Kanjana-Opas. Department of Industrial Biotechnology, Faculty of Agro-Industry, Prince of Songkla University, Hat-Yai, Songkhla, 90112, Thailand.
K. Chantrapromma. Research Unit of Natural Products Utilization, Walailak University, Thasala, Nakhon Si Thammarat, 80160, Thailand.
H.-K. Fun. X-ray Crystallography Unit, School of Physics, Universiti Sains Malaysia, 11800 USM, Penang, Malaysia.

[1]Corresponding author (e-mail: chatchanok.k@psu.ac.th or chatchanok_k@yahoo.com).

 doi:10.1139/V07-031 © 2007 NRC Canada

Table 1. NMR (300 MHz) spectroscopic data of bianthrones J **1a** and **1b** in $CDCl_3$.

		Compound **1a**				Compound **1b**		
Position	DEPT	δ_C	δ_H, (*J* in Hz)	COSY	HMBC	δ_C	δ_H, (*J* in Hz)	HMBC
1, 1′	C	161.7				161.3		
2, 2′	C	113.4				113.4		
3, 3′	C	162.0				162.0		
4, 4′	CH	103.1	5.65, s		$C_{2/2'}$, $C_{9/9'}$, $C_{9a/9'a}$, $C_{10/10'}$	103.0	5.89, s	$C_{2/2'}$, $C_{9/9'}$, $C_{9a/9'a}$, $C_{10/10'}$
4a, 4′a	C	140.1				140.6		
5, 5′	CH	120.7	6.34, br s	H_7, H_{16} / $H_{7'}$, $H_{16'}$	$C_{7/7'}$, $C_{10/10'}$, $C_{8a/8'a}$, $C_{10a/10'a}$, $C_{16/16'}$	120.7	6.04, br s	$C_{7/7'}$, $C_{10/10'}$, $C_{8a/8'a}$, $C_{10a/10'a}$, $C_{16/16'}$
6, 6′	C	146.9				146.7		
7, 7′	CH	117.0	6.68, br s	H_5, H_{16} / $H_{5'}$, $H_{16'}$	$C_{5/5'}$	117.0	6.62, br s	$C_{5/5'}$
8, 8′	C	161.7				161.9		
8a, 8′a	C	114.7				114.4		
9, 9′	C	190.7				190.6		
9a, 9′a	C	110.6				111.1		
10, 10′	C	56.8	4.26, s		$C_{4/4'}$, $C_{5/5'}$, $C_{4a/4'a}$, $C_{10a/10'a}$	57.0	4.25, s	$C_{4/4'}$, $C_{5/5'}$, $C_{4a/4'a}$, $C_{10a/10'a}$
10a, 10′a	C	141.5				140.6		
11, 11′	CH	115.6	6.53, dd, 6.6, 0.7	H_{12}, H_{13} / $H_{12'}$, $H_{13'}$	$C_{2/2'}$, $C_{12/12'}$	115.6	6.47, dd, 6.6, 0.7	$C_{2/2'}$, $C_{12/12'}$
12, 12′	CH	143.6	6.68, t, 6.6	H_{11}, H_{13} / $H_{11'}$, $H_{13'}$	$C_{2/2'}$, $C_{11/11'}$, $C_{13/13'}$	143.6	6.63, t, 6.6	$C_{2/2'}$, $C_{11/11'}$, $C_{13/13'}$
13, 13′	CH	33.1	2.48, m	H_{12}, H_{14}, H_{15} / $H_{12'}$, $H_{14'}$, $H_{15'}$	$C_{11/11'}$, $C_{12/12'}$	33.1	2.48, m	$C_{11/11'}$, $C_{12/12'}$
14, 14′	CH_3	22.2	1.20, d, 6.6	H_{13} / $H_{13'}$	$C_{12/12'}$, $C_{13/13'}$	22.2	1.20, d, 6.6	$C_{12/12'}$, $C_{13/13'}$
15, 15′	CH_3	22.2	1.20, d, 6.6	H_{13} / $H_{13'}$	$C_{12/12'}$, $C_{13/13'}$	22.2	1.20, d, 6.6	$C_{12/12'}$, $C_{13/13'}$
16, 16′	CH_3	22.0	2.34, s		$C_{5/5'}$, $C_{6/6'}$, $C_{7/7'}$	22.0	2.29, s	$C_{5/5'}$, $C_{6/6'}$, $C_{7/7'}$
3, 3′-OMe	CH_3	55.5	3.71, s		$C_{3/3'}$	55.6	3.80, s	$C_{3/3'}$
1,1′-OH	C		12.63, s		$C_{1/1'}$, $C_{2/2'}$, $C_{9a/9'a}$		12.68, s	$C_{1/1'}$, $C_{2/2'}$, $C_{9a/9'a}$
8, 8′-OH	C		11.91, s		$C_{7/7'}$, $C_{8/8'}$, $C_{8a/8'a}$		11.85, s	$C_{7/7'}$, $C_{8/8'}$, $C_{8a/8'a}$

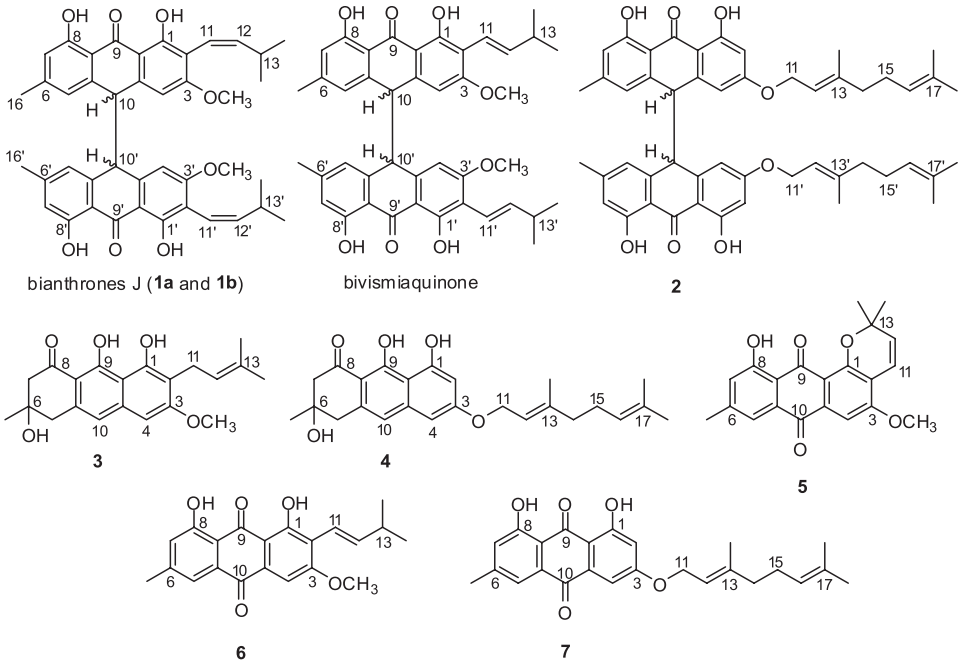
half structure of bianthrones J. The UV spectrum showed absorption bands at 273 and 360 nm. The IR absorption band at 1640 cm^{-1} indicated the presence of the conjugated carbonyl groups. These results suggested a bianthrone type. In this case, the bianthrones J were optically inactive (a mixture of (±) and meso forms). The ^1H and ^{13}C NMR spectral data (Table 1) showed two sets of the signals of (±) and meso forms that were similar to those of bivismiaquinone except for the appearance of the *cis*-olefinic protons of 3-methyl-1-butenyl groups at δ 6.53 (2H, dd, *J* = 0.7, 6.6 Hz, H-11/11′), 6.68 (2H, t, *J* = 6.6 Hz, H-12/12′), 6.47 (2H, dd, *J* = 0.7, 6.6 Hz, H-11/11′), and 6.63 (2H, t, *J* = 6.6 Hz, H-12/12′) instead of the corresponding *trans*-olefinic protons of bivismiaquinone (10) at δ 6.51 (2H, d, *J* = 16.2 Hz, H-11/11′), 6.66 (2H, dd, *J* = 6.6, 16.2 Hz, H-12/12′), 6.45 (2H, d, *J* = 16.2 Hz, H-11/11′), and 6.60 (2H, dd, *J* = 6.6, 16.2 Hz, H-12/12′). The olefinic protons signals at δ 6.68 and 6.63 were assigned to H-12 and H-12′ from HMBC correlation to δ_C 113.4 (C-2/2′), 115.6 (C-11/11′), and 33.1 (C-13/13′), whereas signals at δ 6.53 and 6.47 were assigned to H-11 and H-11′, as they exhibited correlations with δ_C 143.6 (C-12/12′) and 113.4 (C-2/2′). The two signals of 1,1′-OH at δ 12.63 and 12.68 showed HMBC correlation with δ_C 161.7 (C-1/1′), 113.4 (C-2/2′), 110.6 (C-9a/9′a) and 161.3 (C-1/1′), 113.4 (C-2/2′), 111.1 (C-9a/9′a), respectively, which confirmed the attachment of the 3-methyl-1-butenyl moiety at C-2 and C-2′. The locations of all substituents were confirmed by HMBC correlations as shown in Table 1. This mixture was designated as bianthrones J (**1a** and **1b**), a related geometrical isomer of bivismiaquinone, previously isolated from *Psorospermum febrifugum* (11).

The remaining known compounds were identified as bianthrone A_1 (**2**) (11, 12), vismone E (**3**) (13), vismone D (**4**) (13, 14), 11-hydroxy-5-methoxy-2,2,9-tri-methyl-2*H*-anthra[1,2-b]pyran-7,12-dione (**5**) (15), vismiaquinone (**6**) (16), and 3-geranyloxy-6-methyl-1,8-dihydroxyanthraquinone (**7**) (13) (see Fig. 1) by comparison of their spectral data with those published in the literature. Moreover, compounds **2–4** were isolated for the first time from this genus.

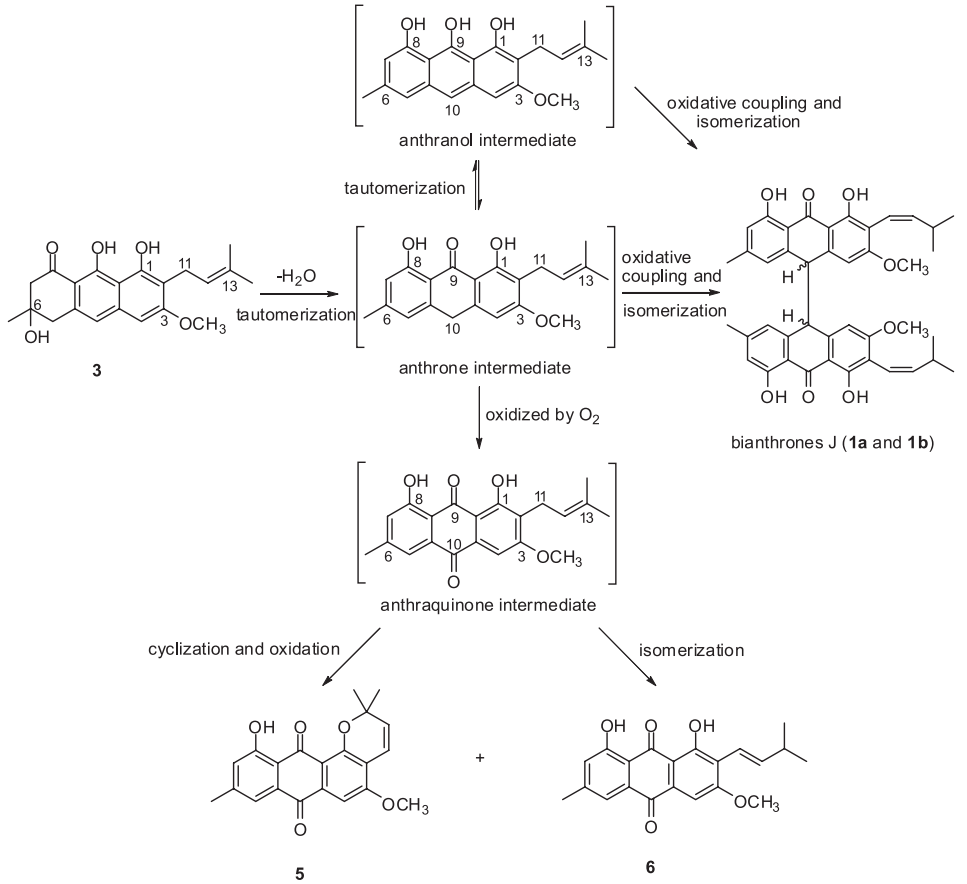
As previously reported (13), vismones with β-hydroxy carbonyl functionality are acid-sensitive under mild conditions, such as prolonged contact with SiO_2 during chromatographic purification. Those vismones with a C-6 hydroxyl group are easily dehydrated and further tautomerized to yield anthrone and anthranol intermediates, which are possibly further oxidized by O_2 to produce anthraquinones and bianthrones (17). We proposed that compound **3** was chemically transformed to an anthrone intermediate (Scheme 1),

© 2007 NRC Canada

Fig. 1. Structures of isolated compounds.



Scheme 1. Plausible biogenetic pathway of the quinonoid compounds.



which was further oxidized at C-10 to form an anthraquinone skeleton. Subsequent cyclization followed by oxidation of the side chain of the anthraquinone intermediate yielded compound **5**, whereas compound **6** was generated by isomerization. Oxidative coupling of two molecules of anthrone or anthranol intermediate, followed by side chain isomerization, presumably produced bianthrones J (**1a** and **1b**). We also suggested that compounds **2** and **7** were de-

© 2007 NRC Canada

Table 2. Antibacterial activity of compounds isolated from *C. formosum* subsp. *pruniflorum*.

	MIC (μg/mL)					
Compound	*B. substilis*	*S. aureus*	*S. faecalis*	*S. typhi*	*S. sonnei*	*P. aeruginosa*
3	—[a]	150	<1.1	9.4	2.3	—[a]
4	—[a]	75	<1.1	<1.1	2.3	—[a]
Vancomycin	75	75	75	75	75	75

Note: Inactive: > 50 μg/mL; highly active: < 5 μg/mL.
[a]Inactive.

Table 3. Cytotoxic activity of compounds isolated from *C. formosum* subsp. *pruniflorum*.

	Cell lines – IC_{50} (μg/mL)			
Compound	MCF-7	HeLa	HT-29	KB
3	—[a]	—[a]	—[a]	4.0
4	0.7	0.6	—[a]	0.2
Camptothecin	0.2–2.0	0.2–2.0	0.2–2.0	0.2–2.0

Note: Highly active: <1 μg/mL; inactive: >10 μg/mL.
[a]Inactive.

rived from compound **4** by the similar pathway as shown in Scheme 1. Therefore, compound **3** should be a precursor of bianthrones J (**1a** and **1b**) and compounds **5** and **6**, while compound **4** is a precursor of compounds **2** and **7**.

The antibacterial and cytotoxic activities of compounds **3** and **4** are shown in Tables 2 and 3, respectively, in which compounds **3** and **4** showed potent antibacterial activities against *Streptococcus faecalis* and *Shigella sonnei*. Compound **4** also exhibited strong antibacterial activity against *Salmonella typhi*. In addition, compound **4** was highly active for cytotoxicity against all tested cell lines except for the HT-29 cell line, whereas compound **3** was moderately active against only the KB cell line. Bianthrones J (**1a** and **1b**) and compounds **2** and **5–7** were found to be inactive for both antibacterial and cytotoxic activities. From the plausible biosynthetic routes (Scheme 1) and biological activity results (Tables 2 and 3), we speculate that if the transformation processes of compound **3** to bianthrones J (**1a** and **1b**) and compounds **5** and **6**, and compound **4** to compounds **2** and **7**, are inhibited, it might be possible to obtain larger amounts of bioactive compounds **3** and **4**, which may be used as starting materials for partial synthesis or biotransformation to develop compounds with enhanced antibacterial and cytotoxic activities.

Experimental section

General experimental procedures

Melting points were determined on a Fisher-Johns melting point apparatus. Optical rotations were measured on a JASCO P-1020 digital polarimeter. UV and IR spectra were recorded on a SPECORD S 100 (Analytik Jena) and a PerkinElmer FTS FT-IR spectrophotometer, respectively. The ^1H and ^{13}C NMR spectra were recorded on a 500 MHz Varian UNITY INOVA and 300 MHz Bruker FT NMR Ultra Shield spectrometers in $CDCl_3$ or CD_3OD with TMS as the internal standard. Chemical shifts were reported in δ (ppm) and coupling constants (*J*) expressed in Hz. EI and HREI mass spectra were measured on a Kratos MS 25 RFA spectrometer. Quick column chromatography (QCC) and column chromatography (CC) were carried out on silica gel 60 F_{254} (Merck) and silica gel 100 (Merck), respectively.

Plant material

The barks of *C. formosum* subsp. *pruniflorum* were collected in May 2004 from Nong Khai Province in the northeastern part of Thailand. The voucher specimen (No. 0012677) has been deposited at Prince of Songkla University Herbarium, Biology Department, Faculty of Science, Prince of Songkla University, Thailand.

Extraction and isolation

The air-dried and finely chopped barks of *C. formosum* subsp. *pruniflorum* (4.0 kg) were successively extracted with CH_2Cl_2 and acetone (each 2 × 20 L, for 5 days) at room temperature. The crude extracts were evaporated to dryness under vacuum to afford CH_2Cl_2 (76.28 g) and acetone (21.74 g) extracts. The crude CH_2Cl_2 extract was subjected to QCC (column size: 12 × 16 cm) and eluted with increasing polarity of CH_2Cl_2 and acetone in hexane to afford 10 fractions (F1–F10). Fraction F2 (58.06 g) was separated by CC using a gradient of hexane–EtOAc to afford 8 subfractions (F2A–F2H). Subfraction F2C (120.02 mg) was further purified by CC with EtOAc–hexane (1:4 *v*/*v*) to give compound **7** (68.20 mg). The subfraction F2F was separated by CC with $CHCl_3$–hexane (3:7 *v*/*v*) to give 3 fractions (F2FA–F2FC) and the subfraction F2FB was further purified by prep TLC with $CHCl_3$–hexane (3:7 *v*/*v*) to yield compound **6** (3.30 mg). Subfractions F2G and F2H were each further separated by CC eluting with acetone–hexane (1:9 *v*/*v*) and CH_2Cl_2–hexane (2:3 *v*/*v*) to give compounds **2** (30.20 mg) and bianthrones J (**1a** and **1b**) (35.50 mg), respectively. The fraction F4 was fractionated by CC using EtOAc–hexane (3:7 *v*/*v*) as eluents to afford 7 fractions (F4A–F4G). The subfraction F4E was further purified by prep TLC with EtOAc–hexane (1:3 *v*/*v*) to give compound **4** (7.40 mg), while the subfraction F4F was purified by CC with EtOAc–hexane (1:4 *v*/*v*) to give compound **3** (15.20 mg). The acetone extract was subjected to QCC (column size: 12 × 16 cm) using a gradient of hexane with acetone to afford 12 fractions (FA1–FA12). The fraction FA2 (1.98 g) was further separated by CC with acetone–hexane (3:97 *v*/*v*) to give 6 fractions (FA2A–FA2F) and then the subfraction FA2B (422.00 mg) was purified by CC with acetone–hexane (1:19 *v*/*v*) to give compound **5** (3.00 mg).

Bianthrones J (1a and 1b)

Yellow-green powder; mp 208 to 209 °C. $[\alpha]_D^{27}$ 0° (*c* 0.65, $CHCl_3$). UV (MeOH) λ_{max} (log ε): 273 (3.91), 360 nm (3.59). IR (KBr, cm^{-1}) ν_{max}: 3335, 1685, 1640. For ^1H NMR

© 2007 NRC Canada

($CDCl_3$, 300 MHz,) and ^{13}C NMR ($CDCl_3$, 75 MHz) spectral data, see Table 1. EIMS *m/z* 674 (1) $[M]^+$: 338 (50), 336 (28), 323 (40), 295 (100), 283 (56), 69 (12). HR EIMS *m/z* calcd. for $C_{42}H_{42}O_8$: 674.2880 $[M]^+$; found: 674.2864.

Bioassays

Antibacterial assay

The isolated compounds from the barks of *C. formosum* subsp. *pruniflorum* were tested against the microorganisms *Bacillus substilis* (obtained from Department of Industrial Biotechnology, PSU), *Staphylococcus aureus* (TISTR517) (obtained from Microbial Resources Center (MIRCEN), Bangkok, Thailand), *S. faecalis*, *S. sonnei*, *S. typhi*, and *Pseudomonas aeruginosa*. The last four microorganisms were obtained from Department of Pharmacognosy and Botany, PSU. The antibacterial assay employed was the same as described in Boonsri et al. (18). Vancomycin, which was used as a standard, showed antibacterial activity of 75 µg/mL.

Cytotoxic assay

The procedure for cytotoxic assay was performed by the sulphorhodamine B (SRB) assay as described by Skehan et al. (19). In this study, four cancer cell lines obtained from the National Cancer Institute, Bangkok, Thailand, were used, MCF-7 (breast adenocarcinoma), KB (human oral cancer), HeLa (Human cervical cancer), and HT-29 (colon cancer). Camptothecin, which was used as a standard, showed cytotoxic activity in the range of 0.2–2.0 µg/mL.

Acknowledgements

We are greatly indebted to the Directed Basic Research in Medicinal Chemistry (Thailand Research Fund) for research grant No. DBG4880019. NB thanks the Development and Promotion of Science and Technology Talents Project, Center for Innovation in Chemistry: Postgraduate Education and Research Program in Chemistry, and the Graduate School, Prince of Songkla University for financial support.

References

1. G.M. Kitanov and I. Assenov. Pharmazie, **43**, H12 (1988).
2. G.L. Sia, G.J. Bennett, L.J. Harrison, and K.Y. Sim. Phytochemistry, **38**, 1521 (1995).
3. L.H.D. Nguyen and L.J. Harrison. Phytochemistry, **50**, 471 (1998).
4. E.-K. Seo, N.-C. Kim, M.C. Wani, M.E. Wall, H.A. Navarro, J.P. Burgess, K.Kawanishi, L.B.S. Kardono, S. Riswan, W.C. Rose, C.R. Fairchild, N.R. Farnsworth, and A.D. Kinghorn. J. Nat. Prod. **65**, 299 (2002).
5. V. Kumar, V. Brecht, and A.W. Frahm. Planta Med. **70**, 646 (2004).
6. Z.H. Mbwambo, S. Apers, M.J. Moshi, M.C. Kapingu, S.V. Miert, M. Claeys, R. Brun, P. Cos, L. Pieters, and A. Vlietinck. Planta Med. **70**, 706 (2004).
7. P. Pattanaprateeb, N. Ruanggrungsi, and G.A. Cordell. Planta Med. **71**, 181 (2005).
8. N. Boonnak, C. Karalai, S. Chantrapromma, C. Ponglimanont, H.-K. Fun, A. Kanjana-Opas, and S. Laphookhieo. Tetrahedron, **62**, 8850 (2006).
9. M. Iinuma, H. Tosa, T. Ito, T. Tanaka, and M. Aqil. Phytochemistry, **40**, 267 (1995).
10. A.A. Hussein, B. Bozzi, M. Correa, T.L. Capson, T.A. Kursar, P.D. Coley, P.N. Solis, and M.P. Gupta. J. Nat. Prod. **66**, 858 (2003).
11. S. Sibanda, C. Nyanyira, M. Nicoletti, and C. Galeffi. Phytochemistry, **34**, 1650 (1990).
12. B. Botta, F. Delle Monache, G. Delle Monache, G.B. Marini Bettolo, and J.D. Msonthi. Phytochemistry, **24**, 827 (1985).
13. B. Botta, F. Delle Monache, G. Delle Monache, G.B. Marini Bettolo, and J.U. Oguakwa. Phytochemistry, **22**, 539 (1983).
14. S. Sibanda, C. Nyanyira, M. Nicoletti, and C. Galeffi. Phytochemistry, **34**, 1650 (1993).
15. F. Delle Monache, F. Ferrari, G.B. Marini-Bettolo, P. Maxfield, P.S. Cerrini, W. Fedeli, E. Gavuzzo, and A. Vaciago. Gazz. Chim. Ital. **109**, 301 (1979).
16. M.L.S. Goncalves and W.B. Mors. Phytochemistry, **20**, 1947 (1981).
17. P.M. Dewick. Medicinal natural products: A biosynthetic approach. John Wiley & Sons Ltd., London, UK. 2002. pp. 66–67.
18. S. Boonsri, C. Karalai, C. Ponglimanont, A. Kanjana-Opas, and K. Chantrapromma. Phytochemistry, **67**, 723 (2006).
19. P. Skehan, R. Storeng, D. Scudiero, A. Monks, J. McMahon, D. Vistica, J.T. Warren, H. Bokesch, S. Kenney, and M.R. Boyd. J. Natl. Cancer Inst. **82**, 1107 (1990).

© 2007 NRC Canada

Formation of monofluorophosphate from fluoride in phosphoric acid – water and phosphoric acid – sulfuric acid – water mixtures

Kenneth E. Newman, Raymond E. Ortlieb, Nicole Pawlik, and Jason Reedyk

Abstract: When dissolved in concentrated phosphoric acid, sodium fluoride reacts rapidly to form monofluorophosphate. In less concentrated acid, the reaction does not proceed to completion, and the reaction kinetics become very much slower. The equilibrium and rate constants for the reaction have been determined. In ternary mixtures of phosphoric acid, sulfuric acid, and water, the formation of monofluorophosphate is considerably enhanced, and the kinetics are rapid. The results are interpreted in terms of the very low water activity coefficients in strong-acid solutions.

Key words: monofluorophosphate, monofluorophosphoric acid, ^{19}F NMR, ^{31}P NMR, phosphoric acid, sulufric acid, equilibria, kinetics.

Résumé : Lorsqu'il est dissout dans de l'acide phosphorique concentré, le fluorure de sodium réagit rapidement pour former le monofluorophosphate. Dans de l'acide moins concentré, la réaction n'est pas complète et la cinétique de la réaction est ralentie. On a déterminé les constantes d'équilibre et de vitesse de la réaction. Dans des mélanges ternaires d'acide phosphorique, d'acide sulfurique et d'eau, la formation du monofluorophosphate est très accélérée et la cinétique est rapide. On interprète les résultats en fonction des très faibles coefficients d'activité de l'eau dans des solutions fortement acides.

Mots-clés : monofluorophosphate, acide monofluorophosphorique, RMN du ^{19}F, RMN du ^{31}P, acide phosphorique, acide sulfurique, équilibre, cinétique.

[Traduit par la Rédaction]

Introduction

Mono-, di-, and hexafluorophosphates, along with their corresponding acids, were first synthesized and characterized by Lange and co-workers in a series of papers starting in 1926 (1). As part of this extended study, they reported that sodium fluoride, when dissolved in concentrated phosphoric acid, gave a mixture of HF and monofluorophosphoric acid (MFP), H_2PO_3F.[2] The ratio of MFP to HF increased with increasing phosphoric acid concentration. The patent literature suggests that sodium monofluorophosphate (Na_2PO_2F) is commercially manufactured using very forcing conditions. For example, the 1993 patent of Swidersky et al. involves mixing H_3PO_4, NaOH, and NaF in stoichiometric amounts, together with a small amount of water, at temperatures between 150 and 400 °C (2). The anhydrous acid itself can be made under much less forcing conditions, namely room temperature reaction of anhydrous metaphosphoric acid (HPO_3) and gaseous hydrogen fluoride (3).

MFP salts find uses in the treatment of osteoporosis, control of corrosion (particularly in steel reinforcing in concrete), and as fungicides and bactericides. However, the major use of MFP salts is as anticaries agents in toothpastes. The hydrolysis of MFP to fluoride is extremely slow at near neutral pH values, although it is hydrolyzed readily by phosphatase enzymes, including those found in saliva (4). The addition of an acid has also been shown to significantly enhance the reaction rate (5).

Phosphoric acid is manufactured by the reaction of the ore (apatite), $Ca_5(PO_4)_3(OH)$, with concentrated sulfuric acid in the temperature range of 70–80 °C (the so-called "wet process") according to the simplified reaction [1] (6).

$$[1] \quad Ca_5(PO_4)_3(OH) + 5H_2SO_4 = 5CaSO_4(s) + 3H_3PO_4 + H_2O$$

The ore is invariably contaminated with fluoroapatite, $Ca_5(PO_4)_3(F)$, with the total fluoride content of the feedstock in the range of 3.5%–4%. The strongly acidic reaction conditions favor the formation of HF, which dissolves silica and silica-like impurity minerals in the ore. Products of this reaction are various fluorosilicates, including the volatile silicon

Received 31 July 2006. Accepted 5 February 2007. Published on the NRC Research Press Web site at canjchem.nrc.ca on 5 May 2007.

K.E. Newman,[1] R.E. Ortlieb, N. Pawlik, and J. Reedyk. The King's Centre for Molecular Structure, The King's University College, 9125 50th Street, Edmonton, AB T6B 2H3, Canada.

[1]Corresponding author (e-mail: ken.newman@kingsu.ca).

[2]Given the strongly acidic media of interest in this paper, the extent of protonation of monofluorophosphate will not always be obvious. Thus, we will refer to the species as MFP regardless of its form except where noted.

 doi:10.1139/V07-027 © 2007 NRC Canada

tetrafluoride (SiF_4), as well as hexafluorosilicic acid (H_2SiF_6) and (or) its salts. Phosphoric acid reactor vessels are thus typically scrubbed to remove the volatile HF and SiF_4. The other product of reaction [1], calcium sulfate (gypsum) is typically pumped as a slurry to tailings ponds; process water is also stored for recycle in storage ponds. These ponds are typically fairly acidic (pH < 2) with very high dissolved solids content, and with fluoride levels in the range of 0.35%–1.35% (7). Probably, the fluoride is mostly in the form of HF and SiF_6^{2-}, but the latter species may partially hydrolyze to SiF_4. Fugitive emissions of gaseous HF and SiF_4 from the ponds are thus of environmental concern.

The work reported here is the first part of an extended study to explore and understand in detail the chemistry and fate of the fluoride impurities as they pass through the "wet process" manufacture of phosphoric acid. The ready formation of MFP in phosphoric acid under benign conditions led us to focus initially on the conditions that determine its formation. Given the central role of sulfuric acid on the manufacturing process, its effect on MFP formation was clearly important to the study.

Experimental

NaF (Fisher, ACS grade), Na_2PO_3F (Alfa Aesar, >99%), H_3PO_4 (Aldrich, 100%), H_3PO_4 (Sigma, 85%, ACS), H_2SO_4 (95%–98%, ACS grade), and D_2O (Cambridge Isotope Laboratories, 99%) were used as received. All solutions were prepared by weight in polyethylene or Teflon containers and were typically 0.01 *m* total fluoride. Solutions typically contained 10%–15% D_2O, although a few solutions were prepared with 40%–50% D_2O. Some of the most-acidic solutions were prepared without D_2O and thus were run unlocked. NMR spectra were obtained with a Bruker 400 Avance NMR spectrometer using a Bruker ATMA multinuclear probe operating at 161.98 MHz for ^{31}P and 376.46 MHz for ^{19}F. All NMR spectra were run at 22.0 ± 0.1 °C. Samples were contained in 5 mm NMR tubes with polytetrafluoroethylene – fluorinated ethylene polypropylene copolymer (PTFE–FEP) liners (Wilmad LabGlass, NJ, USA).

Results

The ^{19}F NMR spectrum of a 0.01 *m* solution of NaF in 85%[3] H_3PO_4 solution consists of a doublet, centered at –75.1 ppm with a coupling constant of 937 Hz, and a somewhat broad peak at ~147 ppm. The ^{31}P NMR spectrum of a similar solution consists of a very large peak centered at ~0 ppm, a small doublet centred at –7.4 ppm with a coupling constant of 937 Hz, and another small peak at –12.8 ppm. The spectra are readily interpreted in terms of a mixture of MFP and HF. The doublet feature in each spectrum is due to $J_{12}(^{19}F–^{31}P)$ coupling in the MFP. The large peak at ~0 ppm in the ^{31}P spectrum is due to H_3PO_4, and the small peak at –12.8 ppm is due to a small amount of pyrophosphate ($P_2O_7^{4-}$). These assignments are consistent with literature values (8). It is worth noting that the ^{19}F chemical shifts of both MFP and HF and the MFP coupling constant show considerable variation, as the phosphoric acid concentration is varied from 5% to 85% H_3PO_4.

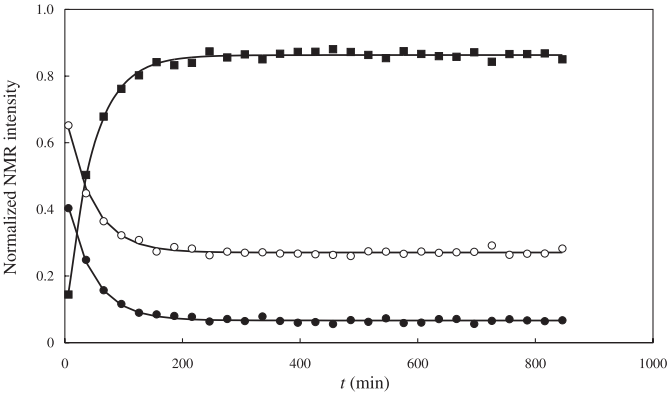


Fig. 1. Variation of normalized NMR intensities of each peak of the monofluorophosphate doublet (closed and open circles) and hydrogen fluoride (closed squares) for a 0.0078 *m* of sodium monfluorophosphate solution in a phosphoric acid – water mixture of the composition $x(H_3PO_4) = 0.254$. The D_2O/H_2O fraction was 0.41. For clarity, the data for the component of the MFP doublet represented by the open circles were displaced vertically by 0.2 units. The smooth curves are the fitted values, obtained as described in the text.

We may define α as the fraction of the fluorine-containing species in the form of MFP

$$[2] \qquad \alpha = \frac{c_{MFP}}{c_{MFP} + c_{HF}}$$

where c_i is the concentration (expressed as either molality or molarity). At 85% H_3PO_4, the value of α from the integration of the ^{19}F spectrum is 0.81. As the phosphoric acid concentration is decreased, not only does α decrease, but also the kinetics of interconversion of HF and MFP become surprisingly slow. The dependence of α on phosphoric acid concentration was thus determined as the infinite-time values obtained from a study of the kinetics of the reaction of 0.01 *m* Na_2MFP in aq. phosphoric acid solutions. Figure 1 shows a typical kinetic ^{19}F NMR run. The integrated NMR peak intensities were normalized by dividing through by the sum of the intensities. The normalized intensities were fitted to a first-order kinetic equation by a non-linear least-squares approach, using the "Solver" facility of Microsoft® Excel. Each NMR peak was fitted to a unique time-zero and time-infinity intensity, but with a common value for the rate constant. For H_3PO_4 compositions greater than 80% [$x(H_3PO_4) > 0.42$], the kinetics were too fast to measure by this NMR method, and thus, only the equilibrium values could be measured. For $x(H_3PO_4) < 0.04$, the infinity values for the MFP peaks were too small to be measured reliably and were thus constrained to zero. Although no extended study was performed, the kinetics do not appear to exhibit any strong isotope effects as the D_2O fraction is changed. Figure 2 shows the values of α as a function of $x(H_3PO_4)$. For the two points

[3] Throughout this work, "% *i*" refers to the weight% of solvent species *i*, calculated excluding the solutes. $x(i)$ refers to the mole fraction of solvent species *i*, calculated excluding the solutes.

© 2007 NRC Canada

Fig. 2. Equilibrium fraction (α) of monofluorophosphate as a function of the mole fraction of H_3PO_4. ●: Experimental values; ——— : Fitted values (see Discussion for details).

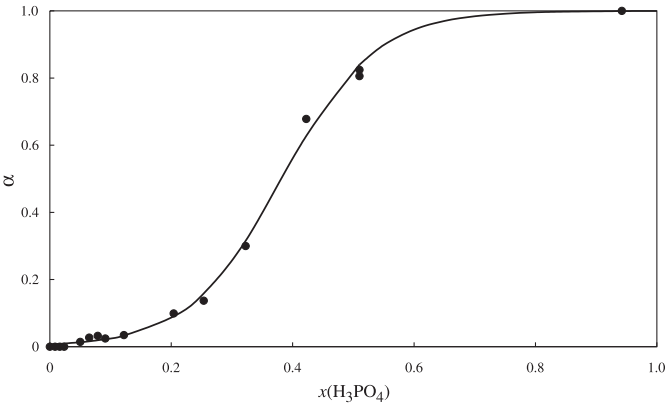
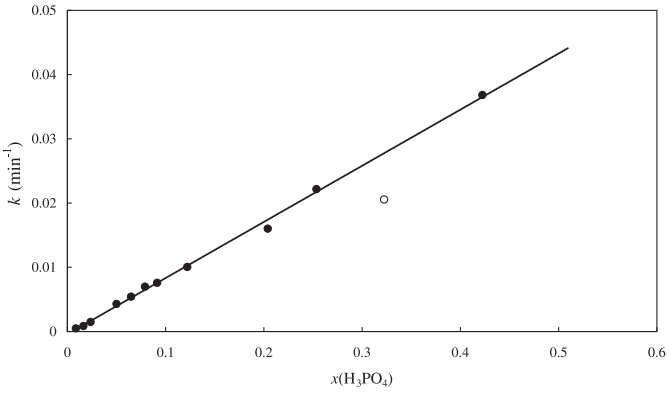


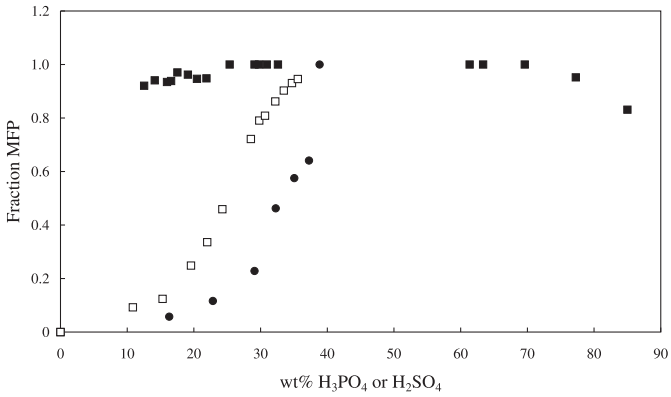
Fig. 3. Apparent first-order rate constants for the interconversion of HF and MFP as a function of the mole fraction of H_3PO_4. The line represents the best straight-line fit, excluding the open-circle data point.



in the figure at $x(H_3PO_4) \approx 0.51$, one was obtained using NaF as the initial reactant, the other using Na_2MFP. The origin of the smooth line through the data will be discussed later. Figure 3 shows the apparent first-order rate constants for the kinetics of formation of MFP as a function of $x(H_3PO_4)$. Quite remarkably, the values obtained were linear with $R^2 = 0.997$.[4]

For the phosphoric acid – sulfuric acid – water mixtures, it is more difficult to survey adequately the solvent composition range. In addition to the H_3PO_4 – H_2O binary mixtures (i.e., the 0% H_2SO_4 isopleth), measurements were also made along the following ternary diagram isopleths: ~43% phosphoric acid, 15% H_2O, and 50% H_2SO_4. The results are shown in Fig. 4. In the ~ 43% H_3PO_4 series, the weight

Fig. 4. Equilibrium fraction (α) of monofluorophosphate in H_3PO_4 – H_2SO_4 – H_2O mixtures. □: 15% H_2O, plotted vs. % H_2SO_4; ●: 50% H_2SO_4, plotted vs. % H_3PO_4; ■: ~ 43% H_3PO_4, plotted vs. % H_2SO_4 (see text for information on this series).



composition varied slightly (from 42.3 to 45.5), which accounts for the slightly scattered results. It is remarkable that sulfuric acid has such a large effect on MFP formation. For example, a H_3PO_4–H_2SO_4 – H_2O (42:38:20) mixture yields 100% MFP, whereas a H_3PO_4 – H_2O (42:58) mixture yields only 10% MFP. The results are even more dramatic in the low-water (15%) mixtures where a H_3PO_4 – H_2SO_4 – H_2O (20:60:15) mixture yields 100% MFP, whereas in a 20% H_3PO_4 solution in the absence of H_2SO_4, the yield is ~ 1%. The kinetics in the sulfuric acid solution were typically too fast to measure by our relatively slow NMR method.

Discussion

Formation of MFP in H_3PO_4 – H_2O mixtures

Theory

For the reaction of HF to give MFP, we can write

[3] $$H_3PO_4 + HF \rightleftharpoons H_2PO_3F + H_2O$$

In terms of the reaction conditions of interest here, both phosphoric acid and water are the predominant species (the solvent), whereas HF and MFP are considered solutes. We have written both of the reactants in their protonated forms because phosphoric acid is a weak acid in water and HF is even weaker. We have no reliable knowledge about the ionization state of MFP. Certainly, it is a stronger acid (in water) than phosphoric acid. However, in the strongly acidic solvents of interest here, we will assume that it is also protonated.

In general, an equilibrium constant is only a "constant" in any given solvent or solvent mixture. For example, in mixtures of ethanol–water, weak acids become considerably weaker as the alcohol content of the solvent increases. One approach to this problem is to define our equilibrium constant K(P–W) for reaction [3] in solvent mixture P–W as

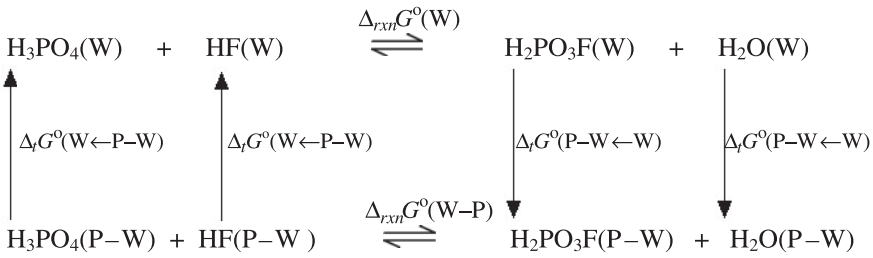
[4] Most texts on error analysis give a definition for R, see for example ref. 9.

© 2007 NRC Canada

$$[4]\qquad K(\mathrm{P-W}) = \left[\frac{c(H_2PO_3F)}{c(HF)}\frac{\gamma(H_2PO_3F)}{\gamma(HF)}\frac{x(H_2O)}{x(H_3PO_4)}\right] = \left[\frac{\alpha}{1-\alpha}\frac{\gamma(H_2PO_3F)}{\gamma(HF)}\frac{x(H_2O)}{x(H_3PO_4)}\right]$$

where the γ terms are the conventional concentration-dependent activity coefficients, which can be ignored, providing the concentrations are low enough. This equilibrium constant changes when the solvent composition is changed because the standard chemical potentials of the reactants and products are solvent-dependent. This is often referred to as the "primary medium effect". One approach to this problem is to use "free energies of transfer". Thus, we can write, for the thermodynamic cycle involving reaction [3] in two different solvents, W and P–W

[5]



where Δ_tG^o(P–W ← W) are called the free energies of transfer of the species from solvent W (in this case, water) to the solvent mixture P–W. Straightforward analysis of the thermodynamic cycle allows us to write the standard free energy of reaction in solvent mixture P–W as

$$[6]\qquad \Delta_{rxn}G^o(\mathrm{P-W}) = \Delta_{rxn}G^o(\mathrm{W}) + \sum_{\text{products}}\Delta_tG^o(\mathrm{P-W} \leftarrow \mathrm{W}) - \sum_{\text{reactants}}\Delta_tG^o(\mathrm{P-W} \leftarrow \mathrm{W}) = -RT\ln K(\mathrm{P-W})$$

The great utility of this equation is that, in principle, the various free energy of transfer terms can be obtained for individual species by thermodynamic measurements such as vapor pressure or solubility. Thus, we can obtain the solvent-composition dependence of the equilibrium constant.

For the reaction of interest, it is not obvious how one would measure the free energy of transfer of HF from H_2O to H_3PO_4. Even if one could find a suitable experimental technique, HF reacts too rapidly in phosphoric acid. It is also not immediately obvious how one would measure this quantity for H_2PO_3F. However, for the purposes of this analysis, we wish to explore the crucial role of the free energy of transfer terms for the two-solvent components, i.e., H_2O and H_3PO_4. The free energy of transfer of species W from W to solvent mixture P–W can be written more formally as

$$[7]\qquad \Delta_tG^o[\mathrm{W(P-W)} \leftarrow \mathrm{W(W)}] = [\mu(\mathrm{W}) - RT\ln x_w]_{\mathrm{P-W}} - [\mu(\mathrm{W}) - RT\ln(x_w = 1)]_{\mathrm{W}}$$

The usual definition for activity coefficients in binary solvent mixtures is

$$[8]\qquad \mu(\mathrm{W}) = \mu^o(\mathrm{W}) + RT\ln x_w + RT\ln\gamma_w$$

with $\ln\gamma_w \to 1$, as $x_w \to 1$; thus, eq. [7] becomes (as we might expect)

$$[9]\qquad \Delta_tG^o[\mathrm{W(P-W)} \leftarrow \mathrm{W(W)}] = RT\ln\gamma_w$$

Applying a similar approach to eqs. [7] and [8] to the transfer of species P from W to a P–W mixture, we obtain

$$[10]\qquad \Delta_tG^o[\mathrm{P(P-W)} \leftarrow \mathrm{P(W)}] = [\mu(\mathrm{P}) - RT\ln x_p]_{\mathrm{P-W}} - [\mu(\mathrm{P}) - RT\ln(x_p = 0)]_{\mathrm{W}}$$

This equation yields

$$[11]\qquad \Delta_tG^o[\mathrm{P(P-W)} \leftarrow \mathrm{P(W)}] = RT\ln\gamma_P - RT\ln\gamma_P(0)$$

where $\gamma_P(0)$ is the limiting activity coefficient of P in pure W.

Solvent-activity coefficients are frequently expressed in terms of an equation of the form (10)

$$[12]\qquad \ln\gamma_w = Ax_p^2$$

and

$$[13]\qquad \ln\gamma_P = A(1 - x_P)^2$$

By combining eqs. [9], [11], [12], and [13], we readily obtain

$$[14]\qquad \Delta_tG^o[\mathrm{W(P-W)} \leftarrow \mathrm{W(W)}] - \Delta_tG^o[\mathrm{P(P-W)} \leftarrow \mathrm{P(W)}] = 2RT\,Ax_P$$

Combining eqs. [6] and [14] (ignoring contributions from free energy of transfer of the two solutes) we obtain

$$[15]\qquad \ln K(\mathrm{P-W}) = \ln K(\mathrm{W}) - 2Ax_P$$

predicting a linear dependence of ln K with phosphoric acid mole fraction.

Comparison with experiment

The values of K(P–W), obtained from the data in Fig. 2 using eq. [4], vary from 0.28 to 4.5 over the solvent composition range $x(H_3PO_4)$ = 0.049–0.51. A plot of ln(K) vs. $x(H_3PO_4)$ is predicted to be linear by eq. [15]. To see how well the values for α obey this prediction, they were fitted by a non-linear least-squares approach, using Microsoft® Excel Solver, to eq. [4] with the γ terms set to unity and with ln(K) as a linear function of $x(H_3PO_4)$. Thus, the two fitting parameters were the slope and intercept. Figure 2 shows a comparison between observed and calculated values of α. The large variation of K with solvent composition is the

© 2007 NRC Canada

cause of the sigmoid shape of Fig. 2. The values obtained for ln K(W) and 2A in eq. [15] were –2.7 and –8.5, respectively. No attempt was made to assess the uncertainties in these parameters because the data were obtained over a narrow range of x_p.

The activity coefficients of both W and P in phosphoric acid mixtures can be obtained from vapor-pressure measurements. The calculation is straightforward because, for this system, the vapor contains no phosphoric acid. The 20 °C vapour-pressure data (11) after conversion to water activity coefficients were fitted to eq. [12] to obtain a value of –10.7 for 2A.[5]

Thus, we conclude that the majority of the large increase in equilibrium constant for the formation of MFP, going from pure water to pure phosphoric acid, is due to the extreme thermodynamic non-ideality of the mixture. In particular, the reaction is strongly promoted by the low water activities, which manifest themselves in the negative value for A in eqs. [12] to [15]. However, the previously mentioned analysis has not included free energy of transfer terms for the two solutes. We also caution that experimental measurements on which the previously mentioned analysis was performed are not of the highest precision.

Formation of MFP in H_3PO_4 – H_2SO_4 – H_2O

To obtain an analytical and graphical representation of the variation of α with solvent composition for the H_3PO_4 – H_2SO_4 – H_2O mixtures, the experimental values for α were fitted using a non-linear least-squares approach to equations of the form:

$$[16] \quad K_{app} = \frac{\alpha}{1-\alpha}\frac{x(H_2O)}{x(H_3PO_4)}$$

with

$$[17] \quad \ln K_{app} = P_1 w_P(1 + S_{11}w_S + S_{12}w_S^2) + P_2 w_P^2(1 + S_{21}w_S + S_{22}w_S^2)$$

and with w_P and w_S being the wt% of phosphoric and sulphuric acids in the ternary solvent mixture, respectively. The optimal values for the fitting parameters are shown in Table 1.

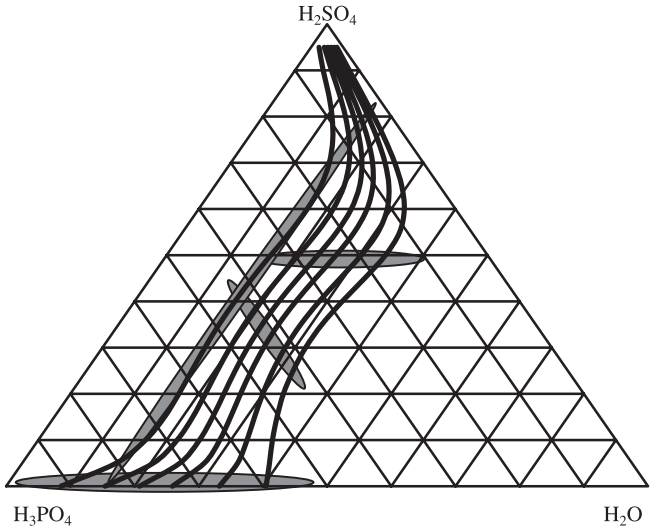
There is no particular theoretical reason for choosing the previously mentioned equations, which are simply convenient representations of the data. With the addition of extra terms, slightly improved fits can be obtained. Figure 5 shows the triangular contour plot from the fit. Whilst the accuracy of the fit may be doubtful in the solvent region that is low in both H_2O and H_3PO_4 (i.e., the H_2SO_4 apex), the form of the graph is unmistakable. Formation of MFP is determined most strongly by the water content of the solution: the lower the water content, the larger the formation of MFP. Quite remarkably, this is a much stronger determinant than the phosphoric acid content of the solution. Thus, we conclude that, as in the case of the binary solvent mixture H_3PO_4 – H_2O, the reaction is being driven by the strong ability of sulphuric acid to depress the thermodynamic activity of water. From the water-activity data for the simple binary mixture H_2SO_4 – H_2O (12), we obtain a value of –24.3 for 2A.[6] This is, of course, simply a manifestation of the strong dehydrating ability of this acid. This effect is used to advantage in many chemical processes such as the production of concentrated nitric acid (13). HNO_3 – H_2O mixtures form an azeotrope, and thus the acid cannot be concentrated by simple distillation. It is concentrated by extractive distillation using concentrated sulphuric acid. It is interesting to note that phosphoric acid has also been suggested as an extractive distillation agent to concentrate nitric acid. (14).

Table 1. Fitting parameters for the determination of α in H_3PO_4 – H_2SO_4 – H_2O mixtures from eqs. [11] and [12].

P_1	-9.298×10^{-2}
P_2	1.298×10^{-3}
S_{11}	1.189×10^{-1}
S_{12}	-2.473×10^{-3}
S_{21}	1.529×10^{-1}
S_{22}	-1.753×10^{-3}

Note: The fit included 65 data points (as shown in Figs. 2 and 4). The standard deviation between observed and calculated points is 0.04.

Fig. 5. A triangular graph that shows contour plot of the fraction α of MFP formed in H_3PO_4 – H_2SO_4 – H_2O mixtures (see text for details). Moving from left to right across the figure, the contours represent fractions of 0.95, 0.8, 0.6, 0,4, 0.2, and 0.1. The ellipses represent the composition regions where the measurements were taken.



Acknowledgements

We acknowledge helpful discussions with Mr. Ken Larlee of Agrium Inc. (Redwater, AB) and with all of the members

[5] Vapor-pressure data are probably not extensive enough to justify including higher-fitting terms to this equation. Including these terms does not make a significant difference to the results given here.

[6] To get a good fit, it is necessary to take into account that for the first deprotonation step, sulfuric acid is strong; thus, we define the mole fraction of water as $x_w = n_w/(n_w + 2n_s)$ where n is the number of moles of i, and i is water or sulfuric acid.

© 2007 NRC Canada

of the King's Centre for Molecular Structure. We thank the King's University College for financial support of this research. R.E.O. thanks the Natural Sciences and Engineering Research Council of Canada (NSERC) for the provision of an Undergraduate Student Research Award (USRA).

References

1. The early work by Lange is well reviewed by W. Lange. *In* Fluorine chemistry. Vol. 1. *Edited by* J.H. Simons. Academic Press, NY. 1950. pp. 140–149.
2. H.-W. Swidersky, R. Werner., U. Hartmann, F. Moewius, V. Radonz, and M. Meisel. US Patent 5-393-506, 07 October 1993.
3. W. Lange and R. Livingston. US Patent 2-408-784, 08 October 1946.
4. Y. Ericsson. Caries Res. **1**, 144 (1967).
5. P.W. Heidbuchel. Pharm. Acta Helv. **66**, 290 (1991).
6. P. Becker. Phosphates and phosphoric acid: raw materials, technology, and economics of the wet process. 2nd ed. Marcel Dekker, NY. 1989.
7. G.A. Kennedy, M.M. Soraczak, S.J. Meischen, and J.D. Clayton. Chemistry of gypsum pond systems. Florida Institute of Phosphate Research Publication No. 05–025–100, August 1992. Available from http://www.fipr.state.fl.us/pondwatercd/05–025–100Final.pdf [cited January 2007].
8. J.W. Emsley, J. Feeney, and L.H. Sutcliffe. High resolution nuclear magnetic resonance spectroscopy. Vol. 2. Pergamon Press, Oxford. 1966. Chap. 11 and 12.
9. J.R. Taylor. An Introduction to error analysis. University Science Books, Mill Valley, CA. 1982. Chap. 9.
10. See for example: E.A. Guggenheim. Thermodynamics. North Holland, Amsterdam. 1988. Chap. 4.
11. Kirk-Othmer. Encyclopedia of chemical technology. 2nd ed. Vol. 15. Interscience Publishers, NY. 1968. p. 236.
12. R.A. Robinson and R.H. Stokes. Electrolyte solutions. 2nd ed. (revised). Butterworths, London. 1965.
13. J.G. Sloan. Adv. Chem. Ser. 1976, 155, 128.
14. R. Flatt and J. Bonnet. Chimia, 1958, 11,343.

© 2007 NRC Canada

An efficient synthesis of carboxaldehyde derivatives of 4*H*-pyran-4-one

Reza Teimuri-mofrad and Fatemeh Abrishami

Abstract: We developed a general method for the synthesis of various 2-mono- and 2,6-di-carboxaldehyde substituted derivatives of 3,5-diphenyl-4*H*-pyran-4-one and 4*H*-pyran-4-one. 3,5-Diphenyl-6-methyl-4-oxo-4*H*-pyran-2-carboxaldehyde (**4a**), 6-methyl-4-oxo-4*H*-pyran-2-carboxaldehyde (**4b**), 3,5-diphenyl-4-oxo-4*H*-pyran-2,6-dicarboxaldehyde (**5a**), 4-oxo-4*H*-pyran-2,6-dicarboxaldehyde (**5b**), 3,5-diphenyl-6-hydroxymethyl-4-oxo-4*H*-pyran-2-carboxaldehyde (**10a**), and 6-hydroxymethyl-4-oxo-4*H*-pyran-2-carboxaldehyde (**10b**) were obtained from the corresponding di-, tri-, and tetra-bromo derivatives of 2,6-dimethyl-3,5-diphenyl-4*H*-pyran-4-one (**1a**) and 2,6-dimethyl-4*H*-pyran-4-one (**1b**) by treatment with silver acetate followed by hydrolysis. Compounds **4a** and **4b** were also obtained by the oxidation of **10a** and **10b** with barium manganate.

Key words: 4*H*-pyran-4-one, hydroxymethyl and carboxaldehyde derivatives, acetoxylation, hydrolysis, oxidation.

Résumé : On a développé une méthode de synthèse générale pour divers 2-mono- et 2,6-di-carboxaldéhydes dérivés de la 3,5-diphényl-4*H*-pyran-4-one et la 4*H*-pyran-4-one. On a ainsi préparé la 3,5-diphényl-6-méthyl-4-oxo-4*H*-pyrane-2-carboxaldéhyde (**4a**), la 6-méthyl-4-oxo-4*H*-pyrane-2-carboxaldéhyde (**4b**), la 3,5-diphényl-4-oxo-4*H*-pyrane-2,6-dicarboxaldéhyde (**5a**), la 4-oxo-4*H*-pyrane-2,6-dicarboxaldéhyde (**5b**), la 3,5-diphényl-6-hydroxyméthyl-4-oxo-4*H*-pyrane-2-carboxaldéhyde (**10a**) et la 6-hydroxyméthyl-4-oxo-4*H*-pyrane-2-carboxaldéhyde (**10b**) en soumettant les dérivés di-, tri- et tétra-bromés correspondants de la 2,6-diméthyl-3,5-diphényl-4*H*-pyran-4-one (**1a**) et de la 2,6-diméthyl-4*H*-pyran-4-one (**1b**) à un traitement par de l'acétate d'argent suivi par une hydrolyse. Les composés **4a** et **4b** ont aussi été obtenus par oxydation des produits **10a** et **10b** par le manganate de baryum.

Mots-clés : 4*H*-pyran-4-one, dérivés hydroxyméthyles et carboxaldéhydes, acétoxylation, hydrolyse, oxydation.

[Traduit par la Rédaction]

Introduction

4*H*-Pyran-4-one and its derivatives have been the subject of intensive research because of their importance in various applications and their widespread biological significance (1–3). They are widely distributed in nature (4–6), and consequently, have become accessible in laboratories by a variety of synthetic methods (7–9). These compounds are useful as fungicides, herbicides, and in the treatment of hypersensitivity conditions, such as asthma and allergies (10, 11).

Functionalized heterocycles are often used for the synthesis of the target organic compounds. Some 4*H*-pyran-4-ones, containing a carboxaldehyde group, may be prepared by the oxidation of hydroxymethyl group in derivatives of kojic acid (12–14) and by the formylation of pyrones in the presence of trifluoroacetic acid (15). Recently, Ghandi and co-workers prepared some mono- and di-carboxaldehyde derivatives of 4*H*-pyran-4-one, substituted at positions 2 and 6 by the condensation of mono- and dimethyl derivatives of 4*H*-pyran-4-one with benzaldehyde, followed by the oxidation of the corresponding mono- and di-styryl derivatives in the presence of osmium tetroxide and potassium periodate (Scheme 1) (16).

It is important to explore an efficient method for the synthesis of carboxaldehyde derivatives of 4*H*-pyran-4-ones because these compounds are potentially useful and carry out a wide range of reactions that would make them suitable for the synthesis of a number of 4*H*-pyran-4-one derivatives. For example, host macrocycles, such as azacrown ethers, could be obtained from their dicarboxaldehyde derivatives.

We report a novel method for the synthesis of mono- and di-carboxaldehyde derivatives of 4*H*-pyran-4-one, substituted at positions 2 and 6, from the acetoxylation and hydrolysis of the corresponding di-, tri-, and tetra-bromo derivatives of 4*H*-pyran-4-one.

Results and discussion

2-Dibromomethyl-6-methyl-4*H*-pyran-4-one (**6b**), 6-bromomethyl-2-dibromomethyl-4*H*-pyran-4-one (**7b**), 2,6-bis(dibromomethyl)-4*H*-pyran-4-one (**8b**), and 3,5-dibromo-2,6-bis(dibromomethyl)-4*H*-pyran-4-one (**8c**) were first prepared in 1997 by Lowe and co-workers through the bromination of 2,6-dimethyl-4*H*-pyran-4-one (**1b**) with 2.1 equiv. of *N*-bromosuccinimide in 10%, 3.1%, 3.4%, and 0.3% yields, respectively, (17). As a result, we tried to synthesize 2-dibromomethyl-3,5-diphenyl-6-methyl-4*H*-pyran-

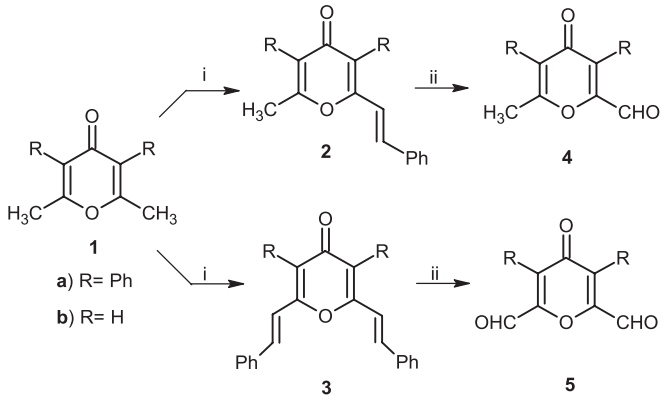
Received 28 November 2006. Accepted 14 March 2007. Published on the NRC Research Press Web site at canjchem.nrc.ca on 12 May 2007.

R. Teimuri-mofrad[1] and F. Abrishami. Department of Chemistry, Faculty of Materials, Malek-ashtar University of Technology, Tehran, P.O. Box 16765–3454, Iran.

[1]Corresponding author (e-mail: teimuri@mut.ac.ir).

 doi:10.1139/V07-034 © 2007 NRC Canada

Scheme 1. (*i*) PhCHO, NaOMe, 1,4-Dioxane; (*ii*) OsO_4, KIO_4.



4-one (**6a**), 6-bromomethyl-2-dibromomethyl-3,5-diphenyl-4*H*-pyran-4-one (**7a**), and 2,6-bis(dibromomethyl)-3,5-diphenyl-4*H*-pyran-4-one (**8a**) from 2,6-dimethyl-3,5-diphenyl-4*H*-pyran-4-one (**1a**) by means of Wohl–Ziegler bromination (18, 19). Bromination of **1a** with 5 equiv. of *N*-bromosuccinimide in the presence of dibenzoyl peroxide in tetrachloromethane produced a mixture of **6a**, **7a**, and **8a**, as major products, and other minor products. The crude product was chromatographed on silica gel and eluted with ethyl acetate – petroleum ether (1:9) to yield **8a**, **7a**, and **6a** as the first, second, and third fractions in 43%, 32%, and 17% yields, respectively. The mixture of other minor products was obtained as the fourth fraction (Scheme 2).

As a second result, we attempted to synthesize **6b**, **7b**, and **8b**, in accordance with Lowe and co-workers report (17), by means of Wohl–Ziegler bromination in the presence of excess *N*-bromosuccinimide. Since Lowe and co-workers were looking to obtain 2,6-bis(bromomethyl)-4*H*-pyran-4-one, they merely used 2.1 equiv. of *N*-bromosuccinimide, but they further got **6b**, **7b**, and **8b** as well. Therefore, to increase the yields of compounds **6b**, **7b**, and **8b**, we tried to use excess amount of *N*-bromosuccinimide, longer reaction time, and sun lamps during the reaction. Bromination of **1b** (20) with 8 equiv. of *N*-bromosuccinimide in presence of dibenzoyl peroxide in tetrachloromethane under radiation of IR lamps produced a mixture of **6b**, **7b**, and **8b**, as major products, and other minor products. The crude product was chromatographed on silica gel and eluted with ethyl acetate – petroleum ether (4:1). The first fraction was **8c** in 0.8% yield, which was produced from further bromination of the nuclear 4*H*-pyran-4-one positions in **8b** (17). The compounds **8b**, **7b**, and **6b** were obtained as the second, third, and fourth fractions in 31%, 23%, and 9% yields, respectively. Additionally, the mixture of other minor products was afforded as the fifth fraction (Scheme 2).

Treatment of **6a**, **7a**, and **8a** with silver acetate in refluxing glacial acetic acid, followed by the reaction with aq. acetic acid (21), produced 2-mono- and 2,6-di-carboxaldehyde derivatives of 3,5-diphenyl-4*H*-pyran-4-one, 6-methyl-3,5-diphenyl-4-oxo-4*H*-pyran-2-carboxaldehyde (**4a**), 6-acethoxymethyl-3,5-diphenyl-4-oxo-4*H*-pyran-2-carboxaldehyde (**9a**), and 3,5-diphenyl-4-oxo-4*H*-pyran-2,6-dicarboxaldehyde (**5a**) in 86%, 71%, and 75% yields, respectively. Under the same conditions, **6b**, **7b**, and **8b** produced 2-mono- and 2,6-di-carboxaldehyde derivatives of 4*H*-pyran-4-one, 6-methyl-4-oxo-4*H*-pyran-2-carboxaldehyde (**4b**), 6-acethoxymethyl-4-oxo-4*H*-pyran-2-carboxaldehyde (**9b**), and 4-oxo-4*H*-pyran-2,6-dicarboxaldehyde (**5b**) in 73%, 66%, and 70% yields, respectively.

Acidic hydrolysis (hydrochloric acid, water, tetrahydrofuran) of **9a** and **9b** produced 3,5-diphenyl-6-hydroxymethyl-4-oxo-4*H*-pyran-2-carboxaldehyde (**10a**) and 6-hydroxymethyl-4-oxo-4*H*-pyran-2-carboxaldehyde (**10b**) in 89% and 81% yields, respectively.

In addition, we decided to oxidize the monohydroxymethyl derivatives of 4*H*-pyran-4-one, **10a** and **10b**, to the corresponding dicarboxaldehyde derivatives, **5a** and **5b**, with barium manganate in dichloromethane and tetrahydrofuran at room temperature. Compounds **5a** and **5b** were obtained in 91% and 82% yields, respectively, (Scheme 2).

The data obtained from Mass spectrometry, IR, ^{1}H and ^{13}C NMR spectra, and elemental analyses are fully consistent with the proposed structures.

In conclusion, we developed a new efficient method for the preparation of mono- and di-carboxaldehyde derivatives of 3,5-diphenyl-4*H*-pyran-4-one and 4*H*-pyran-4-one, substituted at positions 2 and 6, resulting in the compounds **4a**, **4b**, **5a**, **5b**, **9a**, **9b**, **10a**, and **10b**. Our method offers some advantages over the previous one. For instance, it uses cheaper reagent and has higher total yields. Some of these compounds can be used as precursors to synthesize the host molecules. This work is now under investigation.

Experimental

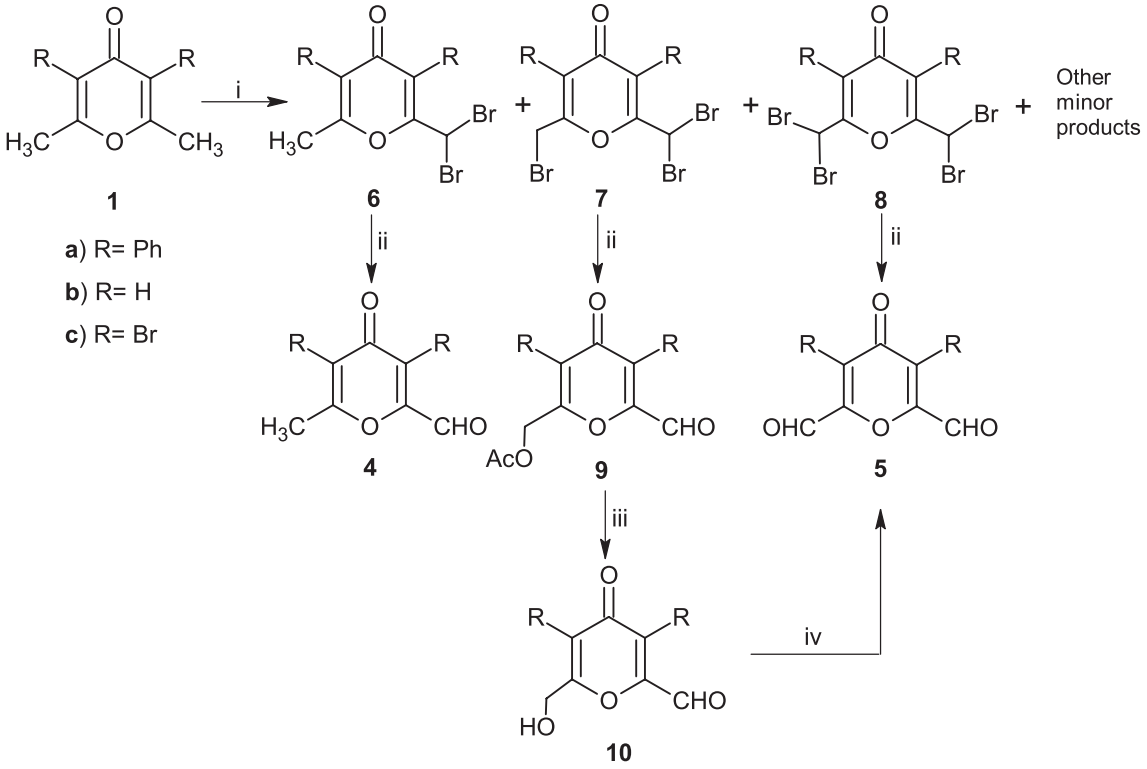
Melting points were determined with an Electrothermal Instrument model 9100 and are uncorrected. IR spectra were run on a Shimadzu FTIR-4300 Spectrophotometer as KBr disks or as smears between salt plates. The ^{1}H and ^{13}C NMR spectra were recorded on a FT-NMR Bruker 300 MHz spectrometer. Chemical shifts (δ) were reported in ppm using TMS as internal standard. Mass spectra were recorded on a Shimadzu MS-QP 1100 EX mass spectrometer. Elemental analyses were performed on a Heareus, CHN-O-RAPID, analyzer.

Reaction of 1a with excessive *N*-bromosuccinimide — Synthesis of di-, tri-, and tetra-bromo derivatives 6a, 7a, and 8a

2,6-Dimethyl-3,5-diphenyl-4*H*-pyran-4-one (**1a**) was prepared according to a published procedure (18). A mixture of **1a** (5.52 g, 0.02 mol), *N*-bromosuccinimide (17.8 g, 0.1 mol), and dibenzoyl peroxide (0.4 g) in tetrachloromethane (60 mL) was refluxed for 96 h. After cooling, the reaction mixture was filtered. The filtrate was concentrated in vacuum, and then dichloromethane (150 mL) was added to the residue. The mixture was washed with several portions of satd. sodium hydrogen carbonate and then water (3 × 50 mL). The organic layer was dried over magnesium sulfate and concentrated in vacuum. The resulting solid was purified by column chromatography on silica gel with ethyl acetate – petroleum ether (1:9) as eluent. Compounds **6a, 7a**, and **8a** were obtained as major products in 0.4:0.74:1 molar ratio, respectively. Specific details are given for each compound.

© 2007 NRC Canada

Scheme 2. (*i*) NBS (for **1a**: 5 equiv. and for **1b**: 8 equiv.), BPO, CCl_4 (for **1a**: reflux, 96 h and for **1b**: reflux under IR lamps radiation (3 × 400 W), 96 h); (*ii*) AgOAc, AcOH (reflux, 16 h); (*iii*) HCl – THF – H_2O (0.03:2:1) (reflux, 15 h); (*iv*) $BaMnO_4$, CH_2Cl_2 – THF (1:1) (RT, 2 h).



*2-Dibromomethyl-3,5-diphenyl-6-methyl-4*H*-pyran-4-one (6a)*

Light-brown crystals (1.48 g, 17%); mp 211.2–212.8 °C. IR υ (cm^{-1}): 1250, 1395, 1640, 3025. ^1H NMR ($CDCl_3$): 2.19 (3H, s, $–CH_3$), 6.33 (1H, s, $–CHBr_2$), 7.15–7.55 (10H, m, phenyl H). ^{13}C NMR ($CDCl_3$): 16.0 ($–CH_3$), 31.1 ($–CHBr_2$), 122.4 (pyran C-5), 127.2 (pyran C-3), 128.2–131.3 (m, phenyl C), 157.2 (pyran C-6), 159.3 (pyran C-2), 176.5 (pyran C-4). MS *m*/*z*: 436, 434, 432 [M^+]. Anal. calcd. for $C_{19}H_{14}Br_2O_2$ (434.126) %: C 52.57, H 3.25; found: C 52.83, H 3.33.

*6-Bromomethyl-2-dibromomethyl-3,5-diphenyl-4*H*-pyran-4-one (7a)*

Light-brown crystals (3.28 g, 32%); mp 219.7–221.3 °C. IR υ (cm^{-1}): 1253, 1392, 1638, 3031. ^1H NMR ($CDCl_3$): 4.21 (2H, s, $–CH_2Br$), 6.32 (1H, s, $–CHBr_2$), 7.35 (10H, s, phenyl H). ^{13}C NMR ($CDCl_3$): 26.0 ($–CH_2Br$), 31.1 ($–CHBr_2$), 122.8 (pyran C-5), 127.6 (pyran C-3), 128.4, 128.7, 129.1, 129.3, 129.5, and 130.2 (phenyl-C), 157.0 (pyran C-6), 158.9 (pyran C-2), 177.0 (pyran C-4). MS *m*/*z*: 516, 514, 512, 510 [M^+]. Anal. calcd. for $C_{19}H_{13}Br_3O_2$ (513.022) %: C 44.48, H 2.55; found: C 44.81, H 2.63.

*2,6-Bis(dibromomethyl)-3,5-diphenyl-4*H*-pyran-4-one (8a)*

Light-brown crystals (5.09 g, 43%); mp 228.1–230.0 °C. IR υ (cm^{-1}): 1250, 1396, 1650, 3028. ^1H NMR ($CDCl_3$): 6.35 (2H, s, $–CHBr_2$), 7.10–7.60 (10H, m, phenyl H). ^{13}C NMR ($CDCl_3$): 31.1 ($–CHBr_2$), 122.7 (pyran C-3,-5), 129.2 (br, phenyl C), 157.3 (pyran C-2,-6), 175.7 (pyran C-4). MS *m*/*z*: 596, 594, 592, 590, 588 [M^+]. Anal. calcd. for $C_{19}H_{12}Br_4O_2$ (591.918) %: C 38.55, H 2.04; found: C 38.70, H 2.0.

Reaction of 1b with excessive *N*-bromosuccinimide — Synthesis of di-, tri- and tetra-bromo derivatives 6b, 7b, and 8b

2,6-Dimethyl-4*H*-pyran-4-one (**1b**) was prepared according to a published procedure (20). A mixture of **1b** (2.48 g, 0.02 mol), *N*-bromosuccinimide (28.48 g, 0.16 mol), and dibenzoyl peroxide (0.5 g) in tetrachloromethane (80 mL) was refluxed under the radiation of IR lamps for 96 h. After cooling, the reaction mixture was filtered. The filtrate was concentrated in vacuum, and then dichloromethane (180 mL) was added to the residue. The mixture was washed with several portions of satd. sodium hydrogen carbonate and then water (3 × 50 mL). The organic layer was dried over magnesium sulfate and concentrated in vacuum. The resulting solid was purified by column chromatography on silica gel with ethyl acetate – petroleum ether (4:1) as eluent. Compounds **6b**, **7b**, **8b**, and **8c** were obtained in 0.29:0.74:1:0.026 molar ratio, respectively. Specific details are given for each compound.

*2-Dibromomethyl-6-methyl-4*H*-pyran-4-one (6b)*

Light-yellow crystals (0.51 g, 9%); mp 131.2–132.8 °C (lit. 132 °C) (17). IR υ (cm^{-1}): 1248, 1655. ^1H NMR (DMSO-d_6): 2.36 (3H, s, $–CH_3$), 6.28 (1H, s, $–CHBr_2$), 6.37

© 2007 NRC Canada

(1H, s, pyran CH-5), 7.22 (1H, s, pyran CH-3). ^{13}C NMR (DMSO-d_6): 17.0 (–CH_3), 32.2 (–$CHBr_2$), 111.5 (pyran C-5), 116.1 (pyran C-3), 158.5 (pyran C-6), 163.8 (pyran C-2), 180.1 (pyran C-4). MS *m*/*z*: 284, 282, 280 [M^+]. Anal. calcd. for $C_7H_6Br_2O_2$ (281.930) %: C 29.82, H 2.1; found: C 29.94, H 2.21.

6-Bromomethyl-2-dibromomethyl-4*H*-pyran-4-one (7b)

Colorless crystals (1.66 g, 23%); mp 85.1–85.9 °C (lit. 85 °C) (17). IR υ (cm^{-1}): 1250, 1400, 1648. ^{1}H NMR (DMSO-d_6): 4.61 (2H, s, –CH_2Br), 6.42 (1H, s, –$CHBr_2$), 6.68 (1H, s, pyran CH-5), 7.22 (1H, s, pyran CH-3). ^{13}C NMR (DMSO-d_6): 26.5 (–CH_2Br), 31.9 (–$CHBr_2$), 112.8 (pyran C-5), 116.5 (pyran C-3), 158.2 (pyran C-6), 163.5 (pyran C-2), 179.8 (pyran C-4). MS *m*/*z*: 364, 362, 360, 358 [M^+]. Anal. calcd. for $C_7H_5Br_3O_2$ (360.826) %: C 23.30, H 1.40; found: C 23.82, H 1.48.

2,6-Bis(dibromomethyl)-4*H*-pyran-4-one (8b)

Colorless crystals (2.73 g, 31%); mp 159.2–161.3 °C (lit. 161 °C) (17). IR υ (cm^{-1}): 1250, 1396, 1655. ^{1}H NMR (DMSO-d_6): 6.50 (2H, s, –$CHBr_2$), 7.30 (2H, s, pyran CH-3,-5). ^{13}C NMR (DMSO-d_6): 31.2 (–$CHBr_2$), 116.1 (pyran C-3,-5), 158.3 (pyran C-2,-6), 179.7 (pyran C-4). MS *m*/*z*: 444, 442, 440, 438, 436 [M^+]. Anal. calcd. for $C_7H_4Br_4O_2$ (439.723) %: C 19.12, H 0.92; found: C 19.33, H 0.89.

3,5-Dibromo-2,6-bis(dibromomethyl)-4*H*-pyran-4-one (8c)

Light-yellow crystals (0.095 g, 0.8%); mp 206.7–207.8 °C (lit. 207.0 °C) (17). IR υ (cm^{-1}): 1251, 1396, 1658. ^{1}H NMR (DMSO-d_6): 7.46 (2H, s, –$CHBr_2$). Anal. calcd. for $C_7H_2Br_6O_2$ (597.515) %: C 14.07, H 0.34; found: C 14.15, H 0.32.

Reaction of 6a, 7a, and 8a with silver acetate — Synthesis of 4a, 9a, and 5a

A mixture of **6a** (3 mmol), **7a** (2 mmol) or **8a** (1.5 mmol), and silver acetate (1.17 g, 6.9 mmol) in glacial acetic acid (20 mL) was refluxed for 16 h. After cooling, the mixture was filtered, and the precipitate was washed with dichloromethane (30 mL). Then, cold water (30 mL) was added to the filtrate, and the mixture was stirred and separated. The aqueous layer was extracted with dichloromethane (2 × 20 mL). The combined organic layer was washed with cold water (4 × 20 mL) and then concentrated in vacuum. A solution of acetic acid (20 mL) and water (20 mL) was added to the residue. The mixture was refluxed for 3 h and then concentrated in reduced pressure. Dichloromethane (30 mL) was added to the residue, and the mixture was washed with water (3 × 20 mL). Organic layer was dried over magnesium sulfate, and the solvent was evaporated in vacuum. Specific details are given for each compound.

3,5-Diphenyl-6-methyl-4-oxo-4*H*-pyran-2-carboxaldehyde (4a)

From 1.3 g of **6a**, pale-yellow crystals (0.75 g, 86%) were obtained; mp 188.6–189.7 °C (lit. 189.6 °C) (16). IR υ (cm^{-1}): 800, 980, 1260, 1640, 1700, 2820, 2920, 3010. ^{1}H NMR ($CDCl_3$): 2.40 (3H, s, –CH_3), 7.40 (10H, m, phenyl H), 9.80 (1H, s, –CHO). ^{13}C NMR ($CDCl_3$): 21.1 (–CH_3), 128.3, 128.6, 130.2, 132.0, and 133.0 (phenyl C), 134.5 (pyran C-5), 138.9 (pyran C-3), 149.0 (pyran C-6), 153.0 (pyran C-2), 183.9 (pyran C-4), 202.0 (–CHO). MS *m*/*z*: 290 [M^+]. Anal. calcd. for $C_{19}H_{14}O_3$ (290.317) %: C 78.60, H 4.86; found: C 77.93, H 4.93.

3,5-Diphenyl-4-oxo-4*H*-pyran-2,6-dicarboxaldehyde (5a)

From 0.89 g of **8a**, pale-yellow crystals (0.34 g, 75%) were obtained; mp 195.9–196.8 °C (lit. 196.9 °C) (16). IR υ (cm^{-1}): 1650, 1710, 2880, 3030. ^{1}H NMR (acetone-d_6): 7.35 (10H, s, phenyl H), 9.59 (2H, s, –CHO). ^{13}C NMR (acetone-d_6): 128.5, 129.0, 130.2, 132.0, and 134.1 (phenyl C), 136.0 (pyran C-3,-5), 152.5 (pyran C-2,-6), 185.0 (pyran C-4), 205.7 (–CHO). MS *m*/*z*: 304 [M^+]. Anal. calcd. for $C_{19}H_{12}O_4$ (304.300) %: C 74.99, H 3.98; found: C 75.15, H 4.09.

6-Acethoxymethyl-3,5-diphenyl-4-oxo-4*H*-pyran-2-carboxaldehyde (9a)

From 1.03 g of **7a**, pale-yellow crystals (0.5 g, 71%) were obtained; mp 211 °C. IR υ (cm^{-1}): 1631, 1700, 1745, 3054. ^{1}H NMR ($CDCl_3$): 2.05 (3H, s, –$OOCCH_3$), 4.91 (2H, s, –CH_2O–), 7.35 (10H, s, phenyl H), 9.60 (1H, s, –CHO). ^{13}C NMR ($CDCl_3$): 20.5 (–$OOCCH_3$), 62.3 (–CH_2OOC–), 127.8, 128.2, 130.0, 130.8, 132.1, and 132.8 (phenyl C), 133.9 (pyran C-5), 138.1 (pyran C-3), 151.0 (pyran C-6), 155.5 (pyran C-2), 169.8 (–$OOCCH_3$), 184.2 (pyran C-4), 204.5 (–CHO). MS *m*/*z*: 348 [M^+]. Anal. calcd. for $C_{21}H_{16}O_5$ (348.352) %: C 72.41, H 4.63; found: C 73.60, H 4.52.

Reaction of 6b, 7b, and 8b with silver acetate — Synthesis of 4b, 9b, and 5b

A mixture of **6b** (1.5 mmol), **7b** (1 mmol) or **8b** (0.75 mmol), and silver acetate (0.585 g, 3.45 mmol) in glacial acetic acid (10 mL) was refluxed for 16 h. After cooling, the mixture was filtered, and the precipitate was washed with dichloromethane (40 mL). Then, cold water (20 mL) was added to the filtrate, and the mixture was stirred and separated. The aqueous layer was concentrated under reduced pressure, and the residue, after complete drying, was extracted with dichloromethane (3 × 20 mL). The combined organic layer was washed with cold aqueous solution of satd. sodium chloride (2 × 5 mL) and concentrated in vacuum. A solution of acetic acid (10 mL) and water (10 mL) was added to the residue. The mixture was refluxed for 4 h and then concentrated in reduced pressure. The residue, after complete drying, was extracted with acetone (3 × 10 mL). The combined organic solution was concentrated in vacuum after drying over sodium sulfate. Specific details are given for each compound.

6-Methyl-4-oxo-4*H*-pyran-2-carboxaldehyde (4b)

From 0.42 g of **6b**, white crystals (0.15 g, 73%) were obtained; mp 117.9–118.6 °C (lit. 118.4 °C) (16). IR υ (cm^{-1}): 1285, 1560, 1640, 1710, 2990. ^{1}H NMR ($CDCl_3$): 2.40 (3H, s, –CH_3), 6.30 (1H, s, pyran CH-3), 6.65 (1H, s, pyran CH-5), 9.65 (1H, s, –CHO). ^{13}C NMR ($CDCl_3$): 20.5 (–CH_3), 118.0 (pyran C-5), 121.5 (pyran C-3), 157.2 (pyran C-6), 168.0 (pyran C-2), 179.1 (pyran C-4), 187.0 (–CHO). MS *m*/*z*: 138 [M^+]. Anal. calcd. for $C_7H_6O_3$ (138.121) %: C 60.87, H 4.38; found: C 60.61, H 4.29.

© 2007 NRC Canada

4-Oxo-4H-pyran-2,6-dicarboxaldehyde (5b)

From 0.33 g of **8b**, yellow oil (0.08 g, 70%) was obtained. IR υ (cm^{-1}): 1100, 1280, 1425, 1615, 1675, 1720, 3010. ^1H NMR (acetone-d_6): 7.05 (2H, s, pyran CH-3,-5), 9.75 (2H, s, –CHO). ^{13}C NMR (acetone-d_6): 123.5 (pyran C-3,-5), 168.0 (pyran C-2,-6), 181.0 (pyran C-4), 188.0 (–CHO). MS *m/z*: 152 [M^+]. Anal. calcd. for $C_7H_4O_4$ (152.105) %: C 55.28, H 2.65; found: C 55.19, H 2.73.

6-Acethoxymethyl-4-oxo-4H-pyran-2-carboxaldehyde (9b)

From 0.36 g of **7b**, colorless oil (0.13 g, 66%) was obtained. IR υ (cm^{-1}): 1635, 1705, 1750, 2990. ^1H NMR ($CDCl_3$): 2.10 (3H, s, $–OOCCH_3$), 4.90 (2H, s, $–CH_2O–$), 6.32 (1H, s, pyran CH-3), 6.62 (1H, s, pyran CH-5), 9.68 (1H, s, –CHO). ^{13}C NMR ($CDCl_3$): 20.0 ($–OOCCH_3$), 61.9 ($–CH_2OOC–$), 118.5 (pyran C-5), 122.1 (pyran C-3), 158.0 (pyran C-6), 167.2 (pyran C-2), 180.1 (pyran C-4), 188.2 (–CHO). MS *m/z*: 196 [M^+]. Anal. calcd. for $C_9H_8O_5$ (196.157) %: C 55.11, H 4.11; found: C 54.99, H 4.0.

3,5-Diphenyl-6-hydroxymethyl-4-oxo-4H-pyran-2-carboxaldehyde (10a)

A mixture of **9a** (0.435 g, 1.25 mmol), tetrahydrofuran (6 mL), water (3 mL), and concentrated hydrochloric acid (0.1 mL) was refluxed for 15 h. The mixture was concentrated under reduced pressure, and then water (5 mL) was added to the residue. The mixture was extracted with dichloromethane (3 × 10 mL), and the combined organic layer was washed with water (3 × 10 mL), dried over magnesium sulfate, and the solvent was distilled under reduced pressure. Pale-brown crystals (0.34 g, 89%) were obtained; mp 215.1–216.5 °C. IR υ (cm^{-1}): 1648, 1700, 3439 (br). ^1H NMR ($CDCl_3$): 2.60 (1H, br, $–CH_2OH$), 4.46 (2H, s, $–CH_2OH$), 7.25–7.50 (10H, m, phenyl H), 9.58(1H, s, –CHO). MS *m/z*: 306 [M^+]. Anal. calcd. for $C_{19}H_{14}O_4$ (306.316) %: C 74.50, H 4.61; found: C 73.91, H 4.71.

6-Hydroxymethyl-4-oxo-4H-pyran-2-carboxaldehyde (10b)

A mixture of **9b** (0.118 g, 0.6 mmol), tetrahydrofuran (3 mL), water (1.5 mL), and concentrated hydrochloric acid (0.05 mL) was refluxed for 15 h. The mixture was concentrated under reduced pressure and the residue, after complete drying, was extracted with acetone (3 × 10 mL). The combined organic solution was concentrated in vacuum after drying over magnesium sulfate. Colorless oil (0.075 g, 81%) was obtained. IR υ (cm^{-1}): 1642, 1705, 3450 (br). ^1H NMR (DMSO-d_6): 2.95 (1H, br, $–CH_2OH$), 4.49 (2H, s, $–CH_2OH$), 6.35 (1H, s, pyran CH-3), 6.68 (1H, s, pyran CH-5), 9.63 (1H, s, –CHO). MS *m/z*: 154 [M^+]. Anal. calcd. for $C_7H_6O_4$ (154.120) %: C 54.55, H 3.92; found: C 53.89, H 3.99.

Oxidation of 10a and 10b with barium manganate — Synthesis of 5a and 5b

The fine powder of barium manganate (0.84 g) was added immediately to a stirred solution of **10a** or **10b** (0.3 mmol) in dichloromethane–tetrahydrofuran (1:1) (6 mL). The mixture was stirred at room temperature for 2 h. Inorganic byproducts were removed by filtration of the reaction mixture through Celite. The Celite was washed with dichloromethane, and the latter solution was added to the previously obtained dichloromethane–tetrahydrofuran filtrate. Evaporation of dichloromethane–tetrahydrofuran in vacuum gave a pale-yellow residue. Specific details are given for each compound.

Compound 5a

From 0.092 g of **10a**, 0.09 g pale-yellow residue was obtained, which recrystallized from ethylacetate and petroleum ether. Pale-yellow crystals (0.083 g, 91%) were obtained; mp 195.7–197.1 °C (lit. 196.9 °C) (16). The physical and spectral properties were identical to that of **5a** reported earlier.

Compound 5b

From 0.046 g of **10b**, pale-yellow oil (0.037 g, 82%) was obtained. The physical and spectral properties were identical to that of **5b** reported earlier.

Acknowledgement

We gratefully acknowledge the financial support for this work by the Research Council of Malek-ashtar University of Technology.

References

1. D.E. Fenton, W.D. Parkin, R.F. Newton, I.W. Nowell, and P.E. Walker. J. Chem. Soc., Dalton Trans. 327 (1982).
2. A. Shahrisa and R. Tabrizi. Iran. J. Chem. Chem. Eng. **18**, 91 (1999).
3. J. Zamocka, E. Misikova, and J. Durinda. Pharmazie, **46**, 610 (1991).
4. T. Moriguchi, H. Matsuvra, Y. Itakura, H. Katsuki, H. Saito, and N. Nishiyama. Life Sci. **61**, 1413 (1997).
5. E. Ochoa De Aspuru and A.M.L. Zaton. J. Enzym. Inhib. **8**, 87 (1994).
6. R.D.H. Murray. Aromat. Heteroaromat. Chem. **5**, 472 (1978).
7. G.P. Ellis. *In* Comprehensive heterocyclic chemistry. Vol. 3. *Edited by* A.J. Boulton and A. Mckillop. Pergamon Press, Oxford. 1984. Chap. 2.23.
8. R. Livingstone. *In* Rodd's Chemistry of carbon compounds. Vol. IV. *Edited by* S. Coffey. Elsevier, Amsterdam. 1977. Chap. 20.
9. S. Yamamura and S. Nishiyama. Bull. Chem. Soc. Jpn. **70**, 2025 (1997).
10. B.P. Clark, W.J. Ross, and A. Todd. US Patent 4 471 129, 11 September 1984.
11. B.P. Clark, W.J. Ross, and A. Todd. US Patent 4 364 956, 21 December 1982.
12. (*a*) M. Saad and A. El-Naby. Afr. J. Mycol. Biotechnol. **4**, 59 (1996); (*b*) K. Sato and A. Sakaida. Japanese Patent 09 220095. 26 August 1997.
13. D.H.R. Barton, B.D. Brown, D.D. Ridley, D.A. Widdowson, A.J. Keys, and C.J. Leaver. J. Chem. Soc., Perkin Trans. 1, 2069 (1975).
14. J. Bransova, M. Uher, and J. Brtko. Chem. Pap. – Chem. Zvesti, **48**, 341 (1994).
15. J. Bransova, M. Uher, and J. Brtko. Chem. Pap. – Chem. Zvesti, **47**, 316 (1993).
16. M. Ghandi, Y. Bayat, and R. Teimuri-mofrad. Org. Prep. Proced. Int. **34**, 525 (2002).
17. W. Lowe, S. Bratter, C. Dietrich, M. Weber, and P. Luger. J. Heterocycl. Chem. **34**, 1173 (1997).

© 2007 NRC Canada

18. T.L. Emmick and R.L. Letsinger. *In* Organic syntheses collective. Vol. V. *Edited by* H.E. Baumgarten. John Wiley & Sons, New York. 1973. pp. 450–452.
19. (*a*) A. Wohl, Ber. **52**, 51 (1919); (*b*) K. Ziegler, A. Spath, E. Schaaf, W. Schumann, and F. Winkelmann. Liebigs Ann. Chem. **551**, 80 (1942).
20. A. Shahrisa, R. Tabrizi, and H.R. Ahsani. Org. Prep. Proced. Int. **32**, 47 (2000).
21. D.J. Cram and R.C. Helgeson. J. Am. Chem. Soc. **88**, 3515 (1966).

© 2007 NRC Canada

Solvent effects on the reactions of copper chlorides with $OP(NH\text{-}t\text{-}Bu)_3$ — Formation of the novel $[Cu_5Cl_{10}]^{5-}$ anion via in situ templation

Zhiyong Fu and Tristram Chivers

Abstract: X-ray structural investigations have shown that the products of the reaction of $CuCl_2{\cdot}2H_2O$ and $OP[NH\text{-}t\text{-}Bu]_3$ are markedly dependent on solvent and temperature. The polymeric ionic complex $[(t\text{-}BuNH_3)_2(Cu_3(OH)(H_2O)Cl_7)]_\infty$ (**1**), containing a trinuclear anionic repeating unit, is obtained from toluene at 80 °C, whereas the 2:1 adduct $Cu(t\text{-}BuNH_2)_2Cl_2$ (**4**) is formed at 150 °C. By contrast, a neutral tetranuclear cluster $Cu_4[PO(NH\text{-}t\text{-}Bu)_3]_4(\mu_4\text{-}O)Cl_6$ (**2**) or the one-dimensional chain $[Cu(Py)_2Cl_2]_\infty$ (**3**) is produced when the reaction is carried out in hexane or pyridine, respectively, at 80 °C. The reaction of a mixture of CuCl and $CuCl_2{\cdot}2H_2O$ (2:1 molar ratio) with $OP[NH\text{-}t\text{-}Bu]_3$ at 80 °C in toluene produces $[t\text{-}BuNH_3]_5[Cu_5Cl_{10}]$ (**5**), in which the anion is a pentanuclear cluster with both terminal and bridging chloride ions. The removal of the chloride ions from the reaction mixture by the addition of $AgNO_3$ yields the 2:1 adduct $Cu[OP(NH\text{-}t\text{-}Bu)_3]_2(NO_3)_2$ (**6**).

Key words: copper halides, templation, P–N compounds, cluster complexes, one-dimensional framework

Résumé : Des études par diffraction des rayons X ont montré que les produits obtenus par réaction du $CuCl_2{\cdot}2H_2O$ et le $OP[NH\text{-}t\text{-}Bu]_3$ dépendent fortement du solvant et de la température. Le complexe ionique polymère $[(t\text{-}BuNH_3)_2(Cu_3(OH)(H_2O)Cl_7]_4$ (**1**) contenant une maille élémentaire anionique trinucléaire est obtenu à partir du toluène à 80 °C alors que l'adduit 2:1 $Cu(t\text{-}BuNH_2)_2Cl_2$ (**4**) est le produit qui se forme à 150 °C. Par opposition à ces résultats, lorsqu'on effectue les réactions dans l'hexane ou la pyridine à 80 °C, ce sont respectivement un agrégat tétranucléaire neutre de formule $Cu_4[PO(NH\text{-}t\text{-}Bu)_3]_4(\mu_4\text{-}O)Cl_6$ (**2**) et la chaîne unidimensionnelle $[Cu(Py)_2Cl_2]_4$ (**3**) qui se forment. La réaction d'un mélange de CuCl et de $CuCl_2{\cdot}2H_2O$ (rapport molaire de 2:1) avec le $OP[NH\text{-}t\text{-}Bu]_3$, à 80 °C dans le toluène, conduit à la formation de $[t\text{-}BuNH_3]_5[Cu_5Cl_{10}]$ (**5**) dans lequel l'anion est un agrégat pentanucléaire dans lequel les anions terminaux et formant le pont sont des chlorures. L'élimination des ions chlorures du mélange réactionnel par addition de $AgNO_3$ conduit à la formation de l'adduit 2:1 $Cu[OP(NH\text{-}t\text{-}Bu)_3]_2(NO_3)_2$ (**6**).

Mots-clés : halogénures de cuivre, formation de maquette, composés P–N, complexes agrégés, squelette unidimensionnel.

[Traduit par la Rédaction]

Introduction

The direct addition of organic ammonium cations to a reaction mixture (known as templation) is a common technique for the syntheses of inorganic materials with new structural motifs in either hydrothermal or solvothermal processes (1, 2). A variety of factors including the length, structure, and conformation of the cation, as well as interactions with the counter-anions, play important roles in determining the structures and properties of the inorganic materials formed in this way (3–21). Although facile P–N bond cleavage is an impediment in the preparation of metal imidophosphates (22, 23), this liability provides an opportunity to generate novel inorganic compounds by an in situ templation approach (24–27). Recently, it has been demonstrated through the use of P–N compounds as sources of amines or organic ammonium cations that this strategy produces materials that are structurally different from those obtained by the direct templation method. Neeraj and Cheetham (24) obtained two new zinc phosphates, $[Me_2NH_2][Zn_3(PO_4)(HPO_4)_2]{\cdot}H_2O$ and $[(Me_2NH_2)(H_3O)][Zn_4(PO_4)_3(H_2O)]_2{\cdot}H_2O$, by using hexamethylphosphoramide $OP(NMe_2)_3$ as an in situ source of both amine and phosphoric acid under hydrothermal conditions at 180 °C. More recently, we have shown that *n*-propylimidodiphosphonic anhydride $[O(OH)P(\mu\text{-}O)PO(OH)(\mu\text{-}N\text{-}n\text{-}Pr)]_2{\cdot}2NH_2\text{-}n\text{-}Pr$, which contains an eight-membered $P_4N_2O_2$ ring, provides a source of phosphate under either hydrothermal or solvothermal conditions (25). The primary amine $n\text{-}PrNH_2$ or the alkylammonium cation $[n\text{-}PrNH_3]^+$ formed as a result of P–N bond cleavage may function as a pH controller or as a structure-directing agent, respectively, in the formation of zinc phosphates.

The application of in situ templation has also furnished novel results for copper halide systems (26, 27). For example, the concurrent release of the templating cation $[RNH_3]^+$ and chloride ions via in situ P–N and P–Cl bond cleavage in the precursors $Cl_3P{=}NR$ results in new copper chloride complexes, which cannot be produced by direct templation (26).

Received 18 January 2007. Accepted 10 April 2007. Published on the NRC Research Press Web site at http://canjchem.nrc.ca on 18 May 2007.

Z. Fu[1] and T. Chivers.[2] Department of Chemistry, University of Calgary, Calgary, AB T2N 1N4, Canada.

[1]Present address: College of Chemistry, South China University of Technology, Guangzhou, P.R. China, 510641.

[2]Corresponding author (e-mail: chivers@ucalgary.ca).

 doi:10.1139/V07-038 © 2007 NRC Canada

Table 1. Crystal data and structure refinement for **2**, **4**, **5**, and **6**.

Compound	**2**	**4**	**5**	**6**
Empirical formula	$C_{48}H_{120}Cl_6Cu_4N_{12}O_5P_4$	$C_8H_{22}Cl_2CuN_2$	$C_{20}H_{60}Cl_{10}Cu_5N_5$	$C_{24}H_{60}CuN_8O_8P_2$
Formula mass (g)	1536.30	280.72	1042.93	714.28
T (K)	173(2)	173(2)	173(2)	173(2)
Crystal system	Monoclinic	Monoclinic	Orthorhombic	Monoclinic
Space group	$P21/n$	$P21/n$	$Pnma$	$P2_1/n$
a (Å)	14.240(3)	10.853(2)	20.155(4)	14.940(3)
b (Å)	28.460(6)	12.318(3)	20.939(4)	14.900(3)
c (Å)	19.360(4)	10.983(2)	10.017(2)	17.260(4)
β (°)	93.26(3)	110.87(3)	90	101.19(3)
V (Å3)	7833(3)	1372.0(5)	4227.3(15)	3769.1(13)
Z	4	4	4	4
D_{calcd} (g cm^{-3})	1.303	1.359	1.639	1.259
μ (mm^{-1})	1.402	1.948	3.127	0.714
F (000)	3240	588	2120	1532
θ_{min}–θ_{max} (°)	2.58–25.03	2.58–25.01	4.09–25.03	3.07–25.03
Reflections collected	25 407	4602	6970	12 135
Independent reflections	13 705	2378	3738	6610
Observed reflections	9307	1128	2432	5055
R (int)	0.0487	0.0268	0.0514	0.0357
Goodness-of-fit on F^2	1.094	1.013	1.029	1.019
Final R indices[$I > 2\sigma(I)$] (R_1, wR_2)	0.0642, 0.1622	0.0257, 0.0592	0.0544, 0.1305	0.0563, 0.1353
R indices (all data) (R_1, wR_2)	0.1018, 0.1775	0.0675, 0.0732	0.0946, 0.1509	0.0768, 0.1503
Largest diff. peak and hole (e Å^{-3})	0.761, –1.026	0.243, –0.289	1.152, –0.856	0.679, –0.571

More significantly, the use of OP(NH-*t*-Bu)$_3$ as an in situ source of [*t*-BuNH$_3$]$^+$ generates the novel copper halide chain {[Cu$_3$(OH)(H$_2$O)Cl$_7$]$^{2-}$}$_\infty$ (**1**), which contains an antiferromagnetically coupled trinuclear fragment (27). Identification of the other products of this solvothermal process demonstrated that, in addition to providing a source of [*t*-BuNH$_3$]$^+$, the tris(alkylamido)phosphate OP(NH-*t*-Bu)$_3$ serves as a proton acceptor to adjust the pH value of the reaction medium (27).

These examples indicate that the use of P–N compounds as precursors for in situ templation is a potentially versatile method for the preparation of new inorganic materials. In hydrothermal processes it is well established that the formation of anionic networks is kinetically controlled and highly sensitive to reaction conditions (24). Thus, it can be anticipated that the variation of reaction conditions will affect the outcome of the in situ templation processes. Systematic studies of this new approach may provide insights into the reaction pathways. In this contribution we have investigated the influence of solvent and the addition of M$^+$ ions (M = Cu, Ag) on the outcome of the reaction of CuCl$_2$·2H$_2$O and OP(NH-*t*-Bu)$_3$. Six different copper complexes were obtained under a variety of solvothermal reaction conditions and their structures have been determined by X-ray crystallography.

Experimental section

Reagents and general procedures

The reagent OP(NH-*t*-Bu)$_3$ was prepared according to the literature procedure (28). Toluene, hexane, pyridine, CuCl$_2$·2H$_2$O, and CuCl were used as received. IR spectra were recorded as NaCl pellets on a Nicolet Nexus 470 FTIR spectrometer in the range 4000–350 cm^{-1}. Elemental analyses were obtained with a Control Equipment Corporation model 440 instrument by the Analytical Services Laboratory, Department of Chemistry, University of Calgary and by the Analytical Services of Fujian Institute of Research on the Structure of Matter, China.

All syntheses were carried out in a sealed 23 mL polytetrafluoroethylene-lined Parr acid digestion vessel. The vessel was allowed to cool to room temperature upon completion of the reaction before isolation of the products.

Preparation of {[*t*-BuNH$_3$]$_2$[Cu$_3$(OH)(H$_2$O)Cl$_7$]}$_\infty$ (1)

A mixture of CuCl$_2$·2H$_2$O (0.170 g, 1.00 mmol) and OP[NH-*t*-Bu]$_3$ (0.263 g, 1.00 mmol) in toluene (10 mL) was heated at 80 °C for 38 h. Yellow platelike crystals of **1** were obtained (0.093 g, 45%). IR (cm^{-1}) ν: 3515 [O – H], 3123 [N – H]. Anal. calcd. for C$_8$H$_{27}$Cl$_7$Cu$_3$N$_2$O$_2$: C 15.45, H 4.38, N 4.50; found: C 16.12, H 4.10, N 4.86.

Preparation of Cu$_4$[PO(NH-*t*-Bu)$_3$]$_4$(μ$_4$-O)Cl$_6$ (2)

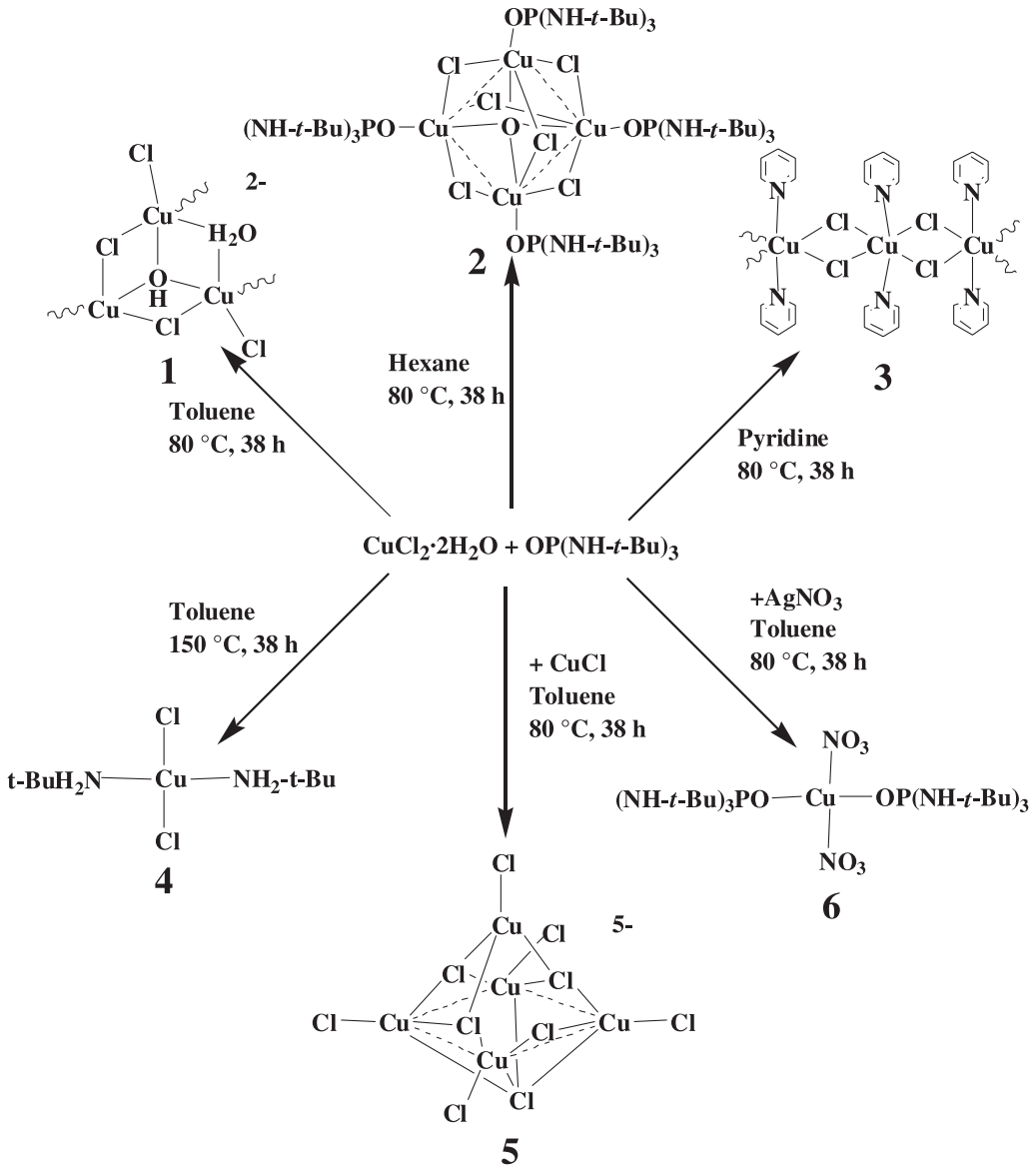
A mixture of CuCl$_2$·2H$_2$O (0.170 g, 1.00 mmol) and OP[NH-*t*-Bu]$_3$ (0.263 g, 1.00 mmol) in hexane (10 mL) was heated at 80 °C for 38 h. Yellow blocklike crystals of **2** were obtained (0.120 g, 31%). Anal. calcd. for C$_{48}$H$_{120}$Cl$_6$Cu$_4$N$_{12}$O$_5$P$_4$: C 37.53, H 7.87, N 10.94; found: C 37.93, H 7.62, N 10.51.

Preparation of [Cu(Py)$_2$Cl$_2$]$_\infty$ (3)

A mixture of CuCl$_2$·2H$_2$O (0.170 g, 1.00 mmol) and OP[NH-*t*-Bu]$_3$ (0.263 g, 1.00 mmol) in pyridine (10 mL) was heated at 80 °C for 38 h. Blue blocklike crystals of **3** were obtained (0.226 g, 77%). Anal. calcd. for

© 2007 NRC Canada

Scheme 1.



$C_{10}H_{10}Cl_2CuN_2$: C 41.04, H 3.44, N 9.57; found: C 41.52, H 3.26, N 10.05.

Preparation of $Cu(t\text{-}BuNH_2)_2Cl_2$ (4)

A mixture of $CuCl_2{\cdot}2H_2O$ (0.170 g, 1.00 mmol) and $OP[NH\text{-}t\text{-}Bu]_3$ (0.263 g, 1.00 mmol) in toluene (10 mL) was heated at 150 °C for 38 h. Blue blocklike crystals of **4** were obtained (0.207 g, 73%). Anal. calcd. for $C_8H_{22}Cl_2CuN_2$: C 34.23, H 7.90, N 9.98; found: C 34.39, H 7.96, N 9.85.

Preparation of $[t\text{-}BuNH_3]_5[Cu_5Cl_{10}]$ (5)

A mixture of $CuCl_2{\cdot}2H_2O$ (0.85 g, 0.500 mmol), CuCl (0.99 g, 1.00 mmol), and $OP[NH\text{-}t\text{-}Bu]_3$ (0.263 g, 1.00 mmol) in toluene (10 mL) was heated at 80 °C for 38 h. Colourless platelike crystals of **5** were obtained (0.090 g, 43%) by manual separation of **5** from the other products. Despite several attempts, satisfactory CHN analyses could not be obtained owing to the necessity to separate the crystals of **5** by hand. A few crystals of **1** were also isolated and identified by determination of unit cell dimensions.

Preparation of $Cu[OP(NH\text{-}t\text{-}Bu)_3]_2(NO_3)_2$ (6)

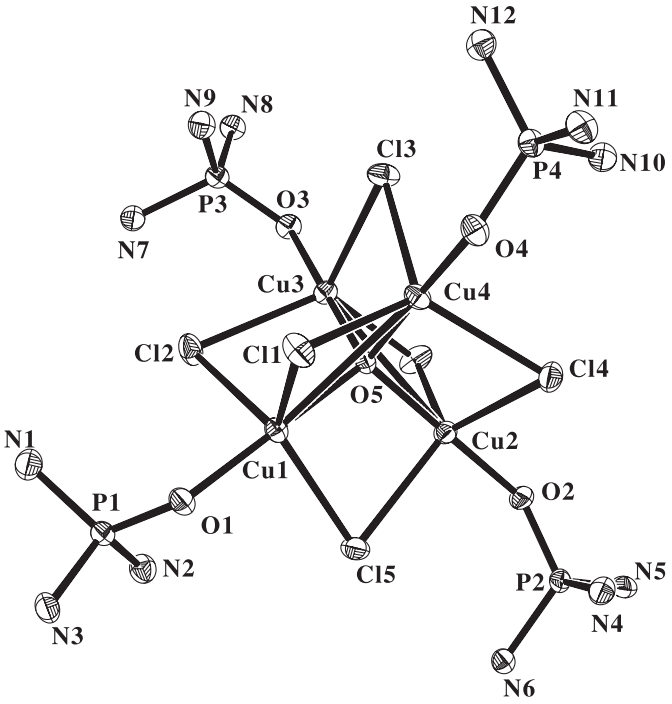
A mixture of $CuCl_2{\cdot}2H_2O$ (0.170 g, 1.00 mmol), $AgNO_3$ (0.340 g, 2.00 mmol), and $OP[NH\text{-}t\text{-}Bu]_3$ (0.263 g, 1.00 mmol) in toluene (10 mL) was heated to 80 °C for 38 h. Blue blocklike crystals of **6** were obtained (0.183 g, 51%). Anal. calcd. for $C_{24}H_{60}CuN_8O_8P_2$: C 40.36, H 8.47, N 15.69; found: C 39.97, H 8.31, N 15.47.

X-ray analyses

Suitable crystals of the complexes [**2**, yellow block (0.28 × 0.16 × 0.16 mm^3); **3**, blue block (0.20 × 0.16 × 0.16 mm^3) ; **4**, blue block (0.16 × 0.12 × 0.06 mm^3); **5**, colourless plate (0.24 × 0.1 × 0.06 mm^3); **6**, blue block (0.18 × 0.12 × 0.12 mm^3)] were selected, coated with oil (Paratone 8277, Exxon), and mounted on glass fibres. The measurements were made on a Nonius Kappa CCD diffractometer with

© 2007 NRC Canada

Fig. 1. Molecular structure of **2** (30% thermal ellipsoids); *tert*-butyl groups and hydrogen atoms attached to the nitrogen atoms have been omitted for clarity.



graphite-monochromated Mo Kα radiation. Data were collected at –100 °C, using the ω and ϕ scans to a maximum θ value of 25.03°, 25.02°, 25.01°, 25.03°, and 25.03° for **2**, **3**, **4**, **5**, and **6**, respectively. The unit cell parameters were calculated and refined from the full data sets. Crystal cell refinement and data reduction were carried out using the Nonius DENZO package. After data reduction, the data were corrected for absorption based on equivalent reflections using SCALEPACK (29). The structure was solved by direct methods (30) and refined by full-matrix least-squares methods with SHELXL-97 (31).

The Cu3 and Cl3 atoms in **5** were disordered over four positions with unequal site occupancy factors in an approximate ratio of 5.4:2:1.6:1; the Cl1 atom in **5** was disordered over two positions with unequal site occupancy factors in an approximate ratio of 9:1. All non-hydrogen atoms were treated anisotropically with the exception of the disordered atoms. All hydrogen atoms were included at geometrically idealized positions.

Crystallographic data for **2**, **4**, **5**, and **6** are summarized in Table 1.[3]

Table 2. Selected bond lengths and angles for **2**

Bond lengths (Å)	
Cu(1)—O(1)	1.915(4)
Cu(1)—Cl(1)	2.3420(19)
Cu(1)—Cl(5)	2.3956(19)
Cu(2)—O(5)	1.900(4)
Cu(2)—Cl(4)	2.4586(19)
Cu(3)—O(3)	1.916(4)
Cu(3)—Cl(3)	2.4635(19)
Cl(2)—Cu(3)	2.4227(19)
Cu(4)—O(5)	1.894(4)
Cl(3)—Cu(4)	2.4567(19)
Cu(1)—Cu(4)	3.0319(12)
Cu(1)—Cu(3)	3.172(2)
P(1)—O(1)	1.496(5)
P(3)—O(3)	1.497(5)
Cu(1)—O(5)	1.913(4)
Cu(1)—Cl(2)	2.5125(19)
Cu(2)—O(2)	1.902(4)
Cu(2)—Cl(5)	2.4622(19)
Cu(2)—Cl(6)	2.354(2)
Cu(3)—O(5)	1.898(4)
Cu(3)—Cl(6)	2.3654(19)
Cu(4)—O(4)	1.911(4)
Cu(4)—Cl(4)	2.4570(19)
Cl(1)—Cu(4)	2.3680(19)
Cu(2)—Cu(3)	3.0453(12)
Cu(2)—Cu(4)	3.124(1)
P(2)—O(2)	1.502(5)
P(4)—O(4)	1.492(5)
Bond angles (°)	
O(5)–Cu(1)–O(1)	179.16(19)
Cl(1)–Cu(1)–Cl(5)	127.63(8)
O(5)–Cu(2)–O(2)	178.7(2)
Cl(4)–Cu(2)–Cl(5)	114.66(7)
O(5)–Cu(3)–O(3)	179.44(19)
Cl(2)–Cu(3)–Cl(3)	119.92(8)
O(5)–Cu(4)–O(4)	177.0(2)
Cl(1)–Cu(4)–Cl(4)	125.42(8)
Cl(1)–Cu(1)–Cl(2)	112.25(8)
Cl(5)–Cu(1)–Cl(2)	117.87(8)
Cl(6)–Cu(2)–Cl(4)	120.37(8)
Cl(6)–Cu(2)–Cl(5)	122.95(8)
Cl(6)–Cu(3)–Cl(2)	121.95(8)
Cl(6)–Cu(3)–Cl(3)	116.24(8)
Cl(1)–Cu(4)–Cl(3)	116.70(8)
Cl(3)–Cu(4)–Cl(4)	116.16(7)

Results and discussion

In the solid state, tris(*tert*-butylamido)orthophosphate $OP(NH\text{-}t\text{-}Bu)_3$ adopts a one-dimensional chain structure in which individual molecules are connected by hydrogen bonds (28). Under solvothermal conditions with toluene as solvent this P–N compound does not decompose at 120 °C;

[3] Supplementary data for this article are available on the journal Web site (http://canjchem.nrc.ca) or may be purchased from the Depository of Unpublished Data, Document Delivery, CISTI, National Research Council Canada, Ottawa, ON K1A 0R6, Canada. DUD 5166. For more information on obtaining material refer to http://cisti-icist.nrc-cnrc.gc.ca/irm/unpub_e.shtml. CCDC 643920–643923 contain the crystallographic data for this manuscript. These data can be obtained, free of charge, via http://www.ccdc.cam.ac.uk/conts/retrieving.html (Or from the Cambridge Crystallographic Data Centre, 12 Union Road, Cambridge CB2 1EZ, UK; fax +44 1223 336033; or deposit@ccdc.cam.ac.uk).

© 2007 NRC Canada

Fig. 2. Molecular structure of **4** (30% thermal ellipsoids); hydrogen atoms have been omitted for clarity.

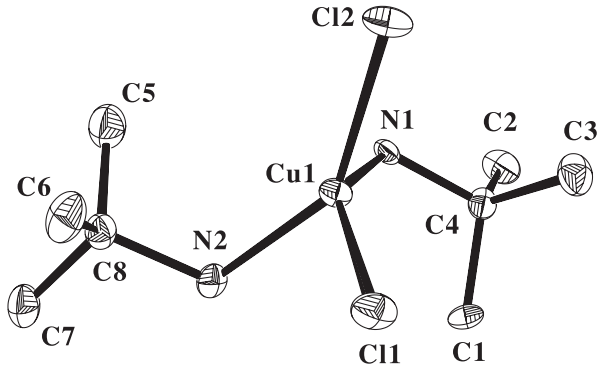
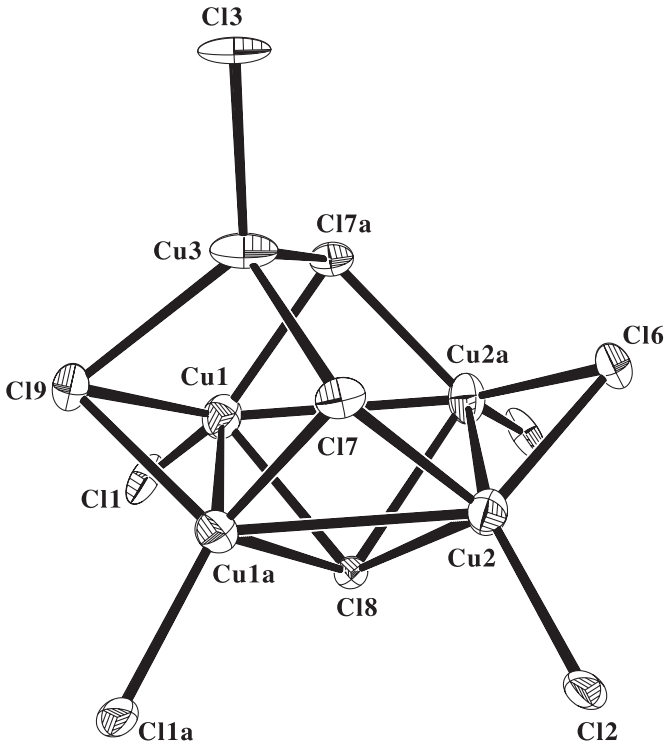


Table 3. Selected bond lengths and angles for **4** and **6**.

Compound Cu(*t*-BuNH$_2$)$_2$Cl$_2$ (**4**)	
Bond lengths (Å)	
Cu(1)—N(1)	1.997(4)
Cu(1)—N(2)	2.003(4)
Cu(1)—Cl(2)	2.2449(15)
Cu(1)—Cl(1)	2.2569(15)
Bond angles (°)	
N(1)–Cu(1)–N(2)	95.81(8)
N(2)–Cu(1)–Cl(2)	144.19(13)
N(2)–Cu(1)–Cl(1)	94.02(13)
N(1)–Cu(1)–Cl(2)	95.41(14)
N(1)–Cu(1)–Cl(1)	144.78(13)
Cl(2)–Cu(1)–Cl(1)	96.10(3)
Compound Cu[OP(NH-*t*-Bu)$_3$]$_2$(NO$_3$)$_2$ (**6**)	
Bond lengths (Å)	
Cu(1)—O(2)	1.900(3)
Cu(1)—O(6)	1.945(3)
P(1)—O(1)	1.501(3)
Cu(1)—O(1)	1.911(3)
Cu(1)—O(3)	2.047(4)
P(2)—O(2)	1.504(3)
Bond angles (°)	
O(1)–Cu(1)–O(6)	86.16(13)
O(1)–Cu(1)–O(3)	93.45(13)
O(2)–Cu(1)–O(1)	174.01(12)
O(2)–Cu(1)–O(6)	92.24(13)
O(2)–Cu(1)–O(3)	88.59(13)
O(6)–Cu(1)–O(3)	175.60(16)

however, partial decomposition is observed upon heating at 150 °C for 38 h. The reaction of $CuCl_2 \cdot 2H_2O$ and OP(NH-*t*-Bu)$_3$ in a 1:1 molar ratio was carried out under different solvothermal conditions to evaluate the effect of (*i*) solvent and (*ii*) the addition of M^+ ions (M = Cu, Ag) on the nature of the products obtained. As indicated in Scheme 1, a variety of products are formed and their structures have been determined by single-crystal X-ray diffraction studies. Under certain conditions, P–N bond cleavage occurs with the release of *t*-BuNH$_2$ and the subsequent formation of [*t*-BuNH$_3$]$^+$ under the influence of HCl present in the reaction mixture. In other cases, the intact OP(NH-*t*-Bu)$_3$ ligand is observed in the reaction product.

Fig. 3. Molecular structure of the $[Cu_5Cl_{10}]^{5-}$ anion in **5** (30% thermal ellipsoids) showing the most important contributor to the disordered structure. Symmetry transformations used to generate equivalent atoms are $a = x, 3/2 - y, z$.



Effect of solvent

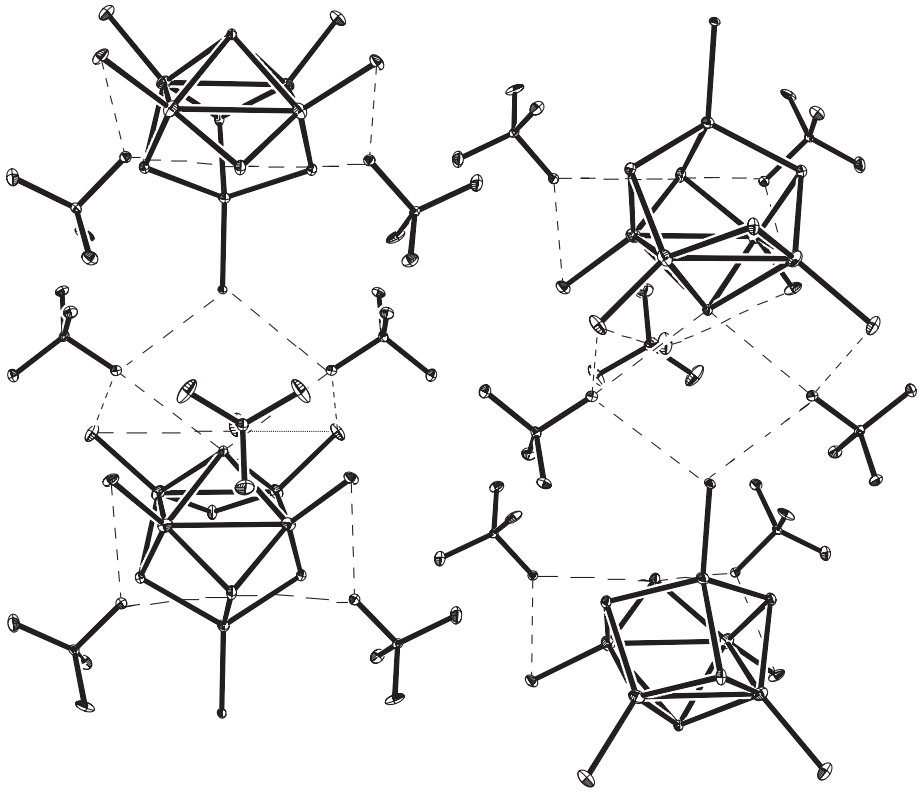
The reaction of $CuCl_2 \cdot 2H_2O$ and OP(NH-*t*-Bu)$_3$ in a 1:1 molar ratio was carried out in three different solvents, viz. toluene, hexane, and pyridine, under similar reaction conditions (80 °C, 38 h). In toluene, P–N bond cleavage takes place with the in situ formation of the templating cation [*t*-BuNH$_3$]$^+$, which directs the assembly of the copper halide chain $[Cu_3(\mu_3\text{-}OH)(\mu_2\text{-}H_2O)Cl_7]^{2-}\}_\infty$ (Scheme 1) (27). Interestingly, when the same reaction is carried out in toluene at 150 °C, the primary amine *t*-BuNH$_2$ formed by P–N bond cleavage is trapped by coordination to the Cu^{2+} centres to give the 2:1 adduct Cu(*t*-BuNH$_2$)$_2$Cl$_2$ (**4**), rather than by protons with the formation of [*t*-BuNH$_3$]$^+$.

By contrast, P–N bond scission is not observed when hexane is employed as the reaction medium. In this solvent at 80 °C, the major product is the oxo-centred tetranuclear cluster Cu$_4$[OP(NH-*t*-Bu)$_3$]$_4$(μ_4-O)Cl$_6$ (**2**), in which the four copper centres are each coordinated by an *O*-monodentate OP(NH-*t*-Bu)$_3$ ligand.

A third type of behaviour is observed when pyridine is used instead of a hydrocarbon solvent. In this case, the strongly coordinating solvent molecules replace the water ligands in $CuCl_2 \cdot 2H_2O$, resulting in the formation of the one-dimensional chain $[Cu(Py)_2Cl_2]_\infty$ (**3**). In this transformation the reagent OP(NH-*t*-Bu)$_3$ remains unchanged in the mother liquid as revealed by a ^{31}P NMR spectrum.

© 2007 NRC Canada

Fig. 4. Packing diagrams for **5** viewed along the [001] direction showing the most important contributor to the disordered structure; hydrogen atoms have been omitted for clarity.



Effect of the addition of M^+ (M = Cu, Ag)

No reaction takes place between cuprous chloride (CuCl) and OP(NH-*t*-Bu)$_3$ at 80 °C in toluene under solvothermal conditions owing to the insolubility of CuCl. However, the addition of CuCl (2 equiv.) to equimolar quantities of $CuCl_2 \cdot 2H_2O$ and OP(NH-*t*-Bu)$_3$ in toluene at 80 °C results in the production of the ion-separated salt [*t*-BuNH$_3$]$_5$[Cu_5Cl_{10}] (**5**), which contains a novel pentanuclear penta-anion (vide infra). Thus, the presence of CuCl has a significant influence on the outcome of the in situ templation process, cf. the formation of **1** in the absence of CuCl.

In view of the foregoing observation, the effect of the addition of 2 equiv. of Ag^+ (in the form of silver nitrate) on the reaction of $CuCl_2 \cdot 2H_2O$ and OP(NH-*t*-Bu)$_3$ in toluene at 80 °C was also investigated. In this case, P–N bond cleavage does not occur. Instead, the silver ions remove the chloride ligands from the copper centre via ion-exchange and intact OP(NH-*t*-Bu)$_3$ ligands are observed in the formation of the 2:1 adduct Cu[OP(NH-*t*-Bu)$_3$]$_2$(NO_3)$_2$ (**6**).

X-ray structures

The details of the X-ray structure of **1** were discussed in a preliminary communication (27). The structure of **2** is shown in Fig. 1, and selected metrical parameters are summarized in Table 2. It is a tetranuclear copper cluster similar to those reported for $Cu_4[(NCH_3)_2CHO]_4(\mu_4\text{-}O)Cl_6$, $Cu_4[C_6H_{12}N_4]_4(\mu_4\text{-}O)Cl_6$, $Cu_4[OP(C_6H_5)_3]_4(\mu_4\text{-}O)Cl_6$, and $Cu_4[OPEt_3]_4(\mu_4\text{-}O)Cl_6$ (32–34). In contrast to the observation of one linear and three bent Cu–O–P coordination linkages (Cu2–O2–P2 = 141.02(46)°) in the complex $Cu_4[OPEt_3]_4(\mu_4\text{-}O)Cl_6$ (34), all Cu–O–P connections in **2** are bent significantly (Cu–O–P = 130.1(3)°–136.7(3)°). The six Cl^- ions bridge (μ_2) the edges of the tetrahedron formed by the four copper ions. A single μ_4-O^{2-} ion is embedded in the centre of the tetrahedron. The propellerlike structure is comprised of three seco-cubes each of which has six unique Cu–Cl edges and shares three Cu–O edges with another seco-cube. Each copper atom exhibits distorted trigonal bipyramidal geometry with three chlorine atoms in the equatorial plane and two oxygen donors in the axial positions. The bond angles O–Cu–O are approximately linear (177.0(2)° to 179.44(19)°). The bond angles Cl–Cu–Cl vary from 112.25(8)° to 127.63 (8)°. The Cu—Cl distances, which lie in the range 2.3420(19)–2.5125(19) Å, and the Cu—O bond lengths (1.894(4)–1.915(4) Å) are similar to previously reported values for related tetranuclear copper halide clusters (32–34). As expected, the P—O distances in **2** (1.492(5) –1.502(5) Å) are slightly longer than that in the free ligand OP(NH^{t}Bu)$_3$ (1.474(3) Å) (28) as a result of coordination to the copper centres. The tetrahedron defined by the four copper atoms in **2** is more distorted than that in the complex $Cu_4[OPEt_3]_4(\mu_4\text{-}O)Cl_6$ and adopts approximately C_{2v} symmetry; the Cu—Cu distances have typical values ranging from 3.0319(12) to 3.172(2) Å.

X-ray quality blue crystals of **3** were grown from a pyridine solution and identified as the one-dimensional chain $[Cu(Py)_2Cl_2]_\infty$, with the two pyridine molecules in a trans arrangement, by comparison of the unit cell parameters with those of the published structure (35).

In contrast to the square-planar structure of $CuCl_2 \cdot 2H_2O$

© 2007 NRC Canada

Table 4. Selected bond lengths and angles for **5**.

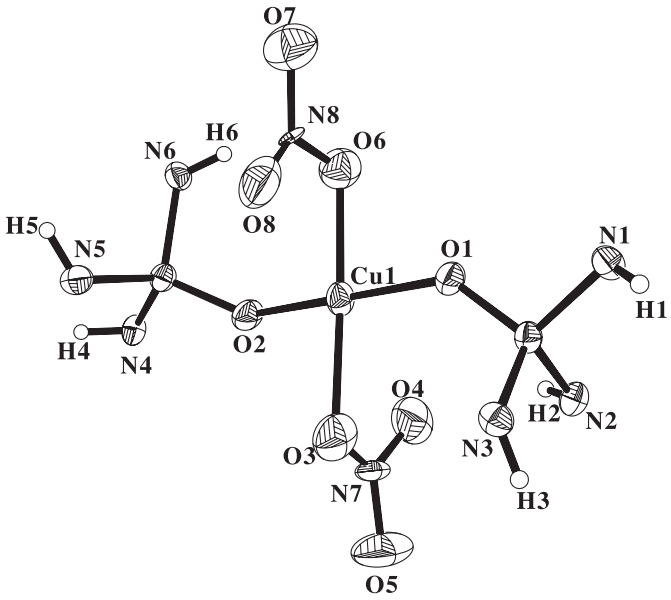
Bond lengths (Å)	
Cu(1)—Cl(1)	2.2824(19)
Cu(1)—Cl(7a)	2.3179(17)
Cu(2)—Cl(2)	2.2517(17)
Cu(2)—Cl(7)	2.3450(17)
Cu(3)—Cl(3)	2.308(7)
Cu(3)—Cl(7)	2.368(3)
Cu(2)—Cu(2a)	2.9435(17)
Cu(1)—Cl(9)	2.4561(18)
Cu(1)—Cl(8)	2.5033(17)
Cu(2)—Cl(6)	2.3785(17)
Cu(2)—Cl(8)	2.5775(17)
Cu(3)—Cl(9)	2.553(6)
Cu(1)—Cu(1a)	2.9258(18)
Cu(1)—Cu(2a)	2.9612(13)
Bond angles (°)	
Cl(1)–Cu(1)–Cl(7a)	132.03(8)
Cl(1)–Cu(1)–Cl(9)	108.70(7)
Cl(7a)–Cu(1)–Cl(9)	100.08(7)
Cl(7)–Cu(2)–Cl(6)	105.38(7)
Cl(2)–Cu(2)–Cl(8)	107.51(6)
Cl(2)–Cu(2)–Cl(7)	120.98(7)
Cl(7a)–Cu(3)–Cl(7)	113.19(18)
Cl(3)–Cu(3)–Cl(7)	111.18(17)
Cl(7)–Cu(3)–Cl(9)	96.05(1)
Cl(1)–Cu(1)–Cl(8)	105.07(7)
Cl(7a)–Cu(1)–Cl(8)	101.80(6)
Cl(9)–Cu(1)–Cl(8)	107.24(5)
Cl(7)–Cu(2)–Cl(8)	98.90(6)
Cl(6)–Cu(2)–Cl(8)	106.09(5)
Cl(2)–Cu(2)–Cl(6)	115.83(7)
Cl(3)–Cu(3)–Cl(9)	127.9(2)
Cl(7a)–Cu(3)–Cl(9)	96.05(17)

Note: The symmetry transformations used to generate equivalent atoms for **5** are $a = x, -y + 3/2, z$. Bond distances and angles are given for the most important contributors only.

(36), the 2:1 adduct Cu(*t*-BuNH$_2$)$_2$Cl$_2$ (**4**) adopts a distorted tetrahedral structure involving two neutral *t*-BuNH$_2$ ligands and two chloride ions (Cu1—N1 = 1.997(4) Å, Cu1—N2 = 2.003(4) Å, Cu1—Cl1 = 2.2569(15) Å, Cu1—Cl2 = 2.2449(15) Å) (Fig. 2). The preference for tetrahedral geometry (see Table 3) presumably reflects the need to minimize steric interactions between bulky *t*-BuNH$_2$ ligands.

The structure of [*t*-BuNH$_3$]$_5$[Cu$_5$Cl$_{10}$] (**5**) incorporates a pentanuclear penta-anion in which the five copper atoms form a square pyramid (Fig. 3); a search of the Cambridge structural data base indicates that this is the first example of the [Cu$_5$Cl$_{10}$]$^{5-}$ penta-anion. Selected bond lengths and angles for **5** are given in Table 4. Each copper centre is coordinated by a distorted tetrahedral arrangement of four Cl$^-$ ligands. The unique copper atom (Cu3) is connected to three μ_3-Cl bridges and one terminal chloride ligand (Cu3—Cl3 = 2.308(7) Å, Cu3—Cl7 = 2.368(3) Å, Cu3—Cl7a = 2.368(3) Å, Cu3—Cl9 = 2.553(6) Å). The bond angles Cl–Cu3–Cl range from 96.05(1)° to 127.9(2)°. By contrast, the copper centres located in the square plane interact with two

Fig. 5. Molecular structure of **6** (30% thermal ellipsoids); *tert*-butyl groups attached to nitrogen have been omitted for clarity.



μ_3-Cl bridges, one μ_4-Cl bridge, and one terminal chloride ligand (Cu–^{t}Cl = 2.2517(17)– 2.2824(19) Å (t = terminal), Cu—μ_3Cl = 2.3179(17)–2.4561(18)Å, Cu—μ_4Cl = 2.5033(17)–2.5775(17) Å). The distances between the copper centers (Cu–Cu) lie in the range of 2.9258(18) to 2.9612(13). The bond angles Cl–Cu–Cl vary from 98.90(6)° to 132.03(8)°. In contrast to the related pentanuclear copper chloride cluster Cu$_5$[(C$_3$H$_5$)$_2$O]$_2$Cl$_5$, which contains diallyl ether as well as chloride ligands (37), the [Cu$_5$Cl$_{10}$]$^{5-}$ unit in **5** is surrounded by five [*t*-BuNH$_3$]$^+$ cations, which engage in weak N···Cl interactions with the anion (3.20–3.30 Å) (Fig. 4). These anion–cation interactions may help to stabilize the penta-anionic cluster.

The monomeric compound **6** has a distorted square-planar structure formed by two [NO$_3$]$^-$ ions and two neutral OP(NH-*t*-Bu)$_3$ ligands (Cu—O = 1.900(3)–2.047(4) Å, and the angle O–Cu–O = 86.16(13)°–93.45(13)°) (Fig. 5). Other structural parameters are given in Table 3.

Conclusions

This study has shown that the reaction medium has an important effect on the outcome of the reaction of CuCl$_2$·2H$_2$O and OP(NH-*t*-Bu)$_3$ under solvothermal conditions. With toluene as the reaction medium, P–N bond cleavage occurs with the in situ formation of *t*-BuNH$_2$ or the templating agent [*t*-BuNH$_3$]$^+$, which directs the formation of copper halide clusters, whereas P–N bond cleavage is not observed in hexane under similar conditions. The production of the pentanuclear cluster [Cu$_5$Cl$_{10}$]$^{5-}$ upon addition of CuCl to this reaction mixture is noteworthy and suggests that other novel cluster aggregations may be formed by in situ templation under solvothermal conditions when two different metal salts are used.

© 2007 NRC Canada

Acknowledgements

We thank Dr. G. Schatte (University of Saskatchewan) for the X-ray data collection of compound **6** and the Alberta Ingenuity Fund (ZF) and Natural Sciences and Engineering Research Council of Canada (NSERC) for financial support.

References

1. A.K. Cheetham, G. Férey, and T. Loiseau. Angew. Chem. Int. Ed. **38**, 3268 (1999).
2. J.D. Martin, A.M. Dattelbaum, T.A. Thornton, R.M. Sullivan, J. Yang, and M.T. Peachey. Chem. Mater. **10**, 2699 (1998).
3. C.N.R. Rao, S. Natarajan, and S. Neeraj. J. Am. Chem. Soc. **122**, 2810 (2000).
4. M. Wei, R.D. Willett, D. Teske, K. Subbaraman, and J.E. Drumheller. Inorg. Chem. **35**, 5781 (1996).
5. S. Haddad and R.D. Willett. Inorg. Chem. **40**, 809 (2001).
6. C. Horn, I. Dance, D. Craig, M. Scudder, and G. Bowmaker. J. Am. Chem. Soc. **120**, 10549 (1998).
7. M. Wei, R.D. Willett, and. C.J. Gómez-García. Inorg. Chem. **43**, 4534 (2004).
8. M. Wei and R. D. Willett. Inorg. Chem. **35**, 6381 (1996).
9. M. Wei, R.D. Willett, and K.W. Hipps. Inorg. Chem. **35**, 5300 (1996).
10. S. Haddad, F. Awwadi, and R.D. Willett. Cryst. Growth Des. **3**, 501 (2003).
11. M.R. Bond, H. Place, Z. Wang, R.D. Willett, Y. Liu, T.E. Grigereit, J.E. Drumheller, and G.F. Tuthill. Inorg. Chem. **34**, 3134 (1995).
12. K.E. Halvorson, T. Grigereit, and R.D. Willett. Inorg. Chem. **26**, 1716 (1987).
13. T.E. Grigereit, B.L. Ramakrishna, H. Place, R.D. Willett, G.C. Pellacani, T. Manfredini, L. Menabue, A. Bonomartini-Corradi, and L.P. Battaglia. Inorg. Chem. **26**, 2235 (1987).
14. A. Colombo, L. Menabue, A. Motori, G.C. Pellacani, W. Porzio, F. Sandrolini, and R.D. Willett. Inorg. Chem. **24,** 2900 (1985).
15. R.J.J. Hansen, J. Livermore, and R.D. Willett. Inorg. Chem. **22**, 330 (1983).
16. M.R. Bond, R.D. Willett, R.S. Rubins, P. Zhou, C.E. Zaspel, S.L. Hutton, and J.E. Drumheller. Phys. Rev. B, **42**, 10280 (1990).
17. B.F. Abrahams, M.G. Haywood, and R. Robson. J. Am. Chem. Soc. **127**, 816 (2005).
18. S. Fernández, J.L. Mesa, J.L. Pizarro, L. Lezama, M.I. Arriortua, and T. Rojo. Angew. Chem. Int. Ed. **41**, 3683 (2002).
19. Y.D. Xia, W.X. Wang, and R. Mokaya. J. Am. Chem. Soc. **127**, 790 (2005).
20. V. Spetzler, C. Nather, and W. Bensch. Inorg. Chem. **44**, 5805 (2005).
21. P. Vaqueiro, A.M. Chippindale, A.R. Cowley, and A.V. Powell. Inorg. Chem. **42**, 7846 (2003).
22. L.D. Quin and S. Jankowski. J. Org. Chem. **59**, 4402 (1994).
23. Z. Fu and T. Chivers. Inorg. Chem. **44**, 7292 (2005).
24. S. Neeraj and A. K. Cheetham. Chem. Commun. 1738 (2002).
25. T. Chivers, Z. Fu, J. Grebinski, and M. Parvez. Z. Anorg. Allg. Chem. **631**, 2601 (2005).
26. Z. Fu and T. Chivers. Can. J. Chem. **84**, 140 (2006).
27. T. Chivers, Z. Fu, and L. K. Thompson. Chem. Commun. (Cambridge), 2339 (2005).
28. T. Chivers, M. Krahn, G. Schatte, and M. Parvez. Inorg. Chem. **42**, 3994 (2003).
29. SCALEPACK [computer program]. Nonius BV, Delft, The Netherlands. 1998.
30. A. Altomare, M. Cascarano, C. Giacovazzo, and A. Guagliardi. J. Appl. Crystallogr. **26**, 343 (1993).
31. G.M. Sheldrick. SHELXL-97 [computer program]. University of Göttingen, Göttingen, Germany. 1997.
32. G.A. Nifontova, I.P. Lavrentev, V.I. Ponomarev, O.S. Filipenko, O.N. Krasochka, L.O. Atovmyan, and M.L. Khidekel. Russ. Chem. Bull. 1691 (1982).
33. O.S. Filipenko, V.I. Ponomarev, and L.O. Atovmyan. Koord. Khim. **12**, 991 (1986).
34. M.R. Churchill, B.G. Deboer, and S.J. Mendak. Inorg. Chem. **14**, 2496 (1975).
35. B. Morosin. Acta Crystallogr. Sect. B, **31**, 632 (1975).
36. M. Kakiuchi, T. Abe, and H. Nakayama. Geochem. J. **35,** 285 (2001).
37. B.M. Mikhalichko, V.V. Olijnik, M.G. Myskiv, and P.Y. Zavalii. Koord. Khim. **13**, 1536 (1987).

© 2007 NRC Canada

Efficient regio- and stereo-selective cleavage of aziridines and epoxides using an ionic liquid as reagent and reaction medium

Brindaban C. Ranu, Laksmikanta Adak, and Subhash Banerjee

Abstract: Ionic liquids, containing a variety of functionalities such as halo, azido, and thiocyano, efficiently cleave aziridines and epoxides to the corresponding products in high yields. The cleavages are regio- and stereo-selective. The reactions are complete in 1 h at 60 °C and do not require any other catalyst or organic solvent. Thus, a convenient synthetic route to 1,2-haloamines, 1,2-azidoamines, 1,2-thiocyanoamines, 1,2-azidoalcohols, and 1,2-thiocyanoalcohols is developed.

Key words: aziridine, epoxide, ionic liquid, cleavage, regioselectivity, stereoselectivity

Résumé : Des liquides ioniques contenant diverses fonctions, telles halogéno, azido ou thiocyano, permettent de cliver efficacement les aziridines et les époxydes pour fournir les produits correspondants avec des rendements élevés. Les clivages sont régio- et stéréosélectifs. Les réactions sont complètes en moins d'une heure, à 60 °C, et elles ne nécessitent pas l'utilisation d'autres catalyseurs ou solvants organiques. On a donc développé une voie de synthèse commode pouvant conduire aux 1,2-halogénoamines, 1,2-azidoamines, 1,2-thiocyanoamines, 1,2-azidoalcools et 1,2-thiocyanoalcools.

Mots clés : aziridine, époxyde, liquide ionique, clivage, régiosélectivité et stéréosélectivité.

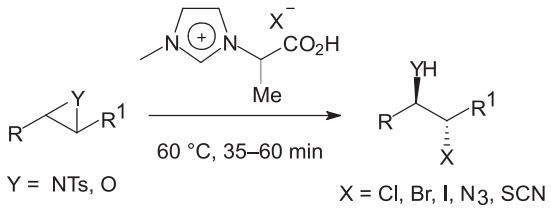
[Traduit par la Rédaction]

Introduction

Ionic liquids are attracting increasing attention in organic synthesis because of their unique advantages as reaction media (1), compared with organic solvents, and efficient promoters for a variety of reactions (2). However, the potential of ionic liquids as reagents has been less explored, and as a part of our activities in this area (3) we initiated an investigation to explore the utility of ionic liquids as efficient reagents (3*a*) for useful transformations.

Aziridines (4) and epoxides (5) are very useful synthetic intermediates. Because of their ring strain and high reactivity, their reactions with various nucleophiles lead to regio- and stereo-selective synthesis of various important synthons. Considerable progress towards the development of several procedures (6) has been achieved in the nucloephilic ring-opening reactions of aziridines and epoxides. The nucleophilic reagents involved in these procedures include tributylphosphine in H_2O (6*a*), $CeCl_3$ in CH_3CN (6*b*), NaN_3–$CeCl_3$ in CH_3CN (6*c*), Me_2SBr_2 in CH_3CN (6*d*), $LiClO_4$–NaX (where X = N_3, CN) in CH_3CN (6*e*), KSCN–sulfated zirconia in CH_3CN (6*f*), zinc halides in CH_2Cl_2 (6*g*), KSCN–$LiClO_4$ in CH_3CN (6*h*), KSCN–β-cyclodextrin in H_2O (6*i*), TBAX–β-cyclodextrin in H_2O (6*j*), $^nBu_4NF$–Me_3SiX in THF (6*k*), $TMSN_3$–$Sn(OTf)_2$ in benzene (6*l*), InX_3 in CH_3CN (6*m*), NaN_3 or KCN–SiO_2 in H_2O (6*n*), $TMSN_3$ in THF (6*o*), NaN_3 in ionic liquid H_2O (6*p*), activated DMF complexes (6*q*), NaX–$Ce(OTf)_4$ in micelle (6*r*), fluoride anion (6*s*), and aminosaccharides (6*t*) in the ionic liquid *N*-methylpyridinium tosylate, among others. However, most of these procedures involve a nucleophilic reagent (usually metal salts), an acid catalyst, and organic solvents like CH_3CN and CH_2Cl_2. We report here a new strategy for the cleavage of aziridines and epoxides with a variety of nucleophiles using a core ionic liquid, 1-(1-carboxy-ethyl)-3-methyl-3*H*-imidazolium derivative [PnMIm]X [where X = N_3, SCN, Cl, Br, I] without any additional reagent, catalyst, or organic solvent (Scheme 1).

Scheme 1.



Results and discussion

The general experimental procedure is very simple and convenient. A mixture of aziridine (or epoxide) and ionic liquid [PnMIm]X was heated at 60 °C for a certain period of time, as required to complete the reaction (TLC). The usual

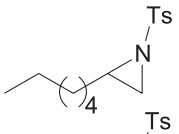
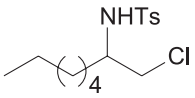
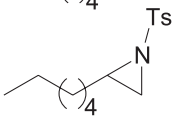
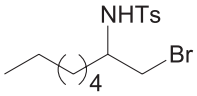
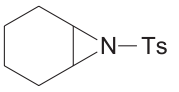
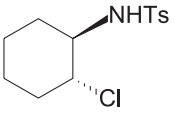
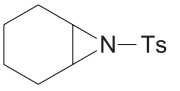
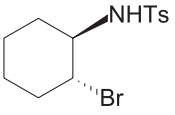
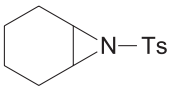
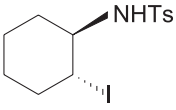
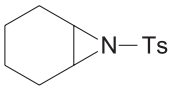
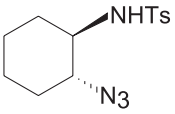
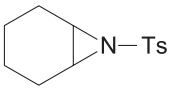
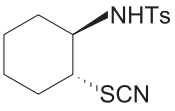
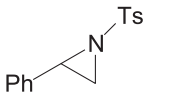
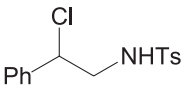
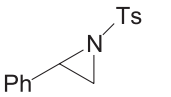
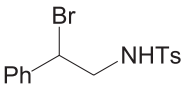
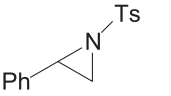
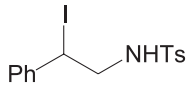
Received 5 March 2007. Accepted 23 April 2007. Published on the NRC Research Press Web site at http://canjchem.nrc.ca on 18 April 2007.

B.C. Ranu,[1] L. Adak, and S. Banerjee. Department of Organic Chemistry, Indian Association for the Cultivation of Science, Jadavpur, Kolkata 700 032, India.

[1]Corresponding author (e-mail: ocbcr@iacs.res.in).

 doi:10.1139/V07-040 © 2007 NRC Canada

Table 1. Ring opening of aziridines by ionic liquids [PnMlm]X.

Entry	Aziridine	X	Product	Time (min)	Yield (%)[a]	Ref.
1		Cl		50	90	6q
2		Br		45	93	6q
3		Cl		40	92	6q
4		Br		35	95	6q
5		I		35	95	6b
6		N_3		35	91	6c
7		SCN		45	90	6f
8		Cl		45	92	6q
9		Br		45	94	6q
10		I		40	95	6b

work-up and purification by column chromatography provided the product.

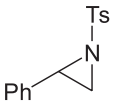
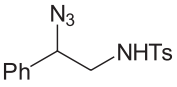
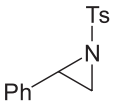
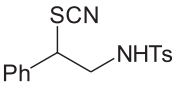
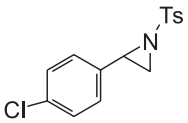
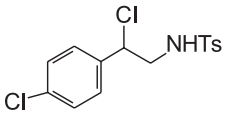
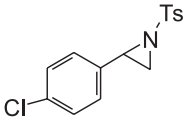
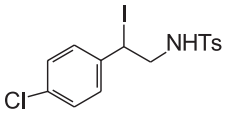
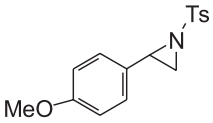
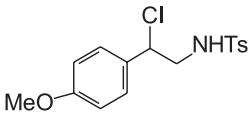
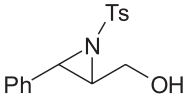
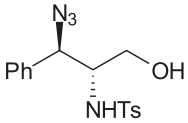
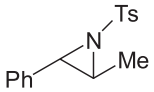
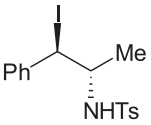
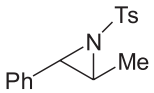
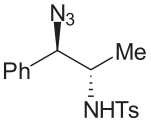
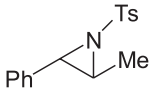
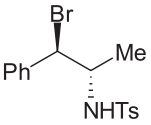
Several structurally diverse aziridines underwent cleavages by this procedure using a core ionic liquid [PnMIm]X (where X = Cl, Br, I, N_3, SCN) to provide the corresponding 2-chloro-, bromo-, iodo-, azido-, and thiocyano-amines. The results were summarized in Table 1. Both alkyl- and aryl-substituted aziridines participated in this reaction. The alkyl-substituted aziridines underwent nucleophilic attack at the less hindered (substituted) carbon atom (Table 1, entries 1 and 2), whereas in aryl-substituted aziridines nucleophiles attacked at the benzylic positions (Table 1, entries 8–23) because of their electronic factor. The cyclohexene azide provided trans isomers by this cleavage, as indicated by the ^{1}H NMR spectra of the corresponding amines (Table 1, entries 3–7). The disubstituted aziridines also furnished trans-functionalized amines (Table 1, entries 16–23).

The epoxides also underwent cleavages by this ionic liquid, producing 2-azido-, nitro-, and thiocyano-alcohols under this procedure. The cleavages by halo-bearing ionic liquids were reported earlier (3*a*). The reactions of alkyl- and aryl-substituted as well as cyclohexene epoxides proceeded smoothly. The results are reported in Table 2. The epoxide of an α,β-unsaturated ketone underwent nucleophilic attack at the α-carbon atom followed by subsequent dehydration to furnish the corresponding α-azido α,β-unsaturated ketone (Table 2, entry 9) under the reaction conditions.

In general, the reactions were very clean, fast, and high-

© 2007 NRC Canada

Table 1 (*concluded*).

Entry	Aziridine	X	Product	Time (min)	Yield (%)[a]	Ref.
11		N_3		40	93	6c
12		SCN		45	89	6f
13		Cl		60	86	6b
14		I		55	90	6b
15		Cl		45	84	-
16		N_3		60	80	9
17		I		45	91	-
18		N_3		40	94	10
19		Br		45	87	11

[a]Yields of pure isolated products characterized by IR, ^{1}H NMR, and ^{13}C NMR spectroscopic data.

yielding. The cleavages of both aziridines and epoxides by this reagent were highly regioselective, affording a single product. The stereochemistry of products was determined as trans by the coupling constant (*J* value) of the hydrogens at the cleaved carbon atoms. It has been observed that nucleophilic attack occurred at the less-substituted carbon atoms of the alkyl-substituted terminal aziridines and epoxides, whereas aryl-substituted substrates underwent attack at the benzylic position, being dictated by the electronic factor. It may be anticipated that these cleavage reactions proceed through the usual S_N2 path as outlined in our earlier paper on epoxide cleavage (3*a*). Several functional groups, such as Cl, OMe, and OPh, remained unaffected during this reaction. The ionic liquids were easily prepared by substitution reaction of the core imidazolium bromide with the sodio-salt of the corresponding anion.

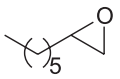
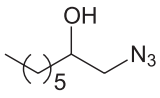
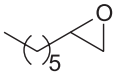
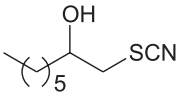
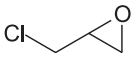
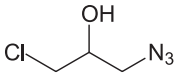
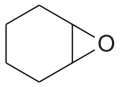
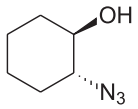
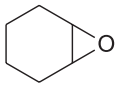
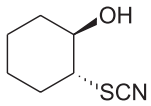
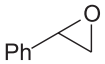
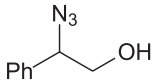
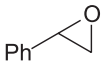
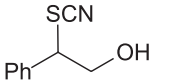
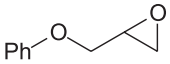
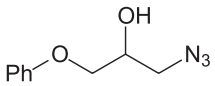
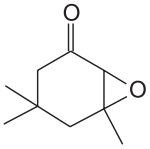
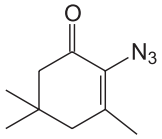
The products of this cleavage reaction, 2-azidoalcohols, 2-thiocyanoalcohol, 2-azido amines, 2-haloamines, and 2-thiocyanoamines are very useful intermediates and have wide applications in organic synthesis (7, 8).

Conclusion

In conclusion, the present procedure provides a novel and

© 2007 NRC Canada

Table 2. Ring opening of epoxides by ionic liquids [PnMlm]X.

Entry	Epoxide	X	Product	Time (min)	Yield (%)[a]	Ref.
1		N_3		45	95	6p
2		SCN		50	89	12
3		N_3		40	90	13
4		N_3		35	94	6c
5		SCN		50	88	12
6		N_3		40	95	6p
7		SCN		45	90	12
8		N_3		45	91	6p
9		N_3		40	87	14

[a]Yields of pure isolated products characterized by IR, ^{1}H NMR, and ^{13}C NMR spectroscopic data.

general route to the cleavage of epoxides and aziridines by a variety of nucleophiles carried out by an inexpensive and easily accessible ionic liquid [PnMIm]X, which itself works as reagent, catalyst, and reaction medium. The other significant advantages offered by this method are operational simplicity, considerably fast reaction time (30–60 min), high isolated yields of products, general applicability to a wide variety of substrates, excellent regio- and stereo-selectivity, thus providing a better and practical alternative to the existing procedures (6). Moreover, this demonstrates the potential of ionic liquids as efficient reagents and shows promise for further useful applications.

Experimental

General

IR spectra were taken as thin films for liquid compounds and as KBr pellets for solids using a Shimadzu 8300 FTIR spectrophotometer. ^{1}H and ^{13}C NMR spectra were recorded in $CDCl_3$ and d_6-DMSO solution at 300 and 75 MHz, respectively (Bruker 300 DPX instrument).

General experimental procedure for the preparation of ionic liquid [PnMIm]x

2-Bromopropionic acid (3.06 g, 20 mmol) was added dropwise to a cooled (0–5 °C) solution of *N*-methylimidazole (1.64 g, 20 mmol) in dry acetonitrile (10 mL). The reaction mixture was then stirred for 12 h at room temperature (RT). The crude product, obtained by evaporation of solvent, was washed with Et_2O (2 × 5 mL) and dried under vacuum to provide the bromo ionic liquid, [PnMIm]Br, ready to be used for cleavage reactions.

The iodo and chloro analogues were prepared from the corresponding 2-iodopropionic acid and 2-chloropropionic acid following the same procedure.

*1-(1-Carboxy-ethyl)-3-methyl-3*H*-imidazol-1-ium bromide [PnMIm]Br*

Viscous liquid. IR (neat, cm^{-1}) ν: 3389, 3001, 2945, 1745, 1579, 1454, 1176, 1091. ^{1}H NMR (DMSO-d_6 + $CDCl_3$) δ:

© 2007 NRC Canada

1.73 (d, J = 7.4 Hz, 3H), 3.92 (s, 3H), 5.48 (quartet, J = 7.35 Hz, 1H), 7.49 (s, 1H), 7.65 (s, 1H), 9.25 (s, 1H), 9.60 (broad, 1H). ^{13}C NMR (DMSO-d_6 + $CDCl_3$) δ: 15.8, 34.0, 55.4, 117.9, 121.4, 133.8, 168.5. HRMS calcd. for $[M + H]^+$ – Br: 156.0899; found: 155.0284. HRMS calcd. for $[M + Na]^+$ – Br: 178.0719; found: 177.0060. Anal. calcd. for $C_7H_{11}BrN_2O_2$: C 35.76, H 4.72, N 11.92; found: C 35.65, H 4.62, N 11.83.

1-(1-Carboxy-ethyl)-3-methyl-3*H*-imidazol-1-ium iodide [PnMIm]I

Viscous liquid. IR (neat, cm^{-1}) ν: 3417, 3107, 2984, 1715, 1620, 1454, 1393, 1281, 1177. ^{1}H NMR (DMSO-d_6 + $CDCl_3$) δ: 1.84 (d, J = 7.1 Hz, 3H), 3.95 (s, 3H), 5.20 (q, J = 7.42 Hz, 1H), 7.31 (s, 1H), 7.45 (s, 1H), 7.68 (s, 1H), 9.57 (broad, 1H). ^{13}C NMR (DMSO-d_6 + $CDCl_3$) δ: 16.8, 34.1, 57.7, 119.7, 120.3, 134.5, 169.8. HRMS calcd. for $[M + H]^+$ – I: 156.0899; found: 155.0193. HRMS calcd. for $[M + Na]^+$ – I: 178.0719; found: 177.0168. Anal. calcd. for $C_7H_{11}IN_2O_2$: C 29.81, H 3.93, N 9.93; found: C 29.70, H 3.81, N 9.79.

1-(1-Carboxy-ethyl)-3-methyl-3*H*-imidazol-1-ium chloride [PnMIm]Cl

Viscous liquid. IR (neat, cm^{-1}) ν: 3391, 3105, 2951, 2897, 2750, 1740, 1580, 1427, 1176. ^{1}H NMR δ: 1.78 (d, J = 7.2 Hz, 3H), 4.04 (s, 3H), 5.25 (q, J = 7.41 Hz, 1H), 7.35 (s, 1H), 7.48 (s, 1H), 8.79 (s, 1H), 10.04 (broad, 1H). ^{13}C NMR δ: 16.1, 33.5, 55.9, 121.1, 122.2, 135.9, 167.2. HRMS calcd. for $[M + H]^+$ – Cl: 156.0899; found: 155.0481. HRMS calcd. for $[M + Na]^+$ – Cl: 178.0719; found: 177.0191. Anal. calcd. for $C_7H_{11}ClN_2O_2$: C 44.10, H 5.82, N 14.70; found: C 43.93, H 5.71, N 14.56.

The bromo ionic liquid was then used for the preparation of other derivatives (X = N_3, SCN) by treatment with NaN_3 (or NaSCN) (30 mmol) in acetonitrile (5 mL) under stirring for 24 h at RT. The precipitated NaBr was filtered and the filtrate was evaporated under vacuum to give the crude product, which was washed with Et_2O (2 × 5 mL) and thoroughly dried under vacuum to furnish the pure ionic liquid characterized by spectroscopic data provided in the following sections.

1-(1-Carboxy-ethyl)-3-methyl-3*H*-imidazol-1-ium thiocyanate

Yellow viscous liquid. IR (neat, cm^{-1}) ν: 3420, 3147, 2058, 1693, 1614, 1394, 1172. ^{1}H NMR (DMSO-d_6 + $CDCl_3$) δ: 2.20 (d, J = 7.2 Hz, 3H), 4.36 (s, 3H), 5.56 (quartet, J = 7.29 Hz, 1H), 7.82 (s, 1H), 7.91 (s, 1H), 9.01 (broad, 1H), 9.12 (s, 1H). ^{13}C NMR (DMSO-d_6 + $CDCl_3$) δ: 16.8, 33.6, 57.6, 120.6, 120.9, 134.4, 170.1. HRMS calcd. for $[M + H]^+$ – SCN: 156.0899; found: 154.9482. HRMS calcd. for $[M + Na]^+$ – SCN: 178.0719; found: 176.9132. Anal. calcd. for $C_8H_{11}N_3O_2S$: C 45.06, H 5.20, N 19.70; found: C 44.95, H 5.30, N 19.58.

1-(1-Carboxy-ethyl)-3-methyl-3*H*-imidazol-1-ium azide

Colourless viscous liquid. IR (neat, cm^{-1}) ν: 3419, 3099, 2104, 1738, 1614, 1583, 1394, 1176. ^{1}H NMR δ: 2.19 (d, J = 7.0 Hz, 3H), 4.36 (s, 3H), 5.57 (quartet, J = 7.21 Hz, 1H), 7.74 (s, 1H), 7.84 (s, 1H), 7.98 (broad, 1H), 9.0 (s, 1H). ^{13}C NMR δ: 17.5, 34.9, 58.3, 120.8, 121.4, 135.2, 170.8. HRMS calcd. for $[M + H]^+ - N_3$: 156.0899; found: 155.0016. HRMS calcd. for $[M + Na]^+ - N_3$: 178.0719; found: 176.9774. Anal. calcd. for $C_7H_{11}N_5O_2$: C 42.64, H 5.62, N 35.51; found: C 42.54, H 5.51, N 35.40.

General experimental procedure for the ring opening of aziridines. Representative procedure for the ring opening of 2-hexyl-1-(toluene-4-sulfonyl)-aziridine with [PnMIm]Cl (Table 1, entry 1)

A mixture of 2-hexyl-1-(toluene-4-sulfonyl)-aziridine (281 mg, 1 mmol) and [PnMIm]Cl (225 mg, 1.3 mmol) was heated at 60 °C with stirring for 50 min (TLC). The reaction mixture was quenched with saturated brine and extracted with ether (3 × 10 mL). Evaporation of ether left the crude product, which was purified by column chromatography over silica gel (hexanes–Et_2O 50:50) to provide the pure *N*-(1-chloromethyl-heptyl)-4-methyl-benzenesulfonamide as a colourless liquid (285 mg, 90%), whose spectroscopic data (IR, ^{1}H, and ^{13}C NMR) are in good agreement with those reported (6*q*).

This procedure was followed for the nucleophilic cleavage of all aziridines listed in Table 1. The known compounds (referenced in Table 1) were identified by the comparison of their spectroscopic data with those reported. The unknown compounds (Table 1, entries 15 and 17) were properly characterized by its spectroscopic data and elemental analysis.

N-*[2-Chloro-2-(4-methoxy-phenyl)-ethyl]-4-methyl-benzenesulf onamide (Table 1, entry 15)*

Colourless viscous liquid. IR (neat, cm^{-1}) ν: 3493, 3282, 2922, 1612, 1514, 1454, 1326, 1250, 1159. ^{1}H NMR δ: 2.38 (s, 3H), 2.97–3.24 (m, 2H), 3.76 (s, 3H), 4.74 (dd, J_1 = 3.72 Hz, J_2 = 8.64 Hz, 1H), 5.10 (t, J = 4.75 Hz, 1H), 6.85 (d, J = 8.64 Hz, 2H), 7.19 (d, J = 8.64 Hz, 2H), 7.29 (d, J = 7.98 Hz, 2H), 7.72 (d, J = 8.34 Hz, 2H). ^{13}C NMR δ: 21.9, 50.6, 55.7, 72.8, 114.4 (2C), 127.5 (2C), 127.5 (2C), 130.1 (2C), 133.3, 137.1, 143.9, 159.9. Anal. calcd. for $C_{16}H_{18}ClNO_3S$: C 56.55, H 5.34, N 4.12; found: C 56.48, H 5.25, N 4.01.

N-*(2-Iodo-1-methyl-2-phenyl-ethyl)-4-methyl-benzene sulfonamide (Table 1, entry 17)*

Colourless viscous liquid. IR (neat, cm^{-1}) ν: 3500, 3273, 1596, 1450, 1326, 1161, 1091. ^{1}H NMR δ: 1.13 (d, J = 6.54 Hz, 3H), 2.42 (s, 3H), 3.57–3.64 (m, 1H), 4.93 (d, J = 8.37 Hz, 1H), 5.05 (d, J = 5.73 Hz, 1H), 7.15–7.33 (m, 7H), 7.73 (d, J = 8.16 Hz, 2H). ^{13}C NMR δ: 19.9, 21.5, 38.5, 56.1, 127.0 (2C), 128.5 (2C), 129.0, 129.3 (2C), 129.7 (2C), 139.0, 139.3, 143.6. Anal. calcd. for $C_{16}H_{18}INO_2S$: C 46.27, H 4.37, N 3.37; found: C 46.16, H 4.29, N 3.28.

General experimental procedure for the ring opening of epoxides. Representative procedure for the ring opening of 2-hexyl-oxirane by [PnMIm]N_3 (Table 2, entry 1)

A mixture of 2-hexyl-oxirane (128 mg, 1 mmol) and [PnMIm]N_3 (256 mg, 1.3 mmol) was heated at 60 °C with stirring for 45 min (TLC). The reaction mixture was quenched with saturated brine and extracted with ether (3 × 10 mL). Evaporation of ether left the crude product, which was purified by column chromatography over silica gel (hexane–Et_2O 80:20) to provide the pure 1-azido-octan-2-ol

© 2007 NRC Canada

as a colourless liquid (162 mg, 95%). The product was identified by comparison of its IR, ^{1}H, and ^{13}C NMR spectroscopic data with those previously reported (6p).

This procedure was followed for the nucleophilic cleavage of all oxiranes listed in Table 2. The products were all known compounds (referenced in Table 2) and were identified by comparison of their spectroscopic data with those reported.

Acknowledgements

This investigation has enjoyed financial support from the Council of Scientific and Industrial Research, New Delhi (CSIR) [Grant No. 01(1936)/04]. LA and SB thank CSIR for their fellowships.

References

1. (*a*) T. Welton. Chem. Rev. **99**, 2071 (1999); (*b*) P. Wasserscheid and W. Keim. Angew. Chem. Int. Ed. **39**, 3773 (2000); (*c*) J.S. Wilkes. Green. Chem. **4**, 73 (2002); (*d*) H.M. Zerth, N.M. Leonard, and R.S. Mohan. Org. Lett. **5**, 55 (2003); (*e*) A. Kumar and S.S. Pawar. J. Org. Chem. **69**, 1419 (2004); (*f*) D.-G. Gu, S.-J. Ji, Z.-Q. Jiang, M.-F. Zhou, and T.-P. Loh. Synlett, 959 (2005).
2. (*a*) J.A. Boon, J.A. Levinsky, J.I. Pflug, and J.S. Wilkes. J. Org. Chem. **51**, 480 (1986); (*b*) J.R. Harjani, S.J. Nara, and M.M. Salunkhe. Tetrahedron Lett. **43**, 1127 (2002); (*c*) V.V. Namboodiri and R.S. Varma. Chem. Commun. (Cambridge), 342 (2002); (*d*) W. Sun, C.-G. Xia, and H.-W. Wang. Tetrahedron Lett. **44**, 2409 (2003); (*e*) K. Qiao and C. Yakoyama. Chem. Lett. **33**, 472 (2004); (*f*) T. Akaiyama, A. Suzuki, and K. Fuchibe. Synlett, 1024 (2005).
3. (*a*) B.C. Ranu and S. Banerjee. J. Org. Chem. **70**, 4517 (2005); (*b*) B.C. Ranu, S. Banerjee, and R. Jana. Tetrahedron, **63**, 776 (2007) and refs. cited therein.
4. (*a*) J.E.G. Kemp. *In* Comprehensive organic synthesis. *Vol. 7. Edited by* B.M Trost and I. Fleming. Pergamon, Oxford, UK. 1991. pp. 469–513; (*b*) H.M.I. Osborn and J. Sweeney. Tetrahedron: Asymmetry, **8**, 1693 (1997); (*c*) R.S. Coleman. Synlett, 1031 (1998).
5. (*a*) R.E. Parker and N.S. Isaacs. Chem. Rev. **59**, 737 (1959); (*b*) C. Bonini and G. Righi. Synthesis, 225 (1994); (*c*) M. Shimizu, A. Yoshida, and T. Fujisawa. Synlett, 204 (1992); (*d*) J.U.G. Smith. Synthesis, 629 (1984).
6. (*a*) R.-H. Fan and X.-L. Hou. J. Org. Chem. **68**, 726 (2003); (*b*) G. Sabitha, R.S. Babu, M. Rajkumar, Ch. S. Reddy, and J.S. Yadav. Tetrahedron Lett. **42**, 3955 (2001); (*c*) G. Sabitha, R.S. Babu, M. Rajkumar, and J.S. Yadav. Org. Lett. **4**, 343 (2002); (*d*) B. Das, M. Krishnaiah, and K. Venkateswarlu. Tetrahedron Lett. **47**, 4457 (2006); (*e*) J.S. Yadav, B.V.S. Reddy, G. Parimala, and P.V. Reddy. Synthesis, 2383 (2002); (*f*) B. Das, R. Ramu, B. Ravikanth, and K.R. Reddy. Tetrahedron Lett. **47**, 779 (2006); (*g*) M.K. Ghorai, K. Das, A. Kumar, and K. Ghosh. Tetrahedron Lett. **46**, 4103 (2005); (*h*) J.S. Yadav, B.V.S. Reddy, B. Jyothirmai, and M.S.R. Murty. Tetrahedron Lett. **46**, 6385 (2005); (*i*) M.S. Reddy, M. Narender, Y.V.D. Nageswar, and K.R. Rao. Tetrahedron Lett. **46**, 6437 2005); (*j*) M. Narender, K. Surendra, N.S. Krishnaveni, M.S. Reddy, and K.R. Rao. Tetrahedron Lett. **45**, 7995 (2004); (*k*) J. Wu, X.-L. Hou, and L.-X. Dai. J. Org. Chem. **65**, 1344 (2000); (*l*) M. Chandrasekhar, G. Sekar, and V.K. Singh. Tetrahedron Lett. **41**, 10079 (2000); (*m*) J.S. Yadav, B.V.S. Reddy, and G.M. Kumar. Synlett, 1417 (2001); (*n*) S. Minakata, D. Kano, Y. Oderaotoshi, and M. Komatsu. Angew. Chem. Int. Ed. **43**, 79 (2004); (*o*) H. Konno, E. Toshiro, and N. Hinoda. Synthesis, 2161 (2003); (*p*) J.S. Yadav, B.V.S. Reddy, B. Jyothirmai, and M.S.R. Murty. Tetrahedron Lett. **46**, 6559 (2005); (*q*) M.K. Pandey, A. Bisai, and V.K. Singh. Tetrahedron Lett. **45**, 9661 (2004); (*r*) N. Iranpoor, H. Firouzabadi, and M. Shekarize. Org. Biomol. Chem. **1**, 724 (2003); (*s*) J. Kroutil and K. Jenistova. Collect. Czech. Chem. Commun. **70**, 2075 (2005); (*t*) J. Kroutil and M. Budesinsky. Carbohydr. Res. **342**, 147 (2007).
7. (*a*) J. Schubert, R. Schwesinger, and H. Prinzbach. Angew. Chem. Int. Ed. Engl. **23**, 167 (1984); (*b*) G.A. Jacobs, J.A. Tino, and R. Zahler. Tetrahedron Lett. **30**, 6955 (1989); (*c*) E.F.V. Scriven and K. Turnbull. Chem. Rev. **88**, 297 (1988).
8. (*a*) M.T. Reets, R. Jaeger, R. Drewlies, and M. Hubel. Angew. Chem. Int. Ed. Engl. **30**, 103 (1991); (*b*) D. Lucet, T. Le Gall, and C. Mioskowski. Angew. Chem. Int. Ed. **37**, 2850 (1998).
9. G.D.K. Kumar and S. Baskaran. Synlett, 1719 (2004).
10. J. Wu, X. Sun, and H.-G. Xia. Eur. J. Org. Chem. 4769 (2005).
11. V.V. Thakur, S.K. Talluri, and A. Sudalai. Org. Lett. **5**, 861 (2003).
12. H. Sharghi, M.A. Nasseri, and K. Niknam. J. Org. Chem. **66**, 7287 (2001).
13. G.D.K. Kumar and S. Baskaran. J. Org. Chem. **70**, 4520 (2005).
14. M. Mizuno and T. Shioiri. Tetrahedron Lett. **40**, 7105 (1999).

© 2007 NRC Canada

Synthesis and characterization of $[M(DMSO)_6][SnCl_6]$ complexes (M = Fe^{2+}, Co^{2+}, and Ni^{2+}) — An old mystery solved

Andrew P. White, Katherine N. Robertson, T. Stanley Cameron, Bernard V. Liengme, Daniel B. Leznoff, Simon Trudel, and Manuel A.S. Aquino

Abstract: The synthesis of an "unknown" Fe(II) complex originally reported in 1973 and formulated then as $[Fe(DMSO)_5Cl][SnCl_4]$ was thoroughly reproduced and the compound reformulated as the novel $[Fe(DMSO)_6][SnCl_6]$ double complex salt. Current elemental analysis and IR and Mössbauer spectroscopy matched the original 1973 data, and Raman spectroscopy and single crystal X-ray diffraction provided additional confirmation of our reformulation. $[Fe(DMSO)_6][SnCl_6]$ (**1**) crystallizes in the trigonal space group $R\bar{3}$ with octahedral $[Fe(DMSO)_6]^{2+}$ and $[SnCl_6]^{2-}$ complex ions with an Fe—O bond length of 2.121(3) Å. The same synthesis was extended to Co(II) and Ni(II) to generate the novel $[Co(DMSO)_6][SnCl_6]$ (**2**), which crystallizes in the triclinic space group $P\bar{1}$ with a Co—O bond length of 2.093(4)–2.113(5) Å, and $[Ni(DMSO)_6][SnCl_6]$ (**3**), which crystallized in the trigonal $R\bar{3}$ space group and has a Ni—O bond length of 2.062(2) Å. The Sn—Cl bond length in all three complexes ranged from 2.421(2) to 2.448(2) Å.

Key words: DMSO complexes of Fe(II), Co(II) and Ni(II), $SnCl_6^{2-}$ salts, IR, Raman and Mössbauer spectroscopy, X-ray crystal structures.

Résumé : La synthèse d'un complexe "inconnu" de Fe(II), qui avait originalement été rapportée en 1973 et pour lequel la formule $[Fe(DMSO)_5Cl][SnCl_4]$ avait alors été proposée, a été complètement reproduite et on peut maintenant lui attribuer la formule $[Fe(DMSO)_6][SnCl_6]$, un double sel complexe. Les données obtenues au cours de ce travail pour les analyses élémentaires, les spectres infrarouge et de Mössbauer correspondent à celles qui avaient été obtenues dans le travail original de 1973; on a par ailleurs déterminé le spectre Raman et la structure cristalline par diffraction des rayons X sur un cristal unique et ces données ont permis de confirmer notre reformulation. Le complexe $[Fe(DMSO)_6][SnCl_6]$ (**1**) cristallise dans le groupe d'espace trigonal $R\bar{3}$ avec un ion octaédrique $[Fe(DMSO)_6]^{2+}$ et des ions complexes $[SnCl_6]^{2-}$; la longueur de la distance Fe—O est de 2,121(3) Å. On a étendu cette synthèse au Co(II) et au Ni(II) pour générer la formation du complexe $[Co(DMSO)_6][SnCl_6]$ (**2**) qui cristallise dans le groupe d'espace triclinique $P\bar{1}$ avec une longueur de la liaison Co—O de 2,093(4)–2,113(5) Å et du complexe $[Ni(DMSO)_6][SnCl_6]$ (**3**) qui cristallise dans le groupe d'espace trigonal $R\bar{3}$ avec une longueur de la liaison Ni—O de 2,062(2) Å. La longueur de la liaison Sn—Cl dans les trois complexes est de 2,421(2)–2,448(2) Å.

Mots-clés : complexes du Fe(II), du Co(II) et du Ni(II) avec le DMSO, sels complexes du $SnCl_6^{2-}$, spectroscopie Raman et de Mössbauer, structures cristallines par diffraction des rayons X.

[Traduit par la Rédaction]

Introduction

A number of years ago Fred Wen, a Master's student of one of the authors (BVL), reported on a reaction involving $FeCl_2$, $SnCl_2$, and dimethylglyoximate anion ($dmgH^-$) in dimethylsulfoxide (DMSO) (1), while investigating the chemistry and spectroscopy (IR and Mössbauer) of Fe–Sn complexes. The red product of this reaction was reported to have the formulation $[Fe(DMSO)_5Cl][SnCl_3]$ and was reportedly only produced when $dmgH_2$ was present.

$$FeCl_2 + SnCl_2 \xrightarrow[DMSO]{dmgH_2} [Fe(DMSO)_5Cl][SnCl_3]$$

This formulation was consistent with the elemental analysis and IR spectroscopy performed at the time. However, while the ^{57}Fe Mössbauer spectrum did reveal a high-spin Fe(II) center to be present, the ^{119}Sn Mössbauer results pointed unequivocally to an oxidized Sn(IV) center, which was *not* consistent with the above formulation.

We report here a thorough re-investigation of this reaction, both in the presence and absence of $dmgH^-$ and compare our elemental analysis, IR, and ^{57}Fe Mössbauer results with those reported by Wen. In addition, we extend the synthetic method to include Co(II) and Ni(II) (along with the

Received 7 March 2007. Accepted 23 April 2007. Published on the NRC Research Press Web site at http://canjchem.nrc.ca on 18 May 2007.

K.N. Robertson and T.S. Cameron. Department of Chemistry, Dalhousie University, Halifax, NS B3H 4J3, Canada.
D.B. Leznoff and S. Trudel. Department of Chemistry, Simon Fraser University, 8888 University Drive, Burnaby, BC V5A 1S6, Canada.
A.P. White, B.V.Liengme, and M.A.S. Aquino.[1] Department of Chemistry, St. Francis Xavier University, P.O. Box 5000, Antigonish, NS B2G 2W5, Canada.

[1]Corresponding author (e-mail: maquino@stfx.ca).

 doi:10.1139/X07-042 © 2007 NRC Canada

Fe(II)) and report on the IR and Raman spectroscopy and the X-ray crystallography of all three complexes. We show them to have the formulation $[M(DMSO)_6][SnCl_6]$, where M = Fe(II) (**1**), M = Co(II) (**2**), and M = Ni(II) (**3**). These double complex salts have not been reported previously, and in fact there have been only a limited number of structures reported containing the $[M(DMSO)_6]^{2+}$ dication with these metal centers (2–10), with only one for M = Fe(II) (2) and two others, $[Co(DMSO)_6][CoCl_4]$ (4) and $[Ni(DMSO)_6][NiCl_4]$ (6), reported as double complex salts (neither of which contain two octahedra).

Experimental

Reagents

$FeCl_2{\cdot}4H_2O$, $CoCl_2{\cdot}6H_2O$, $NiCl_2{\cdot}6H_2O$, and $SnCl_2{\cdot}2H_2O$ (Sigma-Aldrich) were used as received. Dimethylsulfoxide and 2,2′-dimethoxypropane (Sigma-Aldrich) were used without further purification.

Synthesis

$[M(DMSO)_6][SnCl_6]$, M = Fe(II) (1), Co(II) (2), and Ni(II) (3)

Complexes **1**, **2**, and **3** were all prepared in a similar fashion. $FeCl_2{\cdot}4H_2O$ (**1**) (2.10 g, 10 mmol), $CoCl_2{\cdot}6H_2O$ (**2**) (2.50 g, 10 mmol), or $NiCl_2{\cdot}6H_2O$ (**3**) (2.50 g, 10 mmol) and $SnCl_2{\cdot}2H_2O$ (4.30 g, 20 mmol) were dissolved in 150–200 mL of dimethylsulfoxide (DMSO) at room temperature. The resulting solution was gravity filtered to yield a yellow-green (**1**), light purple (**2**), or yellow-green (**3**) solution. Ten milliliters of 2,2′-dimethoxypropane was then added and the solution was heated under Ar at 100–120 °C for 3 to 4 h until the solution changed to pale yellow (**1**), dark purple (**2**), or dark green (**3**). The solution was then allowed to cool and diethyl ether was added until a pale yellow (**1**), light blue (**2**), or light green (**3**) precipitate formed. The precipitate was vacuum filtered, washed with 20 mL of diethyl ether, and dried in vacuo. In all three cases, crystals could be grown by cooling and slow evaporation from hot DMSO solutions. Yields were 8.2 g (91%) for **1**, 8.3 g (92%) for **2**, and 7.9 g (87%) for **3**.

Physical Methods

IR spectra were run as KBr discs on a Bio-Rad FTS-175 spectrophotometer. Raman spectra were acquired on a Renishaw InVia Raman Microscope (Prospect Scientific, Toronto, Canada) equipped with a 514.5 nm laser, a 1800 l/mm grating, a CCD detector, and a 50 × 0.75 NA objective. Samples were deposited on glass slides and the laser power used on the sample was 5 mW. Mössbauer spectra were run at 80 K on a WEB Mössbauer spectroscopy system connected to a Janis Research variable temperature SHI-850 Cryostat and a closed cycle refrigerator. A ^{57}Co (in rhodium matrix) source was used with a source strength of ~40 mCi (1 Ci = 37 GBq). The detector was a Reuters–Stokes Kr–CO_2 proportional counter. Samples were loaded into a custom-made Teflon holder and the velocity scanned between 4 and –4 mm/s using a constant acceleration triangle waveform. The measured isomer shifts (δ) are relative to an Fe foil measured at 295 K in zero magnetic field. Fitting of the data was performed using WMOSS software. C, H, and Cl elemental analysis was performed by Canadian Microanalytical Service Ltd. (Delta, BC, Canada).

X-ray structure determinations for **1** and **3** were performed on a Rigaku AFC5R diffractometer with graphite monochromated Mo Kα radiation and a rotating anode generator, whereas **2** was analyzed using a Rigaku Saturn CCD area detector with graphite monochromated Mo Kα radiation. The crystal data and structure refinement parameters for all three complexes are given in Table 1. All structures were solved by direct methods (11) and expanded using Fourier techniques (12). For complexes **1** and **3** the non-hydrogen atoms were refined anisotropically. Hydrogen atoms were included but not refined. They were placed in geometrically calculated positions and allowed to ride on the heavy atom to which they were bonded with U_{iso} equal to 1.5 × U_{eq} of the heavy atom. In complex **1** the dimethylsulfoxide (DMSO) ligands, of which only one was unique, were found to be disordered. The sulfur and carbon atoms of the ligand were split over two positions and the occupancy of each refined (Part 1 (A) 92.9% and Part 2 (B) 7.1%). The atomic displacement parameters of C1a/C1b and of C2a/C2b were restrained to be equal. A rigid bond restraint and a restraint for similar atomic displacements were applied to the entire molecule. Finally, restraints were applied to certain of the bond lengths and 1,3 distances in the cation. These restraints were applied to both part A and part B atoms. The C—S bond lengths were restrained to 1.73 (0.015) Å and the O—S bond lengths to 1.50 (0.01) Å. The distance between C1 and C2 atoms in both A and B was restrained to 2.64 (0.02) Å and the O1 to C distances were restrained to 2.60 (0.02) Å. For complex **2**, the non-hydrogen atoms were refined anisotropically. Hydrogen atoms were refined using a riding model, with U_{iso} of hydrogen equal to 1.2 × U_{eq} of the heavy atom to which each was bonded.

For all complexes the neutral atom scattering factors were taken from Cromer and Waber (13). Anomalous dispersion effects were included in F_{calc} (14); the values for $\Delta f'$ and $\Delta f''$ were those of Creagh and McAuley (15). The values for the mass attenuation coefficients are those of Creagh and Hubbell (16). All calculations for complexes **1** and **3** were performed using the teXsan (17) crystallographic software package of Molecular Structure Corporation except for the refinement, which was performed using SHELXL-97 (18). All calculations on complex **2** were performed using the CrystalStructure (19, 20) crystallographic software package. ORTEP diagrams were prepared using ORTEP-3 (version 1.076) (21) and POV-Ray (version 3.6.0) (22).

Additional details are provided in the Supplementary data.[2]

[2] Supplementary data for this article are available on the journal Web site (http://canjchem.nrc.ca) or may be purchased from the Depository of Unpublished Data, Document Delivery, CISTI, National Research Council Canada, Ottawa, ON K1A 0R6, Canada. DUD 5170. For more information on obtaining material refer to http://cisti-icist.nrc-cnrc.gc.ca/irm/unpub_e.shtml. CCDC 637505, 637506, and 637507 contain the crystallographic data for this manuscript. These data can be obtained, free of charge, via http://www.ccdc.cam.ac.uk/conts/retrieving.html (Or from the Cambridge Crystallographic Data Centre, 12 Union Road, Cambridge CB2 1EZ, UK; fax +44 1223 336033; or deposit@ccdc.cam.ac.uk).

© 2007 NRC Canada

Table 1. Crystal and structure refinement data for complexes **1–3**.

Compound	**1**	**2**	**3**
Formula	$C_{12}H_{36}Cl_6FeO_6S_6Sn$	$C_{12}H_{36}Cl_6CoO_6S_6Sn$	$C_{12}H_{36}Cl_6NiO_6S_6Sn$
Formula weight	856.01	859.11	858.88
Temperature (K)	213(2)	193(1)	213(2)
Wavelength (Å)	0.71070	0.71070	0.71070
Crystal system	Trigonal	Triclinic	Trigonal
Space group	$R\bar{3}$	$P\bar{1}$	$R\bar{3}$
a (Å)	13.611(2)	9.026(2)	13.542(5)
b (Å)	13.611(2)	9.338(2)	13.542(5)
c (Å)	15.366(3)	9.666(2)	15.416(5)
α (°)	90	93.602(4)	90
β (°)	90	93.047(5)	90
γ (°)	120	92.287(6)	120
V (Å^3)	2465.4(7)	811.3(2)	2448.2(14)
Z	3	1	3
$D_{calcd.}$ (mg/m^3)	1.730	1.76	1.747
μ (mm^{-1})	2.093	2.185	2.241
F(000)	1290	431	1296
Crystal size (mm^3)	0.34 × 0.17 × 0.17	0.02 × 0.15 × 0.15	0.50 × 0.30 × 0.30
θ range (°)	2.99–30.08	2.1–30.0	3.01–30.04
Index ranges	$-19 \le h \le 19$, $-19 \le k \le 19$, $-21 \le l \le 21$	$-12 \le h \le 10$, $-11 \le k \le 12$, $-13 \le l \le 13$	$-19 \le h \le 19$, $-19 \le k \le 19$, $-21 \le l \le 21$
Reflections collected	1762	19 334	1745
Independent reflections	1607	3800	1596
R_{int}	0.0285	0.040	0.0232
Data, restraints, params.	1607, 82, 66	2480, 0, 166	1596, 0, 52
Goodness of fit on F^2	1.047	1.644	1.053
Final R indices [$I > 2\sigma(I)$]	$R_1 = 0.0338$, $wR_2 = 0.0888$	$R = 0.066$, $R_w = 0.083$	$R_1 = 0.0301$, $wR_2 = 0.0784$

Results and discussion

Synthesis

Since it is puzzling why Wen used $dmgH_2$ in his preparations, we have repeated his synthesis of the iron complex (as closely as possible) in the presence and absence of 30 mmol of $dmgH_2$. In both cases a product is formed. The colour of the crude product in the presence of the $dmgH^-$ is pink to red and in the absence of the $dmgH^-$ it is yellow. After recrystallization from hot DMSO *both* products appear yellow and crystalline and have the proposed formulation, $[Fe(DMSO)_6][SnCl_6]$ (**1**) (see more later). The small amount of red impurity, almost certainly due to $[Fe(dmgH)_2(DMSO)_2]$, is easily removed by recrystallization. In fact, the longer the heating in DMSO is allowed to proceed (>5 h) the fainter the red colour of the crude product. The presence of $[Fe(dmgH)_2(DMSO)_2]$ would not be unusual as numerous $[Fe(dmgH)_2L_2]$-type complexes (with L = pyridine, phosphines, CO, and isocyanides, for example) have been documented in the literature (23). When we undertake an identical reaction, using $CoCl_2$ as our starting material, we obtain a purple coloured crude product (with or without $dmgH^-$ present) that, upon recrystallization, yields a light blue crystalline product **2**. Only in the case of $NiCl_2$ as our starting reactant do we encounter two distinct products. With $dmgH^-$ present, only the bright red $Ni(dmgH)_2$ is formed. In the absence of $dmgH^-$, only **3** is formed.

Another significant feature of these reactions that should be noted is that the correct stoichiometric amount of chloride ion must be present, i.e., 2 equiv. from the 10 mmol $FeCl_2$ and 4 equiv. from the 20 mmol $SnCl_2$. If only 10 mmol of $SnCl_2$ is used, no significant amount of solid is produced. It is odd that Wen used 20 mmol of $SnCl_2$ in his reaction as his proposed formulation, $[Fe(DMSO)_5Cl][SnCl_3]$ only requires 4 equiv. of Cl^-.

Finally, the issue of the presence of Sn(IV) vs. Sn(II) that Wen noted and that contradicts his formulation needs to be addressed. Under the reaction conditions, which we have tried to reproduce closely, air has not been excluded rigorously. Even though the reaction heating is performed under an atmosphere of argon, the initial dissolution of reagents and the final workup (addition of diethylether) is not. In addition, none of the solvents have been degassed. These conditions are certainly enough to prevent the oxidation of the Fe(II) but not Sn(II), as it is very sensitive to even small amounts of O_2 in solution (24).

Table 2 compares the C, H, and Cl elemental analysis results for all three complexes obtained in this current work, with and without the addition of $dmgH^-$ for **1** and **2**, to those obtained by Wen (1).

It is clear that the elemental analyses for **1** and **2** are identical whether the synthetic procedure employed $dmgH^-$ or not. As mentioned earlier, complex **3** only forms in the absence of $dmgH^-$. Comparing the results for complex **1** to those of Wen we see reasonable agreement of the %C and

© 2007 NRC Canada

Table 2. Elemental analysis results for **1, 2**, **3**, and Wen's product.

Sample	%C	%H	%Cl
Wen's product[a]	17.5[b]	4.40	19.99
$[Fe(DMSO)_5Cl][SnCl_3]$[a]	17.0[b]	4.24	20.06
1 (with $dmgH^-$)	16.84	4.43	24.69
1 (without $dmgH^-$)	17.13	4.27	24.46
$[Fe(DMSO)_6][SnCl_6]$	16.84	4.24	24.85
2 (with $dmgH^-$)	16.96	4.20	24.81
2 (without $dmgH^-$)	16.77	4.23	24.68
$[Co(DMSO)_6][SnCl_6]$	16.77	4.23	24.75
3 (without $dmgH^-$)	16.72	4.35	24.91
$[Ni(DMSO)_6][SnCl_6]$	16.76	4.23	24.76

[a]Ref. 1.
[b]Only one decimal reported.

%H values but the %Cl of Wen's product is lower. As Wen provides no evidence that he recrystallized his crude product, the slight disparity in the elemental analysis values could be due to a small amount of $[Fe(dmgH)_2(DMSO)_2]$ impurity, which would substantially lower the %Cl and slightly raise the %C and %H. It should also be noted that even small amounts of DMSO of solvation would raise the %C and %H and lower the %Cl.

IR, Raman, and Mössbauer spectroscopy

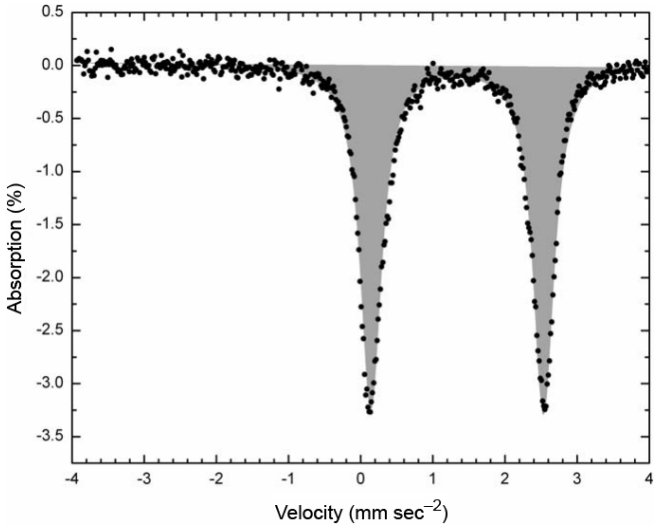
The IR and Raman spectra for complexes synthesized in the presence or absence of $dmgH^-$ were identical (see Table S1 in the Supplementary material).[2] All three complexes show very similar IR and Raman spectra that are predominated by modes associated with the DMSO ligand (25). As well, the data for our complex **1** is essentially identical to the data for Wen's complex. Briefly, the major features are bands around 2900–3000 cm^{-1} due to ν_{as} and ν_s (C–H); δ_{as} and δ_s (C–H) at 1290–1440 cm^{-1}; a very strong ν (S=O) at 1005 cm^{-1} in the IR (very weak in the Raman); and ν_{as} and ν_s (C–S) in the range 670–720 cm^{-1}. A key feature of the IR spectra is the decrease in ν (S=O) of about 45 cm^{-1} in the complexes from that of free DMSO, which is indicative of binding through the oxygen (26).

The ^{57}Fe Mössbauer spectrum of complex **1**, determined at 80 K, is shown in Fig. 1. Fitting the data yielded an isomer shift (δ) of 1.34 mm s^{-1} vs. Fe foil and a quadropolar splitting (ΔE_q) of 2.39 mm s^{-1}. These parameters are consistent with a high-spin Fe(II) center (27) and are very similar to the values Wen determined for his complex. Wen's parameters were δ = 1.56 mm s^{-1} and ΔE_q = 2.12 mm s^{-1}, using nitroprusside as reference (instead of Fe foil). Using a correction of 0.26 mm s^{-1} for Fe foil vs.nitroprusside (27), our isomer shift value for complex **1** is δ = 1.60 mm s^{-1}. We have not been able to measure the ^{119}Sn Mössbauer spectrum; however, Wen's results pointed to an Sn(IV) center (δ = 0.47 mm s^{-1}, ΔE_q = 0 vs. SnO_2), which already contradicted his proposed formulation of $[Fe(DMSO)_5Cl][SnCl_3]$ (which would contain an Sn(II) center) and supports ours, $[Fe(DMSO)_6][SnCl_6]$, which contains an Sn(IV) center.

Structure of $[Fe(DMSO)_6][SnCl_6]$ (1)

Complex **1** crystallizes in an R-centered trigonal cell with a space group of $R\bar{3}$. The structure is shown in Fig. 2, crystal parameters in Table 1, and selected bond lengths and angles in Table 3. The structure consists of an octahedral $[Fe(DMSO)_6]^{2+}$ cation containing Fe(II) and an $[SnCl_6]^{2-}$ anion containing Sn(IV). As mentioned in the Experimental section, the DMSO ligands are disordered and the S and C atoms are averaged between two positions with 92.9% and 7.1% occupancy (see Fig. 2*A*). The bond angles for both ions are consistent with essentially undistorted octahedral coordination. There are no surprises in any of the bond lengths (ranging from 2.102(3) to 2.149(3) Å (2)), with the Fe—O bond length of 2.121(3) Å comparing well with the values seen in the only other complex containing $Fe(DMSO)_6^{2+}$ that we have been able to find that has been crystallographically characterized $[Fe(DMSO)_6][Cl_2Fe(MoS_4)]$.

Fig. 1. ^{57}Fe Mössbauer spectrum (with fitting) of $[Fe(DMSO)_6][SnCl_6]$ at 80 K.



Structure of $[Co(DMSO)_6][SnCl_6]$ (2)

Complex **2** crystallizes in a primitive triclinic cell with space group $P\bar{1}$. The structure is shown in Fig. 3, crystal parameters in Table 1, and selected bond lengths and angles in Table 3. As in **1** this complex consists of two essentially undistorted octahedra. Most bond lengths and angles are identical to those in **1** and the Co—O bond length is in the range 2.093(4)–2.113(5) Å. Three previous structures containing the $[Co(DMSO)_6]^{2+}$ cation have been reported, including $[Co(DMSO)_6](ClO_4)_2$·DMSO (3), $[Co(DMSO)_6](CoCl_4)$ (4), and $[Co(DMSO)_6]I_4$ (5), with Co—O bond lengths ranging from 2.083(2) to 2.113(4) Å.

Structure of $[Ni(DMSO)_6][SnCl_6]$ (3)

Complex **3** (similar to complex **1**) crystallizes in the R-centered trigonal cell with a space group of $R\bar{3}$, with no disorder of the DMSO ligands. The structure is shown in Fig. 4, crystal parameters in Table 1, and selected bond lengths and angles in Table 3. Its characteristics are very similar to those of **1** and **2**. A number of X-ray structures, which include the $[Ni(DMSO)_6]^{2+}$ cation, have been previously reported (6–10). The Ni—O bond length in our complex is 2.062(2) Å, which is close to the values seen, for example, in $[Ni(DMSO)_6]Cl_2$·DMSO (2.041(3)–2.085(3) Å) and $[Ni(DMSO)_6][NiCl_4]$ (2.059(3)–2.079(3) Å) (6).

© 2007 NRC Canada

Fig. 2. (*A*) ORTEP diagram of the molecular structure of $[Fe(DMSO)_6][SnCl_6]$ (**1**). The disorder is shown, where the "A" DMSO are in orange and the "B" DMSO are in blue. Hydrogen atoms are removed for clarity. (*B*) "A" form of the $Fe(DMSO)_6^{2+}$ ion. The ellipsoids represent the 50% probability of finding the atom at that position.

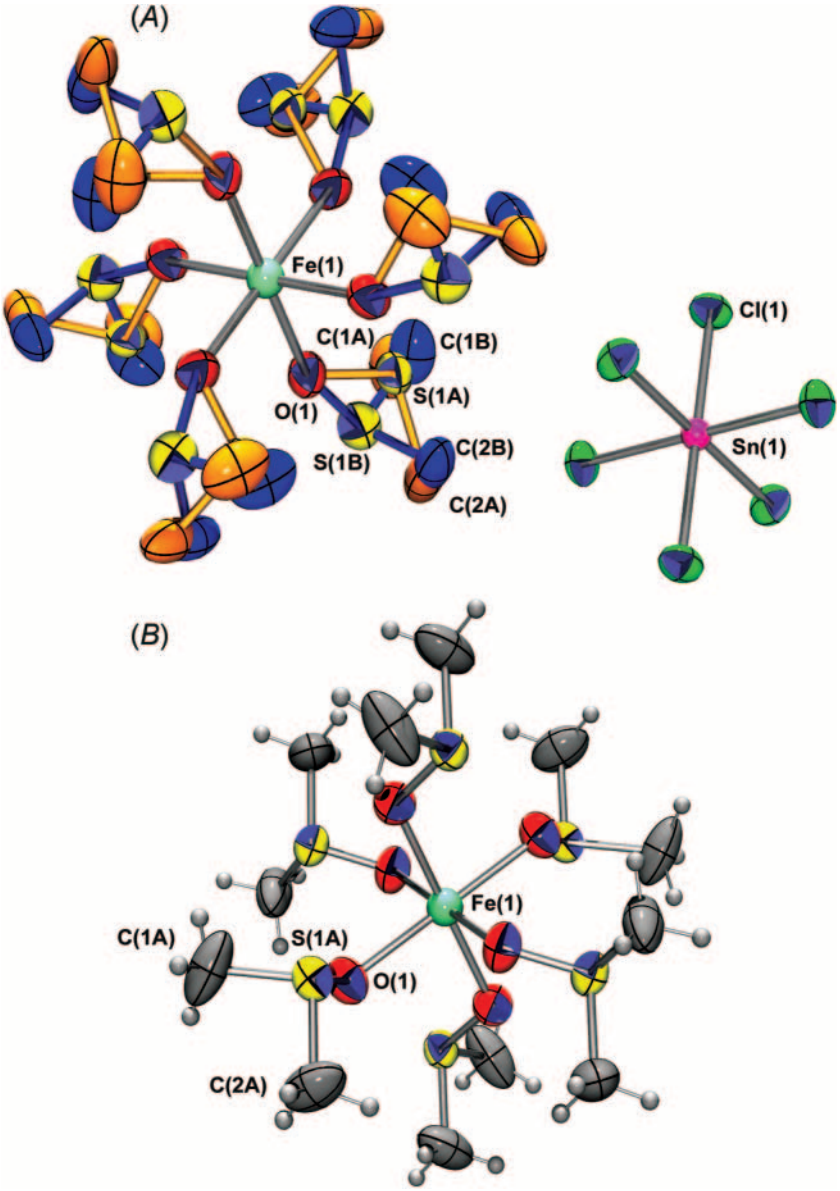


Table 3. Selected bond lengths and angles for complexes **1**, **2**, and **3**.

	M = Fe(II) (**1**)	M = Co(II) (**2**)	M = Ni(II) (**3**)
Bond lengths (Å)			
M—O	2.121(3)	2.093(4)–2.113(5)	2.062(2)
S=O	1.530(3), 1.532(9)	1.516(6)–1.532(6)	1.526(3)
C—S	1.739(5), 1.744(6)	1.73(1)–1.76(1)	1.750(4), 1.761(5)
Sn—Cl	2.4230(9)	2.421(2)–2.448(2)	2.4270(11)
Bond angles (°)			
O–M–O (cis O's)	89.55(12), 90.45(12)	89.0(2)–90.0(2)	89.68(10), 90.32(10)
M–O–S	117.06(17), 161.7(7)	115.7(3)–117.5(3)	116.94(14)
O–S–C	104.7(2), 104.6(3) 103.8(4), 103.2(4)	104.0(4)–105.4(4)	104.5(2), 104.59(19)
C–S–C	98.4(3), 98.0(3)	98.3(4)–99.6(5)	98.7(3)
Cl–Sn–Cl (cis Cl's)	89.80(4), 90.20(4)	89.48(7)–89.58(7)	89.83(4), 90.17(4)

© 2007 NRC Canada

Fig. 3. Molecular structure of $[Co(DMSO)_6][SnCl_6]$ (**2**). The ellipsoids represent the 50% probability of finding the atom at that position.

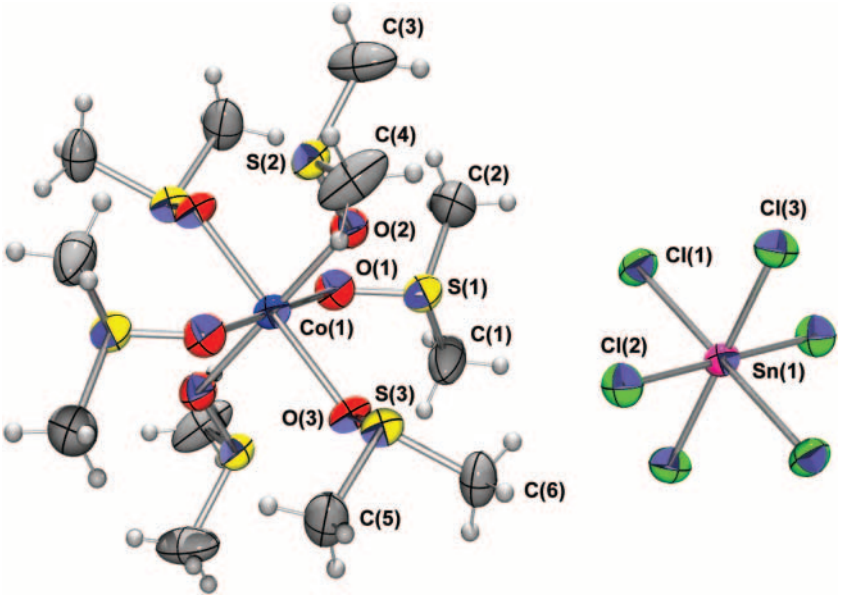
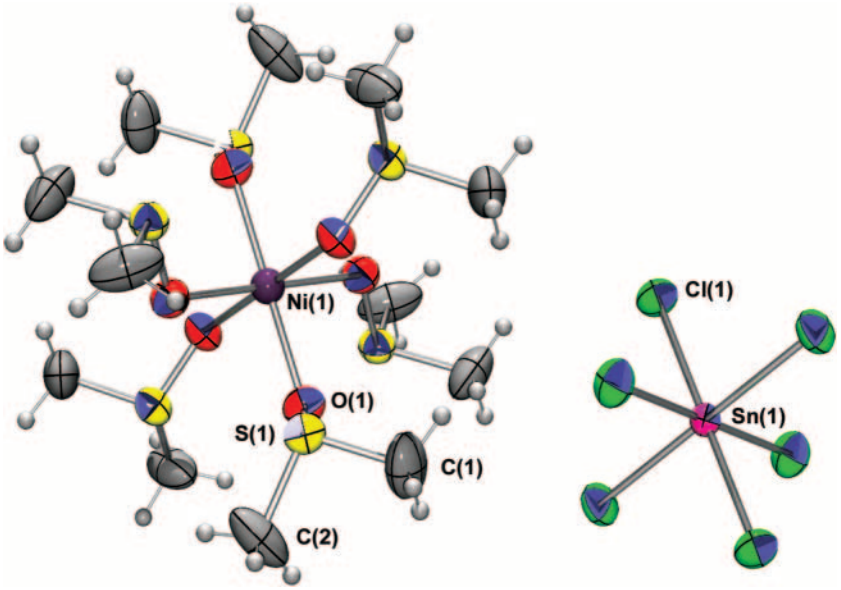


Fig. 4. Molecular structure of $[Ni(DMSO)_6][SnCl_6]$ (**3**). The ellipsoids represent the 50% probability of finding the atom at that position.



The Sn—Cl bond length for the three complexes ranges from 2.421(2) Å to 2.448(2) Å, typical of $SnCl_6^{2-}$ complexes (28), and the decrease in M—O bond length on going from Fe(II) to Co(II) to Ni(II) is consistent with the increase in effective nuclear charge and decrease in the ionic radii for octahedral (high-spin) ions, Fe(II) > Co(II) > Ni(II), as per the Irving–Williams series for first-row $[M(H_2O)_6]^{2+}$ complexes (29).

Conclusion

We have succeeded in reproducing Wen's synthesis of the unknown iron–tin complex both in the presence and absence of $dmgH^-$ and have shown that the same compound is produced in both cases. The original reddish colour Wen reported was most likely due to an $[Fe(dmgH)_2(DMSO)_2]$ impurity that is easily removed by recrystallization from hot DMSO. The elemental analysis (allowing for the $[Fe(dmgH)_2(DMSO)_2]$ impurity in Wen's sample) and IR and Mössbauer spectroscopy of our iron–tin complex match Wen's results very well. From the additional Raman data and the single crystal X-ray diffraction results, we conclude that the correct formulation for the complex is $[Fe(DMSO)_6][SnCl_6]$. We were able to extend the synthesis to include Co(II) and Ni(II) and the structures of both $[Co(DMSO)_6][SnCl_6]$ and $[Ni(DMSO)_6][SnCl_6]$ were also elucidated. None of the three complexes have been previously reported, and while the $[Co(DMSO)_6]^{2+}$ and

© 2007 NRC Canada

$[Ni(DMSO)_6]^{2+}$ ions have been reported in X-ray structures on a few occasions, surprisingly, ours is only the second reported structure containing the $[Fe(DMSO)_6]^{2+}$ complex ion.

The mystery of Wen's unknown iron–tin complex has therefore been solved and we hope this may encourage other researchers to re-investigate past experiments to clear up unsolved problems. We are currently trying to extend the synthesis even further to Cr(II) and Ru(II), as neither the $[Cr(DMSO)_6]^{2+}$ or $[Ru(DMSO)_6]^{2+}$ have been structurally characterized.

Acknowledgements

The authors would like to thank Professor Rich Dunlap of Dalhousie University for helpful discussions and preliminary Mössbauer measurements and Dr. Christophe Sandt and Mr. Stephen Smith for assistance with the Raman spectroscopy. Thanks are also due to the Natural Sciences and Engineering Research Council of Canada (NSERC) and the University Council for Research (UCR) at St. Francis Xavier University for funding.

References

1. F.Y.-P. Wen. M.Sc. Thesis. 1973. St. Francis Xavier University, Antigonish, N.S.
2. A. Müller, H. Bögge, U. Schimanski, M. Penk, K. Nieradzik, M. Dartmann, E. Krickemeyer, J. Schimanski, C. Römer, M. Römer, H. Dornfeld, U. Wienböker, W. Hellmann, and M. Zimmermann. Monatsh. Chem. **120**, 367, (1989).
3. C. Comuzzi, A. Melchior, and P. Polese. Eur. J. Inorg. Chem. 2194 (2002).
4. A. Ciccarese, D.A. Clemente, A. Marzotto, and G. Valle. J. Crystallogr. Spectrosc. Res. **23**, 223 (1993).
5. V.V. Tkachev, E.A. Lavrent'eva, O.S. Rosschupkina, I.P. Lavrent'ev, and L.O. Atovmyan. Koord. Khim. **20**, 674 (1994).
6. D. Bobicz, O. Kristiansson, and I. Persson. J. Chem. Soc. Dalton Trans. 4210 (2002).
7. A.J. Blake, M. Felloni, P. Hubbertstey, M. Schroder, and C. Wilson. Acta Crystallogr. Sect. E, **57**, m556 (2001).
8. O. Kristiansson, I. Persson, D. Bobicz, and D. Xu. Inorg. Chim. Acta, **344**, 15 (2003).
9. J.H. Reibenspies and J.S. Kim. Z. Kristallogr. **211**, 418 (1996).
10. D.-L. Long, H.-M. Hu, J.-T. Chen, and J.-S. Huang. Acta Crystallogr. Sect. C, **55**, 339 (1999).
11. A. Altomare, G. Cascarano, C. Giacovazzo, A. Guagliardi, M. Burla, G. Polidori, and M. Camalli. J. Appl. Crystallogr. **27**, 435 (1994).
12. P.T. Beurskens, G. Admiraal, G. Beurskens, W.P. Bosman, R. de Gelder, R. Israel, and J.M.M. Smits. DIRDIF-99 [computer program]. Technical report of the crystallography laboratory, University of Nijmegen, The Netherlands. 1999.
13. D.T. Cromer and J.T. Waber. International tables for X-ray crystallography. Vol. IV. The Kynoch Press, Birmingham, England. 1974. Table 2.2A.
14. J.A. Ibers and W.C. Hamilton. Acta Crystallogr. **17**, 781 (1964).
15. D.C. Creagh and W.J. McAuley. International tables for crystallography. Vol C. *Edited by* A.J.C. Wilson. Kluwer Academic Publishers, Boston, Mass. 1992. pp. 219–222, Table 4.2.6.8.
16. D.C. Creagh and J.H. Hubbell. International tables for crystallography. Vol C. *Edited by* A.J.C. Wilson. Kluwer Academic Publishers, Boston, Mass. 1992. pp. 200–206, Table 4.2.4.3.
17. teXsan [computer program]. Version 1.06. Crystal structure analysis package, Molecular Structure Corporation, The Woodlands, Tex. 1997.
18. G.M. Sheldrick. SHELXL97 [computer program]. University of Göttingen, Göttingen, Germany. 1997.
19. CrystalStructure [computer program]. Version 3.5.1. Crystal structure analysis package, Rigaku, The Woodlands, Tex. 2000.
20. D.J. Watkin, C.K. Prout, J.R. Carruthers, and P.W. Betteridge. CRYSTALS [computer program]. Issue 10. Chemical Crystallography Laboratory, Oxford, UK. 1996.
21. L.J. Farrugia. J. Appl. Crstallogr. **30**, 565 (1997).
22. T.D. Fenn, D. Ringe, and G.A. Petsko. J. Appl. Crystallogr. **36**, 944 (2003); POV-Ray [computer program]. Version 3.6.0. Persistence of Vision Raytracer Pty. Ltd. Available from http://www.povray.org.
23. H.E. Toma and L.A.Morino. Transition Met. Chem. **15**, 66 (1990) and refs. cited therein.
24. F.A. Cotton, G. Wilkinson, C.A. Murillo, and M. Bochmann. Advanced inorganic chemistry. 6th ed. John Wiley and Sons Inc., New York. 1999.
25. C.J. Pouchert. The Aldrich library of FT-IR Spectra (Ed. 1). Vol. 1. The Sigma-Aldrich Chemical Company, Milwaukee, Wisconsin. 1985. p. 879A.
26. K. Nakamoto. Infrared and Raman spectra of inorganic and coordination compounds. Part A. 5th Ed. John Wiley and Sons Inc., New York. 1997.
27. V.I. Goldanskii and R.H. Herber. Chemical applications of Mössbauer spectroscopy. Academic Press, New York. 1968.
28. I. Wharf and D.F. Shriver. Inorg. Chem. **8**, 914 (1969).
29. C.E. Housecroft, and A.G. Sharpe. Inorganic chemistry. 2nd ed. Pearson Ed. Ltd., Harlow, U.K. 2005.

© 2007 NRC Canada

Improvement of hydrothermal stability of an ordered mesoporous molecular sieve via multistage recrystallization

Yong M. Luo, Zhao Y. Hou, Rong T. Li, and Xiao M. Zheng

Abstract: A highly ordered mesoporous aluminosilicate molecular sieve, designated as MSAMS-4, has been synthesized via multistage recrystallization. Hydrothermal-stability tests revealed that MSAMS-4 has retained a well-ordered hexagonal-symmetry mesostructure both after treatment with 100 °C water for 120 h and after steaming at 800 °C for 6 h.

Key words: aluminosilicates molecular sieves, mesoporous materials, multistage recrystallization, hydrothermal stability.

Résumé : Faisant appel à des recristallisations en plusieurs étapes, on a réalisé la synthèse d'un tamis moléculaire d'aluminosilicate mésoporeux fortement ordonné, dénommé MSAMS-4. Des essais de stabilité hydrothermique démontrent que le MSAMS-4 maintient sa mésostructure de symétrie hexagonale bien ordonnée après avoir été traité à 100 °C pendant 120 heures ou par de la vapeur d'eau à 800 °C pendant 6 heures.

Mots-clés : tamis moléculaires d'aluminosilicates, matériaux mésoporeux, recristallisation en plusieurs étapes, stabilité hydrothermique.

[Traduit par la Rédaction]

Introduction

The hydrothermal stability and the acidity of mesoporous molecular sieves are far lower than those of microporous aluminosilicate zeolites. This could be attributed to the amorphous nature of the mesopore walls, which severely hinders them from practical applications, e.g., acting as catalytic supports or catalysts in petroleum refining and fine-chemical synthesis (1–3). Therefore, many efforts have been focused on improving both the hydrothermal stability and the acidity of mesoporous molecular sieves (4–13). One might expect both to be improved if zeolite-like order could be introduced into the mesopore walls. The amorphous walls of the mesostructure could indeed be converted to a partially zeolitic product. For example, Kloetstra et al. reported the transformation of the walls of Al-HMS and Al-MCM-41 into partially zeolitic structures by ion-exchanging them with a microporous zeolites-structure template, such as TPA^+ (4). Hydrothermally stable mesoporous materials have been synthesized via the assembly of zeolite seeds of ZSM-5, BEA, TS-1, FAU, and so forth, using cetyltrimethylammonium bromide (CTAB) or $HO(CH_2CH_2O)_{20}(CH_2CH(CH_3)O)_{70}(CH_2CH_2O)_{20}H$ (P123) as a structure-directing agent (5–11).

Results and discussion

In this paper, we describe the synthesis of a highly ordered mesoporous aluminosilicate molecular sieve, designated as MSAMS-4, via multistage recrystallization, using ordered mesoporous SBA-15 and aluminosilicates sol–gel diluted solution. Its hydrothermal stability might be attributed to the synergistic effect of the thicker wall, the higher condensation of silanol groups, insertion of non-framework Al atoms, and the formation of zeolites-like subunits within the mesoporous framework.

Figure 1A illustrates the XRD patterns of MSAMS-4 before and after hydrothermal-stability tests. An intense (100) diffraction peak and three well-resolved higher-order (110), (200), and (210) peaks are observed for all three samples. Figure 1B provides the N_2 adsorption–desorption isotherms for MSAMS-4 before and after hydrothermal treatment, and the corresponding pore-size-distribution curves of them are

Received 4 January 2007. Accepted 30 March 2007. Published on the NRC Research Press Web site at canjchem.nrc.ca on 23 May 2007.

Y.M. Luo.[1] Faculty of Environmental Science and Engineering, Kunming University of Science and Technology, Kunming 650093, People's Republic of China; Institute of Catalysis, Department of Chemistry, Zhejiang University (Xixi campus), Hangzhou 310028, People's Republic of China.
Z.Y. Hou and X.M. Zheng.[2] Institute of Catalysis, Department of Chemistry, Zhejiang University (Xixi campus), Hangzhou 310028, People's Republic of China.
R.T. Li. Faculty of Chemical and Bioengineering, Kunming University of Science and Technology, Kunming 650093, People's Republic of China.

[1]Corresponding author (email: luoyongming@tsinghua.org.cn).

[2]Corresponding author (email: xmzheng@zju.edu.cn).

 doi:10.1139/V07-032 © 2007 NRC Canada

Fig. 1. (A) XRD patterns and (B) N_2-adsorption isotherms of MSAMS-4 before and after the hydrothermal-stability test: (*a*) before, (*b*) after treatment with 100 °C water for 120 h, and (*c*) after steaming at 800 °C for 6 h (20% H_2O in N_2 (*v*/*v*)). The isotherms of (*b*) and (*c*) are offset by 200 and 400 cm^3/g for clarity.

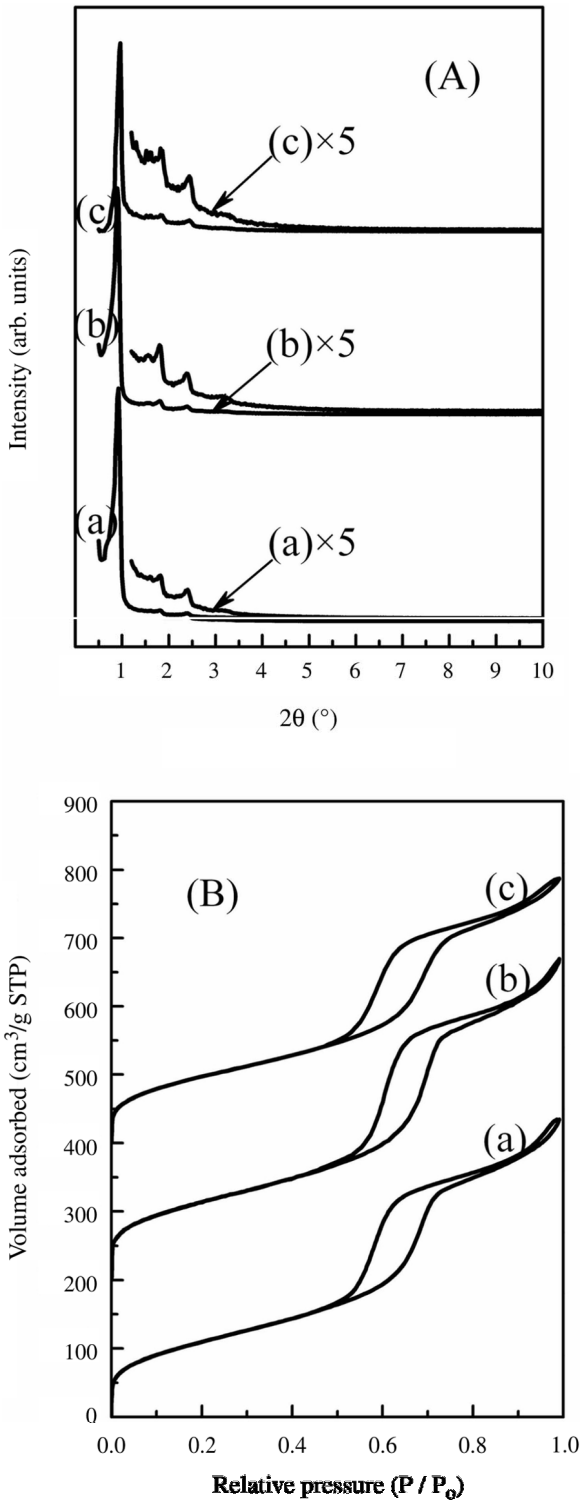
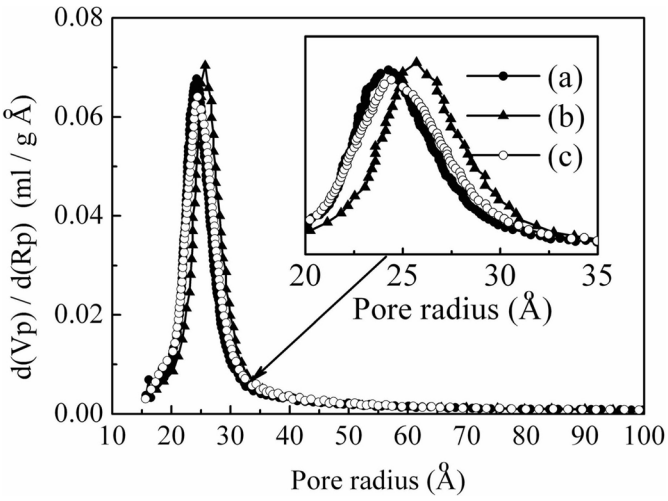


Fig. 2. BJH pore-size-distribution curves of MSAMS-4 before and after the hydrothermal-stability test: (*a*) before, (*b*) after treatment with 100 °C water for 120 h, and (*c*) after steaming at 800 °C for 6 h (20% H_2O in N_2 (*v*/*v*)).



presented as BJH plots in Fig. 2. All samples exhibit type IV isotherms with H_1 hysteresis loops, and a relatively narrow pore-size distribution is observed for each of them. In addition, no obvious changes for the specific surface area and micropore and mesopore volumes of MSAMS-4, before and after hydrothermal-stability tests, are observed (see Table S1 in supplementary data).[3] XRD and N_2 adsorption–desorption results indicate that MSAMS-4 maintained a perfect ordered mesostructure after the hydrothermal-stability tests.

From Fig. S1 (see Supplementary data),[3] the absorption branch of isotherm for MSAMS-4 shows the inflection point at a lower relative-pressure value than that of SBA-15, suggesting a smaller mean pore size for MSAMS-4. On the other hand, compared with SBA-15, no changes in the basal spacing (d_{100}) and linewidth are observed for MSAMS-4. The smaller pore size and the unchanged basal spacing indicate a thicker pore wall (~1.0 nm). In addition, the intensity ratio of the (200)/(110) diffraction peaks of MSAMS-4 is higher than that of SBA-15, indicating a thicker pore wall in case of the MSAMS-4 (14). The thicker MSAMS-4 pore wall might be attributed to the five-membered ring subunits, overgrowing within the channels of SBA-15 with the aid of microporous-zeolites structure template TEA^+, which are expected to provide significantly improved hydrothermal stability to MSAMS-4 (3).

Figure 3 exhibits a band centered at 960 cm^{-1}, observed for both MSAMS-4 and the parent SBA-15, which is characteristic of noncondensed silanol groups (15, 16). However, the intensity of the band for MSAMS-4 is much weaker than that for SBA-15, suggesting a higher condensation degree of the silanol groups in case of MASMS-4, which was further confirmed by ^{29}Si NMR. On the other hand, the band in the 550–600 cm^{-1} region, assigned to the characteristic vibration of five-membered ring subunits (17), is well-expressed in the spectrum of MSAMS-4, but not for the parent SBA-15. The

[3] Supplementary data for this article are available on the journal Web site (canjchem.nrc.ca) or may be purchased from the Depository of Unpublished Data, Document Delivery, CISTI, National Research Council Canada, Ottawa, ON K1A 0S2, Canada. DUD 5160. For more information on obtaining material, refer to http://cisti-icist.nrc-cnrc.gc.ca/irm/unpub_e.shtml.

© 2007 NRC Canada

Fig. 3. FTIR spectra of (*a*) SBA-15 and (*b*) MSAMS-4.

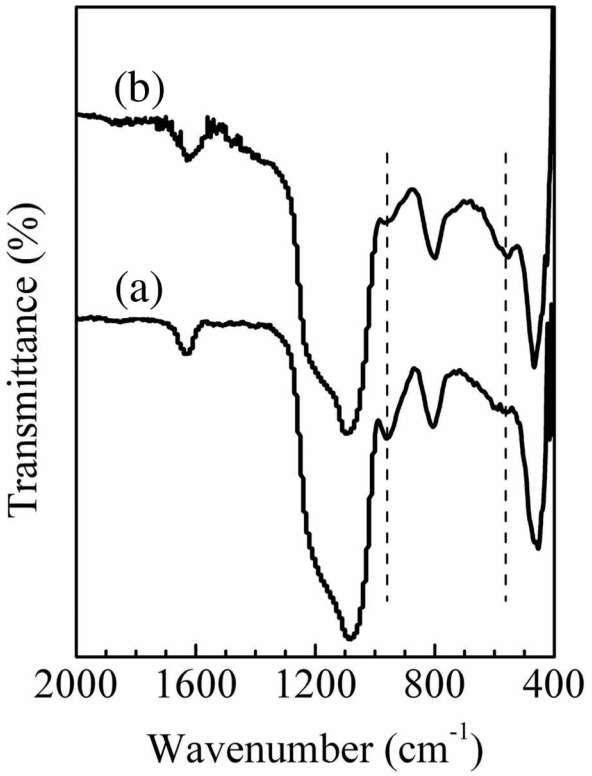
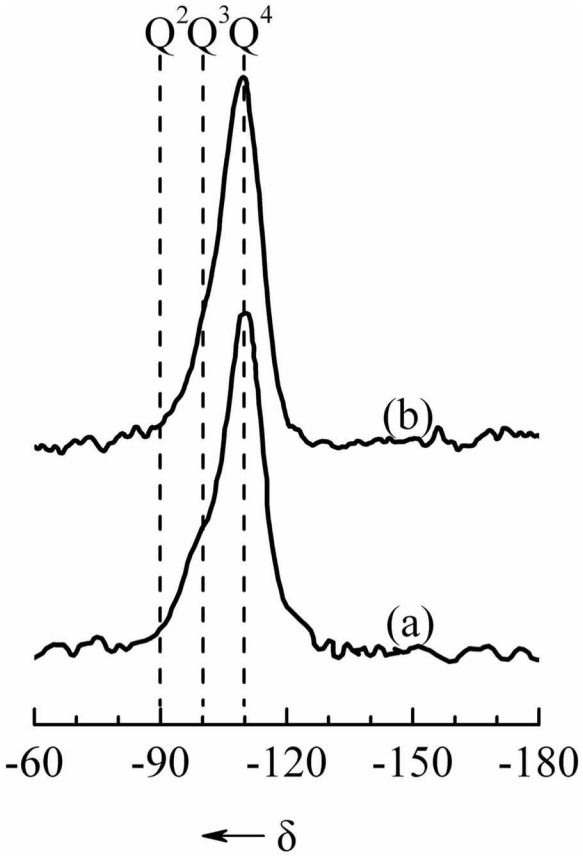


Fig. 4. ^{29}Si MAS NMR spectra of MSAMS-4: (*a*) as-synthesized and (*b*) calcined.



presence of this band indicates the formation of zeolite-like subunits, comprised of AlO_4 and SiO_4 tetrahedra, within the framework of the ordered mesoporous material, which should play an important role in improving its hydrothermal stability (6).

Generally, ordered mesoporous silicate materials show three ^{29}Si NMR resonances, centered at –110, –100, and –90 ppm, which might be attributed to $Si(OSi)_4$ (Q^4), $(HO)Si(OSi)_3$ (Q^3), and $(HO)_2Si(OSi)_2$ (Q^2) framework units, respectively. ^{29}Si MAS NMR spectra of the as-synthesized and calcined MSAMS-4 are presented in Fig. 4. Notably, the as-synthesized MSAMS-4 is primarily composed of fully condensed Q^4 silica units (δ = –110 ppm) and a smaller fraction of incomplete cross-linked Q^3 units (δ = –100 ppm). Normally, surfactant-containing silica mesostructures, whether assembled from ionic or neutral surfactants, exhibit Q^4/Q^3 ratios that are <2.0, and their calcined derivatives typically have values near 3.0 (1, 18). The Q^4/Q^3 ratio of the as-synthesized MSAMS-4 approximates 6.5, and the ratio does not change greatly after calcination, suggesting that the SiOH groups might be site-isolated and buried in the framework. Normally, the high degree of condensation of the silanol groups is responsible for significantly improving the hydrothermal stability of mesoporous molecular sieves (19).

^{27}Al MAS NMR spectrum of MSAMS-4 shows a single resonance centered near 55 ppm (Fig S2, see Supplementary data),[3] characteristic of tetrahedral aluminum centers. This ^{27}Al NMR result indicates that all the Al atoms of MSAMS-4 are incorporated into the framework via multistage recrystallization. This is likely because the octahedrally coordinated Al interacts with the silanol groups of SBA-15, which not only further reduces silanol-groups concentration, but it also acts to heal defect sites in the structure of the parent SBA-15 (20), thus stabilizing the structure.

Conclusions

In conclusion, we synthesized a highly ordered mesoporous molecular sieve, MSAMS-4, via multistage recrystallization. MSAMS-4 exhibits extraordinary stability both in 100 °C water and in high-temperature steam. Its hydrothermal stability may be attributed to the synergistic effect of the thicker wall, the higher condensation of silanol groups, insertion of non-framework Al atoms, and the formation of zeolites-like subunits within the mesoporous framework.

Experimental

Synthesis of MSAMS-4

The following general procedure, described in the literature (12, 13), was used to prepare MSAMS-4:

(*i*) SBA-15 was synthesized using P123, phosphomolybdic acid (HPMo), and tetraethyl orthosilicate (TEOS) as a structure-directing agent, a promoter, and a silica source, respectively. In a typical synthesis batch, 4.0 g of P123 was dissolved in 105 mL of distilled water with vigorous stirring at RT for 3 h, then the calculated amount of HPMo (0.64 g) was added into the solution to keep the molar ratio of Si/Mo at 12.4. After dissolv-

© 2007 NRC Canada

ing P123 and HPMo completely, 8.55 g of TEOS and 0.75 mL of concd. HCl (36 wt%) were added dropwise to the reaction mixture. The chemical composition of the reaction mixture was 4 g of P123 copolymer, 0.041 mol of TEOS, 0.00028 mol of HPMo, 0.0087 mol of HCl, and 5.83 mol of H_2O. Subsequently, the mixture was stirred at 38 °C for 20 h and then thermally treated at 96 °C for 6 h. The reaction products were filtered, washed, and dried at 45 °C for 48 h. Finally, the samples were calcined at 550 °C in air for 8 h.

(*ii*) 9.0 mmol tetraethylammonium bromide (TEA^+) was dissolved in 9.6 mL deionized water. Next, 21.6 mmol TEOS, 25 mL H_2O, and the calculated sodium aluminate ($NaAlO_2$) were added to the solution, and the solution was stirred at RT overnight. Then, the solution was diluted with denionized water to yield 150 mL aluminosilicate sol–gel diluted solution, and the final chemical composition of this solution was 1 mol of TEA^+, 0.06 mol of Al_2O_3, 2.6 mol of SiO_2, 0.06 mol of Na_2O, and 316 mol of H_2O.

(*iii*) the calcined SBA-15 (about 5 g) was added to the diluted solution, and the mixture was vigorously stirred at RT for 2 h. After that, the reaction product was crystallized at 110–130 °C for 12–36 h, followed by filteration, washing, and drying. Subsequently, the dried product was suspended in glycerol and crystallized at 130–150 °C for 24–48 h. Finally, the product was filtered, washed, dried, and calcined at 550 °C in air for 8 h.

Characterization of MSAMS-4

Powder XRD patterns were performed on a Rigaku D/max 2550PC diffractometer, operating at 40 kV and 300 mA and using Cu Kα radiation. BET surface area and N_2 adsorption–desorption isotherms were carried out on an Omnisorp-100CX apparatus at –196 °C. FTIR spectra of the samples in the form of KBr pellets were recorded by using a Nicolet 560 IR spectrometer. The ^{27}Al and ^{29}Si MAS NMR spectra were recorded on a Bruker DSX 300 spectrometer with spinning frequencies of 12 kHz and 4 kHz, respectively.

Acknowledgement

We gratefully acknowledge the financial support by Key Program of National Natural Science Foundation of China (Grant No.: 20433030), National High Technology Research and Development Program of China (Grant No.: 2006AA03Z328), National Natural Science Foundation of China (Grant No.: 90610002), and Natural Science Foundation of Zhejiang Province (Grant No.: Z406142).

References

1. (*a*) C.T. Kresge, M.E. Leonowicz, W.J. Roth, J.C. Vartuli, and J.S. Beck. Nature (London), **359**, 710 (1992); (*b*) J.S. Beck, J.C. Vartuli, W.J. Roth, C.T. Kresge, K.D. Schmitt, C.T.-W. Chu, D.H. Olson, E.W. Sheppard, S.B. McCullen, J.B. Higgins, and J.L. Schlenker. J. Am. Chem. Soc. **114**, 10834 (1992).
2. A. Corma, Chem. Rev. **97**, 2373 (1997).
3. (*a*) D. Zhao, J. Feng, Q. Huo, N. Melosh, G.H. Fredrickson, B.F. Chmelka, and G.D. Stucky. Science (Washington, D.C.), **279**, 548 (1998); (*b*) D. Zhao, Q. Huo, J. Feng, B.F. Chmelka, and G.D. Stucky. J. Am. Chem. Soc. **120**, 6024 (1998).
4. K.R. Kloetstra, H. van Bekkum, and J.C. Jansen. Chem. Commun. 2281 (1997).
5. Y. Liu, W. Zhang, and T.J. Pinnavaia. J. Am. Chem. Soc. **122**, 8791 (2000).
6. Y. Liu, W. Zhang, and T.J. Pinnavaia. Angew. Chem., Int. Ed. **40**, 1255 (2001).
7. Y. Liu and T.J. Pinnavaia. Chem. Mater. **14**, 3 (2002).
8. Z. Zhang, Y. Han, L. Zhu, R. Wang, Y. Yu, S. Qiu, D. Zhao, and F.-S. Xiao. Angew. Chem., Int. Ed. **40**, 1258 (2001).
9. F.S. Xiao, Y. Han, Y. Yu, X. Meng, M. Yang, and S. Wu. J. Am. Chem. Soc. **124**, 888 (2002).
10. Y. Han, S. Wu, Y. Sun, D. Li, and F.S. Xiao. Chem. Mater. **14**, 1144 (2002).
11. Y. Han, F.S. Xiao, S. Wu, Y. Sun, X. Meng, D. Li, S. Lin, F. Deng, and X. Ai. J. Phys. Chem. B. **105**, 7963 (2001).
12. D. Trong On and S. Kaliaguine. Angew. Chem., Int. Ed. **41**, 1036 (2002).
13. D. Trong On and S. Kaliaguine. J. Am. Chem. Soc. **125**, 618 (2003).
14. (*a*) M. Kruk, M. Jaroniec, C.H. Ko, and R. Ryoo. Chem. Mater. **12**, 1961 (2000); (*b*) M. Kruk, M. Jaroniec, and A. Sayari. Chem. Mater. **11**, 492 (1999); (*c*) P. Ågren, M. Lindén, J.B. Rosenholm, R. Schwarzenbacher, M. Kriechbaum, H. Amenitsch, P. Laggner, J. Blanchard, and F. Schüth. J. Phys. Chem. B. **103**, 5943 (1999); (*d*) P. Feuston and J.B. Higgins. J. Phys. Chem. B. **98**, 4459 (1994); (*e*) D. Li, Y. Han, J. Song, L. Zhao, X. Xu, Y. Di, and F.S. Xiao. Chem. Eur. J. **10**, 5911 (2004).
15. X.G. Wang, K.S.K. Lin, J.C.C. Chan, and S.F. Cheng. J. Phys. Chem. B. **109**, 1763 (2005).
16. M. Llusar, G. Monrós, C. Roux, J.L. Pozzo, and C. Sanchez. J. Mater. Chem. **13**, 2505 (2003).
17. (*a*) J.C. Jansen, F.J. van der Gaag, and H. van Bekkum. Zeolite **4**, 369 (1984); (*b*) R. Ravishankar, C. Kirschhock, B.J. Schoeman, P. Vanoppen, P.J. Grobet, S. Storck, W.F. Maier, J.A. Martens, F.C. De Schryver, and P.A. Jacobs. J. Phys. Chem. B. **102**, 2633 (1998); (*c*) E.A. Kirschhock, R. Ravishankar, F. Verspeurt, P.J. Grobet, P.A. Jacobs, and J.A. Martens. J. Phys. Chem. B. **103**, 4965 (1999).
18. P.T. Tanev and T.J. Pinnavaia. Chem. Mater. 8, 2068 (1996).
19. (*a*) S.S. Kim, W.Z. Zhang, and T.J. Pinnavaia. Science (Washington, D.C.), **282**, 1302 (1998); (*b*) Y. Han, D. Li, L. Zhao, J. Song, X. Yang, N. Li, Y. Di, C. Li, S. Wu, X. Xu, X. Meng, K. Lin, and F.-S. Xiao. Angew. Chem., Int. Ed. **42**, 3633 (2003); (*c*) R. Mokaya. J. Phys. Chem. B. **103**, 10204 (1999).
20. W. Breck. Zeolite molecular sieves. R.E. Krieger Company, New York. (1974). P. 441.

© 2007 NRC Canada

Intermolecular interactions and electronic properties in phosphino-(oligothiophene) palladium(II) and platinum(II) complexes

Tracey L. Stott, Michael O. Wolf, and Brian O. Patrick

Abstract: A series of Pt(II) and Pd(II) complexes containing diphenylphosphino-substituted oligothiophene ligands ranging from 1 to 3 thiophene rings in length have been prepared. Crystal structures of four of these complexes were determined via single X-ray crystal diffraction and the solid-state packing arrangements found to vary with both the metal and the thiophene-containing ligand. In some cases, π-stacking between thiophene rings are found for the oligothiophene ligands. Solution and solid-state absorption spectra of these complexes are reported.

Key words: oligothiophenes, metal complexes, structural properties, electronic spectra.

Résumé : On a préparé une série de complexes du Pt(II) et du Pd(II) contenant des ligands oligothiophènes substitués par des groupes diphénylphosphino dans lesquels le nombre de noyaux thiophènes varie de un à trois. On a déterminé les structures cristallines de quatre de ces complexes par diffraction des rayons X par un cristal unique et on a observé que les arrangements de l'empilement à l'état solide varient en fonction de la nature du métal ainsi que du ligand contenant le thiophène. Dans quelques cas, on a observé un empilement π pour les ligands oligothiophènes. On a aussi mesuré les spectres d'absorption en solution et à l'état solide de ces complexes.

Mots-clés : oligothiophènes, complexes métalliques, propriétés structurales, spectres électroniques.

[Traduit par la Rédaction]

Introduction

Conjugated oligomers are of significant interest for application in electroluminescent devices (1), solar cells (2), and field-effect transistors based on molecular materials (3). Solid-state packing and intermolecular interactions are known to influence the emission properties (4) and charge mobility (5) of these materials. In π-conjugated oligomers such as oligothiophenes, π-stacking (6, 7) has been shown to influence the charge mobility as well as the excitation and emission energy of the material (4, 8). The degree of conjugation may also be influenced by solid-state packing, and unsubstituted oligothiophenes adopt a planar, fully conjugated arrangement in the solid state (5).

The solid-state packing of conjugated oligomers, such as oligothiophenes, can be influenced by the use of different organic substituents (5, 9–12) or by a combination of electron-rich and electron-poor groups (13). A novel approach in controlling the solid-state packing is through the use of coordination chemistry where the conjugated groups are positioned as ligands on metal complexes giving a defined local geometrical arrangement, which may predispose the molecule towards specific packing arrangements. Intramolecular geometry may be controlled with coordination chemistry approaches; for example, our group has recently reported the use of pendant Ru(II) complexes to control the coplanarity of rings in a terthiophene derivative (14, 15). In the present work, we have selected palladium(II)- and platinum(II)-bis(phosphine) complexes to further explore these effects. These were chosen because they are readily synthesized, are stable in air, crystallize easily (16), and exist in both cis- and trans-substituted square planar geometries (16–22). Our group has previously reported the synthesis and characterization of several β-substituted phosphinothiophene palladium(II) complexes (23–25). The metal was found to affect both the electronic properties and the structure of the oligothiophene. Au(I) complexes of the α-phosphinothiophene ligands used here have also been reported (26).

Metal centers may create quenching sites within the crystal (27, 28) thus limiting the immediate utility of these materials for application in optoelectronic devices; however, these studies still allow exploration of solid-state effects. The crystal structures of a series of phosphinothiophene palladium(II) and platinum(II) complexes are reported in this paper. The effects of the metal geometry and the length of the thiophene ligand on the structure and electronic spectra are explored. Gray and co-workers (29) recently reported the third-order nonlinear optical behavior of one of the Pd com-

Received 19 January 2007. Accepted 27 March 2007. Published on the NRC Research Press Web site at http://canjchem.nrc.ca on 18 May 2007.

T.L. Stott, M.O. Wolf,[1] and B.O. Patrick. Department of Chemistry, University of British Columbia, Vancouver, BC V6T1Z1, Canada.

[1]Corresponding author (e-mail: mwolf@chem.ubc.ca).

 doi:10.1139/V07-033 © 2007 NRC Canada

pounds ($Pd(PT_3)_2Cl_2$) and one of the Pt compounds ($Pt(PT_3)_2Cl_2$) described here; however, the solid-state structures of these complexes have not been reported.

Experimental

General

^1H and $^{31}P\{^1H\}$ NMR experiments were performed on either a Bruker AV-300 or a Bruker AV-400 spectrometer. Spectra were referenced to a residual solvent (^1H) or external 85% H_3PO_4 (^{31}P). Isomer ratios were determined from ^{31}P NMR spectra obtained with a delay time of 2 s. Electronic spectra were obtained on a Cary 5000 in HPLC grade CH_2Cl_2. Solid-state absorption spectra were obtained by drop casting the compound from a CH_2Cl_2 solution onto a quartz slide. Microanalyses were performed at UBC. Electrospray mass spectra were obtained by infusion of 10 μmol/L of a methanol solution at ~10 μL/min into the electrospray source of a Bruker Esquire ion trap mass spectrometer. The spectra were acquired in positive ion mode. MALDI-TOF mass spectra were obtained on a Bruker Biflex IV mass spectrometer. Samples were prepared from dichloromethane in a dithranol matrix. $PdCl_2$ and K_2PtCl_4 were purchased from Strem and used as received. THF was dried over Na and benzophenone and was distilled before use. CH_2Cl_2 was dried by passing over an alumina column. Acetonitrile was dried over 3 Å molecular sieves and was degassed by sparging with N_2 for 20 min. No special precautions for the exclusion of oxygen were taken during synthesis. The phosphine ligands 2-diphenylphosphinothiophene (PT), 2-diphenylphosphino-5,2′-bithiophene (PT_2) and 2-diphenylphosphino-5,2′:5′,2′′-terthiophene (PT_3) were prepared as described previously (30, 31).

Synthesis

$Pd(PT)_2Cl_2$ (1)

$PdCl_2$ (0.033 g, 0.19 mmol) was dissolved in an HCl–H_2O solution (0.2:3 *v*/*v*), which was then added dropwise to a solution of 0.10 g (0.39 mmol) PT dissolved in an ethanol–acetonitrile mixture (5:4 *v*/*v*). A yellow precipitate formed immediately, and the yellow slurry was stirred for 1 h. The solvent was then removed via rotary evaporation, and the resulting sticky material was dissolved in CH_2Cl_2 and acetone, then filtered, and a yellow powder was precipitated in hexanes. The product was recrystallized in hexanes–CH_2Cl_2, yielding an analytically pure product. Yield 80%. Anal. calcd. for $C_{32}H_{26}Cl_2P_2PdS_2$: C 53.83, H 3.67; found: C 53.67, H 3.67. ^1H NMR ($CDCl_3$) δ: 7.80 (m, 1H), 7.69–7.62 (m, 5H), 7.46–7.34 (m, 6H), 7.13 (m, 1H). $^{31}P\{^1H\}$ NMR ($CDCl_3$) δ: 13.6 (s), 23.9 (s).

$Pd(PT_2)_2Cl_2$ (2)

$PdCl_2$ (0.025 g, 0.14 mmol) and PT_2 (0.10 g, 0.29 mmol) were mixed together in a 1:2 mixture of CH_3CN–CH_2Cl_2 for 3 h. The solvent was removed, and the resulting yellow powder was dissolved in CH_2Cl_2, gravity filtered, and precipitated with hexanes. The product was recrystallized in hexanes–CH_2Cl_2. Yield 40%. Anal. calcd. for $C_{40}H_{30}Cl_2P_2PdS_4$: C 54.71, H 3.44; found: C 54.31, H 3.58. ^1H NMR (CD_2Cl_2) δ: 7.73–7.66 (m, 5H), 7.47–7.38 (m, 6H), 7.31 (dd, J = 5.0, 1.2 Hz, 1H), 7.18 (dd, J = 1.2, 3.5 Hz, 2H), 6.98 (dd, J = 5.0, 3.6 Hz, 1H). $^{31}P\{^1H\}$ NMR ($CDCl_3$) δ: 14.0 (s), 24.2 (s).

$Pd(PT_3)_2Cl_2$ (3)

Results obtained by using a different synthesis were previously reported by our group (24). $PdCl_2$ (0.021 g, 0.12 mmol) was dissolved in an HCl–H_2O solution (0.2:3 *v*/*v*). This was added dropwise to a solution of 0.10 g (0.23 mmol) of PT_3 in THF, and a yellow precipitate began to form almost immediately. The yellow slurry was stirred for 1 h, and the solvent was then removed via rotary evaporation. The resulting sticky material was dissolved in CH_2Cl_2, filtered, and precipitated in hexanes. The product, a bright yellow powder, was recrystallized in hexanes–CH_2Cl_2. Yield 86%. Anal. calcd. for $C_{48}H_{34}Cl_2P_2PdS_6$: C 55.30, H 3.29; found: C 55.06, H 3.29. ^1H NMR ($CDCl_3$) δ: 7.70–7.63 (m, 4H), 7.46–7.38 (m, 6H), 7.28–7.20 (m, 6H, includes $CHCl_3$), 7.18 (d, J = 3.6 Hz, 1H), 7.15 (d, J = 3.6 Hz, 1H), 7.08 (d, J = 3.6 Hz, 1H), 7.04 (d, J = 3.6 Hz, 1H), 6.99 (dd, J = 5.2, 3.6 Hz, 1H). $^{31}P\{^1H\}$ NMR (CD_2Cl_2) δ: 14.3 (s), 24.4 (s).

General procedure for the synthesis of $Pt(PT_n)_2Cl_2$ complexes

The appropriate ligand was dissolved in 50 mL of CH_2Cl_2 and stirred with a solution of 0.5 equiv. of K_2PtCl_4 in 10 mL of H_2O. The reaction was monitored both by the disappearance of the red color in the H_2O layer due to K_2PtCl_4 and by the disappearance of the ligand via TLC. When the reaction was complete the layers were separated, the organic layer was dried over $MgSO_4$ and gravity filtered, and the solvent was removed via rotary evaporation. A minimal amount of CH_2Cl_2 was added to dissolve the resulting solid, which was then precipitated in 300 mL hexanes. The resulting powder was collected via suction filtration and either dried under vacuum or recrystallized from CH_2Cl_2–hexanes to yield an analytically pure sample.

$Pt(PT)_2Cl_2$ (4).

Yield 67%. Anal. calcd. for $C_{32}H_{26}Cl_2P_2PtS_2$: C 47.89, H 3.27; found: C 47.78, H 3.57. ^1H NMR ($CDCl_3$) δ: 7.65–7.59 (m, 2H), 7.47–7.41 (m, 4H), 7.32–7.28 (m, 2H), 7.17–7.13 (m, 4H), 7.04–7.01 (m, 1H). $^{31}P\{^1H\}$ NMR ($CDCl_3$) δ: 5.6 (s), $^1J_{P-Pt}$ = 3680 Hz. MS (MALDI-TOF) *m*/*z*: 766 (MW-Cl).

$Pt(PT_2)_2Cl_2$ (5)

Yield 73%. Anal. calcd. for $C_{40}H_{30}Cl_2P_2PtS_4$: C 49.69, H 3.13; found: C 49.72, H 3.39. ^1H NMR ($CDCl_3$) δ: 7.58–7.53 (m, 4H), 7.43–7.40 (dd, J = 7.7, 3.8 Hz, 1H), 7.36–7.32 (m, 2H), 7.24–7.19 (m, 6H, includes $CHCl_3$), 7.07 (dd, J = 3.6, 0.9 Hz, 1H), 7.01 (dd, J = 3.6, 1.1 Hz, 1H), 6.97 (dd, J = 5.1, 3.7 Hz, 1H). $^{31}P\{^1H\}$ NMR ($CDCl_3$) δ: 5.1 (s), $^1J_{P-Pt}$ = 3690 Hz. MS (ESI) *m*/*z*: 931 (MW-Cl).

$Pt(PT_3)_2Cl_2$ (6).

Previously reported by Gray and co-workers (29). Yield 81%. Anal. calcd. for $C_{48}H_{34}Cl_2P_2PtS_6$: C 50.97, H 3.03; found: C 50.61, H 3.27. ^1H NMR (CD_2Cl_2) δ: 7.68–7.57 (m, 8H), 7.51–7.38 (m, 6H), 7.32–7.19 (m, 11H), 7.15 (dd, J =

© 2007 NRC Canada

3.51, 1.1 Hz, 2H), 7.07–6.98 (m, 7H). $^{31}P\{^{1}H\}$ NMR (CD_2Cl_2) δ: 4.9 (s), $^{1}J_{P-Pt}$ = 3700 Hz. MS (ESI) *m/z*: 1095 (MW-Cl).

X-ray Crystallography

Suitable crystals of **2**, **3**, **5**, and **6** were mounted in oil on a glass fiber, and the data for each compound were collected at 173(1) K. The structures were solved using direct methods (32, 33) and refined using SHELXL-97 (34). All measurements were made on a Bruker X8 APEX diffractometer with graphite monochromated Mo Kα radiation. For each of the four structures, one terminal thiophene ring was disordered in two orientations. In each case, the disordered fragments were modeled using the simple restraints (SADI or SAME) found in SHELXL.

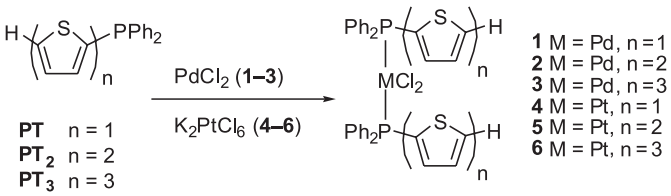
The data for **2** were collected to a maximum 2θ value of 55.8°. Data were collected in a series of ϕ and ω scans in 0.50° oscillations with 10.0 s exposures. Data were collected and integrated using the Bruker SAINT (35) software package and were corrected for absorption effects using the multiscan technique (SADABS) (36). The data were corrected for Lorentz and polarization effects. The material crystallizes with one half-molecule residing on an inversion center. One thiophene ring in the asymmetric unit is disordered and was modeled in two orientations. The atoms of the major disordered fragment were refined anisotropically, while the atoms of the minor fragment (with a relative population of approximately 0.23) were refined isotropically. Restraints were used to ensure the disordered thiophene fragments had reasonable geometries. All other nonhydrogen atoms were refined anisotropically. All hydrogen atoms were included in calculated positions but not refined.

The data for **3** were collected to a maximum 2θ value of 55.6°. Data were collected in a series of ϕ and ω scans in 0.50° oscillations with 10.0 s exposures. Data were collected and integrated using the Bruker SAINT (35) software package and were corrected for absorption effects using the multiscan technique (SADABS) (36). The data were corrected for Lorentz and polarization effects. All nonhydrogen atoms were refined anisotropically, while all hydrogen atoms were included in calculated positions but not refined. The terminal thiophene ring containing S(3) was disordered and modeled in two orientations with relative populations of 0.77 and 0.23 for the major and minor fragments, respectively.

The data for **5** were collected to a maximum 2θ value of 50.2°. Data were collected in a series of ϕ and ω scans in 0.50° oscillations with 20.0 s exposures. Data were collected and integrated using the Bruker SAINT (35) software package, were corrected for absorption effects using the multiscan technique (SADABS) (36), and were corrected for Lorentz and polarization effects. One thiophene ring is disordered in two orientations. All atoms except the two sulfur fragments and one carbon were refined anisotropically. All hydrogen atoms were included in calculated positions but not refined.

The data for **6** were collected to a maximum 2θ value of 52.8°. Data were collected in a series of ϕ and ω scans in 0.50° oscillations with 12.0 s exposures. Data were collected and integrated using the Bruker SAINT (35) software package. Data were corrected for absorption effects using the multiscan technique (SADABS) (36). The data were corrected for Lorentz and polarization effects. All nonhydrogen atoms were refined anisotropically. All hydrogen atoms were included in calculated positions but not refined. The thiophene ring containing S (6) was disordered and modeled in two orientations with the populations of the major and minor fragments refined to an approximate 2:1 ratio.

Scheme 1.



Results and discussion

Synthesis of complexes

The palladium complexes **1**–**3** were synthesized by one of two methods. The ligand and $PdCl_2$ were either stirred together in a mixture of CH_2Cl_2 and CH_3CN, or $PdCl_2$ was dissolved in dilute HCl and subsequently added dropwise to a solution of the ligand in an appropriate solvent (Scheme 1). The crude products were crystallized in CH_2Cl_2–hexanes to yield analytically pure materials in reasonable yields. Complex **1** has been reported previously (37, 38), and the synthesis and structure of **3** was previously communicated by our group (39). Palladium bis(phosphine) complexes of this type are known to exhibit cis–trans equilibria in solution (20), which can be observed by ^{31}P NMR spectroscopy. The ^{31}P NMR signals for the trans complexes are generally found at a lower chemical shift than those of the cis isomer (40–45). The ^{31}P NMR spectra of **1**–**3** in CD_2Cl_2, $CDCl_3$, and DMSO indicate that although both cis and trans isomers exist in solution, the trans isomer predominates in these solvents (as determined by integration of ^{31}P NMR spectra).

As a single species is desirable for solution characterization, we also chose to synthesize the more inert Pt (16, 46) analogs **4**–**6**. These were prepared by stirring together a solution of K_2PtCl_4 in H_2O and the appropriate ligand dissolved in CH_2Cl_2. The progress of the reaction was monitored by the disappearance of the dark red color of $[PtCl_4]^-$ in the water layer. The crude product obtained was either crystallized in CH_2Cl_2–hexanes or dried under vacuum. Complex **4** has been previously synthesized (37, 38, 47), and the synthesis of **6** was reported by Gray and coworkers (29).

The ^{195}Pt satellites in the ^{31}P NMR spectra of **4**–**6** may be used to determine the geometry at the metal (18, 48). Complexes **4** (δ 6), **5**(δ 5), and **6** (δ 6) have ^{195}Pt–^{31}P coupling constants of 3681, 3685, and 3700 Hz, respectively, which indicate that these are cis-substituted complexes. A second less intense peak was observed in the ^{31}P NMR spectra of analytically pure **6** at δ 11.5. This peak is assigned to the trans isomer, expected to appear downfield to the signal from the cis isomer (48). However, because of the low intensity, no ^{195}Pt satellites are observed for this signal. It may be

© 2007 NRC Canada

Table 1. Selected crystal structure data for **2**, **3**, **5**, and **6**.

Compound	**2**	**3**	**5**	**6**
Formula	$C_{40}H_{30}Cl_2P_2S_4Pd$	$C_{48}H_{34}P_2S_6Cl_2Pd$	$C_{40}H_{30}P_2S_4Cl_2Pt$	$C_{48}H_{34}S_6P_2PtCl_2$
Colour, habit	Yellow, plate	Orange, rod	Colorless, prism	Yellow-orange, plate
Dimension (mm)	0.15 × 0.05 × 0.02	0.25 × 0.10 × 0.10	0.25 × 0.20 × 0.08	0.25 × 0.25 × 0.10
T (K)	173	173	173	173
Crystal system	Monoclinic	Monoclinic	Monoclinic	Monoclinic
Space group	$P2_1/c$ (#14)	$P2_1/n$ (#14)	$P2_1/c$ (#14)	$P2_1/n$ (#14)
a (Å)	9.489(1)	11.8648(8)	14.7543(5)	11.749(1)
b (Å)	17.637(2)	20.875(1)	14.7758(2)	29.282(2)
c (Å)	11.2772(9)	18.270(1)	17.5571(6)	12.609(1)
α (°)	90.0	90.0	90.0	90
β (°)	100.667(4)	98.054(4)	107.868(1)	93.704(3)
γ (°)	90.0	90.0	90.0	90
V (Å^3)	1854.7(3)	4480.4(4)	3642.9(2)	4328.9(6)
Z	2	4	4	4
D_{calc} (g cm^{-3})	1.572	1.545	1.763	1.735
Unique data	4056	10 054	6425	8887
μ (Mo Kα) (cm^{-1})	9.86	9.20	43.46	37.65
$R(F)^a$ ($I > 2\sigma(I)$)	0.098	0.033	0.064	0.041
$R_w(F^2)^b$ (all data)	0.093	0.074	0.078	0.094

$^aR = \Sigma||F_o| - |F_c|| / \Sigma|F_o|$
$^bR_w = (\Sigma(F_o^2 - F_c^2)^2/\Sigma w(F_o^2)^2)^{1/2}$

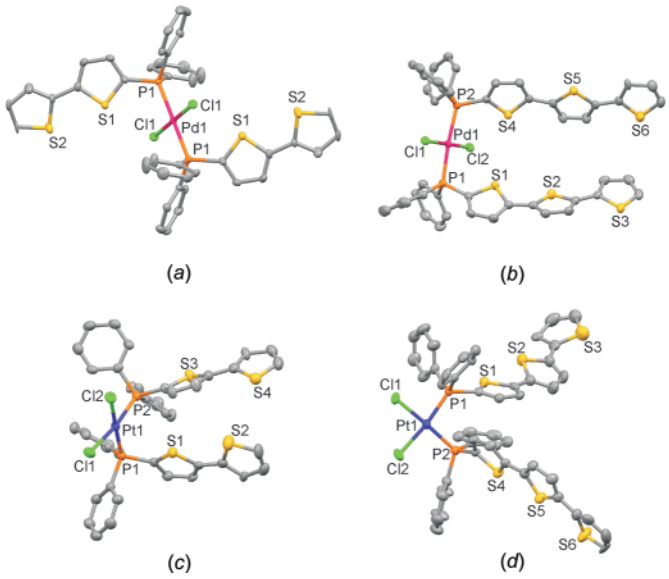
that the increased steric bulk of the terthienyl group results in the formation of some trans isomer.

Molecular solid-state structures

Four of the complexes have been characterized by single crystal X-ray diffraction and selected data is shown in Table 1.[2] Complex **3** was reported in a preliminary communication; however, comparisons are included here. The molecular structures of the four complexes are shown in Fig. 1.

All four complexes **2**, **3**, **5**, and **6** are close to a square planar geometry at the metal center. The largest distortion is observed in **5** where one of the Cl–Pt–P angles is 170.85(5)°. In the two Pd complexes the ligands are arranged in trans geometry, whereas the Pt complexes both exhibit cis geometry at the metal. The metal–Cl, metal–P, and P–C bond lengths are similar to those observed for other complexes of this type. The bond lengths in the thiophene rings range from 1.666(8) to 1.752(7) Å for the S–C bonds and from 1.332(8) to 1.519(10) Å for the C–C bonds. The arrangement and coplanarity of adjacent thiophene rings can be assessed by the S–C–C–S torsion angle. A syn coplanar arrangement is indicated by an S–C–C–S angle of 0°, while an anti coplanar arrangment gives an angle of 180°. Unsubstituted thiophene oligomers typically crystallize in a nearly completely anti coplanar arrangement (5). In all the structures here, adjacent thiophene rings are not completely coplanar (S–C–C–S angle is between 7.6(7)° and 175.40(14)°), and both syn and anti arrangements are found, sometimes within the same molecule. Table 2 summarizes these angles. The largest deviation from coplanarity between adjacent rings is found in **6** where rings containing S2 and S3 have an interannular angle of approximately 40°.

Fig. 1. Molecular structures of complexes (*a*) **2**, (*b*) **3**, (*c*) **5**, and (*d*) **6**.



[2] Supplementary data for this article are available on the journal Web site (http://canjchem.nrc.ca) or may be purchased from the Depository of Unpublished Data, Document Delivery, CISTI, National Research Council Canada, Ottawa, ON K1A 0R6, Canada. DUD 5158. For more information on obtaining material refer to http://cisti-icist.nrc-cnrc.gc.ca/irm/unpub_e.shtml. CCDC 252088, 626550, 626551, and 626552 contain the crystallographic data for this manuscript. These data can be obtained, free of charge, via http://www.ccdc.cam.ac.uk/conts/retrieving.html (Or from the Cambridge Crystallographic Data Centre, 12 Union Road, Cambridge CB2 1EZ, UK; fax +44 1223 336033; or deposit@ccdc.cam.ac.uk).

© 2007 NRC Canada

Table 2. S–C–C–S torsion angles for complexes **2**, **3**, **5**, and **6.**

Complex	Bonds	Torsion angle (°)
2	S1–C4–C5–S2	10(2)
3	S1–C4–C5–S2	24.4(3)
3	S2–C8–C9–S3	162.21(16)
3	S4–C28–C29–S5	169.15(14)
3	S5–C32–C33–S6	175.40(14)
5	S1–C4–C5–S2	14.1(8)
5	S3–C24–C25–S4	153.8(4)
6	S1–C4–C5–S2	22.9(7)
6	S2–C8–C9–S3	140.4(4)
6	S4–C28–C29–S5	7.6(7)
6	S5–C32–C33–S6	8.3(8)

Fig. 2. Packing diagrams of **2** showing (*a*) the arrangement of bithienyl and phenyl groups with the hydrogen atoms omitted and (*b*) looking down the *c* axis, with the hydrogen atoms omitted.

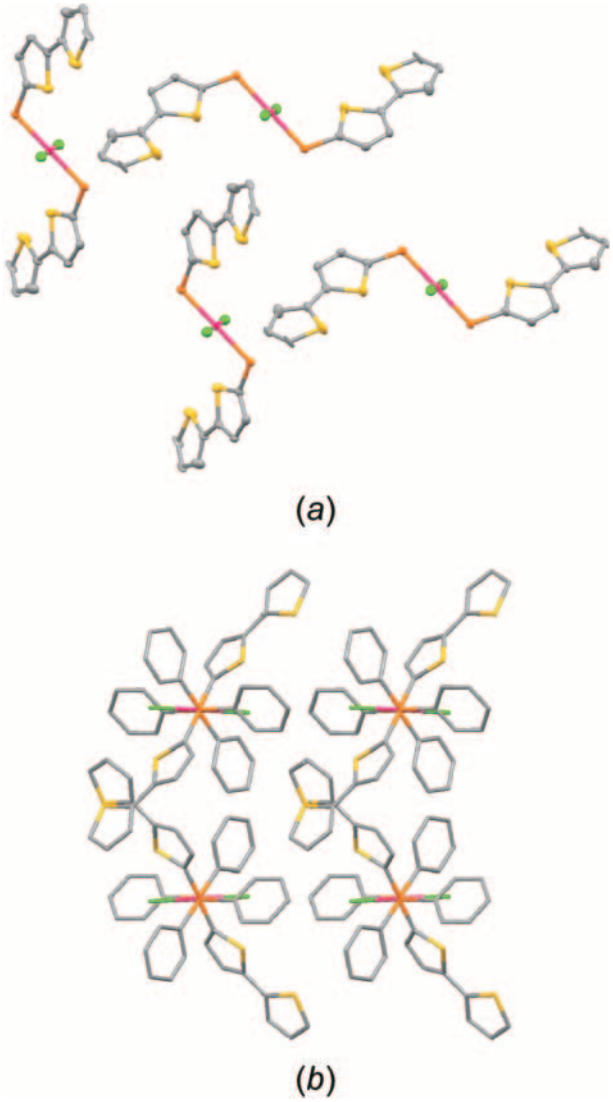
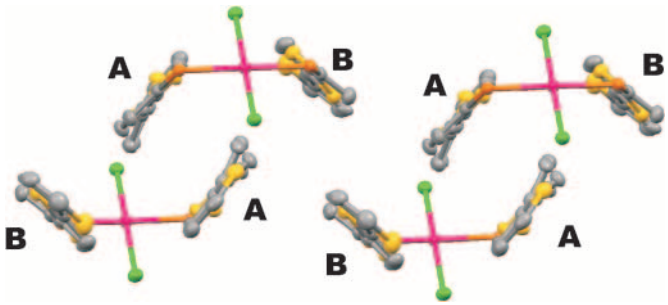


Fig. 3. Packing diagram for **3**, viewed down the long molecular axis of the terthienyl groups. Phenyl groups and hydrogen atoms are omitted for clarity.



Solid-state packing of Pd complexes

Complex **2** crystallizes in the $P2_1/n$ point group. The bithienyl groups are arranged on opposite sides of the plane passing through the Pd, P, and Cl atoms (Fig. 2*a*). The bithiophene groups are arranged in interlocking stacks with adjacent bithienyl groups twisted relative to one another by approximately 90°. When the structure is examined looking down the *c* axis (Fig. 2*b*), it is apparent that the phenyl groups form a tube surrounding the bithienyl stacks, separating the stacks from each other. No π-stacking of thiophene rings is observed in this structure. Short S–S interactions are believed to be important in facilitating charge-transfer in the oligothiophenes (5), however here the shortest intermolecular S–S distance is ~5.6 Å, precluding any interactions between sulfur atoms.

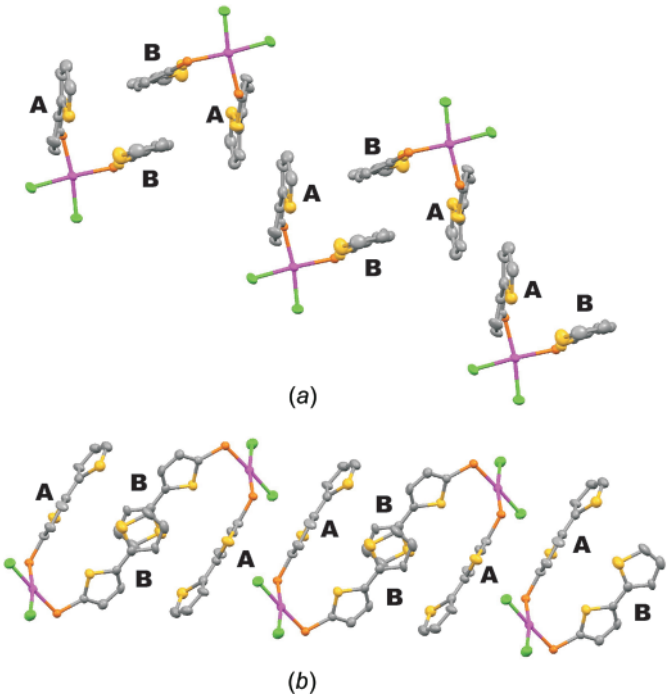
Complex **3** was previously reported but the solid-state packing is discussed here for comparative purposes. This complex crystallizes in the $P2_1/n$ point group. In contrast to **2**, the terthienyl groups are oriented on the same side of the metal plane in this case. In the crystal lattice, the arrangement of the terthienyl groups may be examined by considering the crystallographically distinct terthienyl groups **A** and **B** (Fig. 3). Pairs of terthienyl groups **A** are arranged with interplanar distances, for the inner thiophene rings of the terthienyl groups, within the range of π-stacking (3.65 Å) (13, 49). The π orbital overlap between aromatic groups is greatest if they are arranged in a stack perpendicular to the molecular plane. The two **A** groups are slightly slipped relative to one another, with the slip greater along the short axis of the groups. The degree of slip along the long and short axis may be quantified via pitch and roll angles, as discussed for organic conjugated oligomers by Curtis et al. (13). The interactions between the other pair of coplanar terthienyl groups (**B** and **B**) are much weaker, since these groups are slipped much more substantially (large roll angle) relative to each other despite having little slip along the long axis (small pitch angle). Pairs of groups **A** and **B** are arranged face-to-edge, similar to the motif found in herringbone stacks of organic oligomers (13). The shortest S–S distance in the lattice is 4.13 Å, again too long for any significant S–S interactions in this structure (5).

Solid-state packing of Pt complexes

Complex **5** crystallizes in the $P2_1/c$ point group. The structure shows some similarities to that of the Pd terthienyl complex **3**. The bithienyl groups in **5** are also arranged on the same side of the plane containing the metal, and weak intermolecular π-stacking (3.76 Å) between the outer thienyl

© 2007 NRC Canada

Fig. 4. Packing diagram of **5** viewed (*a*) down the long molecular axis of the bithienyl groups and (*b*) down the short molecular axis of bithienyl groups **A**. Phenyl groups and hydrogen atoms are omitted for clarity.



rings in group **B** on adjacent molecules is observed (Fig. 4*a*). However, these groups show substantial slip along the long molecular axis (large pitch angle) relative to what is observed in **3** (Fig. 4*b*). The **A** groups are rather far apart in the structure and do not interact. Some intramolecular π-stacking of phenyl groups is observed (not shown), with a plane-to-plane distance between the centroids of the rings of 3.63 Å.

Complex **6** crystallizes in the $P2_1/n$ point group. The terthienyl groups (**A**) in this structure are arranged in an approximately coplanar fashion to each other with an intermolecular plane-to-plane distance (between the centroids of the rings) of 3.45 Å (Fig. 5). The rings are slightly slipped along both the long and short molecular axis. The other terthienyl groups (**B**) are arranged so that the edges of the pair of **A** groups point towards the plane of **B** with the **A** and **B** groups twisted 90° relative to each other. Thus in Fig. 5 the view is down the long axes of the two **A** groups, with the long axis of the **B** groups perpendicular to these. Intramolecular π-stacking is also observed between thienyl and phenyl rings (Fig. 6), with a plane-to-plane distance between the centroids of the rings of 3.52 Å.

Absorption spectra

The solution and solid-state absorption spectra of complexes **1–6** are shown in Figs. 7 and 8 respectively, and the data is summarized in Table 3. Although both cis and trans isomers are present in solutions of the Pd complexes **1–3**,

Fig. 5. Packing diagram of **6**. Phenyl groups and hydrogen atoms are omitted for clarity.

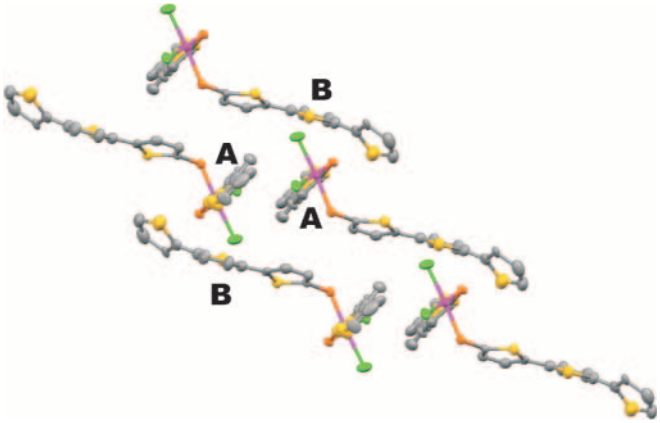


Fig. 6. Intramolecular stacking between phenyl ring and inner thiophene ring in group **B** of **6**. Hydrogen atoms are omitted for clarity.

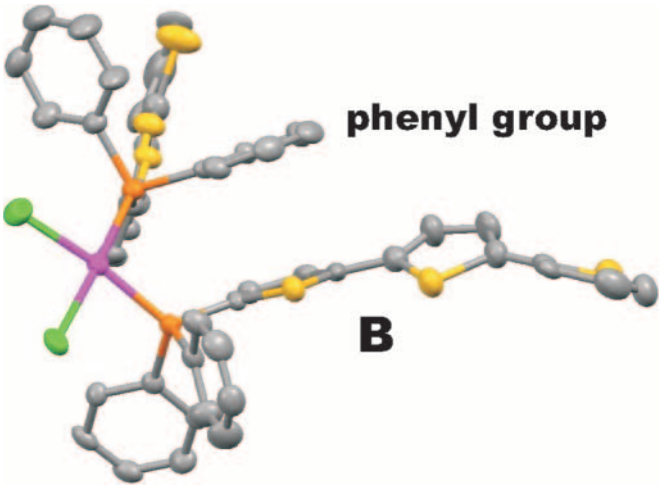
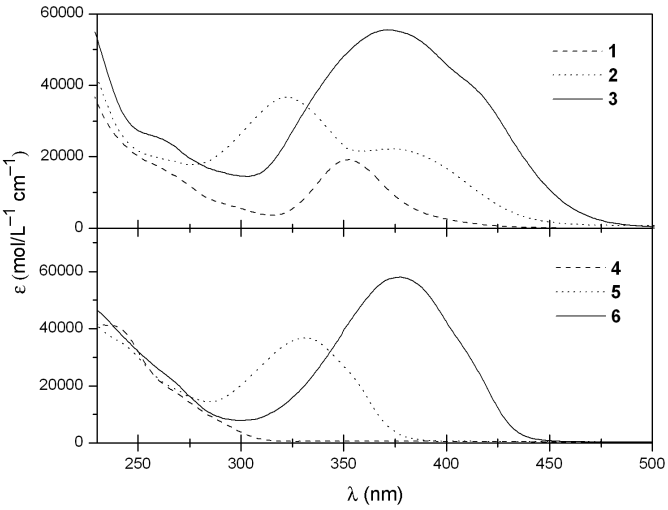


Fig. 7. Solution absorption spectra of palladium and platinum complexes **1–6**.



© 2007 NRC Canada

Table 3. Solution and solid-state absorption data for **1–6.**

Complex	λ_{max} (nm), ε_{max} (mol/L cm)$^{-1}$	λ_{max} (nm) (solid state)
1	267 (sh), 1.4×10^4; 296 (sh), 5.7×10^3; 352, 1.9×10^4	269 (sh), 355
2	264 (sh), 1.8×10^4; 322, 3.7×10^4; 374 (sh), 2.3×10^4	328, 384 (sh)
3	264 (sh), 2.2×10^4; 372, 5.5×10^4; 415 (sh), 3.9×10^4	380, 428 (sh)
4	269 (sh), 1.6×10^4; 277 (sh), 1.2×10^4	250 (sh)
5	270 (sh), 1.7×10^4; 277 (sh), 1.5×10^4; 331, 3.6×10^4	250 (sh), 340, 364 (sh)
6	269 (sh), 2.1×10^4; 277 (sh), 1.6×10^4; 377, 5.8×10^4	270 (sh), 396

Fig. 8. Solid-state absorption spectra of palladium complexes **1–6**.

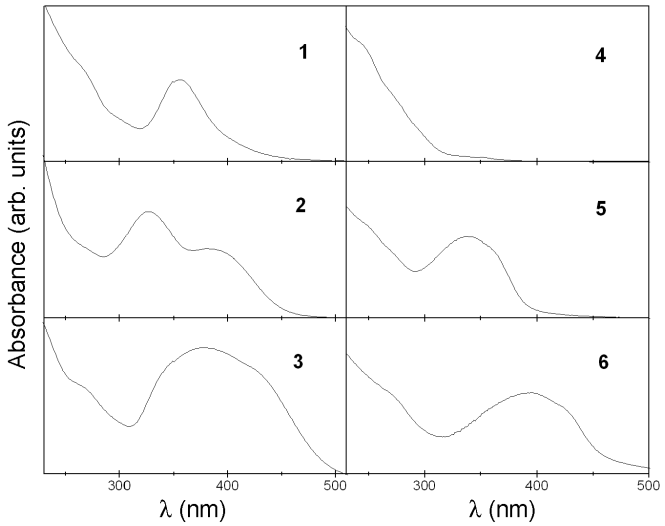
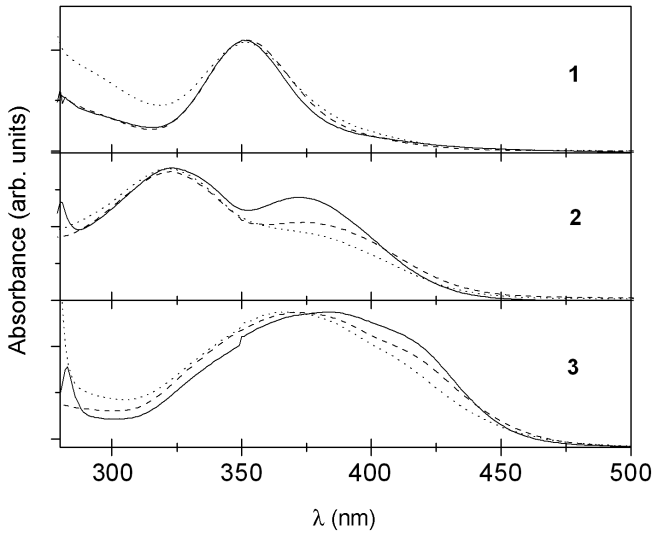


Fig. 9. Solution absorption spectra of palladium complexes **1**, **2**, and **3** in CH_3CN (dotted line), CH_2Cl_2 (broken line), and toluene (solid line).



the amount of cis is low in CH_2Cl_2 (ca. 5% as determined by integration of the ^{31}P NMR spectrum) and should not significantly affect the spectra. In the solution spectrum of **1**, there are shoulders between 250 and 300 nm and a distinct peak at 352 nm. The higher energy bands are assigned to n→π* and π→π* transitions of the ligands and are not substantially shifted from the spectra of the uncoordinated PT (31). The band at 352 nm is not seen in the spectra of PT or in the analogous gold (26) or platinum (**4**) complexes. A band at comparable energy and molar absorptivity is seen in the spectra of other dichlorobis(phosphine) palladium complexes (40, 50–55) and is usually assigned to a LMCT transition (Cl→Pd). The energy of charge transfer bands typically change with the polarity of the solvent (56); however, for **1** no significant shift was observed for this band when comparing the spectra in toluene, CH_2Cl_2, and CH_3CN (Fig. 9). In the solid state the band does shift slightly (3 nm).

Two overlapping bands can be seen in both the solution (322 nm and 374 nm) and solid-state (328 and 384 nm) absorption spectra of **2**. Presumably, one of these peaks is due to a π→π* transition in the bithienyl group and the other to a Cl→Pd charge transfer band, similar to that seen in the spectrum of **1**. The higher energy band is assigned as the π→π* transition, as it is very similar in energy to PT_2 (λ_{max} = 333 nm) (31). The Pd center appears to have little effect on the absorbance of the thiophene group. The lower energy band is assigned to the LMCT transition, which is shifted by 22 nm when compared with the spectrum of **1**. This indicates that the phosphinothiophene ligand has some influence on the LMCT transition. Although the shift is surprisingly large, it is known that there is a significant contribution from triphenylphosphine to the LMCT band of *trans*-dichlorobis(triphenylphosphine) palladium (II), as determined by resonance Raman spectroscopy (51). When the solution spectra for **2** taken in toluene, CH_2Cl_2, and CH_3CN are compared, (Fig. 9) a shift in energy and a change in the intensity of the lower energy band are observed.

The solution spectrum of **3** consists of a broad band at 372 nm with a shoulder at 415 nm. The peak is assigned to a terthiophene-based π→π* transition. As in the spectrum of **2**, it is very similar in energy to the ligand (λ_{max} = 374 nm), indicating little influence of the Pd center on the conjugated moiety. This has also been noted by Gray and co-workers (29). The solid-state spectrum of **3** appears much the same as the solution spectrum, but the peak broadens and shifts to lower energy (380 and 428 nm). These effects may be due to the π-stacking of the terthienyl groups observed in the crystal structure or to the increased planarity of the terthienyl groups in the solid state (57–60). As was seen in the β-substituted phosphinothiophene palladium(II) complexes previously reported (24), no distinct LMCT band is observed here. It is likely that this band overlaps with the terthienyl π→π* transition, which would also indicate some phosphinothiophene character in the LMCT. There appears to be a small decrease in the energy of the band, as the polarity of the solvent is increased and the shoulder at 415 nm becomes more prominent (Fig. 9). This may be due to conformational effects or, if the LMCT overlaps with the terthienyl π→π*

© 2007 NRC Canada

transition, it may be solvatochromism of the LMCT transition.

The spectra of platinum complexes **4**–**6** are dominated by the $\pi \rightarrow \pi^*$ transitions of the oligothiophene moieties. The spectra of these complexes in solution and in the solid state are very similar to those of the corresponding ligands, indicating little electronic effect of the metal center on the thienyl moiety. The shoulders in the spectra of **5** and **6** have been assigned to conformational effects (57, 60).

Conclusions

The series of palladium (II) and platinum (II) phosphinothiophene complexes reported here show interesting variation in their solid-state crystal structures. Although both cis and trans species are observed in the ^{31}P NMR spectra of the palladium complexes **1**–**3**, the isolated crystals of both **2** and **3** exhibit trans geometry exclusively. The platinum complexes **4**–**5** exist in solution only as the cis isomer, as evidenced by their respective ^{31}P–^{195}Pt coupling constants, while **6** appears to have a small amount of the trans isomer present. Only cis isomers are seen in the solid state.

We have focused on the intermolecular interactions between the oligothiophene groups and have found that in contrast to most organic oligothiophenes that pack in a herringbone fashion (5), these metal complexes adopt a variety of structures in the solid state depending on both the metal and the oligothiophene ligand. Interestingly, we find similarities in the structures of **3** and **5**, both of which pack with the oligothiophene groups interlocked and on the same side of the metal plane. The overlap between the terthienyl groups is greater in **3** and it is tempting to speculate that if the bithienyl groups in **5** were extended by one ring, the overlap would improve to give a structure similar to **3**. However, this is not observed and the Pt terthienyl complex **6** exhibits quite a different structure, although also one in which π-stacking between terthienyl groups is observed.

Acknowledgement

We thank the Natural Sciences and Engineering Council of Canada for funding of this work. TLS thanks the Walter C. Sumner Foundation for a fellowship.

References

1. G. Gigli, M. Anni, M. Theander, R. Cingolani, G. Barbarella, L. Favaretto, and O. Inganas. Synth. Met. **119**, 581 (2001).
2. J.L. Segura, N. Martin, and D.M. Guldi. Chem. Soc. Rev. **34**, 31 (2005).
3. F. Garnier. Chem. Phys. **227**, 253 (1998).
4. G. Zhang, Y. Pei, J. Ma, K. Yin, and C.-L. Chen. J. Phys. Chem. B, **108**, 6988 (2004).
5. D. Fichou and C. Ziegler. *In* Handbook of oligo- and polythiophenes. *Edited by* D. Fichou. Wiley-VCH, Weinheim, Germany. 1999. p. 183.
6. C.A. Hunter, K.R. Lawson, J. Perkins, and C.J. Urch. J. Chem. Soc. Perkin Trans. 2, 651 (2001).
7. C.A. Hunter and J.K.M. Sanders. J. Am. Chem. Soc. **112**, 5525 (1990).
8. S. Tsuzuki, K. Honda, and R. Azumi. J. Am. Chem. Soc. **124**, 12200 (2002).
9. A. Facchetti, M. Mushrush, M.-H. Yoon, G.R. Hutchison, M.A. Ratner, and T.J. Marks. J. Am. Chem. Soc. **126**, 13859 (2004).
10. A. Facchetti, M.-H. Yoon, C.L. Stern, G.R. Hutchison, M.A. Ratner, and T.J. Marks. J. Am. Chem. Soc. **126**, 13480 (2004).
11. P. Leclère, M. Surin, P. Viville, R. Lazzaroni, A.F.M. Kilbinger, O. Henze, W.J. Feast, M. Cavallini, F. Biscarini, A.P.H.J. Schenning, and E.W. Meijer. Chem. Mater. **16**, 4452 (2004).
12. U. Mitschke, T. Debaerdemaeker, and P. Bäuerle. Eur. J. Org. Chem. 425, (2000).
13. M.D. Curtis, J. Cao, and J.W. Kampf. J. Am. Chem. Soc. **126**, 4318 (2004).
14. C. Moorlag, O. Clot, M.O. Wolf, and B.O. Patrick. Chem. Commun. (Cambridge), **24**, 3028, (2002).
15. C. Moorlag, M.O. Wolf, C. Bohne, and B.P. Patrick. J. Am. Chem. Soc. **127**, 6382 (2005).
16. F.R. Hartley. The chemistry of platinum and palladium. Halsted Press, New York. 1973.
17. A. Babai, G.B. Deacon, and G. Meyer. Z. Anorg. Allg. Chem. **630**, 339 (2004).
18. W.E. Hill, D.M.A. Minahan, J.G. Taylor, and C.A. McAuliffe. J. Am. Chem. Soc. **104**, 6001 (1982).
19. M.H. Johansson and S. Otto. Acta. Crystallogr. Sect. C, e12 (2000).
20. G.K. Anderson and R.J. Cross. Chem. Soc. Rev. **9**, 185 (1980).
21. D.A. Redfield and J.H. Nelson. Inorg. Chem. **12**, 15 (1973).
22. A.W. Verstuyft and J.H. Nelson. Inorg. Chem. **14**, 1501 (1975).
23. O. Clot, M.O. Wolf, and B.O. Patrick. J. Am. Chem. Soc. **122**, 10456 (2000).
24. O. Clot, M.O. Wolf, and B.O. Patrick. J. Am. Chem. Soc. **123**, 9963 (2001).
25. O. Clot, Y. Akahori, C. Moorlag, D.B. Leznoff, M.O. Wolf, R.J. Batchelor, B.O. Patrick, and M. Ishii. Inorg. Chem. **42**, 2704 (2003).
26. T.L. Stott and M.O. Wolf. Inorg. Chem. **44**, 620 (2005).
27. C.B. Murphy, Y. Zhang, T. Troxler, V. Ferry, J.J. Martin, and W.E. Jones, Jr. J. Phys. Chem. B, **108**, 1537 (2004).
28. Y. Liu, S. Jiang, and K.S. Schanze. Chem. Commun. (Cambridge), 650 (2003).
29. R.D. Myrex, G.M. Gray, A.G. VanEngen Spivey, and C.M. Lawson. Organometallics, **25**, 5045 (2006).
30. J.S. Field, R.J. Haines, E.I. Lakoba, and M.H. Sosabowski. J. Chem. Soc. Perkin Trans. 1, 3352 (2001).
31. T.L. Stott and M.O. Wolf. J. Phys. Chem. **108**, 18815 (2004).
32. A. Altomare, M. Cascarano, C. Giacovazzo, and A. Guagliardi. J. Appl. Crystallogr. **26**, 343 (1993).
33. A. Altomare, M.C. Burla, G. Camalli, M. Cascarano, C. Giacovazzo, A. Guagliardi, A.G.G. Moliterni, G. Polidori, and R. Spagna. J. Appl. Cryst. **32**, 115 (1999).
34. SHELXTL [computer program]. Bruker AXS, Inc., Madison, Wis. 1997.
35. SAINT [computer program]. Bruker Analytical X-ray Systems Inc., Madison, Wis. 1999.
36. G.M. Sheldrick. SADABS. Version 2.05 [computer program]. Bruker AXS, Inc., Madison, Wis. 1996.
37. V.K. Jain, H.C. Clark, and L. Jain. Indian J. Chem. Sect A, **40**, 135 (2001).
38. A. Varshney and G.M. Gray. Inorg. Chim. Acta, **148**, 215 (1988).
39. T.L. Stott, M.O. Wolf, and A. Lam. J. Chem. Soc. Dalton Trans. 652 (2005).
40. A.W. Verstuyft, L.W. Cary, and J.H. Nelson. Inorg. Chem. **14**, 1495 (1975).

© 2007 NRC Canada

41. N.A. Al-Salem, H.D. Empsall, R. Markham, B.L. Shaw, and B. Weeks. J. Chem. Soc. Dalton Trans. 1972 (1979).
42. W.E. Hill, C.A. McAuliffe, I.E. Niven, and R.V. Parish. Inorg. Chim. Acta, **38**, 273 (1980).
43. D.C. Smith, Jr. and G.M. Gray. Inorg. Chem. **37**, 1791 (1998).
44. D.C. Smith, Jr. and G.M. Gray. J. Chem. Soc. Dalton Trans. 677 (2000).
45. J.M.J. Paulusse and R.P. Sijbesma. Chem. Commun. (Cambridge), 1494, (2003).
46. F.A. Cotton, G. Wilkinson, C.A. Murillo, and M. Bochmann. Advanced inorganic chemistry. John Wiley & Sons Inc., New York. 1999.
47. D.W. Allen and B.F. Taylor. J. Chem. Soc. Dalton Trans. 51 (1982).
48. S.O. Grim, R.L. Keiter, and W. McFarlane. Inorg. Chem. **6**, 1133 (1967).
49. T. Yamamoto, D. Komarudin, T. Maruyama, M. Arai, B.-L. Lee, H. Suganuma, N. Asakawa, Y. Inoue, K. Kubota, S. Sasaki, T. Fukuda, and H. Matsuda. J. Am. Chem. Soc. **120**, 2047 (1998).
50. D. Berglund and D.W. Meek. Inorg. Chem. **8**, 2602 (1969).
51. C.L. Choi and D.L. Phillips. Mol. Phys. **94**, 547 (1998).
52. M. Cusumano, G. Guglielmo, V. Ricevuto, S. Sostero, O. Traverso, and T.J. Kemp. J. Chem. Soc. Dalton Trans. 302 (1981).
53. K.H. Leung, W. Szulbinski, and D.L. Phillips. Mol. Phys. **98**, 1323 (2000).
54. C.B. Pamplin, S.J. Rettig, B.O. Patrick, and B.R. James. Inorg. Chem. **42**, 4117 (2003).
55. A.M. Trzeciak, H. Bartosz-Bechowski, Z. Ciunik, K. Niesyty, and J.J. Ziólkowski. Can. J. Chem. **79**, 752 (2001).
56. A.B.P. Lever. Inorganic electronic spectroscopy. Elsevier, New York. 1984.
57. N. DiCésare, M. Belletête, C. Marrano, M. Leclerc, and G. Durocher. J. Phys. Chem. A, **103**, 803 (1999).
58. B. Gombojav, N. Namsrai, T. Yoshinari, S. Nagasaka, H. Itoh, and K. Koyama. J. Solid State Chem. **177**, 2827 (2004).
59. A. Tabet, A. Schröder, H. Hartmann, D. Rohde, and L. Dunsch. Org. Lett. **5**, 1817 (2003).
60. A. Yassar, G. Horowitz, P. Valat, V. Wintgens, M. Hmyene, F. Deloffre, P. Srivastava, P. Lang, and F. Garnier. J. Phys. Chem. **99**, 9155 (1995).

© 2007 NRC Canada

Synthesis, characterization, and reactivity of Pd(II) salicylaldimine complexes derived from aminophenols

Bennett J. Tardiff, Joshua C. Smith, Stephen J. Duffy, Christopher M. Vogels, Andreas Decken, and Stephen A. Westcott

Abstract: Schiff bases, derived from the condensation of salicylaldehydes with 3- and 4-aminophenol, reacted with palladium(II) acetate to give the corresponding bis(*N*-arylsalicylaldiminato)palladium(II) complexes. These complexes have been found to be active catalysts for the Suzuki–Miyaura cross-coupling of aryl bromides and iodides with aryl boronic acids, using water as a solvent.

Key words: cross-coupling, green chemistry, palladium, salicylaldimines, Schiff base, Suzuki–Miyaura.

Résumé : Les bases de Schiff résultant de la condensation de salicylaldéhydes avec les 3- et 4-aminophénols réagissent avec l'acétate de palladium(II) pour conduire aux complexes correspondants bis(*N*-arylsalicylaldiminato)palladium(II). On a trouvé que ces complexes sont actifs dans les réactions de couplages croisés de Suzuki–Miyaura des bromures et des iodures d'aryles avec les acides arylboroniques, en présence d'eau comme solvant.

Mots-clés : couplage croisé, chimie verte, palladium, salicylaldimines, base de Schiff, Suzuki–Miyaura.

[Traduit par la Rédaction]

Introduction

The use of palladium complexes to catalyze the coupling of organoboron compounds with aryl or vinyl halides has become one of the most widely used tools in organic synthesis. The scope and utility of the Suzuki–Miyaura reaction have been the subject of several excellent reviews (1). Indeed, the Suzuki–Miyaura cross-coupling reaction has become an attractive route to generating biaryls, compounds with vast applications ranging from pharmaceutical chemistry to materials science. The use of boronic acids in this cross-coupling process is especially advantageous, as these compounds are relatively nontoxic and thermally, air-, and moisture-stable (2).

Numerous advances have been made to this reaction since its discovery. For instance, the use of aryl chlorides as substrates and the ability to conduct the reaction at low temperature and at low catalyst loading have greatly increased the versatility of the Suzuki–Miyaura cross-coupling reaction. Catalyst development has also played a significant role in improving this reaction (3), as traditional palladium complexes used to catalyze this transformation contained air-sensitive phosphine ligands. Recently, catalysts, containing *N*-heterocyclic carbenes (4), and "ligandless" systems (5), as well as heterogeneous systems (6), have also been employed. A considerable amount of research has also focused on designing water-soluble catalysts to provide a greener and more environmentally benign alternative to this reaction (4*i*, 7). In a recent elegant study by Hong et al., it was found that (*N*-arylsalicylaldiminato)palladium(II) complexes are active catalysts for the Suzuki–Miyaura cross-coupling reaction of a wide array of aryl bromides (8*a*). However, reactions were carried out in organic solvents (THF and toluene), and high yields were only achieved after long periods of time (days). Likewise, trinuclear triphenylphosphine Au(I) complexes with *N,N,O*-tridentate unsymmetrical Schiff base ligands catalyzed the Suzuki–Miyaura cross-coupling reaction to afford nonsymmetrical biaryls in good yields, whereas the Au(III) complexes gave only arylboronic homocoupling products (8*b*). As part of our ongoing investigation into designing new metal Schiff base complexes, we prepared several palladium complexes derived from salicylaldehydes and aminophenols and examined their ability to be used as catalysts for the green Suzuki–Miyaura cross-coupling reaction.

Received 28 February 2007. Accepted 10 April 2007. Published on the NRC Research Press Web site at canjchem.nrc.ca on 18 May 2007.

B.J. Tardiff, J.C. Smith, S.J. Duffy, C.M. Vogels, and S.A. Westcott.[1] Department of Chemistry, Mount Allison University, Sackville, NB E4L 1G8, Canada.
A. Decken.[2] Department of Chemistry, University of New Brunswick, Fredericton, NB E3B 5A3, Canada.

[1]Corresponding author (e-mail: swestcott@mta.ca).
[2]Corresponding author for X-ray crystallography (e-mail: adecken@unb.ca).

 doi:10.1139/V07-036 © 2007 NRC Canada

Experimental

General

Reagents and solvents used were purchased from Aldrich Chemicals. $Pd(OAc)_2$ was purchased from Precious Metals Online Ltd. (Melbourne, AU). NMR spectra were recorded on a JEOL JNM-GSX270 FT spectrometer or a Varian Mercury Plus 200 NMR spectrometer. ^{1}H NMR chemical shifts are reported in ppm and are referenced to the residual solvent protons in the deuterated solvent at 270 and 200 MHz, respectively. ^{13}C NMR chemical shifts are referenced to the solvent carbon resonances as internal standards at 68 and 50 MHz, respectively, and are reported in ppm. Multiplicities are reported as singlet (s), doublet (d), triplet (t), multiplet (m), broad (br), and overlapping (ov). Infrared spectra were obtained using a Mattson Genesis II FTIR spectrometer. Melting points were determined using a Mel-Temp apparatus and are uncorrected. Microanalyses for C, H, and N were carried out at Guelph Chemical Laboratories (Guelph, ON). GC–MS analyses were conducted using a Varian Saturn 2000 MS, coupled to a CP-3800 GC. The GC was equipped with both the 1177 injection port with a CP-8410 liquid autoinjector connected to an SPB-1 (Supelco) fused-silica column (30 m × 0.25 mm i.d. × 0.25 μm) and the 1079 solid-injector chromatoprobe, attached to a 50 cm transfer line. The GC–MS spectrometer is controlled by the Saturn Workstation software, Version 5.51. Imines were prepared by established procedures (9).

X-ray crystallography

Crystals of **2b** were grown from a DMSO solution at 20 °C, **2e** from a saturated THF solution at 5 °C, and **2f** from a saturated CH_2Cl_2 solution at 5 °C. Single crystals were coated with Paratone-N oil, mounted using a glass fibre, and frozen in the cold stream of the goniometer. A hemisphere of data was collected on a Bruker AXS P4/SMART 1000 diffractometer using ω and θ scans with a scan width of 0.3° and exposure times of 10 s (**2b**), 30 s (**2e**), and 80 s (**2f**). The detector distances were 5 cm. The data were reduced (10*a*) and corrected for absorption (10*b*). The structures were solved by direct methods and refined by full-matrix least-squares on F^2 (10*c*). All non-hydrogen atoms were refined anisotropically. Hydrogen atoms were located in Fourier difference maps and refined isotropically (**2b**) or included in calculated positions and refined using a riding model (**2e** and **2f**).

Complex 2a

Palladium(II) acetate (100 mg, 0.45 mmol) was added to a solution of 2-((*E*)-(3-hydroxyphenylimino)methyl)phenol (200 mg, 0.94 mmol) in EtOH (15 mL). The solution was heated at reflux for 2 h, at which point the solvent was removed under vacuum, leaving a brown powder, which was washed with Et_2O (3 × 5 mL). Yield: 170 mg (71%); mp 284–286 °C dec. IR (Nujol): 3433 (br, OH), 2933 (s), 2910 (s), 2856 (s), 1608 (w), 1538 (w), 1457 (w), 1376 (w), 1272 (w), 1145 (w), 846 (w). Spectroscopic NMR data (in DMSO-d_6): ^{1}H δ: 9.61 (br s, O*H*, 2H), 8.02 (s, N=C*H*, 2H), 7.43 (d, *J* = 7.4 Hz, Ar, 2H), 7.23–7.13 (ov m, Ar, 4H), 6.78–6.73 (ov m, Ar, 6H), 6.50 (t, *J* = 7.4 Hz, Ar, 2H), 6.02 (d, *J* = 8.4 Hz, Ar, 2H). ^{13}C{^{1}H} δ: 164.6, 163.7, 157.6, 150.6, 135.8, 135.6, 129.2, 120.7, 120.4, 115.8, 115.2, 113.8, 112.4. Anal. calcd. for $C_{26}H_{20}N_2O_4Pd$ (%): C 58.82, H 3.80, N 5.28; found: C 58.43, H 3.49, N 5.12.

Complex 2b

Palladium(II) acetate (100 mg, 0.45 mmol) was added to a solution of 2-((*E*)-(4-hydroxyphenylimino)methyl)phenol (200 mg, 0.94 mmol) in EtOH (15 mL). The mixture was heated at reflux for 2 h, at which point the solvent was removed under vacuum. The resulting brown solid was washed with Et_2O (3 × 5 mL). Yield: 155 mg (65%); mp 306 °C dec. IR (Nujol): 2919 (s), 2854 (s), 1606 (w), 1542 (w), 1462 (m), 1376 (m), 1178 (w), 842 (w), 759 (w). Spectroscopic NMR data (in DMSO-d_6): ^{1}H δ: 9.49 (br s, O*H*, 2H), 7.99 (s, N=C*H*, 2H), 7.42 (d, *J* = 7.4 Hz, Ar, 2H), 7.23–7.14 (ov m, Ar, 6H), 6.83–6.76 (ov m, Ar, 4H), 6.48 (t, *J* = 7.2 Hz, Ar, 2H), 6.06 (d, *J* = 8.4 Hz, Ar, 2H). ^{13}C{^{1}H} δ: 164.6, 163.7, 146.3, 141.3, 135.7, 135.3, 126.2, 120.8, 120.2, 115.1, 114.8. Anal. calcd. for $C_{26}H_{20}N_2O_4Pd$ (%): C 58.82, H 3.80, N 5.28; found: C 58.46, H 3.47, N 5.27.

Complex 2c

Palladium(II) acetate (100 mg, 0.45 mmol) was added to a solution of 2-((*E*)-(3-hydroxyphenylimino)methyl)-4-bromophenol (264 mg, 0.90 mmol) in EtOH (15 mL). The mixture was heated at reflux for 2 h, at which point the solvent was removed under vacuum. The resulting dark-brown powder was washed with Et_2O (3 × 5 mL). Yield: 199 mg (64%); mp 223 °C dec. IR (Nujol): 3164 (br, OH), 2950 (s), 2900 (s), 1591 (m), 1459 (s), 1376 (m), 1294 (w), 1145 (w), 960 (w), 827 (w). Spectroscopic NMR data (in DMSO-d_6): ^{1}H δ: 9.63 (br s, O*H*, 2H), 8.03 (s, N=C*H*, 2H), 7.65 (d, *J* = 7.4 Hz, Ar, 2H), 7.26–7.15 (ov m, Ar, 4H), 6.72–6.65 (ov m, Ar, 6H), 5.94 (d, *J* = 8.4 Hz, Ar, 2H). ^{13}C{^{1}H} δ: 163.5, 163.2, 157.6, 150.3, 137.8, 136.9, 129.3, 122.6, 122.5, 115.7, 114.1, 112.2, 105.3. Anal. calcd. for $C_{26}H_{18}Br_2N_2O_4Pd$ (%): C 45.34, H 2.64, N 4.07; found: C 44.93, H 2.80, N 4.16.

Complex 2d

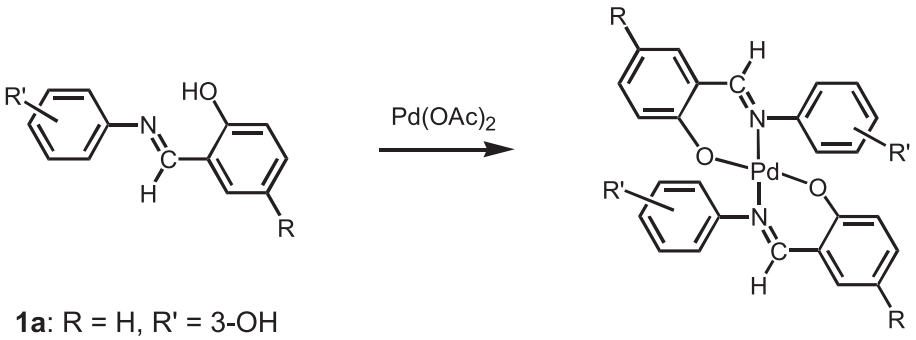
Palladium(II) acetate (120 mg, 0.53 mmol) was added to a solution of 2-((*E*)-(4-hydroxyphenylimino)methyl)-4-bromophenol (312 mg, 1.07 mmol) in EtOH (15 mL), and the solution was heated at reflux for 2 h. Following the removal of the solvent under vacuum, the resulting orange powder was washed with Et_2O (3 × 5 mL). Yield: 150 mg (41%); mp 246–247 °C dec. IR (Nujol): 3242 (br, OH), 3220 (br, OH), 2923 (s), 2854 (s), 1612 (w), 1504 (w), 1462 (m), 1375 (w), 1288 (w), 1213 (w), 1166 (w). Spectroscopic NMR data (in DMSO-d_6): ^{1}H δ: 9.62 (br s, O*H*, 2H), 8.02 (s, N=C*H*, 2H), 7.65 (d, *J* = 1.7 Hz, Ar, 2H), 7.26 (d of d, *J* = 8.7, 1.7 Hz, Ar, 2H), 7.13 (d, *J* = 8.4 Hz, Ar, 4H), 6.78 (d, *J* = 8.4 Hz, Ar, 4H), 5.97 (d, *J* = 8.7 Hz, Ar, 2H). Anal. calcd. for $C_{26}H_{18}Br_2N_2O_4Pd$ (%): C 45.34, H 2.64, N 4.07; found: C 45.10, H 2.45, N 4.01.

Complex 2e

Palladium(II) acetate (100 mg, 0.45 mmol) was added to a solution of 1-((*E*)-(3-hydroxyphenylimino)methyl)naphthalen-2-ol (237 mg, 0.90 mmol) in EtOH (10 mL). The mix-

© 2007 NRC Canada

Scheme 1. Synthesis of Schiff base palladium complexes **2a**–**2f**.



1a: R = H, R' = 3-OH
1b: R = H, R' = 4-OH
1c: R = Br, R' = 3-OH
1d: R = Br, R' = 4-OH
1e: R = naphthyl, R' = 3-OH
1f: R = naphthyl, R' = 4-OH

2

ture was heated at reflux for 2 h, at which point an orange-brown solid was collected by suction filtration. The solid was dissolved in hot THF (10 mL), filtered, hexane (5 mL) was added, and the solution was stored at 5 °C for 2 d. The resulting orange precipitate was collected by suction filtration. Yield: 200 mg (70%); mp 310 °C dec. IR (Nujol): 3183 (br, OH), 2956 (w, ov), 2917 (s), 2852 (m), 1594 (m), 1538 (w), 1462 (m), 1376 (w), 1288 (w), 1149 (w). Spectroscopic NMR data (in DMSO-d_6): ^{1}H δ: 9.66 (br s, O*H*, 2H), 8.60 (s, N=C*H*, 2H), 8.05 (d, *J* = 8.4 Hz, Ar, 2H), 7.68 (d, *J* = 8.4 Hz, Ar, 4H), 7.43 (t, *J* = 6.9 Hz, Ar, 2H), 7.30–7.21 (ov m, Ar, 4H), 6.92–6.90 (ov m, Ar, 4H), 6.82 (d, *J* = 7.7 Hz, Ar, 2H),), 6.27 (d, *J* = 9.2 Hz, Ar, 2H). ^{13}C{^{1}H} δ: 165.8, 157.8, 157.4, 151.5, 136.2, 134.6, 129.6, 129.4, 128.6, 126.9, 123.5, 123.2, 120.9, 116.3, 114.0, 112.9, 111.0. Anal. calcd. for $C_{34}H_{24}N_2O_4Pd$ (%): C 64.71, H 3.84, N 4.44; found: C 64.93, H 3.63, N 4.45.

Complex 2f

Complex 2f was prepared by the modification of a known procedure (11). Palladium(II) acetate (100 mg, 0.45 mmol) was added to a solution of 1-((*E*)-(4-hydroxyphenylimino)methyl)naphthalen-2-ol (237 mg, 0.90 mmol) in EtOH (10 mL). The mixture was heated at reflux for 2 h, at which point an orange- brown precipitate was collected by suction filtration. The solid was dissolved in hot THF (50 mL), filtered, hexane (20 mL) was added, and the solution stored at 5 °C for 5 d. The resulting orange precipitate was collected by suction filtration. Yield: 125 mg (44%); mp 300 °C dec. IR (Nujol): 2917 (s), 2854 (m), 1612 (w), 1592 (w), 1454 (m), 1376 (w), 1000 (w). Spectroscopic NMR data (in DMSO-d_6): ^{1}H δ: 9.58 (br s, O*H*, 2H), 8.57 (s, N=C*H*, 2H), 8.05 (d, *J* = 8.6 Hz, Ar, 2H), 7.68 (d, *J* = 8.6 Hz, Ar, 4H), 7.41 (t, *J* = 7.7 Hz, Ar, 2H), 7.32 (d, *J* = 8.4 Hz, Ar, 4H), 7.23 (t, *J* = 7.2 Hz, Ar, 2H), 6.83 (d, *J* = 8.4 Hz, Ar, 4H), 6.29 (d, *J* = 9.4 Hz, Ar, 2H). Anal. calcd. for $C_{34}H_{24}N_2O_4Pd$ (%): C 64.71, H 3.84, N 4.44; found: C 64.48, H 3.52, N 4.32.

Suzuki–Miyaura cross-coupling reactions

An aryl halide (1 mmol) and a boronic acid (1 mmol) were added to a solution of H_2O (10 mL), K_2CO_3 (276 mg, 2 mmol), and palladium complex (0.5 mol %). The solution was heated at reflux for 2 h. An organic extraction was performed using dichloromethane (2 × 10 mL), whereupon the solution was diluted by a factor of 100 and analyzed in duplicate using GC–MS spectroscopy.

Results and discussion

Salicylaldimines

Schiff bases are remarkable compounds that have been utilized extensively in organic syntheses (12). For instance, a recent report describes a highly diastereo- and enantioselective asymmetric aldol reaction of glycinate Schiff bases with aldehydes (12*a*). In this study, we have found that salicylaldehydes add to 3- and 4-aminophenol to give compounds having spectroscopic data consistent with the Schiff bases **1a**–**1f**. As expected, the proton, initially assigned to the aldehyde group, shifts from 10 to 9 ppm in the ^{1}H NMR spectra upon conversion to the imine functionality, and a resonance at ~160 ppm in the ^{13}C NMR spectra corresponds to the N=CH methine carbon. Likewise, formation of these compounds can be monitored by the diagnostic C=N stretching band in the IR spectra at ~1620 cm^{-1} (12*b*). Attempts to make the corresponding Schiff bases from 2-aminophenol led to products arising from a competing oxidative cyclization reaction (13).

Metal complexes

We have found that addition of **1a**–**1f** to $Pd(OAc)_2$ afforded bis(*N*-arylsalicylaldiminato)palladium(II) complexes (Scheme 1) in moderate yields (41%–71%). Complexes **2a**–**2f** have been characterized by a number of physical methods, including multinuclear NMR spectroscopy. A significant upfield shift in the ^{1}H NMR spectra is observed for the imine methine proton, from ~9 ppm to ~8 ppm, upon coordination of the ligand to the d^8 metal centre. The diagnostic

© 2007 NRC Canada

Fig. 1. Inert-atmosphere MALDI-MS spectra (pyrene matrix) showing simulated (top) and observed (bottom) isotope patterns for **2a**.

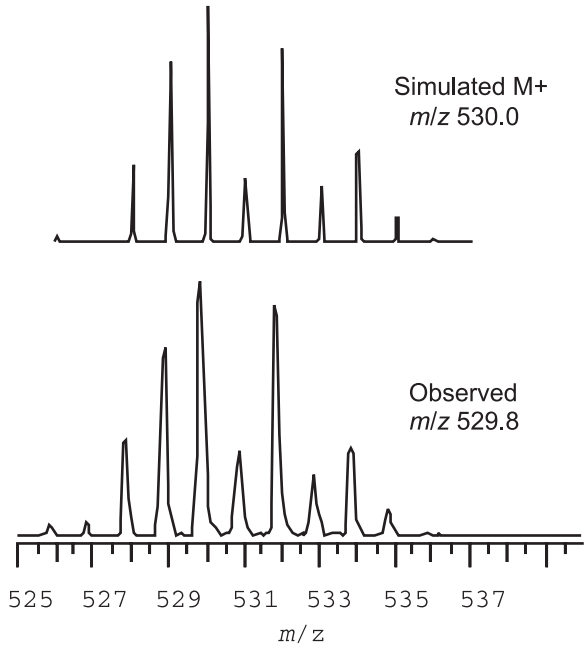
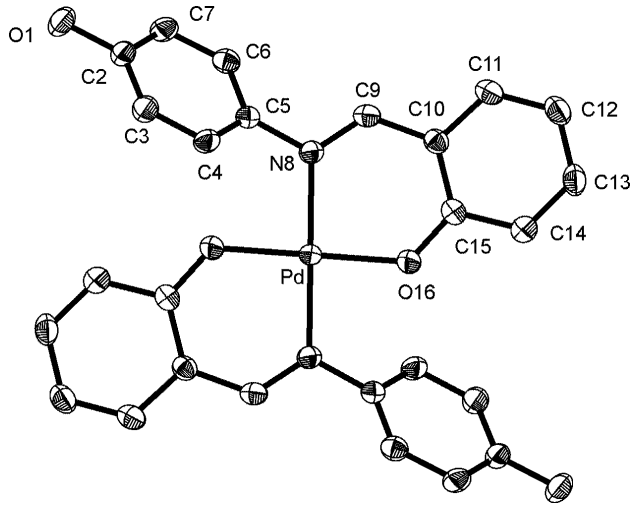


Fig. 2. The molecular structure of **2b** with ellipsoids drawn at the 50% probability level. Hydrogen atoms were omitted for clarity. Selected bond lengths (Å) and angles (°) for **2b**: Pd—O(16) No. 1, 1.9842(13); Pd—O(16), 1.9843(13); Pd—N(8) No. 1, 2.0256(14); Pd—N(8), 2.0257(14); O(1)—C(2), 1.367(2); C(5)—N(8), 1.439(2); N(8)—C(9), 1.292(2); C(15)—O(16), 1.311(2); O(16) No. 1–Pd–O(16), 180.00(6); O(16) No. 1–Pd–N(8) No. 1, 90.89(5); O(16)–Pd–N(8) No. 1, 89.11(5); O(16) No. 1–Pd–N(8), 89.11(5); O(16)–Pd–N(8), 90.89(5); N(8) No. 1–Pd–N(8), 180.00(7); C(2)–O(1)–H(1), 111.8(19); O(1)–C(2)–C(3), 121.90(17); O(1)–C(2)–C(7), 118.57(17).



C=N stretching band in the FTIR spectra has also shifted from ~1620 cm^{-1} to ~1595 cm^{-1} upon coordination to the metal centre (14). Elemental analyses are also consistent with bis Schiff base formulation, and complex **2a** has also been characterized by a mass spectrometry IA-MALDI-TOF study (15), which showed an excellent match between simulated and observed isotope patterns (Fig. 1).

Complex **2b** has been characterized by a single-crystal X-ray diffraction study (Fig. 2). Crystallographic data are provided in Table 1.[3] The environment about Pd is square-planar, supplemented by hydrogen bonds of 2.679(2) Å, resulting in an octahedral environment and a two-dimensional network. DMSO molecules hydrogen bond at a distance of 1.93(3) Å and long S···O bonds of 3.2437(15) Å complete the formation of the two-dimensional sheets. The Pd—O and Pd—N distances of 1.9843(13) Å and 2.0257(14) Å, respectively, are similar to those seen in related complexes (8*a*, 9). Similar copper complexes have recently been reported to be active catalysts in the polymerization of norbornene (16).

Interestingly, the molecular structure of **2e** (Fig. 3) has also been characterized by a single-crystal X-ray diffraction study, and in this case, the metal lies in a distorted square-planar geometry with a cis-N_2O_2 donor set. The naphthyl groups are distorted from the $Pd(N,O)_2$ plane and result in a parallel alignment of the phenol groups. The C(6)—C(25) distance of 3.349(8) Å suggests that intramolecular arene–arene stacking may be important (17). While it is unclear at this time why these ligands lie in a cis configuration, this unusual arrangement has been observed recently in bulky bis(*N*-3,5-Bu^t-2-phenyl-(*R*)-salicylaldiminato)copper(II) complexes, where small changes in the substituents resulted in drastic changes in the molecular structure and in the corresponding redox properties (18). Attempts to obtain single crystals of the corresponding 4-hydroxyl derivative **2f** were complicated by crystal twinning and the deposition of very thin plates from solutions of **2f**. However, the preliminary structure of **2f** clearly shows the trans-arrangement of the ligands (Fig. 4). As these conformers are indistinguishable by NMR spectroscopy, further structural studies are therefore needed to understand the nature of these discrepancies.

Catalytic activity

As mentioned previously, Hong et al. found that cross-coupling reactions of aryl bromides and phenyl boronic acids could be catalyzed by $Pd(OAc)_2$ and 2-[1-(2,4,6-trimethylphenylimino)ethyl]phenol (HL) (8*a*). Reactions were carried out in organic solvents (THF and toluene) at

[3] Supplementary data for this article are available on the journal Web site (canjchem.nrc.ca) or may be purchased from the Depository of Unpublished Data, Document Delivery, CISTI, National Research Council Canada, Ottawa, ON K1A 0S2, Canada. DUD 5163. For more information on obtaining material, refer to http://cisti-icist.nrc-cnrc.gc.ca/irm/unpub_e.shtml. CCDC 637015, 637101, and 637199 contain the crystallographic data for this manuscript. These data can be obtained, free of charge, via http://www.ccdc.cam.ac.uk/conts/retrieving.html (or from the Cambridge Crystallographic Data Centre, 12 Union Road, Cambridge CB2 1EZ, UK; fax +44 1223 336033; or deposit@ccdc.cam.ac.uk).

© 2007 NRC Canada

Table 1. Crystallographic data collection parameters for **2b**, **2e**, and **2f**.

Complex	**2b**·2DMSO	**2e**·THF	**2f**·CH_2Cl_2
Chemical formula	$C_{30}H_{32}N_2O_6PdS_2$	$C_{38}H_{32}N_2O_5Pd$	$C_{35}H_{26}Cl_2N_2O_4Pd$
Formula mass	687.10	703.06	715.88
Crystal dimensions (mm^3)	0.30 × 0.25 × 0.075	0.20 × 0.15 × 0.05	0.23 × 0.10 × 0.03
Crystal system	Monoclinic	Monoclinic	Triclinic
Space group	$P2_1/c$	$P2_1/c$	$P1$
Z	2	4	2
a (Å)	13.8014(6)	12.015(6)	10.697(11)
b (Å)	10.7869(5)	19.479(10)	12.002(12)
c (Å)	9.9018(5)	14.427(7)	12.527(12)
α (°)	90	90	86.302(16)
β (°)	97.226(1)	108.093(7)	80.518(15)
γ (°)	90	90	72.555(16)
Volume ($Å^3$)	1462.42(12)	3210(3)	1513(3)
$D_{calcd.}$ (mg m^{-3})	1.560	1.455	1.571
T (K)	173(1)	173(1)	198(1)
Radiation	Mo Kα (λ = 0.71073 Å)	Mo Kα (λ = 0.71073 Å)	Mo Kα (λ = 0.71073 Å)
μ (mm^{-1})	0.824	0.625	0.833
Total reflections collected	9941	8823	9729
Total unique reflections	3278	8823	6352
No. of variables	251	418	402
θ (°)	1.49–27.50	1.78–27.49	1.65–27.49
Goodness-of-fit on F^2	1.089	1.135	1.052
$R_1{}^a$ [$I > 2\sigma(I)$]	0.0232	0.0667	0.0893
$wR_2{}^b$ (all data)	0.0660	0.2025	0.2922
Largest diff. Peak and hole (e $Å^{-3}$)	0.598 and –0.415	1.216 and –0.903	3.542 and –2.704

[a] $R_1 = \Sigma||F_o| - |F_c||/\Sigma|F_o|$.

[b] $wR_2 = [\Sigma w(F_o^2 - F_c^2)^2/\Sigma(F_o^4)]^{1/2}$ where $w = 1/[\sigma^2(F_o^2) + (0.0359 \times P)^2 + (0.485 \times P)]$ for **2b**, $w = 1/[\sigma^2(F_o^2) + (0.0868 \times P)^2]$ for **2e**, and $w = 1/[\sigma^2(F_o^2) + (0.1616 \times P)^2]$ for **2f** where $P = [\max(F_o^2, 0) + 2 \times F_c^2]/3$.

room temperature, and high yields of the desired products were only achieved after long periods of time (days). Interestingly, only one molar equivalent of the N,O-bidentate Schiff base ligand was used in this study, although the catalyst resting state appears to be the corresponding bis Schiff base compound PdL_2. Reduced catalytic activity was observed for reactions using this bis Schiff base compound, as the active catalyst precursor was believed to be the mono Schiff base compound PdL(OAc)(solvent). It is also possible that palladium nanoparticles, formed by the decomposition of the catalyst precursor during the reaction, are responsible for the observed catalytic activity in these systems (7*o*).

In this preliminary study, preformed complexes **2a**–**2f** were examined for their ability to catalyze the coupling of 4-iodotoluene and phenyl boronic acid in water. Reactions were conducted in air using 0.5 mol% catalyst loading and potassium carbonate at reflux. Remarkably, all reactions with these bis Schiff base complexes gave near-quantitative yield of the unsymmetrical biaryl cross-coupling product after only 2 h (Table 2, entry 1). Complex **2f** gave the most consistent results with minimal amount of catalyst decomposition; therefore, it was used in all the catalytic studies. While reactions with bromotoluene also gave high yields of the desired biaryl product (Table 2, entry 2), these catalysts failed to couple reactions with chlorotoluene (Table 2, entry 3). The electronic nature of the aryl group had little effect on activity, as both the methoxy- (Table 2, entry 4) and fluoro-substituted iodobenzene (Table 2, entry 5) derivatives gave excellent yields of the desired product. Reactions of 4-iodotoluene and naphthalboronic acid using 0.5 mol% of **2f** also gave near-quantitative yields of the corresponding cross-coupling product.

Conclusion

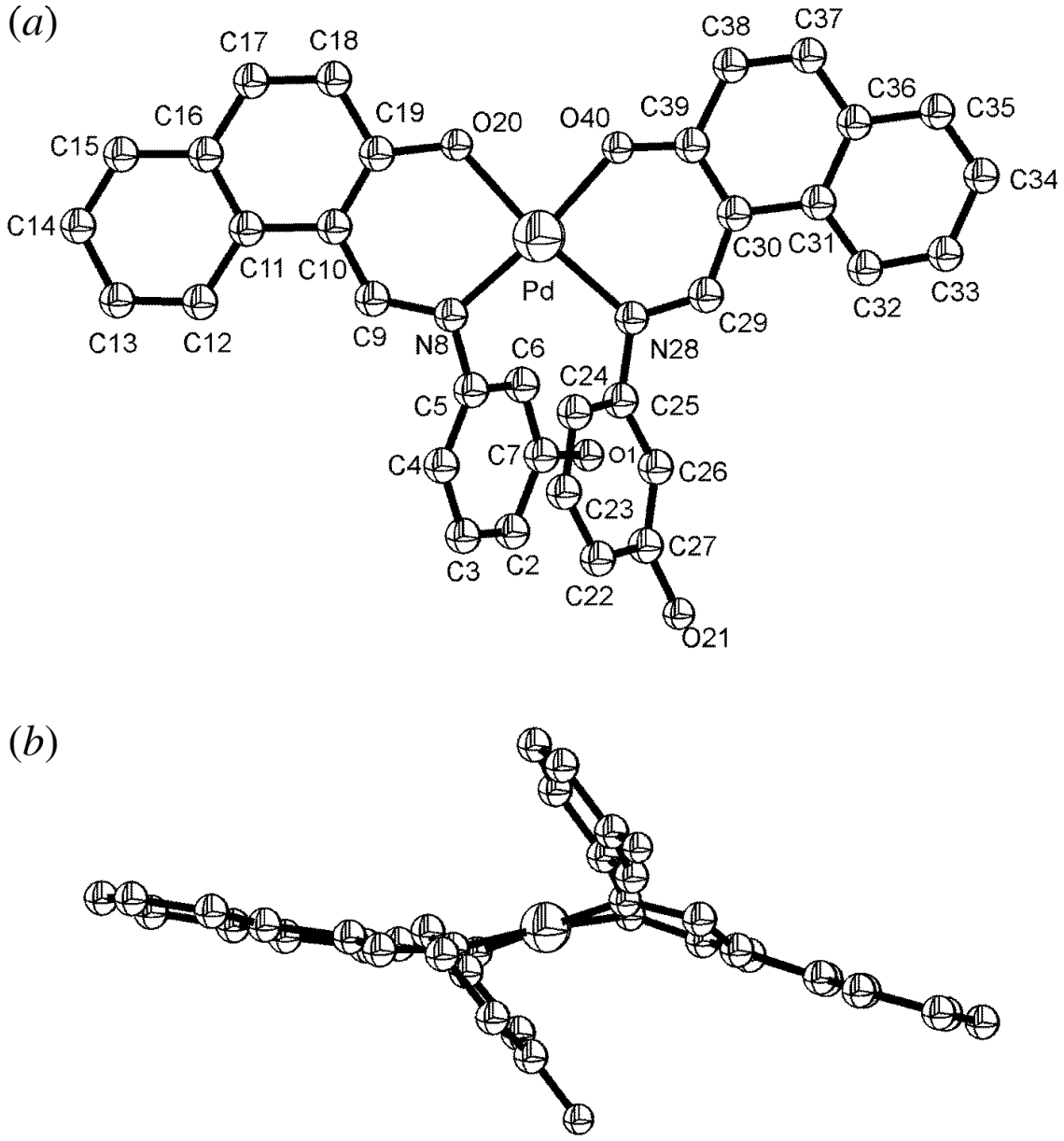
In summary, we have prepared a series of (*N*-arylsalicylaldiminato)palladium(II) complexes, derived from aminophenols, and examined their ability to catalyze the Suzuki–Miyaura cross-coupling reaction. Although no significant activity is observed with aryl chlorides, these complexes effectively catalyze the coupling of both aryl bromides and aryl iodides. Further work is needed to expand the scope of this reaction, the results of which will be published in due course.

Acknowledgements

Thanks are gratefully extended to the American Chemical Society-Petroleum Research Fund (Grant No. 37824-B1), Canada Research Chairs Program, Canadian Foundation for Innovation (CFI)-Atlantic Innovation Fund, Natural Science and Engineering Research Council of Canada (NSERC), and

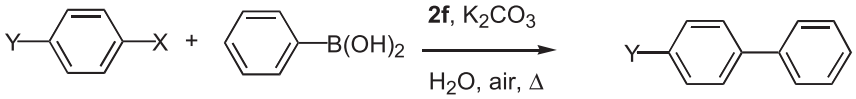
© 2007 NRC Canada

Fig. 3. (*a*) The molecular structure of **2e** with ellipsoids drawn at the 30% probability level. Hydrogen atoms and a molecule of THF were omitted for clarity. (*b*) An alternate side-on view of **2e** showing the distortion of the $Pd(N,O)_2$ backbone and the parallel arrangement of the phenol groups. Selected bond lengths (Å) and angles (°) for **2e**: Pd—O(40), 1.997(5); Pd—O(20), 2.012(4); Pd—N(8), 2.015(5); Pd—N(28), 2.029(5); O(1)—C(7), 1.378(8); N(8)—C(9), 1.318(8); C(19)—O(20), 1.331(7); N(28)—C(29), 1.312(8); C(39)—O(40), 1.320(8); O(40)–Pd–O(20), 83.92(18); O(40)–Pd–N(8), 173.1(2); O(20)–Pd–N(8), 89.9(2); O(40)–Pd–N(28), 89.2(2); O(20)–Pd–N(28), 173.1(2); N(8)–Pd–N(28), 97.0(2); C(5)–N(8)–Pd, 120.9(4); C(9)–N(8)–Pd, 122.7(5); C(29)–N(28)–Pd, 120.0(5); C(25)–N(28)–Pd, 122.1(4).



© 2007 NRC Canada

Table 2. Suzuki–Miyaura cross-coupling reactions catalyzed by complex **2f**.

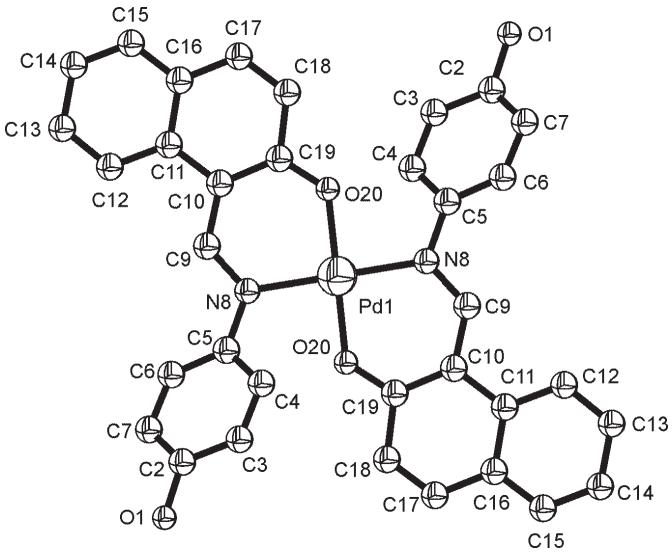


Entry	X	Y	Yield (%)[a]
1	I	CH_3	>95
2	Br	CH_3	>95
3	Cl	CH_3	5
4	I	OMe	>95
5	I	F	>95

Note: Reaction conditions: 1 mmol of 4-halotoluene, 1 mmol of phenyl boronic acid, and 10 mL H_2O.

[a]Yields were determined by GC–MS, with respect to an internal standard, from an average of at least two runs and product formation was confirmed by multinuclear NMR spectroscopy.

Fig. 4. The molecular structure of one of the independent molecules of **2f** with ellipsoids drawn at the 30% probability level. Selected bond lengths (Å) and angles (°) for **2f**: Pd(1)—O(20), 1.990(6); Pd(1)—N(8), 2.015(8); Pd(2)—N(28), 1.943(10); Pd(2)—O(40), 1.980(7); O(20)–Pd(1)–O(20) No. 1, 180.000(1); O(20)–Pd(1)–N(8), 89.3(3); O(20) No. 1–Pd(1)–N(8), 90.7(3); O(20)–Pd(1)–N(8) No. 1, 90.7(3); O(20) No. 1–Pd(1)–N(8) No. 1, 89.3(3); N(8)–Pd(1)–N(8) No. 1, 180.0(4); N(28)–Pd(2)–N(28) No. 2, 180.000(1); N(28)–Pd(2)–O(40) No. 2, 90.7(3); N(28) No. 2–Pd(2)–O(40) No. 2, 89.3(3); N(28)–Pd(2)–O(40), 89.3(3); N(28) No. 2–Pd(2)–O(40), 90.7(3); O(40) No. 2–Pd(2)–O(40), 180.0(4).



Mount Allison University for financial support. JCS thanks NSERC for an Undergraduate Student Research Award (USRA). We also thank Dan Durant and Roger Smith for their expert technical assistance, Johanna M. Blacquiere and Dr. Deryn E. Fogg (University of Ottawa) for the MALDI-TOF spectra, and anonymous reviewers for helpful suggestions.

References

1. (*a*) A. Suzuki. Proc. Jpn. Acad., Ser. B, **80**, 359 (2004); (*b*) A. Suzuki. Chem. Commun. 4759 (2005); (*c*) A. Suzuki. J. Organomet. Chem. **576**, 147 (1999).
2. D.G. Hall. Boronic acids. Wiley-VCH, Weinheim. 2005.
3. (*a*) F. Bellina, A. Carpita, and R. Rossi. Synthesis, 2419 (2004); (*b*) J. Spencer, D.P. Sharratt, J. Dupont, A.L. Monteiro, V.I. Reis, M.P. Stracke, F. Rominger, and I.M. McDonald. Organometallics, **24**, 5665 (2005); (*c*) F. Kerins and D.F. O'Shea. J. Org. Chem. **67**, 4968 (2002); (*d*) G.A. Grasa, A.C. Hillier, and S.P. Nolan. Org. Lett. **3**, 1077 (2001); (*e*) R. Nishio, M. Sugiura, and S. Kobayashi. Org. Lett. **7**, 4831 (2005); (*f*) J.-H. Li, W.-J. Liu, and Y.-XD. Xie. J. Org. Chem. **70**, 5409 (2005); (*g*) Z. Weng, S. Teo, L.L. Koh, and T.S.A. Hor. Organometallics, **23**, 4342 (2004); (*h*) A.F. Littke, C. Dai, and G.C. Fu. J. Am. Chem. Soc. **122**, 4020 (2000); (*i*) S. Paul and J.H. Clark. J. Mol. Catal. A: Chem. **215**, 107 (2004); (*j*) K.L. Billingsley, K.W. Anderson, and S.L. Buchwald. Angew. Chem., Int. Ed. **45**, 3484 (2006); (*k*) E. Ferrer Flegeau, M.E. Popkin, and M.F. Greaney. Org. Lett. **8**, 2495 (2006); (*l*) A.S. Guram, A.O. King, J.G. Allen, X. Wang, L.B. Schenkel, J. Chan, E.O. Bunel, M.M. Faul, R.D. Larsen, M.J. Martinelli, and P.J. Reider. Org. Lett. **8**, 1787 (2006); (*m*) L. Ackermann, C.J. Gshrei, A. Althammer, and M. Riederer. Chem. Commun. 1419 (2006); (*n*) T.E. Bader, S.D. Walker, J.R. Martinelli, and S.L. Buchwald. J. Am. Chem. Soc. **127**, 4685 (2005); (*o*) B. Tao and D.W. Boykin. J. Org. Chem. **69**, 4330 (2004); (*p*) S. Ishikawa and K. Manabe. Chem. Commun. 2589 (2006); (*q*) O. Piechaczyk, M. Doux, L. Ricard, and P. le Floch. Organometallics, **24**, 1204 (2005); (*r*) A.A.C. Braga, G. Ujaque, and F. Maseras. Organometallics, **25**, 3647 (2006); (*s*) V. Poláčková, S. Toma, and I. Augustínová. Tetrahedron, **62**, 11675 (2006); (*t*) S.-D. Cho, H.-K. Kim, H.-S. Yim, M.-R. Kim, J.-K. Lee, J.-J. Kim, Y.-J. Yoon. Tetrahedron, **63**, 1345 (2007).
4. (*a*) C.W.K. Gstöttmayr, V.P.W. Böhm, E. Herdtweck, M. Grosche, and W.A. Herrmann. Angew. Chem., Int. Ed. **41**, 1363 (2002); (*b*) G. Altenhoff, R. Goddard, C.W. Lehmann, and F. Glorius. Angew. Chem., Int. Ed. **42**, 3690 (2003); (*c*) O. Navarro, R.A. Kelly, III, and S.P. Nolan. J. Am. Chem. Soc. **125**, 16194 (2003); (*d*) M.B. Andrus and C. Song. Org. Lett. **3**,

© 2007 NRC Canada

3761 (2001); (*e*) D. Benito-Garagorri, E. Becker, J. Wiedermann, W. Lackner, M. Pollak, K. Mereiter, J. Kisala, and K. Kirchner. Organometallics, **25**, 1900 (2005); (*f*) A.I. Moncada, S. Manne, J.M. Tanski, and L.M. Slaughter. Organometallics, **25**, 491 (2006); (*g*) C.J. O'Brien, E.A.B. Kantchev, C. Valente, N. Hadei, G.A. Chass, A. Lough, A.C. Hopkinson, and M.G. Organ. Chem. Eur. J. **12**, 4743 (2006); (*h*) O. Navarro, N. Marion, J. Mei, and S.P. Nolan. Chem. Eur. J. **12**, 5142 (2006); (*i*) H.V. Huynh, Y. Han, J.H.H. Ho, and G.K. Tan. Organometallics, **25**, 3267 (2006).

5. (*a*) T.I. Wallow and B.M. Novak. J. Org. Chem. **59**, 5034 (1994); (*b*) D. Zim, A.L. Monteiro, and J. Dupont. Tetrahedron Lett. **41**, 919 (2000); (*c*) D. Ma and Q. Wu. Tetrahedron Lett. **42**, 5279 (2001); (*d*) G.W. Kabalka, V. Namboodiri, and L. Wang. Chem. Commun. 775 (2001); (*e*) C.R. LeBlond, A.T. Andrews, Y. Sun, and J.R. Sowa. Org. Lett. **3**, 1555 (2001); (*f*) G.A. Molander and B. Biolatto. J. Org. Chem. **68**, 4302 (2003).
6. (*a*) A. Houdayer, R. Schneider, D. Billaud, J. Ghanbaja, and J. Lambert. Appl. Organomet. Chem. **19**, 1239 (2005); (*b*) Y. Li, X.M. Hong, D.M. Collard, and M.A. El-Sayed. Org. Lett. **2**, 2385 (2000); (*c*) M. Moreno-Mañas, R. Pleixats, and S. Villarroya. Organometallics, **20**, 4524 (2001); (*d*) S.-W. Kim, M. Kim, W.Y. Lee, and T. Hyeon. J. Am. Chem. Soc. **124**, 7642 (2002); (*e*) P.D. Stevens, J. Fan, H.M.R. Gardimalla, M. Yen, and Y. Gao. Org. Lett. **7**, 2085 (2005); (*f*) S.-W. Kim, M. Kim, W.Y. Lee, and T. Hyeon. J. Am. Chem. Soc. **124**, 7642 (2002); (*g*) J. Lemo, K. Heuzé and D. Astruc. Inorg. Chim. Acta. **359**, 4909 (2006); (*h*) J.-H. Li, X.-C. Hu, and Y.-X. Xie. Tetrahedron Lett. **47**, 9239 (2006).
7. (*a*) R. Franzén and Y. Xu. Can. J. Chem. **83**, 266 (2005); (*b*) S. Ogo, Y. Takebe, K. Uehara, T. Yamazaki, H. Nakai, Y. Watanabe, and S. Fukuzumi. Organometallics, **25**, 331 (2006); (*c*) M. Lysén and K. Köhler. Synthesis, 692 (2006); (*d*) B.D. DeVasher, L.R. Moore, and K.H. Shaughnessy. J. Org. Chem. **69**, 7919 (2004); (*e*) C. Baleizão, A. Corma, H. García, and A. Leyva. J. Org. Chem. **69**, 439 (2004); (*f*) A.M. Deveau and T.L. Macdonald. Tetrahedron Lett. **45**, 803 (2004); (*g*) R.W. Friesen and L.A. Trimble. Can. J. Chem. **82**, 206 (2004); (*h*) K.W. Anderson and S.L. Buchwald. Angew. Chem., Int. Ed. **44**, 6173 (2005); (*i*) R.K. Arvela, N.E. Leadbeater, T.L. Mack, and C.M. Kormos. Tetrahedron Lett. **47**, 217 (2006); (*j*) G. Lu, R. Franzén, Q. Zhang, and Y. Xu. Tetrahedron Lett. **46**, 4255 (2005); (*k*) D. Schöfelder, O. Nuyken, and R. Weberskirch. J. Organomet. Chem. **690**, 4648 (2005); (*l*) D.N. Korolev and N.A. Bumagin. Tetrahedron Lett. **46**, 5751 (2005); (*m*) K. Shimizu, R. Maruyama, S. Komai, T. Kodama, and Y. Kitayama. J. Catal. **227**, 202 (2004); (*n*) Q. Yang, S. Ma, J. Li, F. Xiao, and H. Xiong. Chem. Commun. 2495 (2006); (*o*) C.-L. Chen, Y.-H. Liu, S.-M. Peng, and S.-T. Liu. Organometallics, **24**, 1075 (2005); (*p*) W.-Y. Wu, S.-N. Chen, and F.-Y. Tsai. Tetrahedron Lett. **47**, 9267 (2006); (*q*) G.Y. Li, P.J. Fagan, and P.L. Watson. Angew. Chem., Int. Ed. **40**, 1106 (2001); (*r*) I.P. Beletskaya, A.G. Bessmertnykh, A.D. Averin, F. Denat, and R. Guilard. Eur. J. Org. Chem. 261 (2005); (*s*) J.P. Wolfe and J.S. Thomas. Curr. Org. Chem. **9**, 625 (2005); (*t*) E. Peris, J.A. Loch, J. Mata, and R.H. Crabtree. Chem. Commun. 201 (2001); (*u*) C.R. Eisnor, R.A. Gossage and P.N. Yadav. Tetrahedron, **62**, 3395 (2006); (*v*) I.D. Kostas, F.J. Andreadaki, D. Kovala-Demertzi, C. Prentjas, and M.A. Demertzis. Tetrahedron Lett. **46**, 1967 (2005); (*w*) C.-L. Chen, Y.-H. Liu, S.-M. Peng, and S.T. Liu. Organometallics, **24**, 1075 (2005); (*x*) A. Decken, R.A. Gossage, and P.N. Yadav. Can. J. Chem. **83**, 1185 (2005).
8. (*a*) Y.-C. Lai, H.-Y. Chen, W.-C. Hung, C.-C. Lin, F.-E. Hong. Tetrahedron, **61**, 9484 (2005), and refs. cited therein; (*b*) C. González-Arellano, A. Corma, M. Iglesias, F. Sánchez. J. Catal. **238**, 497 (2006); (*c*) N. T. S. Phan, J. Khan, P. Styring. Tetrahedron, **61**, 12065 (2005).
9. (*a*) J.M. Bindlish, S.C. Bhatia, P. Gautam, and P.C. Jain. Ind. J. Chem. **16A**, 279 (1978); (*b*) V.W. Day, M.D. Glick, and J.L. Hoard. J. Am. Chem. Soc. **90**, 4803 (1968); (*c*) A. Doadrio, D. Craciunescu, and C. Ghirvu. An. Real. Acad. Farm. **46**, 153 (1980); (*d*) Y.-S. Uh, H. Zhang, C.M. Vogels, A. Decken, and S.A. Westcott. Bull. Korean Chem. Soc. **25**, 986 (2004).
10. (*a*) SAINT 6.02 [computer program]. Bruker AXS, Inc., Madison, Wisconsin, USA. 1997–1999; (*b*) G.M. Sheldrick. SADABS [computer program]. Bruker AXS, Inc., Madison, Wisconsin, USA. 1999; (*c*) G.M. Sheldrick. SHELXTL 5.1 [computer program]. Bruker AXS, Inc., Madison, Wisconsin, USA. 1997.
11. N.M. Sampat and B.H. Mehta. Asian J. Chem. **8**, 261 (1996).
12. (*a*) T. Ooi, M. Kameda, M. Tanigushi, and K. Maruoka. J. Am. Chem. Soc. **126**, 9685 (2004); (*b*) H. Höpfl, M. Sánchez, N. Farfán, and V. Barba. Can. J. Chem. **76**, 1352 (1998); (*c*) I.B. Sivaev, A.B. Bruskin, V.V. Nesterov, M. Yu. Antipin, V.I. Bregadze, and S. Sjöberg. Inorg. Chem. **38**, 5887 (1999); (*d*) F. Firooznia, C. Gude, K. Chan, N. Marcopulos, and Y. Satoh. Tetrahedron Lett. **40**, 213 (1999); (*e*) H.E. Sailes, J.P. Watts, and A. Whiting. Tetrahedron Lett. **41**, 2457 (2000); (*f*) M.P. Hughes and B.D. Smith. J. Org. Chem. **62**, 4492 (1997); (*g*) M.P. Groziak, A.D. Ganguly, and P.D. Robinson. J. Am. Chem. Soc. **116**, 7597 (1994).
13. J. Chang, K. Zhao, and S. Pan. Tetrahderon Lett. **43**, 951 (2002).
14. (*a*) R.H. Holm, G.W. Everett, Jr., and A. Chakravorty. Prog. Inorg. Chem. **7**, 83 (1966); (*b*) J.S. Kim and B.K. Koo. Bull. Korean Chem. Soc. **13**, 507 (1992).
15. M.D. Eelman, M.M. Moriarty, and D.E. Fogg. Educ. Adv. Chem. **10**, 213 (2006).
16. C. Carlini, S. Giaiacopi, F. Marchetti, C. Pinzino, A.M.R. Galletti, and G. Sbrana. Organometallics, **25**, 3659 (2006).
17. (*a*) X. Mei and C. Wolf. J. Org. Chem. **70**, 2299 (2005); (*b*) J. C. Collings, A. S. Batsanov, J. A. K. Howard, and T. B. Marder. Can. J. Chem. **84**, 238 (2006); (*c*) R. Glaser, N. Knotts, P. Yu, L. Li, M. Chandrasekhar, C. Martin, and C. L. Barnes. J. Chem. Soc., Dalton Trans. 2891 (2006); (*d*) S. Bacchi, M. Benaglia, F. Cozzi, F. Demartin, G. Filippini, and A. Gavezzotti. Chem. Eur. J. **12**, 3538 (2006); (*e*) F. D. Lewis, J.-S. Yang, and C. L. Stern. J. Am. Chem. Soc. **118**, 12029 (1996); (*f*) H. Shiigi, Y. Yamamoto, N. Yoshi, H. Nakao, and T. Nagaoka. Chem. Commun. 4288 (2006); (*g*) H. Sigel, B. P. Operschall, S. S. Massoud, B. Song, and R. Griesser. J. Chem Soc., Dalton Trans. 5521 (2006); (*h*) T. Yajima, R. Takamido, Y. Shimazaki, A. Odani, Y. Nakabayashia, and O. Yamauchi. J. Chem. Soc., Dalton Trans. 299 (2007).
18. V.T. Kasumov, A. Bulut, F. Köksal, M. Aslanoğlu, I. Uçar and C. Kazak. Polyhedron, **25**, 1133 (2006).

© 2007 NRC Canada

Aqua-mediated one-pot synthesis and aromatization of pyrimido-fused 1,4-dihydropyridine derivatives using ammonium salts

Mazaahir Kidwai and Kavita Singhal

Abstract: Dipyrimidine-fused pyridine derivatives were synthesized using 1,3-diketone, aldehyde, different ammonium salts, and water, as the solvent. Aromatization was observed when ammonium nitrate was used as the source of nitrogen, and thus, dipyrimidine-fused pyridine derivatives were synthesized in one-pot synthetic procedure. This environmentally benign procedure leads to high yield of products (80%–90%) in a single step, with greater purity using water as the solvent.

Key words: water, aromatization, dipyrimidopyridine, ammonium salts.

Résumé : On a effectué les synthèses de dérivés de la dipyrimidine condensée à de la pyridine en utilisant une 1,3-dicétone, un aldéhyde, divers sels d'ammonium et de l'eau comme solvant. On observe l'aromatisation lorsqu'on utilise du nitrate d'ammonium comme source d'azote et dans de telles conditions les synthèses des dérivés de la dipyrimidine condensées à de la pyridine sont réalisées par une méthode monotope. Cette méthode environnementalement bénigne conduit à des rendements élevés (80 % à 90 %) de produits d'une grande pureté, en une seule étape et utilisant de l'eau comme solvant.

Mots-clés: eau, aromatisation, dipyrimidopyridine, sels d'ammonium.

[Traduit par la Rédaction]

Introduction

The use of toxic and volatile organic solvents has led to immense environmental deterioration. This entails a challenge for chemists to develop new alternatives that can meet the promises of green chemistry. One of the recent advances in this area where substantial progress has been made is the use of water as reaction medium (1). Various advantages offered by the use of water as the solvent, such as the increased rate of reaction (2), have been explained on the basis of its permanent dipole moment and its behavior as pseudo-organic solvent at elevated temperature. Hence, water has become an attractive medium for many organic reactions. Not only one can avoid the use of dry reactants and solvents, but also the use of water provides unique reactivity and selectivity.

Multicomponent one-pot synthetic protocols (3), such as Hantzsch reaction (4), and their products, 1,4-dihydropyridines (DHPs) (5), have attracted considerable attention because of their recognition as a core structure in calcium antagonists (6). In the case of the structure–activity relationship, the effect of substitution on the DHPs ring has been thoroughly studied (7), and its usefulness has led to recent developments. Furthermore, the scope of this pharmacophore, especially dipyrimidopyridines (DPPs) (8), which are structurally cyclized compounds of the amino analogues of the Hantzsch esters, has been increased by the identification of them as 5-deazaflavin derivatives (Fig. 1, **I**) (9). 5-Deazaflavins were considered to be $NAD(P)^+$ models (NAD: nicotinamide dinucleotide), which oxidize alcohols and exhibit efficient autorecycling oxidation in approximately 100% yield. Furthermore, one of the canonical forms has been regarded as model of the nicotinamide nucleotide-protected by annelation "masked NAD^+ analogue", i.e., as NAD-type redox catalysts (10) (Fig. 1, **II**). The fusion of the two pyrimidine rings (i.e., ureido and thioureido groups) to the pyridine nucleus improved the antiviral activity (11), and the products have also shown antibacterial activities (12).

Aromatization of 1,4-DHPs has also attracted considerable attention because of the reported in vivo studies (13) and their important role in the biomimetic oxidation reactions (14). Dihydropyridines are often produced in a synthetic sequence and need to be oxidized to pyridines. Many oxidizing agents, such as HNO_3, DDQ (15), ceric ammonium nitrate (16), $Mn(OAc)_3$ (17), $Bi(NO_3)_3{\cdot}5H_2O$ (18), $Cu(NO_3)_2$ (19), $RuCl_3/O_2$ (20), activated carbon/O_2 (21), I_2/MeOH (22), $FeCl_3$ (23), and Pd/C (24), have been documented for the aromatization of Hantzsch esters. Most of the existing methods suffer from drawbacks, including two steps, tedius workup, the use of hazardous organic solvents (e.g., dichloromethane, chloroform, and xylene), expensive complex catalysts under strong acidic conditions, and poor

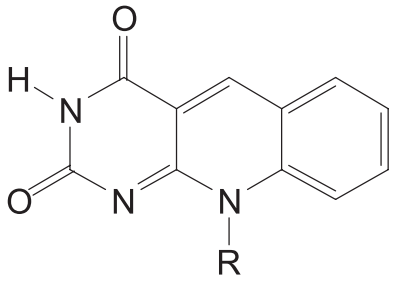
Received 10 February 2007. Accepted 23 April 2007. Published on the NRC Research Press Web site at canjchem.nrc.ca on 25 May 2007.

M. Kidwai[1] and K. Singhal. Green Chemistry Research Laboratory, Department of Chemistry, University of Delhi, Delhi 110007, India.

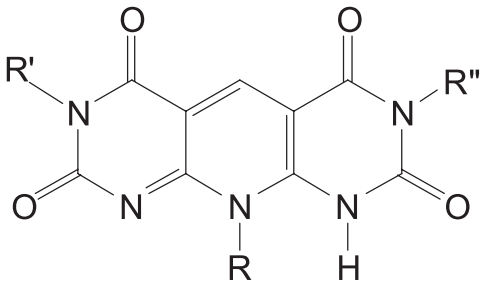
[1]Corresponding author: (e-mail: kidwai.chemistry@gmail.com).

 doi:10.1139/V07-041 © 2007 NRC Canada

Fig. 1.



5-Deazaflavins (**I**)



Dipyrimidopyridine Analogues (**II**)

yields. Therefore, developing a one-pot protocol, using water as the solvent, that could omit any harmful catalyst seems highly desirable.

In our endeavor to develop an environmentally benign protocol (25) and continuing our interest in nitrogen heterocycles with biopotentiality using aqueous-mediated synthetic methodologies (26), we attempted to synthesize dipyrimidine-fused pyridines in appreciable yields using barbituric acid or 2-thiobarbituric acid as alternates to β-ketoesters (27) in water. In this paper, water is used as a solvent together with the ammonium salts, ammonium acetate and ammonium nitrate, for a one-pot synthesis of dipyrimido-fused pyridines using Hantzsch reaction; most of the disadvantages in reported methods were resolved.

Results and discussion

Ammonium acetate as a nitrogen source

The choice of solvent has always been the biggest challenge facing the eco-efficient processes. In search for the optimal solvent, refluxing 1 mol of the aromatic or heteroaromatic aldehyde **2a**–**2e**, 2 mol of barbituric acid (BA) (**1a**) or 2-thiobarbituric acid (TBA) (**1b**), and 4 mol of ammonium acetate (**3**) in water would provide 5-aryl-3,5,7,9,10-pentahydro-(1*H*)-pyrimido[5′,4′:5,6]pyrido[2,3-*d*] pyrimidine-2,4,6,8-tetrone (**4a**–**4f**) or 5-thienyl-2,8-dithioxo-3,5,7,9,10-pentahydro-(1*H*)–pyrimido[5′,4′:5,6]pyrido[2,3-*d*]pyrimidine-4,6-diones (**4g**) (Scheme 1) in synthetically advantageous manner (Table 1).

The process proved to be quite simple in all respects with easy workup. At the completion of the reaction, water-insoluble organic compounds crystallized out immediately. All products were identified using the spectroscopic data and elemental analysis.

Ammonium carbonate as a nitrogen source

To study the conditional aspects of Hantzsch reaction, we used different ammonium salts as alternative nitrogen sources to improve the catalyzing conditions. To achieve the target, the previously mentioned method was performed using ammonium carbonate in place of ammonium acetate. Because of the release of carbonate ions, the aqueous solution of ammonium carbonate becomes basic; thus, it expectedly solubilizes the barbituric acid (BA) or 2-thiobarbituric acid (TBA) completely, and the reaction proceeds faster. However, we were unsuccessful in restoring the product from the reaction mixture by acidification workup, and even the evaporation of water led to the contamination of the catalyst in the product. Thus, the use of ammonium carbonate is inconvenient, as the desired product cannot be isolated.

Ammonium nitrate as a nitrogen source

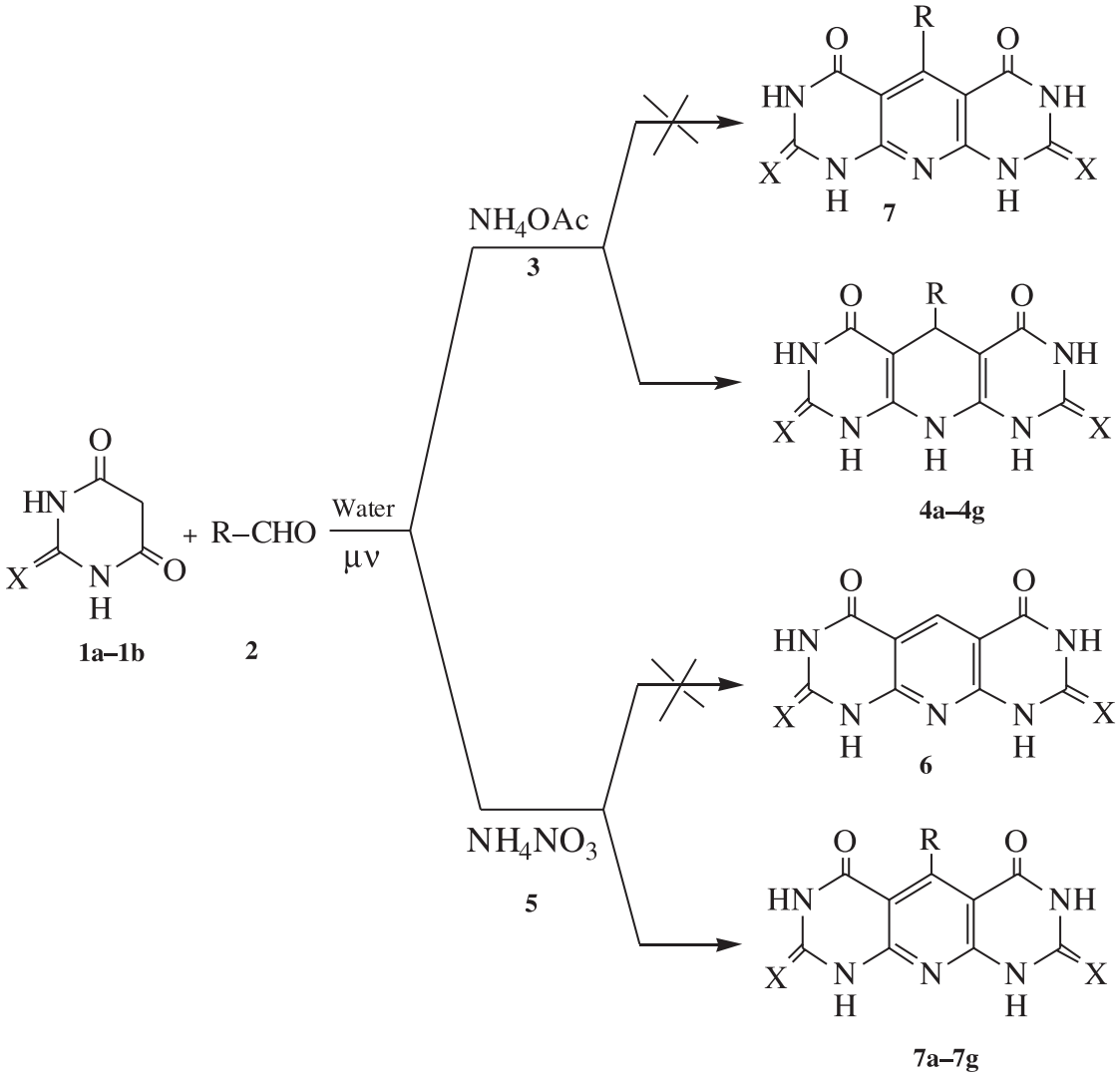
In another trial to standardize the reaction, we employed another ammonium salt, ammonium nitrate, which afforded the aromatized product using the similar optimized reaction conditions. Accordingly, 1 mol of the aromatic or heteroaromatic aldehydes **2a**–**2e** was treated with 2 mmol of BA or TBA in the presence of 4 mol of ammonium nitrate (**5**) in refluxing water (Scheme 1). On completion of the reaction, the solvent was removed using vacuum filtration. An 84%–90% yield of the aromatized product **7a**–**7g** was obtained and identified as 5-aryl-3,7,9-trihydro-(1*H*)-pyrimido-[5′,4′:5,6]pyrido[2,3-*d*]pyrimidine-2,4,6,8-tetrone (**7a**–**7f**) or 5-thienyl-2,8-dithioxo-3,7,9-trihydro-(1*H*)-pyrimido [5′,4′:5,6]pyrido[2,3-*d*]pyrimidine-4,6-dione (**7g**) from the mp, elemental analysis, and spectroscopic data. In ^{1}H NMR spectra, no signal for C_5–H was obtained, this suggested the aromatization of the dihydropyridine ring, and the appearance of the IR band at 1550 cm^{-1}, which was attributed to C=N, confirmed the final product. From the literature, the aromatization of 1,4-DHPs using reagents such as nitrous fumes and $KMNO_4$ resulted in either the dealkylated or the alkylated product or both. When ammonium nitrate was used, only alkylated pyridine ring derivatives (**7a**–**7g**) were isolated, and the nature of the isolated product was further confirmed by the presence of ^{1}H NMR spectral peaks in the aromatic region.

Owing to the green credentials of microwave irradiation (MWI) and utilizing the property of water as a polar solvent, the same reaction was performed under MWI. An Erlenmeyer flask, containing BA or TBA (2 mmol), aldehyde (1 mmol), ammonium nitrate (3 mmol), and the sufficient amount of water for making the slurry of reaction media, was subjected to MWI for the required time (Method D). Notably, there is a remarkable decrease in reaction time with the increased yields of products compared with the conventional methodology (Table 2).

To optimize the reaction temperature, the synthesis of **7e** was performed in water at temperatures ranging from 70 to 130 °C, at different MW powers, i.e., 400, 480, 560, 640, and 800 W. At low power (400 and 480 W), the time needed for the temperature to reach 100 °C was too long. Micro-

© 2007 NRC Canada

Scheme 1. Synthesis of dipyrimidopyridine.



wave irradiation at 560 W in 2 mL of water furnished the highest yield of 5-thienyl-3,7,9-trihydro-(*1H*)-pyrimido[5′,4′:5,6]pyrido[2,3-*d*]pyrimidine-2,4,6,8-tetrone (**7e**) (Scheme 1), without evaporation of the solvent. Thus, a microwave power of 560 W was chosen as the optimal one. The ease of separation of dipyrimidopyridine derivatives from the reaction media is the foremost advantage of this process in aqueous media.

In the synthesis of Hantzsch esters using ammonium nitrate as catalyst, sometimes the reaction does not proceed or exhibit sluggish nature. Notably, we have examined the smooth oxidation using a mild oxidizing agent, ammonium nitrate, and this can be attributed to the fact that this particular system could become more susceptible to oxidation than the unfused pyridines.

Looking at the success of this approach in which no external catalyst was required, it was worthwhile to attempt the reaction in neat reaction conditions under MWI, i.e., omitting the solvent and the catalyst, but no proper results were obtained, as the absence of water lead to some charring on prolonged heating, thus emphasizing the importance of water, which acts as a solvent and provides a media for the transfer of energy. Despite the insolubility of the reactants, an example has been established for the condensation reaction in water.

Conclusion

In conclusion, we have explored the reactivity of various ammonium salts for the Hantzsch reaction. We have found ammonium nitrate to be the best and least expensive catalyst, acting as a nitrogen donor as well as an oxidizing agent in a one-pot protocol for the synthesis of dipyrimidopyridines. The present procedure is equally effective for both BA and TBA; thus, it can be adopted for the synthesis of a library of bioactive compounds in a greener way ensuring the atom economy. Furthermore, we have proved that water could be used as a suitable green solvent for MW-irradiated Hantzsch reaction, resulting in the desired products. The current procedure does not use an organic solvent or an external catalyst; thus, it could be established as a more-straightforward method to synthesize dipyrimido-fused pyridine derivatives. These results may stimulate interest among researchers involved in the industrial-scale reactions.

© 2007 NRC Canada

Table 1. Comparison of the yield and reaction time for the synthesis of **4a**–**4g**.

Compound	R	X	Yield %[a] (%)[b]	Reaction time min[c] (h)[d]
4a	2-OH-Phenyl	O	90 (75)	2.0 (1.5)
4b	4-OCH_3-Phenyl	O	82 (76)	1.5 (1.5)
4c	Phenyl	O	82 (70)	2.0 (2.0)
4d	Piperonyl	O	85 (72)	2.5 (3.5)
4e	Thienyl	O	87 (80)	2.5 (3.0)
4f	2-Cl-Quinolinyl	O	80 (68)	3.2 (2.0)
4g	Thienyl	S	82 (70)	2.8 (3.0)

[a]Obtained using MW.
[b]Obtained conventionally.
[c]MW heating (min).
[d]Conventional heating (h).

Table 2. Comparison of the yield and reaction time for the synthesis of **7a**–**7g**.

Compound	R	X	Yield %[a] (%)[b]	Reaction time min[c] (h)[d]
7a	2-OH-Phenyl	O	88 (70)	2.0 (1.5)
7b	4-OCH_3-Phenyl	O	90 (72)	1.5 (1.5)
7c	Phenyl	O	80 (70)	1.5 (2.5)
7d	Piperonyl	O	90 (68)	2.5 (2.0)
7e	Thienyl	O	92 (68)	1.5 (2.0)
7f	2-Cl-Quinolinyl	O	80 (74)	2.5 (3.0)
7g	Thienyl	S	85 (70)	2.0 (2.5)

[a]Obtained using MW.
[b]Obtained conventionally.
[c]MW heating (min).
[d]Conventional heating (h).

Experimental

Melting points were recorded on a Thomas Hoover melting-point apparatus and are uncorrected. IR spectra (Nujol) were recorded on a PerkinElmer FTIR-1710 spectrophotometer. ^{1}H NMR spectra were recorded on a Bruker Avance Spectrospin 300 (300 MHz) using TMS as internal standard. Elemental analysis was performed on a Heraeus CHN Rapid Analyser. The purity of compounds was checked on silica-gel-coated aluminium plates (Merck). A Kenstar microwave oven, model No. OM9925E (at 2450 MHz, 800W) was used for MWI. Temperature of the reaction mixture was measured through AZ, Mini Gun Type, non-contact IR Thermometer, model No. 8868. All reactants were purchased from Sigma-Aldrich and Lanchester and used without further purification.

General procedure for the synthesis of 5-aryl-3,5,7,9,10-pentahydro-1*H*-pyrimido [5′,4′:5,6]pyrido[2,3-*d*]pyrimidine-2,4,6,8-tetrone (4a–4f) or 5-thienyl-2,8-dithioxo-3,5,7,9,10-pentahydro-1*H*–pyrimido[5′,4′:5,6]pyrido[2,3-*d*]pyrimidine-4,6-diones (4g)

Method A (conventional heating)

To the mixture of barbituric acid (**1a**) or 2-thiobarbituric acid (**1b**) (2 mol), aromatic or heteroaromatic aldehydes (**2a**–**2e**) (1 mol), and 4 mol of ammonium acetate (**3**) was added 10 mL of water. The reaction mixture was refluxed for the appropriate time (as shown in Table 1) with constant stirring. The progress of the reaction was monitored by TLC. Upon completion of the reaction, the solid obtained was filtered and washed with water and ethanol.

Method B (microwave irradiation)

In an Erlenmeyer flask, barbituric acid (**1a**) or 2-thiobarbituric acid (**1b**) (2 mol), aromatic or heteroaromatic aldehydes (**2a**–**2e**) (1 mol), and ammonium acetate (**3**) (2 mol) were mixed with 2 mL of water. The reaction mixture was subjected to MWI for a specific time (Table 1). The progress of the reaction was monitored at 30 s intervals. Upon completion of the reaction, the mixture was cooled, filtered, washed with water, and dried.

Compound 4a

Curdy white solid; mp 210–212 °C. IR (Nujol, cm^{-1}) ν_{max}: 3484, 3121, 3068, 1740, 1695, 1655, 1630. ^{1}H NMR (300 MHz, $CDCl_3$ – TFA, TMS) δ: 5.28 (s, 1H, C_5–H), 6.81–7.02 (m, 4H, Ar–H), 10.21 (s, 3H, NH), 11.43 (s, 2H, NH). Anal. calcd. for $C_{15}H_{11}N_5O_5$: C 52.71, H 3.29, N 20.46; found: C 52.78, H 3.22, N 20.52.

Compound 4b

Yellow solid; mp 226–228 °C. IR (Nujol, cm^{-1}) ν_{max}: 3460, 3130, 3082, 1754, 1690, 1657, 1625. ^{1}H NMR (300 MHz, $CDCl_3$ – TFA, TMS) δ: 3.80 (s, 3H, OCH_3), 5.80 (s, 1H, C_5–H), 7.12 (d, 2H, J = 7.0 Hz, Ar–H), 7.16 (d, 2H, J = 7.0 Hz, Ar–H), 10.19 (s, 3H, NH), 11.45 (s, 2H, NH). Anal. calcd. for $C_{16}H_{13}N_5O_5$: C 54.64, H 3.57, N 19.42; found: C 54.59, H 3.62, N 19.29.

Compound 4c

Yellow solid; mp 165–168 °C. IR (Nujol, cm^{-1}) ν_{max}: 3472, 3120, 3036, 1736, 1678, 1657, 1615. ^{1}H NMR (300 MHz, $CDCl_3$ – TFA, TMS) δ: 5.81 (s, 1H, C_5–H), 7.12–7.26 (m, 5H, Ar–H), 10.21 (s, 3H, NH), 11.41 (s, 2H,

© 2007 NRC Canada

NH). Anal. calcd. for $C_{15}H_{11}N_5O_4$: C 55.38, H 3.38, N 21.53; found: C 55.51, H 3.33, N 21.40.

Compound 4d

Brown solid; mp 202–204 °C. IR (Nujol, cm^{-1}) ν_{max}: 3472, 3121, 3049, 1740, 1673, 1655, 1610. ^1H NMR (300 MHz, $CDCl_3$ – TFA, TMS) δ: 5.80 (s, 1H, C_5–H), 5.89 (s, 2H, OCH_2O), 6.72 (d, 1H, *J* = 8.0 Hz, Ar–H), 6.82 (d, 1H, *J* = 8.0 Hz, Ar–H), 7.10 (s, 1H, Ar–H), 10.24 (s, 3H, NH), 11.45 (s, 2H, NH). Anal. calcd. for $C_{16}H_{11}N_5O_6$: C 52.71, H 2.87, N 18.81; found: C 52.54, H 2.94, N 18.76.

Compound 4e

Brown solid; mp 164 °C dec. IR (Nujol, cm^{-1}) ν_{max}: 3478, 3124, 3062, 1746, 1682, 1654 1622. ^1H NMR (300 MHz, $CDCl_3$ – TFA, TMS) δ: 5.81 (s, 1H, C_5–H), 7.48–7.51 (t, 1H, thienyl), 8.10 (d, 1H, *J* = 3.1 Hz, thienyl), 8.31 (d, 1H, *J* = 4.5 Hz, thienyl), 10.20 (s, 3H, NH), 11.41 (s, 2H, NH). Anal. calcd. for $C_{13}H_9N_5O_4S$: C 47.10, H 2.82, N 21.04; found: C 47.12, H 2.71, N 21.14.

Compound 4f

Brown solid; mp 188–190 °C. IR (Nujol, cm^{-1}) ν_{max}: 3466, 3130, 3087, 1740, 1688, 1655, 1620. ^1H NMR (300 MHz, $CDCl_3$ – TFA, TMS) δ: 5.78 (s, 1H, C_5–H), 7.72–7.76 (m, 5H, Ar–H), 10.21 (s, 3H, NH), 11.40 (s, 2H, NH). Anal. calcd. for $C_{18}H_{11}N_6O_4Cl$: C 52.47, H 2.70, N 20.38; found C 52.61, H 2.67, N 20.46.

Compound 4g

Green solid; mp 276 °C dec. IR (Nujol, cm^{-1}) ν_{max}: 3472, 3121, 3076, 1754, 1695, 1662, 1610. ^1H NMR (300 MHz, $CDCl_3$ – TFA, TMS) δ: 5.81 (s, 1H, C_5–H), 7.51 (t, 1H, thienyl), 8.12 (d, 1H, *J* = 3.1 Hz, thienyl), 8.29 (d, 1H, *J* = 4.5 Hz, thienyl), 10.19 (s, 3H, NH), 11.43 (s, 2H, NH). Anal. calcd. for $C_{13}H_9N_5O_2S_3$: C 42.90, H 2.52, N 19.39; found C 42.97; H 2.47; N 19.28.

General Procedure for the synthesis of 5-aryl-3,7,9-trihydro-(1*H*)-pyrimido [5′,4′:5,6]pyrido[2,3-*d*]pyrimidine-2,4,6,8-tetrone (7a–7f) or 5-thienyl-2,8-dithioxo-3,7,9-trihydro-(1*H*)-pyrimido[5′,4′:5,6]pyrido[2,3-*d*]pyrimidine-4,6-dione (7g)

Method C (conventional heating)

To the mixture of barbituric acid (**1a**) or 2-thiobarbituric acid (**1b**) (2 mol), aromatic or heteroaromatic aldehydes (**2a**–**2e**) (1 mol), and 4 mol of ammonium nitrate (**5**) was added 10 mL of water. The reaction mixture was refluxed for the appropriate time with constant stirring. The solid obtained was filtered and washed with water and ethanol.

Method D (microwave irradiation)

In an Erlenmeyer flask, barbituric acid (**1a**) or 2-thiobarbituric acid (**1b**) (2 mol), aromatic or heteroaromatic aldehydes (**2a**–**2e**) (1 mol), and ammonium nitrate (**5**) (3 mol) were mixed with 2–3 mL of water. The reaction mixture was subjected to MWI for a specific time (Table 1). The progress of the reaction was monitored at 30 s intervals. Upon completion of the reaction, the mixture was cooled, filtered, washed with water, and dried.

Compound 7a

Curdy white solid; mp > 320 °C. IR (Nujol, cm^{-1}) ν_{max}: 3354, 3272, 3193, 1723, 1672, 1614, 1536. ^1H NMR (300 MHz, $CDCl_3$ – TFA, TMS) δ: 6.84–7.11 (m, 4H, Ar–H), 10.21 (s, 2H, NH), 11.43 (s, 2H, NH). Anal. calcd. for $C_{15}H_9N_5O_5$: C 53.01, H 2.74, N 20.60; found: C 53.09, H 2.65, N 20.64.

Compound 7b

Yellow solid; mp 270–272 °C. IR (Nujol, cm^{-1}) ν_{max}: 3360, 3211, 3097, 1723, 1685, 1639, 1548. ^1H NMR (300 MHz, $CDCl_3$ – TFA, TMS) δ: 3.81 (s, 3H, OCH_3), 7.14 (d, 2H, *J* = 7.0 Hz, Ar–H), 7.20 (d, 2H, *J* = 7.0 Hz, Ar–H), 10.19 (s, 2H, NH), 11.47 (s, 2H, NH). Anal. calcd. for $C_{16}H_{11}N_5O_5$: C 54.87, H 3.11, N 19.54; found C 54.90, H 3.08, N 19.60.

Compound 7c

Curdy white solid; mp 202–204 °C. IR (Nujol, cm^{-1}) ν_{max}: 3218, 3200, 3082, 1730, 1671, 1614, 1549. ^1H NMR (300 MHz, $CDCl_3$ – TFA, TMS) δ: 7.21–7.34 (m, 5H, Ar–H), 10.20 (s, 2H, NH), 11.43 (s, 2H, NH). Anal. calcd. for $C_{15}H_9N_5O_4$: C 55.72, H 2.78, N 21.67; found: C 55.64, H 2.71, N 21.78.

Compound 7d

Yellow solid; mp 290–292 °C. IR (Nujol, cm^{-1}) ν_{max}: 3210, 3193, 3082, 1733, 1667, 1614, 1541. ^1H NMR (300 MHz, $CDCl_3$ – TFA, TMS) δ: 5.89 (s, 2H, OCH_2O), 6.71 (d, 1H, *J* = 8.0 Hz, Ar–H), 6.87 (d, 1H, *J* = 8.0 Hz, Ar–H), 7.14 (s, 1H, Ar–H), 10.24 (s, 2H, NH), 11.43 (s, 2H, NH). Anal. calcd. for $C_{16}H_9N_5O_6$: C 52.77, H 2.40, N 18.29; found: C 52.83, H 2.42, N 18.86.

Compound 7e

Yellow solid; mp 210–214 °C. IR (Nujol, cm^{-1}) ν_{max}: 3211, 3086, 1724, 1685, 1640, 1548. ^1H NMR (300 MHz, $CDCl_3$ – TFA, TMS) δ: 7.48 (t, 1H, thienyl), 8.18 (d, *J* = 3.1 Hz, 1H, thienyl), 8.42 (d, *J* = 4.5 Hz, 1H, thienyl), 10.21 (s, 2H, NH), 11.43 (s, 2H, NH). Anal. calcd. for $C_{13}H_7N_5O_4S$: C 47.38, H 2.18, N 21.32; found: C 47.41, H 2.21, N 21.27.

Compound 7f

Rust color solid; mp 210–213 °C. IR (Nujol, cm^{-1}) ν_{max}: 3348, 3204, 3080, 1736, 1680, 1628, 1540. ^1H NMR (300 MHz, $CDCl_3$ – TFA, TMS) δ: 7.76–7.84 (m, 5H, Ar–H), 10.19 (s, 2H, NH), 11.44 (s, 2H, NH). Anal. calcd. for $C_{18}H_9N_6O_4Cl$: C 52.79, H 2.14, N 20.54; found: C 52.87, H 2.20, N 20.56.

Compound 7g

Yellow solid; mp 276 °C dec. IR (Nujol, cm^{-1}) ν_{max}: 3352, 3228, 3092, 1728, 1692, 1634, 1552. ^1H NMR (300 MHz, $CDCl_3$ – TFA, TMS) δ: 7.48 (t, 1H, thienyl), 8.16 (d, *J* = 3.0 Hz, 1H, thienyl), 8.42 (d, *J* = 4.5 Hz, 1H, thienyl), 10.19 (s, 2H, NH), 11.40 (s, 2H, NH). Anal. calcd. for $C_{13}H_7N_5O_2S_3$: C 43.08, H 1.86, N 19.25; found: C 43.21, H 1.93, N 19.39.

© 2007 NRC Canada

Acknowledgements

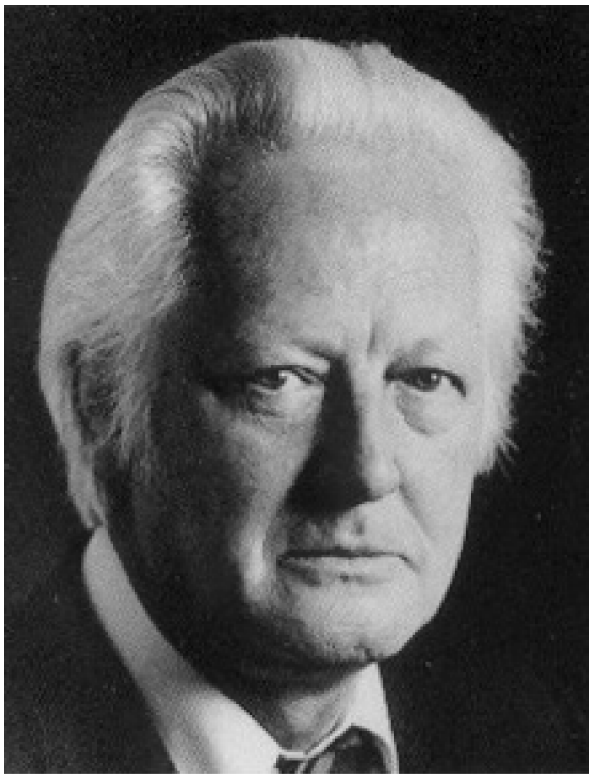
Kavita singhal acknowledges the financial assistance by the Council of Scientific and Industrial Research (CSIR), New Delhi.

References

1. (*a*) P.A. Grieco (*Editor*). Organic synthesis in water. Chapman & Hall, New York. 1998. pp. 1–41; (*b*) P.A. Grieco, E.B. Brands, S.Mc. Cann, and J.D. Clark. J. Org. Chem. **54**, 5489 (1989).
2. D.C. Rideout and R. Breslow. J. Am. Chem. Soc. **102**, 7816 (1980).
3. (*a*) J.F. Cheng, M. Chen, T. Arthenius, and A. Nadzen. Tetrahedron Lett. **43**, 6293 (2002); (*b*) D. Dallinger, N.Y. Gorobets, and C.O. Kappe. Org. Lett. **5**, 1205 (2003).
4. (*a*) M. Kidwai, S. Saxena, R. Mohan, and R. Ventakaramanan. J. Chem. Soc., Perkin Trans. 1, 1845 (2002); (*b*) M. Kidwai, R. Mohan, and S. Saxena. Russ. Chem. Bull. 2460 (2003); (*c*) A. Hantzsch. Liebigs Ann. Chem. **215**, 1 (1882).
5. B. U-hyon, K. Ji-han, L. Jae-hyong, and L. Jae-sung. KR Patent 9 500 215; Chem. Abs. **133**, 73950 (2000).
6. A.C. Gaudio, A. Korolkovas, and Y. Takahata. J. Pharm. Sci. **83**, 1110 (1994).
7. (*a*) B.M. Khadilkar, H.G. Jaisinghani, M.N. Sraf, and S.K. Desai. Indian J. Chem., Sect. B, **40**, 82 (2001); (*b*) F. Bossert, A. Heise, S. Kazda, E. Klauke, and K. Stoepal. Ger. Patent DE2 753 946 (A1) (1979); Chem. Abstr. **92**, 76294 (1980).
8. (*a*) V.K. Ahluwalia and U. Das. Indian J. Chem., Sect. B, **35**, 852 (1996); (*b*) K. Singh, J. Singh, and H. Singh. Tetrahedron, **54**, 935 (1998).
9. F. Yoneda, Y. Sakuma, and P. Hemmerich. J. Chem. Soc., Chem. Commun. 825 (1977).
10. N. Tomohisha, Y. Hirotake, O. Masami, T. Shigeki, and Y. Fumio. J. Chem. Soc., Perkin Trans. 1, 2101 (1992).
11. M.N. Nasr and M.M. Gineinah. Arch. Pharm. Pharm. Med. Chem. **6**, 289 (2002).
12. (*a*) K.B. Beranadetta and A.W. Judith. J. Heterocycl. Chem. **12**, 1221 (1975); (*b*) R.N. Kumar, T. Suresh, and P.S. Mohan. Indian J. Chem., Sect. B, **42**, 1734 (2003).
13. R.H. Bocker and F.P. Guengerich. J. Med. Chem. **29**, 1596 (1986).
14. N. Tomohisha, S. Yoshihara. Synthesis, 93 (1983).
15. J.-J. Vanden Eynde, F. Delfosse, A. Mayence, and Y.V. Haverbeke. Tetrahedron, **51**, 6511 (1995).
16. J.R. Pfister. Synthesis, 689 (1990).
17. R.S. Varma and D. Kumar. Tetrahedron Lett. **40**, 21 (1999).
18. S.H. Mashraqui and M.A. Karnik. Synthesis, 713 (1998).
19. A. Maquestian, A. Mayence, and J.-J. Vanden Eynde. Tetrahedron Lett. **32**, 3839 (1991).
20. S.H. Mashraqui and M.A. Karnik. Tetrahedron Lett. **39**, 4895 (1998).
21. N. Nakamichi, Y. Kawashita, and M. Hayashi. Synthesis, 1015 (2004).
22. J.S. Yadav, B.V.S. Reddy, G. Sabitha, and G.S.K.K. Reddy. Synthesis, 1532 (2000).
23. J.-J. Xia and G.-W. Wang. Synthesis, 2379 (2005), and refs. cited therein.
24. N. Nakamichi, Y. Kawashita, and M. Hayashi. Org. Lett. **4**, 3955 (2002).
25. (*a*) M. Kidwai, M. Preeti, and K.R. Bhushan. Chem. Lett. **6**, 487 (1999); (*b*) M. Kidwai, K. Singhal, and S. Rastogi. J. Heterocycl. Chem. **43**, 1231 (2006); (*c*) M. Kidwai, Priya, S. Rastogi, and K. Singhal. Can. J. Chem. Accepted for publication.
26. (*a*) M. Kidwai, S. Saxena, M.K.R. Khan, and S.S. Thukral. Bioorg. Med. Chem. Lett. **15**, 4295 (2005); (*b*) M. Kidwai, K. Singhal, S. Kukreja. Z. Naturforsch. B, In press.
27. J.B. Sainani, A.C. Shah, and V.P. Arya. Indian J. Chem., Sect. B, **34**, 17 (1995).

© 2007 NRC Canada

OBITUARY / NÉCROLOGIE



Professor Keith Yates

Can. J. Chem. Downloaded from www.nrcresearchpress.com by Sichuan Normal University on 09/13/12
For personal use only.

In Memoriam KEITH YATES 1928–2006

Keith Yates has passed away at the age of 78. He had had a heart attack and stroke in May 2005, which left him mostly paralyzed, and then a second fatal heart attack on December 2, 2006. He died in Victoria, BC, not far from his home on Mayne Island and is survived by his wife of 53 years, June, and his three daughters Alison, Robyn, and Nicola. He never wanted to leave Mayne Island and he now rests there in the cemetery at St. Mary Magdalene.

He was born on October 22, 1928, in Preston in Lancashire, England, and was raised mostly in Blackpool. After World War II, he followed his parents to British Columbia and married June in 1953. He then began his studies in organic chemistry. A brief summary of his various degrees includes a B.A. from the University of British Columbia in 1956, an M.Sc. (1957), and a Ph.D. (1959), also from UBC (his supervisor was Ross Stewart, who survives him), with numerous scholarships and awards along the way. He then went to England to do postdoctoral research with R.P. Bell at Oxford University, and this work eventually led to being awarded an Oxford D. Phil. degree in 1961. Following this, he was appointed as an Assistant Professor at the University of Toronto in 1961, and rose through the ranks to full Professor in 1968. He remained there, apart from sabbati-

Nécrologie — KEITH YATES 1928–2006

Keith Yates est mort à l'âge de 78 ans. En mai 2005, il avait subi une crise cardiaque et un accident cérébrovasculaire qui l'avaient laissé pratiquement paralysé; une deuxième crise cardiaque, le 2 décembre 2006 lui a été fatale. Il est mort à Victoria, BC, près de sa résidence à Mayne Island; il laisse dans le deuil June, son épouse depuis 53 ans, ainsi que ses trois filles Alison, Robyn, and Nicola. Il n'a jamais voulu quitter Mayne Island et il repose maintenant en paix dans le cimetière de St. Mary Magdalene.

Il est né le 22 octobre 1928, à Preston dans le Lancashire, en Angleterre, et il a été élevé principalement à Blackpool. Après la deuxième guerre mondiale, il s'est déplacé avec sa famille vers la Colombie britannique où il s'est marié à June en 1953. Il a alors commencé ses études en chimie organique. Des études à l'Université de British Columbia lui ont permis d'obtenir successivement un B.A. (1956), un M.Sc. (1957), and un Ph.D. (1959) sous la supervision de Ross Stewart qui lui survit; dans ce processus, il a obtenu de nombreuses bourses et prix. Il est allé en Angleterre pour faire des travaux de recherches postdoctorales avec R.P. Bell à l'Université d'Oxford qui lui ont éventuellement permis d'obtenir en 1961 un D. Phil. d'Oxford. À son retour au Canada en 1961, il a été nommé assistant professeur à l'Université de Toronto in 1961 où il est

© 2007 NRC Canada

Can. J. Chem. Downloaded from www.nrcresearchpress.com by Sichuan Normal University on 09/13/12
For personal use only.

cals, until he retired (two years early) in 1991. During his distinguished research career (summarized in the following) he received numerous awards, among them the Syntex Award (1984) and the CIC Medal (1991), and he was appointed a Fellow of the Royal Society of Canada in 1984.

With Ross Stewart he began his long-term interest in aqueous acidic systems and the organic reactions that take place in them. He measured the basicities of amides, ketones, and other carbonyl compounds, using the techniques of the time, applied the Hammett equation to the results, and studied deuterium isotope effects in organic cations. (I will not cite references here as there would be just too many of them.) With R.P. Bell in Oxford he studied the details of the halogenations of carbonyl compounds in buffers, determining which reaction was significant at low and which at high halogen concentrations. Eventually he followed this with his own study of the acid-catalyzed process and of brominations in the presence of added salts. Later in Toronto, he studied many electrophilic brominations with his students and associates.

In Toronto he measured an acidity function for amides, HA, in aqueous sulfuric and hydrochloric acid media, having found that the Hammett H0 function did not work well for the determination of the basicities of carbonyl compounds (and thus showing the basicities that he had determined earlier with Ross Stewart were incorrect). He measured and extended the H0 function in aqueous perchloric acid solutions. His students also measured activity coefficients and water activities in some of these media. He determined several acidity functions in the 70% aqueous dimethyl sulfoxide medium. Eventually, the acidity function concept with a different function for each class of compounds was abandoned in favour of the simpler two-parameter excess acidity treatment, using just one function with a numerical value being used to express the class of compound involved.

He wrote seminal papers and reviews on ester hydrolysis in acid media; the mechanisms he proposed for some of these still stand up today. The hydrolyses of many other functional groups were also studied. He developed the transition state activity coefficient method to help distinguish between different mechanistic possibilities. Amide hydrolysis proved more difficult; when he began work it was still not clear whether amides protonated on oxygen or nitrogen. Oxygen protonation was eventually established, but several proposed hydrolysis mechanisms were subsequently found wanting. The actual experimental measurements withstood the test of time well, however, and form the basis of current mechanistic theories. The excess acidity treatment was also applied to kinetic measurements and proved invaluable in mechanistic determinations.

Later in his career he became interested in photochemistry, studying the photochemical oxidations of nitrobenzyl alcohols and the photohydrations of aromatic alkenes and alkynes, among many other reactions, showing that the course of several reactions in water is different from that in organic solvents. Many reactions were shown to involve intramolecular proton transfers. He determined some excited state dipole moments and polarizabilities, which was very difficult work.

He was always interested in theoretical calculations and published many papers using them over the years, as they became more and more accurate, on a wide variety of molecules and ions in collaboration with his friend and colleague Imre Csizmadia. He wrote a book entitled *Hückel Molecular Orbital Theory* in 1978 (while he was Depart-

devenu professeur titulaire en 1968. À part ses années sabbatiques, il est resté à Toronto pour toute sa carrière, jusqu'à sa retraite en 1991 prise avec deux années d'avance. Au cours de sa carrière exceptionnelle, résumée plus loin, il a reçu de nombreux prix, dont le Syntex Award (1984) et la médaille de l'Institut de chimie du Canada (1991); il a aussi été nommé Fellow de la Société Royale du Canada en 1984.

C'est avec Ross Stewart qu'a commencé son intérêt à long terme pour les systèmes acides aqueux et pour les réactions organiques qui s'y déroulent. Il a mesuré les basicités des amides, des cétones et d'autres composés carbonylés en faisant appel à des techniques de temps, il a appliqué les résultats à l'équation de Hammett et il a étudié les effets isotopiques du deutérium dans les cations organiques (Je ne présenterai pas ici de références car il y en aurait trop). Avec R.P. Bell à Oxford, il a étudié les détails des réactions d'halogénation des composés carbonylés dans des tampons et il a ainsi déterminé quelles sont les réactions significatives à des concentrations faibles et élevées d'halogène. Il a éventuellement poursuivi ces travaux par des études personnelles des processus acidocatalysés et des réactions de bromation en présence de sels additionnés. Plus tard, à Toronto, avec ses étudiants et ses associés, il a étudié plusieurs réactions de bromation électrophiles.

À Toronto, il a aussi mesuré une fonction d'acidité pour les amides, HA, dans des milieux aqueux d'acide sulfurique et d'acide chlorhydrique; il trouvé que la fonction H0 de Hammett ne fonctionne pas bien pour la détermination des basicités des composés carbonyles (et il a ainsi montré que les basicités qu'il avait déterminées antérieurement avec Ross Stewart étaient incorrectes). Il a mesuré et étendu le fonction H0 aux solutions en milieu acide perchlorique aqueux. Ses étudiants ont aussi mesuré les coefficients d'activité et les activités de l'eau dans un certain nombre de ces milieux. Il a déterminé plusieurs fonctions d'acidité dans un milieu aqueux à 70% de diméthylsulfoxyde. Éventuellement, le concept d'une fonction d'acidité comportant une fonction différente pour chaque classe composés a été abandonnée en faveur d'un traitement de l'excès d'acidité à deux paramètres beaucoup plus simple qui ne fait appel qu'à une seule fonction comportant une valeur numérique qui est utilisée pour exprimer la classe de composé impliqué.

Il a écrit plusieurs articles et revues fondamentales sur l'hydrolyse des esters en milieu acide; les mécanismes qu'il a proposé pour un certain nombre de ces cas sont encore reconnus aujourd'hui. Il a aussi étudié les hydrolyses de plusieurs autres groupes fonctionnels. Il a développé la méthode du coefficient d'activité dans l'état de transition qui permet de distinguer entre divers mécanismes possibles. L'hydrolyse des amides s'est avéré un sujet plus difficile; lorsqu'il a commencé à travailler sur ce sujet, il n'était pas clair si les amides se protonent sur l'oxygène ou sur l'azote. Il a éventuellement été établi que la protonation se fait sur l'oxygène, mais subséquemment plusieurs mécanismes se sont avérés incomplets. Toutefois, les valeurs expérimentales obtenues ont bien soutenu les assauts du temps et elles forment aujourd'hui la base des théories mécanistiques actuelles. Le traitement par l'excès d'acidité a aussi été appliqué aux mesures cinétiques et il s'est avéré d'une valeur inestimable dans les déterminations mécanistiques.

Plus tard dans sa carrière, il est devenu intéressé à la photochimie et il a été amené, en autre, à étudier les oxydations photochimiques des alcools nitrobenzyliques et les réactions de photohydratation d'alcènes et d'alcynes aromatiques; il a ainsi été amené à démontrer que le cours de plusieurs de ces réactions varie suivant la nature aqueuse ou organique du solvant utilisé. Il a été démontré que plusieurs réaction impliquent des

© 2007 NRC Canada

Can. J. Chem. Downloaded from www.nrcresearchpress.com by Sichuan Normal University on 09/13/12
For personal use only.

ment Chairman; being Chairman never slowed his research output in the slightest), and while now outdated it still surprises me that these simple calculations can give the same reactivity order for a series of molecules or ions as do the much more elaborate modern calculations. He also became interested in the (still neglected) principle of least nuclear motion, following a suggestion made by Ossie Tee. When he became interested in photochemistry he applied theoretical calculations to many excited state processes. The last thing he studied, by himself without any associates, was a simple approach to the application of Marcus theory to photochemical proton transfers, using an intersecting parabola model.

This necessarily brief and incomplete summary may help to show the incredibly wide-ranging scope of his interests. He was interested in all aspects of physical organic chemistry, among many other subjects, and contributed mightily to many of them. I do not have an accurate count, but he published well over 150 research papers as well as several review articles and book chapters.

The number of current or recently retired academics who were Keith's Ph.D. students, or post-doctoral fellows in his group, is phenomenal, being at least fourteen, which may be a Canadian record. For this reason alone his influence on Chemistry teaching and research was vast, not only in Canada but in at least four other countries. In no particular order these academics are (with their institution), Alan Hopkinson (York University, Toronto), Bob McClelland (Toronto), Jim Pincock (Dalhousie), Bob McDonald (Mount Saint Vincent University, Halifax), Linda Sweeting (Towson University, Maryland), Julie Altmann (Kings College and Imperial College, University of London), Jacques Périé (Université Paul Sabatier, Toulouse), Tom Modro (University of Pretoria, South Africa), Ossie Tee (Concordia), Steve Anderson (University of Wisconsin at Whitewater), Peter Wan (Victoria), Mary Boyd (now at Georgia Southern University), Paul Mezey (now at Memorial), and myself (Toronto). Some of the theoretical people were supervised jointly by Keith and by Imre Csizmadia. There are second-generation people too, Judy Bolton (now at the University of Illinois at Chicago), Bruce Lennox (McGill), and Fran Cozens (Dalhousie) who were all Bob McClelland's Ph.D. students; one of my former graduate teaching assistants has just been appointed to an academic post in California.

Keith was Chairman of the Department of Chemistry at the University of Toronto for two terms, 1974–1985, (with a sabbatical year between terms), and the Department was happier then than at anytime before or since. He had an open door policy; anyone could come and see him and say what they wanted. He would listen to everyone and then decide to do what he wanted to do anyway, but everyone was happy because he had listened to them.

Keith will be sorely missed, but I am sure that he will want to be remembered as the highly intelligent, fun-loving man that he was. He was a longtime supporter of this journal; he was the Physical Organic Editor for a time while he was Chairman. He published much of his best work here, and what would be a better memorial to him than to have it chosen as the journal of first choice for all current and future physical organic chemists.

Robin A. Cox

(The photograph is courtesy of the University of Toronto.)

transferts intramoléculaires de proton. Il a déterminé les moments dipolaires et les polarisabilités de quelques états excités, ce qui s'est avéré un travail très difficile.

Il a toujours été très intéressé par les calculs théoriques et, au cours de sa carrière, il a publié plusieurs articles faisant appel à cette méthode, principalement quand elle est devenue de plus en plus précise; ces travaux couvrant une grande variété de molécules et ions ont souvent été réalisés en collaboration avec son collègue et ami Imre Csizmadia. Il est l'auteur d'un livre intitulé Hückel Molecular Orbital Theory publié en 1978 (alors qu'il était directeur du Département de chimie; ces fonctions n'ont jamais ralenti ses activités de recherche); même si ce livre est maintenant désuet, il me surprend encore par le fait que ces calculs simples puissent, pour une série de molécules ou ions, conduire au même ordre de réactivité que les méthodes modernes beaucoup plus élaborées. Il a aussi développé un intérêt pour le principe (toujours négligé) du principe du mouvement nucléaire minimal qui avait été suggéré par Ossie Tee. Quand il a pris de l'intérêt pour la photochimie, il a appliqué les calculs théoriques à plusieures processus d'états excités. La dernière chose qu'il a étudié, seul et sans associé, a été une approche simple à l'application de la théorie de Marcus aux transferts photochimiques de protons qui faisait appel à un modèle de parabole à intersection.

Ce résumé nécessairement bref et incomplet devrait quand même permettre de démontrer l'étendue incroyable de ses intérêts scientifiques. Il a été intéressé, entre autre, par tous les aspects de la chimie organique physique, et il a grandement contribué à plusieurs d'entre eux. Je n'ai pas un total exact, mais il a publié plus de 150 articles de recherches ainsi que plusieurs articles de revue et de chapitres de livres.

Le nombre de professeurs d'université encore en fonction ou qui se sont retirés récemment qui ont été des élèves ou des chercheurs postdoctoraux dans le groupe de Keith est phénoménal, soit au moins quatorze, qui pourrait être un record canadien. Pour cette seule raison, son influence sur l'enseignement de la chimie et de la recherche a été énorme, non seulement au Canada, mais dans au moins quatre autres pays. Sans ordre particulier, ces professeurs d'université sont (avec leur institution): Alan Hopkinson (York University, Toronto), Bob McClelland (Toronto), Jim Pincock (Dalhousie), Bob McDonald (Mount Saint Vincent University, Halifax), Linda Sweeting (Towson University, Maryland), Julie Altmann (Kings College et Imperial College, University of London), Jacques Périé (Université Paul Sabatier, Toulouse), Tom Modro (University of Pretoria, South Africa), Ossie Tee (Concordia), Steve Anderson (University of Wisconsin à Whitewater), Peter Wan (Victoria), Mary Boyd (maintenant à Georgia Southern University), Paul Mezey (maintenant à Memorial), and moi (Toronto). Plusieurs des personnes impliquées en chimie théorique se trouvaient sous la direction conjointe de Keith et d'Imre Csizmadia. Il y a aussi des gens de deuxième génération, telle Judy Bolton (maintenant à l'Université d'Illinois à Chicago), Bruce Lennox (McGill), et Fran Cozens (Dalhousie) qui ont tous été des étudiants au Ph.D. de Bob McClelland; un de mes assistants a récemment été à un poste académique en Californie.

Keith a été directeur du Département de chimie de l'Université de Toronto pour deux termes, 1974–1985, (avec une année sabbatique entre les deux termes); cette période a été la plus heureuse pour le département. Il avait une politique de porte ouverte et chacun pouvait aller le voir pour lui dire ce qu'il pensait. Il écoutait tout le monde et décidait alors de faire malgré tout ce qu'il avait choisi de faire; tout le monde était toutefois heureux parce qu'il les avait écouté.

Keith sera grandement regretté, mais je suis certain qu'il voudrait qu'on se souvienne de lui comme l'homme qu'il était,

© 2007 NRC Canada

très intelligent, et qui aimait s'amuser. Il a été pendant longtemps défenseur de ce journal; il en a été l'éditeur de la section de chimie organique physique alors qu'il était directeur du département. Il a publié la plus grande partie de ses travaux dans ce journal; pour les praticiens actuels et futurs de la chimie organique physique, une façon appropriée d'honorer sa mémoire, serait de choisir régulièrement ce journal comme premier choix pour leurs publications.

Robin A. Cox

(La photographie a gracieusement été fournie par l'University of Toronto.)

Can. J. Chem. Downloaded from www.nrcresearchpress.com by Sichuan Normal University on 09/13/12
For personal use only.

© 2007 NRC Canada

Preparation of ABC triblock copolymers of *N*-alkyl substituted acrylamides by RAFT polymerization

Ya Cao and X.X. Zhu

Abstract: Reversible addition-fragmentation chain transfer (RAFT) polymerization of *N*-alkyl substituted acrylamides has been carried out by the use of a trithiocarbonate (2-dodecylsulfanylthiocarbonyl-sulfanyl-2-methyl propionic acid) as the RAFT reagent. The *N*-alkyl groups of the acrylamide monomers are important in the RAFT process. *N*-alkyl monosubstituted polyacrylamides are found to be active macro-chain transfer agents, while *N,N*-disubstituted monomers can react easily with them to form a sequent block. We have designed a synthetic pathway to successfully prepare ABC triblock copolymers of *N*-alkyl substituted acrylamides with low polydispersities (PDI < 1.20) by a three-step RAFT polymerization process.

Key words: block copolymers, RAFT polymerization, *N*-alkyl substituted acrylamides, thermosensitive polymers.

Résumé : Utilisant le trithiocarbonate de l'acide (2-dodécylsulfanylthiocarbonylsulfanyl-2-méthylpropionique) comme réactif TCAR, on a effectué la polymérisation par transfert de chaîne avec addition-fragmentation réversible (TCAR) d'acrylamides substitués par un groupe *N*-alkyle. Les groupes *N*-alkyles des monomères acrylamides sont important dans le processus TCAR. On a trouvé que les polyacrylamides portant un seul substituant *N*-alkyle sont actives comme agents de transfert de la chaîne macromoléculaire alors que les monomères *N,N*-disubstitués peuvent facilement réagir avec celles-ci pour former un bloc séquentiel. Faisant appel à un processus de polymérisation TCAR à trois étapes, on a mis au point une méthode de synthèse permettant de préparer avec succès des copolymères à trois blocs ABC d'acrylamides substitués par un groupe *N*-alkyle de faible polydispersité (PDI < 1,20).

Mots-clés : copolymères à bloc, polymérisation par transfert de chaîne avec addition-fragmentation réversible, acrylamides substitués par un groupe *N*-alkyle.

[Traduit par la Rédaction]

Introduction

Polymers based on *N*-alkyl substituted polyacrylamides possess interesting thermosensitive properties. They are soluble in water at low temperatures but become insoluble as the temperature rises above a certain lower critical solution temperature (LCST) (1). A great deal of interest has been focused on the preparation of complex thermosensitive polymers that exhibit temperature-tunable self-assembled morphologies with potential applications in nanotechnology, biomedicine, and membrane separations (2, 3). We have reported previously that the LCST of *N*-alkyl substituted acrylamide polymers can be easily tuned by a radical copolymerization of appropriate comonomers. These random copolymers exhibited only one LCST (1, 4), while diblock copolymers have been found to exhibit double thermosensitivity (5, 6). In more sophisticated systems, precise multiple transitions may be required. It is useful to make well-defined multiblock copolymers in which each block presents a different LCST and aggregates at a different temperature, thus forming a stepwise aggregation process with multiple thermosensitivity.

Recently, controlled radical polymerization has been applied to prepare polymers and block copolymers with well-defined structures and possible reactivation for further chain extension. Reversible addition-fragmentation chain transfer (RAFT) polymerization seems well-suited for polymerizing acrylamide derivatives (7, 8). To date, there have been several acrylamide derivatives synthesized via RAFT polymerization, including *N,N*-dimethylacrylamide (DMA) (9, 10), *N*-isopropylacrylamide (iPA) (11–15), *N*-*tert*-butylacrylamide (tBA) (16), acrylamide (AM) (17,18), *N*-acryloyl morpholine (19). Most reports focus only on the controlled polymerization of iPA and AM (8). RAFT copolymerization of different kinds of neutral acrylamide monomers still proves to be challenging (20). It is even more difficult to prepare ABC triblock copolymers by the RAFT technique. Extending polymerization time or using multiple synthesis steps would produce an increasing amount of dead polymers or cause the loss of chain transfer activity of macro-chain transfer agents (CTAs). To avoid this problem, some researchers used bifunctional CTAs to synthesize ABA triblock copolymers in two steps (20, 21) or PEO-based macro-CTAs as the first segment with subsequent chain extension with acrylamide monomers (22–24). However, to

Received January 8 2007. Accepted April 23 2007. Published on the NRC Research Press Web site at canjchem.nrc.ca on 30 May 2007.

Y. Cao[1] and X.X. Zhu.[2] Department of Chemistry, Université de Montréal, C.P. 6128, Succursale Centre-ville, Montreal, QC H3C 3J7, Canada

[1]Present address: State Key Laboratory of Polymer Materials Engineering, Sichuan University, Chengdu 610065, P.R. China

[2]Corresponding author (e-mail: julian.zhu@umontreal.ca).

 doi:10.1139/V07-043 © 2007 NRC Canada

prepare thermosensitive ABC triblock copolymers based totally on *N*-alkyl acrylamides, the above-mentioned approach is not applicable. To the best of our knowledge, the use of a three-step RAFT polymerization to synthesize ABC triblock copolymers of acrylamide derivatives has not been reported.

Here we report the first successful synthesis of ABC triblock copolymers based on *N*-alkyl acrylamides utilizing the RAFT polymerization technique. To facilitate this three-step synthesis, we chose to use a trithiocarbonate with a very high chain transfer efficiency as the RAFT reagent to reduce the reaction time. A difference in reactivity was found to exist among the *N*-alkyl substituted acrylamide monomers.

Experimental

Materials

All reagents were purchased from Sigma-Aldrich and used without further purification unless otherwise stated. 2,2-Azoisobutyronitrile (AIBN) was recrystallized from methanol. iPA was recrystallized from toluene–hexane (3:2, *v*/*v*). *N*,*N*-Dimethylacrylamide (DMA) was vacuum distilled prior to use. Other *N*-substituted acrylamide monomers (*N*,*N*-ethylmethylacrylamide, MEA; *N*,*N*-diethylacrylamide, DEA; *N*-*n*-propylacrylamide, nPA) were prepared from the corresponding alkylamines and acryloyl chloride according to a similar procedure reported by Shea et al. (25). A trithiocarbonate (2-dodecylsulfanylthiocarbonyl-sulfanyl-2-methyl propionic acid, DMP) was used as the RAFT reagent and was prepared according to a previously reported procedure (26).

General RAFT polymerization

With AIBN as an initiator and DMP as the RAFT reagent, all polymerizations were conducted in dimethyl sulfoxide (DMSO) at 70 or 80 °C in septasealed vials that were bubbled with nitrogen for 20 min before the reaction. The typical [DMP]/[AIBN] ratio was 5. Samples were periodically withdrawn from the reaction mixture for analyses.

Synthesis of macro-CTAs

nPA (13.2 g, 0.117 mol), DMP (0.284 g, 0.779 mmol), and AIBN (25.6 mg, 0.156 mmol) were added along with DMSO (30 mL) to a 100 mL flask. After purging with N_2 for 20 min, the copolymerization proceeded at 70 °C for 50 min and the product PnPA was purified by precipitation in warm water (conversion = 64.4%, M_n = 8100, PDI = 1.07).

RAFT copolymerization of the second block

With the macro-CTA as the RAFT reagent, the second block was added similarly. We describe here a typical procedure to add a block of iPA to a poly(*N*-*n*-propylacrylamide) (PnPA) macro-CTA derived from DMP. iPA (6.28 g, 0.056 mol), macro-CTA PnPA (3.0 g, 0.370 mmol), AIBN (9.14 mg, 0.056 mmol), and DMSO (40 mL) were added to a 100 mL round-bottomed flask equipped with a magnetic stir bar. The mixture was purged with N_2 for 20 min prior to being immersed in a preheated oil bath at 70 °C. The copolymerization was allowed to proceed for 45 min before termination by exposure to air. The product was then dialyzed and lyophilized (conversion = 85.8%, M_n = 20 900, PDI = 1.14).

Synthesis of the triblock copolymer P(nPA-*b*-iPA-*b*-MEA)

MEA (1.081 g, 9.57 mmol), P(nPA-*b*-iPA) (2.5 g, 0.120 mmol), and AIBN (3.94 mg, 0.024 mmol) were added along with 30 mL DMSO to a 100 mL flask. After purging with N_2 for 20 min, the copolymerization proceeded at 70 °C for 3 h and the products were isolated by dialysis and subsequent lyophilizaion (conversion = 92.3%, M_n = 30 900, PDI = 1.16).

Polymer Characterization

Average molecular weights and molecular weight distributions (PDI) were obtained by size exclusion chromatography (SEC) on a Waters 1525 system equipped with three Waters Styragel columns and a refractive index detector (Waters 2410). THF was used as the mobile phase (1.0 mL/min), and the system was calibrated with polystyrene standards. The NMR spectra of the monomers and polymers in $CDCl_3$ were recorded on a Bruker AV400 spectrometer operating at 400 MHz for protons. Monomer conversions were determined by comparing the integration of the NMR signals (5.0–6.5 ppm) of the protons of the vinyl group of the residual monomers with the integration of the characteristic NMR signals of the polymer. Matrix-assisted laser desorption ionization time-of-flight (MALDI-TOF) mass spectrometry of the polymers was performed on an AutoFlex MALDI-TOF (Bruker Daltonics) equipped with a nitrogen laser (337 nm) and with an accelerating potential of 20 kV. Samples were prepared with 3-β-indole acrylic acid (IAA) as matrix

Results and discussion

RAFT homopolymerization of *N*-alkyl acrylamides

RAFT homopolymerization of several *N*-alkyl acrylamides including three *N*,*N*-disubstituted (DMA, MEA, and DEA) and two *N*-monosubstituted (iPA and nPA) acrylamides has been carried out easily in the presence of trithiocarbonate DMP as chain transfer agent in DMSO. The general synthetic scheme of the homopolymer and block copolymers is outlined in Fig. 1.

Figure 2*A* shows SEC chromatograms for the homopolymerization of DEA, indicating the good control of the RAFT polymerization with unimodal traces. The polydispersity indices of the polymers are mostly lower than 1.2 in most cases. The polymerization proceeded at very fast rates and the monomer conversion was greater than 90% within 1 h. In all cases, to keep the activity of polymer chains it is important to keep the reaction time relatively short (within 90 min in this case).

Shown in Fig. 2*B* are the respective M_n and PDI (M_w/M_n) values as a function of monomer conversion. For samples of relatively low molecular weight, the M_n determined by SEC agreed well with that determined by MALDI-TOF mass spectrometry and NMR, indicating the validity of the M_n values obtained by SEC. The PDI values throughout the polymerization are below 1.2 even at high conversions. The observed molecular weights are consistent with the theoretical values (calculated from the monomer to CTA molar ra-

© 2007 NRC Canada

Table 1. Reaction conditions, conversions, molecular weights, and PDI values for the *N*-alkyl acrylamide homopolymers prepared by RAFT polymerization.

Sample	$[M]_0$:$[DMP]_0$:$[I]_0$	T (°C)	t (min)	Conversion[a] (%)	M_n[b] theory	M_n [c] SEC	PDI[c]
PDMA1	400:1:0.2	80	20	60.5	24 300	23 100	1.10
PDMA2	400:1:0.2	80	180	99.9	39 900	27 800	1.14
PDEA1	400:1:0.2	80	20	54.0	27 800	28 800	1.13
PDEA2	400:1:0.2	80	60	91.0	46 600	40 200	1.12
PDEA3	400:1:0.2	70	120	84.5	43 300	32 200	1.07
PMEA	200:1:0.2	80	40	84.5	19 100	18 100	1.12
PiPA1	100:1:0.2	80	40	88.5	10 000	9 600	1.10
PiPA2	400:1:0.2	80	90	94.7	43 200	31 100	1.20
PiPA3	400:1:0.2	70	180	91.0	41 500	32 100	1.12
PnPA1	400:1:0.2	70	60	52.6	24 100	16 900	1.11
PnPA2	400:1:0.2	80	60	58.7	26 900	20 400	1.23
PnPA3	400:1:0.2	80	240	94.7	43 200	28 400	1.38

[a]Determined by ^{1}H NMR spectroscopy.
[b]Calculated from $M_{n,th} = M_{CTA} + ([monomer]/[CTA]) \times M_{monomer} \times$ conversion%, where M_{CTA} and $M_{monomer}$ are the molecular weights of the RAFT agent and monomers, respectively, and [monomer] and [CTA] the initial monomer and CTA concentrations, respectively.
[c]Determined by SEC.

Fig. 1. The synthetic scheme for the RAFT polymerization of *N*-alkyl acrylamides. Further chain extension should lead to a multiblock copolymer. Monomers used include nPA (R = nPr), iPA (R = iPr), DMA (R′ = R′′ = Me), DEA (R′ = R′′ = Et), and MEA (R′ = Me, R′′ = Et).

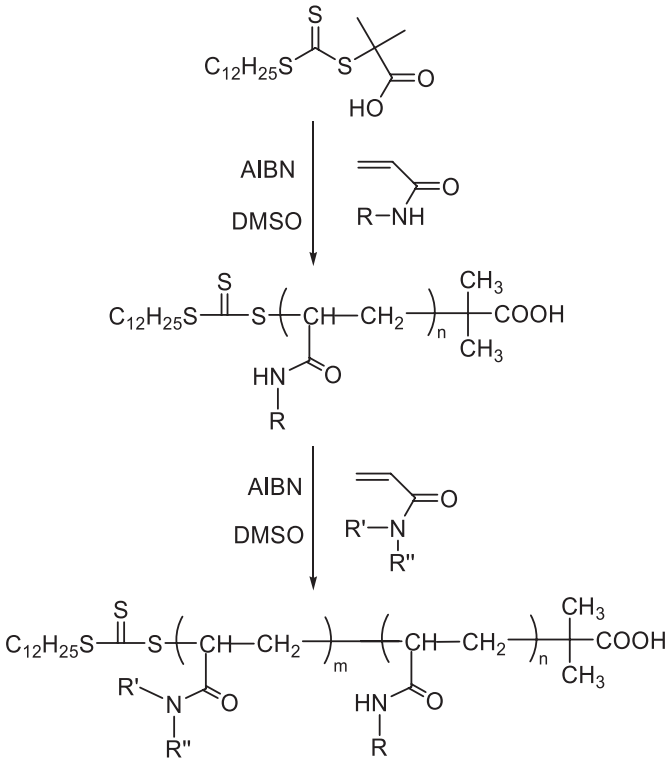
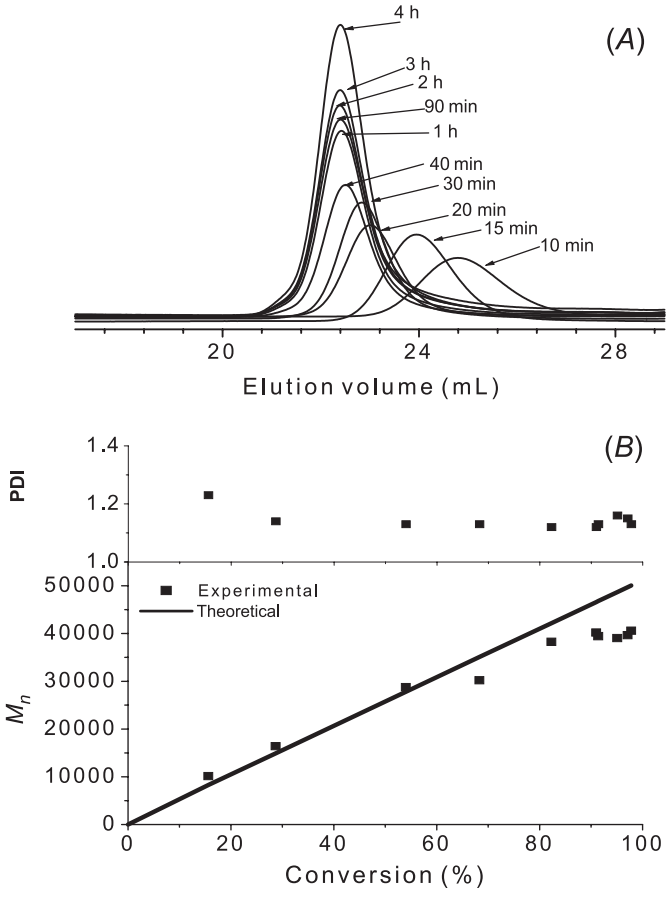


Fig. 2. (*A*) SEC traces of PDEA obtained by RAFT at 80 °C with different reaction times (molar ratio [DEA]/[DMP]/[AIBN] 400:1:0.2). (*B*) Plots of PDI and M_n vs. conversion for RAFT homopolymerization of DEA at 80 °C in DMSO.



tio) initially, with a negative deviation at high conversions. According to the classic RAFT mechanism, this negative deviation of molecular weight may indicate there are other sources of radicals, such as initiator-derived chains (8). A decrease in the amount of AIBN and a lower reaction temperature helped very little to improve the negative deviation, indicating that there may be other causes for the loss of chain transfer activity of the propagating chains.

Several acrylamide derivatives can be synthesized similarly via RAFT polymerization. Data for the homopolymerization (Table 1) did not show any obvious retardation, and high conversion was obtained within a short time suggesting a high chain transfer efficiency of the RAFT reagent DMP.

© 2007 NRC Canada

In all cases, experimental molecular weights were lower than theoretically predicted. However, there is a good agreement between the theoretical and experimental molecular weights when conversions or the molar ratios of monomers to RAFT reagents are low (Table 1, PDMA1, PDEA1, PMEA, and PiPA1). In general, as shown in Table 1, higher temperatures can accelerate the RAFT polymerization process but also result in larger PDI values. Higher conversions can be achieved with longer reaction time but also lead to more polydisperse samples.

Preparation of ABC triblock copolymers

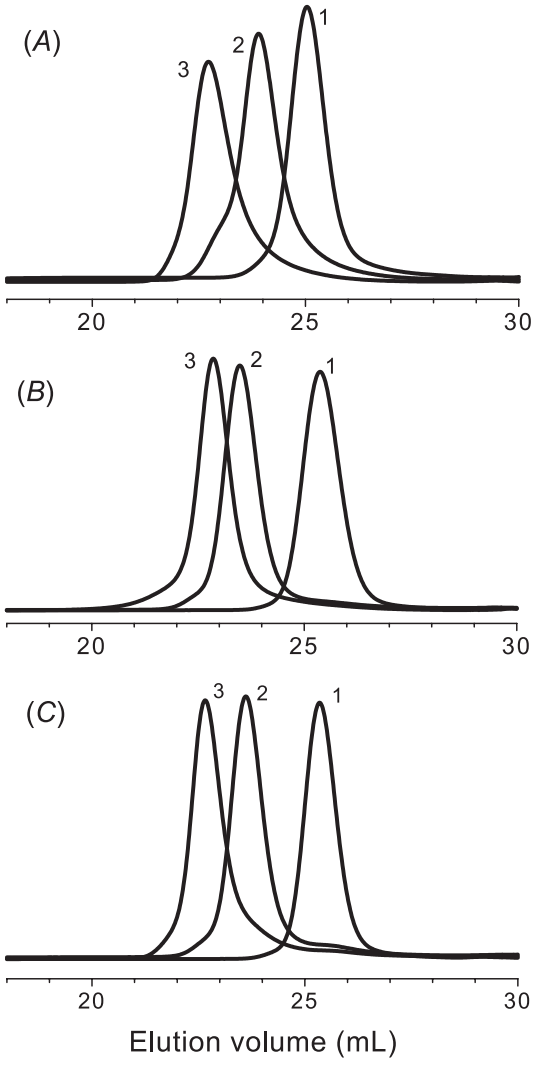
Diblock copolymers can be made by using the homopolymer as a macro-CTA to react with a second monomer. As shown in Fig. 3*A*, PiPA was used to add onto *N*-*n*-propylacrylamide to prepare the corresponding block copolymer. The copolymer P(iPA-*b*-nPA) exhibits a monomodal SEC trace. The clear shifts of the copolymer peaks (M_n = 17 200, PDI = 1.15 and M_n = 28 500, PDI = 1.17) away from the peak of the macro-CTA PiPA (M_n = 9600, PDI = 1.10) confirm the formation of block copolymers. We found that the use of the macro-CTA made of *N*-alkyl monosubstituted acylamide is a good choice and can easily chain-extend with other monomers, especially the *N,N*-disubstituted acrylamides, while the macro-CTAs made of some disubstituted acrylacrylamides may not chain-extend as easily (dead chains). This indicates that a reactivity difference exists among the acrylamide derivatives though they have similar chemical structures. Generally, macro-CTAs of PiPA and PnPA have high transfer constants and they are good leaving groups in the subsequent block copolymerization step. With this knowledge, we have designed a copolymerization pathway to synthesize ABC triblock copolymers. For a copolymer with multiple thermosensitivity, the cloud points of the homopolymer blocks should be taken into consideration. PnPA was used as the first block and macro-CTA to react with iPA to form a diblock copolymer P(nPA-*b*-iPA). ABC triblock copolymers were then synthesized by chain extension of with the macro-CTA P(nPA-*b*-iPA) with MEA or DMA (Figs. 3*B* and 3*C*). The SEC traces of diblock copolymers indicate that most of diblock macro-CTAs chain-extended with third comonomers to convert into the triblock copolymers. Even after three steps of RAFT polymerizations, the triblock copolymers obtained still had very low polydispersities (below 1.20).

Figure 4 shows the typical NMR spectra of some of the homopolymers obtained (PnPA, PiPA, PMEA) and of the triblock copolymer P(nPA-*b*-iPA-*b*-MEA). The characteristic peaks of the three homopolymers are all clearly found in the spectrum of the corresponding block copolymer at nearly the same chemical shift, confirming the chemical composition of the ABC block copolymers obtained.

Conclusions

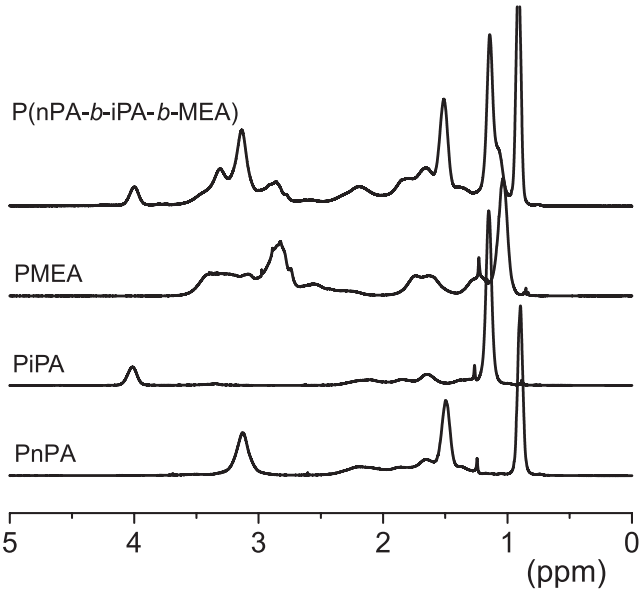
RAFT polymerizations of several *N*-alkyl substituted acrylamides have been successfully carried out in the presence of a trithiocarbonate DMP as chain transfer agent. Selected homopolymers can be used as macro-CTAs to be subsequently chain-extended with other acrylamide-based monomers to form diblock copolymers. We found that the polymers of *N*-monosubstituted acylamides such as iPA and nPA are active macro-chain transfer agents, while *N,N*-disubstituted monomers react easily with them to form a sequent block. Further studies are needed to better understand the difference in their reactivities. ABC triblock copolymers were synthesized successfully. We believe that this method can be used in the preparation of other well-defined multiblock copolymers. The thermal properties of the copolymers are being studied and the triblock copolymer manifests a three-step aggregation process in water. The details of the variable temperature studies will appear in a forthcoming report.

Fig. 3. SEC traces of the macro-CTAs and the corresponding chain-extended block copolymers obtained by RAFT at 70 °C in DMSO. (*A*) Trace 1: macro-CTA PiPA, M_n = 9600, PDI = 1.10; trace 2: P(iPA-*b*-nPA), M_n = 17 200, PDI = 1.15; trace 3: P(iPA-*b*-nPA), M_n = 28 900, PDI = 1.17. (*B*) Trace 1: PnPA, M_n = 8100, PDI = 1.07; trace 2: P(nPA-*b*-iPA), M_n = 20 900, PDI = 1.14; trace 3: P(nPA-*b*-iPA-*b*-MEA), M_n = 30 900, PDI = 1.16. (*C*) Trace 1: PnPA, M_n = 8300, PDI = 1.07; trace 2: P(nPA-*b*-iPA), M_n = 20 100, PDI = 1.11; trace 3: P(nPA-*b*-iPA-*b*-DMA), M_n = 30 000, PDI = 1.18.



© 2007 NRC Canada

Fig. 4. ^{1}H NMR spectra of the homopolymers PnPA, PiPA, PMEA, and the triblock copolymer P(nPA-*b*-iPA-*b*-MEA) in $CDCl_3$.



Acknowledgements

Financial support from Natural Sciences and Engineering Research Council of Canada (NSERC) and Fonds québécois de la recherche sur la nature et les technologies (FQRNT) of Quebec is gratefully acknowledged. YC thanks the China Scholarship Council for a scholarship.

References

1. H.Y. Liu and X.X. Zhu. Polymer, **40**, 6985 (1999).
2. Y. Osada and J.-P. Gong. Adv. Mater. **10**, 827 (1998).
3. R. Bussels, C. Bergman-Goettgens, J. Meuldijk, and C. Koning. Polymer, **46**, 8546 (2005).
4. X.X. Zhu, D. Avoce, H.Y. Liu, and A. Benrebouh. Macromol. Symp. **207**, 187 (2004).
5. M. Arotcarena, B. Heise, S. Ishaya, and A. Laschewsky. J. Am. Chem. Soc. **124**, 3787 (2002).
6. S. Sugihara, S. Kanaoka, S. Aoshima. Macromolecules, **38**, 1919 (2005).
7. S. Perrier and P. Takolpuckdee. J. Polym. Sci. Part A: Polym. Chem. **43**, 5347 (2005).
8. G. Moad, E. Rizzardo, and S. H. Thang. Aust. J. Chem. **58**, 379 (2005).
9. S. Perrier, P. Takolpuckdee, J. Westwood, and D. M. Lewis. Macromolecules, **37**, 2709 (2004).
10. A. J. Convertine, B.S. Lokitz, A.B. Lowe, C.W. Scales, L.J. Myrick, and C.L. McCormick. Macromol. Rapid Commun. **26**, 791 (2005).
11. Q. Liu, P. Zhang, and M. Lu. J. Polym. Sci. Part A: Polym. Chem. **43**, 2615 (2005).
12. A.J. Convertine, N. Ayres, C.W. Scales, A.B. Lowe, and C.L. McCormick. Biomacromolecules, **5**, 1177 (2004).
13. F. Ganachaud, M.J. Monteiro, R.G. Gilbert, M.-A. Dourges, S.H. Thang, and E. Rizzardo. Macromolecules, **33**, 6738 (2000)
14. B. Ray, Y. Isobe, K. Matsumoto, S. Habaue, Y. Okamoto, M. Kamigaito, and M. Sawamoto. Macromolecules, **37**, 1702 (2004)
15. Q. Liu, P. Zhang, A. Qing, Y. Lan, and M. Lu. Polymer, **47**, 2330 (2006).
16. B. De Lambert, M.-T. Charreyre, C. Chaix, and C. Pichot. Polymer, **46**, 623 (2005).
17. D.B. Thomas, A.J. Convertine, L.J. Myrick, C.W. Scales, A.E. Smith, A.B. Lowe, Y.A. Vasilieva, N. Ayres, and C.L. McCormick. Macromolecules, **37**, 8941 (2004).
18. D.B. Thomas, B.S. Sumerlin, A.B. Lowe, C.L. McCormick. Macromolecules, **36**, 1436 (2003).
19. A. Favier, F. D'Agosto, M.-T. Charreyre, and C. Pichot. Polymer, **45**, 7821 (2004).
20. A.J. Convertine, B.S. Lokitz, Y. Vasileva, L.J. Myrick, C.W. Scales, A.B. Lowe, and C.L. McCormick. Macromolecules, **39**, 1724 (2006).
21. M.K. Mahanthappa, F.S. Bates, and M.A. Hillmyer. Macromolecules, **38**, 7890 (2005).
22. Y. Li, B.S. Lokitz, and C.L. McCormick. Macromolecules, **39**, 81 (2006).
23. C. Hong, Y. You, and C.-Y. Pan. J. Polym. Sci. Part A: Polym. Chem. **42**, 4873 (2004).
24. Y. Li, B.S. Lokitz, S.P. Armes, and C.L. McCormick. Macromolecules, **39**, 2726 (2006).
25. K.J. Shea, G.J. Stoddard, D.M. Shavelle, F. Wakui, and R.M. Choate. Macromolecules, **23**, 4497 (1990).
26. J.T. Lai, D. Filla, and R. Shea. Macromolecules, **35**, 6754 (2002).

© 2007 NRC Canada

Iodine-promoted Prins-cyclization of ketones — A facile synthesis of spirocyclic-4-iodo-tetrahydropyrans and 5,6-dihydro-2*H*-pyrans

J.S.Yadav, B.V. Subba Reddy, V. Hari Krishna, T. Swamy, and G.G.K.S. Narayana Kumar

Abstract: Homoallylic and homopropargylic alcohols undergo smooth coupling with ketones in the presence of molecular iodine at ambient temperature to produce spirocyclic-4-iodotetrahydropyrans and 5,6-dihydro-2*H*-pyrans, respectively, in high yields in a short reaction time with high selectivity. The use of molecular iodine makes this procedure quite simple, more convenient, and cost-effective.

Key words: Prins-cyclization, iodine, homopropargylic alcohol, spirocyclic-4-iodopyrans.

Résumé : Sous l'influence d'iode moléculaire, à la température ambiante, les alcools homoallyliques et homopropargyliques conduisent à un couplage en douceur avec les cétones pour conduire respectivement à la formation, avec des rendements élevés et une sélectivité élevée, de 4-iodotétrahydropyranes et de 5,6-dihydro-2*H*-pyranes spirocycliques après de temps de réactions courts. L'utilisation de l'iode moléculaire rend cette méthode très simple, plus commode et plus efficace au point de vue des coûts.

Mots-clés : cyclisation de Prins, iode, alcool homopropargylique, 4-iodopyranes spirocycliques.

[Traduit par la Rédaction]

Introduction

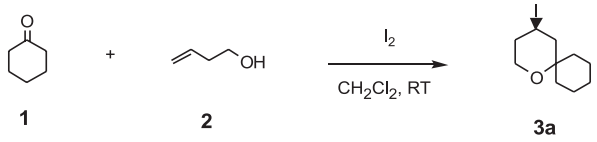
The tetrahydropyran ring system is a core unit in a number of natural products such as avermectins, aplysiatoxins, oscillatoxins, latrunculins, talaromycins, and acutiphycins (1). In particular, spirocyclic-tetrahydropyran derivatives are found in various biologically active molecules. Generally, tetrahydropyran derivatives are prepared via Prins-cyclization using acid catalysis (2–4). Although a large number of methods are available for the Prins-cyclization of aldehydes, only a few procedures are reported for ketones (5–7). Therefore, the development of a simple and convenient method involving inexpensive and readily available reagents would extend the scope of the Prins-cyclization in natural product synthesis (8). Recently, molecular iodine has received considerable attention as an inexpensive, nontoxic, readily available catalyst for various organic transformations, affording the corresponding products with high selectivity in excellent yields (9). The mild Lewis acidity associated with iodine enhanced its usage in organic synthesis to perform several organic transformations using stoichiometric levels to catalytic amounts. Owing to advantages associated with this ecofriendly catalyst, molecular iodine has been explored as a powerful reagent for various organic transformations (10).

Received December 16 2007. Accepted April 23 2007. Published on the NRC Research Press Web site at http://canjchem.nrc.ca on 6 June 2007.

J.S.Yadav,[1] B.V.S. Reddy, V.H. Krishna, T. Swamy, and G.G.K.S.N. Kumar. Division of Organic Chemistry, Indian Institute of Chemical Technology, Hyderabad 500 007, India.

[1]Corresponding author (e-mail: yadavpub@iict.res.in).

Scheme 1.



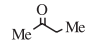
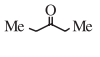
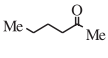
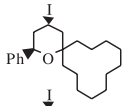
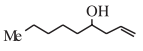
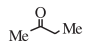
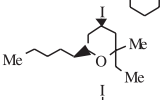
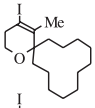
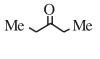
Results and discussion

In this article, we report an efficient and metal catalyst free Prins-cyclization for the rapid synthesis of spirocyclic-tetrahydropyrans from homoallylic alcohols and ketones using molecular iodine under neutral conditions. Accordingly, treatment of 3-buten-1-ol with cyclohexanone in the presence of molecular iodine at ambient temperature for 30 min gave the corresponding 4-iodotetrahydropyran in 96% yield (Scheme 1).

Similarly, various ketones such as cyclopentanone, cyclododecanone, acetone, 2-butanone, 3-pentanone, 2-hexanone, and 2-adamantanone underwent smooth coupling with 3-buten-1-ol to give the respective spirocyclic-4-iodotetrahydropyrans in excellent yields (Table 1, entries **b**–**h**). Encouraged by the results obtained with 3-buten-1-ol, we turned our attention to various substituted homoallylic alcohols. Interestingly, 1-phenyl-3-buten-1-ol reacted efficiently with cyclohexanone and cyclododecanone to produce 2,4,6-trisubstituted pyran derivatives (Table 1, entries **i** and **j**). Likewise, the coupling of 2-butanone with 1-nonen-4-ol

 doi:10.1139/V07-048 © 2007 NRC Canada

Table 1. Iodine-catalyzed preparation of spirocyclic-4-iodotetrahydropyran derivatives.

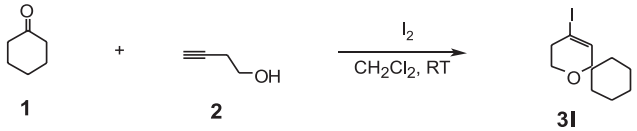
Entry	Alcohol	Ketones	Pyrans[a]	Time (min)	Yield (%)[b]
a				30	96
b				35	94
c				50	88
d				40	90
e				45	89[c]
f				50	92
g				60	91[c]
h				70	85
i				50	94
j				50	86
k				45	90[c]
l				60	90
m				60	88
n				65	92
o				65	85
p				65	84

[a]All products were characterized by ^{1}H NMR, ^{13}C NMR, IR, and mass spectroscopy.
[b]Isolated and upoptimized yields.
[c]cis–trans ratio 2:1

gave the corresponding trisubstituted pyran in 90% yield (Table 1, entry **k**). Furthermore, simple homopropargylic alcohol underwent smooth coupling with cyclohexanone to produce spirocyclic dihydropyran derivative **3l** (Scheme 2).

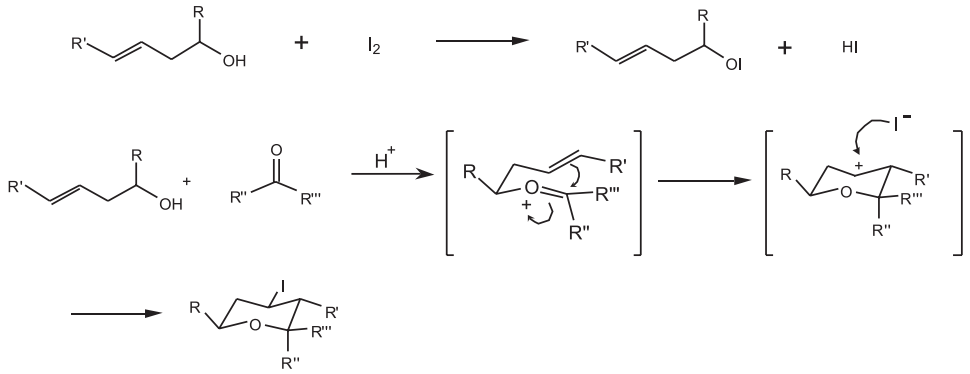
Similarly, 3-pentyn-1-ol also reacted well with several ketones such as cyclopentanone, cyclohexanone, cyclododecanone, and 3-pentanone to generate 2,3,4-trisubstituted pyran derivatives in high yields under similar conditions (Table 1, entries **m**–**p**). However, no reaction was observed in

Scheme 2.



© 2007 NRC Canada

Scheme 3.



the absence of a catalyst even after a long reaction time (12 h). As solvent, dichloromethane appeared to give the best result. In all cases, the reactions proceeded rapidly at room temperature under mild conditions. The reactions were clean and the products were obtained in excellent yields with high diastereoselectivity. Only a single isomer was obtained in each reaction, the structure of which was confirmed by ^{1}H NMR and also by comparison with authentic samples (6). The formation of the products may be further explained by hemi-acetal formation and subsequent Prins-type cyclization (Scheme 3).

Other iodide sources such as LiI, *t*-Bu_4NI, and NaI failed to produce the desired product. Cyclic ketones gave slightly higher yields when compared with acyclic ketones. As depicted in Table 1, a variety of ketones participated in Prins-cyclization under these reaction conditions. The scope and generality of this process is illustrated with respect to various ketones and homoallylic and homopropargylic alcohols, and the results are presented in Table 1.

In summary, we describe a rapid and efficient Prins-cyclization of ketones to produce spirocyclic-4-iodo-tetrahydropyrans in high yields with high selectivity. The use of inexpensive and readily available molecular iodine has made this procedure simple, convenient, and practical. In addition to its simplicity, efficiency, and milder reaction conditions, this method provides a rapid access for spirocyclic-4-iodo tetrahydropyran derivatives with diverse chemical structures.

Experimental

Melting points were recorded on Buchi R-535 apparatus and are uncorrected. IR spectra were recorded on a PerkinElmer FT-IR 240-c spectrophotometer using KBr optics. ^{1}H, ^{13}C NMR spectra were recorded on Gemini-200 spectrometer in $CDCl_3$ using TMS as internal standard. Mass spectra were recorded on a Finnigan MAT 1020 mass spectrometer operating at 70 eV. TLC was monitored on 0.25 mm precoated silica gel plates (60F-254).

General procedure

A mixture of homoallylic alcohol (2 mmol), ketone (1 mmol), and iodine (1 mmol) in dichloromethane (5 mL) was stirred at 23 °C for a specified time (Table 1). After completion of the reaction as indicated by TLC, the reaction mixture was quenched with water and extracted with ether (2 × 10 mL). The combined organic layers were washed with aqueous sodium thiosulfate and brine and dried over anhydr. Na_2SO_4. The removal of solvent, followed by purification on silica gel (Merck, 100–200 mesh, ethyl acetate – hexane, 0.5:9.5), gave pure 4-iodotetrahydropyran. The products thus obtained were characterized by IR and NMR spectroscopy. The characterization data was found to be consistent with the authentic samples (6).

4-Iodo-1-oxaspiro[5.5]undecane (a)

Liquid. IR (KBr, cm^{-1}) ν: 2924, 2853, 1630, 1457, 1075. ^{1}H NMR (200 MHz, $CDCl_3$) δ: 1.19–1.66 (m, 10H), 1.99 (d, *J* = 12.8 Hz, 2H), 2.19–2.24 (m, 2H), 3.51–3.60 (m, 2H), 4.37–4.38 (m, 1H). ^{13}C NMR (75 MHz, $CDCl_3$) δ: 21.0, 21.2, 26.0, 29.2, 39.8, 39.8, 40.3, 49.6, 61.9, 74.6. LCMS: 279 (M – 1). Anal. calcd for $C_{10}H_{17}OI$: C 42.87, H 6.12; found: C 42.92, H 6.08.

4-Iodo-2-phenyl-1-oxaspiro[5.5]undecane (i)

Liquid. IR (KBr, cm^{-1}) ν: 3063, 3028, 2926, 2853, 1637, 1492, 1448, 1059, 757, 698. ^{1}H NMR (200 MHz, $CDCl_3$) δ: d 1.25–1.75 (m, 10H), 2.08–2.16 (m, 2H), 2.33 (dd, *J* = 4.5, 12.8 Hz, 1H), 2.56 (d, *J* = 12.8 Hz, 1H), 4.52–4.62 (m, 2H), 7.23–7.33 (m, 5H). ^{13}C NMR (75 MHz, $CDCl_3$) δ: 21.5, 26.2, 26.2, 30.1, 30.1, 40.0, 47.4, 49.2, 72.3, 75.5, 125.6, 125.6 125.6, 125.6, 128.5, 128.5. LCMS: 355 (M – 1). Anal. calcd for $C_{16}H_{21}OI$: C 53.94, H 5.94; found: C 53.99, H 5.89.

4-Iodo-1-oxaspiro[5.5]undec-4-ene (l)

Liquid. IR (KBr, cm^{-1}) ν: 2927, 2854, 1633, 1452, 1333, 1268, 1208, 1084, 759. ^{1}H NMR (200 MHz, $CDCl_3$) δ: 1.25–1.72 (m, 10H), 2.51 (td, *J* = 2.2, 5.2 Hz, 2H), 3.76 (t, *J* = 5.2 Hz, 1H), 6.26 (s, 1H). ^{13}C NMR (75 MHz, $CDCl_3$) δ: 21.4, 21.4, 25.5, 35.2, 39.4, 39.4, 60.2, 60.2, 91.1, 144.2. LCMS: 277 (M – 1). Anal. calcd for $C_{10}H_{15}OI$: C 43.18, H 5.44; found: C 43.24, H 5.39.

Acknowledgements

VHK, TS, and GGKSNK thank the Council of Scientific and Industrial Research (CSIR, New Delhi) for the award of fellowships.

© 2007 NRC Canada

References

1. K.C. Nicolaou and E.J. Sorensen. Classics in total synthesis. Wiley-VCH, Weinheim, Germany. 1996.
2. (*a*) H.J. Prins. Chem. Weekbl. **16**, 1072 (1919); (*b*) D.R. Adams and S.P. Bhatnagar. Synthesis, 661 (1997); (*c*) S. Chandrasekhar and B.V.S. Reddy. Synlett, 851 (1998).
3. (*a*) Z.Y. Wei, J.S. Li, D. Wang, and T.H. Chan. Tetrahedron Lett. **28**, 3441 (1987); (*b*) F. Perron and K.F. Albizati. J. Org. Chem. **52**, 4130 (1987); (*c*) Z.Y. Wei, D. Wang, J.S. Li, and T.H. Chan. J. Org. Chem. **54**, 5768 (1989); (*d*) L. Coppi, A. Ricci, and M. Taddei. J. Org. Chem. **53**, 913 (1988).
4. (*a*) J. Yang, G.S. Viswanathan, and C.J. Li. Tetrahedron Lett. **40**, 1627 (1999); (*b*) J. Yang and C.J. Li. Synlett, 717 (1999); (*c*) K.-P. Chan and T.-P. Loh. Tetrahedron Lett. **45**, 8387 (2004); (*d*) P.O. Miranda, D.D. Diaz, J.I. Padron, M.A. Ramirez, and V.S. Martin. J. Org. Chem. **70**, 57 (2005).
5. E. Hanschke and I. Mitteil. Chem. Ber. **88**, 1053 (1955).
6. (*a*) J. Li and C.J. Li. Heterocycles, **53**, 1691 (2000); (*b*) G.S. Viswanathan, J. Yang, and C.J. Li. Org. Lett. **1**, 993 (1999); (*c*) G. Sabitha, K.B. Reddy, M. Bhikshapathi, and J.S. Yadav. Tetrahedron Lett. **47**, 2807 (2006).
7. N.A. Nikolic, C.P.D. Longford, N.T. Lane, and D.W. Thompson. J. Org. Chem. **54**, 2748 (1989).
8. (*a*) J.S. Yadav, M.S. Reddy, P.P. Rao, and A.R. Prasad. Tetrahedron Lett. **47**, 4397 (2006); (*b*) J.S. Yadav, M.S. Reddy, and A.R. Prasad. Tetrahedron Lett. **47**, 4937 (2006); (*c*) J.S. Yadav, M.S. Reddy, and A.R. Prasad. Tetrahedron Lett. **47**, 4995 (2006).
9. (*a*) H. Togo and S. Iida. Synlett, 2159 (2006); (*b*) X.-F. Lin, S.-L. Cui, and Y.-G. Wang. Tetrahedron Lett. **47**, 4509 (2006); (*c*) W.-Y. Chen and J.Lu. Synlett, 1337 (2005); (*d*) L. Royer, S.K. De, and R.A. Gibbs. Tetrahedron Lett. **46**, 4595 (2005); (*e*) B.K. Banik, M. Fernandez, and C. Alvarez. Tetrahedron Lett. **46**, 2479 (2005); (*f*) S.-Y. Wang. Synlett, 2642 (2004); (*g*) S. Ko, M.N.V. Sastry, C. Lin, and C.-F. Yao. Tetrahedron Lett. **46**, 5771 (2005).
10. (*a*) J.S. Yadav, B.V.S. Reddy, and S.R. Hashim. J. Chem. Soc. Perkin Trans. 1, 3025 (2000); (*b*) J.S. Yadav, B.V.S. Reddy, K. Premalatha, and T. Swamy. Tetrahedron Lett. **46**, 2687 (2005); (*c*) H.M.S. Kumar, B.V.S. Reddy, E.J. Reddy, and J.S. Yadav. Chem. Lett. 857 (1999); (*d*) J.S. Yadav, B.V.S Reddy, C.V. Rao, P.K. Chand, and A.R. Prasad. Synlett, 1638 (2001).

© 2007 NRC Canada

A solvent-free protocol for facile condensation of indoles with carbonyl compounds using silica chloride as a new, highly efficient, and mild catalyst

Alireza Hasaninejad, Abdolkarim Zare, Hashem Sharghi, Mohsen Shekouhy, Reza Khalifeh, Alireza Salimi Beni, and Ahmad Reza Moosavi Zare

Abstract: A simple and efficient solvent-free procedure for the preparation of bis(indolyl)methanes via electrophilic substitution reactions of indoles with aldehydes and ketones is described. The reactions took place in the presence of a catalytic amount of silica chloride at room temperature. The advantages of this method are high yields, short reaction times, low cost, and compliance with green-chemistry protocols.

Key words: silica chloride, indole, carbonyl compound, solvent-free, bis(indolyl)methane.

Résumé : On décrit une méthode très simple et efficace n'impliquant pas de solvant pour la préparation de bis(indolyl)méthanes qui s'effectue par le biais d'une réaction de substitution électrophile d'indoles avec des aldéhydes et des cétones, à la température ambiante, en présence d'une quantité catalytique de chlorure de silicium. Les avantages de cette méthode sont ses rendements élevés, ses courts temps de réaction, ses coûts peu élevés et leur appariement avec des protocoles de chimie verte.

Mots-clés : chlorure de silicium, indole, composés carbonylés, sans solvant, bis(indolyl)méthane.

[Traduit par la Rédaction]

Introduction

Indole derivatives are known for their vast applications in material sciences (1), agrochemicals (2), and pharmaceuticals (3). Among these compounds, the substrates including bis(indolyl)methane moieties, such as secondary metabolites (4) and marine-sponge alkaloids (5), are important classes of bioactive metabolites. Therefore, there is a great interest in the synthesis of this class of compounds. Electrophilic substitution reaction of indole with carbonyl compounds has been used as a useful route toward the synthesis of bis(indolyl)methanes. Different reagents and catalysts have been employed to accomplish this transformation, such as acetic acid (6*a*), $InCl_3$ (6*b*), $In(OTf)_3$ (6*c*), InF_3 (6*d*), $Dy(OTf)_3$ (6*e*), $Ln(OTf)_3$ (6*f*), $FeCl_3$ (6*g*), NBS (6*h*), $PPh_3{\cdot}HClO_4$ (TPP) (6*i*), trichloro-1,3,5-triazine (6*j*), $AlPW_{12}O_{40}$ (6*k*), $ZrOCl_2{\cdot}8H_2O$ (6*l*), and Ru(III) (6*m*). The synthesis of bis(indolyl)methanes in the absence of a catalyst has been also reported (6*n*). However, some of the reported methods are associated with the following drawbacks: (*i*) the use of expensive reagents (6*c*, 6*e*, 6*f*, 6*k*), (*ii*) long reaction times (6*a*, 6*b*, 6*d*), (*iii*) low yields (6*a*), and (*iv*) the use of an additional microwave oven (6*g*). Because of the wide range of biological, industrial, and synthetic applications of bis(indolyl)methanes, their preparation has received renewed interest.

Solvent-free organic reactions have been used as a useful technique in organic synthesis. Solid-state protocols often lead to shorter reaction times, higher yields, easier workup, compliance with green-chemistry protocols, and may enhance the regio- and stereo-selectivity of the reactions (7). Solvent-free condensation of indoles with carbonyl compounds is scarce in the literature (6*l*, 8). Having those aspects in mind and also in continuation of our previous studies to explore new applications of silica chloride (9), we report a new, clean, and efficient solvent-free method for the condensation of indoles with carbonyl compounds. The method involves the use of a catalytic amount of silica chloride under extremely mild conditions (Scheme 1).

Results and discussion

First, to optimize the reaction conditions, silica chloride was used as a catalyst for the condensation of indole (2.1 mmol) with benzaldehyde (1 mmol), as a model reac-

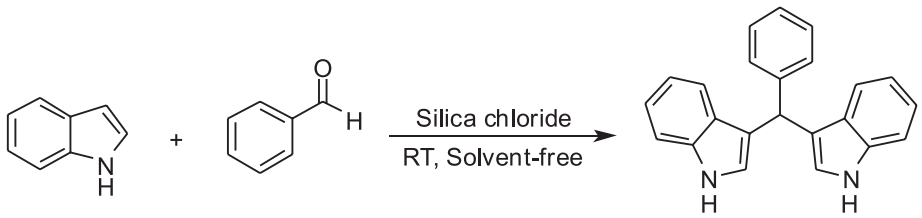
Received 25 February 2007. Accepted 9 May 2007. Published on the NRC Research Press Web site at canjchem.nrc.ca on 9 June 2007.

A. Hasaninejad[1] **and M. Shekouhy.** Department of Chemistry, Faculty of Sciences, Persian Gulf University, Bushehr 75169, Iran.
A. Zare.[2] Department of Chemistry, Payam Noor University of Bushehr, Bushehr 1698, Iran.
H. Sharghi,[3] **R. Khalifeh, A. Salimi Beni, and A.R. Moosavi Zare.** Department of Chemistry, College of Sciences, Shiraz University, Shiraz 71454, Iran.

[1]Corresponding author (e-mail: ahassaninejad@yahoo.com).
[2]Corresponding author (e-mail: abdolkarimzare@yahoo.com).
[3]Corresponding author (e-mail: shashem@susc.ac.ir).

 doi:10.1139/V07-051 © 2007 NRC Canada

Scheme 1. Condensation of indole with benzaldehyde.



tion under solvent-free conditions (Scheme 1). Interestingly, the reaction proceeded efficiently at room temperature, and the desired bis(indolyl)methane was isolated in 93% yield after 10 min. The reaction was also examined in the presence of silica gel without using silica chloride. In these conditions, the reaction was unsuccessful, and 55% of the starting materials remained intact plus an undesired product, which has not been identified. Therefore, silica chloride was used as a catalyst for all reactions in the absence of solvent.

To compare the efficiency of the solvent-free vs. solution conditions, a model reaction was examined in several solvents, including CH_2Cl_2, $CHCl_3$, MeCN, THF, benzene, DMF, and DMSO. Thus, a mixture of indole (2.1 mmol), benzaldehyde (1 mmol), and silica chloride (0.5 g) in the appropriate solvent (10 mL) was stirred at room temperature for 4 h. Moderate yields of the product were obtained in these conditions; therefore, the solvent-free method is more efficient.

To investigate the capacity and efficiency of our catalyst, the condensation of indoles with a variety of aromatic and aliphatic aldehydes and ketones was carried out using this catalyst (Table 1). As Table 1 indicates, the reactions proceeded efficiently, and the desired products were obtained in good to excellent yields and in short reaction times.

Notably, the electronic properties of the aromatic ring of carbonyl compounds affected the results of the reaction. When an electron-withdrawing substituent, such as NO_2, was present on the aromatic ring, reaction times were decreased; however, the yields did not change significantly (Table 1, entries 2, 3, and 14). Electron-donating substituents (e.g., Me or OMe) had negligible effect on reaction times, but caused the reaction yields to decrease (Table 1, entries 6 and 7). Aliphatic aldehydes as well as ketones needed longer reaction times in comparison with aromatic aldehydes (Table 1, entries 10, 11, 12, and 15).

In conclusion, we have introduced a highly efficient catalyst for the condensation of indoles with aldehydes and ketones in the absence of solvent under mild reaction conditions. The promising points for the presented methodology are high conversion, ease of handling and low cost of the catalyst, cleaner reaction profile, and short reaction times, which make it a useful and attractive process for the rapid synthesis of substituted bis(indolyl)methanes.

Experimental

All chemicals were purchased from Merck or Fluka Chemical Companies. Silica chloride was prepared by the reaction of silica gel (item 7731 for TLC from Merck, Darmstadt, FRG) with thionyl chloride according to the literature procedure (10). ^{1}H NMR (250 MHz) and ^{13}C NMR (62.5 MHz) were run on a Bruker AVANCE DPX-250 FTNMR spectrometer. Melting points were recorded on a Büchi B-545 apparatus in open capillary tubes and are uncorrected.

General procedure for condensation of indole with benzaldehyde

To a mixture of indole (0.25 g, 2.1 mmol) and benzaldehyde (0.11 g, 1 mmol) was added silica chloride (0.5 g) and grinded at room temperature for 10 min. Afterward, the reaction mixture was suspended in acetone (20 mL) and filtered. The solvent was evaporated, and the crude product was purified by plate chromatography or recrystallization.

*3-((1*H*-Indol-3-yl)(phenyl)methyl)-1*H*-indole (1)*

Recrystallization from chloroform – petroleum ether (1:1) gave pink solid; yield: 0.301 g (93%); mp 140–142 °C (lit. 142–144 °C) (9). IR (KBr, cm^{-1}): 3402, 3051, 1618, 1600. ^{1}H NMR ($CDCl_3$, ppm) δ: 5.86 (s, 1H, ArCH), 6.66 (s, 2H), 7.11 (t, 2H, *J* = 6.9 Hz), 7.14–7.22 (m, 3H), 7.28–7.31 (m, 2H), 7.35–7.42 (m, 6H), 7.93 (br, 2H, NH). ^{13}C NMR ($CDCl_3$) δ: 31.6, 110.9, 111.9, 118.4, 119.5, 121.2, 124.0, 126.3, 127.1, 128.5, 128.6, 137.0, 145.2.

*3-((1*H*-Indol-3-yl)(4-nitrophenyl)methyl)-1*H*-indole (2)*

Recrystallization from EtOAc – petroleum ether (1:1) gave yellow needles; yield: 0.352 g (96%); mp 217–219 °C (lit. 220–222 °C) (6*c*). IR (KBr, cm^{-1}): 3423, 3051, 1593, 1510, 1458, 1337. ^{1}H NMR ($CDCl_3$, ppm) δ: 6.01 (s, 1H, ArCH), 6.72 (s, 2H), 7.02–7.08 (m, 4H), 7.36 (d, 2H, *J* = 8.1 Hz), 7.41 (d, 2H, *J* = 8.1 Hz), 7.49 (d, 2H, *J* = 8.6 Hz), 8.05 (br, 2H, NH), 8.17 (d, 2H, *J* = 8.6 Hz).

*3-((1*H*-Indol-3-yl)(3-nitrophenyl)methyl)-1*H*-indole (3)*

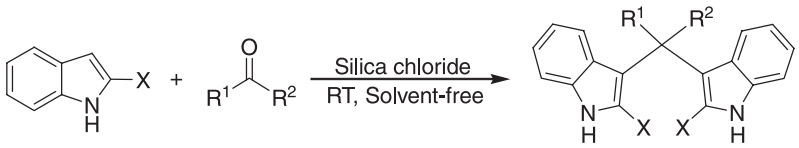
Recrystallization from EtOAc – petroleum ether (1:1) gave yellow solid; yield: 0.350 g (95%); mp 220–222 °C (lit. 221–223 °C) (11). IR (KBr, cm^{-1}): 3403, 3045, 2917, 1520, 1453, 1350. ^{1}H NMR ($CDCl_3$, ppm) δ: 6.23 (s, 1H, ArCH), 7.01 (t, 2H, *J* = 7.3 Hz), 7.06 (s, 2H), 7.22 (t, 2H, *J* = 7.0 Hz), 7.45 (d, 2H, *J* = 7.5 Hz), 7.53 (d, 2H, *J* = 8.0 Hz), 7.75 (m, 1H), 8.02 (d, 1H, *J* = 7.6 Hz), 8.26 (d, 1H, *J* = 7.7 Hz), 8.33 (s, 1H), 8.09 (s, 2H, NH).

*3-((4-Chlorophenyl)(1*H*-indol-3-yl)methyl)-1*H*-indole (4)*

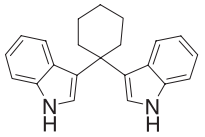
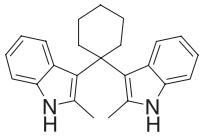
Recrystallization from chloroform – petroleum ether (1:1) gave pink solid; yield: 0.328 g (92%); mp 78–80 °C (lit. 76–78 °C) (12). IR (KBr, cm^{-1}): 3412, 3056, 1483. ^{1}H NMR ($CDCl_3$, ppm) δ: 5.86 (s, 1H, ArCH), 6.65 (s, 2H), 6.85–7.96 (m, 12H), 8.00 (br, 2H, NH).

© 2007 NRC Canada

Table 1. Condensation of indoles with aldehycdes and ketones using silica chloride.



1–15

Entry	Product[a]	Time (min)	Yield[b] (%)
1	X = H, R^1 = C_6H_5, R^2 = H (**1**)	10	93
2	X = H, R^1 = *p*-$NO_2C_6H_4$, R^2 = H (**2**)	5	96
3	X = H, R^1 = *m*-$NO_2C_6H_4$, R^2 = H (**3**)	7	95
4	X = H, R^1 = *p*-ClC_6H_4, R^2 = H (**4**)	10	92
5	X = H, R^1 = *o*-ClC_6H_4, R^2 = H (**5**)	20	81
6	X = H, R^1 = *p*-MeC_6H_4, R^2 = H (**6**)	10	87
7	X = H, R^1 = *p*-$OMeC_6H_4$, R^2 = H (**7**)	12	84
8	X = H, R^1 = 4-Pyridyl, R^2 = H (**8**)	8	92
9	X = H, R^1 = 2-Furyl, R^2 = H (**9**)	15	90
10	X = H, R^1 = *n*-Butyl, R^2 = H (**10**)	20	85
11	X = H, R^1 = C_6H_5, R^2 = Me (**11**)	20	70
12	 (**12**)	20	75
13	X = Me, R^1 = C_6H_5, R^2 = H (**13**)	15	91
14	X = Me, R^1 = *p*-$NO_2C_6H_5$, R^2 = H (**14**)	10	92
15	 (**15**)	25	73

[a]All compounds were identified by comparison of their melting points with the authentic samples and (or) IR as well as ^{1}H NMR data.
[b]Isolated yield.

3-((2-Chlorophenyl)(1H-indol-3-yl)methyl)-1H-indole (5)

Recrystallization from chloroform – petroleum ether (1:1) gave pink solid; yield: 0.288 g (81%); mp 74–76 °C (lit. 78–80 °C) (12). IR (KBr, cm^{-1}): 3412, 3053, 1617, 1455. ^{1}H NMR ($CDCl_3$, ppm) δ: 6.32 (s, 1H, ArCH), 6.67 (s, 2H), 7.02 (t, 2H, *J* = 7.8 Hz), 7.10–7.22 (m, 6H), 7.38–7.43 (m, 4H), 7.98 (br, 2H, NH).

3-((1H-Indol-3-yl)(p-tolyl)methyl)-1H-indole (6)

Recrystallization from chloroform – petroleum ether (1:2) gave pink solid; yield: 0.293 g (87%); mp 95–97 °C (lit. 94–96 °C) (12). IR (KBr, cm^{-1}): 3411, 3040, 2932, 1603, 1512. ^{1}H NMR ($CDCl_3$, ppm) δ: 2.33 (s, 3H, $ArCH_3$), 5.87 (s, 1H, ArCH), 6.69 (s, 2H), 7.04 (t, 2H, *J* = 7.1 Hz), 7.12 (d, 2H, *J* = 7.1 Hz), 7.23–7.28 (m, 6H), 7.41 (d, 2H, *J* = 7.2 Hz), 7.94 (br, 2H, NH).

3-((1H-Indol-3-yl)(4-methoxyphenyl)methyl)-1H-indole (7)

Recrystallization from chloroform – petroleum ether (1:1) gave brown solid; yield: 0.295 g (84%); mp 186–188 °C (lit. 187–189 °C) (13). IR (KBr, cm^{-1}): 3410, 2930, 1610, 1508. ^{1}H NMR ($CDCl_3$, ppm) δ: 3.76 (s, 3H, OCH_3), 5.85, (s, 1H, ArCH), 6.68 (s, 2H), 6.91 (d, 2H, *J* = 8.2 Hz), 7.02 (t, 2H, *J* = 7.3 Hz), 7.16 (t, 2H, *J* = 7.3 Hz), 7.20 (m, 2H), 7.35–7.41 (m, 4H), 7.95 (br, 2H, NH).

3-((1H-Indol-3-yl)(pyridin-4-yl)methyl)-1H-indole (8)

Purification by plate chromatography, eluted with EtOAc – petroleum ether (1:1), gave brown solid; yield: 0.299 g

© 2007 NRC Canada

(92%); mp 161–163 °C (lit. 163–165 °C) (6*j*). ^{1}H NMR ($CDCl_3$, ppm) δ: 5.96 (s, 1H, ArCH), 6.67 (s, 2H), 7.08–7.15 (m, 4H), 7.36 (d, 2H, *J* = 8.1 Hz), 7.43 (d, 2H, *J* = 8.1 Hz), 7.37 (d, 2H, *J* = 7.9 Hz), 7.99 (br, 2H, NH), 8.34 (d, 2H, *J* = 7.9 Hz).

3-(Furan-2-yl(1*H*-indol-3-yl)methyl)-1*H*-indole (9)

Recrystallization from EtOAc – petroleum ether (1:1) gave brown solid; yield: 0.282 g (90%); mp > 300 °C (lit. >300 °C) (12). IR (KBr, cm^{-1}): 3410, 1712, 1450. ^{1}H NMR ($CDCl_3$, ppm) δ: 5.97 (s, 1H, ArCH), 6.90 (s, 2H), 7.08–7.43 (m, 11H), 8.00 (br, 2H, NH).

3-(1-(1*H*-Indol-3-yl)pentyl)-1*H*-indole (10)

Purification by plate chromatography, eluted with EtOAc – petroleum ether (1:2), gave colorless solid; yield: 0.256 g (85%); mp 80–82 °C (6*l*). IR (KBr, cm^{-1}): 3448, 3070, 2962, 1510. ^{1}H NMR ($CDCl_3$, ppm) δ: 0.91 (t, 3H, *J* = 6.8 Hz), 1.29 (m, 2H), 1.61 (m, 2H), 2.30 (m, 2H), 4.75 (t, 1H, *J* = 6.7 Hz), 6.89 (s, 2H), 7.05–7.13 (m, 4H), 7.28 (d, 2H, *J* = 7.9 Hz), 7.52 (d, 2H, *J* = 7.9 Hz), 7.91 (br, 2H, NH).

3-(1-(1*H*-Indol-3-yl)-1-phenylethyl)-1*H*-indole (11)

Purification by plate chromatography, eluted with EtOAc – petroleum ether (1:1), gave colorless solid; yield: 0.236 g (70%); mp 164–166 °C (lit. 165–167 °C) (11). IR (KBr, cm^{-1}): 3400, 3065, 2973, 1595. ^{1}H NMR ($CDCl_3$, ppm) δ: 2.41 (s, 3H, CH_3), 6.65 (s, 2H), 6.95 (t, 2H, *J* = 7.5 Hz), 7.16 (t, 2H, *J* = 7.5 Hz), 7.27–7.44 (m, 9H), 7.92 (br, 2H, NH).

3-(1-(1*H*-Indol-3-yl)cyclohexyl)-1*H*-indole (12)

Purification by plate chromatography, eluted with chloroform – petroleum ether (1:1), gave colorless solid; yield: 0.247 g (75%); mp 163–165 °C (11). IR (KBr, cm^{-1}): 3442, 3055, 2972, 1512. ^{1}H NMR ($CDCl_3$, ppm) δ: 1.61 (m, 2H), 1.69 (m, 4H), 2.54–2.57 (m, 4H), 6.91 (s, 2H), 7.05–7.12 (m, 4H), 7.34 (d, 2H, *J* = 7.8 Hz), 7.58 (d, 2H, *J* = 7.5 Hz), 7.94 (br, 2H, NH).

2-Methyl-3-((2-methyl-1*H*-indol-3-yl)(phenyl)methyl)-1*H*-indole (13)

Purification by plate chromatography, eluted with chloroform – petroleum ether (1/2), gave pink solid; yield: 0.319 g (91%); mp 245–247 °C (6*l*). IR (KBr, cm^{-1}): 3405, 3064, 1595, 1512. ^{1}H NMR ($CDCl_3$, ppm) δ: 2.05 (s, 6H), 5.88 (s, 1H, ArCH), 6.78–7.01 (m, 6H), 7.14–7.22 (m, 5H), 7.28–7.31 (m, 2H), 8.02 (br, 2H, NH).

2-Methyl-3-((2-methyl-1*H*-indol-3-yl)(4-nitrophenyl)methyl)-1*H*-indole (14)

Recrystallization from EtOAc – petroleum ether (1:1) gave yellow solid; yield: 0.364 g (92%); mp 241–243 °C (6*l*); IR (KBr, cm^{-1}): 3398, 3051, 1590, 1515. ^{1}H NMR ($CDCl_3$, ppm) δ: 2.13 (s, 6H), 5.96 (s, 1H), 6.71–6.96 (m, 6H), 7.21 (d, 2H, *J* = 8.0 Hz), 7.47 (d, 2H, *J* = 8.5 Hz), 8.03 (d, 2H, *J* = 8.5 Hz), 8.04 (br, 2H, NH).

2-Methyl-3-(1-(2-methyl-1*H*-indol-3-yl)cyclohexyl)-1*H*-indole (15)

Purification by plate chromatography, eluted with chloroform – petroleum ether (1:1) gave colorless solid; yield: 0.262 g (73%); mp 81–84 (6*l*). IR (KBr, cm^{-1}): 3450, 3043, 2981, 1515. ^{1}H NMR ($CDCl_3$, ppm) δ: 1.55 (d, 2H, *J* = 4.1 Hz), 1.73 (d, 4H, *J* = 4.0 Hz), 2.11 (s, 6H), 2.52–2.56 (m, 4H), 6.71–6.96 (m, 6H), 7.22 (d, 2H, *J* = 7.9 Hz), 7.98 (br, 2H, NH).

Acknowledgements

We gratefully acknowledge the support of this work by Persian Gulf University Research Councils.

References

1. K.W Lo, K.H.K. Tsang, W.K. Hui, and N. Zhu. Chem. Commun. 2704 (2003).
2. J.R. Plimmer, D.W. Gammon, and N.N. Ragsdale. Encyclopedia of agrochemicals. Vol. 3. John Wiley and Sons, New York. 2003.
3. A. Ramirez and S. Garcia-Rubio. Curr. Med. Chem. 1891 (2003).
4. S. Zhao, X. Liao, and J.M. Cook. Org. Lett. 687 (2002), and refs. cited therein.
5. B. Jiang, C.G. Yang, and J. Wang. J. Org. Chem. **67**, 1396 (2002).
6. (*a*) A. Kamal and A.A. Qureshi. Tetrahedron, **19**, 513 (1963); (*b*) G. Babu, N. Sridhar, and P.T. Perumal. Synth. Commun. **30**, 1609 (2000); (*c*) R. Nagarajan and P.T. Perumal. Tetrahedron, **58**, 1229 (2002); (*d*) B.P. Bandgar and K.A. Shaikh. J. Chem. Res. Synop. 34 (2004); (*e*) X.L. Mi, S.Z. Luo, J.Q. He, and J.P. Cheng. Tetrahedron Lett. **45**, 4567 (2004); (*f*) D. Chen, L. Yu, and P.G. Wang. Tetrahedron Lett. **37**, 4467 (1996); (*g*) M. Xia, S.B. Wang, and W.B. Yuan. Synth. Commun. **34**, 3175 (2004); (*h*) H. Koshima and W. Matsuaka. J. Heterocycl. Chem. **39**, 1089 (2002); (*i*) R. Nagarajan and P.T. Perumal. Synth. Commun. **32**, 105 (2002); (*j*) G.V.M. Sharma, J.J. Reddy, P.S. Lakshmi, and P.R. Krishna. Tetrahedron Lett. **45**, 7729 (2004); (*k*) H. Firouzabadi, N. Iranpoor, and A.A. Jafari. J. Mol. Catal. A: Chem. **244**, 168 (2006); (*l*) H. Firouzabadi, N. Iranpoor, M. Jafarpour, and A. Ghaderi. J. Mol. Cat. A: Chem. **253**, 249 (2006); (*m*) K. Tabatabaeian, M. Mamaghani, N. Mahmoodi, and A. Khorshidi. Can. J. Chem. **84**, 1541(2006); (*n*) M.L. Deb and P.J. Bhuyan. Tetrahedron Lett. **47**, 1441 (2006).
7. (*a*) D. Habibi, N. Mahmoodi, and O. Marvi. Can. J. Chem. **85**, 1 (2007); (*b*) K.A. Stephenson, S.R. Banerjee, N. McFarlane, D.R. Boreham, K.P. Maresca, J.W. Babich, J. Zubieta, and J.F. Valliant. Can. J. Chem. **83**, 2060 (2005); (*c*) K. Tanaka. Solvent-free organic synthesis. Wiley-VCH, GmbH and KGaA, Weinheim. 2004; (*d*) A. Loupy. Microwave in Organic synthesis. Wiley-VCH, Weinheim. 2004; (*e*) A. Zare, A. Hasaninejad, A. Khalafi-Nezhad, A.R. Moosavi Zare, A. Parhami, and G.R. Nejabat. Arkivoc, **i**, 58 (2007); (*f*) A. Khalafi-Nezhad, A. Zare, A. Parhami, M.N. Soltani Rad, and G.R. Nejabat. Phosphorus, Sulfur Silicon Relat. Elem. **182**, 657 (2007); (*g*) A. Hasaninejad and A. Zare. J. Sulfur Chem. In press; (*h*) A. Khalafi-Nezhad, A. Zare, A. Parhami, M.N. Soltani Rad, and G.R. Nejabat. Synth. Commun. **36**, 3549 (2006); (*i*) A. Khalafi-Nezhad, A. Zare, M.N. Soltani Rad, B. Mokhtari, and A. Parhami. Synthesis, 419 (2005).
8. (*a*) M. Chakrabarti and S. Sarkar. Tetrahedron Lett. **43**, 1351 (2002); (*b*) M. Chakrabarti, N. Gosh, R. Basak, and Y. Harigaya. Tetrahedron Lett. **43**, 4075 (2002).
9. (*a*) H. Sharghi and A.R. Hassani Nejad. J.Chem. Res. Synop. 87 (2003); (*b*) A. Hasaninejad and H. Sharghi. Phosphorus, Sulfur Silicon Relat. Elem. **182**, 873 (2007).

© 2007 NRC Canada

10. H. Firouzabadi, N. Iranpoor, B. Karimi, and H. Hazarkhani. Synlett, 263 (2000).
11. X. Zeng, S. Ji, and S. Wang. Tetrahedron, **61**, 10235 (2005).
12. S.J. Ji, M.F. Zhou, D.G. Gu, Z.Q. Jiang, and T.P. Loh. Eur. J. Org. Chem. 1584 (2004).
13. D.M. Du, S.M. Meng, Y.M. Wang, J.B. Meng, and X.Z. Zhou. Chin. J. Chem. **13**, 520 (1995).

© 2007 NRC Canada

Concerted rate-limiting proton transfer to sulfur with nucleophilic attack at phosphorus — A new proposed mechanism for hydrolytic decomposition of the P=S pesticide, Diazinon, in moderately acidic sulfuric acid media

Doreen Churchill, Julian M. Dust, and Erwin Buncel

Abstract: We report herein the first kinetic study of a P=S containing organophosphorus pesticide, Diazinon (**1**), in the moderately concentrated acid region. Product analyses (^{31}P NMR) show that reaction occurs only at the P centre. The rate-acidity profile (k_{obs} vs. molarity of H_2SO_4) appears as a curve in which the initial slight downward trace (molarity = 1 to ca. 5) is followed by sharper upward curve (molarity ca. 5 to 14). Using treatments involving the excess acidity (*X*) method, the A-1 and A-2 mechanistic possibilities were found to be inoperative over the full acidity range. A novel mechanism is proposed for the higher acidity (*X* ca. 2–6) region. This mechanism involves proton transfer to P=S from hydronium ion with concomitant proton transfer from water, which effectively delivers hydroxide to the P centre in a variant of the A-S_E2 process. A putative A-2 mechanism in this region is supplanted by the proposed A-S_E2 variant where the cyclic array results in proton transfer being efficiently coupled with nucleophilic attack involving water. This constitutes the first report of rate-limiting proton transfer at the P=S functionality in acid hydrolysis of this class of organophosphorus neutroxins. A 600 000-fold acceleration in the decomposition of Diazinon is associated with the change of medium from neutral aqueous solution to the most acidic medium studied (*X* ca. 6).

Key words: phosphorothioate ester hydrolysis, acid catalysis, rate-limiting proton transfer at P=S, excess acidity analysis, new A-S_E2 variant mechanism.

Résumé : Dans ce travail, on présente les résultats de la première étude cinétique d'un pesticide organophosphoreux contenant une liaison P=S, le Diazinon (**1**), dans la région acide modérément concentrée. L'analyse des produits (RMN du ^{31}P) montrent que la réaction ne se produit qu'au centre réactionnel comportant le P. Le profile de la réactivité en fonction de l'acidité (k_{obs} vs. molarité de H_2SO_4) s'apparente à une courbe dans laquelle la pente initiale légèrement vers le bas (molarité allant de 1 à environ 5) est suivie par une courbe beaucoup plus prononcée vers le haut (molarité allant d'environ 5 à 14). Utilisant des traitements impliquant la méthode de l'acidité en excès (*X*), on a trouvé que les possibilités mécanistiques A-1 et A-2 ne s'appliquent pas à l'ensemble de la plage d'acidité. On propose donc un nouveau mécanisme pour la région supérieure d'acidité (valeur de *X* d'environ 2 à 6). Ce mécanisme implique transfert de proton à la liaison P=S à partir de l'ion hydronium avec un transfert concomitant de proton de l'eau qui permet de transférer d'une façon efficace l'hydroxyde au centre P dans un processus apparenté au mécanisme A-S_E2. Un mécanisme putatif A-2 dans cette région est supplanté par la variante A-S_E2 proposée lorsque les arrangements cycliques conduisent à un transfert de proton couplé à une attaque nucléophile impliquant de l'eau. Ceci correspond au premier rapport d'un transfert de proton cinétiquement limitant au niveau de la fonctionnalité P=S dans l'hydrolyse acide de cette classe de neutroxines organophosphorées. La décomposition du diazinon est 600 000 fois plus rapide lorsqu'on passe d'un milieu impliquant une solution aqueuse neutre au milieu plus acide étudié (*X* d'environ 6).

Mots-clés : hydrolyse d'esters phosphorothioates, catalyse acide, transfert de proton cinétiquement limitant au P=S, analyse par excès d'acidité, mécanisme nouveau, une variante du mécanisme A-S_E2.

[Traduit par la Rédaction]

Received 26 February 2007. Accepted 12 April 2007. Published on the NRC Research Press Web site at canjchem.nrc.ca on 8 June 2007.

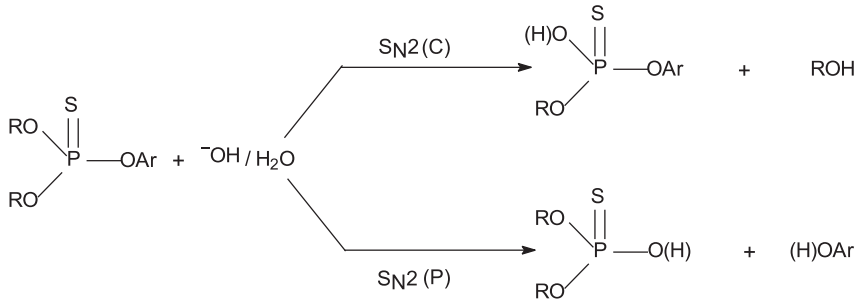
This article is dedicated to the memory of Keith Yates, a good friend, who masterfully changed physical organic chemistry.

D. Churchill[1] and E. Buncel.[2] Department of Chemistry, Queen's University, Kingston, ON K7L 3N6, Canada.
J.M. Dust. Departments of Chemistry and Environmental Science, SWGC, Corner Brook, NL A2H 6P9, Canada.

[1]Present address: Centre of Environmental Excellence, c/o Sir Wilfred Grenfell College (SWGC), Corner Brook, NL A2H 6P9, Canada.
[2]Corresponding author (e-mail: buncele@chem.queensu.ca).

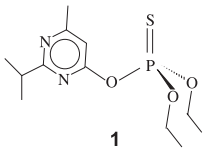
 doi:10.1139/V07-049 © 2007 NRC Canada

Scheme 1. Major reaction pathways of organophosphorothioate insecticides, where the protons in parentheses may or may not be present depending on the acidity of the medium.



Introduction

Diazinon (**1**) is a member of a class of organophosphorothioate insecticides whose mechanism of action is acetylcholinesterase inhibition (1). In principle, such esters may exhibit two main pathways of reaction in neutral or alkaline aqueous solution, as shown in Scheme 1, where hydroxide is taken to be the dominant nucleophilic species under alkaline environmental conditions (2, 3). As shown, the dichotomy of attack involves C or P centres. On the aliphatic carbons (R = CH_3 or CH_2CH_3, typically) an S_N2(C) displacement occurs to give the corresponding organophosphorothioate anion and the alcohol. Attack at phosphorus in a presumably S_N2(P) mechanism (4) produces the aryloxide as a leaving group and the organophosphorothioic acid or its conjugate base (Scheme 1).



1

We, among other groups (5–7), have been engaged in the study of the degradation pathways and reactivities of a number of organophosphorus neurotoxins. In the case of fenitrothion (Scheme 1, R = CH_3, Ar = 3-methyl-4-nitrophenyl) with alkali metal ethoxides in ethanol, we dissected the pathways and found that S_N2(P) was dominant, S_N2(C) also contributed significantly, while the S_NAr attack on the aromatic ring constituted ca. 7% of the reaction (8). More recently (9), the regioselectivity of nucleophilic attack on fenitrothion was used to infer the location and orientation of fenitrothion in cationic micellar (9*a*) α-nucleophilic (9, 10) systems. These studies have highlighted the importance of the medium on pathways of reaction for these neurotoxins.

The research on Diazinon **1** (Scheme 1, R = CH_2CH_3, Ar = 2-isopropyl-6-methyl-pyrimidin-4-yl) for the most part has involved environmental studies, as it is an insecticide that has been applied for agricultural, silvicultural, and horticultural control of various insects (11). Most of these studies have focused on the half-life for disappearance of this insecticide in nonsterilized natural waters at various temperatures. Product analyses have emphasized biological breakdown rather than abiotic hydrolysis. In summary, few studies have examined the hydrolysis of **1** to fully elucidate reaction pathways of degradation in pure sterile water. However, a study by Ku et al. (12) involved the analysis of the products arising from hydrolysis under the pH range 2 to 9 and found 2-isopropyl-6-methylpyrimidin-4-ol (**2**) and *O*,*O*-dimethylphosphorothioate (or its conjugate acid) (**3**) as the only products.

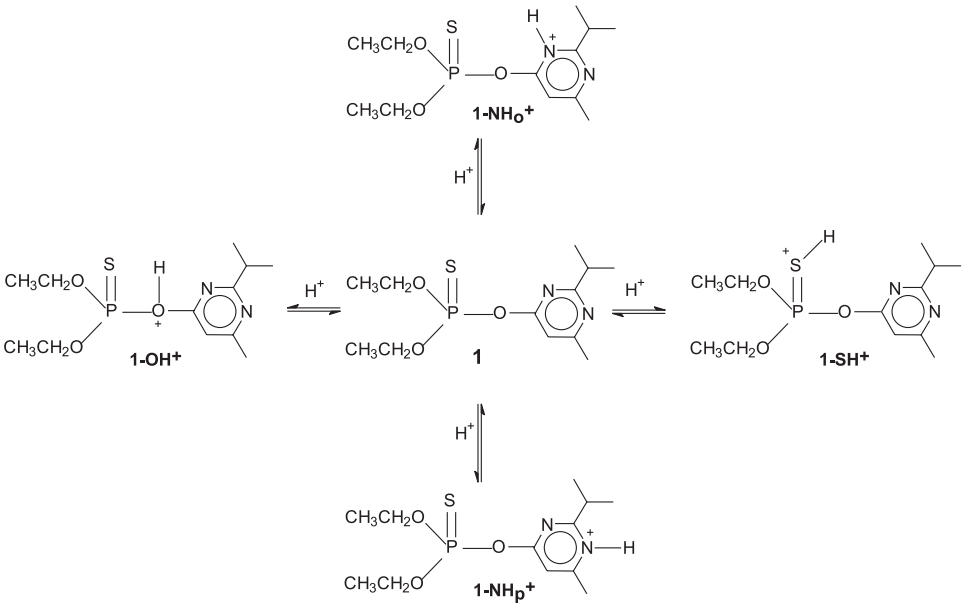
One theme of our program of research has been the effect of reaction media on the reactivity and pathways of organic substrates (13), while the effect of acidic media (e.g., moderately concentrated sulfuric acid solutions) form a sub-theme (14). A third area of study in our group is environmental chemistry and the study of pesticide decomposition mechanisms (8, 9, 15). Our study of Diazinon **1** falls under this rubric. Our initial finding of a rate increase in the low pH region (16*a*) has now led to a study of the behaviour of **1** over a wide range of sulfuric acid solutions (H_2SO4 1–14 mol/L). Unlike previous work on organophosphorothioate ester degradation in alkaline media, the much weaker nucleophile H_2O will operate here. In this regard, attack at the aliphatic carbon could become more favourable here, since H_2O, as a softer nucleophile, would be expected to prefer attack at the softer carbon site (17).

In acidic media, the potential for catalysis would open up new and potentially faster pathways for decomposition. We note that the practical utility of acid hydrolysis of Diazinon formulations (that may also contain other bioactive agents) was examined by Dennis et al. (18) and emphasized the need for a mechanistic evaluation of such acidic systems. Scheme 2 highlights the multiplicity of protonation sites. Protonation of **1** on the aryloxy oxygen, giving rise to **1**-OH^+, would enhance the reaction by providing a better leaving group following the attack at phosphorus. Alternatively, protonation of the ring nitrogens of the pyrimidinyl moiety of **1** to give **1**-NH_o^+ or **1**-NH_p^+ would also produce a better leaving group and so may enhance the reaction. Protonation at P=S to give **1**-SH^+ would increase P electrophilicity, enhancing the attack by nucleophiles at phosphorus. Catalysis in moderately acidic media could be due to any one of these protonations or through the interplay of several simultaneously.

In this paper we report the acidity-rate constant profile for **1** in 1–14 mol/L sulfuric acid. The results will be discussed in terms of the excess acidity analysis, modes of acid catalysis, and potential mechanistic changeover (19, 20). The interesting rate-excess acidity profile has led us to propose a new variant of the A-S_E2 mechanism in the higher acidity medium in which rate-limiting proton transfer to the sulfur

© 2007 NRC Canada

Scheme 2. Protonation pathways of Diazinon.



of the P=S ester bond may occur in a concerted fashion with nucleophilic attack on the phosphorus centre.

Experimental

Materials and instruments

Common solvents and reagents (e.g., 95%–98% H_2SO_4, 99.8% D_2O, 85% H_3PO_4, and dimethyl sulfoxide-d_6) were purchased in the highest purity available and used without further treatment. Diazinon **1** was either obtained from Chem Services Inc. (99.5%) and used as obtained or synthesized as outlined later. *O*,*O*-diethylphosphorothioic acid **3** and triethyl thiophosphate were prepared in our laboratories and purified prior to use by column chromatography as described previously (16). Other reagents were purchased commercially but purified before use (vide infra).

Routine NMR spectra were recorded using a Bruker 300 MHz Avance spectrometer. For NMR spectrometric product analyses or kinetic studies, a Bruker 500 MHz Avance instrument was used. Melting points were determined on a Thomas-Hoover melting point apparatus and are uncorrected. For UV–vis spectrophotometric measurements and for kinetic runs, the following instruments were used: Varian CARY 3, Hewlett-Packard 8452A, or PerkinElmer Lambda-20. Temperature was maintained at 25 °C with a Peltier effect device in the case of the CARY 3 or with a circulating water bath in the case of the other spectrophotometers.

Diazinon (1)

Synthesis

Diazinon was synthesized by a method modified from Gysin and Margot (21). First, a weighed quantity of **2** (5.0 g; 0.033 mol) was reacted with KOH (1.9 g; 0.034 mol) in hot absolute ethanol to generate the potassium salt of **2**. Excess ethanol was removed at reduced pressure (rotovap), and then benzene (70 mL) was added. The solution was distilled to azeotropically remove water; residual benzene was removed using a rotovap. Dry acetone (100 mL) was then added. To this solution was added diethyl chlorothiophosphate (6.20 mL; 0.039 mol), and the mixture was heated at ~35 °C for 2 days under nitrogen. The solution was cooled and filtered through Celite® to remove KCl. The solvent was distilled from the filtrate (rotovap) to give an oil that was purified by column chromatography using methylene chloride as eluent. Two fractions were recovered, the starting material and crude **1**. When dried, the crude **1** was found to contain a white solid impurity (possibly unmodified **2**). The crude sample was dissolved in hexanes (40 mL) and purified by extraction with H_2O (4 × 20 mL). The hexanes layer was dried with anhydr. $MgSO_4$ and filtered to remove the drying agent. The solvent was removed using a rotovap and dried further overnight under reduced pressure and at ambient temperature. The final product was obtained in 50% yield and its purity was verified by ^1H, ^{31}P, and ^{13}C NMR (*J*-modulated and DEPT) spectroscopy. All spectra were consistent with that of Diazinon and contained no peaks ascribable to impurities. ^1H NMR ($CDCl_3$, ppm) δ: 6.64 (s), 4.33 (d of q, $J_{H\text{-}H}$ = 7.1 Hz, $J_{H\text{-}P}$ = 11.2 Hz), 3.10 (sept, $J_{H\text{-}Hf}$ = 6.9 Hz), 2.47(s), 1.37 (t, $J_{H\text{-}H}$ = 7.1 Hz) and 1.30 (d, $J_{H\text{-}H}$ = 6.9 Hz). ^{31}P NMR δ: 61.5 (s). ^{13}C NMR δ: 176 (s), 170 (s), 165 (d, $J_{C\text{-}P}$ = 4.6 Hz), 107 (d, $J_{C\text{-}P}$ = 6.4 Hz), 65.6 (d, $J_{C\text{-}P}$ = 5.1 Hz), 37.7 (s), 24.5 (s), 21.8 (s), 16.2 (d, $J_{C\text{-}P}$ = 8.0 Hz).

*p**K**a Values for the conjugate acids of 1 (1-NH$_p^+$, 1-NH$_o^+$, 1-SH$^+$) and models*

Attempts were made to determine pK_a values for the conjugate acids of Diazinon (Scheme 2, **1**-NH_p^+, **1**-NH_o^+, **1**-SH^+) and of 2-isopropyl-6-methyl-4-pyrimidinol **2** using ^1H (side chain and ring protons), ^{31}P NMR, as well as UV–vis spectrophotometric measurements (λ = 230, 254, and 260 nm). Generally, the methods yielded the same average values for the macroscopic acidity constants. These determinations involved recording spectra of **1** in a series of H_2SO_4 solutions (1–18 or 1–14 mol/L), and relevant chemical shifts

© 2007 NRC Canada

(or λ_{max} values) were plotted against the $-H_0$ acidity function for the acid solutions; H_0 is anchored to the aqueous pH scale. From these titration curves (fitted using the Origin® 7.0 program) the macroscopic pK_a value for **1**-NH_p^+ and (or) **1**-NH_o^+ (= 2.40) was determined and found to be similar to that for the same site in the product 2-isopropyl-6-methyl-4-pyrimidinol measured in the same way (i.e., pK_a = 2.84), which is also similar to that reported for the same site in 2,6-dimethyl-4-pyrimidinol (3.06) (22). These studies also set a limit for the pK_a ascribable to diprotonation at –7.3; higher acidity solutions led to the rapid decomposition of **1** and precluded a more precise assessment. A comparable ^{31}P NMR titration of *O*,*O*-diethyl phosphorothioic acid **3** yields a value for pK_a of the conjugate acid (S-site) of –5.14.

Purification of solvents and reagents and preparation of stock solutions

2-Isopropyl-6-methyl-4-pyrimidinol (2)

Commercial **2** (Sigma-Aldrich, 99%) was recrystallized from either acetone or ethanol to remove a fine black solid impurity. Melting point 172–173.5 °C (lit. value 172–175 °C (23)). The ^{1}H NMR spectrum (300 MHz) contained no extraneous peaks; (D_2O, ppm) δ: 6.09 (s, 1H, ring H-3), 4.72 (sept, 1H, *J* = 7.0 Hz, CH of 2-isopropyl), 2.19 (s, 2H, 6-CH_3), 1.19 (d, 6H, *J* = 7.0 Hz, CH_3 of 2-isopropyl). Exchange of the OH proton with solvent precludes its observation.

Stock solutions

In general, all stock solutions were prepared in volumetric flasks sealed with rubber septa or, alternatively, with a glass stopper and Parafilm®. Aqueous solutions were prepared with distilled, deionized, and degassed water (9). All stock solutions were stored in a refrigerator.

Sulfuric acid solutions

In each case, the calculated required amount of purified water was first transferred to the volumetric flask, and then the H_2SO_4 solutions were made up by mass. In general, the flasks were cooled in an ice bath and the calculated amount of concentrated (ca. 98%) H_2SO_4 was weighed and slowly added. The acid solutions were titrated against NaOH that had been standardized against anhydrous potassium hydrogen phthalate.

Diazinon (1)

An aliquot (15 μL) of **1** was dissolved in purified 1,4-dioxane (5 mL) to give the stock solution (1.10×10^{-2} mol/L). The 1,4-dioxane was purified prior to use by standard methods (24) and stored until use under nitrogen at low temperature (ca. –10 °C, freezer).

UV–vis spectrophotometric kinetic studies of the decomposition of 1 in acidic media

All kinetic runs were carried out under pseudo first-order conditions with the concentration of acid in large excess relative to Diazinon **1**. For experiments that used the stock solution of **1** in 1,4-dioxane, an aliquot (20 μL) of the stock solution was injected (via 25 μL gas-tight syringe) into the quartz UV cuvettes containing the sulfuric acid solution (2.50 mL added by pipette) with an initial (time = 0) concentration of **1** of 8.73×10^{-5} mol/L. The monitoring of this reaction solution spectrophotometrically revealed two processes, an initial fast process followed by a slow one; these were ascribed, respectively, to decomposition of the dioxane and of the substrate **1**. The rate data, however, could be readily dissected to yield the separate rate constants (25). The latter were validated by preparation of reaction solutions (in large volume) free of dioxane and the kinetic results here showed good agreement with those for the slower process.

In either case the rate of appearance of product **2** was followed at 230 nm, the approximate wavelength of maximum absorbance for **2** (or protonated derivatives), under acidic conditions (increased to 234 nm at higher acid concentrations). Reactions were monitored for at least three half-lives and the absorbance at infinite time (A_∞) noted at 10 $t_{1/2}$. Plots of $\log(A_\infty - A_t)$ vs. *t*, using suitable spectrophotometric data as described earlier for systems in which dioxane was present, afforded the pseudo first-order rate constants k_{obs} reported herein.

^{31}P NMR spectrometric studies of the decomposition of 1 in acidic media

Kinetic studies

The reaction was initiated by addition of 4 μL of Diazinon (no solvent) to 1 mL of sulfuric acid solution (4.9–9.5 mol/L) in an NMR tube containing a sealed capillary tube that contained either 5% (*v*/*v*) trimethyl phosphate in DMSO-d_6 or 20% (*v*/*v*) 85% phosphoric acid in D_2O; these capillaries served as external chemical shift standards and supplied the needed lock signal. Spectrometric parameters were optimized (e.g., suitable relaxation delays are given in ref. 26) as previously reported (9). After placement of the tube in the probe of the NMR (at 25 °C), spectra were acquired at regular intervals and the rate constant determined on the basis of the integral of the ^{31}P NMR signal for Diazinon and that of the product signal (normalized versus trimethyl phosphate or phosphoric acid). The plot of natural log (signal area) vs. time yielded the rate constant k_{obs} according to a first-order treatment,

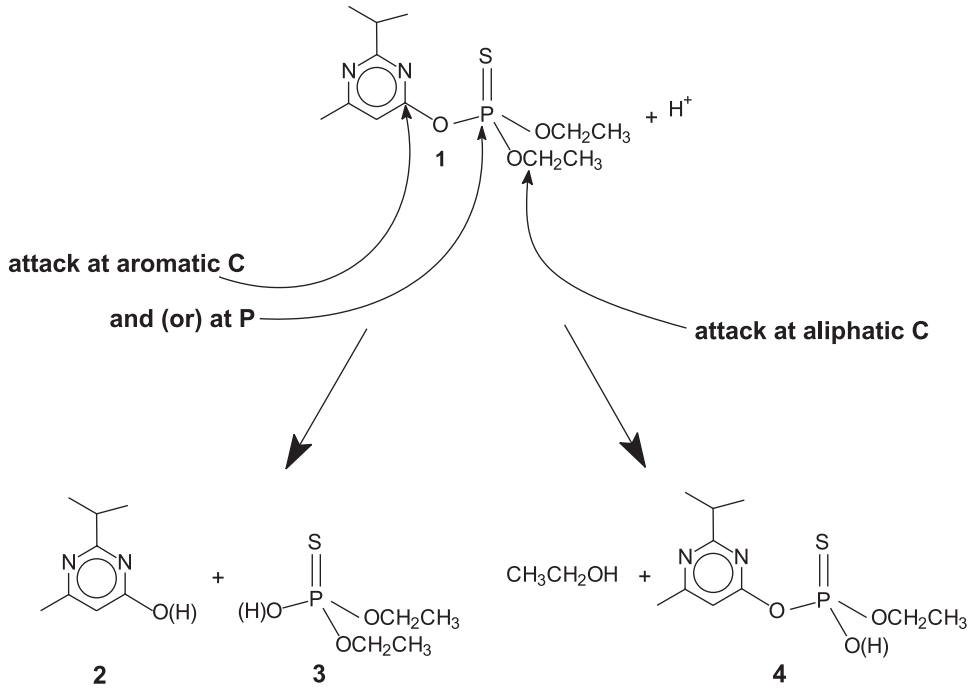
$$[1] \quad \ln(\text{Integral } \mathbf{1}_{initial} - \text{Integral } \mathbf{2}_{time}) = -k_{obs}t + \text{constant}$$

Product analysis

NMR tubes were prepared as outlined for the kinetic experiments. Each tube contained a concentration of sulfuric acid (ranging from 1 to 17 mol/L). The reaction was initiated by injection of 4 μL of **1**. The lower acidity tubes (1–13 mol/L) were set aside to permit reaction for 48 h, while the reaction was allowed for 20 min for the higher acidity (14–17 mol/L) samples. Once the reaction was deemed complete, a ^{31}P NMR spectrum was obtained. Only one product peak was observed; its identity was confirmed as *O*,*O*-diethylphosphorothioic acid **3** through spiking the tubes with authentic compound and re-recording the ^{31}P spectrum.

© 2007 NRC Canada

Scheme 3. Pathways of Diazinon hydrolysis under acidic conditions, where attack at aromatic carbon and (or) phosphorus contrasts with attack at aliphatic carbon.



Results

Acid-catalyzed hydrolysis of Diazinon 1 — UV–vis kinetic study.

Rate data for the hydrolysis of Diazinon in 1–14 mol/L H_2SO_4 solutions were determined spectrophotometrically by following the production of the pyrimidinol leaving group **2** (Scheme 3). The observed rate constants k_{obs} at 25 °C were calculated through application of eq. [2],

$$[2] \qquad \log (A_\infty - A_t) = -k_{obs}t + \text{constant}$$

where A_t is the absorbance at time t and A_∞ at infinite time (i.e., 10 $t_{1/2}$). The pseudo first-order rate constants for the decomposition of **1** at each sulfuric acid concentration and corresponding excess acidity X are given in Table 1.

^{31}P NMR study — Kinetics and product identification.

The reaction was also studied by ^{31}P NMR spectrometry, a method that provides simultaneous rate and product identification data. The pseudo first-order rate constants k_{obs}, in the H_2SO_4 range 4.9–9.5 mol/L, were calculated from the integration of the peak area of **1** or its P-containing product according to eq. [1] (see Experimental section).

The rate data obtained from ^{31}P NMR spectrometry (Table 1) were in good agreement with results using UV–vis spectrophotometry. ^{31}P NMR spectrometry also demonstrated that the only phosphorus-containing product of Diazinon hydrolysis is *O*,*O*-diethylphosphorothioic acid **3** (Scheme 3).

Table 1. Kinetic data for the acid-catalyzed hydrolysis of Diazinon in H_2SO_4 solutions at 25 °C.

$[H_2SO_4]$ (mol/L)	X^a	k_{obs} ($\times 10^{-4}$ s^{-1})^b	$t_{1/2}$ (min)
1.03[c]	0.22	0.686±0.007	168
2.26[d]	0.56	0.349±0.001	331
3.51[c]	0.96	0.174±0.006	663
3.63[d]	1.01	0.170±0.006	676
4.92[e]	—	0.152±0.008	760
4.99[c]	1.51	0.164±0.003	704
5.23[d]	1.60	0.156±0.006	736
6.50[c]	2.10	0.337±0.001	343
6.67[e]	—	0.320±0.016	361
6.85[c]	2.24	0.334±0.007	349
7.64[c]	2.57	0.558±0.001	207
7.64[e]	2.57	0.536±0.027	216
8.43[e]	—	1.04±0.05	111
8.57[c]	2.97	1.05±0.01	110
9.48[c]	3.39	2.15±0.01	53.7
9.48[e]	3.39	2.30±0.12	50.2
10.8[c]	4.07	4.89±0.03	23.6
11.7[c]	4.59	18.2±0.2	6.35
12.9[c]	5.35	90.6±0.70	1.28
13.9[c]	6.03	615±14	0.19 (11 s)

Discussion

Overview

The rate constants determined for the decomposition of **1** in moderately acidic media (Table 1, UV–vis determinations) were plotted as k_{obs} vs. the concentration of sulfuric acid (mol/L) (Fig. 1) and also plotted as log k_{obs} vs. the excess acidity function X, as the appropriate measure of the acidity of the medium (19, 27, 28) (Fig. 2). While the full scale plot in Fig. 1 (1 – ca. 14 mol/L) appears almost flat until about 11 mol/L where the curve swings upward, an enlargement (Fig. 1 inset) of the lower acidity region (1–8 mol/L) more clearly shows the initial decline in rate with

© 2007 NRC Canada

Fig. 1. Plot of pseudo first-order rate constants k_{obs} vs. sulfuric acid concentration (mol/L) for the hydrolysis of **1**. The enlarged inset of the concentration region from ca. 1 to 8 mol/L shows the initial decline and subsequent rise in reactivity with sulfuric acid concentration.

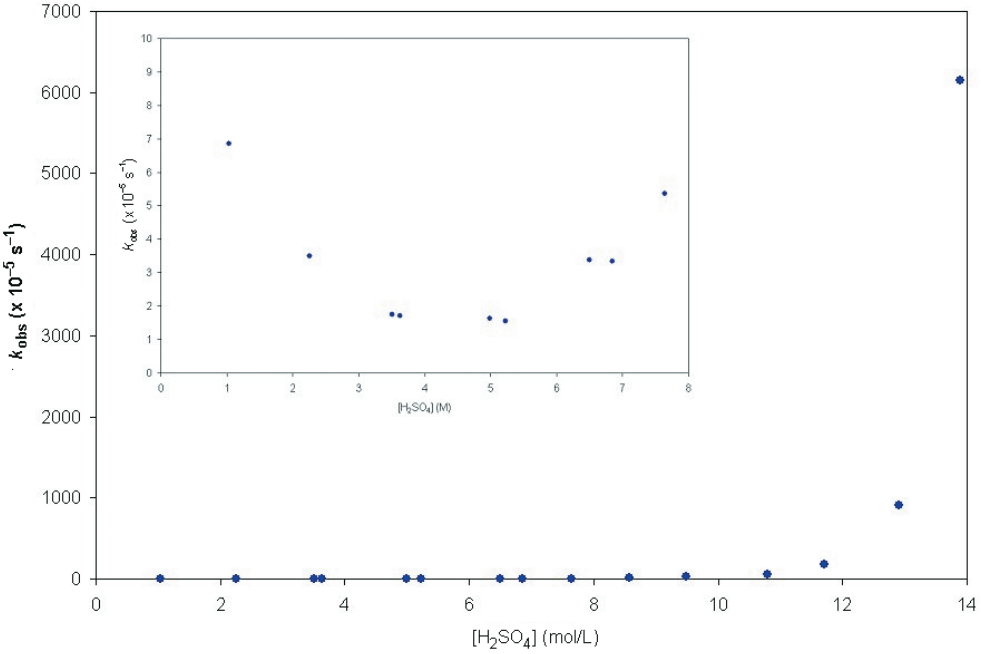
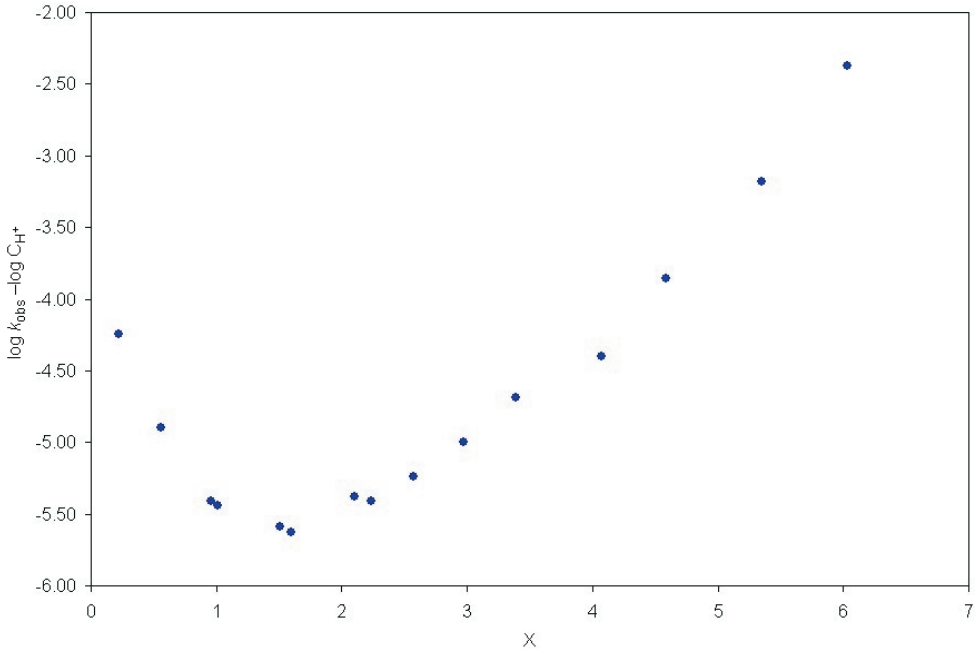


Fig. 2. Rate-excess acidity plot (log k_{obs} – log concentration of H^+ vs. X) for the hydrolysis of **1**.



increasing sulfuric acid concentration (1–5 mol/L), with the sharper increase commencing at a concentration of about 5 mol/L. The profile in Fig. 2 highlights this interesting initial decline in rate with increasing sulfuric acid concentration (X = 0–1.6). Note, however, that even the lowest reaction rate determined (k_{obs} = 1.52 × 10^{-5} s^{-1} corresponding to X ~ 1.6) is 150-fold greater than the rate previously reported at pH 7.0 (k_{obs} = 1 × 10^{-7} s^{-1} (29)). From X = 1.6 onward, the rate rises more steeply; a rate constant of 6.15 × 10^{-2} s^{-1} is attained at X ~ 6, the most acidic solution studied (13.9 mol/L H_2SO_4), i.e., an acceleration of the rate of decomposition by a factor of 600 000 as compared with that found at pH 7.0. These results, and especially the initial decline in rate constant with acidity and later steep rise in reactivity, suggest the intervention of more than one mechanism over this acid range.

As noted earlier, Diazinon contains several sites for potential protonation and these are identified in Scheme 2 as **1**-OH^+, **1**-SH^+, and **1**-NH_o^+ and **1**-NH_p^+ for the ortho- and para-nitrogens, respectively. By considering suitable model

© 2007 NRC Canada

compounds (e.g., pyrimidinol derivatives (30)), protonation of one of the ring nitrogens would plausibly be expected for monoprotonation. It is then also plausible to expect the formation of **1**-NH_p^+ to be favoured over the formation of the isomeric **1**-NH_o^+. (Also see the Experimental section where NMR and spectrophotometric titrations yielded a macroscopic pK_a of 2.40 for **1**-NH_p^+ and **1**-NH_o^+ and a limiting composite pK_a of –7.3 for diprotonation). Henceforth, therefore, in the acid media examined, **1**-NH_p^+ is taken as the starting species for further reaction.

Reaction pathways

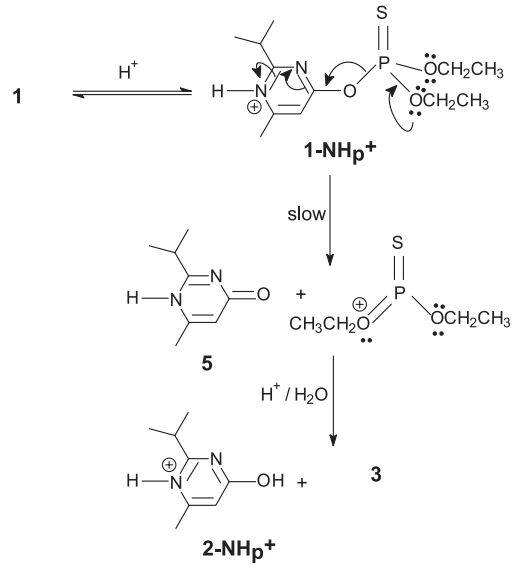
For the hydrolysis of Diazinon, three possible reaction sites can be envisioned; these include an attack at phosphorus as well as an attack at carbon, as outlined in Scheme 3. Attack at the aliphatic carbon of **1** would produce ethanol and de-ethyl Diazinon (**4**) as products; however, ^{31}P NMR spectrometry did not detect any **4**, and hence this pathway will not be considered further. This leaves the possibilities of attack at the aromatic carbon and (or) at phosphorus.

Considering first the S_NAr pathway, we note that generally two or more strongly electron-withdrawing substituents, such as nitro groups in the aromatic ring, are required for this route to be favoured. For example, in the case of the reaction of methyl 2,4-dinitrophenyl phosphate monoanion with amines, where nucleophilic attack at phosphorus is electrostatically suppressed, the reaction follows the S_NAr path (31). Differences in the reactivity of comparable P=S esters, as compared with this P=O example, would be expected to have little effect on this result (32). In contrast, with fenitrothion (Scheme 1, R = CH_3, Ar = 3-methyl-4-nitrophenyl) reacting with ethoxide, where the aryl ring of the leaving group is activated with only a single nitro group and where P-attack is not suppressed, ethanolysis via S_NAr occurs to a small (ca. 7%) extent, and P-attack is the dominant route (8). Thus, considering that a ring nitrogen is normally less effective in promoting S_NAr displacement compared with NO_2 (33), albeit recognizing that an unprotonated N is less activating than protonated N, it is reasonable to conclude that the reaction of Diazinon should proceed preferentially via P-attack rather than by S_NAr. Further discussion will, therefore, focus on reaction of **1** at the P-site.

Mechanisms of acid catalysis

In acidic media, reactions are most commonly catalyzed via mechanisms classified according to types A-1, A-2, or A-S_E2 (19, 27, 28*a*, 34–36). An A-1 process involves a unimolecular rate-determining step, where fast equilibrium protonation of the substrate S results in the formation of a reactive intermediate SH^+. In the current system, protonation facilitates the departure of the leaving group and SH^+ decomposes unimolecularly, and so here the A-1 pathway would involve the unimolecular breakdown of **1**-NH_p^+ with the formation of a metaphosphate-like intermediate, stabilized by resonance, that reacts further with water to give **3** (Scheme 4). On the other hand, in the A-2 mechanism fast equilibrium protonation of the substrate enhances the attack

Scheme 4. A-1 type mechanism for hydrolysis of Diazinon.



of a nucleophile in the bimolecular rate-determining step. Here, the rate-determining attack of water on the monoprotonated substrate 1-NH_p^+ with concomitant P–O bond scission leads to a protonated form **3**-H^+ that equilibrates to give **3** as the final product (Scheme 5). In contrast, *rate-limiting protonation* leading to the SH^+ intermediate that then decomposes in a separate fast step comprises the A-S_E2 pathway. A variant of this mechanism is proposed below.

The excess acidity treatment affords insight into the mechanistic pathways of acid catalysis.

A-1 process

For an A-1 mechanism (Scheme 4), the appropriate excess acidity relationship is expressed in eq. [3], where it is assumed that any diprotonation over the range of H_2SO_4 studied will be negligible (19),

$$[3] \qquad \log k_{obs} - \log C_{H^+} = \log[k/K_{SH_2^{++}}] + m^{\ddagger}m^{*}X$$

However, as Fig. S4 (Supplementary material) shows, the resultant plot, instead of being linear with positive slope, displays strong curvature with a broad minimum (at values of *X* between 1 and 2), thus ruling out this mechanism as the sole process involved in the current system throughout the range of acidity studied.[3] The plot could be described as a "broad upward parabola".

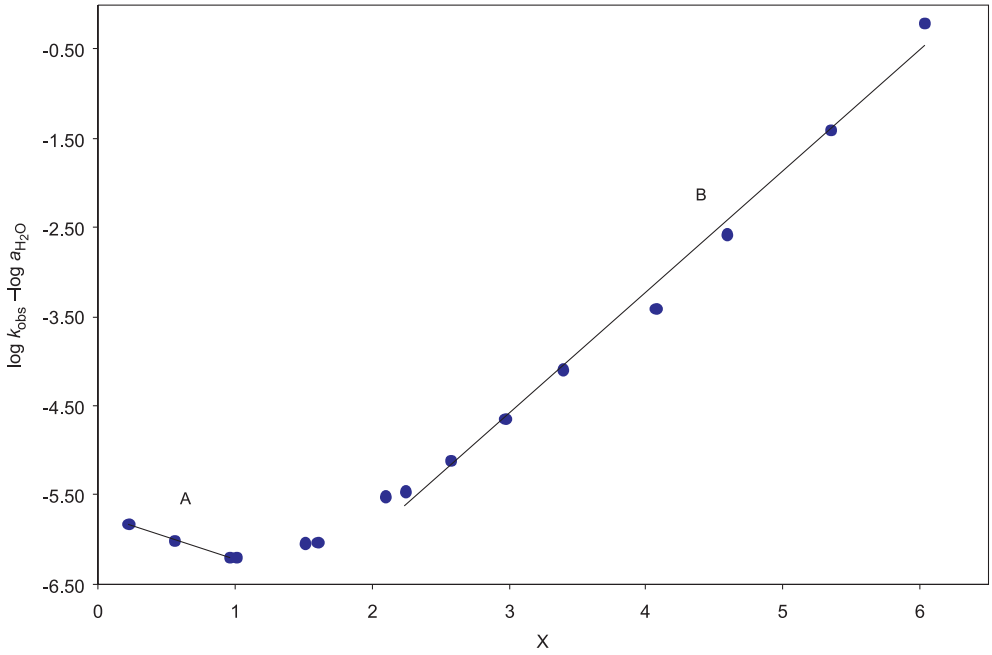
A-2 process

A-2 mechanistic types have been observed in a number of systems involving phosphorus-containing substrates (36–38). In an A-2 process one or more molecules of water may be involved in a rate-determining step that occurs after rapid equilibrium protonation of the substrate (19). Scheme 5 shows the case where a single molecule of water acts as nucleophile. For an A-2 mechanism, any general excess acidity plot (i.e., one obtained from an equation similar to eq. [3]) should yield a downward arc that achieves a maxi-

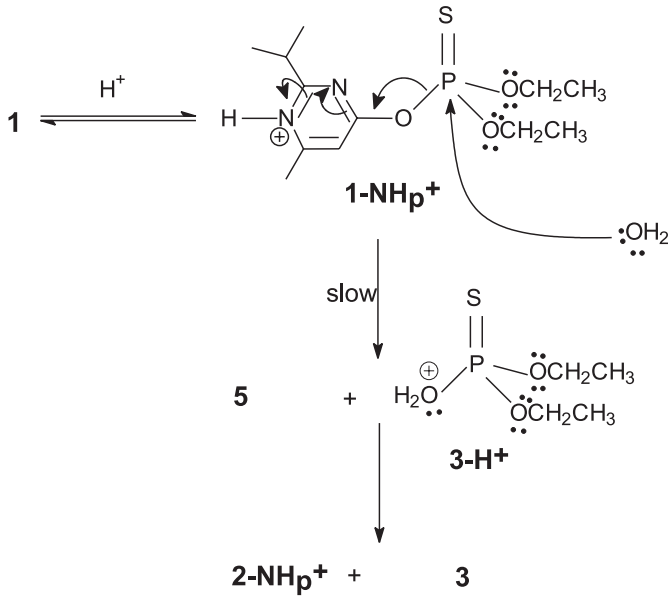
[3] Supplementary data for this article are available on the journal Web site (http://canjchem.nrc.ca) or may be purchased from the Depository of Unpublished Data, Document Delivery, CISTI, National Research Council Canada, Ottawa, ON K1A 0R6, Canada. DUD 5175.

© 2007 NRC Canada

Fig. 3. Rate-excess acidity plot for the hydrolysis of **1** showing a possible mechanistic switch from an A-2 process (line A) at lower X values to an A-1 (or A-S_E2 variant) process (line B) at higher X values. The equations of the lines are given in the text.



Scheme 5. A-2 type mechanism for hydrolysis of Diazinon.



mum near the point where the acidity of the medium would have fully converted the substrate to its protonated form. The decrease in rate that occurs with increasing acidity reflects the decreasing activity of water (a_{H_2O}) at higher acid concentrations.

The kinetic data were treated using eq [4], which involves one water as nucleophile (i.e., Nu = H_2O), and eq. [5], which involves two waters, neither of which however, yielded linear plots (Figs. S5 and S6; see Supplemental Data).[3]

$$[4] \quad \log k_{obs} - \log C_{H^+} - \log a_{Nu} = \log[k/K_{SH_2^{++}}] + m^{\ddagger}m^{*}X$$

$$[5] \quad \log k_{obs} - \log C_{H^+} - 2\log a_{Nu} = \log[k/K_{SH_2^{++}}] + m^{\ddagger}m^{*}X$$

However, even though the entire data do not fit either a single A-1 or A-2 mechanism, it is plausible that there is a change in mechanism when the plot switches from a decrease in rate with increasing acid concentration to an increase in rate with increasing acid concentration.

Switch from an A-2 to an A-1 process

Based on the pK_a values found for Diazinon (2.40 for **1**-NH_p^+ and **1**-NH_o^+ and –7.3 as a limit for diprotonation), it was presumed (vide supra) that Diazinon was protonated at all values of X studied and that **1**-NH_p^+ was, therefore, the starting species for any further discussion. It follows then, that instead of finding a full downward arc, as expected for an A-2 process, the region of the rate-excess acidity profile bounded by $X = 0$ to about $X = 2$ represents the portion of the expected A-2 process where the rate declines as a function of the decreasing amount of free water present. In effect, the expected A-2 arc is truncated so that only the downward portion is seen. An empirical straight line, using one molecule of water as the simplest case (Fig. 3), was fit to the data ($X = 0$ to ca. 1), and for the limited number of points involved the fit is good ($r^2 = 0.998$). The equation of the line is,

$$[6] \quad \log k_{obs} - \log a_{H_2O} = -0.493X - 5.721$$

Similarly, the region defined by $X = 2$ to about 6 yields an empirical straight line treatment (Fig. 3) where the fit is also good ($r^2 = 0.992$) and the equation of the line is,

$$[7] \quad \log k_{obs} - \log a_{H_2O} = 1.366X - 8.688$$

This second line could represent an A-1 mechanism, and therefore overall there would be a switch from an A-2 to an A-1 type mechanism. Such changeovers are far from unprec-

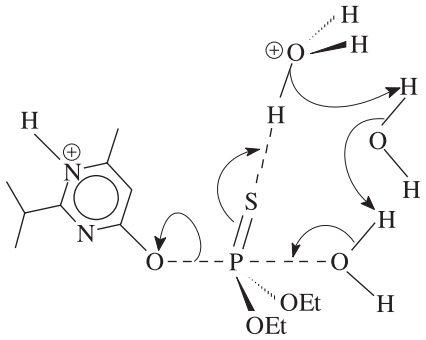
© 2007 NRC Canada

edented and are found for a number of esters, thiobenzoate, and thionobenzoate esters, among other systems (19, 27). However, there is a paucity of examples of acid catalysis of the breakdown of P=S pesticides with structures clearly analogous to **1** (36) in the higher acidity (*X* ca. 2–6) region, and hence, comparison to related systems cannot be made. Moreover, it is difficult to envisage the mechanism of A-1 *catalysis* with increasing acidity, since with **1** the initial N-protonation of the ring is already complete in the dilute acid region. In short, while it is apparent that the A-2 mechanism should become less effective as the concentration of free water declines, it is not apparent that the A-1 mechanism should lead to catalysis as the acidity of the medium increases.

A concerted rate-limiting proton transfer to S with nucleophilic attack at P — An A-S_E2 variant mechanism

An essential part of the reactivity of Diazinon must be associated with the P=S moiety (32). However, it is noteworthy that neither the A-2 nor A-1 mechanisms involve protonation of P=S, even though these mechanisms do not explain the kinetic behaviour throughout the full acidity range.

As a variant of the A-S_E2 class, a mechanism can be proposed where rate-limiting proton transfer to the P=S function occurs in a cyclic array involving hydronium ion as proton donor to S but as proton acceptor from water, which effectively delivers hydroxide to P. A transition state structure for this A-S_E2 variant mechanism is illustrated in structure **6**, where the dotted lines indicate partial bond formation and rupture. In this structure, a bridging water molecule is included as has often been found in such acid-catalysed hydrolyses.[4] To our knowledge, this would be the first instance in which rate-limiting proton transfer to S in a molecule containing the P=S functionality has been proposed.



6

On the other hand, a comparison can be made with the pertinent studies of Cox and Yates (39) on the hydrolytic decomposition of a range of three sets of SC=O and OC=S substrates: four thiobenzoic acids (Ar-CO-SH), eight ethyl thiobenzoates (Ar-CO-SCH_2CH_3), and eight ethyl thionobenzoates (Ar-CS-OCH_2CH_3) in aqueous sulfuric acid media. In general, all of these substrates exhibited two (or more) mechanisms of decomposition. For example, with the parent ethyl thiobenzoate three mechanistic regions could be defined: (*i*) an A-2 mechanism involving two water molecules (*X* ca. 1–2), (*ii*) an A-S_E2 region where hydronium ion was found to be the proton source (*X* ca. 2.5–4) that switches over to (*iii*) an A-S_E2 mechanism where the proton source was assigned to undissociated sulfuric acid (*X* ca. 5–10). In contrast to the behaviour of ethyl benzoate that follows an A-2 mechanism that changes over to an A-1 pathway at about *X* = 6 with acylium ion formation, all of these S-containing substrates exhibit mechanistic changeover at significantly lower acidities (ca. *X* = 2–3) (39). Note that the mechanistic switch (A-2 → A-S_E2) suggested here for Diazinon also occurs at an excess acidity value (*X*) of about 2. Cox and Yates (39) concluded "that proton transfer to sulfur in involved in the slow step of the reaction at least some of the time, for all three types of sulfur-containing substrate in the study" This conclusion may also extend to **1** in moderately acidic sulfuric acid media.

Returning to the Diazinon – aq. H_2SO_4 system, in a (hypothetical) A-2 mechanism involving protonation at S, the pK_a of the P=S group is a dominant consideration. Such protonation in the current system corresponds to protonation at S of the monoprotonated substrate, **1**-NH_p^+, i.e., diprotonation overall. In our estimate (see the Experimental section), the lower limit for the pK_a for diprotonation is –7.3. Therefore, the acidity in our study should be insufficient to produce diprotonation. Note as well that *O*,*O*-diethyl thiophosphoric acid, a model for protonation at P=S, was found to have a pK_a of –5.14. Unfortunately, Diazinon undergoes rapid degradation in media with higher acidities.

An important aspect concerning the proposed (A-S_E2) mechanism, which is to be emphasized, is that the concerted nature of the process makes it accessible in a lower acid region compared to the A-2 mechanism discussed above. In this acid region (*X* = 2–6), although a_{H_2O} continues to decline, this is more than compensated for by the increasing acidity, as evidenced by the sharp upward curve of the rate-excess acidity profile.

Since P=S is a defining feature of a large class of pesticides in use, and the proposed mechanism is directly tied to this structural feature, a broad avenue is opened for the study of the general behaviour of these biocides in acid media.

Conclusions

Whereas in pesticides the lowered hydrolytic activity of P=S triesters relative to their P=O analogues confers lowered mammalian toxicity on these biocides (1), this lowered reactivity opens up the possibility of other routes of reaction. In the current case, we propose that acid catalysis occurs via the less common A-S_E2 type rather than the traditional A-2 or A-1 paths outlined (Schemes 4 and 5). Therefore, in simple ester or amide hydrolysis in acid, the A-2 or changeover of A-2 to A-1 mechanisms (19, 27) are supplanted in Diazinon hydrolysis by the concerted variant of the A-S_E2 process involving partial rate-determining proton transfer to P=S from hydronium ion with concomitant proton transfer from water and effective attack of hydroxide at the P centre

[4] We thank a referee for drawing our attention to this point. The current treatment does not permit definitive assignment of the number of water molecules involved in the transition state.

© 2007 NRC Canada

(structure **6**). In nature, for example in enzymatic processes (e.g., chymotrypsin), rate-determining proton transfers involving relays, in which proton transfer is central to the catalysis are the norm.

Acknowledgements

Financial support of this work was provided by the Natural Sciences and Engineering Research Council of Canada (to EB) and PGS A and PGS B scholarships (to DC) are gratefully acknowledged. Thanks are also extended to the sponsors of the Pestcon Scholarship (granted to DC) administered by the Chemical Institute of Canada, which assisted these studies in pesticide chemistry. Support of the Sir Wilfred Grenfell College Principal's Research Fund (to JMD) is also noted. Helpful comments of the referees are cheerfully acknowledged.

References

1. Handbook of pesticide toxicology. Vol. 2: Classes of pesticides. *Edited by* W.J. Hayes, Jr. and E.R. Laws, Jr. Academic Press, Toronto. 1991.
2. S.D. Faust and H.M. Gomaa. Environ. Lett. **3**, 171 (1972).
3. R.F. Hudson. Structure and mechanism in organophosphorus chemistry. Academic Press, Toronto. 1965.
4. G.R.J. Thatcher and R. Kluger. Adv. Phys. Org. Chem. **25**, 99 (1989).
5. (*a*) R.S. Brown, A.A. Neverov, J.S.W. Tsang, G.T.T. Gibson, and P.J. Montoya-Pelaez. Can. J. Chem. **82**, 1791 (2004) and refs. cites therein; (*b*) J.S.W. Tsang, A.A. Neverov, and R.S. Brown. Org. Biomol. Chem. **2**, 3457 (2004); (*c*) A.A. Neverov and R.S. Brown. Org. Biomol. Chem. **2**, 2245 (2004); (*d*) W. Desloges, A.A. Neverov, and R.S. Brown. Inorg. Chem. **43**, 6752 (2004); (*e*) A.A. Neverov, N. Sunderland, and R.S. Brown. Org. Biomol. Chem. **3**, 65 (2005).
6. (*a*) C.A. Bunton, G. Cerichelli, Y. Ihara, and L. Supelveda. J. Am. Chem. Soc. **101**, 2429 (1979); (*b*) C.A. Bunton, P. Scrimin, and P. Tecilla. J. Chem. Soc. Perkin Trans. 2, 419 (1996); (*c*) C.A. Bunton, N.D. Gillitt, and A. Kumar. J. Phys. Org. Chem. **14**, 221 (1997); (*d*) P. Scrimin, P. Tecilla, U. Tonatello, and C.A. Bunton. Colloids Surf. A, 144, 71 (1998); (*e*) R. Greenhalgh, K.L. Dhawan, and P. Weinberger. J. Agric. Food Chem. **28**, 102 (1980).
7. (*a*) M.J. Pregel, E.J. Dunn, R. Nagelkerke, G.R. Thatcher, and E. Buncel. Chem. Soc. Rev. **24**, 449 (1995); (*b*) E. Buncel, K.G. Albright, and I. Onyido. Org. Biomol. Chem. 601 (2004); (*c*) J.E. Omakor, I. Onyido, G.W. vanLoon, and E. Buncel. J. Chem. Soc. Perkin Trans. 2, 324 (2001); (*d*) J.M. Dust and C.S. Warren. Water Qual. Res. J. Canada **36**, 589 (2001); (*e*) I.S. Enerji, E. Buncel, and G.W. vanLoon. J. Agric. Food Chem. **50**, 5634 (2002); (*f*) E. Buncel, R. Nagelkerke, and G.R.J. Thatcher. Can. J. Chem. **81**, 53 (2003).
8. V.K. Balakrishnan, J.M. Dust, G.W. vanLoon, and E. Buncel. Can. J. Chem. **79**, 157 (2001).
9. (*a*) V.K. Balakrishnan, X. Han, G.W. vanLoon, J.M. Dust, J. Toullec, and E. Buncel. Langmuir, **20**, 6586 (2004); (*b*) V. K. Balakrishnan, E. Buncel, and G.W. vanLoon. Environ. Sci. Technol. **39**, 5824 (2005).
10. (*a*) E. Buncel and S. Hoz. Isr. J. Chem. **26**, 313 (1985); (*b*) E. Buncel and I.H. Um. Tetrahedron, **60**, 7801 (2004); (*c*) I.H. Um and E. Buncel. J. Org. Chem. **65**, 577 (2000); (*d*) G. Moutier, E. leGuevel, C. Cannes, F. Terrier, and E. Buncel. Eur. J. Org. Chem. 3279 (2001); (*e*) I.H. Um and E. Buncel, J. Am. Chem. Soc. **123**, 11111 (2001); (*f*) I.H. Um, J.Y. Lee, S.Y. Bae, and E. Buncel. Can. J. Chem. **83**, 1365 (2005); (*g*) I.H. Um, S.M. Chun, and S.K. Bae. Bull. Korean Chem. Soc. **26**, 457 (2005); (*h*) I.H. Um, S.J. Hwang, and E. Buncel. J. Org. Chem. **71**, 915 (2006).
11. (*a*) S.Y. Szeto and P.M. Price. J. Agric. Food Chem. **39**, 1679 (1991); (*b*) R. Frank, H.E. Braun, N. Chapman, and C. Burchat. Bull. Environ. Contam. Toxicol. **47**, 374 (1991); (*c*) S.K. Lee, D, Freitag, C. Steinberg, A. Kettrup, and Y.U. Kim. Water Res. **27**,199 (1993); (*d*) D.J. Larkin and R.S. Tjeerdema. Rev. Environ. Contam. Toxicol. **166**, 49 (2000); (*e*) P.C.H. Li, E.J. Swanson, and F.A.P.C. Gobas. Bull. Environ. Contam. Toxicol. **69**, 59 (2002); (*f*) A. Prieto, D. Molero, G. Gonzalez, I. Buscema, G. Ettiene, and D. Medina. Bull. Environ. Contam. Toxicol. **69**, 479 (2002); (*g*) M. Bavcon, P. Trebse and L. Zupancic-Kralj. Chemosphere, **50**, 595 (2003).
12. Y. Ku, J-L. Change, and S-C. Cheng. Water, Air, Soil Pollut. **108**, 445 (1998).
13. (*a*) E. Buncel, R. Stairs, and H. Wilson. The role of the solvent in chemical reactions. Oxford University Press, Oxford, UK. 2003; (*b*) E. Buncel and S. Rajagopal. Acc. Chem. Res. **23**, 226 (1990); (*c*) E. Buncel and E.A. Symons. *In* Advances in solution chemistry. *Edited by* I. Bettini, L. Lunazzi, and A. Dei. Plenum Press, New York. 1981. pp 355–371.
14. (*a*) E. Buncel. Can. J. Chem. **78**, 1251 (2000); (*b*) R.A. Cox and E. Buncel. *In* The chemistry of the hydrazo, azo and azoxy groups. Vol. 2. *Edited by* S. Patai. Wiley, Chichester, NY. 1997. pp. 569–602; (*c*) R.A. Cox, K.S. Cheon, and E. Buncel. Can. J. Chem. **76**, 896 (1998); (*d*) E. Buncel and K.S. Cheon. J. Chem. Soc. Perkin Trans 2, 1241 (1998); (*e*) K.S. Cheon, R.A. Cox, S.R. Keum, and E. Buncel. J. Chem. Soc. Perkin Trans. 2, 1231 (1998); (*f*) R.A. Cox, I. Onyido, and E. Buncel. J. Am. Chem. Soc. **114**, 1358 (1992).
15. (*a*) G.W. vanLoon and S. Duffy. Environmental chemistry: A global perspective. Oxford University Press, New York. 2000; (*b*) M.T. Annandale, G.W. VanLoon, and E. Buncel. Can. J. Chem. **76**, 873 (1998); (*c*) J.F. Omakor, I. Onyido, G.W. vanLoon, and E. Buncel. J. Chem. Soc. Perkin Trans. 2, 324 (2001); (*d*) S. Shirin, E. Buncel, and G.W. vanLoon. Can. J. Chem. **81**, 45 (2003).
16. (*a*) D.C. Pieda. M.Sc. Thesis, Queen's University, Kingston, Ont. 2001; (*b*) D.C. Churchill. Ph.D. Thesis, Queen's University, Kingston, Ont. 2004.
17. N.L. Wolfe. Chemosphere, **9**, 571 (1980).
18. W.H. Dennis Jr., A.B. Rosencrance, W. F. Randell, and E.P. Meier. J. Environ. Sci. Health, Part B, **15**, 47 (1980).
19. R.A. Cox. Adv. Phys. Org. Chem. **35**, 1 (2000).
20. R.A. Cox, M.F. Goldman, and K. Yates. Can J. Chem. **57**, 2960 (1979).
21. M. Gysin and A. Margot. J. Agri. Food Chem. **6**, 900 (1958).
22. M. Maderia, L.M. Hunsicker, and V.J. DeRose. Biochemistry, **39**, 12113 (2000).
23. Sigma-Aldrich Ltd. Materials safety data sheet. 1998.
24. D.D. Perrin and W.L.F. Armarego. Purification of laboratory chemicals. 3rd ed. Pergamon Press, New York. 1988.
25. (*a*) E. Buncel and C. Chuaqui. Can. J. Chem. **53**, 1275 (1975); (*b*) E. Buncel, C. Chuaqui, P. Forsythe, S. Mahoney, A. Raoult, and J.F. Wiltshire. J. Chem. Soc. Perkin Trans. 2, 478 (1975); (*c*) E. Buncel, A. Raoult, and J. F. Wiltshire. J. Chem. Educ. **51**, 814 (1974); (*d*) E. Buncel, A. Raoult, and J.F. Wiltshire. J. Am. Chem. Soc. **95**, 799 (1973).
26. (*a*) F. Benoit-Marquie, C. De Montety, V. Gilard, R. Martino, M.T. Maurette, and M. Malet-Martino. Environ. Chem. Lett. **2**,

© 2007 NRC Canada

93 (2004); (*b*) V. Gilard, R. Martino, R. Malet-Martino, U. Niemeyer, and J. Pohl. J. Med. Chem. **42**, 2542 (1999); (*c*) Z. Talebpour, A. Ghazzempour, M. Zendehzaban, H. R. Bijanzadeh, and M.H. Mirjalili. Anal. Chim. Acta. **576**, 290 (2006).
27. R.A. Cox. Can. J. Chem. **83**, 1391 (2005).
28. (*a*) J.F. Bunnett. J. Am. Chem. Soc. **83**, 4956 (1961); (*b*) J.F. Bunnett and F.P. Olsen. Can. J. Chem. **44**, 1899 (1966); (*c*) J.F. Bunnett and F.P. Olsen. Can. J. Chem. **44**, 1917 (1966); (*d*) J.F. Bunnett, J.O. Edwards, D.V. Wells, H.J. Brass, and R. Curci. J. Org. Chem. **38**, 2703 (1973); (*e*) K. Yates and J.C. Riordan. Can. J. Chem. **43**, 2328 (1965); (*f*) R.A. Cox and K. Yates. Can. J. Chem. **59**, 1560 (1981).
29. J.R. Marshall and J. Walker. J. Chem. Soc. 1004 (1951).
30. (*a*) A. Albert, D.J. Brown, and G. Cheeseman. J. Chem. Soc. 474 (1951); (*b*) D.J. Brown and B.T. England. J. Chem. Soc.C. 1922 (1967); (*c*) D.J. Brown. The pyrimidines. John Wiley and Sons, N.Y. 1962; (*d*) D.J. Brown. The pyrimidines. Supplement II. John Wiley and Sons. N.Y. 1985.
31. A.J. Kirby and M. Younas. J. Chem. Soc. B, 1165 (1970).
32. (*a*) A.C. Hengge and I. Onyido. Curr. Org. Chem. **9**, 61 (2005); (*b*) J. Purcell and A.C. Hengge. J. Org. Chem. **70**, 8437 (2005).
33. F. Terrier. Nucleophilic aromatic displacement. The influence of the nitro group. Wiley-VCH, New York. 1991. pp 11–13.
34. R.A. Cox. Can. J. Chem. **76**, 649 (1998).
35. T.H. Lowry and K.S. Richardson. Mechanism and theory in organic chemistry. Harper and Row, New York. 1987.
36. (*a*) R.D. Cook and M. Metni. Can. J. Chem. **63**, 3155 (1985); (*b*) R.D. Cook and M. Metni. J. Chem. Soc. Chem. Comm. 832 (1985).
37. P. Haake and G. Hurst. J. Am. Chem. Soc. **88**, 2544 (1966).
38. (*a*) C.A. Bunton, S.J. Farber, and E.J. Fendler. J. Org. Chem. **33**, 29 (1968); (*b*) C.A. Bunton. Acc. Chem. Res. **3**, 257 (1970).
39. R.A. Cox and K. Yates. Can. J. Chem. **60**, 3061 (1982).

© 2007 NRC Canada

A reinterpretation of the unusual barochromism of azulene

Masami Okamoto, Satoshi Hirayama, and Ronald P. Steer

Abstract: The UV–vis spectra of azulene in methylcyclohexane and acetonitrile solution at room temperature have been measured as a function of applied pressure in the 0.1–600 MPa range. The solvatochromic shifts are normal, but the barochromic shifts are unusual (hypsochromic shift in the S_1–S_0 absorption bands vs. normal bathochromic shifts in its S_2–S_0 and S_3–S_0 absorption bands). An analytical relationship between the barochromic shift and the differences in the polarizabilities and dipole moments of the two radiatively coupled electronic states has been derived. The unusual barochromism of azulene has been reinterpreted in terms of differences in the polarizabilities of azulene in its ground and excited states and the dominance of dispersive interactions in barochromism.

Key words: barochromism, solvatochromism, azulene, polarizability, dipole moment.

Résumé : On a mesuré les spectres UV-vis de l'azulène en solutions dans le méthylcyclohexane et l'acétonitrile, à la température ambiante, en fonction de la pression appliquée de 0,1 à 600 Mpa. Les déplacements solvatochromes sont normaux, mais les déplacements barochromes sont inhabituels (déplacement hypsochrome des bandes d'absorption S_1–S_0 par rapport aux déplacements bathochromes des bandes d'absorption S_2–S_0 et S_3–S_0). On a développé une relation analytique entre le déplacement barochrome et les différences dans les polarisabilités et les moments dipolaires de deux états électroniques couplés d'une façon radiative. On a réinterprété la barochromie inhabituelle de l'azulène en fonction de différences dans les polarisabilités de l'azulène dans des états fondamental et excité et de la dominance d'interactions dispersives dans la barochromie.

Mots-clés : barochromie, solvatochromie, azulène, polarisabilité, moment dipolaire.

[Traduit par la Rédaction]

Introduction

The spectroscopic and photophysical properties of azulene continue to elicit interest because this nonalternant aromatic hydrocarbon provides one of only a few chromophores that fluoresce strongly from a second excited singlet state, S_2 (2^1A_1 in C_{2v} symmetry) (1). The lifetimes of this excited state are determined primarily by its rate of radiationless relaxation to lower electronic states. For azulene and many of its simply substituted derivatives, S_2–S_1 internal conversion is the dominant relaxation path, and the rate of this process follows the energy gap law of radiationless transition theory (2). Thus, the S_2 radiationless decay rates of these compounds vary directly with their Franck-Condon factors, $F = < \chi(s_2)|\chi(s_1) >^2$, which in turn are proportional to exp–[ΔE] when the electronic energy gap, $\Delta E = E(S_2) - E(S_1)$, is sufficiently large. In fluid solution, azulene's electronic energy gap can be tuned by solvatochromism (3), by choice of substituent (3, 4), and by the application of large hydrostatic pressures (5) (barochromism).

The overall effects of the application of a high pressure on the electronic spectrum of azulene have been known (6, 7) for many years; the S_1–S_0 transition in the visible undergoes an unusual blue shift with increasing pressure whereas the S_2–S_0 transition in the near UV undergoes a red shift. The result is a net decrease in ΔE with increasing pressure and an exponential increase in S_2's rate of radiationless decay (5). Although both the S_1–S_0 the S_2–S_0 spectra of azulene have been extensively studied in recent years (8, 9), the barochromic effects on them have received no attention. In fact, the original explanation for the observed barochromism (7), involving differences in the electric dipole moments of azulene in its ground and excited singlet states, has remained unchallenged for many years and has been propagated in the review literature (10, 11).

Recently, we carefully remeasured the effects of applying high hydrostatic pressures on the UV–vis spectra of azulene in solution, and in light of recent additional measurements of its excited state properties (vide infra) offer a reinterpretation of the observed barochromism.

Experimental section

Azulene (Fig. 1, C_s structure and coordinate axis system) was obtained from Sigma-Aldrich, and spectroscopic grade methylcyclohexane and acetonitrile solvents were obtained from Dojin Pure Chemicals Co. All were used as received.

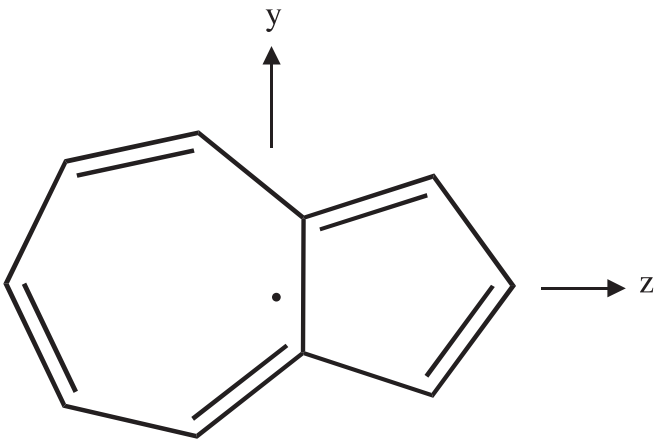
Received March 21 2007. Accepted May 14 2007. Published on the NRC Research Press Web site at canjchem.nrc.ca on 8 June 2007.

M. Okamoto and S. Hirayama. Kyoto Institute of Technology, Matsugasaki, Sakyo-ku, Kyoto 606, Japan
R. P. Steer.[1] Department of Chemistry, University of Saskatchewan, 110 Science Place, Saskatoon, SK S7N 5C9, Canada

[1]Corresponding author (e-mail: ron.steer@usask.ca).

 doi:10.1139/V07-052 © 2007 NRC Canada

Fig. 1. Azulene (C_s structure).



The absorption spectra were taken on a Shimadzu UV 260 spectrophotometer. Data were acquired digitally every 0.05 or 0.10 nm, usually at a spectral resolution of 2 nm. Several spectra were also taken at the substantially higher resolution of 0.2 nm; they exhibited small changes in the widths and apparent relative absorbances of resolved bands but no significant differences in the wavenumbers of band maxima, which were extracted manually from the data files. The differences in the spectra at the two resolutions are illustrated in the Supplementary Information for this paper.[2]

The high pressure cell was made of SUS 316 stainless steel, was fitted with sapphire windows, and had an optical path length of 0.6 cm and an aperture of 0.5 cm. The spectra were measured separately in the S_1–S_0, S_2–S_0, and $S_{3,4}$–S_0 ranges, using solution concentrations that gave a convenient absorbance in the wavelength range of interest. No evidence of solute aggregation was observed at any pressure in any of these solutions. The spectrum of the solvent alone was also measured separately and was deemed independent of pressure up to at least 600 MPa. The pressure was measured using a calibrated Manganin wire. Details may be found in ref. (12). All measurements were taken at a room temperature of 22 °C.

Results and discussion

The S_1–S_0 and S_2–S_0 spectra of azulene in methylcyclohexane as a function of pressure in the 0.1 to 600 MPa range are shown in Figs. 2a and 2b. All the resolved and partly resolved features in the S_1–S_0 spectrum exhibit blue shifts with increasing pressure in both solvents, whereas those in the S_2–S_0 spectrum exhibit red shifts, in qualitative agreement with the original measurements by Robertson and King (6). Graphs of the wavenumbers of the maxima of the origin bands of the S_1–S_0 and S_2–S_0 transitions in methylcyclohexane vs. pressure in this range are shown in Fig. 3.

Drickamer and co-workers (7) have shown that at much higher pressures the wavenumbers of the S_1–S_0 bands reach a maximum (near 6 000 MPa in azulene crystals) and then decrease quite rapidly with further increases in pressure. A hint of nonlinearity in the graphs of transition energy vs. pressure is evident in the present work (Fig. 3). Nevertheless, in the 0.1 to 600 MPa pressure range explored here, only a marginal statistical improvement is obtained when a second order polynomial is used to fit the data compared with a linear function. We therefore use the data from the linear fits: the slopes ($d\bar{\nu}_{u,0}/P$) of such plots and the observed intercepts ($\bar{\nu}_0$) for all the resolved features in the spectra in methylcyclohexane are given in Table 1.

The spectra as a function of applied pressure in acetonitrile (Fig. 2*c* shows the S_1–S_0 spectra) are not well-resolved and yield graphs qualitatively similar to those in Fig. 3 but with slopes and intercepts with large statistical error. The intrinsic broadening of the spectra in the polar solvent, not the spectral resolution employed, prevents the extraction of statistically meaningful barochromic data. Nevertheless, both the expected "normal" solvatochromic blue shift (of the singlet–singlet absorption systems) at any given pressure and the unusual barochromic shift of the S_1–S_0 origin are observed qualitatively in the polar solvent.

The apparent absorbances (and half-widths) of all resolvable bands increase with increasing pressure, albeit by different relative amounts for different features in the spectrum. The largest increase in absorbance is due to the increasing density of the solution (and hence molar concentration of the solute). The remaining small differences in the absorbances and half-widths of different features in the spectrum are real and are not due to increases in the molar absorptivity with increasing refractive index (13). However, these small changes cannot readily be quantified at the spectral resolution employed ($\Delta\lambda$ = 2.0 or 0.2 nm), given the fact that almost all of the observed vibrational structure in these spectra results from the overlap of several bands that are completely unresolved in solution at room temperature. Values of $\bar{\nu}_0$ (Table 1) are obtained by extrapolation of the data such as those in Fig. 3 to P = 0. However, owing to broadening in solution and the effects of band overlap these values will not correspond exactly to the wavenumbers of the same bands in the electronic spectra of the isolated molecule (8, 9).

The magnitudes of the measured slopes of the wavenumber vs. pressure plots (Table 1, $\bar{\nu}_{n,0}/dP$) for all of the vibronic bands in both the S_1–S_0 and S_2–S_0 systems may also be determined in part by the effects of overlapping transitions, so we ascribe significance only to the sign and range of values of these quantities. However, the lowest energy bands in both absorption systems are quite well-resolved from the rest of the spectrum at all pressures up to 600 MPa. We therefore ascribe significance to both the sign and magnitude of their barochromic slopes, despite the fact that these "origin" bands will actually consist of the true inhomogeneously broadened 0–0 transition overlapped by a number of weaker, hot, sequence bands ($\Delta v = v'' - v' = 0$, $v'' = 1, 2, 3, \ldots$). In both electronic band systems, the totally symmetric vibrations (a_1 in C_{2v}) are most active (8, 9), and the most intense of these weaker, hot, sequence bands are expected to be those of lowest frequency. The lowest frequency a_1 vibration in the ground state of azulene is $\bar{\nu}_{17}$ =

[2] Supplementary data for this article are available on the journal Web site (http://canjchem.nrc.ca) or may be purchased from the Depository of Unpublished Data, Document Delivery, CISTI, National Research Council Canada, Ottawa, ON K1A 0R6, Canada. DUD 5177. For more information on obtaining material refer to http://cisti-icist.nrc-cnrc.gc.ca/irm/unpub_e.shtml.

© 2007 NRC Canada

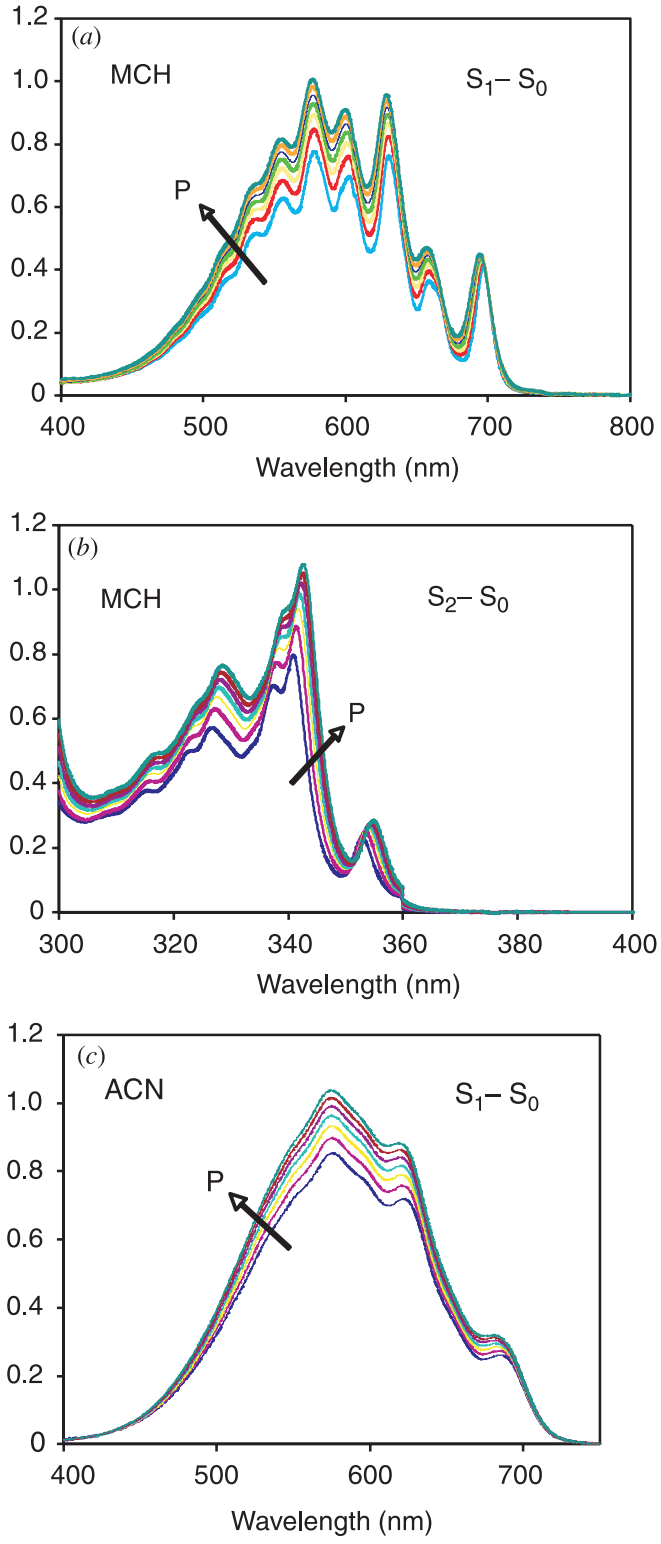


Fig. 2. (*a*) Visible (S_1–S_0) and (*b*) UV (S_2–S_0) spectra of azulene in methylcyclohexane, and (*c*) S_1–S_0 spectra of azulene in acetonitrile as a function of pressure. Apparent absorbance increases with increasing pressure in the 0.1 to 600 MPa range for methycyclohexane and in the 0.1 to 300 MPa range for acetonitrile. The discontinuity in the S_2–S_0 spectra near 360 nm is due to a change of excitation source in the spectrophotometer. The S_2–S_0 spectra in acetonitrile also exhibit no fully resolved vibrational features at any pressure.

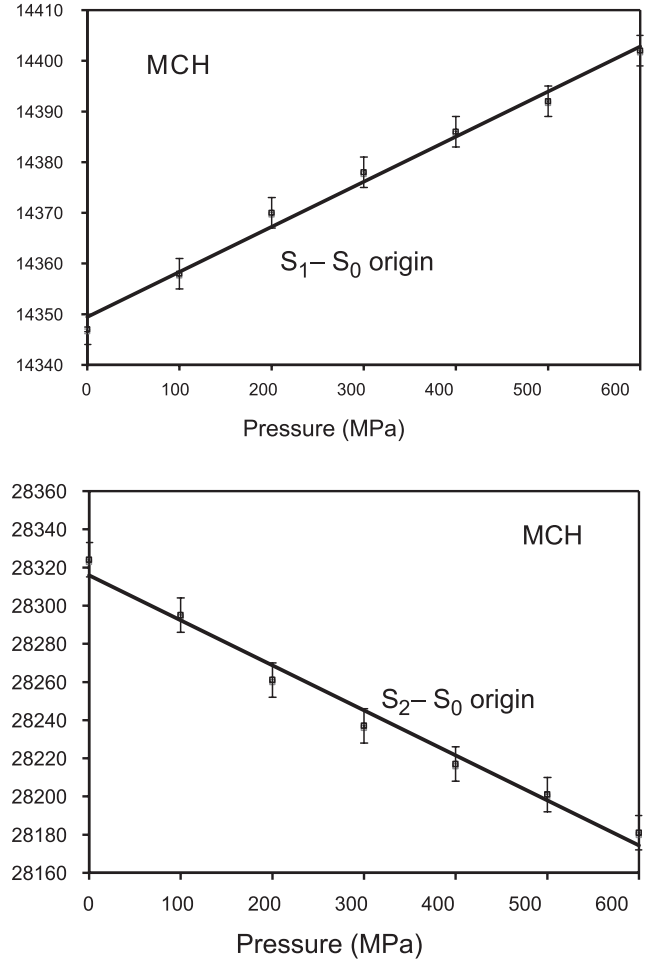
401 cm^{-1} ($\bar{\nu}_{16}$ = 680 cm^{-1}) (14), so if the relative intensity of the $\Delta v_{17} = 0$ sequence band is determined primarily by the thermal population of $v''_{17} = 1$, the intensity of this strongest sequence band should be only about 15% of that of the origin band itself. Note particularly that in methylcyclohexane, the observed ratio of $d\bar{\nu}_{n,0}/dP$ for the origin band of the S_2–S_0 system to that of the origin of the S_1–S_0 system is $R_{obs} = (d\bar{\nu}_{2,0}/dP)/(d\bar{\nu}_{1,0}/dP) = -2.9 \pm 0.3$, and that this ratio is almost independent of pressure in this pressure range. If a second-order polynomial in P is used to fit the data in Fig. 3, the ratio of the first-order pressure coefficients yields a value of R_{obs} within 10% of this value.

We now seek an explanation for these effects. The "anomalous" blue barochromic shift of the S_1–S_0 system of azulene (as distinct from the "normal" red shift seen in the S_2–S_0 spectrum) was originally ascribed to differences in the magnitudes of the dipole moments in its excited states compared with the ground state (6, 7, 10, 11). However, Baumann's accurate measurements (15), recently confirmed by high-level ab initio calculations (16–18), show that in nonpolar cyclohexane solution the dipole moments of azulene in its S_1 and S_2 states are both smaller in magnitude (and are both opposite in direction) compared with that in its ground state. Baumann's data (15) are reproduced in Table 2. In nonpolar solvents at modest applied pressures, such as those used here, the relative barochromic shift of the S_2–S_0 and S_1–S_0 origin bands originating solely in changes in the molecule's static electric dipole moments may be estimated from the ratio of the differences in the squares of the dipole moments in each pair of radiatively coupled states (19, 20), i.e., $R_{dipole} = (\mu^2_{S_2} - \mu^2_{S_0})/(\mu^2_{S_1} - \mu^2_{S_0}) = +1.3$. Thus, both the magnitude and sign of R_{obs} are inconsistent with a dominant solute electric dipole – solvent induced dipole origin of the barochromism in nonpolar solvents.

Baumann also provides experimental data for the ground and excited state polarizabilities of azulene in cyclohexane (15). These data (Table 2) suggest that the observed barochromism is due primarily to differences in azulene's polarizabilities in its S_0, S_1, and S_2 states. If the relative barochromic shift of the S_2–S_0 and S_1–S_0 origin bands at these modest applied pressures were due solely to changes in the molecule's polarizability, then to a good approximation $R_{obs} \approx R_{pol} = (\alpha_{S_2} - \alpha_{S_0})/(\alpha_{S_1} - \alpha_{S_0})$, i.e., the ratio of the differences in the frequency-weighted polarizabilites of each pair of radiatively coupled states (20). While Baumann (15) provides experimental data on all three of the polarizability tensor components for both S_0 and S_1, he is only able to obtain an accurate value of the z (long axis, largest) component, a_z, of that tensor for S_2. Nevertheless, it is clear that for each measured tensor component in the three states, $\alpha_i(S_2) > \alpha_i(S_0) > \alpha_i(S_1)$, ($i = x, y, z$), so the sign of R_{obs} may be accounted for by the fact that the polarizability of S_1 is smaller than that of S_0, whereas the polarizability of S_2 is greater than that of S_0. In fact, using the z (largest) component of the polarizability tensor in each state as representative of the full molecular polarizability results in $R_{pol,z} = (\alpha_{S_2,z} - \alpha_{S_0,z})/(\alpha_{S_1,z} - \alpha_{S_0,z}) = -2.6$. The reasonable

© 2007 NRC Canada

Fig. 3. $\bar{\nu}_{u,l}$ (solution) vs. pressure for the origin bands of azulene in methylcyclohexane. Errors are ±1.5, data channels (±3 cm^{-1} at 700 nm and 0.1 nm per channel; ±8 cm^{-1} at 350 nm and 0.05 nm per channel), representing the average error in selecting the channel of maximum intensity.



agreement between the magnitude of $R_{pol,z}$ and R_{obs} must be considered fortuitous given the errors in the tensor components quoted by Baumann, the errors in the measured barochromic slopes, and the approximations made in the above analysis. Nevertheless, both sign and magnitude agree and it is therefore tempting to ascribe the observed barochromism of azulene mainly to differences in its ground and excited state polarizabilities and not to differences in its dipole moments. This may be surprising, since the solvatochromism of azulene *at constant pressure* is "normal" (i.e., a blue shift in more polar solvents) in all of its visible and near UV absorption systems. We explore the source of this apparent discrepancy in the following section.

A comprehensive, quantitative analysis of the solvatochromism and barochromism of all three UV–vis absorption systems of azulene starts with the theory of solvatochromism of Bayliss and McRae (19, 20). Using second-order perturbation theory and the point dipole approximation, McRae (19) has derived a general four-term expression for the electronic transition energies of a solute embedded in a solvent continuum that is characterized by its refractive index, n, and its dielectric constant, D. Each of the four terms represents a

Table 1. Barochromism of resolved features in the S_1–S_0, S_2–S_0, and S_3–S_0 absorption spectra of azulene in methylcyclohexane at room temperature.

Band[a]	$\bar{\nu}_0$ (cm^{-1})	$\nu_{n,0}/dP$ (cm^{-1}/MPa)	R^2	
S_1–S_0	origin	14347	0.088(9)	0.976
	15^1, 16^1	15184	0.049	0.891
	8^1,91 15^116^1	15860	0.074	0.974
	7^117^1, 9^116^1, 10^115^1	16599	0.149	0.992
	$15^116^117^135^1$	17297	0.078	0.966
S_2–S_0	origin	28336	–0.262	0.971
	979, 993 (a_1)	29324	–0.232	0.969
	1300, 1315 (a_1)	29624	–0.405	0.987
	2272 (?)	30600	–0.259	0.962
	3330 (?)	31655	–0.349	0.970
S_3–S_0	origin	33790	–0.083	0.750

[a]Assignments of the S_1–S_0 bands are from ref. 8. Only the wavenumbers are given for the S_2–S_0 bands, which are vibronically tangled (9).

Table 2. Dipole moments and polarizabilities of azulene in its S_0, S_1, and S_2 states (from ref. 15).

		Polarizability (× 10^{-40} $CV^{-1}m^2$)[a]			
State	μ(× 10^{-30} Cm)[b]	α_x	α_y	α_z	α^c_{av}
S_0	3.31	6.4	19	26.4	17.3
S_1	–1.88	–1.9[d]	16.2	23.9	12.7
S_2	–1.16	—	—	33.0	—

Note: Conversion factors are: 1 D = 3.336 × 10^{-30} Cm; 1 $Å^3$ = 1.113 × 10^{-40} $CV^{-1}m^2$.

[a]Based on an ellipsoidal model.

[b]Colinear with the z axis. Positive values of μ are for the dipole pointing from the five-member ring (δ–) to the seven-member ring (δ+) (cf. Fig. 1).

[c]$\alpha_{av} = 1/3\mathrm{Tr}\{\alpha_i\}$

[d]With large error.

contribution to the solvatochromism resulting from dispersive and static dipole interactions. Simplifying to isolate the dipole moment and polarizability of the solute and retain the solvent continuum parameters, we obtain eq. [1] for the solvent shift of the electronic transition energy,

$$[1]\qquad \Delta\bar{\nu}_{u,l} = \bar{\nu}_{u,l}(\text{solution}) - \bar{\nu}_{u,l}(\text{gas})$$
$$= -Q(\alpha_u - \alpha_l)f_1 - R(\mu_u^2 - \mu_l^2)f_1 - S\mu_l(\mu_u - \mu_l)f_2 - T\mu_l^2(\alpha_u - \alpha_l)f_2^2$$

where $f_1 = (n^2 - 1)/(2n^2 + 1)$, $f_2 = (D - 1)/(D + 2) - (n^2 - 1)/(n^2 + 2)$, l and u designate lower and upper states respectively, and Q, R, S, and T are all positive constants. The derivation of the first term in eq. [1] from the expressions given by McRae (19) is not obvious and is therefore included in the Supplementary material for this paper.[2]

Thus, assuming that the polarizabilities and dipole moments of the solute are independent of pressure (a good assumption in the low hydrostatic pressure regime employed here),

© 2007 NRC Canada

$$[2]\quad d\Delta\bar{\nu}_{u,l}/dP = d\bar{\nu}_{u,l}(\text{solution})/dP$$
$$= -Q(\alpha_u - \alpha_l)df_1/dP - R(\mu_u^2 - \mu_l^2)df_1/dP$$
$$- S\mu_l(\mu_u - \mu_l)df_2/dP - 2f_2T\mu_l^2(\alpha_u - \alpha_l)df_2/dP$$

at constant temperature, where $df_1/dP = 6n/(2n^2 + 1)^2\, dn/dP \geq 0$ and $df_2/dP = [3/(D+2)^2]_n^2\,(\partial D/\partial P)_n^2 - [3/(n^2+2)^2]_D\,(\partial n^2/\partial P)_D$, a term that may be either positive or negative.

For nonpolar solvents, $f_2 \approx 0$, and only the first two terms in eqs. [1] and [2] are of importance. For sufficiently polar solvents, $D >> n$ and $df_2/dP \approx -6n/(n^2 + 2)^2(\partial n/\partial P)_D < 0$. Thus, the results for azulene's barochromism in nonpolar methylcyclohexane are consistent with the dominance of dispersion, the first term in eqs. [1] and [2], with a smaller contribution from dipole-induced dipole interactions, the second term. At constant pressure, the blue shift resulting from replacing a nonpolar solvent by a polar one is consistent with the dominant influence of term three in eq. [1], which contributes to an increase in both the S_1–S_0 and S_2–S_0 transition energies in azulene since both excited state dipole moments are opposite in sign (and smaller in magnitude) compared with the ground state. Term two in eq. [1] is expected to make a slightly smaller blue shift contribution to the solvatochromism in acetonitrile than in methylcyclohexane due to its smaller refractive index, and the term four makes no significant contribution. Finally, the fact that the S_1–S_0 transition of azulene retains its unusual barochromic behaviour in acetonitrile reflects the fact that dispersive interactions dominate the pressure-induced frequency shifts even in this polar solvent. Note that (*i*) df_1/dP is always positive in solution, (*ii*) df_2/dP is negative when $D >> n$, (*iii*) both df_1/dP and df_2/dP are functions of only n when $D >> n$, and (*iv*) df_2/dP is ca. 1.5 times larger in magnitude than df_1/dP for acetonitrile. Thus term three in eq. [2] represents a red barochromic shift that partially offsets the dominant (term one) dispersion-induced blue shift for the S_1–S_0 transition and that augments the dispersion-induced red barochromic shift of the S_2–S_0 transition. Unfortunately, the intrinsic broadening of the spectra in acetonitile precludes analysis that would further quantify these interactions.

Using the above analysis, one should be able to predict the polarizability of the S_3 state from its measured barochromism and the polarizabilities of the lower electronic states. Using the measured values of $d\bar{\nu}_{n,0}/dP$ (Table 1) and the experimentally measured polarizabilities of the ground, S_1 and S_2 states (Table 2 of ref. 15), one calculates $\alpha_z(S_3) = 28 \times 10^{-40}$ $CV^{-1}m^2$ ignoring dipolar contributions, a value that is only slightly larger than that of the ground state.

These results can be compared with the solvatochromic measurements of Renge (21) who recognized that changes in azulene's polarizability are primarily responsible for its solvatochromism in n-alkanes. Renge determined that $\Delta\alpha_{av} = 1/3\text{Tr}\{\Delta\alpha\} = (0\pm2) \times 10^{-40}$ $CV^{-1}m^2$, $(4.5\pm2) \times 10^{-40}$ $CV^{-1}m^2$, and $(3.8\pm2) \times 10^{-40}$ $CV^{-1}m^2$ for the S_1–S_0, S_2–S_0, and S_3–S_0 transitions, respectively, but based this on a rather limited $\bar{\nu}_{1,0}$ vs. $f(n^2)$ correlation for azulene's S_1–S_0 solvatochromism and used uncorrected (gas phase) values of the ground (and by extension excited) state dipole moments in his analysis (21). Renge's data are nevertheless consistent with the foregoing analysis when error limits and corrections are taken into account.

The hypsochromic barochromism of the S_1–S_0 absorption system of azulene is unusual and therefore of importance in testing theories of the effects of intermolecular interactions on molecular spectra. The preceding analysis supports recent models of the solvatochromism, barochromism, and thermochromism of polyatomic chromophores embedded in condensed media in which dispersive interactions are prominent (22–24). Unfortunately, the present state of both multireference CI and TDDFT calculations seems to preclude a definitive ab initio computation of the polarizabilities of a molecule the size of azulene, particularly in states such as S_1 and S_2, which are strongly coupled with still higher singlet states (9). It would, however, be interesting to ask if the Lennard–Jones potential model recently proposed by Renge (25) can reproduce the unusual barochromism of azulene at very high pressures (in excess of 6 000 MPa), where repulsive interactions at hard sphere intermolecular separations are expected to dominate.

Conclusions

The barochromism of azulene in fluid solution at room temperature has been re-examined. The unusual hypsochromic shift of the S_1–S_0 band system with increasing pressure, compared with the normal bathochromic shifts of the S_2–S_0 and S_3–S_0 band systems, is properly ascribed mainly to a decrease in the polarizability of the molecule in its S_1 state. This work illustrates the value of barochromism in obtaining experimental values of excited state polarizabilities and in testing theories of solvatochromic, barochromic, and thermochromic effects.

Acknowledgements

The authors are grateful to the Natural Sciences and Engineering Research Council of Canada (NSERC) for continuing financial support of this research. This work was supported in part by grant-in-aid 17550010 to MO.

References

1. For a review see: G. Burdzinski, J. Kubicki, A. Maciejewski, R.P. Steer, S. Velate, and E.K.L. Yeow. *In* Molecular and supramolecular photochemistry. Vol. 14. *Edited by* V. Ramamurthy and K.S. Schantze. Taylor and Francis, New York. 2005. p. 1.
2. R. Englman and J. Jortner. Mol. Phys. **18**, 145 (1970).
3. N. Tétreault, R.S. Muthyala, R.S.H. Liu, and R.P. Steer. J. Phys. Chem. A, **103**, 2524 (1999).
4. S. Murata, C. Iwanaga, T. Toda, and H. Kokobun. Ber. Bunsen-Ges. **76,** 1176 (1972).
5. D.J. Mitchell, H.G. Drickamer, and G.B. Schuster. J. Am. Chem. Soc. **99**, 7489 (1977).
6. W.W. Robertson and A.D. King, Jr. J. Chem. Phys. **34**, 1511 (1960).
7. R.B. Aust, W.H. Bentley, and H.G. Drickamer. J. Chem. Phys. **41**, 1856 (1964).
8. A.A. Ruth, E.-K. Kim, and A. Hese. Phys. Chem. Chem. Phys. **1**, 5121 (1999).
9. W.D. Lawrance and A.E.W. Knight. J. Phys. Chem. **94**, 1249 (1990).
10. H.G. Drickamer and C.W. Frank. Annu. Rev. Phys. Chem. **23**, 39 (1972).

© 2007 NRC Canada

11. H.W. Offen. *In* Organic molecular photophysics. Vol. 1. *Edited by* J.B. Birks. Wiley, New York. 1973. p. 103.
12. M. Okamoto and M. Sasaki. J. Phys. Chem. **95**, 6548 (1991).
13. S. Hirayama, H. Yasuda, M. Okamoto, and F. Tanaka. J. Phys. Chem. **95**, 2971 (1991); S. Hirayama and D. Phillips. J. Photochem. **12**, 139 (1980).
14. F. Negri and M.Z. Zgierski. J. Chem. Phys. **99**, 4318 (1993).
15. W. Baumann. Chem. Phys. **20**, 17 (1977).
16. P. Foggi, F.V.R. Neuwahl, L. Moroni, and P.R. Salvi. J. Phys. Chem. A, **107**, 1689 (2003).
17. A. Murakami, T. Kobayashi, A. Goldberg, and S. Nakamura. J. Chem. Phys. **120**, 1245 (2004).
18. A. Hinchliffe and H.J. Soscun. Chem. Phys. Lett. **412**, 365 (2005).
19. E.G. McRae. J. Chem. Phys. **61**, 562 (1957).
20. M.F. Nicol. Appl. Spectrosc. Rev. **8**, 183 (1974) and refs. cited therein.
21. I. Renge. Chem. Phys. **167**, 173 (1992).
22. J.E. Brady and P.W. Carr. J. Phys. Chem. **89**, 5759 (1985).
23. P. Suppan. J. Photochem. Photobiol. A, **50**, 293 (1990).
24. E. Leontidis, U.W. Suter, M. Schütz, H.-P. Lüthi, A. Renn, and U.P. Wild. J. Am. Chem. Soc. **117**, 7493 (1995).
25. I. Renge. J. Phys. Chem. B, **108**, 10596 (2004).

© 2007 NRC Canada

Zinc oxide as a new, highly efficient, green, and reusable catalyst for microwave-assisted Michael addition of sulfonamides to α,β-unsaturated esters in ionic liquids

Abdolkarim Zare, Alireza Hasaninejad, Ahmad Reza Moosavi Zare, Abolfath Parhami, Hashem Sharghi, and Ali Khalafi-Nezhad

Abstract: A simple, clean, and efficient procedure for the green synthesis of some *N*-alkyl derivatives of sulfonamides is described. Microwave-assisted Michael addition of sulfonamides to α,β-unsaturated esters, in the presence of catalytic amount of zinc oxide (ZnO) in 1-butyl-3-methylimidazolium bromide ([bmim]Br), affords the title compounds in high yields and short reaction times.

Key words: zinc oxide, green chemistry, microwave, Michael addition, sulfonamide, ionic liquid.

Résumé : On décrit une méthode simple, propre et efficace pour la synthèse verte de quelques dérivés *N*-alkyles des sulfonamides. L'addition de Michael assistée par micro-ondes de sulfonamides sur des esters α,β-insaturés, en présence d'une quantité catalytique d'oxyde de zinc (ZnO) dans le bromure de 1-butyl-3-méthylimidazolium ([bmim]Br) conduit à la formation des produits mentionnés dans le titre, avec des rendements élevés et de courts temps de réaction.

Mots-clés : oxyde de zinc, chimie verte, micro-onde, addition de Michael, sulfonamide, liquide ionique.

[Traduit par la Rédaction]

Introduction

Currently, ionic liquids are the subject of considerable interest as benign reaction media in organic synthesis because of their unique properties, such as non-volatility, non-flammability, recyclability, and ability to dissolve a wide range of materials (1). During the past decade, a variety of ionic liquids have been demonstrated as efficient and practical alternatives to organic solvents for many important organic transformations (1). Catalytic activity has been also reported for these green solvents (2). Together with the substitution of common molecular solvents, non-conventional activation methods, mainly microwave irradiation (MWI), have emerged as powerful techniques to reduce reaction times and to enhance reaction rates (3). As part of our drive to avoid the use of volatile organic solvents in reactions (4), we have initiated a program to explore the use of ionic liquids as efficient reaction media for useful organic transformations at room temperature.

N-Alkyl derivatives of sulfonamides are important because they have various biological activities, including their antidepressant, psychostimulant, analgesic, anti-ulcer, antiemetic, and anti-inflammatory properties (5). These compounds can be prepared via aza-conjugate addition of sulfonamides to α,β-unsaturated compounds (6). Michael reaction of sulfonamides with α,β-unsaturated esters also affords protected β-amino acids. This class of compounds (β-amino acids) are essential components in many bioactive compounds and drugs scaffolds, such as β-peptides (7), imeriamine (hypoglycemic and antiketogenic agent, Fig. 1) (8), vitamin B_3 (Fig. 1) (9), cryptophycin (antitumor) (10), and TAN-1057 A (antibiotic) (11). Indeed, to the best of our knowledge, there are only a few reports of Michael addition of sulfonamides. Reitz et. al have used alumina to carry out this reaction (6). However, in their report, the reaction times are long, and the yields are moderate. Moreover, they applied more reactive α,β-unsaturated ketones.

In aza-conjugate reactions, the nucleophilic nitrogen is usually among the powerful nucleophiles, such as amines (12), which, if used in the reaction, can lead to side products, e.g., amides via nucleophilic attack of amine to carbonyl group of α,β-unsaturated esters (12*a*). Furthermore, 1,2- and 1,4-condensation of a β-amino residue to α,β-unsaturated esters caused polymerization or tar formation (12*a*). Moreover, some procedures often require a large excess of reagents (12*b*). Therefore, in this context, using sulfonamides instead of amines in Michael reaction with

Received 6 March 2007. Accepted 9 May 2007. Published on the NRC Research Press Web site at canjchem.nrc.ca on 12 June 2007.

A. Zare.[1] Department of Chemistry, Payam Noor University of Bushehr, Bushehr 1698, Iran.
A. Hasaninejad.[2] Department of Chemistry, Faculty of Sciences, Persian Gulf University, Bushehr 75169, Iran.
A.R. Moosavi Zare, A. Parhami, H. Sharghi, and A. Khalafi-Nezhad. Department of Chemistry, College of Sciences, Shiraz University, Shiraz 71454, Iran.

[1]Corresponding author (e-mail: abdolkarimzare@yahoo.com).
[2]Corresponding author (e-mail: ahassaninejad@yahoo.com).

 doi:10.1139/V07-050 © 2007 NRC Canada

Scheme 1. Michael addition of benzenesulfonamide to *n*-butyl acrylate.

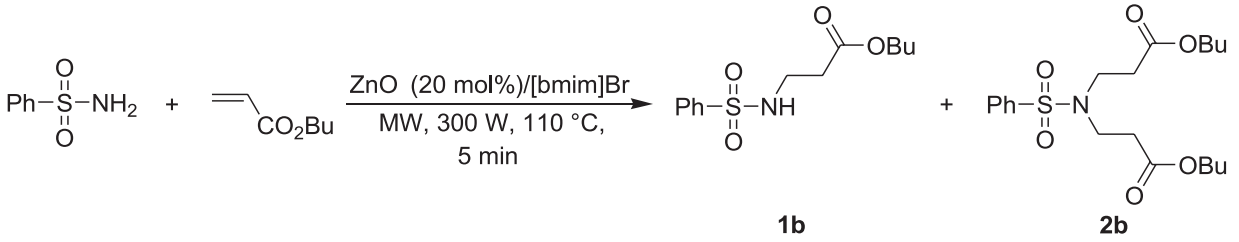
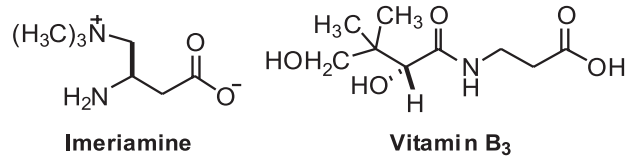


Fig. 1. The structures of imeriamine and vitamin B_3.



α,β-unsaturated esters seems to be more favorable, since lower nucleophilicity of nitrogen leads to less side reactions.

Recently, mineral oxides have proved to be useful to chemists both in the laboratory and in the industry because of the good activation of adsorbed compounds, reaction rate enhancement, selectivity, easier workup, recyclability of the supports, and the eco-friendly reaction conditions (13, 14). Zinc oxide (ZnO) is certainly one of the most interesting of these oxides because it has surface properties that can accomodate rich organic reactions (14). Zinc oxide is an inexpensive, moisture stable, reusable, commercially available, and environmentally benign catalyst. This catalyst has been used in several transformations, such as Beckmann rearrangement (14*a*), Friedel–Crafts acylation (14*b*), benzylic oxidation (14*c*), conversion of oximes to nitriles (14*d*), synthesis of cyclic ureas (14*e*), and acylation of alcohols and amines (14*f*, 14*g*).

Herein, we report a clean, facile, and rapid method for Michael addition of sulfonamides to α,β-unsaturated esters in the presence of catalytic amount of zinc oxide in [bmim]Br under MWI (Scheme 1). In this method, *N*,*N*-dialkyl sulfonamides formed together with the N-alkylated products in very low yields.

Results and discussion

To optimize reaction conditions, Michael addition of benzenesulfonamide to *n*-butyl acrylate was studied as a model reaction to provide compounds **1b** and **2b** (Scheme 1). First, the efficiency of several ionic liquids, including [bmim]Br, [bmim]Cl, [bmim]BF_4, and [bmim]PF_6, was investigated in the presence of ZnO (20 mol%) under MWI (300 W, max. 110 °C). Interestingly, all examined ionic liquids afforded almost similar yields and reaction times. However, [bmim]Br was applied as solvent for all reactions because the preparation of this ionic liquid was easy, compared with other ionic liquids.

In another study, the influence of various inorganic and organic basic catalysts on the model reaction was studied. The results are summarized in Table 1. Clearly, higher selectivity in shorter reaction time was attained when ZnO was used. Therefore, ZnO was the catalyst of choice in all reactions. Moreover, the effect of using different amounts of ZnO was investigated (Table 1). The optimum amount of ZnO was found to be 20 mol%.

Table 1. The effect of different basic catalysts on Michael addition of benzenesulfonamide (2 mmol) with *n*-butyl acrylate (2.2 mmol) in [bmim]Br (2 g) under MW conditions (300 W, max. 110 °C).

		Yield[a] (%)	
Catalyst	Time (min)	N-Alkylated product	N,N-Dialkylated product
ZnO (10%)	8	67	6
ZnO (15%)	8	75	8
ZnO (20%)	5	86	9
ZnO (30%)	5	77	13
ZnO (50%)	5	63	22
ZnO (100%)	5	50	29
K_2CO_3 (20%)	6	57	8
Cs_2CO_3 (20%)	5	68	13
t-BuOK (20%)	5	67	11
Basic Al_2O_3 (20%)	7	58	9
NBu_3 (20%)	8	22	<3
DABCO (20%)	8	17	<3

[a]Isolated yield.

To select the appropriate MW power, conjugate addition of benzenesulfonamide to *n*-butyl acrylate was examined at different MW powers (100–600 W), with controlled temperature (max. 110 °C), in the presence of ZnO, and in [bmim]Br. The best results were observed at 300 W.

To compare the efficiency of the ionic liquid with that of the conventional solvents, the model reaction was examined in various conventional solvents. Thus, a mixture of benzenesulfonamide (2 mmol), ZnO (0.4 mmol), and *n*-butyl acrylate (2.2 mmol) was irradiated in a MW oven (300 W, max. 110 °C) in different solvents (5 mL) (Table 2). Clearly, conventional solvents exhibited lower selectivities and longer reaction times compared with [bmim]Br. Therefore, the ionic-liquid-accelerated method is more efficient.

The capability and efficiency of MW heating, compared with conventional heating, on Michael reaction was also investigated. For this purpose, compounds **1b** and **2b** as well as **1g** and **2g** were prepared via Michael reaction between benzenesulfonamide and α,β-unsaturated esters in the presence of ZnO in [bmim]Br under thermal conditions (110 °C) (Table 3). As Table 3 demonstrates, MW conditions gave better results compared with thermal conditions. This can be attributed to the efficient performance of the reactions with more polar transition state relative to the ground state under MWI (3*a*–3*c*).

© 2007 NRC Canada

Table 2. Comparative Michael addition of benzenesulfonamide (2 mmol) to *n*-butyl acrylate (2.2 mmol) in the presence of ZnO (0.4 mmol) in conventional solvents (5 mL) vs. [bmim]Br (2 g) under MWI (300 W, max. 110 °C).

		Yield[a] (%)	
Solvent	Time (min)	N-Alkylated product	N,N-Dialkylated product
—	25	37	8
DMSO	20	68	12
DMF	20	63	10
HMPTA	25	50	9
o-Xylene	25	44	11
[bmim]Br	5	86	9

[a]Isolated yield.

Table 3. Comparative synthesis of compounds **1b** and **2b** as well as **1g** and **2g** using conventional heating (Δ, 110 °C) vs. the MW method (MW, 300 W, max. 110 °C).

Compound	Time (min)		Yield[a] (%)	
	Δ	MW	Δ	MW
1b	240	5	65	86
2b			16	9
1g	300	9	53	78
2g			9	6

[a]Isolated yield.

After optimizing the reaction conditions, Michael addition of sulfonamides was examined with structurally diverse α,β-unsaturated esters. The results are depicted in Table 4. The reactions proceeded efficiently, and the desired Michael adducts were obtained in high yields.

To study the structural influence of the alkoxy groups (–OR) of α,β-unsaturated esters (Michael acceptors) on the reaction, we have investigated the reaction of benzenesulfonamide with esters containing sterically hindered alkoxy groups. The results showed that the bulkiness of the alkoxy group had no significant effect on the yields, the selectivities, and the reaction times (Table 4, entries 1–6). The structural effect of α,β-unsaturated esters on Michael-addition reaction was also studied. Lower yields of the products and longer reaction times were observed when benzenesulfonamide was added to sterically hindered α,β-unsaturated esters (ethyl methacrylate and ethyl crotonate) (Table 4, entries 7 and 8). However, in these cases, the selectivity increased. Interestingly, the reaction of benzenesulfonamide as well as naphthalene-2-sulfonamide with ethyl crotonate afforded only the monoalkylated product (Table 4, entries 8 and 10). When 4-methylbenzenesulfonamide was used instead of benzenesulfonamide, the yields decreased (Table 4, entries 2 and 9).

The interesting behavior of [bmim]Br–ZnO system lies in the fact that it can be re-used after simple washing with Et_2O, thus rendering the process more economic. The yields of compounds **1b** and **2b** (model compounds) in the second, third, fourth, and fifth uses of the [bmim]Br/ZnO were almost as high as in the first use.

In conclusion, we have introduced a highly efficient catalyst for ionic-liquid-accelerated Michael addition of sulfonamides with α,β-unsaturated esters under MWI. The promising points for the presented methodology are high conversion, ease of handling and low cost of the catalyst, cleaner reaction profile, and short reaction times, which makes it a useful and attractive process for the rapid synthesis of *N*-alkyl sulfonamides as biologically interesting compounds.

Experimental

All chemicals were purchased from Merck or Fluka chemical companies. The progress of the reactions was followed with TLC using silica gel SILG/UV 254 plates. Silica gel 60, 0.063–0.200 mm (70–230 mesh ASTM) was used for column chromatography. All reactions were carried out using CEM MARS 5^{TM} MW oven. IR spectra were run on a Shimadzu FTIR-8300 spectrophotometer; ν_{max} values are reported in cm^{-1}. The ^1H NMR (250 MHz) and ^{13}C NMR (62.5 MHz) were run on a Bruker AVANCE DPX-250 FTNMR spectrometer. Mass spectra were recorded on a Shimadzu GC MS-QP 1000 EX apparatus. Microanalyses were performed on a PerkinElmer 240-B microanalyzer. Melting points were recorded on a Büchi B-545 apparatus in open capillary tubes and are uncorrected.

General procedure for the preparation of compounds 1b and 2b

To a mixture of benzenesulfonamide (0.31 g, 2 mmol), well-ground ZnO (0.033 g, 0.4 mmol), and *n*-butyl acrylate (0.28 g, 2.2 mmol) in a MW vessel was added [bmim]Br (2 g) and mixed carefully. The resulting mixture was irradiated in a MW oven at 300 W for 5 min. The oven was programmed to give a maximum internal temperature of 110 °C. Afterward, the reaction mixture was cooled to room temperature and was extracted with Et_2O (3 × 25 mL). The organic extracts were then combined. After the removal of the solvent, the crude product was purified by column chromatography on silica gel with EtOAc–*n*-hexane (1:3) to give **1b** and **2b** as colorless oils. After isolating the products and evaporating the remainder Et_2O in ionic liquid, the ionic liquid containing the catalyst ZnO ([bmim]Br–ZnO) was used for the next run under identical reaction conditions.

Ethyl 3-(phenylsulfonamido)propanoate (1a)

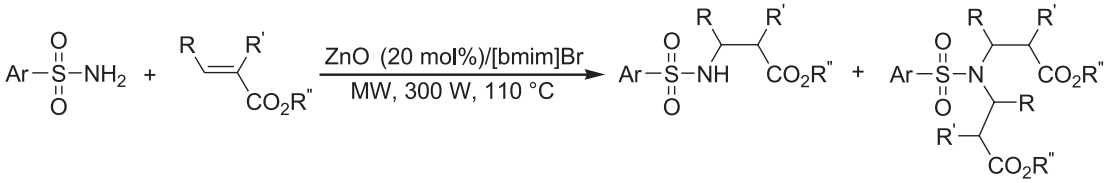
Colorless oil; isolated yield: 0.433 g (84%). IR (neat, cm^{-1}): 3286, 3059, 2975, 1732, 1447, 1329. ^1H NMR ($CDCl_3$, ppm) δ: 1.16 (t, 3H, J = 7.0 Hz, CH_3), 2.48 (t, 2H, J = 5.0 Hz, O=CCH_2), 3.15 (t, 2H, J = 5.0 Hz, O=CCH$_2$CH_2), 4.02 (q, 2H, J = 7.0 Hz, OCH_2), 5.56 (s, 1H, N*H*, exchangeable with D_2O), 7.42–7.52 (complex, 3H, H_3–H_5 of the aromatic ring), 7.80 (m, 2H, H_2 and H_6 of the aromatic ring). ^{13}C NMR ($CDCl_3$) δ: 14.0, 34.1, 38.7, 60.7, 127.0, 128.7, 132.6, 138.8, 171.7. MS *m/z*: 257 [M^+]. Anal. calcd. for $C_{11}H_{15}NO_4S$: C 51.35, H 5.88, N 5.44; found: C 51.52, H 6.01, N 5.30.

Compound 2a

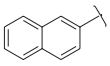
Colorless oil; isolated yield: 0.072 g (10%). IR (neat, cm^{-1}): 3028, 2984, 1733, 1447, 1317. ^1H NMR ($CDCl_3$, ppm) δ: 1.22 (t, 6H, J = 7.1 Hz, 2CH_3), 2.59 (t, 4H, J = 5.0 Hz, 2O=CCH_2), 3.45 (t, 4H, J = 5.0 Hz, 2O=CCH$_2$CH_2), 4.08 (q, 4H, J = 7.1 Hz, 2OCH_2), 7.46–7.57 (complex, 3H, H_3–H_5 of

© 2007 NRC Canada

Table 4. Ionic-liquid-accelerated Michael addition of sulfonamides to α,β-unsaturated esters using ZnO under MWI (300 W, 110 °C).



1a–1j **2a–2g and 2i**

Entry	Ar	R	R'	R"	Product	Time (min)	Yield[a] (%)
1[b]	C_6H_5	H	H	CH_3CH_2	**1a**	5	84
					2a	5	10
2	C_6H_5	H	H	$CH_3(CH_2)_2CH_2$	**1b**	5	86
					2b	5	9
3	C_6H_5	H	H	$CH_3(CH_2)_4CH_2$	**1c**	5	85
					2c	5	9
4	C_6H_5	H	H	$C_6H_5CH_2$	**1d**	6	84
					2d	6	8
5	C_6H_5	H	H	$C_6H_5CH_2CH_2$	**1e**	6	85
					2e	6	8
6	C_6H_5	H	H	$C_6H_5CH{=}CHCH_2$	**1f**	7	82
					2f	7	9
7	C_6H_5	H	CH_3	CH_3CH_2	**1g**	9	78
					2g	9	6
8[c]	C_6H_5	CH_3	H	CH_3CH_2	**1h**	12	73
9	*p*-$CH_3C_6H_4$	H	H	$CH_3(CH_2)_2CH_2$	**1i**	7	77
					2i	7	8
10[c]		CH_3	H	CH_3CH_2	**1j**	12	70

[a]Isolated yield.
[b]In this reaction, the molar ratio of α,β-unsaturated ester/sulfonamide was 1.3:1.
[c]In this case, only monosubstituted Michael adduct was produced.

the aromatic ring), 7.87 (m, 2H, H_2 and H_6 of the aromatic ring). ^{13}C NMR ($CDCl_3$) δ: 13.9, 32.8, 44.7, 60.4, 127.2, 129.1, 132.6, 138.9, 170.9. MS *m/z*: 357 [M^+]. Anal. calcd. for $C_{16}H_{23}NO_6S$: C 53.77, H 6.49, N 3.92; found: C 53.98, H 6.33, N 4.08.

Butyl 3-(phenylsulfonamido)propanoate (1b)

Colorless oil; isolated yield: 0.492 g (86%). IR (neat, cm^{-1}): 3271, 3048, 2960, 1733, 1447, 1330. ^{1}H NMR ($CDCl_3$, ppm) δ: 0.90 (t, 3H, *J* = 6.5 Hz, CH_3), 1.34 (m, 2H, CH_3CH_2), 1.56 (m, 2H, $CH_3CH_2CH_2$), 2.51 (t, 2H, *J* = 5.0 Hz, O=CCH_2), 3.19 (t, 2H, *J* = 5.0 Hz, O=CCH_2CH_2), 4.03 (t, 2H, *J* = 7.0 Hz, OCH_2), 5.68 (s, 1H, N*H*, exchangeable with D_2O), 7.48–7.57 (complex, 3H, H_3–H_5 of the aromatic ring), 7.79 (m, 2H, H_2 and H_6 of the aromatic ring). ^{13}C NMR ($CDCl_3$) δ: 13.5, 18.9, 30.4, 34.1, 38.7, 64.6, 126.8, 129.0, 132.5, 139.9, 172.7. MS *m/z*: 285 [M^+]. Anal. calcd. for $C_{13}H_{19}NO_4S$: C 54.72, H 6.71, N 4.91; found: C 54.48, H 6.92, N 5.06.

Compound 2b

Colorless oil; isolated yield: 0.075 g (9%). IR (neat, cm^{-1}): 3036, 2966, 1732, 1447, 1317. ^{1}H NMR ($CDCl_3$, ppm) δ: 0.92 (t, 6H, *J* = 6.5 Hz, 2CH_3), 1.33 (m, 4H, 2CH_3CH_2),

© 2007 NRC Canada

1.56 (m, 4H, $2CH_3CH_2CH_2$), 2.63 (t, 4H, J = 5.1 Hz, $2O{=}CCH_2$), 3.45 (t, 4H, J = 5.1 Hz, $2O{=}CCH_2CH_2$), 4.06 (t, 4H, J = 6.9 Hz, $2OCH_2$), 7.51–7.60 (complex, 3H, H_3–H_5 of the aromatic ring), 7.82 (m, 2H, H_2 and H_6 of the aromatic ring). ^{13}C NMR ($CDCl_3$) δ: 13.5, 18.9, 30.5, 34.2, 44.4, 64.2, 126.9, 129.0, 132.4, 138.9, 171.1. MS *m/z*: 413 [M^+]. Anal. calcd. for $C_{20}H_{31}NO_6S$: C 58.09, H 7.56, N 3.39; found: C 58.20, H 7.69, N 3.25.

Hexyl 3-(phenylsulfonamido)propanoate (1c)

Colorless oil; isolated yield: 0.532 g (85%). IR (neat, cm^{-1}): 3275, 3044, 2967, 1732, 1447, 1328. ^{1}H NMR ($CDCl_3$, ppm) δ: 0.90 (t, 3H, J = 6.7 Hz, CH_3), 1.28–1.34 (complex, 6H, CH_3CH_2, $CH_3CH_2CH_2$ and $CH_3(CH_2)_2CH_2$), 1.57 (m, 2H, $CH_3(CH_2)_3CH_2$), 2.56 (t, 2H, J = 5.1 Hz, $O{=}CCH_2$), 3.16 (t, 2H, J = 5.1 Hz, $O{=}CCH_2CH_2$), 4.09 (t, 2H, J = 6.9 Hz, OCH_2), 5.63 (s, 1H, NH), 7.41–7.48 (complex, 3H, H_3–H_5 of the aromatic ring), 7.78 (m, 2H, H_2 and H_6 of the aromatic ring). ^{13}C NMR ($CDCl_3$) δ: 13.5, 22.5, 25.5, 27.9, 30.6, 34.1, 38.5, 64.9, 126.5, 128.7, 132.2, 139.5, 171.8. MS *m/z*: 313 [M^+]. Anal. calcd. for $C_{15}H_{23}NO_4S$: C 57.48, H 7.40, N 4.47; found: C 57.26, H 7.58, N 4.62.

Compound 2c

Colorless oil; isolated yield: 0.084 g (9%). IR (neat, cm^{-1}): 3031, 2974, 1733, 1447, 1316. ^{1}H NMR ($CDCl_3$, ppm) δ: 0.89 (t, 6H, J = 6.6 Hz, $2CH_3$), 1.26–1.32 (complex, 12H, $2CH_3CH_2$, $2CH_3CH_2CH_2$ and $2CH_3(CH_2)_2CH_2$), 1.58 (m, 4H, $2CH_3(CH_2)_3CH_2$), 2.61 (t, 4H, J = 5.0 Hz, $2O{=}CCH_2$), 3.41 (t, 4H, J = 5.0 Hz, $2O{=}CCH_2CH_2$), 4.05 (t, 4H, J = 6.9 Hz, $2OCH_2$), 7.43–7.50 (complex, 3H, H_3–H_5 of the aromatic ring), 7.74 (m, 2H, H_2 and H_6 of the aromatic ring). ^{13}C NMR ($CDCl_3$) δ: 13.8, 22.3, 25.5, 28.0, 30.4, 33.9, 44.5, 64.4, 126.4, 128.9, 132.1, 139.4, 171.4. MS *m/z*: 392 [$M^+ - C_6H_5$], 368 [$M^+ - C_6H_{13}O$), 328 [$M^+ - C_6H_5SO_2$]. Anal. calcd. for $C_{24}H_{39}NO_6S$: C 61.38, H 8.37, N 2.98; found: C 61.13, H 8.23, N 3.11.

Benzyl 3-(phenylsulfonamido)propanoate (1d)

Pale yellow oil; isolated yield: 0.535 g (84%). IR (neat, cm^{-1}): 3286, 3031, 2954, 1733, 1447, 1328. ^{1}H NMR ($CDCl_3$, ppm) δ: 2.65 (t, 2H, J = 5.1 Hz, $O{=}CCH_2$), 3.17 (t, 2H, J = 5.1 Hz, $O{=}CCH_2CH_2$), 5.00 (s, 2H, OCH_2), 5.71 (s, 1H, NH), 7.26–7.31 (complex, 5H, H_1–H_5 of the alkoxy groups of the aromatic ring), 7.45–7.51 (complex, 3H, H_3–H_5 of the aromatic ring of sulfonamide), 7.82 (m, 2H, H_2 and H_6 of the aromatic ring of sulfonamide). ^{13}C NMR ($CDCl_3$) δ: 34.2, 38.7, 66.6, 126.9, 128.2, 128.4, 128.6, 129.2, 132.7, 135.4, 139.9, 171.7. MS *m/z*: 319 [M^+]. Anal. calcd. for $C_{16}H_{17}NO_4S$: C 60.17, H 5.37, N 4.39; found: C 59.94, H 5.56, N 4.26.

Compound 2d

Pale yellow oil; isolated yield: 0.081 g (8%). IR (neat, cm^{-1}): 3051, 2965, 1734, 1447, 1316. ^{1}H NMR ($CDCl_3$, ppm) δ: 2.58 (t, 4H, J = 5.0 Hz, $2O{=}CCH_2$), 3.36 (t, 4H, J = 5.0 Hz, $2O{=}CCH_2CH_2$), 5.00 (s, 4H, $2OCH_2$), 7.22–7.25 (complex, 10H, H_1–H_5 of the alkoxy groups of the aromatic ring), 7.39–7.48 (complex, 3H, H_3–H_5 of the aromatic ring of sulfonamide), 7.72 (m, 2H, H_2 and H_6 of the aromatic ring of sulfonamide). ^{13}C NMR ($CDCl_3$) δ: 33.3, 43.9, 65.5, 126.2, 127.7, 128.1, 128.9, 129.5, 131.8, 134.4, 137.8, 171.4. MS *m/z*: 404 [$M^+ - C_6H_5$], 374 [$M^+ - C_7H_7O$], 340 [$M^+ - C_6H_5SO_2$). Anal. calcd. for $C_{26}H_{27}NO_6S$: C 64.85, H 5.65, N 2.91; found: C 65.04, H 5.48, N 2.80.

Phenethyl 3-(phenylsulfonamido)propanoate (1e)

Pale yellow oil; isolated yield: 0.564 g (85%). IR (neat, cm^{-1}): 3285, 3063, 2957, 1732, 1447, 1329. ^{1}H NMR ($CDCl_3$, ppm) δ: 2.48 (t, 2H, J = 5.2, $O{=}CCH_2$), 2.88 (t, 2H, J = 6.8 Hz, $ArCH_2$), 3.14 (t, 2H, J = 5.2 Hz, $O{=}CCH_2CH_2$), 4.24 (t, 2H, J = 6.8 Hz, OCH_2), 5.43 (s, 1H, NH), 7.15–7.28 (complex, 5H, H_1–H_5 of the alkoxy groups of the aromatic ring), 7.47–7.52 (complex, 3H, H_3–H_5 of the aromatic ring of sulfonamide), 7.84 (m, 2H, H_2 and H_6 of the aromatic ring of sulfonamide). ^{13}C NMR ($CDCl_3$) δ: 34.1, 34.9, 38.7, 65.2, 126.6, 126.9, 128.5, 128.8, 129.1, 132.7, 137.5, 139.9, 171.7. MS *m/z*: 333 [M^+]. Anal. calcd. for $C_{17}H_{19}NO_4S$: C 61.24, H 5.74, N 4.20; found: C 60.97, H 5.89, N 4.29.

Compound 2e

Pale yellow oil; isolated yield: 0.083 g (8%). IR (neat, cm^{-1}): 3045, 2942, 1733, 1447, 1331. ^{1}H NMR ($CDCl_3$, ppm) δ: 2.51 (t, 4H, J = 5.2 Hz, $2O{=}CCH_2$), 2.82 (t, 4H, J = 6.9 Hz, $2ArCH_2$), 3.30 (t, 4H, J = 5.2 Hz, $2O{=}CCH_2CH_2$), 4.19 (t, 4H, J = 6.9 Hz, $2OCH_2$), 7.10–7.19 (complex, 10H, H_1–H_5 of the alkoxy groups of the aromatic ring), 7.42–7.45 (complex, 3H, H_3–H_5 of the aromatic ring of sulfonamide), 7.78 (m, 2H, H_2 and H_6 of the aromatic ring of sulfonamide). ^{13}C NMR ($CDCl_3$) δ: 34.3, 34.9, 44.9, 65.2, 126.6, 126.7, 126.9, 128.6, 128.8, 129.2, 132.8, 137.5, 171.0. MS *m/z*: 432 [$M^+ - C_6H_5$], 388 [$M^+ - C_8H_9O$], 368 [$M^+ - C_6H_5SO_2$]. Anal. calcd. for $C_{28}H_{31}NO_6S$: C 65.99, H 6.13, N 2.75; found: C 65.87, H 6.26, N 2.89.

Cinnamyl 3-(phenylsulfonamido)propanoate (1f)

Pale yellow oil; isolated yield: 0.568 g (82%). IR (neat, cm^{-1}): 3287, 3059, 2964, 1732, 1447, 1329. ^{1}H NMR ($CDCl_3$, ppm) δ: 2.55 (t, 2H, J = 5.2 Hz, $O{=}CCH_2$), 3.19 (t, 2H, J = 5.2 Hz, $O{=}CCH_2CH_2$), 4.69 (m, 2H, OCH_2), 5.50 (s, 1H, NH), 6.23 (m, 1H, PhCH=CH), 6.63 (d, 1H, J = 15.7 Hz, PhCH), 7.29–7.35 (complex, 5H, H_1–H_5 of the alkoxy groups of the aromatic ring), 7.45–7.50 (complex, 3H, H_3–H_5 of the aromatic ring of sulfonamide), 7.95 (m, 2H, H_2 and H_6 of the aromatic ring of sulfonamide). ^{13}C NMR ($CDCl_3$) δ: 34.2, 38.8, 65.8, 122.6, 122.9, 126.6, 126.9, 128.1, 128.6, 129.0, 132.7, 134.6, 139.9, 171.7. MS *m/z*: 345 [M^+]. Anal. calcd. for $C_{18}H_{19}NO_4S$: C 62.59, H 5.54, N 4.06; found: C 62.82, H 5.39, N 4.21.

Compound 2f

Pale yellow oil; isolated yield: 0.094 g (9%). IR (neat, cm^{-1}): 3026, 2981, 1732, 1448, 1317. ^{1}H NMR ($CDCl_3$, ppm) δ: 2.51 (t, 4H, J = 5.1 Hz, $2O{=}CCH_2$), 3.41 (t, 4H, J = 5.1 Hz, $2O{=}CCH_2CH_2$), 4.73 (m, 4H, $2OCH_2$), 6.15 (m, 2H, 2PhCH=CH), 6.54 (d, 2H, J = 15.7 Hz, 2PhCH), 7.28–7.36 (complex, 10H, H_1–H_5 of the alkoxy groups of the aromatic ring), 7.41–7.47 (complex, 3H, H_3–H_5 of the aromatic ring of sulfonamide), 7.94 (m, 2H, H_2 and H_6 of the aromatic ring of sulfonamide). ^{13}C NMR ($CDCl_3$) δ: 33.8, 43.2, 65.4, 122.4, 123.0, 126.7, 126.9, 127.9, 128.5, 129.4, 132.4, 134.1, 139.3, 171.5. MS *m/z*: 400 [M^+ –

© 2007 NRC Canada

C_9H_9O], 392 [$M^+ - C_6H_5SO_2$]. Anal. calcd. for $C_{30}H_{31}NO_6S$: C 67.52, H 5.86, N 2.62; found: C 67.40, H 5.71, N 2.78.

Ethyl 2-methyl-3-(phenylsulfonamido)propanoate (1g)

Pale yellow oil; isolated yield: 0.421 g (78%). IR (neat, cm^{-1}): 3283, 3034, 2966, 1732, 1447, 1328. ^1H NMR ($CDCl_3$, ppm) δ: 1.17–1.26 (complex, 6H, $2CH_3$), 2.73 (m, 1H, O=CC*H*), 3.14–3.20 (complex, 2H, O=CCH(CH_3)CH_2), 4.12 (q, 2H, *J* = 7.0 Hz, OCH_2), 5.65 (s, 1H, N*H*), 7.55–7.64 (complex, 3H, H_3–H_5 of the aromatic ring), 7.93 (m, 2H, H_2 and H_6 of the aromatic ring). ^{13}C NMR ($CDCl_3$) δ: 14.0, 14.7, 39.6, 45.4, 60.8, 126.8, 129.1, 132.5, 139.9, 174.7. MS *m*/*z*: 271 [M^+]. Anal. calcd. for $C_{12}H_{17}NO_4S$: C 53.12, H 6.32, N 5.16; found: C 53.31, H 6.57, N 5.01.

Compound 2g

Pale yellow oil; isolated yield: 0.048 g (6%). IR (neat, cm^{-1}): 3042, 2982, 1732, 1447, 1316. ^1H NMR ($CDCl_3$, ppm) δ: 1.09–1.19 (complex, 12H, $4CH_3$), 2.78 (m, 2H, 2O=CC*H*), 3.22–3.27 (complex, 4H, 2O=CCH(CH_3)CH_2), 4.03 (q, 4H, *J* = 7.0 Hz, 2OCH_2), 7.44–7.53 (complex, 3H, H_3–H_5 of the aromatic ring), 7.75 (m, 2H, H_2 and H_6 of the aromatic ring). ^{13}C NMR ($CDCl_3$) δ: 14.1, 15.3, 39.2, 52.4, 60.7, 127.3, 129.1, 132.7, 139.0, 174.7. MS *m*/*z*: 385 [M^+]. Anal. calcd. for $C_{18}H_{27}NO_6S$: C 56.08, H 7.06, N 3.63; found: C 55.80, H 7.23, N 3.77.

Ethyl 3-(phenylsulfonamido)butanoate (1h)

Pale yellow solid; isolated yield: 0.394 g (73%); mp 60–62 °C. IR (KBr, cm^{-1}): 3285, 3044, 2953, 1732, 1447, 1329. ^1H NMR ($CDCl_3$, ppm) δ: 1.14–1.23 (complex, 6H, $2CH_3$), 2.38–2.43 (complex, 2H, O=CCH_2), 3.68 (m, 1H, O=CCH_2C*H*), 4.04 (q, 2H, *J* = 7.1 Hz, OCH_2), 5.39 (s, 1H, N*H*), 7.49–7.59 (complex, 3H, H_3–H_5 of the aromatic ring), 7.89 (m, 2H, H_2 and H_6 of the aromatic ring). ^{13}C NMR ($CDCl_3$) δ: 14.0, 21.0, 40.7, 46.6, 60.7, 126.9, 129.0, 132.5, 140.9, 171.1. MS *m*/*z*: 271 [M^+]. Anal. calcd. for $C_{12}H_{17}NO_4S$: C 53.12, H 6.32, N 5.16; found: C 53.30, H 6.19, N 5.31.

Butyl 3-(4-methylphenylsulfonamido)propanoate (1i)

Pale yellow oil; isolated yield: 0.460 g (77%). IR (neat, cm^{-1}): 3286, 3044, 2960, 1732, 1330. ^1H NMR ($CDCl_3$, ppm) δ: 0.89 (t, 3H, *J* = 6.8 Hz, $CH_2(CH_2)_2CH_3$), 1.33 (m, 2H, CH_3CH_2), 1.56 (m, 2H, $CH_3CH_2CH_2$), 2.40 (s, 3H, ArCH_3), 2.51 (t, 2H, *J* = 5.3 Hz, O=CCH_2), 3.16 (t, 2H, *J* = 5.3 Hz, O=CCH_2CH_2), 4.04 (t, 2H, *J* = 7.0 Hz, OCH_2), 5.76 (s, 1H, N*H*), 7.33 (d, 2H, *J* = 7.9 Hz, H_3 and H_5 of the aromatic ring), 7.72 (d, 2H, *J* = 7.9 Hz, H_2 and H_6 of the aromatic ring). ^{13}C NMR ($CDCl_3$) δ: 13.5, 18.9, 21.3, 30.3, 34.1, 38.7, 64.5, 126.9, 129.6, 135.8, 143.2, 172.7. MS *m*/*z*: 299 [M^+]. Anal. calcd. for $C_{14}H_{21}NO_4S$: C 56.16, H 7.07, N 4.68; found: C 55.97, H 7.18, N 4.55.

Compound 2i

Pale yellow oil; isolated yield: 0.071 g (8%). IR (neat, cm^{-1}): 3056, 2975, 1734, 1317. ^1H NMR ($CDCl_3$, ppm) δ: 0.92 (t, 6H, *J* = 6.9 Hz, $2CH_2(CH_2)_2CH_3$), 1.32 (m, 4H, $2CH_3CH_2$), 1.57 (m, 4H, $2CH_3CH_2CH_2$), 2.42 (s, 3H, ArCH_3), 2.63 (t, 4H, *J* = 5.2 Hz, 2O=CCH_2), 3.43 (t, 4H, *J* = 5.2 Hz, 2O=CCH_2CH_2), 4.02 (t, 4H, *J* = 7.0 Hz, 2OCH_2), 7.31 (d, 2H, *J* = 7.9 Hz, H_3 and H_5 of the aromatic ring), 7.72 (d, 2H, *J* = 7.9 Hz, H_2 and H_6 of the aromatic ring). ^{13}C NMR ($CDCl_3$) δ: 13.6, 19.0, 21.4, 30.4, 33.9, 45.0, 64.5, 126.9, 129.5, 135.9, 143.5, 172.5. MS *m*/*z*: 427 [M^+]. Anal. calcd. for $C_{21}H_{33}NO_6S$: C 58.99, H 7.78, N 3.28; found: C 59.15, H 7.68, N 3.14.

Ethyl 3-(naphthalene-2-sulfonamido)butanoate (1j)

Colorless buff; isolated yield: 0.453 g (70%). IR (neat, cm^{-1}): 3284, 3051, 2970, 1732, 1447, 1329. ^1H NMR ($CDCl_3$, ppm) δ: 1.07–1.12 (complex, 6H, $2CH_3$), 2.31–2.35 (complex, 2H, O=CCH_2), 3.67 (m, 1H, O=CCH_2C*H*), 3.99 (q, 2H, *J* = 7.0 Hz, OCH_2), 5.38 (s, 1H, N*H*), 7.52–7.57 (complex, 4H), 7.79–7.90 (complex, 3H). ^{13}C NMR ($CDCl_3$) δ: 14.0, 21.1, 40.6, 46.7, 60.7, 122.3, 127.5, 127.7, 127.9, 128.1, 128.3, 128.8, 129.2, 129.5, 132.1, 171.1. MS *m*/*z*: 321 [M^+]. Anal. calcd. for $C_{16}H_{19}NO_4S$: C 59.79, H 5.96, N 4.36; found: C 59.90, H 6.11, N 4.51.

Acknowledgements

We are grateful to Payam Noor University of Bushehr, Persian Gulf University, and Shiraz University Research Councils for the financial support of this work.

References

1. (*a*) K. Mikami. Green reaction media in organic synthesis. Blackwell Publishing, Oxford, UK. 2005; (*b*) R. D. Rogers. Ionic Liquids as green solvents: progress and prospects. An American Chemical Society Publication. 2005; (*c*) P. Wasserscheid and T. Welton. Ionic liquids in synthesis. Wiley-VCH, Weinheim. 2003; (*d*) T. Welton. Chem. Rev. **99**, 2071 (1999); (*e*) M.S. Rasalkar, S.V. Bhilare, A.R. Deorukhkar, N.B. Darvatkar, and M.M. Salunkhe. Can. J. Chem. **85**, 1 (2007); (*f*) X. Fan, Y. Li, X. Zhang, G. Qu, and J. Wang. Can. J. Chem. **84**, 794 (2006); (*g*) G. Karthikeyan and P.T. Perumal. Can. J. Chem. **83**, 1746 (2005).
2. (*a*) J.R. Harjani, S.J. Nara, and M.M. Salunkhe. Tetrahedron Lett. **43**, 1127 (2002); (*b*) V.V. Namboodiri and R.S. Varma. Chem. Commun. 342 (2002); (C) V.R. Koch, L.L. Miller, and R.A. Osteryoung. J. Am. Chem. Soc. **98**, 5277 (1976); (*d*) D.S. Kim and W.S. Ahn. Korean J. Chem. Eng. **39**, 20 (2003); (*e*) D.S. Newman, R.E. Winans, and R.L. McBeth. J. Electrochem. Soc. **131**, 1079 (1984); (*f*) C.J. Adams, M.J. Earle, G. Roberts, and K.R. Seddon. Chem. Commun. 2097 (1998); (*g*) P.A.Z. Suarez, J.E.L. Dullius, S. Einloft, R.F. de Souza, and J. Dupont. Polyhedron, **15**, 1217(1996).
3. (*a*) A. Loupy. Microwaves in organic synthesis. Wiley-VCH, Weinheim. 2004; (*b*) L. Perreux and A. Loupy. Tetrahedron, **57**, 9199 (2001); (C) A. Dandia, M. Sati, K. Arya, R. Sharma, A. Loupy. Chem. Pharm. Bull. **10**, 1137 (2003); (*d*) A. Loupy. Microwaves in organic synthesis. Wiley-VCH, Weinheim. 2006; (*e*) K. Tanaka. Solvent-free organic synthesis. Wiley-VCH, GmbH and KGaA, Weinheim. 2004; (*f*) A. Khalafi-Nezhad, A. Zare, A. Parhami, M.N. Soltani Rad, and G.R. Nejabat. Can. J. Chem. **84**, 979 (2006); (*g*) R.S. Varma. Advances in green chemistry: chemical synthesis using microwave irradiation. Astra Zeneca Research Foundation, Kavitha Printers, Bangalore, India. 2002; (*h*) B.L. Hayes. Microwave synthesis: chemistry at the speed of light. CEM Publishing: Mathews, NC. 2002; (*i*) H.M. Kingston and S.J. Haswell. Microwave-enhanced chemistry: fundamentasls, sample prepa-

© 2007 NRC Canada

ration, and applications. American Chemical Society: Washington, D.C. 1997; (*j*) J. Yin, X. Li, X. Wu, B. Chen, Z. Liu, and Q. Song. Can. J. Chem. **83**, 2140 (2005); (*k*) B. P. Joshi, A. Sharma, and A. K. Sinha. Can. J. Chem. **83**, 1826 (2005); (*l*) G. Qu, S. Han, Z. Zhang, M. Geng, and F. Xue. Can. J. Chem. **84**, 819 (2006); (*m*) S. Singh, M.P.S. Ishar, G. Singh, and R. Singh. Can. J. Chem. **83**, 260 (2005); (*n*) M. Kidwai, and R. Mohan. Can. J. Chem. **82**, 427 (2004).

4. (*a*) A. Khalafi-Nezhad, A. Zare, A. Parhami, M.N, Soltani Rad, and G.R. Nejabat. J. Iran. Chem. Soc. In press; (*b*) G.H. Imanzadeh, A. Khalafi-Nezhad, A. Zare, A. Hasaninejad, A.R. Moosavi Zare, and A. Parhami. J. Iran. Chem. Soc. **4**, 229 (2007); (*c*) A. Khalafi-Nezhad, A. Zare, A. Parhami, M.N. Soltani Rad and G.R. Nejabat. Phosphorus, Sulfur Silicon Relat. Elem. **182**, 657 (2007); (*d*) A. Khalafi-Nezhad, A. Zare, A. Parhami, M.N. Soltani Rad, and G.R. Nejabat. Synth. Commun. **36**, 3549 (2006); (*e*) A. Khalafi-Nezhad, A. Parhami, M.N. Soltani Rad, and A. Zare, Tetrahedron Lett. **46**, 6879 (2005); (*f*) A. Khalafi-Nezhad, A. Zare, M.N. Soltani Rad, B. Mokhtari, and A. Parhami. Synthesis, 419 (2005); (*g*) A. Khalafi-Nezhad, M.N. Soltani Rad, and A. Khoshnood. Synthesis, 583 (2004); (*h*) A. Khalafi-Nezhad, M.N. Soltani Rad, and G.H. Hakimelahi. Helv. Chim. Acta. **86**, 2396 (2003); (*i*) A. Khalafi-Nezhad, B. Mokhtari, and M.N. Soltani Rad. Tetrahedron Lett. **44**, 7325 (2003); (*j*) A. Khalafi-Nezhad, and A. Hashemi. Iran. J. Chem. Chem. Eng. **20**, 9 (2001); (*k*) A. Khalafi-Nezhad, F. Alamdari, and N. Zekri. Tetrahedron, **56**, 7503 (2000); (*l*) A. Khalafi-Nezhad, and A. Hashemi. J. Chem. Res. Synop. 720 (1999).
5. M.J. O'Neil, A. Smith, T.E. Heckelman, and F. Dudavari (*Editors*). The Merck index: an encyclopedia of chemicals, drugs, and biologicals. 13th Ed. Merck: Whitehouse Station, NJ. 2001.
6. A. Reitz, M. Verlander, and M. Goodman. Tetrahedron Lett. **23**, 751 (1982).
7. S. H. Gellman. Acc. Chem. Res. **31**, 173 (1998).
8. S. Shinagawa, T. Kanamaru, S. Harada, M. Asai, and H. Okazaki. J. Med. Chem. **30**, 1458 (1987).
9. M. Windholz, S. Budavari, L.Y. Stroumtsos, and M.N. Fertig (*Editors*). The Merck index, an encyclopedia of chemicals and drugs. 9th ed. Merck, Rahway, NJ. 1976.
10. C. Shih, L.S. Gossett, J.M. Gruber, C.S. Grossman, S.L. Andis, R.M. Schultz, J.F. Wor.0zalla, T.H. Corbett, and J.T. Metz. Bioorg. Med. Chem. Lett. **9**, 69 (1999).
11. C. Yuan and R.M. Williams. J. Am. Chem. Soc. **119**, 11777 (1997).
12. (*a*) N. Azizi and M.R. Saidi. Tetrahedron, **60**, 383 (2004); (*b*) F. Palacios, D. Aparicio, Y. Lopez, and J.M. de los Santos. Tetrahedron Lett. **45**, 4345 (2004); (C) C. Magnier-Bouvier, J.-C. Blazejewski, C. Larpent, and E. Magnier. Tetrahedron Lett. **47**, 9121 (2006); (*d*) H. Firouzabadi, N. Iranpoor, M. Jafarpour, and A. Ghaderi. J. Mol. Catal. A.: Chem. **252**, 150 (2006); (*e*) M. Molteni, A. Volonterio, G. Fossati, P. Lazzarib, and M. Zandac. Tetrahedron Lett. **48**, 589 (2007); (*f*) H. Firouzabadi, N. Iranpoor, and F. Nowrouzi. Chem. Commun. 789 (2005); (*g*) H. Firouzabadi, N. Iranpoor, and A. A. Jafari. Adv. Synth. Cat. **347**, 655 (2005); (*h*) B. Tamami, A. Fadavi, and M. Tamami. Iran. Polym. J. **15**, 799 (2006).
13. (*a*) M.M. Khodaei, K. Bahrami, and M. Khedri. Can. J. Chem. **85**, 7 (2007); (*b*) R.S. Varma. Tetrahedron, **58**, 1235 (2002); (C) B.M. Choudary, R.S. Mulukutla, and K. Klabunde. J. Am. Chem. Soc. **125**, 2020 (2003); (*d*) T.F. Dossin, M.-F. Reyniers, R.J. Berger, and G.B. Marin. Appl. Catal. B. **67**, 136 (2006); (*e*) B.M. Choudary, L. Chakrapani, T. Ramani, K.V. Kumar, and M.L. Kantam. Tetrahedron, **62**, 9571 (2006); (*f*) T. Seki, H. Tachikawa, T. Yamada, and H. Hattori. J. Catal. **217**, 117 (2003); (*g*) B.M. Choudary, M.L. Kantam, K.V.S. Ranganath, K. Mahendar, and B. Sreedhar. J. Am. Chem. Soc. **126**, 3396 (2004); (*h*) B.M. Choudary, K.V.S. Ranganath, U. Pal, M.L. Kantam, and B. Sreedhar. J. Am. Chem. Soc. **127**, 13167 (2005).
14. (*a*) H. Sharghi, and M. Hosseini. Synthesis, 1057 (2002); (*b*) M. Hosseini Sarvari, and H. Sharghi. J. Org. Chem. **69**, 6953 (2004); (C) M. Gupta, S. Paul, R. Gupta, and A. Loupy. Tetrahedron Lett. **46**, 4957 (2005); (*d*) M. Hosseini Sarvari. Synthesis, 787 (2005); (*e*) Y.J. Kim and R.S. Varma. Tetrahedron Lett. **45**, 7205 (2004); (*f*) M. Hosseini Sarvari and H. Sharghi. Tetrahedron, **61**, 10903 (2005); (*g*) F. Tamaddon. M.A. Amrollahi, and L. Sharafat, Tetrahedron Lett. 46, 7841 (2005).

© 2007 NRC Canada

Radical-mediated cyclization reactions leading to spiro and [6,6]-fused heterocycles

K.C. Majumdar, P. Debnath, A.K. Pal, S.K. Chattopadhyay, and A. Biswas

Abstract: Regiochemical study of $^{n}Bu_3SnH$–AIBN-mediated aryl-radical cyclization of different 3-(2-bromophenylsulfenylmethyl)coumarins, 3-(2-bromophenylsulfonyl-methyl)coumarins, and 6-[(2-bromophenoxy)methyl]-4-methoxypyran-2-ones have been investigated with the formation of different [6,6]-fused and spirocylic heterocycles. The sulfides and ethers were prepared from 3-chloromethyl coumarin and 6-(bromomethyl)-4-methoxy pyran-2-one with different 2-bromothiophenol and 2-bromophenols under classical alkylation condition. The corresponding sulfones were prepared by oxidation of the sulfides with *m*-CPBA.

Key words: aryl-radical cyclization, coumarin and pyrone derivatives, 5-exo-trig, 5-endo-trig, $^{n}Bu_3SnH$, sulfur heterocycles.

Résumé : On a effectué des réactions de cyclisation radicalaires aryliques, catalysées par le Bu_3SnH–AIBN, de diverses 3-(2-bromophénylsulfénylméthyl)coumarines, de 3-(2-bromophénylsulfonylméthyl)coumarines et de 6-[(2-bromophénoxy)méthyl]–4-méthoxypyran-2-ones et on a étudié leur régiochimie par rapport à la formation d'hétérocycles divers spirocycliques ou à fusion [6,6]. On a préparé les sulfures et les éthers de la 3-chlorométhylcoumarine et de la 6-(6-bromométhyl)-4-méthoxypyran-2-one à l'aide de divers 2-bromothiophénols et de 2-bromophénols, dans des conditions d'alkylation classique. Les sulfones correspondantes ont été préparées par oxydation des sulfures à l'aide d'acide *m*-chloroperbenzoïque.

Mots-clés : cyclisation radicalaire arylique, dérivés de la coumarine et des pyrones, 5-exo-trig, 6-endo-trig, Bu_3SnH, hétérocycles sulfurés.

[Traduit par la Rédaction]

Introduction

Recently, free-radical cyclizations have been regarded as a versatile route for the construction of carbocycles as well as heterocycles (1). In particular, the synthesis of sulfur heterocycles by radical pathway presents a major challenge in organic synthesis. A survey of the literature revealed a few reports on the preparation of sulfur heterocycles by free-radical pathways, which include the cyclizations where the sulfur functionality either constitute the part of the hexenyl chain (2) or is placed outside (3) the 5-hexenyl system. Intramolecular homolytic substitution by an alkyl or aryl radical at the sulfur atom in the alkyl sulfides and sulfoxides have also been widely acceptable for the construction of sulfur heterocycles (4). To the best of our knowledge, no reports on the construction of benzothiophene and benzothiopyran heterocycles by free-radical methodology, employing 2-bromothiophenol as aryl-radical precursor, are available in literature.

We previously reported the synthesis of several novel five- and six-membered sulfur heterocycles by the application of sigmatropic rearrangement (5). Recently, we were successful in synthesizing quinolone-annulated (6) [6,6]-fused sulfur heterocycles by $^{n}Bu_3SnH$-mediated radical cyclization where small amount of β-scission (6, 7) product was formed along with 5-endo cyclization. It has been recognized that a stereoelectronically favored 5-exo cyclization is generally preferred over a 5-endo ring closure in those system, having an alkenic bond at the 5 position relative to the radical center. This regiochemical preference can be altered by the attachment of a suitable stabilizing group to the acceptor double bond (8). An extensive investigation by Della and Graney (2*f*) on the 5-hexenyl radical, where the sulfur functionality is in the α position to the radical center, revealed a dramatic effect on the regiochemistry of radical cyclization. Therefore, we studied the radical cyclization of 3-(2-bromo phenylsulfenylmethyl)coumarins, 3-(2-bromophenylsulfinyl methyl)coumarins, and 3-(2-bromophenylsulfonyl methyl)-coumarins. Here, we report the results of our investigation.

Received 7 December 2006. Accepted 2 April 2007. Published on the NRC Research Press Web site at canjchem.nrc.ca on 9 June 2007.

K.C. Majumdar,[1] P. Debnath, A.K. Pal, S.K. Chattopadhyay, and A. Biswas. Department of Chemistry, University of Kalyani, Kalyani 741235, West Bengal, India

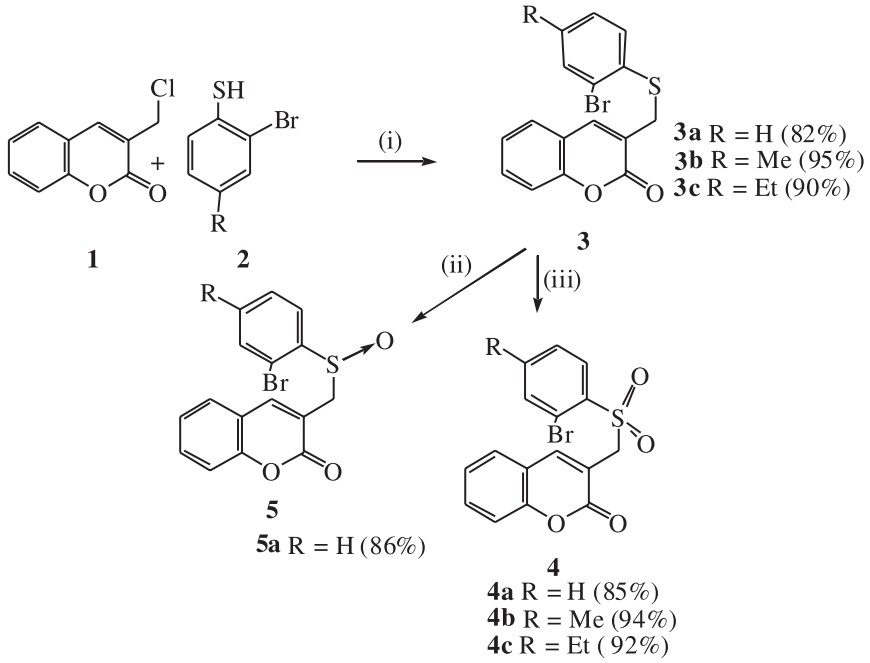
[1]Corresponding author (e-mail: kcm_ku@yahoo.co.in).

Results and discussion

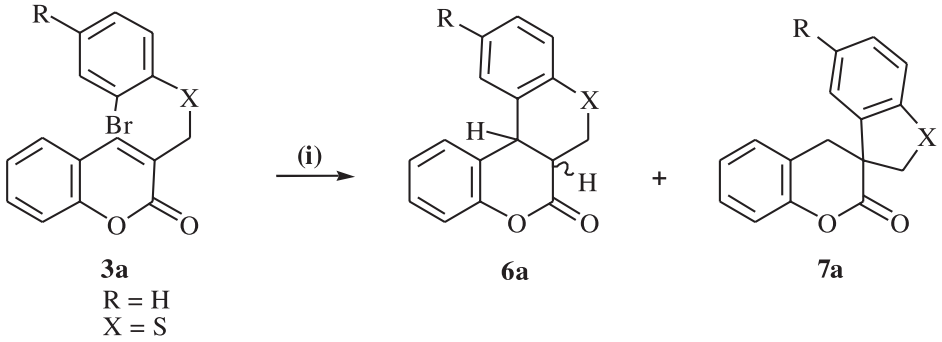
The precursors 3-(2-bromophenylsulfenylmethyl)coumarins (**3a**–**3c**) were prepared in 82%–95% yield by treating 3-chloromethyl coumarin (**1**) with 2-bromothiophenol (**2**) in refluxing acetone (dry) in the presence of anhyd. potassium carbonate for 8 h (Scheme 1). The corresponding sulfones **4a**–**4c** and sulfoxide **5a** were synthesized in 85%–94% and 86% yields, respectively, from the sulfides **3a**–**3c** by the oxidation with *m*-CPBA (Scheme 1). Compounds **3a**–**3c** and

 doi:10.1139/V07-046 © 2007 NRC Canada

Scheme 1. Reagents and conditions: (*i*) anhyd. K_2CO_3, dry acetone, 8 h, and reflux; (*ii*) *m*-CPBA (1 equiv.), CH_2CL_2, 0 °C, and 1 h; (*iii*) *m*-CPBA (excess), CH_2Cl_2, and 0 °C to reflux.



Scheme 2. Reagents and conditions: (*i*) $^nBu_3SnH$, AIBN, toluene, N_2, 55–60 °C, and 1 h.



4a–**4c** were characterized by elemental analysis and spectroscopic data.

We initiated our study on the radical cyclization with the sulfide **3a**. Compound **3a**, when heated for 1 h at 55–60 °C with $^nBu_3SnH$ in dry degassed toluene in the presence of a catalytic amount of AIBN, afforded the two cyclized products **6a** and **7a** in 72% and 20% yield, respectively (Scheme 2).

Similarly, other sulfides **3b**–**3c** were treated to give the cyclic products **6b**–**6c** and **7b** in 85%–88% and 5% yields, respectively (Table 1). Sulfones **4a**–**4c**, when subjected to radical cyclization under similar conditions as the previously described, furnished the spirocyclic compounds **8a**–**8c** in 76%–85% yield, exclusively (Table 1), instead of the expected 5-endo cyclized product **9** (Scheme 3). The structure of the compounds **6a**–**6c**, **7a**–**7b**, and **8a**–**8c** were established from their elemental analysis and spectroscopic data. We observed that compounds **3** and **4**, when subjected to radical cyclization under refluxing conditions, underwent extensive decomposition without giving any cyclized products. To extend the scope of this reaction, we also attempted a similar radical reaction with 3-(2-bromophenylsulfinylmethyl)coumarins (**5a**), employing similar reaction condition. Unfortunately, we were unable to obtain any cyclized products, as the starting material decomposed under the reaction conditions.

The mechanistic rationalization for the formation of products **6a**–**6c** and **7a**–**7b** can be explained by assuming a 5-endo followed by a 5-exo cyclization of the aryl radical onto the double bond of a coumarin moiety, as depicted in Scheme 3. An alternative pathway, via 5-exo cyclization followed by neophyl rearrangement (9), has also been considered for the formation of products **6a**–**6c**. In the case of phenylsulfonylmethyl congener **4a**–**4c**, the generated aryl radicals undergo 5-exo cyclization exclusively to produce the spirocylic products **8a**–**8c**. However, 5-exo cyclization with subsequent neophyl rearrangement pathway is highly unlikely with the present system. The stability and nonnucleophilicity (10) of the intermediate benzylic radical, attributed to the excellent overlapping (11) of a p orbital of the radical center with the adjacent aromatic π system, might prevent further attack, and hence, the production of the intermediate cyclohexadienyl radical **11**.

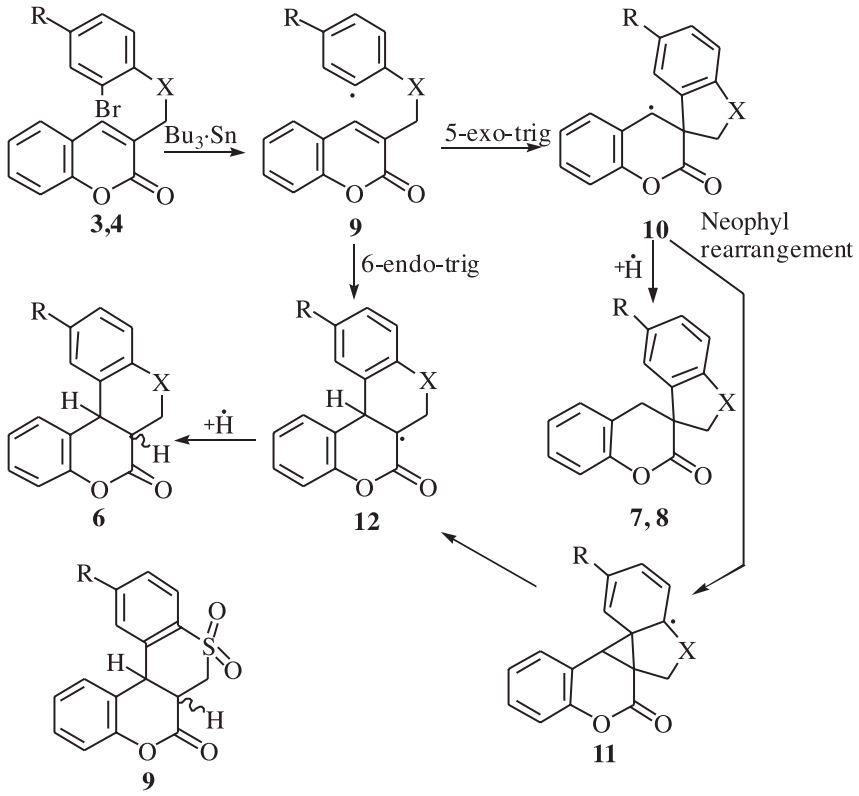
As $^nBu_3SnH$-mediated cyclization of the substrates de-

© 2007 NRC Canada

Table 1. Radical cyclization of sulfides and sulfones

Entry	Precursor	X	R	Product 5-exo/6-endo	Yield (%) 5-exo/6-endo
1	**3a**	S	H	**7a/6a**	20/72
2	**3b**	S	CH_3	**7b/6b**	5/85
3	**3c**	S	CH_2CH_3	**–/6c**	–/88
4	**4a**	SO_2	H	**8a/–**	76/–
5	**4b**	SO_2	CH_3	**8b/–**	78/–
6	**4c**	SO_2	CH_2CH_3	**8c/–**	85

Scheme 3.



rived from benzo[1]pyran-2-ones afforded a mixture of [6,6]-fused and (or) spiro heterocycles, we wanted to examine the radical cyclization of the substrates containing pyran-2-one moiety. For this purpose, 6-[(2-bromophenoxy)methyl]-4-methoxypyran-2-ones (**15a**–**15e**) were synthesized in 77%–89% yields from 6-(bromomethyl)-4-methoxy pyran-2-one (**13**) and 2-bromophenols (**14a**–**14e**) (Scheme 4). Substrates **15a**–**15e** were characterized from their spectral data.

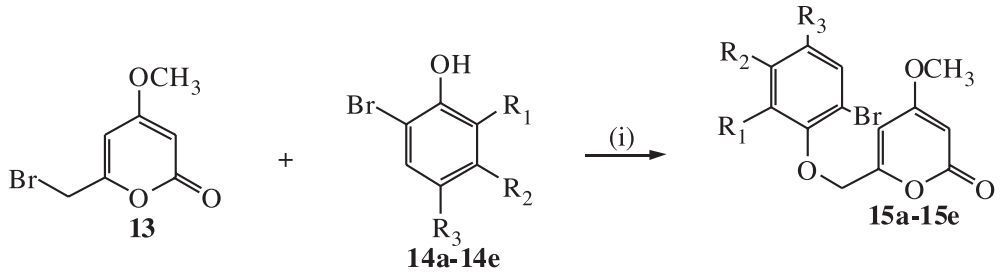
We then carried out the ^{n}Bu$_3$SnCl-mediated cyclization of compound **15a**. We applied the optimal reaction conditions used earlier (12), i.e., ^{n}Bu$_3$SnCl, Na(CN)BH$_3$, AIBN, in dry toluene, and under nitrogen atmosphere at 80 °C for 5 h. Surprisingly, intramolecular cyclization occurred to give only 11% of the cyclized product **16a**, and 76% of the starting material **15a** was recovered. However, changing the solvent, reagents, and raising the temperature of this reaction improved the yield. The best result was achieved by carrying out the reaction in toluene at 110 °C and using ^{n}Bu$_3$SnH instead of ^{n}Bu$_3$SnCl, which furnished **16a** in 79% yield. Similarly, compounds **15b**–**15e** afforded **16b**–**16e** in 68%–76% yields (Scheme 5).

The exclusive formation of five-membered spiro heterocycles **16a**–**16e** from **15a**–**15e** may easily be explained by the generation of the aryl radical **17** followed by a 5-exo-trig cyclization to give the allyl-radical intermediate **18**, which in turn abstracts the hydrogen from ^{n}Bu$_3$SnH to afford the spiro heterocycles **16a**–**16e**. The exclusive formation of five-membered heterocyclic compounds **16a**–**16e** from the substrates **15a**–**15e** may be attributed to the stability of the intermediate allylic radical **18.** There are precedents of Michael-type addition of a radical to the substrates containing Michael acceptors, giving Michael-type addition products; otherwise, α-*oxo* radical would be expected (13) (Scheme 6).

Although a stereoelectronically favored 5-exo-trig ring

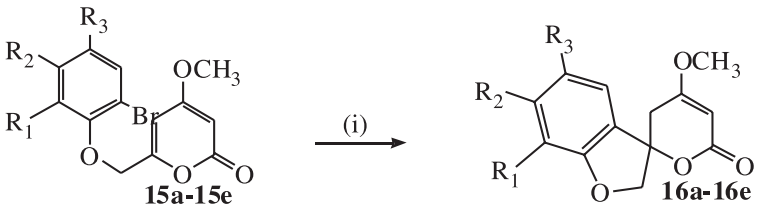
© 2007 NRC Canada

Scheme 4. Reagents and conditions: (*i*) dry acetone, K_2CO_3, and reflux 3–4 h.



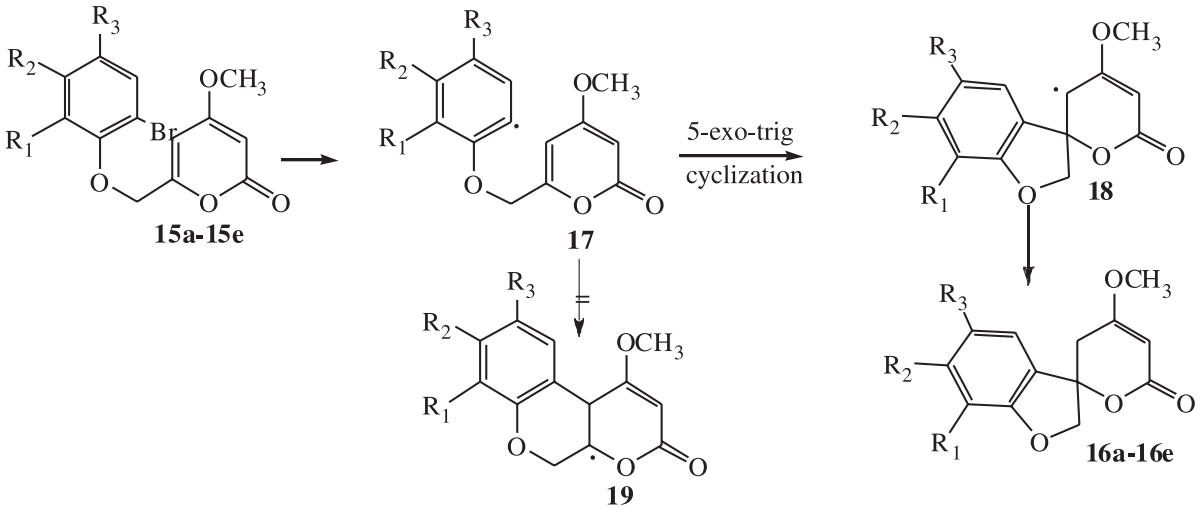
	R_1	R_2	R_3	Yield (%)
15a	H	H	H	82
b	Me	H	H	85
c	H	Me	H	81
d	Me	H	Me	77
e	H	H	OCH_3	89

Scheme 5. Reagents and conditions: (*i*) $^nBu_3SnH$, AIBN, dry toluene, reflux, 3–4 h, and N_2 atmosphere.



	R_1	R_2	R_3	Yield (%)
16a	H	H	H	79
b	Me	H	H	74
c	H	Me	H	68
d	Me	H	Me	71
e	H	H	OCH_3	76

Scheme 6.



closure is preferred for α-sulfenyl-5-hexenyl and α-sulfonyl-5-hexenylsystem, a significant amount of 5-endo-trig product is also formed, because of the longer C–S bond (8), to facilitate the easier approach of the radical center to accommodate the 5-endo transition state. This is quite evident for compounds **3a**–**3c** where products **6a**–**6c** were formed predominantly along with a small amount of the 5-membered products **7a**–**7b**. The stabilization of the intermediate tertiary radical **12** by the adjacent carbonyl group may also be responsible for the formation of the 5-endo product. However, this longer C–S bond for the facile 5-endo ring closure will no longer hold for the sulfones **4a**–**4c**. The presence of the two oxygen atoms attached to sulfur may be expected to favor the stereoelectronically favored 5-exo attack with the formation of highly stable spiro heterocyclic radical intermediate, which, by abstracting H-radicals, produces spirocyclic compounds **8a**–**8c** in excellent yield. However, in the case of compound **15**, the stabilization of the radical intermediate **18** by extended conjugation with the enone part might be responsible for the exclusive formation of the spiro product.

Interestingly, we found that the ratios of the spirocyclic to [6,6]-fused products from compounds **3a**–**3c** were different, depending on the group attached to the thiophenol. However, this ratio is increased by the presence of an activating group attached to the thiophenol moiety. With the *p*-ethyl-substituted phenylsulfenyl precursor, the [6,6]-fused product was produced exclusively. In contrast, this substituent effect on the mode of ring closure was completely absent for the precursors **4** and also from compound **15**. The explanation of the effect of the activating substituent, attached to the thiophenol moiety, is quite unknown. However, this study revealed that the choice of suitable precursors can be utilized for the selective formation of spirocyclic or [6,6]-fused sulfur heterocycles.

© 2007 NRC Canada

Conclusion

In summary, we have described $^{n}Bu_3SnH$-mediated mild and efficient synthesis of coumarin and pyrone-annulated heterocycles. All the reactions were clean with moderate to good yield. The use of 2-bromothiophenol provides an easy access to benzothiophene as well as benzothiopyran derivatives, which are of synthetic utility in organic synthesis.

Experimental

Melting points were determined in an open capillary and are uncorrected. IR spectra were recorded on a PerkinElmer L120–000A spectrometer (ν_{max} in cm^{-1}) using KBr discs. UV-absorption spectra were recorded in EtOH on a Shimadzu UV-2401PC spectrophotometer (λ_{max} in nm). ^1H NMR (300 MHz, 400 MHz, and 500 MHz) and ^{13}C NMR (75.5 MHz and 125 MHz) spectra were recorded on a Bruker DPX-300, Varian-400 MHz FTNMR, and Bruker DPX-500 spectrometer in $CDCl_3$ (chemical shifts in δ) with TMS as internal standard. Silica gel (60–120 mesh; Spectrochem, India) was used for chromatographic separation. Silica gel G (E-Merck, India) was used for TLC. Petroleum ether refers to the fraction boiling between 60 °C and 80 °C.

General procedure for the preparation of 3-(2-bromophenylsulfenylmethyl)coumarins

To a solution of 3-chloromethylcoumarin (**1**) (1 g, 5.15 mmol) in dry acetone (100 mL), 2-bromothiophenol (**2a**–**2c**) (5.15 mmol) and anhyd. potassium carbonate (2 g) were added, and the reaction mixture was refluxed for 8 h. The reaction mixture was then cooled, filtered, and the solvent was removed. The residual mass was extracted with CH_2Cl_2 (3 × 15 mL). The organic layer was washed with 5% Na_2CO_3 solution (2 × 10 mL), then with water (3 × 10 mL), and finally with brine (10 mL). After the removal of the solvent, the residue was subjected to column chromatography over silica gel. Elution of the column with 25% ethyl acetate in petroleum ether afforded 3-(2-bromophenylsulfenylmethyl)coumarins (**3a**–**3c**). All compounds were recrystalized from chloroform – petroleum ether (60–80 °C).

Compound 3a

Yield: 82%. Colourless crystalline solid; mp 100 °C. IR (KBr) ν_{max} (cm^{-1}): 1715, 1604, 743. ^1H NMR (400 MHz, $CDCl_3$) δ: 4.07 (s, 2H, $-SCH_2$), 7.02–7.07 (m, 1H, ArH), 7.18–7.25 (m, 3H, ArH), 7.31 (d, 1H, *J* = 8.28 Hz, ArH), 7.36 (d, 1H, *J* = 7.5 Hz, ArH), 7.47–7.51 (m, 1H, ArH), 7.54 (d, 1H, *J* = 7.87 Hz, ArH), 7.57 (s, 1H, =CH). ^{13}C NMR (125 MHz, $CDCl_3$) δ: 33.2, 116.9, 119.4, 124.6, 124.9, 125.3, 128.1, 128.2, 128.4, 130.5, 131.8, 133.6, 136.6, 140.5, 153.6, 161.4. MS *m*/*z*: 346, 348 [M^+]. Anal. calcd. for $C_{16}H_{11}O_2SBr$: C 55.33, H 3.17; found: C 55.55, H 3.27.

Compound 3b

Yield: 95%. Colourless crystalline solid; mp 98 °C. IR (KBr) ν_{max} (cm^{-1}): 1712, 1603, 756. ^1H NMR (400 MHz, $CDCl_3$) δ: 2.27 (s, 3H, $ArCH_3$), 4.03 (s, 2H, $-SCH_2$), 6.99 (d, 1H, *J* = 7.78 Hz, ArH), 7.14 (d, 1H, *J* = 7.9 Hz, ArH), 7.21 (d, 1H, *J* = 7.4 Hz, ArH), 7.31–7.36 (m, 2H, ArH), 7.40 (s, 1H, ArH), 7.46 (d, 1H, *J* = 7.4 Hz, ArH), 7.5 (s, 1H, =CH). MS *m*/*z*: 360, 362 [M^+]. Anal. calcd. for $C_{17}H_{13}O_2SBr$: C 56.51, H 3.60; found: C 56.26, H 3.47.

Compound 3c

Yield: 90%. Colourless crystalline solid; mp 85–86 °C. IR (KBr) ν_{max} (cm^{-1}): 1702, 1607, 751. ^1H NMR (400 MHz, $CDCl_3$) δ: 1.15 (t, 3H, *J* = 7.5 Hz, $-CH_2CH_3$), 2.53 (q, 2H, *J* = 7.5 Hz, $-CH_2CH_3$), 4.03 (s, 2H, $-SCH_2$), 7.01 (d, 1H, *J* = 7.1 Hz, ArH), 7.1 (d, 1H, *J* = 7.98 Hz, ArH), 7.21 (d, 1H, *J* = 7.43 Hz, ArH) 7.31–7.35 (m, 2H, ArH), 7.41 (s, 1H, ArH), 7.46 (d, 1H, *J* = 7.4 Hz, ArH), 7.49 (s, 1H, =CH). MS *m*/*z*: 374, 376 [M^+]. Anal. calcd. for $C_{18}H_{15}O_2SBr$: C 57.60, H 4.00; found: C 57.67, H 4.12.

General procedure for the preparation of 3-(2-bromophenylsulfonylmethyl)coumarins

To a stirred solution of compound 3-(2-bromophenylsulfenylmethyl)coumarin (**3a**–**3c**) (1.44 mmol) in CH_2Cl_2 (10 mL), a solution of *m*-CPBA (77%, 621 mg, 1.79 mmol, 2.5 equiv.) was added over a period of 1 h. After the addition of *m*-CPBA, the reaction mixture was refluxed for another 2 h for complete conversion (TLC observation). The mixture was then cooled and washed with satd. sodium carbonate (3 × 10 mL) and brine (10 mL) and dried (Na_2SO_4). The mixture was then concentrated, and the crude mass obtained was purified by column chromatography using 20% ethyl acetate in petroleum ether as eluant to afford 3-(2-bromophenylsulfonylmethyl)coumarins (**4a**–**4c**), which were recrystalized from chloroform – petrolium ether (60–80 °C).

Compound 4a

Yield: 85%. Colourless crystalline solid; mp 148 °C. IR (KBr) ν_{max} (cm^{-1}): 1722, 1318, 749. ^1H NMR (400 MHz, $CDCl_3$) δ: 4.71 (s, 2H, $-SO_2CH_2$), 7.25–7.29 (m, 2H, ArH), 7.39–7.56 (m, 4H, ArH), 7.79 (d, 1H, *J* = 7.9 Hz, ArH), 7.95 (s, 1H, =CH), 7.98 (d, 1H, *J* = 7.6 Hz, ArH). MS *m*/*z*: 378, 380 [M^+]. Anal. calcd. for $C_{16}H_{11}O_4SBr$: C 50.66, H 2.90; found C 50.74, H 2.84.

Compound 4b

Yield: 94%. Colourless crystalline solid; mp 151 °C. IR (KBr) ν_{max} (cm^{-1}): 1722, 1313, 763. ^1H NMR (400 MHz, $CDCl_3$) δ: 2.39 (s, 3H, $ArCH_3$), 4.68 (s, 2H, $-SO_2CH_2$), 7.18 (d, 1H, *J* = 7.98 Hz, ArH), 7.27–7.31 (m, 2H, ArH), 7.50–7.56 (m, 2H, ArH), 7.61 (s, 1H, ArH), 7.83 (d, 1H, *J* = 8.08 Hz, ArH), 7.95 (s, 1H, =CH). MS *m*/*z*: 392, 394 [M^+]. Anal. calcd. for $C_{17}H_{13}O_4SBr$: C 51.91, H 3.31; found: C 52.07, H 3.39.

Compound 4c

Yield: 92%. Colourless crystalline solid; mp 160 °C. IR (KBr) ν_{max} (cm^{-1}): 1726, 1313, 766. ^1H NMR (400 MHz, $CDCl_3$) δ: 1.22 (t, 3H, *J* = 7.5 Hz, $-CH_2CH_3$), 2.66 (q, 2H, *J* = 7.4 Hz, $-CH_2CH_3$), 4.69 (s, 2H, $-SO_2CH_2$), 7.21(d, 1H, *J* = 8.3 Hz, ArH), 7.27–7.31 (m, 2H, ArH), 7.50–7.56 (m, 2H, ArH), 7.62 (s, 1H, ArH), 7.88 (d, 1H, *J* = 8.1 Hz, ArH), 7.95 (s, 1H, =CH). MS *m*/*z*: 406, 408 [M^+]. Anal. calcd. for $C_{18}H_{15}O_4SBr$: C 53.07, H 3.69; found: C 53.28, H 3.81.

© 2007 NRC Canada

General procedure for the preparation of 3-(2-bromophenylsulfinylmethyl)coumarin

To a stirred solution of 3-(2-bromophenylsulfenylmethyl)coumarin (**3a**) (1.44 mmol) in CH_2Cl_2 (10 mL) at 0 °C, a solution of *m*-CPBA (77%, 249 mg, 1.44 mmol) was added over a period of 1 h. After the complete addition of *m*-CPBA, the reaction was stirred for another 1 h for complete conversion (TLC observation). The mixture was then washed with satd. solution of sodium carbonate (3 × 10 mL) and brine (10 mL) and dried (Na_2SO_4). The mixture was then concentrated, and the crude mass obtained was purified by column chromatography using 25% ethyl acetate in petroleum ether as eluant to afford 3-(2-bromophenylsulfinylmethyl)coumarin (**5a**), which was recrystallized from chloroform – petrolium ether (60–80 °C).

Compound 5a

Yield: 92%. Colourless crystalline solid; mp 170–172 °C. IR (KBr) ν_{max} (cm^{-1}): 1709, 1057, 756. ^1H NMR (300 MHz, $CDCl_3$) δ: 4.09 (d, 1H, *J* = 12.85 Hz, $–SOCH_2$), 4.28 (d, 1H, *J* = 12.85 Hz, $–SOCH_2$), 7.27–7.32 (m, 2H, ArH), 7.35–7.42 (m, 2H, ArH), 7.48–7.56 (m, 3H, ArH), 7.57–7.60 (m, 1H, ArH), 7.72 (s, 1H, =CH). MS *m*/*z*: 362, 364 [M^+]. Anal. calcd. for $C_{16}H_{11}O_3SBr$: C 52.91, H 3.05; found C 53.06, H 3.14.

General procedure for the radical-cyclization reactions

A suspension of the compounds **3a**–**3c** and **4a**–**4c** (0.430 mmol), $^nBu_3SnH$ (0.174 mL, 0.648 mmol), and AIBN (20 mg) in dry degassed toluene (10 mL) was stirred at 55–60 °C for 1 h under N_2. The solvent was removed under reduced pressure. Water (10 mL) was added to the residue, and the mixture was extracted with CH_2Cl_2 (3 × 10 mL). The organic layer was washed with water (2 × 10 mL) and brine (10 mL) and dried (Na_2SO_4). Evaporation of the solvent furnished a crude material, which was then subjected to column chromatography over silica gel. The column was eluted with 8% and 25% ethyl acetate in petroleum ether to give the cyclized products **6a**–**6c**, **7a**, **7b**, and **8a–8c**. All compounds were recrystalized from chloroform – petrolium ether (60–80 °C).

Compounds 6a

Yield: 72%. Colourless crystalline solid; mp 128 °C. IR (KBr) ν_{max} (cm^{-1}): 1758, 1455, 1148. ^1H NMR (400 MHz, $CDCl_3$) δ: 3.12 (dd, 1H, *J* = 5.9 and 12.6 Hz, $–SCHH_a$), 3.30–3.31 (m, 1H, $–C–H_c$), 3.51 (dd, 1H, *J* = 5.7 and 13.0 Hz, $–SCHH_b$), 4.35 (d, 1H, *J* = 4.9 Hz, $–C–H_d$), 6.86 (d, 1H, *J* = 7.6 Hz, ArH), 7.04–7.20 (m, 5H, ArH), 7.18(d, 1H, *J* = 7.3 Hz, ArH), 7.32–7.36 (m, 1H, ArH). ^{13}C NMR (125 MHz, $CDCl_3$) δ: 24.68, 39.15, 39.75, 117.24, 124.57, 124.89, 125.16, 127.70, 128.10, 129.0, 129.19, 129.70, 131.41, 133.20, 150.60, 168.51. MS *m*/*z*: 268 [M^+]. Anal. calcd. for $C_{16}H_{12}O_2S$: C 71.64, H 4.48; found: C 71.73, H 4.53.

Compounds 6b

Yield: 85%. Colourless crystalline solid; mp 130 °C. IR (KBr) ν_{max} (cm^{-1}): 1756, 1610, 1142.^1H NMR (400 MHz, $CDCl_3$) δ: 2.22 (s, 3H, $ArCH_3$), 3.09 (dd, 1H, *J* = 6.28 and 13.0 Hz, $–SCHH_a$), 3.29–3.34 (m, 1H, $–C–H_c$), 3.49 (dd, 1H, *J* = 6.02 and 13.3 Hz, $–SCHH_b$), 4.31 (d, 1H, *J* = 5.17 Hz, $–C–H_d$), 6.65 (s, 1H, ArH), 6.99 (d, 1H, *J* = 7.0 Hz, ArH), 7.08–7.20 (m, 4H, ArH), 7.44–7.46 (m, 1H, ArH). ^{13}C NMR (125 MHz, $CDCl_3$) δ: 21.42, 25.24, 39.65, 40.45, 117.61, 124.94, 125.29, 128.11, 129.41, 129.45, 129.57, 130.07, 130.56, 132.02, 135.51, 151.04, 169.14. MS *m*/*z*: 282 [M^+]. Anal. calcd. for $C_{17}H_{14}O_2S$: C 72.34, H 4.96; found: C 72.26, H 5.03.

Compounds 6c

Yield: 88%. Colourless crystalline solid; mp 192 °C. IR (KBr) ν_{max} (cm^{-1}): 1763, 1612, 1140.^1H NMR (400 MHz, $CDCl_3$) δ: 1.09 (t, 3H, *J* = 7.8 Hz, $–CH_2CH_3$), 2.49 (q, 2H, *J* = 7.5 Hz, $–CH_2CH_3$), 3.08 (dd, 1H, *J* = 6.0 and 12.6 Hz, $–SCHH_a$), 3.26–3.32 (m, 1H, $–C–H_c$), 3.49 (dd, 1H, *J* = 5.7 and 13.7 Hz, $–SCHH_b$), 4.34 (d, 1H, *J* = 5.12 Hz, $–C–H_d$), 6.69 (s, 1H, ArH), 7.03–7.20 (m, 5H, ArH), 7.32–7.38 (m, 1H, ArH). ^{13}C NMR (100 MHz, $CDCl_3$) δ: 15.90, 25.11, 28.75, 39.62, 40.36, 117.59, 125.0, 125.31, 128.09, 128.20, 129.39, 129.54, 129.67, 130.20, 131.69, 141.88, 150.99, 169.17. MS *m*/*z*: 296 [M^+]. Anal. calcd. for $C_{18}H_{16}O_2S$: C 72.97, H 5.41; found: C 73.11, H 5.36.

Compound 7a

Yield: 20%. Colourless crystalline solid; mp 126 °C. IR (KBr) ν_{max} (cm^{-1}): 1759, 1458, 1143. ^1H NMR (400 MHz, $CDCl_3$) δ: 3.13 (d, 1H, *J* = 11.52 Hz, –SCH), 3.21 (d, 1H, *J* = 16.12 Hz, ArCH), 3.26 (d, 1H, *J* = 16.08 Hz, ArCH), 3.88 (d, 1H, *J* = 11.48 Hz, –SCH), 6.97–7.03 (m, 2H, ArH), 7.09–7.15 (m, 3H, ArH), 7.17–7.22 (m, 2H, ArH), 7.30–7.34 (m, 1H, ArH). ^{13}C NMR (75.5 MHz, $CDCl_3$) δ: 34.6, 40.7, 55.9, 116.5, 121.1, 122.8, 124.6, 124.8, 124.9, 128.8, 128.9, 129.1, 139.0, 140.5, 151.4, 169.3. MS *m*/*z*: 268 [M^+]. Anal. calcd. for $C_{16}H_{12}O_2S$: C 71.64, H 4.48; found: C 71.86, H 4.60.

Compound 7b

Yield: 5%. Colourless crystalline solid; mp 108 °C. IR (KBr) ν_{max} (cm^{-1}): 1766, 1457, 1167. ^1H NMR (400 MHz, $CDCl_3$) δ: 2.22 (s, 3H, $ArCH_3$), 3.12 (d, 1H, *J* = 11.4 Hz, –SCH), 3.20 (d, 1H, *J* = 16.32 Hz, ArCH), 3.24 (d, 1H, *J* = 16.4 Hz, ArCH), 3.79 (d, 1H, *J* = 11.40 Hz, –SCH), 6.84 (s, 1H, ArH), 6.98–7.0 (m, 1H, ArH), 7.07–7.16 (m, 4H, ArH), 7.29–7.33 (m, 1H, ArH). MS *m*/*z*: 282 [M^+]. Anal. calcd. for $C_{17}H_{14}O_2S$: C 72.34, H 4.96; found: C 72.18, H 5.10.

Compound 8a

Yield: 76%. Colourless crystalline solid; mp 120 °C. IR (KBr) ν_{max} (cm^{-1}): 1756, 1310, 1149. ^1H NMR (500 MHz, $CDCl_3$) δ: 3.42 (d, 1H, *J* = 13.4 Hz, $–SO_2CH$), 3.43 (d, 1H, *J* = 16.17 Hz, ArCH), 3.49 (d, 1H, *J* = 16.2 Hz, ArCH), 4.00 (d, 1H, *J* = 13.4 Hz, $–SO_2CH$), 7.17–7.23 (m, 4H, ArH), 7.36–7.41 (m, 1H, ArH), 7.55–7.61 (m, 2H, ArH), 7.78–7.80 (m, 1H, ArH). ^{13}C NMR (75.5 MHz, $CDCl_3$) δ: 37.6, 48.15, 58.0, 117.2, 122.3, 125.9, 126.5, 129.5, 129.9, 130.7, 131.0, 134.5, 137.7, 138.6, 151.5, 167.3. MS *m*/*z*: 300 [M^+]. Anal. calcd. for $C_{16}H_{12}O_4S$: C 64.00, H 4.00; found: C 64.21, H 4.08.

Compound 8b

Yield: 78%. Colourless crystalline solid; mp 92–93 °C. IR (KBr) ν_{max} (cm^{-1}): 1756, 1310, 1149. ^1H NMR (500 MHz,

© 2007 NRC Canada

$CDCl_3$) δ: 2.36 (s, 3H, $ArCH_3$), 3.38 (d, 1H, *J* = 13.08 Hz, –SO_2CH), 3.43 (d, 1H, *J* = 15.97 Hz, ArCH), 3.50 (d, 1H, *J* = 16.02 Hz, ArCH), 3.90 (d, 1H, *J* = 13.32 Hz, –SO_2CH), 6.83(s, 1H, ArH), 7.18–7.38 (m, 5H, ArH), 7.65–7.66 (m, 1H, ArH). MS *m/z*: 314 [M^+]. Anal. calcd. for $C_{17}H_{14}O_2S$: C 64.97, H 4.46; found: C 65.19, H 4.55.

Compound 8c

Yield: 85%. Colourless crystalline solid; mp 78 °C. IR (KBr) ν_{max} (cm^{-1}): 1766, 1302, 1121. ^1H NMR (500 MHz, $CDCl_3$) δ: 1.09 (t, 3H, *J* = 7.6 and 15.0 Hz, –CH_2CH_3), 2.60 (q, 2H, *J* = 7.5 and 14.8 Hz, –CH_2CH_3), 3.39 (d, 1H, *J* = 13.4 Hz, –SO_2CH), 3.40 (d, 1H, *J* = 16.17 Hz, ArCH), 3.46 (d, 1H, *J* = 16.2 Hz, ArCH), 3.99 (d, 1H, *J* = 13.38 Hz, –SO_2CH), 6.97 (s, 1H, ArH), 7.16–7.20 (m, 3H, ArH), 7.36–7.39 (m, 2H, ArH), 7.66–7.68 (m, 1H, ArH). MS *m/z*: 328 [M^+]. Anal. calcd. for $C_{18}H_{16}O_4S$: C 65.85, H 4.88; found: C 65.99, H 4.98.

General procedure for the preparation of 15a–15e

6-(Bromomethyl)-4-methyl-2*H*-pyran-2-one (**13**) (1.05 g, 4.82 mmol) and different *o*-bromophenols (**14a–14e**) (4.82 mmol) were refluxed in dry acetone (100 mL) in the presence of anhyd. potassium carbonate (3 g) for 3–4 h. The reaction mixture was then cooled, filtered, and the solvent was removed. Residual mass was extracted with CH_2Cl_2 (3 × 50 mL), and the extract was washed with water (3 × 30 mL) and then with brine (30 mL) and dried (Na_2SO_4). The residual mass after the removal of the solvent was subjected to column chromatography over silica gel (60–120 mesh). The column was eluted with petroleum ether – chloroform (1:9) to give compounds **15a**–**15e**. Attempts to recrystallize the products from different solvents, such as methanol, chloroform – petroleum ether (60–80 °C), benzene – petroleum ether (60–80 °C), acetonitrile–methanol, failed to give any crystalline compounds. All compounds were found to be amorphous in nature and hence white as paper.

Compound 15a

Yield: 82%. White amorphous solid; mp 117 °C. IR (KBr) ν_{max} (cm^{-1}): 2951, 1740, 1259, 1033. ^1H NMR ($CDCl_3$, 300 MHz) δ: 3.83 (s, 3H), 4.85 (d, *J* = 0.90 Hz, 2H), 5.47 (d, *J* = 2.25 Hz, 1H), 6.33–6.35 (m, 1H), 6.87–6.94 (m, 2H), 7.28–7.31(m, 1H), 7.56 (dd, *J* = 1.59 and 7.83 Hz, 1H). MS *m/z*: 310, 312 [M^+]. Anal. calcd. for $C_{13}H_{11}BrO_4$: C 50.18, H 3.56; found: C 50.43, H 3.63.

Compound 15b

Yield: 85%. White amorphous solid; mp 109–110 °C. IR (KBr) ν_{max} (cm^{-1}): 2920, 1732, 1260, 1049. ^1H NMR ($CDCl_3$, 400 MHz) δ: 2.29 (s, 3H), 3.83 (s, 3H), 4.64 (s, 2H), 5.49 (d, *J* = 1.88 Hz, 1H), 6.29 (s, 1H), 7.24–7.53 (m, 3H). MS *m/z*: 324, 326 [M^+]. Anal. calcd. for $C_{14}H_{13}BrO_4$: C 51.71, H 4.03; found: C 51.66, H 4.21.

Compound 15c

Yield: 81%. White amorphous solid; mp 121 °C. IR (KBr) ν_{max} (cm^{-1}): 2920, 1730, 1260, 1033. ^1H NMR ($CDCl_3$, 400 MHz) δ: 2.54 (s, 3H), 3.82 (s, 3H), 4.73 (s, 2H), 5.49 (d, *J* = 2.04 Hz, 1H), 6.37 (t, *J* = 0.94 Hz, 1H), 6.94 (d, *J* = 8.21 Hz, 1H), 7.39 (d, *J* = 8.16 Hz, 1H), 7.75 (s, 1H). MS *m/z*: 324, 326 [M^+]. Anal. calcd. for $C_{14}H_{13}BrO_4$: C 51.71, H 4.03; found: C 51.88, H 4.12.

Compound 15d

Yield: 77%. White amorphous solid; mp 126 °C. IR (KBr) ν_{max} (cm^{-1}): 2920, 1733, 1259, 1035. ^1H NMR ($CDCl_3$, 400 MHz) δ: 2.25 (s, 3H), 2.27 (s, 3H), 3.83 (s, 3H), 4.63 (d, *J* = 0.94 Hz, 2H), 5.49 (d, *J* = 2.44 Hz, 1H), 6.32–6.34 (m, 1H), 6.93 (s, 1H), 7.05 (s, 1H). MS *m/z*: 338, 340 [M^+]. Anal. calcd. for $C_{15}H_{15}BrO_4$: C 53.12, H 4.46; found: C 52.90, H 4.52.

Compound 15e

Yield: 89%. White amorphous solid; mp 132 °C. IR (KBr) ν_{max} (cm^{-1}): 2921, 1733, 1259, 1053. ^1H NMR ($CDCl_3$, 300 MHz) δ: 3.75 (s, 3H), 3.81 (s, 3H), 4.77 (s, 2H), 5.45 (d, *J* = 2.0 Hz, 1H), 6.30 (s, 1H), 6.78–6.85 (m, 2H), 7.11 (d, *J* = 2.68 Hz, 1H). MS *m/z*: 340, 342[M^+]. Anal. calcd. for $C_{14}H_{13}BrO_5$: C 49.29, H 3.84; found: C 49.38, H 3.70.

General procedure for the radical cyclization of compound 15a–15e

The appropriate compound **15a**–**15e** (0.32 mmol) was dissolved in dry toluene (10 mL), and the solution was purged with nitrogen for 30 min. AIBN (26 mg) and $^nBu_3SnH$ (0.104 mL, 0.38 mmol) were added, and the reaction mixture was refluxed for 3–4 h under nitrogen atmosphere. The reaction mixture was allowed to cool down to room temperature, and the solvent was removed under reduced pressure. Water (10 mL) was added to the residual mass, and the mixture was extracted with CH_2Cl_2 (3 × 10 mL). The CH_2Cl_2 solution was stirred with 10% KF solution (10 mL) for 1 h. The organic phase was washed with water (2 × 20 mL) and then brine (1 × 20 mL) and dried (Na_2SO_4). The solvent was distilled off, and the crude solid was purified by column chromatography over silica gel (230–400 mesh). Elution of the column with petroleum ether – ethyl acetate (4:1) gave pure solids **16a**–**16e**. Attempts to recrystallize the products from different solvents, such as methanol, chloroform – petroleum ether (60–80 °C), benzene – petroleum ether (60–80 °C), and acetonitrile–methanol, failed to give any crystalline compounds. All compounds were found to be amorphous in nature and hence white as paper

Compound 16a

Yield: 79%. White amorphous solid; mp 152–154 °C. IR (KBr) ν_{max} (cm^{-1}): 2998, 1697, 1261, 1015. ^1H NMR ($CDCl_3$, 400 MHz) δ: 2.78 (d, *J* = 17.18 Hz, 1H), 3.05 (d, *J* = 17.19 Hz, 1H), 3.83 (s, 3H), 4.37 (d, *J* = 10.6 Hz, 1H), 4.71 (d, *J* = 10.60 Hz, 1H), 5.30 (s, 1H), 6.87–7.38 (m, 4H). ^{13}C NMR (125 MHz) δ: 36.5, 56.8, 81.4, 85.7, 91.3, 111.5, 121.6, 124.3, 126.8, 132.1, 160.9, 165.8, 171.5. MS *m/z*: 232 [M^+]. Anal. calcd. for $C_{13}H_{12}O_4$: C 67.23, H 5.21; found: C 67.45, H 5.08.

Compound 16b

Yield: 74%. White amorphous solid; mp 147 °C. IR (KBr) ν_{max} (cm^{-1}): 2922, 1714, 1238, 1060. ^1H NMR ($CDCl_3$, 400 MHz) δ: 2.19 (s, 3H), 2.78 (d, *J* = 17.18 Hz, 1H), 2.98 (d, *J* = 17.23 Hz, 1H), 3.82 (s, 3H), 4.36 (d, *J* = 10.72 Hz, 1H), 4.72 (d, *J* = 10.74 Hz, 1H), 5.29 (s, 1H), 7.19–7.29 (m,

© 2007 NRC Canada

3H). MS *m*/*z*: 246 [M^+]. Anal. calcd. for $C_{14}H_{14}O_4$: C 68.28, H 5.73; found: C 68.11, H 5.62.

Compound 16c

Yield: 68%. White amorphous solid; mp 162 °C. IR (KBr) ν_{max} (cm^{-1}): 2920, 1720, 1240, 1035. ^1H NMR ($CDCl_3$, 500 MHz) δ: 2.33 (s, 3H), 2.77 (d, *J* = 17.16 Hz, 1H), 3.03 (d, *J* = 17.18 Hz, 1H), 3.83 (s, 3H), 4.36 (d, *J* = 10.58 Hz, 1H), 4.67 (d, *J* = 10.66 Hz, 1H), 5.29 (s, 1H), 6.69–6.75 (m, 2H), 7.24 (s, 1H). MS *m*/*z*: 246 [M^+]. Anal. calcd. for $C_{14}H_{14}O_4$: C 68.28, H 5.73; found: C 68.55, H 5.65.

Compound 16d

Yield: 71%. White amorphous solid; mp 143–144 °C. IR (KBr) ν_{max} (cm^{-1}): 2928, 1716, 1230, 1025. ^1H NMR ($CDCl_3$, 300 MHz) δ: 2.17 (s, 3H), 2.24 (s, 3H), 2.74 (d, *J* = 17.22 Hz, 1H), 3.03 (d, *J* = 17.21 Hz, 1H), 3.82 (s, 3H), 4.33 (d, *J* = 10.60 Hz, 1H), 4.68 (d, *J* = 10.64 Hz, 1H), 5.28 (s, 1H), 6.92 (s, 1H), 6.97 (s, 1H). MS *m*/*z*: 260 [M^+]. Anal. calcd. for $C_{15}H_{16}O_4$: C 69.22, H 6.20; found: C 69.07, H 6.43.

Compound 16e

Yield: 76%. White amorphous solid; mp 166–167 °C. IR (KBr) ν_{max} (cm^{-1}): 2922, 1717, 1266, 1026. ^1H NMR ($CDCl_3$, 400 MHz) δ: 2.76 (d, *J* = 17.18 Hz, 1H), 3.03 (d, *J* = 17.18 Hz, 1H), 3.74 (s, 3H), 3.82 (s, 3H), 4.36 (d, *J* = 10.52 Hz, 1H), 4.68 (d, *J* = 10.51 Hz, 1H), 5.28 (s, 1H), 6.78–6.90 (m, 3H). MS *m*/*z*: 262 [M^+]. Anal. calcd. for $C_{14}H_{14}O_5$: C 64.12, H 5.38; found: C 64.03, H 5.43.

Acknowledgements

We thank the Council of Scientific and Industrial Research (CSIR; New Delhi) for financial assistance. P.D. and A.K.P. are thankful to CSIR for a Senior and a Junior Research Fellowship, respectively.

References

1. (*a*) B. Giese. *In* Radicals in organic synthesis: formation of carbon–carbon bonds. Pergamon Press, Oxford. 1986; (*b*) P. Renaud and M.P. Sibi (*Editors*). *In* Radicals in organic synthesis. Vol. 1. Wiley-VCH, Weinheim. 2001; (*c*) M. Malacria. Chem. Rev. **96**, 289 (1996); (*d*) C.P. Jasperse, D.P. Curran, and T.L. Fevig. Chem Rev. **91**, 1237 (1991); (*e*) K.C. Majumdar and P.K. Basu. Heterocycles, **57**, 2413 (2002); (*f*) W.R. Bowman, A. J. Fletcher, and G.B.S. Pots. J. Chem. Soc., Perkin Trans. 1, 2747 (2002); (*g*) K.C. Majumdar, P.K. Basu, and P.P. Mukhopadhyay. Tetrahedron, **60**, 6239 (2004).
2. (*a*) B. Vacher, A. Samat, F. Alouche, A. LAknifli, A. Baldy, and M. Chanon. Tetrahedron Lett. **44**, 2925 (1988); (*b*) A.C. Serra and C.M.M. Da Silva Corea. Tetrahedron Lett. **32**, 6653 (1991); (*c*) L.M. Matalia, B.B. Vacher, A. Samat, and M. Chanon. J. Am. Chem. Soc. **114**, 4111 (1992); (*d*) A.A. Ponaras, and O. Zaim. Tetrahedron Lett. **41**, 2279 (2000); (*e*) L. Benati, R. Calestani, R. Leardini, M. Minozzi, D. Nanni, P. Spangolo, and S. Strazzari. Org. Lett. **5**, 1313 (2003); (*f*) E.W. Della and S.D. Graney. J. Org. Chem. **69**, 3824 (2004); (*g*) K.C. Majumdar, A. Biswas, and P.P. Muhopadhyay. Synthesis, 2385 (2003).
3. (*a*) B.-W. Ke, C.-H. Lin, and Y.-M. Tsai, Tetrahedron, **53**, 7805 (1997); (*b*) G. Keum, S.B. Kang, and E. Lee. Org Lett. **6**, 1895 (2004).
4. (*a*) C.H. Schiesser and L.M. Wild. Tetrahedron, **52**, 13265 (1996); (*b*) A.L.J. Beckwith and D.R. Boate. J. Org. Chem. **53**, 4339 (1988); (*c*) A.L.J. Beckwith and D.R. Boate. J. Chem. Soc., Chem. Commun. 189 (1986); (*d*) A.L.J. Beckwith and S.A.M. Duggan. J. Chem. Soc., Perkin Trans. 2, 1509 (1994).
5. (*a*) K.C. Majumdar, M. Ghosh, M. Jana, and D. Saha. Synthesis, **43,** 2111 (2002); (*b*) K.C. Majumdar, U.K. Kundu, and S.K. Ghsoh. Org. lett. **4**, 2629 (2002); (*c*) K.C. Majumdar and S.K. Ghosh. Tetrahedron Lett. **43**, 2115 (2002); (*d*) K.C. Majumdar, S.K. Chattopadhay, and M. Ghosh. Lett. Org. Chem. **2**, 231 (2005).
6. K.C. Majumdar, P.P. Muhopadhyay, and A. Biswas. Tetrahedron Lett. **46**, 6655 (2005).
7. (*a*) A. Studer and M. Bossart. Tetrahedron, **57**, 9649 (2001); (*b*) M. Minozzai, D. Nanni, and J.C. Walton. Org. Lett. **5**, 901 (2003); (*c*) C. Chatgilialoglu, A. Altieri, and H. Fischer. J. Am. Chem. Soc. **124**, 12816 (2002).
8. (*a*) A.A. Ponaras and O. Zaim. Tetrahedron Lett. **34**, 2879 (1993); (*b*) S.A. Ahmad–Juhan and D.A. Whiting. J. Chem. Soc., Perkin Trans. 1, 418 (1990); (*c*) A.L.J. Beckwith, I.A. Blair, and G. Phillipou. Tetrahedron Lett. **15**, 2251 (1974).
9. (*a*) C.S. Aureliano Antunes, M. Bietti, G. Ercolani, O. Lanzalunga and M. Salamone. J. Org. Chem. **70**, 3884 (2005); (*b*) K.A. Parker, D.M. Spero, and K.C. Inman. Tetrahedron Lett. **27**, 2833 (1986); (*c*) A.N. Abeywickrema, A.L.J. Beckwith, and S. Gerba. J. Org. Chem. **52**, 4072 (1987).
10. H. Ishibashi, T. Kobayashi, S. Nakashima, and O. Tamura. J. Org. Chem. **65**, 9022 (2000).
11. (*a*) D.C. Spellmeyer and K.N. Houk. J. Org. Chem. **52**, 959 (1987); (*b*) A.L.J. Beckwith and C.H. Schiesser. Tetrahedron, **41**, 3925 (1985); (*c*) D.A. Struble, A.L. Beckwith, and G.A. Gream. Tetrahedron Lett. 3701 (1968); (*d*) B. Giese. Angew Chem., Int. Ed. Engl. **22**, 753 (1983).
12. (*a*) K.C. Majumdar, P.K. Basu, P.P. Mukhopadhyay, S. Sarkar, S.K. Ghosh, and P. Biswas. Tetrahedron, **59**, 2151 (2003); (*b*) K.C. Majumdar and P.P. Mukhopadhyay. Synthesis, 97 (2003).
13. (*a*) Y. Araki, T. Endo, Y. Arai, M. Tanji, and Y. Ishido. Tetrahedron Lett. **30**, 2829 (1989); (*b*) K. Ogura, N. Sumitani, A. Kayano, H. Iguchi, and M. Fujita. Chem. Lett. 1487 (1992); (*c*) K.C. Majumdar and P.P. Mukhopadhyay. Synthesis, 1864 (2004).

© 2007 NRC Canada

OBITUARY / NÉCROLOGIE



Professor Nick J. Taylor

Memoriam Nick J. Taylor 1944–2006

Nicholas (Nick) J. Taylor, MCIC, passed away suddenly in his home in Drumbo, Ontario on November 23, 2006, at the age of 61. He is survived by his brothers, Ronald and David, and their families. The University of Waterloo and the larger chemical community have lost an accomplished crystallographer, a mentor and teacher to numerous undergraduate and graduate students, a gentleman in the true sense of that word, and a close friend.

Nick was born in Purley, Surrey, UK on December 12, 1944, and completed his formal education at Whyteleafe Primary School (1950–1956), followed by a scholarship to Caterham School (1956–1961), and on passing the O-Level examinations, completed A-level examinations at Croydon Technical College (1961–1964) in Pure Mathematics, Applied Mathematics, Physics and Chemistry, and the S-level examination in Chemistry. He completed B. Sc. and Ph. D. degrees at the University of Surrey, graduating in 1971.

His Ph. D. research was in the area of phosphorus halide and metal halide chemistry, featuring both main-group and transition-metal halides, under the supervision of Professor Joseph I. Bullock. Nick was initially trained by Frederick W. Parrett, and his first paper is co-authored with Dr. Parrett, who had since moved to Royal Military College in Kingston,

Nécrologie Nick J. Taylor 1944–2006

Nicholas (Nick) J. Taylor, MCIC, est décédé subitement à son domicile de Drumbo (Ontario), le 23 novembre 2006, à l'âge de 61 ans. Il laisse dans le deuil ses frères, Ronald et David, ainsi que leurs familles. L'Université de Waterloo et le milieu élargi de la chimie perdent un cristallographe accompli, professeur et mentor de nombreux étudiants au baccalauréat et aux études supérieures, un « gentleman » au sens propre du terme et un ami très cher.

Nick est né à Purley (Surrey), au R.-U., le 12 décembre 1944. Il a amorcé sa formation scolaire à l'école primaire de Whyteleafe (1950-1956), puis a obtenu une bourse d'études pour entreprendre ses études secondaires à l'école de Caterham (1956-1961), jusqu'aux examens du niveau O. Par la suite, il a poursuivi ses études au collège de Croydon (1961-1964) jusqu'aux examens du niveau A en mathématiques pures, mathématiques appliquées, physique et chimie, et a aussi réussi l'examen du niveau S en chimie. L'Université de Surrey lui a d'abord décerné un B.Sc., puis un Ph.D. en 1971.

Ses recherches de doctorat, sous la direction du professeur Joseph I. Bullock, portaient sur la chimie des halogénures de phosphore et de métaux, particulièrement les halogénures des métaux des groupes principaux et de transition. Nick a fait ses premières armes avec Frederick W. Parrett. Il a aussi cosigné

© 2007 NRC Canada

Ontario. That paper (F.W. Parrett and N.J. Taylor, J. Inorg. Nucl. Chem. **32**, 2458 (1970)) is concerned with the IR spectra of polyhalide ions. It is interesting to note that many years later Nick collected, solved, and refined a number of structures of ammonium poly-iodide salts in collaboration with Professor Donald E. Irish. Regrettably, this work is currently unpublished because of the premature deaths of both chemists.

Nick moved to Royal Military College in 1971 and worked briefly as a post-doctoral fellow with Professor Parrett before moving to the University of Waterloo to work with Professor Arthur J. Carty (FCIC, FRS), initially as a post-doctoral fellow in 1973. Nick was appointed as a permanent staff member in 1981 and was Adjunct Professor of Chemistry and manager of the department's X-ray crystallographic facility until his untimely death.

In our early days at the University of Waterloo, X-ray diffraction data were collected on an aging Syntex $P2_1$ instrument (purchased in 1978), and at one point, before our arrival, punch cards had to be laboriously collated and read into the University's mainframe computer prior to solution and refinement! One of us still has a glossy 8½ × 11 inch print of the first structure Nick collected on our behalf (S. Collins, B.A. Kuntz, N.J. Taylor, and D.G. Ward. J. Organomet. Chem. **342**, 21 (1988)).

Of these early days his ex-wife Lynda remarks, "I remember Nick babysitting the old X-ray machine a lot in the early years of our marriage; we would walk into the Chemistry Department in all wind and weather to check that all was well when he was collecting data. On one occasion, late at night, we went in when a blizzard was blowing, and by the time we arrived at the door to the Chemistry Department, we looked like characters out of a scene in Dr. Zhivago".

A Nicolet-Siemens P4 diffractometer, along with much updated computing equipment, were purchased in the late 1980s and early 1990s, and a modern Apex 3000 CCD-based instrument was acquired in 2000. So a majority of the structures Nick collected, solved, and refined were obtained on conventional 4-circle instruments.

Nick was *personally responsible* for the collection, solution, and refinement of over 1300 structures during his tenure at Waterloo and is a co-author on 289 refereed journal publications. In an age of modern instruments where a data set can now be collected and a structure obtained in a matter of hours, his legacy may seem inconsequential. However, he was one of Canada's more prolific and accomplished crystallographers, especially given that he had neither a research group nor independent grant funding for much of his career. Many chemists may also be unaware that Nick was a largely self-taught crystallographer, having received no advanced training in the subject prior to moving to Waterloo.

Further, those of us who worked with him, and this includes a host of undergraduate, graduate students, and faculty at Waterloo, as well as other chemists and crystallographers from around the world, will remember Nick as being meticulous and a true craftsman. He was never satisfied with simply obtaining a structure, he always strived for the best result possible. Indeed, his care and attention to detail resulted in structural data from "old" diffractometers with esd values that rival those for many structures collected on modern CCD-equipped systems.

In a 20+ year association with Nick, we only encountered a couple of problems that were insoluble due to disorder, or "indifferent", or incommensurate crystals. In these cases, students were encouraged to try again, often under the direct tutelage of Nick as to the proper techniques for single

sa première publication avec M. Parrett, qui était alors au Collège militaire royal de Kingston (Ontario). L'article en question (F.W. Parrett et N.J. Taylor, J. Inorg. Nucl. Chem. **32**, 2458 (1970)) portait sur le spectre IR d'ions polyhalogénures. Il est intéressant de noter que, plusieurs années plus tard, Nick a recueilli, élucidé et affiné plusieurs structures de sels de polyiodure d'ammonium en collaboration avec le professeur Donald E. Irish. Malheureusement, ces travaux n'ont jamais été publiés à cause du décès prématuré des deux chimistes.

Nick s'est joint au Collège militaire royal en 1971, où il a brièvement occupé un poste de chercheur postdoctoral dans le groupe du professeur Parrett, avant de se joindre à celui du professeur Arthur J. Carty (FCIC, FRS), d'abord comme chercheur postdoctoral, à l'Université de Waterloo, en 1973. En 1981, Nick est devenu membre permanent du personnel; il a été nommé professeur adjoint et a occupé le poste de directeur du service de radiocristallographie jusqu'à son décès prématuré.

A nos débuts à l'Université de Waterloo, les données obtenues par diffraction des rayons X étaient recueillies sur un vieux diffractomètre Syntex $P2_1$ (acheté en 1978), et, quelque temps avant notre arrivée, des cartes poinçonnées devaient être laborieusement colligées et soumises à l'ordinateur central de l'Université avant que l'on puisse élucider et affiner les données! Un de nous possède encore une photo glacée de la première structure que Nick a recueillie pour lui (S. Collins, B.A. Kuntz, N.J. Taylor et D.G. Ward. J. Organomet. Chem. **342**, 21 (1988)).

Au sujet de cette époque, Lynda, son ex-épouse, raconte : « Je me souviens qu'au début de notre mariage, Nick prenait grand soin de cette machine. Beau temps, mauvais temps, nous allions à l'Université pour nous assurer que la cueillette des données se passait bien. A l'une de ces occasions, tard la nuit, nous nous y sommes rendus en pleine tempête de neige; lorsque nous sommes enfin parvenus au département de chimie, nous avions l'air de deux personnages sortis d'une scène de *Docteur Jivago*. »

Un diffractomètre Nicolet-Siemens P4 et de l'équipement informatique plus à jour ont été acquis à la fin des années 1980 et au début des années 1990. De plus, un détecteur bidimensionnel CCD Apex 3000 a été acheté en 2000. Ainsi, la majorité des structures recueillies, élucidées et affinées par Nick l'ont été sur un instrument traditionnel à quatre cercles.

Nick a été personnellement responsable de recueillir, d'élucider et d'affiner plus de 1300 structures à Waterloo. Il est coauteur de 289 articles dans des publications à comité de lecture. A l'âge de l'instrumentation moderne où un ensemble de données peut être recueilli et une structure obtenue en quelques heures, son œuvre peut sembler sans conséquence. Il a cependant été l'un des cristallographes canadiens les plus prolifiques et les plus accomplis, surtout si l'on considère que, pour une bonne partie de sa carrière, il n'a ni dirigé de groupe de recherche ni obtenu de subventions indépendantes. De nombreux chimistes ignorent probablement que Nick était un cristallographe autodidacte et qu'il n'avait reçu aucune formation avancée dans le domaine de la cristallographie avant d'arriver à Waterloo.

De plus, ceux qui ont travaillé avec lui, y compris un grand nombre d'étudiants au baccalauréat et aux études supérieures, et les professeurs de Waterloo, ainsi que d'autres chimistes et cristallographes du monde entier, se souviendront que Nick était très méticuleux et un véritable artisan. La simple obtention d'une structure ne le satisfaisait jamais; il s'efforçait toujours d'obtenir le meilleur résultat possible. En effet, il a réussi à soutirer de « vieux » diffractomètres des données structurales dont les valeurs d'écarts-types rivalisaient avec

© 2007 NRC Canada

crystal growth. It is gratifying that a number of these students, who now hold faculty appointments in Canada, continued to collaborate with Nick.

Nick had passions other than crystallography. He was an avid gardener (of both fruits and vegetables) and horticulturist (his day, hosta, and true lilies grace the gardens of friends and the University of Waterloo). In addition, he played the violin *con brio* and was a collector of vintage wines and ports. Finally, Nick had a deep interest in the natural world that dated back to his childhood, collecting fossil ammonites and other “ites” while on holiday along the seacoast between Cornwall and Dorset. It is there, amongst the wind and waves off Dodman Point in Cornwall, that Nick J. Taylor will find peace. We will all sorely miss him.

Scott Collins and Todd B. Marder (MCIC, FRSC-UK)y of Toronto.)

celles de plusieurs structures recueillies sur des détecteurs bidimensionnels CCD modernes.

En plus de 20 ans de collaboration avec Nick, nous n’avons croisé que quelques problèmes insolubles en raison du désordre ou de cristaux incommensurables, ou indiscernables. Dans ces cas, les étudiants étaient encouragés à essayer de nouveau, souvent sous la tutelle de Nick, pour apprendre les meilleures techniques de croissance d’un monocristal. Il est d’intérêt de constater que plusieurs de ces étudiants, maintenant professeurs dans des universités canadiennes, ont continué à collaborer avec Nick par la suite.

Nick avait d’autres passions que la cristallographie. Il cultivait fruits et légumes avec ferveur, et était un horticulteur de talent; encore aujourd’hui, ses hémérocalles, ses hostas et ses lis ornent les jardins de ses amis et de l’Université de Waterloo. De plus, il jouait du violon avec brio et collectionnait les grands vins et les portos. Enfin, Nick, ayant développé un vif intérêt pour la nature dès son enfance, collectionnait les fossiles (ammonites et autres « ites »), lorsqu’en vacances, il séjournait sur les côtes de Cornouailles et du Dorset. C’est à cet endroit, dans le vent et les vagues de Dodman Point en Cornouailles, que Nick J. Taylor reposera. Il nous manquera beaucoup.

Scott Collins, Todd B. Marder (MCIC, FRSC-UK)
Traduit par Anne Brunelle.of Toronto.)

© 2007 NRC Canada

The mechanism and kinetics of the HCO + HONO → HCHO + NO_2 reaction — A DFT study

Xiaomin Sun, Zhengting Cai, Dachang Feng, Wenshang Bian, Qing'an Qiao, and Wenxing Wang

Abstract: The hydrogen-transfer reaction of HCO + HNO_2 → HCHO + NO_2 has been studied using both the density function theory (DFT) and high-level ab initio method. Three complete reaction paths have been located for the transfer reaction. Geometry optimization and frequency calculation have been performed at the B3LYP/6–311++G** level. QCISD(T) and G3B3 methods have been used to verify the single-point energy. On the basis of the ab initio data, the rate constants have been deduced over a temperature range of 300–3000 K using the transition-state theory and canonical variational transition-state theory with small-curvature tunneling effect. The calculated rate constants have been compared with the previous reported values.

Key words: density function theory, reaction mechanism, variational transition-state theory, rate constant.

Résumé : Faisant appel à la théorie de la densité fonctionnelle et à des calculs ab initio de haut niveau, on a étudié la réaction de transfert d'hydrogène du HCO + HNO_2 → HCHO + NO_2. On a décelé trois voies réactionnelles complètes pour la réaction de transfert. On a effectué l'optimisation de la géométrie et le calcul de la fréquence au niveau B3LYP/6-311++G**. On a utilisé les méthodes QCISD(T) et G3B3 pour vérifier l'énergie du point unique. Sur la base des données obtenues par les calculs ab initio, on a dérivé les constantes de vitesse pour les températures allant de 300 à 3000 K; pour ce faire, on a utilisé la théorie de l'état de transition et la théorie de l'état de transition à variations canoniques modifiées par une faible courbure d'effet tunnel. On a comparé les constantes de vitesse calculées avec les valeurs rapportées antérieurement.

Mots-clés : théorie de la densité fonctionnelle, mécanisme réactionnel, théorie de l'état de transition variationnel, constante de vitesse.

[Traduit par la Rédaction]

Introduction

In the combustion of hydrocarbons and nitramine propellants, the reactions of CH_2O and NO_x can generate many reactive species, such as HCO, HNO, HONO, HNOH, and so forth (1–3). Moreover, the consequent reactions of HCO with HNO, HONO, and HNOH may play a significant role in the overall kinetics of these chemical systems. The reaction of HNO_2 with HCO has been studied by several groups in both experimental and theoretical calculations. In 1991, Tsang and Herron (4) investigated the kinetics of the reaction, and by combining the results from other work (5, 6) for the reverse reaction, they reported the rate constants of the HCO + HNO_2 → HCHO + NO_2 reaction.

Thus, $k(T) = 2.0 \times 10^{-21} T^{2.37} \exp(-1940/T)$ cm^3 molecule^{-1} s^{-1}; 300 K < T < 1000 K with an uncertainty factor of five. In 1996, to elucidate the mechanism and the kinetics of the forward reaction theoretically, Feng (7) first reported the transition-state (TS) and the intrinsic-reaction coordinates (IRC) with the ab initio UHF/6–31G method and the computed thermal rate constants, involving the tunneling effect, by calculating the microcanonical probability fluxes at the TS. On the basis of the agreement between the theoretical and experimental data, the results were excellent and cited in a textbook (8). However, Veszpremi also pointed out some drawbacks of Feng's study. First, the results, including the geometries and the energies, were derived at a relatively low level of theory with a modest basis set that excluded the polarization and diffuse functions. Second, the spin contamination should be verified to stay at a negligible level during the calculation. Also, it should be pointed out that the reaction path reported by Feng was not the fastest reaction path. Recently, Xu and Lin (9, 10) reported the kinetics and mechanisms of the title reaction on G2M level. Among the mentioned studies, there are still some aspects that are worth discussing. For example, the reaction mechanism is not uniform, the previously reported temperature dependency of the total rate constants is disputed, and large discrepancy exists

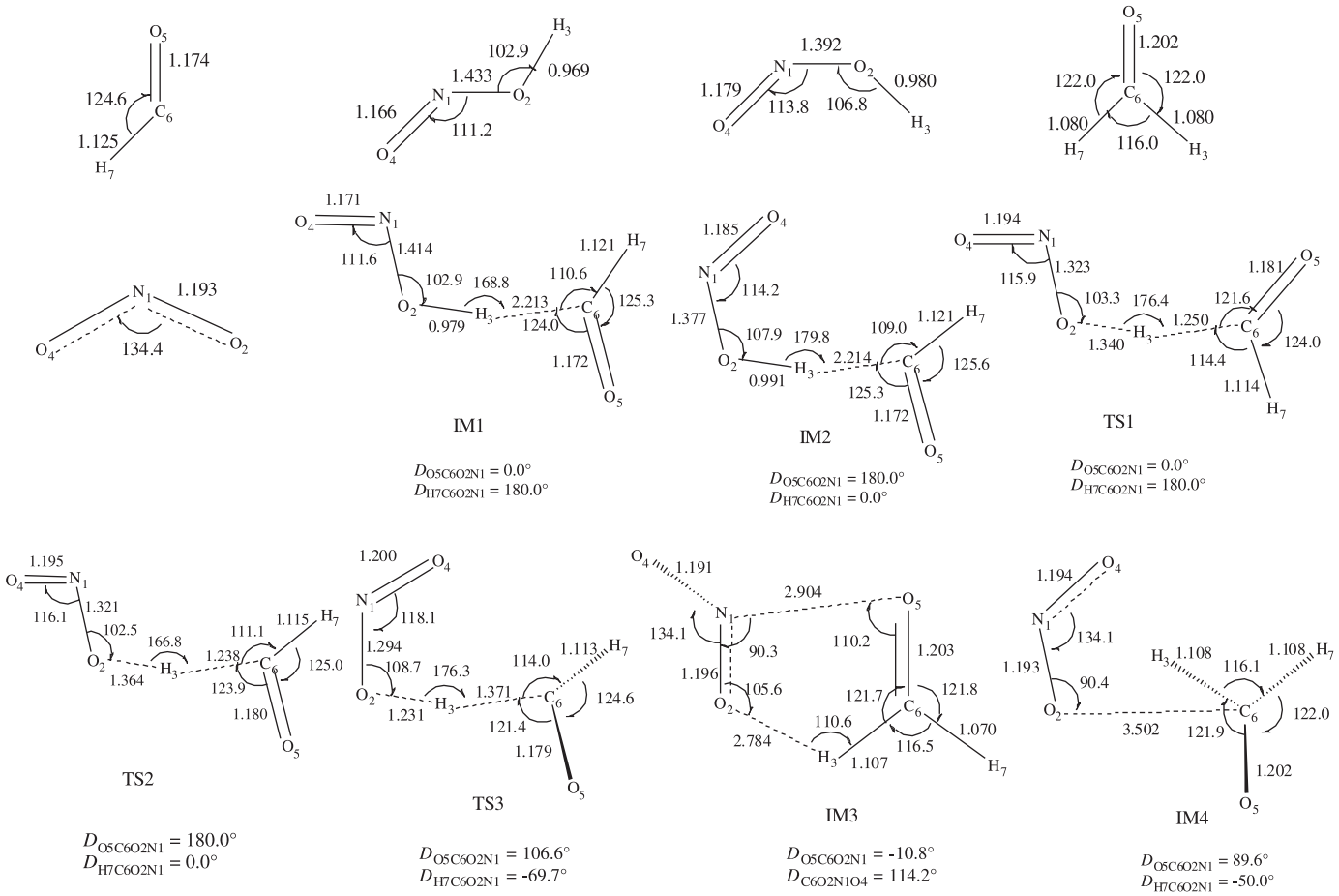
Received 16 January 2007. Accepted 26 April 2007. Published on the NRC Research Press Web site at canjchem.nrc.ca on 14 June 2007.

X. Sun and W. Wang.[1] Environment Research Institute, Shandong University, Jinan 250100, People's Republic of China.
Z. Cai and D. Feng. Institute of Theoretical Chemistry, Shandong University, Jinan 250100, People's Republic of China.
W. Bian. State Key Laboratory of Molecular Reaction Dynamics, Institute of Chemistry, Chinese Academy of Science, Beijing 100080, People's Republic of China.
Q. Qiao. School of Chemistry and Materials Science, Ludong University, Yantai 264025, People's Republic of China.

[1]Corresponding author (e-mail: wxwang@sdu.edu.cn).

 doi:10.1139/V07-044 © 2007 NRC Canada

Fig 1. Geometry parameters of stationary points along three reaction paths at the B3LYP/6-311++G** level.



between the experimental and theoretical results in wider temperature range. It is necessary to perform the mechanism and kinetics studies.

In this paper, the mechanism for the reaction of HNO_2 (including trans- and cis-) with HCO was revealed. Next, kinetic calculations were carried out. Several important features of this study include (*i*) performing the density functional theory (DFT) calculations for the minimum energy paths (MEP) to obtain potential energy information, (*ii*) studying the kinetic nature in the temperature range from 300 to 3000 K using interpolated canonical variational transition-state theory (CVT) and the centrifugal-dominant, small-curvature tunneling approximation (SCT), including information at the reactants, intermediates, transition-states, products, and extra points along the MEP, (*iii*) fitting the non-Arrhenius expression, and (*iv*) comparing the calculated rate constants with the previous results.

Computation methods

For systems with a multiplicity > 1, the spin contamination is one of the aspects that should be considered. In DFT calculations, it is less common to find any significant spin contamination. In addition, recent developments in DFT (11) enabled the modification and improvement of the performance in geometrical optimizations and vibrational-frequency calculations. For hydrogen-bonded systems, it has long been recognized that the basis sets should include diffuse and polarization functions. Thus, combining B3LYP method (12) with 6–311++G** basis set should give satisfactory results.

The geometries of the reactants, intermediates, transition states, and products have been optimized at the B3LYP/6–311++G** level. To determine the nature of the stationary points, the zero-point energy (ZPE), and the thermal contribution to the free energy of activation, we have calculated the vibrational frequencies at the same level. An IRC calculation confirmed that the transition state connects the designated intermediates. At the B3LYP/6–311++G** level, a gradient step size of 0.02 amu bohr^2 was used to obtain the MEP in mass-weighted Cartesian coordinates. Then, we computed both the force-constant matrices of the stationary points and selected non-stationary points near the transition state along the MEP. The geometrical parameters and the frequencies of various species can be determined satisfactorily at the B3LYP/6–311++G** level. The single-point energies obtained at the QCISD(T)/6–311++G** level are chosen for the kinetic calculations. All ab initio calculations have been carried out using GAUSSIAN 03 programs (13) on SGI workstation.

The initial information obtained from the ab initio calculations allowed us to calculate the rate constants, including the tunneling effects. POLYRATE 9.3 program was used to perform all the kinetic calculations (14). Classical calculations were used for the rotational partition functions, and the vibrational modes were treated as quantum-mechanical separable harmonic oscillators. The centrifugal-dominant SCT

© 2007 NRC Canada

correction method was used in our calculations of the rate constants. The total rate constants are obtained as the sum of the calculated rate constants for the three reaction paths.

Results and discussion

Figure 1 shows the optimized geometries of the reactants, intermediates, transition states, and products. The rotational constants and vibrational frequencies of the reactants, products, intermediates, and transition states are listed in Table 1. The hyperfine coupling constants of the intermediates are listed in Table 2. The energies of the stationary points obtained with different methods are summarized in Table 3 and Table 4. The total forward rate constants obtained from different methods are listed in Table 5. The potential energy profile of the HCO + HNO_2 → HCHO + NO_2 system is drawn in Fig. 2. Figure 3 shows the classical potential energy, the ZPE curves, and vibrationally adiabatic potential energy as functions of s on the ^2A potential energy surface. The changes of the generalized normal-mode vibrational frequencies as functions of s are drawn in Fig. 4. Finally, the forward rate constants, including theoretical and previous results, are shown in Fig. 5.

Reaction mechanism

The reaction path

For the title reaction, three product paths on the doublet electronic-state potential energy surface have been identified from the calculations (shown in Fig. 2).

[1] HCO + *trans*-HNO_2 → IM1 → TS1 → IM4 → HCHO + NO_2

[2] HCO + *trans*-HNO_2 → IM1 → TS2 → IM3 → HCHO + NO_2

[3] HCO + *cis*-HNO_2 → IM2 → TS3 → IM4 → HCHO + NO_2

where IM is the intermediate, IM1 and IM2 are the precomplexes, and IM3 and IM4 are the post-complexes. All reactants have planar structures. It should be noted that the reactant HNO_2 has two isomers, i.e., *trans*-HNO_2 and *cis*-HNO_2. The former is more stable than the latter because the former has a lower energy, which can be explained by the stereo effect. In the optimization process, reactants first form a prior complex with low energy, which is a barrierless process. Then, the complex crosses a potential barrier and turns into the other complex. Finally, the products formed after the second complex are decomposed into two particles. There are three reaction paths, which have the similar processes, namely, path 1, path 2, and path 3. Path 3 is chosen to discuss its reaction mechanism because it has the lowest barrier. For convenience, the atoms are labeled according to the sequence of H3O2N1O4 and H7C6O5.

The whole path 3 includes HCO, *cis*-HNO_2, IM2, TS3, IM4, HCHO, and NO_2. The reaction process can be described as follows: first, when planar reactants, i.e., HCO and *cis*-HNO_2, approach each other, the H-bond complex IM2 is formed directly, then the energy decreases, and the potential well comes into being. Then, the H-bond between O7–H1 breaks

Table 1. The rotational constants and frequencies of the stationary points on the different reaction paths obtained at B3LYP/6–311++G** level.

	A	B	C (GHz)	ν (cm^{-1})
HCO	720.3	44.9	42.3	1100.0, 1934.6, 2653.4
trans-HONO	94.5	12.5	11.1	579.4, 613.5, 811.3, 1291.1, 1785.4, 3763.5
cis-HONO	84.9	13.2	11.4	625.7, 683.7, 871.1, 1322.6, 1715.1, 3585.1
IM1	25.5	1.4	1.3	6.1, 35.5, 80.9, 86.6, 150.3, 314.7, 649.6, 715.5, 840.2, 1086.9, 1354.0, 1764.2, 1942.1, 2710.9, 3548.8
IM2	12.7	1.7	1.6	8.2, 51.3, 78.7, 106.5, 162.5, 325.0, 658.3, 789.8, 908.0, 1085.5, 1363.1, 1688.7, 1939.1, 2717.2, 3345.3
IM3	11.3	2.0	1.8	20.6, 26.6, 46.2, 61.1, 88.6, 107.1, 767.4, 1203.1, 1259.3, 1395.1, 1530.6, 1706.4, 1813.0, 2892.2, 2953.8
IM4	11.0	2.5	2.0	36.9, 57.6, 65.4, 116.3, 118.6, 144.9, 765.8, 1205.8, 1260.0, 1390.3, 1524.6, 1702.9, 1808.5, 2896.1, 2960.9
TS1	17.4	2.1	1.8	1571.1i, 62.6, 62.8, 159.0, 328.4, 454.2, 540.1, 721.7, 973.8, 1164.9, 1189.8, 1500.8, 1610.8, 1884.8, 2844.8
TS2	31.8	1.7	1.6	1372.0i, 54.5, 74.4, 175.9, 295.6, 450.0, 528.5, 717.0, 990.0, 1173.6, 1190.7, 1535.2, 1627.6, 1893.0, 2833.4
TS3	11.8	2.5	2.2	1517.0i, 57.0, 113.6, 149.6, 295.5, 487.6, 579.2, 834.0, 1125.2, 1152.2, 1307.2, 1404.7, 1574.6, 1809.6, 2836.5
H_2CO	283.8	39.0	34.3	1202.2, 1259.7, 1531.0, 1814.9, 2884.5, 2942.4
NO_2	242.4	13.6	12.4	764.8, 1391.3, 1702.3

© 2007 NRC Canada

Table 2. Hyperfine coupling constants (in Gauss) on each atom (Mülliken atomic-spin populations are given in parentheses).

	IM1	IM2	IM3	IM4
N1	+0.22 (–0.002)	+0.83 (+0.009)	+49.81 (+0.494)	+52.14 (+0.61)
O2	–1.60 (+0.010)	–0.55 (+0.007)	–16.48 (+0.255)	–12.84 (+0.260)
H3	–4.10 (+0.040)	–4.35 (+0.406)	+0.08 (0.000)	+0.34 (+0.001)
O4	–0.11 (+0.002)	–0.13 (+0.001)	–16.50 (+0.256)	–13.00 (+0.276)
O5	–9.79 (+0.284)	–9.79 (+0.278)	–0.81 (–0.004)	–1.28 (+0.002)
C6	+105.60 (+0.507)	+106.51 (+0.505)	+0.05 (–0.000)	–0.32 (–0.002)
H7	+124.61 (+0.159)	+122.46 (+0.160)	0.00 (–0.000)	+0.77 (0.000)

up, and the HCO encircles another bond between C2 and H4 and approaches *cis*-HNO_2, simultaneously. Subsequently, the transition state is formed. After the system crosses the potential barrier, another five-membered complex (IM4) comes into being as HCO continues to approach *cis*-HNO_2. If (IM4) yields to be clockwise, then its mirror-image conformer appears to be anticlockwise. There are two kinds of isomers in the potential well of the IM4. Thus, the detailed reaction paths become obvious.

Next, the transition states are considered; a more detailed analysis is performed for the transition states. As mentioned previously, the hydrogen-transfer reaction of HCO with HNO_2 proceeds over three potential energy surfaces (PESs), corresponding to the three paths, namely, surface 1, 2, and 3, respectively. At the B3LYP/6–311++G** level, three transition states were located, whose geometrical structures are shown in Fig. 1. The transition states are denoted as TS1, TS2, and TS3. The transition states were different both in energy and in the orientation angle of O–C–H. The C atom of HCO group abstracts the H atoms of HNO_2 from the *trans*-position of the O atom via TS1 or TS2. The breaking N–H bonds are elongated by 35.8% and 39.2%, while the forming C–H bonds in the corresponding transition states are longer than the equilibrium value of 1.107 Å by 12.9% and 11.8%. According to Hammond's postulate (15), these two transition states are product-like, and the H-transfer reaction from HNO_2 to HCO molecule occurs via later transition states. Nevertheless, the reaction still has a high barrier and a high exothermicity. For the TS3, the breaking N–H bonds in the *cis*-HNO_2 molecule are elongated by 25.6%, while the forming C–H bonds in the corresponding transition states are longer than the equilibrium value of 1.107 Å by 23.8%. This reaction path has a lower barrier and a higher exothermicity.

As shown in Table 1, at the B3LYP/6–311++G** level, three transition states have one, and only one, imaginary frequency. The values of the imaginary frequencies are large, which implies that the quantum tunneling effect may be significant and may play an important role in the calculation of the rate constants.

To prove that a particular transition state connects two specific intermediates or products, the intrinsic-reaction coordinate calculation is needed to relocate the minimal-energy reaction path from a transition state down to the nearest local minima in the forward and reverse directions.

The role of intermediates

Recently, several evidences (16, 17) indicated that the intermediates (IM) played an important role in the ground-state reaction dynamics even though these complexes occur at considerably larger internuclear distances than those of the transition states. Accordingly, many works are performed concerning the issue (18).

In this paper, four intermediates are found, whose formations change the topological properties of the PES. Therefore, attention should be paid to them.

The geometries of the intermediates are fully optimized, and the optimized parameters are listed in Fig. 1. Obviously, IM1 and IM2 have similar structures, which are composed of the HCO radical with the HONO molecule (t*rans*- and *cis*-). The H3—C6 distances are 2.214 Å in IM1 and IM2 . However, IM3 and IM4 compose the HCHO and NO_2 groups. The N1—O5 distance in IM3 is 2.987 Å, and the O2—H3 distance in IM4 is 2.593 Å. All the intermediates are weakly bonded complexes. The main difference is that IM1 and IM2 have the reactant-like structures, while IM3 and IM4 have the product-like ones.

The harmonic vibrational frequencies of the intermediates are shown in Table 1. Taking IM1 for example, the vibrational mode of highest frequency, 3548.8 cm^{-1}, corresponds to the H3–O2 stretching mode. This value is slightly smaller than that of the free *trans*-HONO molecule (3763.5 cm^{-1}). This result means that H3–O2 bond becomes weaker in the IM1 formation. In addition, the intermolecular stretching mode between the HCO radial and *trans*-HONO molecule is calculated to be 150.3 cm^{-1}, which is significantly small because of the weak interaction. This result implies that the structure of IM1 may be easily deformed by the thermal activation. Similar analysis can also be applied to the other intermediates.

By using the optimized structures, the hyperfine coupling constants (HFCCs) are calculated at B3LYP/6–311++G** level (19). The results are listed in Table 2 together with Mülliken atomic-spin densities on the atoms in parentheses. Taking the IM1 for example, the O2, H3, O4, and O5 atoms have negative HFCCs; whereas N1, C6, and H7 atoms have positive ones. A simple Mülliken spin densities calculation shows that the unpaired electron is mainly located on the HCO radical, especially on the C atom (spin densities on the carbon atom is calculated to be 0.507). The HFCCs of IM2 has the same trend as those of IM1. However, the HFCCs of IM3 and IM4 are very different from those of IM1 and IM2. In IM3, the O2, O4, and O5 atoms have negative HFCCs; whereas N1, H3, C6, and H7 atoms have positive ones. In IM4, the O2, O4, O5, and C6 atoms have negative HFCCs; whereas N1, H3, and H7 atoms have positive ones. Mülliken spin densities suggest that, both in IM3 and IM4, the unpaired electron is mainly located on the NO_2 molecule, espe-

© 2007 NRC Canada

Table 3. The total energies (a.u.) of the stationary points on the different reaction paths obtained from different methods.

	B3LYP[a]	G3B3[a]	HF[b]	MP2[b]	MP3[b]	MP4SDQ[b]	QCISD[b]	QCISD(T)[b]	B3LYP[b]
HCO	–113.80517	–113.79409	–113.28224	–113.59915	–113.59765	–113.60916	–113.61206	–113.62210	–113.89133
trans-HONO	–205.69522	–205.60838	–204.70010	–205.28749	–205.27442	–205.29231	–205.29256	–205.31676	–205.77176
cis-HONO	–205.69680	–205.60732	–204.69927	–205.28573	–205.27291	–205.29075	–205.29090	–205.31486	–205.77005
IM1	–319.55211	–319.40459	–317.98285	–318.89157	–318.87646	–318.90563	–318.90649	–318.94307	–319.66736
IM2	–319.55409	–319.40399	–317.98331	–318.88919	–318.87438	–318.90355	–318.90441	–318.94089	–319.66555
IM3	–319.57673	–319.42022	–317.99232	–318.91250	–318.88638	–318.91836	–318.91846	–318.95762	–319.68474
IM4	–319.57674	–319.42020	–317.99192	–318.91188	–318.88592	–318.91589	–318.91577	–318.95574	–319.68505
TS1	–319.53124	–319.37327	–317.91805	–318.83018	–318.81772	–318.85248	–318.86287	–318.90335	–319.64277
TS2	–319.53212	–319.37416	–317.91683	–318.83295	–318.81839	–318.85410	–318.86363	–318.90452	–319.64358
TS3	–319.53556	–319.38694	–317.94191	–318.86094	–318.84231	–318.87341	–318.87754	–318.91785	–319.65490
H_2CO	–114.46114	–114.43375	–113.90167	–114.24158	–114.24551	–114.25503	–114.25550	–114.26735	–114.54185
NO_2	–204.98745	–204.98402	–204.08743	–204.66754	–204.63721	–204.65978	–204.65930	–204.68651	–205.14069

[a]6–31G*.
[b]6–311++G**.

cially on the N atom. The reliability of the HFCCs is expected to be verified by the experimental results, such as ESR and FTIR methods combined with the matrix-isolation technique. Other properties of the intermediates, such as the trajectory calculation, time-dependence of HFCC, and temperature-dependence of HFCCs, will be studied in the future.

Energy

Tables 3 and 4 summarize the potential energies at various theory levels, including HF, B3LYP, G3B3 (20), MP_n (n = 2, 3, and 4), QCISD, and QCISD(T). The energies are calculated by taking the zero of energy at the reactants (HCO + *trans*-HONO). From Tables 3 and 4, all the reaction paths have a double-well structure as a whole. The depth of the first well ranges from 0.32 kcal/mol to 5.46 kcal/mol, while the second well locates from 0.68 kcal/mol to 2.46 kcal/mol, measured by taking the zero of energy of NO_2 + H_2O. Although the potential-barrier values are different for the three reaction paths at the same computational level, the values for the same reaction path have the same trend obtained at the HF, B3LYP, and G3B3 levels. The effect of basis set on the potential barrier can be observed from our B3LYP result with two different basis sets, namely, 6–31G and 6–311++G**. The barrier height increases by 3.88 and 3.98 kcal/mol with the increase in basis sets at the B3LYP level for paths 1 and 2, respectively, while for path 3, the barrier height decreases by 1.20 kcal/mol. After comparison, the potential barriers and the reaction enthalpy, calculated at the QCISD(T)/6–311++G** level, are adopted for the following kinetic calculations.

The barrier of path 2, reported by Feng (7), is 11.53 kcal/mol. As for Lin's result (9), the barriers are 19.5 and 10.90 kcal/mol for paths 2 and path 3, respectively. Neither of them reported path 1. According to our calculations, the barriers are 22.28, 21.54, and 13.18 kcal/mol for paths 1, 2, and 3, respectively.

Kinetic calculations

Reaction path properties

The reaction kinetics for the three paths has been calculated independently. The three paths have similar features, and further discussion will refer only to path 3. The MEP is calculated at the B3LYP/6–311++G** level, and the energies along the IRC are calculated at the QCISD(T)/6–311++G** level. Figure 3 shows the changes of the classical potential energy V_{MEP} and the ground-state vibrational adiabatic potential energy V_a^G with the reaction coordinate s on path 3. From $s = -\infty$ to –10.0 amu bohr^2, the potential curves decrease very slowly. From s = –10.0 to –2.0 amu bohr^2, the curves increase gradually, and from s = –2.0 to 2.0 amu bohr^2, the curves increase and decrease quickly on passing the transition state. The V_{MEP} and V_a^G curves are similar in shape. The ZPE, which is the difference between V_a^G and V_{MEP}, is also shown in Fig. 3. The zero-point energy curve is almost unchanged as s varies except from s = –1.0 to 1.0 amu bohr^2 where a gentle valley appears. To analyze this behavior in detail, we have shown the variation of the generalized normal-mode vibrational frequencies of the hydrogen-transfer reaction in Fig. 4. When $s = -\infty$, the frequencies are associated with the reactants HCO and HNO_2, while in the positive

© 2007 NRC Canada

Table 4. The energies (kcal/mol) of the stationary points on the different reaction paths obtained from different methods (measured by taking the zero of energy at HCO + *trans*-HONO).

	B3LYP[a]	G3B3[a]	HF[b]	MP2[b]	MP3[b]	MP4SDQ[b]	QCISD[b]	QCISD(T)[b]	B3LYP[b]
HCO + *trans*-HONO	0.0	0.0	0.0	0.0	0.0	0.0	0.0	0.0	0.0
HCO + *cis*-HONO	+0.8911	+0.6652	+0.5208	+1.1044	+3.4575	+0.9789	+1.0417	+1.1923	1.0730
IM1	–4.2231	–1.3303	–0.3200	–3.2065	–2.7547	–2.6104	–1.1734	–2.6418	–2.6794
IM2	–5.4655	–0.9538	–0.6087	–1.5939	–1.4495	–1.3052	–0.1318	–1.2738	–1.5437
IM3	–19.6721	–11.1381	–6.2625	–16.3527	–8.9795	–10.5985	–8.6846	–11.7719	–13.5854
IM4	–19.6784	–11.1256	–6.0115	–15.8381	–8.6909	–9.0486	–6.9966	–10.5922	–13.7799
TS1	+8.8728	+18.3230	+40.3420	+35.4287	+34.1046	+30.7012	+26.1981	+22.2825	+12.7508
TS2	+8.2579	+17.7645	+41.1075	+33.6905	+33.6842	+31.4189	+25.7212	+21.5484	+12.2425
TS3	+6.1621	+9.7451	+25.3698	+16.1263	+18.6744	+17.6077	+16.9727	+13.1838	+5.1391
$H_2CO + NO_2$	–17.1308	–9.6008	–4.2419	–14.1062	–6.6954	–8.3709	–6.3880	–9.4125	–12.1421

[a]6–31G*.
[b]6–311++G**.

Table 5. The total forward rate constants $k_1 + k_2 + 2k_3$ (cm^3 $molecule^{-1}$ s^{-1}) obtained from different methods.

T	TST	CVT	CVT/ZCT	CVT/SCT
300.0	3.15E–19	3.06E–19	3.92E–19	4.20E–19
350.0	2.21E–18	2.14E–18	2.50E–18	2.64E–18
400.0	1.01E–17	9.72E–18	1.07E–17	1.11E–17
450.0	3.52E–17	3.28E–17	3.47E–17	3.57E–17
500.0	9.63E–17	8.99E–17	9.24E–17	9.46E–17
550.0	2.29E–16	2.11E–16	2.12E–16	2.16E–16
600.0	4.83E–16	4.40E–16	4.36E–16	4.44E–16
700.0	1.67E–15	1.47E–15	1.43E–15	1.45E–15
750.0	2.79E–15	2.45E–15	2.36E–15	2.38E–15
800.0	4.51E–15	3.87E–15	3.71E–15	3.75E–15
900.0	1.02E–14	8.56E–15	8.19E–15	8.25E–15
950.0	1.47E–14	1.21E–14	1.16E–14	1.16E–14
1000.0	2.05E–14	1.67E–14	1.59E–14	1.60E–14
1150.0	4.94E–14	3.88E–14	3.69E–14	3.71E–14
1200.0	6.38E–14	4.96E–14	4.72E–14	4.74E–14
1500.0	2.31E–13	1.67E–13	1.59E–13	1.61E–13
1700.0	4.51E–13	3.15E–13	3.03E–13	3.04E–13
1900.0	7.99E–13	5.42E–13	5.19E–13	5.21E–13
2000.0	1.32E–12	8.67E–13	8.32E–13	8.36E–13
2500.0	3.03E–12	1.89E–12	1.83E–12	1.86E–12
3000.0	6.95E–12	4.14E–12	4.00E–12	4.03E–12

limit of *s*, the frequencies are associated with the products HCHO and NO_2. The frequency of mode 1, which connects the frequency of O–H stretching vibration in HNO_2 with the frequency of the C–H stretching vibration in HCHO, drops sharply from $s = -1.0$ to $s = +1.0$ amu $bohr^2$; this behavior is similar to that found in other hydrogen-transfer reactions (21–24). If changes in other frequencies were small, this drop could cause a considerable fall in the zero-point energy near the transition state. The four lowest harmonic frequencies corresponding to free rotations and translations of the reactants evolve to vibrations at about $s = 0.0$ amu $bohr^2$, and they present a maximum near the saddle point. The behavior of these four lowest frequencies compensates for the fall in the zero-point energy caused by modes 1, 3, and 4. Therefore, there is only a slight change in the zero-point energy with *s*, and the ground-state vibrational adiabatic potential energy V_a^G curve is similar in shape to the classical potential energy V_{MEP} curve.

Rate constants

As mentioned previously, the title reaction has three paths to the products. However, the barriers of path 1 and path 2 are higher than that of path 3. The barrier for path 3 can be interpreted as follows: The reactants, HCO and *cis*-HONO, have planar structures. The dihedral angel between the planes of the two reactants in TS3 is 106.88°. The distance between H7 and O4 is 3.230 Å, which is shorter than 3.281 Å in IM2, suggesting the formation of a hydrogen-bond. It is the hydrogen-bond that stabilizes the structure of TS3, i.e., lowers the barrier of path 3. In addition, path 3 has an equivalent path because the HCO has two permutations with *cis*-HONO to form two transition states that are mirror images. Thus, the total rate constant is $k_1 + k_2 + 2k_3$.

The TST and CVT with a SCT, which have been successfully applied to several analogous reactions (25–27), are effective methods to calculate the rate constants. In this paper, these methods are used to study the title reaction over a wide temperature range of 300–3000 K. To calculate the rate constants, 30 points near the transition state along the MEP were selected; 15 points on the reactants side and 15 points on the products side. Figure 5 shows the total rate constant vs. the temperature for the reaction of HCO with HNO_2. For comparison, the previous values, TST rate constants, and the CVT rate constants with the small curvature tunneling (SCT) correction are also shown in Fig. 5. All the values of $k_1 + k_2 + 2k_3$ obtained from various methods are listed in Table 5. The rate constants of each path are listed in the supplementary data.[2] The calculated rate constants have several important features: (*i*) The rate constants of TST and CVT are nearly the same over the temperature range of 300–3000 K, which enables us to conclude that the variational effect is small for

[2] Supplementary data for this article are available on the journal Web site (canjchem.nrc.ca) or may be purchased from the Depository of Unpublished Data, Document Delivery, CISTI, National Research Council Canada, Ottawa, ON K1A 0S2, Canada. DUD 5174. For more information on obtaining material, refer to http://cisti-icist.nrc-cnrc.gc.ca/irm/unpub_e.shtml.

© 2007 NRC Canada

Fig. 2. Schematic energy diagram of the HCO + HNO_2 → HCHO + NO_2 system predicted at the QCISD(T)||B3LYP/6-311++G** level.

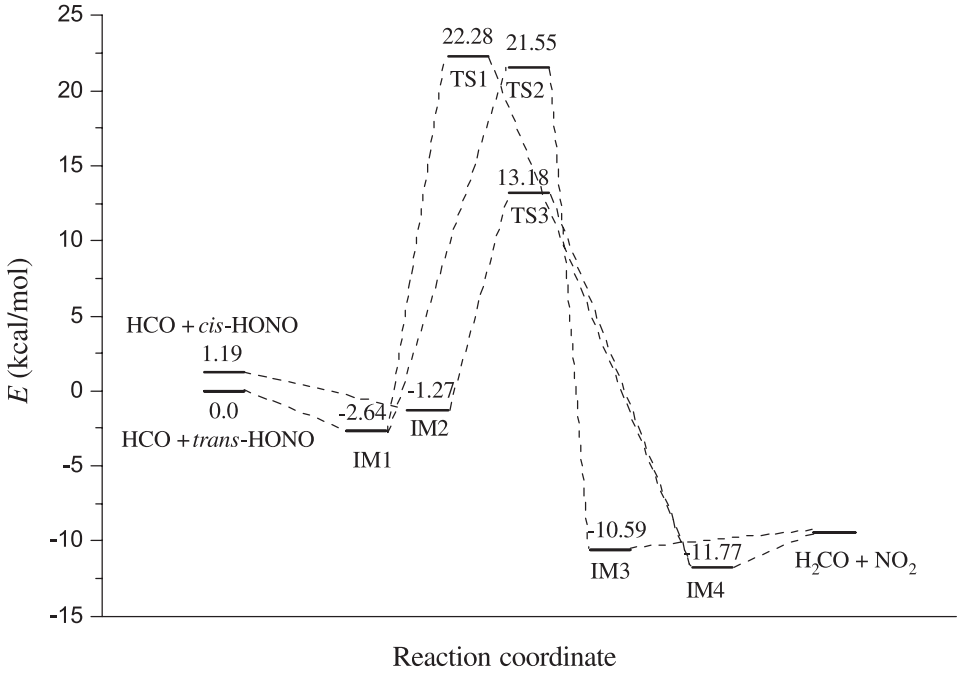


Fig. 3. The classical potential energy V_{MEP}, the ZPE curves, and vibrationally adiabatic potential energy V_a^G as functions of s at the B3LYP/6-311++G** level on path 3.

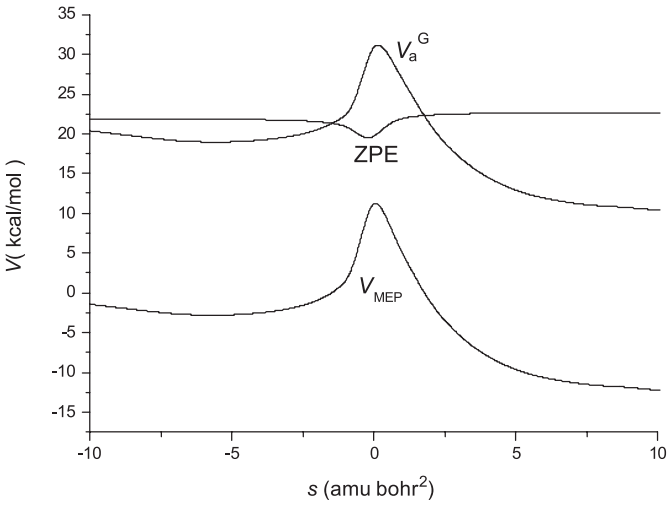
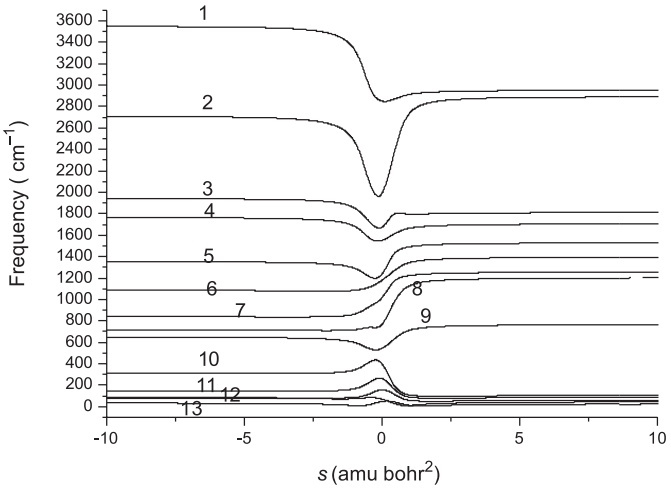


Fig. 4. The changes of the generalized normal-mode vibrational frequencies as functions of s at the B3LYP/6-311++G** level on path 3.



this reaction. (*ii*) When computing reaction rate constants for reactions involving hydrogen-atom transfer, tunneling effects must be taken into account. In the present case, the CVT/SCT rate constants are larger than the CVT ones over the temperature range of 300–3000 K; for example, at 300 K, the CVT rate constant is 3.06×10^{-19} cm^3 molecule^{-1} s^{-1}, while the CVT/SCT rate constant is 4.20×10^{-19} cm^3 molecule^{-1} s^{-1}. The latter is 1.37 × the former. The higher the temperature is, the less the ratio is, which means that the SCT correction plays an important role for the calculation of the rate constants only in the low-temperature range. For TST and CVT/ZCT, the same trend is observed. Another phenomenon is that the CVT/SCT rate constants are asymptotic to the rate constants of TST and CVT/ZCT in the high-temperature range. (*iii*) Comparing the calculated rate constants with the previous values for the title reaction, the CVT/SCT rate constants agree with experimental values for a wide temperature range. Therefore, the CVT/SCT method is a good choice to calculate accurate rate constants for the title reaction. (*iv*) Obviously, a non-Arrhenius behavior is exhibited by the calculated rate constants. The rate constants of the title reaction are fitted by two three-parameter formulas over the temperature range of 300–3000 K and given in units of cm^3 molecule^{-1} s^{-1} as follows:

$$k(T) = 4.58 \times 10^{-23.15}\ T^{2.55}\exp(-2369.25/T)$$

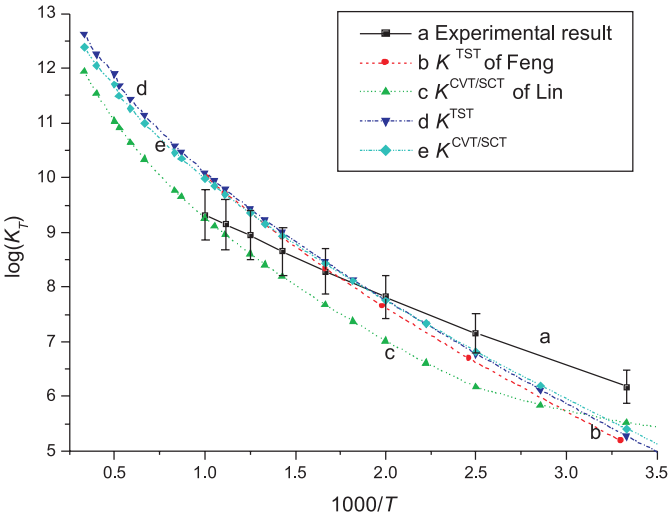
where 300 K < T < 3000 K for TST rate constants, and

$$k(T) = 2.59 \times 10^{-22.68}\ T^{2.34}\exp(-2247.56/T)$$

where 300 K < T < 3000 K for CVT/SCT rate constants.

© 2007 NRC Canada

Fig. 5. Forward rate constants as a function of the temperature (T) in the range of 300–3000 K for the HCO + HNO_2 → HCHO + NO_2 reaction. Line a is the experimental result (4), line b represents TST with correction of the tunneling effect in Feng's results (7), and line c is Lin's result (9).



Conclusion

In this paper, we have studied the reaction of HNO_2 with HCO at the QCISD(T)//B3LYP/6–311++G** level and TST (CVT) with the SCT approximation. Rate constants were reported over the temperature range of 300–3000 K. The structure of reaction paths includes the reactants, the prior-complex, the transition state, the post-complex, and the product. The complexes should not be ignored, as they are helpful to show the complete topological structure of the PES. The modified mechanism is more detailed and integrated. For this H-atom transfer reaction, three paths are calculated, and path 3 is verified to be the fastest. The reasonable interpretation is that the formation of a hydrogen bond in TS3 stabilizes the structure, i.e., lowers the barrier of path 3, which leads to $k_3 >> k_1$ (or k_2). The total forward rate constants are $k_1 + k_2 + 2k_3$ because path 3 has an equivalent path. A typical non-Arrhenius behavior is exhibited by the calculated rate constants. The calculated CVT/SCT rate constants agree with the limited previous reports.

Acknowledgements

This work was supported by National Natural Science Foundation of China (NSFC; project No. 20507013, 20603030) and Post-doctor Research Foundation of Shandong Province (No. 200601007).

References

1. W.C. Gardiner. Combustion chemistry. Springer-Cerlag, Berlin. 1984.
2. T.L. Boggs. Progress in astronautics and aeronautics: on fundamentals of solid-propellant combustion. American Institute of Astronautics and Aeronautics, New York. **90**, 121 (1984).
3. B.J. Finalayson-Pitts and J.N. Pitts., Jr. Atmospheric chemistry: fundamentals and experimental techniques. Wiley, New York. 1986.
4. W. Tsang and J.T. Herron. J. Phys. Chem. Ref. Data, **20**, 609 (1991).
5. C.Y. Lin, H.T. Wang, M.C. Lin, and C.F. Melius. Int. J. Chem. Kinet. **22**, 455 (1990).
6. J.H. Rhomas. Trans. Faraday Soc. **49**, 630 (1953).
7. S.W. Zhang, W.L. Feng, Y. Wang, and X.Y. Pang, J. Mol. Struct.: THEOCHEM. **365**, 215 (1996).
8. T. Veszpremi and M. Feher. Quantum chemistry: fundamentals to applications. Plenu Publishing, New York. 1999. p.281.
9. Z.F. Xu and M.C. Lin. Int. J. Chem. Kinet. **36**, 178 (2004).
10. Z.F. Xu and M.C. Lin. Int. J. Chem. Kinet. **35**, 184 (2003).
11. R.I. Kaiser and A. M. Mebel. Int. Rev. Phys. Chem. **21**, 307 (2002).
12. A.D. Becke. J. Chem. Phys. **98**, 5648 (1993).
13. M.J. Frisch, G. W. Trucks, H.B. Schlegel, G.E. Scuseria, M. A. Robb, J.R. Cheeseman, J.A. Montgomery, T. Vreven, Jr., K.N. Kudin, J.C. Burant, J.M. Millam, S.S. Iyengar, J. Tomasi, V. Barone, B. Mennucci, M. Cossi, G. Scalmani, N. Rega, G.A. Petersson, H. Nakatsuji, M. Hada, M. Ehara, K. Toyota, R. Fukuda, J. Hasegawa, M. Ishida, T. Nakajima, Y. Honda, O. Kitao, H. Nakai, M. Klene, X. Li, J.E. Knox, H.P. Hratchian, J.B. Cross, C. Adamo, J. Jaramillo, R. Gomperts, R.E. Stratmann, O. Yazyev, A.J. Austin, R. Cammi, C. Pomelli, J.W. Ochterski, P.Y. Ayala, K. Morokuma, G.A. Voth, P. Salvador, J.J. Dannenberg, V.G. Zakrzewski, S. Dapprich, A.D. Daniels, M.C. Strain, O. Farkas, D.K. Malick, A.D. Rabuck, K. Raghavachari, J.B. Foresman, J.V. Ortiz, Q. Cui, A.G. Baboul, S. Clifford, J. Cioslowski, B.B. Stefanov, G. Liu, A. Liashenko, P. Piskorz, I. Komaromi, R.L.Martin, D.J. Fox, T. Keith, M.A. Al-Laham, C.Y. Peng, A. Nanayakkara, M. Challacombe, P.M.W. Gill, B. Johnson, W. Chen, M.W. Wong, C. Gonzalez, and J.A. Pople. Gaussian [computer program]. Gaussian, Inc., Pittsburgh, PA. 2003.
14. J.C. Corchado, Y.Y. Chuang, P.L. Fast, J. Villa, W.P. Hu, Y.P. Liu, G.C. Lynch, K.A. Nguyen, C.F. Jackels, V.S. Melissas, B.J. Lynch, I. Rossi, E.L. Coitino, A.F. Ramos, J. Pu, T.V. Albu, R. B.C. Garrett, and D.G. Truhlar. POLYRATE [computer program]. version 9.3. 2003.
15. G.S. Hammond. J. Am. Chem. Soc. **77**, 334 (1955).
16. D.G. Truhlar. J. Comput. Chem. **12**, 266 (1991).
17. D.M. Neumark. Phys. Chem. Commun. **5**, 76 (2002).
18. R.L. Wilson, Z.M. Loh, D.A. Wild, E.J. Bieske, and A.A. Buchachenko. J. Chem. Phys. **121**, 2085 (2004).
19. H. Tachikawa. J. Phys. Chem. A. **102**, 7065 (1998).
20. A.G. Baboul, L.A. Curtiss, P.C. Redfern, and K. Raghavachari. J. Chem. Phys. **110**, 7650 (1999).
21. D.G. Truhlar and A.D. Isaacson. J.Chem. Phys. **77**, 3516 (1982).
22. J. Espinosa-Garcia and J.C. Corchado. J. Phys. Chem. **100**, 16561 (1996).
23. J.C. Corchado and J. Espinosa-Garcia. J. Chem. Phys. **106**, 4013 (1997).
24. Q.Z. Zhang,; S.K. Wang and Y.S. Gu. Chem. Phys. Lett. **369**, 145 (2003).
25. V.S. Melissas and D.G.Truhlar. J. Phys. Chem. **98**, 875 (1994).
26. Y.X.Yu, S.M. Li, Z.F. Xu, Z.S. Li, and C.C. Sun. Chem. Phys. Lett. **320**, 123 (2000).
27. Y.X.Yu, S.M. Li, Z.F. Xu, Z.S. Li, and C.C. Sun. Chem. Phys. Lett. **302**, 281 (1999).

© 2007 NRC Canada

Structures of the 2:1 adducts of benzyne with 2-methylanisole and benzene

Christopher O. Bender, René T. Boeré, Peter W. Dibble, and Ryan T. McKay

Abstract: The 2:1 adduct of benzyne with 2-methylanisole is shown to have the bisbenzotricyclic structure 6,6a,11,11a-tetrahydro-5-methoxy-6-methyl-5,6,11-metheno-5*H*-benzo[*a*]fluorene by a single-crystal X-ray diffraction study ($C_{20}H_{18}O$: *Pca*2$_1$, a = 15.0497(17), b = 9.87783(11), c = 9.6846(11); Z = 4; 1672 data points, R_1 = 0.0325). This structure is compared to an unpublished crystal structure of the parent hydrocarbon 6,6a,11,11a-tetrahydro-5,6,11-metheno-5*H*-benzo[*a*]fluorene, $C_{18}H_{14}$. Both structures have also been computed by DFT methods at the B3LYP/6–311(d,p) level of theory. Bond distances and angles between the solid-state measurements and gas-phase calculations are found to agree well; average deviations are well below 1%. The ^{1}H NMR spectra show surprisingly small $^3J_{HH}$ couplings in the central tricyclic cage, but can be assigned using 2D spectroscopy.

Key words: Hydrocarbon cages, strained rings, cyclopropane, X-ray crystallography, NMR.

Résumé : Faisant appel à la diffraction des rayons X par un cristal unique, on a montré que l'adduit 2:1 de benzyne sur le 2-méthylanisole possède la structure 6,6a,11,11a-tétrahydro-5-méthoxy-6-méthyl-5,6,11-méthéno-5*H*-benzo[*a*]fluorène [$C_{2o}H_{18}O$: *Pca*2$_1$, a = 15,04997(17), b = 9,8778(11) et c = 9,6846(11); Z = 4; 1672 données; R_1 = 0,325). On compare cette structure à une structure cristalline non publiée de l'hydrocarbure fondamental 6,6a,11,11a-tétrahydro-5,6,11-méthéno-5*H*-benzo[*a*]fluorène, $C_{18}H_{14}$. On a aussi calculé les deux structures par des méthodes de la théorie de la fonctionnelle de densité au niveau B3LYP/6-311(d,p) de la théorie. On a trouvé que les distances et les angles de liaison des mesures de l'état solide et des calculs en phase gazeuse concordent bien; les déviations moyennes sont bien en dessous de 1%. Les spectres RMN du ^{1}H présentent des couplages $^3J_{HH}$ qui sont très faibles dans la cage tricyclique centrale, mais qui peuvent être attribués en faisant appel à la spectroscopie 2D.

Mots-clés : cages d'hydrocarbures, cycles tendus, cyclopropane, diffraction des rayons X, RMN.

[Traduit par la Rédaction]

Introduction

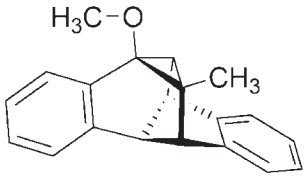
Compound **1** is obtained as a major side-product in the preparation of 2-methyl-1-methoxy-4-hydro-1,4-ethenonaphthalene from the reaction of benzyne in neat 2-methylanisole (1). The structure of **1** is not readily deduced from the spectroscopic data; therefore, a single-crystal X-ray diffraction study was initiated. In this paper, we report the structure of **1**, 6,6a,11,11a-tetrahydro-5-methoxy-6-methyl-5,6,11-metheno-5*H*-benzo[*a*]fluorene and compare it to that reported for the parent hydrocarbon **2**, 6,6a,11,11a-tetrahydro-5,6,11-metheno-5*H*-benzo[*a*]fluorene. Since the initial reports of the synthesis of **2** (2, 3), it has been of interest for the preparation of benzannelated annulenes (4–6). Although the structure of **2** has also been determined by X-ray crystallography (7),[4] the details are neither in the open literature nor in the Cambridge Crystallographic Database. Therefore, we report here the derived geometric parameters of **1** and **2**, as well as a comparison between those common to both structures. In view of the unique structure of the central tricyclic cage common to both **1** and **2**, which also contains a highly strained 3-membered ring, we have computed the structure using hybrid DFT methods at the B3LYP/6–311(d,p) level of theory. There is excellent agreement between the calculated gas-phase and the measured solid-state geometries.

Received 14 February 2007. Accepted 30 May 2007. Published on the NRC Research Press Web site at canjchem.nrc.ca on 22 June 2007.

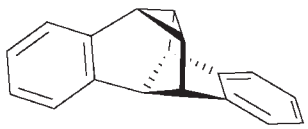
C.O. Bender,[1] R.T. Boeré,[2] P.W. Dibble, and R.T. McKay.[3] Department of Chemistry and Biochemistry, University of Lethbridge, Lethbridge, AB T1K 3M4, Canada.

[1]In retirement.
[2]Corresponding author (e-mail: boere@uleth.ca).
[3]Present address: NANUC Building, Room 105, University of Alberta, Edmonton, AB T6G 2E1, Canada.

[4]$C_{18}H_{14}$: Orthorhombic, $P2_12_12_1$ (No. 19), a = 9.947(5), b = 15.064(2), c = 8.073(2); collected with Cu Kα radiation using the oscillation method.



1



2

Experimental

Compound **1** was prepared as reported in ref. 1. Its high-resolution mass spectrum (EI, 70 eV) is consistent with the proposed formula, displaying only five high-intensity peaks

 doi:10.1139/V07-058 © 2007 NRC Canada

as follows: 274.1356 (calcd. for $C_{20}H_{18}O^+$ 274.1358, 81%); 259 ($C_{19}H_{15}O^+$, 100%); 244 ($C_{18}H_{12}O^+$, 64%); 228 ($C_{18}H_{12}^+$, 74%); and 215 ($C_{17}H_{11}^+$, 70%). Significantly, there is no peak resulting from a retro Diels–Alder process. NMR data (^{1}H, ^{13}C, ^{1}H–^{1}H COSY, HMBC, and HSQC experiments) of **1** were collected on a Bruker AVANCE-II spectrometer operating at 300.13 MHz for ^{1}H and 75.41 MHz for ^{13}C and are reported w.r.t. the $CHCl_3$ (^{1}H: 7.29 ppm) and $CDCl_3$ (^{13}C: 77.23 ppm) resonances. ^{1}H: δ 1.07 (s, 3H), 1.29 (t, J = 1.3 Hz, 1H), 2.44 (s, 1H), 2.75 (s, 1H), 2.93 (s, 1H), 3.55 (s, 3), 7.04–7.26 (m, 7H), 7.5–9 (d, J = 8.0 Hz, 1H). Selective decoupling at 2.93 and 2.75 ppm collapsed the 1.29 ppm triplet to a doublet, while decoupling the singlet at 2.44 ppm had no effect. Irradiation of the singlet at 2.93 ppm sharpened the signal at 2.44 ppm. ^{13}C: δ 10.92, 35.05, 38.41, 44.52, 49.82, 56.95, 57.76, 74.97, 121.80, 121.88, 123.24, 124.71, 124.83, 125.03, 125.29, 126.57, 135.28, 136.00, 149.34, 149.54.

Details of the crystal and the structure determination of **1** are summarized in Table 1. The space-group determination was problematic. Statistics favored *Pbcm*, but we were unable to solve the structure in this space group. The second choice $Pca2_1$, No. 29, is a polar non-centrosymmetric space group. The structure was solved by direct methods using SHELXS (8), expanded using Fourier techniques, and refined with SHELXL (9). Non-hydrogen atoms were refined anisotropically. Hydrogen atoms were included using a riding model. Neutral atomic-scattering factors were taken from the International Tables (10). Selected bond distances and angles are presented in Table 2, and an exhaustive listing is provided in the Supplementary Materials.[5] A thermal ellipsoids plot showing the structure of **1** and the atom-numbering sequence used for both **1** and **2** throughout the discussion is presented in Fig. 1. Since all H atoms are placed by geometry, their positions are only approximate. The approximate shortest contacts in the structure are between C3 and H7 (2.73 Å), C4A and H6A (2.88 Å), C3 and H10 (2.88 Å), and C9 and H3 (2.86 Å), all just slightly shorter than the sums of the van der Waals radii of C and H (2.90 Å).

The starting point for the DFT calculations was the crystal geometry of **1**, imported via Mercury 1.4.1 (11) into GaussView (12). Calculations were performed in the Gaussian 98W suite of programs (13), and the converged minimum structures were confirmed by frequency calculations, which report no imaginary frequencies.

Table 1. Crystal data and structure refinement for **1**.

Crystal	$C_{20}H_{18}O$
Formula weight	274.34
Crystal system	Orthorhombic
Space group	$Pca2_1$ (No. 29)
a (Å)	15.0497(17)
b (Å)	9.7783(11)
c (Å)	9.6846(11)
V (Å^3)	1425.2(3)
Z	4
D_m	Not measured
D_x (Mg/m^3)	1.279
Appearance	Colourless needles
Crystal size (mm^3)	0.48 × 0.26 × 0.14
Temperature (K)	173(2) K
Wavelength (λ) (Å)	0.71073
Absorption coefficient (μ) (mm^{-1})	0.077
Radiation	Mo Kα
Crystallization solvent	Hexanes
Instrument for data collection	Bruker APEX II
θ range for data collection (°)	2.08–27.11
Completeness to θ = 27.11°	100%
Scans	ω
h	–19 → 19
k	–12 → 12
l	–12 → 12
Measured reflections	15181
Independent reflections	1672 (R_{int} = 0.0213)
Reflections with $I > 2\ \sigma(I)$	1672
Absorption correction	None
Intensity decay	None
Refinement method	Refinement on F^2
H atoms	Constrained
GOF on F^2	1.054
restraints/parameters	1/193
R [$F^2 > 2\sigma(F^2)$]	0.0325
R [F^2, all data]	0.0341
$wR(F^2)$	0.0935
$(D/\sigma)_{max}$	0.000
$D\rho_{max}$ (e Å^{-3})	0.232
$D\rho_{min}$ (e Å^{-3})	–0.181

Results and Discussion

The structure of **1** is depicted in Fig. 1 (one enantiomer). The central tricylic structure consists of two cyclohexane rings in twist-boat conformations that share four adjacent atoms along one "side" of the boat. One end of each boat participates in a fused cyclopentane ring, which itself is in an envelope conformation; the other end is bridged on the non-fused side by a single bond, thereby creating a cyclopropane ring. Angles within the six-membered rings deviate considerably from the ideal tetrahedral angle (avg. deviation = 7 ± 2°) mostly to expanded values, while in the five-membered ring, the angles are highly compressed (avg. deviation = 8 ± 5°). The cyclopropane ring is close to ideal (avg. angles = 60.0 ± 0.7°).

The crystal structure of **2** was determined many years ago by photographic methods (7), but it is only available in a

[5] Supplementary data for this article (crystallographic disorder modeling attempts, details of ^{1}H NMR assignments, and full bond-lengths and bond-angles data) are available on the journal Web site (canjchem.nrc.ca) or may be purchased from the Depository of Unpublished Data, Document Delivery, CISTI, National Research Council Canada, Ottawa, ON K1A 0S2, Canada. DUD 5179. For more information on obtaining material refer to http://cisti-icist.nrc-cnrc.gc.ca/irm/unpub_e.shtml. CCDC 635872 contains the crystallographic data for this manuscript. These data can be obtained, free of charge, via www.ccdc.cam.ac.uk/conts/retrieving.html (or from the Cambridge Crystallographic Data Centre, 12 Union Road, Cambridge CB2 1EZ, UK; fax: +44 1233 336033; or deposit@ccdc.cam.ca.uk).

© 2007 NRC Canada

Table 2. Selected inter-atomic distances (Å) and (°) for **1** and **2** from crystallography and DFT calculations.

	1 (Crystal)[a]	**1** (DFT)[a]	**2** (Crystal)[b]	**2** (DFT)[a]
Bond lengths (Å)				
C4A—C11B	1.398(2)	1.4006	1.385(4)	1.4016
C4A—C5	1.480(2)	1.4807	1.464(5)	1.4742
C5—C6	1.523(3)	1.5395	1.517(5)	1.5304
C5—C12	1.529(2)	1.5351	1.516(4)	1.5304
C6A—C6B	1.519(2)	1.5196	1.520(4)	1.5205
C6A—C6	1.544(3)	1.5524	1.532(4)	1.5413
C6A—C11A	1.560(2)	1.5711	1.564(4)	1.5737
C6B—C10A	1.403(2)	1.4088	1.394(4)	1.4089
C10A—C11	1.521(3)	1.5194	1.517(4)	1.5205
C11—C12	1.536(2)	1.5397	1.522(4)	1.5413
C11—C11A	1.564(3)	1.5725	1.558(4)	1.5737
C11A—C11B	1.487(2)	1.4901	1.498(4)	1.4918
C6—C12	1.508(3)	1.5131	1.480(5)	1.5052
Bond angles (°)				
C11B–C4A–C5	114.56(15)	115.18	115.5(4)	115.19
C4A–C5–C6	118.76(15)	118.84	119.4(4)	119.38
C4A–C5–C12	119.74(15)	119.65	119.3(4)	119.38
C6–C5–C12	59.23(12)	58.97	58.4(2)	58.91
C6B–C6A–C6	103.59(15)	105.11	105.3(3)	105.30
C6B–C6A–C11A	99.13(15)	99.27	99.1(3)	99.38
C6–C6A–C11A	102.19(15)	102.29	100.7(3)	101.30
C10A–C6B–C6A	106.89(18)	106.67	106.6(3)	106.67
C6B–C10A–C11	106.73(17)	106.62	106.8(3)	106.67
C10A–C11–C12	103.93(15)	105.34	104.7(3)	105.3
C10A–C11–C11A	99.23(14)	99.33	99.6(3)	99.38
C12–C11–C11A	101.24(14)	101.01	101.2(3)	101.30
C11B–C11A–C6A	112.95(15)	115.18	114.7(3)	114.44
C11B–C11A–C11	114.39(15)	113.60	113.8(3)	114.44
C6A–C11A–C11	93.89(13)	92.95	93.1(2)	92.90
C4A–C11B–C11A	115.93(15)	115.44	115.0(3)	115.22
C12–C6–C5	60.60(13)	60.37	60.8(3)	60.54
C12–C6–C6A	103.91(16)	103.13	104.9(3)	104.58
C5–C6–C6A	116.39(16)	116.19	118.2(4)	117.65
C6–C12–C5	60.17(13)	60.66	60.8(2)	60.54
C6–C12–C11	105.21(16)	105.57	105.0(3)	104.58
C5–C12–C11	118.13(16)	118.27	118.1(3)	117.65

[a]This work.
[b]From ref. 14.

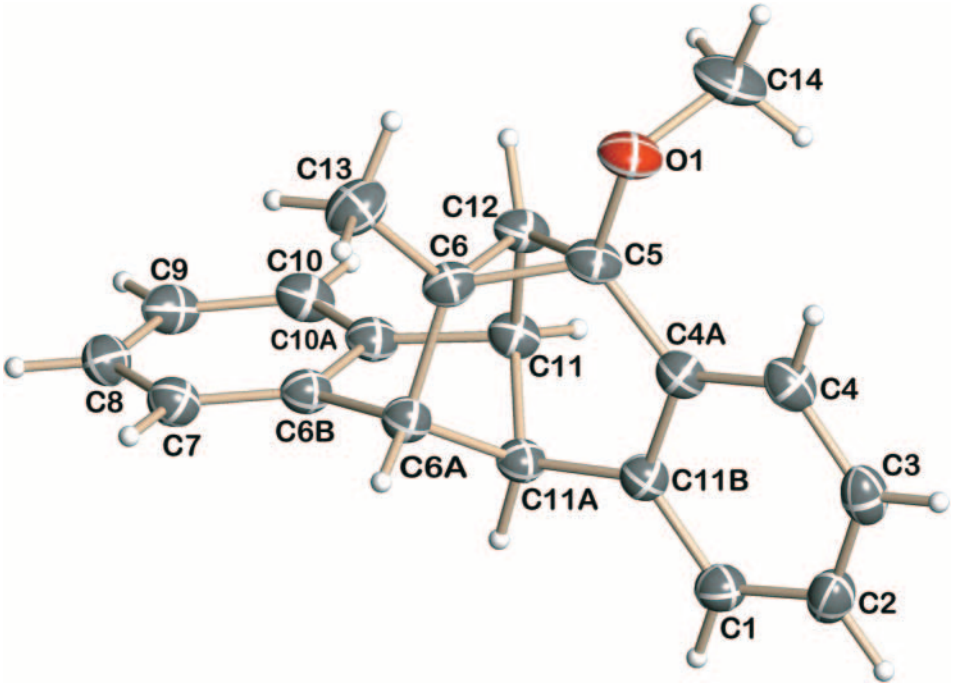
Ph.D. thesis (14). In Table 2, we compare bond lengths and angles for this structure with those that we obtained for **1**. As expected, the more-recent structure determination is more precise: the average value of the standard deviations in bond distances is 0.18% in **1** and 0.31% in **2**, while for bond angles, these values are 0.14% and 0.32%, respectively (15). While significant, the small absolute differences speak to good precision for the older structure. The largest deviation between the two X-ray structures is in the C6—C12 cyclopropane-ring bond, which in **2** is 0.09 Å shorter than in **1** (1.9% deviation). Only three other bond distances deviate by more than 1%: C6B—C7, C4A—C5, and C4A—C11B. Similarly, only six internal bond angles differ between the two X-ray structures by more than one percent, and these are all angles associated with atoms of the central cage (C5, C6, C6A, C11A, and C12).

The structures of **1** and **2** are due to Diels–Alder addition of benzyne to a benzene derivative (Scheme 1). The first step is a 1,4-cycloaddition to give a benzobarrelene **5**; it is well-known that tetrahalobenzynes react with toluene to give adducts in which the non-bridgehead product predominates; whereas in the addition to anisole, the bridgehead adducts predominate (16, 17). The proposed intermediate **5** (X = OCH_3, Y = CH_3) is therefore the expected product from the addition of benzyne, **3**, to 2-methylanisole, **4** (X = OCH_3, Y = CH_3). Subsequent 1,3-cycloaddition by a second molecule of benzyne to the 3,5 carbon atoms gives the observed products (Scheme 1).

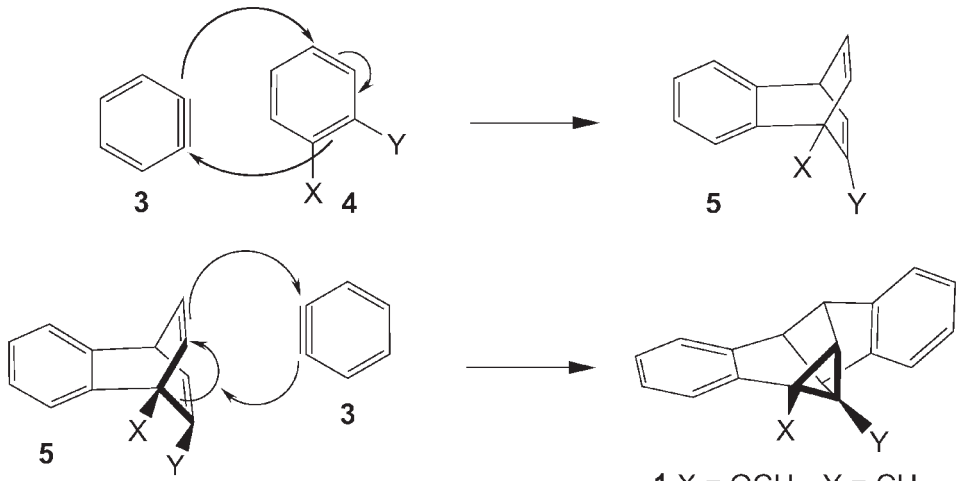
The closest-related structure to **1** and **2** in the Cambridge Database is that of dimethyl-1-cyano-1,1a,2,8,8a,8b-hexahydro-2,3,8-methanetriylcyclopropa[*a*]fluorene-3,3a-dicarboxylate (**6**) (18, 19). This molecule shares the same

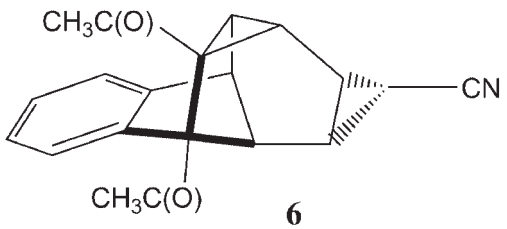
© 2007 NRC Canada

Fig. 1. Thermal ellipsoid plot (50% probability, except H) produced in XSHELL 6.3.1 (Bruker, 2005) showing the structure of one enantiomer of **1** and the atom-numbering sequence used for both **1** and **2**. The H-atom radii are arbitrary.



Scheme 1. Proposed mechanism for the synthesis of **1** and **2**.





central-cage structure, the "horizontal" fused benzo group, and a single substituent on the C6 atom of the cyclopropane ring.

There is notable agreement among the three X-ray structures (**1**, **2**, and **6**) that contain the same strained central carbon cage. The greatest variance is found within the fused cyclopropane rings. To further characterize this unusual strained cage structure, we have performed full structure optimizations using modern DFT methods. The geometrical results of these calculations are also included in Table 2. The normalized average deviations between calculated bond distances from the gas-phase theoretical and the solid-state experimental structure determinations is 0.41% for **1** and 0.72% for **2**. For the bond angles, these values are 0.44% and 0.35%, respectively. The computed structure of **2** adopts

© 2007 NRC Canada

Table 3. NMR peak assignments for **1** and **2**.

	1		**2**[a]	
Position	δ(^{1}H)	δ(^{13}C)	δ(^{1}H)	δ(^{13}C)
5	—	74.97	2.95	31.7
6	—	38.41	1.70	25.8
6A	2.44	49.82	2.70[b]	43.0[c]
11	2.75	44.52	2.70[b]	43.0[c]
11a	2.93	57.76	3.32	56.4[d]
12	1.29	35.05	1.70	25.8
Me	1.07	10.92	—	—
OMe	3.55	56.95	—	—
4	7.59	121.80	—	—
4A	—	135.48	—	—
6B	—	149.34	—	—
10A	—	149.54	—	—
11B	—	136.00	—	—

Note: Atom-numbering scheme is the same as that used in the crystal structure. Hydrogen atoms are attached to carbons of the same number.

[a]Taken from ref. 6 (^{1}H in CD_2Cl_2, ^{13}C in $CDCl_3$); quart: 151.0, 151.0, 136.5, 135.5; tert: 126.8, 125.8, 125.6, 124.9, 124.5, 122.0.

[b]Compare with 2.8 ppm for the bridgehead position in norbornene.

[c]Compare with 42 ppm in norbornene.

[d]Compare with 49 ppm in norbornene.

C_s symmetry naturally; the computed structure of **1** has a remarkably similar orientation of the flexible O1–C14 methoxy substituent groups to that found in the solid-state structure, though the angles associated with this group had the largest normalized deviation in the case of **1**. In contrast to the good agreement to the DFT calculations, the geometry reported for **2** obtained from a Consistent Valence Force Field contains deviations as high as 6% among the seven internal bond distances listed for comparison (normalized avg. deviation = 2.7%) (4).

The NMR spectra of **2** are consistent with the structure determined from the X-ray diffraction study. Taken as a whole, the 1D and 2D NMR experiments support the assignments in Table 3.

Acknowledgements

We thank the Natural Sciences and Engineering Research Council of Canada (NSERC) and the University of Lethbridge for funding. Dr. M. Parvez (University of Calgary) collected an earlier data set on **1**.

References

1. C.O. Bender, D.L. Bengtson, D. Dolman, and R.T. McKay. Can. J. Chem. **72**, 1556 (1994).
2. L. Friedman. J. Am. Chem. Soc. **89**, 3071 (1967).
3. M. Stiles, U. Burckhardt, and G. Freund. J. Org. Chem. **32**, 3718 (1967).
4. M. Banciu, D. Elian, M. Elian, L. Stanescu, and A. Cioranescu. Rev. Roum. Chim. **31**, 503 (1986).
5. M.D. Banciu, C. Hada, D. Albaiu, and C. Drachigi. Rev. Roum. Chim. **34**, 1907 (1989).
6. C. Hada, J.-C. Roussel, P. Beccat, R. Boulet, and M.D. Banciu. Rev. Roum. Chim. **42**, 777 (1997).
7. J.W. Schilling and C.E. Norman. Abstracts of the American Crystallographic Association Meeting. Atlanta, Ga. 1967. p 22.
8. G. Sheldrick. SHELXS-97 [computer program]. University of Göttingen, Göttingen, Germany. 1997.
9. G. Sheldrick. SHELXL-97 [computer program]. University of Göttingen, Göttingen, Germany. 1997.
10. D.C. Creagh and W.J. McAuley. International Tables for X-ray Crystallography, Vol. C. Table 4.2.6.8. Kluwer Academic Publishers, Boston. 1992. p. 219.
11. Mercury 1.4.1 [computer program]. Cambridge Crystallographic Data Centre (2001–2005).
12. Semichem. GaussView 2.1 [computer program]. Gaussian, Inc., Pittsburg, PA, USA. 2001.
13. M.J. Frisch, G.W. Trucks, H.B. Schlegel, G.E. Scuseria, M.A. Robb, J.R. Cheeseman, V.G. Zakrzewski, J.A. Montgomery, Jr., R.E. Stratmann, J.C. Burant, S. Dapprich, J.M. Millam, A.D. Daniels, K.N. Kudin, M.C. Strain, O. Farkas, J. Tomasi, V. Barone, M. Cossi, R. Cammi, B. Mennucci, C. Pomelli, C. Adamo, S. Clifford, J. Ochterski, G.A. Petersson, P.Y. Ayala, Q. Cui, K. Morokuma, D.K. Malick, A.D. Rabuck, K. Raghavachari, J.B. Foresman, J. Cioslowski, J.V. Ortiz, B. B. Stefanov, G. Liu, A. Liashenko, P. Piskorz, I. Komaromi, R. Gomperts, R.L. Martin, D.J. Fox, T. Keith, M.A. Al-Laham, C.Y. Peng, A. Nanayakkara, C. Gonzalez, M. Challacombe, P.M.W. Gill, B. Johnson, W. Chen, M.W. Wong, J. L. Andres, C. Gonzalez, M. Head-Gordon, E.S. Replogle, and J.A. Pople. Gaussian 98 [computer program]. Revision a.6. Gaussian, Inc., Pittsburg, PA, USA. 1998.
14. J.W. Schilling. Ph.D. Thesis, University of Michigan. 1968.
15. G.H. Stout and L.H. Jensen. X-ray structure determination: a practical guide. 2nd ed. Wiley, NY. (1989). p. 404.
16. P.C. Buxton, N.J. Hales, B. Hankinson, H. Heaney, S.V. Ley, and R.P. Sharma. J. Chem. Soc., Perkin I. 1974 (1974).
17. Hankinson and H. Heaney. Tetrahedron. Lett. 1355 (1970).
18. K. Saito, M. Kozaki, A. Imai, Y. Hara, and K. Takahashi. Chem. Lett. 1769 (1994).
19. K. Saito, K. Ono, T. Takeda, S. Kiso, K. Uenishi, and M. Kozaki. Tetrahedron. **58**, 9081 (2002).

© 2007 NRC Canada

Diastereoselective formation of 18-membered ring BINOL-hydrogen phosphonate dimers — Quasi-covalent hydrogen bonds?

Hossein A. Dabbagh, Nader Noroozi-Pesyan, Ali R. Najafi-Chermahini, Brian O. Patrick, and Brian R. James

Abstract: Diastereoselective syntheses of the unusual dimers, 4-heptyl-2-(2′-hydroxy-binaphthyl)hydrogen phosphonate (**5**) and the cyclohexyl analogue (**7**), are achieved by hydrolysis of 4-(3,5-dioxa-4-phosphacyclohepta[2,1-α;3,4-α′]-dinaphthalene-4-yloxy)heptane (**4**) and the cyclohexane analogue (**6**), respectively. Two out of eight possible pairs of monomers units are involved in the stereoselective formation of the dimer **5a** of configuration $BINOL_R$-P_S:$BINOL_R$-P_S; this is determined by X-ray crystallographic data, which reveal a centrosymmetric, 18-membered ring structure with C_i symmetry, consisting of two monomers strongly hydrogen-bonded between the oxygen of P=O units and hydroxyl hydrogen atoms. Mass spectrometric, melting point, and thermal decomposition point data, as well as NMR data, support the presence of strong, quasi-covalent hydrogen bonds. Computational analysis suggests that the diastereoselectivity is controlled by molecularly constrained geometry of the monomer. Compound **7**, although not characterized crystallographically, appears to be analogous to **5**.

Key words: 18-membered ring, phosphonate dimer, diastereoselectivity, hydrogen-bonds, computational analysis.

Résumé : On a réalisé les synthèses diastéréosélectives des dimères inhabituels du phosphonate acide de 4-heptyl-2-(2N-hydroxybinaphtyle) (**5**) et de son analogue cyclohexyle (**7**) par le biais de l'hydrolyse respectivement du 4-(3,5-dioxa-4-phosphacycloheptane[2.1-α;3,4-α′]dinaphtalène-4-yloxy)heptane (**4**) et de son analogue cyclohexane (**6**). Deux des huit paires possibles d'unités monomères sont impliquées dans la formation stéréosélective du dimère **5a** de configuration $BINOL_R$-P_S:$BINOL_S$-P_R; cette conclusion est basée sur des données de diffraction des rayons X qui mettent en évidence l'existence d'une structure cyclique centrosymétrique à 18 chaînons de symétrie C_i, formée de deux monomères reliés fortement par une liaison hydrogène entre l'oxygène des unités P=O et les atomes d'hydrogène des hydroxyles. Les données de spectrométrie de masse, de point de fusion et de point de décomposition thermique ainsi que les données de la RMN sont en accord avec la présence de liaisons hydrogènes fortes et de nature pratiquement covalentes. Une analyse par des calculs théoriques suggère que la diastéréosélectivité est contrôlée par la géométrie fixée d'une façon moléculaire du monomère. Même si le composé **7** n'a pasété caractérisé d'une façon cristallographique, il semble être analogue au composé **5**.

Mots-clés : cycle à 18 chaînons, dimère de phosphonate, diastéréosélectivité, liaisons hydrogènes, analyse par des calculs théoriques.

[Traduit par la Rédaction]

Introduction

During studies aimed at developing new chiral phosphine ligands based on the binaphthol backbone, we accidentally discovered a dimeric structure maintained by two exceptionally strong hydrogen bonds, and this work is described here.

Hydrogen bonding plays a key role in biology and chemistry and remains a topic of intense current interest, as judged by an enormous continuing amount of literature. A few selected recent articles exemplify the general scope of the topic, ranging from the role of H bonding in: weak interactions in the gas phase (1), supramolecular assemblies (2), helical structures (3), promoting catalytic enantioselective reactions (4), molecular rotors (5), through to measurement of H-bond acidity of organics (6). Important consequences of both inter- and intra-molecular H bonding have long been recognized in the physiochemical behavior of DNA and RNA (7), while H bonding within phosphorus systems, of

Received 24 April 2007. Accepted 25 May 2007. Published on the NRC Research Press Web site at canjchem.nrc.ca on 27 June 2007.

H.A. Dabbagh. Department of Chemistry, Isfahan University of Technology, P.O. Box: 84155, Isfahan, Iran.
N. Noroozi-Pesyan. Department of Chemistry, Faculty of Science, Urmia University, 57159, Urmia, Iran.
A.R. Najafi-Chermahini. Department of Chemistry, Yasuj University, Yasuj, Iran.
B.O. Patrick and B.R. James.[1] Department of Chemistry, The University of British Columbia, Vancouver, BC V6T 1Z1, Canada.

[1]Corresponding author (e-mail: dabbagh@cc.iut.ac.ir; brj@chem.ubc.ca).

 doi:10.1139/V07-060 © 2007 NRC Canada

Table 1. Classification of hydrogen bonds within P-containing systems.

Linkages	Bond distance [range, donor---H---acceptor] (Å)	Strength
P-O-H---O-P	2.39–2.50	Very strong
P-OH---O-P	2.50–2.70	Strong
P-O-H---O-C	2.41–2.82	Strong
P-H---OH_2	2.56–3.15	Moderate
P-O---H-N	2.65–3.10	Moderate
C-O-H---O=P[a]	2.70	Strong

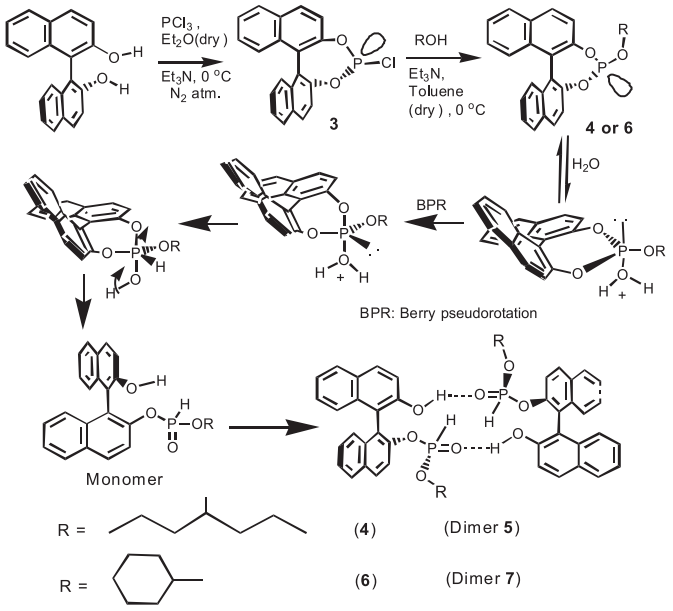
Note: Data taken from from refs. 8*a*, 10*b*, 10*f*, and 11*a*.
[a]Determined by an X-ray crystallographic study of **5a** (see Scheme 2 and Fig. 1).

relevance to our paper, is also well documented (8). Some contributions from our collaborative group have also demonstrated the importance of hydrogen bonding in determining the structure, conformation, energy, and reactivity properties of a molecule (9).

The factors determining the strength of a hydrogen bond, other than electronegativities of the donor and acceptor atoms, remain of interest. Homonuclear linear O---H---O bonds are well understood and display a practically continuous range of O---H---O distances from 2.36 to 3.69 Å: the upper value is the sum of the van der Waals radii and not a physical limit of the hydrogen-bond interaction that has been qualitatively defined as very strong (<2.50 Å), strong (2.41–2.82 Å), medium (2.56–3.15 Å), or weak (>3.15 Å); see Table 1 (8*a*, 10, 11). The strongest hydrogen bonds are seen in homonuclear linear or nearly linear systems with an O–H–O angle > 165°; the energies of bent O–H–O systems have been evaluated computationally and are 90%, 60%, and 10% of the linear system value for angles of 165°, 149°, and 110°, respectively (10*b*, 11*a*). A unified hydrogen bond theory has been presented in which O---H---O bonds are divided into five classes: negative charge-assisted $[–O---H---O–]^-$ (a strong H bond); positive charge-assisted $[=O---H---O=]^+$ (strong); resonance-assisted [-O–H---O=] (strong), where the two oxygens are connected by a π-conjugated system of variable length, including cases where the oxygens are attached to P or As atoms; polarization-assisted [---O(R)–H---O(R)H---] (moderate); and isolated H bonds [-O-H---O(R)(R)] (weak) (11*a*). Of note, a recently reported variable-temperature X-ray crystallographic and DFT computational study of the N-H---O/N---H-O tautomeric competition in 1-(arylazo)-2-naphthol has led to a transition-state hydrogen bond theory (12).

Our current work, based on designing chiral phosphines, prompted us to synthesize 4-(3,5-dioxa-4-phosphacyclohepta[2,1-α;3,4-α′]-dinaphthalene-4-yloxy)heptane (**4**) and the corresponding cyclohexane analogue (**6**) (see Scheme 1). During the attempted purification of **4** and **6**, we discovered their hydrolysis products, which proved to be the dimeric

Scheme 1. Formation of the dimeric phosphonates.



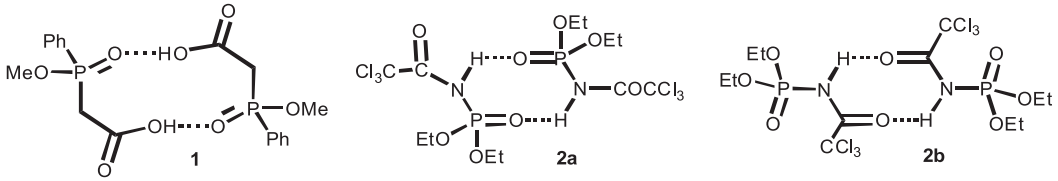
structures, 4-heptyl-2-(2′-hydroxybinaphthyl)hydrogen phosphonate (**5a**) and the cyclohexyl analogue (**7a**) (the "**a**" label refers to a particular stereoisomer of these dimers — see later). The 18-membered ring structure of these dimeric compounds is maintained by the presence of two strong hydrogen bonds, as discussed later (see Scheme 1).

Results and discussion

Prior to a discussion of compounds **5a** and **7a** and their unusual structures, it is best to introduce some general comments about H bonding in phosphorus compounds. The degree of such bonding, which is seen in the solid, liquid, and solution states, varies depending on the solvent, temperature, and the nature of the substituent group on the P atom. Most phosphorus acids form dimers with strong H bonds within a 6- to 10-membered ring (8*a*), although the esters $(RO)PO(OH)_2$ (R = 3-methylhexyl or *n*-octyl) are polymers containing intermolecular H bonding (8_a). Relevant to our paper, aryl H-phosphonates have been synthesized and characterized by ^{31}P NMR spectroscopy (13).

Dimeric centrosymmetric ring structures are quite common within phosphorus chemistry: **1** and **2** exemplify 12- and 8-membered ring structures, respectively (8*a*), and according to spectroscopic evidence, esters of (trichloroacetyl)amidophosphoric acid exist as **2a** rather than **2b**, which suggests that the H bond in N-H---O=P is more stable than that in N-H–O=C (8*a*).

Although lower oxy-acids of phosphorus were initially



© 2007 NRC Canada

thought to exist primarily in tautomeric forms in which the central atom was trivalent, it is now well-established that the majority of such compounds prefer structures that incorporate formally pentavalent phosphorus (8*a*, 14). A detailed analysis of bond and contact distances has suggested that when the O---O interaction is decreased from 2.80 to 2.40 Å, the H bond is transferred from a symmetrical O---H---O electrostatic interaction to a covalent unsymmetrical O–H---O bond (10*b*, 11*a*).

Synthesis of the BINOL phosphonates and solution NMR characterization (Scheme 1)

Hydrolysis of the phosphate esters 4-(3,5-dioxa-4-phosphacyclohepta[2,1-α;3,4-α′]-dinaphthalene-4-yloxy)heptane (**4**) and the cyclohexane analogue (**6**) produced what initially are the respective monomers, 4-heptyl-2-(2′-hydroxybinaphthyl)hydrogen phosphonate (**5m**) and the 4-cyclohexyl analogue (**7m**). The monomers, being chiral at phosphorus coupled with the axial chirality of the BINOL moiety, can exist theoretically in four possible configurations ($BINOL_R$-P_R, $BINOL_R$-P_S, $BINOL_S$-P_S, $BINOL_R$-P_S). Of interest, both precursor monomers appear to dimerize selectively with their mirror images to form the 18-membered ring dimers; certainly, the structurally characterized **5a** (see later) has the configuration $BINOL_R$-P_S:$BINOL_R$-P_S, maintained by two strong hydrogen bonds, while a second stereoisomer seen in solution (**5b**, see later) could be the $BINOL_R$-P_R:$BINOL_S$-P_S form. The analogous system based on **7** is considered from NMR data to behave similarly.

The necessary precursor reagent 4-chloro-3,5-dioxa-4-phosphacyclohepta[2,1-α;3,4-α′]-dinaphthalene (**3**) was prepared by reaction of PCl_3 with 2,2′-dihydroxy-1,1′-binaphthyl (BINOL) in dry Et_2O under an N_2 atmosphere, using procedures from the literature (15). This chloro compound was used without purification in the next step for the production of the phosphate esters **4** and **6** by treatment with the appropriate alcohol, 4-heptanol, or cyclohexanol, respectively. The esters were isolated in 70%–80% yields as yellow powders. The heptyl ester **4** was characterized in solution by ^1H NMR (with signals assigned for the methyl, methylene, and methyne protons of the heptyl group and the 12 binaphthyl protons) and a $^{31}P\{^1H\}$ singlet at δ 146. The corresponding cyclohexyl analogue **6** similarly showed three sets of ^1H signals for the 10 methylene protons, the single CH proton, and binaphthyl protons, as well as a $^{31}P\{^1H\}$ singlet at δ 150.

The remarkable hydrolysis products from **4** and **6** were accidentally synthesized by leaving acetone solutions of the esters in air at ambient temperatures for several days. After work-up procedures and purification by recrystallization, the respective yellow solid products 4-heptyl-2-(2′-hydroxybinaphthyl)hydrogen phosphonate (**5**) and the cyclohexyl analogue (**7**) were isolated as dimeric forms, based on NMR and MS data and an X-ray analysis of **5a**.

Analysis of crude samples of **5** by solution ^1H, $^1H\{^{31}P\}$, ^{31}P, and $^{31}P\{^1H\}$ NMR spectroscopy (see Experimental section) showed two major components **5a** and **5b**, two minor components **5c** and **5d**, and a trace amount of an unknown compound **5x** (Figs. S1–S8).[2] The ^{31}P NMR spectrum of pure **5a** (grown as a single crystal from a cyclohexane-CH_2Cl_2 solution of crude **5**) is a doublet of doublets centered at δ 3.80 because of coupling to two protons ($^1J_{PH}$ = 707, $^3J_{PH}$ = 10.7 Hz), as confirmed by a ^1H-decoupled spectrum that generates a $^{31}P\{^1H\}$ singlet; the $^1J_{PH}$ value is in the expected range (16). The ^1H NMR spectrum for **5a**, showing signals for the heptyl and binaphthyl protons, is consistent with the solid-state structure described later; the PH proton of **5a** is seen as a doublet at δ 6.65 ($^1J_{PH}$ = 703 Hz), which collapses to a singlet in the $^1H\{^{31}P\}$ spectrum. A $^{13}C\{^1H\}$ NMR spectrum of **5a** shows 27 signals corresponding to the number of binaphthyl and heptyl carbon atoms (20 and 7, respectively). Although **5a** was the only compound isolated in a pure state, it was not difficult (e.g., from the relative peak heights of the doublet of doublet patterns seen in the $^{31}P\{^1H\}$ spectra and relative intensities of the various ^1H resonances) to determine the NMR assignments (from data for mixtures) associated with what are possibly other stereoisomers (i.e., **5b**, **5c**, and **5d**, see later); similar reasoning allowed for the determination of resonances associated with each of **7a**–**7d**.

The NMR spectra of **5b** are similar to those of **5a**, and similar data are seen for **5c**, but for this species the ^{31}P shift is centered at δ 8.80; **5d** is characterized by just a doublet centered at δ 5.45 in the ^{31}P spectrum with a $^1J_{PH}$ value of 720 Hz. The structure of **5a** was elucidated by X-ray crystallography, while relevant EI and ES mass spectrometric data were also measured (see later).

The cyclohexyl-2-(2′-hydroxybinaphthyl)hydrogen phosphonate (**7**), like **5**, was isolated as a pale yellow solid. ^{31}P, $^{31}P\{^1H\}$, ^1H, and $^1H\{^{31}P\}$ NMR analysis revealed again the presence of two major components, **7a** (40%) and **7b** (38%), and two minor components, **7c** (18%) and **7d** (4%); Figs. S9 and S10.[2] Unfortunately, we were unsuccessful in obtaining any crystals of **7** suitable for X-ray analysis. However, the NMR data correspond closely to those measured for the **5a**–**5d** mixture (after allowance for the replacing of the 4-heptyl by a cyclohexyl moiety), and the structure of **7a** is likely to be analogous to that of **5a** but with a different R group (Scheme 1).

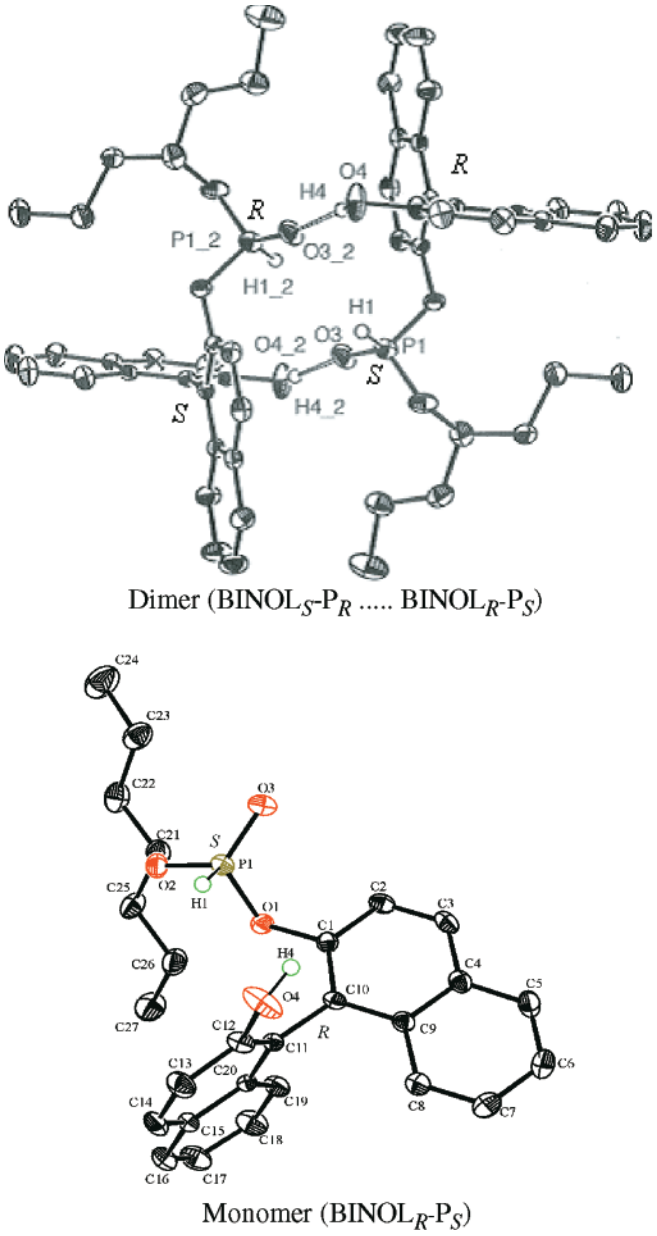
X-ray structure of 5a

The X-ray crystallographic analysis of **5a** reveals the essential monomer structure **5m** shown in Fig. 1 (see also Scheme 1), while the unit cell reveals two such monomer units interacting strongly via two hydrogen bonds between phosphonate P=O moieties and the OH groups of the BINOL; an overall centrosymmetric dimer structure for **5a** is seen with an 18-membered ring with C_i symmetry (Fig. 1

[2] Supplementary data for this article are available on the journal Web site (http://canjchem.nrc.ca) or may be purchased from the Depository of Unpublished Data, Document Delivery, CISTI, National Research Council Canada, Ottawa, ON K1A 0R6, Canada. DUD 5180. For more information on obtaining material refer to http://cisti-icist.nrc-cnrc.gc.ca/irm/unpub_e.shtml. CCDC 623091 contains the crystallographic data for this manuscript. These data can be obtained, free of charge, via http://www.ccdc.cam.ac.uk/conts/retrieving.html. Figs. S1–S13 include: $^{31}P\{^1H\}$, ^{31}P, ^1H, and $^1H\{^{31}P\}$ NMR spectra of **5a**, **5b**, **5c**, and **5d**; $^{31}P\{^1H\}$, ^{31}P, and ^1H NMR spectra of **7a**, **7b**, **7c**, and **7d**; computer-generated minimum configurations for the six pairs of **5m** monomers; and computer-generated minimum configuration for a **5b** dimer.

© 2007 NRC Canada

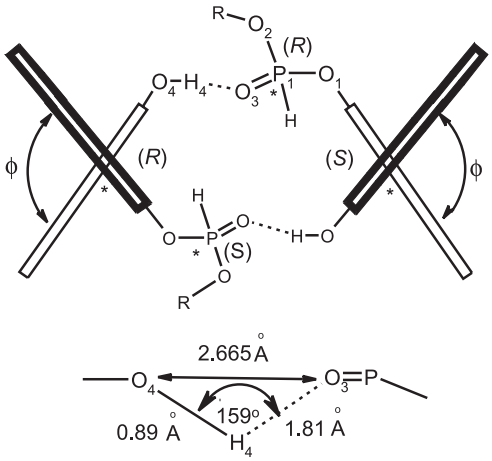
Fig. 1. Molecular structure of dimer **5a** (top) and monomer **5m** (bottom).



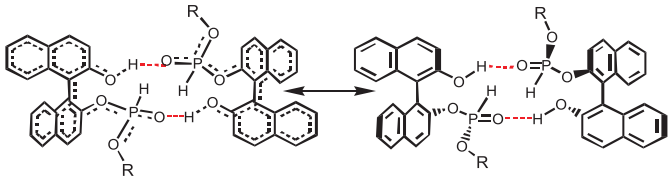
and Schemes 2 and 3). The torsion angles between the two BINOL rings are ~96°, favoring the *s*-transoid conformation. One of the BINOL units in the dimer structure necessarily has *R* axial symmetry and the other unit has *S* symmetry.

As expected, the P=O bond is some 0.1 Å shorter than the P–O bonds in the binaphthyl and heptyl groups, which are 1.58 and 1.55 Å, respectively. Within the hydrogen bonds, the distance between the hydroxyl-H and the acceptor-O atom is 1.81(2) Å, while the bond length for the hydroxyl group is 0.89(2) Å, and the O–H---O bond angle is 159°; the distance between the oxygens of the O---H-O moiety is ~2.70 Å, implying the presence of a strong hydrogen bond within this P=O---H-O-C system (Scheme 2 and Table 1). The strength of hydrogen bonding in the dimer may result from contributions of resonance-assisted and (or) polarization-assisted hydrogen bonds (see Introduction and Table 1),

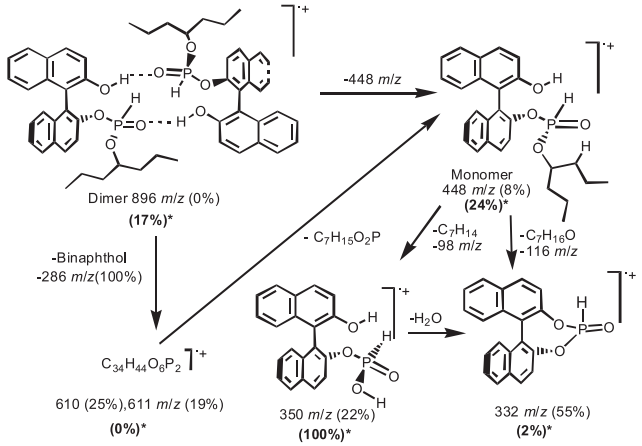
Scheme 2. Diagram showing hydrogen bonding within the dimer.



Scheme 3. Diagram showing resonance-assisted hydrogen bonding.



Scheme 4. Summary of the mass spectral data. Values in parentheses are the % base peak from EI. Values in boldface marked with asterisks (*) are the % base peak from TOF MS Electron Spray (ES$^+$).



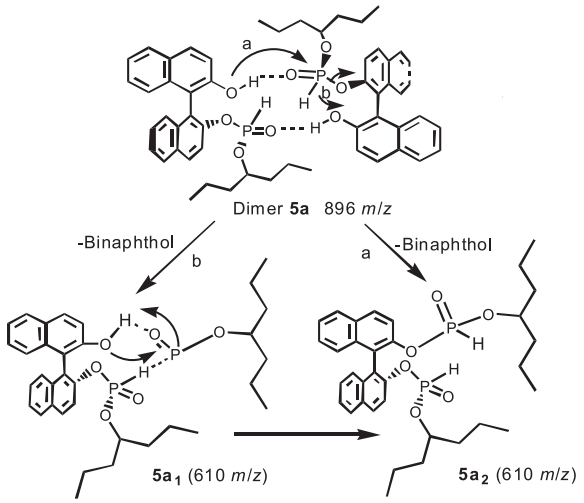
while the deviation from linearity of the O–H---O angle likely allows for a decrease in strain energy of the dimer structure (Scheme 3). More information supporting the presence of strong hydrogen bonds in **5a** was gleaned from mass spectrometric data.

Mass spectroscopic analysis

Positive ion electrospray mass spectral data for a solution of **5a** in CH_3OH–$CHCl_3$ showed molecular ions of *m/z* values around 897 corresponding to the dimer formulation M_2^+, 449 corresponding to the monomer M^+, and a 100% base peak at 350 corresponding to [BINOL + PO_2H]. Electron

© 2007 NRC Canada

Scheme 5. Plausible pathways for fragmentation of dimer 5a.

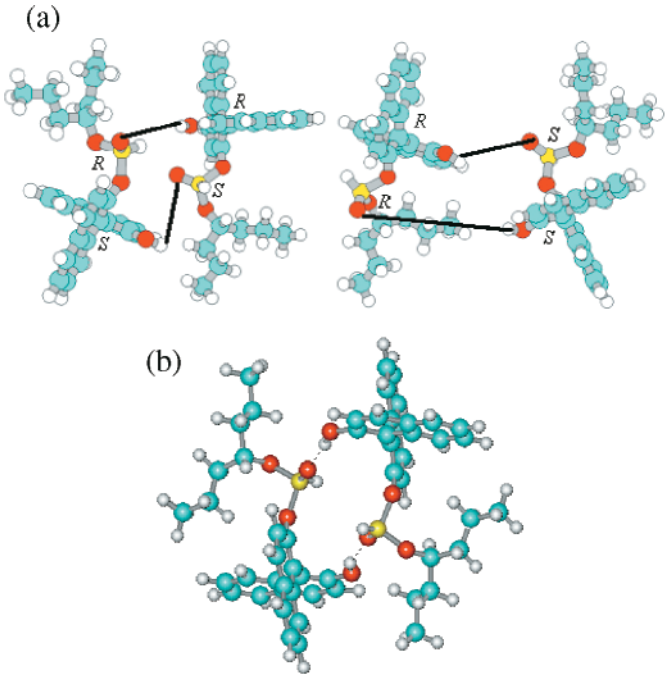


impact MS data did not show M_2^+ and instead revealed a 610/611 fragment (not detected by the ES analysis), a peak for M^+, the 350 peak, a peak at 332, and a 100% base peak at 286 for binaphthol. Scheme 4 summarizes these MS data and the formulations that correspond to the *m/z* values.

The percent abundance in the EI spectrum of the M^+ 448 peak is only about a fifth that of the 610/611 fragment, implying that cleavage of one P–O_{BINOL} bond and one [O–H---O] H-bond to form the 610/611 fragment takes preference over cleavage of the two H bonds to form the monomer; this suggests that the hydrogen bonding is strong (as indicated by the O---H---O structural data) and indeed even implies strength comparable to that of a P–O bond (at least under the EI conditions!). The reverse situation pertains to ES conditions where the monomer is formed exclusively (with the 350/332 fragments) from the dimer with respect to the 610/611 fragment; presumably, methanol breaks down most of the dimer structure by hydrogen-bond formation and prevents the intramolecular rearrangement required to produce the 610 fragment (Scheme 4).

Plausible mechanisms for the conversion of dimer **5a** to fragment 610 *m/z* (depicted by structures **5a$_1$** and **5a$_2$**) are outlined in Scheme 5 and involve direct loss of binaphthol from the dimer to give **5a$_1$** (step b), rearrangement of **5a$_1$** to **5a$_2$**, or direct nucleophilic attack by a binaphthol oxygen of one monomer at the phosphorus of the second monomer to give **5a$_2$** again with loss of binaphthol (step a). The facts that (*i*) the 610 fragment is not seen in the ES-MS, (*ii*) the polar methanol solvent does not break up completely the hydrogen bonds of the dimer, and (*iii*) judging by the sharp melting point at 144 to 145 °C (the hydrogen bonds likely remain intact at this temperature) are all consistent with the [O---H---O=P] hydrogen bond of the dimer being as strong as the P-O_{BINOL} bond. The loss of BINOL would then release strain to give **5a$_1$**, which could rearrange to **5a$_2$**. Justification of the direct rearrangement of the dimer **5a$_1$** to **5a$_2$** rearrangement is less obvious: a direct intramolecular nucleophilic attack by an oxygen of a BINOL hydroxyl group is unlikely because methanol is a better nucleophile and should interact more readily with the dimer to breakup the H bonds. However, the strength of H bonds between methanol and

Fig. 2. (*a*) Computer-generated minimum configuration of monomers **5m** using the HF/STO-3G program. Black lines (——) indicate hypothetical points of interactions to form dimers **5a** (left) and **5b** (right). (*b*) Computer-generated minimum configuration of dimer **5a** ($BINOL_R$-P_S---$BINOL_S$-P_R). Dotted lines show computed H bonds.



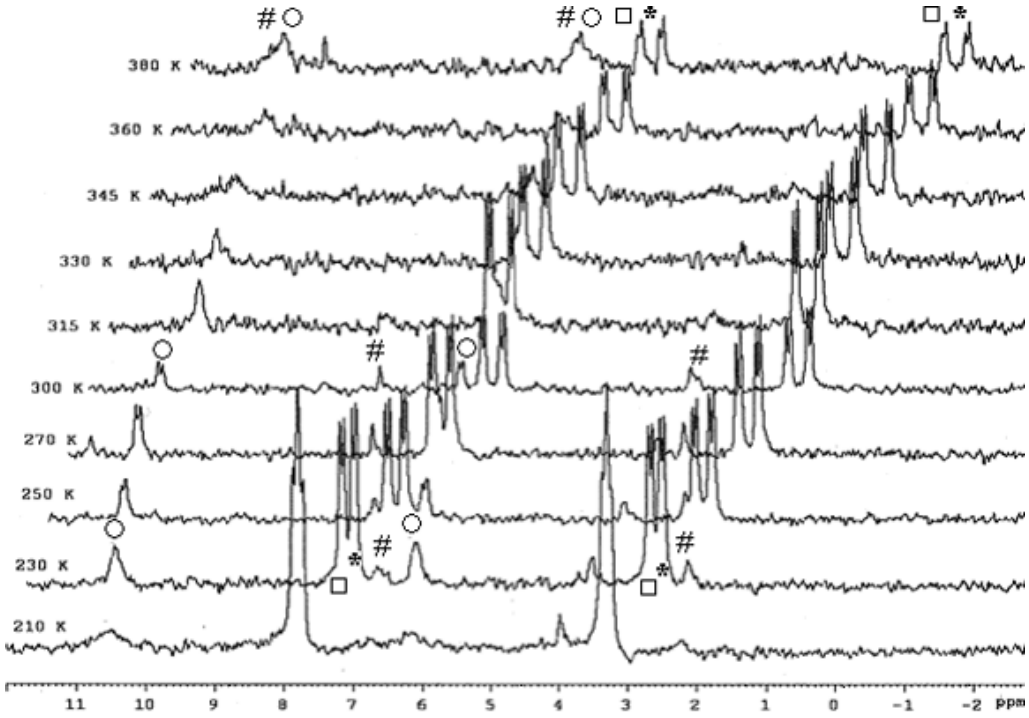
monomer is considered to be less than that of the H bonding in the dimer (judging by the observation of the M_2^+ ion). As evidenced by the high melting point, the boiling point (~180 °C in air), and thermal stability up to 250 °C (clear liquid at boiling point temperature with no color change), the stability of the dimer that results from the strong ("quasi-covalent") H bonds is remarkable. Liquid dimer, when cooled to room temperature (RT), re-melts again at 144 to 145 °C; when the dimer is placed under vacuum in a sealed capillary tube, decomposition becomes apparent at ~260 °C, with darkening of the color. A $CDCl_3$ solution of the dimer slowly decomposes in air (likely via hydrolysis) at RT to an unknown mixture as shown by ^{31}P NMR spectroscopy (Fig. S11).[2]

Diastereoselectivity of the dimer formation

Monomer **5m** has a chiral P center and axial chirality within the BINOL unit, while the dimer correspondingly has twice as many chiral moieties. The X-ray data of **5a** show the presence of the diastereomers $BINOL_S$-P_R:$BINOL_R$-P_S (meso form), and the NMR data of the crystal dissolved in $CDCl_3$ are consistent with the same structure. The solution NMR spectra of the crude sample show that the major component corresponds to **5a**; seen also are very similar resonances for the other major component (**5b**) and those of two minor ones (**5c** and **5d**), which have the same ^1H and ^{31}P NMR patterns as **5a** and **5b**, but as noted earlier the ^{31}P shifts are about 4 and 1 ppm downfield, respectively, from those of **5a** and **5b** (Figs. S1-S5).[2]

© 2007 NRC Canada

Fig. 3. Variable temperature ^{31}P NMR spectra of crude mixture of 4-n-heptyl-2-(2′-hydroxybinaphthyl)hydrogen phosphonate **5a** (*), **5b** (□), **5c** (○), and **5d** (#) in $CDCl_3$.



Computational analysis of the molecular geometry of the monomers predicts that only two enantiomeric pairs of these, with configurations $BINOL_R$-P_S:$BINOL_R$-P_S and $BINOL_R$-P_R:$BINOL_S$-P_S, have the appropriate geometry to interact and form the dimers (see Figs. 2, S12 and S13).[2] The first combination ($BINOL_R$-P_S:$BINOL_R$-P_S) is that found experimentally for **5a**, while the non-isolated **5b** is most likely of the $BINOL_R$-P_R:$BINOL_S$-P_S configuration. Other double combinations of monomers via hydrogen bonding to form the six other diastereomers are not possible because the monomers do not have the appropriate configurations, as seen in Fig. S12.[2]

Variable temperature ^{31}P NMR data from 210–380 K (Fig. 3) indicate that the chemical shifts of the major components (**5a** and **5b**) do not vary much with temperature, while those of the minor components (**5c** and **5d**) do. The NMR behavior is reversible, and the original ratio of isomers was seen on cooling the solution to 230 K; the data are qualitatively consistent with reversible conversion of dimers to monomers with increasing temperature, and so speculatively **5c** and **5d** might be monomeric diastereomers.

NMR and MS data on the mixture of major species **7a** and **7b** and minor species **7c** and **7d**, in which the 4-heptyl group of **5** has been replaced by cyclohexyl, suggest behavior similar to that found for the 4-heptyl system.

Conclusions

The dimer 4-heptyl-2-(2′-hydroxybinaphthyl)hydrogen phosphonate, accidentally synthesized by hydrolysis of 4-(3,5-dioxa-4-phosphacyclohepta[2,1-α;3,4-α′]-dinaphthalene-4-yloxy)heptane at RT, is a centrosymmetric 18-membered ring structure consisting of monomers, strongly hydrogen bonded via two P=O---H–O moieties; a corresponding cyclohexyl analogue appears to behave similarly. Racemic BINOL was used as a precursor reagent, but only two out of the eight possible diastereomeric dimers are formed from the racemic mixture of monomers. The diastereoselective formation of the H-bonded dimers is controlled by molecularly constrained geometry of the monomer.

Experimental

The various NMR spectra were recorded at RT (~20 °C) in $CDCl_3$ solution (unless stated otherwise) on Varian 90 MHz or Bruker AV 300 or 400 MHz instruments; singlet (s), doublet (d), triplet (t), multiplet (m), quintet (quin), broad (br); *J* values are given in Hz. FT-IR spectra (KBr, reported in cm^{-1}) were obtained on a Shimadzu IR-470 instrument. MS data (stated as *m*/*z* values) were acquired on Kratos Concept IIHQ LSIMS or Bruker Esquire ESI instruments. The computational analyses were performed using HyperChem pro 6.0, with PM3 calculations optimized by Polak-Ribiere algorithms. The PM3 optimized geometries were then taken for further optimization with the HF/STO-3G basis set. Racemic 1,1′-bi-2-naphthol (BINOL) was either purchased or prepared by a reported method (17).

X-ray crystallographic analysis of 5a

Measurements were made at –100 °C on a Rigaku ADSC CCD area detector with graphite monochromated Mo Kα radiation (λ = 0.710 60 Å). The final unit-cell parameters were based on 7004 reflections with 2θ = 4.2°–55.7°. The data were collected and processed using the d*TREK program (18). The structure was solved by direct methods (19) and

© 2007 NRC Canada

Table 2. Crystal data for **5a**.

Emprical formula	$C_{27}H_{29}O_4P$
Formula weight	448.50
Crystal size (mm^3)	0.20 × 0.20 × 0.20
Crystal system	Triclinic
Space group	$P\bar{1}$ (#2)
a (Å)	1.6440(2)
b (Å)	11.3196(3)
c (Å)	11.4692(2)
α (°)	67.535(9)
β (°)	86.23(1)
γ (°)	67.544(8)
Volume ($Å^3$)	1175.0(1)
Z	2
D_{calcd} (mg m^{-3})	1.268
F(000)	476
μ cm^{-1}	1.48
Reflections collected	10 620
Unique reflections	4785 (*R*(int) = 0.032)
No. of observations	($I > 2\sigma(I)$) 3759
Data, parameters	4785, 335
Goodness-of-fit (all data)	1.00
Final *R* indices	($I > 2\sigma(I)$) $R_1 = 0.040$, $wR_2 = 0.103$
R indices (all data)	$R_1 = 0.055$, $wR_2 = 0.109$

Table 3. Selected bond lengths of **5a** (esds in parentheses).

Bond[a]	Length (Å)
P(1)—O(3)	1.4578(11)
P(1)—O(2)	1.5544(12)
P(1)—O(1)	1.5865(11)
P(1)—H(1)	1.295(16)
O(1)—C(1)	1.4073(17)
O(2)—C(21)	1.5006(19)
O(4)—C(12)	1.3634(18)
O(4)—H(4)	0.89(2)
O(3)—H(4)	1.81(2)
C(10)—C(11)	1.4942(19)

[a]Atom numbers correspond to those shown in Fig. 1.

expanded using Fourier techniques (20). The non H atoms were refined anisotropically, while the H atoms were included but not refined. Some of the crystallographic data are given in Table 2, while selected bond lengths and angles are given in Tables 3 and 4, respectively.

4-Chloro-3,5-dioxa-4-phosphacyclohepta-[2,1-α;3,4-α′]-dinaphthalene (3)

In a 250 mL, two-necked flask, maintained at ~0 °C and equipped with a magnetic stirrer, freshly redistilled PCl_3 (1.5 mL, 17.2 mmol) was dissolved in 50 mL of dry Et_2O under N_2. To this solution was added BINOL (3.67 g, 13 mmol) in 100 mL of dry Et_2O, followed by Et_3N (4.3 mL, 14.9 mmol) dropwise, and the solution was stirred for 20 h at ~0 °C. The reaction mixture was then filtered, and the residue was washed with 5 mL of dry Et_2O; solvent was evaporated under vacuum from the filtrate to yield a yellow solid. IR: 3500 (m), 3100 (m), 1620 (s), 1590 (s), 1500 (s), 1210 (s), 960 (s), 820 (s), 750 (s). ^{1}H NMR (CCl_4) δ: 7.3–7.7 (m, 8H), 8.0–8.3 (m, 4H). ^{31}P NMR ($CDCl_3$) δ: (s, 178.8). Compound **3** was used without further purification for the synthesis of **4**.

Table 4. Selected bond angles of **5a** (esds in parentheses).

Bond[a]	Angle (°)
O(4)–H(4)–O(3)	159(2)
O(3)–P(1)–O(2)	118.32(7)
O(3)–P(1)–O(1)	113.50(7)
O(2)–P(1)–O(1)	102.16(6)
O(3)–P(1)–H(1)	112.7(7)
O(2)–P(1)–H(1)	103.9(7)
O(1)–P(1)–H(1)	104.7(8)
C(1)–O(1)–P(1)	122.24(9)
C(21)–O(2)–P(1)	122.27(10)
C(12)–O(4)–H(4)	114.4(14)
C(10)–C(1)–C(2)	123.47(14)
C(10)–C(1)–O(1)	117.78(13)
C(2)–C(1)–O(1)	118.66(13)
C(9)–C(10)–C(11)	120.98(12)
O(4)–C(12)–C(11)	124.08(14)
O(4)–C(12)–C(13)	114.68(13)
O(2)–C(21)–C(22)	107.92(12)
O(2)–C(21)–C(25)	111.86(18)
C(22)–C(21)–C(25)	108.84(18)
O(2)–C(21)–H(21)	109.4
C(22)–C(21)–H(21)	109.4
C(25)–C(21)–H(21)	109.4

[a]Atom numbers correspond to those shown in Fig. 1.

4-(3,5-Dioxa-4-phosphacyclohepta[2,1-α;3,4-α′]-dinaphthalene-4-yloxy)heptane (4)

Under conditions used for the preceding synthesis, to compound **3** (1.50 g, 4.3 mmol) dissolved in 20 mL dry toluene was added 4-heptanol (0.50 g, 4.3 mmol). To this solution at 0 °C, Et_3N (2.5 mL, 8.6 mmol) was added dropwise, and the mixture was stirred for 48 h, with the reaction progress being monitored by TLC. The white solid $[Et_3NH]^+Cl^-$ was removed by filtration, and the filtrate evaporated to dryness to give a light yellow solid, which was then washed through a silica gel column using cyclohexane – ethyl acetate (9:1); the fraction containing **4** was evaporated to dryness and the solid residue was recrystallized from the same solvent mixture to yield pure **4** in 80% yield. Melting point 124–126 °C. IR: 3050 (w), 2900 (m), 2850 (m), 1620, (m), 1580 (s), 1500 (s), 1375 (s), 1320 (s), 1060 (m), 950 (s), 930 (s), 820 (s), 750 (s), 695 (m), 640 (m), 550 (m). ^{1}H NMR δ: 0.8–1.7 (m, 6H, C*H*$_3$; and 8H, C*H*$_2$), 4.1–4.5 (m, 1H, C*H*), 7.2–8.2 (m, 12H, binaphthyl). ^{31}P{^{1}H} δ: (s, 146.0).

4-*n*-Heptyl-2-(2′-hydroxybinaphthyl)-hydrogen-phosphonate (5)

The compound was prepared by allowing compound **4** to stand in air at ambient temperature for days, either in the solid state or in acetone solution. A mixture of species is formed but one, labeled **5a**, was isolated as pale yellow crys-

© 2007 NRC Canada

tals (mp 144 to 145 °C, bp. ~180 °C), which were grown by slow evaporation of solvent at RT from a 9:1 mixture of cyclohexane–CH_2Cl_2 solution of the crude isolated product. Characterization data of **5a** were as follows. ^{1}H NMR $\delta_{binaphthyl}$: 8.08 (d, 1H, J = 9), 8.02 (d, 1H, J = 8.98), 7.97 (d, 1H, J = 8.91), 7.89 (d, 1H, J = 7.42), 7.69 (dd, 1H, J = 8.94, J = 1.0), 7.47 (t, 1H, J = 8.0), 7.39 (d, 1H, J = 8.90), 7.30 (m, 4H, one due to O*H*?), 7.25 (d, 1H, J = 8.3), δ: 7.20 (d, 1H, J = 9.0), 6.65 (d, 1H, $^1J_{HP}$ = 703, O=P-*H*; seen as a singlet in the ^{1}H{^{31}P} spectrum), 3.64 (m, 1H, C*H*), 1.27–1.07 (m, 8H, CH_2), 0.60 (t, 3H, J = 7.30, CH_3), 0.72 (t, 3H, J = 7.30, CH_3); Fig. S6. ^{31}P NMR δ: 3.80 (dd, $^1J_{PH}$ = 707, $^3J_{PH}$ 10.7); Fig. S7. ^{31}P{^{1}H} NMR δ: 3.80 (s); Fig. S7. ^{13}C{^{1}H} NMR (1:1 CD_3COCD_3–$CDCl_3$) δ: 18.08, 18.34, 28.50, 37.36, 37.40, 37,44, 77.50, 114.6, 118.7, 121.5, 121.5, 123.5, 124.8, 125.9, 126.2, 126.9, 127.2, 128.3, 128.5, 130.2, 130.4, 132.0, 134.2, 134.4, 146.5, 146.6, 153.1. MS (EI): dimer M^+ = 896 (0%); M – 286 = 610 (25%), 611 (19%); monomer M^+ 448 (8%), 350 (22%), 332 (55%), 286 (100%), 268 (40%), 239 (40%). Low-resolution ESI MS (CH_3OH–$CHCl_3$): dimer M^+ 897.3 (17%), 898.3 (6.5%), 899.3 (1.1%), 610 (0%); monomer M^+ = 449.1 (24%), 450.1 (4.2%), 352.0 (10.8%), 351.0 (100%), 333.0 (2%), 338.3 (2.2%), 287.1 (2%), 269.1 (1.86%).[2]

Species present in the crude product were **5a** (45%), **5b** (36%), **5c** (13%), **5d** (5%), and **5x** (2%). NMR data for the other species were as follows: ^{1}H NMR δ: 8.0–6.98 (m, binaphthyl) 6.65 (d, ^1J = 703), 6.58 (d, ^1J = 703), 6.575 (d, $^1J_{HP}$ = 705), 6.21 (d, $^1J_{HP}$ = 706); δ: 4.32 (m), at 3.95 (m), at 3.65 (m), and 3.53 (m), 1.60–0.40 (m, CH_3 and CH_2); Figs. S3, S5, and S8. ^{31}P NMR (**5b**) δ: 4.20 (dd, $^1J_{PH}$ = 720, $^3J_{PH}$ = 8.4); (**5c**) δ: 8.80 (dd, $^1J_{PH}$ = 704, $^3J_{PH}$ = 9.0); (**5d**) δ: 5.45 (d, br, $^1J_{PH}$ = 720); and an unknown (**5x**) δ: 3.35 (d, br); Figs. S2. ^{31}P{^{1}H} NMR δ: 4.20 (s, **5b**), 8.80 (s, **5c**), 5.45 (s, **5d**), and unknown compound at δ 3.35 (s, **5x**); Fig. S1. ^{1}H{^{31}P} NMR δ: 8.05–6.97 (m), 6.63 (s), 6.59 (s), 6.57 (s), and 6.62 (s), 4.40 (quin), 4.10 (quin), 3.65 (quin), 3.45 (quin), 1.60– 0.40 (m, CH_3 and CH_2); Fig. S8. Recrystallization of the crude solid from Et_2O–cyclohexane (1:9) gave mainly the two major components (**5a** and **5b**); Figs. S4 and S5.[2]

3,5-Dioxa-4-phosphacyclohepta[2,1-α;3,4-α′]-dinaphthalene-4-yloxy)cyclohexane (6)

The synthesis of **6** was identical to that used for the synthesis of **4** except that cyclohexanol (0.43 g, 4.3 mmol) was used. The crystallization produced **6** in 70% yield, mp 64–66 °C. IR: 3100 (w), 2900 (s), 2800 (m), 1720, (s), 1620 (m), 1590 (s), 1510 (s), 1460 (s), 1370 (m), 1330 (s), 1230 (s), 1080 (m), 980 (s), 940 (s), 820 (s), 750 (s), 690 (s), 600 (s). ^{1}H NMR δ: 1.0–1.90 (m, 10H), 4.1– 4.5 (m, 1H), 7.5–8.3 (m, 12H). ^{31}P{^{1}H} NMR δ: (s, 150.0).

Cyclohexyl-2-(2′-hydroxybinaphthyl)-hydrogen phosphonate (7)

The compound was prepared by allowing compound **6** to stand at ambient temperature for several days in the solid state or in solution. Crystallization of the isolated crude residue from a 19:1 mixture of cyclohexane–acetone solution produced a pale yellow solid. ^{1}H NMR (for mixture) δ: 8.00–6.94(m), 6.91 (d, $^1J_{HP}$ = 720), 6.55 (d, $^1J_{HP}$ = 705), 6.43 (d, $^1J_{HP}$ = 720), 4.31 (m), 4.02 (m), 3.78 (m), 3.42 (m) and 1.70–0.70 (m); Fig. S10. ^{31}P{^{1}H} NMR analysis showed components at δ: 3.94 (**7a**, 40%), 4.23 (**7b**, 38%), 8.55 (**7c**, 18%), 5.50 (**7d**, 4%), and a trace amount of an unknown component; Fig. S9. ^{31}P NMR for **7a**–**7d**, respectively, δ: 3.95 (dd, $^1J_{PH}$ = 720, $^3J_{PH}$ = 9.9); 4.29 (dd, $^1J_{PH}$ = 720, $^3J_{PH}$ = 9.3); 8.60 (dd, $^1J_{PH}$ = 704, $^3J_{PH}$ = 9.0); 5.50 (br d, $^1J_{PH}$ = 725); Fig. S9. Low-resolution ESI MS (CH_3OH–$CHCl_3$): dimer M^+ 866.1 (10%), 865.3 (26%), 863.0 (8.8%), 795.3 (3%), 770.3 (3.8%), 707.3 (6.6%), 693.3 (6.6%), 619.3 (8.6%), 605.3 (1.16%), 561.2 (12.9%), 534.1 (26.5%), 532.1 (23%), 517.2 (10.1%); monomer M^+ = 433.1 (32.99%), 351 (40.74%), 311 (8.68%), 237 (100%).

Acknowledgments

We thank the Isfahan University of Technology (Research Council Grant number 85/500/9143) and the Natural Sciences and Engineering Research Council of Canada (NSERC) for financial support.

References

1. For example please see: (*a*) M. Nishio. Tetrahedron, **61**, 6923 (2005); (*b*) X.-B. Wang, H.K. Woo, B. Kiran, and L.-S. Wang. Angew. Chem. Intern. Ed. **44**, 4968 (2005).
2. For example please see: (*a*) Supramolecular assembly via hydrogen bonds II. Structure and bonding. Vol. 111. *Edited by* D.M.P. Mingos. Springer-Verlag, Berlin/Heidelberg, Germany. 2004; (*b*) A. Facchetti, E. Annoni, L. Beverina, M. Morone, P. Zhu, T.J. Marks, and J.A. Pagani. Nature Material, **3**, 910 (2004); (*c*) R.M. McKinlay, P.K. Thallapally, G.W.V. Cave, and J.L. Atwood. Angew. Chem. Intern. Ed. **44**, 5733 (2005); (*d*) H. Gong and M.J. Krische. J. Am. Chem. Soc. **127**, 1719 (2005); (*e*) A. Tessa ten Cate, P.Y.W. Dankers, R.P. Sijbesma, and E.W. Meijer. J. Org. Chem. **70**, 5799 (2005); (*f*) P. Prabhakaran, V.G. Puranik, and G.J. Sanjayan. J. Org. Chem. **70**, 10067 (2005).
3. I. Azumaya, D. Uchida, T. Kato, A. Yokoyama, A. Tanatani, H. Takayanagi, and T. Yokozawa. Angew. Chem. Int. Ed. **43**, 1360 (2004).
4. (*a*) Y. Zhu and D.G. Drueckhammer. J. Org. Chem. **70**, 7755 (2005); (*b*) C.P. Price and A.J. Matzger. J. Org. Chem. **70**, 1 (2005); (*c*) X. Zhang, H. Du, Z. Wang, Y.-D. Wu, and K. Ding. J. Org. Chem. **71**, 2862 (2006).
5. I. Alfonso, M.I. Burguete, and S.V. Luis. J. Org. Chem. **71**, 2242 (2006).
6. M.H. Abraham, R.J. Abraham, J. Byrne, and L. Griffiths. J. Org. Chem. **71**, 3389 (2006).
7. G.A. Jeffery and W. Saenger. Hydrogen bonding in biological structures. Springer-Verlag, Berlin, Germany. 1991.
8. (*a*) D.E.C. Corbridge. Phosphorus: An outline of its chemistry, biochemistry and technology. 4th ed. Elsevier, Amsterdam. 1990. Ch. 14; (*b*) S. Cruz-Gregorio, M. Sanchez, A. Clara-Sosa, S. Bèrnes, L. Quintero, and F. Sartillo-Piscil. J. Org. Chem. **70**, 7107 (2005).
9. (*a*) H.A. Dabbagh, A. Modaresei-Alam, A. Tajarodi, and A. Taeb. Tetrahedron, **58**, 2621 (2000); (*b*) H.A. Dabbagh, N. Noroozi-Pesyan, B.O. Patrick, and B.R. James. Can. J. Chem. **82**, 1179 (2004); (*c*) H.A. Dabbagh, A.R. Najafi Chermahini, and A.R. Modarresi-Alam. Bull. Korean Chem. Soc. **26**, 1229 (2005); (*d*) H.A. Dabbagh, A.R. Najafi Chermahini, A.R.

© 2007 NRC Canada

Modarresi-Alam, and A. Teimouri. J. Iran. Chem. Soc. **3**, 51 (2006).
10. (*a*) F. Hibbert and J. Emsley. Adv. Phys. Org. Chem. **26**, 255 (1990); (*b*) P. Gilli, V. Bertolasi, V. Ferretti, and G. Gilli. J. Am. Chem. Soc. **116**, 909 (1994); (*c*) G.A. Jeffery. An introduction to hydrogen bonding. Oxford University Press, Oxford, UK. 1997; (*d*) P. Gilli, V. Bertolasi, V. Ferretti, and G. Gilli. J. Am. Chem. Soc. **122**, 10405 (2000); (*e*) C.C. Wilson. Single crystal neutron diffraction from molecular materials. 1st ed. Vol. 1. World Scientific Co. Pte. Ltd., Singapore. 2000. p. 211; (*f*) T. Steiner. Angew. Chem. Int. Ed. **41**, 48 (2002).
11. (*a*) G. Gilli and P. Gilli. J. Mol. Struc. **552**, 1 (2000); (*b*) P.A. Frey. Magn. Reson. Chem. **39**, S190 (2001).
12. P. Gilli, V. Bertolasi, L. Pretto, L. Antonov, and G. Gilli. J. Am. Chem. Soc. **127**, 4943 (2005).
13. J. Cieślak, J. Jankowska, J. Stawiński, and A. Kraszewski. J. Org. Chem. **65**, 7049 (2000), and refs. cited therein.
14. W.J. Pietro, W.J. Hehre. J. Am. Chem. Soc. **104**, 3594 (1982).
15. (*a*) G. Franciò, C. Arena, F. Faraone, C. Graiff, M. Lanfranchi, and A. Tripicchio. Eur. J. Inorg. Chem. 1219 (1999); (*b*) S. Yao, J.-C. Meng, G. Siuzdak, and M.G. Finn. J. Org. Chem. **68**, 2540 (2003).
16. A. Troev. Heteroat. Chem. **11**, 205 (2000).
17. (*a*) D. Cai, D.L. Hughes, T.R. Verhoeven, and P.J. Reider. Tetrahedron Lett. **36**, 7991 (1995); (*b*) D. Xiao, Z. Zhang, and X. Zhang. Org. Lett. **1**, 1679 (1999).
18. d*TREK [computer program]. Version 7.1I. Molecular Structure Corporation, The Woodlands, Tex. 2001.
19. A. Altomare, M.C. Burla, G. Cammalli, M. Cascarano, C. Giacovazzo, A. Guagliardi, A.G.G. Moliterni, G. Polidori, and A. Spagna. J. Appl. Crystallogr. **32**, 115 (1999).
20. P.T. Beurskens, G. Admiraal, G. Beurskens, W.P. Bosman, R. de Gelder, R. Israel, and J.M.M. Smits. DIRDIF-94 [computer program]. University of Nijmegen, The Netherlands. 1994.

© 2007 NRC Canada

Electrocatalytic hydrogenation of octyl aldehyde over Pd catalysts

Ciprian M. Cirtiu and Hugues Ménard

Abstract: The electrocatalytic hydrogenation (ECH) of octyl aldehyde (octanal) to octyl alcohol (octan-1-ol) was investigated using commercial Pd/alumina catalysts in aqueous ethanol. The influence of different parameters, such as catalyst support, current intensity, polarity of solvent, supporting electrolyte, and octanal concentration, on the electrocatalytic hydrogenation of octanal was studied.

Key words: octanal, octan-1-ol, Pd/alumina catalyst, electrocatalytic hydrogenation.

Résumé : L'hydrogénation électrocatalytique de l'aldéhyde d'octyl (octanal) à l'alcool d'octyl (octan-1-ol) a été étudiée en utilisant des catalyseurs commerciaux de Pd/alumine en éthanol aqueux. L'influence de différents paramètres, tels que le support catalytique, l'intensité de courant, la polarité du solvant, l'électrolyte support et la concentration en octanal, sur l'hydrogénation électrocatalytique de l'octanal, a été étudiée.

Mots-clés : octanal, octan-1-ol, catalyseur Pd/alumine, hydrogénation électrocatalytique.

Introduction

It is confirmed in the literature (1) that electrocatalytic hydrogenation (ECH) can form the basis of unusually selective electrosynthetic reactions. As demonstrated recently (2), ECH can be a very efficient alternative to the catalytic hydrogenation (CH) of organic compounds. Electrochemical generation of adsorbed hydrogen provides an interesting means to hydrogenate organic compounds. The development of various specific electrodes, which allowed for selective hydrogenation of different classes of organic compounds (3), has improved the ECH technique.

To our knowledge, there are no studies on the ECH of octanal using palladium catalysts. It is well known that palladium catalysts are usually not active for the CH of saturated aliphatic aldehydes (4, 5). However, palladium catalysts are the most active for the CH of aromatic aldehydes under mild conditions. Ruthenium catalysts are very efficient for the hydrogenation of saturated aliphatic aldehydes (4). A promoting effect of stannous chloride has been observed with supported ruthenium and platinum catalysts in the hydrogenation of heptanal (6). Octan-1-ol is obtained in very high yields by the reduction of octanal via BINOL-Zr complex (7).

The difficulty to hydrogenate octanal comes from the stability of the C=O group, which is thermodynamically more stable, in comparison with the C=C group. The development of selective and efficient catalysts is an important requirement for the implementation of ECH in the pharmaceutical and chemical industries. In the ECH mechanism over supported catalysts, adsorption of target molecules onto the inorganic matrix that supported the metallic nanoaggregates represents a crucial step, as demonstrated recently (8). The adsorption, and implicitly the ECH efficiency, can be enhanced by the functionalization of the catalyst matrix.

In the present work, parameters that affect the ECH efficiency, including catalyst support, current intensity, water percentage, supporting electrolyte, and octanal concentration, are studied to obtain preliminary results. This study was motivated by the results obtained previously for the ECH of organic compounds, such as cyclohexanone and benzophenone, which are known to be difficult or completely non-hydrogenable over Pd catalysts.

Received 15 February 2007. Accepted 30 May 2007. Published on the NRC Research Press Web site at canjchem.nrc.ca on 28 June 2007.

C.M. Cirtiu and H. Ménard.[1] Département de Chimie, Centre de Recherche en Electrochimie et Electrocatalyse, Université de Sherbrooke, Sherbrooke, QC J1K 2R1, Canada. [1]Corresponding author (e-mail: hugues.menard@usherbrooke.ca).

Experimental

Chemicals

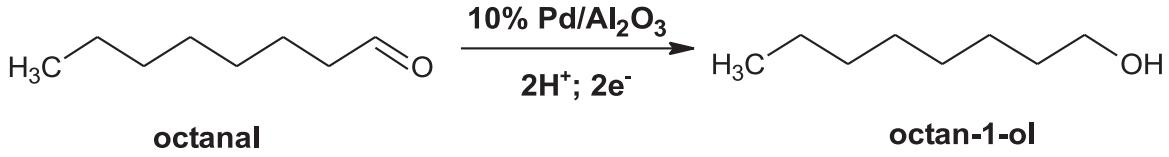
Octanal and octan-1-ol (both from Aldrich) were of 99% grade of purity and were used as received. Ethyl alcohol (anhyd.) and high purity water (from a Milli-Q® unit) were used to prepare the solutions. Reticulated vitreous carbon (RVC) (100 pores per inch) (1 inch = 25.4 mm) purchased from Electrolytica Inc. was used as cathode; commercial 10% (*w*/*w*) Pd/alumina powder (reduced, Aldrich) and finely divided Pd (1.1–2.0 μm APS, Alpha Aesar) were used as catalysts in the present study. Glacial acetic acid (HPLC grade, Caledon), butyric (99%, Aldrich), and NaOH solution (10 mol/L) were used for the preparation of the electrolyte solutions.

ECH procedure

All the electrolyses were conducted at ambient pressure and temperature in a two-compartment electrochemical reactor (9). The compartment of the cathode was filled with

 doi:10.1139/V07-059 © 2007 NRC Canada

Scheme 1. Reaction scheme for the electrocatalytic hydrogenation of octanal to octan-1-ol.



30 mL of 0.25 mol/L supporting electrolyte (acetate or butyrate buffer solution) in aq. ethanol (variable compositions of H_2O + CH_3CH_2OH). The pH was previously adjusted to 5 with 10 mol/L NaOH. The catalyst (200 mg of 10% Pd/alumina or finely divided Pd) was added to the cathodic compartment solution and dynamically circulated through the RVC cathode. The anodic compartment was filled with 1 mol/L solution of acid buffer in water. All the electrolyses were carried out under galvanostatic conditions (I = 10 mA or 20 mA) using an Agilent galvanostat/potentiostat (6634 B model). The RVC cathode was polarized under an applied constant current (10 or 20 mA); the corresponding charge being equal to 15 °C. The coulometer was reset after polarization; octanal was added in the cathodic compartment (2.6 or 5.2 mmol/L final concentration, depending on the experimental conditions), and 0.5 mL aliquot of mixed solution was immediately removed as reference sample (0 °C) and treated as described in the next section.

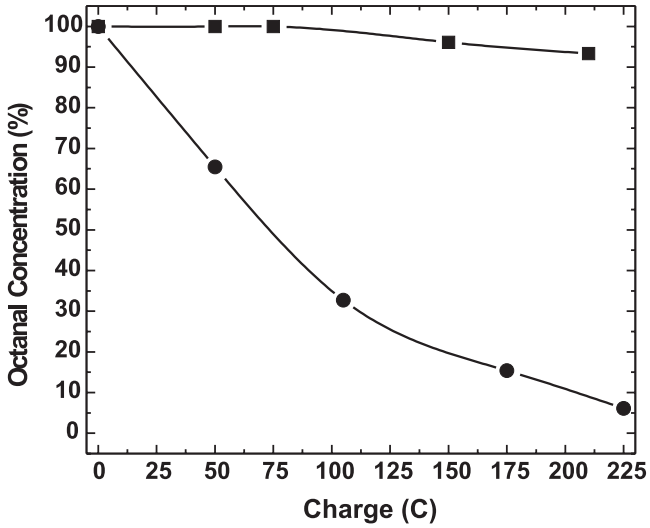
Products analyses

The progress of the reaction was monitored by GC. Quantitative analyses were performed on an Agilent 6890 Series chromatograph, equipped with an FID detector and HP-Innowax (crosslinked polyethylene glycol) capillary column (50 m × 0.22 mm × 0.4 μm). Aliquots of 0.5 mL were withdrawn from the electrochemical reactor at different times of electrolysis and were treated as follows: sample was filtered on Millex-HN syringe-driven filter (0.45 μm, Millipore); at 0.4 mL of filtered solution, 0.1 mL external standard (cyclohexanol) was added, and the mixture was injected in the GC. The conversion percentages presented in this study are determined from the GC yields. Both octanal and octan-1-ol were determined by GC. Kinetic curves, represented as relative concentrations vs. charge consumed, are reproducible with a standard deviation of ±3.1%.

Results and discussion

Adsorbed hydrogen is generated at the palladium surface by the electrochemical reduction of water. The brief electrical contact between the RVC cathode and the Pd/alumina particles, or finely divided Pd particles, is enough to charge the metallic aggregates and to produce the atomic hydrogen, which is implied in the hydrogenation process (10). The ECH efficiency, defined as the amount of transformed target species vs. the cumulative charge passed, is determined by the competition among the hydrogenation of the unsaturated compound (Scheme 1), hydrogen evolution, and, in some cases, the direct reduction of the substrate on the electrode surface. Figure 1 presents the remaining fraction of octanal for the ECH over 10% Pd/alumina and finely divided Pd catalysts under identical experimental conditions. Clearly, the supported catalyst is much more effective (nearly 100% conversion) than the non-supported. The same effect was observed in the ECH and CH of other organic compounds (2, 8, 11). The poor yield of hydrogenation using finely divided Pd catalyst is explained by the absence of the adsorption sites located on the catalyst support (alumina in the case of Pd/alumina catalyst) where the organic target molecule is adsorbed (8).

Fig. 1. ECH of octanal (5.2 mmol/L) over finely divided Pd (■) and 10% Pd/alumina (●) catalysts. Supporting electrolyte: 0.25 mol/L acetate buffer solution (pH 5) in aq. ethanol (50% H_2O *v*/*v*); I = 10 mA.



The relative rates of these processes are not only affected by the adsorption of target species, but also by the current intensity, the polarity of solvent, or the electrolyte nature, as discussed further. We have verified the influence of current intensity on the ECH of octanal over Pd/alumina catalyst in acidic aq. ethanol. One expects to have a decrease in the ECH efficiency because hydrogen evolution reactions are favored. As observed in Fig. 2, the higher the current intensity, the lower the ECH efficiency, which indicates that concurrent hydrogen evolution is more significant for a current intensity of 20 mA. In addition to the kinetic aspect, the current intensity influences the cell flow, by the formation of many cavities of hydrogen gas, as observed experimentally at high intensity of current. To limit the current loss, associated with the hydrogen-evolution reaction, the current must be adjusted to optimize the ECH reaction, while preserving a suitable reaction time; this is why all the reactions were carried out using a current intensity of 10 mA.

Another parameter, which can affect the ECH process, is the supporting electrolyte. It was demonstrated earlier that the acid used as supporting electrolyte intervenes in the ECH process by the change in the surface properties of the catalyst matrix (8), i.e., by fixation at the alumina surface. This

© 2007 NRC Canada

Fig. 2. ECH of octanal (5.2 mmol/L) over 10% Pd/alumina catalyst for different current intensities: (●) I = 10 mA and (■) I = 20 mA. Supporting electrolyte: 0.25 mol/L acetate buffer solution (pH 5) in aq. ethanol (50% H_2O *v*/*v*).

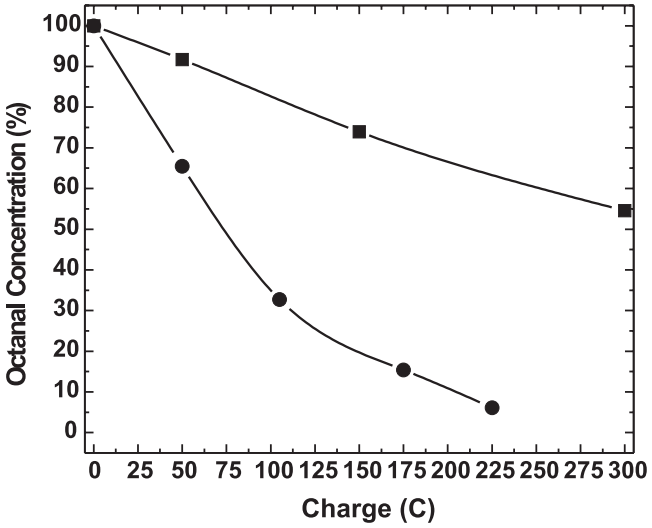
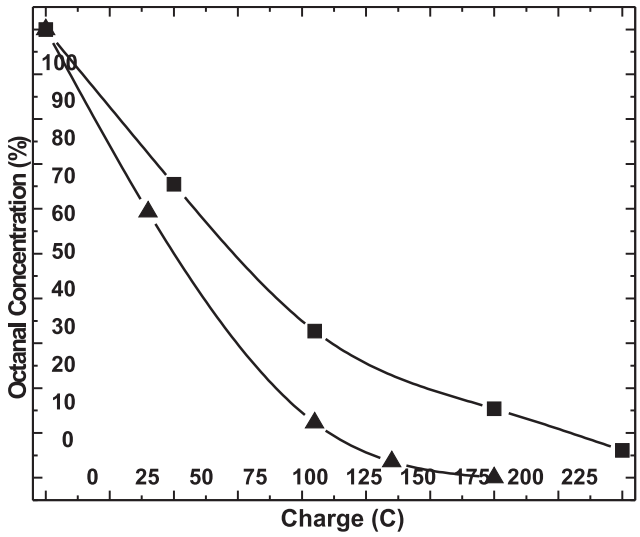


Fig. 3. ECH of octanal (5.2 mmol/L) over 10% Pd/alumina catalyst. Supporting electrolyte: 0.25 mol/L of (■) acetate buffer solution (pH 5) and (▲) butyrate buffer solution (pH 5) in aq. ethanol (50% H_2O *v*/*v*); I = 10 mA.



modification of the surface can affect the adsorption properties, and implicitly the process efficiency, because the adsorption is a key step in the ECH mechanism. Figure 3 presents the depletion curves for the octanal hydrogenation with two aliphatic carboxylic acids used as supporting electrolytes. These results are interpreted while being based on the principle of "in situ functionalized materials" introduced by our group (8). One observes a different behavior when the butyrate replaced the acetate. The nature of adsorption sites onto the catalyst matrix changes because of the carboxylate, which fixes on alumina. The polar surface of the alumina is transformed in a less polar surface by the acetate, which adsorbs onto the alumina via the carboxylate function. When the butyrate replaced the acetate, the alumina surface became less polar, increasing in this way the adsorption capacity. The polarity of solvent can also affect the adsorption equilibrium; this is why different water–ethanol mixtures were tested for the ECH of octanal over 10% Pd/alumina catalyst using acetate as the modifier of the alumina surface. The lower-polarity (ethanol-rich) solutions can reduce the adsorption of the target molecule onto the functionalized alumina and affect in this way the ECH efficiency (Table 1).

It is clear from Table 1 (entries 1–3) that as the ethanol concentration increases, the hydrogenation of octanal becomes less efficient. Again, we suggest that this behavior is principally due to the adsorption phenomena, which modulates the ECH process.

St. Pierre et al. observed a similar effect in their study of the ECH of cyclohexanone with nickel supported on functionalized-silica catalysts (12).

The effect of concentration on the ECH of octanal can be observed by comparing entries 1 and 4 in Table 1. As expected, the ECH is more efficient by increasing the octanal concentration. For a higher concentration of octanal than that used in the present study, one can expect to have an increase in the ECH efficiency, but a very concentrated solution of octanal must be avoided because of the low solubility of octanal in solutions rich in water.

Table 1. Remaining fraction of octanal after 200 °C.

Entry	Ethanol (%)	Octanal (%)
1	50	41
2	65	52
3	80	72
4	50	11[a]

Note: Experimental conditions: supporting electrolyte: 0.25 mol/L acetate buffer solution (pH 5); solvent: ethanol–water; I = 10 mA; octanal concentration: 2.6 mmol/L.
[a]Octanal concentration: 5.2 mmol/L.

Conclusion

The present work demonstrates that octanal can be hydrogenated to octan-1-ol over Pd/alumina catalyst. Effectively, the catalyst matrix plays an important role in the ECH process of octanal, but other parameters, such as current intensity, the polarity of solvent (water concentration), supporting electrolyte, and substrate concentration, also affect the process. These results show that ECH provides a good tool for the hydrogenation of saturated aliphatic aldehydes in mild conditions without the necessity of high pressure and temperature or hydrogen supply.

Acknowledgements

Authors thank the Natural Sciences and Engineering Research Council of Canada (NSERC) and le Fonds Québécois de la Recherche sur la Nature et les Technologies (FQRNT). C.M. Cirtiu thanks ALCAN Inc. company for the institutional fellowship.

© 2007 NRC Canada

References

1. A.M. Couper, D. Pletcher, and F.C. Walsh. Chem. Rev. **90,** 837 (1990).
2. C.M. Cirtiu, A. Brisach-Wittmeyer, and H. Ménard. J. Catal. **245,** 191 (2007).
3. F. Beck. Int. Chem. Eng. **19**, 1 (1979).
4. S. Nishimura. Handbook of heterogeneous catalytic hydrogenation for organic synthesis. John Wiley & Sons, Inc., New York. 2001. p.173.
5. S.J.C. Cleghorn and D. Pletcher. Electrochim. Acta. **38**, 425 (1993).
6. P.N. Rylander and J. Kaplan. Engelhard. Ind. Tech. Bull. **2**, 48 (1961).
7. M. Lorca, D. Kuhn, and M. Kurosu. Tetrahedron Lett. **42**, 6243 (2001).
8. C.M. Cirtiu, H. Oudghiri Hassani, N.-A. Bouchard, P.A. Rowntree, and H. Ménard. Langmuir, **22**, 6414 (2006).
9. A. Bannari, C. Cirtiu, F. Kerdouss, P. Proulx, and H. Ménard. Chem. Eng. Process. **45**, 471 (2006).
10. F. Laplante, L. Brossard, and H. Ménard. Can. J. Chem. **81**, 258 (2003).
11. C. Cirtiu, A. Brisach-Wittmeyer, and H. Ménard. Catal. Commun. **8**, 751 (2007).
12. G. St-Pierre, A. Chagnes, N.-A. Bouchard, P.D. Harvey, L. Brossard, and H. Ménard. Langmuir, **20**, 6365 (2004).

© 2007 NRC Canada

One-pot multicomponent synthesis of β-acetamidoketones catalysed by *p*TSA[1]

Biswanath Das, Kongara Ravinder Reddy, Yallamalla Srinivas, and Rathod Aravind Kumar

Abstract: A catalytic amount of *p*TSA has been found to be effective to carry out a one-pot three-component coupling of aromatic aldehydes, enolizable ketones or ketoesters, and acetonitrile in the presence of acetyl chloride to afford β-acetamidoketones in high yields. Short reaction times and inexpensive catalyst are main advantages of this protocol.

Key words: β-acetamidoketone, *p*TSA, multicomponent reaction, diastereoselectivity.

Résumé : On a trouvé qu'une quantité catalytique d'acide *p*-toluènesulfonique suffit pour effectuer une réaction monotope à trois composants qui permet d'effectuer le couplage d'aldéhydes aromatiques, de cétones ou de cétoesters énolisables et d'acétonitrile et d'acétonitrile, en présence de chlorure d'acétyle, et obtenir des β-acétamidocétones avec des rendements élevés. Des temps de réaction courts et un catalyseur peu coûteux sont les avantages de principaux de ce protocole.

Mots-clés : β-acétamidocétone, acide *p*-toluènesulfonique, réaction à plusieurs réactifs, diastéréosélectivité.

[Traduit par la Rédaction]

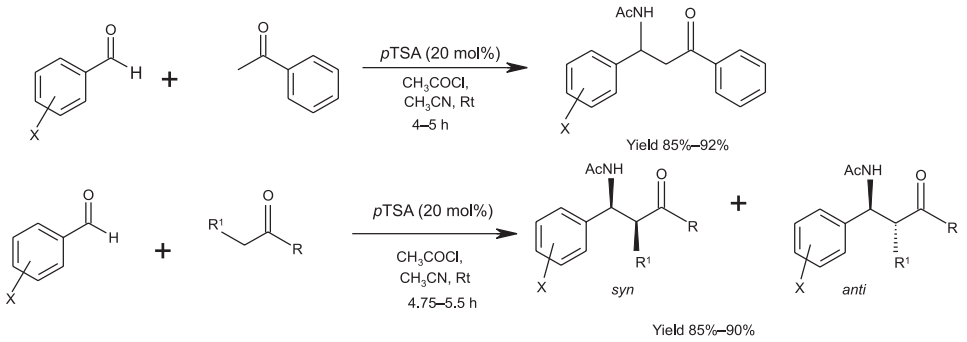
Introduction

Synthesis of β-acetamidoketones has attracted much attention in organic synthesis because of their multifunctional nature and the existence of their skeletons in various biologically important molecules (1). They act as building blocks for the preparation of compounds like 1,3 amino alcohols (2) and fragments of the natural nucleoside peptide antibiotics such as nikkomycins and neopolyoxins (3). Previously, Iqbal and co-workers (4) achieved the synthesis of β-acetamidoketones through a multicomponent reaction applying Lewis acids, $CoCl_2$, polyaniline $Co(OAc)_2$, and Montmorrilonite K-10 clay. Recently, other methods have also been reported involving $Sc(OTf)_3$, $ZrOCl_2$, BiOCl, or I_2 (5). However, most of the methods require expensive catalysts, long reaction times, or high temperature. The catalytic activity of a protic acid in the preparation of β-acetamidoketones has not yet been fully explored.

Results and discussion

In continuation of our studies (6) directed towards the development of useful synthetic methodologies, we recently found that *para* toluene sulfonic acid can efficiently catalyse the one-pot coupling of aromatic aldehydes, enolizabe ketones or ketoesters, and acetonitrile in the presence of acetyl

Scheme 1.



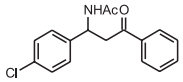
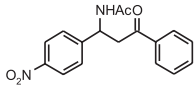
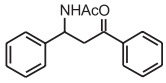
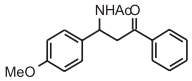
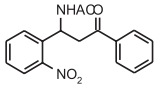
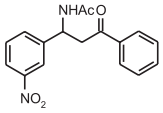
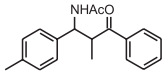
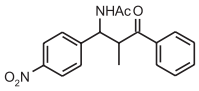
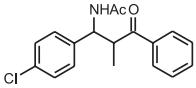
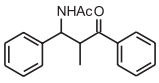
Received 27 March 2007. Accepted 23 May 2007. Published on the NRC Research Press Web site at canjchem.nrc.ca on 28 June 2007.

B. Das,[2] K.R. Reddy, Y. Srinivas, and R.A. Kumar. Organic Chemistry Division-I, Indian Institute of Chemical Technology, Hyderabad 500 007, India.

[1]This article is part 128 in the series "Studies on novel synthetic methodologies". IICT Commu. No. 070520.
[2]Corresponding author (e-mail: biswanathdas@yahoo.com).

 doi:10.1139/V07-062 © 2007 NRC Canada

Table 1. Synthesis of β-acetamidoketones catalysed by *p*TSA.

Entry	β-acetamidoketone (**1**)	Time (h)	Yield (%)	syn–anti [a]
a		4.0	89	–
b		4.5	90	–
c		5.0	87	–
d		4.25	89	–
e		4.5	90	–
f		4.25	92	–
g		4.5	85	12:88
h		5.0	85	17:83
i		4.75	89	9:91
j		5.0	87	25:75

chloride to afford β-acetamidoketones at room temperature in high yields (Scheme 1).

A variety of aromatic aldehydes were converted into the corresponding β-acetamidoketones following the above procedure in the presence of 20 mol% of *p*TSA. The conversion afforded the desired products within 4–5.5 h (Table 1).

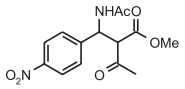
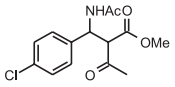
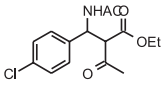
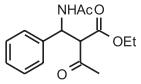
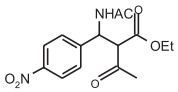
The aromatic aldehydes containing both electron-donating and electron-withdrawing groups worked well. The reaction with propiophenones (Table 1, entries g–j) or ketoesters (Table 1, entries k–o) is diastereoselective. In such cases, anti and syn products were formed. The amount of these anti and syn products was determined by ^{1}H NMR spectra. The coupling constant between H-2 and H-3 is 7–9 Hz for an anti isomer, while 2–5 Hz for a syn isomer (4). In most of the cases, an anti isomer was found to be major. Several functional groups, such as NO_2, alkyl, halogen, and ether, were compatible under the present reaction conditions (Table 1). The structures of the products were settled from spectral (^{1}H NMR and MS) data. The possible mechanism of the reaction is given (4) in the accompanying diagram following Table 1.

Conclusion

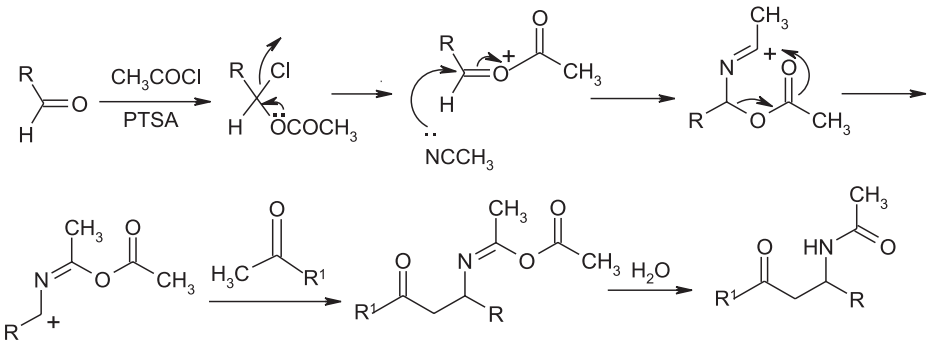
In conclusion, we have demonstrated an alternative and simple method for the synthesis of β-acetamidoketones using an organic Brønsted acid, *p*TSA, for the first time. The application of an inexpensive catalyst, high yields, short reaction times, and mild reaction conditions are the main ad-

© 2007 NRC Canada

Table 1 (*concluded*).

k		5.0	89	32:68
l		5.25	86	40:60
m		5.0	90	44:56
n		5.5	86	50:50
o		5.0	88	38:62

Note: The structures of the products were settled from spectral (^{1}H NMR and MS) data.
[a]Ratio obtained from the ^{1}H NMR spectrum of the crude reaction mixture.



vantages of this protocol. We feel that the method will find practical application in the synthesis of β-acetamidoketones.

Experimental

To a mixture of an aldehyde (1 mmol), a ketone or ketoester (1mmol), and AcCl (1 mmol) in MeCN (5 ml), *p*TSA (20 mol%) was added. The mixture was stirred at room temperature and the reaction was monitored by TLC. After completion, the mixture was poured on water and extracted with ethyl acetate (3 × 20 ml). The extract was dried over Na_2SO_4, and the solvent was concentrated under reduced pressure. The residue was subjected to column chromatography (SiO_2; hexane – ethyl acetate) to afford the pure β-acetamidoketone.

When ketoesters were used, the reaction was conducted under N_2 atmoshere. The analytical data of some representative products are given in the following.

N-(3-Oxo-1,3-diphenyl-propyl)-acetamide (1c)

^{1}H NMR ($CDCl_3$, 200 MHz) δ: 7.87 (2H, d, *J* = 8.0 Hz), 7.56–7.12 (9H, m), 5.50 (1H, m), 3.66 (1H, dd, *J* = 17.0, 4.5 Hz), 3.31 (1H, dd, *J* = 17.0, 5.3 Hz), 1.89 (3H, s). FABMS *m/z*: 268 $[M + H]^+$. Anal. calcd. for $C_{17}H_{17}NO_2$: C 76.40, H 6.37, N 5.24; found: C 76.32, H 6.31, N 5.29.

N-[1-(3-Nitrophenyl)-3-oxo-3-phenylpropyl]acetamide (1f)

^{1}H NMR ($CDCl_3$, 200 MHz) δ: 8.21 (1H, brs), 8.10 (1H, d, *J* = 8.0 Hz), 7.92 (2H, d, *J* = 8.0 Hz), 7.72–7.44 (5H, m), 7.01 (1H, d, *J* = 8.5 Hz), 5.64 (1H, m), 3.81 (1H, dd, *J* = 17.0, 4.4 Hz), 3.48 (1H, dd, *J* = 17.0, 5.2 Hz), 2.07 (3H, s). FABMS *m/z*: 313 $[M + H]^+$. Anal. calcd. for $C_{17}H_{16}N_2O_4$: C 65.39, H 5.13, N 8.97; found: C 65.48, H 5.21, N 8.91.

Ethyl-2-acetyl-3-acetamido-3-(4′-chlorophenyl)-propionate (1m, anti)

^{1}H NMR ($CDCl_3$, 200 MHz) δ: 7.36–7.22 (4H, m,), 6.98 (1H, d, *J* = 8.9 Hz), 5.69 (1H, dd, *J* = 8.9, 5.9 Hz), 4.21 (2H,

© 2007 NRC Canada

q, J = 7.0 Hz), 4.01 (1H, d, J = 5.9 Hz), 2.19 (3H, s), 2.04 (3H, s), 1.28 (3H, d, J = 7.0 Hz). FABMS m/z: 314, 312 $[M + H]^+$. Anal. calcd. for $C_{15}H_{18}ClNO_4$: C 57.79, H 5.78, N 4.49; found: C 57.70, H 5.84, N 4.41.

Acknowledgements

The authors thank the Council of Scientific and Industrial Research (CSIR) and University Grants Commission (UGC), New Delhi, for financial assistance.

References

1. (*a*) J.R. Casimir, C. Turetta, L. Ettouati, and J. Paris, Tetrahedron Lett. **36**, 4797 (1995); (*b*) A.G. Godfrey, D.A. Brooks, L.A. Hay, M. Peters, J.R. McCarthy, and D. Mitchell. J. Org. Chem. **68**, 2623 (2003).
2. (*a*) J. Barluenga, A.L. Viado, E. Aguilar, S. Fustero, and B. Olano. J. Org. Chem. **58**, 5972 (1993); (*b*) D. Enders, M. Moser, and M. Laufer. Synthesis, 2040 (2003).
3. K. Kobinata, M. Uramoto, M. Nishii, H. Kusakabe, G. Nakamura, and K. Isono. Agric. Biol. Chem. **44**, 1709 (1980).
4. (*a*) B. Bhatia, M.M. Reddy, and J. Iqbal. J. Chem. Soc. Chem. Commun. 713 (1994); (*b*) M. Mukhopadhyay, B. Bhatia, and J. Iqbal. Tetrahedron Lett. **38**, 1083 (1997); (*c*) I.N. Rao, E.N. Prabhakaran, S.K. Das, and J. Iqbal. J. Org. Chem. **68**, 4079 (2003); (*d*) D. Bahulayan, S.K. Das, and J. Iqbal. J. Org. Chem. **68**, 5735 (2003).
5. (*a*) G. Pandey, R.P. Singh, A. Garg, and V.K Singh. Tetrahedron Lett. **46**, 2137 (2005); (*b*) R. Ghosh, S. Maiti, and A. Chakraborty. Synlett, 115 (2005); (*c*) R. Ghosh, S. Maiti, A. Chakraborty, S. Chakraborty, and A.K. Mukherjee. Tetrahedron, **62**, 4059 (2006); (*d*) B. Das, K.R. Reddy, R. Ramu, P. Thirupathi, and B. Ravikanth. Synlett, 1756 (2006).
6. (*a*) B. Das, K. Laxminarayana, B. Ravikanth, and B. Ramarao. Tetrahedron Lett. **47**, 9103 (2006); (*b*) B. Das, K. Venkateswarlu, M. Krishnaiah, and H. Holla. Tetrahedron Lett. **47**, 8693 (2006); (*c*). B. Das, R. Ramu, M.R. Reddy, and G. Mahender. Synthesis, 250 (2005); (*d*) B. Das, H. Holla, K. Venkateswarlu, A. Majhi. Tetrahedron Lett. **46**, 8895 (2005).

© 2007 NRC Canada

Synthesis and characterization of intramolecularly coordinated alanes with new sterically demanding trisyl-based ligands

Clinton L. Lund, Olimpiu Stanga, J. Wilson Quail, and Jens Müller

Abstract: Five new intramolecularly coordinated aluminum species, whose molecular structures have been elucidated in solution by NMR spectroscopy and in the solid state by single crystal X-ray analysis, are described. All species are equipped with a trisyl-based ligand with a pyridyl donor group [Pytsi stands for -C(SiMe$_3$)$_2$SiMe$_2$(2-C$_5$H$_4$N)]. While the compound (Pytsi)AlMeCl was accessible either from Li(THF)(Pytsi) and MeAlCl$_2$ or from (Pytsi)AlCl$_2$ and LiMe, the *tert*-butyl derivative (Pytsi)Al*t*BuCl could only be obtained from Li(THF)(Pytsi) and *t*BuAlCl$_2$. Attempted synthesis of (Pytsi)Al*t*BuCl from (Pytsi)AlCl$_2$ and Li*t*Bu or from (Pytsi)AlCl$_2$ and *t*BuMgCl failed. Three other compounds (**3**–**5**) were synthesized and can be described as derivatives of (Pytsi)AlMe$_2$ with additional groups in the ortho position of the pyridyl group. Compound **3** carried a Me group in the ortho position, while compounds **4** and **5** were equipped with Ph and 2,6-diisopropylphenyl moieties, respectively.

Key words: aluminum, trisyl ligands, methyl alanes.

Résumé : On décrit cinq nouvelles espèces d'aluminium à coordination intramoléculaire dont on a déterminé les structures en solution par RMN et à l'état solide par diffraction des rayons X. Toutes les espèces incluent un ligand à base d'un groupe trisyle comportant un groupe donneur pyridyle [Pytsi = -C(SiMe$_3$)$_2$SiMe$_2$(2-C$_5$H$_4$N)]. Alors que le composé (Pytsi)AlMeCl est accessible à partir du Li(THF)(Pytsi) et du MeAlCl$_2$ ou du (Pytsi)AlCl$_2$ et du LiMe, le dérivé *tert*-butylé n'est disponible que par la réaction du Li(THF)(Pytsi) et du *t*-BuAlCl$_2$. On n'a pas pu réaliser la synthèse du (Pytsi)Al*t*-BuCl à partir du (Pytsi)AlCl$_2$ et du Li*t*-Bu ou par réaction du (Pytsi)AlCl$_2$ et du *t*-BuMgCl. On a réalisé la synthèse de trois autres composés (**3**–**5**) qui peuvent être décrits comme des dérivés du (Pytsi)AlMe qui comportent des groupes additionnels en position ortho du groupe pyridyle. Le composé **3** porte un groupe méthyle en position ortho alors que les composés **4** et **5** portent respectivement des groupes phényle et 2,3-diisopropylphényle.

Mots-clés : aluminium, ligands trisyles, méthylalanes.

[Traduit par la Rédaction]

Introduction

Group 13 element compounds EX$_3$ are textbook examples of Lewis acids. Usually, the electronic needs of the heavier group members Al, Ga, and In cannot be satisfied intramolecularly through π bonds and, hence, oligomers are found throughout their structural chemistry. By employing ligands that are equipped with donor groups, Lewis acid–base adducts are formed intramolecularly and oligomers can be prevented. One of the most commonly used intramolecularly coordinating ligands is the "one-armed" phenyl ligand (Fig. 1, Ar′). For example, employing the Ar′ ligand gives access to well-defined, monomeric aluminium halides (1). Azides of the heavier group 13 elements are usually oligomers (2), however, the application of Ar′ and Pr′ (Fig. 1), respectively, allowed for the preparation of the first monomeric aluminum azides (3–5). The use of the Pr′ ligand usually results in species of higher volatility than those equipped with Ar′ ligands and respective Al, Ga, and In azides had been employed as single-source precursors for chemical vapor deposition (CVD) of nitrides (2, 6).

The tris(trimethylsilyl)methyl ligand, commonly referred to as the trisyl ligand, is a widely used sterically demanding ligand with electron-donor properties provided by three silyl groups (β silyl effect) (7). Eaborn and co-workers (8) developed a series of trisyl-based ligands in which one of the methyl groups is formally replaced by a substituent with σ donor abilities. Modifications included ligands of the type -C(SiMe$_3$)$_2$(SiMe$_2$R) with R being MeO (7), Ph$_2$P (7), CH$_2$PPh$_2$ (7), Me$_2$N (Fig. 1, Me$_2$Ntsi) (7), and 2-C$_5$H$_4$N (Fig. 1, Pytsi). Recently, we had shown that Pytsi and Me$_2$Ntsi (Fig. 1) stabilized alanes and gallanes can be used for the preparation of [1]metallacyclophanes such as [1]ferrocenophanes (9–11), [1]chromarenophanes (11), and [1]vanadarenophanes (11). The type of intramolecularly co-

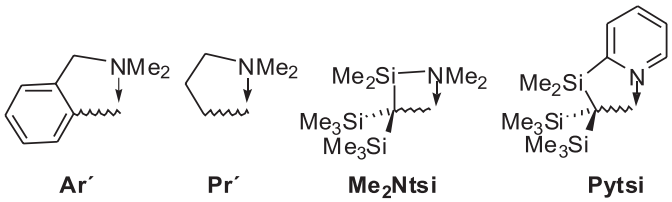
Received 21 March 2007. Accepted 4 May 20007. Published on the NRC Research Press Web site at canjchem.nrc.ca on 11 July 2007.

C.L. Lund, O. Stanga[1], and J. Müller.[2] Department of Chemistry, University of Saskatchewan, 110 Science Place, Saskatoon, SK S7N 5C9, Canada.
J.W. Quail. Saskatchewan Structural Sciences Centre, University of Saskatchewan, 110 Science Place, Saskatoon, SK S7N 5C9, Canada.

[1]Present address: Akzo Nobel Polymer Chemicals bv, Stationsstraat 77, 3811 MH Amersfoort, The Netherlands.
[2]Corresponding author (email: jens.mueller@usask.ca).

 doi:10.1139/V07-063 © 2007 NRC Canada

Fig. 1. Intramolecularly coordinating ligands.



ordinating ligand is of crucial importance for getting strained organometallic species: a change from the sterically demanding Pytsi and MeNtsi, respectively, to the slimmer Ar′ ligand (Fig. 1) resulted in unstrained [1.1]ferrocenophanes (12, 13).

Because of the bulkiness and the β silyl effect, trisyl-type ligands might be ideal to stabilize low-coordinated Lewis-acid metal complexes. Starting with this working hypothesis, we set out to explore cationic aluminum species equipped with the Pytsi ligand. Cationic low-coordinated aluminum compounds are potential catalysts or initiators for olefin polymerizations (14–19). Recently, we described the synthesis of a saltlike compound [(Pytsi)AlMe][$MeB(C_6F_5)_3$] (19). This species was obtained by a methyl abstraction reaction from (Pytsi)$AlMe_2$ with the perfluorinated borane $B(C_6F_5)_3$, however, this compound slowly decomposed in toluene at ambient temperature. We planned to increase its stability by shielding the Al centre more effectively with sterically demanding groups, either attached to aluminum directly or attached to the backbone of the chelating ligand.

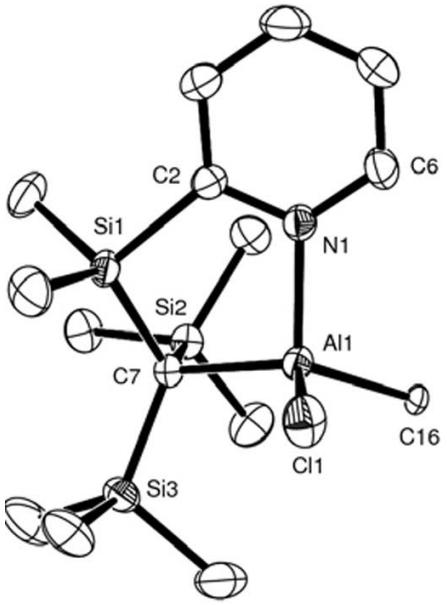
In this paper, we describe the synthesis and characterization of new alanes equipped with trisyl-based intramolecularly coordinating ligands.

Results and discussion

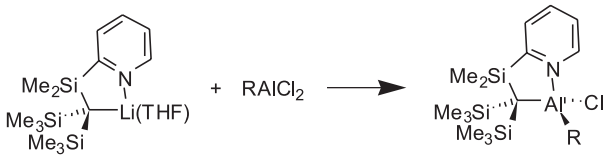
Cations are commonly synthesized through halide abstraction reactions from suitable halogen containing precursors. Often, silver salts of weakly coordinating anions are employed (20). Against this background, we intended to prepare precursor species of the type (Pytsi)AlClR. First, we prepared (Pytsi)AlClMe (**1**) from Li(THF)(Pytsi) and $MeAlCl_2$ (eq. [1]). A similar route had been previously employed for Ar′AlClMe (1). Compound **1** can also be synthesized by a substitution reaction from (Pytsi)$AlCl_2$ and LiMe. Both routes to species **1** work comparably well (see Experimental section). In accordance with the known synthesis of Ar′AlCl*t*Bu (1), we attempted the synthesis of (Pytsi)AlCl*t*Bu (**2**) from (Pytsi)$AlCl_2$ (21) and Li*t*Bu in Et_2O or with *t*BuMgCl in Et_2O. Both reactions proved unsuccessful. In the case of Li*t*Bu, a very rich ^1H NMR spectrum hinted at complex reactions and showed that the target compound **2** had not been formed. In the case of the Grignard reagent, no reaction happened at all. However, the target molecule **2** was accessible in a moderate isolated yield of 54% by reacting Li(THF)(Pytsi) with *t*Bu$AlCl_2$ (eq. [1]).

Compounds **1** and **2** are asymmetric species as revealed by NMR spectroscopy. For example, for both compounds the $SiMe_2$ and the two $SiMe_3$ moieties give rise to two singlets, each in ^1H NMR as well as in $^{13}C\{^1H\}$ NMR spectra. Compounds **1** and **2**, respectively, crystallize in the monoclinic space group $P\ 2_1/c$. Figs. 2 and 3 depict their molecular structures, and Table 1 shows their structural parameters.

Fig. 2. Molecular structure of **1** with thermal ellipsoids at the 50% probability level. H atoms are omitted for clarity. Selected bond lengths (Å) and angles (°): Al1–N1 = 1.962(2), Al–Cl1 = 2.1813(9), Al1–C7 = 2.008(2), Al1–C16 = 1.978(2), N1–Al1–Cl1 = 98.98(7), N1–Al1–C16 = 109.28(9), N1–Al1-C7 = 98.34(9), C7–Al1–Cl1 = 113.42(7), C7–Al1–C16 = 125.37(10), Cl1–Al1–C16 = 107.68(7).



[1]



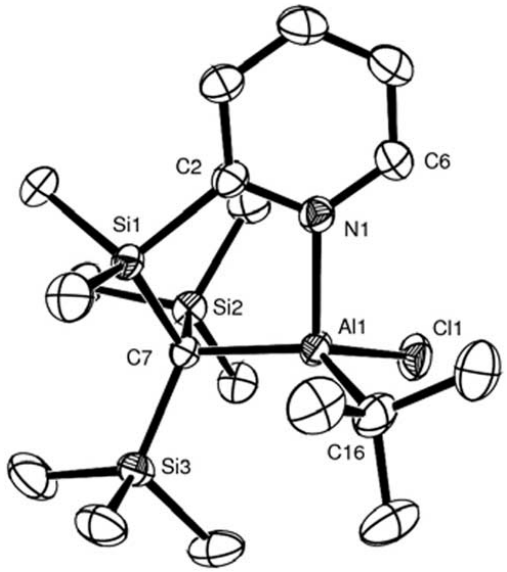
R = Me (**1**)
*t*Bu (**2**)

Expectedly, the molecular structures are very similar. The Al atoms are four-fold coordinated by two C atoms, one Cl atom, and one N atom with nearly identical bond lengths (Figs. 2 and 3). The major difference between **1** and **2** is due to a different folding of the five-membered ring. For both compounds, the five-membered ring adopts an envelope conformation with C7 being the tip of the envelope. However, because of the stereogenic Al centre two different folding directions of C7 are possible. While in compound **1** C7 is folded away from the Cl atom, in compound **2** C7 is folded towards the Cl atom. The conformer found for **2** places the *t*Bu group in an axial position and allows a maximum distance towards the two neighbouring $SiMe_3$ groups, indicating that steric factors play the major role in finding a particular isomer.

As mentioned in the introduction, we attempted to shield the Al centre more effectively with sterically demanding groups. Therefore, we synthesized derivatives of (Pytsi)$AlMe_2$ (19, 21) in which the ortho position of the pyridine ring carries a Me (**3**), Ph (**4**), or Dipp group (**5**) (Dipp = 2,6-diisopropylphenyl). As illustrated in Scheme 1,

© 2007 NRC Canada

Fig. 3. Molecular structure of **2** with thermal ellipsoids at the 50% probability level. H atoms are omitted for clarity. Selected bond lengths (Å) and angles (°): Al1–N1 = 1.9765(14), Al–Cl1 = 2.1787(6), Al1–C7 = 2.0340(15), Al1–C16 = 2.0077(18), N1–Al1–Cl1 = 103.92(4), N1–Al1–C16 = 103.92(7), N1–Al1–C7 = 96.43(6), C7–Al1–Cl1 = 115.31(5), C7–Al1–C16 = 127.95(7), Cl1–Al1–C16 = 105.48(6).



compounds **3**–**5** have been prepared similarly as the known (Pytsi)$AlMe_2$ (19, 21). Of course, the methyl group in the 6 position of the pyridine ring is too small to sterically protect the aluminum atom. However, compound **3** was the first test case to determine if a small change to the pyridyl group has an influence on the synthesis of the respective dimethyl alane.

The preparation of **3**–**5** differs mainly in the way we synthesized the ortho-lithiated pyridine (Scheme 1). In all cases the ortho-lithiated pyridine derivative was prepared in situ. However, for compounds **3** and **4**, we generated it from a respective bromopyridine and LiBu. For compound **5**, we first used a nickel catalyst cross-coupling of a Grignard reagent (22, 23) followed by a selective deprotonation in the ortho position, a method that had been previously applied to other phenylpyridine derivatives (24) (Scheme 2).

The dimethylalanes **3**–**5** were isolated in moderate to good yields of 51% to 86% as crystalline colorless solids. All three compounds reveal patterns in their ^1H and ^{13}C NMR spectra that are consistent with time-averaged C_s symmetrical species. The most noteworthy feature in all the spectra is the appearance of the two isopropyl groups of the Dipp ligand of compound **5**. They show two doublets for the Me groups (δ 0.82 and 1.34) and one multiplet for the CH group (δ 2.40) in the ^1H NMR spectrum and two singlets for the Me groups and one singlet for the CH groups in the $^{13}C\{^1H\}$ NMR spectrum. This shows that both isopropyl groups are chemically equivalent, but the methyl groups are nonequivalent for each isopropyl group. As already mentioned above, the NMR spectra can be rationalized by assuming compound **5** is a time-averaged C_s symmetrical species; e.g., the $SiMe_3$ and the $AlMe_2$ moieties each give rise to one singlet. All facts combined prove that the Dipp ligand is oriented perpendicular to the pyridiyl moiety and is not rotating rapidly on the NMR time scale.

The molecular structures of compounds **3**–**5** were determined with single crystal X-ray analysis (Figs. 4–6 and Table 1). All species exhibit an envelope conformation of the five-membered heterocycle with C7 being the tip of the envelope. In all compounds, aluminum is tetrahedrally surrounded by a set of three C atoms and one N atom with very similar bond lengths and angles (Figs. 4–6). For example, the Al–N bond lengths are found in the narrow range between 2.0393(16) and 2.0587(15) Å, even though these donor bonds are expected to be the most flexible bonds in the molecules. A similar but slightly shorter Al–N bond was found for (Pytsi)$AlEt_2$ (Al-N = 2.0034(18) Å) (19). Reliable bond lengths and angles are not available for the closely related dimethylalane (Pytsi)$AlMe_2$, because it is disordered about a plane of symmetry that bisects the molecule along the Si_2C plane in the $C(SiMe_3)_2$ group (19). In both halves of the molecule the Me_2Al- and the Me_2Si moieties on one side and the two halves of the pyridine ring on the other side have similar sizes and shapes, which makes the disordering understandable (19). Both halves of (Pytsi)$AlMe_2$ can be made dissimilar by either changing the alkyl groups at aluminum or adding a substituent to the pyridyl moiety; neither (Pytsi)$AlEt_2$ (19) nor compound **3** are disordered in the crystal lattice.

Conclusion

We synthesized five new intramolecularly coordinated aluminum species, whose molecular structures have been elucidated in solution by NMR spectroscopy and in the solid state by single crystal X-ray analysis. All species **1**–**5** are equipped with a trisyl-based ligand with a pyridyl donor group (Fig. 1, Pytsi). While the monomethyl compound (Pytsi)AlMeCl (**1**) is accessible either from Li(THF)(Pytsi) and $MeAlCl_2$ (eq. [1]) or from (Pytsi)$AlCl_2$ and LiMe, the *tert*-butyl derivative (Pytsi)Al*t*BuCl (**2**) could only be obtained from Li(THF)(Pytsi) and *t*Bu$AlCl_2$ (eq. [1]). The latter result is in contrast to the synthesis of the related species Ar′Al*t*BuCl (Fig. 1, Ar′), which was synthesized from Ar′$AlCl_2$ and Li*t*Bu (1). The different substitution behavior of (Pytsi)$AlCl_2$ and Ar′$AlCl_2$ towards Li*t*Bu can be interpreted as being due to the higher steric demand of Pytsi compared with Ar′ (Fig. 1).

Compounds **3**–**5** can all be described as derivatives of (Pytsi)$AlMe_2$ with additional groups in the ortho position of the pyridyl group. From the molecular structures of the Ph-substituted compound **4** (Fig. 5) and the 2,6-diisopropylphenyl derivative **5** (Fig. 6) one gets the impression that the aromatic group in the ortho position of the pyridyl ring might serve as a shield to help protect the Al atom and, consequently, we intend to employ these species as precursors for cationic aluminum compounds.

Experimental

General procedures

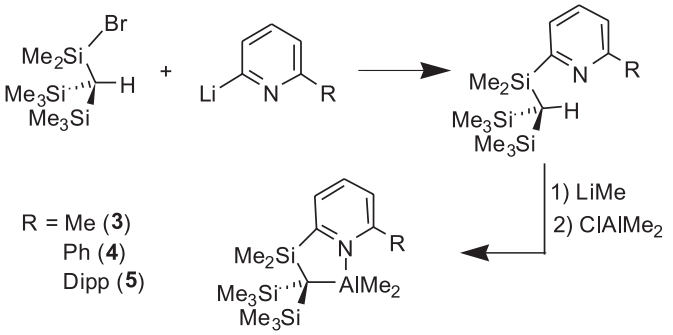
All manipulations were carried out using standard Schlenk techniques. Solvents were dried using a Braun Solvent Purification System and stored under nitrogen over 4 Å

© 2007 NRC Canada

Table 1. Crystal and structural refinement data for compounds **1–5**.

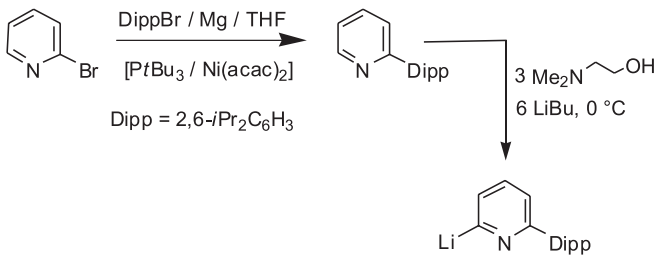
Compound	**1**	**2**	**3**	**4**	**5**
Empirical formula	$C_{15}H_{31}AlClNSi_3$	$C_{18}H_{37}AlClNSi_3$	$C_{17}H_{36}AlNSi_3$	$C_{22}H_{38}AlNSi_3$	$C_{28}H_{50}AlNSi_3$
Formula weight	372.11	414.19	365.72	427.78	511.94
Wavelength (Å)	0.710 73	0.710 73	0.710 73	0.710 73	0.710 73
Crystal system	Monoclinic	Monoclinic	Monoclinic	Monoclinic	Triclinic
Space group	$P\ 2_1/c$	$P\ 2_1/c$	$P\ 2_1/c$	$P\ 2_1/c$	$P\bar{1}$
Z	4	4	4	4	2
a (Å)	9.046 30(10)	9.0520(2)	17.1251(3)	13.8716(4)	8.5860(2)
b (Å)	9.315 60(10)	16.7560(4)	9.1309(2)	9.7136(3)	12.0067(4)
c (Å)	25.5316(4)	18.2311(3)	15.5683(3)	18.6390(8)	16.6488(6)
α (°)	90	90	90	90	71.2665(15)
β (°)	94.8075(5)	118.6060(10)	111.7240(10)	90.394(2)	80.8750(18)
γ (°)	90	90	90	90	75.5988(17)
Volume (Å^3)	2144.02(5)	2427.67(9)	2261.48(8)	2511.42(15)	1568.51(9)
D_{calcd} (mg/m^3)	1.153	1.133	1.074	1.131	1.084
Temperature (K)	173(2)	173(2)	173(2)	173(2)	173(2)
Abs coeff. (mm^{-1})	0.382	0.344	0.247	0.232	0.195
θ range (°)	2.26 to 27.55	2.55 to 30.00	2.57 to 28.20	2.78 to 27.48	2.74 to 27.48
Reflections collected	17 648	13 876	42 198	10 258	13 539
Independent reflections	4921 [R(int) = 0.0631]	7071 [R(int) = 0.0298]	5491 [R(int) = 0.0799]	5732 [R(int) = 0.0457]	7178 [R(int) = 0.0238]
Absorption correction	Semi-empirical from equivalents	Semi-empirical from equivalents	Semi-empirical from equivalents	Semi-empirical from equivalents	Semi-empirical from equivalents
Ref. method	Full-matrix least-squares on F^2	Full-matrix least-squares on F^2	Full-matrix least squares on F^2	Full-matrix least squares on F^2	Full-matrix least-squares on F^2
Data, restraints, parameters	4921, 0, 199	7071, 0, 228	5491, 0, 242	5732, 0, 254	7178, 0, 312
Goodness-of-fit on F^2	1.043	1.058	1.042	1.024	1.001
Final R indices [$I > 2\sigma(I)$]	R_1 = 0.0454, wR_2 = 0.1053	R_1 = 0.0418, wR_2 = 0.0956	R_1 = 0.0442, wR_2 = 0.0943	R_1 = 0.0477, wR_2 = 0.1027	R_1 = 0.0448, wR_2 = 0.1096
R indices (all data)	R_1 = 0.0749, wR_2 = 0.1242	$R1$ = 0.0634, wR_2 = 0.1050	$R1$ = 0.0637, wR_2 = 0.1020	$R1$ = 0.0843, wR_2 = 0.1205	$R1$ = 0.0604, wR_2 = 0.1191
Largest diff. peak and hole (e, Å^{-3})	0.635, –0.462	0.417, –0.275	0.369, –0.291	0.310, –0.355	0.503, –0.384

Scheme 1. Synthesis of compounds **3–5**.



molecular sieves. All solvents for NMR spectroscopy were degassed prior to use and stored under nitrogen over 4 Å molecular sieves. $HC(SiMe_3)_2(SiMe_2Br)$ (8), Li(THF)(Pytsi) [Pytsi = $C(SiMe_2)(SiMe_3)_2C_5H_4N$)] (8), (Pytsi)$AlCl_2$ (21), 2-bromo-6-methylpyridine (25), 2-bromo-6-phenylpyridine (24), and bromo-2,6-diisopropylbenzene (26) were synthesized as described in the literature. *t*Bu$AlCl_2$ was synthesized similar to *t*Bu$AlBr_2$ (27). 2-(2,6-Diisopropylphenyl)pyridine was synthesized similar to 2-(2,6-diisopropylphenyl)-6-methylpyridine (22). Me_2AlCl and $MeAlCl_2$ were purchased from Sigma-Aldrich and used as received. LiMe (Sigma-

Scheme 2. Synthesis of the lithiopyridine for **5**.



Aldrich) and LiBu (VWR) were titrated with 2,6-di-*tert*-butylphenol–fluorene before usage (28). Silica Gel 60 (particle size 0.040–0.063 mm) was purchased from EMD Chemicals. ^{1}H, ^{13}C, and ^{27}Al NMR spectra were recorded on a Bruker 500 MHz Avance at 25 °C in C_6D_6 unless noted differently. ^{1}H chemical shifts were referenced to the residual protons of the deuterated solvents (C_6D_6 at δ 7.15; $CDCl_3$ at δ 7.26), ^{13}C chemical shifts were referenced to the deuterated solvent (C_6D_6 signal at δ 128.0; $CDCl_3$ signal at δ 77.0), and ^{27}Al NMR spectra were referenced to [Al(acac)$_3$] dissolved in C_6D_6. Mass spectra were measured on a VG 70SE (m/z > 10% are listed for signals of the most abundant

© 2007 NRC Canada

Fig. 4. Molecular structure of **3** with thermal ellipsoids at the 50% probability level. H atoms are omitted for clarity. Selected bond lengths (Å) and angles (°): Al1–N1 = 2.0393(16), Al1–C7 = 2.0416(17), Al1–C16 = 1.976(2), Al1–C17 = 1.980(2), C16–Al1–C17 = 110.30(10), C7–Al1–C16 = 116.94(8), C7–Al1–C17 = 118.49(8), N1–Al1–C16 = 112.74(8), N1–Al1–C17 = 99.94(8), N1–Al1–C7 = 96.01(6).

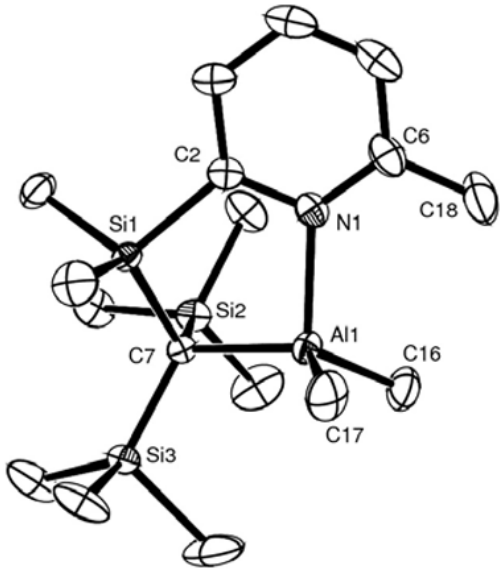
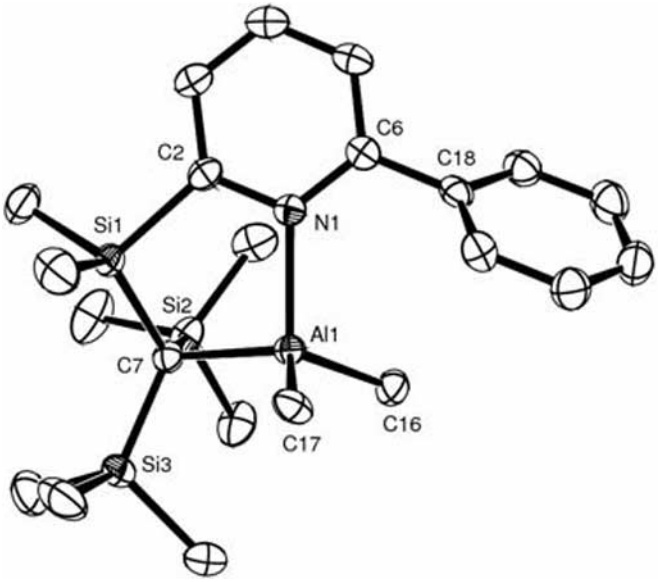
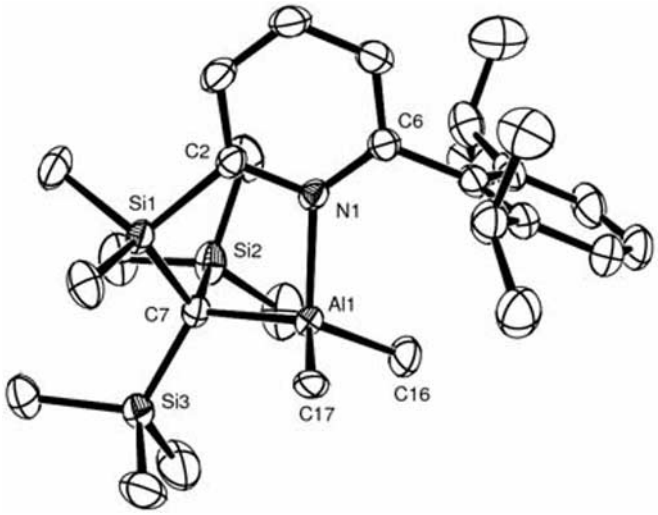


Fig. 5. Molecular structure of **4** with thermal ellipsoids at the 50% probability level. H atoms are omitted for clarity. Selected bond lengths (Å) and angles (°): Al1–N1 = 2.0537(19), Al1–C7 = 2.054(2), Al1–C16 = 1.983(2), Al1–C17 = 2.002(2), C16–Al1–C17 = 111.50(11), C7–Al1–C16 = 117.62(9), C7–Al1–C17 = 113.27(9), N1–Al1–C16 = 110.26(9), N1–Al1–C17 = 106.83(9), N1–Al1–C7 = 95.71(8).



ions). Elemental analyses were performed on a PerkinElmer 2400 CHN Elemental Analyzer using V_2O_5 to promote complete combustion.

Fig. 6. Molecular structure of **5** with thermal ellipsoids at the 50% probability level. H atoms are omitted for clarity. Selected bond lengths (Å) and angles (°): Al1–N1 = 2.0587(15), Al1–C7 = 2.0595(17), Al1–C16 = 1.965(2), Al1–C17 = 2.0390(19), C16–Al1–C17 = 109.25(9), C7–Al1–C16 = 118.47(9), C7–Al1–C17 = 117.17(7), N1–Al1–C16 = 114.48(8), N1–Al1–C17 = 99.89(7), N1–Al1–C7 = 95.32(6).



Chloro{[dimethyl(pyrid-2-yl)silyl]bis(trimethylsilyl)methyl}methylaluminum (1)

Route 1: A solution of $MeAlCl_2$ (4.2 mL, 1.0 mol/L in hexane, 4.2 mmol) was added to a solution of Li(THF)(Pytsi) (1.577 g, 4.220 mmol) in hexane at –78 °C. After stirring for 20 min, the reaction mixture was allowed to warm to ambient temperature and stirred for 16 h. The solid was filtered off, extracted with Et_2O (3 × 10 mL), the combined organic extracts were reduced in volume to 10 mL, and crystallization at ca. –30 °C resulted in colorless crystals of **1** (1.395 g, 88%).

Route 2: LiMe (4.4 mL, 0.93 mol/L, 4.1 mmol) was added to (Pytsi)$AlCl_2$ (1.625 g, 4.140 mmol) in Et_2O (50 mL) at –78 °C. The slurry was stirred for 30 min at –78 °C, allowed to warm to ambient temperature, and stirred for 16 h. The white solid was filtered off and the product extracted with Et_2O (3 × 10 mL). The combined extracts were reduced in volume to 20 mL and kept at –30 °C to give colorless crystals of **1** (1.257 g, 82%).

^{1}H NMR (500 MHz) δ: 0.01 (s, 3H, AlMe), 0.15 (s, 9H, $SiMe_3$), 0.33 (s, 3H, $SiMe_2$), 0.44 (s, 9H, $SiMe_3$), 0.49 (s, 3H, $SiMe_2$), 6.31 (pst, 1H, H-5), 6.77 (pst, 1H, H-4), 6.88 (d, 1H, H-3), 8.06 (d, 1H, H-6). ^{13}C NMR (125.8 MHz) δ: 3.2 (SiMe), 4.2 (SiMe), 5.8 ($SiMe_3$), 6.2 ($SiMe_3$), 124.4 (C-5), 129.0 (C-3), 138.9 (C-4), 145.8 (C-6), 173.1 (*ipso*-C). ^{27}Al NMR (130.3 MHz) δ: 157 ($w_{1/2}$ = 2000 Hz). MS (70 eV) *m/z* (%): 356 (61) [$M^+ - CH_3$], 295 (13) [$MH^+ - Al - Cl - CH_3$], 280 (37) [$MH^+ - Al - Cl - 2CH_3$], 264 (100) [$C_{12}H_{22}NSi_3^+$], 73 (11) [$SiMe_3^+$]. Anal. calcd. for $C_{15}H_{31}AlClNSi_3$ (372.104): C 54.64, H 9.74, N 3.98; found: C 54.67, H 10.11, N 3.75.

***tert*-Butylchloro{[dimethyl(pyrid-2-yl)silyl]bis(trimethylsilyl)methyl}aluminum (2)**

Li(THF)(Pytsi) (2.200 g, 5.887 mmol) was dissolved in

© 2007 NRC Canada

hexane (40 mL) and cooled to –78 °C. A solution of *t*BuAlCl$_2$ (0.913 g, 5.890 mmol) in hexane (30 mL) was filled into a dropping funnel and added to the cooled solution of Li(THF)(Pytsi) over a period of 5 min. This resulted in the formation of a slightly yellow solution with a white precipitate. After stirring the reaction mixture for 30 min, the cooling bath was removed and the solution was stirred for another 2 h. The formed dark brown solution was filtered and all volatiles were removed in high vacuum. Sublimation at 150 °C in high vacuum produced a yellow-orange solid. The sublimed solid was dissolved in hexane (35 mL) and crystallization at ca. –30 °C resulted in pale yellow crystals of **2** (1.322 g, 54%). ^{1}H NMR (500 MHz) δ: 0.30 (s, 9H, SiMe$_3$), 0.36 (s, 9H, SiMe$_3$), 0.40 (s, 3H, SiMe$_2$), 0.44 (s, 3H, SiMe$_2$), 1.25 (s, 9H, C(CH$_3$)$_3$), 6.37 (pst, 1H, H-5), 6.81 (d, 1H, H-3), 6.92 (pst, 1H, H-4), 8.45 (d, 1H, H-6). ^{13}C{^{1}H} NMR (125.8 MHz) δ: 1.15 [br, C(SiMe$_3$)$_2$], 4.41 (SiMe$_2$), 4.61 (SiMe$_2$), 6.94 (SiMe$_3$), 7.10 (SiMe$_3$), 17.1 [C(CH$_3$)$_3$], 31.2 [C(CH$_3$)$_3$], 124.1 (C-5), 129.5 (C-3), 139.1 (C-4), 146.9 (C-6), 172.61 (*ipso*-C). ^{27}Al (130.3 MHz) δ: 150 ($w_{1/2}$ = 4300 Hz). MS (70 eV) *m*/*z* (%): 398 (6) [M$^+$ – CH$_3$], 356 (72) [M$^+$ – *t*Bu], 336 (16) [C$_{15}$H$_{31}$AlNSi$_3^+$], 264 (100) [C$_{12}$H$_{22}$NSi$_3^+$]. Anal. calcd. for C$_{18}$H$_{37}$AlClNSi$_3$ (414.184): C 52.20, H 9.00, N 3.38; found: C 52.88, H 8.96, N 3.18.

[Dimethyl(6-methylpyrid-2-yl)silyl]bis(trimethylsilyl)methane

LiBu (15.0 mL, 2.7 mol/L in hexane, 40.5 mmol) was added dropwise to a solution of 2-bromo-6-methylpyridine (8.796 g, 37.12 mmol) in Et$_2$O (30 mL) at –78 °C to give a dark red solution. The solution was stirred for 20 min before being added to a cold solution (–78 °C) of HC(SiMe$_3$)$_2$(SiMe$_2$Br) (11.751 g, 39.505 mmol) in Et$_2$O (100 mL), which gave a brown solution. The cold bath was removed and the reaction mixture was stirred for 16 h. After the solvent was removed in vacuum, a dark-brown oil remained, which was transferred onto a dry silica column. The product was eluted with ethyl acetate and a subsequent flask-to-flask condensation under inert gas atmosphere yielded a light yellow oil [bp 82–84 °C, 10^{-3} mbar (1 bar = 100 kPa), 8.920 g, 77%]. ^{1}H NMR (500 MHz) δ: 0.10 (s, 18H, SiMe$_3$), 0.46 (s, 6H, SiMe$_2$), 2.43 (s, 3H, o-Me), 6.64 (d, 1H, H-5), 7.06 (pst, 1H, H-4), 7.11 (d, 1H, H-3). ^{13}C NMR (125.8 MHz) δ: 1.5 (SiMe$_2$), 3.4 (SiMe$_3$), 24.8 (CH$_3$), 121.8 (C-5), 125.7 (C-3), 134.0 (C-4), 158.0 (*ipso*-C-6), 169.2 (*ipso*-C-2).

{[Dimethyl(6-methylpyrid-2-yl)silyl]bis(trimethylsilyl)methyl}dimethylaluminum (3)

LiMe (6.6 mL, 1.0 mol/L in THF–cumene, 6.6 mmol) was added dropwise to [dimethyl(6-methylpyrid-2-yl)silyl]bis(trimethylsilyl)methane (1.866 g, 6.026 mmol) in THF (30 mL) at ambient temperature to give a red solution. Gas was given off immediately. After 1 h of stirring, the solvent was removed in vacuum to leave an oily residue behind, which was dissolved in hexane (20 mL). The solution was cooled to –78 °C and Me$_2$AlCl (6.6 mL, 1.0 mol/L in hexane, 6.6 mmol) was added dropwise over 10 min. The cold bath was removed and the reaction mixture stirred for 16 h at ambient temperature. Removal of all volatiles from the solution in high vacuum gave a white solid, which was extracted with hexane (3 × 15 mL). The combined organic fractions were separated from the solid remains by filtration. The organic phase was concentrated to 20 mL and kept at –30 °C to give light yellow crystalline plates of **3** (1.132 g, 51%). ^{1}H NMR (500 MHz) δ: –0.17 (s, 6H, AlMe$_2$), 0.29 (s, 18H, SiMe$_3$), 0.42 (s, 6H, SiMe$_2$), 2.26 (s, 3H, Me), 6.22 (d, 1H, H-5), 6.78 (pst, 1H, H-4), 6.88 (d, 1H, H-3). ^{13}C NMR (125.8 MHz) δ: –1.9 (AlMe$_2$), 4.5 (SiMe$_2$), 6.4 (SiMe$_3$), 23.0 (CH$_3$), 125.3 (C-5), 126.3 (C-3), 138.1 (C-4), 157.4 (*ipso*-C-6), 173.8 (*ipso*-C-2). ^{27}Al NMR (130.3 MHz) δ: 174.3 ($w_{1/2}$ = 2750 Hz). MS (70 eV) *m*/*z* (%): 350 (100) [M$^+$ – CH$_3$], 278 (37) [M$^+$ – Al – 4CH$_3$], 262 (15) [C$_{12}$H$_{20}$NSi$_3^+$]. Anal. calcd. for C$_{17}$H$_{36}$AlNSi$_3$ (365.713): C 55.83, H 9.92, N 3.83; found: C 55.16, H 10.57, N 3.63.

[Dimethyl(6-phenylpyrid-2-yl)silyl]bis(trimethylsilyl)methane

LiBu (2.2 mL, 2.8 mol/L in hexane, 6.2 mmol) was added dropwise to a stirring solution of 2-bromo-6-phenylpyridine (1.321 g, 5.643 mmol) in Et$_2$O (15 mL) at –78 °C. The resulting red solution was stirred for 20 min before a cold solution (–78 °C) of CH(Me$_3$Si)$_2$(SiMe$_2$Br) (1.712g, 5.755 mmol) in Et$_2$O (15 mL) was added. The cold bath was removed and the reaction mixture stirred overnight. The red-brown liquid phase was separated from the solids by filtration. Removal of all volatiles at ambient temperature in high vacuum from the liquid phase gave a red oil. The product was collected as a golden yellow oil by a flask-to-flask condensation (bp 145–150 °C, 10^{-3} mbar, 1.339 g, 64%). The fraction collected at 65–95 °C was discarded. ^{1}H NMR (500 MHz) δ: 0.11 (s, 18H, SiMe$_3$), 0.17 (s, 1H, CH), 0.52 (s, 6H, SiMe$_2$), 7.17(m, 2H, Py H-4, Ph H-5), 7.21 (d, 1H, Py, H-3 or H-5), 7.27 (t, 2H, Ph, H-3, H-4), 7.30 (d, 1H, Py, H-5 or H-3) 8.17 (d, 2H, Ph, H-2, H-6). ^{13}C NMR (125.8 MHz) δ: 1.4 (SiMe$_2$), 1.7 (CH), 3.3 (SiMe$_3$), 119.1 (Py, C-3 or C-5), 127.1 (Py, C-3 or C-5), 127.2 (Ph, C-2, C-6), 128.8 (Ph, C-3, C-5), 129.0 (Py, C-4), 134.6 (Ph, C-4), 140.3 (Ph, *ipso*-C), 156.7 (Py, *ipso*-C-6), 169.8 (Py, *ipso*-C-2).

{[Dimethyl(6-phenylpyrid-2-yl)silyl]bis(trimethylsilyl)methyl}dimethylaluminum (4)

LiMe (4.0 mL, 1.0 mol/L in THF–cumene, 4.0 mmol) was added dropwise to a stirring solution of [dimethyl(6-phenylpyrid-2-yl)silyl]bis(trimethylsilyl)methane (1.339 g, 3.602 mmol) in THF (30 mL) at ambient temperature resulting in the formation of gas and a red solution. After 1 h of stirring at ambient temperature, the red solution was cooled to 0 °C and Me$_2$AlCl (5.0 mL, 1.0 mol/L in hexane, 5.0 mmol) was added dropwise to give a clear brown solution that was stirred for 16 h at ambient temperature. Removal of all volatiles in high vacuum at ambient temperature yielded a light brown solid. The solid was extracted with ether (3 × 20 mL), and the solvent was removed to give a light brown solid, which was subsequently sublimed (140 °C, 10^{-3} mbar) to give a white solid (1.171 g, 76%). Crystallization from diethyl ether at –30 °C yielded colorless crystals of **4** (1.095 g, 71%). ^{1}H NMR (500 MHz) δ: –0.58 (s, 6H, AlMe$_2$), 0.26 (s, 18H, SiMe$_3$), 0.51 (s, 6H, SiMe$_2$), 6.62 (d, 1H, H-5), 6.90 (pst, 1H, H-4), 7.05 (d, 1H, H-3), 7.10–7.11 (m, 3H, Ph), 7.20–7.22 (m, 2H, Ph). ^{13}C NMR

© 2007 NRC Canada

(125.8 MHz) δ: –2.3 ($AlMe_2$, br), 4.7 ($SiMe_2$), 6.3 ($SiMe_3$), 125.7, (C-5), 127.7 (C-3), 128.4 (Ph), 129.1 (Ph) 129.7 (Ph, *ipso*-C), 138.0 (C-4), 160.3 (*ipso*-C-6), 174.8 (*ipso*-C-2). ^{27}Al NMR (130.3 MHz) δ: 182 ($w_{1/2}$ = 4500 Hz). MS (70 eV) *m/z* (%): 412 (100) [$M^+ - CH_3$], 340 (24) [$M^+ - Al - 4CH_3$], 217 (16). Anal. calcd. for $C_{22}H_{38}AlNSi_3$ (422.804): C 61.77, H 8.95, N 3.27; found: C 61.09, H 8.88, N 3.18.

2-(2,6-Diisopropylphenyl)pyridine

Bromo-2,6-diisopropylbenzene (6.115 g, 25.36 mmol) in THF (10 mL) was added to Mg turnings (0.740 g, 30.45 mmol) in THF (20 mL) in a flask equipped with reflux condenser. Heat was used to start the Grignard reaction. The mixture was refluxed for 24 h before being added to a mixture of P*t*Bu_3 (0.1472 g, 0.7376 mmol), $Ni(acac)_2$ (0.1684 g, 0.6555 mmol), and 2-bromopyridine (3.388 g, 21.44 mmol) in THF (100 mL) cooled to 0 °C, which resulted in a brown solution. The solution refluxed for 24 h and was subsequently poured into dilute HCl (200 mL; 0 °C). The organic phase was discarded and the aqueous phase was extracted with Et_2O (2 × 50 mL) and the Et_2O phase was discarded. K_2CO_3 was added to the aqueous phase until the evolution of CO_2 ceased during which the color of the solution went from brown to yellow. The aqueous phase was extracted with dichloromethane (3 × 150 mL) followed by the removal of volatiles in high vacuum from the combined organic phases to leave a brown oil behind. Flask-to-flask condensation under high vacuum at 120–125 °C yielded a viscous yellow oil (2.467 g, 48%). ^{1}H NMR (500 MHz, $CDCl_3$) δ: 1.06 (6 H, d, $HC(CH_3)CH_3$), 1.10 (d, 6 H, $HC(CH_3)CH_3$), 2.46 (m, 2H, $HC(CH_3)CH_3$), 7.19 (d, 1H, Ph), 7.25 (m, 2H, Py H-4, H-3), 7.33 (pst, 1H, Ph), 7.71 (pst, 1H, Py H-5), 8.70 (d, 1H, Py H-6). ^{13}C NMR (125.8 MHz, $CDCl_3$) δ: 23.9 ($HC(CH_3)CH_3$), 24.2 ($HC(CH_3)CH_3$), 30.3 (2 $HC(CH_3)CH_3$), 121.5 (Py, C-3 or C-4), 122.6 (Ph, C-3, C-5), 124.9 (Py, C-4 or C-3), 128.5 (Ph, C-4), 135.6 (Py, C-5), 138.6 (Ph, C-1), 146.4 (Py, *ipso*-C-6), 149.3 (Ph, C-2, C-6), 160.0 (Py, *ipso*-C-2).

{[6-(2,6-Diisopropylphenyl)pyrid-2yl]dimethylsilyl}bis(trimethylsilyl)methane

LiBu (22.0 mL, 2.87 mol/L in hexane, 63.1 mmol) was added dropwise to a solution of 2-dimethylaminoethanol (2.802 g, 31.43 mmol) in hexane (30 mL) cooled to 0 °C, and the resulting yellow solution was stirred for an additional 30 min. 2-(2,6-Diisopropylphenyl)pyridine (2.499 g, 10.44 mmol) in hexane (30 mL) was added and the color of the reaction mixture changed immediately to red. After 1 h of stirring at 0 °C, the mixture was cooled to –78 °C and $HC(SiMe_3)_2(SiMe_2Br)$ (11.355 g, 38.17 mmol) in hexane (30 mL) was added dropwise. The mixture was kept at –78 °C for 1 h before the cold bath was removed and stirring was continued for 16 h at ambient temperature. Deionized H_2O (100 mL) was added, and the aqueous phase was extracted with Et_2O (3 × 100 mL). The combined extracts were dried over $MgSO_4$, filtered, and the volatiles from the organic phase were subsequently removed in vacuum. Flask-to-flask condensation of the orange oil at high vacuum gave two fractions. The fraction at 85–125 °C was discarded. The product was received as an oil (bp 135–140 °C, 10^{-3} mbar, 3.214 g, 68%), which turned into a light yellow solid upon cooling to ambient temperature. ^{1}H NMR (500 MHz) δ: 0.10 (s, 18H, $SiMe_3$), 0.21 (s, 1H, CH), 0.47 (s, 6H, $SiMe_2$), 1.12 (d, 6H, $CH(CH_3)CH_3$), 1.23 (d, 6H, $CH(CH_3)CH_3$), 2.72 (m, 2H, $CH(CH_3)CH_3$, 6.92 (d, 1H, Py, H-3 or H-5), 7.12 (pst, 1H, Ph, H-4), 7.20 (m, 3H, Ph H-3, H-5, Py H-3 or H-5), 7.30 (pst, 1H, Py H-4). ^{13}C NMR (125.8 MHz) δ: 0.8 (CH), 1.3 ($SiMe_2$), 3.3 (2 $SiMe_3$), 23.9 ($HC(CH_3)CH_3$), 25.0 ($HC(CH_3)CH_3$), 30.7 ($HC(CH_3)CH_3$), 122.9 (Ph, 3-C, 5-C), 123.6 (Py, C-3 or C-5), 126.2 (Py, C-5 or C-3), 128.8 (Ph, C-4), 133.6 (Py, C-4), 140.2 (Ph, *ipso*-C-1), 146.7 (Ph, *ipso*-C-2, *ipso*-C-6), 160.3 (Py, *ipso*-C-6), 169.9 (Py, *ipso*-C-2).

{{[6-(2,6-Diisopropylphenyl)pyrid-2yl]dimethylsilyl}bis(trimethylsilyl)methyl}dimethylaluminum (5)

LiMe (2.6 mL, 1.0 mol/L in THF–cumene) was added dropwise to {[6-(2,6-diisopropylphenyl)pyrid-2yl]dimethylsilyl}bis(trimethylsilyl)methane (0.984, 2.158 mmol) in THF (20 mL). The solution was stirred for 4 h during which the solution turned brown and gas evolved. Subsequently, the flask was cooled to –78 °C and Me_2AlCl (2.6 mL, 1.0 mol/L in hexanes) was added dropwise. The cold bath was removed and the reaction mixture stirred overnight. After removal of volatiles from the clear yellow solution a yellow solid remained, which was extracted with ether (10 mL), the extract was filtered and volatiles were removed in vacuum from the filtrate to give a light yellow solid. The solid was dissolved in warm hexane (10 mL) and kept at –30 °C to give colorless crystals of **5** (0.953 g, 86%). ^{1}H NMR (500 MHz) δ: –0.62 (s, 6H, $AlMe_2$), 0.31 (s, 18H, $SiMe_3$), 0.50 (s, 6H, $SiMe_2$), 0.82 (d, 6H, $HC(CH_3)CH_3$), 1.34 (d, 6H, $HC(CH_3)CH_3$), 2.40 (m, 2H, $HC(CH_3)CH_3$), 6.91 (t, 1H, Py, H-4,), 6.96 (d, 1H, Py, H-3 or H-5), 7.08 (d, H, Py, H-5 or H-3), 7.11 (d, 2H, Ph, H-3, H-5), 7.26 (pst, 1H, Ph, H-4). ^{13}C NMR (125.8 MHz) δ: –2.5 ($AlMe_2$), 4.7 ($SiMe_2$), 6.5 (2 $SiMe_3$), 22.2 ($HC(CH_3)CH_3$), 26.4 ($HC(CH_3)CH_3$), 30.9 ($HC(CH_3)CH_3$), 123.1 (Ph, C-3, C-5), 127.8 (Py, C-3 or C-5), 128.3 (Py, C-5 or C-3), 130.7 (Ph, C-4), 134.9 (Ph, C-1), 136.7 (Py, C-4), 147.3 (Ph, C-2, C-6), 159.5 (Py, C-6), 175.5 (Py, C-2). ^{27}Al NMR δ: 179 ($w_{1/2}$ = 4300 Hz). MS (70 eV) *m/z* (%): 496 (10) [$M^+ - CH_3$], 455 (100) [$MH^+ - Al - 2CH_3$], 440 (35) [$MH^+ - Al - 3CH_3$], 73 (13) [$SiMe_3^+$]. Anal. calcd. for $C_{28}H_{50}AlNSi_3$ (511.94): C 65.69, H 9.84, N 2.74; found: C64.89, H 9.42, N 2.38.

X-ray structural analysis for 1–5.[3]

Data was collected at –100 °C on a Nonius Kappa CCD diffractometer, using the COLLECT program (29). Cell refinement and data reductions used the programs DENZO and SCALEPACK (30). The program SIR97 (31) was used to solve the structure and SHELXL97 (32) was used to refine the structure. ORTEP-3 for Windows (33) was used for

[3] Supplementary data for this article are available on the journal Web site (canjchem.nrc.ca) or may be purchased from the Depository of Unpublished Data, Document Delivery, CISTI, National Research Council Canada, Ottawa, ON K1A 0R6, Canada. DUD 5183. For more information on obtaining material refer to cisti-icist.nrc-cnrc.gc.ca/irm/unpub_e.shtml. CCDC 641212 and 641216 contain the crystallographic data for this manuscript. These data can be obtained, free of charge, via www.ccdc.cam.ac.uk/conts/retrieving.html (Or from the Cambridge Crystallographic Data Centre, 12 Union Road, Cambridge CB2 1EZ, UK; fax +44 1223 336033; or deposit@ccdc.cam.ac.uk).

© 2007 NRC Canada

molecular graphics and PLATON (34) was used to prepare material for publication. H atoms were placed in calculated positions with U_{iso} constrained to be 1.5 times U_{eq} of the carrier atom for all methyl H atoms and 1.2 times U_{iso} for all other H atoms.

The three methyl groups on Si3 (compound **3**) are disordered and were modeled with occupancies of 0.72 and 0.28 for the two components. Only one position for the methyl groups is shown in Fig. 4.

Acknowledgments

We thank the Natural Sciences and Engineering Research Council of Canada (JM, NSERC Discovery Grant), the Department of Chemistry, and the University of Saskatchewan for their generous support. We thank the Canada Foundation for Innovation (CFI) and the government of Saskatchewan for funding of the X-ray and NMR facilities in the Saskatchewan Structural Sciences Centre (SSSC).

References

1. J. Müller and U. Englert. Chem. Ber. **128**, 493 (1995).
2. J. Müller. Coord. Chem. Rev. **235**, 105 (2002).
3. R.A. Fischer, A. Miehr, H. Sussek, H. Pritzkow, E. Herdtweck, J. Müller, O. Ambacher, and T. Metzger. Chem. Commun. (Cambridge), 2685 (1996).
4. J. Müller, R.A. Fischer, H. Sussek, P. Pilgram, R. Wang, H. Pritzkow, and E. Herdtweck. Organometallics, **17**, 161 (1998).
5. J. Müller and R. Boese. J. Mol. Struct. **520**, 215 (2000).
6. A. Devi, R. Schmid, J. Müller, and R.A. Fischer. *In* Topics in organometallic chemistry. Vol. 9. Edited by R.A. Fischer. Springer, Heidelberg, Germany. 2005. p 49.
7. C. Eaborn and J.D. Smith. J. Chem. Soc. Dalton Trans. 1541 (2001).
8. S.S. Al-Juaid, C. Eaborn, P.B. Hitchcock, M.S. Hill, and J.D. Smith. Organometallics, **19**, 3224 (2000).
9. J.A. Schachner, C.L. Lund, J.W. Quail, and J. Müller. Organometallics, **24**, 785 (2005).
10. J.A. Schachner, C.L. Lund, J.W. Quail, and J. Müller. Organometallics, **24**, 4483 (2005).
11. C.L. Lund, J.A. Schachner, J.W. Quail, and J. Müller. Organometallics, **25**, 5817 (2006).
12. H. Braunschweig, C. Burschka, G.K.B. Clentsmith, T. Kupfer, and K. Radacki. Inorg. Chem. **44**, 4906 (2005).
13. J.A. Schachner, G.A. Orlowski, J.W. Quail, H.-B. Kraatz, and J. Müller. Inorg. Chem. **45**, 454 (2006).
14. M. Bochmann and D.M. Dawson. Angew. Chem. Int. Ed. **35**, 2226 (1996).
15. M.P. Coles and R.F. Jordan. J. Am. Chem. Soc. **119**, 8125 (1997).
16. M. Bruce, V.C. Gibson, C. Redshaw, A. Solan, J.P. White, and D. J. Williams. Chem. Commun. (Cambridge), 2523 (1998).
17. D.A. Atwood. Coord. Chem. Rev. **176**, 407 (1998).
18. K.C. Kim, C.A. Reed, G.S. Long, and A. Sen. J. Am. Chem. Soc. **124**, 7662 (2002).
19. O. Stanga, C.L. Lund, H. Liang, J.W. Quail, and J. Müller. Organometallics, **24**, 6120 (2005).
20. I. Krossing and I. Raabe. Angew. Chem. Int. Ed. **43**, 2066 (2004).
21. J. Howson, C. Eaborn, P.B. Hitchcock, M.S. Hill, and J.D. Smith. J. Organomet. Chem. **690**, 69 (2005).
22. F. Speiser, P. Braunstein, and L. Saussine. Organometallics, **23**, 2633 (2004).
23. V.P.W. Böhm, T. Weskamp, C.W.K. Gstöttmayr, and W.A. Herrmann. Angew. Chem. Int. Ed. **39**, 1602 (2000).
24. P. Gros and Y. Fort. J. Org. Chem. **68**, 2028 (2003).
25. U.S. Schubert, C. Eschbaumer, and M. Heller. Org. Lett. **2**, 3373 (2000).
26. R.R. Schrock, M. Wesolek, A.H. Liu, K.C. Wallace, and J.C. Dewan. Inorg. Chem. **27**, 2050 (1988).
27. W. Uhl and J.E.O. Schnepf. Z. Anorg. Allg. Chem. **595**, 225 (1991).
28. C.A. Brown. Synthesis, **427** (1974).
29. Nonius. Nonius BV, Delft, The Netherlands. 1998.
30. Z. Otwinowski and W. Minor. *In* Macromolecular crystallography. Vol. 276. Part A. Edited by C.W. Carter and R.M. Sweet. Academic Press, London, UK. 1997. p 307.
31. A. Altomare, M.C. Burla, M. Camalli, G. Cascarano, C. Giacovazzo, A. Guagliardi, A.G.G. Moliterni, G. Polidori, and R. Spagna. J. Appl. Crystallogr. **32**, 115 (1999).
32. G.M. Sheldrick. University of Göttingen, Göttingen, Germany. 1997.
33. L.J. Farrugia. J. Appl. Crystallogr. **30**, 565 (1997).
34. A.L. Spek. University of Utrecht, Utrecht, The Netherlands. 2001.

© 2007 NRC Canada

A new microwave-assisted synthetic approach to novel pyrimido[4,5-*d*]pyrimidines

Mazaahir Kidwai, Priya, Shweta Rastogi, and Kavita Singhal

Abstract: An environmentally benign approach for the synthesis of novel 7-substituted 5-aryl-1*H*-pyrimido[4,5-*d*]pyrimidine-2,4-diones, using mineral supports for their catalytic role and as energy transfer media, is described. The methodology eliminates the usage of solvent during the reaction. The rate enhancement and high yield is attributed to the coupling of solvent-free conditions with microwaves. Further, the role of various supports is studied during the reaction and it is concluded that a MW-assisted basic alumina catalysed reaction is the best in terms of catalysis as well as reaction time and yield.

Key words: microwave (MW) irradiation, SBT, pyrimido[4,5-*d*]pyrimidines, alumina, environmentally benign.

Résumé : On a mis au point une approche environnementalement bénigne à la synthèse de nouvelles 5-aryl-1*H*-pyrimido[4,5-d]pyrimidine-2,4-diones substituées en position 7 dans laquelle on utilise un support minéral joue aussi un rôle catalytique par le biais d'un milieu à transfert d'énergie. La méthodologie élimine l'utilisation d'un solvant pour la réaction. L'augmentation de la vitesse de réaction ainsi que son rendement élevé sont attribués au couplage de conditions sans solvant et de microondes. De plus, on a étudié le rôle de divers supports dans les réactions et on en conclut que la meilleures est la réaction catalysée par l'alumine basique, assistée par les microondes en termes de catalyse, de temps de réaction et de rendement.

Mots-clés : irradiation par microonde (MO), pyrimido[4,5-*d*]pyrimidines, alumine, environnementalement bénigne.

[Traduit par la Rédaction]

Introduction

An important class of annulated uracils with biological significance, as they have a connection with purine-pteridine systems (1), is associated with pyrimido[4,5-*d*]pyrimidines. Various derivatives of this scaffold have remained in high demand as they can be used for different biological activities in bronchodilators (2), vasodilators (3) and in antiallergic (2, 4), antihypertensive (5), and anticancer agents. Recently, pyrimido[4,5-*d*]pyrimidine analogues of folic acid have been found to provide antitumour activity (6). Further, its derivatives also display a wider range of pharmacological inhibitory properties; e.g., 5-phosphoribosyl-1-pyrophosphate synthetase (7), dihydrofolate reductase (8), and the tyrosine kinase domain of epidermal growth factor receptor (9) have been fully demonstrated. The derivatives of the barbituric acid constitute an important class of hypnotic, sedative, and anaesthetic compounds (10). Arylidene barbituric acids or chalcones of barbituric acid are useful intermediates in the synthesis of derivatives (11), heterocyclic compounds(12) and behave as electrically neutral Lewis acids (13). Recently, they were studied as nonlinear optical materials (14).

Received 30 November 2006. Accepted 10 June 2007. Published on the NRC Research Press Web site at canjchem.nrc.ca on 11 July 2007.

M. Kidwai,[1] Priya, S. Rastogi, and K. Singhal. Green Chemistry Research Laboratory, Department of Chemistry, University of Delhi, Delhi 110007, India.

[1]Corresponding author (e-mail: kidwai.chemistry@gmail.com).

Motivated by the aforementioned findings and in continuation of our ongoing studies (15) on versatile heterocycles of pharmacological and biological importance, it was thought worthwhile to design the synthesis of novel derivatives that can be envisaged as the new lead compounds.

In the present communication, aiming at the preparation of 7-substituted 5-aryl-2-yl-1*H*-pyrimido[4,5-*d*]pyrimidine-2,4-diones, we investigated, for the first time, a three-component condensation of heterocyclic chalcones of barbituric acid **1** with SBT and heterocyclic amines **3** as base. Moreover, the versatility of different solid supports was investigated under microwaves for this synthetic approach. The methodology utilizes facile and rapid one-pot condensation of barbituric acid, aromatic aldehydes, SBT (S-benzyl thiouronium chloride), and heterocyclic amines. The development of MW-assisted solid phase synthesis (16) has added a new dimension to organic synthesis, because high-yielding protocols offer the benefits of greater selectivity and experimental ease. A paradigm shift away from using solvent in organic functional group transformations, leading to environmentally benign solvent-free synthesis of novel pyrimidopyrimidines under MWs, is explored.

Results and discussion

A different approach to the synthesis of novel pyrimido[4,5-*d*]pyrimidine derivatives **4a**–**4l** with high pharmaceutical activity is sought. Thus, we contemplate an environmentally benign strategy in which the requisite moiety may be constructed by using the functionality in the chalcones of barbituric acid **1**, SBT, and heterocyclic base **3**.

 doi:10.1139/V07-065 © 2007 NRC Canada

Until now, the literature reports of the synthesis of such a skeleton involve phenyl isocyanate (17), 4-chlorophenyl diazonium chloride (18), and $POCl_3$ (19). But these procedures are tedious and require hazardous chemicals with catalyst loading that contaminated the final product. To obtain the desired product with high purity and optimized timing successfully, we describe herein a MW-assisted one-pot solid support synthesis. Different experimental trials were carried out to standardize the reaction under microwave irradiation. To the chalcones of barbituric acid **1** were added SBT and heterocyclic secondary amine **3** (morpholine–piperidine–pyrrolidine) adsorbed over basic alumina and irradiated under MW (Scheme 1, method C).

The products **4a**–**4l** were obtained in 70%–85% yield within 4–5 min of irradiation (Table 1.) Choosing an optimal solvent for adsorption is the primary requirement for successful synthesis. Thus, various reagents were tried, such as acetone, ethanol, acetic acid, and DMF. On the basis of solubility, the best solvent system was found to be a 1:1 mixture of ethanol and THF (tetrahydrofuran). The initial attempt to synthesize the products **4a**–**4l** consisted of two steps: (Step 1) the S-benzyl derivative **2** was prepared by irradiating chalcones **1** and SBT loaded over basic alumina under MW, followed by an elution and evaporation; (Step 2) this intermediate **2** obtained was then again adsorbed with secondary amines **3** over basic alumina and irradiated under MW to afford products **4a**–**4l**. The yield obtained by this two-step procedure was quite low, 40%–50%. The isolation of the intermediate **2** and its re-employment as a reactant or substrate for target moiety synthesis led to yield losses, as compared with one-pot MW-assisted solid support synthesis (method C). On other hand, a neat reaction with the same substrates was attempted but found to be unsuccessful. The α,β-unsaturated ketones **1**, possessing high melting points (>220 °C), could not be melted even after prolonged irradiation by microwaves; being in salt form, SBT could not be reacted because of the absence of solvent, thus charring occurred after a few minutes.

The role of base was also explored, and the reactions were attempted over different solid supports using basic alumina and neutral alumina under MW irradiation. It was observed that the amount of base required in the case of basic alumina was just ~0.1 mL, instead of 0.5–0.8 mL as was required in neutral alumina with comparable yields (Table 1). It was also found that the increase in the amount of solid support enhanced the product yields to a certain extent, but that further increase in the amount of solid support resulted in the reduction of product yields (Fig. 1).

As a solid support plays the role of energy transfer medium, increases in its amount results in more energy transfer to the reactant molecules, leading to a significant improvement in reactivity. Increase in solid support provides more active reagent sites and enhanced collision rates between reactants because of either the reduced dimensionality on solid reaction sites or a boost in their local concentration, due to trapping in the interstitial spaces of microporous solids. Further increase in the solid support decreases the concentration of reactants per unit surface area of solid support and thus reduces the collision frequency leading to a decrease in the yields (Fig. 1).

Furthermore, the characteristics of surface adsorption on the solid support result in the binding of the product to the solid support and, hence, in the incomplete elution of the product. After a certain point, the adsorption of product on a solid support dominates over its role as energy transfer medium, which results in incomplete elution and leads to lower yields. The compounds **4a**–**4l** were also synthesized classically by refluxing α,β-unsaturated ketones **1** with SBT and heterocyclic secondary amines **3** in ethanol and THF for 12–18 h (method A). The yield is poor compared with the one-pot synthesis (Table 1). One-pot synthesis over solid support not only reduces the reaction time of 12–18 h in method A to few minutes in methods B and C, but also act as a catalyst and energy transfer medium. In the mechanistic approach, SBT, being highly reactive in its salt form, attacks at the carbonyl moiety next to the arylidene part of the chalcone of barbituric acid **1** and leads to the formation of an imine system. As soon as this imine system forms, it facilitates the displacement of electron density towards the NH group of SBT, and the NH again attacks at the arylidene carbon. After cyclisation, the S-benzyl derivative **2** forms as an intermediate. The S-benzyl group, as substituent at position C_2, was found to perform an important role in the formation of the nucleus of pyrimido[4,5-*d*]pyrimidines. This is attributed to the requirement of basic conditions for nucleophilic displacement, since the secondary amine has a lone pair to attack, so that displacement takes place and S-benzyl is a good leaving group in furnishing an unstable intermediate, which finally results in our target moiety **4**. Had primary amine been the attacking species, the reaction would have been sluggish because of the lower basicity in the latter case. The structure of the novel compounds **4a**–**4l** was established on the basis of spectroscopic data and elemental analysis. The synthesized derivatives **4a**–**4l** are low melting crystalline light-yellow substances. Their IR spectra contain characteristic absorption bands of stretching vibrations of the C=N group at 1590–1620 cm^{-1}. The stretching vibrations of alkyl groups and alicyclic C–H bonds give rise to absorption in the region of 2960–2870 cm^{-1}, and those of the C–H bonds in the aromatic ring appear at 3060–3030 cm^{-1}. In the IR spectra of compounds **4a, 4d, 4g**, and **4j** the bands of the fragment C–O–C are observed in the region 1080–1200 cm^{-1}. Also, the ^1H NMR spectrum showed the absence of the singlet of the arylidene proton of chalcone at δ: 8.2–8.5. Apart from IR and ^1H NMR, CHN analysis and mass spectra also supported the proposed product. The chemical shifts of the ^{13}C NMR spectra are in accordance with the desired synthesized product.

Conclusion

The proposed methodology provides an facile, practical, convenient, and environmentally benign one-pot synthesis of bioactive pyrimido[4,5-*d*]pyrimidines. The MW-assisted procedure is modified in such a way that one-pot condensation is the best methodology in view of the fact that the excess of base used in conventional neutral alumina procedure is eliminated by using basic alumina. However, basic alumina further catalysed the reaction, in comparison with neutral alumina, further reducing the reaction time with comparable

© 2007 NRC Canada

Scheme 1.

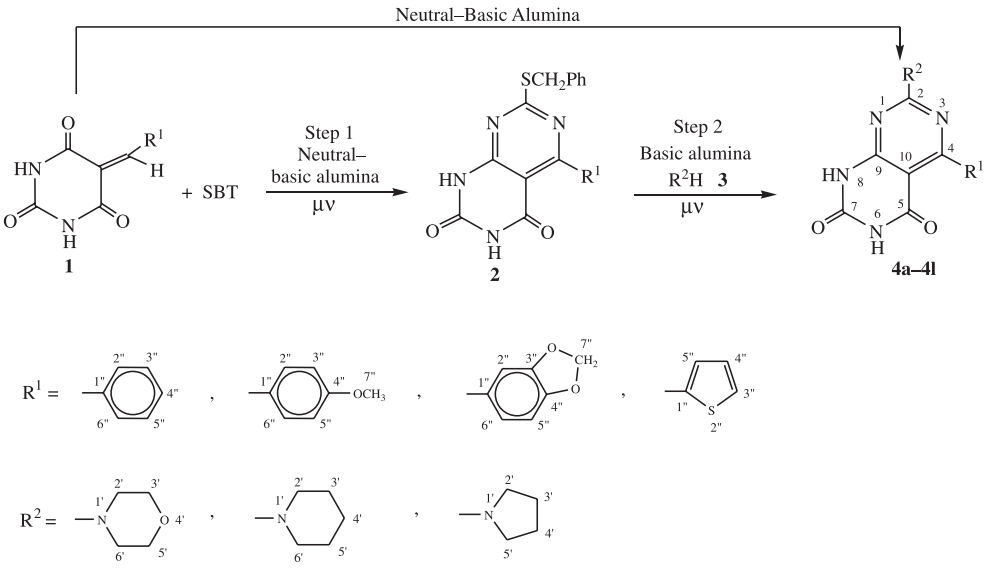
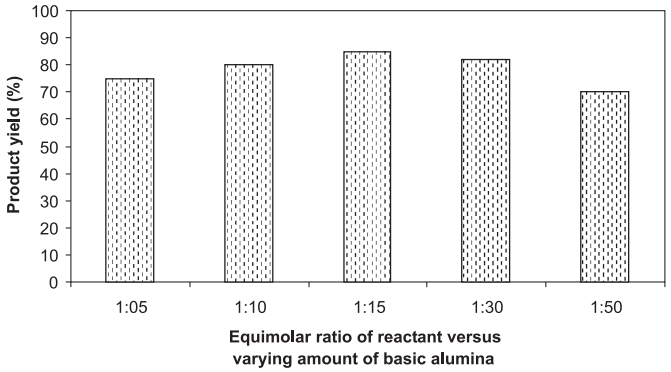


Table 1. Comparison of reaction time and yields of compounds **4a**–**4l**.

Entry No.	R^1	R^2	Method A time and yield[a] (hr, %)	MW irradiations: Method B time and yield[a] (min, %)	MW irradiations: Method C time and yield[a] (min, %)
4a	Phenyl	Morpholinyl	14, 45	3.0, 90	4.5, 85
4b	Phenyl	Piperidinyl	12, 40	2.5, 88	3.5, 82
4c	Phenyl	Pyrrolidinyl	11, 40	2.5, 85	3.0, 78
4d	4-OCH_3-C_6H_4	Morpholinyl	16, 50	4.0, 93	5.5, 85
4e	4-OCH_3-C_6H_4	Piperidinyl	14, 45	3.5, 85	5.0, 80
4f	4-OCH_3-C_6H_4	Pyrrolidinyl	14, 40	3.5, 80	4.5, 72
4g	Piperonyl	Morpholinyl	13, 50	3.0, 85	4.5, 80
4h	Piperonyl	Piperidinyl	12, 55	3.0, 90	4.0, 85
4i	Piperonyl	Pyrrolidinyl	12, 40	3.5, 80	5.0, 72
4j	Thienyl	Morpholinyl	15, 55	4.0, 85	5.5, 75
4k	Thienyl	Piperidinyl	15, 60	4.5, 88	5.5, 80
4l	Thienyl	Pyrrolidinyl	13, 45	2.5, 83	3.5, 78

[a]Isolated and unoptimized yields.

Fig. 1. Study of the effect of different amounts of basic alumina on yields.



yields, and thus emerged as the best solid support. These results also illustrate that the heterocyclic chalcones of barbituric acid **1** are useful substrates for the generation of an array of fused nitrogen heterocycles with two points of diversity, and SBT derivatives as good intermediates for nucleophilic displacement.

Experimental

MW irradiation was carried out on a Kenstar-OM 9925E MW Oven (800 W, 2450 MHz). The temperature of the reaction mixture was measured with a noncontact mini-Gun type IR thermometer (model 8868). IR spectra were recorded on a PerkinElmer FTIR-1710 spectrometer using KBr pellets. ^{1}H NMR spectra were obtained on a Bruker Avance Spectrospin 300 (300 MHz) using TMS as internal standard and chemical shifts are in δ. Elemental analysis was performed on a Heraeus CHN-Rapid analyzer. The melting points (uncorrected) were determined on a Thomas Hoover Melting point apparatus. ^{13}C NMR spectra were recorded at 300 MHz on a Bruker Topsin Spectrometer (300 MHz). Mass spectra were recorded on a TOF MS. All reactants

© 2007 NRC Canada

were purchased from Sigma-Aldrich and Lanchester and used without further purification. Solvents used in reaction are double distilled using vaccum distillation.

General procedure for the synthesis of 7-substituted 5-aryl-1*H*-pyrimido-[4,5-*d*]pyrimidine-2,4-diones (4a–4l)

Method A — Conventional solution phase

A mixture of chalcone **1** (0.01 mol), SBT (0.25 mol), morpholine–piperidine–pyrrolidine (0.76 mol) in 1:1 mixture of THF and ethanol (20 mL) refluxed for 10–18 h. The progress of the reaction was monitored by TLC (Merk TLC: mean particle size 10–12 μm; particle size distribution 5–20 μm; layer thickness 250 μm; plate height 30 μm). The product was evaporated in vacuo to leave an oily residue, which was triturated with methanol and recrystallized from an ethanol and benzene mixture.

Method B — One pot solid support MW (neutral alumina)

To the solution of chalcone **1** (0.02 mol), SBT (0.25 mol), and morpholine–piperidine–pyrrolidine (0.76 mol, 7–8 mL) in a mixture of THF and ethanol, neutral alumina (15 g) (Aldrich: 150 mesh; 58 Å; surface area 55 m^2/g; pH of aqueous suspension is 7.0 ± 0.5) was added with stirring and air dried. It was then placed in an alumina bath used as heat sink and subjected to MW intermittently. The progress of the reaction was monitored by TLC examination. Upon completion of the reaction, the product was eluted from dichloromethane. Recovering the solvent under reduced pressure gave the required products (**4a**–**4l**), which were then recrystallized from an ethanol and benzene mixture.

Method C — One pot solid support MW (basic alumina)

To the solution of chalcone **1** (0.02 mol), SBT (0.25 mol), and morpholine–piperidine–pyrrolidine (0.04 mol) basic alumina (Aldrich: 150 mesh; 58 Å; surface area 55 m^2/g; pH of aqueous suspension 8.5 ± 0.5) was added with stirring and air dried. The rest of the experimental procedure is same as described earlier in method B.

7-Morpholin-4-yl-5-phenyl-1*H*-pyrimido[4,5-*d*]pyrimidine-2,4-dione (4a)

The recrystalization solvent was an ethanol and benzene mixture (1:1 *v*/*v*). Melting point 80–82 °C. IR (KBr, C=N, cm^{-1}) ν_{max}: 1595. ^{1}H NMR (300 MHz, $CDCl_3$) δ: 2.81 (t, 4H, CH_2OCH_2), 3.62 (t, 4H, CH_2NCH_2), 6.51–8.01 (m, 5H, Ar-H), 11.06 (s, 1H, NH), 11.10 (s, 1H, NH). ^{13}C NMR (300 MHz, $CDCl_3$) δ: C2 170.33, C4 170.31, C5 170.72, C7 162.72, C9 177.91, $C_1$0 112.52, C2 55.91, $C_{3'}$ 76.52, $C_{5'}$ 76.53, $C_{6'}$ 55.91, $C_{1''}$ 136.91, $C_{2''}$ 127.20, $C_{3''}$ 129.08, $C_{4''}$ 128.51, $C_{5''}$ 129.08, $C_{6''}$ 127.20. HRMS: M^+ 325.5. Anal. calcd. for $C_{16}H_{15}N_5O_3$: C 59.07, H 4.61, N 21.50; found: C 59.06, H 4.62, N 21.51.

5-Phenyl-7-piperidin-1-yl-1*H*-pyrimido[4,5-*d*]pyrimidine-2,4-dione (4b)

Melting point 67–69 °C. IR (KBr, C=N, cm^{-1}) ν_{max}: 1594. ^{1}H NMR (300 MHz, $CDCl_3$) δ: 1.61 (m, 6H, 3′,4′,5′-CH_2), 2.92 (t, 4H, CH_2NCH_2), 7.31–8.22 (m, 5H, Ar-H), 10.90 (s, 1H, NH), 10.99 (s, 1H, NH). HRMS: M^+ 323.0. Anal. calcd. for $C_{17}H_{17}N_5O_2$: C 63.15, H 5.26, N 21.60; found: C 63.17, H 5.25, N 21.63.

5-Phenyl-7-pyrrolidin-1-yl-1*H*-pyrimido[4,5-*d*]pyrimidine-2,4-dione (4c)

Melting point 60–62 °C. IR (KBr, C=N, cm^{-1}) ν_{max}: 1610. ^{1}H NMR (300 MHz, $CDCl_3$) δ: 2.01 (t, 4H, 3′,4′-CH_2), 3.71 (t, 4H, CH_2NCH_2), 6.92–8.21 (m, 5H, Ar-H), 10.92 (s, 1H, NH), 11.06 (s, 1H, NH). HRMS: M^+ 309.72. Anal. calcd. for $C_{16}H_{15}N_5O_2$: C 62.13, H 4.85, N 22.65; found: C 62.14, H 4.86, N 22.63.

5-(4-Methoxy-phenyl)-7-morpholin-4-yl-1*H*-pyrimido[4,5-*d*]pyrimidine-2,4-dione (4d)

Melting point 75–77 °C. IR (KBr, C=N, cm^{-1}) ν_{max}: 1598. ^{1}H NMR (300 MHz, $CDCl_3$) δ: 2.91 (t, 4H, CH_2OCH_2), 3.63 (t, 4H, CH_2NCH_2), 3.94 (s, 3H, OCH_3), 7.04 (2H, d, *J* = 7.3 Hz, Ar-H), 7.49 (2H, d, *J* = 7.2 Hz, Ar-H), 10.89 (s, 1H, NH), 11.13 (s, 1H, NH). HRMS: M^+ 355.80. Anal. calcd. for $C_{17}H_{17}N_5O_4$: C 57.46, H 4.78, N 19.70; found: C 57.45, H 4.79, N 19.71.

5-(4-Methoxymethyl-phenyl)-7-piperidin-1-yl-1*H*-pyrimido[4,5-*d*]pyrimidine-2,4-dione (4e)

Recrystalization solvent was an ethanol and benzene mixture (1:1 *v*/*v*). Melting point 70–73 °C. IR (KBr, C=N, cm^{-1}) ν_{max}: 1599. ^{1}H NMR (300 MHz, $CDCl_3$) δ: 1.71 (m, 6H, 3′,4′,5′-CH_2), 2.93 (t, 4H, CH_2NCH_2), 3.84 (s, 3H, OCH_3), 6.94 (2H, d, *J* = 7.3 Hz, Ar-H), 7.78 (2H, d, *J* = 7.2 Hz, Ar-H), 10.79 (s, 1H, NH), 11.03 (s, 1H, NH). ^{13}C NMR (300 MHz, $CDCl_3$) δ: C2 169.33, C4 168.39, C5 170.12, C7 162.41, C9 178.99, $C_1$0 112.12, $C_{2'}$ 51.13, $C_{3'}$ 22.17, $C_{4'}$ 23.16, $C_{5'}$ 22.17, $C_{6'}$ 51.13, $C_{1''}$ 135.53, $C_{2''}$ 126.97, $C_{3''}$ 128.42, $C_{4''}$ 117.32, $C_{5''}$ 128.42, $C_{6''}$ 126.52, $C_{7''}$ 51.47. HRMS: M^+ 352.7. Anal. calcd. for $C_{18}H_{19}N_5O_3$: C 61.18, H 5.38, N 19.83; found: C 61.16, H 5.38, N 19.84.

5-(4-Methoxymethyl-phenyl)-7-pyrrolidin-1-yl-1*H*-pyrimido[4,5-*d*]pyrimidine-2,4-dione (4f)

Recrystalization solvent was an ethanol and benzene mixture (1:1 *v*/*v*). Melting point 64–66 °C. IR (KBr, C=N, cm^{-1}) ν_{max}: 1600. ^{1}H NMR (300 MHz, $CDCl_3$) δ: 2.01 (t, 4H, 3′,4′-CH_2), 3.71 (t, 4H, CH_2NCH_2), 3.81 (s, 3H, OCH_3), 6.87 (d, 2H, *J* = 7.3 Hz, Ar-H), 7.69 (d, 2H, *J* = 7.2 Hz, Ar-H), 10.67 (s, 1H, NH), 11.02 (s, 1H, NH). HRMS: M^+ 339.0. Anal. calcd. for $C_{17}H_{17}N_5O_3$: C 60.17, H 5.01, N 20.64; found: C 60.16, H 5.01, N 20.64.

5-Benzo[1,3]dioxol-4-yl-7-morpholin-4-yl-1*H*-pyrimido[4,5-*d*]pyrimidine-2,4-dione (4g)

Melting point 71–73 °C. IR (KBr, C=N, cm^{-1}) ν_{max}: 1598. ^{1}H NMR (300 MHz, $CDCl_3$) δ: 2.86 (t, 4H, CH_2OCH_2), 3.26 (t, 4H, CH_2NCH_2), 5.94 (s, 2H, OCH_2O), 6.82 (1H, *J* = 8.0 Hz, Ar-H), 6.89 (1H, d, *J* = 8.0 Hz, Ar-H), 7.12 (s, 1H, Ar-H), 10.72 (s, 1H, NH), 11.14 (s, 1H, NH). HRMS: M^+ 369.0. Anal. calcd. for $C_{17}H_{15}N_5O_5$: C 55.28, H 4.06, N 18.90; found: C 55.27, H 4.05, N 18.88.

© 2007 NRC Canada

5-Benzo[1,3]dioxol-4-yl-7-piperidin-1-yl-1*H*-pyrimido[4,5-d]pyrimidine-2,4-dione (4h)

Melting point 79–81 °C. IR (KBr, C=N, cm^{-1}) ν_{max}: 1595. ^1H NMR (300 MHz, $CDCl_3$) δ: 1.72 (m, 6H, 3′,4′,5′-CH_2), 2.99 (t, 4H, CH_2NCH_2), 5.93 (s, 2H, OCH_2O), 6.84 (1H, d, *J* = 8.1 Hz, Ar-H), 6.89 (1H, d, *J* = 8.1 Hz, Ar-H), 7.11 (1H, s, Ar-H), 10.71 (s, 1H, NH), 11.20 (s, 1H, NH). HRMS: M^+ 366.5. Anal. calcd. for $C_{18}H_{17}N_5O_4$: C 58.85, H 4.63, N 19.07; found: C 58.86, H 4.64, N 19.06.

5-Benzo[1,3]dioxol-4-yl-7-pyrrolidin-1-yl-1*H*-pyrimido[4,5-*d*]pyrimidine-2,4-dione (4i)

Melting point 84–86 °C. IR (KBr, C=N, cm^{-1}) ν_{max}: 1600. ^1H NMR (300 MHz, $CDCl_3$) δ: 2.03 (t, 4H, 3′,4′-CH_2), 3.74 (t, 4H, CH_2NCH_2), 5.93 (s, 2H, OCH_2O), 6.79 (d, 1H, *J* = 8.1 Hz, Ar-H), 6.86 (d, 1H, *J* = 8.1 Hz, Ar-H), 7.09 (d, 1H, *J* = 8.1 Hz, Ar-H), 10.69 (s, 1H, NH), 11.11 (s, 1H, NH). HRMS: M^+ 353.4. Anal. calcd. for $C_{17}H_{15}N_5O_4$: C 57.79, H 4.24, N 19.83; found: C 57.78, H 4.25, N 19.84.

7-Morpholin-4-yl-5-thiophen-2-yl-1*H*-pyrimido[4,5-*d*]pyrimidine-2,4-dione (4j)

Melting point 79–81 °C. IR (KBr, C=N, cm^{-1}) ν_{max}: 1598. ^1H NMR (300 MHz, $CDCl_3$) δ: 2.91 (t, 4H, CH_2OCH_2), 3.87 (t, 4H, CH_2NCH_2), 7.45 (m, 1H, Ar-H), 8.31 (m, 2H, Ar-H), 10.86 (s, 1H, NH), 11.03 (s, 1H, NH). HRMS: M^+ 330.8. Anal. calcd. for $C_{14}H_{13}N_5O_3S$: C 50.75, H 3.92, N 21.14, S 9.66; found: C 50.73, H 3.91, N 21.16, S 9.64.

7-Piperidin-1-yl-5-thiophen-2-yl-1*H*-pyrimido[4,5-*d*]pyrimidine-2,4-dione (4k)

Melting point 68–70 °C. IR (KBr, C=N, cm^{-1}) ν_{max}: 1595. ^1H NMR (300 MHz, $CDCl_3$) δ: 1.69 (m, 6H, 3′,4′,5′-CH_2), 2.86 (t, 4H, CH_2NCH_2), 7.41 (m, 1H, Ar-H), 8.01 (m, 2H, Ar-H), 10.86 (s, 1H, NH), 11.01 (s, 1H, NH). HRMS: M^+ 329.5. Anal. calcd. for $C_{15}H_{15}N_5O_2S$: C 54.71, H 4.56, N 21.27, S 9.72; found: C 54.72, H 4.55, N 21.28, S 9.75.

7-Pyrrolidin-1-yl-5-thiophen-2-yl-1*H*-pyrimido[4,5-*d*]pyrimidine-2,4-dione (4l)

Melting point 64–67 °C. IR (KBr, C=N, cm^{-1}) ν_{max}: 1595. ^1H NMR (300 Mhz, $CDCl_3$) δ: 2.13 (t, 4H, 3′,4′-CH_2), 3.94 (t, 4H, CH_2NCH_2), 7.38 (m, 1H, Ar-H), 7.99 (m, 2H, Ar-H), 10.85 (s, 1H, NH), 11.02 (s, 1H, NH). ^{13}C NMR (300 MHz, $CDCl_3$) δ: C2 170.12, C4 169.99, C5 170.42, C7 161.72, C9 177.59, $C_1$0 112.42, $C_{2'}$ 50.97, $C_{3'}$ 21.49, $C_{4'}$ 21.49, $C_{5'}$ 50.97, $C_{1''}$ 142.67, $C_{3''}$ 125.49, $C_{4''}$ 127.54, $C_{5''}$ 122.82. HRMS: M^+ 315.0. Anal. calcd. for $C_{14}H_{13}N_5O_2S$: C 53.33, H 4.12, N 22.22, S 9.84; found: C 53.34, H 4.13, N 22.21, S 9.89.

Acknowledgements

The authors are thankful to Council for Scientific and Industrial Research (CSIR), New Delhi, for their financial assistance.

References

1. (*a*) E. Lunt. *In* Comprehensive organic chemistry. Vol. 4. *Edited by* D. Barton, W.D. Ollis. Pergamon, Oxford, UK. 1974. p. 493; (*b*) J.D. Brown. *In* Comprehensive heterocyclic chemistry. Vol. 3. *Edited by* A.R. Katritzky, C.W. Rees. Pergamon, Oxford, UK. 1984. p. 57; (*c*) E.D. Clercq and R. Beraerts. J. Biol. Chem. **262**, 14905 (1987).
2. (*a*) W.J. Coates. Eur. Patent 351058. 17 January 1990; (*b*) Chem. Abstr. **113**, 40711 (1990); (*c*) A.A. Ramsey. U.S. Patent 3830812. 20 August 1974; (*d*) FMC Corp. Chem. Abstr. **81**, 136174 (1974).
3. (*a*) E.C. Taylor, R.J. Knopf, R.F. Meyer, A. Holmes, and M.L. Hoefle. J. Am. Chem. Soc. **82**, 5711 (1960); (*b*) J.D. Figueroavillar, C.L. Carneiro, and E.R. Cruz. Heterocycles, **34**, 891 (1992).
4. N. Kitamura and A. Onishi. Eur. Patent 163599. 4 December 1985; Chem. Abstr. **104**, 186439 (1984).
5. P. Raddatz and R. Bergmann. Ger. Patent DE3601731. 23 July 1987; Chem. Abstr. **109**, 54786 (1988).
6. T.J. Delia, M. Baumann, and A. Bunker. Heterocycles, **35**, 1397 (1993).
7. G.W. Rewcastle, A.J. Bridges, D.W. Fry, J.R. Rubin, and W.A. Denny. J. Med. Chem. **40**, 1820 (1997).
8. D.W. Fry, M.A. Becker, and R.L. Switzer. Mol. Pharmacol. **47**, 810 (1995).
9. J.E. Gready, C. McKinlay, and M.G. Gebauer. Eur. J. Med. Chem. **38**, 719 (2003).
10. The Merck Index. 10th ed. *Edited by* M. Windholz. Merck, Rahway, N.J. 1983.
11. (*a*) A.F.A. Shalaby and I.I. Abd EI-Gaward. J. Prakt. Chem. 1022 (1971); (*b*) Y. Frangin, C. Guimbal, F. Wissocq, and H. Zamarlick. Synthesis, 1046 (1986).
12. (*a*) J.T. Bojarski, J.L. Mokrocz, H.J. Barton, and M.H. Paluchowska. Adv. Heterocycl. Chem. **38**, 229 (1985); (*b*) D.J. Brown. *In* Comprehensive heterocyclic chemistry. Vol. 3. *Edited by* A.R. Katrizky and C.W. Rees. Pergamon Press, Oxford, UK. 1984. p. 57.
13. R. Bednar, O.E. Polansky, P. Wolschann. Z. Naturforsch. B. Anorg. Chem. Org. Chem. **30B**, 582 (1975); Chem. Abstr. **83**, 192338z.
14. H. Ikeda, Y. Kawabe, T. Sakai, and K. Kawasaki. Chem. Lett. 1803 (1989).
15. (*a*) M. Kidwai, V. Bansal, and R. Thakur. J. Sulfur Chemistry, **27**, 57 (2006); (*b*) M. Kidwai and P. Mothsra. Tetrahedron Lett. **47**, 5029 (2006); (*c*) M. Kidwai and K. Singhal. Synth. Commun. **36**, 188 (2006); (*d*) M. Kidwai and R. Mohan. Can. J. Chem. **82**, 427 (2004).
16. A. Ben Alloum, B. Labiad, and D. Villemin. J. Chem. Soc. Chem. Commun. 386 (1989).
17. D. Prajapati and A.J. Thakur. Tetrahedron Lett. **46**, 1433 (2005).
18. P. Sharma, N. Rane, and V.K. Gurram. Bioorg. Med. Chem. Lett. **14**, 4185 (2004).
19. K. Hirota, Y. Kitade, H. Sajiki, and Y. Maki. Synthesis, 589 (1984).

© 2007 NRC Canada

EFGShield — A program for parsing and summarizing the results of electric field gradient and nuclear magnetic shielding tensor calculations

Samyuktha Adiga, Dominic Aebi, and David L. Bryce

Abstract: A computer program (EFGShield) is described that simplifies and summarizes the output from electric field gradient (EFG) and nuclear magnetic shielding tensor calculations performed independently using existing quantum chemical software. In addition to summarizing tensor magnitudes according to conventions commonly used by solid-state NMR spectroscopists, the program provides Euler angles relating the orientations of the EFG and shielding tensor principal axis systems (PAS). An atomic coordinate file is generated that also contains dummy atoms representing the orientations of the EFG and shielding tensor PASs in the molecular framework. We demonstrate the functionality of the program using calculations of the chlorine EFG and shielding tensors for strontium chloride dihydrate and calcium chloride dihydrate. Several models of the chloride environment in these compounds are tested, including those where point charges are used to represent the extended three-dimensional lattices within the self-consistent charge field perturbation approach. The results highlight both the shortcomings and successes of traditional localized orbital-based basis sets in the description of the NMR properties of extended systems. We anticipate that EFGShield will be a useful tool for spectroscopists using quantum chemical software to aid in the interpretation of experimental data.

Key words: quantum chemical calculations, computer program, electric field gradient tensor, quadrupolar coupling constant, nuclear magnetic shielding tensor, Euler angles, alkaline earth chloride hydrates.

Résumé : On a mis au point un logiciel (« EFGShield ») qui simplifie et résume les résultats de calculs de gradient de champ électrique (GCE) et de tenseur de blindage magnétique nucléaire effectués d'une façon indépendante à l'aide d'un programme existant de chimie quantique. En plus de résumer les amplitudes des tenseurs en fonction des conventions généralement utilisées par les spectroscopistes de RMN, le programme fournit aussi les angles de Euler qui permettent de relier les orientations du GCE avec les systèmes d'axes principaux (SAP) du tenseur de blindage. Un fichier de coordonnées est généré qui contient aussi les atomes fictifs qui représentent les orientations des SAP du GCE et le tenseur de blindage par rapport au squelette moléculaire. On a effectué une démonstration de la fonctionnalité du programme à l'aide de calculs du GCE et des tenseurs de blindage du chlore du dihydrate du chlorure de strontium et du dihydrate du chlorure de calcium. On a évalué plusieurs modèles d'environnement du chlore dans ces composés, y compris ceux dans lesquels on utilise les charges ponctuelles pour représenter les réseaux tridimensionnels étendus à l'intérieur d'une approche autocohérente à la perturbation de champ de charge. Les résultats mettent en évidence les défauts et les qualités des ensembles de base traditionnels découlant d'orbitales localisées dans la description des propriétés RMN de systèmes étendus. On prévoit que le programme EFGShield sera un outil utile pour les spectroscopistes qui utilisent des logiciels de chimie quantique pour les aider dans l'interprétation de données expérimentales.

Mots-clés : calculs de chimie quantique, logiciel, tenseur du gradient de champ électrique, constante de couplage quadripolaire, tenseur de blindage magnétique nucléaire, angles de Euler, hydrates de chlorures de métaux alcalino-terreux.

[Traduit par la Rédaction]

Introduction

Solid-state nuclear magnetic resonance (SSNMR) spectroscopy is a useful and versatile technique for the characterization of diverse materials of chemical and biochemical interest. Much information is available on molecular structure and dynamics through the orientation-dependent chemical shift interaction and, for nuclei with spins greater than 1/2, the quadrupolar interaction. It is becoming increasingly popular to use quantum chemistry to aid in the interpretation of these experimentally accessible quantities. There are many different quantum chemistry software packages available that may be used to calculate NMR properties including the Gaussian suite of programs (1), the Amsterdam Density Functional (ADF) Program (2), CASTEP (3–5), and Dalton (6), among others.

Received 30 April 2007. Accepted 14 June 2007. Published on the NRC Research Press Web site at canjchem.nrc.ca on 13 July 2007.

S. Adiga, D. Aebi, and D.L. Bryce.[1] Department of Chemistry and Centre for Catalysis Research and Innovation, University of Ottawa, Ottawa, ON K1N 6N5, Canada.

[1]Corresponding author (e-mail: dbryce@uottawa.ca).

 doi:10.1139/V07-069 © 2007 NRC Canada

While these programs generally provide complete descriptions of computed electric field gradient (EFG) and nuclear magnetic shielding ($\boldsymbol{\sigma}$) tensors (i.e., the complete 3 × 3 matrices that include all tensor components), we have found it convenient in our laboratory to develop a program to further treat the raw output from quantum chemical packages. For example, Gaussian 03 does not directly provide quadrupolar coupling constants, quadrupolar asymmetry parameters, or a set of Euler angles to describe the relative orientations of the EFG and shielding tensors. However, it is precisely these parameters, among others, that are required to properly simulate SSNMR spectra of quadrupolar nuclei in powdered solids (7). In cases where one is analyzing computational output for a large series of calculations, e.g., the results of a basis set study, it is convenient to have an automated analysis tool such as the one described herein.

As an example of the utility of the program, we address a question of interest concerning the NMR properties of solids that consist of extended interconnected networks of ions, rather than molecular crystals that consist of an ordered collection of essentially isolated molecular units. How well can traditional orbital-based basis sets describe the EFG and shielding tensors of nuclei in such systems? The chlorine NMR interaction tensors in the alkaline earth chlorides $SrCl_2 \cdot 2H_2O$ and $CaCl_2 \cdot 2H_2O$ are studied in the present work and the results of a series of quantum chemical calculations using various models of the chloride ion environment are analyzed using EFGShield. Comparisons to experimental data (8) and the results of plane-wave pseudopotential based calculations of the chlorine EFG and shielding tensors (8) are made in an effort to determine the usefulness of the orbital-based approach.

Tensor conventions

We briefly present the definitions and conventions used in the discussion of the EFG and shielding tensor magnitudes and orientations.

The electric field gradient tensor and quadrupolar parameters.

In an arbitrary molecule-fixed axis system the EFG tensor, $\boldsymbol{V}$, may be written in Cartesian form as,

$$[1] \qquad \boldsymbol{V} = \begin{bmatrix} V_{xx} & V_{xy} & V_{xz} \\ V_{yx} & V_{yy} & V_{yz} \\ V_{zx} & V_{zy} & V_{zz} \end{bmatrix}$$

The EFG tensor is symmetric, meaning that $V_{\alpha\beta} = V_{\beta\alpha}$ ($\{\alpha,\beta\} \in \{x, y, z\}$). Diagonalization of the tensor, so that it is expressed in its principal axis system (PAS), yields three eigenvalues (or principal components) and three corresponding eigenvectors that describe the orientation of the PAS relative to the initial molecule-fixed axis system. The principal components are denoted and ordered as follows,

$$[2] \qquad |V_{33}| \geq |V_{22}| \geq |V_{11}|$$

Since the trace of the EFG tensor is zero ($V_{33} + V_{22} + V_{11} = 0$), there are only two independent principal components. The asymmetry of the EFG tensor is described by the following asymmetry parameter,

$$[3] \qquad \eta_Q = (V_{11} - V_{22}) / V_{33}$$

In SSNMR experiments, one observes the result of an interaction between the EFG at a particular nucleus and the nuclear electric quadrupole moment (Q) specific to the nuclide under observation. The nucleus must be quadrupolar ($I > 1/2$) to possess a nonzero ground-state quadrupole moment. The nuclear quadrupolar coupling constant (C_Q) involves a product of the largest principal component of the EFG tensor and Q,

$$[4] \qquad C_Q = eV_{33}Q/h$$

Here, e, is the fundamental electronic charge, $1.602176487 \times 10^{-19}$ C; Q is the nuclear electric quadrupole moment specific to the nucleus of interest; h is Planck's constant, $6.62606896 \times 10^{-34}$ J s. Currently, all nuclear electric quadrupole moments used in EFGShield are from the 2001 collection of Pyykkö (9). All fundamental constants are the most up-to-date values from the National Institute of Standards and Technology (10). The following formula shows more explicitly how the value of C_Q (in MHz) is calculated from the value of V_{33} in Gaussian 03 (which is in atomic units, au) within EFGShield,

$$\begin{aligned} [5] \qquad C_Q[\text{MHz}] = {} & (1.602176487 \times 10^{-19}\ \text{C})(-V_{33}\ [\text{au}]) \\ & \times (Q\ [\text{fm}^2])(9.71736166 \times 10^{21}\ \text{JC}^{-1}\text{m}^{-2}\text{au}^{-1}) \\ & \times (10^{-6}\ \text{MHz Hz}^{-1})(10^{-30}\ \text{m}^2\text{fm}^{-2}) \\ & / (6.62606896 \times 10^{-34}\ \text{Js}) \end{aligned}$$

where the three additional values are included for unit conversions. A negative sign is included in front of the value of V_{33} obtained from Gaussian because an opposite sign convention is used in this program. This opposite sign convention has been noted previously in the literature (11, 12) and is most easily recognized by comparing experimental quadrupolar coupling constants for nuclei in diatomic molecules obtained from molecular beam or high-resolution microwave spectroscopy (where the experimental sign is available) to those calculated using Gaussian (11, 13).

Sometimes, the Greek symbol "χ" or "QCC" is also used to denote the quadrupolar coupling constant. For most quadrupolar nuclei typically observed in SSNMR experiments, C_Q is on the order of MHz.

The nuclear magnetic shielding tensor

The nuclear magnetic shielding tensor may be expressed in an arbitrary molecule-fixed axis system as follows, with up to nine independent elements (14, 15):

$$[6] \qquad \boldsymbol{\sigma} = \begin{bmatrix} \sigma_{xx} & \sigma_{xy} & \sigma_{xz} \\ \sigma_{yx} & \sigma_{yy} & \sigma_{yz} \\ \sigma_{zx} & \sigma_{zy} & \sigma_{zz} \end{bmatrix}$$

The shielding tensor is in principle antisymmetric, meaning that $\sigma_{\alpha\beta}$ is not in general equal to $\sigma_{\beta\alpha}$ ($\{\alpha,\beta\} \in \{x, y, z\}$). The symmetric ($\boldsymbol{\sigma}^{\text{sym}}$) and antisymmetric ($\boldsymbol{\sigma}^{\text{antisym}}$) parts of the tensor may be separated as follows:

© 2007 NRC Canada

$$[7]\qquad \boldsymbol{\sigma}^{\mathrm{sym}} = \frac{1}{2}(\boldsymbol{\sigma} + \boldsymbol{\sigma}^{\mathrm{t}})$$

$$= \begin{bmatrix} \sigma_{xx} & \left(\frac{\sigma_{xy}+\sigma_{yx}}{2}\right) & \left(\frac{\sigma_{xz}+\sigma_{zx}}{2}\right) \\ \left(\frac{\sigma_{yx}+\sigma_{xy}}{2}\right) & \sigma_{yy} & \left(\frac{\sigma_{yz}+\sigma_{zy}}{2}\right) \\ \left(\frac{\sigma_{zx}+\sigma_{xz}}{2}\right) & \left(\frac{\sigma_{zy}+\sigma_{yz}}{2}\right) & \sigma_{zz} \end{bmatrix}$$

$$[8]\qquad \boldsymbol{\sigma}^{\mathrm{antisym}} = \frac{1}{2}(\boldsymbol{\sigma} - \boldsymbol{\sigma}^{\mathrm{t}})$$

$$= \begin{bmatrix} 0 & \left(\frac{\sigma_{xy}-\sigma_{yx}}{2}\right) & \left(\frac{\sigma_{xz}-\sigma_{zx}}{2}\right) \\ -\left(\frac{\sigma_{xy}-\sigma_{yx}}{2}\right) & 0 & \left(\frac{\sigma_{yz}-\sigma_{zy}}{2}\right) \\ -\left(\frac{\sigma_{xz}-\sigma_{zx}}{2}\right) & -\left(\frac{\sigma_{yz}-\sigma_{zy}}{2}\right) & 0 \end{bmatrix}$$

where the superscript "t" denotes the transpose. The symmetric part of the tensor is therefore characterized by up to six independent quantities and the antisymmetric part is characterized by up to three independent variables (14). The symmetric part of the tensor is of paramount interest since the antisymmetric part does not influence NMR spectra to first order (16).

When the symmetric part of the shielding tensor is diagonalized, three eigenvalues and three eigenvectors are obtained. The eigenvalues are labelled and ordered as follows: $\sigma_{11} \leq \sigma_{22} \leq \sigma_{33}$; they are unitless but since they are typically on the order of 10^{-6}, these shielding values are normally expressed in ppm. The eigenvectors describe the orientation of the PAS in the molecule-fixed axis system.

The isotropic shielding constant is given by,

$$[9]\qquad \sigma_{\mathrm{iso}} = \left(\frac{1}{3}\right)(\sigma_{11} + \sigma_{22} + \sigma_{33})$$

The anisotropy and asymmetry of the symmetric part of the shielding tensor may be conveniently described by the span (Ω) and the skew (κ), respectively,

$$[10]\qquad \Omega = \sigma_{33} - \sigma_{11}$$

$$[11]\qquad \kappa = \frac{3(\sigma_{\mathrm{iso}} - \sigma_{22})}{\Omega}$$

This is the "Maryland convention" (17) and has also been referred to as the "Halifax convention" (18). Although these are the preferred representations, the reader should be aware that there are alternative descriptions of the anisotropy and asymmetry of the shielding tensor in use (14, 16, 19). We refer the reader to Eichele's webpage (20) and WSOLIDS software (21) for descriptions and tools for converting between different sets of conventions.

Euler angles

Diagonalization of the EFG and shielding tensors provides two sets of eigenvectors: one which relates the EFG PAS to the molecule-fixed axis system and one which relates the shielding tensor PAS to the molecule-fixed axis system. The relationship between the two PASs may be expressed by a series of three Euler angles α, β, and γ. Here, we adhere to the convention used by Eichele (20, 21) and Arfken (22), among others. We choose the EFG PAS to be the reference coordinate system. The two tensors are considered to be "coincident" when the following three pairs of axes lie in the same direction (see Fig. 1): (*i*) V_{33} and σ_{33}, (*ii*) V_{22} and σ_{22}, (*iii*) V_{11} and σ_{11}. Therefore, starting with coincident tensor PASs, the angles α, β, and γ describe the rotations of the shielding tensor PAS away from the EFG reference PAS (see Fig. 1*a*). (Starting with the final relative tensor orientations, an equivalent use of the same Euler angles describes the rotations of the EFG PAS required to bring it into coincidence with the shielding tensor PAS (see Fig. 1*b*).) Using the first description, starting with coincident tensors, the sequential rotations are as follows: rotation of the shielding tensor PAS by an angle α about the σ_{33} direction, followed by rotation of β about the new direction of σ_{22}, followed by rotation of γ about the new direction of σ_{33}. The angle β may always be easily visualized as the angle between the largest components of the two tensors, i.e., V_{33} and σ_{33}. All rotations are counterclockwise, i.e., mathematically positive. Further discussion of how the Euler angles are determined is presented later.

Description of the program

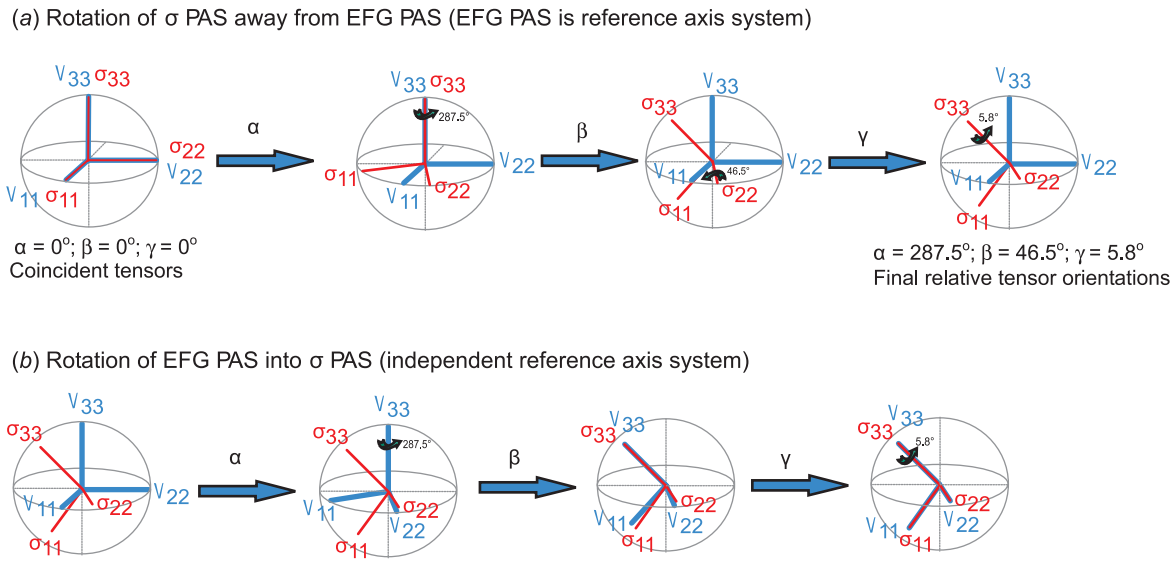
The program is currently compatible with output generated from Gaussian 03 (1) using the "NMR" and "Prop" keywords to calculate nuclear magnetic shielding and EFG tensors, respectively. EFGShield was written using C and is compiled to run under the Windows XP operating system. G03 output files generated either from Windows or Linux/Unix versions of Gaussian will work with EFGShield; the file needs to be in a "plain text" (ANSI encoding) format beforehand (this can be accomplished using MS Wordpad, for example).

EFGShield takes as input the entire G03 output file and then asks the user to indicate the "Center number" of the atom of interest. For example, if one is interested in the EFG and shielding tensor properties of atom No. 6 in the G03 output, then "6" is entered. EFGShield then automatically parses the G03 output to find the full EFG tensor and the full shielding tensor for the atom of interest (see Fig. 2). A summary of the results for atom number 6 is subsequently displayed instantaneously on the screen (Fig. 2). Additionally, a more detailed summary of the results is appended to the source file (see Fig. 3). Finally, an *xyz* molecular coordinate file is also created, with the two PASs centred on the chosen atom.

The EFG tensor is diagonalized to yield the EFG tensor eigenvalues and eigenvectors. Quadrupolar coupling constants are determined for the one or two most abundant quadrupolar isotopes of the atom chosen (depending on whether more than one quadrupolar isotope exists). The shielding tensor is symmetrized and then diagonalized to

© 2007 NRC Canada

Fig. 1. Depiction of the conventions used for the Euler angles α, β, and γ in the present work. (*a*) This series of rotations shows the rotation of the shielding tensor PAS away from the EFG PAS; the EFG PAS is used as the reference axis system. In this example, the first rotation is by α = 287.5° counterclockwise about σ_{33}; the second rotation is by β = 46.5° counterclockwise about the new direction of σ_{22}; the final rotation is by γ = 5.8° counterclockwise about the final direction of σ_{33}. The orientations depicted on the far right of part (*a*) are therefore described by the Euler angles α = 287.5°, β = 46.5°, γ = 5.8°. (*b*) Alternatively, the same set of angles may be used to rotate the EFG PAS into coincidence with the shielding tensor PAS. In this case the orientations depicted at the far left of part (*b*) are described by the Euler angles α = 287.5°, β = 46.5°, γ = 5.8° (the same orientations and same angles as in part (*a*)). The rotations depicted (successively about V_{33}, the new direction of V_{22}, and the final direction of V_{33}) will result in the coincidence of the tensors shown at the far right.



generate the shielding tensor eigenvalues and eigenvectors. The Jacobi routine from *Numerical Recipes* (23) is used to perform the diagonalizations. Eigenvectors are reported with respect to the Gaussian "Standard Orientation" axis system. Similarly, antisymmetric components of the shielding tensor are reported with respect to this axis system.

The next step is to ensure the right-handedness of the set of three eigenvectors corresponding to a particular PAS. This is done by finding the cross product between, for example, the eigenvectors corresponding to V_{11} and V_{22} in the case of the EFG tensor and requiring the eigenvector corresponding to V_{33} to lie along the resulting cross product vector. More specifically, let us define the components of the eigenvectors corresponding to the three principal components of the EFG tensor as follows:

[12] eigenvector for $V_{11} = (V_{11}x,\ V_{11}y,\ V_{11}z)$

eigenvector for $V_{22} = (V_{22}x,\ V_{22}y,\ V_{22}z)$

eigenvector for $V_{33} = (V_{33}x,\ V_{33}y,\ V_{33}z)$

where x, y, and z refer to the Gaussian "Standard Orientation" axis system. The cross product between the eigenvectors for V_{11} and V_{22} is calculated as follows:

$$[13]\quad (V_{11}x,\ V_{11}y,\ V_{11}z) \times (V_{22}x,\ V_{22}y,\ V_{22}z) = (V_{11}yV_{22}z - V_{11}zV_{22}y,\ V_{11}zV_{22}x - V_{11}xV_{22}z,\ V_{11}xV_{22}y - V_{11}yV_{22}x)$$

We then take the dot product of this resulting vector with the eigenvector corresponding to V_{33},

$$[14]\quad \text{dot product} = ((V_{11}yV_{22}z - V_{11}zV_{22}y)(V_{33}x) + (V_{11}zV_{22}x - V_{11}xV_{22}z)(V_{33}y) + (V_{11}xV_{22}y - V_{11}yV_{22}x)(V_{33}z))$$

If the dot product is unity then the EFG PAS is already right-handed. If the dot product is –1 then the EFG PAS is left-handed. We correct this latter situation by inverting the direction of the eigenvector corresponding to V_{33} (i.e., $V_{33}x$, $V_{33}y$, and $V_{33}z$ are replaced by $-V_{33}x$, $-V_{33}y$, and $-V_{33}z$). The same check of right-handedness is performed for the shielding tensor.

The Euler angles relating the two PASs are determined as follows. β is found by simply calculating the positive angle between the eigenvectors corresponding to V_{33} and σ_{33}. This is accomplished using a dot product operation. If the resulting value of β is greater than 90° then the signs of the components of the eigenvectors corresponding to σ_{33} and σ_{22} are inverted so that β will always be less than or equal to 90° and so that a right-handed coordinate system is maintained. α is found by calculating the angle between the V_{11} eigenvector and the projection of the σ_{33} eigenvector onto the plane comprising the eigenvectors corresponding to V_{11} and V_{22}. More explicitly, the projection vector (proj(x), proj(y), proj(z)) is calculated as follows:

$$[15]\quad \text{proj}(x) = \sigma_{33}x - (V_{33}x)\{(V_{33}x)(\sigma_{33}x) + (V_{33}y)(\sigma_{33}y) + (V_{33}z)(\sigma_{33}z)\}$$

$$\text{proj}(y) = \sigma_{33}y - (V_{33}y)\{(V_{33}x)(\sigma_{33}x) + (V_{33}y)(\sigma_{33}y) + (V_{33}z)(\sigma_{33}z)\}$$

© 2007 NRC Canada

Fig. 2. Top: Image of the introductory EFGShield screen. Users are asked to input a filename and a center number. Bottom: EFGShield's "results" screen, which provides quadrupolar and shielding tensor information for the chosen atomic center of interest. The example shown here is from a B3LYP/cc-pVQZ calculation using model 1 for strontium chloride dihydrate.

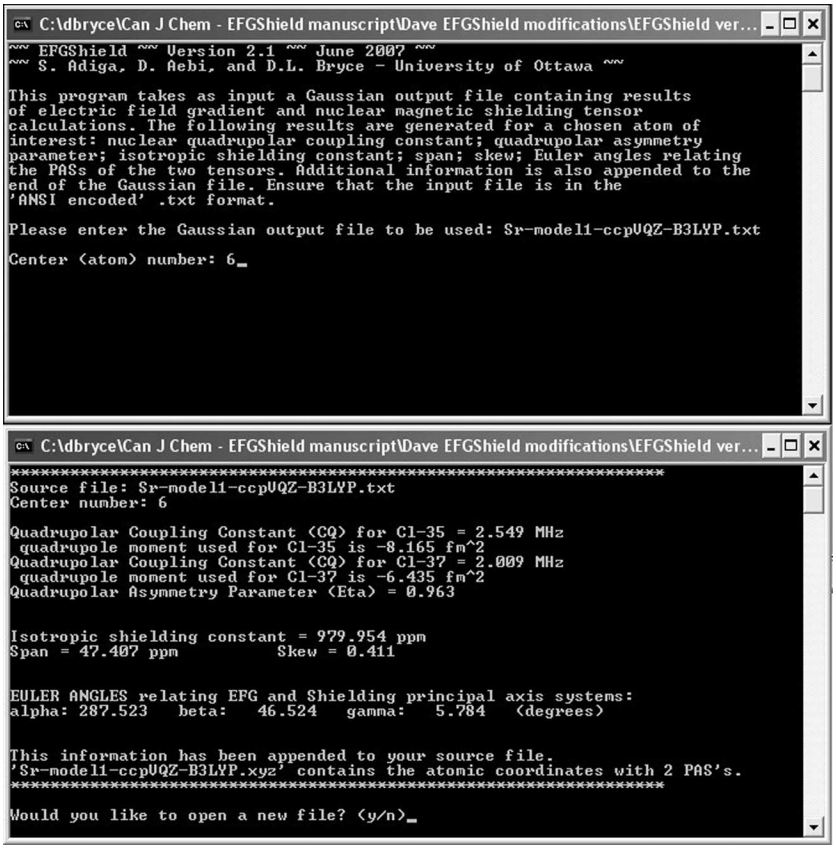
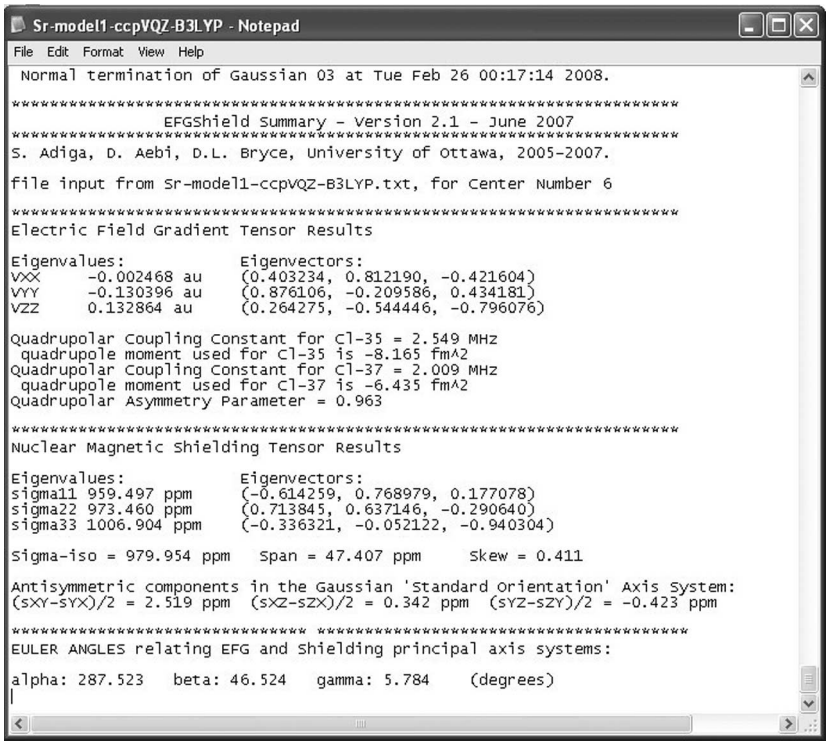


Fig. 3. An "EFGShield Summary" is appended to the end of the Gaussian source file. The example shown here is from a B3LYP/cc-pVQZ calculation using model 1 for strontium chloride dihydrate.



© 2007 NRC Canada

$$\text{proj}(z) = \sigma_{33}z - (V_{33}z)\{(V_{33}x)(\sigma_{33}x) + (V_{33}y)(\sigma_{33}y) + (V_{33}z)(\sigma_{33}z)\}$$

and the angle is then found between this projection vector and the eigenvector corresponding to V_{11} using a dot product operation. To ensure that the value obtained conforms with the convention that α should represent a counterclockwise rotation away from the direction of the V_{11} eigenvector, a check is made to determine whether the angle between the projection vector (eq. [15]) and the V_{22} eigenvector is greater than or less than 90°. If this angle is greater than 90°, then the value of α is replaced with $360° - \alpha$.

The final angle to be found is γ. The components of the vector representing the node line formed by the intersection of the plane defined by the V_{11} and V_{22} eigenvectors and the plane defined by the σ_{11} and σ_{22} eigenvectors is determined as follows:

$$\text{node}(x) = \det\begin{bmatrix} V_{33}y & V_{33}z \\ \sigma_{33}y & \sigma_{33}z \end{bmatrix}$$

$$\text{node}(y) = -\det\begin{bmatrix} V_{33}x & V_{33}z \\ \sigma_{33}x & \sigma_{33}z \end{bmatrix} \quad [16]$$

$$\text{node}(z) = \det\begin{bmatrix} V_{33}x & V_{33}y \\ \sigma_{33}x & \sigma_{33}y \end{bmatrix}$$

The value of γ is calculated as the positive angle between this node line vector and the eigenvector corresponding to σ_{22}. As in the case of α, a check is made to ensure that γ describes a counterclockwise rotation away from the node line. This is done by checking whether the angle between σ_{11} and the node line is greater than 90°, if this is the case then the value of γ is replaced with $360° - \gamma$.

In practice, if the two tensors are coincident then the Euler angles are immediately set to 0, 0, 0 and the above manipulations are skipped.

After finding the Euler angles, the lengths of the unit eigenvectors are uniformly scaled up by a factor of eight to prevent undue overlap of the dummy atoms with actual atoms during subsequent visualization. The resulting *xyz* file is readily opened with existing software, e.g., gOpenMol (24), RasMol (25), or the Chime (26) plug-in, to visualize the tensor orientations in the molecular frame.

Examples and Results

We consider EFG and shielding tensor calculations performed with Gaussian 03 (1) on the chlorine nuclei in calcium chloride dihydrate and strontium chloride dihydrate. The goal of these calculations is to explore the capability of orbital-based quantum chemical calculations in the prediction of NMR properties for systems that are inherently comprised of extended three-dimensional ionic networks in the solid state. EFGShield was used for the rapid and convenient analysis of the calculations performed on these systems. Precise experimental values for the magnitudes and relative orientations of the EFG and chemical shift tensors were recently reported from solid-state $^{35/37}$Cl NMR studies (8).

The results of both B3LYP and RHF calculations with a range of basis sets are summarized in Tables 1 and 2. Several models of the chloride environment in $SrCl_2{\cdot}2H_2O$ and $CaCl_2{\cdot}2H_2O$ were constructed based on their known diffraction structures (27, 28). For $SrCl_2{\cdot}2H_2O$, model 1 consisted simply of a chloride ion coordinated to three water molecules and five Sr^{2+} cations that are within 5 Å of the chloride ion (see Fig. 4). No additional point charges were included in model 1; this model therefore completely neglects the effects of the lattice beyond 5 Å. Model 2 consisted of the same atoms as model 1, plus seven additional point charges in the locations of the seven closest chloride ions in the surrounding lattice. Model 3 expanded on model 2 by adding point charges representative of Sr^{2+} and Cl^- ions out to a distance of 6 Å from the central chloride ion; this represents the addition of two new point charges representing Sr^{2+} and three additional point charges representing chloride ions. Model 4 consists again of the same fifteen central atoms used in model 1, with point charges representative of Sr^{2+} and Cl^- added out to a distance of 10 Å from the central chloride ion. In total there are 68 point charges representing chloride ions and 29 point charges representing strontium ions included in model 4. Models 1 and 4 are depicted in Figs. 4*a* and 4*b*. For all calculations on $SrCl_2{\cdot}2H_2O$, the five strontium cations closest to the central chloride ion were treated with the 3–21G* basis set.

For calculations on $CaCl_2{\cdot}2H_2O$, model 1 was the minimal model with no point charges. In addition to the central chloride ion, this model consists of two nearest-neighbour calcium ions and two water molecules to which the Cl^- ion is hydrogen-bonded. Model 2 included point charges out to 10 Å from the central chloride ion: 32 point charges representing Ca^{2+} and 68 point charges representing Cl^-. The two models are depicted in Figs. 4*c* and 4*d*.

In cases where point charges were used as part of the model, the self-consistent charge field perturbation (SC-CFP) procedure detailed by Zhang et al. (29) was employed. Briefly, this procedure involves an iterative series of quantum chemical calculations where the values assigned to point charges modeling the lattice are adjusted to the value obtained for the central chloride ion from the quantum chemical calculation. The iteration proceeds until the calculated charge on the central chloride ion matches (within 0.01*e*) that assigned to the point charges. Typically this required three to six iterations.

The chlorine NMR interaction tensor results obtained for strontium chloride dihydrate (Table 1) indicate both strengths and weaknesses of the calculations in reproducing the experimental solid-state NMR data. One weakness is an overestimation of $C_Q(^{35}\text{Cl})$ for most methods used and for all models used. The best agreement with the experimental value of $C_Q(^{35}\text{Cl}) = \pm(1.41 \pm 0.02)$ MHz is –2.06 MHz, which was obtained from an RHF/6–311++G(3df, 3pd) calculation on model 1. This result is comparable to the value of –2.00 MHz obtained from plane-wave pseudopotential calculations (8). Unfortunately, however, the agreement with experiment seen in Table 1 worsens as the model used for the calculations is enlarged in an attempt to incorporate more of the effects of the surrounding crystal lattice (models 2–4). This result showcases the difficulties in building a model for the lattice that properly reproduces the EFG at the central chloride ion of interest. The results for $C_Q(^{35}\text{Cl})$ using the largest model are all more than 100% in excess of

© 2007 NRC Canada

Table 1. Orbital-based SC-CFP quantum chemical results for the chlorine-35 quadrupolar and nuclear magnetic shielding tensors in $SrCl_2 \cdot 2H_2O$.

Model	Method[a]	C_Q (MHz)	η_Q	σ_{iso} (ppm)	δ_{iso} (ppm)[b]	Ω (ppm)	κ	α (°)	β (°)	γ(°)
1	RHF/6–311G*	–2.03	0.73	1030.1	–10.7	28.4	0.74	95.1	60.5	222.0
	RHF/6–311++G**	–2.12	0.74	1018.9	0.5	25.4	–0.55	83.6	26.4	314.0
	RHF/6–311++G(3df, 3pd)	–2.06	0.82	1003.0	16.4	31.6	0.52	84.1	41.2	18.2
	B3LYP/6–311G*	–2.77	0.85	998.5	20.9	48.2	0.45	109.3	58.3	305.5
	B3LYP/6–311++G**	–2.83	0.87	982.7	36.7	44.1	–0.49	90.2	21.1	309.7
	B3LYP/6–311++G(3df, 3pd)	2.55	0.92	968.8	50.6	47.4	0.24	270.1	54.0	27.5
	RHF/cc-pVDZ	–2.08	0.82	1013.6	5.8	40.4	0.19	124.8	47.6	212.8
	RHF/cc-pVQZ	–2.10	0.81	1010.4	9.0	34.6	0.52	104.0	48.1	209.4
	B3LYP/cc-pVDZ	2.54	0.84	992.9	26.5	53.6	0.35	300.0	48.2	337.1
	B3LYP/cc-pVQZ	2.55	0.96	980.0	39.4	47.4	0.41	287.5	48.2	337.1
2	RHF/6–311++G**	4.44	0.89	1020.1	–0.7	30.2	–0.59	38.0	85.6	140.7
	RHF/6–311++G(3df, 3pd)	–5.88	0.90	1001.4	18.0	60.4	–0.40	346.0	60.3	265.9
	B3LYP/6–311++G**	5.42	0.87	978.2	41.2	55.7	–0.40	60.3	85.4	140.7
	B3LYP/6–311++G(3df, 3pd)	6.62	1.00	959.1	60.3	78.1	–0.19	51.5	78.4	156.0
3	RHF/6–311++G**	2.79	0.64	1029.0	–9.6	23.2	0.34	231.4	68.3	8.8
	RHF/6–311++G(3df, 3pd)	3.23	0.92	1026.4	–7.0	39.0	0.04	345.8	73.3	5.4
	B3LYP/6–311++G**	3.44	0.49	998.2	21.2	33.3	0.13	249.0	71.4	16.6
	B3LYP/6–311++G(3df, 3pd)	3.98	0.50	993.3	26.1	50.7	0.23	330.3	74.3	177.5
4	RHF/6–311++G**	3.02	0.97	1024.5	–5.1	17.3	0.69	133.8	69.0	333.2
	RHF/6–311++G(3df, 3pdf)	–3.22	0.93	1022.1	–2.7	25.8	–0.04	213.8	52.4	260.4
	B3LYP/6–311++G**	3.43	0.70	995.1	24.3	21.3	0.47	137.3	72.4	325.4
	B3LYP/6–311++G(3df, 3pd)	3.45	0.78	992.3	27.1	28.9	0.18	144.0	67.6	2.8
Experimental (Ref. 8)	Solid-state NMR	±(1.41±0.02)	0.80±0.10	—	142.1±1.0	41±10	0.50±0.20	86±15	75±5	37±10

[a]The listed method refers to how the central chloride ion and three coordinated water molecules were treated. For the five strontium cations within 5 Å of the central chloride ion, the 3–21G* basis set was used in all cases.

[b]Chemical shifts with respect to solid powdered NaCl are determined from the magnetic shielding constants according to the following relationships: (*i*) δ_{iso}(wrt NaCl(aq)) = 974 ppm–σ_{iso} (M. Gee, R.E. Wasylishen, and A. Laaksonen. J. Phys. Chem. A, **103**, 10805 (1999)); (*ii*) δ_{iso}(wrt NaCl(s)) = δ_{iso}(wrt NaCl(aq)) + 45.4 ppm (D.L. Bryce, M. Gee, and R.E. Wasylishen. J. Phys. Chem. A, **105**, 10413 (2001)).

© 2007 NRC Canada

Table 2. Orbital-based SC-CFP quantum chemical results for the chlorine-35 quadrupolar and nuclear magnetic shielding tensors in $CaCl_2{\cdot}2H_2O$.

Model	Method	C_Q (MHz)	η_Q	σ_{iso} (ppm)	δ_{iso} (ppm)[a]	Ω (ppm)	κ	α (°)	β (°)	γ(°)
1	B3LYP/6–311++G**	16.2	0.71	684.5	334.9	396.0	0.47	88.9	88.5	1.2
	B3LYP/6–311++G(3df, 3pd)	15.7	0.69	648.3	371.1	429.0	0.51	90.0	88.8	0.6
	RHF/6–311++G**	14.2	0.73	935.0	84.4	171.6	0.16	91.4	89.4	5.5
	RHF/6–311++G(3df, 3pd)	13.6	0.71	917.6	101.8	190.0	0.30	92.3	89.6	5.8
2	B3LYP/6–311++G**	11.4	0.66	831.7	187.7	252.9	0.37	91.1	85.4	356.3
	B3LYP/6–311++G(3df, 3pd)	11.1	0.61	823.6	195.8	263.2	0.44	89.9	84.1	356.0
	RHF/6–311++G**	9.56	0.65	981.5	37.9	125.0	0.13	96.4	85.4	359.6
	RHF/6–311++G(3df, 3pd)	9.24	0.58	978.7	40.7	128.9	0.28	95.0	83.3	0.1
Experimental (Ref. 8)	Solid-state NMR	±(4.26±0.03)	0.75±0.03	—	110.0±2.0	72±15	0.60±0.20	90±10	82±5	0±20

[a]Chemical shifts with respect to solid powdered NaCl are determined from the magnetic shielding constants according to the following relationships: *(i)* δ_{iso}(wrt NaCl(aq)) = 974 ppm–σ_{iso} (M. Gee, R.E. Wasylishen, and A. Laaksonen. J. Phys. Chem. *A*, **103**, 10805 (1999)); *(ii)* δ_{iso}(wrt NaCl(s)) = δ_{iso}(wrt NaCl(aq)) + 45.4 ppm (D.L. Bryce, M. Gee, and R.E. Wasylishen. J. Phys. Chem. *A*, **105**, 10413 (2001)).

the experimental value. The calculations reproduce the value of η_Q with some consistency regardless of the model used; many of the results are within the experimental range of 0.80 ± 0.10.

Another strength of the calculations is in the prediction of the span of the CS tensor for $SrCl_2{\cdot}2H_2O$. Again, many results for the various models are within error of the experimental value of 41 ± 10 ppm. However, a systematic improvement with basis set size or with the size of the model used is not evident. The calculations fail dramatically in the calculation of the chlorine isotropic chemical shifts, and again no systematic improvement with the size of the model is seen. The largest calculated chemical shift, 60.3 ppm for a B3LYP/6–311++G(3df, 3pd) calculation on model 2, is not close to the experimental value of 142.1 ± 1.0 ppm. The chronic overestimation of the shielding constant by these calculations is in direct contrast to the results of plane-wave pseudopotential calculations, where the shielding constants were found to be significantly underestimated (8). An example of the tensor orientation information for model 1 of $SrCl_2{\cdot}2H_2O$ is presented in Fig. 5 (B3LYP/cc-pVQZ). Opening the *xyz* file generated by EFGShield using a program such as gOpenMol(24) provides an image of the molecule and the tensor orientations.

The results for calcium chloride dihydrate (Table 2) confirm the conclusions reached on the basis of the strontium chloride dihydrate data. In this case, however, the strengths and weaknesses of the calculations are emphasized even more. The quadrupolar asymmetry parameter is well-reproduced by most of the calculations. The relative tensor orientations are in outstanding agreement with experiment, despite the lack of a symmetry element requiring such orientations. However, the experimental value of $C_Q(^{35}Cl)$ is strongly overestimated as is the span of the CS tensor. This is true regardless of the model used. Interestingly, the magnitude of $C_Q(^{35}Cl)$ decreases by several MHz as a result of the inclusion of point charges out to 10 Å (model 2). Nevertheless the smallest calculated value, 9.24 MHz (RHF/6–311++G(3df, 3pd) on model 2), is still greater than 100% in excess of the experimental value of ±(4.26 ± 0.03) MHz. For comparison, our previous plane-wave calculations provided a value of 6.69 MHz (8).

Concluding Remarks

We anticipate that EFGShield will be useful to solid-state NMR spectroscopists seeking to use quantum chemical calculations to help with the interpretation of experimental spectra, particularly in the case of quadrupolar nucleus NMR in static powdered samples. The examples presented herein demonstrate the functionality of the program.

For strontium chloride dihydrate and calcium chloride dihydrate, local orbital-based quantum chemical calculations have difficulty in reproducing much of the experimental chlorine SSNMR data, despite the inclusion of point charges to model the extended crystal lattice. However, it has been shown that some parameters obtained from the calculations, such as the quadrupolar asymmetry parameter and the Euler angles describing the relative orientations of the EFG and shielding tensors, may be useful in the fitting and interpretation of experimental spectra. Clearly, theoretical models that

© 2007 NRC Canada

Fig. 4. Some of the models of strontium chloride dihydrate and calcium chloride dihydrate that were used. (*a*) Model 1 for $SrCl_2 \cdot 2H_2O$. (*b*) Model 4 for $SrCl_2 \cdot 2H_2O$. (*c*) Model 1 for $CaCl_2 \cdot 2H_2O$. (*d*) Model 2 for $CaCl_2 \cdot 2H_2O$. See text for a description of all models used and which ions were treated as point charges. In parts (*b*) and (*d*), the central chloride ion is highlighted in blue.

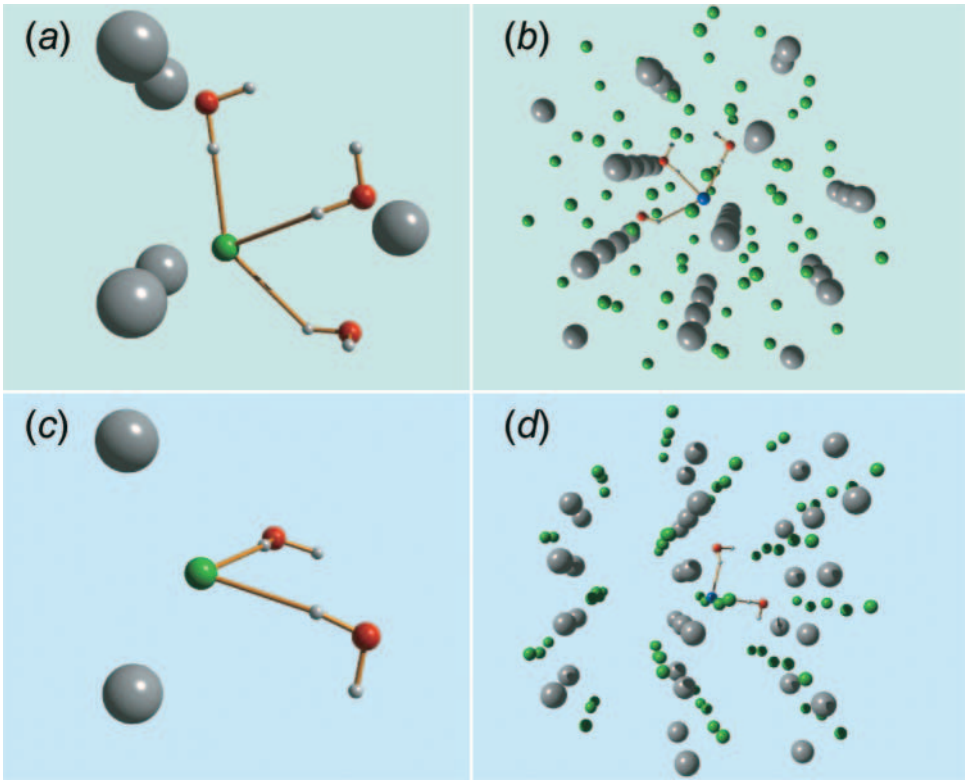
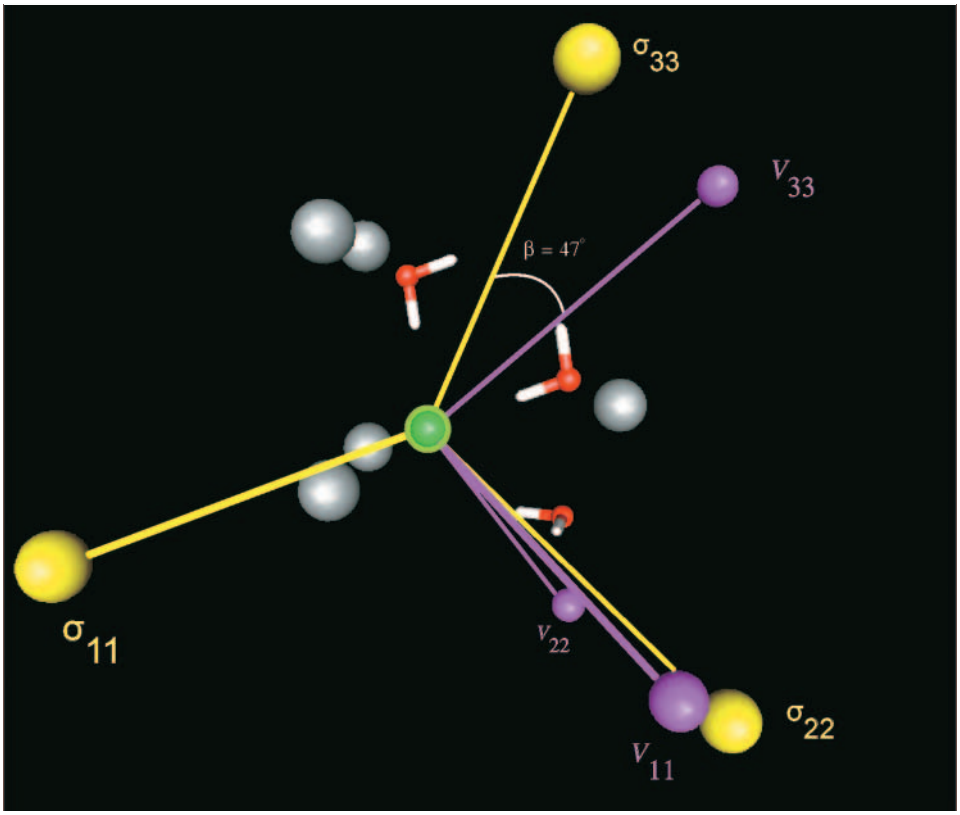


Fig. 5. An example of the EFG and shielding tensor orientations for a B3LYP/cc-pVQZ calculation using model 1 for strontium chloride dihydrate. EFG tensor components are given in purple and shielding tensor components are given in yellow. These are the same relative tensor orientations shown in Fig. 1 ($\alpha = 287.5°$, $\beta = 46.5°$, $\gamma = 5.8°$).



© 2007 NRC Canada

treat the whole crystal lattice, such as plane-wave based calculations, are valuable for describing the NMR parameters of systems such as those examined presently (8, 30, 31, 32).

Availability

The program is available on request from the authors by email (dbryce@uottawa.ca). No warranty is expressed or implied. As of May 2007, EFGShield runs under Windows XP and is compatible with Gaussian 03 output files generated with the "NMR" and "Prop" keywords.

Acknowledgments

We are grateful to the solid-state NMR group at the University of Ottawa for assistance with testing the program. We are also grateful to an anonymous reviewer for helpful comments. SA thanks the Natural Sciences and Engineering Research Council of Canada (NSERC) for an Undergraduate Summer Research Award. DLB thanks NSERC for generous funding.

References

1. M.J. Frisch, G.W. Trucks, H.B. Schlegel, G.E. Scuseria, M.A. Robb, J.R. Cheeseman, J.A. Montgomery, Jr., T. Vreven, K.N. Kudin, J.C. Burant, J.M. Millam, S.S. Iyengar, J. Tomasi, V. Barone, B. Mennucci, M. Cossi, G. Scalmani, N. Rega, G.A. Petersson, H. Nakatsuji, M. Hada, M. Ehara, K. Toyota, R. Fukuda, J. Hasegawa, M. Ishida, T. Nakajima, Y. Honda, O. Kitao, H. Nakai, M. Klene, X. Li, J.E. Knox, H.P. Hratchian, J.B. Cross, V. Bakken, C. Adamo, J. Jaramillo, R. Gomperts, R.E. Stratmann, O. Yazyev, A.J. Austin, R. Cammi, C. Pomelli, J.W. Ochterski, P. Y. Ayala, K. Morokuma, G. A. Voth, P. Salvador, J.J. Dannenberg, V.G. Zakrzewski, S. Dapprich, A.D. Daniels, M.C. Strain, O. Farkas, D.K. Malick, A.D. Rabuck, K. Raghavachari, J.B. Foresman, J.V. Ortiz, Q. Cui, A.G. Baboul, S. Clifford, J. Cioslowski, B.B. Stefanov, G. Liu, A. Liashenko, P. Piskorz, I. Komaromi, R.L. Martin, D.J. Fox, T. Keith, M.A. Al-Laham, C.Y. Peng, A. Nanayakkara, M. Challacombe, P.M. W. Gill, B. Johnson, W. Chen, M.W. Wong, C. Gonzalez, and J.A. Pople. Gaussian 03 [computer program]. Revision C.02. Gaussian Inc., Wallingford, CT. 2004.
2. Amsterdam density functional program [computer program]. Version 2006.01. 2006. Available from www.scm.com.
3. M.D. Segall, P.J.D. Lindan, M.J. Probert, C.J. Pickard, P.J. Hasnip, S.J. Clark, and M.C. Payne. J. Phys. Condens. Matter, **14**, 2717 (2002).
4. C.J. Pickard and F. Mauri. Phys. Rev. B, **63**, 245101 (2001).
5. M. Profeta, F. Mauri, and C.J. Pickard. J. Am. Chem. Soc. **125**, 541 (2003).
6. DALTON [computer program]. Release 2.0. 2005. Available from http://www.kjemi.uio.no/software/dalton/dalton.html.
7. W.P. Power, R.E. Wasylishen, S. Mooibroek, B.A. Pettitt, and W. Danchura. J. Phys. Chem. **94**, 591 (1990).
8. D.L. Bryce and E.B. Bultz. Chem. Eur. J. **13**, 4786 (2007).
9. P. Pyykkö. Mol. Phys. **99**, 1617 (2001).
10. Available from http://www.nist.gov. Accessed 12 June 2007.
11. D.L. Bryce and R.E. Wasylishen. J. Chem. Educ. **78**, 124 (2001).
12. D.L. Bryce, M. Gee, and R.E. Wasylishen. J. Phys. Chem. A, **105**, 10413 (2001).
13. D.L. Bryce and R.E. Wasylishen. Acc. Chem. Res. **36**, 327 (2003).
14. A.D. Buckingham and S.M. Malm. Mol. Phys. **22**, 1127 (1971).
15. F.A.L. Anet and D.J. O'Leary. Concepts Magn. Reson. **3**, 193 (1991).
16. U. Haeberlen. *In* Advances in magnetic resonance. Suppl. 1. *Edited by* J. S. Waugh. Academic Press, New York. 1976. Chap. II.
17. J. Mason. Solid State Nucl. Magn. Reson. **2**, 285 (1993).
18. T. Vosegaard, J. Skibsted, and H.J. Jakobsen. J. Phys. Chem. A, **103**, 9144 (1999).
19. K. Schmidt-Rohr and H.W. Spiess. Multidimensional solid-state NMR and polymers. Academic Press, London, UK. 1994. Chap. 2.
20. Available from http://casgm3.anorg.chemie.uni-tuebingen.de/klaus/nmr/index.html.
21. K. Eichele and R.E. Wasylishen. WSOLIDS NMR Simulation Package [computer program]. Version 1.17.30. Universität Tübingen, Tübingen, Baden-Württemberg, Germany. 2001.
22. G. Arfken. Mathematical methods for physicists. 3rd ed. Academic Press, Orlando, Fla. 1985. pp 198–200 (see Fig. 4.3).
23. (*a*) W.T. Vetterling, S.A. Teukolsky, W.H. Press, and B.P. Flannery, Numerical recipes — Example book [C]. 2nd ed. Cambridge University Press, Cambridge, UK. 1992. Chap. 11; (*b*) W.H. Press, S.A. Teukolsky, W.T. Vetterling, and B.P. Flannery. Numerical recipes in C++: The art of scientific computing. 2nd ed. Cambridge University Press, Cambridge, UK. 2002. Chap. 11.
24. K. Boyd, E. Häkkinen, and L. Laaksonen. gOpenMol [computer program]. Version 3.00. Copyright Leif Laaksonen. Espoo, Finland. 1997–2005.
25. R. Sayle. RasMol 2.6 with RasWin Molecular Graphics [computer program]. Windows version 2.6-ucb. University of California, Berkeley, Calif. 1993–1995.
26. MDL Chime [computer program]. Elsevier MDL, San Ramon, Calif. USA. Available from http://www.mdl.com/products/framework/chime/.
27. H. Möller and H.D. Lutz. Acta Crystallogr. Sect. C, **49**, 944 (1993).
28. A. Leclaire and M.M. Borel. Acta Crystallogr. Sect. B, **33**, 1608 (1977).
29. Y. Zhang, S. Mukherjee, and E. Oldfield. J. Am. Chem. Soc. **127**, 2370 (2005).
30. C.J. Pickard, F. Mauri. *In* Calculation of NMR and EPR parameters — Theory and Applications. *Edited by* M. Kaupp, M. Bühl, V.G. Malkin. Wiley-VCH, Weinheim, Germany. 2004. Chap. 16.
31. R.K. Harris, S.A. Joyce, C.J. Pickard, S. Cadars, and L. Emsley. Phys. Chem. Chem. Phys. **8**, 137 (2006).
32. J.W. Zwanziger, J.L. Shaw, U. Werner-Zwanziger, and B.G. Aitken. J. Phys. Chem. B, **110**, 20123 (2006).

© 2007 NRC Canada

Isolation and characterization of an unusually stable formamidinium-containing macrotricyclic complex of lithium ion formed during the synthesis of 14-thia-1,4,8,11-tetraaza-bicyclo[9,5,3]nonadecane

Tosha M. Barclay, Alexander McAuley, and S. Subramanian

Abstract: Using 1,3-bis(chloroacetamido)propane (**5**) as the common intermediate, an efficient route is described to the stepwise syntheses of 1-thia-4,8-diazacyclodecane, [10]aneN_2S (**8**), and the pentadentate macrobicycle 17-thia-1,4,8,11-tetraazabicyclo[9,5,3]-nonadecane (**11**). During the investigation of the condensation of (**5**) with (**8**), with Li_2CO_3 used as a base the Li^+ cation is carried over as the complex of the dioxo intermediate (**10**) and survives further reduction. Prolonged contact of these complexes with $CHCl_3$ during cyclisation and extraction (in the presence of Li_2CO_3 and NaOH, respectively), leads to the formation of the complex cation $[Li(\mathbf{4})]^{2+}$ as a byproduct in which the cationic macrocycle (**4**), containing a formamidinium ring, is formed through bridging of the 1,11-nitrogens in the macrobicycle (**11**) by a -CH= group that is derived from $CHCl_3$. This renders the cavity in (**4**) too small for the inclusion of transition metal ions. Reaction of the lithium cation $[Li(\mathbf{4})]^{2+}$ with $PdCl_2$ yielded the trimetallic salt $[(Li(\mathbf{4})]\text{-}PdCl_2\text{-}[(Li(\mathbf{4})])](ClO_4)_4$ in which two $[Li(\mathbf{4})]^{2+}$ ions are bridged by a $PdCl_2$ unit through coordination of the pendant thioether donors. A crystal structure of this trimetallic salt confirms the formation of $[Li(\mathbf{4})]^{2+}$. In contrast, if triethylamine is used as a base during the cyclisation reaction leading to the formation of (**11**) and contact with aqueous NaOH and $CHCl_3$ during its isolation is minimized, the formation of (**4**) is prevented and the yield of (**11**) improved.

Key words: macrobicycle synthesis, lithium, formamidinium, paaladium, complex.

Résumé : Utilisant le 1,3-bis(chloroacétamido)propane (**5**) comme intermédiaire commun, on a réalisé une synthèse efficace des synthèses par étape du 1-thia-4,8-diazacyclodécane, du [10]aneN_2S (**8**) et du macrobicyle pentadentate 17-thia-1,4,8,11-tétraazabicyclo[9.5.3]nonadécane (**11**). Au cours de l'étude de la condensation du produit **5** avec le produit **8**, en utilisant le Li_2CO_3 comme base, le cation Li^+ est entraîné sous la forme de complexe de l'intermédiaire dioxo (**10**) et il survit à une réduction ultérieure. Un contact prolongé de ces complexes avec le $CHCl_3$ pendant la cyclisation et l'extraction (en présence respectivement de Li_2CO_3 et de NaOH) conduit à la formation d'un sous-produit, le cation complexe $[Li(\mathbf{4})]^{2+}$, un macrocycle cationique (**4**) qui contient un cycle formamidinium formé par le biais d'un pontage des atomes d'azote 1,11 du macrobicyle **11** avec un groupe "-CH=" dérivé du $CHCl_3$. Cette cyclisation rend la cavité du produit **4** trop petite pour l'inclusion d'ions de métaux de transition. La réaction du cation complexe $[Li(\mathbf{4})]^{2+}$ avec le $PdCl_2$ conduit à la formation du sel trimétallique $[Li(\mathbf{4})\text{-}PdCl_2\text{-}[Li(\mathbf{4})](ClO_4)_4$ dans lequel deux ions $[Li(\mathbf{4})]^{2+}$ sont réunis par un pont de coordination du $PdCl_2$ avec les groupes thioéthers donneurs latéraux. Une étude de la structure cristalline de ce sel trimétallique confirme la formation du $[Li(\mathbf{4})]^{2+}$. Toutefois, si on utilise de la triéthylamine comme base dans la réaction de cyclisation, il y a formation du composé **11** alors que si on minimise le contact avec le NaOH aqueux ou le $CHCl_3$ lors de l'isolation des produits, il est possible d'éliminer la formation du composé **4** et d'améliorer le rendement en produit **11**.

Mots-clés : synthèse de macrobicycles, lithium, formamidinium, palladium, complexe.

[Traduit par la Rédaction]

Received 26 March 2007. Accepted 1 May 2007. Published on the NRC Research Press Web site at canjchem.nrc.ca on 11 July 2007.

T.M. Barclay. Department of Chemistry, North Harris College, Houston, Texas, 77073, USA.
A. McAuley.[1] Department of Chemistry, University of Victoria, Victoria, BC V8W 3V6, Canada.
S. Subramanian. Department of Chemistry, University of British Columbia, Vancouver, BC V6T 1Z1, Canada.

[1]Corresponding author (e-mail: amcauley@uvic.ca).

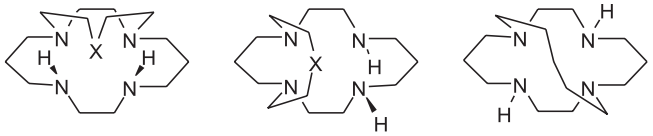
Introduction

The macrocyclic ligand, cyclam (1,4,8,11-tetraazacyclotetradecane), has been used extensively as a fundamental framework from which new ligand structures have been derived (1). This should not be surprising considering the extraordinarily high thermodynamic stability and kinetic inertness of cyclam and cyclam-based complexes of a wide range of metal ions (2) and also the extensive chemistry developed during the past decade for selective functionalization of such macrocycles (3). As a result, such derivatives

 doi:10.1139/V07-066 © 2007 NRC Canada

have been used extensively in supramolecular chemistry (4) and also in diagnostic and pharmaceutical applications (5). In this laboratory, efforts have been directed towards the synthesis of three isomeric macrobicyclic ligands, (**1**), (**2**), and (**3**). Each of these ligands (a [9]ane, a [10]ane, and a hemicryptate structure, respectively) is incorporated into a cyclam frame with an ether (-O-) (6), a secondary amine (-NH-) (7), or a thioether (-S-) (8) donor in one of the axial positions. The objective of these investigations is to study the effect of structure on the kinetics of substitution on the only axial site available in the penta-coordinate complexes of these ligands (9). Also, these macrobicycles may act as precursors to fully developed hexa-coordinate cryptate ligands.

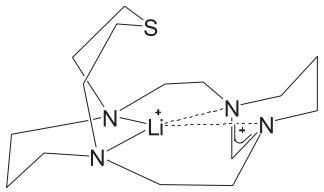
The syntheses of the macrobicycles and their complexes have been reported from this laboratory for (**1**) (6–8*a*), (**2**) (8*b*), and (**3**) (9) with, in the case of (**1**) and (**2**), use being made of the precursors 1,4-diaza-7X-cyclononane, [9]aneN_2X and 1,5-diaza-8X-cyclodecane, [10]aneN_2X, respectively, where X = O or S. Access to a series of [9]aneX_3 ligands (X = O, NH, and S or a combination of these donors) is well-documented (10). However, the corresponding [10]aneX_3 analogues were prepared by a procedure developed by Richman and Atkins (11), where harsh conditions are associated with the removal of tosyl protecting groups causing cleavage in the ether and thioether systems leading to low yields (12). A recent report from this laboratory described the synthesis and structure of a Ni(II) complex of (**11**) (8*b*) in which (**8**) and (**11**) were prepared from different reagents. To prepare reasonable quantities of (**11**), an efficient route to (**8**) is required. This paper describes a procedure that uses 1,3-bis(chloroacetamido)propane (**5**), as a common intermediate, in the syntheses of both (**8**) and (**11**).



(**1**) (**2**) (**3**)

X = O, NH, S

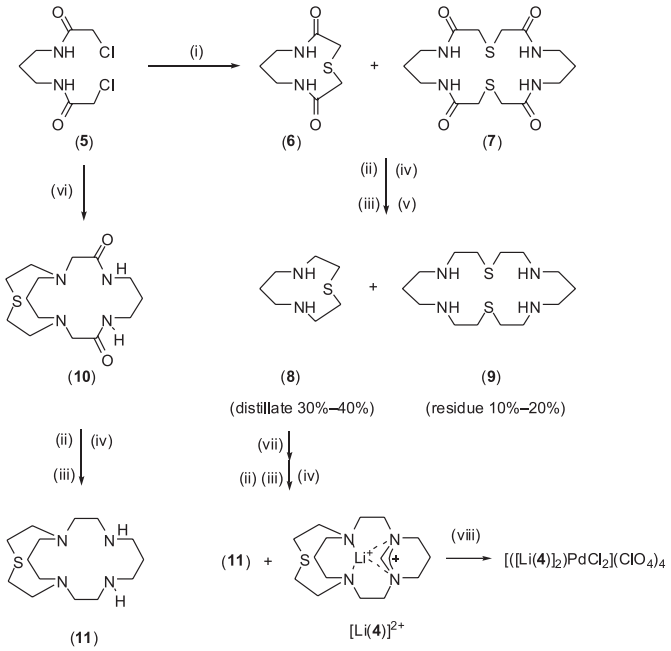
Also presented in this report are details of the formation of the unusual cationic complex, $[Li(\mathbf{4})]^{2+}$ that is formed under some conditions as a major by-product during the synthesis and isolation of (**11**). The $[Li(\mathbf{4})]^{2+}$ ion has been isolated as a Pd(II) bridged species and the single crystal X-ray structure of the trimetallic species is reported here.



Experimental

NMR spectra were obtained on a Bruker AMX360 or AC300 high-field spectrometer using $CDCl_3$ for the final macrocylic ligands and DMSO-d_6 for the precursor oxo species. Mass spectra were recorded on a Finnegan 330 GC-MS instrument either by methane chemical ionization or using a low-energy electron impact method for the ligands and on a Kratos Concept instrument by FAB or LSIMS method for the complexes. 1,2-Diaminoethane (anhydr.), 1,3-diaminopropane, triethylamine, chloroacetyl chloride, and $Na_2S{\cdot}9H_2O$ purchased from Sigma-Aldrich Chemical Co. were used without further purification. 1,2-Bis(chloroacetamido)ethane and 1,3-bis(chloro-acetamido)propane (**5**) were prepared by a method similar to that described by Bradshaw and co-workers (13) and were purified by recrystallization from hot dry acetonitrile at 60 °C and dried under vacuum.

Scheme 1. Reaction conditions: (*i*) Na_2S (1:1 *v*/*v*), aq. CH_3CN; (*ii*) BH_3–THF (1 mol/L); (*iii*) HCl (3 mol/L); (*iv*) NaOH (3 mol/L); (*v*) Kruegler distillation to separate (**8**); (*vi*) (**8**)–Et_3N–CH_3CN; (vii) (**5**)–Li_2CO_3–CH_3CN–$CHCl_3$; (viii) $PdCl_2$–CH_3CN–$HClO_4$.



Caution! Perchlorate salts of organic ligand-containing transition metal complexes are potentially explosive. Use sintered funnels for filtration and vacuum techniques for drying samples. Prepare and handle only small quantities.

In Scheme 1 it is seen that a common intermediate (**5**) is used in the syntheses of both the precursor macrocycle (**8**) and the final macrobicycle (**11**).

3,9-Dioxo-1-thia-4,8-diazacyclodecane (6) and 3,9,13,19-tetraoxo-1,11-dithia-4,8,14,18-tetraazaeicosane (7)

To a dry colorless powder of 1,3-bis(chloroacetamido)propane (**5**) (65.0 g, 0.28 mol) placed in a 5 L round-bottomed flask, 2.5 L of a mixture of acetone–water (1:1 *v*/*v*) was added and the mixture was refluxed under nitrogen yielding a clear solution. To minimize photolytic hydrolysis of (**5**), the glass vessel was covered with aluminum foil. A solution of 98% pure $Na_2S{\cdot}9H_2O$ (70 g, 0.30 mol) in 0.5 L of water was added very quickly through a dropping funnel and the mixture (pH 11.0) was refluxed for 40 h. Acetone was re-

© 2007 NRC Canada

moved under vacuum in a rotary evaporator. After reduction of the aqueous solution to about 300 mL, the solution was neutralized with HCl to pH 7, and the resulting crystalline colorless powder was filtered under suction. This solid was found not to be hygroscopic although it retained large amounts of water. It was dried in a vacuum oven at 80 °C for at least 24 h. The filtrate was further concentrated and any colorless precipitate that formed was recovered. This process was repeated until about 47 g of the product was recovered. Yield 88% (based on **6**). ^{1}H NMR δ: 1.62 (m, 2H, C-CH_2-C), 3.08 (d of t, 4H, N-CH_2), 3.18 (s, 4H, CO-CH_2-S), 3.3 (broad, NH). ^{13}C NMR δ: 28.2 (C-CH_2-C), 36.4 (N-CH_2), 39.9 (S-CH_2), 171.7 (C=O). MS (CH_4 CI): 189 (M + 1), 217 (M + 29), 229 (M + 41). A second set of ^{13}C NMR peaks at 27.8, 35.8, 37,2, and 171.6 was also observed and assigned to the dimeric species 3,9,13,19-tetraoxo-1,11-dithia-4,8,14,18-tetraazaeicosane (**7**).

1-Thia-4,7-diazacyclodecane (8) and 1,11-dithia-4,8,14,18-tetraazaeicosane (9)

A vacuum-oven dried mixture of compounds (**6**) and (**7**) (24 g, 120 mmol based on (**8**)) was ground to a fine powder and charged into a 1 L round-bottomed flask. Under N_2, 350 mL of BH_3·THF (1 mol/L) was added under gentle stirring and subsequent heating to a gentle reflux for 24 h. The reaction mixture was cooled to room temperature. While vigorously stirring the mixture, the excess reductant was decomposed by the slow addition of methanol. Removal of the volatile solvents and addition of an aqueous solution with HCl (3 mol/L) was followed by reflux for 1 h. After cooling the solution and concentration to dryness, the residual solids were dissolved in about 300 mL of water and transferred to a 1 L beaker. The solution was made strongly basic (to about 3 mol/L) with solid NaOH while cooling in an ice bath. This basic solution was extracted with six aliquots of $CHCl_3$ (50 mL) at room temperature. The $CHCl_3$ extracts were dried and concentrated under vacuum, yielding a viscous oil (12.3 g, 78 mmol based on (**8**)). Using a Kugelrohr apparatus, the oil was distilled at 20 mmHg (1 mmHg (0 °C) = 133.322 4 Pa) pressure at 60–70 °C. This yielded 5.5 g (34 mmol, 28%) of a pale yellow oil that was identified to be pure (**8**). ^{1}H NMR δ: 1.60 (m, 2H, C-CH_2-C), 2.71 (d of t, 4H, S-CH_2), 2.89 (m, 8H, CH_2-N-CH_2), 3.1 (broad, NH). ^{13}C NMR δ: 28.6 (C-CH_2-C), 35.3 (S-CH_2), 48.3 and 49.8 (N-CH_2). MS (CH_4 CI): 161 (M + 1), 189 (M + 29), 201 (M + 41).

The remaining 14.3 g of dark brown residue was identified as impure (**9**). ^{1}H NMR δ: 1.67 (m, 2H, C-CH_2-C), 2.71 (d of t, 4H, S-CH_2), 2.76 (m, 8H, CH_2-N-CH_2), 3.3 (broad, NH). ^{13}C NMR δ: 29.4 (C-CH_2-C), 32.8 (S-CH_2), 47.9 and 48.7 (N-CH_2). MS (CH_4 CI): 321 (M + 1), 349 (M + 29), 361 (M + 41).

14-Thia-1,4,8,11-tetraazabicyclo[9,5,3]-nonadecane-3,9-dione (10)

To a solution of (**5**) (2.96 g, 13 mmol) in 500 mL of dry acetonitrile was added distilled [10]aneN_2S (**8**) (1.66 g, 10.4 mmol) in 50 mL of dry acetonitrile. This clear solution was added to a refluxing mixture of 2.5 L of anhydrous acetonitrile and 10 mL of Et_3N at the rate of 60 mL/min under a N_2 atmosphere. After completion of addition, the reaction mixture was refluxed for a period of 20 h. Most of the acetonitrile was distilled off in a rotary evaporator yielding a viscous oil that was extracted with acetone. An acetone insoluble fraction that consisted mostly of $[Et_3NH]^+Cl^-$ was filtered off. The acetone extracts were concentrated to obtain a colorless solid (2.0 g, 6.4 mmol). Yield 57% based on (**8**). ^{1}H NMR δ: 1.67 (m, 2H, C-CH_2-C), 2.71 (d of t, 4H, S-CH_2), 2.76 (m, 8H, CH_2-N-CH_2), 3.3 (broad, NH). ^{13}C NMR δ: 29.4 (C-CH_2-C), 32.8 (S-CH_2), 47.9 and 48.7 (N-CH_2), 169.1 (C=O). MS (CH_4 CI): 321 (M + 1), 349 (M + 29), 361 (M + 41).

14-Thia-1,4,8,11-tetraazabicyclo-[9,5,3]-nonadecane (11)

Crude, powdered, and vacuum dried bicyclic diamide (**10**) (2.20 g, 6.9 mmol) was placed in a 1 L round-bottomed flask into which 400 mL of THF·BH_3 (1 mol/L) was siphoned. The reaction mixture was gently stirred and refluxed for 24 h under N_2. The mixture was cooled and transferred to a 2 L beaker, and while stirring, methanol was added dropwise to decompose excess borane. After a HCl (3 mol/L) work-up, the solution was concentrated to dryness on a rotary evaporator. The resulting mass was suspended in 150 mL of water and a solution of NaOH (10 mol/L) was added a little at a time until a clear solution of pH 13 was obtained. This solution was extracted with 5 × 60 mL of $CHCl_3$, the combined extracts were dried over anhydr. Na_2SO_4, and concentrated to dryness. Traces of solvents were removed under vacuum to get a viscous oil (1.0 g, 3.5 mmol) of the ligand. Yield 51%.

Purification of (11)

Though ligand (**8**) prepared by the preceding method was pure, traces of impurities could be removed only by forming a Cu(II) complex and separating the pure cation $[Cu(\mathbf{11})]^{2+}$ from the impurities on a Sephadex CM C-25 cation exchange column. In a typical procedure, (**11**) (1.0 g, 3.5 mmol) in 25 mL of ethanol was added to a solution of $CuCl_2$·$2H_2O$ (0.6 g, 3.5 mmol) in 25 mL of water. The solution was refluxed for 2 h, diluted with 150 mL of distilled water, and loaded onto a sephadex CM C-25 column (10 cm × 50 cm) fitted with a medium frit, and eluted with a NaCl (0.1 mol/L) solution. Traces of initial impurities were collected with 500 mL of NaCl (0.1 mol/L) and discarded. The main fraction containing $[Cu(\mathbf{11})]^{2+}$ was collected as a single band with 300 mL of NaCl (0.15 mol/L). This fraction was concentrated to about 100 mL, treated with 25 mL of a 10% solution of Na_2S·$9H_2O$, and refluxed for 1 h. The precipitated CuS was filtered under gravity and the ligand was extracted with three 25 mL aliquots of $CHCl_3$. The $CHCl_3$ extracts were collected, dried with anhydr. Na_2SO_4, and evaporated to dryness. Traces of solvents were removed under vacuum. The resulting oily product crystallized into a waxy solid. Recovered yield 0.9 g. ^{1}H NMR δ: 1.60 and 1.67 (m, 2H each, C-CH_2-C), 2.41 (d of t, 4H, S-CH_2), 2.62 (broad multiplet, 16H, CH_2-N-CH_2), 2.98 (broad, 2HNH). ^{13}C NMR δ: 27.9 and 28.3 (-CH_2-CH_2-CH_2-), 30.3 (-S-CH_2-), 47.6 and 48.1 (-CH_2-CH_2-CH_2-), 55.8, 55.9, and 56.7 (-N-CH_2). MS (CH_4 CI): 287 (M + 1), 315 (M + 29), 327 (M + 41). FAB MS showed a very clean peak at 287.2 (M + 1).

© 2007 NRC Canada

[[Li(4)]-$PdCl_2$-[Li(4)]]$(ClO_4)_2$

To Li_2CO_3 (1.0 g, 13.5 mmol) and NaI (1.25 g, 8.3 mmol) in a 5 L three-necked round-bottomed flask was added 2 L of reagent grade acetonitrile. Upon refluxing this mixture, solutions of distilled [10]aneN_2S (**8**) (0.98 g, 6.1 mmol) dissolved in 500 mL of $CHCl_3$–CH_3CN (1:1 *v*/*v*) and (**5**) (1.39 g, 6.1 mmol) in 20% aq. CH_3CN were added separately and simultaneously using pressure equalized dropping funnels. The rate of addition was maintained at about 50 mL/h and the reaction mixture was maintained under an atmosphere of N_2. After 48 h of refluxing, insoluble materials, mostly of unused Li_2CO_3 and NaCl, were filtered off and the reaction mixture concentrated to obtain 2.5 g of a colorless solid, which was soluble only in water. This solid was dried in a vacuum oven and reduced with 150 mL of BH_3–THF using a procedure similar to that described earlier for the preparation of (**11**). After acid hydrolysis and basification, the product was extracted with $CHCl_3$ in a continuous liquid–liquid extractor to yield 1.2 g of a plastic hygroscopic solid.

To a solution of 100 mg dissolved in 2 mL of $CHCl_3$ was added under reflux a solution of $PdCl_2$ (62 mg, 0.35 mmol) in 25 mL of CH_3CN. The reaction mixture was refluxed for 48 h. Some Pd black that formed was removed by gravity filtration and to the clear filtrate, $HClO_4$ (1 mL, 1.0 mol/L) was added from which the trimetallic product crystallized (60 mg, 0.05 mmol). MS by use of a solution of the complex in CH_3CN–H_2O (8:2 *v*/*v*), two prominent peaks were observed in LSIMS (*m*/*e* = 454.1 (100%) for $[C_{30}H_{54}N_8S_2Li_2PdCl_2O_8]^{2+}$ and *m*/*e* = 297.1 (55%) for $[C_{15}H_{29}N_4S]^+$ ion) confirm the existence of both the trimetallic ion and the lithium-containing macrocycle (**4**).

X-Ray crystal structure determination

Single crystals of $[(Li(\mathbf{4}))_2PdCl_2](ClO_4)_2 \cdot H_2O$ were obtained by vapor diffusion or layering of Et_2O into solutions of the complex in CH_3CN. Data were collected on a Smart 1000 CCD area detector diffractometer with graphite-monochromated Mo Kα (λ = 0.710 73 Å) radiation. The cell parameters were determined from a nonlinear least-squares fit of the data. The data were corrected for absorption by the SADABS method (14). The structures was solved by direct methods by use of the SHELX 97 program (15), and refined by full-matrix least-squares on F^2 by use of all reflections. Hydrogen atom positions were initially determined by geometry and refined by a riding model. Non-hydrogen atoms were refined with anisotropic displacement parameters. Crystal structure parameters for $[(Li(\mathbf{4}))_2\ PdCl_2](ClO_4)_4 \cdot H_2O$ is presented in Table 1 and selected bond lengths and angles are listed in Table 2.

Discussion

Formation of the formamidinium complex

The formation of the formamidinium moiety within both triaza (16) and cyclam (3, 16*c*) rings has been observed previously. Such a configuration has been prepared in $CHCl_3$ and used in the selective functionalization of cyclam (3*b*). Under the prolonged exposure to strongly alkaline conditions used in this as well as the previous study (8*b*), $CHCl_3$ is known to form the dichlorocarbene $:CCl_2$ through the loss of HCl. As shown in scheme 1, in macrocycles containing 1,3-diaminopropane moieties, insertion of the dichlorocarbene into an N–H bond followed by elimination of HCl can lead to the formation of a $>N^+{=}CH{-}NH:$ functional group. The formation of the formamidinium moiety also reduces the 14-membered macrocyclic cavity to a 12-membered ring that is asymmetric and too small to permit incorporation of a transition metal ion (Scheme 2). However, a small cation such as Li^+ is retained within a thermodynamically stable complex. Relatively recently, we reported the structure of an encapsulated Li^+ complex in the macrotricyclic ligand [9]aneN_4S_2 that is derived from the 14-membered cyclam unit (8*c*). The presence of Li^+ during the preparation of this ligand led to its incorporation into [9]aneN_4S_2, and attempts to replace the Li^+ by transition metal ions have not been successful. It would appear that once present within the dioxo precursor (**10**), the Li^+ ion is held sufficient strongly to withstand the reduction process.

Structure of [[Li(4)]-$Pd(Cl)_2$-[Li(4)]]$(ClO_4)_4 \cdot H_2O$ [2]

An ORTEP diagram of the complex cation is presented in Fig. 1. The interesting aspects of this structure are the confirmation of the formamidinium group within the macrocyclic ring and the binding of the Li^+ ion.

The introduction of the formamidinium ring introduces an asymmetry into the macrocycle and that is reflected in the following two features: (*i*) the introduction of a conformational rigidity to the cyclam framework that renders the resulting 12-membered macrocycle a powerful chelating agent for Li^+ ion and (*ii*) this in turn forces the thioether donor to coordinate in an exodentate fashion. As seen in Fig. 1, the Li^+ is four coordinate, situated within bonding distances to the four nitrogens of the macrocycle, while the pendant thioether, in an exodentate fashion, coordinates to the square planar Pd(II) center.

Structural and molecular aspects of the coordination chemistry of Li^+ ion have been reviewed (17*a*). In an open frame formamidinium complex in which Li^+ adopts tetrahedral geometry, Li–N distances vary between 2.0 and 2.3 Å (17*b*). The Li–N distances in the trimetallic species described here can be divided into two distinct types. The bond distances Li–N1 (1.853(9)) and Li–N4 (1.839(9)) associated with the free-standing tertiary N donors of the "1,3-diaminopropane" moiety are substantially shorter than the Li–N2 (2.143(10)) and Li–N3 (2.214(9)) distances associated with the formamidinium ring nitrogens. An important aspect to note is that owing to the presence a single positive charge and its delocalization over the two nitrogen atoms, the formamidinium nitrogens might be described effectively

[2] Supplementary data for this article are available on the journal Web site (canjchem.nrc.ca) or may be purchased from the Depository of Unpublished Data, Document Delivery, CISTI, National Research Council Canada, Ottawa, ON K1A 0R6, Canada. DUD 5188. For more information on obtaining material refer to cisti-icist.nrc-cnrc.gc.ca/irm/unpub_e.shtml. CCDC 640897 contains the crystallographic data for this manuscript. These data can be obtained, free of charge, via www.ccdc.cam.ac.uk/conts/retrieving.html (Or from the Cambridge Crystallographic Data Centre, 12 Union Road, Cambridge CB2 1EZ, UK; fax +44 1223 336033; or deposit@ccdc.cam.ac.uk).

© 2007 NRC Canada

Table 1. Structure determination parameters for [(Li(4)]-$PdCl_2$-[(Li(4))]$(ClO_4)_4$·H_2O.

Formula	$PdLi_2Cl_6S_2O_{17}N_8C_{30}H_{58}$
Formula weight	1199.94
Crystal size (mm)	0.22 × 0.25 × 0.44
Cystal color	Orange
Crystal mount	On glass fiber with silicone glue
a (Å)	9.8067(17)
b (Å)	13.411(2)
c (Å)	18.736(3)
β (°)	103.439(3)
V (Å^3)	2396.6(7)
Cell detn, refls	789
D_{calcd} (g cm^{-3})	1.66
Space group	$P2_1/n$
Z	2
*F*000	1232
Radiation	Mo Kα (graphite monochromated)
λ (Å)	0.710 73
Temperature (K)	293
Linear absorption coeff. (mm$^{-1)}$	0.88
Diffractometer	Smart 1000
Scan technique	Omega
2θ range (°)	4–50
Collection ranges	$-11 < h < 10$, $-15 < k < 14$, $-19 < l < 22$
Crystal decay (%)	0.08
Absorption correction	Sadabs
Absorption range	0.84–1.00
Reflections	12 531
Unique reflections	4235
R for merge	0.028
Reflections in refinement $I > 2.0\sigma(I)$	2927
Solution method	SHELX-97
Parameters refined	332
R_1, wR_2	0.046, 0.126
R_1 for $I > 0.0\sigma(I)$	0.073
GOF	1.07
Largest Δ/σ	0.00
Final diff map (e Å$^{-3)}$	–0.46, +0.95
Programs	SHELX-97
Scattering factors	Int. tables for crystallography. Vol C
H atom treatment	Riding

as 1e$^-$ electron donors, while the free-standing tertiary nitrogens provide regular lone pairs. The presence of an asymmetric 12-membered macrocycle is also reflected in a comparison with the regular 14-membered macrocycle (Li–N 2.080(3)) (8*c*). Also, within the small penta aza-[5,5,5]-cryptate (18) that selectively incorporates Li^+ ions, there is no distinction between two axial tertiary Li–N distances (Li–N(1) 2.008(13) and Li–N(3) 2.037(13)) and the three equatorial nitrogens (Li–N(2) 2.083(12), Li–N(5) 2.015(11), and Li–N(4) 2.056(11)) one of which is a secondary nitrogen. Again, the difference with the current system is the presence of a delocalized double bond within the formamidinium ring. In contrast to the current investigation, a nickel(II) complex of a formamidinium-containing cyclam ring (16*c*) has been described. In the nickel(II) complex, only one formamidinium and two secondary nitrogens are coordinated the metal centre. This again illustrates how the presence of a formamidinium ring influences coordination geometry within such macrocycles.

Synthesis

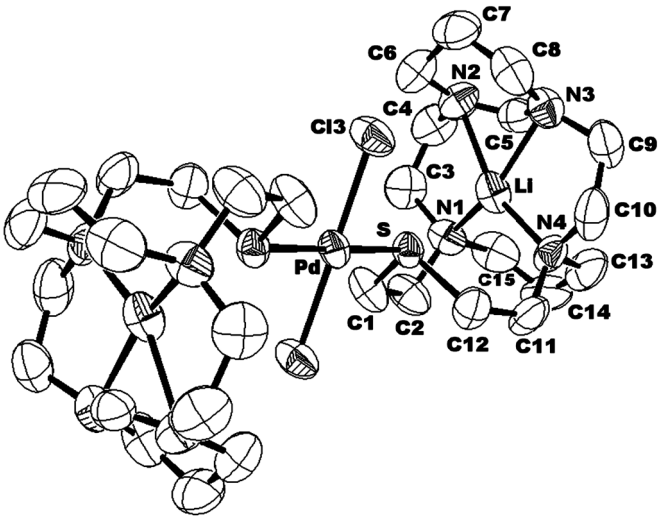
Generally, procedures reported for the formation of thioether macrocycles involve the reaction of a dithiolate anion with an appropriate α,ω-disubstituted halide (19). The use of Na_2S to form thioether macrocycles is relatively rare (8*c*). In the procedure presented here, an aqueous solution of

© 2007 NRC Canada

Table 2. Important structural data for [(Li(8))-$PdCl_2$-[(Li(8))])$(ClO_4)_4$.

Bond lengths (Å)	
Pd(1)—Cl(3)	2.2993(14)
Pd(1)—S(3)	2.3076(10)
Li(1)—N(4)	1.839(9)
Li(1)—N(1)	1.853(9)
Li(1)—N(2)	2.143(10)
Li(1)—N(3)	2.214(9)
Bond Angles (°)	
N(4)–Li–N(1)	102.7(5)
N(4)–Li–N(2)	158.2(5)
N(1)–Li–N(2)	96.5(4)
N(4)–Li–N(3)	94.6(4)
N(1)–Li–N(3)	159.2(5)
N(2)–Li–N(3)	64.7(3)
Cl(3)′–Pd–Cl(3)	180.0
S(3)–Pd–S(1)′	180.0
Cl(3)′–Pd–S(1)	87.51(4)
Cl(3)′–Pd–S(1)′	92.49(4)
Cl(3)′–Pd–Cl(3)	180.0
Cl(3)′–Pd–Cl(3)	180.0

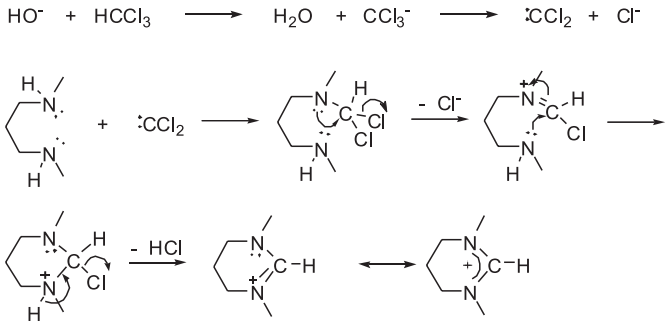
Fig. 1. ORTEP diagram of the cation [(Li(4))-$PdCl_2$-(Li(4))]$^{4+}$.



sodium sulfide is used in the intramolecular cyclisation of the chloroacetamido groups in (**5**) to form the precursor [10]aneN_2S (**8**). Under moderately dilute conditions (0.1 mol/L) and in a large batch, again a mixture of cyclic amides (**6**) and (**7**) were formed in good yields. However, no attempt was made to separate these amides (8*b*). The crude product was reduced directly to a mixture of [10]aneN_2S (**8**) and [20]aneN_4S_2 (**9**). The yield of this mixture varied within 60%–75%. In a subsequent microdistillation under vacuum, (**8**) was distilled off a clear pale yellow liquid and (**9**) was recovered from the residue. The fact that (**8**) can be obtained by a simple distillation, both in high purity and in large quantities makes this procedure more attractive.

In the modified procedure reported here for the macrocycle (**11**), the alkali metal carbonates used were replaced with triethylamine. The advantages of using Et_3N as a base are threefold: (*i*) the absence of alkali metal ions eliminates formation of complexes of cyclic diamide intermediate (**10**) and thus facilitates its separation from the reaction mixture; (*ii*) the nearly identical boiling points of acetonitrile and triethylamine results in most of the base being in the vapor phase while making available sufficient amounts in the liquid as the reaction progressed; and (*iii*) triethylamine hydrochloride, being highly insoluble in an acetone–acetonitrile mixture, is easily removed during the isolation of (**10**). Another advantage of the modified procedure are the shorter reaction times (less than 20 h) and the absence of chloroform during the cyclisation reaction of (**8**) with (**5**).

Scheme 2. Formation of formamidinium ring from $CHCl_3$ in the presence of NaOH.



While developing simpler routes to [10]aneN_2S (**8**) attempts were also made to synthesize the macrocycle [9]aneN_2S using the reaction of 1,2-bis(chloroacetamido)ethane with aq. Na_2S. However, only an insoluble polymeric species was isolated. The difference in the reactivities of 1,2-bis(chloroacetamido)ethane and 1,3-bis(chloroacetamio)propane (**5**) may arise from their conformation. 1,3-Disubstituted propanes in general tend to be adopted by a "w" conformation, in contrast to transoid conformations generally found in most 1,2-disubstituted ethanes in which the reactive groups are oriented in an unfavorable direction for cyclisation to be successful (20).

Summary

In summary, in the synthesis of bi- and tri-macrocycles of this type, the use of tertiary amines instead of alkali metal carbonates appears to eliminate many of the problems normally encountered. In particular, the tendency of the oxo derivatives such as (**10**) to complex alkali metal ions is a significant factor. Many of these macrocycles are also strong Lewis bases in weakly polar nonhydroxylic solvents such as $CHCl_3$. Prolonged contact and heating leads to the formation of formamidinium ring with chelation of small metal ions like Li^+.

Acknowledgements

The authors acknowledge funding from Natural Sciences and Engineering Research Council of Canada (NSERC) and support from the University of Victoria.

© 2007 NRC Canada

References

1. (*a*) S. Subramanian, T.M. Barclay, K.R. Coulter, and A. McAuley. Coord. Chem. Rev. **245**, 65 (2003); (*b*) A. Ingham, M. Rodopoulos, K. Coulter, T. Rodopoulos, S. Subramanian, and A. McAuley. Coord. Chem. Rev. **233–234**, 255 (2002); (*c*) A. McAuley and S. Subramanian. Coord. Chem. Rev. **300**, 75 (2000) and refs. cited therein; (*d*) T.J. Huin, J.M. McCormick, S.R. Collinson, N.W. Alcock, and D.H. Busch. Chem. Commun. (Cambridge), 1765 (1998).
2. (*a*) E. Tfouni, K.Q. Ferreira, F.G. Doro, R.S. da Silva, and Z.N. da Rocha. Coord. Chem. Rev. **249**, 405 (2005); (*b*) G. De Santis, L. Fabbrizzi, M. Licchelli, N. Sardone, and A.H. Velders. Chem. Eur. J. **2**, 1243 (1996); (*c*) A. McAuley and S. Subramanian. Inorg. Chem. **30**, 371 (1990); (*d*) E.J. Bounsall and S.R. Koprich. Can. J. Chem. **48**, 1481 (1970); (*e*) T.J. Collins, B.G. Fox, Z.G. Hu, K.L. Kostka, E. Münck, C.E. F. Rickard, and L.J. Wright. J. Am. Chem. Soc. **114**, 8724 (1992); (*f*) I. Costa, L. Fabbrizzi, P. Pallavicini, A. Poggi, and A. Zani. Inorg. Chim. Acta, **275–276**, 117 (1998); (*f*) T. Ito, H. Ito, and K. Toriumi. Chem. Lett. 1101 (1981).
3. (*a*) J.-J. Yaouanc, N. Le Bris, G. Le Gail, J.-C. Clement, H. Handel, and H. des Abbayes. J. Chem. Soc. Chem. Commun. 206 (1991); (*b*) P.J. Davis, M.R. Taylor, and K.P. Wainwright. Chem. Commun. (Cambridge), 827 (1998) and refs. cited therein; (*c*) F. Boschetti, F. Denat, E. Espinosa, and R. Guilard. Chem. Commun. (Cambridge), 312 (2002); (*d*) S. Brandes, S. Lancour, F. Denat, P. Pulumbi, and R. Guilard. J. Chem. Soc. Perkin Trans. 1, 639 (1998).
4. (*a*) P.V. Bernhardt and L.A. Jones. Chem. Commun. (Cambridge), 655 (1997); (*b*) P.V. Bernhardt. Inorg. Chem. **38**, 3481 (1999); (*c*) S. Sun, J. Saltmarsh, S. Mallik, and K. Thomasson. Chem. Commun. (Cambridge), 519 (1998).
5. (*a*) J.W. Silbert, A.H. Cory, and J.G. Cory. Chem. Commun. (Cambridge), 154 (2002); (*b*) P.V. Bernhardt and P.C. Sharpe. Inorg. Chem. **39**, 412 (2000); (*c*) M. Gaspar, R. Grazina, A. Bodor, E. Farkas, and M.A. Santos. J. Chem. Soc. Dalton. Trans. 799 (1999); (*d*) G.J. Bridger, R.T. Skerlj, D. Thornton, S. Padmanabhan, S.A. Martellucci, G.W. Henson, M.J. Abrams, N. Yamamoto, K. De Vreese, R. Pauwels, and E. De Clercq. J. Med. Chem. **38**, 366 (1995).
6. (*a*) K.A. Beveridge, A. McAuley, and C. Xu. Can. J. Chem. **30**, 2074 (1991); (*b*) M. Rodopoulos, T. Rodopoulos, J.N. Bridson, L.-I. Elding, S.J. Rettig, and A. McAuley. **40**, 2737 (2001).
7. D.G. Fortier and A. McAuley. J. Am. Chem. Soc. **112**, 2640 (1990).
8. (*a*) D.G. Fortier and A. McAuley. Inorg. Chem. **28**, 655 (1989); (*b*) K.R. Coulter, A. McAuley, and S. Rettig. Can. J. Chem. **79**, 930 (2001); (*c*) T.M. Barclay, A. McAuley, and S. Subramanian. Chem. Commun. (Cambridge), 170 (2002).
9. (*a*) A.M. Ingham, C. Xu, T.W. Whitcombe, C. Xu, J.N. Bridson, and A. McAuley. Can. J. Chem. **80**, 155 (2002); (*b*) T. Rodopoulos, K. Ishihara, M. Rodopoulos, M.J. Zaworotko, M. Maeder, and A. McAuley. Can. J. Chem. **83**, 894 (2005).
10. P. Chaudhuri and K. Wieghardt. *In* The Chemistry of 1,4,7-triazacyclononane and related tridentate macrocyclic compounds. Progress in inorganic chemistry. Vol. 35. J. Wiley, New York. 1987. pp. 329–436.
11. J.E. Richman and T.J. Atkins. J. Am. Chem. Soc. **96**, 2268 (1974).
12. A. McAuley and S. Subramanian. Inorg. Chem. **29**, 2830 (1990) and refs. cited therein.
13. K.E. Krakowiak, J.S. Bradshaw, and R.M. Izatt. J. Org. Chem. **55**, 3364 (1990).
14. G.M. Sheldrick. SADABS [computer program]. University of Göttingen, Göttingen, Germany. 1996.
15. G.M. Sheldrick. SHELX-97 [computer program]. University of Göttingen, Göttingen, Germany. 1997.
16. (*a*) T.J. Atkins. J. Am. Chem. Soc. **102**, 6364 (1980); (*b*) G.R. Weisman, D.J. Vachon, V.B. Johnson, and D.A. Gronbeck. J. Chem. Soc. Chem. Commun. 866 (1987); (*c*) A.S. Batsanov, A.E. Goeta, J.A.K. Howard, D. Maffeo, H. Puschmann, and J.A.G. Williams. Polyhedron, **20**, 981 (2001).
17. (*a*) U. Olsher. Chem. Rev. **91**, 137 (1991); (*b*) F.A. Cotton, S.C. Haefner, J.H. Matonic, X. Wang, and C.A. Murillo. Polyhedron, **16**, 541 (1997).
18. A. Bencini, A. Bianchi, A. Borselli, M. Ciampolini, M. Micheloni, N. Nardi, P. Paoli, B. Valtancoli, S. Chimichi, and P. Dapporto. J. Chem. Soc. Chem. Commun. 174 (1990).
19. (*a*) G.D.H. Dijkstra and R.M. Kellog. J. Org. Chem. **52**, 4230 (1987); (*b*) P.R. Ashton, A.L. Burns, C.G. Classens, G.H.K. Shimizu, K. Small, J.F. Stoddart, A.J.P. White, and D.J. Williams. J. Chem. Soc. Dalton Trans. 1493 (1997).
20. (*a*) J.A.E. Pratt, I.O. Sutherland, and R.F. Newton. J. Chem. Soc. Perkins Trans 1, 13 (1988); (*b*) S. Subramanian and M.J. Zaworotko. Can. J. Chem. **71**, 433 (1993).

© 2007 NRC Canada

Fluorescence quenching of gramicidin D in model membranes by halothane

Anna Carnini, Trinh T. Nguyen, and David T. Cramb

Abstract: Inhaled anesthetics were introduced in surgery over a century ago. To this day, the molecular mechanism of anesthetic action remains largely unknown. However, ion-channels of neuronal membranes are believed to be the most-likely molecular targets of inhaled anesthetics. In the study presented here, we investigated the interaction of a simplified ion-channel system, gramicidin, with halothane, a small haloalkane inhaled anesthetic in various environments. Fluorescence-quenching experiments of gramicidin D in dioleoylphosphatidylcholine (DOPC) large unilamellar vesicles (LUVS) have shown that halothane can directly interact with the ion channel (K_{SV} = 66 M^{-1}). Halothane quenched the fluorescence from tryptophan residues located at the lipid bilayer – aqueous interfaces as well as those tryptophans located deeper in the bilayer. Quenching data from gramicidin D in sodium dodecyl sulfide (SDS) micelles revealed that the tryptophan residues located at the micelle–solvent interface were preferentially quenched by halothane (K_{SV} = 22 M^{-1}). In 1-octanol, fluorescence quenching was observed, but with a lower K_{SV} value (K_{SV} = 6 M^{-1}) than in DOPC LUVS and SDS micelles. Taken together, these results indicate that halothane interactions with gramicidin, mediated by a lipid bilayer, are the strongest, and that the mechanism of anesthetic action may also be lipid-mediated.

Key words: anesthetics, lipid bilayer, membrane protein, fluorescence quenching.

Résumé : Les anesthésiants absorbés par inhalation ont été introduits en chirurgie il y a plus de cent ans. À ce jour, le mécanisme moléculaire de l'action anesthésique demeure toujours largement inconnu. Toutefois, on croit généralement que les membranes neuronales à canaux ioniques sont les cibles moléculaires les plus probables des anesthésiants absorbés par inhalation. Dans l'étude présentée ici, on a étudié l'interaction d'un système à canal ionique simplifié, la gramicidine, avec l'halothane, une petite molécule d'alcane halogéné utilisée comme anesthésiant dans divers environnements. Des expériences de piégeage de la fluorescence de la gramicidine D dans de grosses vésicules unilamellaires (GVUL) de dioléoylphosphatidylcholine (DOPC) ont permis de montrer que l'halothane peut interagir directement avec le canal ionique (K_{SV} = 66 M^{-1}). L'halothane permet de piéger la fluorescence des résidus de tryptophane situés aux interfaces de la bicouche lipide – eau ainsi que celles des tryptophanes situés dans des portions plus profondes de la bicouche. Les données du piégeage de la gramicidine D dans des micelles de dodécylsulfure de sodium (DSS) révèlent que les résidus de tryptophane situés à l'interface micelle–solvant sont piégés d'une façon préférentielle par l'halothane (K_{SV} = 22 M^{-1}). Dans le 1-octanol, on a observé du piégeage; toutefois la valeur de K_{SV} (K_{SV} = 6 M^{-1}) est beaucoup plus faible que celles observées dans les micelles de GVUL DOPC ou de DSS. Considérés dans leur ensemble, ces résultats suggèrent que les plus fortes interactions sont celles de l'halothane avec la gramicidine qui sont catalysées par une bicouche lipidique et que le mécanisme de l'action anesthésique pourrait aussi être catalysé par les lipides.

Mots-clés : anesthésiques, bicouche lipidique, membrane de protéine, piégeage de la fluorescence.

[Traduit par la Rédaction]

Introduction

Inhaled anesthetics were introduced in surgery over a century ago. To this day, the molecular mechanism of anesthetic action remains elusive. At the beginning of the twentieth century, Overton and Meyer noted a strong correlation between oil solubility of general anesthetics and their anesthetic potency (1, 2) (Overton–Meyer correlation). As a result of the Overton–Meyer correlation, it was hypothesized that inhaled anesthetics exert their action by targeting the lipid matrix of neuronal cell membranes (3).

In recent years, a protein-mediated mechanism of general anesthesia has been favored over the solely lipid-mediated mechanism. Ion channels of neuronal membranes are believed to be the most-likely molecular targets of inhaled anesthetics (4, 5). Emerging evidence suggests that anesthetics

Received 27 February 2007. Accepted 17 May 2007. Published on the NRC Research Press Web site at canjchem.nrc.ca on 20 July 2007.

A. Carnini,[1] T.T. Nguyen, and D.T. Cramb.[2] Department of Chemistry, University of Calgary, 2500 University Drive N.W., Calgary, AB T2N 1N4, Canada.

[1]Present address: Departments of Anesthesia and Critical Care, University of Pennsylvania School of Medicine, Philadelphia, PA 19104, USA.
[2]Corresponding author (e-mail: dcramb@ucalgary.ca).

 doi:10.1139/V07-064 © 2007 NRC Canada

might also interact directly with G-protein-coupled receptors (GPCRs) (6, 7). However, a specific receptor for general anesthetics has yet to be identified.

A molecular understanding of the mechanism of anesthesia will require detailed structural information regarding anesthetic–protein complexes. This presents a challenge when working with membrane proteins, since structural information is scarce. To overcome this problem, novel approaches have included using well-defined water-soluble model systems, such as synthetic four α-helix bundles (8) and the naturally occurring serum albumin proteins. These studies have indicated that inhaled anesthetics bind to pre-existing hydrophobic cavities or defects found within water-soluble protein model systems. Within these cavities, dipole – induced dipole interactions between anesthetics and hydrophobic side chains, such as tryptophan and phenylalanine, have been found to further stabilize and increase binding affinities (9, 10). The current consensus is that inhaled anesthetics interact with proteins via weak hydrogen and van der Waals bonding. Recent work by Liu et al. has shown that in the case of ferritin, a natural 4-helix bundle containing protein, weak polar interactions can in fact confer significant anesthetic selectivity (11).

Despite the significant insights into inhaled anesthetic – protein interactions obtained from water-soluble protein studies, the structural requirements for optimal anesthetic binding in membrane proteins is unclear. In the study presented here, we investigate the interaction of a simplified ion-channel system, gramicidin, with halothane, a small haloalkane-inhaled anesthetic. Halothane, although seldom used in clinical work today, is frequently used in veterinary medicine and in drug–protein binding studies. Gramicidin is a well-characterized small polypeptide composed of alternating D- and L-amino acids (12, 13). Gramicidin D is a mixture of three main isoforms, with the sequence of the most abundant (~85%) gramicidin A being HCO–L-Val_1–Gly_2–L-Ala_3–D-Leu_4–L-Ala_5–D-Val_6–L-Val_7–D-Val_8–L-Trp_9–D-Leu_{10}–L-Trp_{11}–D-Leu_{12}–L-Trp_{13}–D-Leu_{14}–L-Trp_{15}–$NHCH_2CH_2OH$. The lower-abundance isoforms, gramicidin B and C, differ at residue 11 (Trp_{11}(gA):Phe_{11}(gB):Tyr_{11}(gC) is 85:15:5 mol%, respectively). Gramicidin's secondary structure is solvent-dependent (14, 15). In lipid bilayers, gramicidin forms dimeric ion channels by the association of two right-handed, single stranded beta-helical monomers, each of which spans a single-bilayer leaflet (16). In organic solvents, gramicidin can adopt a variety of conformers: monomer or left-handed and right-handed double helices. In SDS micelles, gramicidin has been shown to adopt the single-stranded beta-helical monomer conformation (17). The structures of gramicidin are depicted in Fig. 1, which also includes a space-filling model of halothane for comparison. Gramicidin has been previously used as a model in anesthetic – ion-channel studies using NMR (17), photoaffinity (18) labeling, and molecular dynamics simulations (19, 20).

Presently, we have investigated the gramicidin-inhaled anesthetic interaction in a DOPC lipid bilayer in sodium dodecyl sulphate (SDS) micelles and in octanol by steady-state fluorescence quenching. Fluorescence-quenching experiments have been previously used to determine the binding of halothane to serum albumin (21). Halothane quenching of aromatic side chains (tryptophan, tyrosine, and phenylalanine) fluorescence is thought to occur as a result of an increase in intersystem crossing, which arises by spin–orbit coupling between the excited singlet state of the aromatic ring and the heavy atoms of chlorine and bromine (22). Our results indicate that the strongest interaction between gramicidin and halothane occurs in the lipid-bilayer environment. This suggests that although anesthetics may directly bind with membrane proteins, it is likely they do so mediated by lipids in the cell membrane.

Materials and methodology

1,2-Dioleoyl-sn-3-glycero-3-phosphocholine (DOPC) was purchased from Avanti Polar Lipids (Alabaster, AL). 2-Bromo-2-chloro-1,1,1-trifluoroethane (Halothane) 99% (0.01% thymol), sodium dodecyl sulfate (SDS), and gramicidin D were purchased from Sigma-Aldrich Chemical Co. (St. Louis, MO). All reagents were used as delivered. Ultrapure water was used in the preparation of buffers and aqueous solutions using a Mega Pure™ System ACS (Corning, NY).

Preparation of gramicidin-containing large unilamellar DOPC vesicles (LUVS) and SDS micelles

Solutions of large unilamellar vesicles (LUVS) were prepared from a chloroform lipid stock (2.5 mg/mL). An appropriate aliquot of chloroform–lipid stock was transferred to a 10 mL volumetric flask to give a final lipid concentration of 0.1 mmol/L (0.25 mg/mL lipid). Stock solutions of gramicidin D were prepared in methanol (1 mmol/L final concentration). An aliquot of the protein stock was mixed with an aliquot of the lipid–chloroform stock. The organic solvents were evaporated using nitrogen. The final gramicidin concentration was 1 μmol/L, giving a DOPC:gramicidin molar ratio of 100:1. The lipid – gramicidin D film was resuspended in 10 mmol/L phosphate buffer (pH = 7.0) by stirring for 1 h. Under very similar conditions, gramicidin was found to adopt a right-handed, single-stranded beta-helical conformation (23). Large unilamellar vesicles were prepared by sonication using a sonicator bath (Laboratory Supplies Co, Inc.) followed by extrusion through a 100 nm polycarbonate membrane using an Avanti MiniExtruder. Alternatively, DOPC LUVS were prepared using a probe sonicator. The lipid solutions were kept on ice to prevent overheating because of the sonication energy. The solutions were sonicated in 10 s pulses to a total of five sonication cycles at which point the lipid solution was clear.

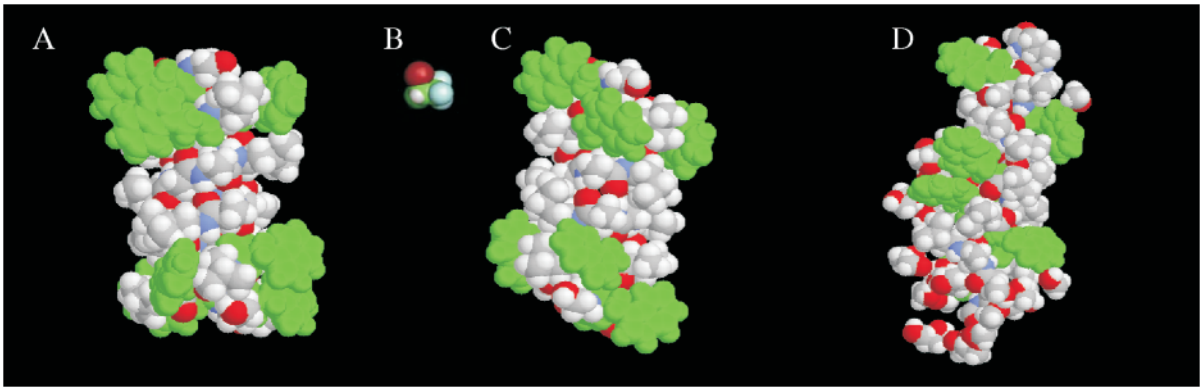
SDS micelles were prepared by dissolving the detergent in ultrapure water to a final concentration of 80 mmol/L. Solutions were allowed to stir for 1.5 h and then sonicated up to 30 min. Aliquots of gramicidin stock in methanol were added to a volumetric flask, and the organic solvent was evaporated with nitrogen gas. The protein film was resuspended with the micelle solution by stirring for an hour and sonicating for 5 min.

Acquisition of spectra and fluorescence-quenching analysis

The four tryptophan residues that gramicidin contains are the only fluorescent moieties in the polypeptide. Fluorescence experiments were performed using a Cary-Eclipse fluorimeter. Protein emission spectra were collected by exciting samples

© 2007 NRC Canada

Fig. 1. Space-filling models of: A) Gramicidin A in DMPC. Ion-channel conformation of gramicidin A, the major component of gramicidin D, in a hydrated DMPC bilayer, obtained by solid-state NMR (minimized energy structure). This structure was obtained from the Protein Data Bank (File: 1MAG.pdb). The channel length is approximately 5.2 nm (bilayer not shown). B) halothane. C) gramicidin A dimer in an SDS micelle, obtained by solid-state NMR (minimized energy structure). This structure was obtained from the Protein Data Bank (File: 1JNO). D) gramicidin A double-helix dimer in methanol, obtained by X-ray diffraction of a crystal obtained in methanol (resolution 1.3 A). This structure was obtained from the Protein Data Bank (File: 1ALX.pdb). The images of gramicidin A were generated using RASMOL. The tryptophan residues are shown in green. The image of halothane was generated using PyMol (DeLano Scientific, San Carlos, CA, USA).



with 280 nm, and emission and excitation slit widths were set at 5 nm. Fluorescence-quenching data for 1-octanol solution was analyzed using the Stern–Volmer equation

$$[1] \qquad F_0/F = 1 + K_{SV}[Q]$$

where F_0 and F are the integrated fluorescence intensities of the main tryptophan fluorescence peak in the absence and presence, respectively, of the quencher, Q; and K_{SV} is the Stern–Volmer quenching constant.

Fluorescence-quenching data in LUV and micelle media were analyzed using a modified Stern–Volmer equation, which accounts for the partitioning of halothane into the LUVs and micelles (24)

$$[2] \qquad \frac{F_0}{F} = \left(1 + \frac{K_{SV}K_{part}[Q]_{tot}}{1 + K_{part}\gamma_L[L]}\right)$$

where K_{part} is the water–lipid partition constant, $[Q]_{tot}$ is the total quencher concentration for the entire solution, $[L]$ is the lipid (or surfactant) concentration, and γ_L is the partial molar volume of the lipid (or surfactant).

Results

Since a large amount of evidence suggests a protein-mediated mechanism of general anesthesia, we investigated the interaction of halothane with the peptide ion channel, gramicidin, within bilayers and bilayer-mimetic environments. This was done to ascertain the effect of the local environment on halothane–gramicidin interactions. In previous work, we examined the location of inhaled anesthetic in a fluorescently labeled DOPC lipid bilayer (25). We found that halothane locates on the acyl chain side, near the headgroup region of the bilayer (25). Therefore, we might anticipate a heterogeneous distribution of halothane around gramicidin in bilayer environments.

Fluorescence quenching in DOPC unilamellar vesicles

The quenching of gramicidin D by halothane in a lipid bilayer was studied using DOPC LUVS (50 nm radius). Analysis of the emission spectra indicated that halothane preferentially quenches the long-wavelength-emitting tryptophans. Figure 2 shows the emission spectrum of tryptophan in the presence of halothane over a range of concentrations (0.1 mmol/L to 20 mmol/L). A large fraction of the accessible tryptophan residues is extensively quenched at halothane concentrations as low as 0.1 mmol/L. At 10 mmol/L halothane, the fluorescent signal was almost entirely quenched. The emission maximum of tryptophan in DOPC LUV occurred at 335 nm, indicative of a partial hydrophobic-residue environment. The quenching of tryptophan in DOPC LUVS resulted in a shift of the λ_{max} to longer wavelengths. Normalization of the spectra shows that the λ_{max} shifted by 20 nm to longer wavelengths (335 nm to 355 nm) (inset of Fig. 2). The small feature at 450 nm is likely a halogenated photoproduct. The integrated emission intensities of the λ_{max} feature were plotted vs. the quencher concentration (Fig. 3) and analyzed according to eq. [2]. From the value of the slope, the Stern–Volmer constant, K_{SV}, was calculated to be 66 M^{-1}.

Fluorescence quenching in SDS micelles

Since the LUV work showed that direct quenching of the ion channel by halothane is possible, we decided to investigate the direct halothane–peptide interaction in SDS micelles. Halothane concentrations ranged from 0.1 mmol/L to 20 mmol/L. The emission spectrum of gramicidin D in the presence of halothane at different concentrations is shown in Fig. 4. The emission maximum of gramicidin occurred at 334 nm in the absence of halothane. At 20 mmol/L halothane concentration, 56% of tryptophan emission was quenched. Quenching of the fluorescence by higher halothane concentrations was accompanied by a significant shift of the emission maximum to shorter wavelengths. Normalization of the emission spectra, as shown in the inset of Fig. 4, revealed that greatest effects on the position of the

© 2007 NRC Canada

Fig. 2. Quenching of gramicidin D by halothane present at different concentrations in DOPC LUVs. The tryptophan λ_{max} in DOPC LUVs was at 335 nm in the absence of the anesthetic (λ_{ex} = 280 nm). Halothane was used at 0.1, 0.5, 1, 10, and 20 mmol/L. The normalized spectra are shown in the inset. Note the shift in λ_{max} to longer wavelengths. The prominent shoulder at ~450 nm is likely a photoproduct.

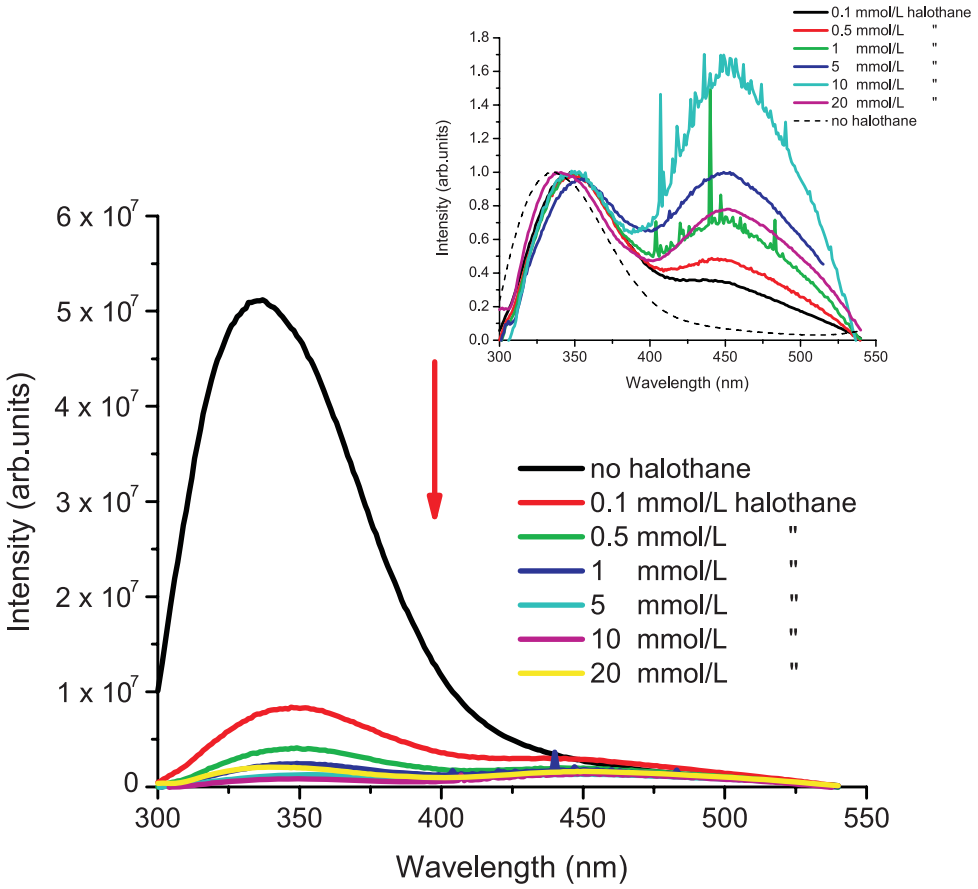
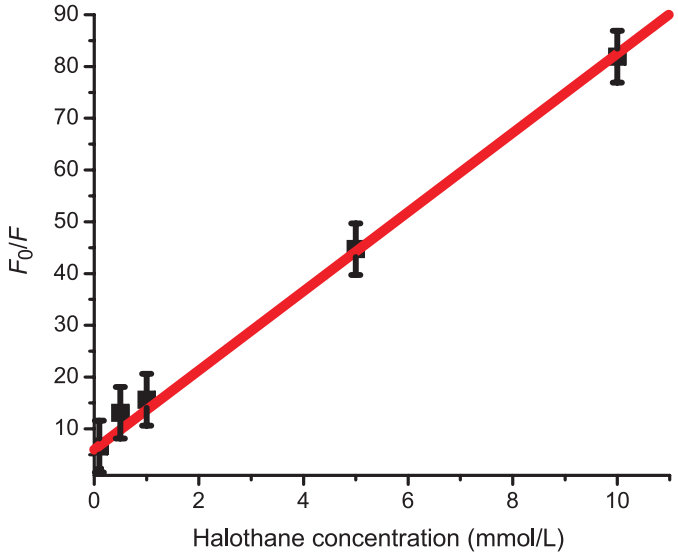
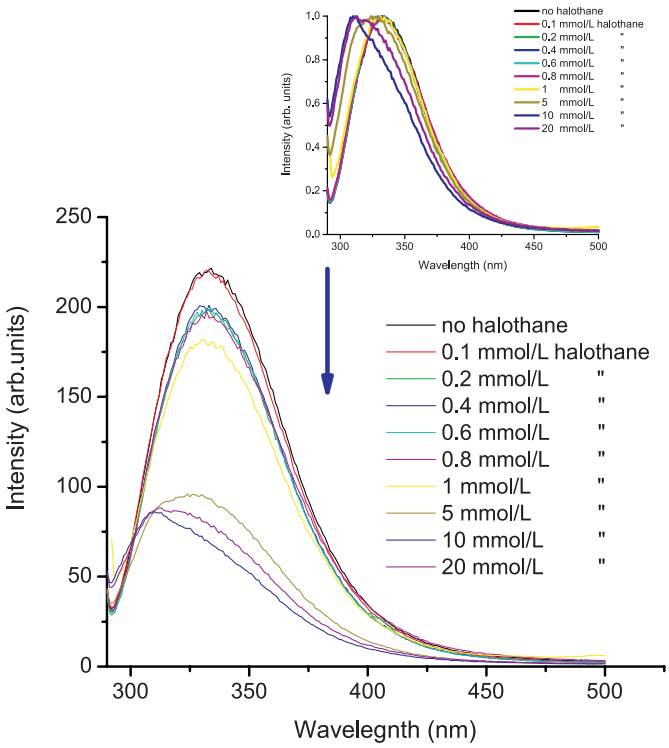


Fig. 3. Stern–Volmer plot for the quenching of gramicidin in DOPC LUVS. The calculated K_{SV} was 66 M^{-1}, using eq. [2].



© 2007 NRC Canada

Fig. 4. Quenching of gramicidin D in SDS micelles. The tryptophan λ_{max} in SDS micelles was 334 nm in the absence of the anesthetic (λ_{ex} = 280 nm). The normalized spectra are shown in the inset. Note the large blue shift of λ_{max} from 334 nm to 312 nm at higher halothane concentrations.



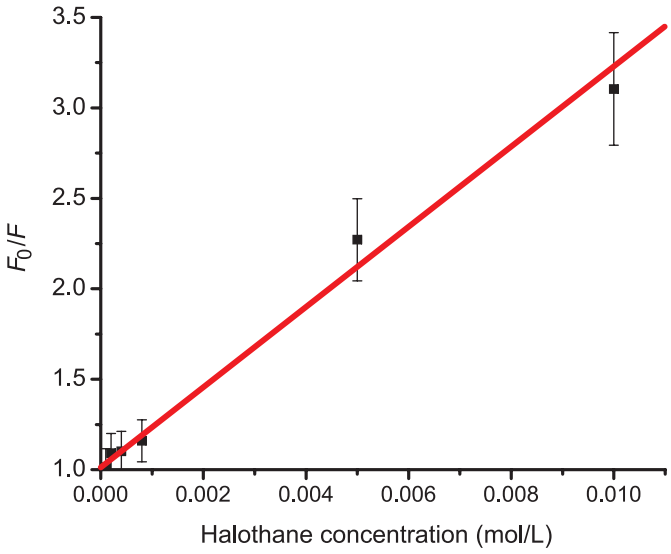
λ_{max} was observed at 10 mmol/L and higher halothane concentration. At these concentrations, λ_{max} shifted 22 nm to shorter wavelength (334 nm to 312 nm) because of an increased influence of the SDS micelle CH Raman-scattering peak (26). At 5 mmol/L halothane, λ_{max} shifted only 5 nm to shorter wavelengths, whereas at lower concentrations (0.1 mmol/L to 1 mmol/L), the emission maximum remained unchanged at 334 nm. Similar to the study in LUVS, the Stern–Volmer plot was linear (Fig. 5). The K_{SV} calculated using eq. [2] was 22 M^{-1}.

Quenching of gramicidin D in octanol

To ascertain if conformation can affect halothane–gramicidin interactions, we investigated halothane quenching in 1-octanol. Gramicidin can be present in different conformers, depending on the organic solvent used (14). An equilibrium mixture of both parallel and antiparallel double helices is present in octanol, and above the dimerization constant for gramicidin, the predominant conformer is expected to be the left-handed antiparallel double helix (14). In our 1-octanol study, gramicidin concentration was below the peptide-dimerization constant (2 μmol/L). As a result, gramicidin monomers were almost exclusively present in solution.

Figure 6 shows the emission spectrum of gramicidin D in 1-octanol in the presence of 0.2 mol/L to 1.2 mol/L halothane. Quenching of the emission maximum at 340 nm increased with increasing halothane concentration. A blue-shifted peak in octanol appears after halothane is added as evidenced by an additional feature at 0.2 mol/L halothane

Fig. 5. Stern–Volmer plot for the quenching of gramicidin in SDS micelles. The calculated K_{SV} from eq. [2] was 22 M^{-1}.



(Fig. 6). By 0.4 mol/L halothane, the emission spectrum has shifted entirely over to the feature at 310 nm, which then decreases in intensity with increasing halothane. This feature is Raman-scattering peak for OH stretch (3300 cm^{-1}) of 1-octanol (26, 27), which was revealed as the fluorescence of tryptophan was quenched. Plotting of the integrated emission intensity vs. quencher concentrations yielded a linear Stern–Volmer plot with a K_{SV} value of 6 M^{-1} determined using eq. [1] (Fig. 7).

Discussion

To elucidate some of the molecular details of anesthetic – membrane protein interactions, we studied the halothane-induced quenching of tryptophan fluorescence in gramicidin. Gramicidin has been shown to create an ion channel through the association of two monomers, each of which spans one leaflet in a lipid bilayer. Each of the four tryptophan residues per monomer has a unique orientation in the lipid bilayer as indicated by several studies (28–31) (see Fig. 1). Tryptophan at position 9 is buried deepest in the membrane, and the remaining three tryptophan residues are located closer to the lipid – aqueous phase interface. The quenching experiments in LUV environments revealed that most tryptophans were equally accessible to halothane, independent of the anesthetic concentrations used, otherwise a sublinear Stern–Volmer plot would result. This suggests that the lipid bilayer mediates anesthetic–gramicidin interactions. The quenching was accompanied by a slight shift of λ_{max} to longer wavelengths. This shift may be the result of halothane increasing the net polarity within the bilayer such that the remaining unquenched tryptophans experience a slightly more-polar environment.

The previous observations agree with findings from recent molecular-dynamics-simulations studies of the gramicidin–halothane system in a fully hydrated DMPC bilayer (20). In this study, Tang et al. showed that halothane targeted the anchoring residues at the channel–lipid interface. Halothane molecules (6 out of 10) were found to migrate towards the

© 2007 NRC Canada

Fig. 6. Quenching of gramicidin D in 1-octanol. The tryptophan λ_{max} in 1-octanol was 337 nm in the absence of the anesthetic (λ_{ex} = 280 nm). Halothane was used at 0.1, 0.2, 0.4, 0.8, 1, and 1.2 mol/L.

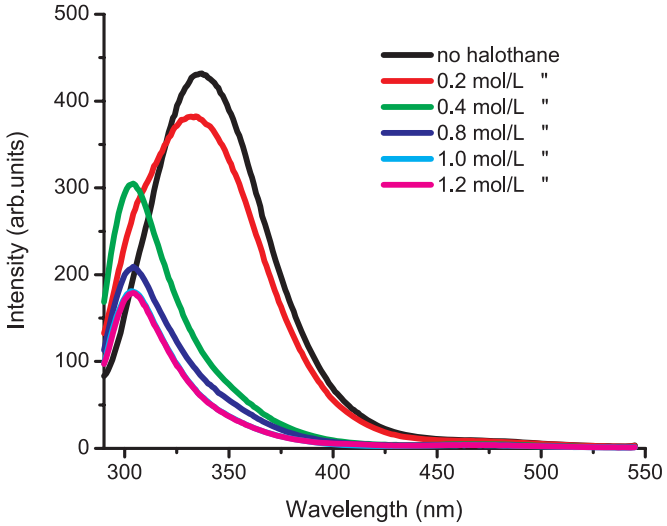
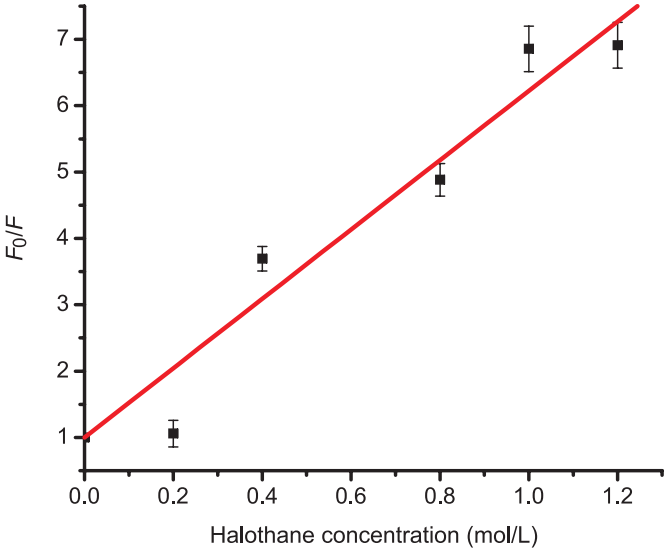


Fig. 7. Stern–Volmer plot for the quenching of gramicidin in 1-octanol. The calculated K_{SV} from eq. [1] was 6 M^{-1}.



membrane interface. It has been previously shown that this interaction requires gramicidin to be in the channel conformation promoted by the lipid environment (18, 32, 33). Tang et al. (18) found that tryptophan 9 and 15 create an amphiphilic pocket in the space between the side chain and lipid headgroups. Such an amphiphilic pocket is an optimal binding site for the slightly polar anesthetic molecule, halothane.

Since we saw evidence of a direct peptide–anesthetic interaction, we were compelled to investigate the halothane–gramicidin system in SDS micelles. As in the case of DOPC LUVS, halothane was found to interact with tryptophan when brought in close proximity in SDS micelles, as indicated by tryptophan fluorescence quenching. Preferential partitioning of halothane at the solvent–micelle interface has been previously reported (25), which suggests that there may be a selective quenching of the tryptophans. Indeed, there appears to be enhanced quenching of the red portion of fluorescence spectrum at lower halothane concentrations in Fig. 3.

Significantly, Tang et al. observed a similar tryptophan-residue arrangement in SDS micelles (18). Moreover, our observation that the preferred interaction between halothane and the tryptophans in gramicidin occurs near the micelle–solvent interface region is corroborated by earlier studies by others (34, 35). Using ^{19}F NMR, Yoshida et al. (34) showed that halothane interacted with SDS micelles at the interfacial region. A later study by Yoshino et al. (35), using the ^{19}F NMR, ^{1}H NMR, and NOE, further confirmed that halothane interacted with the hydrophilic moieties of the SDS micelles.

The quenching of gramicidin in octanol also resulted in a blue shift of the emission maximum. However, in this case the blue-shifted peak arises from Raman scattering.

To gain further insight into the anesthetic binding affinity to gramicidin in its ion channel, we analyzed the quenching data using Stern–Volmer plots. In DOPC LUVS, the Stern–Volmer plot revealed a linear relationship between halothane concentration and the amount of fluorescence quenching. From the slope, the K_{SV} value for the anesthetic–peptide interaction was determined to be 66 M^{-1}. The Stern–Volmer plot for the SDS experiments was also linear. In SDS micelles, the K_{SV} value was found to be 22 M^{-1}.

The presence of the lipid bilayer increased the interaction of halothane by approximately 3-fold (66 M^{-1} in DOPC LUVS vs. 22 M^{-1} in SDS micelles). This increased quenching may lay in different accessibilities of the tryptophans to halothane in the different environments (lipid bilayer vs. micelle).

In organic solvents, gramicidin is present in its non-channel conformation. The different conformation of gramicidin did not prevent halothane quenching from occurring. In the case of 1-octanol, relatively high halothane concentrations (0.1 mol/L to 1.2 mol/L) were required to see an effect on tryptophan emission. The K_{SV} value in 1-octanol is 6 M^{-1}, which is one order of magnitude lower than the value obtained in DOPC LUVs.

The Stern–Volmer quenching constants measured in the current study are similar to those measured for halothane interactions with plasma membrane Ca^{2+}-ATPase (36). However, in contrast to the study by Lopez and Kosk-Kosicka (36), we observe a 3-fold difference between lipid and detergent environments. The fact that the lowest K_{SV} was observed in octanol, which also has the lowest viscosity (η_{oct} = 0.07 P vs. η_{DOPC} = 0.8 P; 1 P = 1 dyn s/cm^2 = 0.1 Pa s), suggests that the quenching is not collisional. Interestingly, the quenching of gramicidin in POPC liposomes by acrylamide produced a K_{SV} of 0.95 M^{-1} (28). Because acrylamide is an aqueous quencher, it is not expected to partition significantly into the bilayer. Thus, the quenching from the study of Rawat et al. (28) was suggested to be collisional, and therefore the Stern–Volmer constant may not be directly comparable to the one determined in the present study.

The value of K_{SV} for halothane–gramicidin interactions in DOPC found in the present work suggests a free energy of binding $\Delta G_{association} \leq -10$ kJ/mol, which is in the range of

© 2007 NRC Canada

van der Waals bonding. The differences between the K_{SV}'s measured here for different environments should reflect the changes in free energy between free and bound halothane in DOPC vs. SDS vs. octanol.

Conclusions

Fluorescence-quenching experiments of gramicidin D in DOPC LUVS have shown that halothane can directly interact with gramicidin. Halothane quenched the fluorescence from tryptophan residues located at the lipid bilayer – aqueous interfaces as good as those located deeper in the bilayer. The partition of halothane in the vesicles may cause an increase in the local polarity as shown by the shift in the tryptophan emission maximum to longer wavelengths. SDS-quenching data revealed that the tryptophan residues located at the micelle–solvent interface were preferentially quenched by halothane. Tryptophan residues located deeper in the bilayer remained partly inaccessible to halothane. The effect of the non-channel conformation on halothane binding to the peptide was investigated in 1-octanol. In 1-octanol, higher anesthetic concentrations were required to detect changes in tryptophan fluorescence emission. Fluorescence quenching was observed, but with a lower K_{SV} value than in DOPC LUVS and SDS micelles.

Taken together, our data suggest that halothane can interact more strongly with gramicidin in the conformation promoted by the lipid bilayer. In turn, this suggests that the lipid matrix may be an important determinant in creating the optimal motif for inhaled-anesthetics binding to other membrane proteins.

Acknowledgements

This work was financially supported by the Natural Sciences and Engineering Research Council of Canada (NSERC).

References

1. E. Overton. Studien über die narkoese zugleich ein beitrag zur allgemeinen pharmakologie. Verlag von Gustav Fisher. Jena, Germany. 1901.
2. H. Meyer. Arch. Exp. Pathol. Pharmakol. **42**, 109 (1899).
3. K.W. Miller. Int. Rev. Neurobiol. **27**, 1 (1985).
4. J.A. Campagna, K.W. Miller, and S.A. Forman. N. Eng. J. Med. **348**, 2110 (2003).
5. N.P. Franks and W.R. Lieb. Nature (London), **367**, 607 (1994).
6. Y. Ishizawa, P.A. Liebman, and R.G. Eckenhoff. Biophys. J. **78**, 154A (2000).
7. Y. Ishizawa, R. Pidikiti, P.A. Liebman, and R.G. Eckenhoff. Mol. Pharmacol. **61**, 945 (2002).
8. J.S. Johansson and R.G. Eckenhoff. Pharmacol. Rev. **49**, 343 (1997).
9. J.S. Johansson, D. Scharf, L.A. Davies, K.S. Reddy, and R.G. Eckenhoff. Biophys. J. **78**, 982 (2000).
10. G.A. Manderson and J.S. Johansson. Biochemistry, **41**, 4080 (2002).
11. R.Y. Liu and R.G. Eckenhoff. Anesthesiology, **102**, 799 (2005).
12. G.A. Woolley and Wallace. Membrane protein structure: lessons from gramicidin. Oxford University Press. 1994. p. 314.
13. B.A. Wallace. J. Struct. Biol. **121**, 123 (1998).
14. Y. Chen and B.A. Wallace. Biopolymers, **42**, 771 (1997).
15. Y. Chen and B.A. Wallace. Biophys. Chem. **65**, 65 (1997).
16. M. Goulian, N.O. Mesquita, D.K. Fygenson, C. Nielsen, O.S. Andersen, and A. Libchaber. Biophys J. **74**, 328 (1998).
17. P. Tang, P.K. Mandal, and M. Zegarra. Biophys. J. **83**, 1413 (2002).
18. P. Tang, R.G. Eckenhoff, and Y. Xu. Biophys. J. **78**, 1804 (2000).
19. Z.W. Liu, Y. Xu, and P. Tang. Biophys. J. **88**, 3784 (2005).
20. P. Tang and Y. Xu. Proc. Natl. Acad. Sci. USA. **99**, 16035 (2002).
21. J.S. Johansson, R.G. Eckenhoff, and P.L. Dutton. Anesthesiology, **83**, 316 (1995).
22. J.R. Lakowicz. Principles of fluorescence spectroscopy. Kluwer Academic/Plenum Publishers. NY. 1999.
23. S.V. Sychev, L.I. Barsukov, and V.T. Ivanov. Eur. Biophys. J. **22**, 279 (1993).
24. N.C. Santos, M. Prieto, and M.A.R.B. Castanho. Biochim. Biophys. Acta, **1612**, 123 (2003).
25. A. Carnini, H. Phillips, L. Shamrakov, and D. Cramb. Can. J. Chem. **82**, 1139 (2004).
26. K. Kamogawa, K. Tajima, K. Hayakawa, and T. Kitagawa. J. Phys. Chem. **88**, 2494 (1984).
27. F. Palombo, M. Paolantoni, S. Paola, A. Morresi, and R.S. Cataliotti. J. Mol. Liq. **125**, 139 (2006).
28. S.S. Rawat, D.A. Kelkar, and A. Chattopadhyay. Biophys. J. **87**, 831 (2004).
29. T.W. Allen, O.S. Andersen, and B. Roux. J. Am. Chem. Soc. **125**, 9868 (2003).
30. R.R. Ketchem, B. Roux, and T.A. Cross. Structure, **5**, 1655 (1997).
31. R.R. Ketchem, W. Hu, and T.A. Cross. Science (Washigton D.C.), **261**, 1457 (1993).
32. P. Tang, J. Hu, S. Liachenko, and Y. Xu. Biophys. J. **77**, 739 (1999).
33. P. Tang, V. Simplaceanu, and Y. Xu. Biophys. J. **76**, 2346 (1999).
34. T. Yoshida, K. Takahashi, H. Kamaya, and I. Ueda. J. Colloid Interface Sci. **124**, 176 (1988).
35. A. Yoshino, K. Murate, T. Yoshida, H. Okabayashi, P.R. Krishna, H. Kamaya, and I. Ueda. J. Colloid Interface Sci. **166**, 375 (1994).
36. M.M. Lopez and D. Kosk-Kosicka. Biophys. J. **74**, 974 (1998).

© 2007 NRC Canada

Synthesis, characterization, and crystal structures of novel oligomeric Zn(II) and Cd(II) complexes with *N,N′*-dimethyl-2,2′-biimidazole

Letitia M. Gruia, Fernande D. Rochon, and André L. Beauchamp

Abstract: Zn(II) and Cd(II) complexes with *N,N′*-dimethyl-2,2′-biimidazole (Me_2biim) were synthesized and characterized by IR spectroscopy and by X-ray crystallographic methods. The reaction of zinc perchlorate with Me_2biim produced the dinuclear compound $[(Me_2biim)Zn(\mu\text{-}Me_2biim)_3Zn(Me_2biim)](ClO_4)_4$, containing two monodentate and three bridging Me_2biim ligands bonded to Zn atoms in a distorted tetrahedral environment. A related neutral $(NO_3)_2Cd(\mu\text{-}Me_2biim)_3Cd(NO_3)_2$ complex, containing only bridging Me_2biim ligands, was also synthesized, in which the distorted octahedral coordination of each Cd atom is completed by one monodentate and one bidentate nitrato ligand. Two ionic trinuclear Cd compounds were also obtained, which include two sets of three bridging Me_2biim ligands connecting a central Cd atom to two terminal Cd centers. An extra Me_2biim ligand is chelated to each terminal metal, and the sixth coordination site is occupied by water molecules in the symmetric $[(Me_2biim)(H_2O)Cd(\mu\text{-}Me_2biim)_3Cd(\mu\text{-}Me_2biim)_3Cd(H_2O)(Me_2biim)](ClO_4)_6$ complex, whereas the aqua ligand is replaced by methanol at one of the terminal units in the non-symmetric $[(Me_2biim)(H_2O)Cd(\mu\text{-}Me_2biim)_3Cd(\mu\text{-}Me_2biim)_3Cd(CH_3OH)(Me_2biim)](ClO_4)_6$ compound. In the chelating ligands, dihedral angles of ~38° between the two imidazole rings reduce repulsion between the *N*-methyl groups, but considerable strain remains, as evidenced from one of the Cd–N bonds being much longer than the other. In the various compounds, dihedral angles of 60–80° are found between the imidazole rings in the bridging ligands, and intramolecular inter-ligand π–π stacking contributes to stabilization.

Key words: zinc, cadmium, dimethylbiimidazole, crystal structure, dinuclear, trinuclear.

Résumé : Des complexes de Zn(II) et Cd(II) avec le *N,N′*-diméthyl-2,2′-biimidazole (Me_2biim) ont été synthétisés et caractérisés par spectroscopie IR et par diffraction des rayons X. La réaction du perchlorate de zinc avec Me_2biim conduit au composé dinucléaire $[(Me_2biim)Zn(\mu\text{-}Me_2biim)_3Zn(Me_2biim)](ClO_4)_4$, qui renferme deux ligands Me_2biim monodentates et trois pontants, définissant un environnement tétraédrique déformé autour du métal. Dans le composé neutre analogue $(NO_3)_2Cd(\mu\text{-}Me_2biim)_3Cd(NO_3)_2$ comportant seulement des ligands Me_2biim pontants, la coordination octaédrique déformée de chacun des atomes de Cd est complétée par deux ligands nitrato, l'un monodentate, l'autre bidentate. Deux composés ioniques trinucléaires de Cd ont aussi été obtenus. Ils renferment deux séries de trois ligands Me_2biim pontants reliant un atome de Cd central à deux atomes de Cd terminaux. Un ligand Me_2biim additionnel est chélaté à chacun des atomes terminaux. Le sixième site de coordination est occupé par des molécules d'eau dans le complexe symétrique $[(Me_2biim)(H_2O)Cd(\mu\text{-}Me_2biim)_3Cd(\mu\text{-}Me_2biim)_3Cd(H_2O)(Me_2biim)](ClO_4)_6$, alors que le ligand aqua est remplacé par le méthanol pour l'un des motifs terminaux dans le composé non-symétrique $[(Me_2biim)(H_2O)Cd(\mu\text{-}Me_2biim)_3Cd(\mu\text{-}Me_2biim)_3Cd(CH_3OH)(Me_2biim)](ClO_4)_6$. Dans les ligands chélatants, des angles dièdres de ~38° entre les cycles imidazoles diminuent la répulsion entre les groupements *N*-méthyles, mais la présence d'une liaison Cd-N beaucoup plus longue que l'autre indique qu'il reste beaucoup de tension dans le chélate. Dans les différents composés, les angles dièdres entre les cycles imidazole dans les ligands pontants sont de 60–80° et des interactions inter-ligand intramoléculaires de type « π–π stacking » contribuent à la stabilization.

Mots-clés : zinc, cadmium, diméthylbiimidazole, structure cristallographique, dinucléaire, trinucléaire.

Introduction

Imidazole is an aromatic moiety that can be protonated or deprotonated without losing its aromaticity, and the connection of two such units in 2,2′-biimidazole (H_2biim, Chart 1) opens a variety of possible protonation patterns and chelating and (or) bridging coordination modes. Because of this broad versatility, this ligand has received much attention in recent years for eventual applications, such as electron transport materials (1), molecular arrays with desirable topology (2), systems with interesting catalytic properties (3, 4), polymers with good thermal stability (5), and anticancer agents (6).

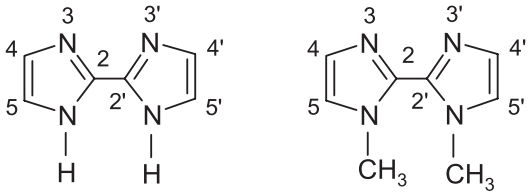
Received 2 February 2007. Accepted 6 June 2007. Published on the NRC Research Press Web site at canjchem.nrc.ca on 20 July 2007.

L.M. Gruia and A.L. Beauchamp.[1] Département de Chimie, Université de Montréal, C. P. 6128, Succ. Centre-Ville, Montréal, QC H3C 3J7, Canada.
F.D. Rochon. Département de Chimie, Université du Québec à Montréal, C. P. 8888, Succ. Centre-Ville, Montréal, QC H3C 3P8, Canada.

[1]Corresponding author (e-mail: andre.beauchamp@umontreal.ca).

 doi:10.1139/V07-061 © 2007 NRC Canada

Chart 1. Syn conformation shown.



H_2biim **Me_2biim**

The 2,2′-biimidazole molecule has the anti conformation in the solid state, forming one-dimensional hydrogen-bonded ribbons with extensive inter-chain π–π stacking (7). It can coordinate to metals as a non-deprotonated, mono-deprotonated or bi-deprotonated ligand (8). In the neutral form, it usually binds in a chelating fashion, which imposes a syn conformation and appreciable strain to the metal complex, since the "bite" angle is ~75° (9). In these compounds, H_2biim remains planar, which maximizes aromaticity, and it forms numerous hydrogen bonds with its environment, which contribute to the stabilization of these systems. Occasionally, H_2biim binds as a bridging ligand, for instance in $[Zn_2(\mu\text{-}H_2biim)(H_2biim)_4](ClO_4)_4$ (10), despite the fact that the imidazole rings are no longer coplanar (dihedral angle ≈ 50°).

The chemistry of the *N*,*N*′-dimethyl derivative (Me_2biim) is very different. The free molecule exists as the anti conformer (11), and in the syn conformation required for chelate formation, steric hindrance between the methyl groups forces the two imidazole rings out of planarity. This characteristic reduces its chelating ability, but promotes a bridging role. In the literature, Me_2biim was reported to act as a chelating bidentate ligand in the mononuclear $PtI_2(Me_2biim)$, $PtCl_4(Me_2biim)$, and $SnMe_2Br_2(Me_2biim)$ complexes (12–14), but as a bridging ligand in $\{OReCl_2\}_2(\mu\text{–}O)(\mu\text{–}Me_2biim)_2$ (15), $\{PtBr(DMSO)\}_2(\mu\text{-}Me_2biim)$ (16), $[Ag(\mu\text{-}Me_2biim)]NO_3$ (17), $[\{Cu(H_2O)\}_2(\mu\text{-}Me_2biim)_4](NO_3)_4$ (18), and $[\{Cu(H_2O)\}_2(\mu\text{-}Me_2biim)_4](ClO_4)_4$ (19).

We recently described the synthesis and crystal structures of various Zn(II) and Cd(II) compounds with H_2biim (9). These two metal centers were selected because they cannot be readily oxidized or reduced; they are devoid of ligand-field effects, and their plastic coordination spheres can adjust to a certain extent to the coordinating preferences of the ligands. All these H_2biim complexes contained chelated ligands and were stabilized by an elaborate hydrogen-bonding system, but no appreciable π–π stacking was observed. This study was extended to Me_2biim, and several Zn(II) and Cd(II) di- or trinuclear compounds were prepared, containing both bridging and terminal monodentate or bidentate Me_2biim ligands. While this work was in progress, Sang and Xu (20) reported on various Cd(II) and Zn(II) compounds of different compositions with the same ligand.

Experimental section

The zinc and cadmium salts (Aldrich), the solvents, and all other chemicals were used as received. Me_2biim was synthesized following the method of Mohanty et al. (21), by methylation of 2,2-biimidazole obtained as described by Fieselmann et al. (22).

The IR spectra were recorded from 4000 to 300 cm^{-1} on a PerkinElmer 783 spectrophotometer as KBr or CsI pellets. Elemental analyses were performed in the Laboratoire d'analyse élémentaire de l'Université de Montréal. Mass spectra for the Zn compounds were recorded in the FAB^+ mode in nitrobenzyl alcohol at the Centre régional de spectrométrie de masse de l'Université de Montréal. Mononuclear and dinuclear fragments were distinguished from isotope distribution. The most intense component is due to the ^{64}Zn isotopomer for monomeric fragments; whereas two peaks of comparable heights corresponding to $^{64}Zn^{66}Zn$ and $^{64}Zn^{68}Zn/^{66}Zn^{66}Zn$ are observed for dinuclear species. Good mass spectra were not obtained for the Cd compounds.[2]

$[(Me_2biim)Zn(\mu\text{-}Me_2biim)_3Zn(Me_2biim)](ClO_4)_4\cdot 1/2H_2O$ (1)

The zinc salt and the ligand were reacted in a 1:2 molar ratio. Accordingly, $Zn(ClO_4)_2\cdot 6H_2O$ (37.2 mg; 0.10 mmol) was dissolved in 10 mL of water, and Me_2biim (32.4 mg; 0.20 mmol) was added while stirring. The reaction was stopped after 3 h, and the clear solution was evaporated under reduced pressure to a volume of 2 mL, from which colorless crystals deposited upon standing at room temperature for one week. Anal. calcd. for $Zn_2Cl_4O_{16}N_{20}C_{40}H_{50}\cdot 1/2H_2O$: C 35.63, H 3.81, N 20.77; found: C 35.32, H 3.83, N 20.61. FAB^+-MS: m/z = 487 $[^{64}Zn(Me_2biim)_2(ClO_4)]^+$.

$[(H_2O)Zn(\mu\text{-}Me_2biim)_3Zn(H_2O)](NO_3)_4\cdot H_2O$ (2)

$Zn(NO_3)_2\cdot 6H_2O$ (29.7 mg; 0.10 mmol) was dissolved in 10 mL of methanol, and Me_2biim (32.4 mg; 0.20 mmol) was added while stirring. After 3 h, the reaction was stopped, and the clear solution was concentrated to 2 mL and kept in a refrigerator. Colorless crystals deposited after 48 h. Anal. calcd. for $Zn_2N_{16}C_{24}H_{34}O_{14}$: C 31.98, H 3.80, N 24.86; found: C 32.38, H 3.88, N 25.11. FAB^+-MS: m/z = 802/804 (36%) $[Zn_2(Me_2biim)_3(NO_3)_3]^+$; 640/642 (30%) $[Zn_2(Me_2biim)_2(NO_3)_3]^+$; 450 (55%) $[Zn(Me_2biim)_2(NO_3)]^+$; 288 (100%) $[Zn(Me_2biim)(NO_3)]^+$. The preparation of this compound by a slightly different method was recently reported (20).

$(NO_3)_2Cd(\mu\text{-}Me_2biim)_3Cd(NO_3)_2$ (3)

$Cd(NO_3)_2\cdot 4H_2O$ (30.8 mg; 0.10 mmol) was dissolved in 2.5 mL of methanol, and Me_2biim (32.4 mg; 0.20 mmol) was added while stirring. After 2 h, the clear solution was left in a refrigerator. A homogeneous sample of colorless crystals deposited after 24 h. The composition was obtained from the X-ray diffraction study.

$[(Me_2biim)(H_2O)Cd(\mu\text{-}Me_2biim)_3Cd(\mu\text{-}Me_2biim)_3Cd(H_2O)(Me_2biim)](ClO_4)_6$ (4)

$Cd(ClO_4)_2\cdot 6H_2O$ (41.9 mg; 0.10 mmol) was dissolved in 5 mL of water, and Me_2biim (32.4 mg; 0.20 mmol) was added while stirring. The reaction was stopped 3 h later.

[2] Safety note: Although no problems were encountered, perchlorate salts of cadmium and zinc with organic ligands and solvents are potentially explosive and should be handled only in small quantities.

© 2007 NRC Canada

Colorless crystals deposited after one week at room temperature. Anal. calcd. for $Cd_3Cl_6O_{26}N_{32}C_{64}H_{84}$: C 33.90, H 3.73, N 19.77; found: C 33.69, H 3.60, N 19.55.

[$(Me_2biim)(H_2O)Cd(\mu\text{-}Me_2biim)_3Cd(\mu\text{-}Me_2biim)_3Cd(CH_3OH)(Me_2biim)](ClO_4)_6$ (5)

The cadmium salt and Me_2biim were reacted in a 1:4 molar ratio. Accordingly, $Cd(ClO_4)_2{\cdot}6H_2O$ (104.8 mg; 0.25 mmol) was dissolved in a mixture of 8 mL methanol and 1 mL water. Me_2biim (162 mg; 1.00 mmol) was added while stirring. The clear solution was then transferred into a Teflon autoclave and heated at 115 °C for 12 h. The solution obtained after gradual cooling was kept in a refrigerator, and the crystals were collected after 24 h.

Crystallographic measurements and structure determination

Diffraction intensities for crystals **1**, **3**, and **5** were measured on a Bruker SMART diffractometer with a CCD 2K area detector controlled by the SMART software (23). The graphite-monochromatized Cu Kα radiation was used. Sets of 30 oscillation frames of 0.3° over a range of 9° were recorded in four regions of the reciprocal space, from which the reduced cell was determined by least-squares refinement. The data were collected at room temperature, using a narrow-frame method with scan widths of 0.30° in ω, exposure times being 5 s/frame for **1**, 10 s/frame for **3**, and 8 s/frame for **5**. Frames were recorded for different orientations of the crystal and detector so as to cover at least 95% of the reciprocal sphere. The first 101 frames were remeasured at the end of the data collection to monitor instrument and crystal stability. The data were integrated using SAINT (24), and the intensities were corrected for the Lorentz effect, polarization, and air absorption. A SADABS (25) absorption correction was applied based on the entire data sets. For crystal **5**, two data sets were measured, and redundant reflections were averaged.

For crystal **4**, an Enraf-Nonius CAD-4 diffractometer operating with graphite-monochromatized Cu Kα radiation was used, under the control of the CAD-4 software (26). The reduced cell was initially determined from 25 spots located on a preliminary rotation photograph and centered in the detector aperture. Accurate cell parameters were then determined from the positions of 25 high-angle reflections centered with the SETANG and DETTH procedures. The intensities were recorded at room temperature over the whole sphere by ω/2θ scan, and five standard reflections were measured every hour. An absorption correction based on the crystal geometry was applied using NRCVAX (27). The data were finally corrected for the effects of Lorentz and polarization and averaged.

All structures were solved by direct methods and refined on F^2 by full-matrix least squares. The SHELXTL system (28) was used for all calculations. Unless otherwise stated, all non-hydrogen atoms were refined anisotropically. Hydrogens were added to the model at idealized positions with standard C—, N—, O—H distances. Their isotropic displacement factors U_{iso} were adjusted to 20%–50% above the U_{eq} value for the bonded atom. At the end of the refinement, the VOID routine of PLATON (29) was used to check for the presence of unoccupied space in the structure. Individual details for each structure are given later. The crystal data are summarized in Table 1.[3]

For crystal **3**, the 2/*m* Laue symmetry and the systematic absences (*hkl*, $h + k \neq 2n$; *h0l*, $l \neq 2n$) were consistent with space groups *Cc* and *C*2/*c*. The structure was solved in the centric *C*2/*c* space group. Direct methods revealed the presence of two structural motifs per asymmetric unit; each consisting of a pair of Cd atoms bridged by three Me_2biim ligands. Peaks were found in the Δ*F* map for two well-defined nitrate ions (centered on N3, N4, N5, and N6) bonded to one of the Cd atoms in each motif. The nitrates close to the second Cd atom (centered on N1, N2, N7, and N8) were disordered, and they were described by two or three orientations. The ordered part of the structure was refined anisotropically. Constraints were applied to the nitrates in the refinement to maintain reasonable thermal parameters, to retain a planar structure, and to link the occupancies of nitrates belonging to the same local structural pattern. In the last cycles, the nitrates were refined anisotropically, except those with low occupancies (centered on N1′, N1″, N2′, N7′, and N8′).

Compounds **4** and **5** are isomorphous. Space group $P2_1/c$ was determined unambiguously from the 2/*m* Laue symmetry and systematic absences (*0k0*, $k \neq 2n$; *h0l*, $l \neq 2n$). Structure resolution raised no particular problems in both cases. In compound **4**, obtained from water, the sixth coordination site on each of the two terminal Cd atoms is occupied by an aqua ligand. In **5**, which was prepared from a 8:1 methanol–water solution, the water bonded to one of the terminal Cd atoms is replaced by a methanol ligand. In both cases, some of the ClO_4^- ions show high thermal motion. Attempts were made to use multiple disordered orientations to describe them, but this did not result in a significant improvement. The non-disordered model was retained, but constraints (DFIX) were applied to keep the Cl—O bond lengths and the intra-ionic O···O contacts close to the ideal values.

Compound **1** was found to be triclinic from the Laue symmetry, and resolution took place normally in the centric $P\bar{1}$ space group. No particular problems were encountered with the cationic part of the structure, but the four ClO_4^- ions were severely disordered. They were described by means of three orientations, using constraints as mentioned previously to maintain the tetrahedral geometry and to keep the occupancies normalized to unity. The Δ*F* map finally revealed a peak of 2.5 e/Å^3, suitably positioned to be a lattice water molecule, whose occupancy refined to 0.50. The atoms in the ClO_4^- ions and water molecule were refined

[3] Supplementary data for this article are available on the journal Web site (canjcehm.nrc.ca) or may be purchased from the Depository of Unpublished Data, Document Delivery, CISTI, National Research Council Canada, Ottawa, ON K1A 0R6, Canada. DUD 5181. For more information on obtaining material, refer to cisti-icist.nrc-cnrc.gc.ca/irm/unpub_e.shtml. CCDC 636536 (**1**), 636538 (**3**), 636537 (**4**), and 636539 (**5**) contain the crystallographic data for this manuscript. These data can be obtained, free of charge, via www.ccdc.cam.ac.uk/conts/retrieving.html (Or from the Cambridge Crystallographic Data Centre, 12 Union Road, Cambridge CB2 1EZ, UK; fax +44 1223 336033; or deposit@ccdc.cam.ac.uk).

© 2007 NRC Canada

Table 1. Crystallographic data.

Crystal	**1**	**3**	**4**	**5**
Chemical formula	$C_{40}H_{51}Cl_4N_{20}O_{16.5}Zn_2$	$C_{24}H_{30}Cd_2N_{16}O_{12}$	$C_{64}H_{84}Cd_3Cl_6N_{32}O_{26}$	$C_{65}H_{86}N_{32}O_{26}Cl_6Cd_3$
M_w	1348.54	959.44	2267.53	2281.56
Space group	$P\bar{1}$ (No. 2)	$C2/c$ (No.15)	$P2_1/c$ (No. 14)	$P2_1/c$ (No. 14)
a (Å)	12.7575(2)	27.2842(6)	27.692(1)	27.6075(4)
b (Å)	14.3387(2)	30.5986(7)	13.7910(5)	13.7873(2)
c (Å)	18.2190(3)	20.6720(6)	24.739(1)	24.6723(4)
α (°)	73.382(1)	—	—	—
β (°)	75.400(1)	123.143(2)	108.48(1)	108.443(1)
γ (°)	65.465(1)	—	—	—
Volume (Å^3)	2871.01(8)	14450.4(6)	8960.7(8)	8908.8(2)
Z	2	16	4	4
ρ_{calcd} (g cm^{-3})	1.560	1.764	1.681	1.701
μ (mm^{-1})	3.502	10.142	8.088	8.139
λ (Å)	1.54178	1.54178	1.54178	1.54178
Reflections collected	34991	86386	67269	107945
Independent reflections (R_{int})	10971 (0.030)	14294 (0.074)	16986 (0.097)	17580 (0.122)
Observed reflections ($I > 2\sigma_I$)	8400	8859	7982	13592
Ranges of h, k, l	$-15 \le h \le 15$	$-33 \le h \le 33$	$-33 \le h \le 31$	$-34 \le h \le 33$
	$-17 \le k \le 17$	$-37 \le k \le 37$	$-16 \le k \le 16$	$-15 \le k \le 16$
	$-22 \le l \le 22$	$-23 \le l \le 25$	$-30 \le l \le 30$	$-30 \le l \le 30$
R_1[a] ($I > 2\sigma_I$)	0.0675	0.0524	0.0613	0.0599
wR_2[b] (all data)	0.1985	0.1402	0.1566	0.1845
S[c]	1.068	0.954	0.918	01.086

[a] $R_1 = \sum(||F_o| - |F_c||)/\sum|F_o|$.
[b] $wR_2 = \{\sum[w(F_o^2 - F_c^2)^2]/\sum[w(F_o^2)^2]\}^{1/2}$.
[c] $S = \{\sum[w(F_o^2 - F_c^2)^2]/(N_{reflections} - N_{parameters})\}^{1/2}$.

isotropically. The fractional hydrogens of the water molecule were neglected.

Results and discussion

Synthesis

The reaction between $Zn(ClO_4)_2{\cdot}6H_2O$ and Me_2biim in water in a 1:2 proportion produced colorless crystals, which were identified by X-ray diffraction as the dinuclear compound $[(Me_2biim)Zn(\mu\text{-}Me_2biim)_3Zn(Me_2biim)](ClO_4)_4{\cdot}1/2H_2O$ (**1**), containing three bridging Me_2biim ligands and a terminal monodentate Me_2biim ligand on each Zn atom. When the reaction was performed with $Zn(NO_3)_2{\cdot}6H_2O$ in wet methanol, the dinuclear compound $[(H_2O)Zn(\mu\text{-}Me_2biim)_3Zn(H_2O)](NO_3)_4{\cdot}H_2O$ (**2**) was isolated. Complex **2** contains only bridging Me_2biim ligands; the terminal monodentate Me_2biim ligands of **1** being replaced by aqua ligands. The crystal structure of **2** has been reported recently (20). These compounds were characterized by elemental analysis and by mass spectrometry. In the FAB$^+$ mass spectrum of the aqua species (**2**), peaks corresponding to the $[Zn_2(Me_2biim)_3(NO_3)_3]^+$ and $[Zn_2(Me_2biim)_2(NO_3)_3]^+$ species suggest that the dinuclear framework is rather robust, stabilized by nitrate ions, which have displaced the aqua ligands. For complex **1**, only the mononuclear fragment $[Zn(Me_2biim)_2(ClO_4)]^+$ was detected, perhaps because the dinuclear unit is not efficiently stabilized by the poor donor perchlorate ion.

The reaction of 2 equiv. of Me_2biim with $Cd(NO_3)_2{\cdot}4H_2O$ in methanol produced a neutral dinuclear compound, identified as $\{Cd(NO_3)_2\}_2(\mu\text{-}Me_2biim)_3$ (**3**), in which all Me_2biim ligands are bridging. A similar reaction with $Cd(ClO_4)_2{\cdot}6H_2O$ in water produced colorless crystals of the trinuclear species $[(Me_2biim)(H_2O)Cd(\mu\text{-}Me_2biim)_3Cd(\mu\text{-}Me_2biim)_3Cd(H_2O)(Me_2biim)](ClO_4)_6$ (**4**), containing a central Cd atom bonded to six bridging Me_2biim ligands. In addition, each terminal Cd atom is bonded to a chelated Me_2biim ligand and to an aqua ligand. When the same reaction is performed in a methanol–water mixture with a Cd:Me_2biim proportion of 1:4, an unsymmetrical trinuclear compound $[(Me_2biim)(H_2O)Cd(\mu\text{-}Me_2biim)_3Cd(\mu\text{-}Me_2biim)_3Cd(CH_3OH)(Me_2biim)](ClO_4)_6$ (**5**) is isolated. Similar trinuclear frameworks were observed in crystals of a different perchlorate salt reported recently (20).

All reactions of the Zn(II) and Cd(II) salts with Me_2biim produced oligomeric species containing bridging ligands. In this respect, the dimethylated ligand differs strikingly from H_2biim, which produced monomers containing chelated bidentate ligands only. A major difference between these two ligands is the much greater solubility of Me_2biim, which makes it possible to run the reactions directly with the metal salts under relatively mild conditions. In contrast, many H_2biim complexes had to be synthesized using the silver(I)-assisted transmetallation route involving the intermediate silver complex $[Ag(H_2biim)](NO_3)$ (30).

The five oligomeric Zn(II) and Cd(II) compounds with Me_2biim were characterized by IR spectroscopy and by X-ray crystallography.

© 2007 NRC Canada

IR spectroscopy

The IR spectra (4000–300 cm^{-1}) of free Me_2biim and its complexes were recorded in the solid state, and the frequencies are provided in the Supplementary data (Table S-1).[3] The approximate assignments proposed are based on earlier studies by Perchard and Novak (31–33) on *N*-methylimidazole and its metal complexes.

The spectra of the perchlorate complexes **1**, **4**, and **5** show the characteristic features for the free anion: very strong and broad ν_3 band at ~1090 cm^{-1} and less intense sharp peak for ν_4 at 624 cm^{-1} (10, 34, 35). The ν_1 and ν_2 vibrations are not observed in IR spectroscopy. The free NO_3^- anions in $[(H_2O)Zn(\mu\text{-}Me_2biim)_3Zn(H_2O)](NO_3)_4$ (**2**) give rise to the usual very strong ν_3 absorption at 1391 cm^{-1}, together with a weaker ν_2 band at 827 cm^{-1} (35). The ν_4 vibration is probably hidden by the strong band of Me_2biim at 737 cm^{-1}. In the complex $Cd(NO_3)_2(\mu\text{-}Me_2biim)_3Cd(NO_3)_2$ (**3**), all nitrato units are coordinated, one monodentate and one bidentate. Although the coordination state can sometimes be identified from vibrational spectra, the bands observed here at 1384 and 830 cm^{-1} do not differ from those of a free nitrate anion.

The presence of aqua ligands and water molecules was detected by the characteristic OH stretching mode. While the relatively high ν(O–H) frequency (3621 and 3552 cm^{-1}) observed for **1** indicates that this solvent is not coordinated, the lower ν(O–H) frequency (3480 cm^{-1}) observed in compound **2** confirms the coordination of the molecule and its involvement in hydrogen bonding (8). The aqua ligands in the $[(Me_2biim)(H_2O)Cd(\mu\text{-}Me_2biim)_3Cd(\mu\text{-}Me_2biim)_3Cd(L')(Me_2biim)](ClO_4)_6$ compounds with $L' = H_2O$ (**4**) or CH_3OH (**5**) also give a ν(O–H) band at relatively low frequency (3424 cm^{-1}). The presence of methanol can usually be detected by a characteristic band at 1030 cm^{-1} (9), but it is masked here by the very strong ν_3 band of the ClO_4^- ion.

The Me_2biim bands undergo various displacements, intensity variations, and splittings upon coordination, but most of these changes are relatively small. More significant modifications in two regions may be useful as a diagnostic for the coordination of the imidazole ring, although they cannot discriminate between the bidentate-chelating, bidentate-bridging, and monodentate binding modes. As noted by Perchard and Novak for the complexation of 1-methylimidazole (32), the highest-frequency ring mode occurring at 1511 cm^{-1} in the free ligand is shifted by 15–26 cm^{-1} to higher frequency in the complexes. These authors also noted that another ring mode at ~910 cm^{-1} is displaced by +45 cm^{-1}. The corresponding vibration is found here at 917 cm^{-1} in free Me_2biim and in the 935–970 cm^{-1} range for the complexes. The weak peak at 918 cm^{-1} for complex **1** would be consistent with the presence of an uncoordinated imidazole ring in the monodentate ligand, although it might also origin from a weak ν_4 vibration of ClO_4^- (35).

Owing to the lack of absorption in the 600–400 cm^{-1} range for uncoordinated Me_2biim, absorptions occurring between 400 and 495 cm^{-1} may be assumed to result from metal coordination. Similar vibrations were found at 420 and 490 cm^{-1} for Zn and Cd complexes of H_2biim (9). However, they are probably not due to metal–ligand vibrations, since the ν(M–N) and ν(M–O) modes are expected to show at lower frequency. For instance, the Zn–N bands were reported at ~225 cm^{-1} for $ZnCl_2(py)_2$ (36, 37), 255 and 239 cm^{-1} for $ZnCl_2(imidazole)_2$ (38), 259 and 244 cm^{-1} for $ZnCl_2(1\text{-methylimidazole})_2$ (33), and 271 cm^{-1} for $[Zn(imidazole)_4]^{2+}$ (39). Our bands between 400 and 500 cm^{-1} are believed to result from low-frequency ligand modes involving mainly torsion and (or) deformation motions about the central C2–C2′ bond, whose energy would be raised in the constrained arrangement resulting from the closure of the chelate ring and the anchoring to the metal atoms in the bridging ligand. These modes might involve some motion of the metal, but this contribution is probably modest, since the frequencies are not sensitive to the replacement of Zn by Cd in the complexes.

Crystal structures

Crystal **1** consists of discrete $[(Me_2biim)Zn(\mu\text{-}Me_2biim)_3Zn(Me_2biim)]^{4+}$ ions (Fig. 1) separated by perchlorate anions. The dinuclear cation contains a $Zn(\mu\text{-}Me_2biim)_3Zn$ skeleton, in which three ligands form bridges between the two Zn atoms. An extra Me_2biim ligand is coordinated in a monodentate fashion to each metallic center. There is no binding contact around the free nitrogen atom of the non-bridging ligands. The Zn···Zn separation of 3.88 Å is too large for any significant interaction to take place directly between the metal centers.

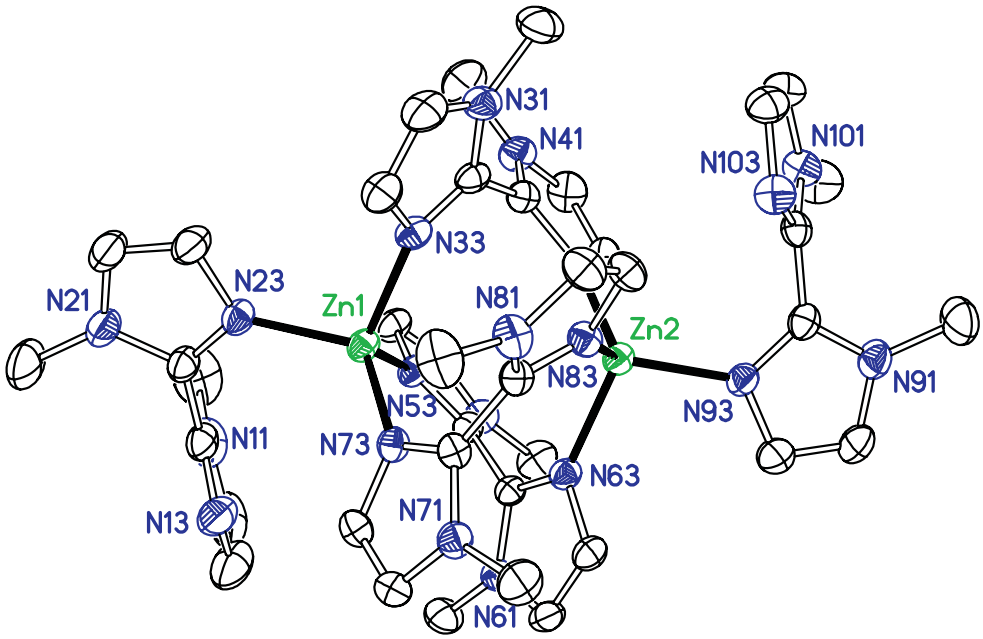
The coordination geometry around each Zn atom is best described as distorted tetrahedral, with the metal atoms exclusively N-coordinated. Selected bond lengths and angles are listed in Table 2. The Zn—N bond lengths are between 1.993(4) and 2.020(4) Å, and there is no difference between the monodentate and bridging distances. They compare well with those found in the tetrahedral $ZnCl_2(imidazole)_2$ complex (1.995(11) and 2.020(11) Å) (40), and they are definitely shorter than those noted for the four-coordinate $ZnCl_2(biimidazole)$ molecule (2.064(3) Å) (9). The $N3_{br}$–Zn–$N3_{br}$ angles (105.1(2)–113.0(2)°) for the bridging ligands are all close to the ideal value. With the terminal monodentate ligands, two of the $N3_t$–Zn–$N3_{br}$ angles vary between 99.8(2)° and 105.0(2)°, while the third one is ~121°. The latter large angles (N23–Zn1–N73 and N83–Zn2–N93) are next to the uncoordinated imidazole ring.

The Me_2biim molecules are not planar; the imidazole rings being rotated with respect to one another about the C2–C2′ bond as a result of steric hindrance between the *N*-methyl groups. For the bridging ligands, the dihedral angle is ~66°, similar to those observed in $\{OReCl_2\}_2(\mu\text{-}O)(\mu\text{-}Me_2biim)_2$ (~62°) (15) and $[(H_2O)Zn(\mu\text{-}Me_2biim)_3Zn(H_2O)](NO_3)_4$ (67–76°) (20). In the terminal ligands, the angles are ~72° and ~57°, respectively. In this conformation, the two Me groups are far apart, and steric hindrance between the uncoordinated imidazole ring and the bridging ligands is minimized.

The bond distances observed in the imidazole moiety and the intra-ring angles are normal, and no appreciable differences are noted between the bonded and the non-coordinated rings. In contrast with chelates of non-methylated biimidazole, where ring closure reduces the C2′–C2–N3 angle ~15° below C2′–C2–N1, these angles in **1** show no appreciable differences for both the bridging and non-bridging ligands. The internal angles Zn–N3–C2 (avg. 131.1(3)°) are systematically larger than the external angles Zn–N3–C4 (avg. 122.4(3)°) for the bridging ligands, as reported for

© 2007 NRC Canada

Fig. 1. ORTEP drawing of the $[(Me_2biim)Zn(\mu\text{-}Me_2biim)_3Zn(Me_2biim)]^{4+}$ cation (**1**). Ellipsoids correspond to 30% probability. Hydrogen atoms are omitted for clarity.



$\{OReCl_2\}_2(\mu\text{-}O)(\mu\text{-}Me_2biim)_2$ (15) and $[(H_2O)Zn(\mu\text{-}Me_2biim)_3Zn(H_2O)](NO_3)_4$ (20). For the terminal monodentate ligands, the difference is much smaller; the average angle being 128.1(3)° for Zn–N3–C2 and 125.4(4)° for Zn–N3–C4.

The conformation of the bridging ligands makes it possible for one ring of each ligand to be parallel to and facing a ring in another ligand (Fig. 1). The ring–ring distances of ~3.3 Å, slightly smaller than the van der Walls distance for aromatic rings, suggest the presence of significant π–π interactions, which undoubtedly reinforce the structural integrity of the $Zn(\mu\text{-}Me_2biim)_3Zn$ unit.

A view of the unit cell is provided in the Supplementary data (Fig. S-1).[3] The complex cations are seen to pack as well-separated entities, surrounded by ClO_4^- counterions.

Compound **3** consists of the neutral dinuclear species $(NO_3)_2Cd(\mu\text{-}Me_2biim)_3Cd(NO_3)_2$ (Fig. 2), in which the two Cd atoms are bridged by three Me_2biim ligands. This framework, observed before in the dinuclear zinc compound, has not been reported so far for cadmium. Furthermore, in this case, the metal is six-coordinated, two nitrato ligands forming altogether three Cd–O bonds with each Cd atom. The asymmetric unit includes two independent molecules, but their stereochemistry and overall structures are very similar. Two of the four independent nitrato ligands in each molecule are disordered over two or three positions. However, these various local arrangements always correspond to one monodentate and one bidentate nitrate. Two of the three local structures for the Cd1/Cd2 molecule are represented in Fig. 2. They differ by the arrangement of the nitrato ligands attached to Cd2 (right-hand side of the figure): in **a** (32% occupancy), the bidentate nitrates are on the same side of the Cd–Cd axis, whereas in **b** (45% occupancy), they are on opposite sides. The third local structure (23% occupancy) is similar to **b** with the monodentate nitrate adopting a slightly different orientation.

The coordination geometry around the Cd(II) centers can be described as a very distorted octahedron. Details of the coordination sphere are given in Table 3 for the most-abundant local structures; the other components of the disorder are showing very similar structural features. Most of the Cd—N bond lengths are between 2.251(5) and 2.325(5) Å (mean = 2.287 Å), which compares well with the values found in biimidazole compounds (9). There is no obvious explanation for the greater distance (2.372(4) Å) found for one of the Cd—N bonds, and this may be an artifact created by the disorder. The shortest Cd—O distances correspond well with the Cd—O(nitrate) bond of 2.381(6) Å found in one of the biimidazole complexes (9), but they cover a broad range attaining 2.592(4) Å.

The angles around the metal show large deviations from the ideal octahedral values. The N–Cd–N bond angles are systematically greater than 90°, ranging from 93.1(2)° to 104.5(2)°. This is consistent with the small steric requirement of the nitrato ligands across the metal center. The trans bond angles range from 134.1(2) to 173.2(4)°, which is not unexpected considering the very small bite angle (~51°) of the bidentate nitrate.

Certain structural features of the bridging ligands noted in compound **1** are again observed here. However, the strain at the ring junction, as measured by the difference between the C2′–C2–N1 and the C2′–C2–N3 angles, is somewhat greater (~4.9°) than for the Zn compound (<1°), although definitely less than for chelated Cd-biimidazole compounds (~7°) (9). The internal Cd–N3–C2 angles are, on average, ~10° greater than the external Cd–N3–C4 angles, compared with ~8.7° for the Zn compound. Again, the two imidazole rings are not coplanar; the dihedral angle being ~80°, which is ~15° greater than for the Zn compound **1**. The Cd···Cd separation of 4.83 Å is ~1 Å greater than the Zn···Zn distance in **1**.

A simplified representation of the dinuclear molecule with the nitrates removed is presented in Fig. 3. Clearly, each of

© 2007 NRC Canada

Table 2. Selected interatomic distances (Å), bond angles (°), and torsion angles (°) in [(Me_2biim)Zn(μ–Me_2biim)$_3$Zn(Me_2biim)](ClO_4)$_4$·½H_2O (**1**). Average values within brackets.

Bond lengths (Å)			
Zn1—N23	2.012(3)	Zn2—N43	2.024(3)
Zn1—N33	2.018(3)	Zn2—N63	2.018(3)
Zn1—N53	2.014(3)	Zn2—N83	2.011(3)
Zn1—N73	1.995(3)	Zn2—N93	2.011(3)
Bond angles (°)			
N23–Zn1–N33	104.7(2)	N93–Zn2–N43	105.1(2)
N23–Zn1–N53	103.3(2)	N93–Zn2–N63	99.8(2)
N23–Zn1–N73	120.3(2)	N93–Zn2–N83	121.9(2)
N33–Zn1–N53	112.9(2)	N43–Zn2–N63	113.0(2)
N33–Zn1–N73	105.8(2)	N43–Zn2–N83	111.5(2)
N53–Zn1–N73	110.0(2)	N63–Zn2–N83	105.2(2)
Terminal ligands			
C22–N23–Zn1	128.2(3)	C92–N93–Zn2	127.6(3)
C24–N23–Zn1	124.8(4)	C94–N93–Zn2	126.1(4)
C22–C12–N11	123.1(5)	C102–C92–N91	124.7(4)
C22–C12–N13	124.6(4)	C102–C92–N93	124.8(4)
C12–C22–N21	122.4(4)	C92–C102–N101	125.6(4)
C12–C22–N23	127.3(4)	C92–C102–N103	123.3(4)
Torsion angles (°)			
N11–C12–C22–N21	72.1(7)	N13–C12–C22–N23	73.0(7)
N91–C92–C102–N101	61.3(6)	N93–C92–C102–N103	53.6(6)
Bridging ligands			
C2–N3–Zn1	130.7(3)–131.4(3)	C2–N3–Zn2	130.4(3)–131.5(3)
—	[131.1(3)]	—	[130.8(3)]
C4–N3–Zn1	121.9(3)–122.9(3)	C4–N3–Zn2	121.3(3)–122.9(3)
—	[122.4(3)]	—	[122.3(3)]
C2′–C2–N1	123.1(3)–125.2(3)	C2′–C2–N3	124.4(3)–127.4(3)
—	[124.5(4)]	—	[125.5(4)]
Torsion angles (°)			
N31–C32–C42–N41	–68.4(5)	N33–C32–C42–N43	–58.9(6)
N51–C52–C62–N61	–69.6(5)	N53–C52–C62–N63	–63.0(5)
N71–C72–C82–N81	–67.5(6)	N73–C72–C82–N83	–67.1(6)

the imidazole rings is parallel to a similar ring in an adjacent ligand, and the overlap is fairly large. The average ring–ring distance (~3.3 Å), smaller than the sum of the van der Walls thickness of an aromatic ring, is indicative of appreciable π–π stacking interactions.

Views of the unit cell provided in the Supplementary data (Figs. S-2 and S-3) show that the molecules crystallize as layers parallel to the *ac* plane.[3] Any given layer contains well-separated molecules of symmetry-equivalent molecules; layers of Cd1/Cd2 molecules are alternating with layers of Cd3/Cd4 molecules in the direction of the *b* axis.

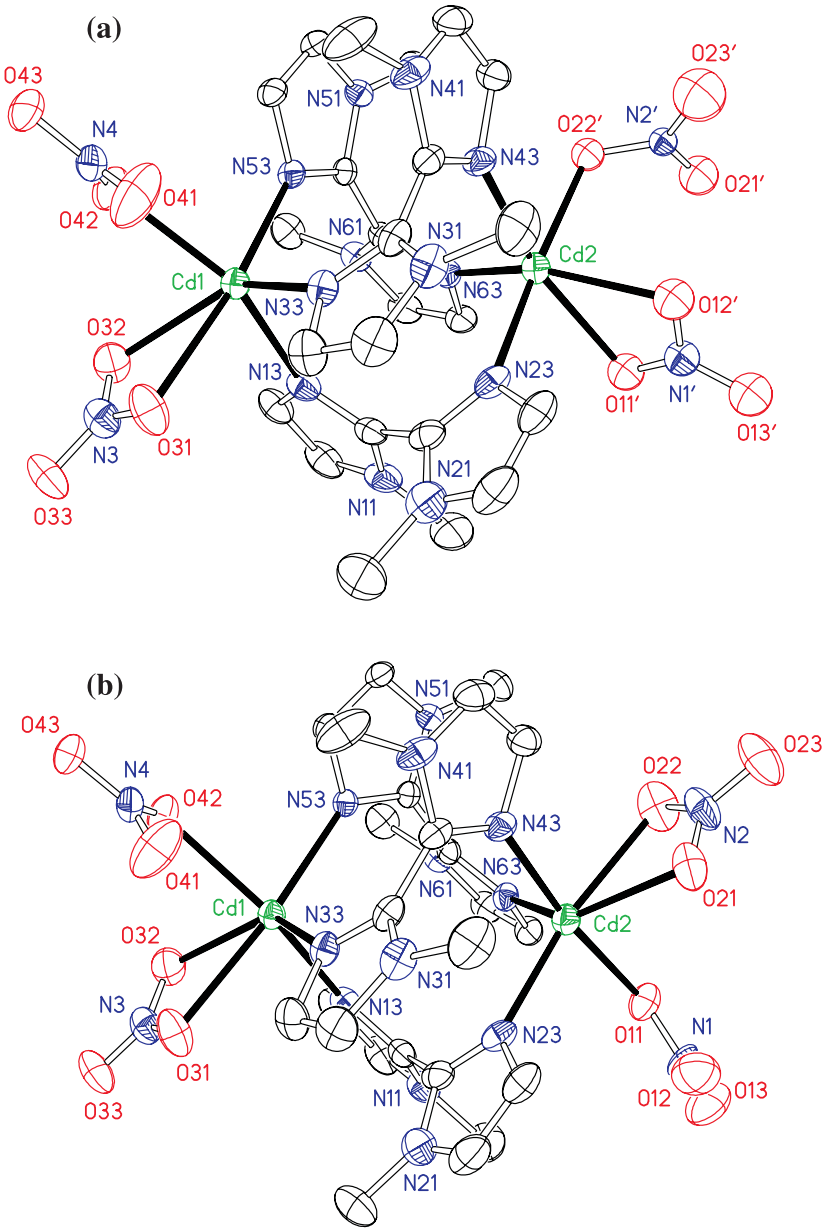
Crystals **4** and **5** are isostructural, consisting of discrete perchlorate anions and trinuclear cations [(Me_2biim)(L)Cd(μ-Me_2biim)$_3$Cd(μ-Me_2biim)$_3$Cd(L′)(Me_2biim)]$^{6+}$. Figure 4 shows the symmetric diaqua cation **4** (L = L′ = H_2O), whereas the aqua–methanol cation **5** (L = H_2O, L′ = CH_3OH) is illustrated in Fig. 5.

A crystal recently studied by Sang and Xu (20) was found to contain, in the same unit cell, the diaqua cation **4**, together with a related bisperchlorato (L = L′ = ClO_4^-) species, both lying on crystallographic inversion centers. In the present case, the cations do not possess crystallographic symmetry, but the trinuclear units are approximately centrosymmetric. They consist of two sets of three bridging ligands connecting the central Cd_c atom with terminal Cd_t atoms. Each Cd_t atom forms extra bonds to one water–methanol ligand and a chelating bidentate Me_2biim ligand. In both of our compounds, one of the $Cd_c\cdots Cd_t$ separations (4.79 Å) is the same as in the dinuclear complex **3**, while the other is somewhat greater (5.02 Å). The three Cd atoms are approximately collinear, with Cd1–Cd2–Cd3 angles of 178.32(2)° for **4** and 177.43(1)° for **5**. In the mixed diaqua–diperchlorato crystals (20), symmetry imposed that the three Cd atoms be perfectly collinear and that the $Cd_c\cdots Cd_t$ distances (~4.94 Å) be equal.

The three metal centers are six-coordinated. The selected distances and angles for **4** and **5**, given in Table 4, are in good agreement with those reported by Sang and Xu (20). The coordination around the central Cd2 atom includes six nitrogen atoms, belonging to six bridging Me_2biim ligands. In the two crystals, the Cd2—N bond distances vary between 2.373(4) and 2.432(4) Å (avg. 2.404 Å). Departure from the octahedral angles is small, the cis N–Cd2–N angles ranging from 86.0(2)° to 94.1(2)°, and trans angles from

© 2007 NRC Canada

Fig. 2. ORTEP drawings of $(NO_3)_2Cd(\mu\text{-}Me_2biim)_3Cd(NO_3)_2$ (**3**). Ellipsoids correspond to 30% probability, and hydrogens are omitted for clarity. The two represented local structures differ by the orientation on the nitrato ligands N1 and N2 (right-hand side).



176.0(2)° to 178.6(2)°. The less regular octahedra around the two terminal Cd_t atoms include five nitrogen atoms from three bridging and one chelated Me_2biim ligands. The sixth position is occupied by an aqua ligand in the symmetric crystal **4** and by an aqua ligand on Cd1 and a methanol ligand on Cd3 in the non-symmetric compound **5**. The two O-bonded ligands in **4** and **5** point in opposite directions, as clearly shown in Figs. 4 and 5.

Each bridging ligand is bonded to two Cd atoms. The Cd_t—N_{br} bond distances with the bridging ligands (2.245(6)–2.315(6) Å, mean = 2.282 Å) are ~0.12 Å shorter than those around the central Cd2 atom, whereas the N_{br}–Cd_t–N_{br} angles (mean = 102.2°) are substantially above 90°. This clearly reflects the less-crowded environment of the terminal Cd atoms, where much less space is occupied by the small H_2O–MeOH and the chelated Me_2biim ligands. The Cd—N_{ch} bonds with chelated Me_2biim are less uniform: each ligand forms one short bond (2.316(6)–2.337(5) Å), while the second bond is longer and covers a broader range (2.435(6)–2.572(7) Å). The long Cd—N_{ch} bonds does not lie close to the plane of the imidazole ring, as evidenced from the Cd-to-plane distance averaging 1.45 Å, compared with 0.60 Å for the short bond.

The Cd—OH_2 bonds in **4** are 2.503(6) and 2.567(8) Å, while in crystal **5**, the Cd—O(H)CH_3 bond (2.552(7) Å) is longer than the Cd—OH_2 bond (2.485(4) Å). These bonds are appreciably longer than the typical distance of 2.318 Å for a Cd—OH_2 bond (41).

The N_{ch}–Cd–N_{ch} bite angles in the chelate rings are ~72°, a value similar to those found in the Zn(II) and Cd(II) com-

© 2007 NRC Canada

Table 3. Selected interatomic distances (Å), bond angles (°), and torsion angles (°) for complex **3**. Average values within brackets.

Bond lengths (Å)			
Cd1—N13	2.317(5)	Cd3—N73	2.372(4)
Cd1—N33	2.256(4)	Cd3—N93	2.290(4)
Cd1—N53	2.317(4)	Cd3—N113	2.251(5)
Cd1—O31	2.487(5)	Cd3—O51	2.592(4)
Cd1—O32	2.486(5)	Cd3—O52	2.351(4)
Cd1—O42	2.414(5)	Cd3—O61	2.448(6)
Cd2—N23	2.276(6)	Cd4—N83	2.266(5)
Cd2—N43	2.325(5)	Cd4—N103	2.299(5)
Cd2—N63	2.275(4)	Cd4—N123	2.289(5)
Cd2—O11	2.444(12)[a]	Cd4—O71	2.515(10)[a]
Cd2—O21	2.349(7)[a]	Cd4—O81	2.423(11)[a]
Cd2—O22	2.534(11)[a]	Cd4—O82	2.470(8)[a]
Bond angles (°)			
N3–Cd1–N3	94.6(2)–103.7(2)	N3–Cd3–N3	93.1(2)–102.6(2)
N3–Cd2–N3	95.0(2)–104.5(2)	N3–Cd4–N3	100.2(2)–102.0(2)
O–Cd1–O (chelate)	49.8(2)	O–Cd3–O (chelate)	50.8(2)
O–Cd2–O (chelate)	50.7(2)[a]	O–Cd4–O (chelate)	51.3(3)[a]
N3–Cd1–O (bident.)	136.6(2), 169.4(2)	N3–Cd3–O (bident.)	148.9(2), 158.7(2)
N3–Cd1–O (monodent.)	142.5(2)	N3–Cd3–O (monodent.)	167.1(2)
N3–Cd2–O (bident.)	134.1(2), 171.0(3)[a]	N3–Cd4–O (bident.)	137.9(3), 168.7(3)[a]
N3–Cd2–O (monodent.)	173.2(4)[a]	N3–Cd4–O (monodent.)	167.3(3)[a]
C2–N3–Cd1	132.2(4)–134.4(4)	C2–N3–Cd3	131.4(4)–135.7(4)
—	[133.0(4)]	—	[133.6(4)]
C4–N3–Cd1	118.3(4)–122.4(4)	C4–N3–Cd3	118.6(4)–122.0(4)
—	[120.7(4)]	—	[119.8(4)]
C2–N3–Cd2	130.3(4)–133.6(4)	C2–N3–Cd4	131.5(4)–133.2(4)
—	[131.5 (4)]	—	[133.1(4)]
C4–N3–Cd2	120.0(4)–123.7(4)	C4–N3–Cd4	122.4(4)–122.5(4)
—	[122.1(4)]	—	[122.4(4)]
C2′–C2–N1	121.5(6)–123.3(5)	C2′–C2–N3	126.5(6)–129.9(5)
—	[122.4(6)]	—	[127.3(6)]
Torsion angles (°)			
N11–C12–C22–N21	–76.8(8)	N13–C12–C22–N23	–84.2(9)
N31–C32–C42–N41	–71.6(8)	N33–C32–C42–N43	–82.8(9)
N51–C52–C62–N61	–78.1(7)	N53–C52–C62–N63	–85.9(8)
N71–C72–C82–N81	73.8(8)	N73–C72–C82–N83	80.9(9)
N91–C92–C102–N101	86.5(7)	N93–C92–C102–N103	93.1(8)
N111–C112–C122–N121	72.3(9)	N113–C112–C122–N123	78.7(9)

[a]For the most abundant disordered pattern (45% about Cd2 and 58% about Cd4).

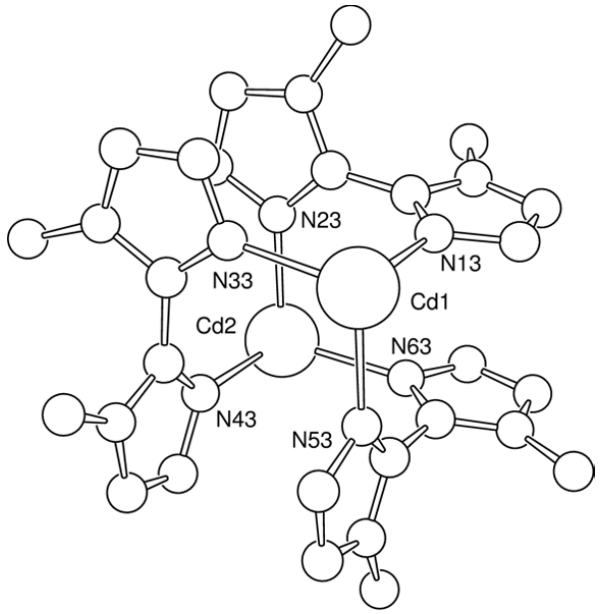
plexes with H_2biim (9, 42). This small angle, the small size of the O-bonded ligand, and the steric constraints imposed by the bridging ligands result in important distortions of the octahedral coordination around the two terminal Cd atoms: the trans angles around Cd1 and Cd3 vary between 154.6(2)° and 168.7(3)°.

The dihedral angles between the two imidazole rings in the bridging ligands are ~70°, a value similar to those observed for the Zn compounds **1** (~66°) and **2** (67° and 76°) (20), although slightly smaller than the one found in the Cd crystal **3** (80°). In this conformation, no methyl–methyl repulsion remains. On the other hand, in the chelated Me_2biim ligands, steric hindrance between the methyl groups twists the molecule by 32–46° about the C2–C2′ inter-ring bond and brings the two imidazole rings out of the plane. This angle is probably a good compromise to minimize the methyl–methyl interactions, while preserving some π connection between the two aromatic imidazole rings (43). A similar twisting of 28° is observed in $SnMe_2Br_2(Me_2biim)$ (12).

Even when they are bridging, the Me_2biim ligands are appreciably distorted. The internal and external Cd–N–C angles show large differences. Details are provided in the Supplementary data (Table S-2).[3] Although they differed by only 4° in the *oxo*-rhenium compound $[\{ORECl_2\}_2(\mu\text{-}O)(\mu\text{-}biimMe_2)_2]$ (15), very large differences are noted in the present Cd complex. The effect is particularly large around the central Cd2 atom, where the Cd2–N3–C2 angles are ~20° larger than Cd2–N3–C4 (mean values: 137.2° vs. 116.7°). The difference remains large for the terminal units (131° vs. 122°). Furthermore, the Cd—N bond is usually displaced

© 2007 NRC Canada

Fig. 3. Diagram of the $(NO_3)_2Cd(\mu\text{-}Me_2biim)_3Cd(NO_3)_2$ molecule (**3**) without the nitrato ligands, showing the parallel orientations of the imidazole rings.



significantly from the plane of the imidazole ring about all three Cd centers. The Cd-to-plane distances average 0.27 Å and may reach 0.50 Å. The distortion at ring junction is less important than in chelates, since the internal and external angles at C2 differ by ~9° for the non-bridging ligands and by only ~3° for the bridging ligands. Thus, the presence of chelated ligands in the molecule introduces important strain in the structure of these trinuclear compounds. On the other hand, many intramolecular π–π stacking interactions of the type shown in Fig. 3 are found between the imidazole rings with an average distance of ~3.2 Å between the ring centers.

Six perchlorate ions are incorporated in the lattice and held by Coulomb forces and hydrogen bonds to the aqua and methanol ligands. A packing diagram is available in the Supplementary data (Fig. S-4).[3]

Discussion

The coordination of Me_2biim with Zn(II) and Cd(II) differs strikingly from the behavior observed for the same metal centers with H_2biim (9, 44). This can be ascribed to two main factors:

(*i*) coordinated H_2biim participates in extended intermolecular hydrogen bonding, whereas coordinated bidentate Me_2biim is unable to form hydrogen bonds; (*ii*) the *N*-methyl groups of Me_2biim rotate the imidazole rings out of the plane, which changes the relative orientation of the *N*-donor lone pairs and leads to different structural preferences.

In the solid state, free H_2biim molecules in the anti conformation are connected into infinite ribbons by pairs of complementary N–H···N bonds (7). Further cohesion via π–π stacking between parallel ribbons results in very low solubility. As a consequence, long reaction times and vigorous conditions have to be used to produce a reaction with the undissolved ligand. In contrast, since Me_2biim is unable to form hydrogen bonds with itself, it dissolves in usual solvents, and reactions can be run in homogeneous media under much milder conditions.

Unsubstituted H_2biim usually acts as a chelating agent in monomeric species, where it is forced into the syn arrangement. The two imidazole rings are coplanar, and the resonance between the two aromatic π systems is maintained. These complexes participate in elaborate hydrogen-bonding systems, where the two N–H groups form strong hydrogen bonds with anions or solvent molecules, which is an important stabilizing factor in the structure of the metal complexes. In contrast, because of the proximity of the two N–Me groups, the two imidazole rings of Me_2biim are twisted out of the plane, and the ligand prefers to bridge two metal centers, although chelate formation remains possible.

In an undistorted H_2biim molecule acting as a bidentate chelating ligand, the vectors along the idealized lone pairs would meet at 4.9 Å from the N3 donors (Chart 2). To favor metal coordination, the five-membered rings are displaced in the ligand plane, so as to bring the N3 donors closer to each other. In a variety of complexes, this displacement reduces the θ angles at the connecting C2–C2′ bond from 125° to ~117°. Then, the metal atoms are found to bind at normal M—N distances, but the M—N vector deviates by ~13° from the idealized lone-pair direction (ϕ ~115°, ϕ′ ~140°).

To form chelates, Me_2biim, which exists as the anti conformer in the solid state (11), has to adopt a conformation on the syn side. Therefore, repulsion between the methyl groups becomes a crucial factor. In an undistorted Me_2biim molecule with a perfectly planar syn arrangement, the C_{Me}—C_{Me} distance would be extremely short (2.13 Å). The distances of 3.30–3.36 Å observed in the polymeric $[Ag(Me_2biim)]NO_3$ complex (17) can be regarded as a "normal" intramolecular Me–Me contact, since the helical structure of the chain likely leaves enough freedom for any severe local strain to be relieved. The slightly smaller distances of ~3.22 Å found in other non-chelate compounds, namely, the tetra-bridged $[Cu_2(\mu\text{-}Me_2biim)_4]^{4+}$ complex (18) and $\{PtBr(DMSO)\}_2(\mu\text{-}Me_2biim)$ (16), probably represent the lower limit for this contact.

Reduction of Me–Me repulsion can be achieved via two main structural parameters: the θ angles (C2′–C2–N3) at the ring junction and the dihedral angle between the imidazole rings. Inspection of an idealized Me_2biim molecule reveals that the contact limit of 3.20 Å occurs at a dihedral angle of 57° for the ideal θ angle (126°), but the dihedral angle is 33° when θ is 117°. Even the latter case represents a large departure from coplanarity, but the structure of $SnBr_2Me_2(Me_2biim)$ (12) suggests that it remains acceptable, since the dihedral angle in this compound is 27° for θ values of 115°. In this typical chelated ligand, some direct Me–Me repulsion is absorbed by a displacement of the methyl groups away from each other; the C2–N1–Me angles becoming 8° greater than C5–N1–Me. On the other hand, non-coplanarity implies that the M–N3 bond cannot lie in the plane of the ring. The Sn-to-plane distances observed are quite large (0.37 and 0.94 Å), which corresponds to angles of 9° and 22°, respectively, between the Sn–N bond and the imidazole plane. Nevertheless, this departure from ideality does not seem to be very energy costly, since the Sn—N bond lengths are normal. Qualitatively similar features are

© 2007 NRC Canada

Fig. 4. ORTEP drawing of the $[(Me_2biim)(H_2O)Cd(\mu\text{-}Me_2biim)_3Cd(\mu\text{-}Me_2biim)_3Cd(H_2O)(Me_2biim)]^{6+}$ cation (**4**). Ellipsoids correspond to 30% probability. Hydrogen atoms are omitted for clarity.

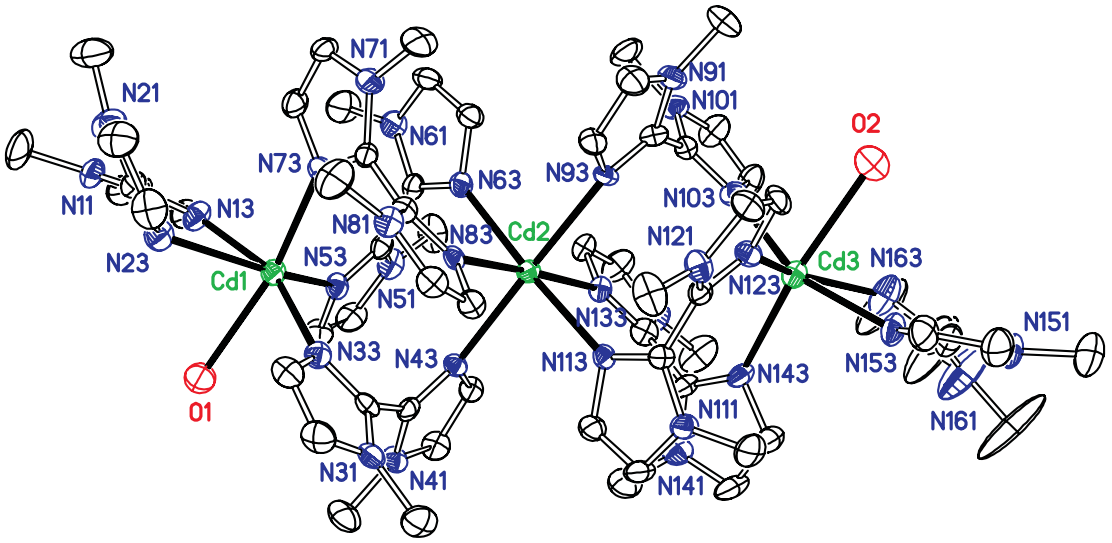
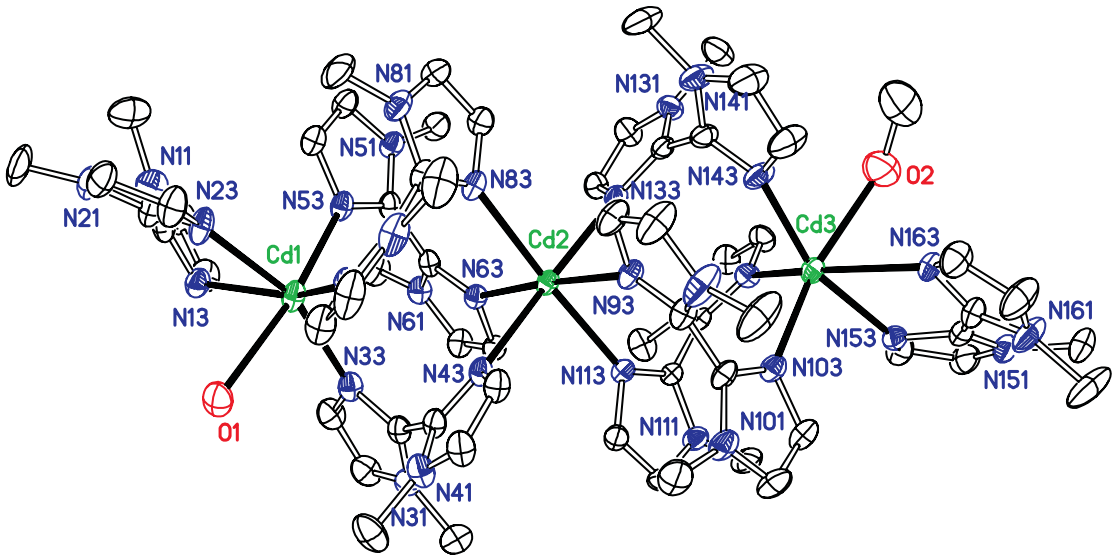


Fig. 5. ORTEP drawing of the $[(Me_2biim)(H_2O)Cd(\mu\text{-}Me_2biim)_3Cd(\mu\text{-}Me_2biim)_3Cd(CH_3OH)(Me_2biim)]^{6+}$ cation (5). Ellipsoids correspond to 30% probability. Hydrogen atoms are omitted for clarity.



observed for the chelating ligands bound to the terminal metal atoms of the $[Cd_3(Me_2biim)_8LL']^{6+}$ units described before and those reported by Sang and Xu (20). The θ angles (117–123°) are comparable, whereas the dihedral angles (21–44°) and the Cd-to-plane distances (0.54–1.33 Å) tend to be somewhat greater. For one of the rings in a terminal ligand of **4** and **5**, the Cd-to-plane distance reaches 1.74 Å. However, in this case, the Cd—N bond becomes 0.24 Å longer than the other. Surprisingly, chelating ligands were reported to be almost planar in $PtI_2(Me_2biim)$ and $PtCl_4(Me_2biim)$ (dihedral angles of 2° and 11°, respectively) (13, 14). A dihedral angle similar to that of $SnBr_2Me_2(Me_2biim)$ is expected, since the θ angles in the Pt compounds are also 115°. A possible explanation would be that in the presence of the very electron-rich Pt and halogen atoms, it may be difficult for X-ray diffraction to distinguish between a flat Me_2biim ligand and two puckered conformations averaged by disorder across the $PtX_2(Me_2biim)$ plane.

For dihedral angles greater than ~50°, methyl–methyl repulsion is no longer a significant factor. Extended polymeric chains are anticipated to develop when the conformation changes from syn to anti, and this type of structures is indeed observed for $[CdX_2(Me_2biim)]_n$ complexes (X = Cl, Br, I) (20), where the N3–C2–C2′–N3′ torsion angles range from 90° to 112°. Below 90°, small di- or trinuclear species are obtained, in which pairs of metal atoms are bridged by up to four ligands. On the basis of the structural data available at the moment, this is the preferred binding mode for Me_2biim, which has been observed in discrete dinuclear species with Cu(II), Zn(II), Cd(II), Re(V), and Pt(II) and trinuclear units with Cd(II). In all these compounds, the absence of direct repulsion between the N–Me groups is reflected by the fact

© 2007 NRC Canada

Table 4. Selected interatomic distances (Å), bond angles (°), and torsion angles (°) for compounds **4** and **5**.

Compound	**4**	**5**
Bond lengths (Å)		
Cd1—N_{br}	2.249(7)–2.316(7)	2.252(5)–2.310(5)
Cd2—N_{br}	2.378(6)–2.433(7)	2.378(4)–2.432(4)
Cd3—N_{br}	2.276(6)–2.285(6)	2.257(5)–2.293(5)
Cd1—N_{ch}	2.311(7), 2.567(8)	2.321(5), 2.559(5)
Cd3—N_{ch}	2.335(7), 2.465(9)	2.321(5), 2.431(6)
Cd—O (H_2O)	2.509(7), 2.572(8)	2.484(4)
Cd—O (CH_3OH)	—	2.556(7)
Bond angles (°)		
N_{br}–Cd2–N_{br} cis	85.9(2)–94.2(2)	86.0(2)–93.4(2)
N_{br}–Cd2–N_{br} trans	176.6(2)–178.5(2)	176.3(2)–177.3(2)
N_{br}–Cd1–N_{br}	100.9(2)–105.4(3)	101.3(2)–104.2(2)
N_{ch}–Cd1–N_{ch}	71.6(3)	72.0(2)
N_{ch}–Cd1–O	82.8(2), 84.1(3)	82.6(2), 84.5(2)
N_{br}–Cd1–O cis	77.7(3), 91.6(2)	78.1(2), 91.5(2)
N_{br}–Cd1–O trans	165.3(2)	164.9(2)
N_{br}–Cd1–N_{ch} cis	82.9(3)–97.5(3)	82.6(2)–98.8(2)
N_{br}–Cd1–N_{ch} trans	154.7(2), 159.9(3)	154.5(2), 161.3(2)
N_{br}–Cd3–N_{br}	99.6(3)–103.0(3)	98.9(2)–105.2(2)
N_{ch}–Cd3–N_{ch}	71.3(3)	73.3(2)
N_{ch}–Cd3–O	78.6(3), 82.5(3)	79.8(2), 80.0(2)
N_{br}–Cd3–O cis	77.1(3), 88.5(3)	77.8(2), 90.8(2)
N_{br}–Cd3–O trans	168.6(3)	166.1(2)
N_{br}–Cd3–N_{ch} cis	86.7(3)–97.6(3)	86.2(2)–97.5(2)
N_{br}–Cd3–N_{ch} trans	155.6(3), 158.5(3)	157.0(2), 158.9(2)
Torsion angles (°)		
N1–C2–C2′–N1′ chelate (avg.)	45(2)	46(2)
N3–C2–C2′–N3′ chelate (avg.)	32(2)	35(2)
N1–C2–C2′–N1′ bridging (avg.)	69(2)	68(2)
N3–C2–C2′–N3′ bridging (avg.)	71(2)	71(2)

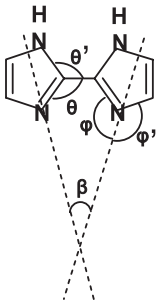
that the C2–N1–Me and C5–N1–Me angles differ by ≤2°. The average metal-to-plane distance of 0.21 Å is still relatively small, although values as high as 0.50 Å are occasionally found. In the bridging ligands, the θ angles (128–138°) are systematically *greater* than the ideal 126° value. This slightly larger angle is not expected to weaken the metal–N3 bond appreciably, since the same angle is systematically *decreased* by the same amount in H_2biim complexes. The larger angle contributes to reduce steric hindrance around the metal center by displacing the C5-bonded hydrogen away from the other ligands.

Optimal adjustment of the structural parameters of Me_2biim results in a coordination environment close to tetrahedral around the Zn(II) center in $[(Me_2biim)Zn(\mu\text{-}Me_2biim)_3Zn(Me_2biim)]^{4+}$. Although Zn(II) can reach five- and six-coordination with H_2biim (9, 10), only four-coordination is found with Me_2biim. Apparently, the constraints imposed by the bridging ligands make it difficult for a fifth ligand to bind to the relatively small Zn center, since otherwise, the terminal Me_2biim ligand would have been chelating bidentate, as found for the Cd trinuclear compounds. The N_{br}–Zn–N_{br} angles within the dinuclear framework are all close to the ideal 109.5° value. The angles involving the terminal ligand average 109.2°, but one N_t–Zn–N_{br} angle (~121°) is greater than the other two (102° and 105°) because of the particular steric requirement of the imidazole ring. Similar features were found in $[(H_2O)Zn(\mu\text{-}Me_2biim)_3Zn(OH_2)]^{4+}$, although the terminal angles are closer to 109.5° (104/116/117° pattern) because the terminal aqua ligand is sterically less demanding.

The larger Cd(II) atom shows a preference for six-coordination. In the $[Cd(\mu\text{-}Me_2biim)_3Cd]^{4+}$ unit, the torsion angles between the imidazole rings are greater than those of the corresponding Zn frameworks (~80° vs. ~65°). Some steric hindrance is suggested by the N–Cd–N angles being all greater than 90° (93–105°), but this could be simply due to the small space required by one bidentate and one monodentate terminal nitrate, since in the trinuclear $[(Me_2biim)Cd(\mu\text{-}Me_2biim)_3Cd(\mu\text{-}Me_2biim)_3Cd(Me_2biim)]^{6+}$ framework, the N–Cd–N angles around the central Cd atom lie between 86° and 94°. At the terminal Cd atoms, the N–Cd–N angles are all greater than 90° (100–105°). The for-

© 2007 NRC Canada

Chart 2.



mation of a dinuclear unit with nitrates, but not with perchlorates, may be related to the better donating ability of the nitrate, which can efficiently close the ends of the molecule at the dinuclear stage. It would be more difficult for perchlorates to play a similar role, because they are bigger and poorer donors, especially in a bidentate role. It can be speculated that in the perchlorate system, the Lewis acidity of the Cd center is better satisfied by introducing extra Me_2biim ligands and extending the chain. Why the chain does not extend beyond the trinuclear stage may be related to the fact that greater steric crowding about the central metal is achieved at the expense of some structural accommodation around the terminal metal atoms, so it may become difficult for two consecutive CdN_6 centers to coexist.

Interestingly, the imidazole rings in all di- and trinuclear units participate in intramolecular π–π stacking between the bridging ligands. These interactions are particularly clear in the Cd compounds. The loss of aromaticity because of the large torsion angles in the bridging ligands is likely balanced by these π–π interactions.

Conclusion

The di- and trinuclear frameworks observed in the present work are particularly interesting, since they consist of tube-like species, containing two or three metal centers maintained at an unbonded, but not very large distance, where the surface of the tubes consist of non-polar groups and the ends are polar. Stable units were produced with three Me_2biim ligands bridging triangular faces of octahedra or tetrahedra, as well as four ligands bridging square planes (with Cu(II)). Since most metal centers can adopt at least one of these coordination geometries, it may be anticipated that a variety of metal atoms can be similarly encapsulated by Me_2biim to develop materials in which a fairly large, but controlled metal—metal distance would be desirable.

Acknowledgment

The authors are grateful to the Natural Sciences and Engineering Research Council of Canada (NSERC) for financial support of the project. We thank F. Bélanger-Gariépy and M. Simard for assistance with the X-ray diffraction studies.

References

1. F. Mao, N. Mano, and A. Heller. J. Am. Chem. Soc. **125**, 4951 (2003).
2. M. Tadokoro, H. Kanno, T. Kitajima, H. Shimada-Umemoto, N. Nakanishi, K. Isobe, and K. Nakasuji. Proc. Nat. Acad. Sci. USA. **99**, 4950 (2002).
3. M.A. Esteruelas, M.P. Garcia, A.M. Lopez, and L.A. Oro. Organometallics, **10**, 127 (1991).
4. M.A. Esteruelas, M.P. Garcia, A.M. Lopez, and L.A. Oro. Organometallics, **11**, 702 (1992).
5. W. Chi and H.L. Collier. J. Macromol. Sci. Chem. **A25**, 1543 (1988).
6. M.J. Bloemink, H. Engelking, S. Karentzopoulos, B. Krebs, and J. Reedijk. Inorg. Chem. **35**, 619 (1996).
7. D.T. Cromer, R.R. Ryan, and C.B. Storm. Acta Crystallogr. **C43**, 1435 (1987).
8. M.A. Martinez Lorente, F. Dahan, Y. Sanakis, V. Petrouleas, A. Bousseksou, and J.-P. Tuchagues. Inorg. Chem. **34**, 5346 (1995).
9. L.M. Gruia, F.D. Rochon, and A.L. Beauchamp. Inorg Chim. Acta. **360**, 1825 (2007).
10. C. Kirchner and B. Krebs. Inorg. Chem. **26**, 3569 (1987).
11. B. Therrien and A.L. Beauchamp. Acta Crystallogr. **C55**, IUC 9 900 054 (1999).
12. C. López, A. Sánchez-González, M.E. García, J.S. Casas, J. Sordo, R. Graziani, and U. Casellato. J. Organomet. Chem. **434**, 261 (1992).
13. J. S. Casas, A. Castiñeiras, Y. Parajó, A. Sánchez, A. Sánchez-González, and J. Sordo. Polyhedron, **24**, 1196 (2005).
14. J.S. Casas, A. Castineiras, Y. Parajo, J. Sordo, and J.M. Varela. Acta Crystallogr. **C54**, 1777 (1998).
15. S. Fortin and A.L. Beauchamp. Inorg. Chem. **39**, 4886 (2000).
16. J.S. Casas, A. Castineiras, Y. Parajo, M.L. Perez-Paralle, A. Sanchez, A. Sanchez-Gonzalez, and J. Sordo. Polyhedron, **22**, 1113 (2003).
17. L. Gruia, F.D. Rochon, and A.L. Beauchamp. Acta Crystallogr. **E61**, m1604 (2005).
18. L. Gruia, F.D. Rochon, and A.L. Beauchamp. Acta Crystallogr. **E62**, m617 (2006).
19. P. Yang, Y. Li, C. Yin, and X. Gao. Zh. Strukt. Khim. **46**, 781 (2005).
20. R. Sang and L. Xu. Inorg. Chem. **44**, 3731 (2005).
21. R.R. Mohanty, K.C. Rout, S. Jena, and K.C. Dash. Polyhedron, **13**, 2945 (1994).
22. B.F. Fieselmann, D.N. Hendrickson, and G.D. Stucki. Inorg. Chem. **17**, 2078 (1978).
23. SMART [computer program]. Release 5.059. Bruker AXS Inc., Madison, WI. 1999.
24. SAINT [computer program]. Release 6.06. Bruker AXS Inc., Madison, WI. 1999.
25. G. M. Sheldrick. SADABS [computer program]. Bruker AXS Inc., Madison, WI. 1996.
26. Enraf-Nonius. CAD-4 Software [compter program]. Version 5.0. Enraf-Nonius, Delft, The Netherlands. 1989.
27. E.J. Gabe, Y. LePage, J.P. Charland, F.L. Lee, and P.S. White. J. Appl. Crystallogr. **22**, 384 (1989).
28. SHELXTL [computer program]. Release 5.10. Bruker AXS Inc., Madison, WI. 1997.
29. A.L. Spek. PLATON [computer program]. University of Utrecht, Utrecht, The Netherlands. 2000.
30. P. Majumdar, S.-M. Peng, and S. Goswami. J. Chem. Soc., Dalton Trans. 1569 (1998).
31. C. Perchard and A. Novak. Spectrochim. Acta. **23A**, 1953 (1967).
32. C. Perchard and A. Novak. J. Chim. Phys. **65**, 1964 (1968).
33. C. Perchard and A. Novak. Spectrochim. Acta. **26A**, 871 (1970).

© 2007 NRC Canada

34. J. Reedijk. Recl. Trav. Chim. Pays-Bas. **88**, 1451 (1969).
35. K. Nakamoto. Infrared and raman spectra of inorganic and coordination compounds. Wiley-Interscience, New York. 1997.
36. M.-A. Buhannic and J.E. Guerchais. Bull. Soc. Chim. France, 55 (1971).
37. Y. Saito, M. Cordes, and K. Nakamoto. Spectrochim. Acta. **28A**, 1459 (1972).
38. B. Cornilsen and K. Nakamoto. J. Inorg. Nucl. Chem. **36**, 2467 (1974).
39. J.B. Hodgson, G.C. Percy, and D. Thornton. J. Mol. Struct. **66**, 81 (1980).
40. B.K.S. Lundberg. Acta Crystallogr. **21**, 901 (1966).
41. A.G. Orpen, L. Brammer, F.H. Allen, O. Kennard, D.G. Watson, and R. Taylor (*Editors*). International tables for crystallography, Volume C. Kluwer Academic Press, Dordrecht, The Netherlands. 1995.
42. C.A. Hester, H.L. Collier, and R.G. Baughman. Polyhedron, **15**, 4255 (1996).
43. E.C. Constable. Tetrahedron, **48**, 10013 (1992).
44. R.-L. Sang and L. Xu. Polyhedron, **22**, 2167 (2006).

© 2007 NRC Canada

Synthesis and characterization of bis(ferrocenylcarboxylato)telluranes

Prakash C. Srivastava, Sangeeta Bajpai, Rajesh Kumar, Shikha Srivastava, Vikas Singh, Shrinkhala Dwivedi, and Ray J. Butcher

Abstract: A convenient route to the synthesis of the first bis(ferrocenyl carboxylato) telluranes has been developed. Reactions of 1,1,2,3,4,5,6-heptahydro-1,1-(dihydroxo)tellurane and 1,1,2,3,4,5-hexahydro-1,1-(dihydroxo)tellurophene with ferrocene carboxylic acid give 1,1,2,3,4,5,6-heptahydro-1,1-bis(ferrocenyl carboxylato)tellurane (**3**) and 1,1,2,3,4,5,-hexahydro-1,1-bis(ferrocenyl carboxylato)tellurophene (**5**), respectively. The X-ray structure of **3** shows that it contains a tellurium heterocycle ($C_5H_{10}Te$), present in a chair conformation, sandwiched between two ferrocene units with carboxylate groups acting as spacers. Compound **3** also exhibits modest second harmonic generation (SHG) efficiency. The electrochemical studies of **3** and **5** through cyclic voltammetry show only one oxidation wave, indicating the presence of independent redox centers leading to reversible single-step two-electron redox systems.

Key words: tellurane, ferrocenylcarboxylate, SHG efficiency, electrochemistry.

Résumé : On a mis au point une méthode pratique de synthèse des premiers bis(ferrocénylcarboxylato)telluranes. La réaction du 1,1,2,3,4,5,6-heptahydro-1,1-(dihydroxo)tellurane et du 1,1,2,3,4,5-hexahydro-1,1-(dihydroxo)tellurophène avec l'acide carboxylique du ferrocène conduit respectivement à la formation de 1,1,2,3,4,5,6-heptahydro-1,1-bis(ferrocénylcarboxylato)tellurane (**3**) et de 1,1,2,3,4,5-hexahydro-1,1-bis(ferrocénylcarboxylato)tellurophène (**5**). La structure du composé **3** telle que déterminée par diffraction des rayons X montre qu'elle contient un hétérocycle de tellure ($C_5H_{10}Te$) qui est présent sous une conformation chaise et qui est pris en sandwich entre deux unités de ferrocène auxquelles il est retenu par des groupes carboxylates agissant comme cales. Le composé **3** possède aussi une faible efficacité dans la génération de la deuxième harmonique (GDH). Les études électrochimiques des composés **3** et **5** réalisées par le biais de voltampérométrie cyclique ne présentent qu'une seule vague d'oxydation, ce qui indique la présence de centres redox indépendants qui conduisent à des systèmes redox à deux électrons impliquant une seule étape réversible.

Mots-clés : tellurane, ferrocénylcarboxylate, efficacité dans la génération de la deuxième harmonique, électrochimie.

[Traduit par la Rédaction]

Introduction

Bridged ferrocenes containing main group (13–16) (p-block) elements are known and generally exist as polymers or oligomers (1–9). Ferrocene derivatives containing boron bridges have been synthesized by the reaction of dilithiated ferrocene and bis(dimethylboryl) ferrocene or bis(trimethylstannyl) ferrocene with $PhBCl_2$ (1, 2). A multinuclear ferrocene derivative with aluminium substitution has been synthesized by the reaction between dilithiated ferrocene with $AlEt_2Cl$ (3). The reaction of 1,1′-bis(trichlorostannyl) ferrocene with Me_3Ga results in the formation of 1,1′-digallyl ferrocene (4). Ring-opening polymerization (ROP) of main group element bridged [1]- and [2]-ferrocenophanes by thermal or anionic methods results in high molecular weight polymers containing ferrocene groups alternating with either boron, carbon, silicon, germanium, tin, or phosphorous atoms (5–7). A hexa-ferrocene unit on a tin–oxygen cluster has been synthesized by the reaction of *n*-butylstannonic acid with ferrocene monocarboxylic acid (8). A chalcogen (sulphur) bridged polymer has been synthesized by the reaction of trithia ferrocenophanes with Bu_3P (9). The interactions between main group elements and transition elements of the periodic table lead to useful precursors for ceramics, electronic materials, and catalysts (10, 11); if the transition metal containing entities are metallocenes (particularly ferrocenes), such combinations exhibit novel electrical, optical, chemical, and magnetic characteristics (12, 13). These include redox active materials for modification of electrodes (14) or materials that can function as multi-electron redox systems (15), biosensors (16*a*, 16*b*), or variable refractive index sensor materials (16*c*, 16*d*). The extent of interaction between ferrocene groups is largely dependent on the nature of the bridge linking the adjacent

Received 5 April 2007. Accepted 15 June 2007. Published on the NRC Research Press Web site at canjchem.nrc.ca on 27 July 2007.

P.C. Srivastava[1], **S. Bajpai, R. Kumar, S. Srivastava, V. Singh, S. Dwivedi.** Chemistry Department, Lucknow University, Lucknow, 226007, India.
R.J. Butcher. Chemistry Department, Howard University, Washington, DC 20059, USA.

[1]Corresponding author (e-mail: pcsrivastava31@rediffmail.com).

 doi:10.1139/V07-073 © 2007 NRC Canada

ferrocene centers (14). However, since polymers are often less well-defined the investigations are best carried out with di- or tri-nuclear model compounds, but such species are often very difficult to prepare and crystallize for X-ray diffraction studies (17, 18). On the other hand, organotelluriums are useful precursors for semiconductors, tellurite glasses, and optoelectronic materials (19–21).

In view of the above, our work is directed to the synthesis of bis(ferrocenyl carboxylato) telluranes by a convenient route in which the complex **3** corresponds to new structural type where a cyclic tellurane ($C_5H_{10}Te$) is (formally) sandwiched between ferrocenes separated by carboxylate spacer groups. We also present preliminary results of their second harmonic generation (SHG) efficiency and electrochemistry.

Experimental

All manipulations were carried out at room temperature. The reagents were obtained from commercial sources and used as received unless otherwise noted. Benzene was dried over $CaCl_2$ and distilled before use. $C_5H_{10}TeI_2$ and $C_4H_8TeI_2$ were prepared according to literature methods (22, 23). ^{1}H NMR spectra were recorded on a Bruker WM 400 (400 MHz.) FT NMR spectrometer in $CDCl_3$ using TMS as an internal standard. Elemental analyses were performed on an Heraeus Carlo Erba 1108 elemental analyser. Cyclic voltammetry (CV) was performed with a CH-1660 scanning potentiostat–galvanostat interfaced to a desktop computer using the EG & G model 270 software package. Cyclic voltammograms of telluranes **3** and **5** were obtained by using a platinum working electrode, a platinum coil counter electrode and as Ag/AgCl (non-aq.) reference electrode. The scan rate was 100 mV/s and full IR compensation was employed in all measurements. Tetraethyl ammonium perchlorate (0.1 mol/L) in acetonitrile was used as supporting electrolyte and the sample concentration was in the order of 10^{-4} mol/L. Cyclic voltammetric studies were carried out at the IIT Bombay and SHG efficiency was measured at IISc, Bangalore.

Preparation of $C_5H_{10}Te(OH)_2$ (1) and $C_4H_8Te(OH)_2$ (4)

To 1,1,2,3,4,5,6-heptahydro-1,1-diiodo tellurane (1.00 g, 2.214 mmol), was added freshly prepared silver hydroxide (0.554 g, 4.432 mmol) in a mortar and ground with a small amount of deionized water to make a thin paste. This was ground for 45 min more, upon which the reddish brown crystals of 1,1,2,3,4,5,6-heptahydro-1,1-diiodo tellurane disappeared. The paste was filtered with hot water. The filtrate was $C_5H_{10}Te(OH)_2$ (**1**) (in situ). Compound **4** was similarly prepared using $C_4H_8TeI_2$ (1.00 g, 2.285 mmol) and silver hydroxide (0.571 g, 4.568 mmol) and the filtrate was $C_4H_8Te(OH)_2$ (**4**) (in situ).

Reaction of 1 with $HOOCC_5H_4FeC_5H_5$

A mixture of ~0.252 g (1.088 mmol) of $C_5H_{10}Te(OH)$**2 1** (in situ) and $HOOCC_5H_4FeC_5H_5$ (**2**) (0.500 g, 2.1753 mmol) in benzene (500 mL) was heated under reflux for 7 h using a Dean–Stark apparatus to remove the water formed in the reaction by azeotropic distillation. The mixture was filtered and reduced (~10 mL) to afford orange-yellow crystals, which were shown to be $C_5H_{10}Te(OCOC_5H_4FeC_5H_5)_2$ (**3**). Yield 0.686 g (96%), mp 194 °C. ^{1}H NMR ($CDCl_3$) δ: 4.21 (s, 10H, C_5H_5), 4.75–4.35 (m, 8H, C_5H_4), 3.21 (t, 4H, CH_2Te), 2.02–1.83 (m, 6H, CH_2C). Anal. calcd. for $Fe_2TeC_{27}H_{28}O_4$: C 49.4, H 4.3, Te 19.5; found: C 49.4, H 4.2, Te 19.5.

Reaction of 4 with $HOOCC_5H_4FeC_5H_5$

Using a procedure similar to that described earlier, the reaction of **4** (~0.173 g, 0.796 mmol) (in situ) with $HOOCC_5H_4FeC_5H$**5 2** (0.344 g, 1.496 mmol) in benzene gave $C_4H_8Te(OCOC_5H_4FeC_5H_5)_2$ (**5**). Yield 0.486 g (95%), mp 200 °C. ^{1}H NMR ($CDCl_3$) δ: 4.22 (s, 10H, C_5H_5), 4.75–4.31 (m, 8H, C_5H_4), 3.31 (t, 4H, CH_2Te), 2.72 (m, 4H, CH_2C). Anal. calcd. for $Fe_2TeC_{26}H_{26}O_4$: C 48.6, H 4.0, Te 19.9; found: C 48.6, H 4.0, Te 19.8.

Crystal structure determination

The orange-yellow crystal of **3** was mounted on a Bruker SMART CCD diffractometer using graphite-monochromated Mo Kα radiation (λ = 0.71073 Å). The data were corrected for Lorentz, polarization, and absorption effects. The structure was solved by the routine heavy atom method SHELXS-97 (24) and Fourier methods. Non-hydrogen atoms were refined anisotropically by full-matrix least-squares using the SHELXL-97 program (24) with hydrogen atoms in idealized positions. A summary of crystallographic parameters is presented in Table 1 (24).[2]

Results and discussion

1,1,2,3,4,5,6-heptahydro-1,1-bis(ferrocenyl carboxylato) tellurane (**3**) was synthesized by the reaction of 1,1,2,3,4,5,6-heptahydro-1,1-(dihydroxo)tellurane **1** with ferrocene monocarboxylic acid **2** in (1:2) stoichiometry in benzene, which yielded orange crystals of 1,1,2,3,4,5,6-heptahydro-1,1-bis(ferrocenyl carboxylato) tellurane (**3**). 1,1,2,3,4,5-Hexahydro-1,1-bis(ferrocenyl carboxylato) tellurophene (**5**) was similarly prepared by the reaction of 1,1,2,3,4,5-hexahydro-1,1-(dihydroxo) tellurophene **4** with **2** in benzene in 1:2 molar ratio (eq. [1], Fc = Ferrocenyl). The products (**3** and **5**) were obtained in nearly quantitative yields.

[1] $$\underset{\substack{\mathbf{1}:R_2=C_5H_{10}\\ \mathbf{4}:R_2=C_4H_8}}{R_2Te(OH)_2} + 2\underset{\mathbf{2}}{FCOOH} \xrightarrow[80\ ^\circ C]{C_6H_6} \underset{\substack{\mathbf{3}:R_2=C_5H_{10}\\ \mathbf{5}:R_2=C_4H_8}}{R_2Te(OCOFc)_2} + 2H_2O$$

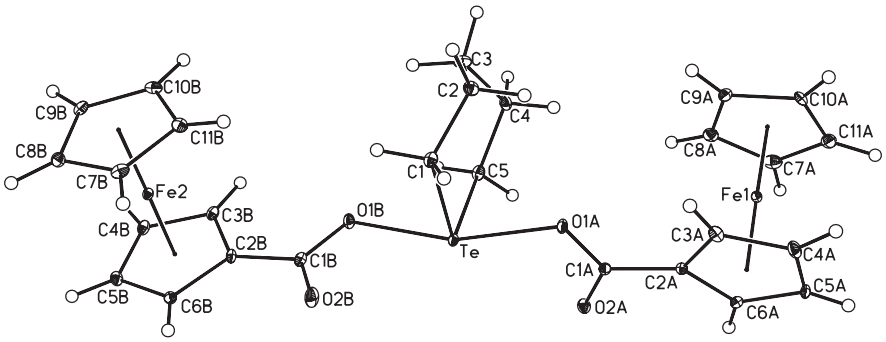
[2] Supplementary data for this article are available on the journal Web site (canjchem.nrc.ca) or may be purchased from the Depository of Unpublished Data, Document Delivery, CISTI, National Research Council Canada, Ottawa, ON K1A 0R6, Canada. DUD 5190. For more information on obtaining material refer to cisti-icist.nrc-cnrc.gc.ca/irm/unpub_e.shtml. CCDC 280463 contains the crystallographic data for this manuscript. These data can be obtained, free of charge, via www.ccdc.cam.ac.uk/conts/retrieving.html (Or from the Cambridge Crystallographic Data Centre, 12 Union Road, Cambridge CB2 1EZ, UK; fax +44 1223 336033; or deposit@ccdc.cam.ac.uk).

© 2007 NRC Canada

Table 1. Crystal data and structure refinement for **3**.

Crystal	**3**
Empirical formula	$C_{27}H_{28}Fe_2O_4Te$
Molecular weight	655.79
Colour, habit	Orange-yellow, plate
Crystal dimensions (mm)	0.58 × 0.35 × 0.08
Crystal system	Monoclinic
Space group	$P2_1/c$
a (Å)	9.6391(12)
b (Å)	7.2254(9)
c (Å)	34.400(4)
α (°)	90
β (°)	91.068(2)
γ (°)	90
V (Å^3)	2395.4(5)
Z	4
D_{calcd} (Mg m^{-3})	1.818
Temperature (K)	93(2)
Absorption coeff. μ (mm^{-1})	2.438
Absorption correction	Semi-empirical from equivalents
F(000)	1304
θ range for data collection (°)	1.18–28.28
Radiation	Mo Kα
λ (Å)	0.710 73
Index ranges	$-12 \le h \le 12$, $-9 \le k \le 8$, $-45 \le l \le 44$
Reflections collected	18 246
Independent reflections	5826 (R_{int} = 0.0370)
Data, restraints, parameters	5826, 0, 362
Max and min transmission	1.0000 and 0.7444
Goodness-of–fit on F^2	1.041
Final R indices [$I > 2\sigma(I)$]	R_1 = 0.0296, wR_2 = 0.0636
R indices (all data)	R_1 = 0.0410, wR_2 = 0.0677
Extinction coefficient	0.000 17(6)
Largest diff. peak, hole (e Å^{-3})	1.111, –1.267

Fig 1. Structure of $C_5H_{10}Te$ $(OCOFc)_2$ (**3**).



Compound **3** contains two ferrocene units and the tellurium heterocycle [1,1,2,3,4,5,6-heptahydro tellurane, $C_5H_{10}Te$] is sandwiched between these, with carboxylate groups acting as spacers (Fig 1; Table 2). The $C_5H_{10}Te$ ring has a chair conformation in which part of the ring is flattened and a part is considerably puckered (25). Of the five methylene groups, two methylene carbon atoms of the C_5H_{10} group are bonded to Te(IV) atoms with bond lengths Te–C(1) = 2.124(3) Å and Te–C(5) = 2.134(3) Å. The coordination geometry formed by the four closest atoms C(1), C(5), O(1A), and O(1B) is approximately trigonal bipyramidal with the oxygen atoms of the unidentate ferrocenecarboxylate groups in the apical positions [Te–O(1A) = 2.145(2) Å, Te–O(1B) = 2.175(2) Å] and the two methylene carbon at-

© 2007 NRC Canada

Table 2. Selected bond lengths (Å) and angles (°) in **3**.

Bond lengths (Å)	
Te—C(1)	2.124(3)
Te—O(1A)	2.145(2)
Fe(1)—C(10A)	2.034(3)
Fe(1)—C(3A)	2.037(3)
Fe(1)—C(8A)	2.045(3)
Fe(1)—C(6A)	2.045(3)
Fe(1)—C(4A)	2.047(3)
Fe(2)—C(2B)	2.034(3)
Fe(2)—C(8B)	2.040(3)
Fe(2)—C(7B)	2.042(3)
Fe(2)—C(10B)	2.044(3)
Fe(2)—C(3B)	2.046(3)
O(1A)—C(1A)	1.313(3)
O(1B)—C(1B)	1.312(4)
C(1A)—C(2A)	1.475(4)
Te—C(5)	2.134(3)
Te—O(1B)	2.175(2)
Fe(1)—C(11A)	2.036(3)
Fe(1)—C(9A)	2.044(3)
Fe(1)—C(2A)	2.045(3)
Fe(1)—C(5A)	2.047(3)
Fe(1)—C(7A)	2.053(3)
Fe(2)—C(6B)	2.035(3)
Fe(2)—C(5B)	2.040(3)
Fe(2)—C(9B)	2.043(3)
Fe(2)—C(11B)	2.046(3)
Fe(2)—C(4B)	2.048(3)
O(2A)—C(1A)	1.229(3)
O(2B)—C(1B)	1.224(3)
C(1B)—C(2B)	1.481(4)
Bond angles (°)	
C(1)–Te–C(5)	97.56(11)
C(5)–Te–O(1A)	87.19(10)
C(5)–Te–O(1B)	81.30(10)
C(3A)–Fe(1)–C(7A)	168.36(14)
C(1B)–O(1B)–Te	110.83(17)
C(1)–Te–O(1A)	82.53(10)
C(1)–Te–O(1B)	87.20(10)
O(1A)–Te–O(1B)	163.43(8)
C(1A)–O(1A)–Te	111.69(17)
C(2B)–Fe(2)–C(9B)	162.58(12)

oms in the equatorial plane [$\cdots$ C(1)–Te –C(5) = 97.56(11)°]. The fifth coordination position in the equatorial plane is apparently occupied by a stereochemically active electron pair. The O(1B)–Te –O(1A) angle of 163.43(8)° deviates considerably from linearity, with oxygen atoms pushed away from the equatorial tellurium lone pair (25, 26). In the unit cell diagram (withheld for sake of brevity) of **3**, no intermolecular interactions are seen between the molecules of **3**, in contrast to other organotellurium carboxylates (26) where a variety of supramolecular associations are present because of Te$\cdots$O secondary bonds formed through the intermolecular interactions between Te and O of the carboxylate groups.

To our knowledge, **3** and **5** are the first ferrocenyl carboxylato tellurium derivatives and their properties are noteworthy: they are virtually inert towards hydrolysis, even in boiling water, and they do not undergo any change until 194 °C. Their NLO (nonlinear optical) and electrochemical properties are being reported for the first time in this investigation.

Table 3. Second harmonic generation (SHG) data for bis(ferrocenyl carboxylato) telluranes.

Complex	SHG effciency[a]
$C_5H_{10}Te(OCOFc)_2$	0.13
$C_4H_8Te(OCOFc)_2$	0.018
$[N{\equiv}W(OCMe_3)_3]n$[29]	0.20
KH_2PO_4(KDP)[28]	0.16

[a]Efficiency (urea = 1) of unsized powders (λ_{ex} = 1064 nm).

Determination of the relative efficiency of second harmonic generation (SHG) using the Kurtz and Perry method (27) shows that 1,1,2,3,4,5,6-heptahydro-1,1-bis(ferrocenyl carboxylato) tellurane **3** is 0.13 times as efficient as urea. This is comparable to the SHG efficiency of potassium dihydrogen phosphate (KDP) (28) (Table 3). The SHG efficiency of **3** is also comparable to the tungsten nitrido $[N{\equiv}W(OCMe_3)_3]_n$ polymer (29) (Table 3). The SHG efficiency of **3** is modest in view of the fact that **3** should, in principle, possess large molecular hyperpolarisability (β) as it contains ferrocene units that are necessarily electrochemically charge–transfer active in nature. The closest analogue to complex **3** is 2-dicyanomethylene-1,3-bis(ferrocenylmethyl)-1,3-diazolidine, which also shows a SHG signal by the Kurtz powder technique with low efficiency (30).

The SHG efficiency of 1,1,2,3,4,5-hexahydro-1,1-bis(ferrocenylcarboxylato) tellurophene **5** is only 0.018 times as that of urea (Table 3), which is much lower than the SHG efficiency of **3.** In spite of our repeated efforts, we have not been able to grow the crystals of **5** for X-ray diffraction studies, and because of the absence of crystal structure data for **5** it is very difficult to comment on the large difference in SHG efficiency values of **3** and **5**. The irradiation of laser light for the evaluation of SHG efficiency through $C_5H_{10}TeI_2$ and $C_4H_8TeI_2$ resulted in their decomposition. This observation, coupled with SHG efficiencies of **3** and **5**, indicates that the attachment of FcCOO groups in place of iodide groups to $C_5H_{10}Te$ or C_4H_8Te heterocycles, probably confers stability to these tellurium heterocycles with respect to irradiation of laser light.

Cyclic voltammetric studies on **3** and **5** show a single quasi-reversible peak with an $E_{1/2}$ value of 0.27 V for **3** and 0.29 V for **5** (vs. Ag/AgCl). A representative cyclic voltammogram of **3** is reproduced in Fig. 2. Comparison of the $E_{1/2}$ value with those of some biferrocene molecules with different spacer groups is shown in Table 4. In biferrocene [A] (31), two oxidation waves are present [$E_{1/2}$ = 0.46 V and $E_{1/2}$ = 0.80 V and ΔE = 0.34 V (vs. Ag/AgCl)] as oxidation of the first ferrocenyl moiety makes subsequent removal of an electron more difficult. Similarly in bridged ferrocenes containing S(9), [P, Ge, Sn] (17*b*), and Si_n [n = 1, 2, 3] (31, 17*b*) bridges, two oxidation waves are observed because of electronic communication between ferrocene units. However, the presence of $(\text{-}CH_2\text{-})_n$ (n > 1) (17*b*) and $(SiMe_2)_n$ (n = 6) [D] (Table 4) (31) units serve as insulating units

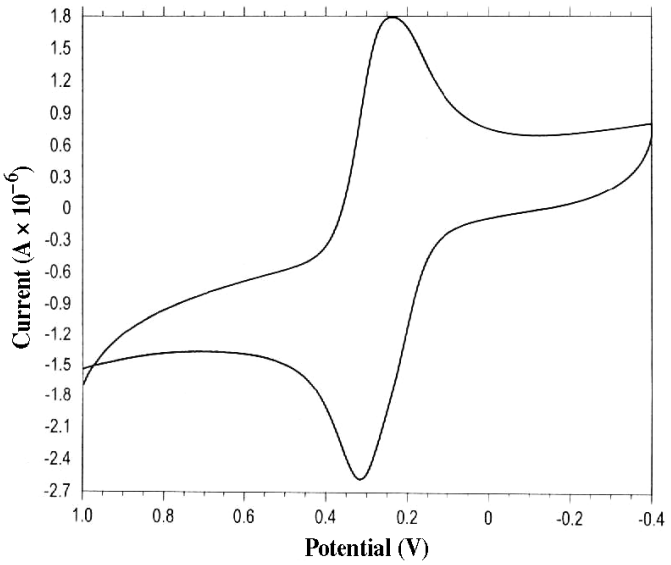
© 2007 NRC Canada

Table 4. CV data for **3**, **5**, and some other biferrocene derivatives.

No.	Compound	$E_{1/2}$ [V][a]	$E_{1/2}$ [V][a]	Ref.
A	Fc-Fc	0.46	0.80	31
B	Fc-$(SiMe_2)_2$-Fc	0.56	0.67	31
C	Fc-$(SiMe_2)_3$-Fc	0.54	0.62	31
D	Fc-$(SiMe_2)_6$-Fc	0.58	—	31
E	Fc-C(O)O-C_5H_{10}Te-O(O)C-Fc (**3**)	0.27	—	Present work
F	Fc-C(O)O-C_4H_8Te-O(O)C-Fc (**5**)	0.29	—	Present work
G	Fc	0.05	—	Present work

[a]Vs. Ag/AgCl

Fig 2. Cyclic voltammogram of $C_5H_{10}Te(OCOFc)_2$ (**3**).



and only one oxidation wave is detected because of little interaction between the two ferrocene groups. Similarly, in the present investigation when a ferrocene group is separated from another ferrocene group by the spacer group [-C(=O)O-Te(R_2)-O-C(=O), R_2 = C_5H_{10}, C_4H_8], the spacer groups act as insulating units and only one oxidation wave is detected. The results are consistent with the earlier conclusions that noninteracting electroactive centers will involve as many electrons as there are centers and will yield a voltammetric wave with a slope matching to that of the corresponding molecule with a single electroactive center (14, 15). The current study opens routes to a convenient method of synthesis of ferrocenylcarboxylato telluranes with independent redox centers and leads to fully reversible single-step two-electron redox systems. Further efforts are directed towards (*i*) the attachment of different tellurium heterocycles, (*ii*) the incorporation of different (spacer) groups in the system, and (*iii*) extension of this chemistry to other transition metallocene carboxylates and investigation of their electrochemical and NLO properties.

Conclusions

We have synthesized the first organotellurium derivatives (**3** and **5**) containing ferrocene carboxylate groups. The structure of $C_5H_{10}Te(OCOFc)_2$ (**3**) has been confirmed by X-ray diffraction and it corresponds to a new structural type. The relative SHG efficiency of **3** is modest. The electrochemical measurements of **3** and **5** reveal them to be fully reversible single-step two-electron redox systems.

Acknowledgements

PCS thanks the Department of Science and Technology (DST) and the Council of Scientific and Industrial Research (CSIR) for financial support. SB is thankful to DST for Women Scientist Programme.

References

1. (*a*) M. Scheibitz, R.F. Winter, M. Bolte, H.-W. Lerner, and M. Wagner. Angew. Chem. Int. Ed. **42**, 924 (2003); (*b*) M. Scheibitz, J.B. Heilmann, R.F. Winter, M. Bolte, J.W. Bats, and M. Wagner. Dalton Trans. 159 (2005).
2. K. Venkatasubbaiah, L.N. Zakharov, W.S. Kassel, A.L. Rheingold, and F. Jäkle. Angew. Chem., Int. Ed. **44**, 5428 (2005).
3. H. Braunschweig, C. Burschka, G.K.B. Clentsmith, T. Kupfer, and K. Radacki. Inorg. Chem**. 44**, 4906 (2005).
4. A. Althoff, P. Jutzi, N. Lenze, B. Neumann, A. Stammler, and H.-G. Stammler. Organometallics, **21**, 3018 (2002).
5. (*a*) J.B. Heilmann, M. Scheibitz, Y. Qin, A. Sundararaman, F. Jäkle, T. Kretz, M. Bolte, H.-W. Lerner, M.C. Holthausen, and M. Wagner. Angew. Chem. Int. Ed. **45**, 920 (2006); (*b*) J.M. Nelson, H. Rengel, and I. Manners. J. Am. Chem. Soc. **115**, 7035 (1993); (*c*) D.A. Foucher, B.Z. Tang and I. Manners. J. Am. Chem. Soc. **114**, 6246 (1992).
6. (*a*) D.A. Foucher, R. Ziembinski, B.Z. Tang, P.M. Macdonald, J. Massey, R. Jaeger, G.J. Vancso, and I. Manners. Macromolecules, **26**, 2878 (1993); (*b*) W. Finckh, B.Z. Tang, D.A. Foucher, D.B. Zamble, R. Ziembinski, A. Lough, and I. Manners. Organometallics, **12**, 823 (1993); (*c*) B.Z. Tang, R. Petersen, D.A. Foucher, A. Lough, N. Coombs, R. Sodhi, and I. Manners. J. Chem. Soc. Chem. Commun. 523 (1993); (*d*) R. Ziembinski, C. Honeyman, O. Mourad, D.A. Foucher, R. Rulkens, M. Liang, Y. Ni, and I. Manners. Phosphorus, Sulfur, Silicon Relat. Elem. **76**, 219 (1993); (*e*) C. Honeyman, D.A. Foucher, O. Mourad, R. Rulkens, and I. Manners. Polymer Prepr. (Am. Chem. Soc. Div. Polym. Chem.) **34**, 330 (1993); (*f*) D.A. Foucher and I. Manners. Makromol. Chem. Rapid Commun. **14**, 63 (1993); (*g*) R. Rulkens, A.J. Lough, and I. Manners, J. Am. Chem. Soc. **116**, 797 (1994) ; (*h*) I. Manners. Chem. Commun. 857 (1999); (*i*) Y. Hatanaka, S. Okada, T. Minami, M. Goto, and K. Shimada. Organometallics, **24**, 1053 (2005); (*j*) W.Y. Chan, A.J. Lough and I. Manners. Organometallics, **26**, 1217 (2007); (*k*) T. Baumgartner, F.

© 2007 NRC Canada

Jäkle, R. Rulkens, G. Zech, A.J. Lough, and I. Manners. J. Am. Chem. Soc. **124**, 10062 (2002); (*l*) R. Rulkens, A.J. Lough and I. Manners. Angew. Chem. Int. Ed. Engl. **35**, 1805 (1996); (*m*) F. Jäkle, R. Rulkens, G. Zech, D.A. Foucher, A.J. Lough, and I. Manners. Chem. Eur. J. **4**, 2117 (1998); (*n*) H.K. Sharma, F. Cervantes-Lee, J.S. Mahmoud, and K.H. Pannell. Organometallics, **18**, 399 (1999); (*o*) A. Bartole-Scott, R. Resendes, F. Jäkle, A.J. Lough, and I. Manners. Organometallics, **23**, 6116 (2004); (*p*) R. Resendes, J.M. Nelson, A. Fischer, F. Jäkle, A. Bartole, A.J. Lough, and I. Manners. J. Am. Chem. Soc. **123**, 2116 (2001); (*q*) N.P. Reddy, H. Yamashita, and M. Tanaka. J. Chem. Soc. Chem. Commun. 2263 (1995); (*r*) M. Tanaka and T. Hayashi. Bull. Chem. Soc. Jpn. **66**, 334 (1993); (*s*) K.H. Pannell, V.V. Dementiev, H. Li, F. Cervantes-Lee, My. T. Nguyen, and A.F. Diaz. Organometallics **13**, 3644 (1994).

7. (*a*) D. Seyferth and H.P. Withers. Organometallics **1**, 1275 (1982); (*b*) H.P. Withers, D. Seyferth, J.D. Fellmann, P. Garrou, and S. Martin. Organometallics, **1**, 1283 (1982).
8. V. Chandrasekhar, S. Nagendran, S. Bansal, M.A. Kozee, and D.R. Powell. Angew. Chem. Int. Ed. Engl. **39**, 1833 (2000).
9. P.F. Brandt and T.B. Rauchfuss. J. Am. Chem. Soc. **114**, 1926 (1992).
10. H.W. Roesky and M. Lücke. Angew. Chem. Int. Ed. Engl. **28**, 493 (1989).
11. (*a*) F.L. Carter. *In* Molecular electronic devices. Marcel Dekker, New York. 1982; (*b*) L.L. Hench and D.R. Ulrich. *In* Ultrastructure processing of ceramics, glasses and composites. Wiley, New York. 1984; (*c*) H.W. Roesky. Chem. Soc. Rev. **15**, 309 (1986).
12. (*a*) M.E. Wright and M.S. Sigman. Macromolecules, **25**, 6055 (1992); (*b*) H.B. Fyfe, M. Mlekuz, D. Zargarian, N.J. Taylor, and T.B. Marder. J. Chem. Soc. Chem. Commun. 188 (1991); (*c*) S.J. Davies, B.F.G. Johnson, M.S. Khan, and J. Lewis. J. Chem. Soc. Chem. Commun. 187 (1991); (*d*) S.C. Tenhaeff and D.R. Tyler. J. Chem. Soc. Chem. Commun. 1459 (1989); (*e*) E.W. Neuse and L. Bednarik. Macromolecules, **12**, 187 (1979); (*f*) R. Bayer, T. Pohlmann, and O. Nuyken. Makromol. Chem. Rapid Commun. **14**, 359 (1993); (*g*) K. Gonsalves, L. Zhanru, and M.V. Rausch. J. Am. Chem. Soc. **106**, 3862 (1984); (*h*) H.M. Nugent, M. Rosenblum, and P. Klemarczyk. J. Am. Chem. Soc. **115**, 3848 (1993); (*i*) L. Espada, K.H. Pannell, V. Papkov, L. Leites, S. Bukalov, I. Suzdalev, M. Tanaka, and T. Hayashi. Organometallics, **21**, 3758 (2002); (*j*) K.H. Pannell, J.M. Rozell, and J.M. Zeigler. Macromolecules, **21,** 276 (1988); (*k*) A. Diaz, M. Sevmour, K.H. Pannell, and J.M. Rozell. J. Electrochem. Soc. **137**, 503 (1990).
13. (*a*) S. Barlow and S.R. Marder. Chem. Commun. (Cambridge), 1555 (2000); (*b*) N.J. Long. Angew. Chem. Int. Ed. Engl. **34**, 21 (1995); (*c*) J.E. Sheats, C.E. Carraher, and C.U. Pittman. *In* Metal containing polymer systems. Plenum, New York. (1985).
14. (*a*) J.B. Flanagan, S. Margel, A.J. Bard, and F.C. Anson. J. Am. Chem. Soc. **100**, 4248 (1978); (*b*) F.G. Bordwell, G.D. Cooper, and H. Mortina. J. Am. Chem. Soc. **79**, 376 (1957); (*c*) T.W. Smith, J.E. Kuder, and D. Wychick. J. Polym. Sci. **14**, 2433 (1976).
15. (*a*) D. Astruc. New. J. Chem. **16**, 305 (1992); (*b*) D. Astruc. Top. Curr. Chem. **160**, 47 (1991); (*c*) J.-L. Fillaut, J. Linares, and D. Astruc. Angew. Chem. Int. Ed. Engl. **33**, 2460 (1994).
16. (*a*) H.A.U. Hill, D.J. Page, and N.J. Walton. J. Electroanal. Chem. **217**, 141 (1987); (*b*) Y. Degani and A. Heller. J. Phys. Chem. **91**, 1285 (1987); (*c*) K.H. Pannell and J. Robillard. U.S. Patent No. 5-472-786. 5 December 1995; (*d*) L. Espada, J. Robillard, M. Shadaram, and K.H. Pannell. Inorg. Organomet. Polym. **10**, 169 (2000).
17. (*a*) I. Manners. Adv. Mater. **6**, 62 (1994); (*b*) D.A. Foucher, C.H. Honeyman, J.M. Nelson, B.Z. Tang, and I. Manners. Angew. Chem. Int. Ed. Engl. **32**, 1709 (1993).
18. B. Grossmann, J. Heinze, E. Herdtweck, F.H. Köhler, H. Nöth, H. Schwenk, M. Spiegler, W. Wachter, and B. Weber. Angew. Chem. Int. Ed. Engl. **36**, 387 (1997).
19. M.L. Steigerwald and C.R. Sprinkle. J. Am. Chem. Soc. **109**, 7200 (1987).
20. A.H. Cowley and R.A. Jones. Angew. Chem. Int. Ed. Engl. **28**, 1208 (1989).
21. (*a*) J.S. Aitchison, J.D. Prohaska, and E.M. Vogel. Met. Mater. Processes, **8**, 277 (1996); (*b*) J.W. Zwanziger. Int. Rev. Phys. Chem. **17**, 65 (1998); (*c*) A. Pierre, F. Duboudin, B. Tanguy, and J. Portier. Solid State Ionics, **53**, 1200 (1992); (*d*) H. Citeau, K. Kirschbaum, C. Conrad, and D.M. Giolando. Chem. Commun. (Cambridge), 2006 (2001); (*e*) H.B. Singh and N. Sudha. Polyhedron, **15**, 745 (1996); (*f*) P.C.Srivastava, S. Bajpai, C. Ram, R. Kumar, and R.J. Butcher. J. Organomet. Chem. **692**, 2482 (2007).
22. G.T. Morgan and H. Burgess. J. Chem. Soc. 321 (1928).
23. G.T. Morgan and F.H. Burstall. J. Chem. Soc. 180 (1931).
24. G.M. Sheldrick. SHELXS 86, SHELXS 97, SHELXL 97 [computer programs]. University of Göttingen, Göttingen, Germany. 1987 and 1997.
25. (*a*) P.C. Srivastava, S. Bajpai, R. Lath, C. Ram, Sm. Bajpai, R.J. Butcher, M. Veith, and M. Zimmer. J. Organomet. Chem. **658**, 34 (2002); (*b*) P.C. Srivastava, S. Bajpai, R. Lath, and R.J. Butcher. J. Organomet. Chem. **608**, 96 (2000); (*c*) J.B. Lambert and R.G. Keske. Tetrahedron Lett. **47**, 4755 (1967).
26. (*a*) P.C. Srivastava, A. Sinha, S. Bajpai, H.G. Schmidt, and M. Noltemeyer. J. Organomet. Chem. **575**, 261 (1999); (*b*) P.C. Srivastava, S. Bajpai, R. Lath, C. Ram, Sm. Bajpai, R.J. Butcher, M. Veith, and M. Zimmer. J. Organomet. Chem. **649**, 70 (2002); (*c*) P.C. Srivastava, S. Bajpai, Sm. Bajpai, R. Kumar, and R.J. Butcher. Inorg. Chim. Acta, **358**, 227 (2005); (*d*) N.W. Alcock, W.D. Hamson, and C. Homes. J. Chem. Soc. Dalton Trans. 1709 (1984); (*e*) N.W. Alcock, J. Culver, and S.M. Roe. J. Chem. Soc. Dalton Trans. 1477 (1992).
27. S.K. Kurtz and T.T. Perry. J. Appl. Phys. **39**, 3798 (1968).
28. (*a*) P.A. Franken, A.E. Hill, and C.W. Peters. Phys. Rev. Lett. **7**, 118 (1961); (*b*) R.C. Miller, D.A. Kleinman, and A. Savage. Phys. Rev. Lett. **11**, 146 (1963); (*c*) R.C. Miller. Appl. Phys. Lett. **5**, 17 (1964); (*d*) G.D. Boyd, R.C. Miller, K. Nassau, W.L. Bond, and A. Savage. Appl. Phys. Lett. **5**, 234 (1964); (*e*) R.C. Miller, G.D. Boyd, and A. Savage. Appl. Phys. Lett. **6**, 77 (1965); (*f*) C. Chen and G. Liu. Annu. Rev. Mater. Sci. **16**, 203 (1986).
29. T.P. Pollagi, T.C. Stoner, R.F. Dallinger, T.M. Gilbert, and M.D. Hopkins. J. Am. Chem. Soc. **113**, 703 (1991).
30. A. Benito, J. Cano, R. Martinez-Manez. J. Paya, J. Soto, M. Julve, F. Lloret, M.D. Marcos, and E. Sinn. J. Chem. Soc. Dalton Trans. 1999 (1993).
31. V.V. Dementiev, F. Cervantes-Lee, L. Parkanyi, H. Sharma, K.H. Pannell, My. T. Nguyen, and A. Diaz. Organometallics, **12**, 1983 (1993).

© 2007 NRC Canada

Self-assembled coating for modification of the electro-osmotic flow in nonaqueous capillary electrophoresis using formamide

Abebaw G. Diress and Charles A. Lucy

Abstract: The use of pure nonaqueous solvents in capillary electrophoresis (CE) can alter the separation selectivity and enhance the solubility of hydrophobic compounds and enables the use of higher voltages. However, control of the electro-osmotic flow (EOF) is essential. In this work, we report the use of self-assembled coatings for EOF modification and elimination of analyte adsorptions onto silica capillaries in pure formamide. Bilayer capillary coatings derived from the double chain cationic surfactant dimethyldioctadecylammonium bromide ($2C_{18}$DAB) reverses the EOF in buffers such as acetate, formate, and phosphate. Reversed EOF of $>1.1 \times 10^{-4}$ cm^2/Vs enables the separation of the pharmaceutical drugs propranolol, metoprolol, chloroquine, and chloropheniramine in less than 5 min with efficiencies of 0.2–0.5 million plates/m (66 000 to 165 000 plates). Chemical and physical factors affecting the coating stability and their influence on separation speed and efficiency of the cationic drugs in formamide are also investigated.

Key words: capillary electrophoresis, cationic surfactants, electro-osmotic flow, formamide, nonaqueous solvents.

Résumé : L'utilisation de solvants non aqueux purs dans l'électrophorèse capillaire (EC) peut altérer la sélectivité des séparations et augmenter la solubilité des composés hydrophobes et elle peut aussi permettre d'utiliser des voltages plus élevés. Toutefois, il est essentiel de contrôler l'écoulement électroosmotique (EEO). Dans ce travail, on a utilisé des enduits auto assemblés pour modifier l'écoulement électroosmotique et pour éliminer les adsorptions d'analyse sur les capillaires de silice dans le formamide pur. Des enduits capillaires à double couche dérivés d'une double chaîne de l'agent de surface, bromure de diméthyldioctadécylammonium ($2C_{18}$DAB) permet de renverser l'écoulement électrostatique dans des tampons, tels ceux de l'acétate, du formiate ou du phosphate. Des EEO inversés de $>1.1\times 10^{-4}$ cm^2/Vs permettent d'effectuer la séparation de médicaments tels, le propranolol, le métoprolol, la chloroquine et la chlorophéniramine en moins de 5 min avec des efficacités allant de 0.2–0.5 million plateaux/m (66 000 à 165 000 plateaux). On a aussi examiné les facteurs chimiques et physiques qui affectent la stabilité des enduits et leur influence sur la vitesse et l'efficacité de séparation des médicaments cationiques

Mots-clés : électrophorèse capillaire, agents de surface cationiques, écoulement électroosmotique, formamide, solvants non aqueux.

[Traduit par la Rédaction]

Introduction

Electrophoresis is the migration of ions under an applied electric field (E). The simplest expression for the velocity of this migration (ν) is given in eq. [1],

$$[1] \qquad \nu = \mu_e E = \frac{q}{6\pi\eta r_s} E$$

where μ_e is the electrophoretic mobility, which is directly related to the charge of the ion (q) and inversely related to the solvent viscosity (η) and the Stokes radius of the ion (r_s). In capillary electrophoresis (CE) the use of narrow (10–100 μm) capillaries enables electric fields of 100–500 V/cm to be applied, which results in rapid electrophoretic separations. However to achieve separation, the mobility of two ions must be different. Mobility differences between analytes may be intrinsic or can result from adjustment of (*i*) the charge of the ion (e.g., through acid–base equilibria or ionic screening (1)), (*ii*) the size of the ion (e.g., through complexation (2–4)), or (*iii*) the solvation of the ion by using mixed organic–water media. Advantages asserted for organic–water media over pure aqueous systems include altering the electrophoretic mobility (and thus possibly selectivity) of analytes, increased solubility of hydrophobic analytes, and the ability to use higher separation voltages and (or) high BGE ionic strengths because of lower electric current compared with water (5–8). The validity of these and other more speculative claims (e.g., increased efficiency) have recently been critically evaluated (9).

A wide range of solvents have been used in nonaqueous CE including methanol, ethanol, butanol, acetonitrile, nitromethane, and mixtures of two or more of these solvents (8, 10, 11). Formamide (FA) is one of the few organic sol-

Received 1 February 2007. Accepted 24 May 2007. Published on the NRC Research Press Web site at canjchem.nrc.ca on 26 July 2007.

A.G. Diress and C.A. Lucy.[1] Department of Chemistry, Gunning–Lemieux Chemistry Centre, University of Alberta, Edmonton, AB T6G 2G2, Canada.

[1]Corresponding author (e-mail: charles.lucy@ualberta.ca).

 doi:10.1139/V07-077 © 2007 NRC Canada

vents possessing a dielectric constant greater than that of water (109.5 vs. 78.5). This property makes ion pairing of analyte ions with buffer counter-ions negligible, whereas ion pairing is often observed in low dielectric organic solvents such as acetonitrile (5, 11). FA also has a 3-dimensional hydrogen-bonded structure that is even more pronounced than that of water. Sahota and Khaledi (12) reported the first investigation of FA as a CE medium in 1994. Since then, FA or FA–aqueous buffers have been used for CE separations of enantiomers (13, 14), for control of the electro-osmotic flow (EOF) (15), as a solvent in MEKC (16–19), and for other applications (15, 20, 21). However, the potential of FA as a pure or mixed solvent in CE has not been fully achieved because of a lack of understanding of the influence of the solvent on mobility, low absorbance detection sensitivity since FA has a UV cut-off of 275 nm, and the slow EOF and mobilities in FA due to its high viscosity (3.3 cP). Recently, Porras and Kenndler (21) addressed the first issue in their thorough investigation of intrinsic mobilities, ionic strength, and pH on mobilities in FA. They also addressed the issue of detection by employing both indirect UV detection and contactless conductivity detection (21). However, they observed EOF values of only $+(0.8–1.5) \times 10^{-4}$ cm^2/Vs (21), approximately a factor of five lower than in aqueous buffers. Coupled with the low mobilities observed in FA (21), long analysis time would be expected, particularly under counter-EOF conditions where highest resolution is achieved. In this paper we focus on the control and modification of the EOF in buffers containing formamide. Double-chained cationic surfactants are employed to reverse the EOF. The reversed EOF conditions enable counter-EOF separations of basic analytes, which have previously only been studied under co-EOF conditions (12, 13).

Results and discussion

Both the migration time and resolution depend upon the apparent mobility (μ_a), which is directly dependent on the mobility of the electro-osmotic flow (μ_{eof}).

$$[2] \qquad \mu_a = \mu_e + \mu_{eof}$$

where μ_e is the electrophoretic mobility of the analyte as defined in eq. [1]. In general, most analytes separated by CE possess an electrophoretic mobility smaller than the EOF mobility (μ_{eof} is typically $+(2–8) \times 10^{-4}$ cm^2/(Vs) in aqueous buffers). This allows for the simultaneous determination of both positively and negatively charged species when the detector is placed at the cathodic (negative) end of the capillary. In this case, cations migrate in the same direction as the EOF (co-EOF) and anions migrate opposite to the direction of the EOF (counter-EOF). The greatest separation speed is achieved under co-EOF separation conditions, while greatest resolution is achieved using counter-EOF conditions. Thus, EOF plays a key role in electrophoretic separations (22).

The magnitude of the EOF mobility is expressed by the von Smoluchowski equation,

$$[3] \qquad \mu_{eof} = -\frac{\varepsilon\zeta}{\eta}$$

where ε and η are the dielectric constant and viscosity of the solvent and ζ is the zeta potential of the capillary surface. The zeta potential is the potential at the plane of shear and is a function of the surface charge and the ionic strength of the buffer. The EOF can be adjusted by alteration of the dielectric constant or viscosity (23, 24), but most often the focus is on controlling the surface charge of the capillary. Approaches include control of the deprotonation of silanols on the capillary surface, covalent coatings (25), and dynamic adsorption (ion exchange) of strongly retained cations (22). Dynamic coatings are attractive relative to covalently bonded polymer coatings because of their simplicity, versatility, and low cost.

Surfactants are a flexible and effective means of suppressing (26) or reversing (27) the EOF. Indeed, rapid and high efficiency separations of inorganic anions was made possible by reversal of the EOF using tetradecyltrimethylammonium bromide (TTAB) (28). EOF reversal by cationic surfactants involves the self-assembly of poly-cationic aggregates that adsorb onto the capillary surface. Single-tailed cationic surfactants such as TTAB form spherical micelles in water, which adsorb to reverse the EOF (27, 29). However, the surfactant must be in the electrolyte to maintain the EOF. Double-chain surfactants such as didodecyldimethylammonium bromide (DDAB or $2C_{12}$DAB) self-assemble to form vesicles in water, which adsorb onto the capillary as a bilayer (29). Bilayer coatings are much more effective at preventing protein adsorption and are sufficiently stable that the surfactant does not need to be present in the separation buffer (30). The use of long-chained dimethyldioctadecylammonium bromide ($2C_{18}$DAB) enhances the stability of the bilayer such that 60 replicate runs could be performed over 12 days using aqueous buffers that did not contain surfactant (31).

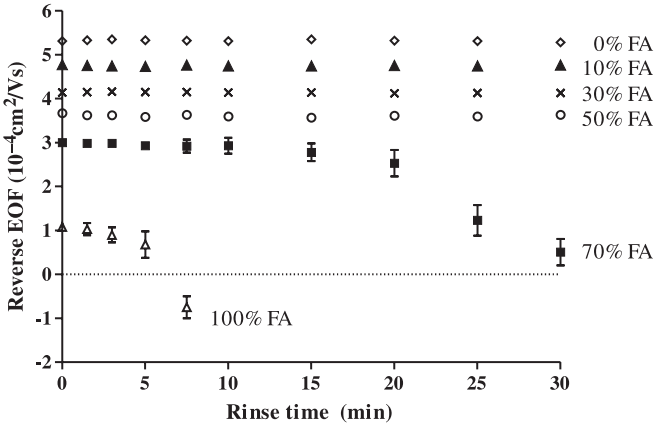
We have shown that long-chained two-tailed surfactants form bilayer coatings that are stable for a number of runs in buffers containing up to 60% *v*/*v* of organic solvents such as methanol, acetonitrile, ethanol, propanol, and butanol (32). As a continuation of that work, our interest in this study was to evaluate whether these long doubly chained surfactants could be used in buffers prepared in pure formamide (FA). Duval and Warr (33) observed that the single-chained surfactant tetradecyltrimethyl ammonium chloride (TTAC) formed similar micellar aggregates in FA as in pure water. This similarity in aggregation behavior is believed to be due to the combined effect of the high dielectric constant of FA and the hydrogen-bonding nature of the amide proton (34–36). However, there have been no studies of two-tailed surfactants in mixed FA–water or pure FA solvent systems.

Bilayer stability in formamide–water media

In Fig. 1 the stability of the coating was assessed by monitoring the electro-osmotic flow mobility (μ_{eof}) as the capillary was rinsed with surfactant-free buffer with varying amounts of FA (37, 38). Surfactant coatings were formed simply by rinsing the capillary with a 1.0 mmol/L aqueous surfactant solution for 10 min, followed by a brief rinse with a surfactant-free electrophoretic buffer to remove any nonsorbed surfactant. Both the initial value of the EOF and the coating stability depend on the volume fraction of FA in the separation buffer. The magnitude of the initial EOF (at zero

© 2007 NRC Canada

Fig. 1. Coating stability of $2C_{18}$DAB in formamide–aqueous phosphate buffers. 0% FA (◇), 10% FA (▲), 30% FA (×), 50% FA (○), 70% FA (■), 100% (△). Experimental conditions are: 25 mmol/L sodium phosphate buffer at pH 7.0; applied voltage –20 kV; capillary 37 cm × 50 μm i.d. (28.5 cm to the detector); neutral marker 0.5 mmol/L mesityl oxide at 254 nm; temperature 25 °C. The coating was prepared by rinsing the capillary with 1.0 mmol/L $2C_{18}$DAB prepared in water for 10 min at 93.8 kPa. The time on the *x*-axis represents the duration for which the coating is then subjected to a high-pressure (93.8 kPa) rinse of buffer not containing surfactant. The capillary was regenerated by rinsing with 1 mol/L NaOH and recoated with $2C_{18}$DAB solution prior to another rinse with separation buffer without surfactant. Error bars indicate the standard deviation of at least three runs. For points with no error bars the standard deviation is smaller than the symbol.



time) decreases as the amount of FA is increased. This is due in part to a decrease in the dielectric constant to viscosity ratio (i.e., lower ϵ/η value, Table 1). Both ϵ and η increase with increasing percentage of FA, with ϵ reaching a maximum value at ~65% and slightly decreasing thereafter, but the overall ϵ/η ratio decreases (39). Rearrangement of eq. [3] allows estimation of the ζ, which is constant at –68 ± 2 mV between 0% and 70% but then decreases by about half in pure FA.

In buffers containing 0%–50% FA (Fig. 1), the $2C_{18}$DAB coating displays a constant EOF value (%RSD < 0.8%) with no noticeable drift over 30 min of continuous rinsing with the surfactant-free buffer. The results in pure aqueous buffer are consistent with those observed previously (31), which allowed protein separations to be performed for 12 days in aqueous buffers without the need to regenerate the coating. In 70% FA (■ in Fig. 1), the EOF remains constant for 15 min of rinsing ($RSD_{0–15\ min}$ = 1.2%) and thereafter decreases rapidly, indicating degradation of the $2C_{18}$DAB coating. In 100% FA, a small reversed EOF of 1.22×10^{-4} cm^2/Vs is obtained with no rinsing (t = 0), but the EOF decreases rapidly, generating a normal EOF after only a 5 min rinse (~6 capillary volumes).

The $2C_{18}$DAB degradation behavior observed in 70% and 100% FA (Fig. 1) differs from that observed previously in aqueous solutions (30). In aqueous solution, the $2C_{12}$DAB bilayer degradation follows first order kinetics such that the EOF decreases exponentially to a residual EOF value. The more drastic behavior in Fig. 1 may be due to a collapse of the bilayer structure because of the lower zeta potential. A similar dramatic decrease in EOF to that in Fig. 1 has been observed for double-chain surfactants in high ionic strength aqueous solutions where the zeta potential was substantially lowered (31). Valkó et al. (40) reported that under unbuffered conditions the zeta potential of fused silica was a factor of two lower in formamide than in water, although others have seen essentially no change in zeta potential under similar conditions (18). The zeta potential of the fused silica might be lowered further by a change in the true pH of our buffer upon addition of FA. Alternately, the dramatic decrease in EOF at high %FA might be due to an increased value of the critical micelle concentration (cmc) with increasing concentrations of FA There are no literature cmc values for double-chain surfactants in FA or in FA–water mixtures. However, the cmc for single-chain surfactants increase significantly in formamide relative to the value in water (41, 42).

Effect of surfactant concentration on EOF

In aqueous buffers the EOF has been observed to be unaffected by low concentrations of cationic surfactant. The EOF undergoes a rapid transition to the reversed direction at a surfactant concentration near the cmc in the bulk solution or the critical surfactant aggregation concentration (csac) at the capillary surface (27, 43–45). Figure 2 shows that in pure FA $2C_{18}$DAB reverses the EOF, and that increased concentrations of surfactant gradually increase the magnitude of the EOF. This behavior is similar to our previous observations of C_{16}TAB in MeOH–water under conditions where the zeta potential of the capillary was low (45).

Effects of capillary size and buffer type

Capillary diameter significantly affects the stability of bilayer coatings (30, 46). Figure 3 shows the coating stability for 25 μm and 50 μm internal diameter $2C_{18}$DAB-coated capillaries in formamide. The 25 μm capillary was coated with 1.0 mmol/L surfactant solution for 25 min (compared with 10 min rinse for the 50 μm capillary) to ensure that same volume of surfactant solution had passed through both capillaries. As expected, both capillaries display the same initial reversed EOF (~1.12×10^{-4} cm^2/Vs) indicating that similar bilayers are produced. However, the coating shows poorer stability with the wider capillary. The larger volume-to-surface ratio of the wider capillary shifts the adsorption–desorption equilibrium towards desorption of more surfactant from the surface (30). Hence, the degradation in the bilayer structure results in the reduction of the EOF. This is similar to the bilayer degradation observed when the coating is subjected to longer rinsing times (e.g., longer than 20 min flushing in 70% FA buffer in Fig. 1).

The nature and concentration of the buffer influences the stability of surfactant coatings (30, 47). Aqueous acetate and formate buffers yield significantly lower stability surfactant coatings than phosphate buffer (30, 48). This is because the weaker attraction of acetate and formate to the surfactant head groups increases the electrostatic repulsion between the charged head groups, which results in a higher cmc and consequently a less stable bilayer. Hence, the coating stability was also examined in two other common buffers, ammonium acetate (NH_4Ac) and ammonium formate (NH_4Fo) buffers

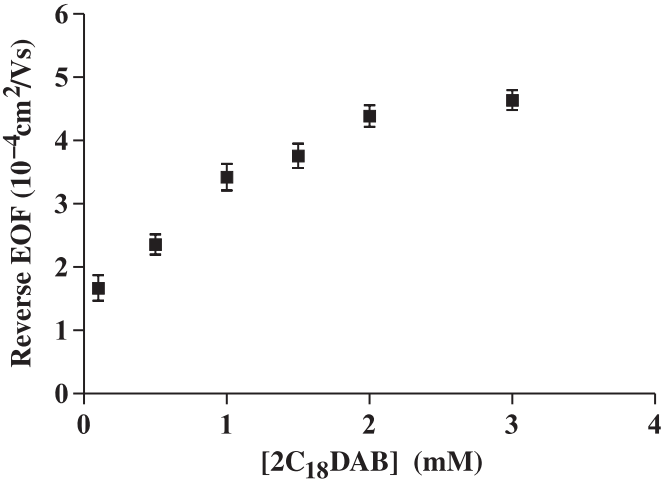
© 2007 NRC Canada

Table 1. Effect of organic buffer solvent content on solvent parameters and electro-osmotic flow at 25 °C.

FA (% *v*/*v*)	ϵ^a	η (mPa·s)	ϵ/η	Reversed EOF[b] ($\times 10^{-4}$ cm^2/Vs) (n = 4)
0	78.5	0.89	88.2	5.3 ± 0.3
10	82.8	1.01	81.9	4.9 ± 0.2
30	93.5	1.27	73.6	4.1 ± 0.4
50	101.8	1.62	62.8	3.8 ± 0.3
70	111	2.13	52.1	3.0 ± 0.1
100	109.5	3.26	32.9	1.1 ± 0.2

[a]Values obtained from interpolation of literature data (39).
[b]Initial EOF values obtained without rinsing the coatings with the electrophoretic buffer. All other experimental conditions are as described in Fig. 1.

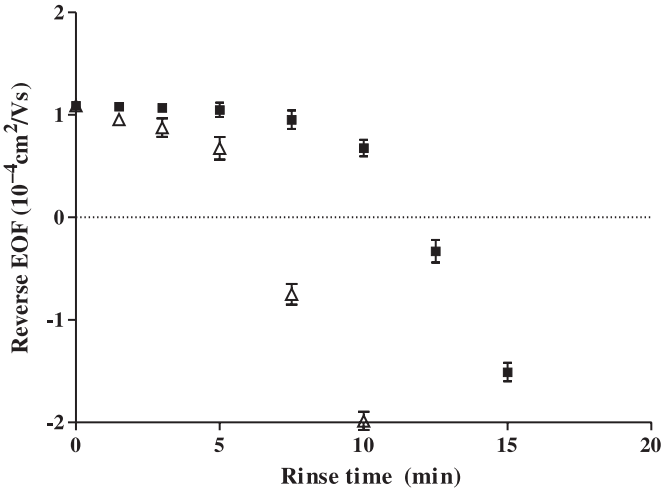
Fig. 2. Effect of $2C_{18}$DAB concentration on the reversed EOF mobility in formamide. Experimental conditions are: buffer 25 mmol/L sodium phosphate buffer (pH 7.0) prepared in formamide; applied voltage –20 kV; capillary 37 cm × 50 µm i.d. (28.5 cm to the detector); neutral marker 0.5 mmol/L mesityl oxide at 254 nm; temperature 25.0 °C. All the $2C_{18}$DAB solutions were prepared in formamide. All other conditions are as described in Fig. 1. Error bars indicate the standard deviation of at least three runs.



prepared in FA at pH 4.0. Under the conditions studied (0.1–2.0 mmol/L surfactant; 25 and 50 mmol/L ammonium acetate and ammonium formate in FA) reversed EOF was not achieved after rinsing of the capillary to remove non-sorbed surfactant. Instead, partially suppressed normal EOF (4.31×10^{-4} and 4.85×10^{-4} cm^2/Vs for 25 mmol/L NH_4Fo and NH_4Ac, respectively) was observed, indicating some surfactant adsorption but no bilayer formation. Complete removal of the surfactant (indicated by a return of the EOF to ~8.0×10^{-4} cm^2/Vs was achieved by flushing the capillary with 1.0 mmol/L NaOH followed by FA. Thus, $2C_{18}$DAB was ineffective as a semipermanent coating in FA in the presence of acetate or formate buffers.

However, when 1.0 mmol/L $2C_{18}$DAB was added to acetate or formate separation buffers as a dynamic additive, a strongly reversed EOF was obtained (Table 2). Also, over the surfactant concentration range studied, the magnitude of the EOF was independent of the surfactant concentration kept in the separation buffer. The magnitude of the reversed

Fig. 3. Effect of capillary i.d. on the stability of a double-chain surfactant coating in nonaqueous solvent: 25 µm i.d. (■); 50 µm i.d. (△). Experimental conditions are: 25 mmol/L sodium phosphate buffer (pH 7.0) and 1.0 mmol/L C_{18}DAB surfactant both prepared in formamide. All other conditions are as described in Fig. 1. Error bars indicate the standard deviation of at least three



EOF decreases as the buffer concentrations are increased, consistent with the expected inverse dependence on the ionic strength (21).

Separations of basic drugs in nonaqueous buffers

The utility of the coating in the presence of nonaqueous solvent was investigated by analyzing cationic drugs. Figure 4 shows the separation of four basic drugs (propranolol, metoprolol, chloroquine, and chloropheniramine) in sodium phosphate buffer prepared in pure formamide. There was no difference in the coating stability at pH 3.0 and pH 7.0, so a lower pH was used for the separation in Fig. 4 to ensure that all the drugs were positively charged. With the bare capillary (Fig. 4*a*), both separation efficiency (N < 150 000 plates/m) and migration time reproducibility (%RSD = 3.2–4.4) are poor. The peaks also are severely tailed (the asymmetry factor B/A ranges from 0.86 to 1.4) because of strong interactions between the positively charged analytes and the negatively charged wall.

Figure 4*b* shows the analogous separation in FA using a $2C_{18}$DAB-coated capillary. The separation was obtained with no surfactant in the separation buffer as the $2C_{18}$DAB

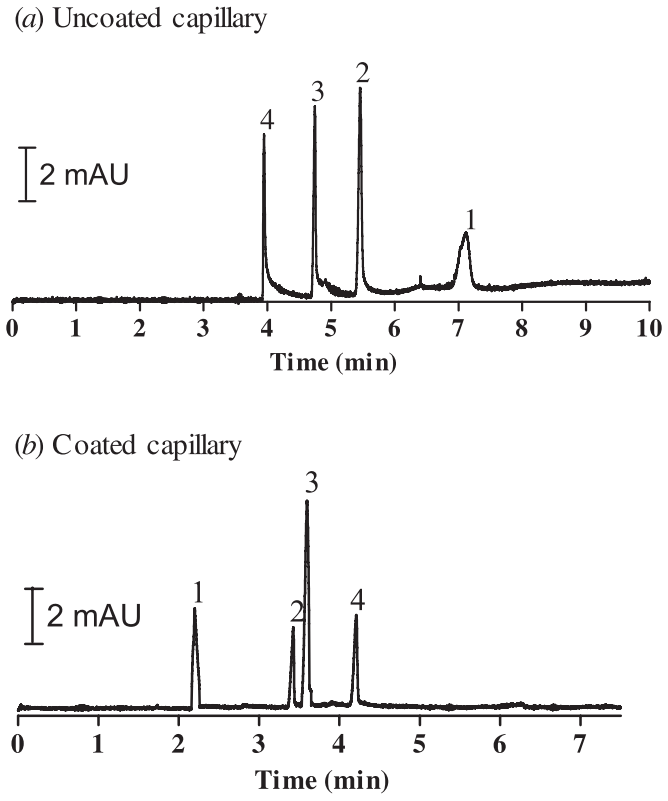
© 2007 NRC Canada

Table 2. Effect of buffer type and surfactant concentration on the value of EOF using $2C_{18}$DAB as a dynamic coating in formamide.

		Reversed EOF ($\times 10^{-4}$ cm^2/Vs) (n = 4)		
Buffer system	C (mmol/L)	0.1 mmol/L C_{18}DAB	1.0 mmol/L $2C_{18}$DAB	2.0 mmol/L $2C_{18}$DAB
NH_4Ac	25	6.3±0.4	6.7±0.4	6.4±0.4
NH_4Ac	50	4.7±0.2	5.0±0.3	4.9±0.1
NH_4Fo	25	7.6±0.1	7.3±0.3	7.8±0.3
NH_4Fo	50	5.8±0.2	6.1±0.4	5.7±0.2

Note: Experimental conditions: applied voltage –15 kV; capillary 37 cm × 50 μm (28.5 cm to the detector); 1.0 mmol/L $2C_{18}$DAB was maintained in the pH 4.0 separation buffer; neutral marker 1.0 mmol/L mesityl oxide dissolved in formamide; 25.0 °C.

Fig. 4. Electropherogram of basic drugs in FA using (*a*) bare silica capillary and (*b*) $2C_{18}$DAB-coated capillary. Experimental conditions are: buffer 25 mmol/L sodium phosphate at pH 3.0 prepared in FA, detection at 210 nm; in (*a*) bare silica capillary 40.5 cm (32 cm to the detection window); applied voltage +20 kV; sample concentration 0.5 mmol/L; in (*b*) $2C_{18}$DAB coated capillary 33 cm (24.5 cm to the detection window); applied voltage –25 kV; 1.0 mmol/L $2C_{18}$DAB, sample concentration 0.5 mmol/L (except metoprolol 0.25 mmol/L). Peaks are (1) chloropheniramine, (2) metoprolol, (3) propranolol, and (4) chloroquine.



coating has good stability in phosphate buffers. The migration order is reversed relative to Fig. *4a* because the $2C_{18}$DAB-coating generates a strong reversed EOF. Peak efficiencies range from 0.2–0.5 million plates/m (66 000 to 165 000 plates) with no tailing (B/A = 0.98–1.1), indicating that analyte adsorption onto the capillary wall has been eliminated. Migration time and peak area reproducibilities on the $2C_{18}$DAB-coated capillary (rinsed with 1.0 mmol/L surfactant for 10 min at 93.8 kPa) in FA without regeneration are <0.8% and <3.5% RSD, respectively, for 5 replicate injections. The coating was regenerated after every five runs, as performance declined gradually with further runs.

One drawback with FA is its high UV absorbance. As a consequence, high analyte concentrations had to be used in Fig. 4. Other detection techniques such as electrochemistry or mass spectroscopy could be employed to improve the detection sensitivity. Nonetheless, the $2C_{18}$DAB bilayer coating is promising for rapid and efficient separation of cationic drugs in pure FA. FA would be suitable for the analysis of substances with low aqueous solubility and for separation that cannot be achieved in aqueous buffers. As shown in this study, however, appropriate choice of the capillary diameter, buffer type and content of FA are essential to achieve the desired result.

Conclusions

The double-chained surfactant dimethyldioctadecylammonium bromide ($2C_{18}$DAB) has been demonstrated to be a noncovalent coating for EOF modification and elimination of analyte adsorptions in pure formamide. The coating is generated simply by rinsing the capillary with a 1.0 mmol/L $2C_{18}$DAB in formamide. High efficiencies and migration time reproducibility of <0.8% RSD are achieved over 5 replicate injections without the regeneration of the coating. This is the first demonstration of the ability to reverse EOF and eliminate analyte adsorption using buffer additives in pure FA.

Experimental section

Apparatus

All capillary electrophoresis experiments were performed on an Agilent HP 3DCE instrument (Agilent Technologies, Palo Alto, California, USA) equipped with an on-column diode array UV absorbance detector. Data acquisition (20 Hz) and control were performed using ChemStation software (Agilent Technologies) on an HP personal computer. Untreated fused silica capillaries (Polymicro Technologies, Phoenix, Arizona, USA) with an inner diameter of 25 or 50 μm, an outer diameter of 365 μm, and a total length of 37 cm (effective length of 28.5 cm to the detector) were used. The polyimide coating at the detection window and at both ends of the capillary was removed by burning to avoid capillary blockage because of swelling of the polyimide

© 2007 NRC Canada

coating in organic solvents (49). In all experiments, the capillary cassette was thermostatted at 25.0 °C with forced-air cooling

Chemicals and reagents

All chemicals were reagent grade or better and were used without further purification. All solutions were prepared with Nanopure 18 MΩ water (Barnstead, Chicago, Illinois, USA). Phosphate buffers were prepared from sodium salts of orthophosphate (BDH, Darmstadt, Germany) and adjusted to the desired pH with reagent grade sodium hydroxide (BDH). Ammonium formate and acetate buffers were prepared from ammonium formate salt (BDH) and ammonium acetate (BDH), respectively. Buffers were prepared by dilution of a 1.0 mol/L stock buffer solution. The pH meter was calibrated with aqueous standards solutions immediately prior to use. For 10%–70% (*v*/*v*) formamide, the required amount of buffer and required volume of formamide (FA; Fisher, Fair Lawn, USA) were added before final dilution with Nanopure water. For 100% FA, the calculated amounts of reagents to make the buffers at specified pH were dissolved in FA and no pH adjustment was made. A 1.0 mmol/L mesityl oxide (Sigma-Aldrich, Milwaukee, Wisconsin, USA), dissolved in the solvent being studied, was used as the neutral EOF marker. The cationic surfactant dimethyldioctadecylammonium bromide ($2C_{18}$DAB) was used as received from Sigma-Aldrich. The $2C_{18}$DAB solutions in water or FA were prepared by a 30 min sonication of the buffer–surfactant mixture at a temperature of 50 °C, which is well above the chain melting temperature (32). Then the solutions were cooled to room temperature (24 °C) with stirring for 15 min. This sonication–stirring cycle was repeated until a clear solution was obtained. Typically, no more than three cycles were needed. The drugs propranolol, metoprolol, chlorpheniramine, and chloroquine were a gift from Pars Minoo pharmaceutical company (Tehran, Iran) and were of >99.98% purity.

EOF measurements

To avoid hysteresis effects, fresh capillaries were used with each new buffer system. New capillaries were rinsed under high pressure (93.8 kPa) with 1 mol/L NaOH for 10 min and then with distilled water for 5 min. For buffers prepared in pure FA, the capillary was rinsed for 5 min with pure FA instead of distilled water. After the preconditioning steps, the capillary was rinsed at high pressure (93.8 kPa) for 10 min with surfactant solution to coat the capillary. Then the excess surfactant was flushed out from the capillary using a 3 min high-pressure (93.8 kPa) rinse with the separation buffer.

To measure the EOF, the neutral marker (1 mmol/L mesityl oxide in water or FA) was injected into the capillary using hydrodynamic injection for 2 s at 5.0 kPa. The electroosmotic flow (μ_{eof}) was calculated from the migration time using,

$$[4] \qquad \mu_{eof} = \frac{L_t L_d}{t_{eof} V}$$

where L_t and L_d are the total length of the capillary (37.0 cm) and the capillary length to the detector (28.5 cm), respectively, t_{eof} is the migration time of the neutral EOF marker (in seconds), and V is the applied voltage (in volts). All the voltages used herein were experimentally verified to be within the linear region of the Ohm's plot. In all experiments, the EO*F* values were the average of three or more measurements. In cases where the observed EOF are slow (less than 2×10^{-4} cm^2/Vs) the pressure-mediated three injections technique developed by Williams and Vigh was employed (50).

Coating stability studies

The coating stabilities were examined using two techniques as described previously (30, 32). In the first method, hydrodynamic rinsing, the stability of the surfactant coatings was indirectly evaluated by monitoring the EOF as a function of high-pressure rinsing time with the separation (electrophoretic) buffer. In this procedure, the coated capillary was flushed with the electrophoretic buffer (in the absence of surfactant) at a constant pressure (93.4 kPa) for an initial period of 3 min. A neutral marker (1 mmol/L mesityl oxide) was injected and the EOF was measured as described earlier. The coating was then regenerated first by rinsing with aq. 1 mol/L NaOH at high pressure (93.8 kPa) for 5 min, followed by distilled H_2O for 5 min at 93.8 kPa and then with 1.0 mmol/L aqueous surfactant solution for 10 min at 93.8 kPa. For buffers prepared in pure FA, the capillary was rinsed for 5 min with pure FA instead of distilled water, and 1.0 mmol/L surfactant dissolved in FA was used for coating. Then, the capillary was subjected to a longer rinsing time with the electrophoretic buffer (e.g., 5 min) and the EOF was again determined as described earlier. This flushing–regeneration procedure was successively repeated for rinsing times up to 30 min at 93.8 kPa. The stability of the coating (i.e., the EOF) was then evaluated by plotting the values of EOF obtained vs. the high-pressure rinsing times.

In the second method, the stability of the coatings was assessed based on separation of basic drugs. These repetitive electrophoretic runs were carried out to test the long-term reproducibility and the capillary coating performance.

Separation of basic drugs

A 5.0 mmol/L stock solution of the drug samples propranolol, metoprolol, chloroquine, and chlorpheniramine, were prepared in Nanopure water or pure FA and stored at 6 °C. The chiral drugs were analyzed as racemic mixtures. The sample solutions were filtered through a 0.2 μm polypropylene membrane filter (Whatman) prior to injection. The final sample solutions were prepared from the stock solutions by diluting to concentrations of 1.0 and 0.25 mmol/L with the separation buffer. For the drug separations, a fresh capillary was flushed first with aq. 1 mol/L NaOH for 15 min at 93.8 kPa, followed by water or FA for 5 min at 93.8 kPa. Then the capillary was coated by rinsing for 10 min with 1.0 mmol/L $2C_{18}$DAB solution (prepared in water or FA) followed by a 3 min rinse at 93.8 kPa with the electrophoretic buffer to remove the excess surfactant from the capillary. A mixture of the drugs was injected for 2.0 s at 5.0 kPa. Detection for the drugs was performed using the direct UV mode at 210 nm. The peak asymmetry factor (B/A) was determined from the ratio of the width of the right half (B) over left half (A) of the analyte peak at 10% of its maxi-

© 2007 NRC Canada

mum height. B/A value equal to 1 corresponds to a symmetrical peak, greater than 1 is a tailing peak, and less than 1 is a fronting peak. The efficiencies were computed using the peak width at baseline.

Acknowledgments

This work was supported by the Natural Sciences and Engineering Research Council of Canada (NSERC) and the University of Alberta.

References

1. C.A. Lucy, K.K.C. Yeung, S.L. Fu, D.M. Li, T.L. Henselwood, and R.S. Underhill. Can. J. Chem. **77**, 281, (1999).
2. X.J. Peng, G.M. Bebault, S.L. Sacks, and D.D.Y. Chen. Can. J. Chem. **75**, 507, (1997).
3. C. Stathakis and R.M. Cassidy. Can. J. Chem. **76**, 194, (1998).
4. X.C. Le, V. Pavski, and H.L. Wang. Can. J. Chem. **83**, 185, (2005).
5. M.T. Bowser, A.R. Kranack, and D.D.Y. Chen. TrAC, Trends Anal. Chem. **17**, 424, (1998).
6. V.L. Ward and M.G. Khaledi. J. Chromatogr. A, **859**, 203, (1999).
7. S.P. Porras, M.L. Riekkola, and E. Kenndler. Electrophoresis, **23**, 1485, (2003).
8. F. Steiner and M. Hassel. Electrophoresis, **21**, 3994, (2000).
9. S.P. Porras and E. Kenndler. Electrophoresis, **26**, 3203, (2005).
10. A. Karbaum and T. Jira. Electrophoresis, **20**, 3396, (1999).
11. H. Salimi-Moosavi and R.M. Cassidy. Anal. Chem. **68**, 293, (1996).
12. R.S. Sahota and M.G. Khaledi. Anal. Chem. **66**, 1141, (1994).
13. F. Wang and M.G. Khaledi. Anal. Chem. **68**, 3460, (1996).
14. Y. Mori, K. Ueno, and T. Umeda. J. Chromatogr. A, **757**, 328, (1997).
15. L. Geiser, S. Cherkaoui, and J.L. Veuthey. J. Chromatogr. A, **979**, 389, (2002).
16. J.M. Lin, M. Nakagawa, K. Uchiyama, and T. Hobo. Electrophoresis, **23**, 421, (2002).
17. J.M. Lin, M. Nakagawa, K. Uchiyama, and T. Hobo. Chromatographia, **50**, 739, (1999).
18. P.B. Wright, A.S. Lister, and J.G. Dorsey. Anal. Chem. **69**, 3251, (1997).
19. F. Steiner and M. Hassel. Electrophoresis, **24**, 399, (2003).
20. I. Bjornsdottir and S.H. Hansen. J. Pharm. Biomed. Anal. **13**, 687, (1995).
21. S.P. Porras and E. Kenndler. Electrophoresis, **25**, 2946, (2004).
22. J.E. Melanson, N.E. Baryla, and C.A. Lucy. TrAC, Trends Anal. Chem. **20**, 365, (2001).
23. A.M. MacDonald, M.A.W. Sheppard, and C.A. Lucy. Electrophoresis, **26**, 4421, (2005).
24. C. Schwer and E. Kenndler. Anal. Chem. **63**, 1801, (1991).
25. E.A.S. Doherty, R.J. Meagher, M.N. Albarghouthi, and A.E. Barron. Electrophoresis, **24**, 34, (2003).
26. K.K.C. Yeung and C.A. Lucy. Anal. Chem. **69**, 3435, (1997).
27. C.A. Lucy and R.S. Underhill. Anal. Chem. **68**, 300, (1996).
28. W.R. Jones and P. Jandik. J. Chromatogr. **546**, 445, (1991).
29. N.E. Baryla, J.E. Melanson, M.T. McDermott, and C.A. Lucy. Anal. Chem. **73**, 4558, (2001).
30. M.M. Yassine and C.A. Lucy. Anal. Chem. **76**, 2983, (2004).
31. M.M. Yassine and C.A. Lucy. Anal. Chem. **77**, 620, (2005).
32. A.G. Diress, M.M. Yassine, and C.A. Lucy. Electrophoresis. **28**, 1189 (2007).
33. F.P. Duval and G.G. Warr. Chem. Commun. (Cambridge), 2268, (2002).
34. G.G. Warr, R. Sen, D.F. Evans, and J.E. Trend, J. Phys. Chem. **92**, 774, (1988).
35. J.B. Evans and D.F. Evans. J. Phys. Chem. **91**, 3828, (1987).
36. T. Perche, X. Auvray, C. Petipas, R. Anthore, I. Rico-Lattes, and A. Lattes. Langmuir, **13**, 1475, (1997).
37. J.E. Melanson, N.E. Baryla, and C.A. Lucy. Anal. Chem. **72**, 4110, (2000).
38. E. Cordova, J. Gao, and G.M. Whitesides. Anal. Chem. **69**, 1370, (1997).
39. P. Rohdewald and M. Moldner. J. Phys. Chem. **77**, 373, (1973).
40. I.E. Valko, H. Siren, and M.L. Riekkola. J. Microcolumn Sep. **11**, 199, (1999).
41. I. Rico and A. Lattes. J. Phys. Chem. **90**, 5870, (1986).
42. M. Sjoberg, U. Henriksson, and T. Warnheim. Langmuir, **6**, 1206, (1990).
43. M.F.M. Tavares, R. Colombara, and S. Massaro. J. Chromatogr. A, **772**, 171, (1997).
44. J.F. Liu and W.A. Ducker. J. Phys. Chem. B, **103**, 8558, (1999).
45. A.G. Diress and C.A. Lucy. J. Chromatogr. A, **1027**, 185, (2004).
46. S. Mohabbati and D. Westerlund. J. Chromatogr. A, **1121**, 32, (2006).
47. M. Bostrom, D.R.M. Williams, and B.W. Ninham. Langmuir, **18**, 6010, (2002).
48. S. Mohabbati, S. Hjerten, and D. Westerlund. J. Chromatogr. A, **1053**, 201, (2004).
49. F. Baeuml and T. Welsch. J. Chromatogr. A, **961**, 35, (2002).
50. B.A. Williams and G. Vigh. Anal. Chem. **68**, 1174, (1996).

© 2007 NRC Canada

The chemistry of the processes involved in the production of lanthanide titanates by the polymerized-complex method

Dimitr S. Todorovsky, Miroslava M. Getsova, Maria M. Milanova, Masato Kakihana, Nikolina L. Petrova, Michail G. Arnaudov, and Venelin G. Enchev

Abstract: The composition, some spectral characteristics, and thermal decomposition of solid lanthanide–titanium (lanthanide (Ln) = Y, La, Ce) and lanthanide–titanium citrates (CA) and tartrates (TA) have been studied. The complexes have been prepared in ethylene glycol medium at conditions modeling those of the polymerized-complex method applied for $Ln_2Ti_2O_7$ preparation. Special attention has been paid to the chemical nature of the bimetallic products as well as to the factors influencing the deprotonation of the alcoholic OH groups of the acidic ligands. The results contribute to further elucidation of the complexation and thermal decomposition processes involved in the polymerized-complex method.

Key words: inorganic compounds, sol–gel chemistry, infrared spectroscopy, nuclear magnetic resonance, thermogravimetric analysis (TGA).

Résumé : On a étudié la composition, quelques caractéristiques spectrales et la décomposition thermique de dérivés solides lanthanide–titane (lanthanide (Ln) = Y, La, Ce) et de citrates et tartrates de lanthanide–titane. On a préparé les complexes dans de l'éthylèneglycol, dans des conditions qui imitent celles de la méthode du complexe polymérisé appliquée à la préparation du $Ln_2Ti_2O_7$. On a porté une attention particulière à la nature chimique des produits bimétalliques ainsi qu'aux facteurs qui influencent la déprotonation des groupes OH alcooliques des ligands acidiques. Les résultats contribuent à une meilleure compréhension des processus de complexation et de décomposition thermique impliqués dans la méthode du complexe polymérisé.

Mots-clés : composés inorganiques, chimie gel–sol, spectroscopie infrarouge, résonance magnétique nucléaire, analyse thermogravimétrique (ATG).

[Traduit par la Rédaction]

Introduction

The polymerized-complex method (PCM) is widely used for the preparation of a number of multicomponent materials, including $Ln_2Ti_2O_7$ (Ln = lanthanide) (1, 2), which are highly effective ferroelectrics (Ln = La, Nd) or ionic conductors (Ln = Y). The PCM is based on the Pechini reaction (3), and its general nature is well-known: the formation of polymeric resin as a result of polyesterification between a metal complex of hydroxopolycarboxylic acid (preferably citric acid, CA) and a polyvalent alcohol (most often ethylene glycol, EG). The main advantage of the method is a homogeneous distribution of the metal ions in the resin formed. The limited ions mobility as well as the close contact between them ensure an insignificant segregation and favor the complete interaction leading to the production (at relatively low temperature) of homogeneous phase, fine dispersive material with a perfect crystal structure. The understanding of the processes involved (especially of the metal-complexes formation) is pointed out (3) as a key function for the successful use of this method.

Data on the processes involved as well as on the chemical nature of the formed intermediates, especially in the preparation of titanates, are given in the literature (1–16). The formation of a mixed-metal complex in the EG solution is supposed to be one of the main factors, which ensures the mixing of the different metal ions at the atomic level. The proofs of its existence are indirect (1–12), obtained by the study of the solutions containing a significant excess of CA and EG. Some other important problems cannot be considered as fully solved, i.e., (*i*) the reasons for the distinguished (1, 2, 10, 12, 16) deprotonation of the CA alcoholic OH group proceeding along with the complexation process at surprisingly low pH, even in some cases in the presence of

Received 15 February 2007. Accepted 13 April 2007. Published on the NRC Research Press Web site at canjchem.nrc.ca on 27 July 2007.

D.S. Todorovsky,[1] M.M. Getsova, M.M. Milanova, N.L. Petrova, and M.G. Arnaudov. Faculty of Chemistry, Sofia University, 1 J. Bourchier Blvd., Sofia 1164, Bulgaria.
M. Kakihana. Institute of Multidisciplinary Research for Advanced Materials, Tohoku University, 1,1 Katahira, 2-Chome, Aobaku, Sendai 980–8577, Japan.
V.G. Enchev. Instistute of Organic Chemistry, Bulgarian Academy of Sciences, Acad. G. Bonchev Street, bl. 9., Sofia 1113, Bulgaria.

[1]Corresponding author (e-mail: nhdt@wmail.chem.uni-sofia.bg).

 doi:10.1139/V07-067 © 2007 NRC Canada

protonated COOH groups; (*ii*) the significant decrease (in comparison with the solid-state reactions) of the temperature and the time needed for a perfect final product obtaining is either due to the formation of mixed-metal precursors or due to the proper homogenization of the highly dispersive individual carbonates and (or) oxides formed at the pyrolysis.

It is rather difficult to solve the problems mentioned (and to look deeper inside the mechanism of the processes) via studying the real systems obtained in the course of the PCM. The great excess of CA and EG in the solutions or in the polyesters resins makes systems rather complicated and impedes a detailed investigation. Our approach of isolating the complexes formed and their study offers new possibilities in solving these problems. The need of investigations on the isolated complexes was pointed out by Kakihana et al. (2). Few previous papers reported results obtained following this approach. La–, Y–, Ti(IV)–, La–Ti–, and Y–Ti–citrates (CA) (17–19) and La–, Ti–, and La–Ti–tartrates (TA) (20), formed in the course of PCM, were isolated after relatively short heating at 40–135 °C of the EG–, CA–, or TA–Ln(III) and (or) Ti(IV) systems. Their composition, some spectral characteristics, morphology, and thermochemical behavior (17, 18, 20–22) were studied. The interaction between EG and CA in the temperature interval 40–120 °C was elucidated (23). Some results on Ce(III or IV)– and Ce(III or IV)–Ti(IV) complexes were reported in the literature (24, 25); more details are published elsewhere (26, 27). These results reveal different aspects of the studied processes and systems.

In the present paper, the results are generalized in an attempt to build up a complete picture of the chemistry of the processes involved in PCM. Direct proofs, both for the heterometalic nature of the complexes formed in the course of the PCM and on the chemistry of the processes involved in their thermal decomposition, are obtained. The results could be of assistance for (*i*) the processes of mechanism clarification in other similar citric or tartaric systems. The importance of the citrate systems and particularly of Ti–citrates is recently considerably increased, mainly because of the Ti expanded applications in ceramic materials, alloys, and composites in medical technologies (28–30); (*ii*) the understanding of the nature of the complexes formed in non-aqueous systems.

Experimental

Materials

$Ln(NO_3)_3{\cdot}6H_2O$, $(NH_4)_2Ce(NO_3)_6$, anhyd. citric acid, (D,L)-tartaric acid, ethylene glycol, Ti-tetraisopropilate (Merck), and acetone of extra pure grade were used. The exact content of Ln in the respectie nitrates was determined complexometrically.

Synthesis of the complexes

The citric complexes were synthesized under conditions close to the ones used in the PCM application for the preparation of $La_2Ti_2O_7$ (1). To the EG solution of CA, metal source(s) was (were) added with stirring at temperatures below 40 °C. The molar ratio EG:CA:metal(s) was adjusted, modeling the one used at $Ln_2Ti_2O_7$ preparation, by the PCM ($EG:CA:Ti^{4+}:Ln^{3+}$ = 40:10:1:1) (1, 2) and accounting for (*i*) the number of COOH in the acid (CA or TA) molecule; (*ii*) the overall charge of the cation(s) (mono- or bimetallic complex preparation in the system). In all of the synthetic procedures, the molar ratio of COOH:overall electrical charge of the cation(s) was kept constant. Thus, the EG:(CA or TA):Ti^{4+}:Ln^{3+} molar ratios at citrates preparation were set up as follows: Ln(III)–Ti(IV), 40:10:1:1; Ln(III), 40:10:2.3; Ti(IV), 40:10:1.7. However, at the preparation of the Ce(IV) and Ce(IV)–Ti(IV) complexes, the relative content of Ce^{4+} was kept the same as of Ln^{3+} to evaluate the effect of the lanthanide oxidation state on the complex composition. At tartrates preparation, the molar ratios were 40:15:1:1.1 for Ln(III)–Ti(IV), 40:15:1.1 for Ln(III), and 40:15:1.7 for Ti(IV).

Preparing the solutions, precautions were taken to prevent the Ti^{4+} hydrolysis. The typical synthetic procedure was performed as follows (for the preparation of La(III)–Ti(IV)–citrate complex): To 124.14 g (2 mol) EG, 96.06 g (0.5 mol) anhyd. CA was added. After complete dissolution, 14.21 g (0.05 mol) Ti-tetraisopropilate and 21.64 g (0.05 mol) $La(NO_3)_3{\cdot}6H_2O$ were added with stirring until clear solution was obtained. The system was agitated in thermostatically heated vessel for 30 min at 120 °C. Such heating conditions ensure the complex(es) formation, but are insufficient for polyesterification processing taking place at the PCM at much longer times. To study the complexes formation, in some experiments the heating conditions (time and temperature) were varied, later mentioned in the proper places in the text. After cooling down to room temperature, acetone as desalting agent was added in a volume of 10 times as much as the solution itself. After the separation of the precipitates obtained, they were soaked for 24 h in fresh acetone and then filtered, washed again with acetone, dried at room temperature, and stored in tightly closed vessels. No differences in the complexes compositions were found if ethanol was used as a desalting agent, but the yield was lower.

Similar citrates and tartrates were also synthesized in water medium (17, 22), mainly to test some spectral and thermogravimetric-data interpretations.

Analysis

By common organic analysis methods, the C, H, N, and Cl contents in the separated compounds were determined. The contents of Ln and Ti were determined by an ICP-AES in solutions, obtained after melting of ~0.5 g of the sample with ~10 g of $KHSO_4$ and dissolving the melt in H_2SO_4 (5%). The analytical lines, 323.657 nm (Ti), 408.672 nm (La), 360 nm (Y), and 413.38 nm (Ce), were singled out based on earlier results (31).

IR spectra in the range 400–4000 cm^{-1} were recorded by a Bomem–Michelson 100 FTIR or Specord IR75 (Carl–Zeis) spectrometers in KBr pellets. ^{13}C and ^{1}H NMR spectra of the complex D_2O solutions were taken using a Bruker 250 MHz spectrometer. ^{13}C cross polarization (CP) magic angle spinning (MAS) spectra of the solids were recorded on a Bruker MSL-300 instrument at 75.5 MHz; the samples were spun at 8.4 kHz in 4 mm ZrO_2 rotor.

SEM analysis of the samples coated with gold was carried out on a JOEL JSM-5300 instrument, and energy dispersive X-ray microanalysis was performed by a JOEL Superprobe 733 microanalyzer with 25 kV accelerating voltage. X-ray photoelectron spectroscopy studies were performed in an

© 2007 NRC Canada

Table 1. Proposed formula of the isolated products.

Sample symbol	Synthesis: Temperature (°C)	Synthesis: Time (min)	Formula proposed[a]
TiCit40	40	30	$Ti(HCitH^{2-})_{0.1}(HCit^{3-})_{0.8}(HCitROH^{2-})_{0.4}(CitROH^{3-})_{0.2}\cdot 0.4HOROH.\ 3H_2O$
TiCit120	120	30	$Ti(HCitROH^{2-})_{0.3}(HCitROH.R.HCit^{3-})_{0.6}[Cit(ROH)_2{}^{2-}]_{0.2}[(CitROH)_2R^{4-}]_{0.3}\cdot 2HOROH\cdot 4H_2O$
YCit40	40	30	$Y(HCitH^{2-})_{0.6}(HCitROH^{2-})_{0.8}[(HCitROH)_2R^{2-}]_{0.1}\cdot 0.5HOROH\cdot 3.5H_2O$
YCit120	120	30	$Y(HCitROH^{2-})(HCitROH.R.HCit^{3-})_{0.2}[(HCitROH)_2R^{2-}]_{0.2}\cdot 0.1HOROH\cdot 3H_2O$
LaCit40	40	30	$La(HCitH^{2-})_{0.2}(HCit^{3-})_{0.6}(HCitROH^{2-})_{0.4}\cdot 0.1HOROH\cdot 3H_2O$
LaCit120	120	30	$La(HCit^{3-})_{0.1}(HCitROH^{2-})_{0.6}(HCitROH.R.HCit^{3-})_{0.5}\cdot 0.1HOROH\cdot 3H_2O$
CeNCit40[b]	40	30	$Ce^{3+}(HCitH^{2-})_{0.2}(HCit^{3-})_{0.6}(HCitROH^{2-})_{0.4}\cdot 0.1HOROH\cdot 3H_2O$
Ce(N)Cit65[b]	65	20	$Ce^{4+}(HCit^{3-})(HCitROH^{2-})_{0.5}\cdot 0.1HOROH\cdot 3.5H_2O$
Ce(N)Cit85[b]	85	20	$Ce^{4+}(HCit^{3-})0.33(HCitROH^{2-})_{1.5}\cdot 1.2HOROH\cdot 3H_2O$
CeNCit100[b]	100	30	$Ce^{4+}(HCit^{3-})(HCitROH^{2-})_{0.5}\cdot 0.1HOROH\cdot 3H_2O$
Ce(Cl)Cit80	80	30	$Ce^{3+}[HCit(ROH)_2{}^{-}]_{0.2}[Cit(ROH)_2{}^{2-}]_{0.6}Cl_{1.6}\cdot 3.2HOROH\cdot 3H_2O$
Ce(Cl)Cit110[c]	110	20	$Ce^{3+}{}_{0.95}Ce^{4+}{}_{0.05}[HCit(ROH)^{-}{}_2]_{0.45}[Cit(ROH)^{2-}{}_2]_{0.7}Cl_{1.2}\cdot 2HOROH\cdot 2H_2O$
Ce(Cl)Cit135[c]	135	20	$Ce^{3+}{}_{0.9}Ce^{4+}{}_{0.1}[HCit(ROH)^{-}{}_2]_{0.4}[Cit(ROH)^{2-}{}_2]_{1.1}Cl_{0.5}\cdot HOROH\cdot 2H_2O$
YTiCit40	40	20	$YTi(HCitH^{2-})_{1.2}(HCit^{3-})(HCitROH^{2-})_{0.8}\cdot 1.2HOROH\cdot 5.2H_2O$
YTiCit120	120	20	$YTi(HCitROH.R.HCit^{3-})_{0.6}(CitROH^{3-})_{1.6}[(CitROH)_2R^{4-}]_{0.1}\cdot 0.7HOROH\cdot 6H_2O$
LaTiCit40/15	40	15	$LaTi(HCitH^{2-})_{1.2}(HCit^{3-})[(HCitH)_2R^{2-}]_{0.2}(CitROH^{3-})_{0.4}\cdot 1.6HOROH\cdot 8H_2O$
LaTiCit40	40	30	$LaTi(HCitH^{2-})_{0.8}(HCit^{3-})_{1.2}(HCitROH^{-})_{0.2}[(HCitROH)_2R^{2-}]_{0.2}(CitROH^{3-})_{0.4}\cdot 2HOROH\cdot 7H_2O$
LaTiCit120/15	120	15	$LaTi(HCitROHRHCIt^{3-})_{0.2}(HCitROHRCit^{4-})_{0.2}(CitROH^{3-})_{1.2}[(CitROH)_2R^{4-}]_{0.5}\cdot 0.2HOROH\cdot 6H_2O$
LaTiCit120	120	30	$LaTi[HCit(ROH)_2RCitRHCit^{4-}]_{0.5}[HCit(ROH)_2RCitRCitROH^{4-}]_{0.5}(CitROH^{3-})\cdot 0.4HOROH\cdot 5H_2O$
LaTiCit40w[d]	40	30	$(NH_4)_{4.5}LaTi(HCit^{3-})_{2.5}(Cit^{4-})\cdot 10H_2O$
NH_4CeCit100[e]	100	30	$(NH_4)_{0.6}Ce^{4+}(HCit^{3-})_{1.2}(HCitROH^{2-})_{0.5}\cdot 0.1HOROH\cdot 3H_2O$
NH_4CeTiCit100[e]	100	30	$(NH_4)_{1.6}Ce^{4+}Ti^{4+}(HCitROH^{2-})_{0.3}(CitROH^{3-})_3\cdot HOROH\cdot 5.2H_2O$
LaTar120	120	30	$La(H_2TarH^{-})(H_2Tar^{2-})_{0.5}(H_2TarROH^{-})\cdot 0.5HOROH\cdot 2H_2O$
TiTar120	120	30	$Ti(H_2Tar^{2-})_{1.4}(H_2TarROH)_{0.2}(HTarROH^{2-})_{0.5}\cdot 0.4HOROH\cdot H_2O$
LaTiTar120	120	30	$LaTi(H_2Tar^{2-})_2(HTarROH^{2-})_{1.5}\cdot 0.5HOROH\cdot 3H_2O$

[a]Cit = $CH_2COOC(O)COOCH_2COO$; HCit = $CH_2COOC(OH)COOCH_2COO$; R = CH_2CH_2, Tar = $CH(O)COOCH(O)COO$; H_2Tar = $CH(OH)COOCH(OH)COO$.
[b]$Ce(NO_3)_3$ is used as stating material.
[c]$CeCl_3$ is used as a starting material.
[d]Prepared in H_2O medium.
[e]$(NH_4)_2Ce(NO_3)_2$ is used as a starting material.

Escalab II electron spectrometer using Mg Kα radiation with energy of 1253.6 eV. All binding energies were referenced to the C1s photoelectron peak of CH_2 species at 285 eV.

DTA, DTG, and TG curves were recorded by a Paulik–Paulic–Erdey (MOM, Hungary) derivatograph in synthetic corundum crucible in static air at heating rate of 5 or 10 K min^{-1}. X-ray powder diffractograms were taken by a TUR-M62 (Germany) diffractometer at Cu Kα, 30 kV, 20 mA, at a scan rate of 0.03°/2 s. In some cases, the exact position of the peaks was determined using Lorenzian curve fit of the experimental data. The relative error in the determination of the interplanar distances was in the limits of 0.1%–0.03%.

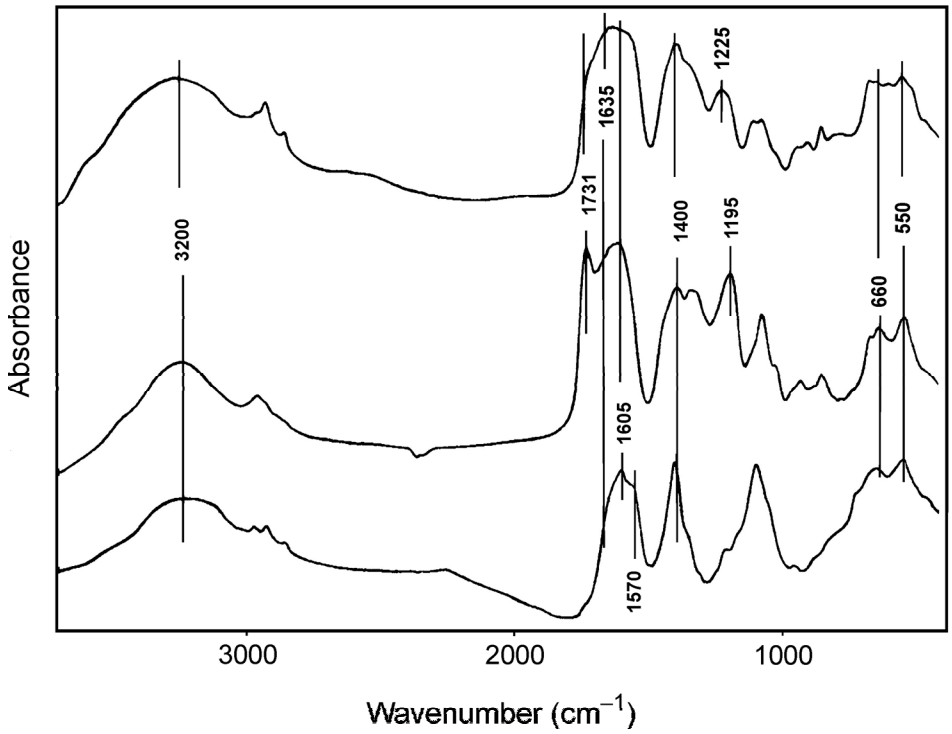
Results and discussion

Composition and spectral characteristics of the complexes

The composition of the isolated products varies in narrow limits from one preparation to another, mainly because of the variation of the degree of the ligand esterification. On the basis of elemental-composition data, thermogravimetrically determined water content, and spectral data, complexes may be described by the formulae reported in Table 1. The data for Ti–, Y–, La–, Y–Ti–, La–Ti–citrates and tartrates are taken from the literature (17, 18, 20). The esterification degree, the relative amount of EG bonded as adduct, and the esterification mode of EG (with one or with both OH groups) are derived from the intensity ratios of the proton signals of the CH_2 groups in EG and CH in TA in the ^1H NMR spectra of the samples in D_2O solution. These data are reported only for the complexes that are satisfactory soluble and stable in D_2O. Some of the Ce(IV)-containing complexes suffer hydrolysis, and a precipitate enriched with Ce (in comparison with the initial complex) is formed shortly after dissolution. The yields of the synthetic procedures were estimated (on the basis of the masses of the metals introduced in the starting solution) as a ratio between the real mass of the obtained product and the mass expected according to the proposed formula. The yields vary in rather wide

© 2007 NRC Canada

Fig. 1. The IR spectrum of La–Ti–citric complex obtained at 40 °C (1, LaTiCit40) and at 120 °C (2, LaTiCit120).



interval from ~95% to 35%, obviously depending on the solubility of the products in EG–acetone mixture.

The spectral data confirm the formulae proposed in Table 1:

(*i*) The presence of H_2O in all of the prepared complexes is proved by the broad absorption bands at 3400–3200 cm^{-1} and 1635 cm^{-1} in the IR spectra (Fig. 1), and by the TG analysis. Non-dissociated OH groups of the citric ligands and from EG, bonded as adduct with CA, also contribute to 3400–3200 cm^{-1} band intensity. The presence of H_2O is also confirmed by the ^{1}H NMR spectra taken in C_2HCl_3.

(*ii*) A well-defined shoulder at 1040 cm^{-1}, belonging to ν(C–OH) of EG (23), in the IR spectra of the samples (Fig. 1) as well as the peaks at 65.5 ppm in the ^{13}C (Fig. 2) and at 3.6 ppm in the ^{1}H NMR spectra (Fig. 3) are associated with CH_2 groups of EG bonded as adduct.

(*iii*) The presence of resonance signals at 62 and 70 ppm in the ^{13}C (Fig. 2) and at 3.8 and 4.2 ppm in the ^{1}H (Fig. 3) NMR spectra, assigned to OCH_2 and $HOCH_2$ groups of EG, proves the formation of esters. The interpretation of the ^{1}H spectra was confirmed by a ^{13}C–^{1}H HMQC analysis. The difference in the intensity of the signals in the ^{1}H spectrum shows the presence of double-esterified EG and permits its relative content in the complex to be calculated. In some of the spectra, a signal at 4.35 ppm is also registered. Its association with the ^{13}C shifts of the EG urged us to assign it to the CH_2 from EG bonded as ester with the COOH belonging to the central C atom in CA. The spectrum simulation confirmed such an interpretation (18).

The IR spectral data also contribute to the elucidation of the interaction between the EG and the CA.

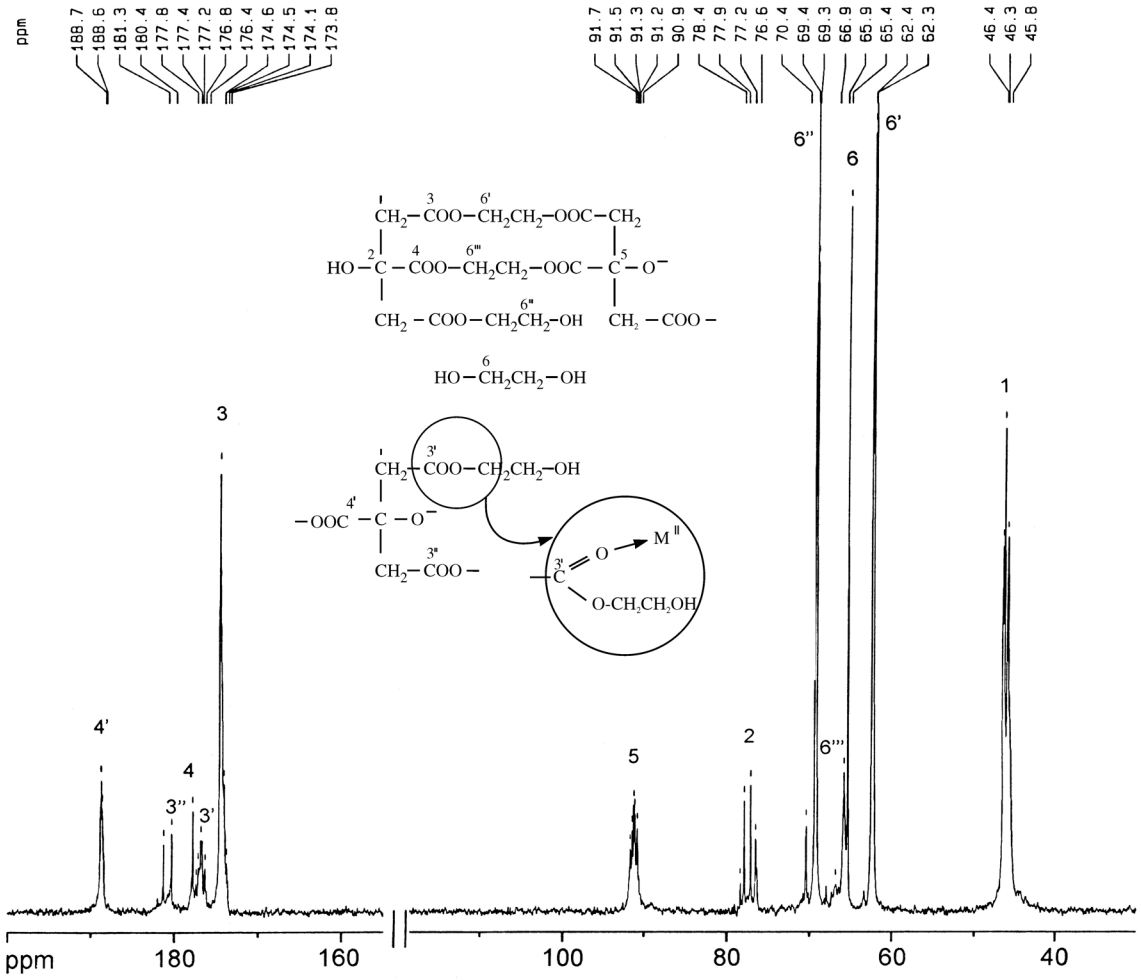
Our spectral study shows that the mixing of the compounds even at room temperature affects the bands of δ(O–H) at 1400 cm^{-1}, ν(C–O) at 1200 cm^{-1}, and the ones of C=O stretching vibration in CA. Applying the curve deconvolution and subtraction of the IR spectra by the so-called stepwise reduction procedure (32), it is possible to overcome the strong overlapping of the bands. In this way, it was shown that the band caused by the ν(O–H) in the CA alcoholic OH group is practically not disturbed, suggesting that, most probably, the latter does not take part in the association. In the same time, the 1750–1700 cm^{-1} spectral range clearly shows the differences between the C=O stretching vibration in the free COOH (1710 cm^{-1}), adducts (1725 cm^{-1}), and in the ester groups (1750 cm^{-1}), and permits the two types of bonding to be distinguished.

The ν(C–O) from the ester (1195 cm^{-1}) and from the adduct (1225 cm^{-1}) contribute to the band appearance around 1200 cm^{-1}.

(*iv*) The complexation is proved by bands of $\nu_{as}(COO^-)$ appearing around 1600 cm^{-1} (1605 cm^{-1} in La–Ti–citrate; 1600 cm^{-1} in the Y, Y–Ti, and Ce complexes; 1631–1605 cm^{-1} in Ce–Ti; 1630 and 1545 cm^{-1} in Ti ones) and $\nu_s(COO^-)$ around 1400 cm^{-1} (1400 cm^{-1} for La–Ti; 1437 cm^{-1} for Y and Y–Ti; 1390–1385 cm^{-1} and 1440–1380 cm^{-1} for Ce; 1450–1317 cm^{-1} for Ce–Ti; and 1385 cm^{-1} for Ti one). The shift of $\upsilon\gamma_{as}$ bands to the higher frequencies compared with those of the sodium citrate (1591 cm^{-1}) suggests that COO^- groups coordinate to the metal ions as monodentate ligands. The difference $(\nu_{as} - \nu_s)$ confirms such assumption,

© 2007 NRC Canada

Fig. 2. ^{13}C NMR spectrum of La–Ti–citric complex obtained at 120 °C (LaTiCit120).



which agrees with the observation in the literature (28) for Ti–citrates prepared in aqueous medium. However, the shoulder observed near 1575 cm^{-1} in some Ce–Ti–citrates might be assigned to a terminal carboxylate group from the bridging ligand (27).

Monodentate coordination can be accepted for Ti–Tar and La–Ti–Tar (Tar denotes tetraionized tartrate) ($\nu_{as}(COO^-)$ at 1630 cm^{-1}, $\nu_{as}(COO^-)$ at 1392 cm^{-1}, respectively). Ionic bonds are probable for La–Tar ($\nu_{as}(COO^-)$ = 1595 cm^{-1}). This difference is confirmed by the positions of the peaks for COO^- groups in the solid state ^{13}C NMR spectra near 181 and 183 ppm and is probably due to the fact that in La–Tar, each ligand is coordinated only via one of its COO^- groups, and the other one is protonated or esterified (20).

(*v*) The presence of citric and tartaric ligands with deprotonated alcoholic OH groups is confirmed by the shift at 85–91 ppm (1, 2, 18) in ^{13}C NMR spectra. The comparison of the solid-state ^{13}C NMR spectra with those taken in D_2O solution (20) leads to the conclusion that Ti–tartrate undergoes some reconstruction in D_2O solution with recovery of the initial protonated alcoholic OH group. Similar effect is observed for the citric complexes of the other easily hydrolyzed ion – Ce (IV) (27).

Actually, most of the isolated products are mixtures of complexes that are principally analogous to the ones formed in water medium (33) and differing by the esterification and deprotonation degree of the COOH and OH groups of the ligands. For example, the sample, labeled as LaCit40 (Table 1), most probably represents [3LaHCit + $La_2(HCitH)(HCitROH)_2$]·0.5HOROH·15H_2O, where HCit and Cit denote triionized and tetraionized citrates, respectively, and R–C_2H_4 group in EG. (The composition of some of the citric compounds is represented in Table 2).Variable degrees of protonation among the bound citrates within the same complex and within different species were reported by Kefalas et al. (28) and also by Collins et al. (30). Nevertheless, the presentation mode used in Table 1 (accounting for the overall composition of the formed precipitates) is useful for the analysis of the factors influencing the composition of the products. Some main characteristics of the complexes are listed in Table 3, and these data may be useful for some discussion.

As the elemental, IR, and TG analyses show that the complexes are isolated as hydrates with molar ratio H_2O:Cit ≈ 2 ± 0.5 and H_2O:Tar ≈ 1 ± 0.5. The only significant deviation (Ce3(Cl)Cit80) is probably due to the very low number of citric ligands and the necessity for the coordination satu-

© 2007 NRC Canada

Fig. 3. ^{1}H NMR spectrum of La–Ti–citric complex obtained at 120 °C (LaTiCit120).

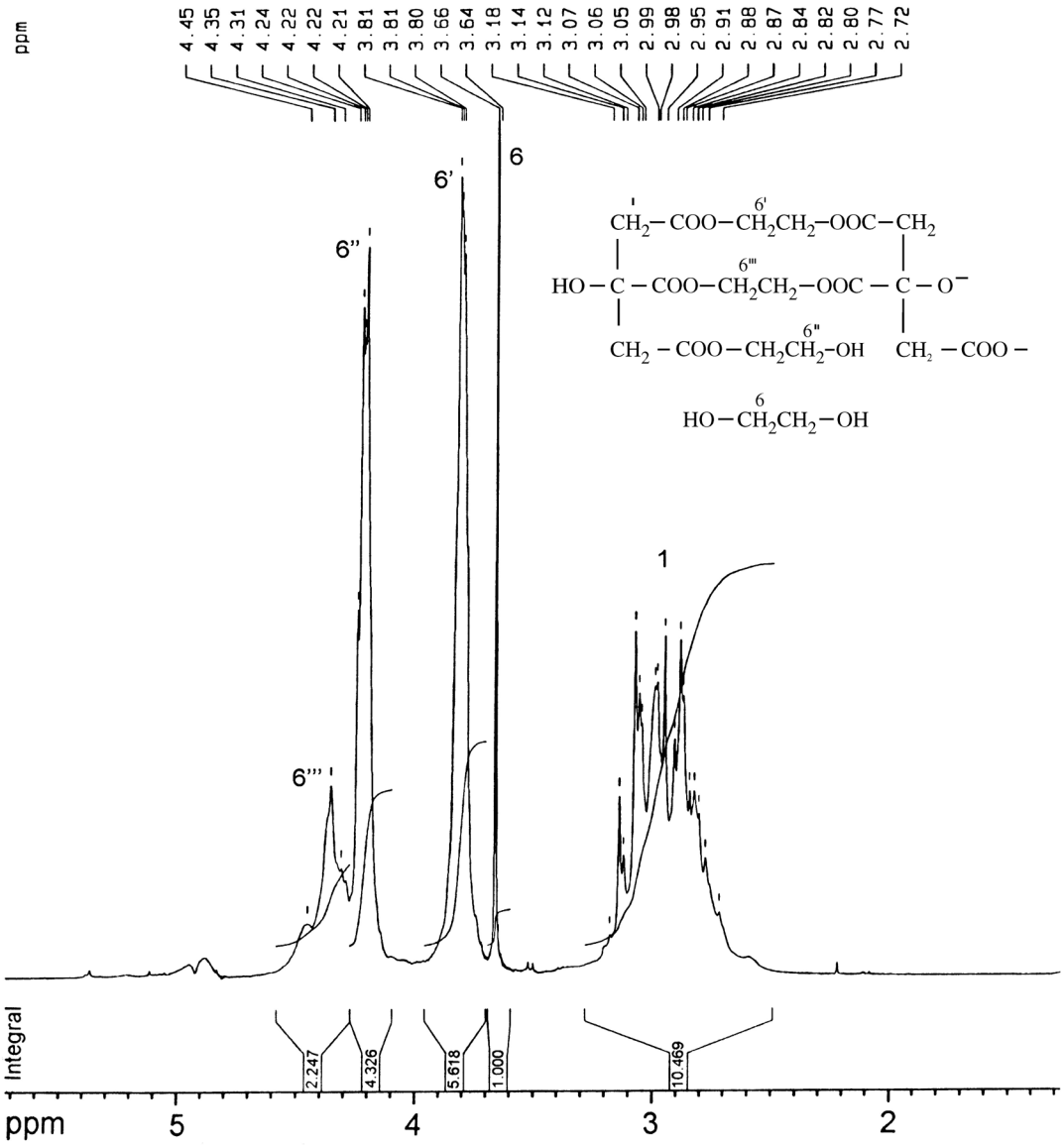


Table 2. Composition of some of the isolated citric compounds.

Sample Symbol[a]	Content[b]
TiC120	$\{3Ti_2(HCitROH)(HCitROHRHCit)_2 + Ti(Cit/ROH/_2)_2 + 3Ti(CitROH/R_2)\}\cdot 20HOROH\cdot 40H_2O$
LaC120	$\{La(HCit) + 5La(HCitROHRHCit) + 2La_2(HCitROH)_3\}\cdot HOROH\cdot 30H_2O$
LaTiC120	$\{LaTi(HCit/ROH/R_2CitRHCit)(CitROH) + LaTi(HCit/ROH/R_2CitRCitROH)(CitROH)\}\cdot 0.8HOROH\cdot 10H_2O$
$NH_4Ce4Ti100$	$\{NH_4CeTi(CitROH)_3 + 0.3(NH_4)_2(HCitROH)\}\cdot HOROH\cdot 5.2H_2O$

[a]See Table 1.
[b]HCit = $CH_2COOC(OH)COOCH_2COO$; Cit = $CH_2COO(O)COOCH_2COO$; R = CH_2CH_2.

ration of the Ce^{3+} to be reached. As a rule, the water relative content decreases with the increase of the temperature and time of heating (Table 3, column 10).

The presence of the ester-bonded EG in the samples prepared at 40 °C (Table 3, column 6) is a little bit unexpected from the point of view of the common notion for the temperature range (> 80–100 °C) in which the esterification is taking place. This fact is in coincidence with the earlier observation (1, 2) and proves a catalytic effect of the studied metal ions on the esterification. This effect could be observed in the IR spectra by the decrease of the intensity of the band at 1040 cm^{-1} corresponding to ν_{as}(C–O) in the EG (Fig. 4). As can be expected, the relative content of the esters in the isolated complexes quite sharply increases with the temperature of the synthesis (Table 3, column 6–8). The only exception is the Ce-complex, produced from $CeCl_3$.

© 2007 NRC Canada

Table 3. Main characteristics of the isolated products.

			Molar ratio[b]											
					ROH/*L*		R/*L*		(ROH+2R)/*L*		HOROH/*L*		H_2O/*L*	
Sample symbol[a]	*L*	Z_L	L_H/*L*	L^-/*L*	*C*[c]	*F*[c]	*C*	*F*	*C*	*F*	*C*	*F*	*C*	*F*
TiCit40	1.5	2.67	0.07	0.13	0.40	0.34	0	0	0.40	0.34	0.27	0.28	2.00	1.96
TiCit120	2.3	1.74	0	0.35	0.83	0.84	0.39	0.46	1.61	1.76	0.87	0.90	1.74	1.67
YCit40	1.6	1.88	0.38	0	0.62	0.71	0.06	0.10	0.74	0.91	0.03	0.04	2.19	2.05
YCit120	1,8	1.67	0	0	0.89	0.89	0.22	0.26	1.33	1.41	0.06	0.09	1.67	1.40
LaCit40	1.2	2.50	0.17	0	0.33	0.34	0	0	0.33	0.34	0.08	0.11	2.50	2.46
LaCit120	1.7	1.76	0	0	0.65	0.83	0.29	0.33	1.23	1.49	0.06	0.10	1.76	1.40
CeNCit40[d]	1.2	2.50	0.17	0	0.33	—	0	—	0.33	—	0.08	—	2.50	2.71
Ce3Cit65[d]	1.5	2.67	0	0	0.33	0.4	0	0	0.33	0.4	0.07	0.1	2.33	2.33
Ce3Cit85[d]	1.83	2.18	0	0	0.82		0	0	0.82		0.66		1.64	1.51
Ce(N)Cit100[d]	1.5	2.67	0	0	0.33	—	0	—	0.33	—	0.07	—	2.00	2.20
Ce(Cl)Cit110[e]	1.5	1.75	0	0.61	2.00	2.00	0	0	2.00	2.00	1.74	1.6	1.33	1.23
Ce(Cl)Cit135[e]	1.5	1.73	0	0.73	2.00	2.00	0	0	2.00	2.00	0.67	0.7	1.33	1.28
YTiCit40	3.0	2.33	0.40	0	0.27	0.26	0	0	0.27	0.26	0.40	0.38	1.73	1.87
YTiCit120	3.0	2.33	0	0.60	0.80	0.82	0.23	0.23	1.03	1.05	0.23	0.23	2.00	1.85
LaTiCit40/15	3.0	2.33	0.43	0.07	0.13	0.13	0.03	0.03	0.19	0.19	0.43	0.42	2.33	2.35
LaTiCit40	3.0	2.33	0.27	0.13	0.33	0.33	0.07	0.07	0.47	0.45	0.67	0.68	2.33	2.40
LaTiCit120/15	3.0	2.33	0	0.80	0.87	0.89	0.30	0.29	1.47	1.47	0.07	0.08	2.00	1.98
LaTiCit120	3.0	2.33	0	0.83	0.50	0.83	0.50	0.52	1.50	1.87	0.13	0.13	1.67	1.67
NH_4CeNCit100[f]	1.5	2.67	0	0	0.33	—	0	—	0.33	—	0.07	—	2.00	2.18
CeNTiCit100[d]	2.7	2.96	0	0.96	1.00	—	0	—	1.00	—	0.04	—	2.11	2.11
NH_4CeTiCit100[f]	3.0	2.67	0	1.00	1.00	0.98	0	0	1.00	0.98	0.33	0.23	1.73	1.73
LaTar120	2.5	1.20	0.40	0	0.40	—	0	0	0.40	—	0.20	—	0.80	0.76
TiTar120	2.1	1.90	0	0.24	0.33	—	0	—	0.33	—	0.19	—	0.48	0.57
Ce3Tar65	1.7	1.76	0	0	0.23	0.3	0	0	0.23	0.3	0.76	1.0	1.76	1.85
Ce3Tar85	2.2	1.36	0	0	0.18	0.2	0.23	0.2	0.64	0.6	0.95	1.0	1.36	1.44
LaTiTar120	3.5	2.00	0	0.43	0.43	—	0	—	0.43	—	0.14	—	0.86	0.93

[a]See Table 1.
[b]*L*: number of ligands; L_H: number of ligands with protonated COOH groups; L^-: number of ligands with deprotonated alcoholic OH groups; Z_L: average charge of the ligands; R = CH_2CH_2.
[c]C: calculated according to the formulae proposed in Table 1; F: experimentally found.
[d]$Ce(NO_3)_3$ is used as a starting material.
[e]$CeCl_3$ is used as a starting material.

Obviously, the starting compound has a greatest catalytic effect on the esterification process, a high esterification degree is reached at relatively low heating temperature, and its further increase with the temperature increasing is impossible.

At lower heating temperature (40 °C), the esterification degree increases with the increase of heating time from 15 to 30 min. At higher temperature (120 °C), the degree of esterification is still established in the first 15 minutes of heating.

The ^{1}H NMR spectra analysis (18) suggests that at 120 °C (particularly at longer heating time), the EG can interact with both of its OH groups bridging the citrate ligand (Table 3, column 7). IR spectral data show that the TA interacts with the EG much weaker than the CA (20). Accordingly, the tartaric-complexes esterification degree is significantly lower than that of the citrate ones, but double EG esterification is also possible (Table 3, columns 6–8).

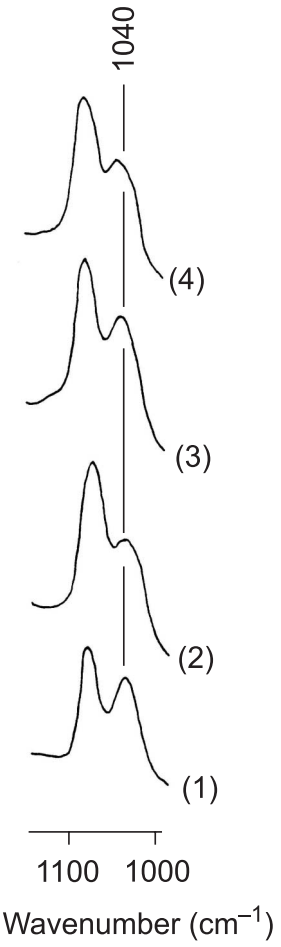
Generally, the studied complexes composition (Table 3) depends on the nature of the metal ion(s) (oxidation state, ionic radii, coordination number, and catalytic activity on the esterification), the nature of the acid (size of the molecule, dissociation and esterification ability, and number of COOH groups), and the synthetic conditions (heating temperature and time). No difference in the complexes composition was found using different desalting agents (17).

The experimental data suggest that four main concurrent processes determinate the composition of the complexes formed at lower temperatures (40 °C): dissociation of the acids, adduct formation, complexation, and esterification; mainly, the latter two are of significant importance at elevated temperatures (100–120 °C) when the deprotonation of all COOH groups has already happened. The steric limitations are of primary importance in determining bimetallic products composition all over the temperature range studied. No more than three citric and (at conditions applied by us) 3.5 tartaric ligands can be coordinated to Ln(III or IV) and Ti(IV) ions. This observation is in line with the ones for solid Ba–Ti–citrate (5, 16) and La–Ti–citrate existing in solution (2), prepared by the Pechini's method as well as for Ti(IV)–citrates, obtained in aqueous medium (28–30).

It is hard to distinguish the effect of every one of the listed processes and factors. The higher average charge of the ligands in LaCit40 in comparison with YCit40 is due to both higher catalytic activity of Y^{3+} (leading to higher lig-

© 2007 NRC Canada

Fig. 4. IR spectra in the range 1100–1000 cm^{-1} of ethylene glycol solutions of (*a*) CA, (*b*) CA–La^{3+}, (*c*) CA–Ti^{4+}, and (*d*) CA–La^{3+}–Ti^{4+}; heated for 30 min at 120 °C.



ands esterification degree; Table 3, column 8) and the stronger basicity of La^{3+} (contributing to the higher deprotonation degree; Table 3, column 5). The smaller ionic radii of Ce^{4+} compared with that of La^{3+} might be a factor, but not the only one determining the smaller ligand number in Ce4TiCit100 complex.

The experiments on the La–Ti–CA–EG system at different heating temperatures and times reveal the growth of the complexes. The progress of the esterification degree with the increase of the temperature and time of synthesis forces all of the COOH groups to take part in the esterification or complexation processes. After consumption of all of the available COOH groups, only oligomerization takes place without further principal reconstruction of the complexes.

Our results suggest that namely the esterification is the most important factor determining the complexes composition. The data in Tables 1 and 3 contain a number of facts supporting this supposition: the almost equal esterification degree in YCit120 and LaCit120 leads to similar composition of the complexes; the similarity in the esterification caused by Ti^{4+} and La^{3+} at 40 °C leads to similar main characteristics of the respective complexes (accounting for the difference in the ions oxidation state); the weaker esterification of the TA in comparison with the CA causes smaller ligand number in TiTar120 than in TiCit120 (Table 3, column 2) in spite of the smaller size of the TA and the different number of COOH groups.

Chemical nature of the bimetallic complexes

Two main experimental evidences for the suggested mixed-metal nature of the bimetallic complexes are reported in the literature (10): (*i*) The IR spectra of the complexes existing in the bimetallic solutions do not result from simple superposition of the respective individual complexes spectra; (*ii*) the shift at 91 ppm in ^{13}C NMR spectra appears in bimetallic systems only.

It was established (Fig. 5, Table 3), however, that deprotonation of the alcoholic OH group is not a unique feature of the bimetallic systems (the same process takes place in the Ti–citric or tartaric–EG (19, 20) and aq. Ti–citric (28, 30) systems). On the other hand, the formation of mixed-metal Y–Fe(III) complexes is not accompanied with the deprotonation of the alcoholic group (34). This peculiarity is not specific for Ti–citrates. The same effect has been observed in Y–Zr–citrates (35) and is very probable in La–Mn ones (36). Nevertheless, the parallel study of mono- and bimetallic products, taken by us, provided a number of proves for mixed-metal nature of the latter ones:

(*i*) The detailed analysis of the IR spectra for the positions of $\nu_{as}(COO^-)$ and $\nu_{as}(COO^-)$ confirms the mentioned assertion (10) and shows that monodentate bridging exists in the LaCit120 ($\nu_{as}(COO^-)$ = 1600 cm^{-1}, $\nu_{as}(COO^-)$ = 1380 cm^{-1}); the frequency of the asymmetric vibration is in agreement with the expected intermediate ionic-coordination nature of the Ln complexes and of LaTiCit120 ($\nu_{as}(COO^-)$ = 1638 cm^{-1}, $\nu_{as}(COO^-)$ = 1383 cm^{-1}). Bridging type of bonding presents in TiCit120 ($\nu_{as}(COO^-)$ = 1635 and 1549 cm^{-1}, $\nu_{as}(COO^-)$ = 1380 cm^{-1}) as well (22).

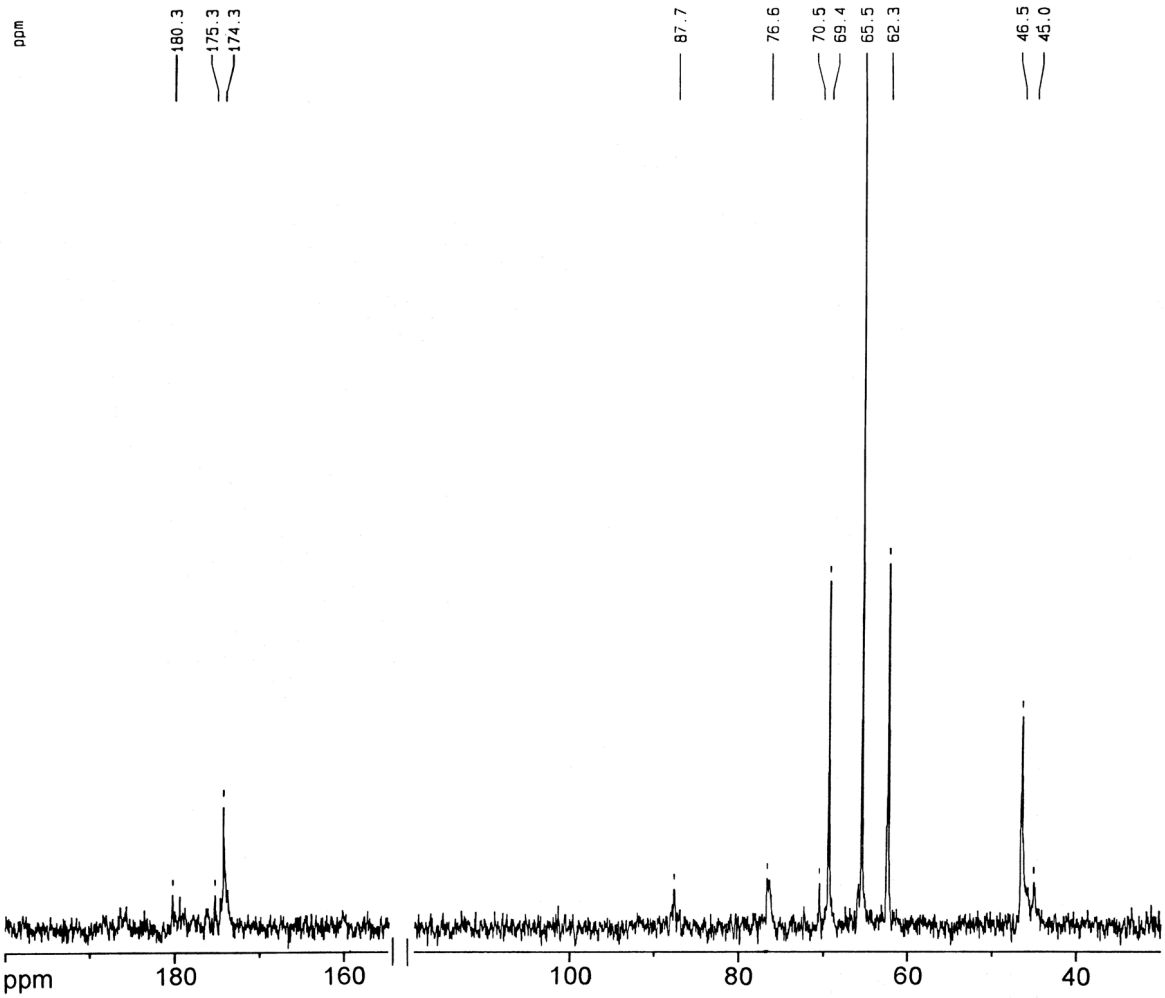
(*ii*) The data in Table 3 concerning some of the main characteristics of the complexes exclude the possibility that the bimetallic products could be mixtures of the individual complexes. Indeed, the average charge and the esterification degree of the ligands and the relative content of the ligands with deprotonated alcoholic OH groups in the bimetallic products cannot be derived by averaging the respective values of the individual complexes (compare for example average charge of the ligands for TiCit120, LaCit120, and LaTiCit120 and similar tartaric systems; the esterification degree of the same type of complexes, synthesized at 40 °C; the relative content of the ligand with deprotonated alcoholic OH groups).

(*iii*) The ^{13}C solid-state NMR spectrum of the bimetallic LaTiCit120 (19) and of LaTiTar120 (20) cannot be represented as a simple superposition of the spectra of the monometallic complexes.

(*iv*) Analogous conclusion could be drawn from the analysis of electronic absorption spectra (19). The broad weak band near 33 500 cm^{-1} observed in the spectrum of La–citric complex does not appear in the bimetallic-complex spectrum, while the band at 44 000 cm^{-1} in the spectrum of TiCit120 is keeping its position. The latter fact suggests that, in the bimetallic product,

© 2007 NRC Canada

Fig. 5. ^{13}C NMR spectrum of Ti–citric complex obtained at 120 °C (TiCit120).



Ti(IV) preserves its coordination like in the individual complex.

(*v*) XPS analysis (19) shows that the covalence of the COO–M^{n+} bonds in the LaTiCit120 is higher than in both La- and Ti-monometallic complexes. Some partial charge transfer from ligands to Ti^{4+} ions is registered by the shift of Ti 2p3/2 lines to a lower binding energy for LaTiCit120 relative to TiCit120. Such a shift is not observed in a La 3d doublet position.

(*vi*) Even the morphology of the individual and mixed-metal complexes is rather different: aggregates of spherical particles with a size of 200–500 nm (LaCit120) and 500–800 nm (TiCit120) are typical for monometallic complexes, but blocks of few micrometers are formed in LaTiCit120 with uniform distribution of the both metals (the content of La and Ti is 50.18 and 49.82 mole% (relatively to the sum of the metals) as the energy dispersive X-ray microanalysis shows (19).

Deprotonation of the alcoholic OH group

Recently, formation of Ti(IV)–citrates by the coordination via deprotonated OH^- group was reported by several authors (28–30). All of the isolated compounds had been produced in aqueous medium at pH = 2 ($MMg_{1/2}[Ti(CitH_2)_3]\cdot 6H_2O$, M = K^+ or NH_4^+ (29)), pH = 6 (28) or pH = 7–8 ($(Na_8[Cit)_3]\cdot 17H_2O$ (30)).

However, the capability of the metals to decrease the pKa of bound ligands could not be the only reason for the deprotonation of the citric OH^- group, taking place at conditions applied in the present and earlier (1, 2, 10, 12) studies, when the complexation is taking place along and in competition with the esterification.

The results reported in the present paper lead to some additional elucidation of this process.

As it was already mentioned, our data show that all mixed-metal citrates, studied by us, can be satisfactory described as complexes with three ligands. It may be supposed that the steric factor is in charge of this limitation. The number of the ligands in the individual complexes is L < 3. If bimetallic complexes are formed, the increased total charge of the complexing agents can be "compensated" by (*i*) an increase of the ligand number, keeping the steric limitations; (*ii*) an increase of the COOH deprotonation degree; (*iii*) a decrease of the ligands esterification degree; (*iv*) deprotonation of the alcoholic OH groups.

According to our data, in all of the studied bimetallic citric systems, the ligand number reaches its upper limit. The YTiCit40 formation, for example, becomes possible only with the esterification-degree decrease (in comparison with

© 2007 NRC Canada

the individual systems), i.e., at 40 °C, the complexation is more advantageous than the esterification. At 120 °C, however, the esterification takes place rather intensively, and all of the COOH groups are fully exhausted by either esterification or complexation. In such conditions, the complex formation becomes possible only on behalf of the coordination through C–O$^-$. Higher esterification degree in LaTiCit120 (in comparison with YTiCit120) leads to higher portion of the ligand with deprotonated alcoholic OH groups. The increase in the complexing-agents charge at substitution of Ln(III) with Ce(IV), along with the relatively high esterification degree of the ligands, causes deprotonation of all of the OH groups available.

On the other hand, in spite of the lower number of COOH and higher number of alcoholic H groups in TA (compared with the CA), the deprotonation degree of the OH groups in the formed complex is lower because of higher ligand number (because of the smaller ligand size and smaller steric hindrance) and, mainly, lower esterification degree.

Our attempt for computer simulation of the complex formation, although not fully successful, shows that in some conditions the complexation via OH deprotonation leads to a sharp decrease of the system energy. This was particularly shown in the case of Ti complex, prepared at 40 °C, in which a trace of ligands with deprotonated OH group exist in spite of the relatively low esterification degree and the presence of COOH groups. The results for LaTiCit40 (Table 3) are similar: the ^{13}C NMR spectra (17) definitely show the presence of deprotonated alcoholic groups in spite of the COOH groups present. These results are consistent with the recent ones for Ti–citrates obtained at higher pH values (28–30). It is established that protonated COOH groups take part in strong hydrogen-bonding interactions between themselves or with lattice water molecules. It may be supposed that in EG systems studied in the present work, the adduct-bonded EG will block these groups and, in this way, impede their participation in the complexation process. Probably, the same COOH···EG interaction exists also in YTiCit40, but the lower esterification degree excludes the OH groups participation in the complexation via deprotonation (Table 3).

Based on indirect data and other assumptions, it had been evaluated (2) that Y–Ti–citrate existing in solution contains 2.5 ligands with deprotonated and 0.5 ligand with protonated alcoholic OH$^-$ groups, i.e., L$^-$/L = 0.83. Our results for the solid YTiCit120 (0.60) and for LaTiCit120 (0.80) (Table 3, column 5) are quite close to the evaluation made in (2).

The difference concerning Y–Ti–citrate could be explained with much-longer heating time (several hours) applied in (2) compared with this work (30 min). Lower portion of deprotonated OH$^-$ groups is observed in our experiments at lower heating temperature (LaTiCit40/15 and LaTiCit40, Table 3), but it may be expressed in Y–Ti systems at higher temperature also because of lower catalytic efficiency of these metals to esterification and, respectively, the necessity of longer heating time for the complex to reach its final chemical form.

Structure of the complexes

X-ray amorphous products were obtained at the experimental conditions applied in this study. The only exception was the complex $NH_4Ce4TiCit100$ (27), but even for this compound, the attempt to grow single crystal, suitable for X- ray study, failed. That is why high resolution solid state NMR and IR spectral analysis were used for evaluation of the complexes structure (19, 27).

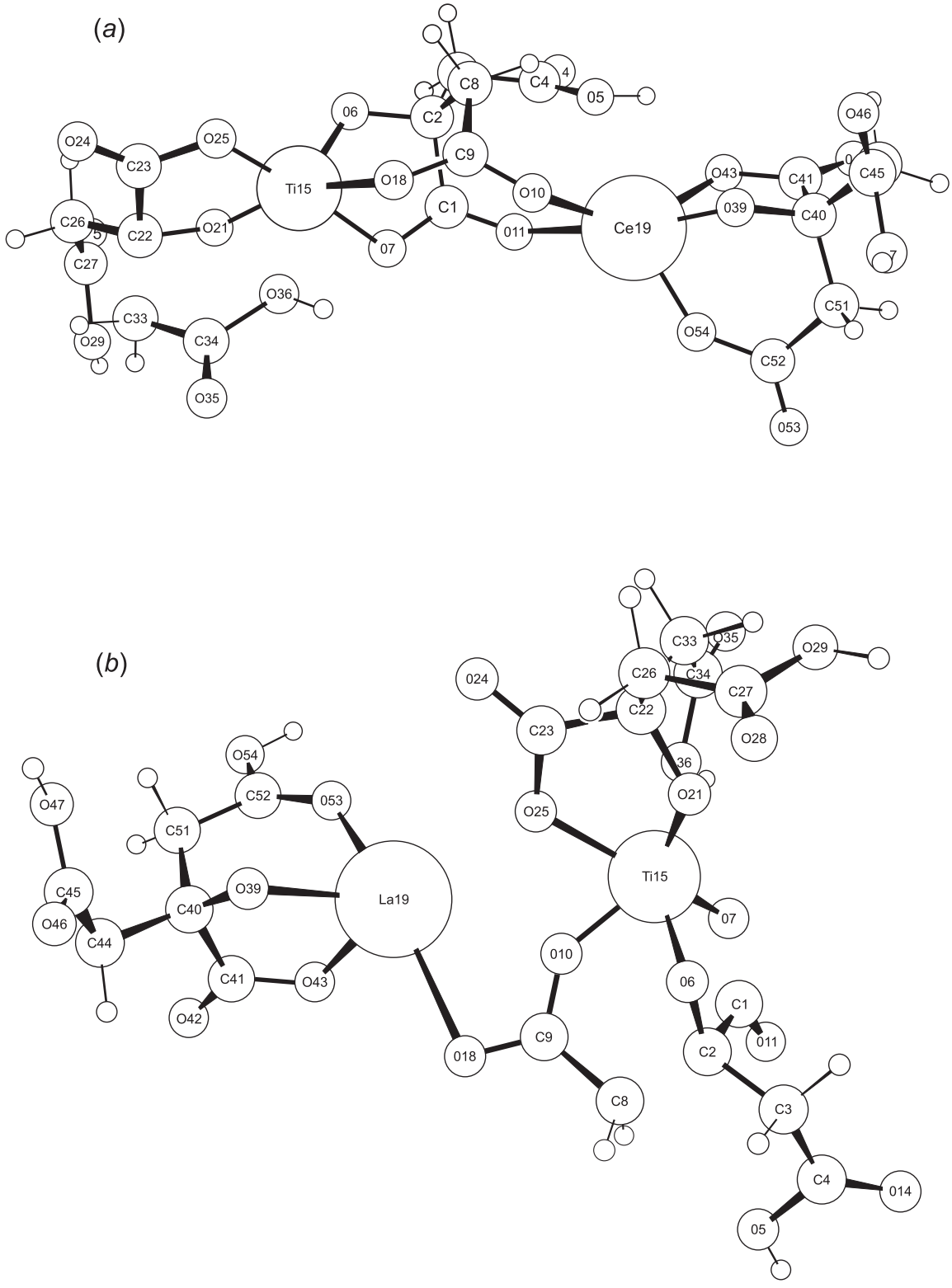
The main experimental facts lying in the base of the hypothesis were (*i*) according to the thermogravimetric analysis data, one water molecule is coordinated to one of the metal ions in each structural units, (*ii*) as it was mentioned previously, IR spectrum proves the monodentate coordination of COO$^-$ groups in the mixed-metal complex, (*iii*) in the ^{13}C solid state NMR spectrum of the bimetallic complex, signals for ionized and esterified terminal and central COOH groups are observed. Shifting of the hydroxyl–carbon signals in the spectra of the individual and bimetallic citrates (74–76 ppm) in comparison with citric acid (72.3 ppm) suggests the coordination of La(III) with alcoholic group and of Ti(IV) with C–O$^-$ (19). Thus, the interpretation of the spectrum leads to the assumption that five- and six-membered rings are formed in the mixed-metal complex with the participation of terminal or central COO$^-$ and alcoholic or alkoxy groups.

The structure optimization of the LaTiCit120 and $NH_4Ce_4TiCit100$ complexes, shown in Fig. 6, was performed at ab initio level. Geometric structures were optimized at Hartree–Fock level without any symmetry constrains. The calculations were carried out with the Stewens–Basch–Krauss–Jasien effective core potentials and their concomitant basis set (CEP-31G) for all the atoms using GAUSSIAN 03 quantum-chemistry program package. On the basis of the experimental data, the scheme of bonding in La–Ti and Ce(IV)–Ti bimetallic complexes can be proposed (Fig. 6) (19, 27) with the following main peculiarities: (*i*) The carboxylic groups of the ligands are monodentate-coordinated to the metal ions. (*ii*) The Ln^{n+} and Ti^{4+} ions are joined together by bridging carboxyl groups of the citric ligands. (*iii*) The central COO$^-$ and alkoxide groups are coordinated to the metal ions, forming five-membered chelate ring. (*iv*) In the case of the La–Ti–citrate, in contrast to the Ce–Ti one, where alcoholic OH groups also exist, the latter are coordinated only to La^{3+} ions. (*v*) Terminal COOH groups (esterificated or deprotonated) together with alkoxide alcoholic OH group form six-membered chelate ring. (*vi*) As it was mentioned, the TG results prove the presence of a molecule of water, coordinated to the metal ions. In spite of that, the metal ions coordination saturation is reached, probably by intermolecular interaction with the participation of the esterificated terminal COOH groups.

Similar six-membered rings are accepted in the amorphous structure isolated from alkaline water solution $BaTi(C_6H_6O_7)_3{\cdot}4H_2O$ (where with $C_6H_6O_7$ is labeled doubly ionized citric ligand with deprotonated alcoholic OH group and one terminal COOH group) (16). In contrast to our results and the X-ray data for other Fe– and Ni–citrates (37, 38), the authors (16) assert that the central COOH group does not participate in the coordination. The assertion is based on the analysis of the Raman spectrum of the Ba–Ti complex and the existence of a resonance in the solid-state ^{13}C NMR spectrum near 188 ppm, assigned to the non-coordinated central COOH group. Protonated COOH groups do not exist in the discussed La–Ti and Ce–Ti

© 2007 NRC Canada

Fig. 6. Ab initio calculated structures of (*a*) Ce–Ti–citric and (*b*) La–Ti–citric complexes.



mixed-metal complexes, and this may be the reason for the difference in the structures. However, the detailed structural studies based on ^{13}C NMR (29) and X-ray diffractometry (28) undoubtly proved the possibility for the citrate groups to chelate to the Ti^{4+} through their negatively charged α-carbonyl oxygen atoms.

Thermal decomposition of the complexes

A number of papers dealing mainly with the synthetic aspects of the PCM report also some data on the thermochemical behavior of the polyester-resins precursors of the prepared compounds, including $Ln_2Ti_2O_7$ (1, 2). Hennings and Mayr (5) studied the thermal decomposition

© 2007 NRC Canada

of Ba–Ti–citrate in details; some thermochemical data are given about Li–Co–, NH_4–Li–Co– (39), and Li–Ni– (40) citrates; all of these complexes are prepared in water solution. The study of Ln–, Ti–, and bimetallic Ln–Ti–citrates and –tartrates prepared in EG medium (17, 21, 22, 27) permits the scheme of the thermochemical processes to be proposed. Some water-prepared compounds were also investigated aiming to compare the behavior of the two types of complexes.

The decomposition of EG-containing citrates proceeds in few stages:

(*i*) Dehydration (from 50 °C to 170–190 °C), taking place usually in two steps (as in Ba–Ti–citrate (5)). Usually only ~1 mol H_2O/mol (approximately ¼ from water found in the complexes) is stronger bounded, probably coordinated.

(*ii*) Intramolecular dehydration (from 170–190 °C to 200–215 °C) leads to a formation of a C=C double bond, i.e., to partial transformation of the citrates to aconitates/ $CH_2(COOH)C(COOH)=CH(COOH)$ aconitic acid and of tartrates to derivatives of the hydroxomaleinic acid. The process is common for all of the citric complexes (5, 6, 16, 37).

(*iii*) Separation of the EG bonded as adduct and as ester (from 200–215 °C to approximately 300 °C) proceeds stepwisely. The separation of the main part of the adduct-bonded EG takes place up to 235 °C; the decomposition of the esters of the type $–COO(CH_2)_2OH$ up to 250–280 °C. As a rule, the destruction of bridge-type esters $^{-}COO(CH_2)_2OOC^{-}$ proceeds simultaneously with the decarboxylation of the COOH groups (existing or formed as a result of deesterification). The higher temperature of a decomposition of the later type of esters explains the higher thermal stability of the polyester resins (6) (comparing with the complexes) in which they are dominant.

(*iv*) The decarboxylation of the citrates is completed at 320–355 °C and leads to transformation of the aconitates to itaconates ($CH_2(COOH)C(COOH)=CH_2$, itaconic acid), observed in other complexes (5, 6, 16). However, we did not find evidences for the formation of the itaconic anhydride reported in the literature (5). The decarboxylation of the TA COOH groups proceeds simultaneously with the deesterification and is completed at ~315 °C.

(*v*) It is hard to determine the nature of the few steps in which the complete destruction of the organic skeleton (from 320–380 °C to 420–520 °C) proceeds. Clearly, one of the reaction products is residual carbon. The nature of the formed metal-containing compound(s) is one of the main problems discussed in the literature (4–8, 12) for the Ba(Sr)–Ti–citrates. The assumption of Hennings and Mayr (5) for the destruction of the complex to $BaCO_3$ and TiO_2, taking part further in a solid-state reaction (enhanced by their high dispersity and intimate mixing), is not confirmed in the following works. The formation of $Ba_2Ti_2O_5CO_3$ is accepted (7) and thermodynamical consideration, IR spectra, and X-ray data (7) support this proposition. TiO_2 was not found in the residue obtained in the systems studied by us (22). The IR spectra confirm the presence of CO_3^{2-} or, more likely, oxycarbonate ions. In the same time at 485 °C, $LaTi[CH_2(O)CH(O)CH_3]_{1.5}[CH_2(O)C(O)=CH_2]_{0.5}[CH_2(O)C(O)OCH_3]$ is formed as intermediate. In the 485–535 °C temperature interval, the latter is destroyed to oxycarbonate. Judging from the experimentally found mass loss in this stage (22), it has to be accepted that X-ray amorphous $La_2Ti_2O_5(CO_3)_2$ is formed in the bimetallic system (but not $La_2Ti_2O_6CO_3$ as could be expected, comparing with the cited results for Ba–Ti system. Such intermediates formed are responsible for the higher temperatures of obtaining final products in lanthanide or Ln–Ti–systems, comparing with the pure Ti–citrate. In the IR spectrum of the intermediate, obtained after heating of the tartrates up to 480 °C, a band at 656 cm^{-1} is observed (20). This absorption maximum is rather close to the characteristic one (640 cm^{-1}) for the TiO_2 (anatase). This fact suggests that the mixed-metal compound is decomposed, and monometallic compounds (most probably $La_2(CO_3)_3$ and TiO_2) are formed.

(*vi*) The burning of the residual carbon starts at 420–520 °C and is completed at about 750 °C. The mass loss found for this stage (20) suggests that in the same temperature region, carbonate, obtained from the tartrate, transforms into $La_2O_2CO_3$. The possibility for such a transformation is proved in the literature (41).

(*vii*) The decomposition of the citrate-originated mixed-metal oxycarbonates proceeds at 750–850 °C. The stage can be better distinguished in samples with lower carbon content (water-prepared or with a lower degree of esterification) (22). As a difference, an exothermic (clearly observed on TG and DTG curves) process takes place around 750 °C in the residue obtained after tartaric-complex heating and leads to $La_2Ti_2O_7$ formation, quite likely as a result of solid-state reaction between TiO_2 and $Ln_2(CO_3)_3$ (20).

(*viii*) The heating changes the bonding nature (20). According to the IR data above 200 °C along with the dominating monodentate coordinated COO^{-} groups, bridging type of coordination exists. In the intermediate, obtained at 350 °C, the carboxylate groups are ionic-bonded with metal ions.

(*ix*) The final products of the individual citrates and tartrates heating are oxides; the bimetallic complexes heating (excluding Ce–Ti–citrates) leads to phase-homogeneous $Ln_2Ti_2O_7$ (17, 23). A good crystal structure from mixed-metal citric complexes is reached at times (4 h for Ln=La, 5 h for Ln=Y) and temperatures (750 °C and 850 °C, respectively) close to the ones of PCM (1, 2) and rather lower in comparison with the solid-state reactions (1100 °C (1)). Longer heating time (up to 8 h) is needed to obtain $La_2Ti_2O_7$ with perfect crystal structure if tartaric complexes are used as a starting material (20).

Conclusion

Some important details of the processes happening in Ln–Ti–CA(TA)–EG systems, leading to a more-precise picture of the complexation, esterification, and thermal decomposition of the complexes formed, are reported. The main factors

© 2007 NRC Canada

governing the composition of the Ln–Ti–citrate and tartrate complexes are determined. The data reported prove the mixed-metal nature of the bimetallic citrates and tartrates produced in the studied systems. One of the peculiarities of the complexation process, coordination via deprotonated CA or TA alcoholic OH group, seems to be an energetically advantageous way of complexation at high esterification degree of the ligands. EG, bonded as adduct to COOH groups, may prevent the latter ones to take part in the complexation (at relatively low temperature of synthesis) via deprotonation.

A difference in the final stages of the thermal decomposition of La–Ti–citrates and tartrates is observed. The final product of the burning, $La_2Ti_2O_7$, is a result of La–Ti–oxocarbonate decomposition in the case of the citrates, and of solid-state reaction between La–oxocarbonate and TiO_2 in the case of the tartrate.

The studied complexes can be used as precursors for the production of the respective materials instead of the polyester resin used in the common PCM. Such an approach ensures a decrease of the organic-components relative content in the precursor, keeping the principal advantages of the PCM: mixing the metals at atomic level. The EG solution of complexes was successfully used for the production of thin films of Y_2O_3, CeO_2, and La_2TiO_7.

Acknowledgments

Solid-state NMR analysis was done by Professor I. Wawer (The Medical University of Warsaw).

References

1. M. Milanova, M. Kakihana, M. Arima, M. Yashima, and M. Yoshimura. J. Alloys Compd. **242**, 6 (1996).
2. M. Kakihana, M. Milanova, M. Arima, M. Yashima, and M. Yoshimura. J. Am. Ceram. Soc. **79**, 1673 (1996).
3. M. P. Pechini. US Patent 3 330 697 (1967).
4. M. Kakihana, M. Arima, M. Yashima, M. Yoshimura, Y. Nakamura, H. Mazaki, and H. Yasuoka. *In* Ceramic transactions: Vol. 55. Sol–gel science and technology. Edited by E.J.A. Popoe, S. Sakka, L.C. Klein. Am. Ceram. Soc. Westerville, OH. 1995.
5. D. Hennings and W. Mayr. J. Solid State Chem. **26**, 329 (1978).
6. S. G. Cho, P. F. Johnson, and R.A. Condrate. J. Mater. Sci. **25**, 4738 (1990).
7. S. Kumar, G.L. Messing, and W.B. White. J. Am. Ceram. Soc. 76, 617 (1993).
8. S. Kumar and G.L. Messing, J. Am. Ceram. Soc. **77**, 2940 (1994).
9. M. Kakihana, M. Arima, M. Yashima, M. Yoshimura, H. Mazaki, and H. Yasuoka. Trans. Mat. Res. Soc. Jpn. **14A**, 801 (1994).
10. M. Arima, M. Kakihana, Y. Nakamura, M. Yashima, and M. Yoshimura. J. Am. Ceram. Soc. **79**, 2847 (1996).
11. M. Kakihana and M. Arima. Appl. Phys. Lett. **69**, 2053 (1996).
12. M. Kakihana, T. Okubo, M. Arima, O. Ushiama, M. Yashima, M. Yoshimura, and Y. Nakamura. Chem. Mater. **9**, 451 (1997).
13. J. Ma, M. Yoshimura, M. Kakihana, and M. Yashima, J. Mater. Res. **13**, 939 (1998).
14. S. Ikeda, M. Hara, J. Kando, K. Domen, H. Takahashi, T. Okubo, and M. Kakihana. J. Mater. Res. **13**, 852 (1998).
15. S. Ikeda, M. Hara, J. Kando, K. Domen, H. Takahashi, T. Okubo, and M. Kakihana. Chem. Mater. **10**, 72 (1998).
16. M. Kakihana, M. Arima, Y. Nakamura, M. Yashima, M. Yoshimura. Chem. Mater. **11**, 438 (1999).
17. M. Milanova, M. Arnaudov, M. Getsova, and D. Todorovsky. J. Alloys Compd. **264**, 95 (1997).
18. M. Getsova, D. Todorovsky, and M. Arnaudov. Z. Anorg. Allg. Chem. **626**, 1488 (2000).
19. D. Todorovsky, M. Getsova, I. Wawer, P. Stefanov, and V. Enchev. Mater. Lett. **58**, 3559 (2004).
20. M. Getsova, D. Todorovsky, and M. Milanova. Synth. React. Inorg. Met.-Org. Chem. **33**, 223 (2003).
21. M. Getsova and D. Todorovsky. Bulg. Chem. Commun. **32**, 89 (2000).
22. D. Todorovsky, M. Getsova, and M. Vasileva. J. Mater. Sci. **37**, 4029 (2002).
23. M. Arnaudov, M. Getsova, D. Todorovsky, and M. Milanova. Anal. Lab. **7**, 70 (1998).
24. D. Todorovsky, N. Petrova, M. Getsova, R. Todorovska, I. Manolov, and St. Groudeva-Zotova. Key Eng. Mater. 264–268, 359 (2004).
25. D. Todorovsky, M. Milanova, M. Getsova, and N. Petrova. Ann. Univ. Sofia, Fac. Chim. **97**, 169 (2004).
26. D. Todorovsky, N. Petrova, S. Angelova, and D. Mehandjiev. J. Alloys Compd. doi:10.1016/j.jallcom.2007.01.005.
27. M. Getzova, D. Todorovsky, V. Enchev, and I. Wawer. Monatsch. Chemie. **138**, 389 (2007).
28. E.T. Kefalas, P. Panagiotidis, C.P. Raptopoulu, A. Terzis, T. Mavromustakos, and A. Salifoglou. Inorg. Chem. **44**, 2596 (2005).
29. Z.-H. Zhou, Y.-Fu Deng, Ya-Qi Jiang, H.-L. Wan, and S.-W.Ng. Dalton Trans. 2636 (2006).
30. J.M. Collins, R. Uppal, C.D. Incarvito, and A.M. Valentine. Inorg. Chem. **44**, 3431 (2005).
31. N. Daskalova, S. Velichkov, P. Slavova, E.L. Ivanova, and O. Vasileva. Spectrochim. Acta, B. **52**, 257 (1997).
32. M. Arnaudov and Y. Dimitriev. Phys. Chem. Glasses. **42**, 99 (2001).
33. K.B. Yatsimirskij, N.A. Kostromina, Z.A. Scheka, N.K. Davidenko, E.E. Kriss, and V.I. Ermolenko. Khimiya kompleksnykh soedinenij redkozemel·nykh elementov (Chemistry of the rare earth complexes). Naukova dumka, Kiev. 1966, p. 224. [in Russian.]
34. D.S. Todorovsky, D.G. Dumanova, R.V. Todorovska, and M.M. Getsova. Croat. Chem. Acta, **75**, 155 (2002).
35. N. Petrova, D. Todorovsky, R. Todorovska, and D. Schopova. Key Eng. Mater. **264–268**, 427 (2004).
36. N.L. Petrova, D.S. Todorovsky, and V.G. Vasileva. Centr. Eur. J. Chem. **3**, 263 (2005).
37. J. Strouse, S.W. Layten, and C.E. Strouse. J. Am. Chem. Soc. **99**, 562 (1977).
38. T. Fudjita. Chem. Pharm. Bull. **30**, 3461 (1982).
39. E. Zhecheva, R. Stoyanova, M. Gorova, R. Alcantara, J. Morales, and J.L. Tirado. Chem. Mater. **8**, 1429 (1996).
40. R. Alcantara, P. Lavela, J.L. Tirado, R. Stoyanova, E. Kuzmanova, and E. Zhecheva. Chem. Mater. **9**, 2145 (1997).
41. R.P.Turcotte, J.O.Sayer, and L.R.Eyring. Inorg. Chem. **8**, 238 (1969).

© 2007 NRC Canada

Substituent effects in the intramolecular photoredox reactions of benzophenones in aqueous solution

Nikola Basarić, Devin Mitchell, and Peter Wan

Abstract: A number of α-hydroxy-3-benzylbenzophenones **7**–**11** have been synthesized for the purpose of studying the effect of a phenyl substituent on the intramolecular photoredox reaction of 3-(hydroxymethyl)benzophenone (**5**) discovered in our laboratory. This latter compound was found to undergo a unimolecular (formal) intramolecular redox reaction upon photolysis in aqueous acid that results in clean reduction of the benzophenone ketone (to secondary alcohol) and oxidation of the alcohol to aldehyde. Three of the phenyl-substituted compounds with simple phenyl (**7**), *p*-methylphenyl (**8**), and *p*-methoxyphenyl (**9**) were found to undergo the acid-catalyzed intramolecular photoredox reaction with the observation that **9** also undergoes a residual photoredox reaction that is not acid-mediated and may involve initial photoinduced electron transfer, which is supported by LFP data. The *m*-methoxyphenyl (**10**) compound did not undergo the reaction. The trend in observed relative reactivity may be partially rationalized by examining changes in molecular orbital coefficients observed in the calculated HOMOs and LUMOs. The photoredox reaction has also been applied twice in succession in a single compound **11**, demonstrating that the photoredox reaction may be useful for sequential photoredox reactions in a multifunctional compound.

Key words: intramolecular photoredox, acid catalysis, meta effect, benzophenone photochemistry.

Résumé : On a synthétisé un certain nombre de α-hydroxy-3-benzylbenzophénones (**7**–**11**) pour pouvoir étudier l'effet d'un substituant phényle sur la réaction de photoredox intramoléculaire de la 3-(hydroxyméthyl)benzophénone (**5**) qui a été découverte dans notre laboratoire. On a trouvé que lorsque ce dernier composé en solution acide aqueuse est soumis à une photolyse, il subit une réaction redox intramoléculaire qui conduit à une réduction propre du groupement carbonyle de la benzophénone en alcool secondaire avec oxydation concomitante de l'alcool en aldéhyde. On a observé que, en solution aqueuse acidulée, trois des composés substitués par un groupe phényle, soit le dérivé phényle non substitué (**7**), le *p*-méthylphényle (**8**) et le *p*-méthoxyphényle (**9**), subissent la réaction photoredox intramoléculaire qui est accompagnée dans le cas du produit **9** d'une réaction photoredox résiduelle qui n'est pas catalysée par les acides et qui peut impliquer un transfert initial d'électron qui est photoinduit et cette hypothèse est supporter par des données de « LPF ». Le composé méthoxyphényle (**10**) ne subit pas la réaction. La tendance dans les réactivités relatives observées peut être partiellement expliquée par un examen des changements dans les coefficients d'orbitales moléculaires qui sont observés dans les valeurs calculées des orbitales moléculaires HO et BV. On a aussi appliqué la réaction photoredox deux fois en succession à un composé unique, **11**; ce résultat démontre que la réaction photoredox pourrait être utile pour des réactions photoredox séquentielles dans un composé multifonctionnel.

Mots-clés : photoredox intramoléculaire, catalyse acide, effet méta, photochimie des benzophénones.

[Traduit par la Rédaction]

Introduction

The photochemistry and photophysics of benzophenone (**1**) and its derivatives have been studied for over a century (1, 2). Indeed, benzophenone photoreduction was one of the first photoreactions described in the literature (3). Despite the many studies on this reaction, it was not until about 60 years later that the mechanism was shown to proceed via the triplet excited state (4, 5). Although many studies have examined benzophenone (**1**) photoreduction in various organic solvents, fewer studies have examined its photochemical and photophysical behavior in aqueous solution. It is known that the benzophenone triplet excited state is quenched by acid. This was first reported by Ledger and Porter (6) who noted that the phosphorescence of benzophenone (**1**) was quenched by added protons, although the detailed mechanism was not understood at that time. Initially, it was thought that the quenching was due to the formation of the protonated triplet **2** (protonation at the carbonyl) and Wyatt and co-workers (7, 8) assigned a pK_a of 1.5 ± 0.1 for the protonated triplet excited state using Förster cycle analysis. That is, the benzophenone triplet is more basic by sev-

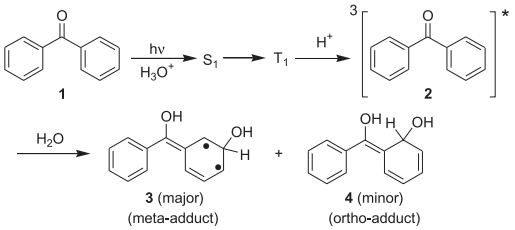
Received 13 June 2007. Accepted 3 July 2007. Published on the NRC Research Press Web site at canjchem.nrc.ca on 1 August 2007.

N. Basarić,[1] D. Mitchell, and P. Wan.[2] Department of Chemistry, University of Victoria, Victoria, BC V8W 3V6, Canada.

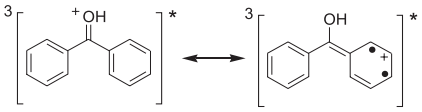
[1]On leave from the Ruder Boskovic Institute, Zagreb, Croatia.
[2]Corresponding author (e-mail: pwan@uvic.ca).

 doi:10.1139/V07-081 © 2007 NRC Canada

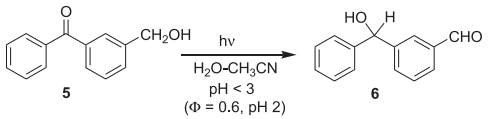
eral orders of magnitude (at the carbonyl oxygen) compared with the ground state ($pK_a(S_o) = -5.7$ (7)). In a recent study, Wirz and co-workers (9) established that protonation (at the carbonyl) of triplet benzophenone results in an overall *photohydration* reaction, to give water-adducts **3** and **4** with a preference for **3**, i.e., hydration at the meta position (eq. [1]). This reaction was unexpected and has probably missed detection in the past because of the instability of the hydration products, which readily revert back to **1**. In addition, Wirz and co-workers (9) assigned a pK_a of –0.4 for the protonated triplet excited state; thus, the triplet is somewhat less basic than originally estimated by Wyatt and co-workers (7, 8).

[1] 

The mechanism (9) of photohydration presumably involves initial protonation of the carbonyl oxygen of triplet excited benzophenone, to generate an excited triplet state conjugate acid that has its positive charge significantly delocalized to the ortho and meta positions of the benzene ring (e.g., as shown in eq. [2]), as would be anticipated based on the Zimmerman "ortho-meta" effect for benzene ring site activation in photochemical reactions (10, 11). Attack by water at these sites of positive charge would lead to the observed hydration products, which upon deactivation to their ground states would not be expected to be long-lived and would readily return to benzophenone (**1**) by dehydration (and re-aromatization).

[2] 

Although the described acid-catalyzed photohydration of benzophenone itself reported by Wirz and co-workers (9) gave no isolable *stable* product, it seemed reasonable to assume that the protonation of triplet excited benzophenone (**1**) might lead to other acid-catalyzed chemistry still to be discovered considering the known range and diversity of chemistry for ground state carbonyl compounds that are acid-catalyzed. Indeed, Wirz and co-workers (9) reported the acid-catalyzed photohydrolysis of *m*-fluoroacetophenones and benzophenones to give the corresponding phenols as proceeding via a protonated triplet. We recently reported two photochemical reactions of benzophenones that require acid-catalysis and appear to require prior protonation (at carbonyl) of triplet benzophenone: (*i*) photochemical deuterium exchange of the meta-substituted methyl group of 3-methylbenzophenone and 3-methylacetophenone (12) in deuterated aqueous acid and (*ii*) formal intramolecular redox reaction of some 3-(hydroxymethyl)benzophenones (13) (e.g., eq. [3] with the parent 3-(hydroxymethyl)benzophenone (**5**)). Notably, all the para isomers studied in these reactions were unreactive; the ortho isomers were not studied because of complications that would arise from the known competing intramolecular hydrogen abstraction pathway.

[3] 

In our view, the intramolecular photoredox chemistry of benzophenones deserves further study. Under appropriate dilution and at pH < 3, the reaction was found to be clean with very high quantum yield (eq. [3], $\Phi = 0.6$ at pH 2) (13). The reaction is mediated by water and acid and is unimolecular in substrate: the reaction becomes cleaner on dilution. At high substrate concentrations ($>10^{-5}$ mol/L), bimolecular (via bimolecular hydrogen abstraction, carbonyl abstracting the benzylic hydrogens of the benzyl alcohol) reactions compete giving rise to oligomeric and polymeric products. Photoproduct **6** does not itself undergo a photoredox reaction to give **5**, indicating that not all aromatic carbonyl chromophores can mediate the chemistry and that the question of photoredox reversibility would be an interesting issue to address in other compounds. Moreover, the reaction itself may be viewed as a formal transfer of electrons through the meta positions of the benzene ring, which cannot be accomplished in the ground state. In this paper we report the details of a study that addresses two aspects: (*i*) the structural and electronic effects on the photoredox reaction as ascertained by placing a phenyl and substituted phenyl groups at the benzyl alcohol carbon of **5** (i.e., α-hydroxy-3-benzylbenzophenones **7**–**10**) and (*ii*) the possibility that the photoredox reaction can be induced twice (one after another) in the same substrate on extended photolysis, by studying model compound **11**.

Results and discussion

Materials

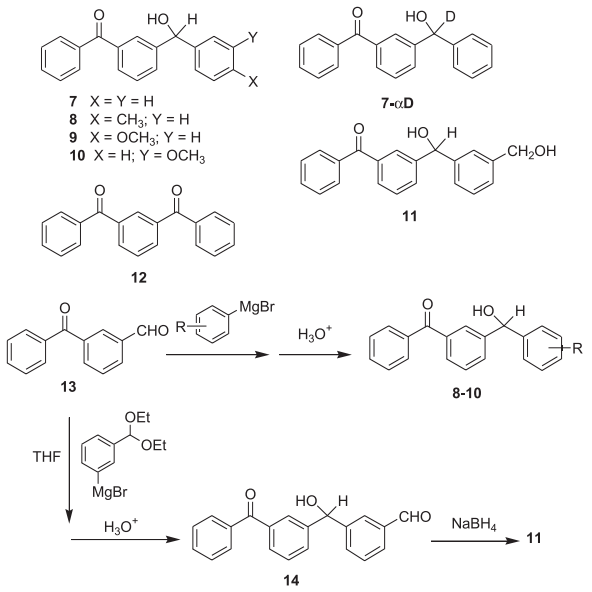
Whereas α-hydroxybenzylbenzophenones **7** and **7-αD** were readily synthesized by $NaBH_4$ ($NaBD_4$) reduction of commercially available 3-benzoylbenzophenone (**12**), **8**–**11** were synthesized according to the reactions outlined in Scheme 1, all starting from 3-formylbenzophenone (**13**). Compounds **8**–**10** were made by the reaction of **13** with the appropriate Grignard reagent with isolated yields in the 14%–80% range. The synthesis of **11** required the intermediate aldehyde **14**, which was readily made by the reaction of **13** with the Grignard reagent derived from commercially available 3-bromobenzaldehyde diethyl acetal (Sigma-Aldrich). This step proceeded in about 20% isolated yield. The subsequent $NaBH_4$ reduction gave the desired benzophenone diol **11** in 50%.

UV–vis and product studies

In view of the previous finding for the photoredox chemistry of **5** (13) in which higher substrate concentrations increased the proportion of side products because of a bimolecular hydrogen abstraction pathway, photolysis runs were carried out at the most dilute substrate concentrations deemed practical for NMR analysis. Most runs were carried out at 10^{-4} mol/L (10 mg in 400 mL, 1:1 H_2O–CH_3CN, pH 7 and 2, Rayonet RPR 100 reactor, 300 nm lamps, argon

© 2007 NRC Canada

Scheme 1.



purged), and some selected runs were carried out 10^{-5} mol/L (2 mg in 600 mL). Product studies were initially carried out with compounds **7** and **7-αD**. The anticipated photoredox chemistry for these compounds (in aqueous acid solution) would give no observable changes in their UV–vis as the reaction would only interchange the benzophenone ketone and benzhydrol alcohol moieties (with no overall change in molecular structure). To follow the reaction, photolyses of **7** (**7-αD**) were carried out in acidic D_2O (H_2O) and after work-up, NMR spectra were recorded. Photolysis (10^{-4} mol/L) of **7-αD** in 1:1 H_2O–CH_3CN (pH 2, argon purged) resulted in formation of the methine peak at δ 5.9 as would be expected on formation of **7** (≅20% yield) (eq. [4]). The reaction shown interconverts the ketone and alcohol carbons. Although this was not proven in the case of **7** (or **7-αD**), the same reaction for the phenyl-substituted compounds **8** and **10** (vide infra) conclusively shows that the reaction does interchange the carbons concerned. Accompanying the reaction was the formation of broad aromatic signals in the δ 7–7.3 region, indicative of oligomeric material resulting from photoreduction of the benzophenone moiety (Fig. 1) and a trace of the simple photooxidation product **12** (this is the major product when photolyzed with an oxygen or air purge). This oligomeric material proved to be intractable and appears to be a mixture of products. Photolysis at 10^{-5} mol/L gave a cleaner product mixture although the broad peaks observed at δ 7–7.3 could not be completely eliminated. In comparison, the photoredox reaction of **5** under these conditions (i.e., at 10^{-5} mol/L or lower) were exceptionally clean (13). As expected, photolysis of **7** in D_2O–CH_3CN (pD 2) (after H_2O wash before NMR analysis) showed the loss of the methine peak at δ 5.9 with essentially no change in the aromatic region except for growth of broad δ 7–7.3 region due to the formation of oligomers. Thus, **7**

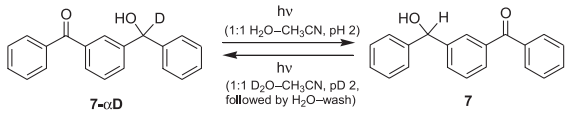
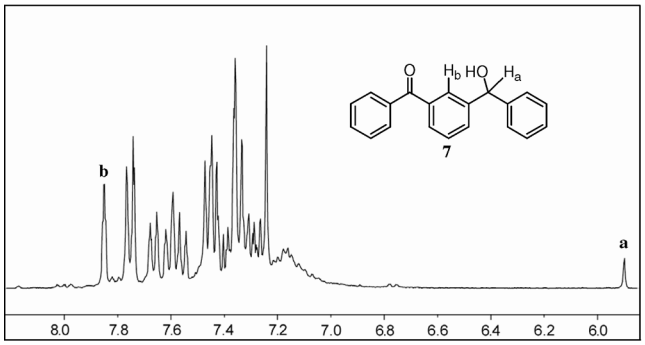
[4] 

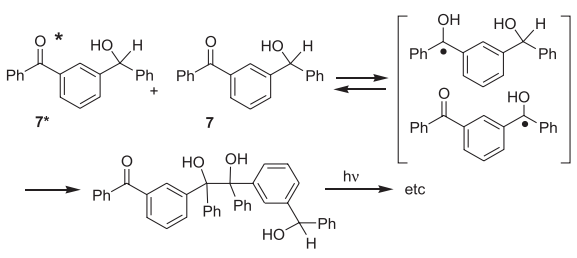
Fig. 1. Product mixture observed after photolysis of **7-αD** (10^{-4} mol/L) in 1:1 H_2O–CH_3CN (pH 2) for 2 min at 300 nm. Formation of **7** was determined by observation of a methine peak at δ 5.9 (H_a). Relative ratios of **7** and **7-αD** were calculated by using the H_b proton at δ 7.85 common to both compounds.



and **7-αD** are photochemically interconvertible (eq. [4]). Noteworthy was the fact that photolysis of **7** or **7-αD** in neat CH_3CN or in 1:1 H_2O–CH_3CN above pH 3 did not result in the photoredox reaction shown in eq. [4]; only the broad signals in δ 7–7.3 were observed.

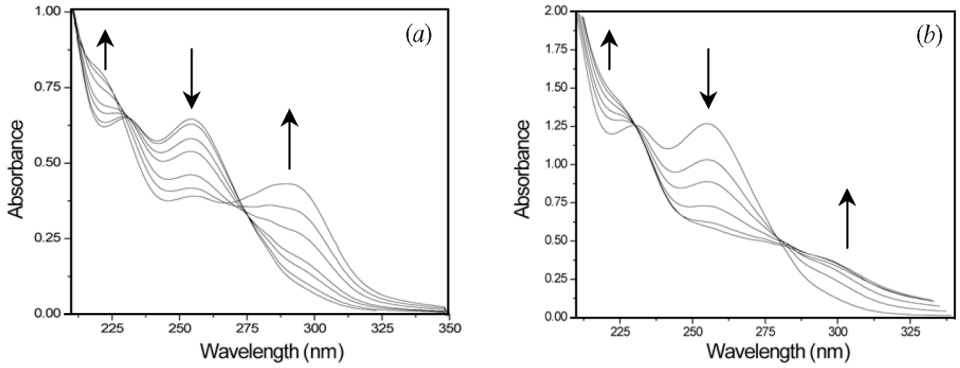
The photoredox reaction of **5** was found to be exceptionally efficient with Φ = 0.6 at pH 2 (13). Using the reaction of **5** as a secondary reference, we have estimated a quantum yield of reaction for **7-αD** to be about 0.3 at pH 2, which further confirms the general high reactivity of these compounds in acid.

As will be shown, all of the photoredox reactions for the phenyl-substituted systems studied in this work (**7**–**11**), regardless of their relative efficiency with respect to the photoredox reaction itself, are accompanied by the formation of oligomeric material as already discussed for **7** and **7-αD**. This is in contrast to what was observed for **5** in which the reaction was exceptionally clean at 10^{-5} mol/L. We believe that the competing reaction(s) are bimolecular in nature and probably involve the triplet benzophenone-like ketone abstracting hydrogen from the benzylic hydrogens of another substrate. In the case of the phenyl-substituted compounds **7**–**11**, the hydrogen to be abstracted is of the benzhydrol type and hence even *more* prone to this reaction. A possible reaction sequence initiated by intermolecular hydrogen abstraction is shown in eq. [5]. Note that in this mechanism one would anticipate a mixture of products in which the benzophenone moiety would suffer "reduction", consistent with the observed NMR (aromatic signals only in the δ 7–7.3 region). This offers a reasonable explanation for the observed concentration-dependent formation of oligomeric products for all of these compounds.

[5] 

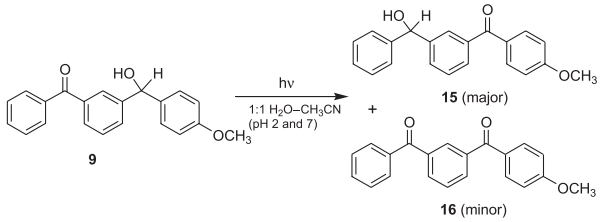
© 2007 NRC Canada

Fig. 2. UV–vis traces observed on the photolysis of **9** in 1:1 H_2O–CH_3CN at (*a*) pH 2 and (*b*) pH 7, purged with N_2, at 300 nm. Traces were taken after initial irradiation of 1 min followed by increasing photolysis times of up to 20 min.



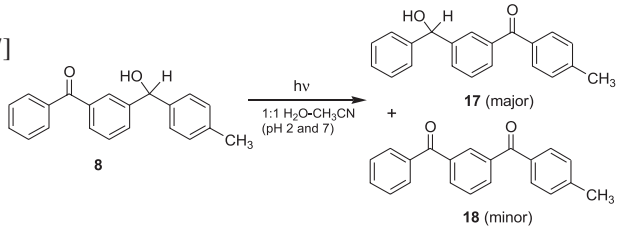
The anticipated photoredox reactions for the methoxy-substituted derivatives **9** and **10** were studied next since reaction would result in significant UV–vis changes. Photolysis of the meta-isomer **10** (pH 2 and 7) resulted in only the loss of substrate and the formation of oligmeric material as noted above for **7**, with no evidence of photoredox reaction. On the other hand, photolysis of the para-isomer **9** resulted in the expected photoredox reaction (eq. [6]) giving **15** (major) and **16** (minor). Notably, at 10^{-5} mol/L substrate, the reaction was much cleaner than **7**, with reaction being observed at pH 7 ($\Phi \cong 0.007$) *and* pH 2 ($\Phi \cong 0.02$), although the quantum yields are both much lower than for **5** and **7**. UV–vis traces carried out for **9** were informative (Fig. 2): photolysis in pH 2 resulted in the formation of a band at 290 nm that is assignable to the expected photoredox product **15**; at pH 7 a much lower yield of this product was observed. Both spectral traces show competing decomposition of the substrate, which is more pronounced at pH 7. Interestingly, **15** was found to be photoinert; that is, the photoredox reaction for **9** (eq. [6]) is not photoreversible. A possible reason for this is provided later.

[6]



The last compound studied in this series was the *p*-methyl-substituted derivative **8**. The intramolecular photoredox reaction was observed at pH 2 (eq. [7]), but it was observed that this compound gave the highest proportion of oligomeric products compared with the other reactive systems discussed so far. Even at 10^{-5} mol/L, low conversion runs gave 10%–20% of the oligomeric products (estimated by comparing the intensity of the signal corresponding to the entire methyl proton region at δ 2.2–2.6 and the sum of the intensities at δ 2.31 and 2.42 corresponding to **8** and **17**, respectively). This is consistent with the greater availability of abstractable benzylic hydrogens (total of 4) in this molecule and the earlier proposal (eq. [5]) that the main competing reaction is due to bimolecular hydrogen abstraction by the benzophenone ketone of another substrate. To further test this assertion, we have carried out the photolysis of **8** in the presence of added naphthalene (a known efficient triplet quencher of benzophenone (1)) at pH 2. The presence of 10^{-4} mol/L naphthalene resulted in a much less efficient reaction and longer photolysis times (up to ten fold) were required, consistent with triplet state reactivity of the benzophenone chromophore of **8**. However, the photoredox reaction was much cleaner and could be taken to almost completion with formation of up to 20%–30% oliogomeric materials as estimated by NMR. This was a significant improvement over runs without added naphthalene. The results are consistent with a photoredox reaction that is unimolecular in substrate (although requiring water and acid mediation) and a competing reaction that is bimolecular in substrate. The addition of naphthalene reduces the lifetime of the reactive triplet state and hence all photochemical pathways. Noteworthy is the finding that in this case, the proportion of bimolecular pathway is retarded more than the unimolecular photoredox pathway, although we do not completely understand why this is so.

[7]

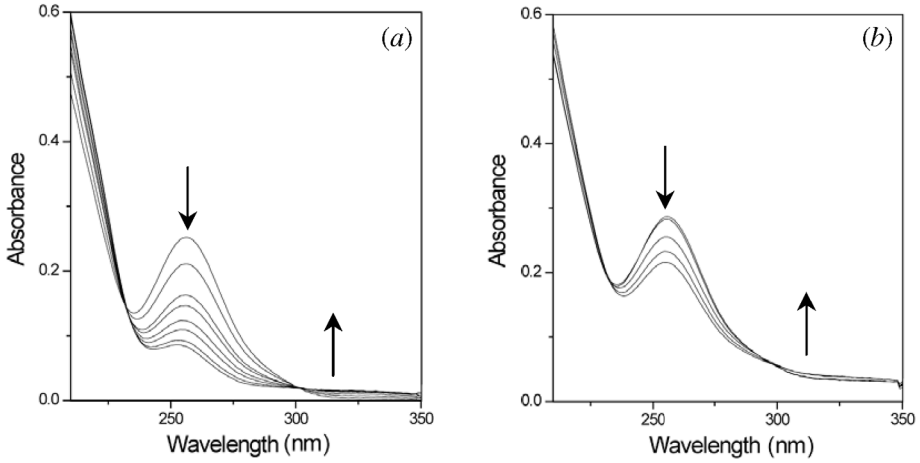


The photoredox product **17** could not be completely separated from substrate **8** using chromatography. The best that could be achieved was a mixture consisting of 92% **17** and 8% **8** from photolysis in the presence of added naphthalene. Subsequent photolysis of this mixture at pH 2 (300 nm) resulted in no observable change in the ratio of these compounds. Although in principle **17** could undergo the photoredox reaction returning to **8**, this result suggests that the return is very inefficient, and that at this photolysis wavelength the photostationary state has already been attained.

Compound **11** was designed with two oxidizable benzylic alcohol moieties. The idea was that this compound might undergo two photoredox reactions in succession, first forming **19** and then **20** as shown in eq. [8]. Initial studies by UV–vis (Fig. 3) spectra show that photolysis of **11** in acid

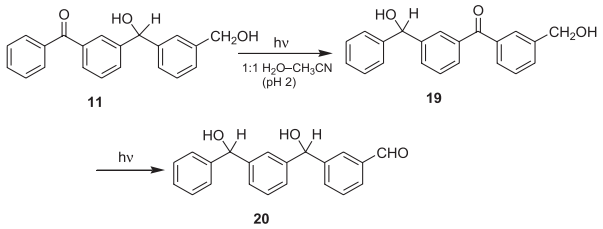
© 2007 NRC Canada

Fig. 3. UV–vis traces of the photolysis of **11** in 1:1 H_2O–CH_3CN at 300 nm at (*a*) pH 2 and (*b*) pH 7, purged with N_2. Traces were taken after 1 min of photolysis in each run, with latter runs requiring 2 min photolysis to produce noticeable spectral change.

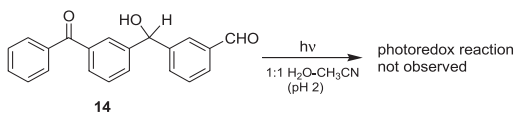


(pH 2) resulted in significantly greater loss of the benzophenone chromphore absorption vs. runs in pH 7, consistent with the acid-catalyzed photoredox reaction. Since **11** and **19** have essentially the same benzophenone chromophore, it was not possible to follow their interconversion using UV–vis. The UV–vis traces are consistent with the eventual formation of **20**, which lacks the benzophenone moiety. Photolysis of **11** at pH 7 gave **14** (up to 10% yield) and oligomeric material. Compound **14** was also observed in all runs carried out in acid (pH 2). Its observation at pH 7 suggests that it is formed via some residual oxidation pathway because of traces of oxygen in the irradiated solution. Interestingly, **14** was found to be photoinert with respect to the photoredox reaction (eq. [9]), as was also the case for the m-methoxyphenyl derivative **10** (vide supra). In addition to **14**, photolysis of **11** in acid (pH 2) did give *both* **19** and **20** shown in eq. [8], although the yield of **20** was always higher than **19** even at the lowest conversions that we were able to conveniently carry out. Thus **19** could not be isolated in pure form and its presence was indicated by NMR assignment of product mixtures that were enriched in **19** by chromatography. It is clear that the reaction scheme shown in eq. [8] can be achieved, in that the end product is formed. Our data suggests that **19** is more reactive than **11** and preferentially undergoes a photoredox reaction to give **20**, although additional studies are warranted to show this in a direct way.

[8]



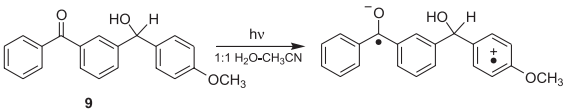
[9]



Nanosecond laser flash photolysis (LFP) studies

LFP studies were carried out using a Nd-Yag laser at 266 nm (pulse width ≅ 20 ns). Based on our initial LFP studies of the photoredox chemistry of **5** (13), transients assignable to reactive intermediates other than the reactive triplet state were not anticipated. Indeed, LFP of **7** and **8** gave the typical triplet state absorption expected for the benzophenone chromophore with maxima at 325 and 525 nm for **7** and **8** (Fig. 4) (9, 13). However, closer analysis of the spectra observed for both of the methoxyphenyl-substituted compounds **9** and **10** show that in addition to the triplet state signal, bands at ≅450 and >600 nm were also observed superimposed on the triplet signal. Shizuka and co-workers (14) have shown that benzophenone radical anion (450 nm) and methoxybenzene radical cations (630 nm) are produced from electron transfer from methoxybenzenes to triplet excited benzophenone. That the same signals were observed for **9** and **10** under dilute conditions and that the triplet signal itself was the dominant one indicate that intramolecular electron transfer from the methoxybenzene to the triplet excited benzophenone is a competing channel for these two compounds (eq. [10]).

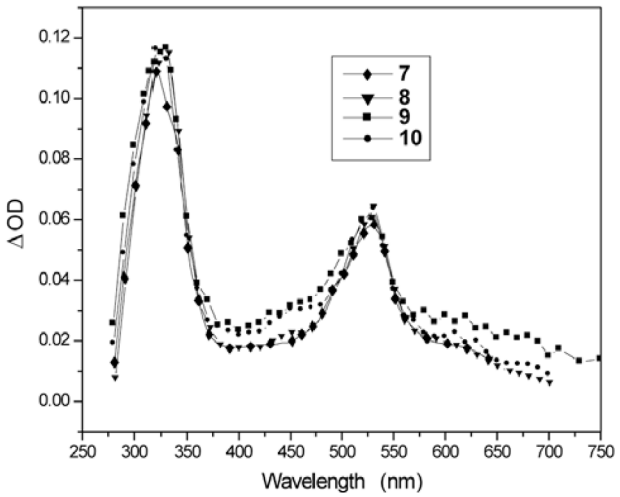
[10]



With respect to the triplet absorption signal itself, the following general findings apply: (*i*) apparent lifetimes were sensitive to oxygen and acid (pH < 3). For **9** the apparent triplet lifetime was 5.2 μs at pH 7 and was reduced to 220 ns at pH 2; for **10** the lifetime was 5.3 μs at pH 7 and 660 ns at pH 2. The addition of oxygen (1 atm; 1 atm = 101.325 kPa) to all samples reduced triplet lifetimes to <100 ns in all cases; (*ii*) most decays could not be fitted to first-order decays and typically required a sum of two first-order decays, especially at pH 7 where there is no quenching of the triplet by acid. This is consistent with competitive pseudo first-order decays (including hydrogen abstraction) pathways. In addition, the benzophenone ketyl absorbs at 545 nm (15) and this overlaps with the 525 nm band of the triplet, mak-

© 2007 NRC Canada

Fig. 4. Triplet absorption spectra of **7**, **8**, **9**, and **10** detected by LFP (Nd-YAG, λ_{ex} = 266 nm) in 1:1 H_2O–CH_3CN (pH 7, N_2 purged) immediately after the laser pulse (≅20 ns).



ing kinetic analysis even more complex. The competition of bimolecular pathways of triplet decay can best be documented for **8** at pH 7 where dilution of the solution induced significantly longer triplet lifetimes: the apparent lifetime at 8.8×10^{-5} mol/L was 2.2 μs whereas at 1.4×10^{-5} mol/L it was 9.1 μs. In view of these complexities, LFP data was used only to infer that the triplet excited state is the reactive state and that it is subject to acid quenching, consistent with photoprotonation at the benzophenone carbonyl (vide supra).

Mechanisms of reaction

As discussed in the Introduction section, the protonation of the oxygen of triplet excited benzophenone in aqueous solution is an important primary photochemical pathway in acid (pH < 3). The more basic carbonyl oxygen in the triplet excited state implies considerable charge transfer from the benzene rings on electronic excitation that is probably enhanced in aqueous solution. Perhaps surprising is the fact that the triplet excited state also retains its ability to abstract hydrogen, as evidenced by the competing hydrogen abstraction pathway observed in this work.

We have carried out simple HOMO and LUMO (Chem 3D, MOPAC/AM1) calculations of the compounds studied in this work to gain possible insights into their relative reactivity. To our pleasant surprise, the experimental observations we have made can be rationalized by the results of these calculations. Shown in Fig. 5 are the calculated HOMOs and LUMOs for the unsubstituted phenyl derivative **7**. The excited state (singlet or triplet) may be viewed in the simplest approximation as attained by promoting an electron from the HOMO to the LUMO. Thus, there would be charge migration from two of the benzene rings (the benzophenone benzene ring with the attached PhCH(OH) group and the benzene ring of the attached Ph(CH)OH itself) to the benzophenone carbonyl and the other benzophenone benzene ring. One would therefore predict the increased basicity of the carbonyl oxygen. Subsequent protonation of the ketone oxygen would give rise to the conjugate acid, which one could argue would retain the electronic distribution of its precursor. A closer examination of Fig. 5 would predict that the benzene ring carbon bearing the PhCH(OH) substituent would be expected to bear most of positive charge in the (redistributed) electronic structure of the excited state (compared with the initial ground state). This is shown in Scheme 2 in which protonation of triplet **7** would give rise to a conjugate acid (carbocation) that may be represented by structures **21a** and **21b**. These predictions are also consistent with the mechanism of photohydration of benzophenone reported by Wirz and co-workers (9). In the case of the photohydration reaction (9), water would attack the carbocation of structure **21b**. This may indeed occur, leading to a product that would eventually return to substrate. However, another possible pathway that is not available in the parent benzophenone studied by Wirz and co-workers (9) is the deprotonation pathway leading to the double enol intermediate **22**. This is perhaps a pathway that initially seems unusual, but one can quickly see that ketonization of this double enol leads back to substrate or to a formal intramolecular redox product that was indeed observed for most of these compounds. Oxygen is expected to trap biradicals of the type **22** leading to the oxidized product **12**, although other mechanisms for photooxidation (photooxygenation) are not excluded.

HOMO and LUMO calculations for the *p*-methylphenyl derivative **8** gave similar results. However, this was not the case for the methoxy-substituted derivatives **9** and **10**. As shown in Fig. 6 for compound **9**, examination of the HOMO and LUMO characteristics would imply that electronic excitation of this compound would transfer charge from only the methoxybenzene ring to *both* of the benzene rings of the benzophenone. This is consistent with the photoinduced single electron transfer to form the benzophenone radical anion and methoxyphenyl radical cation that was inferred in the LFP results for this compound (and **10**). A residual formal photoredox pathway was observed for this compound at pH 7 and pH 2. Indeed, initial photoinduced electron transfer can lead to such a reaction (Scheme 3), and we believe that it is the pathway taken at pH 7. At lower pH, one would still expect protonation of the benzophenone carbonyl, and this may lead to an overall photoredox pathway as well, which is consistent with the higher quantum yield for this reaction at lower pH. The question remains as to why the *m*-methoxy-substituted compound **10** did not undergo photoredox reaction at any pH. Clearly in this case the photoinduced electron transfer appears to take place for **10** as indicated by the LFP data. We believe the explanation lies in the electronic structure of the radical cation shown in Scheme 3. A meta-substituted methoxy group (instead of the para-substituted methoxy group shown) would cause the cation and radical to be more localized at benzene positions that are ortho and para to the methoxy group (for resonance stabilization). This will have the effect of reducing the degree of positive charge that would be localized at the benzene ring carbon adjacent to the Ar(HO)CH moiety. This in term will reduce the acidity of the CH proton of the Ar(HO)CH group and hence the overall efficiency of the formal redox reaction. A similar argument may also be used to explain why photoredox chemistry was not observed when **10** is photoprotonated at pH 2.

Finally, we have also carried out HOMO and LUMO calculations for the photoredox product **15**. As noted earlier, this compound did not undergo the photoredox chemistry

© 2007 NRC Canada

Fig. 5. HOMO (left) and LUMO (right) of **7** calculated using Chem 3D (AMI).

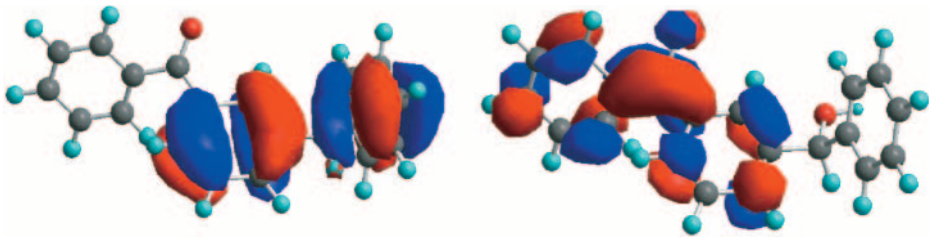
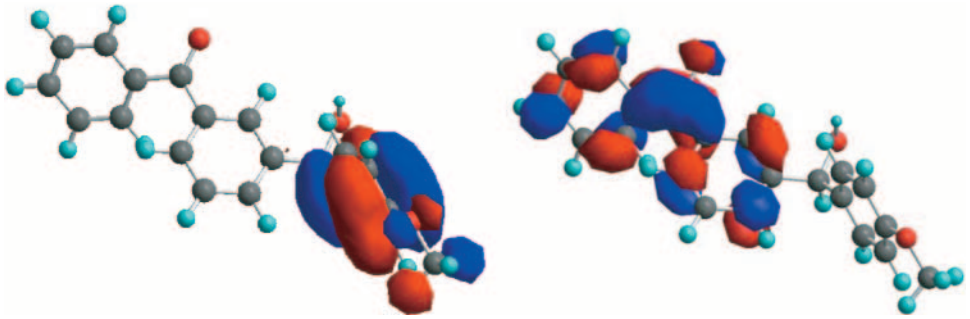
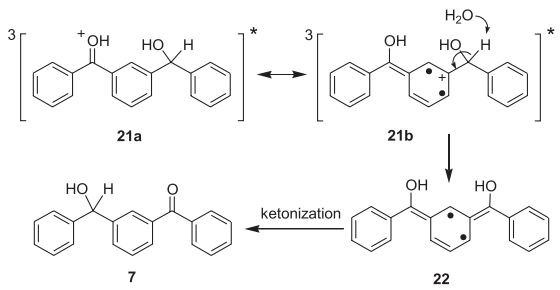


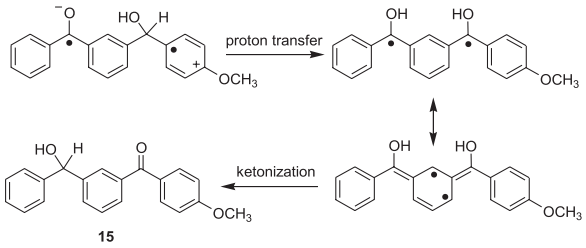
Fig. 6. HOMO (left) and LUMO (right) of **9** calculated using Chem 3D (AM1).



Scheme 2.



Scheme 3.



that would have returned it back to **9**. As shown in Fig. 7, electronic excitation of this compound would result in charge migration from the benzophenone benzene ring substituted with the methoxy group to the carbonyl and the other adjacent benzophenone benzene ring. Although this would make the benzophenone carbonyl more basic (hence photoprotonated by acid), it does not predict that the Ph(HO)CH moiety would be activated with respect to deprotonation, as would be required for the photoredox reaction to proceed and that was predicted in similar HOMO and LUMO calculations for **7** and **8**. Thus, it would appear that simple low level HOMO and LUMO calculations offer a useful parallel study for the intramolecular photoredox chemistry of the benzophenones studied in this work, and we will be applying similar theoretical studies on related chemistry that can arise from acid–base chemistry of electronically excited states of other aromatic compounds.

Experimental section

Instrumentation

^{1}H NMR spectra were recorded on Bruker 300 or 500 MHz instruments. Mass spectra were obtained on a Kratos Concept H instrument. UV–vis spectra were recorded on a Varian Cary 5 instrument. Preparative photolyses were performed using a Rayonet RPR 100 photochemical reactor equipped with 300 nm lamps.

Common laboratory reagents

All solvents used for synthesis (ACS grade) were purchased from Sigma-Aldrich and used as received unless otherwise noted. HPLC grade acetonitrile and distilled water were used in photolyses in mixed H_2O–CH_3CN solutions. D_2O and $CDCl_3$ were purchased from Cambridge Isotope laboratory and D_2SO_4 was obtained from Sigma-Aldrich. Preparative TLC was carried out on 20 cm × 20 cm silica gel GF Uniplates (Analtech).

Materials

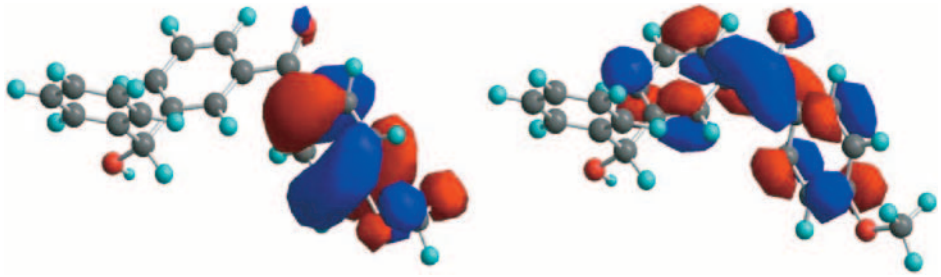
All readily available organic and inorganic reagents required in the synthesis reported below were purchased from Sigma-Aldrich and used as received.

α-*D*-α-Hydroxy-3-benzylbenzophenone (7-αD)

3-Benzoylbenzophenone (0.30 g, 1.1 mmol) was dissolved in 60 mL of 2-propanol and sodium borodeuteride (0.024 g, 0.56 mmol) in 25 mL of 2-propanol was added slowly with stirring at room temperature (RT). The solution was then refluxed for 45 min, cooled and quenched with 100 mL of

© 2007 NRC Canada

Fig. 7. HOMO (left) and LUMO (right) of **15** calculated using Chem 3D(AM1).



H_2O. Upon extraction with 100 mL of CH_2Cl_2 and removal of the organic solvent, a yellow oil was obtained. Pure **7-αD** was obtained via preparative TLC using 1:24 ether–CH_2Cl_2 to give 0.25 g (oil 50%) of material. ^{1}H NMR (500 MHz, $CDCl_3$) δ: 7.84 (t, 2H, 1.8 Hz), 7.74 (dd, 2H, 8.2 Hz and 1.4 Hz), 7.65 (dt, 1H, 7.6 Hz and 1.5 Hz), 7.60 (dt, 1H, 7.7 Hz and 1.6 Hz), 7.56 (tt, 1H, 7.5 and 1.3 Hz), 7.46–7.40 (m, 3H), 7.37–7.35 (m, 2H), 7.34–7.31 (m, 2H), 7.28–7.24 (m, 1H). ^{13}C NMR ($CDCl_3$, 125 MHz) δ: 196.9 (s), 144.4 (s), 143.6 (s), 137.8 (s), 137.6 (s), 132.7 (s), 130.6 (s), 130.3 (s), 129.5 (s), 128.8 (s), 128.6 (s), 128.4 (s), 128.2 (s), 128.0 (s), 126.7 (s). EIMS *m/z*: 289 (M^+, 40), 273 (40), 209 (80), 196 (35), 184 (100), 166 (40), 152 (20). HRMS calcd. for $C_{20}H_{15}DO_2$: 289.1212; found 289.1206.

α-Hydroxy-3-benzylbenzophenone (7)

This compound was prepared the same as the preceding except that sodium borohydride was used. ^{1}H NMR (500 MHz, $CDCl_3$) δ: 7.84 (t, 2H, 1.8 Hz), 7.74 (dd, 2H, 8.2 Hz and 1.4 Hz), 7.65 (dt, 1H, 7.6 Hz and 1.5 Hz), 7.60 (dt, 1H, 7.7 Hz and 1.6 Hz), 7.56 (tt, 1H, 7.5 and 1.3 Hz), 7.46–7.40 (m, 3H), 7.37–7.35 (m, 2H), 7.34–7.31 (m, 2H), 7.28–7.24 (m, 1H). 5.90 (s, 1H), OH signal too broad for detection. ^{13}C NMR ($CDCl_3$, 75 MHz) δ: 196.8 (s), 144.4 (s), 143.7 (s), 137.9 (s), 137.7 (s), 132.7 (s), 130.7 (s), 130.3 (s), 129.5 (s), 128.9 (s), 128.7 (s), 128.5 (s), 128.3 (s), 128.1 (s), 126.8 (s). EIMS *m/z:* 288 (M^+, 15), 272 (10), 209 (30), 195 (10), 183 (50), 105 (100), 77 (60). HRMS calcd. for $C_{20}H_{16}O_2$: 288.1150; found 288.1152.

3-Formylbenzophenone

3-Methylbenzophenone (9.1 mL, 51 mmol) was combined with 2.5 equiv. of *N*-bromosuccinimide (22.8 g, 128 mmol) and benzoyl peroxide (0.11 g, 0.80 mmol) in 100 mL benzene. The reaction mixture was refluxed overnight for 17 h under N_2. After the mixture cooled, it was washed twice with 50 mL of distilled H_2O, dried with anhydr. $MgSO_4$, filtered, and the solvent removed in vacuo. The crude 3-(dibromomethyl)benzophenone was then combined with 5 equiv. of $CaCO_3$ (25.8 g, 258 mmol) in 300 mL 1:1 H_2O–dioxane and refluxed overnight for 17 h. After the reaction mixture had cooled, the solvent was removed under vacuum. Subsequently, 200 mL of CH_2Cl_2 and ~400 mL of 1 mol/L HCl was added with stirring to dissolve the solid. The organic phase was separated and the aqueous phase extracted twice with 100 mL of CH_2Cl_2. The organic fractions were combined and washed twice with 200 mL satd. $NaHCO_3$. The organic fraction was dried with anhydr. $MgSO_4$, filtered, and the solvent removed. Pure white crystals were obtained after chromatography (silica gel, 1:1 ether–hexanes), to yield 2 g (35%) of 3-formylbenzophenone (16). ^{1}H NMR (300MHz, $CDCl_3$) δ: 10.08 (s, 1H), 8.27 (s, 1H), 8.12–8.05 (m, 2H), 7.82–7.78 (m, 2H), 7.69–7.58 (m, 2H), 7.53–7.48 (m, 2H). This material was used without further treatment in the synthesis of **8–10** and **14**.

General procedure for the preparation of benzophenone derivatives 8–10 and 14

For the preparation of the Grignard reagents, 1.2 equiv. of magnesium turnings were reacted with 1.1 equiv. of the corresponding bromobenzene derivative dissolved in dry THF. The Grignard reagents were prepared in the following way. Magnesium turnings and ≅10 mL of dry THF were placed in a dry three-necked flask equipped with a nitrogen inlet, a dropping funnel, and a condenser. The corresponding bromobenzene derivative was dissolved in dry THF and placed in the dropping funnel. Several drops were added to the flask from the dropping funnel. The reaction was initiated by the addition of a crystal of iodine followed by heating. After initiation of the reaction, the remaining solution in the dropping funnel was added slowly to the reaction mixture over 45 min, while the reaction mixture was maintained at ≅40 °C. After the addition was completed, the reaction mixture was heated at reflux for one additional hour. The reaction was cooled to RT and cannulated to the dropping funnel for the next step. In the next reaction, a dry three-necked flask was equipped with a nitrogen inlet, a septum, and a dropping funnel. In this flask was placed a solution of 1 equiv. of 3-formylbenzophenone dissolved in THF. The solution was cooled to –78 °C. The prepared Grignard reagent was added slowly over the period of 2 h to the cooled solution, taking care that the temperature of the reaction mixture remained at –78 °C. After the addition of the reagent, the mixture was stirred for an additional 2 h at –78 °C and allowed to slowly reach RT overnight. The next day water was added to the reaction mixture followed by the addition of 1 mol/L HCl. The reaction mixture was extracted twice with diethyl ether, the organic fraction washed with water and dried over anhydr. $MgSO_4$. The solvent was then evaporated and the residue purified on a column of silica gel using CH_2Cl_2 as the initial eluent followed with CH_2Cl_2–EtOAc mixtures of increasing polarity (up to 20% of EtOAc).

α-*Hydroxy-3-(4′-methylbenzyl)benzophenone (8)*

Starting from 1.2 g (5.7 mmol) of 3-formylbenzophenone and 4-bromotoluene, the reaction furnished 400 mg (23%) of the product, a colorless oil. IR (neat from CH_2Cl_2 solution, salt plates, cm^{-1}) ν: 3434, 1656. ^{1}H NMR ($CDCl_3$,

© 2007 NRC Canada

300 MHz) δ: 7.83 (s, 1H), 7.74 (d, 2H, *J* = 7.4 Hz), 7.64 (d, 1H, *J* = 7.4 Hz), 7.52–7.61 (m, 2H,), 7.43 (dd, 2H, *J* = 7.4 Hz, *J* = 7.7 Hz), 7.39 (t, 1H, *J* = 7.7 Hz), 7.23 (d, 2H, *J* = 8.0 Hz), 7.12 (d, 2H, *J* = 8.0 Hz), 5.82 (s, 1H), 2.65 (br s, 1H), 2.31 (s, 3H). ^{13}C NMR ($CDCl_3$, 75 MHz) δ: 196.9 (s), 144.6 (s), 140.8 (s), 137.7 (s), 137.7 (s), 137.6 (s), 132.6 (d), 130.6 (d), 130.2 (d), 129.5 (d), 129.3 (d), 128.5 (d), 128.4 (d), 128.1 (d), 126.7 (d), 75.8 (d), 21.3 (q). EIMS *m/z*: 303 (M^+, 10), 302 (M^+, 45), 287 (20), 209 (30), 183 (50), 119 (50), 105 (100), 91 (30), 77 (70). HRMS calcd. for $C_{21}H_{18}O_2$: 302.1307; found 302.1306.

α-Hydroxy-3-(4′-methoxybenzyl)benzophenone (9)

Starting from 2.1 g (10 mmol) of 3-formylbenzophenone and 4-bromoanisole, the reaction furnished 460 mg (14%) of the product, a colorless oil. IR (neat from CH_2Cl_2 solution, salt plates, cm^{-1}) ν: 3446, 1653. ^{1}H NMR ($CDCl_3$, 300 MHz) δ: 7.82 (s, 1H), 7.74 (d, 2H, *J* = 7.5 Hz), 7.64 (dd, 1H, *J* = 1.4 Hz, *J* = 7.4 Hz), 7.52–7.61 (m, 2H), 7.44 (dd, 2H, *J* = 7.5 Hz, *J* = 8.1 Hz), 7.41 (t, 1H, *J* = 8.1 Hz), 7.22 (d, 2H, *J* = 8.8 Hz), 6.84 (d, 2H, *J* = 8.8 Hz), 5.83 (s, 1H), 3.76 (s, 3H), 2.50 (br s, 1H). ^{13}C NMR ($CDCl_3$, 75 MHz) δ: 196.9 (s), 159.4 (s), 144.6 (s), 137.8 (s), 137.7 (s), 136.0 (s), 132.7 (d), 130.5 (d), 130.3 (d), 129.4 (d), 128.5 (d), 128.5 (d), 128.1 (d), 128.1 (d), 114.2 (d), 75.6 (d), 55.5 (q). EIMS *m/z*: 319 (M^+, 10), 318 (M^+, 60), 182 (40), 137 (50), 105 (100), 86 (75), 77 (88), 69 (100). HRMS calcd. for $C_{21}H_{18}O_3$: 318.1256; found 318.1255.

α-Hydroxy-3-(3′-methoxybenzyl)benzophenone (10)

Starting from 2.65 g (12.6 mmol) of 3-formylbenzophenone and 3-bromoaniosle, the reaction furnished 3.2 g (80%) of the product, a colorless oil. IR (neat from CH_2Cl_2 solution, salt plates, cm^{-1}) ν: 3435, 1656. ^{1}H NMR ($CDCl_3$, 300 MHz) δ: 7.83 (s, 1H), 7.74 (d, 2H, *J* = 8.1 Hz), 7.64 (d, 1H, *J* = 7.4 Hz), 7.52–7.61 (m, 2H), 7.43 (dd, 2H, *J* = 7.7 Hz, *J* = 8.1 Hz), 7.41 (t, 1H, *J* = 7.7 Hz), 7.23 (dd, 1H, *J* = 8.1 Hz, *J* = 8.3 Hz), 6.90–6.95 (m, 2H), 6.78 (d, 1H, J = 8.3 Hz), 5.83 (s, 1H), 3.76 (s, 3H), 2.50 (br s, 1H). ^{13}C NMR ($CDCl_3$, 75 MHz) δ: 196.8 (s), 160.0 (s), 145.3 (s), 144.3 (s), 137.8 (s), 137.6 (s), 132.7 (d), 130.6 (d), 130.3 (d), 129.9 (d), 129.5 (d), 128.6 (d), 128.5 (d), 128.2 (d), 119.0 (d), 113.4 (d), 112.3 (d), 75.9 (d), 55.4 (q). EIMS *m/z*: 319 (M^+, 25), 318 (M^+, 100), 209 (25), 183 (40), 109 (55), 105 (78), 77 (60). HRMS calcd. for $C_{21}H_{18}O_3$: 318.1256; found 318.1254.

α-Hydroxy-3-(3′-formylbenzyl)benzophenone (14)

Starting from 2.0 g (9.5 mmol) of 3-formylbenzophenone, 255 mg of Mg (10.5 mmol), and 2.71 g of 3-bromobenzaldehyde diethyl acetal (10.5 mmol) (Sigma-Aldrich), the reaction furnished 560 mg (19%) of the product, a colorless oil. IR (neat from CH_2Cl_2 solution, salt plates, cm^{-1}) ν: 3434, 1695, 1653. ^{1}H NMR ($CDCl_3$, 300 MHz) δ: 9.98 (s, 1H), 7.91 (s, 1H), 7.84 (s, 1H), 7.78 (d, 1H, *J* = 7.8 Hz), 7.74 (d, 2H, *J* = 8.1 Hz), 7.63–7.70 (m, 2H), 7.53–7.62 (m, 2H), 7.50 (t, 1H, *J* = 7.6 Hz), 7.44 (dd, 1H, *J* = 7.6 Hz, *J* = 8.1 Hz), 7.40–7.48 (m, 1H), 5.98 (s, 1H), 2.10 (br s, 1H). ^{13}C NMR ($CDCl_3$, 75 MHz) δ: 196.7 (s), 192.4 (d), 144.8 (s), 143.9 (s), 138.2 (s), 137.5 (s), 136.9 (s), 132.8 (d), 132.7 (d), 130.7 (d), 130.3 (d), 129.9 (d), 129.6 (d), 129.4 (d), 128.9 (d), 128.5 (d), 128.2 (d), 127.7 (d), 75.5 (d). EIMS *m/z*: 317 (M^+, 5), 316 (M^+, 20), 270 (25), 239 (30), 212 (25), 183 (70), 165 (15), 135 (20), 122 (20), 105 (100), 77 (85). HRMS calcd. for $C_{21}H_{16}O_3$: 316.1099; found 316.1097.

α-Hydroxy-3-[3′-(hydroxymethyl)benzyl]benzophenone (11)

The aldehyde **14** (450 mg, 1.4 mmol) was dissolved in 30 mL of MeOH and cooled under ice. To this solution was added a solution of $NaBH_4$ (40 mg, 1 mmol) in 10 mL of MeOH. The reaction mixture was stirred at 0 °C for 15 min and quenched by the addition of 50 mL of saturated ammonium chloride. Extractions with CH_2Cl_2 were carried out and the collected extracts were dried over anhydr. $MgSO_4$. After evaporation of the solvent, the residue was chromatographed on silica using CH_2Cl_2 as the initial eluent followed with CH_2Cl_2–EtOAc mixtures of increasing polarity (up to 30% of EtOAc). The product was obtained as a colorless oil, 215 mg, yield 48%. IR (neat, NaCl plates, cm^{-1}) ν: 3390, 1651. ^{1}H NMR ($CDCl_3$, 300 MHz) δ: 7.85 (s, 1H), 7.75 (d, 2H, *J* = 7.4 Hz), 7.66 (d, 1H, *J* = 7.8 Hz), 7.53–7.63 (m, 2H), 7.45 (dd, 1H, *J* = 7.4 Hz, *J* = 7.6 Hz), 7.43 (t, 1H, *J* = 7.6 Hz), 7.39 (s, 1H), 7.25–7.35 (m, 3H), 5.91 (s, 1H), 4.67 (s, 2H), 2.57 (br s, 2H). ^{13}C NMR ($CDCl_3$, 75 MHz) δ: 197.0 (s), 144.4 (s), 144.0 (s), 141.6 (s), 137.8 (s), 137.6 (s), 132.8 (d), 130.7 (d), 130.3 (d), 129.5 (d), 129.0 (d), 128.6 (d), 128.5 (d), 128.2 (d), 126.6 (d), 126.0 (d), 125.2 (d), 75.9 (d), 65.2 (t). EIMS *m/z*: 319 (M^+, 5), 318 (M^+, 20), 209 (38), 183 (35), 135 (28), 105 (100), 77 (50). HRMS calcd. for $C_{21}H_{18}O_3$: 318.1256; found 318.1254.

General photolysis procedure

A 10 mg sample of the benzophenone derivative was dissolved in 400 mL of 1:1 CH_3CN–H_2O and placed in a 600 mL quartz tube, which was continuously cooled with a cold finger to ~15 °C. The pH of the water portion was adjusted by the addition of H_2SO_4. The solution was purged with argon and irradiated at 300 nm in a Rayonet RPR 100 photochemical reactor using 2 or 16 lamps for different times (1–30 min). After irradiation, the solution was neutralized by the addition of $NaHCO_3$ and extracted using CH_2Cl_2. The combined extracts were dried over $MgSO_4$ and the solvent was evaporated. After evaporation of the solvent, photolysis mixtures were analyzed by NMR and (or) chromatographed on a thin layer of silica using CH_2Cl_2–EtOAc as eluent to separate photoproducts.

Photolysis of α-hydroxy-3-(4′-methylbenzyl)benzophenone (8)

A solution of **8** (10 mg in 400 mL, pH 2) was photolyzed (300 nm, 2 lamps) in a quartz tube for up to 20 min. After work-up the residue was chromatographed on prep. TLC to give **18** and a mixture of **8** and **17** (maximum isolated yield of **17** was 20%). The highest content of **17** (92%) was obtained on photolysis in the presence of naphthalene. IR (neat from CH_2Cl_2 solution, salt plates, cm^{-1}) ν: 3434, 1652. ^{1}H NMR ($CDCl_3$, 500 MHz) δ: 7.82 (dd, 1H, *J* = 1.7 Hz, *J* = 1.9 Hz), 7.66 (d, 2H, *J* = 8.1 Hz), 7.64 (ddd, 1H, *J* = 1.2 Hz, *J* = 1.6 Hz, *J* = 7.5 Hz), 7.58 (ddd, 1H, *J* = 1.1 Hz, *J* = 1.6 Hz, *J* = 7.7 Hz), 7.41 (t, 1H, *J*= 7.7 Hz), 7.37 (d, 2H, *J* = 8.5 Hz), 7.33 (dd, 2H, *J* = 7.7 Hz, *J* = 8.5 Hz), 7.25–7.28 (m, 1H), 7.24 (d, 2H, *J* = 8.1 Hz), 5.89 (s, 1H), 2.42 (s, 3H),

© 2007 NRC Canada

2.35 (br s, 1H). ^{13}C NMR ($CDCl_3$, 125 MHz) δ: 196.5 (s), 144.3 (s), 143.7 (s), 143.5 (s), 138.3 (s), 135.0 (s), 130.5 (d), 130.4 (d), 129.4 (d), 129.2 (d), 128.9 (d), 128.6 (d), 128.1 (d), 128.1 (d), 126.8 (d), 76.2 (d), 21.9 (q). EIMS *m/z*: 303 (M^+, 10), 302 (M^+, 30), 279 (10), 223 (15), 212 (40), 197 (50), 165 (20), 149 (30), 133 (50), 119 (60), 105 (100), 91 (30), 77 (70). HRMS calcd. for $C_{21}H_{18}O_2$: 302.1307; found 302.1307.

The oxidized product **18** was also isolated from the preparative TLC as a colorless oil. IR (neat from CH_2Cl_2 solution, salt plates, cm^{-1}) ν: 1659. ^{1}H NMR ($CDCl_3$, 500 MHz) δ: 8.13 (dd, 1H, *J* = 1.8 Hz, *J* = 1.7 Hz), 7.96–8.00 (m, 2H), 7.79 (dd, 2H, *J* = 1.7 Hz, *J* = 8.0 Hz), 7.70 (d, 2H, *J* = 8.1 Hz), 7.59 (dt, 1H, *J* = 1.7 Hz, *J* = 7.7 Hz), 7.58 (ddd, *J* = 1.5 Hz, *J* = 7.0 Hz, *J* = 7.5 Hz), 7.47 (dd, 2H, *J* = 7.7 Hz, *J* = 8.0 Hz), 7.26 (d, 2H, *J* = 8.1 Hz), 2.41 (s, 3H). ^{13}C NMR ($CDCl_3$, 125 MHz) δ: 196.1 (s), 195.8 (s), 144.0 (s), 138.4 (s), 138.0 (s), 137.3 (s), 134.5 (s), 133.6 (d), 133.5 (d), 133.1 (d), 131.3 (d), 130.5 (d), 130.3 (d), 129.4 (d), 128.7 (d), 21.9 (q). EIMS *m/z*: 301 (M^+, 10), 300 (M^+, 60), 279 (10), 223 (15), 209 (10), 167 (20), 149 (35), 119 (100), 105 (50), 91 (30), 77 (30). HRMS calcd. for $C_{21}H_{16}O_2$: 300.1150; found 300.1152.

Photolysis of 8 in the presence of naphthalene

A 400 mL of the CH_3CN–H_2O solution (pH 2) containing 10 mg of **8** and 50 mg of naphthalene was purged with argon and irradiated for 1 h at 300 nm (16 lamps). After irradiation, extractions with CH_2Cl_2 were carried out. The collected extracts were dried over anhydr. $MgSO_4$ and the solvent evaporated. The residue obtained from 3 photolyses was chromatographed on a prep. TLC (silica gel; CH_2Cl_2–EtOAc (2.5%)). The following fractions were isolated: ~10 mg of **18** and ~ 7 mg of the mixture containing 92% of **17** and 8% of the starting material **8**.

Photolysis of α-hydroxy-3-(4′-methoxybenzyl)benzophenone (9)

A solution of **9** (10 mg in 400 mL, pH 2) was photolyzed (300 nm, 16 lamps) in a quartz tube for up to 10 min. After work-up the residue was chromatographed on prep. TLC to give pure **15** as a colorless oil (maximum isolated yield of **15** was 40%–50%). IR (neat, NaCl plates, cm^{-1}) ν: 3429, 1646. ^{1}H NMR ($CDCl_3$, 300 MHz) δ: 7.77 (s, 1H), 7.76 (d, 2H, *J* = 8.8 Hz), 7.60 (d, 1H, *J* = 7.5 Hz), 7.57 (d, 1H, *J* = 8.1 Hz), 7.22–7.44 (m, 6H), 6.92 (d, 2H, *J* = 8.8 Hz), 5.86 (s, 1H), 3.86 (s, 3H), 2.76 (br s, 1H). ^{13}C NMR ($CDCl_3$, 75 MHz) δ: 195.7 (s), 163.4 (s), 144.3 (s), 143.7 (s), 138.5 (s), 132.8 (d), 130.3 (s), 130.2 (d), 129.1 (d), 128.8 (d), 128.5 (d), 128.0 (d), 126.7 (d), 113.7 (d), 76.1 (d), 55.7 (q). EIMS *m/z*: 319 (M^+, 10), 318 (M^+, 60), 279 (15), 256 (15), 239 (15), 213 (50), 165 (20), 149 (70), 135 (100), 121 (30), 105 (100), 97 (30), 77 (87). HRMS calcd. for $C_{21}H_{18}O_3$: 318.1256; found 318.1257.

The oxidized product **16** was also isolated as a colorless oil. IR (neat from CH_2Cl_2 solution, salt plates, cm^{-1}) ν: 1654. ^{1}H NMR ($CDCl_3$, 300 MHz) δ: 8.10 (s, 1H), 7.97 (d, 1H, *J* = 7.2 Hz), 7.95 (d, 1H, *J* = 7.5 Hz), 7.76–7.84 (m, 4H), 7.54–7.62 (m, 2H), 7.47 (dd, 2H, *J* = 7.0 Hz, *J* = 7.8 Hz), 6.94 (d, 2H, *J* = 8.8 Hz), 3.86 (s, 3H). ^{13}C NMR ($CDCl_3$, 75 MHz) δ: 196.2 (s), 196.1 (s), 163.8 (s), 138.7 (s), 137.9 (s), 137.2 (s), 133.4 (d), 133.2 (d), 133.0 (d), 132.8 (d), 131.1 (d), 130.3 (d), 129.8 (s), 128.7 (d), 114.0 (d), 55.8 (q). EIMS *m/z*: 317 (M^+, 5), 316 (M^+, 20), 279 (30), 212 (25), 167 (40), 149 (100), 135 (95), 105 (30), 77 (35). HRMS calcd. for $C_{21}H_{16}O_3$: 316.1099; found 316.1101.

Photolysis of α-hydroxy-3-[4′-(hydroxymethyl)benzyl]benzophenone (11)

A solution of **11** (10 mg in 400 mL, pH 2) was photolyzed at 300 nm for up to 15 min. After work-up, the residue was separated by prep. TLC. The main product was **20** (maximum isolated yield 5%–10%) as a mixture of diastereomers (colorless oil). IR (neat, NaCl plates, cm^{-1}) ν: 3402, 1694. ^{1}H NMR ($CDCl_3$, 500 MHz) δ: 9.96 (s, 1H), 9.95 (s, 1H), 7.86 (2d, 2H, *J* = 1.8 Hz), 7.76 (2dd, 2H, *J* = 1.4 Hz, *J* = 7.7 Hz), 7.62 (2dd, 2H, *J* = 1.8 Hz, *J* = 7.6 Hz), 7.47 (2dd, 2H, *J* = 7.6 Hz, *J* = 7.7 Hz), 7.42–7.45 (m, 2H), 7.12–7.34 (m, 16H), 5.87 (s, 2H), 5.81 (s, 2H). ^{13}C NMR ($CDCl_3$, 125 MHz) δ: 192.5 (d), 145.0 (s), 144.6 (s), 144.6 (s), 143.8 (s), 143.8 (s), 143.7 (s), 143.7 (s), 136.8 (s), 132.7 (d), 129.4 (d), 129.2 (d), 129.1 (d), 128.8 (d), 128.0 (d), 127.9 (d), 127.9 (d), 127.9 (d), 126.8 (d), 126.8 (d), 126.5 (d), 126.4 (d), 126.1 (d), 126.0 (d), 125.0 (d), 76.4 (d), 76.3 (d), 75.9 (d), 75.9 (d). EIMS *m/z*: 319 (M^+, 7), 318 (M^+, 35), 239 (30), 211 (20), 183 (20), 167 (30), 133 (20), 105 (100), 77 (45). HRMS calcd. for $C_{21}H_{18}O_3$: 318.1256; found 318.1254.

Also found were **14** (identified by comparison to an authentic sample made above) and a trace amount of **19** was detected in the photomixture, which could not be purified. ^{1}H NMR of an enriched TLC fraction assignable to **19** is as follows: ($CDCl_3$, 500 MHz) δ: 7.83 (s, 1H), 7.73 (s, 1H), 7.67 (d, 2H, *J* = 7.4 Hz), 7.62 (d, 1H, *J* = 7.7 Hz), 7.58 (d, 1H, *J* = 7.4 Hz), 7.40–7.48 (m, 2H), 7.24–7.40 (m, 5H), 5.90 (s, 1H), 4.73 (s, 2H).

Nanosecond laser flash photolysis (LFP)

All LFP studies were conducted at the University of Victoria LFP facility employing a Nd-YAG laser with a pulse width of 20 ns and excitation wavelength of 266 nm. Flow cells (0.7 cm) were used and solutions were purged with nitrogen or oxygen for 30 min prior to measurements. Optical densities at 266 nm were ~0.1–0.7.

Acknowledgments

This research was supported by the Natural Sciences and Engineering Research Council (NSERC) of Canada and the University of Victoria.

References

1. N.J. Turro. Modern molecular photochemistry. University Science Books, Mill Valley, Calif. 1991.
2. W.M. Horspool and P.-S. Song. CRC Handbook of organic photochemistry and photobiology. CRC Press, Boca Raton, Fla. 1995.
3. G. Ciamician and P. Silber. Ber. **33**, 2911 (1900).
4. G.S. Hammond and W.M. Moore. J. Am. Chem. Soc. **81**, 6334 (1959).
5. W.M. Moore, G.S. Hammond, and R.P. Foss. J. Am. Chem. Soc. **83**, 2789 (1962).

© 2007 NRC Canada

6. M.B. Ledger and G. Porter. J. Chem. Soc., Faraday Trans. 1, **68**, 539 (1972).
7. J.F. Ireland and P.A.H. Wyatt. J. Chem. Soc., Faraday Trans. 1, **69**, 161 (1973).
8. D.M. Rayner and P.A.H. Wyatt. J. Chem. Soc., Faraday Trans. 2, **70**, 945 (1974).
9. M. Ramseier, P. Senn, and J. Wirz. J. Phys. Chem. A, **107**, 3305 (2003).
10. H.E. Zimmerman. J. Am. Chem. Soc. **117**, 8988 (1995).
11. H.E. Zimmerman. J. Phys. Chem. A, **102**, 5616 (1998).
12. L.A. Huck and P. Wan. Org. Lett. **6**, 1797 (2004).
13. D. Mitchell, M. Lukeman, D. Lehnherr, and P. Wan. Org. Lett. **7**, 3387 (2005).
14. K. Okada, M. Yamaji, and H. Shizuka. J. Chem. Soc., Faraday Trans. **94**, 861 (1998).
15. K. Takeda, Y. Kajii, K. Shibuya, and K. Obi. J. Photochem. Photobiol. A, **115**, 109 (1998).
16. P. Miziak, J. Zon, N. Amrhein, and R. Gancarz. Phytochemistry, **68**, 407 (2007).

© 2007 NRC Canada

Thermal and microwave assisted synthesis of *N*-aroylamino acridinediones

T. Josephrajan and V.T. Ramakrishnan

Abstract: A series of *N*-aroylamino acridinediones (**3a**–**3d** and **6a**–**6e**) have been synthesized from tetraketones (**1** and **4**) and benzoic hydrazides (**2a**–**2d** and **5a**–**5e**) under thermal and microwave irradiation conditions with solid supports.

Key words: acridine, hydrazide, microwave irradiation.

Résumé : On a réalisé la synthèse d'une série de *N*-aroylaminoacridinediones (**3a**–**3d** et **6a**–**6e**) à partir des tétracétones (**1** et **4**) et d'hydrazides benzoïques (**2a**–**2d** et **5a**–**5e**) sur des supports solides et en faisant appel à des conditions thermiques ou d'irradiation aux microondes.

Mots-clés : acridine, hydrazide, irradiation aux microondes.

[Traduit par la Rédaction]

Introduction

The acridinedione ring is a important heterocyclic unit present in many biologically active compounds (1*a*, 1*b*). These 1,4-dihydropyridines are structurally similar to the NADH molecule, which acts as a coenzyme in biological systems and plays a crucial role in brain-targeted chemical delivery systems (1*c*, 2). The importance of the acridinedione ring system as a DNA intercalator (3) and as a laser dye has been established in our earlier reports (4). Recently, by using nanosecond laser flash photolysis, Lindqvist et al. studied (5) the radical intermediates involved in the oxidation of the 1,4-dihydropyridine derivative of AZT as related to AIDS dementia. These dyes operate in the blue-green region and they have a lasing properties that is comparable to that of the well-known standard coumarin-102. Acridinedione dyes have been reported as very good photoinitiators for the photo polymerization of acrylates and methacrylates (6) and are used as photosensitizers in onium salt decomposition (7).

Results and discussion

In continuation of our studies on the synthesis of acridinediones (8), we were interested to synthesize *N*-aroylamino acridinediones by using acid hydrazides. The acid hydrazides are a prominent structural motif found in numerous pharmaceutically active compounds (9). They have been found to possess a wide spectrum of medicinal activities such as anti-tubercular, antibacterial, and anti-fungal activities. Sugimoto et al. (10) reported the anti-acetylcholinesterase activity of a series of *N*-aroylamino compounds.

The exploitation of microwave irradiation for enhancing the rate of organic reactions has been gaining more importance in recent years (11). Recently, Suarez et al. (12) reported the microwave-assisted synthesis of acridinediones. However, there is no report in the literature for the synthesis of *N*-aroylamino acridinediones. We report herein the synthesis of various acridinediones from acid hydrazides and tetraketones under microwave irradiation as well as by a conventional method using P_2O_5 in ethanol under refluxing conditions.

The reaction of methylene bis(cyclohexane-1,3-dione) (**1**) and benzoic hydrazide (**2a**) in ethanol, with a catalytic amount of P_2O_5 under microwave irradiation, afforded the 10-(benzoylamino)-3,4,6,7,9,10-hexahydro-1,8(2H,5H) acridinedione (**3a**) in 85% yield. The reaction was completed in 5 min. However, conventional heating of the above reaction mixture required 35 h to give the product **3a** in 80% yield. In the above lines, microwave-assisted synthesis was also extended to other substrates **3b**–**3d** (Scheme 1, Table 1). In all cases, the reaction was completed in 4 to 5 min, affording the product in good yields. We also extended our study for the reaction of methylene bisdimedone **4** with various hydrazides **5a**–**5e**, which afforded the corresponding acridinediones **6a**–**6e** in good yields, as shown in Scheme 2 and Table 2.

The solvent-free "green" approach involves the exposure of neat reactants to microwave irradiation with the use of supported reagents or catalysts that are of mineral origin. Clay minerals, alumina, and supported reagents are commonly employed to synthesize a wide range of compounds. Hence, we have carried out the above synthesis in the presence of montmorrilonite K-10 clay with microwave irradiation. In this condition, the reaction required about 15–17 min to give the respective product with a slight increase in the yield. The results are presented in Tables 1 and 2. Thus, microwave irradiation assisted synthesis of

Received 12 August 2006. Accepted 7 June 2007. Published on the NRC Research Press Web site at canjchem.nrc.ca on 1 August 2007.

T. Josephrajan and V.T. Ramakrishnan.[1] Department of Organic Chemistry, University of Madras, Guindy Campus, Chennai, 600 025, India.

[1]Corresponding author (e-mail: vtrk28@yahoo.com).

 doi:10.1139/V07-075 © 2007 NRC Canada

Scheme 1.

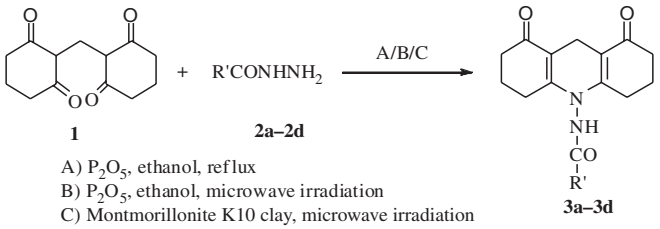


Table 1. Comparative results for the synthesis of acridinediones **3a**–**3d**.

2, 3	R′	Method	Solvent	Reaction time	Yield (%)
a	C_6H_5	A	Ethanol	35 h	80
		B	Ethanol	5 min	85
		C	—	17 min	93
b	4-HO-C_6H_4	A	Ethanol	32 h	81
		B	Ethanol	4 min	86
		C	—	17 min	92
c	4-CH_3-C_6H_4	A	Ethanol	35 h	86
		B	Ethanol	5 min	84
		C	—	15 min	90
d	4-CH_3O-C_6H_4	A	Ethanol	35 h	81
		B	Ethanol	5 min	84
		C	—	15 min	90

acridinedione systems has been found to be highly efficient for the synthesis of multifunctional acridinediones.

The IR spectrum of these compounds showed characteristic peaks around 1650 and 1380 cm^{-1} for the vinylogous amide and amide carbonyl groups. In the ^1H NMR spectrum of **3a**, the C-3 and C-6 methylene protons appeared as a multiplet at δ 1.80–2.10; the C-2, C-4, C-5, C-7, and C-9 methylene protons appeared in the range δ 2.30–3.30 as a multiplet; the aryl protons resonated at δ 7.50–7.70 as a multiplet; the NH proton appeared as a singlet at δ 10.90. The signals in the ^{13}C NMR spectrum at δ 167.0 and 197.7 indicate the presence of an amide (ArCONH) and keto group, respectively; the C-4a and C-9a carbons appeared at δ 155.6 and 111.4. In the X-ray crystal structure of compounds **3a** (13), **3d** (13), and **3b** (14), the central ring adopts boat conformation (14). However, in the tetramethyl-substituted acridine **6d** (15), the central ring is nearly planar. In all of the cases the outer rings adopts sofa conformation. The absorption and fluorescence spectra of the acridinedione dyes **3a**–**3d** and **6c** in different solvents show the absorption maximum around 370 nm. Fluorescence lifetime of the dyes varies with substituents on the nitrogen atom and with the solvents. These dyes are more polar in the excited state than in the ground state (4).

Experimental

Melting points were determined using a Toshniwal melting point apparatus in an open capillary tube and are uncorrected. IR spectra were recorded in Nicolet Impact 400 FT-IR spectrophotometer. ^1H NMR and ^{13}C NMR spectra were recorded on Jeol GSX (400 MHz), Bruker DPX (200 MHz), and Varian EM 390 (90 MHz) spectrometers, using TMS as internal standard. GC-MS data were obtained from a Jeol-DX-303 spectrometer. Microanalyses were performed on a PerkinElmer 240B element analyzer. Microwave reactions were performed using a Kenstar microwave oven (800 W).

The hydrazides **2** were prepared from the esters of the corresponding acids by treatment with hydrazine hydrate. The tetraketones **1** and **4** were prepared from cyclohexane-1,3-dione and dimedone, respectively, on treatment with formaldehyde (12).

General procedure for 10-(benzoylamino)-3,4,6,7,9,10-hexahydro-1,8(2*H*,5*H*)acridinedione (3a)

Method A

To a solution of 2,2′-methylene-bis(cyclohexane-1,3-dione) (**1**) (1.0 g, 4.2 mmol) and benzoic hydrazide (0.58 g, 4.2 mmol) in ethanol (40 mL), a catalytic amount of P_2O_5 was added and the mixture refluxed on a steam bath for 35 h. The reaction mixture was concentrated and poured into ice; the yellow solid was filtered, dried, and crystallized from a mixture of chloroform and ethanol (1:1) to obtain the title compound **3a** (1.25 g, 88%).

Method B

To a solution of 2,2′-methylene-bis(cyclohexane-1,3-dione) (**1**) (0.1 g, 0.42 mmol) and benzoic hydrazide (0.058 g, 0.42 mmol) in ethanol (10 mL), a catalytic amount of P_2O_5 was added and was irradiated in a microwave oven (75–78 °C) for 5 min. The reaction mixture was concentrated and poured into ice; the yellow solid obtained was filtered, dried, and crystallized from a mixture of chloroform and ethanol (1:1) to obtain the title compound **3a** (0.12 g, 85%).

Method C

A homogenized mixture of 2,2′-methylene-bis(cyclohexane-1,3-dione) (**1**) (0.1 g, 0.42 mmol) benzoic hydrazide (0.058 g, 0.42 mmol) and montmorillonite K-10 clay (0.1 g) was irradiated in a microwave oven (60–65 °C) for 17 min. The resulting product was dissolved in a methanol–chloroform mixture and the clay was filtered off. The solvent was distilled off and the product **3a** isolated and crystallized (0.13 g, 93%).

10-(Benzoylamino)-3,4,6,7,9,10-hexahydro-1,8(2*H*,5*H*) acridinedione (3a)

Brown solid; yield 88%; mp 138–140 °C. IR (KBr, cm^{-1}) 3506, 1658, 1625, 1587, 1386. ^1H NMR (400 MHz, $CDCl_3$) δ: 1.80–2.10 (m, 4H, C_3 and C_6-CH_2), 2.30–3.30 (m, 10H, C_2, C_4, C_5, C_7, and C_9-CH_2), 7.50–7.70 (m, 3H, Ar-H), 8.00 (d, 2H, J = 8 Hz, Ar-H), 10.90 (s, 1H, NH). ^{13}C NMR (100 MHz, $CDCl_3$) δ: 18.7, 20.9, 24.6, 36.1, 111.4, 127.7, 129.0, 130.5, 133.1, 155.6, 167.0, 197.7. MS *m*/*z* (%): 366 (M^+, 0.1), 216 (5.7), 215 (12), 198 (0.4), 187 (25.4), 159 (4.6), 131 (13.6), 121 (25), 105 (51.3), 103 (11.4), 77 (100). Anal. calcd. for $C_{20}H_{20}N_2O_3$ (%): C 71.41, H 5.99, N 8.33; found: C 71.44, H 6.04, N 8.38.

© 2007 NRC Canada

Scheme 2.

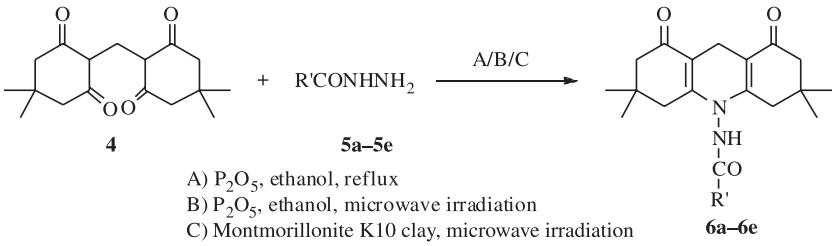


Table 2. Comparative results for the synthesis of acridinediones **6a–6e**.

5, 6	R′	Method	Solvent	Reaction time	Yield (%)
a	2-Cl-C_6H_4	A	Ethanol	35 h	80
		B	Ethanol	5 min	85
		C	—	17 min	93
b	2,4-Cl_2-C_6H_3	A	Ethanol	32 h	81
		B	Ethanol	4 min	86
		C	—	17 min	92
c	2-CH_3-C_6H_4	A	Ethanol	35 h	86
		B	Ethanol	5 min	84
		C	—	15 min	90
d	2-HO-C_6H_4	A	Ethanol	35 h	81
		B	Ethanol	5 min	84
		C	—	15 min	90
e	$C_6H_5CH_2$	A	Ethanol	35 h	76
		B	Ethanol	5 min	80
		C	—	16 min	82

10-(4-Hydroxybenzoylamino)-3,4,6,7,9,10-hexahydro-1,8(2*H*,5*H*)acridinedione (3b)

Pale yellow solid; yield 81%; mp 268–270 °C. IR (KBr, cm^{-1}) 3519, 3159, 1640, 1622, 1579, 1386. ^{1}H NMR (400 MHz, $CDCl_3$-DMSO-d_6) δ: 1.80–1.95 (m, 4H, C_3 and C_6-CH_2), 2.19–2.60 (m, 8H, C_2, C_4, C_5, and C_7- CH_2), 2.85 and 2.98 (2d, 2H, J = 20 Hz, C_9-CH_2), 6.90 (d, 2H, J = 8 Hz, Ar-H), 7.80 (d, 2H, J = 8 Hz, Ar-H), 10.30 (br s, 1H, Ar-OH), 11.00 (s, 1H, NH). MS *m*/*z* (%): 352 (M^+, 15), 306 (2), 216 (6), 215 (8), 198 (4), 187 (97), 159 (16), 137 (34), 121 (51), 93 (18). Anal. calcd. for $C_{20}H_{20}N_2O_4$ (%): C 68.17, H 5.72, N 7.95; found: C 68.22, H 5.77, N 7.96.

10-(4-Methylbenzoylamino)-3,4,6,7,9,10-hexahydro-1,8(2*H*,5*H*)acridinedione (3c)

Greenish yellow solid; yield 86%; mp 148–150 °C. IR (KBr, cm^{-1}) 3450, 1681, 1624, 1577, 1384. ^{1}H NMR (90 MHz, $CDCl_3$-DMSO-d_6) δ: 1.80–2.10 (m, 7H, C_3, C_6-CH_2 and Ar-CH_3), 2.20–2.40 (m, 8H, C_2, C_4, C_5 and C_7-CH_2), 3.00 (br s, 2H, C_9-CH_2), 7.30 (d, 2H, J = 8 Hz, Ar-H), 7.80 (d, 2H, J = 8 Hz, Ar-H), 9.50 (s, 1H, NH). ^{13}C NMR (100.4 MHz, $CDCl_3$-DMSO-d_6) δ: 18.3, 20.7, 21.3, 24.2, 35.8, 111.2, 127.5, 129.1, 154.3, 166.7, 196.5. MS *m*/*z* (%): 350 (M^+, 18.3), 293 (6.1), 216 (100), 215 (97.9), 214 (90.4), 187 (93.5), 135 (51.8), 119 (100), 91 (73.4). Anal. calcd. for $C_{21}H_{22}N_2O_3$ (%): C 71.98, H 6.33, N 7.99; found: C 72.01, H 6.38, N 8.03.

10-(4-Methoxybenzoylamino)-3,4,6,7,9,10-hexahydro-1,8(2*H*,5*H*)acridinedione (3d)

Pale brown solid; yield 81%; mp 228–230 °C. IR (KBr, cm^{-1}) 3471, 1654, 1614, 1585, 1388. ^{1}H NMR (90 MHz, $CDCl_3$) δ: 2.01 (m, 4H, C_3 and C_6-CH_2), 2.33 (m, 8H, C_2, C_4, C_5, and C_7- CH_2), 3.11 (m, 2H, C_9-CH_2), 3.86 (s, 3H, OCH_3), 7.01 (d, 2H, J = 8 Hz, Ar-H), 7.90 (d, 2H, J = 8 Hz, Ar-H). ^{13}C NMR (50 MHz, $CDCl_3$-DMSO-d_6) δ: 18.7, 20.8, 24.53, 36.0, 55.6, 111.2, 114.2, 122.5, 129.7, 155.8, 163.4, 166.6, 197.7. MS *m*/*z* (%): 216 (0.32), 215 (1.9), 187 (9.8), 159 (3.2), 151 (8.1), 135 (29.6), 107 (9.4), 104 (10), 103 (16.8), 77 (76.5). Anal. calcd. for $C_{21}H_{22}N_2O_4$ (%): C 68.84, H 6.05, N 7.64; found: C 68.88, H 6.07, N 7.67.

10-(2-Chlorobenzoylamino)-3,3,6,6-tetramethyl-3,4,6,7,9,10-hexahydro-1,8(2*H*,5*H*)acridinedione (6a)

Yellow solid; yield 76%; mp 228–230 °C. IR (KBr, cm^{-1}) 3410, 1680, 1640, 1550, 1380. ^{1}H NMR (400 MHz, $CDCl_3$-DMSO-d_6) δ: 1.05 and 1.08 (2s, 12H, *gem*-dimethyl), 2.18–2.33 (2d, 4H, J = 16 Hz, C_2 and C_7-CH_2), 2.33–2.48 (2d, 4H, J = 16.6Hz, C_4 and C_5-CH_2), 3.00–3.25 (2d, 2H, J = 20 Hz, C_9-CH_2), 7.31–7.52 (m, 4H, ArH), 10.41 (s, 1H, NH). ^{13}C NMR (100.4 MHz, $CDCl_3$-DMSO-d_6) δ: 18.2, 28.1, 28.9, 31.7, 38.22, 49.5, 110.2, 125.7, 126.9, 129.0, 130.2, 131.0, 137.4, 152.1, 169.1, 196.4. MS *m*/*z* (%): 425 (M^+, 1.5), 411 (2), 398 (2), 397 (3), 396 (19), 395 (20), 273 (32), 272 (37), 271 (40), 256 (1.1), 243 (21), 216 (19), 215 (100), 155 (36), 141 (20), 139 (61), 111 (24). Anal. calcd. for $C_{24}H_{27}N_2O_3Cl$ (%): C 67.51, H 6.37, N 6.56; found: C 67.65, H 6.47, N 6.69.

10-(2,4-Dichlorobenzoylamino)-3,3,6,6-tetramethyl-3,4,6,7,9,10-hexahydro-1,8(2*H*,5*H*)acridinedione (6b)

Yellow solid; yield 83%; mp 212–214 °C. IR (KBr, cm^{-1}) 3440, 1700, 1640, 1590, 1390. ^{1}H NMR (400 MHz, $CDCl_3$-DMSO-d_6) δ: 1.07 and 1.12 (2s, 12H, *gem*-dimethyl), 2.19–2.30 (2d, 4H, J = 16 Hz, C_2 and C_7-CH_2), 2.35–2.49 (2d, 4H, J = 16 Hz, C_4 and C_5-CH_2), 3.11 (bs, 2H, C_9-CH_2), 7.43–7.66 (m, 3H, Ar-H), 10.89 (s, 1H, NH). ^{13}C NMR (100.4 MHz, $CDCl_3$-DMSO-d_6) δ: 17.6, 27.2, 28.1, 31.1, 37.5, 48.9, 109.5, 126.8, 129.5, 129.6, 130.7, 131.7, 136.5, 151.5, 165.2, 195.7. MS *m*/*z* (%): 460 [(M^+, 12), 462 (10), 464 (1)], 459 (2), 272 (92), 271 (50), 243 (2), 216 (20), 215 (100), 189 (21), 173 (47), 145 (16). Anal. calcd. for $C_{24}H_{26}N_2O_3Cl_2$ (%): C 62.50, H 5.63, N 6.07; found: C 62.24, H 5.89, N 6.09.

© 2007 NRC Canada

10-(2-Methylbenzoylamino)-3,3,6,6-tetramethyl-3,4,6,7,9,10-hexahydro-1,8(2*H*,5*H*)acridinedione (6c)

Yellow solid; yield 87%; mp 224–226 °C. IR (KBr, cm^{-1}) 3490, 1695, 1620, 1580, 1388. ^{1}H NMR (200 MHz, $CDCl_3$) δ: 1.02 and 1.07 (2s, 12H, *gem*-dimethyl), 2.11–2.31 (2d, 4H, J = 16 Hz, C_2 and C_7-CH_2), 2.28–2.50 (2d, 4H, J = 19Hz, C_4 and C_5-CH_2), 2.54 (s, 3H, Ar-CH_3), 2.86–3.29 (2d, 2H, J = 19.6 Hz, C_9-CH_2), 7.26–7.58 (m, 4H, Ar-H), 9.01 (s, 1H, NH). MS *m*/*z* (%): 406 (M^+, 24.6), 389 (5.7) 273 (45), 272 (77.6), 271 (100), 270 (10), 257 (9), 256 (30), 243 (57.7), 231 (10), 216 (39.7), 215 (100), 200 (7), 187 (3), 173 (3), 172 (2), 135 (15.2), 119 (43.5), 91 (4.1). Anal. calcd. for $C_{25}H_{30}N_2O_3$ (%): C 73.86, H 7.43, N 6.89; found: C 73.59, H 7.56, N 6.63.

10-(2-Hydroxybenzoylamino)-3,3,6,6-tetramethyl-3,4,6,7,9,10-hexahydro-1,8(2*H*,5*H*)acridinedione (6d)

Pale brown solid; yield 77%; mp 244–246 °C. IR (KBr, cm^{-1}) 3476, 1685, 1625, 1575, 1380. ^{1}H NMR (400 MHz, $CDCl_3$) δ: 0.98 and 1.03 (2s, 12H, *gem*-dimethyl), 1.91–2.21(m, 8H, C_2, C_4, C_5, and C_7-CH_2), 2.77–3.20 (2d, 2H, C_9-CH_2), 6.93–8.12 (m, 4H, Ar-H), 10.84 (s, 1H, NH), 11.51 (s, 1H, OH). ^{13}CNMR (100.4 MHz, $CDCl_3$) δ: 18.5, 27.4, 28.7, 32.1, 38.1, 49.8, 110.4, 128.3, 129.0, 129.3, 132.9, 135.5, 154.1, 169.1, 197.8. MS *m*/*z* (%): 408 (M^+, 6), 407 (15), 393 (20), 314 (9), 313 (24), 272 (69), 271 (51), 243 (9), 216 (20), 215 (100), 137 (12), 121 (54), 93 (13). Anal. calcd. for $C_{24}H_{28}N_2O_4$ (%): C 70.57, H 6.91, N 6.86; found: C 70.76; H 6.91, N 6.63.

10-(Phenacetylamino)-3,3,6,6-tetramethyl-3,4,6,7,9,10-hexahydro-1,8(2*H*,5*H*)acridinedione (6e)

Yellow solid; yield 76%; mp 250–252 °C. IR (KBr, cm^{-1}) 3480, 1695, 1616, 1585, 1380. ^{1}H NMR (200 MHz, $CDCl_3$) δ: 0.85 and 0.97 (2s, 12H, *gem*-dimethyl), 1.91–2.21(m, 8H, C_2, C_4, C_5, and C_7- CH_2), 2.77–3.20 (2d, 2H, J = 19 Hz, C_9-CH_2), 3.56 (s, 2H, Ar-CH_2), 7.27–7.52(m, 5H, Ar-H), 9.91(s, 1H, NH). ^{13}C NMR (100.4 MHz, $CDCl_3$) δ: 18.4, 27.8, 28.7, 31.8, 37.9, 41.6, 49.8, 110.1, 127.7, 129.0, 129.2, 133.8, 153.5, 170.8, 197.3. Anal. calcd. For $C_{25}H_{30}N_2O_3$ (%): C 73.86, H 7.43, N 6.89; found: C 73.75, H 7.29, N 6.82.

Acknowledgements

We thank the Council of Scientific and Industrial Research (CSIR), New Delhi, and the University Grants Commission - Special Assistance Programme (UGC-SAP) for financial support for this department.

References

1. (*a*) T.L. Su, Y.W. Lin, and T.C. Chou. J. Med. Chem. **49**, 3710 (2006); (*b*) I. Sanchez, R. Reches, D.H. Caignard, P. Renard, and M.D. Pujol. Eur. J. Med.Chem. **41**, 340 (2006); (*c*). D.M. Stout and A.I. Meyers. Chem. Rev. **82**, 223 (1982).
2. A. Sausins and G. Duburs. Heterocycles, **27**, 291 (1998).
3. K. Sivaraman, K. Subramanian, S. Ganesan, and V.T. Ramakrishnan. J. Biomol. Struct. Dyn. **13**, 119 (1995).
4. V. Karunakaran, P. Ramamurthy, T. Josephrajan, and V.T. Ramakrishnan. Spectrochim. Acta Part A, **58**, 1443 (2001).
5. L. Lindqvist, B. Czochralska, and W. Kawczynski. J. Photochem. Photobiol. B, **23**, 207 (1994).
6. H.J. Timpe, S. Uldrich, C. Decker, and J.P. Fouassier. Macromolecules, **26**, 4560 (1993).
7. H.J. Timpe, S. Uldrich, and J. P. Fouassier. J. Photochem. Photobiol. A, **73**, 139 (1993).
8. T. Josephrajan, V.T. Ramakrishnan, G. Kathiravan, and J. Muthumary. ARKIVOK, (**xi**), 124 (2005) and refs. cited therein.
9. B.R. Rani, U.T. Bhalerao, and M.F. Rahman. Indian J. Chem. Sect. B, **29**, 995 (1990).
10. H. Sugimoto, Y. Tsuchiya, K. Higurashi, N. Karibe, Y. Iimura, A. Sasaki, Y. Kawakami, and S. Araki. J. Med. Chem. **33**, 1880 (1990).
11. R.S. Varma. Green Chemistry, **2**, 43 (1999).
12. M. Suarez, A. Loupy, E. Salfran, L. Moran, and E. Rolando. Heterocycles, **51**, 21 (1999).
13. J. Jeyakanthan, S. Shanmuga Sundara Raj, D. Velmurugan, H.-K. Fun, T. Josephrajan, and V.T. Ramakrishnan. Acta Crystallogr. Sect. C, **56**, 1109 (2000).
14. J. Jeyakanthan, S. Shanmuga Sundara Raj, D. Velmurugan, H.-K. Fun, T. Josephrajan, and V. T. Ramakrishnan. Cryst. Res. Technol. **37**, 1029 (2002).
15. A. Subbiah Pandi, D. Velmurugan, M.M. Govind, J. Kim, and T. Josephrajan. Cryst. Res. Technol. **37**, 293 (2002).

© 2007 NRC Canada

A comparison of the energetic and topological properties of weak interactions in molecular organic crystals

David J. Wolstenholme and T. Stanley Cameron

Abstract: Several molecular organic crystals [tetraphenylphosphonium squarate, bianthrone, and bis(benzophenone) azine] have been analyzed topologically following a multipole refinement of each compound. This has resulted in the complete characterization of all the weak interactions present in these systems (C-H···O, C-H···C, and C-H$^{\delta+}$···$^{\delta+}$H-C). Correlations have been found to exist between the energetic and topological properties for each type of interaction. The coexistence of the three types of interactions provides a unique opportunity to examine their energetic differences and similarities. This examination can also be used to help understand the complex nature of C-H$^{\delta+}$···$^{\delta+}$H-C type interactions, in particular those characterized as H–H bonds. All this leads to a better understanding of the role H–H bonds play in molecular organic crystals compared with other weak interactions such as hydrogen bonds and van der Waals interactions.

Key words: energetics, multipole refinement, H–H bonds, hydrogen bonds.

Résumé : Faisant appel pour chaque composé à une méthode de raffinement multipolaire, on a fait une analyse topologie de plusieurs cristaux moléculaires organiques, dont le squarate de tétraphénylphosphonium, la bianthrone et la bis(benzophénone)azine. Ces analyses ont permis de faire une caractérisation complète de toutes les interactions faibles qui sont présentes dans ces systèmes, telles C-H···O, C-H···C et C-H$^{\delta+}$···$^{\delta+}$H-C. On a trouvé qu'il existe des corrélations entre les énergies et les propriétés topologiques de chaque type d'interaction. La coexistence de ces trois types d'interaction fournit une opportunité unique d'examiner les similarités et les différences dans les énergies. Cet examen peut aussi être utilisé pour mieux comprendre la nature complexe des interactions du type C-H$^{\delta+}$···$^{\delta+}$H-C, en particulier celles caractérisées par des liaisons H–H. Tout ceci conduit à une meilleure compréhension du rôle des liaisons H–H dans les cristaux moléculaires organiques par comparaison avec d'autres interactions faibles, telles les liaisons hydrogènes traditionnelles et les interactions de van der Waals.

Mots-clés : énergie, raffinement multipolaire, liaisons H–H, liaisons hydrogènes.

[Traduit par la Rédaction]

Introduction

The study of hydrogen bonds and other weak interactions in molecular organic crystals has been a key area of research in organic chemistry. This is a result of the important role these interactions play in solid-state chemical processes (1, 2). Until recently, only classical strong hydrogen bonds (O-H···O, N-H···O, and N-H···N) were studied in any great detail. However, over the past 20 years weaker C-H···O and C-H···N interactions have gained considerable attention (3–6). These types of weak interactions have been shown to play an important role in the formation and stability of molecular organic crystals lacking stronger intermolecular interactions (3). During the early 1990s a new type of weak interaction of the form C-H$^{\delta+}$···$^{\delta-}$H-M, where M represents a transition metal, was discovered (7). These interactions were shown to possess properties similar to those of weak to moderately strong hydrogen bonds and were classified as dihydrogen bonds. Since that time, a number of experimental and theoretical studies have been conducted on the topology and energetics of these weak interactions (8, 9). This in turn has lead to experimental and theoretical studies of interactions containing two hydrogen atoms of similar charge (C-H$^{\delta+}$···$^{\delta+}$H-C and C-H$^{\delta-}$···$^{\delta-}$H-C) (10–15). Early studies performed by Cioslowski and Mixon proposed that these types of interactions were best classified as classical nonbonding steric interactions (16). However, an overwhelming number of experimental (17–26) and theoretical (27–36) studies have provided evidence for a bonding interaction between the two hydrogen atoms in this class of H–H interaction. These H–H interactions were initially believed to be dihydrogen bonds, however, observations made by Matta et al. (10, 14) have shown that the electronic properties of the two hydrogen atoms in these interactions differ significantly from those of dihydrogen bonds (or hydrogen bonds in general). Therefore, this new category of weak interactions was given the name H–H bonds.

Received 10 May 2007. Accepted 10 July 2007. Published on the NRC Research Press Web site at canjchem.nrc.ca on 4 August 2007.

D.J. Wolstenholme[1] and T.S. Cameron. Department of Chemistry, Dalhousie University, Halifax, NS B3H 4J3, Canada.

[1]Corresponding author (e-mail: dwolsten@dal.ca).

 doi:10.1139/V07-090 © 2007 NRC Canada

The experimental examination of the electron density in molecular organic crystals commonly uses the atoms in molecules (AIM) methodology, particularly when intermolecular interactions (hydrogen bonds or van der Waals interactions) are involved (37–39). The AIM theory states that in a bound equilibrium molecular state, the nuclei of the bonded atoms are linked by a line in which the electron density is a maximum with respect to any neighboring lines, which is referred to as a bond path (BP) (40). Along this BP, the minimum in the electron density represents a (3, –1) critical point that can be thought of as the gateway between two bonded atoms. According to the quantum theory of atoms in molecules (QTAM), both the BP and BCP are considered essential for a bond to exist between two atoms (40). Thus, the interpretation of BCP properties provides useful information about the nature of chemical bonding in weak interactions.

Several properties of the electron density at the BCP can be used to characterize and understand these weak interactions. The rho value, $\rho(r_{cp})$, represents the amount of electron density accumulated at the critical point between the two bonded atoms. In the case of an open-shell interaction (covalent bonds) $\rho(r_{cp})$ values are greater than 0.5 eÅ^{-3}, whereas in closed-shell interactions (hydrogen bonds or van der Waals interactions) $\rho(r_{cp})$ values are generally less than 0.5 eÅ^{-3}. The Laplacian, $\nabla^2\rho(r_{cp})$, contains a wealth of information with respect to the charge concentration accumulated in any particular type of bond. If the $\nabla^2\rho(r_{cp})$ value > 0, the charge concentration is locally depleted at the BCP, as occurs in closed-shell interactions. If the $\nabla^2\rho(r_{cp})$ value < 0, then the charge concentration is locally concentrated at the BCP, which is typical of a covalent bond (41). Additional parameters used to characterize weak interactions are the potential energy density, $V(r_{cp})$, and the kinetic energy density, $G(r_{cp})$ (42). Both the potential and kinetic energy densities can be calculated for closed-shell interactions using Abramov's approximations as follows:

$$[1] \qquad G(r_{cp}) = (3/10)(3\pi^2)^{2/3}\ \rho^{5/3}(r_{cp}) + (1/6)\ \nabla^2\rho(r_{cp})$$

$$[2] \qquad V(r_{cp}) = (\hbar^2/4m)\ \nabla^2\rho(r_{cp}) - 2G(r_{cp})$$

These equations show that closed-shell interactions are dominated by a local excess in the kinetic energy and open-shell interactions are dominated by a lowering of the potential energy (14). It should also be noted that the bond energies for closed-shell interactions can be approximated from their potential energy density through the following relationship (37),

$$[3] \qquad \text{Bond energy} = (1/2)\ V(r_{cp})$$

These bond energy estimates have been shown to be in very good agreement with Hartree–Fock calculations for interactions in the medium range from the atomic nuclei, which falls in the region of weak interactions (42).

This study evaluates 50 weak intra- and inter-molecular interactions examined experimentally using X-ray crystallographic charge density studies. These interactions range from C-H···O hydrogen bonds to H–H bonds as found in three molecular crystals: (tetraphenylphosphonium squarate [TPS], bianthrone [BIAN], and bis(benzophenone) azine [AZINE]) (Figure 1). With these 50 interactions a series of correlations have been obtained between the energetic and topological properties of the electron density for each type of interaction. Analysis of these results has led to a better understanding of the electronic and energetic nature of C-H$^{\delta+}\cdots^{\delta+}$H-C interactions and how they relate to other weak interactions.

Experimental

The three organic crystals (TPS, BIAN, and AZINE) were all found to be colorless prisms. They were each mounted on the end of a Lindemann glass capillary, since a tube has a greater resistance to vibration than a fiber of the same cross-section. The low-temperature high-resolution single crystal X-ray diffraction data were collected on a Rigaku RAPID area detector [TPS] and a Saturn 70 CCD diffractometer [BIAN and AZINE] using Mo Kα radiation (6, 15). The crystallographic details of the refinement can be found in Table 1. The details of the collection and treatment of the crystals in order to obtain high resolution, large redundancy, and better completeness in all three of the data sets have been explained in detail elsewhere (6, 15). The CIF files are available in the Supplementary data.[2]

Multipole refinement

Charge density studies require high-resolution X-ray data obtained at low temperature. The electron density used to topologically evaluate the electron distribution in a crystal can be obtained through the multipole expansion method, which incorporates the Hanson–Coppens model (43). Where ρ_{core} and $\rho_{valence}$ are spherically averaged Hartree–Fock core and valence densities, $d_{lm\pm}$ represents the spherical harmonic angular functions, R_l is the radial function, κ and κ′ are the expansion–contraction parameters, and P_v and $P_{lm\pm}$ represent the population parameters.

$$[4] \qquad \rho(\boldsymbol{r}) = P_c\rho_{core}(\boldsymbol{r}) + P_v\kappa\rho_{valence}(\kappa\boldsymbol{r}) + \sum_{1=0}^{I_{max}}\kappa'^3\rho_{valence}(\kappa\boldsymbol{r})\sum_{m=0}^{I_{max}}P_{lm\pm}d_{lm\pm}(\theta,\phi)$$

The multipole refinement of the three molecules was carried out with the XDLSM module, which is incorporated in the XD software package (44). Any residual bonding density not modeled in the conventional spherical refinement was taken into account in the multipole refinement. The scattering factors used throughout the three multipole refinements were those derived by Clementi and Raimondi for all atoms (45). The least-squares refinements involved the minimization of

[2] Supplementary data for this article are available on the journal Web site (canjchem.nrc.ca) or may be purchased from the Depository of Unpublished Data, Document Delivery, CISTI, National Research Council Canada, Ottawa, ON K1A 0R6, Canada. DUD 5196. For more information on obtaining material refer to cisti-icist.nrc-cnrc.gc.ca/irm/unpub_e.shtml. CCDC entries 654318–20 contain the crystallographic data for this manuscript. These data can be obtained, free of charge, via www.ccdc.cam.ac.uk/conts/retrieving.html (Or from the Cambridge Crystallographic Data Centre, 12 Union Road, Cambridge CB2 1EZ, UK; fax +44 1223 336033; or deposit@ccdc.cam.ac.uk).

© 2007 NRC Canada

Fig. 1. ORTEP diagram with labels for the molecules tetraphenylphosphonium squarate, bianthrone, bis(benzophenone) azine at 113 K with 50% ellipsoid probability.

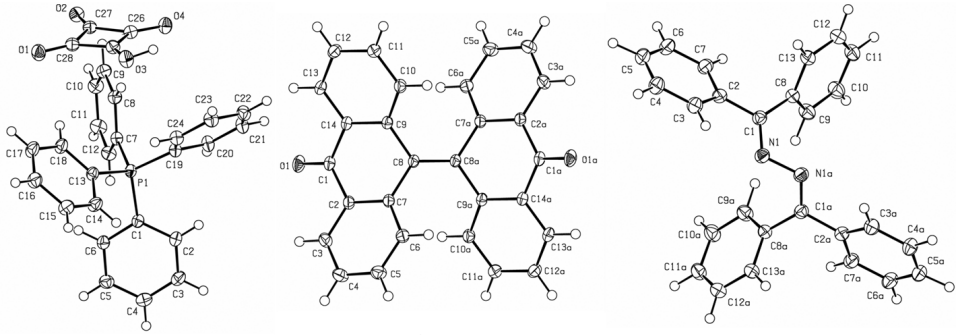


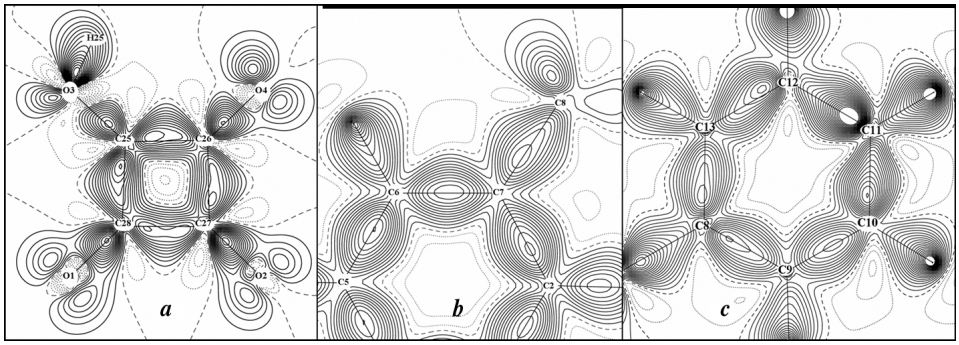
Table 1. Experimental X-ray data.

Compound	Tetraphenylphosphonium squarate	Bianthrone	Bis(benzophenone) azine
Formula	$C_{28}H_{21}O_4P$	$C_{28}H_{16}O_2$	$C_{26}H_{20}N_2$
Crystal sizes	0.2 × 0.2 × 0.2	0.24 × 0.2 × 0.18	0.2 × 0.2 × 0.22
Formula weight	452.45	192.22	180.23
Space group	*P*21/*n* (#14)	*P*21/*n* (#14)	*C*2/*c* (#15)
Temperature (°C)	–180	–160	–160
a (Å)	13.2849(3)	10.155(9)	21.909(7)
b (Å)	12.1411(2)	8.327(7)	5.415(2)
c (Å)	14.6423(3)	11.656(11)	16.063(5)
α (°)	90.0	90.0	90.0
β (°)	109.7180(12)	109.47(3)	94.427(4)
γ (°)	90.0	90.0	90.0
V (Å^3)	2223.23(8)	929.3(14)	1899.9(10)
Z	4	2	4
D_{calcd} (g/cm)	1.352	1.374	1.260
F(000)	944.00	400.00	760.00
μ (mm^{-1})	1.57	0.85	0.74
Radiation	Mo Kα	Mo Kα	Mo Kα
Unique reflections	12107	5943	5628
R(*F*)	1.94%	4.75%	5.72%
GOF	2.1484	2.2058	2.6053
Collection range	$-26 \le h \le 26$, $-23 \le k \le 24$, $-29 \le l \le 29$	$-18 \le h \le 18$, $-15 \le k \le 14$, $-20 \le l \le 16$	$-39 \le h \le 36$, $-6 \le k \le 9$, $-29 \le l \le 29$
Max. resolution (2θ)	90.9	82.9	82.2

the $\sum w(|F_o| - K|F_c|)^2$ function for all reflections with $I > 3\sigma(I)$. Only a general procedure for the multipole refinement of the three compounds will be presented here, since a more detailed description has been included in our previous work (6, 15). Initially, the positional, thermal parameters, and the scale factor were refined to make sure the data was transferred from the conventional spherical refinement to the XD program correctly. This was followed by a high-order refinement (sin θ/λ ≥ 0.6 or 0.7 Å) to obtain accurate positional and thermal parameters for the heavy atoms. Next, a low-order refinement (sin θ/λ ≤ 0.6 or 0.7 Å) was carried out to obtain initial positions and accurate isotropic thermal parameters for the hydrogen atoms. The bond lengths involving the hydrogen atoms were fixed to the distance reported from accurate neutron diffraction data of similar compounds (C_{ar}-H = 1.08 Å) since neutron diffraction data was not available for these compounds (46, 47). The next step in the refinements involved releasing the monopole, dipole, quadrupole, octapole, and, if necessary, the hexadecapole populations with all the heavy atom κ parameters in a stepwise manner. This was followed by a single κ′ term for each of the chemically unique heavy atoms in each structure being refined. Finally, all parameters were combined and refined except the κ′ parameters. This procedure was then cycled through until convergence was achieved. Throughout the multipole refinement, the κ and κ′ parameters for the hydrogen atoms in all three compounds were left fixed at the default XDLSM value of 1.2. The XDPROP module incorporated into the XD package was then used to evaluate the topological properties of the electron density for all three

© 2007 NRC Canada

Fig. 2. (*a*) Static map of the squarate portion of the tetraphenylphosphonium squarate complex. (*b*) Static map of the C6-C7-C8 plane of bianthrone. (*c*) Static map of a phenyl ring in bis(benzophenone) azine. All contours are in increments of 0.05 eÅ^{-3}. Positive contours are represented by solid lines, negative contours by dotted lines, and the zero contour line by a dashed line.



compounds (44). The quality of the refinements can be seen in the static deformation maps of the three compounds, examples of which are shown in Fig. 2. All static, residual, dynamic, and deformation maps were produced using the XDGRAPH option in the XD package (44).

Results and discussion

In previous publications, we have reported a large set of experimental data in which the topological properties of 16 C-H···O interactions (13 TPS and 3 BIAN), 22 C-H···C interactions (11 TPS, 7 BIAN, and 4 AZINE), and 12 C-H$^{\delta+}$···$^{\delta+}$H-C interactions (3 TPS, 4 BIAN, and 5 AZINE) were characterized as either hydrogen bonds, H–H bonds or van der Waals interactions (6, 15). The TPS structure was shown to contain seven weak hydrogen bonds (5 C-H···O and 2 C-H···C), 2 H–H bonds, and 18 van der Waals interactions. Similarly, the BIAN structure was shown to contain 2 C-H···O hydrogen bonds, one H–H bond, and 11 van der Waals interactions. Finally, the AZINE study showed that the crystal contained 2 unique H–H bonds and 10 unique van der Waals interactions. It should be noted that there are two types of interactions classified as C-H···C interactions. The first type (C-H···C$_\pi$) involves a bond path starting off in the direction of a "carbon–carbon" π system then terminating at a carbon acceptor (Fig. 3*a*). The second type (C-H···C) involves a bond path directly from a hydrogen donor to a carbon acceptor (Fig. 3*b*). These two types of C-H···C interaction are grouped together for this study since they possess similar topological and energetic properties. A large variety of interactions are therefore available to study correlations between the energetic and topological properties of the electron density for the three types of weak interactions. The relevant topological values for the H–H interactions can be found in Table 2.

The pioneering work on the topological and energetic correlations of weak interactions has been carried out by Espinosa et al. (37–39). These studies focused on the correlations of weak interactions of the form C-H···O, C-H···N, and C-H···C.

Recently, these types of correlations have been extended to a variety of theoretical dihydrogen bonds (48). However, experimental energetic correlations of H–H interactions, in particular C-H$^{\delta+}$···$^{\delta+}$H-C interactions, have not been investigated in much detail. This subclass of weak interactions has also been found to produce similar correlations between the properties of the electron density at the BCP and the energetic properties. These correlations can be used to understand the electronic and energetic nature of C-H$^{\delta+}$···$^{\delta+}$H-C interactions and H–H bonds, as well as provide insight into the energetic similarities or differences of these interactions from other weak interactions.

According to the second criterion proposed for hydrogen bonding by Koch and Popelier (49, 50), there must be a certain accumulation of electron density at the BCP for an interaction to be considered a hydrogen bond. This has recently been applied to interactions of the form C-H$^{\delta+}$···$^{\delta+}$H-C to characterize them as H–H bonds (15). Thus, a reasonable place to begin looking for correlations between the bond energies and the properties of the electron density is with a correlation involving $\rho(r_{cp})$. Figure 4 shows the correlations between the electron density at the BCP and the bond energies for the C-H$^{\delta+}$···$^{\delta+}$H-C, C-H···C, and C-H···O interactions. It is clear that the bond energies increase in a linear fashion as $\rho(r_{cp})$ increases for all three types of interactions. It can also be observed that the H–H correlation is almost identical to that of the C-H···O correlation. This indicates that the H–H interactions and C-H···O interactions accumulate similar amounts of electron denity when the interactions are of similar energy. This may indicate that they adopt similar roles in the crystal packing of small organic molecules. Interestingly, only the H–H interactions classified as H–H bonds fall in the same region as the C-H···O interactions. This would seem to further indicate that H–H bonds are uniquely different from other forms of C-H$^{\delta+}$···$^{\delta+}$H-C interactions. In addition, it can be seen that the bond energies increase at a slower rate for C-H···C interactions than they do for the other two types of interactions. This seems to be consistent with the fact that C-H···C interactions are usually weaker than interactions of the C-H···O type and are generally classified as van der Waals interactions. These correlations also indicate that at a certain point the C-H$^{\delta+}$···$^{\delta+}$H-C interactions start to become stronger than C-H···C interactions. The point at which the C-H$^{\delta+}$···$^{\delta+}$H-C interactions start to become stronger then the C-H···C interactions is where the H–H interactions begin to be classified as H–H bonds. This progression from C-H$^{\delta+}$···$^{\delta+}$H-C interactions in the van der Waals region (same region as C-H···C interactions) to the

© 2007 NRC Canada

Fig. 3. (*a*) Bond path in bianthrone showing the critical point location along a C-H···C_π interaction. (*b*) Bond path in bis(benzophenone) azine showing the critical point along a C-H···C interaction.

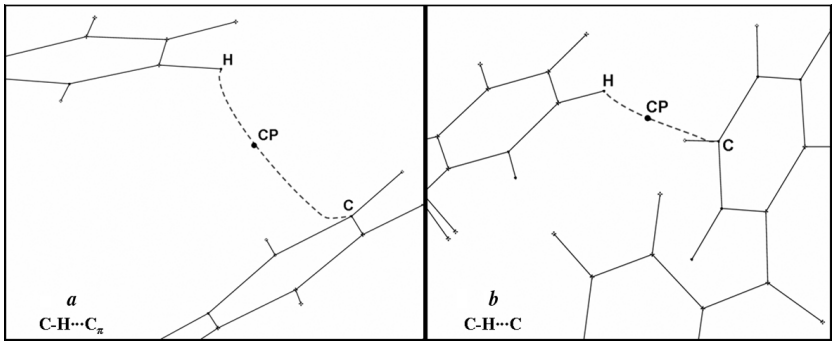


Table 2. Properties of the H–H interactions critical points.

Molecule	Interaction	$\rho(r_{cp})$ (eÅ^{-3})	$\nabla^2\rho(r_{cp})$ (eÅ^{-5})	R_{ij} (Å)	$\lambda_1+\lambda_2$ (eÅ^{-5})	λ_3 (eÅ^{-5})	$\Delta r_H + \Delta r_B$ (Å)	Bond energy (kJ mol^{-1} bohr^{-3})
TPS	H(3)···X2_H(21)[a]	0.047	0.724	2.17	–0.35	1.08	0.229	–5.20
TPS	H(18)···X2^1_H(5)[a]	0.035	0.53	2.35	–0.22	0.75	0.050	–3.58
TPS	H(12)···X3_H(12)	0.013	0.166	3.07	–0.04	0.2	–0.673	–0.98
BIAN	H(3)···X3^1_H(3)	0.018	0.306	2.57	–0.09	0.39	–0.166	–1.78
BIAN	H(3)···X3^1_H(4)	0.012	0.237	2.71	–0.03	0.27	–0.306	–1.27
BIAN	H(5)···X3^2_H(5)	0.006	0.08	3.28	–0.02	0.1	–0.875	–0.43
BIAN	H(6)···X4_H(12)[a]	0.022	0.494	2.28	–0.14	0.63	0.119	–2.78
AZINE	H(3)···X6_H(12)	0.016	0.285	2.67	–0.07	0.35	–0.271	–1.61
AZINE	H(4)···X6_H(12)	0.016	0.322	2.58	–0.09	0.41	–0.179	–1.78
AZINE	H(6)···X4_H(13)	0.016	0.349	2.44	–0.11	0.45	–0.042	–1.90
AZINE	H(9)···X2^2_H(9)[a]	0.078	1.127	1.91	–0.67	1.80	0.487	–9.57
AZINE	H(10)···X5_H(10)[a]	0.034	0.671	2.18	–0.26	0.93	0.219	–4.16

Symmetry				
Interaction	*xyz*	TA	TB	TC
X2	1/2 – *x*, 1/2 + *y*, 1/2 – *z*	0	–1	1
X2^1	1/2 – *x*, 1/2 + *y*, 1/2 – *z*	0	–1	0
X2^2	–*x*, + *y*, 1/2 – *z*	1	0	0
X3	–*x*, –*y*, –*z*	1	0	1
X3^1	–*x*, –*y*, –*z*	1	1	0
X3^2	– *x*, –*y*, –*z*	1	1	1
X4	1/2 – *x*, 1/2 + *y*, 1/2 – *z*	0	0	0
X5	–*x*, +*y*, 1/2 – *z*	1	0	0
X6	+*x*, –*y*, 1/2 + *z*	0	0	–1

Note: kJ mol^{-1} bohr^{-3} = 6.748×10^{30} kJ mol^{-1} m^{-3}
[a]H–H interactions that are classified as H–H bonds

H–H bonding region (similar to weak C-H···O hydrogen bonds) seems to indicate a change in the way the two positively charged hydrogen atoms interact. This provides further evidence of a bonding interaction occurring between the two positive hydrogen atoms.

A recent theoretical study on a wide range of dihydrogen bonds has shown a similar linear fit between $\rho(r_{cp})$ and the bond energies as the C-H$^{\delta+}$···$^{\delta+}$H-C interactions in the three crystals of interest (48). These authors conclude that there is no actual clear separation between hydrogen bonds and dihydrogen bonds when comparing $\rho(r_{cp})$ values, consistent with the observations made for H–H interactions involving two positively charged atoms. This provides further support for the energetic and topological nature of H–H interactions, compared with other weak interactions.

The third Koch and Popelier criterion (49, 50) requires that a certain amount of charge depletion must occur at the BCP for an interaction to be classified as a hydrogen bond. This criterion has also been successfully used to distinguish between H–H bonds and van der Waals interactions of the form C-H$^{\delta+}$···$^{\delta+}$H-C (15). Figure 5 shows the correlations between the Laplacian of the electron density at the BCP, $\nabla^2\rho(r_{cp})$, and the bond energy for the three types of interactions present in the compounds of interest. The bond ener-

© 2007 NRC Canada

Fig. 4. Linear dependence of the bond energy [kJ mol^{-1} bohr^{-3}] on the electron density at the BCP, ρ_{cp}, [eÅ^{-3}] ($y = ax + b$) for all the weak interactions of TPS, BIAN, and AZINE. The dashed lines represent the fitting of the C-H···C and C-H···O interactions ($R^2 = 0.94$ and 0.97, respectively). The solid line represents the fitting of the C-H$^{\delta+}$···$^{\delta+}$H-C interactions ($R^2 = 0.99$).

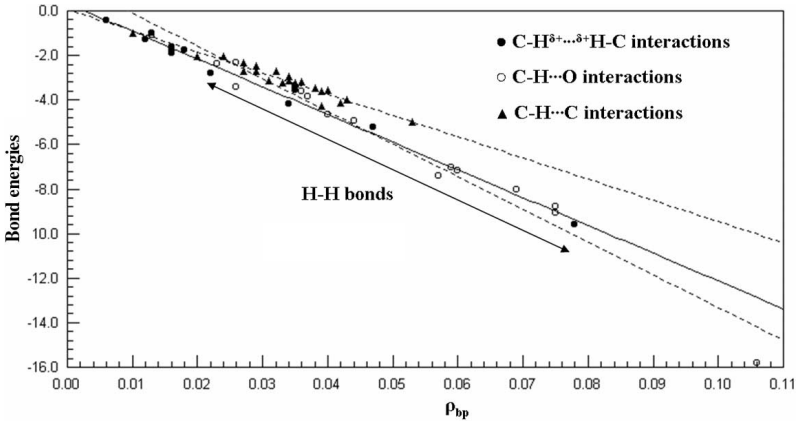
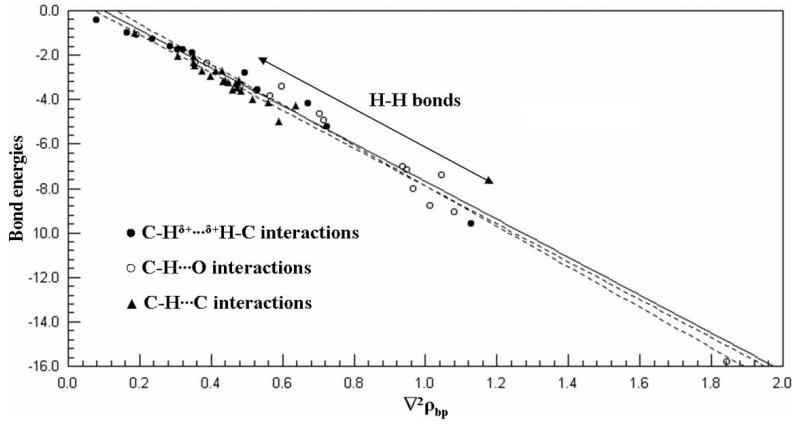


Fig. 5. Linear dependence of the bond energy [kJ mol^{-1} bohr^{-3}] on the $\nabla^2\rho_{cp}$ at the BCP [eÅ^{-5}] ($y = ax + b$) for all the weak interactions of TPS, BIAN, and AZINE. The dashed lines represent the fitting of the C-H···C and C-H···O interactions ($R^2 = 0.92$ and 0.98, respectively). The solid line represents the fitting of the C-H$^{\delta+}$···$^{\delta+}$H-C interactions ($R^2 = 0.99$).



gies associated with all three types of interactions increase in a linear fashion with increasing $\nabla^2\rho(r_{cp})$ values. Unlike the correlation between the bond energy and $\rho(r_{cp})$, the $\nabla^2\rho(r_{cp})$ correlations for each of the three types of interactions show almost identical fits. Previous studies of the correlation between $\nabla^2\rho(r_{cp})$ and R_{ij} (interaction length) have shown that depletion of the charge density for C-H$^{\delta+}$···$^{\delta+}$H-C interactions is less than that for other weak interactions of similar R_{ij} values (15). Since no difference between the $\nabla^2\rho(r_{cp})$ and bond energy correlations is observed for each type of interaction, this seems to indicate that the strength of an interaction is an important factor in the amount of charge density accumulated or depleted in a bond. This seems reasonable since the overlap in R_{ij} values falls in the weaker portion for H–H interactions and in the stronger portion of the C-H···C and C-H···O interactions. It should also be noted that theoretical results on dihydrogen bonds show no significant difference from hydrogen bonds (48).

Correlations between interaction lengths, R_{ij}, and the other properties of the electron density at the BCP are not part of Koch and Popelier's criteria for hydrogen bonding (49, 50). However, they are still commonly used to distinguish between hydrogen bonds, H–H bonds, and van der Waals interactions (4, 5, 15). It has previously been shown that correlations exist between the internuclear distance (the direct distance between two atoms) and the bond energies for C-H$^{\delta+}$···$^{\delta+}$H-C interactions (9). However, the experimental correlations between R_{ij} and the bond energies have yet to be investigated in any great detail for interactions of this form.

Figure 6 shows the exponential correlations ($y = a\exp(bx)$) between the bond energies and the R_{ij} values for all three types of interactions. It can be seen that the bond energies for each type of interaction increase as the R_{ij} values decrease. The C-H···O and C-H···C interactions appear to follow almost the same exponential curve, with the only difference being in the R^2 values. In the case of the C-H···O interactions the R^2 value is 88.6% and for the C-H···C interactions it is 66.2%, which appears to show a trend in the data but no clear correlation. The C-H···C interactions follow the same curve as the C-H···O interactions for the larger R_{ij} values and possess similar R^2 values. However the lack of interactions below 2.7 Å for the C-H···C interactions gives rise to a poor exponential fit, while the inclusion of points below 2.7 Å for the C-H···O interactions gives rise to a rea-

© 2007 NRC Canada

Fig. 6. Exponential dependence of the bond energy [kJ mol^{-1} bohr^{-3}] on the interaction length, R_{ij}, [Å] ($y = a \exp(bx)$) for all the weak interactions of TPS, BIAN, and AZINE. The dashed lines represent the fitting of C-H···C and C-H···O interactions ($R^2 = 0.66$ and 0.89, respectively). The solid line represents the fitting of the C-H$^{\delta+}$···$^{\delta+}$H-C interactions ($R^2 = 0.97$).

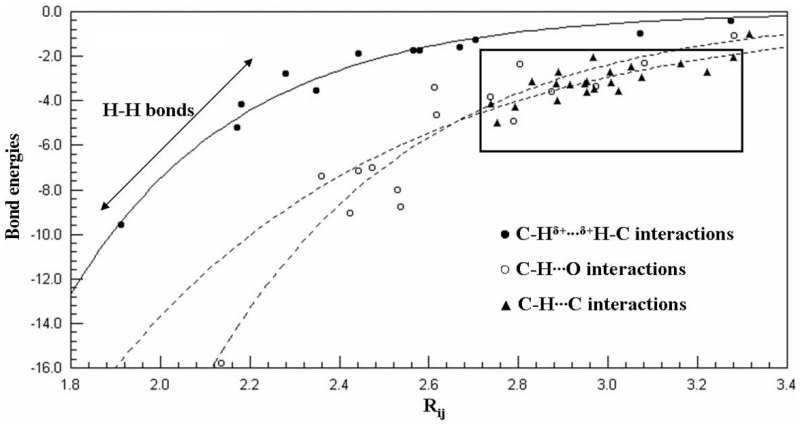
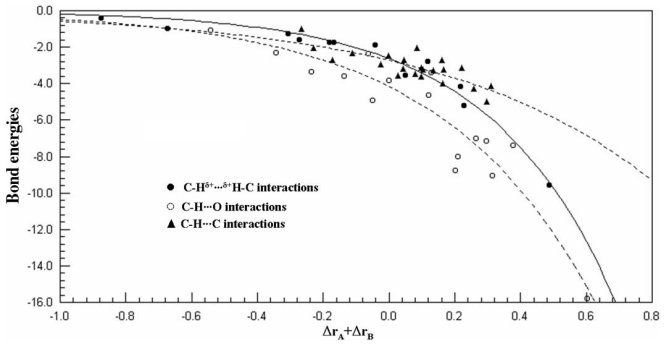


Fig. 7. Exponential dependence of the bond energy [kJ mol^{-1} bohr^{-3}] on the ($\Delta r_A + \Delta r_B$) [Å] ($y = a \exp(bx)$) for all the weak interactions of TPS, BIAN, and AZINE. The dashed lines represent the fitting of the C-H···O interactions ($R^2 = 0.89$) and the C-H···C interactions ($R^2 = 0.66$). The solid line represents the fitting of the C-H$^{\delta+}$···$^{\delta+}$H-C interactions ($R^2 = 0.97$).



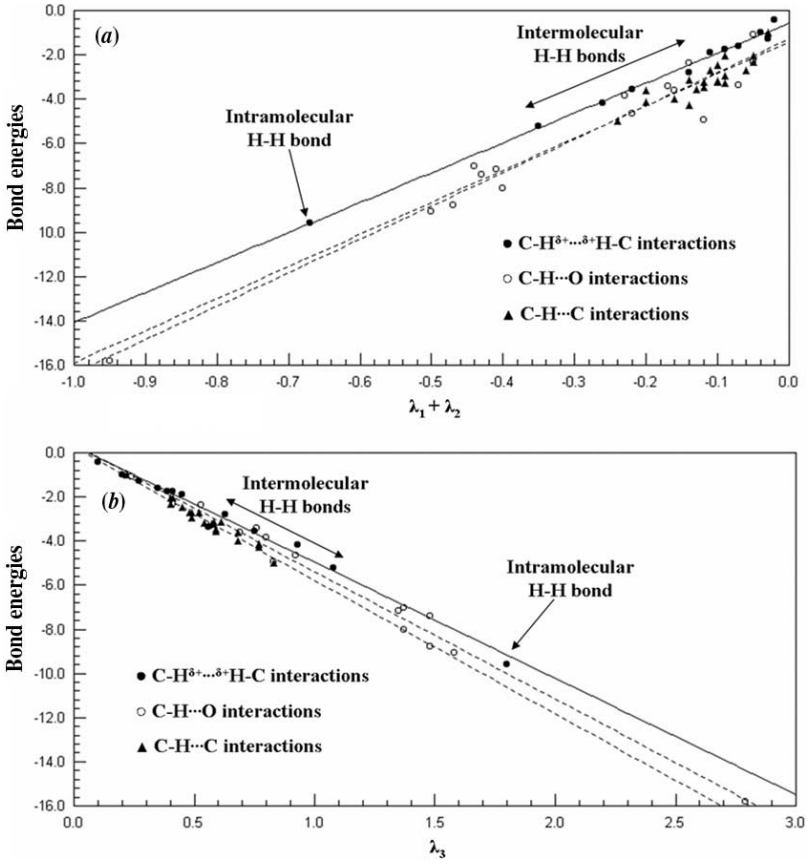
sonable exponential fit (Fig. 6). The lack of C-H···C interactions below 2.7 Å is a direct result of the weak nature of this type of interaction.

A comparison of the correlations between the bond energies and R_{ij} for the C-H$^{\delta+}$···$^{\delta+}$H-C interactions and the other types of weak interactions further demonstrates the fact that the H–H interactions are part of a different population (15). It is clear from Fig. 6 that C-H$^{\delta+}$···$^{\delta+}$H-C interactions require smaller R_{ij} values to obtain similar bond energies to those of C-H···O and C-H···C interactions. This can be attributed to the smaller size of the donor and acceptor atoms involved in C-H$^{\delta+}$···$^{\delta+}$H-C interactions, where the other types of weak interactions involve larger heteroatoms such as oxygen or carbon. Again, the theoretical results for dihydrogen bonds involving intermolecular distances show similar exponential trends as those observed in the R_{ij} correlations for the above interactions (48). Interestingly, the theoretical results extend to shorter intermolecular distances for the H–H interactions but still maintain the expected exponential fit.

The fourth Koch and Popelier criterion for hydrogen bonding (the mutual penetration of the two atoms concerned) is crucial for the characterization of weak hydrogen bonds (49, 50). This criterion has also been shown to be essential for the characterization of H–H bonds (15). Thus, it is important to establish correlations between the mutual penetration values ($\Delta r_H + \Delta r_A$) and the bond energies when looking at the nature of the three interactions of interest. This type of correlation is also important in comparing the energetic differences between H–H bonds and hydrogen bonds. In this work, the nonbonding radius for carbon is taken as 1.85 Å, oxygen as 1.54 Å, and hydrogen as 1.2 Å (51, 52). Figure 7 shows the exponential dependence of the bond energies on the $\Delta r_H + \Delta r_B$ values for all three types of interactions. These correlations show that the bond energies for each type of interaction increase as the $\Delta r_H + \Delta r_B$ values increase. Again, all three types of interactions appear to fit different exponential curves. A direct comparison between the C-H$^{\delta+}$···$^{\delta+}$H-C correlation and the C-H···C correlation cannot be made because of the poor fit made by the C-H···C type interactions. However, it appears that the bond energies increase at a faster rate for the C-H$^{\delta+}$···$^{\delta+}$H-C interactions than for the C-H···C interactions. This seems to indicate that at a certain point the C-H$^{\delta+}$···$^{\delta+}$H-C interactions will require less penetration to achieve bond energies similar to those of C-H···C interactions. One of the possible reasons for the C-H···C interactions possessing a poor exponential goodness of fit (R^2 value) could be the lack of points in the higher mutual penetration area of the plot, a direct reflection of their weak nature. The opposite trend is observed between the C-H$^{\delta+}$···$^{\delta+}$H-C correlation and the C-H···O correlation, where the C-H···O bond energies increase at a faster rate than those of the C-H$^{\delta+}$···$^{\delta+}$H-C interactions. This justifies the idea that

© 2007 NRC Canada

Fig. 8. (*a*) Linear ($y = ax + b$) relationship between the bond energy [kJ mol^{-1} bohr^{-3}] on the sum of the negative curvatures, $\lambda_1 + \lambda_2$ [eÅ^{-5}] for all the weak interactions of TPS, BIAN, and AZINE. The dashed line represents the fitting of the C-H···C and C-H···O interactions ($R^2 = 0.74$ and 0.95, respectively). The solid line represents the fitting of the C-H$^{\delta+}$···$^{\delta+}$H-C interactions ($R^2 = 0.99$). (*b*) Linear ($y = ax + b$) relationship between the bond energy [kJ/mol bohr^3] on the positive curvature, λ_3 [eÅ^{-5}] for all the weak interactions of TPS, BIAN, and AZINE. The dashed lines represent the fitting of the C-H···C and C-H···O interactions ($R^2 = 0.96$ and 0.99, respectively). The solid line represents the fitting of the C-H$^{\delta+}$···$^{\delta+}$H-C interactions ($R^2 = 0.99$).



H–H bonds fit somewhere between C-H···O and C-H···C hydrogen bonds in the hierarchy of weak interactions.

Linear correlations can be observed between the bond energies and the sum of the negative curvatures ($\lambda_1 + \lambda_2$) and the positive curvature (λ_3) for the three types of weak interactions. Figures 8*a* and 8*b* show that intermolecular H–H bonds tend to possess bond energies similar to C-H···C interactions and intramolecular H–H bonds tend to fall in the middle region of the C-H···O hydrogen bonds. This shows that the geometry of a crystalline compound plays a significant role in the formation and strengths of H–H bonds. These two linear relationships show that H–H bonds require larger λ_1, λ_2, and λ_3 values than C-H···O and C-H···C hydrogen bonds of equivalent bond energies. This is not the case for H–H interactions classified as van der Waals interactions, which have similar curvatures to those of other van der Waals interactions.

It has previously been shown that $V(r_{cp})$ and $G(r_{cp})$ are related to the deconvoluted contributions of the concentration or depletion of electrons at the BCP for hydrogen bonds, since they represent the pressures exerted on the atomic basins on the electrons around the BCP and vice versa (37, 38). It has also been found that the energy densities are intrinsically related to the curvatures of the electron density at the BCP in a linear fashion. This has also been observed for the three types of weak interactions of interest in this study (see Supplementary data).[2] Thus, $\lambda_1 + \lambda_2$ and λ_3 can be used to measure directly the amount of deconvoluted concentration and depletion of electrons at the BCP for weak interactions either along or perpendicular to the bond path. The values of both the positive and negative curvatures of the electron density for the H–H bonds are significantly larger then those of the corresponding C-H···C and C- H···O interactions of similar energy. In this way, H–H bonds lead to a thinner topological overlap to obtain similar energies. This is a result of an increase in the repulsive $G(r_{cp})$ magnitude along the bond path, which increases λ_3 and depletes the electron density to the atomic basin. A larger repulsive $G(r_{cp})$ magnitude would be expected for H–H bonds, since they involve two positively charged atoms, which will result in greater repulsion between the two atoms. The larger $\lambda_1 + \lambda_2$ values [or $V(r_{cp})$] for H–H bonds indicates a greater concentration contribution perpendicular to the bond path than that of C-H···C and C-H···O interactions of similar energy.

Conclusion

The use of high-resolution X-ray data for the topological

© 2007 NRC Canada

study of three organic molecules has led to investigations of a series of correlations between the bond energies and several properties of the electron density at the BCP for C-H$^{\delta+}$...$^{\delta+}$H-C, C-H···C, and C-H···O interactions. It has been shown that the bond energies for H–H bonds fall within the range of weak to moderate hydrogen bonds depending on the geometry present in the crystalline state. This study has also shown that a comparison of $\rho(r_{cp})$ values between the three types of interactions leads to a progression of H–H interactions that are van der Waals in nature to H–H bonds. The curvatures at the BCP for H–H bonds have also been shown to have thinner topological overlap than other weak interactions of similar energy. These correlations have helped to show that the bond energies associated with H–H bonds have a wide range and are comparable to those of weak hydrogen bonds. Finally, this study has led to a better understanding of how the energetic properties of C-H$^{\delta+}$...$^{\delta+}$H-C interactions play a significant role in the formation and stability of molecular organic crystals.

Acknowledgements

We are indebted to Rigaku/MSC, The Woodlands, Texas, for provision of the low-temperature data collection facilities during a sabbatical leave fellowship to TSC. We thank the Natural Sciences and Engineering Research Council (NSERC) of Canada for financial support. We also thank Dr. K.N. Robertson for helpful advice and discussion of the topic, Dr. M.A.S. Aquino for providing the TPS crystals, and Dr. J. Ferrara for help with the data collection.

References

1. S.J. Grabowski. J. Phys. Org. Chem. **17**, 18 (2004).
2. G.R. Desiraju. Crystal engineering — The Design of organic solids. Elsevier, Amsterdam, The Nethrelands. 1989.
3. (*a*) G.R. Desiraju. Acc. Chem. Res. **24**, 290 (1991); (*b*) C.B. Aakeroy and K.R. Sneddon. Chem. Soc. Rev. **22**, 397 (1993); (*c*) G.R. Desiraju, S. Kashino, M.M. Coombs, and J. Glusker. Acta Crystallogr. Sect. B, **49**, 880 (1993).
4. P.R. Mallinson, G.T. Smith, C.C. Wilson, E. Grech, and K. Wozniak. J. Am. Chem. Soc. **125**, 4259 (2003).
5. P. Munshi and T.N.G. Row. J. Phys. Chem. A, **109**, 659 (2005).
6. D. Wolstenholme, M.A. Aquino, T.S. Cameron, J.D. Ferrara, and K.N. Robertson. Can. J. Chem. **84**, 804 (2006).
7. T.B. Richardson, S. de Gala, R.H. Crabtree, P.E.M. Siegbahn. J. Am. Chem. Soc. **117**, 12875 (1995).
8. P. Lipkowski, S.J. Grabowski, T.L. Robinson, and J. Leszczynski. J. Phys. Chem. A, **108**, 10865 (2004).
9. K.N. Robertson, O. Knop, T.S. Cameron. Can. J. Chem. **81**, 727 (2003).
10. C.F. Matta, J. Hernandez-Trujillo, T.H. Tang, R.F.W. Bader. Chem. Eur. J. **9**, 1940 (2003).
11. L. Damodharan and V. Pattabhi. Tetrahedron Lett. **45**, 9427 (2004).
12. M. Montejo, A. Navarro, G.J. Kearley, J. Vázquez, and J.J. López-González. J. Am. Chem. Soc. **126**, 15087 (2004).
13. A. Bacchi, E. Bosetti, M. Carcelli, P. Pelagatti, and D. Rogolini. Eur. J. Inorg. Chem. 1985 (2004)
14. C.F. Matta. *In* Hydrogen bonding — New insight (Challenges and advances in computational chemistry and physics series) *Edited by* S. Grabowski. Springer, NY. 2006.
15. D.J. Wolstenholme and T.S. Cameron. J. Phys. Chem. A, **110**, 8970 (2006).
16. J. Cioslowski and S.T. Mixon. Can. J. Chem. **70**, 443 (1992).
17. S.G. Bodige, D. Sun, A.P. Marchand, N.N. Namboothiri, R. Shukla, and W.H. Watson. J. Chem. Crystallogr. **29**, 523 (1999).
18. O. Ermer and S.A. Mason. J. Chem. Soc., Chem. Commun. 53 (1983).
19. M. Domagala, S. Grabowski, K. Urbaniak, and G. Mloston. J. Phys. Chem. A, **107**, 2730 (2003).
20. C.-C. Wang, T.-H. Tang, L.-C. Wu, and Y. Wang. Acta Crystallogr. Sect. A, **60**, 488 (2004).
21. A. Bacchi, E. Bosetti, M. Carcelli, P. Pelagatti, and D. Rogolini. Eur. J. Inorg. Chem. 1985 (2004).
22. C.G. Pozzi, A.C. Fantoni, A.E. Goeta, C.C. Wilson, J.C. Autino, and G. Punte. J. Mol. Struct. **753**, 173 (2005).
23. G.C. Nemes, L. Silaghi-Dumitrescu, I. Silaghi-Dumitrescu, J. Escudié, H. Ranaivonjatovo, K.C. Molloy, M.F. Mahon, and J. Zukerman-Schpector. Organometallics, **24**, 1134 (2005).
24. L.J. Farrugia, C.S. Frampton, J.A.K. Howard, P.R. Mallinson, R.D. Peacock, G.T. Smith, and B. Stewart. Acta Crystallogr. Sect. B, **62**, 236 (2006).
25. E.A. Zhurova, V.G. Tsirelson, V.V. Zhurov, A.I. Stash, and A.A. Pinkerton. Acta Crystallogr. Sect. B, **62**, 513 (2006).
26. E.A. Zhurova, C.F. Matta, N. Wu, V.V. Zhurov, and A.A. Pinkerton. J. Am. Chem. Soc. **128**, 8849 (2006).
27. F. Cortés-Guzmán, J. Hernández-Trujillo, and G. Cuevas. J. Phys. Chem. A, **107**, 9253 (2003).
28. M. Montejo, A. Navarro, G.J. Kearley, J. Vázquez, and J.J. López-González. J. Am. Chem. Soc. **126**, 15087 (2004).
29. I.V. Glukhov, M.Y. Antipin, and K.A. Lyssenko. Eur. J. Inorg. Chem. 1379 (2004).
30. I.V. Glukhov, K.A. Lyssenk, A.A. Korlyukov, and M.Y. Antipin. Russ. Chem. Bull. **54**, 547 (2005).
31. A. Vila and R.A. Mosquera. J. Phys. Chem. A, **109**, 6985 (2005).
32. T. Peña Ruiz, A. Navarro, G.J. Kearley, and M. Fernández Gómez. Chem. Phys. **317**, 159 (2005).
33. C.J. O'Brien, E.A.B. Kantchev, G.A. Chass, N. Hadei, A.C. Hopkinson, M.G. Organ, D.H. Setiadi, T.-H. Tang, and D.-C. Fang. Tetrahedron, **61**, 9723 (2005).
34. P.C. Singh and G.N. Patwari. Chem. Phys. Lett. **419**, 265 (2005).
35. P.C. Singhand Patwari G.N. Chem. Phys. Lett. **419**, 5 (2005).
36. H.S. Rzepa. Org. Lett. **7**, 4637 (2005).
37. E. Espinosa, E. Molins, and C. Lecomte. Chem. Phys. Lett. **285**, 170 (1998).
38. E. Espinosa, C. Lecomte, and E. Molins. Chem. Phys. Lett. **300**, 745 (1999).
39. E. Espinosa, M. Souhassou, H. Lachekar, and C. Lecomte. Acta Crystallogr. Sect. B, **55**, 563 (1999)
40. R.F.W. Bader. Atoms in molecules: a quantum theory. Oxford University Press, Oxford, UK. 1990.
41. P. Popelier. Atoms in molecules. An introduction. Prentice Hall, UK. 2000.
42. Y.A. Abramov. Acta Crystallogr. Sect. A, **53**, 264 (1997).
43. P. Coppens. X-Ray charge densities and chemical bonding. Oxford University Press Inc. Oxford, UK. 1997.
44. T.S. Koritsanszky, S. Howard, P. Macchi, C. Gatti, L.J. Farrugia, P.R. Mallinson, A.Volkov, Z. Su, T. Richter, and N.K. Hansen. XD. Version 4.10 [computer program]. Free University of Berlin, Germany; University of Wales, Cardiff, UK; Universita di Milano, UK; CNR-ISTM, Milano, UK; University of Glasgow, UK; State University of New York, Buffalo, USA; University of Nancy, France. 2003

© 2007 NRC Canada

45. E. Clementi and D.L. Raimondi. J. Chem. Phys. **38**, 2686 (1963).
46. F.H. Allen. Acta Crystallogr. Sect B, **42**, 512 (1986).
47. J. Semmingsen. J. Chem. Phys. **66**, 4405 (1977).
48. D. Hugas, S. Simon, M. Duran. J. Phys. Chem. A, **111**, 4505 (2007).
49. P. Popelier. Atoms in molecules. An introduction. Prentice Hall, UK. 2000.
50. U. Koch and P. Popelier. J. Phys. Chem. **99**, 9747 (1995).
51. A. Bondi. J. Phys. Chem. **68**, 441 (1964).
52. S.C. Nyburg and C.H. Faerman. Acta Crystallogr. Sect. B, **41**, 274 (1985).

© 2007 NRC Canada

X-Ray structures and binding properties of molecular clips based on diethoxycarbonyl glycoluril

Bao H. Zhou, Li P. Cao, Guo D. Yin, M. Gao, and An X. Wu

Abstract: The crystal structures of two molecular clips derived from diethoxycarbonyl glycoluril were reported. Their unique binding behavior towards hydroquinone, which is different from Nolte's clips (high affinity for resorcinol), has been characterized through ^{1}H NMR and IR. Job-plot analyses provide good evidence of a 1:1 stoichiometry for the complexes.

Key words: crystal structure, molecular clips, binding properties

Résumé : On a déterminé les structures cristallines de deux clips moléculaires dérivés du diéthyoxycarbonylglycouril. Faisant appel à la spectroscopie IR et à la RMN du ^{1}H, on a caractérisé leur comportement de liaison unique vis-à-vis de l'hydroquinone qui est différent de celui des clips de Nolte qui ont une grande affinité pour le résorcinol. De plus, une analyse à l'aide de courbes de Job permet d'obtenir de bonnes indications à l'effet que la stoechiométrie de ces complexes est 1:1.

Mots-clés : structure cristalline, clips moléculaires, propriétés de fixation.

[Traduit par la Rédaction]

Introduction

The design and synthesis of host molecules for the binding of neutral guests continues to be an area of great interest in supramolecular chemistry (1–3). Research in Nolte's laboratory has for some time been focused on the development of receptors derived from the concave molecule diphenylglycoluril (4–8), which show high affinity for resorcinol by means of hydrogen bonding between the hydroxyl groups of the guest and the urea carbonyl groups of the host and by π–π stacking interactions between the guest and the host side walls. In addition, similar clips synthesized by Chen and coworkers (9) also showed high affinity for resorcinol but no conspicuous complexation with hydroquinone.

Here, we report the crystal structures of two molecular clips (Figs. 1, 2) derived from diethoxycarbonyl glycoluril with larger cavities compared with Nolte's 3U clip. In addition, their unique binding behavior towards hydroquinone has been investigated.

Results and discussion

According to the general procedure in our laboratory, we synthesized two clips **4U-CC** and **4U-(±)CT** (for the complexation studies, the racemate was used) (10–12) and obtained their crystal structures. Both molecular clips can self-associate into the dimer (Fig. 3) in the crystal but as monomer in the solution of $CDCl_3$, which has been verified by the crystallographic study and ^{1}H NMR analysis (10). In the self-associated dimer, the cavity of one monomer is filled by one of the two aromatic side walls of its dimeric partner and vice versa.

In X-ray single-crystal structure, either from the centroid distance of the side walls or from the height of the cavity, both revealed that the two molecular clips have larger cavities than those of Nolte's 3U clips (4–8) (Fig. 2, Table 1). In addition, the distances of the oxygen atoms O10···O11 or O4···O5, as hydrogen-binding sites on the two clips, are longer than that of Nolte's 3U clip. We assumed that larger clips such as **4U-CC** and **4U-(±)CT** might be as optimal synthetic receptors for different guests from Nolte's 3U clip.

With the aid of ^{1}H NMR, the binding properties of the two molecular clips were studied, and it was found that addition of hydroquinone to the solution of **4U-CC** or **4U-(±)CT** caused the NMR signals of the aromatic protons of the guest and the signals of the cavity-wall protons of the host to shift upfield (Fig. 4, Table 2), whereas the proton signals of the OH groups moved downfield (the Figures of

Received 04 February 2007. Accepted 05 July 2007. Published on the NRC Research Press Web site at canjchem.nrc.ca on 15 August 2007.

B.H. Zhou, L.P. Cao, G.D. Yin, M. Gao, and A.X. Wu.[1] Key Lab of Pesticide & Chemical Biology, Ministry of Education, Department of Chemistry, Central China Normal University, Wuhan 430079, People's Republic of China.

[1]Corresponding author (email: chwuax@mail.ccnu.edu.cn).

 doi:10.1139/V07-084 © 2007 NRC Canada

Fig. 1. Structures of molecular clips and guest (R = COOEt, R_1 = Ph).

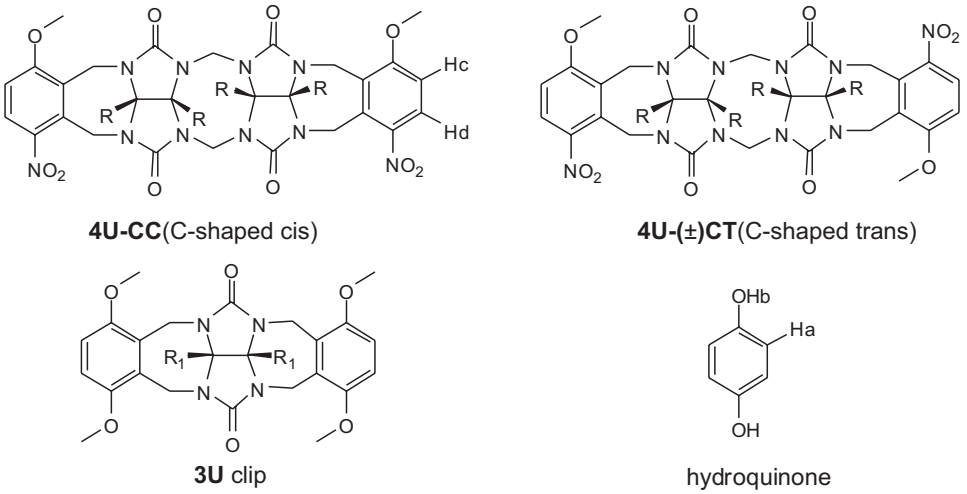
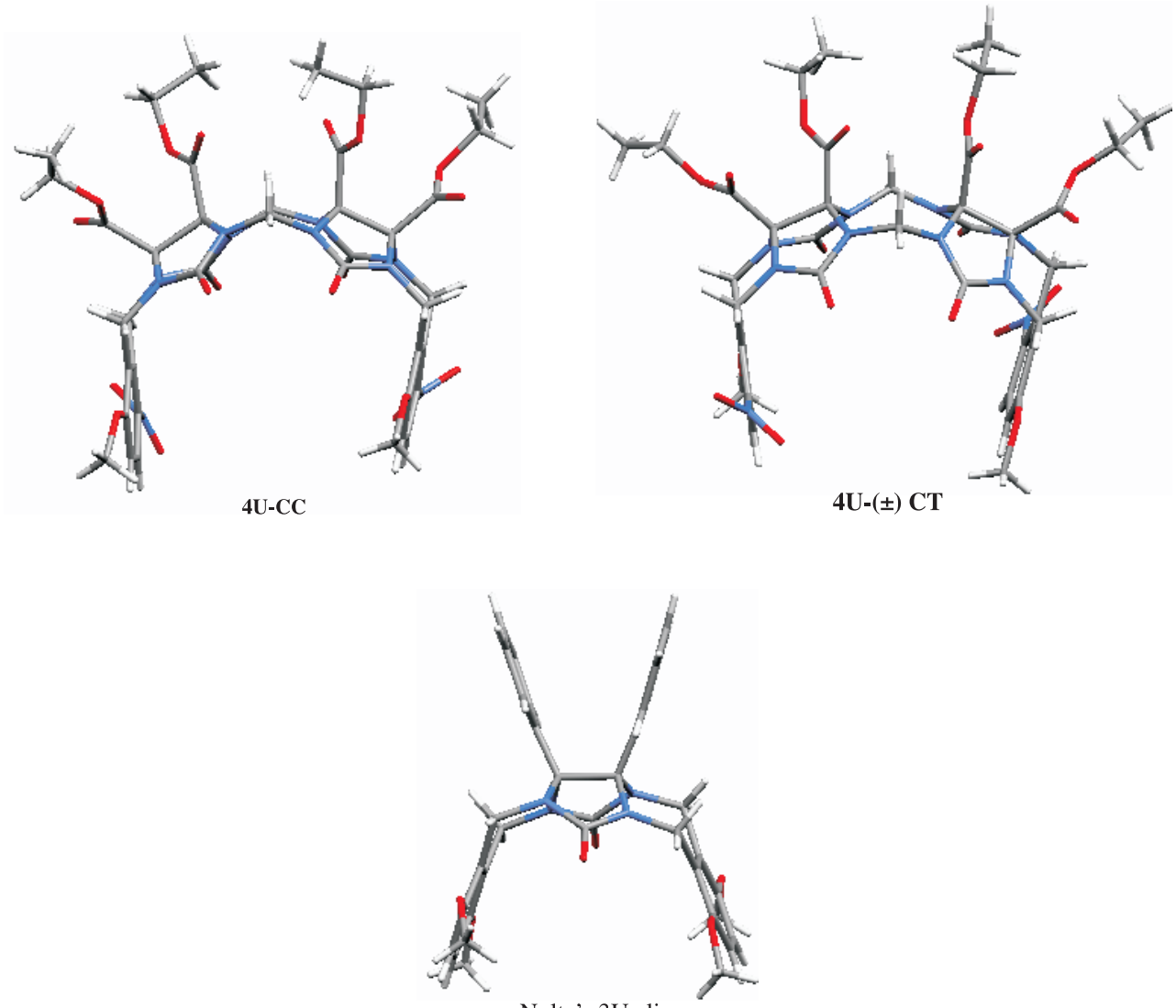


Fig. 2. Single-crystal structure analyses of **4U-CC**, **4U-(±)CT**, and Nolte's 3U clip.



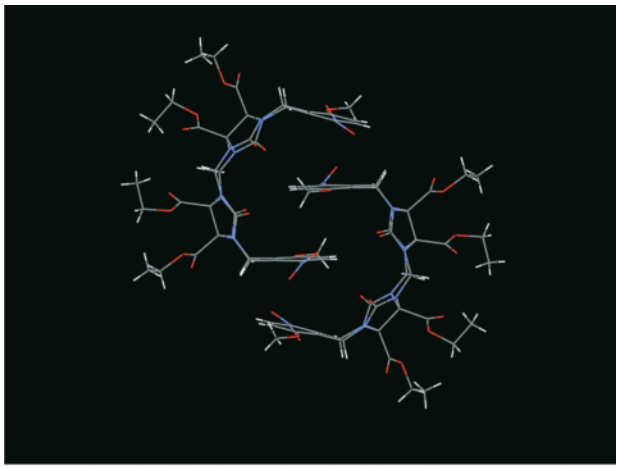
© 2007 NRC Canada

Table 1. Selected parameters from the X-ray crystal structures of **4U-CC**, **4U-(±)CT**, and Nolte's 3U clip.

Compound	=O···O= distance (Å)	Ar···Ar centroid distance (Å)	The height of the cavity (Å)
4U-CC	5.910(O11···O10) 5.793(O4···O5) 3.352(O4···O10) 3.384(O11···O5)	7.58	6.33
4U-(±)CT	5.753(O11···O10) 5.757(O4···O5) 3.729(O4···O10) 3.347(O11···O5)	7.58	6.07
Nolte's clip[a]	5.509	6.68	4.65

[a]As representative examples.

Fig. 3. X-ray structures showing dimers of **4U-CC** and **4U-(±)CT**.



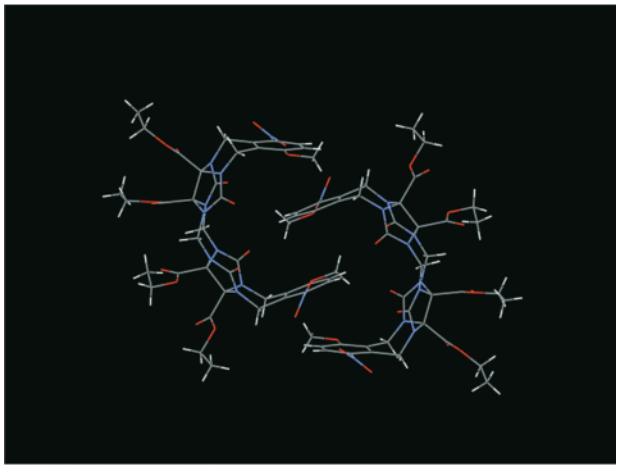
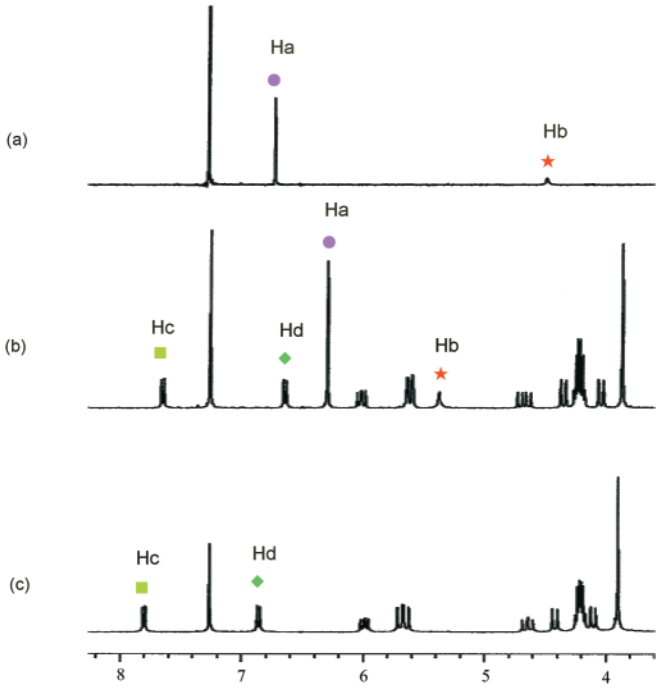


Fig. 4. Partial ^{1}H NMR spectra (400 MHz, $CDCl_3$, 298K) of (*a*) free guest hydroquinone, (*b*) the mixture of host **4U-CC** and guest hydroquinone (1:1), and (*c*) free host **4U-CC**.



complexes **4U-(±)CT** and hydroquinone have been deposited as Supplementary data).[2] These shifts indicate that complexes are formed, involving hydrogen bonds between the OH groups of the guest and the carbonyl groups of the host. Furthermore, they suggest that the aromatic moiety of the guest is wedged between the walls of the cavity. Only one signal was observed for the free and bound forms of the host and guest, implying that the exchange process is fast on the NMR time-scale.

Infrared spectroscopy was also used to investigate hydrogen bonding between hosts and guests (Fig. 5). The host carbonyl stretching vibration band is influenced by hydrogen bonding. IR spectra of compounds **4U-CC** mixed with hydroquinone shows that ν(C=O) splits into two bands (1760 and 1726 cm^{-1}) and **4U-(±)CT** mixed with hydroquinone shows that ν(C=O)

[2] Supplementary data for this article are available on the journal Web site (canjchem.nrc.ca) or may be purchased from the Depository of Unpublished Data, Document Delivery, CISTI, National Research Council Canada, Ottawa, ON K1A 0S2, Canada. DUD 5194. For more information on obtaining material, refer to cisti-icist.nrc-cnrc.gc.ca/irm/unpub_e.shtml. CCDC 286892 (compound **4U-(±)CT**) and 286896 (compound **4U-CC**) contain the crystallographic data for this manuscript. These data can be obtained, free of charge, via www.ccdc.cam.ac.uk/conts/retrieving.html (Or from the Cambridge Crystallographic Data Centre, 12 Union Road, Cambridge CB2 1EZ, UK; fax +44 1223 336033; or deposit@ccdc.cam.ac.uk).

© 2007 NRC Canada

Table 2. Free and complexation-induced ^{1}H NMR chemical shifts of hosts and guests.

Compounds	Ha (ppm)	Hb (ppm)	ΔδHa (ppm)	ΔδHb (ppm)	Hc (ppm)	Hd (ppm)	ΔδHc (ppm)	ΔδHd (ppm)
Free hydroquinone	6.715	4.476						
Free **4U-CC**					7.799	6.857		
4U-(±)CT-hydroquinone	6.297	5.377	0.418	0.901	7.652	6.648	0.147	0.209
Free **4U-(±)CT**					7.816	6.895		
4U-(±)CT-hydroquinone	6.103	5.843	0.612	1.367	7.603	6.598	0.213	0.397

Fig. 5. IR spectra of (*a*) hydroquinone, (*b*) **4U-CC**, and (*c*) a mixture of hydroquinone and **4U-CC**.

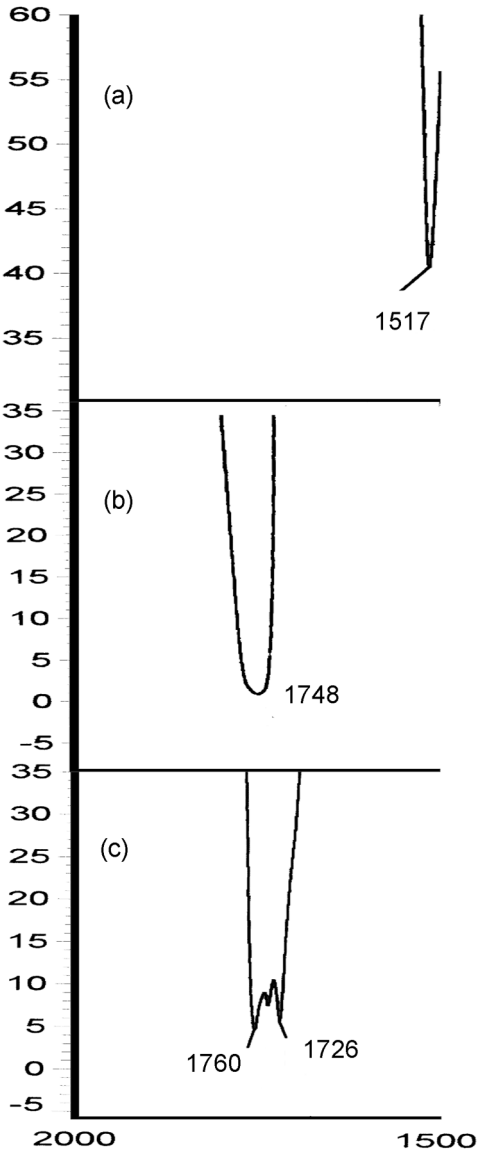
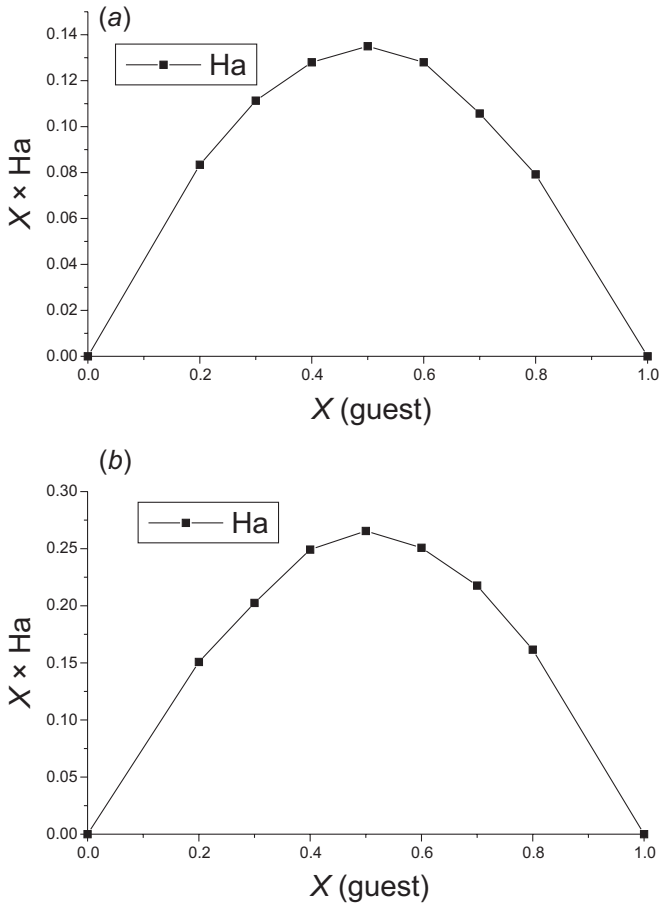


Fig. 6. Job-plot analysis of the stoichiometry between (*a*) **4U-CC** and hydroquinone and (*b*) **4U-(±)CT** and hydroquinone at 25 °C in $CDCl_3$.



splits into two bands (1759 and 1737 cm^{-1}, Supplementary data).[2] This splitting indicates that the carbonyl groups of some hosts in the complexes are involved in hydrogen bonding. The Δν (24 and 22 cm^{-1}, respectively) values agree with values reported in the literature for hydrogen-bonded complexes of other urea derivatives with phenols (13).

Job-plot analyses (14, 15) were performed to determine the stoichiometry of the complexes **4U-CC** and hydroquinone as representative examples. The plot of the mole fraction *X* vs. the mole fraction multiplied by the complexation-induced ^{1}H NMR shift of the substrate shows a maximum at *X* = 0.5 (Fig. 6*a*). This provides good evidence of a 1:1 stoichiometry for the complexes, which is the same for the complex of **4U-(±)CT** and hydroquinone (Fig. 6*b*).

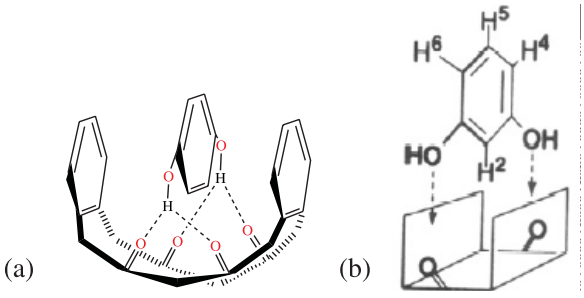
The results show that there exists hydrogen bonds and π–π stacking interactions in a binding process similar to Nolte's clips. But compared with Nolte's clip binding of resorcinol guest molecule, our molecular clips possess four oxygen atoms as binding sites, which strengthen the affinity for guests. According to the calculated distances of the oxygen atoms (Table 1), we assumed that our molecular clips might bind hydroquinone through bifurcated hydrogen bonds and π–π stacking interactions (Fig. 7)

© 2007 NRC Canada

Table 3. Crystal data for the compounds **CC** and **(±)CT**.

Compound	**CC**	**(±)CT**
formula weight	982.88	950.84
Temperature (K)	292(2)	292(2)
λ (Å)	0.71073	0.71073
Crystal system	orthorhombic	orthorhombic
Space group	*Pbca*	*Pbca*
a (Å)	18.9205(11)	16.3310(13)
b (Å)	17.3357(10)	21.5355(17)
c (Å)	27.4073(16)	27.074(2)
α (°)	90	90
β (°)	90	90
γ (°)	90	90
V (Å^3)	8989.6(9)	9521.8(13)
Z	8	8
Density (Mg m^{-3})	1.452	1.327
μ (Mo Kα) (mm^{-1})	0.117	0.106
F (000)	4112	3968
θ range (°)	1.76–25.00	1.5–25.00
Reflections collected	83273	88309
Unique reflections	7883	8397
Data/restraints/parameters	7883/15/660	8397/21/639
GOF on F^2	0.980	1.071
final *R* indices ($I > 2\sigma$ (*I*))	R_1 = 0.0671, wR_2 = 0.1883	R_1 = 0.0573, wR_2 = 0.1657
R indices (all data)	R_1 = 0.1071, wR_2 = 0.2085	R_1 = 0.0753, wR_2 = 0.1762
Largest diffraction peak and hole (e Å^{-3})	0.587 and –0.273	0.370 and –0.237

Fig. 7. (*a*) Model of insertion of hydroquinone in our clips and (*b*) model of insertion of resorcinol in Nolte's clip.



Conclusion

The crystal structures of two clips derived from diethoxycarbonyl glycoluril have been presented. These molecules show high affinity for hydroquinone, which is different from Nolte's clips. In addition, the binding properties of the molecular clips with other guests were being investigated. The details will be reported later.

Experimental part

Crystal data for compounds **CC** and **(±)CT** are given in Table 3. Single crystals, suitable for X-ray crystallographic analyses, were obtained from a slow evaporation of the 1, 2-dichloroethane and methanol solutions. The crystal data of compounds were collected on Bruker SMART APEX CCD diffractometer. The SMART (version 5.628) program was used for collecting data frames, and SAINT Plus (version 6.45) was used for integration of the intensity of reflections and scaling. SADABS was used for absorption correction (16). Structures **CC** and **(±)CT** were solved by direct methods using the programs SHELXS-97 and refined by full matrix least-squares methods against F^2 with SHELXL-97 (17). During the refinement of the **(±)CT** structure, electron-density peaks were located so that they were believed to be highly disordered solvent molecules (possibly methanol). Attempts made to model the solvent molecule were not successful. The SQUEEZE option (18) in PLATON indicated there was a solvent cavity of volume 261.0 A^3 containing approximately 18 electrons. In the final cycles of refinement, this contribution to the electron density was removed from the observed data. All the hydrogen atoms were fixed at the calculated positions, and the positions of hydrogen atoms were refined by a riding model. All non-hydrogen atoms were refined with anisotropic displacement parameters.

Acknowledgement

This work was supported by Central China Normal University, National Natural Science Foundation of China (Grant No. 20472022, 20672042).

References

1. R.J. Jansen, A.E. Rowan, R. De Gelder, H.W. Scheeren, and R.J.M. Nolte. Chem. Commun. 121 (1998).

© 2007 NRC Canada

2. R.M. Izatt, J.S. Bradshaw, K. Pawlak, R.L. Bruening, and B.J. Tarbet. Chem. Rev. **92**, 1261 (1992).
3. B.S. Creaven, J.F. Gallagher, J.P. McDonagh, J. McGinley, B.A. Murray, and G.S. Wheland. Tetrahedron, **60**, 137 (2004).
4. R.P. Sijbesma, S.S. Wijmenga, and R.J.M. Nolte. J. Am. Chem. Soc. **114**, 9807 (1992).
5. R.P. Sijbesma, A.P.M. Kentgens, E.T.G. Lutz, J.H.V. der Mass, and R.J.M. Nolte. J. Am. Chem. Soc. **115**, 8999 (1993).
6. J.N.H. Reek, A.H. Priem, H. Engelkamp, A.E. Rowan, J.A.A.W. Elemans, and R.J.M. Nolte. J. Am. Chem. Soc. **119**, 9956 (1997).
7. R.J. Jansen, J.A.A.W. Elemans, R. de Gelder, A.E. Rowan, and R.J.M. Nolte. Chem. Commun. 1553 (1998).
8. R.J. Jansen, R. de Gelder, A.E. Rowan, H.W. Scheeren, and R.J.M. Nolte. J. Org. Chem. **66**, 2643 (2001).
9. Q.S. Liu, S.L. Gong, Y. Ding, Y.Y. Chen, and X.J. Wu. Synlett, **13**, 2385 (2004).
10. B.H. Zhou, G.D.Yin, X.P. Liu, and A.X. Wu. Chem. J. Chinese U**. 27**, 58 (2006). [in Chinese].
11. B.H. Zhou, G.D. Yin, Z.G. Wang, Y.F. Chen, J. Wan, and A.X. Wu. Chinese Science Bulletin, **51**, 2164 (2006).
12. A.X. Wu, A. Chakraborty, D. Witt, J. Lagona, F. Damkaci, M.A. Ofori, J.K. Chiles, J.C. Fettinger, L. Isaacs. J. Org. Chem. **67**, 5817 (2002).
13. J.P. Muller, G. Vercruysse, Th. Zeeger-Huyskens. J. Chim. Phys. Phys.-Chim. Biol. **69**, 1439 (1912).
14. C.Y. Huang. Methods Enzymol. **87**, 509 (1982).
15. W. Likussar and D.F. Boltz. Anal. Chem. **43**, 1265 (1971).
16. SHELXTL [computer program] (Version 5.10); SMART [computer program] (Version 5.054); and SAINT [computer prograam] (Version 6.01). Bruker AXS Inc., Madison, Wisconsin, USA. 1997.
17. G.M. Sheldrick. SHELXS97 and SHELXL97 [computer programs]. University of Göttingen, Germany. 1997.
18. P.V.D. Sluis and A.L. Spek. Acta Crystallogr., Sect. C: Cryst. Struct. Commun. **A46**, 194 (1990).

© 2007 NRC Canada

Pyrazolo[3,4-*b*]pyridine in heterocyclic synthesis: synthesis of new pyrazolo[3,4-*b*]pyridines, imidazo[1′,2′:1,5]pyrazolo[3,4-*b*]pyridines, and pyrido[2′,3′:3,4]pyrazolo[1,5-*a*]pyrimidines

Mohamed A.M. Gad-Elkareem, Azza M. Abdel-Fattah, and Mohamed A.A. Elneairy

Abstract: Pyrazolo[3,4-*b*]pyridine derivatives **7** and **9** were synthesized via the reaction of 3-amino-1*H*-pyrazolo-[3,4-*b*]pyridine derivative **2** with ω-bromoacetophenones. Reaction of **7** and **9** with Ac_2O afforded the imidazo[1′,2′:1,5]pyrazolo[3,4-*b*]pyridine derivative **8** and pyrazolo[3,4-*b*]pyridine derivative **10**, respectively. Reaction of **2** with chloroacetonitrile followed by DMF–DMA gave imidazo[1′,2′:1,5]pyrazolo[3,4-*b*]pyridines **4** and **5**, respectively. Acetylacetone and 1,1-dicyano-2,2-dimethylthioethene were reacted with **2** to afford the pyrido[2′,3′:3,4]pyrazolo-[1,5-*a*]-pyrimidines **11** and **14**, respectively. Also, **2** reacted with DMF–DMA to yield the formamidine **15**, which in turn, reacted with active methylene reagents, yielding the corresponding pyrido[2′,3′:3,4]pyrazolo[1,5-*a*]pyrimidines **18** and **23a**–**23d**.

Key words: 1*H*-pyrazolo[3,4-*b*]pyridines, imidazo[1′,2′:1,5]pyrazolo[3,4-*b*]pyridines, pyrido[2′,3′:3,4]pyrazolo[1,5-*a*]pyrimidines.

Résumé : On a réalisé la synthèse des dérivés pyrazolo[3,4-*b*]pyridines **7** et **9** par le biais d'une réaction de la 3-amino-1*H*-pyrazolo-[3,4-*b*]pyridine **2** avec des ω-bromoacétophénones. Les réactions de composés **7** et **9** avec l'anhydride acétique conduisent respectivement à la formation de la imidazo[1′,2′:1,5]pyrazolo[3,4-*b*]pyridine **8** et de la pyrazolo[3,4-*b*]pyridine **10**. La réaction du composé **2** avec le chloroacétonitrile, suivie d'un traitement avec du DMF et du DMA conduit à la formation respectivement des imidazo[1′,2′:1,5]pyrazolo[3,4-*b*]pyridines **4** et **5**. Les réactions de l'acétylacétone et du 1,1-dicyano-2,2-diméthylthioéthène avec le composé **2** conduisent respectivement à la formation des pyrido[2′,3′:3,4]pyrazolo-[1,5-*a*]pyrimidines, **11** et **14**. Le produit **2** réagit aussi avec le mélange DMF–DMA pour conduire à la formation d'une formamidine **15** qui réagit ensuite avec des réactifs portant des groupes méthylènes actifs pour conduire à la formation des [2′,3′:3,4]pyrazolo[1,5-*a*]pyrimides, **18** et **23a**–**23d**.

Mots-clés : 1*H*-pyrazolo[3,4-*b*]pyridines, imidazo[1′,2′:1,5]pyrazolo[3,4-*b*]pyridines, pyrido[2′,3′:3,4]pyrazolo[1,5-*a*]pyrimidines.

[Traduit par la Rédaction]

Introduction

1*H*-Pyrazolo[3,4-*b*]pyridines comprise a very interesting class of compounds because of their significant and versatile biological and pharmacological activities, such as antimalarial (1), antiproliferative (2), antimicrobial (3–5), inhibition of cyclin-dependent kinases (6), and cardiovascular (7–9), antiviral (10, 11), and antileishmanial (12) activities. Moreover, pyridopyrazolopyrimidines revealed antiproliferative activity (13) and are used as potent kinase inhibitors (14). In view of these reports and as a continuation of our pervious work (4, 5, 15–19) directed towards the synthesis of substituted condensed pyrazoles, we report a new and convenient method for the synthesis of such ring systems that are required in medicinal chemistry, utilizing 3-amino-1*H*-pyrazolo-[3,4-*b*]pyridine derivative **2**.

Received 06 April 2007. Accepted 09 July 2007. Published on the NRC Research Press Web site at canjchem.nrc.ca on 16 August 2007.

M.A.M. Gad-Elkareem.[1] Department of Chemistry, Faculty of Science, Al-Azhar University (Assiut branch), Assiut 71524, Egypt.
A.M. Abdel-Fattah and M.A.A. Elneairy. Department of Chemistry, Faculty of Science, Cairo University, Giza 12613, Egypt.

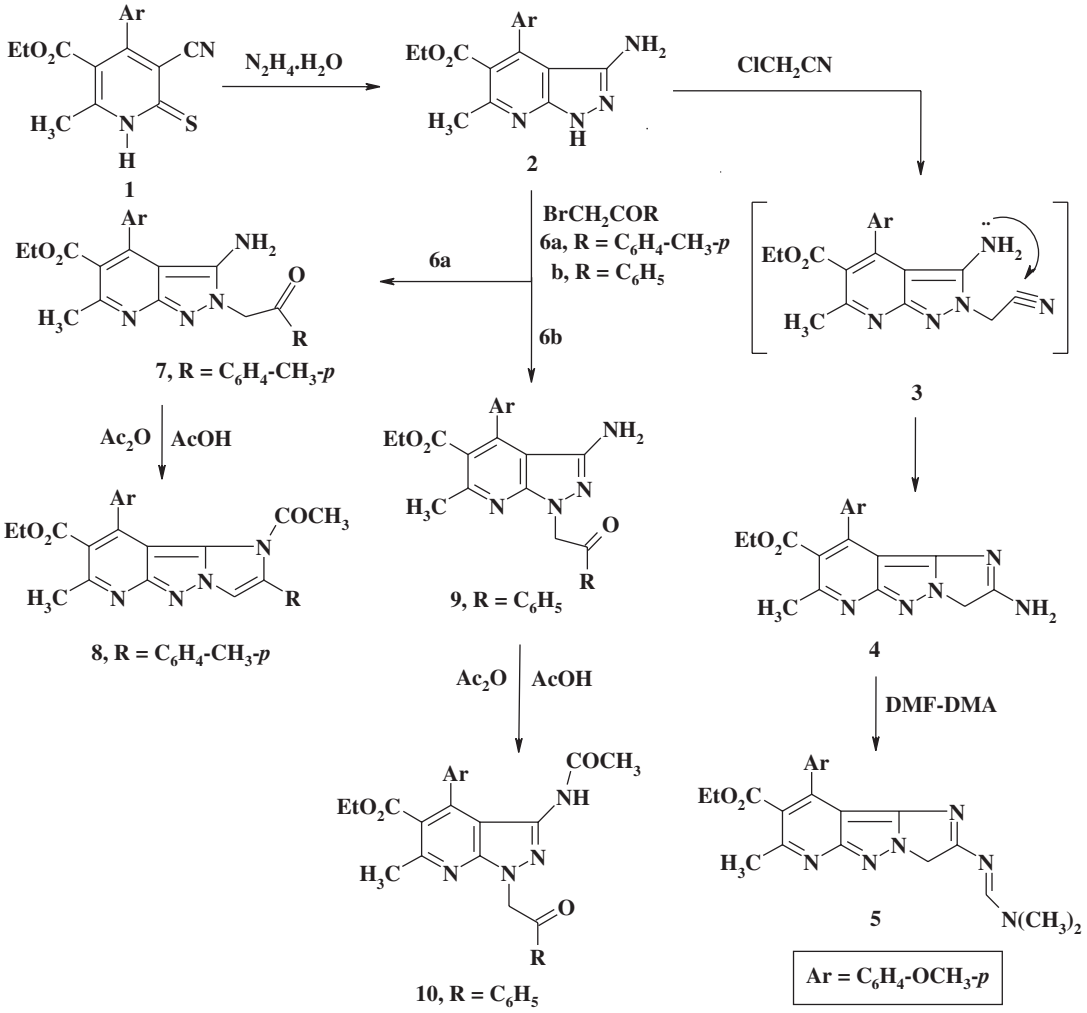
[1]Corresponding author (e-mail: m65gad@yahoo.com).

Results and discussion

Pyridine-2(1*H*)-thione derivative **1** reacted with hydrazine hydrate to afford the corresponding 3-amino-1*H*-pyrazolo[3,4-*b*]pyridine derivative **2** (20). The reactivity of compound **2** towards halo-reagents is studied in this paper. Thus, compound **2** reacted with chloroacetonitrile in potassium hydroxide – dimethyl formamide (DMF) solution to afford a reaction product **4**, which exhibited NH_2 (3454 and 3313 cm^{-1}) absorption bands in its IR spectrum with the absence of any absorption band due to C≡N function. The ^1H NMR spectrum of **4** revealed the singlet signal of two protons at δ = 3.91 ppm, assignable for NH_2, and a singlet signal of two protons at δ = 5.2 ppm characterized for CH_2. Based on the data obtained, the reaction product was formulated as 2-amino-3-hydroimidazo[1′,2′:1,5]pyrazolo[3,4-*b*]pyridine derivative **4**. The formation of **4** was assumed to

 doi:10.1139/V07-089 © 2007 NRC Canada

Scheme 1.



proceed via initial N-2 alkylation (21) of the ring nitrogen in compound **2** to give the non-isolable intermediate **3**, which underwent cyclization via addition of the amino group to the nitrile function to afford the final product, compound **4**. Condensation of **4** with dimethylformamide–dimethylacetal (DMF–DMA) in dry dioxane under reflux yielded the formamidine derivative **5**. The IR spectrum of compound **5** revealed the absence of the NH_2 group, and its ^1H NMR spectrum exhibited the absence of the signal due to the NH_2 group (at δ = 3.91 ppm in compound **4**) and the presence of the signals of $N(CH_3)_2$ at δ = 2.74 and 2.84 ppm and the signal of N=CH at δ = 7.70 ppm (cf. Scheme 1 and Experimental Section).

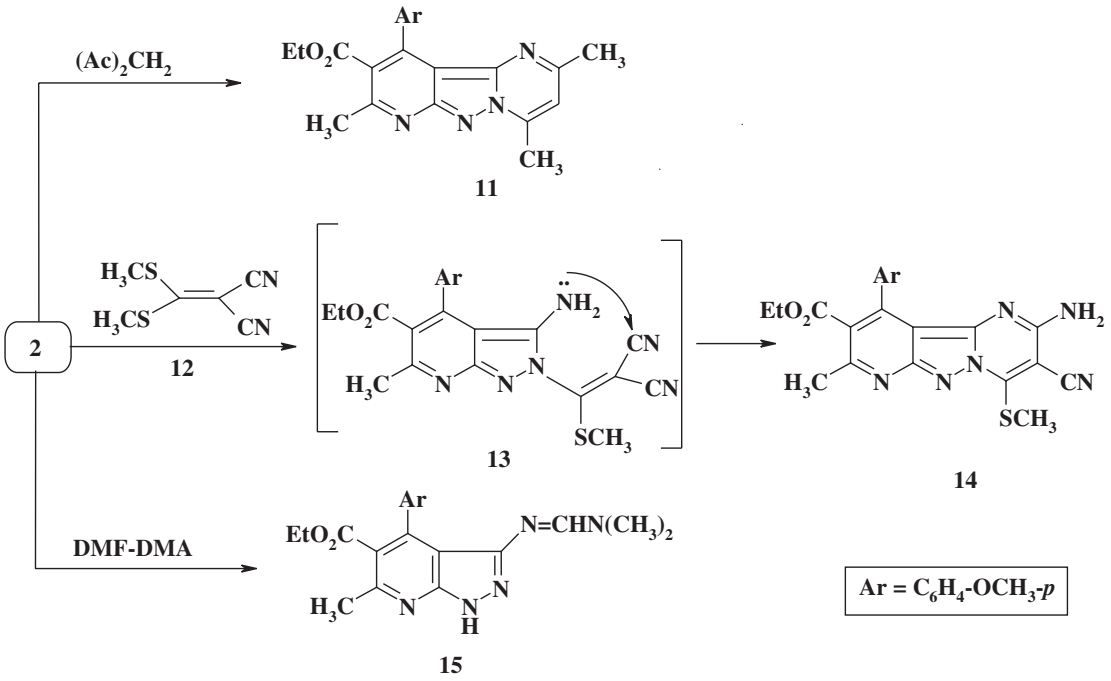
Also, compound **2** reacted with *p*-methyl-ω-bromoacetophenone (**6a**) under the same reaction conditions to give the *N*-2-alkyl product **7**. The IR spectrum of compound **7** showed the presence of the absorption bands of NH_2 and two carbonyl groups. Moreover, the ^1H NMR spectrum of compound **7** revealed the presence of NH_2 and CH_2 protons (cf. Scheme 1 and Experimental Section).

Reaction of compound **7** with acetic anhydride in glacial acetic acid under reflux afforded a reaction product **8** of the molecular formula $C_{28}H_{26}N_4O_4$. IR spectrum of **8** showed the disappearance of the absorption bands of NH_2 group, and its ^1H NMR spectrum revealed the absence of CH_2 and NH_2 protons, and instead, the signal of $C_{(3)}$–H of the imidazole moiety and $COCH_3$ was detected at δ = 7.28 and 2.42 ppm, respectively. Based on the data obtained, the reaction product was formulated as ethyl-1-acetyl-9-(4-methoxyphenyl)-7-methyl-2-(4-*p*-tolyl)-1*H*-imidazo-[1′,2′:1,5]pyrazolo[3,4-*b*]pyridine-8-carboxylate (**8**). The formation of **8** was assumed to proceed via the cyclization of **7** with the loss of water molecule followed by acetylation of the imidazole ring nitrogen (cf. Scheme 1 and Experimental Section).

On the other hand, compound **2** reacted with ω-bromoacetophenone (**6b**) to give the *N*-1-alkyl product **9**, which established on the basis of the elemental analysis, spectral data, and chemical evidence. Treatment of **9** with acetic anhydride in glacial acetic acid under reflux afforded the corresponding acetylation product ethyl-3-acetylamino-4-(4-methoxyphenyl)-6-methyl-2-(2-oxo-2-phenylethyl)-1*H*-pyrazolo[3,4-*b*]pyridine-5-carboxylate (**10**). The structure of **10** was established on the basis of the elemental and spectral data, which showed the presence of NH, CH_2, and three C=O groups. The failure of all the attempts to cyclize **10** as in case of **8** led to the conclusion that the alkylation first took place at N-1 at compound **2** (cf. Scheme 1 and Experimental Section).

© 2007 NRC Canada

Scheme 2.



Condensation of compound **2** with acetyl acetone in glacial acetic acid (22) under reflux afforded the corresponding pyrido[2′,3′:3,4]pyrazolo[1,5-*a*]pyrimidine derivative **11**, its structure was confirmed by elemental analysis and spectral data, which showed the disappearance of NH and NH_2 protons, indicating their participation in the condensation process (cf. Scheme 2 and Experimental Section).

The reactivity of compound **2** towards ketene dithioacetal was also investigated; thus, 1,1-dicyano-2,2-dimethylthioethene (**12**) (23) reacted with compound **2** in dimethylformamide under reflux in the presence of potassium carbonate as a catalyst to afford the corresponding pyrido[2′,3′:3,4]pyrazolo[1,5-*a*]pyrimidine derivative **14**. The IR spectrum of compound **14** showed the presence of NH_2 (3444 and 3324 cm^{-1}) and C≡N (2214 cm^{-1}) groups. The ^1H NMR spectrum of compound **14** exhibited a signal at $\delta = 2.97$ ppm assignable to methylsulfanyl group. The formation of **14** was preceded via initial alkylation (21) at N-2 to give the non-isolable intermediate **13** and subsequent ring closure to yield the final product **14** (cf. Scheme 2 and Experimental Section).

Condensation of **2** with DMF–DMA in dry dioxane under reflux afforded the ethyl 3-{[(*N*,*N*-dimethylamino)methylene]amino}-4-(4-methoxyphenyl)-6-methyl-1*H*-pyrazolo-[3,4-*b*]pyridine-5-carboxylate (**15**). Structure **15** was inferred from its spectral data, elemental analysis, and chemical transformations. ^1H NMR spectrum of **15** confirmed the presence of CH_3 protons and disappearance of NH_2 protons, indicating that the condensation was carried out on the amino group not the methyl group (cf. Scheme 2 and Experimental Section).

The chemistry of the dimethylaminomethyleneaminopyrazole derivatives is now receiving considerable attention as one of the major routes to synthesize the biologically active pyrazolo[1,5-*a*]pyrimidines (24–26) and pyrimido-[2,3:4,3]pyrazolo[1,5-*a*]pyrimidines (27). Thus, treatment of dimethylaminomethyleneaminopyrazolo[3,4-*b*]pyridine derivative **15** with cyanothioacetamide (**16a**) in ethanol containing catalytic amount of piperidine afforded a condensation product via dimethylamine elimination. Two structures were considered for this reaction product: compounds **18** and **19**. Elemental analysis of this reaction product indicated the absence of sulfur; the IR spectrum showed the absorption band of C≡N (2223 cm^{-1}) group, and its ^1H NMR spectrum indicated the presence of only one NH_2 group at $\delta = 9.27$ ppm. Based on these data, structure **19** was excluded, and structure **18** could be readily established for the main reaction product (cf. Scheme 3 and Experimental Section).

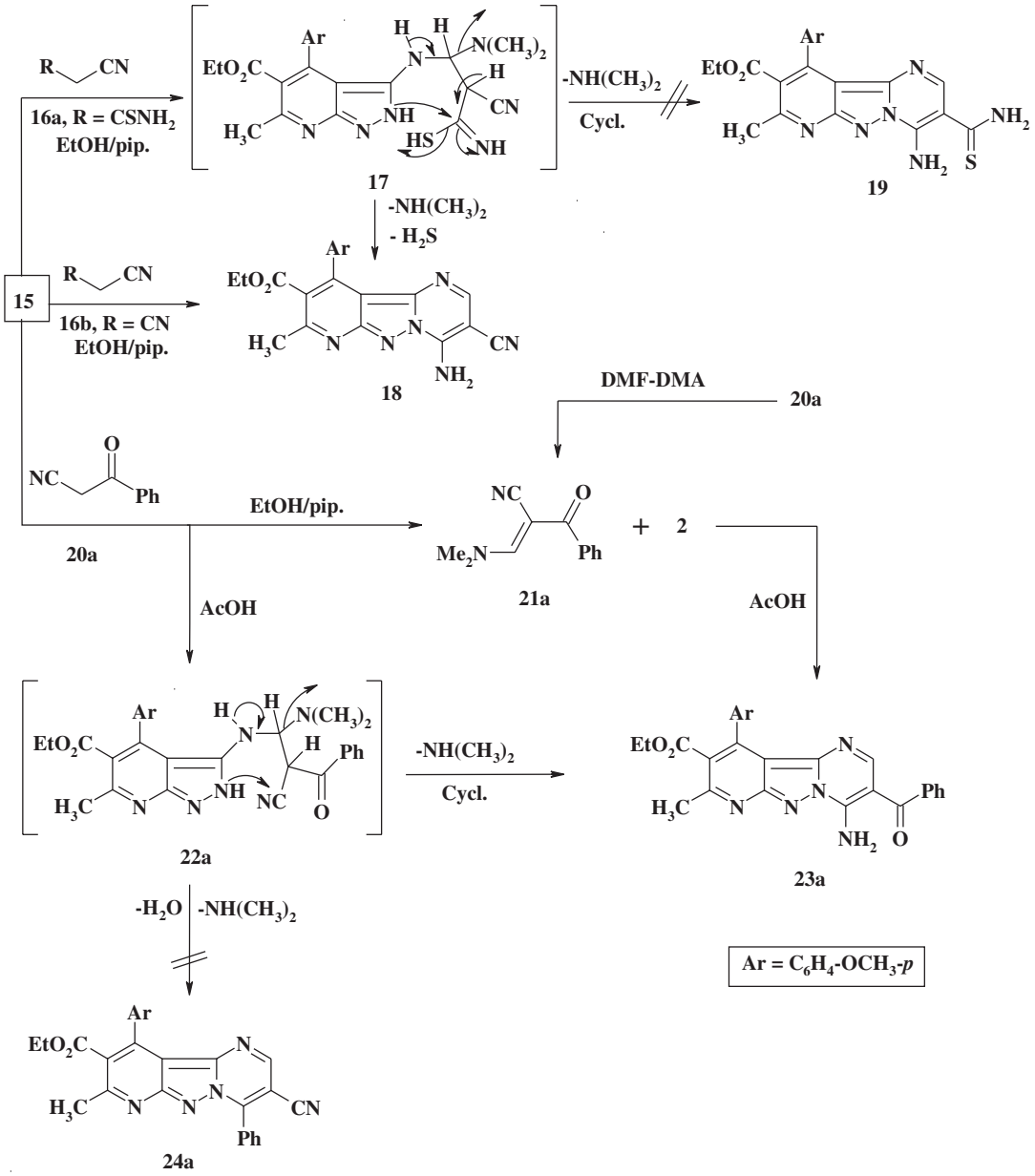
The formation of compound **18** in this reaction product can be assumed to proceed via the formation of the non-isolable adduct **17**, followed by intramolecular cyclization involving the loss of one molecule of H_2S (28) (turned lead acetate paper into black during the reaction) and $HN(CH_3)_2$ to yield compound **18** (cf. Scheme 3).

A solid evidence for the structure of compound **18** came from its authentic synthesis by the reaction of compound **15** with malononitrile (**16b**) under the same reaction conditions to afford one and the same reaction product **18**. Compound **18**, prepared via this route, was found to be completely identical in all aspects (mp, mixed mp, and TLC) with compound **18** prepared via the first route (cf. Scheme 3).

On the other hand, compound **15** reacted with benzoylacetonitrile (**20a**) in ethanol containing catalytic amount of piperidine under reflux to give 3-aminopyrazolo[3,4-*b*]pyridine derivative **2** (20) and 3-phenyl-2-[(*N*,*N*-dimethylamino)methylene]-3-oxopropanenitrile (**21a**) (25) instead of the addition product that would be expected by analogy with the earlier reports (24–27). The formation of compounds **2** and **21a** in this reaction is assumed to proceed via *N*,*N*-dimethylaminomethylene exchange under the

© 2007 NRC Canada

Scheme 3.



applied reaction conditions leading to the regeneration of the amino group (17, 29) and hence the formation of **2** (cf. Scheme 3).

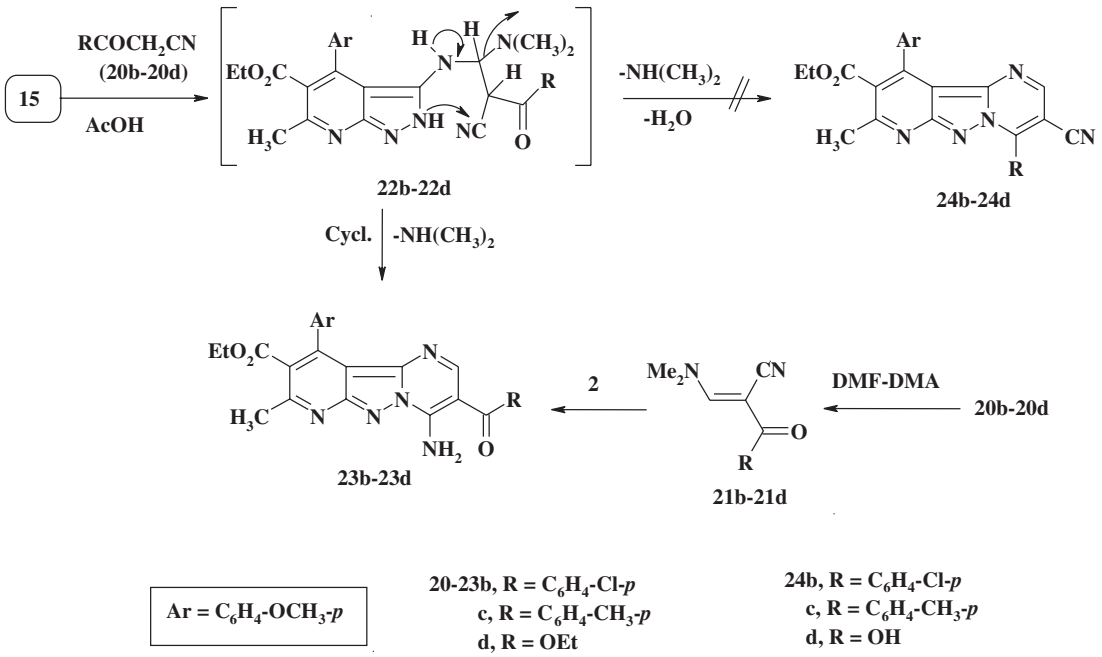
The reaction of **15** with **20a** in glacial acetic acid under reflux afforded an addition product with dimethylamine elimination. Two structures seemed possible for this reaction product: **23a** and **24a**. The IR spectrum of the reaction product indicated the presence of absorption bands due to NH_2 (3369 and 3235 cm^{-1}) and COPh (1647 cm^{-1}) groups and the absence of any absorption band that might be attributed to the C≡N group. The ^1H NMR spectrum of the reaction product exhibited the signal of NH_2 protons at δ = 9.67 ppm (D_2O-exchangeable), and its ^{13}C NMR spectrum revealed the signal of C=O at δ = 195.78 ppm. Moreover, the mass spectrum of this reaction product showed the molecular ion peak M^+ at *m*/*z* = 481 (63.9%), corresponding to the molecular formula $C_{27}H_{23}N_5O_4$; also, the base peak in the spectrum was found at *m*/*z* = 105 (100%), which was attributed to the benzoyl radical ($PhCO^+$). Based on the data obtained, the reaction product was formulated as 4-amino-3-benzoylpyrido[2′,3′:3,4]pyrazolo[1,5-*a*]pyrimidine derivative **23a** rather than the possible alternative 3-cyano-4-phenylpyrido[2′,3′:3,4]pyrazolo[1,5-*a*]pyrimidine derivative **24a** (cf. Scheme 3 and Experimental Section).

The formation of compound **23a** proceeds via first the formation of the non-isolable adduct **22a** followed by the cyclization involving addition to the nitrile function group with the loss of one molecule of dimethylamine to afford compound **23a** rather than the loss of water molecule that gives compound **24a** as we would expect by analogy with the earlier reports (24–27) (cf. Scheme 3).

An unequivocal support for the structure of **23a** was achieved via its synthesis through other route, i.e., condensing **20a** with DMF–DMA and subsequent condensation of

© 2007 NRC Canada

Scheme 4.



the so-formed 3-phenyl-2-[(*N*,*N*-dimethylamino)methylene]-3-oxopropanenitrile (**21a**) (25) with **2** in glacial acetic acid to afford a product that is identical in all respects (mp, mixed mp, and spectral data) to compound **23a** (cf. Scheme 3).

Similarly, compound **15** reacted with aroylacetonitriles **20b**–**20c** and ethyl cyanoacetate (**20d**) in glacial acetic acid under reflux to yield the corresponding 4-amino-3-aroylpyrido[2′,3′:3,4]pyrazolo[1,5-*a*]-pyrimidine derivatives **23b** and **23c** and 4-amino-3-ethoxycarbonylpyrido[2′,3′:3,4]pyrazolo[1,5-*a*]pyrimidine derivative **23d,** respectively, instead of the 3-cyano-4-arylpyrido[2′,3′:3,4]pyrazolo[1,5-*a*]pyrimidine derivatives **24b** and **24c** and 3-cyano-4-hydroxypyrido[2′,3′:3,4]pyrazolo[1,5-*a*]pyrimidine derivative **24d** (cf. Scheme 4).

The reactions of **15** with **20b**–**20c** in this study did not take place as would have been expected by analogy with the earlier reports (24–27).

Also, the structure of compounds **23b**–**23d** was established on the basis of the elemental analysis and spectral data. A further support for the structure of **23b**–**23d** was achieved via its synthesis through other routes, i.e., via condensing **2** with **21b–21d** (25, 26) in glacial acetic acid to afford a product identical in all respects (mp, mixed mp, and spectral data) to those corresponding to compounds **23b**–**23d** (cf. Scheme 4).

Conclusion

The reaction of 3-amino-1*H*-pyrazolo[3,4-b]pyridine derivative **2** with ω-bromoacetophenones gave either N-1 or N-2 alkylation products, and the reaction of dimethylaminomethyleneaminopyrazolo[3,4-b]-pyridine derivative **15** with β-keto nitrile was found to be highly dependent on the reaction mediums whether it is a basic medium (ethanol–pipredine), which gave dimethylaminomethylene group exchange or acidic (acetic acid), which afforded addition followed by cyclocondensation reaction involving the nitrile function instead of loss of water molecule as would be expected by analogy with the earlier reports (24–27).

Experimental

Melting points were measured with a Gallenkamp apparatus and are uncorrected. IR spectra (KBr discs) were recorded on BRUKER Vector 22 FT-IR spectrophotometer. ^{1}H and ^{13}C NMR spectra were determined in DMSO-d_6 and $CDCl_3$ at 300 MHz on Varian Mercury VX spectrometer using TMS as an internal standard. Chemical shifts are expressed as δ ppm and *J* as Hz units. Mass spectra were recorded on GCMS-QP 1000 EX spectrometer at 70 eV. Elemental analyses were carried out at the Microanalytical Center of Cairo University. Compounds **1** (20), **2** (20), **12** (23), and **21a**–**21d** (25, 26) were prepared according to the literature procedures.

Reactions of compound 2 with halo-reagents

General procedure

A mixture of compound **2** (10 mmol) and each of chloroacetonitrile and compounds **6a** and **6b** (10 mmol) was stirred in DMF (30 mL) containing 10 mmoles of KOH at room temperature for 2 h. The reaction mixtures were poured on cold water and acidified with dilute HCl. The solid products obtained were collected by filtration and crystallized from ethanol to afford compounds **4**, **7**, and **9**, respectively.

*Ethyl-2-amino-3-hydro-9-(4-methoxyphenyl)-7-methyl-imidazo[1′,2′:1,5]pyrazolo[3,4-*b*]pyridine-8-carboxylate (4)*

Yellow crystals (65%) from ethanol, mp 146 °C. IR υ (cm^{-1}): 3454, 3313 (NH_2), 1718 (C=O), 1612 (C=N). ^{1}H NMR ($CDCl_3$): δ 0.99 (t, *J* = 7.23 Hz, 3H, $CH_2\underline{CH_3}$), 2.66 (s, 3H, CH_3), 3.86 (s, 3H, OCH_3), 3.91 (s, 2H, $\underline{NH_2}$), 4.07

© 2007 NRC Canada

(q, J = 7.2 Hz, 2H, CH_2CH_3), 5.20 (s, 2H, CH_2, $C_{(3)}$–H), 6.99 (d, J = 8.8 Hz, 2H, Ar–H), 7.31 (d, J = 8.8 Hz, 2H, Ar–H). ^{13}C NMR ($CDCl_3$): δ 13.79 (CH_3CH_2), 23.14 (7-CH_3), 55.44 (OCH_3), 61.59 (OCH_2CH_3), 77.21 (C-3), 114.19 (C-9a), 118.85 (C-9b), 125.45 (C-8), 143.8 (C-9), 149.32 (C-5a), 156.35 (C-7), 161.38 (C-2), 167.45 (C=O), 114.75, 127.63, 130.03, 160.62 (arom. C's). Anal. calcd. for $C_{19}H_{19}N_5O_3$ (365): C 62.46, H 5.20, N 19.17; found: C 62.15, H 5.49, N 18.85.

Ethyl-3-amino-4-(4-methoxyphenyl)-6-methyl-2-(2-oxo-2-*p*-tolylethyl)-2H-pyrazolo[3,4-b]pyridine-5-carboxylate (7)

Yellow crystals (65%) from ethanol, mp 172 °C. IR υ (cm^{-1}): 3432, 3354 (NH_2), 1724 (ester C=O), 1699 (Ar. C=O), 1610 (C=N). ^{1}H NMR ($CDCl_3$): δ 1.02 (t, J = 7.0 Hz, 3H, CH_2CH_3), 2.43 (s, 3H, CH_3-*p*-tolyl), 2.69 (s, 3H, CH_3), 3.89 (s, 3H, OCH_3), 4.05 (q, J = 7.0 Hz, 2H, CH_2CH_3), 5.16 (s, 2H, CH_2, N–CH_2CO), 6.69 (br, 2H, NH_2), 7.03 (d, J = 8.1 Hz, 2H, Ar–H), 7.26–735 (m, 4H, Ar–H), 7.74 (d, J = 7.8 Hz, 2H, Ar–H). Anal. calcd. for $C_{26}H_{26}N_4O_4$ (458): C 68.12, H 5.67, N 12.22; found: C 67.83, H 5.98, N 12.00.

Ethyl-3-amino-4-(4-methoxyphenyl)-6-methyl-2-(2-oxo-2-phenylethyl)-1H-pyrazolo[3,4-b]pyridine-5-carboxylate (9)

Yellow crystals (69%) from ethanol, mp 192–193 °C. IR υ (cm^{-1}): 3462, 3334 (NH_2), 1719 (ester C=O), 1701 (PhC=O), 1613 (C=N). ^{1}H NMR ($CDCl_3$): δ 0.98 (t, J = 7.2 Hz, 3H, CH_2CH_3), 2.62 (s, 3H, CH_3), 3.61 (br., 2H, NH_2), 3.85 (s, 3H, OCH_3), 4.07 (q, J = 7.2 Hz, 2H, CH_2CH_3), 5.75 (s, 2H, CH_2, N–CH_2COPh), 6.98 (d, J = 8.4 Hz, 2H, Ar–H), 7.34 (d, J = 8.4 Hz, 2H, Ar–H), 7.45–7.60 (m, 3H, Ar–H, COPh), 8.01 (d, J = 7.2 Hz, 2H, Ar–H, COPh). Anal. calcd. for $C_{25}H_{24}N_4O_4$ (444): C 67.56, H 5.40, N 12.61; found: C 67.30, H 5.65, N 12.31.

Ethyl-2-{[(N,N-dimetylamino)methylene]amino}-3-hydro-9-(4-methoxy-phenyl)-7-methylimidazo[1′,2′:1,5]pyrazolo-[3,4-b]pyridine-8-carboxylate (5)

A mixture of compound **4** (10 mmol) and DMF–DMA (12 mmol) in dry dioxane (30 mL) was heated under reflux for 3 h. The solid product thus formed after cooling was collected by filtration and crystallized from ethanol to yield compound **5** as yellow crystals (63%), mp 122 °C. IR υ (cm^{-1}): 1722 (C=O), 1627 (C=N). ^{1}H NMR ($CDCl_3$): δ 1.00 (t, J = 7.16 Hz, 3H, CH_2CH_3), 2.66 (s, 3H, CH_3), 2.74 (s, 3H, CH_3, $N(CH_3)_2$), 2.84 (s, 3H, CH_3, $N(CH_3)_2$), 3.83 (s, 3H, OCH_3), 4.07 (q, J = 7.16 Hz, 2H, CH_2CH_3), 5.28 (s, 2H, CH_2, $C_{(3)}$–H), 6.89 (d, J = 8.6 Hz, 2H, Ar–H), 7.35 (d, J = 8.6 Hz, 2H, Ar–H), 7.70 (s, 1H, N=CH). ^{13}C NMR ($CDCl_3$): δ 13.61 (CH_3CH_2), 23.29 (7-CH_3), 33.88, 34.04 ($N(CH_3)_2$), 39.84 (C-3), 55.23 (OCH_3), 61.10 (OCH_2CH_3), 106.97 (C-9a), 114.47 (C-9b), 123.69 (C-8), 144.79 (C-9), 151.05 (C-5a), 154.23 (C-7), 156.17 (C-2 and C=NH), 169.06 (C=O), 112.64, 127.19, 131.06, 159.81 (arom. C's). Anal. calcd. for $C_{22}H_{24}N_6O_3$ (420): C 62.85, H 5.71, N 20.00; found: C 62.53, H 5.46, N 19.73.

Reaction of compounds 7 and 9 with acetic anhydride

A solution of each of compounds **7** and **9** (10 mmol) in glacial acetic acid (30 mL) was treated with acetic anhydride (5 mL) and heated under reflux for 6 h. The reaction mixture was then cooled and poured onto cold water. The solid products thus formed were filtered off and crystallized from ethanol to give compounds **8** and **10**, respectively.

Ethyl-1-acetyl-9-(4-methoxyphenyl)-7-methyl-2-(4-p-tolyl)-1H-imidazo[1′,2′:1,5]pyrazolo[3,4-b]pyridine-8-carboxylate (8)

Yellowish brown crystals (53%) from ethanol, mp 324–326 °C. IR υ (cm^{-1}): 1724 (ester C=O), 1676 (amide C=O). ^{1}H NMR ($CDCl_3$): δ 1.09 (t, J = 7.2 Hz, 3H, CH_2CH_3), 2.42 (s, 6H, CH_3-tolyl and $NCOCH_3$), 2.77 (s, 3H, CH_3, $C_{(7)}$), 3.97 (s, 3H, OCH_3), 4.17 (q, J = 7.2 Hz, 2H, CH_2CH_3), 7.09 (d, J = 8.4 Hz, 2H, Ar–H), 7.28 (s, 1H, $C_{(3)}$–H), 7.65–7.76 (m, 4H, Ar–H), 7.87 (d, J = 8.4 Hz, 2H, Ar–H). Anal. calcd. for $C_{28}H_{26}N_4O_4$ (482): C 69.71, H 5.39, N 11.62; found: C 69.40, H 5.11, N 11.91%.

Ethyl-3-acetylamino-4-(4-methoxyphenyl)-6-methyl-2-(2-oxo-2-phenyl-ethyl)-1H-pyrazolo[3,4-b]pyridine-5-carboxylate (10)

Yellow crystals (60%) from ethanol, mp 224–226 °C. IR υ (cm^{-1}): 3183 (NH), 1723 (ester C=O), 1698 (Ar. C=O), 1664 (amide C=O). ^{1}H NMR (DMSO-d_6): δ 0.97 (t, J = 7.0 Hz, 3H, CH_2CH_3), 1.54 (s, 3H, $COCH_3$), 2.55 (s, 3H, CH_3), 3.82 (s, 3H, OCH_3), 4.05 (q, J = 7.0 Hz, 2H, CH_2CH_3), 6.13 (s, 2H, CH_2, N–CH_2COPh), 7.0–726 (m, 4H, Ar–H), 7.59–7.75 (m, 3H, Ar–H), 8.12 (d, J = 7.25 Hz, 2H, Ar–H), 9.75 (s, 1H, NH). ^{13}C NMR (DMSO-d_6): δ 13.38 (CH_3CH_2), 22.89 (6-CH_3), 32.56 (CH_3CO), 53.09 (NCH_2COPh), 55.17 (OCH_3), 60.89 (OCH_2CH_3), 107.03 (C-3a), 123.66 (C-5), 138.29 (C-4), 142.79 (C-3), 154.81 (C-6 and C-8a), 159.49 (CO_2Et), 192.91 ($COCH_3$), 197.19 (COPh), 113.15, 126.06, 128.06, 128.84, 129.74, 132.06, 132.89, 159.49 (arom. C's). Anal. calcd. for $C_{27}H_{26}N_4O_5$ (486): C 66.66, H 5.34, N 11.52; found: C 66.92, H 5.20, N 11.22.

Ethyl-10-(4-methoxyphenyl)-2,4,8-trimethylpyrido-[2′,3′:3,4]pyrazolo[1,5-a]pyrimidine-9-carboxylate (11)

A mixture of compound **2** (10 mmol) and acetylacetone (10 mmol) in glacial acetic acid (30 mL) was heated under reflux for 3 h then cooled. The solid product thus formed was filtered off and crystallized from acetic acid to afford compound **11** as yellow crystals (58%), mp 168 °C. IR υ (cm^{-1}): 1721 (C=O), 1622 (C=N). ^{1}H NMR ($CDCl_3$): δ 1.07 (t, J = 7.02 Hz, 3H, CH_2CH_3), 2.61 (s, 3H, CH_3), 2.83 (s, 3H, CH_3), 2.94 (s, 3H, CH_3), 3.86 (s, 3H, OCH_3), 4.16 (q, J = 7.02 Hz, 2H, CH_2CH_3), 7.00 (d, J = 8.4 Hz, 2H, Ar–H), 7.15 (s, 1H, $C_{(3)}$–H), 7.56 (d, J = 8.4 Hz, 2H, Ar–H). Anal. calcd. for $C_{22}H_{22}N_4O_3$ (390): C 67.69, H 5.64, N 14.35; found: C 67.42, H 5.33, N 14.10

Ethyl-2-amino-3-cyano-10-(4-methoxyphenyl)-8-methyl-4-methylsulfanylpyrido[2′,3′:3,4]pyrazolo[1,5-a]pyrimidine-9-carboxylate (14)

A mixture of compound **2** (10 mmol) and compound **12** (10 mmol) in dimethylformamide (30 mL) containing 1.0 g of anhyd. potassium carbonate was heated under reflux for 5 h. The reaction mixture was then cooled, poured onto ice-cold water, and acidified with dilute HCl. The solid product obtained was filtered off and crystallized from ethanol to give compound **14** as brown crystals (55%), mp 201–202 °C. IR υ (cm^{-1}): 3445, 3335 (NH_2), 2214 (C≡N), 1718 (C=O), 1637 (C=N). ^{1}H NMR ($CDCl_3$): δ 1.05 (t, J = 7.2 Hz, 3H, CH_2CH_3), 2.76 (s, 3H, CH_3), 2.97 (s, 3H, SCH_3), 3.87 (s,

© 2007 NRC Canada

3H, OCH_3), 4.13 (q, *J* = 7.2 Hz, 2H, CH_2CH_3), 6.97–7.44 (m, 6H, Ar–H and NH_2). Anal. calcd. for $C_{22}H_{20}N_6O_3S$ (448): C 58.92, H 4.46, N 18.75, S 7.14; found: C 58.64, H 4.18, N 18.99, S 6.88.

Ethyl-3-{[(N,N-dimethylamino)methylene]amino}-4-(4-methoxyphenyl)-6-methyl-1H-pyrazolo[3,4-b]pyridine-5-carboxylate (15)

This compound was synthesized from compound **2** (10 mmol) and DMF–DMA (12 mmol) in a manner similar to that described for the preparation of compound **5**. It was crystallized from ethanol to give yellow crystals (76%), mp 174 °C. IR υ (cm^{-1}): 3195 (NH), 1734 (C=O). 1632 (C=N). ^1H NMR ($CDCl_3$): δ 0.99 (t, *J* = 7.2 Hz, 3H, CH_2CH_3), 2.72 (s, 3H, CH_3), 2.75 (s, 3H, CH_3, $N(CH_3)_2$), 2.80 (s, 3H, CH_3, $N(CH_3)_2$), 3.83 (s, 3H, OCH_3), 4.08 (q, *J* = 7.2 Hz, 2H, CH_2CH_3), 6.91 (d, *J* = 8.6 Hz, 2H, Ar–H), 7.38 (d, *J* = 8.6 Hz, 2H, Ar–H), 7.63 (s, 1H, N=CH), 11.74 (s, 1H, NH). Anal. calcd. for $C_{20}H_{23}N_5O_3$ (381): C 62.99, H 6.03, N 18.37; found: C 62.70, H 5.80, N 18.09.

Synthesis of ethyl-4-amino-3-cyano-10-(4-methoxyphenyl)-8-methylpyrido[2′,3′:3,4]pyrazolo[1,5-a]pyrimidine-9-carboxylate (18)

A mixture of compound **15** (10 mmol) and either of cyanothioacetamide (**16a**) or malononitrile (**16b**) (10 mmol) in ethanol (30 mL) containing 0.5 mL of triethylamine, as a catalyst, was heated under reflux for 2 h. The solid product obtained on hot was filtered off and crystallized from dioxane to give compound **18** as yellow crystals (67%), mp 309–310 °C. IR υ (cm^{-1}): 3427, 3391 (NH_2), 2223 (C≡N), 1722 (C=O), 1645 (C=N). ^1H NMR ($CDCl_3$): δ 1.08 (t, *J* = 7.2 Hz, 3H, CH_2CH_3), 2.86 (s, 3H, CH_3), 3.91 (s, 3H, OCH_3), 4.16 (q, *J* = 7.2 Hz, 2H, CH_2CH_3), 7.02 (d, *J* = 8.6 Hz, 2H, Ar–H), 7.51 (d, *J* = 8.6 Hz, 2H, Ar–H), 8.426 (s, 1H, $C_{(2)}$–H), 9.27 (br, 2H, NH_2). ^{13}C NMR (DMSO-d_6): δ 13.41 (CH_3CH_2), 24.07 (8-CH_3), 55.09 (OCH_3), 60.97 (OCH_2CH_3), 78.73 (C-3), 101.72 (C-10a), 113.23 (CN), 122.84 (C-9), 143.78 (C-10b), 144.90 (C-10), 149.29 (C-6a), 158.89 (C-8), 159.78 (C-2), 160.01 (C-4), 168.16 (CO), 114.93, 126.42, 130.26, 155.22 (arom. C's). Anal. calcd. for $C_{21}H_{18}N_6O_3$ (402): C 62.68, H 4.47, N 20.89; found: C 62.39, H 4.21, N 20.62.

Reaction of compound 15 with compounds 20a–20d and 2 with 21a–21d

General procedure

A mixture of compound **15** (10 mmol) and each of compounds **20a**–**20d** (10 mmol) in glacial acetic acid (30 mL) was heated under reflux for 3 h. The solid products obtained after cooling were filtered off and crystallized from the proper solvent to afford compounds **23a**–**23d**, respectively. Reaction of **2** with **21a**–**21d** was preceded in a similar manner to give the same reaction products **23a**–**23d**.

Ethyl-4-amino-3-benzoyl-10-(4-methoxyphenyl)-8-methylpyrido[2′,3′:3,4]pyrazolo[1,5-a]pyrimidine-9-carboxylate (23a)

This compound was formed as yellow crystals from acetic acid (68%), mp 297–298 °C. IR υ (cm^{-1}): 3369, 3235 (NH_2), 1714 (ester C=O), 1647 (PhC=O), 1622 (C=N). ^1H NMR ($CDCl_3$): δ 1.05 (t, *J* = 7.2 Hz, 3H, CH_2CH_3), 2.80 (s, 3H, CH_3), 3.85 (s, 3H, OCH_3), 4.12 (q, *J* = 7.2 Hz, 2H, CH_2CH_3), 7.25–7.57 (m, 9H, Ar–H), 8.62 (s, 1H, $C_{(2)}$–H), 9.67 (br, 2H, NH_2, lost after D_2O-exchange). ^{13}C NMR ($CDCl_3$): δ 13.80 (CH_3CH_2), 24.73 (8-CH_3), 55.20 (OCH_3), 61.41 (OCH_2CH_3), 102.55 (C-10a), 102.87 (C-3), 123.95 (C-9), 138.34 (C-10b), 143.98 (C-10), 145.91 (C-6a), 149.27 (C-2), 151.98 (C-8), 162.15 (C-4), 169.06 (CO_2Et), 195.78 (COPh), 113.44, 126.95, 128.51, 128.81, 130.61, 131.82, 160.31 (arom. C's). MS: (M^+) 481 (63.9%), 105 (100%). Anal. calcd. for $C_{27}H_{23}N_5O_4$ (481): C 67.36, H 4.78, N 14.55; found: C 67.06; H 4.45, N 14.30.

Ethyl-4-amino-3-(4-chlorobenzoyl)-10-(4-methoxyphenyl)-8-methylpyrido[2′,3′:3,4]pyrazolo[1,5-a]pyrimidine-9-carboxylate (23b)

Yellow crystals from acetic acid (65%,), mp 301–302 °C. IR υ (cm^{-1}): 3373, 3237 (NH_2), 1711 (ester C=O), 1648 (Ar. C=O), 1626 (C=N). ^1H NMR (DMSO-d_6): δ 1.02 (t, *J* = 7.25 Hz, 3H, CH_2CH_3), 2.65 (s, 3H, CH_3), 3.81 (s, 3H, OCH_3), 4.08 (q, *J* = 7.25 Hz, 2H, CH_2CH_3), 7.02–7.74 (m, 8H, Ar–H), 8.34 (s, 1H, $C_{(2)}$–H), 9.25 (br., 2H, NH_2). Anal. calcd. for $C_{27}H_{22}N_5O_4Cl$ (515.5): C 62.85, H 4.26, N 13.57, Cl 6.88; found: C 63.15, H 4.00, N 13.27, Cl 6.61.

Ethyl-4-amino-3-(4-methylbenzoyl)-10-(4-methoxyphenyl)-8-methylpyrido[2′,3′:3,4]pyrazolo[1,5-a]pyrimidine-9-carboxylate (23c)

Yellow crystals, (63%, dioxane), mp 317–318 °C. IR υ (cm^{-1}): 3376, 3238 (NH_2), 1713 (ester C=O), 1648 (Ar. C=O). ^1H NMR ($CDCl_3$): δ 1.05 (t, *J* = 7.2 Hz, 3H, CH_2CH_3), 2.44 (s, 3H, CH_3, aroyl), 2.82 (s, 3H, CH_3), 3.87 (s, 3H, OCH_3), 4.15 (q, *J* = 7.2 Hz, 2H, CH_2CH_3), 7.28 (d, *J* = 8.4 Hz, 2H, Ar–H), 7.53–7.59 (m, 6H, Ar–H), 8.66 (s, 1H, $C_{(2)}$–H), 9.46 (br., 2H, NH_2, lost after D_2O-exchange). Anal. calcd. for $C_{28}H_{25}N_5O_4$ (495): C 67.87, H 5.05, N 14.14; found: C 67.60, H 5.36, N 14.39.

Diethyl-4-amino-10-(4-methoxyphenyl)-8-methylpyrido-[2′,3′:3,4]pyrazolo[1,5-a]pyrimidine-3,9-dicarboxylate (23d)

Yellow crystals, (66%, dioxane), mp 258–259 °C. IR υ (cm^{-1}): 3402, 3284 (NH_2), 1715 (ester C=O, $C_{(9)}$), 1700 (ester C=O, $C_{(3)}$), 1642 (C=N). ^1H NMR ($CDCl_3$): δ 1.04 (t, *J* = 7.2 Hz, 3H, CH_2CH_3), 1.41 (t, *J* = 7.1 Hz, 3H, CH_2CH_3), 2.79 (s,3H, CH_3), 3.89 (s, 3H, OCH_3), 4.17 (q, *J* = 7.2 Hz, 2H, CH_2CH_3), 4.44 (q, *J* = 7.1 Hz, 2H, CH_2CH_3), 7.0 (d, *J* = 8.8 Hz, 2H, Ar-H), 7.52 (d, *J* = 8.8 Hz, 2H, Ar–H), 7.75 (br, 2H, NH_2), 8.88 (s, 1H, $C_{(2)}$–H). ^{13}C NMR (DMSO-d_6): δ 13.41 ($2CH_3CH_2$), 23.02 (8-CH_3), 55.16 (OCH_3), 60.53 ($2CH_2CH_3$), 101.43 (C-10a), 120.68 (C-3), 126.87 (C-9), 130.52 (C-10b), 147.81 (C-10), 151.38 (C-6a), 153.04 (C-2), 158.61 (C-8), 159.57 (C-4), 168.27 ($2CO_2Et$), 113.83, 129.39, 142.82, 154.46 (arom. C's). Anal. calcd. for $C_{23}H_{23}N_5O_5$ (449): C 61.46, H 5.12, N 15.59; found: C 61.72, H 5.39, N 15.88.

References

1. C.M.S. Menezes, C.M.R. Sant'Anna, C.R. Rodrigues, and E.J.J. Barreiro. THEOCHEM. **579**, 31 (2002).
2. K. Poreba, A. Oplski, and J. Wietrzyk. Acta Pol. Pharm. **59**, 215 (2002).

© 2007 NRC Canada

3. F.E. Goda, A.A.M. Abdel-Aziz, and O.A. Attef. Bioorg. Med. Chem. **12**, 1845 (2004).
4. F.A. Attaby and A.M. Abdel-Fattah. Phosphorus, Sulfur Silicon Relat. Elem. **155**, 253 (1999).
5. M.A.A. Elneairy, F.A. Attaby, and M.S. Elsayed. Phosphorus, Sulfur Silicon Relat. Elem. **167**, 161 (2000).
6. R.N. Misra, H.Y. Xiao, D.B. Rawlins, W. Shan, K.A. Kellar, J.G. Mulheron, J.S. Sack, J.S. Tokarski, S.D. Kimball, and K.R. Webster. Bioorg. Med. Chem. Lett. **13**, 2405 (2003).
7. J.P. Stasch, K. Dembowsky, E. Perzborn, E. Stahl, and M. Schramm. Br. J. Pharmacol. **135**, 344 (2002).
8. G. Boerrigter, L.C. Costello-Boerrigter, A. Cataliotti, T. Tsuruda, G.J. Harty, H. Lapp, J.P. Stasch, and J.C. Burnett. Circulation, **107**, 686 (2003).
9. D.U. Bawankule, K. Stathishkumar, K.K. Sardar, D. Chanda, A.V. Krishna, V.R. Prakash, and S. K. Mishra. J Pharmacol. Exp. Ther. **314**, 207 (2005).
10. (*a*) F.A. Attaby, A.H.H. Elghandour, M.A. Ali, and Y.M. Ibrahem. Phosphorus, Sulfur Silicon Relat. Elem. **181**, 1087 (2006); (*b*) F.A. Attaby, A.H.H. Elghandour, M.A. Ali, and Y.M. Ibrahem. Phosphorus, Sulfur Silicon Relat. Elem. **182**, 133 (2007).
11. A.R. Azevedo, V.F. Ferreira, H. de Mello, L.R. Leao-Ferreira, A.V. Jabor, I.C.P.P. Frugulhetti, H.S. Pereira, N. Moussatche, A.M.R. Bernardino. Heterocycl. Commun. **8**, 427 (2002).
12. H. de Mello, A. Echevarria, A.M. Bernardino, M. Canto-Cavalheiro, and L.L. Leon. J. Med. Chem. **47**, 5427 (2004).
13. K. Poreba, A. Opolski, J. Wietrzyk, and M. Kowalska. Arch. Pharm. **334**, 219 (2001).
14. M.J. Alberti, E.P. Auten, K.E. Lackey, O.B. McDonald, E.R. Wood, F. Preugschat, G.J. Cutler, L. Kane-Carson, W. Liu, and D.K. Jung. Bioorg. Med. Chem. Lett. **15**, 3778 (2005).
15. M.A.A. Elneairy, M.A.M. Gad-Elkareem, and A.M. Taha. J. Sulfur Chem. **26**, 381 (2005).
16. M.A.M. Gad-Elkareem and A.O. Abdelhamid. Afinidad, **61**, 427 (2004).
17. (*a*) M.A.A. Elneairy, M.A.M. Gad-Elkareem, and A.M. Taha. Heteroat. Chem. 1**8**, 399 (2007); (*b*) A.M. Abdel Fattah, M.A.A. Elneairy, and M.A.M. Gad-Elkareem. Phosphorus, Sulfur Silicon Relat. Elem. **182,** 1351 (2007).
18. M.A.A. Elneairy and A.M. Abdel-Fattah. Phosphorus, Sulfur Silicon Relat. Elem. **175**, 15 (2001).
19. M.A.M. Gad-Elkareem, A.M. Abdel-Fattah, and M.A.A. Elneairy. Phosphorus, Sulfur Silicon Relat. Elem. **181**, 891 (2006).
20. F.A. Attaby, L.I. Ibrahim, S.M. Eldin, and A.K.K. El-Louh. Phosphorus, Sulfur Silicon Relat. Elem. **73**, 127 (1992).
21. M.S.A. El-Gaby, N.M. Taha, J.A. Michy, and M.A.M.Sh. El-Shareif. Acta Chim. Slov. **49**, 159 (2002).
22. A.M.S. Youssef and M.M. Youssef. Indian J. Chem. **37B**, 948 (1998).
23. H.D. Edward and J.D. Kendall. US Patent 2 533 233 (1950) [Chem. Abstr. **45**, 2804a (1951)].
24. A. Al-Enezi, B. Al-Saleh, and M.H. Elnagdi. J. Chem. Res., Synop. 4 (1997).
25. K.M. Al-Zaydi, M.A. Al-Shiekh, and E.A. Hafez. J. Chem. Res., Synop. 13 (2000).
26. S.M. Al-Mousawi, M.A. Mohammad, and M.H. Elnagdi. J. Heterocycl. Chem. **38**, 989 (2001).
27. Y.W. Ho and C.T. Yao. J. Chin. Chem. Soc. **50**, 283 (2003).
28. M.A.A. Elneairy. Phosphorus, Sulfur Silicon Relat. Elem. **178**, 2201 (2003).
29. V.A. Makarov, O.B. Ryabova, L.M. Alekseeva, A.S. Shashkov, and V.G. Granik. Chem. Heterocycl. Compd. **39**(2), 238 (2003).

© 2007 NRC Canada

Chromatographic enantiomer separation and circular dichroism (CD) spectra of three 4-endosubstituted-3,6-diphenyl-3,6-phenylphosphorylcyclohexenes

Martin B. Hocking and Aga Z-Q. Khan

Abstract: Three enantiomeric pairs of Diels–Alder adducts of 2,5-diphenylphosphole-1-oxide have been resolved by elution of each of the enantiomers with 95% ethanol from a swollen microcrystalline triacetylcellulose stationary phase. The degree of separation achieved in each case was confirmed by comparing the absorbance maximum of the UV spectrum of each separated enantiomer with that of a similar concentration of the relevant racemic mixture. The circular dichroism (CD) spectrum of each of the separated enantiomers was recorded, and spectral parameters are listed.

Key words: enantiomer separations, three 4-endosubstituted phosphorus-bridged cyclohexenes (phosphanorbornenes), ethanol, microcrystalline triacetylcellulose.

Résumé : On a effectué la résolution de trois paires énantiomères d'adduits de Diels–Alder du 1-oxyde de 2,5-diphénylphosphole en faisant l'élution de chaque énantiomère à l'aide d'éthanol à 95% à partir d'une phase stationnaire formée de triacétylcellulose microcristalline gonflée. Le degré de séparation obtenu pour dans chaque cas a été confirmé en procédant à une comparaison du maximum d'absorbance dans le spectre UV de chaque énantiomère séparé avec celui à une concentration similaire du mélange racémique approprié. On a enregistré les spectres de DC de chacun des énantiomères séparés et on rapporte les paramètres spectraux.

Mots-clés : séparation d'énantiomères, trois cyclohexènes à pont de phosphore et substitués en position 4 endo (phosphanorbornènes), éthanol, triacétylcellulose microcristalline.

[Traduit par la Rédaction]

Introduction

A number of chiral drugs and pesticides are in commercial use as their racemic mixtures because of either the lack of a suitable stereospecific synthetic route to the respective enantiomers or the practical difficulties attached to the resolution of these materials on a large scale at the time of their development. Growing recognition of the important differences in the bioactivity of isolated enantiomers, compared with the activity of their racemic mixtures in the same applications, has spurred the development of viable stereospecific synthetic routes to individual enantiomers (1). Recently, difficulties with some enantiomer syntheses scale have stimulated the mastery of several racemate separation techniques on a preparative scale (2). In particular, enantiomer separations by chromatographic techniques using solvent elution from chiral stationary phases (CSPs) have been substantially refined (3). Among the available stationary phases, swollen microcrystalline triacetylcellulose (TAC) has been found to be among the most versatile of CSPs for both analytical and preparative separations (4, 5).

In connection with another synthetic project, we had prepared racemic mixtures of three phosphorus-containing heterocycles by the addition of the appropiate dienophile to 1,2,5-triphenylphosphole-1-oxide (6) (Chart 1).[2] In this paper, we examine the efficacy of a few of the resolution methods outlined here for the separation of these racemic mixtures (7–9).

Received 30 January 2007. Accepted 05 July 2007. Published on the NRC Research Press Web site at canjchem.nrc.ca on 21 August 2007.

M.B. Hocking.[1] Department of Chemistry. University of Victoria, Victoria, BC V8W 3V6, Canada.
A. Z-Q. Khan. Organic Chemistry 3, University of Lund, Box 124, S-221 00 Lund, Sweden. (Present address: Glycorex AB, Sölvegatan 41, SE-223 70, Lund, Sweden.)

[1]Corresponding author (e-mail: hockingm@uvic.ca).
[2]Martin B. Hocking. Unpublished results.

Experimental section

Chromatographic separations

Thirty milligrams of each of compounds **1**–**3** was dissolved in ethanol (95%, 1 mL), and the solution was injected into the chromatographic system. This consisted of two 60 × 1.0 cm steel columns, packed with swollen microcrystalline triacetylcellulose (TAC) and connected in series. The eluate (mobile phase: 95% ethanol, flow rate 1 mL/min) was passed through an UV detector (LKB Uvicord, 224 nm) followed by a polarimeter detector (PerkinElmer 241 MC, 365 nm, Hg lamp) in series. The output from the detector was fed to a two-channel recorder (LKB Model 2210) to obtain the chromatogram. The eluate was collected after its passage through the polarimeter tube. Further experimental

 doi:10.1139/V07-088 © 2007 NRC Canada

Table 1. Direction of rotation and separation parameters of the resolved enantiomers.

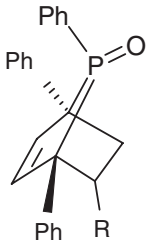
Compound	Optical rotation of the first-eluted enantiomer	k_1'	k_2'	α
1	–	0.51	0.64	1.25
2	+	1.02	1.21	1.19
3	+	0.38	0.47	1.25

Table 2. CD spectra of the first-eluted enantiomers of compounds **1**–**3** in 95% ethanol.

Compound	λ_{max}(nm)($\Delta\epsilon$)[a]
1	274 (–0.3), 267 (–0.2), 224 (+8.2), 207 (–4.7)
2	256 (+0.7), 231 (+7.2), 217 (–5.3)
3	271.5 (+2.0), 265 (+2.6), 252 (+1.6), 259 (+2.1), 217 (+38.0)

[a]Corrected to 100% enantiomeric excess.

Chart 1. Structures of the racemates of novel compounds examined for their ease of resolution by chiral chromatography.



1. R = CO_2Et
2. R = CN
3. R = Ph

details of the resolution methodology are given in the literature (10).

Circular dichroism (CD) spectral methods

The CD spectra of the first-eluted enantiomers (El) were recorded directly from the eluted chromatographic fractions containing them, using a JASCO Model J-500A spectropolarimeter. Concentrations were measured from their UV spectra obtained using a Cary Model 2290 spectrophotometer by comparing the absorbances of the resolved compounds at 261 nm with those of spectra recorded on solutions of the pure racemic compounds of about the same concentration in the same solvent.

Results and discussion

Resolutions achieved

After only a single pass through the resolution columns, initially all three compounds **1**–**3** were only poorly resolved, as evidenced by no resolved elution peaks in the continuous UV trace taken of the column effluent. Recycling improved the separation to give well-resolved samples after three cycles. Enantiomeric excesses were checked by recording their solution ^{1}H NMR spectra on a Varian Model XL-300 NMR spectrometer in the presence of the chiral-shift reagent "Pirkle's alcohol" (11), (+)-1-(9-anthryl)-2,2,2-trifluoroethanol (**4**). Spectra of racemic **1** with one equivalent of **4** in $CDC1_3$ showed two partly resolved triplets for the ester methyl group, whereas **2** and **3** showed two completely separated multiplets for 4-H. The ^{1}H NMR spectrum of the fully resolved **3** under the same conditions showed only one 4-H multiplet even when the plot gain was increased, indicating a 98%–99% optical purity. The less well-resolved ester **1** showed two overlapping methyl triplets with unequal intensities, and the cyano compound **2** showed two 4-H multiplets with unequal intensities. The measured ratios of enantiomers in the latter two samples were 0.73:0.27 and 0.67:0.33, respectively, corresponding to 46% and 34% enantiomeric excess for **1** and **2**. The evaluation was performed by calculation of theoretical NMR spectra and then adjusting the ratios to obtain the best fit with the experimental spectra.

A measure of the quantitative efficiency of the chromatograpic separation was obtained by substituting t_1, t_2, and t_0, which are the retention times of the first and second enantiomers eluted, and the non-retained reference (1,3,5-tri-*t*-butylbenzene), respectively, into eq. [1] and [2]. The capacity factors k_1' and k_2' were then used to obtain the selectivity factor α by substitution into eq. [3] (12).

$$[1] \qquad k_1' = \frac{t_1 - t_0}{t_0}$$

$$[2] \qquad k_2' = \frac{t_2 - t_0}{t_0}$$

$$[3] \qquad \alpha = \frac{k_2'}{k_1'}$$

The results are given in Table 1.

Other stationary phases tested

Attempts to resolve compounds **1**–**3** by elution with 60:35:5 *n*-hexane:dioxane:isopropanol or 50:50 hexane:dioxane on HIBAR (13) columns (from Alltech Associates Inc., Deerfield, Illinois) were fruitless. Likewise, using 75:25 or 50:50 *n*-hexane:dioxane on TRIM (14) columns (rigid macroporous particles prepared by suspension polymerization of trimethylolpropane trimethacrylate) were also unsuccessful.

The CD spectral parameters of the first-eluted enantiomers obtained as described in the Experimental Section are given in Table 2. The CD spectra of the second enantiomers were also recorded and were found to be mirror images of

© 2007 NRC Canada

the first enantiomers, which confirmed that no decomposition had occurred during the chromatography.

Because of the complexity of the chromophoric system, a detailed analysis of the CD spectra was not feasible. Without a substituent in the 4 position, the molecule is achiral with a plane of symmetry through the phosphorus atom bisecting the 1–2 and 4–5 bonds. Introduction of the 4-substituent creates a chiral center at C-4 and also renders the phosphorus atom stereogenic. However, ^{1}H NMR spectra of the various isolated chiral fractions showed no evidence of more than two enantiomers. Presumably, rates of interconversion of the two phosphorus substituents in each of these examples were sufficiently high to reduce the number of isolable enantiomers observed to two. The rotational strengths of the various electronic transitions in the molecule arise mainly by interaction through space between the transition moments in the individual chromophores. The CD bands of **3** are more intense than the bands of **1** and **2** because the 4-phenyl group has electronic transitions in the near UV region, which interact much more strongly with the transitions of the other phenyl groups in the same wavelength region than do the far-UV transitions of the ester and cyano groups.

Acknowledgements

Financial support by the Swedish Natural Science Research Council and the Knut and Alice Wallenberg Foundation to Aga Khan (courtesy of Professor Jan Sandstrom, Lund University) is gratefully acknowledged. Roland Isaksson (L. U.) is thanked for valuable discussion.

References

1. B. Waldeck. Pharmacol. Toxicol. **93**, 203 (2003).
2. Y. Okamoto and E. Yashima. Angew. Chem., Int. Ed. **37**, 1020 (1998).
3. W.H. Pirkle and T.C. Pochapsky. Chem. Rev. **89**, 347 (1989).
4. G. Hesse and R. Nagel. Chromatographia, **9**, 62 (1976).
5. A. Mannschreck, H. Koller, and R. Wernicke. Kontakte (Darmstadt) **1**, 40 (1985); and refs. cited therein.
6. I.G.M. Campbell, R.C. Cookson, M.B. Hocking, and A.N. Hughes. J. Chem. Soc. 2184, (1965).
7. R. Isaksson, P. Erlandsson, L. Hansson, A. Holmberg, and S. Berner, J. Chromatogr. **498**, 257 (1990).
8. A. Ichida and T. Shibat. *In* Chromatographic chiral separations. *Edited by* M. Zeif and L.J. Crane. Marcel Decker, New York – Basle. 1988. Chap. 9.
9. G. Blaschke. J. Liq. Chromatogr. **9,** 341 (1986).
10. R. Isaksson and J. Roschester. J. Org. Chem. **50**, 2519 (1985).
11. W.H. Pirkle, D.L. Sikkenga, and M.S. Pavlin. J. Org. Chem. **42**, 384 (1977).
12. S. Allenmark. Chromatographic Enantioseparation: methods and applications. Ellis Horwood Ltd., Chichester. 1991. Chap. 4.
13. J.N. Kinkel, W. Fraenkel, and G. Blaschke. Kontakte (Darmstadt) **1**, 3 (1987).
14. T. Hargitai, P. Reinholdsson, B. Tornell, and R. Isaksson. J. Chromatogr. **540**, 145 (1991).

© 2007 NRC Canada

Efficient preparation of chiral non-racemic sulfur compounds

Joannie Minville, Mélina Girardin, and Claude Spino

Abstract: *p*-Menthane-3-carboxaldehyde serves as an efficient chiral auxiliary in the preparation of chiral non-racemic *S*-alkylthiocarbamates or *S*-dithiocarbonates via the 3,3-sigmatropic rearrangement of the corresponding alkylthionocarbamates or xanthates. The transfer of chirality during rearrangement is complete, and the final products possess a chiral tertiary or quaternary carbon bearing sulfur. The rearranged products are then transformed into enantiopure cyclic or acyclic sulfur-containing products, depending on the means of clivage of the auxiliary. The synthesis of a potent MMP-13 inhibitor is presented.

Key words: 3,3-sigmatropic rearrangement, *p*-menthane-3-carboxaldehyde, *S*-alkylthiocarbamate, *S*-dithiocarbonate, alkylthionocarbamate, xanthate, ring-closing metathesis.

Résumé : Le *p*-menthane-3-carboxaldéhyde est un auxiliaire chiral efficace dans la préparation de *S*-alkylthiocarbamates ou de *S*-dithiocarbonates non chiraux par le biais d'un réarrangement sigmatropique-3,3 des alkylthionocarbamates ou des xanthates correspondants. Le transfert de chiralité durant ce réarrangement est total et les produits finaux possèdent un atome de carbone tertiaire ou quaternaire chiral portant un atome de soufre. Suivant les méthodes utilisées pour cliver l'auxiliaire, es produits réarrangés sont alors transformés en produits cycliques ou acycliques énantiopurs contenant du soufre. On rapporte la synthèse d'un puissant inhibiteur MMP-13.

Mots-clés : réarrangement sigmatropique-3,3, *p*-menthane-3-carboxaldéhyde, *S*-alkylthiocarbamate, *S*-dithiocarbonate, alkylthionocarbamate, xanthate, métathèse accompagnant une fermeture de cycle.

[Traduit par la Rédaction]

Introduction

Many natural and man-made products, containing a sulfur atom, have huge potential in medicinal chemistry (1). Figure 1 lists some examples. Montelukast **1** (singulair) is a potent antagonist of the cysteinyl leukotriene receptor and serves as a prophylactic, once-a-day, anti-asthma agent (2). Compound **3** is a potent inhibitor of phosphodiesterases (PDE4) at nanomolar concentrations (3). Natural products, containing a chiral sulfide moiety, include the fatty-acid synthetase inhibitors thiolactomycin **4** and thiotetromycin **5** (4), gliotoxin **6** (5), with antiviral, antibacterial, and immunosuppressive activities, and biotin **2** (6).

The construction of chiral C–O and C–N bonds has reached a higher level of sophistication than the making of chiral C–S bonds (7). In fact, chiral C–S bonds are often made by displacement of the corresponding chiral C–O bonds (8). When displacing a chiral allylic C–O bond, transposition may or may not occur. With Mitsunobu reactions, transposition is usually not observed (9), whereas 3,3-sigmatropic rearrangements provide products with a transposed double bond (10).

Received 18 May 2007. Accepted 03 July 2007. Published on the NRC Research Press Web site at canjchem.nrc.ca on 21 August 2007.

J. Minville, M. Girardin, and C. Spino.[1] Département de Chimie, Université de Sherbrooke, Sherbrooke, QC J1K 2R1, Canada.

[1]Corresponding author (email: Claude.Spino@USherbrooke.ca).

In that regard, we viewed our chiral scaffold derived from *p*-menthane-3-carboxaldehyde **7** as ideal to implement a methodology aimed at preparing chiral sulfur-containing compounds (Scheme 1) (11). First, the bulky menthyl moiety allows rearrangements reactions to occur at low temperatures (11*b*). Thus, the 3,3-sigmatropic rearrangement of allylic thionocarbamates (12, 13), phosphonothionates (12*b*), xanthates (14), or similar precursors should proceed smoothly to give the desired chiral C–S bond, even in the case of trisubstituted double bonds. Second, the chiral auxiliary is cleavable by two completely different methods, giving rise to cyclic or acyclic products. Last, either stereochemistry of the targeted chiral C–S bond can be selected by controlling the stereochemistry of the alcohol (both are easily obtained) and (or) the geometry of the alkene and (or) the absolute configuration of **7** (both enantiomers are readily available and inexpensive). This flexibility is a great asset for synthesis.

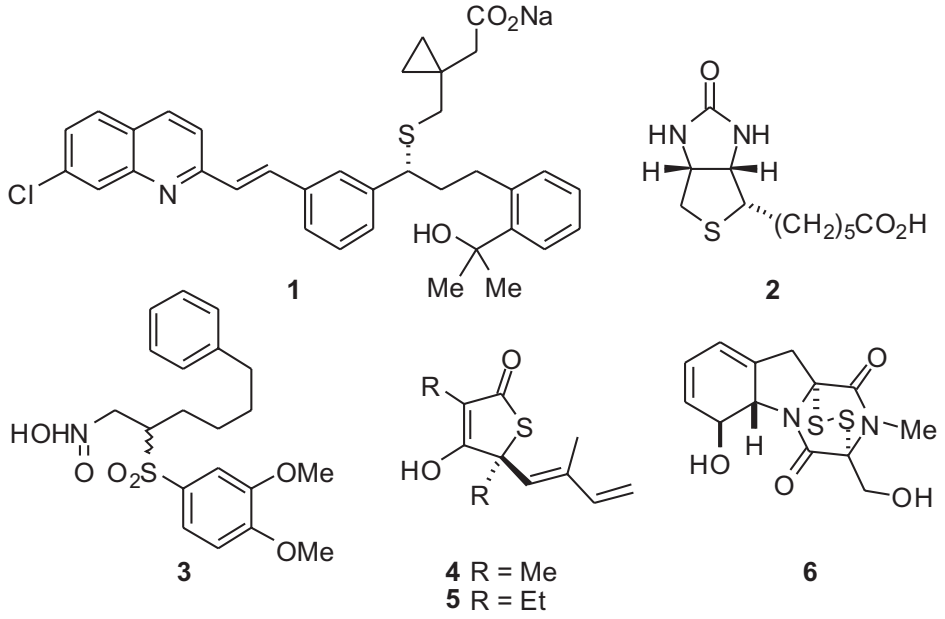
Results and discussion

Building the thiocarbamates and xanthates

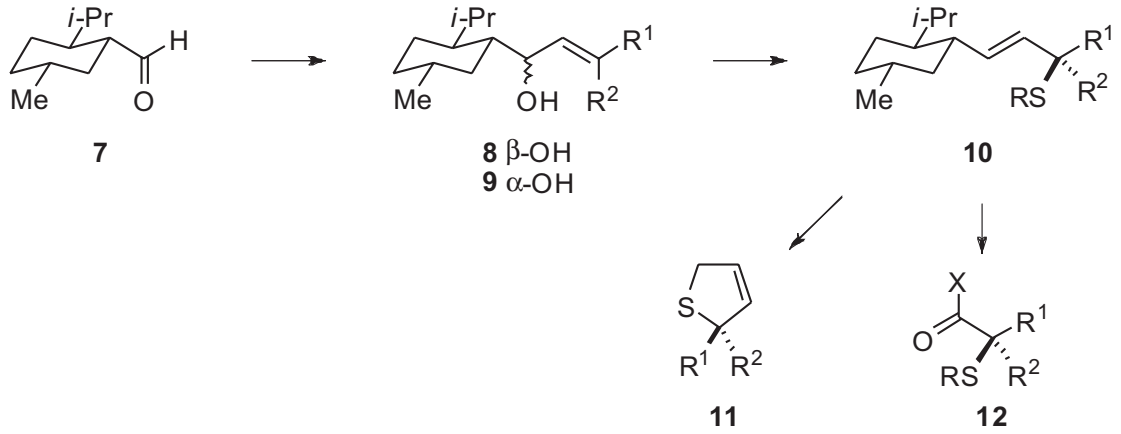
Our strategy starts with the synthesis of allylic alcohols **8**, which were prepared by one of methods A, B, or C (Scheme 2). Method A involves the preparation of vinyl iodides **17** using Schwartz' hydrozirconation or hydroboration of the substituted acetylenes **13**. After submitting vinyl iodides **17** to a metal-halogen exchange using *t*-butyllithium, the resulting vinyllithiums **18a** were stereoselectively added to (–)-*p*-menthane-3-carboxaldehyde **7** in the presence of

 doi:10.1139/V07-091 © 2007 NRC Canada

Fig. 1. Biologically active sulfur-containing natural and unnatural products.



Scheme 1. Strategy to obtain chiral sulfur compounds.



trimethylaluminium (15). The major alcohols **8a**, **c**, **d**, and **f** result from the addition of the vinyllithiums to aldehyde **7** following Felkin–Ahn's model of stereoselectivity (16). Trimethylaluminium renders this addition highly stereoselective, and the Felkin adducts **8** were isolated essentially as a single isomer (52 to 200:1; Table 1, entries 1, 3, 4, and 6). Method B uses the stereoselective addition of vinylalanes **18b**, made from the zirconium-catalyzed carboalumination (17) of alkynes **13**, to aldehyde **7**. While this method is slightly less stereoselective than method A, it is nonetheless the excess trimethylaluminium used during the carbolumination process that provides this level of stereoselection (11 to 30:1; Table 1, entries 2, 7, and 8). Evaporation of the excess trimethylaluminium prior to addition to **7** leads to lower stereoselectivities. Method C involves the addition of lithium acetylides **14** to **7**. Propargyl alcohol **15**, isolated as a 2:1 mixture of diastereomers, was then converted to the desired allylic alcohol **8** using Red-Al. All mixtures of alcohols **8** and **9** were easily separated by flash chromatography, and the sequence was continued with isomerically pure alcohols as determined by GC or HPLC.

The minor diastereomer **9** (α-OH) could be prepared in sufficient quantities first by oxidizing the major isomer **8** to the corresponding enone **19** and then by reducing the latter using Super-Hydride™ (Scheme 3). This reduction is completely diastereoselective and gives **9** as the sole diastereomer (11*a*). Having access to both alcohols **8** and **9** in large quantities allowed us to measure the diastereoselectivities of the subsequent reactions. Moreover, both enantiomers of the final chiral sulfur compounds can be prepared from a single enantiomer of the chiral auxiliary **7** via alcohols **8** or **9**, since they lead to enantiomeric products after cleavage of the chiral auxiliary, respectively.

Starting from the allylic alcohols **8** or **9**, we procured the allylic thionocarbamates as intermediates (not shown), using *N*-phenylisothiocyanate as reagent to make them. They rearranged to the *S*-allylthiocarbamates **20** or **21**, respectively, upon acidification of the reaction mixture with PPTS (Table 2). The rearrangement does not proceed (or proceeds very slowly) while the allylthionocarbamates are still under basic conditions. However, once the solution is acidified, the rearrangement takes place within a few hours at 66 °C.

© 2007 NRC Canada

Scheme 2. Preparation of alcohols **8**.

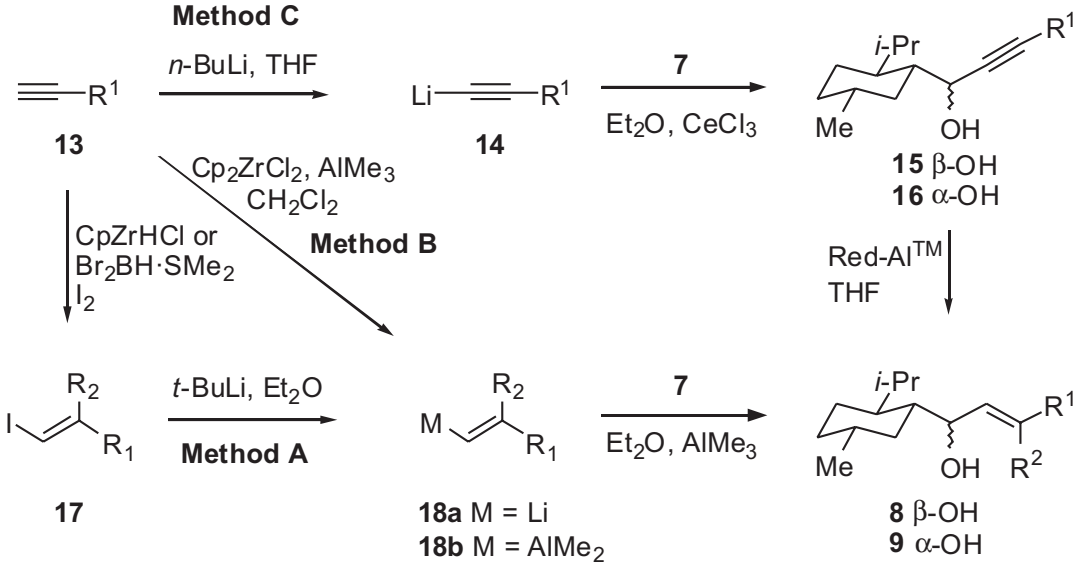
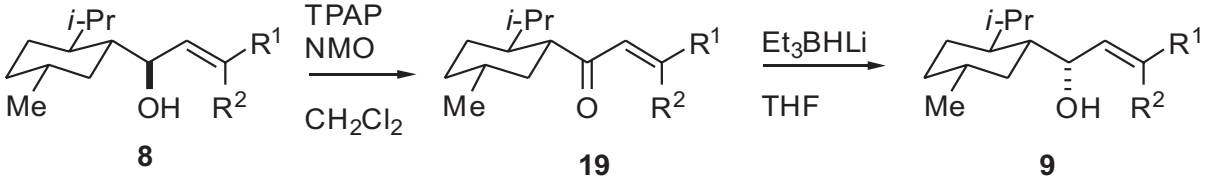


Table 1. Yields and % de of alcohols **8**.

Entry	**13**	R^1	R^2	Method	Yield (%)[a]	de (%)[b]
1	**a**	*n*-Pr	H	A	72	98
2	**b**	*n*-Pr	Me	B	87	94
3	**c**	*t*-Bu	H	A	66	>99
4	**d**	Me_3Si	H	A	46	>99
5	**e**	Ph	H	C	97	90
6	**f**	$Ph(CH_2)_4$	H	A	68	96
7	**g**	$Ph(CH_2)_4$	Me	B	82	88
8	**h**	Bn	Me	B	81	92

[a]Isolated yield.
[b]Measured by GC or HPLC on crude mixtures.

Scheme 3. Preparation of the diastereomeric alcohols **9**.



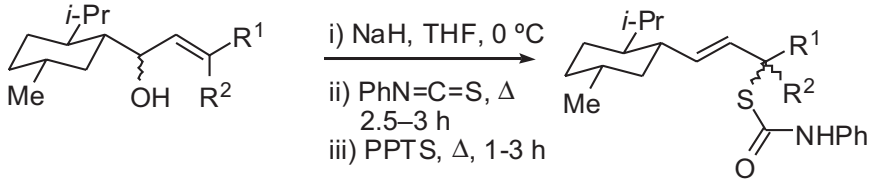
Many substrates underwent the rearrangement slowly at room temperature within several days. This sequence allowed us to prepare various *S*-allylthiocarbamates **20a**–**20h** and **21a**–**21h** in good to excellent yields with diastereomeric excesses (de) > 90%. We believe that the de of compound **21f** reported in Table 2, entry 12 is > 76%. The lower-than-expected value may be due to an impurity that co-elutes with the diastereomer of **21f**, and that we could neither identify nor remove. The structure of **20c** was confirmed by single crystal X-ray diffraction analysis, and it was consistent with a concerted rearrangement of **8c** via a chair-like transition state (TS) **20**-*E*-chair (Scheme 4).

The minor *S*-thiocarbamates in the rearrangement of the thionocarbamates derived from **8** or **9** do not come from a competing concerted transition state (18) but must instead be derived from ionic pathways competing with the concerted one. Indeed, a close look at the possible transition states (Scheme 4, only the chair-like TS are represented) (19) leads us to the conclusion that to attack the alkene face leading to the minor *S*-thiocarbamate, the thionocarbamate must maximize its $A^{1,3}$ strain, which would give a product having a *Z* double bond. There is no concerted pathway leading to **21** from **8** or to **20** from **9**. Ionic intermediates, on the other hand, would collapse to a mixture of **20** and **21** regardless of their origin.

One might wonder why we did not observe the formation of regioisomers **23** as a minor product if ionic intermediates are involved. However, it is our experience that the menthyl moiety is very efficient at preventing attack at the β position. For example, when alcohol **8g** is submitted to an acidic environment, some regioisomer **24g** was isolated as a mixture of diastereomers, but the recovered alcohol **8g** was diastereo-

© 2007 NRC Canada

Table 2. Yields and % de of thiocarbamates **20** and **21**.



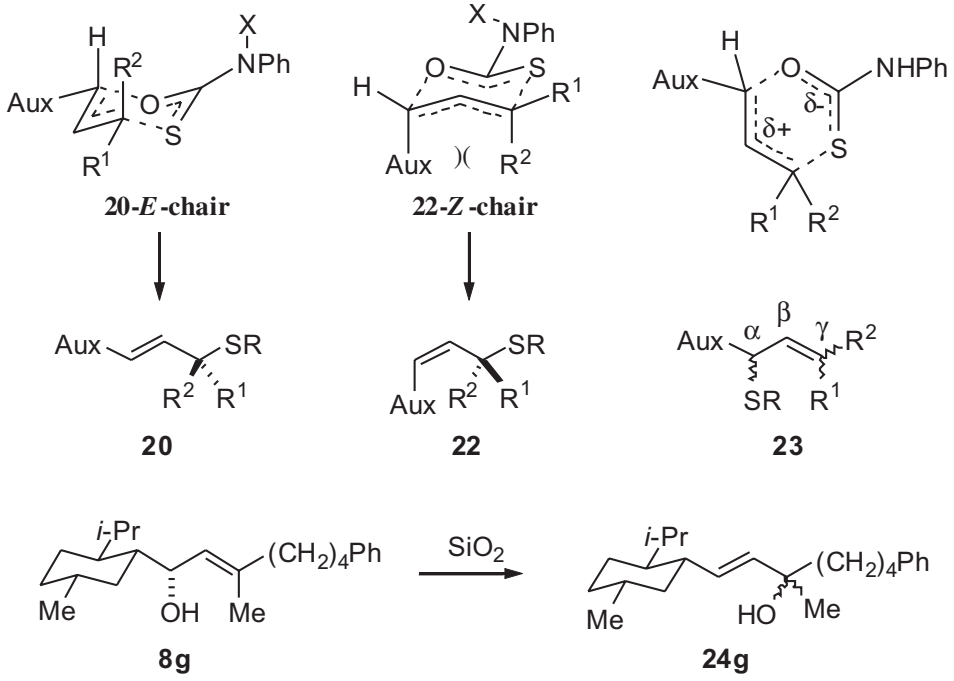
8 β-OH
9 α-OH

20 β-SC(O)NHPh
21 α-SC(O)NHPh

Entry	Alcohol	R^1	R^2	Product	Yield (%)[a]	de (%)[b]
1	**8a**	*n*-Pr	H	**20a**	97	98
2	**9a**	*n*-Pr	H	**21a**	99	>99
3	**8b**	*n*-Pr	Me	**20b**	75	>99
4	**9b**	*n*-Pr	Me	**21b**	65	98
5	**8c**	*t*-Bu	H	**20c**	96	98
6	**9c**	*t*-Bu	H	**21c**	99	>99
7	**8d**	Me_3Si	H	**20d**	99	>99
8	**9d**	Me_3Si	H	**21d**	87	>99
9	**8e**	Ph	H	**20e**	81	93
10	**9e**	Ph	H	**21e**	97	90
11	**8f**	$Ph(CH_2)_4$	H	**20f**	99	97
12	**9f**	$Ph(CH_2)_4$	H	**21f**	94	76[c]
13	**8g**	$Ph(CH_2)_4$	Me	**20g**	87	98
14	**9g**	$Ph(CH_2)_4$	Me	**21g**	67	>99
15	**8h**	Bn	Me	**20h**	88	99
16	**9h**	Bn	Me	**21h**	85	>99

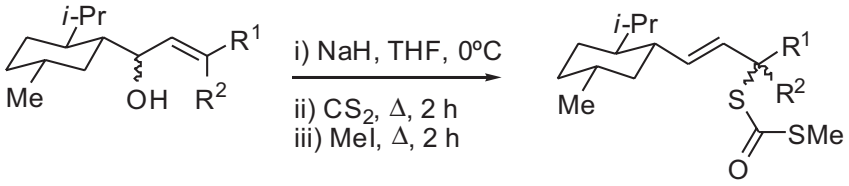
[a]Isolated yield.
[b]Measured by GC or HPLC on crude mixture.
[c]Presence of impurity with same retention time as diastereomer makes % de appear lower than actual value.

Scheme 4. Chair-like transition state for the rearrangement.



© 2007 NRC Canada

Table 3. Yields and % de of *S*-thiocarbonates **25** and **26** and *S*-thiocarbamates **27** and **28**.



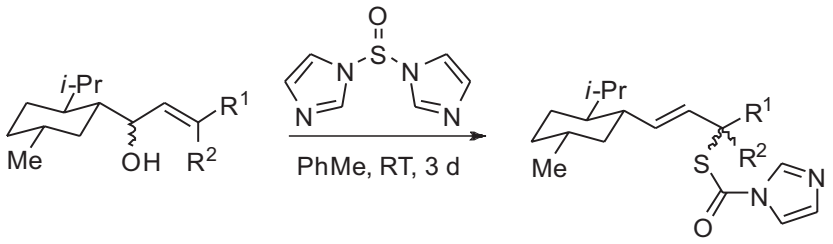
8 β-OH
9 α-OH

25 β-SC(O)SMe
26 α-SC(O)SMe

Entry	Alcohol	R^1	R^2	Product	Yield (%)[a]	de (%)[b]
1	**8b**	*n*-Pr	Me	**25b**	59	99
2	**9b**	*n*-Pr	Me	**26b**	39	98
3	**8c**	*t*-Bu	H	**25c**	99	>99
4	**9c**	*t*-Bu	H	**26c**	90	98
5	**8f**	$Ph(CH_2)_4$	H	**25f**	85	>99
6	**9f**	$Ph(CH_2)_4$	H	**26f**	85	96
7	**8c**	*t*-Bu	H	**27c**	78	97
8	**9c**	*t*-Bu	H	**28c**	42	99
9	**8e**	Ph	H	**27e**	0	—
10	**9e**	Ph	H	**28e**	0	—

[a]Isolated yield.
[b]Measured by GC or HPLC on crude mixture.

Scheme 5. Imidazole variant of the thiocarbamate rearrangement.



8 β-OH
9 α-OH

27 β-SC(O)imid
28 α-SC(O)imid

merically pure. This implies that the ionic intermediates collapsed exclusively to the regioisomer **24g**.

Our observation that the thionocarbamates (Scheme 4, X = H) rearrange much faster than the metallated thionocarbamates (X = Na) is in line with observations by Nakai and Zaim that electron donors (e.g., R_2N) at that position slowed the rearrangement, while an electron-withdrawing group such as Cl increased the reaction rate (18). Possibly, the proton sits exclusively on the nitrogen atom in the thionocarbamate, while the metal is perhaps on sulfur. According to Nakai and Ari-Izumi, a higher bond order for the thiocarbonyl is found in precursors that undergo fast reactions (18*a*).

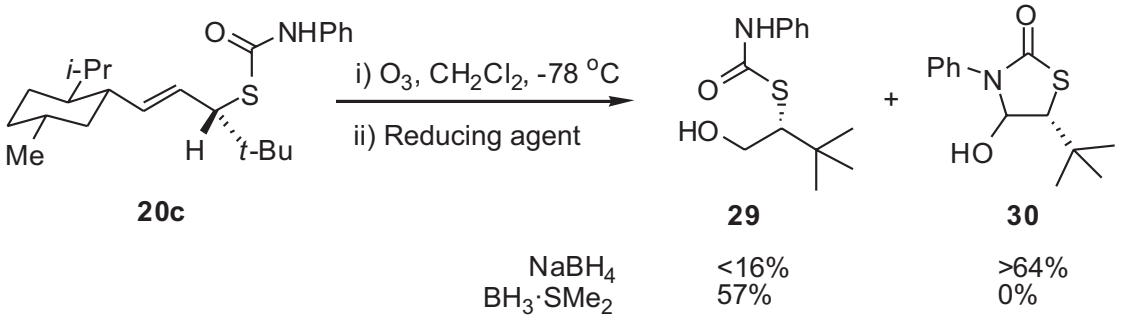
Also, these authors found that substitution on the allylic fragment increased the reaction rate. Although we have not measured the actual rate constants of our reactions, we have qualitatively observed that the thionocarbamates derived from the trisubstituted allylic alcohols **8b**, g, h and **9b**, g, h rearranged substantially faster than the others. For example, the thionocarbamates derived from **8g** and **9g** rearranged in 53% and 67% yield, respectively, at room temperature in 24 h. The analogous thionocarbamates made from **8f** and **9f** did not rearrange after the same time at room temperature. Several days later, some rearrangement was observed for **8f** and **9f**, but the reaction had not reached completion. This same trend was observed for **8a** and **8c**.

Xanthates derived from alcohols **8** or **9** rearranged to allylic dithiocarbonates **25** or **26** (Table 3, entries 1–6). The reaction conditions and times were very similar to the ones used for the thionocarbamates. Table 3 reveals that yields and diastereoselectivities are also comparable. The main difference resides in the subsequent cleavage of the chiral auxiliary (see later).

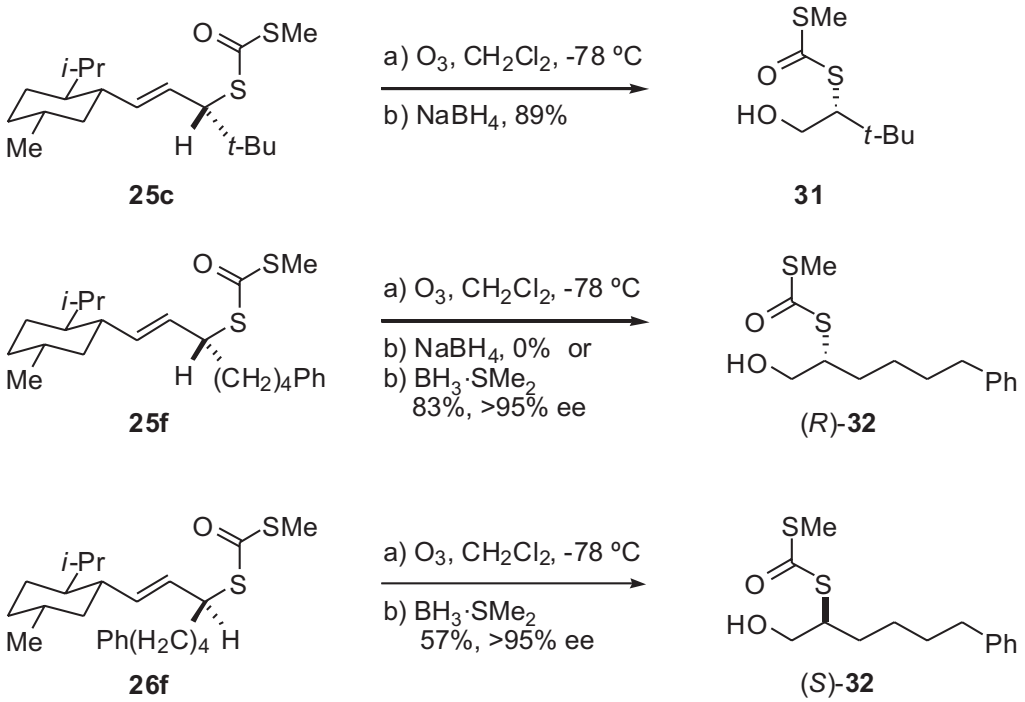
We also tested the rearrangement on the imidazole variant of thionocarbamates because they are supposed to proceed at lower temperatures, which could be an advantage for some thermally unstable substrates (Scheme 5 and Table 3, entries 7–10) (20). Indeed, we obtained a 78% yield of **27c** from **8c** after stirring for 3 days at room temperature (Table 3, entry 7). However, while the rearrangements were somewhat faster than their *N*-phenyl carbamate analogs, it proved to be less general. For example, alcohols **8e** and **9e** yielded only elimi-

© 2007 NRC Canada

Scheme 6. Oxidative cleavage of the *S*-thiocarbamate **20c**.



Scheme 7. Oxidative cleavage of *S*-thiocarbonates **25c**, **25f**, and **26f**.



nation and other decomposition products under those conditions.

The low temperature at which all of these rearrangements take place is noteworthy and likely the result of the steric volume of the menthyl fragment (steric decompression).[2] Some thionocarbamates derived from **8** or **9** undergo rearrangement at room temperature, albeit rather slowly. Usually, such compounds require heating in excess of 100 °C for the rearrangement to take place. For example, Thomas and co-workers used, in their synthesis of thiotetronic acids, a xanthate to thiocarbonate rearrangement that occurred at 145 °C during distillation (10).

Cleaving the chiral auxiliary

Oxidative cleavage

Cleavage of the auxiliary in *S*-thiocarbamate **20c** with ozone, the usual method by which we cleave this chiral auxiliary (11), resulted in the efficient conversion of the starting material. Indeed, a reductive work-up with $NaBH_4$ led to the formation of a mixture of the desired alcohol **29** and thiazolidinone **30** in 80% combined yield (Scheme 6). When $BH_3 \cdot SMe_2$ was used as the reducing agent, only alcohol **29** was formed in 57% yield. The Lemieux protocol ($OsO_4/NaIO_4$) or similar methodologies are less efficient and often lead to a mixture of products.

The yields of cleavage products were consistently better from *S*-thiocarbonates **25** or **26**. Here too, the use of $BH_3 \cdot SMe_2$ usually gives superior results, though sodium borohydride can give good yields of products (Scheme 7). This is the protecting group of choice for sulfur if oxidative cleavage is needed. We verified the stereochemical integrity of the alcohols **32** by making the Mosher ester derivatives on both enantiomers and found no racemization. Aldehydes can be prepared using dimethylsulfide as reducing agent but α-thioaldehydes are sensitive to racemization and must be used without purification, unless of course the α-position is dialkylated (see later).

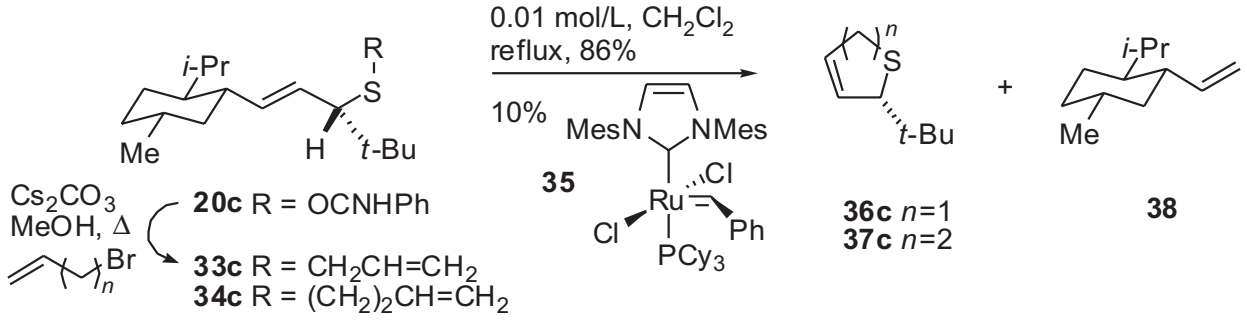
Cleavage by ring-closing metathesis

We have recently discovered that it is possible to generate

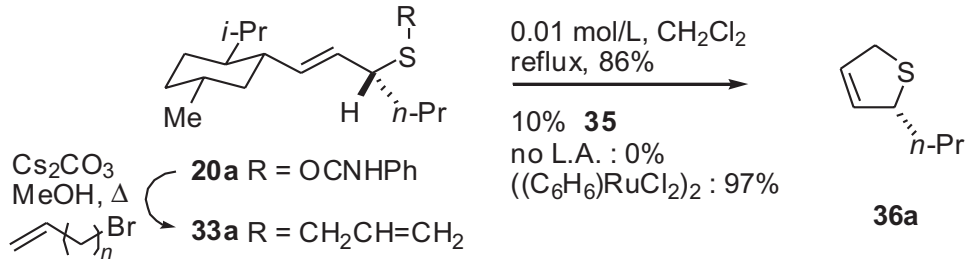
[2] We have observed the same phenomenon for the Claisen rearrangement, see ref. 11.

© 2007 NRC Canada

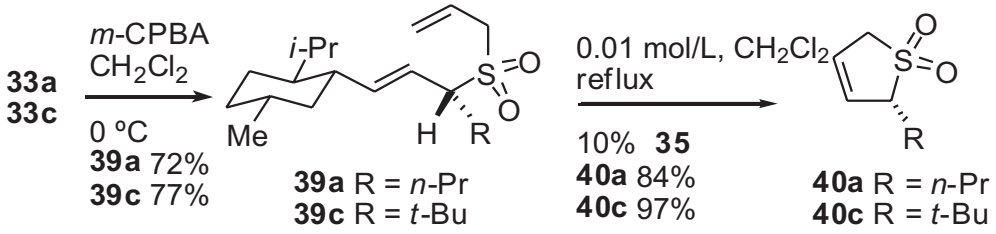
Scheme 8. RCM cleavage of allylic sulfide **33c** and **34c**.



Scheme 9. RCM cleavage of allylic sulfide **33a**.



Scheme 10. RCM cleavage of allylic sulfones **39a** and **39c**.



chiral nonracemic cycloalkenes by ring-closing metathesis (21) starting from dienes that still possess the menthyl moiety (22). To the best of our knowledge, this was the first example of a chiral auxiliary that could be cleaved by RCM. However, several heteroatoms, sulfur in particular (21, 23), may cause problems by coordinating to the metal center, and it was unclear at the onset if chiral *S*-heterocycles could be prepared by this method.

Thus, the carbamate functionality in **20c** was hydrolyzed and the resulting thiol alkylated in a one-pot procedure to give the precursor **33c** in 84% yield. To our delight, 2,5-dihydrothiophene (24) **36c** was obtained in 86% yield from **33c** using the Grubbs–Nolan catalyst **35** (25) (Scheme 8). It appeared that catalyst poisoning was not going to be a problem, or so we thought. Compound **38** is very conveniently recovered by evaporation and distillation. It can be converted back to the chiral auxiliary **7** by ozonolysis.

To our surprise, the very similar precursor **33a**, prepared in the same way from **20a**, gave no cyclic product under identical conditions (Scheme 9). Instead, some dimer (not shown) was isolated. We had to add an external Lewis acid to get the reaction to go (97% conversion by NMR).[3] A ruthenium(II) dimer was the Lewis acid that gave the best results.

3,6-Dihydrothiopyrans **37c** could not be prepared from of the corresponding precursors **34c**, after testing several solvents, catalysts, Lewis acids, and other additives (Scheme 8).

Sulfolenes **40a** and **40c** were efficiently prepared by RCM cleavage of **39a** and **39c**, respectively (Scheme 10). The low temperature used for RCM cleavage in this case was essential, since higher temperatures lead to the slow cheletropic extrusion of SO_2 in the sulfolene product to give the corresponding 1,3-dienes. Again, we were unable to prepare the analogous six-membered cyclic sulfones.

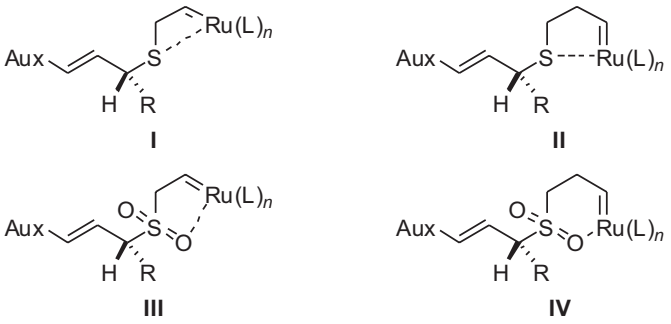
There seem to be several factors controlling the rate of RCM in our system. It is plausible that the formation of 3,6-dihydrothiopyrans **37** is prevented by the formation of a stable chelate **II** between sulfur and ruthenium (Fig. 2). The allylic sulfides do not form a stable chelate (cf. **I** in Fig. 2), and in those cases, poisoning of the catalyst probably occurs intermolecularly. In this case, bulky R groups such as *t*-Bu in **33c** or external Lewis acids are enough to allow the reaction to proceed.

We have shown previously that the formation of six-membered carbo- or *N*-heterocycles is kinetically less favored than the formation of the analogous five-membered rings (22). We suggest that under the reaction conditions and time used, the RCM reaction does not reach equilibrium and

[3] Isolated yield was low because of the high volatility of the product.

© 2007 NRC Canada

Fig. 2. Possible chelates in RCM of allylic sulfides and sulfones.



that the difference in efficiency of formation of dihydrothiophenes and dihydrothiopyrans is kinetically driven. We think that perhaps the longer C–S bond (>1.8 Å) hampers the ring-closing metathesis for six-membered ring formation and that poisoning of the catalyst is not the sole problem in this case, since a fair amount of dimer was isolated in each case.

Sulfones do form internal chelates with ruthenium, but the oxygen–ruthenium bond is weaker such that allylic sulfones (**III**, Fig. 2) undergo RCM fast enough, while homoallylic sulfones yield mostly dimer because of the slower rate of six-membered ring formation (**IV**, Fig. 2).

Synthesis of a potent MMP inhibitor

Several sulfonylhydroxamic acids are potent matrix metalloproteinase (MMP) inhibitors that have been studied in the clinic for the treatment of cancer and osteoarthritis (Fig. 3) (26). The overexpression of MMPs may result in the degradation of cartilage and may lead to medical conditions, such as osteoarthritis and rheumatoid arthritis. Compounds **41** and **43** are two highly selective inhibitors of MMP-13 in the nanomolar concentration (27) that may offer protection against cartilage degradation and potentially better treatment of osteoarthritis (28). Compounds **41** and **42** were previously prepared as racemic mixtures, but a small amount of **41** was resolved by preparative HPLC on a chiral column, and it was shown that (+)**–41** was 20 times as active as (–)**–41** (27). Their asymmetric synthesis thus becomes interesting.

We synthesized **42** as shown in Scheme 11. Alcohol **8h** was easily prepared in two steps from the commercially available propynylbenzene **43**. The ratio of β- and α-alcohols **8h** and **9h** was excellent, and their chromatographic separation was easy. Diastereomerically pure alcohol **8h** was submitted to the rearrangement conditions to give **20h** in 88% yield as essentially a single diastereomer. The *S*-thiocarbamate function could be directly coupled to iodide **45** using Tamaru's allylsulfenylation conditions to give a good yield of **46** (29). The synthesis was continued by first oxidizing the sulfur in **46**, then oxidatively cleaving the chiral auxiliary with ozone. Acid **47** could be obtained directly in one step by treating **46** with ozone, but this procedure led to lower yield of **47** and many decomposition products. Alternatively, when dimethylsulfide was used in the ozonolysis work-up, the α-sulfonylaldehyde was obtained and could be purified. Its treatment with Jones' reagent gave **47** in 53% yield for the two steps. Carrying out the two previoulsy reported steps (27) completed the synthesis of **42** for a total of eight steps and 12% overall yield from **43**.

In conclusion, we have successfully extended our *p*-menthane-3-carboxaldehyde based methodology to include the formation of chiral sulfur-bearing tertiary and quaternary carbons. This methodoly is becoming highly versatile and compares favorably to methodologies based on the classical alkylation of chiral enolates (30). Furthermore, carbo-, *N*-hetero-, and *S*-heterocyclic compounds are now directly accessible using RCM without the need for an extra step to cleave the auxiliary.

Experimental[4]

General

Flash chromatography was performed using Merck silica gel (230–400 Mesh ASTM) with solvents distilled prior to use. NMR spectra were recorded on a Bruker AC-300 spectrometer (^{1}H NMR at 300 MHz, ^{13}C NMR at 75.5 MHz). Infrared spectra were recorded on a PerkinElmer 1600 FTIR spectrometer with a thin layer of the product on a NaCl disc. HPLC analyses were performed on a HP 1100 apparatus; GC analyses were performed on a Agilent 6890 series apparatus; GCMS analyses were performed on a HP 5890 serie II instrument (25 m length, 25μ OD, capillary Stabiliwax-DB5 column) coupled with a mass spectrometer (HP 5971). High-resolution spectrometry was performed on a ZAB-1F micromass spectrometer. Optical rotations $[\alpha]^{20}_{D}$ were measured on a PerkinElmer 343 polarimeter.

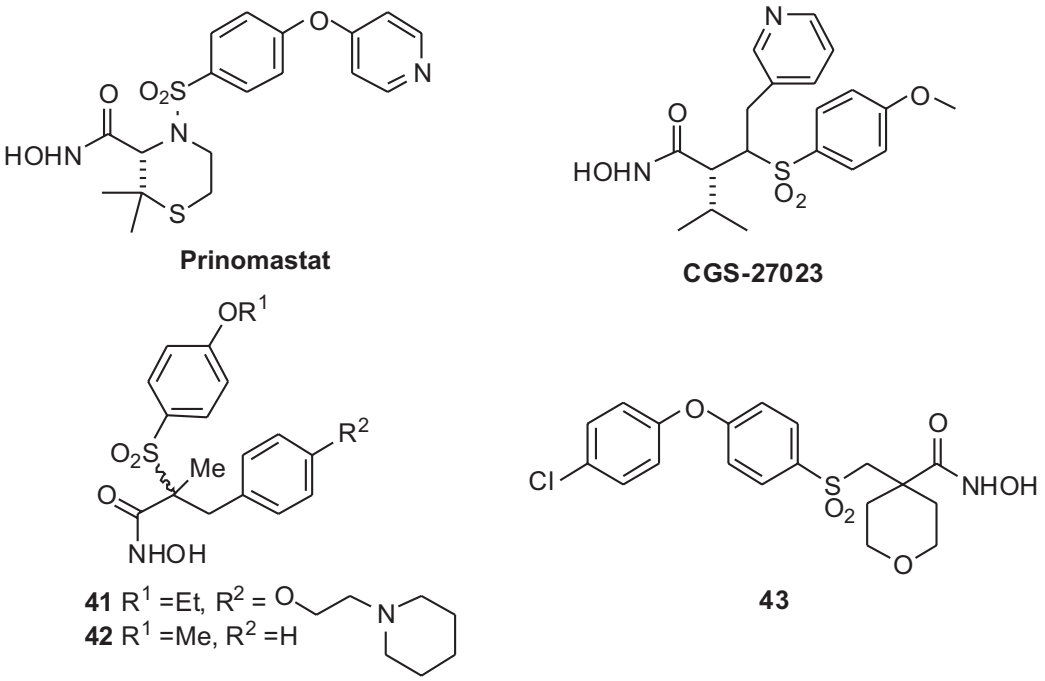
Alcohol 8f (method A)

Vinyliodide **17f** (5.50 g, 19.2 mmol) was dissolved in diethyl ether (70.0 mL), and the solution was cooled to –78 °C. A solution of *t*-BuLi in pentane (38.4 mmol) was added dropwise to the mixture. The reaction mixture was stirred at –78 °C for 30 min and then at RT for 1 h. It was again cooled to –78 °C before the addition of trimethylaluminium (2.0 mol/L in hexanes, 24.0 mL, 48.0 mmol) followed by a solution of (–)-*p*-menthane-3-carboxaldehyde **7** (2.70 g, 16.0 mmol) in diethyl ether (10.0 mL). The reaction mixture was stirred at –78 °C for 2 h and then at RT overnight. The reaction was quenched with an aqueous solution of sodium bicarbonate (100 mL) at 0 °C. The two phases were separated, and the aqueous phase was extracted with diethyl ether (3 × 100 mL). The combined organic portions were washed with brine, dried with anhyd. magnesium sulfate, and evaporated under reduced pressure. The crude product (**8f**:**9f** 52:1 by GC) was purified by flash chromatography on silica gel eluting with a mixture of hexanes/ethyl acetate (100: 0 to 95:5). A colorless oil was obtained (3.44 g, 55%).

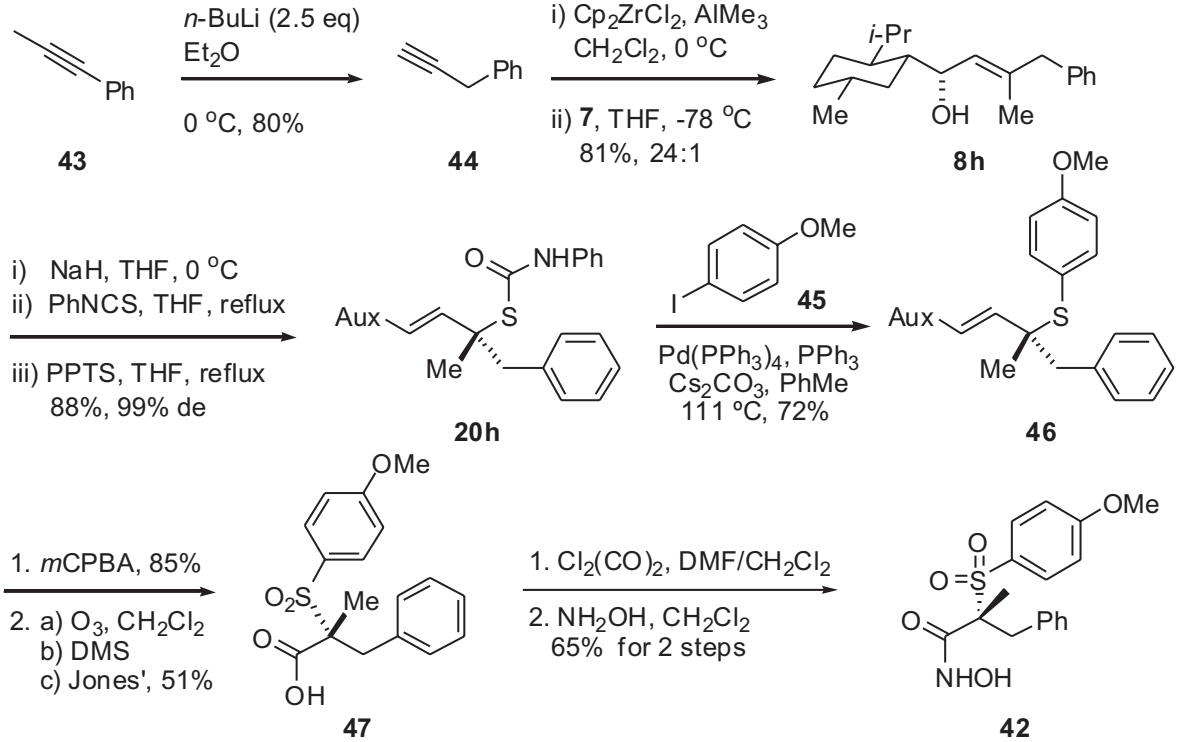
[4] Supplementary data for this article are available on the journal Web site (canjchem.nrc.ca) or may be purchased from the Depository of Unpublished Data, Document Delivery, CISTI, National Research Council Canada, Ottawa, ON K1A 0R6, Canada. DUD 5199. For more information on obtaining material, refer to cisti-icist.nrc-cnrc.gc.ca/irm/unpub_e.shtml.

© 2007 NRC Canada

Fig. 3. Biologically active sulfonylhydroxamic acids.



Scheme 11. Synthesis of MMP-13 inhibitor **42**.



Compound 8f

^{1}H NMR (300 MHz, $CDCl_3$) δ (ppm): 7.30–7.25 (m, 2H), 7.19–7.15 (m, 3H), 5.66–5.49 (m, 2H), 4.41–4.31 (m, 1H), 2.61 (t, 2H, *J* = 7.5 Hz), 2.15–2.06 (m, 3H), 1.70–1.58 (m, 5H), 1.44 (dt, 2H, *J* = 14.9, 7.5 Hz), 1.35–1.21 (m, 4H), 1.06–0.78 (m, 2H), 0.93 (d, 3H, *J* = 7.2 Hz), 0.87 (d, 3H, *J* = 6.6 Hz), 0.76 (d, 3H, *J* = 7.2 Hz). ^{13}C NMR (75.5 MHz, $CDCl_3$) δ (ppm): 142.7 (s), 132.5 (d), 130.4 (d), 128.4 (d), 128.2 (d), 125.7 (d), 71.3 (d), 44.8 (d), 43.0 (d), 35.8 (q), 35.1 (t), 33.8 (q), 32.8 (d), 32.2 (t), 31.0 (t), 28.9 (t), 26.3 (d), 24.3 (q), 22.8 (t), 21.6 (t), 15.5 (t). IR (neat) ν (cm^{-1}): 3395, 2927, 2857, 1454, 966, 698. LRMS (*m*/*z*, relative in-

© 2007 NRC Canada

tensity) 328 (M^+, 18), 285 (4), 171 (95), 83 (100). HRMS calcd. for $C_{23}H_{36}O$: 328.2766, found: 328.2769. $[\alpha]^{20}_D$ –9.2 (c = 1.39, $CHCl_3$).

Compound 9f

^1H NMR (300 MHz, $CDCl_3$) δ (ppm): 7.36–7.31 (m, 2H), 7.26–7.21 (m, 3H), 5.75–5.66 (m, 1H), 5.61–5.53 (m, 1H), 4.45–4.41 (m, 1H), 2.69 (t, 2H, J = 7.7 Hz), 2.23–2.13 (m, 3H), 2.08–1.99 (m, 2H), 1.81–1.62 (m, 3H), 1.56–1.32 (m, 2H), 1.13–0.70 (m, 6H), 1.01 (d, 3H, J = 6.6 Hz), 0.94 (d, 3H, J = 6.6 Hz), 0.88 (d, 3H, J = 6.6 Hz). ^{13}C NMR (75.5 MHz, $CDCl_3$) δ (ppm): 142.6 (s), 132.7 (d), 129.3 (d), 128.4 (d), 128.3 (d), 125.7 (d), 72.1 (d), 44.7 (d), 44.0 (d), 35.9 (q), 35.3 (t), 34.0 (q), 32.6 (d), 32.4 (t), 31.0 (t), 29.1 (t), 26.1 (d), 24.3 (q), 23.0 (t), 21.6 (t), 15.3 (t). IR (neat) ν (cm^{-1}): 3342, 2929, 2856, 1453, 971, 698. LRMS (*m*/*z*, relative intensity) 328 (M^+, 20), 267 (12), 171 (100), 91 (90). HRMS calcd. for $C_{23}H_{36}O$: 328.2766, found: 328.2762. $[\alpha]^{20}_D$ –20.5 (c = 1.71, $CHCl_3$). 98% de (GC).

Alcohol 8g (method B)

A flask containing a solution of *bis*(cyclopentadienyl)zirconium dichloride (129 mg, 0.44 mmol) in 6.3 mL of dichloromethane was put under vacuum and then filled with argon (3×). Trimethylaluminium (545 μL, 5.69 mmol) was added using a sass equipped with a syringe under an argon atmosphere. The solution was stirred 10 min at RT and then 5 min at 0 °C before the dropwise addition of hex-5-ynylbenzene (300 mg, 1.90 mmol). The mixture was stirred at RT overnight. A solution of (–)-*p*-menthane-3-carboxaldehyde **7** (246 mg, 1.46 mmol) in 4.9 mL of tetrahydrofuran was added dropwise to the reaction mixture at –78 °C. The reaction was warmed to RT and stirred overnight. A saturated aqueous solution of potassium carbonate was added dropwise until gas evolution stopped. The white precipitate was dissolved in a 1 N aq. solution of HCl. Then a 5 N aq. solution of HCl was added until the two layers were clear. The two phases were separated, and the aqueous layer was extracted three times with dichloromethane (50 mL). The organic layers were combined, washed with a saturated aqueous solution of sodium bicarbonate, dried over $MgSO_4$, filtered, and evaporated under reduced pressure. The crude compound was determined to be a mixture of the two diastereomers **8g** and **9g** in a ratio of 94:6 (88% de). The crude product was purified by flash chromatography on silica gel (100% hexanes to 5% EtOAc in hexanes). Two colorless oils were isolated (major diastereomer **8g**, 132 mg, 75%, >99% de by HPLC.; minor diastereomer **9g**, 12 mg, 7%, >99% de).

Compound 8g

^1H NMR (300 MHz, $CDCl_3$) δ (ppm): 7.30–7.25 (m, 2H), 7.19–7.15 (m, 3H), 5.34 (d, 1H, J = 7.7 Hz), 4.67 (d, 1H, J = 8.3 Hz), 2.62 (t, 2H, J = 7.7 Hz), 2.23–2.14 (m, 1H), 2.04 (t, 2H, J = 7.4 Hz), 1.71–1.42 (m, 7H), 1.63 (s, 3H), 1.35–1.24 (m, 3H), 1.14 (br s, 1H), 1.04–0.79 (m, 2H), 0.94 (d, 3H, J = 7.1 Hz), 0.88 (d, 3H, J = 6.6 Hz), 0.79 (d, 3H, J = 6.6 Hz). ^{13}C NMR (75.5 MHz, $CDCl_3$) δ (ppm): 142.7 (s), 136.5 (s), 128.4 (d), 128.2 (d), 127.2(d), 125.7 (d), 67.6 (d), 44.9 (d), 43.2 (d), 39.5 (t), 35.8 (t), 35.2 (t), 34.1 (t), 32.8 (d), 31.0 (t), 27.2 (t), 26.3 (d), 24.3 (t), 22.9 (q), 21.7 (q), 16.5 (q), 15.6 (q). IR (neat) ν (cm^{-1}): 3362, 2927, 2857, 1453, 1001, 698. LRMS (*m*/*z*, relative intensity) 342 (M^+, 8), 324 (M^+ - H_2O, 4), 203 (81), 185 (49), 91 (100). HRMS calcd. for $C_{24}H_{38}O$: 342.2922, found: 342.2924. $[\alpha]^{20}_D$ –25.9 (c = 1.01, $CHCl_3$).

Compound 9g

^1H NMR (300 MHz, $CDCl_3$) δ (ppm): 7.36–7.25 (m, 2H), 7.19–7.16 (m, 3H), 5.32 (d, 1H, J = 9.4 Hz), 4.59 (dd, 1H, J = 9.4, 3.9 Hz), 2.62 (t, 2H, J = 7.7 Hz), 2.06 (t, 2H, J = 7.1 Hz), 1.94 (dd, 1H, J = 12.7, 2.8 Hz), 1.84–1.77 (m, 1H), 1.69 (s, 3H), 1.72–1.18 (m, 8H), 1.07–0.70 (m, 10H), 0.90 (d, 3H, J = 6.6 Hz). ^{13}C NMR (75.5 MHz, $CDCl_3$) δ (ppm): 142.5 (s), 140.5 (s), 128.4 (d), 128.2 (d), 125.6(d), 123.4 (d), 67.8 (d), 44.5 (d), 44.1 (d), 39.7 (t), 35.7 (t), 35.2 (t), 34.0 (t), 32.6 (d), 30.8 (t), 27.3 (t), 26.4 (d), 24.1 (t), 22.8 (q), 21.5 (q), 16.4 (q), 15.3 (q). IR (neat) ν (cm^{-1}): 3355, 2931, 2858, 1453, 1020, 698. LRMS (*m*/*z*, relative intensity) 342 (M^+, 14), 324 ($M^+ - H_2O$, 4), 203 (100), 185 (75), 91 (79). HRMS calcd. for $C_{24}H_{38}O$: 342.2922, found: 342.2924. $[\alpha]^{20}_D$ –27.3 (c = 0.70, $CHCl_3$).

General procedure for the preparation of *S*-allylthiocarbamates

To a solution of the allylic alcohol **8** or **9** (0.198 mmol) in THF (2 mL) at 0 °C was added NaH 60% *w*/*w* in oil (15 mg, 0.372 mmol), and the mixture was stirred for 1 h at this temperature before the addition of phenylisothiocyanate (47 μL, 0.396 mmol). The reaction was heated to reflux and stirred for 3 h. It was then cooled down to RT before the addition of pyridinium *p*-toluenesulfonate (124 mg, 0.495 mmol) in THF (3.3 mL). The reaction was then heated to reflux for 2–3 h. Then, the reaction was stopped by the addition of water (5 mL) and Et_2O (5 mL). The two phases were separated, and the aqueous layer was extracted with Et_2O (3 × 10 mL). The combined organic layers were washed with brine, dried with anhyd. $MgSO_4$, and concentrated under reduced pressure. The crude product was purified by flash chromatography on silica gel (100% hexanes to 5% EtOAc in hexanes) to afford the desired product.

S-allylthiocarbamate 20c

Prepared following the general procedure for the synthesis of *S*-allylthiocarbamates. Reaction time after the addition of pyridinium *p*-toluenesulfonate: 2 h. Compound **20c** was isolated as a white solid (74 mg, 96%, 98% de by GC), mp 102–103 °C. ^1H NMR (300 MHz, $CDCl_3$) δ (ppm): 7.41 (d, 2H, J = 8.3 Hz), 7.30 (t, 2H, J = 8.0 Hz), 7.11–7.07 (m, 2H), 5.50–5.47 (m, 2H), 3.97–3.94 (m, 1H), 1.91–1.78 (m, 2H), 1.70 (dm, 1H, J = 12.1 Hz), 1.62–1.53 (m, 2H), 1.36–1.21 (m, 1H), 1.01 (s, 9H), 0.98–0.78 (m, 4H), 0.85 (d, 3H, J = 7.2 Hz), 0.82 (d, 3H, J = 6.6 Hz), 0.70 (d, 3H, J = 7.2 Hz). ^{13}C NMR (75.5 MHz, $CDCl_3$) δ (ppm): 165.1 (s), 138.1 (d), 137.9 (s), 129.0 (d), 127.0 (d), 124.1 (d), 119.5 (d), 59.9 (d), 47.0 (s), 44.9 (d), 42.9 (t), 35.1 (t), 34.4 (d), 32.5 (d), 28.2 (d), 27.9 (q), 23.9 (t), 22.5 (q), 21.4 (q), 15.1 (q). IR ($CHCl_3$) ν (cm^{-1}): 3395–3210 (br), 2958, 2922, 2869, 1659, 1440, 1143, 750. LRMS (*m*/*z*, relative intensity) 387 (M^+, 5), 330 ($(M - C_4H_9)^+$, 3), 177 (64), 97 (100). HRMS calcd. for $C_{24}H_{37}ONS$: 387.2596, found: 387.2591. $[\alpha]_D^{20}$ –118.7 (c = 1.31, $CHCl_3$).

© 2007 NRC Canada

S-allylthiocarbamate 20g

Prepared following the general procedure for the synthesis of *S*-allylthiocarbamates. Reaction time after the addition of pyridinium *p*-toluenesulfonate: 3 h. Compound **21g** was isolated as a colorless oil (83 mg, 87%, 80% de by HPLC). ^{1}H NMR (300 MHz, $CDCl_3$) δ (ppm): 7.39 (d, 2H, *J* = 7.7 Hz), 7.32–7.24 (m, 4H), 7.18–7.03 (m, 5H), 5.66 (d, 1H, *J* = 15.6 Hz), 5.39 (dd, 1H, *J* = 15.6, 9.1 Hz), 2.61 (t, 2H, *J* = 7.7 Hz), 2.07–1.94 (m, 2H), 1.93–1.55 (m, 6H), 1.62 (s, 3H), 1.45–1.32 (m, 3H), 1.04–0.71 (m, 5H), 0.85 (d, 3H, *J* = 7.2 Hz), 0.84 (d, 3H, *J* = 6.1 Hz), 0.67 (d, 3H, *J* = 6.6 Hz). ^{13}C NMR (75.5 MHz, $CDCl_3$) δ (ppm): 165.0 (s), 142.5 (s) 137.7 (s), 135.7 (d), 133.2 (d), 129.0 (d), 128.2 (d), 125.7 (d), 124.2 (d), 119.6 (d), 55.3 (s), 47.1 (d), 45.0 (d), 43.2 (t), 40.6 (t), 35.9 (t), 35.1 (t), 32.4 (d), 31.6 (t), 28.2 (d), 24.5 (q), 24.0 (t), 22.5 (q), 21.4 (q), 15.2 (q). IR (neat) ν (cm^{-1}): 3456, 2925, 2865, 1660, 1436, 1139, 750. LRMS (*m*/*z*, relative intensity) 477 (M^+, 4), 325 (60), 137 (60), 119 (100). HRMS calcd. for $C_{31}H_{43}ONS$: 477.3065, found: 477.3056. $[\alpha]^{20}_D$ –37.0 (*c* = 1.30, $CHCl_3$).

S-allylthiocarbamate 20h

Prepared following the general procedure for the synthesis of *S*-allylthiocarbamates. Reaction time after the addition of pyridinium *p*-toluenesulfonate: 3 h. Compound **21h** was isolated as a colorless oil (77 mg, 88%, 99% de by HPLC). ^{1}H NMR (300 MHz, $CDCl_3$) δ (ppm): 7.44 (d, 2H, *J* = 8.3 Hz), 7.34 (d, 2H, *J* = 7.2 Hz), 7.35–7.22 (m, 4H), 7.15–7.09 (m, 2H), 5.82 (d, 1H, *J* = 15.4 Hz), 5.32 (dd, 1H, *J* = 15.4, 9.4 Hz), 3.35 (ABq, 2H), 2.01–1.90 (m, 1H), 1.76–1.57 (m, 4H), 1.61 (s, 3H), 1.46–1.30 (m, 1H), 1.08–0.78 (m, 4H), 0.86 (d, 3H, *J* = 6.6 Hz), 0.83 (d, 3H, *J* = 7.1 Hz), 0.74 (d, 3H, *J* = 6.6 Hz). ^{13}C NMR (75.5 MHz, $CDCl_3$) δ (ppm): 165.1 (s) 137.7 (s), 137.1 (s), 136.2 (d), 132.4 (d), 131.0 (d), 129.1 (d), 127.7 (d), 126.5 (d), 124.3 (d), 119.7 (d), 55.6 (s), 47.0 (d), 46.6 (t), 44.9 (d), 43.3 (t), 35.1 (t), 32.4 (d), 28.0 (d), 24.3 (q), 24.0 (t), 22.5 (q), 21.4 (q), 15.5 (q). IR (neat) ν (cm^{-1}): 3310, 3029, 2922, 1666, 1514, 1438, 1139. LRMS (*m*/*z*, relative intensity) 435 (M^+, 1), 344 (8), 283 (23), 145 (85), 84 (100). HRMS calcd. for $C_{28}H_{37}ONS$: 435.2596, found: 435.2593. $[\alpha]^{20}_D$ –49.2 (*c* = 1.03, $CHCl_3$).

S-allylthiocarbamate 21c

Prepared following the general procedure for the synthesis of *S*-allylthiocarbamates. Reaction time after the addition of pyridinium *p*-toluenesulfonate: 2 h. Compound **21c** was isolated as a colorless oil (77 mg, >99%, >99% de by GC). ^{1}H NMR (300 MHz, $CDCl_3$) δ (ppm): 7.40 (d, 2H, *J* = 7.7 Hz), 7.30 (t, 2H, *J* = 7.7 Hz), 7.08 (t, 1H, *J* = 7.7 Hz), 7.04 (s, 1H), 5.47–5.44 (m, 2H), 3.94–3.91 (m, 1H), 1.87–1.78 (m, 2H), 1.69 (d, 1H, *J* = 12.1 Hz), 1.61–1.54 (m, 2H), 1.38–1.26 (m, 1H), 1.01 (s, 9H), 0.98–0.80 (m, 4H), 0.86 (d, 3H, *J* = 6.6 Hz), 0.71 (d, 3H, *J* = 7.2 Hz), 0.62 (d, 3H, *J* = 6.6 Hz). ^{13}C NMR (75.5 MHz, $CDCl_3$) δ (ppm): 164.9 (s), 138.0 (s), 138.0 (d), 129.0 (d), 126.9 (d), 124.1 (d), 119.4 (d), 60.2 (d), 47.2 (s), 44.8 (d), 43.1 (t), 35.1 (t), 34.2 (d), 32.5 (d), 28.0 (d), 27.8 (q), 24.0 (t), 22.6 (q), 21.2 (q), 15.1 (q). IR (neat) ν (cm^{-1}): 3298, 2954, 2914, 2869, 1659, 1499, 1439, 1147, 749. LRMS (*m*/*z*, relative intensity) 387 (M^+, 12), 330 ($(M - C_4H_9)^+$, 8), 177 (71), 97 (100). HRMS calcd. for $C_{24}H_{37}ONS$: 387.2596, found: 387.2591. $[\alpha]^{20}_D$ –165.1 (*c* = 1.03, $CHCl_3$).

S-allylthiocarbamate 21g

Prepared following the general procedure for the synthesis of *S*-allylthiocarbamates. Reaction time after the addition of pyridinium *p*-toluenesulfonate: 3 h. Compound **21g** was isolated as a colorless oil (64 mg, 67%, 98% de by HPLC). ^{1}H NMR (300 MHz, $CDCl_3$) δ (ppm): 7.37 (d, 2H, *J* = 7.7 Hz), 7.32–7.24 (m, 4H), 7.18–7.14 (m, 3H), 7.08 (t, 1H, *J* = 7.7 Hz), 6.98 (br s, 1H), 5.62 (d, 1H, *J* = 15.7 Hz), 5.39 (dd, 1H, *J* = 15.7, 9.4 Hz), 2.61 (t, 2H, *J* = 7.7 Hz), 2.04–1.79 (m, 3H), 1.73–1.45 (m, 6H), 1.64 (s, 3H), 1.43–1.25 (m, 3H), 1.04–0.78 (m, 4H), 0.85 (d, 3H, *J* = 6.6 Hz), 0.81 (d, 3H, *J* = 7.2 Hz), 0.64 (d, 3H, *J* = 7.2 Hz). ^{13}C NMR (75.5 MHz, $CDCl_3$) δ (ppm): 164.9 (s), 142.5 (s) 137.6 (s), 135.7 (d), 133.2 (d), 129.0 (d), 128.4 (d), 128.2 (d), 125.6 (d), 124.1 (d), 119.4 (d), 53.6 (s), 47.2 (d), 44.8 (d), 43.2 (t), 40.7 (t), 35.7 (t), 35.1 (t), 32.4 (d), 31.6 (t), 28.0 (d), 24.5 (q), 24.3 (t), 24.0 (t), 22.5 (q), 21.4 (q), 15.2 (q). IR (neat) ν (cm^{-1}): 3302, 2947, 2928, 2869, 1660, 1513, 1435, 1137, 749. LRMS (*m*/*z*, relative intensity) 477 (M^+, 1), 357 (1), 325 (95), 119 (100). HRMS calcd. for $C_{31}H_{43}ONS$: 477.3065, found: 477.3056. $[\alpha]^{20}_D$ –175.6 (*c* = 0.52, $CHCl_3$).

General procedure for the preparation of thiocarbonates

To a solution of the allylic alcohol **8** or **9** (0.099 mmol) in THF (1 mL) at 0 °C was added NaH 60% *w*/*w* in oil (7 mg, 0.198 mmol), and the mixture was stirred for 1 h at this temperature before the addition of carbon disulfide (24 μL, 0.396 mmol). The reaction was heated to reflux and stirred for 2 h. It was then cooled down to RT before the addition of methyl iodide (25 μL, 0.396 mmol) and was again heated to reflux for 45 min. Then, the reaction was stopped by the addition of water (5 mL) and Et_2O (5 mL). The two phases were separated, and the aqueous layer was extracted with Et_2O (3 × 10 mL). The combined organic layers were washed with brine, dried with anhyd. $MgSO_4$, and concentrated under reduced pressure. The crude product was purified by flash chromatography on silica gel (100% hexanes to 2% EtOAc in hexanes) to afford the desired product.

Thiocarbonate 25b

Prepared following the general procedure for the synthesis of thiocarbonates. Compound **25b** was isolated as a colorless oil (90 mg, 59%, >99% de by HPLC). ^{1}H NMR (300 MHz, $CDCl_3$) δ (ppm): 5.56 (d, 2H, *J* = 16.0 Hz), 5.34 (dd, 1H, *J* = 15.7, 9.1 Hz), 2.33 (s, 3H), 1.94–1.68 (m, 6H), 1.62–1.52 (m, 2H), 1.58 (s, 3H), 1.38–1.23 (m, 2H), 1.01–0.76 (m, 7H), 0.86 (d, 6H, *J* = 6.6 Hz), 0.67 (d, 3H, *J* = 7.1 Hz). ^{13}C NMR (75.5 MHz, $CDCl_3$) δ (ppm): 188.7 (s), 135.7 (d), 132.4 (d), 58.0 (s), 47.1 (d), 44.9 (d), 43.1 (t), 35.1 (t), 32.4 (d), 30.9 (t), 28.2 (d), 24.5 (q), 24.0 (t), 22.5 (q), 21.4 (q), 18.0 (t), 15.2 (q), 14.4 (q), 12.8 (q). IR (neat) ν (cm^{-1}): 2955, 2927, 2871, 1641. LRMS (*m*/*z*, relative intensity) 343 (MH^+, 4), 250 (8), 235 (100). HRMS calcd. for $C_{19}H_{35}OS_2$ (MH^+): 343.2129, found: 343.2135. $[\alpha]^{20}_D$ –46.9 (*c* = 0.73, $CHCl_3$).

© 2007 NRC Canada

Thiocarbonate 25c

Prepared following the general procedure for the synthesis of thiocarbonates. Compound **25c** was isolated as a colorless oil (135 mg, 99%, >99% de by GC). ^{1}H NMR (300 MHz, $CDCl_3$) δ (ppm): 5.43–5.40 (m, 2H), 4.04–4.06 (m, 1H), 2.40 (s, 3H), 1.87–1.75 (m, 2H), 1.74–1.68 (m, 1H), 1.62–1.50 (m, 3H), 1.36–1.25 (m, 1H), 0.99–0.77 (m, 3H), 0.95 (s, 9H), 0.85 (d, 3H, J = 7.2 Hz), 0.84 (d, 3H, J = 6.6 Hz), 0.68 (d, 3H, J = 6.6 Hz). ^{13}C NMR (75.5 MHz, $CDCl_3$) δ (ppm): 188.8 (s), 138.7 (d), 126.1 (d), 59.8 (d), 47.0 (d), 44.9 (d), 42.8 (t), 35.1 (t), 34.4 (s), 32.4 (d), 28.3 (d), 27.7 (q), 23.9 (t), 22.5 (q), 21.4 (q), 15.0 (q), 13.1 (q). IR (neat) ν (cm^{-1}): 2956, 2927, 2869, 2360, 2340, 1646, 1366, 861. LRMS (*m/z*, relative intensity) 342 (M^+, 6), 267 (23), 235 (84), 177 (82), 97 (100). HRMS calcd. for $C_{19}H_{34}OS_2$: 342.2051, found: 342.2044. $[\alpha]^{20}_D$ +85.3 (c = 0.83, $CHCl_3$).

Thiocarbonate 26b

Prepared following the general procedure for the synthesis of thiocarbonates. Compound **26b** was isolated (60 mg, 39%, >96% de by HPLC) as a colorless oil. ^{1}H NMR (300 MHz, $CDCl_3$) δ (ppm): 5.55 (d, 2H, J = 15.4 Hz), 5.35 (dd, 1H, J = 15.4, 9.4 Hz), 2.32 (s, 3H), 1.98–1.72 (m, 6H), 1.70–1.50 (m, 2H), 1.60 (s, 3H), 1.43–1.24 (m, 2H), 1.01–0.66 (m, 7H), 0.86 (d, 6H, J = 6.6 Hz), 0.66 (d, 3H, J = 7.2 Hz). ^{13}C NMR (75.5 MHz, $CDCl_3$) δ (ppm): 188.6 (s), 135.7 (d), 132.5 (d), 58.0 (s), 47.2 (d), 44.8 (d), 43.3 (t), 35.1 (t), 32.4 (d), 30.9 (t), 28.0 (d), 24.3 (q), 24.0 (t), 22.5 (q), 21.4 (q), 18.0 (t), 15.2 (q), 14.3 (q), 12.7 (q). IR (neat) ν (cm^{-1}): 2955, 2927, 2871, 1642. LRMS (*m/z*, relative intensity) 343 (MH^+, 3), 250 (5), 235 (100). HRMS calcd. for $C_{19}H_{35}OS_2$ (MH^+): 343.2129, found: 343.2135. $[\alpha]^{20}_D$ –22.9 (c = 0.74, $CHCl_3$).

Thiocarbonate 26c

Prepared following the general procedure for the synthesis of thiocarbonates. Compound **26c** was isolated as a colorless oil (122 mg, 90%, 98% de by GC). ^{1}H NMR (300 MHz, $CDCl_3$) δ (ppm): 5.41–5.38 (m, 2H), 4.05 (dd, 1H, J = 5.5, 3.3 Hz), 2.38 (s, 3H), 1.95–1.75 (m, 2H), 1.73–1.60 (m, 1H), 1.58–1.51 (m, 3H), 1.36–1.28 (m, 1H), 0.99–0.78 (m, 9H), 0.96 (s, 9H), 0.65 (d, 3H, J = 6.6 Hz). ^{13}C NMR (75.5 MHz, $CDCl_3$) δ (ppm): 188.7 (s), 138.7 (d), 126.0 (d), 60.0 (d), 47.2 (d), 44.7 (d), 43.0 (t), 35.1 (t), 34.2 (s), 32.4 (d), 27.8 (d), 27.8 (q), 24.0 (t), 22.5 (q), 21.4 (q), 15.3 (q), 13.0 (q). IR (neat) ν (cm^{-1}): 2955, 2927, 2869, 1647. LRMS (*m/z*, relative intensity) 342 (M^+, 5), 235 (38), 177 (35), 97 (100). HRMS calcd. for $C_{19}H_{34}OS_2$: 342.2051, found: 342.2044. $[\alpha]^{20}_D$ –157.3 (c = 0.49, $CHCl_3$).

General procedure for the preparation of *S*-allylimidazoyl thiocarbonates

To a solution of the allylic alcohol (0.099 mmol) in acetonitrile (0.5 mL) was added thiocarbonyldiimidazole (53 mg, 0.297 mmol), and the mixture was stirred for 3 days at RT. Then, the reaction was stopped by the addition of water (5 mL) and Et_2O (5 mL). The two phases were separated, and the aqueous layer was extracted with Et_2O (3 × 10 mL). The combined organic layers were washed with brine, dried with anhyd. $MgSO_4$, and concentrated under reduced pressure. The crude product was purified by flash chromatography on silica gel (100% hexanes to 5% EtOAc in hexanes) to afford the desired product.

Imidazoyl thiocarbonate 27c

Prepared following the general procedure for the synthesis of imidazoyl thiocarbonates. Compound **27c** was isolated as a colorless oil (28 mg, 78% yield, 97% de by HPLC). ^{1}H NMR (300 MHz, $CDCl_3$) δ (ppm): 8.18 (s, 1H), 7.45 (s, 1H), 7.06 (s, 1H), 5.58–5.41 (m, 2H), 4.10 (d, 1H, J = 9.3 Hz), 1.91–1.66 (m, 3H), 1.60–1.45 (m, 2H), 1.34–1.23 (m, 2H), 1.02 (s, 9H), 1.01–0.62 (m, 3H), 0.84 (d, 3H, J = 7.2 Hz), 0.81 (d, 3H, J = 6.6 Hz), 0.68 (d, 3H, J = 6.6 Hz). ^{13}C NMR (75.5 MHz, $CDCl_3$) δ (ppm): 165.3 (s), 140.0 (d), 135.4 (d), 130.6 (d), 125.3 (d), 115.9 (d), 60.9 (d), 47.0 (d), 44.9 (d), 42.7 (t), 35.0 (t), 34.5 (s), 32.4 (d), 28.3 (d), 27.8 (q), 23.9 (t), 22.5 (q), 21.4 (q), 15.0 (q). IR (neat) ν (cm^{-1}): 3125, 2954, 2924, 1762, 1693. LRMS (*m/z*, relative intensity) 362 (M^+, 3), 306 (39), 107 (100). HRMS calcd. for $C_{21}H_{34}ON_2S$: 362.2392, found: 362.2386. $[\alpha]^{20}_D$ –47.3 (c = 0.64, $CHCl_3$).

Imidazoyl thiocarbonate 28c

Prepared following the general procedure for the synthesis of imidazoyl thiocarbonates. Compound **27c** was isolated as a colorless oil (17 mg, 42% yield, 99% de by HPLC). ^{1}H NMR (300 MHz, $CDCl_3$) δ (ppm): 8.20 (s, 1H), 7.48 (s, 1H), 7.08 (s, 1H), 5.58–5.41 (m, 2H), 4.10 (d, 1H, J = 9.3 Hz), 1.93–1.81 (m, 1H), 1.72–1.52 (m, 4H), 1.39–1.22 (m, 2H), 1.04 (s, 9H), 0.98–0.65 (m, 3H), 0.86 (d, 3H, J = 6.6 Hz), 0.76 (d, 3H, J = 7.2 Hz), 0.57 (d, 3H, J = 7.2 Hz). ^{13}C NMR (75.5 MHz, $CDCl_3$) δ (ppm): 165.4 (s), 139.8 (d), 135.6 (d), 130.6 (d), 125.2 (d), 116.1 (d), 61.1 (d), 47.2 (d), 44.7 (d), 42.9 (t), 35.1 (t), 34.4 (s), 32.4 (d), 28.0 (d), 27.8 (q), 24.0 (t), 22.5 (q), 21.2 (q), 15.1 (q). IR (neat) ν (cm^{-1}): 2955, 2927, 2869, 1695, 1467. LRMS (*m/z*, relative intensity) 362 (M^+, 10), 306 (62), 95 (100). HRMS calcd. for $C_{21}H_{34}ON_2S$: 362.2392, found: 362.2386. $[\alpha]^{20}_D$ –98.8 (c = 1.42, $CHCl_3$).

Alcohol 31

Thiocarbonate **25c** (50 mg, 0.146 mmol) was solubilized in 4.9 mL of dichloromethane and Sudan III (1 mg) was added. The mixture was cooled down to –78 °C. Ozone was bubbled through the solution until the indicator color passed from red to pale pink or from red to violet. Then, dry nitrogen was bubbled through the solution for 5 min before sodium borohydride (55 mg, 1.459 mmol) was added. The mixture was stirred at –78 °C for 30 min and was slowly warmed to RT overnight. Then, the reaction was stopped by the addition of water (5 mL) and dichloromethane (5 mL). The two phases were separated, and the aqueous layer was extracted with dichloromethane (3 × 10 mL). The combined organic layers were washed with brine, dried with anhyd. $MgSO_4$, and concentrated under reduced pressure without heating. The crude product was purified by flash chromatography on silica gel (100% hexanes to 10% EtOAc in hexanes) to afford the desired product. Menthyl alcohol was also recovered in 80% yield. Compound **31** was isolated as a colorless oil (27 mg, 89%, 93% ee by HPLC). ^{1}H NMR (300 MHz, $CDCl_3$) δ (ppm): 4.00 (dd, 1H, J = 11.3, 3.6 Hz), 3.72 (dd, 1H, J = 8.8, 3.9 Hz), 3.62 (dd, 1H, J = 11.6, 8.8 Hz), 2.44 (s, 3H), 1.90–1.50 (br s, 1H), 1.02 (s, 9H). ^{13}C NMR (75.5 MHz, $CDCl_3$) δ (ppm): 190.3 (s), 62.6 (t), 60.3 (d), 34.4 (s), 28.1 (q), 13.3 (q). IR (neat) ν (cm^{-1}): 3430,

© 2007 NRC Canada

2962, 2931, 1646. LRMS (*m/z*, relative intensity) 266 (M + NH_4^+, 7), 209 (MH^+, 1), 195 (24), 178 (100). HRMS calcd. for $C_8H_{16}O_2S_2$: 209.0670, found: 209.0667. $[\alpha]^{20}_D$ +9.5 (*c* 0.86, $CHCl_3$).

Alcohol (R)-32

The substrate (68 mg, 0.239 mmol) was solubilized in 2.4 mL of dichloromethane. The mixture was cooled down to –78 °C. Ozone was bubbled through the solution until TLC showed completion. Nitrogen was then bubbled through the solution for 5 min before a borane-methylsulfide solution (2 mol/L in THF, 0.48 mL, 0.955 mmol) was slowly added. The mixture was stirred at –78 °C for 30 min and was slowly warmed to RT overnight. Then, the reaction was stopped by the addition of water (5 mL) and dichloromethane (5 mL). The two phases were separated, and the aqueous layer was extracted with dichloromethane (3 × 10 mL). The combined organic layers were washed with brine, dried with anhyd. $MgSO_4$, and concentrated under reduced pressure without heating. The crude product was purified by flash chromatography on silica gel (100% hexanes to 20% EtOAc in hexanes) to afford 56 mg of the desired product (83%) as a colorless oil. ^{1}H NMR (300 MHz, $CDCl_3$) δ (ppm): 7.28 (m, 2H), 7.20–7.16 (m, 3H), 3.79–3.66 (m, 3H), 2.62 (t, 2H, *J* = 7.7 Hz), 2.43 (s, 3H), 1.97 (s, 1H), 1.84–1.72 (m, 1H), 1.70–1.37 (m, 5H). ^{13}C NMR (75.5 MHz, $CDCl_3$) δ (ppm): 190.2 (s), 142.3 (s), 128.3 (d), 125.7 (d), 65.4 (t), 48.9 (d), 35.7 (t), 31.1 (t), 30.5 (t), 26.6 (t), 13.3 (q) IR (neat) ν (cm^{-1}): 3600–3200 (br), 3025, 2931, 2857, 1644, 869. LRMS (*m/z*, relative intensity) 285 (MH^+, 15), 159 (70), 117 (75), 91 (100). HRMS calcd. for $C_{14}H_{21}O_2S_2$ (MH^+): 285.0983, found: 285.0980. $[\alpha]^{20}_D$ +4.5 (*c* = 2.37, $CHCl_3$).

General procedure for the preparation of RCM precursors

The thiocarbamate (0.064 mmol) and the bromide (0.322 mmol) were solubilized in 1 mL of methanol, and cesium carbonate (0.322 mmol) was added. The mixture was stirred and heated overnight at 80 °C in a sealed tube. Water (5 mL) and diethyl ether (5 mL) were added to the reaction mixture. The two layers were separated, and the aqueous layer was extracted three times with diethyl ether. The combined organic layers were washed with brine, dried over anhyd. $MgSO_4$, filtered, and evaporated under reduced pressure. The crude product was purified by flash chromatography on silica gel (100% hexanes to 4% EtOAc in hexanes).

Sulfide 33c

Prepared following the general procedure for the synthesis of RCM precursors. Compound **33c** was isolated as a colorless oil (54 mg, 79% yield). ^{1}H NMR (300 MHz, $CDCl_3$) δ (ppm): 5.76 (dddd, 1H, *J* = 15.9, 10.6, 8.4, 5.7 Hz), 5.31 (dd, 1H, *J* = 15.9, 10.6 Hz), 5.12–5.04 (m, 3H), 3.07 (dd, 1H, *J* = 13.9, 5.7 Hz), 2.99 (dd, 1H, *J* = 13.9, 8.4 Hz), 2.83 (d, 1H, *J* = 9.9 Hz), 2.03–1.56 (m, 4H), 1.43–1.32 (m, 1H), 1.25–0.67 (m, 11H), 0.97 (s, 9H), 0.71 (d, 3H, *J* = 7.2 Hz). ^{13}C NMR (75.5 MHz, $CDCl_3$) δ (ppm): 137.6 (d), 135.2, (d), 127.5 (d), 116.5 (t), 58.8 (d), 47.2 (d), 45.2 (d), 44.2 (t), 35.1 (t), 33.8 (t), 33.2 (s), 32.6 (d), 28.2 (q), 28.1 (d), 23.8 (t), 22.6 (q), 21.4 (q), 15.0 (q). IR (neat) ν (cm^{-1}): 2955, 2920, 2871, 1641, 1458, 1366, 971, 912. LRMS (*m/z*, relative intensity) 308 (M^+, 6), 267 ((M – C_3H_5)$^+$, 24), 257 ((M – C_4H_9)$^+$, 100), 177 (78), 97 (88). HRMS calcd. for $C_{20}H_{36}S$: 308.2538, found: 308.2543. $[\alpha]^{20}_D$ +9.6 (*c* = 1.31, $CHCl_3$).

Sulfide 34c

Prepared following the general procedure for the synthesis of RCM precursors. Compound **34c** was isolated as a colorless oil (54 mg, 75% yield.) ^{1}H NMR (300 MHz, $CDCl_3$) δ (ppm): 5.82 (ddt, 1H, *J* = 16.8, 10.3, 6.6 Hz), 5.31 (dd, 1H, *J* = 15.1, 10.3 Hz), 5.15–5.07 (m, 2H), 5.02–4.99 (m, 1H), 2.88 (d, 1H, *J* = 10.3 Hz), 2.48–2.38 (m, 2H), 2.36–2.21 (m, 2H), 1.98–1.80 (m, 2H), 1.74–1.70 (m, 1H), 1.65–1.56 (m, 3H), 1.40–1.25 (m, 1H), 0.98–0.77 (m, 3H), 0.97 (s, 9H), 0.87 (d, 3H, *J* = 7.2 Hz), 0.86 (d, 3H, *J* = 6.6 Hz), 0.71 (d, 3H, *J* = 6.6 Hz). ^{13}C NMR (75.5 MHz, $CDCl_3$) δ (ppm): 137.3 (d), 137.1, (d), 127.6 (d), 115.5 (t), 60.1 (d), 47.2 (d), 45.0 (d), 44.0 (s), 35.1 (t), 34.0 (t), 33.8 (q), 32.5 (d), 29.8 (t), 28.2 (d), 28.0 (q), 23.9 (t), 22.5 (q), 21.4 (t), 15.0 (q). LRMS (*m/z*, relative intensity) 322 (M^+, 25), 265 (95), 205 (69), 177 (72), 127 (100). HRMS calcd. for $C_{21}H_{38}S$: 322.2694, found: 322.2705. $[\alpha]^{20}_D$ –12.3 (*c* = 0.86, $CHCl_3$).

(S)-2-tert-Butyl-2,5-dihydrothiophene 36c

A solution of sulfide **33c** (92 mg, 0.30 mmol) in dichloromethane (30 mL, 0.01 mol/L), was brought to reflux and then degassed by passing a stream of argon for 15 min while refluxing. The Grubbs–Nolan catalyst **35** (25 mg, 10 mol%) was quickly added while the solution was still under reflux. The resulting pale pink solution was refluxed for 18 h. It was cooled to room temperature, and volatiles were removed under reduced pressure without heating. Analysis of the crude reaction mixture showed complete conversion to **36c** and auxiliary by-product **38**. The crude product was purified by flash chromatography on silica gel (100% pentane) to afford the desired product **36c** (36 mg, 85%) as a colorless oil. ^{1}H NMR (300 MHz, $CDCl_3$) δ (ppm): 5.86 (tt, 1H, *J* = 6.6, 2.2 Hz), 5.77 (tt, 1H, *J* = 6.6, 2.2 Hz), 4.12 (br s, 1H), 3.64 (br s, 2H), 0.94 (s, 9H). ^{13}C NMR (75.5 MHz, $CDCl_3$) δ (ppm): 130.9 (d), 128.9 (d), 68.0 (d), 38.4 (t), 35.5 (s), 27.1 (q). IR (neat) ν (cm^{-1}): 2956, 2868, 1712, 1691, 1463. LRMS (*m/z*, relative intensity) 142 (M^+, 20), 85 (100), 77 (10). HRMS calcd. for $C_8H_{14}S$: 142.0816, found: 142.0814. $[\alpha]^{20}_D$ –43.1 (*c* = 1.23, $CHCl_3$).

Sulfone 39c

The allylic sulfide **33c** (192 mg, 0.622 mmol) was solubilized in 3 mL of dichloromethane, and *m*-chloroperbenzoic acid (215 mg, 1.24 mmol) was added to the solution. The mixture was stirred for 10 min at RT and was then cooled to 0 °C before the addition 5 mL of a saturated aqueous solution of $NaHCO_3$ and 5 mL of dichloromethane. The two layers were separated. The aqueous layer was extracted with dichloromethane (3 × 5 mL). The combined organic layers were washed with brine, dried over anhyd. $MgSO_4$, filtered, and evaporated under reduced pressure. The crude product was purified by flash chromatography on silica gel (5% to 10% EtOAc in hexanes). The desired product was isolated as a white solid (163 mg, 77%), mp 107–108 °C. ^{1}H NMR (300 MHz, $CDCl_3$) δ (ppm): 5.88 (dddd, 1H, *J* = 16.0, 10.3, 9.0, 6.1 Hz), 5.60 (dd, 1H, *J* = 15.1, 10.3 Hz), 5.49–5.31 (m, 3H), 3.85 (dd, 1H, *J* = 13.8, 9.0 Hz), 3.41 (dd, 1H, *J* = 13.8, 6.1 Hz), 3.32 (d, 1H, *J* =

© 2007 NRC Canada

10.5 Hz), 2.11–2.00 (m, 1H), 1.76–1.59 (m, 4H), 1.43–1.17 (m, 1H), 1.14 (s, 9H), 1.05–0.78 (m, 4H), 0.86 (d, 3H, J = 6.1 Hz), 0.85 (d, 3H, J = 7.7 Hz), 0.69 (d, 3H, J = 6.6 Hz). IR (CHCl3) ν (cm^{-1}): 3028, 2957, 1310, 1126. LRMS (*m/z*, relative intensity) 358 (MNH_4^+, 30), 235 (100), 97 (70). HRMS calcd. for $C_{20}H_{40}NO_2S$ (MNH_4^+): 358.2780, found: 358.2784. $[\alpha]^{20}_D$ –73.5 (c = 0.73, $CHCl_3$).

Sulfolene 40c

A solution of **39c** (50 mg, 0.15 mmol) in dichloromethane (147 mL, 0.001 mol/L) was brought to reflux and then degassed by passing a stream of argon for 15 min while refluxing. The Grubbs–Nolan catalyst **35** (12 mg, 10 mol%) was quickly added while the solution was still under reflux. The resulting pale pink solution was refluxed for 18 h. It was cooled to room temperature, and volatiles were removed under reduced pressure without heating. Analysis of the crude reaction mixture showed complete conversion to **40c** and auxiliary by-product **38**. The crude product was purified by flash chromatography on silica gel (100% hexanes to 30% EtOAc in hexanes) to afford the desired product **40c** (21 mg, 84%) as a colorless oil. ^{1}H NMR (300 MHz, $CDCl_3$) δ (ppm): 6.17–6.06 (m, 2H), 3.75–3.56 (m, 2H), 3.55–3.53 (m, 1H), 1.18 (s, 9H). ^{13}C NMR (75.5 MHz, $CDCl_3$) δ (ppm): 129.1 (d), 124.0 (d), 74.4 (d), 56.4 (t), 34.5 (s), 27.1 (q). IR (neat) ν (cm^{-1}): 2963, 2868, 1298, 1245, 1109. LRMS (*m/z*, relative intensity) 192 (MNH_4^+, 40), 175 (MH^+, 5), 110 (100), 96 (95). HRMS calcd. for $C_8H_{15}SO_2$ (MH^+): 175.0793, found: 175.0790. $[\alpha]^{20}_D$ –15.2 (c = 1.96, $CHCl_3$).

Sulfonylhydroxamic acid 42

Carboxylic acid **47** (45 mg, 0.135 mmol) was dissolved in dichloromethane (20 mL), and one drop of *N,N*-dimethylformamide was added. The mixture was cooled to 0 °C, and oxalyl chloride (151 μL, 1.73 mmol) was added dropwise. The reaction mixture was stirred at 0 °C for 1 h. The solution was concentrated under reduced pressure, and the residue was taken up in dichloromethane (2 mL).

In a separate flask, the hydrochloride salt of hydroxylamine (435 mg, 6.26 mmol) was dissolved in a 5:1 mixture of tetrahydrofuran and water (6.2 mL), and it was cooled to 0 °C. Triethylamine (1.1 mL, 7.9 mmol) was added dropwise, and the reaction mixture was stirred 1 h at 0 °C.

The acyl chloride solution previously prepared was added to the hydroxylamine solution at 0 °C. The resulting mixture was stirred 2 h, then water (10 mL) and chloroform (10 mL) were added. The two phases were separated, and the aqueous phase was extracted with chloroform (3 × 10 mL). The combined organic phases were washed with brine, dried over anhyd. magnesium sulfate, and concentrated under reduced pressure. Flash chromatography on silica gel, eluting with ethyl acetate, gave a white solid (31 mg, 65%), mp 48–51 °C. ^{1}H NMR (300 MHz, $CDCl_3$) δ (ppm): 9.72 (br s, 1H), 7.77 (d, 2H, J = 8.5 Hz), 7.23–7.22 (m, 3H), 7.13–7.11 (m, 2H), 7.02 (d, 2H, J = 8.5 Hz), 3.88 (s, 3H), 3.58 (d, 1H, J = 13.8 Hz), 3.10 (d, 1H, J = 13.8 Hz), 1.65 (br s, 1H), 1.35 (s, 3H). ^{13}C NMR (75.5 MHz, $CDCl_3$) δ (ppm): 164.8 (s), 164.5 (s), 133.5 (s), 132.4 (d), 130.3 (d), 128.6 (d), 127.6 (d), 125.7 (s), 114.5 (d), 71.6 (s), 55.7 (q), 38.7 (t), 16.1 (q). IR (CHCl3) ν (cm^{-1}): 3650–3500 (br), 3500–3175 (br), 3028, 2934, 2845, 1656, 1595, 1141. LRMS (*m/z*, relative intensity) 349 (M^+, 3), 285 (20), 155 (100). HRMS calcd. for $C_{17}H_{19}NO_5S$ (M^+): 349.0984, found: 349.0990. $[\alpha]^{20}_D$ –12.9 (c = 1.80, $CHCl_3$).

Arylsulfide 46

Thiocarbamate **20h** (94 mg, 0.22 mmol) and the aryl iodide **45** (66 mg, 0.28 mmol) were dissolved in toluene (1.0 mL). Cesium carbonate (91 mg, 0.28 mmol) and triphenylphosphine (17 mg, 0.065 mmol) were added, and argon was bubbled through the solution for 5 min prior to the addition of $Pd(PPh_3)_4$ (25 mg, 0.022 mmol). The reaction mixture was stirred and heated to reflux temperature overnight. The mixture was filtered through Celite®, and the filtrate was concentrated under reduced pressure. The crude product was purified by flash chromatography on silica gel (100% hexanes to 10% EtOAc in hexanes). A colorless oil was isolated (66 mg, 72%). ^{1}H NMR (300 MHz, $CDCl_3$) δ (ppm): 7.39 (d, 2H, J = 8.5 Hz), 7.24–7.11 (m, 5H), 6.81 (d, 2H, J = 8.5 Hz), 5.56 (d, 1H, J = 15.5 Hz), 4.62 (dd, 1H, J = 15.5, 9.1 Hz), 3.80 (s, 3H), 3.03 (d, 1H, J = 12.9 Hz), 2.87 (d, 1H, J = 12.9 Hz), 1.92–1.81 (m, 1H), 1.67 (br d, 1H, J = 12.1 Hz), 1.54–1.21 (m, 4H), 1.18 (s, 3H), 1.07–0.51 (m, 4H), 0.84 (d, 3H, J = 6.6 Hz), 0.72 (d, 3H, J = 6.6 Hz), 0.68 (d, 3H, J = 6.6 Hz). ^{13}C NMR (75.5 MHz, $CDCl_3$) δ (ppm): 160.2 (s), 139.2 (d), 137.4 (s), 134.9 (d), 133.7 (d), 130.6 (d), 127.5 (d), 126.2 (d), 122.9 (s), 113.7 (d), 55.2 (q), 54.1 (s), 48.0 (t), 47.0 (d), 44.7 (d), 43.0 (t), 35.0 (t), 32.4 (d), 27.7 (d), 23.9 (t), 23.6 (q), 22.5 (q), 21.4 (q), 15.5 (q). IR (neat) ν (cm^{-1}): 2953, 2923, 1588, 1493, 1246. LRMS (*m/z*, relative intensity) 422 (M^+, 1), 283 (18), 145 (100). HRMS calcd. for $C_{28}H_{38}OS$: 422.2643, found: 422.2637. $[\alpha]^{20}_D$ –42.2 (c = 1.45, $CHCl_3$).

Carboxylic acid 47

Arylsulfide **46** was treated as per the preparation of sulfone **39c**. A white solid was obtained after chromatography (834 mg, 85%), mp 137–138 °C. ^{1}H NMR (300 MHz, $CDCl_3$) δ (ppm): 7.76 (d, 2H, J = 8.8 Hz), 7.26–7.18 (m, 3H), 7.11–7.08 (m, 2H), 6.95 (d, 2H, J = 8.8 Hz), 5.73 (d, 1H, J = 15.8 Hz), 4.81 (dd, 1H, J = 15.8, 9.3 Hz), 3.86 (s, 3H), 3.34 (d, 1H, J = 12.9 Hz), 3.23 (d, 1H, J = 12.9 Hz), 2.02–1.90 (m, 1H), 1.67 (br d, 1H, J = 12.6 Hz), 1.55–1.19 (m, 4H), 1.16 (s, 3H), 0.84 (d, 3H, J = 6.6 Hz), 0.80–0.47 (m, 4H), 0.68 (d, 3H, J = 6.0 Hz), 0.66 (d, 3H, J = 6.0 Hz). IR ($CHCl_3$) ν (cm^{-1}): 2922, 1595, 1497, 1458, 1289. LRMS (*m/z*, relative intensity) 455 (MH^+, 1), 437 (8), 283 (100), 145 (85). HRMS calcd. for $C_{28}H_{39}O_3S$ (MH^+): 455.2620, found: 455.2622. $[\alpha]^{20}_D$ –75.9 (c = 0.69, $CHCl_3$).

The resulting sulfone (35 mg, 0.079 mmol) was solubilized in dichloromethane (1.0 mL). The mixture was cooled down to –50 °C, then ozone was bubbled through the solution for 4 h. Nitrogen was then bubbled through the solution for 10 min before Jones' reagent was added dropwise until the orange color persisted. The reaction mixture was stirred for 60 min at RT. Then, 2-propanol was added dropwise until the solution became blue-green. The mixture was concentrated under reduced pressure, and the resulting solids were dissolved in a minimum amount of water (1 mL). Dichloromethane (1 mL) was added, and the two phases were separated. The aqueous layer was extracted

© 2007 NRC Canada

with dichloromethane (3 × 1 mL). The combined organic fractions were washed with brine, dried over anhyd. magnesium sulfate, and concentrated under reduced pressure. The crude product was purified by flash chromatography on silica gel (10% methanol in dichloromethane). A colorless oil was isolated (13 mg, 51%). ^{1}H NMR (300 MHz, CD_3OD) δ (ppm): 7.89–7.85 (m, 2H), 7.19 (br s, 5H), 7.11 (d, 2H, J = 9.3 Hz), 3.90 (s, 3H), 3.72 (d, 1H, J = 12.6 Hz), 2.86 (d, 1H, J = 12.7 Hz), 1.24 (s, 3H). IR (neat) ν (cm^{-1}): 3700–3100 (br), 2925, 2851, 1709, 1595, 1265, 1141. LRMS (*m/z*, relative intensity) 335 (MH^+, 5), 317 (10), 163 (70), 91 (100). HRMS calcd. for $C_{17}H_{19}O_5S$ (MH^+): 335.0953, found: 335.0946. $[\alpha]^{20}_D$ –17.7 (*c* = 0.56, $CHCl_3$).

Acknowledgements

Financial support from Bristol-Myers Squibb, the Natural Sciences and Engineering Research Council of Canada (NSERC), and the Université de Sherbrooke is gratefully acknowledged.

References

1. (*a*) H. Cho and B.V. Plapp. Biochemistry, **37**, 4482 (1998); (*b*) M. Mitchard. Drug Met. Drug Inter. **6**, 183 (1988); (*c*) L.A. Damani. *In* Sulfur-containing drugs and related organic compounds: chemistry, biochemistry, and toxicology. Vol 1. Part B. Ellis Horwood Ltd., Chichester, UK, 1989.
2. R. Young. Prog. Med. Chem. **38**, 249 (2001).
3. C.J. Burns, R.D. Groneberg, J.M. Salvino, G. McGeehan, S.M. Condon, R. Morris, M. Morrissette, R. Mathew, S. Darnbrough, K. Neuenschwander, A. Scotese, S.W. Djuric, J. Ullrich, and R. Labaudinière. Angew. Chem., Int. Ed. **37**, 2848 (1998).
4. (*a*) P. Kim, Y.-M. Zhang, G. Shenoy, Q.-A. Nguyen, H.I. Boshoff, U.H. Manjunatha, M.B. Goodwin, J. Lonsdale, A.C. Price, D.J. Miller, K. Duncan, S.W. White, C.O. Rock, C.E. Barry, III, and C.S. Dowd. J. Med. Chem. **49**, 159 (2006); (*b*) R.A. Slayden, R.E. Lee, J.W. Armour, A.M. Cooper, and I.M. Orme. Antimicrob. Agents Chemother. **40**, 2813 (1996); (*c*) H. Sasaki, H. Oishi, T. Hayashi, I. Matsuura, K. Ando, and M. Sawada. J. Antibiotics, **35**, 396 (1982); (*d*) S. Omura, A. Nakagawa, R. Iwata, and A. Hatano. J. Antibiotics, **36**, 1781 (1983); (*e*) L.A. Dolak, T.M. Castle, S.E. Truesdell, and O.K. Sebek. J. Antibiotics, **39**, 26 (1986); (*f*) M.S. Chambers, E.J. Thomas, and D.J. Williams. J. Chem. Soc., Chem. Commun., 1228 (1987); (*g*) I. Nishida, A. Kawaguchi, and M. Yamada. J. Biochem. **99**, 1447 (1986); (*h*) T. Hayashi, O. Yamamoto, H. Sasaki, A. Kawaguchi, and H. Okazaki. Biochem. Biophys. Res. Commun. **115**, 1108 (1983).
5. (*a*) T. Fukuyama and Y. Kishi. J. Am. Chem. Soc. **98**, 6723 (1976); (*b*) E. De Clercq, A. Billiau, H.C. Ottenheijm, and J.D. Herscheid. Biochem. Pharmacol. **27**, 635 (1978); (*c*) W.A. Rightsel, H.G. Schneider, B.J. Sloan, P.R. Graf, F.A. Miller, O.R. Bartz, J. Ehrlich, and G.J. Dixon. Nature (London), **204**, 1333 (1964); (*d*) P. L. Rodriguez and L. Carrasco, J. Virol. **66**, 1971 (1992); (*e*) A. Mullbacher and R.D. Eichner. Proc. Natl. Acad. Sci. USA. **81**, 3835 (1984); (*f*) A. Mullbacher, P. Waring, and R.D. Eichner. J. Gen. Microbiol. **131**, 1251 (1985); (*g*) A. Mullbacher, P. Waring, U. Tiwari-Palni, and R.D. Eichner. Mol. Immunol. **23**, 231 (1986); (*h*) J.P. Beaver and P. Waring. Immunol. Cell Biol. **72**, 489 (1994).
6. (*a*) P. V. Attwood and J. C. Wallace. Acc. Chem. Res. **35**, 113 (2002); (*b*) P.J. De Clercq. Chem. Rev. **97**, 1755 (1997).
7. The Michael addition of thiols to α,β-unsaturated esters or amides has been successfully utilized for the stereoselective formation of chiral sulfides; see for example: (*a*) C. Palomo, M. Oiarbide, R. López, P.B. González, E. Gómez-Bengoa, J.M. Saá, and A. Linden. J. Am. Chem. Soc. **128**, 15236 (2006); (*b*) C. Palomo, M. Oiarbide, F. Dias, R. López, and A. Linden. Angew. Chem., Int. Ed. **43**, 3307 (2004); (*c*) P. McDaid, Y. Chen, and L. Deng. Angew. Chem., Int. Ed. **41**, 338 (2002); (*d*) M. Saito, M. Nakajima, and S. Hashimoto. Chem. Commun. 1851 (2000); (*e*) V. van Axel Castelli, A. Dalla Cort, L. Mandolini, D.N. Reinhoudt, and L. Schiaffino. Chem. Eur. J. **6**, 1193 (2000); (*f*) E. Emori, T. Arai, H. Sasai, and M. Shibasaki. J. Am. Chem. Soc. **120**, 4043 (1998); (*g*) K. Nishimura and K. Tomioka. J. Org. Chem. **67**, 431 (2002); (*h*) N. Prabagaran and G. Sundararajan. Tetrahedron Assym. **13**, 1053 (2002).
8. For a review on the preparation of sulfides, sulfoxides, sulfones, and their selenium counterparts, see: (*a*) D.J. Procter. J. Chem. Soc., Perkin Trans. 1, 335–354 (2001), and refs. cited therein; for metal catalyzed C–S bond formation: (*b*) T. Kondo and T. Mitsudo. Chem. Rev. **100**, 3205–3220 (2000).
9. For example, see: A. Dion, P. Dubé, and C. Spino. Org. Lett. **7**, 5601 (2005).
10. (*a*) M.S. Chambers and E.J. Thomas. J. Chem. Soc., Perkin Trans. 1, 417 (1997); (*b*) Y. Tamaru, Z.-i. Yoshida, Y. Yamada, K. Mukai, and H. Yoshioka. J. Org. Chem. **48**, 1293 (1983); for palladium-catalyzed rearrangements: (*c*) A. Böhme and H.-J. Gais. Tetrahedron: Asymmetry, **10**, 2511 (1999), and see also reference 6*f*.
11. (*a*) C. Spino, C. Godbout, C. Beaulieu, M. Harter, and T.M. Mwene-Mbeja. J. Am. Chem. Soc. **126**, 13312 (2004); (*b*) C. Beaulieu and C. Spino. Angew. Chem., Int. Ed. **39**, 1930 (2000).
12. R.E. Hackler and T.W. Balko. J. Org. Chem. **38**, 2106 (1973).
13. (*a*) T. Nakai, T. Mimura, and A. Ari-Izumi. Tetrahedron Lett. **28**, 2425 (1977); (*b*) T. Nakai, T. Mimura, and T. Kurokawa. Tetrahedron Lett. **32**, 2895 (1978); (*c*) T. Mimura, Y. Kimura, and T. Nakai. Chem. Lett., 1361 (1979); (*d*) For an example of mercury-catalyzed rearrangement of thionocarbamate, see: (e) L.E. Overman, C.B. Campbell, and F.M. Knoll. J. Am. Chem. Soc. **100**, 4822 (1978).
14. (*a*) R.J. Ferrier and N. Vethauiyasar. J. Chem. Soc. D, 1385 (1970); (*b*) B.M. Trost and H. Hiemstra. J. Am. Chem. Soc. **104**, 886 (1982).
15. C. Spino, M.-C. Granger, and M.-C. Tremblay. Org. Lett. **4**, 4735 (2002).
16. A. Mengel and O. Reiser. Chem. Rev. **99**, 1191 (1999).
17. E.-i. Negishi and D.Y. Kondakov. Chem. Soc. Rev. 417 (1996), and s. cited therein.
18. (*a*) T. Nakai and A. Ari-Izumi. Tetrahedron Lett. **27**, 2335 (1976); (*b*) Ö. Zaim. Tetrahedron Lett. **40**, 8059 (1999).
19. K. Banert and J. Schlott. Tetrahedron, **56**, 5413 (2000).
20. (*a*) K.C. Nicolaou, R.D. Groneberg, T. Miyazaki, N.A. Stylianides, T.J. Schulze, and W. Stahl. J. Am. Chem. Soc. **112**, 8193 (1990); (*b*) K.C. Nicolaou and R.D. Groneberg. J. Am. Chem. Soc. **112**, 4085 (1990).
21. For selected reviews: (*a*) R.H. Grubbs (*Editor*). Handbook of metathesis. Vol. 1–3. Wiley-VCH, New York, NY. 2003; (*b*) K.C. Nicolaou, P.G. Bulger, and D. Sarlah. Angew. Chem., Int. Ed. **44**, 4490 (2005); (*c*) R.H. Grubbs. Tetrahedron, **60**, 7117 (2004).
22. (*a*) L. Boisvert, F. Beaumier, and C. Spino. Can. J. Chem. **84**, 1290 (2006); (*b*) C. Spino, L. Boisvert, J. Douville, S. Roy, S.

© 2007 NRC Canada

Lauzon, J. Minville, D. Gagnon, F. Beaumier, and C. Chabot. J. Organomet. Chem. **691**, 5336 (2006).

23. For selected examples of RCM involving sulfides, see: (*a*) G.J. Rowlands and J. Singleton. J. Chem. Res. 247 (2004); (*b*) Y.S. Shon and T.R. Lee. Tetrahedron Lett. **38**, 1283 (1997); (*c*) J.F. Miller, A. Termin, K. Koch, and A.D. Piscopio. J. Org. Chem. **63**, 3158 (1998); (*d*) J.D. Moore, K.T. Sprott, and P.R. Hanson. Synlett, 605 (2001); (*e*) J.A. Smulik, A.J. Giessert, and S.T. Diver. Tetrahedron Lett. **43**, 209 (2002); (*f*) G. Spagnol, M.P. Heck, S.P. Nolan, and C. Mioskowski. Org. Lett. **4**, 767 (2002); (*g*) R.V. Anand, S. Baktharaman, and V.K. Singh. J. Org. Chem. **68**, 3356 (2003); For selected examples involving sulfoxides or sulfones, see: (*h*) D.K. Bates, X. Li, and P.V. Jog. J. Org. Chem. **69**, 2750 (2004); (*i*) A. Fürstner, T. Gastner, and H. Weintritt. J. Org. Chem. **64**, 2361 (1999).
24. For selected methods to prepare chiral dihydrothiophenes, see: (*a*) A.M. Ponce and L.E. Overman. J. Am. Chem. Soc. **122**, 8672 (2000); (*b*) D. Desmaële, S. Delarue-Cochin, C. Cavé, J. d'Angelo, and G. Morgant. Org. Lett. **6**, 2421 (2004); (*c*) V. Popsavin, O. Beric, S. Velimirovic, and D. Miljkovic. J. Serb. Chem. Soc. **9**, 717 (1993); (*d*) A.V.R. Rao, K.A. Reddy, N.R. Srinivas, M.K. Gurjar, N. Padmaja, S. Ramakumar, M.A. Viswamitra, G.V.T. Swapna, B. Jagannadh, and A.C. Kunwar. J. Chem. Soc., Perkin Trans. 1, 1255 (1993); (*e*) E.V. Dehmlow and R. Westerheide. Synthesis, **10**, 947 (1992); (*f*) S. Brandau, E. Maerten, and K.A. Jørgensen. J. Am. Chem. Soc. **128**, 14986 (2006).
25. (*a*) J. Huang, E.D. Stevens, S.P. Nolan, and J.L. Peterson. J. Am. Chem. Soc., **121**, 2674 (1999); (*b*) M. Scholl, T.M. Trnka, J.P. Morgan, and R.H. Grubbs. Tetrahedron Lett. **40**, 2247 (1999).
26. (*a*) M. Whittaker, C.D. Floyd, P. Brown, and A.J.H. Gearing. Chem. Rev. **99**, 2735 (1999); (*b*) H. Nagase and J.F.Woessner. J. Chem. Biol. **274**, 21491 (1999).
27. V. Aranapakam, G.T. Grosu, J.M. Davis, B. Hu, J. Ellingboe, J.L. Baker, J.S. Skotnicki, A. Zask, J.F. DiJoseph, A. Sung, M.A. Sharr, L.M. Killar, T. Walter, G. Jin, and R. Cowling. J. Med. Chem. **46**, 2361 (2003), and s. cited therein.
28. T. Walter, M.A. Sharr, C.E. Roth, F.J. Moy, R. Powers, G. Jin, R. Cowling, and J.S. Skotnicki. Bioorg. Med. Chem. Lett. **11**, 235 (2001).
29. H. Harayama, T. Nagahama, T. Kozera, M. Kimura, K. Fugami, S. Tanaka, and Y. Tamaru. Bull. Chem. Soc. Jpn. **70**, 445 (1997).
30. C. Spino. Org. Prep. Proc. Int. **35**, 1 (2003).

© 2007 NRC Canada

Comparative studies of univariate and multivariate optimizations for manganese determination in antihypertensive drugs by electrothermal atomic absorption spectrometry

Josianne Nicácio Silveira, Paulo Celso Pereira Lara, Michelle Batista Dias, Clésia Cristina Nascentes, Cynthia Demicheli, and José Bento Borba da Silva

Abstract: Comparative studies using the univariate and multivariate optimizations (factorial design) were undertaken to determine manganese in antihypertensive drugs by electrothermal atomic absorption spectrometry (ET AAS). For the univariate method, the optimum pyrolysis and atomization temperatures were 500 and 2200 °C, and for multivariate analysis, the temperatures were 500 and 2400 °C, respectively. No differences were observed between the methods with respect to the slopes of the calibration curves, recoveries, results for certified urine samples for the two levels, and the averages of the intra- and inter-assay coefficients of variation (CV) using Student *t* and *F* tests as a statistical tool ($P < 0.05$). Calibration was performed by matrix matching. All other studies were made using the optimized multivariate conditions. The characteristic mass was of 0.68 ± 0.17 pg (the recommended mass is 0.60 pg). The limits of detection and quantification were 0.23 and 0.77 μg L^{-1}, respectively. Intra- and inter-assay studies on the drug spiked with 0.5, 1.0, and 1.5 μg L^{-1} of Mn yielded mean results of 3.6 ± 1.9% and 9.6 ± 2.2%, respectively. For the intra-assay evaluation, seven samples of each concentration were evaluated for Mn on the same day, whereas, for the inter-assay study, these solutions were analyzed in three replicates during three consecutive days. Recovery studies on the drug spiked with three levels of Mn ($n = 7$ for each level) furnished results between 101.4 ± 17.2% and 106.6 ± 7.5%. The results of a certified urine sample analysis (two levels of Mn) agreed at a 95% level of confidence. Forty eight antihypertensive drug samples were analyzed, and the drug contents varied between 2.9 ng and 1.9 μg $capsule^{-1}$.

Key words: manganese, antihypertensive drugs, electrothermal atomic absorption spectrometry, multivariate optimization.

Résumé : Afin de déterminer le manganèse dans les médicaments hypertensifs par spectrométrie d'absorption atomique électrothermique (SAA ET), on a effectué des études comparatives en faisant appel à des optimisations à une et à plusieurs variables (modèle factoriel). Pour la méthode à une variable, les températures optimales pour la pyrolyse et l'atomisation sont de 500 et 2200 °C alors que pour l'analyse à plusieurs variables, elles sont respectivement de 500 et 2400 °C. On n'a observé aucune différence entre les méthodes en ce qui a trait aux pentes des courbes de calibration, aux résultats pour des échantillons certifiés d'urine pour deux niveaux et pour les moyennes des coefficients de variation (CV) intra- et inter-essais en utilisant les tests de Student *t* et *F* comme outil statistique ($P < 0,05$). On a effectué la calibration en procédant par appariement de matrice. Toutes les autres études ont été réalisées en utilisant des conditions à variables multiples optimisées. La masse caractéristique était de 0,68 ± 0,17 pg (la masse recommandée est de 0,60 pg). Les limites de détection et de quantification sont respectivement de 0,23 et 0,77 μg L^{-1}. Les études intra- et inter-essais effectuées sur le médicament fortifié dans lequel on a ajouté 0,5, 1,0 et 1,5 μg L^{-1} de manganèse ont conduit à des résultats moyens respectifs de 3,6 ± 1,9% et 9,6 ± 2,2%. Pour l'évaluation intra-essai, on a évalué le même jour la quantité de manganèse de sept échantillons de chaque concentration, alors que pour l'évaluation intra-essai on a analysé trois duplicata de ces solutions durant trois jours consécutifs. Les études de récupération sur le médicament fortifié à trois niveaux de manganèse ($n = 7$ pour chaque niveau) ont conduit à des résultats entre 101,4 ± 17,2% et 106,6 ± 7,5%. Les résultats pour l'analyse d'un échantillon certifié d'urine (deux niveaux de manganèse) correspondent au niveau de 95% de confiance. On a analysé quarante-huit échantillons de médicament hypertensif et le contenu de ces médicaments en manganèse varie de 2,9 à 1,9 μg par capsule.

Received 13 January 2007. Accepted 30 May 2007. Published on the NRC Research Press Web site at canjchem.nrc.ca on 28 August 2007.

J.N. Silveira[1] and M.B. Dias. Laboratório de Toxicologia Ocupacional, Faculdade de Farmácia, Universidade Federal de Minas Gerais, Belo Horizonte 31270–901, MG. Brazil.
P.C.P. Lara, C.C. Nascentes, C. Demicheli, and J.B.B. da Silva.[2] Departamento de Química, Universidade Federal de Minas Gerais, Belo Horizonte 31270–901, MG. Brazil.

[1]Corresponding author (e-mail: nicacio@ufmg.br).
[2]Corresponding author (e-mail: bentojb@terra.com.br).

 doi:10.1139/V07-086 © 2007 NRC Canada

Mots-clés : manganèse, médicaments antihypertension, spectrométrie d'absorption atomique électrothermique, optimisation à plusieurs variables.

[Traduit par la Rédaction]

Introduction

Manganese is an essential element for humans and animals. It is largely distributed as particles in the earth's crust, in water, and in the atmosphere (1). Normal human blood and urine levels are 2–8 μg dL^{-1} and 0.1–0.8 μg dL^{-1}, respectively, (2). Individuals exposed to high levels of manganese can suffer deterioration of neurological functions, beginning with unspecific symptoms and neurological signals (3).

The Recommended Daily Ingestion (RDI) of manganese is 5.0 mg for normal adults and from 2.0 to 5.0 mg for pregnant and lactating women. Certain groups of the population in general are more extensively exposed to manganese through some foods, from living close to industrial areas, by occupational exposure, and from other sources such as medicines (3).

According to Flores et al. (4), the control of heavy metals in the most-diverse samples (biological tissues, water, soil, foods, and so forth) is currently a relevant subject, principally for evaluating the degree of exposure and possible consequences for the human health. In this respect, control of contamination in medicines is of vital importance, since such contamination may constitute a public health problem. Quality control is necessary to prevent eventual risk of intoxication by contaminants in medicines and for the control of medicines where this type of element is present as the main constituent or as an adjuvant.

Electrothermal atomic absorption spectrometry (ET AAS) can be employed for the direct analysis of liquid samples and slurries with the advantages of low time consumption and a simple pre-treatment process with reduced contamination problems (5). Frequently, the optimization of experimental conditions for ET AAS determinations (chemical modifiers, pyrolysis time, pyrolysis and atomization temperatures) requires a large number of experiments in addition to being time-consuming and expensive. Moreover, the interactions between optimized variables are not evaluated. Multivariate optimization would seem to be a more adequate approach when many variables are involved. Factorial design (6, 7) is a good and simple statistical tool that can be used to verify the effects of variables and their interactions based on a small number of experiments.

Choudhary et al. (8) has studied multi-mineral pharmaceutical formulations of twelve drugs produced in Pakistan to determine calcium, copper, iron, magnesium, manganese, potassium, and zinc contents by AAS. In another work (9), Acar determined lead, chromium, manganese, and zinc as slurries of botanical and other biological samples by ET AAS, using tungsten-containing chemical modifiers.

In the present work, a factorial design was employed to optimize experimental conditions for the direct determination of manganese in antihypertensive drugs by electrothermal atomic absorption spectrometry. The results were compared with those of conventional pyrolysis- and atomization-temperature curves (univariate method).

Experimental

Instrumentation

All measurements were performed on a Varian (Victoria, Australia) SpectrAA Z-220 atomic absorption spectrometer equipped with a graphite furnace, an autosampler (PSD – 31–972), and the Polarized Zeeman Background correction procedure. The atomic signal was measured in peak-height mode. A single element, hollow cathode lamp for Mn from IST (Imaging & Sensing Technology, Horseheads, NY, WL 22936, serial No. 12774) was used as the light source; it was operated at 15.0 mA with a spectral band-pass of 0.2 nm at 279.5 nm. Unless otherwise specified, the conditions recommended by the manufacturer were employed. Argon (99.999%) from Air Liquide® (Contagem, MG, Brazil) was used as the purge gas. Graphite-coated pyrolytic tubes without a platform (Varian, part No. 63–100012–00) were employed throughout this work.

Reagents and solutions

All of the solutions were prepared using deionized water from a Milli-Q system (Millipore, Bedford, MA, USA). Nitric acid (65% *w*/*w*, Suprapur®, Merck, Darmstadt, Germany, part No. 1.00441.0250) was used. The calibration solutions were prepared from a stock manganese solution containing 1000 ± 0.002 mg L^{-1} (Titrisol–Merck) in 5% *v*/*v* HNO_3. The final solutions contained 0.4% *v*/*v* HNO_3. In all of the studies, a standard solution of 1000 mg L^{-1} tungsten (Titrisol–Merck) was used for the graphite-tube treatment.

Plastic bottles, autosampler cups, and glassware materials were cleaned by soaking in 20% (*v*/*v*) HNO_3 for 1 day, rinsing many times with Milli-Q water, and drying. The autosampler washing solution, containing 0.1% (*v*/*v*) Triton X–100 (Merck) plus 0.2% (*v*/*v*) nitric acid, was used to avoid analyte adsorption onto the surface of the container, to avoid clogging the autosampler pipette, and to improve the dispersion of sample solution onto the platform.

Sampling and sample treatment

Samples (capsules) were obtained from 20 manipulation pharmacies. Industrial samples (tablets) were obtained from a local drugstore. Two kinds of antihypertensive drugs were selected from those most consumed by patients in Belo Horizonte, MG, Brazil. The active principles of these two drugs were enalapril maleate and anlodipine besilate. Since different pharmacies use different excipients, a capsule (reference sample A) was produced that contained all the excipients and the two active pharmaceutical ingredients, as used and sold in the manipulation pharmacies that participated in this project.

The sample capsules or tablets were weighed in a tube with a threaded cover, and 300 μL of concentrated nitric acid

© 2007 NRC Canada

Table 1. Factorial design experiments of the pyrolysis and atomization temperatures and type of graphite furnace.

Experiment	Pyrolysis temperatures (°C)	Atomization temperatures (°C)	Type of graphite furnace[a]	Mean absorbances (peak height)
1	500	2000	N	0.391
2	500	2000	Y	0.194
3	500	2400	N	0.421
4	500	2400	Y	0.257
5	1500	2000	N	0.254
6	1500	2400	N	0.308
7	1500	2400	Y	0.048
8	1500	2000	Y	0.031
9	1000	2200	N	0.360
10	1000	2200	Y	0.189

[a]N = graphite tube without modifier; Y = graphite tube with modifier.

was added with subsequent stirring for one minute, followed by the addition of 2.5 mL of Milli-Q water with one more minute of stirring. The volume of the solution was increased quantitatively to 25.0 mL with water, resulting in a homogeneous slurry.

Graphite-tube treatment

The graphite tubes were treated with a permanent W modifier. The treatment with 520 μg of tungsten was accomplished by applying 40 μL of the solution of the metal ion (1.0 g L^{-1}) onto the tube and submitting it to a furnace temperature program 13 times, with 13 injections of 40 μL of Milli-Q water to cleanse the tube (10) after each temperature program.

Optimization

The reference sample (A) spiked with 3.0 μg/L of Mn in 1.2% HNO_3 was employed to obtain the most appropriate temperatures for both methods (uni- and multivariate). The volume of sample introduced into the graphite tube was 22 μL for both methods.

Univariate optimization

In the conventional method, the pyrolysis- and atomization-temperature curves were obtained independently. To obtain the pyrolysis-temperature curve, the atomization temperature used was that recommended by the manufacturer, and measurements were obtained between 500 °C and 1000 °C (at intervals of 100 °C). These studies were performed without the use of a modifier. Previous results for the determination of manganese in human urine and serum by ET AAS with comparison of several modifiers indicated that the the best results were obtained without the use of a modifier (11). The pyrolysis temperature utilized to obtain the atomization-temperature curve was the one that gave the best results in the previous study (500 °C), varying of 100 °C between 1900 °C and 2400 °C. Sensitivity, absorption-pulse forms, background absorption, and the lowest-atomization temperature (to increase the lifetime of the graphite tube) were criteria for selection of the best conditions. Matrix-matching calibration curves and analytical characteristics were obtained under the optimized conditions.

Multivariate optimization

A factorial design (2^3 plus two center points) was performed to determine the optimal experimental conditions and to evaluate the influence of and the interaction between the factors studied. The minimum and maximum levels for pyrolysis and atomization temperatures were chosen according to the information furnished by the manufacturer. No modifier was used (11). The selection of tungsten was based on the wide use of that modifier for analytes with a tendency to be refractory. The variables studied were pyrolysis temperatures (500 °C and 1500 °C), atomization temperatures (2000 °C and 2400 °C), and the use or non-use of a permanent modifier (W). The factorial design is presented in Table 1. The Mn absorbance (n = 3) was analyzed using the Statgraphics Plus software that supplies the best condition of Mn determination. The highest-absorbance signal was selected, and the background was corrected, showing a good removal from the matrix. Matrix-matching calibration curves and analytical characteristics were obtained using the optimized conditions.

Results and discussion

Determination of the temperature program by the univariate and multivariate methods

The results obtained for the pyrolysis- and atomization-temperature curves using the conventional method are presented in Fig. 1, while the time for pyrolysis is presented in Fig. 2. The highest-sensitivity and the lowest-background signals were obtained with a pyrolysis temperature of 500 °C and an atomization temperature of 2200 °C.

The results obtained using the multivariate method are shown in Figs. 3 and 4. The Pareto chart (Fig. 3) presents the variables that have a significant effect on the response obtained at a 95% significance level. The effects of the variables (modifier and pyrolysis temperature) were statistically significant. The effect of the atomization temperature was not significant. On the other hand, the atomization temperature of 2400 °C was more effective than that of 2000 °C for the determination of manganese (Fig. 4, main-effects plot) in spite of the fact that no statistically significant difference between 2000 °C and 2400 °C was observed. For that reason,

© 2007 NRC Canada

Fig. 1. Pyrolysis- and atomization-temperature curves obtained for manganese in reference sample A, using the conditions optimized by the univariate method.

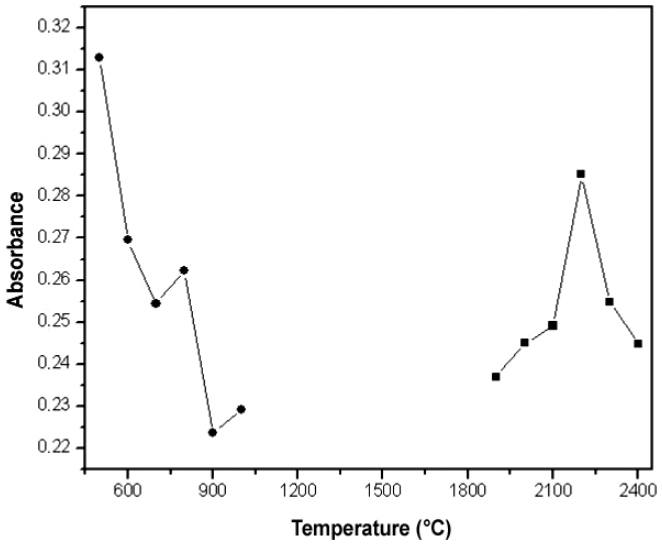


Fig. 2. Pyrolysis-time curve for manganese in reference sample A, using univariate optimization.

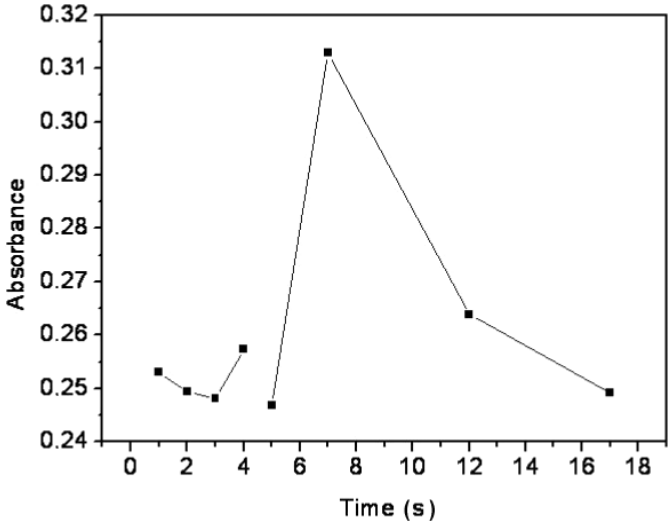


Fig. 3. Pareto chart showing the results of the factorial design (multivariate method) for the variables pyrolysis and atomization temperatures, modifier, and their interactions for Mn determination in reference sample A by ET AAS.

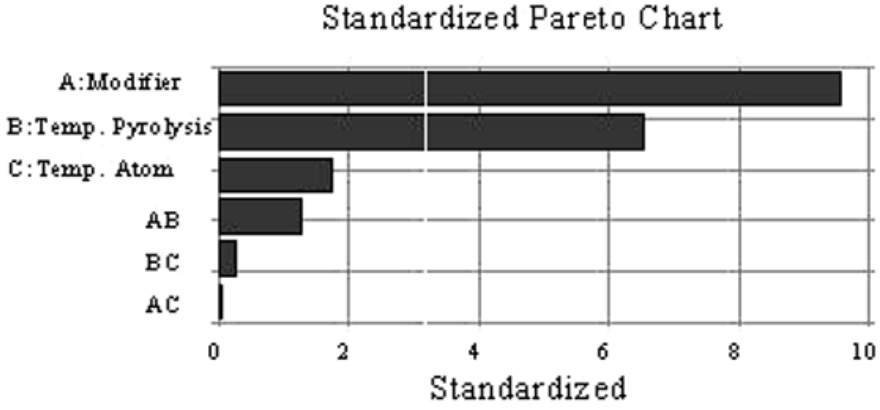
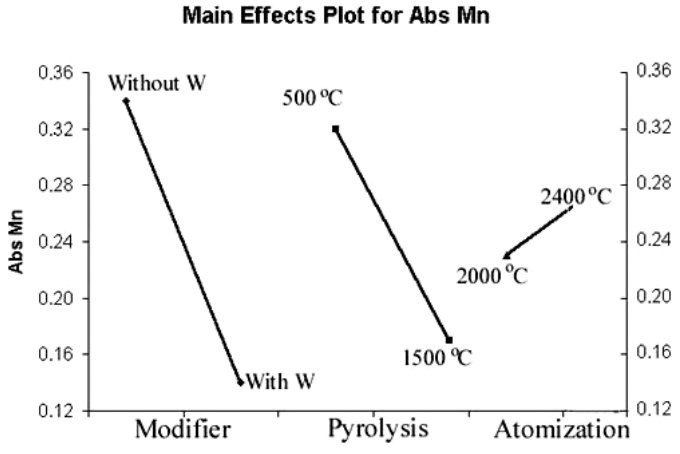


Fig. 4. Main-effects plot showing the results of the factorial design (multivariate method) of the variables pyrolysis and atomization temperatures and modifier for manganese in reference sample A.



2400 °C was chosen as the atomization temperature, and this temperature should not significantly reduce the life-time of the graphite furnace. According to the absorbance results, the pyrolysis temperature of 500 °C was better than that of 1500 °C. In the estimated response surface (Fig. 5) obtained with the Mn absorbance data, there is a tendency for a low pyrolysis temperature in combination with the highest atomization temperature. Under these conditions (500 and 2400 °C), the background was around 0.16 absorbance units. The optimal conditions obtained by the conventional and multivariate methods were very similar, since the best atomization temperature was 2200 °C for the univariate method and, in the multivariate optimization, the best analytical signal was obtained at an atomization temperature of 2400 °C. The results show that the multivariate method presents advantages because of the smaller number of experiments. The temperature program for manganese determination obtained after optimization of the analytical conditions is shown in Table 2.

© 2007 NRC Canada

Fig. 5. Estimated response surface for the factorial design of reference sample A.

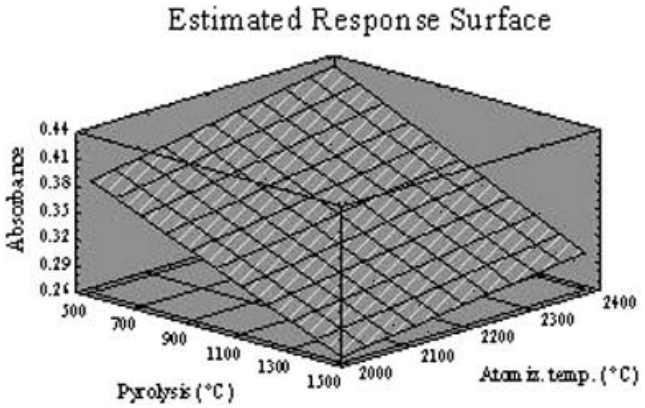


Table 2. Temperature program for Mn determination in antihypertensive drugs by ET AAS.

Step	Temperature (°C)	Ramp (s)	Hold (s)	Air flow rate (L min^{-1})
1	85	5.0	–	3.0
2	95	40.0	–	3.0
3	120	10.0	–	3.0
4	500	1.0	7.0	3.0
5[a]	2200[b], 2400[c]	0.9	3.0	0.0
6	2400	–	2.0	3.0

[a]Read in this step.
[b]Univariate method.
[c]Multivariate method.

Table 3. Analytical characteristics for the determination of Mn in antihypertensive drugs obtained by ET AAS under the optimized uni- and multivariate experimental conditions.

Parameter	Univariate optimization	Multivariate optimization
Regression equation	$Y = 0.0475(\pm0.003)x + 0.0407(\pm0.027)$	$Y = 0.0448(\pm0.018)x + 0.0314(\pm0.008)$
R^2	0.9962 ± 0.0026	0.9965 ± 0.0016
Linear range (μg L^{-1})	0.5–4.0	0.5–4.0
LOD (μg L^{-1})	0.23	0.23
LQ (μg L^{-1})	0.77	0.77
Mass (pg)	0.70 ± 0.14	0.68 ± 0.17
CV[a] intra (%)	2.8 ± 1.3	3.6 ± 1.9
CV inter (%)	6.5 ± 3.9	9.6 ± 2.2
Mean recovery (%)	106.3 ± 8.7	104.1 ± 2.6

[a]CV is the coefficient of variation.

Analytical figures of merit

Optimized conditions obtained by conventional and multivariate procedures were employed to determine the analytical characteristics presented in Table 3.

The limit of detection (LOD, μg L^{-1}) was calculated using the equation: LOD = 3 × $S_{0.5}/b$, where $S_{0.5}$ is the standard deviation for 10 measurements of the first point of the matrix-matching calibration curve, and b is the slope of the calibration curve, whereas the limit of quantification was calculated using the equation: LOQ = 10 × $S_{0.5}/b$.

The accuracy of the method was evaluated by the use of certified urine samples (Bio-Rad Laboratories, Lyphochek® Urine Metals Control level 1 – 69081 and level 2 – 69082, Irvine, CA, USA) with two manganese concentration levels and through recovery studies on the drugs.

Sample A (reference sample), spiked with 0.5, 1.0, and 1.5 μg L^{-1} of Mn, was used for the recovery study, which was performed in seven replicates and read in triplicate.

The precision was evaluated through intra- and inter-assay studies. The intra-assay variation coefficient was calculated using the standard deviation of the 0.5, 1.0, and 1.5 μg L^{-1} concentrations of Mn added to the reference sample (A), divided by the average of the respective concentrations, and multiplied by 100. These analyses were performed separately in seven replicates on the same day and read in triplicate. To calculate the inter-assay variation coefficient, the same procedure was repeated with three replicates of the sample and read in triplicates on three different days.

The optimized conditions obtained by conventional and multivariate procedures were employed to determine the analytical characteristics presented in Table 3. No differences were found between the methods concerning the slopes of the calibration curves, recoveries, and certified urine samples for the two levels and the average of the CV's for the intra- and inter-assays ($P < 0.05$) when statistical tools (Student F and t tests) were employed.

Considering that the multivariate procedure simultaneously evaluates all the variables studied and requires a smaller number of experiments for the development of a method, thereby requiring less time and expense, this procedure was adopted for determining Mn in the samples. Seven matrix-matching calibration curves were constructed by applying the temperature program presented in Table 2. All calibration curves were constructed in the range between 0.5 and 4.0 μg L^{-1} of Mn (Fig. 6) and presented an $R^2 > 0.99$. The results for uni- and multivariate methods were very similar, as is shown Table 3.

The recoveries and deviations ($n = 7$) for the spiked samples are presented in Table 4. The recovery values obtained were nearly 100%; a result that shows the high degree of accuracy of both methods.

The accuracy was also evaluated in a study performed using certified urine samples (Table 5). For both methods, the

© 2007 NRC Canada

Fig. 6. Absorption signal for manganese in reference sample A spiked with 4.0 μg L^{-1} of manganese (last point of the matrix-matching calibration curve).

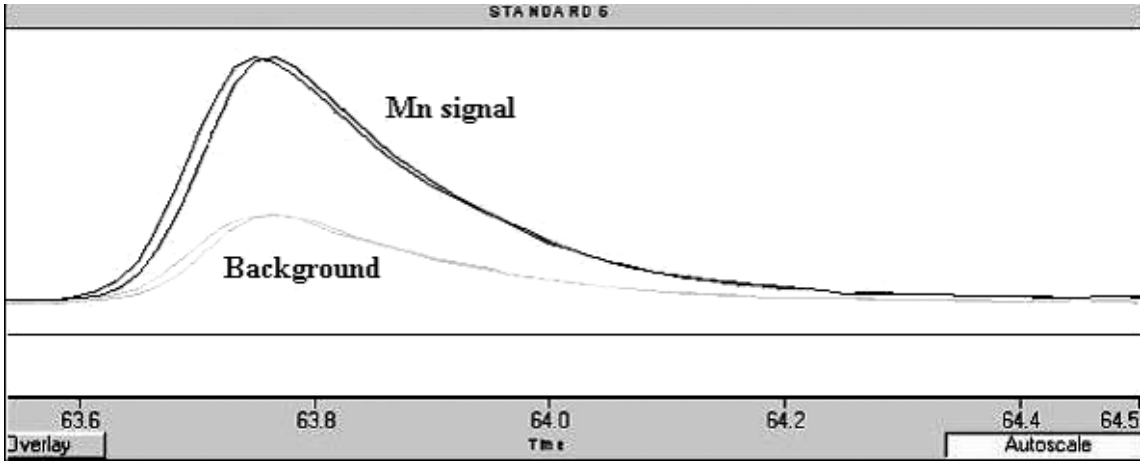


Table 4. Recovery of Mn in antihypertensive drugs by conventional and multivariate methods (n = 7).

Concentration of Mn (μg L^{-1})	Recovery (univariate method) (%)	Recovery (multivariate method) (%)
0.5	116.3 ± 9.7	101.4 ± 17.2
1.0	101.0 ± 4.5	106.6 ± 7.5
1.5	101.6 ± 1.3	104.2 ± 6.8

Table 5. Certified and determined values (μg L^{-1}) for Mn in the urine sample (n = 7).

	Certified	Univariate	Multivariate
Level 1	5.9–8.9	7.4 ± 1.0	7.7 ± 1.2
Level 2	15.9–23.8	21.4 ± 2.5	21.3 ± 0.6

Table 6. Intra- and inter-assay studies of the precision.

	CV intra (%, n = 7)		CV inter (%, n = 3)	
Concentration of Manganese (μg L^{-1})	Univariate	Multivariate	Univariate	Multivariate
0.5	3.4	3.4	2.8	7.2
1.0	3.5	5.6	10.6	11.5
1.5	1.3	1.8	6.3	10.0
Average	2.8 ± 1.3	3.6 ± 1.9	6.5 ± 3.9	9.6 ± 2.2

results obtained for both Mn concentration levels were in agreement with the certified values. This result again demonstrates the accuracy of the proposed methods.

The averages of the intra-assay variation coefficients (Table 6) were 2.8 ± 1.3% and 3.6 ± 1.9% for the conventional and multivariate methods, respectively. The averages of the inter-assay variation coefficients were 6.5 ± 3.9% and 9.6 ± 2.2%, respectively, thus demonstrating the high precision of both methods.

Determination of manganese in antihypertensive drugs

Manganese concentration in different antihypertensive drugs was determined using the experimental conditions optimized by the multivariate method and matrix-matching calibration curves.

The manganese levels of 48 antihypertensive drugs were analyzed, and the levels encountered varied from 2.9 ± 0.6 to 1921.7 ± 211.4 ng $capsule^{-1}$ or $tablet^{-1}$. The highest manganese levels were found in the tablets and in the amlodipine besilate. The levels of manganese in the medicines analyzed are not worrisome, since the oral absorption is low, being 3% to 5% of the ingested dose with rapid elimination ($t_{1/2}$ of 37 days). Thus, in agreement with the Brazilian legislation, the average RDI is 5 mg. On the other hand, because of the inherent toxicity of each metal, the development of methods that are specific and sensitive for their determination in medicines is still necessary for quality control.

Conclusions

The factorial design is a simple procedure for evaluating ET AAS conditions for manganese determination in antihypertensive drugs with a reduced number of experiments. The results indicate that there are no significant differences between the figures of merits obtained by the two methods. The manganese levels in the analyzed samples varied from 2.9 ± 0.6 to 1921.7 ± 211.4 ng $capsule^{-1}$ or $tablet^{-1}$. The highest manganese levels were found in the tablets and in the anlodipine besilate.

The simplicity of the method of preparation and of the set of instrumental and analytical conditions resulted in a rapid,

© 2007 NRC Canada

precise, and accurate determination of manganese in antihypertensive-drug samples.

The levels of manganese in the medicines analyzed are not worrisome. However, the proposed method was simple, fast, specific, and sensitive, which is advantageous when compared with the tests based on the reaction with the sulfide ion proposed by the pharmacopeias in general. The proposed method can be applied to the investigation of other medicines of continuous use.

Acknowledgements

The authors are thankful to the Conselho Nacional de Pesquisa e Desenvolvimento Tecnológico (CNPq), Fundação de Amparo à Pesquisa do Estado de Minas Gerais (FAPEMIG), and to the Laboratório de Toxicologia Ocupacional da Faculdade de Farmácia (LATO/FAFAR/UFMG). P.C.P. Lara, C.C. Nascentes, and J.B.B. Silva received scholarships from the CNPq.

References

1. H.A. Waldron. Metals in the environment. *Edited by* K. Kadish, K.M. Smith, and R. Guilard. Academic Press, New York. 1980.
2. WHO. World Health Organization. Manganese and its compounds: concise international chemical assessment document. Geneva. 1999.
3. D.G. Barceloux. J. Toxicol., Clin. Toxicol**. 37**, 293 (1999).
4. E.M.M. Flores, C.F.L. Bittencourt, V. Laporta, and J.S. Barin. Pharm. Technol. **24**, 9 (2000).
5. C. Bendicho and M.T.C. Loos-Vollebregt. J. Anal. At. Spectrom. **6**, 353 (1991).
6. G.E.P. Box, W.G. Hunter, and J.S. Hunter. Statistics for experiments: an introduction to design, data analysis, and model building. Willey Publishing, New York. 1978.
7. B. Barros Neto, I.S. Scarminio, and R.E. Bruns. Planejamento e Otimização de Experimentos; Editora da Unicamp: Campinas, 1996. [Book in Portuguese].
8. F. Choudhary, Z. Iqbal, T. Khan, and M. Ashraf Park. J. Pharm. Sci. **18**, 40 (2005).
9. O. Acar. Mikrochim. Acta. **151**, 53 (2005).
10. J.B.B. Silva, M.A.M. Silva, A.J. Curtius, and B. Welz. J. Anal. At. Spectrom. **14**, 1737 (1999).
11. F.G. Pinto, U.V. Rey, E.F. Fernandes, J.N. Silveira, L.C.A. Amorim, and J.B.B. Silva. Anal. Sci. **21**, 1605 (2006).

© 2007 NRC Canada

Glycosides from the North Atlantic sea cucumber *Cucumaria frondosa* V — Structures of five new minor trisulfated triterpene oligoglycosides, frondosides A_7-1, A_7-2, A_7-3, A_7-4, and isofrondoside C

Alexandra S. Silchenko, Sergey A. Avilov, Anatoly I. Kalinovsky, Pavel S. Dmitrenok, Vladimir I. Kalinin, Jeffrey Morre, Max L. Deinzer, Carl Woodward, and Peter D. Collin

Abstract: Seven highly polar trisulfated triterpene glycosides belonging to the frondoside A_7 group have been isolated from the North Atlantic sea cucumber *Cucumaria frondosa*. The structures of five new glycosides, frondosides A_7-1 (**1**), A_7-2 (**2**), A_7-3 (**3**), A_7-4 (**4**), and isofrondoside C (**5**) were elucidated, three of which contained lanostane aglycons without a lactone-ring. Three pairs of the glycosides proved to be isomers by virture of the positions of double bonds in the aglycons nuclei; two pairs of the glycosides differed from each other by the character of the oxygen functionality at C-22. The results from these studies provided the basis for postulating the biosynthetic pathways of norlanostane glycosides in the sea cucumber.

Key words: Cucumaria frondosa, sea cucumbers, frondosides, triterpene glycosides.

Résumé : Au départ de concombres de mer, *Cucumaria frondosa*, du nord l'Atlantique, on a isolé plusieurs glycosides de triterpène trisulfatés très polaires qui appartiennent au groupe frondoside A_7. On a élucidé les structures de cinq nouveaux glycosides, les frondosides A_7-1 (**1**), A-2 (**2**), A_7-3 (**3**), A_7-4 (**4**) et l'isofrondoside C (**5**), dont trois contiennent des aglycones de lanostane sans noyau lactonique. Trois paires de glycosides sont des isomères de position de doubles liaisons dans les noyaux des aglycones; les deux autres paires de glycosides diffèrent l'un de l'autre par le caractère de la fonctionnalité oxygène en C-22. Les résultats de ces études fournissent les bases nécessaires pour postuler les voies de biosynthèse des glycosides du norlanostane dans les concombres de mer.

Mots-clés : Cucumaria frondosa, concombres de mer, frondosides, glycosides de triterpène.

[Traduit par la Rédaction]

Introduction

Our investigations on the triterpene glycosides from the North Atlantic sea cucumber *Cucumaria frondosa* (1–4) have continued and the structures of highly polar trisulfated glycosides are being presented. Structurally, these glycosides are diverse with different aglycon moieties, including holostane and nonholostane skeleton systems with shortened and unshortened side chains. These compounds contain identical trisulfated pentaoside-branched carbohydrate chains, and they are refered to the A_7 group by analogy with cucumariosides of the A_7 group from *C. japonica* (5).

In spite of the predominance of these trisulfated glycosides, which distinguish them from the mono- and disulfated glycosides in *C. frondosa*, this compound class has not been thoroughly investigated to date because of the very complicated multicomponent composition. Moreover, the presence of three polar sulfate groups affects the chromatographic behaviour of the glycosides, thus complicating the isolation of the individual components by HPLC. There are some good examples in the literature that demonstrate the difficulties in the isolation procedure of trisulfated glycosides. Frondoside F, a trisulfated pentaoside obtained from *C. frondosa* (6), has a saturated polycyclic nucleus in the aglycon moiety and an 18(22)-lactone instead of the more common 18(20)-lactone. These structural features for sea cucumber glycosides have not been reported before. However, experimental data in the paper by Yayli (6) raise many questions including the absence of a quasi-molecular ion in the FAB mass spectrum, the absence of any correla-

Received 28 April 2007. Accepted 3 July 2007. Published on the NRC Research Press Web site at canjchem.nrc.ca on 28 August 2007.

A.S. Silchenko, S.A. Avilov, A.I. Kalinovsky, P.S. Dmitrenok, and V.I. Kalinin.[1] Pacific Institute of Bioorganic Chemistry, Far East Division of the Russian Academy of Sciences, Vladivostok, 690022, Russia.
J. Morre and M.L. Deinzer. Department of Chemistry, Oregon State University, 153 Gilbert Hall, Corvallis, Oregon 97331–4003, USA.
C. Woodward and P.D. Collin. Coastside Bio Resources Inc., P.O. Box 151, Stonington, ME 04681, USA.

[1]Corresponding author (e-mail: kalininv@piboc.dvo.ru).

 doi:10.1139/V07-087 © 2007 NRC Canada

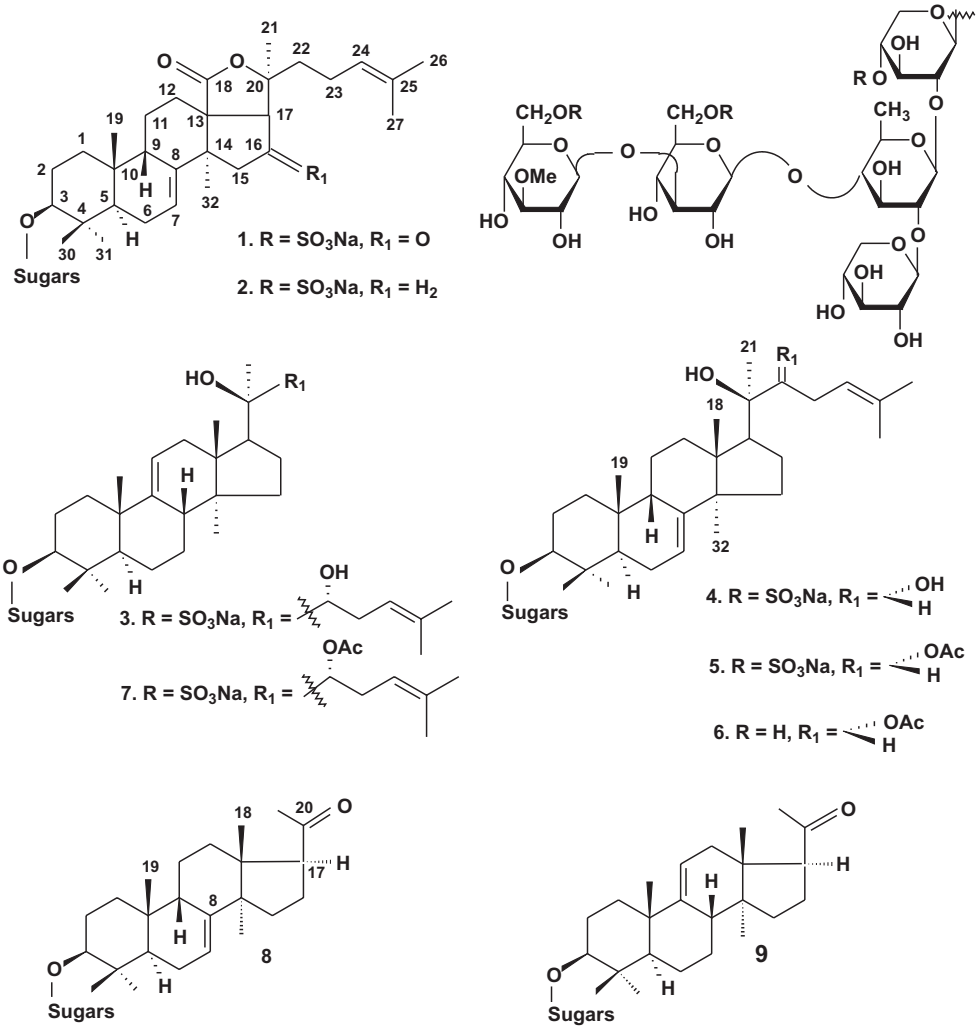
tion between protons at C-8 and C-9 in the ^{1}H-^{1}H-COSY spectrum, and the absence of graphic explanation of the NOESY data. A simple explanation could be that the investigator was working with a complicated mixture of glycosides having both 7(8) and 9(11) double bonds. As a result, not all the signals of the constituents were accumulated and indicated in the ^{13}C NMR spectrum (7). In other cases, the investigation of trisulfated glycosides were carried out only after the desulfation of the corresponding fraction and isolation of the desulfated derivatives (2). Only the use of modern isolation techniques and modified HPLC conditions have allowed us to isolate the pure natural substances belonging to this group of glycosides.

The sea cucumber *C. frondosa* was collected in the Gulf of Maine, Penobscot Bay, Maine, USA. The fraction of trisulfated frondosides (glycosides belonging to the frondoside A_7 group) (5) observed to be homogeneous by TLC was obtained from the ethanolic extract of the organism after column chromatography on polychrom-1 (powdered Teflon) and silica gel. Further separation of this fraction by HPLC yielded 10 individual glycosides, five of which were previously unreported. These are named here as frondosides A_7-1 (**1**), A_7-2 (**2**), A_7-3 (**3**), A_7-4 (**4**), and isofrondoside C (**5**).

Results and Discussion

Three of the glycosides were identified on the basis of NMR data as known frondoside C (**7**), which had been isolated earlier from *C. frondosa* (2), koreoside A (**8**) from *C. koraiensis* (8), and isokoreoside A (**9**) from *C. conicospermium* (9). Frondoside C (**7**) and isokoreoside A (**9**) were isolated as native substances, in contradistinction to earlier works (refs. 2 and 9), where the structures of the natural products, **7** and **9**, were elucidated on the basis of their desulfated derivatives. The spectra of these desulfated derivatives were compared with the spectra of the corresponding nonseparable fractions of thisulfated glycosides with identical carbohydrate chains to determine the number and positions of sulfate groups.

The signals of the carbohydrate moieties in the NMR spectra of all the isolated glycosides **1**–**5** and **7**–**9** of the frondoside A_7 group were identical. The corresponding data are discussed here only for one of these glycosides, namely for frondoside A_7-1 (**1**) (Table 1). The presence of five anomeric carbon signals at 102.2–105.2 ppm in the ^{13}C NMR spectrum of frondoside A_7-1 (**1**) and the corresponding doublets at 4.96–5.29 ppm (J = 7.0–8.0 Hz) of the anomeric protons in the ^{1}H NMR spectrum were consistent



© 2007 NRC Canada

Table 1. ^{13}C and ^{1}H NMR chemical shifts and selected HMBC and NOESY correlations of the carbohydrate moiety of **1**–**5** and **7**–**9**.

Position	δ_C [a,b,c]	δ_H mult. (*J* in Hz)[d]	HMBC	NOESY
Xyl1 (1→C-3)				
1	104.5	4.86 d (7.0)	C: 3	H-3,5 Xyl1, H-3, H-31
2	**81.7**	4.08 t (9.0)	C: 1-Qui, 1,3-Xyl1	
3	75.0	4.42 t (8.9)	C: 2, 4-Xyl1	H-1,5 Xyl1
4	*76.1*	5.13 m	C: 3-Xyl1	
5	64.1	4.93 m	C: 1,3-Xyl1	H-1,3 Xyl1
		4.01 m	C: 1,3-Xyl1	
Qui (1→2Xyl1)				
1	102.2	5.29 d (7.9)	C: 2-Xyl1	H-3, 5 Qui
2	**82.6**	4.03 m	C: 1,3-Qui, 1-Xyl2	
3	75.0	4.08 m	C: 2,4-Qui	H-1 Qui
4	**86.5**	3.54 t (8.9)	C: 1-Glu, 3-Qui	H-1 Glc, H-6 Qui
5	70.8	3.69 m		H-1 Qui
6	17.8	1.68 d (6.0)	C: 4,5-Qui	H-4 Qui, H-30
Glc (1→4Qui)				
1	103.9	4.90 d (7.8)	C: 4-Qui	H-4 Qui, H-3,5 Glc
2	73.4	3.93 t (8.0)	C: 1-Glc	
3	**86.5**	4.28 t (9.0)	C: 2,4-Glu, 1-MeGlu	H-1 MeGlc, H-1 Glc
4	69.1	3.91 t (9.1)	C:6 Glc	
5	74.8	4.22 m		H-1 Glc
6	*67.3*	4.72 dd (6.8, 11.3)	C: 5-Glc	
		5.09 brd (10.5)	C: 5-Glc	
MeGlc (1→3Glu)				
1	104.7	5.29 d (8.0)	C: 3-Glc	H-3 Glc, H-3,5 MeGlc
2	74.3	3.90 t (9.1)	C:1-MeGlc	
3	86.3	3.76 t (8.6)	C: 2,4-MeGlc, OMe	H-1,5 MeGlc
4	69.8	4.14 m	C:5-MeGlc	
5	75.5	4.13 m		H-1,3 MeGlc
6	*67.0*	4.89 m	C: 4-MeGlc	
		5.06 brd (10.6)	C: 4-MeGlc	
OMe	60.4	3.87 s	C: 3-MeGlcu	
Xyl2 (1→2 Qui)				
1	105.2	5.29 d (7.6)	C: 2-Qui	H-3,5 Xyl 2, H-2 Qui
2	74.8	4.04 t (7.9)	C: 1-Xyl2	
3	76.3	4.20 t (8.5)	C: 2,4 Xyl2	H-1 Xyl2
4	70.0	4.16 m		
5	66.5	4.37 dd (4.7; 11.0)	C: 1,3,4 Xyl2	
		3.75 t (10.0)	C: 1,3,4 Xyl2	H-1 Xyl2

Note: The spectra of frondoside A_7-1 (**1**) is presented; the spectra of **2**–**5** and **7**–**9** had only minimal differences.
[a]Recorded at 125 MHz in C_5D_5N–D_2O (4:1).
[b]Boldface = interglycosidic positions.
[c]Italic = sulfate position.
[d]Recorded at 500 MHz in C_5D_5N–D_2O (4:1).

with those of a pentasaccharide chain with β-configuration for the glycosidic linkages (10). Positions of interglycosidic bonds were elucidated by the analysis of HMBC spectra of frondoside A_7-1 (**1**) with correlations found between H-1 of the first xylose residue and C-3 of the aglycon, H-1 of quinovose and C-2 of the first xylose, H-1 of the glucose residue and C-4 of quinovose, H-1 of terminal 3-O-methyl glucose and C-3 of glucose, and between H-1 of the terminal xylose residue and H-2 of quinovose. Analogous correlations were revealed in the NOESY spectrum that confirmed the sequence of monosaccharide units in carbohydrate moieties of glycosides belonging to the frondoside A_7 group.

To confirm the presence of three sulfate groups in the carbohydrate moieties of all the isolated substances, isofrondoside C (**5**) was desulfated to give a derivative **6**. The sugar resonances in the NMR spectrum of **6** were compared with those of isofrondoside C (**5**) (Tables 1 and 2). Because of α- and β-effects of the sulfate group, the C-4 and C-5 signals of the first xylose residue in the ^{13}C NMR spectrum of **5** were shifted downfield by 6.8 ppm and upfield by 2.5 ppm, respectively, in comparison to these signals in the spectrum of desulfated derivative **6**. The same effects were observed for the C-5 (3.1 ppm upfield) and C-6 (5.5 ppm downfield) signals of the glucose residue and C-5 (2.68 ppm

© 2007 NRC Canada

Table 2. ^{13}C and ^{1}H NMR chemical shifts and selected HMBC and NOESY correlations of of desulfated isofrondoside C (**6**).

Position	δ_C[a]	Position	δ_C[a]	δ_H mult. (*J* in Hz)[b]	HMBC	NOESY
C-1 Xyl1	105.1	1	35.69	1.50 m		
C-2 Xyl1	82.6	2	27.23	1.96 m, 2.23 m		
C-3 Xyl1	78	3	88.84	3.35 dd (3.8, 10.0)		
C-4 Xyl1	70.2	4	39.54			
C-5 Xyl1	66.5	5	49.42	1.05 dd (3.6, 11.1)		
		6	23.21	1.83 m, 2.07 m		
C-1 Qui	103	7	121.43	5.75 m		
C-2 Qui	83.3	8	148.89			
C-3 Qui	75.7	9	48.32	2.45 m		H-18, H-19
C-4 Qui	86.6	10	35.69			
C-5 Qui	71	11	23.05			
C-6 Qui	18	12	35.56	1.86 m, 1.95 m		
		13	45.15			
C-1 Glu	104.7	14	53.06			
C-2 Glu	73.5	15	33.55	1.70 m, 1.79 m		
C-3 Glu	87.9	16	22.47	1.93 m, 2.50 m		
C-4 Glu	69.6	17	52.26	2.10 m		H-32
C-5 Glu	78	18	25.02	1.50 s	C: 12, 13, 14, 17	H-9, H-19
C-6 Glu	62	19	24.59	1.09 s	C: 5, 9, 10	H-9, H-18
		20	75.66			
C-1 MeGlu	105.5	21	21.9	1.58 s	C: 17, 20, 22	
C-2 MeGlu	74.9	22	79.46	5.37 dd (4.1, 9.3)		
C-3 MeGlu	87.9	23	30.12	2.44 m, 2.53 m		
C-4 MeGlu	70.4	24	122.15	5.40 m		
C-5 MeGlu	78.2	25	133.08			
C-6 MeGlu	62	26	17.69	1.71 s	C: 24, 25, 27	
OMe	60.6	27	25.6	1.72 s	C: 24, 25, 26	
		30	17.43	1.18 s	C: 3, 4, 5, 31	
C-1 Xyl2	105.8	31	28.68	1.33 s	C: 3, 4, 5, 30	
C-2 Xyl2	75.7	32	30.68	1.18 s	C: 8, 13, 14, 15	
C-3 Xyl2	77.8	$OCOCH_3$	170.54			
C-4 Xyl2	70.4	$OCOCH_3$	20.98	2.03 s		
C-5 Xyl2	66.9					

[a]Recorded at 125.77 MHz in C_5D_5N–D_20 (4:1).
[b]Recorded at 500 MHz in C_5D_5N–D_20 (4:1).

upfield) and C-6 (4.99 ppm downfield) signals of the 3-O-methyl glucose residue in the ^{13}C NMR spectrum of **5** in comparison with that of **6**. These data indicated the presence of three sulfate groups attached to C-4 of the first xylose residue and to C-6 of glucose and 3-O-methyl glucose residues in the studied glycosides. The NMR resonances of carbons of the carbohydrate parts of glycosides **1**–**5** and **7**–**9** were found to be identical to those of the cucumariosides A_7-1, A_7-2, and A_7-3 from *C. japonica* (5), which confirms the identity of carbohydrate chains of these substances.

The HR ESI MS (negative ion mode) of the frondoside A_7-1 (**1**) exhibited a pseudomolecular ion peak $[M_{3Na} - Na]^-$ at *m/z* 1499.4215, which compared with that calculated for $C_{59}H_{89}O_{35}S_3Na_2$ of 1499.4142. Thus, the molecular formula of frondoside A_7-1 (**1**) is $C_{59}H_{89}O_{35}S_3Na_3$.

The MALDI TOF MS (positive ion mode) of glycoside **1** exhibited a pseudomolecular ion peak $[M_{3Na} + Na]^+$ at *m/z* 1545, which confirmed the molecular formula $C_{59}H_{89}O_{35}S_3Na_3$ and the fragment ion peaks at *m/z* 1443 $[M_{3Na} - SO_3Na + Na + H]^+$ and 1341 $[M_{3Na} - 2SO_3Na + Na + 2H]^+$. These latter peaks correspond to elimination of sulfate groups and confirm the structure of carbohydrate chain of **1**.

The signals of the aglycon of frondoside A_7-1 (**1**) were assigned by extensive NMR spectroscopic studies (^1H, ^{13}C, HSQC, HMBC, COSY, NOESY, TOCSY) (Table 3) to be similar with those of the known frondoside A_2-1 from *C. frondosa* (3), which contains a holostane aglycon with a 7(8) double bond, a keto-group at the C-16 position, and a 24(25) double bond in the side chain that confirms the identity of the aglycons in these saponins. The correlation between H-19 and H-9 in the NOESY spectrum of **1** indicated a β-configuration for H-9. Hence, the structure of frondoside A_7-1 (**1**) is 3-*O*-{6-*O*-sodium sulfate-3-*O*-methyl-β-D-glucopyranosyl-(1→3)-6-*O*-sodium sulfate-β-D-glucopyranosyl-(1→4)-[β-D-xylopyranosyl-(1→2)]-β-D-quinovopyranosyl-(1→2)-4-*O*-sodium sulfate-β-D-xylopyranosyl}-3β-hydroxy-16-oxo-9β-holosta-7,24-diene.

The HR ESI MS (negative ion mode) of the frondoside A_7-2 (**2**) exhibited a pseudomolecular ion peak $[M_{3Na} - Na]^-$ at *m/z* 1485.4450, which calculated as 1485.4350 *m/z* for

© 2007 NRC Canada

Table 3. ^{13}C and ^{1}H NMR chemical shifts and selected HMBC and NOESY correlations of aglycon moiety of frondoside A_7-1 (**1**).

Position	δ_C[a]	δ_H mult. (*J* in Hz)[b]	HMBC	NOESY
1	35.7	1.43 m		
2	26.7	1.89 m (a) 2.05 m (e)		H-19, H-30
3	88.9	3.28 dd (4.0, 12.0)		H-5, H-31, H-1 Xyl1
4	39.3			
5	48.3	1.02 m		H-3
6	23.1	2.05 m		H-19, H-30
7	121.8	5.79 m		
8	143.8			
9	47.0	3.63 m		H-19
10	35.5			
11	22.3	1.92 m, 1.65 m		
12	29.5	2.33 m		H-17
13	56.8			
14	45.6			
15	51.9	2.44 d (15.9) 2.79 d (15.9)	C: 14, 16, 32 C: 13, 16, 32	H-32
16	214.2			
17	63.5	3.03 s	C: 12, 13, 16, 20, 21	H-12, H-21, H-32
18	179.2			
19	23.9	1.21 s	C: 1, 5, 9, 10	H-2, H-6, H-9
20	83.6			
21	26.0	1.62 s	C: 17, 20, 22	H-17
22	38.6	1.72 m, 1.90 m		
23	23.0	2.13 m, 2.42 m		
24	123.9	5.13 m	C: 26, 27	
25	132.0			
26	17.5	1.63 s	C: 24, 25, 27	
27	25.5	1.66 s	C: 24, 25, 26	
30	17.3	1.13 s	C: 3, 4, 5, 31	H-2, H-6, H-6 Qui
31	28.7	1.30 s	C: 3, 4, 5, 30	H-3, H-1 Xyl1
32	31.9	1.30 s	C: 8, 13, 14, 15	H-15, H-17

[a]Recorded at 125.77 MHz in C_5D_5N–D_2O (4:1).
[b]Recorded at 500 MHz in C_5D_5N–D_2O (4:1).

$C_{59}H_{91}O_{34}S_3Na_2$ and allowed the determination of the molecular formula of frondoside A_7-2 (**2**) as $C_{59}H_{91}O_{34}S_3Na_3$.

The positive ion mode MALDI TOF MS of the frondoside A_7-2 (**2**) exhibited a pseudomolecular ion peak at *m/z* 1531 $[M_{3Na} + Na]^+$ that corresponded to the molecular formula and the fragment ion peaks at *m/z* 1429 and 1327 analogous to those of frondoside A_7-1 (**1**). The ion peak at *m/z* 1195 observed in the spectrum of frondoside A_7-2 (**2**) was due to the loss of two sulfate groups along with the terminal xylose residue.

The NMR spectra of the aglycon moiety of frondoside A_7-2 (**2**) were found to be very similar to the spectra of frondoside A_2-4 from *C. frondosa* (4), indicating that the same holostane aglycons were present with 7(8) and 24(25) double bonds and no functionality at C-16 (Table 4). Indeed, the high-field signal of 24.4 ppm for C-16 observed in the ^{13}C NMR spectrum of frondoside A_7-2 (**2**) corresponded to two protons in the HSQC spectrum (signals at 1.87 (m, H – 16″) and 2.11 (m, H – 16″) ppm). Moreover, the signals of the isolated spin system CH_2(15)-CH_2(16)-CH(17) were observed in the COSY spectrum of frondoside A_7-2 (**2**), corroborating the aglycon structure of **2** (Table 4). The correlation between H-19 and H-9 in the NOESY spectrum of **2** confirmed the β-configuration for H-9. Hence, frondoside A_7-2 (**2**) is 3-*O*-{6-*O*-sodium sulfate-3-*O*-methyl-β-D-glucopyranosyl-(1→3)-6-*O*-sodium sulfate-β-D-glucopyranosyl-(1→4)-[β-D-xylopyranosyl-(1→2)]-β-D-quinovopyranosyl-(1→2)-4-*O*-sodium sulfate-β-D-xylopyranosyl}-3β-hydroxy-9β-holosta-7,24-diene.

The HR ESI MS (negative ion mode) of frondoside A_7-3 (**3**) exhibited a pseudomolecular ion peak $[M_{3Na} - Na]^-$ at *m/z* 1489.4768 that calculated as 1489.4662 *m/z* for $C_{59}H_{95}O_{34}S_3Na_2$ and allowed the assignment of the molecular formula for frondoside A_7-3 (**3**) as $C_{59}H_{95}O_{34}S_3Na_3$.

The MALDI TOF MS (positive ion mode) of frondoside A_7-3 (**3**) exhibited a pseudomolecular ion peak $[M_{3Na} + Na]^+$ at *m/z* 1535 that also corresponded to the molecular formula $C_{59}H_{95}O_{34}S_3Na_3$. In the MALDI TOF MS (negative ion mode) of glycoside **3,** ion peaks at *m/z* 1387 and 1285 were due to the elimination of two sulfate groups.

The signals of the polycyclic nucleus of the aglycon part in the NMR spectra of frondoside A_7-3 (**3**) were similar to those of frondoside C from *C. frondosa* (2), which has the nonholostane aglycon without a lactone. The ^{13}C NMR spectrum shows signals at 148.7 (C-9) and 114.9 (C-11) ppm, and the ^{1}H NMR spectrum shows a multiplet at 5.33 (H-11) ppm for the 9(11) double bond (Table 5). The signals for the tertiary carbon at 123.1 (C-24) ppm and quaternary carbon

© 2007 NRC Canada

Table 4. ^{13}C and ^{1}H NMR chemical shifts and selected HMBC and NOESY correlations of aglycon moiety of frondoside A_7-2 (**2**).

Position	δ_C[a]	δ_H mult. (*J* in Hz)[b]	HMBC	NOESY
1	36.0	1.44 m		H-19
2	26.7	1.87 m, 2.05 m		
3	89.0	3.25 dd (4.2, 11.6)		H-1, H-5, H-31
4	39.2			
5	47.9	1.05 m		H-3
6	23.2	2.08 m		
7	119.9	5.80 m		H-15
8	146.6			
9	47.3	3.46 brd (13.0)		H-1, H-19
10	35.4			
11	22.8	1.57 m, 1.82 m		
12	30.2	2.13 m		
13	58.7			
14	51.2			
15	34.2	1.92 m		
16	24.4	1.87 m, 2.11 m	C: 18	
17	53.0	2.34 dd (4.2, 10.2)	C: 18	H-21, H-32
18	180.9			
19	23.9	1.21 s	C: 1, 5, 9, 10	H-1, H-9
20	84.6			
21	25.9	1.54 s	C: 17, 20, 22	H-17
22	39.4	1.69 m, 1.79 m		
23	22.9	2.03 m		
24	121.1	5.16 m	C: 23, 26, 27	H-27
25	132.1			
26	17.5	1.66 s	C: 24, 25, 27	
27	25.5	1.74 s	C: 24, 25, 26	H-24
30	17.3	1.13 s	C: 3, 4, 5, 31	
31	28.7	1.32 s	C: 3, 4, 5, 30	H-3, H-1 Xyl1
32	30.8	1.25 s	C: 8, 13, 14, 15	H-15, H-17

[a]Recorded at 125.77 MHz in C_5D_5N–D_2O (4:1).
[b]Recorded at 500 MHz in C_5D_5N–D_2O (4:1).

at 132.1 (C-25) ppm were indicative of a 24(25) double bond in the side chain of glycoside **3**. However, in comparison with frondoside C (2) the signals of C-22 and H-22 of frondoside A_7-3 (**3**) were shifted upfield (δ_C 77.0 ppm and δ_H 2.88 ppm), and signals for an O-acetic group were absent. These data indicated the presence of a tertiary carbon (C-22) bearing a hydroxyl group (Table 5). The asymmetric center at C-20 in frondoside A_7-3 (**3**) was determined as the R configuration by analogy with frondoside C and confirmed by the presence of the cross peaks H-21/H-12 and H-22/H-16 in the NOESY spectrum of **3**. The asymmetric center at C-22 was deduced as the R, the most probable from the C-20 and C-22 signals in the ^{13}C NMR spectrum of glycoside **3** on the basis of a comparison of this spectrum with that of model substances where the signals of C-20 and C-22 were characteristic for R,R-configuration at C-20 and C-22, which had the same values of chemical shifts and differed by 2 ppm from each other in the case of R,S-configuration (11). Hence the structure of frondoside A_7-3 was determined to be 3-*O*-{6-*O*-sodium sulfate-3-*O*-methyl-β-D-glucopyranosyl-(1→3)-6-*O*-sodium sulfate-β-D-glucopyranosyl-(1→4)-[β-D-xylopyranosyl-(1→2)]-β-D-quinovopyranosyl-(1→2)-4-*O*-sodium sulfate-β-D-xylopyranosyl}-3β,20(*R*),22(*R*)-trihydroxylanosta-9,24-diene.

The HR ESI MS (negative ion mode) of the frondoside A_7-4 (**4**) exhibited a pseudomolecular ion peak $[M_{3Na} - Na]^-$ at *m/z* 1489.4851, which calculated as 1489.4662 *m/z* for $C_{59}H_{95}O_{34}S_3Na_2$. The molecular formula of frondoside A_7-4 (**4**) was determined to be $C_{59}H_{95}O_{34}S_3Na_3$.

The MALDI TOF MS (positive ion mode) of the frondoside A_7-4 (**4**) exhibited a pseudomolecular ion peak at *m/z* 1535 $[M_{3Na} + Na]^+$ that also was consistent with the molecular formula $C_{59}H_{95}O_{34}S_3Na_3$. In the MALDI TOF MS (negative ion mode), fragment ion peaks at *m/z* 1387 and 1285 corresponding to sequentual elimination of two sulfate groups were observed.

The NMR spectra of the aglycon part of frondoside A_7-4 (**4**) clearly indicates that this substance is an isomer of frondoside A_7-3 (**3**) by the double bond position in the aglycon nucleus (Table 6). Indeed, the signals at 122.1 (C-7) and 149.1 (C-8) ppm in the ^{13}C NMR spectrum are characteristic of a 7(8) double bond in **4**. The comparison of the ^{13}C NMR spectra of frondosides A_7-4 (**4**) and A_7-3 (**3**) showed similar side chains signals that indicated that their side chains have 24(25) double bond and a hydroxyl group at C-22. The presence of the cross-peaks H-9/H-18 and H-9/H-19 in the NOESY spectrum of **4** indicated a β-configuration of H-9 and showed that the C ring in the aglycon was

© 2007 NRC Canada

Table 5. ^{13}C and ^{1}H NMR chemical shifts and selected HMBC and NOESY correlations of aglycon moiety of frondoside A_7-3 (**3**).

Position	δ_C[a]	δ_H mult. (*J* in Hz)[b]	HMBC	NOESY
1	36.3	1.42 m, 1.80 m		
2	26.7	1.92 m, 2.09 m		
3	88.7	3.23 dd (4.0, 11.8)		H-1, H-5, H-31
4	39.7			
5	52.9	0.93 m		H-3
6	21.3	1.44 m		
7	29.6	1.60 m		
8	41.4	2.24 m		H-18, H-19
9	148.7			
10	39.2			
11	114.9	5.33 m		
12	37.8	2.14 m, 2.26 m		H-21, H-32
13	45.4			
14	46.9			
15	33.7	1.47 m, 1.61 m		H-17
16	22.1	1.78 m 2.32 m		H-22
17	49.7	2.32 m		H-15, H-21, H-32
18	16.4	1.20 s	C: 12, 13, 14, 17	H-8
19	22.2	1.09 s	C: 1, 5, 9, 10	H-8
20	77.1			
21	20.3	1.59 s	C: 17, 20, 22	H-12, H-17
22	77.0	2.88 m		H-16
23	31.6	2.39 m, 2.53 m		
24	123.1	5.60 brt (7.5)		
25	132.1			
26	25.8	1.72 s	C: 24, 25, 27	
27	17.8	1.75 s	C: 24, 25, 26	
30	16.7	1.13 s	C: 3, 4, 5, 31	
31	28.1	1.30 s	C: 3, 4, 5, 30	H-3, H-1 Xyl1
32	18.6	0.90 s	C: 8, 13, 14, 15	

[a]Recorded at 125.77 MHz in C_5D_5N–D_2O (4:1).
[b]Recorded at 500 MHz in C_5D_5N–D_2O (4:1).

largely in the "boat" conformation. The boat conformation for the C ring in holostane-type aglycons was observed earlier by X-ray analysis (12). Hence the structure of frondoside A_7-4 (**4**) was elucidated as 3-*O*-{6-*O*-sodium sulfate-3-*O*-methyl-β-D-glucopyranosyl-(1→3)-6-*O*-sodium sulfate-β-D-glucopyranosyl-(1→4)-[β-D-xylopyranosyl-(1→2)]-β-D-quinovopyranosyl-(1→2)-4-*O*-sodium sulfate-β-D-xylopyranosyl}-3β,20(*R*),22(*R*)-trihydroxy-9β-lanosta-7,24-diene.

The HR ESI MS (negative ion mode) of the isofrondoside C (**5**) exhibited a pseudomolecular ion peak $[M_{3Na} - Na]^-$ at *m/z* 1531.4817. The calculated mass for $C_{61}H_{97}O_{35}S_3Na_2$ is 1531.4766 from which the molecular formula of isofrondoside C (**5**) $C_{61}H_{97}O_{35}S_3Na_3$ was established.

The MALDI TOF MS (positive ion mode) of the isofrondoside C (**5**) exhibited a pseudomolecular ion peak at *m/z* 1577 $[M_{3Na} + Na]^+$ that confirmed the molecular formula $C_{61}H_{97}O_{35}S_3Na_3$. In the MALDI TOF MS (negative ion mode) the ion peaks at *m/z* 1429 and 1327 corresponded to the sequential elimination of two sulfate groups.

The structure of glycoside **5** was deduced on the basis of NMR data of its desulfated derivative **6** (Table 7). The NMR spectra of **6** showed signals characteristic of the lanostane aglycon containing a 7(8) double bond (25.0 (CH_3-18), 121.4 (C-7), and 148.9 (C-8) ppm in ^{13}C NMR spectrum). The signals of the acetate group at C-22 (79.5 (C-22), 170.5 ($OCOCH_3$), and 21.0 ($OCOCH_3$) ppm in ^{13}C NMR spectrum) and 24(25) double bond (signals at 122.1 (C-24) and 133.1 (C-25) ppm) in the side chain were also detected. The correlation between H-19 and H-9 in the NOESY spectrum of **5** yielded evidence for a β-configuration of H-9. Thus, the new glycoside **5** is an isomer of the known frondoside C (**7**) by the position of the double bond in the aglycon nucleus. The aglycon structure was confirmed by the corresponding HMBC and NOESY correlations (Table 2). The 20*R*,22*R* configurations for the hydroxy group at C-20 and the acetoxy group at C-22 in **5** were suggested as most probable by the almost coincident corresponding carbon chemical shifts of **6** and the known 2β,3β,22(*R*)-triacetoxy-14α,20(*R*),25-trihydroxy-5β-cholest-7(8)-en-6-one (13). Hence, the structure of isofrondoside C (**5**) was deduced as 3-*O*-{6-*O*-sodium sulfate-3-*O*-methyl-β-D-glucopyranosyl-(1→3)-6-*O*-sodium sulfate-β-D-glucopyranosyl-(1→4)-[β-D-xylopyranosyl-(1→2)]-β-D-quinovopyranosyl-(1→2)-4-*O*-sodium sulfate-β-D-xylopyranosyl}-3β,20(*R*)-dihydroxy-22(*R*)-acetoxy-9β-lanosta-7,24-diene.

In most cases, sea cucumbers have been reported to accumulate glycosides with one type of polycyclic system for the aglycons that contain either the 7(8) or 9(11) double bond.

© 2007 NRC Canada

Table 6. ^{13}C and ^{1}H NMR chemical shifts and selected HMBC and NOESY correlations of aglycon moiety of frondoside A_7-4 (**4**).

Position	δ_C[a]	δ_H mult. (*J* in Hz)[b]	HMBC	NOESY
1	35.6	1.42 m		
2	27	1.90 m, 2.07 m		
3	89	3.29 dd (5.0, 10.9)		H-5, H-31, H-1 Xyl1
4	39.5			
5	49.4	1.02 m		H-3
6	23.2	2.04 m		
7	122.1	5.78 m		
8	149.1			
9	48.3	2.41 m		H-18, H-19
10	35.6			
11	23	1.94 m, 2.04 m		
12	35.3	1.86 m, 1.97 m		H-21, H-32
13	44.9			
14	53			
15	33.4	1.72 m, 1.78 m		
16	22.3	1.84 m 2.35 m		H-22
17	51.9	2.17 m		H-32
18	25	1.47 s	C: 12, 13, 14, 17	H-9, H-19
19	24.5	1.06 s	C: 1, 5, 9, 10	H-9, H-18
20	77			
21	20.9	1.60 s	C: 17, 20, 22	
22	76.9	3.86 m		
23	31.6	2.40 m, 2.55 m		
24	123.1	5.61 m		
25	132.1			
26	17.8	1.73 s	C: 24, 25, 27	
27	25.8	1.76 s	C: 24, 25, 26	
30	17.4	1.16 s	C: 3, 4, 5, 31	
31	28.7	1.31 s	C: 3, 4, 5, 30	
32	30.7	1.19 s	C: 8, 13, 14, 15	

[a]Recorded at 125.77 MHz in C_5D_5N–D_2O (4:1).
[b]Recorded at 500 MHz in C_5D_5N–D_2O (4:1).

Table 7. The quantitative content of components of the glycosidic fraction in different body parts of *C. Frondosa*.

	Quantitative content of glycosides (%)					
	Body wall and the integumental epithelium		Integumental epithelium		Buccal tentacles with calcareous ring	
Glycosides	d.r.[a]	s.g.[b]	d.r.[a]	s.g.[b]	d.r.[a]	s.g.[b]
Frondoside A_1	0.02	3	0.04	3	—	—
Frondoside A	0.07	12	0.24	17	0.02	4
Frondoside A_2 group	0.06	10	0.04	3	0.03	9
Frondoside A_3/A_6 group	0.17	29	0.31	22	0.12	29
Frondoside A_7 group	0.28	46	0.77	55	0.23	58
Sum	0.6		1.4		0.4	

Note: The material is not statistically processed.
[a]From the weight of dry residue.
[b]From the sum of glycosides.

There are only four known species of sea cucumbers that contain both glycosides with the 7(8) and 9(11) double bond simultaneously. These are, *C. conicospermium* (9), *Pentacta australis* (14), *Neothyonidium magnum* (15, 16), *Psolus fabricii* (17–19). However, only two pairs of glycosides from *C. conicospermium* were isomeric by such double bond positions. Thus, when compared with other sea cucumbers it is very unusual that *C. frondosa* contains three pairs of isomers, i.e., frondosides A_7-3 (**3**) and A_7-4 (**4**), and frondoside C (**7**) and isofrondoside C (**5**), koreoside A (**8**) and

© 2007 NRC Canada

isokoreoside A (**9**), that differ only in the positions of the double bonds in the polycyclic systems of their aglycons.

Moreover, there are two pairs of glycosides in *C. frondosa* that differ in the character of the oxygen function at C-22 in the aglycon side chains. Actually, hydroxyl groups in frondosides A_7-3 (**3**) and A_7-4 (**4**) are replaced by the O-acetate groups in frondoside C (**7**) and isofrondoside C (**5**). Probably, the biosynthetic pathway from lanostane (no lactone ring) glycosides with unshortened side chains to non-lanostane glycosides with shortened side chains occurs through the introduction of a hydroxyl or acetate group at C-22 that is followed by the cleavage of a side chain. Such a biosynthetic pathway of biosynthesis is evident because of the presence of substances with shortened side chains in the aglycon, such as koreoside A (**8**) and isokoreoside A (**9**) in the fraction of trisulfated glycosides of *C. frondosa*. The analogous biosynthetic transformations are known for the biogenesis of steroid hormones from cholesterol in vertebrates (20).

The quantitative content of the main components of the glycosidic fraction in some body parts of *C. frondosa* collected in March 2003 in the Gulf of Maine was investigated (Table 7). The integumental epithelium of the sea cucumbers, the body walls with epithelium, and the buccal tentacles with calcareous ring were extracted separately, Then, the glycoside fractions were obtained from each extract by column chromatography on Teflon and silica gel.

The spawning season of *C. frondosa* near the eastern shore of the US and Canada is during April and May (21). The quantitative predominance of trisulfated glycosides (of the A_7 group) collected in March (46%–58% from glycosidic fraction of *C. frondosa*) for all investigated parts of the organism, when compared with the content of monosulfated glycosides (13%–25%, frondosides A, A_1 and glycosides belonging to the A_2 group) and disulfated glycosides (22%–29%, glycosides of A_3 and A_6 groups) (Table 7), could be explained by the accumulation of this group of substances before spawning as regulators of the pubescence process in the population. Therefore, the biological role of monosulfated and trisulfated glycosides could be different. The hemolytic activity of the glycosides correlated with their toxicity (22). Monosulfated frondosides show high hemolytic activity and probably provide a biochemical defense mechanism towards predators. However, the hemolytic activity of trisulfated glycosides is much less than that of the monosulfated ones (22). It was reported earlier that triterpene glycosides of sea cucumbers perform a hormonelike function and may regulate the process of oocyte maturation in the sea cucumber population (23). So, it is likely that just trisulfated glycosides perform a hormonelike regulatory function in the organism of *C. frondosa*. However, to confirm this point it seems to be necessary to carry out investigations on seasonal variations of the different groups of the saponins in different organs and tissues of *C. frondosa*.

Experimental section

General experimental procedures

All melting points were determined with a Kofler Thermogenerate apparatus. Specific rotation was measured on a PerkinElmer 343 polarimeter. NMR spectra were recorded on a DRX-500 Bruker spectrometer at 500.12 and 125.67 MHz for ^1H and ^{13}C, respectively, in C_5D_5N–D_2O (4:1) with TMS as an internal reference ($\delta = 0$). The HMBC experiments were optimized on the long-range coupling constant $J = 8$ Hz, and the mixing time in the NOESY experiments was 350 ms. The MALDI TOF MS (positive and negative ion modes) were recorded using a Bruker mass spectrometer, model BIFLEX III with impulse extraction of ions, on an α-cyano-4-hydroxycinnamic acid matrix. The ESI MS (negative ion mode) measurements were performed on a ESI TOF (LCT, Micromass, Altrincham, UK) mass spectrometer fitted with a standard two-spray source. HPLC was performed using an Agilent 1100 chromatograph equipped with a differential refractometer on a Zorbax ODS and Diasphere-110 C_8 columns.

Animal material

The sea cucumber *C. frondosa* (family Cucumariidae, order Dendrochirotida) was collected in Penobscot Bay (Gulf of Maine, Maine, USA) in September 2000 by commercial dragging. Taxonomic identification was carried out by Dr. E.N. Gudimova. A voucher specimen is on a deposit in the collection of the Murmansk Marine Biological Institute of the Kolsky Scientific Center of the Russian Academy of Sciences, Murmansk, Russia.

Extraction and isolation of the subfraction of trisulfated glycosides

Body walls of the sea cucumbers were separated, cut very small, lyophilized to dryness, and extracted twice with hot ethanol (dry weight of the residue was 943 g). The combined extracts were concentrated to dryness and chromatographed on a polychrom-1 column (powdered Teflon, Biolar, Latvia) previously loaded in EtOH and washed by water to remove inorganic salts and polar impurities. The fraction containing glycosides was eluted with 50% acetone. This fraction was chromatographed on silica gel columns eluted with a $CHCl_3$–EtOH–H_2O (100:125:25) solvent system to obtain a TLC homogenous crude subfraction of trisulfated glycosides belonging to the A_7 group (1942 mg).

Isolation of glycosides 1–5 and 7–9

The fraction of trisulfated frondosides (1942 mg) was submitted for HPLC (followed by desalting on a Teflon column as described previously) on a Zorbax ODS (10 × 250) [mobile phase MeOH–water–($Na_2HPO_4 \cdot 12H_2O$ (358 mg) + $NaH_2PO_4 \cdot 2H_2O$ (156 mg) in 100 mL of water) (59:38:3)] column to give the subfractions **I**–**V** that were subsequently chromatographed on a Diasphere-110 C_8 (4 × 250) column. The different ratios of the solvents MeOH–H_2O–[$Na_2HPO_4 \cdot 12H_2O$ (358 mg) + $NaH_2PO_4 \cdot 2H_2O$ (156 mg) in 100 mL of water] were used as mobile phase. Ratio 40:57:3 for subfraction **I**. Ratio 42:54:4 for subfraction **II** to obtain 8 mg of koreoside A (**8**), mp 250 °C, $[\alpha]_D^{20}$ –48° (*c* 0.1, pyridine) and 6 mg of isokoreoside A (**9**), mp 238 °C, $[\alpha]_D^{20}$ –64° (*c* 0.1, pyridine). Ratio 45:53:2 for subfraction **III** to give 3 mg of frondoside A_7-1 (**1**), mp 213–215 °C, $[\alpha]_D^{20}$ –11° (*c* 0.1, pyridine). See Tables 1 and 3 for NMR data. MALDI TOF MS (positive ion mode) *m*/*z*: 1545 ($C_{59}H_{89}O_{35}S_3Na_4$ $[M_{3Na} + Na]^+$, 1), 1443 ([$M_{3Na} - SO_3Na$ +

© 2007 NRC Canada

Na + H]$^+$, 0.3), 1341 ([M_{3Na} – 2SO_3Na + Na + 2H]$^+$, 0.2). MALDI TOF MS (negative ion mode) *m/z*: 1499 ($C_{59}H_{89}O_{35}S_3Na_2$ [M_{3Na} – Na]$^-$, 1), 1397 ([M_{3Na} – Na – SO_3Na + H]$^-$, 0.3), 1295 ([M_{3Na} – Na – 2SO_3Na + 2H]$^-$, 0.2). 4.5 mg of frondoside A_7-3 (**3**), mp 205 to 206 °C, $[\alpha]_D^{20}$ – 18° (*c* 0.1, pyridine). See Tables 1 and 5 for NMR data. MALDI TOF MS (positive ion mode) *m/z*: 1535 ($C_{59}H_{95}O_{34}S_3Na_4$ [M_{3Na} + Na]$^+$, 1), 1433 ([M_{3Na} – SO_3Na + Na + H]$^+$, 0.4), 1331 ([M_{3Na} – 2SO_3Na + Na + 2H]$^+$, 0.2). MALDI TOF MS (negative ion mode) *m/z*: 1489 ($C_{59}H_{95}O_{34}S_3Na_2$ [M_{3Na} – Na]$^-$, 1), 1387 ([M_{3Na} – Na – SO_3Na + H]$^-$, 0.4), 1285 ([M_{3Na} – Na – 2SO_3Na + 2H]$^-$, 0.2). Six mg of frondoside A_7-4 (**4**), mp 240 °C, $[\alpha]_D^{20}$ –42° (*c* 0.1, pyridine). See Tables 1 and 6 for NMR data. MALDI TOF MS (positive ion mode) *m/z*: 1535 ($C_{59}H_{95}O_{34}S_3Na_4$ [M_{3Na} + Na]$^+$, 1). MALDI TOF MS (negative ion mode) *m/z*: 1387 ([M_{3Na} – Na – SO_3Na + H]$^-$, 0.3). Ratio 48:49:3 for subfraction **IV** to obtain 10 mg of isofrondoside C (**5**), mp 210 °C, $[\alpha]_D^{20}$ –23° (*c* 0.1, pyridine). MALDI TOF MS (positive ion mode) *m/z*: 1577 ($C_{61}H_{97}O_{35}S_3Na_4$ [M_{3Na} + Na]$^+$, 1). MALDI TOF MS (negative ion mode) *m/z*: 1429 ([M_{3Na} – Na – SO_3Na + H]$^-$, 0.4); 1327 ([M_{3Na} – Na – 2SO_3Na + 2H]$^-$, 0.3). 24 mg of frondoside C (**7**), mp 243 °C, $[\alpha]_D^{20}$ –52° (*c* 0.1, pyridine). Ratio 50:47:3 for subfraction **V** to obtain 6 mg of frondoside A_7-2 (**2**), mp 195–197 °C, $[\alpha]_D^{20}$ –28° (*c* 0.1, pyridine). See Tables 1 and 4 for NMR data. MALDI TOF MS (positive ion mode) *m/z*: 1531 ($C_{59}H_{91}O_{34}S_3Na_4$ [M_{3Na} + Na]$^+$, 1), 1429 ([M_{3Na} – SO_3Na + Na + H]$^+$, 0.3), 1327 ([M_{3Na} – 2SO_3Na + Na + 2H]$^+$, 0.2), 1195 ([M_{3Na} – 2SO_3Na – Xylose + Na + 3H]$^+$, 0.2). MALDI TOF MS (negative ion mode) *m/z*: 1485 ($C_{59}H_{91}O_{34}S_3Na_2$ [M_{3Na} – Na]$^-$, 1), 1383 ([M_{3Na} – Na – SO_3Na + H]$^-$, 0.4), 1281 ([M_{3Na} – Na – 2SO_3Na + 2H]$^-$, 0.2).

Desulfation of isofrondoside C (5).

Glycoside **5** (10 mg) was dissolved in a mixture of pyridine–dioxane (1:1) and refluxed for 1 h. The obtained mixture was concentrated in vacuo. The residue was chromatographed on a Si gel column with $CHCl_3$–EtOH–H_2O (100:50:4) to give the desulfated derivative **6**: 7 mg, mp 224 °C, $[\alpha]_D^{20}$ –36° (*c* 0.1, pyridine); see Table 2 for NMR data.

Determination of the quantitative content of different groups of frondosides in some parts of *C. frondosa*

Sea cucumbers were collected in the Penobscot Bay (Gulf of Maine, Maine, USA) in March 2003 and were disintegrated into body wall and integumentary epithelium, integumentary epithelium, and buccal tentacles with the calcareous ring. The freeze-dried parts of the sea cucumbers were extracted twice with hot ethanol. The combined extracts of corresponding parts were concentrated to dryness and chromatographed on a polychrom-1 column (powdered Teflon, Biolar, Latvia) as described earlier to give the summarized fractions of triterpene glycosides. These fractions were chromatographed on silica gel columns with a $CHCl_3$–EtOH–H_2O (100:75:10, 100:100:17, and 100:125:25) solvent system to obtain frondoside A_1 and frondoside A (as individual substances), the subfractions of monosulfated frondosides that belongs to the A_2 group, disulfated frondosides that belong to the A_3/A_6 group, and trisulfated frondosides that belongs to A_7 group in different ratios for each part (Table 7).

Acknowledgements

The authors acknowledge the financial support from a grant of the Presidium of the Russian Academy of Sciences for Molecular and Cell Biology and grants of the President of the Russian Federation No. NSH-6491.2006.4, RFBR grant No. 06–04–96016, FEB RAS grant No. 06-III-B-05–128, and FEBRAS-UBRAS No. 06–2Y-0–05–009, NATO grant No. CBP.NR.CLG 982737, and support from grant number P30 ES00210 from the National Institute of Environmental Health Sciences, NIH (USA) is acknowledged. Finally, the authors wish to acknowledge the Mass Spectrometry Facility of the Environmental Health Sciences Center at Oregon State University.

References

1. S.A. Avilov, V.I. Kalinin, O.A. Drozdova, A.I. Kalinovsky, V.A. Stonik, and E.N. Gudimova. Khim. Prir. Soedin. **2**, 260 (1993).
2. S.A. Avilov, O.A. Drozdova, V.I. Kalinin, A.I. Kalinovsky, and V.A. Stonik. Can. J. Chem. **76**, 137 (1998).
3. A.S. Silchenko, S.A. Avilov, A.S. Antonov, A.I. Kalinovsky, P.S. Dmitrenok, V.I. Kalinin, V.A. Stonik, C. Woodward, and P.D. Collin. Can. J. Chem. **83**, 21 (2005).
4. A.S. Silchenko, S.A. Avilov, A.S. Antonov, A.I. Kalinovsky, P.S. Dmitrenok, V.I. Kalinin, V.A. Stonik, C. Woodward, and P.D. Collin. Can. J. Chem. **83**, 2120 (2005).
5. O.A. Drozdova, S.A. Avilov, A.I. Kalinovsky, V.A. Stonik, Yu. M. Milgrom, and Ya. V. Rashkes. Khim. Prir. Soedin. **3**, 369 (1993).
6. N. Yayli. Indian J. Chem. **40**, 399 (2001).
7. V.I. Kalinin, A.S. Silchenko, S.A. Avilov, V.A. Stonik, and A.V. Smirnov. Phytochem. Rev. **4**, 221 (2005).
8. S.A. Avilov, A.I. Kalinovsky, V.A. Stonik, V.I. Kalinin, R. Riguero, and C. Jimenes. J. Nat. Prod. **60**, 808 (1997).
9. S.A. Avilov, A.S. Antonov, A.S. Silchenko, V.I. Kalinin, A.I. Kalinovsky, P.S. Dmitrenok, V.A. Stonik, R. Riguera, and C. Jimenes. J. Nat. Prod. **66**, 910 (2003).
10. A.S. Shashkov and O.S. Chizhov. Bioorg. Khim. **2**, 437 (1976).
11. H. Hikino, T. Okuyama, S. Arihara, Y. Hikino, T. Takemoto, H. Mori, and K. Shibata. Chem. Pharm. Bull. **23**, 1458 (1975).
12. S.G. Ilyin, B.L. Taropolsky, Z.I. Safina, A.N. Sobolev, A.K. Dzizenko, and G.B. Elyakov. Dokl. AN SSSR. **230**, 860 (1976).
13. H. Hikino, T. Okuyama, C. Konno, and T. Takemoto. Chem. Pharm. Bull. **23**, 125 (1975).
14. T. Miyamoto, K. Togawa, R. Higuchi, T. Komori, and T. Sasaki. J. Nat. Prod. **55**, 940 (1992).
15. M.B. Zurita, A. Ahond, C. Poupat, P. Potier, and J.L. Menou. J. Nat. Prod. **49**, 809 (1986).
16. S.A. Avilov, A.I. Kalinovsky, and V.A. Stonik. Khim. Prir. Soedin. **1**, 53 (1990).
17. F.-X. Garneau, J.L. Simard, O. Harvey, J.W. Apsimon, and M. Girard. Can. J. Chem. **61**, 1465 (1983).
18. V.I. Kalinin, A.I. Kalinovsky, and V.A. Stonik. Khim. Prir. Soedin. **2**, 212 (1985).
19. V.I. Kalinin, A.I. Kalinovsky, V.A. Stonik, P.S. Dmitrenok, and Y.N. Elkin. Khim. Prir. Soedin. **3**, 361 (1989).

© 2007 NRC Canada

20. Lukner M. Secondary metabolism of microorganisms, plants and animals. Mir, Moscow, Russia. 1979.
21. V.M.M. David and B.A. MacDonald. J. Mar. Biol. Assoc. UK. **82**, 141 (2002).
22. V.I. Kalinin, N.G. Prokofieva, G.N. Likhatskaya, E.B. Schentsova, I.G. Agafonova, S.A. Avilov, and O.A. Drozdova. Toxicon, **34**, 475 (1996).
23. D.L. Aminin and M.M. Anisimov. *In* Recent advances in toxinology research. Vol. II. *Edited by* P. Gopalakrishnakone and C. Tan. National University of Singapore, Singapore. 1992. pp. 562–575.

© 2007 NRC Canada

PERSPECTIVE / PERSPECTIVE

The Canadian Synchrotron Radiation Facility (CSRF) in Madison — Twenty-five years of soft X-ray research[1]

G. Michael Bancroft

Abstract: The first beamline at the Canadian Synchrotron Radiation Facility (CSRF) was established with NSERC funding in 1982 at the Tantalus synchrotron outside Madison, Wisconsin, after many years of work at the University of Western Ontario to establish a synchrotron facility in Canada. The CSRF facility expanded to three very productive soft X-ray beamlines over the next twenty years. The planning, funding, and construction of the three beamlines is outlined; and the dedicated work of the scientists who set up the laboratory, along with those who conducted important research there, are described. CSRF has produced over 500 publications in many different scientific areas from 11 different Canadian Universities. One of the CSRF beamlines, and several CSRF personnel have been transferred to the Canadian Light Source in Saskatoon, and CSRF will formally close in March, 2008.

Keywords: CSRF at the University of Wisconsin Madison, synchrotron radiation, soft X-ray research, materials science.

Resume : Le premier faisceau lumineux de l'Institut canadien du rayonnement synchrotron (ICRS) a été établi en 1982, avec le support financier du CRSNG, en marge du synchrotron Tantalus à l'extérieur de Madison, Wisconsin, après plusieurs années de travaux à l'Université de Western Ontario dans le but de créer un synchrotron au Canada. Sur une période de vingt ans, l'ICRS a été l'objet d'expansions qui ont porté à trois le nombre des faisceaux très productifs de rayons X doux. La planification, le financement et la construction des trois faisceaux sont décrite dans ce travail et on décrit le travail dévoué des scientifiques qui ont mis le laboratoire sur pieds ainsi que celui des personnes qui y ont réalisé d'importants travaux de recherches. L'ICRS a produit plus de 500 publications dans divers domaines scientifiques; ils provenaient de chercheurs attachés à onze universités canadiennes différentes. L'un des faisceaux de l'ICRS et plusieurs membres du personnel de l'ICRS ont été transférés au Centre canadien de rayonnement synchrotron [Canadian Light Source (CLS)] à Saskatoon et l'ICRS sera formellement fermé en mars 2008.

Mots-clés : ICRS à l'Université de Wisconsin Madison, rayonnement synchrotron, recherches avec des rayons X doux, science des matériaux.

Introduction

The Canadian Synchrotron Radiation Facility (CSRF) began operation with one soft X-ray beamline in 1982 at the low-energy 240 MeV Tantalus synchrotron at the University of Wisconsin outside Madison, Wisconsin. CSRF was then transferred to the "new" second generation 1 GeV Aladdin synchrotron in January 1986, after Aladdin had been delayed for over three years because of technical problems. Three soft X-ray CSRF beamlines were funded by Canadian organizations between 1979 and 1995, and several hundred Canadian scientists, along with many international scientists, have routinely and successfully used these Canadian facilities since 1983. The CSRF facility has produced over 50 Ph.D. and M.Sc. theses from 11 different Canadian Universities and well over 500 publications in refereed journals. The total capital and operating funding has been incredibly small for such a productive facility. Two of the three CSRF beamlines have been duplicated at the third generation Canadian Light Source (CLS) in Saskatoon with great improvements in intensity and resolution. The newest CSRF beamline was transferred to CLS in 2004 and modified for greatly enhanced performance at the CLS. The third CSRF beamline will be duplicated at the CLS within a year. Several of the CSRF employees are now employed at the CLS and many of the students, postdoctoral fellows (postdocs), and faculty that did a lot of their research at CSRF are now CLS users. Funding for the CSRF from the Natural Sciences

Received April 27 2007. Accepted April 27 2007. Published on the NRC Research Press Web site at canjchem.nrc.ca on 13 June 2007.

G.M. Bancroft.[2] Department of Chemistry, *The* University *of* Western Ontario, London, ON N6G 1V5, Canada

[1]This article is part of a Special Issue dedicated to Professor G. Michael Bancroft.
[2]Corresponding author (e-mail: gmbancro@uwo.ca).

 doi:10.1139/V07-047 © 2007 NRC Canada

and Engineering Research Council of Canada (NSERC) and the National Research Council (NRC) terminates on March 31, 2008, and CSRF will formally cease operations on March 31, 2008.

T.K. Sham approached me to suggest that it might be interesting to write an article on the history of the CSRF in this issue of Canadian Journal of Chemistry. CSRF history is dominated by: first, excellent cooperation and teamwork from a large number of very talented Canadian faculty, post-doctoral fellows, and students from a number of Canadian universities; second, a remarkable international collaboration and cooperation from the Synchrotron Radiation Centre (SRC) outside Madison, Wisconsin; and third, a number of good decisions (with a significant amount of luck!) on the selection of CSRF beamline equipment and beamline personnel. These three characteristics, along with excellent support from NSERC and NRC after 1988, enabled CSRF to be a very cost-effective, world-class, soft X-ray synchrotron facility for over 20 years. Before looking at the CSRF history, it is important to review first my early scientific history that led me to synchrotron radiation (SR) studies, and second, the history of SR in Canada in the 1970s before CSRF was formed.

My early road to "see the light"

I arrived in the Department of Chemistry at UWO in July 1970 to continue a strong research program using Mössbauer spectroscopy that began in 1964 as a Ph.D. student at the University of Cambridge (1). In 1969, I attended an inorganic chemistry Faraday Society discussion in Cambridge and presented a paper on the use of Mössbauer spectra for obtaining bonding and structure in Fe(II) low-spin compounds (2). This meeting also featured papers on the use of photoelectron spectroscopy for studying bonding and structure in inorganic compounds in the gas and solid phases (3). I became very interested in this new spectroscopic area and after setting up my Mössbauer program at UWO in 1970 and 1971, I began to plan for a photoelectron spectrometer, a McPherson ESCA 36 (ESCA = electron spectroscopy for chemical analyses) to perform both UPS (UV photoelectron spectroscopy) and XPS (X-ray photoelectron spectroscopy) on gases and solids. This spectroscopy had been developed in the 1960s mainly by groups at Uppsala University in Sweden (4) and Oxford University in England (5).

In early 1972, I proposed to my department head, Howard Clark, that I would like to apply for a photoelectron spectrometer at UWO. I was not even aware of synchrotron radiation (SR) at the time! Howard Clark strongly supported a $140 000CAN application (a very large grant at the time) to NRC in October 1972, sent me to a photoelectron workshop in Cardiff, Wales, in the summer of 1972, and did a substantial amount of the grant writing. He suggested that the operating funds (including a technician's salary) for the facility would come from income from contracts with private industry and also suggested that we get support from other interested universities to strengthen the application. It is important to emphasize that he was not directly interested in the technique and was not on the application. Such support from senior administration is not common! I received support from the Universities of Windsor and Toronto for the southwestern Ontario ESCA facility, the grant was awarded in March 1973, and the McPherson ESCA 36 spectrometer was working very long hours with full-time technician Bob Lazier in early 1974. This same versatile (but non-UHV) spectrometer was purchased by other groups in Canada (e.g., R.G. Cavell in Alberta and N.S. McIntyre at AECL, Pinawa) at about the same time. The UWO instrument supported a very diverse program of investigation using UV and X-ray photons on gases, solids, and surfaces: from the observation and characterization of a new effect in the spectra, ligand field splitting; to determining the order of molecular orbitals and chemical shifts in organic, inorganic, and organometallic molecules; to the absorption of metals on minerals; to applied industrial surface science with support from a number of steel companies.

Fortuitously, Bill McGowan, the first Director of the Centre for Chemical Physics (CCP) at UWO, initiated the Canadian SR effort just as I began planning for the photoelectron purchase in 1972. Gerhard Herzberg and several of his close NRC spectroscopic colleagues (along with Ed Rowe, the Director of the Madison, Wisconsin, Tantalus SR facility) attended the first Canadian workshop organized by Bill McGowan on the uses of synchrotron radiation (SR) at UWO in October 1972. At this workshop, I realized the power of SR to improve the resolution of photoelectron spectra and to change the photon energy to vary cross-sections. Dr. McGowan pushed extremely hard for a Canadian synchrotron in the period 1972–1977. For example, he applied in July 1973 to the NRC for a feasibility study for a Canadian SR source. As there were *no* known Canadian users at the time (very limited international SR work at Stanford, Tantalus, Cornell, and several European sites had only begun in about 1969), that request (and later requests, see later) was rejected. In January 1975, Dr. McGowan hosted a CCP SR workshop to consider a design from Roger Servranckx of the University of Saskatchewan for a Canadian low-energy synchrotron, and Dr. McGowan suggested a possible site for the synchrotron at the University of Western Ontario to the UWO senior administration.

Canadian scientists began to use synchrotron radiation in the USA in 1974. Probably, the first Canadian user was Daryl Crozier from Simon Fraser University who set up a beamline at the Stanford synchrotron in 1974 for high-energy EXAFS studies. In late 1974, I made an application to Ed Rowe and the Tantalus synchrotron at the University of Wisconsin Physical Sciences Laboratory to obtain photoelectron spectra of volatile organometallics. For one week in March 1975, I went to Madison with my new Ph.D. graduate T.K. Sham to collaborate with Dean Eastman from IBM, who was very well-known for recent SR photoemission studies of semiconductors. He had a UHV photoemission system and was extremely flexible and helpful in obtaining spectra of organometallic films by subliming my volatile compounds onto metal substrates to avoid charging problems. This one week of *very* intense work changed my career! I decided to do part of my sabbatical (July 1975 to January 1976) working with Dean Eastman and postdoc Wolfgang Gudat, and I was greatly encouraged by Eastman and Rowe to spend at least six months at Tantalus studying the valence band and core level spectra of organometallics. I was able to do some good science in that six months (6), but

© 2007 NRC Canada

in addition I learned a lot about synchrotron beamlines and had good discussions with the optics group at Tantalus, especially Charlie Pruett.

In September 1975, Dr. McGowan submitted a very large proposal entitled, *A National Laboratory for SR Studies* to Paul Redhead, the Director of the Physics Division at the NRC. Paul Redhead chaired an ad-hoc NRC committee on SR, and that committee met in June, August, and October of 1976. I spent the second six months of my sabbatical at Siegbahn's lab in Uppsala, Sweden, using his new monochromatic X-ray spectrometer for high resolution core level studies of volatile gases (7), and I returned to Ottawa from Sweden for the first two meetings. The Canadian chemists on that committee were Camille Sandorfy, Chris Brion, and me. Bill McGowan also organized the first very large international SR workshop at Laval University in June 1976. There were 55 attendees at this workshop, with just 11 Canadian scientists. A 624 page report on the many uses of SR was submitted to Paul Redhead's ad-hoc committee. There was still very little Canadian involvement at this time, but it was obvious even then to nearly all the committee members that SR research was going to be very important for Canadian science, and that Canada should be a major player in SR research along with all the other G7 countries that already had SR facilities (8, 9). However, because there were still very few Canadian users, and Canada is averse to taking "risks", this proposal was turned down.

The Beginning of CSRF

It was apparent that establishing a Canadian synchrotron was years away, so the next best thing was to construct a beamline or beamlines at a facility in the USA. As the new Director of the Centre for Chemical Physics at UWO, I headed up a $541 000CAN application (co-applicants were Bill McGowan and Bill Ware, both from UWO) to NRC in October 1977 for the Canadian Synchrotron Radiation Facility (CSRF) to construct one Canadian soft X-ray beamline and three endstations for the existing Tantalus and newly designed Aladdin SR sources at the University of Wisconsin in Madison. I had a very cordial invitation from Ed Rowe (including a 100% use of a SR port on Aladdin at *no* charge in perpetuity!), great technical support at UWO from postdocs Raj Gupta and Leighton Coarsworth, and excellent scientific and technical support from Ed Rowe and Charlie Pruett from Tantalus.

In July 1978, the newly created NSERC awarded $320 000CAN in capital for the Canadian Synchrotron Radiation Facility in Madison, a soft X-ray beamline ($200 000CAN), and two endstations (my photoelectron spectroscopy and Bill McGowan's X-ray microscopy of cells). The visiting committee, chaired by Boris Stoicheff from the University of Toronto, complimented the UWO group for their initiative "on behalf of researchers in Canada" and went on to say that, "their persistent efforts during the last several years to stimulate interest in and acquire funding for a Canadian Synchrotron Facility have led to the current unique opportunity for Canadian science". It is interesting to contrast the cost of this beamline with present more sophisticated beamline costs, at all third generation synchrotrons including CLS, of several million dollars! Not enough capital money was awarded to do the job and it was necessary to arrange multiple sources of funding with concomitant huge amounts of time and effort. With strong support from Dean John Bancroft, I was able to obtain $100 000CAN from the UWO Academic Development Fund and another $40 000CAN from NSERC in the next year to complete the two experimental endstations.

I was appointed the Scientific Director of CSRF (and I continued until 1999), and Norman Sherman was also appointed the NRC manager for close to two decades. But who was paying the operating costs for CSRF? NRC was "to own, staff, and manage the facility" (from NSERC President Gordon McNabb's letter of July 7, 1978). This sounded very promising, but then NRC allotted $5 000CAN annually to own, operate, and maintain the equipment!! After months of correspondence with both NRC and NSERC, the $5 000CAN was not increased. (It is important to note that, as I show later, both NRC and NSERC became very supportive of CSRF financially and scientifically, and that NRC personnel, such as Norman Sherman and later Arthur Carty and Walter Davidson, were enormously helpful). This small operating contribution created enormous problems for me and for the development of CSRF. Fortunately and again coincidentally, UWO (with John Bancroft, George Connell, and Howard Baldwin being enormously helpful) scraped together enough funding by 1980, mostly through the newly announced UWO 2nd Century Fund (a fund which was launched well after the UWO Centenary in 1977), mainly to hire Kim Tan in January 1980 for most of five years as the CSRF Operations Manager based in Madison. Kim Tan did his Ph.D. work with Bill McKonkey at the University of Windsor and a postdoc with Chris Brion in EELS at UBC. He had no synchrotron experience, but had a lot of spectroscopic experience in high vacuum conditions, and more importantly an excellent attitude. He was the only CSRF employee at CSRF from 1980 till 1987 and was the glue that held things together, especially in the first 10 years.

All the initial purchases were funneled through the NRC, with Norman Sherman guiding them and in constant contact with me. We ordered the beamline momochromator from Baker Engineering, a company near Madison in Evansville, Wisconsin, that was marketing a unique soft X-ray monochromator (so-called "Grasshopper" monochromator) that had been designed and built by Neil Lien and Charlie Pruett of the Physical Sciences Laboratory and Fred Brown, a physicist from the University of Illinois (10). Neil Lien joined Baker Engineering, and our monochromator was the first one that Baker made and the fourth that had been manufactured; it was labeled Mark IV. This monochromator was state-of-the-art in the energy region from 20 eV to 200 eV, and it had proven to be easy to use, rugged, and dependable at the Tantalus ring. This $200 000CAN beamline is still working routinely as I write in 2007!!

Kim Tan worked closely with Baker Manufacturing in Evansville, Wisconsin, (with excellent cooperation and collaboration with the monochromator designers Charlie Pruett, Fred Brown, and Niel Lien) in assembling the soft X-ray Grasshopper monochromator; in one year the monochromator was successfully tested at Tantalus (Fig. 1), the first publication appeared in 1982 (11), and the beamline plus XPS was working routinely at Tantalus by January, 1983 (12).

© 2007 NRC Canada

Fig. 1. The official opening ceremony of the first CSRF beamline (the Grazing incidence "Grasshopper" beamline) at the Tantalus synchrotron in October 1983. From left to right: Norman Sherman (NRC, the CSRF Manager), Bill McGowan (Professor, UWO), Brian Yates (graduate student, UWO), Ed Rowe (Tantalus Director, Physical Sciences Laboratory), Brenda Addison (graduate student, UWO), Mike Bancroft (CSRF Scientific Director, UWO), and Kim Tan (CSRF Operations Manager, UWO).



However, we needed Aladdin to get the best results. Aladdin was significantly delayed so that my first graduate student, Brian Yates (now at CLS), had to use Tantalus for all his excellent gas phase Ph.D. results [e.g., (13)]. Doug Shinozaki and Bill McGowan also had a very strong program on soft X-ray microscopy of biological specimens on Tantalus (14). Very fortunately, Seppo and Helena Aksela, sponsored by the Centre for Chemical Physics in 1984, wanted to begin synchrotron studies of the rare gas atoms, and our beamline was as good as any in the world at the time for these studies. Seppo doggedly recorded most of the initial resonance Auger spectra of atoms at the CSRF on Tantalus, and these spectra were interpreted by Helena (15). The resulting series of papers on Ne, Ar, Kr, and Xe are widely cited and formed the basis for their much higher resolution studies in the 1990s on higher intensity synchrotron beamlines. With seven publications in 1984 and 1985 and 16 publications in 1986 (see the publication list in the Supplementary data), the CSRF facility was taking off, and operating money from NSERC and NRC increased greatly.[3] NSERC introduced infrastructure grants in 1983, and Norman Sherman strongly supported increased funding from the NRC. The NSERC and NRC grants of $32 000CAN and $16 000CAN allotted in April 1984 came closer to paying Kim Tan's salary and maintenance costs; by 1987–1988, NSERC and NRC were contributing $82 000CAN and $35 000CAN, and UWO funding was no longer required. Remember that we were paying *nothing* for the use of Aladdin, and Kim Tan was very skillful in accessing technical help from the Aladdin facility for reasonable fees. This saga to gain reasonable operating funding again illustrates the difficulty of getting anything really novel started in Canada — or outside Canada in this case. Exchange rate issues (the US dollar has varied from $1.10CAN to $1.60CAN over the years!) have made budgets very difficult, and long term visa and healthcare issues for employees have been problematic. Fortunately, Norman Sherman at the NRC and the UWO Dean's office were always helpful.

Travel to Madison was a problem, especially in the first 10 years. It took 6–8 h by plane (via Toronto and Chicago) until regular flights from London to Detroit began. I was in Madison at least 4 times a year from 1980 to 1998 and I always enjoyed these trips for the exciting science with dedicated, talented, students and postdocs, and rather few problems at CSRF. I especially enjoyed the rural farm atmosphere (cows, tobacco, and corn) surrounding the SRC, the residence 12 miles from Madison near Stoughton, and the easy country walk to and from SRC and the residence.

CSRF on Aladdin — Towards three beamlines

Aladdin was supposed to be operational in 1982, but multiple problems seriously delayed the commissioning of this new second generation 1 GeV ring. Indeed by 1985, there was considerable concern that the funding would collapse for Aladdin, and that the Canadian program could not reach its potential on Tantalus. Fortunately by late 1985, most of

[3] Supplementary data for this article are available on the journal Web site (http://canjchem.nrc.ca) or may be purchased from the Depository of Unpublished Data, Document Delivery, CISTI, National Research Council Canada, Ottawa, ON K1A 0R6, Canada. DUD 5178. For more information on obtaining material refer to http://cisti-icist.nrc-cnrc.gc.ca/irm/unpub_e.shtml.

© 2007 NRC Canada

Fig. 2. The official opening ceremony for the second CSRF beamline (the Double Crystal Monochromator (DCM) beamline) in 1990. From left to right (front row): Fred Middleton (Physical Sciences Laboratory (PSL)), Jim Taylor (Director, Synchrotron Radiation Centre, University of Wisconsin), Norman Sherman, Kim Tan, John Hicks (PSL), T.K. Sham (Professor, UWO), Jing-Ming Chen (CSRF postdoc), and Masoud Kasrai (Senior scientist, UWO); (back row): Bing Xing Yang (CSRF beamline manager), M. Bissen (SRC), Dan Wallace (SRC), Tim Sailor (PSL), Mike Bancroft, Bengt Olsson (UWO postdoc), Leon Silverling (SRC), Brian Yates (UWO research scientist), Ron Cavell (Professor, University of Alberta), and Glen Caldwell (Vice-President Research, UWO).



Aladdin's problems were solved, and reasonable electron currents could be stored with good lifetimes. We decided to transfer the CSRF beamline to Aladdin (with Ed Rowe still promising us 100% use in perpetuity!) in early 1986 — one of the first beamlines installed on Aladdin. This switch to Aladdin opened up a lot of new science for CSRF users on the Grasshopper beamline because the Aladdin X-ray intensity was much higher than on Tantalus over a broader energy range from 10 to 4 keV. The Grasshopper beamline became useful up to over 300 eV on Aladdin, but most importantly the higher energies could be available using other higher energy monochromators (see later). Many new users became involved on the Grasshopper beamline (see refs. cited in ref. 16), and the scientific program expanded greatly from the two initial programs of Mike Bancroft and Bill McGowan/Doug Shinozaki, mainly to absorption studies (XANES) of gases and solids of all kinds along with high resolution XPS studies of gases and solids. Ron Cavell very generously gave the CSRF one of his ESCA 36 XPS instruments, which was extensively modified by John Bozek and Jeff Cutler for the highest resolution gas phase XPS and Auger studies on a second generation synchrotron; John Bozek and Tolek Tylisczczak (courtesy of Adam Hitchcock) did most of the hardware and software development to scan the Grasshopper monochromator for XANES studies.

With the higher energies available from Aladdin, I planned in 1987 (after becoming Chair of Chemistry at UWO) for a new beamline to cover the energy range from 1.5 keV to 4 keV. Fortuitously again, the Ontario Centre for Materials Research (OCMR) was formed in 1987, and I submitted a $2.1CAN million application to the OCMR for this beamline (cost of about $500 000CAN), endstations for solid-state spectroscopy, and several five-year appointments — a new Professor in my Department and a postdoc for the beamline. My former excellent Ph.D. student, T.K Sham, was hired (after 11 years at Brookhaven National Laboratory doing synchrotron research) to design the beamline at CSRF in 1987 in expectation of the grant. The grant was successful, T.K. Sham was hired as an Associate Professor in Chemistry at UWO, and B.X. Yang from Brookhaven was hired as a postdoc to construct the beamline in 1988. The monochromator ($210 000US) was built by the local PSL group headed by Fred Middleton, and Bing Xing Yang did a remarkable job (with some help in 1989 from the PSL group, Jin-Min Chen, and a postdoc Bengt Olsson) to get the whole beamline working in less than 18 months (Fig. 2) (17). It is interesting to note that Baker Engineering also bid on our monochromator, and apparently their design at Brookhaven National Lab never worked well! In contrast, the unique PSL DCM has worked routinely for almost 20 years! Another hire in my group in 1987 also made a fundamental difference to the CSRF effort. A former colleague from the University of Cambridge in 1964–1968, Masoud Kasrai, became a Senior Chemical Physics Fellow at UWO in early 1987, and he has spent the last 20 years at UWO researching at CSRF for many weeks every year, helping un-

© 2007 NRC Canada

Fig. 3. The official opening of the third CSRF beamline (the Spherical Grating Monochromator (SGM) beamline) in 1999. From left to right: Ron Cavell, Brian Yates (CSRF beamline manager), Nils Petersen (Vice-President Research, UWO), Walter Davidson (NRC, the CSRF Manager), T.K. Sham, Mike Bancroft, Kim Tan, and Jim Taylor. The SGM was shipped to CLS in 2004 for the CLS SGM beamline.



selfishly in many ways with the many students and postdocs in my group and other UWO groups. The two dedicated SR appointments at UWO, T.K. Sham and Masoud Kasrai, became absolutely critical to the ensuing success of CSRF. The productivity of CSRF increased enormously at that point. For example, as shown in ref. 18, over 40 scientists from over 10 Canadian laboratories and universities did experiments at CSRF from 1990 to 19992, and the productivity of the facility increased dramatically to over 30 papers per year in 1992 in a wide variety of scientific areas (see ref. 18, Table 4). We were guaranteed 80% of the beamtime on the DCM, and users came from the following Canadian organizations: the Universities of Alberta, British Columbia, Carleton, Laval, McMaster, Simon Fraser, Toronto, Waterloo, and Western Ontario; also from AECL, CANMET, ESSO, INRS, and NRC. Foreign users came from: Oulu and Turku, Finland, SRC in Madison, and Brookhaven National Laboratory. The research interests of this group varied widely: development of new techniques such as soft X-ray SAXS, EXAFS in liquids from photoconductivity measurements, X-ray excited optical luminescence (XEOL), and soft X-ray fluorescence detection; radiation damage of polymers, reflectivity of muti-layer mirrors, XANES and EXAFS studies of a huge range of gases, solids, and surfaces — semiconductors, coals, glasses, multi-layers, metallo-proteins, tribofilms; and high-resolution XPS–Auger measurements of simple molecules and organometallics.

The funding for the facility from NSERC and NRC was now stable and adequate; (e.g., in 1993–1994 the amounts received were $173 000CAN and $50 000CAN, respectively); as is the international norm, there were *no* user charges of any kind to use the two beamlines.

The intermediate energy range from 300 to 1500 eV was still lacking at CSRF, and I applied to NSERC for $1.4CAN million in 1992 for a third beamline using a so-called spherical grating monochromator (SGM) to give CSRF high resolution capabilities between 250 and 700 eV. The funding was obtained in 1994, my first SR graduate student Brian Yates was hired to construct the beamline, and the entire beamline was ordered from Baker Engineering in 1995. Again, Brian did a marvelous job, mostly on his own. The beamline was somewhat delayed at the Baker end, but it began working to specifications in 1998 for general users (19) (Fig. 3). This beamline enabled very high-resolution studies at the C, N, and O K-edges. Adam Hitchcock donated his photo-ionization chamber for coincidence measurements, and this was used by Adam and John Neville.

Under the direction of Walter Davidson (of NRC) and T.K. Sham since 1999, the Grasshopper and DCM beamlines are still working well at CSRF. The SGM was shipped to the Canadian Light Source in 2004 and forms the basis for a very fine third generation line (the beam team leader is T.K. Sham at UWO) that is working as well as any in the world. It is hoped that the Grasshopper beamline will be shipped to CLS as a museum piece, and that the DCM line will remain at the SRC for general use. The DCM replacement at CLS (again headed by T.K. Sham) should be ready for use by the end of 2007.

Conclusions

After the usual difficult "teething period" from 1980 to 1984, CSRF became a very successful SR facility in the soft X-ray region, with a small fraction of the funds required by most international SR facilities. Several hundred researchers

© 2007 NRC Canada

Table 1. M.Sc. and Ph.D. theses from CSRF.

Ph.D.	1985	P.C. Cheng (UWO and Illinois), Soft X-ray Contact Microscopy using Synchrotron Radiation
Ph.D.	1986	B.W. Yates (UWO), Atomic and Molecular Photoelectron Studies using Synchrotron Radiation
Ph.D.	1987	J.E. Bice (UWO), Gas Phase Photoelectron Studies using HeI, HeII, and Synchrotron Radiation
Ph.D.	1989	D.S. Yang (UWO), Gas Phase Photoelectron Studies of Organoplatinum Complexes using He I, He II, and Synchrotron Radiation
Ph.D.	1991	J.D. Bozek (UWO), High Resolution Core Level Spectroscopies of Molecular Silicon Compounds using Monochromatized Synchrotron Radiation
Ph.D.	1993	J.N. Cutler (UWO), High Resolution Photoelectron Spectroscopy using Synchrotron Radiation: Ligand Field and Vibrational Splittings and Chemical Effects on Linewidths
Ph.D.	1993	M. Kuhn (UWO), Charge Redistribution and Electronic Behaviour of Au-Cu Alloys
Ph.D.	1993	R.W.M. Kwok (UWO), Fabrication of InP MISFET
Ph.D.	1993	Z.F. Liu (UWO), High Resolution Gas Phase Studies of Inner Shell Excitations and Decay
Ph.D.	1993	D.G.J. Sutherland (UWO), High Resolution Gas Phase Si 2p Core Level Spectroscopy using Synchrotron Radiation
Ph.D.	1994	D. Li (UWO), Al, Si, P and S K- and L-edge X-ray Absorption Spectroscopy of Minerals and Glasses: Applications in Mineralogy and Geochemistry
Ph.D.	1995	A. Bzowski (UWO), Electronic Structure of Au-Ag Bimetallics
Ph.D.	1995	Z. Gui (UWO, Spectroscopic Studies on Silver Binding to Metallothionein
Ph.D.	1995	X. Li (UWO), Photoelectron Spectra of Late Transition Metal Organometallic Compounds
Ph.D.	1995	C. Montcalm (INRS/NRC), XUV Mutilayer Mirrors for Wavelenghts Below 13 nm
M.Sc.	1995	M.S. Moghaddam (Carleton), Study of the Correlation States of Molecular Systems by Synchrotron Photoelectron Spectroscopy
Ph.D.	1995	C. Turci (McMaster), Molecular Inner Shell Excitation
Ph.D.	1995	T. Van Buuren (UBC), Electronic and Optical Properties of Porous Silicon
Ph.D.	1995	B. Way (Simon Fraser), Boron-doped Carbon for Advanced Battery Applications
Ph.D.	1995	Z. Yin (UWO), Chemistry of Antiwear Films from X-ray Absorption Spectroscopy
Ph.D.	1996	J. Aubry (McMaster), X-ray Absorption of Si-Ge Semiconductors
Ph.D.	1996	J. Francis (McMaster), Dipole and Non-dipole Core Excitation
Ph.D.	1996	Y.F. Hu (UWO), Photoelectron Spectra of Organometallic Carbonyl Compounds
Ph.D.	1996	J.Z. Xiong (UWO), Structure and Bonding of Organ-Silicon Compounds Containg Si-Si and Si-Ge Bonds
M.Sc.	1997	J. Wu (UWO), Photoelectron Spectra of Organometallic Compounds
Ph.D.	1997	S. Urquhart (McMaster), Core Excitation Spectroscopy of Molecules and Polymers
Ph.D.	1997	A. Wilson (Simon Fraser), Lithium Insertion in Carbonaceous Materials Containing Silicon
M.Sc.	1997	J.C. St Amour (Toronto), The Structure of Titanium Silicate Glasses
Ph.D.	1998	I. Coultard (UWO), X-ray Excited Optical Luminescence and Chemical Properties of Porous Silicon
Ph.D.	1998	M. Suominen-Fuller (UWO), Chemistry of Surface Films from ZDDP by X-ray Absorption Spectroscopy
M.Sc.	1999	G.W. Canning (UWO), Soft X-ray Spectroscopic Studies of Surface Films from Oil Additives
Ph.D.	1999	A. Jurgensen (Alberta), Probing Electronic Structure and Chemical Bonding with X-ray Spectroscopy
Ph.D.	1999	S. Naftel (UWO), Interactions of Transition Metals with Si(100)
Ph.D.	1999	R. Yang (Toronto), Advanced High Dielectric Constant Films
Ph.D.	2000	A. Khoueir (Toronto), RTP Nitride and Oxynitride as Gate Dielectrics
Ph.D.	2001	P. Brodersen (McMaster), Structural Studies of Single Crystal Semicoonductor Surfaces
Ph.D.	2001	S.P. Farrell (UWO), S K- and L-edge XANES Spectroscopy of Metal Sulphides
Ph.D.	2001	Y.Yu (Toronto), Interfacial Engineering for Organic High-emitting Diodes
Ph.D.	2003	C. Morin (McMaster), Biomaterials Studied by X-ray Microscopy
Ph.D.	2003	M.N. Najman (UWO), Chemical Interactions of Metal-free Oil Additives with 52100 Steel
Ph.D.	2003	P. Zhang (UWO), Synthesis, Structure, and Bonding of Some Nanocrystals
M.Sc.	2003	L.Li (New Brunswick), Core Excitation Spectroscopy and the Subsequent Fragmentation Processes of Aromatic Molecules
Ph.D.	2004	M.A. Nicholls (UWO), Microscale Chemical and Mechanical Characterization of ZDDP Antiwear Films on Steel and Al-Si Alloys
Ph.D.	2005	P.S. Grace Kim (UWO), XAFS and XEOL Studies of Light Emitting Materials
Ph.D.	2005	H. Wang (Toronto), An Investigation of the relationship between Opstical Basiciity and Structure in Alkali-Borosilicate Glasses
Ph.D.	2005	L.Soltay (Toronto), Comparison of the Structure of Lithium Containing Silicate and Germanate Glasses
M.Sc.	2006	S. Lam (UWO), XAFS and XEOL Studies of Light Emitting Materials

© 2007 NRC Canada

Table 1. (*concluded*).

Ph.D.	2006	G. Pereira (UWO), Nanoscale Characterization of ZDDP Antiwear Films
Ph.D.	2006	L. Yang (New Brunswick), Inner Shell Excitation Spectroscopy and Ionic Fragmentation of Small Alkynes
M.Sc.	2006	S. Odoh (New Brunswick), Core Excitation Spectroscopy and Photofragmentation of *N*-Heterocycles
M.Sc.	2006	Y.Fan (New Brunswick), Ionic Fragmentation Study of Inner Shell Excited Molecules
In progress		J. Zhou, M. Murphy, J.Y. Ko, N. Grawberg, O. Lobacheva, Y.Li, H. Wang

have used CSRF over the 25 years; over 50 Ph.D. and M.Sc. theses (Table 1) have been produced with at least 7 still expected, and over 500 papers have been published (please see the Supplementary material for the complete list).[3] The *total* capital cost for the three beamlines and all endstations was just over $3CAN million, and the *total* operating cost from 1980 to 1999 was $2.6CAN million. Since 1999, under the direction of T.K. Sham and Walter Davidson, the operating costs (from NSERC and NRC) have been over $2CAN million (over $400 000 per year for several years, but decreasing as CLS comes on stream) as the success of the facility became well-known. As expected, the initial use of the facility was dominated by UWO users, but a quick perusal of the CSRF theses and publications shows that users from 10 other Canadian universities and organizations contributed over 50% of the theses since 1993. Not only are the quantity of CSRF publications remarkable for the amount of money spent, but the high quality of these publications is indicated by the large number of citations for many of them.

But probably most importantly, the CSRF provided first SR training and experience for a lot of present CLS employees (mostly in beamline design and construction) and CLS users. For example, former CSRF employees now employed at CLS include Kim Tan, Brian Yates, and Yongfeng Hu. Other CLS employees, Ian Coulthard, Jeff Cutler, Detong Jiang (now at the University of Guelph) did their Ph.D. or postdoctoral work at CSRF, and Emil Hallin from the Saskatchewan Accelerator Group was introduced to SR beamlines at CSRF. Many faculty members who are strong users of CLS did their first SR research at CLS. For example, Stephen Urquhart and John Tse, at the University of Saskatchewan, did a lot of research at CSRF, and other Canadian faculty such as Adam Hitchcock, Ron Cavell, T.K. Sham, and Grant Henderson did most of their initial SR work at CSRF. And, of course T.K. Sham — the most productive of any Canadian SR researcher — did an enormous amount of his SR work at CSRF from 1987 until recently. The first publications from the CLS from the two replacement CSRF beamlines originated mostly from the above group of outstanding researchers.

It is extremely pleasing for me to see CLS become an excellent international SR facility and to see that the former CSRF users are critical to the CLS development. Many of the papers referred to here come from the above group of people. Finally, I have to thank again the enormous number of talented students, postdocs, senior scientists, and faculty, who have put great effort into the success of the remote CSRF facility. And all of us must thank the SRC staff and management at the Aladdin synchrotron for their outstanding cooperation. Certainly, this must be a model for international cooperation of all kinds.

References

1. G.M. Bancroft. Mössbauer spectroscopy — An introduction for inorganic chemists and geochemists. McGraw-Hill, London, UK. 1973.
2. G.M. Bancroft, M.J. Mays, and B.E. Prater. Disc. Far. Soc. **47**, 136 (1969).
3. S. Evans, J.C. Green, M.L.H. Green, A.F. Orchard, and D.W. Turner, Discuss, Faraday Soc. **47**, 112 (1969).
4. K. Siegbahn, C. Nordling, G. Johansson, J. Hedman, P.F. Heden, K. Hamrin, U. Gelius, T. Bergmark, L.O. Werme, R. Manne, and Y. Baer. ESCA applied to free molecules. North Holland Press, Amsterdam-London. 1971.
5. D.W. Turner, C. Baker, A.D. Baker, and C.R. Brundle. Molecular photoelectron spectroscopy. Wiley-Interscience, London. 1970.
6. G.M. Bancroft, T.K. Sham, D.E. Eastman, and W. Gudat. J. Am. Chem. Soc. **99**, 1752 (1977).
7. G.M. Bancroft, P.A. Malmquist, S. Svensson, E. Basilier, U. Gelius, and K. Siegbahn. Inorg. Chem. **17**, 1595 (1978).
8. G.M. Bancroft and P.W.M. Jacobs. Science Forum. 21 December 1975.
9. J. Wm. McGowan. Phys. Canada, **31**, 67 (1975).
10. F.C. Brown, R.Z. Bachrach, and N. Lien. Nucl. Instrum. Methods Phys. Res. **152**, 73 (1978).
11. K.H. Tan, G.M. Bancroft, L.L. Coatsworth, and B.W. Yates. Can. J. Phys. **60**, 131 (1982).
12. G.M. Bancroft, B.W. Yates, K.H. Tan, and L.L. Coatsworth. J. Chem. Soc. Chem. Comm. 1613 (1984).
13. B.W. Yates, K.H. Tan, G.M. Bancroft, L.L. Coatsworth, and J.S. Tse. J. Chem. Phys. **83**, 4906 (1985).
14. P.C. Cheng, H.B. Peng, K.H. Tan, J. Wm. McGowan, R.Feder, and D.M. Shinozaki. Springer Ser. Opt. Sci. **43**, 285 (1984).
15. H. Aksela, S. Aksela, G.M. Bancroft, K.H. Tan, and H. Pulkkinen. Phys. Rev. A, **33**, 3867 (1986).
16. G.M. Bancroft, K.H. Tan, and J.D. Bozek. Phys. Canada, **113**, July (1987).
17. B.X. Yang, F.H. Middleton, B.G. Olsson, G.M. Bancroft, J.M. Chen, T.K. Sham, K.H. Tan, and D. Wallace. Nucl. Instrum. Methods, **316**, 422 (1992).
18. G.M. Bancroft. Chem. Can. **44**(6), 15 (1992).
19. B.W. Yates, Y.F. Hu, K.H. Tan, G. Retzlaff, R.G. Cavell, T.K. Sham, and G.M. Bancroft. J. Synchrotron Rad. **7**, 296 (2000).

© 2007 NRC Canada

Chemical vapor deposition of nickel-group metals on multiwall carbon nanotubes[1]

Maoqi Feng and Richard J. Puddephatt

Abstract: Chemical vapor deposition (CVD) of Ni, Pd, and Pt films and of Ni/Pd and Pd/Pt bimetallic films on multiwall carbon nanotubes (MWCNTs) can be effected at low temperature if the nanotubes are pretreated by CVD of titanium carbide. In the absence of the pretreatment, the CVD leads to formation of isolated nanoparticles of the nickel-group metals. The metallized MWCNTs are curved or kinked, as a result of the interaction with the metal. Preliminary oxidation of the carbon nanotubes allows easier metallization, and the bending of the metallated nanotubes is not observed in this case.

Key words: Chemical vapor deposition, platinum, palladium, nickel, carbon, nanotube.

Résumé : Si on opère avec des nanotubes qui ont été prétraités par un dépôt de vapeur chimique (DVC) de carbure de titane, on peut effectuer à basse température des dépôts de vapeurs chimiques de films de Ni, Pd et Pd et de films bimétalliques de Ni/Pd et Pd/Pt sur des nanotubes de carbone à parois multiples (NCPM). En l'absence d'un prétraitement, le DVC conduit à la formation de nanoparticules isolées du métal du groupe du nickel. Les NCPM métallisées sont recourbées ou déviées en raison de l'interaction avec le métal. Une oxydation préliminaire des nanotubes de carbone facilite la métallisation et, dans ce cas, on n'observe pas de courbure dans les nanotubes métallisés.

Mots-clés : dépôt de vapeur chimique, platine, palladium, nickel, carbone, nanotube.

[Traduit par la Rédaction]

Introduction

The surface metallization of inorganic and organic materials has relevance in areas such as geochemistry and nanoelectronics, so it is an active area of research (1, 2). For example, there has been much interest in the use of chemical vapor deposition (CVD) to form thin films of transition metals (3), including nickel (4), palladium (5), and platinum (6), on metals, semiconductors, and insulating materials. The metallization of carbon nanotubes to give a hybrid material for potential applications in electronic devices or catalysis is rapidly developing; however, although transition-metal nanoparticles are often used as catalysts for forming carbon nanotubes (7), the use of CVD as a method of metallizing carbon nanotubes has been neglected (8, 9). Instead, carbon nanotubes are usually coated by solution methods, such as electroless deposition, or by metal evaporation–sputtering methods (8, 9). In all coating methods, it is important to recognize that most late transition metals bind only weakly to the nanotube surface; hence, metal deposition tends to give isolated nanoparticles, which are often located at defect sites of the nanotube. One method that has been successful in coating nanotubes with metals by electron-beam evaporation is to apply a preliminary coating of titanium, which forms a stable carbide at the interface, so it gives a continuous and uniform coating (9). Subsequent evaporation of other metals onto the titanium-coated carbon nanotubes can then give uniform metal coatings (9). This article reports the metallization of multiwall carbon nanotubes (MWCNT's) with the metals nickel, palladium, and platinum or with the bimetallics Ni/Pd and Pd/Pt by CVD techniques. Because direct deposition of the metals led to the formation of isolated metal nanoparticles, a new method was developed in which preliminary CVD of titanium carbide was carried out to give a continuous coating, followed by CVD of the nickel-group metal. An unexpected discovery was that the CVD on the MWCNT can lead to the bending of the carbon nanotube. We have previously reported the low-temperature CVD of palladium and platinum on organic materials, including deposition on polystyrene beads to give macroporous films of the metal (10).

Received 17 November 2006. Accepted 26 January 2007. Published on the NRC Research Press Web site at canjchem.nrc.ca on 11 April 2007.

Dedicated to Mike Bancroft, friend, colleague, and distinguished scientist.

M. Feng and R.J. Puddephatt.[2] Department of Chemistry, University of Western Ontario, Chemistry Building, Room 100, London, ON N6A 5B7, Canada.

[1]This article is part of a Special Issue dedicated to Professor G. Michael Bancroft.

[2]Corresponding author (e-mail: pudd@uwo.ca).

Results and discussion

Direct deposition experiments

The atmospheric-pressure CVD experiments were conducted by using a hot-wall CVD apparatus (10) with the multiwall carbon nanotubes supported on the surface of a silicon wafer and using hydrogen as the carrier gas. Initial experiments were carried out to deposit nickel, using the precursor [$Ni(Cp)_2$]; palladium, using the precursor [$Pd(hfac)_2$]; and platinum, using the precursor [$Pt(COD)Me_2$], with the

 doi:10.1139/V07-014 © 2007 NRC Canada

precursor warmed to 60 °C and the substrate heated to 200–250 °C. CVD of bimetallic alloys Ni/Pd and Pd/Pt was carried out by using equimolar amounts of the appropriate precursors. The metallized MWCNT's were then structurally characterized by imaging, SEM or TEM, and the composition of the film was studied by XPS and XRD.

The metallic phases were characterized by the binding energies of Pt $4f_{7/2}$ at ~71.2 eV, Pd $3d_{5/2}$ at 335 eV, and Ni $2p_{3/2}$ at 853 eV, with only minor variations as a function of film thickness and alloy formation. It has previously been shown that the metals are formed in high purity by CVD on silicon or glass by using hydrogen as a carrier gas (6). In the present experiments, CVD was carried out on carbon nanotubes, and XPS analysis always showed the presence of carbon. For example, a sample of carbon nanotubes coated with palladium was analyzed as (atom%): Pd, 35; C, 65 atom%, but the composition varied across the sample. It is shown later by SEM or TEM imaging that the nanotubes are not evenly coated by the direct CVD route, so it is clear that much of the detected carbon is the nanotube substrate (and graphitic impurity in the commercial samples of MWCNT). The composition of the Ni/Pd and Pd/Pt alloys, formed by CVD, was determined by XPS analysis to be Ni:Pd ≈ 1:1 and Pd:Pt ≈ 3:1, which reflects the relative ease of decomposition of the two precursors in an individual CVD experiment. The nickel-coated MWCNT samples gave significant oxygen analysis (Table 1), although NiO was not detected by XRD analysis. It is likely that the nickel surface is oxidized during storage and transfer, prior to XPS analysis.

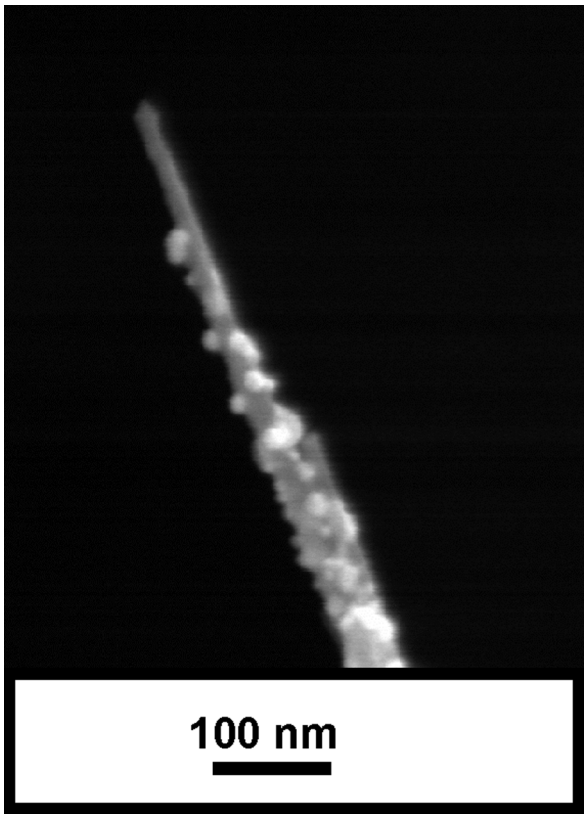
SEM examination of the metallized carbon nanotubes showed the presence of isolated metal nanoparticles in all cases. For example, Fig. 1 shows an SEM image of a carbon nanotube coated with nickel, and Fig. 2 shows a TEM image of a carbon nanotube coated with palladium. They are representative of similar images obtained for nanotubes coated with nickel, palladium, or platinum or with Ni/Pd or Pd/Pt alloys. Clearly, there is no continuous coating, but isolated nanoparticles of nickel or palladium are formed, with average diameter of ~20 nm. This structure arises because the nucleation rate is low, and growth at the forming metal surface is fast, while the metal – carbon nanotube interactions are relatively weak. The autocatalysis of the CVD of nickel, palladium, and platinum by the reactive metal surface is well documented (5, 6).

Table 1. Surface compositions (atom%) of the metallized MWCNTs determined by XPS.

	Metal	C	O
Ni[a]	69	17	14
Ni[b]	66	18	16
Pd[a]	85	15	0
Pd[b]	87	13	0
Pt[a]	79	21	0
Pt[b]	80	20	0
Ni/Pd[a]	Ni,38; Pd,35	19	8
Ni/Pd[b]	Ni,33; Pd,34	25	8
Pd/Pt[a]	Pd,60; Pt,22	18	0
Pd/Pt[b]	Pd,61; Pt,23	16	0

[a,b]Values for films on unoxidized and oxidized carbon nanotubes, respectively.

Fig. 1. SEM image of a MWCNT coated with nickel nanoparticles.



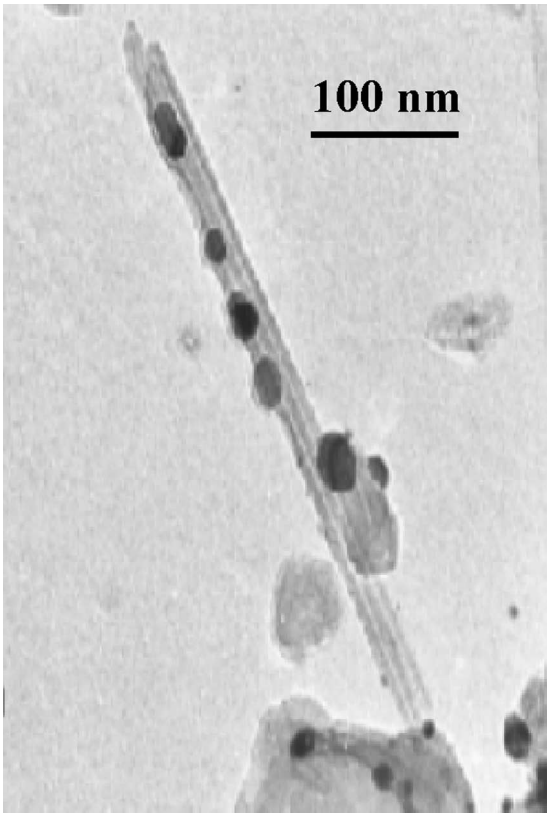
Pre-coating with titanium carbide

Titanium carbide can be formed at high temperature (>800 °C) by the reaction of titanium atoms with carbon nanotubes, and it has been used to connect individual nanotubes (11). In the present work, titanium carbide was deposited by CVD at 400 °C on carbon nanotubes, using $[Cp_2TiCl_2]$ as a precursor (12). The film formed this way was analyzed by XPS and XRD. The Ti $2p_{3/2}$ peak for TiC was broad with components from 455–459 eV, whereas crystalline TiC is reported at 455.1 eV and TiO_2 (anatase or rutile) at 459 eV (13). The data are similar to those reported for partially oxidized TiC(O) films, for which components with Ti $2p_{3/2}$ = 456 and 458 eV were observed (13). In confirmation, an O 1s peak at 530 eV was observed, close to the literature values for TiO_2 of 529.7–529.9 eV. The C 1s peak was dominated by the peak for the carbon nanotubes at 284.5 eV, but there was a lower-energy peak at ~283.5 eV, close to the value reported for carbide in Ti–O–C films at 283.45 eV (13). Finally, XRD analysis confirmed the presence of a crystalline TiC phase (13). XPS analysis gave (atom%) Ti:C:O (49:40:11). Thus, the thin films are identified as partially oxidized TiC.

An unexpected feature of the images obtained by SEM or TEM was that many of the TiC-coated carbon nanotubes were curved or kinked, whereas all of the uncoated nanotubes were linear. Figure 3 shows a TEM image of one such curved nanotube. The deposition of titanium carbide on fullerenes has been shown to cause surface reconstruction (9, 14), while the bending of carbon nanotubes may be

© 2007 NRC Canada

Fig. 2. TEM image of a MWCNT coated with palladium nanoparticles.



caused by replacement of carbon hexagons by pentagons (14), so it is possible that the bending observed in Fig. 3 arises as a result of surface reconstruction of the carbon nanotube, caused by the deposition of titanium carbide.

Nickel-group elements were deposited on the titanium carbide-coated carbon nanotubes by CVD, as previously described; however, under these conditions, the coatings were continuous and more even. Qualitatively, the deposition of nickel-group metals was faster on the TiC-coated nanotubes because the induction period for nucleation on the carbon surface of the pure nanotube was no longer present. Thus, it is shown that TiC is an effective intermediate layer because it can interact strongly with both the carbon nanotube substrate and the nickel-group metal. Figure 4 shows an SEM image of a carbon nanotube coated first with TiC and then with Pd/Pt alloy. Comparing with Fig. 1, it is clear that the metal coating is more continuous and even, with no isolated metal nanoparticles.

Some typical analytical data by EDX for the continuous nickel-group coatings obtained are listed in Table 1. In samples with thicker coatings, the TiC buffer layer was not detected, but the samples always contained residual carbon impurity in the range of 15–21 atom%. It is not obvious whether the carbon impurity arises from the substrate, from carbon in the ligands used, or from a combination of both. The samples containing Ni or Ni/Pd coatings also gave significant oxygen content, indicating partial oxidation of the surface nickel. XPS binding energies showed that Ni, Pd, and Pt coatings contained the elements in the metallic state.

Fig. 3. A TEM image of a MWCNT coated with TiC, showing the curvature induced by the CVD process.

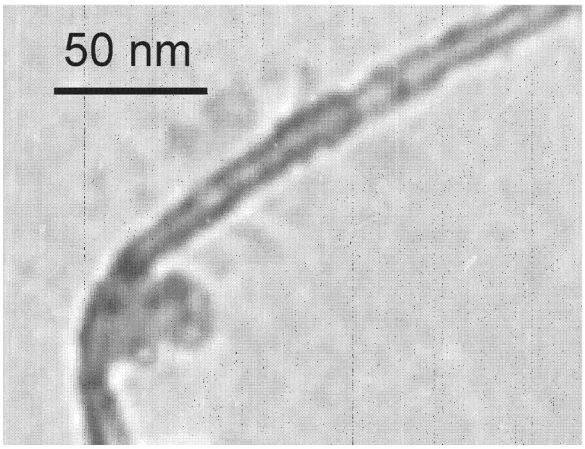


Fig. 4. An SEM image of a carbon nanotube coated first with TiC and then with Pd/Pt alloy. The background material arises from a graphitic impurity in the carbon nanotubes.

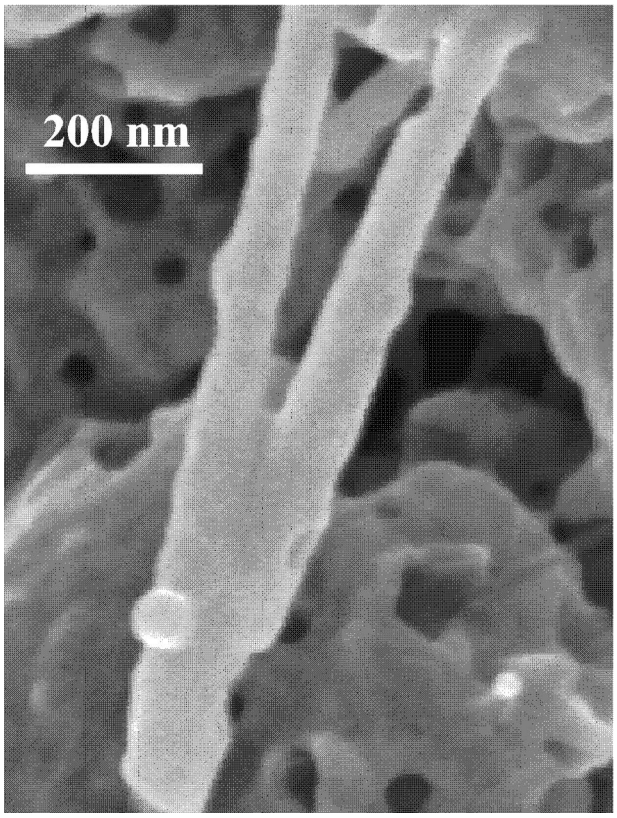


Figure 5 shows TEM images of nanotubes coated with TiC and then with a nickel-group metal. Figure 5(*a*) shows a nanotube coated with TiC and then with a thin coat of nickel. The kink in the nanotube and the even coating of the nanotube with nickel are obvious features. Less obvious is the presence of a helical appearance along the nanotube. Figure 5*b* shows CVD-coated nanotubes first with TiC and then with a thicker coating of Ni/Pd alloy. The apparent helical structure is now very pronounced and appears to arise

© 2007 NRC Canada

Fig. 5. TEM images of MWCNTs coated by CVD: (*a*) TiC, followed by Ni; (*b*) TiC, followed by Pd/Ni alloy.

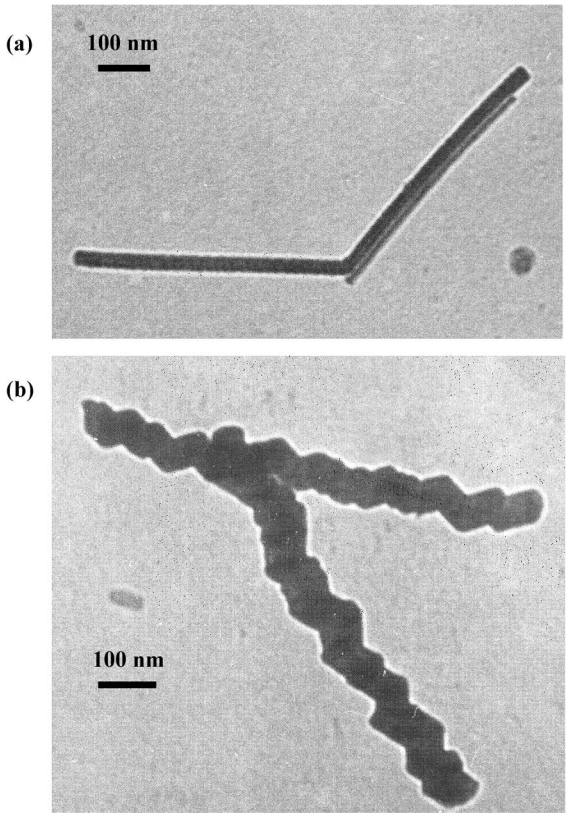
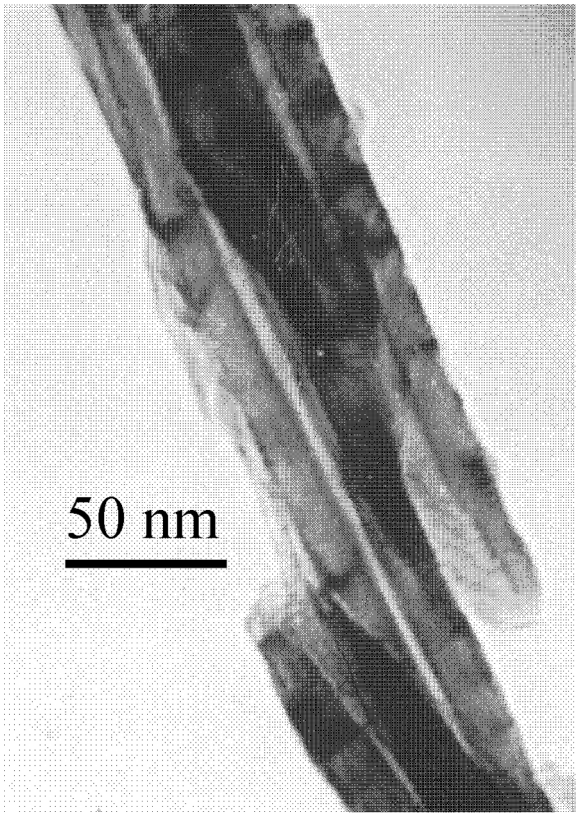


Fig. 6. A TEM image of a bundle of oxidized carbon nanotubes with buffer layer of TiC/TiO_2 and final coating of palladium.



from multiple bends of the coated nanotubes. The metallic coating is again uniform and continuous along the length of the nanotube. These images further show that the problem of forming disconnected particles of Ni, Pd, Pt, and Ni/Pd or Pd/Pt bimetallic alloys by direct CVD onto the MWCNTs (Fig. 2) is overcome by precoating the nanotubes with TiC (Figs. 4, 5), which forms a strong interaction with the MWCNTs and gives a high nucleation rate for subsequent metal deposition.

Pre-oxidation of the carbon nanotubes

Oxidation of carbon nanotubes by nitric acid is known to introduce carboxylic acid, carbonyl, and hydroxyl groups at the surface, and these functional groups can act as nucleation centres in the deposition of metals, such as silver, gold, and platinum from solution (15).

CVD onto the oxidized carbon nanotubes, using $[Cp_2TiCl_2]$ as a precursor, gave a mixture of TiC and TiO_2 in a ratio of roughly 1:3, as determined by XRD and XPS analyses. XRD peaks for TiO_2 are broadened, indicating the formation of small particles, and the average particle size is estimated to be about 6 nm, as calculated from the Scherrer equation (16). The much greater degree of oxidation of titanium to form TiO_2 on the oxidized compared with the untreated carbon nanotubes indicates that the oxophilic titanium abstracts oxygen atoms from the oxygen-containing functional groups on the nanotube walls. Nevertheless, it is possible to deposit nickel-group metals by CVD to give continuous coatings on these treated nanotubes, and the compositions for thick films are very similar to those for films on unoxidized carbon nanotubes (Table 1). However, no bending or kinking of the coated nanotubes was observed by SEM or TEM imaging, in contrast to the observations with unoxidized carbon nanotubes described earlier. Figure 6 shows a TEM image of a bundle of oxidized carbon nanotubes coated first with TiC/TiO_2 and then with palladium, showing that the nanotubes remained linear.

The uniform coating of the oxidized carbon nanotubes with TiC/TiO_2 suggested that it might be possible to coat the nanotubes with a pure metal oxide (15, 17). This hypothesis was tested by CVD of zirconium dioxide, using $[Zr(DPM)_4]$ as a precursor (DPM = dipivaloylmethanate). Zirconia formed a continuous coating on the oxidized carbon nanotubes (Fig. 7*a*), and it was identified by XRD (Fig. 8). Further coating with nickel gave a continuous film (though with some visible imperfections) rather than isolated nanoparticles (Fig. 7*b*). A thick film gave the composition (atom%) of Ni:C:O (62:19:19), similar to that obtained for direct deposition on the oxidized carbon nanotubes. Again, no bending or kinking of the oxidized carbon nanotubes was observed as a result of the CVD-coating processes.

Conclusions

The deposition of the transition metals Ni, Pd, and Pt, and of the alloys Ni/Pd and Pd/Pt, on MWCNTs by CVD, using a buffer layer of TiC, provides a viable method for the metallization of carbon nanotubes, with potential uses as nanowires etc. The unusual bending of the MWCNTs, observed during CVD, is caused by the interaction of

© 2007 NRC Canada

Fig. 7. TEM images of carbon nanotubes coated with (*a*) ZrO_2 and (*b*) ZrO_2, followed by Ni.

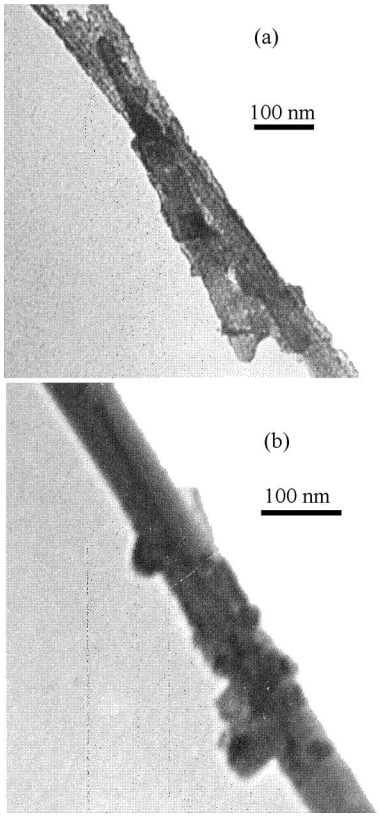
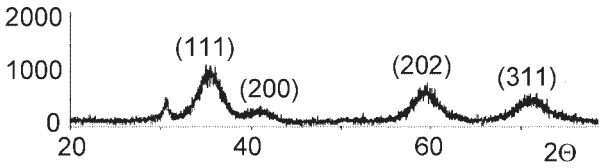


Fig. 8. XRD of carbon nanotubes coated with ZrO_2. The broadening of the ZrO_2 peaks is attributed to the nanocrystalline nature of the zirconia.



the MWCNTs with the adsorbate. Thus, although a detailed explanation is not possible at this stage, it appears likely that adsorbate-induced reconstruction of the nanotube surface occurs, and that the distortions are amplified by the subsequent epitaxial growth of the metal films.

Experimental

The precursors used for CVD of TiC, Ni, Pd, and Pt were $[Cp_2TiCl_2]$, $[Ni(Cp)_2]$, $[Pd(hfac)_2]$ and $[Pt(COD)Me_2]$. $[Cp_2TiCl_2]$ and $[Ni(Cp)_2]$ (Cp = η-C_5H_5) were commercial samples (Aldrich, Strem), and $[Pd(hfac)_2]$ (hfac = hexafluoroacetylacetonate) and $[Pt(COD)Me_2]$ (COD = 1,5-cyclooctadiene) were prepared as described previously {$[Pd(hfac)_2]$, $[Pt(COD)Me_2]$} (5, 6). Multiwall carbon nanotubes (MWCNT, 7–12 nm outer diameter, 0.5–10 μm long) were purchased from Alfa Aesar in the form of a suspension in toluene. The substrates for CVD were prepared by adding a drop of the MWCNT suspension in toluene to a section of silicon wafer (1 cm in diameter), followed by evaporation of the solvent at 60 °C.

CVD was conducted at atmospheric pressure by using a horizontal glass hot-wall CVD apparatus (10). The carrier gas was ultra-high purity H_2 at a flow rate of 100 mL min^{-1}. The precursor was heated to 60 °C to give a suitable rate of evaporation in the carrier-gas stream. The substrate was heated as follows: deposition of TiC at 400 °C, Ni at 200 °C, Pd or Pt (or alloys of these elements) at 250 °C. Under these conditions, a typical CVD experiment was complete in 2 h. After the deposition, the silicon wafer was removed from the reactor, and the metallized MWCNTs were removed from the silicon surface and stored in vacuum for further analysis. For CVD of alloy materials, a mixture of $[Ni(Cp)_2]$–$[Pd(hfac)_2]$ or $[Pd(hfac)_2]$–$[Pt(COD)Me_2]$ was used for the deposition of Ni/Pd or Pd/Pt, respectively.

XPS spectra were recorded by using a SSL SSX-100 small-spot XPS surface-analysis instrument with a monochromatized Mg Kα X-ray source (1253.6 eV); binding energies were reproducible to within 0.1 eV. X-ray diffraction (XRD) profiles were measured using a Rigaku diffractometer with Co Kα radiation (wavelength = 1.790210 Å) at 40 kV and 40 mA, operating over a $2° < 2\theta < 82°$ angular range. TiC was identified by comparison to standard data from the Joint Committee for Powder Diffraction Studies (JCPDF) card 32–1383. SEM images were obtained using a Hitachi S-4500 scanning electron microscope. TEM images were obtained using a Philips EM300 transmission electron microscope system, operating at 80 keV.

Acknowledgments

We thank Surface Science Western for SEM measurements and EMK (Ontario) and the Natural Sciences and Engineering Research Council of Canada (NSERC) for financial support. RJP thanks the Government of Canada for a Canada Research Chair.

References

1. (*a*) G.E. Jean and G.M. Bancroft. Geochim. Cosmochim. Acta, **50**, 1455 (1986); (*b*) Z. Zhang, E.S. Yamaguchi, M. Kasrai, and G.M. Bancroft. Tribology Lett. **19**, 211 (2005).
2. Y. Zhou. Curr. Nanosci. **2**, 123 (2006).
3. (*a*) T.T. Kodas and M.J. Hampden-Smith. The chemistry of metal CVD. VCH, New York. 1994; (*b*) R.J. Puddephatt. Polyhedron, **13**, 1233 (1994); (*c*) J.C. Hierso, R. Feurer, and P. Kalck. Chem. Mater. **12**, 390 (2000); (*d*) J.R.V. Garcia and T. Goto. Mater. Trans. **44**, 1717 (2003).
4. (*a*) L. Mond, C. Langer, and F. Quincke. J. Chem. Soc., Trans. 749 (1890); (*b*) L. Brissoneau and C. Vahlas. Chem. Vap. Deposition, **5**, 135 (1999); (*c*) V.V. Bakovets, V.N. Mitkin, and N.V. Gelfond. Chem. Vap. Deposition, **11**, 112 (2005).
5. (*a*) W. Lin, S.R. Wilson, and G.S. Girolami. Inorg. Chem. **33**, 2265 (1994); (*b*) Z. Yuan, D. Jiang, S.J. Naftel, T.-K. Sham, and R.J. Puddephatt. Chem. Mater. **6**, 2151 (1994); (*c*) Y. Zhang and R.J. Puddephatt. Chem. Vap. Deposition, **3**, 81 (1997); (*d*) Y. Zhang, Z. Yuan, and R.J. Puddephatt. Chem. Mater. **10**, 2293 (1998); (*e*) Y. Zhang, S.W.-K. Choi, and R.J. Puddephatt. J. Am. Chem. Soc. **119**, 9295 (1997); (*f*) Y.H. Liu, Y.C. Cheng, Y.L. Tung, Y. Chi, Y.L. Chen, C.S. Liu, S.M. Peng, and G.H. Lee. J. Mater. Chem. **13**, 135 (2003); (*g*) U.

© 2007 NRC Canada

Weckenmann, S. Mittler, S. Kramer, A.K.A. Aliganga, and R.A. Fischer. Chem. Mater. **16**, 621 (2004); (h) Q.-H. Wu, M. Gunia, T. Strunskus, G. Witte, M. Muhler, and C. Woell. Chem. Vap. Deposition, **11**, 355 (2005).

6. (*a*) R. Kumar, S. Roy, M. Rashidi, and R.J. Puddephatt. Polyhedron, **8**, 551 (1989); (*b*) Z. Xue, M.J. Strouse, D.K. Shuh, C.B. Knobler, H.D. Kaesz, R.F. Hicks, and R.S. Williams. J. Am. Chem. Soc. **111**, 8779 (1989); (*c*) N.H. Dryden, R. Kumar, E. Ou, M. Rashidi, S. Roy, P.R. Norton, and R.J. Puddephatt. Chem. Mater. **3**, 677 (1991); (*d*) B. Nixon, P.R. Norton, E.C. Ou, R.J. Puddephatt, S. Roy, and P.A. Young. Chem. Mater. **3**, 222 (1991); (*e*) Z. Xue, H. Thridandam, H.D. Kaesz, and R.F. Hicks. Chem. Mater. **4**, 162 (1992); (*f*) T.P. Martin, C.P. Tripp, and W.J. DeSisto. Chem. Vap. Deposition, **11**, 170 (2005); (*g*) G.A. Battiston, R. Gerbasi, and A. Rodriguez. Chem. Vap. Deposition, **11**, 130 (2005).
7. (*a*) J.F. Geng, D. Jefferson, and B.F.G. Johnson. J. Mater. Chem. **15**, 844 (2005); (*b*) S.Y. Lee, M. Yamada, and M. Miyake. Sci. Tech. Adv. Mater. **6**, 420 (2005).
8. (*a*) L.M. Ang, T.S.A. Hor, G.Q. Xu, C.H. Tung, S.P. Zhao, and J.L.S. Wang. Chem. Mater. **11**, 2115 (1999); (*b*) X.R. Ye, Y.H. Lin, and C.M. Wai. Chem. Commun. 642 (2003); (*c*) C.H. Yen, X.L. Cui, H.B. Pan, S.F. Wang, Y.H. Lin, and C.M. Wai. J. Nanosci. Nanotechnol. **5**, 1852 (2005); (*d*) Y. Wang, X. Xu, Z.Q. Tian, Y. Zong, H.M. Cheng, and C.J. Lin. Chem. Eur. J. **12**, 2542 (2006).
9. (*a*) Y. Zhang and H.J. Dai. Appl. Phys. Lett. **7**, 3015 (2000); (*b*) Y. Zhang, N.W. Franklin, R.J. Chen, and H.J. Dai. Chem. Phys. Lett. **33**, 35 (2000).
10. M. Feng and R.J. Puddephatt. Chem. Mater. **15**, 2696 (2003).
11. (*a*) Y. Zhang, T. Ichihashi, E. Landree, F. Nihey, and S. Ijima. Science (Washington, D.C.), **285**, 1719 (1999); (*b*) J.-O. Lee, C. Park, J.-J. Kim, J. Kim, J.W. Park, and K.-H. Yoo. J. Phys. D: Appl. Phys. **33**, 1953 (2000).
12. J. Slifirski, G. Huchet, A. Reynes, A. Marty, and F. Teyssandier. Chem. Mater. **7**, 622 (1995).
13. (*a*) Handbook of X-ray Photoelectron spectroscopy. PerkinElmer Corp., 1992; (*b*) V. Schier, H.-J. Michel, and J. Halbritter. Fres. J. Anal. Chem. **346**, 227 (1993); (*c*) L. Ramqvist, K. Hamrin, G. Johansson, A. Fahlman, and C. Nordling. J. Phys. Chem. Solids, **30**, 1835 (1969); (*d*) H. Ihara, Y. Kumashiro, A. Itoh, and K. Maeda. Jpn. J. Appl. Phys. **12**, 1462 (1973); (*e*) U. Muller and R Hauert. Thin Solid Films, **290–292**, 323 (1996); (*f*) G.A. Swift and R. Koc. J. Mater. Sci. **34**, 3083 (1999).
14. (*a*) A.J. Maxwell, P.A. Bruhwiler, S. Andersson, N. Martensson, and P. Rudolf. Chem. Phys. Lett. **247**, 257 (1995); (*b*) M. Terrones. Annu. Rev. Mater. Res. **33**, 419 (2003); (*c*) L. Chico, V.H. Crespi, L.H. Benedict, S.G. Louie, and M.L. Cohen. Phys. Rev. Lett. **76**, 971 (1996).
15. (*a*) T.W. Ebbesen, H. Hiura, M. E. Bisher, M.M.J. Treacy, J.L. Shreeve-Keyer, and R.C. Haushalter. Adv. Mater. **8**, 155 (1996); (*b*) M. Kosaka, T.W. Ebbesen, H. Hiura, and K. Tanigaki. Chem. Phys. Lett**. 233**, 47 (1995).
16. A.D. Krawitz. Introduction to diffraction in materials science and engineering. Wiley, New York. 2001.
17. (*a*) W.-Q. Han and A. Zettl. Nano Lett. **3**, 681 (2003); (*b*) D.F. Johnson, B.J. Craft, and S.M. Jaffe. J. Nanopart. Res. **3**, 63 (2001).

© 2007 NRC Canada

Precipitation of gold by the reaction of aqueous gold(III) chloride with cyanobacteria at 25–80 °C — Studied by X-ray absorption spectroscopy[1]

Maggy F. Lengke, Bruce Ravel, Michael E. Fleet, Gregory Wanger, Robert A. Gordon, and Gordon Southam

Abstract: The mechanisms of gold precipitation by the interaction of cyanobacteria (*Plectonema boryanum* UTEX 485) and gold(III) chloride aqueous solutions (7.6 mmol/L final gold) have been studied at 25, 60, and 80 °C, using both laboratory and real-time synchrotron radiation absorption spectroscopy experiments. Addition of aqueous gold(III) chloride to the cyanobacterial culture initially promoted the precipitation of amorphous gold(I) sulfide at the cell walls and finally caused the formation of octahedral (111) platelets (<1 to 6 μm) of gold metal near cell surfaces and in solutions. X-ray absorption spectroscopy results confirmed that the reduction mechanism of gold(III) chloride to elemental gold by cyanobacteria involves the formation of an intermediate Au(I) species, gold(I) sulfide, with sulfur originating from cyanobacterial proteins, presumably cysteine or methionine. Although the bioreduction of gold(III) chloride to gold(I) sulfide was relatively rapid at all temperatures, the reaction rate increased with the increase in temperature. At the completion of the experiments, elemental gold was the major species present at all temperatures.

Key words: gold, X-ray absorption spectroscopy (XAS), cyanobacteria, transmission electron microscopy (TEM), precipitation, biosynthesis.

Résumé : Opérant à 25, 60 et 80 °C et faisant appel à des expériences tant de laboratoire que de spectroscopie d'absorption de rayonnement d'un synchrotron en temps réel, on a étudié les mécanismes de précipitation de l'or par l'interaction de la cyanobactérie (*Plectonema boryanum* UTEX 485) et de solutions (7,6 mmol/L finale d'or) aqueuses de chlorure d'or(III). L'addition de la solution aqueuse de chlorure d'or(III) à la culture cyanobactérienne provoque initialement une précipitation de sulfure d'or(I) amorphe sur les surfaces de la cellule et ultérieurement la formation de plaquettes (<1 à 6 μm) octaédriques (111) d'or métallique près des surfaces de la cellule et dans les solutions. Les résultas de la spectroscopie d'absorption de rayons X confirment que le mécanisme de réduction du chlorure d'or(III) en or élémentaire par la cyanobactérie implique la formation d'une espèce intermédiaire Au(I), le sulfure d'or(I), dans lequel le soufre provient de la cystéine ou de la méthionine des protéines de la cyanobactérie. Même si la bioréduction du chlorure d'or(III) en sulfure d'or(I) se fait relativement rapidement à toutes les températures, la vitesse de réaction augmente avec une augmentation de la température. Quelle que soit la température, à la fin des expériences, l'or élémentaire est l'espèce principale.

Mots-clés : or, spectroscopie d'absorption des rayons X (SAX), cyanobactérie, microscopie électronique en transmission (MET), précipitation, biosynthèse.

[Traduit par la Rédaction]

Received 10 December 2006. Accepted 27 February 2007. Published on the NRC Research Press Web site at canjchem.nrc.ca on 30 May 2007.

We are pleased to contribute this paper to the Special Issue recognizing the scientific career of G. Michael Bancroft, particularly in light of his pioneering work on gold geochemistry and X-ray absorption spectroscopy.

M.F. Lengke,[2,3] M.E. Fleet, G. Wanger, and G. Southam. Department of Earth Sciences, The University of Western Ontario, London, ON N6A 5B7, Canada.
B. Ravel. Argonne National Laboratory, Argonne, IL 60439, USA.
R.A. Gordon. Simon Fraser University, Burnaby, BC V5A 1S6, Canada.

[1]This article is part of a Special Issue dedicated to Professor G. Michael Bancroft.
[2]Present address: Geomega Inc., 2995 Baseline Road, Suite 202, Boulder, CO 80303, USA.
[3]Corresponding author (e-mail: maggylengke@yahoo.com).

 doi:10.1139/V07-024 © 2007 NRC Canada

Table 1. Starting proportions for the cyanobacterial experiments at 25, 60, and 80 °C at The University of Western Ontario (UWO) and Argonne National Laboratory (APS).

Final Au (mmol/L)	Mixture	Total volume (mL)
Laboratory experiments at UWO		
7.6 mmol/L	20 mL of 26.6 mmol/L Au + 50 mL of cyanobacteria	70
XAS experiments at APS		
7.6 mmol/L	0.2 mL of 26.6 mmol/L Au + 0.5 mL of cyanobacteria	0.7

Note: Stock solutions contained ~20 mg/mL cyanobacteria (dry weight).

Introduction

Gold particles have many important applications in industry and nanotechnology. Therefore, it is essential to find simple and effective methods to synthesize gold particles, and it is also important to develop clean, nontoxic, and environment-friendly procedures. Consequently, biological processes that lead to the formation of gold particles are appealing as possible environment-friendly nanofactories.

Biological methods using organisms, such as bacteria and cyanobacteria, for the synthesis of gold particles are relatively new areas that are currently being explored (1–9). A number of laboratory experiments have been conducted to understand the interaction of gold with bacteria (e.g., *Bacillus subtilis* 168, Fe(III)-reducing bacteria, magnetotactic cocci, *Lactobacillus* sp., *Arthrobacter tumescens* IAM 1447, *Bacillus subtilis* IAM 1026, *Brevibacterium helovolum* IAM 1637, *Corynebacterium equi* IAM 1038, *Deinococcus proteolyticus* IAM 1214, *Escherichia coli* IAM 1264, *Pseudomonas maltophilia* IAM 1554, *Zooglea ramigera* IAM 12136) and cyanobacteria (e.g., *Plectonema terebrans*, *Plectonema boryanum* UTEX 485), using gold(III) chloride ($AuCl_4^-$) (1–9). Studies by Southam and Beveridge (2, 3) demonstrated the formation of metallic octahedral gold, possibly by organic sulfur and phosphate compounds from bacteria. Similarly, Lengke et al. (8, 9) observed the precipitation of metallic octahedral gold by the reaction with *Plectonema boryanum* UTEX 485 at pH 1.9–2.2 and at 25–200 °C and investigated the mechanisms of gold precipitation by X-ray absorption spectroscopy (XAS) at 25 °C. XAS results indicated that the interaction of cyanobacteria with gold(III) chloride initially promoted the precipitation of gold(I) sulfide and finally caused the formation of metallic octahedral gold. Fe(III)-reducing bacteria reduced gold(III) chloride prior to, or simultaneously with, the adsorption of gold onto the cell surfaces at pH 7.0, and the reactions involved the hydrogenase enzyme from these bacteria (4). The formation of gold by magnetotactic cocci was observed inside granules containing phosphorus, sulfur, and iron, and it was suggested that the sulfur-containing component of the granules is much more important in gold reduction than the phosphorus-containing component (7). Gold has also been observed within the cells of *Lactobacillus* sp., but the mechanisms of gold reduction were not discussed (5). The precipitation of gold by other bacteria (e.g., *Bacillus subtilis*, *Escherichia coli* IAM 1264, *Pseudomonas maltophilia* IAM 1554) at pH 1–6 and the precipitation of gold on the sheaths of *Plectonema terebrans* were hypothesized to take place through adsorption on the cells, although the precise mechanisms were poorly understood (1, 6).

Biosynthesis of gold particles by the reaction of aqueous gold(III) chloride ($AuCl_4^-$) with bacteria and cyanobacteria have been intensively studied (1–9); however, only one study has investigated the mechanisms of gold precipitation using cyanobacteria at 25 °C (9). Therefore, the goal of this study was to elucidate the mechanisms of gold precipitation using gold(III) chloride ($AuCl_4^-$) and cyanobacteria at 25–80 °C and to determine whether the mechanisms at 25 °C and higher temperatures are similar. This study was conducted using a combination of laboratory-based cyanobacterial experiments, supported by transmission electron microscopy (TEM), and real-time experiments by XAS. X-ray absorption near edge structure (XANES) provides information on the changes in oxidation state and coordination chemistry of gold during bioreduction, which is required to understand the chemical mechanisms of gold precipitation by cyanobacteria.

Experimental

Cyanobacterial cultures

The filamentous cyanobacterium, *Plectonema boryanum* UTEX 485 (obtained from the culture collection at the University of Texas at Austin, Texas, USA), was grown in batch cultures in BG-11 medium (10) and buffered with 10 mmol/L *N*-2-hydroxyethylpiperazine-*N*′-2-ethanesulfonic acid (HEPES) at a control temperature of 29 °C under ambient CO_2 conditions. The pH of the medium was adjusted to 8.0 using 1 mol/L NaOH solution. Before experimentation, the culture was transferred (20% (*v*/*v*) of inoculum), and grown for 6–8 weeks to reach stationary "growth" phase. It was then centrifuged and washed three times with sterile distilled, deionized water to remove salts and trace metals from the medium.

Laboratory-based cyanobacterial and abiotic experiments

The cyanobacterial experiments were conducted at The University of Western Ontario (UWO) to examine the role of cyanobacteria in the bioaccumulation of gold from aqueous solutions of gold(III) chloride [$HAuCl_4 \cdot 3H_2O$; Alfa Aesar Company, Ward Hill, Massachusetts, USA]. To initiate the experiments, gold solutions (7.6 mmol/L final gold; Table 1) were added to a washed cyanobacterial culture (~20 mg/mL dry weight). The experiments were conducted at 25 °C for 48 h, and 60 and 80 °C for 24 h. pH, E_h, total gold, sulfur, phosphorus, and cyanobacterial populations were measured with time. All experiments were conducted in duplicate. Because there was no significant variation between duplicates for the first six experiments, triplicate experiments were

© 2007 NRC Canada

unnecessary. Abiotic control experiments, consisting of 7.6 mmol/L gold, were conducted using $AuCl_4^-$ solutions without the cyanobacteria.

Bacterial viability and total bacterial counts

The effects of $AuCl_4^-$ solution on the cyanobacteria were monitored during the course of the cyanobacterial experiments by determining bacterial viability using the LIVE/DEAD® BacLight™ bacterial viability kit (L-7007; Molecular Probes, Inc., Eugene, Oregon, USA). When viewed with a fluorescence microscope, viable bacteria, stained with the LIVE/DEAD® BacLight™ reagents, appear green, whereas dead bacteria appear red. The total number of bacteria in the cultures was determined by the direct counting method using a Petroff–Hauser counting chamber and a phase-contrast light microscope (Nikon Labophot microscope).

Chemical analyses

The pH and E_h were monitored using a Denver Instrument Basic pH/ORP/temperature meter. The pH electrode was calibrated using buffer solutions 4, 7, and 10 with analytical uncertainties in the pH measurements of ±0.05 pH unit. The E_h was measured using an ORP electrode and calibrated using ZoBell's solution (11).

Total gold, sulfur, and phosphorus concentrations were measured over the course of the experiments with a PerkinElmer 3300-DV inductively coupled plasma optical emission spectrometer (ICP-OES). The uncertainty in measured gold, sulfur, and phosphorus is ~5%, with detection limits of 0.25 μmol/L, 0.03 mmol/L, and 0.02 mmol/L for gold, sulfur, and phosphorus, respectively.

Transmission electron microscopy (TEM)

Unstained whole sample mounts of cyanobacteria and gold particles from the experiments were examined with a Phillips CM-10 transmission electron microscope (TEM), operated at 80 kV, and a Phillips EM400T transmission electron microscope (TEM) with energy dispersive X-ray spectrometer (EDS), operated at 100 kV. The whole mounts were prepared by floating Formvar carbon-coated 200 mesh copper grids on a drop of culture for several minutes to allow the bacteria and any fine-grained particles to attach to the grid. Selected-area electron-diffraction (SAED) patterns of the precipitated solids were obtained by TEM from unstained whole mounts to ascertain the crystallinity of the solids.

X-ray Absorption Spectroscopy (XAS)

XAS data collection

All XAS measurements were performed at the Pacific Northwest Consortium (PNC/XOR) bending magnet beamline, 20-BM, at the Advanced Photon Source, Argonne National Laboratory, Argonne, Illinois, USA. The Au-L_3 edge XAS measurements were collected using a Si(111) double-crystal monochromator under standard conditions of 7.0 GeV and 102 mA beam current. The energy of each scan was calibrated to the inflection of the Au-foil edge (11919 eV).

All XAS measurements for the cyanobacterial samples were conducted under in situ and real-time reaction conditions. Cyanobacterial samples contained a mixture of gold(III) chloride solution and cyanobacteria (7.6 mmol/L final gold; Table 1) and were prepared in an acid-resistant Teflon fluid cell (3.5 cm × 1 cm × 0.5 cm) with Teflon-coated Kapton film windows. XAS measurements were recorded in transmission mode at 25 °C and in fluorescence mode at 60 and 80 °C, and at intervals that were up to approximately 40 h at 25 °C and 60 min at 60 and 80 °C.

Model compounds, namely, gold(III) chloride ($HAuCl_4 \cdot 3H_2O$), gold(III) thiocyanate ($KAu(SCN)_4$), gold(I) chloride (AuCl), gold(I) cyanide (AuCN), gold(I) thiosulfate ($Na_3Au(S_2O_3)_2 \cdot 2H_2O$), gold(I) sulfide ($Au_2S$), gold(I) thiomalate ($NaO_2CCH_2CH(SAu)CO_2Na.xH_2O$), gold(I) chloro(triphenylphosphine) ($C_{18}H_{15}AuClP$), and gold foil (Au), were measured in the solid form in transmission mode. All model compounds contained a purity of at least 99.9% and were acquired from either Alfa Aesar Company, Ward Hill, Massachusetts, USA or Sigma-Aldrich Inc., St. Louis, Missouri, USA. The model compounds, except for gold foil, were ground and mixed with boron nitride and then pressed as a pellet prior to the measurement to achieve an edge step near unity in transmission. XAS spectra for all standards other than the gold foil and gold(I) sulfide were also collected in solution in transmission mode. The liquids were prepared from the solid compounds and diluted with distilled, deionized water without pH adjustment. Gold(III) hydroxide was prepared, as a model compound, by diluting solid gold(III) chloride with distilled, deionized water, and the pH of the solution was adjusted to pH 11 using NaOH. These model compounds were chosen as reference because they represent the most stable oxidation states of gold, Au(0), Au(I), and Au(III), and were used to qualitatively illustrate the environment expected to be found in the cyanobacterial samples.

Transmission spectra were collected from the cyanobacterial samples and model compounds, using 1 atm (1 atm = 101.325 kPa) nitrogen-gas-filled ionization chambers. A reference spectrum was measured for each sample using a third-ionization chamber and gold foil. The spectra were monitored for radiation-induced chemical effects, but none were found in any sample.

XAS data analysis

XAS data were processed using the ATHENA program (12, 13). Individual scans were calibrated and aligned using the reference gold foil spectrum, then averaged to improve signal quality. XANES spectra were analyzed by fitting with linear combinations of standard spectra. XANES spectra for both the standards and the cyanobacterial samples were normalized and then corrected before analysis to remove variation in the shape of the background. Normalization is done by regressing polynomials to the data regions before and after the edge step. The pre-edge line is subtracted from the data to place the baseline at 0. The post-edge line is extrapolated back to the edge energy of 11919 eV. The difference between the pre- and post-edge lines at 11919 eV is the "edge step". The pre-edge-subtracted data are normalized by dividing by this step height at each energy interval. A background correction is made by subtracting the slope of the

© 2007 NRC Canada

pre-edge line from the post-edge polynomial and then subtracting this difference function from the normalized data. This has the effect of flattening the XANES spectra such that the oscillatory fine structure oscillates about unity. With flattened spectra, the linear combination analysis does not require any additional terms to account for the different background shapes of the standards and data.

Results

Cyanobacterial and abiotic experiments

At 25 °C

Upon the addition of gold(III) chloride (7.6 mmol/L final gold) to the cyanobacterial culture, the soluble gold concentration significantly decreased after 48 h at 25 °C (Fig. 1). Total soluble sulfur and phosphorus concentrations increased from 0.00 to ~0.82 mmol/L and ~0.38 mmol/L, respectively, after 48 h (Fig. 1). The pH and E_h values were relatively constant at ~1.9 and ~1.11 V, respectively. All cyanobacteria were killed within several minutes upon the addition of gold(III) chloride, with concomitant change in color of the cyanobacteria from green to brown, while the solution color remained yellow until the end of the experiments.

At 60 °C

The soluble gold concentration decreased with the increase in reaction time (Fig. 1). Total soluble sulfur and phosphorus concentrations increased from 0.00 to ~0.91 mmol/L and to ~0.47 mmol/L, respectively, after 24 h (Fig. 1). The pH and E_h values were relatively constant at ~1.9 and ~1.10 V, respectively. Cyanobacteria were killed within several minutes. Development of a brown color on cyanobacteria was taken as macroscopic evidence of gold precipitation.

At 80 °C

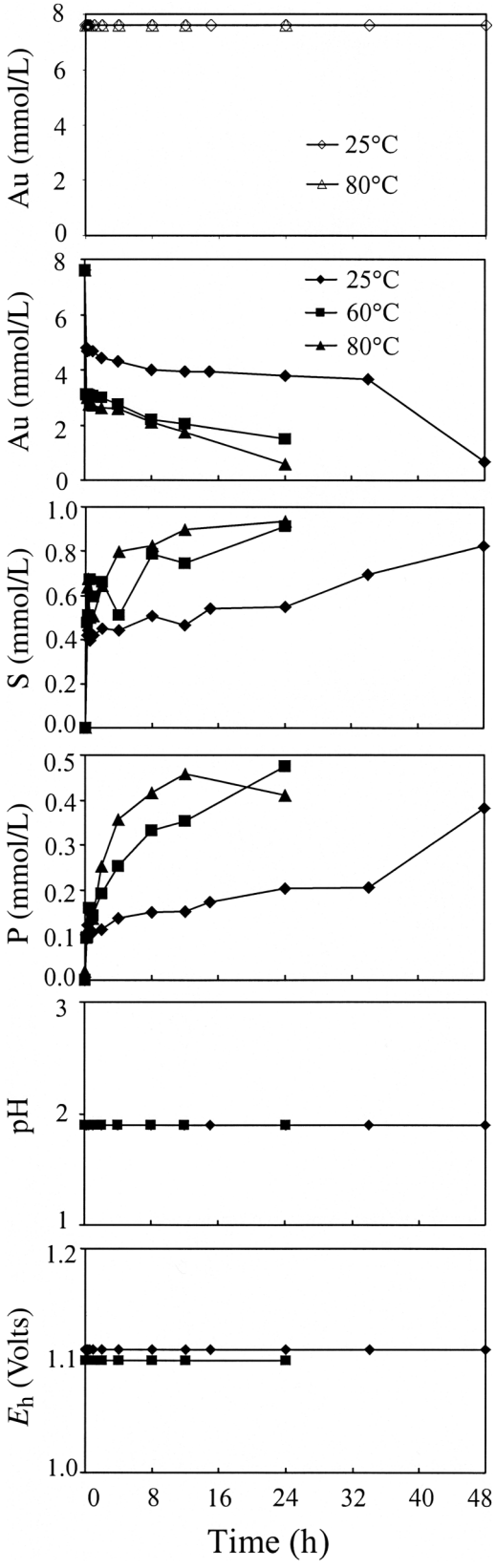
The soluble gold concentration decreased with the increase in reaction time by about 7 mmol/L (Fig. 1). During the course of experiments, total soluble sulfur and phosphorus concentrations increased gradually from 0.00 to ~0.93 mmol/L and ~0.41 mmol/L, respectively (Fig. 1). The pH and E_h values were relatively constant at ~1.9 and ~1.10 V, respectively. All cyanobacteria were killed within several minutes at 80 °C, with concomitant change in color of the cyanobacteria from green to brown, while the solution color became light-yellow at the end of the experiments.

For abiotic experiments using aq. $AuCl_4^-$ at 25, 60, and 80 °C, total soluble gold concentrations were relatively constant (Fig. 1), and pH and E_h values also remained relatively constant until the end of experiments.

TEM

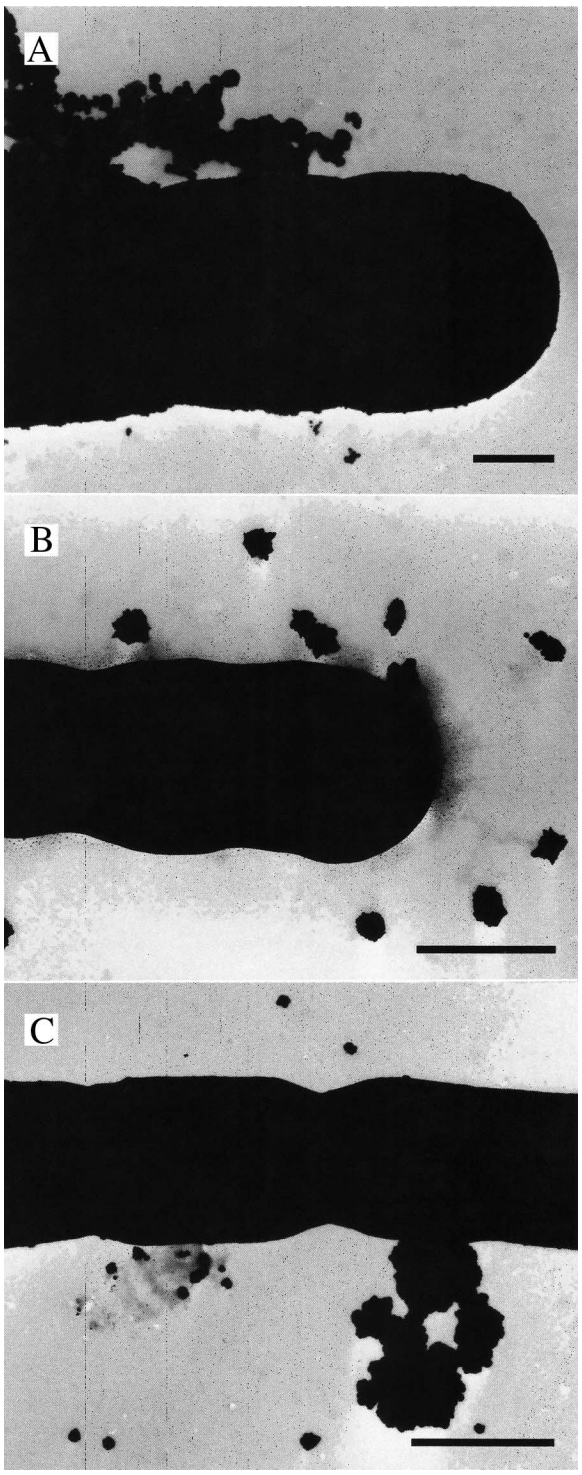
TEM observations on products of cyanobacteria – gold(III) chloride experiments at 25, 60, and 80 °C are presented in Figs. 2 and 3. Addition of gold(III) chloride to the cyanobacteria resulted in the precipitation of nanoparticles at the cell surfaces and at the cell wall – solution interface within several minutes (Fig. 2). These early formed nanoparticles were amorphous to electron diffraction (data not shown) and by TEM–EDS, gold was associated with sul-

Fig. 1. Variation of total soluble gold, sulfur, phosphorus, pH, and E_h with time for cyanobacterial experiments at The University of Western Ontario (UWO) with gold(III) chloride solution at 25, 60, and 80 °C; gold contents in abiotic experiments (open symbols) are included for comparison.



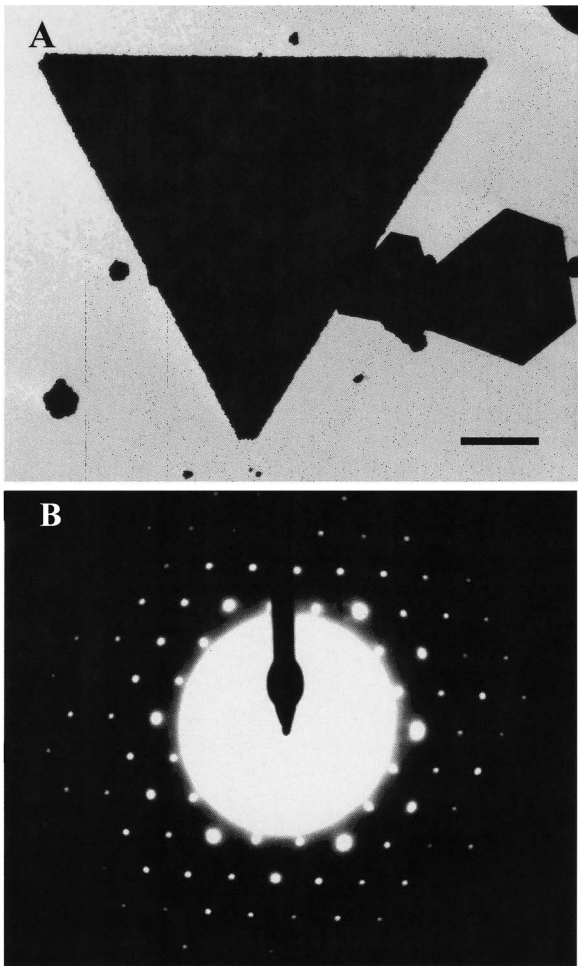
© 2007 NRC Canada

Fig. 2. TEM micrographs of whole mounts of cyanobacterial cells cultured in the presence of gold(III) chloride at 2 h at UWO: (A) precipitation of nanoparticles of gold at cell boundary at 2 h at 25 °C, (B) precipitation of nanoparticles of gold in the vicinity of the cell at 60 °C, (C) precipitation of nanoparticles at cell boundary and near the cell at 80 °C. Scale bars in A, B, and C are 0.5, 1.0, and 0.3 μm, respectively.



fur, phosphorus, and nitrogen. After several minutes, the dead cyanobacteria released cytoplasmic material around the cells, causing further precipitation of gold nanoparticles,

Fig. 3. TEM micrographs and the corresponding TEM–SAED diffraction patterns of whole mounts of nanoparticles of gold metal in the cyanobacteria – gold(III) chloride system at 60 °C and 24 h: (A) octahedral gold, and (B) TEM–SAED twinned diffraction pattern consistent with crystalline gold metal. Scale bar in A is 1.5 μm.



which were characterized by TEM–SAED and TEM–EDS as gold metal. Initially, these second-generation gold nanoparticles were anhedral in shape, but ultimately octahedral shapes with sizes ranging from <1 to 6 μm were formed (Fig. 3A). TEM–SAED patterns were consistent with octahedral gold(111) crystals (Fig. 3B).

XAS

XANES spectra of model compounds

XANES spectra of the model compounds, gold(III) chloride, gold(III) hydroxide, gold(III) thiocyanate, gold(I) chloride, gold(I) cyanide, gold(I) thiosulfate, gold(I) sulfide, gold(I) thiomalate, gold(I) chloro(triphenylphosphine), and gold foil, are presented in Figs. 4 and 5. The absorption edge of gold(III) and gold(I) compounds shifts to lower energy compared with the gold foil. The unusual edge shift for Au(III) is readily attributed to the low-energy dipole-allowed 2p to 5d transition, which is allowed for the d^8 species and forbidden for d^{10} Au(0) (14). Oxidation states of gold are determined from the position and appearance of the intense

© 2007 NRC Canada

Fig. 4. XANES Au-L_3 edge spectra of the gold model compounds measured in the solid and aqueous forms. The vertical solid line indicates the tabulated edge energy, 11919 eV. The vertical dashed lines mark distinctive features of the gold foil and gold(I) sulfide spectra, indicative of the presence of those species in the LC–XANES fitting.

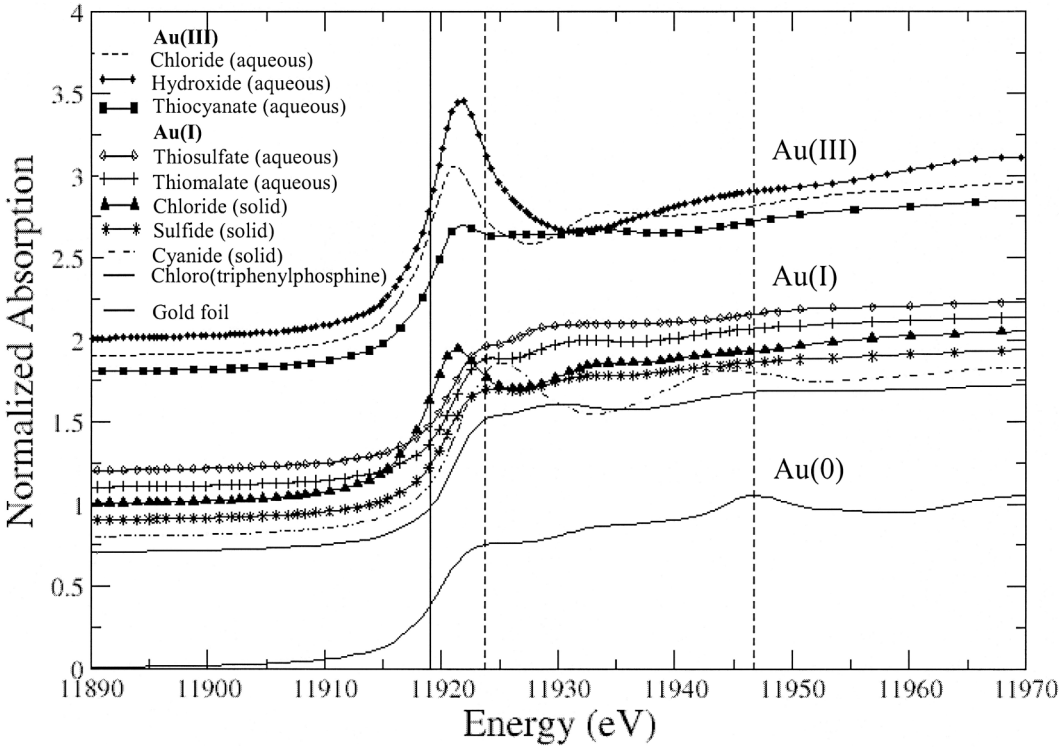
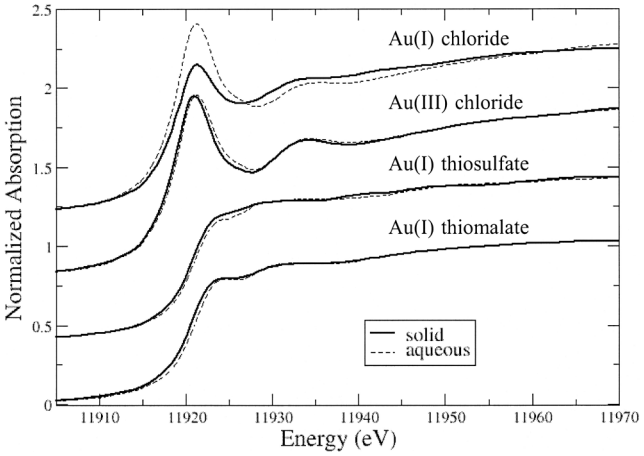


Fig. 5. Comparison of XANES Au-L_3 edge spectra of the gold(I) chloride, gold(III) chloride, gold(I) thiosulfate, and gold(I) thiomalate model compounds measured in the solid form and in solution. Gold(I) chloride clearly disproportionates in solution.



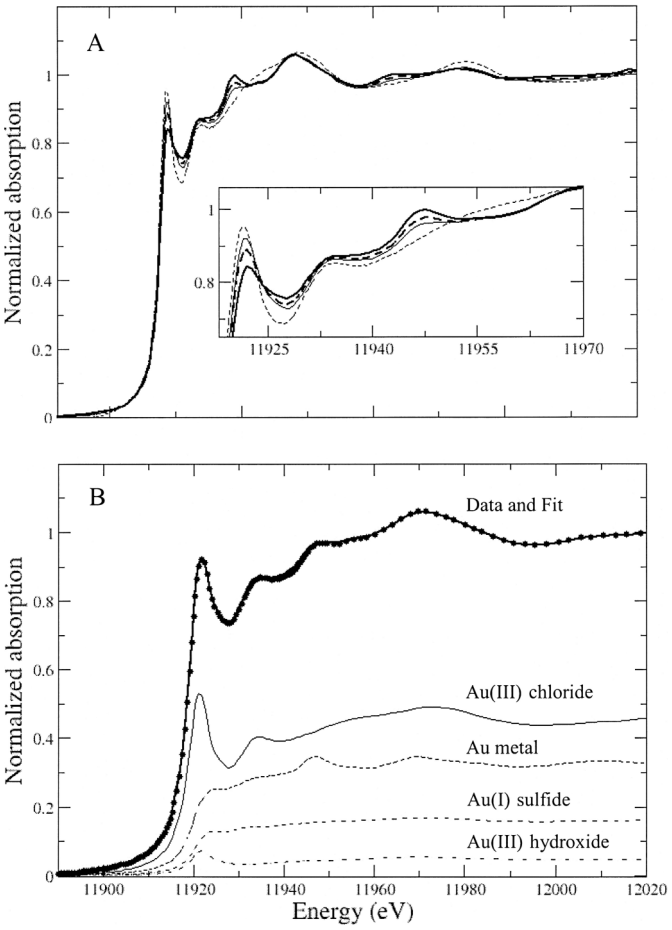
and sharp Au-L_3 edge feature (15). The white-line feature appears at approximately 11921 eV for Au(III) (e.g., gold(III) chloride, gold(III) hydroxide, and gold(III) thiocyanate), but it shifts to higher photon energy with the decreasing oxidation state of gold, as presented in Fig. 4. The white-line feature should only be observed in Au(III) because of the unfilled final-state 5d orbital in the electron configuration of gold (Table 2). However, some Au(I) compounds (e.g., gold(I) chloride and gold(I) cyanide) show a white-line feature with less intensity because of the incorporation of electrons from the closed 5d orbital in chemical bonding (15). The possible incorporation of d electrons from the closed d^{10} subshell for chemical bonding suggests that the electron configuration of Au(I) is $5d^{10-\delta}6s^{\delta}$ (15,16). In a linear 2-fold coordination such as gold(I) cyanide, it has been proposed that hybridization between the 5d and 6s orbitals leads to a valence-electron distribution of $5d^{10-\delta}6s^{\delta}$. This implies the presence of unoccupied d states above the Fermi level, similar to the electron configuration in Au(III) compounds. The occurrence of an edge peak confirms the presence of the vacancies in the 5d valence level. In case of Au(0), the 5d orbital is filled, and no electrons can be added (Table 2); therefore, the white line is absent. For gold foil, the post-edge XANES peaks at approximately 11947 eV are characteristic of Au(0) (Fig. 4). Thus, the white-line feature and its intensity were used for the determination of the oxidation state of gold. The Au-L_3 XANES spectra for the solutions of the selected model compounds (gold(III) chloride, gold(I) thiosulfate, and gold(I) thiomalate) show similar spectra to the solids, confirming that the Au atoms remain complexed in aqueous solution (Fig. 5). We observed no changes in energy shifts of the edge position for measurements in solutions compared with corresponding solids.

Table 2. Electron configurations of gold.

Au(0)	$[Xe]4f^{14}5d^{10}6s^{1}$
Au(I)	$[Xe]4f^{14}5d^{10}6s^{0}$
Au(III)	$[Xe]4f^{14}5d^{8}6s^{0}$

© 2007 NRC Canada

Fig. 6. (A) Evolution of the XANES Au-L_3 edge spectral shift from the beginning to the end of the cyanobacterial experiments at 7.6 mmol/L final gold; thin dashed line, thin solid line, thick dashed line, and thin solid line are measurements after at 10 min, 2 h and 40 min, 8 h and 15 min, and 40 h, respectively. The inset shows the details of the main XANES features. (B) Example of an LC–XANES fit at 5 h and 12 min. The weighted components are displayed below the fit.



However, the spectrum of gold(I) chloride in solution is not similar to the solid, indicating that gold(I) chloride is unstable in solution (Fig. 5). At 25 °C and high concentration, gold(I) chloride disproportionates to a mixture of gold(III) chloride and gold metal (17), via the following reaction:

[1] $3AuCl_2^- \leftrightarrow 2Au_{(s)} + AuCl_4^- + 2\ Cl^-$

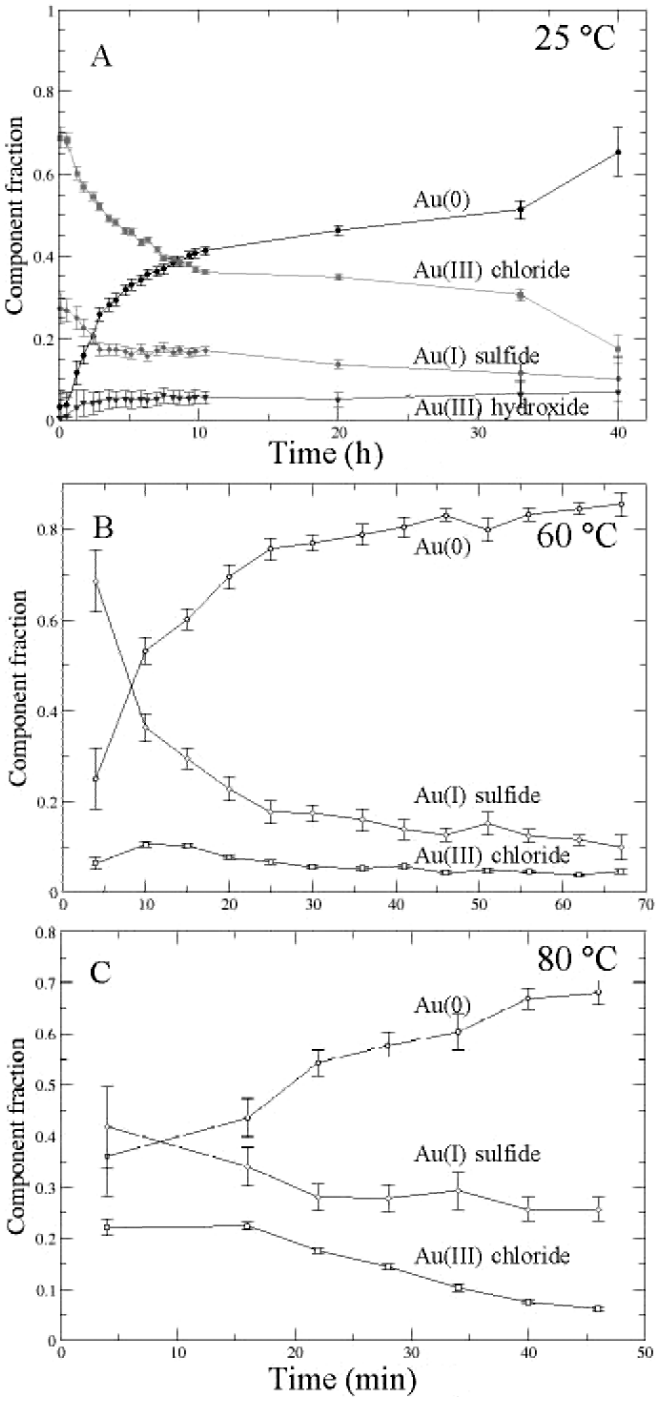
XANES spectra of cyanobacterial samples

XANES spectra and the results of linear-combination fits (LC–XANES) for the cyanobacteria that reacted with gold(III) chloride (7.6 mmol/L final gold) at 25, 60, and 80 °C are presented in Figs. 6 and 7.

At 25 °C

The in situ, real-time experiments were conducted on the cyanobacterial samples at 25 °C for approximately 40 h. During the course of experiments, the spectra showed significant change from the first to the last scans; therefore, an average of every five scans was used for data analysis. The

Fig. 7. Evolution of gold oxidation states and species with time at 7.6 mmol/L final gold in solution, deduced from LC–XANES fits: (A) 25 °C, (B) 60 °C, and (C) 80 °C.



evolution of the data from the beginning to the completion of experiments is shown in Fig. 6A. With the increase in reaction time, the Au-L_3 edge position moved to higher energy, the white line intensity became smaller, and the peak at 11947 eV became higher (Fig. 6A), indicating progressive change in the oxidation state from Au(III) to Au(0). Four model compounds, namely, gold foil (Au), gold(III) chloride, gold(I) sulfide, and gold(III) hydroxide, showed the best match in the (linear-combination) LC–XANES fits

© 2007 NRC Canada

(Fig. 6B). The results of the fits as a function of time are presented in Fig. 7A. Gold(III) chloride and gold(I) sulfide decreased as gold(0) increased with time. Data reduction indicated that trace gold(III) hydroxide consistently improved the fits, although the pH was very low (pH 1.9). The presence of gold(III) hydroxide in the sample was attributed to the replacement of Cl^- by O-containing ligands during the hydration of gold(III) chloride because the XAS measurements for cyanobacterial samples were conducted in aqueous solution in the presence of unreduced gold(III) chloride.

At 60 °C

The in situ, real-time experiments were conducted on a cyanobacterial sample at 60 °C for approximately 68 min. During the course of experiments, changes in spectra were observed; therefore, an average of every five scans was used for data analysis. Three model compound, namely, gold foil (Au), gold(III) chloride, and gold(I) sulfide, showed the best match in the LC–XANES fits. The proportion of gold(III) chloride decreased sharply after the addition of cyanobacteria within the first 4 min, and then remained constant for the duration of the experiment. Gold(I) sulfide decreased in proportion to the increase in gold(0), i.e., gold(I) sulfide and gold(0) distributions were inversely correlated.

At 80 °C

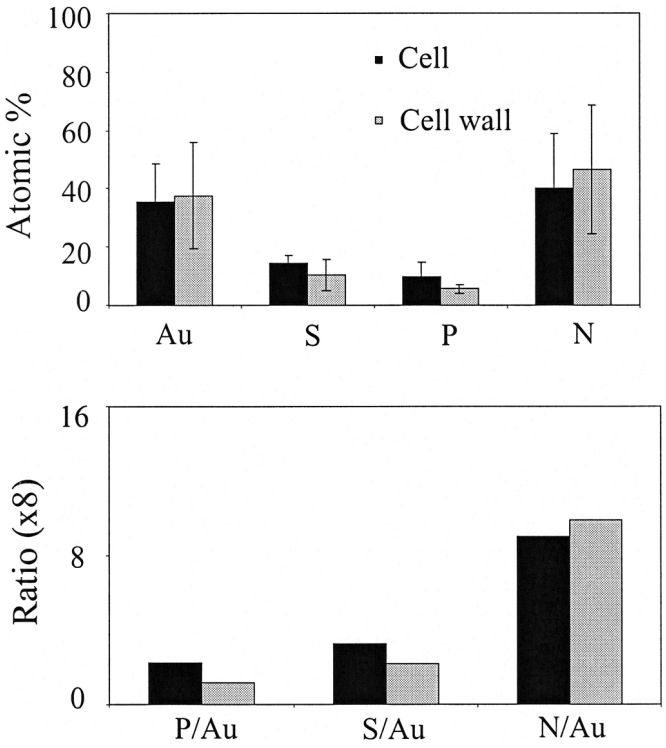
The in situ, real-time experiments were conducted on the cyanobacterial sample at 80 °C for approximately 47 min. During the course of experiments, the spectra showed change from the first to the last scans; therefore, an average of every five scans was used for data analysis. Three model compounds, namely, gold foil (Au), gold(III) chloride and gold(I) sulfide, showed the best match in the LC–XANES fits. As in the 60 °C experiments, gold(III) chloride decreased sharply after the addition of cyanobacteria within the first 4 min, and then slightly decreased until the end of the experiments. Also, gold(I) sulfide and gold(0) showed linear changes with time and were inversely correlated (Fig. 7C).

Discussion

Based on the results of the laboratory cyanobacterial experiments, total gold concentrations decreased significantly at all three temperatures (25, 60, and 80 °C) after the addition of gold(III) chloride to the cyanobacterial culture, whereas total soluble sulfur and phosphorus concentrations increased with time until the completion of the experiments (Fig. 1). The TEM–EDS for the cyanobacterial samples at 25 °C after 2 h reaction time showed the association of gold with sulfur, phosphorus, and nitrogen in the cyanobacterial cells and at the cell walls (Fig. 8). This suggests that sulfur, phosphorus, nitrogen, and gold were involved in the formation of gold nanoparticles precipitated in the early stages of the experiments.

LC–XANES fits confirm that elemental gold was present as a major phase at the completion of all experiments, and that gold(III) chloride was present as a major component in the 25 °C experiments. Gold(III) chloride could undergo ligand-exchange reactions with the O-containing ligands in the 25 °C experiments. However, at 60 and 80 °C, gold(III) chloride was largely reduced by the cyanobacteria, and the

Fig. 8. Histograms of the normalized contents of gold, sulfur, phosphorus, and nitrogen (atomic weight %) by TEM–EDS in the reacted cyanobacterial cells and cell walls, with corresponding ratios of P:Au, S:Au, and N:Au, at 7.6 mmol/L final gold in solution and 25 °C.



binding occurred via a ligand-exchange mechanism, forming gold(I) sulfide by a very fast reaction (Fig. 7). The only source of sulfur in the experimental vessels for the formation of gold(I) sulfide was organic sulfur from the cyanobacteria. Thus, sulfur from cyanobacteria was released to the bulk solutions, and immediately bound with the reduced gold, forming gold(I) sulfide. The fast reduction of Au(III) to Au(I) and the fast release of organic sulfur from the dying and dead cyanobacteria at the higher temperatures investigated (60 and 80 °C) resulted in the presence of gold(I) sulfide as a major phase at the initial stage in the reaction. The reduction of gold(I) sulfide to elemental gold was slower at 25 °C than at 60 and 80 °C. This reduction step was also somewhat slower at 80 °C than at 60 °C, presumably reflecting the increase in stability of aq. gold(I) sulfide at the higher temperature (18, 19).

We noted that the mechanisms for the interaction of bacteria and cyanobacteria with gold(III) chloride have not been investigated in detail in previous studies (1–7). The present XAS results show that Au(III) was reduced to Au(I) bound as gold(I) sulfide, with the sulfide being of organic (cyanobacterial) origin, in a very fast reaction (within minutes). Within the cyanobacteria, sulfur presumably was present as cysteine or methionine groups of the outer membrane or periplasmic proteins (20). These proteins also contain phosphorus and nitrogen, and this may explain the indirect relationship between nitrogen and gold (TEM–EDS results). As soft acids, gold(III) and gold(I) ions readily form com-

© 2007 NRC Canada

plexes with non-polar soft bases such as sulfur and phosphorus. Therefore, the interaction of a gold cation with sulfur would be expected. The reduction of Au(I) to Au(0) was a slower process than the formation of gold(I) sulfide, and occurred after most of the gold(III) chloride had been consumed by the reaction with the cyanobacterial culture (Fig. 7). Thus, we deduce that the steps for the bioaccumulation of gold from gold(III) chloride solution by cyanobacteria are

[2] gold(III) chloride ($AuCl_4^-$) $\rightarrow$

gold(I) sulfide (Au_2S) $\rightarrow$ gold(0) (Au)

Acknowledgment

We thank Dr. Marianna Krol for providing the cyanobacterial cultures and access to the incubation chamber, Ronald Smith for his help during TEM analysis, and Dr. Steve Heald, Dr. Mahalingam Balasubramanian, and Michael Pape for their technical assistance during XAS measurements. We thank Dr. TK Sham and two anonymous reviewers for their constructive comments. Experiments at the PNC/XOR facilities, Advanced Photon Source, Argonne National Laboratory, and research at these facilities were supported by the United States Department of Energy–Basic Energy Sciences, a major facilities access grant from the Natural Sciences and Engineering Research Council of Canada (NSERC), the University of Washington, Simon Fraser University, the Pacific Northwest National Laboratory, and the Advanced Photon Source. Use of the Advanced Photon Source was also supported by the United States Department of Energy, Office of Science, Office of Basic Energy Sciences, under Contract No. DE-AC02-06CH11357. Support for synchrotron efforts was also provided by the United States Department of Energy, Office of Science, Biological and Environmental Research, Environmental Remediation Science Program. The research at The University of Western Ontario was supported in part by the National Science Foundation LExEn Program and NSERC Discovery Grants to G. Southam and M. E. Fleet.

References

1. B.D. Dyer, W.E. Krumbein, and D.J. Mossman. Geomicrobiol. J. **6**, 33 (1988).
2. G. Southam and T.J. Beveridge. Geochim. Cosmochim. Acta, **58**, 4527 (1994).
3. G. Southam and T.J. Beveridge. Geochim. Cosmochim. Acta, **60**, 4369 (1996).
4. K. Kashefi, J.M. Tor, K.P. Nevin, and D.R. Lovley. Appl. Environ. Microbiol. **67**, 3275 (2001).
5. B. Nair and T. Pradeep. Crys. Growth Des. **2**, 293 (2002).
6. A. Nakajima. World J. Microbiol. Biotechnol. **19**, 369 (2003).
7. C.N. Keim and M. Farina. Geomicrobiol. J. **22**, 55 (2005).
8. M.F. Lengke, M.E. Fleet, and G. Southam. Langmuir, **22**, 2780 (2006).
9. M.F. Lengke, B. Ravel, M.E. Fleet, G. Wanger, R.A. Gordon, and G. Southam. Environ. Sci. Technol. **40**, 6304 (2006).
10. R. Rippka, J. Deruelles, J. Waterbury, M. Herdman, and R.Y. Stanier. J. Gen. Microbiol. **111**, 1 (1979).
11. D.K. Nordstrom. Geochim. Cosmochim. Acta, **41**, 1835 (1977).
12. M. Newville. J. Synchrotron Rad. **8**, 322 (2001).
13. B. Ravel and M. Newville. J. Synchrotron Rad. **12**, 537 (2005).
14. J.L. Gardea-Torresdey, K.J. Tiemann, G. Gamez, K. Dokken, I. Cano-Aguilera, L.R. Furenlid, and M.W. Renner. Environ. Sci. Technol. **34**, 4392 (2000).
15. A. Pantelouris, G. Kuper, J. Hormes, C. Feldmann, and M. Jansen. J. Am. Chem. Soc. **117**, 11749 (1995).
16. M.T. Czyzik, R.A. de Groot, G. Dalba, P. Fornasini, A. Kisiel, F. Rocca, and E. Burattini. Phys. Rev. B: Solid State, **39**, 9831 (1989).
17. C.H. Gammons, Y. Yu, and A.E. Williams-Jones. Geochim. Cosmochim. Acta, **61**, 1971 (1997).
18. D.M. Shenberger and H.L. Barnes. Geochim. Cosmochim. Acta, **53**, 269 (1989).
19. S.A. Wood, P. Pan, Y. Zhang, and A. Mucci. Miner Deposita, **29**, 309 (1994).
20. T.D. Brock, M.T. Madigan, J.M. Martinko, and J. Parker. Biology of microorganisms. Prentice Hall, Englewood Cliffs, New Jersey. 1994.

© 2007 NRC Canada

Synthesis and characterization of fluorinated phosphonium ionic liquids[1]

Jocelyn J. Tindale, Chris Na, Michael C. Jennings, and Paul J. Ragogna

Abstract: A wide variety of phosphonium ionic liquids containing fluorous ponytails R_{fn} (R_{fn} = $-(CF_2)_{n-1}CF_3$; n = 4, 6, 10) are synthesized by the reaction of R_{fn}-$(CH_2)_2$-I with trialkylphosphines (R_3P; R = Me, ^{n}Bu, ^{n}Oct). The efficacy of multiple metathetical routes to anion exchange have been investigated, thus the corresponding BF_4^-, PF_6^-, tosylate (OTs^-) and triflate (OTf^-) derivatives have also been prepared. All compounds have been comprehensively characterized by multinuclear NMR spectroscopy, ESI-MS, DSC, and TGA/SDTA, and in the case of $[Me_3PCH_2CH_2R_{f4}][I]$ by single crystal X-ray diffraction. These materials range from high melting solids (e.g., $[Me_3P(CH_2)_2R_{f4}][I]$ T_m = 195 °C) to very low melting liquids (e.g., $[^nOct_3P(CH_2)_2R_{f4}][OTf]$ T_g = –64 °C), and they all have high thermal decomposition points (295 to 394 °C). Incorporation of the more weakly coordinating BF_4^- and PF_6^- yielded a significant increase in the melting point of the materials, in contrast to OTf^- and OTs^- derivatives, which all exhibited significantly depressed melting points.

Key words: phosphonium ionic liquids, alternative solvents, fluorine, phosphorus, fluorous ponytails.

Résumé : On a réalisé la synthèse d'une grande variété de liquides ioniques du phosphonium portant des queux de cheval fluorées [R_{fn} = $-(CF_2)_{n-1}CF_3$; n = 4, 6, 10] en faisant réagir des R_{fn}-$(CH_2)_2$-I avec des trialkylphosphines (R_3P; R = méthyle, butyle, octyle). On a étudié l'efficacité des voies de métathèses multiples conduisant à un échange d'anion; pour cette raison, on a aussi préparé les dérivés BF_4^-, PF_6^-, tosylate (OTs^-) et triflate (OTf^-). Tous les composés ont été caractérisés par spectroscopie RMN multinucléaire, par spectrométrie de masse avec ionisation par électronébulisation, par analyse calorimétrique différentielle et par analyse thermogravimétrie et analyse thermique simultanée et, dans le cas du cristal $[Me_3PCH_2CH_2R_{f4}][I]$, par diffraction des rayons X par un cristal unique. Au point de vue physique, ces produits varient de solides à points de fusion élevés pour des composés comme le $[Me_3P(CH_2)_2R_{f4}][I]$ (T_m = 195 °C) à liquides à points de fusion très faibles des composés comme le $[octyl_3P(CH_2)_2R_{f4}][OTf]$, ($T_g$ = –64 °C); ils ont toutefois tous des points de décomposition thermique élevés (295 à 394 °C). L'incorporation des anions plus faiblement coordinants BF_4^- et PF_6^- conduit à une augmentation substantielle dans les points de fusion de ces matériaux; ce résultat est en opposition avec ce qui est observé avec les dérivés OTf^- et OTs^- qui présentent tous des diminutions significatives des points de fusion.

Mots-clés : liquides ioniques du phosphonium, solvants alternatifs, fluor, phosphore, queux de cheval fluorées.

[Traduit par la Rédaction]

Introduction

"Reduce, reuse, and recycle" waste are considered cornerstone ideas for living "green" (1). This philosophy is becoming increasingly more important in terms of developing cleaner processes for chemical synthesis and manufacturing (2). Many synthetic methods and chemical reactions are carried out in the solution phase, which is considered to be one of the most difficult areas for developing a more environmentally benign process. The identification of ionic liquids as ideal media in which to perform a vast array of solution phase chemistry has been a crucial development for overcoming the difficulties associated with making this area of chemistry "greener".

Ionic liquids possess remarkable properties, which make them ideal candidates as alternative solvents for synthesis (3), catalysis (4), and chemical separations (5) (e.g., negligible vapor pressure, high thermal stability, large liquid range) (6–12). In addition to these more familiar applications, ionic liquids have been reported as highly versatile media for use as electrolytes in various electrochemical devices such as solar cells (13, 14) and lithium batteries (11), as electrochemical capacitors (15), matrices for MALDI mass spectrometry (16, 17), surfactants (18), electropolishing agents (13), phase

Received 25 January 2007. Accepted 12 March 2007. Published on the NRC Research Press Web site at canjchem.nrc.ca on 12 June 2007.

J.J. Tindale, C. Na, and P.J. Ragogna.[2] Department of Chemistry, *The* University *of* Western Ontario, 1151 Richmond St., London, ON N6A 5B7, Canada.
M.C. Jennings. X-ray Crystallography Laboratory, Department of Chemistry, *The* University *of* Western Ontario, 1151 Richmond St., London, ON N6A 5B7, Canada.

[1]This article is part of a special issue dedicated to Professor G. Michael Bancroft.
[2]Corresponding author (e-mail: pragogna@uwo.ca).

 doi:10.1139/V07-035 © 2007 NRC Canada

Fig. 1. Common cations in ionic liquids.

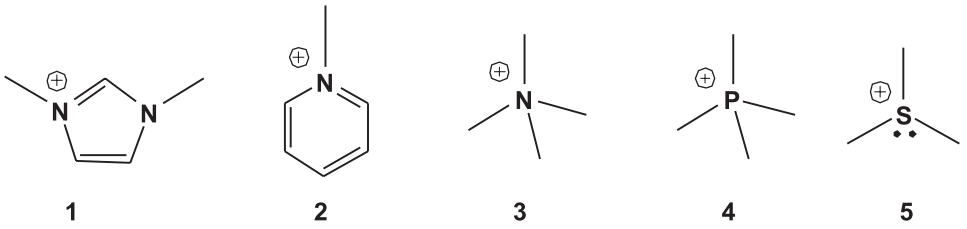


Fig. 2. Ionic liquids featuring unusual functionalities.

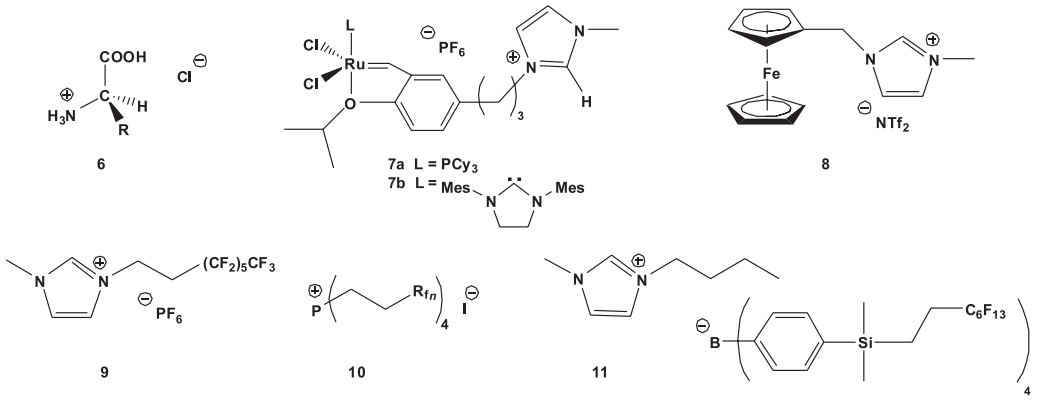
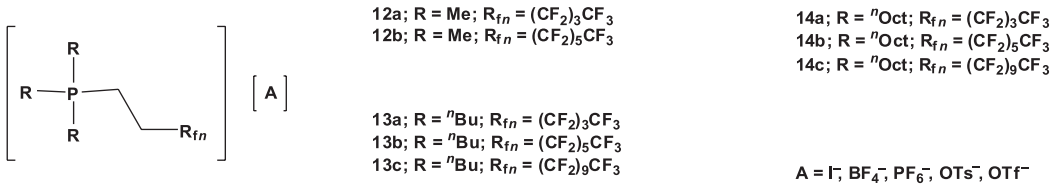


Fig. 3. Numbering scheme for the ionic liquids containing one fluorous chain. Compound numbers refer to the composition of the phosphonium cation.



transfer catalysis (19), and as highly resilient media in radiation intensive environments (20). The overwhelming majority of these ionic liquids employ nitrogen-based cations (**1**–**3**), while there have been limited reports on the use of phosphonium or sulphonium ionic liquids (**4**, **5**, Fig. 1).

Despite their greater thermal stability, propensity for forming multiphasic systems, increased resilience in basic environments, and demonstrated utility in a variety of catalytic and other synthetic applications, reports on the development of new phosphonium ionic liquids are relatively uncommon (19, 21–27).

Incorporating unusual but potentially useful functionalities into the cation or anion pair can impart these materials with attractive properties not observed in more conventional systems. For example, ammonium-based systems derived from natural amino acids generate biodegradable, chiral-solvent media **6** (28). Other functionalities integrated into the ionic liquid frameworks include catalytically active organometallic complexes (e.g., **7**), such as the Grubbs generation I (**7a**) and generation II catalysts (**7b**) or ferrocenyl substituents that are tethered to an imidazolium cation (**8**). These materials proved to be highly effective in ring-closing olefin metathesis (RCM) or as novel media for the study of electron transfer dynamics, respectively (Fig. 2) (29–33). However, these substituents can limit the environmental compatibility of the end materials.

Ionic liquids integrated with perfluoroalkyl chains, also referred to as fluorous ponytails (R_{fn} = $-(CF_2)_{n-1}CF_3$) (**9**, **10**), have shown excellent utility as surfactants or as a solvents for phase transfer catalysis (18, 19, 34–37). Systems containing heavily fluorinated anions paired with imidazolium cations (**11**) have displayed temperature dependent solvent miscibilities similar to those observed for highly fluorinated organic solvents (34) and will likely have applications in fluorous biphasic catalysis (38, 39) as a nonvolatile fluorous phase, a distinct advantage over current technologies.

In this context, we report the synthesis and characterization of a wide range of phosphonium ionic liquids that contain a diverse array of highly fluorinated alkyl chains as a component of the cation (Fig. 3). In all cases, the products are air stable, hygroscopic, exhibit high decomposition points, are soluble in a variety of polar organic or fluorinated solvents (acetone, CH_2Cl_2, α,α,α-trifluorotoluene), have wide liquid ranges, and are a promising new alternative solvent media.

Experimental section

General

Trialkylphosphines ($^nBu_3P$, $^nOct_3P$) were donated by Cytec Corporation and distilled prior to use (0.01 torr, 1 torr = 133.322 4 Pa; 80 and 160 °C, respectively). Sodium

 doi:10.1139/V07-035 © 2007 NRC Canada

hexafluorophosphate, AgOTs, $NaBF_4$, HBF_4, HPF_6, HOTs, NaOTs (Sigma-Aldrich), and TMS-OTf (Alfa Aesar) were used as received. Fluorinated alkyl iodides (Fluorous Technologies Inc.) were used without further purification, except for $CF_3(CF_2)_9CH_2CH_2I$, which was sublimed prior to use (0.05 mmHg, 1 mmHg = 133.322 4 Pa; –20 °C cold finger). The purity of all reagents was assessed by multinuclear NMR spectroscopy (^1H, $^{19}F\{^1H\}$, $^{31}P\{^1H\}$) where appropriate, and they were stored in a nitrogen-filled MBraun Labmaster 130 glove box. Solvents were obtained from Caledon Laboratories and dried using an Innovative Technologies Inc. Controlled Atmospheres Solvent Purification System, which utilizes dual-alumina columns. The dried solvents were collected under vacuum and stored under a nitrogen or argon atmosphere in Strauss flasks or stored in the drybox over 4 Å molecular sieves. Deuterated solvents were dried by stirring for a minimum of 2 days over CaH_2, then vacuum distilled and stored over 4 Å molecular sieves in the drybox. Solution ^1H and $^{31}P\{^1H\}$ NMR spectra were recorded on either a Varian INOVA 400 MHz, a Varian INOVA 600 MHz, or a Varian Mercury 400 MHz spectrometer (^1H: 400.09, 599.49, and 400.1 MHz, respectively; ^{31}P: 161.82, 242.67, and 161.96 MHz, respectively). Proton decoupled ^{19}F NMR spectra were recorded on either a Varian INOVA 400 MHz or Varian Mercury 400 MHz spectrometer (376.15 MHz, 376.46 MHz, respectively).

All samples for ^1H NMR spectroscopy were referenced to the residual protons in the solvent relative to $(CH_3)_4Si$ (δ (ppm): chloroform-*d* 7.26; pyridine-d_5 8.71; 7.55, 7.20; acetonitrile-d_3 1.94; acetone-d_6 2.05). Phosphorus-31 chemical shifts were reported relative to an external standard (85% H_3PO_4, 0.00 ppm) and ^{19}F NMR data were referenced to an external standard ($CF_3(C_6H_5)$, –63.9 ppm) relative to $CFCl_3$, 0.00 ppm. Mass spectrometry measurements were recorded in positive and negative ion modes using an electrospray ionization Micromass LCT spectrometer. Melting and glass transition points were determined using differential scanning calorimetry (DSC) on a DSC 822e Mettler Toledo instrument. A 0.005–0.010 g sample was heated at a rate of 10 °C/min over a temperature range of –70 to 120 °C. Ionic liquids that were liquid at room temperature (RT) were cooled to –70 °C for 15 min, followed by increasing the heating rate to 10 °C/min until reaching 120 °C. The decomposition temperatures were determined using thermal gravimetric analysis (TGA) on a TGA/SDTA 851e Mettler Toledo instrument. A 0.005–0.010 g sample was heated at a rate of 10 °C/min over a temperature range of 100 to 600 °C. Decomposition temperatures were confirmed by DSC, in that no exotherm indicative of a decomposition with zero mass loss was observed below the decomposition points noted. Single crystal X-ray diffraction data were collected on a Nonius Kappa CCD area detector using Mo K_α radiation (λ = 0.710 73 Å). Single crystals of [**12a**][I] were successfully grown via vapour diffusion of Et_2O into a CH_2Cl_2 solution of the salt, yielding colourless needles of sufficient quality for X-ray diffraction analysis. They were selected under oil, mounted on a glass fiber, and then placed in a cold stream of N_2. Structures were solved by direct methods and refined using full-matrix least-squares on F^2. Representative samples were tested for their water content by Karl Fischer titration on a 684 KF coulometer by Metrohm.

Crystal data for [12a][I]

$C_9H_{13}F_9I_1P_1$, M = 450.06 g mol^{-1}, Rhombohedral, $R3$, a = 19.6596(6) Å, c = 21.4939(9) Å, V = 7194.4(4) Å^3, T = 150(2) K, Z = 18, D_c = 1.870, measured reflections = 23 068, unique 2827, refined parameters 237, $R[I > 2\sigma I]$ = 0.0446, $wR_2(F^2)$ = 0.1236, R_1 (all data) = 0.0571, wR_2 (all data) 0.1307.

General procedure for the synthesis of $[R_3P(CH_2)_2R_{fn}]$[I] reactions involving ^{n}Bu$_3$P or ^{n}Oct$_3$P

A vial (27.7 × 57 mm, 4 dr.) was charged with $I(CH_2)_2R_{fn}$, where n = 4, 6, 10 (2.72 mmol), R_3P where R = n-C_4H_9, n-C_8H_{17} (2.47 mmol), and a Teflon stir bar. The neat reaction mixture was stirred at RT for 48 h. The residual reagents were removed in vacuo (0.05 mmHg, 100 °C) resulting in viscous liquids or waxy solids [**13**][I] and [**14**][I].

Variations to the general procedure — Reactions involving $(CH_3)_3P$

These were carried out in THF (5 mL) and were stirred for 42 h at RT. An off-white solid precipitated from the reaction mixture, which was filtered and the residual solvent removed in vacuo to give [**12**][I].

General procedure for [13–14][A] salts (A = PF_6^-, BF_4^-, OTs^-) via the parent Brønstead acids

A vial was charged with [**13–14**][I] (0.433 mmol) in CH_2Cl_2 (5 mL). The solution was stirred vigorously and the respective Brønstead acid (0.866 mmol) required to give the desired ionic liquid was dissolved in distilled water (2 mL) and added dropwise. The mixture was stirred for 20 h. The resulting mixture was washed with cold distilled water (4 × 5 mL), and after each wash the aqueous layer was tested with a 10% solution of $AgNO_3$ to confirm the absence of I^- (21). The dichloromethane fraction was dried with $MgSO_4$, and the volatiles were removed in vacuo (0.05 mmHg, 115 °C) for 20 h to give colourless to slightly yellow viscous liquids or solids.

General procedure for [13–14][A] salts via sodium salts (A = PF_6^-, BF_4^-, OTs^-)

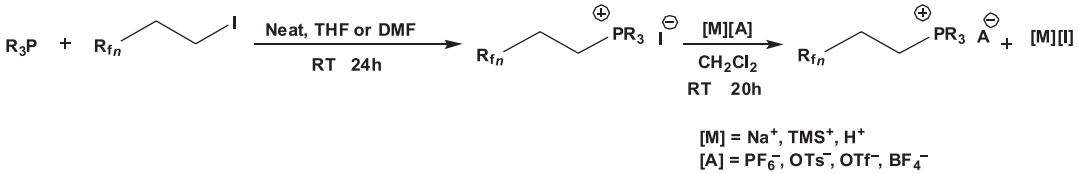
The required phosphonium iodide (0.250 g) and sodium salt (30% mol excess) in CH_2Cl_2 (5 mL) were stirred vigorously (24 h, RT). The NaI precipitate was filtered and the organic fraction was extracted with water (4 × 5 mL). A 10% solution of $AgNO_3$ was added to each aqueous phase to confirm the absence of I^-. The dichloromethane fraction was dried with $MgSO_4$ to remove residual water. Volatiles were removed in vacuo (0.05 mmHg, 115 °C) for 20 h to give colourless to slightly yellow viscous liquids or solids.

General procedure for [13–14][OTf] salts via trimethylsilyl triflate (Me_3Si-OTf)

The required phosphonium iodide (0.250 g) in CH_2Cl_2 (4 mL) and trimethlsilyl triflate (30% mol excess) in CH_2Cl_2 (1 mL) were stirred vigorously under nitrogen (24 h, RT). The resulting Me_3Si-I was removed in vacuo (0.05 mmHg, 115 °C) yielding viscous liquids, tacky solids, or in the case of [**14c**][OTf], a waxy solid.

© 2007 NRC Canada

Scheme 1.



Procedure for [(14c][OTs] salt via AgOTs

[**14c**][I] (0.182 g, 0.174 mmol) in CH_2Cl_2 (5 mL) was added to AgOTs (0.073 g, 0.261 mmol) and stirred for 4 days at RT. The resulting solid was centrifuged and the supernatant was filtered through Celite. The solvent was removed in vacuo resulting in a yellow viscous liquid. The liquid was redissolved in acetone and filtered through Celite until a colourless liquid remained and all traces of AgI were removed. The volatiles were removed in vacuo to give a colourless, viscous liquid. Upon standing for elongated periods (5 days), the material formed a colourless, waxy solid, [**14c**][OTs].

Multinuclear NMR spectroscopy

The $^{31}P\{^1H\}$ NMR spectra of the trimethyl phosphonium series [**12**][I] all exhibited a singlet at δ 29.6 ppm. The *n*-butyl (**13**) and *n*-octyl (**14**) substituted series displayed chemical shifts further downfield at δ 35.2 ppm. Proton NMR spectra were identical for all the *n*-butyl and *n*-octyl phosphonium series (**13**–**14**) except in the case of those containing OTs^- anions, for which the aryl and methyl resonances were observed for that anion. Therefore, proton NMR data for [**13a**][I] and [**14a**][I] only are listed in the following section. The $^{19}F\{^1H\}$ NMR spectra for each fluorous chain (**a**–**c**) are identical, and therefore only one example of each R_{fn} chain is reported.[3]

[13a][I]

^1H NMR ($CDCl_3$, ppm) δ: 0.98 (t, 9H, J = 6.8, CH_3), 1.55 (m, 12H, $CH_2CH_2CH_3$), 2.61–2.54 (m, 8H, PCH_2 CH_2CF_2, $PCH_2(CH_2)CH_3$), 2.76–2.72 (m, 2H, PCH_2CH_2). $^{19}F\{^1H\}$ NMR ($CDCl_3$, ppm) δ: –81.5 (t, 3F, J = 9.4, CF_3), –115.0 (m, 2F), –123.9 (m, 2F), –126.5 (m, 2F).

[13b][I]

$^{19}F\{^1H\}$ NMR ($CDCl_3$, ppm) δ: –81.4 (t, 3F, J = 9.4, CF_3), –114.8 (m, 2F), –122.4 (m, 2F), –123.0 (m, 2F), –123.4 (m, 2F), –126.7 (m, 2F).

[13c][I]

$^{19}F\{^1H\}$ NMR ($CDCl_3$, ppm) δ: –81.18 to –81.30 (t, 3F, J = 9.4 Hz, CF_3), –114.5 (m, 2F), –122.3 (m, 10F), –122.9 (m, 2F), –123.2 (m, 2F), –126.6 (m, 2F).

[14a][I]

^1H NMR ($CDCl_3$, ppm) δ: 0.87 (t, 9H, J = 6.8 Hz, CH_3), 1.33–1.19 (m, 24H, $(CH_2)_3(CH_2)_4CH_3)_3$), 1.58–1.43 (m, 12H $(CH_2(CH_2)_2(CH_2)_4CH_3)_3$), 2.62–2.50 (m, 8H, $PCH_2CH_2CF_2$ and $PCH_2(CH_2)_6CH_3$), 2.85–2.76 (m, 2H, PCH_2CH_2).

Results and discussion

Synthesis

The synthesis of the phosphonium ionic liquids involves the quaternization of an alkyl phosphine by a haloalkane in a S_N2 reaction (Scheme 1). A mixture of neat R_3P (R = ^{n}Bu, ^{n}Oct) and I-$(CH_2)_2R_{fn}$ at RT was slowly converted (48 h) to form viscous liquids or solids at RT. Phosphorus-31 NMR spectra of the resulting material indicated that there was complete consumption of the alkyl phosphine (δ (ppm): ^{n}Bu$_3$P = –32, ^{n}Oct = –35) to the quantitative formation of a single phosphorus-containing product with a chemical shift consistent with that of a phosphonium cation, 35 ppm (cf. ^{n}Bu$_4$P$^+$ δ = 32) (40). Excess I-$(CH_2)_2R_{fn}$ was removed in vacuo and the resulting material was purified, if necessary, by precipitation from concentrated CH_2Cl_2 solutions using *n*-hexane or by washing with *n*-pentane. Reaction times can be reduced to as little as 12 h by heating the neat mixtures to 80 °C or by adding polar solvents (THF, DMF; 10 mL) and heating to 60 to 80 °C; however, the resulting material was found to be of inferior purity.

It has been well-established that ionic liquids can be "tuned" to achieve a target property (e.g., viscosity, melting point, hydrophobicity, or hydrophilicity) by way of pairing different anions with a given cation. This is readily achieved via metathetical routes, using the appropriate Ag^+, Na^+, or Li^+ salts or Brønstead acids (Scheme 1). A facile anion exchange reaction with the sodium salts of PF_6^-, BF_4^-, OTs^- (OTs^- = tosylate; tolylsulphonate) or with the corresponding Brønstead acids HPF_6, HBF_4, HOTs or with trimethylsilyl (TMS) derivates TMS-OTf (OTf = triflate; trifluoromethanesulphonate) have provided access to a range of fluorinated phosphonium salts with varying anions.

Anion exchange reactions carried out by salt metathesis using Ag^+ salts of the desired anion ([A^-], where A = PF_6^-, BF_4^-, OTs^-, OTf^-) were successful; however, there was significant contamination of the resulting ionic liquid with [Ag][I], which could not be removed. A substantial quantity of [Ag][I] remained in the isolated ionic liquid, which would subsequently turn black upon exposure to light, in which the contamination is a consequence of its very low solubility in water (K_{sp} ([Ag][I]) = 8.51×10^{-17}) (41). Extraction of the CH_2Cl_2 solutions with distilled H_2O was found to be an integral step in ensuring that the resulting ionic liquids remain

[3] Supplementary data for this article are available on the journal Web site (http://canjchem.nrc.ca) or may be purchased from the Depository of Unpublished Data, Document Delivery, CISTI, National Research Council Canada, Ottawa, ON K1A 0R6, Canada. DUD 5162. For more information on obtaining material refer to http://cisti-icist.nrc-cnrc.gc.ca/irm/unpub_e.shtml. CCDC 640596 contain the crystallographic data for this manuscript. These data can be obtained, free of charge, via http://www.ccdc.cam.ac.uk/conts/retrieving.html (Or from the Cambridge Crystallographic Data Centre, 12 Union Road, Cambridge CB2 1EZ, UK; fax +44 1223 336033; or deposit@ccdc.cam.ac.uk).

© 2007 NRC Canada

Table 1. Summary of characterization data for **12–14**.

	Anion				
Cation	I^-	BF_4^-	PF_6^-	OTs^-	OTf^-
[**12a**]	Solid 1.11, 80 (323) [773]				
[**12b**]	Solid 0.82, 63 (423) [973]				
[**13a**]	Liquid 5.54, 97 (449) [1025]	Liquid 0.19, 83 [985]	Solid 0.20, 77 [1043]	Liquid 0.18, 68 [1069]	Liquid 3.53, 88 [1047]
[**13b**]	Solid 0.93, 56 (549) [1225]	Solid 0.15, 65 [1185]	Liquid 0.11, 43 [1244]	Liquid 0.17, 65 [1269]	Liquid 0.08, 31 [1247]
[**13c**]	Solid 1.48, 68 (749) [1625]	Solid 0.16, 65 [1585]	Solid 0.20, 80 [1643]	Solid 0.19, 70 [1669]	Liquid 0.12, 48 [1647]
[**14a**]	Solid 0.53, 52 (617) [1361]	Solid 0.12, 72 [1321]	Solid 0.21, 82 [1379]	Liquid 0.17, 63 [1405]	Liquid 0.25, 98 [1383]
[**14b**]	Solid 0.79, 76 (717) [1561]	Solid 0.10, 70 [1521]	Solid 0.19, 75 [1579]	Liquid 0.23, 88 [1605]	Liquid 0.24, 94 [1583]
[**14c**]	Solid 0.58, 41 (917) [1967]	Solid 0.55, 60 [1921]	Solid 0.21, 84 [1979]	Solid 0.14, 74 [2005]	Solid 0.06, 75 [1983]

Note: Second row contains yield (g, %); third row contains ESI MS, $[M^+ - A]$ in parenthesis () and $[M_2A^+]$ in brackets [].

free of the metathesis by-products (see later). Removing the residual [Ag][I] from the ionic liquid is possible via successive filtrations of a solution of the contaminated product through tightly packed Celite or silica gel columns. However, this is much more labour intensive and will reduce the overall yields appreciably.

Subsequent methodologies for anion exchange involving Brønstead acids, sodium salts, or trimethylsilyl derivatives were considerably more successful. A stoichiometric excess of an aqueous solution of a Brønstead acid containing the desired anion was added to a CH_2Cl_2 solution of the $[R_3PCH_2CH_2R_{fn}][I]$ forming a two-phase system, which was vigorously stirred for 24 h. Similarly, the corresponding sodium salt was added to a mixture of $[R_3PCH_2CH_2R_{fn}][I]$ in CH_2Cl_2 and stirred for 24 h. The sodium salt approach resulted in a NaI precipitate, which was filtered, and the CH_2Cl_2 solutions were extracted with water to remove any remaining NaI. Workup for the Brønstead acid method involved the separation of the organic layer followed by extraction with H_2O, which gave the desired $[R_3PCH_2CH_2R_{fn}][A]$ product in good yields. For all anion exchange methodologies, the absence of residual halide was confirmed by testing the aqueous wash layers with $AgNO_3$ (21). All materials that were subjected to an aqueous wash were dried at 100 °C for a minimum of 12 h.

Anion exchange via the sodium salts was more facile than using the corresponding Brønstead acid approach given that the precipitation and filtration of NaI removed the bulk of the unwanted metathesis by-product. Further extraction of any remaining NaI with water yielded a highly pure product (solubility of NaI = 1.84 g/mL in cold water) (42). Overall, the TMS-I elimination method (from the reaction of [**13–14**][I] with TMS-OTf) gave products with the greatest yields and purity, as minimal reaction workup was required. Identification of all phosphonium ionic liquid derivatives was confirmed by multinuclear NMR spectroscopy and ESI-MS. In all ESI mass spectra the free cation $[M^+ - A]$ and complex ions $[M_2A^+]$ (A = I^-, PF_6^-, BF_4^-, OTs^-, OTf^-) were positively identified (Table 1) and the absence of remaining phosphonium iodide or NaI were confirmed in both the positive and negative ion mode spectra.

Table 2. Karl–Fischer titration data for selected ionic liquid samples.

Sample	Run 1 av value (mmol/L)[a]	Run 2 av value (mmol/L)[b]
[**13a**][BF_4]	5.403	1.000
[**13b**][OTf]	1.204	0.574
[**14b**][PF_6]	0.500	0.700
[**14b**][Ts]	15.529	3.218
[**14b**][I]	14.592	4.030

[a]Test perfomed on samples that were exposed to the open atmosphere for several months.
[b]Values obtained from samples immediately after drying.

Contamination of the resulting ionic liquids by water is often an issue, given their hygroscopic nature, and this is an especially important consideration as moisture can degrade those derivatives that have BF_4^- or PF_6^- counteranions. After

© 2007 NRC Canada

Table 3. Glass transition points (T_g) or melting points (T_m) and decomposition onset temperatures (T_d) for compounds **12**–**14**.

	Anion				
Cation	I^-	BF_4^-	PF_6^-	OTs^-	OTf^-
[**12a**]	195[a], (305)				
[**12b**]	169[a], (328)				
[**13a**]	–25, (325)	–34, (334)	46[a], (304)	–47, (291)[b]	–45, (379)
[**13b**]	54[a], (295)	51[a], (320)	–30, (297)	–25, (300)	–37, (340)
[**13c**]	94[a], (331)	88[a], (339)	93[a], (312)	70[a], (316)	87[a], (382)
[**14a**]	49[a], (325)	58[a], (329)	71[a], (228)	–64, (296)	—, (353)
[**14b**]	52[a], (323)	63[a],(313)	89[a], (294)	36[a], (319)	–53, (353)
[**14c**]	56[a], (334)	68[a], (333)	92[a], (313)	32[a], (318)	37[a], (394)

Note: Onset of decomposition is considered to be when 98% of the original mass is remaining. The decomposition temperature is shown in parenthesis. All temperatures are given in °C.

[a] T_m

[b] The onset of decomposition when 97% of the original mass remained.

the synthesis, work-up, and drying of the material in vacuo, representative samples, which had been stored in the open air for several weeks after the initial drying process, were selected for Karl–Fischer titrations. The first KF analysis revealed relatively high water content in the range of 0.50 mmol/L ([**14b**][PF_6]) to 15.52 mmol/L ([**14b**][OTs]; Table 2, Run 1). Subsequently, the samples were dried in vacuo at 100 °C and re-analyzed, showing minimal water content (Table 2, Run 2). Multinuclear NMR analysis of these same samples did not indicate decomposition of the material upon sitting in the open atmosphere; however, they should be considered hygroscopic and stored in a dry environment, as the samples slowly take on water from the air.

Differential scanning calorimetry and thermogravimetric analysis

Critical to the classification of a material with a distinct cation–anion pair as an ionic liquid, is a characteristic melting point at or below 100 °C. The melting points (or glass transition temperatures) for compounds **12**–**14** were determined by differential scanning calorimetry (DSC). A vast majority of the ionic liquids were found to be low melting solids or viscous liquids and the melting–glass transition temperatures were observed over a wide temperature range (e.g., [**14a**][OTs]: –64 °C; [**12a**][I]: 195 °C) (Table 3).

Samples that were solids at RT displayed distinct melting peaks; conversely, products that were liquids at RT did not have observable melting curves, but rather exhibited glass transition signals at considerably lower temperatures (–64 to –25 °C). In the case of [**14a**][OTf] no melting or glass transition signals were observed despite many attempts at varying the conditions for obtaining a DSC trace. This is attributed to the melting–glass transition points being lower than –70 °C, which is outside of the range of our current instrumentation.

As expected, compounds [**12**][I] are high melting point solids as a result of the small size of the parent phosphine (PMe_3), which allows for efficient cation–anion packing arrangements. In general, as the alkyl chain length is increased (Me < ^{n}Bu < ^{n}Oct) along the iodide series, the melting points decrease. However, the melting point increases with increasing R_{fn} chain length for both the [**13**][I] and [**14**][I], which is attributed to the ordering of the cations into fluorophilic and fluorophobic regions.

The anion exchange products exhibit an interesting melting and glass transition temperature trend. The more weakly coordinating anions are expected to lower the melting points of the ionic liquids (7). However, this was not observed for the anion exchange products of the cations [**13**] or [**14**] paired with BF_4^- or PF_6^-. These clearly demonstrate that the melting point actually increases in comparison to the iodide analogues despite comparable anion sizes (I^- = 2.2 Å; BF_4^- = 2.2 Å; PF_6^- = 2.4 Å) (7). In contrast, the triflate and tosylate anions lowered the melting point of the ionic liquids substantially because of a combination of a large increase in anion size, charge delocalization, and the reduction in symmetry.

The negligible vapor pressures of phosphonium ionic liquids imply that they remain intact and stable upon heating until the upper thermal limit is obtained, at which point they primarily decompose through elimination pathways. The decomposition temperatures recorded were obtained at the onset of decomposition where 2% mass loss had occurred (Table 2). The decomposition temperatures measured in a dynamic heating environment are higher than those reported for nitrogen based ionic liquids and are in the range or slightly higher than those reported for other nonfluorinated systems (43).

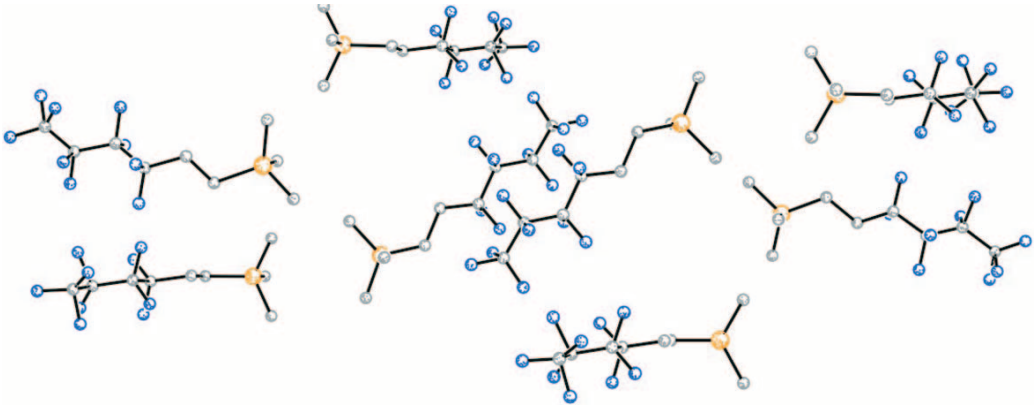
For [**12**–**14**][I], the decomposition temperatures increased with increasing length of the R_{fn} chain as the longer fluorous chains may increase steric hindrance, therefore promoting fluorophilic interactions and imposing higher decomposition points. In general, the stability of the ionic liquid is inversely proportional to the tendency to form stable R_{fn}-A decomposition products, and therefore the decomposition temperatures for the [**13**–**14**][A] series were higher for the more weakly coordinating anions OTf^- and OTs^- than they were for the smaller BF_4^- and PF_6^-, following the expected trends (7).

X-ray crystallography

By definition ionic liquids are low melting point salts; thus, obtaining solid-state structures by way of X-ray diffraction methodologies is not common. This presents difficulties in identifying the dominant interactions in bulk

© 2007 NRC Canada

Fig. 4. A section of the solid-state packing arrangement of [**12a**][I]. Ball and stick drawings have been used and iodide anions have been removed for clarity.



samples of these materials. In this regard, salts that contain cation **13** and **14** are generally liquids or soft waxes at RT, precluding the growth of crystalline materials suitable for X-ray diffraction studies. However, high melting point model compounds of **13** or **14** can be generated by using PMe_3 as the parent phosphine rather than $^{n}Bu_3P$ or $^{n}Oct_3P$. Single crystals of [**12a**][I] (Fig. 4) of sufficient quality for X-ray diffraction analysis were obtained. All other $[Me_3PCH_2CH_2R_{fn}][I]$ samples did not yield single crystals under similar conditions, only microcrystalline powders.

The solid-state structure of [**12a**][I] reveals the expected phosphonium cation with a distorted tetrahedral bonding arrangement about phosphorus with standard $P–C_{Methyl}$ single bond lengths for a trimethylphosphonium cation (1.766(6)–1.780(7) Å) as well as consistent $P–CH_2CH_2R_{fn}$ bond lengths, which are slightly longer (1.802(6) Å; relative to nonfluorinated alkyl C–P bonds) (44–48). The structure is best described as ionic, since the closest cation–anion interaction is an I···H contact at 2.917 Å. The most striking feature of the structure is the packing arrangement for the cation revealing a "head to head" (fluorophobic) and "tail to tail" (fluorophilic) arrangement, where the fluorous ponytails are associated with one another as are the methyl groups on phosphorus. This arrangement is imposed by the long fluorous chains and has previously been observed in highly fluorinated phosphines or in the solid-state structures of partially fluorinated compounds (49). In a bulk sample, it is likely that these are the dominant intermolecular interactions and have a strong influence on the physical properties of these materials.

Conclusions

Phosphonium ionic liquids containing fluorinated ponytails and varying degrees of fluorine content have been synthesized and comprehensively characterized. Efficient anion exchange can be achieved using metathetical routes; however, silver metathesis reagents should be avoided because of significant contamination of the residual AgI byproduct. Trimethylsilyl reagents were preferred as the metathesis was facile and the resulting ionic liquids were obtained in high yield and purity with a minimal workup. Investigating the properties of the series of compounds **12–14** demonstrated that varying the length of alkyl and fluorous chains in the cation influenced the melting and decomposition parameters of the ionic liquids. Increasing the alkyl chain length decreased the melting point, while increasing the length of the fluorous chains resulted in higher melting temperatures. The electron-withdrawing fluorous chains increased the stability of the ionic liquid, as did incorporating weakly coordinating anions.

Acknowledgement

We thank the Natural Science and Engineering Research Council of Canada (NSERC) and *The* University *of* Western Ontario for funding, Cytec Corporation for the generous gift of $^{n}Bu_3P$ and $^{n}Oct_3P$, Professor K.M. Baines for the use of DSC and TGA instrumentation, P. Rupar and Dr. E. Turner for their help on the acquisition of DSC and TGA data, D. Hairsine for the acquisition of mass spectrometry data, Y. Rambour for glassware fabrication, and for the many helpful comments from the referees.

References

1. P. Anastas and J.C. Warner. Green chemistry, theory and practice. Oxford University Press, New York. 1998.
2. J.H. Clark. Green Chem. **1**, 1 (1999).
3. T. Welton. Coord. Chem. Rev. **248**, 2459 (2004).
4. R. Sheldon. Chem. Commun. (Cambridge), 2399 (2001).
5. D.J. Cole-Hamilton. Science (Washington, DC), **299**, 1702 (2003).
6. R.D. Rogers and K.R. Seddon. Science (Washington, DC), **302**, 792 (2003).
7. P. Wasserscheid and T. Welton. Ionic liquids in synthesis. Wiley-VCH, Germany. 2003.
8. K.R. Seddon. J. Chem. Technol. Biotechnol. **68**, 351 (1997).
9. J.S. Wilkes. Green Chem. **4**, 73 (2002).
10. J.H. Davis, Jr. and P.A. Fox. Chem. Commun. (Cambridge), 1209 (2003).
11. Z.-B. Zhou, H. Matsumoto, and K. Tatsumi. Chem. Eur. J. **12**, 2196 (2006).
12. B.M. Quinn, Z. Ding, R. Moulton, and A. Bard. Langmuir, **18**, 1734 (2002).
13. J.D. Holbrey, N.V. Plechkova, and K.R. Seddon. Green Chem. **8**, 411 (2006).
14. H. Matsumoto, T. Matsuda, T. Tsuda, R. Hagiwara, Y. Ito, and Y. Miyazaki. Chem. Lett. **30**, 26 (2001).

© 2007 NRC Canada

15. K. Xu, M.S. Ding, and T.R. Jow. J. Electrochem. Soc. **148**, A267 (2001).
16. D.W. Armstrong, L.-K. Zhang, L. He, and M.L. Gross. Anal. Chem. **73**, 3679 (2001).
17. M. Zabet-Moghaddam, E. Heinzle, M. Lasaosa, and A. Tholey. Anal. Bioanal. Chem. **384**, 215 (2006).
18. T.L. Merrigan, E.D. Bates, S.C. Dorman, J.H. Davis, Jr. Chem. Commun. (Cambridge), 2051 (2000).
19. C. Emnet, K.M. Weber, J.A. Vidal, C.S. Consorti, A.M. Stuart, and J.A. Gladysz. Adv. Synth. Catal. **348**, 1625 (2006).
20. L. Berthon, S.I. Nikitenko, I. Bisel, C. Berthon, M. Faucon, B. Saucerotte, N. Zorz, and P. Moisy. Dalton Trans. 2526 (2006).
21. A. Cieniecka-Roslonkiewicz, J. Pernak, J. Kubis-Feder, A. Ramani, A.J. Robertson, and K.R. Seddon. Green Chem. **7**, 855 (2005).
22. C.J. Bradaric, A. Downard, A. Kennedy, C. Robertson, A.J. Zhou, Y. Green Chem. **5**, 143 (2003).
23. J. McNulty, A. Capretta, J. Wilson, J. Dyck, G. Adjabeng, and A.J. Robertson. Chem. Commun. (Cambridge), 1986 (2002).
24. N. Karodia, S. Guise, C. Newlands, and J.-A. Andersen. Chem. Commun. (Cambridge), 2341 (1998).
25. G.W. Parshall. J. Am. Chem. Soc. **94**, 8716 (1972).
26. J.F. Knifton. J. Mol. Catal. **43**, 65 (1987).
27. J. Kagimoto, K. Fukumoto, and H. Ohno. Chem. Commun. (Cambridge, U.K.), 2254 (2006).
28. G.-H. Tao, L. He, N. Sun, and Y. Kou. Chem. Commun. (Cambridge, U.K.), 3562 (2005).
29. H. Clavier, N. Audic, M. Mauduit, J.-C. Guillemin. Chem. Commun. (Cambridge), 2282 (2004).
30. N. Audic, H. Clavier, M. Mauduit, and J.-C. Guillemin. J. Am. Chem. Soc. **125**, 9248 (2003).
31. Q. Yao and Y. Zhang. Angew. Chem. Int. Ed. **42**, 3395 (2003).
32. Y. Gao, B. Twamley, and J.M. Shreeve. Inorg. Chem. **43**, 3406 (2004).
33. R. Balasubramanian, W. Wang, and R.W. Murray. J. Am. Chem. Soc. **128**, 9994 (2006).
34. (*a*) J. van den Broeke, F. Winter, B.-J. Deelman, and G. van Koten. Org. Lett. **4**, 3851 (2002). There are numerous patents that also incorporate fluorinated alkyl chains. Much of this literature involves fluorinated anions, fluorinated nitrogen-based cations, and one example of a phosphonium cation that contains a fluorinated alkyl chain well-removed from the phosphorus centre. (*b*) N. Ignatyev, U. Welz-Biermann, M. Heckmeier, G. Bissky, and H. Willner. Int. Patent WO 2006/128563 A1, 7 December 2006; (*c*) N. Ignatyev, U. Welz-Biermann, A. Kucheryna, and H. Willner. Int. Patent WO 2006/063655 A1 22 June 2006; (*d*) U. Welz-Biermann, N. Ignatyev, M. Weiden, U. Heider, A. Kucheryna, H. Willner, and P. Sartori. US Patent 7-202-379, 10 April 2007; (*e*) US Patent 2007/0026460 A1; (*f*) U. Heider, M. Schmidt, P. Sartori, N. Ignatev, and A. Kucherna. US Patent 6-582-849, 24 June 2003; (*g*) N. Ignatyev, M. Schmidt, A. Kuhner, V. Hilarius, U. Heider, A. Kucheryna, P. Sartori, and H. Willner. US Patent 7-094-328, 22 August 2006.
35. J.A. Gladysz. Science (Washington, DC), **266**, 55 (1994).
36. H. Xue and J.M. Shreeve. Eur. J. Inorg. Chem. 2573 (2005).
37. (*a*) C. Rocaboy, F. Hampel, and J.A. Gladysz. J. Org. Chem. **67**, 6863 (2002); (*b*) C.S. Consorti, M. Jurisch, and J.A. Gladysz. Org. Lett. **9**, 2309 (2007).
38. I.T. Horváth. Acc. Chem. Res. **31**, 641 (1998).
39. I.T. Horváth, G. Kiss, R.A. Cook, J.E. Bond, P.A. Stevens, J. Rábai, and E.J. Mozeleski. J. Am. Chem. Soc. **120**, 3133 (1998).
40. G.M. Kosolapoff and L. Maier. Organic phosphorus compounds. Vol. 2. John Wiley & Sons, Inc., Toronto. 1972.
41. C.E. Housecroft and A.G. Sharpe. Inorganic chemistry. Pearson Education Ltd., Toronto. 2001.
42. CRC Handbook of chemistry and physics. 58th ed. CRC Press, Inc., Cleveland. 1977.
43. W. Xie, R. Xie, W.-P. Pan, D. Hunter, B. Koene, L.-S. Tan, R. Vaia. Chem. Mater. **14**, 4837 (2002).
44. G. Kociok-Kohn, J.G. Winter, and A.C. Fillipou. Acta Crystallogr. Sect. C: Cryst. Struct. Commun. **55**, 351 (1999).
45. W. Clegg, A.J. Scott, F.J. Lawlor, N.C. Norman, T.B. Marder, C. Dai, and P. Nguyen. Acta Crystallogr. Sect. C: Cryst. Struct. Commun. **54**, 1875 (1998).
46. T.D. Getman, J.A. Krause, and S.G. Shore. Inorg. Chem. **27**, 2389 (1988).
47. J. Fawcett, E.G. Hope, R.D.W. Kemmitt, D.R. Paige, D.R. Russell, A.M. Stuart, D.J. Cole-Hamilton, and M.J. Payne. Chem. Commun. (Cambridge), 1127 (1997).
48. M.-A. Guillevic, A.M. Arif, I.T. Horváth, and J.A. Gladysz. Angew. Chem. Int. Ed. Engl. **36**, 1612 (1997).
49. P. Metrangolo, C. Prasang, G. Resnati, R. Liantonio, A.C. Whitwood, and D.W. Bruce. Chem. Commun. (Cambridge, U.K.), 3290 (2006).

© 2007 NRC Canada

Steady-state photolysis of dimesitylbis(trimethylsilyl)germane[1]

Krysten L. Hurni and Kim M. Baines

Abstract: The photolysis of dimesitylbis(trimethylsilyl)germane (**3**) in hexanes or THF, at low temperature, has been investigated as a potential method for the preparative-scale synthesis of tetramesityldigermene (**5**). A product mixture, consisting of hexamethyldisilane, mesitylene, 2-trimethylsilylmesitylene (**7**), a new germacyclobutene (**8**), and an unidentified polymer, was obtained. No evidence for the formation of tetramesityldigermene (**5**) was observed.

Key words: diaryldisilylgermane, digermene, germylene, germacyclobutene, photolysis.

Résumé : On a étudié la photolyse du dimésitylbis(triméthylsilyl)germane (**3**) dans les hexanes ou le THF, à de faibles températures, comme méthode potentielle de la synthèse à l'échelle préparative de tétramésityldigermène (**5**). On a obtenu un mélange de produits formé d'hexaméthyldisilane, de mésitylène, de 2-triméthylsilylmésitylène (**7**), d'un nouveau germacyclobutène (**8**) et d'un polymère non identifié. On n'a observé aucune formation du tétramésityldigermène (**5**).

Mots-clés : diaryldisilylgermane, digermène, germylène, germacyclobutène, photolyse.

[Traduit par la rédaction]

Introduction

Since the synthesis of the first solid digermene 30 years ago by Lappert et al. (1), followed six years later by the preparation of the first solution-stable digermene by Masamune et al. (2), several methods for the preparation of digermenes have been realized (3). These heavier alkene analogues are important not only because they are useful substrates for the preparation of a variety of organogermanium compounds, but also because they are the molecular analogues of the germanium dimers found on the Ge(100)-2 × 1 surface (3*i*). For some time, our research group has been extensively engaged in the study of the reactivity of digermenes (4). This, and the interest in the emerging applications of digermene chemistry (3*i*, 5), have continuously driven a need for the development of efficient routes for the preparation of digermenes.

In almost every review on digermene chemistry published since 1990, the preparation of tetraaryldigermenes by the irradiation of a diarylbis(trimethylsilyl)germane has been described as one of the primary methods for the synthesis of digermenes (Scheme 1) (3*a*–3*f*, 3*h*). An analogous method is frequently employed in the preparative-scale synthesis of a variety of disilenes (3*b*, 3*e*, 6); however, in the case of tetraaryldigermenes, the photolyses have, in general, only been carried out in a matrix at low temperature on an analytical scale. The presence of the digermene under these conditions has been inferred by the observation of appropriate signals by UV–vis or NMR spectroscopy (7*a*–7*e*). On one occasion, the photolysis of bis(2,4,6-triisopropylphenyl)bis(trimethylsilyl)germane was carried out at room temperature in solution for the subsequent preparation of an adduct of tetrakis(2,4,6-triisopropylphenyl)digermene; however, the adduct was isolated in very low yield (7*f*). The irradiation of diphenylbis(trimethylsilyl)germane (**1**) in solution at room temperature has been investigated, primarily as a source of diphenylgermylene (**2**) for kinetic studies (8); the synthesis of tetraphenyldigermene was not the goal of these studies. Although the generation of diphenylgermylene (**2**) was shown to be the primary reaction pathway followed in the steady-state photolysis of germane **1** at room temperature, the occurrence of other minor reaction pathways was noted (8*b*–8*c*). Similarly, dimesitylbis(trimethylsilyl)germane (**3**) has been investigated as a photochemical precursor of dimesitylgermylene (**4**) for solution-state kinetic studies (9). Both dimesitylgermylene (**4**) and tetramesityldigermene (**5**) were readily detected by UV–vis spectroscopy; however, the weakness of the absorptions precluded the use of germane **3** as an effective source of germylene **4** for kinetic measurements. To date, the viability of using the irradiation

Received 21 January 2007. Accepted 19 April 2007. Published on the NRC Research Press Web site at canjchem.nrc.ca on 7 June 2007.

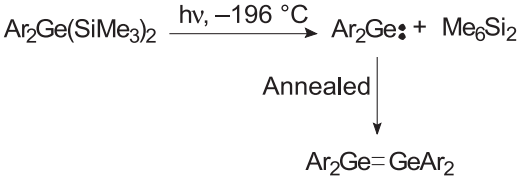
This article is dedicated to G. Michael Bancroft in recognition of his outstanding contributions not only to science and to Canada, but also to the Department of Chemistry at The University of Western Ontario.

K.L. Hurni and K.M. Baines.[2] Department of Chemistry, The University of Western Ontario, London, ON N6A 5B7, Canada

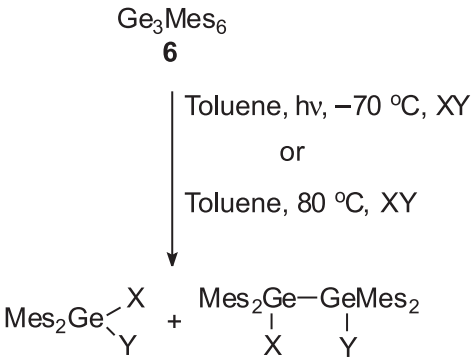
[1]This article is part of a Special Issue dedicated to Professor G. Michael Bancroft.
[2]Corresponding author (e-mail: kbaines2@uwo.ca).

 doi:10.1139/V07-039 © 2007 NRC Canada

Scheme 1.



Scheme 2.



of diarylbis(trimethylsilyl)germanes as a means for the preparation of practical quantities of a digermene has not been demonstrated.

Many of our studies on the reactivity of digermenes employ tetramesityldigermene (**5**) as the prototypical digermene (4). We generate digermene **5** either by thermolysis or by photolysis of hexamesitylcyclotrigermane (**6**) (10). A disadvantage of this method is the concomitant formation of an equivalent of dimesitylgermylene (**4**). In general, germylene **4** and digermene **5** are trapped during the course of the reaction, and the two products are separated by chromatography (Scheme 2) (4*c*). The irradiation of germane **3** as a possible route to tetramesityldigermene (**5**) is particularly attractive, since hexamethyldisilane is a volatile, relatively inert coproduct, which could easily be removed in vacuo from digermene **5** (or the products derived from it) at the end of the procedure. The formation of **5** could be determined either directly, using UV–vis or NMR spectroscopy, or indirectly, by the reaction with a well-known trapping reagent (e.g., methanol). We now report on the results of our investigations of this reaction on a preparative scale.

Results

A colourless solution of **3** was photolyzed (254 nm) at –70 °C for 24 h.[3] The product mixture obtained after removal of the solvent was quite complex. Similar results were obtained when either hexanes or THF were used as the solvent for the photolysis. In the early stages of the photolysis, the colourless solution became yellow and, by the end of the photolysis, the colour of the solution was orange. The crude product mixture was separated by preparative TLC. Five products were isolated, and four were unambiguously identified as mesitylene, 2-trimethylsilylmesitylene (**7**), germacyclobutene **8**, and hexamethyldisilane. An uncharacterized germanium-containing polymer was also obtained (Scheme 3). The relative ratios of the products were determined by GC analysis of the reaction mixture before exposure to air and are given in Table 1. A GC–MS of the headspace gas revealed no additional volatile products. Because of the difficulties encountered during the separation of and loss by evaporation of several products, we were unable to determine the isolated yields.[4] Hexamethyldisilane was identified as a component of the product mixture (prior to its removal in vacuo) by comparison of its ^{1}H chemical shift with that of an authentic sample. The relative amount of hexamethyldisilane could not be determined by GC, since it eluted with the solvent in the gas chromatogram; however, it

Scheme 3.

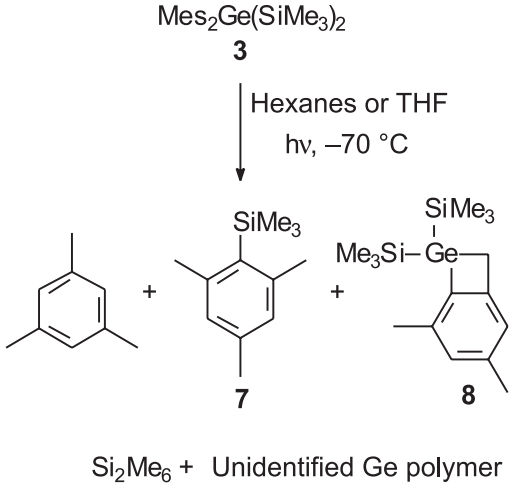


Table 1. Relative ratios of volatile products formed by irradiation of **3** for different time periods, as determined by GC.

Time (h)	Mesitylene	**7**	**8**	**10**	**11**	**3**
0.5[a]	12	2	14	n/a	n/a	72
1[a]	19	3	22	n/a	n/a	54
3[a]	37	7	44	n/a	n/a	12
6[a]	44	9	45	n/a	n/a	2
24[a]	55	11	33	n/a	n/a	0
48[a]	70	12	17	n/a	n/a	0
1[b]	4	6	6	n/a[c]	7	n/a[c]
5[b]	13	21	15	16	17	18
20[b]	21	23	21	17	17	0

Note: n/a: not applicable.
[a]Irradiation (254 nm) of **3** at –70 °C in hexanes.
[b]Irradiation (254 nm) of **3** at –70 °C in hexanes in the presence of 2,3-dimethylbutadiene.
[c]Germane **3** and germacyclopentene **10** initially co-elute in the gas chromatogram. Together, they account for 76%.

[3] Previous work from this laboratory has shown that tetramesityldigermene (**5**) rearranges to (trimesitylgermyl)mesitylgermylene between –70 °C and room temperature (4*a*, 4*b*, 4*e*).
[4] Mesitylene and hexamethyldisilane partially evaporate under ambient conditions. Complete loss of mesitylene occurs upon chromatography. 2-Trimethylsilylmesitylene (**7**) slowly evaporates after extended periods in vacuo.

© 2007 NRC Canada

could be determined by ^{1}H NMR spectroscopy prior to removal of the solvent.[5] Mesitylene was identified in the crude product mixture by ^{1}H NMR spectroscopy and by comparison of the GC retention time with that of an authentic sample. Compounds **7** and **8** could not be completely separated.

An authentic sample of 2-trimethylsilylmesitylene (**7**) was prepared by treatment of bromomesitylene with BuLi, followed by the addition of trimethylsilyl chloride, a variation on the published procedure (11). Thus, **7** was unambiguously identified in the mixture by comparison of the ^{1}H NMR spectroscopic data and of the GC retention time with that of the prepared authentic sample.

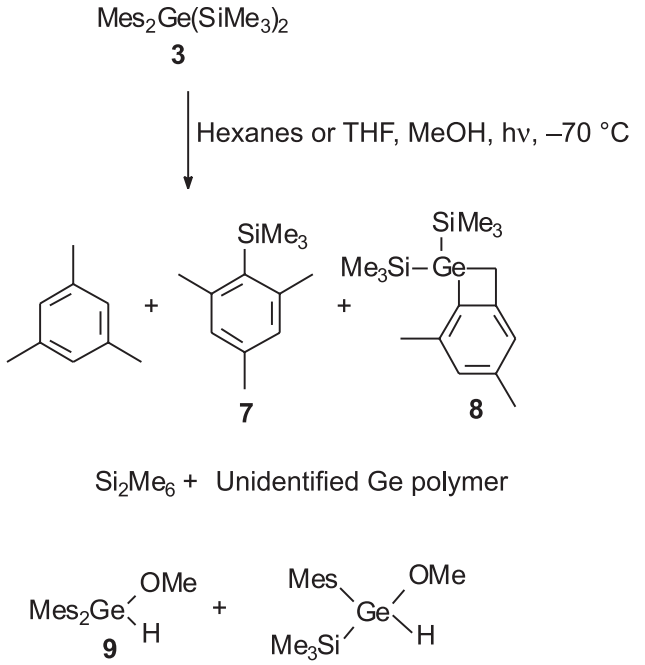
The ^{1}H NMR spectrum of germacyclobutene **8** contained six signals: a singlet at 0.23 ppm assigned to two equivalent trimethylsilyl groups, two singlets (6.85 and 6.70 ppm) assigned to two aryl-*H*'s, and three singlets at 2.19, 2.23, and 2.52 ppm, which were consistent with the presence of two CH_3–Ar groups and a CH_2 group, respectively. Clearly, the mesityl group is no longer symmetric. The ^{1}H–^{29}Si *g*HMBC spectrum of **8** displayed a correlation between the signal assigned to the trimethylsilyl groups in the ^{29}Si dimension and the signal assigned to the CH_2 group in the ^{1}H dimension. The highest-mass ion was located at *m*/*z* 338 in the mass spectrum of **8**. Moreover, the precise mass of *m*/*z* 338 agrees well with the calculated mass of **8**. The structure of **8** is completely consistent with the spectroscopic data.

The relative amount of germacyclobutene **8** in the product mixture varied greatly depending on the length of the irradiation time. The photolysis of germane **3** was monitored hourly by GC; a steady increase in the relative amounts of mesitylene, **7**, and **8** was observed as **3** was consumed, up to a given time period. Interestingly, prolonged irradiation of the sample (24 h) led to a reduction in the relative amount of **8** and an increase in the relative amount of mesitylene (Table 1). Photolysis of a mixture of **7** and **8**, isolated from the reaction mixture, showed complete loss of germacyclobutene **8** by ^{1}H NMR spectroscopy and the appearance of mesitylene by GC, while **7** remained unchanged. Thus, germacyclobutene **8** is photolytically unstable and decomposes to produce mesitylene and other unidentified, nonvolatile products.

A yellow solid precipitated from the crude product mixture (exposed to air) upon the addition of methanol. The signals in the ^{1}H NMR spectrum of this solid were very broad. The chemical shifts of the signals were consistent with the presence of both mesityl groups and trimethylsilyl groups. The same material was also isolated by chromatography from the product mixture in yields of 10–20 wt%. Elemental analysis of the solid by Energy Dispersive X-ray analysis (EDX) confirmed the presence of germanium and silicon in the sample. These observations are consistent with the formation of a polymer, which has been tentatively assigned the structure $(GeR_2)_n$ (R = Mes, Me_3Si).

Photolysis of germane **3** at 10 °C produced the same products in approximately the same ratios. Mes_2GeH_2 was also identified in trace amounts based on a comparison of the GC retention time and the ^{1}H NMR chemical shifts with those of an authentic sample (12).

Scheme 4.



The addition of methanol to the reaction solution (prior to exposure to the ambient atmosphere) at low temperature or at room temperature led to the production of trace amounts of dimesitylmethoxygermane (**9**), identified by comparison of the ^{1}H chemical shifts with the published data (13). No evidence for the formation of the methanol adduct of digermene **5**, ($Mes_2Ge(OMe)GeHMes_2$), and hence, no evidence for the formation of digermene **5** was observed. Co-photolysis of germane **3** with methanol also produced methoxygermane **9** in low yield in addition to mesitylmethoxy(trimethylsilyl)germane, identified by GC–MS analysis (Scheme 4).

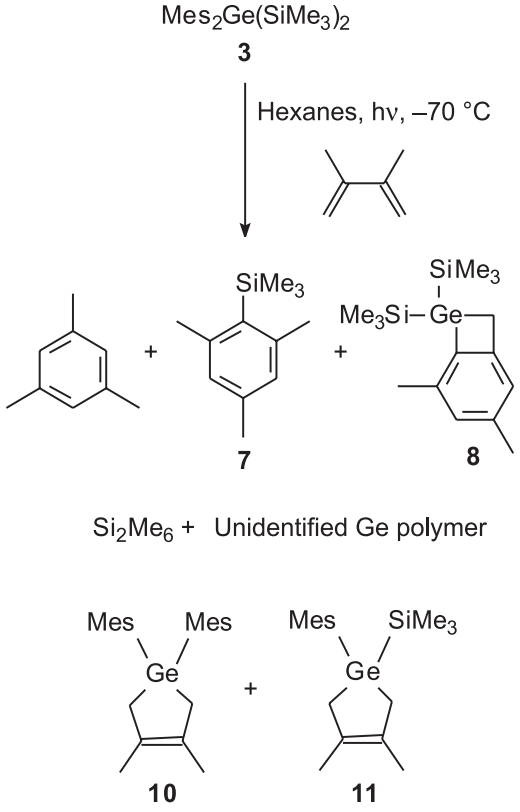
In an attempt to trap any transient germylenes, germane **3** was co-photolyzed with 2,3-dimethylbutadiene, a well-known and efficient trapping agent for germylenes (8*b*, 14, 15). The solution remained clear and colourless throughout the entire irradiation. The resulting product mixture contained both 1,1-dimesityl-3,4-dimethyl-1-germacyclopent-3-ene (**10**) and 1-mesityl-3,4-dimethyl-1-(trimethylsilyl)-1-germacyclopent-3-ene (**11**) in addition to the previously observed products (Scheme 5). There was also a noticeable increase in the relative amount of **7** produced under these conditions (Table 1).

Germacyclopentene **10** was identified by comparison of the GC retention time and the ^{1}H NMR chemical shifts with those of an authentic sample (4*b*, 16). Germacyclopentene **11** was characterized by NMR spectroscopy and mass spectrometry as part of a mixture of **11** with trace amounts of **7** and **8**. The most diagnostic feature of the ^{1}H NMR spectrum of **11** is the two sets of doublets at 1.90 and 2.23 ppm, as-

[5] Supplementary data for this article are available on the journal Web site (canjchem.nrc.ca) or may be purchased from the Depository of Unpublished Data, Document Delivery, CISTI, National Research Council Canada, Ottawa, ON K1A 0S2, Canada. DUD 5172. For more information on obtaining material, refer to http://cisti-icist.nrc-cnrc.gc.ca/irm/unpub_e.shtml.

© 2007 NRC Canada

Scheme 5.



signed to the non-equivalent ^{1}H's of the CH_2 groups. A correlation was observed between these two signals in the ^{1}H dimension of the ^{13}C–^{1}H *g*HSQC spectrum of **11** and one signal in the ^{13}C dimension at 27.59 ppm. The ^{1}H–^{1}H *g*COSY spectrum of **11** revealed a correlation between the signals assigned to the CH_2 groups and the signal assigned to equivalent methyl groups, consistent with the structure of **11**. The mass spectrum of one component of the crude product mixture (separated by GC) exhibited a highest-mass ion at *m*/*z* 347, corresponding to the molecular ion of **11**. Furthermore, the precise mass determination of *m*/*z* 347 agrees with the calculated precise mass of **11**.

Discussion

Clearly, a quick evaluation of the results shows that germane **3** is not a clean source of germylene **4**, and thus, is not a viable precursor for the preparation of digermene **5**. The results can be better understood if we consider the previous report of the steady-state irradiation of the corresponding phenyl derivative, diphenylbis(trimethylsilyl)germane (**1**) (8*c*). Co-photolysis of **1** with 2,3-dimethylbutadiene resulted in the formation of germacyclopentenes **12** (major product) and **13** (minor product) in addition to hexamethyldisilane and trimethylsilylbenzene (Scheme 6) (8*c*). The products are believed to be formed by extrusion of either diphenylgermylene (**2**) or phenyl(trimethylsilyl)germylene, with the concomitant formation of the disilane or arylsilane, respectively, followed by addition of the germylene to the diene (8*c*). Examination of the structures of the products formed during the photolyses of both **1** and **3** in the presence of the diene reveals many similarities. The structures of compounds **10** and **11** are analogous to those of compounds **12** and **13**. Hexamethyldisilane and an aryltrimethylsilane were observed in both reactions. Although the formation of mesitylene is observed during the irradiation of **3**, benzene was not reported as a product of the photolysis of **1**. Not surprisingly, an analogous compound to germacyclobutene **8** was not formed during the photolysis of **1**. Since dienes are known triplet quenchers, and thus, may suppress radical formation (8*c*), the co-photolysis of germane **1** with methanol was also examined. The formation of both methoxydiphenylgermane (**14**) and 1,1,2,2-tetraphenylbis(trimethylsilyl)digermane (**15**) was observed under these conditions in addition to other unidentified products (Scheme 6). Germane **14** was believed to be formed by the insertion of germylene **2** into the OH bond of methanol. On the other hand, the formation of digermane **15** was rationalized by the coupling of two $Ph_2(Me_3Si)Ge$ radicals, which result from the homolysis of a Ge–Si bond (8*c*). An analogous digermane was not observed by ^{1}H NMR spectroscopy or GC–MS upon the photolysis of germane **3** in the presence of methanol. The photolysis of germane **1** in the absence of a trapping agent was not examined.

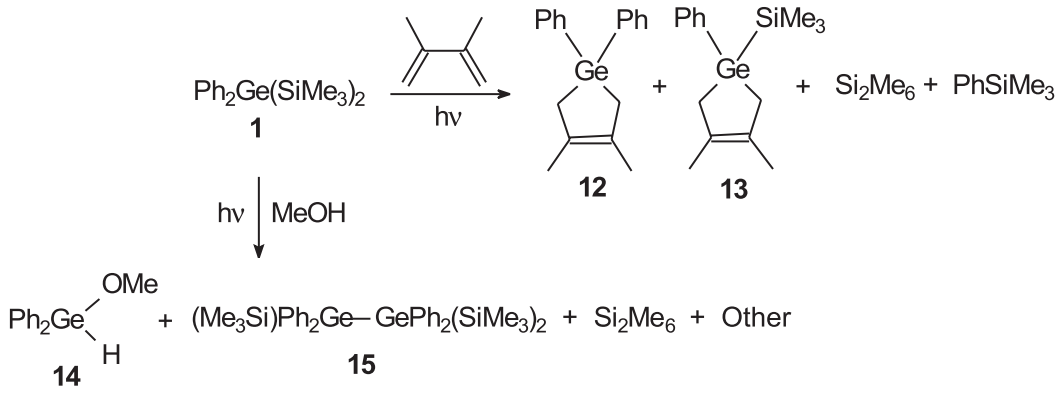
On the basis of the relative amounts of hexamethyldisilane and **7** formed, the extrusion of a germylene from **3** appears to be a minor reaction pathway. We propose a radical-based mechanism to explain the formation of germacyclobutene **8** from the irradiation of dimesitylbis(trimethylsilyl)germane (**3**). Homolysis of the Ge–Mes bond produces a germyl and a mesityl radical. Abstraction of a benzylic hydrogen by the mesityl radical results in the formation of a benzylic radical and mesitylene. Germacyclobutene **8** is reasonably formed by ring closure of the resulting 1,4-biradical (Scheme 7). We note that, at low conversions, mesitylene and **8** are formed in approximately equal amounts, consistent with this proposal (Table 1). To provide some evidence for the proposed mechanism, **3** was irradiated for 5 h in THF-d_8. After irradiation, THF-d_8 was removed and replaced with C_6H_6. A signal at 6.71 ppm, which we attribute to 1,3,5-$(CH_3)_3C_6H_2D$, was observed in the ^{2}H NMR spectrum of the product. The formation of the deuterated mesitylene is consistent with a cage-escaped mesityl radical, which, at least to some extent, abstracts a deuterium from the solvent. We acknowledge that the mesityl radical may result from homolysis of the Ge–Mes bond of **3** or during the secondary photolysis of **8**.

On the other hand, homolysis of the Ge–Si bond could produce a trimethylsilyl and a germyl radical. By following a similar reaction pathway, the formation of germylenes **4** and **16** in addition to **7** and hexamethyldisilane can be accounted for. However, the formation of hexamethyldisilane and **7** by concerted elimination of **4** or **16** is also plausible (Scheme 8) and, perhaps, more likely given that the relative amount of **7** increased when 2,3-dimethylbutadiene was used as a trapping agent.

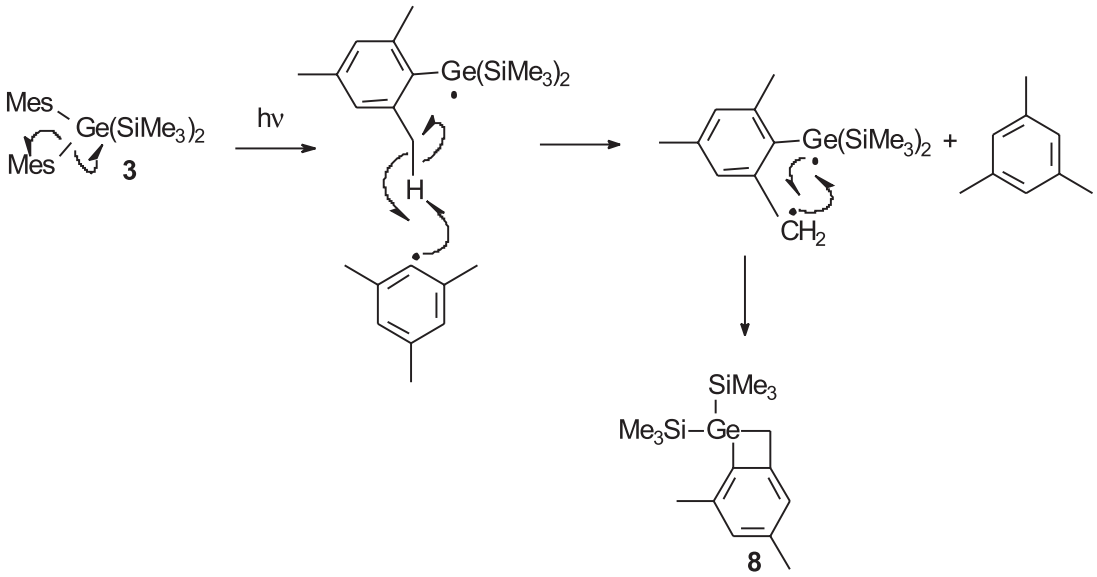
Photolysis of germane **3** in the presence of either 2,3-dimethylbutadiene or methanol gives **10** and **11** or **9**, respectively. This provides convincing evidence for the formation of germylenes **4** and **16** during the reaction. In the absence of a germylene trap, the germylenes may indeed couple to produce digermenes. However, under the given reaction con-

© 2007 NRC Canada

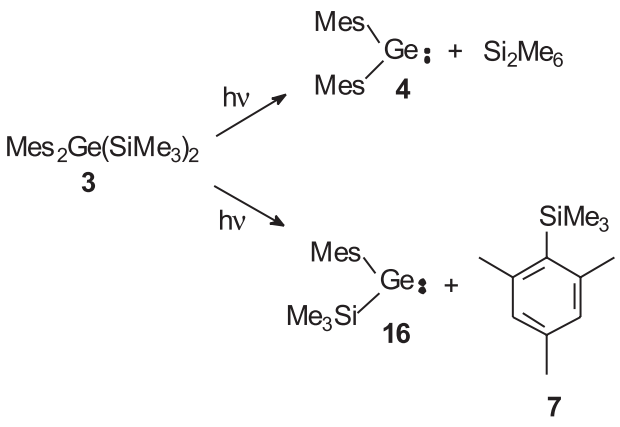
Scheme 6.



Scheme 7.



Scheme 8.



ditions, any digermenes formed apparently polymerize, yielding a germanium-based polymer.

Clearly, our results indicate that the steady-state photolysis of germane **3** in solution is not a feasible route for the preparation of synthetic quantities of digermene **5**. The results were somewhat surprising, given the commonly held belief that the photolysis of diarylbis(trimethylsilyl)germanes is a useful method for the preparation of tetraaryldigermenes. However, our results appear reasonable, given that the observed products of the steady-state solution photolyses of diphenylbis(trimethylsilyl)germane (**1**) demonstrated that cleavage of the germanium–phenyl bond was occurring, at least to some extent, during irradiation, since products, formally derived from phenyl(trimethylsilyl)germylene, were isolated (8*b*, 8*c*). Previous studies of the photolysis of dimesitylbis(trimethylsilyl)germane (**3**), in which both dimesitylgermylene (**4**) and tetramesityldigermene (**5**) were characterized by UV–vis spectroscopy, showed no evidence for the formation of additional products or alternate reaction pathways (7*b*–7*e*, 9). It is unlikely that the absorptions originally assigned to the germylene **4** and digermene **5** are erroneous, as has been shown in the diphenyl case (8*c*, 15), since the assignments for the mesityl system, both in a matrix and in solution, have been corroborated in at least three independent studies (7*b*–7*d*, 9, 17). Possibly, at the low conversions used in the previous experiments, the absorptions of potential radical species could not be observed and (or) are too weak to be observed.

The low yields of germacyclopentenes **10** and **11** obtained

© 2007 NRC Canada

during the photolysis of **3** in the presence of 2,3-dimethylbutadiene are most likely due to secondary photolysis of the germacyclopentene rings (17). However, even at low conversion, the irradiation still yields only relatively low ratios of **10** and **11** (Table 1). Unfortunately, there are few reagents that are known to react quickly with dimesitylgermylene (**4**) under photolytic conditions to give a stable product, and thus, we were limited in our selection of germylene trapping agents.

In summary, the steady-state irradiation of germane **3** in solution is not a feasible route for the preparation of practical quantities of tetramesityldigermene (**5**), contrary to what may be expected based on the numerous reviews written on digermene chemistry (3). Thus, for tetramesityldigermene (**5**), the thermolysis or photolysis of hexamesitylcyclotrigermane (**6**) continues to be the best method for the preparation of this useful digermene. We are continuing our search for alternate large-scale, practical syntheses of tetramesityldigermene (**5**).

Experimental

General details

Unless otherwise indicated, all reactions were carried out in flame-dried glassware under an inert atmosphere of argon using a dual manifold vacuum line or prepared under a nitrogen atmosphere using an MBraun Labmaster 130 glovebox. THF and hexanes were purged with nitrogen and then passed through an alumina column (Innovative Technology Inc., Newburyport, Massachusetts) prior to use. Trimethylsilyl chloride was distilled from calcium hydride prior to use. 2,3-Dimethylbutadiene, BuLi, and 1-bromo-2,4,6-trimethylbenzene were purchased from the Aldrich Chemical Co. and used without further purification. Chromatography was carried out on conventional silica-gel preparative plates. Dimesitylbis(trimethylsilyl)germane (**3**) was prepared according to the previously reported procedure (7*d*).

NMR spectra were recorded on a Varian Mecury 400, a Varian Inova 400, or a Varian Inova 600 NMR spectrometer. The standards used were as follows: residual C_6D_5H (7.15 ppm) for ^{1}H NMR spectra, C_6D_6 central transition (128.00 ppm) for ^{13}C NMR spectra, and Me_4Si as an external standard (0.00 ppm) for ^{29}Si spectra. Mass spectra were recorded on a Finnegan MAT model 8400 mass spectrometer with an ionizing voltage of 70 eV (reported in mass-to-charge units (*m*/*z*) with ion identity and intensity relative to the base peak in parentheses). GC analyses were performed on a polydimethylsiloxane column using an Agilent 6850 Series GC. Photolyses were performed at 254 nm using a Rayonet Photochemical Reactor (Southern New England Co.) typically equipped with 10 bulbs. Samples were cooled by circulating methanol through a vacuum-jacketed quartz immersion well using an Endocal model ULT–70 low-temperature external bath circulator.

Photolysis of dimesitylbis(trimethylsilyl)germane (3)

A clear, colourless solution of germane **3** (100 mg, 0.219 mmol), dissolved in hexanes or THF (8 mL), was placed in a quartz Schlenk tube fitted with a septum. The solution was photolyzed at –70 °C for 24 h; the colour of the solution changed from light yellow to deep orange during the photolysis and reverted to yellow when the solution was warmed to room temperature. Gas chromatograms of both the reaction mixture and the headspace gas were recorded prior to exposure to the ambient atmosphere. In some reactions, methanol was added to the solution either at room temperature or in the cold (dry ice – acetone bath). The solvent was removed by rotary evaporation, yielding a yellow oil. Hexamethyldisilane and mesitylene were removed in vacuo. The resulting crude mixture was purified by preparative TLC (silica gel; hexanes) to give a polymer as a yellow solid and a liquid mixture of **7** (11) and **8**.[5]

2-Trimethylsilylmesitylene (7)

^{1}H NMR (C_6D_6) δ: 6.73 (s, 2H, Mes CH), 2.34 (s, 6H, Mes *o*-CH_3), 2.12 (s, 3H, Mes *p*-CH_3), 0.34 (s, 9H, $Si(CH_3)_3$). ^{13}C NMR (C_6D_6) δ: 144.12 (*o*-MesC), 138.34 (*p*-MesC), 132.90 (*i*-MesC), 129.48 (Mes CH), 24.86 (Mes *o*-CH_3), 20.89 (Mes *p*-CH_3), 3.67 ($Si(CH_3)_3$). ^{29}Si NMR (C_6D_6) δ: –6.1 ($Si(CH_3)_3$). GC–MS (*m*/*z*): 192 (M^+, 25), 177 ($M^+ - CH_3$, 100), 162 ($M^+ - (CH_3)_2$, 12), 149 ($M^+ - SiCH_3$, 10), 119 (Mes, 4), 73 ($Si(CH_3)_3$, 5).

1,1-Bis(trimethylsilyl)-4,6-dimethyl-1-germadihydrobenzocyclobutene (8)

^{1}H NMR (C_6D_6) δ: 6.85 (s, 1H, CH), 6.70 (s, 1H, CH), 2.52 (s, 2H, $GeCH_2$), 2.23 (s, 3H, 6-CH_3), 2.19 (s, 3H, 4-CH_3), 0.23 (s, 18H, $Si(CH_3)_3$). ^{13}C NMR (C_6D_6) δ: 153.77 (CH_2–*C*), 140.59 (CH_2–Ge–*C*), 140.04 (6-CH_3*C*), 138.16 (4-CH_3*C*), 128.29 (5-CH), 124.96 (3-CH), 21.84 (4-CH_3), 21.45 (6-CH_3), 13.69 (CH_2), 0.20 ($Si(CH_3)_3$). ^{29}Si NMR (C_6D_6) δ: –7.3 ($Si(CH_3)_3$). GC–MS (*m*/*z*): 338 (M^+ ^{74}Ge, 25), 323 ($M^+ - CH_3$, 30), 265 ($M^+ - Si(CH_3)_3$, 37), 249 ($M^+ - Si(CH_3)_3 - CH_2$, 15), 73 ($Si(CH_3)_3$, 100). Exact mass calcd. for $C_{15}H_{28}{}^{70}Ge^{28}Si_2$: 334.0973; found: 334.0979.

Co-photolysis of dimesitylbis(trimethylsilyl)germane (3) with 2,3-dimethylbutadiene

A clear, colourless solution of germane **3** (100 mg, 0.219 mmol) and 2,3-dimethylbutadiene (0.1 mL, excess), dissolved in hexanes (8 mL), was irradiated at –70 °C for 24 h. The solution remained clear and colourless throughout the irradiation. The solvent was removed by rotary evaporation to yield a clear, slightly yellow liquid. The crude product mixture was separated by chromatography (silica gel; hexanes) to give a polymer, germacyclopentene **10**, and a mixture of **7**, **8**, and **11**.[5] Compounds **7**, **8**, and **11** were further separated from the mixture using preparative TLC (silica gel; hexanes). Compound **7** was removed under high vacuum to give **11**, which remained contaminated with small amounts of **8**.

1-Mesityl-3,4-dimethyl-1-(trimethylsilyl)-1-germacyclopent-3-ene (11)

^{1}H NMR (C_6D_6) δ: 6.80 (s, 2H, Mes CH), 2.30 (s, 6H, Mes *o*-CH_3), 2.23 (d, 2H, C*H*H, *J* = 15 Hz), 2.17 (s, 3H, Mes *p*-CH_3), 1.90 (d, 2H, CH*H*, *J* = 15 Hz), 1.75 (s, 6H, CH_3), 0.13 (s, 9H, $Si(CH_3)_3$). ^{13}C NMR (C_6D_6) δ: 142.95 (*o*-Mes C), 137.39 (*p*-Mes C), 135.75 (*i*-Mes C), 131.04 (C=C), 128.44 (Mes CH), 27.59 (CH_2), 24.83 (Mes *o*-CH_3), 21.05 (Mes *p*-CH_3), 19.32 (CH_3), –1.07 ($Si(CH_3)_3$). ^{29}Si NMR (C_6D_6) δ: –10.9 ($Si(CH_3)_3$). EI-MS (*m*/*z*): 348 (M^+ ^{74}Ge,

© 2007 NRC Canada

14), 266 ($M^+ - C_6H_{10}$, 44), 193 ($Mes^{74}Ge$, 28), 177 (Mes $Si(CH_3)_2$, 100), 119 (Mes, 8), 73 ($Si(CH_3)_3$, 36). Exact mass calcd. for $C_{18}H_{30}{}^{70}Ge^{28}Si$: 344.1360; found: 344.1366.

Acknowledgements

We thank the Natural Sciences and Engineering Research Council of Canada (NSERC), The University of Western Ontario, and the Ontario Photonics Consortium (OPC) for financial support. We also thank Teck Cominco Ltd. for a generous gift of $GeCl_4$. Finally, we also thank a referee for a useful suggestion.

References

1. P.J. Davidson, D.H. Harris, and M.F. Lappert. J. Chem. Soc., Dalton Trans. 2268 (1976).
2. S. Masamune and Y. Hanzawa. J. Am. Chem. Soc. **104**, 6136 (1982).
3. For reviews on digermene chemistry, see: (*a*) J. Barrau, J. Escudié, and J. Satgé. Chem. Rev. **90**, 283 (1990); (*b*) T. Tsumuraya, S.A. Batcheller, and S. Masamune. Angew. Chem., Int. Ed. Engl. **30**, 902 (1991); (*c*) J. Escudié, C. Couret, H. Ranaivonjatovo, and J. Satgé. Coord. Chem. Rev. **130**, 427 (1994); (*d*) K.M. Baines and W.G. Stibbs. Adv. Organomet. Chem. **39**, 275 (1996); (*e*) M.A. Chaubon, H. Ranaivonjatovo, J. Escudié, and J. Satgé. Main Group Met. Chem. **19**, 145 (1996); (*f*) J. Escudié and H. Ranaivonjatovo. Adv. Organomet. Chem. **44**, 113 (1999); (*g*) M. Weidenbruch. Eur. J. Inorg. Chem. 373 (1999); (*h*) N. Tokitoh and R. Okazaki. *In* The Chemistry of organic germanium, tin, and lead compounds. Vol. 2. *Edited by* Z. Rappoport. John Wiley and Sons Ltd., Chichester. 2002. p. 843; (*i*) J.M. Buriak. Chem. Rev. **102**, 1271 (2002); (*j*) M. Weidenbruch. Organometallics, **22**, 4348 (2003).
4. (*a*) K.M. Baines, J.A. Cooke, and J.J. Vittal. J. Chem. Soc., Chem. Commun. 1484 (1992); (*b*) K.M. Baines, J.A. Cooke, C.E. Dixon, H.W. Liu, and M.R. Netherton. Organometallics, **13**, 631 (1994); (*c*) C.E. Dixon, H.W. Liu, C.M. Vander Kant, and K.M. Baines. Organometallics, **15**, 5701 (1996); (*d*) C.E. Dixon, J.A. Cooke, and K.M. Baines. Organometallics, **16,** 5437 (1997); (*e*) C.E. Dixon, M.R. Netherton, and K.M. Baines. J. Am. Chem. Soc. **120**, 10365 (1998); (*f*) M.S. Samuel, M.C. Jennings, and K.M. Baines. J. Organomet. Chem. **636**, 130 (2001); (*g*) M.S. Samuel, M.C. Jennings, and K.M. Baines. Organometallics, **20**, 590 (2001); (*h*) K.L. Fujdala, D.W.K. Gracey, E.F. Wong, and K.M. Baines. Can. J. Chem. **80**, 1387 (2002); (*i*) M.S. Samuel and K.M. Baines. J. Am. Chem. Soc. **125**, 12702 (2003).
5. (*a*) R.J. Hamers, S.K. Coulter, M.D. Ellison, J.S. Hovis, D.F. Padowitz, M.P. Schwartz, C.M. Greenlief, and J.N. Russell, Jr. Acc. Chem. Res. **33**, 617 (2000); (*b*) Q.-S. Li, R.-H. Lu, Y. Xie, and H.F. Schaefer, III. J. Comput. Chem. **23**, 1642 (2002); (*c*) R. Miotto, R.H. Miwa, and A.C. Ferraz. Phys. Rev. B: Condens. Matter, **68**, 115436 (2003); (*d*) Y.-J. Xu, Y.-F. Zhang, and J.-Q. Li. J. Phys. Chem. B, **110**, 3197 (2006); (*e*) M.A. Filler, J.A. van Deventer, A.J. Keung, and S.F. Bent. J. Am. Chem. Soc. **128**, 770 (2006); (*f*) J.-H. Cho, K.S. Kim, and Y. Morikawa. J. Chem. Phys. **124**, 024716 (2006).
6. (*a*) R. West. Angew. Chem., Int. Ed. Engl. **26**, 1201 (1987); (*b*) M. Weidenbruch. Coord. Chem. Rev. **130**, 275 (1994); (*c*) T.L. Morkin, T.R. Owens, and W.J. Leigh. *In* The chemistry of organic silicon compounds. Vol. 3. *Edited by* Z. Rappoport and Y. Apeloig. John Wiley and Sons Ltd., Chichester. 2001. p. 949; (*d*) K.M. Baines and M.S. Samuel. *In* Science of synthesis. Vol. 4. *Edited by* I. Fleming. Georg Thieme Verlag, Stuttgart. 2002. p. 117; (*e*) M. Kira. J. Organomet. Chem. **689**, 4475 (2004); (*f*) H. Ottosson and P.G. Steel. Chem. Eur. J. **12**, 1576 (2006).
7. (*a*) S. Collins, S. Murakami, J.T. Snow, and S. Masamune. Tetrahedron Lett. **26**, 1281 (1985); (*b*) W. Ando, T. Tsumuraya, and A. Sekiguchi. Chem. Lett. 317 (1987); (*c*) W. Ando, H. Itoh, T. Tsumuraya, and H. Yoshida. Organometallics, **7**, 1880 (1988); (*d*) W. Ando and T. Tsumuraya. Organometallics, **8**, 1467 (1989); (*e*) W. Ando, H. Itoh, and T. Tsumuraya. Organometallics, **8**, 2759 (1989); (*f*) T. Tsumuraya, S. Sato, and W. Ando. Organometallics, **9**, 2061 (1990).
8. (*a*) S. Konieczny, S.J. Jacobs, J.K. Braddock Wilking, and P.P. Gaspar. J. Organomet. Chem. **341**, C17 (1988); (*b*) K.L. Bobbitt, V.M. Maloney, and P.P. Gaspar. Organometallics, **10**, 2772 (1991); (*c*) C.R. Harrington, W.J. Leigh, B.K. Chan, P.P. Gaspar, and D. Zhou. Can. J. Chem. **83**, 1324 (2005).
9. N.P. Toltl, W.J. Leigh, G.M. Kollegger, W.G. Stibbs, and K.M. Baines. Organometallics, **15**, 3732 (1996).
10. W. Ando and T. Tsumuraya. J. Chem. Soc., Chem. Commun. 770 (1989).
11. (*a*) C. Eaborn and R.C. Moore. J. Chem. Soc. 3640 (1959); (*b*) H.J. Sipe, Jr. and R. West. J. Organomet. Chem. **70**, 367 (1974).
12. (*a*) P. Rivière, M. Rivière-Baudet, and J. Satgé. *In* Organometallic syntheses, Vol. 4. *Edited by* R.B. King and J.J. Eisch. Elsevier, New York. 1988. p. 545; (*b*) J.A. Cooke, C.E. Dixon, M.R. Netherton, G.M. Kollegger, and K.M. Baines. Synth. React. Inorg. Met.-Org. Chem. **26**, 1205 (1996).
13. (*a*) M. Lazraq, J. Escudié, C. Couret, J. Satgé, and M. Soufiaoui. J. Organomet. Chem. **387**, 1 (1990); (*b*) K.M. Baines and J.A. Cooke. Organometallics, **10**, 3419 (1991).
14. (*a*) J. Satgé, M. Massol, and P. Rivière. J. Organomet. Chem. **56**, 1 (1973); (*b*) P. Rivière, J. Satgé, and D. Soula. J. Organomet. Chem. **63**, 167 (1973); (*c*) W.P. Neumann and M. Schriewer. Tetrahedron Lett. **21**, 3273 (1980); (*d*) M. Schriewer and W.P. Neumann. J. Am. Chem. Soc. **105**, 897 (1983); (*e*) N. Tokitoh and R. Okazaki. Coord. Chem. Rev. **210**, 251 (2000).
15. W.J. Leigh and C.R. Harrington. J. Am. Chem. Soc. **127**, 5084 (2005)
16. P. Rivière, A. Castel, and J. Satgé. J. Organomet. Chem. **232**, 123 (1982).
17. W.J. Leigh, C.R. Harrington, and I. Vargas-Baca. J. Am. Chem. Soc. **126**, 16105 (2004).

© 2007 NRC Canada

The chemical characterization of tribofilms using XANES — Interaction of nanosize calcium-containing detergents with zinc dialkyldithiophosphate[1]

L.G. Yu, E.S. Yamaguchi, M. Kasrai, and G.M. Bancroft

Abstract: A Plint friction and wear tester was used to investigate the effect of several calcium-containing detergents on the tribological and tribochemical performance of a zinc dialkyldithiophosphate (ZDDP) lubricating oil additive in a low-sulfur base stock, 100N. Thus, the friction and wear behavior of a steel-on-steel contact lubricated by 100N oil containing ZDDP alone and ZDDP–detergent mixtures at 100 °C was evaluated in a pin-on-disc configuration. The wear scar width of the upper steel pins was determined using an optical microscope, while the tribofilms formed on the lower steel discs were analyzed using X-ray absorption near edge structure (XANES) spectroscopy and X-ray photoelectron spectroscopy (XPS). At the same time, the thermal-oxidation films of the oil blends containing different additives were also prepared on the same steel discs and analyzed using XANES spectroscopy for comparative studies. It was found that in simple formulations the three kinds of calcium-containing detergents improved the friction-reducing and antiwear abilities of the 100N base stock. This was related to the individual tribochemical reactions and the deposition (in one case) of nanosized $CaCO_3$ on the rubbing steel surface, indicating that the calcium-containing detergent had a synergistic antiwear performance with the ZDDP tested in the present work. Moreover, the calcium-containing detergents contributed to retarding the thermo-oxidation and friction-induced decomposition of ZDDP in 100N oil and influenced the composition and thickness of the tribofilms, which could be dependent on the molecular structures of the detergents and directly related to the tribochemistry of ZDDPs in mineral oil. The rubbing of the steel–steel pair at 100 °C was more beneficial for the deposition of nanosized calcium carbonate on the steel surface than heating at 150 °C. The calcium-containing detergents alone in the base stock also experienced tribochemical reactions, leading to obvious changes in the oxidation state of S in the corresponding tribofilms. Therefore, it was supposed that the tribochemical reactions of the ZDDP and detergents together with the deposition of nanosized $CaCO_3$ on the rubbing steel surfaces accounted for the good antiwear performance of the blended oils.

Key words: ZDDP, detergent, thermal film, tribofilm, tribochemistry, XANES, XPS.

Résumé : On a utilisé une friction de Pling et un appareil permettant d'évaluer la durée de vie pour étudier l'effet de plusieurs détergents contenant du calcium sur la performance tribologique et tribochimique d'un dithiophosphate dialkyle et de zinc (DPDZ), un additif d'huile de lubrification dans une base ne contenant que de faibles quantités de soufre, 100N. Opérant à 100 °C et faisant appel à une configuration avec pointe sur un disque, on a évalué les comportements de friction et d'usure sur un contact acier sur acier lubrifié avec de l'huile 100N ne contenant que du DPDZ ou des mélanges de DPDZ et de détersif. On a déterminé la largeur de la cicatrice d'usure des pointes d'acier de la partie supérieure en faisant appel à la microscopie optique, alors qu'on a analysé les tribofilms formés sur les disques d'acier inférieurs en procédant à des analyses de spectroscopie d'absorption des rayons X à la périphérie de la surface (« XANES ») ainsi que par spectroscopie photoélectronique des rayons X (SPX). En même temps, on a aussi préparé des films d'oxydation thermique de mélanges d'huile contenant divers additifs sur les mêmes disques d'acier et, à des fins d'études comparatives, on les a analysés par spectroscopie « XANES ». On a trouvé que dans les formulations simples, les trois types de détersifs contenant du calcium augmentent les capacités de réduction de la friction et de l'usure de l'huile de base 100N. Ces qualités sont reliées aux réactions tribochimiques individuelles et, dans un cas, au dépôt sur la surface de friction de l'acier, de $CaCO_3$ de taille nano ce qui indique que, dans le présent travail, le détersif contenant du calcium possède une performance antifriction synergique avec le DPDZ. De plus, les détersifs contenant du calcium contribuent au retardement de la thermooxydation et de la décomposition induite par la friction

Received March 22 2007. Accepted April 19 2007. Published on the NRC Research Press Web site at canjchem.nrc.ca on 7 June 2007.

L.G. Yu, M. Kasrai[2], and G.M. Bancroft. Department of Chemistry, University of Western Ontario, London, ON N6A 5B7, Canada.
E.S. Yamaguchi. Chevron Oronite Company LLC, Richmond, California 94802, USA.

[1]This article is part of a Special Issue dedicated to Professor G. Michael Bancroft.
[2]Corresponding author (e-mail: mkasrai@uwo.ca)

 doi:10.1139/V07-045 © 2007 NRC Canada

du DPDZ dans l'huile 100N et qu'ils influencent l'épaisseur des tribofilms qui pourraient dépendre des structures moléculaires des détersifs et être reliés directement à la tribochimie du DPDZ dans l'huile minérale. Un frottement d'une paire acier–acier, à 100 °C, est plus bénéfique au dépôt sur la surface de l'acier de carbonate de calcium de taille nano qu'un chauffage à 150 °C. Les détersifs ne contenant que du calcium dans l'huile de base donnent aussi lieu à des réactions tribochimiques qui conduisent à des changements évidents dans l'état d'oxydation du S dans les tribofilms correspondants. On suppose donc que les réactions tribochimiques du DPDZ et des détersifs ainsi que le dépôt de $CaCO_3$ de taille nano sur des surfaces frottées d'acier permettent d'expliquer la bonne performance antiusure des huiles d'assemblage.

Mots-clés : DPDZ, détersif, film thermique, tribofilm, tribochimie, « XANES », SPX.

[Traduit par la Rédaction]

Introduction

As the most important multifunctional commercial additives for engine oils, zinc dialkyldithiophosphates (ZDDPs) have been successfully used for over five decades and found to be very effective for antioxidation performance and wear control (1, 2). It has been found that the performance of ZDDPs is closely related to their degradation on metallic surfaces and the subsequent formation of tribofilms thereon (3, 4). Moreover, some dispersants and detergents have been found to exhibit significant effects on the tribological and tribochemical properties of ZDDPs as engine oil additives, which could be attributed to their synergistic and (or) antagonistic effects with ZDDPs (5–8). No doubt, the proper combination of ZDDPs with certain detergents is crucial in keeping the engine clean by preventing the deposition of harmful carbon, lacquer, and sludge. This is why the mutual interactions among ZDDPs and various detergents and dispersants have been highlighted in many studies (6–9).

In the past, researchers have reported that several overbased detergents were able to provide substantial wear protection (7, 8, 10–12), which could be due to the accumulation of calcium carbonate on the metal surface. Willermet et al. (13, 14) reported that the introduction of an overbased detergent led to changes in the composition and chain length of the polyphosphate in the antiwear film derived from ZDDP-containing engine oil. For instance, in the absence of overbased detergents the tribofilms derived from ZDDPs consist of zinc polyphosphate, while in their presence polyphosphate reacts with the metallic cation to produce a lower average phosphate chain length. Recent studies by Kasrai et al. (15, 16) using X-ray absorption near edge structure (XANES) spectroscopy have supported these findings.

Dispersants and detergents may differ from each other regarding their effect on the tribological behavior of ZDDPs, and thus some of the reported results contradict each other. For example, Shirahama and Hirata (17) reported that the introduction of an overbased sulphonate to a ZDDP-containing blend was harmful to the antiwear properties of the tribofilm; this is perhaps because the overbasing component of the sulphonate acts to retard the decomposition of ZDDP that may be the rate-determining step of the antiwear action of ZDDP. On the contrary, Rounds (18) found that overbased sulphonate contributed significantly to the antiwear performance of ZDDP-derived antiwear films, which may be related to the formation of a pastelike structure of residual hydroxide from the detergent in the contact zone. In our previous work, we found that overbased calcium and magnesium sulphonate detergents acted to retard the formation of ZDDP-derived tribofilms under sliding conditions, and that the antiwear film formed from ZDDP-detergents was not simply the mixture of the films formed separately (19). In the study of the effects of various succinic anhydride or polyamine dispersants on the tribological behavior of ZDDPs-derived tribofilms, we also found that mono polyisobutylene succinic anhydride or polyamine, bis polyisobutylene succinic anhydride or polyamine, and polyisobutylene succinic anhydride or pentaerythritol dispersants had little effect on the antiwear performance of ZDDPs, though they did enhance the thermal-oxidative and tribochemical decomposition of ZDDPs (20, 21). However, borated polyisobutylene succinic anhydride or polyamine dispersant alone was capable of significantly increasing the antiwear performance of a mineral base stock. It has been suggested that the retardation of the decomposition of ZDDPs by the overbased calcium and magnesium sulphonate detergents may be related to the competitive adsorption of the degraded products of ZDDPs and to the deposition of the detergent nanocores on the sliding metal surfaces (11, 12). This suggestion may be studied by X-ray photoelectron (XPS) and XANES spectroscopy (22, 23). Thus, we introduced three types of calcium-containing detergents into blends containing a commercial secondary alkyl ZDDP and investigated the effect of the detergents on the tribological behavior and tribochemistry of the ZDDP-derived tribofilms.

There is another important reason for this study. Secondary alkyl ZDDPs have been found to give better wear performance than the primary or aryl ZDDPs, and since the establishment of the GF-3 specification level for automotive engine oils, the amount of allowable phosphorus in the engine oil has steadily decreased from 0.1 wt% phosphorus in GF-3 oils to perhaps 0.05 wt% phosphorus allowed for GF-5 oils. The reason for this is that although phosphorus, particularly the phosphorus delivered by ZDDP, has been the predominant antiwear agent in fully formulated lubricants for decades, studies have suggested that phosphorus may poison catalytic converters used on gasoline-fueled engines to reduce exhaust emissions of unburned hydrocarbons and oxides of nitrogen (24–26). As the environmental regulations governing tailpipe emissions have tightened, the allowable concentration of phosphorus in engine oils has been significantly reduced. Further reductions in the phosphorus content of engine oil require studies such as this one at low levels of phosphorus.

Even though we have been discussing the gasoline engine

© 2007 NRC Canada

oil side of the automotive market, changes are also occurring for diesel engine lubricating oils. Although it is not conclusively proven that phosphorus in diesel engine lubricating oils is detrimental to the emission system, developers of these oils must meet strict new emission standards, new fuel economy standards, and achieve extended drain. Formulators for diesel engine oils have been asked to protect the environment by delivering long drain oils that give good emission control and therefore contain lower levels of sulfated ash, phosphorus, and sulfur, while providing fuel economy.

These trends are not just taking place in the United States. Actually, since 1970 the European Union has been trying to reduce pollutant levels, and the newest Euro IV standard for heavy duty trucks and bus engines requires an approximate 60% reduction in NO_x and a 97% mass reduction in particulates compared with the original Euro I (27). This means that the engine formulations have to be compatible with the aftertreatment system of a diesel engine, and this is a significant change. It requires a reduction in phosphorus, sulfated ash, and sulfur. With regard to phosphorus, more phosphorus is thought to deactivate the catalyst and give rise to increased emissions, which is not favored. With regard to sulfated ash, blockage of the diesel particulate filter and the continuously regenerating trap (CRT) may occur. This can give rise to fuel economy reductions because of increased backpressure on the engine, and may result in greater cost to manufacture. With regard to sulfur, increased levels may give rise to the blockage of the NO_x storage sites, and this leads to increased emissions. It can also give rise to increased sulfate particles affecting the diesel oxidation catalyst, the CRT, selective catalytic reduction, and the catalyzed diesel particulate filter. This can yield increased cost and size of the aftertreatment system. Finally, an increase in sulfur may give rise to a fuel economy penalty because there is a desensitization of the catalytic conversion affecting the $DeNO_x$ traps and selective catalytic reduction. These same kinds of concerns are being voiced around the world, including India (28) and Japan (29). The low level of phosphorus that we used in our tested oil blends addresses these concerns.

Experimental details

Materials and preparation of various oil blends

The oil blends containing secondary alkyl ZDDP with an average alkyl chain length of 4.5, referred to as ZDDP, and (or) various Ca-containing detergents were prepared at the laboratories of Chevron Oronite in Richmond, California, using low-sulfur Chevron 100N as the base stock. The physico-chemical properties of the 100N base stock are given in Table 1, while the constituents of the various oil blends are listed in Table 2.

Table 1. Physico-chemical properties of 100N base stock.

Items	Properties
Density (g/cm^3)	0.859
Viscosity at 40 °C (m^2/s)	1.99×10^{-5}
Viscosity at 100 °C (m^2/s)	4.03×10^{-6}
Viscosity index	97
Pour point (°C)	–9
Sulfur content (wt%)	0.002

Table 2. Constituents of various oil blends made with 100N base stock.

Oil blend	Component
No. 1	Base oil 10N
No. 2	Base oil-8 (mmol/L)/kg ZDDP
No. 3	Base oil-8 (mmol/L)/kg ZDDP/52 (mmol/L)/kg Ca detergent I
No. 4	Base oil-8 (mmol/L)/kg ZDDP/52 (mmol/L)/kg Ca detergent II
No. 5	Base oil-8 (mmol/L)/kg ZDDP/52 (mmol/L)/kg Ca detergent III
No. 6	Base oil-52 (mmol/L)/kg Ca detergent I, TBN ~140
No. 7	Base oil-52 (mmol/L)/kg Ca detergent II, TBN ~160
No. 8	Base oil-52 (mmol/L)/kg Ca detergent III, TBN ~250

Preparation of thermal films and tribofilms of various oil blends

A silicone oil bath was used to prepare thermal-oxidative films (referred to as thermal films) of various oil blends. Thus, the AISI 52100 steel coupons of a size ϕ 19 mm × 4 mm in thickness (HRC 60–64, polished to a mirror finish using 3 μm diamond paste) were separately immersed in 60 mL of each oil blend in 100 mL glass bottles and sealed and heated in the silicone oil bath at 150 °C for 6 h to allow for the formation of the thermal films. After heating, the steel coupons were removed and gently wiped using tissue paper to remove any residual oil on the surface.

A Plint friction and wear tester was used to evaluate the friction-reducing and antiwear performance of the oil blends on a steel–steel contact. The details about the friction and wear tests have been provided elsewhere (30). Briefly, a pin (ϕ 6.2 mm × 11 mm, HRC 60–64) made of AISI 52100 steel was driven by a motor to reciprocate over the steel coupon in a pin-on-disc configuration. The lubrication of the frictional pair was realized by introducing about 30 mL of an oil blend into the steel coupon holder of the Plint machine before commencing the friction and wear test. The sliding friction and wear tests were carried out at a frequency of 25 Hz, stroke of 7 mm, load of 220 N, and temperature of 100 °C, for a duration of 1 h. The friction coefficient was automatically recorded using a sensor connected to a desktop computer. At the end of each sliding test, both the upper steel pin and lower steel coupon were ultrasonically cleaned in hexane for about 5 min and allowed to dry in atmosphere. The wear scar widths of the cleaned upper steel pins were measured using a Nikon® digital camera, while the lower steel coupons were used for the XANES analysis and (or) XPS analysis. Three repeated sliding friction and wear tests were conducted for each oil blend, and the averaged friction coefficients and wear scar widths of the three tests, with rel-

© 2007 NRC Canada

ative errors of ±10% and ±5%, respectively, are reported in this article.

XANES detection methods and analysis

Background

Total electron yield (TEY) has been used to investigate the L-edge XANES of low-Z elements (<300 eV, X-ray region) in thin films, including tribofilms, for many years. On the other hand, the fluorescent yield (FY) method has been the detection technique chosen for K-edge XANES for soft and hard X-ray regions (>1000 eV). During the early work in this area, the FY detection method was developed for very soft X-ray (<300 eV) detection (31). It should be pointed out that the FY yield for this region is at least four orders of magnitude smaller than that for the Auger yield (TEY). Thus, the background noise of the detector must be extremely low to detect the FY yield.

The sampling depth of the TEY and FY detection modes was also investigated using carefully prepared SiO_2-coated Si samples with various thicknesses of SiO_2 (32). It was found that TEY probes the topmost surface information to a film depth of about 5 nm (L-edge) or 50 nm (K-edge), while FY gives the subsurface and bulk film information to a depth of about 500 Å (L-edge) or several microns (K-edge). Therefore, the combination of these detecting modes is a powerful nondestructive technique to differentiate the surface and bulk chemical features of the thermal films and tribofilms prepared from various oil blends (30). As a result of these developments, it was shown for the first time that tribofilms generated from ZDDP on steel are multilayer films (33).

Data acquisition

The P and S K-edge and P, S, and Ca L-edge XANES spectra of the thermal films and tribofilms were recorded using a InSb double-crystal monochromator (DCM) beamline and a Grasshopper grating beamline from the Canadian Synchrotron Radiation Facility (CSRF) situated on the 1 GeV Aladdin storage ring at the University of Wisconsin (Madison, Wisconsin). Both the total electron yield (TEY) and fluorescence yield (FY) raw data were collected for the thermal film and tribofilm made from each oil blend; the photon resolution for the P and S K-edge data on the DCM beamline was about 0.9 eV and that for the P and S L-edge data on the Grasshopper grating beamline was about 0.2 eV. The XANES raw data were processed using a Ban software to remove a linear background and calibrated with respect to the data of carefully selected model compounds with known XANES chemical features.

DLS analysis

Dynamic light scattering (DLS) studies of the oil blends were carried out at 60 °C to determine the size of detergent molecules in suspension because of their high viscosities. A Brookhaven Instruments 90 Plus particle size analyzer, with a 35 mW laser and avalanche photodiode (APD) detector, was used. Analyses for each sample were repeated in triplicate. Figure 1 shows the size distributions of the three Ca detergents and Table 3 lists the effective size of each detergent. In the homodyne photocount autocorrelation method, the scattered light autocorrelation function is compared by

Fig. 1. Particle size distribution of detergents I, II, and III.

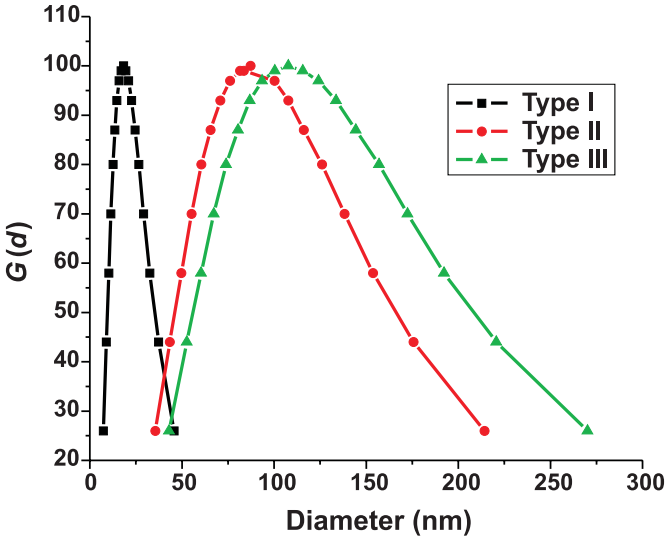


Table 3. Effective diameters of Ca detergents measured by DLS.

Detergent	Viscosity (60 °C) cP	Effective diameter (nm)	Polydispersity
Type I	11.45	18.3	0.364
Type II	10.59	87.3	0.346
Type III	10.57	107.7	0.367

signal-averaging within a digital correlator. The intensity autocorrelation function $I_2(t)$ can be related, for the case of Gaussian statistics (34), to the scattered electric field correlation function $I_1(t)$ as follows,

$$[1] \qquad I_2(t) = \langle I(0)I(t)\rangle = |I_1(0)|^2 + \beta|I_1(t)|^2$$

where β is the detector efficiency. For the simple case of a translationally diffusing particle, $I_1(t)$ is a single exponential decay involving the translational diffusion coefficient D_t,

$$[2] \qquad I_1(t) = A\ \exp[-q^2 D_t]$$

where $q = (4\pi\,\eta_D/\lambda_0)\ \sin(\theta/2)$ is the scattering magnitude at the scattering angle θ, for light of wavelength λ_0 in vacuum, scattered in a medium of index of refraction, η_D.

If there is a distribution of sizes there will be more than one relaxation, each with its own rate, $\Gamma = q^2 D_t$. In that case, $I_1(t)$ can be written as an integral over a relaxation rate distribution function $g(\Gamma)$,

$$[3] \qquad I_1(t) = \int g(\Gamma)\ \exp[-\Gamma t]\ d\Gamma$$

and the problem of determining $g(\Gamma)$ is that of inverting a Laplace transform. This can be done by CONTIN, a computer program developed specifically for DLS by Provencher (35). CONTIN yields $g(\Gamma)$, average values of Γ, and standard deviations that are a measure of the polydispersity. Typically a spherical particle model is used with this method. The effective diameters increase as the TBN number varies from 140 to 250 (see Table 2). The effect of the size of the detergents will be discussed below.

© 2007 NRC Canada

Fig. 2. Variation of friction coefficient for the steel pin-on-disc pair lubricated with base oil and base oil containing various additives (Plint machine, load 220 N, frequency 25 Hz, temperature 100 °C, test duration 1 h).

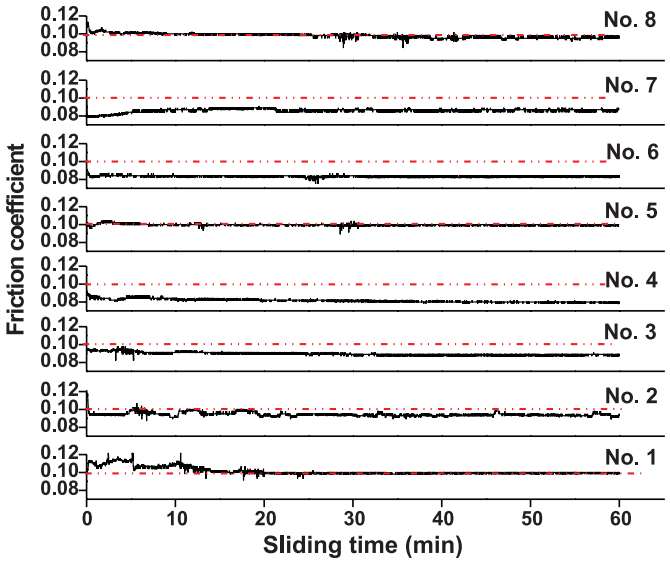
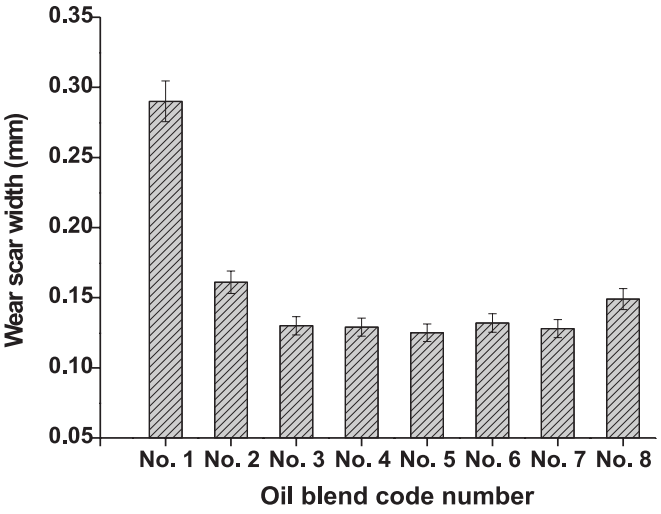


Fig. 3. Comparison of wear scar diameter of steel pin sliding against disc under the lubrication of base oil and base oil containing various additives (see Fig. 2 for rubbing conditions).



Results and discussion

Friction-reducing and antiwear performance of various oil blends

Figure 2 shows the friction coefficients for various oil blends. ZDDP and the calcium-containing detergents were all able to improve the friction-reducing ability of the 100N base stock to some extent. Moreover, the introduction of the calcium-containing detergents to the base stock had some effects on the friction-reducing ability of ZDDP. The steady-state friction coefficients for the base oil (oil blend No. 1), the oil blend containing ZDDP alone (oil blend No. 2), or calcium detergent III alone (oil blend No. 8), and the one containing both ZDDP and calcium detergent III (oil blend No. 5) were all about 0.10, with the difference being within the relative error (±10%) for the measurement of the friction coefficient. However, it was likely that the calcium-containing detergents I and II were able to decrease the friction coefficient of the base oil from ~0.1 to ~0.08 (compare the friction coefficients for oil blends Nos. 3 and 6 with that of No. 1, or those for Nos. 4 and 7 with that of No. 1). The ability of the calcium-containing detergents to decrease friction was greatest for calcium detergent II.

Looking at Fig. 1 and Table 3, we notice that detergent types I and II are smaller in size than detergent type III. In particular, detergent type I has the smallest particle size (but the highest particle concentration). Detergent type II has an intermediate particle size, and detergent type III has the largest particles and the greatest polydispersity. At this stage we cannot explain how the sizes in this range can affect the friction behavior of the detergent.

Figure 3 shows the wear scar widths (WSW) of the upper steel pins lubricated with various oil blends. It is obvious that the base stock gave much larger wear scar width and high wear of the steel pin in the steel–steel contact. In comparison, ZDDP alone and ZDDP combined with each of the three types of calcium detergent additives were very effective in decreasing the wear scar width of the upper steel pin, indicating that they could be good antiwear additives for the steel–steel sliding contact. In particular, the oil blend containing ZDDP alone registered a steel pin wear scar width of 0.165 mm, which is much smaller than that for the base oil and in good agreement with what has been reported elsewhere (18). Furthermore, the blends with ZDDP and each of the three calcium-containing detergents (blends Nos. 3–5) recorded a steel pin wear scar width smaller than that for the blend containing ZDDP alone, indicating that the calcium detergents were beneficial for improving the tribological behavior of ZDDPs. In fact, oil blend No. 5 shows synergistic behavior for antiwear performance. Moreover, it is interesting to note that each of the three calcium detergents alone in the base stock also gave good antiwear protection for the steel–steel contact, indicating that these Ca-type detergents themselves could be promising multifunctional additives for low-sulfur mineral oil. Again, tribofilm generated from detergent type III (no ZDDP) with larger particle size has relatively larger WSW compared with types I and II. Further work is necessary to correlate the structure of these calcium-containing detergents with their effects on the tribochemistry of the tribofilms derived from ZDDPs, especially in full formulations rather than these simple ones.

Film thickness

The relative thickness of thermal films and tribofilms generated from different blends was measured using XANES spectroscopy. We have shown in the past that the intensity of the P K-edge XANES spectra can be used to measure the average thickness of the major phosphate component of ZDDP-derived antiwear films (21). The peak intensity of the FY K-edge spectra is a direct measure of surface coverage (mass thickness) and can be used to monitor the film thickness of the tribofilms (36). Figure 4 shows the relative film thickness for thermal films and tribofilms. It is seen that the oil blend containing ZDDP alone forms a relatively thick thermal film and tribofilm on the steel surface. However, in-

© 2007 NRC Canada

Fig. 4. Comparison of the thickness of thermal films and tribofilms derived from various oil blends.

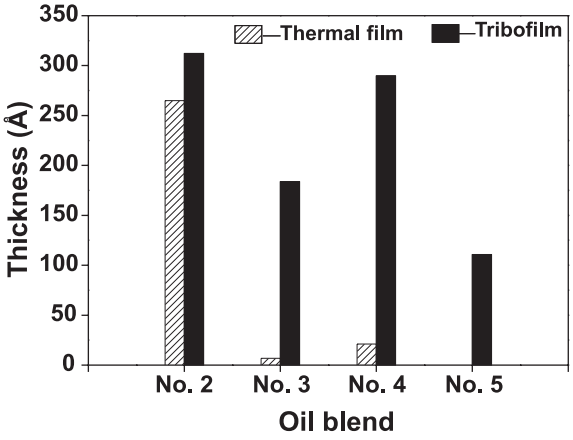
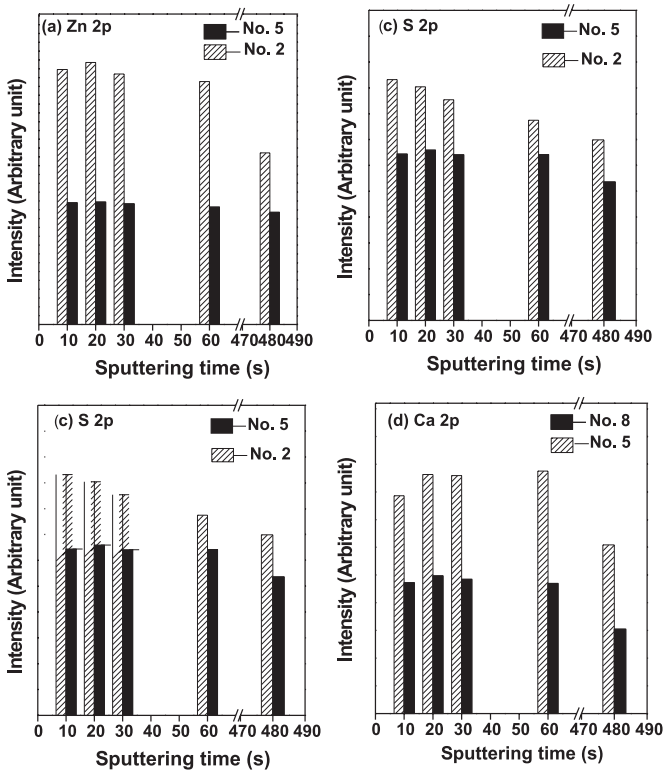


Table 4. XPS elemental composition of the antiwear films derived from various oil blends.

	Elemental composition (%)						
Films	C	Ca	O	P	S	Zn	Fe
No. 2	16.7	—	47.3	11.5	10.6	9.7	1.8
No. 3	28.7	2.5	38.6	9.7	10.2	8.2	0.7
No. 4	26.6	8.6	48.9	9.1	2.0	3.1	1.6
No. 5	11.1	10.4	51.3	17.3	5.0	3.5	1.4
No. 8	20.6	16.3	53.2	—	0.7	0.5	8.7

Fig. 5. Thickness of tribofilms from XPS Ar^+ sputtering for (*a*) Zn2p, (*b*) P2p, (*c*) S2p, and (*d*) Ca2p.



corporation of the Ca-detergent in the blend prevented the formation of a thick thermal films. This is also the case for tribofilm but to a lesser extent.

XPS profiling using Ar^+ sputtering was used to investigate the elemental composition and thickness of tribofilms. The elemental composition of tribofilms Nos. 2–5 and No. 8 are summarized in Table 4. It is very interesting to note that the Ca concentration in tribofilms Nos. 3–5 qualitatively increases as the total base number (TBN) increases from 140 to 250 in the blends. At the same time the proportion of Zn decreases. This suggests that Zn is replaced by Ca in the tribofilms, in agreement with the data in the literature (13, 15). As an example, the Ar^+ sputtering results for tribofilms No. 2 (ZDDP alone) and No. 5 (ZDDP plus detergent III) are presented in Fig. 5. Also, the Ca concentrations for tribofilms No. 5 and No. 8 (detergent III alone) are plotted in Fig. 5. It is obvious that the relative concentration of Zn, P, and S in the tribofilm blended with the Ca detergent is lower than that of No. 2 tribofilm. The sputtering rate has been calibrated using a film of SiO_2 and found to be ~50 Å/60 s. Using this calibration, the films are over 50 nm thick. After 480 s sputtering, the Fe 2p signal increased markedly (not shown), suggesting that the substrate is becoming exposed and we were approaching the maximum film thickness. Another interesting observation is the measurement of Ca in tribofilms No. 5 and No. 8. The film generated from detergent alone is also quite thick and that is why these detergents show such a good antiwear protection (see Fig. 3).

XANES analysis of the thermal films

Fig. 6*a* shows the P K-edge TEY XANES spectra of thermal films made from various oil blends listed in Table 2. The spectra of relevant model compounds are also included in Fig. 6*a*. The P K-edge XANES spectrum of ZDDP in oil (ZDDP) is shifted by ~3 eV to lower energy compared with that of the polyphosphate. The thermal films spectra align very closely with that of polyphosphate, indicating that the ZDDP has been thermally oxidized to a phosphate at 150 °C. The presence of Ca detergents in blends Nos. 3–5 has significantly retarded the oxidation rate of ZDDP, as discussed earlier, in conjunction with the film thickness (Fig. 4). A close inspection of Fig. 6*a* indicates the presence of a broad shoulder (peak a) on the low energy side of the spectrum for No. 5, corresponding to unreacted ZDDP. Another interesting finding in Fig. 6*a* is the absence of a shoulder S, corresponding to $Ca_3(PO_4)_2$ in the spectra for Nos. 3–5 (15, 16, 37). This indicates that the Ca in the detergents does not exchange with Zn in Zn phosphate, and as a result no appreciable amount of Zn–Ca phosphate forms under thermal conditions (see below for tribofilms). The FY XANES spectra, sampling the bulk of the thermal films, were also recorded (not shown). The spectra for Nos. 3–5 were noisy and weak, an indication that the films were very thin (see Fig. 4), with less decomposition of ZDDP to phosphate.

The P L-edge XANES spectra of model compounds and thermal films are presented in Fig. 6*b*. The spectrum of ZDDP in oil is distinct from those of phosphate model com-

© 2007 NRC Canada

Fig. 6. (*a*) P K-edge and (*b*) L-edge XANES spectra of model compounds and thermal films made from various oil blends.

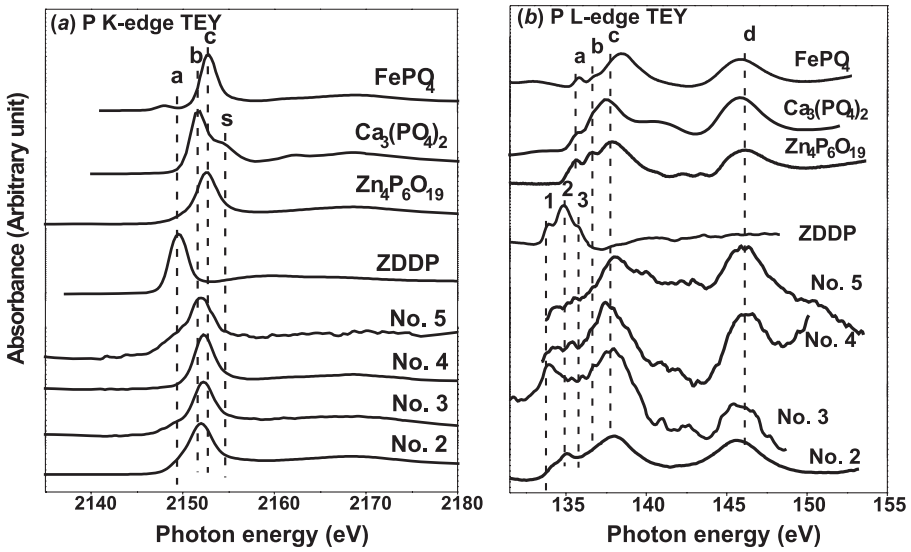
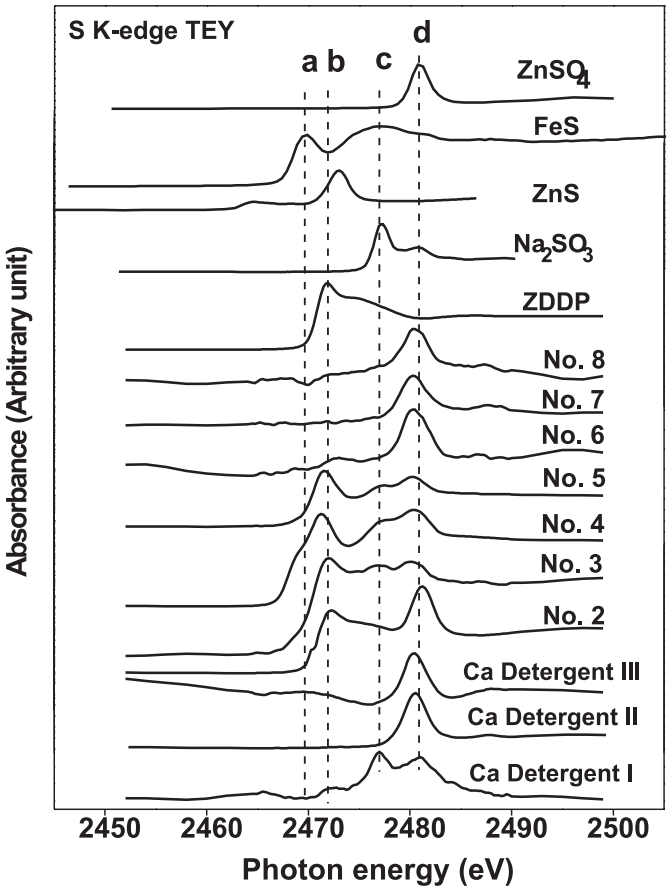


Fig. 7. S K-edge TEY XANES spectra of model compounds and thermal films made from various oil blends.



pounds and is shifted to the lower energies, compared with the phosphate spectrum. Thermal film spectrum of No. 2 shows the characteristic peaks a–d corresponding to a polyphosphate. The spectra of Nos. 3–5 also correspond to a phosphate. However, since the spectra are noisy no detailed information regarding the nature of the phosphates can be derived from the spectra. Therefore, it is concluded that heating of the AISI 52100 steel coupons at 150 °C in the base oil containing the calcium-containing detergents (oil blends Nos. 3–5) and ZDDP led to the formation of a very thin film of phosphate, compared with that of ZDDP alone in base oil.

The sulfur composition of thermal films was investigated using S K-edge and L-edge XANES spectroscopy. Figure 7 shows S K-edge XANES spectra of the thermal films and model compounds, representing sulfur in different oxidation states. The spectra of Ca detergents II and III in oil show a peak corresponding to a sulfate (peak d), whereas detergent I shows peaks corresponding to sulfide (peak b), sulfite (peak c), and sulfate (peak d). Thermal films derived from blends No. 3–5, containing detergents and ZDDP, all show the presence of sulfide (peak b), sulfite (peak c), and sulfate (peak d). However, thermal film generated from ZDDP alone, No. 2, shows no sulfite. Careful inspection of the spectrum for No. 4 shows a shoulder corresponding to a FeS species, which is not found in the other thermal films. This blend contains detergent II and ZDDP. It is not clear how FeS is formed under thermal conditions. Formation of FeS is generally associated with tribofilms generated under extreme pressure (EP) conditions (23).

Thermal films generated from detergents I to III, spectra for Nos. 6–8, show only sulfate (peak d). The FY spectra probing the bulk of the films were also recorded (not shown). They were generally noisy, an indication that the films were very thin. The sulfur L-edge XANES spectra (not shown) were noisy and did provide additional information. From these data, it is clear that sulfur is susceptible to oxidation under thermal film formation conditions. This can partly be due to the length of time (~6 h) that is required to generate the films and the fact that the film is exposed to air in oil at 150 °C (see the later discussion of tribofilms).

XANES analysis of the tribofilms of various oil blends

Figure 8*a* shows the P K-edge XANES spectra of the tribofilms for various oil blends along with the spectra of relevant model compounds. The main peak b of the

© 2007 NRC Canada

Fig. 8. (*a*) P K-edge and (*b*) L-edge XANES spectra of model compounds and tribofilms made from various oil blends.

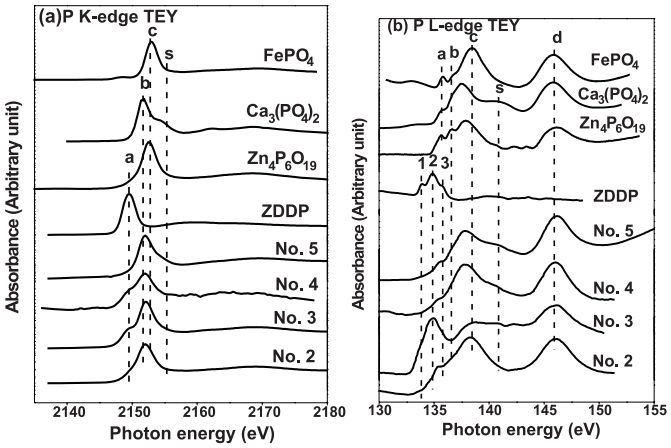
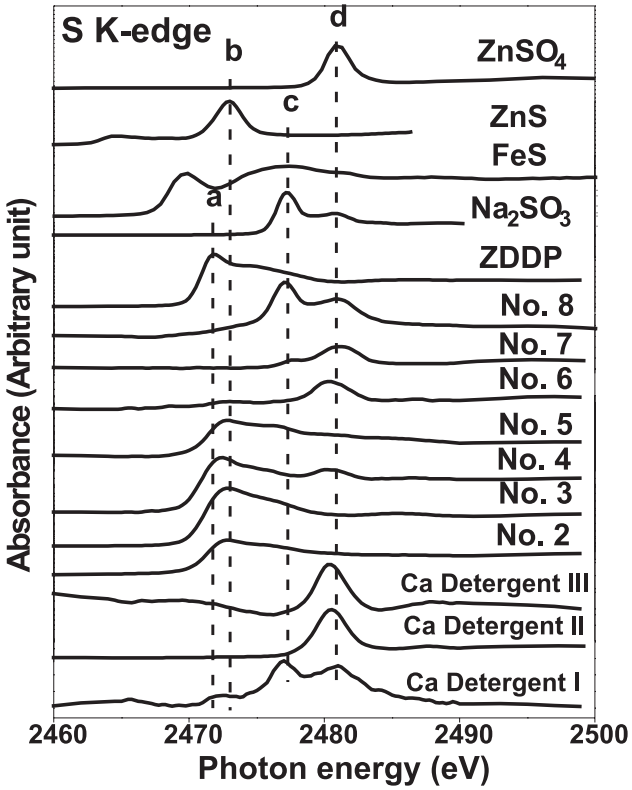


Fig. 9. S K-edge TEY XANES spectra of model compounds and tribofilms made from various oil blends.



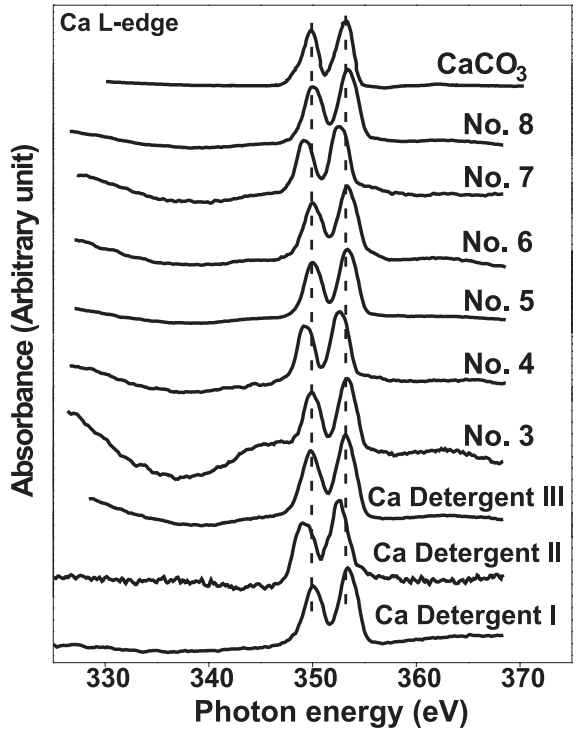
tribofilms aligns closely with that of Zn and Ca phosphate, but is shifted ~1 eV to lower energy compared with that of Fe phosphate (peak c). Peak a of ZDDP aligns very closely with that of the shoulder in the spectra for No. 3 and No. 4, indicating the presence of unreacted ZDDP in these films, generated from Ca detergents and ZDDP. Spectra for No. 5 and No. 2 do not show the shoulder.

The corresponding P L-edge XANES spectra of model compounds and tribofilms are presented in Fig. 8*b*. The spectral features for No. 2 (ZDDP alone) are very similar to those of Zn polyphosphate, whereas the spectral features of the Fe and Ca phosphates are shifted to higher and lower energies compared with Zn phosphate, respectively. The addition of detergents I, II, and III to ZDDP changed the spectral features of the polyphosphates in the tribofilms. First, the ratio of intensity of peaks a/c (0.54) for spectrum No. 2 (ZDDP alone) dropped to 0.3 for the spectra of Nos. 4 and 5 (ZDDP plus detergents). Nicholls et al. (38) provided a calibration curve assigning the a/c and b/c ratios to the number of phosphorous atoms in different polyphosphate glasses. The P L-edge spectra of short chain polyphosphates with 10 or fewer P atoms in a polyphosphate glass exhibit an a/c ratio of ~0.44 or less. Medium chain polyphosphates, which have between 10 and 25 P atoms in each chain in the polyphosphate glass network, exhibit an a/c ratio between ~0.44 and ~0.60. Long chain species, characterized by 25 or more P atoms in the polyphosphate chain, show an a/c ratio of ~0.60 or greater. Thus, the addition of detergents has reduced the polyphosphate chain length from medium to short. Second, peak c of spectra Nos. 4 and 5 shifted to lower energy, approaching that of Ca phosphate. The broad peak s of Ca phosphate is quite apparent in spectra of Nos. 3–5, whereas it is not present in spectrum of No. 2. This is a strong indication that Ca has incorporated into Zn polyphosphate to form Ca–Zn phosphate. This is in good agreement with previous results (14, 15, 32). As noticed in conjunction with P K-edge spectra (Fig. 8*a*), there is a peak or shoulder in the spectra of Nos. 3–5, corresponding to peak 2 of ZDDP. This peak is especially very strong in spectrum of No. 3. These data confirm the observations from the P K-edge data that, along with phosphate, some undecomposed ZDDP is present in the tribofilms. This was also observed in the case of thermal film formation. This information, and the observation that films generated from combination of ZDDP and Ca detergents are thin, strongly suggests that the detergents interact with ZDDP and retard the decomposition of ZDDP to phosphates (17). However, as was shown in Fig. 3, the interaction is a synergistic one and generally improves the antiwear performance of ZDDP. However, detergent size has no significant effect. In the past, we have investigated the effects of Ca sulfonate, phenate, and salicylate detergents in combination with ZDDP. In general the effect has been antagonistic (15, 16, 37). Here we notice that detergent type III (larger size) behaves differently. The spectra of No. 5 in Fig. 8 (K-edge and L-edge) for a film generated from detergent III and ZDDP do not show the shoulder corresponding to unreacted ZDDP. It seems the composition of these particular detergents plays an important role in providing superior antiwear function and friction-reducing performance.

The sulfur composition of tribofilms was investigated using S K-edge and L-edge XANES spectroscopy. Figure. 9 shows the S K-edge XANES spectra of tribofilms and model compounds along with those of detergents in oil. As was shown earlier, the spectra of Ca detergents II and III in oil show a peak corresponding to a sulfate (peak d), whereas detergent I shows peaks corresponding to sulfide (peak b), sulfite (peak c), and sulfate (peak d). Tribofilms generated

© 2007 NRC Canada

Fig. 10. Ca L-edge TEY XANES spectra of model compounds and tribofilms made from various oil blends.



directly from the detergents (no ZDDP), spectra of Nos. 6–8, show sulfite (S^{4+}) and sulfate (S^{6+}) features. The film generated from ZDDP alone, spectrum of No. 2, shows peak b corresponding to ZnS with a broad shoulder corresponding to unreacted ZDDP. The spectra of Nos. 3–5, for films generated from ZDDP in combination with detergent I to III, have a broad peak encompassing unreacted ZDDP (peak a) and ZnS (peak b). In contrast to thermal films (Fig. 7), there is little or no oxidized form of sulfur in the tribofilms.

S L-edge XANES spectra of the tribofilms were also recorded (not shown). The results support the S K-edge findings indicating that the topmost surface chemistry of S is very similar to the near surface and the bulk.

Calcium was also present in both the thermal films and tribofilms. As an example, the Ca L-edge XANES spectra of tribofilms along with those of $CaCO_3$ and detergents in oil are presented in Fig. 10. As is obvious from Fig. 10, the spectral features of tribofilms and detergents in oil align very closely with those of $CaCO_3$. However, close inspection of the spectra clearly shows that the doublet feature in the spectrum of detergent II (in oil) is shifted to lower energy by ~0.5 eV, compared with those of detergents I and III. This indicates that, most likely, the counter ion of Ca^{2+} in detergent II is different from that in detergents I and III. Overall, calcium can be present in the tribofilm as $CaCO_3$, Ca phosphate, and undecomposed detergents. It is very interesting to find that both in thermal films and tribofilms, calcium is present and becomes an integral part of the film. As was shown in Fig. 3, the antiwear properties of the three detergents, regardless of differences in their composition, are very similar.

Conclusions

The effects of three kinds of calcium-containing detergents on the tribological and tribochemical features of a ZDDP additive in 100N base stock was investigated using XANES spectroscopy and XPS. The main conclusions are given in the following.

The three kinds of calcium-containing detergents tested in the present work were all able to improve the friction-reducing performance of the 100N base stock (calcium detergent II was the most effective.) In base stock alone, these calcium-containing detergents gave good antiwear protection for the steel–steel contact, which was dependent on the tribochemical reactions of the detergents themselves.

The mixtures of ZDDP with each of the three types of calcium-containing detergents as additives in 100N oil were more effective in reducing wear of the steel–steel contact than ZDDP alone. These Ca detergents showed synergistic antiwear performance with the ZDDP tested in the present work.

Heating of the AISI 52100 steel coupons in various oil blends at 150 °C only led to the formation of very thin thermal-oxidation films containing Zn phosphate, sulfate, and small amounts of calcium. The calcium-containing detergents contributed to retarding the thermo-oxidation decomposition of ZDDP in 100N oil, which could be dependent on the molecular structures of the detergents and directly related to the tribochemistry of ZDDPs in mineral oil. The reduction of the thickness can also partially be due to the cleaning action of the detergent.

Much more Ca was detected by XANES in the tribofilms as compared with the thermal films, which indicates that the rubbing of the lubricated steel–steel pair enhances formation of tribofilms containing Ca.

The calcium-containing detergents influenced the composition and thickness of the tribofilms. The reciprocating sliding of the steel pin-on-disc pair at 100 °C was more effective than heating at 150 °C to induce the decomposition of ZDDP, leading to incorporation of the active sulfur originating from ZDDP and (or) other additives into the tribofilm.

Each of the three calcium-containing detergents, alone, also produced tribochemical reactions, leading to changes in the oxidation state of S in the corresponding tribofilms. The deposition of nanosized $CaCO_3$ onto the rubbing steel surfaces may account for the good antiwear performance of this oil blend.

Acknowledgements

This study was financially supported by a grant from Chevron Oronite Company. The financial support from the National Research Council of Canada and the Natural Science & Engineering Research Council of Canada is appreciated. The authors are grateful to S. Ajiboye and A. J gensen from CSRF and to the staff of the Synchrotron Radiation Center (SRC) at the University of Wisconsin-Madison for their technical support. The support to the SRC under award No. DMR-0537588 from the National Science Foundation (NSF) is also gratefully acknowledged.

© 2007 NRC Canada

References

1. M.A. Nicholls, T. Do, P.R. Norton, M. Kasrai, and G.M. Bancroft. Tribol. Int. **38**, 15 (2005).
2. H. Spikes. Tribol. Lett. **17**, 469 (2004).
3. F.G. Rounds. ASLE Trans. **18**, 79 (1975).
4. S. Jahanmir. Trans. ASME, J. Tribol. **109**, 577 (1987).
5. K. Inoue and H. Watanabe. ASLE Trans. **26**, 189 (1983).
6. Ph. Kapsa, J.M. Martin, and J.M. Georges. Trans. ASME, J. Tribol. **103**, 486 (1981).
7. S.S.V. Ramakumar, A.M. Rao, and S.P. Srivastava. Wear, **156**, 101 (1992).
8. F.G. Rounds. ASLE Trans. **21**, 91 (1978).
9. Y.L. Wu and B. Dacre. Tribol. Int. **30**, 445 (1997).
10. Y. Yamada, J. Igarashi, and K. Inoue. Lubr. Eng. **48**, 511 (1992).
11. S. Giasson, D. Espinat, and T. Palermo. Lubr. Sci. **5**, 91 (1993).
12. S. Giasson, T. Palermo, T. Buffeteau, B. Desbat, and J.M. Turlet. Thin Solid Films, **252**, 111 (1994).
13. P.A. Willermet, D.P. Dailey, R.O. Carter, P.J. Schmitz, W. Zhu, J.C. Bell, and D. Park. Tribol. Int. **28**, 163 (1995).
14. P.A. Willermet, R.O. Carter, P.J. Schmitz, M. Eveson, D.J. Scholl, and W.H. Weber. Lubr. Sci. **9**, 325 (1997).
15. M. Kasrai, M. Suominen Fuller, G.M. Bancroft, E.S. Yamaguchi, and P.R. Ryason. Tribol. Trans. **46**, 534 (2003).
16. M. Kasrai, M. Suominen Fuller, G.M. Bancroft, E.S. Yamaguchi, and P.R. Ryason. Tribol. Trans. **46**, 543 (2003).
17. S. Shirahama and M. Hirata. Proceedings of the 5th international colloquium on additives for lubricants and operational fluids, Vol. 1 *Edited by* W.J. Bartz. Esslingen, Germany. 1986. pp. 4/4/1–4/4/13.
18. F.G. Rounds. Lubr. Eng. **45**, 761 (1989).
19. E.S. Yamaguchi, P.R. Ryason, S.W. Yeh, and T.P. Hansen. Tribol. Trans. **41**, 262 (1998).
20. E.S. Yamaguchi, Z.F. Zhang, M.Kasrai, and G.M. Bancroft. Tribol. Lett. **15**, 385 (2003).
21. Z.F. Zhang, M. Kasrai, G.M. Bancroft, and E.S. Yamaguchi. Tribol. Lett. **15**, 377 (2003).
22. M.A. Nicholls, G.M. Bancroft, P.R. Norton, M. Kasrai, G.De Stasio, B.H. Frazer, and L.M. Wiese. Tribol. Lett. **17**, 245 (2004).
23. Z.F. Zhang, M. Najman, M. Kasrai, G.M. Bancroft, and E.S. Yamaguchi. Tribol. Lett. **18**, 43 (2005).
24. J.A. Spearot and F. Caracciolo. SAE technical paper 770637. 1977.
25. F. Caracciolo and J.A. Spearot. SAE technical paper 790941. 1979.
26. F. Ueda, S. Sugiyama, K. Arimura, S. Hamaguchi, and K. Akiyama. SAE technical paper 940746. 1994.
27. P.M. Walsh. SAE technical paper 2000–01–0183. 2000.
28. S.K. Singh, A.K. Agarwal, D.K. Srivastava, and M. Sharma. J. Eng. Gas Turbines Power, **128**, 921 (2006).
29. M. Soejima, Y. Ejima, K. Uemori, and M. Kawasaki. JSAE Rev. **23**, 113 (2002).
30. Z.F. Zhang, E.S. Yamaguchi, M. Kasrai, and G.M. Bancroft. Tribol. Trans. **47**, 527 (2004).
31. M. Kasrai, Z. Yin, G.M. Bancroft, and K.H. Tan. J. Vac. Sci. Technol. A, **11**, 2694 (1993).
32. M. Kasrai, W.N. Lennard, R.W. Brunner, G.M. Bancroft, and K.H. Tan. Appl. Surf. Sci. **99**, 303 (1996).
33. Z. Yin, M. Kasrai, M. Fuller, G.M. Bancroft, K. Fyfe, and K.H. Tan. Wear, **202**, 172 (1997).
34. R. Pecora and B.J. Berne. Dynamic light scattering. John Wiley and Sons Inc., New York. 1975.
35. S.W. Provencher. Comput. Phys. Commun. **27**, 229 (1982).
36. M.L. Suominen Fuller, R.L. Fernandez, M.L. Massoumi, W.N. Lennard, M. Kasrai, and G.M. Bancroft. Tribol. Lett. **8**, 187 (2000).
37. Y. Wan, M.L. Suominen Fuller, M. Kasrai, G.M. Bancroft, K. Fyfe, J.R. Torkelson, Y.F. Hu, and K.H. Tan. *In* Boundary and mixed lubrication: Science and applications. Edited by D. Dowson et al. Elsevier B.V., Amsterdam, Netherlands. 2002. pp. 155–166.
38. M.A. Nicholls, P.R. Norton, G.M. Bancroft, M. Kasrai, T. Do, B.H. Frazer, and G.De Stasio. Tribol. Lett. **17**, 205 (2003).

© 2007 NRC Canada

Canadian Light Source — Optical Metrology Facility[1]

Brian W. Yates and Dylan G. Maxwell

Abstract: The Canadian Light Source Optical Metrology Facility serves as a support facility and provides metrological services required by the synchrotron beamlines. The Facility consists of three state-of-the-art instruments: a Micromap 570 surface profiler, an Ocean Optics long trace profilometer, and a Zygo Verifire AT Fizeau interferometer. These three complementary measurement systems permit a complete analysis of the synchrotron beamline optical components. The systems will be discussed in detail, noting synchrotron and industrial applications where possible.

Key words: optics, metrology, surface roughness, slope error, tribology.

Résumé : Le laboratoire de métrologie optique de la source canadienne de lumière sert de support et fournit les services requis par les faisceaux linéaires du synchrotron. Le laboratoire consiste en trois appareils ultramodernes, un profileur de surface Micromap 570, un profilomètre à long tracé Ocean Optics et un interféromètre Zygo Verifire AT Fizeau. Ces trois systèmes de mesure complémentaires permettent de faire une analyse complète des composantes d'un faisceau optique du synchrotron. On discute des systèmes en détail et, lorsqu'on en a noté, on discute aussi des applications industrielles ou celles du synchrotron.

Mots-clés : optique, métrologie, aspérités d'une surface, erreur sur la pente, tribologie.

[Traduit par la Rédaction]

Introduction

The Canadian Light Source (CLS) is the Canadian national synchrotron science facility (1), operating on the University of Saskatchewan campus in Saskatoon, Saskatchewan. The CLS is operated as a not-for-profit corporation wholly owned by the University of Saskatchewan. The facility was constructed with a $173CAN million capital budget starting in 1999 and operations began in early February 2004. The facility is a third generation 2.9 GeV synchrotron light source that produces a high intensity light source of infrared, visible, ultraviolet, and both soft and hard X-ray radiation. The CLS currently has seven operational scientific beamlines and a further seven beamlines in the early stages of construction. The beamlines provide multidisciplinary support in the areas of advanced materials, earth and environmental science, life sciences, and industrial science. Canadian researchers in such diverse areas as chemistry, physics, geology, materials science, soils science, surface science, biochemistry, and engineering can submit scientific proposals and apply for beam time at the CLS.

Received April 18 2007. Accepted May 22 2007. Published on the NRC Research Press Web site at http://canjchem.nrc.ca on 8 June 2007.

This paper is dedicated to Mike Bancroft for his vision and leadership in Canadian synchrotron science, his outstanding contributions to Canadian science in general, and friendship over the years.

B.W. Yates[2] and D.G. Maxwell. Canadian Light Source Inc., University of Saskatchewan, Saskatoon, SK S7N 0X4 Canada.

[1]This article is part of a special issue dedicated to Professor G. Michael Bancroft.

[2]Corresponding author (e-mail: brian.yates@lightsource.ca).

The Optical Metrology Facility (OMF) is a support facility at the CLS that determines the required optical specifications through SHADOW ray-tracing modeling (2, 3) and measures the quality of the optical components prior to beamline installation. However, the OMF has a broader mandate to support scientific researchers or "users" at the CLS and, where possible, researchers across Canada. Therefore, this paper has been written to inform the Canadian scientific community what instrumentation and capabilities are available.

Typical surface parameters measured by the OMF instruments are surface roughness (surface finish), radius of curvature (flatness), height and slope errors, and power spectral density (PSD). Removal of the desired best-fit theoretical figure (e.g., plane, cylinder) from the raw surface height yields the height error and differentiation generates the slope error. A large slope error will result in an undesirable experimental focus, where photon flux, brightness, and spot size have been compromised. Slope error, surface roughness, and mirror coating quality determines the photon flux density, focus characteristics, and photon energy range delivered to the beamline experimental station. Since all measurement methods use visible light, these techniques are noncontact and nondestructive. In general, the surfaces being measured need to be somewhat reflective. Uncoated glass optics with about 4% reflectivity are still suitable for measurement. We have developed tools within the OMF (metrological, software) to improve our understanding of the interplay that these parameters have on the overall focus quality and to deliver optical components to the beamlines that meet or exceed their design specifications.

Optical Metrology Facility

All OMF instruments are housed in a 27 m^2 Class 10 000 clean room with four HEPA units. The metrological instru-

 doi:10.1139/V07-053 © 2007 NRC Canada

Fig. 1. A view of the CLS Optical Metrology Facility with the Micromap 570 surface profiler in the left foreground, the long trace profilometer in the left background, and the Zygo Verifire AT Fizeau interferometer in the right background.



Table 1. Metrology instrument measurement ranges.

Instrument	Horizontal spatial period range (mm)	Height range	Measurement limit (RMS)
Micromap 570 surface profiler	0.0002–1.25[a]	0.01–150000 (nm)[b]	0.03 nm (height error)
Ocean Optics Long Trace profilometer	2–1500	0.1–10000 (μrad)	10 nm (height error)\ 0.45 μrad (slope error)
Zygo Verifire AT Fizeau interferometer	0.039–150 (normal)[c] 0.39–1500 (grazing)[c]	5–1000 (nm)	20 nm (height error) 0.45 μrad (slope error)

[a]Actual spatial period is dependent on the objective magnification used.
[b]Height range is dependent on the mode used — smooth, wave, or focus.
[c]Zoom feature ranges from (1–6)X. Numbers shown reflect the highest zoom factor of 6X.

ments are mounted on vibration isolation tables (Technical Manufacturing Corporation, 780 Series) with pneumatic isolation legs to minimize vibrational effects. Plastic curtains and bellows are used, when required, to minimize air turbulence effects. The temperature in the room is maintained at 23.0±0.2 °C, since temperature changes are extremely critical for metrological measurements. The Micromap 570 surface profiler from Micromap Corporation primarily measures the surface roughness of test optics. The Long Trace Profilometer (LTP) from Ocean Optics Inc. measures the slope error for a one-dimensional line profile and radius of curvature. Finally, a Verifire AT Fizeau interferometer from Zygo Corporation measures the height error map for a surface and radius of curvature. See Fig. 1 for a view of the OMF scientific instrumentation currently available and Table 1 for a summary of their measurement ranges and limitations for surface slope and height errors. Basic metrological equipment such as light sources, optical and micromechanical components, precision height gage, laboratory grade gage and angle blocks, beam profiler, and various NIST-traceable standards are available for routine testing and experiments by users.

Micro-roughness measurements

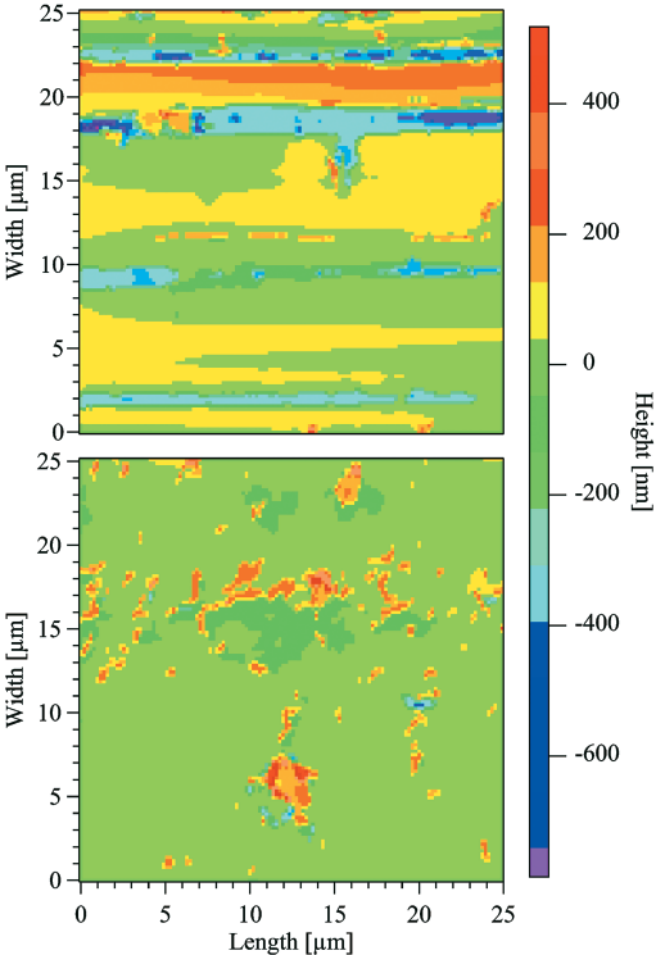
The Micromap 570 surface profiler is a microscope-based instrument that utilizes visible light interferometry (520 nm, white) to measure the surface roughness of reflective optical surfaces. A CCD detector (9.8 μm pixel pitch) mounted on the microscope is used to measure an area on the surface (<1 mm^2, which is dependent on the microscope objective used) with a height resolution of approximately 0.01 nm. Four different objectives are currently available, 5X, 10X, 20X, and 50X, which enables one to cover a wide range of spatial sampling periods (0.0002–1.25 mm) or spatial frequencies (0.0004–2.5 $μm^{-1}$). The electronic noise floor contribution, which limits the achievable surface roughness, has been characterized by measuring calibrated fused silica super smooth mirrors from General Optics (Cat. No. GO-FS100–1R) of ~0.03 nm root-mean-square (RMS) surface roughness. Surface roughness down to 0.03 nm RMS can be routinely measured with some signal averaging.

Three measurement modes are available in the distributed software — smooth phase mode (interferometry phase measurement), wave mode (white light interferometry phase scan), and focus mode (interferometry focus scan). Smooth phase mode is ideal for very smooth surfaces (0.02–100 nm RMS roughness) but is limited to a maximum height measurement of 4 μm (objective focus depth dependent). Wave mode is ideal for smooth surfaces with heights and steps < 5 μm. Focus mode is ideal for rough surface textures with heights and steps > 5 μm (maximum height measurement of 150 μm).

The surface height map shown in the bottom portion of Fig. 2 is for an antiwear film, produced using a four-ball extreme pressure wear machine. In this device a ball is rotated in contact with 3 test spherical balls that are held stationary. The contact surfaces are covered with test lubricant, the central ball is rotated and a load applied, and then a timed test is performed. The map was taken using a 50X objective on an antiwear film and shows the following surface amplitude parameters: 63.12 nm RMS surface roughness (Sq), 32.86 nm

© 2007 NRC Canada

Fig. 2. Surface height maps measured with the Micromap 570 surface profiler using a 50X objective. The bottom map is for an antiwear film with surface amplitude parameters of 63.12 nm RMS surface roughness (Sq), 32.86 nm arithmetical mean deviation (Sa), and 1.013 μm peak-to-valley (St). The top map is outside the wear track region with 131.5 nm RMS Sq, 88.73 nm Sa, and 1.299 μm St.



arithmetical mean deviation (Sa), and 1.013 μm peak-to-valley (St). For comparison purposes, a nearby section outside the wear track region is shown in the top portion of Fig. 2. The unworn surface height map is less homogenous, showing the following surface amplitude parameters: 131.5 nm RMS Sq, 88.73 nm Sa, and 1.299 μm St. A significant reduction in surface roughness and arithmetic mean deviation has occurred in the wear process that produces these antiwear films.

Most modern automotive oils contain many additives, antiwear agents, anti-oxidants, detergents, and dispersants. The most popular antiwear agent is zinc dialkyldithiophosphate (ZDDP). ZDDP decomposes on the hot metal engine surfaces to generate very thin inhomogeneous antiwear films (~100 nm thickness). The chemistry of antiwear films has been studied extensively with conventional XPS surface techniques and using synchrotron sources on the phosphorus L-edge and K-edge XANES, using total electron yield (TEY) and fluorescence yield (FY) (4–6). TEY and FY techniques are well-suited to study these antiwear films since their analysis depths match well. L-edge TEY has an analysis depth of ~5 nm making it surface sensitive, while FY has an analysis depth of ~70 nm making it a bulk measurement technique. Combined with the energy tunability of synchrotron beamlines via crystal or grating diffraction, TEY and FY make very powerful probes into the antiwear film surface chemistry and tribology. The operational variable line spacing plane grating monochromator (VLS-PGM) beamline at the CLS is particularly well suited for phosphorus L-edge studies (at ~135 eV binding energy) because of the high undulator photon flux and very high resolving power (up to 30 000). The soft X-ray microcharacterization beamline (SXRMB) currently under construction at the CLS, which will be commissioned in early 2008, should provide access to the low-Z K-edges of elements like phosphorus and sulphur. The SXRMB beamline will utilize a bending magnet source and a double crystal monochromator, which will use InSb-111 and Si-111 crystal pairs for diffraction to access the photon energy range of ~1.8–10 keV. In addition, antiwear films can be measured for surface amplitude parameters in the CLS OMF using the Micromap 570 surface profiler to gain insight into their tribology.

Height and Slope Error Measurements

The long trace profilometer measures the slope and curvature of optical surfaces along one dimension using a zero path-difference interferometer. Our LTP IV is an improved version of the original LTP (7) and now incorporates a precision linear air bearing and aluminum beam from New Way. Two "folding" mirrors and a reference planar mirror in the optical system have been replaced with super smooth silicon mirrors from General Optics (custom folding mirrors, <0.1 nm RMS roughness and <2 μrad RMS slope error, Cat. No. GO-S100–1). A 3 mW class IIIa solid state laser source (λ = 635 nm) with circular beam source and 0.7 mrad beam divergence from Edmund Industrial Optics (Cat. No. F54–024) is used to probe the test optic. The CLS LTP can measure reflective optical surfaces up to 1.5 meters in length, covering the range of spatial samplings from 2–1500 mm and spatial frequencies of 0.00033–0.25 mm^{-1}. Surfaces of virtually any shape can be measured in situ, as long as the surface slope change is within the ±5 mrad acceptance angle of the LTP optical system. Our current LTP measurement floor is ~0.45 μrad RMS in slope and 10 nm RMS in height (Table 1), being limited by air turbulence and thermal drift during measurement.

Figure 3 shows the LTP signal averaged slope error profile of the CLS spectromicroscopy beamline M2 planar mirror. In this case the desired figure is planar, so the slope error of 0.45 ± 0.13 μrad RMS represents a very slight deviation from "flat". Slope error represents the difference in slope between the surface and the desired figure (e.g., plane, cylinder). In this case the planar mirror, which is a critical component in the plane grating monochromator design for this beamline, met the stringent design goal of 0.5 μrad RMS slope error.

The Verifire AT Fizeau interferometer measures the deviation of height of a test reflective surface from a reference surface, typically a reference flat. It accomplishes this using phase shifting interferometry and a collimated HeNe laser

© 2007 NRC Canada

beam (λ = 632.8 nm) of 150 mm diameter. Three dimensional surface height maps of optical surfaces up to 150 mm in diameter can be measured at normal incidence or up to 1500 mm in grazing incidence using a new optics tip and tilt stage designed at the CLS. The radius of curvature and slope error can be calculated from the measured surface height map. A variable zoom feature allows a particular region to be enlarged by up to six times magnification. The spatial period measured depends on the zoom factor and number of pixels used, the grazing incidence angle, and the test optic length (L). A typical normal incidence spatial period range without zoom is about 0.3–L mm.

A grazing incidence measurement on a far IR beamline M3 planar mirror, in so-called "double pass" mode, is shown in Fig. 4. A collimated HeNe laser beam is output from the Fizeau interferometer through a reference transmission flat (Fig. 4, left side), reflected off the M3 mirror under test on a tip and tilt stage (Fig. 4, right side), and then reflected back with a return flat (top right) to the detector in the interferometer. Double pass refers to the fact that the collimated beam is reflected twice off the test mirror. The transmission and return flats form an optical cavity. Our custom optical cavity purchased from Zygo Corporation is approximately λ/50 in quality, so flatness measurements to ~12.7 nm are certainly possible with this instrument.

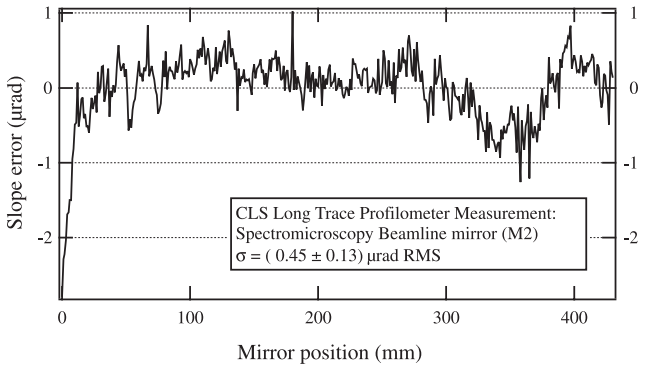
Software Development

Software has been developed to provide advanced analysis functionality beyond that of the control and analysis commercial instrumentation software provided by the vendors. The core functionality includes support for signal averaging, error analysis, curve fitting, and PSD for both profile (1D) (8) and surface (2D) data (9). Signal averaging is frequently beneficial for reducing noise but requires multiple surface height map measurements to be collected and analyzed. The software was developed in C/C++ using the ROOT data analysis framework (10) from CERN.

A data window can be applied to select the desired analysis region of the measured optic. Both height and slope maps are supported and conversions allowed. The software is designed to handle multiple measurements so that a surface uncertainty map can be computed from the variation amongst unique permutations of the original sample measurements. Averaging these measurements generates a mean surface map. A best-fit polynomial to remove piston, tilt, power, and twist can be applied to the data, if desired. The uncertainties in the fitted parameters are calculated from the best-fit differences of the surface with and without the surface uncertainty map. The radius of curvature with uncertainty is calculated from certain fitted parameters and their respective uncertainties. Mean and RMS values of the maps are calculated with their estimated uncertainties. These results are formatted so that they can be combined to generate a comprehensive report.

An example of the output from the software can be seen in Fig. 5. The average of several successive surface height map measurements on the Fizeau interferometer of a Kirkpatrick-Baez (KB) mirror is shown in the center left of Fig. 5, with the best-fit polynomial approximation to a sphere removed. The lower left histogram shows the residuals binned according to height. The surface height uncertainty map is shown in the center right, while the corresponding height uncertainty distribution is displayed in the lower right histogram. The histograms are helpful in visualizing the measurement distributions and showing how closely they follow normal or gaussian statistics. The upper right box shows the radius of curvature and fitted parameter results with their respective errors. This particular KB mirror has a height error of 0.0115 ± 0.0002 μm and a radius of curvature of 42.61 ± 0.6 km, which is considered optically flat for all intents and purposes.

Fig. 3. LTP slope error measurement results for the CLS spectromicroscopy beamline planar mirror (M2), showing a signal averaged slope error of 0.45 ± 0.13 μrad RMS.



Summary

The CLS Optical Metrology Facility is fully operational and all instrumentation is performing well within their design specifications. To reduce the LTP measurement noise floor even further, we are currently studying how to optimize the room temperature feedback control system for temperature derivative instead of temperature bandpass. Replacement of the LTP aluminum beam with a ceramic beam from Coorstek Inc. is also being considered. A ceramic beam would have a substantially better flatness of ~4 μrad, higher stiffness, lower coefficient of thermal expansion, and lower thermal conductivity.

Considerable effort has been spent to build a complete state of the art metrology laboratory that is capable of performing a complete analysis of synchrotron beamline optical components. This is required to deliver synchrotron beamlines that meet or exceed their design specifications with respect to photon flux intensity, density and distribution, brightness, photon energy range and resolution, and focal size.

In the future we look forward to expanding our support to scientific users and their research programs within the CLS and afar, including industrial research like the tribology example shown in this paper.

Acknowledgements

The CLS is supported by Natural Sciences and Engineering Research Council of Canada (NSERC), the National Research Council (NRC), Canadian Institutes of Health Research (CIHR), and the University of Saskatchewan. I would personally like to thank Mike Bancroft for his help as PhD advisor in Chemistry at *The* University *of* Western Ontario and for introducing

© 2007 NRC Canada

Fig. 4. A Fizeau interferometer measurement of an IR mirror using a 45° grazing incidence setup (double pass mode).

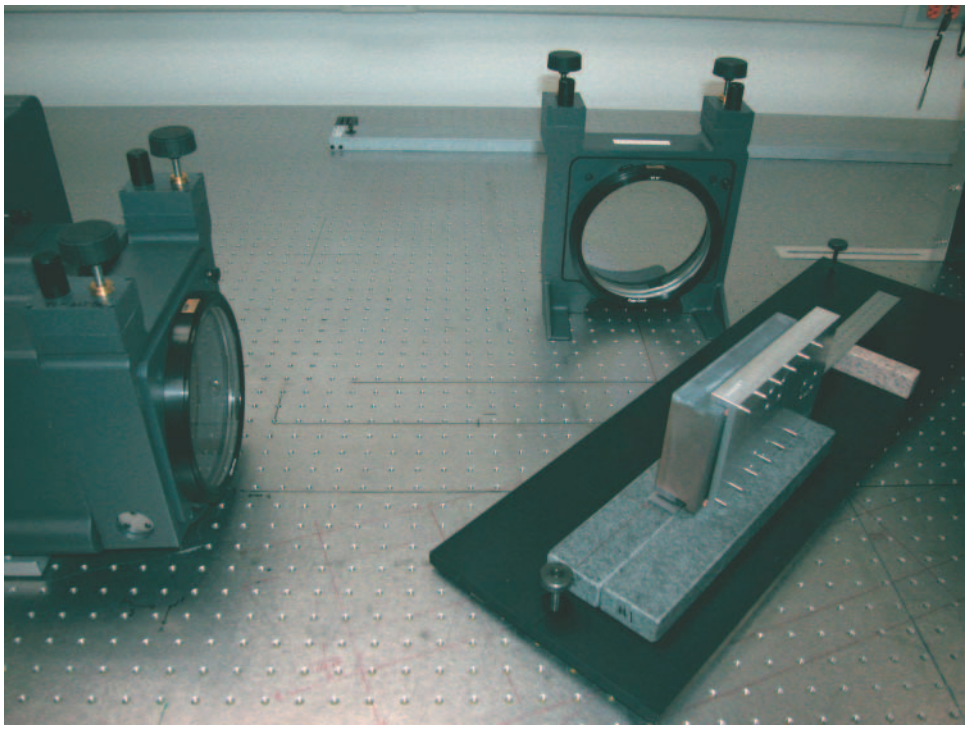
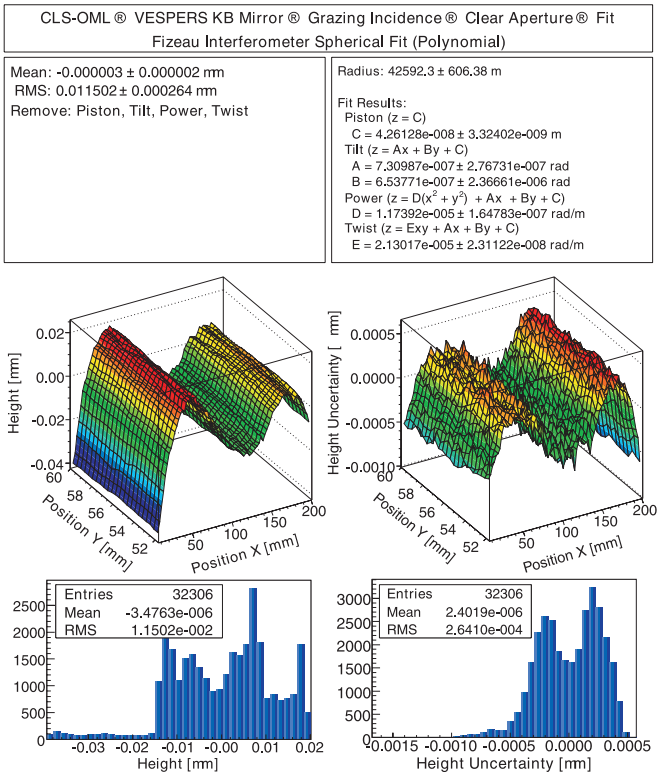


Fig. 5. The results of a spherical fit to a Fizeau interferometer surface height map for a Kirkpatrick-Baez (KB) beamline mirror, using software developed at the CLS OMF.



me early on during that endeavor to synchrotron science. The authors are grateful for helpful advice from Dr. Peter Z. Takacs (Brookhaven National Laboratory) in setting up many aspects of the CLS optical metrology facility and thank Dr. Jeff Cutler at the CLS for providing a sample antiwear film on which to measure surface texture parameters.

References

1. G.M. Bancroft. Can. J. Chem. **82**, 1028 (2004). Also see the CLS and the CLS Optical Metrology Facility websites available from http://www.lightsource.ca and http://ex.lightsource.ca/oml/, respectively.
2. M. Sanchez del Rio and R.J. Dejus. SPIE Proc. **5536**, 171 (2004).
3. C. Welnak, G.J. Chen, and F. Cerrina. Nucl. Instrum. Methods Phys. Res. Sect. A, **347**, 344 (1994).
4. M. Kasrai, R.W. Brunner, G.M Bancroft, J.A. Bardwell, W.N. Lennard, and K.H. Tan. Appl. Surf. Sci. **99**, 303 (1996).
5. Z. Yin, M. Kasrai, G.M. Bancroft, K. Fyfe, and K.H. Tan. Wear, **202**, 172 (1997).
6. Z. Yin, M. Kasrai, M. Fuller, G.M. Bancroft, K. Fyfe, and K.H. Tan. Wear, **202**, 192 (1997).
7. P.Z. Takacs, S.N. Qian, and J. Colbert. Proc. Soc. Photo-Opt. Instrum. Eng. **749**, 59 (1987).
8. E.L. Church and P.Z. Takacs. Brookhaven National Laboratory BNL-49035, Rev. 5/94. 1994.
9. V.V. Yashchuk, A.D. Franck, S.C. Irick, M.R. Howells, A.A. MacDowell, and W.R. McKinney. Lawrence Berkeley National Laboratory LBNL-56757, May 2005. Available from http://repositories.cdlib.org/lbnl/LBNL-56757.
10. R. Brun and F. Rademakers. Nucl. Instrum. Methods Phys. Res. Sect. A, **389**, 81 (1997).

© 2007 NRC Canada

High-resolution gas phase P L-edge photoabsorption spectra of PF_5[1]

Y.F. Hu, L. Zuin, and R. Püttner

Abstract: High-resolution photoabsorption spectra of P 2s and 2p levels of PF_5 are reported. Fine structure, due to spin-orbit and ligand field splittings together with strong vibrational progression, is resolved in the Rydberg region of the P 2p spectrum. A ligand field splitting of 31 meV for the $2p_{3/2}$ orbital is obtained from the fit of the Rydberg transitions. The Franck–Condon fit analysis revealed that the vibrational progression of the higher Rydberg states is different from that of the valence-Rydberg mixed 4s state. In particular, we derived a decrease in P–F bond distances of 12 and 28 pm for the 4s valence-Rydberg mixed state and the high nl Rydberg states, respectively. The natural linewidths of the P 2p levels were determined to be 55 meV.

Key words: PF_5, Rydberg state, vibrational, ligand field splitting, photoabsorption.

Résumé : On a déterminé les spectres photoélectroniques à haute résolution des niveaux 2s et 2p du phosphore dans le PF_5. Dans la région de Rydberg du spectre 2p du phosphore, on a résolu la structure fine qui résulte de couplages spin-orbite et couplages de champ avec une progression vibrationnelle importante. Faisant appel à un ajustement des transitions de Rydberg, on a déterminé que le couplage du champ de ligand de l'orbitale $2p_{3/2}$ est de 31 meV. Une analyse de l'ajustement de Franck–Condon révèle que la progression vibrationnelle des états de Rydberg les plus élevés est différente de celle de l'état 4s de valence de Rydberg mixte. On a, en particulier, mis en évidence des diminutions respectives de 12 et 28 ppm dans les distances des liaisons P–F de l'état 4s de valence de Rydberg mixte et les états élevés nl de Rydberg. On a déterminé que les largeurs de raies naturelles des niveaux 2p du phosphore sont de 55 meV.

Mots-clés : PF_5, état de Rydberg, vibrationnel, dédoublement de champ de ligand, photoabsorption.

[Traduit par la Rédaction]

Introduction

Excitations of the 2p inner shell of gas phase molecules containing second-row elements such as Si, P, S, and Cl have been traditionally studied by electron energy loss spectroscopy (EELS) (1) with resolutions between 50 meV and 1 eV. Recent developments in soft X-ray beamlines has made it possible to record high-resolution photoabsorption spectra of these molecules using synchrotron radiation. This high resolution of ~30 meV has previously been used to resolve fine features such as vibrational structure and ligand field splitting (also called molecular field splitting) in SiF_4 (2, 3), SiH_4 (4), $SiCl_4$ (5), H_2S (6), SO_2 (7), and HCl (8).

Received April 5 2007. Accepted May 4 2007. Published on the NRC Research Press Web site at canjchem.nrc.ca on 16 June 2007.

In honour of Mike Bancroft for his mentorship, friendship, and his leadership in Canadian science, particularly in the synchrotron community.

Y.F. Hu[2] and L.Zuin. Canadian Light Source, University of Saskatchewan, Saskatoon, SK S7N 0X4, Canada.
R. Püttner. Institut für Experimentalphysik, Freie Universität Berlin, Arnimallee14, D-14195 Berlin-Dahlem, Germany.

[1]This article is part of a Special Issue dedicated to Professor G. Michael Bancroft.

[2]Corresponding author (e-mail: yongfeng.hu@lightsource.ca).

For L-edge of P-containing molecules such as PF_5, several studies of modest resolution (50–200 meV) have been carried out to determine general assignment and oscillation strength (9, 10), to study quasi-isotropic fragmentation of PF_5 (11), and to investigate ligand field splitting in the P continuum 3d orbitals (12). In this study, high-resolution photoabsorption spectra of P L-edge of PF_5 are recorded using the newly commissioned VLS-PGM beamline at the Canadian Light Source (13). An improved photon resolution (15 meV at P 2p or a resolving power of >10 000) and signal to noise ratio allowed us to resolve many more Rydberg transitions. Furthermore, vibrational fine structures due to P–F stretching are resolved in these Rydberg transitions. Vibrational progression fit revealed that the higher Rydberg states exhibit a shorter P–F bond distance upon the 2p excitation than the valence-Rydberg mixed 4s states. A ligand field splitting of 31 meV on the $2p_{3/2}$ level was obtained from the fit.

Experimental

The spectra were recorded with the VLS-PGM beamline at the Canadian Light Source (CLS) (13). The beamline employs a 185 mm PPM undulator, and three variable line-spacing plane gratings are used to cover the photon energy of 5.2–250 eV. A 10 μm slit was used for both entrance and exit slits. With these conditions, a resolving power of >10 000 is expected (14) and achieved (13) over the entire

 doi:10.1139/V07-055 © 2007 NRC Canada

range, with a maximum resolving power of ~50 000 reached at 30 eV photon energy (13). The energy scale was calibrated against Kr 3d and Ar 2p lines.

A double ionization gas cell (10 cm active path length in each chamber) was used for the photoabsorption measurements. The PF_5 gas was commercially available (research grade) and used without further purification. Typical gas pressures of a few mbar (1 bar = 100 kPa) were used in the gas cell. A 0.2 μm carbon window was used between the gas cell and the differentially pumped section to protect the UHV of the beamline. PF_5 is vulnerable to hydrolysis, therefore, the sample introduction line and the gas cell were flushed several times to passivate internal surfaces until no feature due to OPF_3 was detectable.

Results and Discussion

Overview of P 2s and 2p regions

The photoabsorption spectrum of PF_5 in the P 2p and 2s regions is shown in Fig. 1. The general features of the spectrum are in good agreement with those of previous studies (9–12). This spectrum can be divided into four regions: the broad feature in the 2p pre-edge (peaks 1 to 4 shown in the insert); the 2p pre-edge Rydberg region with many sharp structures; the 2p post-edge region (between 145 and 165 eV); and the 2s pre-edge region. Assignments of broad features, with exception of the 2p Rydberg region, are well established (9–12), and they are only discussed briefly here. Peaks 1 and 2 are assigned to transitions to the σ* (a_1') valence type antibonding orbitals from the P 2p spin-orbit components, while peaks 3 and 4 are the spin-orbit components of 2p → σ* (e′) transitions. Three broad and intense resonances (peaks 5, 6, and 7 in Fig. 1) are observed in the 2p post-edge region. They are due to transitions from 2p to the P 3d continuum orbitals, which are split by 3d ligand field splitting with an energy order of: $3d_{xz,\ yz}$ (e″) < $3d_{x^2-y^2,\ xy}$ (e′) < $3d_{z^2}$ (a_1'). Peaks 8 and 9 at 197.39 and 201.76 eV, respectively, are due to transitions of 2s to valence antibonding σ* orbitals (9). Peak positions and assignments of the above broad features are given in Table 1. The Rydberg region (between 141.5 and 145 eV) is very complex with many sharp peaks, and a number of new features are resolved. The assignment of the Rydberg states will be discussed in the next section.

Rydberg region

Figure 2 displays the Rydberg region of PF_5 below the P 2p ionization threshold. This spectrum reveals a rich fine structure that is due to the spin-orbit and ligand field splittings of the P 2p level superimposed by strong vibrational progressions. The solid line through the data points represents the results of a fit analysis, which will be described in detail later. For a basic understanding of the spectrum and the performed fit analysis, we first want to summarize the main results.

Due to the spin-orbit and ligand field splittings, Rydberg series converge towards three different P 2p ionization thresholds. The assignment of the resonances is given by the vertical bar diagrams below the spectrum. It is dominated by the 2p → 4s excitations, which exhibit a vibrational fine structure as shown by the subspectrum around 141.7 eV.

Fig. 1. Overview photoabsorption spectrum of P 2s and 2p levels of PF_5. The broad features are labeled as peaks 1–9. Their energies and assignments are given in Table 1. The sharp features between 141.5 and 150 eV belong to the 2p Rydberg transitions. The details are shown in Fig. 2 and discussed in the text.

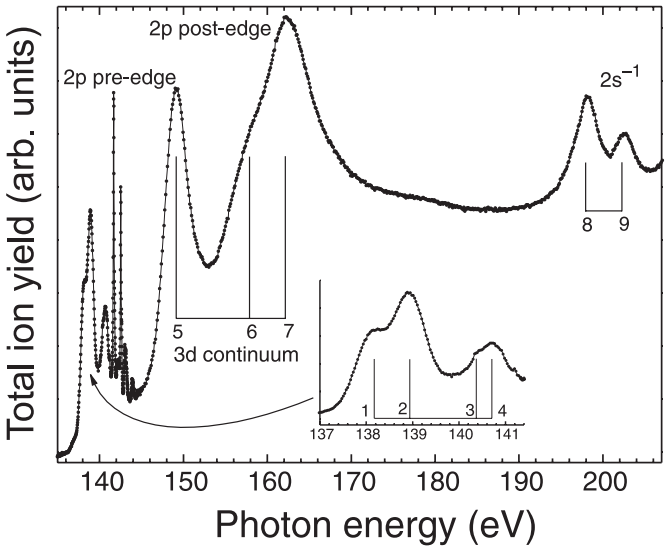


Table 1. Peak energies and assignments of broad features in the P 2s and 2p excitations of PF_5.

Peak	Energy (eV)	Assignment
2p Pre-edge		
1	138.17	$2p_{3/2} \rightarrow (9a_1')^*$
2	138.95	$2p_{1/2} \rightarrow (9a_1')^*$
3	140.40	$2p_{3/2} \rightarrow (7e'')^*$
4	140.72	$2p_{1/2} \rightarrow (7e'')^*$
2p Post-edge		
5	149.12	$2p \rightarrow 3d_{xz,\ yz}$ (e″)
6	157.48	$2p \rightarrow 3d_{x^2-y^2,\ xy}$ (e′)
7	162.16	$2p \rightarrow 3d_{z^2}$ (a_1')
2s Pre-edge		
8	198.09	$2s \rightarrow \sigma^*$ (e′)
9	202.51	$2s \rightarrow \sigma^*$ (a_2'')

This subspectrum is different from that at about 143 eV, which represents the excitations to the higher Rydberg states. This difference in the vibrational progressions is due to the mixed valence-Rydberg character of the 4s orbital, while all higher nl orbitals show a pure Rydberg character. Such a mixed valence-Rydberg character for the lowest Rydberg states was observed for similar molecules such as SiF_4 (2, 3) or SiH_4/SiD_4 (4) and resulted in a vibrational progression different from that for the higher Rydberg states.

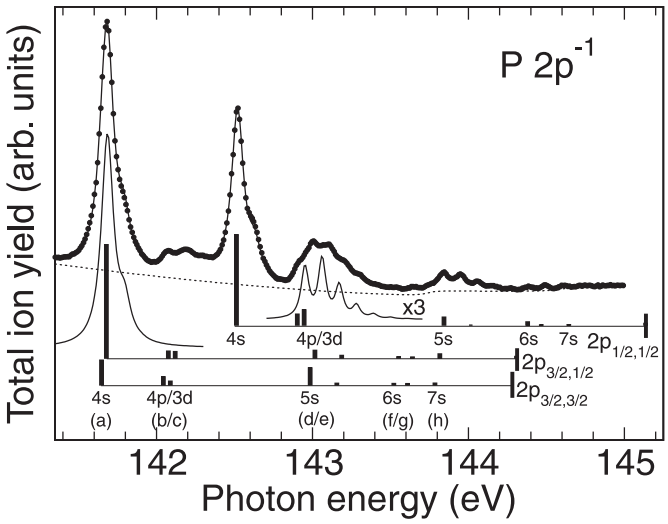
Altogether, eight different 2p → nl Rydberg transitions (as indicated with letters *a* to *h* under the $2p_{3/2,3/2}$ level in Fig. 2) were obtained from the fit analysis. Their energy positions and quantum defects are given in Table 2. Based on the assumption of an almost constant quantum defect for a nl Rydberg series, these transitions can be distinguished into two different groups of series. This also allows us to derive the energy positions of the corresponding ionization thresh-

© 2007 NRC Canada

Table 2. Energies, assignments, and quantum defects (δ) of PF_5 2p Rydberg transitions.

		Excitation energies (eV)			
Transition	Assignment	$2p_{3/2,3/2}$	$2p_{3/2,1/2}$	$2p_{1/2,1/2}$	δ
a	4s	141.647	141.678	142.513	1.73
b	4p(e′) and (or) 3d	142.044	142.076	142.903	1.53 (4p), 0.53 (3d)
c	4p(e′) and (or) 3d	142.088	142.120	142.947	1.51 (4p), 0.51 (3d)
d	5s	142.985	143.016	143.843	1.76
e	5p(e′) and (or) 4d	143.156	143.187	144.014	1.52 (5p), 0.52 (4d)
f	6s	143.521	143.552	144.379	1.77
g	5p(e′) and (or) 4d	143.609	143.641	144.467	1.49 (5p), 0.49 (4d)
h	7s	143.785	143.816	144.643	1.75
Ionization threshold	144.277	144.308	145.135		

Fig. 2. Details of the P 2p Rydberg region. The solid line through the data points represents the results of the fit. The background is represented by the dotted line. The three vertical-bar diagrams in the lower part of the figure represent the energy positions and intensities of Rydberg transitions converging towards the spin-orbit and ligand field split P 2p ionization thresholds. The assignments of the Rydberg transitions (*a* to *h* in brackets) is given in Table 2. The solid subspectra show the vibrational progressions used in the fit analysis. Note that the intensity of the subspectrum indicating the vibrational progressions used for the higher nl Rydberg transitions ($2p_{1/2,1/2}$ → transition *c*) is multiplied by a factor of three.



olds. One series (transitions *a, d, f*, and *h*) results in a quantum defect δ≈1.75 and can be readily assigned to the ns Rydberg series since (*i*) the lowest transition shows a valence-Rydberg mixing, which is typical for low ns states and (*ii*) this quantum defect value is similar to that of the 2p → 4s excitations in SiF_4 (2) and $SiCl_4$ (5). Moreover, the transitions *b, c, e*, and *g* give rise to two more Rydberg series due the small splitting between transitions *b* and *c* of 44 meV. They exhibit a quantum defect of ≈1.50 (≈0.50) by assuming that the lowest state of this series has a 4p (3d) character. A quantum defect value of ≈1.50 for np levels agrees well with the results obtained for tetrahedral SiX_4 molecules (2–5). In addition, considerable contributions of the 2p → np(e′) Rydberg excitations were calculated by different groups (11, 12), so that such an assignment is reasonable. In principle, under the trigonal bipyramidal geometry of PF_5 there exist two different np Rydberg series, namely, np(a_2'') and np(e′). However, excitations of the np(a_2'') Rydberg orbitals from the 2p levels are forbidden by dipole selection rules, so that 2p → np transitions alone cannot explain the observed splitting between transitions *b* and *c*.

The nd levels can split into the sublevels nd(e″), nd(e′), and nd(a_1'). In contrast to the np levels, transitions to all three sublevels are allowed by dipole selection rules, as also seen in the 3d splitting in the continuum of the 2p post-edge region. Such a splitting of the different 3d sublevels was observed in the tetrahedral molecules $SiCl_4$ (5) and $Si(CH_3)_4$ (3) and may explain the observed splitting. However, this leads to a quantum defect of ≈0.50, i.e., a value considerable higher than those observed for nd Rydberg transitions of different SiX_4 molecules (2–5). Nevertheless, at least one of the two series under discussion has to have nd character since (*i*) the ns series is clearly identified and (*ii*) the dipole-allowed np(e′) series alone does not explain the experimental findings. It is, however, at present unclear if the second and third series are caused by both 2p → np(e′) and 2p → nd Rydberg transitions or by 2p → nd transitions alone with an observable splitting between the 2p → 3d transitions of different symmetry.

The vibrational fine structure displayed by the subspectra is due to a change of the P–F equilibrium distance upon core excitation. Although PF_5 possesses 12 vibrational modes (15), the vibrational fine structure for the higher Rydberg states can be described by one mode only. This mode could be identified as the symmetric stretching mode and can be understood by a similar change of all bond distances. To extract detailed information on the change of the bond distance, a Franck–Condon fit analysis was performed by calculating the Franck–Condon factors on the assumption of Morse potentials for the ground and the excited states. For this, an algorithm described by Halman and Laulich (16) as well as Ory et al. (17) was used. To describe the ground-state potential energy curve, equilibrium distances and vibrational energy were taken from the literature (15, 18). We used the same potential energy curve and linewidth for all excited states with the exception of the 4s state because of the observed valence-Rydberg mixing. In addition, the same values of spin-orbit and ligand field splittings were assumed for all transitions. The background is represented by the dotted subspectrum and was described by a quadratic function as well as two arctan functions to simulate the unresolved Rydberg states directly below the ionization thresholds. In

© 2007 NRC Canada

addition, two broad Gaussians were applied to account for the broad structures at ≈141 and ≈148 eV (Fig. 1, peaks 4 and 5). Finally, the spectrum was convoluted with a Gaussian of 15 meV to simulate the experimental resolution.

As stated earlier, the fit result shown in Fig. 2 is represented by the solid lines through the data points. The energy positions of the $v''= 0 \rightarrow v'= 0$ transitions, as well as the intensities, are represented by the vertical-bar diagram. The energy positions are also summarized in Table 2 together with their quantum defects and assignments. The ionization energies derived from the assignment and the Rydberg formula are also given. From the fit, we obtained a splitting between the $2p_{3/2,3/2}$ and $2p_{3/2,1/2}$ as well as $2p_{1/2,1/2}$ ionization thresholds of 31(5) and 858(3) meV, respectively. Fits without a ligand field splitting of the $2p_{3/2,3/2}$ level were also performed. However, they resulted in about 35% higher values for χ^2 so that we see evidence for a ligand field splitting in the order of 30 meV.

The very small ligand field splitting in PF_5 is consistent with the small nuclear quadrupole splittings (QS) observed (and predicted by the partial quadrupole splitting method) from Mössbauer spectra on analogous trigonal pyramidal species. For example, the QS on the isostructural $SnCl_5^-$ species are very small or not resolvable (19). Since the QS is proportional to the ligand field splitting at core levels (20), we expect that the ligand field splitting on the Sn, Sb, or P core levels of isostructural species, such as PF_5, will also be very small. It has been reported that the QS on species such as SnF_3^- are about 4 to 5 times that of the QS on $SnCl_5^-$ (21). By a similar proportion, this 31 meV of ligand field splitting on the $2p_{3/2}$ level of PF_5 compares very favorably with a P $2p_{3/2}$ splitting of 146 meV reported for PF_3 (22).

The vibrational progression for the higher Rydberg states exhibits six vibrational substates and we obtained from this progression an increase of the vibrational energy from 101.2 to 110.0(1.0) meV as well as a decrease of the P–F bond distances by 28(2) pm. In addition, a natural linewidth of 55(3) meV is derived from the fit of all higher Rydberg states with the inclusion of the ligand field splitting and a 15 meV photon width. For the fits without ligand field splitting, this value was much larger, 76(3) meV. The vibrational progression for the 4s states with mixed valence-Rydberg character turned out to be much shorter, and we obtained a vibrational energy of 115(2) meV, a decrease of the bond distance by 12(2) pm and a linewidth of 91(3) meV. A vibrational progression based on these parameters describes the spectrum quite well. Nevertheless, these values have to be considered with caution since it is well-known from SiF_4 (2, 3) and SiH_4/SiD_4 (3, 4) that an admixing can lead to considerable excitations of bending modes. Therefore, we conjecture that the decrease in the bond distance essentially describes the actual change upon excitation. However, the higher vibrational energy and in particular the much larger linewidth are only ways of describing the unresolved vibrational modes.

Summary

With the improved photon resolution and signal to noise ratio on the VLS-PGM beamline at CLS, we were able to resolve many new transitions in the P 2p Rydberg region of PF_5. These vibrationally resolved Rydberg states were assigned to excitations from three spin-orbit and ligand field split 2p core levels. A ligand field splitting of 31 meV for the P $2p_{3/2}$ core levels is determined from the fit analysis. The 4s Rydberg state, which has mixed valence-Rydberg character, was shown to have a vibrational progression that is different from that of the pure, higher nl Rydberg states.

Sophisticated calculations are necessary to assign the additional splittings observed in transitions 2 and 3, as it is still unclear which transition ($2p \rightarrow np(e')$, $nd(e'')$, $nd(e')$, or $nd(a'_1)$) contribute significantly to the higher nl Rydberg region of the P 2p spectrum. It would be interesting to apply this high resolution (<15 meV for P 2p levels) to other P-containing molecules for more experimental data.

Acknowledgement

The research described in this work was performed at the Canadian Light Source (CLS), which is supported by Natural Sciences and Engineering Research Council of Canada (NSERC), National Research Council (NRC), Canadian Institutes of Health Research (CIHR), and the University of Saskatchewan. We thank the CLS staff for the operation of the ring and help with the PGM beamline. We thank Mike Bancroft for his continuous support and fruitful discussions on the P 2p ligand field splitting.

References

1. A.P. Hitchcock and D.C. Mancini. J. Electron Spectrosc. Relat. Phenom. **67**, 1 (1994).
2. R. Püttner, M. Domke, K. Schulz, and G. Kaindl. Chem. Phys. Lett. **250**, 145 (1996).
3. R. Püttner, M. Domke, and G. Kaindl. Phys. Rev. A, **57**, 297 (1998).
4. R. Püttner, M. Domke, D. Lentz, and G. Kaindl. Phys. Rev. A, **56**, 1228 (1997).
5. M. Domke, R. Püttner, K. Schulz, and G. Kaindl. Phys. Rev. A, **52**, 1147 (1995).
6. E. Hudson, D.A. Shirley, M. Domke, G. Remmers, and G. Kaindl. Phys. Rev. A, **49**, 161 7. (1994).
7. E. Gedat, R. Püttner, M. Dormke, and G. Kaindl. J. Chem. Phys. **109**, 4471 (1998).
8. E. Kukk, H. Aksela, O.P. Sairanen, E. Nõmmiste, S. Aksela, S.J. Osborne, A. Ausmees, and S. Svensson. Phys. Rev. A, **54**, 2121 (1996).
9. R.N.S. Sodhi and C.E. Brion. J. Electron Spectrosc. Relat. Phenom. **37**, 125 (1985).
10. J.W. Au and C.E. Brion. Chem. Phys. **221**, 135 (1997).
11. Z.F. Liu, J.N. Cutler, G.M. Bancroft, K.H. Tan, R.G. Cavell, and J.S. Tse. Chem. Phys. **168**, 133 (1992).
12. K. Ueda, Y. Muramatsu, Y. Shimizu, H. Chiba, Y. Sato, M. Kitajima, H. Tanaka, and H. Nakamatsu. Chem. Phys. Lett. **308**, 45 (1999).
13. Y.F. Hu, L. Zuin, R. Reininger, and T.K. Sham. AIP Proceedings for the 9th International Conference on Synchrotron Radiation Instrumentation, **879**, 535 (2007).
14. R. Reininger, K. Tan, and I. Coulthard. Rev. Sci. Instrum. **73**, 1489 (2002).
15. C.L. Lugez, K.K. Irikura, and M.E. Jacox. J. Chem. Phys. **20**, 8381 (1998).
16. M. Halman and J. Laulich. J. Chem. Phys. **43**, 438 (1965).

© 2007 NRC Canada

17. H.A. Ory, A.P. Gittelman, and J.P. Maddox. Astrophys. J. **139**, 346 (1964).
18. K.W. Hansen and L.S. Bartell. Inorg. Chem. **4**, 1775 (1965).
19. G.M. Bancroft and R.H. Platt. Adv. Inorg. Chem. Radiochem. **15**, 59 (1972).
20. R.P. Gupta, J.S. Tse, and G.M. Bancroft. Philos. Trans. R. Soc. **293**, 535 (1980).
21. T.C. Gibb and N.N. Greenwood. Mössbauer spectroscopy. Chapman and Hall, London, UK. 1971. pp. 387 and 392.
22. K.J. Børve, L.J. Sæthre, J.D. Bozek, J. True, and T.D. Thomas. J. Chem. Phys. **111**, 4472 (1999).

© 2007 NRC Canada

Condensation of silicon nanowires from silicon monoxide by thermal evaporation — An X-ray absorption spectroscopy investigation[1]

P.-S. G. Kim, Y.-H. Tang, T.-K. Sham, and S.T. Lee

Abstract: We report a Si K-edge X-ray absorption fine structures (XAFS) study of silicon monoxide (SiO), the starting material for silicon nanowire preparation, its silicon nanowires, and the residue after the preparation of the starting material. The silicon nanowires were condensed onto three different substrates, (*i*) the wall of the furnace quartz tube, (*ii*) a porous silicon substrate, and (*iii*) a Si(100) silicon wafer. It was found that the Si K-edge XAFS of SiO exhibits identifiable spectral features characteristic of Si in 0 and 4 oxidation states as well as in intermediate oxidation states, while the SiO residue primarily shows features of Si(0) and Si(4). The XAFS suggest that SiO is not exactly a simple mixture of Si and SiO_2. The silicon nanowires produced by the process exhibit morphology and luminescence property variations that depend on the nature of the substrate. X-ray excited optical luminescence (XEOL) at the O K-edge suggests an efficient energy transfer to the optical decay channel. The results and their implications are discussed.

Key words: silicon nanowires, thermal evaporation, silicon monoxide, X-ray absorption fine structures, X-ray excited optical luminescence.

Résumé : On a étudié les structures fines d'absorption des rayons X par le silicium à la périphérie K (SFAX) de monoxyde de silicium (SiO), le produit de départ dans la préparation de nanofils de silicium, de son résidu après la préparation et des produits. Les nanofils sont condensés de silicium sur trois substrats différents: (*i*) la surface du tube de quartz de la fournaise, (*ii*) le substrat de silicium poreux et (*iii*) une pastille de Si(100). On a trouvé que les SFAX par le silicium à la périphérie K du SiO présentent les caractéristiques spectrales du silicium dans les états d'oxydation 0 et 4 de même que celles des états d'oxydation intermédiaires alors que le résidu de SiO ne présente que les caractéristiques des états d'oxydation du Si(O) et du Si(4). Les SFAX suggèrent que le SiO n'est pas un simple mélange de Si et de SiO_2. Les nanofils produits par la méthode de préparation présentent une morphologie et des variations de la propriété de luminescence qui dépendent de la nature du substrat. La luminescence optique excitée des rayons X (LOEX) de l'oxygène à la périphérie K suggère qu'il existe un transfert efficace d'énergie vers la voie de désactivation optique. On discute de ces résultats et de leurs implications.

Mots-clés : nanofils de silicium, évaporation thermique, monoxyde de silicium, structures fines d'absorption des rayons X, luminescence optique excitée des rayons X.

Introduction

It is well-established that Si nanowires can be prepared by a number of methods, varying from laser ablation (1, 2), thermal evaporation with or without catalysts (3), and solution chemistry (4). The size, crystal orientation, and morphology vary somewhat depending on the preparation conditions, although all silicon nanowires are inevitably capped with a layer of silicon oxide. Of considerable interest is the thermal evaporation technique using silicon monoxide (SiO) as a starting material. It is generally believed that group IV element monoxides such as CO, SiO, and GeO are good sources for the preparation of elemental nanostructures through disproportionation of MO (M = C, Si, Ge) (3),

$$[1] \qquad 2MO \rightarrow M + MO_2$$

In this study, we tracked the starting material, SiO, its residue, and the products — a Si nanowire web grown on the wall of a quartz furnace tube and two Si nanowire thin films condensed on different substrates, a Si(100) wafer and a po-

Received February 20 2007. Accepted April 15 2007. Published on the NRC Research Press Web site at canjchem.nrc.ca on 16 June 2007.

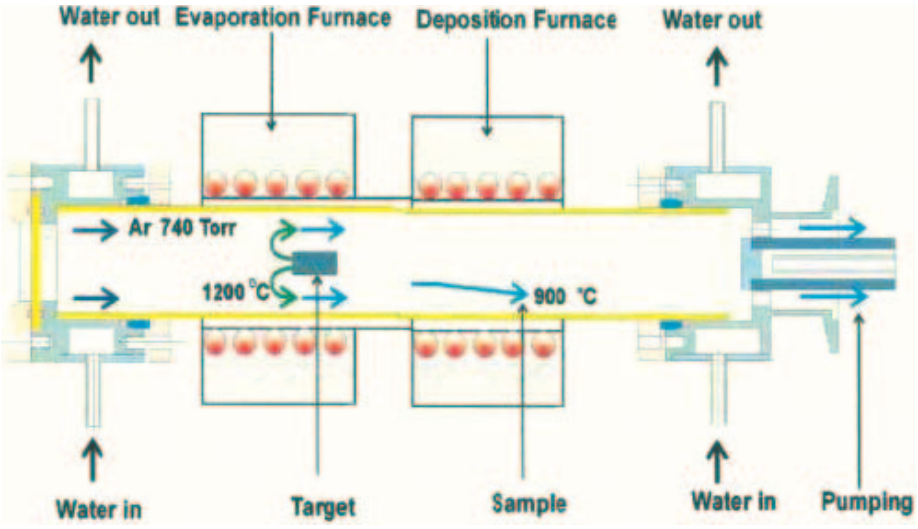
P.-S. G. Kim[2], Y.-H. Tang[3] and T.-K. Sham.[4] Department of Chemistry, *The* University *of* Western Ontario, London, Canada. **S.T. Lee.** Department of Physics and Materials Science and Center Of Super Diamond and Advanced Films (COSDAF), City University of Hong Kong, Hong Kong, P.R. China.

[1]This article is part of a Special Issue dedicated to Professor G. Michael Bancroft.

[2]Present address: Brockhouse Institute for Materials Research (BIMS) and Department of Materials Science and Engineering, McMaster Unversity, Hamilton, ON Canada.
[3]Present address: College of Materials Science and Engineering, Hunan Unversity, Changsha 410082, P.R. China.
[4]Corresponding author (e-mail: tsham@uwo.ca).

 doi:10.1139/ V07-054 © 2007 NRC Canada

Fig. 1. A schematic of the double furnace set up for the experiment (1 Torr = 133.322 4 Pa).



rous silicon film prepared on a silicon wafer — using X-ray absorption fine structure spectroscopy (XAFS) at the Si K-edge. The Si(100) and porous silicon substrate provide a nearly atomically flat and a nanostructure substrate surface morphology of the same element, respectively. Emphasis is placed on the identification of characteristic spectral features of Si and silicon oxide in different oxidation states. XEOL (X-ray excited optical luminescence) with excitation energies at the O K-edge was also used to characterize the optical properties of these Si nanowires (5, 6).

Experimental Procedures

The preparation of silicon nanowires was carried out using a double tube-furnace system, shown in Fig. 1. The reaction took place inside a quartz tube inserted into the furnace. This system provides additional temperature control for the condensation of the products. The starting material SiO was obtained commercially (Alfa, 99.5%). XRD analysis shows that it is amorphous. Several grams of the starting material were placed at one end of the quartz tube reactor set at a high temperature (Fig. 1, furnace to the left, set at 1000 °C). The substrates, an n-type Si(100) wafer and a porous silicon film prepared on a n-type Si wafer (etched electrochemically in HF at 100mA/cm^2 for 20 min) (7, 8) were placed in the middle of the second furnace set at a lower temperature (800 °C). Argon was used as a carrier gas, which flowed through the pre-evacuated tube at a pressure of 740 torr and a rate of 50 sccm during the experiment (1 Torr = 133.322 4Pa). The process was allowed to proceed under these conditions for 20 h, then the furnaces were cooled to room temperature. A brownish ring on the quartz tube and a yellowish brown film on both substrates were clearly visible. SEM images (scanning electron microscopy), recorded at Surface Science Western, and TEM images (transmission electron microscopy), recorded at the Brockhouse Institute of Materials Science of McMaster University, are shown in Fig. 2. They clearly reveal the formation of nanowires with substrate-dependent morphology. The presence of Si and oxygen was revealed by EDX.

The nanowire web condensed on the quartz wall, henceforth denoted SiNW I, is free-standing upon removal from the wall of the quartz tube. The nanowires are relatively short (~1 μm). Silicon nanowires deposited on the Si(100) wafer, henceforth denoted SiNW II, are encapsulated with a thick oxide coating and have an average diameter of >100 nm. Silicon nanowires condensed on porous silicon, henceforth denoted SiNW III, are ~50 nm in diameter on average, typical of most silicon nanowires reported in the literature (3). They are short (~1 μm) and thin (~50 nm), compared with the thick nanowire (>100 nm) on Si(100), denoted SiNW II, while the nanowires condensed on porous silicon, a nanostructured substrate, SiNW III, is the thinnest (<50 nm). After the evaporation process, a significant amount of residue remained and the residue appeared noticeably darker than the brownish starting material. The specimens of interest for XAFS and related studies are summarized in Table 1.

Si K-edge XAFS of SiO, the silicon nanowires film condensed on the three different substrates, the residue of the starting material (henceforth denoted SiO-residue), as well as the three standards, were recorded in total electron yield (TEY) and fluorescence yield (FLY) at the DCM beamline of the Canadian Synchrotron Radiation Facility (CSRF) at the Synchrotron Radiation Center, University of Wisconsin, Madison (800 MeV, ~250 mA injection current). XEOL data, excited with photon energy above the oxygen K-edge, were collected at the CSRF SGM beamline using a JY 100 monochromator equipped with a Hamamutsu photon multiplier as reported previously (9). In all measurements, the substrate's contribution to the TEY is negligible since the thickness of the specimen is larger than the absorption length of Si at the Si K-edge (1.3 μm) and the O K-edge (0.5 μm) (10).

Results and Discussion

Si K-edge XAFS of SiO and its residue

Figure 3*a* shows the Si K-edge XANES (X-ray absorption near edge structure) of SiO, the starting material in the Si nanowire synthesis, in both TEY and FLY together with the

© 2007 NRC Canada

Fig. 2. SEM images of the products from left to right, (*a*) SiNW I, silicon nanowire condensed on the quartz tube, (*b*) SiNW II, silicon nanowire thin films on a Si(100) wafer, and (*c*) SiNW III, silicon nanowire on a porous silicon substrate. Transmission electron microscope images of (*d*) free-standing SiNW I and (*e*) SiNW III (on a porous silicon substrate) show similar results as SEM (obtained with a Philips CM12 operating at the accelerating voltage of 120 KV).

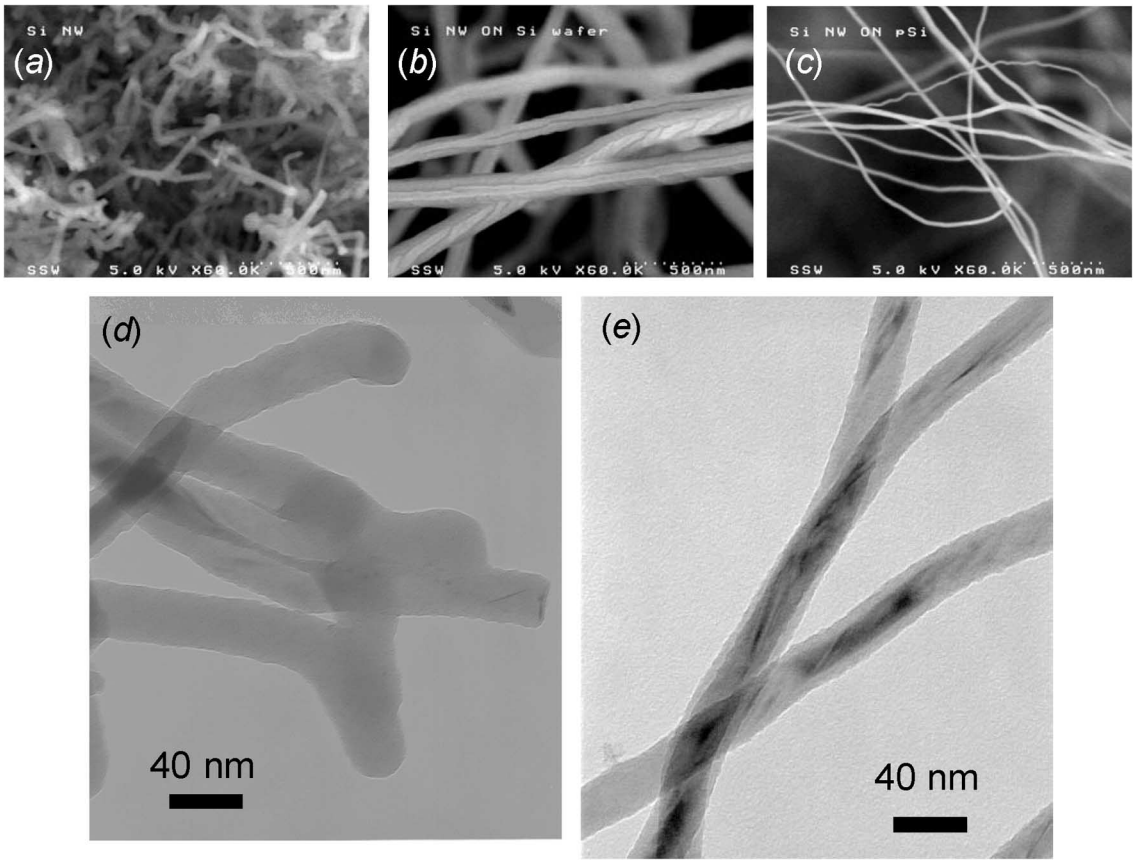
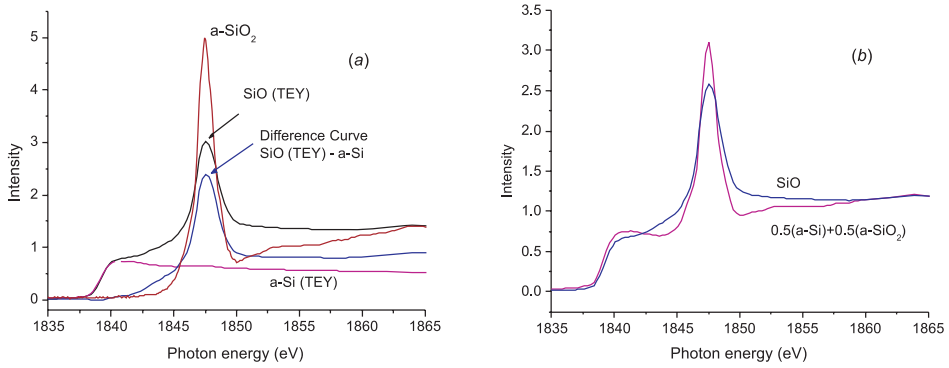


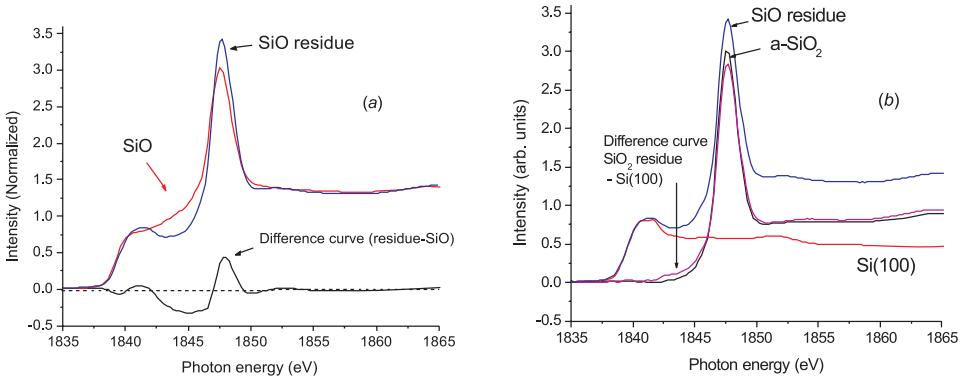
Fig. 3. (*a*) Si K-edge XANES of SiO together with that of amorphous Si and amorphous SiO_2 in TEY; the difference curve between SiO and amorphous Si (normalized to the elemental white line) is also shown. (*b*) A comparison of SiO XANES with a synthesized XANES of 0.5(a-Si) + 0.5(a-SiO_2).



XANES of amorphous Si (a-Si) and amorphous SiO_2 (a-SiO_2) recorded in TEY. The latter two specimens serve as a standard for elemental Si(0) and dioxide Si(4) material with no significant long-range order, respectively. We see from Fig. 3*a* that the resonance characteristics of elemental silicon Si(0) and silicon dioxide Si(4+) are clearly noticeable at 1841 and 1848 eV, respectively, in a-Si and a-SiO_2. The 1841 eV peak arises from the elemental Si 1s to conduction band (p character) dipole transition and is blurred compared with the well-known doublet (band structure) feature of crystalline Si (11). The 1848 eV peak arises from the Si 1s to t_2 transition in a tetrahedral "SiO_4" local environment. These features are clearly present in the SiO XANES, although there is a noticeable broadening. This observation indicates that in SiO, there exists tetrahedral "$SiSi_4$" and "SiO_4" bonding locally with no significant long-range order. Perhaps the most interesting region is the absorption coefficient between 1841 and 1845 eV. This region exhibits con-

© 2007 NRC Canada

Fig. 4. (*a*) Si K-edge XANES of SiO, its residue recorded in TEY, and the difference spectrum. (*b*) Si K-edge XANES of SiO residue, Si(100), and their difference curve; the Si XANES of a-SiO_2 is also shown.



siderable and continuous absorption intensity between the Si(0) and Si(4) white line indicating the existence of a combination of tetrahedral "Si_xSiO_y" (where x + y = 4 or less) bonding environments locally with Si in the intermediate oxidation states (e.g., 1–3). It has been shown in a study of the Si/SiO_2 interface from a thin film of silicon oxide grown on a silicon substrate that all oxidation states (0 to 4) can exist in the Si/SiO_2 interface where the dioxide is often the dominant oxide component (12). The difference curve between the normalized XANES (TEY) of SiO and amorphous Si (at the elemental Si K-edge, 1841 eV) is also shown in Fig. 3*a*. It clearly reveals the continuous region of absorption intensity between 1842 and 1847 eV. This feature is absent in the a-SiO_2 spectrum. Fig. 3*b* displays a comparison of the SiO XANES with the stoichiometric sum of the a-Si and a-SiO_2 XANES. It is apparent from Fig. 3*b* that SiO is not exactly a mixture of Si and SiO_2. The above observations provide convincing evidence for the presence of intermediate oxidation states of Si in SiO, most probably forming a random network of Si-Si and Si-O bonds.

Figure 4*a* compares the Si K-edge XANES of SiO with its residue in some detail. It shows the XANES recorded in TEY and normalized to unit edge jump, together with the difference spectrum. The white lines, characteristic of the elemental Si (1841 eV) and the Si dioxide (1848 eV) and associated features for the SiO-residue, sharpen noticeably at the expense of the intensity between the two peaks for the starting material; i.e., the absorption features of Si, characteristic of the intermediate oxidation states of Si seen in SiO as shown in the 1842–1847 eV region of the difference curve, decreased markedly in the SiO-residue. This is accompanied by an increase in the intensity of the SiO_2 white line.

Figure 4*b* compares the XANES of the SiO-residue with that of a Si(100) wafer of which the white line associated with elemental Si(0) is scaled to the same height as that for the SiO- residue so that the difference curve will remove the elemental Si contribution to SiO. The difference curve is very similar to that of a-SiO_2, although the oxide resonance is less intense and there is still some residue in the 1842–1847 eV region. These observations are consistent with the notion that SiO has undergone disproportionation to form Si and SiO_2.

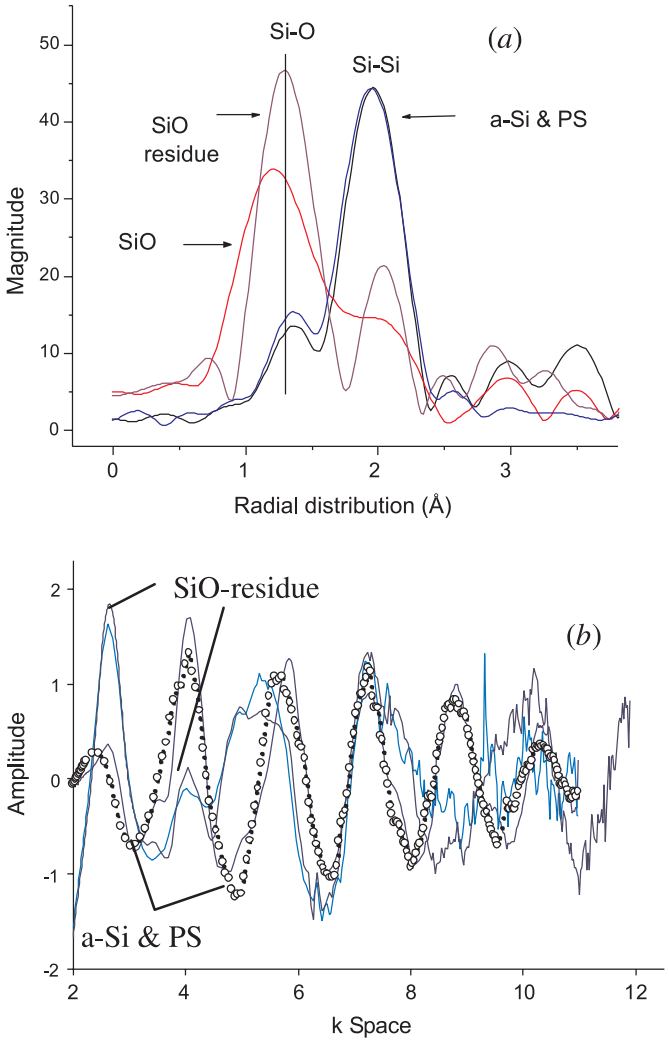
It is interesting to note that the structure of SiO is still being debated. For example, Yasatitis and Kaplow (13) first reported X-ray diffraction results of SiO and suggested that SiO assumed a phase of its own, while others believe that SiO disproportionates into Si and SiO_2. More recently, Holt et al. (14) reported X-ray diffraction results using synchrotron radiation. They showed that the radial pair distribution function is similar to that of a mixture of Si and SiO_2 but did not elaborate pending further analysis.

Let us now revisit the structure of SiO from the EXAFS (extended X-ray absorption fine structures) perspective. The XAFS spectrum is conveniently divided into two regions, (*i*) the XANES region, the first ~50 eV above the edge where bound-to-bound and bound-to-quasi-bound transitions take place and (*ii*) the EXAFS region that appears as oscillations and extends as much as 1 keV above the threshold. EXAFS arises from the modulation of the absorption coefficient at the absorbing atom by the interference of the outgoing and the backscattered photoelectron wave (by neighboring atoms). EXAFS is often denoted by $\chi(k)$, where $k = 0.513\ (E - E_0)^{1/2}$ ($Å^{-1}$), is the wave vector and E and E_0 are the photon energy above and at the threshold, respectively. $\chi(k) = A(k)\Phi(k)$, where the amplitude term $A(k)$ contains information about the coordination number, the bond length of the neighboring atom, and the dynamic behavior (Debye–Waller factor). $\Phi(k)$ is the phase function containing information about the phase shifts of the absorbing and backscattering atom and the bond length. EXAFS can be analyzed with Fourier transform (FT) and curve fitting. FT separates the amplitude and phase and yields the phase modified radial distribution of atomic shells around the absorbing atom. FT was used in our analysis. A fully quantitative analysis is not reported here because the presence of a distribution of elemental silicon wires of difference sizes and surface silicon oxide in these systems will hamper the accuracy of the analysis.

Figure 5*a* and 5*b* shows the FT of the Si K-edge EXAFS and the EXAFS of SiO, SiO-residue, porous silicon (PS), and a-Si (Δk ~ 2.7–12 $Å^{-1}$ with k^2 weighting), respectively. PS and a-Si are used as references because they do not exhibit significant long-range order. From the FT, we see that SiO exhibits two main peaks at 1.29 and 2.08 Å, followed by a couple of weak peaks at 2.84 and 3.32 Å. These peaks are significantly broad compared with that of the SiO residue and a-Si in spite of the fact that similar data length (~2.7 – ~11 $Å^{-1}$) was used in the analysis (Fig. 5*b*). This indicates that there is a distribution of Si–O and Si–Si dis-

© 2007 NRC Canada

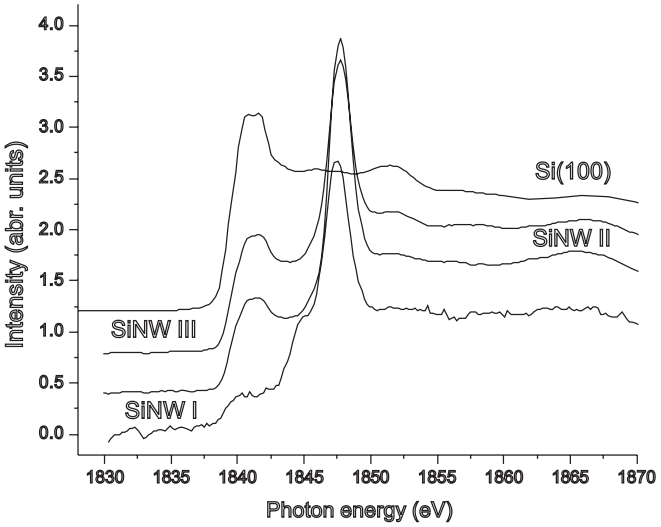
Fig. 5. (*a*) Fourier Transform of the Si K-edge EXAFS (k^2 weighted) of SiO, its residue, porous silicon, and amorphous silicon. The vertical line marks the position of the first Si-O shell in a-SiO_2 (not shown) and the first Si–Si shell in a-Si and PS, which also show the presence of surface oxide. (*b*) The corresponding EXAFS, the open circles represent amorphous silicon; porous siliocn shows similar patterns while SiO and SiO-residue exhibit closely related oscillations as noted.



tances in SiO. The two main peaks correspond to the first shell Si–O and Si–Si interatomic distances in SiO after the usual phase correction (add ~0.3 Å). It is interesting to note that after phase correction, these peak positions, especially the first two peaks, compare favorably with the X-ray diffraction results of SiO of which the radial distribution curve shows peaks at 1.6, 2.41, 3.2, and 3.6 Å (14). The first two peaks in the SiO FT were attributed to the first shell Si–O and Si–Si interatomic distances. Another interesting feature is that the EXAFS Si–Si interatomic distance in SiO, as observed in the FT, deviates towards longer interatomic distance slightly from that in PS and a-Si. This observation supports the notion that SiO is not exactly a mixture of Si and SiO (13).

The FT of the EXAFS of the SiO-residue displays similar radial distribution as that of SiO, except that the first two

Fig. 6. Normalized Si K-edge XANES for SiO residue and the three Si nanowire specimens, SiNW I (quartz), SiNW II (Si wafer), and SiNW III (PS).



peaks in the FT sharpen considerably, consistent with the XANES results. This suggests that the SiO-residue exhibits a higher degree of order and produces more Si(4+) sites upon heating. The Si–O distance in the SiO-residue is similar to that of SiO_2 (not shown for clarity and marked by a vertical line) in the FT, supporting the notion that disproportionation has taken place, although we cannot rule out the presence of unreacted SiO in the residue since a comparison of Fig. 3*b* and Fig. 4*b* indicates that the XANES of SiO-residue, though very similar to, is still not exactly the sum of SiO_2 and Si.

Si K-edge XAFS of SiNW condensed on various substrates

Figure 6 shows the Si K-edge XANES for the three types of Si nanowires collected from the Si nanowire web on the quartz tube (SiNW I) and the two thin films on the Si wafer and porous silicon substrate (SiNW II and SiNW III, respectively) (Table 1). The features are similar to those recorded previously (5–9, 15). All spectra have been normalized to unity edge jump at 1880 eV so that we can compare the relative element and oxide content in these SiNWs by comparing their relative edge jump (5). The absorption at 1880 eV is flat and the absorption coefficient between this energy and the photon energy just below the edge can be used to represent the total edge jump of all Si components (Si in the core of the nanowire and the encapsulating Si oxide) (9, 15). From Fig. 6, we see that the elemental white line at 1841 eV is the least intense in the SINW I specimen (the SiNW removed from the quartz tube) followed by that of SiNW III (the SiNW on porous silicon) and then SiNW II (the SiNW on Si(100)). The silicon oxide to silicon ratio (relative edge jump) estimated from Fig. 6 shows the trend SiNW I > SiNW II > SiNW III, as expected since the shorter and thinner wires have a relatively large surface area of oxides (11). In addition, a significant suboxide feature is observed at 1845 eV in SiNW I, which is not seen in the other samples. This feature is reminiscent of similar features observed in

© 2007 NRC Canada

Table 1. Summary of specimens for XAFS and related investigations.

Specimens	Description
SiO	Commercially obtained powder (Alfa, 99.95%)
SiO-residue	Residue of the starting material
SiNW I	Silicon nanowire removed from the quartz tube, free-standing
SiNW II	Silicon nanowire condensed on the surface of a Si(100) wafer
SiNW III	Silicon nanowire condensed on the surface of a porous silicon film (~10 μm) prepared from a n-type Si(100) wafer. (Refs. 7, 8)
a-Si	Amorphous silicon film prepared by IMS, NRC
a-SiO_2	Amorphous silicon dioxide film prepared by IMS, NRC
PS	p-Type porous silicon (20 mA, 20 min) (Ref. 11)
Si(100)	HF refreshed n-Si(100) wafer with a resistivity of ~ 1–10 Ωcm

SiNW chains with oxide nodules (6) and may be associated with the oxygen from quartz as an oxygen source. This is likely due to the short length morphology of the wires with oxide nodules at the tip (Fig. 2). The Si K-edge feature for Si(0) is most blurred in SiNW I, indicating that it is likely to contain a wider distribution of small Si nanostrucutes with a relatively large Si/SiO_2 interface (5–9, 15).

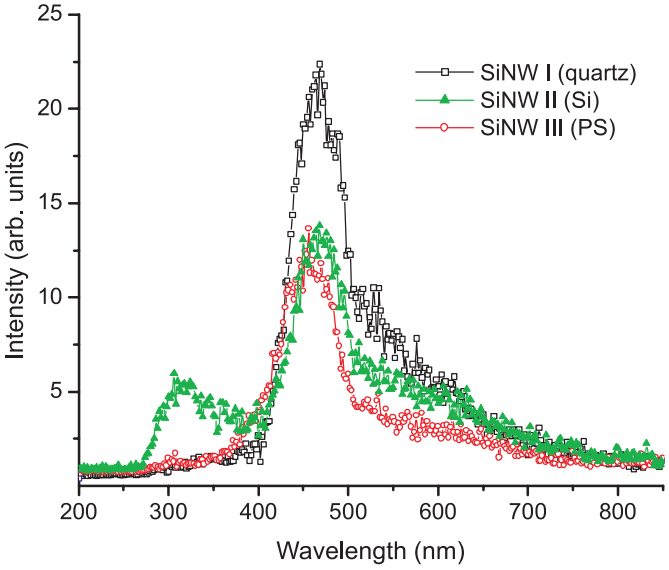
It is worthwhile to comment on the dependence of the morphology on the substrate. It should be noted that no catalyst, such as Au nanoparticles, was used. The quartz surface could be a source of oxygen and be responsible for the relatively high oxide content and the presence of nodules in SiNW I. HF-refreshed Si(100) is a relatively flat surface and the substrate as well as Si from SiO can both serve as the Si source for the growth, leading to thicker wires in SiNW II. Porous silicon is itself a nanosubstrate. Thus, silicon nanowire grown on PS (SiNW III) is expected to be the thinnest, as is observed.

It is generally recognized that as-prepared silicon nanowire is encapsulated by a thick oxide layer with a somewhat rugged Si-oxide interface. It is not too surprising, judging from the SEM (Fig. 2), that the thick SiNW II (diameter of the order of ~10^2 nm) has the least fraction of oxygen since the oxide layer does not thicken dramatically as the size of the nanowire increases, and that the SiNW II is significantly thicker than SiNW I and SiNW III (diameter on the order of ~10 nm), which is significantly longer than SiNW and is without oxide nodules.

XEOL studies of SiNW

Figure 7 shows the XEOL recorded for the three different SiNW specimens with excitation photon energy above the oxygen K-edge (550 eV). The XEOL from SiNW I and SiNW III are very similar to other silicon nanowires, such as oxide-capped silicon nanowire or an alternate Si nanoparticle-silicon oxide chain (5, 6). The emissions at ~460 nm, ~530 nm, and ~630 nm have been attributed to silicon oxide, small nanocrystallites in the nanowire and Si-oxide interface (5, 6). The position of the maximum intensity and branching ratio (peak intensity/total intensity) vary somewhat, reflecting the variation in morphology. The SiNW/Si II specimen exhibits an intense feature at ~310 nm, which is characteristic of emissions from defects of silicon oxide glass (16). It is not absolutely clear at present whether or not this silicon dioxide glass structure is part of the encapsulating oxide on the thick nanowire, since similar emissions in this region are significantly less noticeable from the free-standing SiNW I and SiNW III. This indicates that the morphology and structure of the oxide layer on SiNW II is different from that of the other two SiNW specimens. Returning to the SEM and TEM, we clearly see the unusual textures of the very thick wires in SiNW II. These structures are clearly related to this luminescence in the UV, although the exact details require further investigation.

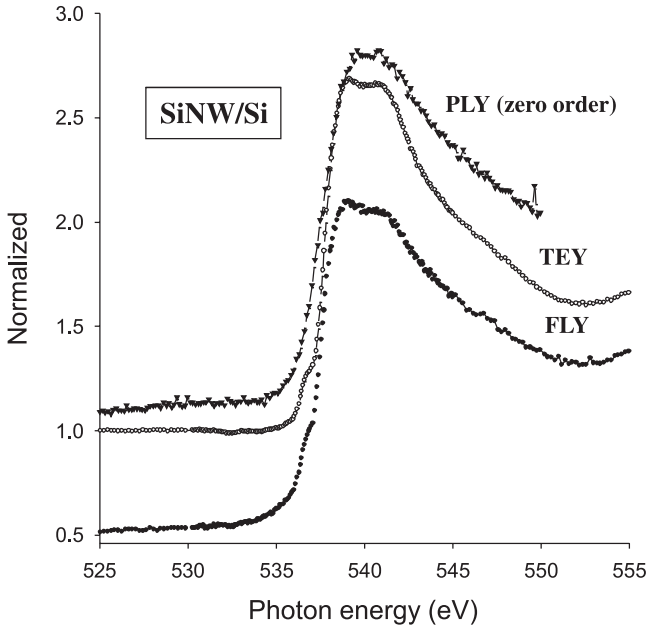
Fig. 7. XEOL of the three Si nanowire samples excited at 550 eV (photon energy).



The corresponding O K-edge XANES in TEY, FLY, and PLY (photoluminescence in zero order) for SiNW III (on a Si wafer substrate) is shown in Fig. 8. The O K-edge spectra recorded at selected wavelengths (~300 nm, 460 nm, 600 nm) are similar, albeit with lower count rates. Similar results are also obtained for the other SiNW samples (not shown). The most noticeable feature in Fig. 8 is the positive edge jump when the absorption is monitored with PLY. This observation indicates that the luminescence is associated with electronic states involving oxygen (17). In other words, the luminescence yield from the specimen with excitation photon energies across the O K-edge tracks the absorption coefficient. Thus the X-ray energy absorbed by oxygen is effectively transferred to the optical decay channel. It must be

© 2007 NRC Canada

Fig. 8. O K-edge XANES of SiNW II (on Si wafer) recorded in TEY, FLY, and PLY (zero order).



noted that neither SiO nor its residue exhibits any detectable XEOL.

Conclusion

We have reported a study of SiO in which we tracked SiO, the starting material in the preparation of silicon nanowires, its residue, SiO-residue, and its products (Si nanowires) deposited on different substrates with X-ray absorption spectroscopy at the Si K-edge and X-ray excited optical luminescence at the O K-edge. We found that despite the similarity, SiO is not exactly a mixture of Si and SiO_2. The chemical reaction leading to the formation of Si nanowire is almost certainly a disproportionation reaction of SiO. The products are silicon oxide encapsulated silicon nanowires with morphology and optical property variations as characterized by SEM, XAFS, and XEOL. While thick Si nanowires with a distinct glassy silicon oxide emission features are formed on a nearly atomic flat Si(100) surface, Si nanowires removed from the quartz tube and deposited on a nanostructured porous silicon surface exhibit typical emission features.

Acknowledgements

Research at *The* University *of* Western Ontario is supported by Natural Sciences and Engineering Research Council of Canada (NSERC), Canada Foundation for Innovation (CFI), and CRC of Canada. Research at CSRF is supported by the National Research Council (NRC) and an NSERC MFA grant. SRC is supported by the NSF (US), Grant No, DMR-0084402. We thank Kim Tan and Brian Yates for their technical assistance. Research at the City University of Hong Kong is supported by a CERG grant (CityU 1294/03E) from the Research Grant Council of Hong Kong, SAR, China. The gifts of amorphous silicon and amorphous silicon oxide specimens from Dr. D.X. Xu of the Institute for Materials Science, National Research Council of Canada (Ottawa) are gratefully acknowledged.

References

1. Y.F. Zhang, Y.H. Tang, N. Wang, D.P. Yu, I. Bello, and S.T. Lee. Appl. Phys. Lett. **72**, 1835 (1988).
2. A. Morales and C.M. Lieber. Science, **279**, 208 (1998).
3. S.T. Lee, N. Wang, Y.F. Zhang, and Y.H. Tang. MRS Bull. **24**, 36 (1999).
4. J.D. Holmes, K.P. Johnson, R.C. Doty, and B.A. Korgel. Science, **287**, 1471 (2000).
5. T.K. Sham, S.J. Naftel, P.-S. G. Kim, R. Sammynaiken, Y.H. Tang, I. Coulthard, A. Moewes, J. W. Freeland, Y. Hu, and S.T. Lee. Phys. Rev. B, **70,** 045313 (2004).
6. X.H. Sun, N.B. Wong, C.P. Li, S.T. Li, and T.K. Sham. J. Appl. Phys. **96**, 3447 (2004).
7. I. Coulthard, Y.-J. Zhu, S. Degan, and T.K. Sham. Can. J. Chem. **76**, 1707 (1999).
8. I. Coulthard, D.-T. Jiang, Y.-J. Zhu, and T.K. Sham. J. Porous Mater. **7**, 165 (2000).
9. Y.-F. Hu, K.H. Tan, P.S. Kim, P. Zhang, S.J. Naftel, T.K. Sham, I. Coulthard and B.W. Yates. Rev. Sci. Instrum. **73**, 1379 (2002).
10. T.K. Sham, S.J. Naftel, and I. Coulthard. Chemical applications of synchrotron radiation. Vol II. *Edited by* T.K. Sham. World Scientific, Hackensack, N.J. (2002).
11. Y.F. Zhang, L.S. Liao, W.H. Chan, R. Sammynaiken, S.T. Lee, and T.K. Sham. Phys. Rev. B, **61**, 8298 (2000).
12. F.J. Himpsel, F.R. McFeely, A. Taleb-Ibrahimi, J. A. Yarmoff, and G. Hollinger. Phys. Rev. B, **38**, 6084 (1988).
13. J.A. Yasaitis and R. Kaplow. J. Appl. Phys. **43**, 995 (1972).
14. A. Holt, T. Wieder, and M. Knapp. HASYLAB Ann. Rep. Available from http://hasyweb.desy.de/science/annual_reports/1999_report/index.html. (1999).
15. Y.F. Zhang, L.S. Liao, W.H. Chan, S.T. Lee, R. Sammynaiken, and T.K. Sham. Phys. Rev. B, **61**, 8298 (2000).
16. J.H. Stathis and M.A. Kastner. Phys. Rev. B, **35**, 2972 (1987).
17. A negative edge jump in PLY is not uncommon if the states are not coupled to the luminescence chromophore. See P.-S. Kim, T.K. Sham, P. Zhang, M.-K. Fung, S.T. Lee, Y.-F. Hu, and B.W. Yates. J. Am. Chem. Soc. **123**, 8870 (2001).

© 2007 NRC Canada

Characterization of the influence of fission product doping on the anodic reactivity of uranium dioxide[1]

Heming He, Peter G. Keech, Michael E. Broczkowski, James J. Noël, and David W. Shoesmith

Abstract: The influence of fission product doping on the structure, composition, and electrochemical reactivity of uranium dioxide has been studied using X-ray diffractometry (XRD), scanning electron microscopy (SEM/EDX), Raman spectroscopy, and X-ray photoelectron spectroscopy (XPS). Experiments were conducted on SIMFUEL specimens with simulated burn-ups (increasing doping levels) of 1.5, 3.0, and 6.0 atom%. As the dopant level increased, the lattice contracted, suggesting the dominant formation of dopant-oxygen vacancy clusters. The smaller than expected lattice contraction can be attributed to the segregation of Zr (one of eleven added dopants) to ABO_3 perovskite-type phases that SEM/EDX shows also contain Ba, Ce, and possibly some U. Raman spectroscopy shows that doping leads to a loss of cubic symmetry, possibly associated with tetragonal distortions. Raman mapping confirms this loss of cubic symmetry and suggests the specimen is not uniformly doped. Electrochemical experiments show that these distortions lead to a decrease in the oxidative dissolution rate of the UO_2 with increased doping density.

Key words: UO_2, X-ray diffraction, electrochemistry, Raman spectroscopy, nuclear fission products.

Résumé : Faisant appel à la diffraction des rayons X (DRX), à la microscopie électronique à balayage (MEB), à la spectroscopie Raman et la spectroscopie photoélectronique des rayons X (SPX), on a étudié l'influence du dopage du produit de fission sur la structure, la composition et la réactivité électrochimique du dioxyde d'uranium. Les expériences ont été réalisées sur des spécimens de SIMFUEL comportant des épuisements simulés (avec augmentation des niveaux de dopage) de 1,5, 3,0 et 6,0 atom%. Une augmentation du niveau de dopant provoque une contraction du réseau cristallin ce qui suggère la formation dominante d'agrégats de dopants et de lacunes d'oxygène. Le fait que la contraction du réseau cristallin soit plus faible que prévu peut être attribué à la ségrégation du Zr (un des onze dopants ajoutés) aux phases ABO_3 de type perovskite pour lesquelles la microscopie électronique à balayage démontre aussi la présence de BA, de Ce et éventuellement d'uranium. La spectroscopie Raman montre que le dopage conduit à une perte de la symétrie cubique qui peut être associée à des distorsions tétragonales. La cartographie Raman permet de confirmer la perte de la symétrie cubique et suggère que le spécimen n'est pas dopé d'une façon homogène. Des expériences électrochimiques montrent que ces distorsions conduisent à une diminution du taux de dissolution oxydante du UO_2 avec une augmentation de la densité du dopage.

Mots-clés : UO_2, diffraction des rayons X, spectroscopie Raman, produits de fission nucléaire.

[Traduit par la Rédaction)

Introduction

A key issue in determining the corrosion performance of nuclear fuel under permanent disposal conditions is the influence of in-reactor burn-up (the amount of thermal energy generated per unit mass of uranium dioxide) on fuel corrosion and dissolution rates leading to the release of radionuclides to groundwater. Fuel burn-up leads to complex and significant changes in the properties of the fuel (1–3) and the extent of burn-up changes with reactor type. For light water reactors (LWR), burn-up is typically in the range 35–45 GWd/MTU, compared with 6 to 12 (average ~8) GWd/MTU for CANDU reactor fuel. However, there is an on-going trend to higher burn-ups (3–6).

Subtle changes in fuel density occur as fabrication sintering porosity is eliminated, and the generation of fission gas bubbles expands the lattice and interlink to form grain boundary tunnels (3, 7). At higher linear power ratings, UO_2 grain growth becomes an important process, and thermal stresses cause cracking of the fuel matrix (3). Collision cascades initiated by fission and alpha recoil events create a large number of atomic defects, but the final defect number is limited through thermal reannealing (8). Inhomogeneity arises at both microscopic and macroscopic levels because of temperature and neutron flux gradients within the fuel as

Received April 11 2007. Accepted May 22 2007. Published on the NRC Research Press Web site at canjchem.nrc.ca on 11 July 2007.

H. He, P.G. Keech, M.E. Broczkowski, J.J. Noël, and D.W. Shoesmith.[2] Department of Chemistry, *The* University *of* Western Ontario, 1151 Richmond St. London, ON N6A 5B7, Canada.

[1]This article is part of a Special Issue dedicated to Professor G. Michael Bancroft.

[2]Corresponding author (e-mail: dwshoesm@uwo.ca).

 doi:10.1139/V07-056 © 2007 NRC Canada

well as through the segregation of fission products that are insoluble in the UO_2 matrix (1, 3). The influence of neutron irradiation was discussed by Spino and Papaiannou (9) and refs. cited therein. Transmission electron microscopy (TEM) has shown that lattice damage is manifested as an increase in dislocation density and increases with increasing burn-up up to ~40 GWd/MTU. This gives rise to a dislocation cell structure leading to grain subdivision in the outer rim of LWR fuel.

These physical effects are not easily reproduced in nonradioactive analogues of spent UO_2. However, the chemical effects of nonvolatile fission products and actinides, which introduce dopants at substitutional and defect sites in the uraninite structure, can be reproduced in simulated spent fuels (i.e., SIMFUEL) (10–12). For these materials, if the free energy of a fission product oxide (conveniently expressed as an electrochemical potential) is more negative than the oxidation potential of the fuel then it is stabilized as an oxide; otherwise, it will be present as a stable element (metal). In the case of Mo, these potentials are close and it can exist in either oxide or elemental forms. Whether or not a specific fission product that is stable as an oxide remains in solid solution or separates into a distinct precipitate can be determined by its compatibility with the face-centered cubic UO_2 matrix. In many cases, fission products can divide between a range of structures, but an abundance of evidence exists to show that actinides and lanthanides remain in solid solution, with UO_2 (13, 14) substituting for U in the fluorite lattice. The chemical composition and microstructure of nuclear fuel have been studied extensively (1, 3, 15–17) and will only be summarized here.

Elements stable in metallic form (Mo, Ru, Pd, Tc, Rh) tend to congregate in alloy precipitates, generally referred to as ε-particles.

Fission products, which are stable as oxides but incompatible with the UO_2 matrix (Rb, Cs, Ba, Zr, Nb, Mo, Te, Sr), separate into precipitates sometimes referred to as grey phases. These phases tend to have the general composition ABO_3 and to adopt a cubic perovskite-type structure with Ba, Sr, and Cs in the A sites and Zr, Mo, U, Pu, and rare earths in the B sites (1).

Elements that remain as substitutional ions within the fuel matrix include the actinides: Np, Pu, Am, and Cm; the rare earths elements (REE): La, Ce, Pr, Nd, Pm, Sm, Eu, Gd, and Y; and Sr, Zr, Ba, Te, and Nb within the limits of their solubility in the UO_2 and to the extent that they have not precipitated in perovskite-type oxides.

Two fission products are worth special mention: Mo, which can be present in both metallic and oxide forms and hence helps to maintain the fuel close to stoichiometry; Zr, which tends to distribute between perovskite-type phases and the fuel matrix, within which it exerts a major influence on lattice dimensions (18).

Despite the fact many of the elements created during fission are of lower oxidation state than U^{IV}, the excess oxygen created is almost completely neutralized by oxidation of elemental Mo and reaction with the inner Zr-cladding surface (19, 20). The approximate change in CANDU fuel stoichiometry has been calculated to be from $UO_{2.000}$ to $UO_{2.007}$ (21), and O/M measurements confirm the absence of significant fuel oxidation in both low (22) and high (23) burn-up LWR fuel. This slight increase in degree of nonstoichiometry, coupled to the substitution of U^{IV} by trivalent or divalent ions, leads to a substantial decrease in electrical resistivity (24–26).

Considerable evidence exists to show that the fission product and actinide–lanthanide doping of the fuel associated with burn-up exerts a significant effect on the air oxidation of fuel (27–30). These studies, as well as studies on the impure natural form of UO_2 (uraninite) (31) show that both the mechanism of oxidation of UO_2 to U_3O_8 and its rate are influenced by the presence of dopants and impurities. A prominent feature of doped UO_2 is the enhanced kinetic stability of the cubic fluorite structure (compared with that of undoped UO_2) with respect to U_3O_8 formation; oxidation experiments on doped UO_2 show that it retains this structure to higher temperatures and for longer times than the undoped material (27), clearly demonstrating a retardation of the oxidation kinetics.

The analysis of X-ray diffraction (XRD) patterns for partially oxidized samples shows that the oxidation of pure UO_2 (or lightly doped UO_2) proceeds via U_3O_7,

$$[1] \qquad UO_2 \rightarrow U_3O_7 \rightarrow U_3O_8$$

whereas UO_2 doped with larger amounts of dopants (such as Gd) proceeds via U_4O_9,

$$[2] \qquad UO_2 \rightarrow U_4O_9 \rightarrow U_3O_8$$

These observations are supported by studies with SIMFUELs (10, 29), LWR fuels (highly doped and following the reaction path [2] (32)) and CANDU fuels (lightly doped and following reaction path [1] (33)). In addition, the studies of Cobos et al. (29) on specimens with simulated burn-ups covering the whole range up to 200 GWd/MTU also suggest that the kinetics of the transformation, $UO_2 \rightarrow U_4O_9$, are slightly retarded as the dopant concentration increases. This effect is virtually negligible for simulated burn-ups below ~25 GWd/MTU (i.e., over the burn-up range anticipated for CANDU fuels).

Weight gain measurements show that the oxidation of doped UO_2 proceeds to a stoichiometry of $UO_{2.4}$ despite XRD evidence demonstrating the retention of the cubic fluorite structure and the peak broadening and shifts characteristic of U_4O_9 ($UO_{2.25}$) (27, 29). A similar stabilization of U_4O_{9+y} has been observed for UO_2 doped with Pu (34) or Th (35). While the reasons for this retained stability of the fluorite phase remain uncertain, it has been suggested that the dopants may disrupt the defect cluster ordering that is thought to be responsible for the tetragonal distortion of the U_3O_7 lattice (30).

Our previous studies show that under oxidizing aqueous conditions, the corrosion of UO_2 proceeds via a surface oxidation step prior to destruction of the lattice and the release of soluble U^{VI}. In the neutral to slightly alkaline conditions anticipated for waste repository groundwater, dissolved uranium then reprecipitates to form corrosion product deposits,

$$[3] \qquad UO_2 \rightarrow UO_{2+x} \rightarrow {UO_2}^{2+} \rightarrow UO_3 \cdot yH_2O$$

While schoepite formation is observed under laboratory conditions, more complex depositions are anticipated under disposal conditions.

© 2007 NRC Canada

Based on the evidence for air oxidation, one might anticipate an influence of lattice doping on the corrosion process, which involves a similar reaction sequence. In this paper we have studied this possibility using a range of simulated spent fuels (SIMFUELs) ranging from 1.5 atom% burn-up (14 GWd/MTU, typical of normal CANDU fuel), to 3.0 atom% (28 GWd/MTU, representing a reasonable high burn-up CANDU fuel), and 6.0 atom% (56 GWd/MTU, corresponding to a high burn-up LWR fuel). Changes in structure and composition have been analyzed by X-ray diffractometry (XRD), Raman spectroscopy, and X-ray photoelectron spectroscopy (XPS); subsequently, the oxidative reactivity has been determined electrochemically.

Experimental

Fuel specimens and electrode preparation

The three electrodes used in this study were made with 1.5, 3, 6 atom% SIMFUEL pellets, fabricated at Chalk River Laboratories, Ontario, and consist of natural UO_2 doped with nonradioactive fission products (Ba, Ce, La, Mo, Sr, Y, Zr, Rh, Pd, Ru, Nd) to replicate the chemical effects of a CANDU reactor irradiation to the corresponding burn-up (10).

The electrical resistivities (l) of the SIMFUEL specimens are compared with that of an almost stoichiometric pure UO_2 ($UO_{2.001}$) in Table 1. These values are obtained using the current interrupt method during electrochemical experiments as described elsewhere (36). Lattice substitution of U^{IV} by lower valent species causes the expected enhancement in conductivity in the 1.5 and 3 atom% SIMFUELS. However, the 6 atom% SIMFUEL has a considerably higher resistivity than the less heavily doped materials. One possibility is that this material contains a degree of substoichiometry as a consequence of over reduction during sintering. The high concentration of lower-valence lattice substituents may have facilitated O^{2-} loss from the UO_2 matrix, which would partly offset their contribution to the conductivity (37).

Electrodes of these materials were prepared using methodology described elsewhere (38). Prior to use, an electrode was polished (wet) with 600 grit SiC paper, rinsed with distilled deionized water (18MΩcm) and re-polished (wet) with 1200 grit SiC paper. Before immersion into the electrochemical cell, the electrode was ultrasonically cleaned with distilled deionized water for 5 min to remove any polishing particles from the fuel surface.

SIMFUEL characterization

X-ray diffraction

X-ray diffraction patterns were recorded over the 2θ range, 20° to 80°, using Co Kα radiation from a Rigaku Rotafex X-ray diffractometer operating at 40 kV and 40 mA. A scanning step of 0.02° and a scanning rate of 0.2° min^{-1} were used. The diffractometer was calibrated using a standard Si sample. The peaks in the XRD patterns were fitted using Pearson VII functions, and the parameters obtained were employed to determine the cell parameters.

Table 1. Resistivities of various uranium dioxide specimens.

Material	Resistivity (Ωcm)	Gwd (MTU)
$UO_{2.001}$	982	0
1.5 atom% SIMFUEL	182	14
3.0 atom% SIMFUEL	81	28
6.0 atom% SIMFUEL	1120	56

Raman spectroscopy

Raman microspectrometric measurements were carried out with a Renishaw 1000 confocal Raman spectrometer (Renishaw PLC., UK). Raman backscattering was excited with a 632.8 nm excitation wavelength helium–neon laser operating at 50% power to avoid oxidation of the UO_2 sample surface during the measurements. When focused on regions subsequently identified as the perovskite-type grey phases, an operating power of 100% was used and multiple scans were performed to ensure maximum sensitivity. Individual spectra were obtained for an exposure of 45 s over the wavenumber range from 120 to 1400 cm^{-1}. The laser was focused onto the sample using 50× uncoated objective lenses, at a sample spot size of ~1 μm. The Raman spectrometer was calibrated using a Si single crystal, and the correct shift was maintained for all samples.

Raman maps were obtained with the same micro Raman spectrometer. The SIMFUEL samples were mounted on a computer-controlled automated *xy* translation stage with 0.1 μm resolution and 1 μm reproducibility. Mapping was performed point-by-point using 2 μm steps over a 40 μm linear region; spectra were acquired for 45 s at each step. To ensure ideal laser focusing on the rough specimens, an autofocusing system with a 50× magnification in the Z (XX) configuration, was used. This system employed a high-precision piezo translator and feedback signal to automatically track and adjust the laser beam focus on the sample. More than 20 individual Raman spectra were collected under nondestructive conditions at room temperature for each SIMFUEL specimen. Individual spectra were then used to obtain an averaged Raman spectrum.

The Raman images were generated via the same HeNe laser (λ = 632.8 nm) beam and a CCD detector with 2–4 cm^{-1} resolution. Three images centered at 450, 570, and 1150 cm^{-1} were accumulated with (121 × 121) pixels. Typically, images were acquired with one accumulation of 600 s. To avoid damage, a laser power less than 200 μW was used to record images. The absence of laser damage was verified by careful comparison of optical images recorded before and after Raman map collection.

Energy dispersive X-ray results (EDX) and elemental imaging

A Hitachi S-4500 field emission scanning electron microscope (SEM) with an energy dispersive X-ray (EDX) analysis system was used to collect images. A high electron beam voltage of 30 kV was used, resulting in a spatial resolution of <2 nm. Micrographs were recorded at various magnifications (100–5000X). EDX mapping was performed to identify the size, distribution, number density, and elemental composition of regions or particles on the surface; EDX was again performed on an individual particle to determine elemental composition.

© 2007 NRC Canada

X-ray photoelectron spectroscopy (XPS)

An SSX-100 spectrometer was used to record XPS spectra. Spectra were excited using Al Kα radiation to bombard the surface with high energy monochromatic X-rays ($h\nu$ = 1486.6 eV). The instrument work function was set to give a value of 84.00 ± 0.05 eV for the binding energy of the Au ($4f_{7/2}$) line of metallic gold. The spectrometer was calibrated such that the energy difference between the Cu ($2p_{3/2}$) and Cu ($3p_{1/2}$) lines of copper metal was 875.5 ± 0.1 eV. The position of the C (1s) line at 285.0 eV was recorded and used, when necessary, to correct for surface charging. The U ($4f_{7/2}$) peaks, satellites associated with U ($4f_{5/2}$) band region, and the valence band region of the UO_2 spectrum were recorded. The procedure used to analyze these regions involved a fitting routine that was 70% Gaussian and 30% Lorentzian with a Shirley background correction. A detailed description of the procedure and spectral fitting methods has been published elsewhere (39).

Electrochemical experiments

Solutions

All experiments were conducted in 0.1 mol/L NaCl (pH 9.5) solutions, prepared with distilled deionized water (resistivity of 18.2MΩcm), purified using a Millipore milli-Q-plus unit to remove organic and inorganic impurities, and subsequently passed through Milli-Q-plus ion exchange columns. All chemicals were reagent grade and purchased from Fisher Scientific.

Electrochemical cell and equipment

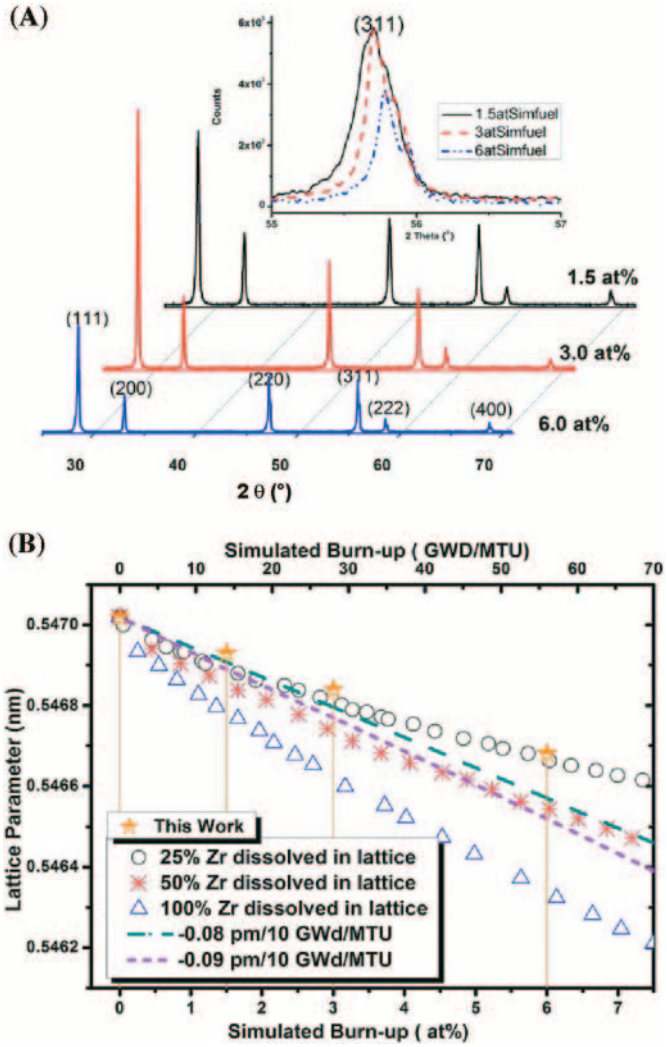
All experiments were conducted in a standard three-electrode, three-compartment cell. The counter electrode was made of Pt foil spot-welded to a Pt wire. All potentials were measured and are quoted against a saturated calomel reference electrode (SCE). All electrochemical experiments were performed with a Solartron 1287 potentiostat controlled by Corrware Version 2.9 Software. Working electrodes were cathodically cleaned at a potential of –1.2 V for 5 min prior to recording voltammograms at a scan rate of 10 mV s^{-1}.

Results and discussion

X-ray diffraction

The XRD patterns of the three simulated UO_2 fuel specimens with burn-ups of 1.5, 3.0, and 6.0 atom% are given in Fig. 1A. (Please note the use of at% for atom% in all figures.) The similarity in patterns shows that the UO_2 fluorite structure, a cubic arrangement of O^{2-} ions with a U^{4+} cation at alternating cubic body-centered positions, is retained in all specimens. Inspection of the insert in Fig. 1A shows that the position of the fluorite (311) peaks for the SIMFUEL specimens differed slightly. These peaks shifted to higher 2θ values with increased simulated burn-up, which is indicative of a decrease in the lattice parameter and hence, the unit cell volume.

Fig. 1. (A) X-ray diffraction patterns of SIMFUELs with different burnup (atom%). (B) Variation of the lattice parameter for UO_2 with percentage of simulated atomic burn-up for sintered SIMFUEL samples. The dashed and short dashed lines are from Kleykamp (42, 43). The three different symbols (○, ✶, △) show the influence of various Zr contents (18).



The effect of fission product dissolution into the UO_2 lattice is shown in Fig. 1B as a function of simulated burn-up, which gives the measured lattice parameter for each SIMFUEL as well as the value for undoped UO_2 of 0.547 02 nm (29, 40). The results show a close to linear decrease in UO_2 lattice constant with an increase in simulated burn-up, which is in approximate agreement with Vegard law[3] (41) and consistent with fission product and actinide dissolution in the UO_2 matrix to form a solid solution. This trend is also consistent with available literature data, which are also summarized in Fig. 1B. Spino and Papaioannou (9) measured an average lattice contraction of 0.087 pm/10GWd/MTU based on measurements over the burn-up range 0–70 GWd/MTU. A similar trend of 0.08–0.09 pm/10GWd/MTU was obtained by Kleykamp (dashed

[3] Vegard's law is an approximate empirical rule, which holds that a linear relation exists, at constant temperature, between the crystal lattice constant of an alloy and the concentrations of the constituent elements.

© 2007 NRC Canada

line and short dashed line in Fig. 1B) for irradiated LWR-fuels (42) and also for FBR-fuels (43).

The influence of dopants on the UO_2 lattice parameter varies depending on their identity. Tsuji et al. (44) showed that the lattice parameter decreased on doping with Pu but increased on doping with Th and La. Kapoor et al. (45) observed a linear reduction in lattice parameter with increasing Gd content, despite Gd^{3+} having the same ionic radius as U^{4+}. According to Park and co-workers (46, 47), Gd^{3+} is effectively negatively charged (in a U^{IV} lattice) and is neutralized by the creation of an oxygen vacancy. As the dopant concentration increases, Gd^{3+} attracts these vacancies to form dopant-vacancy clusters leading to lattice contraction. This appears to be the dominant mechanism in spent and simulated spent fuels.

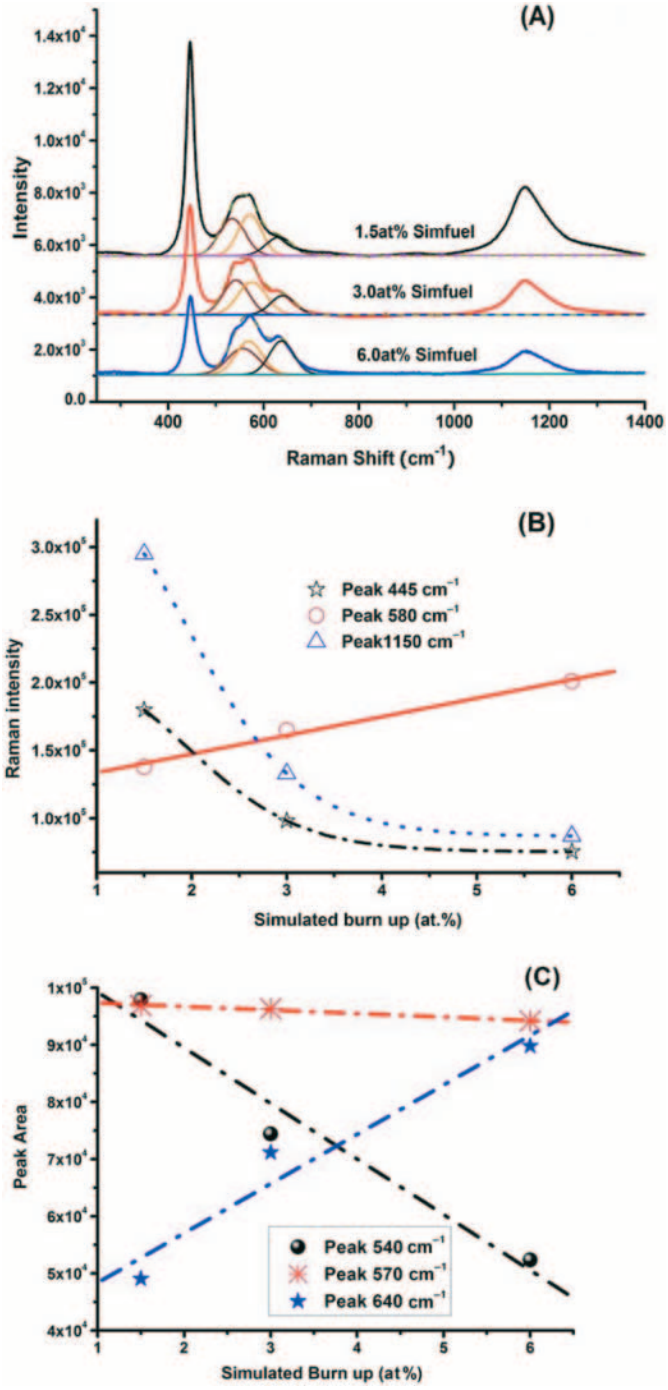
Figure 1B also shows the influence of various Zr contents on the lattice constant, as reviewed by Kleykamp (18). As mentioned earlier, Zr is shared between the UO_2 lattice and the so called grey-phase perovskite (ABO_3). The effective ionic radii of U^{4+} and Zr^{4+} are 114.0 (45) and 84 pm (48), respectively, and because of this significant size differential Zr largely controls the lattice dimension of SIMFUEL and spent fuel. The smaller than expected decrease in lattice parameter with simulated burn-up for our specimens may be attributable to the distribution of Zr, which appears to agree well with the data of Kleykamp if 25% of the Zr is assumed dissolved in the UO_2 lattice (18). Based on an analysis of the composition of grey-phase precipitates in irradiated fuels (1) and on phase equilibrium studies in the system BaO-UO_2-ZrO_2-MoO_2 (49), Kleykamp proposed a maximum of 25% dissolution of Zr in the fuel matrix, the rest being precipitated in the perovskite phase (18). Our data suggests the SIMFUEL UO_2 matrices are only lightly Zr-doped, suggesting major segregation of Zr to an ABO_3 perovskite phase.

Raman spectroscopy

Group theory predicts that UO_2, which possesses a fluorite structure with a space group O_h ($Fm3m$), will possess one Raman active mode (T_{2g}) (50). Consequently, stoichiometric UO_2 should possess a single fundamental vibrational stretch at around 450 cm^{-1}. This peak is triply degenerate (T) with a symmetric (g) stretching mode arising as a result of the fluorite structure (51, 52). A similar vibration at 460 ± 5 cm^{-1} has been reported for other oxides with the fluorite structure (CeO_2, ThO_2) (53). In addition, a broad peak near 1150 cm^{-1} has been observed (54) and attributed to a crystal electric field transition, probably $\Gamma_5 \rightarrow \Gamma_3$. The intensity of this peak was found to increase with a temperature decrease (200 to 5 K), which was taken to be confirmation that it was attributable to electronic scattering (55). These authors claimed this peak could be taken as a fingerprint for a quasi-perfect fluorite lattice, since its intensity decreased as the degree of nonstoichiometry of UO_2 increased, finally disappearing as UO_{2+x} approached $UO_{2.1}$. Experimentally, a very broad peak between 500 and 700 cm^{-1} has been observed and attributed to UO_2 lattice damage, possibly because of the presence of defects leading to a breakdown in selection rules (51). Senanayake et al. (51) showed the presence of two peaks at 578 and 640 cm^{-1} in this region.

Figure 2A shows averaged Raman spectra for the three SIMFUELs obtained by point-by-point (2 μm per step)

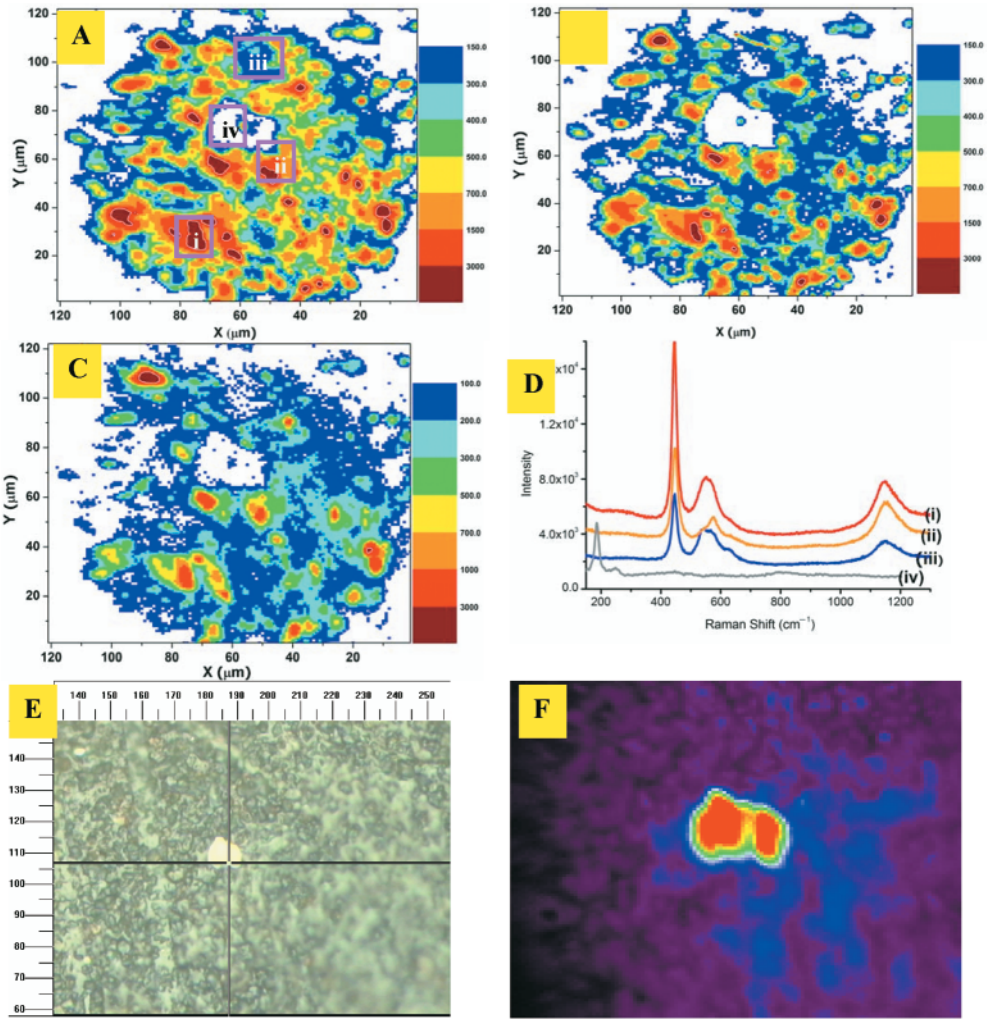
Fig. 2. (A) Averaged Raman spectra for the three different SIMFUELs. (B) Change in intensity of Raman peaks as a function of simulated burn-up. (C) Peak areas calculated from the Raman peaks in the region 500–700 cm^{-1}.



Raman mapping over a 40 μm linear region. All three of the expected spectral features are observed. The characteristic fundamental T_{2g} stretching mode shifts only marginally from 445 to 447 cm^{-1} with increasing simulated burn-up from 1.5 to 6.0 atom%. This shift could be due to the increased concentration of fission products in solid solution with UO_2. Irrespective of whether this shift is significant, both this peak and that at 1140–1150 cm^{-1} show very similar

© 2007 NRC Canada

Fig. 3. Raman imaging of polished 1.5 atom% SIMFUEL: (A) Raman image with the color intensity set for the 450 cm^{-1} fundamental vibration; (B) Raman image for 580 cm^{-1}; (C) Raman image for 1150 cm^{-1}; (D) individual Raman spectra taken at the locations noted on the Raman imaging map (A); (E) optical image of the same area of the surface; (F) white light image.



decreases in intensity with increased doping (Fig. 2B). These decreases are accompanied by a small, but significant, increase in the intensity of the broad peak in the range 500 to 700 cm^{-1}. That the changes in these peaks occur in concert eliminates the possibility that they can be attributed to artifacts (such as variations in surface roughness). Previous deconvolutions of the spectra in this region (51) yielded peaks at 578 and 640 cm^{-1}, but Fig. 2A clearly shows the presence of three peaks, as indicated by the deconvolutions shown at 540, 570, and 640 cm^{-1}. Estimates of the area associated with these peaks are plotted in Fig. 2C and show a decrease in area of the 540 cm^{-1} peak accompanied by an increase in area associated with the 640 cm^{-1} peak as the degree of doping increases. By contrast, the area associated with the peak at 570 cm^{-1} is independent of doping level.

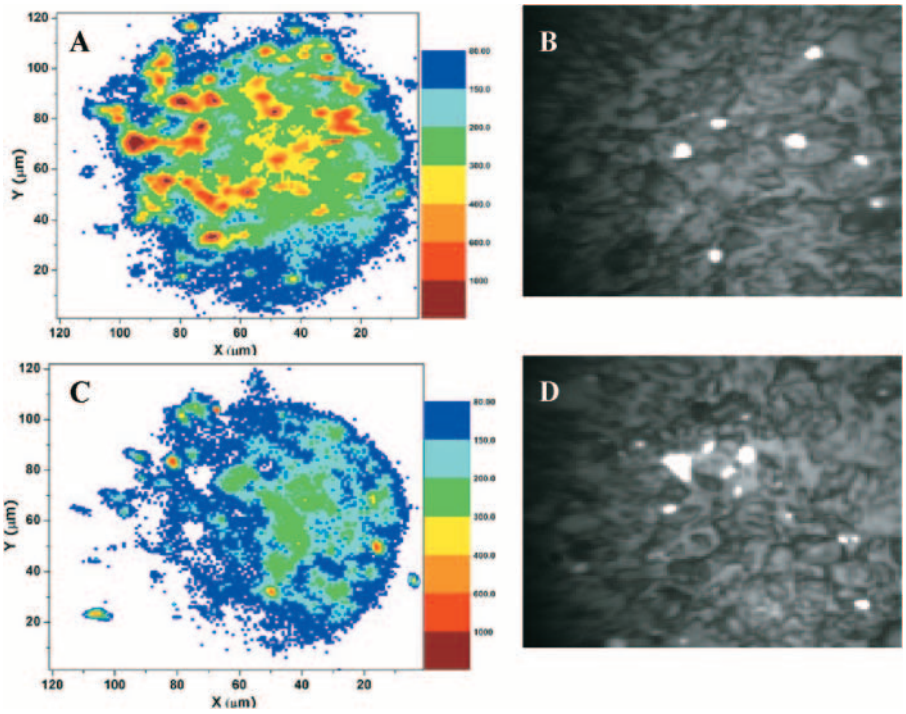
The loss in intensity of the fundamental U–O stretch and the crystal field transition accompanied by the increased relative importance of the broad band associated with lattice damage are clearly attributable to the lattice distortions caused by fission product doping. The subtle changes in the peaks at 540 and 670 cm^{-1} (as shown in Fig. 2C) suggest a consistent influence of doping on the rearranged (damaged) fluorite structure. The distortions of the ideal cubic UO_2 fluorite structure to a tetragonal or even orthorhombic structure because of doping are consistent with the lattice contractions observed by XRD and would be expected to decrease the intensities of the peaks at 445 and 1150 cm^{-1} associated with the perfect lattice. The consistent changes in the two peaks associated with the damaged region suggest a regular change in the nature of the defect clusters formed by the dopants and the oxygen vacancies. The origin of the peak at 540 cm^{-1}, which has not been reported by other researchers, remains unknown, but one possibility is that it is attributable to the perovskite structure (ABO_3) formed by the separation of dopants such as Ba, Sr, Zr, Mo in the so-called grey phase. Evidence exists to show that a cubic perovskite structure can exhibit a peak in this wavelength region (53).

Raman imaging

Figures 3A–3C show the relative Raman intensities for three distinct wavelengths as a function of location within an area (121 × 121 μm) of the surface of a 1.5 atom% SIMFUEL specimen. The three wavelengths chosen are those at which the three distinct spectral features are located

© 2007 NRC Canada

Fig. 4. Raman images obtained on 3.0 atom% (A) and (C) 6.0 atom% SIMFUELs with the colour intensity set for the 450 cm^{-1} fundamental vibration. White light images of the same area of the surface obtained on (B) 3.0 atom% and (D) 6.0 atom% SIMFUELs.



in Fig. 2A (450, 580, 1150 cm^{-1}). Figure 3D shows individual spectra taken at the labeled locations in Fig. 3A, while Fig. 3E shows an optical image of the same area of the surface.

The spectrum recorded at location (*i*) shows that the peak intensities associated with a perfect fluorite lattice (450 and 1150 cm^{-1}) are large compared with that for the peak associated with lattice damage (550 cm^{-1}). Comparison to Fig. 2A indicates that this can be associated with a light doping of this area of the surface. The spectra for the orange and blue sections, labeled (*ii*) and (*iii*) respectively in Fig. 3C, show a decreasing prominence of the peaks at 450 and 1150 cm^{-1} and the splitting of the wide band in the region 500 to 700 cm^{-1}, with an increasing prominence of the peak at 640 cm^{-1}. Comparison to the spectra for the three SIMFUELs in Fig. 2A shows these changes are an indication of increased doping (and therefore, distortion of the cubic lattice structure). Given that the UO_2 grain size in these materials is in the range 8–15 μm (29), the distribution of colour in the Raman image suggests that the SIMFUEL may comprise a network of individual grains with different degrees of doping.

The colour contrast in the white light images Figs. 4B and 4D give some indication of the surface roughness, and comparison to the spectral images shows this contrast does not match the colour distribution, indicating that the differences in Raman features cannot simply be attributable to intensity variations due to differences in surface topography. This indicates that the spectral contrast is primarily associated with the non-uniform doping of the SIMFUEL. Figures 4A and 4C show intensities for the O–U fundamental vibrational stretch (450 cm^{-1}) for the 3 and 6 atom% SIMFUEL specimens, respectively. Comparison of the relative intensities in these maps to the intensity shown for the 1.5 atom% SIMFUEL specimen (Fig. 3A) confirms the destruction of the perfect fluorite lattice as the doping level increases, as implied by the average spectra in Fig. 2A.

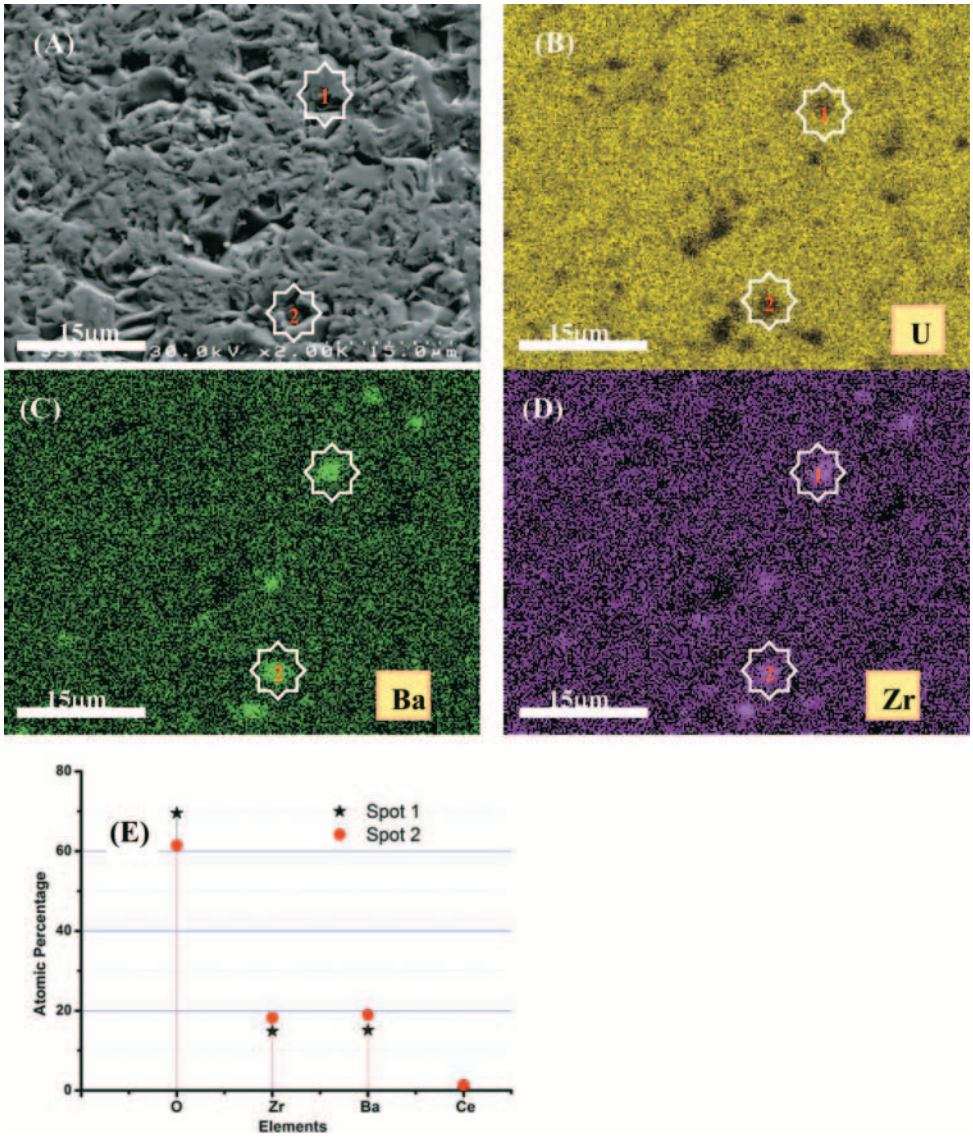
Recalling that the rate and extent of surface oxidation under dry air conditions is influenced by the degree of burn-up, the above observations raise the possibility that the corrosion rates of the surfaces will also vary with degree of doping of the surface region. A second possibility is that variations in degree of doping will also introduce the possibility of the separation of anodes and cathodes on the corroding surface, with the more heavily doped areas of the surface being capable of the sustaining higher cathodic reduction rates (of O_2 and H_2O_2).

The spectrum associated with location (*iv*) (Fig. 3A) did not show spectral features characteristic of doped UO_2, with only a weak band at 189 cm^{-1} being observed. The distinctness of this feature is clearly apparent in the optical image in Fig. 3E and the white light (as opposed to laser) image in Fig. 3F. This area is about 10 μm in size making it too large to be an ϵ-particle, which SEM analyses show to be ≤1 μm.[4] A possibility is that it is a perovskite phase, ABO_3, formed during the sintering process. The cubic perovskite structure would give rise to the optical vibrational modes described as $3F_{1\mu} + F_{2\mu}$. The $F_{1\mu}$ modes are IR active, while the $F_{2\mu}$ mode is silent since there are no Raman-active vibrational modes, so this structure or a slight distortion of it should not

[4] M.E. Broczkowski, P.G. Keech, J.J. Noël, and D.W. Shoesmith. Manuscript in preparation.

© 2007 NRC Canada

Fig. 5. SEM/EDX analyses of a polished 6.0 atom% SIMFUEL specimen. (A) SEM image; (B), (C), and (D) EDX element maps for U, Ba, and Zr, respectively, recorded separately in the same surface region showing the distribution of these different components; (E) EDX spot analysis taken at the locations labelled on the SEM image.



generate a Raman spectrum (53). However, highly nonstoichiometric $BaCe_xZr_{1-x}O_3$ (x = 0.6, 0.8) formed at high pressures, which has a highly distorted perovskite structure, did show a broad band around 200 cm^{-1} (56), i.e., in the range where a band (at 189 cm^{-1}) is observed in our spectra.

Energy dispersive X-ray results (EDX) and elemental imaging

The SEM image in Fig. 5A is a representative example of a polished specimen surface. With the exception of physical defects, there are no defined features in the SEM image. Figures 5B–5D show the U, Ba, and Zr distribution in the surface of 6.0 atom% SIMFUEL, as measured by EDX analysis. A distinguishable attenuation in the U map is observed at locations where bright spots appear for Ba and Zr. This is consistent with the expected formation of perovskite-type oxide precipitates with the chemical form ABO_3 The approximate composition of this phase can be obtained from EDX spot analyses (Fig. 5E), which yield a ratio of Ba–(Zr + Ce)–O of ~1:1:3. It is noteworthy that the O content is higher than expected for the ABO_3 stoichiometry, suggesting the phase may also contain U (57).

X-ray photoelectron spectroscopy

XPS was used to characterize the influence of doping on surface composition. The binding energies of the U4$f_{7/2}$ and U4$f_{5/2}$ peaks are positioned at 379.5 and 390.5 eV (1.5% and 3%), and 379.7 and 390.7 eV (6%), respectively (as shown in Table 2). These positions are comparable to those obtained by others (58) on UO_2 (111) single crystals. The slight shift in the U4f peaks for 6% SIMFUEL is attributable to peak broadening towards the high-binding energy side. The FWHM increases from 2.0 to 2.05 to 2.12 with increasing burn-up, consistent with an increase in multiple oxidation states in the fuel surface.

© 2007 NRC Canada

Table 2. Comparison between the XPS core level parameter values on SIMFUEL specimens with different degrees of simulated burn-up.

	Binding energy (B.E.) (eV)					
SIMFUEL	U $4f_{7/2}$	FWLM	Satellite	U $4f_{5/2}$	FWLM	Satellite
1.5 atom%	379.5	2.00	6.7	390.5	2.00	6.7
3.0 atom%	379.5	2.05	6.7	390.5	2.05	6.7
6.0 atom%	379.7	2.12	6.9	390.7	2.12	6.9

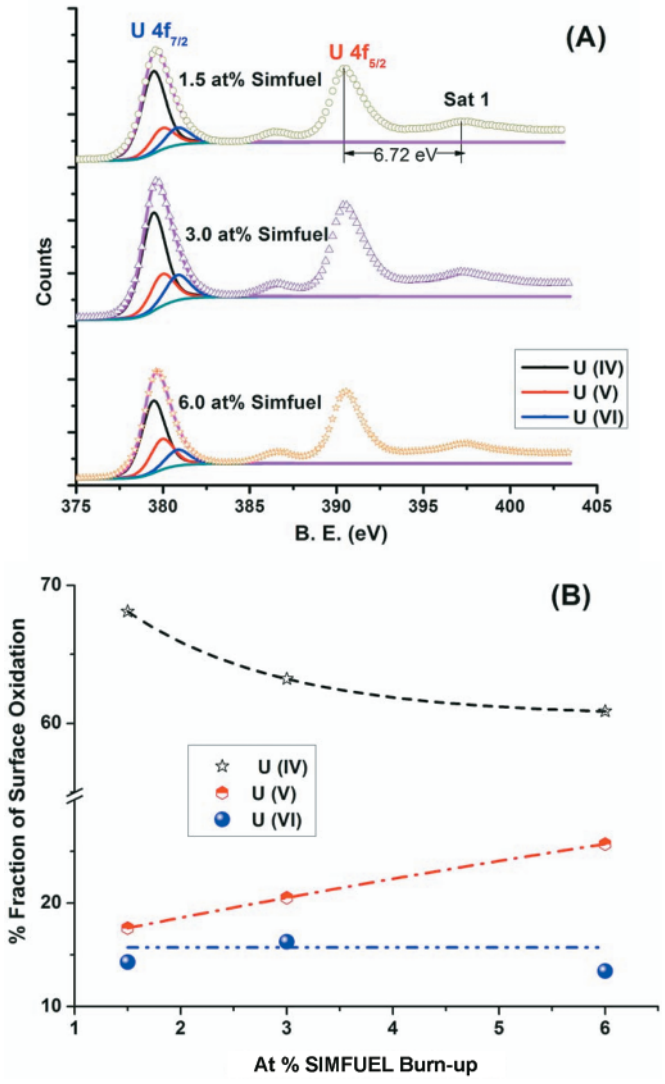


Fig. 6. (A) U $4f_{5/2}$ and U $4f_{7/2}$ regions of the XPS spectra recorded on 1.5, 3.0, and 6.0 atom% burn-up SIMFUELs; (B) relative fractions of all three oxidation states as a function of burn-up.

This change in surface composition is confirmed by the peak deconvolutions shown in Figs. 6A and 6B. The procedure used in peak fitting is described elsewhere (39). The position of the satellite peaks (Fig. 6A) at 6.7 eV (1.5 and 3%) and 6.9 eV (6%) are consistent with the 7 eV expected for reduced UO_2. While the peak deconvolutions (Fig. 6B) show U^{IV} remains the dominant oxidation state, increased doping leads to a measurable increase in the U^V content at the expense of U^{IV}. The U^{VI} content of the surface is independent of the degree of doping and almost certainly arises from air oxidation (on transfer of the specimens from the polishing pad to the vacuum chamber of the XPS spectrometer). An increase in U^V content is to be expected as the level of RE^{3+} cation doping increases.

Our previous studies suggest that an increase in the U^V content of the surface will lead to an increased density of the donor–acceptor sites utilized in cathodic reactions, such as the reduction of O_2 (59) and H_2O_2 (60). Since these two oxidants are the primary products of the alpha radiolysis of water, catalysis of their reduction could increase the fuel corrosion rate. In the case of H_2O_2, rapid chemical oxidation of the surface appears able to create catalytic donor states (U^V states), and hence, we might expect their variation due to the RE^{3+} doping to be relatively insignificant in catalyzing H_2O_2 reduction. However, this may not be the case for other cathodic processes, in particular O_2 reduction.

Electrochemistry

Figures 7A and 7B show voltammograms recorded in unbuffered and borate buffered solutions for the three SIMFUEL specimens. As discussed in detail previously (39), oxidation of UO_2 occurs in two stages. In region 1 (up to 0.2 V vs. SCE), the surface of UO_2 is oxidized to UO_{2+x}, a process that involves injection of O^{2-} into the vacant sites in the fluorite lattice accompanied by the creation of U^V states. In region 2, (>0.2 V vs. SCE), further oxidation of this thin surface layer to the U^{VI} state and its dissolution as UO_2^{2+} occurs. In the neutral to alkaline solution employed in our experiments, UO_2^{2+} has limited solubility and accumulates on the fuel surface as a $UO_3{\cdot}yH_2O$ deposit. The cathodic peak in region 3 on the reverse scan is due to the reduction of this anodically formed dual layer (UO_{2+x} / $UO_3{\cdot}yH_2O$). In unbuffered solution, however, anodic dissolution can lead to the development of locally acidified conditions (due to UO_2^{2+} hydrolysis) in the asperities in the rough electrode surface (Fig. 5A). In buffered solution, this acidification would be expected to be at least partially avoided.

The similarity in the anodic oxidation sequence,

$$[4] \qquad UO_2 \rightarrow UO_{2+x}\ (UO_3{\cdot}yH_20)$$

to that observed under dry air conditions (reaction sequences [1] and [2]) is worth noting. In both cases, the first stage involves modification of the UO_2 fluorite lattice by the incorporation of interstitial O^{2-}, while the second stage involves lattice destruction by recrystallization (in air) or dissolution and redeposition (in aqueous solution). Inspection of Figs. 7A and 7B shows the anodic currents in both region 1 ($UO_2 \rightarrow UO_{2+x}$) and region 2 ($UO_2 \rightarrow UO_2^{2+}$ / $UO_3{\cdot}yH_2O$) decrease as the extent of simulated doping is increased, sug-

© 2007 NRC Canada

Fig. 7. Voltammograms recorded on 1.5, 3.0, and 6.0 atom% burn-up SIMFUELs at room temperature in (A) 0.1 mol/L NaCl at pH 9.5 and in (B) borate buffered solution of 0.1 mol/L NaCl at pH 9.5.

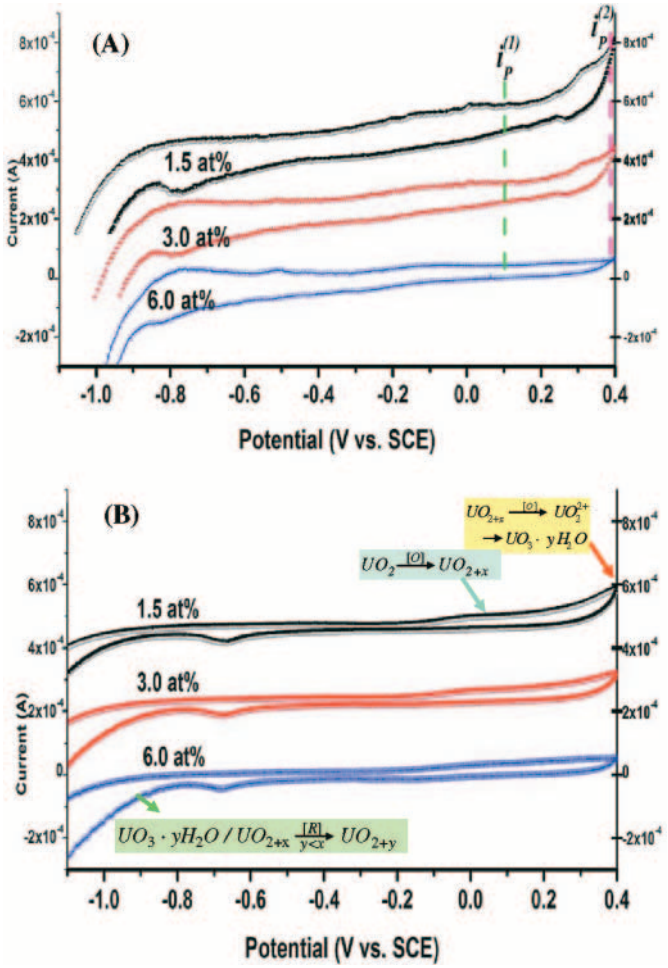
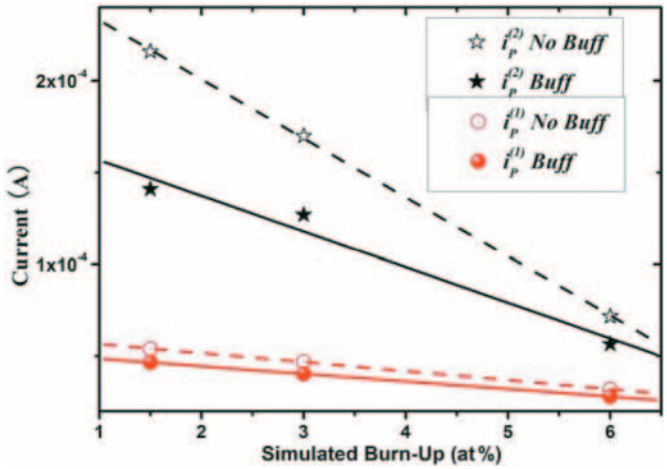


Fig. 8. Current densities for oxidation ($UO_2 \rightarrow UO_{2+x}$, $i_p^{(1)}$) and dissolution ($UO_{2+x} \rightarrow UO_2^{2+}$, $i_p^{(2)}$) in buffered and unbuffered solutions as a function of simulated burn-up (data taken from Fig. 7).



gesting a similar influence of lattice doping on oxidation under aqueous conditions as observed for air oxidation.

To emphasize this influence, we have plotted the currents at 0.1 V (representative of region 1) and 0.4 V (vs. SCE, representative of region 2) for all three SIMFUEL specimens in Fig. 8. At 0.1 V the decrease in current with increase in simulated burn-up is small and effectively independent of solution buffering. This indicates a measurable but marginal influence of doping on the surface modification of the UO_2 fluorite lattice, consistent with the minor influence of doping on the first stage of the air-oxidation process (at these burn-up levels). The lack of any effect of buffering is not surprising, considering the negligible solution pH change caused by the conversion of a thin surface layer to UO_{2+x}.

By contrast, the influence of doping on the anodic destruction by conversion of UO_2 to U^{VI} followed by dissolution is much more marked, similar to the second (recrystallization) stage of the air oxidation process. As expected, the presence of a buffer decreases the current for dissolution of all SIMFUEL specimens (at 0.4 V vs. SCE), and this effect becomes less prominent as the extent of doping is increased. The very small influence of buffering on the anodic dissolution current for 6 atom% SIMFUEL reinforces the argument that doping to this level stabilizes the fluorite surface against anodic oxidation and (or) dissolution, thereby preventing the formation of soluble and hydrolysable UO_2^{2+}.

By analogy to the air oxidation behaviour, it can be speculated that doping stabilizes the UO_{2+x} fluorite structure against further oxidation to produce soluble species by interfering with the defect cluster ordering that would lead to destabilizing tetragonal distortions. Our XRD data demonstrate that the primary influence of dopants is to induce the lattice contraction indicative of the formation of dopant vacancy clusters. It is possible that this retards anodic oxidation at high doping levels by reducing the number-density of available vacancy sites for O^{2-} incorporation, the first step in the anodic oxidation and (or) dissolution process.

Summary and conclusions

The addition of fission product dopants to UO_2 to simulate the influence of in-reactor burn-up leads to a contraction of the fluorite lattice, which is expected if dopant-vacancy (RE^{III}-O^{V}) clustering occurs.

EDX mapping demonstrates the presence in the matrix of ABO_3 perovskite particles containing primarily Ba and Zr, but also a small amount of Ce, and possibly U. The segregation of Zr to such particles accounts for the smaller than expected measured lattice contraction.

Raman spectroscopy confirms that the fluorite lattice structure is significantly disturbed as the doping level is increased. The spectral responses due to the fundamental O–U stretch and a crystal electric field transition, indicative of a cubic fluorite lattice, decrease in intensity with increasing doping level, while responses indicating a damaged lattice increase. Raman imaging at the wavenumbers associated with these responses shows that doping of the matrix is non-uniform, with some grains being more heavily doped than others.

XPS indicates an increase in U^{V} concentration, at the expense of U^{IV}, with increased doping.

© 2007 NRC Canada

Voltammetric experiments show that the currents, due to oxidation first of the fluorite lattice to UO_{2+x} and then to dissolved UO_2^{2+} and deposited $UO_3{\cdot}yH_2O$, are suppressed as the extent of doping increases. This suppression is particularly marked for the 6 atom% SIMFUEL and is consistent with the influence of doping on the air oxidation of SIMFUELs and spent fuels. This affect is tentatively assigned to the formation of dopant-vacancy clusters that stabilize the fluorite lattice against the formation of destabilizing tetragonal distortions and reduce the availability of oxygen vacancies which facilitate oxidation and then dissolution.

Acknowledgements

The authors thank Mary Jane Walzak of *The* University *of* Western Ontario for Raman microscopy determinations, and Surface Science Western for XPS and SEM/EDX facilities. This research was funded under the Industrial Research Chair agreement between the Canadian Natural Sciences and Engineering Research Council (NSERC) and Ontario Power Generation (OPG), Toronto, Canada.

References

1. H. Kleykamp. J. Nucl. Mater. **131**, 221 (1985).
2. I.J. Hastings. Atomic Energy of Canada Limited Report AECL-Misc-249. Atomic Energy of Canada Limited, Mississauga, Ontario. 1982.
3. L.H. Johnson and D.W. Shoesmith. *In* Radioactive waste forms for the future. *Edited by* W. Lutze and R. Ewing. Elsevier, Amsterdam. 1988. Chap. 11.
4. V. Jain, G. Cragnolino, and L. Howard. CNWRA 2004–08. Center for nuclear waste regulatory analyses, San Antonio, Texas. (2004).
5. J.C. Tait, I.C. Gould, and G.B. Wilkin. Atomic Energy of Canada Report AECL-9881. Atomic Energy of Canada Limited, Mississauga, Ontario. 1989.
6. L.O. Werrne, L.H. Johnson, V.M. Ovlisby, F. King, K. Spahin, B. Grambow, and D.W. Shoesmith. SR-Can SKB TR-04–19. Svensk Kärnbränslehantering AB, Stockholm, Sweden. 2004.
7. I.J. Hastings, M.J.F. Notley, and D.H. Rose. J. Nucl. Mater. **75**, 301 (1978).
8. Hj. Matzke. Radiat. Eff. Defect Solids, **64**, 3 (1982).
9. J. Spino and D. Papaioannou. J. Nucl. Mater. **281**, 146 (2000).
10. P.G. Lucuta, R.A. Verrall, Hj. Matzke, and B.J. Palmer. J. Nucl. Mater. **178**, 48 (1991).
11. P.G. Lucuta, B.J.F. Palmer, H. Matzke, and D.S. Hartwig. Proc. Sec. Int. Conf. CANDU Fuel, 132 (1989).
12. Hj. Matzke, P.G. Lucuta, and R.A. Verrall. J. Nucl. Mater. **185**, 292 (1991).
13. J. Belle. Uranium dioxide properties and nuclear applications. United States Atomic Energy Commission, Washington, DC. 1961.
14. P.E. Porter. Proc. Behav. Chem. St. Irrad. Cer. Fuel 1972. International Atomic Energy Agency (IAEA), Vienna, Austria. 1974.
15. H. Kleykamp. Nucl. Technol. **80**, 412 (1988).
16. R.W. Grimes and C.R.A. Catlow. Philos. Trans. R. Soc. London, Ser. A, **335**, 609 (1991).
17. B.D. Hanson. Pacific Northwest National Laboratory Report PNNL-11929. Pacific Northwest National Laboratory, Richland, Wash. 1998.
18. H. Kleykamp. J. Nucl. Mater. **206**, 82 (1993).
19. H. Kleykamp. J. Nucl. Mater. **171**, 181 (1990).
20. M.R. Floyd, J. Novak, and P.T. Truant. Atomic Energy of Canada Report AECL-10636. Atomic Energy of Canada Limited, Mississauga, Ontario. 1992.
21. H.J. Smith, J.C.Tait, and R.E.V. Massow. Atomic Energy of Canada Report AECL-9072. Atomic Energy of Canada Limited, Mississauga, Ontario. 1987.
22. K. Une, Y. Tominaga, and S. Kashibe. J. Nucl. Sci. Technol. **28**, 409 (1991).
23. H.Matzke. J. Nucl. Mater. **223**, vii, (1995).
24. G.J. Hyland and J. Ralph. High Temp. High Pressures, **1**5 179, (1983).
25. P.W. Winter. J. Nucl. Mater. **161**, 38 (1989).
26. N.J. Dudney, R.L. Coble, and H.L. Tuller. J. Am. Ceram. Soc. **64**, 627 (1981)
27. L.E. Thomas, R.E. Einziger, and H.C. Buchanan. J. Nucl. Mater. **201**, 310 (1993).
28. J.W. Choi, R.J. McEachern, P. Taylor, and D.D. Wood. J. Nucl. Mater. **230**, 250 (1996).
29. J. Cobos, D. Papaioannou, J. Spino, and M. Coquerelle. J. Alloys Compd. **271–273**, 610 (1998).
30. R.J. McEachern and P. Taylor. J. Nucl. Mater. **254**, 87 (1998).
31. J. Janeczek and R.C. Ewing. J. Nucl. Mater. **190**, 128 (1992).
32. R.E. Einziger, L.E. Thomas, H.C. Buchanan, and R.B. Stout. J. Nucl. Mater. **190**, 53 (1992).
33. K.M. Wasywich, W.H. Hocking, D.W. Shoesmith, and P. Taylor. Nucl. Technol. **104**, 309 (1993).
34. V.J. Tennery and T.G. Godfrey. J. Am. Ceram. Soc. **56**, 129 (1973).
35. D.N. Bykhovstrii, G.S. Novikov, and L.V. Solntseeva. Radiokhimiya, **34**, 9 (1992).
36. W.H. Hocking, J.S. Betteridge, and D.W. Shoesmith. Atomic Energy of Canada Limited Report AECL-10402. Atomic Energy of Canada Limited, Mississauga, Ontario. 1991.
37. T. Ohmichi, H. Takeshita, S. Fukushima, and A. Malda. J. Nucl. Mater. **151**, 90 (1987).
38. B.G. Santos, J.J. Noël, and D.W. Shoesmith. Corros. Sci. **48**, 3852 (2006).
39. B.G. Santos, H.W. Nesbitt, J.J. Noël, and D.W. Shoesmith. Electrochim. Acta, **49**, 1863 (2004).
40. S.D. Conradson, D. Manara, F. Wastin, D.L. Clark, G.H. Lander, L.A. Morales, J. Rebizant, and V.V. Rondinella. Inorg. Chem. **43**, 14 (2004).
41. A.R. Denton and N.W. Ashcroft. Phys. Rev. A, **43**, 3161 (1991).
42. H. Kleykamp. J. Nucl. Mater. **206**, 82 (1993).
43. H. Kleykamp and R. Pejsa. J. Nucl. Mater. **124**, 56 (1984).
44. T. Tsuji, S. Taguchi, M. Abe, and K. Naito. J. Alloys Compd. **193**, 110 (1993).
45. K. Kapoor, S.V. Ramana, Rao Sheela, T. Sanyal, and A. Singh. J. Nucl. Mater. **321**, 331 (2003).
46. K. Park, M.-S. Yang, and H.-S. Park. J. Nucl. Mater. **247**, 116 (1997).
47. K. Park and D.R. Olander. J. Nucl. Mater. **187**, 89 (1992).
48. Y. Nagai, T. Yamamoto, T. Tanaka, S. Yoshida, T. Nonaka, T. Okamoto, A. Suda, and M. Sugiura. Catal. Today, **74**, 225 (2002).
49. J.O.A. Paschol, H. Kleykamp, and F. Thummler. J. Nucl. Mater. **151**, 10 (1987).
50. P.R. Graves. Appl. Spectrosc. **44**, 1665 (1990).
51. S.D. Senanayake, G.I.N. Waterhouse, A.S.Y. Chan, T.E. Madey, D.R. Mullins, and H. Idriss. Catal. Today, **120**, 151 (2007).

© 2007 NRC Canada

52. P.G. Marlow, J.P. Russel, and J.R. Hardy. Philos. Mag. **14**, 409 (1966).
53. J.R. Schoonover, A. Saab, J. Bridgewater, G.J. Havrilla, C.T. Zugates, and P.J. Treado. Appl. Spectrosc. **54**, 1362 (2000).
54. J. Schoenes. J. Chem. Soc. Faraday Trans. **83**, 1205 (1987).
55. D. Manara and B. Renker. J. Nucl. Mater. **321**, 233 (2003).
56. C. Chemarin, N. Rosman, T. Pagnier, and G. Lucazeau. J. Solid State Chem. **149**, 298 (2000).
57. K. Kurosaki, Y. Saito, M. Uno, and S. Yamanaka. J. Nucl. Mater. **350**, 203 (2006).
58. S.D. Senanayake and H. Idriss. Surf. Sci. **563**, 135 (2004).
59. D.W. Shoesmith, J.S. Betteridge, and W.H. Hocking. J. Electroanal. Chem. **406**, 69 (1996).
60. J.S. Goldik, J.J. Noël, and D.W. Shoesmith. J. Electroanal. Chem. **582**, 241 (2005).

© 2007 NRC Canada

Pulsed-field ionization electron spectroscopy and molecular structures of copper-(pyridine)$_n$ (n = 1, 2) complexes[1]

Xu Wang, Bradford R. Sohnlein, Shenggang Li, Jason F. Fuller, and Dong-Sheng Yang

Abstract: Cu-(pyridine)$_n$ (n = 1, 2) complexes are prepared in a pulsed laser ablation cluster source and identified using laser photoionization time-of-flight mass spectrometry. High-resolution electron spectra of these complexes are obtained using pulsed-field ionization zero electron kinetic energy (ZEKE) photoelectron spectroscopy. Metal-pyridine and pyridine-based vibrational modes are identified by comparing the ZEKE spectra with previous spectroscopic studies of isolated pyridine, pyridine adsorbed on metal surfaces, and other Cu complexes. Ground electronic states and molecular structures are determined by comparing the ZEKE spectra with ab initio and multidimensional Franck–Condon factor calculations. Metal-pyridine bond energies of the neutral complexes are derived from the measured ionization energies and thermochemical relations. The mono-ligand complex has C_{2v} symmetry in both the neutral and ionized forms, whereas the di-ligand complex has an eclipsed pyridine configuration with D_{2h} and C_2 symmetries for the ion and neutral species, respectively. Although both the mono- and di-pyridine Cu complexes are formed by Cu binding to nitrogen atoms, important binding differences are found between these two complexes.

Key words: pulsed-field ionization, ZEKE, photoelectron, ab initio, copper-pyridine complexes.

Résumé : On a préparé des complexes de Cu(pyridine)$_n$ (n = 1, 2) dans une source d'agrégat avec ablation au laser pulsé et on les a identifiés par spectrométrie de masse à temps d'envol avec une photoionisation au laser. On a déterminé les spectres électroniques à haute résolution de ces complexes en faisant appel à la spectroscopie photoélectronique à l'aide d'une ionisation à champ pulsé avec une énergie cinétique électronique égale à zéro (ECEZ). On a identifié les modes vibrationnels du complexe métal-pyridine et ceux à base de pyridine en comparant leurs spectres à ECEZ avec ceux d'études spectroscopiques antérieures de la pyridine seule et de la pyridine adsorbée sur des surfaces métalliques ainsi que ceux d'autres complexes du Cu. On a déterminé les états électroniques fondamentaux et les structures moléculaires en comparant les spectres ECEZ avec des calculs ab initio et des calculs du facteur de Franck–Condon multidimensionnels. On a évalué les énergies de la liaison métal-pyridine de complexes neutres à partir d'énergies d'ionisation mesurées et de relations thermochimiques. Le complexe monocoordonné possède une symétrie C_{2v} tant dans ses formes neutres qu'ionisées alors que le complexe dicoordonné comporte une configuration avec une pyridine éclipsée de symétries D_{2h} et C_2 respectivement pour les espèces ioniques et neutres. Même si les complexes du cuivre comportant un ou deux molécules de pyridine se forment par la fixation du cuivre aux atomes d'azote, on a trouvé qu'il existe d'importantes différences dans les liaisons de ces deux complexes.

Mots-clés : ionisation à champ pulsé, ECEZ, photoélectron, ab initio, complexes du cuivre avec la pyridine.

[Traduit par la Rédaction]

Introduction

Pyridine (C_5H_5N) is the best-known heterocyclic aromatic nitrogen ligand, and its coordination chemistry has been extensively studied in condensed phases (1). The majority of pyridine compounds use the nitrogen electron pair to bind with metal ions in a monodentate mode (1), although aromatic ring coordination is also possible (2). Similar to the condensed-phase coordination chemistry, studies of pyridine adsorption on metal surfaces (3–10) and binding to individ-

Received 26 April 2007. Accepted 14 June 2007. Published on the NRC Research Press Web site at canjchem.nrc.ca on 11 July 2007.

X. Wang,[2] S. Li,[3] J.F. Fuller,[4] B.R. Sohnlein, and D.-S. Yang.[5] Department of Chemistry, University of Kentucky, Lexington, KY 40506–0055, USA.

[1]This article is part of a Special Issue dedicated to Professor G. Michael Bancroft.

[2]Present address: Department of Chemical and Materials Engineering, University of Alberta, 114 Street – 89 Avenue, Edmonton, AB T6G 2E1, Canada.
[3]Present address: Department of Chemistry, The University of Alabama, Box 870166, Tuscaloosa, AL 35487-0166, USA.
[4]Present address: Department of Chemistry, Eastern Kentucky University, 521 Lancaster Avenue, Richmond, KY 40475-3102, USA.
[5]Corresponding author (e-mail: dyang0@uky.edu).

 doi:10.1139/V07-068 © 2007 NRC Canada

ual metal atoms or ions (11–18) have shown both nitrogen and ring binding modes.

Studies of pyridine adsorption on copper surfaces have been reported using surfaced-enhanced Raman spectroscopy (3, 7), reflection-adsorption IR spectroscopy (4), photoelectron diffraction (5), temperature programmed desorption, low energy electron diffraction and electron stimulated desorption ion angular distribution (6), photoelectron spectroscopy (8, 9), and near edge X-ray absorption fine structure analysis (10). In these studies, a number of possible adsorption geometries of pyridine were considered on a metal surface. These geometries included vertical absorption via the N lone-pair electrons, tilted adsorption via both the lone-pair electrons of the N atom and the π electrons of the aromatic ring, flat adsorption via the π electrons, and edge on adsorption through the N and C atoms. Pyridine was found to adsorb on Cu (110) via the nitrogen lone pair orbital. At low coverage, the ring plane of pyridine was perpendicular to the surface; at high coverage, it was tilted away from the surface normal. In the gas phase, the most stable structures of pyridine association complexes with a neutral Cu atom (12, 16), small Cu clusters (18), or a Cu^+ ion (16) were predicted to be formed by metal σ interactions with the nitrogen lone-pair electrons by density functional theory (DFT) or ab initio calculations. The bond dissociation energy of Cu^+-pyridine was determined by photodissociation spectroscopy (274 kJ mol^{-1}) (12) and collision-induced dissociation (CID) [246 (10) kJ mol^{-1}] (11), and that of Cu^+-$(pyridine)_2$ was determined by ion-ligand exchange equilibrium measurements [495 (25) kJ mol^{-1}] (15). The ligand field spectra of Cu^{2+}-$(pyridine)_n$ (n = 4–7) were recorded in the UV region, which indicated d–d transitions in these doubly charged complexes (17, 19). In spite of these experimental and computational studies, very little gas-phase electronic-vibrational spectroscopy has been reported for metal complexes with one or more pyridine molecules, except for a recent study of Cu-pyridine (14). Such spectroscopic measurements should provide direct evidence about the structures and bonding for these interesting systems.

In this work, we report pulsed-field ionization zero electron kinetic energy (ZEKE) photoelectron spectroscopy of Cu-$(pyridine)_n$ (n = 1, 2). The ZEKE spectrum of Cu-pyridine exhibits a number of new features compared with a previous study (14), which allows the identification of additional copper-pyridine and pyridine-based vibrations. The spectrum of Cu-$(pyridine)_2$ is reported for the first time. From this spectrum, the ionization and bond energies of the bis(pyridine) complex are determined. By comparing the spectra of the mono and bis(pyridine) complexes, interesting bonding differences are revealed in these two complexes.

Experimental and computational methods

The experimental setup has been described in a previous publication (20). Copper-$(pyridine)_{1,2}$ complexes were prepared by reactions of copper atoms with the vapor of pyridine (99.9+%, Sigma-Aldrich) in molecular beams. The metal atoms were produced by pulsed laser vaporization of a copper rod (99.9%, Alfa Aesar) with the second harmonic output of a Nd:YAG laser (532 nm, ~3 mJ, Quanta-Ray GCR-3) in the presence of He or Ar carrier gas (ultra high purity, Scott-Gross) at ~50 psi. The carrier gas was delivered by a home-made piezoelectric pulsed valve (21). The metal rod was translated and rotated by a motor-driven mechanism to ensure that each laser pulse ablated a fresh surface. At room temperature, vapor of the ligand was introduced downstream of the ablation by a stainless steel capillary to a small reaction chamber (~1.5 mL), where the pyridine molecules interacted with the metal atoms entrained in the carrier gas.

The copper complexes in the molecular beams were identified by photoionization time-of-flight mass spectrometry. Ionization was carried out by a frequency-doubled dye laser (Lumonics, HD-500), pumped by a XeCl excimer laser (308 nm; Lumonics PM-884). The production of Cu-$(pyridine)_{1,2}$ complexes was maximized by optimizing the timing and power of the vaporization and photoionization lasers, the amount of the ligand vapor, and the backing pressure of the carrier gas. Prior to ZEKE experiments, ionization thresholds of the complexes were measured by recording the ion signals as a function of laser wavelength. ZEKE electrons were produced by phototexcitation of neutral molecules to high-lying Rydberg states, followed by a ~3 μs delayed, pulsed electric field ionization (1.2 V cm^{-1}, 100 ns) of these Rydberg states. A small dc field of ~0.08 V cm^{-1} was applied to help separate ZEKE from kinetic electrons produced by direct photoionization. The pulsed electric field was generated by a delay pulsed generator (Stanford Research System DG535). The ZEKE spectra were recorded by scanning the photoexcitation laser while monitoring the intensity of the ZEKE signal. The ion and electron signals were detected by a dual microchannel plate detector (Galileo), amplified by a preamplifier (Stanford Research System SR445), averaged by a gated integrator (Stanford Research System SR250), and recorded in a laboratory computer. Laser wavelengths were calibrated against titanium or vanadium atomic transitions (22). Field-dependent measurements were not performed because of the limited size of the ZEKE signal.

Calculations of molecular geometries and vibrational frequencies were carried out using the second-order Møller–Plesset (MP2) perturbation theory method and 6–311+G(d,p) basis implemented in the GAUSSIAN 03 program (23). Single-point energy calculations using the MP2 optimized geometries were performed with the coupled cluster CCSD(T) method with correlation-consistent aug-cc-pVDZ basis for H, C, and N, and aug-cc-pVDZ-PP basis for Cu (24). These single-point energy calculations were performed using the MOLPRO 2006.1 program (25). Multidimensional Franck–Condon (FC) factors were computed from the theoretical equilibrium geometries, harmonic frequencies, and normal modes of the neutral and ionic complexes (26). The Duschinsky effect (27) was considered to account for normal mode differences between the neutral molecule and ion in the FC calculations. Spectral broadening was simulated by giving each line a Lorentzian line shape with the linewidth of the experimental spectrum. Boltzmann distributions were used to simulate spectra at specific temperatures.

Results and discussion

Cu-pyridine

Figure 1*a* shows the ZEKE spectrum of Cu-pyridine

© 2007 NRC Canada

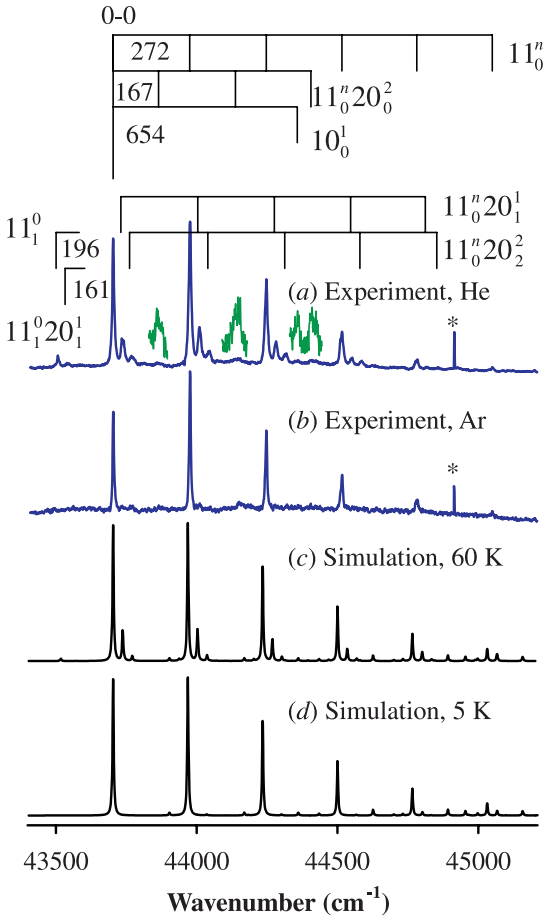


Fig. 1. Experimental ZEKE spectra of Cu-pyridine seeded in (*a*) He, (*b*) Ar, simulations at (*c*) 60 K, and at (*d*) 5 K. The peak with an asterisk is the Cu $^4D^0_{1/2} \leftarrow {}^2S_{1/2}$ atomic transition. Vertical expansions are made in (*a*) to show clearly the $11^n_0\,20^n_0$ and 10^1_0 weak peaks.

seeded in He carrier gas. Major peaks in this spectrum have a spectral linewidth (full width at half maximum) of 7 cm^{-1}. Compared to the spectrum recently recorded by Miyawaki and Sugawara (14), this spectrum shows a number of additional weak transitions and a significantly narrower linewidth. The first strong peak appears at 43 703 (5) cm^{-1}, and corresponds to the 0–0 transition between the zero vibrational levels of the ground electronic states of the neutral and ionized complexes. Above the 0–0 transition, the spectrum displays a major vibrational progression (11^n_0) with five 272 cm^{-1} intervals; a weak signal at 167 cm^{-1} and its combination with two 272 cm^{-1} intervals ($11^n_0\,20^2_0$), and an additional weak peak at 654 cm^{-1} (10^n_0). On the higher energy side of the first five members of the major progression, the spectrum exhibits two peaks separated by 34 cm^{-1} ($11^n_0 20^1_1$, $11^n_0 20^2_2$). Below the 0–0 transition, the spectrum shows two small peaks (11^0_1, $11^0_1 20^1_1$) with the lower energy peak at 196 cm^{-1} from the band origin. In contrast to all these peaks, a peak at 44 915 cm^{-1} has a much narrower linewidth and is easily assigned to be the Cu $^4D^0_{1/2} \leftarrow {}^2S_{1/2}$ atomic transition (22).

The 272 cm^{-1} intervals in the major vibrational progression are very close to the Cu$^+$-diazine stretching frequencies of Cu$^+$-pyrazine (265 cm^{-1}), Cu$^+$-pyrimidine (270 cm^{-1}), and Cu$^+$-pyridazine (273 cm^{-1}) observed in the ZEKE spectra of Cu-diazines (28). It is also comparable to the Cu-pyridine stretching frequency of 244 cm^{-1} measured in the Raman spectrum of pyridine adsorbed on aqueous Cu colloids (Table 1) (3). Thus, the main progression is assigned to the transitions from the zero vibrational level of the neutral complex to excited levels of the Cu$^+$-pyridine stretch in the ionized complex (11^n_0). The 654 cm^{-1} spacing is comparable to the frequency of the pyridine ring inplane asymmetric deformation mode in the gas phase (ν_{6a}, 601 cm^{-1}) (29–31), liquid (618 cm^{-1}) (32), or on the Cu colloid (632 cm^{-1}) (3) and electrode (633 cm^{-1}) (7) surfaces (Table 1). This vibration can thus be assigned to the same vibrational mode in the Cu$^+$-pyridine complex (ν_{10}^+). The blue shift of this pyridine deformation mode is induced by the metal-pyridine interaction, and the extent of such shifts has been found to correlate with the metal-pyridine binding strength (7, 16, 18). The weak peaks below the band origin and on the higher energy side of the major progression disappear when He is replaced by Ar as a carrier gas, as shown in Fig. 1*b*. This observation indicates that the weak peaks are due to the transitions from excited vibrational levels of the neutral complex. Because the supersonic expansion of the heavier Ar gas provide a more efficient cooling than does the lighter He gas, metal complexes seeded in Ar have lower vibrational temperatures than those seeded in He. The use of different carrier gases has been employed to identify the vibrational hot bands in the ZEKE spectra of other metal complexes (28, 33). In addition to the disappearance of the vibrational hot bands, the spectral linewidth is reduced from 7 cm^{-1} in Fig. 2*a* to 5 cm^{-1} in Fig. 1*b*. In PFI-ZEKE experiments, the intrinsic spectral linewidth is determined by the linewidth of the laser used for photoexcitation and the magnitude of the electric pulse used for ionization. The spectral linewidth of the laser is only 0.08 cm^{-1}, and the spectral broadening from the electric field is no more than 1–2 cm^{-1}. The additional spectral broadening measured in Figs. 1*a* and 1*b* is due to the unresolved rotational envelope resulting from the transitions of excited rotational levels (28, 33). The narrower linewidth in Fig. 1*b* vs. 1*a* is due to fewer rotational populations for the molecules seeded in Ar than in He.

For detailed spectral assignments, we will compare the experimental measurements with theoretical calculations. In calculating the geometry of Cu-pyridine, we considered both σ and π structures formed by Cu binding to the nitrogen atom and the six-membered π ring, respectively. However, no minimum energy π structure was found for either neutral or ionic species. Table 2 lists the electronic energies, equilibrium geometries, and harmonic frequencies of the σ structure from the MP2/6–311+G(d,p) calculations. These calculations yield a C_{2v} structure with the metal atom being coplanar to the aromatic ring. The Cu–N distance is predicted to be 2.005 Å and is fairly close to those of the Cu-diazine complexes (2.000–2.021 Å) calculated by the same method and basis (28). The geometry of pyridine shows very little change upon coordination, similar to those of diazine molecules in the Cu-diazine complexes. Upon ionization, the Cu$^+$–N distance (1.889 Å) is shrunk because of the reduced Pauli electron repulsion between Cu 4s^1 and N lone-pair electrons and to the additional charge–dipole attraction in the ionized species. Figures 1*c* and 1*d* show the spectral

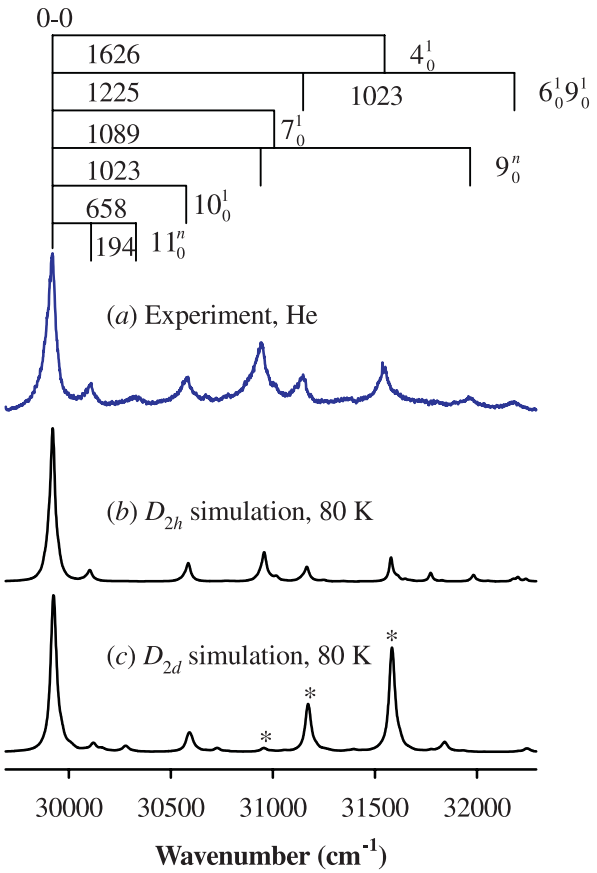
© 2007 NRC Canada

Table 1. Vibrational frequencies (cm^{-1}) of the a_1 modes of pyridine in the gas phase, adsorbed on the Cu surfaces, and in the Cu^+-$(pyridine)_n$ (n = 1,2) complexes.

			Cu surfaces[c]			
a_1 Modes[a]	Description	Gas phase (liquid)[b]	(110)	Colloid	Electrode	$Cu^+(pyridine)_{1,2}$[d]
	Cu–N stretch	—	—	244	—	292, 194
ν_1 (ν_2)	C–H stretch	3094	—	—	—	—
ν_2 (ν_{13})	C–H stretch	3072 (3070)	3058	—	—	—
ν_3 (ν_{20a})	C–H stretch	3030	—	—	—	—
ν_4 (ν_{8a})	C–C, C–N stretch	1583 (1593)	1595	1593	1596	1626
ν_5 (ν_{19a})	C–C, C–N stretch	1483 (1487)	1479	1477	—	—
ν_6 (ν_{9a})	C–H i.p bend	1218 (1220)	—	1212	1214	1225
ν_7 (ν_{18a})	C–H i.p. bend	1072 (1071)	1064	1065	—	1089
ν_8 (ν_{12a})	Asym ring breath	1032 (1036)	1035	1037	—	—
ν_9 (ν_1)	Sym ring breath	991 (1002)	1004	1010	1011	1023
ν_{10} (ν_{6a})	I.p. ring def	601 (618)	—	632	633	654, 658

[a]Labels in parentheses are based on a correlation with the vibrational modes of benzene (29).
[b]The gas phase and liquid values of the free ligand are taken from references (30) and (32), respectively.
[c]The values of pyridine adsorbed on Cu(110), Cu colloid, and Cu electrode surfaces are taken from refs. 4, 3, and 7, respectively.
[d]This work. All values are from the ZEKE spectrum of Cu-$(pyridine)_2$, except for 294 and 654 cm^{-1} that are measured from the ZEKE spectrum of Cu-pyridine.

Fig. 2. Experimental ZEKE spectrum (*a*) seeded in He, (*b*) simulations of eclipsed, and (*c*) staggered structures at 80 K.



simulations of the $^1A_1 \leftarrow {}^2A_1$ transition obtained by using the equilibrium geometries, harmonic frequencies, and force fields of the neutral and ionic states at two different temperatures. In these simulations, the calculated vibrational frequencies are not scaled, while the 0–0 transition energies are shifted to the measured value for easier comparison of the experimental and theoretical spectra. The simulation in Fig. 1*c* was carried out at the vibrational temperature of 60 K and is compared with the experimental spectrum recorded with He carrier, whereas the simulation in Fig. 1*d* was performed at 5 K and is compared with the experimental spectrum with Ar carrier. These simulations are in excellent agreement with the experimental spectra, and thus the spectral assignments based on these comparisons are straightforward. The 272 cm^{-1} progression is due to excitations of the Cu^+-pyridine stretching mode (ν_{11}^+), and the 654 cm^{-1} interval arises from the excitation of the pyridine ring in-plane deformation (ν_{10}^+). Both of these assignments are consistent with those obtained from the comparison of the ZEKE spectrum of Cu-pyridine with the ZEKE spectra of Cu-diazines (28), IR spectra of the free ligand (29–31), and the Raman spectra of pyridine adsorbed on a copper electrode (7). The 167 cm^{-1} interval is assigned to an overtone transition of the Cu^+-pyridine out-of-plane bend (ν_{20}^+). Since this vibrational mode has a b_1 representation, only transitions with $\Delta v = \pm 2, \pm 4, \ldots$ are possible. Thus, the frequency of the Cu^+-pyridine out-of-plane bend is 84 cm^{-1}. All other transitions present in Fig. 1*a*, but not in Fig. 1*b*, are due to either the Cu-pyridine stretching (ν_{11}) or the Cu-pyridine out-of-plane bending (ν_{20}) excitations in the neutral complex. The frequency of the neutral Cu-pyridine stretch, 196 cm^{-1}, is measured from the lowest energy peak (11_1^0), and that of the neutral Cu-pyridine out-of-plane bend, 49 cm^{-1}, is derived from the sequence transitions ($11_1^0 20_1^1$, $11_0^n 20_1^1$, and $11_0^n 20_2^2$), and the ionic Cu^+-pyridine out-of-plane bend (11_0^n). A complete assignment of all the transitions is given in Table 3.

The assignment of the Cu^+–Cu-pyridine stretch vibrations is consistent with a recent ZEKE study by Miyawaki and Sugawara (14). For the sequence transitions, however, our assignment is different. In the previous study, the sequence transitions were attributed to the excitations of the Cu-pyridine in-plane bend (b_2), and the assignment was made

© 2007 NRC Canada

Table 2. Electronic energies, bond lengths, bond angles, and vibrational frequencies of the neutral and ionized Cu-pyridine complexes from MP2/6–311+G(d,p) calculations.

Bond lengths (Å)	Bond angles (°)	Vibrational frequencies (cm^{-1})
$^2A_1$ (C_{2v}), E_e = –1886.875 29 (a.u.)		
Cu–N = 2.005	∠Cu–N–C = 120.9	a_1: 3243, 3222, 3213, 1643, 1508, 1241, 1088, 1047, 1027, 630, 186
N–C = 1.350	∠N–C–C = 122.7	a_2: 938, 878, 361
C–C = 1.396 / 1.397	∠C–C–C = 119.0 / 119.0	b_1: 927, 908, 723, 565, 377, 66
	∠C–N–C = 118.2	b_2: 3237, 3216, 1615, 1481, 1399, 1381, 1178, 1086, 655, 130
$^1A_1$ (C_{2v}), E_e = –1886.690 29 (a.u.)		
Cu–N = 1.899	∠Cu–N–C = 120.7	a_1: 3255, 3239, 3231, 1659, 1517, 1251, 1098, 1063, 1029, 658, 266
N–C = 1.358	∠N–C–C = 122.1	a_2: 943, 878, 368
C–C = 1.393 / 1.397	∠C–C–C = 119.3 / 118.6	b_1: 955, 913, 731, 581, 380, 100
	∠C–N–C = 118.6	b_2: 3252, 3234, 1616, 1496, 1399, 1390, 1191, 1099, 652, 166

Note: The bond lengths (Å) and angles (°) of the free ligand from the MP2/6–311+G(d,p) calculations: N–C = 1.344, C–C = 1.399, 1.397; ∠N–C–C = 123.9, ∠C–C–C = 118.6, 118.3, ∠C–N–C = 116.8.

by comparing the experimental 34 cm^{-1} intervals with B3LYP calculated frequency differences between the ionic and neutral in-plane and out-of-plane bending modes, respectively. Since these metal-ligand bending modes have very low frequencies, the prediction of their values often has relatively large errors and is sensitive to theoretical methods and basis sets. Thus, spectral assignment solely based on the frequency comparison may be tentative as pointed by Miyawaki and Sugawara. Moreover, the observation of the weak transitions ($11_0^n 20_0^2$ and 10_0^1) in our measurements yield three additional vibrational frequencies (ν_{20}^+ = 84 cm^{-1}, ν_{20} = 49 cm^{-1}, and ν_{10}^+ = 654 cm^{-1}), which were not reported in the previous study.

Cu-(pyridine)$_2$

Figure 2*a* presents the ZEKE spectrum of Cu-(pyridine)$_2$ seeded in He carrier gas. This spectrum displays remarkable differences from that of Cu-pyridine. First, the 0–0 transition is shifted to 29 917 cm^{-1}, 13 590 cm^{-1} lower than that of the mono-pyridine complex. Second, the linewidth of each band in the ZEKE spectrum of the Cu-(pyridine)$_2$ complex (~40 cm^{-1} with He and ~27 cm^{-1} with Ar) is much broader than that of the mono-pyridine complex (~7 and 5 cm^{-1} with He and Ar, respectively). Third, many more different vibrational intervals are identified in the spectrum of the di-ligand complex, which include 194, 658, 1023, 1089, 1225, and 1626 cm^{-1}.

The measured vibrational intervals can be assigned by comparing them with the ZEKE spectrum of Cu-pyridine and vibrational frequencies of free pyridine (29) or pyridine absorbed on metal surfaces (4, 7). The 194 cm^{-1} intervals are due to excitations of the pyridine-Cu^+-pyridine stretch mode. This stretching frequency is smaller than that the corresponding stretching mode of the mono-pyridine complex (272 cm^{-1}) as a result of the heavier mass of the di-pyridine complex. The 658 cm^{-1} spacing is almost the same as the frequency of the in-plane ring deformation (654 cm^{-1}) measured for Cu^+-pyridine and thus is assigned to the same pyridine vibrational mode of Cu^+-(pyridine)$_2$. Other vibrational intervals (1023, 1089, 1225, and 1626 cm^{-1}) are compared with the vibrational frequencies of free and absorbed pyridine in Table 1. From this comparison, the 1023, 1089, 1225, and 1626 cm^{-1} intervals are attributed to the symmetric ring breath, in-plane C–H bends, and C–C/C–N stretch, respectively. These pyridine-based vibrational frequencies are slightly larger than those of pyridine in the gas phase, but similar to those of pyridine absorbed on Cu (110) (4) and electrode surfaces (7).

Although the vibrational assignment is straightforward, the identification of the involved electronic transition and molecular structure of this di-ligand complex requires theoretical calculations. In our calculations, the formation of a π structure by Cu binding to one of the pyridine rings was excluded since such a structure was not found for Cu-pyridine. However, the σ structure formed by Cu binding to the nitrogen atom of each pyridine molecule may be in an eclipsed or a staggered configuration, as shown in Fig. 3. The optimized geometries, energies, and vibrational frequencies of both configurations are listed in Table 4. According to the MP2/6–311+G(d,p) calculations, the staggered structure has a lower energy than the eclipsed structure in both the neutral and ionic forms. For the eclipsed structure, a $^2B_{3u}$ neutral state is located in D_{2h} molecular symmetry. The $^2B_{3u}$ state of the eclipsed Cu-(pyridine)$_2$ has significantly shorter Cu–N distances (1.838 Å) than that of the $^2A_1$ state of Cu-pyridine (2.005 Å). Ionization of the $^2B_{3u}$ state yields the ^1A_g state also in D_{2h}. In contrast to the mono-pyridine species where the ionized form has a shorter Cu–N distance, the ionized di-pyridine complex has a longer Cu–N bond (1.862 Å) than the neutral species. Vibrational frequency calculations of both the $^2B_{3u}$ and ^1A_g states reported a small imaginary frequency for a pyridine ring torsion mode in the neutral (27*i* cm^{-1}) and ionized (21*i* cm^{-1}) species, respectively. Additional calculations without symmetry constraints (C_1 point group) still yielded a small imaginary frequency (<30i cm^{-1}) for both the neutral and ionic states. Such small imaginary frequencies are likely due to numerical errors in the calculations, and thus these two states are considered local minima. In contrast to the eclipsed configuration, the staggered structure of the neutral complex has a lower molecular symmetry (C_2), presumably because of Jahn–Teller distortion. A ^2B electronic state is predicted for the C_2 staggered structure. In

© 2007 NRC Canada

Table 3. ZEKE peak positions (cm^{-1}) and assignments of Cu-(pyridine)$_{1,2}$.

Cu-pyridine				Cu-(pyridine)$_2$	
Position	Assignment	Position	Assignment	Position	Assignment
43 507	11_1^0	44 316	$11_0^2 20_2^2$	29 917	0_0^0
43 542	$11_1^0 20_1^1$	44 357	10_0^1	30 111	11_0^1
43 703	0_0^0	44 412	$11_0^2 20_0^2$	30 305	11_0^2
43 737	20_1^1	44 516	11_0^3	30 575	10_0^1
43 771	20_2^2	44 550	$11_0^3 20_1^1$	30 940	9_0^1
43 870	20_0^2	44 585	$11_0^3 20_2^2$	31 006	7_0^1
43 975	11_0^1	44 782	11_0^4	31 142	6_0^1
44 009	$11_0^1 20_1^1$	44 817	$11_0^4 20_1^1$	31 543	4_0^1
44 044	$11_0^1 20_2^2$	44 854	$11_0^4 20_2^2$	31 963	9_0^2
44 146	$11_0^1 20_0^2$	44 915	$^4D_{1/2}^0 \leftarrow {}^2S_{1/2}$	32 165	$6_0^1 9_0^1$
44 247	11_0^2	45 050	11_0^5		
44 281	$11_0^2 20_1^1$				

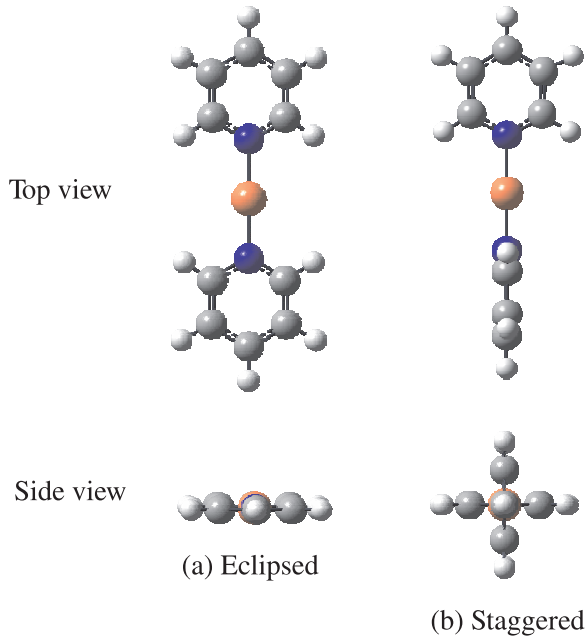


Fig. 3. (*a*) Eclipsed and (*b*) staggered structures of Cu-(pyridine)$_2$. In the web version Cu is shown in red, N in blue, C in grey, and H in white. In the print version Cu is shown in dark grey, N in black, C in light grey, and H in white.

this state, the two Cu–N bond lengths (1.863 and 1.813 Å) are not the same, but their average is identical to the Cu–N distance (1.838 cm^{-1}) of the eclipsed $^2B_{3u}$ state. Ionization of the ^2B state yields a $^1A_1$ ion state in D_{2d} symmetry, and the Cu^+–N distance (1.861 Å) is almost the same as one of the Cu–N bonds in the neutral complex. The ion has a higher molecular symmetry because Jahn–Teller distortion does not exist in a singlet electronic state.

Figures 2*b* and 2*c* show the simulations of the ^1A_g (D_{2h}) ← $^2B_{3u}$ (D_{2h}) transition of the eclipsed structure and the $^1A_1$ (D_{2d}) ← ^2B (C_2) transition of the staggered structure. Again, the calculated frequencies in these simulations are not scaled, but the 0–0 transition energies are shifted to the experimental value for simplicity. Compared to the experimental spectrum, the simulation of the $^1A_1$ (D_{2d}) ← ^2B (C_2) transition of the staggered structure considerably overestimates the intensities of the 1225 and 1626 cm^{-1} peaks, but underestimates the intensity of the 1023 cm^{-1} peak. These peaks are marked with asterisks in Fig. 2*c*. On the other hand, the simulation of the ^1A_g (D_{2h}) ← $^2B_{3u}$ (D_{2h}) transition of the eclipsed structure reproduces the experimental spectrum quite well. Therefore, the observed ZEKE spectrum is attributed to ionization of the eclipsed D_{2h} structure. Spectral assignments derived from the simulation of the eclipsed D_{2h} structure are the same as those from spectral comparisons of Cu-(pyridine)$_2$, Cu-pyridine, free pyridine, and surface-adsorbed pyridine discussed earlier. These assignments are listed in Table 3, where ν_{11}^+ represents for the symmetric pyridine-Cu^+-pyridine stretch, ν_8^+ in-plane pyridine ring deformation, ν_9^+ ring breath, ν_6^+ and ν_7^+ in-plane C–H bends, and ν_4^+ C–C/C–N stretch in the ^1A_g ion state. From the theoretical vibrational analysis, the pyridine-Cu^+-pyridine stretching mode in this di-ligand complex displays different motions from the Cu^+-pyridine stretch in the mono-ligand species. The metal-ligand stretch of the di-ligand complex is largely characterized by the movement of two pyridine molecules along the N–Cu^+–N axis, while that of the mono-ligand species is described by a large Cu^+ displacement. In addition to these ion modes, the spectral simulation indicates that the broad linewidth in the experimental spectrum contains unresolved sequence transitions involving the pyridine ring torsion (ν_{63}) and bending (ν_{56}) modes.

As noted previously, although the ^2B (C_2) state of the staggered structure is predicted to be lower in energy than the $^2B_{3u}$ state of the eclipsed structure, the simulation of the ^1A_g (D_{2h}) ← $^2B_{3u}$ (D_{2h}) transition of the eclipsed structure shows a better match with the experimental spectrum. In attempt to obtain better energies, we carried out CCSD(T) single-point energy calculations at the MP2 optimized geometries of the ^2B (C_2) and $^2B_{3u}$ (D_{2h}) states. However, these higher-level calculations yielded the same energy order for the two electronic states as the MP2 calculations, although the energy difference between these two states was reduced from 46 kJ mol^{-1} (MP2) to 17 kJ mol^{-1} [CCSD(T)]. We also performed calculations for the eclipsed and staggered structures using B3P86 and B3LYP methods. Like

© 2007 NRC Canada

Table 4. Bond lengths, bond angles, and vibrational frequencies of the eclipsed and staggered structures of Cu-(pyridine)$_2$ from MP2/6–311+G(d,p) calculations.

Bond lengths (Å)	Bond angles (°)	Vibrational frequencies (cm^{-1})
Eclipsed D_{2h}, $^2B_{3u}$, E_e = –2134.483 27 (a.u.)		
Cu–N = 1.838	∠N–Cu–N = 180.0	a_g: 3262, 3238, 3217, 1892, 1548, 1285, 1161, 1105, 1060, 667, 209
N–C = 1.358	∠Cu–N–C = 121.8	b_{1g}: 1061, 945, 454
C–C = 1.355, 1.393	∠N–C–C = 123.2	b_{2g}: 1025, 917, 744, 630, 335, 41
	∠C–C–C = 120.0, 117.2	b_{3g}: 3243, 3215, 1622, 1446, 1383, 1268, 1160, 1111, 687, 151
	∠C–N–C = 116.5	a_u: 1063, 947, 458, 27*i*
	∠C–N–N–C = 0.0	b_{1u}: 3264, 3243, 3216, 2326, 1550, 1377, 1247, 1096, 1052, 689, 374
		b_{2u}: 3243, 3214, 1624, 1443, 1385, 1265, 1163, 1103, 688, 267, 36
		b_{3u}; 1027, 919, 748, 628, 377, 218, 15
Eclipsed D_{2h}, ^1A_g, E_e = –2134.400 60 (a.u.)		
Cu–N = 1.862	∠N–Cu–N = 180.0	a_g: 3255, 3240, 3230, 1659, 1517, 1249, 1103, 1069, 1032, 661, 195
N–C = 1.357	∠Cu–N–C = 120.8	b_{1g}: 940, 879, 367
C–C = 1.393, 1.397	∠N–C–C = 122.2	b_{2g}: 950, 910, 728, 586, 380, 96
	∠C–C–C = 119.2, 118.6	b_{3g}: 3251, 3237, 1615, 1493, 1398, 1386, 1189, 1096, 653, 153
	∠C–N–C = 118.4	a_u: 939, 877, 366, 21*i*
	∠C–N–N–C = 0.0	b_{1u}: 3255, 3240, 3230, 1660, 1516, 1247, 1104, 1071, 1031, 673, 354
		b_{2u}: 3251, 3236, 1616, 1494, 1401, 1388, 1189, 1099, 654, 254, 41
		b_{3u}: 950, 911, 729, 583, 395, 178, 34
Staggered C_2, ^2B, E_e = –2134.500 76 (a.u.)[a]		
Cu–N = 1.863	∠N–Cu–N′ = 180.0	3274, 3253, 3249, 3240, 3236, 3233, 3233, 3224, 3208, 3206, 1810, 1653, 1615, 1606, 1511, 1487, 1471, 1393, 1382, 1378, 1326, 1258, 1251, 1245, 1182, 1123, 1098, 1093, 1092, 1068, 1049, 1031, 993, 988, 968, 954, 945, 926, 883, 879, 846, 773, 731, 668, 667, 654, 650, 621, 588, 461, 407, 376, 370, 365, 236, 229, 204, 165, 120, 78, 33, 27, 14
N–C = 1.355	pCu–N–C = 120.9	
C–C = 1.394, 1.397	pN–C–C = 122.4	
Cu–N′ = 1.813	pC–C–C = 119.2, 118.5	
N′–C′ = 1.390	∠C–N–C = 118.2	
C′–C′ = 1.349, 1.424	∠C–N–N′–C′ = 90.0	
	∠Cu–N′–C′ = 122.2	
	∠N′–C′–C′ = 123.2	
	∠C′–C′–C′ = 121.5, 115.0	
	∠C′–N′–C′ = 115.6	
Eclipsed D_{2d}, $^1A_1$, E_e = –2134.401 82 (a.u.)		
Cu–N = 1.861	∠N–Cu–N = 180.0	a_1: 3240, 3230, 1658, 1516, 1249, 1102, 1069, 1031, 662, 196
N–C = 1.358	∠Cu–N–C = 120.8	a_2: 954, 884, 373
C–C = 1.393, 1.397	∠N–C–C = 122.2	b_1: 954, 854, 377, 18
	∠C–C–C = 119.2, 118.6	b_2, 3240, 3230, 1660, 1516, 1247, 1104, 1071, 1031, 674, 354
	∠C–N–N–C = 90.0	e: 3255, 3251, 3236, 1615, 1494, 1399, 1387, 1189, 1097, 959, 926, 735, 653, 623, 402, 226, 121, 36

[a]Two pyridine rings in the ^2B state of the staggered configuration of Cu-(pyridine)$_2$ are not equivalent becasue of Jahn–Teller distorted low molecular symmetry. Thus, the carbon and nitrogen atoms in these two rings are differentiated with single primes.

MP2, the simulations of the ^1A_g (D_{2h}) ← $^2B_{3u}$ (D_{2h}) transition of the eclipsed structure from these density functional methods are in good agreement with the experimental spectrum. However, both the B3P86 and B3LYP calculations failed to locate any staggered structure for the neutral complex. The failure of finding a neutral staggered configuration by the density functional theory may also suggest that the eclipsed structure is more stable, as indicated by the ZEKE measurements.

Comparison of experiment and theory

Table 5 summarizes the ZEKE spectroscopic measurements for the Cu-(pyridine)$_{1,2}$ complexes, along with the values from the MP2 and CCSD(T) calculations. The bond dissociation energies of Cu^+-pyridine were previously measured as 274 kJ mol^{-1} by photodissociation (12) and 246(10) kJ mol^{-1} by CID (11). Although the uncertainty of the photodissociation value was unknown, bond dissociation energies from such measurements are normally considered as the upper limit. Moreover, the bond dissociation energy of Cu^+-pyrimidine was measured to be 250(10) kJ mol^{-1} with CID (34). From the viewpoint of electrostatic interactions, the Cu^+ bonding with pyridine and pyrimidine should be comparable since these two ligands have similar electric dipole moments (pyridine, 2.215 D; pyrimidine, 2.334 D) (35). Based on the above considerations, the CID value of the dissociation energy of Cu^+-pyridine is used in Table 4. The dissociation energy of Cu^+-(pyridine)$_2$ is taken from a

© 2007 NRC Canada

Table 5. Adiabatic ionization energies, AIE (eV), bond dissociation energies, D_0 / D_0^+ (kJ mol^{-1}), and vibrational frequencies (cm^{-1}) of Cu-(pyridine)$_{1,2}$ from ZEKE measurements and MP2/6–311+G(d,p) and CCSD(T)/aug-cc-pVDZ//MP2/6–311+G(d,p) calculations.

		ZEKE	MP2	CCSD(T)
Cu-pyridine				
AIE ($^2A_1$)		5.4185 (6)	5.06	5.31
D_0^+ ($^1A_1$), D_0 ($^2A_1$)		246, 23	259, 47	276, 62
Cu^+, Cu-pyridine stretch	ν_{11}^+/ν_{11}, a_1	272, 196	266, 186	—
Cu^+, Cu-pyridine o.p. bend	ν_{20}^+/ν_{20}, b_1	84, 49	100, 66	—
I.p. ring deformation	ν_{10}^+, a_1	654	658	—
Cu-(pyridine)$_2$				
AIE ($^2B_{3u}$)		3.709(1)	2.13	3.00
D_0^+ (^1A_g), D_0 ($^2B_{3u}$)		495, 107	517, 24	536, 100
Pyridine-Cu^+-pyridine stretch	ν_{11}^+, a_g	194	195	—
I.p. ring deformation	ν_{10}^+, a_g	658	661	—
Ring breath	ν_9^+, a_g	1023	1032	—
C–H i.p. bend	ν_7^+, a_g	1089	1103	—
C–H i.p. bend	ν_6^+, a_g	1225	1249	—
C–C, C–N stretch	ν_4^+, a_g	1626	1659	—

Note: D_0^+ (Cu^+-pyridine → Cu^+ + pyridine) is from ref. 11 with an uncertainty of 10 kJ mol^{-1}; D_0^+ [Cu^+-(pyridine)$_2$ → Cu^+ + 2 pyridine] is from ref. 15 with an uncertainty of 25 kJ mol^{-1}. D_0 (Cu-pyridine→ Cu + pyridine) and D_0 [Cu-(pyridine)$_2$ → Cu + 2 pyridine] are obtained by using the thermodynamic relation discussed in the text.

previous ion-ligand exchange equilibrium measurement (15). The dissociation energies of the mono- and di-pyridine neutral complexes are obtained using the thermochemical relationship: AIE(M – L_{n-1}) – AIE(M – L_n) = D_0^+(M – L_n) – D_0(M – L_n), where D_0^+ and D_0 are the bond energies of M^+ – L_n and M – L_n, respectively, and AIE(M – L_{n-1}) and AIE(M – L_n) are the adiabatic ionization energies of M – L_{n-1} and M – L_n, respectively.

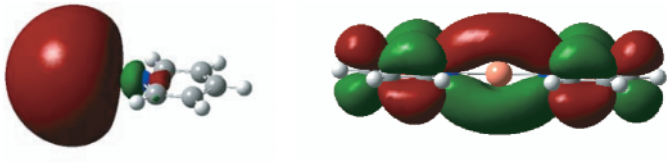
The calculated vibrational frequencies are in very good agreement with those determined experimentally, although slightly larger errors are presented for the low-frequency Cu^+/Cu-pyridine out-of-plane bending modes. However, the agreements between MP2 and ZEKE are very poor for the ionization and dissociation energies of the di-ligand complex. The major reason for this poor agreement was due to the spin contamination of the $^2B_{3u}$ state from a higher energy quartet state. Although it has no significantly adverse effect on the geometry (as indicated by the high quality of simulation in Fig. 2*b*), the spin contamination has considerably raised the total energy of the $^2B_{3u}$ state. As a result, the ionization and dissociation energies of Cu-(pyridine)$_2$ were predicted to be too low compared with the experimental values. In fact, the predicted dissociation energy for Cu-(pyridine)$_2$ → Cu^+ + 2 pyridine was even smaller than that of Cu-pyridine → Cu + pyridine. Apparently, the MP2 calculations for the Cu-(pyridine)$_2$ dissociation energy were wrong. To improve the MP2 values, we carried out single-point energy calculations using the CCSD(T) method for the ^1A_g and $^2B_{3u}$ states of the di-ligand complex. The ionization energy of the $^2B_{3u}$ state from the CCSD(T) calculations is now closer to the experimental value, although it is still low. The dissociation energy of the $^2B_{3u}$ state is inline with the value derived from the thermochemical relation, while the dissociation energy of the ^1A_g state is somewhat overestimated. As a further computational effort, we also calculated ionization and dissociation energies of the mono-ligand species using the CCSD(T) method. The ionization energy of the $^2A_1$ state from the CCSD(T) prediction is in excellent match with the value from the ZEKE measurement, while the dissociation energies of both the $^2A_1$ and $^1A_1$ states are too large compared with the experimental values. Since the CCSD(T) calculations reproduce well the precisely measured ionization energy for the mono-ligand species, we are puzzled by the relatively large differences between the theoretical and experimental dissociation energies of both the $^2A_1$ and $^1A_1$ states, especially the dissociation energy of the $^2A_1$ state. More experimental and computational studies are needed to resolve this discrepancy. Experimentally, more precise measurements for the ion bond energies will definitely be valuable, as these measurements will also reduce the uncertainties of the neutral dissociation energies derived from the thermochemical cycle. Computationally, larger and better basis sets may improve the predictions.

Metal-ligand binding in the mono- and di-pyridine complexes

Although pyridine can function as a σ donor through the nitrogen lone pair or a π donor or acceptor through occupied or empty π orbitals, the formation of the Cu-pyridine σ structure can be described by dative binding from the nitrogen lone pair to Cu 4s or 4pσ orbital. However, this dative bonding is impeded by Pauli electron repulsion between the nitrogen lone pair and Cu $4s^1$ electrons. To reduce the electron repulsion, s-pσ polarization may occur to polarize electron density away to the opposite side of the Cu atom and from pyridine, allowing the ligand to experience a larger effective nuclear charge (11, 36). This s-pσ polarization mechanism is evident from the atomic orbital compositions and electron density map of the highest occupied molecular orbital (HOMO) of Cu-pyridine (Fig. 4*a*), where the electron density is not spherical. However, because of the large energy difference between the Cu 4s and 4p orbitals

© 2007 NRC Canada

Fig. 4. Electron densities of the (*a*) highest occupied molecular orbitals of the Cu-pyridine $^2A_1$ state and (*b*) the Cu-(pyridine)$_2$ $^2B_{3u}$ state from the MP2/6–311+G(d,p) calculations.



(a) Cu-pyridine, $^2A_1$ (b) Cu-(pyridine)$_2$, $^2B_{3u}$

(~3.78 eV) (22), the s-pσ polarization mechanism is not expected to be effective. As a result, the Cu-pyridine bond energy (23 kJ mol^{-1}) is relative small. Ionization of Cu-pyridine removes the Cu 4s-based electron from the HOMO and thus the electron repulsion between Cu 4s and nitrogen lone pair. The removal of this Pauli repulsion greatly enhances the metal-ligand σ dative binding. Moreover, the removal of the Cu-based electron creates a charge–dipole attraction between Cu^+ and pyridine, further increasing the metal-ligand binding. The metal-ligand bond energy of the ionized complex is measured to be about 10 times stronger than that of the corresponding neutral species. Due to the increased ion bonding, the ionization energy of the Cu-pyridine complex (5.4185 eV) is red shifted compared with that of the metal atom (7.7264 eV) (35).

One might think that the binding mechanism between Cu and pyridine in the di-pyridine complex should be similar to that of the mono-ligand species. It is true that the di-pyridine complex is also formed by Cu binding with nitrogen atoms. However, its bond energy is measured to be almost five times stronger than that of the mono-ligand species. This large binding difference cannot be rationalized by the nitrogen lone-pair donation and Pauli repulsion discussed earlier. Although the nitrogen σ donation increases with the number of pyridine molecules, Pauli repulsion is expected to increase as well since the s-pσ polarization mechanism is not operative in the linear Cu-(pyridine)$_2$ complex. Consequently, the dissociation energy of Cu-(pyridine)$_2$ → Cu + 2 pyridine should not be more than twice as that of Cu-pyridine → Cu + pyridine. Thus, there must be additional factors contributing to the larger than expected difference between the mono- and di-ligand bond energies. The major contribution is the significant π bonding in this σ complex. Instead of the largely Cu 4s electron density in the $^2A_1$ HOMO of the mono-pyridine complex, the $^2B_{3u}$ HOMO of the di-pyridine complex consists of the bonding interaction between the Cu 4pπ and nitrogen 2pπ electrons (Fig. 4). This π-bonding interaction reduces the Cu–N distances and thus enhances the pyridine-Cu-pyridine bonding. The Cu–N distances of the Cu-(pyridine)$_2$ $^2B_{3u}$ state are predicted to be 1.838 Å, 0.169 Å shorter than that of the Cu-pyridine $^2A_1$ state (2.005 Å). Ionization of the Cu-(pyridine)$_2$ $^2B_{3u}$ state removes the π-bonding electron and thus increases the Cu–N distances. Like the mono-ligand complex, the ion bond dissociation energy of Cu^+-(pyridine)$_2$ (495 kJ mol^{-1}) is also larger than that of the neutral species (107 kJ mol^{-1}), because of the additional charge–dipole attraction and reduced Pauli repulsion.

Conclusion

Vibrationally resolved ZEKE spectra are reported for the Cu-(pyridine)$_n$ (n = 1,2) complexes. The ZEKE spectrum of the mono-pyridine complex exhibits a narrower linewidth and additional vibrational transitions compared with a previously reported ZEKE spectrum, whereas the ZEKE spectrum of the di-ligand complex is first studied in this work. The ionization energy of the mono-ligand complex is much lower than that of Cu atom, and the ionization energy of the di-ligand complex is further reduced compared with that of the mono-ligand species. These ionization energy shifts are the result of stronger metal-ligand bonding in the ion than in the neutral complex, and the increased ion binding is due to the additional charge–dipole interaction and reduced electron repulsion in the ion. The ion bond energy of the di-ligand complex is about two times stronger than that of the mono-ligand species, whereas the difference of the corresponding neutral bond energies is increased to five times. Copper binds to a single pyridine molecule in a planar C_{2v} structure and to two pyridine molecules in an eclipsed configuration, both through the nitrogen atoms. In addition to the Cu–N σ bonding in the mono- and di-ligand species, important π binding between the Cu and N pπ orbitals greatly enhances the metal-ligand bonding in the di-ligand complex. In comparing the experimental measurements with the theoretical calculations, we find that the geometries and vibrational frequencies predicted by the MP2 calculations are very good for both the mono- and di-ligand species, but the ionization and dissociation energies of the di-ligand neutral complex are underestimated because of the spin contamination in the $^2B_{3u}$ state. The CCSD(T) calculations improve the ionization energies for both the mono- and di-ligand complexes but overestimate the their bond energies, except for the neutral Cu-(pyridine)$_2$ complex.

Acknowledgment

We gratefully acknowledge financial support from the Experimental Physical Chemistry Program of the National Science Foundation. We also acknowledge partial funding from the Petroleum Research Fund of the American Chemical Society and Kentucky Science and Engineering Foundation.

References

1. J. Reedijk. *In* Comprehensive Coordination Chemistry. Vol. II. *Edited by* G. Wilkinson, R.D. Gillard, and J.A. McCleverty. Pergamon, Oxford, UK. 1987. PAGENO
2. J. Ashmore, J.C. Green, L.H. Malcolm, M.L. Smith, C. Mehnert, and E.J. Wucherer. J. Chem. Soc. Dalton Trans. **11**, 1873 (1995).
3. J.A. Creighton, M.S. Alvarez, D.A. Weltz, S. Garoff, and M.W. Kim. J. Phys. Chem. **87**, 4793 (1983).
4. S. Haq and D.A. King. J. Phys. Chem. **100**, 16957 (1996).
5. T. Gießel, O. Schaff, R. Lindsay, P. Baumgartel, M. Polcik, A.M. Bradshaw, A. Koebbel, T. McCabe, M. Bridge, D.R. Lloyd, and D.P. Woodruff. J. Chem. Phys. **110**, 9666 (1999).
6. J.G. Lee, J. Ahner, and J.T. Yates, Jr. J. Chem. Phys. **114**, 8722 (2001).
7. D.-Y. Wu, B. Ren, X. Xu, G.-K. Liu, Z.-L. Yang, and Z.-Q. Tian. J. Chem. Phys. **119**, 1701 (2003).

© 2007 NRC Canada

8. M.E. Bridge, M. Connolly, D.R. Lloyd, J. Somers, P. Jakob, and D. Menzel. Spectrochim. Acta, Part A, **43**, 1473 (1987).
9. B.J. Bandy, D.R. Lloyd, and N.V. Richardson. Surf. Sci. **89**, 344 (1979).
10. M. Bader, J. Haase, K.-H. Frank, C. Ocal, and A. Puschmann. J. Phys. Colloq. **47**, C8 (1986).
11. M.T. Rodgers, J.R. Stanley, and R. Amunugama. J. Am. Chem. Soc. **122**, 10969 (2000).
12. Y.-S. Yang, W.-Y. Hsu, H.-F. Lee, Y.-C. Huang, C.-S. Yeh, and C.-H. Hu. J. Phys. Chem. A, **103**, 11287 (1999).
13. (*a*) Y.-S. Yang and C.-S. Yeh. Chem. Phys. Lett. **305**, 395 (1999); (*b*) H.-C. Hsu, F.-W. Lin, C.-C. Lai, P.-H. Su, and C.-S. Yeh. New J. Chem. **26**, 481 (2002); (*c*) W. Guo, H. Liu, and S. Yang. Int. J. Mass. Spectrom. **226**, 291 (2003); (*d*) D.Y. Wu, M. Hayashi, C.H. Chang, K.K. Liang, and S.H. Lin. J. Chem. Phys. **118**, 4073 (2003); (*e*) C. Guo, Z. Cao, and Q. Zhang. Chem. Phys. Lett. **386**, 448 (2004); (*f*) B. Douglas Edmonds, A.K. Kandalam, S.N. Khanna, X. Li, A. Grubisic, I. Khanna, and K.H. Bowen. J. Chem. Phys. **124**, 074316/1 (2006).
14. J. Miyawaki and K.-i. Sugawara. Chem. Phys. Lett. **386**, 196 (2004).
15. H. Deng and P. Kebarle. J. Am. Chem. Soc. **120**, 2925 (1998).
16. D.-Y. Wu, B. Ren, Y.-X. Jiang, X. Xu, and Z.-Q. Tian. J. Phys. Chem. A, **106**, 9042 (2002).
17. L. Puskar, H. Cox, A. Goren, G.D.C. Aitken, and A.J. Stace. Faraday Discuss. **124**, 259 (2003).
18. D.Y. Wu, M. Hayashi, Y.J. Shiu, K.K. Liang, C.H. Chang, Y.L. Yeh, and S.H. Lin. J. Phys. Chem. A, **107**, 9658 (2003).
19. L. Puskar, P.E. Barran, R.R. Wright, D.A. Kirkwood, and A.J. Stace. J. Chem. Phys. **112**, 7751 (2000).
20. G.K. Rothschopf, J.S. Perkins, S. Li, and D.-S. Yang. J. Phys. Chem. A, **104**, 8178 (2000).
21. D. Proch and T. Trickl. Rev. Sci. Instrum. **60**, 713 (1989).
22. C.E. Moore. Atomic energy levels. National Bureau of Standards, Washington, DC. 1971.
23. M.J. Frisch, G.W. Trucks, H.B. Schlegel, G.E. Scuseria, M.A. Robb, J.R. Cheeseman, J. Montgomery, J.A., T. Vreven, K.N. Kudin, J.C. Burant, J.M. Millam, S.S. Iyengar, J. Tomasi, V. Barone, B. Mennucci, M. Cossi, G. Scalmani, N. Rega, G.A. Petersson, H. Nakatsuji, M. Hada, M. Ehara, K. Toyota, R. Fukuda, J. Hasegawa, M. Ishida, T. Nakajima, Y. Honda, O. Kitao, H. Nakai, M. Klene, X. Li, J.E. Knox, H.P. Hratchian, J.B. Cross, V. Bakken, C. Adamo, J. Jaramillo, R. Gomperts, R.E. Stratmann, O. Yazyev, A.J. Austin, R. Cammi, C. Pomelli, J.W. Ochterski, P.Y. Ayala, K. Morokuma, G.A. Voth, P. Salvador, J.J. Dannenberg, V.G. Zakrzewski, S. Dapprich, A.D. Daniels, M.C. Strain, O. Farkas, D.K. Malick, A.D. Rabuck, K. Raghavachari, J.B. Foresman, J.V. Ortiz, Q. Cui, A.G. Baboul, S. Clifford, J. Cioslowski, B.B. Stefanov, G. Liu, A. Liashenko, P. Piskorz, I. Komaromi, R.L. Martin, D.J. Fox, T. Keith, M.A. Al-Laham, C.Y. Peng, A. Nanayakkara, M. Challacombe, P.M.W. Gill, B. Johnson, W. Chen, M.W. Wong, C. Gonzalez, and J.A. Pople. GAUSSIAN 03 [computer program]. Revision C.02. Gaussian Inc, Wallingford, CT. 2004.
24. K.A. Peterson and C. Puzzarini. Theor. Chem. Acc. **114**, 283 (2005).
25. H.-J. Werner, P.J. Knowles, R. Lindh, F.R. Manby, M. Schütz, P. Celani, T. Korona, G. Rauhut, R.D. Amos, A. Bernhardsson, A. Berning, D.L. Cooper, M.J.O. Deegan, A.J. Dobby, F. Eckert, C. Hampel, G. Hetzer, A. W. Lloyd, S.J. McNicholas, W. Meyer, M.E. Mura, A. Nicklass, P. Palmieri, R. Pitzer, U. Schumann, H. Stoll, A.J. Stone, R. Tarroni, and T. Thorsteinsson. MOLPRO [computer program]. Version 2006.1. Cardiff, UK. 2006.
26. (*a*) D.-S. Yang, M.Z. Zgierski, D.M. Rayner, P.A. Hackett, A. Martinez, D.R. Salahub, P.-N. Roy, and T. Carrington, Jr. J. Chem. Phys. **103**, 5335 (1995); (*b*) A. Berces, M.Z. Zgierski, and D.-S. Yang. Computational molecular spectroscopy. Wiley, New York. 2000. p. 109.
27. F. Duschinsky. Acta Physicochim, **7**, 551 (1937).
28. X. Wang, J.S. Lee, and D.-S. Yang. J. Chem. Phys. **125**, 014309 (2006).
29. K.B. Wiberg, V.A. Walters, K.N. Wong, and S.D. Colson. J. Phys. Chem. **88**, 6067 (1984).
30. K.N. Wong and S.D. Colson. J. Mol. Spectrosc. **104**, 129 (1984).
31. V.A. Walters, D.L. Snavely, S.D. Colson, K.B. Wiberg, and K.N. Wong. J. Phys. Chem. **90**, 592 (1986).
32. H.D. Stidham and D.P. Dilella. J. Raman Spectrosc. **9**, 247 (1980).
33. (*a*) R. Sohnlein Bradford and D.-S. Yang. J. Chem. Phys. **124**, 134305 (2006); (*b*) B.R. Sohnlein, S. Li, and D.-S. Yang. J. Chem. Phys. **123**, 214306/1 (2005); (*c*) S. Li, J.F. Fuller, X. Wang, B.R. Sohnlein, P. Bhowmik, and D.-S. Yang. J. Chem. Phys. **121**, 7692 (2004); (*d*) S. Li, B.R. Sohnlein, G.K. Rothschopf, J.F. Fuller, and D.-S. Yang. J. Chem. Phys. **119**, 5406 (2003); (*e*) X. Wang, J.S. Lee, and D.-S. Yang. J. Phys. Chem. A, **110**, 12777 (2006).
34. R. Amunugama and M.T. Rodgers. J. Phys. Chem. A, **105**, 9883 (2001).
35. D.R. Lide and H.P.R. Frederikse. CRC Handbook of chemistry and physics. 78th ed. CRC, New York. 1997.
36. (*a*) M. Rosi and C.W. Bauschlicher. J. Chem. Phys. **90**, 9264 (1989); (*b*) M. Rosi and C.W. Bauschlicher. J. Chem. Phys. **92**, 1876 (1990); (*c*) P.B. Armentrout. Acc. Chem. Res. **28**, 430 (1995).

© 2007 NRC Canada

Dipole oscillator strength distributions, properties, and dispersion energies for ethylene, propene, and 1-butene[1]

A. Kumar, B.L. Jhanwar, and W. Meath

Abstract: A recommended isotropic dipole oscillator strength distribution (DOSD) has been constructed for the ethylene molecule through the use of quantum mechanical constraint techniques and experimental dipole oscillator strength (DOS) data; the DOS data employed are recent experimental results not available at the time of the original constrained DOSD analysis of this molecule. The constraints are furnished by molar refractivity data and the Thomas–Reiche–Kuhn sum rule. The DOSD is used to evaluate a variety of isotropic dipole oscillator strength sums, logarithmic dipole oscillator strength sums, and mean excitation energies for ethylene. Pseudo-DOSDs for this molecule, and for propene and 1–butene, which are based on an earlier constrained DOSD analysis for these molecules, are developed. They are used to obtain reliable results for the isotropic dipole–dipole dispersion-energy coefficients C_6, for the interactions of the alkenes with each other and with 47 other species, and the triple-dipole dispersion-energy coefficients C_9 for interactions involving any triple of molecules taken from ethylene, propene, and 1–butene.

Key words: alkenes, dipole properties, pseudo-states, dipole–dipole and triple-dipole dispersion energies, long-range additive, non-additive interaction energies.

Résumé : Faisant appel à des techniques de contrainte de mécanique quantique et des données expérimentales de force d'un oscillateur dipolaire (FOD), on a développé une distribution de la force d'un oscillateur dipolaire isotrope (DFOD) recommandée pour la molécule d'éthylène; les données de force d'un oscillateur dipolaire utilisées sont des résultats expérimentaux récents qui n'étaient pas disponibles lors de l'analyse originale contrainte de la DFOD de cette molécule. Les contraintes sont fournies par les données de réfractivité molaire et la règle des sommes de Thomas–Reiche–Kuhn. On utilise la DFOD pour évaluer des sommes de forces d'oscillateurs dipolaires isotropes, des sommes logarithmiques de force d'oscillateur dipolaire et des énergies d'excitation moyenne de l'éthylène. On a développé des valeurs pseudo-DFOD pour cette molécule, pour le propène et le but-1-ène qui sont basées sur une analyse antérieure de ces molécules par une méthode contrainte de type DFOD. Les résultats obtenus sont utilisés pour obtenir des résultats fiables pour les coefficients C_6 de l'énergie de dispersion dipôle–dipôle isotrope, pour les interactions des alcènes les uns avec les autres et avec 47 autres espèces ainsi que pour les coefficients C_9 d'énergie de dispersion triple-dipôle pour les interactions impliquant tout triplet de molécules impliquant de l'éthylène, du propène et du but-1-ène.

Mots-clés : alcènes, propriétés dipolaires, pseudo états, énergies de dispersion dipôle–dipôle et triple-dipôle, énergies d'interaction additives, non-additives à longue portée.

[Traduit par la Rédaction]

Introduction

One of the purposes of this work is to assess the reliability of the results for a wide variety of the isotropic dipole properties of the ground-state ethylene, propene, and 1-butene molecules evaluated previously (1) by using the constrained dipole oscillator strength distribution (DOSD) technique (2–7). The original constrained DOSD calculations (1) were based on the then rather sparse and disjointed (as a function of photon energy) experimental dipole oscillator strength

Received 24 April 2007. Accepted 17 May 2007. Published on the NRC Research Press Web site at canjchem.nrc.ca on 27 July 2007.

This report is dedicated to Professor G. Michael Bancroft, a colleague and friend for a long time, on the occasion of his 65th birthday.

A. Kumar. Department of Physics, Ch. Charan Singh University, Meerut 250004, India.
B.L. Jhanwar. Department of Computer Application, Mody Institute of Technology and Science, Lakshmangarth, Distt. Sikar, Rajasthan 332311, India.
W.J. Meath.[1,2] Department of Chemistry, The University of Western Ontario, London, ON N6A 5B7,Canada.

This article is part of a Special Issue dedicated to Professor G. Michael Bancroft.

[1]Corresponding author (e-mail: wmeath@uwo.ca).
[2]Associated with the Center for Interdisciplinary Studies in Chemical Physics, The University of Western Ontario.

 doi:10.1139/V07-057 © 2007 NRC Canada

(DOS) data for these alkenes, which were drawn from the work of several different experimental groups. Our new calculations for ethylene are based on much more recent, extensive, and reliable experimental DOS data (8). They can be used to directly check the reliability of the original DOSD calculations for this molecule and, in conjunction with a recent study (9) for methanol, ethanol, and propan-1-ol, which involves analogous input DOS data sets for these molecules, to indirectly assess the reliability of the analogous results for propene and 1-butene. We also present new reliable results for the isotropic dipole–dipole dispersion energies for the interaction of the three alkenes with each other and with a variety of other species. Discrete pseudo-state representations (10, 11) of the recommended constrained dipole oscillator strength distributions for the alkenes are constructed, which are useful for the efficient evaluation (10–12) of the dipolar dispersion energies, particularly the triple-double dispersion energies, for interactions involving these molecules; explicit reliable results for the triple-dipole dispersion-energy coefficients are included for all triples of the alkene molecules.

The relationship between molecular dipole oscillator strength distributions (DOSDs) and the isotropic dipole properties of molecules, and the dipole–dipole and the triple-dipole dispersion energies for interactions involving molecules, is well known (2, 13–19). The molecular dipole properties explicitly considered here are the dipole oscillator strength sums S_k, the logarithmic dipole sums L_k, the mean excitation energies I_k, and the molar refractivity R_λ as a function of wavelength λ. The properties S_k, L_k, and I_k, which depend on the value of the index k, and the dipolar dispersion energies find application in many research areas (2, 13–16, 20–32).

A quantum mechanical constraint technique (2–7) is used to construct the DOSDs for ethylene from a base of experimental dipole oscillator strength input data (1, 8) using constraints comprised of the molar refractivity (1, 33, 34) of the molecule for two well-separated wavelengths and the Thomas–Reiche–Kuhn sum rule (14, 35) for the DOSD. Specific results for integrated dipole oscillator strengths for ethylene, over various energy regions, are computed. Recommended values for the dipole sums, S_k, k = –10(2) – 4(1) – 3(½) 0, 1, 2; the logarithmic dipole sums L_k and mean excitation energies I_k, k = –2(1) 2; and the molar refractivities of the molecule are tabulated; those for propene and 1-butane can be found in the literature (1). A ten pseudo-state representation of the recommended DOSD for each of the three alkenes is also constructed and tabulated, and these are used to evaluate the results for the dipole–dipole dispersion-energy coefficients for a variety of interactions involving these molecules, and the triple-dipole dispersion-energy coefficients for the interaction of any combination of the three alkenes. The estimated uncertainties in our results for the dipole properties and dispersion energies, and a comparison with literature values, are included in the discussion. The values obtained from the constrained DOSD approach, either the original (1) or the present calculations, are either the only values or the only reliable values available for most of the dipole molecular properties considered in this paper. The results for the dispersion energies obtained herein are generally the only available reliable values for the interactions considered in this paper.

Relationship between DOSDs and dipole properties and dispersion energies

The differential dipole oscillator strength distribution (DOSD) for a molecule is the differential dipole oscillator strength df/dE as a function of photon energy E from the electronic absorption threshold E_0 for the molecule to very high photon energies. Generally, the dipole properties and dispersion-energy coefficients evaluated using DOSDs are isotropic results, since only orientationally averaged input dipole oscillator strengths are available over the required wide range of photon energies. In some instances (36–40), i.e., CO, H_2, N_2, NO, and O_2, sufficient anisotropic constraints are available to permit the construction of anisotropic DOSDs and hence the evaluation of anisotropic molecular properties.

A variety of important isotropic molecular properties can be evaluated as integrals whose integrands involve the isotropic DOSD weighted by simple functions of the photon energy. These include the dipole oscillator strength sums S_k, the logarithmic dipole sums L_k, and the mean excitation energies I_k, defined by

$$[1] \qquad S_k = \int_{E_0}^{\infty} (E / E_H)^k (df / dE)\, dE$$

$$[2] \qquad L_k = \int_{E_0}^{\infty} (E / E_H)^k (df / dE) \ln(E / E_H)\, dE$$

$$[3] \qquad I_k = E_H \exp(L_k / S_k)$$

where $E_H \approx 4.35975 \times 10^{-18}$ J (≈ 27.21 eV) is the Hartree of energy (2, 13, 14). The index k can take on various integer and half-integer values, and each choice defines a different dipole property via eqs. [1–3]. For example, the straggling (I_1 and S_1), stopping (I_0), and the total (I_{-1}, S_{-1}) inelastic scattering cross-sections of fast charged particles in matter (13, 20, 21); S_2 and I_2 determine (2, 13, 14) charge densities at the nucleus and Lamb shifts, while S_{-1}, S_{-3}, $S_{-3/2}$, S_{-2}, and L_{-2} can be used to obtain estimates for the dipole–dipole dispersion energies between molecules (10, 15, 22, 23). An important property, which is involved as a constraint in the construction of DOSDs, is the molar refractivity R_λ of a dilute molecular gas. It is related (2, 14–16) to the refractive index $n(\lambda)$ of the gas at wavelength λ and to an integral involving the DOSD

$$[4] \qquad R_\lambda = (1 / \rho)[(n^2(\lambda) - 1) / (n^2(\lambda) + 2)]$$

$$= (4\pi / 3) N_A (E_H)^2 a_0^3 \int_{E_0}^{\infty} (df / dE)(E^2 - (hc / \lambda)^2)^{-1} dE$$

$$= (4\pi / 3) N_A \alpha(\lambda)$$

where $a_0 \approx 5.29177 \times 10^{-11}$ m = Bohr, ρ is the molar density of the gas, h is Planck's constant, N_A is Avogadro's constant, c is the speed of light, and $\alpha(\lambda)$ is the wavelength-dependent electronic dipole polarizability of the molecule. The static dipole polarizability is $\alpha_d = \alpha(\lambda = \infty) = a_0^3 S_{-2}$. The S_k, k = –4, –6, –8, … are other moments of the DOSD that occur in the Cauchy expansion of $\alpha(\lambda)$.

© 2007 NRC Canada

The dipole–dipole dispersion energy is the dominant interaction energy at long range for interactions of spherically symmetric systems including freely tumbling molecules. Its importance lies in its use for representing long-range interactions between two atoms or molecules and in constructing potential-energy models that are valid for all intermolecular distances (24–30). The orientationally averaged dipole–dipole dispersion energy (16, 17) for the interaction of molecules A and B is given by $-C_6(\mathrm{A,B})R^{-6}_{\mathrm{AB}}$ where R_{AB} is the distance between species A and B and $C_6(\mathrm{A,B})$ is the dipole–dipole dispersion-energy coefficient for the interaction

$$[5]\qquad C_6 = E_{\mathrm{H}}a_0^6(3/2)\int_{E_0(A)}^{\infty} dE(\mathrm{A})\int_{E_0(B)}^{\infty} dE(B) \times \frac{[df(\mathrm{A})/dE(\mathrm{A})][df(\mathrm{B})/dE(\mathrm{B})](E_{\mathrm{H}})^3}{E(\mathrm{A})E(\mathrm{B})[E(\mathrm{A})+E(\mathrm{B})]}$$

where $E(\mathrm{A})$, $\mathrm{d}f(\mathrm{A})/dE(\mathrm{A})$, and $E_0(\mathrm{A})$ are the excitation energy, the differential dipole oscillator strength, and the electronic absorption threshold for molecule A, respectively.

Analogously, the triple-dipole dispersion energy gives the dominant non-additive interaction energy for an assembly of well-separated spherical or "tumbling" species and can be used to help model non-additive effects for other molecular configurations as well (26, 31, 32). For the interaction of three molecules A, B, and C, the triple-dipole dispersion energy is given by (16, 18, 19)

$$[6]\qquad W^{(3)} = (3\cos\theta_{\mathrm{A}}\cos\theta_{\mathrm{B}}\cos\theta_{\mathrm{C}}+1) \times C_9(\mathrm{A,B,C})R^{-3}_{\mathrm{AB}}R^{-3}_{\mathrm{BC}}R^{-3}_{\mathrm{AC}}$$

where θ_{A} is the angle between R_{AB} and R_{AC}. In terms of the original continuous DOSDs for the interacting molecules A, B, and C, the triple-dipole dispersion-energy coefficient C_9 for "tumbling" molecules is given by

$$[7]\qquad C_9(\mathrm{A,B,C}) = E_{\mathrm{H}}a_0^9(3/2)\int_{E_0(\mathrm{A})}^{\infty}\int_{E_0(\mathrm{B})}^{\infty}\int_{E_0(\mathrm{C})}^{\infty} dE(\mathrm{A})dE(\mathrm{B})dE(\mathrm{C}) \times \frac{[df(\mathrm{A})/dE(\mathrm{A})][df(\mathrm{B})/dE(\mathrm{B})][df(\mathrm{C})/dE(\mathrm{C})]}{E(\mathrm{A})E(\mathrm{B})E(\mathrm{C})} \times \frac{[E(\mathrm{A})+E(\mathrm{B})+E(\mathrm{C})](E_{\mathrm{H}})^5}{[E(\mathrm{A})+E(\mathrm{B})][E(\mathrm{B})+E(\mathrm{C})][E(\mathrm{C})+E(\mathrm{A})]}$$

Clearly, many important molecular properties and dispersion interaction energies can be evaluated if molecular dipole oscillator strength distributions (DOSDs) are available. The basic procedure used here for constructing molecular dipole oscillator strength distributions has been discussed in detail in the literature (2, 6, 7). Briefly, the initial DOS input data is divided, from the UV-absorption threshold E_0 to very large values of the photon energy, into N_0 energy intervals as suggested by the structure of the input DOS data and by the photon-energy regions associated with the individual sources of the DOS data. The number of different initial DOSDs that can be obtained by taking all possible combinations of the input DOS data is given by $N_D = \prod_{j=1}^{N_0} N_j$ *where* N_j is the number of independent sources of DOS data used for the j^{th} input spectral region (41). Each of the initial DOSDs considered is modified by requiring satisfaction of the constraints via application of a constrained least-squares technique (2, 6, 7). The input initial oscillator strength database, $(\mathrm{d}f/\mathrm{d}E)_{\mathrm{initial}}$ vs. E, for each spectral region i, is modified via

$$[8]\qquad (df/dE)^i_{\mathrm{constrained}} = (1+a_i)(df/dE)^i_{\mathrm{initial}}, \quad i = 1,2,\ldots,N_0$$

so that the total constrained DOSD satisfies the imposed constraints through the choice of the a_i. The degree of modification of the initial DOSD data required to satisfy the constraints can be represented by the standard deviation (STD) defined by

$$[9]\qquad \mathrm{STD} = [\sum_{i=1}^{N_0}(a_i-\bar{a})^2/N_0]^{1/2}$$

where $\bar{a}$ is the average of all the a_i values (6, 41). The recommended DOSD is represented by a set of data points E_j and $(\mathrm{d}f/\mathrm{d}E)_j$, for $j = 1, 2, \ldots, N_p >> N_0$, and a set of interpolating functions to connect the points. For very high photon energies, $E \geq 10^8$ eV, $(\mathrm{d}f/\mathrm{d}E)$ is represented by the Born dipole formula (35) $AE^{-2.5}$. The dipole properties of molecules are readily evaluated (2) using such a representation of DOSDs.

Construction of the DOSD for ethylene

The experimental dipole oscillator strength (DOS) data used by Jhanwar, Meath, and MacDonald (1) for constructing the original constrained DOSDs for ethylene, propene, and 1-butene have been reviewed by these authors. Generally, relatively few sources of DOS data were available at that time, the experimental DOS data were sparse as a function of photon energy and from a variety of sources, and no direct experimental data was available for $E > 70$ eV for ethylene, for $E > 27$ eV for propene, and for $E > 24$ eV for 1-butene. We base our new constrained DOSD calculations for ethylene on the extensive DOS data of Cooper, Olney, and Brion (8), which are available from the electronic absorption threshold to 200 eV; both high- and low-resolution measurements are available for $E \leq 50$ eV, while for higher photon energies, only low-resolution measurements were made. Analogous experimental studies have unfortunately not been carried out for propene and 1-butene, and so, for these molecules, our recommended DOSD results remain those of the earlier work (1). For ethylene, these more-recent DOS results are part of an extensive collection of experimental DOS data from the same laboratory that in the past has produced DOS data for other molecules that have proved to be very reliable in the sense that the modifications in the data induced by our constraint procedures have often been less than or on the order of the estimated experimental errors of ≈ 5% (to 10%) (see for example, refs. 9, 42–49).

For higher photon energies, for which the recent experimental DOS data are not available, we use, as input DOS values for ethylene, the recommended values of Jhanwar et

© 2007 NRC Canada

al. (1). These were originally based on additivity rules and then modified by the constraints imposed on the overall initial DOS data collection. For large photon energies, the modifications were generally quite small (1).

Following earlier work (1), the constraints for constructing the DOSDs for ethylene are provided by the Thomas–Reiche–Kuhn sum rule $S_0 = 16$ and by experimental molar-refractivity data. The molar-refractivity constraints are obtained by using refractive-index data for ethylene, measured by Watson and Ramaswamy (33) and Friberg (34) as normalized to Watson and Ramaswamy's value at 5462 Å. The results at two well-separated wavelengths, namely, $R(\lambda = 6440\ \text{Å}) = 10.6362\ \text{cm}^3\ \text{mol}^{-1}$ and $R(\lambda = 2302\ \text{Å}) = 13.7115\ \text{cm}^3\ \text{mol}^{-1}$, are employed as constraints. The percentage difference between these two values of R_λ, namely, $\Delta R_\lambda = 200(R_{\lambda 2} - R_{\lambda 1})/(R_{\lambda 1} + R_{\lambda 2}) = 25.3\%$, is very much larger than the expected experimental error in the refractive-index data, and hence, the least-squares constraint procedure can be used with confidence with this refractivity data to construct the DOSDs for ethylene (41, 50).

The following DOSDs have been constructed for ethylene: (*i*) DOSD1: 6.02 – 50.0 eV (high-resolution data of Cooper et al. (8)), 50.0 – 200.0 eV (low-resolution data of Cooper et al. (8)), 200 eV – ∞ (recommended DOSD of Jhanwar et al. (1)); STD = 2.11. (*ii*) DOSD2: as in DOSD1 except the high-resolution data are replaced by the low-resolution data; STD = 5.14.

DOSD1, with the smallest STD for the input data considered here, is chosen as the recommended DOSD for ethylene. The integrated dipole oscillator strengths for the recommended DOSD, together with those calculated from the initial DOS data used to construct the DOSDs for ethylene, are given in Table 1 together with the corresponding integrated oscillator strengths from the original (1) recommended DOSD for ethylene. The approach used here removes errors in the initial DOSD data in a global sense and is capable of yielding reliable dipole molecular properties and very reasonable integrated oscillator strengths. It does not necessarily lead to constrained DOSDs that are accurate on a point-by-point basis (51).

The integrated oscillator strengths evaluated using the initial high-resolution DOS data of Cooper et al. (8) are higher than our recommended integrated oscillator strengths for $6.02\ \text{eV} \le E \le 20.7\ \text{eV}$ and are lower than our results for $20.7\ \text{eV} \le E \le 50\ \text{eV}$. The maximum modification in the high-resolution data induced by our fitting procedure is about 6.5% in the 6.8–8.0 eV energy region; generally, the modifications in the initial input data in the other energy regions is much smaller than this except for 12.3–18.0 eV where it is 4.7%. Generally, the integrated DOSs obtained from the unmodified experimentral high-resolution DOS data (8) agree with our recommended results to within the estimated experimental error.

The initial low-resolution integrated DOSs are significantly different from the recommended results, and with the integrated DOS's obtained from the unmodified high-resolution data, for $E \le 12.3$ eV. The low-resolution integrated DOS is high from 6.02 to 6.8 eV, and the disagreements with the recommended (initial high-resolution) results are 13.7% (19.0%), –6.5 (–5.0), –26.5 (–25.8), 4.0 (6.4), –12.1 (–11.7), –18.4 (–17.1), and 13.1% (13.8%) for the energy regions 6.8–8.0 eV, 8.0–8.6 eV, 8.6–9.0 eV, 9.0–10.4 eV, 10.4–10.7 eV, 10.7–11.8 eV, and 11.8–12.3 eV, respectively. For higher excitation energies, the agreement between the various integrated oscillator strengths is within 5% except for the 26.7–35.0 eV and the 35.0 eV–50 eV energy regions where the low-resolution result is 6.7% and 5.1% and 9.7% and 7.9% lower than the recommended and high-resolution values, respectively.

The discrepancies between our integrated oscillator strengths and those corresponding to the original (1) DOSD for ethylene are often less than 5% and generally less than 10% with the exception of the 8.0–8.6 eV, 8.6–9.0 eV, and the 20.7–26.7 eV energy intervals where the original integrated DOSs are 12.7, 28.7, and 12.4% lower than our recommended results, respectively, and the 70.0–100.0 eV and the 100.0–200.0 eV energy regions where the original results are 15.2 and 21.8% higher than the new results.

A number of sources of DOS data for ethylene were involved in the construction of the original (1) constrained DOSD for this molecule, and these and other DOSs, and associated integrated DOSs, for the molecule have been discussed extensively earlier (see for example, refs. 1 and 8 and papers cited therein).

Relatively recently, Berkowitz (52) has updated his earlier (53) discussion and compilation of the photoabsorption cross sections for a variety of gaseous atoms and molecules including ethylene. As pointed out by Berkowitz (52), there are several sources of DOS data, in addition to Cooper et al. (8), that were not available at the time of the construction of the original (1) constrained DOSD for ethylene. Those of particular interest in his analysis (52), in addition to Cooper et al. (8), are the measurements of Holland et al. (54) and Kempgens et al. (55) in the energy regions 10.513 eV to 24.8 eV and 284 eV to 340 eV, respectively. Berkowitz presents integrated oscillator strengths for ethylene over different energy intervals than used in Table 1, and so to compare with his results, we have calculated integrated DOSs for our recommended DOSD over appropriate energy regions. Our results are 7.785(–1), 6.189, 4.624, 6.034(–1), 1.287(–1), 8.451(–1), 2.691, 1.364(–1), and 3.448(–3) for the energy regions 6.62–10.513 eV, 10.513–24.8 eV, 24.8–80.0 eV, 80.0–200.0 eV, 200–285 eV, 285–340 eV, 340–1740 eV, 1740–10^4 eV, and 10^4–∞ eV, respectively. Berkowitz's corresponding results, using his raw experimental DOS input, differ from our results by –6.9%, –0.5%, –5.8%, 14.0%, 39.8%, 19.9%, –2.2%, 2.7%, and –7.2%, respectively. He adjusted the experimental data in the 6.62–10.513 eV and the 10.513–24.8 eV regions to obtain good agreement with the experimental result (see next section) for S_{-2} and the Thomas–Reiche–Kuhn sum rule; the corresponding adjusted integrated DOSs in these regions differ by 0.6% and 1.5%, respectively, with our constrained DOSD results. As we shall see in the next section, the dipole sums obtained by Berkowitz agree very well with those obtained by our constrained DOSD approach even though the integrated DOSs in some energy regions differ appreciably. This arises for two reasons: the relevant energy regions do not contribute significantly to the sums or the discrepancies in the DOSs tend to cancel in the calculation of the dipole sums, since they can vary in sign as E changes. Finally, we point out that our DOSs for ethylene begin with an absorption threshold of

© 2007 NRC Canada

Table 1. Integrated dipole oscillator strengths for C_2H_4.

Energy region (eV)	Recommended DOSD1	Unconstrained DOSD1	High-resolution data of Cooper et al. (8)	Low-resolution data of Cooper et al. (8)	Jhanwar et al.(1)
6.020–6.8	8.240(–4)	8.242(–4)	8.242(–4)	2.735(–2)	8.151(–4)
6.8–8.0	2.827(–1)	3.009(–1)	3.009(–1)	2.438(–1)	2.891(–1)
8.0–8.6	1.034(–1)	1.049(–1)	1.049(–1)	1.101(–1)	9.029(–2)
8.6–9.0	5.399(–2)	5.430(–2)	5.430(–2)	6.830(–2)	3.845(–2)
9.0–10.4	3.147(–1)	3.228(–1)	3.228(–1)	3.021(–1)	2.863(–1)
10.4–10.7	5.507(–2)	5.525(–2)	5.525(–2)	6.173(–2)	5.254(–2)
10.7–11.8	2.336(–1)	2.361(–1)	2.361(–1)	2.765(–1)	2.363(–1)
11.8–12.3	2.428(–1)	2.450(–1)	2.450(–1)	2.111(–1)	2.339(–1)
12.3–18.0	2.768	2.898	2.898	2.889	3.011
18.0–19.1	5.570(–1)	5.579(–1)	5.579(–1)	5.685(–1)	5.382(–1)
19.1–20.7	7.541(–1)	7.541(–1)	7.541(–1)	7.577(–1)	7.173(–1)
20.7–26.7	2.180	2.157	2.157	2.137	1.909
26.7–35.0	1.685	1.656	1.656	1.572	1.772
35.0–50.0	1.442	1.414	1.414	1.302	1.441
50.0–70.0	7.285(–1)	7.202(–1)	—	7.202(–1)	7.274(–1)
70.0–100.0	4.197(–1)	4.168(–1)	—	4.168(–1)	4.837(–1)
100.0–200.0	3.743(–1)	3.718(–1)	—	3.718(–1)	4.558(–1)
200.0–300.0	3.849(–1)	3.823(–1)	—	—	3.823(–1)
300.0–500.0	1.926	1.864	—	—	1.864
500.0–1000.0	1.078	1.058	—	—	1.058
1000.0–∞	4.156(–1)	4.125(–1)	—	—	4.125(–1)

Note: Numbers in parentheses indicate a power of ten.

6.02 eV relative to that of 6.62 eV used in ref. 52. The oscillator strength from 6.02 to 6.62 eV is only 1.856(–4) and has no effect on the dipole properties considered by Berkowitz (52).

Dipole properties

Results for the molar refractivity of ethylene evaluated using our recommended DOSD are listed in Table 2 for a variety of wavelengths between 2302 Å and 6709 Å where they are compared with the experimental results of Watson and Ramaswamy (33), Friberg (34), and Lowery (56); for common wavelengths, the agreement between the results from the various sources is excellent as is the agreement with the molar refractivity results evaluated from the original (1) DOSD for ethylene.

The results for the dipole properties of ethylene, namely, the S_k, $k = -10(2) - 4(1) - 3(1/2)\ 0, 1, 2$; and the logarithmic dipole sums L_k and mean excitation energies I_k, $k = -2(1)\ 2$, evaluated using both the constrained and unconstrained ethylene DOSD1, are compared for common properties, with the literature results of Olney et al. (57) in Table 3. Olney et al. (57) computed the dipole properties by employing the photoabsorption spectrum of Cooper et al. (8); the calculations were based on the high-resolution data, augmented by the low-resolution data as needed. In order to obtain absolute values of the DOSs for ethylene, the original experimental data of Cooper et al. (8) were normalized using the valence-shell TKR (VTKR) sum rule (58). Using the normalized data of Cooper et al., Olney et al. obtained $S_{-2} = 28.26$ and then renormalized the distribution of Cooper et al. by satisfying the experimental result $S_{-2} = 27.79$ (59). It is this renormalized distribution that was used to evaluate the dipole properties of ethylene listed in Olney et al. (57). The dipole properties S_k and L_k, corresponding to the absolute scale of the original normalized DOS data of Cooper et al. (8), can be obtained from those of Olney et al. (57) by multiplying the latter by the factor 1.0169, which is the ratio of the S_{-2} evaluated from the Cooper et al. data to that finally used by Olney et al.; the mean excitation energies are unaffected by this normalization procedure.

For the dipole properties S_k, the results of Olney et al. (57) are lower than our values by 2.5% for $k = -1$ and are higher by about 0.3, 1.3, 1.9, 2.7, 3.2, and 3.6% for $k = -2(-1) -10$. For L_{-1} and L_{-2}, they are 13.5% and 2.4% lower than our recommended results. The differences between the two sets of values for common properties are less than the (rather large) uncertainties estimated by Olney et al. Results for S_k with $k = -5/2, -3/2, -1/2, k \geq 0$, and L_k and I_k with $k \geq 0$, are not available in Olney et al. (57); those for I_{-1} and I_{-2}, which can be calculated from their corresponding results for the analogous S_k and L_k sums via eq. [3], are 6.0% and 1.4% lower than our recommended values. For $k \approx 0$ and $k > 0$, the original DOS data of Copper et al. (8), and hence the DOS results of Olney et al. (57), will lead to poor values for the dipole properties unless extended to higher photon energies and constrained to both refractivity data and the full TRK sum rule $S_0 = 16$. For example, the S_0's evaluated from the unconstrained DOSD1 and DOSD2 are 15.98 and 15.75, respectively; using the Cooper et al. data (8) (i.e., up to 200 eV only) yields 12.27 and 12.04, respectively. Using the original DOS data in this way requires an extension of this data to very high photon energies as illustrated in the construction of the DOSDi, $i = 1, 2$.

The values of the dipole properties evaluated using the original (1) recommended DOSD for ethylene are also included in Table 3. The agreement with our new results is ex-

© 2007 NRC Canada

Table 2. Recommended values of the molar refractivity (cm^3 mol^{-1}) of C_2H_4 (ideal gas, STP) evaluated using the recommended DOSD1 and a comparison with literature values.

λ (Å)	Recommended DOSD1	Watson and Ramaswamy (33)	Friberg (34)	Lowery (56)
6709	10.6132	—	—	10.6069
6440	10.6362	10.6362[a]	—	10.6306
5792	10.7065	—	10.7094	—
5462	10.7531	10.7538	10.7538	10.7522
5087	10.8186	10.8202	—	10.8185
4917	10.8539	—	10.8565	—
4801	10.8804	10.8825	—	10.8819
4603	10.9309	—	—	—
4359	11.0043	11.0061	—	11.0079
4109	11.0958	—	11.0991	—
3985	11.1488	—	11.1523	—
3342	11.5515	—	11.5540	—
2968	11.9624	—	11.9363	—
2926	12.0227	—	12.0270	—
2894	12.0713	—	12.0752	—
2857	12.1304	—	12.1349	—
2760	12.3024	—	12.3079	—
2753	12.3159	—	12.3193	—
2675	12.4776	—	12.4823	—
2577	12.7152	—	12.7220	—
2464	13.0522	—	13.0564	—
2447	13.1101	—	13.1140	—
2302	13.7115	—	13.7115[a]	—

[a]Used as constraints in constructing the DOSD.

cellent; to within about 1%, and often to significantly less than 1%, except for S_{-10} where the older result is about 2% higher than our current recommended result.

This table also includes the dipole properties of the molecule obtained using the unconstrained DOSD1. The unconstrained dipole sums S_k are less than the recommended results by 1%, 1.6%, and (only) 0.1% for k = 2, 1, and 0, respectively. For $k < 0$, they are systematically greater than the recommended values by from 0.8% to 5.3% as k decreases from $k = -0.5$ to $k = -10$ in agreement with the greater values of the integrated oscillator strengths for the input DOS data relative to the recommended integrated DOSs for low excitation energies ($E \leq 20.7$ eV); the dipole sum S_k for negative k are dominated by the low-energy part of the DOSD, more so as k decreases (41, 60–62). The unconstrained results for the L_k are less than the recommended results by 0.9%, 1.7%, 4.0%, 4.7%, and 3.8% for $k = 2(-1) -2$, respectively, and the unconstrained average energies I_k agree with the recommended values to within about 1% except for I_0 where the discrepancy is 2.3%.

The results for the dipole properties of ethylene developed here and in the original alkene paper (1), and those for propene and 1-butane obtained earlier by Jhanwar et al. (1), are the most reliable compilation of such properties for these alkenes. References to other literature results for some of these properties have been given previously and other relevant literature can be found in these references. A discussion of a selection of more-recent work follows.

Hohm (59) has determined values of the frequency-dependent dipole polarizability of ethylene and propene by measuring accurate values of the refractive index of these molecules over a limited range of wavelengths relative to those in Table 2. The corresponding molar refractivities (see eq. [4]) for ethylene and propene are higher and lower than the results evaluated from our recommended DOSDs for these molecules by only a maximum of 0.4% and 0.25%, respectively. For the wavelengths 6329.9, 6119.71, 5940.96, 5435.16, and 3251.3 Å, the DOSD results are 10.6465, 10.6680, 10.6881, 10.7531, and 11.6342 cm^3 mol^{-1} for ethylene, respectively, and 15.6571, 15.6873, 15.7156, 15.8129, and 17.0459 cm^3 mol^{-1} for propene, respectively.

Hohm has extracted the dipole sums S_k, $k = -2$, -4, -6, and -8 by fitting a Cauchy series to his frequency-dependent polarizability data. For ethylene, the sums so obtained are 0.3%, 1.7%, and 1.7% higher, and 11.5% lower; and for propene, they are 0.3% lower, 0.5% and 5.1% higher, and 9.0% lower, than the recommended DOSD results of this paper and Jhanwar et al.(1). The larger discrepancies as k decreases, given the excellent agreement for the refractivity data, are probably due to difficulties in fitting the Cauchy series to polarizability data over a limited wavelength range; see for example the discussion in Hohm (59). The evaluation of the dipole sums using the DOSD approach involves no such fitting procedure.

As discussed in the previous section, Berkowitz (52) has analyzed the experimental DOSs for the ethylene molecule. He has evaluated the dipole sums S_k, $k = -2(1)$ 2, using both raw and adjusted experimental DOS data and the value of the S_{-2} used in the adjustment is that due to Holm (59) just discussed. The results obtained for the dipole sums S_k, $k = -2$

© 2007 NRC Canada

Table 3. The dipole sums S_k, logarithmic dipole sums L_k and mean excitation energies I_k for C_2H_4 evaluated using the recommended and unconstrained DOSD1.

Property	Unconstrained DOSD1	Recommended DOSD1	Jhanwar et al. (1)	Olney et al. (57)
S_2	6.553(3)	6.619(3)	6.556(3)	—
S_1	9.956(1)	1.012(2)	1.001(2)	—
S_0	1.598(1)	1.600(1)	1.600(1)	—
$S_{-0.5}$	1.450(1)	1.438(1)	1.438(1)	—
S_{-1}	1.656(1)	1.630(1)	1.631(1)	1.590(1)
$S_{-1.5}$	2.100(1)	2.056(1)	2.057(1)	—
S_{-2}	2.841(1)	2.770(1)	2.770(1)	2.779(1)
$S_{-2.5}$	4.048(1)	3.933(1)	3.930(1)	—
S_{-3}	6.029(1)	5.840(1)	5.828(1)	5.918(1)
S_{-4}	1.496(2)	1.442(2)	1.435(2)	1.470(2)
S_{-6}	1.261(3)	1.207(3)	1.202(3)	1.240(3)
S_{-8}	1.341(4)	1.277(4)	1.286(4)	1.318(4)
S_{-10}	1.588(5)	1.508(5)	1.541(5)	1.562(5)
L_2	3.906(4)	3.940(4)	3.906(4)	—
L_1	3.024(2)	3.075(2)	3.034(2)	—
L_0	9.394	9.781	9.712	—
L_{-1}	–6.480	–6.189	–6.189	–7.011
L_{-2}	–1.873(1)	–1.805(1)	–1.802(1)	–1.848(1)
I_2 (eV)	1.0556(4)	1.0471(4)	1.0535(4)	—
I_1 (eV)	5.672(2)	5.674(2)	5.628(2)	—
I_0 (eV)	4.898(1)	5.015(1)	4.993(1)	—
I_{-1} (eV)	1.840(1)	1.862(1)	1.862(1)	—
I_{-2} (eV)	1.407(1)	1.419(1)	1.420(1)	—

Note: Numbers in parentheses indicate a power of ten.

to 2, respectively, differ from our constrained DOSD results of Table 3 by –3.2%, –2.52%, –0.6%, 1.6%, and –1.6% and by only 0.2%, –0.1%, 0.5%, 1.8%, and –1.6% for the raw vs. the adjusted DOS input, respectively.

Time-dependent Hartree–Fock (TDHF) results for the ethylene S_k, k = –2, –4, and –6, are available from Spackman (63); he employed an 6–31G(+sd +sp) basis set and an ELP (electrical properties) basis set of Liu and Dykstra (64). The ab initio results are 1.7% lower and 4.8% and 16.1% higher for the 6–31G(+sd +sp) basis and 0.5%, 13.3%, and 34.3% higher for the ELP basis set than our recommended results, which are very similar to those of Jhanwar et al. (1) used in the analysis of Spackman (63). Generally, the ELP basis seems to perform better in the calculation of dipole sums and ethylene is one of the exceptions pointed out by Spackman (63).

About a year after Spackman's paper, Maroulis (65) carried out a study of basis set and electron correlation effects in the ab initio calculation of the dipole polarizability (and hyperpolarizability) of ethylene using the self-consistent field and many body-perturbation theory methods. Eight basis sets were discussed/investigated beginning with that due to Dunning (66) and perturbation theory through fourth order, including contributions from single, double, triple, and quadruple substitutions from the zeroth order function were considered. The Hatree–Fock limit of S_{-2} (the dipole polarizability in units of a_0^3) was estimated to be 28.36 ± 0.14, while the best estimate, including correlation effects, was 27.29 ± 0.12, which is within about 1.5% of the then, and the current, recommended result of 27.70. Reference 65 has a nice discussion of the then available theoretical and experimental results for the dipole polarizability of ethylene.

Dalskov and Sauer (67) have evaluated the ethylene dipole sums S_k, k = –2, –4, and –6, using the random phase approximation (RPA), the second-order polarization propagator approximation (SOPPA), the SOPPA with coupled cluster singles and doubles amplitudes (SOPPA(CCSD)), and the coupled cluster singles and doubles linear response function method (CCSDLR); two basis sets were investigated, Sadlej's (68, 69) medium-sized polarization basis set (basis set I) and Dunning's (70) correlation consistent valence triple ζ basis set augmented by two diffuse polarization functions for all angular momenta in the basis added in an even tempered fashion (71, 72) (basis set II). For the first three ab initio methods, the dipole sums were directly evaluated using the approach discussed by Fowler et al. (73), while a Cauchy fit to the frequency-dependent polarizability was used in the case of the CCSDLR calculation.

The discrepancies of the ab initio results with respect to our recommended values for basis set I (and II) are 2.2%, 2.3%, –0.8%, and –0.6% (2.9%, 1.6%, –0.6%, and –0.6%), 15.7%, 13.5%, 6.7%, and –2.4% (15.5%, 9.2%, 4.9%, and –4.7%) and 35.2%, 26.4%, 16.1%, and –6.6% (36.0%, 19.7%, 13.9%, and –9.7%) for S_{-2}, S_{-4}, and S_{-6}, respectively,

© 2007 NRC Canada

in the order RPA through CCSDLR. These results are more or less in agreement with the trend discussed in Dalskov and Sauer (67) that the accuracy of these ab initio approaches increases in the order RPA to CCSDLR. Generally, the dipole sums are more difficult to compute as k decreases. Dalskov and Sauer also computed the frequency-dependent dipolar polarizability of ethylene using basis set II and the CCSDLR method over a limited wavelength range (five values from 6329.9 to 3251.3 Å). Their corresponding results vary from being 0.7% to 1.5% lower than those evaluated from our recommended DOSD, as the λ decreases; the agreement is well within the estimated errors (67) in their calculations.

The ethylene dipole sums S_k, $k = -2$ and -4, have also been evaluated by Caillie and Amos (74) using the self-consistent field (SCF) approach and two variants of density functional theory (DFT), namely, the local density approximation (LDA) and a gradient corrected functional (BLYP); basis sets (see earlier) developed by Sadlej (68, 69) and Woon and Dunning (71, 72) were investigated. The dipole sum S_{-2} was calculated directly, while S_{-4} was determined by a Cauchy fit of the relevant frequency-dependent polarizability through terms varying as λ^{-4}. The ab initio results are all greater than our recommended values; for the Sadlej (Woon and Dunning), basis sets by 2.3%, 5.1%, and 3.6% (2.9%, 5.0%, and 3.8%), and 15.5%, 17.8%, and 17.0% (15.5%, 15.6%, and 15.6%) for S_{-2} and S_{-4}, respectively, in the order: SCF, LDA, BLYP. The DFT results show no improvement relative to the SCF results and, as in the case of the ab initio methods employed by Dalskov and Sauer (67), the more sophisticated basis set shows little improvement over the results obtained from the Sadlej basis.

A recent discussion of the mean excitation energies for the stopping power of some 32 atoms and molecules can be found in Kamakura et al. (75). This includes the evaluation of I_0 for these species using, as a basis, the analysis of the relevant oscillator-strength spectra recently given by Berkowitz (52). A detailed comparison with a variety of literature values of I_0 for the atoms and molecules considered is included in Kamakura et al. (75). Their result for I_0 for ethylene is 51.3 eV, which is 2.3% higher than our recommended result; the older recommended DOSD result of Jhanwar et al. (1), referred to in ref. 75, is 0.5% lower than our recommended result.

The discussion (76) of the radiation interaction parameters (S_k, L_k, I_k, $k = 1,0, -1$, $S_{1/2}$), and their additivity for the alkenes based on the results of ref. 1, is not significantly affected by the results of the current work.

The ab initio quantum mechanically calculated results (63, 65, 67, 74) for the dipole properties discussed earlier do not include vibrational averaging effects, which are included, for example, in the experimentally based results of Hohm (59) and in the DOSD values for these properties. As emphasized, for example, by Russell and Spackman (77), the sizes of these effects are often reasonably small, and so high-quality electronic property calculations are generally required initially before vibrational effects are considered within the ab initio treatment used in the calculation. Ab initio calculations of such properties are complicated by several factors: (*i*) the selection of the nuclear geometry of the molecule (equilibrium or vibrationally averaged geometries, experimental or calculated geometries, calculated geometries that have been calculated previously or those that are consistent with the theoretical approach used in the property evaluation), (*ii*) the choice of the ab inito method, (*iii*) the choice of the basis set used to carry out the calculation, and (*iv*) whether or not vibrational averging effects are included in the calculation. Each of these factors can introduce error into the final ab initio result for the property.

The molecular property most studied in the context of the last paragraph is the polarizability of molecules. For example, two studies (78, 79) indicate that the effects of vibrational averaging on the isotropic dipole polarizabilities of the first-row hydrides CH_4, NH_3, H_2O, and HF varies from being 4%–5.5% to 1.5% higher than the unaveraged values; a study (77) of the second-row hydrides shows similar results. As might be expected, molecules with a number of hydrogen atoms bonded to a common atom show the largest vibrational averaging effect as does H_2 itself. Results for S_{-2}, as a function of the bond length of H_2, are available in the literature (80, 81), and for example, the result at the vibrationally averaged bond length $r_0 = 1.449\ a_0$ is 4% higher than at the equilibrium bond length $r_e = 1.40\ a_0$. Limited results for some of the other dipole properties of H_2, as a function of bond length, are also available in ref. 82.

Vibrational averaging effects, when available for the molecule of interest, have been used from time to time to help reconcile ab initio and constrained DOSD results for molecular properties (see for example, refs. 37, 42, 48). Also, it is relevant to point out that the effects of molecular geometry, including vibrational averaging, can be relatively more significant in the evaluation of the (intrinsically smaller) anisotropy of molecular properties than it is for the isotropic properties of particular interest in this paper (37, 77–82).

Dispersion-energy coefficients

The dipole dispersion-energy coefficients are generally most conveniently evaluated by using discrete representations (pseudo-DOSDs) of the recommended constrained DOSDs for the interacting species (10, 11). This representation of the original DOSD of the molecule is particularly useful for the efficient evaluation of the triple-double dispersion energy, which is given (eq. [7]) in terms of a triple integral involving the original continuous DOSDs of the interacting species (11, 12). The pseudo-DOSD for a given molecule is determined from known values of the dipole sums S_k by requiring

$$[10] \qquad S_k = \sum_{i=1}^{n} (E_i / E_H)^k f_i \quad , k = 2,1,0, -1, -2, \ldots, 3-2n$$

The values of $2n$ dipole sums generate n pseudo-dipole (excitation energy oscillator strength) pairs (E_i, f_i). The ten pseudo-state representation of the constrained DOSD 1 for ethylene is given in Table 4. It is more than adequate for evaluating the dipole–dipole and the triple-dipole dispersion-energy coefficients, for interactions involving the ethylene molecule, to well within the accuracy (≤1% for dipole–dipole, ≤1%–2% for triple-dipole) generally expected (10–12) from using the original constrained DOSD. We have also computed the pseudo-DOSDs for propene and 1-butene using the S_k determined from the recommended DOSDs for

© 2007 NRC Canada

Table 4. The values of the pseudo-DOSD excitation energies (in units of E_H) and oscillator strengths for ground state C_2H_4.

E_i	f_i
2.49559(–1)	7.70604(–3)
2.72445(–1)	2.28700(–1)
3.13376(–1)	2.99037(–1)
4.02588(–1)	8.03816(–1)
5.44545(–1)	2.47268
7.92270(–1)	3.92625
1.33778	3.12855
3.21851	1.43078
1.77416(1)	3.60023
2.31130(2)	1.02252(–1)

Note: Numbers in parentheses indicate a power of ten.

these molecules constructed by Jhanwar et al. (1); they can be found in Tables 5 and 6.

The discretized version of eq. [7], useable for the evaluation of the dipole–dipole dispersion-energy coefficient C_6 by employing the pseudo-DOSDs of the interacting species, is given by (10, 14)

$$[11] \quad C_6(\mathrm{A},\mathrm{B}) = E_H a_0^6 (3/2) \sum_{i=1}^{n_A} \sum_{j=1}^{n_B} \frac{f_i(\mathrm{A}) f_j(\mathrm{B}) (E_H)^3}{E_i(\mathrm{A}) E_j(\mathrm{B}) [E_i(\mathrm{A}) + E_j(\mathrm{B})]}$$

The results for the C_6 coefficients obtained from this result for the interaction of ethylene, propene, and 1-butane with themselves and with some 47 other atoms and molecules, can be found (units of $E_H a_0^6$) in Tables 7, 8, and 9, respectively. In these calculations, the alkene molecules are represented by the pseudo-states listed in Tables 4, 5, and 6, and the pseudo-states for the other species can be found in the literature (6, 7, 9, 10, 12, 42, 46–49, 51, and refs. cited therein). The uncertainties are ≈1%.

The pseudo-DOSD expression for the triple-dipole interaction energy coefficient C_9 is (11, 14)

$$[12] \quad C_9(\mathrm{A},\mathrm{B},\mathrm{C}) = E_H a_0^9 (3/2) \sum_{i=1}^{n_A} \sum_{j=1}^{n_B} \sum_{k=1}^{n_C} \frac{f_i(\mathrm{A}) f_j(\mathrm{B}) f_k(\mathrm{C})}{E_i(\mathrm{A}) E_j(\mathrm{B}) E_k(\mathrm{C})} \times \frac{[E_i(\mathrm{A}) + E_j(\mathrm{B}) + E_k(\mathrm{C})](E_H)^5}{[E_i(\mathrm{A}) + E_j(\mathrm{B})][E_j(\mathrm{B}) + E_k(\mathrm{C})][E_k(\mathrm{C}) + E_i(\mathrm{A})]}$$

Using the pseudo-states given in Tables 4–6, the triple-double dispersion-energy coefficients for the interaction of any three alkenes taken from ethylene, propene, and 1-butene can be evaluated with an estimated error of less than 2%. The results are given, in units of $E_H a_0^9$, in Table 10. The C_9 coefficients for all the interactions involving the alkenes and any of the other species occurring in the earlier tables can be evaluated by using the pseudo-states for the species referred to previously.

Olney et al. (57) have evaluated two dipole–dipole dispersion-energy coefficients using their DOSs for He, Ne, and C_2H_4 and obtained $C_6(\mathrm{He}-C_2H_4) = 19.92$ and $C_6(\mathrm{Ne}-C_2H_4) = 39.96$, which are 0.7% and 1.7% lower than our results.

Table 5. The values of the pseudo-DOSD excitation energies (in units of E_H) and oscillator strengths for ground state C_3H_6.

E_i	f_i
2.45374(–1)	4.44189(–2)
2.65480(–1)	2.19447(–1)
3.17393(–1)	3.49069(–1)
4.02328(–1)	1.35368
5.45075(–1)	3.94058
7.88288(–1)	5.57534
1.33880	4.71831
3.24561	2.34981
1.77062(1)	5.29692
2.31219(2)	1.52409(–1)

Note: Numbers in parentheses indicate a power of ten.

Table 6. The values of the pseudo-DOSD excitation energies (in units of E_H) and oscillator strengths for ground state C_4H_8.

E_i	f_i
2.44401(–1)	5.47815(–2)
2.63912(–1)	2.41008(–1)
3.16143(–1)	4.28545(–1)
4.02901(–1)	1.77394
5.43816(–1)	5.14232
7.90723(–1)	7.48640
1.33569	6.41832
3.22456	3.17907
1.76814(1)	7.07170
2.30866(2)	2.03906(–1)

Note: Numbers in parentheses indicate a power of ten.

Spackman (83) has carried out time-dependent Hartree–Fock (TDHF) calculations for C_6 and C_9, for the dimers and trimers, respectively, of ethylene, propene, and 1-butene, using a 6–31G(+sd +sp) basis set. His results of 285.4, 596.9, 1037.92, 5555.2, 16418.7, and 37286.5, respectively, are 4.9%, 9.8%, 8.2% and 6.6%, 15.2% and 13.0% lower than our recommended results. As thoroughly discussed by Spackman (63, 83, 84), who has used many of our previous constrained DOSD results for C_6 and C_9 for a variety of molecules to assess the situation, this level of TDHF calculation cannot be expected to give accurate results for these dispersion-energy coefficients.

Spackman has discussed the systematics of the deviations of 6–31G(+sd +sp) TDHF results of the dispersion-energy coefficients from the constrained DOSD values and suggested how to correct the TDHF results to obtain values that are generally much closer to the DOSD results if the static dipole polarizabilities of the interacting species are known both at the 6–31G(+sd +sp) TDHF level of approximation and reliably (for example, experimentally or through a constrained DOSD analysis). His equations for the predicted values, written for the interaction of like molecules, have the form

$$[13] \quad C_{6,\mathrm{pre}} = c[\alpha_{d,\mathrm{exp}} / \alpha_{d,\mathrm{TDHF}}]^a C_{6,\mathrm{TDHF}}$$

and

© 2007 NRC Canada

Table 7. Recommended values for the dipole–dipole dispersion-energy coefficients $C_6(C_2H_4, B)$ for the interaction of C_2H_4 with various species B (in units of $E_H a_0^6$).

B	$C_6(C_2H_4, B)$	B	$C_6(C_2H_4, B)$	B	$C_6(C_2H_4, B)$
C_2H_4	300.2	NO	143.1	CH_2O	222.3
H	43.80	N_2O	234.4	CH_3CHO	346.8
Li	418.1	H_2O	115.9	$(CH_3)_2CO$	487.6
He	20.07	SO_2	296.2	CH_3OH	257.5
Ne	40.66	CS_2	507.0	C_2H_5OH	400.2
Ar	138.0	COS	347.2	C_3H_7OH	540.0
Kr	196.8	H_2S	254.6	CH_4	197.2
Xe	292.8	SF_6	403.9	C_2H_6	338.3
H_2	60.23	SiH_4	319.8	C_3H_8	479.9
N_2	147.0	SiF_4	306.1	C_4H_{10}	616.6
O_2	133.9	CCl_4	779.2	C_5H_{12}	755.6
Cl_2	341.7	C_2H_2	247.5	C_6H_{14}	891.2
HF	73.73	C_6H_6	719.1	C_7H_{16}	1028
HCl	197.7	NH_3	163.5	C_8H_{18}	1164
HBr	254.9	CH_3NH_2	301.7	—	—
CO	155.6	$(CH_3)_2NH$	440.6	—	—
CO_2	216.4	$(CH_3)_3N$	564.5	—	—

Table 8. Recommended values for the dipole–dipole dispersion-energy coefficients $C_6(C_3H_6, B)$ for the interaction of C_3H_6 with various species B (in units of $E_H a_0^6$).

B	$C_6(C_3H_6, B)$	B	$C_6(C_3H_6, B)$	B	$C_6(C_3H_6, B)$
C_3H_6	662.1	NO	212.7	CH_2O	330.3
H	65.00	N_2O	348.2	CH_3CHO	515.2
Li	617.3	H_2O	172.2	$(CH_3)_2CO$	724.3
He	29.84	SO_2	440.1	CH_3OH	382.5
Ne	60.48	CS_2	752.3	C_2H_5OH	594.5
Ar	205.0	COS	515.4	C_3H_7OH	802.2
Kr	292.3	H_2S	378.0	CH_4	292.9
Xe	434.9	SF_6	600.5	C_2H_6	502.6
H_2	89.45	SiH_4	474.7	C_3H_8	712.8
N_2	218.5	SiF_4	455.1	C_4H_{10}	915.9
O_2	198.9	CCl_4	1157	C_5H_{12}	1122
Cl_2	507.5	C_2H_2	367.6	C_6H_{14}	1324
HF	109.6	C_6H_6	1068	C_7H_{16}	1527
HCl	293.7	NH_3	242.9	C_8H_{18}	1729
HBr	378.5	CH_3NH_2	448.2	C_2H_4	445.8
CO	231.1	$(CH_3)_2NH$	654.5	—	—
CO_2	321.5	$(CH_3)_3N$	838.5	—	—

[14] $$C_{9,\mathrm{pre}} = d\,[\alpha_{d,\mathrm{exp}} / \alpha_{d,\mathrm{TDHF}}]^b C_{9,\mathrm{TDHF}}$$

where in Spackman's work, the parameters a, b, c, and d are $a = 2$, $b = 3$, $c = 0.9435$, and $d = 0.9283$. Using Spackman's results (63, 83) for $\alpha_{d,\mathrm{TDHF}}$, $C_{6,\mathrm{TDHF}}$, and $C_{9,\mathrm{TDHF}}$, and our recommended values of S_{-2} as $\alpha_{d,\mathrm{exp}}$, one obtains $C_{6,\mathrm{pre}}$ = 278.4, 639.5, and 1100.0 and $C_{9,\mathrm{pre}}$ = 5421.4, 18440.5, and 41206.8 for the like interactions involving ethylene, propene, and 1-butene; these results differ from our recommended results by –7.3%, –3.4%, and –2.7% (avg. = –4.4%), and –8.8%, –4.7%, and –3.8% (avg. = –5.8%), respectively. The improvement relative to the TDHF values is very good except for ethylene where the correction factors multiplying the TDHF results are less than unity.

More recently, Cybulski and Haley (85) have discussed several new approximations for calculating the dispersion-energy coefficients C_6 and C_9, which are based on eqs. [13] and [14] for the interaction of like species. They developed several schemes using our literature DOSD results to determine the parameters a, b, c, and d and tested their approach against our accurate DOSD results for some fourteen interactions involving rare gases, HF, N_2, CO, H_2O, and normal

© 2007 NRC Canada

Table 9. Recommended values for the dipole–dipole dispersion-energy coefficients $C_6(C_4H_8, B)$ for the interaction of C_4H_8 with various species B (in units of $E_H a_0^6$).

B	$C_6(C_4H_8, B)$	B	$C_6(C_4H_8, B)$	B	$C_6(C_4H_8, B)$
C_4H_8	1130	NO	278.2	CH_2O	431.6
H	84.85	N_2O	455.2	CH_3CHO	673.3
Li	802.0	H_2O	225.1	$(CH_3)_2CO$	946.6
He	39.07	SO_2	575.3	CH_3OH	500.0
Ne	79.22	CS_2	982.0	C_2H_5OH	776.9
Ar	268.1	COS	673.2	C_3H_7OH	1048
Kr	382.1	H_2S	493.6	CH_4	382.7
Xe	568.1	SF_6	785.8	C_2H_6	656.7
H_2	116.9	SiH_4	619.8	C_3H_8	931.5
N_2	285.7	SiF_4	595.5	C_4H_{10}	1197
O_2	260.2	CCl_4	1512	C_5H_{12}	1467
Cl_2	663.2	C_2H_2	480.2	C_6H_{14}	1730
HF	143.4	C_6H_6	1395	C_7H_{16}	1995
HCl	383.8	NH_3	317.4	C_8H_{18}	2260
HBr	494.5	CH_3NH_2	585.7	C_2H_4	582.5
CO	302.2	$(CH_3)_2NH$	855.3	C_3H_6	865.0
CO_2	420.4	$(CH_3)_3N$	1096	—	—

Table 10. Recommended values for the triple-dipole dispersion-energy coefficients C_9 for all the three-body interactions involving the A = C_2H_4, B = C_3H_6, and C = C_4H_8 molecules, in units of $(E_H a_0^6)$.

Interaction	C_9	Interaction	C_9
A–A–A	5944.8	B–B–A	13057
A–A–B	8810.1	B–B–C	25220
A–A–C	11481	C–C–C	42837
A–B–C	17016	C–C–A	22176
B–B–B	19351	C–C–B	32868

alkanes. Their approximations have been set up using higher level basis set values for the input TDHF quantities than Spackman's scheme, which is designed for the use of 6–31G(+sd +sp) TDHF results for the input polarizabilities and dispersion-energy coefficients; the TDHF input from refs. 63, 83, and 85, for common molecules are significantly different. Thus, as discussed previously (9), the approximations of Cybulski and Haley, which yield an improvement on the Spackman scheme for the fourteen test interactions, do not necessarily improve the situation for other interactions (partly depending on the nature of the TDHF input).

The alkene ab initio results (83) for the dipole–dipole dispersion-energy coefficients do not contain vibrational averaging effects. Also, all the problems discussed at the end of the last section regarding the ab initio calculation of molecular properties apply to the calculation of the C_6 coefficients as well; various approximations (15, 16) for C_6 indicate that this coefficient qualitatively behaves as the product of the dipole polarizabilities of the two interacting molecules. Results for C_6 for the H_2–H_2 interaction, and for the interaction of H_2 with all the rare gases (R_g), as a function of the H_2 bond length are available in the literature (80–82). For example, the increase in C_6 due to increasing the H_2 bond length from $r_e = 1.40\ a_0$ to $r_0 = 1.449\ a_0$ is about 6% for the H_2–H_2 interaction and about 2.8% to 3.2% for the H_2–R_g interactions. In general, the bond length dependence of the dispersion-energy coefficients, the higher-order coefficients as well as C_6, is important as input for the construction of multi-dimensional potential-energy surfaces that reflect the relevant vibrational motions in a molecular complex, see for example ref. 86 and citations therein.

Discussion and conclusions

Estimates for the uncertainties in our recommended values for molecular dipole properties, evaluated using the constrained dipole oscillator distribution approach, are based on methods developed and used previously (2, 6, 7, 21, 41). The recommended results are compared with those obtained from alternative DOSDs satisfying the same constraints (i.e., DOSD1 and DOSD2 for ethylene in this paper and the various DOSDs considered for all three alkenes in ref. 1). For the properties that depend significantly (21, 41, 50, 60, 61) on energy regions of the DOSD that dominate the constraints used in constructing the DOSDs, that is the S_k, L_k, and I_k for $-6 \le k \le 0$ or 1, the estimated errors are ≤ 1%−2%. The uncertainties will increase, relatively slowly, as k decreases for $k < -6$ because local errors in the DOSD for small photon energies are magnified for these properties (21, 50, 60, 61); they can be as high as 10% to 15% for S_{-10}. These error estimates assume reliable values (errors of a few tenths of a percent) for the molar refractivities used as constraints. For $k \ge 1$, and particularly for $k = 2$, the estimated errors in the dipole properties are related to errors in the high-energy input data used in the construction of the DOSD and generally can be on the order of several percent. These error estimates apply for the three alkene molecules considered in this work and in ref. 1. Because of the analysis of

© 2007 NRC Canada

Berkowitz (52), which includes consideration of relatively recent high-energy DOS data for ethylene, and the agreement between his and our results for S_2 and S_1, we estimate the errors in our recommended results for the S_k, L_k, and I_k, $k = 1, 2$, to be 1%–2% for this molecule.

As indicated earlier, part of motivation for this work was to verify the reliability of the results for the dipole properties of the alkenes obtained in the original (1) constrained DOSD analysis for these molecules. That work was carried out in the early 1980s and was based on the then available DOS data for the molecules, which, as discussed earlier in the present paper, were sparse, from various experimental groups, with no direct experimental DOS data being available for photon energies greater than 50 eV for ethylene, 27 eV for propene, and 24 eV for 1-butene (in ref. 1, the higher-energy DOSs were obtained via mixture rules with ethylene playing a relevant role for propene and 1-butene). The constrained DOSD analysis in the current paper for ethylene, which is based on extensive experimental DOS data from a single experimental group (8), indicates that the results for the properties of these molecules obtained originally are indeed reliable and that the present recommended values for ethylene offer only a marginal improvement. Similarly, the values of the dipole properties of ethylene for $k \leq 1$ obtained by Olney et al. (57), which were obtained in 1997 by using the same experimental molecular DOS database as used in the present paper (with no extension beyond 200 eV using mixture rules) and an energy-independent normalization approach, offer little improvement relative to the original (1) evaluation of these properties. This indicates the power of the constraint procedure used in our work, namely, the reproduction of experimental molar refractivity data and the satisfaction of the full Thomas–Reiche–Kuhn sum rule ($S_0 = N$). The use of both of these constraints normalizes the complete DOSD, from small to very large E, in a smooth, continuous, and energy-dependent manner. Energy-independent normalization (8, 57, 87) and (or) no extension of the DOS database to very high photon energies can lead to difficulties in determining reliable values of atomic and molecular dipole properties even from extensive experimental DOS data sets; this has been discussed in the literature (see for example, refs. 9, 47, 49, and some of the citations therein) and is also illustrated by the discussion of the dipole properties of ethylene given earlier here.

The results for the dipole–dipole and the triple-dipole dispersion energies for the interactions considered in this paper are new and are apparently (essentially) the only reliable values available for these alkenes. They represent prototype interactions involving prototypical molecules containing the alkene group and therefore should be of considerable interest. The estimated errors for the C_6 and C_9 results given in this paper are 1% and 2%, respectively.

Accurate DOSD values of C_6 for important prototype interactions furnish useful checks of other methods for evaluating dispersion-energy coefficients, for example, empirical, non-empirical, ab initio quantum mechanical, and Padé approximant approaches (10, 11, 15, 28, 29, 51, 83, 88–93). In this context, it is relevant to point out that in the construction of potential-energy models (24–30) (mentioned briefly previously), it is necessary to include the dispersion energy to at least terms that vary as R^{-10} at long range. The terms varying as powers of R^{-1} higher than R^{-6} are not accessible by DOSD techniques due to the lack of (experimental) higher multipole (than dipole) oscillator strengths. The method of choice for determining these higher-order dispersion energies is via ab initio quantum mechanical methods analogous to those used for the dipole–dipole case. The reliability of these methods for these energies can be checked indirectly via the checks on the dipole–dipole dispersion energy referred to earlier, since the ab initio calculation of the higher-order terms is not easier than for the dipole–dipole dispersion energy. In any event, as pointed out earlier, the dipole–dipole dispersion energy is the lead or dominant dispersion energy, and the success of the potential-energy models depends (26, 61) on a reliable value of the coefficient C_6.

The pseudo-DOSDs employed in this work to calculate the dipole–dipole and the triple-double dispersion-energy coefficients form a concise representation of the original recommended DOSDs for the alkene molecules, which are continuous functions of the excitation energy from the UV-absorption threshold to many thousands of eV. They give reliable results for the dispersion-energy coefficients and a variety of other molecular properties through the use of discretized analogues of the usual expressions for these properties (10–12). We emphasize that more than ten pseudo-states are needed to reliably evaluate some of these properties,[3] for example, the logarithmic dipole sums L_k for "larger" values of k, which have significant negative and positive contributions (41, 49).

Acknowledgements

The authors wish to thank C.E. Brion, G. Cooper, and T.N. Olney for making their dipole oscillator strengths for ethylene available to us. This research was supported by a grant from the Natural Sciences and Engineering Research Council of Canada (NSERC).

References

1. B.L. Jhanwar, W.J. Meath, and J.C.F. MacDonald. Can. J. Phys. **61**,1027 (1983).
2. G.D. Zeiss, W.J. Meath, J.C.F. MacDonald, and D.J. Dawson. Can. J. Phys. **55**, 2080 (1977).
3. H. Margenau. Phys. Rev. **37**, 1425 (1931); **56**, 1000 (1939).
4. A. Dalgarno and N. Lynn. Proc. Phys. Soc. **70**, 802 (1957); A. Dalgarno and A.E. Kingston. Proc. Phys. Soc. **72**, 1053 (1958); **73**, 455 (1959); **78**, 607 (1961).
5. P.J. Leonard and J.A. Barker. Theor. Chem.: Adv. Perspect. **1**, 117 (1975).
6. A. Kumar, G.R.G. Fairly, and W.J. Meath. J. Chem. Phys. **83**, 70 (1985), and refs. cited therein.
7. R.J. Pazur, A. Kumar, R.A. Thuraisingham, and W.J. Meath. Can. J. Chem. **66**, 615 (1988).
8. G. Cooper, T.N. Olney, and C.E. Brion. Chem.Phys. **194**, 175 (1995).
9. A. Kumar, B.L. Jhanwar, and W.J. Meath. Collect. Czech. Chem. Commun. **70**, 1196 (2005).

[3] Twenty pseudo-states for each of the alkenes are available from the authors (akumar14in@yahoo.co.in).

© 2007 NRC Canada

10. D.J. Margoliash and W.J. Meath. J. Chem. Phys. **68**, 1426 (1978).
11. D.J. Margoliash, T.R. Proctor, and W.J. Meath. Mol. Phys. **35**, 747 (1978).
12. B.L. Jhanwar and W.J. Meath. Mol. Phys. **41**, 1061 (1980).
13. U. Fano and J.W. Cooper. Rev. Mod. Phys. **40**, 441(1968); **41**, 724 (1969).
14. J.O. Hirschfelder, W. Byers Brown, and S.T. Epstein. Adv. Quantum Chem. **1**, 255 (1964).
15. G.D. Zeiss and W.J. Meath. Mol. Phys. **33**, 1155 (1976).
16. J.O. Hirschfelder, C.F. Curtis, and R.B. Bird. Molecular theory of gases and liquids.Wiley, New York. 1954.
17. R. Eisenschitz and F. London. Z. Phys. **60**, 491 (1930).
18. P.M. Axilrod and E. Teller. J. Chem. Phys. **11**, 299 (1943).
19. Y. Muto. Proc. Phys. Math. Soc. Jpn. **17**, 629 (1943).
20. M. Inokuti. Rev. Mod. Phys. **43**, 297 (1971).
21. G. D. Zeiss. W.J. Meath, J.C.F. MacDonald, and D.J. Dawson. Radiat. Res. **63**, 64 (1975); **70**, 284 (1977).
22. H.L. Kramer. J. Chem. Phys. **53**, 2783 (1970).
23. H.L. Kramer and D.R. Herschbach. J. Chem. Phys. **53**, 2792 (1970).
24. C. Douketis, G. Scoles, S. Marchetti, M. Zen, and A.J. Thakkar. J. Chem. Phys. **76**, 3057 (1982).
25. K.T. Tang and J.P. Toennies. J. Chem. Phys. **80**, 3726 (1984).
26. W. J. Meath and M. Koulis. J. Mol. Struct. **226**, 1 (1991), and refs. cited therein.
27. A.K. Dham and W.J. Meath. Mol. Phys. **99**, 991 (2001), and refs. cited therein.
28. M.P. Hodges and R.J. Wheatley. J. Chem. Phys. **114**, 8836 (2001).
29. M.P. Hodges and R.J. Wheatley. J. Mol. Struct.:THEOCHEM. **591**, 67 (2002).
30. R.J. Wheatley, A.S. Tulegenov and E. Bichoutskaia. Int. Rev. Phys. Chem. **23**, 151 (2004).
31. J.A. Barker. Mol. Phys. **57**, 755 (1986).
32. W.J. Meath and R.A. Aziz. Mol. Phys. **52**, 225 (1984), and refs. cited therein.
33. H.E. Watson and K. L. Ramaswamy. Proc. R. Soc. London, Ser. A. **156**, 144 (1936).
34. S. Friberg. Diss. Lund 1933. Reported in Landolt-Börnstein, Zahlenwert and Funktionen, Vol. II, part 8. 6th ed. Springer-Verlag, Berlin, West Germany, 1962, p.884.
35. H.A. Bethe and E.E. Salpeter. Quantum mechanics of one- and two-electron atoms. Academic Press, New York. 1957.
36. W.J. Meath and A. Kumar. Int. J. Quantum Chem. **S24**, 501 (1990).
37. A. Kumar and W.J. Meath. Theor. Chim. Acta. **82**, 131 (1992).
38. A. Kumar and W.J. Meath. Chem. Phys. **189**, 467 (1994).
39.A. Kumar, W.J. Meath, P. Bundgen, and A.J. Thakkar. J. Chem. Phys. **105**, 4927 (1996).
40. P. Bundgen, A.J. Thakkar, A. Kumar, and W.J. Meath. Mol. Phys. **90**, 721(1997).
41. A. Kumar and W.J. Meath. Can. J. Phys. **63**, 417; 1616 (1985).
42. A. Kumar and W.J. Meath. Mol. Phys. **75**, 311 (1992).
43. G.R. Burton, W.F. Chan, G. Cooper, C.E. Brion, A. Kumar, and W.J. Meath. Can. J. Chem. **71**, 341 (1993).
44. G.R. Burton, W.F. Chan, G. Cooper, C.E. Brion, A. Kumar, and W.J. Meath. Can. J. Chem. **72**, 529 (1994).
45. A. Kumar and W.J. Meath. Mol. Phys. **90**, 389 (1997).
46. A. Kumar. J. Mol. Struct.: THEOCHEM. **591**, 91 (2002).
47. M. Kumar, A. Kumar, and W.J. Meath. Mol. Phys. **100**, 3271 (2002).
48. A.Kumar, M.Kumar, and W.J. Meath. Chem. Phys. **286**, 227 (2003).
49. A. Kumar, M. Kumar, and W.J. Meath. Mol. Phys. **101**, 1535 (2003).
50. B.J. Jhanwar, W.J. Meath, and J.C.F. MacDonald. Can. J. Phys. **59**, 185 (1981).
51. B.L. Jhanwar and W.J. Meath. Chem. Phys. **67**, 185 (1982).
52. J. Berkowitz. Atomic and molecular photoabsorption: absolute total cross sections. Academic Press, New York. 2002.
53. J. Berkowitz. Photoabsorption, photoionization, and photoelectron spectroscopy. Academic Press, New York. 1979.
54. D.M.P. Holland, D.A. Shaw, M.A. Hayes, L.G. Shpinkova, E.E. Rennie, L. Karlsson, P. Baltzer, and B. Wannberg. Chem. Phys. **219**, 91 (1997).
55. B. Kempgens, B.S. Itchkawitz, K.J. Randall, J. Feldhaus, A.M. Bradshaw, H. Köpel, F.X. Gadea, D. Nordfors, J. Schirmer, and L.S. Cederbaum. Chem. Phys. Lett. **246**, 347 (1995); B. Kempgens, A. Kivimäki, B.S. Itchkawitz, H.M. Köppe, M. Schmidbauer, M. Neeb, K. Maier, J. Feldhaus, and A.M. Bradshaw. J. Electron. Spectrosc. **93**, 39 (1998).
56. H. Lowery. Proc. R. Soc. London, Ser. A. **133**, 188 (1931).
57. T.N. Olney, N.M. Cann, G. Cooper, and C.E. Brion. Chem. Phys. **223**, 59 (1997)
58. G.R. Burton, W.F. Chan, G. Cooper, and C.E. Brion. Chem. Phys. **177**, 217 (1993).
59 U. Hohm. Mol. Phys. **78**, 929 (1993).
60. G.D. Zeiss, W.J. Meath, J.C. F. MacDonald, and D.J. Dawson. Mol. Phys. **39**, 1055 (1980).
61. W.J. Meath, D.J. Margoliash, B.L. Jhanwar, A. Koide, and G.D. Zeiss. *In* Intermolecular forces. *Edited by* B. Pullman. Reidel, Dordrecht. 1981. p. 101.
62. B.J. Jhanwar, W.J. Meath, and J.C.F. MacDonald. Can. J. Phys. **59**, 185 (1981).
63. M.A. Spackman. J. Chem. Phys. **94**, 1288 (1991).
64. S.-Y. Liu and C.E. Dykstra. J. Phys. Chem. **91**, 1749 (1987); Chem. Phys. Lett. **119**, 407 (1985).
65. G. Maroulis, J. Chem. Phys. **97**, 4188 (1992).
66. T.H. Dunning, Jr. J. Chem. Phys. **53**, 2823 (1970).
67. E.K. Dalskov and S.P.A. Sauer. J. Phys. Chem. **A102**, 5269 (1998).
68. A.J. Sadlej. Theor. Chim. Acta. **79**, 123 (1991).
69. K. Andersson and A.J. Sadlej. Phys. Rev. **A46**, 2356 (1992).
70. T.H. Dunning, Jr. J. Chem. Phys. **90**, 1007 (1989)
71. D.E. Woon and T.H. Dunning, Jr. J. Chem. Phys. **98**, 1358 (1993).
72. D.E. Woon and T.H. Dunning Jr. J. Chem. Phys. **100**, 2975 (1994).
73. P.W. Fowler, P. Jorgensen, and J. Olsen. J. Chem. Phys. **93**, 7256 (1990).
74. C. Van Caillie and R.D. Amos. Chem. Phys. Lett. **291**, 71 (1998).
75. S. Kamakura, N. Sakamoto, H. Ogawa, H. Tsuchida, and M. Inokuti. J. Appl. Phys. **100**, 064905–1(2006).
76. B.L. Jhanwar, W.J. Meath, and J.C.F. MacDonald. Radiat. Res. **106**, 288 (1986).
77. A.J. Russell and M.A. Spackman. Mol. Phys. **90**, 251 (1997)
78. H.-J. Werner and W. Meyer. Mol. Phys. **31**, 855 (1976).
79. A.J. Russell and M.A. Spackman. Mol. Phys. **84**, 1239 (1995).
80. W. Meyer. Chem. Phys. **17**, 27 (1976).
81. P.E.S. Wormer, H. Hettema, and A.J. Thakkar. J. Chem. Phys. **98**, 7140 (1993)
82. A.L. Ford and J.C. Browne. Phys. Rev. **A7**, 418 (1973).
83. M.A. Spackman. J. Chem. Phys. **94**, 1295 (1991).
84. M.A. Spackman. J. Phys. Chem. **93**, 7594 (1989).
85. S.M. Cybulski and T.P. Haley. J. Chem. Phys. **121**, 7711 (2004).

© 2007 NRC Canada

86. H. Wei, R.J. leRoy, R. Wheatley, and W.J. Meath. J. Chem. Phys. **122**, 084321 (2005).
87. R. Feng and C.E. Brion. Chem. Phys. **282**, 419 (2002).
88. M.P. Hodges, R.J. Wheatley, and A.H. Harvey. J. Chem. Phys. **116**, 1397 (2002).
89. S.A.C. McDowell and W.J. Meath. Can. J. Chem. **76**, 483 (1998).
90. F. Mulder, G.F. Thomas, and W.J. Meath. Mol. Phys. **41**, 249 (1980).
91. F. Mulder, G. van Dijk, and A. van der Avoird. Mol. Phys. **39**, 407 (1980).
92. R.M. Berns and A. van der Avoird. J. Chem. Phys. **71**, 6107 (1980).
93. H. Hettema, P.E.S.Wormer, and A.J. Thakkar. Mol. Phys. **80**, 533 (1993).

© 2007 NRC Canada

Chemical forms of calcium in Ca,Zn- and Ca,Cd-containing grains excreted by tobacco trichomes[1]

Géraldine Sarret, Marie-Pierre Isaure, Matthew A. Marcus, Emiko Harada, Yong-Eui Choi, Sébastien Pairis, Sirine Fakra, and Alain Manceau

Abstract: Tobacco (*Nicotiana tabacum* L. cv. Xanthi) plants exposed to toxic levels of zinc and cadmium excrete metals through their leaf trichomes (epidermal hairs) as Zn,Ca- and Cd,Ca-containing grains. Little is known about the nature and formation mechanism of these precipitates. The chemical, crystalline, and noncrystalline compositions of individual grains produced by tobacco were studied by scanning electron microscopy coupled with energy dispersive X-ray analysis (SEM-EDX), micro-X-ray diffraction (μXRD), and calcium K-edge micro X-ray absorption near edge structure (μXANES) spectroscopy. Zinc is predominantly incorporated in calcite and cadmium in calcite and vaterite. Aragonite, which occurs occasionally, does not seem to contain trace metals. In addition to being precipitated in its three possible polymorphic forms, calcite, aragonite, and vaterite, calcium is also speciated as amorphous $CaCO_3$ and possibly organic Ca in some grains. Most often, a particular grain consists of two or more crystalline and noncrystalline phases. The observed variability of intra- and inter-grain elemental and phase composition suggests that this biomineralization process is not constrained by biological factors but instead results from thermodynamically and kinetically controlled reactions. This study illustrates the potential of laterally resolved X-ray synchrotron radiation techniques (μXRD and μXANES) to study biomineralization and metal immobilization processes in plants.

Key words: biomineralization, detoxification, micro-XANES, micro-XRD.

Résumé : Lorsque des plants de tabac (*Nicotiana tabacum* L. cv. Xanthi) sont exposés à des niveaux toxiques de zinc et de cadmium, ils excrètent des métaux par les trichomes (poils épidermiques) de leurs feuilles qu'on retrouve sous la forme de grains contenant du Zn,Ca et du Cd,Ca. On connaît peu de choses sur la nature et le mécanisme de formation de ces précipités. On a étudié les compositions chimiques cristallines et non cristallines de grains individuels produits par le tabac en faisant appel à la microscopie électronique à balayage couplée à l'analyse des rayons X en dispersion d'énergie (MEB-XDE), à la diffraction micro des rayons X (μDRX) et à la micro spectroscopie d'absorption X de type XANES (μXANES) au seuil *K* du calcium. Le zinc est principalement incorporé dans la calcite et le cadmium dans la calcite et la vatérite. L'aragonite qu'on rencontre occasionnellement ne semble pas contenir de traces de métaux. En plus d'être précipité sous ses trois polymorphes possibles, calcite, aragonite et vatérite, le calcium se trouve aussi sous la forme de $CaCO_3$ amorphe et possiblement sous la forme de Ca organique dans certains grains. Le plus souvent, un grain est formé d'au moins deux phases cristallines et non cristallines. La variabilité tant intra- qu'intergrains en terme de composition élémentaire et de nature des phases suggère que ce processus de biominéralisation n'est pas contraint par des facteurs biologiques, mais qu'il résulte plutôt de réactions sous contrôle thermodynamique et cinétique. Cette étude illustre le potentiel des techniques de rayonnement X synchrotron résolues latéralement (μDRX et μXANES) dans l'étude des processus de biominéralisation et d'immobilisation des métaux dans les plantes.

Mots-clés : biominéralisation, détoxification, spectroscopie d'absorption micro-X de type XANES (μXANES), diffraction micro des rayons X (μDRX).

[Traduit par la Rédaction]

Received 19 April 2007. Accepted 18 June 2007. Published on the NRC Research Press Web site at canjchem.nrc.ca on 3 August 2007.

G. Sarret,[2] M.-P. Isaure, E. Harada, and A. Manceau. Environmental Geochemistry Group, LGIT, University of Grenoble and CNRS, BP 53, 38041 Grenoble cedex 9, France.
M.A. Marcus and S. Fakra. Advanced Light Source (ALS), Lawrence Berkeley National Lab, MS 6–100, Berkeley, CA 94720, USA
E. Harada and Y.-E. Choi. Division of Forest Resources, College of Forest Sciences, Kangwon National University, Chunchon 200–701, Kangwon-do, Korea.
S. Pairis. Institut Néel CNRS-UJF, Dept. Matière Condensée, Matériaux et Fonctions, Pôle Instrumentation (Microscopie Electronique), 25 av. des Martyrs, BP 166, 38042 Grenoble cedex 9, France.

[1]This article is part of a Special Issue dedicated to Professor G. Michael Bancroft.
[2]Corresponding author (e-mail: geraldine.sarret@ujf-grenoble.fr).

 doi:10.1139/V07-076 © 2007 NRC Canada

Table 1. Tobacco culture conditions and name of the grains investigated.

Treatment conditions	Cation concentrations in the nutrient solution (mmol/L)			Grain names	Techniques and references				
	Ca	Zn	Cd		SEM-EDX	μXRD	Zn μEXAFS	Cd μXANES	Ca μXANES
Zn	0.28	0.25	0	Zn2	(3) and this work	(3)	(3)	—	This work
				Zn3	—	This work	Unpublished	—	
Zn + Ca	3.28	0.25	0	ZnCa3	(3) and this work	(3)	(3)	—	This work
				ZnCa4	(3) and this work	(3)	(3)	—	This work
				ZnCa5	—	This work	Unpublished	—	This work
Cd	0.28	0.08×10^{-3}	0.025	Cd10	See footnote *a*	See footnote *a*	—	See footnote *a*	This work
Cd + Ca	3.28	0.08×10^{-3}	0.025	CdCa2	See footnote *a*	See footnote *a*	—	See footnote *a*	This work
				CdCa3	See footnote *a*	See footnote *a*	—	See footnote *a*	This work
				CdCa6	See footnote *a*	See footnote *a*	—	See footnote *a*	This work
Ca	3.28	0.08×10^{-3}	0	Ca3	This work	—	—	—	—

[a]Isaure et al., manuscript in preparation.

Introduction

Recently, a novel original mechanism of Zn and Cd detoxification was described in tobacco (*Nicotiana tabacum* L. cv. Xanthi). Tobacco exposed to Cd excreted Cd,Ca-containing grains through leaf trichomes (1, 2), and a similar excretion of Zn,Ca-containing grains was observed under Zn exposure (3). Trichomes are specialized epidermal structures. In tobacco, they are glandular and excrete various organic substances including nicotine and resins. This detoxification process may have implications in human health, since smoking is one of the principal routes of exposure to heavy metals, and also in phytoremediation as tobacco is a candidate species for phytoextraction.

The morphology, elemental composition, mineralogy, as well as Zn and Cd speciation in the grains were investigated by scanning electron microscopy coupled with energy dispersive X-ray analysis (SEM-EDX), micro-X-ray fluorescence (μXRF), micro-X-ray diffraction (μXRD), Zn K-edge micro extended X-ray absorption fine structure (μEXAFS) (3), and Cd L_{III} edge micro X-ray absorption near edge structure (μXANES) spectroscopy (Isaure et al., manuscript in preparation). Calcium was always the major component. μXRD analyses revealed the presence of calcite and less frequently vaterite and aragonite, two other $CaCO_3$ polymorphs. Calcium oxalate mono- and di-hydrate were occasionally found. Calcite and vaterite were substituted by cations, probably Zn, Cd, and possibly Mn and Mg. Zn μEXAFS confirmed the occurrence of Zn-substituted calcite and evidenced Zn associations with other phases including organic compounds, silica, and phosphate (3). Cd μXANES showed that cadmium was a Ca substituent in calcite and vaterite and (or) sorbed on the surface of these minerals (Isaure et al., manuscript in preparation).

The mechanism of formation of these grains remains unclear. Biogenic minerals may result from a controlled biomineralization process leading to well-defined minerals and shapes. They may also be biologically induced, which means that an organism promotes the precipitation but does not control the crystallization process (4). In the present case, grains could result from the exudation of a liquid containing the various metals and substances and the precipitation of the various solid phases because of water evaporation. Alternatively, they might be formed intracellularly and excreted thereafter as suggested by Choi and Harada (5). The purpose of this study is to better characterize the structure and composition of the grains. Grains excreted by tobacco, under various Zn, Cd, and Ca exposure conditions, were investigated by SEM-EDX, μXRD, and Ca K-edge μXANES spectroscopy. Results of these complementary approaches are compared, and a hypothesis for the formation of the grains is proposed in light of these data.

Experimental

Materials

Plant culture and grain collection procedures have been described previously (3). Briefly, tobacco plants were grown in hydroponic conditions and exposed for 5 weeks to Zn or Cd, with or without a supplement of Ca (Table 1). A control condition with Ca only was also tested. Then, grains were

© 2007 NRC Canada

collected by washing the leaves in ultrapure water and centrifugating the suspension. Several Ca-containing reference compounds were used for the Ca XANES data analysis. Calcite, vaterite, and Cd-containing vaterite were synthesized at room temperature (RT) according to a modified protocol of Paquette and Reeder (6, 7). Briefly, an aqueous solution (500 mL) containing 10 mmol/L $CaCl_2$ and 1.8 mol/L NH_4Cl was placed in a glass reactor, an EPPENDORF tube containing solid ammonium carbonate was allowed to float at the surface of the solution, and the reactor was closed and kept unstirred. NH_4Cl was used as a background electrolyte to provide a high ionic strength. Initial pH was 4.9. The decomposition of ammonium carbonate produces NH_3(g) and CO_2(g), which dissolve into the solution simultaneously increasing pH and alkalinity. The supersaturation of the solution induces the formation and growth of $CaCO_3$ crystals. Continuous sublimation of NH_3(g) buffers the solution around pH = 7.9. After 13 days, the reactor contained rhombohedral crystals and spherical particles attached to the surface of the glass. The two types of particles were separated and characterized by XRD. Rhombohedral crystals corresponded to calcite and spherical particles to vaterite. For the synthesis of Cd-containing vaterite, the same procedure was used except that after 13 days, when crystal size amounted to 150–200 μm in diameter, the $CaCl_2$–NH_4Cl solution was progressively doped with 0.1 mol/L $CdCl_2$ to a total concentration of 100 μmol/L Cd to incorporate Cd as a Ca substituent in vaterite (6, 7). The progressive addition of $CdCl_2$ kept the solution undersaturated with respect to otavite ($CdCO_3$). After 7 days, the particles were collected and separated. Spherical particles were identified as Cd-containing vaterite by XRD and μXRF. The Cd content was 1–20 ppm based on μXRF analysis.

Aragonite was a natural specimen. The XANES spectrum for synthetic amorphous $CaCO_3$ was provided by Y. Politi (8). Ca oxalate monohydrate (whewellite) was purchased from Sigma-Aldrich. A solution containing 0.5 mol/L $Ca(NO_3)_2$ at pH 2.6 was used as a reference for aq. Ca^{2+}. The phase purity of all crystalline samples was checked by XRD prior to XANES analysis.

Electron microscopy

The morphology and the chemical composition of the grains were studied by SEM-EDX using a Jeol-JSM 840A equipped with a Kevex Si(Li) detector. The chamber pressure was 10^{-6}–10^{-5} torr (1 torr = 133.322 4 Pa), and the accelerating voltage was 20 kV. Grains were mounted on kapton tape or on carbon tape, then fixed on carbon stubs and coated with carbon. Images were taken at a magnification of 500 to 10 000. EDX spectra were recorded on prominent spots of the grains to optimize the detection.

μXRF, μXRD, and μXANES

The μXRF, μXRD, and Ca K-edge μXANES measurements were performed on beamline 10.3.2 of the Advanced Light Source (ALS, Berkeley, California) (9). The grains were spread on kapton tape and analyzed at RT and pressure. First, each grain was mapped by μXRF. Then, μXANES and μXRD data were recorded on the Zn-richest region for the Zn and Zn + Ca treatments, on the Cd-richest region for the Cd and Cd + Ca treatment, and on the Ca-richest region for the Ca treatment. μXRF data were collected at 10 keV with a beam size of 5 × 5 μm. The same X-ray spot size was used for Ca μXANES. Fluorescence X-ray yield was measured with a 7-element Ge solid-state detector. The spectra were recorded between 3900 to 4400 eV. μXRD patterns were recorded at an incident energy of 17 keV with a beam size of 16 × 7 μm. More experimental details are given in (3). Ca XANES reference spectra were recorded at RT on beamline ID21 at the European Synchrotron Radiation Facility (ESRF, Grenoble, France). Each spectrum is the average of two to three spectra, each about 15 min long.

XRD and XANES data treatment

The XRD data treatment was performed as described previously (3). Briefly, after calibration with alumina, two-dimensional XRD patterns were integrated to one-dimensional patterns for peak assignment. For substituted calcite crystals the unit cell parameters *a* and *c* were refined, and the stoichiometry of the substituent was estimated from these two parameters using the Vegard law (10) with calcite, smithsonite ($ZnCO_3$), and otavite ($CdCO_3$) as end members for the Ca-Zn and Ca-Cd solid solutions. This approach cannot be used for substituted vaterite because of the absence of a $CdCO_3$ structural analogue of vaterite.

XANES spectra were processed using WinXAS (11). All spectra were energy-calibrated with respect to calcite (the inflection point for this reference was set to 4042.6 eV). The collected scans were averaged; the background was subtracted and normalized using linear (pre-edge) or cubic (post-edge) polynomials. XANES spectra were then fitted by linear combinations using calcite, aragonite, vaterite, Cd-containing vaterite, amorphous $CaCO_3$, aq. Ca^{2+}, and Ca oxalate monohydrate reference spectra. The quality of the fits was quantified by the normalized sum-squares residuals $NSS = \sum(\mu_{experimental} - \mu_{fit})^2 / \sum(\mu_{experimental})^2 \times 100$, in the 4000–4150 eV range, where μ is the normalized absorbance. An energy shift of ±0.5 eV maximum and a correction of slope were allowed to account for the energy resolution of the monochromator and for possible inconsistencies in data processing. For some spectra, linear combination (LC) fitting did not provide satisfactory results, and over-absorption effects were suspected based on the comparison of these spectra with the standards. Therefore, each spectrum was fitted with and without a correction of over-absorption using a simple model (12). This model assumes that the smooth part of the resonant absorption is a constant fraction of the nonresonant background (which is a reasonable assumption in the XANES region), and that the sample is infinitely thick, i.e., totally absorbs the incident beam (which is probably true considering the energy range and the size and global composition of the grains). The equation used is,

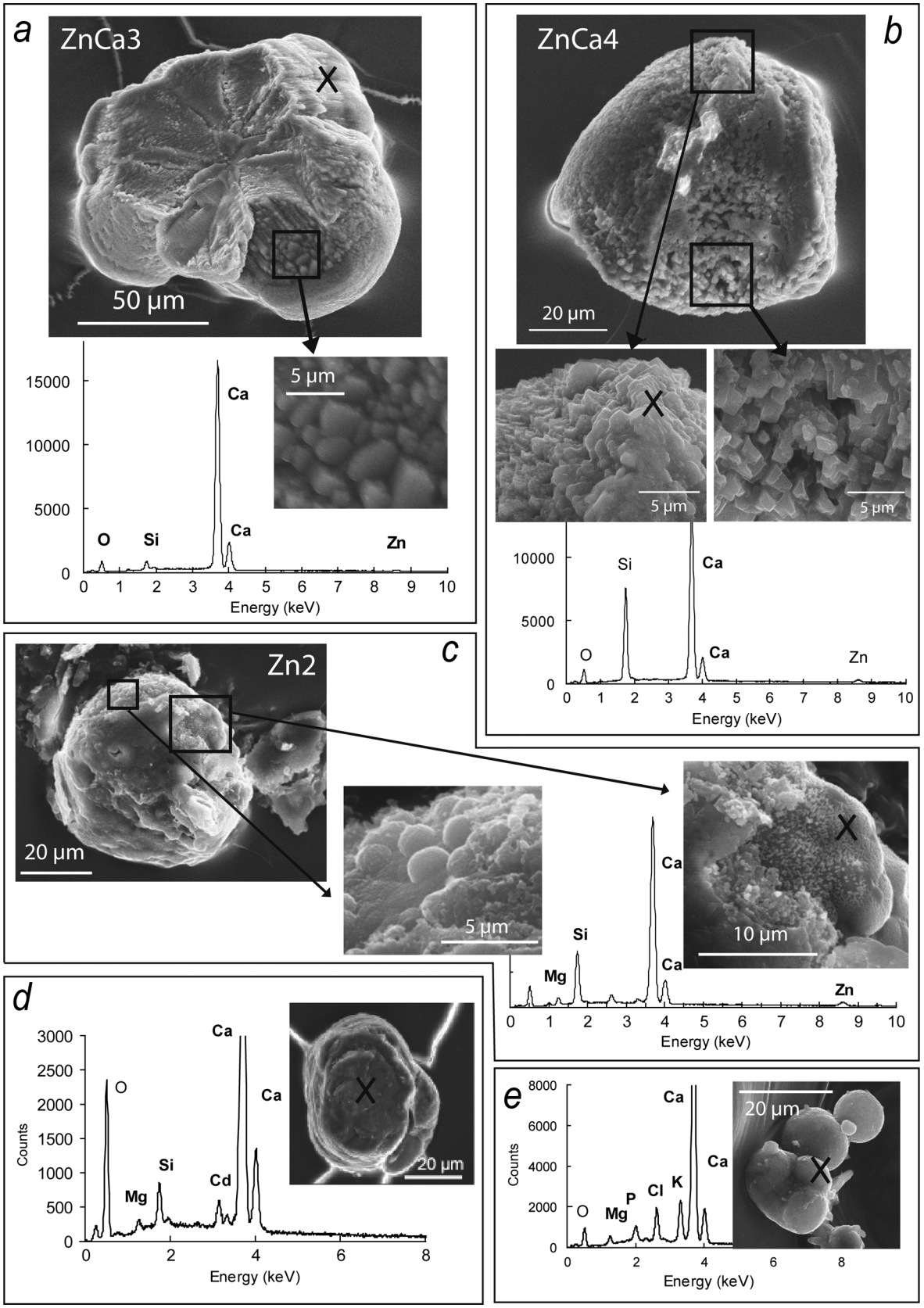
$$[1] \qquad y_{experimental} = (1 + a) / (1 + a y_{corrected})$$

where *y* is the normalized resonant absorbance (which equals 0 below the edge and oscillates around 1 above the edge) and $a = \mu_{resonant} / (\mu_{nonresonant} + \mu_{fluorescence})$, where $\mu_{resonant}$, $\mu_{nonresonant}$, and $\mu_{fluorescence}$ are the three components of the absorbance μ.

Equation [1] can be solved as,

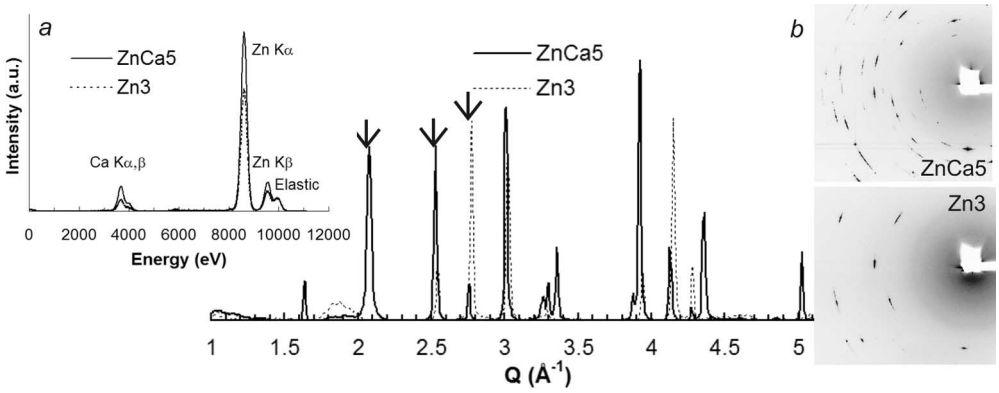
© 2007 NRC Canada

Fig. 1. SEM imaging for the grains (*a*) ZnCa3, (*b*) ZnCa4, (*c*) Zn2, (*d*) CdCa3, and (*e*) Ca3. EDX analyses were performed on the spots marked by a black cross.



© 2007 NRC Canada

Fig. 2. (*a*) μXRF spectrum and (*b*) one- and two-dimensional μXRD patterns for grains ZnCa5 and Zn3. All XRD peaks were attributed to substituted calcite. The positions of three peaks for pure calcite are indicated by arrows.



[2] $$y_{corrected} = y_{experimental} / (1 + a(1 - y_{experimental}))$$

The over-absorption parameter *a* equals 0 in the absence of an over-absorption effect and increases with this effect. Because of the sample heterogeneity, the precise composition of the sample is not known, so *a* is an adjusted parameter.

Results

The morphology of the grains as observed by SEM varied considerably. The grains varied from 10 to 150 μm in diameter. Each grain is an aggregate of different types of particles. The first type is composed of micro-faceted crystallites (insets in Figs. 1*a* and 1*b*), and the second type is composed of globular structures of various sizes (from 2 to 50 μm, see Figs. 1*c*–1*e*). Some grains such as Zn2 (Fig. 1*c*) seem visually less crystalline. The elemental composition of the grains varies from one grain to another and within the same grain. Ca was always the major component regardless of the plant metal treatment conditions. Minor elements include Mg, Si, P, Cl, K, and Zn or Cd depending on the plant treatment (Fig. 1). The high Si peaks observed in Figs. 1*a*–1*d* are attributed to kapton tape on which the grains were mounted. Silicon is not detected in the grain presented in Fig. 1*e* (mounted on carbon tape). However, Si was found in small amounts in some grains (not presented in this study), as was Mn.

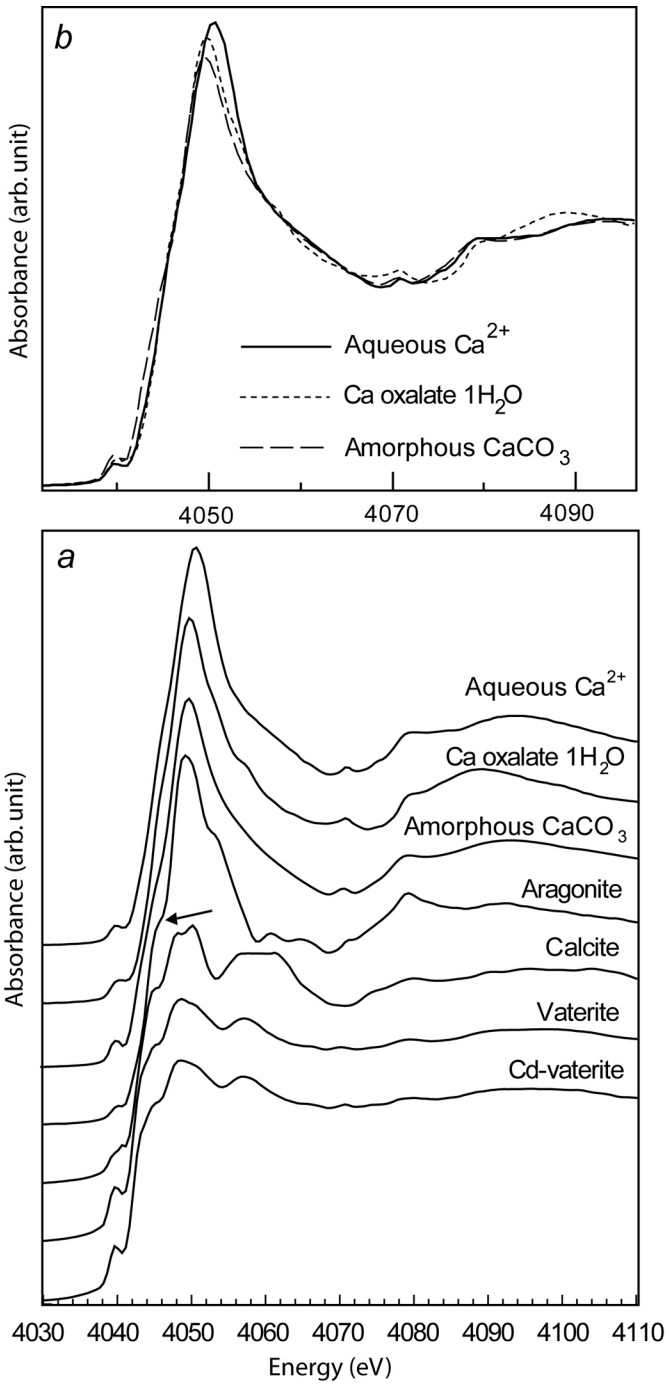
Our previous study using μXRD (3) showed that grain ZnCa3 contained substituted calcite and aragonite, grain ZnCa4 contained substituted calcite, and grain Zn2 did not contain crystalline phases. The two-dimensional μXRD patterns for grains ZnCa5 and Zn3 show that the Bragg reflections for these two grains consist of small arcs of Debye–Scherrer rings, indicating that the grains are composed of micrometer size mosaic crystals (Fig. 2*b*). All reflections correspond to substituted calcite, and the major Ca substituent is Zn, based on μXRF (Fig. 2*a*). Note that although Ca is the major element, the Ca Kα peak has a low intensity relative to the Zn Kα peak due to air absorption and the lower fluorescence yield of Ca vs. Zn. The refined unit cell parameters *a* and *c* for grains ZnCa5 and Zn3 were 4.97 and 16.97 Å and 4.95 and 16.83 Å, respectively, compared with 4.9896 and 17.0610 Å for pure calcite. The calculated formulae using the Vegard law were $Ca_{0.95}Zn_{0.05}CO_3$ and $Ca_{0.89}Zn_{0.11}CO_3$, respectively. The difference in the Zn stoichiometry coefficient obtained using parameters *a* and *c* was ±0.01. The μXRD results for the Cd-containing grains will be presented separately together with Cd L_{III}-XANES data (Isaure et al., manuscript in preparation). Briefly, the grains CdCa2 and Cd10 contain micrometer-sized crystals of substituted calcite and finer (nanometer-sized) crystals of substituted vaterite. Grain CdCa3 contains nanocrystals of substituted vaterite only. Finally, no crystalline phases were detected in grain CdCa6. For Cd-substituted calcite, the Vegard law provides an imprecise estimation of Cd stoichiometry because the contrast in ionic radius between Cd and Ca is small (0.95 Å for Cd^{2+} and 1.00 Å for Ca^{2+} compared with 0.74 Å for Zn^{2+}) (13). For instance, the substitution rate for grain CdCa2 could be anywhere between 30% and 80%. It was not possible to calculate the stoichiometry of Cd in vaterite because of the absence of a Cd end member (see the Experimental section).

Since calcium is the major element in the grains, Ca K-edge μXANES spectroscopy was then performed to get some insight on the composition of the grains and test for the presence of amorphous Ca phases. Fig. 3*a* shows the XANES spectra for several Ca reference compounds. The four $CaCO_3$ species (calcite, vaterite, aragonite, and amorphous $CaCO_3$ (ACC)) have clearly distinct spectra, which enables their identification (14, 15). However, Ca XANES has no sensitivity to substitutional impurities, as seen for instance for low Cd-containing vaterite (Cd content lower than 1%, as estimated by μXRF) and pure vaterite, exhibiting nearly identical spectra. The spectra for aq. Ca^{2+}, Ca oxalate monohydrate, and ACC share some similarities. However, the lower part of the edge is shifted to lower energy for the ACC spectrum, and the maximum of the white line (zero value of the first derivative) increases from 4049.5 (ACC) to 4049.9 eV (Ca oxalate monohydrate), and to 4050.5 eV (aq. Ca^{2+}, Fig. 3*b*). The aragonite spectrum is distinct from the three previous spectra in displaying a shoulder at 4046 eV (arrow in Fig. 3) and a minimum between 4060 and 4070 eV.

Fig. 4 shows the Ca μXANES spectra for the grains. They were fitted by LC using the standard spectra presented earlier, and the results are presented in Table 2. The ZnCa3 spectrum presents strong similarities with the aragonite

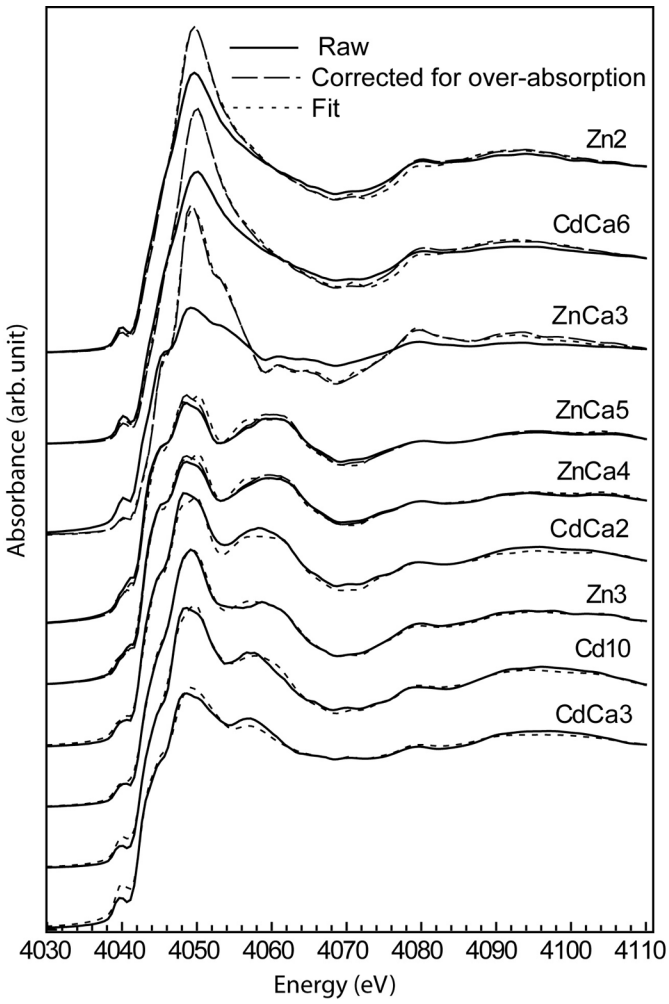
© 2007 NRC Canada

Fig. 3. (*a*) Ca K-edge XANES spectra for the reference compounds used in the linear combination fits and (*b*) enlargement of the main peaks for aq. Ca2+, Ca oxalate monohydrate, and ACC.



spectrum but with markedly lower amplitude. The drop in amplitude suggests some over-absorption effect (12) due to a high Ca content of the analyzed spot. The fit without over-absorption correction (see the Materials section) did not provide a satisfactory result (*NSS* = 0.065% with 68% vaterite and 25% aragonite). Introducing an over-absorption correction greatly improved the fit (Fig. 4, *NSS* = 0.014% with aragonite as the only component). The over-absorption

Fig. 4. Ca K-edge μXANES spectra for the tobacco grains and corresponding linear combination fits. Five spectra (Zn2, CdCa6, ZnCa3, ZnCa5, and ZnCa4) were corrected for over-absorption.



parameter *a* value found (1.38) corresponds to a very strong over-absorption effect. The fit was not improved significantly by introducing a second component (*NSS* decreased by less than 10%). Thus, the spot analyzed by μXANES likely contains aragonite as the sole Ca species.

The grains ZnCa4 and ZnCa5 were fitted with 98% calcite. The fit was slightly improved with a correction for over-absorption (*NSS* = 0.015% and 0.021%, compared with 0.020% and 0.035%, respectively), and the proportions were unchanged. Adding a second component did not significantly improve the fits (*NSS* decreased by less than 10%).

For grains Zn2 and CdCa6, fits without over-absorption correction were not satisfactory (*NSS* = 0.048% and 0.091%, respectively, for two-component fits). Fair one-component fits with over-absorption correction were obtained with ACC (*NSS* = 0.021% and 0.024%, respectively), but the match was not optimal for the first oscillation (around 4080 eV). Ca oxalate monohydrate and aq. Ca^{2+} provided weaker fits (*NSS* = 0.086% and 0.053% for Zn2, and 0.076% and 0.043% for CdCa6, respectively). Adding a second component did improve the reproduction of the first oscillation. Several fits of equivalent qualities were obtained with ACC

© 2007 NRC Canada

Table 2. Ca μXANES results.

Treatment	Grain name	a^a	Proportion of Ca species determined by linear combination fitting of the μXANES spectra (%) Calcite	Vaterite	Aragonite	Amorphous $CaCO_3$	Aq. Ca^{2+}	Ca oxalate 1 H_2O	Sum	*NSS* (%)^b
Zn + Ca	ZnCa3	1.38			97±2				97	0.014^c
	ZnCa4	0.12	98±2						98	0.015^c
	ZnCa5	0.17	98±2						98	0.021^c
Zn	Zn2	0.27			22±10	76±15			97	0.011^c
		0.27				77±15		20±15	97	0.016
		0.27				79±15	17±15		96	0.019
		0.42				(excluded)	55±15	45±15	100	0.050
	Zn3		62±5			29±5			91	0.009^c
			70±5					22±5	92	0.016
			71±5				21±5		92	0.018
Cd+Ca	CdCa2		85±5			13±5			98	0.012^c
			87±5					10±5	97	0.014
			89±5				9±5		98	0.015
	CdCa3			77±5		21±7			98	0.031^c
				79±5				20±7	99	0.036
				82±5			16±7		98	0.037
	CdCa6	0.38				74±15		25±15	99	0.015^c
		0.42				68±15	32±15		100	0.019
		0.28				(excluded)	73±15	25±15	98	0.040
Cd	Cd10		29±7	42±8			25±5		96	0.022^c
			25±7	37±8		34±5			96	0.025
			28±7	42±8				26±5	96	0.028

[a]Coefficient of over-absorption.

[b]Residual between fit and experimental data $NSS = \sum(\mu_{experimental} - \mu_{fit})^2 / \sum(\mu_{experimental})^2 \times 100$ in the 4000–4150 eV range, where μ is the normalized absorbance.

[c]Fit shown in Fig. 4. The error bars on the percentages correspond to the variation needed to increase *NSS* by 20%.

as a major component (about 80% and 70% of total Ca) and various species as secondary components. *NSS* values were more than doubled if ACC was excluded (Table 2 and Fig. 1 in the Supplementary information).[3] Therefore, grains Zn2 and CdCa6 likely contain ACC as major species and an additional species whose nature remains unknown.

For the other grains (Zn3, CdCa2, CdCa3, and Cd10), over-absorption correction did not improve the fits. Calcite was the major form in grains Zn3 and CdCa2, and fits of equivalent quality were obtained with ACC, aq. Ca^{2+}, and Ca oxalate monohydrate as minor species. Aqueous Ca^{2+} is unlikely in solid-state material. ACC and Ca oxalate monohydrate are more likely. In the absence of reference spectra for Ca bound to organic ligands other than oxalate, this latter compound may be considered as a proxy for Ca bound to organic compounds in general. Therefore, this pool is referred to as organic Ca and (or) ACC in Table 3. Vaterite was found in grains CdCa3 and Cd10. For this latter grain only, no satisfactory fit was obtained with two components (*NSS* = 0.046%), so a third component was introduced. Again, a contribution of organic Ca and (or) ACC was found in grains CdCa3 and Cd10.

The speciation of Ca was then compared with the mineralogy and morphology of the grains (Table 3). The percentages were rounded to the nearest ten for clarity. Except for two grains, ZnCa3 and CdCa2, the same crystalline species were identified by μXRD and Ca μXANES. Zn-substituted calcite and Cd-substituted vaterite were identified by μXRD in grains ZnCa3 and CdCa2, respectively, but not by Ca μXANES spectroscopy. This difference likely results from the larger beam size and higher penetration depth of X-rays in μXRD measurements relative to μXANES (16 × 7 μm vs. 5 × 5 μm and a few tens of μm at 17 keV vs. a few μm at 4 keV). Thus, μXRD probes a different material volume than Ca μXANES, even when conducted on the same spot.

Discussion and conclusion

Results showed that besides crystalline calcium carbonates (calcite, vaterite, and aragonite), the tobacco grains contained ACC as well. Whewellite (Ca oxalate monohydrate) did show up in some XANES fits, but its presence could not be firmly attested. Ca oxalate mono- and dehydrate have several XRD peaks in common with calcite but several peaks at distinct positions as well. These two minerals were positively identified by μXRD in other tobacco grains based on the presence of these specific peaks (3). In the present

[3] Supplementary data for this article are available on the journal Web site (canjchem.nrc.ca) or may be purchased from the Depository of Unpublished Data, Document Delivery, CISTI, National Research Council Canada, Ottawa, ON K1A 0R6, Canada. DUD 5191. For more information on obtaining material refer to cisti-icist.nrc-cnrc.gc.ca/irm/unpub_e.shtml.

© 2007 NRC Canada

Table 3. Summary of the information obtained on each grain.

Treatment	Grain name	Ca speciation (μXANES results) [1]	Mineralogy (μXRD results)	Aspect of the grain (SEM results)
Zn + Ca	ZnCa3	100% aragonite	Aragonite, Zn-subst. calcite ($Ca_{0.93}Zn_{0.07}CO_3$)	Faceted
	ZnCa4	100% calcite	Zn-subst. calcite ($Ca_{0.87}Zn_{0.13}CO_3$)	Faceted
	ZnCa5	100% calcite	Zn-subst. calcite ($Ca_{0.95}Zn_{0.05}CO_3$)	Not observed
Zn	Zn2	80% ACC, 20% undetermined	No diffraction peaks	Rounded
	Zn3	70% calcite, 30% organic Ca, and (or) ACC	Zn-subst. calcite ($Ca_{0.89}Zn_{0.11}CO_3$)	Not observed
Cd + Ca	CdCa2	90% calcite, 10% organic Ca, and (or) ACC	Cd-subst. calcite, Cd-subst. vaterite	Not observed
	CdCa3	80% vaterite, 20% organic Ca, and (or) ACC	Cd-subst. vaterite	Rounded
	CdCa6	70% ACC, 30% undetermined	No diffraction peaks	Not observed
Cd	Cd10	30% calcite, 40% vaterite, 30% organic Ca, and (or) ACC	Cd-subst. calcite, Cd-subst. vaterite	Rounded and faceted

Note: The error bar on the percentages varies from 5% to 15% depending on the species (see Table 2).

study, no such peaks were found on the XRD patterns. However, it is still possible that coarse crystals of Ca oxalate mono- or dehydrate are present but produce nonspecific peaks only, or that Bragg conditions were not met for these coarse crystals. Therefore, the presence of Ca oxalate mono- and dehydrate cannot be ruled out. Other undetermined organic ligands may also complex Ca. In addition, mixed mineral and organic Ca compounds such as organic matter containing calcite (16) may occur.

The Ca μXANES analysis showed that strong over-absorption effects may take place and decrease dramatically the amplitude of the spectra. We show that this effect is far from negligible when identifying and quantifying Ca species. For instance, for grain ZnCa3, the uncorrected spectrum was fitted by 68% vaterite and 25% aragonite, and the corrected spectrum was fitted with 100% aragonite. Note that the LC fit without over-absorption correction was relatively bad, which alerted us on the possibility of an over-absorption effect.

In the environment, ACC is thermodynamically unstable and rapidly transforms into vaterite and then calcite (17). However, it is found as a stable compound in plants (e.g., cystoliths) and animals (e.g., cuticle of crustaceans, spicules of ascidiae, granules in molluscs) (18). ACC is probably stabilized by proteins, magnesium, and phosphorus in these organisms (18). In our case, Mg and P were found in the grains.

Biologically controlled biomineralization leads to well-defined mineral species and shapes. Here, the variety of morphologies and of $CaCO_3$ crystal structures, and their coexistence with amorphous and possibly organic forms, supports the hypothesis of a biologically induced (as opposed to biologically controlled) biomineralization. This study illustrates the potential of microfocused X-ray techniques to study biomineralization processes, and strategies of metals immobilization developed by plants to cope with metal toxicity.

Acknowledgements

We acknowledge the ALS (Berkeley, California) and the ESRF (Grenoble, France) for the provision of beamtime. We are grateful to Jean Susini and the staff of beamline ID21 at the ESRF for their technical support during the experiment. The operations of the Advanced Light Source at Lawrence Berkeley National Laboratory are supported by the Director, Office of Science, Office of Basic Energy Sciences, Materials Sciences Division, of the US Department of Energy under Contract No. DE-AC02–05CH11231. We acknowledge Y. Politi and S. Weiner for sharing the ACC Ca XANES spectrum, and two anonymous reviewers.

References

1. Y.E. Choi, E. Harada, M. Wada, H. Tsuboi, Y. Morita, T. Kusano, and H. Sano. Planta, **213**, 45 (2001).
2. Y.E. Choi, E. Harada, G.H. Kim, E.S. Yoon, and H.J. Sano. Plant Biol. **47**, 75 (2004).
3. G. Sarret, E. Harada, Y.E. Choi, M.P. Isaure, N. Geoffroy, M. Birschwilks, S. Clemens, S. Fakra, M.A. Marcus, and A. Manceau. Plant Physiol. **141**, 1021 (2006).
4. H. Lowenstam and S. Weiner. *In* On biomineralization. Oxford University Press, Oxford, UK. 1989.
5. Y.E. Choi and E. Harada. Plant Biol. **48**, 113 (2005).
6. J. Paquette and R.J. Reeder. Geochim. Cosmochim. Acta, **59**, 735 (1995).
7. R.J. Reeder. Geochim. Cosmochim. Acta, **60**, 1543 (1996).
8. Y. Politi, Y. Levi-Kalisman, S. Raz, F. Wilt, L. Addadi, S. Weiner, and I. Sagi. Adv. Funct. Mater. **16**, 1289 (2006).
9. M.A. Marcus, A.A. MacDowell, R. Celestre, A. Manceau, T. Miller, H.A. Padmore, and R.E.J. Sublett. Synchrotron Radiat. **11**, 239 (2004).
10. A. West. Solid state chemistry and its applications. Wiley, New York. 1984.
11. T.J. Ressler. J. Phys. IV, **7**, c2–269 (1997).
12. A. Manceau, M.A. Marcus, and N. Tamura. *In* Applications of synchrotron radiation in low-temperature geochemistry and

© 2007 NRC Canada

rnvironmental science. *Edited by* P. Fenter, M. Rivers, N. Sturchio, and S. Sutton. Mineralogical Society of America, Washington, DC. 2002. pp. 341–428.
13. R.D. Shannon. Acta Crystallogr. A, **32**, 751 (1976).
14. Y. Levi-Kalisman, S. Raz, S. Weiner, L. Addadi, and I. Sagi. Adv. Funct. Mater. **12**, 43 (2002).
15. S. Pattanaik. Nucl. Instrum. Methods Phys. Res., Sect. B, **229**, 367 (2005).
16. B.L. Phillips, Y.J. Lee, and R.J. Reeder. Environ. Sci. Technol. **39**, 4533 (2005).
17. T. Ogino, T. Suzuki, and K.J. Sawada. Cryst. Growth, **100**, 159 (1990).
18. S. Weiner, Y. Levi-Kalisman, S. Raz, and L. Addadi. Connect. Tissue Res. **44**(Suppl. 1), 214 (2003).

© 2007 NRC Canada

Formation of group 12 [Zn, Cd] mixed-chalcogen nanoparticles from the reagent Me_3Si-SeS-$SiMe_3$[1]

Elizabeth A. Turner, Harald Rösner, Yining Huang, and John F. Corrigan

Abstract: Mixed-chalcogen metal chalcogenide nanoparticles (MSe_xS_{1-x}; M = Zn, Cd) have been synthesized using Me_3Si-SeS-$SiMe_3$ as a delivery source of Se^{2-} and S^{2-} to the metal core. This method demonstrates the ease with which mixed-chalcogen particles can be fabricated at low temperature using colloidal techniques. Reaction with Me_3Si-SeS-$SiMe_3$ occurs via a redox pathway resulting in Se–S bond cleavage and ultimately contributing to the non-equivalent Se:S ratio observed in the isolated particles. Subsequent thermolysis of $ZnSe_{0.57}S_{0.43}$ and $CdSe_{0.28}S_{0.72}$ in hexadecylamine gives rise to controlled particle growth while maintaining the observed stoichiometry. Particles are characterized by EDX, TEM, and powder X-ray diffraction analysis in conjunction with UV–vis absorption and photoluminescence (PL) spectroscopy.

Key words: nanoparticles, semiconductors, mixed-chalcogen, quantum confinement, Group 12.

Résumé : On a effectué la synthèse de nanoparticules mixtes comportant un chalcogène et un chalcogénure métallique ($MeSe_xS_{1-x}$; M = Zn, Cd) en utilisant le Me_3Si-SeS-$SiMe_3$ comme source pouvant livrer les groupes Se^{2-} et S^{2-} au métal central. On a fait une démonstration de cette méthode par la facilité avec laquelle des particules de chalcogènes mixtes peuvent être fabriqués à basse température en faisant appel à des techniques colloïdales. La réaction avec le Me_3Si-SeS-$SiMe_3$ se produit par une voie réactionnelle redox qui provoque un clivage de la liaison Se-S et qui contribue éventuellement au rapport non équivalent de Se:S qui est observé dans les particules qui ont été isolées. Une thermolyse subséquente du $ZnSe_{0.57}S_{0,43}$ et du $CdSe_{0.28}S_{0.72}$ dans l'hexadécylamine conduit à une croissance contrôlée des particules tout en maintenant la stoechiométrie observée. On a caractérisé les particules par le biais de la diffraction des rayons X par des poudres et les techniques « EDX » et « TEM » en relation avec les spectres d'absorption UV–vis et la spectroscopie de photoluminescence (PL).

Mots-clés : nanoparticules, semiconducteurs, chalcogènes mixtes, confinement quantique, groupe 12.

[Traduit par la Rédaction]

Introduction

Metal-chalcogenides (ME; M = Zn, Cd, Hg; E = S, Se, Te; or M_2E; M = Cu, Ag) have been of tremendous interest over the past several decades (1). In particular, an extensive amount of research has surrounded both the synthesis (2) and characterization (3) of group 12–16 nanomaterials. Upon constricting the dimensions of a given material to the nanometer-size regime, quantum confinement effects predominate such that electronic, physical, and optical properties become size specific (4). Ultimately, for semiconductors, these phenomena give rise to an increase in band gap energy from that of the bulk material, where the band gap becomes tunable to a desired particle size. As a result, group 12–16 nanomaterials have found potential applications in the fabrication of new devices such as LEDs, photovoltaic, and photoelectrochemical devices (5). The control of particle size and the efficient delivery of chalcogen (E^{2-}) to the metal core, however, are two challenging aspects of nanomaterial synthesis. One means of managing these two synthetic obstacles is through the use of trimethylsilyl-chalcogenide reagents as an easily handled chalcogen source in conjunction with passivating the metal core with long alkyl chain amine (phosphine) ligands, thereby preventing possible aggregation (6).

One of the pioneering methods in controlling particle size is what is commonly referred to as the controlled arrested precipitation method from colloidal solutions where dilute aqueous mixtures of M^{2+} and E^{2-} species are combined together (7). This method was further extended into what is considered to be one of the most notable advances in the formation of discrete nanoparticles, the TOP or TOPO (trioctylphosphine or trioctylphosphine oxide) pyrolysis method. The rapid injection of sources of both M^{2+} and E^{2-} species into a hot coordinating solvent facilitates the development of nanoparticles (8). An extension of this method has been to inject metal clusters, where the metal-chalcogen bond is already prepositioned, into a hot hexadecylamine (HDA) solution (9). By increasing the reaction temperature,

Received 17 May 2007. Accepted 21 June 2007. Published on the NRC Research Press Web site at canjchem.nrc.ca on 3 August 2007.

E.A. Turner, Y. Huang[2], and J.F. Corrigan.[3] Department of Chemistry, *The* University *of* Western Ontario, London, ON N6A 5B7, Canada.
H. Rösner. Institut für Nanotechnologie, Forschungszentrum Karlsruhe GmbH, 76344 Eggenstein-Leopoldshafen, Germany.

[1]This article is part of a Special Issue dedicated to Professor G. Michael Bancroft.
[2]Corresponding author (e-mail: yhuang@uwo.ca).
[3]Corresponding author (e-mail: corrigan@uwo.ca).

 doi:10.1139/V07-083 © 2007 NRC Canada

particles are found to grow via Ostwald ripening (10) where the more soluble smaller particles grow in an effort to form larger particles (11). The large surface area to volume ratio of the smaller particles promotes the number of energetically less stable surface molecules, and larger particles having a greater volume to surface area ratio are of a lower energy state and thus preferentially form at the expense of smaller particles (12).

Manipulating particle size is one means of dictating their physical properties. An additional degree of freedom can be gained by substituting some metal (or chalcogen) atoms with another metal (or chalcogen), thus forming ternary MM′E (or MME′; M ≠ M′ and E ≠ E′) materials. These materials exhibit physical properties whose energies are intermediate between those of ME and M′E (or ME′). Recent studies have focused on the synthesis and characterization of group 12–12′–16 nanoclusters and nanoparticles through the use of trimethylsilyl-chalcogenide reagents (13). The formation of 12–16–16′ nanomaterials, however, remains relatively unexplored (vide infra).

Only a few known examples exist where discrete quantum dots, rather than thin films, of mixed-chalcogen cadmium materials have been synthesized. Quantum dots and tetrapod nanocrystals of $CdSe_xTe_{1-x}$ (14) have been synthesized from cadmium salts and stock solutions of selenium and tellurium using either TOP, TOPO, or stearic acid as surface stabilizing ligands. Homogeneously alloyed zinc-blende $CdSe_xS_{1-x}$ (15) nanocrystals have also been prepared from cadmium oxide, oleic acid, and stock solutions of elemental sulfur and selenium, added in varying proportions. Discrete particles were observed using transmission electron microscopy (TEM) and chemical homogeneity was demonstrated by powder X-ray diffraction (PXRD). By changing the ratio S:Se, the photophysical properties could be altered such that an increasing selenium content leads to a shift to lower energy of the excitonic transition, as observed in the absorption spectra. The majority of reports on mixed-chalcogen ternary alloys, however, involve the preparation of $CdSe_xS_{1-x}$ thin films typically on glass, quartz, GaAs, and silicon. A typical procedure involves the mixture of CdS and CdSe powders combined in a desired ratio (16). Other methods employ $CdCl_2$, thiourea and sodium selenosulfate as precursors (17), while the elemental forms of cadmium, sulfur, and selenium can also be combined with a desired stoichiometry in a glass melt (18). An extension to this synthesis involves the use of elemental sulfur and selenium with cadmium salts (19), while other procedures use a combination of metal salts with various chalcogen precursors (i.e., H_2E and $CS(NH_2)_2$) (20). Regardless of the choice of reagents, the methods involve specialized techniques such as chemical bath deposition, molecular beam epitaxy, or pulsed laser ablation, all of which require extremely high temperatures. The deposited materials typically have nanometer dimensions, where examples of nanowires and nanoribbons have been formed on a Si[111] substrate (21).

Herein we report the synthesis of MSe_xS_{1-x} (M = Zn, Cd) nanoparticles formed from the reagent $Me_3Si\text{-}SeS\text{-}SiMe_3$. The highly reactive nature of this reagent allows for the facile low temperature delivery of both sulfur and selenium to the corresponding metal acetate. The resulting nanoparticles are easily formed in solution at room temperature (RT). Subsequent thermolysis of the zinc and cadmium mixed-chalcogen nanoparticles in hot hexadecylamine is found to provide controlled particle growth. The resulting nanoparticles are analyzed by UV–vis absorption and PL spectroscopy, in addition to TEM, powder X-ray diffraction, and EDX analysis.

Experimental

Materials

All synthetic procedures and manipulations were performed under an inert nitrogen atmosphere using standard Schlenk techniques and gloveboxes, unless otherwise noted. Toluene, pentane, and hexanes (all from Caledon) were dried and collected using an MBraun MB-SPS solvent purification system with tandem activated alumina – activated copper redox catalyst (22). Dichloromethane (EMD) was dried and distilled over P_2O_5. Anhydrous methanol was purchased from Caledon. Cadmium acetate dihydrate (98%), anhydrous zinc acetate (99.99%), *N,N,N′,N′*-tetramethylethylenediamine (TMEDA), *n*-butyl lithium in hexanes (1.6 mol/L), tri(*n*-butyl)phosphine, and hexadecylamine (HDA) were purchased from Sigma-Aldrich. Sulfur (99%) was purchased from EM Science. Cadmium acetate dihydrate was dried under vacuum (10^{-3} torr; 1 torr = 133.322 4 Pa) at 130 °C and stored under inert conditions. TMEDA was dried and distilled over a lump of sodium and stored under inert conditions. The reagent $Se(SiMe_3)_2$ was prepared according to literature procedures (13*c*, 23).

Synthesis of TMEDA Li^+ $^-SeSiMe_3$

In a Schlenk tube with no stir bar, $(SiMe_3)_2Se$ (0.15 mL, 0.7 mmol) and TMEDA (0.1 mL, 0.7 mmol) were added to tetrahydrofuran (10 mL) and cooled to 0 °C, producing a light brown solution. *n*-Butyl lithium (0.44 mL, 0.7 mmol) was added to the reaction, upon which the solution immediately became colourless, and the reaction was kept at 0 °C for 30 min with periodic mixing via agitation. A stir bar was then added to the solution and the reaction was warmed to RT with stirring. The solvent was removed under vacuum (10^{-3} torr for one hour) producing a colourless oil. The anion was used immediately in the subsequent chalcogen insertion as the product has limited stability at RT. ^1H NMR (C_7D_8, 203K) δ: 0.72 (s, $Si(CH_3)_3$), 1.64 (br s, CH_2), 2.11 (s, CH_3). $^{13}C\{^1H\}$ (C_7D_8, 203 K) δ: 8.41 ($Si(CH_3)_3$), 47.08 (CH_2), 56.11 (CH_3). ^{29}Si NMR (C_7D_8, 203 K) δ: 1.1. ^{77}Se NMR (C_7D_8, 203 K) δ: –520.

Synthesis of TMEDA Li^+ $^-SSeSiMe_3$

In a Schlenk tube, sulfur (0.023 g, 0.7 mmol) was suspended in pentane (10 mL) and cooled to -78 °C. Toluene (5 mL) was added to the lithio trimethylsilyl selenolate anion (0.7 mmol) and the solution was cooled to –78 °C. The anion solution was rapidly added to the sulfur suspension at –78 °C upon which a slightly yellow solution developed. The reaction was removed from the cold bath until a bright yellow cloudy solution resulted. The solution was then immediately cooled again to –78 °C and allowed to stir for an additional 20 min. The product was used in situ as removal of the solvent leads to product decomposition; in addition, the lithio trimethylsilyl selenothiolate anion must be used

© 2007 NRC Canada

immediately as it quite reactive to both air and elevated temperatures. ^{1}H NMR (C_7D_8, 203 K) δ: 0.31 (s, Si(CH_3)$_3$), 1.58 (br s, CH_2), 2.12 (s, CH_3). ^{13}C{^{1}H} (C_7D_8, 203 K) δ: 1.22 (Si(CH_3)$_3$), 48.55 (CH_2), 56.00 (CH_3). ^{29}Si NMR (C_7D_8, 203K) δ: 15.3. ^{77}Se NMR (C_7D_8, 203 K) δ: –96.

Synthesis of Me_3Si-SeS-$SiMe_3$

An excess of chlorotrimethylsilane (0.2 mL, 1.4 mmol) was added to lithio trimethylsilyl selenothiolate anion (0.7 mmol) at –78 °C. The reaction was allowed to gradually warm to RT upon which the cloudy solution went through a clear bright yellow stage followed by the development of a cloudy yellow suspension. Upon achieving this stage the reaction was immediately cooled to –78 °C and kept cold until further use. The product cannot be isolated as removal of the solvent leads to rapid decomposition. Furthermore, the generated lithium chloride must be added to subsequent reactions as filtration of the solution also leads to decomposition. The product is exceptionally reactive to air and has only short-term stability at RT. ^{1}H NMR (C_7D_8, C_5D_{12}, 218 K) δ: 0.26 (SSi(CH_3)$_3$), 0.34 (SeSi(CH_3)$_3$). ^{13}C{^{1}H} NMR (C_7D_8, C_5D_{12}, 218 K) δ: 1.27 (SeSi(CH_3)$_3$), 3.86 (Si(CH_3)$_3$). ^{29}Si NMR (C_7D_8, C_5D_{12}, 218 K) δ: 15.9 (Se*Si*(CH_3)$_3$), 16.4 (S*Si*(CH_3)$_3$). ^{77}Se NMR (C_7D_8, C_5D_{12}, 218 K) δ: –100.

Synthesis of $CdSe_xS_{1-x}$ nanoparticles

Anhydrous cadmium acetate (0.320 g, 1.4 mol) was solubilized with 2.2 equiv. of tri(*n*-butyl)phosphine (0.76 mL, 3.05 mol) in toluene (30 mL), producing a turbid solution. After stirring at RT for 1 h, a solution of Me_3Si-SeS-$SiMe_3$ (1.4 mol) was added and the reaction was stirred at RT overnight, resulting in the precipitation of a pale yellow solid. The solid was isolated via removal of the mother liquor, followed by washing (3 × 10 mL methanol), sonication for 15 min at 45 °C, and centrifugation. The resulting solid was dried under vacuum (10^{-3} torr) for 1 h.

Synthesis of $ZnSe_xS_{1-x}$ nanoparticles

Anhydrous zinc acetate (0.255 g, 1.4 mol) was solubilized with 2.2 equiv. of tri(*n*-butyl)phosphine (0.76 mL, 3.05 mol) in CH_2Cl_2 (10 mL). After stirring at RT for one hour, Me_3Si-SeS-$SiMe_3$ (1.4 mol) was added and the reaction was stirred at RT overnight. A resulting white solid precipitated from solution and was isolated via removal of the mother liquor and washing with hexanes (3 × 15 mL), followed by drying under vacuum (10^{-3} torr) for 1 h.

Thermolysis of MSe_xS_{1-x} in hexadecylamine

To the obtained MSe_xS_{1-x} [M = Zn, Cd] nanoparticles, hexadecylamine (HDA; 20 g, 82.8 mmol) was added to the flask and heated to 60 °C, until all of the HDA had melted. The solution was then degassed under vacuum (10^{-3} torr) for 20 min. The mixture was then heated to 240 °C, where at specified temperature intervals an aliquot was taken. At each temperature the reaction was annealed for 15 min, an aliquot was taken, washed with anhydrous methanol (15 mL) thus precipitating the resulting particles, centrifuged at 45 °C, and washed again with methanol. The obtained solids were dried under vacuum (10^{-3} torr) for 15 min and stored in a glovebox.

Characterization

Solution ^{1}H, ^{13}C{^{1}H}, and ^{77}Se NMR spectra were recorded on a Varian Inova 400 spectrometer with an operating frequency of 399.76, 100.53, and 76.24 MHz respectively. ^{29}Si NMR spectra were obtained indirectly as gradient heteronuclear multibond coupling (g-HMBC) experiments to proton ($J_{Si–H}$ = 6 Hz). ^{1}H and ^{13}C{^{1}H} NMR spectra were referenced internally to the respective deuterated solvent as well as externally to TMS, ^{29}Si NMR spectra were referenced to silicon grease (–20 ppm), and ^{77}Se NMR spectra were referenced externally to $PhSeSiMe_3$ (+85.6 ppm) (24). Powder X-ray diffraction (PXRD) patterns were obtained using a Rigaku diffractometer with a Co Kα radiation source (λ = 1.799260 Å). UV–vis absorption spectra for $ZnSe_xS_{1-x}$ nanoparticles were recorded on an Ocean Optics SD2000 UV–vis fiber optic spectrometer equipped with a Mini-D2T light source and a UV2/OFLV-4 detector. The spectra were obtained as a mineral oil mull between two quartz plates. UV–vis absorption spectra of the $CdSe_xS_{1-x}$ nanoparticle series were recorded on a Varian Cary 100 UV–vis absorption spectrometer. The spectra were obtained in a CH_2Cl_2 solution. Luminescence measurements were obtained using a Photo Technology International fluorimeter equipped with an LPS 220B lamp power supply and an 814 photomultiplier detection system. Energy dispersive X-ray (EDX) analyses were carried out by Dr. Brian Hart at Surface Science Western (UWO). A Quartz Xone EDX analysis system coupled to a Leo 440 SEM equipped with a Gresham light element detector was used to obtain semiquantitative analysis of Zn, Cd, S, and Se. Analyses were carried out using a 20 kV electron beam rastered over 100 μm × 100 μm areas and repeated to ensure reproducibility. Samples for high-resolution transmission electron microscopy (HR-TEM) were obtained by dispersing the solid in CH_2Cl_2 and dropping these dilute suspensions on gold-plated grids, allowing the excess solvent to evaporate. TEM investigations were performed in a Philips Tecnai F20 ST operated at 200 kV. The TEM was equipped with an EDAX Energy-Dispersive X-ray SiLi detector with a S-UTW (super ultra-thin window). EDX analyses were carried out in the STEM mode with a HAADF (high angle annular dark field) detector using a nanometer-sized probe (1 nm spot size for the presented measurements). Use of an analytic double tilt holder (Philips) was made. High-resolution micrographs were taken with a 1K × 1K CCD camera and analyzed with the software package Digital Micrographs (Version 3.7.4, Gatan Company) to perform fast Fourier Transformations (FFT).

Results and discussion

Synthesis of mixed-chalcogen nanoparticles

Trimethylsilyl-chalcogen reagents ($RESiMe_3$, $E(SiMe_3)_2$; R = alkyl, aryl, ferrocenyl) are valuable in the formation of structurally characterized nanoclusters (25) and nanoparticles (26). The reactive pendant trimethylsilyl moiety allows for the facile and homogeneous delivery of either chalcogenolate (RE^-) or chalcogenide (E^{2-}) bonding interactions to a metal salt via the generation and elimination of the corresponding trimethylsilane (27). Although the synthesis of binary and ternary mercury chalcogenides has been a syn-

© 2007 NRC Canada

thetically challenging area (28), one recent example involves the formation of $HgSe_xS_{1-x}$ particles from both $S(SiMe_3)_2$ and $Se(SiMe_3)_2$ and mercury acetate, using TOP in a phase separation method, to control particle growth (29). Particles varying in size from 2 to 3 nm were formed.

Traditional trimethylsilyl-chalcogenide reagents (i.e., $E(SiMe_3)_2$; E = S, Se, Te) are well-known and extensively used in synthesis, however, there is recent interest in synthesizing silylated-chalcogen reagents containing two chalcogen elements, whereby both E^{2-} and E'^{2-} are supplied to the metal core. Recently we have communicated the synthesis and characterization of the first mixed-chalcogen silylated reagent $Me_3Si\text{-}SeS\text{-}SiMe_3$ and demonstrated its use in the formation of a $[Cu_{84}Se_{15}S_{27}(PEt_2Ph)_{24}]$ cluster (30).

Bis(trimethylsilyl)selenosulfide $[Me_3Si\text{-}SeS\text{-}SiMe_3]$ is a highly reactive reagent, for which both exposure to atmosphere and elevated temperatures leads to rapid decomposition. In addition, the reagent cannot be isolated and can only be synthesized in dilute solutions. Lithium chloride generated in the formation of $Me_3Si\text{-}SeS\text{-}SiMe_3$ cannot be removed via filtration and must be carried forward in subsequent syntheses. Although $Me_3Si\text{-}SeS\text{-}SiMe_3$ is not a storable precursor, its low temperature stability is ideal for the generation of MSe_xS_{1-x} (M = Zn, Cd) nanoparticles at RT vs. the typically explored high temperature methods.

$CdSe_xS_{1-x}$ nanoparticles

Given the sensitivity of $Me_3Si\text{-}SeS\text{-}SiMe_3$, cadmium acetate $[Cd(OAc)_2]$ can only be introduced in a select number of solvents. The addition of $Me_3Si\text{-}SeS\text{-}SiMe_3$ at RT to a toluene solution of $(P^nBu_3)_2Cd(OAc)_2$ results in the immediate consumption of $Me_3Si\text{-}SeS\text{-}SiMe_3$, as noted by the disappearance of the yellow colour associated with the selenosulfide, in conjunction with the complete solubilization of $Cd(OAc)_2$. This reactivity is then followed by the precipitation of a colourless solid from solution, which gradually develops into a pale yellow colour after stirring overnight. The resulting solid is easily isolated where washing with anhydrous methanol effectively removes any LiCl. Isolated particles were characterized by HR-TEM, however, given their poor solubility a UV–vis absorption spectrum could not be obtained.

To investigate the growth of the resulting $CdSe_xS_{1-x}$ nanoparticles in a coordinating solvent, the solid was added to a hot (60 °C) solution of hexadecylamine (HDA) and heated to 240 °C. Upon increasing the temperature, the sample colour changes from pale yellow to an intense red (Supplementary data, Fig. S1).[4] At specified temperature intervals the sample is annealed (where upon there is no corresponding change in colour) and an aliquot is taken. The resulting nanoparticles are isolated by precipitating from solution using anhydrous methanol.

Lyothermal growth of the nanoparticles results in an increase in particle size without altering the chemical composition (i.e., the ratio between Cd:Se:S). EDX (energy dispersive X-ray) analysis was performed on three separate areas of each sample, where the overall ratio was determined by calculating the average based on the atomic percentages for the corresponding elements. Table 1 clearly demonstrates the nondeviating stoichiometry beginning with the as-synthesized particles and those obtained through thermolysis in HDA. The ratio between Se and S in the isolated particles is not 1:1 although a stoichiometrically precise reagent is used in the synthesis. The reactivity of $Me_3Si\text{-}SeS\text{-}SiMe_3$ however, is expected to occur with Se–S bond cleavage as has previously been established with the synthesis of a $[Cu_{84}Se_{27}S_{15}(PEt_2Ph)_{24}]$ cluster (30). It is necessary to note that the stoichiometry is reproducible and is a reflection of the isolated particles.

The growth in particle size is surveyed using HR-TEM microscopy. Shown in Fig. 1 are the HR-TEM images for as-synthesized, 180 °C, 210 °C, and 240 °C lyothermally grown particles. At 180 °C the particles are found to be ~3.5 nm in diameter, while an increase in thermolysis temperature to 240 °C leads to particles of ~9 nm in diameter. The *d* spacing, as determined by TEM (3.54 Å), is relatively consistent with the *d* spacing associated with the (1 1 1) reflection in the powder X-ray diffraction pattern (3.40 Å).

The photophysical properties of the obtained nanoparticles were analyzed using UV–vis absorption and photoluminescence (PL) spectroscopy. The UV–vis absorption spectra of the thermolysed samples (Fig. 2) distinctly display a red shift in absorption maximum upon increasing thermolysis temperature. At a thermolysis temperature of 160 °C, the absorption maximum is observed at 445 nm (2.79 eV) and shifts by over 100 nm to lower energy upon increasing the thermolysis temperature to 240 °C (560 nm; 2.21 eV). This shift in absorption maximum is consistent with an increase in particle size upon increasing thermolysis temperature. The observed absorption maxima are consistent with what has previously been reported for $CdSe_xS_{1-x}$ having a similar stoichiometry and particle size (15).

The low- and high-energy PL spectra for this series is shown in Fig. 3, where the spectra were obtained by irradiating samples at 468 nm. As is illustrated in Fig. 3*a*, the emission maximum shifts from 488 nm (2.54 eV) to 590 nm (2.10 eV) upon increasing thermolysis temperature and is associated with band-edge emission. At lower energy, two types of emission are observed (Fig. 3*b*) that, although normalized in the figure, are found to increase in intensity (relative to the high energy emission) as the thermolysis temperature is raised. The emission observed at lower energy is much broader in comparison to the sharp band-edge emission and results from deep-trap emission coinciding with nanoparticle defects. The appearance of both band-edge and deep-trap emission is not uncommon for $CdSe_xS_{1-x}$ systems, although several reported examples have developed techniques thereby eliminating deep-trap emission (16–21). One method is to prolong the thermal annealing time, thus forcing defects within the nanoparticle to move to the surface creating a defect-free nanoparticle core. This was investigated for the sample prepared at 230 °C, where, rather than annealing for 15 min, the thermolysis temperature was held for 4 h. Based on the PL spectrum (not shown) after 4 h,

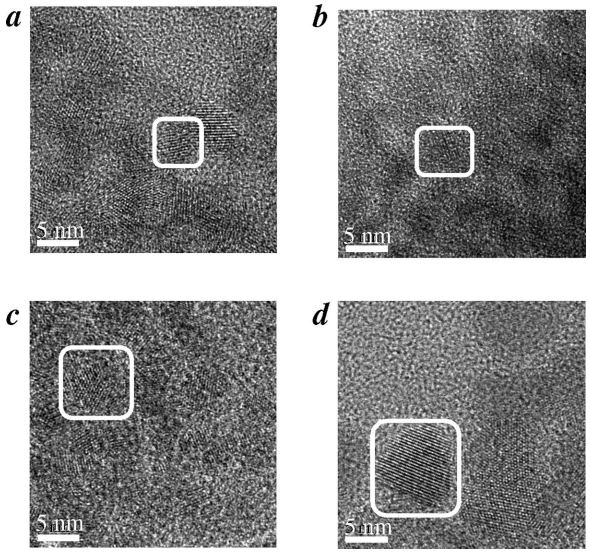
[4] Supplementary data for this article are available on the journal Web site (canjchem.nrc.ca) or may be purchased from the Depository of Unpublished Data, Document Delivery, CISTI, National Research Council Canada, Ottawa, ON K1A 0R6, Canada. DUD 5193. For more information on obtaining material refer to cisti-icist.nrc-cnrc.gc.ca/irm/unpub_e.shtml

© 2007 NRC Canada

Table 1. Cd:Se:S ratios as determined by EDX analysis. Ratios were calculated using atomic percentages.

	Ratio as determined by EDX analysis		
	Cadmium	Selenium	Sulfur
As-synthesized	1	0.31	0.57
160 °C	1	0.34	0.57
180 °C	1	0.32	0.57
200 °C	1	0.31	0.56
210 °C	1	0.30	0.56
220 °C	1	0.31	0.56
230 °C	1	0.31	0.56
240 °C	1	0.30	0.54

Fig. 1. HR-TEM images of (*a*) as-synthesized $CdSe_xS_{1-x}$ and HDA capped particles thermolysed at (*b*) 180 °C, (*c*) 210 °C, and (*d*) 240 °C. Box outlines individual particles.



prolonged annealing times minimized the low energy emission but did not all together eliminate it.

Spectroscopically, the two types of deep-trap emission behave differently. The higher energy emission maximum is red-shifted upon increasing thermolysis temperature from 620 nm (2.00 eV) at 160 °C to 770 nm (1.61 eV) at 240 °C. The lower energy emission however only begins to appear at 200 °C and remains relatively unaltered in peak position upon increasing thermolysis temperature (~790 nm; 1.57 eV). Conversely, the intensity of this low energy emission greatly increases upon raising the thermolysis temperature, where at 240 °C this is the predominant emission observed. Photoluminescence excitation (PLE) measurements confirm the single species nature of the observed emission (Fig. S2).[4] Previous work with CdS and CdSe nanocrystals have described a similar spectroscopic behaviour where the higher energy emission is associated with shallow traps, while the lower energy emission results from deep traps (7*c*, 31).

The powder X-ray diffraction (PXRD) patterns for $CdSe_xS_{1-x}$ (Fig. 4) thermolysed at 200 °C, 220 °C, and 240 °C display two important features. First, the relative

Fig. 2. UV–vis absorption spectra of thermolysed $CdSe_xS_{1-x}$ nanoparticle series. The spectra have been normalized for clarity.

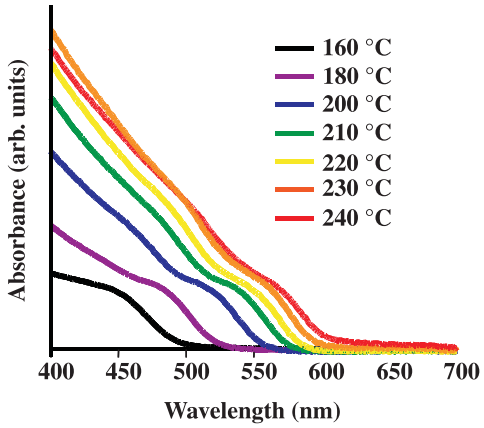
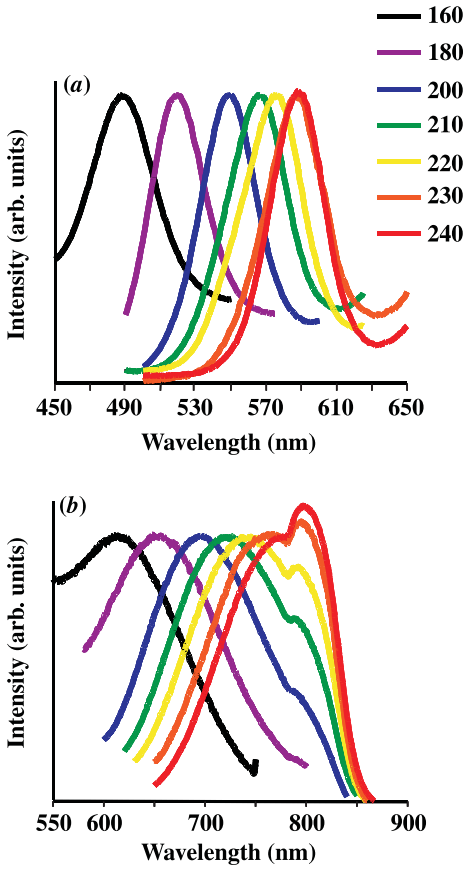


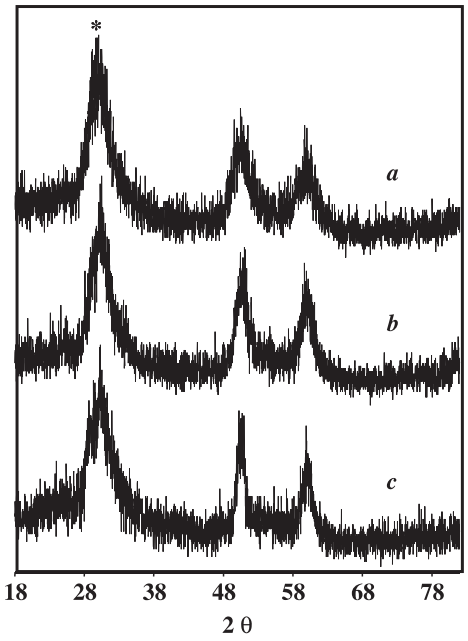
Fig. 3. Photoluminescence spectra of the $CdSe_xS_{1-x}$ thermolysis series at (*a*) high energy and (*b*) low energy. Excitation at 468 nm. The spectra have been normalized for clarity.



peak positions remain unchanged with increasing thermolysis temperature, which is consistent with the chemical composition remaining unaltered. Second, the diffraction peaks become sharper as the thermolysis temperature is raised, consistent with the observed particle growth. The observed PXRD pattern is characteristic of the cubic phases of CdS and CdSe (32). Thus using the (1 1 1) reflection, the lattice parameter *a* can be calculated using eq. [1]. From

© 2007 NRC Canada

Fig. 4. Powder X-ray diffraction patterns of $CdSe_xS_{1-x}$ samples thermolysed at (*a*) 200 °C, (*b*) 220 °C, and (*c*) 240 °C. Asterisk (*) Denotes (1 1 1) reflection.



each PXRD pattern the *d* spacing of (1 1 1) is found to be 3.40 Å and *a* is calculated to be 5.89 Å, where the corresponding lattice parameters for CdS and CdSe are 5.818 and 6.077 Å, respectively (33).

$$[1] \qquad \frac{1}{d^2} = \frac{h^2 + k^2 + l^2}{a^2} = \frac{3}{a^2}$$

Using Vegard's rule (34), which assumes a linear dependence of composition on lattice parameter, the stoichiometry of the obtained $CdSe_xS_{1-x}$ nanoparticle system can be determined using eq. [2],

$$[2] \qquad a(x) = x \cdot a_{CdSe} + (1 - x)a_{CdS}$$

Based on eq. [2], *x* is calculated to be 0.28 (i.e., $CdSe_{0.28}S_{0.72}$), which is similar to what is observed via EDX analysis.

$ZnSe_xS_{1-x}$ nanoparticles

A handful of published examples have investigated the synthesis of $ZnSe_xS_{1-x}$ nanomaterials. $ZnSe_xS_{1-x}$ (where x = 0.05–0.08) is almost perfectly lattice-matched to GaAs and thus improves the blue-green response over the conventionally used ZnSe. Consequently, $ZnSe_xS_{1-x}$ is well-suited for fabricating optoelectronic devices (35). Much like its cadmium counterpart, $ZnSe_xS_{1-x}$ is formed as thin films on either glass or GaAs substrates. The synthesis typically involves the mixing of ZnS and ZnSe powders in a specified ratio (35, 36), although some procedures use dimethylzinc in the presence of gaseous H_2Se and H_2S (37) as well as $ZnCl_2$ with thiourea and selenourea (38). A variety of specialized techniques such as spray pyrolysis, atomic layer epitaxy, and close-space evaporation are used for thin film formation and thus require high operating temperatures. Using Me_3Si-SeS-$SiMe_3$, discrete nanoparticles of $ZnSe_xS_{1-x}$ can be produced.

As previously reported (30), the use of Me_3Si-SeS-$SiMe_3$ imposes limitations with regards to solvent choice and reaction conditions that must be considered when designing a chemical reaction. Employing similar conditions used in the formation of $CdSe_xS_{1-x}$, zinc acetate [$Zn(OAc)_2$] was solubilized in toluene with 2.2 equiv. of tri(*n*-butyl)phosphine. Toluene, however, does not effectively solubilize $Zn(OAc)_2$ and P*n*-Bu_3. As opposed to using phosphine-based ligands to coordinate to $Zn(OAc)_2$ in toluene, an amine ligand (triethylamine) was alternatively employed. Although this leads to the dissolution of $Zn(OAc)_2$, the addition of Me_3Si-SeS-$SiMe_3$ results in the formation of a brightly coloured red solid after a few hours of stirring, suggesting decomposition and the possible precipitation of elemental selenium. In contrast, tri(*n*-butyl)phosphine oxide is able to solubilize $Zn(OAc)_2$ in toluene, however, the addition of Me_3Si-SeS-$SiMe_3$ leads to the immediate formation of a red solid. This reactivity suggests an additional limitation of Me_3Si-SeS-$SiMe_3$ in which hard bases such as amines and oxides should be avoided, while soft bases such as phosphines are less reactive toward Me_3Si-SeS-$SiMe_3$.

An alternative solvent to toluene is to use dichloromethane to solubilize $Zn(OAc)_2$ and P*n*-Bu_3. The addition of Me_3Si-SeS-$SiMe_3$ causes the immediate consumption of the selenosulfide. Although a precipitate does not form initially, continued stirring overnight results in the formation of a white solid. The solid, however, is quite soluble in anhydrous methanol and thus LiCl cannot be removed at this stage and must be carried through to the thermolysis.

The obtained solid is added to a hot (60 °C) HDA solution and gradually heated to 240 °C. At specified temperature intervals the sample is annealed for 15 min, an aliquot is taken, precipitated out with anhydrous methanol, and isolated via centrifugation. By washing with methanol, LiCl is effectively removed from the sample as determined by EDX analysis. The increase in thermolysis temperature does not result in an associated colour change.

To ensure that the chemical composition remains unaltered during the thermolysis, the atomic ratio between zinc, selenium, and sulfur was determined from EDX analysis (Table 2). As is shown in Table 2, the ratio between zinc, selenium, and sulfur remains relatively unaltered throughout thermolysis, however, at 240 °C the quantity of both sulfur and selenium increases, although the ratio between the two elements is similar to what is observed at the lower thermolysis temperatures. The same ratio is not observed in the as-synthesized $ZnSe_xS_{1-x}$ largely because of the presence of chloride within the sample (from LiCl), which consequently affects the overall ratio calculated for the respective elements. Again, the ratio between selenium and sulfur is not 1:1, likely due to the expected Se–S bond cleavage and the presence of both phosphine sulfides and phosphine selenides in the reaction mixture. Phosphine sulfides and selenides are known to form from P*n*-Bu_3 with various chalcogen sources (39). Both sulfur and selenium are however, incorporated into the nanoparticles through the use of the Se–S reagent.

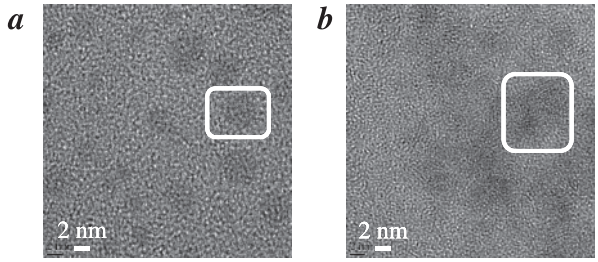
Particle size measurements were calculated based on HR-TEM images (Fig. 5). As can be seen, the particle size increases upon increasing thermolysis temperature. At 200 °C (Fig. 5*a*), individual particles of $ZnSe_xS_{1-x}$ are observed and

© 2007 NRC Canada

Table 2. Zn:Se:S ratio as determined by EDX analysis. Ratios were calculated using atomic percentages.

	Ratio as determined by EDX analysis		
	Zinc	Selenium	Sulfur
As-synthesized	1	0.47	0.36
190 °C	1	0.43	0.49
210 °C	1	0.40	0.44
220 °C	1	0.40	0.48
240 °C	1	0.52	0.59

Fig. 5. HR-TEM images of $ZnSe_xS_{1-x}$ particles thermolysed at (*a*) 200 °C and (*b*) 240 °C. Box outlines individual particles.



are ~4 nm in diameter. Upon increasing the thermolysis temperature to 240 °C, the particles grow to ~8 nm in diameter, however, it appears as though homogeneity is lost at elevated temperatures.

The spectroscopic properties of the obtained nanoparticles were analyzed using UV–vis absorption and PL spectroscopy. The UV–vis absorption spectra of the thermolysis series (Fig. 6) distinctly display a red-shift in absorption maximum with increasing the thermolysis temperature. At a thermolysis temperature of 190 °C, the absorption maximum is found at 305 nm (4.07 eV) and shifts 30 nm to lower energy with increasing the thermolysis temperature to 240 °C (335 nm, 3.70 eV). This shift in absorption maximum is consistent with an increase in particle size.

The PL spectra (obtained by irradiating between 310–320 nm) for the series $ZnSe_xS_{1-x}$ (Fig. 7) differs significantly from the PL spectra of the $CdSe_xS_{1-x}$ series in that one type of emission is observed, corresponding to band-edge emission. The emission maximum shifts from 342 nm (3.63 eV) at 200 °C to lower energy (362 nm, 3.42 eV) with increasing the thermolysis temperature to 240 °C. This red shift in emission maximum upon increasing thermolysis temperature confirms an increase in particle size. PLE measurements confirm the nature of the emitting species (Fig. S3).[4]

Much like the PXRD patterns for $CdSe_xS_{1-x}$, the PXRD patterns for $ZnSe_xS_{1-x}$ thermolysed at 190 °C, 210 °C, and 220 °C (Fig. 8) indicate a sharpening of diffraction peaks with increasing thermolysis temperature, in addition to consistent peak positions. Conversely, the obtained $ZnSe_xS_{1-x}$ nanoparticles display a characteristic hexagonal phase pattern as observed for ZnS and ZnSe (40). Thus, using the (0 0 2) reflection, the lattice parameter *c* can be calculated (double the associated *d* spacing, *d* = 3.2 Å). The obtained *c* parameter (6.4 Å) is found to be intermediate between the *c* parameters for ZnS (6.234 Å) and ZnSe (6.53 Å) (37), and

Fig. 6. UV–vis absorption spectra of thermolysed $ZnSe_xS_{1-x}$ nanoparticle series. The spectra have been normalized for clarity.

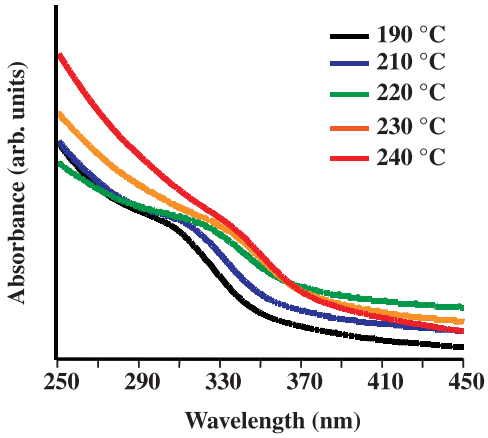
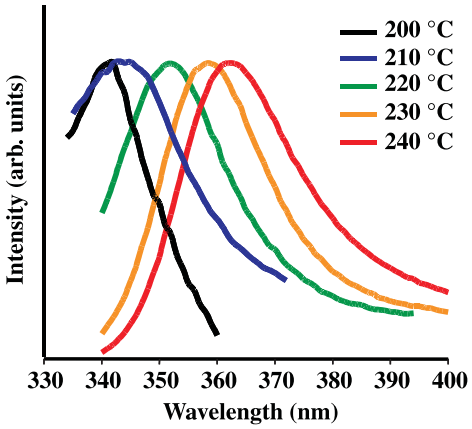


Fig. 7. PL spectra of the $ZnSe_xS_{1-x}$ thermolysis series. Excitation between 310 and 320 nm. The spectra have been normalized for clarity.



using Vegard's rule (eq. [2], substitute *a* for *c*), *x* is found to be an intermediate value.

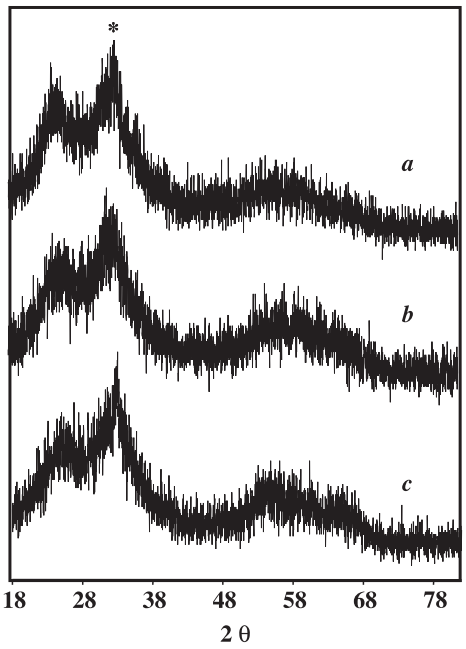
It is noteworthy to mention that the observed stoichiometry in the zinc system varies significantly from the stoichiometry of the cadmium system, thus reflecting a differing reactivity between the two elements.

Conclusions

It has been demonstrated that $Me_3Si\text{-}SeS\text{-}SiMe_3$ is an effective delivery agent of both sulfur and selenium. As such, the reagent has found utility in the synthesis of mixed-chalcogen zinc and cadmium nanoparticles. $Me_3Si\text{-}SeS\text{-}SiMe_3$ serves as a reagent for the distribution of both chalcogen elements at low temperature vs. the conventional methods used for the formation of MSe_xS_{1-x} materials, which typically require two chalcogen reagents and relatively high temperatures. The resulting nanoparticles display a nonstoichiometric amount of both sulfur and selenium as the ensuing chemistry with the corresponding metal acetate leads to Se–S bond cleavage. Thermolysis of both zinc and cadmium nanoparticle species in hexadecylamine leads to controlled particle growth with increasing thermolysis tem-

© 2007 NRC Canada

Fig. 8. Powder X-ray diffraction patterns of $ZnSe_xS_{1-x}$ samples thermolysed at (*a*) 190 °C, (*b*) 210 °C and (*c*) 220 °C. * Denotes (0 0 2) reflection.



perature, as has been noted by the red-shift in both the absorption and emission excitonic transition. An extension of this research will be to investigate the effectiveness of $Me_3Si\text{-}SeS\text{-}SiMe_3$ in the synthesis of $HgSe_xS_{1-x}$ nanoparticles.

Acknowledgements

We gratefully acknowledge the Natural Sciences and Engineering Research Council (NSERC) of Canada for financial support of this research, equipment funding, and for a postgraduate scholarship (EAT). The Government of Ontario Premier's Research Excellence Awards (PREA) program is also acknowledged for financial support and *The* University *of* Western Ontario and the Canada Foundation for Innovation (CFI) are thanked for equipment funding.

References

1. (*a*) R.D. Rauh. Stud. Phys. Theor. Chem. **55**, 277 (1988); (*b*) A.C. Jones, P.J. Wright, and B.J. Cockayne. J. Cryst. Growth, **107**, 297 (1991); (*c*) K. Kamazaki. Two–Six Semicond. Compd. 47 (1993).
2. (*a*) M.T. Swihart. Curr. Opin. Colloid Interface Sci. **8**, 127 (2003); (*b*) K.J. Holmberg. Colloid Interface Sci. **274**, 355 (2004); (*c*) T. Tsuzuki and P.G.J. McCormick. Mater. Sci. **39**, 5143 (2004); (*d*) M.A. Malik and P. O'Brien. Top. Organomet. Chem. **9**, 173 (2005); (*e*) D. Mandal, M.E. Bolander, D. Mukhopadhyay, G. Sarkar, and P. Mukherjee. Appl. Microbiol. Biotechnol. **69**, 485 (2006).
3. (*a*) N.L. Pickett and P. O'Brien. Chem. Rec. **1**, 467 (2001); (*b*) Nanoparticles: from theory to application. *Edited by* G. Schmid. Wiley-VCH, Weinheim, Germany. 2004. Chap. 3.
4. (*a*) L.E. Brus. J. Chem. Phys. **80**, 4403 (1984); (*b*) A.P. Alivisatos. J. Phys. Chem. **100**, 13226 (1996); (*c*) L.E. Brus. Phys. Chem. Solids, **59**, 459 (1998); (*d*) M. Nirmal and L. Brus. Acc. Chem. Res. **32**, 407 (1999); (*e*) T. Trindade, P. O'Brien, and N.L. Pickett. Chem. Mater. **13**, 3843 (2001); (*f*) N.L. Pickett and P. O'Brien. Chem. Rec. **1**, 467 (2001); (*g*) S. Sapra, D.D. Sarma. *In* The chemistry of nanomaterials synthesis, properties and applications. Vol. 2. *Edited by* C.N.R. Rao, A. Müller, and A.K. Cheetham. Wiley-VCH, Verlag GmbH & Co, Weinheim, Germany. 2004. p. 371.
5. (*a*) V.L. Colvin, M.C. Schlamp, and A.P. Alivisatos. Nature (London), **370**, 354 (1994); (*b*) D.E. Fogg, L.H. Radzilowski, B.O. Dabbousi, R.R. Schrock, E.L. Thomas, and M.G. Bawendi. Macromolecules, **30**, 8433 (1997); (*c*) B.A. Ridley, B. Nivi, and J.M. Jacobson. Science (Washington, D.C.), **286**, 746 (1999); (*d*) X. Duan, C. Niu, V. Sahi, J. Chen, J.W. Parce, S. Empedocles, and J.L. Goldman. Nature (London), **425**, 274 (2003); (*e*) J.A. Kloepfer, S.E. Bradforth, and J.L. Nadeau. J. Phys. Chem. B, **109**, 9996 (2005).
6. (*a*) D.V. Talapin, A.L. Rogach, A. Kornowski, M. Haase, and H. Weller. Nano Lett. **1**, 207 (2001); (*b*) Y.-W. Jun, S.-M. Lee, N.-J. Kang, and J. Cheon. J. Am. Chem. Soc. **123**, 5150 (2001); (*c*) R.W. Meulenberg, S. Bryan, C.S. Yun, G.F. Strouse. J. Phys. Chem. B. **106**, 7774 (2002).
7. (*a*) R. Rossetti, S. Nakahara, and L.E. Brus. J. Chem. Phys. **79**, 1086 (1983); (*b*) R. Rossetti, R. Hull, J. M. Gibson, and L.E. Brus. J. Chem. Phys. **83**, 1406 (1985); (*c*) N. Chestnoy, T.D. Harris, R. Hull, and L. E. Brus. J. Phys. Chem. **90**, 3393 (1986); (*d*) M.L. Steigerwald, A.P. Alivisatos, J.M. Gibson, T.D. Harris, R. Kortan, A.J. Muller, A.M. Thayer, T.M. Duncan, D.C. Douglass, and L.E. Brus. J. Am. Chem. Soc. **110**, 3046 (1988); (*e*) C.-C. Chen, C.-Y. Chao, and Z.-H. Lang, Chem. Mater. **12**, 1516 (2000); (*f*) J.O. Winter, N. Gomez, S. Gatzert, C.E. Schmidt, and B.A. Krogel. Colloids Surf. A, **254**, 147 (2005).
8. (*a*) C.B. Murray, D.J. Norris, and M.G. Bawendi. J. Am. Chem. Soc. **115**, 8706 (1993); (*b*) C. B. Murray, M. Nirmal, D. J. Norris, and M. G. Bawendi. Z. Phys. D: At., Mol. Clusters, **26**, S231 (1993); (*c*) T. Trindade and P. O'Brien. Adv. Mater. **8**, 161 (1996); (*d*) T. Trindade, P. O'Brien, and X.-M. Zhang. Chem. Mater. **9**, 523 (1997).
9. (*a*) S.L. Cumberland, K.M. Hanif, A. Javier, G.A. Khitrov, G.F. Strouse, S.M. Woessner, and C.S. Yun. Chem. Mater. **14**, 1576 (2002); (*b*) G.A. Khitrov and G.F. Strouse. J. Am. Chem. Soc. **125**, 10465 (2003).
10. W. Ostwald. Z. Phys. Chem. **22**, 289 (1897).
11. A.D. McNaught and A. Wilkinson. *In* IUPAC Compendium of chemical terminology. 2nd ed. Blackwell Science, Malden, Mass. 1997. p. 286.
12. I.D. Morrison and S. Ross. Colloidal dispersions: suspensions, emulsions and foams. John Wiley & Sons, Inc. New York. 2002. p. 151.
13. (*a*) M.W. DeGroot, N.J. Taylor, and J.F. Corrigan. J. Am. Chem. Soc. **125**, 864 (2003); (*b*) M.W. DeGroot and J.F. Corrigan. Angew. Chem. Int. Ed. **43**, 5355 (2004); (*c*) M.W. DeGroot, N.J. Taylor, and J.F. Corrigan. J. Mater. Chem. **14**, 654 (2004); (*d*) M.W. DeGroot, N.J. Taylor, and J.F. Corrigan. Inorg. Chem. **44**, 5447 (2005); (*e*) M.W. DeGroot, H. Rösner, and J.F. Corrigan. Chem. Eur. J. **12**, 1547 (2006).
14. (*a*) R. Bailey and S. Nie. J. Am. Chem. Soc. **125**, 7100 (2003); (*b*) Y. Li, H. Zhong, R. Li, Y. Zhou, C. Yang, and Y. Li. Adv. Funct. Mater. **16**, 1705 (2006).
15. L.A. Swafford, L.A. Weigand, M.J. Bowers, J.R. McBride, J.L. Rapaport, T.L. Watt, S.K. Dixit, L.C. Feldman, and S.J. Rosenthal. J. Am. Chem. Soc. **128**, 12299 (2006).
16. (*a*) M.M. El-Nahass. J. Mater. Sci. Mater. Electron. **3**, 71 (1992); (*b*) M. Grün, H. Gerlach, T. Breitkopf, M. Hetterich,

© 2007 NRC Canada

A. Reznitsky, H. Kalt, and C. Klingshirn. J. Cryst. Growth, **146**, 414 (1995); (*c*) G. Perna, S. Pagliara, V. Capozzi, M. Ambrico, and T. Ligonzo. Thin Solid Films, **349**, 220 (1999).
17. R.S. Mane and C.D. Lokhande. Thin Solid Films, **304**, 56 (1997).
18. (*a*) A. Uhrig, L. Banyai, Y.Z. Hu, S.W. Koch, C. Klingshirn, and N. Neuroth. Z. Phys. B: Condens. Matter, **81**, 385 (1990); (*b*) P. Verma, L. Gupta, S.C. Abbi, and K.P. Jain. J. Appl. Phys. **88**, 4109 (2000); (*c*) P. Huber, H. Karl, J.K.N. Linder, and B. Stritzker. Nucl. Instrum. Methods Phys. Res., Sect. B, **242**, 170 (2006); (*d*) P. Huber, H. Karl, and B. Stritzker. Appl. Surf. Sci. **252**, 2497 (2006).
19. (*a*) S.-H. Yu, J. Yang, Z.-H. Han, R.-Y. Yang, Y.-T. Qian, and Y.-H. Zhang. J. Solid State Chem. **147**, 637 (1999); (*b*) R. Elbaum, S. Vega, and G. Hodes. Chem. Mater. **13**, 2272 (2001); (*c*) D.R. Mendes, Jr., F. Qu, A.M. Alcalde, and N.O. Dantas. Microelectron. J. **34**, 643 (2003); (*d*) C. Allahverdi, M.H. Yükselici, R. Turan, and A. Seyhan. Semicond. Sci. Technol. **19**, 1005 (2004).
20. (*a*) D.J. Scoberg, F. Grieser, and D.N. Furlong. J. Chem. Soc. Chem. Commun. 515 (1991); (*b*) M. Nogami, A. Kato, and Y. Tanaka. J. Mater. Sci. **28**, 4129 (1993); (*c*) E. Jang, S. Jun, and L. Pu. Chem. Commun. (Cambridge), 2964 (2003); (*d*) Y. Liu, Y. Xu, J.-P. Li, B. Zhang, D. Wu, and Y.-H. Sun. Mater. Res. Bull. **41**, 99 (2006).
21. (*a*) S.J. Kwon, Y.-J. Choi, J.-H. Park, I.-S. Hwang, and J.-G. Park. Phys. Rev. B: Condens. Matter, **72**, 205312–1 (2005); (*b*) A. Pan, H. Yang, R. Yu, and B. Zou. Nanotechnology, **17**, 1083 (2006).
22. A.B. Pangborn, M.A. Giardello, R.H. Grubbs, R.K. Rosen, and F.J. Timmers. Organometallics, **15**, 1518 (1996).
23. J.-H. So and P. Boudjouk. Synthesis, 306 (1989).
24. H. Poleschner, M. Heydenreich, and U. Schilde. Eur. J. Inorg. Chem. **6**, 1307 (2000).
25. (*a*) J.F. Corrigan, S. Balter, and D. Fenske. J. Chem. Soc. Dalton Trans. 729 (1996); (*b*) J.F. Corrigan and D. Fenske. Chem. Commun. (Cambridge), 1837 (1997); (*c*) D.T.T. Tran, N.J. Taylor, and J.F. Corrigan. Angew. Chem. Int. Ed. **39**, 935 (2000); (*d*) A. Lorenz, D. Fenske. Angew. Chem. Int. Ed. **40**, 4402 (2001); (*e*) A.I. Wallbank and J.F. Corrigan. Chem. Commun. (Cambridge), 377 (2001); (*f*) T.P. Lebold, D.L.B. Stringle, M.S. Workentin, and J.F. Corrigan. Chem. Commun. (Cambridge), 1398 (2003); (*g*) J. Olkowska-Oetzel, P. Sevillano, A. Eichhöfer, and D. Fenske. Eur. J. Inorg. Chem. 1100 (2004); (*h*) M.W. DeGroot, N.J. Taylor, and J.F. Corrigan. Inorg. Chem. **44**, 5447 (2005).
26. (*a*) M.L. Steigerwald, A.P. Alivisatos, J.M. Gibson, T.D. Harris, A.R. Kortan, A.J. Muller, A.M. Thayer, T.M. Duncan, D.C. Douglass, and L.E. Brus. J. Am. Chem. Soc. **110**, 3046 (1988); (*b*) S.M. Stuczynski, J.G. Brennan, and M.L. Steigerwald. Inorg. Chem. **28**, 4431 (1989); (*c*) A.R. Kortan, R. Hull, R.L. Opila, M.G. Bawendi, M.L. Steigerwald, P J. Carrol, and L.E. Brus. J. Am. Chem. Soc. **112**, 1327 (1990); (*d*) C.B. Murray, D.J. Norris, and M.G. Bawendi. J. Am. Chem. Soc. **115**, 8706 (1993).
27. M.W. DeGroot and J.F. Corrigan. *In* Comprehensivec coordination chemistry II. Vol. 7. *Edited by* M. Fujita, A. Powell, and C. Creutz. Pergamon, Oxford, UK. 2004. p. 57.
28. (*a*) D.J. Elliot, D.N. Furlong, and F. Grieser. Colloids Surf. A, **155**, 101 (1999); (*b*) J. Zhu, S. Liu, O. Palchik, Y. Koltypin, and A. Gedanken. J. Solid State Chem. **153**, 342 (2000); (*c*) H. Wang, S. Xu, X.-N. Zhao, J.-J. Zhu, and X.-Q. Xin. Mater. Sci. Eng. B, **96**, 60 (2002); (*d*) M. Shao, L. Kong, Q. Li, W. Yu, and Y. Qian. Inorg. Chem. Commun. **6**, 737 (2003); (*e*) T. Ding, J.-J. Zhu, and J.-M. Hong. Mater. Lett. **57**, 4445 (2003); (*f*) P. Sreekumari Nair, T. Radhakrishnan, and N. Revaprasadu. Macromol. Symp. **193**, 227 (2003); (*g*) T. Ding, J.-R. Zhang, S. Long, and J.-J. Zhu. Microelectron. Eng. **66**, 46 (2003); (*h*) Y. Wang, Q.-S. Wu, Y.-P. Ding. J. Nanopart. Res. **6**, 253 (2004); (*i*) H. Wang and J.-J. Zhu. Ultrason. Sonochem. **11**, 293 (2004); (*j*) P. Sreekumari Nair, T. Radhakrishnan, N. Revaprasadu, G.A. Kolawole, and P. O'Brien. J. Mater. Chem. **14**, 581 (2004); (*k*) P. Sreekumari, T. Radhakrishnan, N. Revaprasadu, C.G.C.E. van Sittert, V. Djoković, and A. S. Luyt. Mater. Lett. **58**, 361 (2004); (*l*) T. Ding, J.-R. Zhang, J.-M. Hong, J.-J. Zhu, and H.-Y. Chen. J. Cryst. Growth, **260**, 527 (2004).
29. M. Kuno, K.A. Higginson, S.B. Qadri, M. Yousuf, S.H. Lee, B.L. Davis, and H. Mattoussi. J. Phys. Chem. B, **107**, 5758 (2003).
30. E.A. Turner, Y. Huang, and J.F. Corrigan. Z. Anorg. Allg. Chem. In Press.
31. (*a*) S. Wageh, L. Shu-Man, and X. Xu-Rong. Physica E, **16**, 269 (2003).
32. (*a*) G. Wang, G. Li, C. Liang, and L. Zhang. Chem. Lett. **30**, 344 (2001); (*b*) W. Zhang, C. Wang, L. Zhang, X. Zhang, X. Liu, K. Tang, and Y. Qian. J. Solid State Chem. **151**, 241 (2000).
33. A.R. West. Solid state chemistry and its applications. John Wiley & Sons Ltd., New York. 1984. p. 237.
34. (*a*) L.Z. Vegard. Phys. **5**, 17 (1921); (*b*) A.R. Denton and N.W. Ashcroft. Phys. Rev. A, **43**, 3161 (1991).
35. A. Ganguly, S. Chaudhuri, and A.K. Pal. J. Phys. D: Appl. Phys. **34,** 506 (2001).
36. (*a*) V. Kumar and T.P. Sharma. Opt. Mater. **10**, 253 (1998); (*b*) Y.P. Venkata Subbaiah and K.T. Ramakrishna Reddy. Mater. Chem. Phys. **92**, 448 (2005); (*c*) K.M.M. Abo-Hassan, M.R. Muhamad, and S. Radhakrishna. Thin Solid Films, **491**, 117 (2005); (*d*) K.M.M. Abo-Hassan, M.R. Muhamad, and S. Radhakrishna. Physica B, **358**, 256 (2005).
37. J.H. Song, E.D. Sim, K.S. Baek, S.K. Chang, J. Cryst. Growth, **214–215**, 460 (2000).
38. K.T. Ramakrishna, Y.V. Subbaiah, T.B.S. Reddy, D. Johnston, I. Forbes, and R.W. Miles. Thin Solid Films, **431–432**, 340 (2003).
39. (*a*) R.K. Kumar, G. Aravamuda, and M.R. Udupa. Phosphorus, Sulfur Silicon Relat. Elem. **114**, 39 (1996); (*b*) P. Arsenyan, K. Oberte, S. Belyakov, and E. Lukevics. Chem. Heterocycl. Compd. **40**, 503 (2004).
40. (*a*) M.A. Short and E.G. Steward. Acta Crystallogr. **8**, 733 (1955); (*b*) J.H. Zhan, X.G. Yang, W.X. Zhang, D.W. Wang, Y. Xie, and Y.T. Qian. J. Mater. Res. **15**, 629 (2000).

© 2007 NRC Canada

Electronic structures of CdSe nanocrystals — An X-ray absorption near-edge structure (XANES) investigation[1]

Jigang Zhou, Xingtai Zhou, Xuhui Sun, Michael Murphy, Franziskus Heigl, Tsun-Kong Sham, and Zhifeng Ding

Abstract: CdSe nanocrystals (NCs), capped with trioctylphosphine oxide and 1-octadecanamine, have been synthesized with colloidal methods. Both UV–vis absorption and photoluminescence spectra show that the prepared nanostructures exhibit a quantum confinement effect. X-ray absorption near–edge structure (XANES) at Se K-edge recorded in fluorescence yield mode have been carried out on these NCs, with different size and capping ligands to gain insight into how their electronic structures are affected by the NC size and chemical properties of the ligands. The results indicate that XANES are sensitive to both the NC size and the nature of the capping ligands. The whiteline intensity in XANES spectra can be related to the photoluminescence properties of these NCs.

Key words: CdSe nanocrystals, capping ligands, X-ray absorption near-edge structure, UV–vis spectroscopy, photoluminescence.

Résumé : Faisant appel à des méthodes colloïdales, on a réalisé la synthèse de nanocristaux (NC) de CdSe portant des embouts d'oxyde de trioctylphosphine et d'octadécan-1-amine. Les spectres d'absorption UV-vis et les spectres de photoluminescence montrent que les nanostructures qui ont été préparées présentent un effet de confinement quantique. On a fait appel à la méthode des structures par absorption de rayons X auprès du seuil (XANES, ("X-ray absorption near edge structure") près du seuil K du Se en mode de fluorescence pour déterminer les structures de ces NC portant divers embouts de tailles différentes afin de pouvoir déterminer l'effet de la taille des NC et des propriétés chimiques des ligands sur leurs structures électroniques. Les résultats indiquent que les spectres de type XANES sont sensibles tant à la taille du NC qu'à la nature des ligands servant d'embouts. On peut relier l'intensité de la ligne blanche des spectres de type XANES avec les propriétés de photoluminescence de ces NC.

Mots clés : nanocristaux de CdSe, ligands servant d'embout, structure par absorption de rayons X auprès du seuil, spectroscopie UV–vis, photoluminescence.

[Traduit par la Rédaction]

Introduction

Direct band gap CdSe nanocrystals (NCs) exhibit size-tunable optical properties such as blue shifts in their UV–vis absorption and photoluminescence (PL) spectra with deceasing NC size. This behavior results from the quantum confinement of excitons in the NC to dimensions smaller than the exciton Bohr radius (10 nm in CdSe)(1). The confinement alters the band structure from bulk to molecular character, resulting in the opening of the band gap and ultimately the splitting of bands into discrete energy levels. This leads to a blue shift of the absorption and PL spectra with decreasing NC size. Applications of these CdSe nanostructures in biological imaging (2), novel sensors (3), and potential light emitting devices (4, 5) are anticipated and intensively pursued. A reliable green chemical route (6, 7) was also well-developed for synthesizing free standing CdSe NCs through arresting NCs during growth by the application of capping ligands. The size-dependent optical propeties have been utilized to demonstrate quantum confinement in NCs (1), to characterize NCs,(8), and to monitor NC growth in situ. Since NCs have a very large surface to volume ratio, NC properties are extremely surface sensitive. Surface capping ligands not only halt the growth of NCs and prevent their

Received 19 April 2007. Accepted 15 June 2007. Published on the NRC Research Press Web site at canjchem.nrc.ca on 3 August 2007.

Dedicate to Professor Dr. G. Michael Bancroft for his many years of pioneering research and service in synchroton spectroscopies.

J. Zhou, X. Zhou, X. Sun, M. Murphy, F. Heigl,[2] T.-K. Sham[3], and Z. Ding.[4] Department of Chemistry, *The* University *of* Western Ontario, London, Ontario N6A 5B7, Canada.

[1]This article is part of a Special Issue dedicated to Professor G. Michael Bancroft.
[2]Present adress: CELLS-ALBA, Universitat Autònoma de Barcelona, 08193 Bellaterra, Barcelona, Spain.
[3]Corresponding author (e-mail: tsham@uwo.ca).
[4]Corresponding author (e-mail: zfding@uwo.ca).

 doi:10.1139/V07-080 © 2007 NRC Canada

aggregation, but they also play a critical role in determining the properties of NCs. For instance, hydrophobicity, photochemistry, and optical performance are all dependent on surface capping. PL is believed to be sensitive to the NC size and type of capping ligands (6), because the electronic structure of CdSe NCs is altered by the two factors mentioned.

Although the understanding of the effects of NC size and ligand type on the PL of NCs is crucial to the synthesis and manipulation of these nanomaterials, detailed information on the relationship between electronic structures and ligand–NC interaction still remains scarce because of relatively limited analysis methods.

X-ray absorption near edge structures (XANES) refers to the modulation of the atomic absorption coefficient of a core level of an atom in a specific chemical environment in the region of ~50 eV above the threshold for core electron excitation. It encompasses bound to bound, bound to quasi-bound (virtual molecular orbital, multiple scattering state), and bound to continuum transitions. The absorption coefficient across an absorption edge is a function of (*i*) the dipole transition matrix element <i|r|f> (from the initial state <i|, e.g., Se 1s to the final state |f>, e.g., states with Se 4p character), which increases abruptly at the threshold (edge) and is modulated markedly by the molecular potential around the atom and (*ii*) the density of unoccupied electronic states of appropriate symmetry above the Fermi level in metals, in the conduction band in semiconductors and insulators, and in the LUMO in molecular systems. Thus, XANES is sensitive to the unoccupied electronic densities of states and the local structure. XANES is element specific and can also be sensitive to either the surface or the bulk of the specimen depending on the edge and the detection schemes.

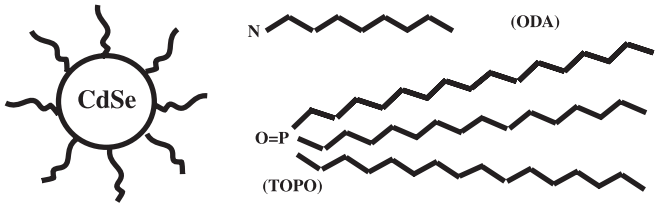
XANES has been increasingly used to study electronic structure, chemical bonding, and surface chemistry of nanostructures (9–18). However, study on free standing NCs has not yet been widely reported. In this work, we report a study on the effects of the size of NCs and the type of capping ligands on the electronic structures of CdSe NCs, using Se K-edge XANES. The electronic structures are correlated to their PL properties.

Experimental section

Synthesis of CdSe NCs

CdSe NCs capped with trioctyl phosphine oxide (TOPO) or octadecanamine (ODA) were synthesized according to procedures reported by Peng and co-workers (6,7) and Bard and co-workers (19) with a modification of the temperature for the Se precursor injection and NC growth, described in the following. Briefly, for ODA capped NCs, 5.00 g of technical grade trioctylphosphine oxide (TOPO), 5.00 g of ODA, 2.00 g of ODE, and 0.10 g of cadmium acetate hydrate were placed into a three-necked round-bottomed flask, stirred and heated to ~140 °C. After degassing with argon for approximately 1 h at this temperature, the solution in the flask was heated to 280 °C. At this temperature, the heating mantle was immediately removed and a cold Se solution (prepared by mixing 0.16 g of Se powder, 4.00 g of trioctylphosphine (TOP), and 80 μL of toluene) was quickly injected into the reaction vessel through a rubber septum. The temperature dropped to ~250 °C after the injection. With continuous stirring, the temperature dropped to ~180 °C. At this point the flask was reheated slowly to 250 °C. Aliquots were taken out of the flask at 5 min time intervals and cooled to ~50 °C with tap water bath. In this way NCs with different sizes were obtained. After addition of 10 mL of $CHCl_3$, the solution was kept in the dark. The NCs were precipitated with a copious amount of methanol and collected by centrifugation and decantation. The precipitate was then dissolved in $CHCl_3$ and re-precipitated. This cycle was repeated three times to increase purity. The product, CdSe NCs, are capped with ODA and denoted as NCs(ODA).

For TOPO-capped CdSe NCs, 12.00 g of technical grade trioctylphosphine oxide (TOPO) was used to replace the mixture of 5 g of technical grade trioctylphosphine oxide (TOPO), 5.00 g of ODA, and 2.00 g of ODE in the NCs(ODA) synthesis. The solution in the flask was heated to 330 °C. At this temperature, the heating mantle was removed immediately and a cold Se solution (prepared by mixing 0.16 g of Se powder, 4.00 g of trioctylphosphine (TOP), and 80 μL of toluene) was quickly injected into the reaction vessel through a rubber septum. The mixed solution was allowed to cool down in the ambient. The purification procedure was the same as described previously. The purified CdSe NCs capped with TOPO are denoted as NCs(TOPO). The ligand passivated NCs are illustrated in the following schematic.



UV–vis absorption and PL spectra of NCs

UV–vis absorption spectra were measured on a Cary 300 Bio spectrometer (Varian, Mississauga, Ontario). The corresponding solvents were used as references. A PTI Flourimeter QM-7/2005 set with an excitation slit width of 0.5 mm and an emission slit width of 0.3 mm was used to excite the samples at 360 nm and to record their PL spectra. A quartz cuvette with a path length of 1.00 cm was used in the UV–vis absorption and PL experiments. Samples were prepared by dispersing NCs in chloroform. The spectra were normalized to the maximum absorption in the UV–vis absorption spectra or the maximum emission peak in the PL spectra for comparison.

XANES of CdSe NCs

The specimens were prepared by depositing a NC-containing solution onto a Si wafer to form a thin film. The solvent was then evaporated. Commercial CdSe powder (Sigma-Aldrich) was pressed into a carbon tape and used as a reference. The Se K-edge XANES spectra were obtained on the PNC-XOR BM line of the Advanced Photon Source (APS). Crystal Si 111 was used as the monochromator with a resolution (FWHM) of 1.5 eV at the Se K-edge. XANES spectra were recorded in X-ray fluorescence yield (FLY) mode using a multichannel solid-state detector (Canberra 12 element Ge solid state detector). A Rh-coated planar har-

© 2007 NRC Canada

monic rejection mirror was used to minimize this contribution of harmonics. Since FLY is collected over a thin sample and the count rate was kept below 50 000 cps/detector element to keep dead time below 10%, the nonlinearities from the detector are negligible. Data were then normalized to the incident photon flux. The incident was recorded by an ionization chamber. After background correction, the spectra at the Se K-edge are normalized to the edge jump, the difference in absorption coefficient just below and at a flat region above the edge (12 710 eV) for quantitative comparison.

Results and discussions

UV–vis and photoluminescence spectroscopy

Figures 1 and 2 show the UV–vis absorption and PL spectra for the purified NCs(TOPO) (dashed line) and NCs(ODA) (solid line) of different sizes, respectively. It should be noted that the absorption peak in the UV–vis spectroscopy and the luminescent peak in the PL spectroscopy are associated with the electronic transition between the conduction band and the valence band. The peak positions can be therefore correlated to the energy separation of the band gap, since quantum confinement effect manifests itself in opening the CdSe NC band gap as the size of the NC decreases. According to the first UV–vis absorption peak position, the size of CdSe NC can be determined using previously established size calibration curves (1, 7). The NC diameters were then estimated from the first absorption peak wavelengths to be 2.3, 2.5, and 2.9 nm for NCs with the first absorption maximum at 498, 511, and 543 nm, respectively, according to sizing curves established by Peng and coworkers (8). As for the NCs(TOPO), the size is estimated to be 2.7 nm according to the first UV–vis absorption peak at 533 nm (8). It should also be noted that in situ UV–vis absorption spectra could be recorded during the synthesis and used to monitor the growth stage in terms of the size of NCs. These NCs also exhibit the size dependent emission peak wavelengths displayed in the PL spectra at longer wavelength as expected (Fig. 2). For instance, NCs(ODA) show emission maximum at 509, 543, and 578 nm corresponding to 2.3, 2.5, and 2.9 nm in diameter, respectively.

Furthermore, as previous reported (1, 6, 7, 20) the size distribution for one batch of NCs can be revealed from the full width at half-maximum (FWHM) in the PL spectrum, since the spectrum is a collective result contributed by individual NCs. The emission peaks in NCs(ODA) are very sharp. The FWHM for NCs with diameter of 2.3, 2.5, and 2.9 nm was only 73, 100, and 111 meV, respectively, which indicates that the size distribution was narrow and the deviation should be less than 10% for all batches. The evolution of size distribution during the growth process reported here is in good agreement with literature (7). The PL FWHM in NCs(TOPO) is 147 meV, indicating that the size distribution is slightly wider than that in NCs(ODA). Additionally, all PL spectra have a nonzero tail in the long wavelength region. This can be best seen in the spectrum of NCs(TOPO) and 2.3 nm NCs(ODA). This means that all samples have emission allowed surface defect related states. It has been extensively reported that primary amine (20), for instance ODA, can provide stronger surface passivation in NCs than TOPO. Thus, surface states that trap electrons, hence reduce

Fig. 1. UV–vis absorption spectra of the CdSe NCs dispersed in chloroform. The dashed line represents TOPO-capped CdSe NCs. The size is estimated to be 2.7 nm. Solid lines correspond to ODA-capped CdSe NCs. The sizes are estimated to be 2.3, 2.5, and 2.9 nm from left to right.

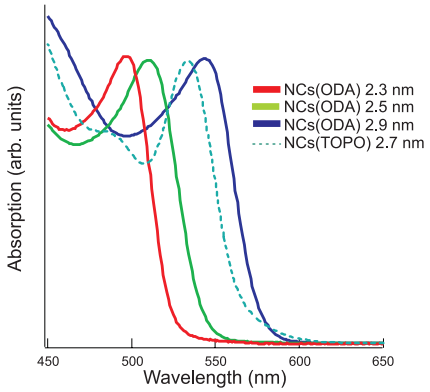
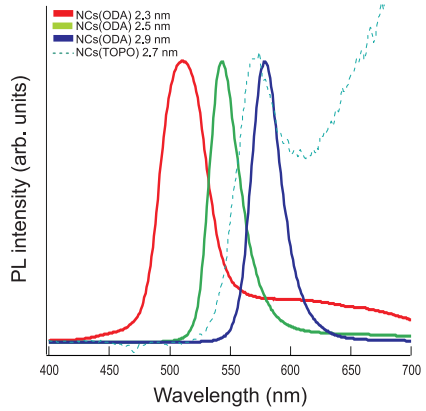


Fig. 2. PL spectra of the CdSe NCs dispersed in chloroform. The dashed line represents TOPO-capped CdSe NCs. Solid lines correspond to ODA-capped CdSe NCs as described in Fig. 1.

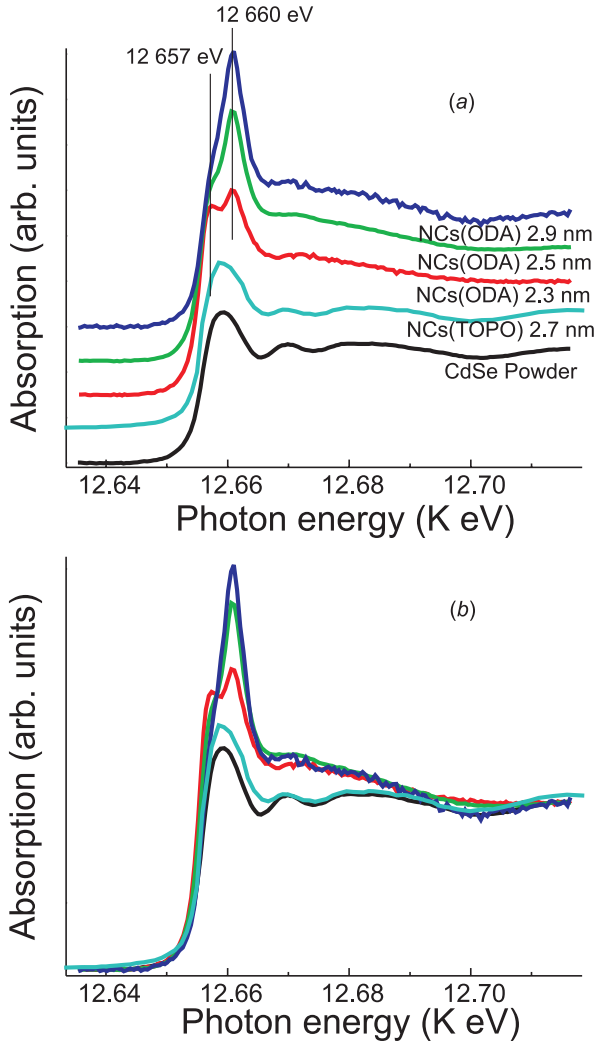


light emission, are quenched more significantly in NCs(ODA) than in NCs(TOPO). Consequently, NCs(ODA) exhibit much higher PL quantum yield than NCs(TOPO). This phenomenon can be understood considering the electron donation ability and structure effect of capping ligands. The amine group in ODA is a considerably better electron donor than the P=O group in TOPO. The linear structure in ODA also facilitates its passivation ability on the targeted NCs.

Interestingly, in contrast to the above generalization we observed that the relative surface states related emission from NCs(TOPO) is much stronger than in the similar-sized NCs(ODA), indicating that emission allowed surface defect related states, rather than traps, in NCs(TOPO) are more pronounced than those in NCs(ODA). Furthermore, the emission allowed surface defect related states in NCs(TOPO) are even more pronounced than in smaller-sized NCs(ODA), as seen in the PL spectra. All of these results allow us to propose that the strong amine–NC interaction induced surface reconstruction in NCs(TOPO) is very different

© 2007 NRC Canada

Fig. 3. (*a*) Se K-edge XANES recorded in FLY modes for the CdSe powder, TOPO-capped CdSe NCs, and ODA-capped CdSe NCs (arranged by increasing the size from bottom to top). (*b*) Whiteline features compared in Se K-edge XANES recorded in FLY modes for the CdSe powder, TOPO-capped CdSe NCs, and ODA-capped CdSe NCs (arranged by increasing the size from bottom to top).



from that in NCs(ODA). This aspect will be addressed in the following section.

XANES spectroscopy

The Se K-edge XANES spectra of the NCs(ODA), NCs(TOPO), and CdSe powder are shown in Fig. 3. The photon energy is calibrated to the Se 1s to 4p transition of a Se film at 12 658 eV. The most noticeable feature is the identical appearance of the XANES for NCs(TOPO) and bulk CdSe confirming that the NC is crystalline and has the same Wurzite structure (18) as that of bulk CdSe. Se K-edge XANES probes the densities of unoccupied states of primarily Se 4p character as well as crystal structure, The 1s 4p dipole transition at the threshold often results in a sharp absorption peak known as the whiteline. The rising edge and the area under the whiteline are related to the formal charge at the Se site and the densities of states of 4p holes in the Se conduction band, respectively. Multiple scattering resonance features up to 50 eV beyond the whiteline are characteristic of the immediate vicinity of the absorbing atom in the crystal (12).

The Se K-edge XANES spectra of the NCs(ODA) are noticeably different from those of CdSe powder and NCs(TOPO). We can see from Fig. 3*a* that replacing the TOPO capping liagnd (weakly bonded P=O based ligand) with the ODA capping ligand (a strongly bonded amine based ligand) shifts the Se K-edge whiteline maximum to higher energy by 2 eV and exhibits more features. This result illustrates the chemical sensitivity of XANES. Close examination reveals that the whiteline splits into two bands at 12 657 and 12 660 eV. This is noticeably different from the single band seen in bulk CdSe and NCs(TOPO). We attribute the whiteline splitting in the XANES spectra to contributions from the surface and core of the NCs induced by strong ligand NC interaction.

Before we proceed further, let us consider for the moment how a ligand interacts with the surface of a CdSe NC, which contains both Cd and Se ions, and the fraction of atoms on the surface (21). In our preparation, although the synthesis of CdSe NCs is performed in a Se-rich environment (the molar ratio of Se to Cd in the precursor is about 10), the ligand–CdSe surface interaction is believed to favour the O-Cd (in TOPO-capped NCs) or the N-Cd (in ODA-capped NCs). As for the surface to bulk atom ratio in the NC, it has been estimated that approximately 1/3 of the atoms are on the surface for a ~3 nm NC.

We now return to the splitting of the whiteline in CdSe(ODA). We attribute the 12 657 and the 12 660 eV peak to surface and core contributions (henceforth denoted S and C), respectively. These assignments are based on the observation that the surface peak decreases in intensity as the size of the NC increases (surface to bulk atom ratio decreases); this is accompanied by the increase in the intensity of peak C. We envision that the strong amine–NC interaction screens the Cd^{2+} ion, considerably reducing its formal oxidation state. Charge neutrality requires corresponding charge depletion at the Se^{2-} site of the NC, giving rise to a 1s-4p shift (peak C) to higher energy. The shift of the surface peak S to lower energy results from amine–Se interaction on the surface. Finally the oscillation beyond 12 680 eV is blurred in NCs(ODA) compared with that in NCs(TOPO). Since it is well-documented (6) that the crystalline characteristic of NCs(ODA) is the same as that of NCs(TOPO), which favored the Wurzite structure, this feature must be also related to the surface reconstruction in NCs(ODA), resulting in a shell that is substantially different from the core, which maintains the crystal structure of bulk CdSe.

A close examination of the whitelines shown in Fig. 3*b* reveals an obvious increase in intensity in the CdSe NCs relative to that of CdSe powder. This is interesting since a more intense whiteline hints at a higher unoccupied density of states (DOS) of 4 p character in the conduction bands. Assuming no countervailing selection rule arguments (reasonable for a randomly oriented NC system), the more intense whiteline in Pt L_3 or M_3 edge is often observed and expected in Pt nanoparticles (PtNPs) supported on nano Si substrates relative to that of bulk Pt, which is due to PtNP–Si oxide interactions that withdraw d charges from Pt (16). The reduc-

© 2007 NRC Canada

tion of DOS of p character in Pt NPs-CNTs relative to that of CNTs has also been reported (22), which provided the evidence that charge redistribution transfer between the environment, the Pt NPs, to C 2p-derived states has occurred. Since the present system does not favor such charge redistribution between NCs and the environment, the intensity variation trend must relate to amine–NC interaction-induced rehybridization of Se s, p, and even d orbitals such that Se loses p charge in these amine-capped NCs. This observation is of considerable interest, although more details await further experimental and theoretical investigations.

The DOS increases from CdSe powder to NCs(TOPO), and NCs(ODA) may be explored further in connection with the intensity of the luminescence. It was reported that the PL quantum yield increased with the size of NCs until the diameter of NCs reached 3.3 nm, then the PL quantum yield decreased as the size of NCs increased during growth of the NCs (6). The size of NCs(ODA) in the present research are smaller than 3.3 nm, so the PL quantum yield for these NCs should increase with size. Therefore the PL quantum yield in those samples should increase from CdSe powder to NCs(TOPO) and then to NCs(ODA). The increase of PL quantum yield follows the same trend in the DOS increase. Our results indicate that surface state emission (PL) from NCs(TOPO) is the strongest, followed by the smallest NCs(ODA), then the large NCs(ODA). This trend also corelates with the DOS variation trend. It should be noticed, however, that this trend should be used with caution since we have taken into account the effect of both size and surface chemistry.

In conclusion, we have synthesized CdSe NCs capped with ODA or TOPO with controlled size. The UV–vis absorption and PL were used to characterize the NCs in terms of size and optical properties. XANES spectra at the Se K-edge were performed to probe the electronic structure, which is found to be dependent on capping ligand and size. This appears to be an emerging phenomenon of NCs with interesting implications (23). A correlation between the whiteline intensity in the XANES spectra and the optical emission intensity was observed. Finally, we have demonstrated that XANES is a very valuable tool to explore the surface and size effects on the electronic structure of CdSe NCs and have anticipated that XANES will be widely used in the characterization of nano systems.

Acknowledgements

This work was supported by the Natural Science and Engineering Research Council of Canada (NSERC), Canadian Research Chair (TKS), Canada Foundation for Innovation, Ontario Innovation Trust, Ontario Photonics Consortium (ZFD), the Premier's Research Excellence Award (ZFD), and *The* University *of* Western Ontario. Work at the PNC-CAT BM line of the Advanced Photon Source (APS) was supported by the US Department of Energy, Office of Basic Sciences, under contract No. W-31–109-ENG-38 and a MFA grant from NSERC.

References

1. C.B. Murray, D.J. Norris, and M.G. Bawendi. J. Am. Chem. Soc. **115**, 8706 (1993).
2. A. Fu, W. Gu, B. Boussert, K. Koski, D. Gerion, L. Manna, M. Le Gros, C.A. Larabell, and A. P. Alivisatos. Nano Lett. **7**, 179 (2007).
3. R.C. Somers, M.G. Bawendi, and D.G. Nocera. Chem. Soc. Rev. **36**, 579 (2007).
4. A.J. Bard, Z. Ding, and N. Myung. *In* Structure and bonding. Vol. 118. Springer, Berlin, Germany. 2005. p. 1.
5. J. Zhou, J. Zhu, and Z. Ding. Proc. Electrochem. Soc. **2005–04**, 129 (2005).
6. L. Qu and X. Peng, J. Am. Chem. Soc. **124**, 2049 (2002).
7. J.J. Li, Y.A. Wang, W. Guo, J.C. Keay, T.D. Mishima, M.B. Johnson, and X. Peng. J. Am. Chem. Soc. **125**, 12567 (2003).
8. W.W. Yu, L. Qu, W. Guo, and X. Peng. Chem. Mater. **15**, 2854 (2003).
9. Y.H. Tang, T.K. Sham, Y.F. Hu, C.S. Lee, and S.T. Lee. Chem. Phys. Lett. **366**, 636 (2002).
10. H.M. Tsai, P.D. Babu, C.W. Pao, J.W. Chiou, J.C. Jan, K.P.K. Kumar, F.Z. Chien, W.F. Pong, M.H. Tsai, C.H. Chen, L.Y. Jang, J.F. Lee, R.S. Chen, Y.S. Huang, and D.S. Tsai. Appl. Phys. Lett. **90**, 042108/1 (2007).
11. Y.H. Tang, P. Zhang, P.S. Kim, T.K. Sham, Y.F. Hu, X.H. Sun, N.B. Wong, M.K. Fung, Y. F. Zheng, C.S. Lee, and S.T. Lee. Appl. Phys. Lett. **79**, 3773 (2001).
12. T.K. Sham, S.J. Naftel, I. Coulthard. J. Appl. Phys. **79**, 7134 (1996).
13. C.W. Pao, P.D. Babu, H.M. Tsai, J.W. Chiou, S.C. Ray, S.C. Yang, F.Z. Chien, W.F. Pong, M.H. Tsai, C.W. Hsu, L.C. Chen, C.C. Chen, K.H. Chen, H.J. Lin, J.F. Lee, and J.H. Guo. Appl. Phys. Lett. **88**, 223113/1 (2006).
14. J.W. Chiou, J.C. Jan, H.M. Tsai, W.F. Pong, M.H. Tsai, I.H. Hong, R. Klauser, J.F. Lee, C.W. Hsu, H.M. Lin, C.C. Chen, C.H. Shen, L.C. Chen, and K.H. Chen. Appl. Phys. Lett. **82**, 3949 (2003).
15. J.W. Chiou, K.P.K. Kumar, J.C. Jan, H.M. Tsai, C.W. Bao, W.F. Pong, F.Z. Chien, M.H. Tsai, I.H. Hong, R. Klauser, J.F. Lee, J.J. Wu, and S.C. Liu. Appl. Phys. Lett. **85**, 3220 (2004).
16. I. Coulthard and T.K. Sham. Solid State Commun. **105**, 751 (1998).
17. H. Dollefeld, C. McGinley, S. Almousalami, T. Moller, H. Weller, and A. Eychmuller. J. Chem. Phys. **117**, 8953 (2002).
18. P. Zhang, X. Zhou, Y. Tang, and T.K. Sham. Langmuir, **21**, 8502 (2005).
19. N. Myung, Z. Ding, and A.J. Bard. Nano Lett. **2**, 1315 (2002).
20. D.V. Talapin, A.L. Rogach, A. Kornowski, M. Haase, and H. Weller. Nano Lett. **1**, 207 (2001).
21. M.A. El-Sayed. Acc. Chem. Res. **37**, 326 (2004).
22. J. Zhou, X. Zhou, X. Sun, R. Li, M. Murphy, Z. Ding, X. Sun, and T.-K. Sham. Chem. Phys. Lett. **437**, 229 (2007).
23. P. Zhang and T.K. Sham. Phys. Rev. Lett. **90**, 245502 (2003).

© 2007 NRC Canada

High-resolution XANES S $L_{3,2}$ edge spectra collected from a series of iron-bearing sphalerite(Zn,Fe)S minerals[1]

Allen Pratt, Lucia Zuin, Y. Mui Yiu, and Sarah Harmer

Abstract: High-resolution S $L_{3,2}$-edge XANES spectra have been collected from a series of high-quality sphalerite samples. Each of the sphalerite samples examined has a characteristic iron concentration, and the range is from <0.01 to 14.79 wt% Fe. The structures of the S $L_{3,2}$-edges are investigated by comparing ab initio calculated spectra with experimentally measured S $L_{3,2}$-edge spectra collected from synthetic ZnS sphalerite. The theoretical and experimental data provide evidence that S 2p electron transitions to empty S 3s and S 3d states can occur across an energy range above the absorption edge. A chemical shift, associated with iron to sulphur bonds, is identified, and for the first time, a pre-edge feature associated with S–Fe bonding in sphalerite is observed.

Key words: XANES, zincblende, sphalerite, characteristic iron content, S L-edge structure, ab initio calculated spectra, density of states, pre-edge peak.

Résumé : On a mesuré les spectres d'absorption synchrotron à haute résolution de type « XANES » près du seuil $L_{3,2}$ d'une série d'échantillons d'excellente qualité de sphalérite. Chacun des échantillons de sphalérite examiné comporte une concentration caractéristique de fer qui se situe entre < 0,01% à 14,7% en poids de fer. On a étudié la structure des seuils $L_{3,2}$ des spectres synchrotron par comparaison de spectres calculés par une méthode ab initio avec les spectres d'absorption synchrotron près du seuil $L_{3,2}$ mesurés expérimentalement avec une sphalérite ZnS de synthèse. Les données théoriques et expérimentales permettent de montrer que les transitions synchrotron des électrons 2p vers les états synchrotrons vides 3s et 3d se produisent à travers une plage d'énergie qui est supérieure au seuil d'absorption. On a identifié le déplacement chimique qui est associé aux liaisons fer-soufre et on a observé pour la première fois la caractéristique pré-seuil associée à la liaison S–Fe de la sphalérite.

Mots-clés : « XANES », zincblende, sphalérite, contenu en fer caractéristique, structure synchrotron au seuil L, spectres calculés par des méthodes théoriques ab initio, pic pré-seuil.

[Traduit par la Rédaction]

Introduction

The results and interpretations presented in this study build on the foundational work conducted by Professor Bancroft's group on metal sulphides using the Canadian Synchrotron Radiation Facility (CSRF) Grasshopper beamline on the Aladdin Storage Ring (1*a*, 1*b*, 2, 3, 4). The focus mineral sulphide for this study is sphalerite, (Zn,Fe)S. Understanding sphalerite mineral chemistry is important because it is the primary source for virtually all of the world's zinc production. Over 7 000 000 tonnes of zinc each year originate from sulphide ores in which sphalerite (Zn,Fe)S is the dominant zinc mineral (5). The purpose of this study is to build on the work conducted previously by Professor Bancroft's group and use the high-resolution capabilities of the recently commissioned VLS-PGM beamline at the Canadian Light Source to investigate the fine structure in the S $L_{3,2}$-edge collected from a series of iron-bearing sphalerite samples. In this work, we interpret the experimental results through comparison with theoretical results obtained using ab initio modeling. The S $L_{3,2}$-edge was chosen to investigate because it has fine structures that are not found in the S K-edge (1*b*).

Sphalerite is in the cubic crystal system. Well-formed individual specimens commonly occur, and when found in natural settings, the most common crystal shape is the tetrahedron (6). The structure of sphalerite is similar to that of diamond with one half of the C atoms replaced by Zn and the other half by S. The Zn is tetrahedrally coordinated by four S atoms, and S is tetrahedrally coordinated by four Zn

Received 28 March 2007. Accepted 14 June 2007. Published on the NRC Research Press Web site at canjchem.nrc.ca on 3 August 2007.

A. Pratt.[2] CANMET Mining and Mineral Sciences Laboratories, Natural Resources Canada, 555 Booth Street, Ottawa, ON K1A 0G1, Canada.
L. Zuin. Canadian Light Source Incorporated, University of Saskatchewan, 101 Perimeter Road, Saskatoon, Saskatchewan S7N 0X4, Canada.
Y.M. Yiu. Department of Chemistry, The University of Western Ontario, London, Ontario N6A 5B7, Canada.
S. Harmer. Ian Wark Research Institute, The University of South Australia, Mawson Lakes, Adelaide, South Australia 5095, Australia.

[1]This article is part of a Special Issue dedicated to Professor G. Michael Bancroft.

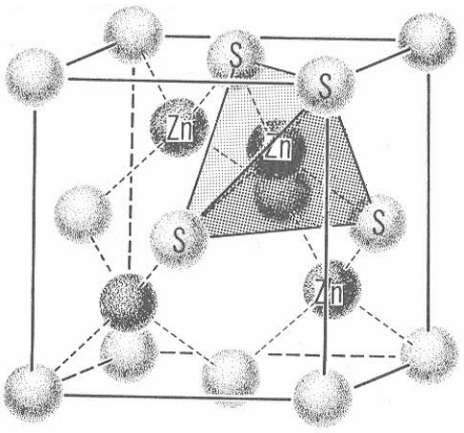
[2]Corresponding author (e-mail: Allen.Pratt@NRCan.gc.ca).

 doi:10.1139/V07-072 © 2007 NRC Canada

atoms (7). Atoms in the sphalerite structure, it is also known as the zincblende structure, form tetrahedrally distributed orbitals of the hybrid sp^3 (8). The sphalerite structure is characterized by two interpenetrating face-centered cubic lattices, with the sulphur atoms being centered on the points of one lattice and zinc atoms on the other (Fig. 1) (7). Sphalerite nearly always contains Fe, substituting in part for Zn. The maximum iron content is about 26 wt%. The iron-rich varieties above 10 wt% Fe are referred to as marmatite, and the most iron-rich varieties are referred to as christophite (6).

In this research, X-ray absorption near-edge structure (XANES) S $L_{3,2}$-edge spectra, collected from a series of sphalerite specimens, are investigated through comparison with the theoretical S $L_{3,2}$-edge of ZnS sphalerite. The characteristic feature of each sphalerite specimen is its respective iron concentration. In this work, sphalerite iron concentrations range from <0.01 to 14.79 wt% Fe.

Fig. 1. Line drawing of sphalerite showing Zn and S coordination and the two characteristic interpenetrating face-centered cubic lattices; sulphur atoms are centered on the points of one lattice and zinc atoms on the other lattice. After Bloss (7).



Methods

XANES spectra were collected from a series of sphalerite samples that each had a characteristic iron concentration. Large crystals and coarse cleavages of sphalerite from Nacia, Chihuahua, Mexico (14.79 wt% Fe); Montaubon, Quebec, Canada (8.14 wt% Fe); Oklahoma, USA (0.19 wt% Fe); and a synthetic specimen (<0.01 wt% Fe) were used in these experiments. Mineralogical examination showed that all the samples were >98% sphalerite. Impurities were largely carbonate minerals and the sulphide mineral species, pyrite and chalcopyrite. Detailed characterizations of the materials used in this work are provided in Dutrizac et al. (5). For this work, small fragments of material were broken from each sphalerite sample. The fragments were examined with a hand lens and a stereo microscope to determine purity. Fragments with traces of other minerals were discarded.

The hand-picked mineral fragments were prepared for XANES analyses by further grinding the samples into a fine powder in an alumina mortar and pestle. Immediately following grinding, the powder was mounted to a metal disc with double-sided carbon tape and placed into the load lock of the XANES analytical chamber. Exposure to air was about 1 min.

Sulphur $L_{3,2}$-edge XANES spectra were collected using the recently commissioned VLS-PGM beamline (9, 10) at the Canadian Light Source (CLS), University of Saskatchewan. The VLS-PGM beamline is Canada's replacement for the CSRF Grasshopper beamline at Aladdin. Three variable line-spacing plane gratings cover the photon energy region 5.2–250 eV. For this work, we used the high-energy grating, 98–250 eV, and 100 μm entrance and 100 μm exit slits. At the time these experiments were conducted, the beamline resolution for 100 μm slits was unknown. For 50 μm slits, the resolution was 117 meV. The resolution was determined from gas-phase measurements made at the Ar L-edge (10). Spectra were collected at room temperature simultaneously in fluorescence yield (FY) and total electron yield (TEY) modes. Detailed information on the detection system is provided in Kasrai et al. (1*a*). Only FY spectra are shown. FY detection was chosen for two reasons: (*i*) FY is the XANES L-edge data collection method with the highest spectral resolution (1*a*); (*ii*) the FY sampling depth is near 100 nm (1*b*), making the FY data collected more bulk-sensitive than surface-sensitive, and this allows for flexibility in the sample preparation. The S L-edge spectra were collected by monitoring the fluorescence yield using a microchannel plate (MCP) detector (1*a*). All the spectra were normalized with respect to the incident photon flux (I_0). I_0 was simultaneously recorded with the FY by monitoring the current emitted from a nickel mesh located downstream from the last refocusing mirror. The spectra presented here are the sum of five scans. The energy scale was calibrated using the four sharp peaks at 162.4, 163.5, 168, and 169.3 (±0.1) eV in the L-edge spectrum for pyrite (1*b*).

In this work, the theoretical structure of the S $L_{3,2}$-edge for ZnS sphalerite is determined using ab initio calculations. Comprehensive and complete details on the calculation are provided in Yiu et al. (11). Briefly, we have used the full potential linearized augmented plane wave (LAPW) method (11), based on the density functional theory (DFT) (12) with generalized gradient approximation (GGA) (13), to calculate the electronic structure of ZnS sphalerite. ZnS in general has four crystal structures, B1 (rocksalt) (14), B2 (CsCl structure) (15), B3 (zincblende structure), and B4 (Wurtzite) structures (16). The naturally occurring crystal, sphalerite, has the zincblende structure with space group $F\bar{4}3m$. It has cubic face-centred lattice with Zn at (0,0,0) and S at (1/4,1/4,1/4), and a lattice constant of 5.41 Å. The B1 and B2 structures of ZnS crystals are the high-pressure phases of these crystals. We model the sphalerite crystals where Zn and S atoms are quenched at the perfect crystal sites of the zincblende structure as shown in Fig. 1 with spatial symmetry of $F\bar{4}3m$. The eigen-states of these ZnS crystal systems have been evaluated self-consistently employing the Wien code (17). Ten thousand k points have been used in the calculation of the irreducible wedge of the Brillouin zone. The XANES spectra are determined using Fermi's golden rule and dipole matrix elements convoluted by the life-time and instrumentation broadenings.

The LAPW method is one of the most-accurate methods for performing electronic-structure calculations for crystals.

© 2007 NRC Canada

The LAPW method is a procedure for solving the Konh–Sham equations for the ground-state density and total energy of a many-electron system. The many-body system consists of non-overlapping atomic spheres and an interstitial region. The eigen function of the atomic sphere is a linear combination of the radial wave function and the spherical harmonics. In the interstitial region, the eigen function consists of plane wave expansions. Core states are treated fully relativistically.

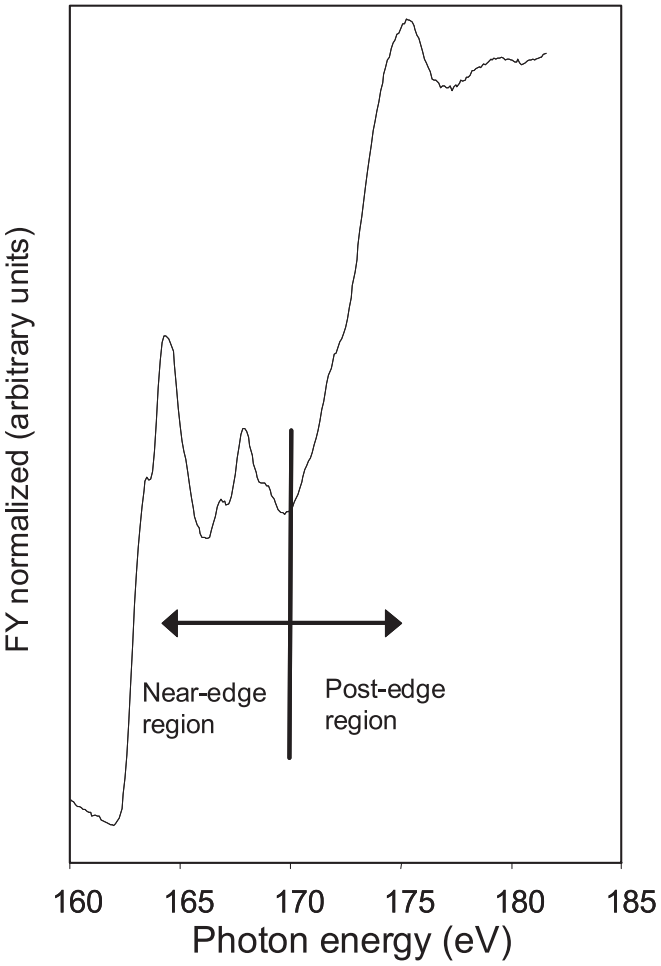
Results and discussion

The S $L_{3,2}$-edge XANES spectrum collected from a synthetic sphalerite sample is shown in Fig. 2. The S L-edge for sphalerite begins at 162.0 eV, and from the leading edge to about 170.0 eV, the XANES spectrum is made up of a series of sharp, well-defined peaks. Beyond 170.0 eV, there is a marked increase in background, and peak structures become diffuse. This dataset nicely shows that an S $L_{3,2}$-edge XANES spectrum can be divided into two basic regions: (*i*) the near-edge region and (*ii*) the post-edge region. The near-edge region is usually found in the first 15 eV above the onset position for absorption; the post-edge region is usually found 15 eV to about 50 eV above the initial absorption position (18). The near-edge region is sensitive to chemical shifts and has fine structure that is due to transitions to unoccupied electron orbitals in the conduction band (3, 4). The XANES post-edge region is sensitive via the multiple scattering of photons to the geometrical arrangement surrounding the absorbing atom (1*b*). Structures in the post-edge region are usually broad and not very well resolved. Following on the example set by Li et al. (2), the division between near- and post-edge regions for sphalerite S $L_{3,2}$-edge spectra is taken at 170 eV.

For all the spectra collected in this study, the post-edge features are very similar, in both position and intensity. This is expected because all the samples have the same crystal structure and tetrahedral coordination of sulphur. In all the spectra collected, there were no features in the post-edge region that could be attributed to oxidized sulphur species, such as sulphite or sulphate. This result shows that the FY XANES spectra examined in this study are representative of fresh sphalerite. Beam damage is not suspected in the data that were collected. No noticeable changes in the spectra were observed during acquisition, and spectra that were collected during two separate beamtime sessions match one another remarkably well.

The S $L_{3,2}$-near-edge XANES spectra acquired from the different sphalerite specimens examined are shown in Fig. 3. Sulphur in all the samples examined is in four-fold coordination, and the electronic configuration is fully occupied, $1s^2 2s^2 2p^6 3s^2 3p^4$ (8). The structure in the near-edge of the S $L_{3,2}$-edge XANES spectra is related to the electronic structure of the conduction band (4, 19, 20). The ab initio calculated S $L_{3,2}$-edges for ZnS sphalerite are shown in Figs. 4 and 5. The theoretical spectra were calculated using the density of states (DOS) for Zn and S in the zincblende structure. The calculated DOS data for sulphur are shown in Fig. 6. The theoretical S L-edge is constructed using L_3 and L_2 line separation of 1.1 eV (4) and an area ratio of 1:1. The calculated spectra as shown do not have a background, whereas the experimental spectra contain background contributions.

Fig. 2. Sulphur L-edge XANES of synthetic sphalerite.

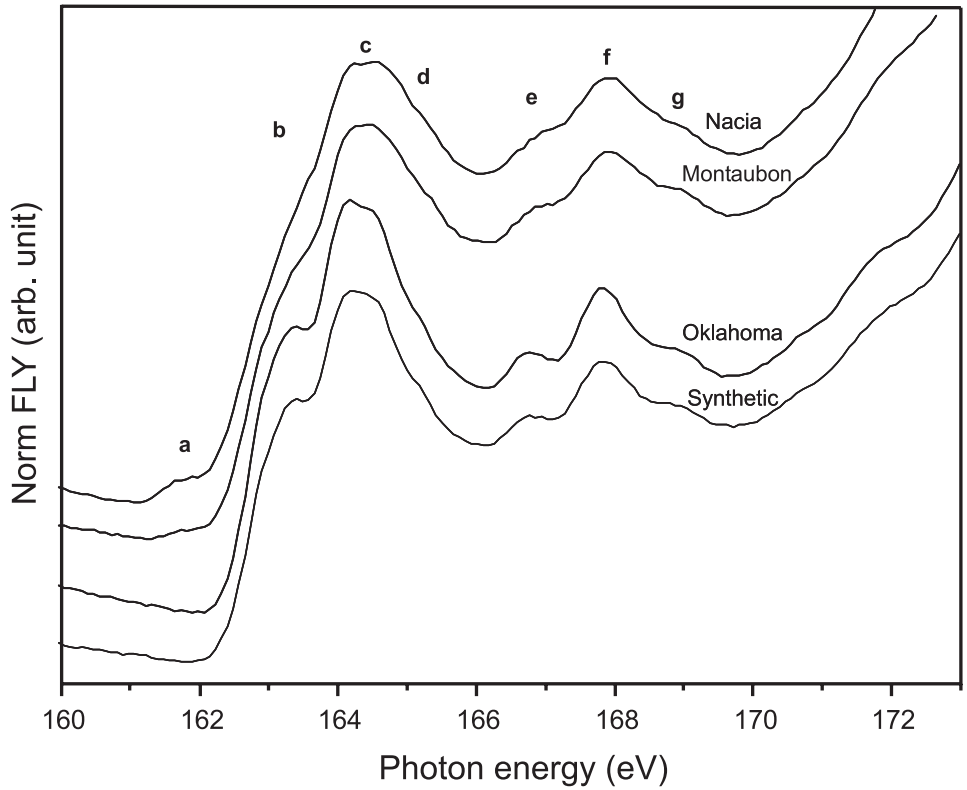


The XANES edge in Fig. 4 was calculated with an intrinsic line broadening of 0.1 eV. Comparison with the experimental data for synthetic sphalerite shows remarkable agreement with regard to individual peak positions. The experimental XANES is however significantly broader than the calculated spectrum. This is in part due to self-absorption and vibrational broadening. The data were collected using FY mode on a relatively concentrated sample, and some self-absorption is expected to occur and broaden the resonance. Limitations in instrument resolution and signal processing electronics also will contribute to line broadening. Broadening will also occur as the lifetime of the core hole increases as a function of increasing photon energy. The calculations do not account for this phenomena; however, for this dataset, the change in photon energy is so small that broadening related to photon-energy-dependent core-hole lifetimes will not be significant.

To account for the broadening influences, a spectrum with a line broadening of 1.0 eV is calculated. Comparison of this calculated spectrum with the measured spectrum shows very reasonable agreement in the XANES structure. (Fig. 5). Most notable are the improvements in agreement in edge structure between experimental and theoretical data on the main-peak slopes near 163 eV and 165 eV (Fig 5, labels b

© 2007 NRC Canada

Fig. 3. Sulphur L-edge XANES of sphalerite samples from Nacia, Chihuahua, Mexico (14.79 wt% Fe); Montaubon, Quebec, Canada (8.14 wt% Fe); Oklahoma, USA (0.19 wt% Fe); and a synthetic specimen (<0.01 wt% Fe).



and d). There is also a considerable improvement in the structure of the two edges between 166 eV and 170 eV (Fig. 5).

We should point out that there is a limitation on the density functional theory. DFT tends to underestimate band gaps of semi-conductors, since it assumes that electron distributions have no singularity inside the crystals. By adding GGA, it corrects its limitation to a certain extent. From the density of state results as indicated in Fig. 6 with GGA, the calculated band gap of the ZnS crystal is 2.09 eV, whereas the experimental band gap is 3.70 eV (21). The ZnS crystals are one of the wide band gap materials.

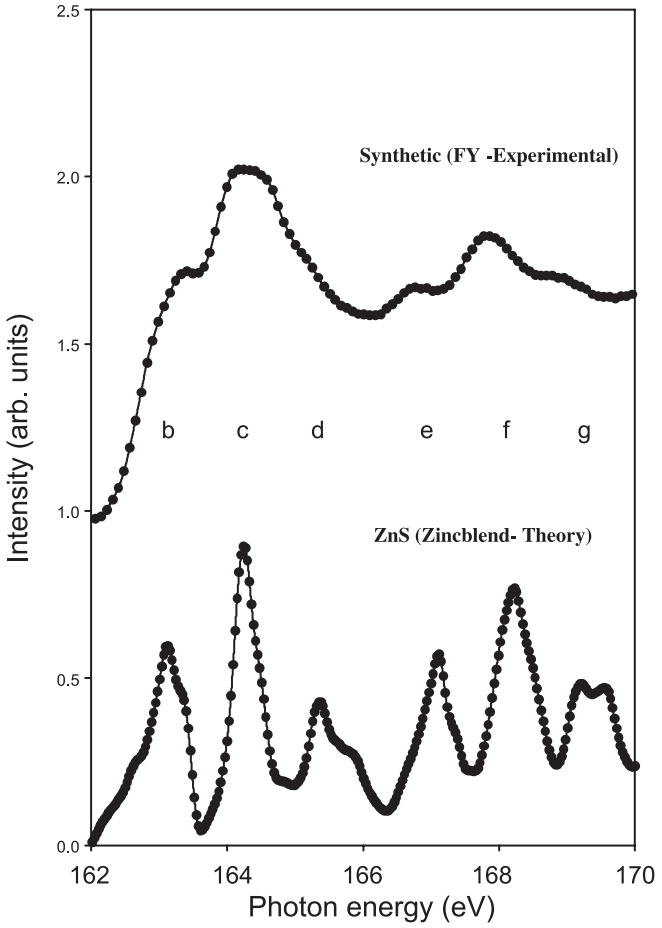
The theoretical absorption edge is made up of six distinct peaks. These peaks are identified with the labels b, c, d, e, and f in Figs. 4 and 5. Each of these peaks has a unique structure, and this structure is due to the overlap and mixing of the L_3 and L_2 edges within each of the peaks. There is one exception, and it is the leading peak in the edge near 163 eV (label b). This peak is exclusively made up of contributions from the L_3 edge. The sharp peak identified by the label c is where the L_2 edge emerges. This peak contains contributions from the L_3 edge as well.

The S 2p electron transitions that contribute to S L-edge of sphalerite can be understood by comparing the calculated density of states, the theoretical, and experimental S $L_{3,2}$-edges. The electrical dipole transitions as modeled for the L_3- and L_2-edges only allow for ΔL (angular momentum quantum number) = ±1. The S L_3 absorption edge is from $2p_{3/2}$ electron transitions to the unoccupied states of d or s, and the L_2 absorption edge results from $2p_{1/2}$ electron transitions to the unoccupied states of d or s. Examination of the positions and intensities of the first DOS peaks near 3.3 eV above the Fermi level (Fig. 6) for S s and S d show S 2p electrons undergo transitions to both states (Fig. 6). Comparison of the DOS peak intensities for S s and S d shows that, at the initiation of absorption, it is the S 2p electron transitions to empty S 3s states that dominate. As the energy difference from the edge is increased, an increase in the S 2p electron transitions to empty S 3d states is observed. At 4.6 eV above the Fermi level, the DOS peaks for S s and S d have near equal intensities. From this point toward higher energies, the DOS data show that transitions to both empty S 3s and S 3d states occur, but it is the transitions to empty S 3d states that are dominant. These results show that S 2p electron transitions to empty S 3s and S 3d states occur across an energy range above the absorption edge.

With increased ferrous iron content, there is an increase in the broadness of the individual absorption contributions in the experimental XANES spectra (Fig. 3). The broadening is systematic and suggests that there is a chemical shift in line positions for S transitions that result from S atoms that are bonded with iron atoms. The broadening of the spectra as Fe content increases shows that the line positions for electron transitions associated with S atoms bonded with iron atoms occur at slightly different energies than the electron transitions that occur when S is bonded with Zn in the zincblende structure. For the Oklahoma sample (0.19 wt% Fe), the broadening is manifested by the decreased resolution of the peak at 163.3 eV. For the Montaubon sphalerite (8.14 wt% Fe), the broadening has been expanded to include the peaks at higher energies (labeled e, f, and g in Fig. 3). In the Nacia sample, which has the highest iron content (14.79 wt% Fe),

© 2007 NRC Canada

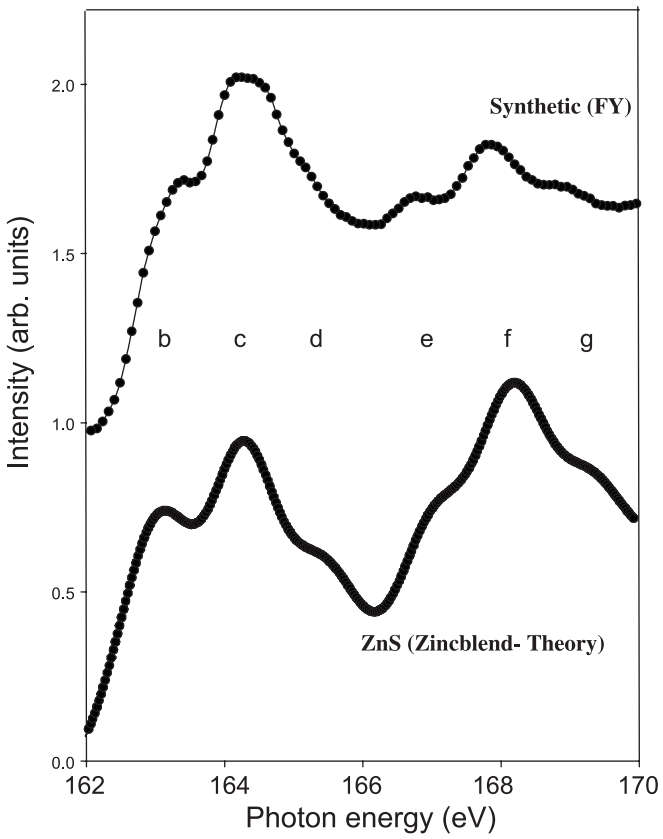
Fig. 4. Ab initio calculated L_3- and L_2-edges for ZnS sphalerite. For the theoretical spectrum, the line broadening was the natural linewidth of 0.1 eV. Peaks in the theoretical and experimental spectra are identified with the lowercase letters.



broadening from electron transitions related to Fe–S bonds has progressed to the extent that "all" individual edge contributions have become diffuse.

Examination of the XANES spectra collected from the sphalerite samples shows that the S L-edge data for the Montaubon and Nacia sphalerite contain a peak at the toe of the edge at 161.7 eV. This low-energy peak has a weak intensity, and it is identified with the label (a) in Fig 3. This peak is in the pre-edge region of the data, and this is the first time that a pre-edge peak has been observed for sphalerite. The peak is only observed in the sphalerite varieties with considerable iron concentrations, and empirically this suggests that it is associated with Fe–S bonding in sphalerite. It may be that the peak is simply the beginning of the L_3-edge for Fe–S bonds in sphalerite. This would indicate that there is a significant chemical shift (1.7 eV) for Fe–S bonds in sphalerite. Another and perhaps more likely possibility is that the peak results from S 2p electron transitions to hybridized Fe 3d – S 3p states. Optical microscopy and XANES studies have shown that this transition occurs in a variety of metal sulphide species (3, 12, 21, 22). If this is indeed the explanation for the pre-edge peak observed here, then this result indicates that there is a strong covalency in the S–Fe bond in sphalerite.

Fig. 5. Ab initio calculated L_3 and L_2 edges for ZnS sphalerite. The line broadening in theoretical spectrum is 1.0 eV. Peaks in the theoretical and experimental spectra are identified with the lowercase letters.



Conclusions

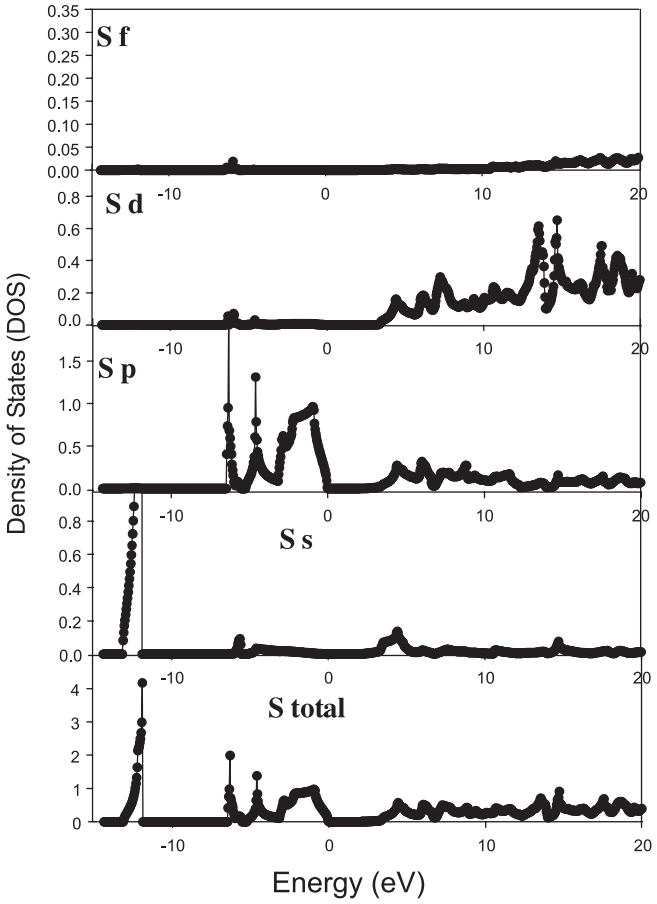
The S L-edge for sphalerite shows remarkable agreement between theory and experiment. Examination of the spectra through comparison with theoretical spectra and the calculated density of states for ZnS sphalerite shows that there is a mixing of S 2p electron transitions to empty 3s and 3d states over a range of energies above the absorption edge. Comparison of the S L-edge spectra collected from sphalerite with characteristic Fe concentrations shows that there is a chemical shift that is associated with transitions linked to Fe–S bonding. For the first time, a pre-edge feature associated with S–Fe bonding in sphalerite is observed.

Acknowledgements

We thank Dr. Yong Feng Hu (CLS) for his assistance and suggestions, Dr. J.E. Dutrizac (CANMET MMSL) for providing us with the sphalerite samples, the staff of the Canadian Light Source for their technical assistance, and the staff at the CANMET Mining and Mineral Sciences Laboratories in sample preparation and sample characterization. We would like to thank I.T.S. of The University of Western Ontario and the SHARNET team of Ontario for computer support. This work research was supported by the CANMET Mining and Mineral Sciences Laboratories, Natural Re-

© 2007 NRC Canada

Fig. 6. Calculated densities of states for sulphur in ZnS sphalerite using the ideal zincblende structure. The Fermi level is set at the zero energy.



sources Canada (NRCan) and Natural Science and Engineering Research Council of Canada (NSERC). The research described in this paper was performed at the Canadian Light Source, which is supported by NSERC, NRCan, Canadian Institutes of Health Research (CIHR), and the University of Saskatchewan. We thank the Editor, Dr. T.K Sham, and two anonymous referees for their constructive reviews of the manuscript.

References

1. (*a*) M. Kasrai, Z. Yin, K.H. Tan, and G.M. Bancroft. J. Vac. Sci. Technol., A. **11**, 2694 (1993); (*b*) M. Kasrai, J.R. Brown, G.M. Bancroft, Z. Yin, and K.H. Tan. Int. J. Coal Geology, **32**, 107 (1996).
2. D. Li, G.M. Bancroft, M. Kasrai, M.E. Fleet, B.X. Yang, X.H. Feng, K. Tan, and M. Peng. Phys. Chem. Miner. **20**, 489 (1994).
3. M.E. Fleet. Can. Mineral. **43**, 1811 (2005).
4. J.G. Chen. Surf. Sci. Rep. **30**, 1 (1997).
5. J.E. Dutrizac, A.R. Pratt, and T.T. Chen. *In* Aqueous and electrochemical processing. Vol. III. Metallurgical and materials processing: principles and technologies. *Edited by* F. Kongoli, C. Yamanchi, and H.Y. Sohn. TMS (The Minerals, Metals & Materials Society). 2003. p. 139.
6. C. Palache, H. Berman, and C. Frondel. Dana's system of mineralogy. 7th ed. Vol. 1. John Wiley and Sons Inc., New York. 1944.
7. F.D. Bloss. Crystallography and crystal chemistry: an introduction. Holt, Rinhart, and Winston Inc., New York. 1971.
8. J.A. Tossel and D.J. Vaughan. Theoretical geochemistry: applications of quantum mechanics in the earth and mineral sciences. Oxford University Press, New York. 1992.
9. R. Reininger, K. Tan, I. Coulthard. Rev. Sci. Instrum. **73**, 1489 (2002).
10. Y.F. Hu, L. Zuin, R. Reininger, and T.K. Sham. AIP proceeding for the 9th international conference on synchrotron radiation instrumentation. **879**, 535 (2007).
11. Y.M. Yiu, Y.F. Hu, and T.K. Sham. Comp. Nanoscience 2001, 169 (2001).
12. P. Hohenberg and W. Kohn. Phys. Rev., B. **136**, 864 (1964).
13. J.P. Perdew and Y. Wang. Phys. Rev., B. **45**, 13244 (1992).
14. J.E. Jaffe, R. Pandey, and M.J. Seel. Phys. Rev., B. **47**, 6299 (1993).
15. S. Ves, U. Schwarz, N.E. Christensen, K. Syassen, and M. Cardona. Phys. Rev. **42**, 9113 (1990).
16. C.Y. Yeh, Z.W. Lu, S. Froyen, and A. Zunger. Phys. Rev., B. **46**, 10086 (1992).
17. P. Blaha, K. Schwarz, and P.I. Sorantin, and S.B. Trickey. Comput. Phys. Commun. **59**, 399 (1990).
18. J.F.W. Mosselman, R.A.D. Pattrick, G. Laan, J.M. Charnick, D.J. Vaughan, C.M.B. Henderson and C.D. Garner. Phys. Chem. Miner. **22**, 311 (1995).
19. P.L. Hansen, R. Brydson, and D.W. McComb. Microsc. Microanal. Microstruct. 3 213 (1992)
20. D.J. Vaughan and J.A. Tossel. Can. Mineral. **18**, 157 (1980).
21. B. Gilbert, B.H. Frazer, H. Zhang, F. Huang, J.F. Banfield, D. Haskel, J.C. Lang, G. Srajer, and G. De stasio. Phys. Rev., B. **66**, 245205 (2002).
22. M. Fujisawa, S. Suga, T. Mizokawa, and A. Fujimori. Phys. Rev., B. **49**, 49 (1994).

© 2007 NRC Canada

Examination of the proposition that Cu(II) can be required for charge neutrality in a sulfide lattice — Cu in tetrahedrites and sphalerite[1]

Alan N. Buckley, William M. Skinner, Sarah L. Harmer, Allan Pring, Robert N. Lamb, Liang-Jen Fan, and Yaw-wen Yang

Abstract: Synchrotron XPS and Cu $L_{2,3}$-edge NEXAFS spectroscopic data for a natural tetrahedrite surface prepared by fracture under UHV were in accord with the composition of the mineral and its expected semiconductivity. The 2p binding energy for the 6-coordinate S atoms was found to be not detectably greater than that for the 4-coordinate S atoms, and surface species were not clearly discernible in either surface-optimized S 2p or Cu 2p spectra. The Cu 2p and Cu $L_{2,3}$-edge spectra indicated that all Cu in the mineral was indisputably Cu(I). The Cu $L_{2,3}$-edge spectra of relatively pure natural sphalerite treated with mildly acidic aqueous cupric solution revealed the presence of Cu(II) in the outermost layer of the fracture surfaces, but it was concluded that most of the Cu near the surface of the mineral was in formal oxidation state Cu(I), albeit with higher than normal d^9 character. The Cu(I) absorption peak was at an energy much lower than for the tetrahedrite absorption edge, but still consistent with Cu(I) in 4-fold coordination by S. The Cu(II) was consistent with Cu bonded both to S atoms in the outermost layer of the sphalerite and to O atoms in chemisorbed water. S 2p spectra determined at different photon energies revealed high binding energy components arising from oligosulfide-like environments in the outermost layers, but not necessarily in a completely restructured lattice and not in a Cu oligosulfide only. The data indicated some loss of Zn in addition to the Zn that had been replaced by Cu in the outermost layers of the sulfide lattice. The presence of these oligosulfide-like environments precluded the detection of S with formal oxidation state greater than (-II) that might have arisen only from Cu(I) in the S lattice. No evidence was obtained for the presence of Cu(II) in a sulfide lattice, but it was not possible to exclude the possibility of a very low concentration because of the presence of the Cu(II) bonded to both S and O at the surface of the treated sphalerite.

Key words: tetrahedrite, sphalerite, copper uptake, XPS, NEXAFS.

Résumé : Les données de spectroscopie photoélectronique aux rayons X par synchrotron et de spectroscopie d'absorption X de type « NEXAFS » près du seuil L_{23} du cuivre pour une surface de tétrahédrite naturelle préparée par fracture sous « UHV » sont en accord avec la composition du minerai et de sa semiconductivité attendue. On a trouvé que l'énergie de liaison 2p des atomes de soufre hexacoordinés n'est pas plus élevée que celle des atomes de soufre tétracoordonnés et que les espèces en surface ne peuvent pas être facilement discernées dans les spectres S 2p ou Cu 2p optimisés pour la surface. Les spectres Cu 2p et ceux près du seuil L_{23} du cuivre indiquent que tous les atomes de cuivre dans l'ensemble du minerai sont de type Cu(I), sans questionnement. Les spectres près du seuil L_{23} du cuivre d'une sphalérite naturelle relativement pure et traitée avec une solution cuprique aqueuse et faiblement acide mettent en évidence la présence de Cu(II) dans la couche externe des surfaces de fracture; on a toutefois conclu que la plupart des atomes de cuivre près de la surface du minerai se trouvent dans un état d'oxydation formel Cu(I) qui possède par ailleurs un caractère d^3 plus élevé que la normale. Le pic d'absorption du Cu(I) se situe à une énergie qui est de beaucoup inférieure à celle observée par absorption près du seuil de la tétrahédrite, mais qui est encore en accord avec un Cu(I) dans une coordination quaternaire avec le soufre. Le Cu(II) est en accord avec un atome de cuivre lié à des

Received 22 March 2007. Accepted 11 June 2007. Published on the NRC Research Press Web site at canjchem.nrc.ca on 3 August 2007.

Dedicated to G.M. Bancroft to mark his 65th year and his contribution to synchrotron science.

A.N. Buckley.[2] School of Chemistry, The University of New South Wales, Sydney, NSW 2052, Australia.
W.M. Skinner and S.L. Harmer. Ian Wark Research Institute, University of South Australia, Mawson Lakes, SA 5095, Australia.
A. Pring. The South Australian Museum, North Terrace, Adelaide, SA 5000, Australia
R. Lamb. Australian Synchrotron, 800 Blackburn Road, Clayton, Vic 3168, Australia
L.-J. Fan and Y.-w. Yang. National Synchrotron Radiation Research Center, Hsinchu 30076, Taiwan.

[1]This article is part of a Special Issue dedicated to Professor G. Michael Bancroft.
[2]Corresponding author (e-mail: a.buckley@unsw.edu.au).

 doi:10.1139/V07-078 © 2007 NRC Canada

atomes de soufre dans la couche extérieure de la sphalérite et à des atomes d'oxygène dans l'eau de chimisorption. Les spectres 2p du soufre déterminés à diverses énergies photoniques ont mis en évidence la présence de composants d'énergie de liaison plus élevée qui découlent d'environnements oligosulfurés dans les couches les plus externes, mais pas nécessairement dans un réseau complètement restructuré et pas seulement dans un oligosulfure de cuivre. Les données indiquent qu'il y a une certaine perte de zinc en plus de l'addition du zinc qui a été remplacé par le cuivre dans les couches les plus externes du réseau de sulfure. La présence de ces environnements de type oligosulfure ne permet pas la détection des atomes de soufre ayant un état d'oxydation formel plus grand que (-II) qui pourraient découler uniquement du Cu(I) dans des réseaux de soufre. On n'a pas pu obtenir de données pouvant permettre de confirmer la présence de Cu(II) dans le réseau de sulfure; il n'est toutefois pas possible d'exclure la possibilité de l'existence d'une très faible concentration en raison de la présence de Cu(II) lié tant à un atome de soufre qu'à un atome d'oxygène à la surface de la sphalérite traitée.

Mots-clés : tétrahédrite, sphalérite, absorption de cuivre, SPX, NEXAFS.

[Traduit par la Rédaction]

Introduction

The classical representation of tetrahedrite is $Cu_{12}Sb_4S_{13}$, but the tetrahedrite group minerals are more generally represented by $(Cu,Ag)_{10}(Cu,Fe,Zn)_2(Sb,As)_4S_{13}$. In each formula unit or half unit cell, the twelve univalent (Cu and Ag) or divalent atoms occupy 6 trigonal planar (^{III}M) sites and 6 tetrahedral (^{IV}M) sites (1). The trivalent atoms also occupy tetrahedral sites, but each is bonded to only 3 S atoms, resulting in a structural vacancy. Twelve of the 13 S atoms are 4-coordinate, whereas the other S atom is 6-coordinate and bonded to ^{III}M atoms. The coordination information can be summarized by $^{III}(Cu,Ag)_6{}^{IV}(Cu,Fe,Zn)_6{}^{III}(Sb,As)_4{}^{IV}S_{12}{}^{VI}S$, although there is some evidence for Fe, especially Fe(III), occupying trigonal sites (2).

The members of the tetrahedrite group of most interest in the present context are those in which the number of Cu atoms is greater than 10 minus the number of Ag atoms. There is general agreement that in natural tetrahedrites of this composition, the Ag preferentially occupies the univalent metal sites and the excess Cu is located in the divalent metal sites, but there is no consensus concerning the formal oxidation state of that Cu. Some consider either explicitly (e.g., 3) or implicitly (e.g., 4) that it is Cu(I), but others maintain that Cu in the divalent metal sites is Cu(II) (e.g., 5, 6), notwithstanding the reported antipathy of Cu(II) for tetrahedral coordination (7). Indeed, it has been argued that when tetrahedrite minerals are deficient in divalent metal atoms such as Fe or Zn, a minor Cu(II) component can be required for "charge neutrality" (6). Support for this hypothesis, which has been reiterated recently (8), was originally provided by the observation of an absorption peak near 931 eV in the total electron yield (TEY) Cu L_3-edge near-edge X-ray absorption fine structure (NEXAFS) spectra of synthetic and natural tetrahedrite samples prepared by grinding under acetone after being mixed with ultra pure graphite (6). For the four natural tetrahedrites studied in that investigation, the correlation between the expected Cu content in the divalent metal sites and the Cu(II) concentration indicated by NEXAFS spectroscopy was not strong. Furthermore, the corresponding fluorescence yield NEXAFS spectra were not determined, which raises the question as to whether the observed Cu(II) might have been associated with Cu-O surface oxidation products of the tetrahedrite specimens rather than Cu(II) in the sulfide lattice. Nevertheless, for synthetic $Cu_{12}Sb_4S_{13}$, electron paramagnetic resonance and related measurements were reported to be consistent with Cu(II) in the divalent metal sites (9). Instead of postulating the presence of Cu(II) for charge neutrality, Charnock et al. (2) proposed that for Fe-containing tetrahedrites in which copper is present in excess of 10 atoms per unit formula, compensation of the valence deficiency is by Fe(III). Fe K-edge extended X-ray absorption fine structure (EXAFS) and Mössbauer spectroscopic data for synthetic specimens were in agreement with that hypothesis, but for natural specimens the Fe was present mainly as Fe(II) in tetrahedral coordination.

Setting aside for the moment the origin of the small concentration of Cu(II) detected in some of the tetrahedrite samples, the proposition that Cu(II) can be required for "charge neutrality" is a contentious one, as it appears to be based on the assumption that the S in the sulfide lattice must remain as S(-II), despite the fact that it cannot have only this formal oxidation state in CuS, nor can the S be only S_2(-II) in CuS_2. In both cases, the deviation from typical S(-II) or S_2(-II) is evident in the S 2p spectra for these materials. As a more subtle example, it has been proposed (10) that djurleite, $Cu_{1.96}S$, can be represented by $Cu(I)_{62}Cu(II)S_{32}$. However, it is now widely accepted that Cu has a formal oxidation state of only Cu(I) in all copper-containing sulfides, including CuS and CuS_2 (11–19), except perhaps for tetrahedrite.

A corollary of the "Cu(II) for charge neutrality" hypothesis is that the Cu initially replacing Zn in the surface layers of sphalerite ("copper activation" of sphalerite for its recovery by flotation), must be present as Cu(II), notwithstanding the counsel by Pattrick et al. (18) that because copper chalcogenides are invariably Cu(I), the Cu incorporated into ZnS is likely to be reduced to Cu(I) with the concomitant oxidation of sulfide to form S^-–S^- bonds and, with increasing substitution of Zn with Cu, the formation of a covellite-like surface layer. However, if it is considered possible for some Cu(II) to be in tetrahedral sites in tetrahedrite, the question arises as to whether it might be possible for the Cu initially replacing Zn in sphalerite to be Cu(II). The Cu 2p spectra obtained in X-ray photoelectron spectroscopy (XPS) studies of the copper activation of sphalerite under conditions not conducive to the formation of $Cu(OH)_2$ have indicated that the Cu is present as Cu(I) regardless of the extent of uptake, although Cu 2p spectra are appreciably less sensitive than Cu L_3-edge spectra for the detection of Cu(II) (6,

© 2007 NRC Canada

20). In the corresponding S 2p spectra, there has been clear evidence for an increase in the formal oxidation state (to those less negative than -II) of some of the S after Cu uptake, but the observed S 2p binding energies have been too large to have arisen from a Cu(I) sulfide phase or S(-I) only (21). Heavily Cu-substituted surface layers would be expected to restructure, although it appears that Cu can be incorporated into an unreconstructed sphalerite lattice at least to a small extent. On the one hand there have been reports of supergene cuprian sphalerite with Cu content up to 10 atom% (22), while on the other hand attempts by Pattrick et al. (23) to substitute (in a silica tube at 600 °C) Cu into a sphalerite lattice without the concomitant introduction of indium produced sphalerite with only ~0.2 atom% Cu. In the latter case, the corresponding Cu $L_{2,3}$-edge spectra were reported to reveal the presence of some (but presumably not all) Cu(II) that was thought to be located in the ZnS lattice (23). It was concluded that Cu substitution at low concentrations can occur without the need for corresponding Zn vacancies, and it was proposed that the limit of Cu substitution is controlled by the aversion of Cu(II) for tetrahedral coordination in sulfides (23).

There is some, although perhaps not incontrovertible, evidence for the existence of Cu(II) in the wurtzite ZnS lattice. The IR emission centre in Cu-doped wurtzite ZnS is normally assigned to the substitution of Zn by Cu(II), whereas the green and blue centres are associated with Cu(I) at substitutional sites (24). There is stronger optical spectroscopic evidence for Cu(II) substituting for Zn at the ppm level in polymorphic (including cubic) crystalline ZnS (25).

Pattrick et al. (18) investigated the Cu activation of 2.5 × 8 cm^2 slabs of polycrystalline synthetic sphalerite and natural Fe-rich sphalerite by 0.5 mol dm^{-3} Cu^{2+} at pH 3.9 primarily by means of fluorescence reflection EXAFS (REFLEXAFS) spectroscopy. The large slabs of ZnS were polished to optical flatness in air, and the ~0.1° angle of incidence corresponded to a penetration depth of ≤5 nm. The Cu K-edge fluorescence REFLEXAFS data indicated that the Cu was bonded to 3 S atoms at 0.225 nm and one O atom at 0.207 nm, distances similar to those obtained by bulk EXAFS for pure ZnS powder similarly Cu-activated. It was reasoned (18) that these results, when averaged over the ~2 layers of Zn exchanged by Cu, suggested that the outermost Cu must be bonded to more than one O, as Cu below the surface would be expected to be fully bonded to S.

There has typically been at least one limitation in previous investigations of the interaction of sphalerite with cupric ions that has prevented a definitive conclusion concerning the possible existence of Cu(II) in the treated mineral. Most notably, Cu L_3-edge absorption spectra have usually not been obtained to complement Cu 2p photoelectron spectra, but other limitations have included the use of impure natural sphalerite, surfaces of relatively pure sphalerite that have been abraded, polished, or cleaved in air prior to treatment with the Cu-containing aqueous phase, treatment in Cu^{2+} solution of concentration in excess of 0.001 mol dm^{-3}, treatment for periods of at least 30 min, or treatment at a pH of ~9, which is of relevance to flotation but which may allow the adsorption of Cu-hydroxy species on the treated surfaces.

In this work, a tetrahedrite surface prepared by the fracture of a single piece specimen under ultra high vacuum (UHV) was characterized by partial electron yield (PEY) and total fluorescence yield (TFY) NEXAFS spectroscopy as well as synchrotron XPS (SXPS). Spectra from the tetrahedrite were sought not only to establish whether they were consistent with the mineral composition and structure, but also because a reference material containing Cu in trigonal planar and tetrahedral S environments was required to assist interpretation of the spectra from Cu-doped sphalerite. Relatively pure sphalerite samples were cleaved while immersed in aqueous solutions of cupric ions and subsequently characterized by SXPS and NEXAFS spectroscopy in such a way as to minimize exposure of the treated mineral surface to oxygen, and hence minimize any oxidative leaching of Zn from the Cu-treated surface or possible oxidation of Cu(I) in the sulfide lattice near the surface to a Cu(II) oxygen species. In both systems, the aim was to identify the source of any Cu(II) present, and to determine whether S of formal oxidation state more positive than (-II) was discernible.

Experimental details

Mineral specimens

The tetrahedrite was a massive polycrystalline specimen from Casapalca, Peru. Specimens of approximate size 3 × 3 × 6 mm were mounted in a vice-like specimen holder, designed for use in the double-blade cleaving stage, attached to the rotary distribution chamber of the Australian Synchrotron Research Program (ASRP) soft X-ray spectroscopy endstation. Preliminary bulk analysis was carried out on the mineral specimen with an FEGSEM, and the tetrahedrite structure was confirmed by XRD. The bulk composition below the fracture surface characterized by SXPS was determined by electron microprobe analysis using a Cameca SX-51 instrument at the Adelaide Microscopy Centre, University of Adelaide. Operating conditions included an accelerating voltage of 20 kV and a beam current of 19.5 nA. Standards used were PbS (S), $CuFeS_2$ (Cu, Fe), ZnS (Zn), CoAsS (As), Ag_2Te (Ag), Sb_2S_3 (Sb), and Bi_2Se_3 (Bi). Apart from slightly low values for Fe and Zn, the analyses were found to be within the composition range reported for other tetrahedrite specimens from Casapalca, viz. $(Cu,Ag)_{10+x}(Fe,Zn)_{2\pm y}(Sb,As)_{4+z}S_{13}$ (26). The compositions of the 16 regions analysed varied by less than 2%. The sphalerite used in the investigation was a relatively pure (almost colourless) mineral specimen from Santander, Spain.

Interaction of aqueous cupric ions with sphalerite

Approximately 3 × 3 mm surfaces of the Santander sphalerite were prepared by fracture while under 10^{-3} mol dm^{-3} Cu sulfate solution at pH 2 or 5, and the fracture surfaces were left immersed for periods ranging from 1 to 5 min prior to being rinsed with water. Adjustment of pH was made with dilute hydrochloric acid. The specimen treatment and rinsing was carried out in a nitrogen-flushed glove box surrounding the introduction chamber of the ASRP endstation with nitrogen-saturated solution and water, respectively, and therefore would have taken place in no more than a low concentration of residual oxygen. The sphalerite specimens, with the treated fracture surface uppermost, were

© 2007 NRC Canada

mounted on a stainless steel specimen stub by means of double-sided conducting adhesive tape.

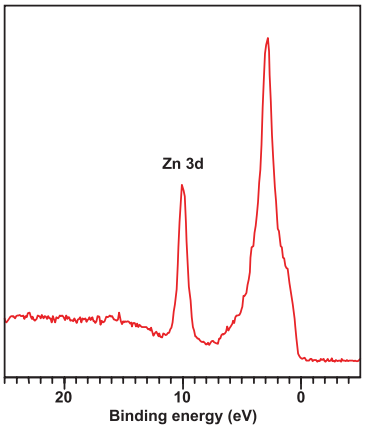
Spectroscopic measurements

The SXPS and NEXAFS spectroscopic measurements were carried out in the ASRP soft X-ray spectroscopy end-station while connected to beamline 24A at the NSRRC in Hsinchu, Taiwan. BL24A is a bending-magnet wide-range beamline incorporating a grating monochromator (27). With 25 μm slits and 400 L/mm grating, the resolution was 0.07 eV at a photon energy of 210 eV. The synchrotron was operated at 300 mA in continuous top-up mode. The ASRP end-station, constructed by OmniVac and PreVac, is equipped with a SPECS Phoibos 150 electron energy analyser and an OmniVac UHV-compatible partial yield detector based on a multichannel plate behind retarding grids. Electron analyser pass energies of 10 eV and 20 eV were used for S 2p and Cu 2p spectra, respectively. A Gammadata Scienta Flood Gun 300, operated at 3 eV energy and 0.05 mA emission, was used for specimen charge compensation only during determination of the tetrahedrite photoelectron spectra. Cu $L_{2,3}$-edge NEXAFS spectra are shown together with the absorption current monitored concomitantly by a Cu metal mesh in the beamline but unnormalized by the flux incident on a Au mesh also in the beamline. The NEXAFS spectroscopic analysis depths in PEY and TFY modes would be ~8 nm and >100 nm, respectively (28). Conventional XPS measurements were undertaken using monochromatised Al K_α X-rays in a Kratos Axis Ultra spectrometer.

Measurement of binding energies in SXPS

The measurement of photoelectron binding energies in SXPS can be complicated by uncertainties in the photon energy arising from any variation in the incidence of the synchrotron beam on the first optical element of the beamline. The situation is even more complicated when an electron flood gun has to be used for charge compensation with poorly conducting materials and when no reference peaks are available, such as when there is negligible carbon present at a fracture surface prepared under clean UHV conditions. Typically, a flood gun electron beam required to minimize photoelectron linewidths overcompensates for the positive charge established as a result of the photoemission, and hence renders the surface negative by a few eV. The degree of overcompensation can be different for different photon energies as charging can depend on the photon flux, and the flux normally varies as the monochromator grating and settings are changed. When the use of a flood gun was necessary in the investigation of a clean fracture surface in the present work, electron energies were measured relative to the top of the valence band. This is effectively the same as measuring the energies relative to the onset of photoemission at the same photon energy, as the top of the valence band is typically estimated by extrapolating the leading edge of the valence band peak to the baseline (29). The method is "calibrated" using a similar well-characterized reference material. Sphalerite is an appropriate reference material for the two systems studied in the present work, as Zn is present in tetrahedral sites in tetrahedrite, and some essentially unaltered sphalerite remains as a substrate within the depth analysed for Cu-treated sphalerite.

Fig. 1. Tetrahedrite Zn 3d and valence band spectrum determined at a photon energy of 210 eV.



Pure cubic ZnS fracture surfaces have been characterized by conventional XPS without a flood gun but with Au decoration for a binding energy reference (29) and a Zn 3d binding energy of 10.1 eV was determined. A S $2p_{3/2}$ binding energy of 161.6 eV was obtained for an Fe-containing mineral sphalerite with a flood gun using a magnetic confinement charge compensation system (30).

Fitting of core photoelectron spectra

The CasaXPS (version 2.0) software was used to fit photoelectron spectra. The constraints used in fitting S 2p spectra were a (3/2, 1/2) splitting of 1.19 eV, intensity ratio 2:1, and equal linewidths. Fitted parameters were not significantly different if a Gaussian–Lorentzian sum SGL(p) of lower Lorentzian character (smaller "p") rather than the more usual product, GL(p), was used to approximate the Voigt profile. However, SGL(10) or GL(50) usually gave slightly better fits at the leading edge compared with GL(30). The asymmetric lineshape proposed by Gelius (31, 32) of general form A(a,b,n)GL(p), where a, b, and n are parameters determining the shape of the tail contribution to the lineshape, was used for the Cu 2p spectra of Cu-treated sphalerite, typically A(0.35, 0.4, 0)GL(50).

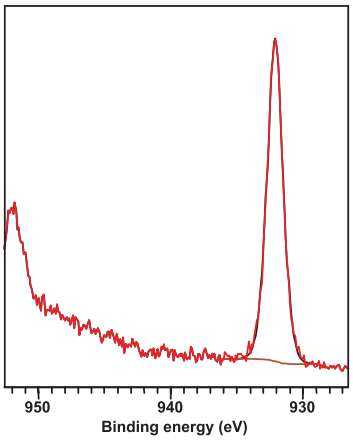
Results

Tetrahedrite

The survey photoelectron spectrum determined at a photon energy of 1100 eV, for a tetrahedrite surface prepared by fracture under ~5 × 10^{-11} torr (1 torr = 133.322 4 Pa) and transferred to the analyser chamber without exposure to a higher pressure, was largely consistent with the electron microprobe analysis of the mineral, viz. $Cu_{10.07}Ag_{0.23}Zn_{1.40}Fe_{0.22}Sb_{2.76}As_{1.35}Bi_{0.01}S_{13}$. In particular, peaks from Cu, Zn, Sb, and S were clearly visible, Fe 2p peaks were barely evident, and Ag 3d peaks were not discernible at all. Peaks from As, such as the 3d at a binding energy near 43 eV, were not quite as intense as expected from the microprobe analysis. A flood gun was required to minimize the effect of charging, consequently photoelectron energies were determined relative to the onset of photoemission as described in the experimental details section. The need for a flood gun indicates that the mineral was a

© 2007 NRC Canada

Fig. 2. Tetrahedrite Cu 2p spectrum determined at a photon energy of 1100 eV and fitted with a single symmetric $2p_{3/2}$ peak.

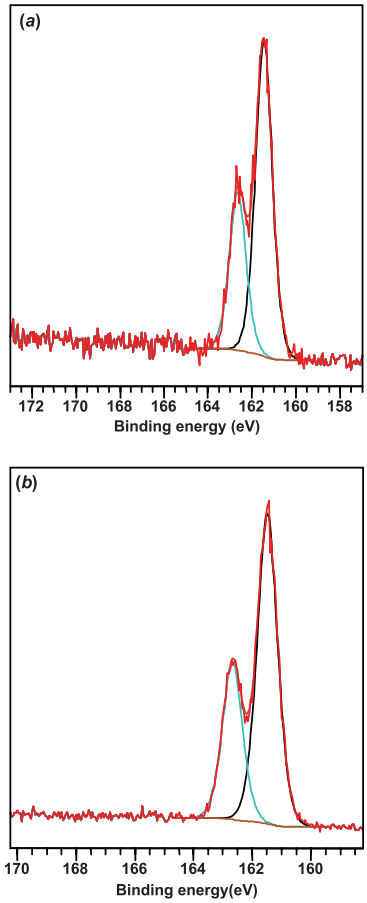


semiconductor with a substantial band gap rather than a conductor and hence with a total number of valence electrons per unit cell close to 208 (33), as expected from the composition, which predicts 207.8 per unit cell. Spectra in the valence region were determined at photon energies of 210 eV (Fig. 1), 400 eV, and 800 eV, and a quite steep valence band edge, estimated to be at a binding energy of ~0.8 ± 0.1 eV, was observed in each case. The Zn 3d binding energy was approximately 10.1 eV.

From the spectra for Cu-treated sphalerite (vide infra), it is expected that the valence band spectrum for tetrahedrite would be dominated by a Cu 3d peak at a binding energy ~7 eV lower than that for the Zn 3d. The valence band would also contain significant contributions from Sb (5p) and As (4p) as well as S, nevertheless, for relative intensity comparison purposes, the Cu 3d peak can be approximated by the relatively sharp central peak in the valence band. The estimated intensity of that peak, relative to the Zn 3d peak, was essentially the same at 800 eV as at 210 eV. In principle, an estimate of the Cu/Zn ratio can be obtained from the relative intensity of the two corresponding 3d peaks and a calculated photoionization cross section ratio at 800 or 210 eV; however, the Cu 3d peak intensity might have been systematically underestimated and the calculated cross sections for the 3d levels of Cu and Zn might not be very accurate, consequently it was preferable for this intensity ratio to be calibrated for tetrahedrite and used later for Cu-treated sphalerite. At a photon energy of 210 eV, the Cu 3d/Zn 3d cross section ratio was estimated to be 1:2.9, while at 800 eV a ratio of 1:2.6 was obtained. By comparison, the Cu 3d/Zn 3d cross section ratio at 1254 eV calculated by Scofield (34) was 1:1.36.

On the same energy reference basis, the Sb $3d_{5/2}$ binding energy was 529.6 eV, an energy also close to the value expected given the corresponding value of 530.1 eV observed for Sb_2S_3 (35). The Sb $3d_{5/2}$ linewidth at a photon energy of 800 eV was 0.94 eV compared with 0.72 eV observed (35) for Sb_2S_3 by means of conventional XPS with a magnetic confinement charge neutralization system. The slightly larger linewidth for tetrahedrite is more likely to have been due to a wider distribution of Sb environments in tetrahedrite compared with stibnite than to broadening arising from incomplete compensation by the flood gun of non-

Fig. 3. S 2p spectrum for a tetrahedrite fracture surface determined at a photon energy of (*a*) 210 eV and (*b*) 400 eV fitted with a single doublet in each case.



uniform charging (given the relatively narrow Cu 2p linewidth; vide infra). It is unlikely to have been due to a larger X-ray linewidth (0.25 eV) provided by the monochromator grating and slit settings used (1600 L/mm, 25/25 μm). The observed width of the Sb 3d peaks is of relevance for evaluating the observed widths of the Cu 2p and S 2p photoelectron peaks. There was no evidence for any O 1s intensity near the Sb $3d_{5/2}$ peak.

The $2p_{3/2}$ peak in the Cu 2p spectrum determined at a photon energy of 1100 eV (Fig. 2) was at a binding energy of 932 eV, close to values previously observed for Cu in other sulfide minerals (e.g., 36). The peak could be fitted with a single symmetrical component of Gaussian–Lorentzian lineshape and of linewidth 1.4 eV, which was at least as narrow as the corresponding peak for other sulfide minerals that had been characterized under the same experimental conditions and that were sufficiently conducting to not require charge compensation with a flood gun. The symmetrical nature of this peak is of considerable relevance in the interpretation of the Cu 2p spectrum from Cu-doped sphalerite (vide infra). As expected from the absence of a Cu $2p_{3/2}$ component between 933 and 934 eV that could have arisen from any Cu(II) present, excited final state satellites were not discernible. Thus, the Cu 2p spectrum was consistent with the presence of only Cu(I) in a sulfide of nonmetallic conductivity.

© 2007 NRC Canada

The S 2p spectrum determined at a photon energy of 210 eV is shown in Fig. 3*a*. The spectrum can be fitted with a single S 2p doublet with symmetrical Gaussian–Lorentzian components of width 0.9 eV and at a $2p_{3/2}$ binding energy of 161.5 eV. This observation is notable for two reasons. First, the absence of any indication of at least one additional doublet at a binding energy noticeably lower than that for the main doublet revealed that surface species (i.e., species expected when covalent bonds are broken on fracture or when the atoms in the outermost layers relax significantly following fracture) either had not been formed or were close in energy to the bulk states. A photon energy of 210 eV corresponds to the value of maximum surface sensitivity for S 2p photoelectrons, and the photon linewidth at 210 eV should have been sufficiently narrow to allow the resolution of surface species such as those observed for covellite (37). However, the 0.9 eV S $2p_{3/2}$ linewidth at a photon energy of 210 eV was broader than values observed for better conducting Cu sulfides under similar experimental conditions, including ~0.55 eV for covellite, ~0.6 eV for cubanite, and ~0.7 eV for bornite, therefore the formation of surface species cannot be precluded. Second, the absence of an additional doublet of intensity ~8% of that of the main doublet and at a binding energy at least 0.5 eV higher indicated that the two 6-coordinate S atoms in the tetrahedrite unit cell do not have a measurably higher binding energy than the 24 4-coordinate S atoms. On the basis of the binding energy difference deduced for 4- and 5-coordinate S in pentlandite (38), Schaufuß et al. (39) had postulated that a unit increase in S coordination would lead to an increase in S 2p binding energy of ~0.8 eV. Subsequently, a binding energy difference of at most 0.3 eV was determined for the 2- and 3-coordinate S atoms in stibnite (35), and a negligible binding energy difference was observed for the 5-coordinate S in millerite (β-NiS) and the 6-coordinate S in α-NiS (40). The negligible difference observed for the S atoms in tetrahedrite provides confirmation that a higher S coordination number does not necessarily lead to higher S core electron binding energies.

The S 2p spectrum observed at a photon energy of 400 eV is shown in Fig. 3*b*. As for the S 2p spectrum excited at 210 eV, the 400 eV spectrum could be fitted with a single doublet of symmetric components of width 0.8 eV. The slightly narrower linewidth of the doublet components in the 400 eV spectrum compared with the 210 eV spectrum (Fig. 3*a*) is not expected to have arisen from a better photon beam resolution. Rather, it is most probably because of a more effective compensation by the flood gun of less specimen surface charging produced by a photon flux that was lower at 400 eV (800 L/mm grating) than at 210 eV (400 L/mm grating), but the narrower linewidth could also have been the result of a contribution from surface species that was lower because of the greater analysis depth. The observed S $2p_{3/2}$ binding energy of 161.5 eV is within 0.1 eV of the value for chalcopyrite. Also, the S K-edge spectrum for a natural tetrahedrite was found to be quite similar to that for chalcopyrite (41).

To demonstrate that the tetrahedrite S 2p spectrum cannot be fitted satisfactorily with a second doublet arising from the 6-coordinate S of intensity 1/13th that of the principal (4-coordinate S) doublet and at a significantly higher binding energy, the spectrum in Fig. 3*b* was fitted with such a second doublet constrained to 1 eV higher binding energy from the principal doublet and with the same component line shape and width (Fig. 4). It can be seen from Fig. 4 that the best fit obtainable on this basis is inadequate. The best fit was also clearly inadequate for a shift of only 0.5 eV. These shifts should be compared with a shift of 1.6 eV that would correspond to an increase of S 2p binding energy of 0.8 eV per unit increase in S coordination number.

Fig. 4. S 2p spectrum shown in Fig. *3b* fitted with a second doublet of intensity 1/13th that of the principal doublet and shifted 1 eV to higher binding energy.

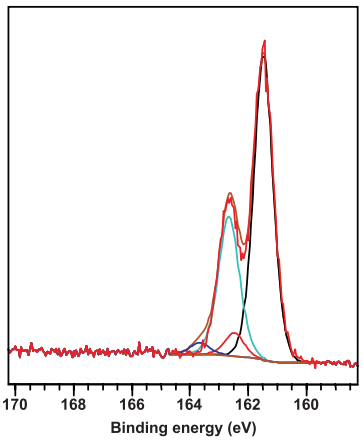
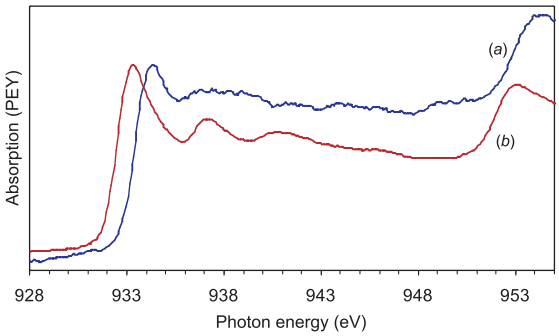


Fig. 5. PEY Cu $L_{2,3}$-edge NEXAFS spectrum for (*a*) a tetrahedrite and (*b*) Cu metal.



TFY and PEY Cu $L_{2,3}$-edge NEXAFS spectra were determined for the same tetrahedrite fracture surface. The NEXAFS spectra were obtained immediately after the photoelectron spectra that had been determined (at a photon energy of 1100 eV) using the same monochromator settings but using several different irradiated areas on the fracture surface to check for any sign of surface chemical degradation brought about by the photon beam. A representative PEY Cu $L_{2,3}$-edge NEXAFS spectrum is shown in Fig. 5 together with the spectrum from Cu metal determined concomitantly. The L_3 absorption edge was at 933.4 eV relative to the edge position for Cu metal of 932.6 eV. An absorption edge energy of 933.4 eV (peak energy of ~934.5 eV) is similar to that observed for chalcocite and ~1.9 eV higher than that for chalcopyrite (36). Thus, the absorption energy for tetrahedrite is in the "indisputably Cu(I)" region rather than being near the lower end of the Cu(I) range adjacent to that for Cu(II) (6). The TFY spectrum was essentially the same

© 2007 NRC Canada

as the PEY spectrum apart from an even flatter baseline before the absorption edge. It is important to note that despite the significant Cu + Ag excess (>10) and comparable Zn + Fe deficiency (<2) in the tetrahedrite investigated, viz. $(Cu,Ag)_{10.3}(Zn,Fe)_{1.6}(Sb,As,Bi)_{4.1}S_{13}$, there was no evidence for an absorption peak near 931.3 eV in the TFY spectrum that could have arisen from a small concentration of Cu(II) in the mineral's divalent metal sites. Even in the corresponding PEY spectrum (Fig. 5*a*), any absorption near 931 eV remained below noise level.

The Cu L_3 peak energy of 934.5 eV is in agreement with the values found by Pattrick et al. (6). In the tetrahedrite specimens they studied that did not contain Te (instead of Sb), the Cu(I) peak energies ranged from 934.0 to 934.6 eV, while the energy of the Cu(II) L_3 peak, when present, was in the slightly narrower range of 930.5 to 930.8 eV. For specimens that did not contain Ag, the Cu(I) range was 934.2 to 934.6 eV. They concluded that the L_3 peak energy for Cu in tetrahedral sites (934.0 eV) was smaller than that for Cu in the trigonal sites (~935 eV), consistent with a longer more ionic Cu–S bond in the former sites and a shorter (0.226 nm), stronger more covalent Cu–S bond in the latter sites. The absorption spectrum observed in the present work is in accord with the findings of Pattrick et al. (6), apart from the absence of a peak from Cu(II).

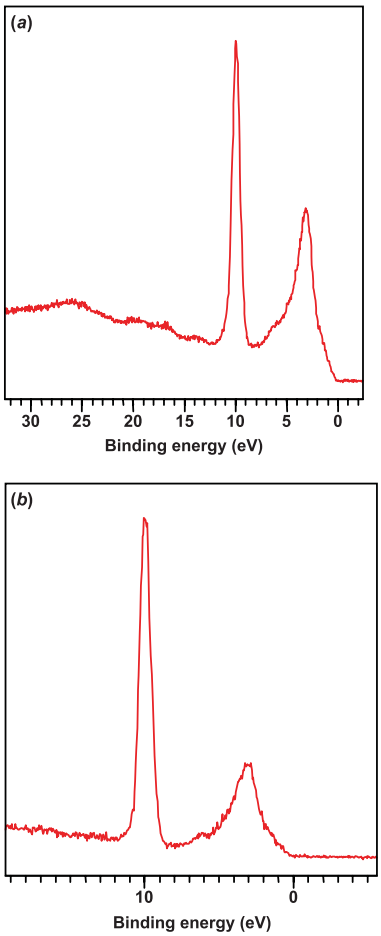
Interaction of sphalerite with mildly acidic aqueous cupric ions

Survey photoelectron spectra, determined at a photon energy of 1100 eV from Santander sphalerite fracture surfaces treated in Cu sulfate solution, revealed peaks from oxygen in addition to those from Zn, S, and Cu, notwithstanding preparation of the specimens in the nitrogen-flushed glove box surrounding the end-station load lock. More O was evident after 1 min treatment than 5 min, suggesting that the O might be associated with adsorbed water; treated surfaces are expected to become increasingly hydrophobic as a result of Cu incorporation (21, 42), and less water adsorption would be expected on a more hydrophobic surface. Indeed, each narrow scan O 1s spectrum determined at a photon energy of 800 eV consisted of a structureless symmetrical peak of width ~2 eV centred at a binding energy of ~532.5 eV, intimating that the probable source of the oxygen was chemisorbed water rather than Cu-O species such as hydroxide (43). The O 1s intensity was clearly lower, and the Cu 2p intensity obviously higher, towards the end of the specimen irradiation period than at the beginning of data collection, indicating that some O was lost from the surface during the measurements and that the Cu was below the oxygen-containing species. The survey spectra also revealed that a flood gun was not necessary to compensate for specimen charging, unlike the situation for the same sphalerite not treated with Cu.

The valence band and Zn 3d spectra determined at photon energies of 210, 400, and 800 eV were all consistent with a Zn 3d binding energy of 10.0 ± 0.1 eV. As for the tetrahedrite studied, this binding energy is close to the 10.1 eV determined for pure cubic ZnS by Ley et al. (29). The low kinetic energy band edge was not noticeably steeper at a photon energy of 210 than 400 eV; a steeper edge might have been expected if a Cu sulfide-like surface layer with high electrical conductivity had been produced. At a photon energy of 210 eV, the central peak in the valence band was noticeably more intense relative to that for the Zn 3d than at the higher photon energies (Fig. 6). This energy variation was much more pronounced than for tetrahedrite, therefore it must have reflected a higher concentration of Cu in the outermost layers rather than a change in the relative Zn and Cu 3d photoionization cross sections with energy. Changes in the concentration of Cu relative to Zn in the outermost layers can be monitored by the Cu 3d/Zn 3d intensity ratio in spectra determined at 210 eV, while changes in the depth analysed by ~790 eV electrons will be reflected in the Cu 3d/Zn 3d intensity ratio in spectra determined at 800 eV (Table 1). It is also possible to estimate Cu/Zn atomic ratios from the Cu 3d/Zn 3d intensity ratios. From the calibration of Zn 3d and estimated Cu 3d peak intensities carried out for tetrahedrite, the Cu/Zn ratio in the depth analysed by ~200 eV electrons after treatment with Cu for 1 min at pH 5 was 2:1. By contrast, the ratio in the depth analysed by ~790 eV electrons was 0.7:1.

Each narrow scan encompassing the Zn 3p, Cu 3p, and Cu $L_3M_{4,5}M_{4,5}$ peaks determined at a photon energy near 1010 eV also enabled an estimate of the Cu/Zn ratio within the depth analysed by electrons of kinetic energy ~925 eV to be made from the Cu 3p/Zn 3p intensity ratio (Table 1). For

Fig. 6. Valence region spectra for a sphalerite fracture surface treated with aq. Cu^{2+} for 1 min at pH 5 determined at a photon energy of (*a*) 210 eV and (*b*) 400 eV.

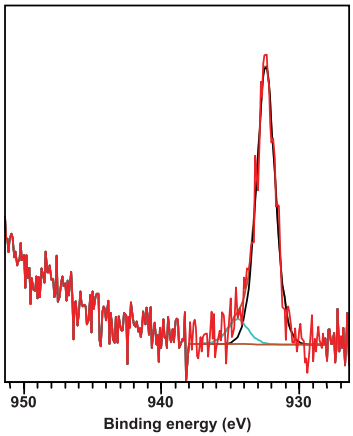


© 2007 NRC Canada

Table 1. Narrow scan photoelectron peak intensities, intensity ratios, and Cu $2p_{3/2}$ component separation [ΔBE] for tetrahedrite and Cu-treated sphalerite.

Mineral	Treatment time (min)	pH	Photon energy (eV)	Other details	Zn 3d (Zn 3d/S 2p)	Cu 3d (Cu 3d/S 2p)	S 2p	Cu 3d/Zn 3d	Cu 3p/Zn 3p	ΔBE – Cu 2p (eV)
Tetrahedrite	—	—	210		4 640 (0.54)	11 378 (1.33)	8559	2.45		
			800		85.7					0
			1100							
Santander sphalerite	1	5	210	Near start	4 412 (4.32)	3 142 (3.07)	1022	0.71	0.71	
	1	5	210	Near end	(3.54)	(2.52)	1248			
	1	5	800		166 (1.25)	44 (0.33)	133	0.27		
	1	5	1100							2.3
Santander sphalerite	5	2	210		12 144 (4.75)	4 954 (1.94)	2 555	0.41		
	5	2	800		262	45		0.17		
	5	2	1100							1.86
Santander sphalerite	5	5	210		2 075 (4.86)	815 (1.91)	427	0.39	0.26	
	5	5	800		194	33		0.17		
	5	5	1100							1.86

Fig. 7. Cu 2p spectrum for a Santander sphalerite surface treated with aq. Cu^{2+} for 1 min at pH 5 determined at a photon energy of 1100 eV and fitted with two components.



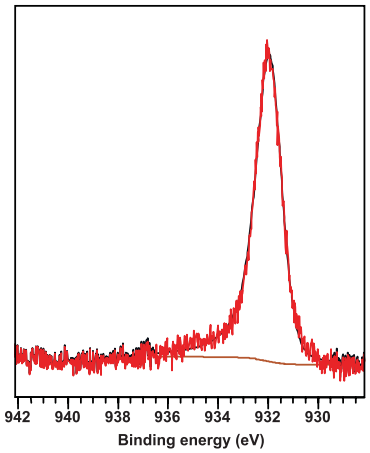
example, the Cu 3p/Zn 3p intensity ratio indicated a Cu/Zn ratio of ~0.5:1 within the surface layer analysed after interaction with aq. Cu^{2+} for 1 min at pH 5, based on calculated values of subshell photoionization cross sections (44) that predicted a Cu 3p/Zn 3p cross section ratio at 1010 eV of 0.88:1. This value is in reasonable agreement with the ratio estimated experimentally from the Cu 3d/Zn 3d intensity ratio at 800 eV.

The principal $2p_{3/2}$ component in the Cu 2p spectrum determined at a photon energy of 1100 eV, shown in Fig. 7 for a surface interacted with cupric ions for 1 min at pH 5, was at a binding energy of ~932.4 eV, close to values previously observed for Cu-activated sphalerite (e.g., 21, 45) and for Cu in other sulfide minerals (e.g., 36). The Cu $L_3M_{4,5}M_{4,5}$ Auger peak kinetic energy and the principal Cu $2p_{3/2}$ peak binding energy, i.e., the modified Auger parameter, was 1850.0 eV, close to the value of 1849.9 eV observed by Perry et al. (46) for presumably pure sphalerite but greater than the value of 1849.3 eV for two Fe-containing sphalerites (21). An Auger parameter of ~1850.0 is entirely consistent with Cu(I) in a sulfide lattice (21), but ~0.3 eV lower than that for covellite (CuS).

It is clear from Fig. 7 that the Cu $2p_{3/2}$ peak could not be fitted adequately with a single component. A better fit could be obtained by including a second minor component at a higher binding energy, however, if the linewidth of the second component was constrained to be no more than 10% greater than that of the principal component, the binding energy of the second component was ~2.3 eV higher than that for the principal component (Table 1). A Cu $2p_{3/2}$ binding energy of 934.8 eV is higher than values normally observed for Cu(I) species or even Cu(II) oxides but similar to values reported for Cu bonded to oxygen in Cu(II) hydroxide (43) and in other oxy-anions. There was no evidence for the excited final state satellites normally associated with Cu(II) species, however for a primary peak of such low intensity excited final state satellites might not be discernible. For the other specimens with the same linewidth constraint, the minor component was at a binding energy 1.85 ± 0.05 eV higher than that for the principal component, nevertheless a binding energy of 934.35 eV is still higher than values nor-

© 2007 NRC Canada

Fig. 8. Cu $2p_{3/2}$ spectrum from a cubanite fracture surface determined at a photon energy of 1025 eV and fitted with a single asymmetric peak.

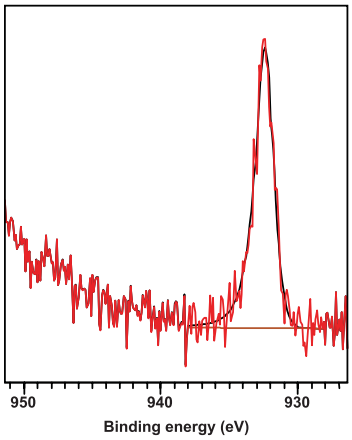


mally observed for Cu(I) species. The intensity of the fitted high binding energy Cu $2p_{3/2}$ component, constrained to have a linewidth no more than 10% greater than that of the principal component, was found to correlate poorly both with the intensity of the principal Cu $2p_{3/2}$ component and with the Cu 3d/S 2p intensity ratio determined at a photon energy of 210 eV.

When the width of the second component was constrained to be no greater than three times the width of the principal component, the best-fit parameters for the second component, which included a significantly lower shift and a higher intensity, suggested that the fit might have been specious. Kartio et al. (45) reported that they required a minor component (intensity ~8%) shifted 1.4 eV to higher binding energy from the principal component and of only slightly greater linewidth to fit the Cu $2p_{3/2}$ peak in their conventional XPS data for Cu activation of sphalerite for 1 h at pH 9. The lower intensity of the higher binding energy component observed by Kartio et al. could be explained by the different pH or by the lower surface sensitivity of the Cu 2p spectrum determined at 1487 eV compared with 1100 eV in the present work.

The Cu 2p spectrum in Fig. 7 resembles the corresponding spectrum from a fracture surface prepared under UHV of some Cu sulfide minerals such as cubanite or covellite determined at similar monochromator and analyser resolution. The Cu $2p_{3/2}$ peak for cubanite ($CuFe_2S_3$) is shown in Fig. 8 fitted with one asymmetric component of shape A(0.3,0.25,0)SGL(20). The Cu $L_{2,3}$-edge NEXAFS spectrum corresponding to the Cu 2p spectrum in Fig. 8 confirmed the expected absence of Cu(II). These observations raise the possibility that the shape of the Cu $2p_{3/2}$ peak from Cu-treated sphalerite arises from a physical effect rather than from the presence of high binding energy Cu environments, such as those in surface species, or with formal oxidation state Cu(II). In this regard it is important to recall that a surface sensitive Cu $2p_{3/2}$ spectrum from tetrahedrite displayed no such high binding energy component, and the corresponding surface optimized S 2p spectrum revealed no discernible low binding energy surface species. If the Cu $2p_{3/2}$ lineshape were to be the result of a physical effect such as a

Fig. 9. Fit to the Cu $2p_{3/2}$ peak in Fig. 7 with a single asymmetric component.

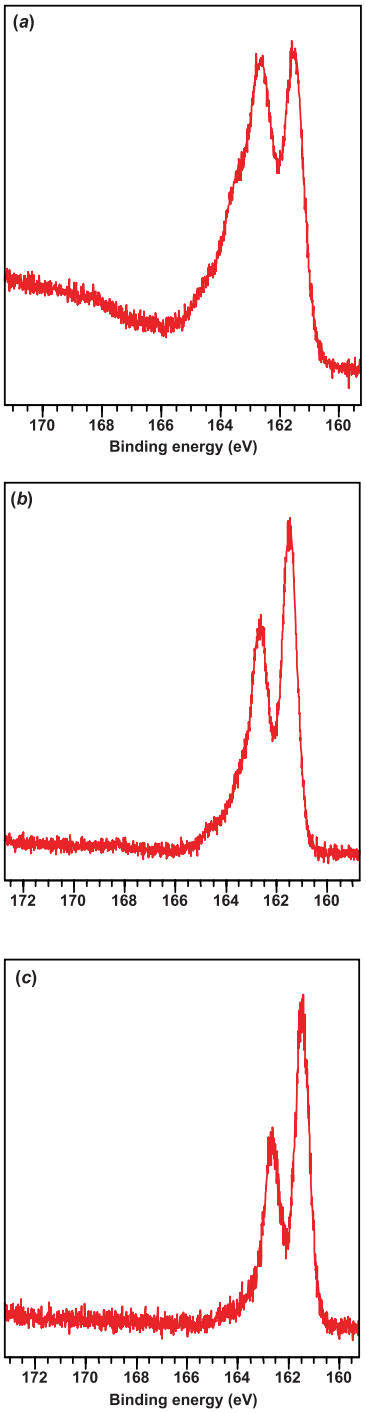


high electron density at the Fermi level, then the Cu $2p_{3/2}$ peak should be able to be fitted with a single asymmetric component. Such a fit is possible, and with the asymmetric lineshapes tried the fits were comparable with, but not better than, those with a higher binding energy component of unconstrained width. An example of a fit with a single asymmetric component of shape A(0.3,0.35,0)GL(50) is shown in Fig. 9. As noted earlier, however, a high electron density at the Fermi level for Cu atoms was not obvious from the shape of the leading edge of the valence band. In principle, surface species for a Cu-Zn-S layer formed by the incorporation of Cu might also be a possible explanation, but as discussed later, there was no evidence for any corresponding S 2p surface species. Another possible reason for the lineshape is a distribution of electronic environments that varies with depth, but this should not be applicable for cubanite or covellite surfaces prepared by fracture under UHV. No definitive explanation for the Cu $2p_{3/2}$ peak shape for the Cu-treated sphalerite can be offered at this stage.

The S 2p spectra for treated surfaces determined at a photon energy of 210 eV (Fig. 10*a*) can be fitted adequately with 3 doublets in the sulfide region (Fig. 11 and Table 2) and the presence of a low concentration of S-O species appeared to be evident from a broad peak near 168.3 eV in the spectrum for the surface treated with Cu^{2+} for 1 min at pH 5. The principal sulfide $2p_{3/2}$ peak was at 161.6 eV. There was no evidence for a S 2p component at a binding energy significantly lower than that for the principal substrate doublet and that might have arisen from identifiable surface species. The reliability of the fitted components was assessed by using different background and line shapes in fitting the same spectrum and by comparing data for spectra obtained at 210 eV near the start and near the end of the accumulation period for all photoelectron and NEXAFS spectra from each specimen (see Table 2 for representative examples). It was found that binding energy shifts and intensities for the fitted components were reproducible to within ±0.1 eV and ±10%, respectively, with significantly higher reproducibility usually observed for fits to the same spectrum on the same basis but starting with different initial parameter estimates. In particular, there was no major difference in the form of the spectra determined near the beginning and end of the specimen X-ray irradiation period, although the relative intensity of

© 2007 NRC Canada

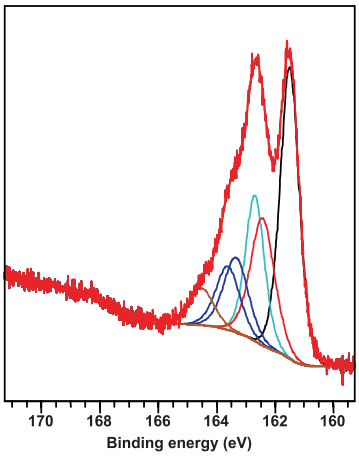
Fig. 10. S 2p spectrum from Santander sphalerite treated for 5 min with aq. Cu^{2+} at pH 2 determined at a photon energy of (*a*) 210 eV, (*b*) 400 eV, and (*c*) 800 eV.



peaks from some elements did change. For example, the S 2p intensity increased towards the end of the measurement period, most probably because of the loss of chemisorbed water from the surface.

As expected, the higher binding energy sulfide components were less obvious in the S 2p spectra obtained at 400 eV (Fig. 10*b*), as was the peak arising from the low concentration of S-O species for the surface treated for 1 min.

Fig. 11. S 2p spectrum in Fig. 1*0a* fitted with three doublet components.



The sulfide region of the 400 eV spectra could be fitted on essentially the same basis as the 210 eV spectra apart from a marginally (~0.1 eV) lower binding energy shift for the highest binding energy doublet. The higher binding energy sulfide components were even less evident in the S 2p spectra determined at 800 eV (Fig. 10*c*), and a peak arising from S-O species was not discernible, confirming that alteration to the sphalerite surface was limited to the outermost few atomic layers. The 800 eV S 2p spectra could be fitted on much the same basis as the 400 eV and 210 eV spectra (Table 2), apart from a further small decrease in the binding energy shift for the highest binding energy doublet.

As evident from Table 2, the S 2p spectra from fracture surfaces treated with Cu^{2+} for 1 and 5 min were broadly similar, although for the surface treated for 5 min at pH 2 there was slightly less higher binding energy sulfide intensity, and the background was flatter. A surface treated with Cu^{2+} for 5 min at pH 5 gave rise to a S 2p spectrum that displayed more high binding energy sulfide intensity than for 1 min interaction with Cu^{2+} solution, but the Cu/Zn ratio revealed by the Cu 3p/Zn 3p intensity ratio determined at a photon energy of 1010 eV was only ~0.3:1, and the Cu 3d/Zn 3d ratio was also lower. Therefore, the concentration of high binding energy sulfide evident in the S 2p spectrum does not appear to be directly related to the concentration of Cu relative to Zn in the surface layer. In the 210 eV S 2p spectrum for the specimen treated for 5 min at pH 5, the intensity of the 1.9 eV shifted component (32%) was greater than the unshifted (24%) with the intermediate about half the unshifted (Table 2). By contrast, for the surface treated for 1 min and for which the corresponding Cu/Zn ratio was 0.7:1, the 1.9 eV shifted S 2p component (14%) was relatively small compared with the unshifted (33%) and intermediate (20%). In particular, the intermediate binding energy sulfide intensity does not appear to be directly related to the Cu concentration, as it should be if a separate Cu oligosulfide phase were formed. It is possible that the concentration of high binding energy S is related to the degree of Zn deficiency which could arise after the initial Cu uptake.

The Cu $2p_{3/2}$ peak shapes near the baseline on the high binding energy side were similar for 1 and 5 min treatment

© 2007 NRC Canada

Table 2. Fitted S $2p_{3/2}$ component relative binding energies, linewidths, and intensities for tetrahedrite and Cu-treated sphalerite.

Mineral	Treatment time (min)	pH	Photon Energy (eV)	Other details	Background	S $2p_{3/2}$ (a) Width, intensity (eV, %)	S $2p_{3/2}$ (b) Position, width, intensity (eV, eV, %)	S $2p_{3/2}$ (c) Position, width, intensity (eV, eV, %)
Tetrahedrite	—	—	210		Shirley	0.9, 100		
Santander sphalerite	1	5	210	Near start	Shirley	0.79, 49	0.87, 0.92, 30	1.85, 0.98, 21
	1	5	210	Near start	Linear	0.76, 44	0.82, 0.92, 29	1.83, 1.19, 27
	1	5	210	Near end	Shirley	0.76, 45	0.85, 1.10, 39	1.91, 0.97, 16
	1	5	400		Shirley	0.73, 63	0.82, 0.88, 20	1.75, 1.22, 17
	1	5	800		Shirley	0.72, 76	0.81, 1.0[a], 15	1.70, 1.3[a], 9
Santander sphalerite	5	2	210	GL(30)	Shirley	0.76, 55	0.89, 0.87, 24	1.77, 1.07, 21
	5	2	"	SGL(10)	Shirley	0.78, 54	0.88, 0.86, 25	1.77, 1.05, 21
	5	2	"	GL(50)	Shirley	0.76, 54	0.93, 0.96, 29	1.84, 0.99, 17
Santander sphalerite	5	5	210	GL(30)	Shirley	1.01, 35	0.77, 1.18, 18	1.94, 1.59, 47
Santander sphalerite	30	9	209	Kartio et al. (45)[b]	Linear	0.8, 34	0.8, 0.8, 23	1.8, 1.1, 43

[a]Constrained to maximum value.
[b]Data estimated from figure.

Fig. 12. PEY Cu L_3-edge NEXAFS spectrum for (*a*, *b*) Santander sphalerite treated with aq. Cu^{2+} at pH 5 for 1 min (*a*) near the start, (*b*) towards the end of the measurement period, and (*c*) Cu metal.

with Cu^{2+}, and the intensity of any higher binding energy component was not obviously influenced by the Cu/Zn ratio in the outermost layers. These observations would be consistent with a physical explanation for the lineshape (such as a high Cu electron density at the Fermi level), but not with the presence of Cu(II) to compensate for loss of Zn. However, only the much greater sensitivity of Cu $L_{2,3}$-edge NEXAFS spectra towards Cu(II) can confirm or preclude the presence of very low concentrations of Cu(II).

Cu $L_{2,3}$-edge NEXAFS spectra were determined in PEY and TEY mode for each Cu-treated sphalerite fracture surface investigated. The slightly more surface sensitive PEY spectra were not significantly different from the corresponding TEY spectra. For the spectra determined soon after the beginning of the measurement period (and start of the irradiation by the X-ray beam), a peak at 930.7 eV, indisputably arising from Cu(II), dominated the spectrum (Fig. 12). A shoulder at ~931.7 eV was also evident, and as this absorption energy is slightly higher than the upper limit of 931.2 eV normally observed for Cu(II) (6, 7, 47, 48), the peak giving rise to the shoulder was probably part of a spectrum from Cu(I). The absorption edge, near 933.6 eV, of the main L_3 peak is consistent with the second part of a spectrum for Cu(I) but not with spectra observed for typical Cu(II) materials (49). Towards the end of the measurement period, the intensity of the Cu(II) peak at 930.7 eV was lower relative to the now resolved peak at 931.7 eV and the main absorption edge from Cu(I), indicating some photoreduction of Cu(II) to Cu(I) had occurred. The fact that the peak near 931.7 eV did not appear to exhibit photoreduction supports its assignment to Cu(I). The photoreduction behaviour was similar for surfaces treated with Cu^{2+} for 1 and 5 min, and there was no obvious dependence on the period between treatment and characterization that might have arisen from a slow conversion of Cu(II) to Cu(I) in the sulfide lattice.

Discussion

Tetrahedrite

Although Charnock et al. (2) cautioned that the delocalization of electrons in many sulfide structures means that assignment of formal oxidation states to the cations represents an over-simplification, they noted that quite different ^{57}Fe Mössbauer spectra were produced by different

© 2007 NRC Canada

tetrahedrite minerals. Also, Pattrick et al. (6) have established that tetrahedrites display different Cu $L_{2,3}$-edge NEXAFS spectra, therefore differences in formal oxidation states for Cu and Fe in the tetrahedrites are not merely semantic differences.

There have been very little XPS data published for tetrahedrite, and most of that information is for surfaces conditioned in alkaline solution. Most importantly for the present study, Mielczarski et al. (50) found that for a natural tetrahedrite immediately after treatment at pH 10, a significant concentration of Cu(II) hydroxide was present at the mineral surface, but Sb-O species were not evident. If the oxidation behaviour of the mineral were similar in air to aq. pH 10 solution, or even if Sb(V)-O as well as Cu(II)-O species were formed, then it would be possible for Cu(II) from surface oxidation of the specimen to be detected in PEY or TEY NEXAFS spectra. This might explain the observation of 2.9% Cu(II) in a finely divided natural tetrahedrite specimen of composition $Cu_{5.84}Ag_{4.22}Zn_{0.43}Fe_{1.59}Sb_{4.10}As_{0.13}S_{13}$ (i.e., with Cu + Ag only marginally greater than 10) by means of TEY NEXAFS spectroscopy (6). However, low-resolution Cu 2p spectra obtained (13) for both tetrahedrite and tennantite specimens, ground under nitrogen but transferred to the spectrometer in air, provided no evidence for the presence of Cu(II). Cu $2p_{3/2}$ and $Sb_{3/2}$ spectra reported (51) for tetrahedrite after 30 min grinding in a planetary mill in air indicated the presence of Cu(II) and Sb-O species at the altered surface, whereas before that treatment only Cu(I) (as well as some Sb-O species) had been evident.

XPS data available for the closely related mineral tennantite, $(Cu,Ag)_{10}(Fe,Zn)_2As_4S_{13}$, suggest a lower reactivity towards oxygen. The absence of Cu 2p excited final state satellites for a tennantite surface prepared by fracture in air, and minimal oxidation of such a surface after further exposure to air for 30 min, have been reported (52). Also, negligible Cu(II) species retained at the surface of tennantite conditioned at pH 10 or polarized in 0.1 mol/L HCl have been observed (50, 53). On the other hand, Cu $2p_{3/2}$ components within the binding energy range 933.9–936.2 eV attributed to Cu(II) were observed (54) at the surface of both natural and synthetic tennantite after it had been conditioned at pH 11.

It is perhaps surprising that no evidence for S 2p surface species was discernible for tetrahedrite. Sulfides of structure similar to sphalerite or wurtzite are expected to undergo considerable relaxation of surface atoms following fracture. For sphalerite, the relaxation involves movement of the outermost Zn and S atoms by up to 0.05 nm (55), and conventional XPS evidence for a S 2p surface state shifted by about –0.5 eV has been reported (30). The fitted S $2p_{3/2}$ linewidth was broader than for Cu sulfides of higher electrical conductivity (and for which charge compensation was not required), but any surface species must have had energies not markedly different from the bulk states, and (or) there was an equal concentration of states with energies higher and lower than the bulk states. A broad leading absorption peak observed in the S K-edge and L-edge NEXAFS spectra for minerals of composition $Cu_{11.06}Fe_{0.99}As_{0.18}Sb_{4.03}S_{13}$ and $Cu_{10.53}Fe_{0.94}As_{2.31}Sb_{1.78}S_{13}$ was attributed (56) to the presence of the 6-coordinate S and (or) the presence of minor Cu(II).

Cu-treated sphalerite

Taking into account the higher $L_{2,3}$ absorption cross-section for Cu(II) relative to Cu(I), and the fact that Cu(II) L_3-edge spectra, such as those for tenorite and azurite (49), usually consist largely of a single narrow peak, it is clear that most of the Cu at the surface of Cu-treated sphalerite was present as Cu(I), nevertheless some Cu(II) was undoubtedly also present. The question is, where was the Cu(II) located? Was it a low concentration of Cu(II) in the sphalerite lattice, or was it from one or more Cu(II)-O species present at the Cu-treated surface, or both? Although the O 1s spectra indicated that the O was probably present as chemisorbed water rather than a hydroxide, which probably would have been associated with Cu(II), the Cu(II) intensity appeared to correlate with the O 1s intensity. This suggests that the outermost layer of Cu may have been between the surface of the sulfide lattice and chemisorbed water. Such an arrangement would be consistent with the REFLEXAFS data of Pattrick et al. (18), who concluded that Cu at the surface of sphalerite was bonded to both S and O atoms. It is also consistent with the ease of removal of the Cu(II); the process may well be one of stimulated desorption of chemisorbed water rather than of simple photoreduction of Cu(II) to Cu(I). Loss of chemisorbed water from the surface would be consistent with the observed lowering of O 1s intensity during the course of the measurements. If this is indeed the case, then it effectively precludes any conclusion on whether a low concentration of Cu(II) can be present in the sulfide lattice.

Some apprehension has been expressed (57) about the accommodation of Cu(I) in the sphalerite lattice on the grounds of a larger ionic radius of Cu(I) compared with Zn(II) and a charge imbalance between Cu(I) and S(-II). Given that the Zn–S bond length (0.234 nm) in sphalerite is similar to tetrahedral Cu–S bond lengths (e.g., 0.234 nm in tetrahedrite, 0.232 nm in chalcopyrite), such that the tetrahedral covalent radii (the radii of relevance here) for Zn and Cu are considered to be 0.131 and 0.135 nm, respectively (58), size would not appear to constitute a problem. Furthermore, the covalent radii of Cu(I) and Fe(II) in tetrahedral S sites are similar, with relevant Fe–S bond lengths of ~0.231 nm (2), and Fe is accommodated easily within the sphalerite lattice therefore Cu(I) should also be easily accommodated. Moreover, there should be no requirement for the actual charge on the S atoms in the sulfide lattice to remain the same after replacement of Zn by Cu.

The remaining question is whether the Cu(I) that was present near the sphalerite surface was in a sphalerite S lattice essentially unchanged apart from the substitution of some Zn by Cu (and a concomitant decrease in the electron density on the S atoms around those Cu atoms) in a sphalerite S lattice containing some Zn vacancies as well as some Cu in Zn sites, or only in a phase restructured to a CuS-like phase (that could be subsequently oxidized to a Cu oligosulfide) similar to that proposed by Kartio et al. (45).

Although the Cu L-edge peak at 931.7 eV attributed to Cu(I) is at an energy slightly lower than the lower limit of

© 2007 NRC Canada

931.9 eV usually associated with Cu(I) and approaching the upper limit of 931.2 eV normally associated with Cu(II), the leading absorption peak energy for Cu(I) in tetrahedral coordination by S is not always as high as the edge peak energy observed for tetrahedrite (934.5 eV) where no "pre-edge" peak is observed. Low energy pre-edge peaks are observed for chalcopyrite (932.6 eV) and bornite (932.7 eV), therefore an even lower energy (931.7 eV) of the pre-edge peak for treated sphalerite is not by itself sufficient reason to rule out Cu in 4-fold coordination by S, but it does indicate a significant difference in electronic environment. In particular, a d^9 character for the Cu atoms larger than normally observed for Cu(I) but not as large as that normally observed for Cu(II) is indicated.

The interaction of aq. Cu^{2+} ions with the surface of sphalerite has been extensively investigated by means of bulk and surface techniques and the findings reviewed by Finkelstein (42). Three of those findings are highly relevant for interaction under weakly acidic conditions. First, the number of Cu^{2+} ions removed from solution by the mineral is the same, within experimental error, as the number of Zn^{2+} ions released to the solution (e.g., 59, 60). Accordingly, at least during the initial stage of the Cu^{2+} treatment and before any restructuring of the sphalerite surface layer to a Cu sulfide phase might occur, the ion exchange reaction [1] forming a metastable surface phase should be applicable (21),

$$[1] \qquad xCu^{2+} + ZnS \rightarrow xZn^{2+} + Zn_{1-x}Cu_xS$$

Second, Cu 2p photoelectron spectra and X-ray excited Cu $L_3M_{4,5}M_{4,5}$ Auger electron spectra determined by conventional XPS have been consistent with the presence of only Cu(I) in the sulfide lattice; no Cu(II) has been discernible (e.g., 21, 45, 46). However, it should be noted that in some nonsulfide systems, small concentrations of Cu(II) have been detected directly by Cu L_3-edge NEXAFS spectra and indirectly by ToF-SIMS when the presence of Cu(II) was not evident in the Cu 2p or Cu $L_3M_{4,5}M_{4,5}$ spectra (20). The observation of some Cu(II) at the surface after treatment in alkaline solutions has normally been attributed to adsorbed Cu(II) hydroxy species. Third, at least one S 2p component at a binding energy at least 0.8 eV higher than that for sphalerite has been observed for the Cu^{2+}-treated mineral, suggesting a formal oxidation state less negative than (-II) for this component.

It should be noted that the metastable surface phase representation $Zn_{1-x}Cu_xS$ implies no particular formal oxidation state for the Cu, just as the chemical formulae CuS and CuS_2 do not. What is implied is a formal oxidation state for S more positive than -II if the Cu is present as Cu(I) and therefore the possible presence of a S 2p component at a binding energy higher than that for sphalerite. It should also be emphasised that a formal oxidation state of S(–II) does not mean an *actual* charge of S^{-2}. Pauling (58) even considered that the actual charge on the S atoms in some metal sulfides might be positive.

The observation of at least one S $2p_{3/2}$ binding energy higher than that for sphalerite has usually been explained by the formation of a CuS-like phase (e.g., 45),

$$[2] \qquad Zn_{1-x}Cu_xS \rightarrow xCuS + (1-x)ZnS$$

As mentioned earlier, any CuS-like phase cannot be the same as covellite, as the Auger parameter is different, as is the high binding energy side of the Cu $2p_{3/2}$ peak. Alternatively, and notwithstanding the fact that the S 2p spectrum provides no evidence for the production of elemental sulfur, a Cu_2S-like phase plus elemental S has been proposed (e.g., 61),

$$[3] \qquad Zn_{1-x}Cu_xS \rightarrow 0.5xCu_2S + 0.5xS^0 + (1-x)ZnS$$

Kartio et al. (45) first resolved the high binding energy S 2p component into two components by determining spectra at 209 eV from Santander sphalerite surfaces wet-polished in air and treated with Cu^{2+} solution at pH 9.2 either in air or under nitrogen. They found that for the nitrogen-purged Cu^{2+} solution the surface Cu concentration relative to Zn and S was greater than for treatment in air, and that the component at +1.8 eV was less intense, but the +0.8 eV component was of comparable intensity, relative to the underlying sphalerite component. They proposed that the S 2p component at a binding energy ~0.8 eV higher than for sphalerite arose from the CuS-like activation product, and the component ~1.8 eV higher arose from oligosulfide. They correctly noted that the formation of a Cu oligosulfide phase requires oxidation following the Cu incorporation and cannot be the result of Cu incorporation alone. However, in an apparent contradiction of that understanding they suggested that the S^0 in eq. [3] could actually be part of a polysulfide chain.

Even if oligosulfide-like electronic environments were established within a modified sphalerite lattice rather than a restructured phase, loss of Zn that was not replaced by Cu would be involved, and that leaching would constitute an oxidation process,

$$[4] \qquad Zn_{1-x}Cu_xS \rightarrow Zn_{1-x-y}Cu_xS + yZn^{2+} + 2ye^-$$

It is expected that the oxidant associated with eq. [4] would be residual oxygen. If such a loss of Zn occurred in the cupric solution, it would not be in agreement with previous observations of the Cu uptake being the same as the Zn release, but if the additional Zn loss was only from the outermost few atomic layers, then it might not be detectable by measuring solution concentrations. It is also possible that Zn loss might occur when a treated sphalerite surface is washed with water after removal from the cupric solution.

If the S 2p component shifted by ~0.8 eV were to arise from a CuS-like Cu-activation product, then its intensity might be expected to be proportional to the concentration of Cu. Indeed, even if a Cu oligosulfide were the Cu-activation product, the component shifted by ~0.8 eV should correlate with the Cu concentration, as that binding energy would be expected to correspond to S atoms nearest the Cu atom of a Cu oligosulfide complex (62). A poor correlation was observed in the present study. The poor correlation could be explained by loss of Zn from the Cu-activated surface that is not replaced by Cu as in eq. [4]. Oligosulfide-like electronic environments could be associated with Zn or Cu atoms (i.e., could be considered part of a Zn or Cu oligosulfide) and could be created by Zn vacancies in a largely unrestructured sulfide lattice. This possibility would be more consistent with a surface layer sufficiently conducting to not need a

© 2007 NRC Canada

flood gun; a "molecular" Cu oligosulfide was found to charge even in conventional XPS (62).

Gerson et al. (57) proposed a model for a Cu-activated sphalerite surface that did not involve the formation of oligosulfide either in a reconstructed phase or in a largely unreconstructed S lattice containing vacancies. They postulated that the Cu atoms would have a distorted trigonal planar geometry (coordinated to 3 S atoms) in both surface and bulk sites where the S would have an "oxidation state" of approximately –1.5 in the former case and –0.5 in the latter, and thereby give rise to the two high binding energy S 2p components observed. However, although an interesting suggestion, their model is inconsistent with the similar binding energies observed for the S atoms associated with the trigonal planar and tetrahedral Cu sites in tetrahedrite, or with the poor correlation between the concentration of high binding energy S environments and the concentration of Cu in the treated sphalerite surface. On the available evidence, loss of some metal atoms from a sphalerite surface that are not replaced by Cu (i.e., oxidation of a Cu-treated surface) is the only plausible explanation for a S-enriched surface that could have oligosulfide-like electronic environments. It has yet to be established whether CuS-like "disulfide" environments can be produced *without* the concomitant formation of oligosulfide-like environments. A more definitive identification of the nature of the Cu-treated sphalerite surface and the mechanism by which it becomes S-rich should result from the research currently in progress by Harmer et al. on the treatment of Fe-containing sphalerites by aq. Cu^{2+}.

Conclusions

The Cu $L_{2,3}$-edge and Cu 2p spectra for a natural tetrahedrite surface prepared by fracture under UHV indicated that all Cu in the mineral was indisputably Cu(I), with no Cu(II) present for "charge neutrality". This was notwithstanding the fact that the mineral characterized had a significant excess of univalent metal atoms and a comparable deficiency in divalent metal atoms. The XPS data provided no evidence for different S or Cu core electron binding energies in tetrahedrite. In particular, the 2p binding energy for the 6-coordinate S atoms was found to be not detectably greater than that for the 4-coordinate S atoms, and there was no measurable difference in the 2p binding energies for the Cu atoms in trigonal planar and tetrahedral sites.

The Cu $L_{2,3}$-edge spectra of relatively pure natural sphalerite treated with mildly acidic aqueous cupric solution revealed the presence of Cu(II) that was consistent with Cu bonded both to S atoms in the outermost layer of the sphalerite and to O atoms in chemisorbed water. Most of the Cu near the surface of the mineral was in formal oxidation state Cu(I), albeit with higher than normal d^9 character. Surface-optimized S 2p spectra revealed high binding energy components from the outermost layers that were consistent with oligosulfide-like environments, but not necessarily in a completely restructured lattice and not in a Cu oligosulfide only. The presence of these oligosulfide-like environments precluded the detection of S with formal oxidation state greater than (-II) that might have arisen only from Cu(I) in the S lattice. The data were consistent with some loss of Zn in addition to the Zn that had been replaced by Cu in the outermost layers of the sulfide lattice. No evidence was obtained for the presence of Cu(II) in a sulfide lattice, but it was not possible to exclude the possibility of a very low concentration because of the presence of the Cu(II) bonded to both S and O at the surface of the treated sphalerite. Accordingly, no support was obtained for the proposition, nor irrefutable evidence for its indictment that Cu(II) can be required for charge neutrality in a sulfide lattice.

Acknowledgements

Access to synchrotron beam time was made possible by support from the Australian Synchrotron Research Program, which is funded by the Commonwealth of Australia under the Major National Research Facilities Program. Use of the Taiwan Light Source, assistance by personnel at the National Synchrotron Radiation Research Center in Hsinchu, electron microprobe analyses by Daniel Yoo-Hyun Sung, and helpful discussions with David French and Angus Netting are gratefully acknowledged.

References

1. N.E. Johnson, J.R. Craig, and J.D. Rimstidt. Am. Mineral. **73**, 389 (1988).
2. J.M. Charnock, C.D. Garner, R.A.D. Pattrick, and D.J. Vaughan. Min. Mag. **53**, 193 (1989).
3. D.W. Bullett and W.G. Dawson. J. Phys. C Solid State Phys. **19**, 5837 (1986).
4. R. Jeanloz and M.L. Johnson. Phys. Chem. Miner. **11**, 52 (1984).
5. E. Makovicky and B.J. Skinner. Can. Mineral. **16**, 611 (1978).
6. R.A.D. Pattrick, G. van der Laan, D.J. Vaughan, and C.M.B. Henderson. Phys. Chem. Miner. **20**, 395 (1993).
7. R.A.D. Pattrick, J.F.W. Mosselmans, J.M. Charnock, K.E.R. England, G.R. Helz, C.D. Garner, and D.J. Vaughan. Geochim. Cosmochim. Acta, **61**, 2023 (1997).
8. C.I. Pearce, R.A.D. Pattrick, D.J. Vaughan, C.M.B. Henderson, and G. van der Laan. Geochim. Cosmochim. Acta, **70**, 4635 (2006).
9. G.P. Bernardini, A. Caneschi, C. Danti, F. Di Benedetto, and M. Romanelli. Proc. Int. Symp. Experimental Mineralogy, Petrology and Geochemistry IX, Zurich, Switzerland. 24–27 March 2002. p. 11.
10. R.J. Goble. Can. Mineral. **23**, 61 (1985).
11. F. Jellinek. In MTP Int. Rev. Sci. Inorg. Chem. Ser. One. Vol 5. Butterworths, London, UK. 1972. pp. 339–396.
12. H. Rupp and U. Weser. Bioinorg. Chem. **6**, 45 (1976).
13. I. Nakai, Y. Sugitani, K. Nagashima, and Y. Niwa. J. Inorg. Nucl. Chem. **40**, 789 (1978).
14. J.C.W. Folmer and F. Jellinek. J. Less-Common Met. **76**, 153 (1980).
15. J.C.W. Folmer and D.K.G. de Boer. Solid State Commun. **38**, 1135 (1981).
16. J.C.W. Folmer, F. Jellinek, and G.H.M. Calis. J. Solid State Chem. **72**, 137 (1988).
17. J.F.W. Mosselmans, R.A.D. Pattrick, G. van der Laan, J.M. Charnock, and D.J. Vaughan. Phys. Chem. Miner. **22**, 311 (1995).
18. R.A.D. Pattrick, K.E.R. England, J.M. Charnock, and J.F.W. Mosselmans. Int. J. Miner. Process. **55**, 247 (1999).
19. H. Ueda, M. Nohara, K. Kitazawa, H. Takagi, A. Fujimori, T. Mizokawa, and T. Yagi. Phys. Rev. B, **65**, 155104 (2002).

© 2007 NRC Canada

20. S.W. Goh, A.N. Buckley, R.N. Lamb, L.-J. Fan, and Y.-w. Yang. ECS Trans. **2**, 107 (2006).
21. A.N. Buckley, R. Woods, and H.J. Wouterlood. Int. J. Miner. Process. **26**, 29 (1989).
22. A.H. Clark and R.H. Sillitoe. Am. Mineral. **55**, 1021 (1970).
23. R.A.D. Pattrick, J.F.W. Mosselmans, and J.M. Charnock. Eur. J. Mineral. **10**, 239 (1998).
24. K.C. Mishra, K.H. Johnson, P.C. Schmidt, B.G. DeBoer, J. Olsen, and E.A. Dale. Phys. Rev. B, **43**, 14188 (1991).
25. T. Telehun, U. Scherz, P. Thurian, R. Heitz, A. Hoffmann, and I. Broser. Phys. Rev. B, **53**, 1274 (1996).
26. I. Wu and U. Petersen. Econ. Geol. **72**, 993 (1977).
27. P.-C. Tseng, C.-C. Chen, T.-E. Dann, S.-C. Chung, C.T. Chen, and K.-L. Tsang. J. Synchrotron Rad. **5**, 723 (1998).
28. B.H. Frazer, B. Gilbert, B.R. Sonderegger, and G. De Stasio. Surf. Sci. **537**, 161 (2003).
29. L. Ley, R.A. Pollak, F.R. McFeely, S.P. Kowalczyk, and D.A. Shirley. Phys. Rev. B, **9**, 600 (1974).
30. S.L. Harmer, L.V. Goncharova, R. Kolarova, W.N. Lennard, M.A. Muñoz-Márquez, I.V. Mitchell, and H.W. Nesbitt. Surf. Sci. **601**, 352 (2007).
31. U. Gelius. 7th Quantitative Surface Analysis Conference, University of Surrey, Surrey, UK. 8–11 September 1992.
32. D. Briggs and N. Fairley. Surf. Interface Anal. **33**, 283 (2002).
33. M.L. Johnson and R. Jeanloz. Am. Mineral. **68**, 220 (1983).
34. J.H. Scofield. J. Electron Spectrosc. **8**, 129 (1976).
35. V.P. Zakaznova-Herzog, S.L. Harmer, H.W. Nesbitt, G.M. Bancroft, R. Flemming, and A.R. Pratt. Surf. Sci., **600**, 348 (2006).
36. S.W. Goh, A.N. Buckley, R.N. Lamb, R.A. Rosenberg, and D. Moran. Geochim. Cosmochim. Acta, **70**, 2210 (2006).
37. K. Laajalehto, I. Kartio, T. Kaurila, T. Laiho, and E. Suoninen. *In* Proc. ECASIA 1995. *Edited by* H.J. Mathieu, B. Reihl, and D. Briggs. Wiley, Chichester, NY. 1996. pp. 717–720.
38. D.L. Legrand, G.M. Bancroft, and H.W. Nesbitt. Int. J. Miner. Process. **51**, 217 (1997).
39. A.G. Schaufuß, H.W. Nesbitt, I. Kartio, K. Laajalehto, G.M. Bancroft, and R. Szargan. J. Electron Spectrosc. **96**, 69 (1998).
40. S.W. Goh, A.N. Buckley, R.N. Lamb, L.-J. Fan, L.-Y. Jang, Y.-w. Yang. Phys. Chem. Miner. **33**, 445 (2006).
41. M.O. Figueiredo, J. Mirão, and J.A. Ferreira. ESRF report on experiment number ME-589. European Synchrotron Radiation Facility, Grenoble, France. 2003.
42. N.P. Finkelstein. Int. J. Miner. Process. **52**, 81 (1997).
43. W.M. Skinner, C.A. Prestidge, and R.StC. Smart. Surf. Interface Anal. **24**, 620 (1996).
44. D.A. Verner, D.G. Yakovlev, I.M. Band, and M.B. Trzhaskovskaya. At. Data Nucl. Data Tables, **55**, 233 (1993).
45. I.J. Kartio, C.I. Basilio, and R.-H. Yoon. Langmuir, **14**, 5274 (1998).
46. D.L. Perry, L. Tsao, and J.A. Taylor. *In* Proc. Int. Symp. Electrochemistry in Mineral and Metal Processing. *Edited by* P.E. Richardson, S. Srinivasan, and R. Woods. The Electrochem. Soc., Pennington, NJ. 6–11 May 1984. pp. 169–184.
47. G. van der Laan, R.A.D. Pattrick, C.M.B. Henderson, and D.J. Vaughan. J. Phys. Chem. Solids, **53**, 1185 (1992).
48. G. van der Laan, R.A.D. Pattrick, J.M. Charnock, and B.A. Grguric. Phys. Rev. B, **66**, 045104 (2002).
49. E.C. Todd and D.M. Sherman. Am. Mineral. **88**, 1652 (2003).
50. J.A. Mielczarski, J.M. Cases, M. Alnot, and J.J. Ehrhardt. Langmuir, **12**, 2519 (1996).
51. P. Balaz, Z. Bastl, and V. Vigdergauz. Fizykochem. Problemy Mineral. **29**, 13 (1995).
52. E.L. Hobson, P. Wincott, D.J. Vaughan, and R.A.D. Pattrick. Min. Mag. **70**, 445 (2006).
53. J. Ásbjörnsson, G.H. Kelsall, D.J. Vaughan, R.A.D. Pattrick, P.L. Wincott, and G.A. Hope. J. Electroanal. Chem. **570**, 145 (2004).
54. D. Fullston, D. Fornasiero, and J. Ralston. Langmuir, **15**, 4530 (1999).
55. D.J. Vaughan, U. Becker, and K. Wright. Int. J. Miner. Process. **51**, 1 (1997).
56. D. Li, G.M. Bancroft, M. Kasrai, M.E. Fleet, X.H. Feng, B.X. Yang, and K.H. Tan. Phys. Chem. Miner. **21**, 317 (1994).
57. A.R. Gerson, A.G. Lange, K.E. Prince, and R.StC. Smart. Appl. Surf. Sci. **137**, 207 (1999).
58. L. Pauling. *In* The nature of the chemical bond and the structure of molecules and crystals. 3rd Ed. Cornell University Press, Ithaca, NY. 1960. Chap. 11. p. 644.
59. J. Ralston and T.W. Healy. Int. J. Miner. Process. **7**, 175 (1980).
60. C.C. Sui, D. Lee, A. Casuge, and J.A. Finch. Miner. Metall. Process. **16**, 53 (1999).
61. C.A. Prestidge, W.M. Skinner, J. Ralston, and R.StC. Smart. Appl. Surf. Sci. **108**, 333 (1997).
62. S.C. Termes, A.N. Buckley and R.D. Gillard. Inorg. Chim. Acta, **126**, 79 (1987).

© 2007 NRC Canada

High resolution O 1s XPS spectral, NMR, and thermodynamic evidence bearing on anionic silicate moieties (units) in $PbO-SiO_2$ and Na_2O-SiO_2 glasses[1]

H.W. Nesbitt and K.N. Dalby

Abstract: Recent technical advances in X-ray photoelectron spectroscopy (XPS) have largely overcome differential charging of insulator surfaces, with the result that O 1s linewidths for silicates can be routinely collected that are 50% to 100% narrower than had been previously obtainable. The bridging and nonbridging oxygen signals of glasses are well resolved and now can be accurately measured by XPS without resorting to ad hoc fitting procedures. All O 1s spectra of silicates collected so far are somewhat asymmetric to the high binding energy side of the peak, a characteristic due primarily to vibrational contributions in the ion state produced by photoemission (electronic excited state). This asymmetry must be considered if the proportion of bridging to nonbridging oxygen ratios are to be accurately determined from the XPS O 1s spectra of silicates. X-ray photoelectron spectroscopy (XPS) and nuclear magnetic resonance (NMR) experiments yield similar silicon-bridging oxygen (Si-**O**-Si) concentrations for $PbO-SiO_2$ glasses. The data are proof that the reaction, $2PbO + SiO_2 \Rightarrow Pb_2SiO_4$, does not go to completion (i.e., one or other reactant is not completely consumed). Instead, the data indicate that an equilibrium exists among these constituents, with the equilibrium constant for the reaction being near 15; ergo, some metal bridging oxygen (MBO or Pb-**O**-Pb), silicon bridging oxygen (BO or Si-**O**-Si), and nonbridging oxygen (NBO or M-**O**-Si) are present over the entire range of binary melt compositions. NMR and XPS spectroscopic techniques yield substantially different Si-**O**-Si concentrations in Na_2O-SiO_2 glasses of intermediate to high Na_2O content. XPS experiments indicate higher proportions of Si-**O**-Si in Na_2O-rich glasses than do the NMR studies. In spite of the different results, three independently collected sets of NMR experiments are similar and yield similar Si-**O**-Si concentrations. Five XPS experimental studies are likewise self-consistent (but different from the NMR studies). Comparison of data from the two spectroscopic techniques indicates that all experimental spectra are of good or reasonable quality, so that systematic experimental problems or the interpretation (i.e., fitting) of these spectra may be incorrect for one or both types of spectral data. Viscosity, conductivity, and the XPS data are consistent with (but not proof for) formation of an $Na_2Si_2O_5$ species in the Na_2O-SiO_2 glasses. The most comprehensive NMR study is, by contrast, consistent with the formation of an orthosilicate species (Na_4SiO_4). The NMR and XPS results cannot yet be reconciled and additional experimental studies are required to resolve and to understand better Na_2O-SiO_2 liquids and glasses.

Key words: XPS, high resolution, silicate glass, NMR.

Résumé : Les progrès techniques récents dans le domaine de la spectroscopie photoélectronique aux rayons X (SPX) ont permis d'éliminer des différences dans les charges des surfaces des isolants et il en résulte que des largeurs de raies 1s de l'oxygène de quelques silicates de 50% à 100% plus fines que celles obtenues antérieurement peuvent maintenant être recueillies d'une façon routinière pour les silicates. Les signaux des atomes d'oxygène qui servent ou qui ne servent pas de pont dans les verres sont maintenant bien résolus et il est alors possible de mesurer d'une façon précise les SPX sans avoir à utiliser des méthodes ad hoc d'ajustements. Tous les spectres 1s des atomes d'oxygène des silicates qui ont été recueillis jusqu'à maintenant sont quelque peu asymétriques et déplacés vers la partie de haute énergie de liaison du pic, une caractéristique qui est principalement due à des contributions de vibration dans l'état ionique produit lors de la photoémission (état électronique excité). On doit considérer cette émission si on veut déterminer avec précision la proportion des rapports des signaux des atomes d'oxygène qui servent ou qui ne servent pas de pont dans les verres à partir des spectres SPX 1s des atomes d'oxygènes des silicates. Des expériences de spectroscopie photoélectronique des rayons X (SPX) et de résonance magnétique nucléaire (RMN) ont permis de déterminer des concentrations similaires d'atomes d'oxygène servant de pont pour le silicium (Si-**O**-Si) de verres du

Received 8 May 2007. Accepted 27 June 2007. Published on the NRC Research Press Web site at canjchem.nrc.ca on 4 August 2007.

H.W. Nesbitt and K.N. Dalby.[2] Department of of Earth Sciences, *The* University *of* Western Ontario, London, ON N6A 5B7, Canada.

[1]This article is part of a Special Issue dedicated to Professor G. Michael Bancroft.
[2]Corresponding author (e-mail: kim.dalby@gmail.com).

 doi:10.1139/V07-085 © 2007 NRC Canada

type PbO-SiO_2. Les données sont une preuve que la réaction 2Pbo + $SiO_2 \Rightarrow Pb_2SiO_4$ n'est pas complète (c'est-à-dire qu'un ou l'autre des réactifs n'est pas complètement utilizé). Les données montrent plutôt qu'il existe un équilibre entre ces constituants, avec une constante d'équilibre de pratiquement 15; en conséquence, sur l'ensemble des combinaisons binaires du produit fondu, on retrouve diverses entités impliquant, entre autre, des atomes d'oxygène liant des métaux (du type Pb-**O**-Pb), des atomes d'oxygène liant des atomes de silicium (du type Si-**O**-Si) et des atomes d'oxygène non liants (du type M-**O**-Si). Les techniques de RMN et de SPX conduisent à des concentrations substantiellement différentes de Si-**O**-Si dans les verres de Na_2O-SiO_2 contenant des quantités allant d'intermédiaires à élevées de Na_2O. Par comparaison avec les résultats obtenus par RMN, les expériences de SPX donnent des proportions supérieures de Si-**O**-Si dans les verres riches en Na_2O. Malgré les différences dans ces résultats, trois expériences indépendantes de RMN ont conduit à des ensembles de données similaires et ont conduit à des concentrations en Si-**O**-Si semblables. De la même manière, cinq expériences de SPX sont autocohérentes, mais différentes des études par RMN. Une comparaison des données obtenues par les deux techniques spectroscopiques indique que tous les spectres expérimentaux sont de qualité qui varie de bonne à raisonnable et qu'on doit en conclure que des problèmes expérimentaux systématiques ou des problèmes d'interprétation (telle l'ajustement) de ces spectres pourraient se présenter pour un ou chacun de ces types de données spectrales. La viscosité, la conductivité et les données de SPX sont en accord le fait, mais n'en sont pas une preuve, que dans les verres Na_2O-SiO_2 il y a formation d'une espèce $Na_2Si_2O_5$. L'étude RMN plus approfondie est, par ailleurs, en accord avec la formation d'une espèce orthosilicate (Na_4SiO_4). Les résultats de la RMN ou des SPX ne peuvent pas encore être réconciliés et des études expérimentales additionnelles s'imposent pour résoudre et comprendre mieux les liquides et les verres Na_2O-SiO_2.

Mots-clés : SPX, haute résolution, verre de silicate, RMN.

[Traduit par la Rédaction]

Introduction

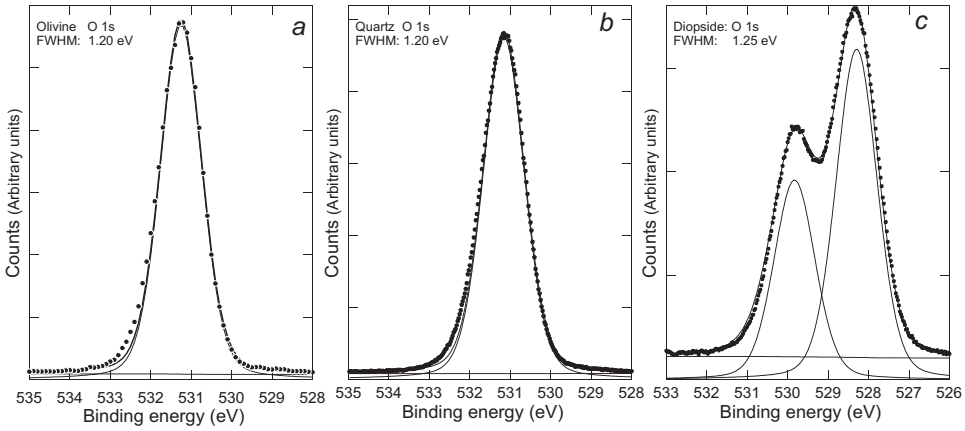
It is a pleasure to contribute to a volume honouring Mike Bancroft's diverse contributions to the understanding of synthetic and natural compounds. His interests in insulators, and silicates particularly, derived from an early and productive encounter with Roger Burns, a postdoctoral fellow at Cambridge University. Mike's interest in natural materials, his enthusiasm and prodding, convinced the senior author to apply X-ray photoelectron spectroscopy to natural semiconductors and insulators in the late 1980s. Although Mike's early forays into XPS studies of insulators were frustrated by poor resolution resulting from surface charging, this interest was re-ignited with the advent of the magnetic confinement charge compensation system of the Kratos Ultra Axis instrument, first produced in the 1990s. With the acquisition of the instrument at *The* University *of* Western Ontario, Mike has been integral to our investigations into the spectroscopic properties of silicates. Here we report some recent findings. His experience of, insight into, and enthusiasm for XPS studies of gaseous and solid materials has had a major impact on the direction of our small group.

The bulk properties of silicate glasses and melts have been studied quantitatively since the early 1950s (1). The thermodynamic properties of silicate glasses have also been evaluated from many perspectives, yet only the last 20 years has seen the application of numerous spectroscopic techniques to silicate liquids and glasses, including Raman, IR, X-ray photoelectron spectroscopy (XPS), and nuclear magnetic resonance spectroscopy (NMR; 2–9). The vibrational spectroscopies (Raman and IR) yield broad signals requiring sophisticated fitting procedures to evaluate the various contributions to the spectra (e.g., 7). The XPS data provide a direct measure of the fraction of bridging oxygen (Si-**O**-Si) relative to total oxygen in liquids and glasses (8), and with appropriate care NMR (^{29}Si and ^{17}O) also provides the proportions of Si-**O**-Si and nonbridging oxygen (M-**O**-Si where M is a metal ion) in silicate liquids and glasses (e.g., 9). The evaluation of bridging and nonbridging abundances in glasses has, however, been hampered by broad O 1s linewidths. The breadth of these lines results either from the charging of surfaces or from the use of nonmonochromatic photon sources, which yield broad peaks. Recent advances in charge compensation incorporated into the Kratos Ultra Axis instrument have overcome charging problems, allowing the use of a monochromated Al Kα source. These advances have resulted in O 1s linewidths some 50% to 100% narrower than has been previously obtainable. The properties of the narrower O 1s spectra of silicates are evaluated here and are found to be asymmetric. The insight gained is used to interpret and accurately quantify measurements in PbO-SiO2 glasses and to interpret better the XPS results from previous studies. Here we compare XPS and NMR data from PbO-SiO_2 and Na_2O-SiO_2 glasses using a measure common to both techniques, the fraction of bridging oxygen (Si-**O**-Si) in silicate glasses. This measure is adopted because the fraction of Si-**O**-Si may be unambiguously evaluated over a wide range of compositions solely from the data collected by each technique.

Electrical conductivity measurements of alkali-, alkaline earth-, and Pb-silicate melts indicate 100% Faradaic yield (1). In the SiO_2-rich portion of these binary melts, conductance is unipolar with the cation transporting all charge, whereas in the metal oxide-rich portion O^{2-} may also contribute to charge transport (1*d*). Viscosity studies corroborate these findings (1*a*, 1*b*). An important conclusion drawn from these and more recent studies is that silicate melts (and glasses) are ionic and must be treated as ionic solutions (e.g., ref. 2). A second conclusion is that the anions of the melt or glass, which are composed of SiO_4 tetrahedra, are effectively immobile, and hence do not contribute to transport of charge; these anionic species, although charged negatively, are apparently too large to be appreciably mobile in melts or glasses. The investigations of Bockris et al. (1*a*–1*c*)

© 2007 NRC Canada

Fig. 1. (*a*) Illustrates the XPS O 1s XPS spectrum of olivine ($[Mg,Fe]_2SiO_4$); (*b*) illustrates the XPS XPS O 1s spectrum of alpha-quartz (SiO_2); (*c*) illustrates the XPS O 1s spectrum of pyroxene ($[Ca,Mg]_2Si_2O_6$). XPS data for (*a*) and (*b*) are from Zakaznova-Herzog et al. (15) and the spectrum for (*c*) is modified after Zakaznova-Herzog et al. (14). The spectra are fitted with a Shirley background (11) and a (80:20 Gaussian-Lorentzian) Voigt line shape (12). Dots represent experimental data, curve mimicing the data is the fit, and the symmetric curves are the peaks used in the fit. Binding Energies have not been corrected to a standard (typically C 1s) value.



proposed that trimeric or tetrameric rings were the basic structures from which these largely immobile anionic species are constructed. The structural aspects of silicate liquids and glasses at the molecular level remain a major source of scientific interest and controversy. Throughout this communication the term "moiety" is used to represent a molecular unit or cluster in a glass or melt. The compositions of the moieties or units are stipulated as required for thermodynamic speciation calculations, but there is no implication of structure with regard to the moiety or the glass (melt).

Thermodynamic arguments have been constructed indicating that silicate-rich liquids are composed of discrete silicate anionic moieties, with their molar mass being dependent primarily on the number of SiO_4 tetrahedra in each moiety (3). Gotz and Masson (4) extracted four discrete anionic silicate species from PbO-SiO_2 glass (at the orthosilicate composition), and although the extraction technique (trimethylsilylation coupled with chromatography) is not quantitative, the study provides strong evidence for a suite of silicate species in silicate liquids and glasses. These efforts culminated in the application of polymer theory to metal oxide silicate liquids (5). The applicability of polymer theory was, however, questioned because silica tetrahedra tend to form networks rather than chains, and new thermodynamic approaches were developed to emphasize the ionic nature of silicate liquids and glasses and speciation within these liquids (6).

XPS O 1s signals of silicates

Linewidths and peak shapes

Previous O 1s and Si 2p XPS studies of insulating silicates have produced linewidths ranging from about 1.5 to 2.5 eV, as apparent from XPS studies cited herein. The lines are sufficiently broad that bridging and nonbridging oxygen signals are sometimes overlapped entirely or one is present as an indistinct shoulder on the other broad peak. The amount and accuracy of chemical state information gleaned from such spectra is consequently limited. Recent advances incorporated into the Kratos Ultra Axis XPS instrument has largely overcome differential charging, resulting in much narrower lines (10). The spectra of Fig. 1 are sufficiently narrow to identify asymmetry on the high binding side of these peaks. With the recognition of asymmetry, appropriate procedures for fitting O 1s spectra are evaluated so that accurate proportions of bridging and nonbridging oxygen abundances can be accurately evaluated, as now discussed.

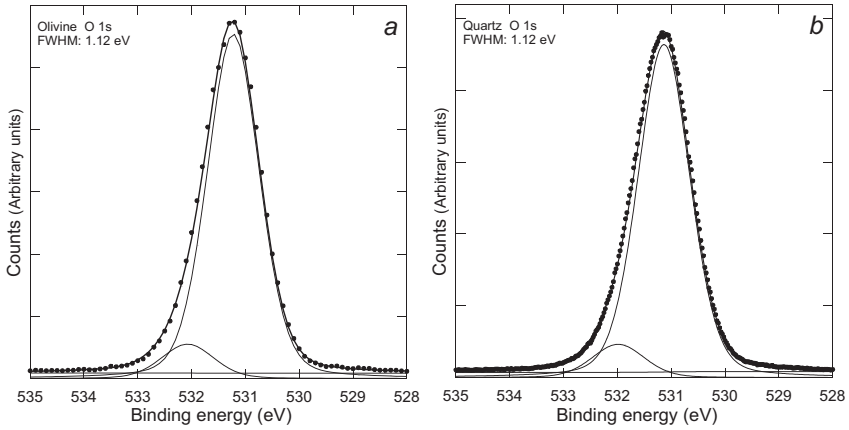
Nesbitt et al. (10) demonstrated that the Si 2p linewidth of crystalline silicates (olivine and quartz) is determined by final state vibrational contributions so that neither inherent nor minimal instrumental linewidths can be achieved for Si 2p lines. The interpretation is consistent with the Si 2p linewidths for the gas phase analogue, tetramethoxysilane ($Si[OCH_3]_4$), where the vibrational contributions have been identified, yet the total Si 2p linewidth is 1.10 eV (10, 13). Nesbitt et al. (10) and Zakaznova-Herzog et al. (14) collected O 1s spectra for a number of crystalline silicates (Fig. 1) and obtained linewidths of about 1.2 eV. Like the Si 2p spectra, neither inherent nor instrumentally controlled O 1s linewidths could be approached and we propose that final state vibrational contributions control the widths of both Si 2p and O 1s lines in silicates.

Final state vibrational contributions also affect peak shape. Because photoemission causes a vertical (Frank–Condon) transition to an excited electronic state, affected peak shapes are controlled by the number of vibrational states accessed in the electronic excited state. The resulting suite of states accessed generally does not give rise to a symmetric spectral manifold because a greater number of high binding energy final states are more likely to be accessed than low binding energy states (e.g., 13). With the high resolution now achievable for insulating samples, the asymmetry of peaks is detectable.

The O 1s line shapes of olivine and quartz are somewhat asymmetric to the high binding energy side (Figs. 1*a*, 1*b*), and this may result from final state effects just as for Si 2p spectra. The asymmetry of the olivine (M_2SiO_4) and quartz (SiO_2) O 1s peaks were simulated by fitting a second peak to

© 2007 NRC Canada

Fig. 2. As for Fig. 1*a* and 1*b* except a second peak has been added to each spectrum to account for peak asymmetry. In both diagrams, the intensity, energy splitting and linewidth of the second peak are fixed by the properties of the respective main peak (see text for details).



the high binding energy side of each spectrum (Fig. 2) where (*i*) it has precisely the same FWHM as the lower energy major peak, (*ii*) it is located at 0.67 eV higher binding energy than the major peak maximum, and (*iii*) its intensity is 15.65% that of the major peak, thus demonstrating the extent of the asymmetry. The second peak is consequently entirely constrained by properties of the major peak. The good fit (Fig. 2) is an indication that the asymmetric characteristics are the same in both the quartz and olivine O 1s spectra and probably arise from the same process (i.e., effectively the same envelope of final state contributions). A more fundamental approach to fitting the O 1s spectra would be to identify the vibrational energy splittings and the properties of the potential energy curves of both ground and excited (electronic) states, so that an appropriate manifold of vibrational contributions could be calculated and used to fit the spectra.

O 1s signals in silicate minerals

Crystalline orthosilicates such as olivines (e.g., $[Mg,Fe]_2SiO_4$) consist of discrete SiO_4 tetrahedra with each apical oxygen bonded to a divalent cation (e.g., Mg; M-**O**-Si). These cations are octahedrally coordinated to six oxygen atoms of adjacent tetrahedra. The Mg–O bonds thus bind the individual tetrahedra and provide structural integrity to the mineral. There should consequently be only M-**O**-Si in olivines, and indeed high-resolution XPS spectra (10, 15) reveal only one type of oxygen (Fig. 1*a*).

Quartz (SiO_2) is composed solely of SiO_4 tetrahedra with each apical oxygen being a bridge to an adjacent tetrahedron (Si-**O**-Si bonding), producing a three-dimensional network. All oxygen atoms are of the Si-**O**-Si type, and as expected the high resolution XPS O 1s spectrum of quartz (Fig. 1*b*) demonstrates the presence of only one contribution (10).

Minerals of metasilicate composition (e.g., pyroxenes) are composed of infinite chains of tetrahedra where two of the four oxygen atoms of each tetrahedron are shared with an adjacent tetrahedra, and the remaining two oxygen atoms of each tetrahedron are typically bonded to alkaline earths or 3d metal cations (e.g., Mg, Ca, Fe); each tetrahedron consequently includes two bridging oxygen (Si-**O**-Si) and two nonbridging oxygen (M-**O**-Si) atoms. A high-resolution XPS O 1s spectrum of diopside ($CaMgSi_2O_6$) reveals two distinct peaks (Fig. 1*c*), the higher binding energy peak representing Si-**O**-Si and the lower energy peak M-**O**-Si. The Ca and Mg atoms have different coordination numbers, complicating the spectrum as explained by Zakaznova-Hertzog et al. (14).

O 1s signals in silicate glasses

The O 1s spectra of $PbO\text{-}SiO_2$ glasses (Fig. 3) display two distinct peaks, but as emphasized by Dalby et al. (8) these glasses include three types of oxygen, Si-**O**-Si (bridging oxygen), M-**O**-Si (nonbridging oxygen), and M-**O**-M (metal-bridging oxygen such as Na-**O**-Na or Pb-**O**-Pb). Dalby et al. (8) note that the lower binding energy peak is composite and includes the signal for the latter two types of oxygen (i.e., M-**O**-Si and M-**O**-M). The three types of oxygen may be found in binary liquids or glasses.

Mass balance considerations affecting oxygen species

Effect of compositional changes on types of oxygen

Viscosity and conductivity studies (1*a*–1*c*) and the NMR and XPS studies here surveyed indicate that the addition of metal oxide (MO, e.g., MgO, CaO, or PbO) to the SiO_2 liquid causes breakdown of the three-dimensional network through formation of M-**O**-Si according to

[1] $$1\text{M-}\mathbf{O}\text{-M} + 1\text{Si-}\mathbf{O}\text{-Si} \Rightarrow 2\text{M-}\mathbf{O}\text{-Si}$$

If reaction [1] proceeds to completion, then all oxygen would be as M-**O**-Si at the orthosilicate composition (e.g., M_2SiO_4); no Si-**O**-Si or M-**O**-M would be present at this composition. The olivine group of silicate minerals are orthosilicates and indeed all oxygen atoms are of the M-**O**-Si type. An alternative representation of reaction (1) is,

[2] $$2MO + SiO_2 \Rightarrow M_2SiO_4$$

One or both of the reactants of [2] are completely consumed if the reaction proceeds to completion. The abundances of M-**O**-Si, Si-**O**-Si, and M-**O**-M have been calculated assuming that the reaction goes to completion, and the results are plotted in Figs. 4*a* and 4*b*.

© 2007 NRC Canada

For monovalent metal oxides (e.g., Na_2O, K_2O), the concentration of M-**O**-Si may be calculated on the assumption that each metal atom produces one M-**O**-Si in silicate liquids and glasses. Reactions may be written that incorporate this constraint, an example being the formation of a disilicate moiety (i.e., $M_2O + 2SiO_2 \Rightarrow M_2Si_2O_5$). Where $M_2O = Na_2O$,

[3] $Na_2O + 2SiO_2 \Rightarrow Na_2Si_2O_5$

Reaction [3] is feasible in that the NMR study of Stebbins (9) noted that a glass of $Na_2Si_2O_5$ composition displayed a spectrum similar to its crystalline equivalent. Furthermore, Bockris et al. (1*a*–1*c*) and Bockris and Mellors (1*d*) propose an $Si_6O_{15}^{6-}$ anionic species in silicate liquids. All such double rings consist of two M-**O**-Si and three Si-**O**-Si per unit formula (i.e., $Na_6Si_6O_{15}$ or $Na_2Si_2O_5$). The proportions of Si-**O**-Si, Na-**O**-Si, and Na-**O**-Na in glass of the Na_2O-SiO_2 binary system have been calculated assuming that Rxn [3] goes to completion and the results are shown in Fig. 4*c*.

Experimental aspects of PbO-SiO_2 glasses

XPS O 1s studies

Dalby et al. (8)

The XPS O 1s spectra of four PbO-SiO_2 glasses range in composition from $X_{PbO} = 0.50$ to 0.667 and display two distinct contributions (Fig. 3). As for diopside (Fig. 1*c*), the high binding energy peak represents the Si-**O**-Si signal (8). The low binding energy peak may include an M-**O**-Si and an M-**O**-M contribution, where M = Pb, as argued by Dalby et al. (8). As evidence, Sorokina et al. (16) quote the O 1s binding energy of PbO (their Table 1) to be on the low binding energy side of the O 1s envelope of their PbO-SiO_2 glasses and a Pb-**O**-Pb signal is consequently expected to be associated with the low binding energy peak of O 1s spectra in PbO-SiO_2 glasses and to overlap with the M-**O**-Si contribution. The Si-**O**-Si contribution should be unaffected by the M-**O**-Si signal so that the fraction of oxygen present as Si-**O**-Si may be calculated whereas fractions of M-**O**-Si and M-**O**-M cannot.

The four spectra (Fig. 3) were fitted with all peaks having the same FWHM (1.25 eV). This constraint is different from that used by Dalby et al. (8) to demonstrate the insensitivity of the calculated fraction of Si-**O**-Si to different fitting constraints. The constraint used here yields Si-**O**-Si percentages of 20.2, 24.9, 36.5, and 41.1 whereas the constraints used by Dalby et al.(8) yielded 19.3, 26.0, 36.9, and 42.6. The resolution of the above referenced spectra is appreciably better than any O 1s spectra previously obtained and are consequently the most reliable so far obtained for PbO-SiO_2 glasses. The bridging oxygen fraction in the PbO-SiO_2 glasses derived from the Dalby et al. (8) data are plotted in Fig. 4.

Smets and Lommen (17)

These XPS O 1s spectra are of lower resolution than those collected by Dalby et al. (8). Smets and Lommen (17) assumed that there were two contributions to these spectra and without evidence assumed that the linewidths of the two contributions were equal. The latter assumption was confirmed by Dalby et al. (8). Their calculated fractions of Si-**O**-Si (Fig. 4*a*) are consistent with those of Dalby et al. (8). Smets and Lommen's (17) use of an achromatic rather than monochromatic source probably accounts for their obtaining reasonable peak shapes and peak areas for these insulating samples.

Gee et al. (18)

Gee et al. (18) collected XPS O 1s spectra using a monochromatized source with a flood gun to compensate for surface charging. Their calculated Si-**O**-Si fractions are plotted in Fig. 4*a*. Two results agree with the results of Smets and Lommen (17) and Dalby et al. (8; i.e., at $X_{PbO} = 0.5$ and 0.6) but the other data do not. The variability of the data may be related to ineffective charge compensation.

Sorokina et al. (16)

This study collected O 1s, Si 2p, and Pb 4f spectra from PbO-SiO_2 glasses. They illustrate fitted O 1s spectra, but there is ambiguity in the reporting of the calculated Si-**O**-Si fraction. As well, their data plot well above the other sets of data. They sputtered the surfaces and may have disrupted the surface. Dalby et al. (8), for example, observed very slow reduction of Pb to the metallic state in the near-surface promoted by the X-ray source.

Other XPS Studies

Wang and Zhang (19) collected the O 1s spectra from glasses ranging in composition from $X_{PbO} = 0.15$ to 0.70 and fitted their spectra with two peaks. The constraints on shape and width were not documented and the results are inconsistent with previously mentioned results. Shakhmin and Tyutikov (20) conducted an XPS study of PbO-SiO_2 glasses with a monochromated source and electron flood gun. Surfaces were exposed to the atmosphere prior to loading the samples into the spectrometer. The results are different from other results, perhaps because of contaminated surfaces or surface charging problems.

Summary of XPS O 1s spectral studies

The survey emphasizes the difficulty of obtaining consistent XPS O 1s results on insulators. The data of Dalby et al. (8) are the best resolved Si-**O**-Si signals of all studies reported and the lineshapes conform to the expected Gaussian–Lorentzian shape. These data are consequently taken as the most accurate of the XPS data. Smets and Lommen (17) assumed that the Si-**O**-Si and M-**O**-Si signals were of equal width when fitting their data, an assumption verified by the study of Dalby et al. (8). It is therefore not surprising that the two sets of data yield consistent results, and these are taken as the most reliable of the XPS data.

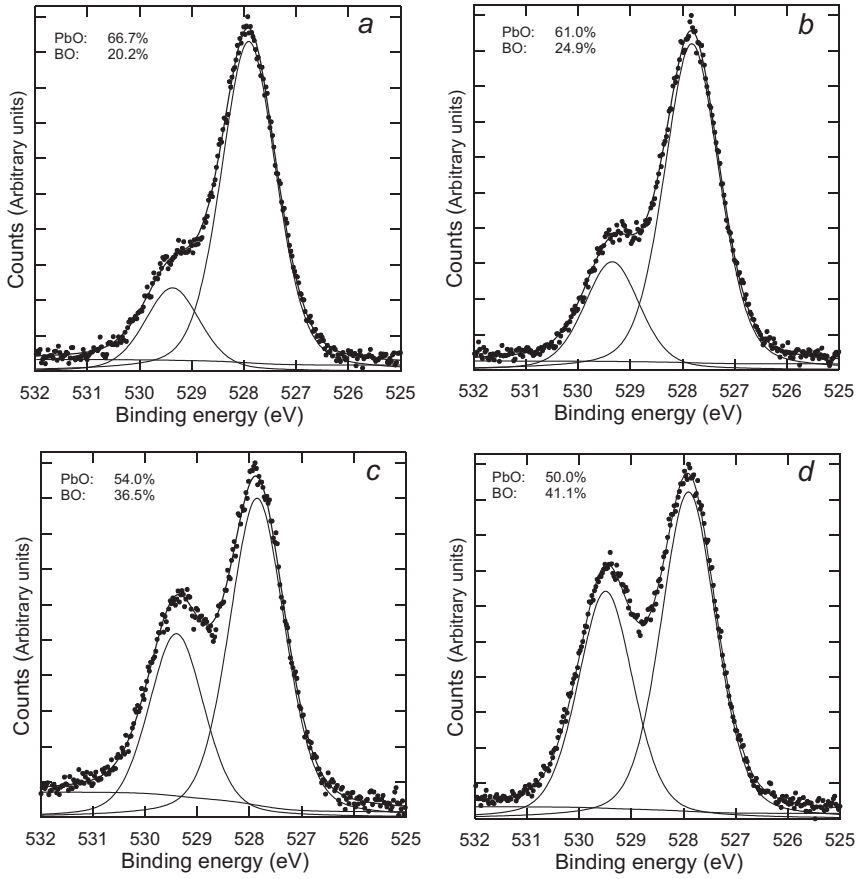
^{29}Si MAS-NMR studies

Fayon et al. (21)

The ^{29}Si MAS-NMR spectral studies report results from PbO-SiO_2 glasses ranging in composition from $X_{PbO} = 0.31$ to 0.73. From the reported distribution of Q species, the fraction of Si-**O**-Si were calculated and plotted in Fig. 4*b*. These data are consistent with the XPS results of Dalby et al. (8) and Smets and Lommen (17). The agreement between the NMR and XPS measurements provides confidence that the Si-**O**-Si content as a function of composition is known

© 2007 NRC Canada

Fig. 3. XPS O 1s spectra of PbO-SiO_2 glasses of compositions: (*a*) PbO:SiO_2 = 66.6:33.3; (*b*) PbO:SiO_2 = 61.0:39.0; (*c*)PbO:SiO_2 = 54.0:46.0; (*d*) PbO:SiO_2 = 50.0:50.0. All XPS data are from Dalby et al. (8) and all spectra were fitted with a Shirley background (34) and Voigt line shapes (35). The low binding energy peak represents NBO and the high binding energy peak BO in all diagrams. Peak widths are discussed in the text.



and that the deconvolution of NMR and XPS spectra is reasonable.

Shrikhande et al. (22)

The Q species distribution reported by this MAS-NMR study was used to calculate Si-**O**-Si concentrations (Fig. 4*b*). The calculated values for X_{PbO} = 0.50 and 0.60 conform to the data of Fayon et al. (21), the XPS data of Dalby et al. (8), and Smets and Lommen (17), but the high silica results (X_{PbO} = 0.125 and 0.25) plot appreciably lower than the trends established by the other studies. Apparently, the abundance of Q species high in Si-**O**-Si was underestimated during fitting of the high-silica glass spectra.

Takaishi et al. (23)

This study provides Q species distributions for three glasses rich in PbO (X_{PbO} = 0.50, 0.667, and 0.89). The Si-**O**-Si calculated for the two most siliceous compositions conforms to the other NMR data (Fig. 4*b*), but the sample richest in PbO is greatly divergent from the trend established by the other data.

Summary of MAS-NMR spectral studies

The NMR data of Fayon et al. (21) are accepted as the most accurate NMR data available, in part because these and the XPS O 1s results are consistent. Nevertheless, there is a need to investigate ambiguities associated with both types of experiment to ensure that neither the NMR nor XPS technique has introduced systematic error related to the analytical technique or the fitting procedures.

Studies of Na_2O-SiO_2 glasses

XPS O 1s spectra

Veal et al. (24)

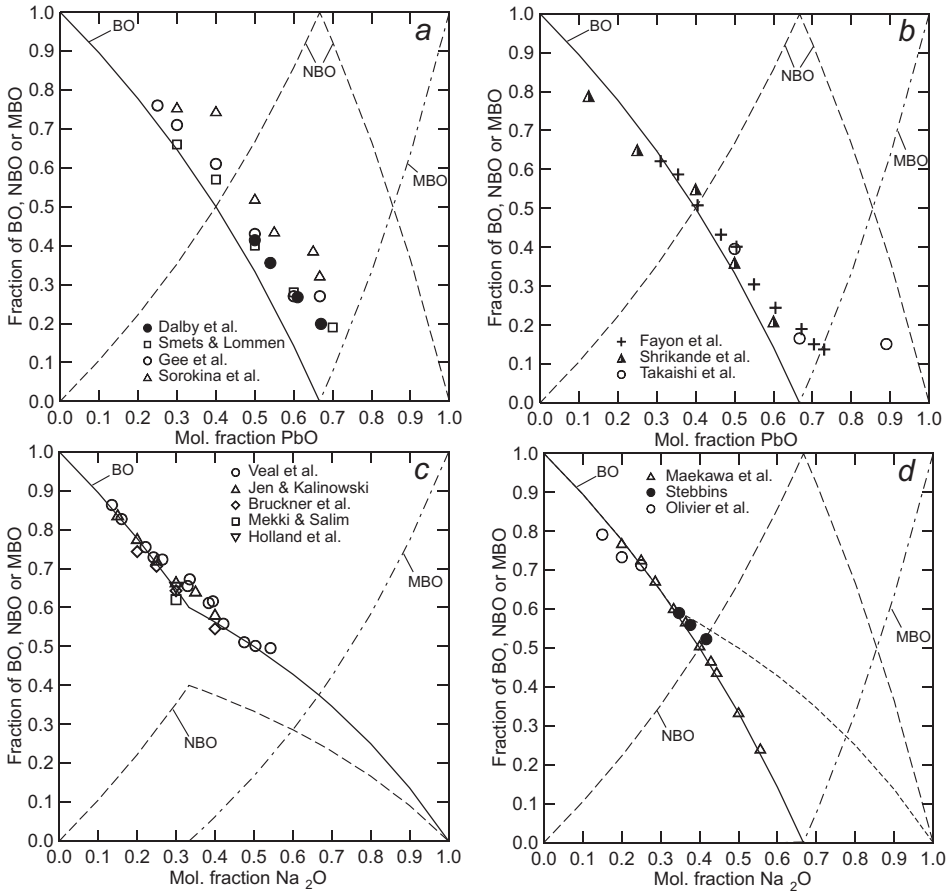
The O 1s spectra of a wide range of glasses are reported in graphical form. The fraction of Si-**O**-Si was calculated from their graphs and plotted in Fig. 4*c*. No information about instrumental equipment, conditions, or settings was provided. Veal et al. (24) noted that their data at high Na_2O content did not confirm the tenet that each Na atom produces a M-**O**-Si bond in the glass. As explanation, they offered that the Na-rich glasses may have become hydrated through absorption of water during preparation. Their sample preparation technique, however, should have removed any hydrated surface layer before analysis.

Jen and Kalinowski (25)

This study took precautions to ensure their glasses were not hydrated. They also used an achromatic source so that charging was minimized. As shown in Fig. 4*c*, their results

© 2007 NRC Canada

Fig 4. (*a*) Experimental XPS O 1s data for PbO-SiO_2 glasses. The curves for BO, NBO and MBO fractions are calculated assuming that the Pb_2SiO_4 moiety has formed in the glass and the reaction (Rxn 4) has gone to completion (see text for details). (*b*) Experimental NMR data for PbO-SiO_2 glasses. The BO, NBO and MBO curves calculated as in (4*a*). (*c*) Experimental XPS O 1s data for Na_2O-SiO_2 glasses. The curves for BO, NBO and MBO fractions are calculated assuming that a disilicate moiety ($Na_2Si_2O_5$) has formed in the glass and the reaction (Rxn 8) has gone to completion (see text for details). (*d*) Experimental NMR data for Na_2O-SiO_2 glasses. The curves for BO, NBO and MBO fractions are calculated assuming that an orthosilicate moiety (Na_2SiO_4) has formed in the glass and the reaction (Rxn 10) has gone to completion (see text for details). The short dashed curve is the BO content calculated assuming the disilicate reaction goes to completion (Rxn 8).



are consistent with those of Veal et al. (25). This careful study consequently demonstrates the reproducibility of the XPS results.

Bruckner et al. (26)

Bruckner et al. fractured their glasses in the vacuum of the XPS instrument ensuring that the surfaces analysed were not hydrated. They also used an achromatic source so that charging was minimized. The measured Si-**O**-Si contents (Fig. 4*c*) are consistent with the data of Veal et al. (26) and Jen and Kalinowski (25).

Other studies

Mekki and Salim (27) and Holland et al. (28) analysed the O 1s signal of Na_2O-SiO_2 glasses of the same composition (X_{Na2O} = 0.30) and obtained the same result (Fig. 4*c*). Mekki and Salim (27) used an achromatic source and their O 1s spectrum was reasonably resolved. Holland et al. (28) reported an identical abundance of Si-**O**-Si in glass of the same composition, but the quoted value may be that measured made by Mekki and Salim (27).

^{29}Si MAS-NMR spectra

Maekawa et al. (29)

Maekawa et al. conducted an ^{29}Si NMR study of Na_2O-SiO_2 glasses over the compositional range X_{Na2O} = 0.20 to 0.556. Calculated Si-**O**-Si fractions derived from reported Q species abundances conform to the XPS data at high silica contents (Fig. 4*d*), but plot below the XPS data at the low SiO_2 content (compare Figs. 4*c* and 4*d*).

Stebbins (9)

Stebbins reported NMR data for three compositions. He quotes the Si-**O**-Si fraction for the Q_4 species. Q_2 and Q_3 species abundances were here calculated from the Q_4 abundance and the equilibrium constants provided by Stebbins. The Si-**O**-Si fractions derived from the data of Stebbins (Fig. 4*d*) plot close to the NMR data of Maekawa et al. (29), but define a somewhat shallower trend. The data plot lower than the XPS data for similar compositions.

Olivier et al. (30)

Their NMR data provide Q-species distributions for three

© 2007 NRC Canada

highly siliceous glasses. The Q-species were used to calculate the fraction of Si-**O**-Si, and these are plotted on Fig. 4*d*. Two points plot below the trend defined by the Maekawa et al. (29) data, but the third does not.

Summary of NMR and XPS results

From the conformity of the five XPS experiments and three sets of NMR data, it is concluded that both types of experimental data are reproducible. There is, however, a serious disparity between the XPS and the NMR data in the compositional range between about X_{Na_2O} = 0.4 and 0.6, which must be explained.

Discussion

$PbO\text{-}SiO_2$ system

Mass balance constraint

The XPS data of Dalby et al. (8) and Smets and Lommen (17) and the NMR data of Fayon et al. (21) indicate that the measured Si-**O**-Si contents of these glasses are accurate to within a few percent of the calculated values (Fig. 5*a*). These Si-**O**-Si contents plot near or above the Si-**O**-Si content calculated assuming that Rxn [1], or its equivalent Rxn [2], goes to completion; consequently, the assumption that the reaction goes to completion may be reasonable in high silica glasses, but it is not reasonable in glasses of intermediate and high PbO content. A more realistic approach must be adopted if Si-**O**-Si, M-**O**-Si, and M-**O**-M contents are to be explained over the entire compositional range of this binary system.

Thermodynamic approach

The limitations of the mass balance arguments may be alleviated by appealing to thermodynamic considerations. If PbO = MO for Rxn [2],

$$[4] \qquad 2PbO + SiO_2 \Rightarrow Pb_2SiO_4$$

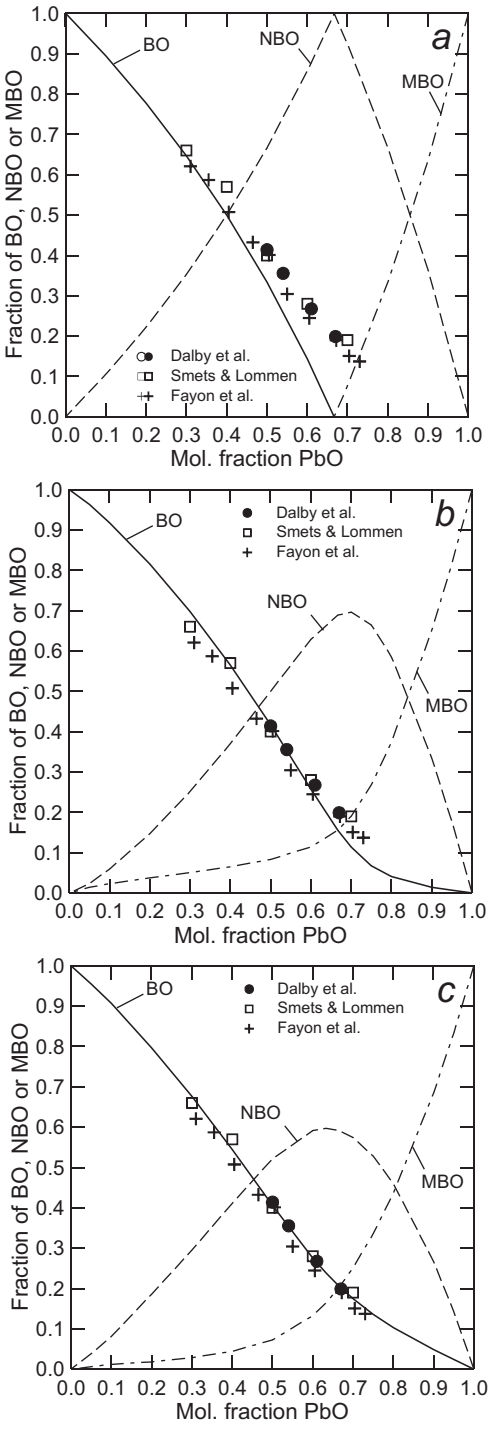
The associated mass action equation with equilibrium constant (K_4) is,

$$[5] \qquad K_4 = (Pb_2SiO_4) \,/\, [(PbO)^2(SiO_2)]$$

where the value of K_4 is infinite, the reaction necessarily goes to completion (one or both reactants is completely consumed), and the concentrations of Si-**O**-Si, M-**O**-Si, and M-**O**-M are those shown by the curves in Fig. 5*a*. If K_4 were finite the reaction would not go to completion, and both reactants then would be present at all binary compositions; that is, all three oxygen species, Si-**O**-Si, M-**O**-Si, and M-**O**-M, would be present over the entire compositional range of the binary. Takaishi et al. (23) provide X-ray and neutron diffraction results demonstrating the existence of M-**O**-M even at 50% SiO_2 (metasilicate composition), justifying the proposed thermodynamic approach to evaluate the distribution of oxygen species.

The most reliable XPS and NMR experimental data indicate greater Si-**O**-Si content than calculated (Fig. 5*a*); hence, the experimental data require K_4 to be finite. A K_4 value has been adopted that duplicates the Si-**O**-Si content in the experimental data at 50% SiO_2, and with this value the abundances of Si-**O**-Si, M-**O**-Si, and M-**O**-M for the entire range

Fig. 5. (*a*) Most reliable XPS O 1s and NMR experimental data for $PbO\text{-}SiO_2$ glasses. The BO, NBO and MBO curves are calculated as for Fig. 4*a* (K_4 = infinite value); (*b*) as for Fig. 5*a* except the BO, NBO and MBO curves were calculated with K_4 = 15 (rather than being infinite) so that Rxn (4) does *not* go to completion; (*c*) as for Fig. 5*a* except the BO, NBO and MBO curves were calculated assuming three distinct Si moieties were present in the glass, a network forming moiety represented by SiO_2, a metasilicate (ring) moiety ($PbSiO_3$) and an orthosilicate moiety (Pb_2SiO_4). See text for details of the calculation.



© 2007 NRC Canada

of composition have been calculated using eq. [5] (K_4 = 15.0) and plotted in Fig. 5*b*. Although a reasonable approximation to the experimental data, the trend of the calculated Si-**O**-Si content (Fig. 5*b*) is nevertheless somewhat steeper than that defined by the experimental measured Si-**O**-Si data at the extremities of composition. No K_4 value yields an appreciably better simulation of the data.

Multiple structures in liquids

There are several studies that indicate ring structures in silicate liquids and glasses (e.g., 8, 1*a*, 1*b*, 1*c*, 1*d*, 31, 32, 33, 34, 35). Bockris et al. (1*b*, 1*c*) proposed the basic anionic unit is $[Si_nO_{2n+3}]^{6-}$ or its neutral equivalent, $M_6Si_6O_9$, the normalized formula of which is $MSiO_3$. The evidence is based on viscosity, molar volume, expansivity, and measured Si-**O**-Si contents. The formation of $MSiO_3$ (metasilicate composition) may be written as,

[6] $PbO + SiO_2 \Rightarrow PbSiO_3$

where the associated mass action equation is,

[7] $K_6 = (PbSiO_3) / [(PbO)(SiO_2)]$

and K_6 is the equilibrium constant. Inclusion of an orthosilicate moiety (Rxn [2]) and a metasilicate moiety (Rxn [6]), with K_4 = 1.50 and K_6 = 4.00, duplicates the measured Si-**O**-Si content at 50% SiO_2 (Fig. 5*c*). The *K* values then were used to calculate Si-**O**-Si, M-**O**-Si, and M-**O**-M over the entire compositional range (Fig 5*c*). The calculations simulate well the Si-**O**-Si measurements.

The simulation includes three types of Si moieties, the orthosilicate moiety (SiO_4^{4-} or Pb_2SiO_4), the metasilicate ring moiety ($PbSiO_3$), and a three-dimensional network moiety represented in these calculations by SiO_2. Bockris et al. (1*a*–1*c*) also argue for a three-dimensional network structural entity in highly siliceous liquids, thus justifying the use of SiO_2 as the moiety representing the network species. This simple thermodynamic treatment requires a minimum of three Si moieties to reproduce the most reliable XPS and NMR experimental data. Although these calculations are consistent with the presence of three Si moieties in the glass, they nevertheless, cannot be taken as proof that these three moieties exist in the glass. Furthermore, if they exist, these liquids and glasses probably contain more than just these three moieties.

Na_2O-SiO_2 system

XPS and NMR experimental data yield similar Si-**O**-Si contents in Na_2O-SiO_2 glasses where the fraction SiO_2 is greater than about 0.66, but the two types of data diverge for glasses of lower SiO_2 content (Figs. 4*c* and 4*d*).

Interpreting XPS results

Brockris et al. (1*a*–1*d*) collected viscosity, volume, and conductivity data on the Na_2O-SiO_2 system and argued strongly for three-membered ring structures in these liquids. Stebbins (9) provided support for the argument by noting the similarity between NMR spectra of Na_2SiO_5 glass and crystals, the crystal having a double ring structure much as proposed by Bockris et al. (1*b*–1*d*). Single and double ring structures contain Q_2 and Q_3 species respectively, and these are the dominant species in the disilicate–metasilicate range of composition. If the disilicate ring structure $[Si_6O_{15}]^{6-}$ were to form in these liquids and noting that $Na_6Si_6O_{15}$ is equivalent to $Na_2Si_2O_5$ (if normalized) then,

[8] $Na_2O + 2SiO_2 \Rightarrow Na_2Si_2O_5$

where the associated mass action equation is,

[9] $K_8 = (Na_2Si_2O_5) / [(Na_2O)(SiO_2)^2]$

and K_8 is the equilibrium constant. The Si-**O**-Si, M-**O**-Si, and M-**O**-M abundances shown in Fig. 6*a* were calculated assuming that Rxn [8] goes to completion (one or both reactants are completely consumed). A K_8 value of 250 was then adopted so that the measured Si-**O**-Si content at $X_{Na_2O} = 0.3$ was reproduced (Fig. 6*b*). The K_8 value was then used to calculate the Si-**O**-Si, M-**O**-Si and M-**O**-M contents at all other compositions of the binary system. The comparison between the Si-**O**-Si XPS measurements and calculation is good, and calculated results are consistent with the existence of such a moiety in Na_2O-SiO_2 liquids (and glasses).

Interpreting NMR results

The NMR measurements of Maekawa et al. (29) are consistent with the studies of Stebbins (9) and Olivier et al. (30). Si-**O**-Si contents derived from these studies are also consistent with the XPS data for glasses with SiO_2 mol fractions greater than 0.66, indicating that the two techniques can yield the similar results for this binary system. Nevertheless, at lower SiO_2 contents the Maekawa et al. (29) NMR data are dramatically different from those obtained by XPS. The NMR data of Stebbins (9) plot between those of Maekawa et al. (29) and the XPS data (Figs. 4*c*, 4*d*). Indeed the Olivier et al. (30) and Stebbins (9) data, if combined, define a trend somewhat shallower than the Maekawa et al. (30) data (Fig. 6*c*). There is consequently no objective experimentally based means to determine which of the NMR or XPS data is correct.

An orthosilicate (Na_4SiO_4) may be proposed for the Na_2O-SiO_2 system in which Na_2O and SiO_2 react to form the moiety,

[10] $2Na_2O + SiO_2 \Rightarrow Na_4SiO_4$

where the associated mass action equation is,

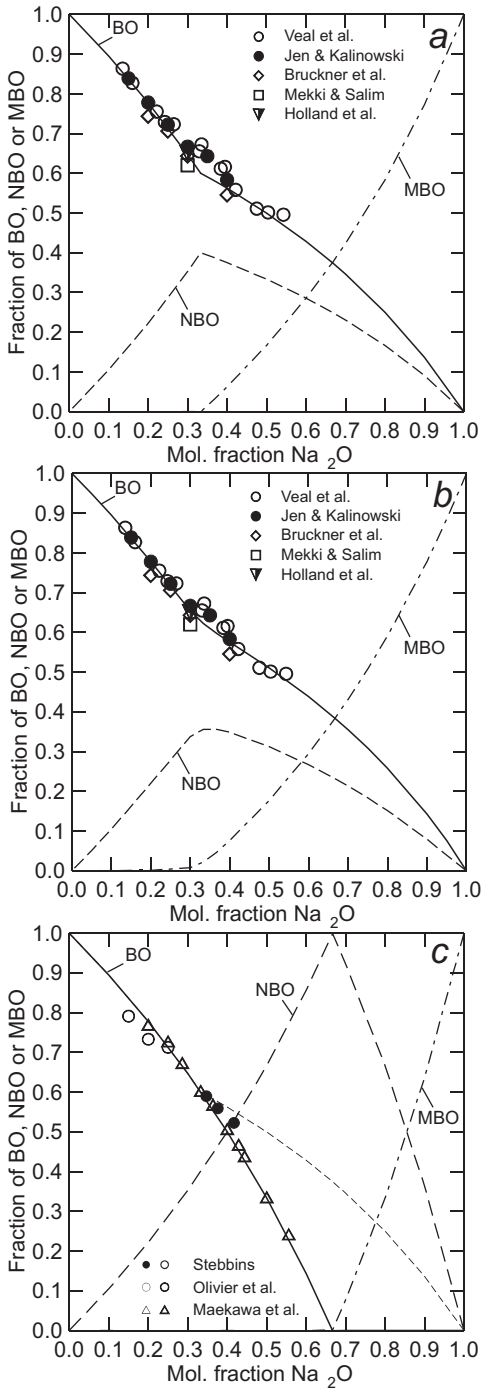
[11] $K_{10} = (Na_4SiO_4) / [(Na_2O)^2(SiO_2)]$

and K_{10} is the equilibrium constant. Where Rxn [10] is assumed to go to completion (i.e., K_{10} has an infinite value) the abundances of Si-**O**-Si, M-**O**-Si, and M-**O**-M were calculated with the results shown as curves in Fig. 6*c*. The calculations mimic the data of Maekawa et al. (29). The implications are that K_{10} is very large, and that, in effect, the reaction has gone to completion in these glasses. The short dashed curve of Fig. 6d is the Si-**O**-Si content calculated assuming Rxn [8] goes to completion (as in Fig. 6*c*).

The Si-**O**-Si results of Stebbins (9) describe a shallower trend (Fig. 6d), and do not support an effectively infinite value for K_{10}. The presence of an orthosilicate moiety, at least in SiO_2-dominated liquids, is also inconsistent with the viscosity and conductivity data of Bockris et al. (1*a*–1*d*). Maekawa et al. (29) noted (p. 59) that their test for Q species assignments assumed the absence of free alkali oxide

© 2007 NRC Canada

Fig. 6. (*a*) XPS O 1s experimental data for Na_2O-SiO_2 glasses. The BO, NBO and MBO curves are calculated as for Fig. 4*c* (K_8 = infinite value); (*b*) as for Fig. 6*a* except the BO, NBO and MBO curves were calculated with K_8 = 250 so that Rxn (8) does *not* go to completion; (*c*) NMR experimental data for Na_2O-SiO_2 glasses. The BO, NBO and MBO curves were calculated assuming an orthosilicate moiety (Na_2SiO_4) formed in the glass and that Rxn (10) goes to completion (K_{10} = infinite value). The short dashed curve indicates BO concentrations if a disilicate species formed (K_8 = infinite value). See text for details of calculations.



ions (M_2O). They justified the assumption by stating that XPS and thermodynamic studies indicate the absence of free Na_2O (hence M-**O**-M) in glasses of the compositional range they studied. The XPS study to which they refer is that of Bruckner et al. (26) who also *assumed* that there was no M-**O**-M contribution to their XPS O 1s spectra, hence the Bruckner et al. (26) publication provides no justification for the assumption. The thermodynamic study to which they refer measured "Na_2O" activities, which were found to be very low in these SiO_2-dominated liquids. At low concentrations of Na_2O, however, activity coefficients may vary greatly from unity in compositions well removed from compositions where Raoult's Law behaviour pertains, so that this evidence for the assumption requires additional testing.

Conclusions

The most reliable XPS and NMR experimental studies of the PbO-SiO_2 glasses yield similar Si-**O**-Si concentrations. Many of the XPS O 1s measurements with poorly resolved peaks overestimate Si-**O**-Si contents of these glasses, whereas one of the NMR studies generally underestimates Si-**O**-Si contents. The most reliable XPS and NMR data proves the assumption that Rxn [4] goes to completion is invalid (i.e., every Pb atom is associated with two M-**O**-Si moieties in these glasses). A thermodynamic treatment, however, reproduces the experimental data.

The NMR and XPS experimental data yield dramatically different results in Na_2O-rich Na_2O-SiO_2 glasses. Five XPS studies are self-consistent but yield much greater Si-**O**-Si contents near the metasilicate composition than do the data from the most comprehensive NMR study. The XPS measurements are compatible with the formation of an $Na_2Si_2O_5$ moiety in the glasses with equilibrium constant of 250. The results of the comprehensive NMR study are consistent with the formation of a Na_2SiO_4 moiety in the solutions where the equilibrium constant has a large value. Additional detailed studies of Si-**O**-Si contents are required of this system to resolve the ambiguity and to understand better the Na_2O-SiO_2 system.

Acknowledgments

We thank V.P. Zakaznova-Herzog for providing the original XPS data for olivine and diopside and G.M. Bancroft for critical and insightful comment on these glass studies and for editing the first draft of the manuscript. The study was funded by the Natural Science and Engineering Research Council of Canada (NSERC). Surface Science Western at the University of Western Ontario, through M. Beisinger, provided exceptional technical support with the Kratos XPS for which we are very grateful.

References

1. (*a*) J.O'M. Bockris, J.W. Kitchener, and A.E Davies. Trans. Faraday Soc. **48**, 536 (1952); (*b*) J.O'M. Bockris, J.D. Mackenzie, and J.A. Kitchener. Trans. Faraday Soc. **51**, 1734 (1955); (*c*) J.O'M. Bockris, J.W. Tomlinson, and J.L. White. Trans. Faraday Soc. **52**, 299 (1956); (*d*) J.O'M. Bockris and G.W. Mellors. J. Phys. Chem. **60**, 1321 (1956); (*e*) F.M. Ezz Eldin and N.A. El Alaily. Mater. Chem. Phys. **52**, 175 (1998).

© 2007 NRC Canada

2. (*a*) G. Calas, G.S. Henderson, and J.F. Stebbins. Elements, **2**, 265 (2006); (*b*) S.J. Lee and J.F. Stebbins. Geochim. Cosmochim. Acta, **66**, 303 (2002); (*c*) B. Mysen and P. Richet. *In* Silicate glasses and melts: properties and structure. Elsevier, Amsterdam, Denmark. 2005. P. 544; (*d*) P. Zhang, P.J. Grandinetti, and J.F. Stebbins. J. Phys. Chem. **101**, 4004 (1997).
3. (*a*) C.R. Masson. Proc. R. Soc. London Ser. A, **287**, 201 (1965); (*b*) C.R. Masson. J. Am. Ceram. Soc. **51**, 134 (1968).
4. J. Gotz and C.R. Masson. J. Chem. Soc. A, 2683 (1970).
5. C.R. Masson, I.B. Smith, and S.G. Whiteway. Can. J. Chem. **48**, 1456 (1970).
6. (*a*) P.C. Hess. Geochim. Cosmochim. Acta, **39**, 671 (1975); (*b*) H.W. Nesbitt and M.E. Fleet. Geochim. Cosmochim. Acta, **45**, 235 (1982).
7. (*a*) B.O. Mysen, D. Virgo, and C.M. Scarfe. Am. Mineral. **65**, 690 (1980); (*b*) K.N. Dalby and P.L King. Am. Mineral. **91**, 1782 (2006).
8. K.N. Dalby, H. W. Nesbitt, V.P. Zakaznova-Herzog, and P.L King. Geochim. Cosmochim. Acta. In press.
9. J.F. Stebbins. Nature, **330**, 465 (1987).
10. H.W. Nesbitt, G.M. Bancroft, R. Davidson, N.S. McIntyre, and A.R. Pratt. Am. Mineral. **89**, 878 (2004).
11. D.A. Shirley. Phys. Rev. B, **5**, 4709 (1972).
12. D. Briggs and M.P. Seah. *In* Practical surface analysis. Vol 1. 2nd ed. Wiley, Chichester, NY. 1990. p. 657.
13. J.D. Bozek, G.M. Bancroft, J.N. Cutler, and K.H. Tan. Phys. Rev. Lett. **65,** 2757 (1990).
14. V.P. Zakaznova-Herzog, H.W. Nesbitt, G.M. Bancroft, and J.S. Tse. Surf. Sci. **600**, 3175 (2006).
15. V.P. Zakaznova-Herzog, H.W. Nesbitt, G.M. Bancroft, J.S. Tse, X. Gao, and W. Skinner. Phys. Rev. B, **72**, 205113 (2005).
16. M.F. Sorokina, O.M. Kanunnikova, F.Z. Gil'mutdinov, and V.I. Kozhevnikov. Glass Ceram. **53**, 11 (1996).
17. M.J. Smets and T.P.A. Lommen. J. Non-Cryst. Solids, **48**, 423 (1982).
18. I.A. Gee, D. Holland, and C.F. McConville. Phys. Chem. Glasses, **42**, 339 (2001).
19. P.W. Wang and I. Zhang. Jour. Non-Cryst. Solids, **194**, 129 (1996).
20. A.L. Shakhmin and A.M. Tyutikov. Fiz. Khim. Stekla, **16**, 833 (1989).
21. F. Fayon, C. Bessada, D. Massiot, I. Farnan, and J.P. Coutures. J. Non-Cryst. Solids, **232–234**, 403 (1998).
22. V.K. Shrikhande, V. Sudarsan, G.P. Kothiyal, and S.K. Kulshreshtha. J. Non-Cryst. Solids, **283**, 18 (2001).
23. T. Takaishi, M. Takahashi, J. Jin, T. Uchino, and Y. Toshinobu. J. Am. Ceram. Soc. **88**, 1591 (2005).
24. B.W. Veal, D.J. Lam, and A.P. Paulikas. J. Non-Cryst. Solids, **49**, 309 (1982).
25. J.S. Jen and M.R. Kalinowski. J. Non-Cryst. Solids, **38–39**, 21 (1989).
26. R. Bruckner, H.-U. Chun, H. Goretzki, and M. Sammet. J. Non-Cryst. Solids, **2,** 49 (1980).
27. A. Mekki and M. Salim. J. Electron. Spectrosc. Relat. Phenom. **101–103**, 227 (1999).
28. D. Holland, I.A. Gee, A. Mekki, M.D. Bowdry, and C.F. McConville. Top. Issues Glass, **2**, 9 (2003).
29. H. Maekawa, T. Maekawa, K. Kawamura, and T. Yokokawa. J. Non-Cryst. Solids, **127**, 53 (1991).
30. L. Olivier, X. Yuan, A.N. Cormack, and C. Jåger. J. Non-Cryst. Solids, **293–295**, 53 (2001).
31. W. Malfait, Y. Morizet, W. Halter, R. Verel, and B. Meier. Geophys. Res. Abst. **7**, 07324 (2005).
32. G.S. Henderson. Can. Mineral. **43**, 1921 (2005).
33. G.S. Henderson, G. Calas, and J.F. Stebbins. Elements, **2**, 269 (2006).
34. K.H. Karlsson and K. Froberg. Chem. Geol. **62**, 1 (1987).
35. J. Shelby. Introduction to glass science and technology. RSC Publishing, New York. 2005. p. 291.

© 2007 NRC Canada

Self-assembly of biomolecules at surfaces characterized by NEXAFS[1]

Xiaosong Liu, Fan Zheng, A. Jürgensen, V. Perez-Dieste, D.Y. Petrovykh, N.L. Abbott, and F.J. Himpsel

Abstract: Surface science has made great strides towards tailoring surface properties via self-assembly of nanoscale molecular adsorbates. It is now possible to functionalize surfaces with complex biomolecules such as DNA and proteins. This brief overview shows how NEXAFS (near edge X-ray absorption fine structure spectroscopy) can be used to characterize the assembly of biological molecules at surfaces in atom- and orbital-specific fashion. To illustrate the range of applications, we begin with simple self-assembled monolayers (SAMs), proceed to SAMs with customized terminal groups, and finish with DNA oligonucleotides and Ribonuclease A, a small protein containing 124 amino acids. The N 1s absorption edge is particularly useful for characterizing DNA and proteins because it selectively interrogates the π^* orbitals in nucleobases and the peptide bonds in proteins. Information about the orientation of molecular orbitals is obtained from the polarization dependence. Quantitative NEXAFS models explain the polarization dependence in terms of molecular orientation and structure.

Key words: NEXAFS, bio-interfaces, ribonuclease A, immobilization, orientation.

Résumé : La chimie des surfaces a fait de grands pas dans la direction de la possibilité d'ajuster les propriétés des surfaces par le biais d'autoassemblages d'adsorbats moléculaires à l'échelle nanométrique. Il est maintenant possible de fonctionnaliser des surfaces avec des biomolécules complexes, tels l'ADN et des protéines. Cette brève revue montre comment on peut appliquer la spectroscopie de la structure fine d'absorption des rayons X près du seuil ("NEXAFS") à la caractérisation d'assemblages de molécules biologiques liés à des surfaces de façon spécifiquement atomique et orbitalaire. Pour illustrer l'éventail des applications, on commence avec des monocouches autoassemblées simples (MAA) à partir desquelles on procède à des MAA portant des groupes terminaux personnalisés et on termine avec des oligonucléotides de l'ADN et la ribonucléase A, une petite protéine comportant 124 acides aminés. L'absorption 1s au seuil de l'azote est particulièrement utile pour caractériser l'ADN et les protéines parce qu'il permet d'interroger sélectivement les orbitales π^* des nucléobases et des liaisons peptidiques des protéines. Les informations relatives à l'orientation des orbitales moléculaires sont obtenues à partir de la dépendance de la polarisation. Des modèles quantitatifs de "NEXAFS" permettent d'expliquer la dépendance de la polarisation en fonction de l'orientation moléculaire et de la structure.

Mots-clés : NEXAFS, bio-interfaces, ribonucléase A, immobilisation, orientation.

[Traduit par la Rédaction]

Motivation

The functionalization of surfaces with biomolecules (1) is becoming a significant part of biochemistry and molecular biology, both of which traditionally have focused on phenomena occurring in bulk solution. Among the major drivers of this technology are DNA microarrays ("DNA chips") used for massively parallel analysis and synthesis of DNA (2), detection of proteins involved in signaling networks in cells ("protein chips") (3), as well as solid-state biosensors for rapid detection of pathogens in the field (4). For the study of protein activity and for achieving optimum sensitiv-

Received 18 April 2007. Accepted 7 June 2007. Published on the NRC Research Press Web site at canjchem.nrc.ca on 14 August 2007.

X. Liu and F. Zheng. Department of Physics, University of Wisconsin-Madison, Madison, Wisconsin 53706, USA.
A. Jürgensen. Canadian Synchrotron Radiation Facility, Synchrotron Radiation Center, Stoughton, Wisconsin 53589–3097, USA.
V. Perez-Dieste. ALBA Synchrotron Light Facility, Universitat Autònoma de Barcelona, Edifici Ciencies, 08193 Bellaterra, Barcelona, Spain.
D.Y. Petrovykh. Physics Department, University of Maryland, College Park, MD 20742 and Naval Research Laboratory, Washington, DC 20375, USA.
N.L. Abbott. Department of Chemical and Biological Engineering, University of Wisconsin-Madison, Madison, Wisconsin 53706, USA.
F.J. Himpsel.[2] Department of Physics, University of Wisconsin-Madison, Madison, Wisconsin 53706, USA.

[1]This article is part of a Special Issue dedicated to Professor G. Michael Bancroft.
[2]Corresponding author (e-mail: fhimpsel@wisc.edu).

 doi:10.1139/V07-079 © 2007 NRC Canada

ity of immunoassays and protein sensors, it is important to control the orientation of proteins adsorbed on a surface (5). Consequently, the development of methods to assess the orientation of proteins on surfaces has been a focus of considerable research activity in recent years. Surface functionalization schemes, such as self-assembled monolayers (SAM) and phospholipid bilayers, make it possible to specifically immobilize proteins on surfaces, control their surface density, increase their orientational order, and prevent them from denaturing.

Biological activity of molecules in solution is typically measured using molecules labeled with tags that can be easily observed and (or) manipulated. These tags can be, for example, fluorescent, radioactive, chemiluminescent, magnetic, and electrochemical. However, in many cases labeled measurements can be difficult or even impossible for biomolecules immobilized on a surface. Surface analysis techniques such as ellipsometry, attenuated total reflection, quartz microbalance, and surface plasmon resonance can be used to measure the wet and dry mass uptake by biologically functionalized surfaces (1, 6). To understand the chemistry and structure of these surfaces, however, it is desirable to obtain element-specific and bond-specific information. This is where sophisticated techniques are required, such as FTIR (Fourier transform IR spectroscopy), XPS (X-ray photoelectron spectroscopy), and NEXAFS (near edge X-ray absorption fine structure spectroscopy) (1, 7, 8).

NEXAFS technique

NEXAFS measures optical dipole transitions from a core level to unoccupied valence orbitals, as shown in Figs. 1 and 2. The binding energy of the core level identifies a specific element and its charge, for example, neutral carbon and positively charged carbon in Fig. 2. The binding energy and its chemical shift can be measured independently by XPS. NEXAFS goes beyond XPS by identifying a specific σ* or π* orbital located at a particular atom (left side of Fig. 2, from ref. 9). Furthermore, the orientation of the orbital can be determined using optical dipole selection rules from the polarization dependence of the transition intensity. Accordingly, NEXAFS measurements require synchrotron radiation because there are no other tunable polarized light sources available in the soft X-ray regime. Typical elements in biomolecules, such as C, N, O, and S, exhibit simple s-to-p transitions, which are dipole-allowed if the electric field vector $\boldsymbol{E}$ of the incident X-rays is parallel to the transition dipole moment, which is perpendicular to the plane of peptide bond in proteins and perpendicular to the plane of the nucleotide bases in DNA. The observed intensity follows a $\cos^2\theta_E$ pattern around that axis. A measurement of the transition intensity makes it possible to determine the amount of certain bonds on a surface.

Usually, the optical absorption is measured indirectly by detecting decay products of the core hole, such as the total electron yield (TEY), the fluorescence yield (FY), or the Auger electron yield (Fig. 1). All of these decay products are proportional to the number of core holes created in the absorption process. The probing depth, however, varies. Electron detection is surface sensitive (typically 1–2 nm), while fluorescence detection probes deeper (typically

Fig. 1. Schematic of various methods to measure X-ray absorption via decay products of the core hole that is created in the absorption process. Detecting energy-selected fluorescence photons provides sensitivity to dilute species. Detecting Auger electrons, photoelectrons, and secondary electrons provides surface sensitivity.

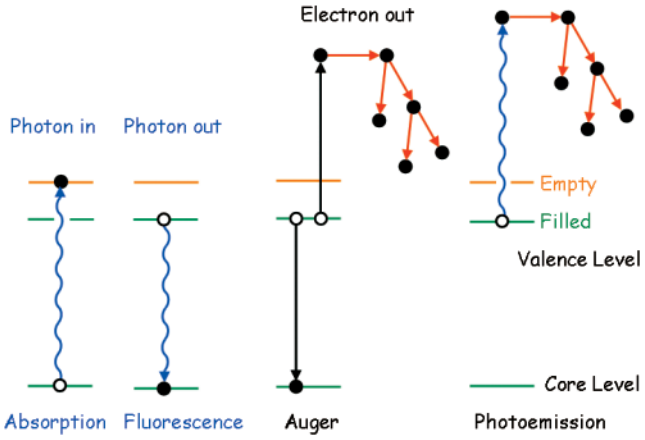
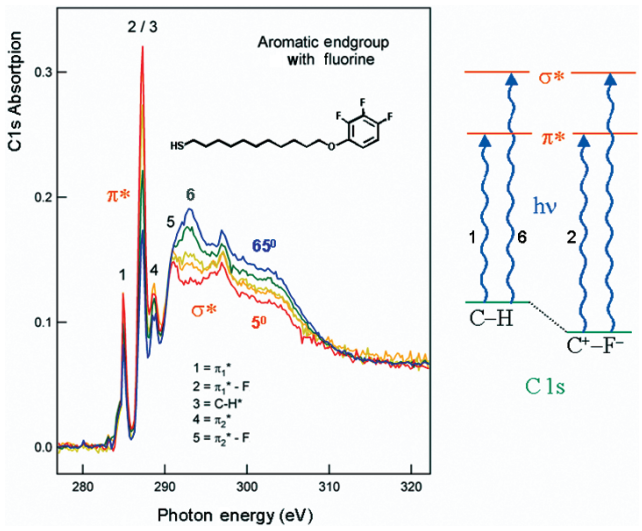


Fig. 2. Chemical selectivity of NEXAFS, demonstrated by a self-assembled monolayer of alkane chains with aromatic terminal groups (9). Transitions from the C 1s core level to unoccupied valence orbitals are observed. Specific atoms can be addressed by selecting the core level and by using its chemical shift to determine the oxidation state (here neutral C^0 in C-H versus C^{1+} in C-F). Specific valence orbitals are addressed via the final state, such as σ* and π*. The orientation of an orbital is obtained from its polarization dependence when changing the angle of incidence θ (measured from the surface normal).

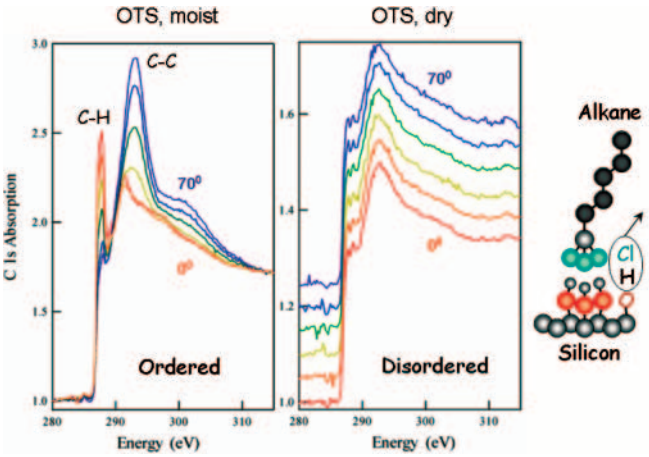


100 nm to several μm, depending on the absorption length at the photon energy of the emitted photons). By simultaneously measuring electron and fluorescence yield, it is possible to obtain a coarse depth profile of the sample.

Electron detection produces a much higher signal than fluorescence, since most of the core holes in the 100–1000 eV binding energy range decay by an Auger process. Fluorescence decay occurs 10^4–10^5 times less frequently. The decay of an Auger electron into multiple secondary electrons am-

© 2007 NRC Canada

Fig. 3. Functionalization of an oxidized silicon surface via siloxane chemistry (11). The coverage can be inferred from the height of the C 1s edge jump relative to the pre-edge background (which is normalized to 1). The orientation of the alkane chains is obtained from the polarization dependence. Both depend strongly on the preparation, with a dry environment leading to low coverage and random orientation.



plifies the signal further in the total electron yield mode (see Fig. 1). Nevertheless, fluorescence detection makes it possible to filter out photons characteristic of the substrate, thereby enhancing the signal-to-noise ratio for dilute systems, such as a fraction of a monolayer of DNA or protein immobilized at a surface. This trade-off between electron and photon detection will be demonstrated in the section on DNA and proteins. A channel plate with an Al filter is able to discriminate against a Si substrate, because Al absorbs the red-shifted Si fluorescence optimally ($Z_{Al} = Z_{Si} - 1$). Unfortunately, there is no good filter material to absorb C 1s fluorescence while transmitting the N 1s edge, which is of interest for DNA and proteins. In that case, a more sophisticated Si–Li detector or a multilayer band pass reflector is called for. Auger electron detection via an electron spectrometer allows some filtering as well. In Auger detection, however, the NEXAFS features are superimposed on the photoemission spectrum of the occupied valence orbitals sweeping through the fixed Auger energy window.

Self-assembled monolayers (SAMs)

Self-assembled monolayers of alkanes are widely used as the first step of chemically functionalizing surfaces. The two prevailing methods of attaching alkanes to a surface utilize thiol groups (on noble metals) or siloxanes (on oxidized silicon) (10). Figure 2 shows the NEXAFS spectrum of an alkanethiol on gold (10), and Fig. 3 of a siloxane on oxidized Si (OTS = octadecyltrichlorosilane) (11). The siloxane chemistry can be applied directly to a silicon wafer but requires stringent control over preparation conditions to achieve reproducible and well-defined surface functionalization. A well-ordered, densely packed SAM requires long soaking in solution (Fig. 3, left side), while quick drying in a nitrogen atmosphere produces a randomly oriented layer with much lower coverage (Fig. 3, right side).

The orientation of molecules in SAMs is inferred from the polarization dependence of NEXAFS. Rotating the sample changes the polar angle of incidence and therefore the angle θ of the electric field vector $\boldsymbol{E}$ with respect to the surface normal (for p-polarized light). The spectra on the left of Fig. 3 exhibit a strong θ-dependence, while the spectra on the right are identical to each other to the extent that they can only be distinguished by a vertical offset. On average, the C-H orbitals are oriented perpendicular to the alkane chain and the C-C orbitals parallel to it. Therefore, the intensity maximum of the C-H signal and the intensity minimum of the C-C orbital at $\theta = 90°$ both imply that the chains are, on average, oriented perpendicular to the surface. The fact that the intensity modulation is not quite 100% is usually taken as a sign that the chains are slightly tilted away from the normal (7), forming many domains with a well-defined polar tilt angle α but randomly distributed azimuthal tilt angles ϕ. Independent information from other techniques supports a tilted geometry for alkane-based SAMs. From the NEXAFS spectra alone, it is difficult to distinguish such a situation from a finite spread of tilt angles α around the surface normal. Examples are single-stranded DNA chains (section on DNA and proteins) and the orientation of the terminal group in Fig. 2 (10). These situations will be discussed more quantitatively in the quantitative analysis section.

The coverage can be estimated by normalizing the NEXAFS spectra to their pre-edge region, which is dominated by the substrate. While the spectra of ordered OTS on the left of Fig. 3 rise by 2 units (from 1 to 3), the spectra of disordered OTS on the right increase by only 0.5 units (from 1 to 1.5, see the red (bottom-most) spectrum with zero offset). Thus, the coverage is four times larger for ordered adsorption. At the highest possible coverage, the alkane chains come within a van der Waal's bond distance of each other and are forced to adopt a tilted geometry with dense packing.

Alkane-passivated surfaces can be further functionalized by adding specific terminal groups on top of a SAM. Two examples of functionalized SAMs are shown in Figs. 2 and 4 (from refs. 10 and 12, respectively). Spectroscopically, the terminal group can be distinguished from the supporting alkane chain by its valence orbital or its core level.

Particularly useful for selecting terminal groups are the sharp π^* orbitals, whose cross-section is large compared with the C-H or C-C orbitals of alkane chains. In Fig. 2, the π^* orbitals of the C=C-H groups in the phenyl group (Peak 1) appear below all the other orbitals. The π^* orbitals of the C=C-F groups in the fluorinated part of the phenyl group (Peak 2) overlap with the C-H orbitals of the alkane chain (Peak 3), but their higher cross section makes them dominant. This can be inferred from the π^* intensity ratio of Peaks 2 and 1, which should be 4:2 (counting =C-O- with =C-F) in this system.

In Fig. 4, the terminal group contains Fe, which can be probed selectively at the sharp Fe 2p absorption edge. The 3d transition metals are involved in many biological systems, such as enzymes and photosystems (12). Their sharpest edge is the 2p edge. It is ideal for probing the oxidation state from the multiplet structure induced by the interaction of the 2p core hole with the 3d valence electrons (13) as well as covalent bonding effects (14, 13). The 1s edges are much broader, but they are needed for probing highly dilute metallo-proteins in solution. The functionalization of alkane

© 2007 NRC Canada

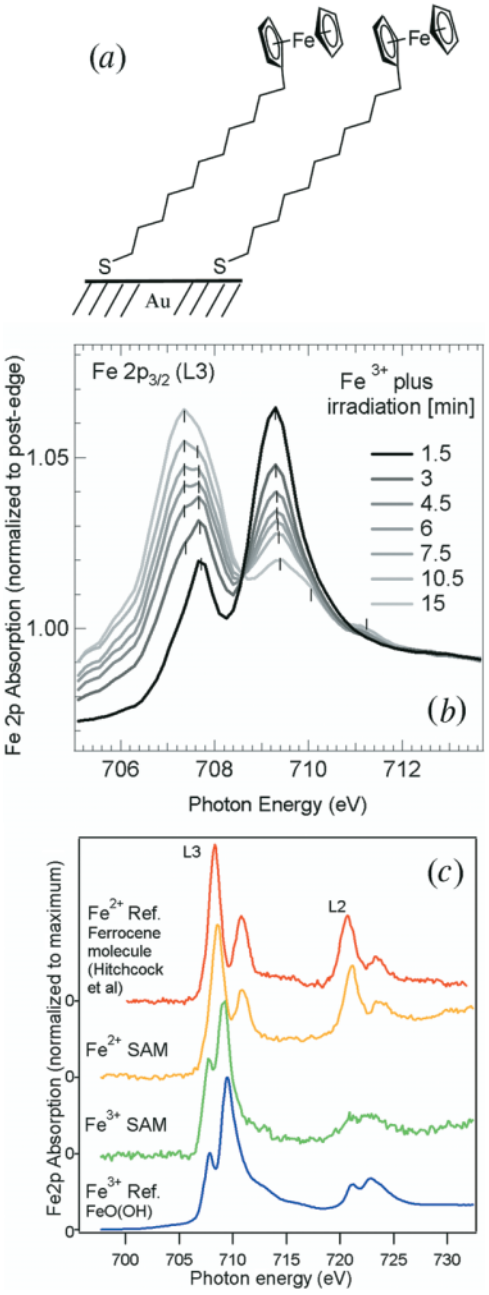
chains by ferrocene in the 2+ and 3+ oxidation states allows for prototypical experiments that investigate electrochemical and photochemical switching of the oxidation state. The multiplet structure of Fe^{2+} and Fe^{3+} and their energy shift are obtained via reference spectra, using molecular ferrocene (14) and a Fe^{3+} mineral (Fig. 4*c*, top and bottom spectra). They compare well to the spectra of two SAMs with ferrocene terminal groups in the 2+ and 3+ oxidation states, which were prepared by electrochemical means (15) (Fig. 4*c*, spectra at the center). Irradiation with intense undulator radiation reduces Fe^{3+} back to Fe^{2+} and further (Fig. 4*b*).

DNA and proteins

Immobilization of DNA and proteins at surfaces is a fast-growing area of research. DNA microarrays are revolutionizing biotechnology by allowing the simultaneous identification of many DNA sequences. They are a critical component of advanced systems for medical diagnostic and pathogen detection. The full potential of chip-based sensors in genomics and proteomics can only be realized if the fragile biomolecules survive the attachment process intact. Furthermore, they must be properly oriented to perform their biological function, for example, binding to a complementary DNA strand in a DNA chip and to a specific protein in an immunosensor. The ability to characterize the chemistry and structure of biomolecules at surfaces facilitates the systematic and controlled development of future generations of DNA chips and protein biosensors.

Despite the complexity of biomolecules, NEXAFS is able to provide information about the attachment process and the orientation of immobilized DNA and proteins. The C 1s edge tends to be difficult to analyze because of the multitude of carbon atoms in different chemical environments. However, the N 1s edge singles out specific atoms and bond orbitals. For both DNA and proteins, the lowest unoccupied N valence orbital is a π*, as shown in Figs. 5 and 6. These orbitals are sharp and have a high cross section, which makes them easy to detect. In DNA, the N π* orbitals are located at the base pairs, and they are all oriented parallel to the axis of the double-helix in double-stranded DNA (Fig. 5*d*). In proteins, the N π* orbitals are located at the peptide bonds, which link amino acids into peptides and eventually proteins. This has been demonstrated very clearly in (16), where the N π* orbital is observed only when amino acids are linked together, not in individual amino acids. Fig. 6 shows this peptide bond as the first major peak at the N 1s absorption edge. It also includes the wave function of the peptide bond orbital, which extends over four atoms (Cα, C, N, O) and forces them into a planar arrangement. Even more selective are the absorption edges of minority elements in proteins. S is the most prominent example. It is only part of a few amino acids, such as cysteine, but these are important in cross-linking proteins and attaching them to a surface. Fig. 6 shows the S 1s edge spectrum. As a second row element, sulfur has little tendency towards π bonding. Therefore, the S 1s edge does not exhibit a π* orbital, only a σ*. However, it is sensitive to the formation of S-S crosslinks, for example between two cysteines (17).

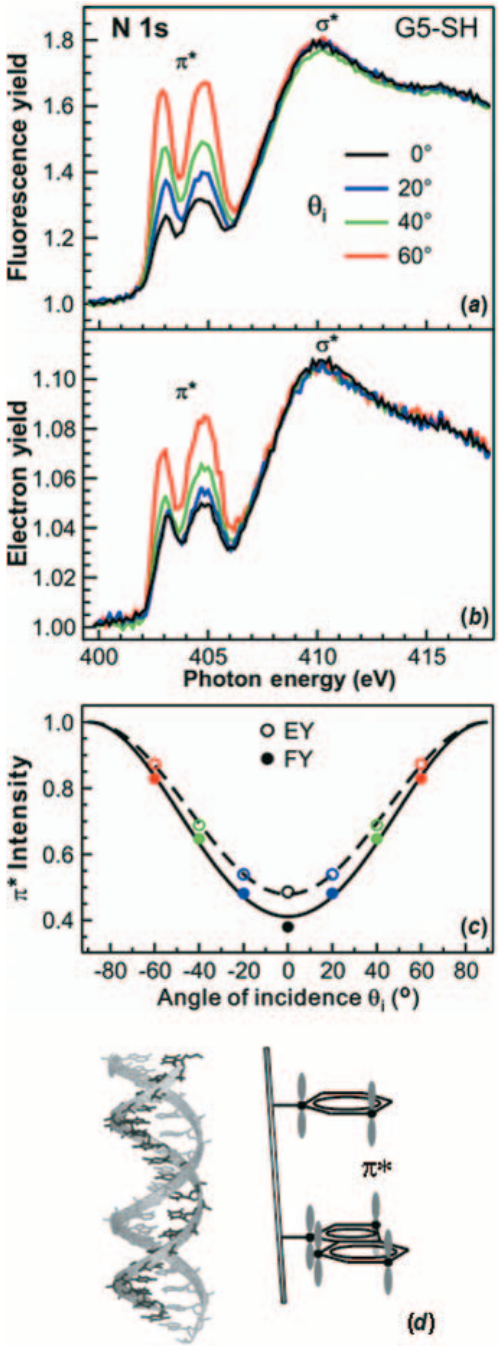
Fig. 4. Determination of the oxidation state of Fe in a self-assembled monolayer functionalized by a ferrocene terminal group (15). The multiplet structure of the Fe 2p to 3d transitions reveals the oxidation state. Spectra for molecular ferrocene (from



The information from NEXAFS becomes more and more selective by going from C to N, S, and other minority elements, such as transition metals in metallo-proteins (12, 13). NEXAFS of the 2p to 3d transitions of 3d transition metals provides very specific information about the oxidation state and spin state (see Fig. 4). The electron yield signal of dilute elements becomes swamped by background absorption from the C 1s core level, the C 2s, 2p valence orbitals, and the substrate. This problem is solved by fluorescence detection, where the background photons from the C 2s, 2p valence orbitals, and from the substrate can be filtered out. Figure 5 demonstrates the effect of a simple Al filter in front of a

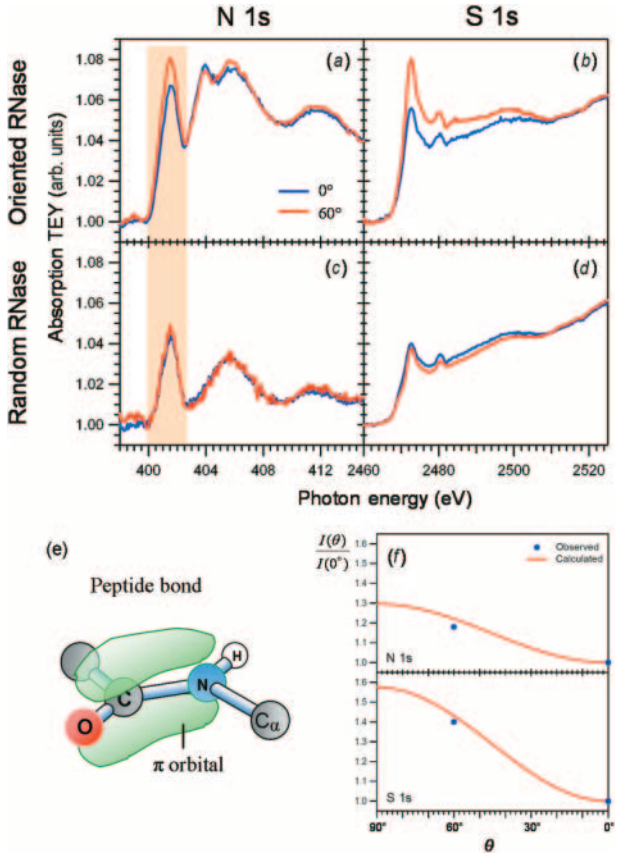
© 2007 NRC Canada

Fig. 5. The π* orbitals of the nucleotide bases in DNA detected at the N 1s edge. The spectra in (*a*)–(*c*) are for single-stranded DNA consisting of 5 guanine nucleotides and attached to a gold surface via a thiol group (18). Fluorescence detection in (*a*) provides a much better signal to background ratio than electron detection in (*b*). The polarization dependence shows that the π* orbitals are oriented perpendicular to the surface (on average). Similar spectra are obtained for double-stranded DNA (19), where the π* orbitals of all base pairs point along the axis of the double helix, as indicated in (*d*).



channel plate detector. After normalizing the data to the pre-edge background, the electron yield in panel 5*b* provides a low signal-to-background ratio of 8%, which increases the noise substantially and makes a reliable background subtraction difficult. The filtered fluorescence measurement in panel 5*a* improves this ratio to 65%, i.e., signal and background become comparable. This ratio can be improved further by using an energy-dispersive Si-Li or Ge detector (not shown). However, it is difficult to maintain the large acceptance angle of a channel plate, and the maximum count rate suffers as the energy resolution of the detector is improved. Detector efficiency is a critical factor with biological samples because radiation damage imposes severe limits on the exposure time.

Fig. 6. Polarization-dependent NEXAFS of a protein (RNase A, from (21)). The N 1s edge reveals the π* orbital of the peptide bond that polymerizes amino acids into a protein (shaded in (*a*), and (*c*)). Despite the summation over 124 amino acids in RNase A, there is substantial polarization dependence at the N 1s and S 1s edges (see (*a*) and (*b*)). A parameter-free calculation is consistent with the data in (*f*). The polarization dependence can be enhanced by choosing a minority species, such as sulfur. The *y*-axis scales are same in panels (*a*) to (*d*). (*a*) and (*b*) are for oriented immobilization, (*c*) and (*d*) for random immobilization (21).



The orientation of DNA nucleobases can be determined from the polarization dependence of the N 1s NEXAFS spectra (18–20). At the C 1s edge, the polarization effects are averaged out because of the many inequivalent C atoms with nearly random bond orientations. Figures 5*a*–5*c* show the polarization dependence for single-stranded DNA oligomers consisting of 5 guanine nucleotides attached to a Au surface via a thiol bond (from ref. 18). Similar measurements have been made for double-stranded DNA (19). The maximum of the π* intensity occurs at grazing incidence, i.e., with the

© 2007 NRC Canada

electric field vector ***E*** perpendicular to the surface. The dipole selection rules lead to the conclusion that the π* orbitals of the bases are preferentially oriented perpendicular to the surface (parallel to ***E***). Therefore, the aromatic rings of the nucleobases are parallel to the surface. A more quantitative evaluation is shown in panel 5*c* for both electron and fluorescence detection. Since the fluorescence measurement is affected by an additional dipole selection rule in the emission process, one has to make sure that the detection geometry does not distort the polarization dependence. This can be achieved by having a large acceptance angle or by placing the detector near the magic angle, where the orientation dependence vanishes. For 100% orientation, one should observe a $\cos^2\theta_E$ dependence of the NEXAFS intensity according to the matrix element for a s to p dipole transition. Experimentally, the $\cos^2\theta_E$ modulation is only 60% of the maximum, which indicates only partial ordering. A quantitative analysis will by given in the section Quantitative analysis. The degree of orientation can be changed (18) by varying the length of the DNA segment, its base sequence, and the preparation conditions. The σ* orbitals generally have a much smaller polarization dependence than the π* orbitals, which can be explained by the fact that an aromatic ring contains σ* orbitals in many in-plane directions, while all the π* orbitals are parallel to each other and perpendicular to the plane.

Proteins are even more complex and less regular than DNA, and yet it has been possible to observe a polarization dependence in RNase A (21), a protein containing 124 amino acids and more than 10^3 atoms (not counting H). The π* orbital at the N 1s edge exhibits a 18% modulation between θ = 0° and 60°, while the S 1s edge is modulated by 41%. This follows the expectation that a less frequent element, such as S, experiences less averaging. The higher σ* orbitals have a much weaker polarization dependence than the π* orbitals, similar to the DNA results. As a further cross-check, RNase A can be immobilized by a different technique that gives random orientation (21). In that case the polarization dependence of the peptide band π* orbital is comparable to the experimental error of a few percent.

The polarization dependence at the N 1s edge is surprisingly strong in view of the 123 peptide bonds contributing to the spectrum. A purely random arrangement of these bonds within one protein molecule (together with perfect orientation of the molecules relative to each other) would give a modulation of $1/\sqrt{123} = 9\%$. Therefore, we have developed a program that sums the dipole matrix elements over all 123 peptide bonds using the atomic coordinates in the protein data base and a specific orientation of the molecules based on the immobilization method. (The protein is bound to the supporting SAM via a S–S bond to the cysteine at the 19th residue, and that bond is assumed to be perpendicular to the surface (21).) The calculated modulation (red curve in Fig. 6*f*) is surprisingly close to the experimental points (blue dots), and the remaining difference goes in the right direction. The data are modulated less than the calculation because the molecules are not perfectly oriented and the polarization of the synchrotron light is not perfect (93% in this experiment). A similar calculation can also be performed for the 12 sulfur atoms in RNase A, and it represents the data equally well. Thus, we conclude that RNase has substantial internal correlations between the orientations of the peptide bonds, which double the statistical polarization dependence. This is quite reasonable in view of the internal structure of proteins, which contain highly regular elements, such as the α-helix and the β-sheet. RNase A, for example, contains 22% α-helices and 46% β-sheets.

Quantitative analysis

NEXAFS has been mostly used for qualitative analysis of the chemical reactions that occur during the immobilization process of biomolecules at surfaces. However, quantitative NEXAFS analysis can be used for determining both coverage and orientation of molecules. Here we mainly address the orientational information that can be obtained from the polarization dependence of the NEXAFS signal. A widely used formula for the polarization dependence (7) assumes a layer of tilted molecules consisting of domains with perfect orientation within each domain. The domains all have the same polar tilt angle α, but a random-distribution of azimuthal angles φ. This leads to the formula,

$$[1] \qquad I(\theta) / I(0°) = 1 + P[(2/\sin^2\alpha) - 3]\sin^2\theta$$

where θ is the angle of incidence from the sample normal ($\theta = 90° - \theta_E$), α is the tilt angle of a p-orbital from normal, and *P* is the degree of polarization of the soft X-rays. These assumptions are reasonable for simple SAMs that are known to be nearly perfectly ordered. However, in more complex systems, such as SAMs with tailored terminal groups, DNA, or proteins, one encounters two phenomena that are not captured by eq. [1].

First, there can be more than a single angle determining the geometry of the system. A terminal group is often able to rotate around the bond that attaches it to the supporting alkane chain. An extreme case is the orientation of a protein at a surface, which requires three angles to be fully characterized. If one allows for different folding patterns, the number of variables increases rapidly.

Second, larger molecules may exhibit a distribution of bond angles instead of being perfectly oriented. That introduces a finite spread σ of the bond angles. Moreover, for a system that contains a distribution of bond orientations, the interpretation of a polarization-dependent measurement in terms of a unique angle, in general, will not result in a value close to the average of that distribution (18, 22, 23).

In all cases, one faces the dilemma that NEXAFS provides at best two experimental numbers for each orbital that characterize the polar and azimuthal polarization dependence of the peak height. Therefore, one needs to carefully select the free parameters when fitting the data and freeze the remaining variables by using other experiments or making judicious assumptions. For example, it makes little sense to assume a fixed polar tilt angle (as in eq. [1]) for characterizing the orientation of floppy molecules, such as single-stranded DNA (18). A more reasonable assumption is a distribution of tilt angles with an average orientation α_0 relative to the surface normal. Using a Gaussian distribution with standard deviation σ leads to the following polarization dependence (24),

© 2007 NRC Canada

[2] $I(\theta) / I(0°) = 1 + P[8z/(3z - 1 - 2\cos(2\alpha_0)) - 3]\sin^2\theta$, where $z = \exp(4\sigma^2)$

With this approach, the free parameter becomes σ, and the average angle α_0 needs to be obtained from symmetry arguments (e.g., $\alpha_0 = 0°$ for DNA (18, 19)), or from other measurements (e.g., X-ray diffraction of the bulk phase (24)).

Another situation occurs in proteins, where the π* signal at the N 1s edge contains contributions from many nitrogen atoms in peptide bonds with different orientations. In that case one needs to sum over the angular dependence of all individual orbitals. Each overall orientation (Θ, Φ) of the protein corresponds to a well-defined polarization dependence $I(\theta, \phi, \Theta, \Phi)$ with respect to the angle of incidence (θ, ϕ). The polarization dependence is calculated by summing over the individual contributions $I_n(\theta, \phi, \Theta, \Phi)$ from the *n*th peptide bond. Each of these follows a $\cos^2\theta_n$ law, where θ_n is the angle between the electric field vector $\boldsymbol{E}$ and the direction $\boldsymbol{e}_n^{\mathrm{N}}(\Theta, \Phi)$ of the π* orbital in the *n*th peptide bond. The vectors $\boldsymbol{e}_n^{\mathrm{N}}$ are obtained from the cross product of the vectors $\boldsymbol{r}_n^{\mathrm{CO}}$ and $\boldsymbol{r}_n^{\mathrm{CN}}$ that define the plane of the peptide bond (see Fig. 6*e*). They connect the carbon atom in the *n*th peptide bond with its neighboring oxygen and nitrogen atoms. For the S 1s edge, the unit vector $\boldsymbol{e}^{\mathrm{S}}{}_m$ connects the *m*th S atom with the adjacent C atom along a σ bond. The atomic coordinates are obtained from the protein databank available from www.pdb.org.

The overall orientation angle Θ of RNase in Figs. 6*a*, 6*b*, and 6*f* is determined by its attachment to the supporting SAM via a S–S bond to the cysteine at the 19th residue. Assuming that this S–S bond is perpendicular to the surface, one needs to rotate the coordinates in the protein data bank such that the vector $\boldsymbol{r}_{19}^{\mathrm{SH}}$ becomes parallel to the surface normal. This is achieved by calculating the transformation matrix for this rotation and applying it to all vectors $\boldsymbol{e}_n$. The azimuthal orientation Φ of the RNase molecules around the S–S bond is assumed to be random. That leads to an average over the azimuthal orientation Φ, which is equivalent to an average over the angle of incidence ϕ with fixed orientation Φ. This approach eliminates the angles Θ, Φ, and ϕ from the problem. The normalized polarization dependence of the NEXAFS signal $I(\theta)/I(0°)$ becomes a function of the angle of incidence θ from the surface normal, without adjustable parameters. For the N 1s and S 1s edges one obtains,

[3*a*]
$$\boldsymbol{e}_n^{\mathrm{N}} = \frac{\boldsymbol{r}_n^{\mathrm{CO}} \times \boldsymbol{r}_n^{\mathrm{CN}}}{\left|\boldsymbol{r}_n^{\mathrm{CO}} \times \boldsymbol{r}_n^{\mathrm{CN}}\right|}$$
$$\frac{I^{\mathrm{N}}(\theta)}{I^{\mathrm{N}}(0°)} = \frac{\int \sum_n [\boldsymbol{E}(\theta)\, \boldsymbol{e}_n^{\mathrm{N}}]^2 \, \mathrm{d}\phi}{\int \sum_n [\boldsymbol{E}(0°)\, \boldsymbol{e}_n^{\mathrm{N}}]^2 \, \mathrm{d}\phi}$$

[3*b*]
$$\boldsymbol{e}_m^{\mathrm{S}} = \frac{\boldsymbol{r}^{\mathrm{SC}}}{\left|\boldsymbol{r}_m^{\mathrm{SC}}\right|}$$
$$\frac{I^{\mathrm{S}}(\theta)}{I^{\mathrm{S}}(0°)} = \frac{\int \sum_m [\boldsymbol{E}(\theta)\, \boldsymbol{e}_m^{\mathrm{S}}]^2 \, \mathrm{d}\phi}{\int \sum_m [\boldsymbol{E}(0°)\, \boldsymbol{e}_m^{\mathrm{S}}]^2 \, \mathrm{d}\phi}$$

Applying these formulas to the N 1s and S 1s data of oriented RNase A in Fig. 6 gives the correct magnitude of the polarization dependence (see panel (*f*)). This calculation could be refined further by including the degree of polarization *P* and a distribution of orientation angles (compare eqs. [1] and [2]). Both would bring the calculation closer to the experimental values.

Apart from the polarization dependence, there are several other quantitative results that can be extracted from NEXAFS data of proteins. Spatially resolved spectromicroscopy (25, 26) maps the distribution of proteins in biological samples.[3] The spectrum of a protein can be modeled (27) by using reference spectra for individual amino acids (28) and taking the changes due to the formation of the peptide bond into account. For the determination of relative concentrations, it is useful to normalize the spectra to the edge jump between the pre-edge and the continuum absorption 20–30 eV above the edge. This normalization provides a signal proportional to the density of C, N, O, and S atoms.

Summary and outlook

In summary, we demonstrate how the element and orbital sensitivity of NEXAFS spectroscopy can be used to investigate the binding properties of biomolecules at surfaces. Simple alkane passivation layers serve as tutorial examples. The complexity is increased systematically by adding customized terminal groups. Eventually, DNA and proteins are tackled. The orientation of the immobilized protein is detected from the polarization dependence of the NEXAFS intensity. The results suggest that NEXAFS can be used to investigate fairly complex biomolecules at surfaces, such as DNA oligomers and proteins containing more than a hundred amino acids. The agreement between the results of complementary NEXAFS, XPS, and FTIR measurements (18) strongly suggests that these ex situ techniques capture salient properties of biomolecules as they are immobilized in solution. Such element-specific surface-sensitive diagnostic methods help to monitor and control the multistep immobilization process of biomolecules.

To have an impact on day-to-day biochemical research, it will be necessary to simplify the access to the required synchrotron light sources and the analysis of the results. Protein crystallography can serve as a model, where automation in sample handling and data processing has become routine. Even remote control data acquisition has become possible, as long as there is a synchrotron staff member available to load the samples. Due to the vacuum requirements for NEXAFS, the sample introduction becomes more complicated. However, it is possible to build sample cells with thin Si or Si_3N_4 windows that separate the sample atmosphere from the detector and the synchrotron, while transmitting enough light to operate in the fluorescence detection mode. In the "water window" between the C 1s and O 1s edges, the mean free path of soft X-rays is only a few μm in liquid water (4 μm at the N 1s edge). This length increases to 0.3 m in saturated water vapor (18 Torr at 100% humidity; 1 torr = 133.322 4 Pa). That makes sample handling much easier. In addition, the radiation damage from radicals created by

[3] C.J. Johnsen, R.M. Olabisi, R.A. Metzler, B.Gilbert, B.H. Frazer, D. McKenzie, J.M. Aiken, and P.U.P.A. Gilbert. Manuscript in preparation.

© 2007 NRC Canada

photodecomposition of the liquid water film between sample and window is avoided. Developing practical "wet" or "humid" sample cells is an important step in bringing NEXAFS closer to a mainstream analytical technique for surface biochemistry.

Looking farther into the future, one could go beyond self-assembled monolayers and consider more complex objects, such as phospholipid membranes, supported by molecular stilts (29). Like a cell wall, such a membrane may contain ion channels, photosynthetic centers, molecular motors, etc. Compared to a natural cell, this is a more controllable environment that can be used for selectively investigating a specific part of the incredibly complex cell machinery.

Acknowledgment

This work was supported by the National Science Foundation (NSF) under awards DMR-0520527 (MRSEC) and DMR-0084402 (SRC), and by the DOE under contracts No. DE-FG02–01ER45917 and No. DE-AC03–76SF00098 (ALS). Financial support for CSRF is provided by Natural Sciences and Engineering Research Council of Canada (NSERC) and NRC–CRNC (National Research Council Canada – Conseil National de Recherches Canada). Work at NRL (DYP) was supported by the Air Force Office of Scientific Research.

References

1. B. Kasemo. Surf. Sci. **500**, 656 (2002); D.G. Castner and B.D. Ratner. Surf. Sci. **500**, 28 (2002).
2. J.D. Hoheisel. Nat. Rev. Genet. **7**, 200 (2006); M.C. Pirrung. Angew. Chem., Int. Ed. **41**, 1277 (2002); S. Draghici, P. Khatri, A.C. Eklund, and Z. Szallasi. Trends Genet. **22**, 101 (2006).
3. H. Zhu, M. Bilgin, R. Bangham, D. Hall, A. Casamayor, P. Bertone. N. Lan, R. Jansen, S. Bidlingmaier, T. Houfek, T. Mitchell, P. Miller, R.A. Dean, M. Gerstein, M. Snyder. Science, **293**, 2101 (2001); G. MacBeath, S.L. Schreiber. Science, **289**, 1760 (2000); C.-H. Jang, M.L. Tingey, N.L. Korpi, G.J. Wiepz, J.H. Schiller, P. Bertics, N.L. Abbott. J. Am. Chem. Soc. **25**, 8912 (2005); A. Guo and X. Zhu. Int. J. Nanosci. **6**, 109 (2007).
4. S.A. Soper, K. Brown, A. Ellington, B. Frazier, G. Garcia-Manero, V. Gau, S.I. Gutman, D. F. Hayes, B. Korte, J.L. Landers, D. Larson, F. Ligler, A. Majumdar, M. Mascini, D. Nolte, Z. Rosenzweig, J. Wang, and D. Wilson. Biosens. Bioelectron. **21**, 1932 (2006); J.J. Gooding. Anal. Chim. Acta, **559**, 137 (2006); V.K. Gupta, J.J. Skaife, T.B. Dubrovsky, N.L. Abbott, Science, **279**, 2077 (1998).
5. Y.Y. Luk, M.L. Tingey, D.J. Hall, B.A. Israel, C.J. Murphy, P.J. Bertics, N.L. Abbott. Langmuir, **19**, 1671 (2003); Y.Y. Luk, M.L. Tingey, D.J. Hall, K.A. Dickson, R.T. Raines, N.L. Abbott. J. Am. Chem. Soc. **126**, 9024 (2004).
6. M. Bally, M. Halter, J. Voros, and H.M. Grandin. Surf. Interface Anal. **38**, 1442 (2006); A. Janshoff, H.-J. Galla, and C. Steinem. Angew. Chem., Int. Ed. **39**, 4004 (2000).
7. J. Stöhr. NEXAFS Spectroscopy. Springer-Verlag, New York. 1996.
8. D.Y. Petrovykh, H. Kimura-Suda, L.J. Whitman, and M.J. Tarlov. J. Am. Chem. Soc. **125**, 5219 (2003); D.Y. Petrovykh, H. Kimura-Suda, M.J. Tarlov, and L.J. Whitman. Langmuir, **20**, 429 (2004).
9. Y.-Y. Luk, N.L. Abbott, J.N. Crain, and F.J. Himpsel. J. Chem. Phys. **120**, 10792 (2004).
10. F. Luderer and U. Walschus. Top. Curr. Chem. **260**, 37 (2005); J.C. Love, L.A. Estroff, J.K. Kriebel, R.G. Nuzzo, and G.M. Whitesides. Chem. Rev. (Washington, DC), **105**, 1103 (2005).
11. R.D. Peters, P.F. Nealey, J.N. Crain, and F.J. Himpsel. Langmuir, **18**, 1250 (2002).
12. S.P. Cramer, J. Chen, S.J. George, J. Vanelp, J. Moore, O. Tensch, J. Colaresi, M. Yocum, O.C. Mullins, C.T. Chen. Nucl. Instrum. Methods Phys. Res., Sect. A, **319**, 285 (1992); X. Wang, M.M. Grush, A.G. Froeschner, S.P. Cramer. J. Synchrotron Rad. **4,** 236 (1997); M.C. Corbett, F.A., Tezcan, O. Einsle, M.Y. Walton, D.C. Rees, M.J. Latimer, B. Hedman, K.O. Hodgson. J. Synchrotron Rad. **12**, 28 (2005).
13. F. De Groot. Coord. Chem. Rev. **249**, 31 (2005).
14. A.P. Hitchcock, A.T. Wen, E. Rühl. Chem. Phys. **147**, 51 (1990).
15. F. Zheng, V. Pérez-Dieste, J.L. McChesney, Y.-Y. Luk, N.L. Abbott, and F.J. Himpsel. Surf. Sci. **587**, L191 (2005).
16. M.L. Gordon, G. Cooper, C. Morin, T. Araki, C.C. Turci, K. Kaznatcheev, A.P. Hitchcock. J. Phys. Chem. A, **107**, 6144 (2003).
17. A. Rompel, R.M. Cinco, M.J. Latimer, A.E. McDermott, R.D. Guiles, A. Quintanilha, R.M. Krauss, K. Sauer, V.K. Yachandra, and M.P. Klein. Proc. Natl. Acad. Sci. USA, **95**, 6122 (1998).
18. D.Y. Petrovykh, V. Perez-Dieste, A. Opdahl, H. Kimura-Suda, J.M. Sullivan, M.J. Tarlov, F.J. Himpsel, and L.J. Whitman. J. Am. Chem. Soc**. 128**, 2 (2006).
19. J.N. Crain, A. Kirakosian, J.-L. Lin, Y. Gu, R.R. Shah, N.L. Abbott, and F.J. Himpsel. J. Appl. Phys. **90**, 3291 (2001).
20. K. Fujii, K. Akamatsu, and A. Yokoya. J. Phys. Chem. B, **108**, 8031 (2004); C.Y. Lee, P. Gong, G.M. Harbers, D.W. Grainger, D.G. Castner, and L.J. Gamble. Anal. Chem. **78**, 3316 (2006); N.T. Samuel, C.Y. Lee, L.J. Gamble, D.A. Fischer, and D.G. Castner. J. Electron Spectrosc. Relat. Phenom. **152**, 134 (2006).
21. X. Liu, C.H. Jang, F. Zheng, A. Jürgensen, J.D. Denlinger, K.A. Dickson, R.T. Raines, N.L. Abbott, and F.J. Himpsel. Langmuir, **22**, 7719 (2006).
22. G.J. Simpson and K.L. Rowlen. J. Am. Chem. Soc. **121**, 2635 (1999).
23. F. Zheng, J.L. McChesney, X. Liu, and F.J. Himpsel. Phys. Rev. B, **73**, 205315 (2006).
24. F. Zheng, B.-N. Park, S. Seo, P.G. Evans, and F.J. Himpsel. J. Chem Phys. **126**, 154702 (2007).
25. L. Li., A.P. Hitchcock, N. Robar, R. Cornelius, J.L. Brash, A. Scholl, and A. Doran. J. Phys. Chem. B, **110**, 16763 (2006).
26. C.S. Chan, G. De Stasio, S.A. Welch, M. Girasole, B.H. Frazer, M.V. Nesterova, S. Fakra, and J.F. Banfield. Science, **303**, 1656 (2004).
27. J. Stewart-Ornstein, A.P. Hitchcock, D. Hernandez-Cruz, P. Henklein, J. Overhage, K. Hilpert, J.D. Hale, and R.E.W. Hancock. J. Phys. Chem. B, **111**, 7691 (2007).
28. Y. Zubavichus, A. Shaporenko, M. Grunze, and M. Zharnikov. J. Phys. Chem. A, **109**, 6998 (2005).
29. B.A. Cornell, V.L.B. Braach-Maksvytis, L.G. King, P.D.J. Osman, B. Raguse, L. Wieczorek, and R.J. Pace. Nature **387**, 580 (1997); M. Tanaka and E. Sackmann. Phys. Status Solidi A, **203**, 3452 (2006); E.T. Castellana and P.S. Cremer. Surf. Sci. Rep. **61**, 429 (2006).

© 2007 NRC Canada

An O K-edge XANES study of calcium aluminates[1]

Grant S. Henderson, Daniel R. Neuville, and Laurent Cormier

Abstract: Oxygen K-edge XANES spectra of crystalline calcium aluminate phases exhibit features that are strongly influenced by orbital mixing between the O 2p antibonding states and Ca and Al orbitals. Specific peaks in the spectra are characteristic of the calcium coordination and can be assigned to Ca in nine-, eight-, seven-, and six-fold coordination. The Q speciation of the AlO_4 tetrahedra also influences the position of the peaks, and several peaks result from a mixture of Ca and Al interactions.

Key words: O K-edge XANES, calcium aluminates, coordination, Q species.

Résumé : Les spectres d'absorption X de type XANES « X-ray absorption near edge structure » près du seuil K de l'oxygène des phases cristallines d'aluminate de calcium présentent des caractéristiques qui sont fortement influencés par la combinaison des orbitales entre les états antiliants 2p de l'oxygène et les orbitales du calcium et de l'aluminium. Des pics spécifiques des spectres sont caractéristiques de la coordination du calcium et ils peuvent être attribués au calcium dans des états de nona-, octa-, hepta- et hexacoordinations. La spéciation Q du tétraèdre du AlO_4 influence aussi la position des pics et plusieurs d'entre eux correspondent à un mélange d'interactions du calcium et de l'aluminium.

Mots-clés : spectres XANES près du seuil K de l'oxygène, aluminates de calcium, coordination, espèces Q.

[Traduit par la Rédaction]

Introduction

In general, X-ray absorption studies of glass structure have focused on investigating the structural environment of the major cations making up the glass of interest. There have been very few studies that have investigated the oxygen environment. However, recent studies (1–2) have shown that the oxygen K-edge can be useful for probing glass structure. Oxygen K-edge XANES result from O 1s transitions to O 2p antibonding states mixed with cation orbitals (1–2, and refs. therein) and are sensitive to interactions with whatever is bound to the oxygen. The spectra are complex and also influenced by a number of factors other than the nature of the cation that is bound to the oxygen. These include whether or not oxygen is bridging or non-bridging, the coordination geometry of the cation, and the bond angles between the oxygen and surrounding cations (cf. (3)). Despite these complexities, the O K-edge XANES has proven useful for determining the coordination of Ti in Ti-silicate glasses (1) and of germanium in alkali germanate glasses (3) where determination of cation coordination can be problematic.

In glass systems that lack the long-range structure and translational symmetry typical of crystalline phases, analysis of XANES spectra requires the use of crystalline standards as a means to make logical assignments of the observed peaks in the spectra. One of the glass systems that are currently of interest to geologists is the calcium aluminosilicate (CAS) ternary. CAS glasses are important geologically and for commercial applications. This is because of their highly refractory nature and excellent optical and mechanical properties (cf. (4), and refs. therein). Furthermore, glasses in this system can be made by conventional melt-quenching techniques in a narrow range of compositions (60–70 mol% CaO) at very low wt% SiO_2 contents, contrary to alkali or Mg aluminosilicate glasses. Addition of small amounts of SiO_2 to CaO–Al_2O_3 (CA) glasses extends the glass-forming region and lowers the liquidus temperature (5), and the macroscopic properties are markedly changed with the introduction of silica, suggesting structural modification of these glasses. Here, we investigate, using O K-edge XANES, a series of calcium aluminate phases used as standards in the studies of the CAS system.

Experimental

The crystalline calcium aluminate phases $Ca_3Al_2O_6$ (C3A), $CaAl_2O_4$ (CA), and $CaAl_4O_7$ (CA2) (the C3A, CA, and CA2 terminology uses the standard notation for cements where C = CaO, A = Al_2O_3) were prepared by melting the appropriate quantities of Al_2O_3, $CaCO_3$, and SiO_2. Approximately 100 g of the stoichiometric mixtures of $CaCO_3$–Al_2O_3–SiO_2 (Rectapur from Merck) were ground for 1 h under alcohol in an agate mortar. The mixtures were heated slowly to decompose the carbonate and then heated up to 1900 K in covered Pt-alloy crucibles for a few hours in equilibrium with air. The samples were quenched in a few sec-

Received 26 March 2007. Accepted 08 June 2007. Published on the NRC Research Press Web site at canjchem.nrc.ca on 14 August 2007.

G.S. Henderson.[2] Department of Geology, University of Toronto, Toronto, ON M5S 3B1, Canada.
D.R. Neuville. Physique des Minéraux et des Magmas, IPGP-CNRS, 4 place Jussieu, 75005 Paris, France.
L. Cormier. IMPMC, Université Paris 6 et Université Paris 7, CNRS, 140 rue de Lourmel, 75015 Paris, France.

[1]This article is part of a Special Issue dedicated to Professor G. Michael Bancroft.
[2]Corresponding author (e-mail: henders@geology.utoronto.ca).

 doi:10.1139/V07-071 © 2007 NRC Canada

onds from high temperature by dipping the bottom of the platinum crucible into distilled water. The crushing, heating, and quenching were repeated four times for each sample and corresponds to heating the samples to 1950 K for 24 h. The crystals were then obtained by thermal treatment near the glass-transition temperatures. All crystals were characterized by X-ray diffraction, electron microprobe analysis (Camparis Center, Paris), and by Raman spectroscopy (JY64000, 514.5 Å). The experimental details of the characterization techniques are given in ref. 4.

The O K-edge spectra were recorded on the SGM beamline at the Canadian Light Source (CLS), University of Saskatoon. The beamline at CLS has three gratings with line spacings of 600, 1100, and 1700 lines/mm, which extend the photon region from 250 to 2000 eV. The energy resolution is approximately 0.05 eV at the O K-edge. The photon flux at 100 mA is 10^{12} photons/s, and the beam size is <1 mm (horizontal) × 100 μm (vertical) (6). The monochromator step size was varied between 0.05 and 0.1 eV to maximize the signal-to-noise ratio, and the scan rate was adjusted according to the step size, based on a scan rate of 0.858 eV min^{-1} for a step size of 0.1 eV. The spectra were collected simultaneously in both fluorescence yield (FY) and total electron yield (TEY) modes, with the latter measured by current yield. Incident photon energy was calibrated at the start of the experimental run using nitrogen (N_2). All samples were crushed, ground, and mounted on carbon tape immediately prior to analysis. The energy ranges of all spectra have been calibrated using the first sharp peak in the O K-edge spectrum of rutile TiO_2 at 531.1 eV. Peak positions are accurate to ±0.1 eV. A background subtraction has been applied using a Victoreen or polynomial function fitted to the pre-edge region. In addition, each spectrum has been normalized to the peak with maximum intensity and with the same intensity scale.

Crystalline calcium aluminates

The structure of $CaAl_2O_4$ (CA) has been determined by Horkner and Muller-Buschbaum (7). It is a tridymite-like structure with AlO_4 tetrahedra making up six-membered rings. Calcium atoms occupy cavities within the fully polymerized AlO_4 network. There are three Ca sites of which two have Ca in octahedral coordination, while the third has Ca bonded to nine oxygens. The AlO_4 tetrahedra are all fully interconnected (Q^4) (Q^n species where n = the number of bridging oxygens). $CaAl_4O_7$ (CA2) has a feldspar-like structure with calcium occupying large cavities within the interconnected AlO_4 tetrahedra (8). Calcium is in a seven-coodinated site, while the aluminium atoms are in tetrahedral sites. The AlO_4 tetrahedra are all Q^4 species, although one of the oxygen atoms is bound to three AlO_4 tetrahedra forming an oxygen tricluster. The structure of $Ca_3Al_2O_6$ (C3A) has been determined by Mondal and Jeffery (9). It consists of puckered six-membered rings of AlO_4 tetrahedra with Ca atoms occupying the holes between the rings. There are two types of slightly distorted AlO_4 tetrahedra that make up the rings; each type alternates around the ring and is a Q^2 species. There are six different Ca sites with three of them containing Ca in six-fold coordination and one each in seven-, eight-, and nine-fold coordination (9).

The O K-edge XANES spectra for the three calcium aluminates are shown in Fig. 1. The FY spectrum for CA (Fig. 1*a*) is comparable to that of Jiang (10); peaks *b*, *c/d*, and *e* of Fig. 1 are the equivalent peaks *a*, *b*, and *c* of Jiang (10) shown in the inset. However the XANES spectrum is of much higher resolution than the ELNES (Electron-loss near-edge spectroscopy) spectrum (10) and exhibits a number of additional peaks not observed in the ELNES spectrum (peak positions are given in Table 1).

The TEY and FY CA spectra are comparable. However, in the TEY spectrum the pre-edge peak (peak *a*) is increased in intensity, while the intensities of peaks *b* and *e* are reduced. In addition, the asymmetry in the FY spectrum at peaks *b′* and *c* is also less apparent. Jiang and Spence (11) assign the pre-edge peak, which is also observed in complex oxides, to π* O–O transitions induced by radiation damage from the incident beam. The reduced intensity of peak *b*, relative to peak *c*, is also attributed to beam damage (Jiang; personal communication), and the increased intensity of the pre-edge peak in the TEY spectrum would support this radiation-induced mechanism. Jiang (10) has carried out theoretical calculations, which show that peak *b*, *c/d*, and *e* are due to O 1s to O 2p antibonding states mixed with s, p, and d orbitals of the cation to which the O is bound. These results are similar to those of other studies involving the O K-edge (1–3, 12). For the $CaAl_2O_4$ phase, the transitions are dominated by states associated with the Ca. Jiang (10) assigns peak *b* to transitions involving oxygen and the nine-coordinated Ca site, and peaks *c* and *e* to oxygen and both calcium and aluminium sites. Furthermore, he suggests that peak *c* should show some asymmetry because of the presence of the two types of Ca sites: the nine-fold Ca site will be at lower energy than the six-fold Ca site. Figure 1 shows that peak *b* of ref. 10 actually consists of three peaks (labelled *b′*, *c*, and *d*). Following ref. 10, we can assign peak *b′* to transitions involving the nine-fold coordinated Ca site. We could then assign peak *c* to the six-fold Ca site and peak *d* to transitions involving Al. However, an assignment of peak *c* to transitions involving Al rather than Ca seems more likely. This is because the O K-edge spectrum of CA2 with increased Al content exhibits higher intensity for peak *c* relative to peak *d*; the latter being more intense in the C3A spectrum.

Peaks *f*, *g*, and *h* are not shown in the study of Jiang (10). However, Mizoguchi et al. (13) have used overlap population diagrams to assign peaks in ELNES and XANES spectra of MgO. Since the O K-edge XANES is dominated by transitions involving the oxygen and Ca, we can use the study of ref. 13 to help assign the higher-energy peaks of Fig. 1*a*. Following Mizoguchi et al. (13), it seems likely that peaks *g* and *h* arise from similar peaks observed in the O K-edge spectrum for MgO (see Fig. 7 of ref. 13). If so, then we can assign peak *g* to transitions of O 2p antibonding states mixed with Ca and Al p orbitals and peak *h* to similar transitions involving Ca and Al d states. The shoulder on peak *g* (peak *f*) may be due to transitions involving Ca and (or) Al orbitals.

The spectrum for CA2 is shown in Fig. 1*b*, and peak positions are given in Table 1. The spectrum is qualitatively similar to that of CA but with subtle differences. Peak *b* is shifted to higher energy by ~0.5 eV. The shift by ~0.5 eV to higher energy is consistent with the shift in energy calcu-

© 2007 NRC Canada

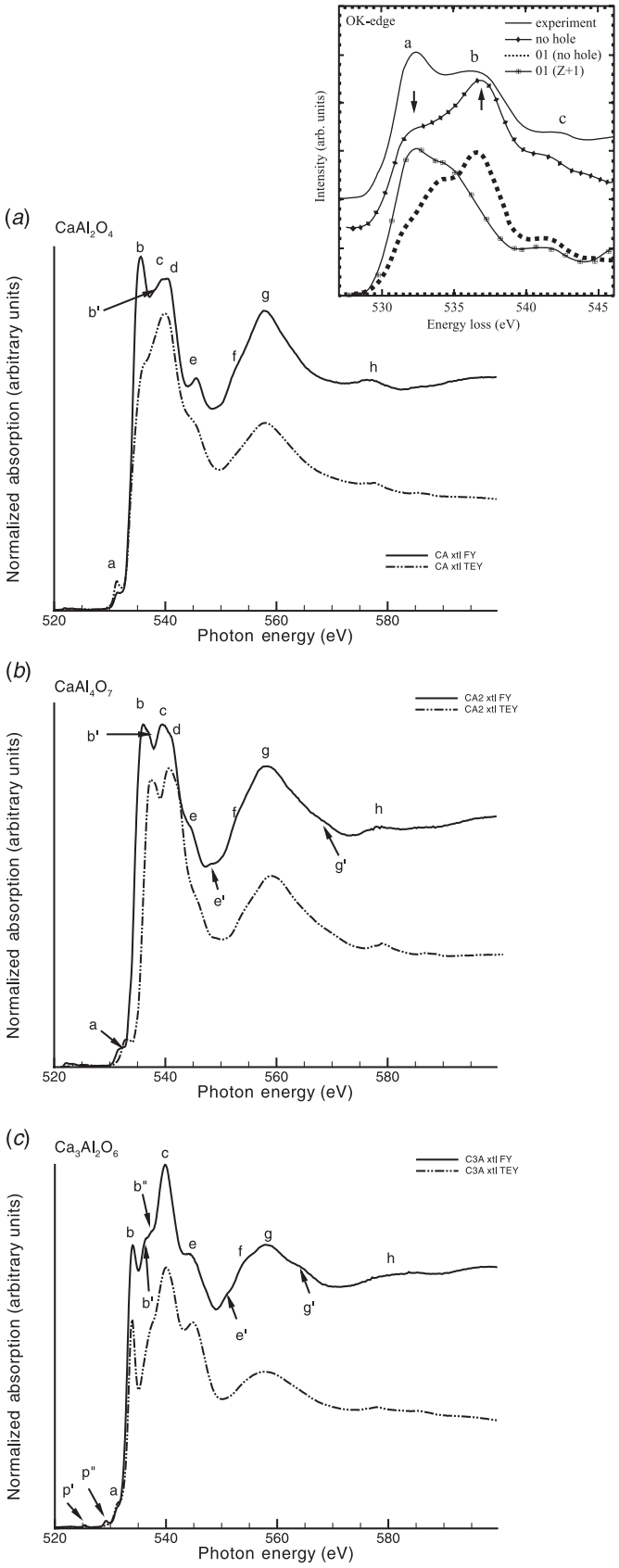


Fig. 1. O K-edge spectra of calcium aluminate phases: (*a*) CA ($CaAl_2O_4$), (*b*) CA2 ($CaAl_4O_7$), and (*c*) C3A ($Ca_3Al_2O_6$). Peak positions are given in Table 1.[3] The peaks *a*, *b,* and *c* in the inset are comparable to peaks *b*, *c/d*, and *e* of the CA spectrum.

lated by Jiang (10) for a change in coordination of Ca. As noted earlier, Ca is nine- and six-fold coordinated in CA but only seven-fold coordinated in CA2. The peak labelled *b′* at 537.0 eV is not equivalent to the peak *b′* (537.8 eV) observed in the CA spectrum. Its appearance, coupled with an increase in intensity of peak *c* relative to peak *d*, suggests that both peaks *b′* and *c* in the CA2 spectrum are due to interactions involving Al not Ca. Peak *e* has also moved to lower energy and been reduced in intensity, although a small weak peak *e′* is observed prior to peak *f*. Peaks *f*, *g*, and *h* are essentially unchanged except for the appearance of a weak shoulder *g′* on the high energy side of peak *g*. The TEY and FY spectra for CA2 are similar, but the pre-edge peak *a* is increased in intensity in the TEY spectrum as is peak *c* (relative to peaks *b* and *d*), while the intensity of peak *e* is greatly reduced in the TEY spectrum

The TEY and FY spectra for C3A are shown in Fig. 1*c* with peak positions given in Table 1. The FY spectrum exhibits three pre-edge features (peaks *a*, *p′*, and *p″*), and peak *b* has moved to lower energy and sharpened considerably (greatly reduced FWHM). Peak *c* has increased in intensity relative to peak *b* and has smaller shoulders labelled *b′* and *b″*. The TEY and FY are, like those of CA and CA2, qualitatively similar to each other. The TEY spectrum exhibits increased intensity of peaks *a*, *b*, and *e* relative to these peak in the FY spectrum. Furthermore, peak *b′* and *b″* appear to have merged into a broad shoulder, while the two pre-edge peaks labelled *p′* and *p″* have been reduced in intensity.

Discussion

The region between 533–543 eV in the crystalline calcium aluminate O K-edge XANES spectra is complex, consisting of at least six individual transitions due to mixing of the O 2p antibonding states with Ca and Al. More specifically, the complexity arises from the close proximity of peaks due to Al in tetrahedral coordination vs. those due to Ca in nine-, eight-, seven- and six-fold coordination. In addition, for C3A, there is a large proportion of Al in Q^2 species. This means that the Al—O bond distances will exhibit a much broader range than the other two phases because the Al—NBO distances will be shorter than the Al—BO distances, leading to broadening of any Al—O contributions. However, using the analysis of Jiang (10) combined with careful examination of the spectra, some preliminary assignments can be made concerning the origin of some of these peaks.

The C3A structure has six different Ca sites of which three are in relatively regular six-fold coordination, while the other three are in distorted seven-, eight-, and nine-fold coordination. The density of state (DOS) calculations of Jiang (10) indicate that the Ca total DOS occur between 0–11 eV of the edge, while those of Al become more important at en-

[3] The inset in Fig. 1*a* is Fig. 1 of ref. 10, reprinted with permission from N. Jiang. Appl. Phys. Lett. **100**, 013703 (2006). Copyright 2006, American Institute of Physics.

© 2007 NRC Canada

Table 1. Peak positions and assignments.

Peak	CA2	Assignment	CA	Assignment	C3A	Assignment
p′					525.4	?
p″					529.2	?
a	531.6	O_2 π*	531.4	O_2 π*	531.3	O_2 π*
b	536.1	Ca seven-fold	535.6	Ca nine-fold	534.0	Ca nine-fold
b′	537.0	Al-BO	537.8	Ca nine-fold	536.5	Al-NBO/Ca eight-fold
b″					537.4	Al-BO/Ca seven-fold
c	539.4	Al-BO	539.4	Al-BO	539.9	Ca nine/eight/seven/six-fold
d	541.1	Ca seven-fold	540.4	Ca nine/six-fold		
e	544.7	Ca seven-fold	545.5	Ca nine-fold	544.1	Ca nine-fold
e′	548.3	Ca/Al			551.2	Ca/Al
f	552.7	Ca/Al	552.5	Ca/Al	554.3	Ca/Al
g	558.2	Ca/Al	557.9	Ca/Al	557.9	Ca/Al
g′	567.6	Ca/Al			564.7	Ca/Al
h	578.6	Ca/Al	576.6	Ca/Al	582.1	Ca/Al

ergies higher than 11 eV. Furthermore, the shorter Al—O bonds push the unoccupied Al DOS several eV above the unoccupied Ca DOS. As Jiang (10) points out, this causes the intensity of the O K-edge near the threshold region to be dominated by Ca–O interactions. Consequently, we can assign the sharp peak for C3A at 534.0 eV (*b*) and the sharp peak at 535.6 eV (*b*) in the CA spectrum to transitions involving the distorted nine-fold Ca sites. For CA2, the peak at 536.1 eV (peak *b*) can also be assigned to interactions involving Ca; more specifically to Ca in seven-fold coordination.

The peak associated with the nine-fold Ca site in C3A is at lower energy than the nine-fold Ca site in CA because the C3A structure is composed of Q^2 AlO_4 tetrahedra, while CA is exclusively Q^4 tetrahedra. Jiang (14) has shown that the presence of non-bridging oxygens (NBO) will also move the O 2p transition to lower energy relative to the one involving bridging oxygens (BO) by about 0.8 eV, which is in the order of the experimental difference of ~1.6 eV. The C3A FY spectra also have narrower peaks than the equivalent CA and CA2 spectra. The smaller widths of the peaks in the C3A spectrum could be due to the fact that the six-fold Ca sites in the C3A structure are relatively regular compared to CA or CA2 (7–9), and this has also been observed in recent Ca K-edge results (15).

A unique characteristic of the CA2 structure is the presence of oxygen atoms that are shared between three Q^4 aluminium atoms: oxygen "triclusters" (8). The triclusters must contribute to peaks involving Al; however, theoretical analysis of the individual O contributions to the peaks is required to understand the explicit contributions from such triclusters.

The other peak observed in all three spectra that is primarily due to O 2p interactions with Ca is the peak at 539.9 eV (peak *c*) in the C3A spectrum. This peak loses intensity relative to other peaks as the amount of Ca is reduced on going from C3A to CA2. However, analysis of its behavior is complicated by the close proximity of peaks due to Al interactions (see later).

The other peaks in the near-edge region of the spectrum (~535–540 eV) can be assigned to interactions with Al and (or) Ca. The peaks that are due primarily to interactions with Al clearly increase in intensity with the addition of Al_2O_3. In C3A, peaks at 536.5 and 537.4 eV (peaks *b′* and *b″*) are likely due to Al, as the relative intensity (compared with peak *c*) in this region is greatly reduced compared with CA and CA2. The C3A structure has Al atoms bonded to both non-bridging oxygens (NBOs) and bridging oxygens (BO). The Al—NBO bonds will be slightly shorter than the Al—BO bonds, and as a consequence, it is likely that the 2 peaks (*b′* and *b″*) are due to Al–NBO and Al–BO interactions, respectively. However, possible contributions to these peaks from the eight- and seven-fold Ca sites cannot be ruled out without a detailed theoretical analysis. For the CA and CA2 spectra, there is only a single peak in this region due to Al–BO interactions as neither of these structures contains NBOs. The observation of a single peak for CA and CA2, supports the previous assignment to Al interactions for C3A.

In both the CA and CA2 spectra, peaks *c* and *d* are a combination of Ca and Al interactions. As noted before, Jiang (10) assigns the peak at 537.8 eV (peak *b′*) in the CA spectrum to interaction with nine-fold Ca and peaks at 539.4 and 540.4 eV (peaks *c* and *d*) to interactions with Ca and Al, respectively. As we pointed out, the peak at 539.4 eV must be due to Al and not Ca, as it increases in intensity in the CA2 spectrum. For the C3A spectrum, there is also a peak due to Ca interactions in the same energy range (peak *c*). However, the peak due to Ca is shifted to higher energy by ~0.5 eV.

The higher-energy peaks (*e*, *f*, *g*, *h*, and so forth) cannot be unambiguously assigned at the present time without at least some initial theoretical analysis of the orbitals contributing to the mixing between the O 2p states and the cations, and any specific assignments would be highly speculative.

Finally, there are some notable differences between the TEY and FY spectra of the individual crystalline phases. The TEY spectra are more representative of the surface structure compared with the FY spectra. While there are no data for the sampling depths for FY and TEY electrons for the O K-edge, data for the Ti L-edge at 464 eV indicate that the TEY sampling depth is ~ 47 Å (16), and for the FY electrons, it will be significantly higher. We would expect the O K-edge sampling depths to be comparable if not slightly higher given that the study by Frazer et al. (16) used samples coated in Cr, which would further attenuate the sampling depth.

For C3A the TEY spectrum exhibits an increase in the rel-

© 2007 NRC Canada

ative intensity of peak *b*, a reduction in intensity of peak *c* and broadening of peaks *b′* to *c*. The increased intensity of peak *b* suggests that the distorted nine-fold Ca site is more prevalent at the surface. Furthermore, the broadening of the peaks may be related to increased contributions from NBOs, which will be in higher abundance at the surface. A point of interest is that peak *e* increases in intensity and evolves into a well-defined peak in the TEY spectra. This would suggest that the dominant interaction with this peak involves oxygens associated with the nine-fold Ca site.

The CA TEY spectrum exhibits a large reduction in the relative intensity of peak *b*, suggesting that the nine-fold Ca site is not in abundance at the surface. In addition, there is some loss of resolution for peak *e*. This supports the suggestion that interactions with oxygens bound to the higher coordinated Ca site in both the C3A and CA structures are primarily responsible for peak *e*.

The CA2 TEY spectrum, compared with the spectra of the other CA phases, shows much less variation compared with the FY spectrum. There is only a small loss of relative intensity of peak *b* accompanied by a similar loss of intensity in peak *e*. Again, this suggests that peak *e* is associated with interactions involving oxygens associated with the Ca site. However, unlike C3A and CA, the CA2 structure only has Ca in a seven-fold site (cf. nine-, eight-, seven-/six-fold for C3A and nine-/six-fold in CA); consequently, there is no interaction between Ca atoms in different coordination geometries and the oxygen atom, and consequently, there is no preference for one Ca site over another at the surface.

In summary, the O K-edge XANES spectra of crystalline calcium aluminates is complex. The details of the spectra are strongly influenced by the cations to which the oxygen atoms are bound. However, the intense peak in the near edge region can be assigned to interactions involving Ca as can a peak at around 539.9 eV. The exact position of the near-edge peak is influenced by the Q speciation of the Al tetrahedra. Peaks due to the presence of Al can also be assigned in a region between ~536–539.4 eV. A peak due to the presence of Ca is almost co-located with the one due to Al in this region; however, the Ca peak is ~0.5 eV higher in energy.

Acknowledgements

Professor Nan Jiang is thanked for helpful comments and for supplying unpublished data. GSH acknowledges funding from the Natural Sciences and Engineering Research Council of Canada (NSERC) in the form of a discovery grant and also thanks “Bonz the Barbarian” for the use of his bushes one or two times. Rob Blythe and Tom Regier are thanked for their help and assistance with the SGM beamline. The Canadian Light Source is supported by NSERC, National Research Council of Canada (NRC), Canadian Institutes of Health Research (CIHR), and the University of Saskatchewan. Two anonymous referees are thanked for their constructive comments.

References

1. G.S. Henderson, Xiaoyang Liu, and M.E. Fleet. Min. Mag. **67**, 597 (2003).
2. H. Wang and G.S. Henderson. Chem. Geol. **213**, 17 (2004).
3. D. Cabaret, F. Mauri, and G.S. Henderson. Phys. Rev. B. **75**, 184205 (2007).
4. D.R. Neuville, L. Cormier, and D. Massiot. Chem. Geol. **229**, 173 (2006).
5. J.E. Shelby. J. Am. Ceram. Soc. **68**, 155 (1985).
6. T. Regier, J. Paulsen, G. Wright, I. Coulthard, K. Tan, T.K. Sham, and R.I.R. Blyth. AIP conference proceedings **879**, 473 (2006).
7. W. Horkner and H.K. Muller-Buschbaum. J. Inorg. Nucl. Chem. **38**, 983 (1976).
8. D.W. Goodwin and A.J. Lindop. Acta Crystallogr., Sect. B. **26**, 1230 (1970).
9. P. Mondal and J.W. Jeffery. Acta Crystallogr., Sect. B. **31**, 689 (1975).
10. N. Jiang. App. Phys. Lett. **100**, 013703 (2006).
11. N. Jiang and J.C.H. Spence. Ultramicroscopy, **106**, 215 (2006).
12. H. Wang and G.S. Henderson. Phys. Chem. Glasses, **46**, 377(2005).
13. T. Mizoguchi, K. Tatsumi, and I. Tanaka. Ultramicroscopy, **106**, 1120 (2006).
14. N. Jiang. Solid State Commun. **122**, 7 (2002).
15. D.R. Neuville, L. Cormier, D. de Ligny, J. Roux, A-M. Flank, P. Lagarde. Am. Mineral. Accepted for publication.
16. B.H. Frazer, B. Gilbert, B.R. Sonderegger, and G. De Stasio. Surf. Sci. **537**, 161 (2003).

© 2007 NRC Canada

Pushing the limit of confocal polarized Raman microscopy[1]

François Lagugné-Labarthet

Abstract: Raman microscopy has emerged as a powerful technique to characterize anisotropic materials with submicrometer resolution. The use of polarized light allows one to obtain precise information about the local organization of the relevant molecular groups through the determination of the most probable distribution function. Such polarization analysis can be conducted under a confocal microscope, but caution must be exercised because of the use of objectives of high numerical value. The molecular orientation can be effectively correlated with the topography of the sample when atomic force microscopy experiments are conducted on the same object. In the present review paper, we present Raman imaging results that have been conducted on mesostructured polymer surfaces and on a single isolated semiconductor nanowire.

Key words: Raman spectroscopy, confocal microscopy, orientation parameters, azopolymers, nanowires.

Résumé : La spectroscopie Raman présente des avantages considérables pour identifier des systèmes moléculaires anisotropiques avec une résolution spatiale inférieure au micromètre. Les propriétés de polarisation de la lumière offrent en outre la possibilité de déterminer précisément l'orientation la plus probable des groupes moléculaires ainsi que de la fonction de distribution associée. De telles mesures peuvent être conduites avec un microscope confocal mais il est alors nécessaire de tenir compte de l'utilisation d un objectif a grande ouverture numérique. L'orientation moléculaire locale peut dès lors être corrélée à la topographie de surface grâce a des mesures annexes en microscopie a force atomique. Dans ce manuscript de revue nous reportons les résultats de notre groupe en imagerie Raman polarisée sur des films de polymères mésostructurés et sur des nanofils semiconducteurs isolés.

Mots-clés : spectroscopie Raman, microscopie confocale, paramètres d'orientation moléculaire, polymères azoïques, nanofils.

Introduction

The macroscopic properties of a material often depend on the degree of local organization and interactions of its elemental molecules. The electrical, mechanical, tribological, optical, and biological functions are strongly influenced not only by the composition of its intrinsic atomic composition, but also by the local orientation and interactions of the molecular arrangements. Such factors are of importance in surface science where the orientational properties of a single monolayer can determine the properties of the surface. For example, surface anisotropy is of great importance in the field of liquid crystal displays, where a rubbed polymer surface will induce an homogenous alignement of liquid crystal molecules deposited on its surface. This is also the case in materials science where the bulk anisotropic growth direction of a crystal will influence the optical and conductive properties of the final material.

Received 19 June 2007. Accepted 22 July 2007. Published on the NRC Research Press Web site at canjchem.nrc.ca on 24 August 2007.

F. Lagugné-Labarthet.[2] Department of Chemistry, *The* University *of* Western Ontario, 1151 Richmond Street, London, ON N6A5B7, Canada.

[1]This article is part of a Special Issue dedicated to Professor G. Michael Bancroft.

[2]Corresponding author (e-mail: flagugne@uwo.ca).

In this context, it is important to precisely assess orientation information in organized systems and to give an accurate representation of the distribution of the anisotropic molecular entities. Vibrational spectroscopy plays an important role since it allows one to quantify the ordering of an anisotropic system at a molecular (vibrational) level. In uniaxial systems where the orientation of a molecule or a functional group is only determined by a single angle θ, polarized IR spectroscopy can provide relevant information through the measurement of the second-order parameter, $\langle P_2 \rangle = 1/2\ (3\ \cos^2\theta - 1)$ (1, 2). In Raman spectroscopy, both order parameters $\langle P_2 \rangle = 1/2\ (3\cos^2\theta - 1)$ and $\langle P_4 \rangle = 1/8\ (35\cos^4\theta - 30\cos^2\theta + 3)$ can be measured and then combined in a distribution function $f(\langle P_2 \rangle, \langle P_4 \rangle)$ to describe more accurately the orientation of active molecular groups (3, 4). These order parameters are determined by performing Raman polarized measurements where both input polarized and analyzer direction are properly selected.

Raman spectroscopy can also be combined with a confocal optical microscope, keeping the polarized flexibility. The spatial resolution of Raman measurements combined with a confocal microscope will be limited to the diffraction limit of light, $1.22\ \lambda$/N.A., where λ and N.A. are the excitation wavelength and the numerical aperture of the microscope objective, respectively. When the laser spot is tighly focussed, one must be careful with the polarized properties of the excitation laser beam and backscattered Raman signal, since the use of a high numerical aperture objective modifies the propagation path of the coupled light. Raman imaging

 doi:10.1139/V07-094 © 2007 NRC Canada

with high spatial resolution can be performed on isolated objects that are smaller than the wavelength. In such experiments great care must be taken with the positioning and scanning of the sample in low vibration environments and with high-precision and reproducible piezoelectric stages. Here again, polarized Raman imaging can be performed giving information on the molecular orientation or directions of the molecular vibrations.

In this paper we review two examples of our recent work emphasizing Raman imaging in confocal microscopy. The first example concerns the study of anisotropic azobenzene polymers. Polarized Raman measurements have been conducted to determine the local orientation of the side chain azobenzene chromophores on micrometer-scale diffraction gratings. The second example shows the imaging capability of a state-of-the-art Raman confocal microscope on a single gallium nitride nanowire.

Polarized Raman imaging of polymer mesostructures

Azobenzene polymers that are substituted in the 4-4′ positions with electron-donating (-NH_2) and electron-accepting (-NO_2) groups possess intense electronic transitions in the visible region. Under irradiation with a linearly and resonant polarized light, the azobenzene side chain chromophores undergo efficient trans–cis photoisomerization and angular reorientation from a $trans_{//}$ to a $trans_{\perp}$ isomer, where // and ⊥ refer to the parallel and perpendicular directions with respect to the polarization of the actinic field (5–7). This property leads to a birefringent–dichroic uniaxial material with preferential orientations of the chromophores perpendicular to the polarized direction of the polarized light (8, 9). In addition, it is also possible to modulate the surface of such azopolymer thin films upon irradiation with an interference pattern, leading to the formation of surface relief diffraction gratings with large diffraction efficiency (8, 10). In the present study, the authors have focused their attention on a grating with 25% efficiency that was holographically inscribed on an azopolymer thin film and then electrically poled using an intense DC field (11, 12). The surface relief amplitude of the grating was about 390 nm as measured by atomic force microscopy, which corresponds nearly to the initial thickness of the film. The poling experiment was conducted to generate nonlinear optical properties of the thin grating by creating a noncentrosymetric arrangement of the chromophores within the grating.

General methods and theoretical approach

The grating was first inscribed using the (p+p) polarized (where p indicates an in-plane polarized beam) configuration, which is known to be very efficient to lead to highly diffractive gratings (11, 13). In such a polarized configuration, the resulting optical field from the interference pattern is always polarized along the same direction, i.e., perpendicular to the grating grooves, which implies that the resulting molecular reorientation of the chromophores would always be in the same direction after $trans_{//}$–cis–$trans_{\perp}$ cycles. Assuming a uniaxial photoinduced reorientation of the rodlike molecules in the direction perpendicular to the actinic optical field, the azobenzene entities will have the same probability to orient in the in-plane (*Y*) and in the out-of-plane (*Z*) directions that are equivalent in the angular hole burning model (Fig. 1a) (14). For such a uniaxial orientation, the molecular orientation can be described by a unique angle θ between the molecular director and the reference axis, which in the present case is the out-of-plane direction (Fig. 1a, *Z*). In this work, the *Z* direction was chosen as the reference because an electrical poling field (3 KV) was also induced perpendicular to the thin film surface, i.e., along the *Z* direction (11, 15).

Assuming this uniaxial orientation and cylindrical symmetry (the molecules have a revolution symmetry along their long molecular axis), the angular distribution function $f(\theta)$ of the chromophores along the out-of-plane *Z* direction can be described on the basis of the Legendre polynomials using information entropy theory. In this general method, the distribution function is obtained by maximizing the information entropy, and the Lagrange method of undetermined multipliers leads to the normalized function, which includes the second ($\langle P_2 \rangle$) and fourth ($\langle P_4 \rangle$) order parameters.

$$[1] \qquad f(\theta) = \frac{\exp(\lambda_2 P_2(\cos\theta) + \lambda_4 P_4(\cos\theta))}{\int_{-1}^{+1} \exp(\lambda_2 P_2(\cos\theta) + \lambda_4 P_4(\cos\theta)) \mathrm{d}(\cos\theta)}$$

and where the coefficients $\langle P_2 \rangle$ and $\langle P_4 \rangle$ are given by,

$$[2] \qquad \langle P_2 \rangle = \int_{-1}^{+1} P_2(\cos\theta) f(\theta) \mathrm{d}(\cos\theta)$$

$$\langle P_4 \rangle = \int_{-1}^{+1} P_4(\cos\theta) f(\theta) \mathrm{d}(\cos\theta)$$

with

$$[3] \qquad P_2(\cos\theta) = \frac{1}{2}(3\cos^2\theta - 1)$$

$$P_4(\cos\theta) = \frac{1}{8}(35\cos^4\theta - 30\cos^2\theta + 3)$$

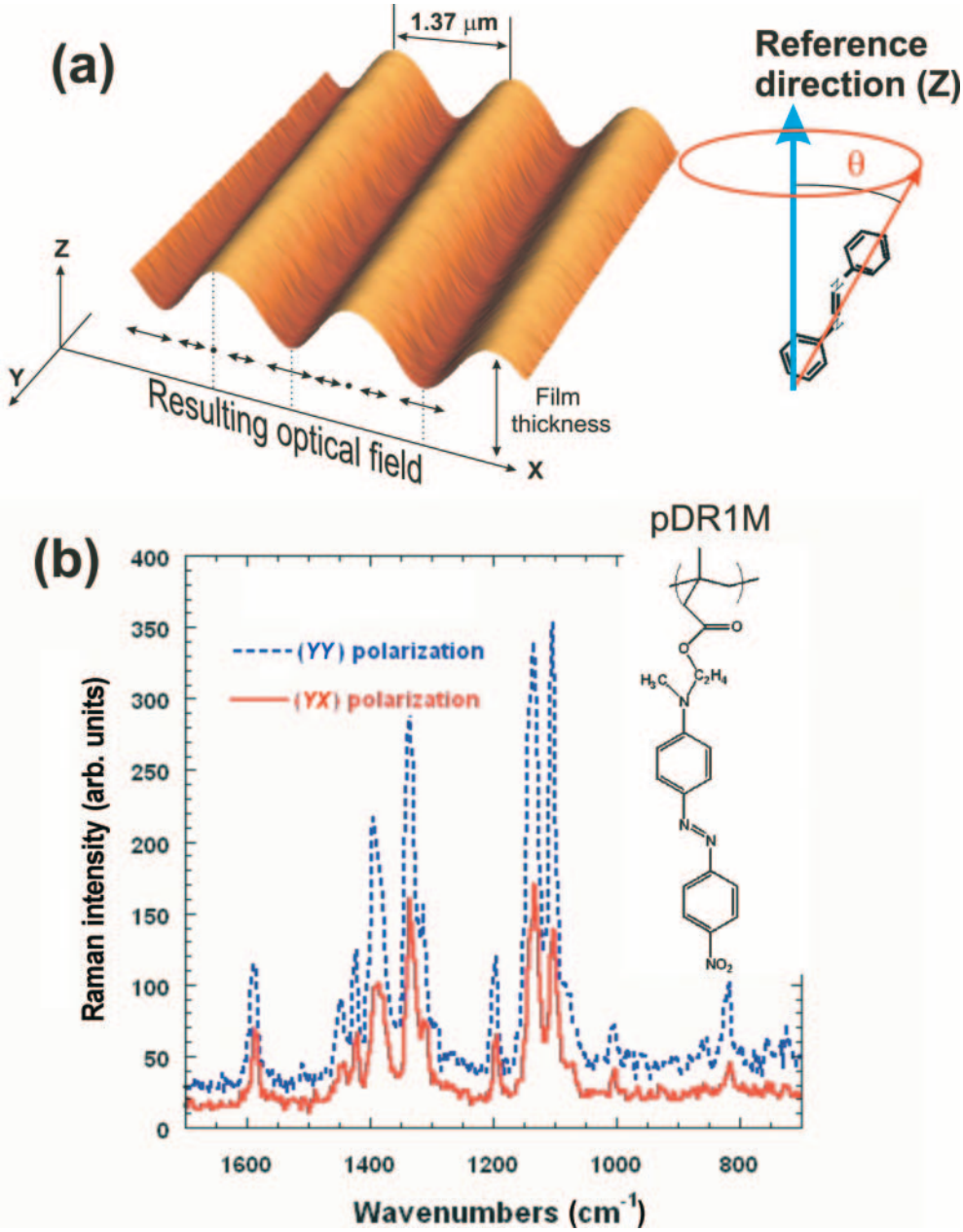
The resulting distribution function can be derived knowing the experimental $\langle P_2 \rangle$ and $\langle P_4 \rangle$. The Lagrange multipliers λ_2 and λ_4 are numerically calculated using eqs. [1] and [2]. The normalized distribution function $f(\theta)$ can be determined for the various area of the gratings where $\langle P_2 \rangle$ and $\langle P_4 \rangle$ have been determined.

The theoretical expressions of polarized Raman intensities, taking into consideration the use of a large N.A. microscope objective, have been exhaustively detailed for gratings inscribed with a (p+p) interference pattern. We recall here the essential expressions to obtain $\langle P_2(\cos\theta) \rangle$ and $\langle P_4(\cos\theta) \rangle$. In previous studies, the two first even order parameters were determined relative to the actinic field polarization, which is along *X* for (p+p) interference pattern (16). However, to compare these parameters with nonlinear optical measurements, a common axis which corresponds to the *Z* or *Y* directions is selected as a proper reference (Fig. 1*a*).

The polarized Raman intensities depend on the average over all orientations in space (17),

© 2007 NRC Canada

Fig. 1. (a) Components of the incident optical field upon grating inscription using the (p+p) polarized configuration of the interfering beams and angular distribution of the azo chromophores relative to the reference direction. (b) Polarized *YY* and *YX* polarized Raman spectra of a pDR1M polymer thin film in the 700–1700 cm^{-1} spectral range.



[4] $$I_{ij} \propto I_0 \langle \alpha_{ij}^2 n_T \rangle$$

where *i*, *j* denote the input and analyzer polarized directions, respectively, and α_{ij} the molecular polarizability tensor elements, and where the quantities,

[5] $$\langle \alpha_{ij}^2 n_T \rangle = \int_0^{2\pi} d\psi \int_0^{2\pi} d\varphi \int_{-1}^{+1} n_T(\theta)[\mathbf{T}(\theta,\varphi,\psi)\vec{\alpha}\mathbf{T}^t(\theta,\varphi,\psi)]^2 d(\cos\theta)$$

are calculated using the normal **T** and transposed $\mathbf{T}^t$ classical Euler matrices. Since the integral involves only the angle θ, the averaged quantities $\langle \alpha_{ij}^2 \rangle$ can be expressed in terms of $\langle \cos^2 \theta \rangle$ and $\langle \cos^4 \theta \rangle$, thus $\langle P_2 \rangle$ and $\langle P_4 \rangle$. In the rigorous treatment, the use of a high N.A. objective must be taken into account. For the grating grooves oriented along the polarized direction of the input beam (along *Y*), we arrive in a first set of experiments with the general intensity equations,

[6] $$I_{YX} = [\langle \alpha_{YX}^2 \rangle A + \langle \alpha_{YZ}^2 \rangle B](2C_0 + C_2) + [\langle \alpha_{ZX}^2 \rangle A + \langle \alpha_{ZZ}^2 \rangle B](4C_1) + [\langle \alpha_{XX}^2 \rangle A + \langle \alpha_{XZ}^2 \rangle B]C_2$$

$$I_{YY} = [\langle \alpha_{YY}^2 \rangle A + \langle \alpha_{YZ}^2 \rangle B](2C_0 + C_2) + [\langle \alpha_{ZY}^2 \rangle A + \langle \alpha_{ZZ}^2 \rangle B](4C_1) + [\langle \alpha_{XY}^2 \rangle A + \langle \alpha_{XZ}^2 \rangle B]C_2$$

© 2007 NRC Canada

In the second set of experiments, the grating is rotated under the microscope with its grooves oriented in the perpendicular direction to the input polarized giving,

$$[7]\quad I_{XY} = [\langle\alpha^2_{XY}\rangle A + \langle\alpha^2_{XZ}\rangle B](2C_0 + C_2) + [\langle\alpha^2_{ZY}\rangle A + \langle\alpha^2_{ZZ}\rangle B](4C_1) + [\langle\alpha^2_{YY}\rangle A + \langle\alpha^2_{YZ}\rangle B]C_2$$

$$I_{XX} = [\langle\alpha^2_{XX}\rangle A + \langle\alpha^2_{XZ}\rangle B](2C_0 + C_2) + [\langle\alpha^2_{ZY}\rangle A + \langle\alpha^2_{ZZ}\rangle B](4C_1) + [\langle\alpha^2_{YX}\rangle A + \langle\alpha^2_{YZ}\rangle B]C_2$$

with

$$[8]\quad A = \pi^2 \int_0^{\theta_m} (\cos^2\theta + 1)\sin\theta\, d\theta = \pi^2\left(\frac{4}{3} - \cos\theta_m - \frac{1}{3}\cos^3\theta_m\right)$$

and

$$B = 2\pi^2\left(\frac{2}{3} - \cos\theta_m + \frac{1}{3}\cos^3\theta_m\right)$$

Here, the expressions A and B come from the integrations of the squares of the electric vector components over the scattering cone, and the constants $C_0 = 5.3825$, $C_1 = 0.1424$, and $C_2 = 5.10^{-4}$ are related to the focalization efficiency and are calculated via the integration of the incident electric field vector components over the effective irradiated volume (18). All these parameters are dependent on the angular semi-aperture of the objective ($\theta_m = 64.16°$ for the 100×, N.A. = 0.9 microscope objective) and the refractive index of the sample n ($n = 1.645$).

Finally, knowing the intensities I_{ij} in the different parts of the grating (δ) and their ratio $R_1(\delta) = I_{XY}/I_{XX}$, and $R_2(\delta) = I_{YX}/I_{YY}$, the two first even order parameters, namely $\langle P_2\rangle$ and $\langle P_4\rangle$, can be estimated.

From the Raman polarized spectra experimentally measured ($\lambda_{excitation} = 752.5$ nm) in the 700–1700 cm^{-1} spectral domain and shown in Fig. 1b, we integrate a particular vibrational mode whose orientation is well known. The $\upsilon_s NO_2$ mode is oriented along the long molecular axis of the trans-shaped azobenzene chromophore and is thus a good probe to estimate the orientation of the rod-shaped azobenzene chromophore. The other modes at 1104 cm^{-1} (υ-N, υ18a), 1134 and 1196 cm^{-1} (δCH ring, υ9a and υ9b), 1392 cm^{-1} (υN=N), and 1589 cm^{-1} (ωC=C, 8a and 8b) are also characteristic of the trans azobenzene chromophores, but their directions are less unidirectional than $\upsilon_s NO_2$. In the following we have arbitrarily selected the whole 1044–1180 cm^{-1} spectral range to calculate the polarized intensities I_{ij}, their ratios $R_1(\delta)$ and $R_2(\delta)$, and finally the order parameters $\langle P_2\rangle$ and $\langle P_4\rangle$. As illustrated in Figs. 2a and 2b, we have thus obtained the polarized Raman images over a (5 μm)^2 area for *YY* and *YX* polarizations, respectively. Under these conditions, the variations over several grating periods of the average polarized Raman intensities are plotted in Fig. 2c for the full set of input and output polarizations. The variation of the final order parameters $\langle P_2\rangle$ and $\langle P_4\rangle$ along the position on the grating are reported in Fig. 2d.

Discussion

First, the $\langle P_2\rangle$ order parameter varies from +0.228 (bottoms) to +0.266 (tops). As expected, these values are positive, but they denote an orientational ordering along the Z reference direction that is far from perfect. For a perfect alignment one should expect $\langle P_2\rangle = 1.0$, since θ would be 0. In contrast, the parameter $\langle P_4\rangle$ is always negative and varies markedly from –0.067 (bottoms) to –0.230 (tops); the influence of $\langle P_4\rangle$ is thus preponderant on the shape of the distribution function. Actually, using only the sets of $\langle P_2\rangle$ and $\langle P_4\rangle$, the polar distribution functions (Fig. 3) are asymmetric and display maxima at ±34° (bottoms), ±39° (intermediates), and ±42°(tops) with respect to the direction of reference. Also, the distribution function in the top regions is significantly narrower than in the bottom regions (the full width at half maximum, fwhm, varies from ±28° to ±60°); this probably indicates the existence of increasing force and pressure constraints during the peak relief formation and during the related chromophore diffusion mechanisms. Because of the large force gradients during the isomerization cycles and the angular reorientations, the chromophore orientation distributions appear significantly perturbed by the polymer migration from areas of high field intensity (that correspond to the bottoms of the grating) to area of lower field intensity (tops of the grating).

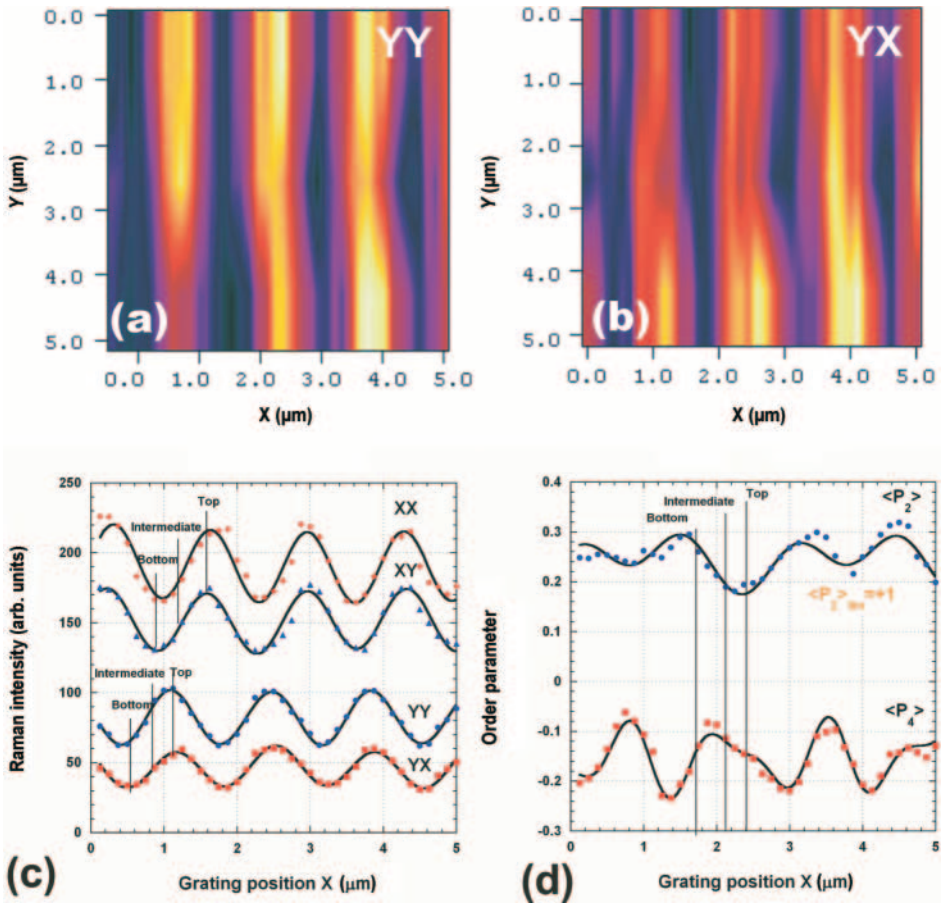
As a demonstration of high-resolution Raman confocal imaging on mesostructured polymer thin films, both atomic force microscopy surface topography and Raman images were conducted on superimposed surface relief gratings (Fig. 4). Raman measurements were recorded with a Labram HR 800 (Horiba, Jobin-Yvon) spectrometer combined with an inverted microscope (Olympus IX 71), and an X,Y Piezoelectric stage to position the sample for the best accuracy and repeatability. A 100× 0.9 NA microscope objective was used. A Raman spectrum (Fig. 4c) was recorded every 100 nm along the X and Y directions with an integration time of 5 s per spectrum ($\lambda_{excitation} = 752.5$ nm). The variation of the Raman signal was integrated over the 1060–1180 cm^{-1} spectral domain (Fig. 4d). It must be pointed out that details on the Raman profile are obtained with a spatial resolution better than $\lambda/2$.

Polarized Raman microscopy of single nanostructures

One-dimensional semiconductor nanowires of gallium nitride (GaN) are prime candidates for future nanoscale devices, such as blue laser and high-power and high-temperature electronics (19). Significant advances in nanostructure synthesis allows controlling not only the size but also the crystallographic orientations of the nanostructure by properly choosing the best substrate with matching lattice constants. GaN wires grown on a (100)-$LiAlO_2$ substrate have their [001] axis perpendicular to the growing direction and display a triangular cross-section, while wires grown on (111)-MgO have their growing axis along the [001] direction with an hexagonal Wurzite-type lattice (19). Consequently, it is of importance to measure the homogeneity and the composition of such nanowires at the individual scale and to correlate them with the dimensions and optical properties of these strongly anisotropic materials. In this context, trans-

© 2007 NRC Canada

Fig. 2. (a and b) Raman polarized images of a mesostructured polymer in the *YY* and *YX* polarized configurations, respectively. (c) Variation of the polarized Raman measurements *YY*, *XX*, *YX*, and *XY* along the grating position *X*. (d) Order parameter along the grating vector (11).



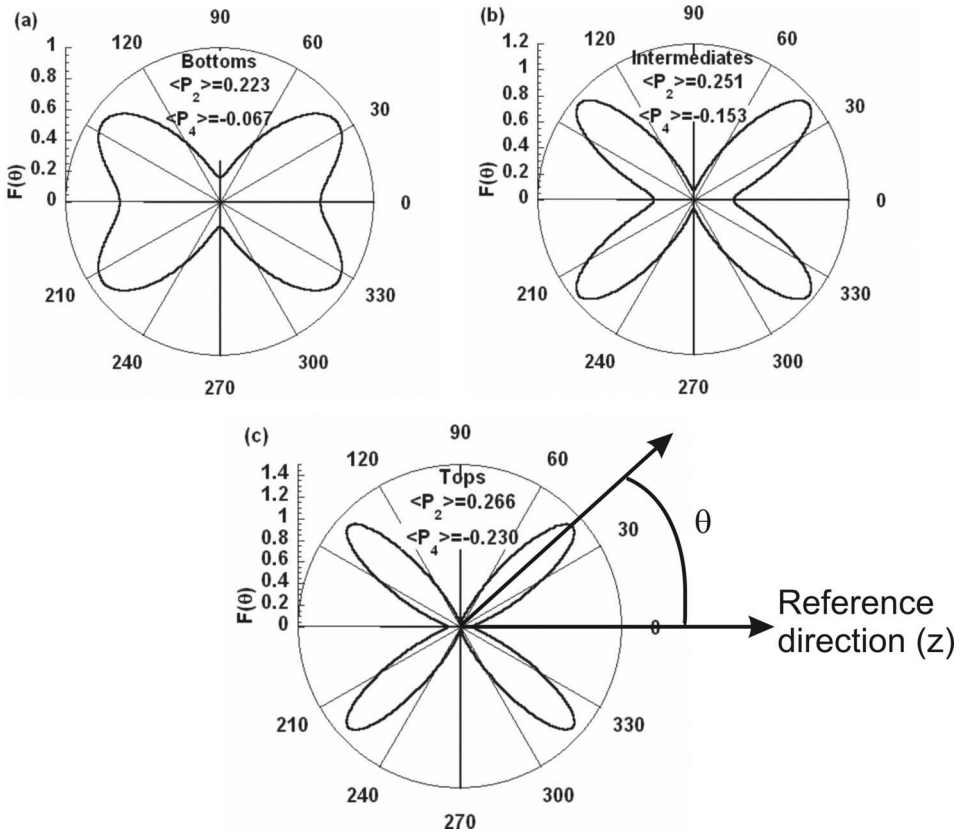
mission electronic microscopy (TEM) and scanning electron microscopy together with electron diffraction play an important role to characterize individual nanowires with an unprecedented resolution. However, optical microscopy and spectroscopy are also able to play a key role in diagnostics that go far beyond visualizing the physical shape of nanoobjects. Molecular optical spectroscopy, such as Raman scattering, can be very helpful to probe the crystallinity, mechanical stress, temperature effects, the confinement of phonons modes, or the lattice dynamics in nanocrystals allowing to correlate the optical measurements with the anisotropy of the nanowire (20). In addition, these optical techniques can be easily implemented in synthesis reactors to monitor in situ and in real time the growing process of the nanoobjects. Raman confocal microscopy has a spatial resolution of roughly one third the excitation wavelength, which often limits its use for the characterization of aggregated bundles of nanowires. However, we have recently shown that polarized imaging of individual isolated nanowires is possible.

General methods

As reported by Lagugné-Labarthet and co-workers (20), a single [001] nanowire with a Wurtzite-like hexagonal cross-section was first cut and positioned on a microscope glass slide (Fig. 5). Atomic force microscopy (AFM) reveals a diameter of about 170 nm and a length of 41 μm. The Raman setup is based on an inverted microscope combined with a spectrometer (grating 600 grooves/mm, resolution 4 cm^{-1}). The sample is scanned with a piezoelectric stage with an intrinsic accuracy of 1 nm in the lateral directions. The light beam input excitation wavelength was fixed at $\lambda = 514.5$ nm from an Ar^+ ion laser and the input polarized was selected with a half-waveplate. Focussing on the sample was done with a 100× objective (NA = 0.90), and the Raman signal was collected under the backscattering geometry. A polarizer serves as an analyzer just in front of the entrance slit of the spectrometer. The laser intensity was fixed to 10 mW at the focal point. The depolarization ratios were checked with a reference sample of liquid CCl_4. The pinhole of the confocal microscope was closed to about 140 μm, which corresponded to a focal volume of about 1 μm^3, limiting significantly the background signal of the glass substrate. The detector was a liquid nitrogen cooled CCD camera and acquisition time was fixed to 1 s/spectrum in the imaging mode, while an acquisition time of 20 s/spectrum was used to record most spectra shown in the present work. Raman spectra under the polarized configurations $Y(ZZ)\bar{Y}$, $Y(XX)\bar{Y}$ and $Y(XZ)\bar{Y}$ are shown in Fig. 5. The nanowire was aligned so that the *Z* polarized direction matches the growing direc-

© 2007 NRC Canada

Fig. 3. Polar representation of the distribution functions $f(\theta)$ calculated at the (a) bottom, (b) intermediate, and (c) ridges of a surface relief grating inscribed on pDR1M polymers. The distribution functions were calculated using even order parameters, $\langle P_2 \rangle$ and $\langle P_4 \rangle$ (11).



tion (i.e., the $\vec{c}$ axis) of the nanowire. Y and $\bar{Y}$ are the directions of the input excitation and the backscattered Raman signal, respectively.

Discussion

As reported by various authors for thin films (21, 22) and for bundles of nanowires (23), GaN that crystallizes in the hexagonal Wurtzite-type structure belongs to the space group C^4_{6v} and has two formula units per primitive cell. According to factor group analysis, the Raman active modes are $1A_1(x^2 + y^2, z^2) + 1E_1(xz, yz)) + 2E_2(x^2 - y^2, xy)$, while $2B_2$ modes are silent. Since GaN Wurtzite structure is noncentrosymmetric, both A_1 and E_1 modes can be split into longitudinal optical (LO) and transverse optical (TO) components. For a GaN single nanowire, four main signals are observed at 142, 530, 557, and 568 cm^{-1}, and they can be assigned to E_2(low), A_1(TO), E_1(TO), and E_2(high) symmetry type modes, respectively. In the $Y(XZ)\bar{Y}$ configuration, only E_1(TO) mode is expected, and the peak at 530 cm^{-1} (A_1 (TO)) denotes a polarization leak. The polarized spectra shown in Fig. 5 allow unambiguous assignments, which is in a good agreement with previous work on GaN thin films (23). Mapping of the nanowire was performed by recording step-spectra at every 200 nm with an integration time of 1s. Such a short acquisition time was required to rule out any thermal effects because of the high laser power. By intensity integration of the 509–552 cm^{-1} spectral domain around the A_1(TO) mode (530 cm^{-1}), the variations of the Raman signal over the full nanowire are investigated. The images shows an excellent lateral resolution better than 200 nm, with a reasonable acquisition time of about 1 h for a polarized image. For the $Y(ZZ)\bar{Y}$ polarized configuration, Fig. 6a shows that the signal is maximum on the straight portions of the nanowire, while it almost disappears on the bent portion of the nanowire. The geometric complementary image (Fig. 6b) is obtained by integration of the E_2 (high) mode at 568 cm^{-1}. In the $Y(XX)\bar{Y}$ polarized configuration, the opposite spectroscopic contrast is observed with a maximum signal of the 568 cm^{-1} mode in the straight portions of the wire, as observed in Fig. 6c, and a maximum signal for the A_1 mode in the horizontal part of the nanowire.

Under this scattering configuration, the optical longitudinal phonon modes were not observed. To complement these polarized spectra, nonpolarized spectra of the end face of an upright GaN nanowire grown on MgO were recorded. Actually, two nanowires stuck together can be seen on Fig. 7, along with the corresponding Raman image integrated over the most intense peak at 568 cm^{-1}. A totally similar spectrum was observed for a single nanowire, which excludes any coupling effects between the two nanowires. In addition to the phonon modes observed earlier, additional broader peaks are detected at 256, 318, 421, 660, and 731 cm^{-1}. The latter can be assigned to the LO type mode of A_1 symmetry (23). The origin of the peaks at 318 and 421 cm^{-1} arises from second-order Raman effects, providing information of the vibrational states over the Brillouin zone; they are assigned to overtone processes of acoustic phonons (24–26). As suggested in previous experimental and theoreti-

© 2007 NRC Canada

Fig. 4. (a) Atomic force microscopy and (b) Raman images from a thin film of azobenzene-containing polymer thin film (300 nm) that is periodically structured (periodicity of ~1 μm). (c) Raman spectra of azobenzene polymer with a 5 s acquisition time. (d) Variation of the Raman intensity over the *X* and *Y* directions.

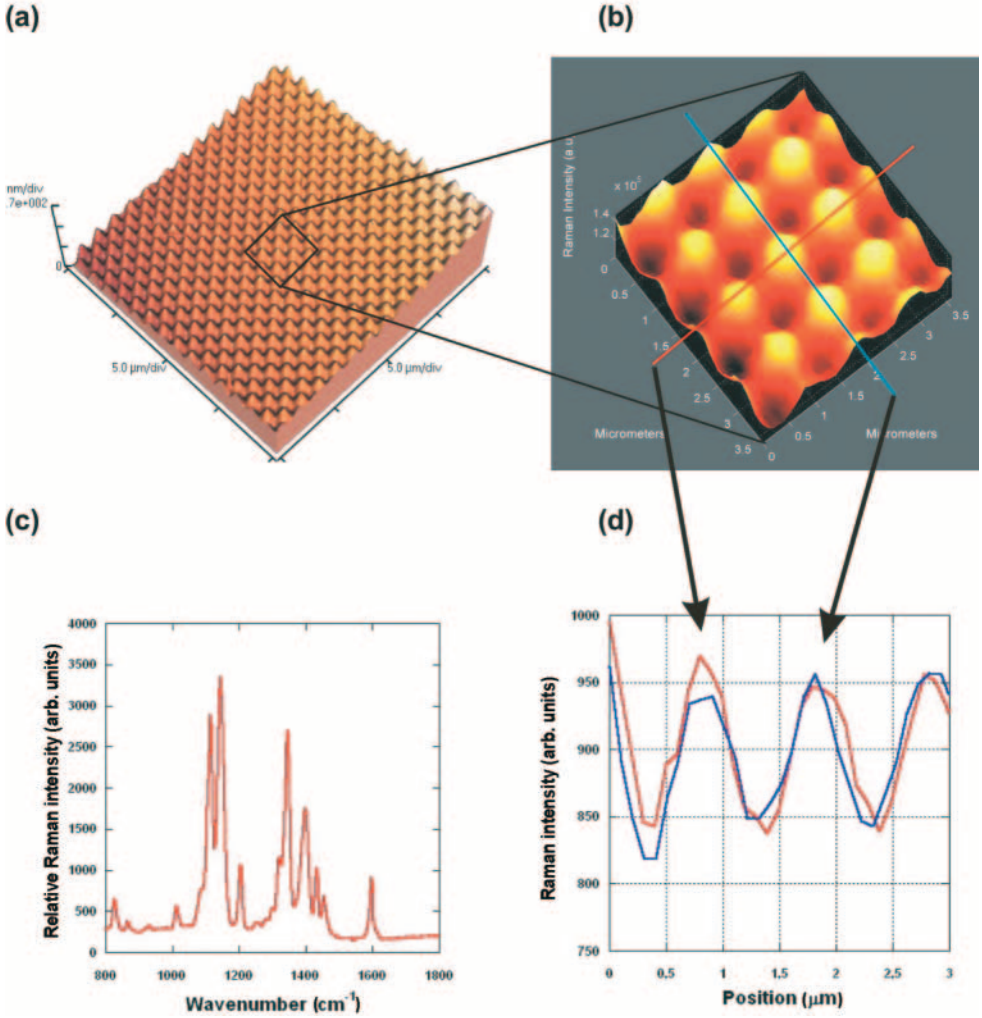
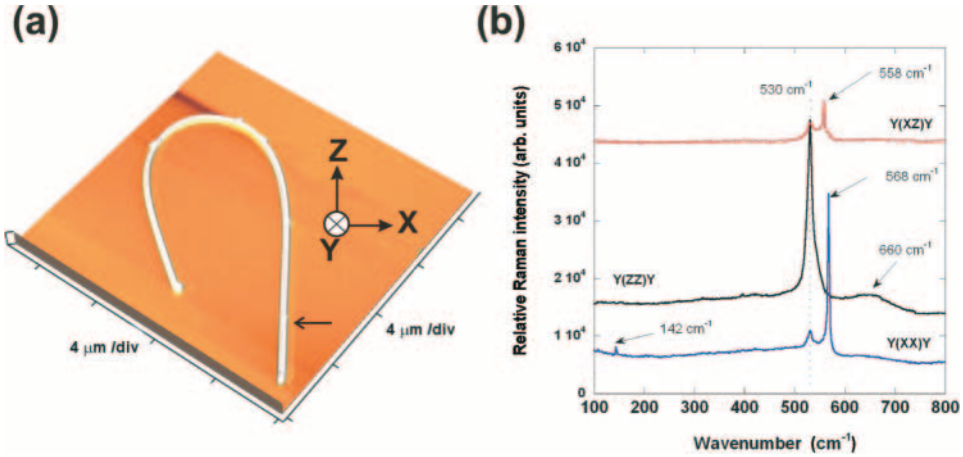


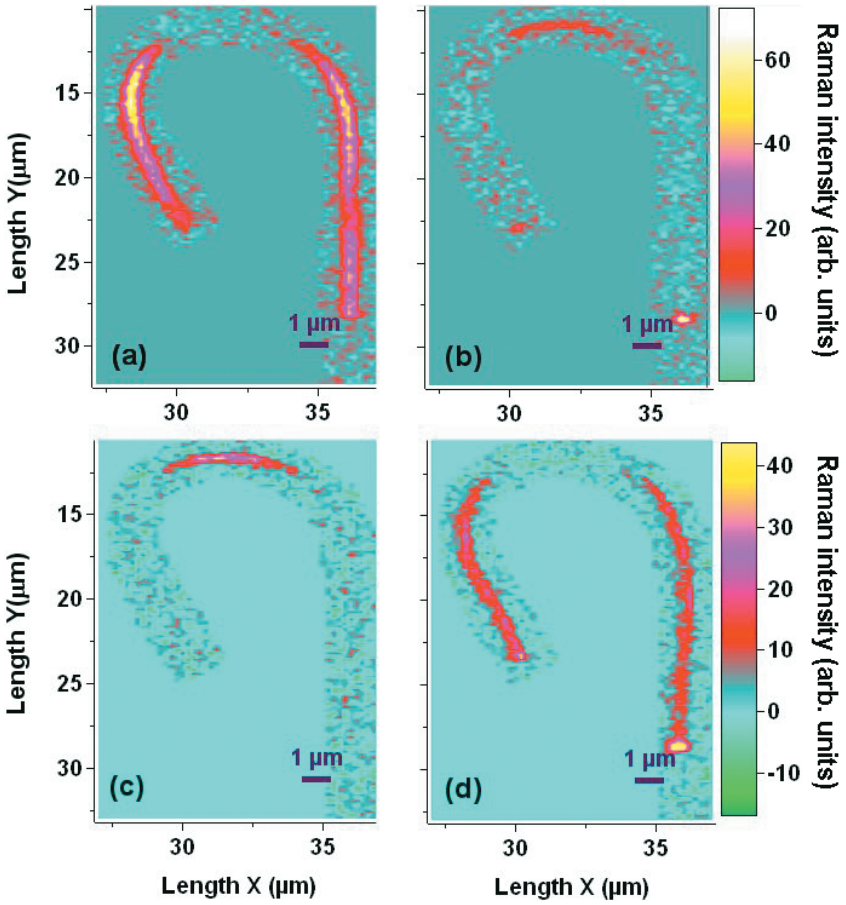
Fig. 5. (a) Atomic force microscope image and (b) polarized Raman spectra of the GaN nanowire in the $Y(ZZ)\overline{Y}$, $Y(XX)\overline{Y}$ and $Y(XZ)\overline{Y}$ polarized configurations, respectively, (20).



cal studies, the 318 cm^{-1} band belongs to the A_1 symmetry class, while the peak at 421 cm^{-1} belongs to E_2 symmetry. The peak at 256 cm^{-1} can be assigned to a zone boundary phonon activated by surface disorder that occurs at the end of the nanowire. From lattice dynamical calculations and phonon dispersion relations for hexagonal GaN, the E_2 opti-

© 2007 NRC Canada

Fig. 6. (a) Polarized Raman images generated by integration of the 509–552 cm^{-1} and (b) 558–575 cm^{-1} spectral ranges for the $Y(ZZ)\bar{Y}$ polarized configuration. (c) Polarized Raman images generated by integration of the 509–552 cm^{-1} and (d) 558–575 cm^{-1} spectral ranges for the $Y(XX)\bar{Y}$ polarized configuration (20).



cal branch produces a peak in the phonon density of states around 250 cm^{-1} (24). It is noteworthy that this peak is observed only from the extremity of a single nanowire but never when the nanowire is flat on the surface. This allows us to conclude that finite-size effects, defects, and phonon confinement phenomena can only be observed at the end(s) of the nanowires. The broad peak at 660 cm^{-1} is observed for both the nanowire extremities and also for the $Y(ZZ)\bar{Y}$ polarization.

As reported by Liu et al. (23), this broad peak is presumably due to a defect state with an energy close to the A_1 (LO), or it can be tentatively assigned to the first overtone of a B_1 silent mode. Furthermore, Raman measurements were also performed on an isolated GaN nanowire grown using the chemical vapour transport synthetic approach (CVT). The wire has a cylindrical cross section with its $\vec{c}$ axis oriented perpendicular to the growing direction $[1\bar{1}0]$. Because of the cylindrical symmetry of the nanowire, the angular position of $\vec{c}$ relative to the substrate plane is not known (Fig. 8a). For $Y(XX+XZ)\bar{Y}$ spectra (Fig. 8c), the input polarization is along the growth direction and no analyzer was used. Only the two E_2 modes (low and high) can be observed at 143 and 568 cm^{-1}, respectively. With an orthogonal polarization input relative to the growth direction, $Y(ZZ+ZX)\bar{Y}$, only E_1 and E_2(high) at 559 and 568 cm^{-1}, respectively, can be observed. It is noteworthy that the A_1 (TO) mode is not clearly defined, and only a broad background can be observed in Fig. 8c. These observations exclude an orientation of the $\vec{c}$ axis in the direction perpendicular relative to the substrate plane (i.e., along the propagation direction of the probe beam) where A_1 mode should be observed along with E_2. Also, the $\vec{c}$ axis cannot be oriented along the substrate plane, as shown in Fig. 8a where A_1 mode should also be observed together with E_1. This is certainly due to a peculiar orientation of the $\vec{c}$ axis, which presumably has a tilted angle with respect to the substrate plane. Because of the $[1\bar{1}0]$ growing direction of this nanowire, the c axis is possibly tilted at an angle of about $\theta = \pm 45°$ relative to the substrate plane. In addition, one must point out that even for the [001] nanowire the A_1 mode is very weak compared with the intensity of the E_2 (high) mode (Fig. 5). This may be an additional source to account for the absent A_1 mode. For such a configuration, only the E_2 modes are expected to be the strongest ones. This emphasizes the tremendous advantage of Raman spectroscopy, allowing to assign not only the crystalline structure of an individual nanowire but also to determine the most probable orientation of its crystallographic axes.

The high spatial resolution of the modern Raman confocal instrument together with a piezoelectric stage demonstrates unambiguously the possibility to image the optical properties of nanoobjects with a resolution better than 200 nm,

© 2007 NRC Canada

Fig. 7. (a) Video and (b) Raman images of the extremities of two nanowires standing upright on a MgO substrate. (c) Raman spectra of the end face without polarized analysis of $Z(YY+YX)\bar{Z}$ integrated over 20 s.

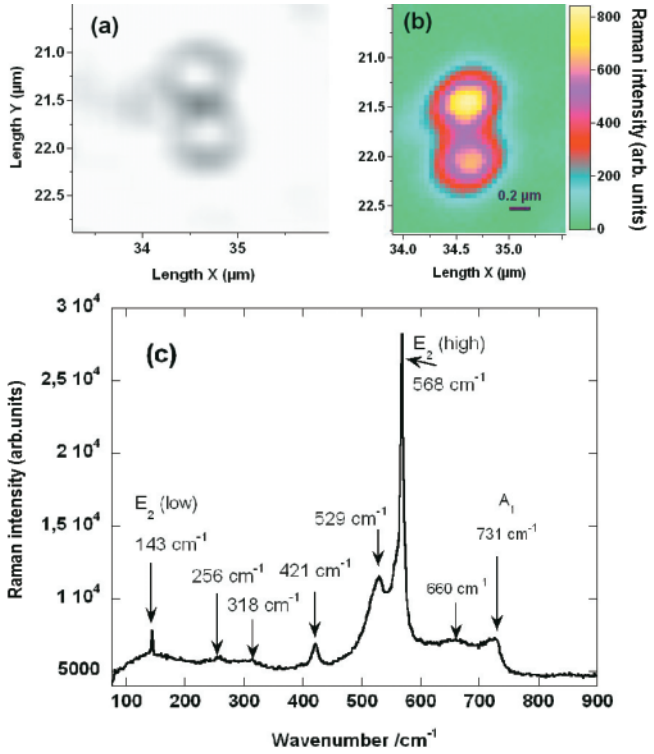
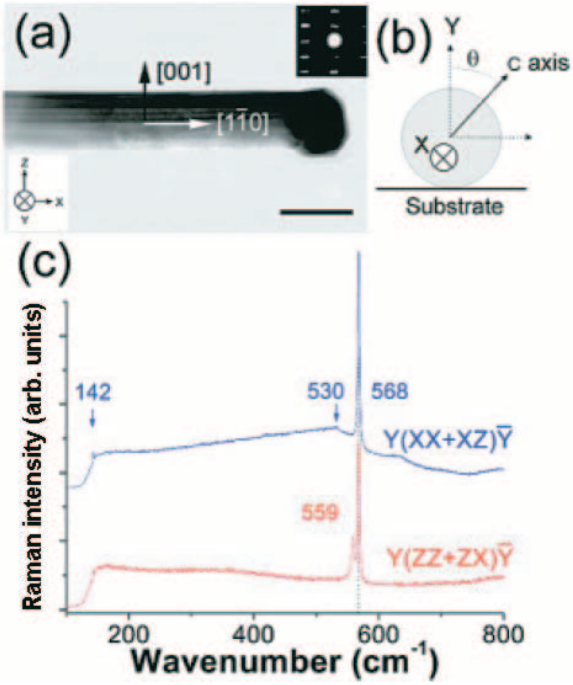


Fig. 8. (a) GaN nanowire grown by chemical vapor transport with a cylindrical cross-section in the [1 $\bar{1}$ 0] direction. For scale the bar = 100 nm. Inset is electron diffraction image of the nanowire taken with large diffraction aperture, illustrating growth direction. (b) Schematic showing possible orientations of the transverse *c*-axis. (c) Raman polarized spectra with input polarized parallel (*XX* + *XZ*) or orthogonal (*ZZ* + *ZX*) to the growing direction (20).



keeping the full control of polarized analysis. With the help of a higher resolution spectrometer, stress-induced shifts and crystallinity modifications at various growing temperatures can be monitored for individual objects.

Summary

In this article, we reviewed two recent examples of polarized Raman measurements conducted by our group on meso and nanoscale objects. The analysis of the polarized measurements was applied to materials such as polymer thin films and inorganic nanostructures. The basis of the theoretical expressions of the polarized intensities as well as the order parameters and associated distribution functions were defined and developed for a given example. The use of a high numerical aperture is also taken into consideration for the microscopic polarized intensities. In the case of nanomaterials, Raman microscopy can provide useful information on the direction of the nanocrystal axes using polarized measurements.

Raman confocal microscopy, in conjunction with polarized analysis recordings, can lead to a better understanding of the optical, mechanical, or biological properties of a sample, emphasizing the importance of using polarized analysis combined with microscopy measurements.

Acknowlegments

The author is grateful to Jean-Luc Bruneel (CNRS, France) and David Talaga (CNRS france) for experimental assistance, and Peidong Yang (UC berkeley, USA) for the nanomaterial project and collaboration.

References

1. X. Bin and J. Lipkowski. J. Phys. Chem. B, **110**, 26430 (2006).
2. T. Buffeteau, A. Natansohn, P. Rochon, and M. Pézolet. Macromolecules, **29**, 8783 (1996).
3. F. Lagugné-Labarthet and C. Sourisseau. J. Raman Spectrosc. **27**, 491 (1996).
4. T. Buffeteau, F. Lagugné-Labarthet, C. Sourisseau, S. Kostromine, and T. Bieringer. Macromolecules, **37**, 2880 (2004).
5. A.M. Makushenko, B.S. Neporent, and O.V. Stolbova. Opt. Spektrosk. **31**, 741 (1971).
6. T. Todorov, L. Nikolova, and N. Tomova. Appl. Opt. **23**, 23 (1984).
7. F. Lagugné-Labarthe and C. Sourisseau. New J. Chem. **21**, 879 (1997).
8. C.J. Barrett, A. Natansohn, and P. Rochon. J. Phys. Chem. B, **100**, 8836 (1996).
9. T. Buffeteau, F. Lagugné-Labarthet, M. Pézolet, and C. Sourisseau. Macromolecules, **34**, 7514 (2001).
10. P. Rochon, E. Batalla, and A. Natansohn. Appl. Phys. Lett. **66**, 136 (1995).
11. F. Lagugné-Labarthet, C. Sourisseau, R.D. Schaller, R.J. Saykally, and P. Rochon. J. Phys. Chem. B, **108**, 17059 (2004).
12. F. Lagugné-Labarthet, F. Adamietz, V. Rodriguez, and C. Sourisseau. J. Phys. Chem. B, **110**, 13689 (2006).
13. F. Lagugné-Labarthet, T. Buffeteau, and C. Sourisseau. J. Phys. Chem. B, **103**, 6690 (1999).
14. Z. Sekkat and M. Dumont. Synth. Met. **54**, 373 (1993).
15. R.D. Schaller, R. Saykally,Y.R. Shen, and F. Lagugné-Labarthet. Opt. Lett. **28**, 1296 (2003).

© 2007 NRC Canada

16. F. Lagugné-Labarthet, T. Buffeteau, and C. Sourisseau. J. Phys. Chem. B, **102**, 5754 (1998).
17. C. Sourisseau. Chem. Rev. **104**, 3851 (2004).
18. C. Brémard, P. Dhamelincourt, J. Laurens, and G. Turell. Appl. Spectrosc. **39**, 1036 (1985).
19. T. Kuykendall, P. Pauzauskie, Y. Zhang, J. Goldberger, D. Sirbully, J. Denlinger, and P. Yang. Nat. Mater. **3**, 524 (2004).
20. P.J. Pauzauskie, D. Talaga, K. Seo, P. Yang, and F. Lagugné-Labarthet. J. Am. Chem. Soc. **127**, 17146 (2005).
21. H. Harima. J. Phys.: Condens. Matter. **14**, R967 (2002).
22. T. Azuhata, T. Sota, K. Suzuki, and S. Nakamura. J. Phys.: Condens. Matter. **7**, L129 (1995).
23. H.-L. Liu, C.-C. Chen, C.-T. Chia, C.-C. Yeh, C.-H. Chen, M.-Y. Yu, S. Keller, and S.P. DenBaars. Chem. Phys. Lett. **345**, 245 (2001).
24. T. Ruf, J. Serrano, M. Cardona, P. Pavone, M. Pabst, M. Krisch, M. D'astuto, T. Suski, I. Grzegory, and M. Leszczynski. Phys. Rev. Lett. **86**, 906 (2001).
25. H. Siegle, L. Kacsmarczyk, L. Filippidis, A.P. Litvinchuk, A. Hoffman, C. Thomsen. Phys. Rev. B, **55**, 7000 (1997).
26. V. Davidov, Y. Kitaev, I. Goncharuk, A. Smirnov, J. Graul, O. Semchinova, D. Uffman, M. Smirnov, A. Mirforodsky, and E. Evarestov. Phys. Rev. B, **58**, 12899 (1998).

© 2007 NRC Canada

The contribution of XANES spectroscopy to tribology[1]

M. Nicholls, M.N. Najman, Z. Zhang, M. Kasrai, P.R. Norton, and P.U.P.A. Gilbert

Abstract: X-ray absorption near edge structure spectroscopy (XANES) analysis has been routinely used to study the complex chemical interactions between additives in engine oil and metallic surfaces during high-temperature and pressure reciprocating wear conditions. XANES analysis provides detailed chemical and structural information on the resultant antiwear and tribo films formed on metallic surfaces. The following review will illustrate how XANES analysis on the macro scale can provide the information required to elucidate complex film formation mechanisms, then describes the use of emerging XANES spectromicroscopy to such systems, and concludes by showing the complementary nature of the macro and micro scale spatially resolved XANES analysis; Professor Bancroft has utilized the combination of these to stay at the forefront of XANES research in the field of tribology and in spectroscopy science in general.

Key words: tribology, XANES, X-ray absorption near edge structure spectroscopy, metals, thiophosphates, spectromicroscopy, tribochemistry.

Résumé : L'analyse des spectres de la structure fine d'absorption des rayons X près du seuil (« XANES ») a été utilisée d'une façon routinière pour l'étude des interactions chimiques complexes entre les additifs des huiles à moteur et les surfaces métalliques, dans des conditions de températures et de pressions élevées qui provoquent des usures réciproques. Les analyses de type « XANES » permettent d'obtenir des informations chimiques et structurales détaillées sur les films anti usure/tribo résultants qui se forment sur les surfaces métalliques. La revue qui est présentée ici permettra d'illustrer comment les analyses de type « XANES » à l'échelle macro peuvent fournir l'information requise pour élucider les mécanismes complexes de formation de films et ensuite décrire l'utilisation de la spectromicroscopie de type « XANES » qui se développe à l'étude de tels systèmes avant de conclure en mettant en évidence la nature complémentaire des études de type « XANES » résolues dans l'espace aux échelles micro et macro; la combinaison qui a été utilisée par le professeur Bancroft pour lui permettre de demeurer à la tête des méthodes de type « XANES » dans le champ de la tribologie et dans le domaine de la spectroscopie en général.

Mots-clés : tribologie; « XANES », spectroscopie de la structure fine d'absorption des rayons X près du seuil, métaux, thiophosphates, spectromicroscopie, tribochimie.

[Traduit par la Rédaction]

Introduction

In 1966 the term tribology was coined by the newly formed Committee on Tribology of the British House of Commons. Tribology can be defined as the science and technology of interacting surfaces in relative motion and of related subjects and practices (1). It encompasses a wide variety of topics and is a truly interdisciplinary field of study. One of the core disciplines of tribology is chemistry, termed tribochemistry, and presents a most challenging approach to understanding the history of a rubbing contact, the dynamic nature of the contact, the protective film formation process, and attrition during wear. In one combination or another, a wide range of chemical and analytical techniques have been used to understand the tribochemistry of a system. These include X-ray photoelectron spectroscopy (XPS) (2–7), Auger electron spectroscopy (AES) (8–12), energy dispersive X-ray (EDX) analysis (13–15), IR spectroscopy (16–21), and transmission electron microscopy (TEM) (8, 22).

It is the formulation and study of engine oils and how they decompose in solution and between rubbing contacts that comprises a vast majority of the associated literature on how additives work. Until 1986, X-ray absorption spectroscopy (XAS) was an unexplored technique in the investigation of tribological contacts (23). X-Ray absorption spectroscopy probes the transition of electrons from core states and is particularly useful for low-Z elements (such as C, N, P, O, and S, common elements found in additive molecules). Spectra allow for the collection of a comprehensive

Received 25 April 2007. Accepted 18 July 2007. Published on the NRC Research Press Web site at canjchem.nrc.ca on 29 August 2007.

M.A. Nicholls.[2] Dofasco Inc., Research and Development, Hamilton, ON L8N 3J5, Canada.
M.N. Najman. Lubrizol Corporation, Wickliffe, OH, USA.
Z. Zhang. Milacron Inc, Cincinnati, OH, USA.
M. Kasrai and P.R. Norton. The University of Western Ontario, Department of Chemistry, London, ON, Canada.
P.U.P.A. Gilbert.[3] Department of Physics, University of Wisconsin-Madison, Madison, WI, USA.

[1]This article is part of a Special Issue dedicated to Professor G. Michael Bancroft.
[2]Corresponding author (e-mail: mark_nicholls@dofasco.ca).
[3]Previously publishing as Gelsomina De Stasio.

 doi:10.1139/V07-093 © 2007 NRC Canada

set of data that provide details on geometry, oxidation state, and quantum numbers of the absorbing atom. Chemical changes, which result from the additives breaking down or interacting during rubbing, are observed as changes in the absorption structures in the recorded spectra (24–26).

Advancements in the area of nanotechnology have demanded an improvement in the spatial resolution of many surface analytical techniques, and XAS is not impervious to these pressures. In fact, XAS has welcomed these advancements and has made some very significant strides towards providing spatially resolved chemical speciation to <100 nanometer spatial resolution (27–30). The first use of spatially resolved XAS, termed X-ray photoelectron emission spectromicroscopy (X-PEEM), was published on the reaction films formed from organo-molybdenum compounds in a tribo-contact in 1997 (31). As the technique evolved and improved, many other groups exploited it in the study of tribology (32–36).

The use of XAS, or more specifically X-ray absorption near edge structure (XANES) spectroscopy, and subsequently X-PEEM began to be embraced by the tribology community after a chance meeting at an Ontario Center for Materials Research (OCMR) meeting in 1990. At that meeting G.M. Bancroft and M. Kasrai from the University of Western Ontario (UWO) introduced XANES to a major lubricant manufacturer, Imperial Oil. At that time, Dr. Kim Fyfe from Imperial Oil was looking for a technique that could easily characterize the chemical form of phosphorus and sulfur. After a short explanation and introduction to the approach, which G.M. Bancroft and M. Kasrai were exploiting at that time to investigate the intricate and detailed chemistry of coals and bitumus materials, an almost 10-year relationship began between the UWO and Imperial Oil. This chance meeting has led to the co-authorship of 15 publications by the three researchers and allowed for the crossing of paths with two other very prominent researchers at Chevron, Dr. Elaine Yamaguchi and Ray Ryason in 1994. The collaboration with Chevron continues today with over 15 joint publications. This has established the UWO group as the leading world experts in the study of tribochemistry by XANES spectroscopy, with a total of 55 publications with associates over the last 15 years. At the root of these publications is the ability of XANES spectroscopy to elucidate the lubrication properties of antiwear additives, determine mechanisms by which certain oil additives perform, but also be able to explain their behavior at a fundamental chemical level.

Examples of the type of work performed over the last 15 years will be briefly discussed in this paper to demonstrate the usefulness of XANES in the study of tribochemistry. The first section will highlight the information XANES spectroscopy has provided about the macrochemistry of the tribofilms generated from dialkyl-dithiophosphates (and derivatives thereof) on steel surfaces, and how this information can be used to explain the growth and wear processes experienced in the rubbing contact. The second section will illustrate the more advanced, spatially resolved, microchemical characterization done with X-PEEM. The section will describe how this approach helps to identify the location and chemical speciation of an antiwear film formed on a high silicon content (~18%) aluminum–silicon alloy, which is beneficial to understanding the applicability of such an alloy in a combustion engine. The final section will demonstrate the value of combining XANES and X-PEEM results to comprehensively evaluate both the tribochemical make-up as well as topographical features of lubricious films generated from ashless phosphorus- and sulfur-containing additives. This introduction presents the wealth of information that XANES spectroscopy has provided to the tribology community, and clearly demonstrates how the group at the UWO has maintained their dominance in the field by exploiting its emerging capabilities.

Experimental

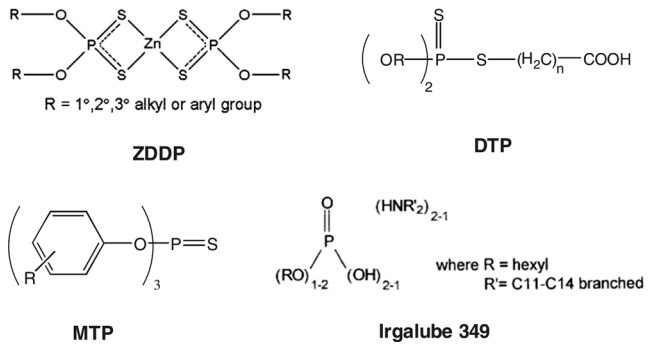
Sample preparation and film formation

The steel samples were manufactured from 52100 steel into square specimens 10 mm × 10 mm × 4 mm or 19 mm diameter discs. The composition of 52100 steel is ~1% C, 1.3%–1.6% Cr, and the remainder primarily Fe. The steel samples were polished with 3 μm diamond paste. The aluminum 390 (A390) material was wire electrode discharge machined to create 10 mm × 10 mm × 4 mm samples. The composition range of A390 is ~4%–5% Cu, 16%–18% Si, with small percentages of Mg, Fe, Zn, and Ti. The A390 samples were polished with 0.3 μm alumina and finished with 0.05 μm silica suspension. The reciprocating cylinders were manufactured from 52100 steel, 6 mm in diameter and 6 mm in length. The steel sample and pins were austenitized and quenched. Their hardness was >60 Rockwell C. The pins were used as is.

The antiwear films were formed in a reciprocating Plint wear tester (37) under boundary lubrication conditions with a cylinder-on-flat test geometry establishing a line contact. The test conditions consisted of rubbing times that varied between 10 s and 10 h, at varying temperatures 60–100 °C, with a frequency of 25 Hz, load between 60–220 N, and a 7 mm stroke length. Chemical structures of the additives used in this study are shown in Fig. 1. A ZDDP commercial concentrate was obtained from Imperial Oil Limited, Canada. The concentrate is a mixture of neutral and basic forms, consisting of 85% secondary (C-4) and 15% primary (C-8) alkyls. The concentrate was diluted using MCT-10 base oil to 1.2 mass% resulting in a phosphorus content of ~0.1% by weight. MCT-10 base oil is a mineral oil with a sulfur content of 0.12 mass%. Two different ashless thiophosphate additives were used. The first additive used was an ashless triaryl monothiophosphate and is referred to as MTP. The second additive used was an ashless dialkyldithiophosphate and is referred to as DTP. The lubricant formulation was achieved by dissolving the additive by weight in the low sulfur base stock. The concentrations used in this study were 0.5 wt% DTP and 1.5 wt% MTP, respectively. The antiwear films were stored as is with their oily protective layer. Before insertion into vacuum the samples were thoroughly rinsed in hexanes. The light hydrocarbon rinse has been found not to alter the antiwear film, which is very robust (38, 39). On the X-PEEM samples, a grid composed of indent marks was created using a Vickers hardness tester. This grid allowed for relocation of the same regions with the multiple techniques discussed below.

© 2007 NRC Canada

Fig. 1. Chemical structures of antiwear additives: zinc dialkyldithiophosphate (ZDDP), triaryl monothiophosphate (MTP), ashless dialkyldithiophosphate (DTP), and commercial additive Irgalube 349.



Surface imaging

Topographical imaging was performed using a Digital Instruments Nanoscope IIIa® atomic force microscope. Images were obtained in constant force mode to investigate the morphology and topography of the blank substrates, wear scars, and antiwear films after formation. A LEO-440 scanning electron microscope with a Quartz Xone Gresham light element detector was used to image the surfaces in field-emission and backscattering modes and to perform X-ray analysis.

XANES and X-PEEM analysis

X-ray absorption spectra provide detailed information about the local environment and oxidation state of elements in a film or on a surface. XANES analysis employs the use of soft X-rays making it a nondestructive technique. XANES spectroscopy was performed at the Canadian Synchrotron Radiation Facility at the 1 GeV Aladdin storage ring, University of Wisconsin, Madison. The data were obtained using the Grasshopper beamline, which has a resolution of ~0.1 eV, and the double crystal monochromator (DCM) beamline with a photon resolution of ~0.9 eV. Spectra were recorded using the total electron yield (TEY) and fluorescence yield (FY) detection modes (details of which can be found elsewhere (40)), and represent the information from a surface several square millimetres in area. The sampling depths of the TEY and FY at the P K-edge are 50 nm and >800 nm, respectively (41), and the sampling depths of the TEY and FY at the P L-edge are 5 and 60 nm, respectively (41). These techniques are ideally suited for measuring antiwear films such as these, which are on the order of 50–100 nm thick. At least two individual scans were recorded for each specimen and digitally combined. The spectra were normalized against I_o, and a linear background was subtracted.

X-ray photoelectron emission spectromicroscopy was performed using the SPHINX (42) microscope (ELMITEC GmbH), with an optimum spatial resolution of 10 nm (42), installed on the 6m-TGM (toroidal grating monochromator) beamline at the 1 GeV Aladdin storage ring, University of Wisconsin, Madison, optimized to give ~0.1 eV resolution at the phosphorus L-edge (for details see refs. 32, 43, and 44). Image intensity in X-PEEM is proportional to the TEY, and the surface sensitivity was limited by the escape depth of the secondary electrons at the phosphorus L-edge (3–5 nm) (41, 43). For the phosphorus L-edge region, a "stack" consisting of 301 images were taken over an energy range of 130–160 eV with an energy spacing of ~0.1 eV. A 100 μm field of view was chosen for the selected areas with a resolution of ~200 nm per pixel. Typical areas examined were <10 μm^2. The images were combined to produce a three-dimensional data set or spectromicroscopy movie (29) that was analysed to extract detailed chemical information about the tribofilm using aXis2000 software (28, 45). The data analysis procedure and the obstacles overcome have been described elsewhere (28, 29, 45, 46). Briefly, the aXis2000 software enables the selection of a single pixel, or regions of interest of several pixels in size, from which XANES spectra are extracted. The resulting spectra are averaged over all the pixels contained in the region of interest. Thus, some spectra are the average of a few pixels (usually with poor signal-to-noise) or several tens or hundreds of pixels.

Contributing evidence to the usefulness of XANES in the study of tribolochemistry

As examples of the value of XANES to the study of tribology, this first section will highlight the information that XANES spectroscopy has provided about the macrochemistry of the tribofilms generated from dialkyldithiophosphates. The second section will illustrate the more advanced, spatially resolved, microchemical characterization done with X-PEEM. The final section will demonstrate the value of combining XANES and X-PEEM results to comprehensively evaluate both the tribochemical make-up as well as topographical features of lubricious films generated from ashless phosphorus- and sulfur-containing additives.

A. Study of the tribochemistry of ZDDP and DTP using XANES

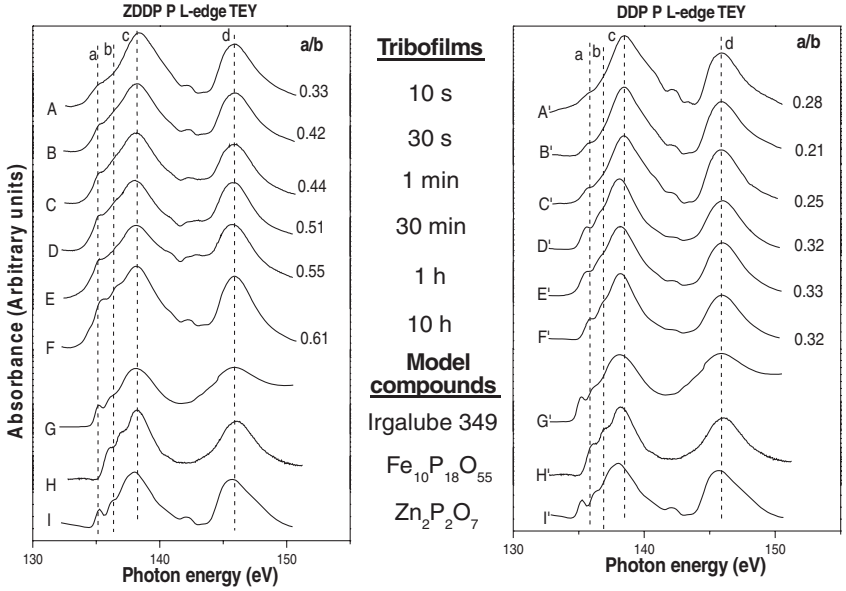
XANES measurements have been found to be ideally suited to the chemical studies of these films. First, most of the important elements in these films (e.g., P and S) have suitable absorption peaks (e.g., P and S L- and K-edges) in the soft-X-ray energy region. Some of these provide better chemical resolution than other analytical techniques. Second, TEY and FY detection modes allow for nondestructive study of the chemical nature of the surface, the near surface region, and the bulk of the film.

Zinc dialkyldithiophosphate (ZDDP) has been used for many years as the most common and the best antiwear (AW) additive for engine lubricant formulations. ZDDP is contained in fully formulated combustion engine oils at less than 0.1 wt% phosphorus content. Current environmental regulations are driving research to develop other AW additives that contain less phosphorus, since this element poisons catalytic converters leading to increased NO_x exhaust emissions. Despite the wide use of ZDDP, the formation, composition, and function of sacrificial wear films produced from its decomposition products are only partially understood. However, it is now widely accepted that ZDDP tribofilms consist mainly of phosphates with some sulfides (47), and the average thickness of the films is less than 100 nm (39).

Sarin et al. (48) showed that ashless thiophosphates gave comparable antiwear and antioxidant properties to those of

© 2007 NRC Canada

Fig. 2. Phosphorus L-edge XANES (in TEY mode) spectra of model compounds and tribofilms generated from 1 wt% ZDDP (left) and DTP (right) for different rubbing times.



ZDDP in bench tests. In contrast to the ZDDP film chemistry, XANES analysis showed that DTP gave short-chain polyphosphates throughout the film, and the sulphide formed was largely FeS (49). It was assumed that the cation in the phosphate glass was Fe^{2+}. This section will describe the use of XANES to the study of ZDDP and DTP tribofilm products and how the detailed chemical and structural data can be interpreted to theorize the decomposition and film formation mechanisms.

Results and discussion

Phosphorus characterization

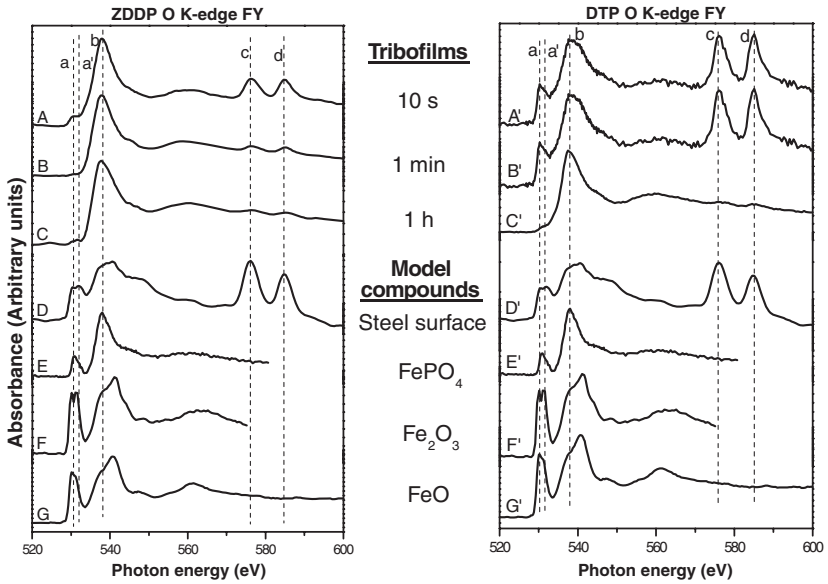
Phosphorus L-edge XANES spectra of tribofilms generated from ZDDP and DTP at different rubbing times and model compounds are shown in Fig. 2. These spectra are characteristic of polyphosphate glasses observed in all of our previous studies of both ZDDP and DTP films (49–55). Comparing the ZDDP spectra in Fig. 2 (left), it can be seen that the peak positions in spectra A to F of the tribofilms generated at different rubbing times are highly similar to the positions for the model compound, zinc polyphosphate ($Zn_2P_2O_7$). In particular, the position of peak a in the tribofilms is much closer to peak a for Zn polyphosphate than for Fe polyphosphate or a phosphate ester, Irgalube 349. This indicates that the major cation in the surface of these films is Zn^{2+} rather than Fe^{2+} or Fe^{3+} and is consistent with our previous findings that films formed for long rubbing times have long-chain Zn polyphosphates at the surface and shorter-chain Zn polyphosphates (with some Fe) in their bulk (50–55). X-ray photoelectron spectroscopy (XPS) also showed that there is no Fe the in surface of the films (56). The peak located at ~142 eV is due to carbon contamination of the beamline optics and is a 2nd order carbon peak (32, 46). The intensity of peaks a or b relative to peak c has been used to indicate the phosphate chain length; an a/c of about 0.3 is representative of a short-chain polyphosphate, and an a/c of about 0.6 indicates a long-chain polyphosphate (57). The FY spectra of ZDDP films provide chemical information about the bulk and indicate that the chain length is shorter (a/c of <0.4) for the long rubbing time films, an a/c of ~0.6 from the surface sensitive TEY measurement as observed previously (e.g., see Figs. 2E, 2F). These spectra show the bi-layer nature of the ZDDP films having short-chain polyphosphates in the bulk and long-chain polyphosphates at the surface.

However, the present results on ZDDP antiwear films show, for the first time, that the polyphosphate chain length at the surface of these films increases with rubbing time. For spectrum A from the 10 s film, the ratio of intensity of peak a/c is 0.33, indicating a short-chain zinc polyphosphate. With increasing rubbing time, the a/c ratio of the spectra (A to F) increases. Thus, for the 10 h film (spectrum F), the a/c ratio is 0.61. Because the Zn/P ratio of 1:2 in ZDDP is much smaller than the Zn/P ratio in a short-chain polyphosphate (e.g., 1:1 in $Zn_2P_2O_7$), the initial formation of a short-chain polyphosphate indicates that substantial Fe must be present in these shorter rubbing time films. The availability of Fe (or Fe oxides) from the steel surface decreases as the film becomes thicker, and the chain length increases with relatively more Zn and less Fe in the surface of the films. Unfortunately, the position of peak a is not sensitive to the differences in the relative proportion of Fe and Zn in these films and therefore no direct evidence supports this.

The spectra of the DTP films (Fig. 2, right) are qualitatively similar to the ZDDP spectra — they are all characteristic of polyphosphates. However, there are two obvious differences. First, the position of peak a in all spectra aligns very well with peak a for $FePO_4$ rather than $Zn_2P_2O_7$, suggesting that, as expected, Fe is the predominant cation in these films (the shoulder in the ZDDP spectra), which appears just before peak a, is due to the presence of a small amount of unreacted ZDDP (50, 51). Second, the ratio a/c in all spectra is close to 0.3, indicating that all films contain short-chain polyphosphates as was found earlier by Najman

© 2007 NRC Canada

Fig. 3. Oxygen K-edge XANES spectra of model compounds and tribofilms generated from 1 wt% ZDDP (left) and DTP (right) for different rubbing times.



(55). It is not easy to rationalize why DTP gives short-chain polyphosphate, especially for the thick films, when the availability of cations for DTP has to be less than that for ZDDP. However, careful examination of spectra shows that position of peak c in spectra D′ to F′ (30 min to 10 h films) shifts slightly (~0.5 eV) to lower energy corresponding to zinc polyphosphate or Irgalube 349 spectrum G′. This suggests that in the absence of Fe as a cation, contaminant zinc and (or) an alkyl group are balancing the charge in these films. The alkyl group may originate from incomplete decomposition of DTP. Our recent studies on phosphate esters indicate that the P L-edge spectra of some of the organic phosphates are similar to those of metal phosphates (55).

Oxygen characterization and the role of Fe in the films

Oxygen K-edge FY XANES spectra of tribofilms generated from ZDDP and DTP at different rubbing times and model compounds are shown in the left and right panels of Fig. 3, respectively. The TEY spectra for all of these samples (not shown) are qualitatively similar. Spectra A (A′) to C (C′) are produced from tribofilms rubbed for 10 s, 1 min, and 1 h, respectively. Peaks c and d in some of these spectra originate from chromium L-edge XANES from a concentration of the 1% Cr in the 52100 steel surface oxide. This may indicate that the probing depth is greater than 500 Å and large enough to detect the steel surface in these very thin films; however, there could also be Cr incorporated into these phosphate films as suggested by XPS broad scans (not shown). Peak a is very weak in the ZDDP spectra (A and B) showing a rather small amount of Fe in these films. In contrast, the spectra A′ and B′ from the DTP films show a very intense peak a without any noticeable a′. This certainly indicates that there is appreciable Fe phosphate in these films, although there is still a contribution to these spectra from the surface Fe oxide. However, after one hour of rubbing (spectrum C′), peak a is very weak (although stronger than in the comparable ZDDP spectrum C), indicating rather little Fe is in the films. If Fe is the only cation (or even the predominant cation due to some Zn incorporation) in these phosphate films, the intensity of peak a should be much larger in spectrum C′. On the other hand, it was shown in Fig. 2 for 30 min to 10 h films, that contaminant zinc cations and alkyl groups may balance the charge for these phosphates. We cannot, at present, explain this apparent discrepancy.

Fe L-edge results for Fe characterization

The iron L-edge spectra of the films and model compounds taken with second-order synchrotron light (24) are shown in Fig. 4 for the ZDDP films (left) and DTP films (right). As for the oxygen K-edge spectra, the $FePO_4$ spectrum (D) is appreciably different from those of the oxides: peak a is very narrow and not split as with the other three Fe standards (spectra E, F, and G). For ZDDP films, the 10 s film (A) shows mostly Fe oxides. However for the thicker 1 min and 1 h ZDDP films (B and C), the spectra are very weak, showing that there is very little Fe in the surface of these films. For the very thin DTP films (A′ and B′) and thick film (C′) the spectra are very similar to the Fe oxide from the steel surface. This is not surprising. As was shown in Fig. 6 of reference (56), the DTP films were very inhomogeneous and are composed of small pads compared to the ZDDP films. Furthermore, scratch marks are quite apparent in these films and obviously the Fe signal may originate from the substrate, although a contribution may also be given by the small amount of iron phosphate that can exist in the film.

Sulfur characterization

Sulfur K-edge XANES spectra of tribofilms generated from ZDDP and DTP at different rubbing time and model compounds are shown in Fig. 5. The spectra of the ZDDP films (spectra A, B, and C) are highly similar to the ZnS spectrum (with peak c dominating), as reported in our previous studies (58, 59). This indicates that the main chemical state of sulfur in the tribofilms generated from ZDDP at all rubbing times is ZnS. However, for the 10 sec film (spec-

© 2007 NRC Canada

Fig. 4. Fe L-edge XANES spectra (recorded with second-order light) of model compounds and tribofilms generated from 1 wt% ZDDP (left) and DTP (right) for different rubbing times.

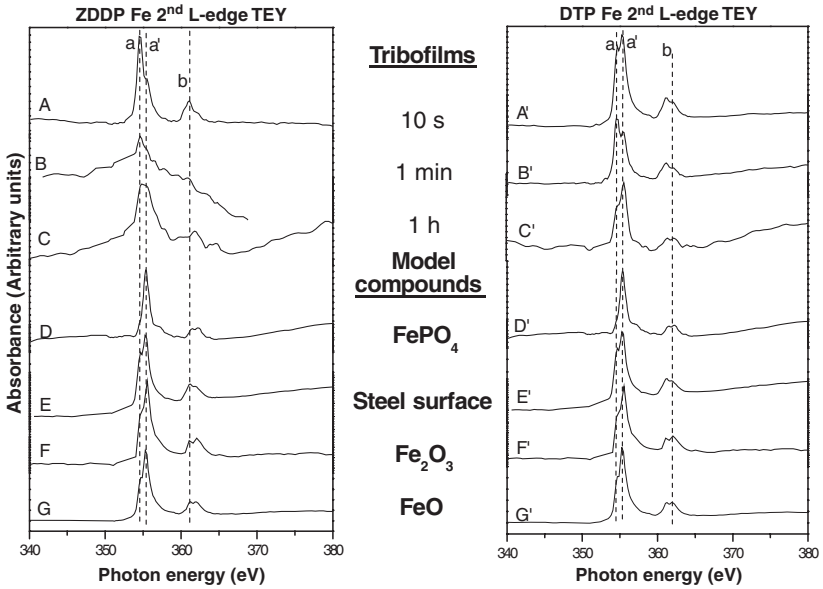
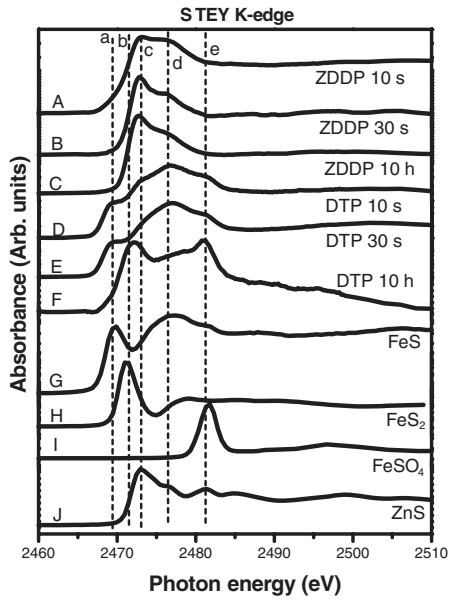


Fig. 5. Sulfur K-edge XANES spectra of model compounds and tribofilms generated from 1 wt% ZDDP and DTP for different rubbing times.



trum A) there are two shoulders, peaks a and d. These two shoulders correspond to the FeS spectrum (spectrum G). This result implies that there are two kinds of sulfides in the tribofilm generated from 10 sec rubbing. Zinc sulfide is the main chemical state of sulfur, but there is also some iron sulfide in the film. Because the concentration of iron sulfide is lower, there are only two shoulders in spectrum A, and this indicates that iron sulfide does exist in the tribofilm at the beginning of rubbing; and more importantly, Fe from the surface is immediately available for reaction with the sulfur and (or) phosphorus generated as the ZDDP decomposes. As rubbing continues, peak a disappears and the intensity of peak d decreases. This indicates that the amount of FeS in the film decreases relative to the amount of ZnS. In the thick films, there is probably only FeS right at the interface between the tribofilm and the steel surface. This is not unexpected from the principle of hard acids and soft bases as outlined by Martin and co-workers (60, 61). The soft base S^{2-} prefers to react with the borderline soft acid Zn^{2+} over the harder acid Fe^{2+} or Fe^{3+}. This principle can also be expressed by thermodynamic predictions. For example, consider the reactions,

[1] $$FeS + Zn^{2+} \rightarrow ZnS + Fe^{2+}$$

or

[2] $$FeS + ZnO \rightarrow FeO + ZnS$$

ΔG^0 is negative for these two reactions because of the very large negative ΔG_f^0 for ZnS (–201.3 kJ/mole) compared with FeS (–100.4 kJ/mole) (62). In the presence of a Zn species, FeS is expected to convert to ZnS. However, the majority of the zinc ends up in Zn polyphosphates rather than ZnS. The very large ΔH_f^0 values (ΔG_f^0 values are not available (62)) for the Zn phosphates (e.g., –2892 kJ/mole for $Zn_3(PO_4)_2$ and –4479 kJ/mole for $Zn_3P_4O_{13}$) indicate that the Zn phosphates are the thermodynamically stable zinc products in this complex system. For example, the ΔG value is –145 kJ for the following reaction,

[3] $$3ZnS + 2\ H_3PO_4 \rightarrow Zn_3(PO_4)_2 + 3H_2S$$

Indeed, the presence of Zn in the DTP films from a very minor zinc contamination shows that Zn phosphates are incredibly stable compounds. The XPS data shown elsewhere (56) support this discussion. In DTP films in the absence of Zn (or very small amount due to contamination), the sulfur proportion (~1%) is very low compared with that of ZDDP films (~8%).

For the DTP films, Najman (55) already reported that substantial FeS was present in these films after rubbing for greater than 5 min. The formation of FeS is much clearer in

© 2007 NRC Canada

the 10 s and 30 s films, as shown in Figs. 5D and 5E; indeed, FeS is the dominant sulfur species in these two spectra.[4] The presence of peak c in these spectra could be due to a small amount of ZnS from the contaminant Zn. The 10 h film shows the presence of sulfate (peak e) and some FeS and FeS_2, with perhaps a small amount of ZnS.

Sulfur K-edge XANES spectra of tribofilms generated from different concentrations of ZDDP were also investigated (not shown). The spectra of sulfur in the different concentration tribofilms are the same and align with zinc sulfide. This indicates that the concentration of ZDDP does not affect the formation of zinc sulfide in the tribofilm.

From the preceding discussion, it can be concluded that the tribofilm generated from ZDDP is a multilayer film. The mechanism of tribofilm formation for both ZDDP and DTP is given in more detail below.

A. ZDDP Mechanism

(Products entering solution are ignored.)
Stage 1. Physical and chemical adsorption.

[4] $Zn[(RO)_2PS_2]_2$ (solution) $\rightarrow Zn[(RO)_2PS_2]_2$ (ZDDP adsorbed)

Stage 2. Initial film formation (~10 nm) on the surface when cations are plentiful.

[5] $Zn(RO)_4P_2S_4 + O_2$ (in oil) + FeO $\rightarrow$ Zn/Fe phosphate (short-chain) + ZnS + FeS

Stage 3. Surface is covered with a thin film and Fe is not accessible from the substrate.

[6] $Zn(RO)_4P_2S_4 + O_2$ (in oil) $\rightarrow$ Zn phosphate (long-chain) + ZnS

In stage 2 based on ΔH_f^0 values, the proportion of FeS will be very small. In stage 3, Zn phosphate formation is preferred over ZnS formation.

Stage 4. Conversion of long-chain polyphosphate to short chain.

[7] Zn phosphate (long-chain) + $6H_2O \rightarrow$ Zn phosphate (short-chain) + $4H_3PO_4$

In stage 4, any water in the system can hydrolyze long-chain polyphosphates to short-chain (53, 63). As a result, the film becomes thicker, composed of short-chain Zn phosphate (with little Fe). We can think of a tri-layer film, with the top layer consisting of longer chain phosphates, a middle layer of predominantly short-chain phosphates, and an inorganic layer of ZnS and (or) FeS.

B. DTP Mechanism

(Products entering solution are ignored.)
Stage 1. Physical/chemical adsorption.

[8] $(RO)_2PSS\text{-}C_2H_4CO_2R$ (solution) $\rightarrow (RO)_2PSS\text{-}C_2H_4COOR$ (DTP adsorbed)

Stage 2. Initial film formation (~10 nm) on the surface when Fe are plentiful.

[9] $(RO)_2PSS\text{-}C_2H_4CO_2R + O_2$ (in oil) + FeO $\rightarrow$ Fe phosphate (short-chain) + FeS

Stage 3. Surface is covered with a thin film of Fe phosphate and no cation is accessible from the substrate.

[10] $(RO)_2PSS\text{-}C_2H_4CO_2R + O_2$ (in oil) + H_2O (in oil) $\rightarrow$ phosphate ester + alkyl sulphide

In stage 3, the alkyl sulphide will be dissolved in oil. However, it is difficult to see how the phosphate ester can remain on the surface.

Conclusions

The macro-scale XANES spectra yield much information about the film chemistry. The phosphorus L-edge spectra (along with the oxygen K-edge spectra and Fe L-edge spectra) have been used for the first time to give information on the role of Fe in the films. For ZDDP, a bi-layer phosphate film develops very quickly. Initially, the film is predominantly short-chain polyphosphate with Zn as the predominant cation, but the film develops to give predominantly long-chain Zn polyphosphate at the surface and a shorter chain polyphosphate with some Fe in the bulk. The average polyphosphate chain length increases with an increase in ZDDP concentration up to a certain point. For DTP, the polyphosphate film is of short-chain character throughout the test, with cations being Fe and alkyl groups. The proportion of alkyl groups is much higher on the surface. At this stage we cannot give a quantitative estimate of the proportion of Fe in the tribofilm. The Fe from the oxide and from solution must become available at the high local temperatures for the phosphate film formation, even for the relatively thick films. Some sulfur from the ZDDP reacts to form ZnS, but in addition the presence of FeS has been identified for the first time in the early films from both ZDDP and DTP.

This study demonstrates how XANES spectroscopy can provide detailed chemical information on complex heterogeneous tribofilms formed on steel. It goes further by illustrating how this information can be interpreted to elucidate complex film formation mechanism. A next step in understanding such complex systems would be able to spatially extract the same comprehensive information from discrete locations on a surface. Synchrotron spectromicroscopy has enabled the acquisition of chemical information on the submicron length scale (27, 29, 32, 44, 64) and opened up the ability to investigate, for the first time, the spatial distribution and chemical speciation of antiwear (AW) films.

[4] In the case of tribofilms, the formation of a pure compound is rarely observed. Typically, intermediate species are incorporated in the film as a result of incomplete chemical reactions. Thus, the use of the term dominant to indicate that the major sulfur component of the film, in this case, is FeS.

© 2007 NRC Canada

B. X-ray photoelectron emission spectroscopy of ZDDP films on Al–Si alloys

Not only are replacement additives for ZDDP being sought to reduce emissions, but automotive manufacturers are also envisioning weight savings by altering the design of the engine block to reduce fuel consumption and therefore also reduce emissions. Aluminum–silicon alloys with high silicon contents (>18%) are currently being investigated as cost effective replacements for cast iron components. The introduction of silicon improves the wear resistance of aluminium through the formation of separate hard phase silicon grains in the aluminum matrix. A long-standing question is the function of the silicon grains. It is generally thought, since very little research exists, that the grains, after honing and etching of the surface, act like riders that bear the load of the conforming surface (65–69). To date no suitable additive has been found which can effectively lubricate Al–Si alloys. It would be ideal if ZDDPs proved to be effective additives to reduce friction and wear of Al–Si alloys.

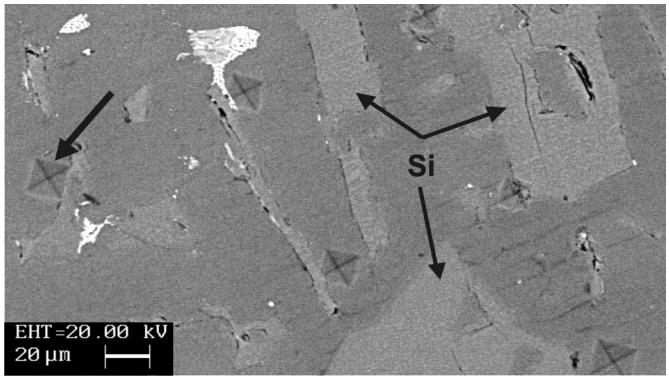
For the first time, the spatial localization,and chemical speciation of ZDDP AW films on high silicon content Al–Si alloys was performed using X-ray photoelectron emission spectromicroscopy (X-PEEM). The ability to spatially resolve features on a surface enables examination of the occurrence (or lack thereof) and location of ZDDP AW film formation under lubricated wear of a high-silicon content (~18%) Al–Si alloys.

Results and discussion

Fiducially placed indents were used to recognize and reanalyse specific areas of interest, using atomic force microscopy (AFM), X-PEEM, and secondary electron microscopy (SEM). These indents were made after the ZDDP AW films were formed on the Al–Si alloy. As was performed previously (70), SEM imaging and EDX elemental mapping were used to understand the heterogeneous nature of the alloy surface and was performed after X-PEEM analysis. A high-resolution SEM image is shown in Fig. 6. The diamond-shaped indents used to identify the regions of interest are clearly observed, as are the distinct grey features that have been identified by EDX as silicon grains (70). Light wisps and blotches are due to the difference in backscattering from the agglomeration of other elements such as iron, copper, and magnesium.

Once a particular silicon grain was pinpointed, the region was then examined by AFM. AFM imaging provides high-resolution topographic information and has been routinely used to observe the varying morphology of AW films (71–73). In this instance, AFM was used to investigate where (if any) ZDDP AW films formed. ZDDP antiwear films on steel have a heterogeneous topography composed of islands and valleys. The islands have been termed AW pads and are thought to act like a cushion preventing the two rubbing surfaces from coming into contact (44). Figure 7A is a mosaic of AFM images that show a large silicon grain running diagonally across the figure. The large "diamond-shaped" indents can also be observed at the top and bottom. In AFM images, objects with a higher elevation appear lighter. Careful examination of the silicon grain shows small, elevated islands, or ZDDP AW pads. The pads have an elongation that is in the direction of the rubbing experienced during the friction test. A 3D AFM image of the AW pads, boxed 1 in Fig. 7A, is shown in Fig. 7B. The padlike morphology can be clearly observed and is quite similar to those formed on steel under identical rubbing conditions (70). Again, the pads are thought to limit the contact between the two rubbing surfaces. Since AFM imaging provides 3D topographic information it is possible to extract useful height information about the surface. A cross-sectional profile along the line (marked 2) in Fig. 7A is shown in Fig. 7C. From this profile the height of the silicon grain can be measured to be ~100 nm; as well, the oscillations on the surface of the grain can be identified as the small AW pads.

Fig. 6. A secondary electron image (in backscattering mode) of the Al–Si surface. Vicker's indents can be identified in the image as well as the distinct silicon grains.

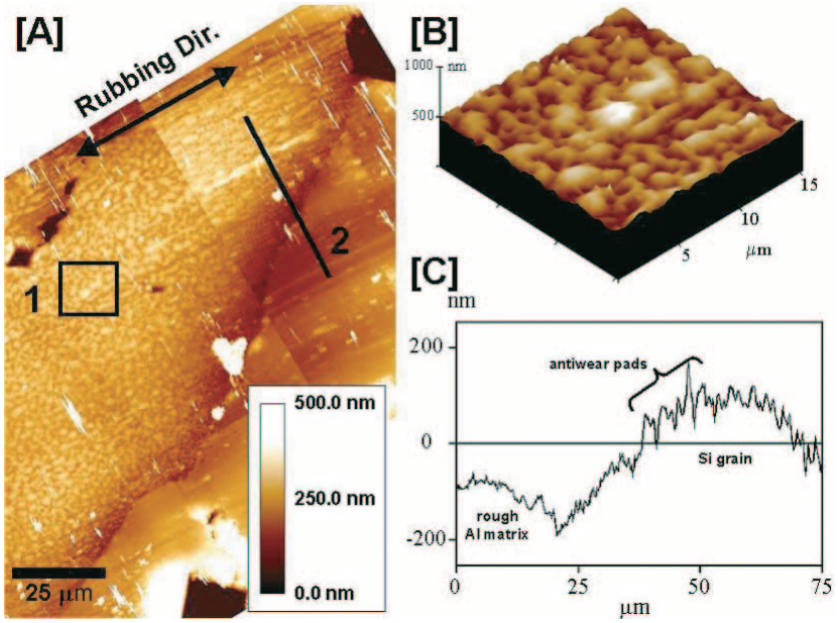


Advancements in X-ray photoelectron emission spectromicroscopy have made it possible to image surfaces similar to a secondary electron microscope. This gives the user the unique ability to distinguish small features on a surface (on a submicron scale), and then determine the chemical nature of the species present using X-ray absorption spectroscopy. This powerful combination of techniques has only become possible (at this resolution) in the last several years and has only been routinely used to analyse ZDDP AW films on steel recently (32, 44, 74). The imaging function of the X-PEEM was used to locate the same fiducial indents identified in with the AFM images. For comparative purposes, the AFM image is reintroduced in Fig. 8A with the X-PEEM image Fig. 8B (with the same orientation and scale as in the AFM image). The large indents can be observed, as well as the large AW pads (circled).

Using the X-PEEM analysis software, an image mask was generated to separate the ZDDP AW pads form all other features (details of the entire procedure can be found elsewhere (44)). Figure 9 shows the mask used to select only the large AW pads. The mask is used to extract and average the phosphorus L-edge spectra obtained from each pixel within the mask. The average spectrum using this procedure is labelled (D), shown in Fig. 10, and is compared with the model spectra from compounds with known oxidation state and elemental geometry around the phosphorus atom. Comparisons to unreacted ZDDP (A), a zinc polyphosphate glass (B), and a ZDDP AW film formed on steel, make interpretation of the film chemistry much easier. The spectrum from the unreacted ZDDP shows its characteristic triplet structure (51). The zinc polyphosphate has peaks a, b, and c that are shifted to higher energy from peaks 1, 2, and 3 of unreacted

© 2007 NRC Canada

Fig. 7. (A) A mosaic of AFM images showing a large silicon grain on the top of which patches of ZDDP antiwear film can be observed. The silicon grain runs diagonally through the image. (B) A 3D topographic image of the antiwear pads found within box 1. (C) A cross-sectional profile taken across 2.



ZDDP. Peaks a and b are the 2p spin-orbit doublet, separated by 0.8 eV. They are assigned to the transitions of electrons from occupied $2p_{3/2}$ and $2p_{1/2}$ levels to unoccupied antibonding orbitals. Peak c is attributed to the transition of the 2p electrons to a p-like t_2* molecular orbital. As described previously, the ratio of the intensities of peaks a/b increase as the polyphosphate chain length increases (44, 57, 75). An *ideal* ZDDP AW film formed on 52100 steel (C) has a polyphosphate structure. Comparison of this spectrum (C) to that of the AW film formed on the Si grain (D) reveals that the AW film does have the characteristic polyphosphate structure as that formed by ZDDP on the steel surface.

In spectrum (D) the ratio is 0.65, and in spectrum (E) the ratio is 0.60. This indicates that the AW pads have a longer polyphosphate chain length than the off-pad areas (44, 57, 75). This would indicate that although the Al matrix is too soft to allow shear forces to reach a sufficient magnitude to decompose ZDDP, polyphosphates can form on the hard silicon grains and must transfer to the Al matrix. The shorter-chain polyphosphates as well as unreacted ZDDP were also found in regions off the silicon grains on the Al matrix (70). This is indicative of the sacrificial nature of ZDDP AW films as they form on steel. Spectrum (F) in Fig. 10 shows a small shoulder (labelled s) to the left of peak a that lines up well with unreacted ZDDP, indicating that ZDDP species are also located in the Al matrix.

These results show that X-PEEM is a powerful tool for the investigation of ZDDP AW action on Al–Si alloys. Topographic imaging has observed that the ZDDP antiwear films are formed of patches (termed antiwear pads), characterized as smooth plateaus between which valleys and *bare* surfaces have been found. X-PEEM analysis at the phosphorus L-edge identified polyphosphates in the ZDDP AW film. It was found that the antiwear pads were located on the hard silicon grains and were oriented in the direction of rubbing; furthermore, the AW pads had a slightly longer polyphosphate chain length than the lower (valley) and surrounding Al matrix regions. This indicates that not only does the ZDDP AW film formed on Al–Si alloys possess a similar polyphosphate structure to films formed on steel, but it also has the same sacrificial characteristic (whereby polyphosphate is transferred from the hard silicon grains to the softer Al matrix) that it does on steel surfaces.

Conclusions

The use of spatially resolved X-PEEM chemical analysis in combination with high-resolution topographic imaging have provided new insight into the location and structure of ZDDP AW films on Al–Si alloys. The combination of these techniques provides researchers with the unique ability to obtain useful data on the chemical nature and wear protection mechanisms of ZDDP, and thus provide insight into how new replacement additives need to function to perform as effectively as ZDDP.

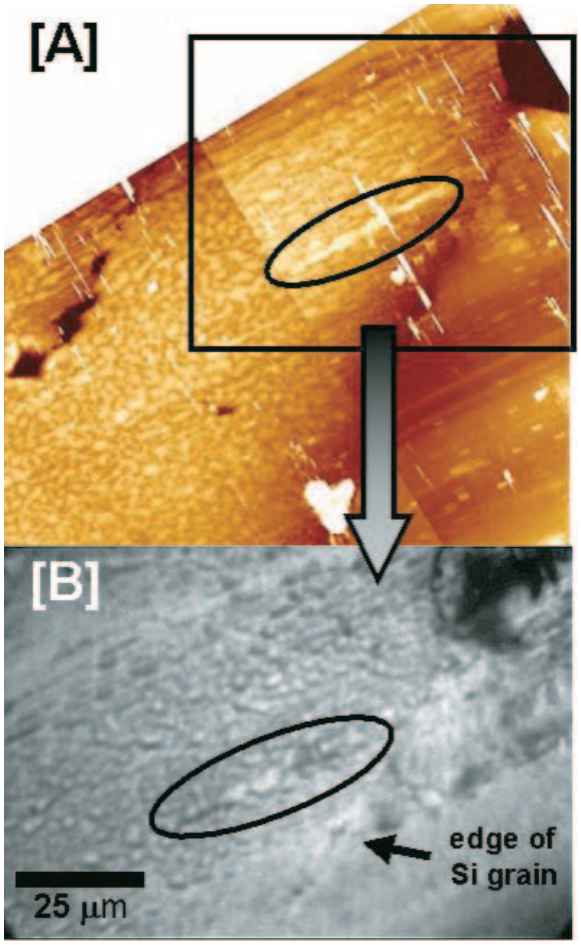
The final section in this review will demonstrate the coupling of the powerful macro-scale XANES analysis (e.g., section A) with the unique X-PEEM ability of spatially resolving where the tribofilms have formed and determine their exact chemical make-up.

C. Investigating the microchemical properties of tribofilms generated from ashless thiophosphate additives

As shown above, XANES has focused primarily on the understanding of tribochemistry from reaction films generated from various types of ZDDPs. However, concerns over some of the potential environmental implications of using ZDDPs have created an increased interest in the understanding of how metal-free lubricant additives function (37, 48,

© 2007 NRC Canada

Fig. 8. The AFM image from Fig. 7 is re-introduced (A) for navigation, along with the (B) secondary electron X-PEEM image showing the silicon grain and antiwear pads. The large antiwear pads are circled in the AFM to aid in identification in the X-PEEM image.



76). As a result, only recently has XANES been extended to that family of additives. Various types of phosphate esters as well as organosulfur compounds, such as sulfurized esters and dialkyldithiocarbamates, have been studied using XANES with much success (77, 78).

This section discusses the complementary use of macroscale XANES and X-PEEM to investigate the microchemical properties of lubricious films generated from ashless thiophosphate oil additives under boundary lubrication. During reciprocating sliding, noticeable differences were seen between an ashless dithiophosphate additive (DTP) and a monothiophosphate additive (MTP). Wear scar width measurements of the pin revealed that the DTP additive at a concentration of 0.5 wt% in sulfur-free base oil provided statistically better wear protection than the MTP additive at a concentration of 1.5 wt%. Preliminary tribochemical film analysis using X-ray photoelectron spectroscopy (XPS) and conventional XANES revealed slight differences in the phosphorus concentration at the near surface, while the polyphosphate structure, from a macrochemical perspective, was relatively the same between the two additives — both the MTP and DTP additives generated a short-chain

Fig. 9. A mask showing the selection of the larger ZDDP antiwear pads only. Spectra were extracted from only these regions to produce the spectrum shown in Fig. 10D.

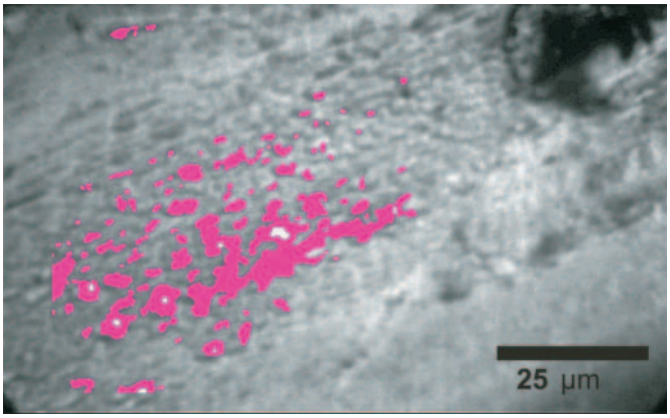
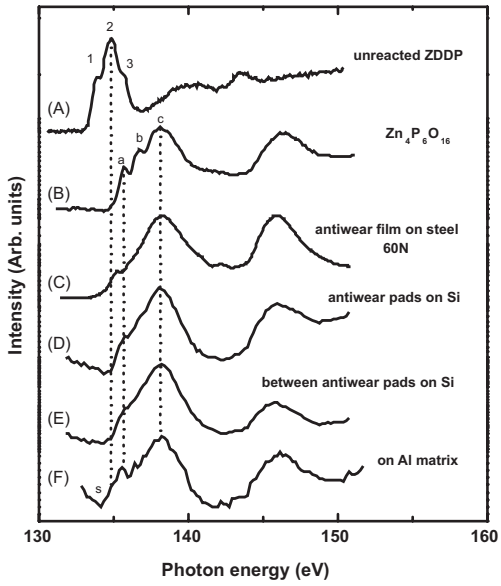


Fig. 10. (A) The XANES spectra for unreacted ZDDP, (B) a zinc polyphosphate, Zn4P6O16, and (C) ZDDP antiwear films formed on steel, (D) on silicon grain, (E) found between the antiwear pads on the silicon grain, and (F) on the aluminum matrix.



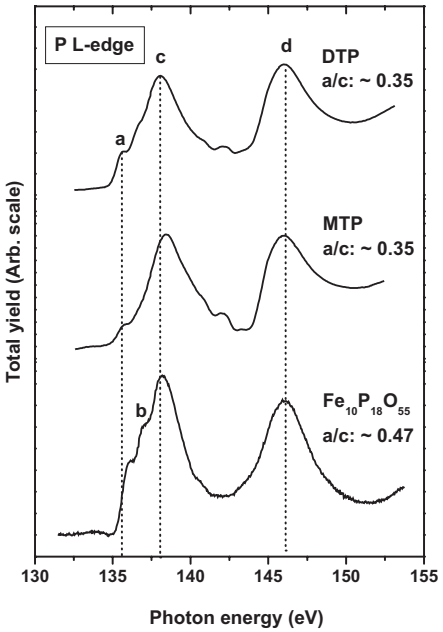
polyphosphate AW film (49, 79). Figure 11 displays the conventional macro XANES spectra (acquired from ~5mm^2 area) at the phosphorus L-edge for the tribochemical films generated from two ashless thiophosphate additives.

Results and discussion

The general topographical features of both MTP and DTP tribofilms were compared using both X-PEEM and AFM and are shown in Fig. 12. Based on the images, differences in the tribofilms are immediately apparent. For DTP, the 120 × 120 µm AFM image reveals a heterogeneous surface with elongated pads oriented in the sliding direction with widths between 2.5–5.0 µm as determined by X-PEEM. Conversely, the MTP tribofilm appears to be very homoge-

© 2007 NRC Canada

Fig. 11. Conventional P L-edge XANES spectra (from ~5 mm^2 area) of tribofilms generated from DTP and MTP in total electron yield (TEY) mode, compared with an iron polyphosphate model compound.



neous topographically, with thin elongated pads oriented in the sliding direction as well. Pad widths for the MTP tribofilm were estimated to be in the range of 1.5–2.0 μm.

Using X-PEEM analysis similar to that shown previously, the P L-edge region data showcase the properties of the AW films in a variety of ways. Figure 13b shows a "difference image" revealing the spatial distribution of polyphosphate from the DTP AW film excluding topographic information. The difference image technique subtracts two different spectral images along the phosphorus L-edge to show image contrast based on chemical and elemental properties. Figure 13a is a PEEM image of area of tribochemical film generated from the DTP additive taken at a photon energy of 137.2 eV. This on-peak image shows topography and chemistry combined. Figure 13b is a digital difference of two images, on-peak and off-peak, taken at 137.2 and 133.7 eV, respectively. Since the off-peak image contains only the topographic contribution, the difference image in Fig. 13b shows only the chemistry. Notice the presence of phosphorus on the surface of the tribofilm and its higher concentration (brighter pixels) where the pads are located. From the stack of difference images that can be created, one of the fascinating observations (not shown) is that the image intensity of the padlike structures begins to increase, eventually reaching a maximum intensity at the absorption edge.

As mentioned above, conventional XANES spectroscopy at the phosphorus L-edge samples an area on the order of several square millimetres, dimensions too large to provide any microchemical information (see Fig. 11 for example). On the SPHINX microscope,where the X-PEEM experiments were conducted with a field of view of 100 μm, in which each pixel represented an ~200 nm × 200 nm area, thereby enabling microchemical analyses. Figure 14 shows the X-PEEM image of an area where local XANES spectra

Fig. 12. Height mode atomic force microscope images and topographical PEEM image for the two AW films prepared: (a) DTP and (a) MTP.

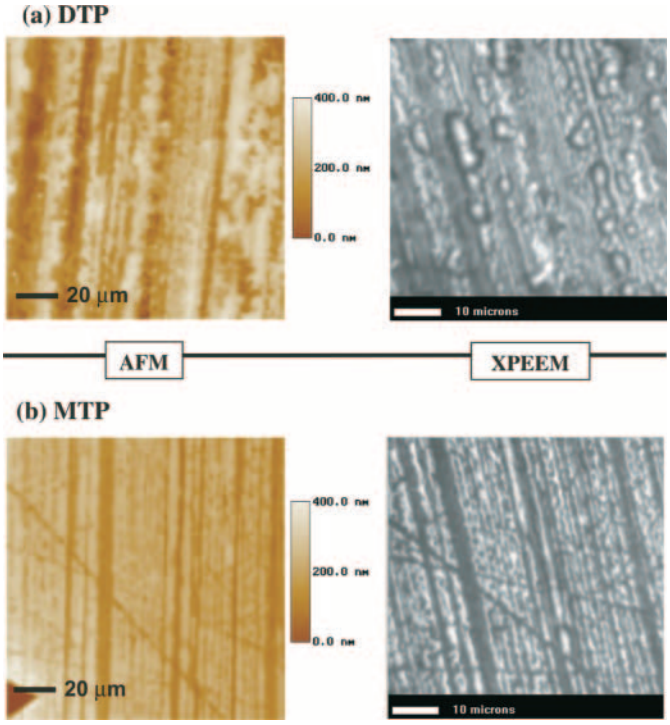
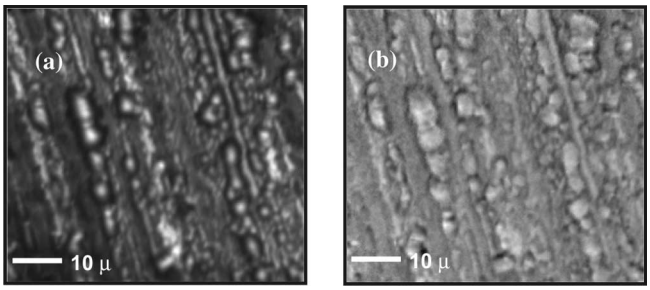


Fig. 13. (a) PEEM image of an area of tribochemical film generated from the DTP additive taken at a photon energy of 137.2 eV. This on-peak image shows topography and chemistry combined. (b) Digital difference of two images, on-peak and off-peak, taken at 137.2 and 133.7 eV, respectively. Since the off-peak image contains only the topographic contribution, the difference image in (b) shows only the chemistry.



at the phosphorus L-edge were taken within the wear scar for the DTP AW film, and can be compared with Fig. 11 that displays the conventional macro XANES spectra. XANES spectra were extracted from several different areas within the respective X-PEEM image and are indicated by the labelled areas. Several regions were analysed to determine notable differences in polyphosphate chain length from pad to pad. Prior work from our group has shown that for phosphorus L-edge XANES spectra, the intensity of peaks a and b relative to peak c correlate very well to polyphosphate chain length i.e., a higher ratio of a/c suggests longer-chain polyphosphates (57) (also see the example in Section A).

© 2007 NRC Canada

Fig. 14. Detailed microchemical analysis of a region within the wear scar of AW film of DTP. (a) PEEM image with labeled areas indicating where local P L-edge XANES spectra were extracted. (b) Corresponding P L-edge XANES spectra.

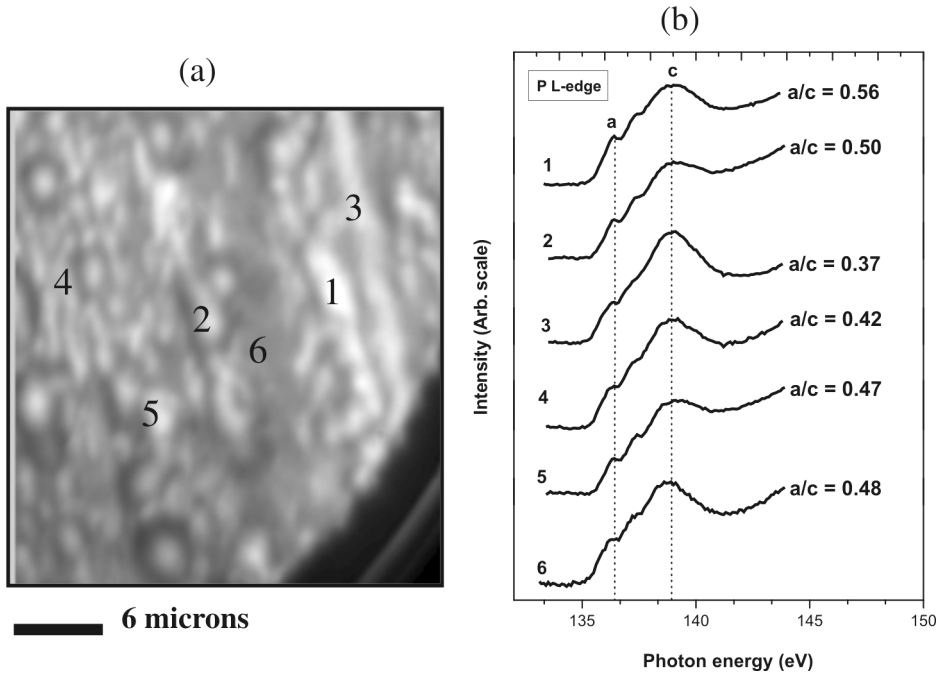
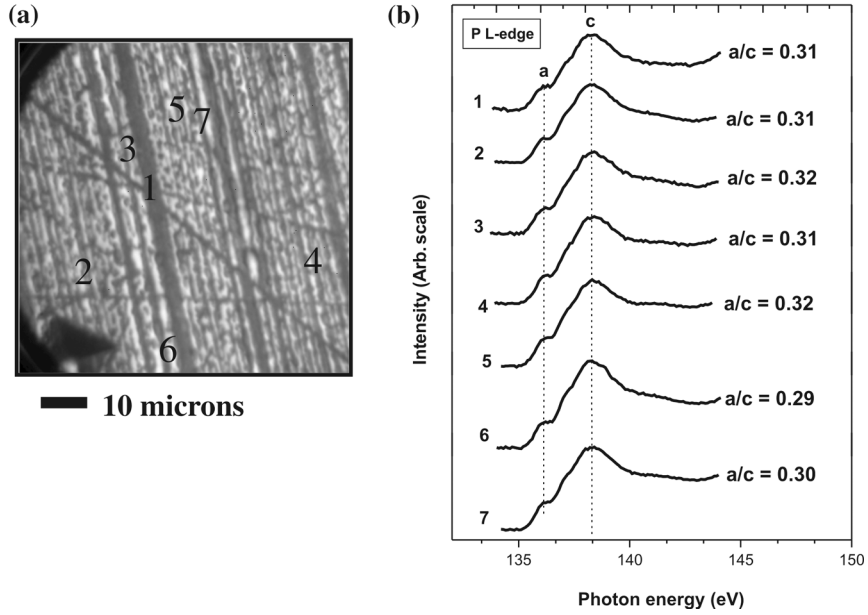


Fig. 15. Detailed microchemical analysis of a region within the wear scar for AW film of MTP. (a) PEEM image with labeled areas indicating where local P L-edge XANES spectra were extracted. (b) Corresponding P L-edge XANES spectra.

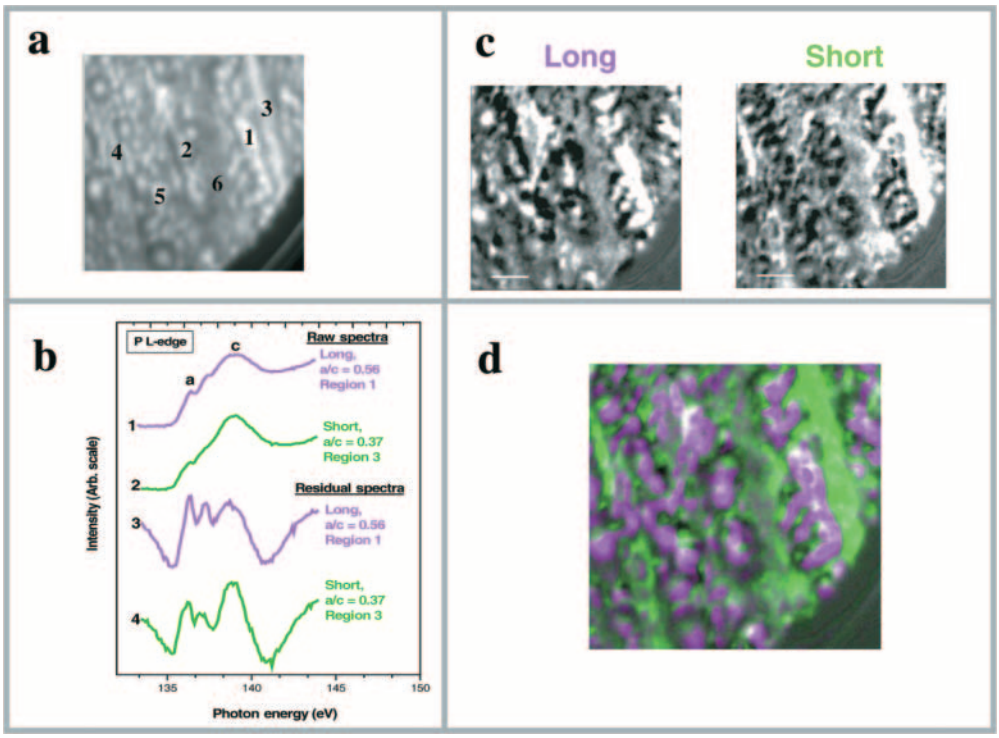


With this in mind, the a/c ratios of the different regions are shown beside the corresponding phosphorus L-edge spectra, 1–6, respectively. Looking at both the local XANES spectra and the corresponding ratios, it is clear that while the different regions do look similar to one another spectrally, there are variations in the microchemical properties of the DTP film, with local areas consisting of varying degrees of polyphosphate chain length.

Focusing on the microchemical properties of the MTP AW film, X-PEEM reveals differences when compared with DTP. The X-PEEM image of the MTP AW film in Fig. 15, along with the corresponding extracted spectra, clearly shows microchemical homogeneity throughout the analysed area of the film (again, these microchemical spectra can be compared with Fig. 11, which displays the conventional macro XANES spectra). Focusing on the a/c ratios, there is little or no change across individual pads. Several different areas were also investigated (not shown) with similar results, thus concluding that the AW pads that are developed during tribofilm formation are predominantly or almost completely

© 2007 NRC Canada

Fig. 16. Example of chemical mapping depicting polyphosphate chain length distribution within an area of AW film generated from DTP. (a) Topographical X-PEEM image displaying selected regions of interest. (b) Spectra 1 and 2 correspond to the raw P L-edge XANES spectra of regions 1 and 3 in (a). Spectra 3 and 4 correspond to residual P L-edge XANES spectra of regions 1 and 3 after a spline background was removed. (c) Derived quantitative chemical maps of the two components used. Spectra 3 and 4 were used as the components to generate the maps. (d) Color-coded composite map displaying polyphosphate chain length distribution. Areas of longer chain polyphosphates are colored in magenta, while green depicts areas of shorter chain polyphosphates.



short-chain polyphosphates. Recalling results obtained from conventional XANES, surprisingly, the polyphosphate chain length between the two AW films was similar (Fig. 11).

The ability to extract local XANES spectra at the submicron level clearly demonstrates the power of X-PEEM and how useful it is in the field of tribology. X-PEEM was able to discriminate between areas of different polyphosphate chain lengths within an AW film for the DTP additive on the basis of intensity ratio of peaks a to c in the phosphorus L-edge. Another advantage of X-PEEM is that the intensity of the peaks observed can also be used as individual components to obtain a chemical distribution map, of varying polyphosphate chain length, from the set of images collected. There are several references in the literature describing the use of quantitative analytical techniques to extract these types of maps from a wide range of materials including polymers and proteins (29, 30, 64). Briefly, a linear regression analysis was applied pixel-by-pixel to the acquired image sequence to derive the component maps. This allows for full spectral variation to be used in deriving the maps. Since the tribofilms studied are not comprised of one pure component but rather a mixture, no quantitative reference standards exist thus making the analysis semiquantitative (80).

Looking at a spatial distribution map of polyphosphate chain length for the DTP AW film in Fig. 16, different regions within the AW film are clearly differentiated visually. To generate the colour-coded map in Fig. 16d, a spline background was removed from the raw phosphorus L-edge XANES spectra, and the spectra depicting areas of both longer- and shorter-chain polyphosphates were used as individual components for the map. The individual components are shown in Fig. 16c. The more intense bright areas reveal concentrated areas of shorter- and longer-chain polyphosphate for each component, respectively. The phosphorus L-edge spectromicroscopy reveals that there are areas of long-chain polyphosphates that are segregated from areas of shorter-chain polyphosphates, and upon closer inspection there are regions where both types coexist (black in Fig. 16d). White regions are where there were difficulties fitting to either spectra (typically because of lack of signal). The consistency of the colour-coded map was evaluated spectroscopically in 19 different areas (data not shown). Here the a/c peak intensity values were extracted from the phosphorus L-edge XANES spectra and tested against the map to determine its validity. It was found that the microchemistry along the various selected areas of interest was in good agreement with the map.

Conclusions

In general, this in-depth analysis of the tribochemical films generated from ashless thiophosphate oil additives clearly demonstrates the powerful capabilities of the X-PEEM technique, a clear extension of the macro XANES information that was originally acquired at the phosphorus L-edge. With X-PEEM, high quality submicron XANES spec-

© 2007 NRC Canada

tra can be obtained with phenomenally high energy and spatial resolution. Coupling the power of this technique with other topographical imaging techniques such as AFM has created an entirely new and exciting way to evaluate tribochemical structure–performance relationships for lubricant additives.

Concluding remarks

Undoubtedly XANES analysis has provided tribologists with a wealth of knowledge over the last 20 years. This brief review illustrates how XANES can probe common elements in additives and provide unique information. The three examples described above take the science from its beginning: macro-scale XANES has provided detailed chemical and structural information on antiwear and tribo films on metallic surfaces with enough illumination that complex and theoretically sound reaction mechanisms could be proposed. The review then reveals the more recent advancements in the field of XANES spectromicroscopy, in which complex surfaces can be imaged with submicron resolution, which enables the user to extract detailed XANES spectra from small discrete features. The last example summarizes the previously described macro- and micro-scale XANES approaches by coupling the methods to provide a complementary and compelling combination to spatially resolve where the tribofilms have formed and to determine their exact chemical make-up.

With this we dedicate our sincere thanks to G.M. Bancroft, a great friend and mentor, for guiding us through our research and ushering us into the forefront of XANES research through its use in tribochemistry at metallic surfaces.

Acknowledgements

The authors would like to personally thank A.P. Hitchcock for his help with aXis2000 and useful discussions about the analysis of the X-PEEM data. The authors would also like to thank K. Tan, A. Jurgensen, and the staff of the Synchrotron Radiation Centre (SRC), University of Wisconsin, Madison, for their technical support. M.A.N. would personally like to thank Heather Bloomfield and Ross Davidson of Surface Science Western, The University of Western Ontario, for acquisition and discussion about the SEM results. We are grateful to the National Science Foundation for supporting the SRC under Award # DMR-0537588. Financial support was provided by General Motors of Canada Ltd. and the Natural Sciences and Engineering Research Council of Canada (NSERC).

References

1. P. Jost. Tribol. Lubr. Technol. **3**, 24 (2006).
2. J.M. Martin, C. Grossiord, K. Varlot, B. Vacher, and J. Igarashi. Tribol. Lett. **8**, 193 (2000).
3. J.A. McGeehan, E.S. Yamaguchi, and J.Q. Adams. SAE Tech. Paper Ser. 852133, 1 (1985).
4. J.C. Bell, K.M. Delargy, and A.M. Seeney. Proc. Leeds–Lyon Symp. Tribol. **21**, 387 (1992).
5. K.J. Bird and G.D. Galvin. Wear, **37**, 143 (1976).
6. H. Spedding and R.C. Watkins. Tribol. Int. **99**, 9 (1982).
7. K. Varlot, J.M. Martin, C. Grossiord, R. Vargiolu, B. Vacher, and K. Inoue. Tribol. Lett. **6**, 181 (1999).
8. C. Grossiord, J.M. Martin, T. Le Mogne, and T. Palermo. Tribol. Lett. **6**, 171 (1999).
9. T.P. Debies and W.G. Johnston. Lubr. Eng. **23**, 289 (1980).
10. S. Jahanmir. J. Tribol. **109**, 577 (1987).
11. M. Kano, Y. Mabuchi, T. Ishikawa, A. Sano, and T. Wakizono. Lubr. Sci. **11**, 365 (1999).
12. P. Kapsa, J.M. Martin, C. Blanc, and J.M. Georges. J. Lubr. Technol. **103**, 486 (1981).
13. J.M. Martin, J.L. Mansot, I. Berbezier, and H. Dexpert. Wear, **93**, 117 (1984).
14. A.F. Alliston-Grenier, J.A. Greenwood, and A. Cameron. IMechE Conf. **178**, 565 (1987).
15. F.T. Barcroft, R.J. Bird, J.F. Hutton, and D. Park. Wear, **77**, 355 (1982).
16. M. Aktary, M.T. McDermott, and J. Torkelson. Wear, **247**, 172 (2001).
17. A. Molina. Lubr. Eng. **30**, 479 (1987).
18. P.A. Willermet, L.R. Mahoney, and C.M. Bishop. Lubr. Eng. **23**, 217 (1979).
19. P.A. Willermet, R.O. Carter III, and E.N. Boulos. Tribol. Int. **25**, 371 (1992).
20. F.M. Piras, A. Rossi, and N.D. Spencer. Tribol. Lett. **15**, 181 (2003).
21. F.G. Rounds. Lubr. Eng. **21**, 91 (1978).
22. J.M. Martin. Tribol. Lett. **6**, 1 (1999).
23. J.M. Martin, M. Belin, J.L. Mansot, H. Dexpert, and P. Lagarde. Lubr. Eng. **29**, 523 (1986).
24. J. Stohr. NEXAFS Spectroscopy. Vol. 25. Springer-Verlag, NY. 1992.
25. D.C. Koningsberger and R. Prins. X-ray absorption: Principles, applications, techniques of EXAFS, SEXAFS, and XANES. Vol 92. John Wiley and Sons, Toronto. 1988.
26. D. Norman. J. Phys. C: Solid State Phys. **19**, 3273 (1986).
27. C. Morin, H. Ikeura-Sekiguchi, T. Tyliszczak, R. Cornelius, J.L. Brash, A.P. Hitchcock, A. Scholl, F. Nolting, G. Appel, D.A. Winesett, K. Kaznacheyev, and H. Ade. J. Electron. Spectrosc. Relat. Phenom. **121**, 203 (2001).
28. L.M. Croll, J.F. Britten, C. Morin, A.P. Hitchcock, and H.D. H. Stoever. J. Synchrotron. Rad. **10**, 265 (2003).
29. C. Jacobsen, S. Wirick, G. Flynn, and C. Zimba. J. Microsc. **197**, 173 (2000).
30. X. Zhang, R. Balhorn, J. Mazrimas, and J. Kirz. J. Struct. Biol. **116**, 335 (1996).
31. H. Ade, A.P. Smith, H. Zhang, G.R. Zhuang, J. Kirz, E.G. Rightor, and A. Hitchcock. J. Electron. Spectrosc. Relat. Phenom. **84**, 53 (1997).
32. M.A. Nicholls, G.M. Bancroft, P.R. Norton, M. Kasrai, G. De Stasio, B.H. Frazer, and L.M. Wiese. Tribol. Lett. **17**, 245 (2004).
33. D.S. Grierson, A.V. Sumant, A.R. Konicek, M. Abrecht, J. Birrell, O. Auciello, J.A. Carlisle, T.W. Scharf, M.T. Dugger, P.U.P.A. Gilbert, and R.W. Carpick. J. Vac. Sci. Technol. A. In press. (2007).
34. A.V. Sumant, P.U.P.A. Gilbert, D.S. Grierson, A.R. Konicek, M. Abrecht, J.E. Butler, T. Feygelson, S.S. Rotter, and R.W. Carpick. Diamond Relat. Mater. In press. (2007).
35. J. Stohr and S. Anders. IBM J. Res. Develop. **44**, 535 (2000).
36. K. Masenelli-Varlot, M. Kasrai, G.M. Bancroft, G. De Stasio, B. Gilbert, E.S. Yamaguchi, and P.R. Ryason. Tribol. Lett. **14**, 157 (2003).
37. U. Wallfahrer and L. Bowen. Lubr. Eng. **53**, 23 (1997).

© 2007 NRC Canada

38. G.M. Bancroft, M. Kasrai, M. Fuller, Z. Yin, K. Fyfe, and K.H. Tan. Tribol. Lett. **3**, 47 (1997).
39. M.L. Suominen Fuller, L.R. Fernandez, G.R. Massoumi, W.N. Lennard, and M. Kasrai. Tribol. Lett. **8**, 187 (2000).
40. M. Kasrai, Z. Yin, G.M. Bancroft, and K. Tan. J. Vac. Sci. Technol. A, **11**, 2694 (1993).
41. M. Kasrai, W.N. Lennard, R.W. Brunner, G.M. Bancroft, J.A. Bardwell, and K.H. Tan. Appl. Surf. Sci. **99**, 303 (1996).
42. B.H. Frazer, M. Girasole, L.M. Wiese, T. Franz, and G. De Stasio. Ultramicroscopy, **99**, 87 (2003).
43. B.H. Frazer, B. Gilbert, B.R. Sonderegger, and G. De Stasio. Surf. Sci. **537**, 161 (2003).
44. M.A. Nicholls, P.R. Norton, G.M. Bancroft, M. Kasrai, T. Do, B.H. Frazer, and G. De Stasio. Tribol. Lett. **17**, 205 (2004).
45. A.P. Hitchcock, P. Hitchcock, C. Jacobsen, C. Zimba, B. Loo, E. Rotenberg, J. Denlinger, and R. Kneedler. aXis2000 [computer program]. Available from http://unicorn.mcmaster.ca/aXis2000.html. 1997.
46. M.A. Nicholls, T. Do, P.R. Norton, G.M. Bancroft, M. Kasrai, T.W. Capehart, Y.-T. Cheng, and T. Perry. Tribol. Lett. **15**, 241 (2003).
47. Z. Yin, M. Kasrai, G.M. Bancroft, K.F. Laycock, and K.H. Tan. Tribol. Int. **26**, 383 (1993).
48. R. Sarin, A.K. Gupta, D.K. Tuli, A.S. Verma, M.M. Rai, and A.K. Bhatnagar. Tribol. Int. **26**, 389 (1993).
49. M.N. Najman, M. Kasrai, and G.M. Bancroft. Tribol. Lett. **17**, 217 (2004).
50. Z. Yin, M. Kasrai, M. Fuller, G.M. Bancroft, K. Fyfe, M.L. Colaianni, and K.H. Tan. Wear, **202**, 192 (1997).
51. Z. Yin, M. Kasrai, M. Fuller, G.M. Bancroft, K. Fyfe, and K.H. Tan. Wear, **202**, 172 (1997).
52. M. Fuller, Z. Yin, M. Kasrai, G.M. Bancroft, E.S. Yamaguchi, P.R. Ryason, P.A. Willermet, and K.H. Tan. Tribol. Int. **30**, 305 (1997).
53. M.L. Suominen Fuller, M. Kasrai, G.M. Bancroft, K. Fyfe, and K.H. Tan. Tribol. Int. **31**, 627 (1998).
54. M.L. Suominen Fuller, M. Kasrai, and G.M. Bancroft. Chemical applications of synchrotron radiation. Vol 12B. World Scientific, NJ. 2002. p. 1091.
55. M.N. Najman. Ph.D. thesis. Chemical interactions of metal-free oil additives with 52100 steel. Department of Chemistry. The Universtiy of Western Ontario, London, Ont., Canada, 2003.
56. Z. Zhang, E. Yamaguchi, M. Kasrai, and G.M. Bancroft. Tribol. Lett. **19**, 211 (2005).
57. Z. Yin, M. Kasrai, G.M. Bancroft, K.H. Tan, and X. Feng. Phys. Rev. B, **51**, 742 (1995).
58. Z. Zhang, M. Kasrai, G.M. Bancroft, and E.S. Yamaguchi. Tribol. Lett. **15**, 377 (2003).
59. E.S. Yamaguchi, Z. Zhang, M. Kasrai, and G.M. Bancroft. Tribol. Lett. **15**, 385 (2003).
60. J.M. Martin, C. Grossiord, T. Le Mogne, S. Bec, and A. Tonck. Tribol. Int. **34**, 523 (2001).
61. C. Minfray, J.M. Martin, C. Esnouf, T. Le Mogne, R. Kersting, and B. Hagenhoff. Thin Solid Films, **447/448**, 272 (2004).
62. D.D. Wagman, W.H. Evans, V.B. Parker, R.H. Schumm, I. Halow, S.M. Bailey, K.L. Churney, and R.L. Nuttall. Journal of physical and chemical reference data. Vol 11. The American Chemical Society and the American Institute of Physics for the National Bureau of Standards, Washington, DC. 1982.
63. D.E.C. Corbridge. Structural chemistry of phosphorus. Elsevier, NY. 1974.
64. I.N. Koprinarov, A.P. Hitchcock, C.T. McCrory, and R.F. Childs. J. Phys. Chem. B, **106**, 5358 (2002).
65. M. Kawamura and K. Fujita. Wear, **89**, 99 (1983).
66. T. Konishi, E.E. Klaus, and J.L. Duda. Tribol. Trans. **39**, 811 (1996).
67. Y. Wan, L.L. Cao, and Q.J. Xue. Tribol. Int. **30**, 767 (1997).
68. M. Fuller, M. Kasrai, J.S. Sheasby, G.M. Bancroft, K. Fyfe, and K.H. Tan. Tribol. Lett. **1**, 367 (1995).
69. M.A. Nicholls, P.R. Norton, G.M. Bancroft, and M. Kasrai. Wear, **257**, 311 (2004).
70. M.A. Nicholls, P.R. Norton, G.M. Bancorft, M. Kasrai, G. De Stasio, K.S.-I. Nicholls, and L.M. Wiese. Tribol. Lett. **18**, 261 (2005).
71. A.J. Pidduck and G.C. Smith. Wear, **212**, 254 (1997).
72. O.L. Warren, J.F. Graham, P.R. Norton, J.E. Houston, and T.A. Michalske. Tribol. Lett. **4**, 189 (1998).
73. S. Bec, A. Tonck, J.M. Georges, R.C. Coy, J.C. Bell, and G. Roper. Proc. R. Soc. London, Ser. A, **455**, 4181 (1999).
74. G.W. Canning, M.L. Fuller, G.M. Bancroft, M. Kasrai, J.N. Cutler, G. De Stasio, and B. Gilbert. Tribol. Lett. **6**, 159 (1999).
75. M. Kasrai, M. Fuller, M. Scaini, Z. Yin, R.W. Brunner, G.M. Bancroft, M.E. Fleet, K. Fyfe, and K.H. Tan. Lubricants and lubrication: Lubrication at the frontier. Vol 30. Elsevier Science B.V., Amsterdam. The Netherlands. 1995. p. 659.
76. K.K. Swami, S. Prakesh, P.K. Mondal, K.C. Dohhen, R. Sarin, D.K. Tuli, and A.K. Bhatnagar. Lubr. Sci. **14**, 385 (2002).
77. M.N. Najman, M. Kasrai, G.M. Bancroft, and A. Miller. Tribol. Lett. **13**, 209 (2002).
78. M.N. Najman, M. Kasrai, and G.M. Bancroft. Tribol. Lett. **14**, 225 (2003).
79. M.N. Najman, M. Kasrai, G.M. Bancroft, B.H. Frazer, and G. De Stasio. Tribol. Lett. **17**, 811 (2004).
80. A.P. Hitchcock, I. Koprinarov, K. Pecher, and E.M. Kneedler. Manuscript in preparation.

© 2007 NRC Canada

Comparison of the distributions of bromine, lead, and zinc in tooth and bone from an ancient Peruvian burial site by X-ray fluorescence[1]

Ronald R. Martin, Steven J. Naftel, Andrew J. Nelson, and William D. Sapp III

Abstract: Synchrotron micro X-ray fluorescence was used to study the distribution of selected trace elements (Zn, Pb, and Br) in tooth and bone samples obtained from an individual from a pre-Columbian archaeological site (Cabur) located on the north coast of Peru. The results show that Zn, Pb, and Br are present in both the teeth and bone samples and that the Zn and Pb seem to be confined to similar regions (cementum and periostium), while Br shows a novel distribution with enrichment close to the Haversian canals and (or) in regions that appear to be Ca deficient.

Key words: teeth, bone, metals, XRF, Br, Zn, and Pb.

Résumé : On a fait appel à la fluorescence de micro rayons X (FRX) à synchrotron pour étudier la distribution d'éléments choisis (Zn, Pb et Br) qui sont présents à l'état de trace dans des échantillons de dents et d'os obtenus à partir des restes d'un individu retrouvé sur un site archéologique précolombien (Cabur) situé sur la côte Nord du Pérou. Les résultats montrent que le Zn, le Pb et le Br sont présents dans les échantillons d'os ainsi que de dents et que le Zn et le Pb semblent confiner dans des régions similaires (cementum et periostium) alors que le Br présente une distribution nouvelle comportant un enrichissement aux abords des canaux haversiens et/ou dans les régions qui apparaissent comme déficientes en calcium.

Mots-clés : dent, os, métaux, FRX, Br, Zn, Pb.

[Traduit par la Rédaction]

Introduction

Human teeth and bone constitute significant reservoirs of trace elements that are potentially indicative of diet, disease, and (or) environmental exposure (1). Bone is a complex tissue, approximately 35% organic (mainly collagen), while the remainder is mineral, principally bioapatite. The outer portion of most bone is dense and is termed compact bone. The structure of compact bone is formed around the cylindrical shaped osteons, or Haversian systems, oriented parallel to the long axis of the bone. The Haversian systems are the sites where remodeling of the bone occurs. Bone density decreases toward the center to yield spongy or trabecular bone (2). The outer surface of bone is covered by a fibrous membrane called the periostium. This term is also used to indicate the outside surface of the bone itself, while the term endostium indicates the center of the bone.

As noted in the preceding, bone is actively remodeled so that the turnover time for any metal deposited in bone represents a confounding factor in the interpretation of bone metal content. In addition, turnover is dependent on bone type. Lead (Pb^{2+}), thought to substitute for Ca^{2+} in calcium carbonate and hydroxyapatite in the mineralized component of bone and teeth (3), has a turnover rate estimated at 1% per year in cortical bone and 8% per year in trabecular bone (4).

Teeth are more robust than bone and are generally well preserved. However, tooth structure is such that the individual component tissues (enamel, dentine, cementum) of teeth have unique potentials as metal reservoirs. Enamel, the hardest structure in the human body, constitutes the tooth crown and is generally believed to be free of remodeling effects and is resistant to diagenesis. Naturally, much analytical effort has been directed at the enamel.

In mammals (and hence humans) there are two sets of dentition, which form at different times in an individual's life. Deciduous teeth begin formation within 14–19 weeks of fertilization and enamel mineralization is complete shortly after birth (5, 6). Thus, analysis of the metal content of deciduous enamel reveals details of a brief period in an individual's life. The permanent dentition is formed from early childhood to approximately 16 years of age. Therefore, analysis of the enamel of permanent teeth reveals details of a much longer period during an individual's development. The

Received 29 March 2007. Accepted 1 August 2007. Published on the NRC Research Press Web site at canjchem.nrc.ca on 6 September 2007.

R.R. Martin, S.J. Naftel.[2] Department of Chemistry, University of Western Ontario, London, ON N6A 5B7, Canada.
A.J. Nelson. Department of Anthropology, University of Western Ontario, London, ON N6A 5B7, Canada.
W.D. Sapp III. Cotsen Institute of Archaeology, UCLA, Los Angeles, CA 90024, USA.

[1]This article is part of a Special Issue dedicated to Professor G. Michael Bancroft.

[2]Corresponding author (e-mail: snaftel@uwo.ca).

 doi:10.1139/V07-100 © 2007 NRC Canada

permanent dentition enamel is often thought to preserve ingested lead (7).

Budd et al. (8) have used laser ablation inductively coupled plasma mass spectrometry (La_ICP/MS) and isotope dilution thermal ionization mass spectrometry (ID/TIMS) to study Pb distributions in cross-sections from ancient and modern teeth. Their results show enhanced Pb content in the outer 30 μm of the enamel. This effect is attributed to exposure to the oral cavity. They also showed the dentine to be enriched in Pb and concluded that enamel was indicative of metal exposure during crown formation if the outer layer was removed before analysis.

Cementum is a connective tissue that surrounds the tooth root in incremental, mineralized layers (9). These layers exhibit a seasonal growth pattern and potentially represent a chronological record of metal exposure throughout an individual's life; for this reason, the cementum is an especially promising tissue for trace metal analysis. Individual cementum ring structures vary in width depending on age, species, and location on the tooth root. In humans, the cementum is of the order of a few hundred micrometres across, with individual rings varying from about 5–20 μm in width (10).

Given the variation in metal content in different components of bones and teeth, meaningful analysis is ideally carried out using techniques that examine small regions (of the order of micrometres) with low detection limits so that the spatial distributions within each component might be resolved. Techniques that have been used include secondary ion mass spectroscopy (SIMS) (11), proton induced X-ray emission (PIXE) (12), and laser ablation inductively coupled plasma mass spectroscopy (La_ICP/MS) (8).

Perhaps the most promising technique for studying metal distributions in teeth and bone is provided by synchrotron radiation analysis (SRA) (13). In SRA, electrons circulating in a central accelerator ring (synchrotron) at relativistic velocities are used to generate electromagnetic radiation at wavelengths from the visible to high energy X-rays at intensities exceeding conventional sources by as much as eight orders of magnitude. In micro-SRA the X-rays produced by the synchrotron may be focused to a spot of the order of 1 μm × 1 μm, inducing element-specific X-ray fluorescence from the metals in a sample with detection limits in the ppb range. Analysis can be carried out under ambient conditions, avoiding artifacts introduced by high vacuum techniques, and, in principle at least, SRA is nondestructive. In addition, synchrotron X-ray microspectroscopy can provide chemical information including oxidation state, coordination number, bond length, X-ray diffraction information, and possible identification of nearest neighbor atoms using X-ray absorption near edge spectra (XANES) and extended X-ray absorption fine structure (EXAFS). Not surprisingly, SRA is widely applied to the study of the chemistry and structure of teeth and bone (14–23).

We have used synchrotron induced X-ray fluorescence to study the trace element distribution in the cementum rings of human teeth (24) showing Zn enrichment in this region, as well as variation in metal content across the ring system. Since diagenesis represents a significant confounding factor in the interpretation of metal distribution in teeth (25), we have also used the element distribution in the cementum ring system to establish criteria for distinguishing between endogenous (derived internally) and exogenous (derived externally) metals (26).

This study focused on four elements. Calcium was used as the best indicator of mineralization within the teeth. Zinc is present in the oral cavity (27), plays an important role in the formation of dental calculus (28), inhibits formation of hydroxyapatite (29), and is readily incorporated in calcium triphosphate (30), one of the mineral components of teeth. In addition, it is sufficiently enriched in the cementum that its X-ray fluorescence can be used to identify the cementum region (24, 26). Lead has been widely studied in anthropology (31), and it is possible that lead originated from pre-Columbian ore smelting (32). Finally, bromine, when present, is indicative of a marine diet (16).

The objectives of this preliminary study of the Cabur sample was limited to determining (*i*) if the X-ray fluorescence from both teeth and bone contained all four elements in the study, (*ii*) what similarities existed between the metal distributions in the teeth and bone, and (*iii*) what inferences might be drawn from the results.

Archaeological context

In this study we examine material from the Cabur site in northern Peru. This site is located in the Jequetepeque Valley on the north coast of Peru. It is the palace of a local lord that was constructed in about 1150 A.D. and was abandoned in 1532 A.D. The site documents the continuity of local power through three cultural phases, including the Chimu and Inka imperial occupations of the Jequetepeque Valley. Three burials, dating to the Chimu period (ca. 1400 A.D.), were excavated from the central part of the site. These burials were of young children who were buried at the same time and were probably sacrificed (33). One tooth and one rib section were selected from one of these individuals (B12-U1-E2). The tooth section was analyzed at both the Advanced Photon Source (APS) and the National Synchrotron Light Source (NSLS), while the bone section was only analyzed at NSLS. The tooth was a lower right first permanent molar, and the sex was undetermined (because of its young age), however a dental eruption age of approximately 12.2 years could be estimated using standard methods (34), while the suggested age from an analysis of the cementum annulations (35) was 15.2 years. Thus, a range of 10–15 years is a reasonable estimate for the age of this individual.

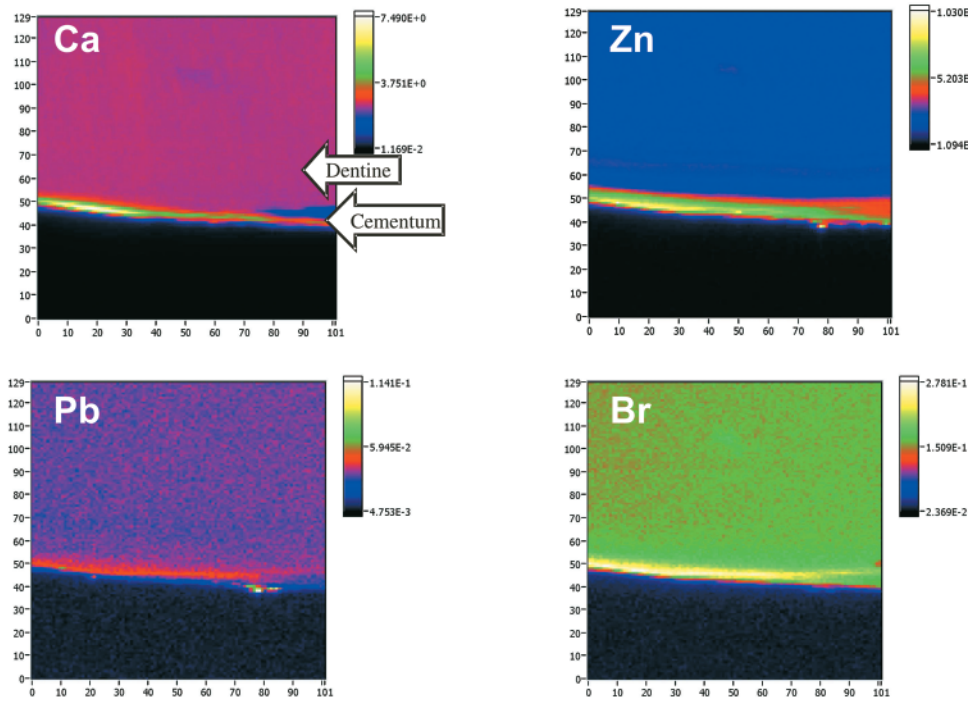
The goal, from the archaeological perspective, was to add information to the osteobiography being constructed for this individual. In this case the information consists of the history of their exposure to trace elements in their diet and environment. When placed in the full osteobiographic and archaeological context, this information has potential implications for our understanding of the organization of craft production, distribution of resources, dietary choices, and population movements among the pre-Columbian Peruvian population.

Experimental

The tooth and rib selected for this experiment were embedded in resin and sectioned with a low speed diamond saw, followed by polishing with diamond grit using isopropanol as lubricant. The final thickness of the samples

© 2007 NRC Canada

Fig. 1. Micro X-ray fluorescence elemental maps of the tooth cross-section obtained at PNC/XOR. The cementum and dentine are indicated. The *x*–*y* scale represents pixel numbers, and the actual image size is 500 μm × 640 μm. The colour scale refers to the XRF intensity normalized to I_0 in total counts/I_0.



was between 50 and 100 μm. The embedded samples were mounted in such a way that no other material was present in the X-ray beam during measurements. The approximate concentrations of the elements of interest (~10 ppm) are too low to cause self-absorption effects in these samples.

Micro X-ray fluorescence maps were collected at the PNC/XOR (Pacific Northwest Consortium – Collaborative Access Team) facility (36), beamline 20-ID-B, located at the APS, Argonne National Laboratory and at beamline X27A (37) located at the NSLS, Brookhaven National Laboratory.

At APS, the incident X-ray energy was selected at 16 200 eV using a Si(111) monochromator, and a pair of Kirkpatrick–Baez mirrors focused the beam to 5 μm × 5 μm. This beam struck the sample at an angle of 45° relative to the sample surface. Emitted fluorescence X-rays were monitored using a 13 element Ge detector placed at 90° relative to the incident X-rays to minimize interference from scattered X-rays. The sample was scanned in 5 μm steps for Ca Kα, Zn Kα, Br Kα, and Pb L emission lines simultaneously. Both the Pb Lα and Pb Lβ lines were monitored, as the As K α line overlaps the lead Lα line but not the Pb Lβ line. The signal was only attributed to Pb if both Lα and Lβ patterns were identical.

At NSLS, the experimental geometry was identical. The incident X-rays were selected at 15 000 eV using a Si(111) monochromator, and focused to 6 μm vertically × 20 μm horizontally. Emitted fluorescence X-rays were monitored using a 13 element Ge detector, which collected Ca Kα, Zn Kα, Br Kα, and Pb L simultaneously.

Results and discussion

Figure 1 shows the tooth distributions of Ca, Zn, Pb, and Br obtained using the APS 20-ID beamline. The images obtained for Ca and Zn are consistent with our observations of other teeth (24, 26). Lead is present in the dentine and enriched in the cementum. In addition, there is a single highly enriched lead inclusion at the surface of the tooth. It is difficult to interpret the lead signal unambiguously. The presence of lead in the dentine and in a narrow band in the cementum might be taken as evidence for lead ingestion, but without clear evidence of banding in the cementum (26) this assignment is uncertain. The local enrichment at the tooth surface might well represent soil lead or metals introduced at burial. However, reports of lead artifacts are very rare in the Andean archaeological record. One galena spindle whorl has been reported for the site of Pampa Grande (38) and isolated artifacts have been reported from the sites of Tucumé (Narvaez, personal communication) and Puruchuco (Cock, personal communication).

Bromine is enriched in the cementum and present within the dentine. This result is consistent with a marine diet. Naturally any analysis showing enriched bromine at the burial site would challenge this interpretation.

Figure 2 shows the results obtained at the National Synchrotron Light Source, beamline X27A. Note that this beamline has a lower photon flux (36, 37) and larger spot size than the APS 20-ID beamline, and that the images were obtained from a different area. The results are an excellent match with those obtained at APS with the exception that the width of the cementum system varies somewhat across the image (this is not a surprising result as cementum thickness varies with location on the tooth), and there is evidence of banding in the calcium and zinc images.

Lead is indicated in the cementum and dentine; as well, there is some local enrichment at the surface. The scale bar

© 2007 NRC Canada

Fig. 2. Micro X-ray fluorescence elemental maps of the tooth cross-section taken on X27A. The cementum and dentine are indicated. The colour scale refers to the XRF intensity normalized to I_0 in total counts/I_0.

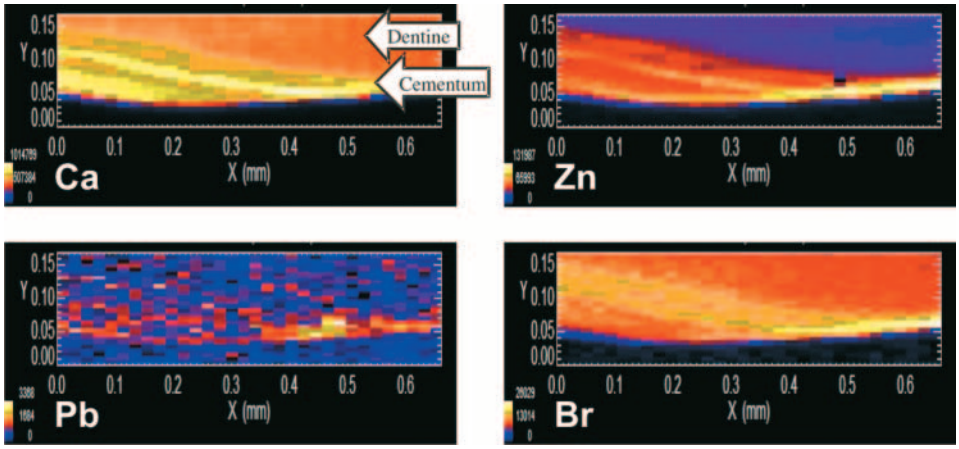
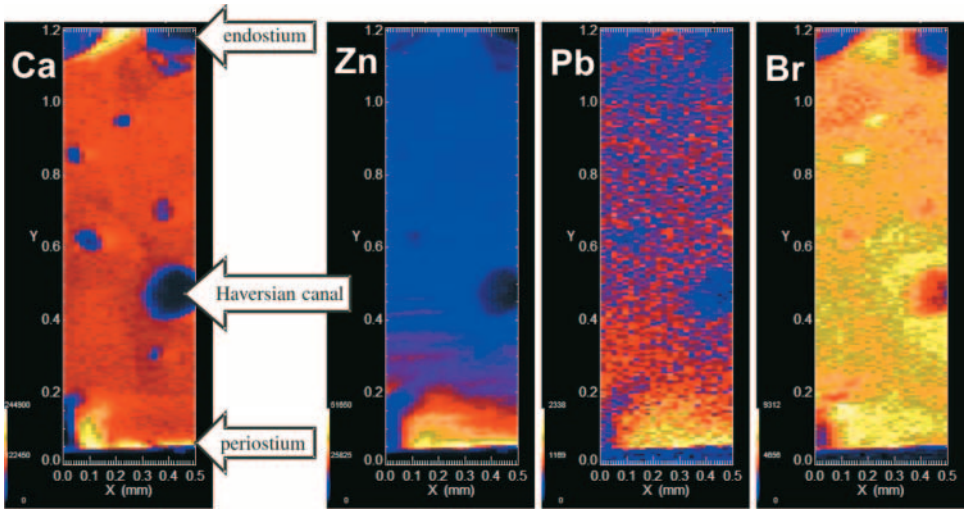


Fig. 3. Micro X-ray fluorescence elemental maps of the rib cross-section. The periostium, endostium, and a Haversian canal are indicated. The colour scale refers to the XRF intensity normalized to I_0 in total counts/I_0.



(see Fig. 2) suggests a 10-fold increase in the cementum relative to the dentine.

Bromine shows evidence for banding in the cementum; however, the interpretation of the results is virtually the same as for the previous area. Taken together, these similar results from different areas of the same tooth, obtained on synchrotron micro-beams with different spot sizes and photon fluxes, increases our confidence in the results.

Interpretation of the tooth data is rendered more difficult because of the young age of the individual. The youth of the individual means that the cementum region will be narrow and pronounced repeated banding would be unlikely.

Figure 3 shows the images obtained from the rib cross-section. The calcium image shows the mineralized portion of the bone with notable enrichment in the periostium, an observation consistent with the known distribution of bone density. There is also some enrichment in the endostium. The areas where calcium is absent are indicative of the Haversian canal systems through which blood vessels and nerves ramify in cortical bone, as well as representing regions where osteons are active. Haversian canals are not permanent at any site so that their distribution changes with time, older canals become mineralized while new ones develop in the process of remodeling. The widths of Haversian canals are indicative of an individual's age (39).

Zinc is enriched in the periostium. Lead is present in the periostium and the cortex. While diagenesis cannot be ruled out as an explanation for this pattern, when combined with the suggestive tooth data the argument for endogenous lead is strengthened. The lead distribution in the periostium is in general agreement with early lead–bone studies using synchrotron radiation (40).

Bromine reveals a complex pattern. It should be noted that bromine is enriched in both the periostium and endostium, where it exhibits the same pattern as calcium. There is also pronounced enrichment around the largest of the Haversian canals and around two of the remaining canals (y = ~0.9). The image appears to place Br within the canal. This is an experimental artifact resulting from the difference between the X-ray escape depths of Br Kα X-rays relative to Ca Kα X-rays (~0.4 mm and ~0.03 mm, respectively). As a result, the Br image is displaced and broadened relative to the Ca image (24). There is little or no bromine deposition near two of the remaining canals (y = ~0.6 and ~0.3). This distribu-

© 2007 NRC Canada

tion may have resulted if no bromine was present when the two bromine-free canals were active; if so, it may be possible to extract endogenous bromine chronologies (dietary shifts) from distribution patterns. This observation fits well with ongoing research on other samples from the Jequetepeque Valley that is using carbon, nitrogen and oxygen isotope analysis to examine patterns of mobility in pre-Columbian times (41).

In general, the results are similar to previous synchrotron microanalysis of bone (40).

Conclusions

Although carried out in different regions and on different beamlines, the depositional patterns in the tooth cross-sections are similar, exhibiting patterns for the individual elements observed in other samples. The distributions within the matching rib sample confirm the presence of all four elements in the bony skeleton.

The widely dispersed bromine signal in both tooth and bone may be ascribed with high confidence to a marine diet. Bromine exhibits a distribution pattern within the bone that suggests an intimate relationship with the Haversian canal system; this may be tentatively assigned to the depositional chronology of the element, which may indicate a significant dietary shift in the individual's lifetime.

Only one individual has been studied because of the difficulties encountered in obtaining well-documented samples from several individuals spread over several sites in Peru. Broad conclusions regarding the entire local population are not warranted at this time. Future work will include quantitative analysis of a significant number of individuals.

The lead signal may be indicative of widespread smelting using lead ores and coincident in time with the Cabur burials. The evidence that the lead is endogenous is strong, but in the absence of extensive banding in the cementum system must be tentative. Given the rarity of lead artifacts in the archaeological record, it is likely that any exposure to lead was the product of the pre-Columbian smelting of lead-bearing galena ore for silver. The deposition of lead in highland lake sediments during the Tiwanaku period has documented the ability of smelting products to spread over a wide area (32). No smelting site has yet been identified in the area of Cabur, but several other sites have been identified on the Peruvian north coast where smelting and (or) metal working took place (42, 43).

The enrichment of zinc in the cementum and in the outer layers of compact bone suggest that zinc may play a role in both tooth and bone mineralization.

The specific roles and (or) origins of the lead, zinc, and bromine will be the subject of future research using matched standards to quantify these species. Efforts will be undertaken to resolve their chemistry using XANES and EXAFS with model compounds.

Acknowledgements

PNC/XOR facilities at the Advanced Photon Source and research at these facilities are supported by the US Department of Energy – Basic Energy Sciences, a major facilities access grant from Natural Sciences and Engineering Research Council of Canada (NSERC), the University of Washington, Simon Fraser University, the Pacific Northwest National Laboratory, and the Advanced Photon Source. Use of the Advanced Photon Source is also supported by the US Department of Energy, Office of Science, Office of Basic Energy Sciences, under Contract DE-AC02–06CH11357.

Brookhaven National Laboratory and the research conducted at its facilities (X27A at the National Synchrotron Light Source) is supported by the US. Department of Energy, Division of Materials Sciences and Division of Chemical Sciences, under Contract No. DE-AC02–98CH10886.

The Social Sciences and Humanities Research Council of Canada provided funding for the fieldwork portion of this research. We acknowledge the assistance of the Instituto Nacional de Cultura of Peru.

References

1. M.L. Carvalho, C. Casaca, T. Pinheiro, J.P. Marques, P. Chevallier, and A.S. Cunha. Nucl. Instrum. Methods Phys. Res., Sect. B, **168**, 559 (2000).
2. K.R. Burns. Forensic anthropology training manual. Prentice Hall, Upper Saddle River, NJ. 1999.
3. P. Brätter, D. Garvlick, J. Lausch, and U. Risick. J. Radioanal. Nucl. Chem. **37**, 393 (1977).
4. B.L. Gulson and B. R. Gillings. Environ. Health Perspect. **105**, 820 (1997).
5. B.S. Kraus. J. Am. Dent. Assoc. **74**, 1128 (1969).
6. B.L. Gulson. Environ. Health Perspect. **104**, 306 (1996).
7. I.M. Shapiro, H.L. Needleman, and O.C. Tuneay. Environ. Res. **5**, 467 (1972).
8. P. Budd, J. Montgomery, A. Cox, P. Krause, B. Barreiro, and R.G. Thomas. Sci. Total Environ. **220**, 121 (1998).
9. D.E. Lieberman. J. Archaeol. Sci. **21**, 525 (1994).
10. S. Hillson. Dental anthropology. Cambridge University Press, Cambridge, UK. 1996.
11. T. Lindgern, L.G. Persson, E.U. Engström, J. Chabala, R. Levi-Setti, and J. G. Norén. Arch. Oral Biol. **43**, 841 (1998).
12. T. Molleson. *In* Trace elements in environmental history. Proceedings Symposium, June 1987 Göttingen 1987. *Edited by* G. Grupe and B. Herrmann. Springer-Verlag, Berlin, Germany. 1987.
13. Chemical applications of synchrotron radiation, advanced series in physical chemistry. Vol. 12A. *Edited by* Tsun-Kong Sham. World Scientific, Singapore. 2002.
14. K.W. Jones, W.J. Berry, D.J. Borsay, H.T. Cline, W.C. Conner Jr., and C. S. Fullmer. X-Ray Spectrom. **26**, 350 (1997).
15. M.L. Carvallo, T. Pinheiro, M.A. Barreiros, C. Casaca, A.S. Cunha, and P. Chevallier. Nucl. Instrum. Methods Phys. Res., Sect. B, **136–138**, 913 (1998).
16. M.A. Barreiros, A.S. Cunha, and P. Chevallier. Nucl. Instrum. Methods Phys. Res., Sect. B, **158**, 393 (1999).
17. M.L. Carvallo, C. Casaca, T. Pinheiro, J.P. Marques, P. Chevallier, and A.S. Cunha.Nucl. Instrum. Methods Phys. Res., Sect. B, **168**, 559 (2000).
18. S. Blau. J. Archaeol. Sci. **29**, 811 (2002).
19. M.L. Carvallo, C. Casaca, J.P. Marques, T. Pinheiro, and A.S. Cunha. X-Ray Spectrom. **30**, 190 (2001).
20. M.L. Carvallo, J.P. Marques, A.F. Marques, and C. Casaca. X-Ray Spectrom. **33**, 55 (2004).
21. A. Ide-Ektessabi, K. Shirasawa, A. Koizumi, and M. Azechi. Nucl. Instrum. Methods Phys. Res., Sect. B, **213**, 761 (2004).

© 2007 NRC Canada

22. K. Shirasawa, A. Ide-Ektessabi, A. Koizumi, M. Azechi, and S. Sie. J. Electron. Spectrosc. Relat. Phenom. **137–140**, 827 (2004).
23. M.J. Anjos, R.C. Barroso, C.A. Pérez, D. Braz, S. Moreira, K.R.H.C. Dias, and R.T. Lopes. Nucl. Instrum. Methods Phys. Res., Sect. B, **213**, 569 (2004).
24. R.R. Martin, S.J. Naftel, A.J. Nelson, A.B. Feilen, and A. Narvaez. J. Environ. Monit. **6,** 783 (2004).
25. M.J. Kohn, M.J. Schoeninger, and W.W. Barker. Geochim. Cosmochim. Acta, **63**, 2737 (1999).
26. R.R. Martin, S.J. Naftel, A.J. Nelson, A.B. Feilen, and A. Narvaez. J. Archaeol. Sci. **34**, 936 (2007).
27. N.K.A. Bakar, D.M. Taylor, and D.R. Williams. Chem. Speciation and Bioavailability, **11**, 95 (1999).
28. R.A. Barrea, C.A. Pérez, and A.Y. Ramos. J. Synchrotron Rad. **8**, 990 (2001).
29. A. Bigi, E. Foresti, M. Gandolfi, M. Gazzano and N. Roveri. J. Inorg. Biochem. **58**, 49 (1995).
30. A. Bigi, E. Foresti, M. Gandolfi, M. Gazzano, and N. Roveri. J. Inorg. Biochem. **66**, 259 (1997).
31. A.C. Aufderheide, L.E.Wittmers, Jr., G. Rapp, Jr., and J. Wallgren. American Anthropologist, New Series, **90**, 931 (1988).
32. M.B. Abbott and A.P. Wolfe. Science, **301**, 1893 (2003).
33. W.D. Sapp, III. The impact of imperial conquest at the palace of a local lord in the Jequetepeque valley, Northern Peru. Ph.D. Thesis. Department of Anthropology, The University of California, Los Angeles. 2002.
34. A.R. Ten Cate. Oral histology: development, structure and function. 4th ed. CV Mosby, St. Louis, MO. 1998.
35. A. Feilen. Reading between the lines: a cementum ring analysis on pre-Hispanic mummies from Peru. Diploma Thesis. Department of Biology, Ludwig-Maximilians-Universität, Munich, Germany. 2004.
36. More information is available from www.pnc.aps.anl.gov.
37. More information is available from http://www.nsls.bnl.gov/beamlines/beamline.asp?blid=X27A
38. I. Shimada. Pampa Grande and the Mochica culture. The University of Texas Press, Austin, TX. 1994.
39. H. Cho and S.D. Stout. *In* Bone loss and osteoporosis: an anthropological perspective. *Edited by* S.C. Agarwal and S.D. Stout. Kluwer Academic/Plenum Publishers, NY. 2003. pp. 207–228.
40. K.W. Jones, G. Schidlovsky, D.E. Burger, F.L. Mider, and H. Hu. *In* Advances In vivo body composition studies. *Edited by* S. Yamsumura and J.E. Harrison. Plenum Press, NY. 1990. pp. 281–286.
41. C.D. White, A.J. Nelson, and F.J. Longstaffe. Long- and short-term dietary change as indicated by isotopic analysis of tissues from Pacatnamu, Peru. Paper presented to the VI World Congress on Mummy Studies, Lanzarote, Spain. 23 February 2007.
42. S.M. Epstein. Cultural choice and technological consequences: constraint of innovation in the Late Prehistoric copper smelting industry of Cerro Huaringa, Peru. Ph.D. Thesis. Department of Anthropology, University of Pennsylvania, Pittsburg, PA. 1993.
43. A. Bezúr. Variability in Sicán copper alloy artifacts: its relation to material flow patterns during the Middel Sicán period in Peru, AD 900–1100. Ph.D. Thesis. Department of Materials Science and Engineering, The University of Arizona, Tucson, AZ. 2003.

© 2007 NRC Canada

Theoretical X-ray absorption investigation of the uniaxial compression of hexagonal graphite[1]

Dawn M. Shaw, Michael Odelius, and John S. Tse

Abstract: The X-ray absorption (XAS) and powder X-ray diffraction (XRD) spectra for the intermediate structures along uniaxial *c*-axis compression of hexagonal graphite are studied with the first-principles pseudopotential plane wave method. Comparison with experiment is made whenever results are available. A transformation from graphite to a new carbon phase was observed in the simulation. The new phase consists of alternating linkages of the graphite layers via the formation of C–C σ bonds. The calculated XAS and XRD reproduced most but not all of the features observed in a recent experiment. Comments are made on the reliability of the computational procedures to reproduce the XAS of these structures.

Key words: graphite, uniaxial compression, ab initio, and X-ray absorption spectroscopy.

Résumé : Faisant appel à la méthode des premiers principes du plan pseudopotentiel, on a étudié la possibilité d'utiliser les spectres d'absorption de rayons X (SAX) et diffraction de rayons X par des poudres (DRX) pour les structures intermédiaires le long de la compression de l'axe c uniaxial du graphite hexagonal. Chaque fois que des résultats sont disponibles, on fait une comparaison avec des données expérimentales. Dans la simulation, on a observé une transformation du graphite en une nouvelle phase de carbone. La nouvelle phase est formée de liaisons alternées de couches de graphite qui résultent de la formation de liaisons σ C–C. Les spectres SAX et DRX calculés reproduisent la plupart des caractéristiques qui ont été observées dans une expérience récente. On fait aussi des commentaires sur la fiabilité des méthodes de calcul pour reproduire les spectres SAX de ces structures.

Mots-clés : graphite, compression uniaxale, ab initio, spectroscopie d'absorption des rayons X.

[Traduit par la Rédaction]

Introduction

It is well known that carbon can participate in sp-, sp^2-, and sp^3-type bonds, and hence exists in a variety of forms. The conversion mechanism between various forms of carbon has long been a topic of interest (1). Much of the work, both theoretically (2–5) and experimentally (6–10), has largely been focused on the conversion of graphite to diamond. However, details on the direct conversion route from graphite to diamond are still unknown. This, in part, is due to the mixture of rhombohedral and hexagonal graphite in the samples used in the experiments (2). Theoretical calculations, on the other hand, are able to distinguish between the chemical behavior of rhombohedral and hexagonal graphite. For this reason, they have been able to provide insight into the different possible conversion pathways for the transformation from graphite to diamond. From the calculations, it is clear that, depending on whether the starting graphite structure is rhombohedral or hexagonal, the conversion route to diamond is different (2). Rhombohedral graphite is shown to transform directly to hexagonal diamond (2, 3) when it is compressed. On the other hand, hexagonal graphite transforms to a superhard phase (4, 5), which is not quench-recoverable at room temperature (10, 11). To convert this superhard phase to diamond, the crystal must be heated to provide energy for lateral motion between the puckered layers (10, 11), which facilitates the formation of interlayer C–C bonds. Very recently, an experimental investigation (10) has shown that this superhard form of graphite is structurally different from the more well-known hexagonal diamond. The formation of this new polymorphic phase has been characterized using inelastic X-ray scattering (IXS) and XRD experiments. IXS provides similar information to XAS but is applicable to in situ studies of materials in a diamond anvil cell.

A number of experimental (10, 12–18) and theoretical (10, 12, 13, 18–21) studies have focused on the assignment of the spectral features in the electronic spectra of graphite and diamond. The assignment of the transitions to higher-energy continuum states in the conduction band is less straightforward. For this reason, assignments for this region are often ambiguous. Lower-energy electronic transitions to the conduction band are well-characterized, but their exact nature is still being debated (14, 15, 17). Apart from the lack

Received 01 May 2007. Accepted 31 July 2007. Published on the NRC Research Press Web site at canjchem.nrc.ca on 15 September 2007.

This paper is dedicated to Prof. G.M. Bancroft to celebrate his retirement.

D.M. Shaw and J.S. Tse.[2] Department of Physics and Engineering Physics, University of Saskatchewan, SK S7N 5E2, Canada.
M. Odelius. FYSIKUM, Stockholm University, Albanova, S-106 91, Stockholm, Sweden.

[1]This article is part of a Special Issue dedicated to Professor G. Michael Bancroft.
[2]Corresponding author (e-mail: john.tse@usask.ca).

 doi:10.1139/V07-102 © 2007 NRC Canada

of a detailed understanding, the electronic spectra are still indispensable for monitoring changes in the chemical bonding as graphite is compressed. As the graphite layers are compressed, some of the carbon will rehybridize from sp^2 to sp^3 with concomitant formation of C–C bonds between layers. As a result, significant changes in the electronic spectra are observed. These changes can be followed and provide evidence of sp^2-to-sp^3 transition of graphite under pressure.

In this study, the structures obtained from uniaxial compression of the *c* axis of hexagonal graphite are reported. Theoretical XAS and XRD patterns are computed, and comparison is made to experiment where possible. The present approach is reasonable, since in the XAS experiment (10), compression was performed in a diamond anvil cell without a hydrostatic medium. The sample preferentially aligned with the graphite layers perpendicular to the compression direction, and this is very similar to uniaxial compression.

Computational methods

The starting structure was constructed from the lattice coordinates of hexagonal graphite. An orthorhombic cell containing 3 × 2 × 2 unit cells was used. The resulting supercell consisted of four graphite layers with a total of 96 carbon atoms. The initial model had lattice constants $a = b = 2.456$ Å and $c = 6.696$ Å, corresponding to a density of 2.28 g cm^{-3}, which is close to the experimental value of 2.265 g cm^{-3} (11). It is noteworthy for subsequent discussion that the length of the "*c*" axis of the model is twice that of the experimental *c* axis of the initial structure. At ambient conditions, it is four times the interplanar graphite distance. Electronic structure calculations and geometry optimizations were performed with the pseudopotential plane wave method implemented in the Car Parrinello (CPMD) suite of programs (22). The Perdew–Burke–Enzerof (PBE) exchange–correlation functional (23) was used in the calculations. The core electrons for the carbon atoms were replaced with the Troullier–Martins pseudopotential (24). In the calculation of the XAS, a similar procedure was used to generate an appropriate pseudopotential representing the screened or unscreened core-hole states. Wave functions of the valence electrons were expanded in a plane-wave basis set with an energy cutoff of 70 Rydberg. The energy sampling was done for the Γ-point only. Although the calculations were performed using a single *k* point, it is expected that the larger supercell used here reduces the need for a larger set of *k* points (25). Geometry optimizations were performed using the preconditioned conjugate gradient (PCG) method. Convergence is achieved so that the largest contribution to the gradient of the nuclei was less than or equal to 0.001 Hartree/Bohr.

It has been shown in a previous XRD study (10) that the change in the *a* axis with uniaxial compression is quite small. Thus, the simulation was performed by gradually reducing the *c* axis of the model system by a selected amount. The atomic positions at each compression step were reoptimized with the cell axes fixed. This process was repeated until the interlayer distance was reduced to less than 2.0 Å. At this point, bonding between the carbon layers was observed, and no further compression was necessary. In total, five compressions were performed. Since the sample was not compressed hydrostatically, we chose not to estimate the applied pressure for each compression.

At each compression, once the structural relaxation had been achieved, the XAS for the intermediate structure was computed. In principle, the XAS intensities (oscillator strengths) should be computed individually for a large number of excitations from the core level to vacant valence, Rydberg, and continuum states. This procedure, however, is prohibitively expensive. An approximation, which may circumvent this problem, is to employ the transition potential method of Slater (26). Within this approximation, electron excitations are computed from wave functions of the initial and final states obtained from the transition-state potential. The transition matrix elements for the excitation from a 1s core orbital $|\phi_{1s}>$ to a final state $|\phi_f>$ with energy ω_f is given by

$$[1] \qquad I = \frac{2}{3}\omega_f \left| \langle \phi_{1s} | \bar{\mu} | \phi_f \rangle \right|^2$$

where μ is the dipole operator and *I* is the intensity of the transition. Spectra are then obtained from the eigenvalues and pseudo-wavefunctions projected onto a numerical basis containing the three functions ($\phi_{1s}x$, $\phi_{1s}y$, $\phi_{1s}z$). The resulting spectra are convoluted in a manner similar to that suggested in ref. 27. Namely, a set of Gaussian broadening functions with full width half maximum (FWHM) estimated from experiment were used to convolute the calculated excitation energies. In addition, an error function was used to mimic effects of the edge jump. To insure the quality of the wave function for the XAS, the cutoff was increased first from 70 to 90 and then to 110 Rydberg. At a 90 Rydberg cutoff, no significant change in the XAS was observed, indicating that convergence in the energy cutoff had been achieved.

Two approaches were used to approximate the final state in the calculations of the near-edge XAS spectra: the half (partially screened) core hole (HCH) (28) and full (unscreened) core hole (FCH). In the half core-hole approach, the wave function is obtained with half an electron removed from the core. Accordingly, a pseudopotential was generated with the same electron configuration. This approach is known to include relaxation effects up to second order and yield spectra in reasonable agreement with experiment (26, 28). The "transition-state" empty orbitals were used in the calculation of the XAS spectra. In the full core-hole approach, one electron is removed from the core. In this case, this is equivalent to an unscreened final core-hole state.

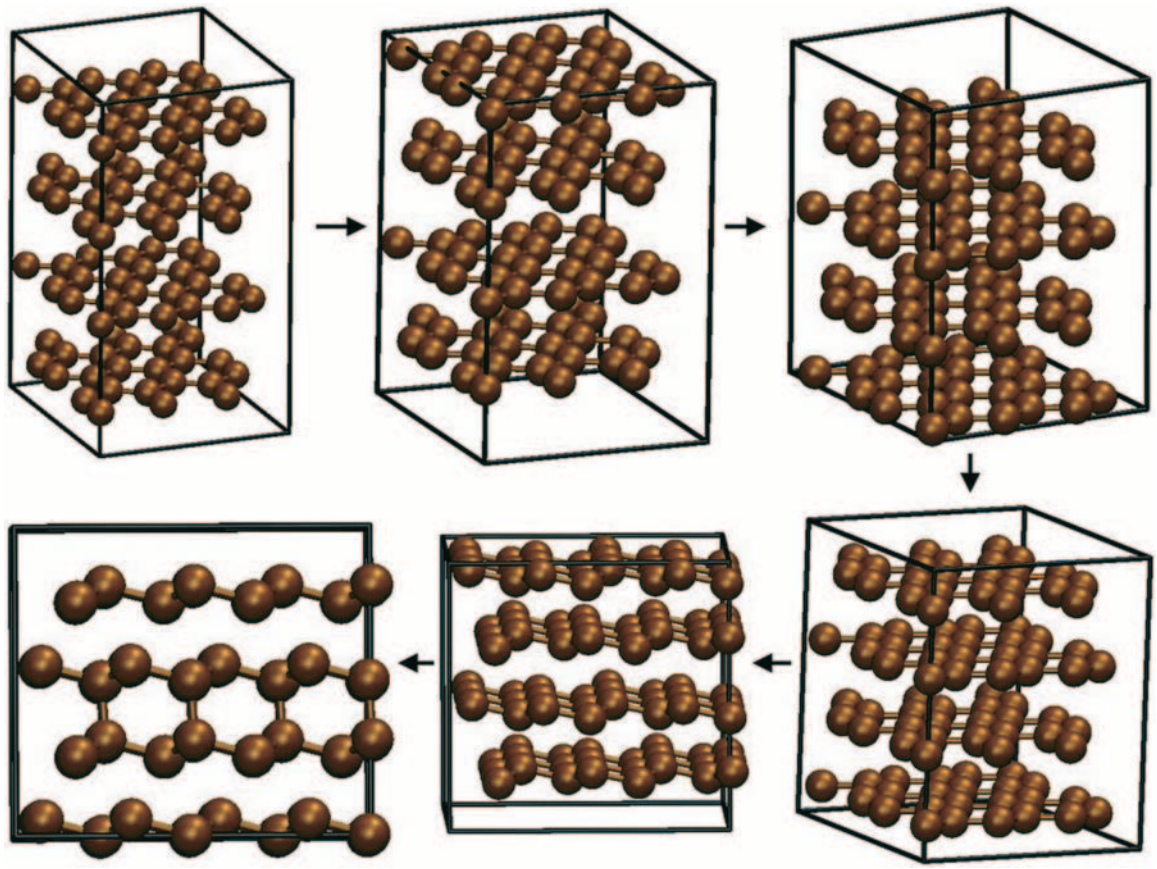
Powder XRD patterns at different stages of compression were generated from the corresponding optimized atomic positions with the program Mercury (29) at the experimental X-ray wavelength $\lambda = 0.331$ Å (10).

Results and discussion

Figure 1 shows the crystal structures obtained at different stages of compression. Arrows in the figure denote the direction of increasing uniaxial pressure. A transition from an sp^2-layered structure to a buckled structure is clearly observed at $c = 7.392$ Å (in the diagram, carbon atoms were connected when their distance was less than 1.5 Å). It is significant to note that interlayer C–C single bonds are observed only between alternate pairs of layers. This structure

© 2007 NRC Canada

Fig. 1. Structures obtained from uniaxial compression of the *c* axis of hexagonal graphite. The compression path follows the arrows shown in the figure, leading from hexagonal graphite to a form where there is significant bonding between alternate layers. Note that the "*c*" axis in the initial structure is twice that of the crystallographic *c* axis.



is clearly different from hexagonal diamond, where the C–C bonds linking adjacent layers are complete, forming a 3D network. This observation is in contrast with the experimental suggestion that the new high-pressure phase obtained at 23 GPa has a 3D structure (10), although details of the structure have not been characterized. Thus, the present theoretical calculations predict a new polymorph of carbon.

Powder XRD patterns corresponding to the intermediate structures are shown in Fig. 2. The predicted diffraction patterns are in reasonable agreement with experimental XRD patterns reported in refs. 8 and 10. Since the experiments may have included both the rhombohedral and hexagonal forms, an exact match to experiment is not possible. Furthermore, since the experimental sample undoubtedly has preferred orientation, a direct comparison of the calculation with the observed Bragg peak intensity is not appropriate.

In the calculation, as the *c* axis is reduced, some of the hexagonal-graphite diffraction peaks disappear. In addition, some weak peaks become more intense and new Bragg peaks appear in the region $8° < 2\theta < 9°$. This observation is indicative of the formation of a new structure different from the hexagonal graphite. Changes to the XRD initiate at c = 11.392 Å (the second compression step). However, significant changes are observed when $c < 10.192$ Å. As shown in Fig. 1, a definite buckling and the formation of interlayer C–C bonds starts to appear when $c = 8.992$ Å (in the fourth compression step). Changes in the calculated XRD patterns reflect the onset of the sp^2-to-sp^3 transition. A detailed examination of the calculated diffraction pattern shows that additional Bragg peaks started to appear at $2\theta \approx 14–16°$. This feature is associated with the shifting of the graphite layers against each other. At the third compression step, a new peak starts to emerge at $2\theta \approx 16.7°$ and becomes more prominent at the fourth compression step. This is due to the puckering of the graphitic layers. The final diffraction pattern shows an additional weak peak at $2\theta \approx 8.8°$, and it corresponds to the complete linking of the adjacent graphite layers. The theory reproduces the experimental results semiqualitatively. In the experiment, as the pressure increases, the [002] peak shifts to higher diffraction angle with decreasing intensity. A broad unresolved band of diffraction peaks starts to develop from $2\theta \approx 8–11°$ with an additional feature at $2\theta \approx 13.5°$. At the highest pressure (23.9 GPa), there appears to be a feature at 8.4° and broad peaks at 9–10° and 15–17°, indicating a mixture of crystalline materials.

Now, we turn to the discussion on the electronic structure associated with the structural changes. Figure 3 shows the powdered average XAS for structures obtained from uniaxial compression along the *c* axis using the HCH approach. The HCH approach is the generally accepted model and has been shown in a recent study to give XAS in almost quantitative agreement with experiment (28). When graphite is compressed, because of the linkage of the graphite layers to form

© 2007 NRC Canada

Fig. 2. Calculated powder XRD for structures obtained via uniaxial compression along the *c* axis. Note that the *c* axis of the simulation model is twice that of the crystallographic cell (see text).

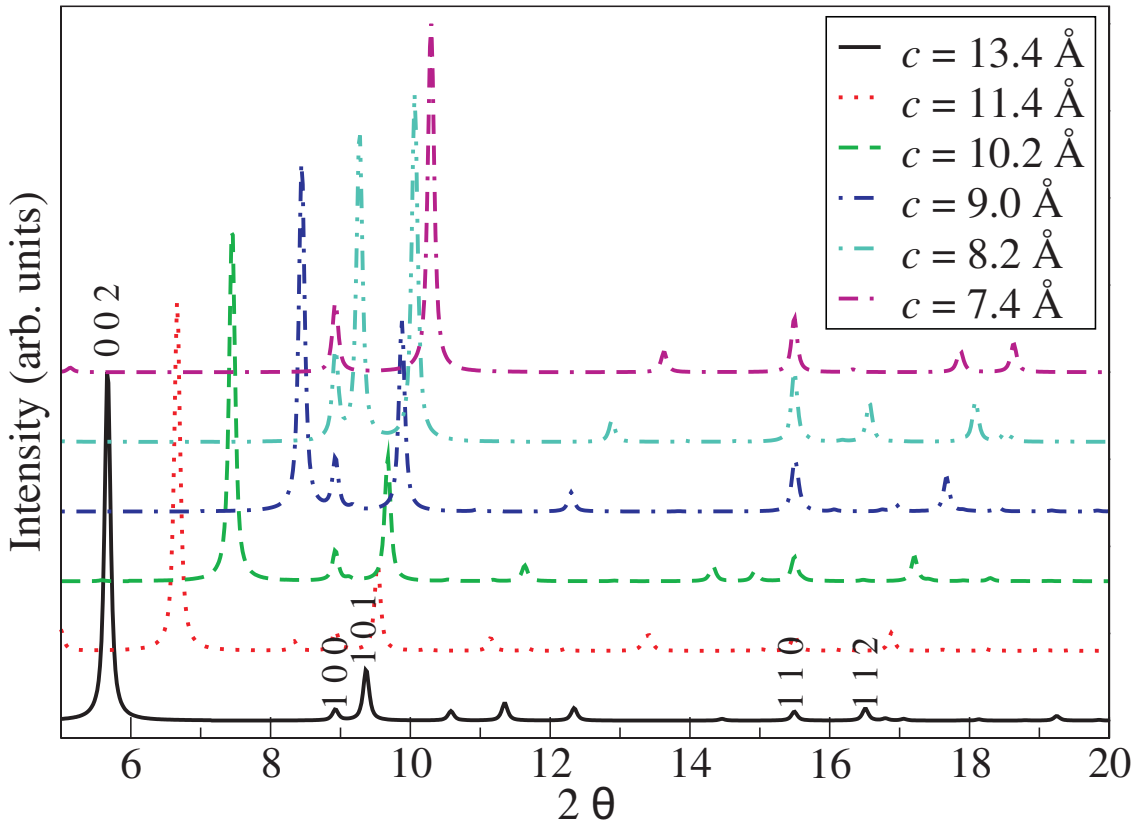
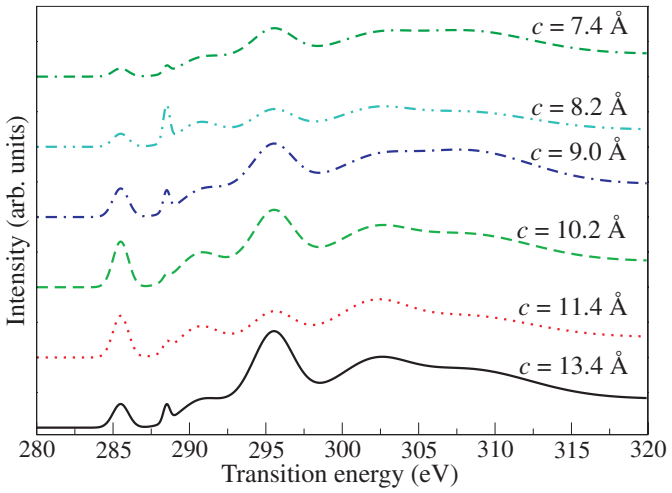


Fig. 3. Powdered average XAS for graphite structures computed via uniaxial compression along the *c* axis using the HCH approach.

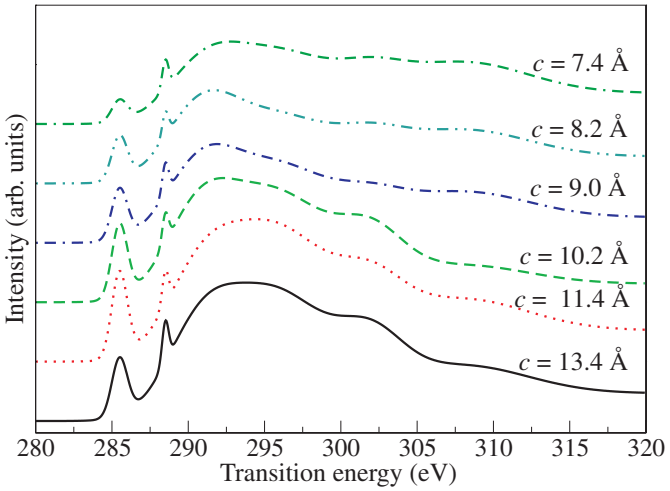


a three-dimensional structure, the intensity of the low-energy pre-edge peak, which is assigned to excitations into the π^* orbital, is expected to decrease gradually, and the intensity of the bands corresponding to the σ^* excitations should increase substantially, as shown in the vertical IXS spectra in ref. 10. This implies a reduction in the π bonding between carbon atoms in the layers with a concomitant increase in σ bonding between the layers. However, as shown in Fig. 3, as uniaxial pressure is applied, the theoretical spectra show an initial increase in the π^* peak, then a decrease as the *c* axis is further compressed. The intermediate structures corresponding to the compression are shown in Fig. 1. The initial increase in the π^* intensity can be traced back to the small shift between the graphite layers. However, the overall agreement of the theoretical XAS spectra computed with the HCH approximation with experiment is rather poor. In the experiment, the intensity of the π^* peak decreases monotonically with pressure. Moreover, the calculated intensity of the π^* to the σ^* bands are significantly underestimated.

A possible cause for the discrepancy may be the improper description of the core-hole state. To this end, calculations of the XAS of uniaxially compressed graphite were repeated using the FCH approximation. Figure 4 shows the XAS obtained using the FCH approach. The spectra show a different trend as predicted by the HCH calculations. The most significant difference is on the computed relative intensity between the π^* and σ^* peaks. The FCH approach has improved the relative π^*/σ^* intensities significantly, and they are now in closer agreement with experiment. Moreover, the behavior of the π^* excitation with increasing compression is now in qualitative agreement with experiment. There is only a slight increase in the π^* intensity in the first compression step. This again is attributed to the relative shift of the graphite layers. However, with increasing compression, the π^* intensity decreases as observed in the experiment. The calculated XAS spectra are still not in quantitative agreement with experiment. The remaining discrepancy, apart from the assumptions made in the theoretical calculations,

© 2007 NRC Canada

Fig. 4. Powdered average XAS for graphite structures computed via uniaxial compression along the *c* axis using the FCH approach.



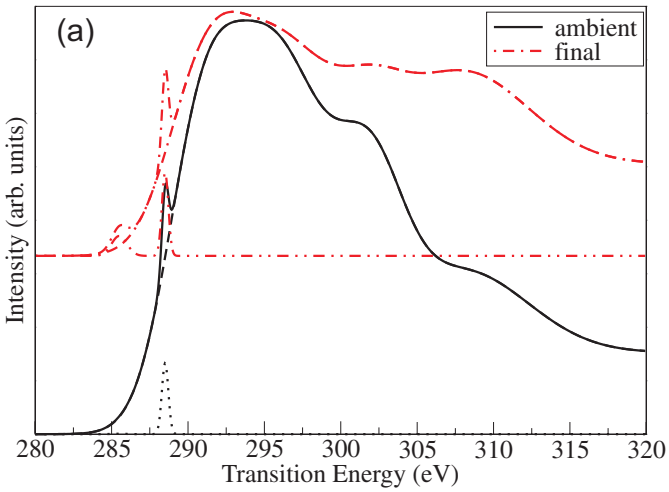
would be due to the fact that the experimental sample may be a mixed phase as commented earlier. Taken in all, there is a qualitative agreement between the FCH results and experiment.

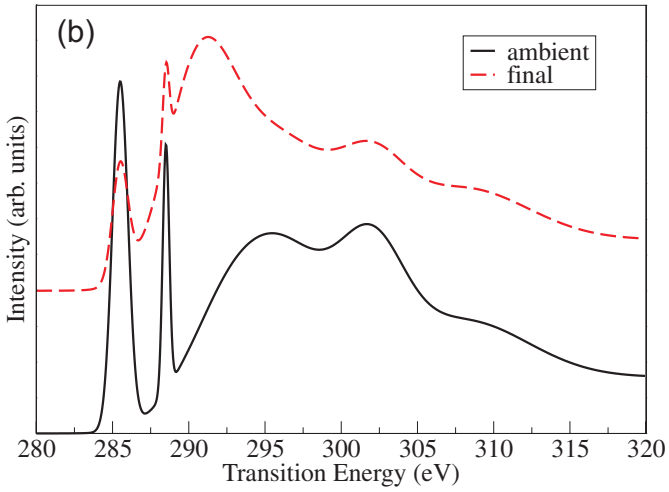
To investigate details of the absorption spectra, polarization-dependent XAS spectra calculated with the FCH approximation are reported in Figs. 5*a* and 5*b*. Using polarized synchrotron radiation, it is possible to resolve contributions from the C_{1s} to π^* transition, which is perpendicular to the graphite plane (i.e., *z*-polarized), and the C_{1s} to σ^* transition, which is parallel to the graphite plane (i.e., *xy*-polarized). We can perform calculations in a similar manner, dividing the XAS into *c* (*z* axis, vertical) and *a*, *b* (*x*–*y* axis, horizontal) components.

At zero pressure, the *xy*-polarized XAS spectrum (Fig. 5*a*) shows a small but sharp pre-edge feature at 288.5 eV and several broad features at 293, 302, and 307 eV. The low-energy peak has been assigned to excitation into a π^* orbital (16). The intensity of this peak is very low in comparison to the σ^* contribution (see dashed line in Fig. 5*a*, where the π^* excitation below 290 eV is plotted separately). This is due to orbital mixing as a result of the lowering of the symmetry when a localized core hole is generated. The broad features are excitations into the σ^* continuum. There is no substantial change in the *xy*-polarized XAS profile when the graphite is compressed.

The *z*-polarized XAS spectrum (Fig. 5*b*) differs significantly from the *xy*-polarized spectrum. Two intense excitations are observed at 286 and 288.5 eV. This is followed by broad features at higher energy. The first sharp peak is undoubtedly assigned to the strong symmetry allowed $C_{1s} \rightarrow \pi^*$ excitation. The second sharp peak at 288.5 eV, which has energy close to the first sharp excitation in the *xy*-polarized spectrum can also be assigned to a π^* excitation (16). In contrast to the *xy*-polarized XAS, the intensity of the π^* excitation decreases substantially when graphite is compressed. This is not surprising. As commented before, this is the consequence of the loss of π bonding in graphite because of cross linkage of adjacent graphite layers under uniaxial pressure.

Fig. 5. Polarized XAS for graphite at ambient pressure and after the fifth (final) compression step, computed using the FCH. Polarization is (*a*) in the *xy* plane and (*b*) along the *z* axis. Note that the absolute magnitudes of the XAS intensities are not the same for both the ambient pressure and the compressed structures. The small peak assigned to the π^* excitation in the *xy*-polarized spectrum is separated from the plot and shown as a dashed line.





The results show that the FCH method may be more appropriate to describe the XAS for graphite. This would imply that the screening of the core hole is not very effective in this case, which is quite surprising for a system with extensively delocalized π electrons. The sensitivity of the calculated spectral features with the approximation for the core-hole state is puzzling and problematic. The HCH approach, which satisfies the Slater transition-state theory and partially accounts for core relaxation effects, should be more theoretically sound. In this case, a direct comparison between calculated and observed spectra of compressed graphite shows that apparently FCH is the preferred approximation for the calculation of the XAS spectra, at least qualitatively. A possible explanation is that dynamical screening effects may be important. Moreover, since energy-dependent self-energy effects are not included, the calculated peak positions and intensities are expected to deviate from experi-

© 2007 NRC Canada

ment. The theoretical reason behind this trend is under investigation.

Conclusions

In conclusion, theoretical XAS and XRD for the uniaxial compression of hexagonal graphite are presented and compared with experiment. The XRD are shown to be in reasonable agreement with experiment and clearly show that sp^2-to-sp^3 transition is achieved once the *c* axis value is reduced beyond roughly 7.2 Å. This corresponds to an interlayer spacing below 1.8 Å, which is close to the C–C single-bond length of 1.5 Å. This observation is supported by the reduction of the π^* and subsequent increase of the σ^* peaks in both the FCH and HCH computed XAS. In all cases, general features of the XAS, particularly in the pre-edge region, are reproduced, but quantitative agreement with the observed spectra has not been achieved. In the graphite system, the relative π^*/σ^* peak intensities in the XAS are not reproduced accurately with both the FCH and HCH approximations. Finally, although cross-linkage of the graphite layers under cold compression was observed in the theoretical calculations, we failed to achieve a completely three-dimensional network, which might otherwise explain the superhardness (10) of the new phase observed in the experiment. The reason for the lack of quantitative agreement with experiment is currently under investigation.

Acknowledgements

Pictures and (or) text taken from the Crystal Lattice Structures Web page, http://cst-www.nrl.navy.mil/lattice/, provided by the Center for Computational Materials Science of the United States Naval Research Laboratory.

References

1. F.P. Bundy, W.A. Bassett, M.S. Weathers, R.J. Hemley, H.K. Mao, and A.F. Goncharov. Carbon, **34**, 141 (1996).
2. S. Fahey, S.G. Louie, and M.L. Cohen. Phys. Rev. B, **34**, 1191 (1986).
3. J. Furthmüller, J. Hafner, and G. Kresse. Phys. Rev. B, **50**, 15606 (1994).
4. M. Bernasconi, G.L. Chiarotti, P. Focher, S. Scandolo, E. Tosatti, and M. Parrinello. J. Phys. Chem. Solids. **56**, 501 (1995).
5. Y. Tateyama, T. Ogitsu, K. Kusakabe, and S. Tsuneyuki. Phys. Rev. B, **54**, 14994 (1996).
6. D.J. Erskine and W.J. Nellis. Nature (London), **349**, 317 (1991).
7. D.J. Erskine and W.J. Nellis. J. Appl. Phys. **71**, 4882 (1992).
8. T. Yagi, W. Utsumi, M. Yamakata, T. Kikegawa, and O. Shimomura. Phys. Rev. B, **46**, 6031 (1992).
9. H. Yusa, K. Takemura, Y. Matsui, H. Morishima, K. Watanabe, H. Yamawaki, and K. Aoki. Appl. Phys. Lett. **72**, 1843 (1998).
10. W.L. Mao, H.-K. Mao, P.J. Eng, T.P. Trainor, M. Newville, C.-C. Kao, D.L. Heinz, J. Shu, Y. Meng, and R. J. Hemley. Science (Washington, DC), **302**, 425 (2003).
11. J. Sung and J. Mater. Sci. **35**, 6041 (2000).
12. E.J. Mele and J.J. Ritsko. Phys. Rev. Lett. **43**, 68 (1979).
13. R.A. Rosenberg, P.J. Love, and V. Rehn. Phys. Rev. B, **33**, 4034 (1986).
14. P.E. Batson. Phys. Rev. B, **48**, 2608 (1993).
15. Y. Ma, P. Skytt, N. Wassdahl, P. Glans, D.C. Mancini, J. Guo, and J. Nordgren. Phys. Rev. Lett. **71**, 3725 (1993).
16. P. Skytt, P. Glans, D.C. Mancini, J.-H. Guo, N. Wassdahl, J. Nordgren, and Y. Ma. Phys. Rev. B, **50**, 10457 (1994).
17. P.A. Brühwiler, A.J. Maxwell, C. Puglia, A. Nilsson, S. Andersson, and N. Mårtensson. Phys. Rev. Lett. **74**, 614 (1995).
18. R. Ahuja, P.A. Brühwiler, J.M. Wills, B. Johansson, N. Mårtensson, and O. Eriksson. Phys. Rev. B, **54**, 14396 (1996).
19. X. Weng, P. Rez, and H. Ma. Phys. Rev. B, **40**, 4175 (1989).
20. Y. Zou and J.C. Tang. J. Phys. Condens. Matter. **6**, 2949 (1994).
21. D.M. Shaw, M. Odelius, and J.S. Tse. Proc. 21st Int. Symp. High Performance Computing Systems and Applications. May 2007. p. 4.
22. CPMD [computer program]. Copyright IBM Corp., 1990–2003; copyright MPI für Festkörperforschung Stuttgart, 1997–2001.
23. J.P. Perdew, K. Burke, and M. Ernzerhof. Phys. Rev. Lett. **77**, 3865 (1996).
24. N. Troullier and J.L. Martins. Phys. Rev. B, **43**, 1993 (1991).
25. X. Wang, S. Scandolo, and R. Car. Phys. Rev. Lett. **95**, 185701 (2005).
26. J.C. Slater. Quantum Theory of molecules and solids. McGraw-Hill, New York, 1974.
27. J. Díaz, S. Anders, X. Zhou, E.J. Moler, S.A. Kellar, and Z. Hussain. Phys. Rev. B, **64**, 125204 (2001).
28. L. Triguero, L.G.M. Pettersson, and H. Ågren. Phys. Rev. B, **58**, 8097 (1998).
29. C.F. Macrae, P.R. Edgington, P. McCabe, E. Pidcock, G.P. Shields, R. Taylor, M. Towler, and J. van de Streek. J. Appl. Cryst. **39**, 453–457 (2006).

© 2007 NRC Canada

Geometries and energetics of methanol–ethanol clusters: a VUV laser/time-of-flight mass spectrometry and density functional theory study[1]

Y. Liu, S. Consta, F. Ogeer, Y.J. Shi, and R.H. Lipson

Abstract: Hydrogen-bonded clusters, formed above liquid methanol (Me) and ethanol (Et) mixtures of various compositions, were entrained in a supersonic jet and probed using 118 nm vacuum ultraviolet (VUV) laser single-photon ionization/time-of-flight mass spectrometry. The spectra are dominated by protonated cluster ions, formed by ionizing hydrogen-bonded Me_mEt_n neutrals, m = 0–4, n = 0–3, and $m + n$ = 2–5. The structures and energetics of the neutral and ionic species were investigated using both the all-atom optimized potential for liquid state, OPLS-AA, and the density functional (DFT) calculations. The energetic factors affecting the observed cluster distributions were examined. Calculations indicate that the large change in binding energy going from trimer to tetramer can be attributed more to pair-wise interactions than to cooperativity effects.

Key words: alcohol clusters, cluster formation, DFT calculations, mass spectrometry, vacuum ultraviolet laser.

Résumé : Les agrégats à liaisons hydrogènes qui se forment au-dessus de mélanges de méthanol (Me) et d'éthanol (Et) liquides de compositions diverses ont été entraînés dans un jet supersonique et on les a étudiés grâce à une combinaison de spectrométrie de masse à temps de vol et d'ionisation à simple photon produite par un laser ultraviolet sous vide (UVV), à 118nm. Les spectres sont dominés par les ions protonés, formés par l'ionisation des espèces neutres qui s'ionisent, Me_mEt_n dans lesquelles m = 0–4, n = 0–3 et $m + n$ = 2–5. On a étudié les structures et les énergies tant des espèces neutres qu'ioniques à l'aide d'une combinaison calculs de la théorie de densité fonctionnelle (TDF) et du potentiel optimisé de l'état liquide pour tous les atomes (POEL-TA). On a examiné les facteurs énergétiques qui affectent les distributions d'agrégats qui ont été observés. Les calculs indiquent que le grand changement d'énergie de liaison qui est observé en passant du trimère au tétramère peut être attribué plutôt à des interactions par paire qu'à des effets de coopération.

Mots-clés : agrégats d'alcools, formation d'agrégats, calculs selon la théorie de la densité fonctionnelle (TDF), spectrométrie de masse, laser UV sous vide.

[Traduit par la Rédaction]

Introduction

Alcohol clusters have attracted considerable experimental and theoretical attention (1–3), since they often serve as prototypical molecules to study molecular association through hydrogen bonding (H-bonding). Compared to water molecules that can form as many as four H-bonds, the alkyl group in an alcohol molecule limits the number of intermolecular H-bonds each hydroxyl group can form. The interplay between the formation of H-bonding and the steric repulsion between alkyl groups determine the structure and stability of alcohol clusters. For small alcohol clusters such as methanol (Me) or ethanol (Et), H-bonds play a key role in determining the most-stable structures (4), whereas the alkyl chains have a more pronounced effect in larger clusters, as shown in our earlier studies of butanols (5). Despite the extensive amount of research that has been done on neat alcohols (1–3), the number of studies on alcohol mixtures, specifically on their vapor cluster compositions, is quite limited. In this work, VUV laser/time-of-flight (TOF) mass spectrometry was used to probe Me–Et clusters formed in the vapor phase above their liquid mixtures. Their structures and energetics were investigated using both the all-atom optimized potential for liquid state, OPLS-AA (3), and the density functional (DFT) calculations.

Received 13 June 2007. Accepted 15 August 2007. Published on the NRC Research Press Web site at canjchem.nrc.ca on 13 September 2007.

Y. Liu. Materials and Process Simulation Center (MSC), California Institute of Technology, 1200 East California Blvd., Pasadena, CA 91125, USA.
S. Consta, F. Ogeer, and R.H. Lipson.[2] Department of Chemistry, The University of Western Ontario, London, ON N6A 5B7, Canada.
Y.J. Shi. Department of Chemistry, University of Calgary, Calgary, AB T2N 1N4, Canada.

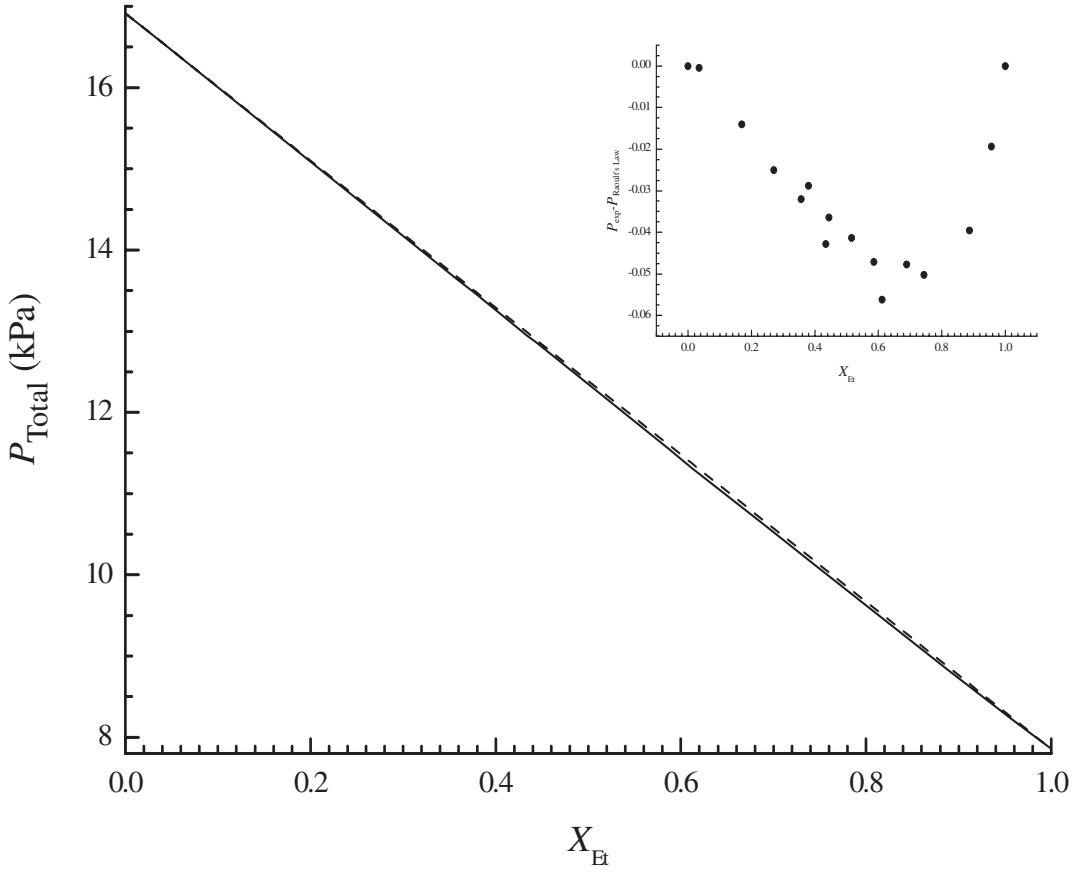
[1]This article is part of a Special Issue dedicated to Professor G. Michael Bancroft.
[2]Corresponding author (e-mail: rlipson@uwo.ca).

Experimental

The experimental arrangement used to record VUV laser mass spectra has been described in detail elsewhere (6). VUV laser mass spectrometry has been shown to be able to yield strong parent-ion signals for a wide variety of organic

 doi:10.1139/V07-104 © 2007 NRC Canada

Fig. 1. A plot of the total vapor pressure of methanol–ethanol mixtures as a function of the mole fraction of ethanol (X_{Et}). The insert shows the deviation between the experimentally determined vapor pressures and those calculated using Raoult's Law.



molecules having different functional groups (7). In this work, ~10 mL of Me:Et liquids with different volume ratios ranging from 10%:90% to 90%:10% was placed in a stainless steel vial. After the vapor–liquid equilibrium was achieved, ~1 atm (1 atm = 101.325 kPa) of He carrier gas was passed through the liquid mixtures. The alcohol vapor entrained in the carrier gas was subsequently expanded as a supersonic jet into the ionization region of the mass spectrometer. As shown in Fig. 1, experimentally measured Me:Et vapor pressures as a function of the mole fraction of Et (8), X_{Et}, are very close to those predicted by Raoult's Law. The negative deviations from Raoult's law (the insert in Fig. 1), while expected for alcohol systems capable of hydrogen-bonding, are at most only ~0.5% of the total vapor pressure at $X_{Et} \approx 0.6$. Thus, it was felt that Raoult's Law could be reliably used to predict the vapor-phase compositions.

The jet was ionized by 118.2 nm VUV light generated by non-resonant third harmonic generation in a phase-matched Xe/Ar gas cell. The positively charged ions were extracted and dispersed in a linear time-of-flight mass spectrometer ($m/\Delta m \approx 500$). The ions were detected at the end of the 1 m flight tube by a microchannel plate (MCP) to produce a mass spectrum of m/z vs. ion intensity.

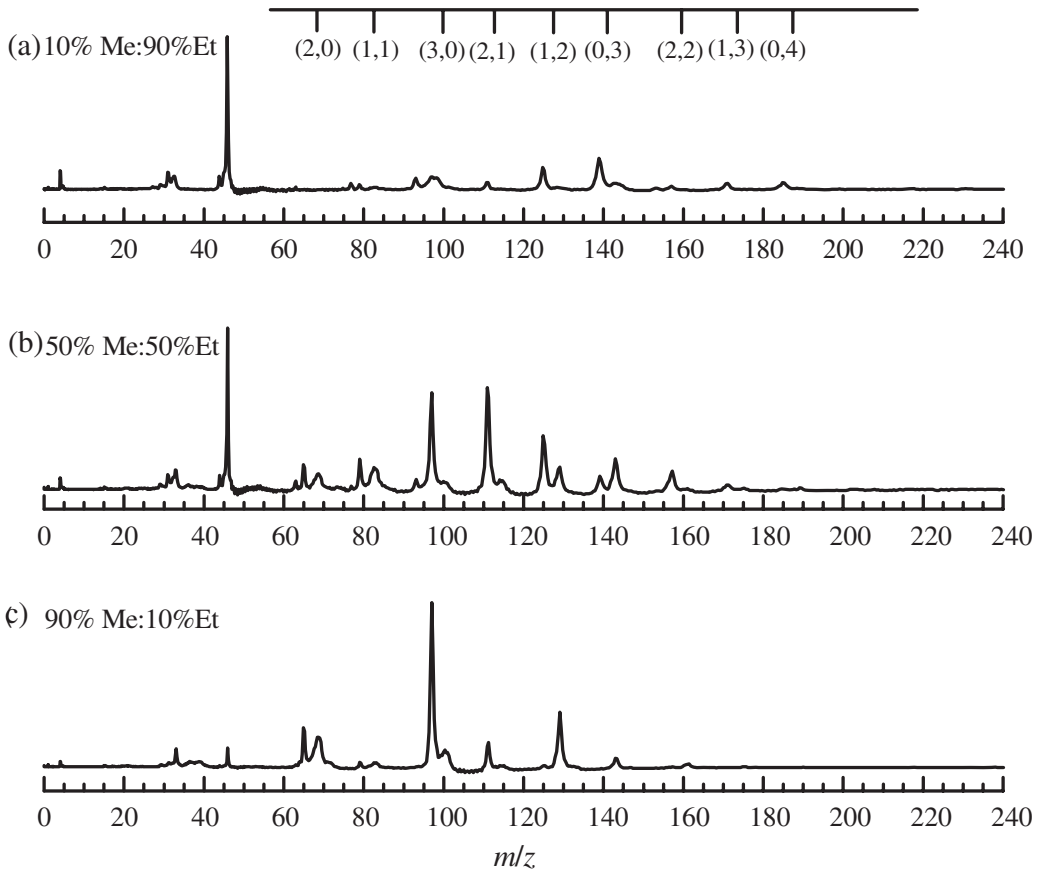
Experimental results

Typical TOF mass spectra of the Me:Et mixtures are shown in Fig. 2. Many more peaks are found in the region $m/z > 46$ (Et monomer) than in the spectra obtained using pure Me or pure Et (4). Peak assignments are listed in Table 1. The main observation is the presence of heterogeneous cluster ions formed from Me and Et, which can be represented by a general formula $HMeEt_n^+$ or (m, n) where m, n = 1–4, and $m + n \leq 5$. The homogenous Me and Et cluster ions are also present, and fit the general formula when either m or n is set to 0. The fragment ion at m/z = 77 is attributed to methyl loss from ethanol dimer to produce $[CH_2{=}OH^+{\cdots}HOC_2H_5]^+$. Most of the peaks have shoulders to slightly higher m/z, which are attributed to metastable decomposition leading to daughter fragment-ion formation inside the drift tube of the mass spectrometer.

The most-striking feature for all the TOF mass spectra of the Me:Et mixtures studied in this work is that the strongest features belong to the trimer ions of the protonated cluster. This agrees with the results obtained using neat alcohol vapors (4). The strongest peak centered at m/z = 139 in the sample with 10% Me can be assigned to Et_3H^+ clusters. In the sample with 50% Me, the dominant features at m/z = 97 and 111, correspond to Me_3H^+ and Me_2EtH^+ clusters, respectively. In the sample with 90% Me, the mass spectrum is dominated by the peak at m/z = 97, corresponding to Me_3H^+. It is interesting to note that the TOF mass spectrum of the 90% Et: 10% Me binary mixture exhibits more heterogeneous cluster ions than that of the 10% Et: 90% Me mixture, which suggests that Me has a higher tendency to self-associate in the gas-phase than Et.

© 2007 NRC Canada

Fig. 2. VUV laser mass spectra of methanol (Me) – ethanol (Et) vapor mixtures found in equilibrium with Me–Et liquid mixtures having volume ratios of (*a*) 10:90, (*b*) 50:50, and (*c*) 90:10. Raoult Law predicts the gas-phase molar percentage ratios to be approximately (*a*) 19:81, (*b*) 70:30, and (*c*) 95:5. The numbers in brackets are (*m*, *n*) values corresponding to the most abundant $Me_mEt_nH^+$ as described in the text.



Previous studies have shown that VUV ionization of neat Me and Et clusters yields a protonated species by the following reaction (9):

[1] $$R_n \xrightarrow{hv} R_{n-1}H^+ + RO^- \text{ or } RO^{\cdot} + e^-$$

where R denotes the alkyl chain. Similar reactions are assumed to hold for the mixed cluster as well:

[2] $$Me_mEt_n \xrightarrow{hv} Me_{m-1}Et_nH^+ + MeO^{\cdot} + e^-$$

$$Me_mEt_n \xrightarrow{hv} Me_{m-1}Et_nH^+ + EtO^{\cdot} + e^-$$

Equations [1] and [2] suggest that the probability of protonated (N – 1)-mer formation can be correlated to the abundance of the neutral N-mer. Such a correlation would be invalid for van der Waals clusters because, upon ionization, they lose monomer units uncontrollably by evaporation (10). Neutral alcohol clusters, however, differ in that hydrogen-bonding is ≥10 times stronger than van der Waals interactions. An ionized alcohol cluster can be viewed as a solvated proton surrounded by monomer units (11). Thus, the combination of evaporative cooling due to the loss of one ligand (eqs. [1] and [2]) and solvated proton–ligand polarization makes further ligand loss difficult. Although this effect will become less important with increasing neutral-cluster size, the ion intensities recorded by VUV laser/mass spectrometry should qualitatively correlate with the neutral-cluster distribution in the supersonic expansion. Moreover, our work on neat methanol (4), ethanol (4), and butanol (5) vapors showed that the cluster distributions are relatively unaffected by changes in the stagnation pressure of the carrier gas used to form the supersonic expansion. This observation is supported by the work of Jackson and co-workers (12) who obtained essentially identical neat-alcohol mass spectra to ours but using very different stagnation pressures. Together, the experimental results suggest that neutral tetramers are the most-abundant clusters prior to ionization.

These neat-alcohol cluster distributions were simulated previously using a Grand Canonical Monte Carlo scheme (4, 5), which established that the dominance of the tetramer could only be understood if the vapor introduced by this experimental method was supersaturated. While the exact level of supersaturation has not been established quantitatively in this work, the design of experimental arrangement used to deliver the gas into the system made such a scenario a distinct possibility.

Theoretical calculations

Density functional (DFT) calculations were carried out using GAUSSIAN-98 program (13). The hybrid density functional B3LYP (14) was used, since it has been shown to provide reliable results for hydrogen-bonded systems, including neat-alcohol clusters (15, 16). Since an accurate de-

© 2007 NRC Canada

Table 1. Cluster ion *m*/*z* assignments observed in 118 nm VUV laser/TOF mass spectra.

	Assignment	
m/*z*	$HMe_mEt_n^+$	(*m*, *n*)
33	HMe^+	(1, 0)
47	HEt^+	(0, 1)
65	HMe_2^+	(2, 0)
79	$HMeEt^+$	(1, 1)
93	HEt_2^+	(0, 2)
97	HMe_3^+	(3, 0)
111	HMe_2Et^+	(2, 1)
125	$HMeEt_2^+$	(1, 2)
129	HMe_4^+	(4, 0)
139	HEt_3^+	(0, 3)
143	HMe_3Et^+	(3, 1)
157	$HMe_2Et_2^+$	(2, 2)
161	HMe_5^+	(5, 0)
171	$HMeEt_3^+$	(1, 3)
175	HMe_4Et^+	(4, 1)
185	HEt_4^+	(0, 4)
189	$HMe_3Et_2^+$	(3, 2)
203	$HMe_2Et_3^+$	(2, 3)
217	$HMeEt_4^+$	(1, 4)
231	HEt_5^+	(0, 5)

scription of H-bonds requires a highly flexible basis set, the 6–311++G(d, p) basis set was used for geometry optimization, followed by single-point energy (SPE) calculations using a larger basis set, 6–311++G(3df, 2p). The energies were corrected for zero-point energy (ZPE) and basis-set superposition error (BSSE) (17). Geometry optimizations were also done using the OPLS-AA force field. Comparison with the DFT results can provide an evaluation of the empirical potentials used in the OPLS-AA force field.

(a) Structures of Me_mEt_n (m = 0–4, n = 0–4, $m + n$ = 2–5) isomers

Alcohol clusters exhibit structural isomerism. For example, the ethanol monomer has a trans (t) and a gauche (g) conformation in which the trans isomer is slightly more stable than the gauche. Global minima on the potential energy surface (PES) for the structural isomers were found by first performing Molecular Dynamics (MD) simulations in a NVT ensemble at T = 100 K using the OPLS-AA force field. Several tens of local minima on the PES were then selected as the initial conformations for geometry optimizations using the OPLS-AA force field. The structures obtained were further optimized by DFT/B3LYP calculations. The optimized structures among the most-stable isomers are shown in Figs. 3*a*–3*d*. Except for the dimers, which form open structures, the most-stable structures for the trimers through to the pentamers are monocyclic rings in which each molecule has two H-bonds. The oxygen atoms in these structures act as both a proton donor and an acceptor. The number of H-bonds is a maximum in the cyclic trimer, which agrees reasonably with intuition. However, cyclic tetramers and pentamers in fact do not have the maximum number of H-bonds possible. For example, the monocyclic pentamer is more stable than the branched cyclic species even though one molecule in the branched cyclic structure has three H-bonds. It should be appreciated that another common feature of the monocyclic structures is that the alkyl groups are arranged to minimize steric hindrance. A similar behavior is found for water clusters (18).

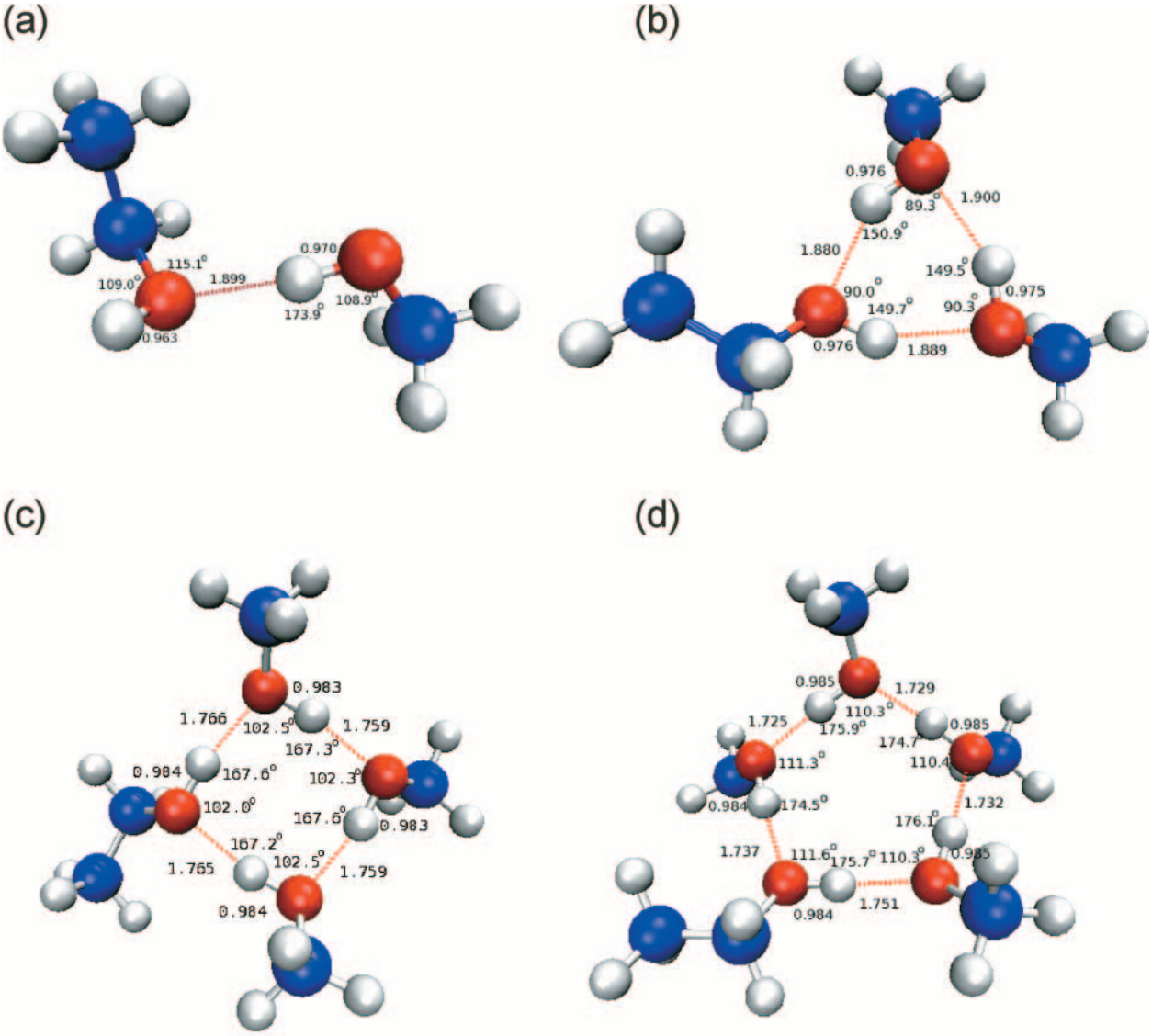
Figures 4*a*–4*d* show the dependences of the nearest-neighbour O–O separations, the H-bonded O–H bond lengths, the covalent O–H bond lengths, and the OHO angles on cluster size. These values were calculated by taking averages over various mixture clusters. As the cluster size increases, the O–O distance ($r_{O–O}$) and the H-bond length ($r_{O–H}$) decrease, while the covalent O–H bond lengths ($r'_{O–H}$) increase slightly. These trends indicate that the monocyclic structures contract because of H-bond shortening as the cluster becomes larger. This structure change implies that H-bonding becomes stronger with the increasing cluster size, which is consistent with the trends of the average binding energies per molecule (see later). On the other hand, the O–O repulsions do not favor the contractions energetically. The interplay between H-bonding and O–O repulsion results in the tetramers and the pentamers having comparable $<E_b>$ and $<r_{O–O}>$. A similar trend was also found in our previous studies of the *n*-butanol and *iso*-butanol isomers, but not for *sec*-butanol and *tert*-butanol (5). Since the *sec*-butanol and *tert*-butanol have short and bulky alkyl chains, steric repulsion makes the O–O separations larger in the pentamers than in the tetramers. The structural changes in small alcohol clusters resemble those of water including a systematic contraction of the nearest-neighbour O–O separation with increasing cluster size, and a red shift of the H-bonded OH stretch frequency (19, 20).

The proton positions were located in this work by measuring the average OHO angle (Fig. 4*d*). In the dimers, the protons lay approximately along the O–O axes to form linear H-bonds. The trimer protons are so close in this cluster that repulsion forces them outward to off-axis positions. The deviations from the O–O axes reduce quickly however with the increasing cluster size, which is indicated by an increasing OHO angle going from the trimer to the pentamer. In the pentamer, the OHO angles are essentially restored to the values found for the dimer. This implies that in the pentamer, the proton–proton separations are sufficiently large that the repulsion between them has become negligible. Extrapolation of these trends suggests that even larger monocyclic structures should have very similar bond distances and average binding energies per molecule. Of course, it may be that these larger clusters would rather adopt more compact shapes, for example, bicyclic or cage-like structures.

Lastly, the cluster structures obtained from the OPLS-AA and the DFT calculations were compared. The OPLS-AA model underestimates cluster covalent O–H bond lengths by at least 0.01 although the trend is similar to that calculated by DFT (Fig. 4*c*). The OPLS-AA also underestimates the H-bond length and the nearest-neighbour O–O distance for the dimer. These deviations correlate with the overestimated OPLS-AA binding energies. Yet, except for the deviations mentioned earlier, the OPLS-AA model predicts the microscopic cluster structures almost as well as DFT.

© 2007 NRC Canada

Fig. 3. Optimized structures of Me_mEt_n (m = 0–4, n = 0–3, $m + n$ = 2–5) clusters found by DFT/B3LYP calculations: (*a*) dimers, (*b*) trimers, (*c*) tetramers, and (*d*) pentamers. The unit of bond length is Å, and the angles are in degrees.



(b) Structures of protonated clusters

As noted earlier, the protonated trimer ions are the most dominant cluster ions detected by VUV laser mass spectrometry. The optimized structures for Me_3H^+, Et_3H^+, and Me_2EtH^+, respectively, are shown in Figs. 5*a*–5*d*. Unlike the neutral clusters, the protonated trimers form open structures that maximize the alkyl group separations and minimize proton–proton repulsions. The H-bonds are noticeably shorter than those in the neutral clusters, and the covalent O–H bonds are slightly stretched. As a result, the nearest-neighbour O–O distances are also contracted in the protonated clusters relative to their neutral counterparts.

Energetics of Me_mEt_n (m = 0–4, n = 0–4, $m + n$ = 2–5) isomers

The binding energy of a cluster, E_b', is defined as the difference between the total energy of the cluster and those of its isolated components:

$$[3] \quad E_b'[Me_mEt_n] = E_{tot}[Me_mEt_n] - mE_{tot}[Me] - nE_{tot}[Et]$$

where $E_{tot}[Me_mEt_n]$, $E_{tot}[Me]$, and $E_{tot}[Et]$ are the total energies of the mixed cluster, methanol monomer, and ethanol monomer, respectively. The binding energy per molecule can be calculated from $E_b[N_{(m+n)}] = E_b'[Me_mEt_n]/(m + n)$. For monocyclic clusters that have the same number of molecules and H-bonds (other than dimer), $E_b[N_{(m + n)}]$ represents the strength of a H-bond. The incremental binding energy is then defined as follows:

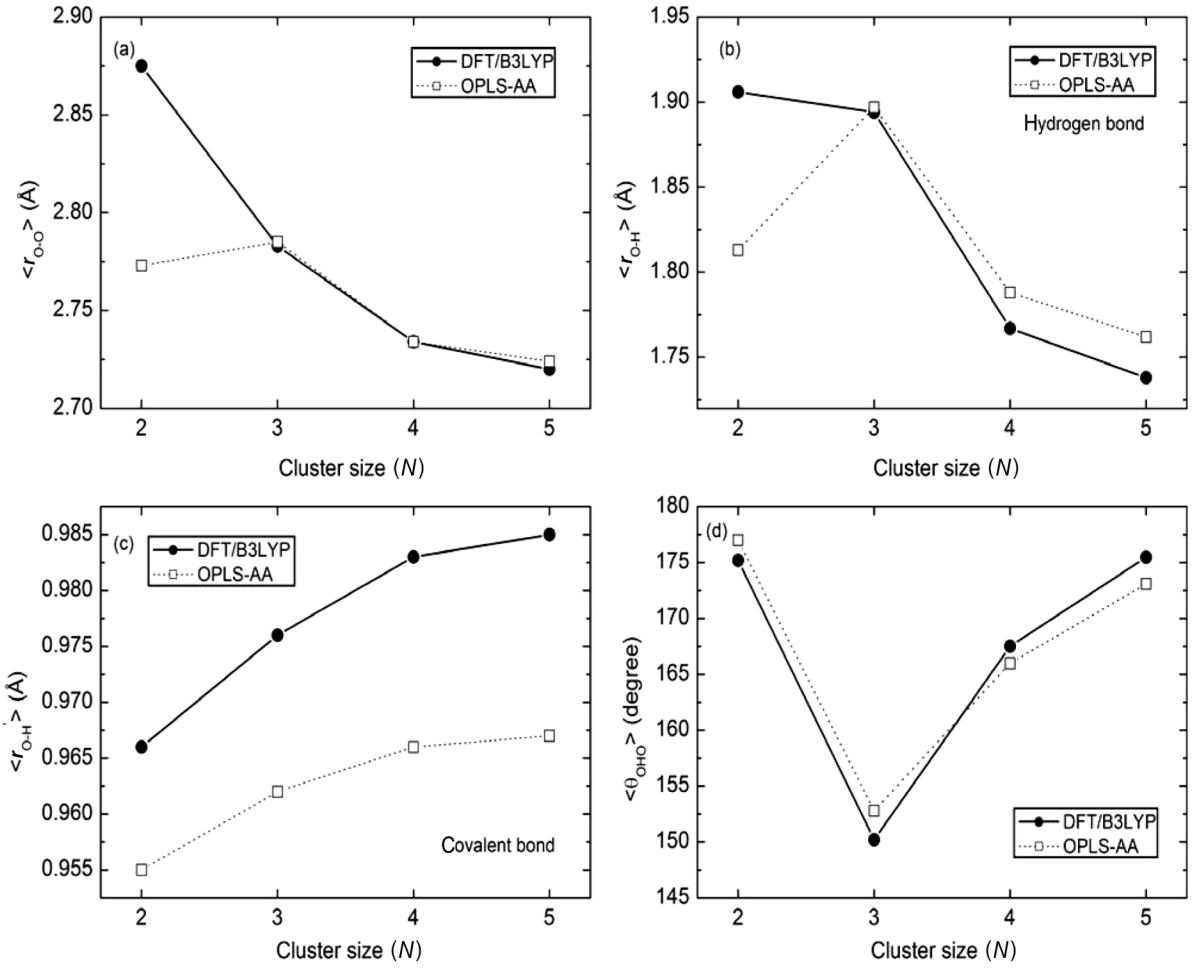
$$[4] \quad E_{ib}[N_{(m+n)}] = E_b[N_{(m+n)}] - E_b[N_{(m+n-1)}]$$

and is a measure of the change in the H-bond strength because of the addition of a monomer to the cluster.

The binding energy can be further understood in terms of many-body interactions. The binding energy of a Me_mEt_n binary cluster can be decomposed as follows (18):

© 2007 NRC Canada

Fig. 4. (*a*) Average O–O distances, (*b*) average H-bond lengths, (*c*) average covalent O–H bond lengths, and (*d*) average OHO angles, as a function of cluster size calculated using the OPLS-AA model and by DFT.



$$[5]\quad E_b'[\mathrm{Me}_m\mathrm{Et}_n] \equiv \sum_{i=1}^{m+n} E(i) - mE_{\mathrm{tot}}(\mathrm{Me}) - nE_{\mathrm{tot}}(\mathrm{Et}) + \sum_{i=1}^{m+n-1}\sum_{j>1}^{m+n}\Delta^2 E(\mathrm{ij}) + \sum_{i=1}^{m+n-2}\sum_{j>1}^{m+n-1}\sum_{k>j}^{m+n}\Delta^3 E(\mathrm{ijk}) + \sum_{i=1}^{m+n-3}\sum_{j>l}^{m+n-2}\sum_{k>j}^{m+n-1}\sum_{l>k}^{m+n}\Delta^4 E(\mathrm{ijkl}) + \cdots + \Delta^{m+n}E(m,n)$$

where E(i), E(ij), E(ijk), and E(ijkl) are the total energies of the monomers, dimers, trimers, and tetramers within a given cluster, respectively. E_{tot}(Me) and E_{tot}(Et) are the total energies of an isolated methanol and ethanol molecule, respectively. The first three terms together are called the relaxation term, and it represents the energy required to change the geometry of the isolated monomers to that found in the cluster. The pair-wise two-body additive terms, three- and four-body non-additive terms are defined as (18):

$$[6]\quad \Delta^2 E(\mathrm{ij}) = E(\mathrm{ij}) - [E(\mathrm{i}) + E(\mathrm{j})]$$

$$[7]\quad \Delta^2 E(\mathrm{ijk}) = E(\mathrm{ijk}) - [E(\mathrm{i}) + E(\mathrm{j}) + E(\mathrm{k})] - [\Delta^2 E(\mathrm{ij}) + \Delta^2 E(\mathrm{ik}) + \Delta^2 E(\mathrm{jk})]$$

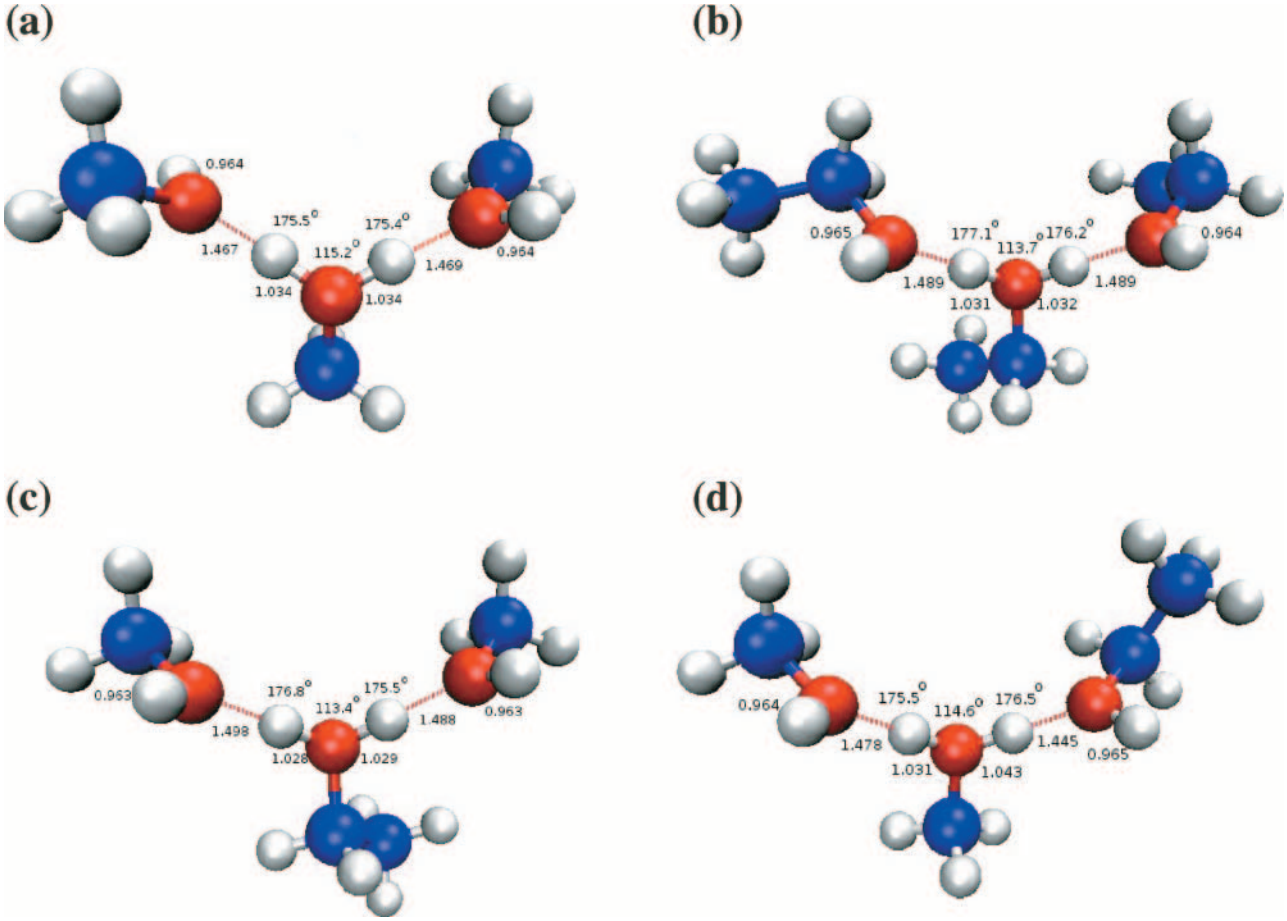
$$[8]\quad \Delta^4 E(\mathrm{ijkl}) = E(\mathrm{ijkl}) - [E(\mathrm{i}) + E(\mathrm{j}) + E(\mathrm{k}) + E(\mathrm{l})] - [\Delta^2 E(\mathrm{ij}) + \Delta^2 E(\mathrm{ik}) + \Delta^2 E(\mathrm{il})] - [\Delta^2 E(\mathrm{jk}) + \Delta^2 E(\mathrm{jl}) + \Delta^2 E(\mathrm{kl})] - [\Delta^3 E(\mathrm{ijk}) + \Delta^3 E(\mathrm{ijl}) + \Delta^3 E(\mathrm{ikl}) + \Delta^3 E(\mathrm{jkl})]$$

The cooperativity is defined as the sum of all non-additive terms with orders higher than the two-body term. The resultant binding energies were computed for $\mathrm{Me}_m\mathrm{Et}_n$ (m = 0–4, n = 0–4, $m + n$ = 2–5) isomers, and are listed in Table 2. Excellent agreement with the experimental values for pure methanol and ethanol dimers (21) were obtained when the binding energies were calculated after geometry optimizations that included corrections for ZPEs but not BSSE. Moreover, the calculated binding energy of methanol dimer differed by only 0.05 kcal/mol from the value obtained from MP2/VTZ(2df, 2p) and MP2/ESPB calculations (15). In general, the binding energies among various isomers are very similar, with energy variations typically <0.3 kcal/mol. The gauche mixed dimer was found to be slightly more stable than the trans species, while the opposite trend was observed for the mixed trimers.

The relative stability of the different clusters was determined by the energy calculations done using both the OPLS-AA and the DFT/B3LYP methods. Plots of the average binding energy/molecule, and the average incremental binding

© 2007 NRC Canada

Fig. 5. Optimized structures of the protonated clusters obtained by DFT/B3LYP calculations: (*a*) Me_3H^+, (*b*) Et_3H^+, (*c*) Me_2EtH^+, and (*d*) Me_2H^+Et. The unit of bond length is Å, and angles are given in degrees.



energy vs. cluster size are shown in Figs. 6*a* and 6*b*, respectively. The energies were averaged per cluster over the different isomers. The average incremental binding energy clearly maximizes at $N_{(m+n)} = 4$. Therefore, the large energy gain due to the formation of the tetramers should be associated with its abundance in the vapor, along with the supersaturation effect discussed before. A similar energy trend has been reported for neat methanol and water vapors (1, 2). It should be noted that methanol prefers to form larger clusters than water (1). This difference implies that entropy as well as energetics may also play a role in determining cluster-size distributions in alcohols.

The results obtained using the empirical force field were compared with those obtained by DFT. As shown in Fig. 6*b*, both the OPLS-AA and DFT calculations predict a similar trend in the size dependence of the incremental binding energy. Strikingly, the incremental binding energies for the tetramer obtained by the two different approaches agree remarkably well. As this value describes the relative stability of the trimers and tetramers, it is critical in understanding the exceptional stability of the tetramer. The OPLS-AA model generally overestimates the binding energy per molecule (Fig. 6*a*). The largest discrepancy is found for the dimer. This should translate into a large deviation of the computed dimer OH stretching modes from the experimental values (2). This disagreement, however, is not surprising because the OPLS-AA potential parameters were originally fitted to reproduce the properties of liquids. The origin of this error probably comes from an overestimation of the static dipole moment in the force field parameters (2). The OPLS-AA model describes the stability of large clusters better because, in the gas-phase, large clusters usually adopt cyclic structures, which closely resemble their liquid-phase counterparts. However, further comparisons with DFT show that the OPLS-AA model fails to predict the relative stabilities among the clusters of equal *N*, and the relative stability of the structural isomers associated with a given cluster composition. Here, the energy differences are generally very small, and this suggests therefore, that the OPLS-AA model is only qualitatively reliable for predicting the stability of clusters of different sizes. While the OPLS-AA model does describe the relative stability between trimers and tetramers well, significant differences between the calculated OPLS-AA and DFT energies exist. Careful tests should therefore be taken when using the OPLS-AA energies to describe the stability of the cluster.

Discussion and conclusions

VUV single-photon ionization and TOF mass spectrometry were used to detect gas-phase protonated methanol and ethanol cluster ions. Optimized structures for these neutral precursors have been calculated. Not surprisingly the most-stable neutral mixed clusters are monocyclic, similar to that

© 2007 NRC Canada

Table 2. Binding energies of Me_mEt_n (m = 0–4, n = 0–4, $m + n$ = 2–5) isomers. The subscript t or g denotes an ethanol molecule with a trans or gauche conformation, respectively. The values in parentheses are the binding energies after ZPE correction. All energies are in units of kcal/mol.

Isomer		E_{b1}[a]	E_{b2}[b]	BSSE
$(MeOH)_2$	A	–5.83 (–4.45)	–4.93 (–3.55)[c]	0.24
$(EtOH)_2$	A_{tt}	–5.61 (–4.31)	–4.48 (–3.17)[c]	0.23
	B_{tg}	–5.71 (–4.43)	–4.60 (–3.33)[c]	0.24
	C_{gg}	–5.49 (–4.31)	–4.41 (–3.23)[c]	0.25
(MeOH)(EtOH)	A_t	–5.81 (–4.40)	–5.05 (–3.63)	0.26
	B_g	–5.83 (–4.42)	–5.15 (–3.74)	0.25
	C_t	–5.65 (–4.35)	–4.76 (–3.45)	0.25
$(MeOH)(EtOH)_2$	A_{tt}	–16.60 (–13.27)	–14.79 (–11.47)	0.78
	B_{tt}	–16.53 (–13.29)	–14.73 (–11.49)	0.87
	C_{tg}	–16.40 (–13.12)	–14.61 (–11.33)	0.78
	D_{tg}	–16.35 (–13.16)	–14.64 (–11.46)	0.74
	E_{gg}	–16.23 (–13.06)	–14.51 (–11.34)	0.72
	F_{gg}	–16.15 (–13.02)	–14.34 (–11.22)	0.72
$(MeOH)_2(EtOH)$	A_t	–16.86 (–13.47)	–14.96 (–11.58)	0.77
	B_g	–16.71 (–13.33)	–14.85 (–11.45)	0.77
	C_g	–16.65 (–13.27)	–14.69 (–11.31)	0.76
$(MeOH)(EtOH)_3$	A_{ttt}	–29.23 (–24.32)	–26.27 (–21.36)	1.25
	B_{ttg}	–29.15 (–24.22)	–26.15 (–21.22)	1.26
$(MeOH)_2(EtOH)_2$	A_{tt}	–29.61 (–24.52)	–26.54 (–21.45)	1.28
	B_{tt}	–29.62 (–24.49)	–26.54 (–21.41)	1.26
$(MeOH)_3(EtOH)$	A_t	–29.97 (–24.82)	–26.76 (–21.61)	1.29
$(MeOH)_2(EtOH)_3$	A_{ttt}	–38.68 (–32.37)	–32.64 (–26.33)	1.51
$(MeOH)_3(EtOH)_2$	A_{tt}	–39.33 (–32.91)	–33.13 (–26.71)	1.53
$(MeOH)_4(EtOH)$	A_t	–39.76 (–33.21)	–33.41 (–26.89)	1.54

[a]Binding energy calculated after geometry optimization using B3LYP/6–311++G(d, p).
[b]Binding energy calculated after geometry optimization using B3LYP/6–311++G(d, p) followed by a single point energy calculation using B3LYP/6–311++G(3df, 2p).
[c]Experimental binding energies for pure methanol and ethanol dimers (23) lie between –3.20 to –3.50 kcal/mol, and –3.39 to –3.99 kcal/mol, respectively.

found for neat-alcohol clusters (4). These structures are also consistent with recent infrared studies that suggest that the OH groups of the monomers involved in neat methanol and ethanol clusters larger than the dimer are all involved in hydrogen bonding (22–24). The protonated trimer ions correspond to the most abundant species detected by VUV laser/time-of-flight mass spectrometry. The correlation shown in eq. [1] between a neutral N-mer and a protonated (N – 1)-mer ion suggests that the mixed alcohol tetramers are "magic" clusters. This conclusion holds for neat methanol and ethanol tetramers because these size clusters (with S_4 symmetry) are expected to exhibit a maximum hydrogen-bonding cooperativity effect, and a minimum ring strain (1, 2).

The neutral mixed cluster binding energies were decomposed into the terms representing the many-body interactions (see eqs. [5–8]) to understand the size-dependence trend found here for the incremental binding energy. Table 3. shows the average binding energies and their components calculated by DFT (without ZPE corrections) for the alcohol clusters ranging from the dimer to the pentamer. It can be seen again that the difference in the binding energies for the N-mer and (N – 1)-mer maximizes for the tetramer. Further examination shows that the differences in the pair-wise additive contributions have the same trend as the binding-energy differences, whereas the differences in the non-additive contributions, often termed cooperativity effects, does not exhibit this trend. This observation suggests that the large change in energy going from the trimer to the tetramer is mainly due to pair-wise interactions rather than higher-order cooperativity effects; that is, the tetramer stability is mainly a balance between the energy gained through attractive H-bonding vs. the repulsion between the oxygen atoms within the cluster.

It is instructive to compare the relative contributions of the pair-wise additive and non-additive terms, rather than their absolute values. Table 4. lists the percentage contribution of the many-body terms to the binding energy, which were averaged over various alcohol clusters, along with the corresponding values for water clusters taken from ref. 18. It can be seen that the repulsive contribution due to the relaxation term becomes more pronounced going from the dimer to the pentamer. This indicates that for the larger clusters, the individual monomers deform considerably relative to their isolated conformations. These deformations include the stretching of the covalent O–H bonds (Fig. 4*c*). The additive

© 2007 NRC Canada

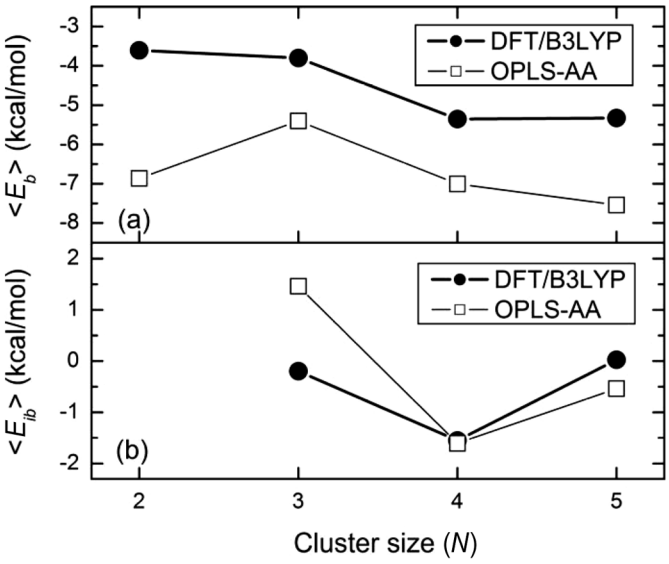
Table 3. Average binding energies and their many-body components for Me_mEt_n (m = 0–4, n = 0–4, $m + n$ = 2–5) clusters (in kcal/mol). The binding energies E_{b2} correspond to those in Table 2 (without ZPE corrections). E_r is the relaxation term defined in eq. [5]. $< {}^nE >$ are the n-body terms defined in eqs. [5–8]. E_c corresponds to the non-additive terms. $< E_{b2} >$, $< {}^2E >$, and E_c are the differences of average binding energies, two-body terms, and non-additive terms, respectively. The positive signs for the relaxation terms denote repulsive contributions to the energy.

$m + n$	$<E_{b2}>$	E_r	$<\Delta^2E>$	$<\Delta^3E>$	$<\Delta^4E>$	$<\Delta^5E>$	E_c	$\Delta<E_{b2}>$	$\Delta<\Delta^2E>$	ΔE_c
2	–4.98	0.14	–5.12	—	—	—	—	–4.98	–5.12	—
3	–14.69	0.56	–12.15	–3.10	—	—	–3.10	–9.71	–7.03	–3.10
4	–26.45	1.43	–21.53	–3.89	–2.46	—	–6.53	–11.76	–9.38	–3.25
5	–33.06	2.44	–25.50	–7.63	–1.76	–0.61	–10.00	–6.61	–3.97	–3.65

Table 4. Percentage contribution of many-body terms to the binding energy of Me_mEt_n (m = 0–4, n = 0–4, $m + n$ = 2–5) clusters. The notations have the same meanings as those in Table 3. The negative sign indicates that the relaxation term has a repulsive contribution. The values in parenthesis are the corresponding values for $(H_2O)n$ (n = 2–5) clusters, which are taken from ref. 19.

$m + n$	Theory level	E_r	$< {}^2E >$	$< {}^3E >$	$< {}^4E >$	$< {}^5E >$	E_c
2	B3LYP(MP2)	–2.8 (–0.8)	102.8 (100.8)	—	—	—	—
3	B3LYP(MP2)	–3.8 (–2.7)	82.7 (85.1)	21.1 (17.6)	—	—	21.1 (17.6)
4	B3LYP(MP2)	–5.4 (–4.1)	81.4 (76.3)	14.7 (25.6)	9.3 (2.2)	—	24.0 (27.8)
5	B3LYP(HF)	–7.4 (–1.4)	77.1 (78.9)	23.1 (20.4)	5.3 (2.1)	1.9 (0.01)	30.2 (22.51)

Fig. 6. (*a*) Average binding energy per molecule, $< E_b >$, and (*b*) average incremental binding energy, $< E_{ib} >$, as a function of cluster size obtained by DFT/B3LYP and OPLS-AA calculations.



contribution to the binding energy represented by the two-body term decreases, while the non-additive contribution increases with the increasing cluster size. The non-additive interactions (cooperativity) can contribute significantly (as high as 20%–30%) in both the alcohol and the water clusters. The four- and five-body terms also provide non-negligible contributions (7%–9%) in the alcohol clusters, whereas these contributions are less than 3% in the water clusters. In other words, the four- and five-body terms in the alcohol clusters contribute ~30% of the cooperativity effect in alcohol clusters. In the water clusters, however, the contributions from these high-order terms are less than 10%. This analysis shows that cooperativity effects in both alcohol and water clusters are significant. Nevertheless, the alcohol-cluster binding energies converge more slowly than those for water clusters. To capture the cooperativity effects in water clusters, it was deemed sufficient to consider terms up to and including three-body interactions to design a force field (18). The effect of even higher-order terms, such as the four-body interaction, must be included for alcohol clusters to obtain a similar accuracy.

It is well known that different levels of theory can have a considerable effect on the decomposition of the binding energy: second-order many-body perturbation (MP2) level that includes electron correlation generally will decrease the additive contribution relative to a Hartree–Fock (HF) calculation (18) but will increase the non-additive contribution. The DFT/B3LYP results here are considered to be comparable to those obtained by MP2.

As noted earlier, the open structure calculated for the mixed ionic trimers and shown in Fig. 5 can be viewed as a solvated proton. This behavior is also observed for the neat protonated dimers (25). The methanol protonated trimer in particular is a "magic" structure, as it can be regarded as a proton with a complete first-solvation shell (11, 26). Infrared spectroscopy reveals that the free and hydrogen-bonded OH stretching frequencies of the neat cluster ions blue-shift with increasing N (22, 24). The mixed protonated ions are expected to exhibit a similar spectroscopic signature.

Acknowledgements

The authors acknowledge the financial support of the Natural Sciences and Engineering Research Council of Canada (NSERC) and Shared Hierarchical Academic Research Computing Network (SHARCNET) at UWO. One of us (S.C.) is grateful for funding through a Premier's Research Excellence Award.

© 2007 NRC Canada

References

1. L.A. Curtiss and M. Blander. Chem. Rev. **88**, 827 (1988).
2. U. Buck, J.-G. Siebers, and R.J. Wheatley. J. Chem. Phys. **108**, 20 (1998).
3. W.L. Jorgensen. J. Phys. Chem. **90**, 1276 (1986).
4. Y.J. Shi, S. Consta, A.K. Das, B. Mallik, D. Lacey, and R.H. Lipson. J. Chem. Phys. **116**, 6990 (2002), and references within.
5. G.S. Fanourgakis, Y.J. Shi, S. Consta, and R.H. Lipson. J. Chem. Phys. **119**, 6597 (2003).
6. R.H. Lipson, S.S. Dimov, P. Wang, Y.J. Shi, D. M. Mao, X.K. Hu, and J. Vanstone. Instrum. Sci. Technol. **28**, 85 (2000).
7. Y.J. Shi and R.H. Lipson. Can J. Chem. **83**, 1891 (2005).
8. Z.S. Kooner and D.V. Fenby. Aust. J. Chem. **33**, 1943 (1980).
9. K.D. Cook, G.G. Jones, and J.W. Taylor. Int. J. Mass. Spectrom. Ion Phys. **35**, 273 (1980).
10. J.M. Soler, J.J. Sáenz, N. García, and O. Echt. Chem. Phys. Lett. **109**, 71 (1984).
11. (*a*) M.S. El-Shall, C. Marks, L.W. Sieck, and M. Meot-Ner (mautner). J. Phys. Chem. **96**, 2045 (1992); (*b*) K. Hirao, M. Sano, and Y. Yambe. Chem. Phys. Lett. **87**, 181 (1982).
12. W.M. Jackson, D. Xu, R.J. Price, K.L. McNesby, and I.A. McLaren. In Imaging in chemical dynamics, ACS Symposium Series 779. *Edited by* A. G. Suits and R. E. Continetti. American Chemical Society, Washington, DC, 2001, p. 103.
13. M.J. Frisch, G.W. Trucks, H.B. Schlegel, G.E. Scuseria, M.A. Robb, J.R. Cheeseman, V.G. Zakrzewski, J.A. Montgomery, Jr., R.E. Stratmann, J.C. Burant, S. Dapprich, J.M. Millam, A.D. Daniels, K.N. Kudin, M.C. Strain, O. Farkas, J. Tomasi, V. Barone, M. Cossi, R. Cammi, B. Mennucci, C. Pomelli, C. Adamo, S. Clifford, J.W. Ochterski, G.A. Petersson, P.Y. Ayala, Q. Cui, K. Morokuma, D.K. Malick, A.D. Rabuck, K. Raghavachari, J.B. Foresman, J. Cioslowski, J.V. Ortiz, A.G. Baboul, B.B. Stefanov, G. Liu, A. Liashenko, P. Piskorz, I. Komaromi, R. Gomperts, R.L. Martin, D.J. Fox, T. Keith, M.A. Al-Laham, C.Y. Peng, A. Nanayakkara, C. Gonzalez, M. Challacombe, P.M.W. Gill, B.G. Johnson, W. Chen, M.W. Wong, J.L. Andres, M. Head-Gordon, E.S. Replogle, and J.A. Pople. GAUSSIAN 98 [computer program]. Revision A.9. Gaussian, Inc. Pittsburgh, PA. 1998.
14. (*a*) A.D. Becke. J. Chem. Phys. **88**, 1053 (1988); (*b*) C. Lee, W. Wang, and R. Parr. Phys. Rev. B **37**, 785 (1988); (*c*) A. D. Becke. J. Chem. Phys. **98**, 5648 (1993).
15. F. Hagmeister, C. Gruenloh, and T. Zwier. J. Phys. Chem. **102**, 82 (1998).
16. S.L. Boyd and R.J. Boyd. J. Chem. Theory Comput. **3**, 54 (2007).
17. S.F. Boys and F. Bernardi. Mol. Phys. **19**, 553 (1970).
18. S.S. Xantheas. Chem. Phys. Lett. **258**, 225 (2000).
19. S.S. Xantheas and T.H. Dunning, Jr. J. Chem. Phys. **99**, 8774 (1993).
20. F. Huisken, M. Kaloudis, and A. Kulcke. J. Chem. Phys. **104**, 17 (1996).
21. L. Gonzáles, O. Mó, and M. Yáńez. J. Chem. Phys. **111**, 3855 (1999).
22. Y.J. Hu, H.B. Fu, and E.R. Bernstein. J. Chem. Phys. **125**, 154306 (2006).
23. R.W. Larsen, P. Zielke, and M.A. Suhm. J. Chem. Phys. **126**, 194307 (2007).
24. Y.J. Hu, H.B. Hu, and E.R. Bernstein. J. Chem. Phys. **125**, 154305 (2006)
25. T.D. Fridgen, L. MacAleese, T.B. McMahon, J. Lemaire, and P. Maitre. Phys. Chem. Chem. Phys. **8**, 955 (2006).
26. K. Hitao, M. Sano, and S. Yamabe. Chem. Phys. Lett. **87**, 181 (1982).

© 2007 NRC Canada

Soft X-ray excited colour-centre luminescence and XANES studies of calcium oxide[1]

J.Y. Peter Ko, Franziskus Heigl, Yun Mui Yiu, Xing-Tai Zhou, Tom Regier, Robert I.R. Blyth, and Tsun-Kong Sham

Abstract: In this study, we show that colour centres can be produced by irradiating calcium oxide with soft X-rays from a synchrotron radiation source. Using the X-ray excited optical luminescence (XEOL) technique, two colour centres, F-centre, and F^+-centre can be identified. These colour centres emit photons at characteristic wavelengths. In addition, by performing time-resolved XEOL (TRXEOL), we are able to reveal timing and decay characteristics of the colour centres. We also present X-ray absorption near-edge structure (XANES) spectra collected across oxygen K-edge, calcium $L_{3,2}$-edge, and calcium K-edge. Experimental results are compared with density functional theory (DFT) calculations.

Key words: calcium oxide, colour centre, synchrotron, X-ray excited optical luminescence, X-ray absorption near-edge structure.

Résumé : Dans ce travail, on démontre qu'on peut produire des centres colorés par irradiation de l'oxyde de calcium avec des rayons X doux obtenus à partir d'une source de radiation de synchroton. Faisant appel à la technique de la luminescence optique excitée par les rayons X (LOEX), on a pu identifier deux centres colorés, le centre-F et le centre-F^+. Ces centres colorés émettent des photons à des longueurs d'onde caractéristiques. De plus, en faisant appel à la technique LOEX en temps résolu (LOEXTR), il a été possible de déterminer les caractéristiques de décroissance des centres colorés. On rapporte aussi les données obtenues par spectroscopie de la structure fine d'absorption des rayons X près du seuil (« XANES ») recueillis à la périphérie K de l'oxygène, $L_{3,2}$ du calcium et K du calcium. On a comparé les résultats expérimentaux avec ceux des calculs d'après la méthode de théorie de la densité fonctionnelle (TDF).

Mots-clés : oxyde de calcium, centre coloré, synchrotron, luminescence optique excitée par les rayons X, spectroscopie de la structure fine d'absorption des rayons X près du seuil.

[Traduit par la Rédaction]

Introduction

Luminescence from oxygen vacancies in calcium oxide has been a subject of considerable interest, both experimentally (1–4) and theoretically (5, 6). Such vacancies lead to the creation of defect states in wide gap oxides and can result in colouration. These vacancy-induced colour centres are referred to as F-centres. Oxygen can be removed from rock-salt structure of calcium oxide (band gap = 6.9 eV) by means of irradiation. The vacancies can be filled with either one electron (F^+-centre) or two electrons (F-centre). These colour centres are produced by either particle bombardment or additive colouration. Depending on the conditions under which the colour centres are formed, optical properties can vary (1). Some of the primary defects become stable and their number increases with radiation dose, thus changing the crystal features. The nature of the radiation source and the method of colour centre production (e.g., radiation vs. thermal process) can affect the relative population of F^+-centres vs. F-centres. It is also important to note that radiation damage can be non-uniform because of a non-uniform concentration of impurities within the crystal and the penetration depth of the radiation (7). Synchrotron radiation, with its full tunability in the soft X-ray region, provides a new

Received 12 May 2007. Accepted 20 August 2007. Published on the NRC Research Press Web site at canjchem.nrc.ca on 15 September 2007.

J.Y.P. Ko, Y.M. Yiu, X.-T. Zhou,[2] and T.-K. Sham.[3] Department of Chemistry, University of Western Ontario, London, ON N6A 5B7, Canada.
F. Heigl.[4] Canadian Synchrotron Radiation Facility, Synchrotron Radiation Center, University of Wisconsin-Madison, Stoughton, WI 53589, USA.
T. Regier, and R.I.R. Blyth. Canadian Light Source, University of Saskatchewan, 101 Perimeter Road, Saskatoon, SK S7N 0X4, Canada.

[1]This article is part of a Special Issue dedicated to Professor G. Michael Bancroft.
[2]Present address: Pohang University of Science and Technology, San 31, Hyoja-Dong, Namgu, Pohang, Gyungbuk, South Korea.
[3]Corresponding author (email: tsham@uwo.ca).
[4]Present address: CELLS-ALBA, Edifici Ciències, C-3 central. Campus Universitari de Bellaterra, Universitat Autònoma de Barcelona, 08193 Bellaterra, Barcelona, Spain.

 doi:10.1139/V07-109 © 2007 NRC Canada

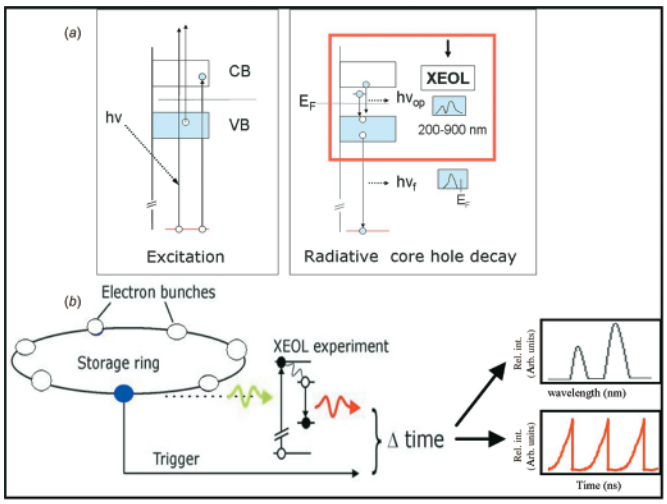
probe for colour-centre study by being able to tune the excitation energy across the absorption edges of elements of interest, such as Ca $L_{3,2}$- and O K-edges. This capability allows for the study of the production of colour centres as well as their luminescence properties.

In this study, we show colour-centre luminescence induced by synchrotron radiation in the soft X-ray region. Radiation damage of crystals is a typical process in which the energy of the intrinsic electronic excitation is converted into lattice defects (i.e., oxygen vacancies) (7). With soft X-rays, one phenomenon is photon-stimulated desorption, in which O^+ ions from the oxide surface can be desorbed as the X-ray is tuned across the O K-edge. This process results from the creation of the O 1s core hole, with subsequent Auger decay and coulomb explosion (two inner valence holes for example). The creation of the oxygen core hole is most efficient at the O K-edge resonance (1s → p transition). Thus, soft X-ray excitation will induce colour centres, and subsequently, energy transfer from X-ray absorption to these centres can lead to luminescence, which in turn will be used to monitor the absorption across the edge. This is sometimes known as optical X-ray absorption near-edge structure (XANES). Here, we present X-ray excited optical luminescence (XEOL) and XANES results of calcium oxide at the Ca $L_{3,2}$- and O K-edges, using total electron yield and luminescence yield detection schemes.

XEOL is an X-ray photon-in/optical photon-out technique in which the optical luminescence excited by tunable X-rays from synchrotron radiation is monitored with an optical spectrometer (8). XEOL deals with the measurement of specific optical de-excitation channels associated with the energy redistribution by a system upon the absorption of an energetic photon. Optical luminescence allows for the system to dissipate the excess energy from a highly excited state (e.g., with a core hole). It can be produced by direct excitation as well as secondary processes in which energetic electrons (photoelectron and Auger electrons for example) thermalize in the solid, producing more secondary electrons and holes. Fig. 1 shows a schematic of the XEOL process in both the energy (Fig. 1*a*) and time domains (Fig. 1*b*), starting from the excitation of a system by an incoming X-ray (Fig. 1*a*, left panel) to the relaxation process (Fig. 1*a*, right panel).

Time-resolved XEOL (TRXEOL) measurements has also been performed, where the lifetime of optical luminescence, which can range from nanoseconds to hundreds of nanoseconds, is studied (9). Also, luminescence within a certain time window after excitation can be used for time-gated XEOL and time-gated photoluminescence yield (PLY) XANES. This method takes advantage of the time structure of a synchrotron storage ring in which electrons are bunched by the radio frequency (RF) cavity, and as a result the emitted light is pulsed, the length of which is much shorter than the time gap between consecutive bunches (10). At the Canadian Light Source (CLS) where this experiment was conducted, the pulse width is ~60 ps, and the repetition rate is 570 ns in a single-bunch mode (11). Figure 1*b* shows a schematic of the TRXEOL process and a synchrotron storage ring with electron bunches. The emitted light pulses are monochromatized to desired excitation energies. Upon absorption, the energy of the excited state is transferred to primary de-excitation channels, such as Auger and X-ray fluorescence (fast), and secondary de-excitation processes, such as thermalization of electrons and holes and XEOL (slow). Within the XEOL time domain, the decay time can span from picoseconds to microseconds. Thus, TRXEOL can be used to study the luminescence properties of a broad variety of light emitting systems, including semiconductor nanostructures, organic light emitting device (OLED) materials, and soft matters.

Fig. 1. Schematic of (*a*) XEOL, showing the excitation and the recombination of holes and electrons leading to optical photon hv_{op} and fluorescent X-rays, hv_f, (*b*) TRXEOL, showing synchrotron radiation from a storage ring, electron bunches, the excitation light pulse (green), and the luminescence (red); the decay curve (stop–start) as well as the time-gated emission are shown in the inset.



XANES probes the local structure and bonding of an atom in a chemical environment by monitoring the atomic absorption coefficient modified by the molecular potential. As the photon energy approaches the threshold, a new excitation channel is switched on and transitions from core to bound, quasi-bound, and continuum states take place. A sharp resonance called whiteline is often observed at the onset of the threshold; it arises from the dipole transition from the core to high densities of unoccupied states, e.g., from 1s to p character at the bottom of the conduction band in ionic and semiconductor solids and to the LUMO in molecules. XANES is an element-specific method, sensitive to oxidation states and coordination chemistry. The detail of XANES is determined by the chemical environment (e.g., crystal field, density of unoccupied states, and the orientation of the specimen with respect to the polarization of the photon).

For light-emitting materials, three different channels can be used in measurements: (*i*) total electron yield (TEY), (*ii*) total fluorescence yield (FLY), and (*iii*) photoluminescence yield (PLY). TEY refers to the total electron yield upon excitation and is generally proportional to the absorption coefficient in a uniform specimen and is surface-sensitive. FLY refers to X-ray fluorescence yield and is bulk-sensitive. PLY refers to optical photon yield; either total (zero order) or partial (selected wavelength) yield (time-gated or ungated) can be used to monitor absorption edges.

© 2007 NRC Canada

In the measurements reported here, the probing depth of PLY is comparable to FLY and is more bulk sensitive than TEY.

Experimental

CaO powder was purchased from Alfa Aesar (Ward Hill, Massachusettes, USA, 99.95% purity, <10 μm particle size). All XEOL and TRXEOL measurements, with the exception of XANES at calcium K-edge, were performed on the spherically grating monochromator (SGM) beamline (undulator energy range: 200–2000 eV, resolution $E/\Delta E$: >5000) at the CLS (operation energy: 2.9 GeV). Operating current for our measurement was 250 mA at injection; a current up to 15 mA was used for the single-bunch measurement. XANES measurements at the calcium K-edge was performed on the double crystal monochromator (DCM) beamline (energy range: 1500–4500 eV, resolution $E/\Delta E$: ~2000) at Canadian Synchrotron Radiation Facility (CSRF) at the Synchrotron Radiation Center (SRC), University of Wisconsin-Madison. Luminescence was measured with a monochromator (JY-100) and a photomultiplier tube (PMT) (Hamamatsu R943–02), which has a range of 160 nm to 930 nm. The sample was prepared by spreading the powdered compound on a piece of double-sided carbon tape on a steel disk (diameter ~1 cm). The steel disk was mounted onto a sample holder. For the colour-centre study, the sample was irradiated at oxygen K-edge, 542 eV, for 1 h, and XEOL measurements were made at a 10 min intervals. The tape was checked to ensure no light-emitting impurity was present. At the set parameter, the flux was approximately 5×10^{10} photons/(s mA). For X-ray absorption measurements, oxygen K-edge and calcium $L_{3,2}$-edge XANES spectra were obtained on the same beamline. TEY, FLY, and PLY were obtained simultaneously using specimen current, a channel plate detector, and the JY-100 described earlier, respectively. For all experiments, the incoming monochromatic beam, I_0, was measured using a gold mesh detector upstream of the sample chamber. Photon flux was calibrated with a silicon photodiode. All experiments were performed at room temperature and under high vacuum conditions.

Results and discussions

XEOL and TRXEOL

XEOL spectra of CaO powder with excitation energy at the oxygen K-edge (542 eV) collected at various time intervals are shown in Fig. 2. The inset shows the spectral range from 250 to 450 nm to highlight the features of interest. All spectra have been normalized to the intensity of the incoming monochromatic photon flux (I_o).

Four peaks can be clearly distinguished at 326, 404, 607, and 808 nm. By performing Gaussian peak fits, shoulder peaks were found at 354 and 652 nm. The peak at 808 nm is the second order of 404 nm; the same can be said for the peak at 652 nm (second order of 326 nm). The peaks at 326 (3.8 eV) and 404 nm (3.1 eV) are attributed to emissions from F^+-centres and F-centres, respectively. At the early stage of irradiation, the number of F^+-centres dominate, although there are also some contributions from F-centres as well. As the sample is irradiated longer, more F-centres appear, causing the relative intensity of the peak at 404 nm to increase. This increase in intensity can be attributed to the creation of new vacancy sites and the conversion of previously created F^+-centres to F-centres. The evidence for the latter was observed previously by Pogatshnik (1), where continuously exposing a sample of calcium oxide under UV light in the region of absorption of the F^+-centre (325 nm) led to photo-conversion of F^+-centres to F-centres.

Fig. 2. XEOL spectra of CaO irradiated by synchrotron radiation at the oxygen K-edge (542 eV) at given time intervals. Inset: close-up view of spectral range from 250 to 450 nm.

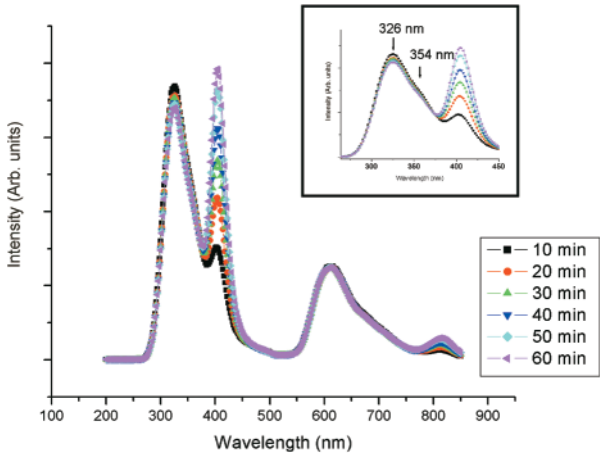
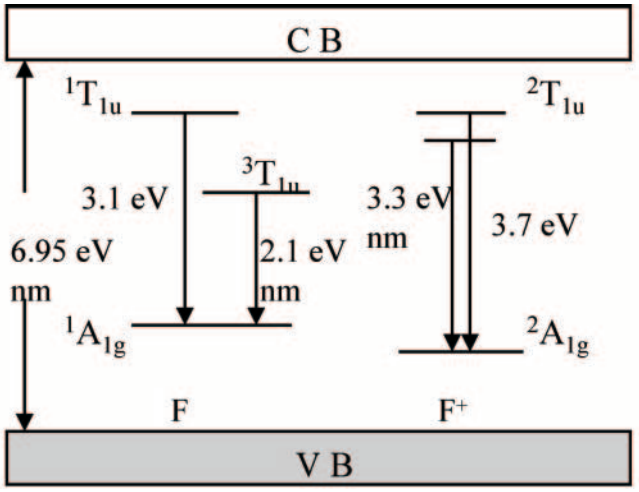


Fig. 3. Schematic for CaO F^+-centre and F-centre emission; arrows indicate possible routes for XEOL. The energy separations are experimental values given in ref. 6.



A schematic energy diagram of CaO colour centers based on previous experimental and theoretical evidence is illustrated Fig. 3. From Fig. 3, we see that F-centers (oxygen vacancy replaced with two electrons) show absorption and emission features at longer wavelengths than the F^+-centers (one electron, unpaired, magnetic). The values are from previous experiments (6). Theory also yields similar results. The origins of these emissions are more or less understood as illustrated. De-excitation from a singlet or triplet in the case of F-centres and from doublet to doublet in the case of the F^+-centres produce the optical emissions. In some cases,

© 2007 NRC Canada

intersystem crossing is involved, leading to slower decays (7).

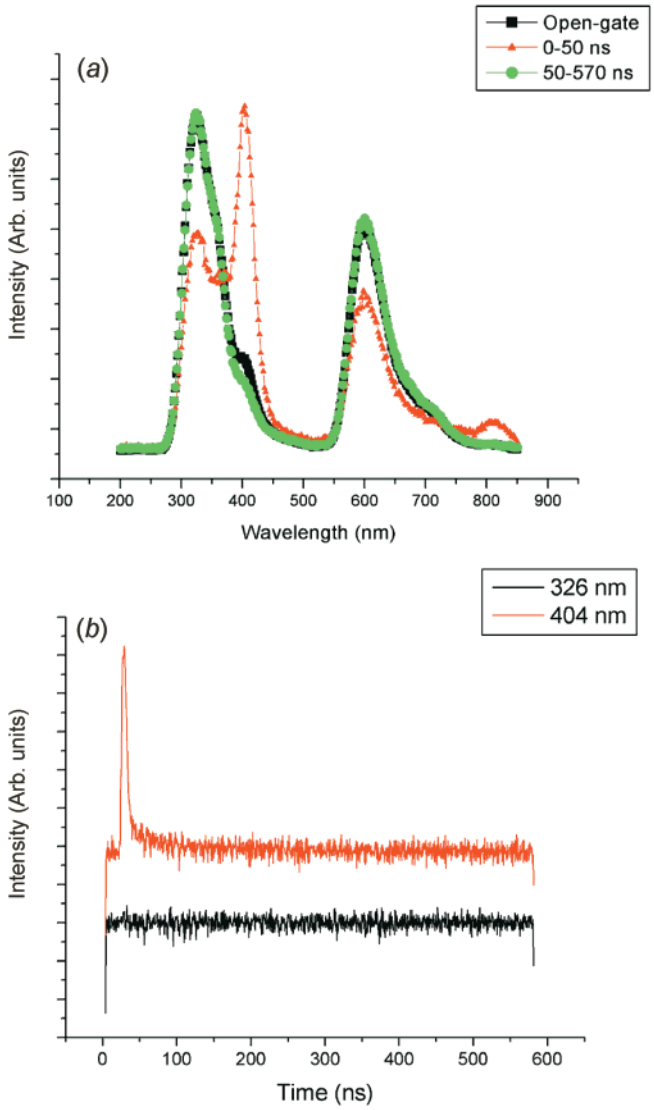
Returning to Fig. 2, the 326 nm (3.8 eV) and 404 nm (3.07 eV) emissions are the $^2T_{1u}(x, z) \rightarrow {}^2A_{1g}$ (F^+) and the triplet $^1T_{1u} \rightarrow {}^1A_{1g}$ (F) transitions, respectively, according to Carrasco et al. (6). The emission at 354 nm (3.5 eV) and 607 nm (2.04 eV) are attributed to fluorescence from the self-absorption of photons emitted from F^+-centres (326 nm) and F-centres (404 nm), respectively, which also closely agree with theoretical and experimental values reported by Carrasco et al. for the $^2T_{1u}(y) \rightarrow {}^2A_{1g}$ (F^+) and $^3T_{1u} \rightarrow {}^1A_{1g}$ (F) transition (6). The latter transitions involve intersystem crossing and have time implication (slow) as confirmed by time-resolved measurements discussed later. It should be mentioned that the XEOL experiment excited at the Ca L-edge (see later) is dominated by F^+-centres and does not produce F-centres as dramatically as that at the oxygen edge. Thus, the time-dependent F-centre production observed in Fig. 2 with excitations at the O K-edge is likely tied to the large absorption coefficient at the O K-edge, enhancing photon stimulated desorption (desorbing O^+ ion following the creation of oxygen core hole), producing surface defects; also, very little luminescence was observed with excitations at the Ca K-edge in a recent measurement; these issues will be addressed elsewhere.

TRXEOL was performed on a new spot of the specimen at three different time windows: open-gate (0–570 ns), fast (0–50 ns), and slow (50–570 ns). The resulting spectra are shown in Fig. 4*a*. At first glance, the F-centre emission (404 nm) is dominant at the fast time window, whereas the F^+-centre emission (354 nm) is more intense at the slow time window, and there is only a very small contribution due to F-centre emission (404 nm). Close examination reveals that the 326 nm channel, which is near the 354 nm channel, is also fast. The results indicate that the F-centre $^1T_{1u} \rightarrow {}^1A_{1g}$ and F^+-centre $^2T_{1u}(x,z) \rightarrow {}^2A_{1g}$ emissions are narrower and decay much faster than the $^3T_{1u} \rightarrow {}^1A_{1g}$ (F) and $^2T_{1u}(y) \rightarrow {}^2A_{1g}$ (F^+) channels. This is expected, as noted earlier, since the slow pathway involves intersystem crossing. Another interesting observation is that at open-gate, the relative intensity of the luminescence of F^+-centres (326 nm) is much greater than that of F-centres (404 nm), which is another indication that there are more F^+-centres present initially. Timing results (Fig. 4*b*) show the decay behaviour at the two main emission wavelengths, 326 and 404 nm. The curve shows much faster decay characteristics at the F-centre emission (404 nm), compared with the F^+-centre emission (326 nm), although, the proximity of the much slower 354 nm emission has undoubtedly interfered with the measurement, as we can see from Fig. 4*a* that the 326 nm emission is faster than the nearby 354 nm emission. The fast decay for the 404 nm emission appears to be comparable to the time-resolution of the PMT. More detailed analysis awaits further investigation.

XANES

It is also interesting to investigate the O K-edge and Ca $L_{3,2}$-edge XANES with photoluminescence yield. Figure 5 shows the XANES spectra (TEY spectrum and PLY spectra at 326 nm, 404 nm, and zero-order) of calcium oxide around the oxygen K-edge. All spectra have been normalized to I_o.

Fig. 4. (*a*) TRXEOL spectra of CaO at three different time windows: open-gate (0–570 ns), fast (0–50 ns), and slow (50–570 ns); (*b*) plots showing decay behaviour at 326 and 404 nm.



On the TEY XANES, the edge jump is at ~537 eV and there is a sharp resonance at 542 eV. Also seen is a broad peak at 548 eV with shoulders on either side. The edge jump and beyond is attributed to the 1s → 2p transition, mapping the unoccupied densities of states. The sharp peak is likely due to localized states, such as OH on the surface. On the PLY, the edge jumps are negative (i.e., inverted spectra), which is similar to observations made by Bianconi et al. (12) and Naftel et al. (13) with calcium fluoride. This is due to saturation (total absorption, sometimes known as the thickness effect) (14). At total absorption (all photons are absorbed), the attenuation length of the X-ray, which is approximately 300 nm at the O K-edge, is much smaller than the sample thickness. Below the edge, the X-ray beam can penetrate much deeper into the sample, irradiating more atoms. At these energies, although all photons are absorbed, the core electrons are not excited. At the absorption edge, core electrons are excited to previously unoccupied levels turning on Auger and fluorescence channels near the surface. Through

© 2007 NRC Canada

Fig. 5. Oxygen K-edge XANES spectra of calcium oxide showing the TEY spectrum and PLY spectra at 326 nm, 404 nm, and zero-order.

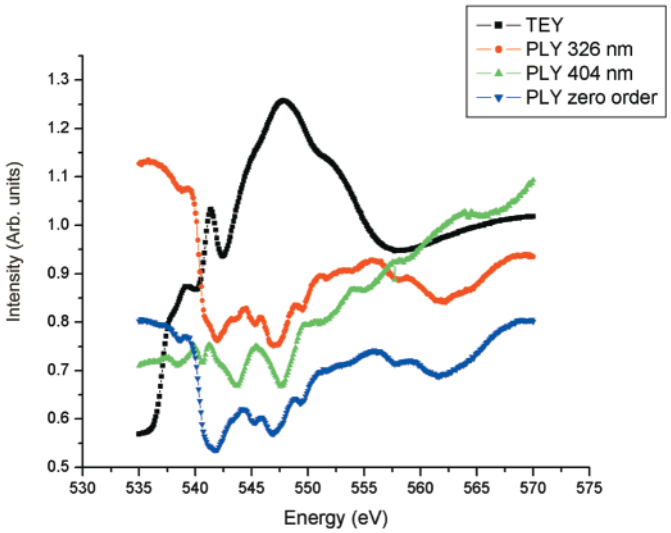


Fig. 6. Calcium $L_{3,2}$-edge XANES spectra of calcium oxide showing the TEY spectrum and PLY spectra at 326 nm, 404 nm, and zero-order.

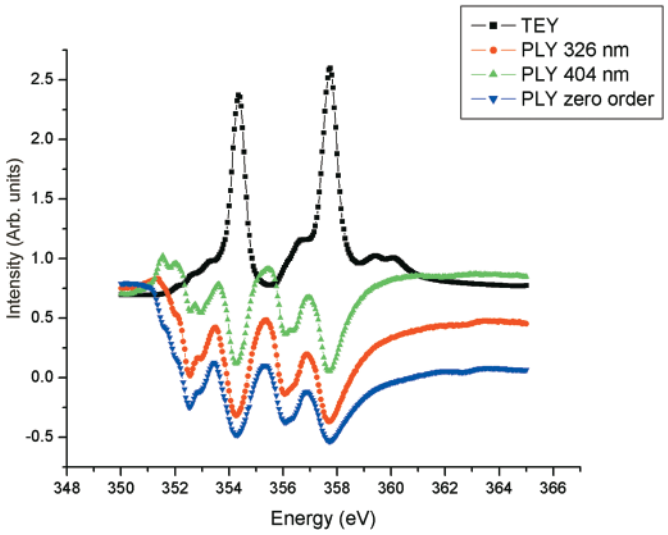
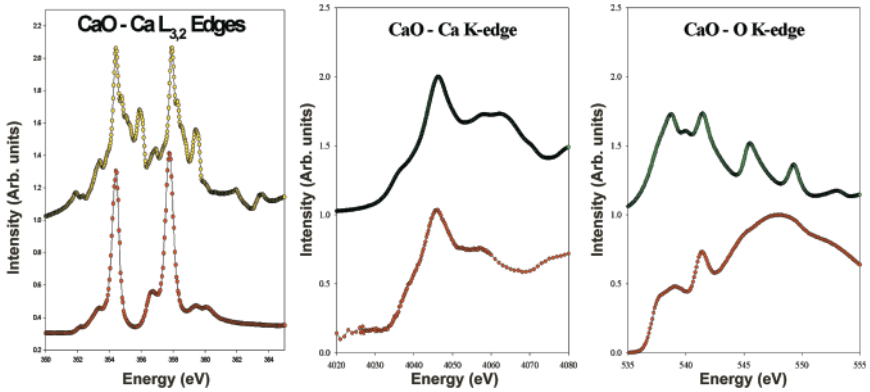


Fig. 7. Comparison of calculated XANES (top) with experiment (bottom) at the Ca $L_{3,2}$–edge (left), Ca K-edge (middle), and O K-edge (right) of CaO. Linewidths used in the convolution are from left to right, 0.1 eV, 5 eV, and 1 eV, respectively.



these channels, the excess energy can be carried by fluorescence X-rays and Auger electrons without contribution to the energy transfer to the medium (conversion to optical channel). In other words, Auger electrons and fluorescence X-rays can leave the sample without being reabsorbed. This reduces the efficiency of optical photons being produced per photon absorbed (i.e., reduced quantum yield, an inversion). In addition to inversion, the spectral features also vary depending on the yield. Although the details of the features are complex and will not be addressed here, one can see that the F-centre emission exhibits a different pattern than that of the F^+-centre.

Figure 6 shows XANES spectra (TEY spectrum and PLY spectra at 326 nm, 404 nm, and zero-order) of calcium oxide around calcium $L_{3,2}$-edge. Two sharp peaks can be seen at 354 and 358 eV. The peaks are due to excitation from core $2p^63d^0$ to $2p^53d^1$ or $2p^54s^1$ (more accurately, densities of states containing these characters) dipole transitions. (15). Smaller peaks that precede the main peaks are sensitive to the symmetry of atoms surrounding the Ca^{2+} ion in the first coordination sphere (16). They also have predominantly triplet characteristics and arise from spin-orbit coupling and Coulombic repulsion (17). The PLY-XANES features at the Ca $L_{3,2}$-edge bear considerable similarity to the TEY, compared with the O K-edge PLY-XANES. Again, the F-centre (404 nm) yield shows an interesting pre-edge feature between 351 and 352 eV, not observed in F^+-centre luminescence, suggesting a delay in the turn-on of the inversion.

XANES from DFT calculations

We have also conducted DFT calculations for the densities of states of CaO and corresponding XANES at the Ca $L_{3,2}$–edge,and Ca and O K-edge using the WIEN code, which solves the Kohn–Sham equation (18–20). These calculations employed the CaO lattice parameter of the rock-salt structure. Figure 7 compares the calculated XANES with experiment. The calculated spectra are broadened with a constant energy window so that the whiteline has about the same width as that of the experiment. It is interesting to note that although these calculations show reasonable agreement with experiment for CaF_2 (13) and at the Ca K-edge for CaO, the higher energy regions (post-whiteline) in the calculated

© 2007 NRC Canada

spectra for the shallower core levels, Ca $L_{3,2}$ and O K-edge of CaO, appear to be spiky and overemphasized. The whiteline and pre-edge features are in reasonable agreement however. The spiky features are due to high densities of l+1 states and should smooth out with an energy-dependent lifetime broadening, which increases significantly above the threshold (21). More details of these comparisons will be discussed elsewhere.

Conclusions

We have shown that luminescence centres (F^+-centre and F-centre) of calcium oxide can be created effectively by irradiating the sample with synchrotron radiation at the O K-edge. At the earlier stage of irradiation there are more F^+-centres, but continuing exposure converts some of these previously created F^+-centres to F-centres. We also observed that these colour centers can effectively convert the excess energy into optical channels. Moreover, using the TRXEOL technique we were able to identify timing characteristics of the colour-centre emissions; that is, that F-centre emission is a faster process than the F^+-centre emission. Experimental XANES and DFT calculations are in reasonable agreement.

Acknowledgements

Part of the research described in this paper was performed at the Canadian Light Source, which is supported by Natural Sciences and Engineering Research Council of Canada (NSERC), the National Research of Canada (NRC), Canadian Institutes of Health Research CIHR, and the University of Saskatchewan. The Synchrotron Radiation Center, University of Wisconsin-Madison, is supported by the National Science Foundation under award No. DMR-0537588. Research at CSRF is supported by NSERC and NRC. Research at UWO is supported by NSERC, Canada Research Chairs CRC (TKS), and Ontario Innovation Trust (OIT). We would like to acknowledge Astrid Jürgensen and Narayana Apathurai for their assistance with experiments at CSRF.

References

1. G.J. Pogatshnik. J. Lumin. **60/61**, 535 (1994).
2. M. Kirm, E. Feldbach, R. Kink, A. Lushchik, Ch. Lushchik, A. Maaroos, and I. Martinson. J. Electron. Spectrosc. Relat. Phenom. **79**, 91 (1996).
3. M.A. Bolorizadeh, V.A. Sashin, A.S. Kheifets, and M.J. Ford. J. Electron. Spectrosc. Relat. Phenom. **141**, 27 (2004).
4. J.L. Park, Y. Chen, G.P. Williams Jr., R.T. Williams, and G.J. Pogatshnik. Phys. Rev. B: Condens. Matter, **43**, 11991 (1991).
5. O.E. Taurian, A.H. Tang Kai, and V. Lobatch. J. Phys. Chem. Solids, **47**, 59 (1986).
6. J. Carrasco, C. Sousa, F. Illas, P.V. Sushko, A.L. and Shluger. J. Chem. Phys. **125**, 074710 (2006).
7. P.A. Rodnyi. Physical processes in inorganic scintillators. CRC Press. NY. 1997. p. 165.
8. T.-K. Sham, D.T. Jiang, I. Coulthard, J.W. Lorimer, X.H. Feng, K.H. Tan, S.P. Frigo, R.A. Rosenberg, D.C. Houghton, and B. Bryskiewicz. Nature, **363**, 331 (1993).
9. R.A. Rosengerg, G.K. Shenoy, F. Heigl, S.-T. Leel, P.-S.G. Kim, X.-T. Zhou, and T.-K. Sham. Appl. Phys. Lett. **86**, 263115 (2005).
10. F. Heigl, A. Jürgensen, X.-T. Zhou, S. Lam, M. Murphy, J.Y.P. Ko, T.-K. Sham, R.A. Rosenberg, R. Gordon, D. Brewe, T. Regier, and L. Armelao. American Institute of Physics Conference Proceedings. Vol. 879. Synchrotron Radiation Instrumentation: Ninth International Conference on Synchrotron Radiation Instrumentation. *Edited by* J.-Y. Choi, and S. Rah. American Institute of Physics, Daegu, Korea. 2006. pp. 1202–1205.
11. F. Heigl, S. Lam, T. Regier, I. Coulthard, and T.-K. Sham. J. Am. Chem. Soc. **128**, 3906 (2006).
12. A. Bianconi, D. Jackson, and K. Monahan. Phys. Rev. B, **17**, 2021 (1978).
13. S.J. Naftel, Y.M. Yiu, T.-K. Sham, and B.W. Yates. J. Electron Spectrosc. Relat. Phenom. **119**, 215 (2001).
14. J.Y.P. Ko, X.-T. Zhou, F. Heigl, T. Regier, R. Blyth, T.-K. Sham. American Institute of Physics Conference Proceedings. Vol. 882. X-ray absorption fine structure – XAFS13: 13th International Conference. *Edited by* B. Hedman, and P. Pianetta. American Institute of Physics, Stanford, CA, USA. 2006. pp 538–540.
15. A. Rogalev and J. Goulon. In Chemical applications of synchrotron radiation. Part II. *Edited by* T.-K. Sham. World Scientific Co., Singapore. 2002. p. 707.
16. S.J. Naftel, T.-K. Sham, Y.M. Yiu, and B.W. Yates. J. Synchrotron Rad. **8**, 255 (2001).
17. F.M.F. de Groot, J.C. Fuggle, B.T. Thole, G.A. Sawatzky, Phys. Rev. B, **41**, 928 (1990).
18. P. Blaha, K. Schwarz, J. Luitz. WIEN 97 [computer program]. Vienna University, Vienna, Austria. 1997.
19. P. Blaha, K. Schwarz, P. Sorantin, S.B. Trickey. Comput. Phys. Commun. **59**, 399 (1990).
20. W. Kohn and Sham. Phys. Rev. A, **104**, 1133 (1965).
21. J.E. Muller, O. Jepsen, and J.W. Wilkins. Solid State Commun. **42**, 365 (1982).

© 2007 NRC Canada

Cross-linking organic semiconducting molecules by preferential C-H cleavage via "chemistry with a tiny hammer"[1]

W.M. Lau, Z. Zheng, Y.H. Wang, Y. Luo, L. Xi, K.W. Wong, and K.Y. Wong

Abstract: In the context of collision-induced dissociation in chemistry and kinematics in physics, we have determined that a beam of hyperthermal protons can be used as tiny hammers to preferentially break the C-H bonds of hydrocarbon precursor molecules adsorbed on a conductive substrate with little damage to other chemical bonds. The activated molecules are thereby converted to a cross-linked molecular network, with its chemical properties tailored by the preservation of the chemical functional groups of the precursors and with its physical properties tuned by the degree of cross-linking. This "chemistry with a tiny hammer" process is adopted to induce inter-chain cross-linking of the semiconducting molecular chains in poly (3,4-ethylenedioxythiophene) molecular films and to raise the electrical conductivity and stability of the molecular films. The results exemplify the unusual reaction design of this process as well as its application in electronic and optoelectronic device fabrication. The application is particularly attractive because the process does not require any chemical additives or catalysts other than a beam of protons, and it needs no thermal budget.

Key words: organic semiconductor, polymeric semiconductor, cross-linking, polymer, collision, dissociative collision, molecular electronics, device fabrication.

Résumé : On a démontré que, dans le contexte d'une dissociation induite par une collision en chimie et de la cinématique en physique, un faisceau de protons hyperthermiques peut être utilisé comme un petit marteau pour briser préférentiellement les liaisons C-H de molécules d'hydrocarbures précurseurs adsorbés sur un substrat conducteur, avec un minimum de dommage aux autres liaisons chimiques. Les molécules activées sont ainsi transformées en un réseau moléculaire réticulé dont les propriétés chimiques sont déterminées par la conservation des groupes fonctionnels chimiques des précurseurs alors que ses propriétés physiques sont ajustées par le degré de réticulation. On a adopté ce processus de chimie avec un minuscule marteau pour induire des réticulations interchaînes de chaînes moléculaires semiconductrices dans des films moléculaires de poly(3,4-éthylènedioxythiophène) et augmenter la conductivité électrique ainsi que la stabilité des films moléculaires. Les résultats obtenus mettent en relief le caractère inhabituel de la réaction impliquée dans ce processus ainsi que ses possibilités d'application dans la fabrication de dispositifs électroniques ou optoélectroniques. L'application est particulièrement intéressante en raison du fait que le processus ne requiert aucun additif ou catalyseur chimique, à l'exception d'un faisceau de photons et ne nécessite aucun budget thermique.

Mots-clés : semiconducteur organique, semiconducteur polymère, réticulation, polymère, collision, collision dissociative, électronique moléculaire, fabrication de dispositifs.

[Traduit par la Rédaction]

Introduction

Polythiophene and its derivatives have drawn much attention in recent materials research because of their potential applications in many electronic and optoelectronic devices, such as photodiodes, polymeric light emitting diodes, and electrochemical actuators (1). The molecular structure is relatively simple, with the thiophene monomers queuing like a long tape with their π units lying on the tape plane. Holes are typically injected electrochemically to convert these materials into p-type semiconductors, and the charged states are balanced with negatively charged chemical additives equiva-

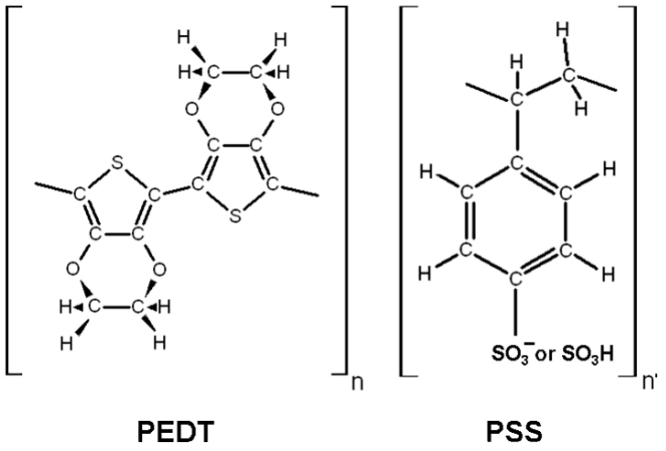
Received 24 April 2007. Accepted 27 June 2007. Published on the NRC Research Press Web site at canjchem.nrc.ca on 21 September 2007.

W.M. Lau,[2] L. Xi. Department of Physics, Chinese University of Hong Kong, Shatin, Hong Kong, China; Surface Science Western, University of Western Ontario, London, Ontario N6A 5B7 Canada.
Z. Zheng. Institute of Surface Micro and Nano Materials, Xuchang University, Xuchang, 461000, China; Department of Physics, The Chinese University of Hong Kong, Shatin, Hong Kong, China.
Y.H. Wang, Y. Luo, K.W. Wong, and K.Y. Wong. Department of Physics, The Chinese University of Hong Kong, Shatin, Hong Kong, China.

[1]This article is part of a Special Issue dedicated to Professor G. Michael Bancroft.
[2]Corresponding author (e-mail: llau22@uwo.ca).

 doi:10.1139/V07-101 © 2007 NRC Canada

Fig. 1. The molecular schematic structure of PEDT and PSS.



lent to the negatively charged p-type dopants in an inorganic semiconductor (such as B^- in p-Si). Among all polythiophenes, poly(3,4-ethylenedioxythiophene) (commonly referred as PEDT), mixed with poly(styrene sulphonate) (commonly referred as PSS) as its "dopant", has received worldwide acceptance as a practical conductive polymer because it possesses good optical and electrical properties and also high processibility in the conventional aqueous form (2–6). The basic molecular structures of PEDT and PSS are shown in Fig. 1. Various PEDT:PSS products with their PEDT/PSS molar ratio, amounts of chemical additives, and physical properties optimized for specific applications are commercially available and comprehensively reviewed (3,7). In general, the ultimate properties of any PEDT:PSS molecular film very much depend on the experimental conditions during preparation, in addition to the choice of a specific PEDT:PSS product (3, 7). For example, the as-deposited molecular film is typically required to be thermally cured in the temperature range of 50–300 °C for it to show the best performance in film stability and electrical conductivity (3, 7, 8). However, the molecular film is also known to be susceptible to degradation by environmental factors like oxygen, moisture, heat, light, and mechanical stress (2–11). Immediately, one sees that the effects of thermal energy are particularly interesting (9–11). On the one hand, excessive input of thermal energy can cause undesirable phase separation, drive oxidation, and compositional degradation and induce undesirable diffusion of materials in the relevant device structure. On the other hand, appropriate thermal treatments are known to drive the residual solvent and impurities out, improve structuring ordering and inter-chain charge transport, and even induce additional cross-linking in the presence of appropriate additives. However, because of the hygroscopic nature of many polymeric semiconductors, particularly PEDT:PSS, some of the improvement in conductivity gained by thermal annealing can be lost very quickly in air (8). In short, it is desirable to develop alternative post-deposition processes to improve the stability and electrical conductivity of the molecular film, particularly dry chemical processes that are compatible to device fabrication and that thus ideally require no thermal budget and no chemical additives.

This article reports on our trials to explore if cross-linking the PEDT molecules in the PEDT:PSS molecular film with a nonthermally driven method can improve its stability and electrical conductivity. Briefly, we adopt the kinematics-driven method (12–14) of using hyperthermal proton bombardment of organic precursor molecules adsorbed on a conductive substrate to preferentially cleave C-H bonds and thereby cross-link the precursors to a stable molecular network. Unlike the typical design considerations of chemical reactions in which chemical additives and catalysts are added to reduce the reaction energy barrier and thermal energy is used to drive the reaction, the design strategy of this kinematics-driven method employs hydrogen projectiles like tiny hammers to preferentially break C-H bonds of the organic precursors, and the reaction is driven by the kinematic energy transfer in the collision (15). Therefore, by nature the method imposes little risks in chemical contamination and virtually no thermal budget. Thus, it is attractive in the development of new fabrication processes for the production of organic electronic and optoelectronic devices.

Explanation of the new cross-linking method using hyperthermal protons

The kinematics-driven method for cross-linking adsorbed organic precursor molecules with hyperthermal proton bombardment is rather unusual in comparison to the conventional synthetic chemistry. The basic physics and chemistry of this method have already been shown elsewhere recently (12–14). Briefly, in the simplest embodiment a high vacuum reactor is used to facilitate the irradiation of the organic precursor molecules adsorbed on a conductive substrate with a beam of protons such that no other undesirable surface contamination reactions including oxidation occur. The kinetic energy of the protons is a reaction variable, but is assumed to be 10 eV in this explanatory example. When such a proton travels to about 0.5 nm from the surface, the probability of electron tunneling from the valence band below the Fermi level of the conductive substrate (including the valence band of the adsorbed molecular film) to the empty 1s level of the proton is very high. Hence, prior to any direct atomic interactions between the proton and the atoms or molecular moieties on the substrate, the proton is converted to an atomic hydrogen projectile with a kinetic energy of 10 eV.[3] Under the first-order approximation of hard-sphere binary collision (16), a projectile colliding head-on with a target transfers its kinetic energy most effectively, with the energy transfer frac-

[3] This clarification is important because the electronic energy carried by a proton amounts to 13.6 eV and is thus significantly higher than the projectile kinetic energy in most of our hyperthermal proton bombardment experiments described in Refs. 12–14 and in this present article. The validity of the expectation of surface neutralization prior to any collision induced dissociation of molecules on the surface is supported by the large and consistent group of experimental data (Refs. 12–14) that shows the observed reaction outcomes from the collision induced dissociation of molecules on the surface are critically dependent on the kinetic energy of the projectile. The optimum energy for cross-linking acrylic acid molecular units with no damage of the COOH group (Ref. 14) was found to be ~5–6 eV, which is much less than 13.6 eV.

© 2007 NRC Canada

tion equal to $4M_pM_t/(M_p + M_t)^2$, where M_p and M_t are the mass of the projectile and target, respectively. Hence, a hydrogen projectile having a kinetic energy of 10 eV can transfer virtually all of its kinetic energy to its collision partner in a head-on collsion if this partner is also a hydrogen atom, but the maximum energy transfer amounts to only 2.8 eV if the partner is a carbon atom. The maximum energy transfer to the collision partner further reduces when the partner is heavier than carbon. Since the bond energy of C-H, C-C, and most other bonds in an organic molecule are typically about 3–5 eV, the collision can break C-H but not other bonds. As such, chemical selectivity can be derived from the nature of the kinematics and chemistry and by controlling the proton energy. In addition, this collision approach of breaking C-H bonds also attractively offers a high reaction yield. The collision cross-section for a projectile energy of 10 eV is typically a few $Å^2$ (16, 17). In comparison, although atomic hydrogen at room temperature (average kinetic energy of about 0.04 eV) is known to cause hydrogen abstraction, which can lead to the cleavage of a C-H bond, the reaction cross-section (18) is merely ~0.05 $Å^2$.

With this kinematics-driven method, precursor molecules such as dotriacontane (12), polyisoprene (13), docosanoic acid (14), and poly(acrylic acid)oligomer (14) have previously been deposited on a substrate such as a silicon wafer and treated with protons at 1–50 eV. The preferential C-H cleavage induced by the proton bombardment produces carbon radicals, and the recombination of them leads to cross-linking of the precursors. The evidence of collision-induced cross-linking has been proven by spectroscopic data, including photoemission evidence of a rising density of branching carbon with increasing proton fluence and secondary ion mass spectrometric evidence of the formation of such branching hydrocarbon chains. In addition, the relative degree of cross-linking has also been estimated by measuring the solubility of the molecular film in an organic solvent because the virgin film is soluble and the solubility decreases because of cross-linking. Indeed, the solubility decreases with increasing proton fluence. Further, the expectation that insufficient proton energy will compromise the C-H cleavage yield and excessive proton energy will lead to C-C bond breakage has also been confirmed by studying the reaction system as a function of the incident proton energy. The optimal proton energy for cross-linking simple saturated hydrocarbon molecules, such as dotriacontane ($CH_3(CH_2)_{30}CH_3$), is indeed around 10 eV, and when the proton energy is raised to 15–50 eV some C-C cleavage becomes detectable (12). At 50 eV, the reactivity of C-H cleavage is high such that a low fluence of less than 1×10^{16} cm^{-2} is enough to cross-link the molecules to the extent that the film is no longer soluble in hexane; yet the chemical selectivity is compromised such that even at this low fluence C-C bond cleavage is no longer negligible, and a loss of about 1 nm in molecular film thickness is evident. Since in the course of our research on cross-linking adsorbed hydrocarbon molecules we have found that most straight chain saturated hydrocarbon molecules with a carbon chain length shorter than 32 carbon atoms readily desorb in ultrahigh vacuum, the material loss induced by proton bombardment at 15–50 eV is likely due to C-C cleavage and fragment desorption. If we assume that one C-C cleavage is enough to lead to fragment desorption, we can estimate from the fluence dependence of molecular film loss that about 100 protons at 50 eV are required to cause one C-C cleavage with the result of fragment desorption. In comparison, from the fluence requirement for cross-linking the adsorbed molecules such that the molecular film becomes insoluble in hexane, we have also estimated that on average 10 protons are required to induce enough C-H cleavage to lead to the degree of cross-linking required for making the molecular film insoluble in hexane (12).

In summary, the expected preferential cleavage of C-H bonds induced by proton bombardment of adsorbed saturated hydrocarbon molecules in the energy range of 1–50 eV has already been verified experimentally. The experimental results indicate that the probability of C-H cleavage rises with increasing proton bombardment energy in this energy range. Although C-C bond cleavage is evident when the bombardment energy is raised to 15–50 eV, the probability of C-C cleavage relative to C-H cleavage is low because most of the collisions are not head-on and the amounts of kinetic energy transfer to a carbon target atom in most of these cases are still not enough for C-C cleavage. For cross-linking adsorbed saturated hydrocarbon molecules with this "chemistry with a tiny hammer" approach, the bombardment energy of ~10 eV seems to give the best combination of chemical reactivity and selectivity (12).

The results of proton bombardment of a molecular film of hydrocarbon molecules containing carboxylic acid functionality show another interesting feature of the new reaction approach because if the kinematics can drive C-H cleavage, it should also drive O-H cleavage (14). If so, the original chemical functionality of the precursor molecules can no longer be preserved and the technological impact is compromised. It turns out that the O-H bond is stronger than the C-H bond; hence, the O-H cleavage yield should drop more than the C-H cleavage yield when the proton energy is lowered. Indeed this has been proven experimentally (14); using a proton energy of around 6 eV with proper fluence control, molecular films of docosanoic acid and poly(acrylic acid)oligomer have been effectively cross-linked with little damage to the carboxylic acid functionality.

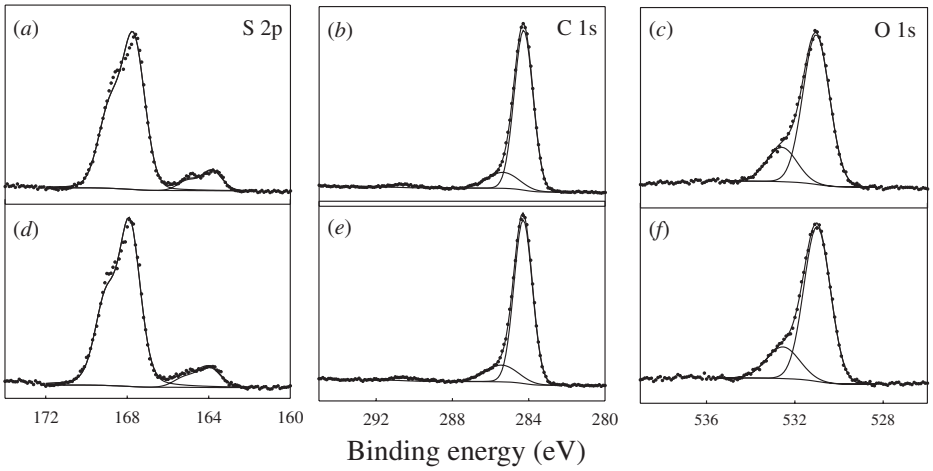
Therefore, with the kinematics-driven method one conducts chemistry with hyperthermal atomic hydrogen as a tiny hammer to preferentially break C-H bonds. Unlike the design of conventional chemical reactions, the design of reactions in this chemistry with a tiny hammer approach does not employ chemical additives, catalysts, and thermal energy to drive the reaction forward. Instead, it uses a beam of protons as the reagent and the proton kinetic energy as the main driving force. The design takes advantage of the ease in precisely controlling the proton fluence and the high collision cross-section. The magic of chemistry is enhanced by these attributes that are common to physicists but uncommon to synthetic chemists

Results and discussion on hyperthermal proton bombardment of PEDT

To test if the chemistry with a tiny hammer is effective in cross-linking the molecules in a PEDT:PSS film, one should track the solubility of the molecular film because it should decrease as a function of proton energy and fluence, as the

© 2007 NRC Canada

Fig. 2. (*a–c*) XPS S 2p, C 1s, and O 1s of the as-prepared PEDT:PSS film; (*d–f*): XPS S 2p, C 1s, and O 1s of the same film after the proton bombardment at 10 eV and a fluence of 2.0×10^{16} cm^{-2}.



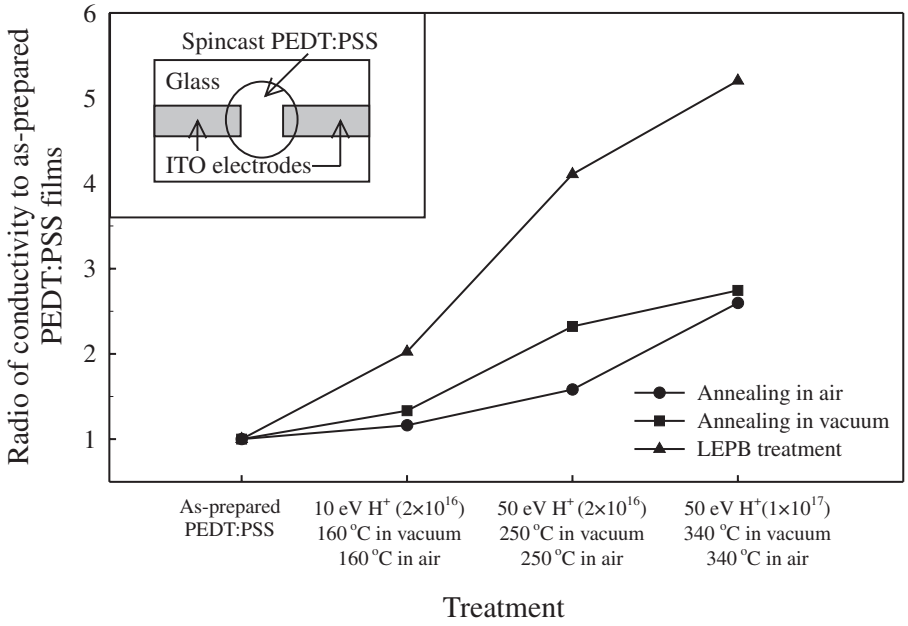
solubility qualitatively reflects the degree of cross-linking. In fact, we have verified this experimentally. Briefly, the as-prepared PEDT:PSS films (~50 nm in thickness, measured by standard profilometry) can be completely removed by dissolution in de-ionized water. For PEDT:PSS films bombarded with hyperthermal protons, the film solubility decreases with increasing fluence for the same bombardment energy. It also decreases with increasing proton energy for the same fluence. For example, for the bombardment with 50 eV protons to a fluence of $2x10^{16}$ cm^{-2}, the average residual film thickness surviving the dissolution test amounts to 80% of the original film thickness. Hence, this implies that most of the molecules in the film have become cross-linked to the extent that they are no longer soluble in water. The bombardment with 10 eV protons can also yield the same results but the fluence has to be about 10 times higher. The correlation between proton bombardment and decrease in solubility, together with no undesirable chemical functionality change as shown later, suggests that the proposed chemistry with a tiny hammer approach to preferentially break C-H bonds and cross-link molecules is indeed applicable to the present work on hyperthermal proton bombardment of PEDT:PSS films. By controlling the degree of cross-linking with the bombardment conditions, the film solubility and stability can be adjusted and improved with no requirement of any thermal treatments.

The core value of the hyperthermal proton bombardment method is its chemical selectivity of breaking C-H bonds and thereby inducing chain cross-linking without compromising the desirable chemical functionalities of the precursor molecules. For the hyperthermal proton bombardment of the PEDT:PSS film, this is demonstrated by the results of chemical state analysis with XPS. Figures 2*a*–2*c* show the XPS C 1s, S 2p, and O 1s spectra of the as-prepared PEDT:PSS film on Au. The spectral features are consistent with the XPS data in the literature (9). Among them, the S 2p spectra are particularly informative. The convoluted doublet at the low binding energy end (163.9 eV) is attributed to the S $2p_{3/2}$ and S $2p_{1/2}$ spectral peaks of the sulfide of PEDT and that at the high-binding energy end to the sulphate of PSS. The latter is about 10 times more intense than the former because (*i*) the as-received PEDT:PSS solution mixture has a PEDT:PSS mixing molar ratio of about 1:4.5 for the optimal solubility and conductivity of the material, (*ii*) the PEDT:PSS film is granular because the as-received PEDT:PSS product comprises of pre-mixed PEDT:PSS gel particulates in an aqueous solution with the hydrophilic PSS orienting towards the particulate surface, and (*iii*) during film formation, the grain surfaces are enriched with PSS. Following this interpretation, we can also assign the small spectral components in the C 1s and O 1s spectra to the carbon atoms and oxygen atoms of the PEDT units and the intense components to those of the PSS units. A comparison of these chemical state data before and after the proton bombardment clearly shows that although the bombardment is effective in breaking C-H bonds and cross-linking the precursors, the overall chemical functionality properties are intact. In fact, the spectral data in Figs. 2*d*–2*f* are commonly found from the films bombarded by protons with a fluence up to $1x10^{17}$ cm^{-2}, no matter whether the energy is 10 or 50 eV. Further, by checking the characteristic energy loss spectral intensity of C 1s at ~292 eV, we have also found no change in the basic π nature of the molecules in the PEDT:PSS film, as any significant damage of the π nature will lead to a decrease of this π–π^* interband energy loss intensity. In this context it is relevant to note that if the protons are replaced with inert gas ions, the kinematics favoring preferential C-H cleavage is replaced with indiscriminating bond cleavage because of the relatively high mass of the inert gas projectiles. For example, it has been shown that by bombarding the same sample with 100 eV Ar^+ to the fluence of $1x10^{17}$ cm^{-2}, the PSS spectral component drops and the PEDT spectral component rises to the extent that the two spectral components have similar spectral intensities (19). Hence, unlike proton bombardment at 10–50 eV, the bombardment of the PEDT:PSS sample with a "heavy and indiscriminating hammer" like 100 eV Ar^+ can cause significant damage of the molecular chains and subsequent molecular fragment desorption. Therefore, we infer that the chemical functionalities of PEDT:PSS survive well in the proton bombardment experiments, and no significant degradation of the molecular chain and its chemical functionality is induced.

In addition to increasing film stability, the common prac-

© 2007 NRC Canada

Fig. 3. Ratio of conductivity of the PEDT:PSS film after different treatments to that of the as-prepared PEDT:PSS film (LEPB means low energy proton bombardment; the lines are drawn to aid readers in following the trends and bear no scientific content; the fluence is always measured as number of ions per cm^2). Inset: schematics of the electrical conductivitiy measurements.



tice of thermal curing as-deposited PEDT:PSS also improves the electrical conductivity of the film. Thus, the main goal of this work is to determine if the hyperthermal proton bombardment treatments can also improve the film conductivity. In this analysis, the current–voltage characteristics of a strip of PEDT:PSS deposited across two electrodes are measured and the analysis is applied to films before and after proton bombardment with different bombardment conditions. The analysis is also repeated for films before and after the common thermal curing treatments. The results are schematically summarized in Fig. 3 and clearly show that the hyperthermal proton bombardment is more effective than the common thermal curing treatments in increasing film conductivity. The observed evidence of raising the electrical conductivity by proton bombardment implies that the chemistry with a tiny hammer has induced some inter-molecular cross-linking of PEDT, since intermolecular cross-linking of PSS molecules and intermolecular cross-linking of PSS and PEDT should not increase the electrical conductivity of the molecular film.

To explain how the chemistry with a tiny hammer can effectively increase the electrical conductivity of the PEDT:PSS molecular film, we resort to the origin of electrical conductivity of the film. The basic conducting element is the polythiophene chain. When holes are injected to the π-conjugated polythiophene chain and stabilized by the PSS dopant unit, the holes can travel along the π-conjugated molecular "tape" with the planar arrangement of each pair of adjacent thiophene units spanning across the width of the tape. Holes from one conductor tape jump to another conductor tape when the two tapes are closely spaced, with their π–π system effectively overlapped at the "tape–tape" crossing point. Ideally, stacking the molecular tapes in an ordered fashion enhances the conductivity, but in many practical systems such as the PEDT:PSS molecular films in this study, its "crystallinity" is known to be weak mainly because it is difficult to accommodate the PSS chains in a crystalline stack of the polythiophene molecules (3, 8, 10, 20). Hence, in the following discussion, the PEDT molecules are assumed to be randomly packed, with many "tape–tape" crossing points having their separations affected by the thermally driven molecular motions in the film.

The main difference between the PEDT chain and the basic polythiophene chain can be simplified to merely widening the molecular tape of the polythiophene chain with an U-shape ethylenedioxy side branch for each thiophene unit (as shown in Fig. 1). This side branch depletes the remaining two C-H bonds of each thiophene unit, and because of this the conjugated backbone has no C-H bonds at all and cannot interact with the low energy proton projectiles (actually atomic hydrogen projectiles, as explained earlier) when the kinematics is not violent enough to break the strong bonds in the conjugated backbone. Experimentally, we find that proton bombardment at 10–50 eV is effective in improving the stability and electrical conductivity of PEDT, with no detectable undesirable effects such as materials loss even with a fluence up to $1x10^{17}$ cm^{-2}. This is not inconsistent with the hyperthermal proton bombardment of a film of adsorbed dotriacontane ($CH_3(CH_2)_{30}CH_3$, film thickness of 11nm). The C-C bond in this straight-chain hydrocarbon molecule is much weaker than the conjugated carbon bonds in the polythiophene units. Since the probability of C-C bond cleavage in dotriacontane has been found (12) to be much lower than that of C-H bond cleavage for proton projectiles with kinetic energy at 10–50 eV, the probability of damaging the conjugated carbon bonds should be even lower.

With the preceding clarification, we postulate several pathways that can lead to the observed increase in electrical conductivity. Further computational and experimental studies are underway to examine the validity of such postula-

© 2007 NRC Canada

tions. Nevertheless, the postulated pathways are summarized as follows:

(*i*) During the cascade collision process, some of the incident proton kinetic energy is dissipated to the PEDT molecules and this promotes molecular diffusion towards energy minimization with more intermolecular π–π overlapping. The effect is similar to enhancing molecule ordering by thermal annealing (8, 10).

(*ii*) Time-of-flight laser-induced ion mass spectrometry has been used to show (3) that the PEDT molecules in the commercially available PEDT:PSS product used in this study are actually relatively small and have not more than ~10 monomer units. If this is true and the head and tail thiophene units are terminated by C-H bonds, these C-H bonds can be cleaved during the hyperthermal proton bombardment. A pathway is thus created for cross-linking small PEDT molecules to larger PEDT molecules with longer conjugated lengths. Intuitively, we judge that the chance of having this rather special cross-linking condition is low. Since this pathway should lead to a significant increase in the average conjugation length and thus to an observable red shift of the optical absorption, we have begun to examine the effects of proton bombardment on the optical properties. Our preliminary results indeed indicate no observable red shift, which implies this cross-linking pathway being unimportant.

(*iii*) The chemistry with a tiny hammer approach can break the C-H bonds of the "ethylenedioxy" side branch and can thereby enable another cross-linking pathway. In the following discussion, we postulate that in the granular PEDT:PSS films studied in this work, each grain contains nominally flat molecular tapes randomly tangling together, with some of them having inter-chain separations as close as the van der Waals bond distance. By chance, inter-chain π–π overlapping may happen, and as explained earlier, electrical conductivity is induced. Thermally driven molecular motions may compromise such π–π overlapping and limit the electrical conductivity. Harnessing the chemistry with a tiny hammer to break C-H bonds without breaking other bonds can lock some of these casual inter-chain junctions by covalently cross-linking the ethylenedioxy side branches of the two nearby ethylenedioxy–thiophene units. Such a lock can thus secure the inter-chain π–π overlapping. This cross-linking reaction can then lead to the observed decrease in solubility and increase in electrical conductivity of the bombarded film. Computational modeling of such inter-chain π–π overlapping is expected to give a more detailed picture of this proposed pathway. In addition, experimental measurements of the proposed bonding changes of some of the ethylenedioxy side chains with NMR and secondary ion mass spectrometry are also informative. These studies are indeed underway in our research group.

Conclusion

In summary, the chemistry with a tiny hammer approach of using hyperthermal proton bombardment to induce preferential C-H cleavage and cross-link adsorbed organic precursors is shown to be applicable to the technologically important PEDT-based molecular films. Proton bombardment in a wide energy window of 10–50 eV is found to be effective in increasing both stability and electrical conductivity. There may be several plausible reaction pathways leading to these observed desirable effects, and further computational modeling and experimental studies are underway to examine the effectiveness of each individual reaction channel. In general, the film improvement method is attractive in that it does not use any chemical additives and catalysts other than protons in a dry process, and it does not require any thermal budget. It is conceivable that the method is applicable to the fabrication of other organic semiconductor films and devices.

Experimental

The PEDT:PSS (Baytron P AI 4083) stocks used in this report were purchased from Bayer AG (7). The PEDT:PSS molar mixing ratio is ~1:4.5. As-received PEDT-PSS was spin-cast on Au/Si substrates. The XPS analysis was conducted with a Kratos AXIS-HS spectrometer equipped with a monochromatic Al Kα source. For the current–voltage measurements of electrical conductivity, PEDT:PSS was spin-cast on patterned ITO electrodes on glass and the film conductivity was characterized with a Keithley 236 source measurement unit. Hyperthermal proton bombardment was performed with a mass-resolved low-energy ion beam system. Both the instrument and the basic hyperthermal ion bombardment process have already been described elsewhere (21). The PEDT-PSS film on an Au/Si substrate was bombarded with 10 and 50 eV proton beams at fluences up to 1×10^{17} cm^{-2}. The film solubility analysis was conducted by rinsing the film sample in de-ionized water for one minute and the change in film thickness was measured by a standard profilometer. For comparison, the film conductivity and solubility of PEDT:PSS films annealed in both air and ultrahigh vacuum (base pressure ~10^{-9} torr; 1 torr = 133.322 4 Pa) were also measured.

Acknowledgement

This work was partially supported by the Physics Department of the Chinese University of Hong Kong, the Research Grant Council of Hong Kong (Grants No. 402803 and No. 401303), the National Natural Science Foundation of China (Grant No. 20574058), NSERC Discovery Grant (Grant No. 327221 06), Surface Science Western, and the Faculty of Science of the University of Western Ontario. The principle author, Leo Lau, has developed his career through the vibrant research activities facilitated by Surface Science Western, which was founded by Professor Mike Bancroft. In addition, he is also grateful to the invaluable scientific and personal advice which he has continuously received from Professor Bancroft since 1983.

References

1. For example, see: Handbook of conducting polymers. 2nd ed. *Edited by* T.A. Skotheim, R.L. Elsenbaumer, and J.R. Reynoids. Marcel Dekker, NY. 1998; Handbook of Oligo- and polythiophenes. *Edited by* D. Fichou. Wiley-VCH, Weinheim, Germany. 1999.

© 2007 NRC Canada

2. L.B. Groenendaal, F. Jonas, D. Freitag, H. Pielartzik, and J.R. Reynolds. Adv. Mater. **12**, 481 (2000).
3. S. Kirchmeyer and K. Reuter. J. Mater. Chem. **15**, 2077 (2005).
4. S.C.J. Meskers, J.K.J. van Duren, R.A.J. Janssen, F.Louwet, and L. B. Groenendaal. Adv. Mater. **15**, 613 (2003).
5. S. Bereznev, I. Konovalov, A. Opik, and J. Kois. Synth. Met. **152**, 81 (2005).
6. A.V. Murugan. J. Power Sources, **159**, 312 (2006).
7. For example, see: The product data sheet of Baytron available from www.baytron.com.
8. (*a*) J. Huang, P.F. Miller, J.C. de Mello, A.J. de Mello, and D.D.C. Bradley. Synth. Met. **139**, 569 (2003); (*b*) H.S. Huang, P.F. Miller, J.S. Wilson, A.J. de Mello, J.C. de Mello, D.D.C. Bradley. Adv. Funct. Mater. **15**, 290 (2005).
9. (*a*) X. Crispin, S. Marciniak, W. Osikowicz, G. Zotti, A.W. Denier van der Gon, F. Louwet, M. Fahlman, L. Groenendaal, F. De Schryver, and W.R. Salaneck. J. Polym. Sci., Part B: Polym. Phys. **41**, 2561 (2003); (*b*) G. Greczynski, Th. Kugler, M. Keil, W. Osikowicz, M. Fahlman, and W.R. Salaneck. J. Electron. Spectrosc. Relat. Phenom. **121**, 1 (2001).
10. J.Y. Kim, E.R. Kim, Y.S. Won, H.S. Lee, and K.S. Suh. Synth. Met. **139**, 485 (2003).
11. L. Lam, J.W. McBride, and J. Swingler. J. Appl. Polym. Sci. **101**, 2445 (2006).
12. Z. Zheng, X.D. Xu, X.L. Fan, W.M. Lau, and R.W.M. Kwok. J. Am. Chem. Soc. **126**, 12336 (2004).
13. Z. Zheng, W.M. Kwok, and W.M. Lau. Chem. Commun. (Cambridge, U.K.), 3122 (2006).
14. Z. Zheng, K.W. Wong, W.C. Lau, R.W.M. Kwok, and W.M. Lau. Euro. J. Chem. In press.
15. "Chemistry with a hammer" was first used by S.T. Ceyer to describe her work on employing hyperthermal argon and kryton projectiles to collide with adsorbed CH_4 molecules on nickel and induce the dissociattion of the adsorbed molecules. See: S.T. Ceyer. Science, 249, **133** (1990).
16. E.S. Parilis. Atomic collisions on solid surfaces. North-Holland Press, Amsterdam, The Netherlands. 1993.
17. R. Martinazzo and G.F. Tantardini. J. Chem. Phys. **124**, 124702 (2006).
18. J. Kuppers. Surf. Sci. Rep. **22**, 251 (1995).
19. Y.H. Wang. Thesis for a Master Degree of Philosophy, Department of Physics, The Chinese University of Hong Kong. August 2005.
20. K.E. Aasmundtveit, E.J. Samuelsen, L.A.A. Pettersson, O. Inganas, T. Johansson, and R. Feidenhans. Synth. Met. **101**, 561 (1999).
21. W.M. Lau, X. Feng, I. Bello, S. Sant, K.K. Foo, and R.P.W. Lawson. Nucl. Instrum. Methods Phys. Res., Sect. B, **59/60**, 316 (1992).

© 2007 NRC Canada

Examining the structural changes in $Fe_2(CO)_9$ under high external pressures by Raman spectroscopy[1]

Muhieddine Safa, Zhaohui Dong, Yang Song, and Yining Huang

Abstract: Pressure-induced structural changes in di-iron nonacarbonyl [$Fe_2(CO)_9$] were examined by in situ Raman spectroscopy with the aid of a diamond anvil cell. Our results indicate that $Fe_2(CO)_9$ undergoes a pressure-induced phase transformation at about 0.9 GPa. Upon further compression, another structural transformation is identified at 7 GPa. In the low-pressure phase below 0.9 GPa, the π back-bonding between metal and carbonyl increases with increasing pressure. In the high-pressure phase above 7 GPa, the combination of high-pressure and laser irradiation induces a change in structure from $Fe_2(CO)_9$ to $Fe_2(CO)_8$. $Fe_2(CO)_8$ appears to adopt a structure with C_{2v} rather than D_{3d} or D_{2h} symmetry. The metal–metal bond is gradually weakened under high pressures, and $Fe_2(CO)_8$ eventually decomposes by breaking the Fe–Fe bond when compressed up to 17.7 GPa.

Key words: metal carbonyl, Raman spectroscopy, high pressure, diamond anvil cell.

Résumé : Faisant appel à la spectroscopie Raman in situ avec l'aide d'une cellule à matrice de diamant, on a étudié les changements structuraux induits par la pression dans le difernonacarbonyle, [$Fe_2(CO)_9$]. Les résultats obtenus indiquent que le $Fe_2(CO)_9$ subit une transformation de phase induite par la pression à environ 0,9 GPa. Par compression subséquente, on a identifié une autre transformation structurale à 7 GPa. Dans la phase à basse pression, en dessous de 0,9 GPa, la liaison en retour π entre le métal et les carbonyles augmente avec une augmentation de pression. Dans la phase à haute pression, au-dessus de 7 GPa, une combinaison de pression élevée et une irradiation au laser induit un changement dans la structure de $Fe_2(CO)_9$ à $Fe_2(CO)_8$. Le $Fe_2(CO)_8$ semble adopter une structure de symétrie C_{2v} plutôt que les symétries D_{3d} ou D_{2h}. La liaison métal–métal s'affaiblit graduellement sous des pressions élevées et le $Fe_2(CO)_8$ se décompose éventuellement par bris de la liaison Fe–Fe lorsqu'on atteint une pression de 17,7 GPa.

Mots-clés : métal carbonyle, spectroscopie Raman, pression élevée, cellule à matrice de diamant.

[Traduit par la Rédaction]

Introduction

Vibrational spectroscopy has long been the method of choice for the characterization of organometallic compounds because it provides invaluable information on the molecular geometry, crystal structures of the solid complexes, and the nature of the bonding interactions in these compounds. Using external pressure as an independent variable to explore the change in molecular geometry and phase behavior of organometallic carbonyls is quite important, since many of the transition metal carbonyls exhibit interesting changes in both molecular and crystal structures under high external pressures (1, 2), but these changes often do not occur upon lowering temperatures.

The high-pressure studies are usually performed with the aid of diamond anvil cells (DACs). Coupling of a DAC to a Raman spectrometer provides an extremely useful approach to examine the metal carbonyls under pressures because the spectra in the CO stretching region (~2000 cm^{-1}) are very sensitive to the change of molecular geometry and crystal structure. The pressure dependences ($d\nu/dP$) of the ν(CO) and ν(M–CO) modes of transition-metal carbonyls provide the information regarding the π back-bonding between metals and the carbonyl groups. The corresponding IR spectroscopy is much less useful, since the strong diamond adsorption completely masks the ν(CO) region (3).

The structures of binuclear transition-metal carbonyls, such as $Mn_2(CO)_{10}$, $Re_2(CO)_{10}$ and $MnRe(CO)_{10}$ have been examined by Raman spectroscopy under high pressures (4, 5). A second-order phase transition was detected, but more interestingly, the molecular geometry changed from the staggered structure (D_{4d}) to an eclipsed configuration (D_{4h}) in each case.

Tri-μ-carbonyl(hexacarbonyl)di-iron(0), $Fe_2(CO)_9$, was one of the earliest known metal carbonyls and remains to be one of the best-known examples for binuclear transition-metal carbonyls. This complex is an important reagent for organic synthesis and is a catalyst as well. The crystal struc-

Received 09 May 2007. Accepted 30 June 2007. Published on the NRC Research Press Web site at canjchem.nrc.ca on 21 September 2007.

This manuscript is dedicated to Professor G. Mike Bancroft in honor of his 65th birthday.

M. Safa, Z. Dong, Y. Song,[2] and Y. Huang.[3] Department of Chemistry, The University of Western Ontario, London, ON N6A 5B7, Canada.

[1]This article is part of a Special Issue dedicated to Professor G. Michael Bancroft.

[2]Corresponding author (e-mail: yang.song@uwo.ca).
[3]Corresponding author (e-mail: yhuang@uwo.ca)

 doi:10.1139/V07-096 © 2007 NRC Canada

ture has been determined by single-crystal X-ray diffraction (6, 7). The unit cell adopts a space group of $P6_3/m$ with two molecules per unit cell residing at C_{3h} sites and a molecular symmetry of D_{3h} (Fig. 1). The vibrational spectra of $Fe_2(CO)_9$ at ambient pressure and low temperature have been assigned (8–10). The low-temperature Raman studies indicated that there is no phase transition occurring at temperatures as low as 15 K (8). In addition, $Fe_2(CO)_9$ exhibits interesting photochemistry. The early study of Poliakoff and Turner showed that this complex undergoes the CO disassociation under irradiation (11, 12). $Fe_2(CO)_8$ was captured as a key product at very low temperature in matrixes. Structures of di-iron carbonyls with different stoichiometry [$Fe_2(CO)_x$] together with their bonding natures between the two irons have been extensively characterized by Xie et al. (13) using various computational approaches. Very recently, the photochemistry of $Fe_2(CO)_9$ was further examined by Bertini et al. (14) using time-dependent DFT theory.

In the present study, we have investigated the behavior of $Fe_2(CO)_9$ under high external pressures up to about 18 GPa. Particular attention was paid to the possible pressure-induced phase transition, the geometry change and the combining effect of laser irradiation and applying high pressure on the photochemical behavior of $Fe_2(CO)_9$.

Experimental

Polycrystalline powder of $Fe_2(CO)_9$ was purchased from Alfa Aesar Chemical Company (purity ≥99%) and was used without further purification. Raman spectra were recorded on a Renishaw Model 2000 Raman spectrometer equipped with a Leica microscope and a thermoelectronically cooled CCD detector. The 632.8 nm line of a HeNe laser was used as the excitation source with an average power of several milliwatts at the sample. The resolution achieved was typically 1 cm^{-1}. The sample and several tiny ruby chips were placed in a stainless steel gasket (250 μm in diameter and 70 μm thick) mounted between two opposing anvils of a symmetric piston-cylinder type DAC. The DAC was then mounted onto an X–Y stage, and the laser beam was focused on the sample via a 4X microscope objective. The pressure was calibrated by using the well-known ruby method (15). No pressure media were used. The uncertainty for pressure determination is estimated as 0.05 GPa.

Results

Raman spectra of $Fe_2(CO)_9$ at 0–7 GPa

The Raman spectrum of $Fe_2(CO)_9$ was collected at ambient pressure and room temperature before compression and is depicted in Fig. 2. The structure of $Fe_2(CO)_9$ at ambient pressure has been well-established and extensively characterized by X-ray diffraction and vibrational spectroscopy. Under factor group analysis (9), 18 modes are predicted to be Raman active and eight modes to be IR active, while 10 modes are both Raman and IR active out of a total of 54 vibrational modes. In general, the Raman active modes are observed in two spectral regions, i.e., 1800–2150 cm^{-1} and below 600 cm^{-1}, corresponding to the carbonyl stretching and iron–carbonyl cluster vibrations, respectively. Our Raman spectrum is consistent with previous vibrational studies (9) with the major characteristic modes being observed. The assignments of these modes are labeled in Fig. 2 and listed in Table 1 in comparison with previous observations. In the carbonyl stretching region, the peaks at 2107, 2013, and 1988 cm^{-1} are attributed to the terminal carbonyls

Fig. 1. Molecular structure of $Fe_2(CO)_9$.

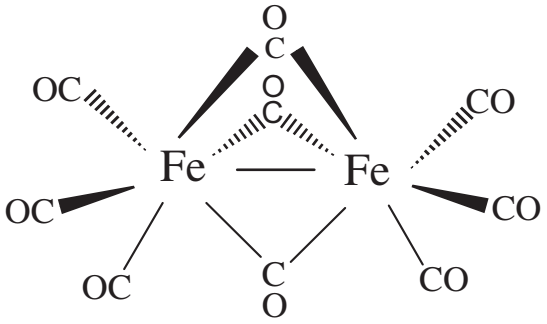
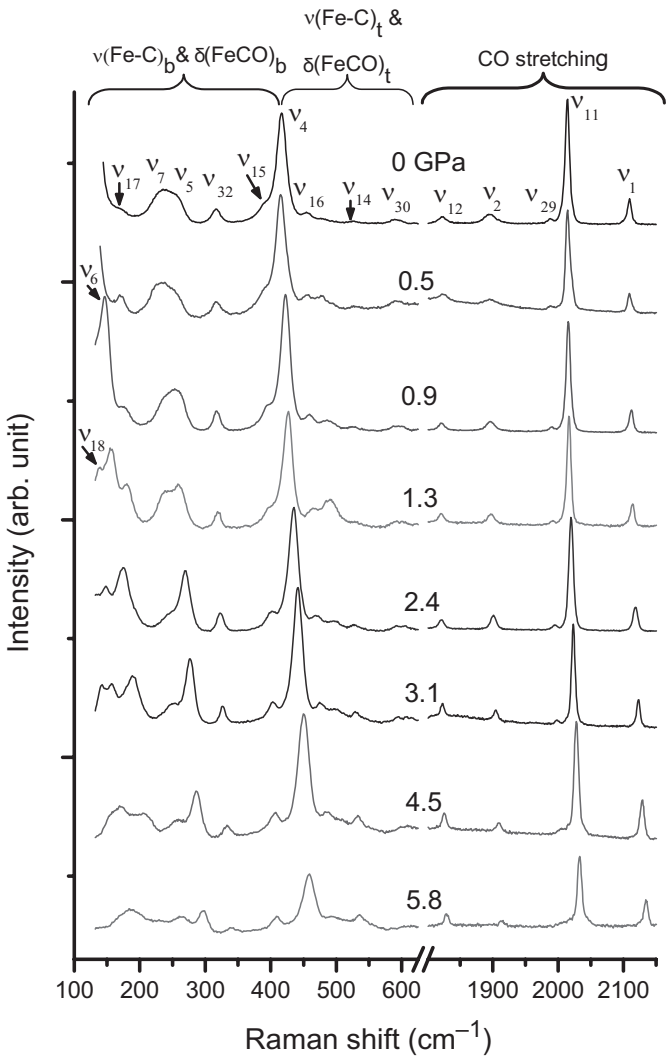


Fig. 2. Selective Raman spectra of $Fe_2(CO)_9$ on compression at 0–5.8 GPa in the spectral regions of 100–650 cm^{-1} and 1800–2150 cm^{-1}. The pressures in GPa are labeled for each spectrum. The assignments of the Raman modes are labeled on the top spectrum collected at ambient pressure. The spectra are normalized to the same scale and offset vertically for clarity.



© 2007 NRC Canada

Table 1. Assignment of Raman active modes of solid $Fe_2(CO)_9$ observed at ambient pressure and room temperature.

Mode	This work (cm^{-1})	Reference 8 (cm^{-1})	Description[a]
ν_1 (A_g)	2107	2112	$\nu(CO)_t$
ν_{11} (E_{2g})	2013	2016	
ν_{29} (E_{1g})	1988	1990	
ν_2 (A_g)	1895	1891	$\nu(CO)_b$
ν_{12} (E_{2g})	1824	1814	
ν_{30} (E″)	594	590	$(Fe–CO)_t$
ν_{14} (E′)	529	528	$\delta(Fe–CO)_t$
ν_{31} (E″)	494	493	
ν_3 (A′)	480	480	
ν_{16} (E′)	457	451	$\nu(Fe–C)_t$
ν_4 (A'_1)	415	415	
ν_{15} (E′)	393	390	$\delta(Fe–CO)_b$
ν_{32} (E″)	316	315	
ν_5 (A′)	248	260	$\nu(Fe–Fe)$, $\nu(Fe–C)_b$
ν_7 (A′)	236	237	
ν_{17} (E′)	171	175	$\nu(Fe–C)_b$
ν_6 (A'_1)[b]	142	137	$\delta(C–Fe–C)$, $\Delta(Fe_2C_3)$
ν_{18} (E′)[c]	138	126	

[a]ν: Stretching; δ: bending; Δ: cluster vibration; t: terminal; and b: bridging.
[b]First observed at 0.9 GPa.
[c]First observed at 1.3 GPa

$[\nu(CO)_t]$, while those at 1895 and 1824 cm^{-1} are associated with bridging carbonyls $[\nu(CO)_b]$. In the spectral region between 600 and 400 cm^{-1}, the vibrations are associated with the bending of the terminal carbonyls $[\delta(Fe–CO)_t]$ and the stretching between iron and terminal carbonyls $[\nu(Fe–C)_t]$. The modes below 400 cm^{-1} are due to the bending of bridging carbonyls $[\delta(Fe–CO)_b]$, the stretching between iron and bridging carbons $[\nu(Fe–C)_b]$, as well as some vibrations from iron-centred cluster $[\Delta Fe_2C_3]$ (9).

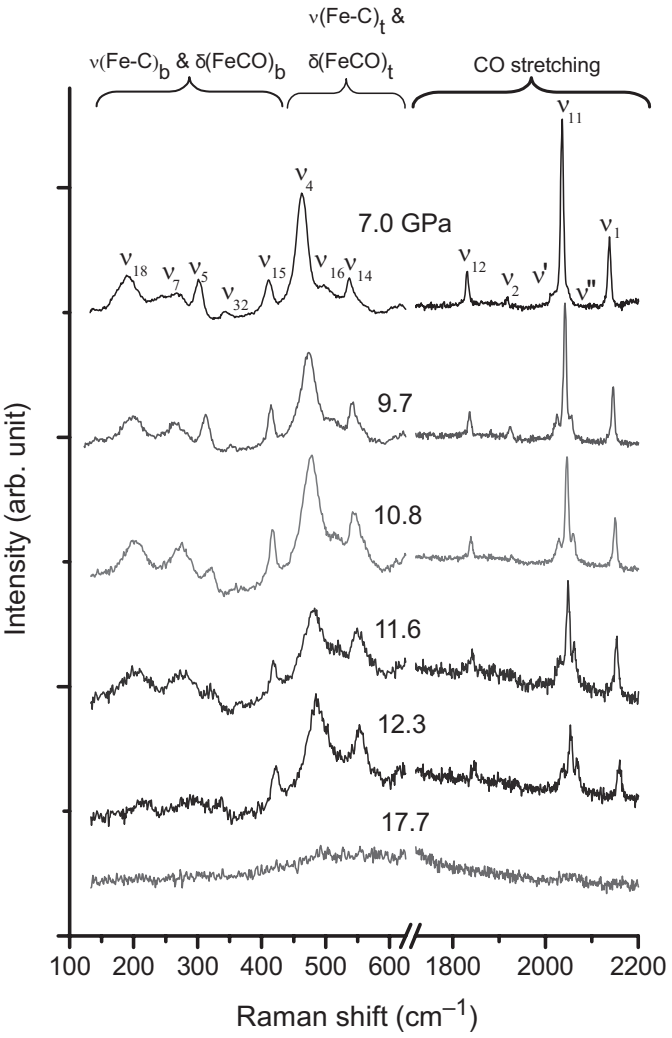
Upon compression, the Raman modes for carbonyl stretching shift to higher frequencies smoothly. The Raman intensities of these modes are relatively insensitive to pressure except for mode ν_{29}, a $\nu(CO)_t$ mode, the intensity of which decreases with pressure significantly. In the lower vibrational frequency region, the major Raman modes are found to shift to higher frequencies markedly. In addition, significant changes in Raman patterns are found in this region. For instance, ν_{15}, a very weak $\delta(FeCO)_b$ mode at 393 cm^{-1} at ambient pressure, becomes a resolvable shoulder of ν_4 mode at 0.9 GPa and is completely deconvoluted from ν_4 mode at 5.8 GPa. Furthermore, the ν_7 and ν_5 modes, which exhibit a broad convoluted peak at ambient pressure, become a resolvable doublet at 1.3 GPa, which further develops into two bands with strongly constrasting intensities. The most drastic changes of the Raman spectra are observed below 200 cm^{-1}. The ν_{17} mode is greatly enhanced by compression between 0.5–1.3 GPa but becomes indiscernible beyond 1.3 GPa. More interestingly, a new Raman mode, which is identified as ν_6 (Table 1), is observed at 0.9 GPa. This mode, which is not observable at lower pressures because of the use of an edge filter in the Raman spectrometer, shifts rapidly to higher frequency until 5.8 GPa when the intensity drops significantly. Other new modes observed include the ν_{18} mode at 138 cm^{-1} at 1.3 GPa and a band at 142 cm^{-1} at 3.1 GPa, which can be assigned as a mode associated with the iron-centred cluster vibration. These low-frequency modes become very weak with increasing pressure up to 5.8 GPa.

Raman spectra of $Fe_2(CO)_9$ at 7–17.7 GPa

Raman spectra of $Fe_2(CO)_9$ at 7–17.7 GPa are depicted in Fig. 3. At 7 GPa, eight Raman modes (ν_{18}, ν_7, ν_5, ν_{32}, ν_{15}, ν_4, ν_{16}, and ν_{14}) are observed in the low-wavenumber region below 600 cm^{-1}. These modes shift to higher wavenumbers with pressure, and their intensities decrease systematically. Concurrent to the weakening of Raman intensities, all bands become significantly broader with only three bands (ν_5, ν_4, and ν_{14}) identifiable at 12.3 GPa. When pressure is increased to 17.7 GPa, the Raman features in this region completely disappeared, indicating the destruction of the Fe–C cluster. The most striking change is observed in the carbonyl stretching region. A new peak at 2018 cm^{-1} is observed at 7.0 GPa, which develops into a relatively intense Raman mode with increasing pressure. When pressure is increased to 9.7 GPa, another new peak at 2056 cm^{-1} was observed all the way to 12.3 GPa. The intensities of these carbonyl stretching modes

© 2007 NRC Canada

Fig. 3. Selective Raman spectra of $Fe_2(CO)_9$ on compression at 7.0–17.7 GPa in the spectral regions 100–650 cm^{-1} and 1800–2200 cm^{-1}. The pressures in GPa are labeled for each spectrum. The assignments of the Raman modes are labeled on the top spectrum collected at 7.0 GPa. The spectra are normalized to the same scale and offset vertically for clarity.



are also reduced by compression with the ν_2 mode being completely unobservable at 11.6 GPa. Similar to the low frequency regions, the carbonyl stretching region exhibits absolutely no Raman feature at 17.7 GPa, indicating the compound has completely decomposed.

Pressure dependence of Raman modes of $Fe_2(CO)_9$

Figure 4 shows the Raman shifts of major modes in both the low-frequency region and the carbonyl stretching region as a function of pressure on compression. The pressure dependences $d\nu/dP$ are also listed in Table 2. As can be seen from the Fig. 4 and Table 2, below 0.9 GPa, all modes exhibit a positive linear dependence with pressure except for two modes, ν_{14} and ν_{12}, which have negative $d\nu/dP$ values. A distinct change in slope at 0.9 GPa is observed for almost all modes. In the region below 0.9 GPa, all modes follow a linear pressure dependence with larger $d\nu/dP$ values than those between 0.9 and 7 GPa, except for ν_{16}, ν_2, and ν_{11} modes, which exhibit larger $d\nu/dP$ values at the higher pressure region. Most significantly, the ν_{29}, ν_{16}, and ν_{32} modes are not observed beyond 7 GPa, while new modes in the carbonyl stretching region are observed above 7 GPa (Fig. 3), indicating a major phase or structural transition.

Discussion

Figure 4 illustrates that in the pressure region below 7 GPa, most of the Raman modes exhibit a distinct break in the slopes of the $\nu - P$ plots at around 0.9 GPa, suggesting that there is a pressure-induced phase transition. Since the discontinuities in Fig. 4 are not abrupt, and there is no change in the number of internal modes at the transition, the observed phase transformation is likely second-order. Previous vibrational studies showed no phase change occurring at low-temperature (8). Therefore, the new phase appears to only exist under high pressures.

In the low-pressure phase, three high-frequency bands at 2107, 2013, and 1988 cm^{-1} due to the terminal carbonyl stretching vibrations [$\nu(CO)_t$] steadily shifted to higher frequencies with increasing pressure. The band at 1895 cm^{-1} is almost pressure-insensitive, while the 1824 cm^{-1} band has a negative pressure-shift rate, i.e., it shifts to lower frequencies with increasing pressure. Both the 1895 and 1824 cm^{-1} bands are due to the bridging carbonyl stretching modes, [$\nu(CO)_b$]. Normally, all the internal modes shift gradually with increasing external pressure because of the anharmonicity of the potential function. Any unusual pressure behavior, such as very large, small, and even negative pressure dependence should be explained in terms of specific intra- and intermolecular interactions. The insensitivities and (or) negative pressure dependences of terminal $\nu(CO)_t$ modes have been reported in the previous high-pressure Raman studies on transition metal carbonyl complexes (16–18). Such observations were interpreted as the pressure-enhanced π back-bonding between the metal centre and the CO groups, i.e., the strengthening of the π back-bonding decreases the carbonyl bond order, which results in a constant or decreasing $\nu(CO)$ frequency. In the present case, the two bridging $\nu(CO)_b$ modes exhibit a very small and a negative pressure dependence, suggesting that in the low-pressure phase, the π back-bonding between iron and bridging carbonyl groups is particularly enhanced under external pressure. It is also worth noting that the broad peak centred at around 260 cm^{-1} exhibits a very prominent positive pressure dependence (41.5 cm^{-1}/GPa) in the low-pressure phase. This band has been previously assigned to the Fe–Fe stretching mode (8, 9). Thus, the very large pressure shift rate of the ν(Fe–Fe) mode implies that the metal–metal bond is significantly shortened by pressure.

All the results indicate that in the low-pressure phase, increasing pressure significantly affects the cluster involving two metal centres and three bridging CO groups [$(Fe_2C_3)_b$]. It appears that the bonding interactions responsible for holding the cluster together, such as metal–metal bond and the bonding between bridging CO and metal centres, are strengthened by pressure. Several binuclear transition-metal carbonyl complexes, such as $Mn_2(CO)_{10}$, $Re_2(CO)_{10}$, and $MnRe(CO)_{10}$, have been examined under high external pres-

© 2007 NRC Canada

Fig. 4. Raman shift of $Fe_2(CO)_9$ with pressure on compression for vibrations involving (*a*) iron–carbonyl and (*b*) bridging and terminal carbonyls. Different symbols denote Raman modes with different origins. The solid lines crossing the solid symbols are linear fit for eye guidance. The vertical dotted lines denote the proposed transition boundary. The assignments are labeled for each Raman active mode.

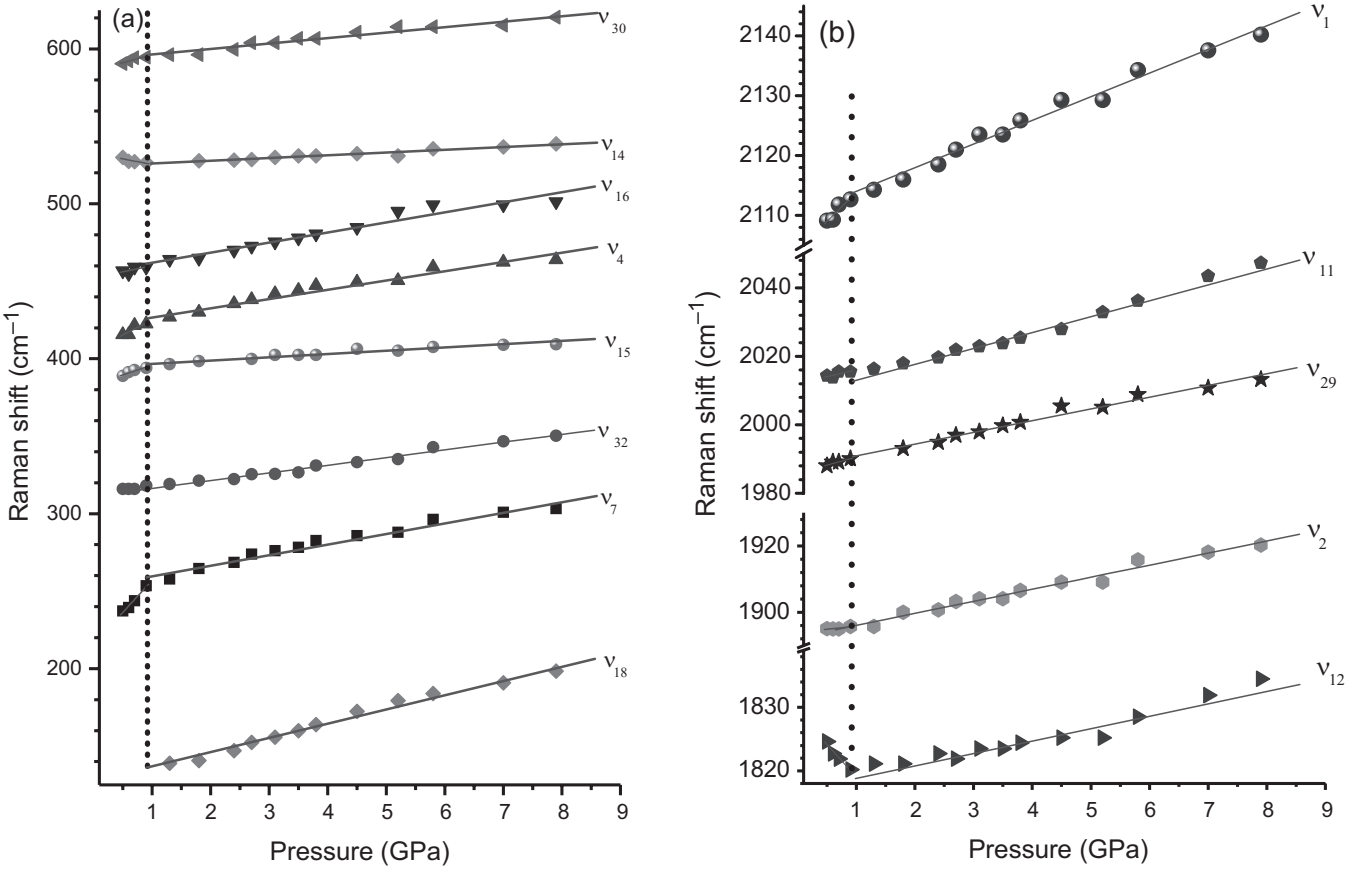


Table 2. Pressure dependence of Raman modes of $Fe_2(CO)_9$ at 0–7.0 GPa.

		$(d\nu/dP)_T$ (cm^{-1}/GPa)	
Raman modes	Frequency at ambient P (cm^{-1})	0–0.9 GPa	0.9–7.0 GPa
ν_{18}	138	—	10.7
ν_7	236	41.5	7.4
ν_{32}	316	5.5	5.0
ν_{15}	393	12.4	2.2
ν_4	415	19.4	6.3
ν_{16}	457	7.9	8.1
ν_{14}	529	–7.1	1.7
ν_{30}	594	10.3	3.8
ν_{12}	1824	–10.5	1.8
ν_2	1895	1.9	3.7
ν_{29}	1988	4.8	3.6
ν_{11}	2013	3.9	4.7
ν_1	2107	9.9	4.2

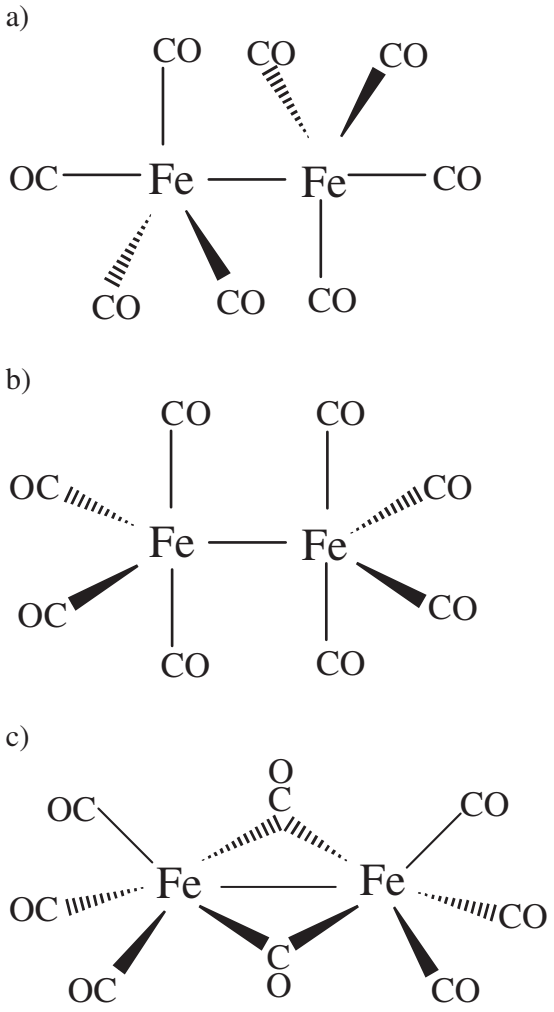
sure by Raman spectroscopy (4, 5). In each case, a change in molecular geometry from staggered (D_{4d}) to eclipsed (D_{4h}) configuration was observed. However, in the present case, the molecular geometry of $Fe_2(CO)_9$ remained as D_{3h}. Apparently, the pressure-strengthened interactions between metal centres and bridging carbonyl groups via π bonding prevents any rotation of $Fe(CO)_3$ fragment around Fe–Fe axis from changing to other configurations.

In the high-pressure phase (0.9–5.8 GPa), all the ν(CO) stretching modes are gradually shifting to the higher frequencies, including the two bands due to the bridging carbonyl groups. Overall, there is no major change in the appearance of the spectra in the ν(CO) region, indicating no change in the molecular geometry in this high-pressure phase. As shown in Fig. 2, in the low-frequency region, all the bands originating from the $(Fe_2C_3)_b$ cluster as well as all the $(Fe–CO)_b$ stretching and bending vibrations are gradually broadened with increasing pressure except for the ν_7 mode, which is mainly due to metal–metal bonding. All these results suggest that in the pressure range of 0.9–5.8 GPa, the $(Fe_2C_3)_b$ core is significantly distorted under pressure, while the $Fe(CO)_3$ groups involving terminal carbonyls are relatively unaffected.

When the pressure was increased to 7 GPa, some distinct changes were observed in the ν(CO) region. In particular, two new bands appeared at 2018 and 2056 cm^{-1} (Fig. 3). The appearance of these new bands in the ν(CO) region implies the formation of a new carbonyl species. The early work by Fletcher et al. showed that irradiation of $Fe_2(CO)_9$

© 2007 NRC Canada

Fig. 5. Proposed structures of $Fe_2(CO)_8$ with (*a*) D_{3d}, (*b*) D_{2h}, and (*c*) C_{2v} symmetries.



with UV light leads to the formation of $Fe_2(CO)_8$ at low temperature according to the following (11):

$$Fe_2(CO)_9 \rightarrow Fe_2(CO)_8 + CO$$

They were able to capture two $Fe_2(CO)_8$ isomers in matrices at 20 K: the CO bridged and unbridged $Fe_2(CO)_8$. The CO bridged isomer is a kinetic product and the unbridged compound is thermodynamically much more stable. The point groups of C_{2v} and D_{3d} were proposed for the CO bridged and unbridged $Fe_2(CO)_8$ species, respectively. The authors later established that the unbridged compound actually has D_{2h} symmetry (12). These symmetries are depicted in Fig. 5.

The work by Butler and co-workers showed that photolysis of $Fe_2(CO)_9$ can also occur during the acquisition of Raman spectra (8). In the present study, the appearance of additional ν(CO) bands suggest that $Fe_2(CO)_8$ is also formed by laser irradiation and stabilized by high external pressure. In particular, the frequencies of these new bands (2018 and 2056 cm^{-1}) are closer to those observed in the bridged $Fe_2(CO)_8$ (2022 and 2055 cm^{-1}) rather than the two high-frequency peaks of the unabridged isomer at 2006 and 2038 cm^{-1} (11). Therefore, the observations of five terminal $\nu(CO)_t$ and two bridging $\nu(CO)_b$ bands are consistent with C_{2v} symmetry (19). We also noticed that the intensity of the $\nu(CO)_b$ band, initially observed at 1895 cm^{-1}, quickly decreased with increasing pressure and is almost depleted completely at 12.6 GPa. It appears that $Fe_2(CO)_8$ may undergo further decomposition by losing one of the two bridging carbonyl groups.

In the low-frequency region, starting from 5.8 GPa, all the vibrations associated with $(Fe_2C_3)_b$ core, including the ν_7(Fe–Fe) mode, become gradually broadened with increasing pressure. At 12.3 GPa, all the previously mentioned bands become extremely broad. All these results suggest that the decomposition begins by breaking the $(Fe_2C_3)_b$ core, while the $Fe(CO)_3$ terminal groups are relatively unaffected in the beginning. Although peak broadening could be induced by structural amorphization or pressure gradients, the irreversible transformation and reasonably sharp ruby profiles rule out these possibilities and suggest that the transformation is chemical in nature. At 17.7 GPa, no Raman bands were observed, indicating that all the metal carbonyl species have completely decomposed.

Conclusions

In the present work, we have examined the behavior of $Fe_2(CO)_9$ under high external pressures. In the low-pressure range of 0–0.9 GPa, the pressure enhances the π back-bonding between the bridging CO ligands and the metal centres. The bonding interactions involving $(Fe_2C_3)_b$ cluster were strengthened upon compression in this pressure range. In the intermediate pressure region of 0.9–7 GPa, the molecular geometry remains as D_{3h}, but the $(Fe_2C_3)_b$ core undergoes distortion with increasing pressure. Above 7 GPa, gradual decomposition induced by the combination of pressure and laser irritation starts to be observed. $Fe_2(CO)_8$ with C_{2v} symmetry was identified as a product. This species at ambient pressure is very unstable and can only be captured at very low temperature in matrices. Apparently, this CO bridged compound is stabilized by high pressure. At higher pressure, further decomposition of $Fe_2(CO)_8$ was detected through losing a bridging CO group.

Acknowledgements

The authors are grateful to M.J. Walzak at Surface Science Western for her assistance with the Raman instrumentation. This work is supported by the Discovery Grants from Natural Sciences and Engineering Research Council of Canada (NSERC) and Academic Development Fund from The University of Western Ontario.

References

1. J.R. Ferraro. Vibrational spectroscopy at high external pressures: the diamond anvil cell. Academic Press, New York – Toronto. 1984.
2. C.M. Edwards and I.S. Butler. Coord. Chem. Rev. **199**, 1 (2000).
3. Z.X. Liu, J.Xu, H.P. Scott, Q. Williams, H.K. Mao, and R.J. Hemley. Rev. Sci. Instrum. **75**, 5026 (2004).
4. D.M. Adams, P.D. Hatton, A.C. Shaw, and T.K. Tan. J. Chem. Soc., Chem. Commun. **5**, 226 (1981).

© 2007 NRC Canada

5. D.M. Adams and I.O.C. Ekejiuba. J. Chem. Phys. **78**, 5408 (1983).
6. H.M. Powell and R.V.G. Ewens. J. Chem. Soc. 286 (1939).
7. F.A. Cotton and J.M. Troup. J. Chem. Soc., Dalton Trans. 800 (1974).
8. I.S. Butler, S. Kishner, and K.R. Plowman. J. Mol. Struct. **43**, 9 (1978).
9. D.M. Adams and I.D. Taylor. J. Chem. Soc., Faraday Trans. **78**, 1551 (1982).
10. S. Onaka and D.F. Shriver. Inorg. Chem. **15**, 915 (1976).
11. J.J. Turner and M. Poliakoff. J. Chem. Soc. A **4**, 654 (1971).
12. S.C. Fletcher, M. Poliakoff, and J.J. Turner. Inorg. Chem. **25**, 3597 (1986).
13. Y. Xie, H.F. Schaefer, and R.B. King. J. Am. Chem. Soc. **122**, 8746 (2000).
14. L. Bertini, C. Greco, L. De Gioia, and P. Fantucci. J. Phys. Chem. A **110**, 12900 (2006).
15. H.K. Mao, J. Xu, and P.M. Bell. J. Geophys. Res. **91**, 4673 (1986).
16. D.M. Adams and I.O.C. Ekejiuba. J. Chem. Phys. **77**, 4793 (1982).
17. Y. Huang, I.S. Butler, D.F.R. Gilson, and D. Lafleur. Inorg. Chem. **30**, 117 (1991).
18. Y. Huang, I.S. Butler, and D.F.R. Gilson. Inorg. Chem. **30**, 1098 (1991).
19. S.H.R. Brienne, R.D. Markwell, S.M. Barnett, I.S. Butler, and J.A. Finch. Appl. Spectrosc. **47**, 1131 (1993).

© 2007 NRC Canada

Solvation and electronic structures of M^+L_n, with $M^+ = Mg^+$ and Ca^+, L = H_2O, CH_3OH, and NH_3, and n = 1–6[1]

Ka Wai Chan, Young Wu, and Zhi-Feng Liu

Abstract: The solvation clusters $M^+(L)_n$, with a singly charged alkaline earth cation Mg^+ or Ca^+ as the solute and with water, methanol, or ammonia as the solvent, are studied systematically in the size range n = 1–6, to compare the variations in the solvation interactions. For clusters with $n \leq 3$, the energies and structural values are compared in details, with both the MP2 and B3LYP methods. For clusters with $n \geq 4$, the solute–solvent and solvent–solvent interaction energies are calculated to explain the relative stability among various isomeric structures, and the contrast in both solvent and electron distribution among these cluster series. Thermal stabilities for these clusters are also examined by ab initio molecular dynamics simulations at finite temperature.

Key words: solvation clusters, ab initio calculations, solute–solvent interactions, size-dependent effects.

Résumé : Afin de pouvoir comparer les variations dans leurs interactions de solvatation, on a effectué une étude systématique des agrégats de solvatation $M^+(L)_n$ (n = 1–6) comportant, comme soluté, un cation alcalino-–terreux avec une seule charge, tel le Mg^+ ou le Ca^+, et de l'eau, du méthanol ou de l'ammoniac comme solvant. Utilisant les méthodes MP2 et B3LYP, on a pu comparer en détails les valeurs structurales ainsi que celles des énergies pour les agrégats dans lesquels $n \leq 3$. Pour les agrégats dans lesquels $n \geq 4$, on a calculé les énergies d'interaction soluté–solvant et solvant–solvant afin de pouvoir expliquer la stabilité relative entre les diverses structures isomères ainsi que le contraste tant dans la distribution de solvant que la distribution électronique entre les diverses séries d'agrégats. On a aussi évalué les stabilités thermiques de ces agrégats en faisant appel à des simulations de dynamique moléculaire ab initio à la température ambiante.

Mots-clés : agrégats de solvatation, calculs ab initio, interactions soluté–solvant, effets reliés à la taille.

[Traduit par la Rédaction]

Introduction

Singly charged alkaline earth cations such as Mg^+ and Ca^+ are interesting solutes in the study of solvation clusters that have provided considerable insights into solvation interactions (1–3). First, they are open shell species with a singly occupied molecular orbital (SOMO), which could reside either on the metal ion or in the solvation shells (in an orbital detached from the metal ion), depending on the solvation environment. Then, there are of course the solvent–solvent and ion–solvent interactions, with the ion either being in +1 or +2 states, again depending on the solvation environment (4–8). Furthermore, these species could only be studied as clusters, since they are unstable in solutions, and thus they provide a fairly unique medium to probe the complex interactions among the three components, electron, cation, and solvents. And finally, it is now well-understood that these interactions lead to rich variations in both the geometrical and electronic structures and also to reactivities that can be controlled by varying the cluster size. Electronically, these ions are isoelectronic to alkali atoms, and spectroscopically, electronic excitations and photo-induced fragmentation have been studied extensively over the years (1, 3). For the ground state, the most interesting observation is the size-dependent reactivity of these clusters. In the case of $Mg^+(H_2O)_n$ and $Ca^+(H_2O)_n$, it is the loss of hydrogen atom and the formation of metal hydroxide (9–11). In the case of $Mg^+(CH_3OH)_n$ and $Ca^+(CH_3OH)_n$, both the hydrogen loss and the methyl loss channels are accessible (12, 13). Hydrogen loss has also been observed in the case of $Mg^+(NH_3)_n$, although the reaction rate is lower (14). More interestingly, these reactions are only observed when the size is within a certain range (typically around 6–18), and such size-dependent reactivities have been studied extensively, both by experiments and theory. In the case of $Mg^+(H_2O)_n$, the switch-on around 6 and switch-off around 18 are now understood to be related to the detachment of the SOMO from the metal orbital into the solvation shell, and the position of this solvated electron relative to the metal ion (4, 5). All these works have demonstrated the intricate links between electron solvation, ion solvation, and chemical reactivity, and have provided interesting examples in which much insights into solvation are gained by detailed studies on solvation clusters.

The solvation environment in these clusters is also dependent on the identity of the metal ion and the solvent molecules. The difference in the ionic radius between Mg^+ and Ca^+ affects both the strength of ion–solvent interaction and the steric ef-

Received 22 April 2007. Accepted 31 July 2007. Published on the NRC Research Press Web site at http://canjchem.nrc.ca/ on 26 September 2007.

K.W. Chan, Y. Wu, and Z.-F. Liu.[2] Department of Chemistry and Centre for Scientific Modeling and Computation, Chinese University of Hong Kong, Shatin, Hong Kong, China.

[1]This article is part of a Special Issue dedicated to Professor G. Michael Bancroft.

[2]Corresponding author (e-mail: zfliu@cuhk.edu.hk).

 doi: 10.1139/V07-103 © 2007 NRC Canada

fects around the first solvation shell. Similarly, as the solvent molecule is changed from water, to methanol, or to ammonia, the ion–solvent, solvent–solvent, and electron–solvent interactions are altered, producing interesting variations in the solvation environment. Although these clusters have been studied individually before, a systematic comparison on the structures and reactivities of these clusters should provide a better understanding on the interplay of these factors. In this paper, we take a first step in this direction by a theoretical study on the $M^+(L)_n$, with M^+ being Mg^+ or Ca^+, L being H_2O, CH_3OH, or NH_3, and n between 1 and 6. Ab initio and density functional theory (DFT) methods are employed in our calculations, and the attention will be focused on the geometrical and electronic structures and their variations across these cluster series, which are the foundation for understanding the structures and reactivities in larger clusters.

Computational details

The energy calculations and the structure optimizations are all performed using the Gaussian 98 Package (15). Two basis sets, 6-31+G** and 6-311+G**, are tested. It is well-understood that diffuse orbitals are needed to account for the solvation around the SOMO. Most of these structures are examined at two levels, MP2 and B3LYP. As discussed later, $Ca^+(L)_3$ is found to be a very difficult case, with its optimized structure being very sensitive to the choice of method and the basis set. As a result, $Ca^+(H_2O)_3$ is treated as a special case and studied extensively using CISD, QCISD, and MP4 for post-Hartree–Fock treatment. As these clusters are radicals, the electron densities are spin-polarized. The calculated $< S^2 >$ values show no problem with spin contamination. All energies include corrections for the basis set superposition error (BSSE), using the counterpoise method (16, 17).

To gauge the strength of solvation interactions, two energetic quantities are calculated. The first is $BE[M^+/L_n]$, with M^+ being the metal ion, and L is the neutral solvent, as defined by

$$BE[M^+/L] = E[M^+] + E[(L)_n] - E[M^+(L)_n]$$

which calculates the difference between the energy of the cluster $M^+(L)_n$, and the energy sum of an isolated metal ion M^+ and a solvent cluster $(L)_n$ taking the same geometry as $M^+(L)_n$ but with the metal ion removed. $BE[M^+/(L)_n]$ measures the solute–solvent interaction energy. The other quantity, $BE[(L)_n]$ measures the solvent–solvent interaction energy, as defined by,

$$BE[(L)_n] = n \times E[L] - E[(L)_n]$$

where L is an isolated solvent molecule, and $(L)_n$ is the same as defined above.

To gauge the extent of electron detachment from the metal ion, we follow the method previously used by Tsurusawa and Iwata (18) to calculate the SOMO centroid, $R\{e^-\}$. The space around a cluster is first divided into small cubic cells with a uniform length of δr, and each cubic cell is labeled by an index ijk to indicate its position, $\mathbf{r}_{ijk} = (x_i, y_j, z_k)$. The SOMO centroid is then calculated by

$$R\{e^-\} = \sum \rho(\mathbf{r}_{ijk})\mathbf{r}_{ijk},$$

where $\rho(\mathbf{r}_{ijk})$ is the electron density due to the SOMO. The difference between the SOMO centroid and the metal position, $R[\{e^-\} - M]$, measures the deviation of the SOMO center from the metal ion. The other quantity calculated is the SOMO extent measure (SEM), also introduced by Tsurusawa and Iwata, which is the volume that contained half the electron on the SOMO. It is calculated by first ranking the density in each cubic cell over the entire grid, and the cell volume is added from the highest density value to the lower ones until the total charge $\sum \rho(\mathbf{r}_{ijk})\Delta V_{ijk}$ is over 0.5. ΔV_{ijk} are the volume elements, which are then added together to produce the SEM that indicates the spacial extent of SOMO.

One of the interesting aspects of solvation clusters is their thermal stability, since their potential energy surfaces are usually flat with many minima and low transition barriers. At finite temperature, the most stable structure may not be the most abundant because of the entropy effects, which has recently been demonstrated in the case of hydrated sulfate clusters (19–21). Ab initio molecular dynamics (AIMD) is the best way to examine this kind of effect, since quality empirical potential surfaces are usually not available to describe the metal ion and solvent interactions. For that purpose, we use the Vienna Ab initio Simulation Package (VASP) (22–25). A cluster is put in a periodic cubic box with a length of 15 Å in order to minimize the interaction between their neighboring images. The electronic wave function is expanded in a planewave basis set with a cutoff energy at 273.9 eV for water and methanol clusters and at 250 eV for ammonia clusters, while the core area is described by PAW pseudopotentials (26). The exchange correlation functional is PW91 (27), while the electron densities are spin-polarized. A constant background charge is subtracted to neutralize the charge on the cluster ion. Only the Γ point is used in the k-space sampling. The AIMD simulations are performed at 300 K as controlled by a Nóse–Hoover thermostat (28, 29) for a total of 10 000 time steps, each of 0.4 fs for the Ca^+ clusters and 0.5 fs for the Mg^+ clusters.

Results and discussion

Interaction energy for $n = 1$–3

For the solvation clusters studied in this report, the two most commonly used methods have been MP2 and DFT/B3LYP (6, 30). Because of the rapid increase in computational cost with the number of water molecules, MP2 is the only affordable post-Hartree–Fock treatment for a cluster with a few water molecules (4, 5, 7, 8). For the same reason, density functional theory based methods are the only choices when n reaches beyond 10. For the basis set, it is generally understood that diffuse functions are needed to describe the solvated electron on the SOMO. In previous studies, we have identified DFT calculations (B3LYP or BPW91) with a basis set of 6-31+G** as the best compromise between computational accuracy and cost in the specific cases of $Mg^+(H_2O)_n$ and $Na(H_2O)_n$ (5, 31). In this study, detailed comparisons are also made for $n = 1$–3 for all the solvated Mg^+ and Ca^+ clusters at four specific levels, MP2/6-31+G**, MP2/6-311+G**, B3LYP/6-31+G**, and B3LYP/6-311+G**, as listed in Tables 1, 2, 3, and 4.

For the Mg^+ clusters with one solvent molecule, the agreement between MP2 and B3LYP results is quite decent. For the interaction energy between Mg^+ and solvent, the difference is around 2 kcal/mol (1 cal = 4.184 J) with slightly higher B3LYP values. The difference in the optimized geometry parameters is fairly small, as listed in Table 1. And the two basis sets

© 2007 NRC Canada

Table 1. Calculated binding energies and geometrical parameters for M^+L clusters.

	Mg^+H_2O				Ca^+H_2O			
Method	BE[Mg^+/H_2O]	r(Mg-O)	r(O-H)	∠(Mg-O-H)	BE[Ca^+/H_2O]	r(Ca-O)	r(O-H)	∠(Ca-O-H)
B3LYP/6-31+G**	32.0	2.08	0.97	126.5	24.5	2.44	0.97	127.2
B3LYP/6-311+G**	31.9	2.08	0.97	126.6	29.1	2.32	0.97	127.0
MP2/6-31+G**	30.6	2.09	0.97	126.8	23.8	2.45	0.97	127.5
MP2/6-311+G**	30.1	2.09	0.97	127.2	25.1	2.37	0.97	127.7
	Mg^+CH_3OH				Ca^+CH_3OH			
Method	BE[Mg^+/CH_3OH]	r(Mg-O)	r(O-H)	∠(Mg-O-H)	BE[Ca^+/CH_3OH]	r(Ca-O)	r(O-H)	∠(Ca-O-H)
B3LYP/6-31+G**	36.3	2.05	0.97	121.5	27.4	2.41	0.97	122.0
B3LYP/6-311+G**	37.4	2.05	0.97	121.7	33.1	2.30	0.97	121.1
MP2/6-31+G**	36.4	2.05	0.97	121.8	27.2	2.42	0.97	122.0
MP2/6-311+G**	35.5	2.06	0.97	122.7	29.0	2.34	0.96	122.4
	Mg^+NH_3				Ca^+NH_3			
Method	BE[Mg^+/NH_3]	r(Mg-N)	r(N-H)	∠(Mg-N-H)	BE[Ca^+/NH_3]	r(Ca-N)	r(N-H)	∠(Ca-N-H)
B3LYP/6-31+G**	39.6	2.20	1.02	113.0	28.0	2.59	1.02	113.6
B3LYP/6-311+G**	39.2	2.20	1.02	113.0	32.9	2.46	1.02	113.4
MP2/6-31+G**	37.9	2.20	1.02	113.2	27.2	2.59	1.02	113.9
MP2/6-311+G**	37.4	2.20	1.02	113.4	28.9	2.51	1.02	114.0

Note: Binding energies are in kcal/mol (1 cal = 4.184 J) and include BSSE corrections. All distances are in Å and all angles in degrees.

Table 2. Calculated binding energies and geometrical parameters for $M^+(L)_2$ clusters.

	$Mg^+(H_2O)_2$				$Ca^+(H_2O)_2$			
Method	BE [$Mg^+/(H_2O)_2$]	BE [$(H_2O)_2$]	r(Mg-O)	∠(O-Mg-O)	BE [$Ca^+/(H_2O)_2$]	BE [$(H_2O)_2$]	r(Ca-O)	∠(O-Ca-O)
B3LYP/6-31+G**	60.2	−2.8	2.10	93.1	46.7	−1.2	2.43	180.0
B3LYP/6-311+G**	60.0	−2.9	2.11	93.6	56.3	−1.3	2.35	180.0
MP2/6-31+G**	58.6	−2.8	2.11	89.4	44.1	−1.2	2.44	180.0
MP2/6-311+G**	57.3	−2.9	2.12	88.8	48.2	−1.3	2.37	180.0
	$Mg^+(CH_3OH)_2$				$Ca^+(CH_3OH)_2$			
Method	BE [$Mg^+/(CH_3OH)_2$]	BE [$(CH_3OH)_2$]	r(Mg-O)	∠(O-Mg-O)	BE [$Ca^+/(CH_3OH)_2$]	BE [$(CH_3OH)_2$]	r(Ca-O)	∠(O-Ca-O)
B3LYP/6-31+G**	67.7	−4.2	2.08	98.2	50.8	−2.3	2.42	178.5
B3LYP/6-311+G**	67.5	−4.3	2.08	98.6	61.9	−2.6	2.33	179.0
MP2/6-31+G**	66.7	−3.5	2.08	91.5	49.3	−2.1	2.42	180.0
MP2/6-311+G**	65.0	−3.3	2.09	91.2	54.0	−2.2	2.35	179.0
	$Mg^+(NH_3)_2$				$Ca^+(NH_3)_2$			
Method	BE [$Mg^+/(NH_3)_2$]	BE [$(NH_3)_2$]	r(Mg-N)	∠(N-Mg-N)	BE [$Ca^+/(NH_3)_2$]	BE [$(NH_3)_2$]	r(Ca-N)	∠(N-Ca-N)
B3LYP/6-31+G**	73.0	−4.6	2.22	103.1	52.4	−1.9	2.59	179.9
B3LYP/6-311+G**	71.9	−4.3	2.23	102.8	62.5	−1.9	2.49	179.7
MP2/6-31+G**	71.6	−5.0	2.22	99.8	49.6	−2.1	2.58	180.0
MP2/6-311+G**	70.2	−4.5	2.23	99.6	54.6	−1.9	2.51	180.0

Note: Binding energies are in kcal/mol and include BSSE corrections. All distances are in Å and all angles in degrees.

also produced fairly small differences in either the energy or the geometric parameters. The same is observed as the number of solvents is increased to 2 and 3, as listed in Tables 2 and 3. The difference in the ion–solvent interaction energy between MP2 and B3LYP is usually under 3 kcal/mol. The agreement is also excellent for the solvent–solvent interaction energy, which is usually positive or just slightly below zero, indicating that the ion–solvent interaction is much more important than the solvent–solvent interaction. For the geometry parameters, only the O-Mg-O and N-Mg-N angles show an appreciable difference around 4°. These comparisons indicate that similar to $Na(H_2O)_n$ and $Mg^+(H_2O)_n$, B3LYP/6-31+G** should

© 2007 NRC Canada

Table 3. Calculated binding energies and geometrical parameters for $Mg^+(L)_3$ clusters.

	$Mg^+(H_2O)_3$						
Method	Isomer	Relative energy	BE[$Mg^+/(H_2O)_3$]	BE[$(H_2O)_3$]	r(Mg-O1)	r(Mg-O3)	∠(O1-Mg-O2)
B3LYP/6-31+G**	3+0	0.0	85.2	−6.7	2.12	2.12	91.2
B3LYP/6-311+G**	3+0	0.0	84.8	−7.0	2.13	2.13	91.5
MP2/6-31+G**	3+0	0.0	83.2	−6.3	2.13	2.13	87.6
MP2/6-311+G**	3+0	0.0	81.4	−6.4	2.14	2.14	87.7
B3LYP/6-31+G**	2+1	2.7	76.9	0.3	2.08	3.89	87.0
B3LYP/6-311+G**	2+1	2.6	76.4	0.2	2.08	3.91	86.7
MP2/6-31+G**	2+1	2.8	75.4	−0.4	2.08	3.92	86.1
MP2/6-311+G**	2+1	2.7	74.1	−1.0	2.09	3.94	85.3
	$Mg^+(CH_3OH)_3$						
Method	Isomer	Relative energy	BE[$Mg^+/(CH_3OH)_3$]	BE[$(CH_3OH)_3$]	r(Mg-O1)	r(Mg-O3)	∠(O1-Mg-O2)
B3LYP/6-31+G**	3+0	0.0	93.3	−8.1	2.11	2.11	91.2
B3LYP/6-311+G**	3+0	0.0	93.1	−8.4	2.12	2.12	91.4
MP2/6-31+G**	3+0	0.0	92.8	−6.9	2.11	2.11	87.6
MP2/6-311+G**	3+0	0.0	90.8	−7.2	2.12	2.12	88.2
B3LYP/6-31+G**	2+1	2.4	84.3	−0.6	2.06	3.83	89.4
B3LYP/6-311+G**	2+1	2.3	84.0	−0.7	2.06	3.84	89.1
MP2/6-31+G**	2+1	3.0	84.4	−0.8	2.06	3.83	88.2
MP2/6-311+G**	2+1	2.9	82.6	−1.1	2.06	3.85	87.2
	$Mg^+(NH_3)_3$						
Method	Isomer	Relative energy	BE[$Mg^+/(NH_3)_3$]	BE[$(NH_3)_3$]	r(Mg-N1)	r(Mg-N2)	r(Mg-N3)
B3LYP/6-31+G**	3+0	0.0	103.7	−12.5	2.23	2.23	2.23
B3LYP/6-311+G**	3+0	0.0	101.7	−11.7	2.24	2.24	2.24
MP2/6-31+G**	3+0	0.0	103.1	−13.2	2.23	2.23	2.23
MP2/6-311+G**	3+0	0.0	100.9	−11.9	2.24	2.24	2.24
B3LYP/6-31+G**	2+1	8.9	86.8	−4.7	2.17	2.23	4.21
B3LYP/6-311+G**	2+1	8.8	85.4	−4.4	2.17	2.23	4.22
MP2/6-31+G**	2+1	10.1	85.1	−5.7	2.17	2.22	4.17
MP2/6-311+G**	2+1	10.1	83.8	−5.2	2.17	2.23	4.18

Note: Binding energies are in kcal/mol and include BSSE corrections. All distances are in Å and all angles in degrees. In the labeling for isomers, $m + n$, m indicates the number of solvents in the first shell and n in the second shell.

be an excellent choice for the study on $Mg^+(CH_3OH)_n$ and $Mg^+(NH_3)_n$ clusters.

For the Ca^+ clusters, the agreements among various levels are less satisfactory than those for the Mg^+ clusters, as shown in Tables 1, 2, and 4. Again, the B3LYP method produces larger solute–solvent interaction energy. For $n = 1$, the difference is around 5 kcal/mol, while for $n = 2$ and 3, the difference could reach around 10 kcal/mol. Basis set is also an important factor, especially for the B3LYP method, with the difference between B3LYP/6-31+G** and B3LYP/6-311+G** values also reaching 10 kcal/mol for $n = 2$ and 3. For MP2 calculations, the change in basis set produces a change of around 4 kcal/mol for the solute–solvent interaction energy. It is also interesting to notice that the B3LYP/6-31+G** results are actually in good agreement with the MP2 results in all cases, which indicates that B3LYP/6-31+G** is a better choice for the study of Ca^+ clusters than B3LYP/6-311+G**. The agreement among various methods is better for the solvent–solvent interaction energies, which are small in their values as the dominant interactions in these clusters are again the solute–solvent interactions. Finally, it should be noted that larger fluctuations are also observed in the optimized bond distances, with difference reaching around 1 Å in some cases, which are more sensitive to the choice of basis set (6-31+G** versus 6-311+G**), rather than the choice of methods (MP2 versus B3LYP).

The structure of Ca^+L_3

While the structural parameters for cluster series are in good agreement with previous findings (4–8), the structures for Ca^+L_3 have turned out to be sensitive to the calculation levels. Previously, Watanabe and Iwata identified a planar D_{3h} structure **Ca^+-W-3a** (30), as shown in Fig. 1, as the most stable for $n = 3$ at the MP2 and MP4 levels with a basis set of 6-31G*, which is reproduced in our calculations at the B3LYP/6-311+G** level. However, when the basis set is 6-31+G** and 6-311+G**, the MP2 optimized structure is changed to **Ca^+-W-3b**, in which the three oxygen atoms are in the same plane, and all three water molecules are squeezed to one side of the plane, opposite to the SOMO, with C_{2v} symmetry. Such a structure was identified before at the Hartree–Fock level (32). The D_{3h} **Ca^+-W-3a** is also predicted as the most stable structure when other functionals (BLYP and PW91) with a basis set of 6-311+G** are used. But when the basis set is lowered to B3LYP/6-31+G**, an imaginary frequency is found for **Ca^+-W-3a** and the most stable structure becomes **Ca^+-W-3c**, which is pyramidal.

© 2007 NRC Canada

Table 4. Calculated binding energies and geometrical parameters for $Ca^+(L)_3$ clusters.

	$Ca^+(H_2O)_3$							
Method	Isomer	Relative energy	BE[$Ca^+/(H_2O)_3$]	BE[$(H_2O)_3$]	r(Ca-O1)	r(Ca-O3)	∠(O1-Ca-O2)	∠(O1-O2-Ca-O3)
B3LYP/6-31+G**	3+0	0.0	69.8	−5.3	2.45	2.45	91.7	53.6
B3LYP/6-311+G**	3+0	0.0	79.8	−5.4	2.36	2.36	120.0	0.0
MP2/6-31+G**	3+0	0.0	66.7	−4.7	2.44	2.48	79.3	0.0
MP2/6-311+G**	3+0	0.0	69.3	−4.8	2.40	2.41	81.6	0.0
B3LYP/6-31+G**	2+1	3.5	61.0	2.2	2.43	4.23	78.6	0.0
B3LYP/6-311+G**	2+1	7.8	67.4	1.7	2.35	4.17	80.2	0.0
MP2/6-31+G**	2+1	1.9	60.4	1.6	2.44	4.29	77.1	0.0
MP2/6-311+G**	2+1	3.3	62.3	0.7	2.38	4.25	77.2	0.0
	$Ca^+(CH_3OH)_3$							
Method	Isomer	Relative energy	BE[$Ca^+/(CH_3OH)_3$]	BE[$(CH_3OH)_3$]	r(Ca-O1)	r(Ca-O3)	∠(O1-Ca-O2)	∠(O1-O2-Ca-O3)
B3LYP/6-31+G**	3+0	0.0	74.1	−6.2	2.45	2.45	88.6	55.7
B3LYP/6-311+G**	3+0	0.0	85.8	−6.8	2.35	2.35	120.0	1.2
MP2/6-31+G**	3+0	0.0	74.1	−5.1	2.46	2.45	94.9	51.0
MP2/6-311+G**	3+0	0.0	76.1	−5.4	2.39	2.41	94.8	64.5
B3LYP/6-31+G**	2+1	2.5	65.0	1.8	2.41	4.18	80.5	1.1
B3LYP/6-311+G**	2+1	6.6	72.9	1.1	2.33	4.09	82.6	0.2
MP2/6-31+G**	2+1	2.5	65.8	1.8	2.42	4.20	78.8	0.1
MP2/6-311+G**	2+1	2.5	68.3	0.9	2.35	4.16	78.7	0.1
	$Ca^+(NH_3)_3$							
Method	Isomer	Relative energy	BE[$Ca^+/(NH_3)_3$]	BE[$(NH_3)_3$]	r(Ca-N1)	r(Ca-N3)	∠(N1-Ca-N2)	∠(N1-N2-Ca-N3)
B3LYP/6-31+G**	3+0	0.0	77.4	−7.6	2.60	2.60	174.4	0.2
B3LYP/6-311+G**	3+0	0.0	86.6	−6.7	2.50	2.53	141.8	0.2
MP2/6-31+G**	3+0	0.0	76.0	−8.5	2.60	2.62	173.4	2.4
MP2/6-311+G**	3+0	0.0	79.4	−7.8	2.53	2.57	180.0	0.0
B3LYP/6-31+G**	2+1	7.8	64.9	−2.4	2.55	4.56	99.4	9.9
B3LYP/6-311+G**	2+1	8.4	73.0	−1.0	2.45	4.65	175.4	0.1
MP2/6-31+G**	2+1	7.0	64.1	−3.3	2.56	4.47	93.6	0.0
MP2/6-311+G**	2+1	8.2	64.8	−1.4	2.47	4.60	171.1	0.3

Note: Binding energies are in kcal/mol and include BSSE corrections. All distances are in Å and all angles in degrees. In the labeling for isomers, $m + n$, m indicates the number of solvents in the first shell and n in the second shell.

Table 5. Bond distances (Å), bond angles (°), and relative energies (in kcal/mol with BSSE and ZPE corrections) in Ca^+-W-3a and Ca^+-W-3b, optimized using post-HF and DFT methods with various basis sets.

	Ca^+-W-3a			Ca^+-W-3b				
Method	Relative energy	r(Ca-O1)	∠(O1-Ca-O2)	Relative energy	r(Ca-O1)	r(Ca-O2)	∠(O1-Ca-O2)	∠(O2-Ca-O3)
MP2/6-311+G**	0.86[i]	2.38	120.0	0.00	2.40	2.41	81.6	163.2
MP2/6-311+G(3df,3pd)	0.04[i]	2.35	120.0	0.00	2.38	2.38	84.2	168.5
CCSD/6-311+G**	1.74[i]	2.39	120.0	0.00	2.41	2.42	80.8	161.5
B3LYP/6-31+G**	0.03[i]	2.43	120.0	0.00	2.44	2.45	88.1	176.3
B3LYP/6-311+G**	0.00	2.36	120.0	0.48[i]	2.38	2.37	95.1	169.9
B3LYP/6-311+G(3df,3pd)	0.00	2.35	120.0	0.98[i]	2.37	2.35	102.3	155.5
BLYP/6-31+G**	0.00[i]	2.45	120.0	0.38	2.46	2.46	91.2	177.6
BLYP/6-311+G**	0.00	2.36	120.0	0.55[i]	2.38	2.36	106.2	147.6
BLYP/6-311+G(3df,3pd)	0.00	2.36	120.0	0.91[i]	2.38	2.35	110.8	138.4
PW91PW91/6-31+G**	0.00[i]	2.43	120.0	0.19	2.43	2.44	89.1	178.2
PW91PW91/6-311+G**	0.00	2.34	120.0	0.58[i]	2.36	2.35	104.8	150.4
PW91PW91/6-311+G(3df,3pd)	0.00	2.34	120.0	0.92[i]	2.35	2.33	110.3	139.4
Single Point energy with 6-311+G(3df,3pd) basis set at MP2/6-311+G(3df,3pd) optimized geometries								
MP4	0.74			0.00				
CCSD	1.19			0.00				
QCISD(T)	1.02			0.00				

Note: The superscript i denotes geometries with imaginary frequencies.

© 2007 NRC Canada

Fig. 1. The optimized structure and the shape of the SOMO for $Ca^+(H_2O)_3$ obtained at various calculation levels. Each row contains two orientations for one structure.

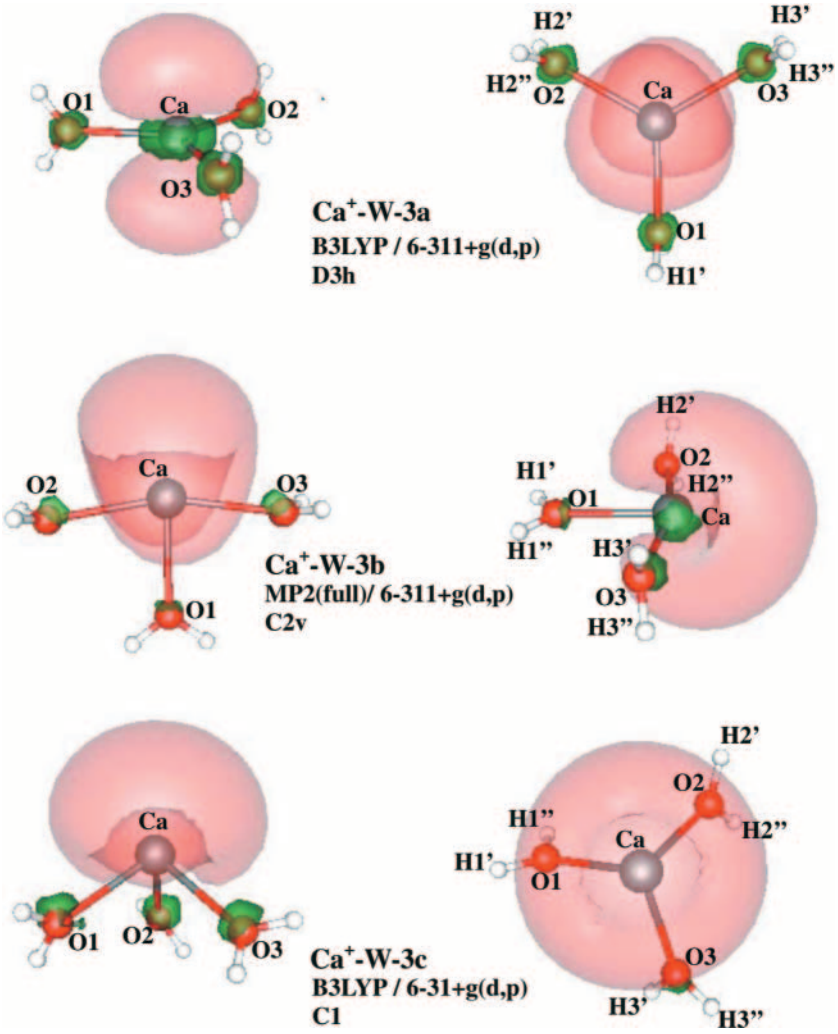


Table 6. Successive binding energies, defined as $[E(M^+L_{n-1}) + E(L) - E(M^+L_n)]$, (in kcal/mol with BSSE and ZPE corrections) for $Ca^+(H_2O)_n$ and $Mg^+(H_2O)_n$ with n up to 3.

	$Ca^+(H_2O)_n$			$Mg^+(H_2O)_n$		
Method	$n = 1$	$n = 2$	$n = 3$	$n = 1$	$n = 2$	$n = 3$
B3LYP/6-31+G**	23.0	19.8	17.2	30.3	23.5	18.8
B3LYP/6-311+G**	27.4	24.6	18.1	30.2	23.3	18.5
MP2/6-31+G**	22.2	17.9	16.9	28.9	23.0	18.6
MP2/6-311+G**	23.6	20.4	15.6	28.3	22.4	18.0
Experiment	28[a]	24[a]	21.5[a]	28.4±3.0[b]	22.4±1.6[b]	17.4±2.1[b]

[a]From Ref. 33.
[b]From Ref. 34.

In their study on $Ca^+(H_2O)_n$, Watanabe and Iwata identified the importance of d orbitals on the Ca atom in the solute–solvent interactions that made the structures of $Ca^+(H_2O)_n$ distinct from the structures of $Mg^+(H_2O)_n$ (30). Our results further show that in the case of $Ca^+(L)_3$, the p orbitals could also play an important role. The relative importance of p and d orbitals is very sensitive to the calculation level, and so are the optimized structures. As shown in Table 5, the DFT methods (with B3LYP, BLYP, and PW91 functionals) all produce the planar D_{3h} **Ca^+-W-3a** as the most stable structure, when triple zeta basis sets are used, while optimization by either MP2 or CISD method leads to the planar C_{2v} **Ca^+-W-3b**. Single point energy calculations performed at the MP4, CCSD, and QCISD levels using the geometry optimized at MP2/6-311+G(3df, 3pd)

© 2007 NRC Canada

also indicate that **Ca^+-W-3b** is more stable. Nonetheless, the energy difference between these two structures is small, typically below 1 kcal/mol, and at each level there is only one stable structure among **Ca^+-W-3a** and **Ca^+-W-3b**, with the other one containing imaginary frequencies. The plot for the SOMO indicates another interesting difference between these structures. In **Ca^+-W-3a**, SOMO takes the shape of a d_{z^2} orbital and indicates sd hybridization. In contrast, the SOMO in **Ca^+-W-3b** stays on the opposite of the three water molecules and indicates sp hybridization. Therefore, while sd hybridization is preferred in DFT calculations, sp hybridization is preferred in post-Hartree–Fock calculations.

Since there is no known experimental geometry for $Ca^+(H_2O)_3$, it is difficult to conclude which structure, **Ca^+-W-3a** or **Ca^+-W-3b**, is more stable. But the small energy difference indicates that water molecules can easily move within the coordination plane. Not only 3d orbitals, but also 4p orbitals can participate in the hybridization to form the SOMO, and the two types of hybridization have comparable effects on the total energy. Therefore, as water molecules move around the coordination plane, the SOMO could change from one type of hybridization into another, with only a small energy cost. It underlies the fact that the optimized structure is very sensitive to the method and basis set used.

Experimental stepwise solvation energy is known for both $Ca^+(H_2O)_n$ and $Mg^+(H_2O)_n$ for $n = 1$–3 (33, 34). As listed in Table 6, the B3LYP/6-311+G** results are in better agreement with experiment than the MP2 results. For $Mg^+(H_2O)_n$, the MP2 results are only slightly better. Similar discrepancies between DFT and post-Hartree–Fock results are also found for both $Ca^+(CH_3OH)_3$ and $Ca^+(NH_3)_3$.

Structures and energies for $n = 4$–6

As shown in our previous study on $Mg^+(H_2O)_n$ (4), the cluster structures for $n > 3$ can be roughly characterized by the number of solvent molecules in the first solvation shell, which varies from 3 to 6. The relative stabilities among these structures are determined by factors such as ion–solvent and solvent–solvent interactions. At finite temperature, entropy could also be an important factor.

In the case of $Mg^+(H_2O)_n$, it was found that the energy difference among these structures were small. This conclusion is corroborated by calculations at the B3LYP level, as shown in Table 7. The energy difference is typically within 5 kcal/mol. However, the solute–solvent and solvent–solvent interaction energies vary considerably among these structures. Using $n = 6$ as an example, when there are 6 water molecules in the first shell (**Mg^+-W6-6**), the solute–solvent interaction energy is the strongest among 4 isomers at an exothermic 151.7 kcal/mol. At the same time, the solvent–solvent interaction between water molecules are endothermic, at −31.2 kcal/mol, indicating repulsion among water molecules. In contrast, when the Mg^+ coordination number is reduced to 3, as in **Mg^+-W6-3**, the solute–solvent interaction energy is only 115.8 kcal/mol, while the solvent–solvent interaction energy is at a much more favorable 4.9 kcal/mol. Therefore, the cluster structure could either favor the solute–solvent interaction, albeit with a considerable increase in solvent–solvent repulsion, or favor the solvent–solvent interaction at a cost to the solute–solvent interaction. As the solvent is changed from water to methanol or ammonia, and the solute is changed from Mg^+ to Ca^+, the relative importance of these interactions are changed too, producing interesting variations in the relative stability among isomer structures.

Table 7. Relative energies (in kcal/mol with BSSE and ZPE corrections), relative Gibbs energies (at 298 K and in kcal/mol), solute–solvent interactions, $BE[Mg^+/(H_2O)_n]$ (in kcal/mol), solvent and solvent interactions, and $BE[(H_2O)_n]$ (in kcal/mol) in $Mg^+(H_2O)_n$, for $n = 5$ and 6 at B3LYP/6-311+G**.

	Relative energy	Relative Gibbs energy	$BE[Mg^+/(H_2O)_n]$	$BE[(H_2O)_n]$
Mg^+-W5-5	0.0	0.0	127.4	−21.8
Mg^+-W5-4	2.1	1.9	114.5	−8.8
Mg^+-W5-3	1.3	3.0	109.5	−1.3
Mg^+-W6-6	0.0	0.0	151.7	−31.2
Mg^+-W6-5	3.8	3.4	138.7	−20.0
Mg^+-W6-4	4.7	6.0	127.7	−7.7
Mg^+-W6-3	4.8	5.8	115.8	4.9

When water is replaced by methanol as the solvent molecule, the change is obvious but small. The solute–solvent interaction is larger for Mg^+–CH_3OH than for Mg^+–H_2O, which has already been noted above for the smaller clusters. At the same time, there is also an increase in the solvent–solvent repulsion, as indicated in Table 8, because of the presence of the methyl group in methanol. The balance of these two factors leaves the structures of $Mg^+(CH_3OH)_5$ and $Mg^+(CH_3OH)_6$ quite similar to their hydrated counterpart, in that as the number of solvent varies in the first shell, the energy does not change much.

More appreciable changes are observed when the solvent molecules are ammonia, as listed in Table 9. Again, both the solute–solvent interaction and solvent–solvent repulsion are stronger, and as compared to water the increase is larger for ammonia than for methanol for both types of interactions, as indicated in Table 8. However, in the case of ammonia, the increase in solute–solvent interaction is larger than the increase in solvent–solvent repulsion. Therefore, structures with high number of solvents in the first shell are energetically favored for $Mg^+(NH_3)_n$, with $n = 5$ and 6.

When the solute Mg^+ is replaced by Ca^+, both the solute–solvent interaction and solvent–solvent repulsion decrease for all three solvents, as shown in Tables 10–12, largely because of the larger ion radius for Ca^+. Not surprisingly, structures with high number of solvents in the first shell are favored for $Ca^+(NH_3)_5$ and $Ca^+(NH_3)_6$. And the same is also true when either water or methanol is the solvent. This is largely because of the fact that the decrease in solvent–solvent repulsion is more substantial, and higher direct coordination around Ca^+, which increases the solute–solvent interaction, is energetically less costly as the solvent–solvent repulsion does not increase to the same extent as in $Mg^+(H_2O)_n$.

Electronic structures for $n = 4$–6

The most interesting feature in the electronic structures of these three cluster series is the electron on the singly occupied molecular orbital (SOMO). It is now well-understood that as the number of solvent molecules increases, this electron is eventually detached from the metal atom and solvated by solvent molecules to form an electron-ion pair, which contributes to the size-dependent reactivities in these clusters.

© 2007 NRC Canada

Table 8. Relative energies (in kcal/mol with BSSE and ZPE corrections), relative Gibbs energies (at 298 K and in kcal/mol), solute–solvent interactions, BE[$Mg^+/(CH_3OH)_n$] (in kcal/mol), solvent and solvent interactions, BE[$(CH_3OH)_n$] (in kcal/mol), R[Mg …e^-] (in Å) and SEM (in Å^3) in $Mg^+(CH_3OH)_n$, for $n = 5$ and 6 at B3LYP/6-311+G**.

	Relative energy	Relative Gibbs energy	BE[$Mg^+/(CH_3OH)_n$]	BE[$(CH_3OH)_n$]	R[Mg …e^-]	SEM
Mg^+-M5-5	3.5	4.4	128.8	−20.9	1.16	19.6
Mg^+-M5-4	0.2	0.0	126.3	−14.6	1.06	15.8
Mg^+-M5-3	0.0	0.1	116.0	−3.1	0.82	11.5
Mg^+-M6-6	0.6	4.5	156.3	−35.6	2.06	25.8
Mg^+-M6-5	2.1	4.9	140.8	−20.0	1.13	19.6
Mg^+-M6-4	1.0	1.8	131.8	−9.9	1.13	14.6
Mg^+-M6-3	0.0	0.0	122.8	0.7	0.82	11.5

Table 9. Relative energies (in kcal/mol, with BSSE and ZPE correction), relative Gibbs energies (at 298K and in kcal/mol), solute-solvent interactions, BE[$Mg^+/(NH_3)_n$] (in kcal/mol), solvent and solvent interactions, BE[$(NH_3)_n$] (in kcal/mol), R[Mg …e^-] (in Å), and SEM (in Å^3) in $Mg^+(NH_3)_n$, n=5 and 6 at B3LYP/6-311+G**.

	Relative energy	Relative Gibbs energy	BE[$Mg^+/(NH_3)_n$]	BE[$(NH_3)_n$]	R[Mg …e^-]	SEM
Mg^+-A5-5	0.0	0.0	153.3	−35.5	0.16	118.1
Mg^+-A5-4	3.6	1.1	135.1	−21.5	0.47	97.5
Mg^+-A5-3	6.0	3.1	125.2	−12.6	0.82	12.7
Mg^+-A6-6	0.0	0.0	182.3	−50.4	0.00	135.9
Mg^+-A6-5	4.5	2.8	163.9	−36.4	0.49	117.5
Mg^+-A6-4	7.9	4.1	146.6	−23.1	0.67	100.4
Mg^+-A6-3	13.8	12.7	129.4	−9.8	0.86	12.7

Table 10. Relative energies (in kcal/mol with BSSE and ZPE corrections), relative Gibbs energies (at 298 K and in kcal/mol), solute–solvent interactions, BE[$Ca^+/(H_2O)_n$] (in kcal/mol), solvent and solvent interactions, and BE[$(H_2O)_n$] (in kcal/mol) in $Ca^+(H_2O)_n$, for $n = 5$ and 6 at B3LYP/6-311+G**.

	Relative energy	Relative Gibbs energy	BE[$Ca^+/(H_2O)_n$]	BE[$(H_2O)_n$]
Ca^+-W5-5	0.0	0.0	123.7	−16.3
Ca^+-W5-4	7.0	8.4	105.8	−2.4
Ca^+-W5-3	12.0	14.7	97.5	2.4
Ca^+-W6-6	0.0	0.0	147.2	−24.1
Ca^+-W6-5	4.1	5.0	136.4	−14.8
Ca^+-W6-4	9.8	12.2	127.1	−3.1
Ca^+-W6-3	16.3	18.3	103.7	8.9

It turns out that the shape and extent of SOMO for the hydrated clusters are quite similar to those for the methanol clusters but in sharp contrast to the ammonia clusters. The contrasts are illustrated in Fig. 2 and by two numbers listed in Tables 7–12, which were previously used by Tsurusawa and Iwata (18) to indicate the detachment of SOMO from the metal ion in hydrated sodium clusters $Na(H_2O)_n$. The first number R[{e^-}–M^+] is the distance between the geometric center of SOMO and the metal ion. The second number is the SEM, which measures the spatial extent of the SOMO. Both quantities have been defined in the previous section on computational details.

In **Mg^+-M6-3**, a $Mg^+(CH_3OH)_6$ cluster with only three methanol molecules in the first shell, the Mg^+ ion is on the surface of the cluster, while the SOMO is largely situated on the Mg, as reflected by an R[{e^-}–Mg^+] distance of only 0.82 Å. As the number of methanol molecules increases in the first shell, the R[{e^-}–Mg^+] value increases to 2.06 Å in **Mg^+-M6-6**, in which all six methanol molecules are directly coordinated with the metal ion. The SEM value also doubled. As shown in Fig. 2, the electron is now detached from the metal and localized on one side of the cluster, which is a typical example of the electron–ion pair.

The SOMO in **Mg^+-A6-3**, a $Mg^+(NH_3)_6$ cluster with three ammonia molecules in the first shell, is quite similar to the SOMO in its methanol counterpart, **Mg^+-M6-3**. The Mg^+ ion is on the cluster surface and so is SOMO situated on the ion, producing comparable R[{e^-}–Mg^+] and SEM numbers. As discussed earlier in the ammonia clusters, a high coordination number around the metal ion is energetically more favorable, and the most stable isomer at $n = 6$ is the one with all six ammonia molecules in the first solvation shell, as in **Mg^+-A6-6**. Its SOMO is in sharp contrast with that in its methanol counterpart, **Mg^+-M6-6**. The SEM for **Mg^+-A6-6** is 135.9 Å^3, compared with a mere 25.8 Å^3 in **Mg^+-M6-6**. The R[{e^-}–Mg^+] value for 0.0 Åcompared with a value of 2.06 Å for **Mg^+-M6-6**. The electron is actually detached from the metal ion, notwithstanding a zero value for R[{e^-}–Mg^+]. As illustrated in Fig. 2, the electron is completely delocalized among the six ammonia molecules, which accounts for the large SEM value, and at the same time produces a geometric center that coincides with the position of the metal ion. Such a contrast has been observed before, in the comparison between $Na(H_2O)_n$ and $Na(NH_3)_n$ clusters (35). It can be understood as due to the difference in dipole moment. The larger dipole moments in water and methanol produce stronger solvation interaction around the electron, which

© 2007 NRC Canada

Fig. 2. The SOMO for a number of methanol (M) and ammonia (A) clusters with six solvent molecules. For structures with 3 solvent molecules in the first shell, the SOMO shapes are similar. For structures with all six solvent molecules in the first shell, there is a sharp contrast between the methanol and the ammonia clusters.

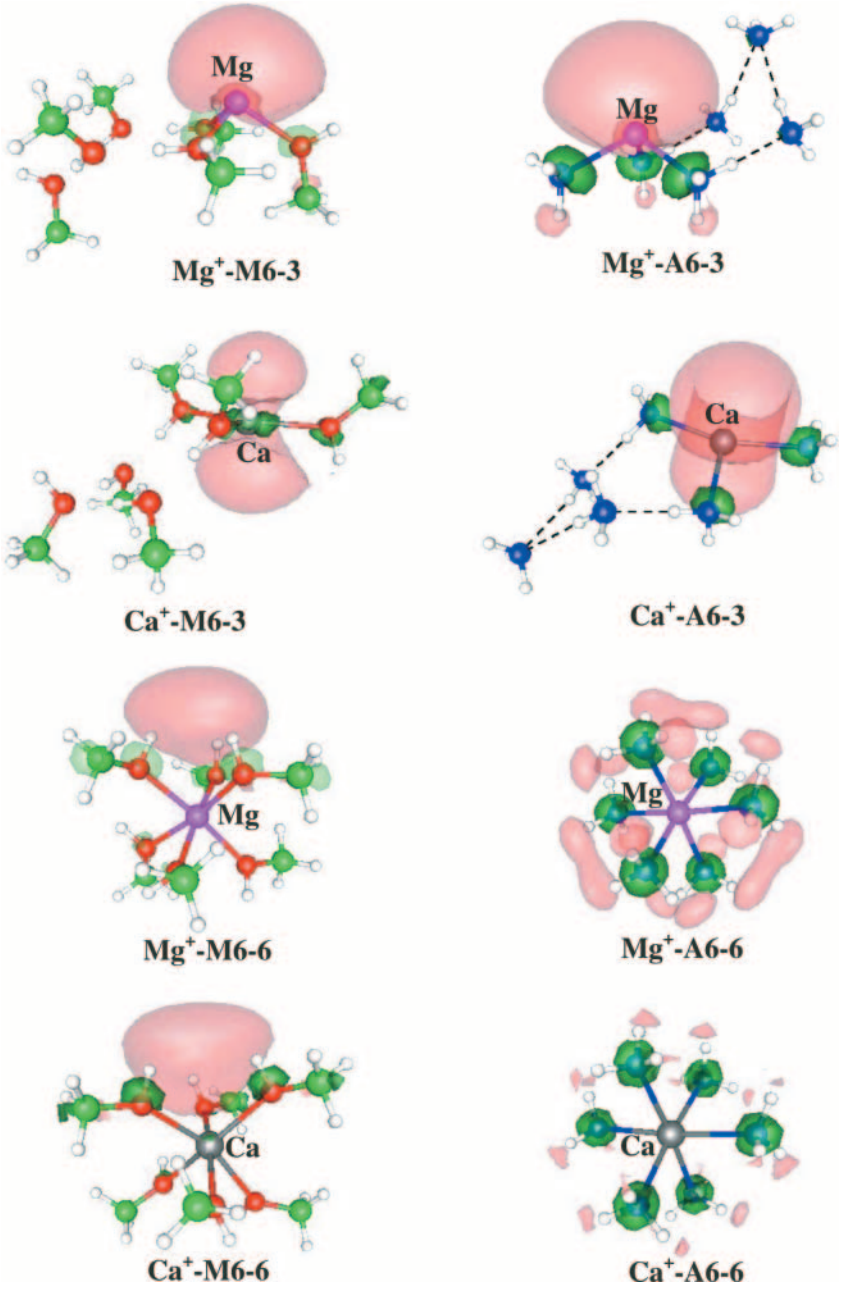


Table 11. Relative energies (in kcal/mol with BSSE and ZPE corrections), relative Gibbs energies (at 298 K and in kcal/mol), solute–solvent interactions, BE[$Ca^+/(CH_3OH)_n$] (in kcal/mol), solvent and solvent interactions, BE[$(CH_3OH)_n$] (in kcal/mol), R[Ca …e^-] (in Å), and SEM (in $Å^3$) in $Ca^+(CH_3OH)_n$, for $n = 5$ and 6 at B3LYP/6-311+G**.

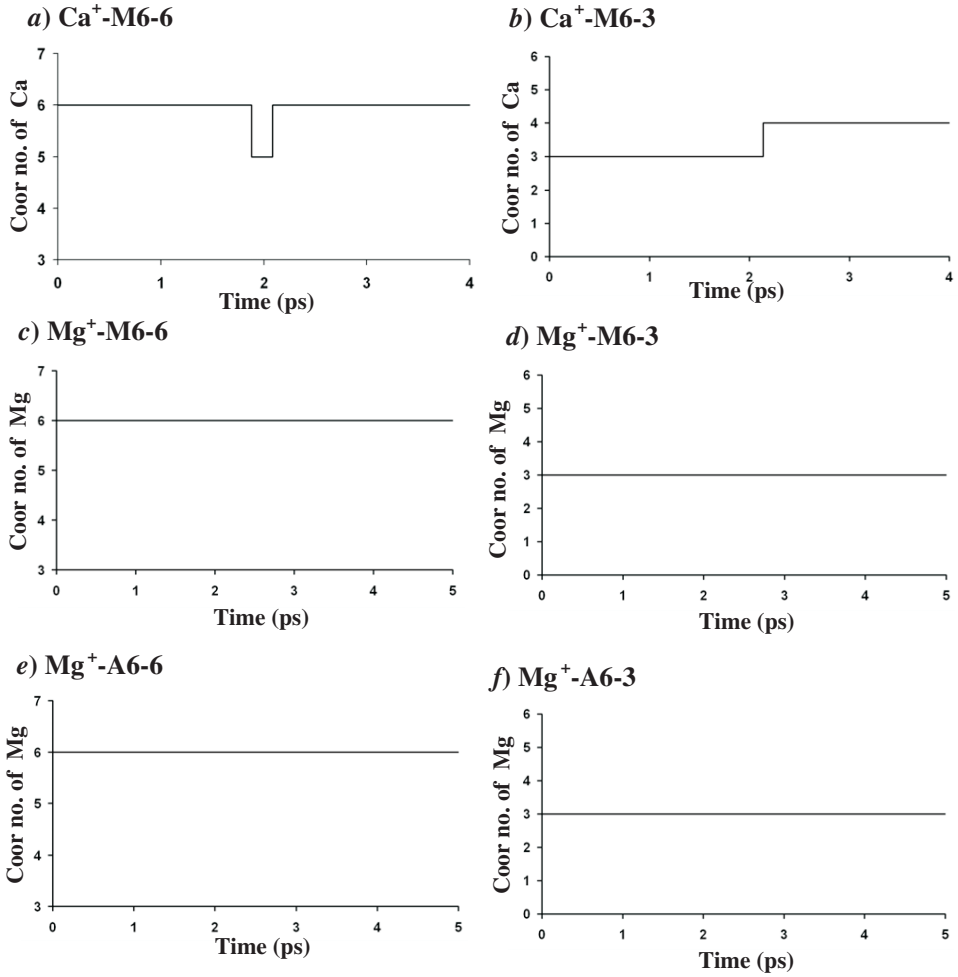
	Relative energy	Relative Gibbs energy	BE[$Ca^+/(CH_3OH)_n$]	BE[$(CH_3OH)_n$]	R[Ca …e^-]	SEM
Ca^+-M5-5	0.0	0.0	123.5	−14.0	1.35	28.6
Ca^+-M5-4	1.1	0.4	118.2	−8.9	1.27	27.3
Ca^+-M5-3	5.9	5.3	104.0	1.3	0.67	24.8
Ca^+-M6-6	0.0	0.0	145.7	−22.1	2.10	26.4
Ca^+-M6-5	2.7	3.8	135.6	−12.9	1.27	30.1
Ca^+-M6-4	5.9	5.7	125.7	−5.7	1.35	26.5
Ca^+-M6-3	10.4	9.7	110.7	5.2	0.43	25.4

© 2007 NRC Canada

Table 12. Relative energies (in kcal/mol with BSSE and ZPE corrections), relative Gibbs energies (at 298 K and in kcal/mol), solute–solvent interactions, $BE[Ca^+/(NH_3)_n]$ (in kcal/mol), solvent and solvent interactions, $BE[(NH_3)_n]$ (in kcal/mol), R[Ca …e$^-$] (in Å), and SEM (in Å^3) in $Ca^+(NH_3)_n$, for $n = 5$ and 6 at B3LYP/6-311+G**.

	Relative energy	Relative Gibbs energy	$BE[Ca^+/(NH_3)_n]$	$BE[(NH_3)_n]$	R[Ca …e$^-$]	SEM
Ca^+-A5-5	0.0	0.0	136.7	−23.6	0.55	86.7
Ca^+-A5-4	6.6	6.6	121.4	−14.2	0.26	42.8
Ca^+-A5-3	14.3	13.2	106.3	−6.4	0.35	29.3
Ca^+-A6-6	0.0	0.0	163.5	−34.4	0.00	158.6
Ca^+-A6-5	7.7	6.8	146.2	−24.1	0.83	86.5
Ca^+-A6-4	14.7	14.0	130.0	−14.2	0.55	43.3
Ca^+-A6-3	24.5	24.2	110.2	−3.7	0.42	29.0

Fig. 3. Time evolution of the coordination number as obtained by AIMD simulations at 300 K.



makes it possible to be localized by a few solvent molecules within the cluster. While the dipole moment for ammonia is smaller, the interaction between ammonia and the metal ion is stronger. The cluster structure is geared toward maximizing the metal–ammonia interaction, while the electron is less well solvated and is delocalized over all the ammonia molecules.

Thermal stability

In our previous study on $Mg^+(H_2O)_n$ and hydrated sulfate clusters $SO_4^{2-}(H_2O)_n$, it was found that structures with large numbers of water molecules in direct coordination with the solute ion could lose water molecules to outer solvation shells during AIMD simulations at finite temperature (5, 20). This is due to the entropy effect, since upon heating the inner solvation shell could be too crowded for the thermal motion of solvent molecules. It is natural to ask if the same could happen for the clusters studied in this report.

Shown in Fig. 3 is the time evolution of the coordination number around the metal ion for six clusters containing six solvent molecules at 300 K. The coordination number is obtained with a cutoff distance of 2.5 Å for Mg^+–O, 2.8 Å for Mg^+–N, and 2.7 Å for Ca^+–O, as obtained from the calculated radial

© 2007 NRC Canada

distribution plots. Fluctuations in the coordination number indicate loose solvation shells with solvent molecules crossing solvation shells during the simulation. It is observed only for the two Ca clusters. In the case of **Ca^+-M6-3**, a $Ca^+(CH_3OH)_6$ cluster with only three methanol molecules in the first shell, the coordination number is increased to 4 after 2 ps, which is in agreement with the energetic data in Table 11 with **Ca^+-M6-3** being the least stable isomer in terms of both the relative energy and the relative Gibbs free energy. In the case of **Ca^+-M6-6**, a $Ca^+(CH_3OH)_6$ cluster with all six solvent CH_3OH molecules in the first shell, there is a short period of time when the coordination number is decreased to 5. It indicates some flexibility in the solvation shell, although **Ca^+-M6-6** is the most stable structure at $n = 6$.

In contrast, the other four Mg clusters, **Mg^+-M6-6** and **Mg^+-M6-3** for $Mg^+(CH_3OH)_6$, and **Mg^+-A6-6** and **Mg^+-A6-3** for $Mg^+(NH_3)_6$, are more rigid, and the coordination number does not change during the simulation. This is not surprising in the case of $Mg^+(CH_3OH)_6$, since energy and free energy differences among its various isomers, as listed in Table 8, are fairly small. But it is somewhat surprising that **Mg^+-A6-3** does not go through any changes during the simulation, since it is considerably less stable than the other isomers and high coordination number should be favored for the ammonia solvated cluster. The possible explanation is that with the Mg^+–NH_3 interaction being relatively strong, the solvation structure is more rigid and shifting an NH_3 solvent between solvation shells is kinetically more difficult.

Conclusion

By a systematic comparison of the solvated Mg^+ and Ca^+ clusters with $n \leq 6$, we find that the solvation interactions produced by the three types of solvent molecules, water, methanol, and ammonia, vary in interesting and important ways. While in terms of solute–solvent interactions, CH_3OH is slightly stronger than H_2O, the repulsion among CH_3OH molecules is also slightly stronger. As a consequence, the geometrical and electronic structures for the methanol-solvated clusters are quite similar to their counterparts for the hydrated clusters. As a solvent molecule, ammonia stands in contrast to water and methanol. Despite the repulsion between ammonia molecules, the solute–ammonia interaction is much stronger for ammonia than for either water or methanol, and therefore ammonia molecules tend to squeeze into the first solvation shell. Furthermore, because of the smaller dipole moment on ammonia, the electron on the SOMO is delocalized among solvent ammonia molecules once it is detached from the metal ion at high coordination number. This is again in sharp contrast with the water and methanol clusters in which the detached electron is localized among a subset of solvent molecules. How such contrasts would affect the structures as cluster size grows over 6, in terms of geometry, electron solvation, and reactivity, should be interesting subjects for further studies.

Acknowledgment

Calculations reported in this paper were performed on the computer clusters operated by the Department of Chemistry, the Chinese University of Hong Kong (CUHK), supported by a Special Equipment Grant, and on the SGI Origin 2000, at the Information Technology Services Center (ITSC), CUHK. We thank Mr. Ka Fai Woo at the Department of Chemistry and Mr. Frank Ng at ITSC, for technical support. We gratefully acknowledge the financial support provided by the Hong Kong SAR Government through the Project CUHK 401604P. One of the authors (ZFL) would like to acknowledge his indebtness to Professor G. Mike Bancroft for his guidance and advice that have deeply influenced his academic career. This paper is dedicated to Professor Bancroft on the occasion of his 65th birthday.

References

1. J.M. Farrar. Int. Rev. Phys. Chem. **22**, 593 (2003).
2. A.W. Castleman, Jr. and K.H. Bowen. J. Phys. Chem. **100**, 12911 (1996).
3. K. Fuke, K. Hashimoto, and S. Iwata. Adv. Chem. Phys. **110**, 431 (1999).
4. C.K. Siu and Z.F. Liu. Chem. Eur. J. **8**, 3177 (2002).
5. C.K. Siu and Z.F. Liu. Phys. Chem. Chem. Phys. **7**, 1005 (2005).
6. H. Watanabe, S. Iwata, K. Hashimoto, F. Misaizu, and K. Fuke. J. Am. Chem. Soc. **117**, 755 (1995).
7. B.M. Reinhard and G. Niedner-Schatteburg. J. Chem. Phys. **118**, 3571 (2003).
8. B.M. Reinhard and G. Niedner-Schatteburg. Phys. Chem. Chem. Phys. **4**, 1471 (2002).
9. A.C. Harms, S.N. Khanna, A.B. Chen, and A.W. Castleman, Jr. J. Chem. Phys. **100**, 3540 (1994).
10. M. Sanekata, F. Misaizu, K. Fuke, S. Iwata, and K. Hashimoto. J. Am. Chem. Soc. **117**, 747 (1995).
11. G. Niedner-Schatteburg and V.E. Bondybey. Chem. Rev. **100**, 4059 (2000).
12. C.A. Woodward, M.P. Dobson, and A.J. Stace. J. Phys. Chem. A, **101**, 2279 (1997).
13. W.Y. Lu and S.H. Yang. J. Phys. Chem. A, **102**, 825 (1998).
14. J.I. Lee, D.C. Sperry, and J.M. Farrar. J. Chem. Phys. **121**, 8375 (2004).
15. M.J. Frisch, G.W. Trucks, H.B. Schlegel, G.E. Scuseria, M.A. Robb, J.R. Cheeseman, V.G. Zakrzewski, J.A. Montogemery, Jr., R.E. Stratmann, J.C. Burant, S. Dapprich, J.M. Millam, A.D. Daniels, K.N. Kudin, M.C. Strain, O. Farkas, J. Tomasi, V. Barone, M. Cossi, R. Cammi, B. Mennucci, C. Pomelli, C. Adamo, S. Clifford, J. Ochterski, G.A. Petersson, P.Y. Ayala, Q. Cui, K. Morokuma, D.K. Malick, A.D. Rabuck, K. Raghavachari, J.B. Foresman, J. Cioslowski, J.V. Ortiz, B.B. Stefanov, G. Liu, A. Liashenko, P. Piskorz, I. Komaromi, R. Gomperts, R.L. Martin, D.J. Fox, T. Keith, M.A. Al-Laham, C.Y. Peng, A. Nanayakkara, C. Gonzelez, M. Challacombe, P.M.W. Gill, B. Johnson, W. Chen, M.W. Wong, , J.L. Andres, C. Gonzalez, M. Head-Gordon, E.S. Replogle, and J.A. Pople. GAUSSIAN 98. Revision a.11 [computer program]. Gaussian, Inc., Pittsburgh, PA. 1998.
16. S. Simon, M. Duran, and J.J. Dannenberg. J. Chem. Phys. **105**, 11024 (1996).
17. S.F. Boys and F. Bernardi. Mol. Phys. **19**, 553 (1970).
18. T. Tsurusawa and S. Iwata. J. Phys. Chem. A, **103**, 6134 (1999).
19. B. Gao and Z.F. Liu. J. Chem. Phys. **123**, 224302 (2005).
20. B. Gao and Z.F. Liu. J. Chem. Phys. **121**, 8299 (2004).
21. B. Gao and Z.F. Liu. J. Phys. Chem. A, **109**, 9104 (2005).
22. G. Kresse and J. Hafner. Phys. Rev. B, **47**, 558 (1993).
23. G. Kresse and J. Hafner. Phys. Rev. B, **49**, 14251 (1994).
24. G. Kresse and J. Furthmüller. Phys. Rev. B, **54**, 11169 (1996).

© 2007 NRC Canada

25. G. Kresse and J. Furthmüller. Comput. Mater. Sci. **6**, 15 (1996).
26. G. Kresse and D. Joubert. Phys. Rev. B, **59**, 1758 (1999).
27. J.P. Perdew, J.A. Chevary, S.H. Vosko, K.A. Jackson, M.R. Pederson, D.J. Singh, and C. Fiolhais. Phys. Rev. B, **46**, 6671 (1992).
28. S. Nosé. J. Chem. Phys. **81**, 511 (1984).
29. W. Hoover. Phys. Rev. A, **31**, 1695 (1985).
30. H. Watanabe and S. Iwata. J. Phys. Chem. A, **101**, 487 (1997).
31. K.W. Chan, C.K. Siu, S.Y. Wong, and Z.F. Liu. J. Chem. Phys. **123**, 124313 (2005).
32. C.W. Bauschlicher, M. Sodupe, and H. Partridge. J. Chem. Phys. **96**, 4453 (1992).
33. E. Kochanski and E. Constantin. J. Chem. Phys. **87**, 1661 (1987).
34. N.F. Dalleska, B.L. Tjelta, and P.B. Armentrout. J. Chem. Phys. **98**, 4191 (1994).
35. B. Gao and Z.-F. Liu. J. Chem. Phys. **126**, 084501 (2007).

© 2007 NRC Canada

Remarkable two-step, four-electron oxidative addition reactions at phosphorus [P(I)–P(V)] in terminal electrophilic phosphinidene complexes[1]

Todd W. Graham, Konstantin A. Udachin, Marek Z. Zgierski, and Arthur J. Carty

Abstract: The reactivity of the terminal phosphinidene complex $[Re(CO)_5\{\eta^1\text{-}P(N^iPr_2)\}]AlCl_4$ towards the oxidants S_8 and Me_3SnN_3 has been investigated. These result in unprecedented four-electron oxidative addition reactions, affording complexes containing the P(V) ligands η^1-P(=S)(Cl)(N^iPr_2) and η^1-P(=NR)(Cl)(N^iPr_2), respectively. DFT calculations support the proposed mechanism.

Key words: electrophilic phosphinidene, low coordinate phosphorus, rhenium, oxidative addition, P(I) ligand.

Résumé : On a étudié la réactivité de phosphinidènes terminaux $[Re(CO)_5\{\eta^1\text{-}P(N^iPr_2\}]AlCl_4$ vis-à-vis des oxydants S_8 et Me_3SnN_3. Ces interactions donnent lieu à des réactions d'addition oxydantes à quatre électrons inconnues jusqu'à maintenant qui conduisent à la formation de complexes comportant respectivement les ligands P(V) η^1-P(=S)(Cl)(N^iPr_2} et η^1-P(=NR)(Cl)(N^iPr_2}. Des calculs selon la théorie de la fonctionnelle de la densité sont en accord avec le mécanisme proposé.

Mots-clés : phosphinidène électrophile, phosphore à faible coordination, rhénium, addition oxydante, ligand P(I).

[Traduit par la Rédaction]

Introduction

Over the years since the isolation and structural characterization of the first terminal, cationic, electrophilic phosphinidene complex of molybdenum in 2001 (1*a*), it has become clear that an extensive range of these phosphinidene-based analogues of Fischer carbenes can be synthesized. Examples of $[L_nM(=PNR_2)]$ complexes with metals from groups VI (1), VII (2), VIII (1*b*, 3), IX (4), and X (5) have been described, and a comprehensive picture of bonding and reactivity in these molecules is beginning to emerge, which complements an extensive reaction manifold already established for transient (6*a*, 6*b*) and nucleophilic (6*c*, 7) phosphinidenes. The bonding in terminal, electrophilic phosphinidene complexes consists primarily of a σ donor interaction from one phosphorus lone pair to the metal center with weak π back donation from the metal into the vacant p orbital on phosphorus. The electrophilicity of the phosphorus is partially alleviated by π donation from the NR_2 group. Structurally, these bonding interactions are typically manifested in slightly shortened M–P bonds, planar geometries at the nitrogen substituents, and short P–N bonds (1*b*, 2–4). Accordingly, aminophosphinidene ligands (P–NR_2) are regarded as isoelectronic to CO, with phosphorus in the +1 oxidation state. Chemically, as expected from the bonding model, such complexes undergo facile nucleophilic addition at the P(I) center forming adducts with Lewis bases (2, 8), in contrast to nucleophilic phosphinidene complexes such as $[Cp^*Ir(PPh_3)(=PMes^*)]$ (9), which react with electrophilic reagents.

The oxidative addition reaction is a key step in many important organometallic transformations (10). It typically proceeds via an addition of a reagent X–Y to a metal complex [M], resulting in the formation of a new complex of the form [M](X)(Y) and in a change of the oxidation state of the metal from $(n)^+$ to $(n + 2)^+$. Many of the reactions with terminal aminophosphinidene complexes we have previously described have resulted in conversion of the P(I) ligand to P(III); for example, conversion to a coordinated phosphaalkene ($R_2NP=CR_2$) or phosphaimine ($R_2NP=N\text{-}N=CPh_2$) ligand (3*b*). We have also observed reactions in which activated X–H bonds (X = SiR_3, OR, or $C_6H_4N_2Ph$) oxidatively add to the P(I) ligand, affording coordinated functionalized phosphines ($P(H)(X)NR_2$) (2, 11).

Received 7 August 2007. Accepted 23 August 2007. Published on the NRC Research Press Web site at canjchem.nrc.ca on 28 September 2007.

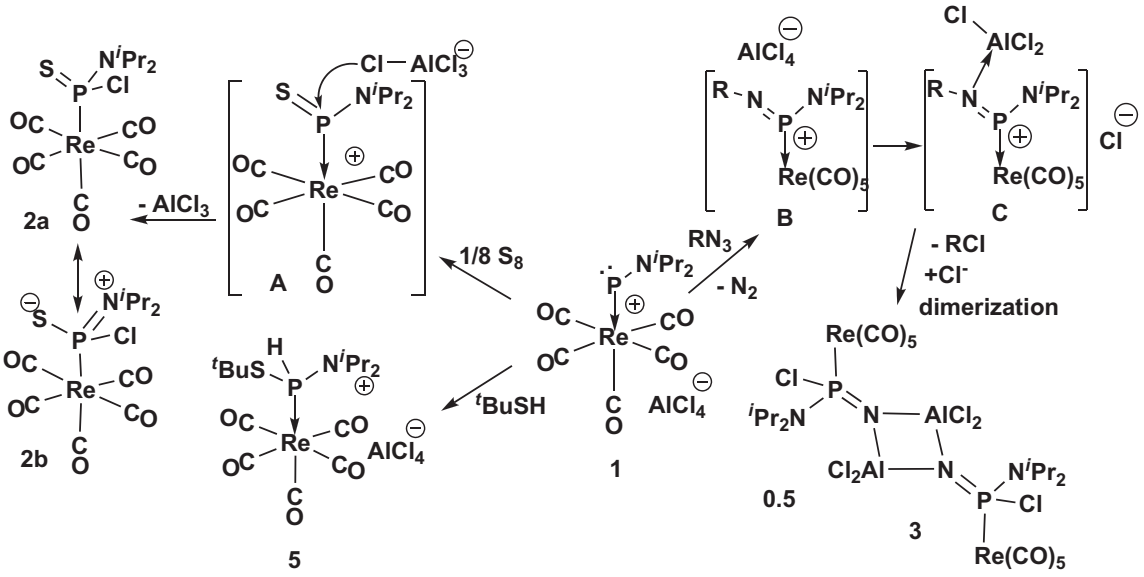
This article is dedicated to Dr. George Michael Bancroft for his pioneering application of Mössbauer and electron spectroscopy to fundamental and applied science and for the leadership he has provided to the Canadian Synchrotron community.

T.W. Graham, K.A. Udachin, M.Z. Zgierski, and A.J. Carty.[2] Steacie Institute for Molecular Sciences, National Research Council of Canada, 100 Sussex Drive, Ottawa, ON K1A 0R6, Canada; The Ottawa–Carleton Chemistry Institute, University of Ottawa, Ottawa, ON K1N 6N5, Canada.

[1]This article is part of a Special Issue dedicated to Professor G. Michael Bancroft.
[2]Corresponding author (e-mail: carty.arthur@ic.gc.ca).

 doi:10.1139/V07-119 © 2007 NRC Canada

Scheme 1.

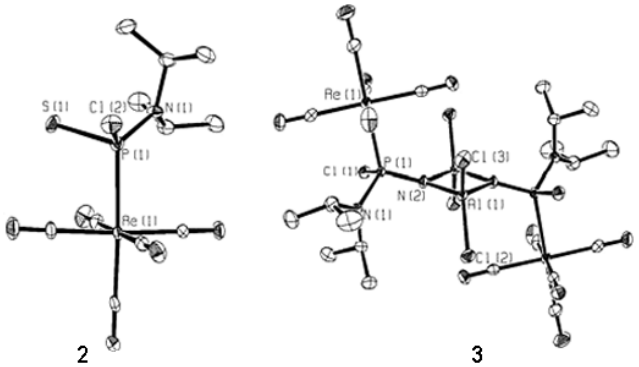


We now wish to report a new and unprecedented type of oxidative addition reaction, which results in the conversion of a P(I) center in cationic $[Re(CO)_5\{\eta^1\text{-}P(N^iPr_2)\}]AlCl_4$ (**1**) to a P(V) ligand in neutral $[Re(CO)_5\{\eta^1\text{-}P(=S)(Cl)(N^iPr_2)\}]$ (**2**) via reaction with S_8. A similar four-electron oxidative addition occurs on reaction of **1** with Me_3SnN_3 affording the novel neutral dimer $[Re(CO)_5\{P(Cl)(N^iPr_2)=N(AlCl_2)\}]_2$ (**3**).

Results and discussion

The complex $[Re(CO)_5\{\eta^1\text{-}P(N^iPr_2)\}]AlCl_4$ (**1**) (2), prepared by halide abstraction from $[Re(CO)_5\{\eta^1\text{-}P(Cl)N^iPr_2\}]$ (**4**) by $AlCl_3$, reacts smoothly with S_8 in dichloromethane, precipitating $AlCl_3$ and affording a quantitative yield of the new compound $[Re(CO)_5\{\eta^1\text{-}P(=S)(Cl)(N^iPr_2)\}]$ (**2**) (Scheme 1), which displays a ^{31}P NMR resonance at δ 100 (see Experimental Section), sharply upfield of that in **1** (δ 956). The ^1H NMR spectrum of **2** shows only resonances due to the ^{i}Pr groups. A single crystal X-ray analysis[3] (Fig. 1) revealed that a new one-electron donor P(V) ligand $P(=S)(Cl)N^iPr_2$ is coordinated to a typical square-pyramidal $Re(CO)_5$ fragment. The Re(1)—P(1) bond length of 2.4972(8) Å is significantly longer than the corresponding Re—P distance in the precursor phosphinidene complex **1** (2) (2.446(3) Å). The P(1)—S(1) separation of 2.181(1) Å is considerably longer than the short P=S separation of Ph_3P=S (1.950(3) Å) (12), which may be attributed to competitive π bonding to phosphorus from the sulfur atom and the nitrogen lone pair of the N^iPr_2 substituent. In agreement with this, the P(1)—N(1) bond length (1.661(3) Å) indicates substantial residual π character (4). While oxidation of R_3P to form R_3P=S is a well-known reaction (13), the direct conversion of P(I) to P(V) is a new reaction pathway for coordinated phosphorus ligands. Complex **2** is likely formed from the intermediate complex **A** (Scheme 1) via oxidative sulfuration; the highly electrophilic phosphorus center in **A** then

Fig. 1. ORTEP diagrams of complexes **2** and **3**. Hydrogen atoms have been omitted for clarity, and thermal ellipsoids are shown at the 50% probability level. Selected bond lengths (Å) and angles (°): **2**: Re(1)—P(1), 2.4972(8); P(1)—S(1), 2.181(1); P(1)—N(1), 1.661(3); Re(1)–P(1)–S(1), 102.16(4); Re(1)–P(1)–Cl(2), 112.31(4); Re(1)–P(1)–N(1), 118.1(1); S(1)–P(1)–Cl(2), 105.28(5); S(1)–P(1)–N(1), 103.6(1); Cl(2)–P(1)–N(1), 113.3(1). **3**: Re(1)—P(1), 2.5249(7); P(1)—Cl(1), 2.1298(9); P(1)—N(1), 1.660(2); P(1)—N(2), 1.600(2); N(2)—Al(1), 1.861(2); Al(1)—Cl(2), 2.143(1); Al(1)—Cl(3), 2.152(1); Re(1)–P(1)–Cl(1), 104.03(3); Re(1)–P(1)–N(1), 118.48(8); Re(1)–P(1)–N(2), 117.11(8); P(1)–N(2)–Al(1), 133.3(1); N(2)–Al(1)–Cl(3), 111.85(8); Cl(2)–Al(1)–Cl(3), 104.80(4).



reacts with chloride ion to form the product. Although we have not been able to observe intermediate **A**, DFT analyses (14) of the cations **1**, **A**, and the neutral product **2** support the proposed mechanism. The energy of intermediate **A** formed by adding sulfur to the phosphinidene cation **1** lies 5.45 eV below the sum of the energies of **1** and atomic S, thus **A** is an energetically stable species. However, addition of chloride ion to **A** provides an additional stabilization energy of 5.82 eV. There is therefore a strong driving force for

[3] X-ray data for **2**: FW 524.91; orthorhombic; *Pna*2(1); a = 24.342(1) Å; b = 7.6634(7) Å; c = 9.2297(8) Å; T = 125(2) K; V = 1721.7(3) Å^3; Z = 4; D_{calcd} = 2.025 Mg/m^3; 4709 independent reflections ($R_{(int)}$ = 0.0234); GOF = 1.150; R_1 = 0.0184; wR_2 = 0.0458.

© 2007 NRC Canada

the oxidation from P(I) in **1** to P(V) in **2**. The minimized geometry of **2** matches the major features of the X-ray data with the HOMO being a localized 3p orbital on the sulfur atom. The LUMO of **A** is centered on phosphorus, which also bears a positive charge (+0.52 e (Mulliken)), consistent with nucleophilic attack by Cl^- at this atom. Experimental and calculated (DFT) P—S and P—N bond lengths in **2** confirm that the ground state has substantial contributions from the mesomeric form **2b** (Scheme 1). Synthetically, we have found that **2** can also be generated directly from the neutral terminal chlorophosphido complex $[Re(CO)_5\{\eta^1\text{-}P(Cl)N^iPr_2\}]$ (**4**) and S_8, although the reaction is qualitatively much slower than with complex **1**. ^{31}P NMR spectroscopy of solutions of **1** showed no indication of the presence of any of the phosphide complex **4**, and exhaustive pentane extractions of solid complex **1** afforded no trace of highly soluble **4**. While we cannot completely eliminate the possibility of trace amounts of **4** in equilibrium with **1**, we believe the experimental evidence coupled with the DFT calculations favor the intermediacy of **A** in the oxidative conversion of **1** to **2**.

By contrast, the reaction of **1** with ^{t}BuSH affords the new P(III) complex $[Re(CO)_5\{P(N^iPr_2)(H)(S^tBu)\}]AlCl_4$ (**5**), which results from oxidative addition of the S–H bond to the P(I) ligand. This compound has been fully characterized (see Experimental Section) and displays a ^{31}P NMR resonance at δ –11. The ^1H NMR spectrum of **5** shows the expected ^{t}Bu and ^{i}Pr resonances, in addition to a characteristic P–H signal at δ 8.62 with a large $^1J_{PH}$ of 424 Hz.

The reaction of **1** with Me_3SnN_3 readily affords the new complex $[Re(CO)_5\{P(Cl)(N^iPr_2)=N(AlCl_2)\}]_2$ (**3**) (Scheme 1). The ^{31}P NMR spectrum of the product shows a high-field resonance at δ 81 (cf. δ 100 in **2**), and the ^1H NMR spectrum shows only the presence of ^{i}Pr signals (see Experimental Section). The X-ray analysis[4] confirms that in the centrosymmetric structure, the rhenium and phosphorus ligand environments in **3** are closely related to those in **2**, with a one electron P(V) fragment coordinated to each octahedral rhenium center in the dimeric molecule. The P–N(2) bonds of the two equivalent P(V) ligands are bound to two $AlCl_2$ units forming an $N_2Al_2Cl_4$ bridge between $[Re(CO)_5\{P(Cl)(N^iPr_2)\}]$ entities. The P(1)—Cl(1) (2.1298(9) Å) and P(1)—N(1) (1.660(2) Å) distances are typical, and the P=N separation (1.600(2) Å) is as expected for an R_3P=N ligand (15). The μ-$AlCl_2$ fragments have an average Al—Cl separation of 2.147 Å and average N—Al distances of 1.855 Å. By analogy with compound **2**, **3** likely forms by initial conversion to the extremely electrophilic intermediate **B**. Nucleophilic attack of the RN nitrogen in **B** on $AlCl_4^-$ forms **C**; subsequent chloride attack on phosphorus with concomitant elimination of RCl and dimerization forms compound **3**.

These results, coupled with previous studies describing facile P=C, P=N, and P=S bond-forming reactions at both terminal (3*b*) and doubly bridging (16) phosphinidene complexes, illustrate the synthetic potential of electrophilic P(I) centres for the generation of new types of coordinated P(III) and P(V) ligands.

Conclusion

In conclusion, we have demonstrated for the first time that terminal electrophilic phosphinidene complexes can undergo two step, four-electron oxidative addition reactions leading to new types of coordinated P(V) ligand systems. We attribute the remarkable and unprecedented reactivity of the phosphinidene complexes to the low oxidation state (i.e., P(I)) and coordination number of the phosphinidene ligand, both of which favor oxidative addition. We note that main-group compounds, which contain phosphorus in low coordination environments (17), are known, and we anticipate exciting and complementary reactivity patterns to emerge.

Experimental[5]

General comments

All procedures were carried out using standard Schlenk techniques or in a glovebox under a nitrogen atmosphere. THF was distilled from Na/benzophenone. Dichloromethane and pentane were purified using solvent purification columns containing alumina (dichloromethane) or alumina and copper catalyst (pentane). $CDCl_3$ and CD_2Cl_2 were vacuum-distilled from $AlCl_3$ and then CaH_2. C_6D_6 was vacuum-distilled from Na/benzophenone. NMR spectra were recorded at 400.13 MHz (^1H), 161.98 MHz ($^{31}P\{^1H\}$), or 100.61 MHz ($^{13}C\{^1H\}$). $Cl_2PN^iPr_2$ (18) was prepared according to the literature procedures. $Re_2(CO)_{10}$ and $AlCl_3$ were obtained from Strem Chemicals. All other reagents were obtained from Aldrich and were used as received.

$[Re(CO)_5\{\eta^1\text{-}P(=S)(Cl)(N^iPr_2)\}]$ (2)

13 mg (0.0507 mmol) of S_8 was added to 250 mg (0.399 mmol) of $[Re(CO)_5\{P(N^iPr_2)\}]AlCl_4$, the mixture was stirred for 1 h, and then the solvent was removed in vacuo. The solid was dissolved in ~3 mL of THF and filtered, and then pentane was added dropwise until the solution became cloudy. Cooling to −45 °C overnight resulted in the formation of large crystals of $AlCl_3(THF)_2$, which were filtered off. This was repeated twice until all $AlCl_3(THF)_2$ was removed from the solution. On standing, compound **2** crystallized in 50% yield. Analytically pure compound **2** may also be prepared by adding 1/8 equiv. of S_8 to $[Re(CO)_5(P(Cl)N^iPr_2)]$ at −45 °C in THF and stirring for 2 h, followed by recrystallization from THF–pentane at −45 °C. Yield: 67%. ^1H NMR (δ, $CDCl_3$, 25 °C): 3.96 (sept., $^3J_{HH}$ = 6.7 Hz, 2H, C*H*$(CH_3)_2$); 1.61 (d, $^3J_{HH}$ =

[4] X-ray data for **3**: FW 2418.97; monoclinic; $P2_1/c$; a = 9.176(1) Å; b = 18.493(2) Å; c = 13.725(1) Å; β = 123.120(6)°; V = 1950.7(4) Å^3; Z = 1; $D_{calcd.}$ = 2.059 Mg/m^3; 5442 independent reflections ($R_{(int)}$ = 0.0240); GOF = 0.945; R_1 = 0.0201; wR_2 = 0.0477.

[5] Supplementary data for this article are available on the journal Web site (canjchem.nrc.ca) or may be purchased from the Depository of Unpublished Data, Document Delivery, CISTI, National Research Council Canada, Ottawa, ON K1A 0R6, Canada. DUD 5219. For more information on obtaining material, refer to cisti-icist.nrc-cnrc.gc.ca/irm/unpub_e.shtml. CCDC 661898, and 661599 contain the crystallographic data for this manuscript. These data can be obtained, free of charge, via www.ccdc.cam.ac.uk/conts/retrieving.html (Or from the Cambridge Crystallographic Data Centre, 12 Union Road, Cambridge CB2 1EZ, UK; fax +44 1223 336033; or deposit@ccdc.cam.ac.uk).

© 2007 NRC Canada

6.7 Hz, 6H, $CH(CH_3)_2$); 1.50 (d, $^3J_{HH}$ = 6.8 Hz, 6H, $CH(CH_3)_2$). ^{31}P NMR (δ, $CDCl_3$, 25 °C): 100. IR (ν_{CO}, cm^{-1}, CH_2Cl_2): 2150 (m, sh); 2087 (m, sh); 2045 (s); 2024 (s). Anal. calcd. for $C_{11}H_{14}ClNO_5PSRe$: C, 25.2; H, 2.7; N, 2.7. Found: C, 25.5; H, 2.5; N, 2.4.

$[Re(CO)_5\{\eta^1\text{-}P(N^iPr_2)(Cl)(=NAlCl_2)\}]_2$ (3)

10 mL of CH_2Cl_2 was added to 55 mg (0.412 mmol) of $AlCl_3$ and 200 mg (0.406 mmol) of $[Re(CO)_5(P(Cl)N^iPr_2)]$, and the mixture was stirred for 5 min. After cooling the suspension to −45 °C, 84 mg (0.404 mmol) of Me_3SnN_3 was added. The mixture was stirred for 4.5 h and was then filtered through Celite. The solution was concentrated in vacuo to ~1 mL and was then cooled to −45 °C overnight resulting in the formation of a white crystalline product, which was collected and dried in vacuo. Yield: 145 mg, 60%. ^{1}H NMR (δ, CD_2Cl_2, −45 °C): 4.53 (m, 4H, $CH(CH_3)_2$); 1.48 (d, $^3J_{HH}$ = 6.8 Hz, 12H, $CH(CH_3)_2$); 1.45 (d, $^3J_{HH}$ = 6.8 Hz, 6H, $CH(CH_3)_2$); 1.44 (d, $^3J_{HH}$ = 6.8 Hz, 6H, $CH(CH_3)_2$). ^{31}P NMR (δ, $CDCl_3$, 25 °C): 80.5 (br, s). IR (ν_{CO}, cm^{-1}, CH_2Cl_2): 2154 (w); 2102 (w); 2093 (w); 2052 (s); 2045 (s); 2030 (m, sh). Anal. calcd. for $C_{22}H_{28}Al_2Cl_6N_4O_{10}P_2Re_2$: C, 21.9; H, 2.3; N, 4.6. Found: C, 21.6; H, 2.3; N, 4.6.

$[Re(CO)_5\{\eta^1\text{-}P(S^tBu)(H)(N^iPr_2)\}]AlCl_4$ (5)

$[Re(CO)_5\{\eta^1\text{-}P(N^iPr_2)\}]AlCl_4$ in 10 mL of dichloromethane was prepared as described earlier from 200 mg (0.406 mmol) of $[Re(CO)_5(P(Cl)N^iPr_2)]$. The suspension was cooled to −80 °C, and then 46 μL (0.408 mmol) of ^{t}BuSH was added. The mixture was warmed to room temperature, resulting in dissolution of the solid, and was stirred for 20 min. The solvent was removed in vacuo, and the residue was recrystallized from dichloromethane–ether at −45 °C. Yield: 60%. ^{1}H NMR (δ, $CDCl_3$, 25 °C): 8.62 (d, $^1J_{PH}$ = 424 Hz, 1H, P-*H*); 3.70 (sept., $^3J_{HH}$ = 6.8 Hz, 2H, $CH(CH_3)_2$); 1.63 (s, 9H, $C(CH_3)_3$); 1.42 (d, $^3J_{HH}$ = 6.7 Hz, 6H, $CH(CH_3)_2$); 1.38 (d, $^3J_{HH}$ = 6.8 Hz, 6H, $CH(CH_3)_2$). ^{31}P NMR (δ, $CDCl_3$, 25 °C): −11. IR (ν_{CO}, cm^{-1}, CH_2Cl_2): 2156 (w); 2053 (s); 2035 (m, sh). Anal. calcd. for $C_{15}H_{24}AlCl_4NO_5PSRe$: C, 25.1; H, 3.4; N, 2.0. Found: C, 24.9; H, 3.0; N, 2.0.

References

1. (*a*) B.T Sterenberg and A. J. Carty. J. Organomet. Chem. **617**, 696 (2001); (*b*) B.T. Sterenberg, K.A. Udachin, and A.J. Carty. Organometallics, **20**, 2657 (2001).
2. T.W. Graham, R.P.-Y. Cariou, J. Sánchez-Nieves, A.E. Allen, K.A. Udachin, and A.J. Carty. Organometallics, **24**, 2023 (2005).
3. (*a*) B.T. Sterenberg, K.A. Udachin, and A.J. Carty. Organometallics, **22**, 3927 (2003); (*b*) T.W. Graham, K.A. Udachin, and A.J. Carty. Chem. Commun. 5890 (2005).
4. J. Sánchez-Nieves, B.T. Sterenberg, K.A. Udachin, and A.J. Carty. J. Am. Chem. Soc. **125**, 2404 (2003).
5. R. Waterman and G.L. Hillhouse. Organometallics, **22**, 5182 (2003).
6. (*a*) F. Mathey. Angew. Chem., Int. Ed. Engl. **26**, 275 (1987); (*b*) F. Mathey, N.H. Tran Huy, and A. Marinetti. Helv. Chim. Acta, **84**, 2938 (2001); (*c*) K. Lammertsma. Top. Curr. Chem. **229**, 95 (2003).
7. (*a*) G. Zhao, F. Basuli, U.J. Kilgore, H. Fan, H. Aneetha, J.C. Huffman, G. Wu, G., and D.J. Mindiola. J. Am. Chem. Soc. **128**, 13575 (2006); (*b*) R. Waterman and G.L. Hillhouse. J. Am. Chem. Soc. **125**, 13350 (2003); (*c*) A.T. Termaten, H. Aktas, M. Schakel, A.W. Ehlers, M. Lutz, A.L. Spek, and K. Lammertsma. Organometallics, **22**, 1827 (2003); (*d*) R. Melenkivitz, D.J. Mindiola, and G.L. Hillhouse. J. Am. Chem. Soc. **124**, 3846 (2002); (*e*) Z. Hou, T.L. Breen, and D.W. Stephan. Organometallics, **12**, 3158 (1993); (*f*) C.C. Cummins, R.R. Schrock, and W.M. Davis. Angew. Chem., Int. Ed. Engl. **32**, 756 (1993).
8. B.T. Sterenberg, K.A. Udachin, and A.J. Carty. Organometallics, **20**, 4463 (2001).
9. A.J. Termaten, T. Nijbacker, M. Schakel, M. Lutz, A.L. Spek, and K. Lammertsma. Organometallics, **21**, 3196 (2002).
10. J.P. Collman, L.S. Hegedus, J.R. Norton, and R.G. Finke. Principles and applications of organotransition metal chemistry. University Science Books, Mill Valley, California. 1987. Vol. 1. pp. 279–353.
11. B.T. Sterenberg, J. Sánchez-Nieves, and A.J. Carty. Unpublished results.
12. P.W. Codding and K.A. Kerr. Acta. Crystallogr., Sect. B: Struct. Sci. **34**, 3785 (1978).
13. H.R. Hayes and D.J. Peterson. *In* Organic phosphorus compounds. *Edited by* G.M. Kosolapoff and L. Maier. Wiley-Interscience, New York. 1972. Vol. 3. p. 341.
14. Density functional calculations were performed with the GAUSSIAN 98 program package with the BP 86: (*a*) A.D. Becke. Phys. Rev. A, **38**, 3098 (1988); (*b*) J.P. Perdew. Phys. Rev. B. **33**, 8822 (1986); set of functionals and cc-pVDZ basis set for all first, second, and third row atoms. For Re, relativistic pseudopotentials for core electrons and a LANL2DZ ECP basis set for all other electrons were used.
15. T.W. Graham, J. Kickham, S. Courtenay, P. Wei, and D.W. Stephan. Organometallics, **23**, 3309 (2004).
16. (*a*) T.W. Graham, K.A. Udachin, and A.J. Carty. Inorg. Chim. Acta, **360**, 1376 (2007); (*b*) T.W. Graham, K.A. Udachin, and A. J. Carty. Chem. Commun. **35**, 4441 (2005).
17. (*a*) N. Burford, T.S. Cameron, K.D. Conroy, B.D. Ellis, M. Lumsden, C.L.B. MacDonald, R. McDonald, A.D. Phillips, P.J. Ragogna, R.W. Schurko, D. Walsh, and R.E. Wasylishen. J. Am. Chem. Soc. **124**, 14012 (2002); (*b*) B.D. Ellis, C.A. Dyker, A. Decken, and C.L.B. MacDonald. Chem. Commun. **15**, 1965 (2005).
18. R.B. King and N.D. Sadanani. Synth. React. Inorg. Met.-Org. Chem. **15**, 149 (1985).

© 2007 NRC Canada

Characterization of metallurgical-grade aluminas and their precursors by ^{27}Al NMR and XRD[1]

Linus M. Perander, Zoran D. Zujovic, Tania Groutso, Margaret M. Hyland, Mark E. Smith, Luke A. O'Dell, and James B. Metson

Abstract: The structure of metallurgical- or smelter-grade aluminas (MGAs) is complex and poorly understood. Ultra-high-field solid-state ^{27}Al NMR results on industrial as well as on laboratory-prepared aluminas are discussed in relation to XRD results. It is demonstrated that high-field NMR can effectively be used to quantify the proportion of the thermodynamically stable alpha-alumina phase in these materials. The results demonstrate that ^{27}Al NMR is a vital adjunct to XRD methods to quantify the transition alumina phases that invariably dominate the MGAs. The nature of the disorder in these materials, determined by ^{27}Al NMR, is also compared with literature data, such as XANES and EXAFS studies, on typical laboratory-prepared materials. The utility of ^{27}Al NMR studies to provide new insight into the structural complexity of metallurgical aluminas is shown.

Key words: solid-state magic-angle-spinning NMR, metallurgical-grade alumina, transition alumina, gamma-alumina, coordination number.

Résumé : La structure des alumines de qualité métallurgique (AQM) ou pour électrolyse est complexe et mal comprise. Opérant à champ élevé et à l'état solide, on a déterminé les spectres RMN du ^{27}Al d'alumines industrielles et d'autres préparées en laboratoire et on discute de ces spectres en relation avec les résultats obtenus par diffraction des rayons X (DRX). On a démontré que la RMN à champ élevé peut effectivement être utilisée pour quantifier la proportion de la phase thermodynamiquement stable d'alumine alpha qui est présente dans ces matériaux. Les résultats démontrent que la RMN du ^{27}Al est une addition absolument nécessaire aux méthodes de DRX pour quantifier les phases d'alumines de transition qui dominent invariablement les AQM. On a aussi comparé la nature du désordre dans ces matériaux, telle que déterminée par RMN du ^{27}Al, avec les résultats déjà publiés dans la littérature et obtenus par des études à l'aide de la spectroscopie d'absorption X de type XANES ou EXAFS sur des matériaux typiques préparés en laboratoire. On démontre donc l'utilité de la RMN du ^{27}Al à fournir de nouvelles indications sur la complexité structurale des alumines métallurgiques.

Mots-clés : RMN à l'état solide et à l'angle magique, alumine de qualité métallurgique, alumine de transition, alumine gamma, indice de coordination de l'aluminium.

[Traduit par la Rédaction]

Introduction

Over 50 million tonnes of metallurgical-grade alumina (MGA) is produced annually, largely as a raw material for the electrolytic production of aluminum. This material is produced almost exclusively by the Bayer process to a reasonably uniform specification across the industry, in terms of specific surface area, particle size and strength, residual hydrogen or moisture as well as impurity and alpha-alumina contents. The microstructure of this material is of considerable interest for a number of reasons; there has, for instance, been interest in the relationship between properties and the behavior of the alumina when used in gas scrubbing systems and when fed to the reduction cell (1, 2). Furthermore, this material can also provide insights into the complex relationship within the family of the so-called "transition aluminas" produced in the calcination of gibbsite $Al(OH)_3$ (3).

In the Bayer process, the calcination step plays an important role in the evolution of microstructural features that can be related to the properties and the performance of the MGA

Received 28 June 2007. Accepted 21 August 2007. Published on the NRC Research Press Web site at canjchem.nrc.ca on 2 October 2007.

L.M. Perander, Z.D. Zujovic, and T. Groutso. Department of Chemistry, University of Auckland, Private Bag 90219, Auckland, New Zealand.
M.M. Hyland. Department of Chemical and Materials Engineering, The University of Auckland, Private Bag 92019, Auckland, New Zealand.
M.E. Smith and L.A. O'Dell. Department of Physics, University of Warwick, Coventry CV4 7AL, UK.
J.B. Metson.[2] Department of Chemistry, University of Auckland, Private Bag 90219, Auckland, New Zealand; MacDiarmid Institute for Advanced Materials and Nanotechnology.

[1]This article is part of a Special Issue dedicated to Professor G. Michael Bancroft.
[2]Corresponding author (e-mail: j.metson@auckland.ac.nz).

 doi:10.1139/V07-106 © 2007 NRC Canada

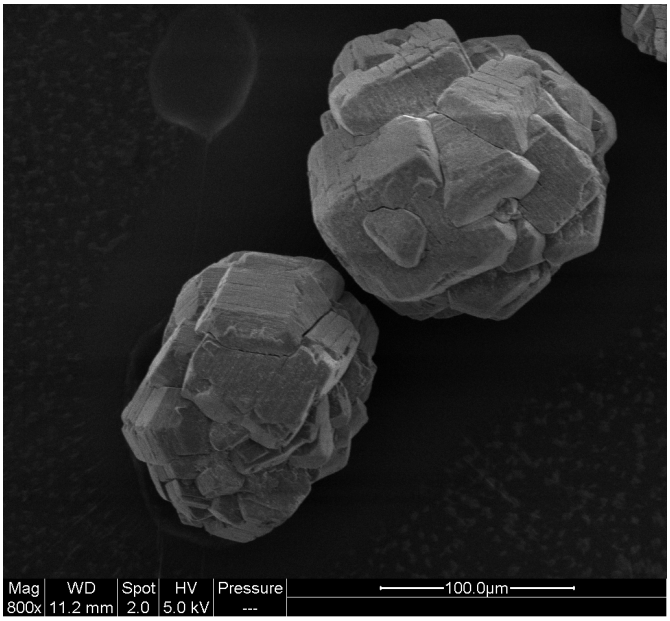
in the aluminum smelter. For the calcination step, production technology has progressively moved from rotary kilns to the more energy-efficient gas suspension or fluid-bed-type rapid-flash calciners, in some cases with capacity in excess of 4 000 tonnes per day (4). Due to the extended residence time, rotary kilns produce a more-homogenous and structurally ordered material. However, the literature and the understanding of the processes operating under flash-calcination conditions are lacking when compared, for example, with the typical gamma-aluminas widely used in catalysis.

The most-authoritative description of the interrelationship of the alumina phases or "forms" during calcination processes is that of Wefers and Misra (3). The speed of the modern calcination process, together with the variation of particle size, velocity, and residence time, produces a far-from-equilibrium phase distribution both between and within individual alumina grains. MGAs can thus be viewed as granular materials comprised of aggregates of intergrown alumina crystals; generally, with a crystallite size of 10–40 μm. Figure 1 shows a scanning electron micrograph of a typical assembly of MGA particles. The precipitation conditions of the precursor gibbsite are selected to maximize yield in the critical size range, thus causing the dominance of heavily intergrown aggregates.

The disorder and complexity of MGA is influenced by the calcination process as well as the gibbsite precipitation stage. The calcination strategy is governed first and foremost by the need to meet a specification for a specific surface area of 70–80 m^2g^{-1}, while maintaining a low residual-moisture content, necessary to limit HF generation when fed into the molten cryolite electrolyte in the reduction cell. Surface area is also critical for effective performance as a gas scrubbing medium and for optimal dissolution in the reduction cell. Surface area is maximized by controlling the transition sequence to limit maximum temperature and residence time. With increasing temperature, the phase sequence moves from the hexagonal gibbsite, $Al(OH)_3$, through the oxyhydroxide boehmite, AlOOH, into the cubic system represented by the spinel structured gamma-alumina (5) (Fig. 2). Neutron diffraction studies indicate that the face-centred cubic oxygen sublattice in the spinel-based transition aluminas tends to be highly ordered in these materials; however, the aluminum ions are quite disordered, leading to the broadened lines typical of their powder X-ray diffraction (XRD) patterns (6).

In gibbsite, aluminum atoms occupy two thirds of the octahedral positions, with hydroxyl groups octahedrally coordinated in double layers. This gives gibbsite a monoclinic symmetry (space group $P2_1/n$) with a hexagonal close packing of the hydroxyl groups. Upon heating, the hydroxyls are progressively lost through the structural channels formed in the gibbsite lattice by the formation of water by proton exchange between neighbouring hydroxyls (7–9). This is accompanied by the structural rearrangement of the crystal lattice, a pseudomorphic transformation (i.e., the original morphology of the parent gibbsite is retained) with little change in the external dimensions, and as a consequence, a large internal porosity develops. The long-range ordering in gibbsite or boehmite is lost, and an amorphous transition-alumina form, gamma-alumina, appears.

Fig. 1. Scanning electron micrograph of "typical" metallurgical-grade alumina particles.



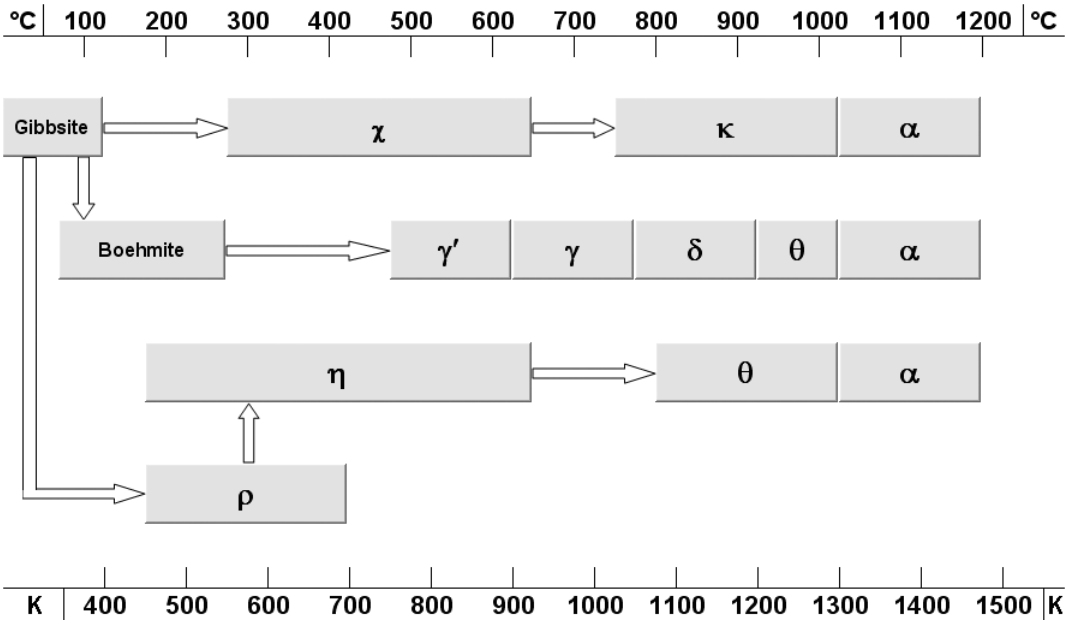
Further heating results in the conversion to delta- and then to theta-alumina, which are also spinel-structured transition-alumina forms. Gamma-, delta- and theta-alumina all have a face-centred cubic packing of the oxygen anions with various amounts of aluminum cations in either the octahedral or tetrahedral interstices. The proportion of tetrahedral sites increases with temperature (10), having 25%–30% of the octahedral sites occupied for gamma-alumina and 50% for theta-alumina (11, 12), until the abrupt disappearance of tetrahedrally coordinated aluminum upon the formation of alpha-alumina (corundum), which marks the end of the transformation sequence. Alpha-alumina has a hexagonal close packing of the oxygen anions, and all of the octahedral aluminum sites are occupied (13).

The mix of "forms" and high levels of disorder in MGAs present significant challenges in understanding their structure with relation to the performance as a raw-material feed for the smelting process (14). The X-ray methods by which we might follow these phase transformations are constrained by the limited long-range order in these materials. Thus, methods, which do not rely on long-range crystallographic order, can provide new insights and improved understanding of these materials. Kato et al. have reported X-ray absorption near-edge studies (XANES) of the Al K-edge in transition aluminas (15). In the manner of NMR studies, this approach appears to provide significant insight into the occupancy of octahedral and tetrahedral sites, i.e., key to understanding the forms and transition points in the alumina samples examined. However, the XANES approach has yet to be applied to MGAs.

A new phase, described as gamma-prime-alumina (γ'-Al_2O_3) was introduced by Paglia et al., which significantly improved the fitting of diffraction data on aluminas from fluid-bed and gas-suspension calciners (16). Ashida et al. developed a model used for fitting XRD data to better accommodate the degree of structural disorder observed for MGAs

© 2007 NRC Canada

Fig. 2. Thermal-decomposition pathways of gibbsite, adapted from ref. 3.



by including the contribution of theta-alumina to the background (14). However, a significant challenge is the broad and diffuse diffraction patterns of amorphous transition alumina phases, making quantitative or structural determinations difficult.

Ingram-Jones et al. compared flash calcining with soak calcining of gibbsite in laboratory trials (17). They used XRD and ^{27}Al magic-angle spinning (MAS) NMR to examine the dehydroxylation sequence, as a function of both the calcination temperature and particle size. They suggested a cross-over of the calcination pathways shown in Fig. 2, where chi-alumina would transform into gamma-alumina for flash-calcined fine gibbsite particles (<0.5 μm) and partially for coarse (~14 μm) particles as well. The remainder of the coarse gibbsite would react via the previously discussed spinel-based (fcc) transformation sequence (i.e., boehmite – gamma – delta – theta alumina) before converting to alpha-alumina. Whittington et al. proposed a similar mechanism based on quantitative X-ray analysis of laboratory aluminas (18). The authors noted that the careful control of the calcination time allows the phase distribution (although perhaps not the degree of structural disorder) of both rotary kiln and fluid-bed-calcined aluminas to be reproduced in the laboratory. Interestingly, Ingram-Jones et al. also found the chi-alumina originating from soak and flash-calcined gibbsites to have different short-range structures.

Solid-state MAS NMR studies can provide significant insight into the occupancy of octahedral and tetrahedral sites (the chemical shifts being characteristic of the oxide (or hydroxide) coordination (AlO_n/$Al(OH)_n$)) (19), which is key to understanding the forms of alumina in the samples tested. ^{27}Al MAS NMR chemical-shift ranges for aluminum in different coordinations with oxygen (or hydroxyls) are typically –10 to 20 ppm for octahedrally coordinated aluminum (AlO_6), 30 to 40 ppm for pentahedrally coordinated aluminum (AlO_5), and 50 to 80 ppm for tetrahedrally coordinated aluminum (AlO_4) (19, 20). The variation in the reported ranges for the chemical shifts reflects the range of possible Al–O bond lengths and angles, and next-nearest-neighbour species. A recently published ^{27}Al NMR study of a sol–gel manufactured theta-alumina reported the NMR parameters of its two aluminum sites (21). Several ^{27}Al studies have made use of the high sensitivity and the relatively minor contribution of particle and crystallite size effects of this technique to explore the transition aluminas (10, 11, 20–25). Furthermore, MAS NMR has also been beneficial in settling some of the ambiguity concerning the onset temperatures of the transition reactions; since XRD relies on the development of nuclei of sufficient size or long-range order for the detection of the phase, the technique does not always give reliable onset-temperature data. However, NMR has not been frequently applied to MGAs because of the low spectral resolution caused by the co-existence of different transition aluminas and the influence of the second-order quadrupolar interaction causing significant spectral broadening. With higher magnetic fields now becoming available, some of these problems may be overcome (26).

This study examines the use of multiple-field ^{27}Al MAS NMR on samples formed from the reaction of model hydroxides and MGAs, as compared to XRD data. Solid-state MAS NMR spectra of quadrupolar nuclei, such as ^{27}Al (nuclear spin I = 5/2), are broadened by the second-order quadrupolar interaction, a mechanism characterized by the quadrupolar coupling constant C_Q, in MHz (26). This second-order quadrupole interaction dominates the usually observed central transition (26) and has an angular dependence that is only partially averaged by conventional MAS. The interaction scales inversely with the applied magnetic field, so that high magnetic fields are normally advantageous, and the magnetic-field dependence can also be used to constrain the fits. In disordered solids, a distribution in bond lengths and angles for a particular site leads to a distribution in C_Q, resulting in asymmetric, rather featureless spectral lineshapes with a tail on the low frequency side. Re-

© 2007 NRC Canada

cording the spectra from samples at multiple magnetic fields can greatly constrain the fitting even of featureless and overlapping lines. The distributions in C_Q in such materials can be simulated as a Gaussian around a central (mean) value, and the FWHM of this distribution can be used as a quantitative measure of the amount of disorder for a particular atomic site (27). In this study, three magnetic fields are applied, including 18.8 T. The aluminum-site distribution in two calcined samples and an MGA are compared using ^{27}Al MAS NMR and discussed in the context of the XRD data.

Experimental

Materials

Two Bayer gibbsites from different refineries but with very similar specifications (in terms of particle and crystallite size, morphology, and purity) were calcined in a fluid-bed-type reactor, with electrically controlled heating to ensure a uniform temperature distribution. The calcination time was 20 min, and the temperature was 1020 °C; X-ray analysis reveals that the disorder in the material is similar to that of an industrially calcined gibbsite, although the higher temperature and longer retention time than normally encountered in an industrial fluid-bed calciner produces a slightly more-crystalline material, indicated by the narrower and more-developed peaks in the X-ray diffractograms, Figs. 3–5.

XRD

X-ray diffractometry was performed on a Bruker D8 apparatus using Cu Kα X-rays, a 2θ range of 10–80°, a stepwidth of 0.02°, and a counting time of 10 s. To obtain quantitative information about the phase composition of the samples, subsequent Rietveld refinement of the X-ray diffractograms was performed using the FullProf software (28–30).

NMR

^{27}Al experiments were carried out using Varian Chemagnetics Infinity (8.45 T), Bruker Avance II (14.1 T), and Varian Infinity Plus (18.8 T) spectrometers. All MAS NMR experiments on Varian spectrometers were performed using the Spinsight program. The spectra at 8.45 T (^{27}Al Larmor frequency 93.81 MHz) were obtained with a 3.2 mm probe at 10 kHz spinning frequency. The pulse width used was 1 μs. ^{27}Al spectra at 14.1 T (^{27}Al Larmor frequency 156.37 MHz) were obtained with a 3.2 mm probe at 15 kHz spinning frequency using the TopSpin program. The pulse width was 2 μs. ^{27}Al spectra at 18.8 T (^{27}Al Larmor frequency 208.24 MHz) were recorded with a 2.5 mm probe at 25 kHz spinning frequency. The pulse width was 1 μs. These pulse lengths meant that the tip angle was in the linear-response regime (26). The repetition delay for all experiments was 5 s, which was sufficient to produce relaxed spectra. The spectra were referenced against YAG (Yttrium Aluminium Garnet) with the signal corresponding to the octahedrally coordinated aluminum site set to 0.7 ppm, so that chemical shifts reported are relative to the primary shift reference of 1 mol/L $[Al(H_2O)_6]^{3+}$ at 0 ppm. The QuadFit program was used to simulate the spectra and fit the peaks (31).

Fig. 3. Rietveld refinement of XRD data for a fluid-bed calcined MGA, illustrating the wide and weak diffraction patterns stemming from the amorphous transition alumina phases present in the material.

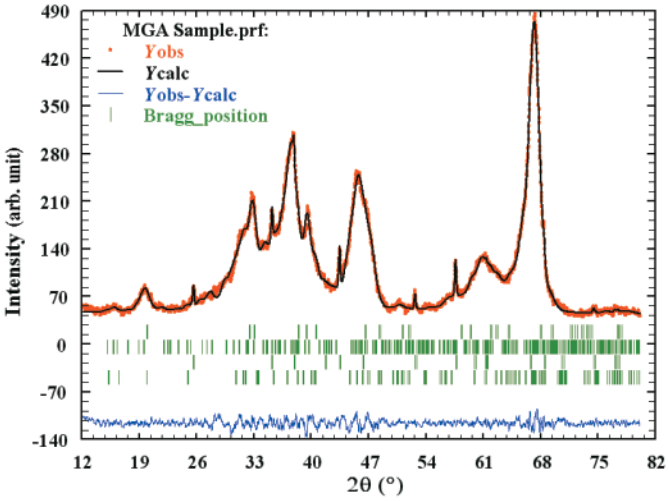
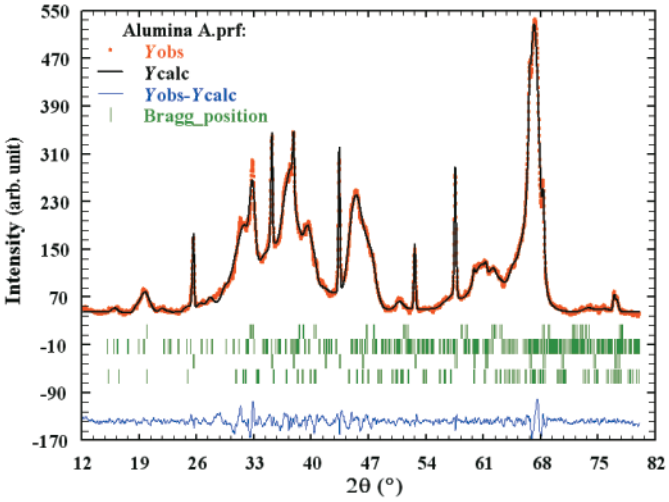


Fig. 4. X-ray diffractogram and Rietveld refinement of XRD data for alumina A (calcined for 20 min at 1020 °C).



Results and discussion

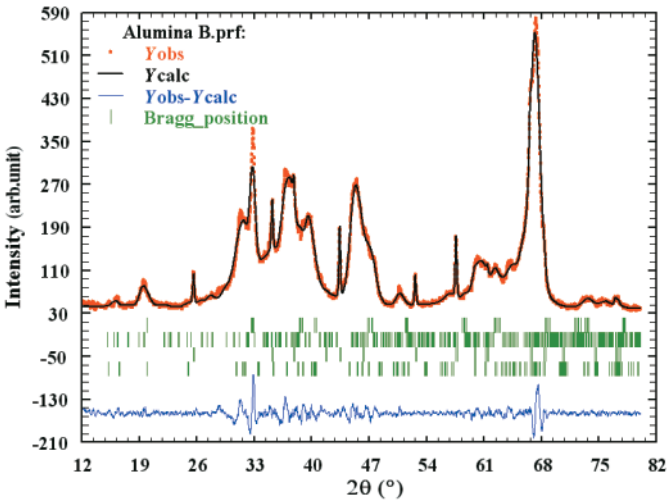
In the last few decades, significant progress in the understanding of the complex structure and phase evolution of MGA has been made possible by advances in the fields of MAS NMR and improvements in structural modelling of diffraction data. However, quantitative measurements are still especially challenging, since the transformation reactions are continuous with several phases co-existing during the rapid heating encountered in modern calciners. Analyses of MGA show that the material is dominated by the poorly defined gamma phase(s); understanding the structure of these phases is key to understanding the properties of MGA. The relatively ill-defined and broad diffraction patterns are exemplified in Fig. 3, where the result from a Rietveld refinement on XRD data from a MGA is shown. In fact, even the structures of most transition aluminas are not fully understood (3,

© 2007 NRC Canada

Table 1. Results from the Rietveld refinement (quantitative phase analysis (%)) of the XRD data for the laboratory-prepared aluminas, A and B, used in this study and for an industrial fluid-bed-calcined MGA sample.

Sample	Gamma-Al_2O_3	Gamma-prime-Al_2O_3	Total gamma-Al_2O_3	Theta-Al_2O_3	Alpha-Al_2O_3
A	28	42	70	22	8
B	26	45	71	25	4
MGA	32	44	76	22	2

Fig. 5. X-ray diffractogram and Rietveld refinement of XRD data for alumina B (calcined for 20 min at 1020 °C).



12, 32). The XRD technique is limited by the need for long-range ordering in the material. Supplementary information, as produced from ^{27}Al MAS NMR, can be very useful in better defining such systems.

In Figs. 3–5, the results from the XRD measurements and the Rietveld refinements for the MGA sample and alumina A and B are displayed. The numerical data from the quantitative phase analysis (using the Rietveld method) are listed in Table 1.

The ^{27}Al MAS NMR spectra obtained from alumina A at three fields are shown in Fig. 6, along with the individual simulated peaks for each aluminum environment. The NMR parameters and relative intensities of each site for both aluminas A and B are shown in Table 2. The ^{27}Al MAS NMR spectrum of the MGA sample is shown in Fig. 7. Integration of the various lineshapes revealed that this sample consists of a much-higher fraction of the gamma-alumina phase (see Table 3). The key to the robustness and uniqueness of these fits, despite significant spectral overlap, is that the same parameters are used to fit the spectra at all three fields. The ability to fit all three fields accurately with spurious parameters would be highly coincidental and is hence unlikely. Also, the positions (and parameters) of several peaks are not arbitrary, as they are largely determined by the known phases that are present in this sample (i.e., gamma-, theta-, and alpha-alumina).

This assignment of the peaks was made by comparison to the chemical-shift positions and NMR parameters previously reported for a sol–gel theta alumina and corundum (21). The chemical shifts and C_Q values for the theta phase are in good agreement with the published data, although the presence of a distribution in C_Q in the theta form present here suggests it is more disordered than the sol–gel formed sample (21, 26). This disorder appears to be present in the corundum phase too, which could explain why the C_Q value is slightly larger here than the commonly accepted value of 2.38 MHz (33).

The peaks at 71 and 16 ppm have much larger ΔC_Q, corresponding to a broader distribution of aluminum environments, as would be expected from a more disordered alumina phase. Hence, these peaks probably belong to the more-disordered gamma-alumina. Wefers et al. considered theta-alumina to be an intermediate between the low-temperature transition aluminas and the energetically favored alpha-alumina (3). Levin et al. showed that a disordering of the gamma phase is required to obtain the lattice parameters for theta-alumina (34). Furthermore, numerous XRD studies show that theta-alumina has narrower and more-developed peaks than gamma-alumina, also indicating a more-crystalline, or ordered structure (e.g., Stumpf et al. (35)). It is therefore assumed that gamma-alumina is more disordered than theta-alumina, and consequently that gamma-alumina has more asymmetric peaks (i.e., a broader distribution of C_Q) and larger mean C_Q.

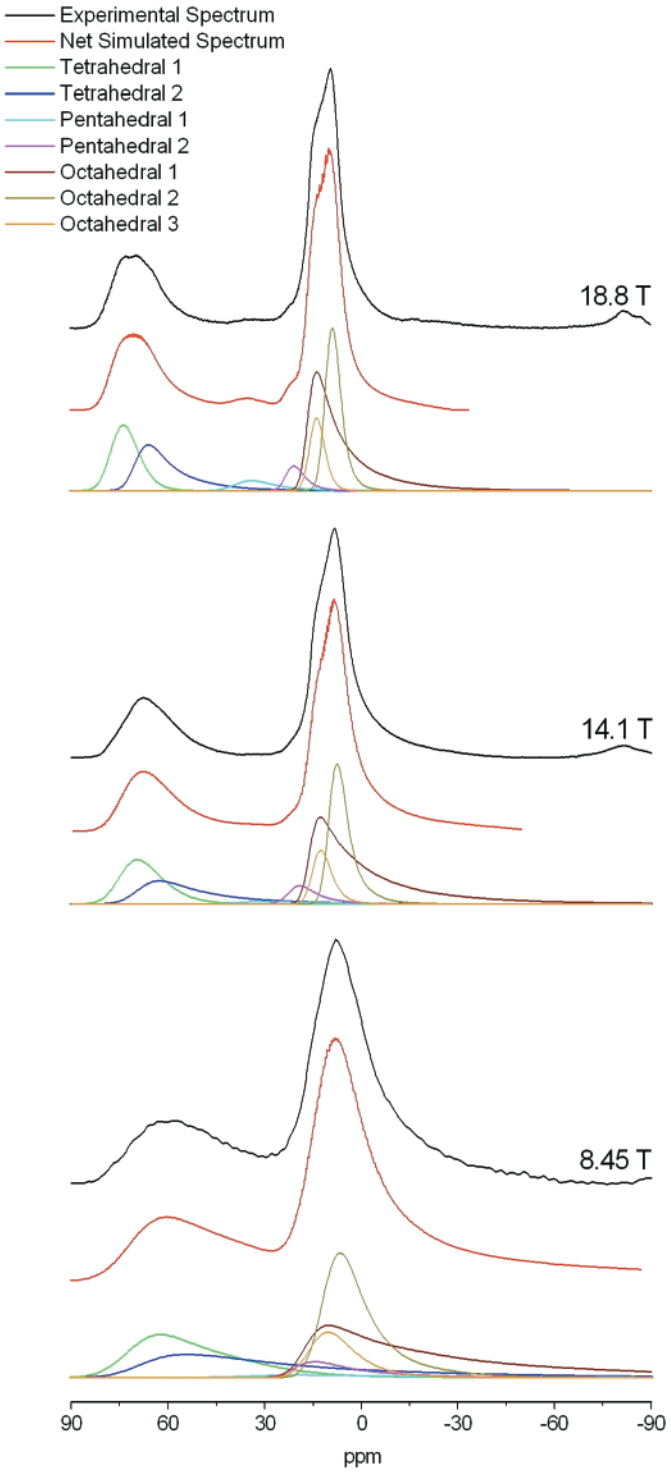
The peak centred at a chemical shift of approximately 38 ppm indicates the presence of pentahedrally coordinated aluminum (AlO_5) in accordance with previously reported values for the chemical shift (20, 23, 36). The presence of penta-coordinated aluminum is consistent with the disordered nature of the MGAs and is thought to originate from more highly distorted (disordered) sites (components) in an X-ray amorphous part. More disordered or even amorphous aluminas, if present in significant quantities, limit the accuracy of XRD methods for quantitative phase measurements of MGAs. In gamma-alumina, penta-coordinated aluminum has also been speculated be present and would originate from aluminum at the external surface and be associated with the Lewis acidity and catalytic activity of the materials (24).

The only remaining question is the small peak at 23 ppm where ΔC_Q is only 4 MHz. This could be associated with a more "ordered" site within the disordered gamma or a small amount of penta-coordinated aluminum perhaps within the theta phase.

The distribution of aluminum cations between octahedral and tetrahedral positions for the transition aluminas has been investigated in several studies. Considering the ideal spinel structure as a basis for the gamma-alumina structure, the fraction of octahedral to tetrahedral aluminum is 0.67. The deformed spinel structures (usually represented as $Al_8^{\square}O_{12}$, where $\square$ represents a vacant Al), either with octahedral or tetrahedral cation vacancies, gives a theoretical fraction of octahedral aluminum of 0.63 and 0.75, for octahedral or tetrahedral vacancies, respectively. Based on the results in this

© 2007 NRC Canada

Fig. 6. Fitted ^{27}Al MAS NMR spectra of alumina A (calcined for 20 min at 1020 °C). The black line is the experimental spectrum, and the red line is the sum of the individual fitted curves.



study (Table 3), it cannot be unambiguously deduced whether octahedral or tetrahedral vacancies are favored. It is generally considered, and also experimentally supported, that aluminum would favor octahedral coordination in gamma-alumina under normal conditions (usually meaning that no hydrogen is included in the structure), leaving tetrahedral vacancies in the spinel-based framework (6, 24). A recent study, however, suggests a preferential distribution of aluminum over tetrahedral sites for gamma-alumina (37). In another study, conducted by Lee et al., the distribution of octahedral and tetrahedral aluminum in gamma and alpha alumina was examined using MAS NMR as well as quantum mechanical calculations; this reported a fraction of 0.7 ± 0.02 (11). It should be noted that in some of the earlier work, the lower magnetic-field strengths and lower MAS frequencies employed result in significant interference of the octahedral spinning sidebands with the peaks stemming from tetrahedrally and pentahedrally coordinated aluminum. This makes accurate quantification of the spectra very difficult. Another possible reason for the significant variation in the observed distribution of aluminum between different sites is the influence of different preparation techniques and precursor materials in the various studies.

Zhou et al. examined eta-, gamma-, and theta-aluminas using profile refinement of neutron diffraction data (6). They suggested that, in gamma-alumina, a fraction of the aluminum cations would also occupy non-spinel sites, aptly labelled as quasi-octahedral, as they lie so close to the octahedral aluminum sites; the distance being only 0.373 Å. They ascribe these sites mainly on the surface of the gamma-alumina where they also would contribute to the catalytic activity of the material. The occupation of non-spinel sites in gamma-alumina is supported in the study by Wolverton et al., who propose that not only surface sites would show this abnormal coordination but also atoms in the bulk (12). One possible explanation of the small 23 ppm peak observed here is that it is the quasi-octahedral aluminum resulting from a distorted gamma-alumina framework resulting from the incomplete transformation or complex-phase composition, which puts further stress on the structure. If the peak at 23 ppm is a quasi-octahedral site belonging to the gamma-alumina, this would correspond to 11% and 8% of the "octahedrally" coordinated aluminum atoms in alumina A and B, respectively. However, the deformed spinel-based crystal structure for gamma-alumina derived by Zhou et al. suggests that 25% of the aluminum atoms would be in quasi-octahedral coordination.

Theoretical and computational studies strongly indicate that cation vacancies in octahedral sites would be energetically favorable in gamma-alumina (12, 38). Krokidis et al. propose an equilibrium structure for gamma- alumina with 69%–75% of the aluminum ions in octahedral positions. The fractions of octahedrally coordinated aluminum (Table 3) show some agreement with this structure. However, the short heating times and the presence of theta- and alpha-alumina could distort the gamma-alumina structure, resulting in an incomplete lattice framework, and perhaps accounts for the AlO_5 observed. Data obtained on crystallographically pure, single phase systems cannot be directly compared to the data obtained for the structurally disordered systems represented by the samples used in this study. Nevertheless, important information on the coordination environment can be deduced from the results.

For the theta-alumina, the ideal structure would give a 50:50 distribution for aluminum over tetrahedral and octahedral sites (12). The experimental results for aluminas A, B,

© 2007 NRC Canada

Table 2. Peak parameters used in the curve fitting of the NMR data, collected at 18.8 T, for alumina A (calcined for 20 min at 1020 °C) and the resulting peak intensities. The relative abundances are approximate, since the spinning sideband intensities were not included in the integration.

^{27}Al NMR Peak	Chemical Shift (±2 ppm)	Mean C_Q (±1 MHz)	ΔC_Q (±1 MHz)	Alumina A Intensity (%)	Alumina B Intensity (%)	Alumina Phase
Tet 1	77	5.5	3	15	20	Theta
Tet 2	71	8	6	15	12	Gamma
Pent 1	38	8	7	2	2	—[b]
Oct[a]	23	5	4	4	3	Gamma
Oct 1	16	7	9.5	33	37	Gamma
Oct 2	14	3.5	3	8	5	Alpha
Oct 3	10	3	3.5	23	22	Theta

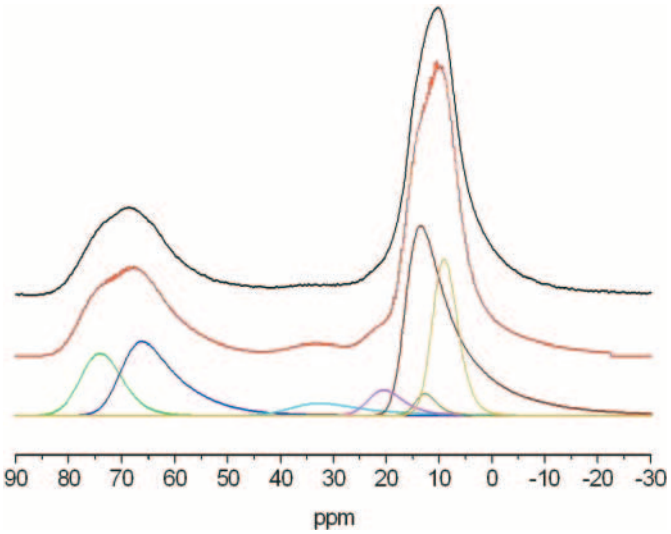
[a]Possibly a quasi-octahedral peak (see discussion).
[b]Small quantity of AlO_5 from some amorphous component of gamma- or other transition alumina (such as the X-ray amorphous chi- or rho-alumina).

Table 3. Total intensities and fraction of octahedrally coordinated aluminum for the various transition alumina phases, for aluminas A and B and the MGA sample.

Sample	Total gamma-Al_2O_3 (±2%)	Total theta-Al_2O_3 (±2%)	Total alpha-Al_2O_3 (±2%)	Fraction of octahedral Al in gamma-Al_2O_3	Fraction of octahedral Al in theta-Al_2O_3
A	50	38	8	0.71	0.61
B	51	42	5	0.67	0.52
MGA	66	28	3	0.82	0.61

Note: The quasi-octahedral peak (at a chemical shift of 23 ppm) is included in the gamma-alumina.

Fig. 7. The ^{27}Al MAS NMR spectrum of MGA obtained at 18.8 T, with simulated peaks (same colors as Fig. 6).



and the MGA show some agreement with the ideal structure. The theta-alumina in alumina B appears to be very close to the ideal structure. In alumina A and the MGA, the complex-phase mixture and severe disorder in the material results in the lineshapes of the associated resonances showing much more disorder than in a crystalline alumina. The "theta" phase present in these two samples may actually be closer to the more-disordered delta-alumina phase, which would explain the lower tetrahedral to octahedral ratio.

Recently, a number of authors report on the use of various synchrotron radiation sources to investigate the transition aluminas and their transformation reactions (15, 39–42) as well as some aluminum-containing minerals and zeolites (43, 44). It seems that by examining the Al K-edge XANES or NEXAFS features, information on the coordination environment can be obtained. The methods clearly show some promise for analyzing disordered systems, such as MGAs. Quantification is made in a similar manner as with the NMR results in this study; i.e., by curve fitting of the obtained spectrum. The results generally give a distribution of octahedral and tetrahedral aluminum closer to unity regardless of the calcination temperature (15, 40), which does not agree well with NMR data nor has there been any report of pentahedrally coordinated aluminum for which there is strong experimental evidence in this and other studies.

It is clear that there still exists considerable ambiguity over several issues relating to the transition aluminas, the variations in structure that occur, and the accurate characterization of these structures. The true structure and the distribution of aluminum cations and vacancies for some of the transition aluminas remain yet to be discovered (3, 32). Another outstanding question is the location of the residual hydroxyl groups, initially thought to be located on the exterior of the alumina structure and at grain boundaries. In gas-suspension or fluid-bed calcined MGAs, the very high heating rates are expected to result in a far more random distribution. Computational studies indicate that for the formation of cubic spinel-based transition alumina forms, protons may have a stabilizing effect on the structure (45), but contradictory results are obtained in neutron diffraction studies (6, 12). It has also been suggested that hydrogen would be present as water from the decomposition reactions of gibbsite and boehmite and located within the amorphous structure (3, 46).

© 2007 NRC Canada

The MGAs must be viewed as a kinetically "frozen" material in which the different phases exist not in a simple binary mixture, but in a continuum of evolving and disappearing phases. Local variations between particles and even within particles further contribute to difficulties and uncertainties with interpreting the data. The structural domains transcend both short-range nanostructures and longer-range ordering; a combination of techniques such as MAS NMR and XAS with XRD will be necessary for a more-complete understanding of these important materials.

Conclusions

It has been shown that ^{27}Al MAS NMR spectroscopy can be used to quantify the distribution of aluminum between different sites in the component phases of MGAs. The use of multiple applied magnetic fields, and especially the availability of higher magnetic fields, is crucial to constrain the simulations. The results also clearly demonstrate that the complementary information obtainable by XRD significantly aids quantification. Amorphous aluminas, if present in significant quantities, can however limit the accuracy of XRD methods for quantitative phase measurements of MGAs. An NMR peak at 23 ppm was detected and could be due to aluminum in a quasi-octahedral coordination, relating to a distorted gamma-alumina form. In conclusion, ^{27}Al MAS NMR has been shown to be an extremely useful part of experimental methodologies to examine the commercially significant and structurally interesting transition aluminas and their precursors.

Acknowledgements

Experimental assistance by the solid-state NMR group at the University of Warwick, which thanks Engineering and Physical Sciences Research Council (EPSRC) for funding, is gratefully acknowledged as is financial support from the MacDiarmid Institute for Advanced Materials and Nanotechnology and Outotec Aluminum Technologies.

References

1. R.G. Haverkamp. Surface studies and dissolution studies of fluorinated alumina. Ph.D. thesis. The University of Auckland. Auckland, New Zealand. 1992.
2. P.N. Østbø. Evolution of alpha phase alumina in agglomerates upon addition to cryolitic melts. Ph.D. thesis. Norwegian University of Science and Technology, Faculty of Natural Sciences and Technology, Trondheim, Norway. 2002. p. 252.
3. K. Wefers and C. Misra. Eds. Oxides and Hydroxides of aluminum. Alcoa Technical Paper No. 19. Aluminum Company of America: Pittsburgh, PA. 1987.
4. B.E. Raahauge. Aluminum (Isernhagen, Germany), **83**, 40 (2007).
5. B.C. Lippens and J.H. de Boer. Acta Crystallogr. **17**, 1312 (1964).
6. R.S. Zhou and R.L. Snyder. Acta Crystallogr., Sect. B: Struct. Sci. **47**, 617 (1991).
7. F. Freund. Ber. Deut. Keram. Ges. **42**, 23 (1965).
8. J. Rouquerol, F. Rouquerol, and M. Ganteaume. J. Catal. **36**, 99 (1975).
9. J. Rouquerol, F. Rouquerol, and M. Ganteaume. J. Catal. **57**, 222 (1979).
10. K.J.D. MacKenzie, J. Temuujin, and K. Okada. Thermochim. Acta, **327**(1–2), 103 (1999).
11. M.H. Lee, C.-F. Cheng, V. Heine, and J. Klinowski. Chem. Phys. Lett. **265**, 673 (1997).
12. C. Wolverton and K.C. Hass. Phys. Rev. B: Condens. Matter. **63**, 024102/1 (2001).
13. M.L. Kronberg. Acta Metall. **5**, 507 (1957).
14. T. Ashida, J.B. Metson, and M.M. Hyland. *In* Light metals. Warrendale, PA, United States. 2004. pp. 93–96.
15. Y. Kato, K.-i. Shimizu, N. Matsushita, T. Yoshida, H. Yoshida, A. Satsuma, and T. Hattori. Phys. Chem. Chem. Phys. **3**, 1925 (2001).
16. G. Paglia, C.E. Buckley, A.L. Rohl, R.D. Hart, K. Winter, A.J. Studer, B.A. Hunter, and J.V. Hanna. Chem. Mater. **16**, 220 (2004).
17. V.J. Ingram-Jones, R.C.T. Slade, T.W. Davies, J.C. Southern, and S. Salvador. J. Mater. Chem. **6**, 73 (1996).
18. B. Whittington and D. Ilievski. Chem. Eng. J. (Amsterdam, Netherlands), **98**, 89 (2004).
19. M.E. Smith. Appl. Magn. Reson. **4**, 1 (1993).
20. R.C.T. Slade, J.C. Southern, and I.M. Thompson. J. Mater. Chem. **1**, 563 (1991).
21. L.A. O'Dell, S.L.P. Savin, A.V. Chadwick, and M.E. Smith. Solid State Nucl. Magn. Reson. **31**, 169 (2007).
22. C.S. John, N.C.M. Alma, and G.R. Hays. Appl. Catal. **6**, 341 (1983).
23. G. Kunath-Fandrei, T.J. Bastow, J.S. Hall, C. Jaeger, and M.E. Smith. J. Phys. Chem. **99**, 15138 (1995).
24. C. Pecharroma, I. Sobrados, J.E. Iglesias, T. Gonzalez-Carreno, and J. Sanz. J. Phys. Chem. B, **103**, 6160 (1999).
25. R.C.T. Slade, J.C. Southern, and I.M. Thompson. J. Mater. Chem. **1**, 875 (1991).
26. K.J.D. MacKenzie and M.E. Smith. Multinuclear solid-state nuclear magnetic resonance of inorganic materials. Pergamon Materials Series 6, Pergamon-Elsevier, Oxford. 2002.
27. L.A. O'Dell, S.L.P. Savin, A.V. Chadwick, and M.E. Smith. Appl. Magn. Reson. In Press.
28. H.M. Rietveld. Acta Crystallogr. **22**, 151 (1967).
29. H.M. Rietveld. J. Appl. Crystallogr. **2**, 65 (1969).
30. J. Rodriguez-Carvajal. FULLPROF [computer program]: A program for Rietveld refinement and pattern matching analysis. *In* Abstracts of the Satellite Meeting on Powder Diffraction of the XV Congress of the IUCr. Toulouse, France. 1990.
31. T.F. Kemp. High-field solid-state ^{27}Al NMR of ceramics and glasses. Masters thesis. The University of Warwick, UK. 2004.
32. I. Levin and D. Brandon. J. Am. Ceram. Soc. **81**, 1995 (1998).
33. H.J. Jakobsen, J. Skibsted, H. Bildsoee, and N.C. Nielsen. J. Magn. Reson. **85**, 173 (1989).
34. I. Levin, L.A. Bendersky, D.G. Brandon, and M. Ruhle. Acta Mater. **45**, 3659 (1997).
35. H.C. Stumpf, A.S. Russell, J.W. Newsome, and C.M. Tucker. J. Ind. Eng. Chem. **42**, 1398 (1950).
36. T.R. Barton, T.J. Bastow, J.S. Hall, B.J. Robson, and M.E. Smith. Light Metals, 71 (1995).
37. H.J. Kim, H.C. Lee, and J.S. Lee. J. Phys. Chem. C, **111**, 1579 (2007).
38. X. Krokidis, P. Raybaud, A.-E. Gobichon, B. Rebours, P. Euzen, and H. Toulhoat. J. Phys. Chem. B, **105**, 5121 (2001).
39. A.W. Chester, R.P.A. Absil, G.J. Kennedy, P. Lagarde, and A.M. Flank. J. Synchrotron Radiation, **6**, 448 (1999).
40. J.F. Larue, B. Moraweck, A. Renouprez, and P. Lagarde. Springer Series in Chemical Physics, **27**, 32 (1983).
41. B.A. Latella, and B.H. O'Connor. J. Am. Ceram. Soc. **80**, 2941 (1997).

© 2007 NRC Canada

42. K.-I. Shimizu, Y. Kato, H. Yoshida, A. Satsuma, T. Hattori, and T. Yoshida. Chem. Commun. (Cambridge), **17**, 1681 (1999).
43. P. Ildefonse, D. Cabaret, P. Sainctavit, G. Calas, A.M. Flank, and P. Lagarde. Phys. Chem. Miner. **25**, 112 (1998).
44. J.A. Van Bokhoven, H. Sambe, D.E. Ramaker, and D.C. Koningsberger. J. Phys. Chem. B, **103**, 7557 (1999).
45. K. Sohlberg, S.J. Pennycook, and S.T. Pantelides. J. Am. Chem. Soc. **121**, 7493 (1999).
46. G. Paglia, E.S. Bozin, and S.J.L. Billinge. Chem. Mater. **18**, 3242 (2006).

© 2007 NRC Canada

Characterization of the conformational changes in recombinant human metallothioneins using ESI-MS and molecular modeling[1]

Jayna Chan, Zuyun Huang, Ian Watt, Peter Kille, and Martin J. Stillman

Abstract: Electrospray ionization mass spectrometry (ESI-MS) data and molecular modeling calculations were used to gain mechanistic, conformational, and domain-specific information from the acid-induced demetallation reactions of human metallothionein. The recombinant proteins studied were the single α- and β-rhMT-1a domains and the βα- and αβ-rhMT-1a two-domain species, based on the human metallothionein 1a sequence. Complete molecular models (MM3/MD) for all the fully metallated and demetallated species using a modified force field are reported for the first time. Basic residues that contribute to the ESI-MS charge states are identified from the molecular models. Demetallation took place under equilibrium conditions within a narrow pH range. For the two-domain proteins, these results support a demetallation mechanism involving the initial complete demetallation of one domain followed by the other for both βα-rhMT and αβ-rhMT. Based on the stability of the separate domains, the β domain is predicted to demetallate first in the two-domain rhMTs. Both the α domain and the β domain were observed to bind an excess of one Cd^{2+} ion. The metallated rhMT structures were shown to have very stable conformations, but only when fully metallated. Two or more conformations were observed at low pH in the ESI-MS data, which are interpreted as arising from the presence of structure, as opposed to a random coil, in the apo-rhMT. This is the first report of the existence of a structure in the two-domain metal-free apo-MT proteins. Only at extremely low pH does the structure open fully to give the highest charge distribution, which is associated with a random coil. Pre-existing structural features in the apo-MT would explain why the metallation reactions occur so rapidly.

Key words: recombinant human metallothionein-1 (rhMT1), electrospray ionization mass spectrometry (ESI-MS), circular dichroism (CD), molecular mechanics/molecular dynamics (MM3/MD).

Résumé : On a utilisé des données de spectrométrie de masse avec ionisation par électronébulisation (SM-IEN) et des calculs théoriques de modélisation moléculaire pour obtenir des informations mécanistiques, conformationnelles et spécifiques au domaine relatifs aux réactions de démétallation induites par des acides de métallothionéines humaines. Les protéines recombinantes étudiées sont les espèces α- et β-rhMT-1a, à un domaine, et les espèces βα- et αβ-rhMT-1a à deux domaines sur la base de la séquence 1a de la métallothionéine humaine. Faisant appel à un champ de forme modifié, on a pu définir pour la première fois les modèles moléculaires complets (MM3/MD) de toutes les espèces métallées et démétallées. Sur la base des modèles moléculaires, on a identifié les résidus basiques qui contribuent aux états chargés de SM-IEN. La démétallation se produit sur une très faible plage de pH. Pour les protéines à deux domaines, ces résultats sont en accord avec un mécanisme de démétallation impliquant une démétallation complète d'un domaine suivie par l'autre pour le βα-rhMT et le αβ-rhMT. Sur la base de la stabilité de chacun des domaines pris séparément, on peut prédire que des rhMT à deux domaines, le domaine β sera le premier à subir une démétallation. On a observé que le domaine α ainsi que le domaine β se lient tous les deux à un excès d'ion Cd^{2+}. On a démontré que les structures rhMT démétallées sont dans des conformations très stables, mais uniquement lorsqu'elles sont complètement démétallées. Dans les données de SM-IEN du apo-rhMT à faible pH, on a observé la présence d'au moins deux conformations qui a été interprétée en fonction de la présence d'une structure par opposition à la pelote statistique. Ceci constitue le premier rapport de l'existence d'une structure dans protéines apo-MT à deux domaines et privées de métal. La structure ne s'ouvre complètement qu'à des valeurs extrêmement faibles du pH et elle conduit alors à la

Received 2 August 2007. Accepted 28 August 2007. Published on the NRC Research Press Web site at canjchem.nrc.ca on 2 October 2007.

A paper in recognition of the outstanding research work of Prof. G. Michael Bancroft in the Department of Chemistry, The University of Western Ontario, London, Ontario, Canada.

J. Chan, Z. Huang, and M.J. Stillman.[2] Department of Chemistry, The University of Western Ontario, London, ON N6A 5B7, Canada.
I. Watt and P. Kille. School of Biosciences, Cardiff University, Wales, UK.

[1]This article is part of a Special Issue dedicated to Professor G. Michael Bancroft.
[2]Corresponding author (e-mail: Martin.Stillman@uwo.ca).

 doi:10.1139/V07-111 © 2007 NRC Canada

plus grande distribution de charge qui est associée à une pelote statistique. Des caractéristiques structurales préexistantes dans l'apo-MT pourquoi leurs réactions de démétallation se produisent si rapidement.

Mots-clés : métallothionéine-1 humaine recombinante (rhMT1), spectrométrie de masse avec ionisation par électronébulisation (SM-IEN), dichroïsme circulaire (DC), mécanique moléculaire/dynamique moléculaire (« MM3/MD »).

[Traduit par la Rédaction]

Introduction

Metal-dependent protein folding is an elaborate reaction that is still not well-understood, having the added complexity of metal coordination chemistry, but is important in our understanding of the relationship between overall structure and metalloprotein function. A major difficulty in probing metal-induced protein folding arises from the speed of the reactions. Spectroscopic measurements, for example, can provide protein structural details, but as a sample average, and data collection is slow to capture these short-lived folding events. In metalloproteins, metal-induced protein folding offers both the chromophores for spectroscopic analysis and speciation data. Metallothionein (1–8) is a metalloprotein for which metal-dependent folding is important. Metal-ion chelation by MT causes the protein to fold into metal-thiolate clusters that define their three-dimensional structure via the coordination of the cysteinyl sulfurs to the metal ions. Stoichiometric and spectroscopic studies of mammalian MTs have shown that the N-terminal β-domain forms M_3S_9 clusters and the C-terminal α-domain forms M_4S_{11} clusters via tetrahedral coordination with divalent metal ions, such as Zn^{2+} and Cd^{2+} (Fig. 1) (6). The structure and metal–cysteine connectivities for Cd_7-MT have been studied by ^{1}H–^{113}Cd NMR (9–11) and by X-ray crystallography (12, 13), and the interatomic distances within the clusters have been refined by X-ray absorption spectroscopy (XAS) (14–16) and molecular modeling (17–34). However, the structures of partially metallated and metal-free, or apo, metallothioneins are extremely difficult to determine.

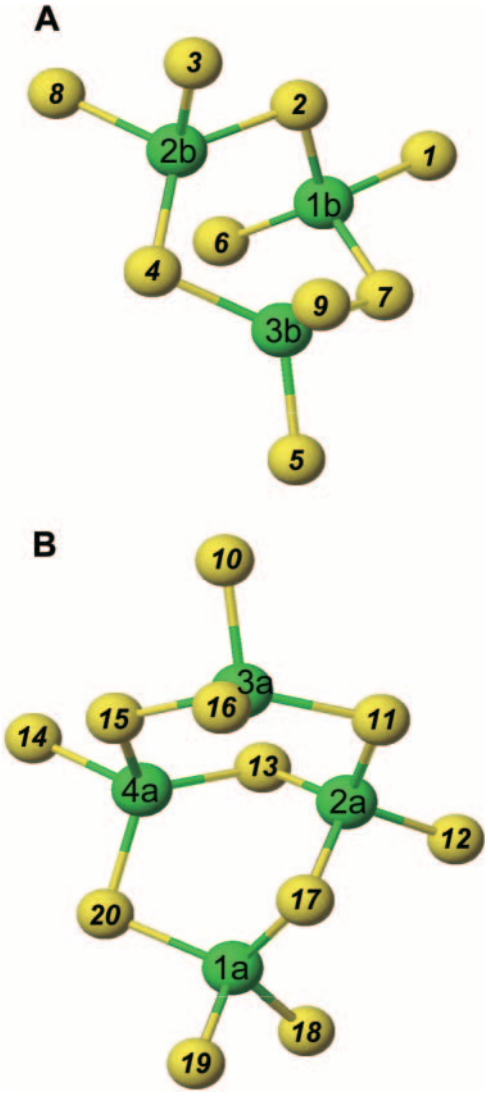
Electrospray ionization mass spectrometry (ESI-MS) provides both speciation and structural information because different ligands change the measured mass, and structural effects are observed from the changes in the number of protonatable sites on the protein observed from the charge distribution (35, 36). The charge distributions change as the protein folds to envelop the incoming metal. In the mass spectrum, the relative abundance of charge states is measured, which leads directly to quantification of the degree of exposure of (in positive-ion measurements) basic sites (37). The number of protonatable sites is related to the three-dimensional structure, which in turn is related to the extent of protein folding. The capability of ESI-MS to analyze samples at various temperatures, pH values, and solvent conditions, which monitors the unique molecular species within a single-sample mixture (38), allowing observation of reaction intermediates that cannot be isolated in significant quantities. These "snapshots" can provide mechanistic information of the protein-folding events. Determination of the protein-surface locations of the acidic and basic sites may provide useful information on the availability of the protonation sites, which may control the unfolding of the protein via electrostatic interactions, and consequently affect the observable charge states seen in the ESI-MS spectra (39). Molecular modeling has made significant progress in elucidating molecular structures and molecular motions (40, 41). Molecular modeling can provide realistic models of the molecules, allowing one to visually interpret the molecular structure (bonding and chemistry) (42–44). Molecular modeling can provide chemical and spectroscopic information that is especially relevant to the interpretation of structures formed in the vacuum space of the mass spectrometer. In addition, molecular modeling has been utilized in simulating chemical reactions and molecular folding.

In this present study, we have probed the cadmium-binding properties of a series of related peptides, each of which are made recombinantly and based on the human MT-1a sequence (rhMT). This series of peptides includes the novel αβ-rhMT, altered from the native sequence by placing the α sequence at the N terminus and the β sequence at the C terminus. This altered peptide will in the future be used to test the question of the significance of the presence of two slightly different domains on metal binding. To explore the metal-dependent structural and functional features of this human metallothionein isoform, the properties of Cd-α-rhMT, Cd-β-rhMT, Cd-αβ-rhMT, and Cd-βα-rhMT recombinant human MT samples were examined by ESI-MS over a wide pH range. The molecular species of metallothionein that exist within the neutral to acidic pH range prove to play physiologically relevant roles in the cytosol, where the pH is neutral, and in lysosomal function, where the pH is strongly acidic (45, 46). Demetallation reactions of the holoproteins as a function of solution pH occur in a very narrow range with specific metallated structures present and allow an understanding of the extent of unfolding as the metals leave the binding site. Changes in charge state distributions and the molecular species present were monitored to gain information regarding solvent accessibility, conformational changes, and the extent of unfolding in response to changes in pH. Structures in the metal-free, apoproteins were also studied from the charge state distributions.

A calibrated MM3/MD force field (26) was applied to simulations of the metallated and demetallated conformations of α-rhMT, β-rhMT, αβ-rhMT, and βα-rhMT to mimic the initial and final conformations expected for the demetallation reaction of metallothionein by acidification. These simulations were carried out to pinpoint the locations of exposed acidic and basic residues on the folded and unfolded conformations for comparison with the charge states measured by ESI-MS. Molecular dynamics simulations of these proteins may also uncover regions of flexibility in the protein that might allow partial access to protonation sites.

© 2007 NRC Canada

Fig. 1. Metal-thiolate cluster models of mammalian metallothioneins determined by NMR spectroscopy (9–11) and X-ray crystallography (14, 16): (A) β domain with a stoichiometric ratio of $M^{II}{}_3S_{Cys9}$ and (B) α domain with a stoichiometric ratio of $M^{II}{}_4S_{Cys11}$ (the green spheres represent tetrahedrally coordinated divalent metal atoms, such as Zn^{2+} and Cd^{2+}, which are numbered based on their NMR chemical shifts and lettered based on the domain in which they are found. The numbering scheme for the S_{Cys} represents the cysteine residues in the order they appear in any general mammalian holoprotein sequences, and are similarly numbered in Fig. 2. The yellow spheres represent sulfur atoms, which are numbered based on the position of the cysteines in the protein sequence of the mammalian MTs.



Materials and Methods

Materials

Sephadex™ G-25 Fine Grade and HiTrap™ SP Sepharose™ HP cation-exchange cartridges were purchased from Amersham Pharmacia. All buffers and reagents used were analytical-grade products. Cadmium sulfate ($3CdSO_4{\cdot}8H_2O$), isopropyl-β-D-thiogalactoside (IPTG) (Biotech Grade), ammonium formate, and guanidine chloride were purchased from Caledon Laboratories Ltd. BL21(DE3) strain of *E. coli* was purchased from Novagen EMD. Kanamycin monosulfate, 5,5-dithio-bis(2-nitro)benzoic acid (DTNB), LB broth (Miller), LB agar (Miller), and tris(hydroxymethyl)aminomethane (Tris) were purchased from Sigma-Aldrich Chemical Company, Inc., and mercaptoethanol (EtSH) was purchased from EM Science. All buffer solutions were pH-adjusted by pH meter (Fisher Scientific) at 25 °C and prepared using water that was deionized to 18 MΩ cm using a Millipore Nanopure Infinity RO System (Barnstead).

Methods

Recombinant human MT plasmid vectors

The plasmid vectors used to express the human metallothionein proteins used here were constructed and transformed into *E. coli* (BL21(DE3)*pLys*S) at Cardiff University, Wales, UK. These vectors were constructed using the pET vector system purchased from Novagen. The recombinant proteins used here were the single-domain α-rhMT-1a and β-rhMT-1a, and the two-domain βα-rhMT-1a and αβ-rhMT-1a, based on the human metallothionein 1a sequence with sequences shown in Fig. 2 and reported by I. Watt (47). All expressed fusion proteins included an S-peptide tag (labeled "S-tag" in Fig. 2) on the N terminus of each protein (48). The S-tag was originally used as an affinity tag for isolation, but currently is retained purely for protein stability during isolation. We have no evidence that the S-tag interacts with the metal binding site, and so we find the data with and without the S-tag to be equivalent.

Protein expression, isolation, and purification

The plasmid vectors were transformed into the *E. coli* bacterial cells using the protocol as described by the supplier (Novagen, EMD Biosciences). The transformed cells were incubated on LB agar culture plates containing 50 μg/mL kanamycin and 50 μmol/L $CdSO_4$ at 37 °C. Large-scale preparations (4 L) of the recombinant proteins were produced by mid-log phase induction in LB media containing 50 μg/mL kanamycin (sterilized by filtration), 50 mmol/L $CdSO_4$, and swabs from the culture plates, incubated at 37 °C for about 3 h until the solution OD_{600} reached 0.6. Protein expression was induced by IPTG and incubation continued for 4 h at 37 °C, during which time the cadmium concentrations in the culture medium were elevated with two additions of $CdSO_4$, to reach a final solution concentration of 250 μmol/L to stabilize the MT via metallation.

The cells were harvested by centrifugation at 6000 rpm for 30 min at 4 °C, and the cellular pellets were resuspended in 40 mL of 50 μmol/L ammonium formate buffer solution at pH 7.4 containing 3 mmol/L mercaptoethanol per liter of induction volume, and the resuspension mixture was rapidly frozen at –70 °C. The cells were partially thawed and then lysed by FRENCH® Pressure Cell (Thermo IEC), using a 40 mL cell. The cellular debris was removed by centrifugation at 13 000 rpm for 1 h at 4 °C. A 5 μL aliquot of 1 mol/L $CdSO_4$ was added to the 40 mL supernatant to stabilize the MT (this is equivalent to adding a reducing agent in that the slight excess of Cd(II) ensures continuing metallation and no free thiolates during isolation). The supernatant was kept

© 2007 NRC Canada

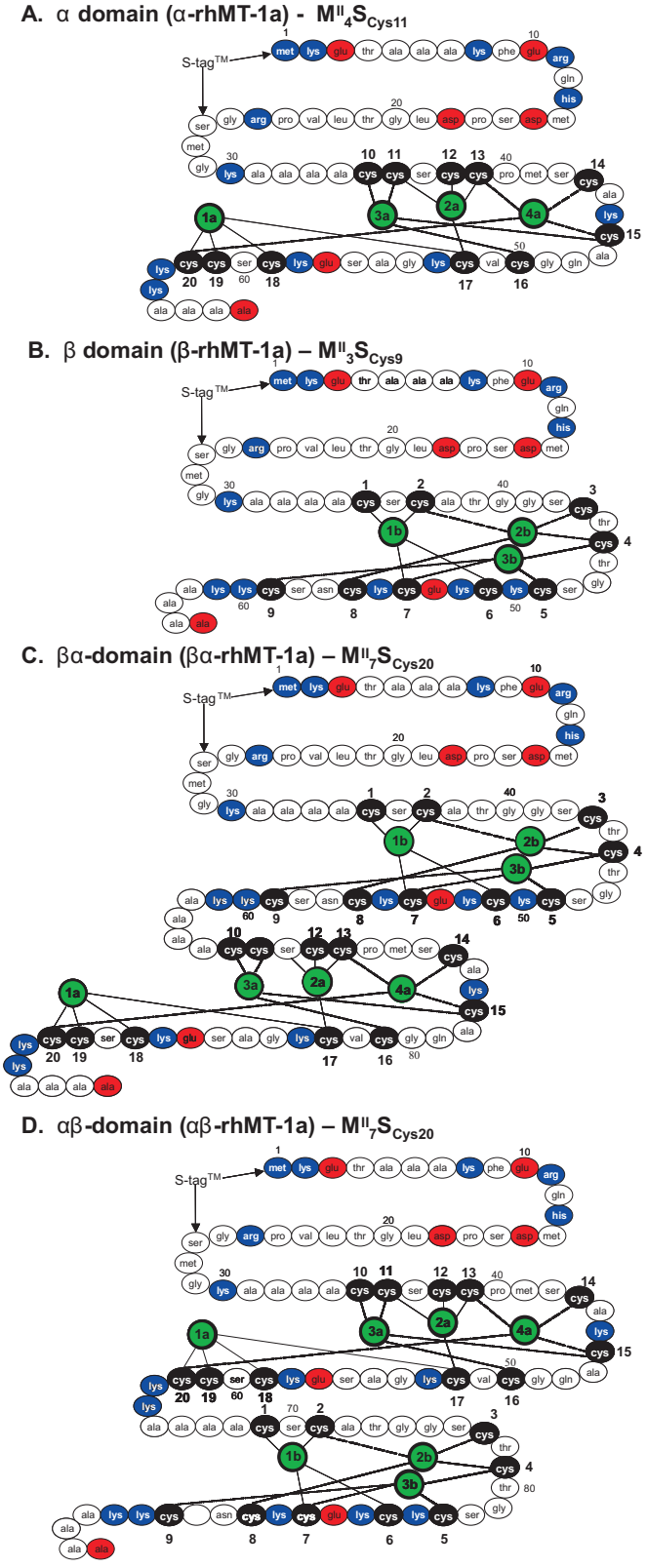


Fig. 2. Amino acid sequences of the recombinant human metallothioneins and their metal-thiolate connectivities, including the N-terminal S-tag sequence. Cysteine residues are represented by the dark ovals, basic residues are represented by blue ovals, and acidic residues are represented by red ovals. The metals are numbered 1a–4a in the α domain and 1b–3b in the β domain, and the cysteine residues are numbered in order of occurrence from the N terminus to the C terminus. (A) Recombinant human MT-1a 11cys α domain; (B) Recombinant human MT-1a 9cys β domain; (C) Recombinant human MT-1a 20cys βα domain; and (D) Recombinant human MT-1a 20cys αβ domain.

cold throughout the rest of the procedure to reduce the chance of oxidation. The protein solution was gravity-filtered followed by isolation by cation exchange using a HiTrap™ SP cartridge coupled to a Millipore Consep™ LC100 system by the following method: All eluents were prepared using cold deionized water, deoxygenated with argon. The effluent was passed through a quartz flow-cell and monitored by absorption spectroscopy (Cary 1E UV–vis Spectrophotometer, Varian Canada Inc.), recording scans continuously over the wavelength range of 200–300 nm. The protein was loaded onto the SP cartridge and then rinsed thoroughly with Tris buffer solution until the absorbance of the effluent went to baseline. The eluents used were 10 mmol/L Tris buffer (pH 7.4) (eluent A) and 1 mol/L NaCl in 10 mmol/L Tris buffer (pH 7.4) (eluent B). Recombinant human MTs were each eluted from the column during a salt gradient that increased from an eluentA:eluentB ratio of 100:0 to 90:10 within 15 min. A Buchler Fractomette Alpha 200™ automated fraction collector was used to collect the effluent in 3–5 mL fractions.

The metallation quality of the strongly absorbing protein fractions were measured by circular dichroism (CD) (Jasco J-500C spectropolarimeter controlled by an IBM 9000 computer using the program CDSCAN) (49). The high-quality fractions were combined and concentrated using an Amicon Stirred Cell filtration system, then desalted using a Sephadex™ G-25 size exclusion column with cold 25 mmol/L ammonium formate buffer as the eluent. The effluent was monitored over the wavelength range of 300 to 200 nm as described earlier. The protein fractions were again isolated, combined, and concentrated using the Amicon Stirred Cell filtration system. The homogeneity of the purified recombinant human MTs was confirmed by CD spectroscopy, absorption spectroscopy, and ESI-MS.

Concentration of recombinant human MTs

Protein concentrations were estimated from measurements of the –SH group by Ellman's method (50, 51), and cadmium concentrations were estimated by atomic absorption spectrometry (AAS). These estimations were based on the assumption that the number of –SH groups in each of the recombinant human MTs bind a specific number of metal ions. Metal content was determined by flame AAS using a Varian model 875 atomic absorption spectrometer with a Varian model 55 programmable sample changer.

ESI-MS measurements

The PerkinElmer SCIEX API 365 triple quadrupole electrospray ionization mass spectrometer (PE-SCIEX, Concord, ON, Canada) was calibrated using polypropylene glycols and myoglobin. The scan conditions for the spectrometer were positive ion mode, ion-spray needle potential = +4.9 and +5.6 kV, and orifice potential = 30 to 40 V. The *m*/*z* range was 500 to 2300, step size of 0.5 Da, and dwell time

© 2007 NRC Canada

Fig. 3. All rhMTs, metallated with Cd^{2+} at neutral pH. Spectra A–D are the charge distributions, and spectra E–H are the reconstructed spectra.

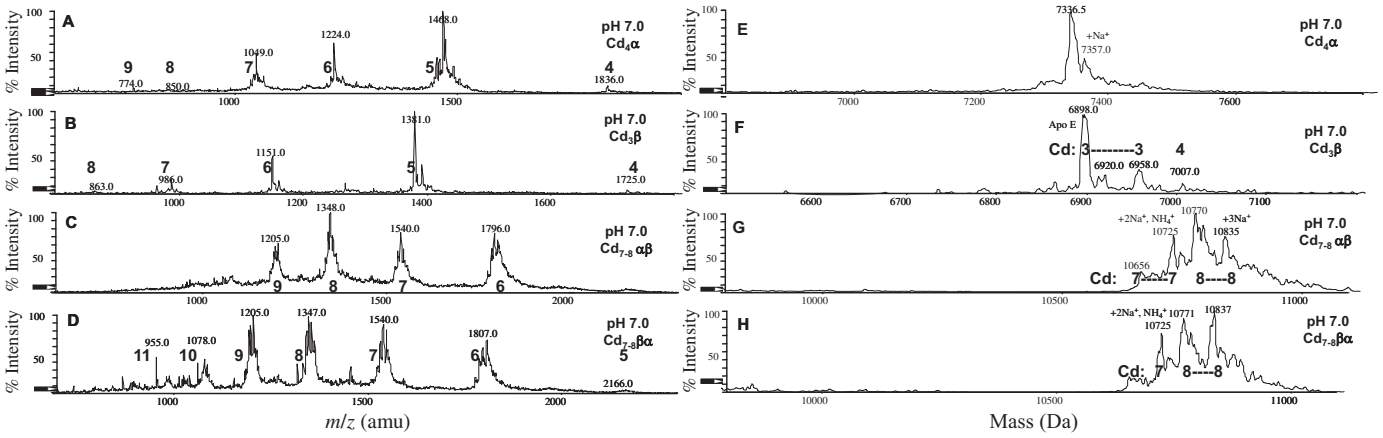
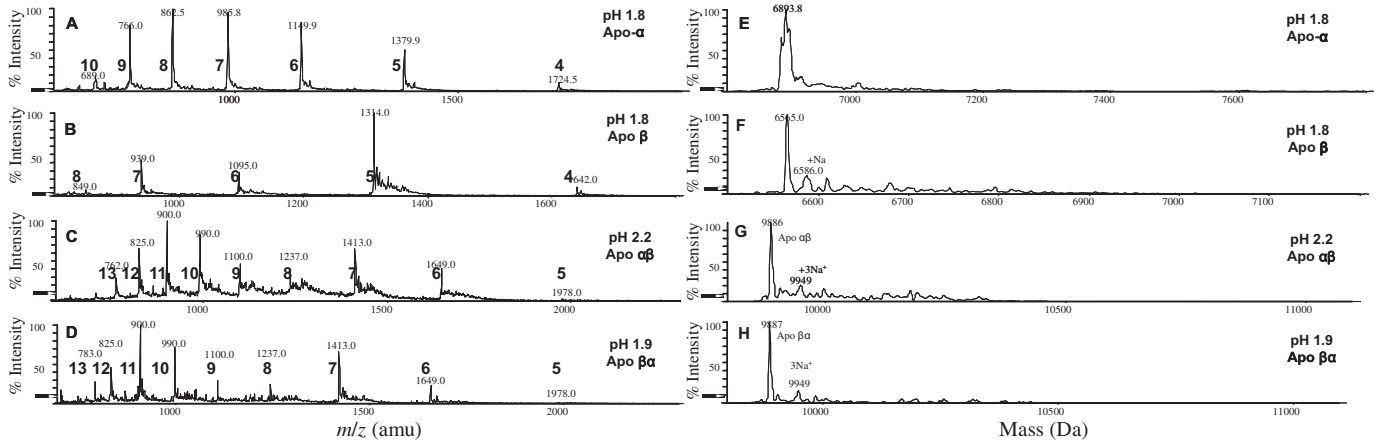


Fig. 4. All rhMTs, metal-free at low pH. Spectra A–D are the charge distributions, and spectra E–H are the reconstructed spectra.



of 1.0 ms. Solutions were delivered through a long fused-silica capillary (I.D. = 75 μm, Polymicro Technologies, Phoenix, AZ) by a syringe pump (Harvard Apparatus, South Natick, MA) with 2.0 and 5.0 μL/min flow rate. Orifice and the focusing ring potentials were also optimized to enhance detector sensitivity and signal stability. The measured spectra were analyzed using BiomultiView Version 1.5.1b. The pH values of the rhMT solutions were adjusted from pH 7.5 to pH 1.80 with formic acid or HCl (for extremely acidic pH). Following treatment with acid, the solutions were allowed to reach equilibrium prior to analysis by ESI-MS.

The AAS measurements were adapted from the Ph.D. thesis by Watt (47). These AAS measurements were carried out on α-rhMT, β-rhMT, and βα-rhMT samples of known cadmium concentration and were pH-adjusted to the desired level. The protein solutions were then separated by size-exclusion chromatography to remove the free metal ions. AAS measurements were carried out on the remaining protein solution and compared to the original cadmium concentration to give the percentage of cadmium recovery. This was carried out over the pH range of 7 to 1.

Molecular models

MM3/MD calculations parameterized using the modified force field described by Chan et al. (26) and the dielectric constant for water (78.4) were carried out to obtain minimum-energy structures of both the metallated (at neutral pH) and the demetallated (at acidic pH) structures of various metallothionein structures. All MM3/MD calculations and model-structure rendering were carried out using CAChe WorkSystem Pro 6.1.1 Software (Fujitsu America). Calculations were carried out using a simple PC (Intel P4 3.0 GHz) with 1.00 Gb RAM. The original metallated MT structure was taken from the RCSB protein databank (52) (1MHU, 2MHU (53)) and was modified using CAChe to produce molecular models for Cd_4-α-rhMT, Cd_3-β-rhMT, Cd_7-αβ-rhMT, and Cd_7-βα-rhMT. The structure was atom-typed and energy-minimized as follows: the structure was energy-minimized using the MM3 calculation followed by the MD simulation at 300 K for 500 ps. MM3 and MD calculations were cycled until no change in energy was observed. The apo-MT structure was energy minimized from the linear sequence as described for metallated MT, with the appropriate residues protonated based on their pKa values.

Results

Protein quality

Samples of Cd_4-α-rhMT, Cd_3-β-rhMT, Cd_7-αβ-rhMT, and Cd_7-βα-rhMT were first characterized by AAS and Ellman's method to determine the stoichiometry of metal

© 2007 NRC Canada

Fig. 5. Effect of pH on the conformation and metallation states of α-rhMT. The left side of this figure shows the measured mass spectra (A–F) labeled with the charge states of the molecular species as the pH was titrated from pH 7.0 to pH 1.8. The right side of this figure shows the reconstructed masses (G–L) that correspond to the measured mass spectra, as labeled. In spectrum D, the masses at 863.0, 986.0, 1150.0, 1380.0, and 1725.0 amu correspond to the charge states that arise from the demetallated α-rhMT where the two maxima are centered on +7 (986.0 amu) and +5 (1380.0).

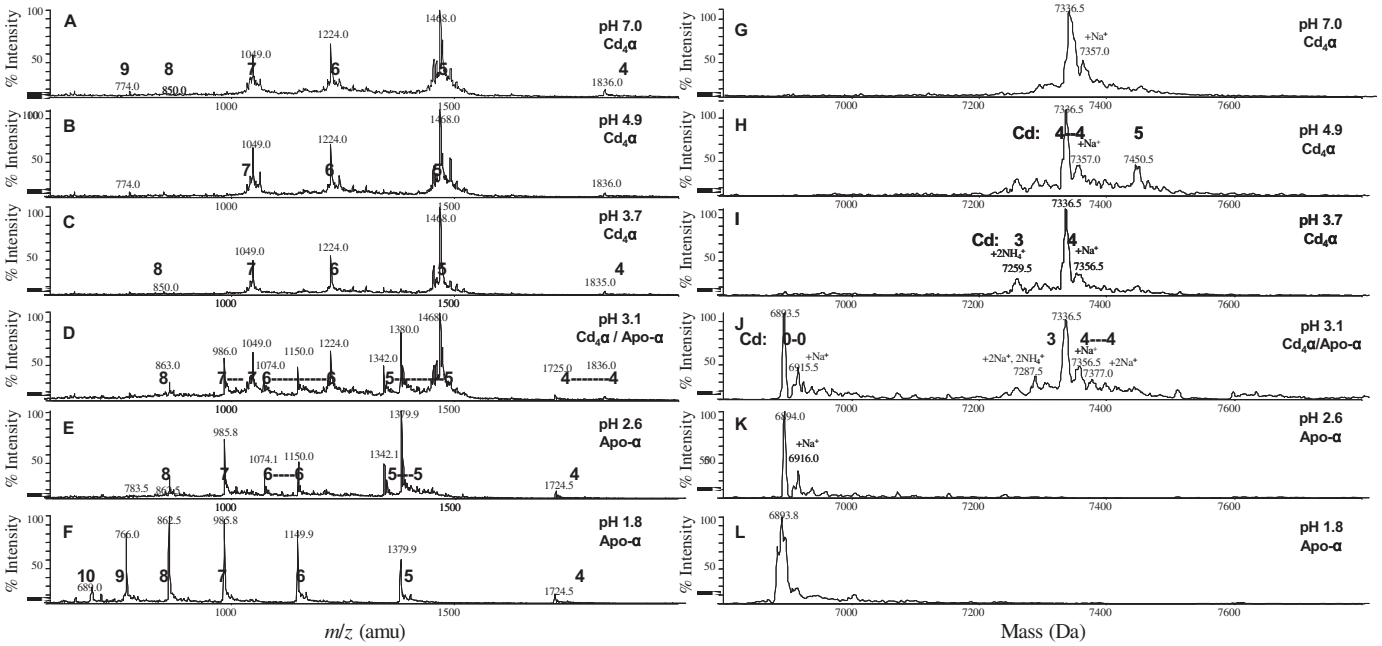
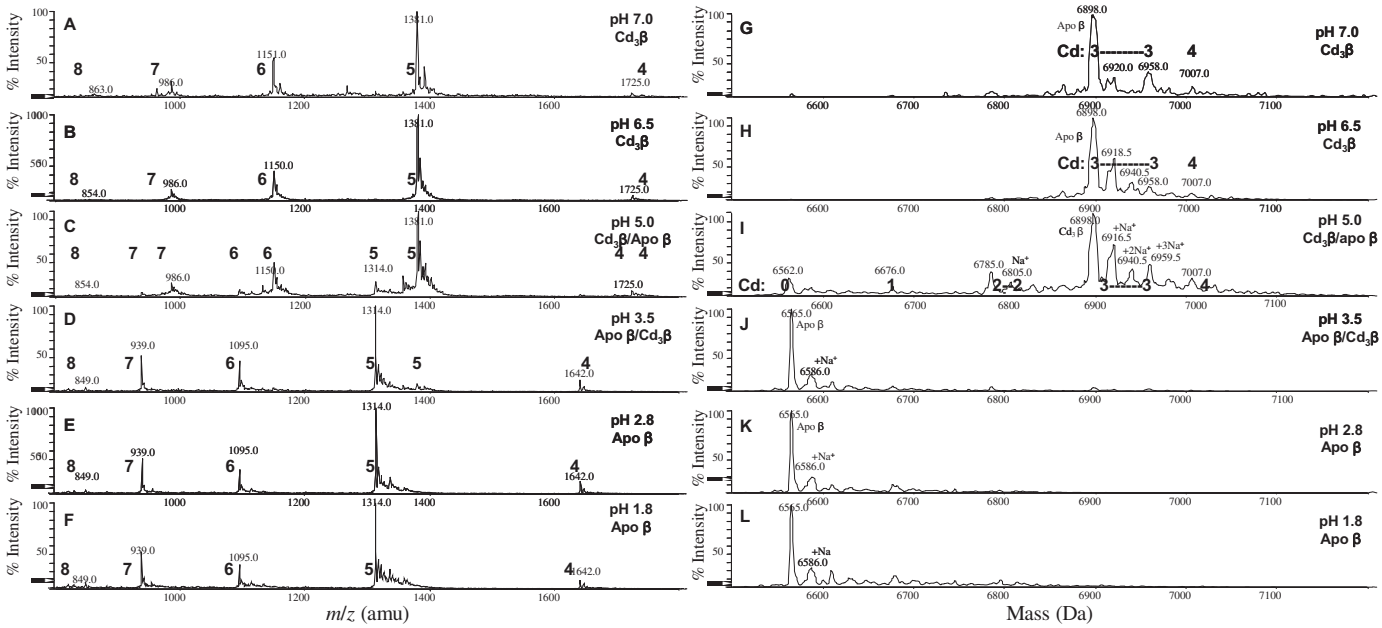


Fig. 6. Effect of pH on the conformation and metallation states of β-rhMT. The left side of this figure shows the measured mass spectra (A–F) labeled with the charge states of the molecular species as the pH was titrated from pH 7.0 to pH 1.8. The right side of this figure shows the reconstructed masses (G–L) that correspond to the measured mass spectra, as labeled.



binding and by absorption and CD spectroscopy to confirm the quality of the rhMT proteins.

ESI-MS spectra

The measured ESI-MS spectra, Figs. 3–8, show the charge distributions on the left and the reconstructed spectra showing the principal masses on the right. Figures 3 and 4 show the spectra for the metallated (pH 7.0) and demetallated (apo, pH < 2.2) states, respectively, for each protein, and Table 1 shows the comparison of calculated and measured masses for each of the rhMTs at high and low pH. These results confirm the stoichiometry of metal binding and the presence of single molecular species within each sample. Figures 5–6 show the spectra for the single-domain rhMTs

© 2007 NRC Canada

Fig. 7. Effect of pH on the conformation and metallation states of αβ-rhMT. The left side of this figure shows the measured mass spectra (A–F) labeled with the charge states of the molecular species as the pH was titrated from pH 7.0 to pH 2.2. The right side of this figure shows the reconstructed masses (G–L) that correspond to the measured mass spectra, as labeled.

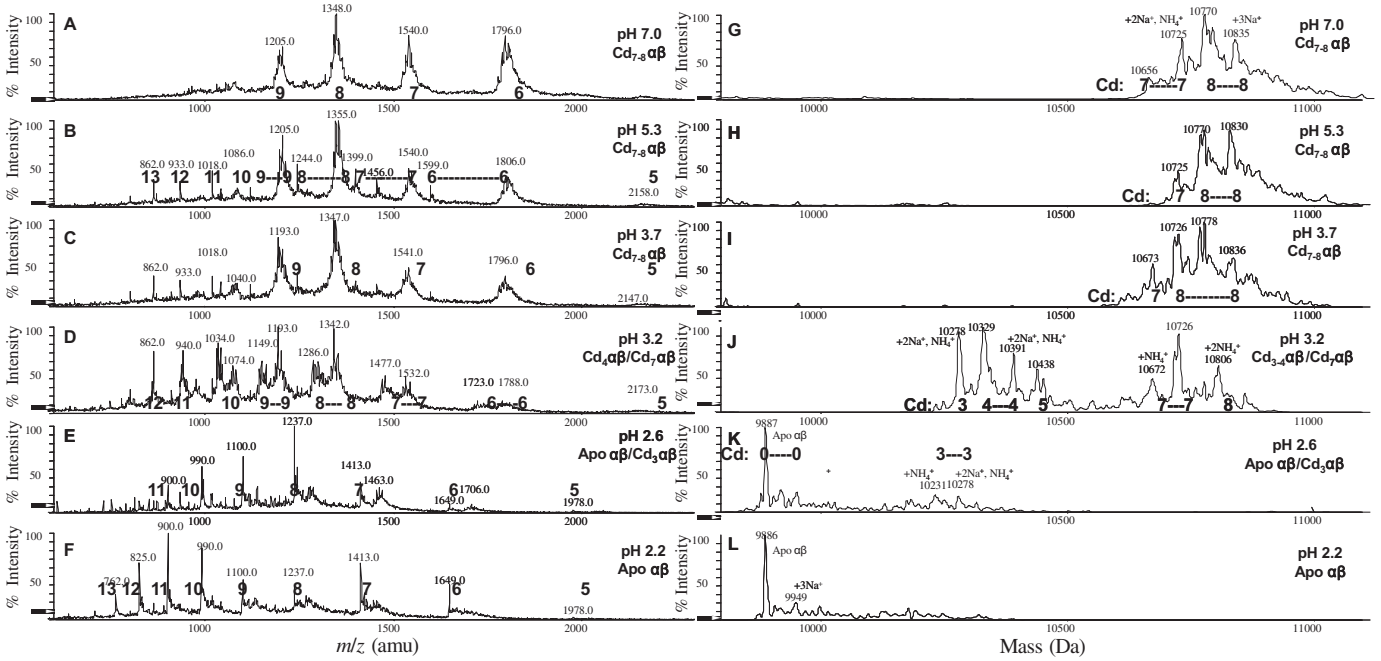
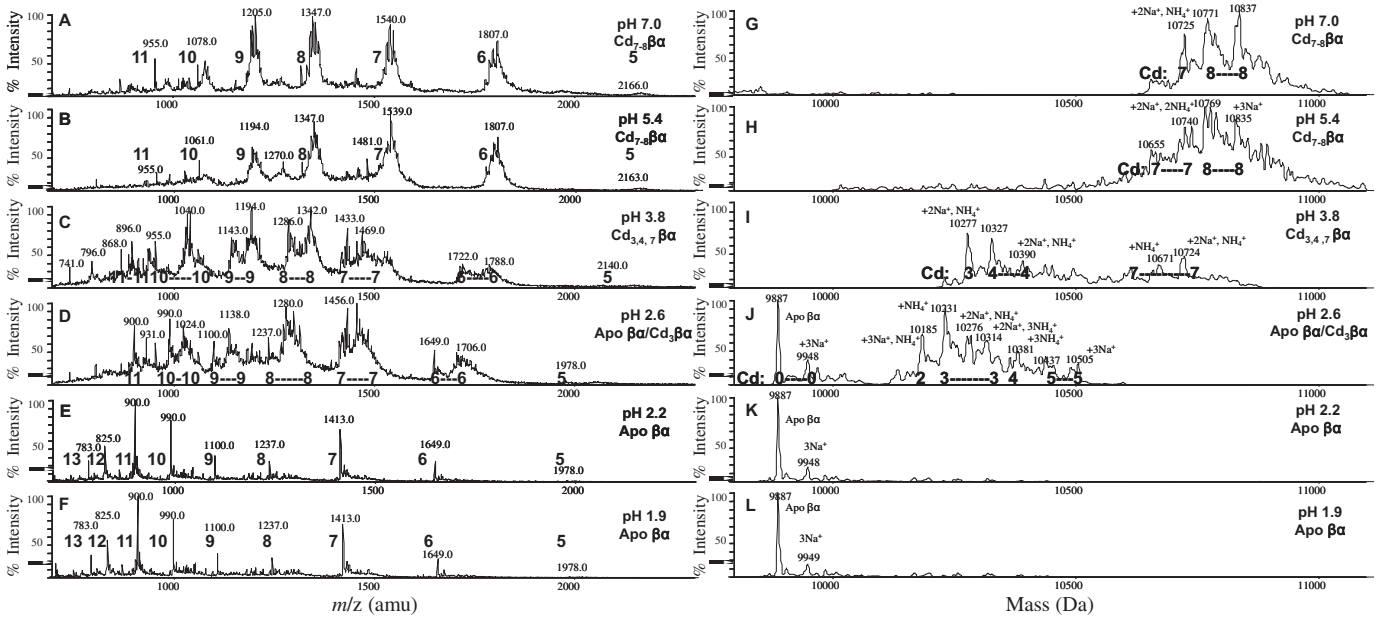


Fig. 8. Effect of pH on the conformation and metallation states of βα-rhMT. The left side of this figure shows the measured mass spectra (A–F) labeled with the charge states of the molecular species as the pH was titrated from pH 7.0 to pH 1.9. The right side of this figure shows the reconstructed masses (G–L) that correspond to the measured mass spectra, as labeled.



and Figs. 7 and 8 show the spectra for the two-domain rhMTs. Spectra were measured at six different pH levels during a pH titration over the range of neutral to acidic pH (~2), and Fig. 9 summarizes the observed metallation states for each rhMT species plotted with the metallation data from AAS measurements over the same pH range.

Species present during acid-induced demetallation

Cd_4-α-rhMT

AAS measurements show that demetallation of Cd_4-α-rhMT begins around pH 4; the point of inflection is at pH 3.1, and complete demetallation is reached by pH 2.4.

© 2007 NRC Canada

Table 1. Mass spectral data for the recombinant human metallothionein proteins used to calculate the stoichiometric ratios of cadmium per MT molecule.

Recombinant human metallothionein	Amino acids[a]	Cysteines	Metal ions	Protons	$Mass_{calc}$ (Da)[a]	$Mass_{meas}$ (Da)[b]
α-rhMT	68	11	0	11	6894.3	6893.8±0.6
			4Cd	3	7335.9	7335.8±0.6
β-rhMT	65	9	0	9	6564.7	6564.6±0.4
			3Cd	3	6895.9	6896.2±0.8
αβ-rhMT	99	20	0	20	9884.8	9886.5±0.5
			7Cd	6	10657.6	10656.2±0.6
βα-rhMT	99	20	0	20	9884.8	9886.5±0.5
			7Cd	6	10657.6	10656.2±0.6

[a]Calculated molecular masses of the rhMTs with a 27 amino acid N terminal S-tag. Calculated masses were based on their polypeptide sequence and the loss of two protons per divalent metal bound.
[b]Measured molecular masses of the rhMTs with S-tag, measured experimentally by ESI-MS.

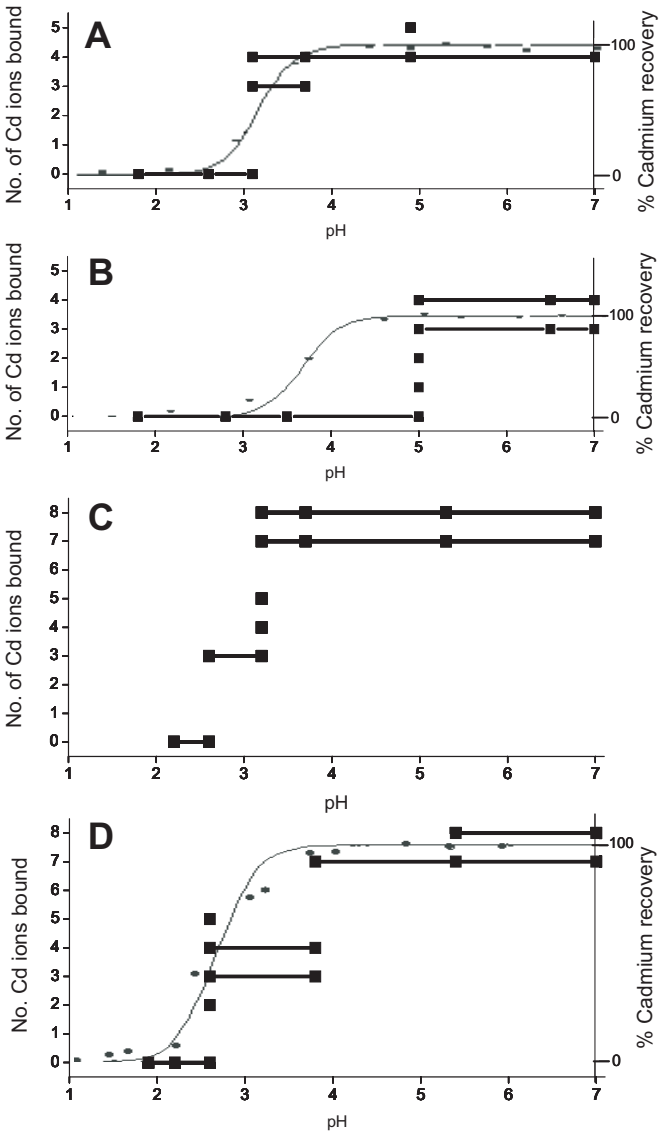


Fig. 9. Summary of the metallation states observed by ESI-MS during pH titration and the associated demetallation curves measured by AAS for (A) α-rhMT, (B) β-rhMT, (C) αβ-rhMT, and (D) βα-rhMT (demetallation curve for αβ-rhMT is not available).

The ESI-MS data indicate that excess metallation of one Cd^{2+} ion is observed, but only as a minor component of the sample. Demetallation of Cd_4-α-rhMT begins at pH 3.7 with the loss of a single Cd^{2+} ion. At pH 3.1, Cd_4-α-rhMT and apo-α-rhMT coexist. The lack of intermediates suggest that protonation of the coordinated thiolates takes place over a very narrow range, and that species with less than a full complement are unstable under the ESI-MS conditions. Full demetallation is achieved by pH 2.6. These findings strongly correlate with the AAS data.

Cd_3-β-rhMT

For Cd_3-β-rhMT, the AAS measurements show that demetallation begins at pH 4.5, the point of inflection is at pH 3.6, and complete demetallation is reached at pH 2.9. The reconstructed ESI-MS spectra show a small fraction of protein with an additional Cd^{2+} ion. Partial demetallation at pH 5.0 is observed where all β-rhMT metallation states from zero to four cadmiums coexist, suggesting that intermediate metallation species exist, and becomes fully demetallated by about pH 3.5. There is a small discrepancy in the pH of demetallation between the ESI-MS results and the AAS results for the β domain, yet both results show that the β domain demetallates at a higher pH than the α domain.

Cd_7-βα-rhMT

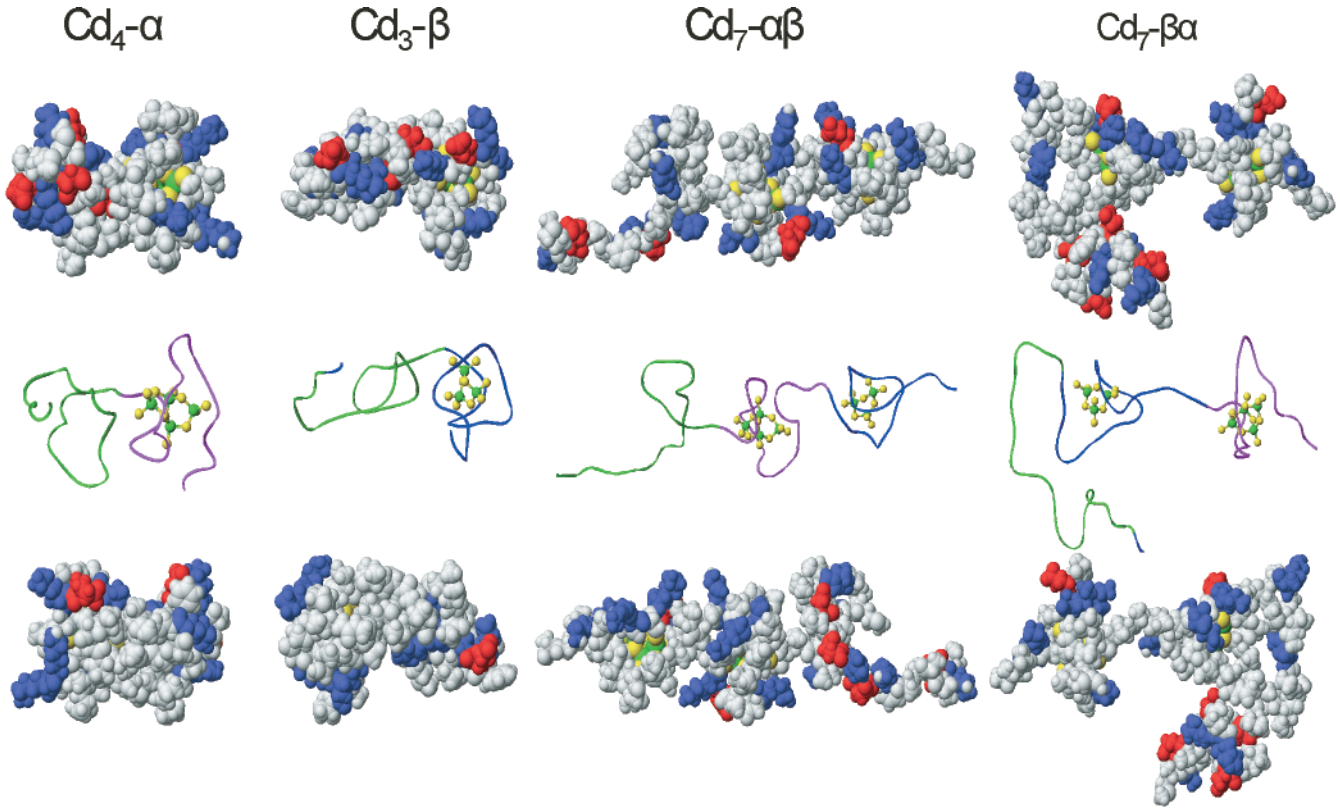
AAS measurements show that demetallation begins at pH 3.9, the point of inflection is at pH 2.7, and complete demetallation is reached by pH 1.9. The reconstructed ESI-MS spectra show that βα-rhMT substantially binds an excess of one Cd^{2+} ion. Partial demetallation is observed at pH 3.8 where metallation states of 3, 4, and 7 coexist, a difference of three to four metal ions. The protein continues to demetallate through pH 2.6 where metallation states of 0 and 2–5 coexist, and is fully demetallated by pH 2.2. These demetallation transitions measured by AAS strongly agree with the results of ESI-MS.

Cd_7-αβ-rhMT

AAS measurements were not available for this protein. Much like Cd_7-βα-rhMT, a substantial amount of the sample shows excess metallation of one Cd^{2+} ion. The reconstructed spectra show that αβ-rhMT is partially demetallated at pH 3.2 where metallation states of 3–5, and 7–8 coexist, and is fully demetallated by pH 2.2; a difference of three to four

© 2007 NRC Canada

Fig. 10. Metallated metallothionein structures generated from MM3/MD calculations. The colored atoms correspond to the residues shown in Fig. 2 where the red atoms represent acidic residues, the blue atoms represent basic residues, the yellow atoms represent the cysteinyl sulfurs, and the green atoms represent the cadmium or zinc ions bound. The top row of structures shows one side of the molecules. The middle row of structures shows the protein backbone where the green represents the S-tag sequence, the purple represents the α-MT sequence, and the blue represents the β-MT sequence, also showing the location of the metal-thiolate cluster. The bottom row of structures represents the other side of the molecules.



metal ions. The metallation states appear as two groups, fully metallated (seven to eight Cd^{2+} ions) and partially demetallated (three to five Cd^{2+} ions), again a difference of three to four metal ions. There is an absence of the Cd_6-αβ-rhMT species. This suggests that αβ-rhMT has a demetallation mechanism that involves the demetallation of one domain at a time. At pH 2.6, there are again two sets of metallation states, 0 Cd^{2+} and 3 Cd^{2+} (1 Cd^{2+} and 2 Cd^{2+} are absent), further supporting initial demetallation of a single domain, and also suggesting that the β-domain is still metallated, but this may be an artifact, as the signal-to-noise level of the Cd_3-αβ-rhMT species is very low. By pH 2.2, αβ-rhMT is completely demetallated.

Molecular models

Molecular models of Cd_4-α-rhMT, Cd_3-β-rhMT, Cd_7-αβ-rhMT, and Cd_7-βα-rhMT were constructed and energy-minimized to mimic the conformations at neutral pH (fully metallated with Cd^{2+}), shown in Fig. 10. Similarly, models of apo-α-rhMT, apo-β-rhMT, apo-αβ-rhMT, and apo-βα-rhMT were prepared to mimic the conformations at low pH (fully demetallated) when the proton concentration in solution is high, shown in Fig. 11. Dynamics simulations of each of the metallated rhMTs show that the metal-thiolate clusters have some short-range freedom of motion, but are otherwise fairly rigid structures. The peptides that wrap around the clusters have more freedom of motion than the clusters, but do not move significantly. Upon removal of the metals, the apo-rhMTs demonstrate significantly higher freedom of movement in the peptide chain, but the overall conformation does not change significantly. In each of the metallated and demetallated molecular models, the majority of the charged residues are located at the protein surface, which would make them solvent-accessible and easily protonatable.

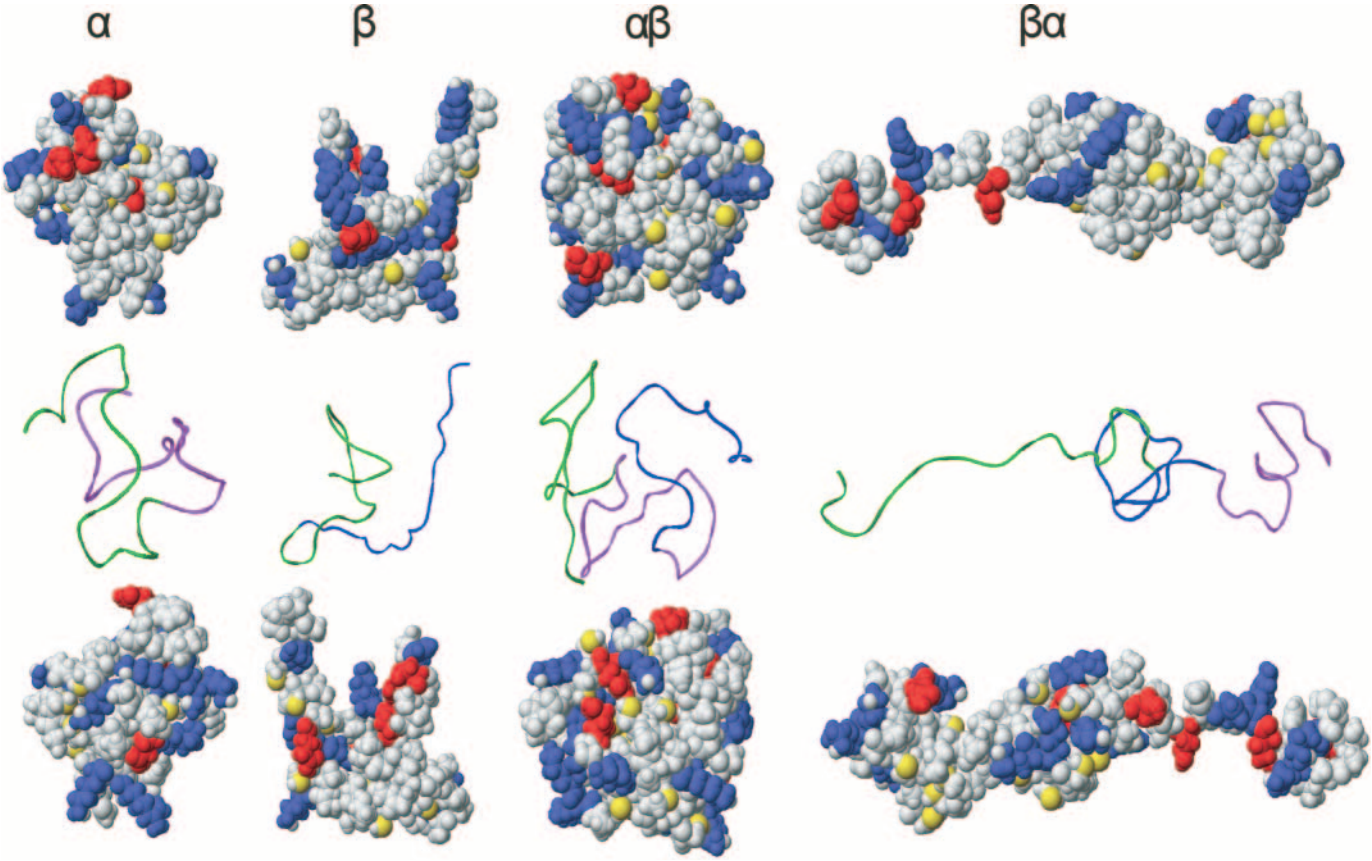
With respect to the S-tag, over many calculations we have found that it is quite fluxional and does not adopt a fixed or even sticky association with the MT peptide chain. Therefore, we believe these MT fusion proteins do adopt well-formed structure even at neutral pHs in the presence of the S-tag.

Correlation of calculated and measured charges

Table 2 summarizes the total charges, the expected charges based on the solvent accessible protonatable groups observed on the molecular models, and the charges measured by ESI-MS (collected from Figs. 5–8) for both the metallated and apo forms for each of the rhMTs. The protonatable residues include the following: N-terminus (pKa 10), C-terminus (pKa 2), Asp (pKa 4), Glu (pKa 4), His (pKa 6), Lys (pKa 10), Arg (pKa 12.5), and Cys (pKa

© 2007 NRC Canada

Fig. 11. Apo metallothionein structures generated from MM3/MD calculations. The colored atoms correspond to the residues shown in Fig. 2 where the red atoms represent acidic residues, the blue atoms represent basic residues, and the yellow atoms represent the cysteinyl sulfurs. The top row of structures shows one side of the molecules. The middle row of structures shows the protein backbone where the green represents the S-tag sequence, the purple represents the α-MT sequence, and the blue represents the β-MT sequence. The bottom row of structures represents the other side of the molecules.



8). However, the data show (Fig. 9) that the pKa of the cysteine groups within metallothionein are significantly lower due to metal-ion coordination, and histidine (only in the S-tag) has a borderline pKa at neutral pH and therefore is likely that the sample only partially contains protonated histidine groups. In addition, the clusters in the metallated structures have a net –3 charge, but it is suspected to be of little influence on the charge, since the cluster is largely shielded inside the core of the protein (54), and hence these clusters are not included in the calculated charge. Lower charge states indicate more compact structures (less solvent-exposed protonatable groups), while higher charge states are associated with more open or unwound structures (more solvent-exposed protonatable groups), of the same peptide chain.

Cd_4-α-rhMT

At neutral pH, the molecular model of Cd_4-α-rhMT has the protein strand tightly wrapped around the cluster, with the S-tag slightly folded but does not appear to interact strongly with the metallated domain. The sulfurs of the cluster are well-buried, though there is a tight crevice site observed that may allow solvent access. The histidine residue in the S-tag is exposed, so it will have an impact on the molecular charge. Of all the protonatable residues, only a single aspartic acid (residue 18) is buried within the protein, which may play a role in protein unfolding at intermediate pH.

Based on this analysis, the expected charge is +6 at neutral pH. The ESI-MS spectra show that one series of charge states is observed ranging from +4 to +7 with the maximum charge intensity centered at +5 and a hint of a maximum at +7. The distribution of charge suggests that there is one principal protein conformation, and one minor protein conformation. The observed charge is comparable to the expected charge of +6.

At pH 3.1, a complex pattern of overlapping charge distributions emerges. The *m*/*z* values belonging to Cd_4-α-rhMT are still present, but the *m*/*z* values of 863.0, 986.0, 1150.0, 1380.0, and 1725.0 amu, arise from apo-α-rhMT and corresponding to charges states ranging from +8 to +4 where there are two maxima centered on +7 (986.0 amu) and +5 (1380.0 amu). At pH 2.6, only the distribution of apo-α-rhMT, consisting of the two maxima, remains.

Further acidification to pH 1.8 results in the charge distribution collapsing to a single distribution ranging from +4 to +10 and centered at +8, corresponding to apo-α-rhMT. The model of the apo structure shows the S-tag folds up close with the α portion of the protein strand, which has a more open structure than the metallated form, and many of the sulfur groups are now found at the protein surface. The basic

© 2007 NRC Canada

Table 2. Charged sites on rhMTs based on the protein sequence (total charges) and the exposed charged sites on molecular models (expected charge), and the number of charges observed by ESI-MS. The charged sites in brackets represent buried charges. The observed charge values are the range of charges in the charge distributions, with the bold, italic values being the charge maxima.

rhMT	Metallation state	Positive sites	Negative sites	Total charges	Expected charge	Observed charge
α-rhMT	Metallated	8 Lys, 2 Arg N-terminus 4 Cd^{2+} 1 His	3 Glu, 2 Asp C-terminus 11 S^-	+3	+6	+4→+5→+7
	Apo	8 Lys, 2 Arg N-terminus		+11	+11	+4→+8→+10
β-rhMT	Metallated	8 Lys, 2 Arg N-terminus 4 Cd^{2+} (1 His)	3 Glu, 2 Asp C-terminus 11 S^-	+3	+5	+4→+5→+8
	Apo	8 Lys, 2 Arg N-terminus		+11	+11	+4→+5, +7→+8
αβ-rhMT	Metallated	13 Lys, 2 Arg N-terminus 3 Cd^{2+} 1 His	4 Glu, 2 Asp C-terminus 9 S^-	+4	+10	+6→+8→+9
	Apo	8 Lys, 2 Arg N-terminus		+16/+17	+16/+17	+5→+7, +10→+13
βα-rhMT	Metallated	13 Lys, 2 Arg N-terminus 3 Cd^{2+} 1 His	4 Glu, 2 Asp C-terminus 9 S^-	+4	+10	+6→+9→+11
	Apo	8 Lys, 2 Arg N-terminus		+16/+17	+16/+17	+5→+7, +11→+13

sites and all the sulfur groups of α-rhMT are therefore accessible, giving a predicted charge of +11 at acidic pH. These results indicate that the measured apo structure is more compact than the calculated structure, suggesting that the demetallated structure is still partially folded.

Cd_3-β-rhMT

At neutral pH, the molecular model of Cd_3-β-rhMT has a structure similar to that of Cd_4-α-rhMT in that the protein wraps around the cluster with a non-interacting S-tag. The protein itself has the equivalent number of acidic and basic residues as the α-domain. An arginine (residue 11) and an aspartic acid (residue 15) are buried within the protein, but are inconsequential at pH 7. The sulfurs appear to be significantly more exposed for solvent access than the α domain, which may explain why the α-domain stability is greater than that of the β domain. The histidine residue of the S-tag is buried in the folded structure so is less likely to be protonated compared to that in the α domain. Therefore, the expected charge is +5 for the metallated β-rhMT. A single-charge distribution is observed for Cd_3-β-rhMT, ranging from +4 to +8 and centered on +5, matching the expected charge. At pH 5.0, masses of the intermediate metallation states emerge, which become more prevalent by pH 3.5, where these masses dominate the spectrum, and the original masses attributed to Cd_3-β-rhMT disappear. The new distribution attributed to apo-β-rhMT has a strong maximum at +5 and a weak maximum at +7.

Further acidification to pH 1.8 refines the double maxima at +5 (major) and +7 (minor). In the molecular model, the β portion of the protein strand becomes linear and significantly less compact than the metallated structure, with the sulfurs exposed at the protein surface. In addition, the S-tag folds up but does not strongly interact with the β portion of the protein. The predicted charge of +11 is significantly higher than observed, suggesting that the apo-protein still has significant structure, and the two distributions measured in the MS data indicate that there are at least two different conformations present.

Cd_7-αβ-rhMT

At neutral pH, the molecular model of Cd_7-αβ-rhMT demonstrates the characteristic dumbbell shape of mammalian MT, and the additional S-tag peptide portion of the protein is non-interacting with the metallated domains. An aspartic acid (residue 18) in the α domain of this metallated protein, the same as in α-rhMT, is also buried. In addition, the arginine (residue 11) and aspartic acid (residue 15) are buried in this metallated protein just as they are in the metallated β-rhMT. The structure exhibits crevice sites similar to those found in the separate α and β domains. The expected charge is +10 at neutral pH. The observed charge states range from +6 to +9 in which the principal maximum is centered at +8, and a secondary maximum is centered at +6, which is lower than the expected charge, suggesting a more-compact structure than expected. At pH 5.3, the charge distribution widens significantly, and several new masses with lower m/z values, associated with αβ-rhMT bound to seven to eight Cd^{2+}, emerge, indicating the inhomogeneity of the sample. At pH 3.2, when metal loss is observed, the

© 2007 NRC Canada

charge distribution becomes even more complicated, but the overall charge distribution shifts to higher charge values. At pH 2.6, the distribution is still rather complicated, but the charge ranges from +5 to +11 with a single maximum observed at +8, which can be correlated to apo-αβ-rhMT.

When the pH is further reduced to pH 2.2, the spectral resolution improves significantly as only apo-αβ-rhMT is observed. However, a splitting of the charge state distributions is observed such that two maxima are centered at +11 and +7 over the range of +5 to +13 charge states. The molecular model shows the protein strand collapsing into a ball, and the sulfur groups again invert to the protein surface. The predicted charge at acidic pH is +16 (or +17, since the acidic pH borderlines the pKa of the C terminus), so the observed charge states are again lower than this, indicating that more compact structures are present with buried charges.

Cd_7-βα-rhMT

Like αβ-rhMT, at neutral pH, the domains of the molecular model of Cd_7-βα-rhMT are distinct from each other, making the structure appear linear. The dumbbell shape of the βα portion is quite distinct, with the S-tag noninteracting. Again, like metallated α-rhMT, the aspartic acid (residue 18) is buried. However, unlike the metallated β-rhMT structure, the arginine (residue 11) and the aspartic acid (residue 15) are exposed. These differences may play a role in the unfolding of the protein and may be the key differences between this two-domain protein and the reverse-domain αβ-rhMT. Again, the crevice sites are quite prominent, as in the Cd_7-αβ-rhMT structure. The expected charge was +10. The observed charge states range from +6 to +11, where the maximum is centered at +9, which is comparable to the expected charge. The solvent exposure of Cd_7-βα-rhMT is similar to that of Cd_7-αβ-rhMT. No significant changes occur to the spectrum until about pH 3.8 where new charge states emerge, and the overall charge distribution shifts to higher charges centered at about +10. Multiple distributions overlap as expected, given the coexistence of multiple species with adducts. At pH 2.6, several new masses emerge and several disappear, but no major shift in the charge distribution is observed.

At pH 2.2, the spectrum resolves significantly as the masses resolve to a mass attributed to apo-βα-rhMT. A charge distribution ranging from +5 to +13 is observed with two maxima centered at +7 and +11, again indicating compact structures with buried charges and two different protein conformations. Further acidification to pH 1.9 results in no significant changes to the spectrum, and the two-maxima distribution remains. The molecular model shows that the strand maintains a similar conformation to that of the metallated structure with the domains remaining folded, which is a significant difference from αβ-rhMT. This implies that the apo structure may have some inherent structure that facilitates metal binding. Like apo-αβ-rhMT, the predicted charge is +16 (or +17), showing the observed conformation of the protein to be more compact than predicted.

Discussion

Protein folding is important because of the implication of the overall three-dimensional structure on biologically significant function and our understanding of factors that change the structure and hence modify function. The recent use of ESI-MS studies has provided details of intermediates not easily obtained by other methods leading to ESI-MS as one of the foremost contributors to this area (55–58). Our interest in this paper is in the structural role of metals in metalloproteins, especially those proteins with structures dominated by the metal coordination (rather than structures where the metal-free or apo-protein is similar to that of the metallated or holoprotein). We are also interested in the possible structure in the metal-free, apoMT, as these structures may play a role in metallation as well as in functions yet to be understood but involving the redox properties of the large numbers of cysteine thiols present.

The ESI-MS data described here identify first the presence of species with intermediate metal loading (partially demetallated) states. These data can be associated with metal-loading values determined by AAS to construct a titration curve that yields the modified pKa values for the coordinating cysteine thiols. The ESI-MS and AAS data correlate extremely well and show that the Cd-rhMTs demetallate at a significantly lower pH (~3) than the pKa of cysteine (pKa = 8), as expected. We should briefly comment on the appearance of one "extra" cadmium in most of the mass spectra. For many years, these additional cadmium atoms have been deduced from spectroscopic data (changes to the Cd spectrum when loading apo-MT with Cd^{2+}, blurring of NMR signals, and so forth) and in the mass spectral data. Generally, the cause has been attributed to adducts. Very recently, Rigby-Duncan and Stillman (unpublished) have determined that Cd_5-α-rhMT1a exists with 5 unique Cd atoms present at high cadmium loadings. We interpret the minor contribution of five Cd in the α, and eight Cd in the αβ mass spectra as arising from Cd_5-α domains.

The changes in the conformation of the protein, deduced from the ESI-MS charge states, in response to systematic pH changes provide information about the mechanism of acid-induced protein unfolding. The key information is contained in the number and intensity distribution of the ESI-MS charge states for each species that exists at each pH. The observed multiple-charge states result from the protonation of exposed basic amino acids. The presence of different numbers of the protonated groups is an indicator of exposure to solvent such that protein conformations with more positive charge indicate a more unfolded structure, though the charge does not provide an absolute number of exposed basic amino acids. The expectation is that there should be a distribution about a single-charge state, representing the equilibrium distribution of protons across all basic amino acids. As the pH is lowered, the less-basic sites will be protonated and the mean charge state will increase in charge. These changes in charge states are a very sensitive indicator of three-dimensional structure, as they are measured in solution and can help characterize intermediate species from the mass and the degree of compactness from the charge state maximum; data that are difficult to quantify from methods such as NMR and CD spectroscopy.

Since the coordination of the metal ions to MT is essential to maintain its structural integrity, demetallation by acidification results in the unfolding of the protein, becoming much less compact and more susceptible to solvent exposure, thus increasing the extent of protonation of additional

© 2007 NRC Canada

basic sites. This is indeed what is observed for each of the rhMTs in the ESI-MS data. In the proteins studied in this work, it is clear that the additional S-tag sequence will provide several exposed sites that will be available for protonation in addition to the peptide in the region of the metal binding site. The histidine residue in the S-tag does not affect the spectroscopy of the rhMTs, so it is not likely to be involved in the metallated metallothionein, since coordination of a metal ion by the histidine and any of the cysteines would be energetically unfavorable for the protein conformation. Table 2 lists the frequency of the basic residues in the MT sequence. Even at neutral pH, many of these residues are protonated as the maximum intensity charge state is +5 for the fragments and +8/+9 for the βα and αβ peptides (Fig. 3). Indeed, the low pH data (Fig. 4) indicate that only the protonation of the cysteines is new at low pH. The pKa of the cys thiolates is clearly reduced from the usual 8 to between 3.7 (β) and 2.8 (βα) (Fig. 9).

The structures calculated using the Molecular Mechanics/Molecular Dynamics (MM3/MD) methods showed the fully metallated and the metal-free protein, the starting and ending structures expected for the metal-release reaction of metallothionein by acidification. We can correlate these findings with the demetallation sequence determined by Rigby et al. (31, 32) The orientation of the cysteinyl sulfurs in the de novo apo protein can be compared to those in the metallated form to determine any potential preexisting three-dimensional structural features of the apo protein in the aqueous environment that may facilitate the metal binding. Following complete demetallation, the peptide may still have some conserved structure because of the non-covalent interactions, such that conformational changes in the apo-protein may also be observed upon further acidification.

Demetallation events

The Cd-rhMTs begin to demetallate around pH 4.5. They are about 50% demetallated (the point of inflection) at about pH 3 and are completely demetallated at around pH 2.9 or lower. Therefore, the Cd-rhMTs have a narrow range of pH for demetallation (1–1.9 pH values), indicating that the demetallation reaction in metallothionein occurs in a fairly concerted manner involving all coordinating cys thiolates. There are obvious differences between the demetallation reactions of the single domains, α-rhMT and the β-rhMT. First, demetallation of the α domain (~pH 4) occurs at a lower pH than the β domain (~pH 4.5), indicating that the α domain is more stable than the β domain as has been previously found by Jiang et al. (59). Second, the ESI-MS data suggest that because the α domain demetallates over such a narrow range of pH, this accounts for the lack of partially metallated species (Fig. 5), whereas the β domain demetallates over a wider range of pH allowing the one Cd and two Cd species to be observed. When the two domains are linked together in the naturally occurring βα-MT, the two-domain structure has comparable stability to that of the α domain, and these results suggest that it has a slightly higher binding constant than the α domain. Reversing the order of the two domains in the αβ-rhMT has surprisingly little effect, and the stability is comparable to that of α-rhMT and βα-rhMT. The data of the αβ and βα proteins suggest that the β domain demetallates completely first leaving the four-metal α domain intact as the pH is lowered. The data provide an excellent example of the metal-induced pKa lowering effect for coordinated amino acid side chains.

Conformational changes

The fully folded, metallated α-rhMT initially exhibits two conformations, the dominant conformation being more compact, both of which are stable until demetallation begins at pH 3.7. Throughout most of the demetallation reaction, α-rhMT maintains these two conformations, showing the apo-rhMT retains some structure. The calculation of the single parent molecular ions for the apo-α-rhMTs from the double maxima shows that the double maxima in the charge states arise from equilibrium between two protein conformations that exhibit different exposures to the protons. Further acidification causes the complete unfolding of α-rhMT to a single, open conformation, as indicated by the shift in the total charge distribution centered at a single, higher charge, showing that the two conformations were in equilibrium and that acidification shifted the equilibrium to the more-stable conformation under low pH conditions.

The initial conformation of β-rhMT, like α-rhMT, is stable until demetallation. When β-rhMT is fully demetallated, two conformations are observed where the dominant conformation is more compact, much like what is observed in demetallated α-rhMT, indicating some retained structure in apo-β-rhMT because of the hydrogen bonding. Further acidification does not cause any changes in conformation, indicating that the hydrogen-bonding network in β-rhMT is stronger than that of α-rhMT.

The charge states of αβ-rhMT are proportionally higher than that of α-rhMT and β-rhMT (αβ-rhMT is about 1/3 larger in size than both α-rhMT and β-rhMT). αβ-rhMT also has a wider charge distribution than α-rhMT and β-rhMT, demonstrating the heterogeneity of the sample. αβ-rhMT has two different metallated conformations of which the dominant conformation has a more-open structure. A decrease in intensity of the minor conformation as the pH is lowered shows that there is some instability in the protein conformation prior to demetallation. This may be the result of the flexibility of the linker region between the two domains. Complete demetallation of αβ-rhMT results in a single conformation with moderate charge. Further acidification results in complete unfolding, as indicated by the shift of the charge distribution to higher charge states, though a minor conformation does exist.

βα-rhMT has a more-open conformation and is more heterogeneous than αβ-rhMT, as indicated by the higher charge. Metallated βα-rhMT appears to have two conformations with the more-open structure being the dominant form, though the dominant conformation may be less stable prior to demetallation, as seen by the decrease in the intensity of the distribution. Complete demetallation results in the formation of two stable conformations of which the dominant conformation has a more-open structure, as is observed for αβ-rhMT.

The molecular models, which were calculated for each of the fully metallated and metal-free species, show the compact nature of the metal-containing proteins, but surprisingly, predict that demetallated structures should exhibit a

© 2007 NRC Canada

structure that is unrelated to the metals. The calculations of the models of the demetallated proteins are quite compact and in fact represent the structures of the metallated species. The models also identify the basic and acidic amino acids on the surface of the protein; the fraction of basic amino acids protonated will increase from pH 7 to low pH. The observation of multiple charge state distributions at low pH for the single parent molecule provide evidence that the metal-free, apoMT do exhibit a structure as predicted by the MM3/MD calculations.

Conclusions

The metallothionein proteins have been very well characterized by many spectroscopic and analytical techniques. ESI-MS provides a way of determining structural details of intermediate structures that cannot be measured by any other method currently. Structure in the apo-proteins is reported for each of the species lending support for the previous proposals that apo-MT may have a specific function. In the future, rapid measurement of ESI-MS data will allow a more detailed view of the folding and unfolding processes.

Acknowledgements

We thank the Natural Sciences and Engineering Research Council of Canada (NSERC) for financial support.

References

1. B.L. Vallee. *In* Metallothionein. *Edited by* J.H.R. Kagi and M. Nordberg. Birkhauser Verlag, Basel. 1979. pp. 31–36.
2. J.H.R. Kagi and M. Nordberg (*Editors*). Metallothionein. Birkhauser, Basel; Boston. 1979.
3. J.H.R. Kagi and Y. Kojima (*Editors*). Metallothionein II. Birkhauser Verlag, Basel; Boston. 1987.
4. M.J. Stillman, C.F. Shaw III, and K.T. Suzuki (*Editors*). Metallothioneins. VCH, New York. 1992.
5. K.T. Suzuki, N. Imura, and M. Kimura (*Editors*). Metallothionein III. Birkhauser Verlag, Basel, Switzerland. 1993.
6. M.J. Stillman. Metallothioneins. Coord. Chem. Rev. **144**, 461 (1995).
7. C. Klaassen (*Editor*). Metallothionein IV. Birkhauser Verlag, Basel, Switzerland. 1999.
8. J.F. Riordan and B.L. Vallee (*Editors*). Methods in enzymology, metallobiochemistry Part B. Metallothionein and related molecules. Academic Press, New York. 1991.
9. B.A. Messerle, A. Schaffer, M. Vasak, J.H.R. Kagi, and K. Wuthrich. J. Mol. Biol. **225**, 433 (1990).
10. J.D. Otvos and I.M. Armitage. Proc. Natl. Acad. Sci. U.S.A. **77**, 7094 (1980).
11. W. Braun, G. Wagner, E. Woergoetter, M. Vasak, J.H.R. Kagi, and K. Wuthrich. J. Mol. Biol. **187**, 125 (1986).
12. A.H. Robbins, D.E. McRee, M. Williamson, S.A. Collett, N.H. Xuong, W.F. Furey, B.C. Wang, and C.D. Stout. J. Mol. Biol. **221**, 1269 (1991).
13. A.H. Robbins and C.D. Stout. *In* Metallothioneins: Synthesis, structure and properties of metallothioneins, phytochelatins and metal-thiolate complexes. *Edited by* K.T. Suzuki. VCH New York. 1992. pp. 31–54.
14. M.J. Stillman, A. Presta, Z. Gui, and D.-T. Jiang. Metal-Based Drugs, **1**, 375 (1994).
15. Z. Gui, A.R. Green, M. Kasrai, G.M. Bancroft, and M.J. Stillman. Inorg. Chem. **35**, 6520 (1996).
16. M.J. Stillman. NATO ASI Series, Series 2: Environment, **26**, 139 (1997).
17. D.A. Fowle and M.J. Stillman. J. Biomol. Struct. Dyn. **14**, 393 (1997).
18. C.C. Chang and P.C. Huang. *In* Metallothionein IV. *Edited by* C. Klaassen. Birkhauser Verlag, Basel, Switzerland. 1999. pp. 45–49.
19. C.-C. Chang, W.-F. Liao, and P.C. Huang. Protein Eng. **11**, 41 (1998).
20. C.-C. Chang and P.C. Huang. Protein Eng. **9**, 1165 (1996).
21. N. Romero, M. Capdevila, P. Gonzalez-Duarte, and B. Oliva. J. Mol. Model. **2**, 417 (1996).
22. H. Wang, Q. Zhang, B. Cai, H. Li, K.-H. Sze, Z.-X. Huang, H.-M. Wu, and H. Sun. FEBS Lett. **580**, 795 (2006).
23. A. Presta, D.A. Fowle, and M.J. Stillman. Dalton Trans. **6**, 977 (1997).
24. Z. Szilagyi and C. Fenselau. Drug Metab. Dispos. **28**, 174 (2000).
25. M.J. Stillman, A.R. Green, Z. Gui, D. Fowle, and P.A. Presta. *In* Metallothionein IV. *Edited by* C.D. Klaassen. Birkhauser Verlag, Basel, Switzerland. 1999. pp. 23–35.
26. J. Chan, M.E. Merrifield, A.V. Soldatov, M.J. Stillman. Inorg. Chem. **44**, 4923 (2005).
27. A.V. Soldatov, G. Smolentsev, G. Yalovega, J. Chan, and M. Stillman. Rad. Phys. Chem. **75**, 1901 (2006).
28. G. Yalovega, G. Smolentsev, A. Soldatov, J. Chan, and M. Stillman. Nucl. Instr. Meth. in Phys. Res., Section A, **575**, 162 (2007).
29. C.D. Berweger. Proteins, **41**, 299 (2000).
30. K.E. Rigby and M.J. Stillman. Biochem. Biophys. Res. Commun. **325**, 1271 (2004).
31. K.E. Rigby, J. Chan, J. Mackie, and M.J. Stillman. Proteins **62**, 159–172 (2006).
32. K.E. Rigby Duncan and M.J. Stillman. J. Inorg. Biochem. 100, 2101 (2006).
33. M. Enescu, J.-P. Renault, S. Pommeret, J.-C. Mialocq, S. Pin. Phys. Chem. Chem. Phys. **5**, 3762 (2003).
34. I.G. Dance. *In* Transition-metal sulfur chemistry. *Edited by* E. Stiefel and K. Matsumoto. Vol. 653. American Chemical Society, Washington, DC. 1996. pp. 135–152.
35. A. Dobo and I.A. Kaltashov. Anal. Chem. **73**, 4763 (2001).
36. R.H. Griffey, K.A. Sannes-Lowery, J.J. Drader, V. Mohan, E.E. Swayze, and S.A. Hofstadler. J. Am. Chem. Soc. **122**, 9933 (2000).
37. P.D. Schnier, D.S. Gross, and E.R. Williams. J. Am. Soc. Mass. Spectrom. **6**, 1086 (1995).
38. F.B. Simpson and D.B. Northrop. *In* Mass Spectrometry in biology and medicine. *Edited by* A.L. Burlingame, S.A. Carr, and M.A. Baldwin. Humana Press, Totowa, New Jersey. 2000. pp. 329–364.
39. L. Konermann. J. Phys. Chem. B, **111**, 6534 (2007).
40. J.S. Fetrow, A. Giammona, A. Kolinski, and J. Skolnick. Curr. Pharm. Biotechnol. **3**, 329 (2002).
41. E. Shakhnovich. Chem. Rev. **106**, 1559 (2006).
42. A.R. Leach. Molecular modelling: Principles and applications. 2nd ed. Prentice Hall, New York, Harlow, England. 2001.
43. T. Schlick. Molecular modeling and simulation: An interdisciplinary guide. Springer, New York. 2002.
44. S. Tsai. An introduction to computational biochemistry. Wiley-Liss, New York. 2001.
45. J.H. Freedman, L. Powers, and J. Peisach. Biochemistry, **25**, 2342 (1986).

© 2007 NRC Canada

46. D. Klein, J. Lichtmannegger, U. Heinzmann, J. Muller-Hocker, S. Michaelsen, and K.H. Summer. Eur. J. Clin. Invest. **28**, 302 (1998).
47. I. Watt. Metallothioneins: Molecular engineering improvements in metal specificity. Ph.D. thesis. School of Biosciences, Cardiff University, Cardiff, Wales. 1999. p. 171.
48. J.H.R. Kagi. *In* Metallothionein III. *Edited by* M. Kimura. Birkhauser Verlag, Basel, Switzerland. 1993. pp. 29–55.
49. Z. Gasyna, W.R. Browett, T. Nyokong, R. Kitchenham, and M.J. Stillman. Chemom. Intell. Lab. Syst. **5**, 233 (1989).
50. G.L. Ellman. Arch. Biochem. Biophys. **82**, 70 (1959).
51. W. Birchmeier and P. Christen. FEBS Lett. **18**, 209 (1971).
52. H.M. Berman, J. Westbrook, Z. Feng, G. Gilliland, T.N. Bhat, H. Weissig, I.N. Shindyalov, and P.E. Bourne. Nucleic Acids Res. **28**, 235 (2000).
53. A. Arseniev, P. Schultze, E. Worgotter, W. Braun, G. Wagner, M. Vasak, J.H. Kagi, and K. Wuthrich. J. Mol. Biol. **201**, 637 (1988).
54. S.J. Lippard and J.M. Berg. Principles of bioinorganic chemistry. University Science Books, Mill Valley, California. 1994.
55. S.J. Eyles, T. Dresch, L.M. Gierasch, and I.A. Kaltashov. J. Mass Spectrom. **34**, 1289 (1999).
56. C.S. Maier, M.I. Schimerlik, and M.L. Deinzer. Biochemistry, **38**, 1136 (1999).
57. L. Konermann and D.A. Simmons. Mass Spectrom. Rev. **22**, 1 (2003).
58. L. Konermann and D.J. Douglas. Rapid Commun. Mass Spec. **12**, 435 (1998).
59. L.J. Jiang, M. Vasak, B.L. Vallee, and W. Maret. Proc. Natl. Acad. Sci. U.S.A. **97**, 2503 (2000).

© 2007 NRC Canada

BIOGRAPHY / BIOGRAPHIE

Mike Bancroft was born in Saskatoon in 1942. He was educated in Winnipeg and obtained his B.Sc. (Honours) and M.Sc. in Inorganic Chemistry at the University of Manitoba, the latter supervised by H.D. Gesser. After obtaining a Shell Postgraduate Scholarship, he went to the University of Cambridge in 1964 for his Ph.D. studies. Under the supervision of A.G. Maddock, he set up one of the first automated Mössbauer spectrometers and used this early spectrometer to study structure and bonding in inorganic compounds and silicate minerals (in a remarkable collaboration with R.G. Burns). After his Ph.D. in early 1967, he did a postdoc with J.B. Westmore at the University of Manitoba before returning to the University of Cambridge as a Research Fellow at Christ's College and Demonstrator in the Chemistry Department. At that time, he obtained contracts to publish a book and a large review article (with R.H. Platt) on Mössbauer spectroscopy, both of which appeared in 1972 and 1973.

In 1970, he joined the University of Western Ontario Department of Chemistry as an Assistant Professor and rose through the ranks, becoming a Professor in 1974, and Chair in 1986–1991 and 1992–1995. As Director of the Centre for Chemical Physics from 1977 to 1981, he established Surface Science Western in 1979 and the Canadian Synchrotron Radiation Facility (CSRF) in Madison, Wisconsin, in 1980, directing the latter facility until 1999.

Bancroft is best known as a pioneer in the use of gamma ray (Mössbauer specroscopy) and X-ray spectroscopies (using laboratory UV and X-ray sources, as well as synchrotron radiation) to record high-resolution spectra of inorganic molecules, minerals, tribochemical films, and other surfaces. He has published over 400 papers, supervised 39 graduate students and 37 postdoctoral fellows, and worked with several large industries. Most of these excellent students and postdocs have had very productive careers in academia, industry, and (or) government.

He has been recognized for his scholarly work by numerous prizes including Western's Florence Bucke and the Hellmuth Research Awards, and others from the Royal Society of Canada (FRSC), the Canadian Society of Chemistry, the American Chemical Society, the British Chemical Society.

His multidecade long dream and effort to establish a national synchrotron facility (beginning with a UWO proposal headed by Bill McGowan in 1975) became a reality when the Canadian Light Source was built at the University of Saskatchewan, and he became its first Director from 1999 to 2001. For this achievement and his productive research and administrative career, he was appointed as Officer of the Order of Canada in 2003, and awarded two Honorary degrees in 2006.

He has had an active love of classical music as a boy and adult chorister, and as a piano and flute player. Global warming is a current passion, and he is currently serving on a committee at UWO to set up a pan-University Liberal Studies program to bring many disciplines together (including science, music, and religion) to discuss important topics such as global warming and evolution and creation.

Mike Bancroft est né à Saskatoon, en 1942. Il a commencé ses études à l'Université du Manitoba, à Winnipeg, où il a obtenu un baccalauréat ès sciences (avec mention), puis une maîtrise en chimie inorganique, sous la direction de H.D. Gesser. Après avoir obtenu une bourse d'études supérieures de la société Shell, il a entrepris ses études de doctorat à l'Université de Cambridge, en 1964. Sous la direction de A.G. Maddock, il a assemblé l'un des premiers spectromètres Mössbauer automatiques et utilisé ce dernier pour étudier la structure et les liaisons chimiques de composés inorganiques et de silicates minéraux (collaboration remarquable avec R.G. Burns). Après l'obtention de son doctorat, au début de l'année 1967, il a effectué un postdoctorat sous la direction de J.B. Westmore, à l'Université du Manitoba, avant de retourner à l'Université de Cambridge à titre de chercheur universitaire au Christ's College et de chargé de travaux pratiques au Département de chimie. A cette époque, il a obtenu des contrats pour publier un livre et un article de synthèse important (en collaboration avec R.H. Platt) sur la spectroscopie Mössbauer, parus respectivement en 1972 et en 1973.

En 1970, il s'est joint au Département de chimie de l'Université Western Ontario (UWO) à titre de professeur adjoint et a gravi les échelons, obtenant le poste de professeur en 1974 et occupant celui de titulaire de la chaire de 1986 à 1991, et de 1992 à 1995. A titre de directeur du Centre for Chemical Physics, de 1977 à 1981, il a mis sur pied Surface Science Western, en 1979, et le Canadian Synchrotron Radiation Facility (CSRF), à Madison (Wisconsin), en 1980. Il a dirigé le CSRF jusqu'en 1999.

M. Bancroft est surtout connu en tant que pionnier de l'utilisation de la spectroscopie des rayons gamma (spectroscopie Mössbauer) et des rayons X (utilisant aussi bien des sources UV et de rayons X en laboratoire que le rayonnement synchrotron) pour enregistrer des spectres à haute résolution de molécules inorganiques, de minéraux, de films tribochimiques ou d'autres surfaces. Il a publié plus de 400 articles, dirigé 39 étudiants diplômés et 37 boursiers postdoctoraux, et a collaboré avec plusieurs grandes entreprises. La plupart de ces excellents étudiants et boursiers postdoctoraux poursuivent des carrières très productives dans le milieu universitaire, industriel ou gouvernemental.

Il a été reconnu pour son travail scientifique en recevant de nombreux prix dont le Florence Bucke et l'Hellmuth Research de l'UWO, ainsi que d'autres distinctions de la Société royale du Canada (MSRC), de la Société canadienne de chimie, de l'American Chemical Society et de la British Chemical Society. Son rêve, caressé depuis plusieurs décennies, et ses efforts pour créer une installation nationale de rayonnement synchrotron (qui a débuté par une proposition de l'UWO dirigée par Bill McGowan, en 1975) se sont concrétisés lorsqu'on a construit le Centre canadien de rayonnement synchrotron, à l'Université de la Saskatchewan, et qu'il est devenu son premier directeur, de 1999 à 2001. En raison de cette réalisation et de sa carrière productive de chercheur et d'administrateur, il a été nommé officier de l'Ordre du Canada, en 2003, et a reçu deux doctorats honorifiques, en 2006.

Son amour indéfectible pour la musique classique se traduit par le chant choral auquel il s'adonne depuis l'enfance ainsi que par la pratique du piano et de la flfte. Le réchauffement climatique est sa passion actuelle et il fait partie d'un comité à l'UWO qui vise à instaurer un programme de formation générale continue panuniversitaire regroupant de nombreuses disciplines (dont les sciences, la musique et la religion) afin de discuter de sujets importants comme le réchauffement climatique ainsi que l'évolution et la création.

© 2007 NRC Canada

TRIBUTE / HOMMAGE

It is an honour and pleasure to present this tribute to Dr. G. Michael Bancroft, an outstanding scientist and colleague whom I have known for 35 years and for whom I have the greatest respect and admiration. Born in Saskatoon in 1942, Mike Bancroft became intrigued by spectroscopy and the practical application of spectroscopic measurements to determine the structure of matter as an undergraduate chemistry student at the University of Manitoba. (Little did he know at the time but his love affair with spectroscopy would eventually bring him back full circle to the city of his birth where the opening of the Canadian Light Source in 2004, a project he had pioneered for almost 30 years, was the crowning achievement of an outstanding scientific career.) A summer spent in Shier Berman's analytical laboratory in the Division of Chemistry at NRC, following his fourth year and a master's degree at Manitoba supervised by Dr. Hymie Gesser, further convinced him that his future lay in spectroscopy. The discovery by chance of a new book on Mössbauer Spectroscopy — the effect that had been only recently observed by German Nobel Laureate Rudolph Mössbauer in 1959 and named after him — was the final icing on the cake for Mike Bancroft. He wrote to Dr. Ian Smith, now of NRC and at that time a Ph.D. student at Cambridge, about the possibility of a Ph.D. studentship in Cambridge and learnt that Dr. A.G. Maddock, a radiochemist planned, to construct a Mössbauer spectrometer and would welcome a new student to build it. With a Shell Commonwealth Scholarship in hand, Bancroft began his research and within six months had a working spectrometer functioning, at that time one of relatively few automated systems in the world. The novelty of a new technique capable of identifying the form, oxidation state, and coordination number of metal atoms (e.g., 57Fe, ^{119}Sn) in complexes and minerals attracted considerable attention worldwide and produced some very fruitful scientific collaborations. It also brought home a lesson that Mike has practiced for the rest of his career — collaborative research in different scientific fields, with both basic and applied components. In his own words, "…with any new spectroscopy there are opportunities to develop the spectroscopic method, discovering new phenomena and devising simple theories to explain and predict new and previously known features. A good understanding of spectroscopy can then be applied to an enhanced understanding in both basic and applied areas".

Over a 20 year period (1964–1984), Bancroft became one of the world's leading experts in Mössbauer spectroscopy producing some 80 papers, a major 200-page review, and an authoritative 252-page textbook *Mössbauer Spectroscopy: An Introduction for Inorganic Chemists and Geochemists.* His distinctive contributions to this field were threefold: (*i*) the demonstration for the first time of the use of Mössbauer spectroscopy to quantitatively analyse the chemical states of metals (e.g., Fe^{2+}/Fe^{3+}) in mineral silicates; (*ii*) the application of Mössbauer chemical shifts and quadrupole splittings to provide structural and bonding information in coordination and organometallic compounds; (*iii*) the development of a simple point charge model for rationalising and predicting quadrupole splittings in Mössbauer spectra. That Bancroft's pioneering work in the 1960s–1970s on Mössbauer studies of ^{57}Fe in minerals, including Apollo lunar samples, has stood the test of time is shown by the presence of a Mössbauer spectrometer aboard the US Mars probe in December 2003.

Following his return to Canada at the University of Western Ontario in 1970 and with the publication of his major review and book on Mössbauer spectroscopy and its applications in 1972 and 1973, Bancroft began to turn his attention to another spectroscopy: UV and X-ray photoelectron spectroscopy to probe the valence and core levels in organic, organometallic, and non-metal compounds. This work, using a new PES spectrometer at UWO purchased via an NRC grant for a team from the universities of Western Ontario, Toronto, and Windsor, produced a wealth of data on the electronic structures and ordering of molecular orbitals in main group and transition metal organometallics. A major discovery here — the observation for the first time of a new parameter in PES, the ligand field splitting — encouraged Bancroft to look to synchrotron radiation as a much more intense and higher resolution source for his photoelectron work.

Between 1975 and 1979, Bancroft and his group carried out preliminary experiments at the Tantalus Synchrotron at the University of Wisconsin and began to realise the truly exciting opportunities for a new era of high-resolution photoelectron, Auger, and absorption spectroscopy. In 1978 the first small step towards a Canadian synchrotron was made with grants from the Natural Sciences and Engineering Research Council (NSERC) and NRC for a soft X-ray beamline at Madison; the Canadian Synchrotron Radiation Facility (CSRF) was created for the use of all Canadian researchers. This facility, now more than 25 years old, has played a pivotal role in the evolution of synchrotron science in Canada: more than 500 papers have been produced by researchers and 120 faculty, students, and postdoctoral fellows have been users of the suite of beamlines, which was expanded to three in 1995. There is no doubt that Mike Bancroft, as the Scientific Director of the CSRF, was not only instrumental in its success but also integral to the development and growth of a significant community of Canadian synchrotron scientists. Bancroft sparked the idea of a uniquely Canadian beamline at Tantalus and spearheaded successful applications for infrastructure funding from NSERC, NRC, Materials and Manufacturing Ontario (part of the Ontario Centres of Excellence), and his own university, UWO. His personal belief and commitment together with that of his many students, postdoctoral fellows, and colleagues who spent countless hours on the road to Madison and gathering data on the CSRF, ensured that not only did the facility produce a great scientific return on the Canadian investment but it also kept the fire burning ever brighter for a national synchrotron light source at home on Canadian soil.

From a personal scientific point of view, Bancroft's hope that the very intense focussed radiation in the far UV and soft X-ray region, from a synchrotron source, would open up new vistas in high resolution PES, Auger, and absorption spectroscopies was not disappointed. Following up on earlier observations in 1976–1978 of electric field gradient splittings in gas phase PES spectra, Bancroft established using synchrotron radiation that ligand field splitting is a fundamental principle in core level spectroscopy (Phys. Rev. Lett. **67**, 1531 (1991)). Another key discovery was the resonant Auger (Raman) effect in a molecule (Phys. Rev. Lett. **72**, 621 (1994)). The CSRF beams also enabled some very successful collaborations, most notably perhaps on variable energy PES studies elucidating the ordering of molecular orbitals for a wide range

© 2007 NRC Canada

of transition metal organometallics. A seminal review of these insights was published in Accounts of Chemical Research **30**, 213 (1997).

An analysis of Bancroft's publications over the period 1980–1999 reveals that he was incredibly prolific with 227 papers in peer-reviewed journals in a diverse range of projects and fields. Although many important contributions were made to advances in state of the art electron and X-ray spectroscopies, Bancroft also collaborated with geologists and mineralogists, surface scientists, tribologists, and industrial scientists on a spectacular array of innovative multi-disciplinary investigations. Typical of this were pioneering studies on X-ray absorption spectroscopy to investigate mechanisms of tribochemical film formation (Tribology Letters, **3**, 47 (1997)), on the details of surface reactivity and surface states in pyrite minerals as determined by synchrotron XPS (Surface Science Letters, **411**, 321 (1998)), and on the deposition of metallic gold on sulphide mineral surfaces (Geochim. Cosmochim. Acta. **49**, 979 (1985)).

With the success of CSRF and the founding of the Canadian Institute for Synchrotron Radiation in 1990, a new thrust towards a dedicated Canadian synchrotron facility began. Following a peer review decision to select the University of Saskatchewan as the preferred site over Bancroft's home institution UWO, the lobbying effort was led by a team consisting of Mike Bancroft, Dennis Skopik, Dennis Johnson, and George Ivany (then President of U of S). One amusing story from this "dog and pony show" was that on one visit, Mike Bancroft, unknowingly at first, turned up for the presentation wearing shoes of different colours, undoubtedly prompting the comment that he still had his feet in two separate camps! Finally in 1999, following a competition for infrastructure grants from the newly created Canada Foundation for Innovation, the announcement came that the University of Saskatchewan would receive $56.4CAN million (40% of total funding) from CFI to build a third generation 2.9 GeV Canadian Light Source (CLS), with other partners (federal agencies, governments, industry) providing the remainder of the funding. At long last the pioneering efforts and leadership of Mike Bancroft were to be fulfilled! That is not of course the end of the story. Bancroft continued to contribute to the CLS project, seconded from UWO to be the first Director of CLS (1999–2001) in its formative years, member of the Board (1999–2006), and Acting Director of Research from 2001–2004). He saw the opening of the new building in 2001 and the official opening of the facility in October 2004. The last of the instruments at the CSRF will be transferred from Madison to the CLS in 2007–2008, thus completing a 28 year gestation and birth for the synchrotron community in Canada.

Mike Bancroft is an inveterate spectroscopist who has spent his entire research career developing, exploring, and exploiting spectroscopies covering almost half of the electromagnetic spectrum from γ-rays (1.24 MeV) to the far IR (12.4 meV). His major contributions have been to Mössbauer, photoelectron, absorption, and Auger spectroscopies, using both laboratory and synchrotron sources. One of his strengths has been an ability to bring a deep fundamental understanding of spectroscopic principles, tools, and experiments to bear in resolving challenging problems across a wide variety of scientific domains and disciplines. His contributions have gone far beyond physical chemistry and some of his most notable work has been at interfaces with mineralogists, tribologists, and industry.

Recognition for Bancroft's talents and work has come from many national and international bodies going back to the award of an NSERC studentship in 1963–1964. In 1972 he won two important British awards for young researchers: the Harrison Memorial Prize from the British Chemical Society and the Meldola Medal from the Royal Institute of Chemistry. An E.W.R. Steacie Fellowship from NRC quickly followed on his return to Canada from Cambridge. He was elected a Fellow of the Royal Society of Canada in 1979 at the almost unprecedented age of 37, received the Rutherford Memorial Medal of the RSC in 1980, and a Guggenheim Fellowship from the US Guggenheim Foundation in 1982–1983. Other Canadian recognitions include: the Alcan Lecture Award in Inorganic Chemistry (1990), the CIC and Montreal Medals of the Chemical Institute of Canada (1996 and 2002), the Herzberg Award of the Spectroscopy Society of Canada (1991), and two awards from the University of Western Ontario (Florence Bucke Science Prize 1983 and Hellmuth Research Award 1999). He received the Morley Medal of the American Chemical Society in 1998. Finally he was honoured by the Saskatchewan Centennial Medal (2005) and recognized by Canada's highest civilian honour, the Order of Canada in 2003. Mike has also served as President and Vice President of the Canadian Society for Chemistry.

With more than 400 publications in refereed journals, 150 invited talks, and a stellar record of funding from granting agencies, industry, and government programs, Bancroft's work has been acclaimed by peers around the world. Finally, 36 doctoral students have completed Ph.D.s under his supervision, and he has overseen the training of some 33 postdoctoral fellows and research associates, most of whom have gone on to positions in academia and industry.

Although Mike Bancroft was born in Saskatoon in 1942, the son of an accountant, the family moved to Winnipeg soon afterwards and he received his school and early University education (B.Sc., M.Sc. Manitoba) in that city. Following his Ph.D. at Cambridge and three years as a teaching fellow at Christ's College, he returned to Canada in 1970 to take up an assistant professorship at the University of Western Ontario. He rose rapidly to full professor in 1974. In 1975–1976 he spent two 6 month periods as a visiting investigator–scientist in the Synchrotron Group at Madison, Wisconsin, and at the University of Uppsala, Sweden, which had a major impact on the development of his career. Dr. Bancroft played important roles at Western as Director of the Centre for Chemical Physics (1977–1981), then Founder and Director of Surface Science Western (1981–1984), and as Chairman of the Department of Chemistry (1986–1991 and 1992–1995). He was the Scientific Director for CSRF from 1981–1999 when he took on the challenging task of leading the construction phase of the Canadian Light Source to 2004. Mike retired from UWO in 2005 becoming Professor Emeritus. He still operates an active research laboratory at the university.

Despite the recognition he has received and his stature and credibility in the community, Mike has remained a modest, generous, and sincere individual, who continues to set an example to all of us for his spirit of collaboration and commitment.

Arthur Carty

© 2007 NRC Canada

TRIBUTE / HOMMAGE

C'est un honneur et un grand plaisir pour moi de présenter cet hommage à monsieur G. Michael Bancroft, Ph.D., chercheur et collègue exceptionnel que je connais depuis 35 ans, et pour qui j'ai le plus grand respect et une admiration sans bornes.

Né à Saskatoon en 1942, Mike Bancroft s'est intéressé à la spectroscopie et à l'application pratique des mesures spectroscopiques pour déterminer la structure de la matière lorsqu'il était étudiant de premier cycle en chimie à l'Université du Manitoba. (A cette époque, il ne se doutait guère que son histoire d'amour avec la spectroscopie le ramènerait finalement dans la ville qui l'a vu naître pour l'entrée en service, en 2004, du Centre canadien de rayonnement synchrotron, un projet dont il a joué le rôle de précurseur pendant près de 30 ans et qui est le point culminant d'une carrière scientifique exceptionnelle). Un été passé dans le laboratoire de chimie analytique de Shier Berman à la Division de la chimie du CNRC, après sa quatrième année d'études, et l'obtention d'une maîtrise à l'Université du Manitoba, sous la direction de monsieur Hymie Gesser, Ph.D., ont renforcé sa conviction selon laquelle son avenir résidait dans le domaine de la spectroscopie. Pour Michael Bancroft, le comble a été la découverte fortuite d'un nouveau livre portant sur la spectroscopie Mössbauer (l'effet nommé en l'honneur de Rudolph Mössbauer, lauréat allemand du prix Nobel en 1959, qui ne l'avait observé que récemment). Il a donc écrit à Ian Smith, maintenant au CNRC, mais qui était alors étudiant de troisième cycle à Cambridge, au sujet de la possibilité d'une bourse d'études de troisième cycle à Cambridge. Ainsi, il a appris qu'un radiochimiste, A.G. Maddock, Ph.D., planifiait de construire un spectromètre Mössbauer et qu'il accepterait d'accueillir un nouvel étudiant pour ce faire. Grâce à une bourse du Commonwealth de Shell, Bancroft a commencé ses recherches et, en moins de six mois, il a réussi à produire un spectromètre fonctionnel qui, à l'époque, figurait parmi les quelques rares systèmes automatisés au monde. La nouveauté d'une technique qui permet d'identifier la forme, l'état d'oxydation et le nombre de coordination d'atomes métalliques (p. ex. ^{57}Fe et ^{119}Sn) dans des complexes et des minéraux a attiré une attention internationale considérable et donné des collaborations scientifiques très fructueuses. Cette technique a permis également de tirer une conclusion que Mike a mise en pratique dès son retour au pays et tout au cours de sa carrière : faire de la recherche en collaboration dans différents domaines scientifiques et qui comprend des composantes autant fondamentales qu'appliquées. Pour reprendre dans ses propres mots : « Dans le cas de toute nouvelle spectroscopie, il est possible de développer la méthode spectroscopique par la découverte de nouveaux phénomènes et l'élaboration de théories simples pour expliquer et prévoir à la fois les nouvelles caractéristiques et celles déjà connues. Une bonne compréhension de la spectroscopie permet ensuite de mieux comprendre des domaines de recherche fondamentale et appliquée. »

Sur une période de 20 ans (1964-1984), Bancroft est devenu l'un des chercheurs les plus éminents du monde dans le domaine de la spectroscopie Mössbauer, ayant produit quelque 80 articles, une recension importante de 200 pages et un manuel rigoureux de 252 pages intitulé *Mössbauer Spectroscopy: An Introduction for Inorganic Chemists and Geochemists*. Ce domaine de recherche a bénéficié de trois contributions remarquables de sa part : *i*) la démonstration pour la première fois de l'utilisation de la spectroscopie Mössbauer pour analyser quantitativement les états chimiques de métaux (p. ex. Fe^{2+}/Fe^{3+}) dans des silicates minéraux; *ii*) l'application des déplacements chimiques et des dédoublements quadrupolaires Mössbauer pour fournir de l'information sur la structure et les liaisons des composés organométalliques et de coordination; *iii*) l'élaboration d'un modèle simple de charge ponctuelle pour trouver une explication logique aux dédoublements quadrupolaires et les prédire dans les spectres Mössbauer. Les travaux précurseurs de Bancroft effectués dans les années 1960-1970 portant sur des études de l'effet Mössbauer sur le ^{57}Fe dans les minéraux, y compris les minéraux d'échantillons lunaires de la mission Apollo, ont résisté à l'épreuve du temps puisqu'en 2003, la sonde spatiale américaine à destination de Mars était équipée d'un spectromètre Mössbauer.

Aprs son retour au Canada à l'Université Western Ontario, en 1970, et la publication de son importante recension ainsi que de son livre portant sur la spectroscopie Mössbauer et ses applications, en 1972 et 1973, Bancroft a commencé à porter son attention sur un autre type de spectroscopie : la spectroscopie photoélectronique (SPE) des rayons X et UV pour examiner de façon approfondie les couches d'électrons internes et de valence dans les composés organiques, organométalliques et non métalliques. Ces travaux, effectués au moyen d'un nouveau spectromètre photoélectronique situé à l'UWO et obtenu grâce à une subvention du CNRC accordée à une équipe de chercheurs des universités Western Ontario, de Toronto et de Windsor, ont produit une énorme quantité de données sur les structures électroniques et la mise en ordre des orbitales moléculaires dans des composés organométalliques du groupe principal et des métaux de transition. On assiste alors, pour la première fois, à l'observation d'un nouveau paramètre en SPE : le dédoublement du champ des ligands. Une découverte majeure qui a encouragé Bancroft à considérer le rayonnement synchrotron comme une source beaucoup plus intense et de meilleure résolution pour ses travaux en photoélectronique.

Entre 1975 et 1979, Bancroft et son équipe ont effectué des expériences préliminaires au synchrotron Tantalus de l'Université du Wisconsin, et se sont rendu compte rapidement des possibilités vraiment exceptionnelles pouvant mener vers une nouvelle ère de la spectroscopie photoélectronique, Auger et d'absorption à haute résolution. En 1978, la première étape, modeste, vers un synchrotron canadien a été franchie grâce à des subventions accordées par le Conseil de recherches en sciences naturelles et en génie du Canada (CRSNG) et le CNRC pour l'obtention d'une source de faisceau de rayons X mous à Madison; le Canadian Synchrotron Radiation Facility (CSRF) a été créé pour Ltre utilisé par tous les chercheurs canadiens. Cette installation, qui existe depuis maintenant plus de 25 ans, a joué un rôle essentiel dans l'évolution de la science du rayonnement synchrotron au Canada : des chercheurs ont écrit plus de 500 articles sur ce sujet et 120 professeurs, étudiants et boursiers postdoctoraux ont utilisé cette série de faisceaux, passée au nombre de trois en 1995. Il n'y a aucun doute que Mike Bancroft, à titre de directeur scientifique du CSRF, a non seulement joué un rôle important dans la réussite de cette installation, mais a été également un élément indispensable à la création et à la croissance d'une com-

© 2007 NRC Canada

munauté importante de chercheurs canadiens intéressés par le rayonnement synchrotron. Bancroft a fait surgir l'idée d'un faisceau exclusivement canadien à Tantalus et a ouvert la voie à des applications fructueuses qui ont apporté des fonds d'infrastructure provenant du CRSNG, du CNRC, de Materials and Manufacturing Ontario (un des centres d'excellence de l'Ontario) et de sa propre université, l'UWO. Sa croyance et son engagement personnels, jumelés à ceux de ses nombreux étudiants, boursiers postdoctoraux et collègues qui ont passé d'innombrables heures sur la route de Madison à recueillir des données au CSRF, ont fait en sorte que non seulement cette installation a produit un grand retour scientifique sur l'investissement canadien, mais a également entretenu davantage le feu qui mènerait plus tard à l'obtention d'une source de rayonnement synchrotron nationale au Canada.

D'un point de vue scientifique personnel, l'espoir de Bancroft a aussi été nourri en ce sens que le rayonnement focalisé très intense dans les régions des ultraviolets lointains et des rayons X mous, provenant d'une source synchrotron, a ouvert de nouvelles perspectives en spectroscopie photoélectronique, Auger et d'absorption à haute résolution. Pour faire suite aux observations antérieures effectuées en 1976-1978 sur les dédoublements des gradients de champ électrique dans les spectres photoélectroniques en phase gazeuse, Bancroft a démontré, en utilisant le rayonnement synchrotron, que le dédoublement du champ des ligands est un principe fondamental en spectroscopie des couches internes d'électrons (*Phys. Rev. Lett*. **67**, 1531 (1991)). L'effet Auger (Raman) de résonance dans une molécule a été une autre découverte importante (*Phys. Rev. Lett*. **72**, 621 (1994)). Les faisceaux du CSRF ont également permis des collaborations très fructueuses, notamment pour des études portant sur la SPE à énergie variable, qui ont permis d'élucider la mise en ordre des orbitales moléculaires de nombreux composés organométalliques des métaux de transition. Une synthèse fondamentale de ces observations a été publiée dans *Accounts of Chemical Research* **30**, 213 (1997).

Une analyse des publications de Bancroft couvrant la période de 1980 B 1999 révèle qu'il a été incroyablement prolifique, ayant produit 227 articles publiés dans des revues à comité de lecture, pour une variété de travaux et dans divers domaines. Bien que de nombreuses contributions importantes à l'avancement des domaines de pointe de la spectroscopie électronique et de la spectroscopie des rayons X aient été apportées, Bancroft a également collaboré à un éventail impressionnant de travaux de recherche multidisciplinaires novateurs avec des géologues et des minéralogistes, des chercheurs de la science des surfaces, des tribologistes ainsi que des chercheurs du secteur industriel. Des études originales portant sur la spectroscopie d'absorption des rayons X pour examiner les mécanismes de formation d'un film tribochimique (*Tribology Letters* , **3** , 47 (1997)), sur les détails de la réactivité de surface et des états de surface dans les pyrites tels que déterminés par la SPE des rayons X au moyen d'un rayonnement synchrotron (*Surface Science Letters*, **411**, 321 (1998)) et sur le dépôt d'or métallique sur des surfaces de minéraux de sulfure (*Geochim. Cosmochim. Acta.* **49**, 979 (1985)) sont des exemples typiques de ces collaborations.

Grâce au succès remporté par le CSRF et la fondation de l'Institut canadien du rayonnement synchrotron en 1990, un nouvel élan à l'égard d'une installation réservée à un synchrotron canadien a été donné. A la suite d'une décision issue d'une évaluation par les pairs désignant l'Université de la Saskatchewan comme site de choix de l'installation au lieu de l'établissement d'attache de Bancroft, l'UWO, une campagne de lobbying a été menée par une équipe composée de Mike Bancroft, Dennis Skopik, Dennis Johnson et George Ivany (alors président de l'Université de la Saskatchewan). Une anecdote amusante est ressortie de cette « tournée de présentation »… Lors d'une des visites, Mike Bancroft, sans le savoir au départ, est arrivé en portant deux chaussures de couleur différente, ce qui a immanquablement soulevé le commentaire qu'il avait encore les pieds dans deux camps distincts! Finalement en 1999, à la suite d'un concours pour l'obtention de subventions d'infrastructures de la Fondation canadienne pour l'innovation (FCI), créée peu avant, il en est ressorti que l'Université de la Saskatchewan recevrait 56,4 millions de dollars canadiens (40 % du financement total) de la part de la FCI pour la construction d'un centre canadien de rayonnement synchrotron comportant un synchrotron de troisième génération de 2,9 GeV, le reste du financement étant assuré par d'autres partenaires (organismes fédéraux, gouvernements, secteur industriel). Enfin, les efforts de pionnier et le rôle de chef de file de Mike Bancroft allaient porter des fruits! Bien sûr, l'histoire est loin d'Ltre terminée. Bancroft a continué d'apporter son concours à la réalisation du CCRS. Il a été détaché de l'UWO pour Ltre le premier directeur du CCRS pendant ses années de formation (1991-2001), membre du conseil d'administration (1999-2006) et directeur intérimaire de la recherche (2001-2004). Il a assisté à l'ouverture du nouvel immeuble, en 2001, et à l'inauguration officielle de l'installation, en octobre 2004. Le dernier des instruments encore présent au CSRF de Madison sera transféré au CCRS en 2007-2008, ce qui mettra fin à une gestation qui aura duré 28 ans pour la communauté canadienne du rayonnement synchrotron.

Mike Bancroft est un spécialiste invétéré de la spectroscopie qui a passé sa carrière scientifique entière à mettre au point, à explorer et à exploiter des types de spectroscopie couvrant près de la moitié du spectre électromagnétique, des rayons γ (1,24 MeV) aux infrarouges lointains (12,4 meV). Ses principales contributions ont été sur le plan des spectroscopies Mössbauer, photoélectronique, d'absorption et Auger, au moyen de sources en laboratoire et de rayonnement synchrotron. L'une de ses forces est sa capacité d'amener une compréhension fondamentale profonde des principes, des outils et des expériences spectroscopiques, et de les appliquer à la résolution de problèmes difficiles dans une grande variété de domaines et de disciplines scientifiques. Ses contributions ont largement dépassé la chimie physique, et certains de ses travaux les plus remarquables l'ont été grâce à des échanges avec des minéralogistes, des tribologistes et le secteur industriel.

La reconnaissance des talents et du travail de Bancroft provient de nombreux organismes nationaux et internationaux, et remonte à l'obtention d'une bourse d'études du CRSNG, en 1963-1964. En 1972, il a gagné deux prix britanniques importants pour jeunes chercheurs : le prix Harrison Memorial de la British Chemical Society et la médaille Meldola du Royal Institute of Chemistry. Une bourse E.W.R. Steacie du CNRC a suivi rapidement après son retour au Canada de Cambridge. Il a été élu membre de la Société royale du Canada, en 1979, à l'âge presque sans précédent de 37 ans; il a aussi reçu la médaille commémorative Rutherford de la SRC, en 1980, et une bourse de recherche Guggenheim de la Guggenheim Foundation des États-Unis, en 1982-1983. Il compte également d'autres distinctions canadiennes : le prix Alcan pour un exposé en chimie inorganique (1990), les médailles ICC et Montréal de l'Institut de chimie du Canada (1996 et 2002), le prix Herzberg de la Société de spectroscopie du Canada (1991) et deux prix de l'Université Western Ontario (le Florence Bucke,

© 2007 NRC Canada

en 1983, et le Hellmuth Research, en 1999). Il a reçu également la médaille Morley de l'American Chemical Society, en 1998. Finalement, on lui a rendu hommage en lui décernant la médaille du centenaire de la Saskatchewan, en 2005, et la plus haute distinction civile au pays, l'Ordre du Canada, en 2003. Mike a également exercé les fonctions de président et de vice-président de la Société canadienne de chimie.

Ayant à son actif plus de 400 publications dans des revues à comité de lecture, 150 présentations invitées et une fiche longue et édifiante de financement provenant d'organismes de subvention, du secteur privé et des programmes gouvernementaux, Bancroft et ses travaux ont été accueillis de façon élogieuse par ses pairs de partout dans le monde. Enfin, 36 étudiants de troisième cycle ont effectué leur doctorat sous sa direction, et il a veillé à la formation de quelque 33 boursiers postdoctoraux et assistants de recherche, la plupart d'entre eux occupant maintenant des postes dans le milieu universitaire ou le secteur privé.

Bien que Mike Bancroft, fils de comptable, soit né à Saskatoon en 1942, sa famille a déménagé à Winnipeg peu de temps après, où il a effectué ses études jusqu'à l'université (B.Sc. et M.Sc. à l'Université du Manitoba). Après avoir fait son doctorat à Cambridge et enseigné trois ans au Christ's College, il est revenu au Canada en 1970 et a accepté un poste de professeur adjoint à l'Université Western Ontario. Il est devenu rapidement professeur titulaire, en 1974. En 1975-1976, il a passé deux périodes de six mois à titre de chercheur invité : l'une au sein du groupe Synchrotron à Madison (Wisconsin), et l'autre à l'Université Uppsala, en Suède. Ces deux invitations ont eu des répercussions importantes sur l'avancement de sa carrière. M. Bancroft, a joué des rôles importants au sein de l'UWO à titre de directeur du Centre for Chemical Physics (1977-1981), ensuite comme fondateur et directeur de Surface Science Western (1981-1984) et directeur du Département de chimie (1986-1991 et 1992-1995). Il a occupé le poste de directeur scientifique du CSRF, de 1981 à 1999, et a accepté le grand défi de piloter la phase de construction du Centre canadien de rayonnement synchrotron jusqu'à son inauguration, en 2004. Mike a pris sa retraite de l'UWO en 2005, devenant ainsi professeur émérite. Par contre, il assure encore le fonctionnement d'un laboratoire de recherche à l'université.

Malgré la reconnaissance qu'il a reçue ainsi que sa stature et sa crédibilité dans la communauté, Mike demeure un homme modeste, généreux et sincère, qui continue à nous donner l'exemple en matière d'esprit de collaboration et d'engagement.

Arthur Carty

© 2007 NRC Canada

Nucleophilic substitution reactions of *N*-alkoxyimidoyl fluorides by carbon nucleophiles

Debra D. Dolliver, David B. Delatte, Derek B. Linder, James E. Johnson, Diana C. Canesco, and Jeffrey E. Rowe

Abstract: Nucleophilic substitutions of *N*-alkoxybenzoimidoyl fluorides [*p*-ClArC(F)=NOR; R = CH_3, *i*-Pr] by enolate-type ions have been performed to produce compounds that can exist in two tautomeric forms: the imine form{*p*-ClArC(Y)=NOR [Y = $CH(CN)_2$, $CH(CN)(CO_2Et)$, $CH(CO_2Et)_2$]}or the enamine form {*p*-ClArC(NHOR)=C(R_1)(R_2) [R_1, R_2 = CN, CO_2Et]}. These compounds display varying ratios of imine–enamine tautomerizm in chloroform: the diester compound exists almost solely in the imine form, the dicyano compound exists solely in the enamine form, and the cyano-ester compound exists in both tautomeric forms. Comparison of the imine–enamine equilibrium in chloroform of the cyano-ester compound to an analogue where the *p*-ClAr group has been replaced by a methyl group reveals that the aromatic ring has a significant effect on the imine–enamine distribution. The former exists in both the imine and enamine form, while the latter exists solely in the enamine form. Complete NMR characterization data for the enamine form of $CH_3C(NHOCH_3)=C(CN)(CO_2Et)$ is also reported. The acidity of *p*-ClArC(NHOR)=C$(CN)_2$ is demonstrated by a high degree of dissociation of the enamine proton in DMSO. Substitution reactions of *p*-ClArC(F)=NO*i*-Pr by Grignard reagents (PhMgBr, CH_3MgBr, and PhCCMgBr) have also been performed to produce single geometric isomers of *p*-ClArC(Ph)=NO*i*-Pr, *p*-ClArC(CCPh)=NO*i*-Pr, and *p*-ClArC(CH_3)=NO*i*-Pr. A modified synthesis of *N*-alkoxyimidoyl fluorides, which prevents a competing reaction of the product with the solvent, is reported.

Key words: *N*-alkoxyimidoyl fluoride, enolate ion substitution, Grignard substitution, imine–enamine tautomerizm, carbon acid.

Résumé : On a effectué des réactions de substitutions nucléophiles de fluorures de *N*-alkoxybenzoimidoyle [*p*-ClArC(F)=NOR; R = CH_3, *i*-Pr] par des ions de type énolate pour obtenir des composés qui existent sous deux formes tautomères: la forme imine {*p*-ClArC(Y)=NOR [Y = $CH(CN)_2$, $CH(CN)(CO_2Et)$, $CH(CO_2Et)_2$]} ou la forme énamine {*p*-ClArC(NHOR)=C(R_1)(R_2) [R_1 = R_2 = CN, CO_2Et]. Dans le chloroforme, ces composés présentent des rapports divers de tautomérie imine–énamine; le composé dicyano existe uniquement sous la forme énamine alors que le composé cyano-ester existe sous les deux formes tautomères. Une comparaison de l'équilibre imine–énamine dans le chloroforme du composé cyano-ester avec celui observé avec un analogue dans lequel le groupe *p*-ClAr a été remplacé par un groupe méthyle révèle que le noyau aromatique joue un rôle important sur la distribution imine–énamine. Le premier existe dans les deux formes imine et énamine alors que le deuxième n'existe que sous la forme énamine. On rapporte aussi les données RMN pour une caractérisation complète de la forme $CH_3C(NHOCH_3)=C(CN)(CO_2Et)$. L'acidité du composé *p*-ClArC(NHOR)=C$(CN)_2$ est démontrée par le degré élevé de dissociation du proton énamine dans le DMSO. On a aussi réalisé des réactions de substitutions en solution du *p*-ClArC(F)=NO*i*Pr par des réactifs de Grignard (PhMgBr, CH_3MgBr et PhCCMgBr) qui ont conduit aux isomères géométriques uniques *p*-ClArC(Ph)=NO*i*Pr, *p*-ClArC(CCPh)=NO*i*Pr et *p*-ClArC(CH_3)=NO*i*Pr. On a aussi mis au point une synthèse modifiée des fluorures de *N*-alkoxyimidoyles qui élimine une réaction compétitive avec le solvant.

Mots-clés : fluorure de *N*-alkoxyimidoyle, substitution par un ion énolate, substitution de Grignard, tautomérie imine–énamine, carbone acide.

[Traduit par la Rédaction]

Received 24 April 2007. Accepted 06 July 2007. Published on the NRC Research Press Web site at canjchem.nrc.ca on 7 September 2007.

D.D. Dolliver,[1] D.B. Delatte, and D.B. Linder. Department of Chemistry and Physics, Southeastern Louisiana University, SLU 10878, Hammond, LA 70402, USA.
J.E. Johnson and D.C. Canseco. Department of Chemistry and Physics, Texas Woman's University, Denton, TX 76204–5859, USA.
J.E. Rowe. School of Chemistry, La Trobe University, Victoria 3086, Australia.

[1]Corresponding author (e-mail: ddolliver@selu.edu).

 doi:10.1139/V07-097 © 2007 NRC Canada

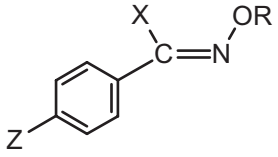
Introduction

Nucleophilic addition–elimination reactions at the C=O bond of acid halides are commonplace in synthetic schemes. This type of reaction has also been studied in imidoyl halides (1), hydrazonyl halides (2), and *N*-alkoxyimidoyl halides (3). These latter reactions, however, have been limited because of the diminished electrophilicity of the azomethine carbon in these compounds and the lability of the N–O bond. In addition, there are synthetic challenges posed because of the existence of possible *E*–*Z* isomeric mixtures around the C=N bond (4). To enhance the electrophilicity of the C=N bond of *N*-alkoxyimine compounds, Lewis acids have sometimes been included in the reaction medium (5). *N*-Alkoxyimidoyl chloride (**2**) and bromide (**3**) compounds (Fig. 1) are known to undergo nucleophilic substitution reactions with nucleophiles, such as amines, amide ions, and alkoxide ions, but these types of substitution reactions are relatively sluggish and are viewed as having limited synthetic utility (3). It has been found, however, that *N*-alkoxyimidoyl fluorides (**1**) are much more electrophilic than their bromo- or chloro-analogues (**2** or **3**) and will undergo nucleophilic attack by methoxide ion at an accelerated rate (3*a*). The tetrahedral intermediate formed from the nucleophilic attack of methoxide then rapidly loses the fluoride ion to reform the C=N bond faster than it undergoes rotation to another conformer. Therefore, the stereochemistry of the product from this reaction is retained exclusively when starting from the *Z* isomer and is predominately retained when starting from the *E*-isomer. This is due to the fact that the tetrahedral intermediate first formed by methoxide attack in the case of the *Z* isomer (**A** in Scheme 1) already has a pair of electrons anti-periplanar to the fluoride leaving group. In the *E*-isomer case, the first-formed intermediate (**B**) must undergo rotation to align lone pair electrons in an anti-periplanar configuration. The rotational barrier 1 is lower than rotational barrier 2, and conformer **B** therefore predominately rotates over the lower rotational energy barrier to a conformation that leads to retained stereochemistry (3*a*). Owing to the enhanced electrophilicity of (*Z*)-*N*-alkoxyimidoyl fluoride compounds, their ability to undergo a methoxide substitution at a much faster rate, and the retention of stereochemistry demonstrated in the product, it was felt that they might be good candidates for synthetically useful routes to specific geometric isomers of oxime ethers.

This paper discusses the nucleophilic substitution of *N*-alkoxyimidoyl fluoride compounds (**1a** and **1b**) by enolate-type anions and Grignard reagents.

The *N*-alkoxyimine or oxime ether moiety has become important in pharmaceutical compounds and as a starting material for the synthesis of asymmetric amines, which are also widely incorporated in pharmaceuticals and agrochemicals (4–6). It has been found that the geometric stereochemistry around the C=N bond (*E* vs. *Z*) has a direct effect on the stereochemical purity of an asymmetric amine derived from an oxime ether (5, 7). Many methods for the synthesis of oximes and oxime ethers produce either a mixture of geometric isomers or allow only the preparation predominantly of the thermodynamically more stable isomer (5, 8). Oftentimes, subsequent separations must be performed to prepare a single geometric isomer (5, 6*b*). This paper discusses a technique by which a specific geometric stereoisomer of an oxime ether may be prepared even when there is little difference in the thermodynamic stability of the two geometric isomers. This can be accomplished by nucleophilic substitution of an *N*-alkoxyimidoyl fluoride by a Grignard reagent. In addition, the nucleophilic substitution reaction of *N*-alkoxyimidoyl fluorides by enolate-type anions will be discussed. The compounds produced by this technique are interesting in that they display varying degrees of imine–enamine tautomerizm.

Fig. 1. (*Z*)-*N*-alkoxyimines.



1a: X = F, Z = Cl, R = CH_3
1b: X = F, Z = Cl, R = *i*-Pr
1c: X = F, Z = H, R = CH_3
2: X = Cl
3: X = Br
4: X = OR

Results and discussion

Enolate-type ion substitution of *N*-alkoxyimidoyl fluorides

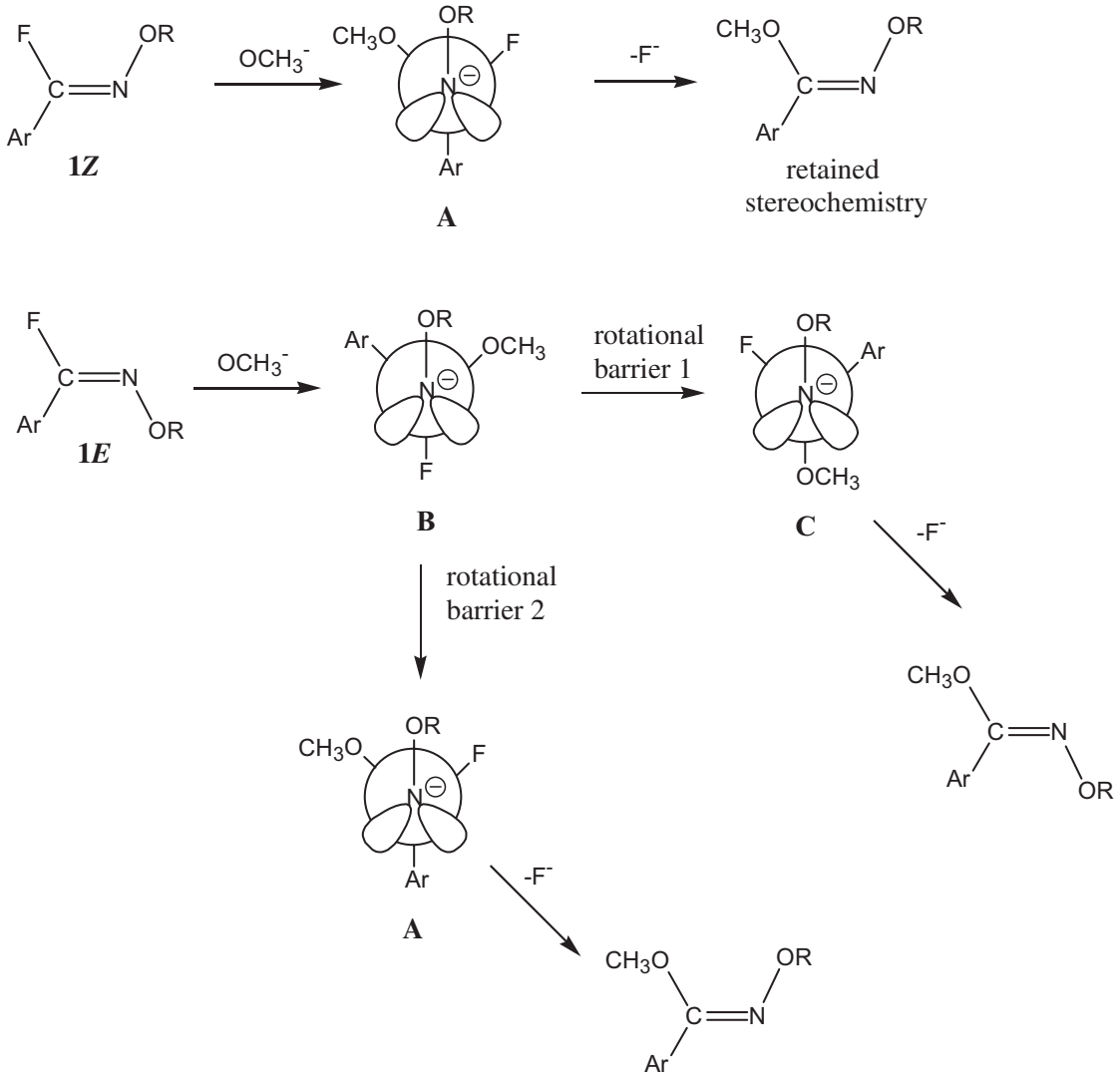
The substitution of the fluorine in (*Z*)-*N*-alkoxy-4-chlorobenzenecarboximidoyl fluoride (**1a** and **1b**) with different enolate-type ions to produce **5** was achieved in moderate yields (Scheme 2). The target molecules of this study are interesting in that they contain three electron-withdrawing groups attached to a single carbon (R_1, R_2, and the oxime ether moiety). Related molecules have been previously synthesized by methods similar to those discussed in this paper with comparable yields. Methanetricarboxylic esters have been made by acylating malonates with various acid chlorides with yields that vary from 30% to 90% (9). In addition, trifluoromethyl imidoyl chlorides have been acylated with lithium enolates (1*a*, 1*b*).

The methine carbon attached to the three electronegative groups in these molecules is felt to have a fairly acidic proton and would exhibit a pKa range similar to that of related compounds. By making comparisons to similar compounds, one may begin to predict pKa ranges for **5a**–**5d** (Table 1). The acidities of **5c** and **5d** were qualitatively demonstrated by low integration for this proton's signal when these compounds were dissolved in d_6-DMSO. This indicates that these compounds are partially ionized in the case of **5d** and extensively ionized in the case of **5c** and would suggest that **5c** and **5d** have pKa's around –1.5 (pKa of protonated DMSO) (12).

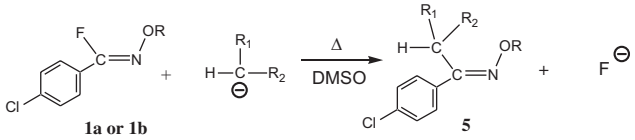
In similar compounds, which contain a carbon attached to three electron withdrawing groups, keto–enol and imine–enamine tautomerizm is seen (1*a*, 1*b*, 13). One would also expect the compounds described in this paper to display

© 2007 NRC Canada

Scheme 1. Tetrahedral intermediates formed by methoxide attack on *N*-alkoxyimidoyl fluorides.



Scheme 2. Enolate-type ion substitution on **1a**.



Compound	R_1	R_2	R	% Yield
5a	CO_2Et	CO_2Et	CH_3	41%
5b	CO_2Et	CN	CH_3	56%
5c	CN	CN	CH_3	46%
5d	CN	CN	*i*-Pr	62%

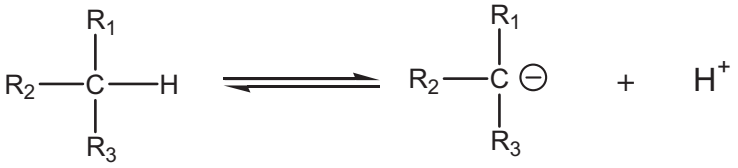
some degree of tautomerizm. Figure 2 displays the theoretically possible tautomeric forms for **5a**, **5b** and **5c**, and **5d**. In addition, the imine tautomers of **5a**–**5d** could theoretically exist in either the *E* or *Z* isomeric form around the C=N bond.

To determine the tautomeric form(s) of each compound, NMR experiments were performed. ^{1}H NMR and ^{13}C NMR of compound **5a** in $CDCl_3$ showed primarily one species in solution. No appreciable signal in the region expected for an enamine (N–H) proton was seen. There was an indication of a methine proton at δ 5.17, which integrated for one proton. In addition, a DEPT experiment in $CDCl_3$ indicated the presence of a C–H bond for the signal at δ 51.73. From these experiments, it appears that compound **5a** exists in the imine tautomeric form in chloroform solution.

^{1}H NMR of compounds **5c** and **5d** also show these molecules to exist in predominantly one tautomeric form in chloroform solution; however, they appear to be in the enamine form rather than the imine form. There is no discernable resonance in the region expected for the methine proton of the imine tautomer. Compound **5c** was so sparingly soluble in $CDCl_3$ that ^{13}C NMR could not be effectively run. Additional ^{1}H NMR and ^{13}C NMR studies on these compounds were therefore run in d_6-DMSO. ^{1}H NMR of compound **5c** in d_6-DMSO revealed no appreciable signal for this acidic proton (either in the enamine or imine tautomeric form). ^{1}H NMR of compound **5d** in d_6-DMSO revealed a signal for the N–H proton of the enamine form (δ 12.09), but it only integrated for 0.7 protons. The absence of this proton signal for

© 2007 NRC Canada

Table 1. Comparison of the predited pKa values for **5a**, **5b**, **5c**, and **5d** to known pKa values for related compounds.



Entry	Compd.	R_1	R_2	R_3	pKa	ref
1		CN	H	H	~ 25	10
2		CN	CN	H	11.2	10
3		CO_2R	CO_2R	CO_2R	~7.8	11
4	**5a**	CO_2Et	CO_2Et	C(*p*-ClAr)=$NOCH_3$	~7.8 *predicted*	this work
5	**5b**	CO_2Et	CN	C(*p*-ClAr)=$NOCH_3$	< 7.8 and > pKa for **5c** *predicted*	this work
6	**5c & 5d**	CN	CN	C(*p*-ClAr)=NOR	< pKa for **5b** and >-2.8 *predicted*	this work
7		CN	CN	CO_2CH_3	-2.8	10
8		CN	CN	CN	-5, -5.13	10

5c and the low integration value for this proton in **5d** could be due to ionization to some degree of this fairly acidic proton. Protonated DMSO has a pKa value of –1.5 (12). It is estimated by comparison with similar compounds that compound **5c** would have a pKa approaching that of methyl-2,2-dicyanoacetate (Table 1, entry 7), which is –2.8. If this is the case, this low or negligible integration value for the N–H proton may actually represent a partial loss of this proton to the solvent. Since **5d** was more soluble in chloroform, it was possible to run the ^{13}C NMR on this compound. The ^{13}C NMR of **5d** showed two signals for the cyano carbons. This observation is consistent with the compound being in the enamine tautomer rather than the imine form. If **5d** existed in the imine form, the two cyano carbons signals would have to be explained by the presence of *Z* and *E* isomers. This explanation is not plausible, since the ^{13}C NMR spectrum of **5d** shows only two signals for the isopropyl carbons.

^1H NMR of compound **5b** in $CDCl_3$ reveals a mixture of the two tautomeric forms. ^{13}C NMR of **5b** in $CDCl_3$ reveals 21 distinct signals, while there are only 11 unique carbons in the molecule. Every non-aromatic carbon appears as two signals, and all of the aromatic carbons are also doubled up except for one quaternary carbon that could not be located. This too suggests that two distinct tautomeric species are present in solution. All the NMR studies suggest that molecule **5b** exists in two predominant tautomeric forms in chloroform solution, and one is the imine form. While the enamine N–H proton resonance for **5c** in chloroform is at δ 8.15, and the proton of interest in compound **5b** has a resonance of δ 11.69, it is not reasonable to rule out the enamine tautomeric form for **5b** because of the rather large difference in the chemical shift. It should be recognized that there are enhanced intramolecular H-bonding capabilities through a six-membered ring system in the enamine tautomer of **5b** compared with that of the enamine tautomer of **5c**, which could account for large differences in the chemical shift of an N–H proton in these species.

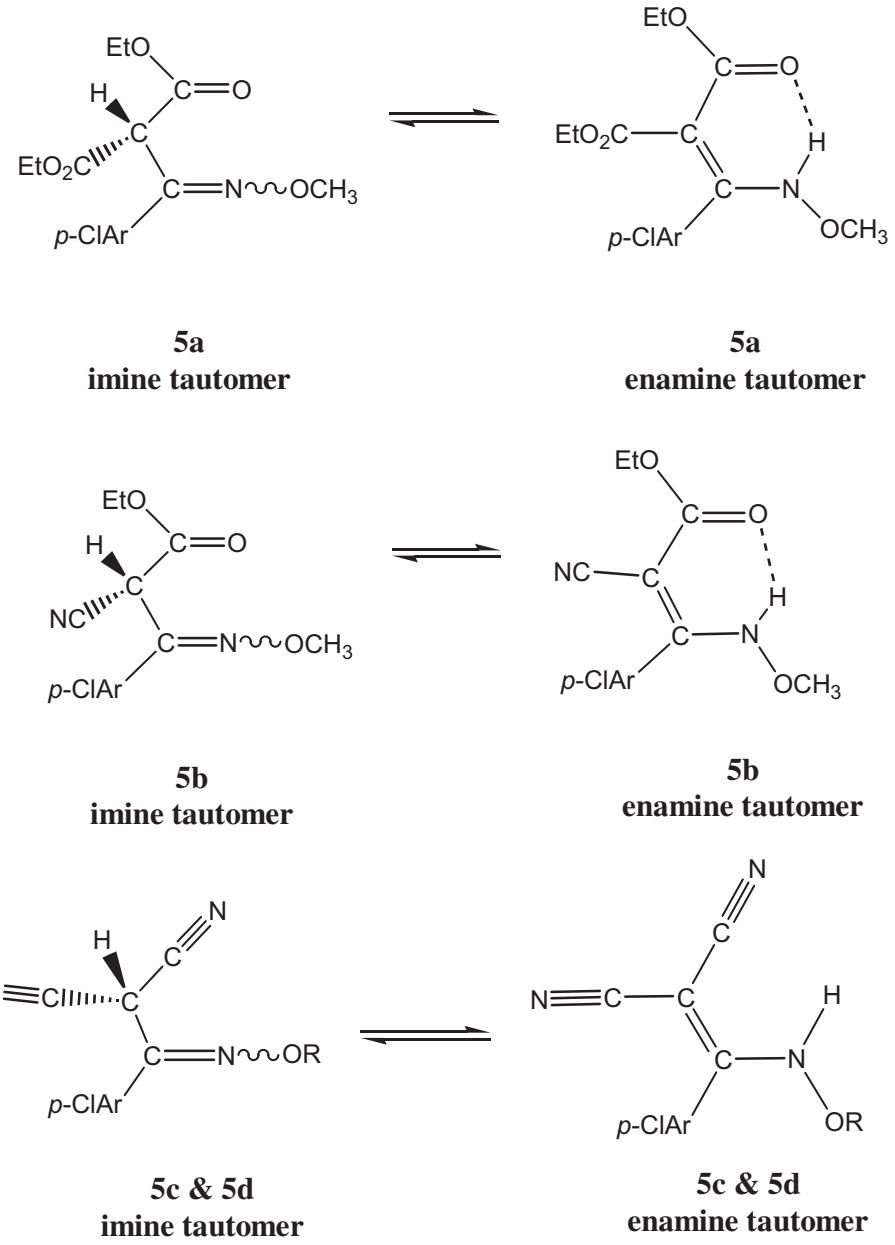
To help solve this problem, X-ray crystallography was performed on a single crystal of **5b**. This showed that **5b** existed in the enamine form in the solid state. This crystal structure shows the intramolecular H-bonding seen in other similar enamine compounds capable of forming a six-membered cyclic N–H···O=C interaction (14).

Interestingly, a similar compound (**6**) has been previously made by reacting ethyl-α-cyano-β-methoxycrotonate with methoxylamine (15) (Scheme 3). Only the chemical shift of the N–H proton of **6** was reported (11.64 ppm in $CDCl_3$) in this work. As compound **6** was reported to only exist in the enamine tautomer in $CDCl_3$ solution, and as the initial report on the synthesis of this compound only supplied limited NMR data, **6** was synthesized in our lab, and its ^1H NMR and ^{13}C NMR data were recorded. Both the ^1H NMR and ^{13}C NMR spectra of **6** showed no evidence of the imine tautomer in solution. Therefore, it appears that the aromatic ring in **5b** has a significant effect on the imine–enamine equilibrium. While both tautomers of **5b** have resonance with the aromatic ring and are thereby stabilized by this resonance effect, the relative stabilizing effect must be more significant in the imine tautomer.

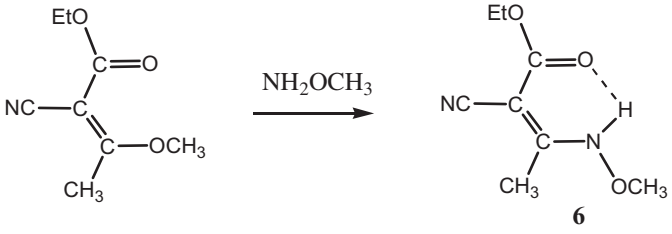
Comparisons with ^1H NMR resonances of other known enamine N–H protons were also made. It appears that the N–H chemical shift for compounds capable of a six-membered cyclic intramolecular H-bond can be found from δ 9.18–15.90 in $CDCl_3$ (13*a*, 13*f*) and δ 9.3–11.99 in d_6-DMSO (13*c*). All of the compounds used for comparison display intramolecular H-bonding through a six-membered cyclic structure. The N–H chemical shift for **5b**, which can form the six-member cyclic intramolecularly H-bonded

© 2007 NRC Canada

Fig. 2. Possible tautomeric forms of **5a**, **5b**, **5c**, and **5d**.



Scheme 3. Synthesis of a similar enamine compound (15).



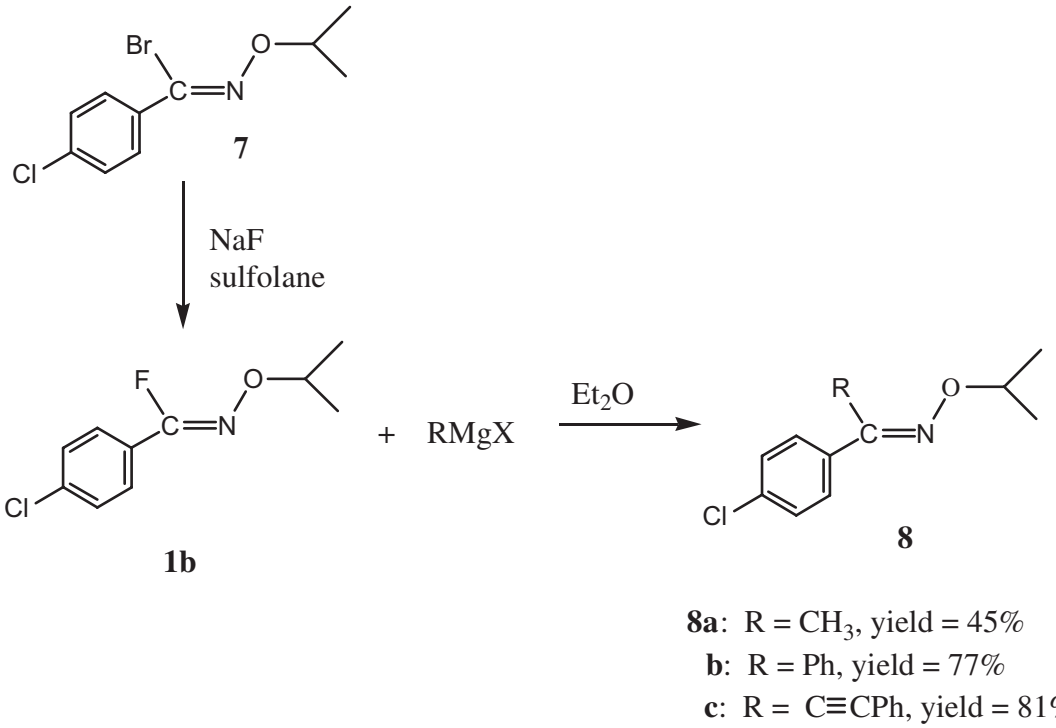
structure is δ 11.69 in $CDCl_3$. This value falls in the middle of those found for the comparison structures. For **5c** and **5d**, the N–H chemical shifts were found to be δ 8.15 and 8.56, respectively, in $CDCl_3$ and δ 12.09 for **5d** in d_6-DMSO. These values fall outside the ranges seen for the structures capable of the intramolecular hydrogen bonding through a six-membered ring, but are still suggestive of a highly deshielded proton, which would be expected for a proton in the enamine form.

Grignard reagent substitution of (*Z*)-*N*-isopropoxy-4-chlorobenzenecarboximidoyl fluoride

Nucleophilic substitution of hydroximates [RC(OR')=NOR', **4**] by Grignard reagents have previously been reported (16). This same type of reaction was initially attempted with **1a**; however, it was found that a competing nucleophilic attack of the Grignard reagent on the *O*-methyl group appeared to account for about 50% of the reaction process. Therefore, the alkyl group attached to oxygen was changed to an isopropyl group to slow down the S_N2 attack at this site. In previous work (17), hydroximoyl fluorides were prepared by heating a hydroximoyl bromide with potassium fluoride in

© 2007 NRC Canada

Scheme 4. Route to nucleophilic substitution of **1b** by a Grignard reagent.



8a: R = CH_3, yield = 45%
b: R = Ph, yield = 77%
c: R = C≡CPh, yield = 81%

DMSO. Under these reaction conditions a methyl *O*-methylbenzothiohydroximate was also formed by reaction of the hydroximoyl fluoride with DMSO. In the present work, (*Z*)-*N*-isopropoxybenzenecarboximidoyl bromide (**7**) was reacted with sodium fluoride in sulfolane to make (*Z*)-*N*-isopropoxybenzenecarboximidoyl fluoride (**1b**). This new synthetic procedure prevents subsequent reaction of the hydroximoyl fluoride with the solvent. Grignard reagents were then reacted with **1b** to make **8a**–**8c** with the yields indicated in Scheme 4.

By NMR and GC–MS, these reactions yield only one geometric stereoisomer of the product (**8a**–**8c**). Substitution of (*Z*)-*N*-methoxybenzenecarboximidoyl fluoride (**1a** and **1c**) by methoxide is known to also yield only one isomer: the product isomer with retained stereochemistry around the C=N bond. This reaction is believed to go through an addition–elimination step in which the nucleophilic attack by methoxide is rate-limiting. The stereochemistry is maintained in this process, despite the formation of a single bond between carbon and nitrogen in the intermediate. This has been found to be due to high barriers to rotation around the C–N bond of the intermediate compared with the barrier for elimination of the fluoride ion from the intermediate (3*a*). With this in mind, it is likely that the isomer produced by nucleophilic substitution of the fluoride of **1b** by a Grignard reagent is also the one with retained stereochemistry.

To demonstrate the difficulty in preparing a single geometric isomer of an oxime ether where the substituents on carbon are similar, the *O*-methyloxime of 4-chlorobenzophenone and 4-nitrobenzophenone were prepared by a commonly used method (5*c*, 18). The reaction of 4-chlorobenzophenone with methoxylamine hydrochloride in pyridine yielded both the *E* and *Z* isomers, which were only discernable by ^{13}C NMR spectra with the two signals for the OCH_3 carbon of each isomer at 61.89 and 61.86 ppm. Because of the poor resolution of these two isomers by 300 MHz NMR, it was difficult to determine the absolute percentages of each isomer. Additionally, these isomers were inseparable by TLC on silica or by GC–MS and therefore would present a considerable challenge for isolation of a single geometric isomer. The reaction to produce the *O*-methyloxime of 4-nitrobenzophenone by the same method also yielded two geometric isomers. These isomers were almost resolvable by 300 MHz ^1H NMR with OCH_3 chemical shifts of 4.04 and 4.00 ppm in a 62%:38% ratio by integration. These isomers were also almost resolvable by GC–MS and yielded approximately the same ratio composition with the first eluted isomer comprising 61%–62% of the mixture. Again, these two isomers did not separate well on TLC and would prove difficult to isolate from each other, thereby demonstrating the potential utility of the substitution of an *N*-methoxyimidoyl fluoride by a Grignard reagent.

Conclusions

N-alkoxyimidoyl fluorides have undergone nucleophilic substitution reactions with enolate-type anions and with Grignard reagents. The products of the enolate-type anion substitutions are compounds that contain a single methine carbon that bears three electron withdrawing groups. The proton on this carbon is therefore believed to be fairly acidic, and these compounds display varying degrees of imine–enamine tautomerizm and ionization in chloroform and DMSO. The products derived from the nucleophilic substitution of *N*-alkoxyimidoyl fluorides by Grignard reagents result in a single geometric configuration about the C=N bond. Comparison studies using common methods to synthesize similar oxime ethers demonstrate that the other methods

© 2007 NRC Canada

would result in mixtures of both geometric isomers, which would prove difficult to separate.

Experimental section

General procedure

All chemicals used in this research were reagent-grade except as noted. The ^{1}H NMR and ^{13}C NMR spectra were performed on either a Varian Mercury 300 MHz spectrometer or a Bruker AC 300 MHz NMR spectrometer using either $CDCl_3$ or d_6-DMSO. Melting points were determined on a Thomas–Hoover capillary melting-point apparatus and are uncorrected. IR spectra were either determined from Nujol mulls between sodium chloride plates for solids or neat on sodium chloride plates for liquids on a Nicolet Magna IR 560 spectrometer or a PerkinElmer 16 PC FTIR over the frequency range of 4000–600 cm^{-1}. Elemental analyses of the new compounds were performed at Midwest Microlab, Indianapolis, Inc. Exact masses were obtained by the Central Science Laboratory at the University of Tasmania.

Preparation of diethyl 2-[2-aza-1-(4-chlorophenyl)-2-methoxyvinyl]propane-1,3-dioate (5a)

Lithium diisopropylamide (2.0 mol/L in heptane, ethylbenzene, and tetrahydrofuran) (6.3 mL, 0.013 mol) was added dropwise with stirring to diethylmalonate (2.67 g, 0.017 mol) under nitrogen purge. (*Z*)-*O*-Methyl-4-chlorobenzohydroximoyl fluoride (**1a**) (1.50 g, 0.0080 mol) in dimethyl sulfoxide (10 mL) was added dropwise to the flask. The reaction mixture was heated under nitrogen at 115 °C for 27 h. The reaction mixture was cooled to room temperature, acidified with concentrated HCl, and placed in a continuous liquid–liquid extractor with chloroform for 50 h. The chloroform was then removed by rotary evaporation to yield a dark brown liquid. Purification was performed on silica gel, 200–300 mesh, with an eluent progressively changing from 1:10 $CHCl_3$:hexane to 7:3 $CHCl_3$:hexane. This yielded a very light yellow viscous oil (1.07 g, 41%). IR (neat); 2986, 2933, 1754, 1739, 1600, 1489, 1370, 1152 cm^{-1}. ^{1}H NMR (300 MHz, $CDCl_3$) δ: 7.55 (d, 2H, *J* = 9.0 Hz, ArH), 7.33 (d, 2H, *J* = 9.0 Hz, ArH), 5.17 (s, 1H, CH), 4.16 (q, 4H, *J* = 7.2 Hz, OCH_2), 4.01 (s, 3H, OCH_3), 1.15 (t, 6H, *J* = 7.2 Hz, OCH_2CH_3). ^{13}C NMR (75.5 MHz, $CDCl_3$) δ: 165.96 (C=O), 149.32 (C=N), 135.16 (Ar C), 132.51 (Ar C), 129.53 (Ar CH), 128.32 (Ar CH), 62.49 (OCH_3), 61.96 (OCH_2), 51.73 (CH), 13.82 (CH_2CH3). Anal. calcd. For $C_{15}H_{18}NO_5Cl$: C, 54.97; H, 5.54; N, 4.27; Cl, 10.82. Found: C, 54.74; H, 5.59; N, 4.19; Cl, 10.73.

Preparation of ethyl 4-aza-3-(4-chlorophenyl)-2-cyano-4-methoxybut-3-enoate (5b)[2]

Lithium diisopropylamide (2.0 mol/L in heptane, ethylbenzene, and tetrahydrofuran) (17.5 mL, 0.035 mol) was added dropwise with stirring to ethylcyanoacetate (8.02 g, 0.071 mol) under nitrogen purge. (*Z*)-*O*-Methyl-4-chlorobenzohydroximoyl fluoride (**1a**) (1.68 g, 0.0090 mol) in dimethyl sulfoxide (5 mL) and hexane (3 mL) was added dropwise to the flask. The reaction mixture was heated under nitrogen at 80 °C for 3 h. The reaction mixture was cooled to room temperature, acidified with concentrated HCl, and placed in a continuous liquid–liquid extractor with chloroform for 24 h. The chloroform was then removed by rotary evaporation to yield a dark brown liquid. Purification was performed on silica gel, 200–300 mesh, with an eluent progressively changing from 3:7 $CHCl_3$:hexane to 1:1 $CHCl_3$:hexane. This yielded very light yellow crystals (1.82 g). These crystals were recrystallized in 2:1 hexane: chloroform to yield whitish crystals (1.41 g, 56%). IR (nujol): 3198, 2203, 1666, 1547, 1461, 1375 cm^{-1}. ^{1}H NMR (300 MHz, $CDCl_3$) δ: 11.69 (s, 0.6 H, NH), 7.60–7.38 (m, 4 H, ArH), 5.32 (s, 0.2 H, CH), 4.26 (q, 2H, *J* = 6.9 Hz, OCH_2), 4.09 (s, 0.7 H, OCH_3), 3.56 (s, 2.3 H, OCH_3), 1.41–1.23 (m, 3H, CH_2CH_3). ^{13}C NMR (75.5 MHz, $CDCl_3$) δ: 167.64 (C=O), 167.16 (C=O), 162.54 [C=C(CN)(CO_2Et)], 145.00 (C=N), 137.09 (Ar C), 136.18 (Ar C), 130.76 (Ar C), 129.74 (Ar CH), 128.85 (Ar CH), 128.70 (Ar CH), 127.59 (Ar CH), 117.16 (CN), 112.87 (CN), 71.50 [C=C(CN)(CO_2Et)], 64.84 (OCH_3), 63.44 (OCH_2), 63.03 (OCH_3), 61.18 (OCH_2), 35.68 (CH), 14.28 (CH_2CH_3), 13.81 (CH_2CH_3).[2] A DEPT experiment showed only C–H attachments belonging to the aromatic ring except for a single C–H bond belonging to the resonance at δ 35.69, indicative of the imine tautomer. Anal. calcd. For $C_{13}H_{13}N_2O_3Cl$: C, 55.62; H, 4.67; N, 9.98; Cl, 12.63. Found: C, 55.67; H, 4.70; N, 9.94; Cl, 12.66.

Preparation of [2-aza-1-(4-chlorophenyl)-2-methoxyvinyl]methane-1,1-dicarbonitrile (5c)

A sodium ethoxide solution was prepared by dissolving sodium metal (1.63 g, 0.071 mol) in absolute ethanol (30 mL). Malononitrile (5.02 g, 0.076 mol) was placed in the sodium ethoxide solution. The mixture was stirred for approximately five minutes, and a visible solid formed in the flask. The remaining ethanol was removed under a vacuum with heating for 1 h. (*Z*)-*O*-Methyl-4-chlorobenzohydroximoyl fluoride (**1a**) (3.25 g, 0.017 mol) and the freshly prepared sodium salt of malononitrile (4.55 g, 0.052 mol) were placed in a 25 mL round-bottomed flask. The flask was sealed and heated to 90 °C with periodic venting at the beginning of the reaction. At 3.5 h, another portion of the dry sodium salt of malononitrile (1.52 g, 0.017 mol) was added. The reaction mixture was then heated at 90 °C for an additional 50 h. The reaction mixture was then cooled to room temperature, placed in 100 mL of ice-cold water, and acidified with concentrated HCl. The reaction mixture was placed in a liquid–liquid continuous extractor with chloroform for 72 h. The chloroform was then removed by rotary evaporation. The crude yield was 3.54 g of light brownish-yellow solid. This solid was recrystallized in 2:1 hexane:chloroform to yield a slightly yellow powder (1.88 g, 46%). IR (nujol) 2217, 2200, 1458, 1377 cm^{-1}. ^{1}H NMR (300 MHz, $CDCl_3$) δ: 8.15 (br s, 0.8 H, NH), 7.51–7.41 (m, 4H, ArH), 3.89 (s, 3H, OCH_3). ^{1}H NMR (300 MHz, *d*6-DMSO) δ: 7.63 (s, 4H, ArH), 3.84 (s, 3H, OCH_3). ^{13}C NMR (75.5 MHz, *d*6-DMSO) δ: 162.23 (C–N), 136.63 (Ar C), 130.59 (Ar CH), 128.67 (Ar CH), 127.60 (Ar C), 116.16 (CN), 64.17 (OCH_3), 46.69 [C($CN)_2$]. A DEPT experiment performed on **5c** revealed no C–H attachments other than those seen in the aromatic system. Anal. calcd. for $C_{11}H_8N_3OCl$: C, 56.55; H, 3.45; N,

[2] This ^{13}C NMR is corrected from a previous erroneous report in ref. 14 where an additional resonance frequency of δ 43.93 is reported.

© 2007 NRC Canada

17.98; Cl, 15.27. Found: C, 56.56; H, 3.27; N, 17.90; Cl, 15.07.

Preparation of [2-aza-1-(4-chlorophenyl)-2-isopropoxyvinyl]methane-1,1-dicarbonitrile (5d)

Malononitrile (1.69 g) was added to a solution of sodium methoxide prepared from 0.545 g (0.0237 mol) of sodium in absolute ethanol (20 mL). After evaporation of the ethanol, a portion of the solid sodium salt of malononitrile (1.5 g, 0.023) was added to O-isopropyl-4-chlorobenzohydroximoyl fluoride (1.2 g, 0.0056 mol) in a sealed flask. The flask was heated to 90 °C in a sand bath with periodic venting. After three hours, the remaining portion of the sodium salt was added to the flask, and the reaction was heated for 50 h at 90 °C. The resulting dark solid was extracted with chloroform (3 × 100 mL). Evaporation of the chloroform gave 1.36 g of a yellowish solid. One recrystallization from 2:1 hexane–chloroform gave a light yellow solid (0.85 g, 62%). Several additional recrystallizations from hexane–chloroform gave a light yellow powder 138–139 °C (dec). IR (nujol): 3190, 2217, 2198,1581, 1541 cm^{-1}. ^1H NMR (300 MHz, $CHCl_3$) δ: 1.33 (6H, d, J = 6 Hz, $(CH_3)_2$), 4.27 (1H, m, CH), 7.40 (2H, d, J = 9 Hz, ArH), 7.48 (2H, d, J = 8.4 Hz, ArH), 8.56 (1H, s, NH). ^{13}C NMR (75.5 MHz, $CDCl_3$) δ: 19.72 [$CH(\underline{C}H_3)_2$], 52.02 [$\underline{C}(CN)_2$], 80.35 [$\underline{C}H(CH_3)_2$], 114.36 (CN), 116.07 (CN), 117.58 (ArC) 127.27 (ArC), 129.65 (ArCH), 129.93 (ArCH), 139.06 (=CNH). ^1H NMR (300 MHz, d_6-DMSO) δ: 1.30 [6H, d, J = 6 Hz, $(CH_3)_2$)], 4.30 (1H, septet, J = 6 Hz, CH), 7.40 (4H, s, ArH), 12.09 (0.7H, broad s, NH). ^{13}C NMR (75.5 MHz, d_6-DMSO) δ: 19.57 [$CH(\underline{C}H_3)_2$], 47.11 [$\underline{C}(CN)_2$], 78.70 [$\underline{C}H(CH_3)_2$], 128.25 (Ar C), 128.93 (ArCH), 130.94 (ArCH) 136.72 (ArC), 163.20 [$\underline{C}$=C(CN)$_2$]. (Found: $M^{+\bullet}$, 261.06685. $C_{13}H_{12}ClN_3O$ requires $M^{+\bullet}$, 261.06688).

Preparation of ethyl α-cyano-β-methoxyaminocrotonate (6)

The procedure for the synthesis of this compound is as that described by Baba et al. (15). ^1H NMR (300 MHz) δ 1.28 (t, J_{HH} = 7.11 Hz, 3H, CH_3), 2.33 (s, 3H, C=CCH_3), 3.77 (s, 3H, OCH_3), 4.17 (q, J_{HH} = 7.11 Hz, 2H, OCH_2), 11.60 (s, 1H, N–H). ^{13}C NMR (75 MHz) δ: 14.14 (CH_3), 15.28 (CH_3), 60.50 (CH_2), 64.73 (OCH_3), 68.95 [C=$\underline{C}$(CN)(CO_2Et)], 117.72 (CN), 166.88 [$\underline{C}$=C(CN)(CO_2Et)], 167.75 (C=O).

Preparation of (*Z*)-*O*-isopropyl-4-chlorobenzohydroximoyl bromide (7)

The procedure for the synthesis of this compound is as that described by Johnson et al. (3*b*) in their synthesis of (*Z*)-*O*-methyl-4-nitrobenzohydroximoyl bromide. This yielded a yellow semi-solid material, which was recrystallized in methanol. The first recrystallization yielded light tan crystals (16.177 g, 73%). A second recrystallization in methanol yielded white crystals (12.210 g, 55%), mp 37.0–37.5 °C. R_f (hexane, alumina): 0.88. IR: 1592, 1583, 1465, 1092, 996 cm^{-1}. ^1H NMR (300 MHz) δ: 1.39 (d, J_{HH} = 6.4 Hz, 6H, CH_3), 4.61 (m, J_{HH} = 6.2, 1H, OCH), 7.36 (d, J_{HH} = 8.6 Hz, 2H, ArH), 7.79 (d, J_{HH} = 8.6 Hz, 2H, ArH). ^{13}C (75 MHz) δ: 21.64 (CH_3), 77.77 (CH), 127.92 (C=N), 128.45 (Ar CH), 129.30 (Ar CH), 132.82 (Ar C), 136.26 (Ar C). GC–MS: *m*/*z* 277 (18%), 275 (M, 13), 235 (11), 233 (9), 198 (4), 196 (14), 156 (32), 154 (100), 139 (11), 137 (35), 125 (11), 123 (20), 113 (9), 111 (29), 102 (23), 75 (18). Anal. calcd. For $C_{10}H_{11}BrClNO$: C, 43.43; H, 4.01; Br, 28.89; Cl, 12.82; N, 5.06. Found: C, 43.22; H, 4.02; Br, 28.51; Cl, 12.66, N, 4.96.

Preparation of (*Z*)-*O*-isopropyl-4-chlorobenzohydroximoyl fluoride (1b)

(*Z*)-*O*-Isopropylbenzohydroximoyl bromide (7) (6.723 g, 0.0243 mol), potassium fluoride (Aldrich, spray-dried, 99%) (10.405 g, 0.179 mol) in 108 mL of sulfolane was placed in a 250 mL round-bottomed flask fitted with a thermometer, a $CaCl_2$ drying tube, and a nitrogren gas inlet. The resulting solution was heated to 146 °C with stirring for 10 days. The reaction mixture was cooled to room temperature. Water (100 mL) was poured into the cooled reaction mixture, and the mixture was continuously extracted with heptane for 4 days. Heptane extract was washed with water (2 × 50 mL), and the heptane extract was dried with anhyd. magnesium sulfate. Heptane was removed by rotary evaporation. This yielded a yellowish liquid (4.938 g). The compound was purified by vacuum distillation to yield a clear, colorless liquid (3.362 g, 64%). IR (neat): 2978, 2933, 1646, 1601, 1494, 1321, 993 cm^{-1}. ^1H NMR (300 MHz) δ: 1.34 (d, J_{HH} = 6.4 Hz, 6H, CH_3), 4.39 (m, J_{HH} = 6.3, 1H, OCH), 7.40 (d, J_{HH} = 8.6 Hz, 2H, ArH), 7.70 (d, J_{HH} = 8.6 Hz, 2H, ArH). ^{13}C (75 MHz) δ: 21.38 (CH_3), 77.32 (d, J_{CONCF} = 1.8, CH), 125.59 (d, J_{CCF} = 31.9 Hz, Ar C), 126.90 (d, J_{CCCF} = 5.0 Hz, Ar CH), 128.80 (d, J_{CCCCF} = 1.8 Hz, Ar CH), 136.76 (Ar C–Cl), 151.00 (d, J_{CF} = 320.0 Hz, C=N). GC–MS: *m*/*z* 217 (9%), 215 (M, 26), 175 (31), 173 (100), 158 (5), 156 (13), 111 (30), 107 (32), 75 (22). (Found: $M^{+\bullet}$, 215.05072. $C_{10}H_{11}ClFNO$ requires $M^{+\bullet}$, 215.05132).

Preparation of the (*E*)-isomer of *O*-isopropyloxime of 4-chloroacetophenone (7a)

Preparation of Grignard reagent

Magnesium metal (1.372 g, 0.0564 mol) was placed in a dry 25 mL round-bottomed flask fitted with a dry Claisen adaptor, a dry dropping funnel, a dry water-cooled condenser with a dry nitrogen inlet and a $CaCl_2$ drying tube-protected outlet. Methyl iodide (4 mL, 0.0640 mol) in 6 mL of anhyd. ether was added dropwise to form Grignard reagent. This resulted in approximately 6 mL of an approximately 10 mol/L methylmagnesium iodide solution.

Reaction of 4-chloro-*O*-methylbenzohydroximoyl fluoride with methylmagnesium iodide

4-Chloro-O-methylbenzohydroximoyl fluoride (0.635 g, 0.00294 mol) in 7 mL of anhyd. ether was added dropwise to approximately 6 mL of ~10 mol/L methylmagnesium iodide in diethyl ether solution. This mixture was refluxed for 4 h. The reaction was then poured onto approximately 40 g of dry ice. The resulting residue was washed with hexane (approximately 300 mL). The hexane was evaporated under reduced pressure. This yielded a light yellow oil (0.280 g, 45%). This was distilled under vacuum with short path distillation apparatus to yield microanalytically pure sample of a colorless oil (0.200 g, 32.1%). IR (neat): 2975, 2930,

© 2007 NRC Canada

1609, 1490, 1369, 1004. ^{1}H NMR (300 MHz) δ: 1.32 (d, J_{HH} = 6.2 Hz, 6H, $C(CH_3)_2$), 2.21 (s, 3H, CH_3), 4.46 (m, J_{HH} = 6.2 Hz, 1H, CH), 7.33 (d, J_{HH} = 8.6 Hz, 2 H, ArH), 7.61 (d, J_{HH} = 8.6 Hz, 2H, ArH). ^{13}C (75 MHz) δ: 12.53 (CH_3), 21.84 (CH_3), 75.74 (CH), 127.13 (Ar CH), 128.41 (Ar CH), 134.59 (Ar C), 135.47 (Ar C), 152.37 (C=N). GC–MS: *m/z* 213 (21%), 211 (M, 64), 171 (32), 169 (100), 154 (22), 152 (51), 137 (29), 130 (17), 128 (56), 113 (28), 111 (77), 103 (42), 77 (31), 75 (65). Anal. calcd. for $C_{11}H_{14}ClNO$: C, 62.41; H, 6.67; Cl, 16.75; N, 6.62. Found: C, 62.47; H, 6.89; Cl, 16.73, N, 6.56.

Preparation of the (*E*)-isomer of *O*-isopropyloxime of 4-chlorobenzophenone (7b)

(*Z*)-*O*-Isopropyl-4-chlorobenzohydroximoyl fluoride (**1b**) (0.308g, 0.00143 mol) was placed in a dry 25 mL round-bottomed flask fitted for distillation under nitrogen purge. Phenylmagnesium bromide (4.7 mL of 1.0 mol/L in THF, 0.00470 mol) was added to the flask, and the mixture was heated to distill off 2.2 mL of THF. Reaction was then heated at reflux for 17 h. Mixture was then cooled to room temperature and quenched in 25 mL of ice-cold water. This was extracted with ether (5 × 50 mL). The ether layer was dried with magnesium sulfate and ether removed by rotary evaporation. This yielded 0.471 g of medium yellow colored oil. This material was purified by column chromatography (silica 63–200 and hexanes) to yield a colorless viscous oil (0.299g, 77%). IR (neat): 3082, 3058, 3029, 2975, 2932, 1577, 1488, 1444, 1369, 1324, 1121, 1092, 971. ^{1}H NMR (300 MHz) δ: 1.27 (d, J_{HH} = 6.2 Hz, 6H, $C(CH_3)_2$), 4.48 (m, J_{HH} = 6.2 Hz, 1H, CH), 7.25–7.43 (m, 9 H, ArH). ^{13}C (75 MHz) δ: 21.88 (CH_3), 76.56 (CH), 128.15 (Ar CH), 128.51 (Ar CH), 128.93 (Ar CH), 129.31 (Ar CH), 129.69 (Ar CH), 133.20 (Ar C), 135.08 (Ar C), 135.79 (Ar C), 154.68 (C=N). GC–MS: *m/z* 275 (19%), 273 (M, 55), 233 (13), 231 (39), 216 (32), 214 (100), 202 (12), 165 (71), 113 (11), 111 (26), 77 (42), 75 (31). (Found: $M^{+\bullet}$, 273.09238. $C_{16}H_{16}ClNO$ requires $M^{+\bullet}$, 273.09204).

Preparation of the (*Z*)-isomer of the *O*-isopropyloxime of 1-(4-chlorophenyl)-3-phenyl-prop-2-yn-1-one (7c)

(*Z*)-*O*-Isopropyl-4-chlorobenzohydroximoyl fluoride (**1b**) (0.240g, 0.00111 mol) was placed in a dry 25 mL round-bottomed flask fitted for distillation under nitrogen purge. Phenylmagnesium bromide (3.7 mL of 1.0 mol/L in THF, 0.00370 mol) was added to the flask, and the mixture was heated to distill off 1.5 mL of THF. Reaction was then heated at reflux for 48 h. Mixture was then cooled to room temperature and quenched in 30 mL of ice-cold satd. ammonium chloride solution. This was extracted with ether (4 × 50 mL). The ether layer was dried with magnesium sulfate and ether removed by rotary evaporation. This yielded 0.778 g of reddish-amber colored liquid. This material was purified by column chromatography (silica 63–200 and hexanes) to yield a colorless viscous oil (0.268g, 81%). IR (neat): 3056, 2976, 2929, 2202, 1598, 1488, 1328, 1120, 1094, 1052, 983. ^{1}H NMR (300 MHz) δ: 1.37 (d, J_{HH} = 6.3 Hz, 6H, $C(CH_3)_2$), 4.55 (m, J_{HH} = 6.2 Hz, 1H, CH), 7.29–7.85 (m, 9 H, ArH). ^{13}C (75 MHz) δ: 21.66 (CH_3), 77.31 (CH), 79.50 (CC), 100.90 (CC), 121.83 (Ar C), 127.50 (Ar CH), 128.35 (Ar CH), 128.44 (Ar CH), 129.37 (Ar C), 132.01 (Ar CH), 132.50 (Ar C), 135.16 (Ar C), 137.90 (C=N). GC–MS: *m/z* 299 (16%), 297 (M, 45), 257 (3), 255 (9), 227 (17), 225 (48), 189 (57), 105 (100), 77 (11), 75 (23). (Found: $M^{+\bullet}$, 297.09206. $C_{18}H_{16}ClNO$ requires $M^{+\bullet}$, 297.09204).

Acknowledgements

Acknowledgment is made to the American Chemical Society Petroleum Research Fund Grant (PRF #44412-GB1), Southeastern Louisiana University's Faculty Development Grant, Southeastern Louisiana University's OSCAR/STAR Grant, the Minority Biomedical Research Support Program of the National Institutes of Health (NIH-MBRS Grant R25-GM55380), The Robert A. Welch Foundation (Grant No. M-0200), and the Texas Woman's University Research Enhancement Program for support of this work.

References

1. (*a*) S. Fustero, B. Pina, and A. Simon-Fuentes. Tetrahedron Lett. **38**, 6771, (1997); (*b*) S. Fustero, B. Pina, M. Garcia de la Torre, A. Navarro, C. Ramirez de Arellano, and A. Simon. Org. Lett. **1**, 977, (1999); (*c*) R. Ta-Shma and Z. Rappoport. J. Am. Chem. Soc. **99**, 1845, (1977); (*d*) R. Ta-Shma and Z. Rappoport. J. Am. Chem. Soc.**98**, 8460, (1976).
2. (*a*) J.E. Rowe and K. Lee. Aust. J. Chem. **50**, 849, (1997); (*b*) J.E. Rowe and D.A. Papanelopoulos. Aust. J. Chem. **48**, 2041, (1995); (*c*) J.E. Rowe and A.F. Hegarty. J. Org. Chem. **49**, 3083, (1984).
3. (*a*) J.E. Johnson, D.D. Dolliver, L. Yu, D.C. Canseco, M.A. McAllister, and J.E. Rowe. J. Org. Chem. **69**, 2741, (2004); (*b*) J.E. Johnson, A. Ghafouripour, M. Arfan, and S.L. Todd, D. Sitz. J. Org. Chem. **50**, 3348, (1985).
4. (*a*) D. Enders and U. Reinhold. Tetrahedron: Asymmetry, **8**, 1895, (1997); (*b*) R. Bloch. Chem. Rev. **98**, 1407, (1998).
5. (*a*) C.J. Moody. Chem.Commun. 1341, (2004); (*b*) C.J. Moody, P.T. Gallagher, A.P. Lightfoot, and A.M.Z. Slawin. J. Org. Chem. **64**, 4419, (1999); (*c*) R.K. Dieter and R. Datar. Can. J. Chem. **71**, 814, (1993).
6. (*a*) K.G. Watson, R.N. Brown, R. Cameron, D.K. Chalmers, S. Hamilton, B. Jin, G.Y. Krippner, A. Luttick, D.B. McConnell, P.A. Reece, J. Ryan, P.C. Stanislawski, S.P. Tucker, W.-Y. Wu, D.L. Barnard, and R.W. Sidwell. J. Med. Chem. **46**, 3181, (2003); (*b*) A. Palani, S. Shapiro, H. Josien, T. Bara, J.W. Clader, W.J. Greenlee, K. Cox, J.M. Strizki, and B.M. Baroudy. J. Med. Chem. **45**, 3143, (2002); (*c*) A. Rossello, S. Bertini, A. Lapucci, M. Macchia, A. Martinelli, S. Rapposelli, E. Herreros, and B. Macchia. J. Med. Chem. **45**, 4903, (2002); (*d*) P.L. Ferrarini, C. Mori, M. Badawneh, V. Calderone, R.Greco, C. Manera, A. Martinelli, P. Nieri, and G. Saccomanni. Eur. J. Med. Chem. **35**, 815, (2000); (*e*) A. Karakurt and S. Dalkara. FABAD J. Pharm. Sci. **24**, 143 (1999).
7. (*a*) E. Fontaine, C. Namane, J. Meneyrol, M. Geslin, L. Serva, E. Roussey, S. Tissandie, M. Maftouh, and P. Roger. Tetrahedron: Asymmetry, **12**, 2185, (2001); (*b*) C. Bolm and M. Felder. Synlett, 655 (1994); (*c*) Y. Sakito, Y. Yoneyoshi, and G. Suzukamo. Tetrahedron Lett. **29**, 223, (1988).
8. (*a*) E. Abele, R. Abele, J. Popelis, and E. Lukevics. Org. Prep. Proced. Int. **32**, 153, (2000); (*b*) P.E. Titus, P.A. Forte, and J.M. Prokipcak. Can. J. Chem. **54**, 647, (1976); (*c*) R.

© 2007 NRC Canada

Andrisano, A.S. Angeloni, F. Del Moro, and M. Tramontini. M. Ann. Chim. (Rome), **55**, 645, (1965).
9. (*a*) J. Skerzewski. Tetrahedron **45**, 4593, (1989); (*b*) G.R. Newkome and G.R. Baker. Org. Prep. Proced. Int. **18**, 117, (1986).
10. J.R. Jones. The ionization of carbon acids. Academic Press, New York, 1973.
11. J.P. Guthrie. Can. J. Chem. **45**, 4593, (1979).
12. T.H. Lowry and K.S. Richardson. Mechanism and theory in organic chemistry 3rd Ed. Harper and Rowe: New York. 1987. p. 297.
13. (*a*) P. Gilli, V. Bertolasi, V. Ferretti, and G. Gilli. J. Am. Chem. Soc. **122**, 10405, (2000); (*b*) V.F. Traven, V.V. Negrebetsky, L.I. Vorobjeva, and E.A. Carberry. Can. J. Chem. **75**, 377, (1997); (*c*) K. Neuvonen, C. Zewi, and H. Lonnberg. Acta Chem. Scand. **50**, 1137, (1996); (*d*) G. Bartoli, C. Cimarelli, T. Calpozzo, and G. Palmieri. Tetrahedron, **51**, 8613, (1995); (*e*) K. Takagi, A. Bajnati, and M.J. Hubert-Habart. Heterocycl. Chem. **31**, 973, (1994); (*f*) A. Arnold, M. Budeshisky, and M. Pankova. Collect. Czech. Chem. Commun. **56**, 1019, (1991); (*g*) A.S. Shawali, N.M. Harb, and K.O. Badahdah. Heterocycl. Chem. **22**, 1397, (1985).
14. J.E. Johnson, D.C. Canseco, D.D. Dolliver, J.E. Rowe, and F.R. Fronczek. J. Chem. Cryst. **36**, 667, (2006).
15. H. Baba, I. Hori, T. Hayashi, and H. Midorikawa. Bull. Chem. Soc. Jpn. **42**, 1653, (1969).
16. J. Pornet and L. Miginiac. Bull. Soc. Chim. Fr. **7–8**, 1849, (1975).
17. J.E. Rowe, K. Lee, D.D. Dolliver, and J.E. Johnson. Aust. J. Chem. **52**, 807, (1999).
18. X. Creary, Y.-X. Wang, and Z. Jiang. J. Am. Chem. Soc. **117**, 3044, (1995).

© 2007 NRC Canada

Methanol electro-oxidation at $Pt_x Ru_{(1-x)}O_y$ electrodes — An in situ FTIR study

Luciene P.R. Profeti, Françoise Hahn, Kouakou B. Kokoh, and Paulo Olivi

Abstract: In this work we investigated the nature of the intermediates adsorbed during the electrooxidation of methanol on $Pt_xRu_{(1-x)}O_y$ electrodes, where $0.5 < x < 0.9$, prepared by the decomposition of polymeric precursors. Thin layer electrodes with different compositions were prepared directly on a gold substrate by thermal decomposition of ethylene glycol – citric acid solutions containing the precursor salts at 400 °C. In situ IR reflectance spectra were obtained using the SPAIRS (single potential alteration infrared reflectance spectroscopy) and SNIFTIRS (subtractively normalized interfacial Fourier transform IR reflectance spectroscopy) techniques. For all the investigated compositions, the SNIFTIRS and SPAIRS spectra displayed three main bands, which were attributed to CO species in the linear (CO_L) and bridged (CO_B) forms adsorbed over Pt and linearly adsorbed over Ru. Formation of CO_2 carbonyl species was also detected. The spectra features were analyzed in terms of the applied potential and they were compared with those reported for Pt–Ru electrodes prepared by other methods.

Key words: methanol, electrocatalytic oxidation, in situ infrared reflectance spectroscopy, $Pt_xRu_{(1-x)}O_y$, adsorption

Résumé : Dans ce travail, on a étudié la nature des intermédiaires adsorbées au cours de l'électrooxydation du méthanol sur des électrodes de $Pt_xRu_{(1-x)}O_y$ dans lesquels $0{,}5 < x < 0{,}9$ et qui ont été préparées par décomposition de précurseurs polymères. On a préparé des électrodes à couches minces de diverses compositions directement sur un substrat d'or en procédant à la décomposition thermique à 400 °C de solutions d'éthylèneglycol et d'acide citrique contenant les sels précurseurs. On a déterminé les spectres de réflectance infrarouge in situ en faisant appel aux techniques de spectroscopie infrarouge de réflexion in situ lors d'une variation linéaire de potentiel (« SPAIRS ») et de spectroscopie de réflectance infrarouge à transformée de Fourier interfaciale normalisée par soustraction (« SNIFTIRS »). Pour toutes les compositions étudiées, les spectres « SPAIRS » et « SNIFTIRS » présentent trois bandes principales qui ont été attribuées aux espèces CO dans les formes linéaire (CO_L) et pontée (CO_B) adsorbées sur le platine et adsorbée d'une façon linéaire sur le ruthénium. On a aussi détecté la présence d'espèces carbonyles CO_2. On a analysé les caractéristiques spectrales en fonction du potentiel appliqué et on les a comparées avec celles rapportées pour des électrodes Pt–Ru préparées par d'autres méthodes.

Mots-clés : méthanol, oxydation électrocatalytique, spectroscopie de réflectance infrarouge in situ; $Pt_xRu_{(1-x)}O_y$, adsorption.

[Traduit par la Rédaction]

Introduction

In the last decades there has been increasing interest in the development of energy conversion devices, including fuel cells (1). In this kind of device, chemical energy is converted into electric energy by fuel anodic oxidation and cathodic oxygen reduction. The electrodes are separated by a suitable electrolyte, and electrons flow in the external circuit to generate electric current. The electrode compositions and the fuel depend on the kind of cell used in the process.

The most promising system for autonomous fuel cell devices is the hydrogen–oxygen system, where hydrogen is oxidized in the anode and power densities as high as 0.7 W cm^{-2} (2) can be achieved. However, the use of hydrogen as fuel may pose some difficulties in terms of storage, not to mention the fact that it is potentially explosive. The possibility of substituting methanol for hydrogen has been largely exploited, since the former fuel can be directly reformatted in certain devices, like automobiles, generating hydrogen in situ. An alternative approach to use methanol as fuel is to oxidize it directly on the anode, so that it could be easily stored and there would be no need for a reformer. Direct methanol fuel cells (DMFC) power densities are lower than those of hydrogen, i.e., 0.15–0.3 W cm^{-2} (2), but the use of methanol as fuel is still interesting.

The best metal for the methanol electrooxidation is platinum (3), but the presence of strongly adsorbed intermediates on this metal restricts its practical use. These intermediates block the electrode surface and prevent adsorption of other

Received 10 May 2007. Accepted 24 July 2007. Published on the NRC Research Press Web site at canjchem.nrc.ca on 12 September 2007.

L.P.R. Profeti and P. Olivi.[1] Departamento de Química, Faculdade de Filosofia, Ciências e Letras de Ribeirão Preto, Universidade de São Paulo, 14040–901 Ribeirão Preto, SP, Brazil.
F. Hahn and K.B. Kokoh. LACCO, Equipe Electrocatalyse, UMR 6503, CNRS – Université de Poitiers, 40 avenue du Recteur Pineau, 86022 Poitiers CEDEX, France.

[1]Corresponding author (e-mail: olivip@ffclrp.usp.br).

 doi:10.1139/V07-098 © 2007 NRC Canada

species. Different authors have identified these "poisoning" species as carbon monoxide adsorbed in distinct forms, namely the linear (CO_L), bridged (CO_B), and multibonded (CO_M) forms (4). These species cannot be oxidized at potentials lower than 0.7 V (vs. RHE) on Pt electrodes, which decreases cell performance.

To overcome this problem, different modifications to Pt electrodes have been suggested. The main adopted strategy is to add another element to Pt to inhibit the CO layer formation or to facilitate its oxidation. Among the elements used as the second metal are Ru, Sn, Mo, and W (5–8). These metals can be applied in their alloy form or as adatoms (9). Different investigations have shown that binary catalysts containing Pt and Ru lead to the best results (10–13). The Ru action mechanism in the catalyst is not exactly established, but the most accepted proposition supposes that the Ru atoms facilitate the oxidation of CO species because of the formation of adsorbed OH, which can combine with CO and lead to CO_2. Another interesting proposition is the possible modification of the electronic structure of Pt upon Ru addition, which can facilitate CO desorption by lowering the bond strength (14–18).

Metal oxides can also be used as catalysts for the electrooxidation of small organic molecules. The use of such oxides with Pt has proven to be a promising system since they can assume different oxidation states. They are also capable of adsorbing large quantities of oxygenated species, which may aid the electrooxidation of strongly adsorbed intermediates (19). The electroactivity of electrodes consisting of metal oxides has been intensively investigated for the Cl_2, O_2, and H_2 evolution reactions (20), but their use as catalyst for the oxidation of organic molecules has not been much exploited (19, 21–24).

Besides electrode composition, the preparation method plays an important role in electroactivity since it determines surface morphology, crystalline structure, and surface composition. We have recently proposed the use of the polymeric precursor method to prepare oxide electrodes containing tin and ruthenium oxides with platinum, to oxidize methanol (25, 26), formic acid and formaldehyde (27), and ethanol (28). Results showed that this method produces electrodes with activity comparable to that of electrodes prepared by other methods, with the advantage of being convenient for the preparation of small particles (26). Results from the characterization of $Pt_xRu_{(1-x)}O_y$ prepared by the polymeric precursor method in powder form and the performance of these materials on DMFC (26) have been recently published. The preparation method leads to a material with low crystallinity, which contains RuO_2 as well as Pt and Ru in their metallic form. Additionally, DMFC results showed that the thermal decomposition of polymeric precursors is a promising alternative route for the preparation of catalysts applicable to DMFC (26).

The development of efficient catalysts for methanol electrooxidation depends on the understanding of the reaction mechanism involving the adsorption of several intermediates. Different in situ IR spectroscopy techniques have been used to identify such species, and they have permitted the proposition of mechanisms for the electrodic process (29–31).

In this work we prepared electrodes containing Pt and Ru by decomposition of polymeric precursors on a gold surface and we investigated the intermediates adsorbed on the electrode surface during methanol oxidation by the SNIFTIRS and SPAIRS techniques. SPAIRS and SNIFTIRS techniques are complementary and allowed the detection of adsorbed species and reaction products at the vicinity of the electrode surface. With the first one, reflectivities were recorded each 50 mV during a slow voltammetric scan (1 mV s^{-1}), each spectrum resulting from the co-addition of 128 interferograms. The acquisition required 20 s, i.e., over 20 mV. Spectra were calculated as $(RE_i - RE_{ref})/RE_{ref}$, where the reference spectrum RE_{ref} was the one recorded at the most negative potential. In this way, SPAIRS technique is more suitable to obtain information about reaction intermediates and reaction products (CO_2 is a good example). With the second, reflectivities were obtained at two electrode potentials (frequency of potential modulation 0.025 Hz and amplitude 200 mV). These reflectivities resulted from the co-addition of 128 interferograms, co-added 30 times at each potential. Final spectra were normalized as $(RE_2 - RE_1) / RE_1$. SNIFTIRS is better adapted to the detection of adsorbed species.

Experimental

Catalyst preparation

In this work, we used the polymeric precursor method, also known as the Pechini method (32), in the preparation of Pt and Ru oxide electrodes. The Pt and Ru precursor solutions were prepared from the dissolution of H_2PtCl_6 or $RuCl_3$ (both in HCl 1:1 *v*/*v*) in a citric acid and ethylene glycol solution under constant stirring at 90–95 °C. The metal/citric acid/ethyleneglycol molar ratio employed in the preparation of these precursor solutions was 1:4:16. Atomic absorption spectrophotometry was used to determine the concentrations of Pt or Ru in the respective precursor solutions. The final solutions were obtained by mixing the precursor solutions in appropriate proportions, to achieve the desired electrode composition. Different Au/$Pt_xRu_{(1-x)}O_y$ molar compositions (x = 0.5, 0.6, 0.7, 0.8, and 0.9) were prepared. The value of y is not known because the formation of different amounts of oxides and metals can be formed. The solutions were carefully brushed on 8 mm diameter gold disc surfaces. The electrodes were finally calcinated at 400 °C. The gold discs had been previously polished with alumina until a 0.05 μm grain size was achieved.

Electrochemical and spectroscopic techniques

Voltammetric experiments were carried out in a conventional three-electrode Pyrex electrochemical cell. The apparatus consisted of a waveform generator (Wenking Model VSG72, Bank Electronik), a potentiostat (Wenking Model LB81), and an X–Y recorder (Linseis LY 17100). The counter electrode was a vitreous carbon plate and a reversible hydrogen electrode (RHE) was used as reference.

The Fourier transform IR spectrometer used in this work was a Bruker IFS 66v equipment containing a modified sample compartment that allowed the IR beam to be reflected on the electrode surface (8mm diameter) with an incidence angle of 65°, after passing through the IR window (CaF_2) of a conventional thin layer spectroelectrochemical cell. The

© 2007 NRC Canada

working electrode was connected to a glass rod fitted through the top of the cell, allowing it to be pressed down against the IR window. The beam path was placed under vacuum (to remove interferences from atmospheric water and CO_2) and a liquid nitrogen-cooled HgCdTe detector (Infrared Associates) was used. The spectral resolution was 4 cm^{-1}.

Using the single potential alteration IR reflectance spectroscopy (SPAIRS) technique, reflectivities were recorded at 100 mV intervals during the first voltammetric scan at a slow sweep rate (1 mV s^{-1}). Each spectrum resulted from the co-addition of 128 interferograms. Data acquisition required 20 s; i.e., over ca. 20 mV. Spectra were calculated as $\Delta R/R = (R_{E2} - R_{E1}) / R_{E1}$, where the "reference" reflectivity R_{E1} was the one recorded at the most negative potential.

Similarly, using the subtractively normalized interfacial Fourier transform IR reflectance spectroscopy (SNIFTIRS) method, reflectivities were obtained at two electrode potentials E1 and E2 (potential modulation frequency = 0.025 Hz) and co-added 30 times at each potential. Final spectra were normalized as $\Delta R/R = (R_{E2} - R_{E1}) / R_{E1}$. For the SNIFTIRS and SPAIRS techniques, $E_2 > E_1$, so that a positive absorption band indicates the species consumption and a negative absorption band corresponds to species production at the electrode surface.

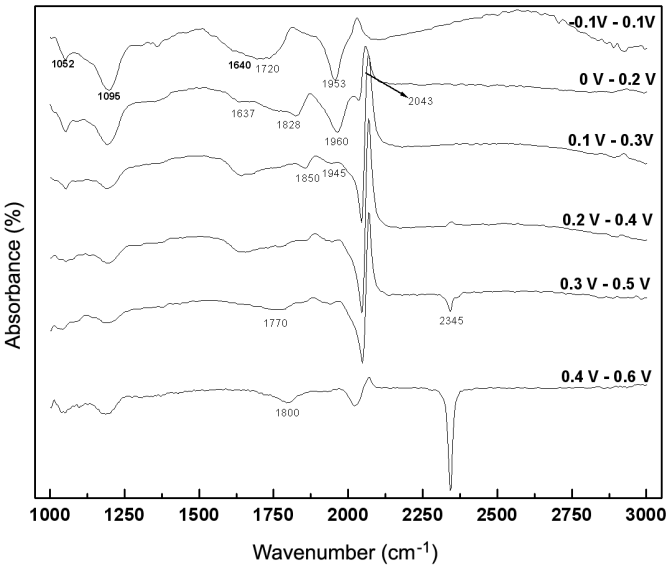
Both techniques allowed the detection of the adsorbed species, reaction intermediates, and reaction products on and in the vicinity of the electrode.

The solutions were prepared from ultrapure water (Millipore Milli-Q System), and Merck Suprapur reagents. Before each experiment, the solutions had been purged with nitrogen (U Quality from Air Liquide) and a nitrogen stream was maintained over the solution during the measurements. All the voltammetric experiments were performed at room temperature.

Results and discussion

Using the SNIFTIRS technique, the surface reflectivity was recorded at two different potential values, E_1 and E_2, with $E_2 - E_1 = +200$ mV. E_1 values were set from –0.1 to 0.4 V, with a 100 mV interval. The spectra obtained for the $Pt_{0.6}Ru_{0.4}O_y$ electrodes are presented in Fig. 1 for the various potential modulation conditions. The bands observed at 1052 and 1195 cm^{-1} in almost all the spectra can be attributed to the symmetric and asymmetric stretching modes (33), respectively, because of the presence of bisulfate ions, HSO_4^-, with C_{3v} symmetry. These bands can be seen because of the subtractive characteristic of the technique. The sulfate species can be present in the small volume between the electrode surface and the CaF_2 window, and if a decrease in the amount of these ions occurs because of a perturbation in the double layer region during the application of one potential value (E_1 or E_2), a positive or negative band is expected. Two main bands at 1720 and 1953 cm^{-1} can be seen (Fig. 1, spectrum 1) in the potential modulation between –0.1 and 0.1 V. The first is a clearly asymmetrical broad band lying between 1500 and 1800 cm^{-1}, which indicates that it is formed by the overlap of at least two bands. Since the band maximum is at 1720 cm^{-1} and because a broad region can be detected at lower wavenumbers, it is very probable that this

Fig. 1. SNIFTIR spectra of 0.1 mol/L methanol in 0.5 mol/L H_2SO_4 on a $Pt_{0.6}Ru_{0.4}O_y$ electrode at various potential modulations and at a constant modulation amplitude of 200 mV.



broad band is a result of the presence of a band at 1720 cm^{-1} and another one around 1640 cm^{-1}. The latter band is due to the water absorption, which is related to the in-plane deformation vibration of adsorbed water. The band at 1720 cm^{-1} is related to the C=O stretching mode of a carbonyl group of either a carboxylic acid or an aldehyde. However, it is not possible to actually distinguish between these two latter species because of the low separation expected between their C=O stretching bands (34). The assignment of the band at 1953 cm^{-1} may be interpreted in different ways. Iwasita et al. (12) have found a similar band at 1965 cm^{-1} on $Pt(111)/Ru_{ads}$ electrodes, and the authors assigned it to CO adsorbed on Ru sites. Meanwhile, Kabbabi et al. (35) found a CO absorption band at 2023 cm^{-1} when CO was adsorbed on pure Ru. Lin et al. (36) have also attributed a band found in the 2000–2045 cm^{-1} region to the linear CO adsorbed on the Ru (0001) surface, which is coincident with that observed by Kabbabi et al. (35). On the other hand, Yajima et al. (37) investigated the methanol oxidation reaction on Pt–Ru sputtered Ru electrodes by using in situ FTIR spectroscopy and they found a band between 1950 and 2010 cm^{-1}, which were assigned to CO linearly adsorbed on Ru. Koper et al. (38) presented the results of a density functional theory study on the adsorption of carbon monoxide (CO) and hydroxyl (OH) on platinum, ruthenium, and a series of platinum–ruthenium alloys. These authors showed that the vibrational frequencies of linearly adsorbed CO on Ru sites may vary between 1950 and 2010 cm^{-1}, depending on the electrode composition. So, in the presence of Pt the stretching frequencies of CO_L adsorbed on Ru shift to lower values. Therefore, we conclude that the band at 1953 cm^{-1} is most probably due to CO adsorbed on Ru sites in its linear form (CO_L).

At potential modulations between 0 and 0.2 V (Fig. 1, spectrum 2), the band at 1720 cm^{-1} practically disappears and a band at 1637 cm^{-1} due to interfacial water can be seen. The band due to CO adsorbed on Ru sites is slightly shifted

© 2007 NRC Canada

to higher wavenumbers, i.e., 1960 cm^{-1}. Two other bands can be seen, one at 1828 cm^{-1} and a bipolar band at 2043 cm^{-1}. The former can be attributed to the presence of CO adsorbed in two Pt sites, normally called bridged CO, CO_B, (39). The bipolar band at 2043 cm^{-1} is related to CO linearly adsorbed on Pt surface, CO_L (39).

When potential modulation between 0.1 to 0.3 V is applied (Fig. 1, spectrum 3), the intensity of the band related to bridged CO decreases, whereas the intensity of the band at 2043 cm^{-1} increases. Apart from the bands attributed to adsorbed water and sulfate, no other bands can be distinguished in the spectrum. The intensities of the bands due to CO_B and CO adsorbed on Ru sites are very small, whereas the intensity of the CO_L band increases when a potential modulation between 0.2 and 0.4 V is applied (Fig. 1, spectrum 4). Another small band can be seen at 2345 cm^{-1}, which can be attributed to CO_2 absorption. The same behavior can be seen for the potential modulation ranging from 0.3 to 0.5 V (Fig. 1, spectrum 5), where an increase in the CO_2 band can be observed, while the intensity of the CO_L band remains practically constant. A small band at 1770 cm^{-1} can be seen, but it is very difficult to ascribe it because of the proximity to the values expected for formic acid or formaldehyde carbonyl bands. However, the three-fold hollow CO appears typically around 1780 cm^{-1} on Pt(111) and related stepped surfaces and may exist in this region (40). This band can also be seen when potential modulation between 0.4 to 0.6 V is applied, but it is slightly shifted to 1800 cm^{-1} (Fig. 1, spectrum 6), which indicates the presence of the three-fold hollow CO. The CO_L band decreases and the CO_2 band increases in this potential modulation condition, i.e., during the oxidation process.

The spectra obtained for $Pt_{0.5}Ru_{0.5}O_y$ (Fig. 2), $Pt_{0.7}Ru_{0.3}O_y$ (Fig. 3), and $Pt_{0.8}Ru_{0.2}O_y$ (Fig. 4) are very similar to those presented in Fig. 1 for the $Pt_{0.6}Ru_{0.4}O_y$ electrode. The main differences lie in the intensities of the bands under different potential modulation conditions and in the small shifts in band positions. The intensities of the CO_L bands are presented in Fig. 5 for the different electrodes in relation to the potential modulation. In this picture, the amplitude of the band was normalized by subtracting the maxima of the bipolar band peak to peak. It can be seen that the band maxima arise at ca. 250 mV for the $Pt_{0.8}Ru_{0.2}O_y$ electrode, at 275 mV for the $Pt_{0.5}Ru_{0.5}O_y$, and $Pt_{0.6}Ru_{0.4}O_y$ electrodes, and at 330 mV for the $Pt_{0.7}Ru_{0.3}O_y$ electrode. It is important and noteworthy that the CO_2 absorption band appears only at potentials higher than the potential corresponding to the maxima of the CO_L band. Another important fact is that the bands related to CO_B decrease in the potential range in which the CO_L band increases, and no CO_2 is detected in this range. This fact indicates that CO_B is transformed into CO_L at high CO surface coverage. However, the CO_B bands do not disappear completely at more positive potentials, but coexist with the CO_2 band.

The spectra obtained with the SPAIRS technique are shown in Fig. 6 for the $Pt_{0.6}Ru_{0.4}O_y$ electrode. In the spectrum for the 0.1 V potential (Fig. 6, spectrum 1) a band is found at 1954 cm^{-1}, which is related to the CO species adsorbed on Ru sites. This band is also seen in all the spectra but with a shift towards lower wavenumbers. Two weak bands can also be found at 1710 and 1744 cm^{-1} as in the case of the SNIFTIRS spectra, and they can be related to the C=O stretching mode of a carbonyl group, which may be due to the presence of either a carboxylic acid or an aldehyde. These bands decrease at higher potentials and disappear completely for potentials higher than 0.5 V. In spectrum 1 (Fig. 6), a band at 2022 cm^{-1} related to the CO adsorbed linearly on Pt sites can also be seen. This band is also observed for the spectra obtained for potentials up to 0.8 V, with an initial increase in intensity for potentials up to 0.4 V and a decrease for higher potentials. At 0.4 V (Fig. 6, spectrum 4), a CO_2 absorption band at 2344 cm^{-1} can be seen and this band is also present in all the spectra re-

Fig. 2. SNIFTIR spectra of 0.1 mol/L methanol in 0.5 mol/L H_2SO_4 on a $Pt_{0.5}Ru_{0.5}O_y$ electrode at various potential modulations and at a constant modulation amplitude of 200 mV.

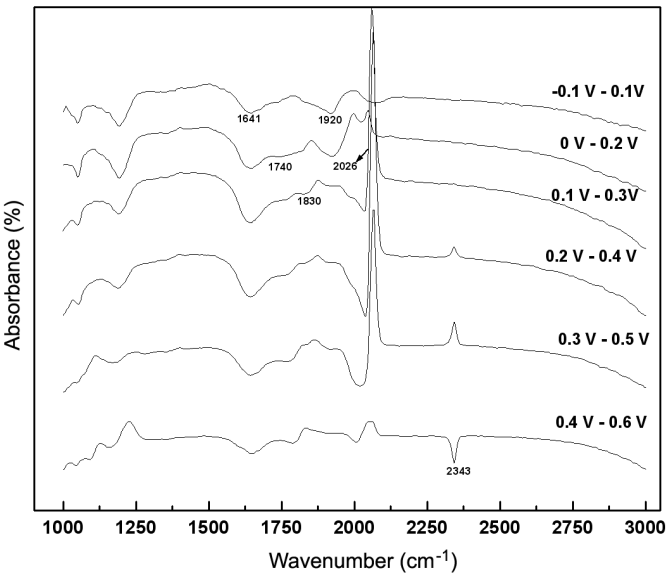
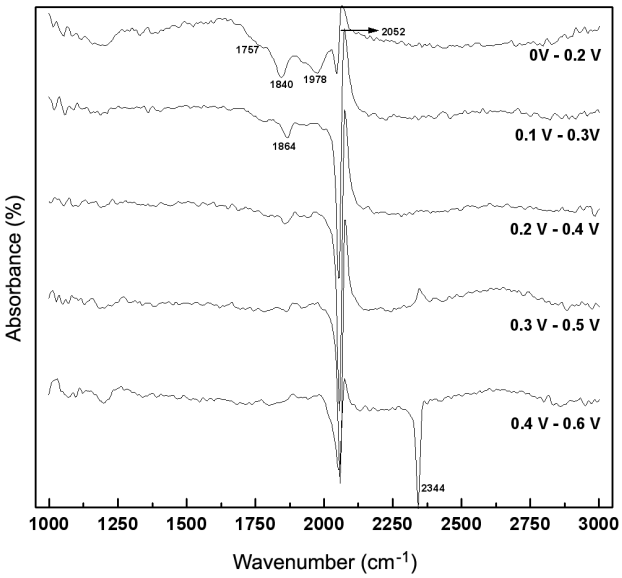


Fig. 3. SNIFTIR spectra of 0.1 mol/L methanol in 0.5 mol/L H_2SO_4 on a $Pt_{0.7}Ru_{0.3}O_y$ electrode at various potential modulations and at a constant modulation amplitude of 200 mV.



© 2007 NRC Canada

Fig. 4. SNIFTIR spectra of 0.1 mol/L methanol in 0.5 mol/L H_2SO_4 on a $Pt_{0.8}Ru_{0.2}O_y$ electrode at various potential modulations and at a constant modulation amplitude of 200 mV.

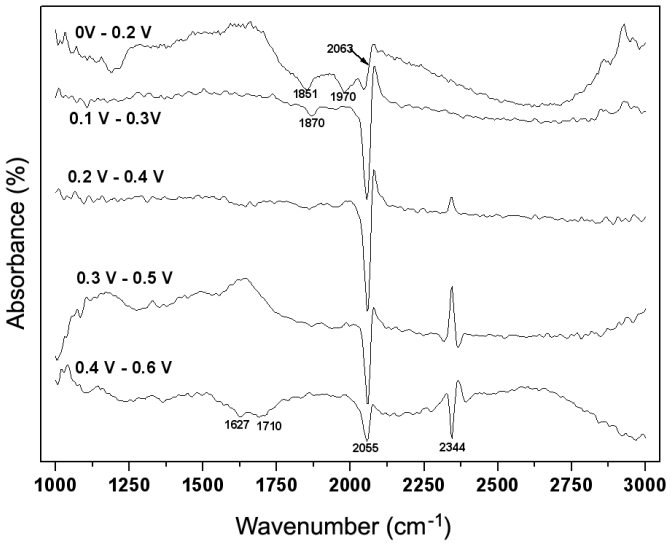
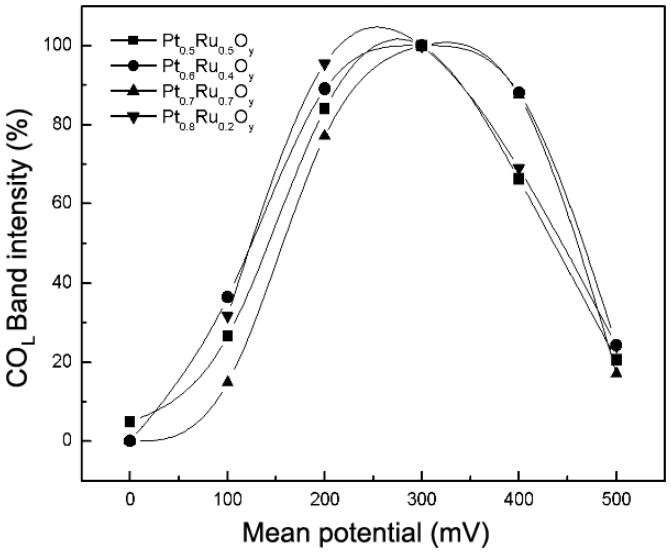
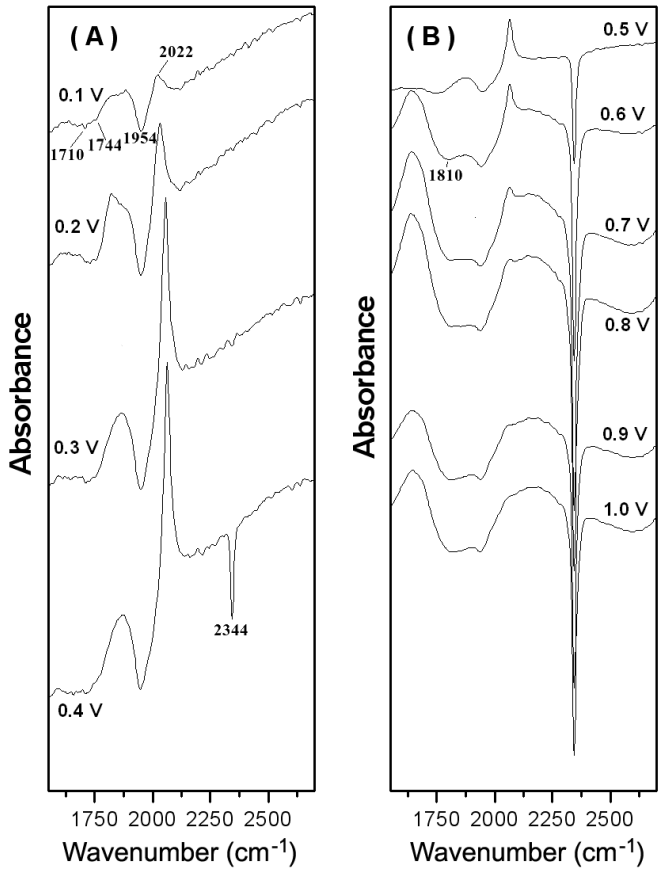


Fig. 5. CO_L band intensity (%) of 0.1 mol/L methanol in 0.5 mol/L H_2SO_4 on a $Pt_xRu_{(1-x)}O_y$ electrodes as a function of potential modulation and at a constant modulation amplitude of 200 mV. Mean potential = $E_2 - E_1$.



corded at potentials up to 1.0 V. The intensities of the CO_2 absorption bands vary with at the different potential values. These results are presented in Fig. 7. In that picture, the intensities of the CO_2 band rapidly increase with increasing potential values, but they reach a maximum around 0.65 to 0.75 V, depending on the electrode composition. A small decrease is observed after the maximum and the potential in which the CO_2 band intensity begins to decrease coincides with the potential values where the CO_L begins to decrease. This suggests that CO_L is being oxidized to CO_2. A band at ca. 1810 cm^{-1} can be seen in all the spectra for potentials higher than 0.6 V and may be assigned to the presence of CO adsorbed in the bridge form. The spectra obtained for

Fig. 6. SPAIR spectra of 0.1 mol/L methanol in 0.5 mol/L H_2SO_4 on a $Pt_{0.6}Ru_{0.4}O_y$ electrode at various potentials. R_{Ref} taken at 0 V vs. RHE.



the other electrode compositions present almost the same behavior.

Figure 6 shows that the bands shift to higher values with increasing applied potential. The wavenumber shifts are presented in Fig. 8. Analysis of Fig. 8 reveals an interesting behavior regarding the band related to the CO_L species adsorbed on Pt. This absorption band apparently presents two linear coefficients, one at low potential values (ca. 165 cm^{-1} V^{-1}) and another one at high potentials (14 $cm^{-1}V^{-1}$). The latter value agrees with the values found in the literature but the coefficient found at low potential values can be considered "anomalous" and does not correspond to the values expected for the Stark effect. To understand this behavior it is necessary to take into account the characteristics of the catalysts. Previous X-ray diffraction results revealed that the electrodes employed in this work consist mainly of metallic platinum, metallic ruthenium, and ruthenium oxide in the RuO_2 form (26), which means that at least three different phases can be present in the electrode surface. Another important characteristic of the catalyst is that small crystals are formed and a homogeneous distribution is obtained (25). In a recent work, Baranova et al. (41) showed that the vibrational wavenumbers for CO linearly adsorbed on Pt depended on the particle size. Pt particles of around 1 nm presented a CO_L absorption band at 2017 cm^{-1}, corresponding to CO adsorbed preferentially on the Pt edges (41). The CO_L wavenumber increased for larger particles, being

© 2007 NRC Canada

Fig. 7. CO_2 band intensity SPAIR spectra of 0.1 mol/L methanol in 0.5 mol/L H_2SO_4 on $Pt_xRu_{(1-x)}O_y$ electrodes.

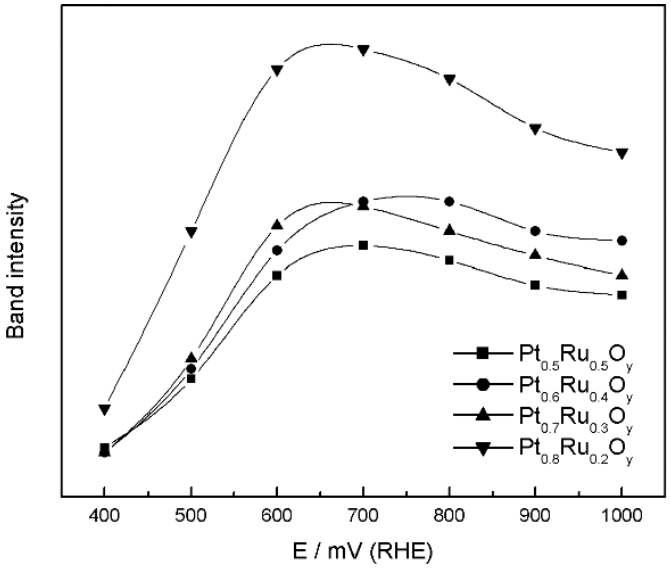
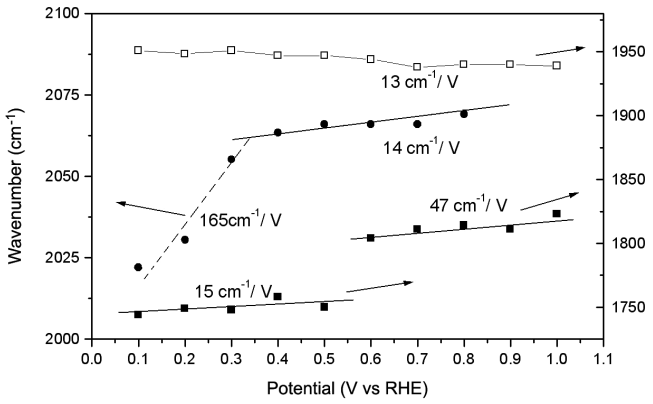


Fig. 8. Band wavenumber of Pt-adsorbed CO_L band as a function of applied potential.



2046 cm^{-1} for particles of around 5.5 nm, where CO must be adsorbed preferentially on Pt terrace sites (41). Arenz et al. (42) also showed that the wavenumber for CO adsorbed on Pt depends on the particle size, and a difference of 15 cm^{-1} was found for particles with sizes of 2 and 5 nm at the same applied potential. In other words, the CO_L band shift shown in Fig. 8 is related to the adsorption of CO in different Pt sites. At low potential values, CO_L is adsorbed mainly in small Pt particles occupying Pt edges. As for higher potential values, CO_L adsorption occurs preferentially at larger particles where the amount of Pt terrace sites is larger.

An analysis of the present results is complicated because the electrode surface is not a well-defined structure (26). Direct comparison of our results with results obtained for Pt–Ru bulk alloys cannot be made, and analysis of the role of RuO_2 is hindered because of the possible presence of a Pt–Ru solid solution. However, some comments may be made. An important point is the detection of the carbonyl band in the ca. 1720–1740 cm^{-1} region, which suggests the existence of an oxidation route involving the formation of either an aldehyde or a carboxylic acid species. Although the presence of these species was not detected in Pt–Ru alloys by some authors (3, 39), Kabbabi et al. (35) reported the presence of a band at 1695 cm^{-1} on Pt–Ru alloys in the presence of methanol. This apparent discrepancy is attributed to the different forms used in the alloy preparations. The presence of this band suggests the occurrence of a parallel path in the methanol oxidation that does not necessarily include the formation of adsorbed CO (39).

The CO_2 absorption band can be seen at 0.4 V potential values in all the electrodes employed in this work, which is the same potential expected for CO_2 detection in Pt–Ru alloys (39). This potential value is more negative than the potential where CO_2 is detected on pure Pt electrodes, a feature that is attributed to the ability of RuO_2, an oxygen donor, to oxidize CO (35). In the case of Pt–Ru alloys, the anodic formation of RuO_2 is seen as inhibitory of electrode activity, since it is believed that it is not capable of donating oxygen to oxidize CO (43). In the present case, RuO_2 was thermally prepared and the present results indicate that this oxide may act also as an oxygen donor. This observation agrees with the behavior observed by J.W. Long et al. (44) that suggests that Pt modified by the addition of hydrous ruthenium oxide presents a high catalytic activity for the methanol electrooxidation.

Conclusion

In this work we investigated the species formed on $Pt_xRu_{(1-x)}O_y$ electrodes in methanol solutions using in situ IR reflectance spectroscopy techniques (SNIFTIRS and SPAIRS). We observed the formation of adsorbed CO species in different geometries, i.e., in the linear and bridged forms. Carbonyl stretching bands in the 1720–1740 cm^{-1} region were also detected, and they were attributed to the possible formation of aldehyde or carboxylic acid intermediates. The detection of the CO_2 absorption band at potential values below the values expected for pure Pt indicates that the electrodes prepared by decomposition of polymeric precursors are promising candidates for use in DMFC. The wavenumber shift for the CO_L adsorbed on Pt sites suggests that this species are adsorbed preferentially on small Pt particles at low potentials and on larger particles at higher potentials.

Acknowledgements

The authors acknowledge Fundação de Apoio a Pesquisa do Estado de São Paulo, Brasil (FAPESP) for the financial support and LPR Profeti acknowledges FAPESP for a fellowship. This work was done under the framework of a collaboration programme between the CAPES (Brasil) and the COFECUB (Comité Français d'Evaluation de la Coopération Universitaire avec le Brésil).

References

1. C. Lamy, A. Lima, V. Le Rhun, F. Delime, C. Coutanceau, and J.-M. Léger. J. Power Sources, **105**, 283 (2002).
2. K. Scott, W.M. Taama, and P. Argyropoulos. J. Power Sources, **79**, 43 (1999).
3. N. Markovic, H.A. Gasteiger, P.N. Ross, I. Villegas, and M.J. Weaver. Electrochim. Acta, **40**, 91 (1995).

© 2007 NRC Canada

4. M.I.S. Lopes, B. Beden, F. Hahn, J.M. Léger, and C. Lamy. J. Electroanal. Chem. **313**, 323 (1991).
5. K.A. Friedrich, K.P. Geyzers, U. Linke, U. Stimming, and J. Stumper. J. Electroanal. Chem. **402**, 123 (1996).
6. W. Chrzanowski and A. Wieckowski. Langmuir, **14**, 1967 (1998).
7. M. Krausa and W. Vielstich. J. Electroanal. Chem. **379**, 307 (1994).
8. M.P. Hogarth, J. Munk, A.K. Shukla, and A. Hamnett. J. Appl. Electrochem. **24**, 85 (1994).
9. T. Frelink, W. Visscher, and J.A.R. Vanveen. Surf. Sci. **335**, 353 (1995).
10. W. Chrzanowski, H. Kin, and A. Wieckowski. Catal. Lett. **50**, 69 (1998).
11. H.A. Gasteiger, N. Markovic, P.N. Ross, and E.J. Cairns. J. Phys. Chem. **98**, 617 (1994).
12. T. Iwasita, H. Hoster, A. John-Anacker, W.F. Lin, and W. Vielstich, Langmuir, **16**, 522 (2000).
13. H.A. Gasteiger, N. Markovic, P.N. Ross, and E.J. Cairns. Electrochim. Acta, **39**, 1825 (1994).
14. H.A. Gasteiger, N. Markovic, P.N. Ross, and E.J. Cairns. J. Phys. Chem. **97**, 12020 (1993).
15. T. Frelink, W. Visscher, and J.A.R. van Veen. Surf. Sci. **335**, 353 (1995).
16. B. Hammer and J.K. Norskov. Surf. Sci. **343**, 211 (1995).
17. E. Herrero, K. Franaszcuk, and A. Wieckowski. J. Electroanal. Chem. **361**, 269 (1993).
18. M. Watanabe and S. Motoo. J. Electroanal. Chem. **60**, 275 (1975).
19. L.D. Burke and O.J. Murphy. J. Electroanal. Chem. **101**, 351 (1979).
20. S. Trasatti. Electrochim. Acta, **29**, 1503 (1984).
21. A. Hamnett. Catal. Today, **38**, 445 (1997).
22. T. Ohmori, Y. Nodasaka, and M. Enyo. J. Electroanal. Chem. **281**, 331 (1990).
23. P.C. Biswas, T. Ohmori, and M. Enyo. J. Electroanal. Chem. **305**, 205 (1991).
24. A. Katayama. J. Phys. Chem. **84**, 376 (1980).
25. M.B. Oliveira, L.P.R. Profeti, and P. Olivi. Electrochem. Commun. **7**, 703 (2005).
26. L.P.R. Profeti, F.C. Simões, P. Olivi, K.B. Kokoh, C. Coutanceau, J.-M. Léger, and C. Lamy. J. Power Sources, **158**, 1195 (2006).
27. L.P.R. Profeti, D. Profeti, and P. Olivi. Ecletica Quím. **30**, 75 (2005).
28. F.C. Simões, D. dos Anjos. F. Vigier, J.-M. Léger, F. Hahn, C. Coutanceau, E.R. Gonzalez, G. Tremiliosi-Filho, A.R. de Andrade, P. Olivi, and K.B. Kokoh. J. Power Sources, **167**, 1 (2007).
29. T. Iwasita. J. Braz. Chem. Soc. **13**, 401 (2002).
30. T. Iwasita. Electrochim. Acta, **47**, 3663 (2002).
31. K. Ashley and S. Pons. Chem. Rev. **88**, 673 (1988).
32. M.P. Pechini and S. Adams. U.S. Patent 3-330-697, 11 July 1967.
33. F.C. Nart and T. Iwasita. J. Electroanal. Chem. **308**, 277 (1991).
34. F. Vigier, C. Coutanceau, F. Hahn, E.M. Belgsir, and C. Lamy. J. Electroanal. Chem. **563,** 81 (2004).
35. A. Kabbabi, R. Faure, R. Durand, B. Beden, F. Hahn, J.-M. Léger, and C. Lamy. J. Electroanal. Chem. **444**, 41 (1998).
36. W.F. Lin, J.M. Jin, P.A. Christensen, and K. Scott. Electrochim. Acta, **48**, 3815 (2003).
37. T. Yajima, H. Uchida, and M. Watanabe. J. Phys. Chem. B, **108**, 2654 (2004).
38. M.T.M. Koper, T.E. Shubina, and R.A. van Santen. J. Phys. Chem. B, **106**, 686 (2002).
39. T. Iwasita. Handbook of fuel cell. Vol. 2. *Edited by* W. Vielstich, H.A. Gasteiger, A. Lamm. Wiley, Chichester, England. 2003. Chap. 41. pp. 603.
40. A. Rodes, R. Gomez, J.M. Feliu, and M.J. Weaver. Langmuir, **16**, 811 (2000).
41. E.A. Baranova, C. Bock, D. Ilin, D. Wang, and B. MacDougall. Surf. Sci. **600**, 3502 (2006).
42. M. Arenz, K.J.J. Mayrhofer, V. Stamenkovic, B.B. Blizanac, T. Tomoyuki, P.N. Ross, and N.M. Markovic. J. Am. Chem. Soc. **127**, 6819 (2005).
43. H. Hoster, T. Iwasita, H. Baumgartner, and W. Vielstich. J. Electrochem. Soc. **148**, A496 (2001).
44. J.W. Long, R.M. Stroud, K.E.S. Lyons, and D.R. Rolison. J. Phys. Chem. B, **10**4 9772 (2000).

© 2007 NRC Canada

DDQ-promoted thiocyanation of aromatic and heteroaromatic compounds

Hamid R. Memarian, Iraj Mohammadpoor-Baltork, and Kobra Nikoofar

Abstract: Thiocyanation of various aromatic and heteroaromatic compounds has been achieved using ammonium thiocyanate in the presence of 2,3-dichloro-5,6-dicyanobenzoquinone (DDQ) in methanol solution at room temperature and under reflux condition. The rate of reaction is influenced by the electron-donor ability of the aromatic nucleus.

Key words: amines, DDQ, indoles, thiocyanation.

Résumé : On a effectué la thiocyanatation de divers composés aromatiques et hétéroaromatiques en utilisant du thiocyanate d'ammonium en présence de 2,3-dichloro-5,6-dicyanobenzoquinone (DDQ), en solution dans le méthanol, à la température ambiante ainsi que sous des conditions de reflux du méthanol. La vitesse de la réaction est influencée par le caractère électrodonneur des substituants sur le noyau aromatique.

Mots-clés : amines, DDQ, indoles, thiocyanatation.

[Traduit par la Rédaction]

Introduction

The electrophilic thiocyanation of aromatic and heteroaromatic compounds is an important process of carbon–sulfur bond formation in organic synthesis, since the nucleophilic attack of the thiocyanate ion to the aromatic nucleus by displacement reactions is not the easy way to form thiocyanated compounds. Thiocyanates constitute an interesting group, which could be readily transformed into other sulfur-bearing functionalities (1–4), especially for producing drugs and pharmaceuticals (5). Therefore, it is important to find new methods for the thiocyanation of aromatic systems. Several methods have been developed for the thiocyanation of aromatic systems using bromine/potassium thiocyanate (6), *N*-thiocyanatosuccinimide (7), cerric ammonium nitrate (CAN) (8), montmorillonite K-10 (9), iodine/methanol (4), oxone (10), and ferric(III) chloride (11). However, some of these methods suffer from disadvantages, such as low yields, especially in the case of aromatic amines, the use of strongly acidic or oxidizing conditions, the use of special conditions (long reaction time and (or) high temperature), and also the use of expensive reagents. In this research, we have developed a new route for the thiocyanation of aromatic and heteroaromatic systems.

2,3-Dichloro-5,6-dicyanobenzoquinone (DDQ) is a versatile reagent for organic synthesis. Owing to its oxidizing ability and also its relative stability under various reaction conditions, this reagent has been used for various organic transformations, e.g., benzylic oxidation of Catechine (12), oxidation of benzhydrols (13), selective oxidation of allylic or benzylic hydroxyl groups (14), anodic oxidation of naphthalenes (15), and oxidation of thioglycosides (16).

DDQ has also been used alone for a wide range of transformations, such as dehydrogenation (17), carbon–carbon bond cleavage (18), and alcoholysis of epoxides (19); or in combination with triphenylphosphine for the conversion of epoxides to halohydrines (20), thiocyanation of α-hydroxy phosphonates (21), and thiocyanation and isothiocyanation of some alcohols and ethers (22). DDQ is also a well-known electron-acceptor species, and its interaction with a variety of electron donors has been the subject of several investigations concerning the formation of charge-transfer (CT) complexes (23–28). Herein, we wish to report an effective and benign method for the thiocyanation of aromatic and heteroaromatic compounds using ammonium thiocayanate, as a thiocyanating agent, in the presence of DDQ at room temperature (Method A) and under reflux conditions (Method B).

Received 14 May 2007. Accepted 13 July 2007. Published on the NRC Research Press Web site at canjchem.nrc.ca on 20 September 2007.

H.R. Memarian,[1] I. Mohammadpoor-Baltork, and K. Nikoofar. Catalysis Division, Department of Chemistry, Faculty of Science, University of Isfahan, 81746–73441, Isfahan, Iran.

[1]Corresponding author (e-mail: memarian@sci.ui.ac.ir).

Results and discussion

Solvent effect and optimization of the reactants

Since the nature of solvent influences the rate of reaction, thiocyanation of 2-methylindole as a model substrate was performed in various solvents at room temperature. According to the data presented in Table 1, methanol has been chosen as the best solvent for this purpose. One reason for the observed different reaction times could be the solubility of the starting materials, especially DDQ, in solvents used in this study. Therefore, we carried out the reaction with the same concentration of the dissolved reactants in *n*-hexane (as non-polar solvent) and methanol (as polar solvent). We found that methanol is the suitable solvent for our reaction.

The next step is the optimization of NH_4SCN:DDQ molar ratio in thiocyanation reaction under two reaction conditions.

 doi:10.1139/V07-092 © 2007 NRC Canada

Table1. Solvent effect on the reaction of 2-methylindole with NH_4SCN in the presence of DDQ at room temperature (method A).

Entry	Solvent	Time (min)	Yield (%)
1	H_2O	180	0
2	H_2O–CH_3OH (1:1)	70	10
3	DMF	75	10
4	CH_3CN	25	99
5	CH_2Cl_2	90	85
6	$CHCl_3$	90	75
7	*n*-hexane	180	40
8	EtOAc	40	93
9	CH_3OH	15	99

Note: All reactions were performed in the presence of 2 mmol of NH_4SCN and 1.5 mmol of DDQ in 5 mL of solvent.

Table 2. Optimization of NH_4SCN:DDQ molar ratio in the thiocyanation of 2-methylindole under two different conditions.

Entry	Molar ratio of NH_4SCN:DDQ	Method A[a] Time (min) [yield (%)]	Method B[b] Time (min) [yield (%)]
1	3:1.5	15 [99]	15 [99]
2	3:0.5	—	90 [35]
3	3:1	40 [75]	70 [85]
4	3:1.25	60 [88]	15 [90]
5	2:1.25	25 [95]	15 [99]
6	1:1.5	—	35 [62]
7	2:1.5	15 [99]	15 [99]
8	2:1	—	40 [78]
9	2.5:1.5	15 [99]	—

Note: In all cases, methanol (5 mL) was used as solvent.
[a]Room temperature conditions.
[b]Under reflux conditions.

The results presented in Table 2 showed that the optimized molar ratio of NH_4SCN:DDQ is 2:1.5 for method A and 2:1.25 for method B. These data also show that an increase of the amount of NH_4SCN did not affect the yield or the rate of the reaction.

Thiocyanation of aromatic and heteroaromatic systems

Under optimized reaction conditions, the thiocyanation of different aromatic and heteroaromatic compounds was investigated under two conditions, at room temperature (method A) and under reflux conditions (method B). The results are summarized in Table 3. Clearly, various compounds were converted to their corresponding thiocyanation products in good to excellent yields. The products were identified by IR, ^1H NMR, and MS spectra. IR spectra showed the characteristic peaks of –SCN between 2120–2150 cm^{-1} and the C–S stretching between 650–750 cm^{-1}. The regiochemistry of substitution was achieved by the interpretation of ^1H NMR spectra and their comparison with the spectra and physical data of authentic samples (see Experimental Section).

According to the results obtained from the control experiment and the results presented in Table 3, we can summarize the following:

(*i*) The presence of DDQ is necessary for the reaction because the reaction of **1b** as a test compound with NH_4SCN in methanol in the absence of DDQ did not proceed at all.

(*ii*) The use of DDQ in a molar ratio of 1.25 and 1.5 to 1 of the aromatic compound indicates that DDQ does not act as a catalyst, since it is consumed during the reaction.

(*iii*) The times and the yields of the reactions are dependent on the electron-donating ability of the aromatic and heteroaromatic compounds.

On the basis of the forgoing results, the following mechanism is proposed for the reaction, by taking (**1a**) as an example (Scheme 1).

According to the proposed mechanism, either the formation of a π complex between the aromatic system and DDQ can occur (path a) or an electron-transfer process leads to the formation of an ion pair, namely, the radical cation of aromatic system and $DDQ^{\bullet-}$ (path b). Nucleophilic attack of one of these intermediates by the thiocyanate ion leads to the formation of a thiocyanated radical system accompanied by $DDQ^{\bullet-}$. An electron transfer from the radical intermediate to $DDQ^{\bullet-}$, followed by the proton abstraction, accomplished the reaction under the formation of the thiocyanated product and $DDQH^-NH_4^+$. The following experiments support the involvement of a π complex (path a) in the reaction rather than the electron-transfer process (path b):

(*i*) The electronic absorption spectra of 0.001 mol/L solutions of the donor molecule **1b** or **1c** with the acceptor molecule DDQ (0.001 mol/L) and also the mixture of either **1b** + DDQ or **1c** + DDQ in methanol show the formation of the weak charge-transfer (CT) complexes between both donor and acceptor molecules (Figs. 1 and 2).

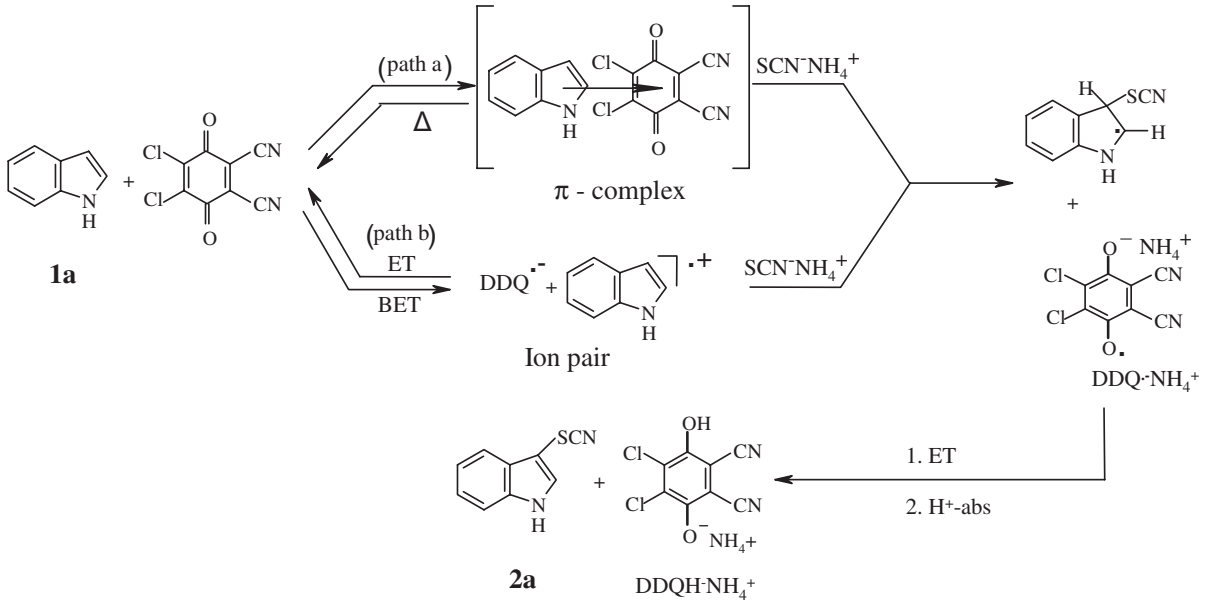
(*ii*) Addition of ammonium thiocyanate to the mixture of either **1b** + DDQ or **1c** + DDQ at room temperature causes a decrease of CT-complex absorption (Figs. 3 and 4).

(*iii*) To obtain more information about the formation of charge-transfer complexes between DDQ and the aromatic and heteroaromatic systems as a key step in the reaction, conductance measurements, as a much sensitive method, was used. Conductance measurements were carried out on the solutions of **1b**, **1c**, DDQ and their mixtures **1b** + DDQ and **1c** + DDQ at three molar ratios (0.5:1, 1:1, and 2:1) at 23 °C and 50 °C. The results are summarized in Table 4.

The results showed that the addition of DDQ to the solutions of **1b** and **1c** causes a sharp increase in the conductivity. The conductivities of the mixture of **1b** with DDQ or **1c** with DDQ are more than the sum of conductivities of the separated compounds. The results clearly indicate that the charge-transfer complexes are more mobile than the individual compounds (29). The differences between the conductivities of the mixture of **1b** with DDQ and (**1c**) with DDQ and the sum of the conductivities of the individual compounds at the same concentration could be related to the extent of CT formation, which is directly related to the electron-donor ability of **1b** compared with **1c**. This is supported by comparing the rate of thiocyanation of **1b** (15 min) with **1c** (30 min). These experiments show clearly that by increasing DDQ ratio from 0.5 to 1 and 2, the difference in conductivity is increased, but there is no difference between the conductivities of the 1:1 and 1:2 molar ratios. This result

© 2007 NRC Canada

Scheme 1.



confirms that a 1:1 complex is formed between the donor and the acceptor molecules (Figs. 5 and 6).

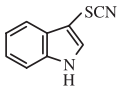
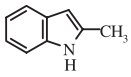
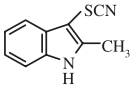
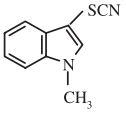
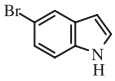
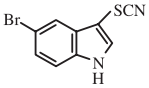
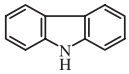
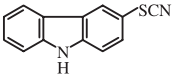
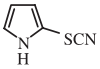
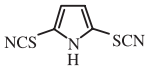
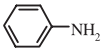
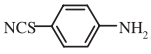
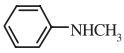
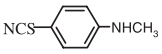
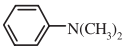
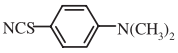
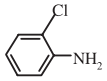
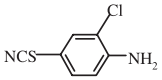
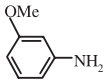
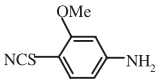
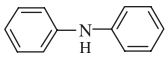
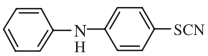
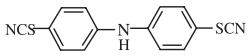
Interestigly, conductivity measurements showed that by increasing the temperature, the conductivities are decreased. This clearly indicates that the cleavage of a π complex occurs by increasing the temperature and supports the reaction path a. In path b and formation of the ionic intermediates, we expected that ion mobility should be increased by increasing temperature. All these observations support the involvement of a π complex in the thiocyanation in our study. These observations are also supported by the fact that the reaction of thiophene, furan, pyridine, and their benzocondenced derivatives, namely, benzothiophene, benzofuran, and quinoline, as less electron-donor compounds compared with the compounds considered in this study, under the same reaction conditions did not result in changing the color of solution (indicating the lack of any CT-complex formation) or in the formation of any product(s) even after stirring the reaction mixture at room temperature for 6 h.

The results presented in Table 3 showed that various aromatic and heteroaromatic compounds are converted to their corresponding thiocyanated derivatives in good to excellent yields. A comparison of the times for the maximum progression of reactions indicates that the electron-donor ability of compounds is an important factor for this reaction. These results indicate that the steric and electronic effects (e.g., the HOMO energy) are responsible for the CT-complex formation, which supports our suggestion of the involvement of the π complex in the rate-determining step. In comparison with the results obtained by the thiocyanation of indolic compounds (Table 3, entries 1–4), we found that the inductive effect of the methyl group at the 2 position (Table 3, entry 2) decreases the time required for the completion of the reaction, compared with compound **1a** (Table 3, entry 1) that does not have this substituent. Contrary to these observations, the presence of the methyl group at position 1 (compound **1c**) increases the time required for the completion of the reaction. It is expected that the presence of the methyl group in position 1, should increase the electron-donating character of the nitrogen; therefore, a reaction-time decrease should be observed for the thiocyanation of compound **1c** (Table 3, entry 3) compared with compound **1a** (Table 3, entry 1). The obtained reaction times do not confirm these suggestions. The reason is probably that because of the rehybridization of the nitrogen atom from sp^3 to sp^2 for better participation of the nitrogen lone pair in a conjugative system, the repulsive effect of the methyl group in position 1 (compound **1c**) with the hydrogen in position 7 is increased, which leads to the aversion of the nitrogen of pushing electron to the pyrrole ring to increase the HOMO energy. Due to cross conjugation of the nitrogen to both phenyl rings in carbazole **1e**, compared with indole **1a**, the energy of the HOMO should lay lower; therefore, a longer reaction time is expected. The most interesting results were obtained for the thiocyanation of aniline and its *N*- and ring substituted derivatives. While the presence of the methyl group(s) on the nitrogen decreases the reaction time, the presence of electron-withdrawing substituents, such as chlorine, methoxy, or phenyl groups, increases the reaction time. The data reported in Table 3 also showed that for pyrrole **1g** and diphenylamine **1l**, both mono- and dithiocyanated products were formed.

Concerning the regiochemistry of thiocyanate-ion addition, especially for indole and its derivatives, two possible radical intermediates **3** (a donor-substituted radical center) and **4** (a benzylic radical center) should be considered (Scheme 2). The stability of these radical intermediates explains the direction of thiocyanate addition to the heteroaromatic ring. The conjugation of a radical center in **4** with the aromatic ring should disturb the aromaticity of ring, whereas the interaction of the nitrogen lone pair with the adjacent radical center in **3** should increase the stabilization of a radical center, while the aromaticity of ring stays intact (30). For other starting materials (Table 3, entries 5–12), the

© 2007 NRC Canada

Table 3. Thiocyanation of aromatioc and heteroaromatic compounds with NH_4SCN in the presence of DDQ under different reaction conditions.

Entry	Substrate		Product(s)[a]		Method A[b]		Method B[c]	
					Time (min)	Yield[d] (%)	Time (min)	Yield[d] (%)
1		**1a**		**2a**	20 (50)[e]	97 (94)[e]	20	99
2		**1b**		**2b**	15 (30)	98 (98)	15	99
3		**1c**		**2c**	30 (60)	98 (97)	30	97
4		**1d**		**2d**	25 (45)	97 (97)	25	99
5		**1e**		**2e**	140 (240)	52 (45)	70	50
6		**1f**		**2fa**	35 (45)	63 (69)	20	54
				**2fb**		32 (25)		41
7		**1g**		**2g**	40 (60)	95 (92)	35	98
8		**1h**		**2h**	30 (45)	98 (95)	20	98
9		**1i**		**2i**	20 (35)	98 (97)	20	98
10		**1j**		**2j**	50 (75)	94 (90)	40	94
11		**1k**		**2k**	30 (40)	96 (94)	25	95
12		**1l**		**2la**	90 (130)	51 (58)	50	53
				**2lb**		29 (22)		29

[a]All products were identified by compariing their physical and spectral data with those of the authentic samples (See also the Experimental Section).
[b]Room temperature, molar ratio of NH_4SCN:DDQ = 2:1.5.
[c]Reflux conditions, molar ratio of NH_4SCN:DDQ = 2:1.25.
[d]Isolated yields.
[e]The numbers in parentheses show the time and yield of the reaction in the presence of 1.25 mmol of DDQ.

© 2007 NRC Canada

Fig. 1. Electronic absorption spectra of **1b**–DDQ reaction in CH_3OH. (A) [**1b**] = 0.001 mol/L, (B) [DDQ] = 0.001 mol/L, (C) **1b**–DDQ mixture: [**1b**] = [DDQ] = 0.001 mol/L.

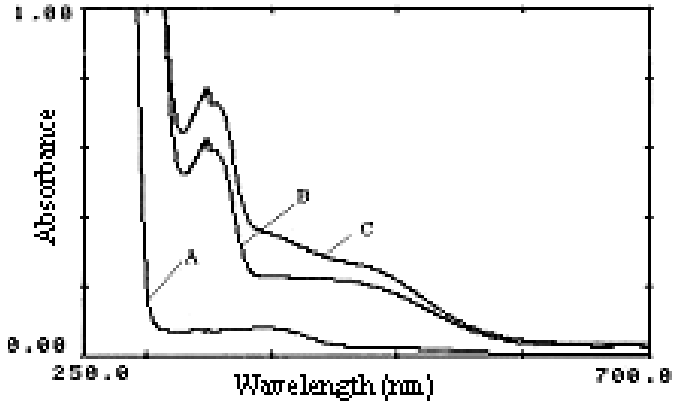


Fig. 2. Electronic absorption spectra of **1c**–DDQ reaction in CH_3OH. (A) [**1c**] = 0.001 mol/L, (B) [DDQ] = 0.001 mol/L, (C) **1c**–DDQ mixture: [**1c**] = [DDQ] = 0.001 mol/L.

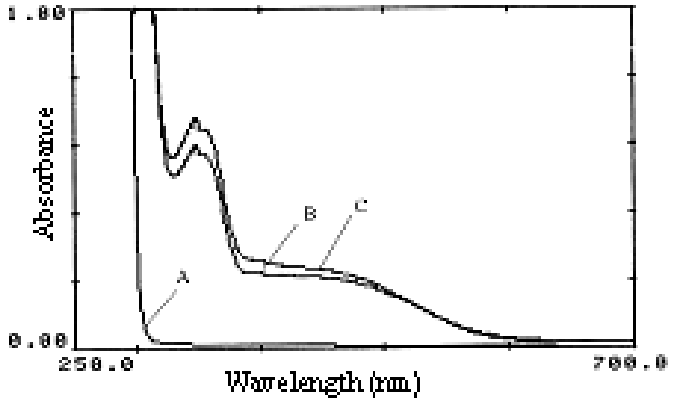


Fig. 3. Time evolution of the UV–vis spectra for the reaction of NH_4SCN with DDQ and 2-methylindole (**1b**) CT-complex at room temperature. The spectra were taken at 2 min intervals.

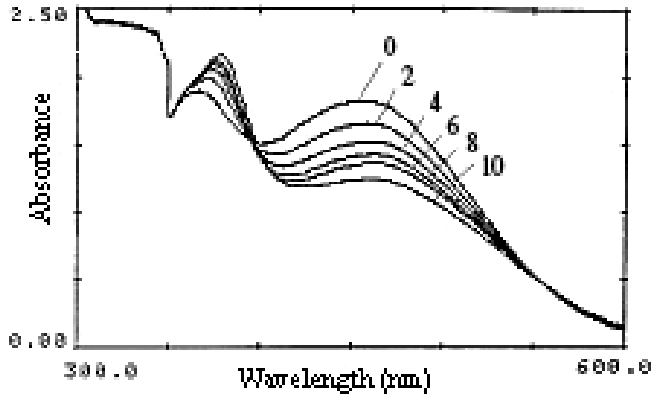
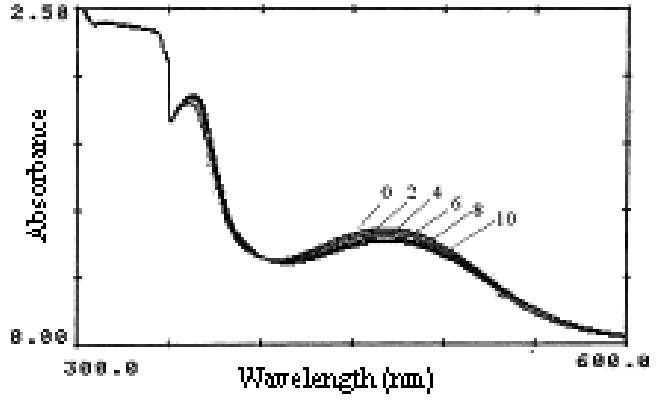


Fig. 4. Time evolution of the UV–vis spectra for the reaction of NH_4SCN with DDQ and 1-methylindole (**1c**) CT-complex at room temperature. The spectra were taken at 2 min intervals.



resonance effect of the nitrogen lone pair directs the position of thiocyanate addition after complexation with DDQ.

Experimental

Melting points were determined using a Stuart Scientific SMP2 capillary apparatus and are uncorrected. IR spectra were recorded from KBr discs (unless otherwise mentioned) on Shimadzu IR-435. ^{1}H NMR spectra were recorded with a Brucker drx 500 (500 MHz) machine. They are reported as follows: chemical shifts (multiplicity, number of protons, coupling constants *J* (Hz), and assignment). Mass spectra were obtained on Platform II spectrometer from Micromass; EI mode at 70 eV. Elemental analysis was run on CHN-O-RAPID analyzer from Heraeus. Conductance measurements were carried out with an ORION (**1c**) Model 180 coductivity meter. A dip-type cell with a cell constant of 0.723 cm^{-1} of platinum blank was used. Stock solutions of **1b** and DDQ were prepared in methanol. Varying concentrations of DDQ were added to a fixed concentration of **1b** and **1c** to prepare the desired DDQ to **1b** or **1c** molar ratios of 0.5:1, 1:1, and 2:1 for conductance measurements at 23 and 50 °C. Preparative layer chromatography (PLC) was carried out on 20 × 20 cm^2 plates, coated with a 1 mm layer of Merck silica gel PF_{254}, prepared by applying the silica gel as a slurry and dying in air.

General procedure for the thiocyanation of aromatic and heteroaromatic compounds at room temperature (method A)

To a solution of the aromatic or heteroaromatic compound (1 mmol) and NH_4SCN (2 mmol) in CH_3OH (5 mL), was added DDQ (1.5 mmol) at room temperature. The reaction mixture was stirred for the appropriate time according to Table 3. The progress of the reaction was monitored by TLC. The solvent was evaporated; the residue was diluted with water (10 mL) and extracted with chloroform (3 × 10 mL). The combined organic layers were dried over $MgSO_4$ and evaporated under reduced pressure. The resulting crude product was purified by plate chromatography on silica gel (PLC; eluent: *n*-hexane–EtOAc, 9:1). Further recrystallization from petroleum ether – EtOAc gives the pure product (Table 3).

General procedure for the thiocyanation of aromatic and heteroaromatic compounds under reflux conditions (method B)

To a solution of the aromatic or heteroaromatic compound (1 mmol) and NH_4SCN (2 mmol) in CH_3OH (5 mL), was

© 2007 NRC Canada

Table 4. Observed conductances (μs/cm^2) of charge-transfer complexes **1b** and **1c** with DDQ at different molar ratios at 23 and 50 °C in methanol solution.

Molar ratio[a]	0:1[b]		0.5:1[c]		1:1[c]		2:1[c]	
T °C	23	50	23	50	23	50	23	50
1b	0.82	15.35	48.34	5.85	81.21	26.05	90.08	30.65
1c	0.79	15.2	47.77	5	68.24	14.9	70.71	21.5

Note: The values refer to the corrected conductances. This means that the conductances of methanol has been subtracted.
[a]Molar ratio of DDQ:**1b** or **1c**.
[b]*C* (**1b** or **1c**) = 0.01 mol/L.
[c]Conductance of DDQ at 23 (50 °C) and 0.005 mol/L, 0.01 mol/L, and 0.02 mol/L was 11.18 (126.41), 23.81 (127.01), and 38.34 (131.41), respectively.

Fig. 5. The plot of conductances vs. DDQ–**1b** in different molar ratios at 23 and 50 °C.

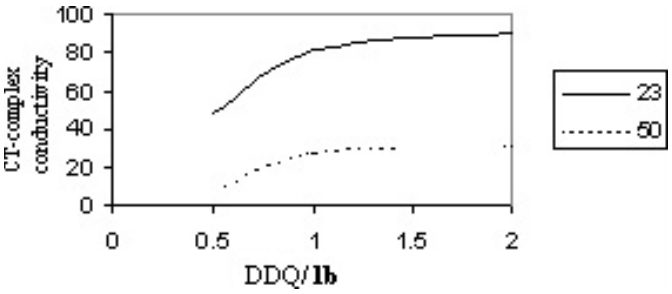
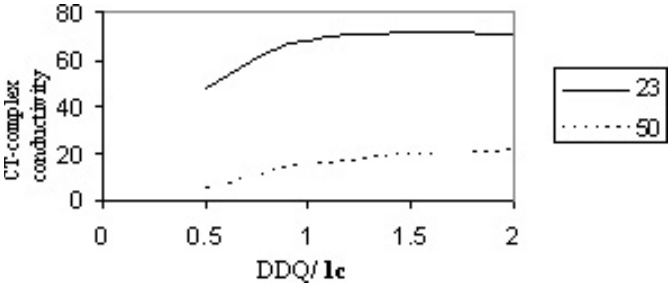


Fig. 6. The plot of conductances vs. DDQ–**1c** in different molar ratios at 23 and 50 °C.

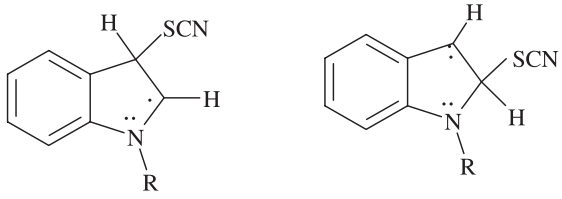


added DDQ (1.25 mmol). The reaction mixture was taken in pre-heated oil bath for the appropriate time according to Table 3. The progress of the reaction was monitored by TLC. The solvent was evaporated; the residue was diluted with water (10 mL) and extracted with chloroform (3 × 10 mL). The combined organic layers were dried over $MgSO_4$ and evaporated under reduced pressure. The resulting crude product was purified by plate chromatography on silica gel (PLC; eluent: *n*-hexane–EtOAc, 9:1). Further recrystallization from petroleum ether – EtOAc gives the pure product (Table 3).

3-Thiocyanatoindole (2a)

Mp 105–106 °C (Lit. (11) 125–127 °C). IR ν: 3334 (NH), 2150 (SCN), 1435, 1410, 1232, 1095, 735 (N–H), 658 (C–S) cm^{-1}. ^{1}H NMR ($CDCl_3$) δ: 7.29–7.42 (m, 4H, 4-, 5-, 6-, 7-H), 7.81 (d, 1H, *J* = 8.72 Hz, 2-H), 8.90 (brd s, 1H, NH). EI-MS *m/z* (%): 174 [M$^+$] (100), 148 [M$^+$ – CN] (63), 116 [M$^+$ – SCN] (28).

Scheme 2.



2-Methyl-3-thiocyanatoindole (2b)

Mp 99–101 °C (Lit. (11) 102–103 °C). IR ν: 3324 (NH), 2140 (SCN), 1582, 1540, 1455, 1408, 1228, 738 (N–H), 658 (C–S) cm^{-1}. ^{1}H NMR ($CDCl_3$) δ: 2.58 (s, 3H, CH_3), 7.23–7.28 (m, 2H, 5-, 6-H), 7.34 (d, 1H, *J* = 7.63 Hz, 4-H), 7.69 (d, 1H, *J* = 7.52 Hz, 7-H), 8.41 (brd s, 1H, NH). EI-MS *m/z* (%): 188 [M$^+$] (100), 173 [M$^+$ – CH_3] (5), 161 [M$^+$ – HCN] (22), 146 [M$^+$ – HCN, – CH_3] (6), 117[M$^+$ – SCN, – CH_3] (15).

1-Methyl-3-thiocyanatoindole (2c)

Mp 83–84 °C. IR ν: 2145 (SCN), 1514, 1240, 748 (C–S), 661 cm^{-1}. ^{1}H NMR ($CDCl_3$) δ: 3.82 (s, 3H, CH_3), 7.31–7.41 (m, 4H, 4-, 5-, 6-, 7-H), 7.81 (d, 1H, *J* = 7.56 Hz, 2-H). EI-MS *m/z* (%): 188 [M$^+$] (100), 173 [M$^+$ – CH_3] (37), 162 [M$^+$ – CN] (27), 146 [M$^+$ – HCN, – CH_3] (40), 130 [M$^+$ – SCN] (12).

5-Bromo-3-thiocyanatoindole (2d)

Mp 127–129 °C. IR ν: 3321 (NH), 2122 (SCN), 1452, 1408, 1106, 794 (N–H), 654 (C–S), 601 cm^{-1}. ^{1}H NMR ($CDCl_3$) δ: 7.31 (d, 1H, *J* = 8.68 Hz, 7-H), 7.41 (dd, 1H, *J* = 8.65 Hz, *J* = 1.71 Hz, 6-H), 7.53 (d, 1H, *J* = 2.79 Hz, 4-H), 7.93 (s, 1H, 2-H), 8.72 (brd s, 1H, NH). EI-MS *m/z* (%): 253 [M$^+$] (27), 227 [M$^+$ – CN] (7), 173 [M$^+$ – Br] (100), 146 [M$^+$ – HCN, – Br] (19), 114 [M$^+$ – HSCN, – Br] (8).

3-Thiocyanatocarbazole (2e)

Mp 80–81 °C (Lit. (6) 76.5–78 °C). IR ν: 3295 (NH), 2155 (SCN), 2925, 1721, 1620, 1472, 1208, 1121, 1062, 734 (N–H), 702 (C–S) cm^{-1}. ^{1}H NMR ($CDCl_3$) δ: 7.41–7.47 (m, 4H, 6-,7-,8-, 9-H), 7.53 (d, 1H, *J* = 8.55 Hz, 2-H), 7.59 (d, 1H, *J* = 3.1 Hz, 5-H), 7.68 (dd, 1H, *J* = 8.53 and 1.86 Hz, 2-H), 8.31 (brd S, 1H, NH). EI-MS *m/z* (%): 224 [M$^+$] (2), 191 [M$^+$ – SH] (4), 165 [M$^+$ – SCN, – H] (100).

© 2007 NRC Canada

2-Thiocyanatopyrole (2fa)

Liquid (Lit. (4) liquid). IR (film) ν: 3395 (NH), 2902, 2126 (SCN), 1462, 1381, 1115, 735 (N–H), 662 (C–S) cm^{-1}. ^1H NMR ($CDCl_3$) δ: 6.29 (dd, 1H, *J* = 5.91 and 2.91 Hz, 4-H), 6.66 (s, 1H, 3-H), 6.99 (s, 1H, 5-H), 8.87 (brd s, 1H, NH). EI-MS *m/z* (%): 124 [M^+] (100), 98 [M^+ – CN] (10).

2,5-Dithiocyanatopyrole (2fb)

Mp 97–99 °C (Lit. (10) 99–102 °C). IR ν: 3392 (NH), 2906, 2122 (SCN), 1623, 1381, 1105, 792 (N–H), 683 (C–S) cm^{-1}. ^1H NMR ($CDCl_3$) δ: 6.71 (d, 2H, *J* = 1.18 Hz, 3-, 4-H), 9.38 (brd s, 1H, NH). EI-MS *m/z* (%): 181 [M^+] (92), 154 [M^+ – HCN] (77), 123 [M^+ – SCN] (99), 96 [M^+ – HCN, – SCN] (100), 64 [M^+ – HSCN, – SCN] (27).

4-Thiocyanatoaniline (2g)

Mp 51–52 °C (Lit. (10) 51–52 °C). IR ν: 3375 (NH_2), 2144 (SCN), 2902, 1595, 1382, 1095, 795 cm^{-1}. ^1H NMR ($CDCl_3$) δ: 3.95 (brd s, 2H, NH_2), 6.68 (d, 2H, *J* = 8.59 Hz, 2-, 6-H), 7.37 (d, 2H, *J* = 8.56 Hz, 3-, 5-H). EI-MS *m/z* (%): 150 [M^+] (33), 134 [M^+ – NH_2] (4), 123 [M^+ – HCN] (14), 91[M^+ – HSCN] (53).

4-Thiocyanato-*N*-methylaniline (2h)

Liquid. IR (film) ν: 3385 (NH), 2908, 2142 (SCN), 1596, 1508, 1305, 1181, 814 (N–H), 745 (C–S) cm^{-1}. ^1H NMR ($CDCl_3$) δ: 2.84 (s, 3H, CH_3), 4.12 (brd s, 1H, NH), 6.58 (d, 2H, *J* = 8.67 Hz, 2-, 6-H), 7.38 (d, 2H,, *J* = 8.64 Hz, 3-, 5-H). EI-MS *m/z* (%): 164 [M^+] (100), 149 [M^+ – CH_3] (820), 138 [M^+ – CN] (69), 105 [(M^+ – SCN, – H] (60), 90 [M^+ – SCN, – H, – CH_3] (21), 77 [M^+ – CH_3, – NH, – SCN] (38).

4-Thiocyanato-*N*,*N*-dimethylaniline (2i)

Mp 71–72 °C (Lit. (4) 72–74 °C). IR ν: 2130 (SCN), 1585, 1504, 1368, 1079, 803 (C–S) cm^{-1}. ^1H NMR ($CDCl_3$) δ: 3.00 (s, 6H, $2CH_3$), 6.68 (d, 2H, *J* = 8.97 Hz, 2-, 6-H), 7.43 (d, 2H, *J* = 8.99 Hz, 3-, 5-H). EI-MS *m/z* (%): 178 [M^+] (100), 163 [M^+ – CH_3] (15), 152 [M^+ – CN] (29), 134 [M^+ – $N(CH_3)_2$] (11), 108 [M^+ – CN, – $N(CH_3)_2$] (23).

2-Choloro-4-thiocyanatoaniline (2j)

Mp 60–61 °C. IR ν: 3457 (NH_2), 3385 (NH_2), 2142 (SCN), 1627, 1595, 1482, 1153, 809, 702 (N–H), 668 (C–S), 563 cm^{-1}. ^1H NMR ($CDCl_3$) δ: 4.39(brd s, 2H, NH_2), 6.77 (d,1H, *J* = 8.47 Hz, 6-H), 7.28 (dd, 1H, *J* = 8.46 and 2.14 Hz, 5-H), 7.50 (d, 2H, *J* = 2.14 Hz, 3-H). EI-MS *m/z* (%): 184 [M^+] (98), 158 [M^+ – CN] (78), 149 [M^+ – Cl] (98), 133 [M^+ – Cl, – NH_2] (18), 125 [M^+ – HSCN] (20). $C_7H_5N_2ClS$ (184.58) calcd.: C 45.54, H 2.71, N 15.17; found: C 45.48, H 2.69, N 15.13.

3-Methoxy-4-thiocyanatoaniline (2k)

Mp 99–100 °C. IR ν: 3368 (NH_2), 3415 (NH_2), 2121 (S–CN), 1627, 1593, 1462, 1327, 1218, 1047, 821 (N–H), 796 (C–S). ^1H NMR ($CDCl_3$) δ: 3.88 (s, 3H, CH_3), 3.99 (s, 2H, NH_2), 6.25 (d, 1H, *J* = 2.12 Hz, 2-H), 6.29 (dd, 1H, *J* = 8.29 and 2.24 Hz, 6-H), 7.30 (d, 1H, *J* = 8.30 Hz, 5-H). EI-MS *m/z* (%):180 [M^+] (100), 164 [M^+ – NH_2] (17), 149 [M^+ – OCH_3] (12), 110[M^+ – HCN, – $COCH_3$] (9), 91 [M^+ – SCN, – OCH_3] (13). $C_8H_8N_2OS$ (180.13) calcd.: C 53.34, H 4.44, N 15.54; found: C 53.40, H 4.41, N 15.49.

4-Thiocyanatodiphenylamine (2la)

Mp 62–64 °C. IR ν: 3332 (NH), 2132 (SCN), 1602, 1578, 1525, 1488, 1330, 820, 745 (N–H), 692 (C–S) cm^{-1}. ^1H NMR ($CDCl_3$) δ: 5.93 (brd s, 1H, NH), 7.03 (d, 2H, *J* = 8.65 Hz, 2-,6-H), 7.07 (t, 1H, *J* = 7.38 Hz, 4′-H), 7.14 (d, 2H, *J* = 7.82 Hz, 2′-, 6′-H), 7.34 (t, 2H, *J* = 7.84 Hz, 3′-, 5′-H), 7.43 (d, 2H, *J* = 8.67 Hz, 3-,5-H). EI-MS *m/z* (%): 226 [M^+] (100), 200[M^+ – CN] (30), 167 [M^+ – H, – SCN] (66), 77 [Ph^+] (36).

4,4′-Dithiocyanatodiphenylamine (2lb)

Mp 110–111 °C. IR ν: 3342 (NH), 2125 (SCN), 1582, 1516, 1482, 1335, 803 (N–H) cm^{-1}. ^1H NMR ($CDCl_3$) δ: 6.09 (brd s, 1H, NH), 7.12 (d, 4H, *J* = 8.68 Hz, 3-, 5-, 3′-, 5′-H), 7.49 (d, 4H, *J* = 8.68 Hz, 2-, 6-, 2′-, 6′-H). EI-MS *m/z* (%): 283 [M^+] (19), 257 [M^+ – CN] (4), 225 [M^+ – SCN] (23), 149[M^+ – PhSCN] (11), 122 [M^+ – PhSCN, – HCN] (22), 90 [M^+ – PhSCN, – HSCN] (4).

Acknowledgments

We are thankful to the Center of Excellence (Chemistry) and Office of Graduate Studies of the University of Isfahan for their financial support.

References

1. J.L. Wood. *In* Organic reactions. Vol. 3. Wiley, New York. 1967. pp. 240–266.
2. T.R. Kelly, M.H. Kim, and A.D.M. Cetris. J. Org. Chem. **58**, 5855 (1993).
3. F.D. Toste, F. Laronde, and I.V.J. Still. Tetrahedron Lett. **36**, 2949 (1995).
4. J.S. Yadav, B.V.S. Reddy, S. Shubashree, and K. Sadashiv. Tetrahedron Lett. **45**, 2951 (2004).
5. (*a*) B.L. Leblanc and B.C. Jursic. Synth. Commun. **28**, 3591 (1998); (*b*) A.A. Newman. Chemistry and biochemistry of thiocyanic acid and its derivatives. 1st Ed. Academic Press. USA. 1975.
6. M.S. Grant and H.R. Synder. J. Am. Chem. Soc. **82**, 2742 (1960).
7. V. Nair, T.G. George, l.G. Nair, and S.B. Panicker. Tetrahedron Lett. **40**, 1195 (1999).
8. F.D. Toste, V.D. Stefano, and I.V.J. Still. Synth Commun. **25**, 1277 (1995).
9. M. Chakrabarty and S. Sarkar. Tetrahedron Lett. **44**, 8131 (2003).
10. G. Wu, Q. Liu, Y. Shen, W. Wu, and L. Wu. Tetrahedron Lett. **46**, 5831 (2005).
11. J.S. Yadav, B.V.S. Reddy, A.D. Krishna, Ch. Suresh Reddy, and A.V. Narsaiah. Synthesis, 961 (2005).
12. N.-E. Es-Safi and P.-H. Ducrot. Lett. Org. Chem. **3**, 231 (2006).
13. G.P. Kalena, S.M. Jadhav, and A. Banerji. Molecules, **5**, 240 (2000).
14. K. Peng, F. Chen, X. She, Ch. Yang, Y. Cui, and X. Pan. Tetrahedron Lett. **46**, 1217 (2005).
15. J.H.P. Utley and G.G. Rozenberg. J. Appl. Electrochem. **33**, 525 (2003).
16. L.O. Kononov, N.N. Malysheva, Y. Ito, and T. Ogawa. Rus. Chem. Bull. **53**, 254 (2004).

© 2007 NRC Canada

17. (*a*) A.J.M. Da Silva, C.D. Netto, and P.R.R. Costa. J. Braz. Chem. Soc. **15**, 979 (2004); (*b*) B.P. Joshi A.A.K. Sharma, and A. Sinha. Tetrahedron, **62**, 2590 (2006).
18. M. Uemura, H. Yorimistu, and K. Oshima. Tetrahedron Lett. **47**, 163 (2006).
19. N. Iranpoor and I. Mohammadpoor-Baltork. Tetrahedron Lett. **31**, 735 (1990).
20. N. Iranpoor, H. Firouzabadi, Gh. Aghapour, and A. Nahid. Bull. Chem. Soc. Jpn. **77**, 1885 (2004).
21. H. Firouzabadi, N. Iranpoor, and S. Sobhani. Synthesis, 290 (2004).
22. N. Iranpoor, H. Firouzabadi, and N. Nowrouzi. Tetrahedron, **62**, 5498 (2006).
23. H. Duymus, M. Arslan, M. Kucukislamoglu, and M. Zengin. Spectrochim. Acta A. **65**, 1120 (2006).
24. M. Pundeeswaran and K.P. Elango. Spectrochim. Acta A. **65**, 1148 (2006).
25. M.S. Refat and A.M. El-Didamong. Spectrochim. Acta A. **65**, 732 (2006).
26. E.H. El-Mossalamy. J. Mol. Liq. **123**, 118 (2006).
27. M. Guber and S.S. Al-Shihry. Spectrochim. Acta A. *62*, 526 (2005).
28. F. Yakuplianoglu, M. Arslan, and S.Z. Yildiz. Opt. Mater. **27**, 1153 (2005).
29. P.C. Dwivedi, A.K. Banga, and R. Agarwal. Electrochom. Acta. **27**, 1697 (1982).
30. F. Bernardi, N.D. Epiotis, W. Cherry, H.B. Schlegel, M.-H. Whangho, and S. Wolfe. J. Am. Chem. Soc. **98**, 469 (1976).

© 2007 NRC Canada

Norcantharidin analogues — Synthesis and evaluation of growth inhibition in a panel of selected tumor-cell lines

Liping Deng, Li Shen, Jing Zhang, Bo Yang, Qiaojun He, and Yongzhou Hu

Abstract: A series of norcantharidin (NCTD) analogues have been synthesized by [3+2]1,3-dipolar cycloaddition reaction of norcantharidin derivatives of substituted aromatic amines with four nitrile oximes. All analogues have been screened for their antiproliferative activity in vitro against a panel of tumor cell lines: KB, SGC-7901, HL60, Bel-7402, HO-8910, and ECA109, producing IC_{50} values from 0.36 μmol/L to >100 μmol/L. Compound **9d** showed potency for the treatment of hepatoma, with IC_{50} value to Bel-7402 cell line comparable to that of norcantharidin.

Key words: norcantharidin analogues, isoxazoline, growth inhibition.

Résumé : On a réalisé la synthèse d'une série d'analogues de la norcantharidine en procédant à une réaction de cycloaddition 1,3-dipolaire [3+2] de dérivés de la norcantharidine d'amines aromatiques substituées avec quatre oximes de nitriles. On a évalué l'activité comme inhibiteur de croissance in vitro de chacun des analogues contre un ensemble de souches de cellules tumorales: KB, SGC-7901, HL60, Bel-7402, HO-8910 et ECA109 pour lesquelles les valeurs de IC_{50} varient de 0,36 μmol/L à plus de 100 μmol/L. Le composé **9d** présente un grand potentiel pour le traitement de l'hépatome, avec une valeur de IC_{50} qui, par comparaison avec celle des cellules Bel-7402, est comparable à celle de la norcantharidine.

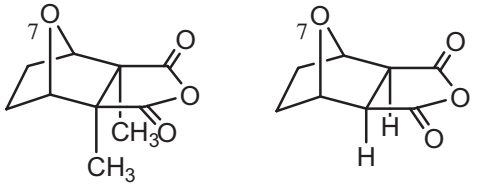
Mots-clés : analogues de la norcantharidine, isoxazoline, inhibition de la croissance.

[Traduit par la Rédaction]

Introduction

Traditional Chinese medicine is a rich source of potential anticancer agents. In particular, cantharidin (CAN; exo, exo-2,3-dimethyl-7-oxabicyclo[2.2.1]heptane-2,3-dicarboxylic acid anhydride; Fig. 1) is the active ingredient of Mylabris, which has been used in China as a medicinal agent for the treatment of cancer, particularly hepatoma (1). Although cantharidin is cytotoxic to cancer cells and stimulatory on the bone marrow, the renal toxicity of this drug has limited its application (2). A series of bioactive analogues have been synthesized in an attempt to increase the utility and to reduce the toxicity of cantharidin. Norcantharidin (NCTD; Fig. 1), the demethylated analogue of cantharidin, has been used to treat human cancers in China since 1984 (2). NCTD appeared to improve the awkward side of cantharidin, making the drug safer in application. It was recently found to be capable of inducing apoptosis in human cervical, tongue, ginival, mucoepidermoid carcinoma, adenocystic carcinoma, neuroblastoma, bone, leukaemia, ovarian, and colon cancer cell lines (3–5); however, the main application so far is treating hepatoma. We have referred to all the known cantharidin SAR data; briefly, no modification of the bicyclo[2.2.1] skeleton is permissible, the 7-oxa bridge is required to maintain activity, and the presence of a double bond (5,6-ene) has little effect on activity (6–10). Replacement of the O-atom (anhydride) with N (as N–H and N–R, where R = aryl or thiazolyl) allows the development of a new series of anhydride-modified cantharidin analogues; some are more potent than CAN or display potency similar to NCTD (11, 12). On the other hand, it is well-known that isoxazoline derivatives possess a wide range of pharmacological activities (13). These observations prompted us to design a new series of norcantharidin analogues by combining isoxazoline with norcantharidin derivatives in one single molecule to improve their antiproliferative activities and to carry out a structure–activity relationship study. In this paper, we describe the synthetic methodology towards the development of a series of norcantharidin analogues and their antiproliferative activities in vitro against various human tumor-cell lines.

Fig. 1. Chemical structures of Cantharidin and Norcantharidin.



Cantharidin Norcantharidin

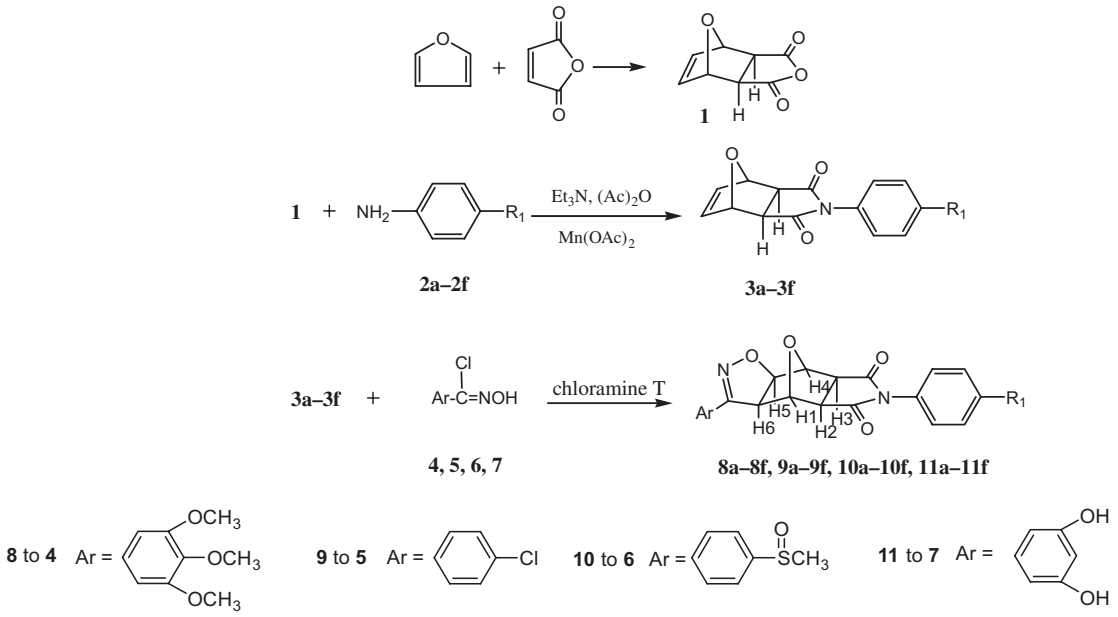
Received 11 September 2006. Accepted 17 May 2007. Published on the NRC Research Press Web site at canjchem.nrc.ca on 3 October 2007.

L. Deng, L. Shen, and Y. Hu.[1] ZJU-ENS joint laboratory of medicinal chemistry, School of Pharmaceutical Sciences, Zhejiang University, Hangzhou 310058, China.
J. Zhang, B. Yang, and Q. He. Department of Pharmacology and Toxicology, School of Pharmaceutical Sciences, Zhejiang University, Hangzhou 310058, China.

[1]Corresponding author (email: huyz@zjuem.zju.edu.cn).

 doi:10.1139/V07-082 © 2007 NRC Canada

Scheme 1. Synthetic route of novel norcantharidin analogues **8a–8f**, **9a–9f**, **10a–10f**, and **11a–11f**.



2a, 3a, 8a–11a R_1 = H; **2b, 3b, 8b–11b** R_1 = F; **2c, 3c, 8c–11c** R_1 = Cl;
2d, 3d, 8d–11d R_1 = Br; **2e, 3e, 8e–11e** R_1 = CH_3; **2f, 3f, 8f–11f** R_1 = OCH_3;

Results and discussion

Synthesis

Norcantharidin analogues were prepared as shown in Scheme 1. Treatment of furan with maleic anhydride resulted in 5,6-dehydronorcantharidin **1**, then compound **1** reacted with substituted phenylamine **2a–2f** to give compounds **3a–3f** according to the published procedure (16). [3+2] Cycloaddition of **3a–3f** with four nitrile oximes **4–7** in the presence of chloramine T yielded target compounds **8a–8f**, **9a–9f**, **10a–10f**, and **11a–11f**. All compounds were tested as racemic mixtures.

To identify the configuration of the norcantharidin analogues (**8a–8f**, **9a–9f**, **10a–10f**, and **11a–11f**), we have studied selective ^{1}H–^{1}H COSY spectra and NOESY spectra of the compounds. ^{1}H–^{1}H COSY spectra showed cross peaks between H-2 and H-3 and H-5 and H-6. NOESY spectra showed cross peaks between H-2 and H-6 and H-3 and H-5. The Diels–Alder adduct 5,6-dehydronorcantharidin of furan with maleic anhydride have the exo configuration exclusively; the endo isomer has never been reported (14, 15), which, combined with ^{1}H–^{1}H COSY and NOESY spectra data, give us a reasonable exo-adduct configuration, as we have proved before similarly (16, 17).

Biological activity

The norcantharidin analogues **8a–8f**, **9a–9f**, **10a–10f**, and **11a–11f** were screened for their antiproliferative activity against a panel of six tumor-cell lines: KB, SGC7901, HL60, Bel7402, HO8910 and ECA109. CAN and NCTD were included as internal standards. IC_{50} values of different compounds are summarized in Table 1.

As shown in Table 1, the synthesized compounds displayed growth inhibition with IC_{50} values ranging from 0.36 μmol/L to >100 μmol/L. Most norcantharidin analogues were antiproliferative against HL60 cell line after 72 h treatment and were inactive to the KB and SGC7901 cell lines. Some norcantharidin analogues exhibited higher growth inhibition than NCTD, e.g., **9c** was more potent than NCTD against HL60 cell line, and **11c** was more potent than NCTD against HL60 and HO8910 cell lines. Also, compound **9d** displayed potency against Bel-7402 cell line comparable to that of NCTD, suggesting that the halogeno group in the aryl moiety (R_1) might be crucial for activity. It is also noteworthy that the presence of the methoxyl (such as **8f**, **9f**, **10f**, and **11f**) appeared to have an unfavorable effect.

The apoptosis-inducing activity of NCTD and its analogues was dose- and time-dependent; for instance, the antiproliferative activity of compound **9d** and cantharidin against Bel-7402 cell line are shown in Fig. 2.

Conclusion

From the data presented, subtle modifications of norcantharidin's skeleton permitted the development of a new series of analogues with alterations in their antiproliferative activity against a panel of tumor-cell lines. The lead compounds cantharidin and norcantharidin are somewhat more potent against tumor-cell lines, respectively. Of the synthesized analogues, the notable exception being **9c**, which showed both good potency and selectivity for the HL60 cell line, and compound **9d** displayed moderate potency for the treatment of hepatoma with IC_{50} values to Bel7402 cell line comparable to that of norcantharidin. We are currently working towards the development of more po-

© 2007 NRC Canada

Table 1. Antiproliferative activity of the skeletally modified norcantharidin analogues (**8a–8f**, **9a–9f**, **10a–10f**, and **11a–11f**).

	IC_{50} (μmol/L)[a, b]					
Compound	KB	SGC7901	HL60	Bel7402	HO8910	ECA109
CAN	21.9	58.2	0.1	1	1.28	0.38
NCTD	32.2	79	5	24	>100	47.4
8a	>100	>100	>100	>100	>100	>100
8b	>100	>100	>100	>100	>100	>100
8c	>100	>100	>100	>100	>100	>100
8d	>100	>100	7.2	>100	>100	>100
8e	>100	>100	60.6	>100	>100	>100
8f	>100	>100	>100	>100	>100	>100
9a	>100	>100	51.2	>100	>100	>100
9b	>100	>100	74.4	>100	>100	>100
9c	>100	>100	0.36	>100	>100	>100
9d	>100	>100	1.9	37.7	>100	88.3
9e	>100	>100	3.4	62.4	>100	87.5
9f	>100	>100	>100	>100	>100	>100
10a	>100	>100	>100	>100	>100	>100
10b	>100	>100	4.9	69.6	>100	>100
10c	>100	>100	4.8	>100	>100	>100
10d	>100	>100	20	>100	>100	>100
10e	>100	>100	>100	>100	>100	>100
10f	>100	>100	>100	>100	>100	>100
11a	>100	>100	1.6	>100	>100	>100
11b	>100	>100	92.3	>100	>100	>100
11c	>100	>100	1.6	>100	16.5	>100
11d	>100	>100	17.8	>100	>100	>100
11e	>100	>100	13	>100	>100	>100
11f	>100	>100	>100	>100	>100	>100

[a]The IC_{50} values represent the concentration that results in a 50% decrease in cell growth after 72 h incubation.
[b]The IC_{50} values were the mean values of three repeated experiments.

tent and selective analogues of this nature and will report the outcome of these studies in due course.

Experimental section

General

All reagents were of commercial quality and were used as received (Aldrich). Solvents were dried and purified using standard techniques. Reactions were monitored by TLC on aluminum plates coated with silica gel with fluorescent indicator (Merck 60 F254). Melting points were obtained on a B-540 Büchi melting-point apparatus and are uncorrected. ^{1}H NMR and NOESY spectra were recorded on a Brucker AM-400 MHz spectrometer with $SiMe_4$ as the internal standard in DMSO-d_6. Mass Spectra were recorded with a HP5989B analyzer. Elemental analyses were performed on an EA-1110 instrument.

General procedure for the preparation of the 5,6-dehydronorcantharidinisoxazoline adducts (8a–8f, 9a–9f, 10a–10f, 11a–11f)

To a solution of 3-acetyl-7-oxa-bicyclo[2.2.1]hept-5-ene-2-carboxylic acid phenylamide **3a** (1 mmol) and **4** (1 mmol) in ethanol (20 mL) was added chloramine T (1.2 mmol), and the reaction mixture was refluxed in ethanol for 4–7 h. Then, it was cooled to room temperature, water (10 mL) was added to the reaction mixture, and it was extracted with dichloromethane (30 mL). The extract was dried over anhyd. sodium sulfate, concentrated in vacuum, and the residue was recrystallized from acetone to give the compound **8a**. The synthesis of compounds **8b–8f, 9a–9f, 10a–10f, 11a–11f** were performed using the same method.

exo,exo-4,8-Epoxy-3a,4,4a,7a,8,8a-hexahydro-6-phenyl-3-(3,4,5-trimethoxyphenyl)-pyrrolo[3,4-f]-1,2-benzisoxazole (8a)

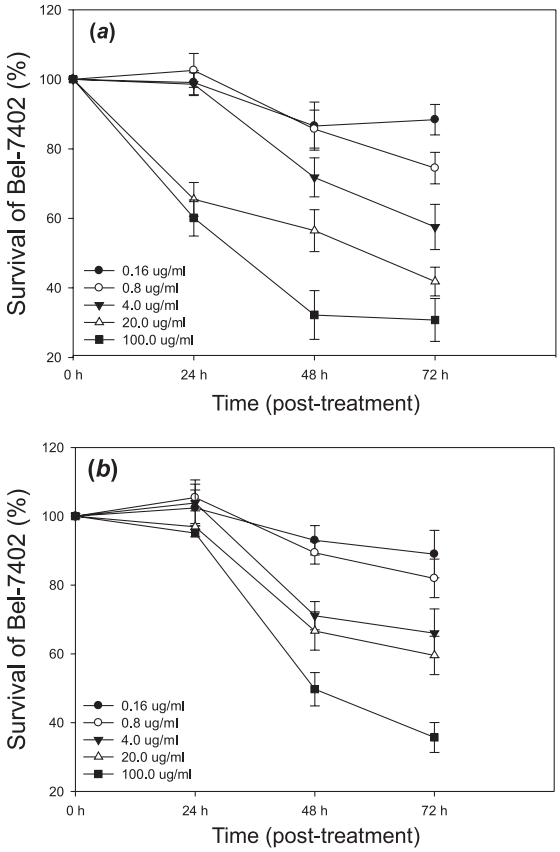
Compound **8a** was obtained as a colorless solid: yield 94%; mp 284 °C. IR ν (KBr, cm^{-1}): 3062 and 3027 (ArH), 1778, 1721 (C=O), 1598 (C=N), 1240 (C–O–C). ^{1}H NMR (DMSO-d_6) δ: 7.83–7.19 (m, 7H, Ar–H), 5.24 (d, J = 7.9 Hz, 1H, H-5), 4.98 (s, 1H, H-4), 4.75 (s, 1H, H-1), 4.52 (d, J = 7.9 Hz, 1H, H-6), 3.77 (s, 9H, 3 × OCH_3), 3.59 (d, J = 7.9 Hz, 1H, H-3), 3.38 (d, J = 7.9 Hz, 1H, H-2). MS m/z: 450 (M^+). Anal. calcd. for $C_{24}H_{22}N_2O_7$: C 63.99, H4.92, N 6.22; found: C 63.80, H 4.99, N 6.18.

exo,exo-6-(4-fluorophenyl)-4,8-epoxy-3a,4,4a,7a,8,8a-hexahydro-3-(3,4,5-trimethoxyphenyl)-pyrrolo[3,4-f]-1,2-benzisoxazole (8b)

Compound **8b** was obtained as a colorless solid: yield 81%; mp 300 °C (Dec.). IR ν (KBr, cm^{-1}): 3121 and 3010

© 2007 NRC Canada

Fig. 2. The antiproliferative activity of (*a*) cantharidin and (*b*) **9d** in Bel-7402 cell line. Cells were treated with various concentrations of cantharidin and **9d** for 24 h, 48 h, and 72 h. The percent of Bel-7402 cell line at each time point (post-treatment) is observed by MTT assay and expressed as the mean *D* of three independent experiments. Antiproliferative activity induced by cantharidin and **9d** is dose- and time-dependent in Bel-7402 cell line.



(ArH), 1777, 1718 (C=O), 1570 (C=N), 1224 (C–O–C). ^{1}H NMR (DMSO-d_6) δ: 7.83–7.25 (m, 6H, Ar–H), 5.23 (d, *J* = 7.9 Hz, 1H, H-5), 4.98 (s, 1H, H-4), 4.76 (s, 1H, H-1), 4.51 (d, *J* = 7.9 Hz, 1H, H-6), 3.59 (d, *J* = 7.9 Hz, 1H, H-3), 3.77 (s, 9H, 3 × OCH_3), 3.38(d, *J* = 7.9 Hz, 1H, H-2). MS *m*/*z*: 468 (M^+). Anal. calcd. for $C_{24}H_{21}FN_2O_7$: C 61.54, H 4.52, N 5.98; found: C 61.60, H 4.55, N 5.95.

*exo,exo-6-(4-Chlorophenyl)-4,8-epoxy-3a,4,4a,7a,8,8a-hexahydro-3-(3,4,5-trimethoxyphenyl)-pyrrolo[3,4-**f**]-1,2-benzisoxazole (8c)*

Compound **8c** was obtained as a colorless solid: yield 83%; mp 279 °C. IR ν (KBr, cm^{-1}): 3072 and 3029 (ArH), 1777, 1716 (C=O), 1571 (C=N), 1248 (C–O–C). ^{1}H NMR (DMSO-d_6) δ: 7.83–7.18 (m, 6H, Ar–H), 5.24 (d, *J* = 7.9 Hz, 1H, H-5), 4.98 (s, 1H, H-4), 4.76 (s, 1H, H-1), 4.51 (d, *J* = 7.9 Hz, 1H, H-6), 3.60 (d, *J* = 7.9 Hz, 1H, H-3), 3.77 (s, 9H, 3 × OCH_3), 3.38 (d, *J* = 7.9 Hz, 1H, H-2). MS *m*/*z*: 484 (M^+), 486 (M^+ + 2). Anal. calcd. for $C_{24}H_{21}ClN_2O_7$: C 59.45, H4.37, N 5.78; found: C 59.51, H 4.38, N 5.75.

*exo,exo-6-(4-Bromophenyl)-4,8-epoxy-3a,4,4a,7a,8,8a-hexahydro-3-(3,4,5-trimethoxyphenyl)-pyrrolo[3,4-**f**]-1,2-benzisoxazole (8d)*

Compound **8d** was obtained as a colorless solid: yield 91%; mp 280 °C. IR ν (KBr, cm^{-1}): 3056 and 3043 (ArH), 1780, 1721(C=O), 1567 (C=N), 1243 (C–O–C). ^{1}H NMR (DMSO-d_6) δ: 7.83–7.25 (m, 6H, Ar–H), 5.24 (d, *J* = 7.9 Hz, 1H, H-5), 4.98 (s, 1H, H-4), 4.75 (s, 1H, H-1), 4.51(d, *J* = 7.9 Hz, 1H, H-6), 3.59 (d, *J* = 7.9 Hz, 1H, H-3), 3.77 (s, 9H, 3 × OCH_3), 3.38 (d, *J* = 7.9 Hz, 1H, H-2). MS *m*/*z*: 528 (M^+), 530 (M + 2). Anal. calcd. for $C_{24}H_{21}BrN_2O_7$: C 54.46, H 4.00, N 5.29; found: C 54.48, H 4.03, N 5.25.

*exo,exo-4,8-Epoxy-3a,4,4a,7a,8,8a-hexahydro-3-(3,4,5-trimethoxyphenyl)-6-(**p**-tolyl)-pyrrolo[3,4-**f**]-1,2-benzisoxazole (8e)*

Compound **8e** was obtained as a colorless solid: yield 90%; mp 261 °C. IR ν (KBr, cm^{-1}): 3072 and 3060 (ArH), 1781, 1721(C=O), 1569 (C=N), 1286 (C–O–C). ^{1}H NMR (DMSO-d_6) δ: 7.83–7.15 (m, 6H, Ar–H), 5.23 (d, *J* = 7.9 Hz, 1H, H-5), 4.97 (s, 1H, H-4), 4.75 (s, 1H, H-1), 4.51 (d, *J* = 7.9 Hz, 1H, H-6), 3.59 (d, *J* = 7.9 Hz, 1H, H-3), 3.35 (d, *J* = 7.9 Hz, 1H, H-2), 3.77 (s, 9H, 3 × OCH_3), 2.33 (–CH_3). MS *m*/*z*: 464 (M^+). Anal. calcd. for $C_{25}H_{24}N_2O_7$: C 64.65, H 5.21, N 6.03; found: C 64.67, H 5.22, N 6.00.

*exo,exo-4,8-Epoxy-3a,4,4a,7a,8,8a-hexahydro-6-(4-methoxyphenyl)-3-(3,4,5-trimethoxypheny)-pyrrolo[3,4-**f**]-1,2-benzisoxazole (8f)*

Compound **8f** was obtained as a colorless solid: yield 91%; mp 279 °C. IR ν (KBr, cm^{-1}): 3051 and 3027 (ArH), 1778, 1714 (C=O), 1568 (C=N), 1250 (C–O–C). ^{1}H NMR (DMSO-d_6) δ: 8.37–7.49 (m, 6H, Ar–H), 5.25 (d, *J* = 7.9 Hz, 1H, H-5), 5.02 (s, 1H, H-4), 4.80 (s, 1H, H-1), 4.53 (d, *J* = 7.9 Hz, 1H, H-6), 3.66 (d, *J* = 7.9 Hz, 1H, H-3), 3.44 (d, *J* = 7.9 Hz, 1H, H-2), 3.77 (s, 9H, 3 × OCH_3), 3.83 (s, 3H, –OCH_3). MS *m*/*z*: 480 (M^+). Anal. calcd. for $C_{25}H_{24}N_2O_8$: C 62.49, H 5.03, N 5.83; found: C 62.51, H 5.02, N 5.81.

*exo,exo-4,8-Epoxy-3a,4,4a,7a,8,8a-hexahydro-6-phenyl-3-(4-chlorophenyl)-pyrrolo[3,4-**f**]-1,2-benzisoxazole (9a)*

Compound **9a** was obtained as a colorless solid: yield 95%; mp 300 °C (Dec.). IR ν (KBr, cm^{-1}): 3046 and 3008 (ArH), 1788, 1721 (C=O), 1567 (C=N), 1258 (C–O–C). ^{1}H NMR (DMSO-d_6) δ: 7.74–7.06 (m, 9H, Ar–H), 5.18(d, *J* = 7.9 Hz, 1H, H-5), 4.95 (s, 1H, H-4), 4.73 (s, 1H, H-1), 4.48 (d, *J* = 7.9 Hz, 1H, H-6), 3.59 (d, *J* = 7.9 Hz, 1H, H-3), 3.36 (d, *J* = 7.9 Hz, 1H, H-2). MS *m*/*z*: 394 (M^+). Anal. calcd. for $C_{21}H_{15}ClN_2O_4$: C 63.89, H 3.83, N 7.10; found: C 63.90, H 3.84, N 7.06.

*exo,exo-6-(4-Fluorophenyl)-4,8-epoxy-3a,4,4a,7a,8,8a-hexahydro-3-(4-chlorophenyl)-pyrrolo[3,4-**f**]-1,2-benzisoxazole (9b)*

Compound **9b** was obtained as a colorless solid: yield 82%; mp 310 °C (Dec.). IR ν (KBr, cm^{-1}): 3055 and 3017 (ArH), 1780, 1721 (C=O), 1543 (C=N), 1252 (C–O–C). ^{1}H NMR (DMSO-d_6) δ: 7.75–7.06 (m, 8H, Ar–H), 5.18 (d, *J* = 7.9 Hz, 1H, H-5), 4.95 (s, 1H, H-4), 4.74 (s, 1H, H-1), 4.47(d, *J* = 7.9 Hz, 1H, H-6), 3.59 (d, *J* = 7.9 Hz, 1H, H-3), 3.37(d, *J* = 7.9 Hz, 1H, H-2). MS *m*/*z*: 412 (M^+). Anal. calcd. for $C_{21}H_{14}ClFN_2O_4$: C 61.10, H 3.42, N 6.79; found: C 61.12, H 3.45, N 6.75.

© 2007 NRC Canada

exo,exo-6-(4-Chlorophenyl)-4,8-epoxy-3a,4,4a,7a,8,8a-hexahydro-3-(4-chlorophenyl)-pyrrolo[3,4-f]-1,2-benzisoxazole (9c)

Compound **9c** was obtained as a colorless solid: yield 84%; mp 309 °C (Dec.). IR ν (KBr, cm^{-1}): 3053 and 3027 (ArH), 1778, 1713 (C=O), 1550 (C=N), 1280 (C–O–C). ^{1}H NMR (DMSO-d_6) δ: 7.75–7.06 (m, 8H, Ar–H), 5.18 (d, *J* = 7.9 Hz, 1H, H-5), 4.95 (s, 1H, H-4), 4.74 (s, 1H, H-1), 4.47 (d, *J* = 7.9 Hz, 1H, H-6), 3.59 (d, *J* = 7.9 Hz, 1H, H-3), 3.37(d, *J* = 7.9 Hz, 1H, H-2). MS *m/z*: 428 (M^+). Anal. calcd. for $C_{21}H_{14}Cl_2N_2O_4$: C 58.76, H 3.29, N 6.53; found: C 58.78, H 3.30, N 6.49.

exo,exo-6-(4-Bromophenyl)-4,8-epoxy-3a,4,4a,7a,8,8a-hexahydro-3-(4-chlorophenyl)-pyrrolo[3,4-f]-1,2-benzisoxazole (9d)

Compound **9d** was obtained as a colorless solid: yield 70%; mp 325 °C (Dec.). IR ν (KBr, cm^{-1}): 3053 and 3029 (ArH), 1778, 1714 (C=O), 1528 (C=N), 1233 (C–O–C). ^{1}H NMR (DMSO-d_6) δ: 7.76–7.02 (m, 8H, Ar–H), 5.17 (d, *J* = 7.9 Hz, 1H, H-5), 4.95 (s, 1H, H-4), 4.74 (s, 1H, H-1), 4.47 (d, *J* = 7.9 Hz, 1H, H-6), 3.59 (d, *J* = 7.9 Hz, 1H, H-3), 3.37 (d, *J* = 7.9 Hz, 1H, H-2). MS *m/z*: 471(M^+), 473 (M^+ + 2). Anal. calcd. for $C_{21}H_{14}ClBrN_2O_4$: C 53.25, H 2.98, N 5.91; found: C 53.27, H 2.32, N 5.89.

exo,exo-4,8-Epoxy-3a,4,4a,7a,8,8a-hexahydro-3-(4-chlorophenyl)-6-(*p*-tolyl)-pyrrolo[3,4-f]-1,2-benzisoxazole (9e)

Compound **9e** was obtained as a colorless solid: yield 68%; mp 342 °C (Dec.). IR ν (KBr, cm^{-1}): 3058 and 3034 (ArH), 1787, 1723 (C=O), 1514 (C=N), 1289 (C–O–C). ^{1}H NMR (DMSO-d_6) δ: 7.77–7.02 (m, 8H, Ar–H), 5.17 (d, *J* = 7.9 Hz, 1H, H-5), 4.93 (s, 1H, H-4), 4.72 (s, 1H, H-1), 4.46 (d, *J* = 7.9 Hz, 1H, H-6), 3.59 (d, *J* = 7.9 Hz, 1H, H-3), 3.37 (d, *J* = 7.9 Hz, 1H, H-2), 2.33 (–CH_3). MS *m/z*: 408 (M^+). Anal. calcd. for $C_{22}H_{17}ClN_2O_4$: C 64.63, H 4.19, N 6.85; found: C 64.65, H 4.23, N 6.85.

exo,exo-4,8-Epoxy-3a,4,4a,7a,8,8a-hexahydro-3-(4-chlorophenyl)-6-(4-methoxyphenyl)-pyrrolo[3,4-f]-1,2-benzisoxazole (9f)

Compound **9f** was obtained as a colorless solid: yield 58%; mp 315 °C(Dec.). IR ν (KBr, cm^{-1}): 3057 and 3021 (ArH), 1786, 1718 (C=O), 1516 (C=N), 1258 (C–O–C). ^{1}H NMR (DMSO-d_6) δ: 7.86–7.22 (m, 8H, Ar–H), 5.19 (d, *J* = 7.9 Hz, 1H, H-5), 4.72 (s, 1H, H-1), 4.46 (d, *J* = 7.9 Hz, 1H, H-6), 3.56 (d, *J* = 7.9 Hz, 1H, H-3), 3.33 (d, *J* = 7.9 Hz, 1H, H-2), 3.83 (s, 3H, –OCH_3). MS *m/z*: 424 (M^+). Anal. calcd. for $C_{22}H_{17}ClN_2O_5$: C 62.20, H 4.03, N 6.59; found: C 62.23, H 4.03, N 6.58.

exo,exo-4,8-Epoxy-3a,4,4a,7a,8,8a-hexahydro-6-phenyl-3-(4-methylsulfinylphenyl)-pyrrolo[3,4-f]-1,2-benzisoxazole (10a)

Compound **10a** was obtained as a colorless solid: yield 95%; mp 310 °C (Dec.). IR ν (KBr, cm^{-1}): 3062, 3028 (ArH), 1778, 1722 (C=O), 1597 (C=N), 1239 (C–O–C). ^{1}H NMR (DMSO-d_6) δ: 7.83–7.20 (m, 9H, Ar–H), 5.24 (d, *J* = 7.9 Hz, 1H, H-5), 4.98 (s, 1H, H-4), 4.75 (s, 1H, H-1), 4.52 (d, *J* = 7.2 Hz, 1H, H-6), 3.59 (d, *J* = 7.9 Hz, 1H, H-3), 3.38 (d, *J* = 7.9 Hz, 1H, H-2), 3.27 (s, 3H, –$SOCH_3$). MS *m/z*: 422 (M^+). Anal. calcd. for $C_{22}H_{18}N_2O_5S$: C 62.55, H 4.29, N 6.63; found: C 62.56, H 4.30, N 6.61.

exo,exo-6-(4-Fluorophenyl)-4,8-epoxy-3a,4,4a,7a,8,8a-hexahydro-3-(4-methylsulfinylphenyl)-pyrrolo[3,4-f]-1,2-benzisoxazole (10b)

Compound **10b** was obtained as a colorless solid: yield 81%; mp 177 °C. IR ν (KBr, cm^{-1}): 3121 and 3011 (ArH), 1778, 1718 (C=O), 1570 (C=N), 1224 (C–O–C). ^{1}H NMR (DMSO-d_6) δ: 7.83–7.25 (m, 8H, Ar–H), 5.23 (d, *J* = 7.9 Hz, 1H, H-5), 4.97(s, 1H, H-4), 4.76 (s, 1H, H-1), 4.51 (d, *J* = 7.9 Hz, 1H, H-6), 3.59 (d, *J* = 7.9 Hz, 1H, H-3), 3.38 (d, *J* = 7.9 Hz, 1H, H-2), 3.27 (s, 3H, –$SOCH_3$). MS *m/z*: 440 (M^+). Anal. calcd. for $C_{22}H_{17}FN_2O_5S$: C 59.99, H 3.89, N 6.36; found: C 59.98, H 3.91, N 6.35.

exo,exo-6-(4-Chlorophenyl)-4,8-epoxy-3a,4,4a,7a,8,8a-hexahydro-3-(4-methylsulfinylphenyl)-pyrrolo[3,4-f]-1,2-benzisoxazole (10c)

Compound **10c** was obtained as a colorless solid: yield 83%; mp 152 °C. IR ν (KBr, cm^{-1}): 3072 and 3030 (ArH), 1774, 1716 (C=O), 1571 (C=N), 1239 (C–O–C). ^{1}H NMR (DMSO-d_6) δ: 7.83–7.23 (m, 8H, Ar–H), 5.24 (d, *J* = 7.9 Hz, 1H, H-5), 4.98 (s, 1H, H-4), 4.77 (s, 1H, H-1), 4.51 (d, *J* = 7.9 Hz, 1H, H-6), 3.60 (d, *J* = 7.9 Hz, 1H, H-3), 3.38 (d, *J* = 7.9 Hz, 1H, H-2), 3.27 (s, 3H, –$SOCH_3$). MS (70 eV) *m/z*: 456 (M^+), 458 (M^+ + 2), 460 (M^+ + 4). Anal. calcd. for $C_{22}H_{17}ClN_2O_5S$: C 57.83, H 3.75, N 6.13; found: C 57.84, H 3.77, N 6.12.

exo,exo-6-(4-Bromophenyl)-4,8-epoxy-3a,4,4a,7a,8,8a-hexahydro-3-(4-methylsulfinylphenyl)-pyrrolo[3,4-f]-1,2-benzisoxazole (10d)

Compound **10d** was obtained as a colorless solid: yield 91%; mp 244 °C. IR ν (KBr, cm^{-1}): 3063, 3041 (ArH), 1779, 1721 (C=O), 1567 (C=N), 1240 (C–O–C). ^{1}HNMR (DMSO-d_6) δ: 7.83–7.25 (m, 8H, Ar–H), 5.24 (d, *J* = 7.9 Hz, 1H, H-5), 4.98 (s, 1H, H-4), 4.76 (s, 1H, H-1), 4.51 (d, *J* = 7.9 Hz, 1H, H-6), 3.59 (d, *J* = 7.9 Hz, 1H, H-3), 3.38 (d, *J* = 7.9 Hz, 1H, H-2), 3.27 (s, 3H, –$SOCH_3$). MS *m/z*: 500 (M^+), 502 (M^+ + 2), 503 (M^+ + 3), 504 (M^+ + 4). Anal. calcd. for $C_{22}H_{17}BrN_2O_5S$: C 52.70, H 3.42, N 5.59; found: C 52.71, H 3.44, N 5.56.

exo,exo-4,8-Epoxy-3a,4,4a,7a,8,8a-hexahydro-3-(4-methylsulfinylphenyl)-6-(*p*-tolyl)-pyrrolo[3,4-f]-1,2-benzisoxazole (10e)

Compound **10e** was obtained as a colorless solid: yield 71%; mp 341 °C (Dec.). IR ν (KBr, cm^{-1}): 3069, 3035 (ArH), 1781, 1721 (C=O), 1568 (C=N), 1256 (C–O–C). ^{1}H NMR (DMSO-d_6) δ: 7.83–7.19 (m, 6H, Ar–H), 5.23 (d, *J* = 7.9 Hz, 1H, H-5), 4.97 (s, 1H, H-4), 4.75 (s, 1H, H-1), 4.51 (d, *J* = 7.9 Hz, 1H, H-6), 3.59 (d, *J* = 7.9 Hz, 1H, H-3), 3.35 (d, *J* = 7.9 Hz, 1H, H-2), 3.27 (s, 3H, –$SOCH_3$), 2.33 (–CH_3). MS *m/z*: 436 (M^+), 437 (M^+ + 1). Anal. calcd. for $C_{23}H_{20}N_2O_5S$: C 63.29, H 4.62, N 6.42; found: C 63.28, H 4.64, N 6.41.

exo,exo-4, 8-Epoxy-3a,4,4a,7a,8,8a-hexahydro-6-(4-methoxyphenyl)-3-(4-methylsulfinylphenyl)-pyrrolo[3,4-f]-1,2-benzisoxazole (10f)

Compound **10f** was obtained as a colorless solid: yield

© 2007 NRC Canada

67%; mp 304 °C (Dec.). IR ν (KBr, cm^{-1}): 3051, 3027 (ArH), 1778, 1717 (C=O), 1568 (C=N), 1246 (C–O–C). ^{1}H NMR (DMSO-d_6) δ: 8.37–7.49 (m, 6H, Ar–H), 5.25 (d, J = 7.9 Hz, 1H, H-5), 5.01 (s, 1H, H-4), 4.79 (s, 1H, H-1), 4.53 (d, J = 7.9 Hz, 1H, H-6), 3.66 (d, J = 7.9 Hz, 1H, H-3), 3.43 (d, J = 7.9 Hz, 1H, H-2), 3.83 (s, 3H, –OCH_3), 3.27 (s, 3H, –$SOCH_3$). MS *m/z*: 452 (M^+), 453 (M^+ + 1). Anal. calcd. for $C_{23}H_{20}N_2O_6S$: C 61.05, H 4.46, N 6.19; found: C 61.03, H 4.46, N 6.18.

*exo,exo-4,8-Epoxy-3a,4,4a,7a,8,8a-hexahydro-6-phenyl-3-(1,3-diolphenyl)-pyrrolo[3,4-**f**]-1,2-benzisoxazole (11a)*

Compound **11a** was obtained as a colorless solid: yield 95%; mp 183 °C. IR ν (KBr, cm^{-1}): 3047, 3018 (ArH), 1782, 1723 (C=O), 1564 (C=N), 1248 (C–O–C). ^{1}H NMR (DMSO-d_6) δ: 7.74–7.07 (m, 8H, Ar–H), 5.25 (s, 2H, OH), 5.18 (d, J = 7.9 Hz, 1H, H-5), 4.96 (s, 1H, H-4), 4.73 (s, 1H, H-1), 4.48 (d, J = 7.9 Hz, 1H, H-6), 3.59 (d, J = 7.9 Hz, 1H, H-3), 3.35 (d, J = 7.9 Hz, 1H, H-2). MS *m/z*: 392 (M^+). Anal. calcd. for $C_{21}H_{16}N_2O_6$: C 64.28, H 4.11, N 7.14; found: C 64.27, H 4.13, N 7.13.

*exo,exo-6-(4-fluorophenyl)-4,8-epoxy-3a,4,4a,7a,8,8a-hexahydro-3-(1,3-diolphenyl)-pyrrolo[3,4-**f**]-1,2-benzisoxazole (11b)*

Compound **11b** was obtained as a colorless solid: yield 82%; mp 176 °C. IR ν (KBr, cm^{-1}): 3054, 3016 (ArH), 1780, 1720 (C=O), 1544 (C=N), 1252 (C–O–C). ^{1}H NMR (DMSO-d_6) δ: 7.75–7.06 (m, 7H, Ar–H), 5.25 (s, 2H, OH), 5.18 (d, J = 7.9 Hz, 1H, H-5), 4.9 (s, 1H, H-4), 4.74 (s, 1H, H-1), 4.47 (d, J = 7.9 Hz, 1H, H-6), 3.59 (d, J = 7.9 Hz, 1H, H-3), 3.37 (d, J = 7.9 Hz, 1H, H-2). MS *m/z*: 410 (M^+). Anal. calcd. for $C_{21}H_{15}FN_2O_6$: C 61.47, H 3.68, N 6.83; found: C 61.46, H 3.69, N 6.81.

*exo,exo-6-(4-Chlorophenyl)-4,8-epoxy-3a,4,4a,7a,8,8a-hexahydro-3-(1,3-diolphenyl)-pyrrolo[3,4-**f**]-1,2-benzisoxazole (11c)*

Compound **11c** was obtained as a colorless solid: yield 84%; mp 191 °C. IR ν (KBr, cm^{-1}): 3053, 3027 (ArH), 1775, 1715 (C=O), 1550 (C=N), 1266 (C–O–C). ^{1}H NMR (DMSO-d_6) δ: 7.75–7.06 (m, 7H, Ar–H), 5.25 (s, 2H, OH), 5.18 (d, J = 7.2 Hz, 1H, H-5), 4.95 (s, 1H, H-4), 4.73 (s,1H, H-1), 4.47 (d, J = 7.9 Hz, 1H, H-6), 3.59 (d, J = 7.9 Hz, 1H, H-3), 3.37 (d, J = 7.9 Hz, 1H, H-2). MS *m/z*: 426 (M^+), 428 (M^+ + 2). Anal. calcd. for $C_{21}H_{15}ClN_2O_6$: C 59.10, H 3.54, N 6.56; found: C 59.11, H 3.55, N 6.53.

*exo,exo-6-(4-Bromophenyl)-4,8-epoxy-3a,4,4a,7a,8,8a-hexahydro-3-(1,3-diolphenyl)-pyrrolo[3,4-**f**]-1,2-benzisoxazole (11d)*

Compound **11d** was obtained as a colorless solid: yield 70%; mp 199 °C. IR ν (KBr, cm^{-1}): 3053, 3028 (ArH), 1778, 1714 (C=O), 1538 (C=N), 1244 (C–O–C). ^{1}H NMR (DMSO-d_6) δ: 7.76–7.02 (m, 7H, Ar–H), 5.25 (s, 2H, OH), 5.17 (d, J = 7.2 Hz, 1H, H-5), 4.96 (s, 1H, H-4), 4.74 (s, 1H, H-1), 4.47 (d, J = 7.9 Hz, 1H, H-6), 3.59 (d, J = 7.9 Hz, 1H, H-3), 3.37 (d, J = 7.9 Hz, 1H, H-2). MS *m/z*: 470 (M^+), 472 (M^+ + 2), 474 (M^+ + 4). Anal. calcd. for $C_{21}H_{15}BrN_2O_6$: C 53.52, H 3.21, N 5.94; found: C 53.52, H 3.23, N 5.92.

*exo,exo-4,8-Epoxy-3a,4,4a,7a,8,8a-hexahydro-3-(1,3-diolphenyl)-6-(**p**-tolyl)-pyrrolo[3,4-**f**]-1,2-benzisoxazole (11e)*

Compound **11e** was obtained as a colorless solid: yield 68%; mp 176 °C. IR ν (KBr, cm^{-1}): 3058, 3034 (ArH), 1780, 1723 (C=O), 1544 (C=N), 1282 (C–O–C). ^{1}H NMR (DMSO-d_6) δ: 7.77–7.02 (m, 7H, Ar–H), 5.25 (s, 2H, OH), 5.17 (d, J = 7.9 Hz, 1H, H-5), 4.94 (s, 1H, H-4), 4.72 (s, 1H, H-1), 4.46 (d, J = 7.9 Hz, 1H, H-6), 3.59 (d, J = 7.9 Hz, 1H, H-3), 3.37 (d, J = 7.9 Hz, 1H, H-2), 2.33 (–CH_3). MS *m/z*: 406 (M^+), 408 (M^+ + 2). Anal. calcd. for $C_{22}H_{18}N_2O_6$: C 65.02, H 4.46, N 6.89; found: C 65.01, H 4.47, N 6.87.

*exo,exo-4,8-Epoxy-3a,4,4a,7a,8,8a-hexahydro-3-(1,3-diolphenyl)-6-(4-methoxyphenyl)-pyrrolo[3,4-**f**]-1,2-benzisoxazole (11f)*

Compound **11f** was obtained as a colorless solid: yield 58%; mp 185 °C. IR ν (KBr, cm^{-1}): 3057, 3021 (ArH), 1786, 1719(C=O), 1536 (C=N), 1238 (C–O–C). ^{1}H NMR (DMSO-d_6) δ: 7.86–7.22 (m, 7H, Ar–H), 5.25 (s, 2H, OH), 5.25 (d, J = 7.9 Hz, 1H, H-5), 4.97 (s, 1H, H-4), 4.73 (s, 1H, H-1), 4.46 (d, J = 7.9 Hz, 1H, H-6), 3.83 (s, 3H, –OCH_3), 3.56 (d, J = 7.9 Hz, 1H, H-3), 3.33 (d, J = 7.9 Hz, 1H, H-2). MS *m/z*: 422 (M^+), 424 (M^+ + 2). Anal. calcd. for $C_{22}H_{18}N_2O_7$: C 62.56, H 4.30, N 6.63; found: C 62.55, H 4.32, N 6.62.

Cell culture and antiproliferative assays

Stock solutions of drugs were prepared as follows (and stored at –20 °C): Cantharidin (Biomol, USA) as a 12 mmol/L solution in dimethylsulphoxide (DMSO); norcantharidin and cantharidin analogues as 10 mmol/L solutions in phosphate buffered saline. All cell lines were cultured at 37 °C in 5% CO_2.

Antiproliferative activity of different compounds was determined by MTT method. Cells in logarithmic growth were plated in triplicate in 100 μL medium at a density of 3 000–5 000 cells/well in 96-well plates. When the cells were in logarithmic growth, 100 μL medium with or without the test compounds were added to each well. After 72 h, MTT solution (5.0 mg/mL) was added (10.0 μL/well), and plates were incubated for a further 4 h at 37 °C. The purple formazan crystals were dissolved in 100.0 μL DMSO. After 5 min, the plates were read on an automated microplate spectrophotometer at 570 nm. Concentration of drug that inhibited 50% of cells (IC_{50}) was calculated using the software of Dose–Effect analysis with Microcomputers.

References

1. J.E. Carrel and T. Eisner. Science (Washington, D.C.), **183**, 755 (1974).
2. G.S. Wang. J. Ethnopharmacol. **26**, 147 (1989).
3. F. Peng, Y.Q. Wei, L. Tien, L. Yang, X. Zhao, and Y. Lu. J. Cancer Res. Clin. Oncol. **128**, 223 (2002).
4. Y.N. Chen, J.C. Chen, S.C. Yin, G.S. Wang, W. Tsauer, S.F. Hsu,and S.L.Hsu. Int. J. Cancer. **100**, 158 (2002).
5. Z.X. Sun, Q.W. Ma, T.D. Zhao, Y.L. Wei, G.S. Wang,and J.S. Li. World J. Gastroenterol. **6**, 263 (2000).
6. A. McCluskey, S.P. Ackland, M.C. Bowyer, M.L. Baldwin, J. Garner,and C.C. Walkom. Bioorg. Chem. **31**, 68 (2003).

© 2007 NRC Canada

7. A. McCluskey, A.T.R. Sim, and J.A. Sakoff. J. Med. Chem. **45**, 1151(2002).
8. A. McCluskey, C. Taylor, R.J. Quinn, M. Suganuma, and H.Fujiki. Bioorg. Med. Chem. Lett. **6**, 1025 (1996).
9. A. McCluskey, M.A. Keane, L.M. Mudgee, A.T.R. Sim, J. Sakoff, and R.J. Quinn. Eur. J. Med. Chem. **35**, 957 (2000).
10. A. McCluskey, M.C. Bowyer, C. Walkom, S.P. Ackland, E.Gardiner, and J.A. Sakoff. Bioorg. Med. Chem. Lett. **11**, 2941 (2001).
11. P.Y. Lin, S.J. Shi, H.L. Shu, H.F. Chen, C.C. Lin, P.C. Liu,and L.F. Wang. Bioorg. Chem. **28**, 266 (2000).
12. F.L. Liu, T. jiang, D.S. Zuo, X. Qin, and X.L. Zhan. Chin. J. Org. chem. **22**, 761 (2002). (In Chinese).
13. J.M. Corral, M. Gordaliza, M.A. Castro, H.B. Broughton, and A.S. Feliciano. Tetrahedron, **53,** 6555 (1997).
14. V.J. Ram, U.K. Singha, and P.Y. Guru. Eur. J. Med. Chem. **25**, 533 (1990).
15. R.B. Woodward and B.J. Harold. J. Am. Chem. Soc. **70**, 1161 (1948).
16. L.P. Deng, F.M. Liu, and H.Y. Wang. J. Heterocycl. Chem. **42**, 13 (2005).
17. L.P. Deng and Y.Z. Hu. J. Heterocycl. Chem. **43**, 1715 (2006).

© 2007 NRC Canada

An ab initio investigation of bismuth hydration

Cory C. Pye, C. Mahesh Gunasekara, and Wolfram W. Rudolph

Abstract: A series of geometry, frequency, and energy calculations of aquabismuth(III) complexes were carried out at up to the MP2/CEP-121G* level. A thorough examination of all species up to and including enneacoordinate species was carried out. The structures of the complexes are compared with experimental data where available. Deviations from the most highly symmetric structures are consistent with the inert-pair effect. In addition, protonated bismuth–oxo clusters of the stoichiometry $Bi_6O_{8-n}(OH)_n^{(2+n)+}$, n = 0–4 are examined. The Raman spectrum of bismuth perchlorate with added perchloric and hydrochloric acid is measured.

Key words: bismuth, aqua complexes, ab initio, Raman spectra.

Résumé : Opérant au niveau MP2/CEP-121G*, on a effectué une série de calculs de géométrie, de fréquence et d'énergie de complexes du aqua(bismuth(III)). On a effectué un examen critique de toutes les espèces, y compris celles qui comportent une enneacoordination et on a comparé les structures des complexes avec les données expérimentales disponibles. Les déviations par rapport aux structures les plus symétriques pourraient correspondre avec l'effet de la paire inerte. On a étudié de plus, les agrégats oxo du bismuth de stoechiométrie $Bi_6O_{8-n}(OH)_n^{(2+n)+}$ dans lesquels n = 0–4. On a mesuré le spectre Raman du perchlorate de bismuth additionné d'acide perchlorique et d'acide chlorhydrique.

Mots-clés : bismuth, aqua, complexes, ab initio, spectre Raman.

[Traduit par la Rédaction]

1. Introduction

Bismuth preparations have been used for medicinal purposes for some time and are currently used mostly in stomach remedies, such as Pepto-Bismol (1). The coordination chemistry of bismuth (III) has recently been reviewed (2). However, the poor solubility and difficult characterization of most of its compounds has hampered efforts to systematically characterize the structure and chemistry of this heavy element. In fact, non-aaquabismuth(III) was only characterized a decade ago as the trifluoromethanesulfonate (triflate) salt (3). In this compound at 133 K, the Bi–O distances are 2.448(2) and 2.577(2) Å for the tricapped trigonal prism of C_{3h} symmetry. A redetermination at 298 K gave 2.435(2) and 2.595(6) Å (4). The corresponding acidified bismuth perchlorate solutions gave a low-angle X-ray scattering (LAXS) result, consistent with an eight-coordinate square antiprism with a mean Bi-O distance of 2.41 Å, with one or two perchlorate ions in the inner coordination shell (4). A recent molecular dynamics study, however, suggested a nine-coordinate tricapped trigonal prism (5), as found in the solid state. Vibrational studies of bismuth(III) nitrate solutions indicate the presence of up to four bidentate nitrates binding to the cation (6). Similar studies of the chlorides and bromides suggest that up to six halides may be associated with the metal (7). In dilute strongly acidic bismuth perchlorate solutions, a weak polarized band at 390 cm^{-1} was assigned to the bismuth–oxygen symmetric stretching mode.

Some polynuclear bismuth compounds based on the common Bi_6O_8 core have also been prepared. The $Bi_6O_4(OH)_4^{6+}$ cation has been explored both as the nitrate monohydrate (8, 9) and tetrahydrate (10) salt and as the perchlorate aqueous solution (11). It was originally thought that this ion was $Bi_6(OH)_{12}^{6+}$ (12–14). A related structure containing a $Bi_6O_5(OH)_3^{5+}$ dimer has also been examined (15). Very recently, much larger bismuth–oxygen clusters have been prepared (16).

In this work, we examine both bismuth aqua complexes and protonated bismuth–oxo clusters using ab initio theory. In the bismuth aqua complexes, several levels of theory were employed and compared and represent the speciation of bismuth at extremely low pH. For the bismuth–oxo clusters, increasing levels of protonation of the "bismuth-oxide-like" clusters should eventually solubilize the oxide and represent the speciation at higher pH. Previous work in this group include studies of other metal–aqua complexes (17–19), hydrated oxoanions (20–22), and metal–anion complexes (23, 24).

2. Method

Calculations were performed using Gaussian 98 (25). As this program version allows, for the first time, analytical frequency calculation of molecules in which core electrons are described by effective core potentials (ECPs), many variants of these were tried. The MP2 calculations utilize the frozen core approximation. The geometries were optimized using a stepping stone approach, in which the geometries at the levels HF/CEP-4G, HF/CEP-31G*, HF/CEP-121G*, HF/LANL2MB, HF/LANL2DZ, and HF/SDD were sequentially optimized. For minimum energy structures, the MP2/CEP-31G* and

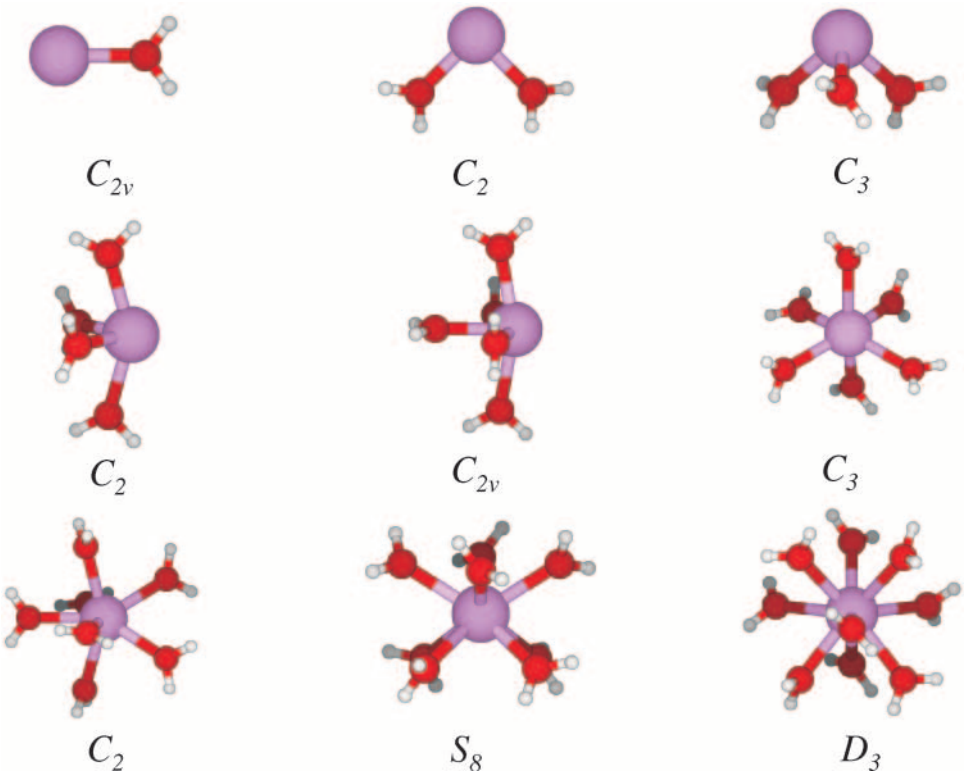
Received 11 June 2007. Accepted 20 August 2007. Published on the NRC Research Press Web site at http://canjchem.nrc.ca/ on 5 October 2007.

C.C. Pye[1] and C.M. Gunasekara. Department of Chemistry, Saint Mary's University, Halifax, NS B3H 3C3, Canada.
W.W. Rudolph. Instituet fuer Virologie im MTZ, Medizinische Fakultaet der TU Dresden, Fiedlerstrasse 42, D01307 Dresden, Germany.

[1]Corresponding author (e-mail: cory.pye@smu.ca).

 doi: 10.1139/V07-108 © 2007 NRC Canada

Fig. 1. Optimized structures of aquabismuth(III) complexes.



MP2/CEP-121G* calculations were also performed. Calculations were also carried out using the 6-31G* (26) and 6-31+G* (27) basis sets on the atoms of the water molecules with an effective core potential and basis set on bismuth. Default optimization specifications were normally used. After each level, where possible, a frequency calculation was performed at the same level and the resulting Hessian used in the following optimization. Z-matrix coordinates constrained to the appropriate symmetry were used as required to speed up the optimizations. Since frequency calculations are done at each level, any problems with the Z-matrix coordinates would manifest themselves by giving imaginary frequencies corresponding to modes orthogonal to the spanned Z-matrix space. The Hessian was evaluated at the first geometry (opt = CalcFC) for the first level in a series to aid geometry convergence.

A stock solution (1.48 mol/L $Bi(ClO_4)_3$ and 2.36 mol/L $HClO_4$) was prepared from bismuth oxide and 6.8 mol/L perchloric acid. This unstable solution precipitated a white solid (presumably BiOOH) so the mixture was diluted with an equal volume of 10.0 mol/L perchloric acid. Details of the spectral measurement are given in ref. 24.

3. Results and literature comparison

3.1. Aquabismuth complexes, $Bi(H_2O)_n^{3+}$

Figure 1 gives the structures of the aquabismuth clusters. Our experience with other trivalent ions suggested that the mono- through ennea-hydrate should have C_{2v}, D_{2d}, D_3, S_4, C_{2v} (trigonal bipyramid), T_h, C_2, S_8, and D_3 symmetries, respectively (17, 28–30), so our initial structures corresponded to these. The optimized structures for the di- through hexa-aquabismuth were actually of C_2, C_3, C_2, C_{2v} (square pyramid), and C_3 symmetries, respectively, as further discussed in the Supplementary material.[2] The distortions relative to other trivalent ions in di- to hexa-aquabismuth(III) are consistent with what has been termed the inert pair effect. The occupied $6s^2$ orbital behaves as if it is a lone pair, from the point of view of VSEPR theory. The ligands then undergo the usual repulsions. For coordination numbers greater than 6, the lone pair stereochemistry is often absent (31). More sophisticated theories on this phenomenon have been developed (32).

The variation of the average Bi–O distance as a function of coordination number is given in Fig. 2. Comparison between the different levels of theory is given in the Supplementary material.[2] Experimentally, the solid-phase bismuth triflate enneahydrate has bond lengths 2.438–2.448 Å (prism) and 2.577–2.595 Å (caps) (3, 4). Although the Bi–O distances (caps) are well described, the CEP-31G* Bi–O distances (prism) seem to be much longer than experimental values (see Table S2 of the Supplementary data).[2] The HF/LANL2DZ, HF/SDD, and the MP2/CEP levels seem to have too short Bi–O (cap) distances and too long Bi–O (prism) distances. The putative octaaquabismuth(III) ion is found to have a Bi–O distance of 2.41 Å by extended X-ray absorption fine structure (EXAFS) and LAXS (4), which is also quite a bit shorter than our calculations (2.48–2.50 Å). The temperature dependence of the structures may account for some of the difference, as the predictions are for

[2] Supplementary data for this article are available on the journal Web site (canjchem.nrc.ca) or may be purchased from the Depository of Unpublished Data, Document Delivery, CISTI, National Research Council Canada, Ottawa, ON K1A 0R6, Canada. DUD 5222. For more information on obtaining material refer to cisti-icist.nrc-cnrc.gc.ca/irm/unpub_e.shtml.

© 2007 NRC Canada

Fig. 2. Average Bi–O distance of aquabismuth(III) complexes as a function of coordination number (pure ECP).

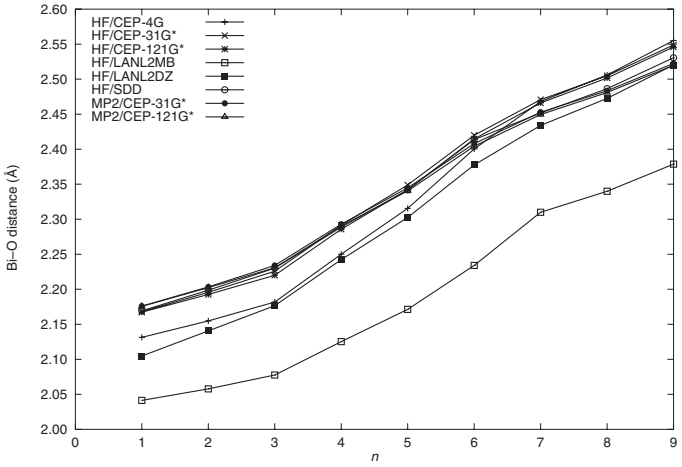


Fig. 3. Average Bi–O distance of aquabismuth(III) complexes as a function of coordination number (mixed).

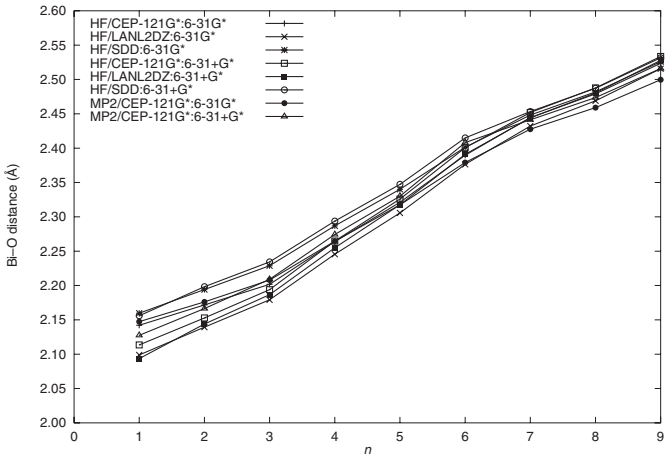


Fig. 4. Incremental hydration energy of bismuth(III), $Bi(H_2O)_{n-1}^{3+} + H_2O \rightarrow Bi(H_2O)_n^{3+}$ (kJ/mol) (pure ECP).

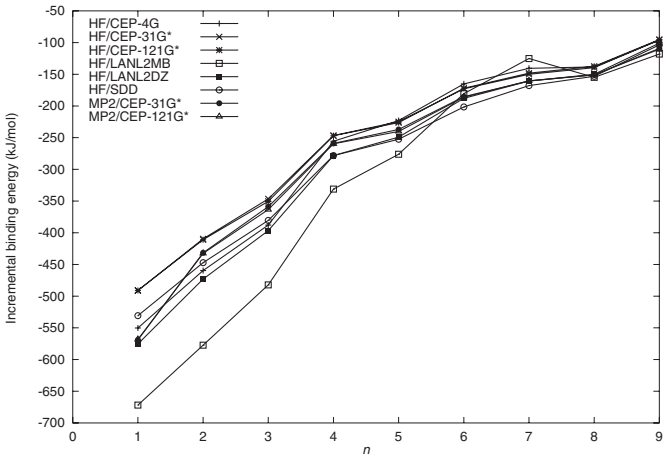
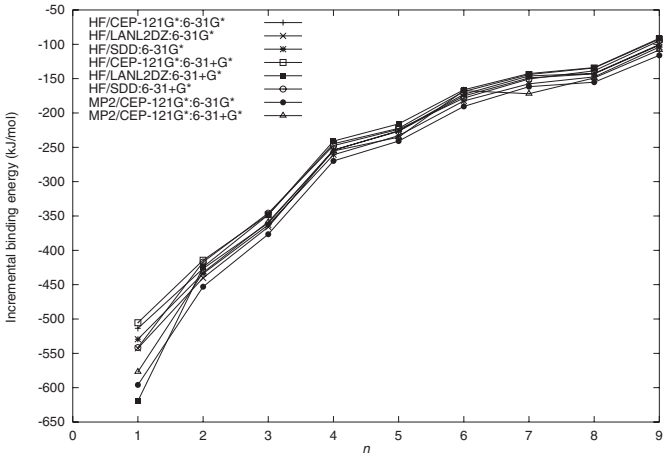


Fig. 5. Incremental hydration energy of bismuth(III), $Bi(H_2O)_{n-1}^{3+} + H_2O \rightarrow Bi(H_2O)_n^{3+}$ (kJ/mol) (mixed).



0 K. The influence of the environment (slight shortening of M–O bonds), omitted in these calculations, and deficiencies in the levels chosen probably account for the rest.

To clarify the role of choice of level, we also carried out mixed basis set calculations where the standard 6-31G* and 6-31+G* basis sets (5d) were used on the oxygen and hydrogen atoms, and the effective core potentials and valence basis sets were used on bismuth (see Fig. 3). When comparing the pure ECP basis sets and the mixed basis sets, we noticed that the Bi–O distances using the CEP type basis sets were shortened by between 0.015–0.030 Å, whereas not much difference was found for LANL2DZ and SDD. Adding a diffuse function tended to shorten the Bi–O distances in the complexes with only a few waters but lengthened it in those with more waters.

The incremental binding energy of bismuth hydration is given in Fig. 4. A pronounced kink at $n = 4$ can be seen, whereas similar plots for other metal ions such as aluminum, scandium, zinc, gallium, and indium show a kink at $n = 5$. This presumably is due to the onset of significant ligand–ligand repulsion for the other metal ions at $n = 5$ and can be interpreted as ligand–inert pair repulsion in bismuth, which would occur at $n = 4$.

We may compare the incremental binding energies (HF) using the ECP basis sets with those using the 6-31G* (5d) basis set on the atoms of the water molecules (see Fig. 5). No general trend was found, only specific trends that changed with each ECP choice, as discussed in the Supplementary material.[2] Within the mixed basis set results, adding a diffuse function typically lowers the magnitude of the binding energy by around 10 kJ/mol for CEP-121G* but slightly more for SDD and LANL2DZ, except for the first incremental binding energy, which is raised by 80 and 12 kJ/mol, respectively. The diffuse functions make a larger difference at the MP2 level. It is anticipated that binding energies will soon be able to be measured for trivalent ions by mass spectrometry, as there has been some recent progress (33).

The Raman spectrum of acidified bismuth perchlorate solution in R-format is given in Fig. 6. In addition to the perchlorate modes at ca. 455 and 625 cm^{-1}, a totally polarized mode is seen at 393 cm^{-1} and is assigned to the Bi–O totally symmetric stretch. If bismuth perchlorate is acidified with excess hydrochloric acid instead (to a 9:1 chloride/bismuth ratio), then the perchlorate modes remain, but the band at 393 cm^{-1} disappears, and a new polarized mode at 266.5 cm^{-1} appears in

© 2007 NRC Canada

Fig. 6. Raman spectra of acidified bismuth perchlorate solution (0.74 mol/L $Bi(ClO_4)_3$ and 6.2 mol/L excess $HClO_4$).

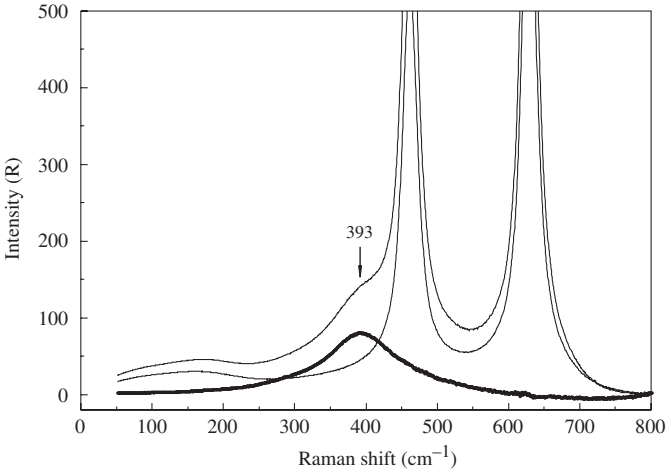
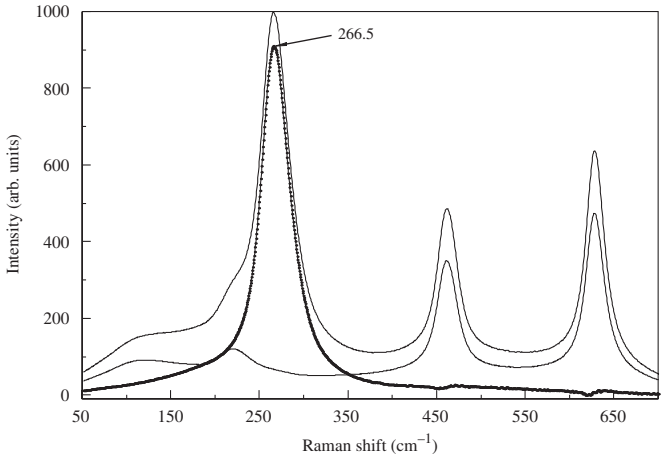


Fig. 7. Raman spectra of acidified bismuth perchlorate solution (0.6 mol/L $Bi(ClO_4)_3$ and 5.5 mol/L excess HCl).



addition to depolarized modes at 120 and 220 cm^{-1} (see Fig. 7). These most likely arise from the formation of a chlorobismuth complex, possibly hexachlorobismuthate(III).

The vibrational frequencies of the Bi–O stretching modes are given in Table 1. The totally symmetric stretching frequency of the octa- and ennea-hydrate complexes differs by only 15 cm^{-1} (Table 1). Based on comparison with other trivalent metal ion hexahydrates using similar quality basis sets, we expect these frequencies to be too low by between 50–70 cm^{-1} (28–30). For bismuth, the ν_1 frequency (HF/SDD) of the T_h hexahydrate is 59 cm^{-1} lower than the corresponding mode in the T octadecahydrate. If the effect of the second hydration sphere can be regarded to be of the same magnitude for both the octa- and ennea-hydrate, then we might be able to differentiate by empirically correcting the ν_1 frequency by 60 cm^{-1} and seeing which gives a closer match to experiment. This suggests (albeit weakly) that the complex in solution is more likely the octahydrate rather than the enneahydrate.

3.2. Polynuclear bismuth–oxo clusters

The $Bi_6O_8^{2+}$ can exist in aqueous solution and the solid state in varying degrees of protonation. The unprotonated form has O_h symmetry (see Fig. 8). A proton inside the cage does not give a stable O_h structure, whereas a proton located on an oxygen gives a stable $Bi_6O_7(OH)^{3+}$ C_{3v} structure. A second proton added to form $Bi_6O_6(OH)_2^{4+}$ can situate itself opposite to the first proton to form a D_{3d} structure, on a different face not opposite to form a C_{2v} # 1 structure, or on the same face to form C_{2v} # 2. The C_{2v} # 1 structure is the most stable, followed by the D_{3d}, with the C_{2v} # 2 structure being the least stable. At some levels the C_{2v} structures desymmetrize to C_s along with a conversion of one μ_3-OH into a μ_2-OH.

A third proton can be added to give either a C_{3v} or one of two different C_s structures. The first C_s structure has all three OH groups interacting with a common Bi atom. The C_{3v} structure is not stable, but it is always lower in energy than the other two forms. It desymmetrizes to either C_3, C_s # 3, or C_1 # 3 structure depending on level. The C_s # 1 and # 2 structures both have an imaginary frequency at all levels and desymmetrize to the corresponding C_1 # 1 and #2 structures. Some of these structures have significantly longer Bi–O distances and have partially opened up the Bi_6O_8 cage. The structure of Lazarini corresponds nominally to the C_{3v} structure, although distortions are evident (15).

A fourth proton can be potentially added to form one of five maximally symmetric structures: T_d, C_{4v}, C_{3v}, D_{2h}, or C_s # 1. For the T_d structure, most levels desymmetrize to either a C_3 or C_1 # 3. The C_{4v} structure descends (C_4) and re-ascends in symmetry to a new stable C_{4v} # 2 structure in which four Bi–O bonds were broken. The C_{3v} structure can convert into two $Bi_3O_2(OH)_2$ fragments or desymmetrize to the stable C_1 # 2 structure. The D_{2h} structure either fragments into Bi_2O_2 and two $Bi_2O(OH)_2$ or desymmetrizes into a stable C_2 or an open C_i structure. The C_s # 1 structure desymmetrizes to the stable C_1 # 1 form. The structure of Lazarini (9, 10) and of Sundvall (8, 11) correspond to the T_d form. In perchlorate solution, the Bi–O (Bi–OH) distance is 2.19 (2.37) Å, and our HF/SDD calculation that predicts this structure to be a minimum gives 2.180 (2.445) Å.

Table 1. Bi–O totally symmetric stretching mode of $Bi(H_2O)_n^{3+}$, $n = 8$, 9.

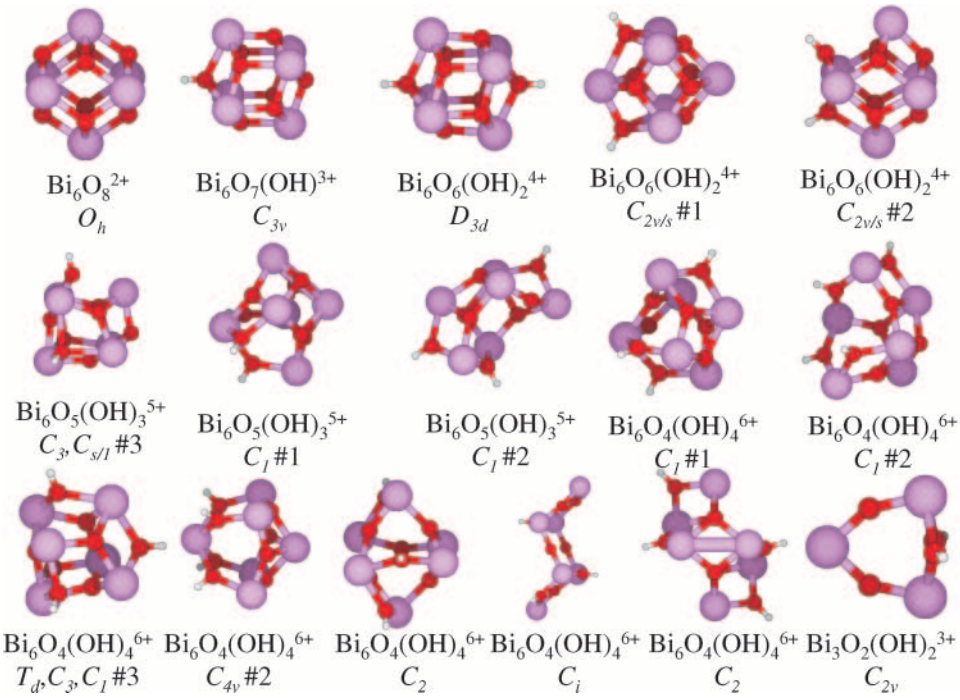
Level	$n = 8$	$n = 9$
HF/CEP-31G*	319	303
HF/CEP-121G*	318	303
HF/LANL2DZ	332	315
HF/SDD	329	311
MP2/CEP-31G*	325	310
MP2/CEP-121G*	324	310
Experiment	393	

4. Conclusions

The structures of bismuth aqua complexes up to the hexaaqua complex are distorted relative to other trivalent metal ions, consistent with the inert pair effect. The earlier kink appearance in the incremental hydration energies is also consistent with the inert pair effect. Fair agreement with experimental Bi–O distances was reached. In solution, our calculations are consistent with either the octa- or ennea-hydrate, with a slight preference for the former. For the bismuth–oxo clusters, good agreement

© 2007 NRC Canada

Fig. 8. Optimized structures of oxobismuth(III) clusters.



was found with the structures found experimentally in terms of symmetry and Bi–O distance, but somewhat poorer agreement for the Bi–OH distance was found.

Acknowledgements

The authors thank the Department of Astronomy and Physics, Saint Mary's University (AP-SMU), for providing access to computing facilities, in particular, to cygnus, a 10-processor Sun server, purchased with assistance from the Canada Foundation for Innovation, Sun Microsystems, the Atlantic Canada Opportunities Agency, and SMU. CCP acknowledges the past support of the Natural Sciences and Engineering Research Council of Canada. CMG acknowledges the support of the Department of Economic Development (Government of Nova Scotia) and the Cooperative Education Program (SMU - Work Term 1, Summer 2001; Work Term 3, Winter 2002).

References

1. G.G. Briand and N. Burford. Chem. Rev. **99**, 2601 (1999).
2. G.G. Briand and N. Burford. Adv. Inorg. Chem. **50**, 285 (2000).
3. W. Frank, G.J. Reiss, and J. Schneider. Angew. Chem. Int. Ed. Engl. **34**, 2416 (1995).
4. J. Naslund, I. Persson, and M. Sandstrom. Inorg. Chem. **39**, 4012 (2000).
5. S. Durdagi, T.S. Hofer, B.R. Randolf, and B.M. Rode. Chem. Phys. Lett. **406**, 20 (2005).
6. R.P. Oertel and R.A. Plane. Inorg. Chem. **7**, 1192 (1968).
7. R.P. Oertel and R.A. Plane. Inorg. Chem. **6**, 1960 (1967).
8. B. Sundvall. Acta Chem. Scand. A, **33**, 219 (1979).
9. F. Lazarini. Acta Crystallogr. Sect. B, **35**, 448 (1979).
10. F. Lazarini. Cryst. Struct. Comm. **8**, 69 (1979).
11. B. Sundvall. Acta Chem. Scand. A, **34**, 93 (1980).
12. H.A. Levy, M.D. Danford, and P.A. Agron. J. Chem. Phys. **31**, 1458 (1959).
13. V.A. Maroni and T.G. Spiro. J. Am. Chem. Soc. **88**, 1410 (1966).
14. V.A. Maroni and T.G. Spiro. Inorg. Chem. **7**, 183 (1968).
15. F. Lazarini. Acta Cryst. B, **34**, 3169 (1978); F. Lazarini. Acta Crystallogr. Sect. A, **34**, S157 (1978).
16. E.V. Dikarev, H. Zhang, and B. Li. Angew. Chem. Int. Ed. **45**, 5448 (2006).
17. M.R. Michels, T.G. Enright, M.R. Tomney, C.C. Pye, and W.W. Rudolph. Can. J. Anal. Sci. Spectrosc. **48**, 64 (2003) and refs. 7–18 therein.
18. Li^+: C.C. Pye, M.R. Tomney, and T.G. Enright. Can. J. Anal. Sci. Spectrosc. **50**, 254 (2005).
19. Cd^{2+}: C.C. Pye, M.R. Tomney, and W.W. Rudolph. Can. J. Anal. Sci. Spectrosc. **51**, 140 (2006).
20. PO_4^{3-}: C.C. Pye and W.W. Rudolph. J. Phys. Chem. A, **107**, 8746 (2003).
21. HPO_4^{2-}: M.R. Michels and C.C. Pye. Can. J. Anal. Sci. Spectrosc. **49**, 175 (2004).
22. $H_2PO_4^-$: M.R. Michels and C.C. Pye. Can. J. Anal. Sci. Spectrosc. **50**, 70 (2005).
23. Sc-Cl complexes: C.C. Pye and C.R. Corbeil. Can. J. Chem. **80**, 1331 (2002).
24. Zn-Cl complexes: C.C. Pye, C.R. Corbeil, and W.W. Rudolph. Phys. Chem. Chem. Phys. **8**, 5428 (2006).
25. M.J. Frisch, G.W. Trucks, H.B. Schlegel, G.E. Scuseria, M.A. Robb, J.R. Cheeseman, V.G. Zakrzewski, J.A. Montgomery, Jr., R.E. Stratmann, J.C. Burant, S. Dapprich, J.M. Millam, A.D. Daniels, K.N. Kudin, M.C. Strain, O. Farkas, J. Tomasi, V. Barone, M. Cossi, R. Cammi, B. Mennucci, C. Pomelli, C. Adamo, S. Clifford, J. Ochterski, G.A. Petersson, P.Y. Ayala, Q. Cui, K. Morokuma, D.K. Malick, A.D. Rabuck, K. Raghavachari, J.B. Foresman, J. Cioslowski, J.V. Ortiz, A.G. Baboul, B.B. Ste-

© 2007 NRC Canada

fanov, G. Liu, A. Liashenko, P. Piskorz, I. Komaromi, R. Gomperts, R.L. Martin, D.J. Fox, T. Keith, M.A. Al-Laham, C.Y. Peng, A. Nanayakkara, M. Challacombe, P.M.W. Gill, B. Johnson, W. Chen, M.W. Wong, J.L. Andres, C. Gonzalez, M. Head-Gordon, E.S. Replogle, and J.A. Pople. Gaussian 98, Revision A.9 [computer program]. Gaussian, Inc., Pittsburgh, Penn. 1999.

26. C-F 6-31G: W.J. Hehre, R. Ditchfield, and J.A. Pople. J. Chem. Phys. **56**, 2257 (1972); H, C-F polarization functions: P.C. Hariharan and J.A. Pople. Theor. Chim. Acta, **28**, 213 (1973).
27. H, Li-F diffuse: T. Clark, J. Chandrasekhar, G.W. Spitznagel, and P.v.R. Schleyer. J. Comput. Chem. **4**, 294 (1983).
28. Al^{3+}: W.W. Rudolph, R. Mason, and C.C. Pye. Phys. Chem. Chem. Phys. **2**, 5030 (2000).
29. Sc^{3+}: W.W. Rudolph and C.C. Pye. J. Phys. Chem. A, **104**, 1627 (2000).
30. In^{3+}: W.W. Rudolph, D. Fischer, M.R. Tomney, and C.C. Pye. Phys. Chem. Chem. Phys. **6**, 5145 (2004).
31. D.T. Richens. The chemistry of aqua ions. Wiley, Chichester, NY. 1997. p. 157.
32. D. Reinen and M. Atanasov. *In* Comprehensive coordination chemistry II. Vol. 1. *Edited by* J.A. McCleverty and T.J. Meyer. Elsevier, Amsterdam, The Netherland. 2003. pp. 661–667.
33. M.F. Bush, R.J. Saykally, and E.R. Williams. Int. J. Mass Spectrom. **253**, 256 (2006).

© 2007 NRC Canada

Synthesis, crystal structure, and growth inhibition of human hepatoma cell (HepG2) of polyphenolic compounds based on gallates

Zhu-Ping Xiao, Rui-Qin Fang, Lei Shi, Hui Ding, Chen Xu, and Hai-Liang Zhu

Abstract: Seven compounds (**1**–**7**) based on gallate were synthesized and characterized by elemental analysis, ^{1}H NMR, and MS spectra. 2-(3,5-Dibenzyloxy-4-methoxy)phenyl-2-propanol (**6**) was a new compound. Methyl 3,5-dihydroxy-4-methoxybenzoate (**3**), methyl 3,5-dibenzyloxy-4-methoxybenzoate (**4**), 3,5-dibenzyloxy-4-methoxybenzyl alcohol (**5**), and compound **6** were structurally determined by single-crystal X-ray diffraction for the first time. Crystallographic data for **3**: space group $P2_12_12_1$; a = 4.0750(8) Å, b = 7.5880(15) Å, c = 29.802(6) Å; V = 921.5(3) Å^3; Z = 4. **4**: space group P-1; a = 10.068(2) Å, b = 10.499(2) Å, c = 11.388(2) Å; α = 76.84(3)°, β = 66.79(3)°, γ = 64.10(3)°; V = 993.0(3) Å^3, Z = 2. **5:** space group P-1; a = 8.1410(16) Å, b = 8.7590(18) Å, c = 12.879(3) Å; α = 91.66(3)°, β = 94.69(3)°, γ = 91.73(3)°; V = 914.4(3) Å^3; Z = 2. **6**: space group $P2_1/c$; a = 5.8100(12) Å, b = 15.778(3) Å, c = 23.237(5) Å; β = 96.09(3)°; V = 2118.1(7) Å^3; Z = 4. All of the seven compounds were evaluated for the inhibition of growth of human hepatoma (HepG2) cells. Comparison with the positive-control 5-fluorouracil (IC_{50} 51.6 μmol/L), **5** showed stronger cytotoxic activity with an IC_{50} around 15.3 μmol/L, while IC_{50} value of **3** was 90.3 μmol/L. The effect of slight structural variations in this series of compounds was found to cause a marked change in their activity against HepG2 cells.

Key words: gallates, benzyl alcohol, human hepatoma cells, crystal structure, anti-cancer activities.

Résumé : On a réalisé la synthèse de sept composés apparentés au gallate (**1**–**7**) dont le 2-(3,5-dibenzoyloxy-4-méthoxy)phénylpropan-2-ol (**6**) est un nouveau produit, et on a les a caractérisés par leur analyse élémentaire, leur spectre de RMN et leur spectre de masse. Faisant appel à la diffraction des rayons X par un cristal unique, on a déterminé pour la première fois les structures du 3,5-dihydroxy-4-méthoxybenzoate de méthyle (**3**), du 3,5-dibenzyloxy-4-méthoxybenzoate de méthyle (**4**), de l'alcool 3,5-dibenzyloxy-4-méthoxybenzylique (**5**) et du composé **6**. Les données cristallographiques sont les suivantes: pour le composé **3**, groupe d'espace $P2_12_12_1$ avec a = 4,0705(8) Å, b = 7,5880(15) Å et c = 29,802(6) Å, V = 921,5(3) Å^3 et Z = 4; pour le composé **4**, groupe d'espace P-1 avec a = 10,068(2) Å, b = 10,499(2) Å et c = 11,388(2) Å, α = 76,84(3)°, β = 66,79(3)° et γ = 64,10(3)°, V = 993,0(3) Å^3 et Z = 2; pour le composé **5**, groupe d'espace P-1 avec a = 8,1410(16) Å, b = 8,7590(18) Å et c = 12,879(3) Å, α = 91,66(3)°, β = 94,69(3)° et γ = 91,73(3)°, V = 914,4(3) Å^3 et Z = 2; pour le composé **6**, groupe d'espace $P2_1/c$ avec a = 5, 8100(12) Å, b = 15,778(3) Å et c = 23,237(5) Å, β = 96,09(3)°, V = 2118,1(7) Å^3 et Z = 4. On a évalué les capacités inhibitrices des sept composés vis-à-vis de la croissance de cellules d'hépatome humain (HepG2). Par comparaison avec le produit de contrôle positif, 5-fluorouracil (IC_{50} = 51,6 μmol/L), le composé **5** présente une activité cytotoxique plus importante (IC_{50} = 15,3 μmol/L), alors que pour le composé **3**, la valeur de IC_{50} = 90,3 μmol/L. On a observé que de faibles changements de structures dans cette série de composés provoque dans changements importants dans leur activité contre les cellules HepG2.

Mots-clés : gallates, alcool benzylique, cellules d'hépatome humain, structure cristalline, activités anticancérigènes.

[Traduit par la Rédaction]

Introduction

Gallic acid and its derivatives are widely present in the plant kingdom and represent a large family of secondary plant polyphenolic metabolites. Toxicological studies showed that the no-observed-adverse-effect-level (NOAEL) of gallic acid is at least 120 mg kg^{-1} day^{-1} for F334 rats, and the level of gallates was reported to be as high as 1000 mg kg^{-1} for mice (1, 2).

Gallic acid and its alkyl esters derivatives are added to foods to prevent oxygen-induced lipid peroxidation (3). The alkyl gallates can inhibit 7,12-dimethylbenz[*a*]anthracene-initiated mammary tumorigenesis (4, 5) and decrease benzo[*a*]pyrene metabolite formation (6) in vivo, and they

Received 16 November 2006. Accepted 20 August 2007. Published on the NRC Research Press Web site at canjchem.nrc.ca on 3 October 2007.

Z.-P. Xiao,[1] R.-Q. Fang, L. Shi, H. Ding, C. Xu, and H.-L. Zhua.[2] Institute of Functional Biomolecules, State Key Laboratory of Pharmaceutical Biotechnology, Nanjing University, Nanjing 210093, P.R. China

[1]Present address: Department of Chemistry, Shangrao Normal College, Shangrao 334000, P.R. China.
[2]Corresponding author (e-mail: zhuhl@nju.edu.cn).

 doi:10.1139/V07-107 © 2007 NRC Canada

protect against hydroperoxide-induced cytotoxicity (7) and mutagenicity (8) in vitro. The ability of the alkyl gallates to induce apoptosis in several tumor-cell lines has recently attracted much interest (9, 10). At the cellular level, they have been shown to inhibit cell adhesion (11) and induce apoptosis of tumor cells (12). Toshihiko Osawa found that alkyl gallates suppress the 3-methylcholanthrene-mediated cytochrome $P_{45}0$ 1A induction in human hepatoma (HepG2) cells. The suppressions were dependent on the length of the alkyl chain of the gallates (13). The cytotoxic activity of phenolic derivatives depends on their rate of incorporation into cells, directly related to their lipophilicity as much as to their antioxidant activity.

The gallates investigated in the literature for their antitumor activity in a human cancer-cell line varied mainly in the number of phenolic substituents and (or) in the length of the alkyl side chain. In the present paper, some structurally distinct derivatives based on gallate were synthesized and evaluated for the inhibition of growth of liver (HepG2) cancer cells. Compounds **4**, **5**, and **6** showed potent anticancer activities with IC_{50} values of 23.1, 15.3, and 20.2, respectively, and crystal structures of **3**–**6** were described to determine the effect of the structural characteristics on their antiproliferative activity.

Experimental

Reagents

MTT cell-proliferation assay kits were purchased from ATCC. Cell-death detection ELISA kits were purchased from Roche. The HepG2 cell line was purchased from ATCC.

Cell cultures and cell viability assay

The HepG2 cells were cultured in ATCC minimum essential medium (Eagle) with 2 mmol/L L-glutamine and Earle BSS adjusted to contain 1.5 g/L sodium bicarbonate, 0.1 mmol/L non-essential amino acids, 1.0 mmol/L sodium pyruvate (90%), and 10% fetal bovine serum. Cells were incubated under 37 °C with 5% CO_2. The medium was changed 2–3 times per week.

After digestion with trypsin-EDTA, uniform amounts ($\sim 2 \times 10^4$) of HepG2 cells in growth media were inoculated into each well of a 96-well flat-bottomed plate. After 24 h of incubation at 37 °C in 5% CO_2, the growth medium was replaced with 100 media, containing different concentrations of compounds **1** to **7**, respectively. DMSO was added initially to the test compounds to help dissolve the sample. After 48 h of incubation, cell population growth was determined using the ATCC MTT cell proliferation assay at 570–655 nm with a Bio-Rad Model 680 Microplate Reader (Hercules, California). Briefly, a mitochondrial enzyme in living cells, succinate dehydrogenase, reduced the yellow tetrazolium salt (MTT) to insoluble purple formazan crystals. Therefore, the amount of formazan produced was proportional to the number of viable cells (14). To better explain the inhibitory results, the inhibition of cell population growth was calculated based on the following formula:

> Inhibition percentage = (cell no. in control – cell no. in treatment) / (cell no. in control – original cell no. before the compounds were added) × 100%.

IC_{50} is the extract concentration under which a 50% inhibition of cell population growth occurs.

Single-crystal analysis

The purified products were dissolved in ethyl acetate, then petroleum ether was added carefully. The crystals suited for X-ray analysis were obtained after 3 to 4 days by volatilization of the solvents.

The crystal data, data collection, and refinement parameters for compounds **3**–**6** are listed in Table 1.[3] The crystal data were collected with a Bruker SMART APEX CCD diffractometer, using graphite monochromatized Mo Kα radiation (λ = 0.71073 Å) (15). All calculations were performed by using the SHELXTL package and refined with full-matrix least-square procedures on desktop computers (16). All non-hydrogen atoms were located from a difference Fourier map and were placed at calculated positions, refined isotropically with riding model position parameters.

Chemistry

The compounds previously reported were synthesized according to the methods in the references with appropriate modifications. Separation of the compounds by column chromatography was carried out with silica gel 60 (200–300 mesh ASTM, E. Merck). The quantity of silica gel used was 50–100 times the weight charged on the column. The eluates were monitored using TLC. Melting points (uncorrected) were determined on a XT4 MP apparatus (Taike Corp., Beijing, China). ESI mass spectra were obtained on a Mariner System 5304 mass spectrometer, and ^{1}H NMR spectra were recorded at DPX500 on a Bruker spectrometer. Elemental analyses were performed on a CHN-O-Rapid instrument and were within ±0.4% of the theoretical values.

Compounds **1** to **5** were synthesized according to refs. 17 and 18.

Methyl 3,4,5-triacetoxybenzoate (1)

Melting point 130 to 131 °C. ^{1}H NMR ($CDCl_3$) δ: 2.29 (s, 9H, C(=O)CH_3), 3.89 (s, 3H, OCH_3), 7.79 (s, 2H, ArH). ESI-MS: $C_{14}H_{15}O_8$ $[M + H]^+$ 311. Anal. calcd. for $C_{14}H_{14}O_8$: C 54.18, H 4.56; found: C 54.20, H 4.55.

Methyl 3,5-diacetoxy-4-methoxybenzoate (2)

Melting point 83–83.5 °C. ^{1}H NMR ($CDCl_3$) δ: 2.32 (s, 6H, C(= O)CH_3), 3.87 (s, 6H, OCH_3). ESI-MS: $C_{13}H_{15}O_7$ $[M + H]^+$ 283. Anal. calcd. for $C_{13}H_{14}O_7$: C 55.35, H 4.98; found: C 55.32, H 5.00.

[3] Supplementary data for this article are available on the journal Web site (canjchem.nrc.ca) or may be purchased from the Depository of Unpublished Data, Document Delivery, CISTI, National Research Council Canada, Ottawa, ON K1A 0R6, Canada. DUD 5214. For more information on obtaining material refer to cisti-icist.nrc-cnrc.gc.ca/irm/unpub_e.shtml. CCDC 642103–642106 contain the crystallographic data for **3**–**6**. These data can be obtained, free of charge, via www.ccdc.cam.ac.uk/conts/retrieving.html (Or from the Cambridge Crystallographic Data Centre, 12 Union Road, Cambridge CB2 1EZ, UK; fax +44 1223 336033; or deposit@ccdc.cam.ac.uk).

© 2007 NRC Canada

Table 1. Crystal data and structure refinement for compounds **3**, **4**, **5**, and **6**.

Compounds	**3**	**4**	**5**	**6**
Empirical formula	$C_9H_{10}O_5$	$C_{23}H_{22}O_5$	$C_{22}H_{22}O_4$	$C_{24}H_{26}O_4$
Formula weight	198.17	378.41	350.40	378.45
Crystal system	Orthorhombic	Triclinic	Triclinic	Monoclinic
Space group	$P2_12_12_1$	P-1	P-1	$P2_1/c$
a (Å)	4.0750(8)	10.068(2)	8.1410(16)	5.8100(12)
b (Å)	7.5880(15)	10.499(2)	8.7590(18)	15.778(3)
c (Å)	29.802(6)	11.388(2)	12.879(3)	23.237(5)
α (°)	90	76.84(3)	91.66(3)	90
β (°)	90	66.79(3)	94.69(3)	96.09(3)
γ (°)	90	64.10(3)	91.73(3)	90
Volume (Å^3)	921.5(3)	993.0(5)	914.4(3)	2118.1(7)
Z	4	2	2	4
Calculated density (Mg/m^3)	1.428	1.266	1.273	1.187
μ (mm^{-1})	0.118	0.089	0.087	0.080
F(000)	416	400	372	808
Reflections collected	2185	4126	3847	4112
Unique reflections	1111	3894	3581	3716
R_{int}	0.0472	0.0131	0.0117	0.0431
Data/restraints/parameters	1111/0/133	3894/0/256	3581/0/238	3716/19/254
Goodness-of-fit on F^2	1.069	1.026	1.026	0.975
R_1; wR_2 [$I > 2\sigma(I)$]	0.0500, 0.1195	0.0580, 0.1412	0.0441, 0.1036	0.0658, 0.1511
R_1; wR_2 (all data)	0.0678, 0.1304	0.1009, 0.1674	0.0682, 0.1179	0.1444, 0.1761
Extinction coefficient	0.145(15)	0.049(6)	0.373(13)	0.028(3)
$\Delta\rho_{max}/\Delta\rho_{min}$ (eÅ^{-3})	0.345/–0.245	0.200/–0.209	0.140/–0.183	0.188/–0.190

$R_1 = \Sigma|(|F_o| - |F_c|)|/\Sigma|F_o|$. $wR_2 = [\Sigma w(|F_o| - |F_c|)^2/\Sigma w|F_o|^2]^{1/2}$, $w = [\sigma^2(F_o)^2 + (0.1(\max(0, F_o^2) + 2F_c^2)/3)^2]^{-1}$.

Methyl 3,5-dihydroxy-4-methoxybenzoate (3)

Melting point 148 to 149 °C. ^{1}H NMR ($CDCl_3$) δ: 3.73 (s, 3H, $ArOCH_3$), 3.77 (s, 3H, OCH_3), 6.94 (s, 2H, ArH), 9.51 (s, 2H, OH). ESI-MS: $C_9H_{11}O_5$ $[M + H]^+$ 199. Anal. calcd. for $C_9H_{10}O_5$: C 54.52, H 5.10; found: C 54.55, H 5.09.

Methyl 3,5-dibenzyloxy-4-methoxybenzoate (4)

Melting point 119 to 120 °C. ^{1}H NMR ($CDCl_3$) δ: 3.88 (s, 3H, $ArOCH_3$), 3.94 (s, 3H, OCH_3), 5.16 (s, 4H, $ArCH_2$), 7.33 (t, 2H, J = 7.0 Hz, benzyl H-4′), 7.31 (s, 2H, H-2, 6), 7.39 (t, 4H, J = 7.3 Hz, benzyl H-3′, 5′), 7.46 (d, 4H, benzyl H-2′, 6′). ESI-MS: $C_{23}H_{23}O_5$ $[M + H]^+$ 379. Anal. calcd. for $C_{23}H_{22}O_5$: C 73.04, H 5.84; found: C 73.00, H 5.86.

3,5-Dibenzyloxy-4-methoxybenzyl alcohol (5)

Melting point 105 to 106 °C. ^{1}H NMR ($CDCl_3$) δ: 1.76 (s, 1H, OH), 3.90 (s, 3H, OCH_3), 4.54 (s, 2H, $HOCH_2$), 5.13 (s, 4H, $ArCH_2$), 6.64 (s, 2H, H-2, 6), 7.32 (t, 2H, J = 7.3 Hz, benzyl H-4′), 7.38 (t, 4H, J = 7.3 Hz, benzyl H-3′, 5′), 7.45 (d, 4H, J = 7.5 Hz, benzyl H-2′, 6′). ESI-MS: $C_{22}H_{23}O_4$ $[M + H]^+$ 351. Anal. calcd. for $C_{22}H_{22}O_4$: C 75.45, H 6.30; found: C 75.41, H 6.33.

2-(3,5-Dibenzyloxy-4-methoxy)phenyl-2-propanol (6)

Methyl iodide (4.26 g, 29.6 mmol) was dissolved in 25 mL of dry ether and the resultant mixture added dropwise with stirring to magnesium turnings (0.68 g, 28.5 mmol) in 5 mL of dry ether. The mixture was heated to reflux for 0.5 h. A solution of 3,5-dibenzyloxy-4-methoxybenzoate (**5**; 3.96 g, 10.5 mmol) in 20 mL dry tetrahydrofuran was added dropwise with stirring. After heating to reflux for 1.5 h, the mixture was cooled and poured into an NH_4Cl solution. The ethereal layer was separated, and the aqueous layer was extracted with ether. The combined ethereal extracts were washed with solutions of $NaHSO_3$, $NaHCO_3$, and water and dried over anhyd. Na_2SO_4. The solvent was removed, and the residue was purified by flash chromatography with EtOAc – petroleum ether (1:4) to afford colorless crystals (3.45 g, 87%). Melting point 63 to 64 °C. ^{1}H NMR ($CDCl_3$) δ: 1.49 (s, 6H, CH_3), 2.05 (s, 1H, OH), 3.90 (s, 3H, OCH_3), 5.14 (s, 4H, $ArCH_2$), 6.77 (s, 2H, H-2, 6), 7.31 (t, 2H, J = 7.3 Hz, benzyl H-4′), 7.38 (t, 4H, J = 7.4 Hz, benzyl H-3′, 5′), 7.46 (d, 4H, J = 7.4 Hz, benzyl H-2′, 6′). ESI-MS: $C_{24}H_{25}O_3$ $[M - H_2O + H]^+$ 361. Anal. calcd. for $C_{24}H_{26}O_4$: C 76.09, H 6.94; found: C 76.17, H 6.92.

3,5-Dibenzyloxy-4-methoxyphenol (7)

Boron trifluoride etherate (83 mmol, 10 mL) was added to a suspension of sodium perborate (15.8 mmol, 2.7 g) in dry tetrahydrofuran (72 mL) contained in a nitrogen-flushed flask cooled to 0 °C. The mixture was stirred for 30 min at room temperature, and then the compound **7** (7.2 mmol, 2.71 g in 20 mL of dry tetrahydrofuran) was added. After stirring for 13 h, the reaction was quenched with sodium sulfite; the product was extracted into ethyl acetate and dried over $MgSO_4$. Removal of the solvent followed by column chromatography (EtOAc – petroleum ether, 1:4) produced compound **7** as colorless crystals (2.25 g, 93%). Melting point 86–88 °C. ^{1}H NMR (DMSO-d_6) δ: 3.64 (s, 3H, OCH_3), 5.04 (s, 4H, $ArCH_2$), 6.14 (s, 2H, H-2, 6), 7.33 (t, 2H, J = 6.9 Hz, benzyl H-4′), 7.40 (t, 4H, J = 7.4 Hz, benzyl H-3′, 5′), 7.44 (d, 4H, J = 7.1 Hz, benzyl H-2′, 6′), 9.22 (s, 1H,

© 2007 NRC Canada

ArOH). ESI-MS: $C_{21}H_{21}O_4$ $[M + H]^+$ 337. Anal. calcd. for $C_{21}H_{20}O_4$: C 75.02, H 5.97; found: C 74.98, H 5.99.

Result and discussion

Chemistry

Gallates are known to display variety of biological functions, including anticancer activity. To investigate the effect of the ester moieties on their antiproliferative and (or) cytotoxic activity, we successfully synthesized compounds **5**–**7** (shown in Scheme 1). Guzmán et al. reported that oxidation of hydroxy and alkoxybenzaldehydes afforded phenols with H_2O_2 and SeO_2 in *t*-butyl alcohol at room temperature (19). Thus, we designed a rout to synthesize compound **7** (shown in Scheme 2). However, compound **8** was obtained in good yield instead of **7** when the route was carried out. Kabalka et al. reported another method to synthesize phenols. Namely, sodium perborate could convert benzylic alcohols to phenols with boron trifluoride etherate in tetrahydrofuran (20). Compound **6** was treated under similar conditions to afford **7** in 93% yields. In contrast, compound **7** was not formed by similarly treating **5**.

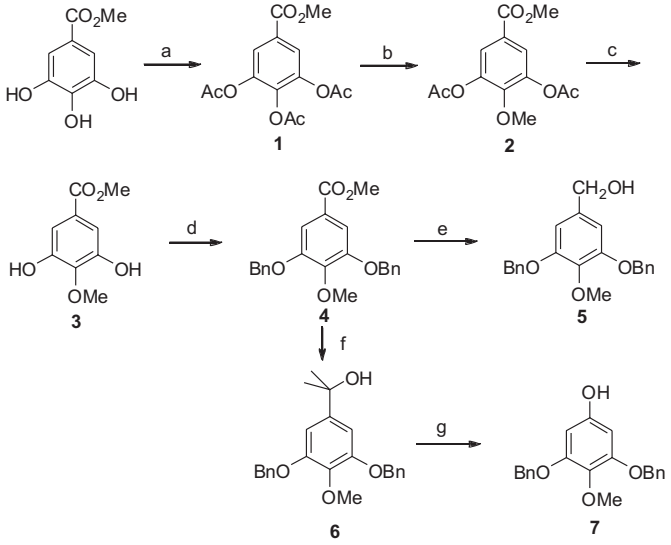
Structure analysis

Figures 1–4 represent the crystal structures of compounds **3**–**6** with thermal ellipsoids at 30% probability, respectively. For compound **6**, the hydroxyl O(4) and the two methyl groups C(23) and C(24) were disordered and were refined in three different orientations. The cause is the rotation about C(1)–C(22) bond. The selected bond lengths and bond angles are listed in Table 2.

In the crystal structures of compounds **4**–**6**, there are three benzene rings for each molecule. Although they are structurally similar, the dihedral angels between the central benzene ring and the two peripheral ones in different compounds have significant differences. In compounds **4**–**6**, C(1), C(2), C(3), C(4), C(5), and C(6) form the first plane, defined as plane I; C(8), C(9), C(10), C(11), C(12), and C(13) form the second plane, defined as plane II; C(16), C(17), C(18), C(19), C(20), and C(21) form the third plane, defined as plane III. Plane II and plane III make dihedral angles of 83.064(84) and 62.153(112)°, respectively, with plane I, and the dihedral angle between plane II and plane III is 88.847(112)° in compound **4**. Whereas, plane II and plane III make dihedral angles of 84.899(61) and 50.761(66)°, respectively, with plane I in compound **5** vs. 36.582(81) and 31.189(98)°, respectively, in compound **6**, and the dihedral angle between plane II and plane III is 53.726(73)° in **5** and 37.767(87)° in **6** (Table 3).

In compound **3**, the bond length of C(8)—O(4) is 1.202(3) Å, which is comparable with the corresponding bond length (C(22)—O(4) = 1.197(3) Å) in compound **4**. This is in good agreement with the standard values of C=O bond. In both compounds **3** and **4**, the bond lengths of C(=O)–O are shorter than that of the other C—O single bond in the ester moieties, and the bond lengths of C(=O)–C(phenyl) are slightly shorter than that of normal C—C single bond (1.530 Å) (Table 2), but they are still within the normal scope. This indicated that p–π conjugation exists between O and C=O and the existence of a week π–π conjugation between C=O group and the benzene ring.

Scheme 1. (a) Ac_2O, Et_3N; (b) K_2CO_3, CH_3I; (c) CH_3OH/H_2O, K_2CO_3; (d) DMF, K_2CO_3, BnCl; (e) THF, $LiAlH_4$; (f) Et_2O, CH_3I, Mg; and (g) THF, $NaBO_3{\cdot}4H_2O$, $BF_3{\cdot}Et_2O$.



Scheme 2. (h) Pyridine/CrO_3, THF and (g) SeO_2, H_2O_2, *t*-butyl alcohol.

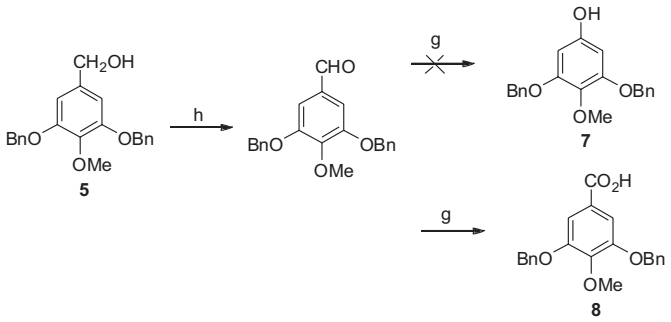
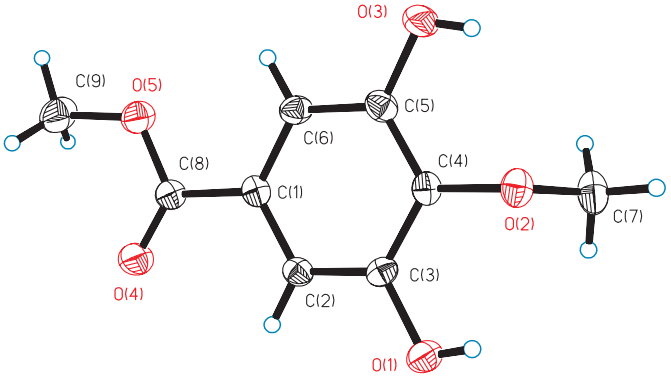


Fig. 1. The crystal structure of compound **3** (30% probability ellipsoids).



In compound **3**, the bond length of C(3)—O(1) (1.373(3) Å) is longer than that of C(5)—O(3) (1.354(3) Å), this difference may be caused by the different type of intermolecular hydrogen bonds. In fact, the intermolecular hydrogen bonds are as follows: O(3)–H(1)···O(4) has length of 2.819(4) Å and an angle of 147(4)°, with symmetry code

© 2007 NRC Canada

Table 2. Selected bond lengths (Å) and angles (°) for compounds **3**, **4**, **5** and 6

Compound **3**		Compound **4**		Compound **5**		Compound **6**	
Bond lengths (Å)							
C(1)—C(8)	1.489(4)	C(1)—C(22)	1.503(3)	C(1)—C(22)	1.508(2)	C(1)—C(22)	1.525(5)
C(3)—O(1)	1.373(3)	C(3)—O(1)	1.367(3)	C(3)—O(1)	1.366(2)	C(3)—O(1)	1.369(4)
C(5)—O(3)	1.354(3)	C(5)—O(3)	1.369(3)	C(5)—O(3)	1.3707(19)	C(5)—O(3)	1.371(4)
C(8)—O(4)	1.202(3)	C(7)—C(8)	1.500(3)	C(7)—C(8)	1.504(2)	C(7)—C(8)	1.504(5)
C(8)—O(5)	1.328(4)	C(15)—C(16)	1.496(4)	C(15)—C(16)	1.495(3)	C(15)—C(16)	1.496(6)
C(9)—O(5)	1.444(4)	C(22)—O(4)	1.197(3)				
		C(22)—O(5)	1.322(3)				
		C(23)—O(5)	1.455(3)				
Bond angles (°)							
O(4)–C(8)–O(5)	123.8(3)	O(3)–C(7)–C(8)	108.87(18)	O(3)–C(7)–C(8)	112.64(14)	O(3)–C(7)–C(8)	109.2(3)
O(4)–C(8)–C(1)	124.2(3)	O(1)–C(15)–C(16)	107.7(2)	O(1)–C(15)–C(16)	109.25(15)	O(1)–C(15)–C(16)	111.3(4)
O(5)–C(8)–C(1)	112.0(2)	O(4)–C(22)–O(5)	123.6(2)	C(3)–O(1)–C(15)	116.78(13)	C(4)–O(2)–C(14)	115.6(2)
C(4)–O(2)–C(7)	113.9(3)	O(4)–C(22)–C(1)	123.2(2)	C(4)–O(2)–C(14)	113.20(16)	C(5)–O(3)–C(7)	116.53(17)
C(8)–O(5)–C(9)	116.8(2)	O(5)–C(22)–C(1)	113.2(2)	C(5)–O(3)–C(7)	118.23(13)	C(22)–O(5)–C(23)	116.7(2)
		C(3)–O(1)–C(15)	118.22(18)			C(3)–O(1)–C(15)	117.8(3)
						C(4)–O(2)–C(14)	114.5(3)
						C(5)–O(3)–C(7)	117.7(3)

Fig. 2. The crystal structure of compound **4** (30% probability ellipsoids).

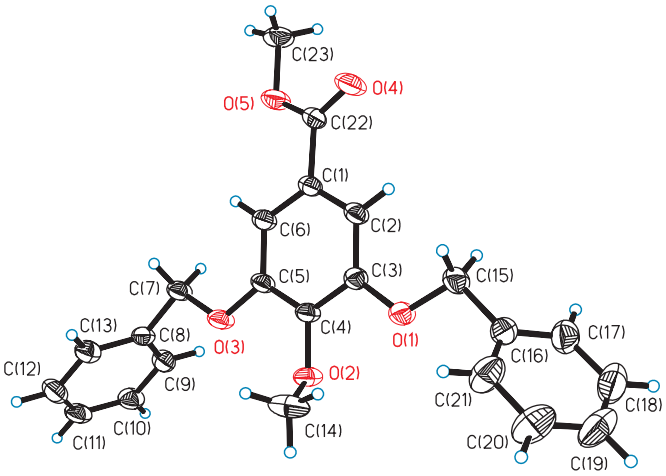


Fig. 3. The crystal structure of compound **5** (30% probability ellipsoids).

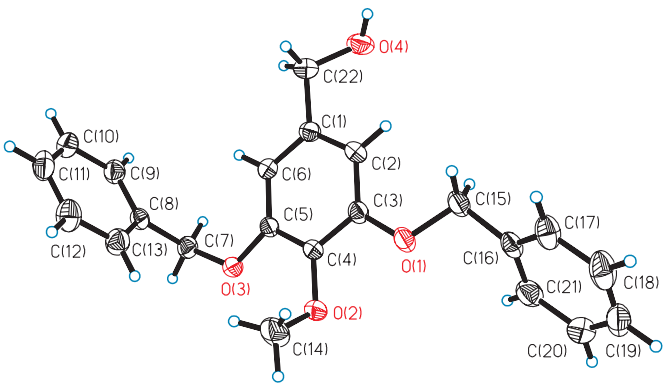
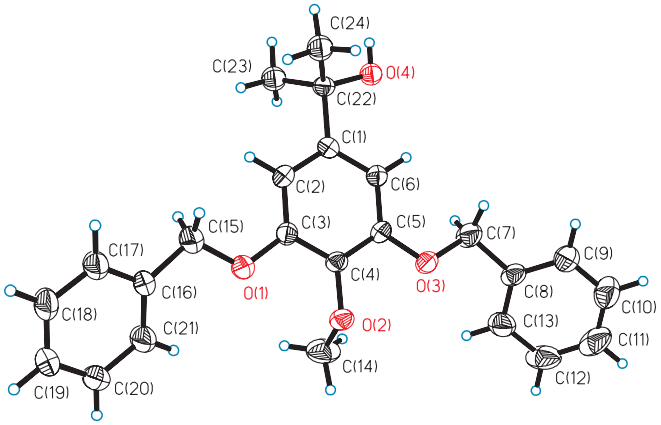


Fig. 4. The crystal structure of compound **6** (30% probability ellipsoids).



x–1, *y*–1, *z*, respectively. On the other hand, O(1)–H(3)···O(1) has length of 2.775(4) Å and an angle of 146(3)°, with symmetry code *x* – 1/2, –*y* + 3/2, –*z*, respectively, (Table 4). One hydrogen bond acceptor is the carbonyl O(4) atom and the other, however, is the phenolic hydroxyl O(1) atom. The corresponding bond lengths of C=O in compounds **4**–**5** verified that hypothesis. The two C=O bond lengths in each compound (**4** or **5**) are almost identical (Table 2). Obviously, the reason is that the hydrogen bonds mentioned do not exist any longer owing to the hydrogen atoms in hydroxyl groups being substituted.

The packing diagrams in Figs. 5 and 6 show the stacking patterns of compounds **3** and **5**, respectively. In the crystal cell of compound **3**, intermolecular hydrogen bonds lead to forming three-dimensional supramolecular network (Fig. 5); meanwhile, the intramolecular hydrogen bonds were also observed between the two hydroxyl groups and O(2) atom. On the other hand, the molecules of compound **5** are linked by the intermolecular hydrogen bonds to form a one-

© 2007 NRC Canada

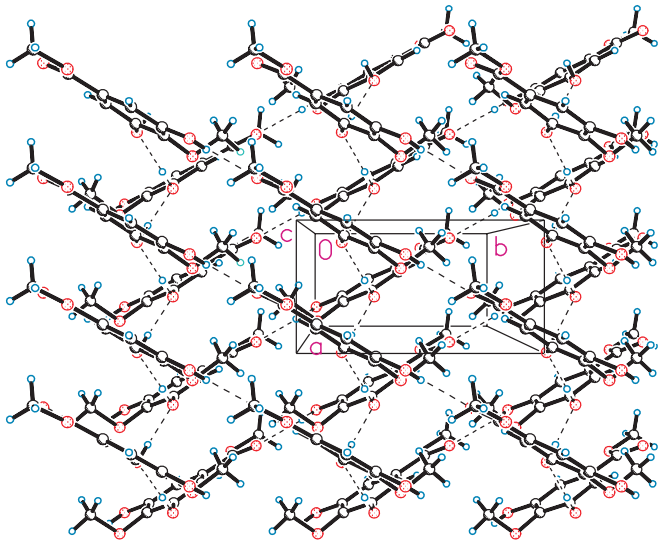
Table 3. Dihedral angles in compounds **4**, **5**, and **6**.

Plane	**4**	**5**	6
C1 to C6 and C8 to C13	83.064(84)°	84.899(61)°	36.582(81)°
C1 to C6 and C16 to C21	62.153(112)°	50.761(66)°	31.189(98)°
C8 to C13 and C16 to C21	88.847(112)°	53.726(73)°	37.767(87)

Table 4. Intra and Intermolecular hydrogen bonds in compounds **3** and **5**.

Compound	D···H	d(D···H)	d(H···A)	<DHA	d(D···A)	A
3	O1···H3	0.77(3)	2.11(3)	146(3)	2.775(4)	O1 [x – 1/2, –y + 3/2, –z]
	O1···H3	0.77(3)	2.35(3)	117(2)	2.779(3)	O2
	O3···H1	0.73(4)	2.18(4)	147(4)	2.819(4)	O4 [x – 1, y – 1, z]
5	O3···H1	0.73(4)	2.41(3)	116(3)	2.804(3)	O2
	O4···H4	0.87(3)	2.17(3)	165(3)	3.016(2)	O2 [x + 1, y, z]
	O4···H4	0.87(3)	2.47(3)	125(2)	3.052(2)	O3 [x + 1, y, z]

Fig. 5. Packing diagram of compound **3**, viewed along the *c* axis, showing the intermolecular hydrogen-bonding scheme (dashed lines).



dimensional hydrogen-bonded linear wire, and the linear wires interact by face-to-face aromatic interactions (Fig. 6). Table 4 shows the hydrogen bonds in compounds **3**–**5**. All the geometrical data fall into the normal range of the hydrogen bonding interactions.

Biological assays

A few studies have evaluated the inhibitory effects of phenolic compounds on HepG2 cancer-cell growth (21) and studied the effects of pure polyphenols (quercetin, chlorogenic acid, and epicatechin) on HepG2 cell population growth and apoptosis. They found that quercetin was the most active with an IC_{50} of 87 μmol/L. Table 5 represented the cytotoxic effect of compounds **1**–**6** against the HepG2 cell lines. Compounds **4**, **5**, and **6** showed more potent-cell-growth inhibitory activities than the positive control 5-FU (IC_{50} 51.6 μmol/L). Compound **5** showed the highest bioactivity with an IC_{50} around 15.3 μmol/L, and compound

Fig. 6. View of the packing diagram of compound **5** showing intermolecular hydrogen bonds. The chains run along the *a* axis.

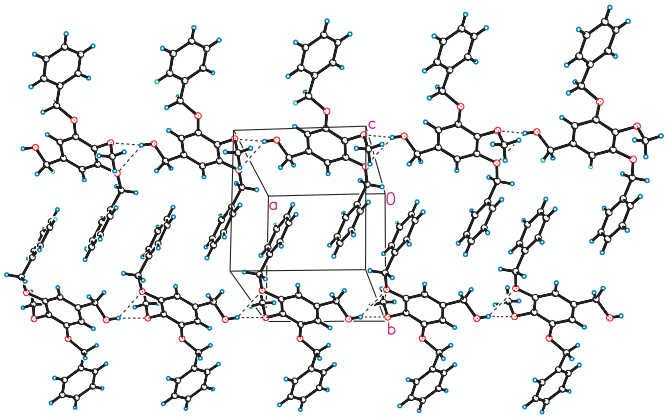


Table 5. Inhibition of HepG2 cells by compounds **1–7**.

Compounds	IC_{50} (μmol/L)
5-UF	51.6±0.2
1	77.8±0.7
2	69.6±0.4
3	90.3±0.6
4	23.1±0.1
5	15.3±0.2
6	20.2±0.5
7	67.8±0.3

4 (IC_{50} 23.1 μmol/L) was as potent as **6** (IC_{50} 20.2 μmol/L). In contrast, other compounds showed intermediate IC_{50} values. This suggested that the lipophilic group makes it easier for the molecule to permeate the cell membrane and interact with the enzymes in the cells. Roy et al. reported that lauryl gallate is able to inhibit protein tyrosine kinases (PTKs) in whole cells and in crude extracts (22). This allows us to make the following consideration: the compounds based on gallates in this paper may exert their proapoptotic activity

© 2007 NRC Canada

through the mechanism mentioned earlier. The study of the detailed mechanism is in progress.

Conclusion

A structural analysis of compounds **3**–**6** was carried out by single-crystal X-ray diffraction. The cytotoxic effects of seven derivatives of gallates tested against the HepG2 cell lines were evaluated. The effect of slight structural variations in this kind of systems was found to cause a marked change in their biological activity. Compound **5** showed the highest bioactivity with an IC_{50} around 15.3 μmol/L. The understanding of the structure–activity relationships ruling their biological function lies in more specific assays, the target particular binding sites, and the mechanisms of action. Further structure–activity relationship study is undergoing and will be reported in due course.

Acknowledgements

The work was financed by grant (Projects 30672516 and 30772627) from National Natural Science Foundation of China.

References

1. C.A. van der Heijden, P.J. Janssen, and J.J. Strik. Food Chem. Toxicol. **24**, 1067 (1986).
2. N. Niho, M. Shibutani, T. Tamura, K. Toyoda, C. Uneyama, N. Takahashi, and M. Hirose. Food Chem. Toxicol. **39**, 1063 (2001).
3. E.R. Sherwin. Food additives. Dekker, New York. 1990. pp. 139–193.
4. N. Ito and M. Hirose. Adv. Cancer Res. **53**, 247 (1989).
5. M. Hirose, A. Masuda, S. Fukushima, and N. Ito. Carcinogenesis, **9**, 101 (1988).
6. J. Gnojkowski, V. Krajka-Kuzniak, and W. Baer-Dubowska. Nutr. Cancer. **39**, 117 (2001).
7. T. Nakayama. Cancer Res. **54**, 1991s (1994).
8. T. Nakayama, M. Hiramitsu, T. Osawa, and S. Kawakishi. Mutat. Res. **303**, 29 (1993).
9. K. Saeki, A. Yuo, M. Isemura, I. I. Abe, T. Seki, and H. Noguchi. Biol. Pharm. Bull. **23**, 1391 (2000).
10. G. Roy, M. Lombardia, C. Palacios, A. Serrano, C. Cespon, E. Ortega, P. Eiras, S. Lujan, Y. Revilla, and P. Gonzalez-Porque. Arch. Biochem. Biophys. **383**, 206 (2000).
11. T. Murase, N. Kume, T. Hase, Y. Shibuya, Y. Nishizawa, I. Tokimitsu, and T. Kita. Arterioscler.Thromb. Vasc. **19**, 1412 (1999).
12. K. Brusselmans, E. De Schrijver, W. Heyns, G. Verhoeven, and J.V. Swinnen. Int. J. Cancer **106**, 856 (2003).
13. Q. Feng, T. Kumagai, Y. Nakamura, K. Uchida, and T. Osawa, Mutat. Res-Gen. Tox. En. **537(1)**, 101 (2003).
14. T. Mosmann. J. Immunol. Methods, **65**, 55 (1983).
15. SMART 5.0 and SAINT 4.0 for Windows NT [computer programs]. Area detector control and integration software. Bruker Analytical X-Ray Systems, Inc.: Madison, WI. 1998.
16. G.M. Sheldrick. SHELXTL [computer program]: Structure determination software programs. Bruker Analytical X-Ray System, Inc.: Madison, WI. 1997.
17. M.L. Cardona, M.I. Fernandez, M.B. Garcia, and J.R. Pedro. Tetrahedron, **42**, 2725 (1986).
18. A.J. Pearson and P.R. Bruhn. J. Org. Chem. **56**, 7092 (1991).
19. J.A. Guzm, V. Mendoxa, E. Garc, C.F. Garibay, L.Z. Olivares, and L.A. Maldonado. Synthetic Commun. **25 (14)**, 2121 (1995).
20. G.W. Kabalka, N. K. Reddy, and C. Narayana. Tetrahedron Lett. **34**, 7667 (1993).
21. S. Ramos, M. Alia, L. Bravo, and L. Goya. J. Agr. Food Chem. **53**, 1271 (2005).
22. G. Roy, M. Lombard, C. Palacios, A. Serrano, C. Cesp, E. Ortega, P. Eiras, S. Lujan, Y. Revilla, and P. Gonzalez-Porqu. Arch. Biochem. Biophys. **38**, 206 (2000).

© 2007 NRC Canada

An exploratory ab initio study of the S_N2 reaction of 1,3,3-trimethyltriazene with halide ions

Katherine G. Doucet, Cory C. Pye, and Thomas G. Enright

Abstract: Methyltriazene and the O6 oxygen of guanine are believed to undergo a bimolecular nucleophilic substitution (S_N2) reaction to form methylguanine, which is proposed to be responsible for the cytotoxic properties of triazene-containing anti-neoplastic agents, such as Dacarbazine. To better understand the proposed mechanism of triazene-containing anti-neoplastic agents, a series of ab initio studies investigating the S_N2 reaction between methyltriazenes and halide ions were undertaken. The results of our investigation of the S_N2 reaction between 1,3,3-trimethyltriazene and the halide ions are presented here.

Key words: triazene, trimethyltriazene, Dacarbazine, Temozolomide, bimolecular nucleophilic substitution reaction.

Résumé : On fait généralement l'hypothèse que le méthyltriazène et l'oxygène O6 de la guanidine donnent lieu à une réaction de substitution nucléophile bimoléculaire (S_N2) qui conduirait à la méthylguanidine et on attribue à cette réaction la responsabilité des propriétés cytotoxiques des agents anti-néoplasiques qui contiennent du triazène, tel le Dacarbazine. Dans le but de mieux comprendre le mécanisme proposé pour l'action des agents anti-néoplasiques contenant du triazène, on a entrepris des études ab initio sur la réaction S_N2 entre les méthyltriazènes et les ions halogénures. On rapporte ici les résultats de notre investigation de la réaction S_N2 entre le 1,3,3-triméthyltriazène et les ions halogénures.

Mots-clés : triazène, triméthyltriazène, Dacarbazine, Temozolomide, réaction de substitution nucléophile bimoléculaire.

[Traduit par la Rédaction]

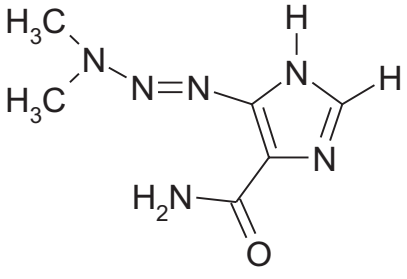
Introduction

Dacarbazine, 5-(3,3-dimethyl-1-triazenyl)imidazole-4-carboxamide (Fig. 1) is the single most-reactive agent known for the treatment of malignant melanoma (1–3). The mechanism of action of these anti-neoplastic agents remains unknown (4). It has been proposed that triazene-containing anti-neoplastic agents, especially Dacarbazine, require demethylation, a process that is known to be carried out by hepatic cytochrome P450 enzymes (5) (Scheme 1). The active metabolite, a monomethyltriazene, is believed to methylate DNA, as other methyltriazenes have been shown to be DNA and RNA methylating agents (6, 7). It has been proposed that monomethyltriazenes methylate the O6 oxygen of guanine to form methylguanine through a carbon-centered bimolecular nucleophilic substitution (S_N2) reaction (8) (Scheme 2).

Previous studies have focused on triazene and its mono-, di-, and tri-methyl analogues (9). In addition to this, more recent studies focused on the S_N2 reaction pathways of monomethyltriazene (10) and dimethyltriazene with halide ions (11). The present study focuses on the S_N2 reaction between 1,3,3-trimethyltriazene (Fig. 2) and the halide ions. 1,3,3-Trimethyltriazene contains three potential sites for attack by a halide ion and can exist as one of two isomers, (*E*) or (*Z*) with respect to the N=N bond of the triazene moiety (9). The (*E*) form is 56–64 kJ mol^{-1} more stable than the (*Z*) form. The S_N2 reaction between the 1-methyl of 1,3,3-trimethyltriazene and halide ions results in halomethane, molecular nitrogen, and dimethylamide ion (Scheme 3). The S_N2 reaction with either 3-methyl of 1,3,3-trimethyltriazene results in halomethane and a dimethyltriazenide ion (Scheme 4).

This series of studies was intended to provide a framework for future studies involving the active metabolite of Dacarbazine and its simple structural analogues. It is believed that these studies will provide a better understanding of the chemistry behind the proposed mechanism of action of triazene-containing anti-neoplastic agents.

Fig. 1. The chemical structure of 5-(3,3-dimethyl-1-triazenyl)imidazole-4-carboxamide (Dacarbazine, DTIC®).



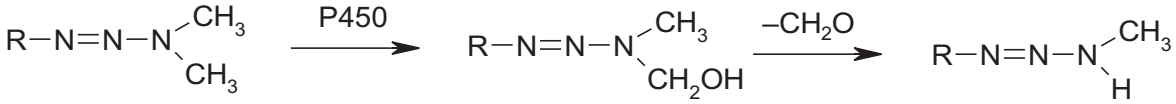
Received 10 July 2007. Accepted 23 August 2007. Published on the NRC Research Press Web site at canjchem.nrc.ca on 11 October 2007.

K.G. Doucet, C.C. Pye,[1] and T.G. Enright. Department of Chemistry, Saint Mary's University, Halifax, NS B3H 3C3, Canada.

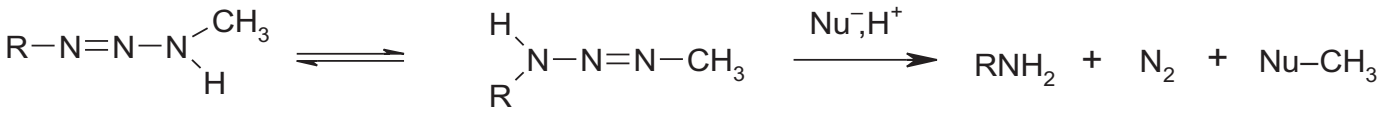
[1]Corresponding author (e-mail: cory.pye@smu.ca).

 doi:10.1139/V07-110 © 2007 NRC Canada

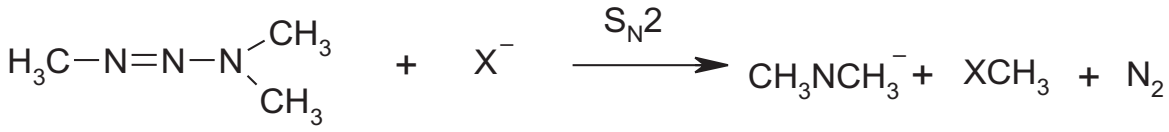
Scheme 1. The metabolic formation of monomethyltriazene from Dacarbazine through hepatic cytochrome P450 enzymatic oxidation.



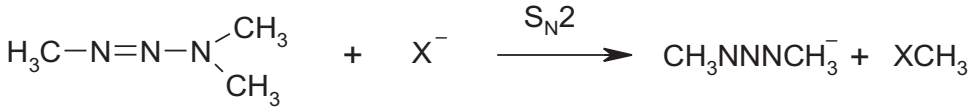
Scheme 2. The proposed mechanism of action for DNA methylation by a methyltriazene occurs through a bimolecular nucleophilic substitution reaction resulting in molecular nitrogen, aryl amine, and methylated DNA.



Scheme 3. The S_N2 reaction between 1-methyl of 1,3,3-dimethyltriazene and a halide ion results in a halomethane, molecular nitrogen, and $CH_3NCH_3^-$.



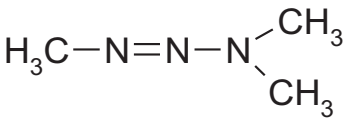
Scheme 4. The S_N2 reaction between 3-methyl of 1,3,3-dimethyltriazene and a halide ion results in a halomethane and dimethyltriazenes ion.



Method

Gaussian 98 (12) or Gaussian 03 (13) were used to perform all calculations for this computational study. Geometry optimizations were sequentially performed at the HF/STO-3G, HF/3–21G, HF/6–31G(d), HF/6–31+G(d), MP2/6–31G(d), and MP2/6–31+G(d) levels of theory. For MP2 calculations, the frozen-core approximation was utilized. Harmonic vibrational frequencies and zero-point vibrational energy (ZPVE) corrections were performed sequentially at the previously mentioned levels of theory. Harmonic vibrational frequency calculations characterized the geometry optimizations. A previously determined scaling factor was used to correct the ZPVE (14). Modified Huzinaga basis sets were used for iodine (15, 16). Only the results at MP2/6–31+G(d) will be presented; the rest are given in the Supplementary Data.[2] Because the halide ions were chosen as a very simple model for guanine in this initial survey, errors resulting from this choice would overshadow errors from neglecting temperature, free-energy, and solvation corrections. To allow direct comparison with our previous work (10, 11), we do not invoke these corrections.

Fig. 2. The chemical structure of 1,3,3-dimethyltriazene.



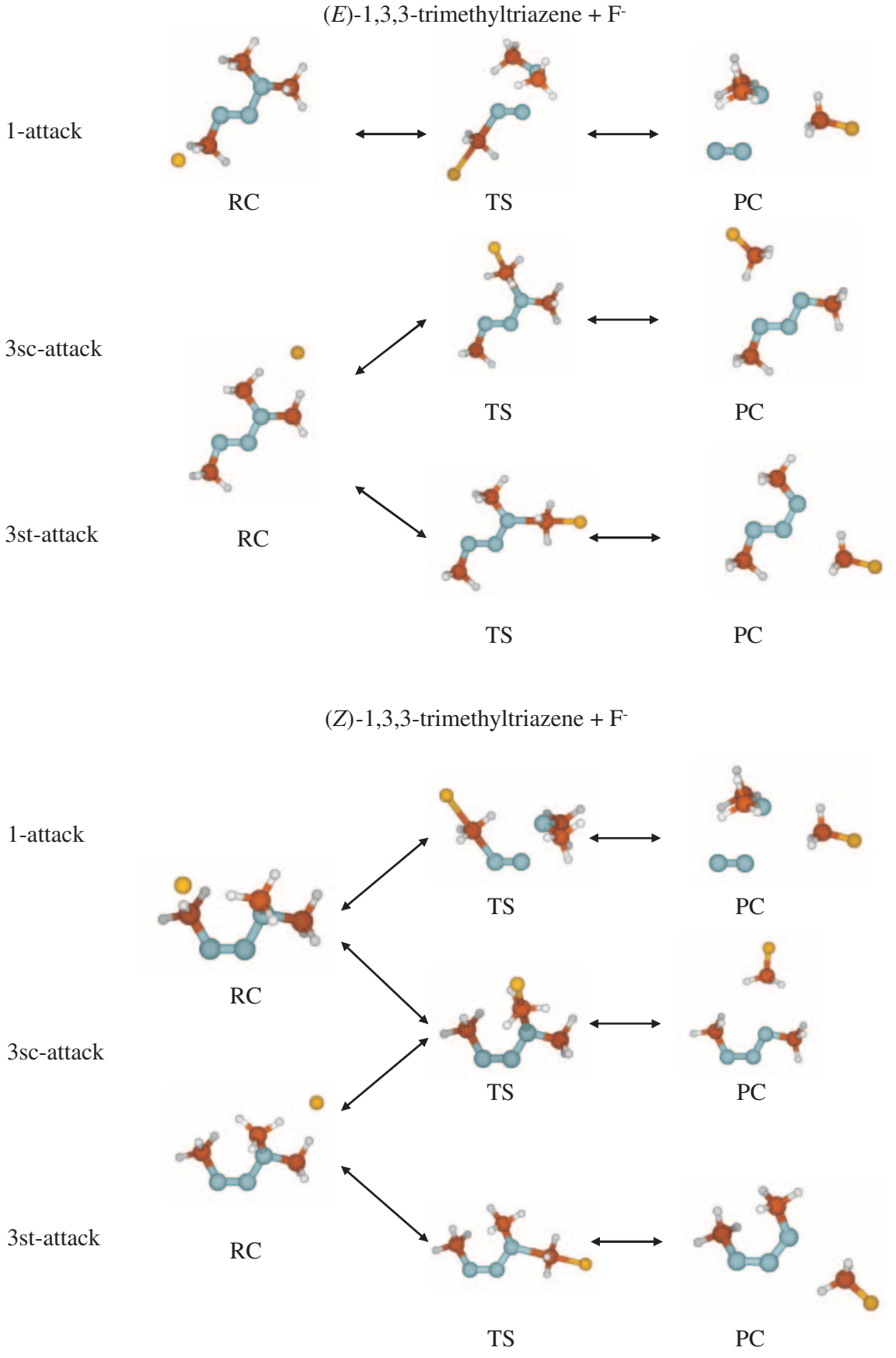
Results and discussion

Each reaction pathway passes through five stationary structures; the separated reactants (SR), a reactant complex (RC), a transition structure (TS) that corresponds to the characteristic Walden inversion of the methyl group, a product complex (PC), and the separated products (SP). The separated reactants and products are assumed to be at an infinite distance. For the (*E*) structures, the RC is the same for both syn-periplanar (sp, "s-cis") and anti-periplanar (ap, "s-trans") attack, whereas for the (*Z*) structures, each of the two RCs leads to one of two TSs, with the 3 sp TS being arrived at from either RC (see Fig. 3). We consider the net barriers, the energy difference between separated reactants and transition state, unless otherwise specified.

[2] Supplementary data for this article are available on the journal Web site (canjchem.nrc.ca) or may be purchased from the Depository of Unpublished Data, Document Delivery, CISTI, National Research Council Canada, Ottawa, ON K1A 0S2, Canada. DUD 5215. For more information on obtaining material, refer to cisti-icist.nrc-cnrc.gc.ca/irm/unpub_e.shtml.

© 2007 NRC Canada

Fig. 3. The structures on the reaction pathways of attack of halide upon (*E*)- and (*Z*)-1,3,3-trimethyltriazene.

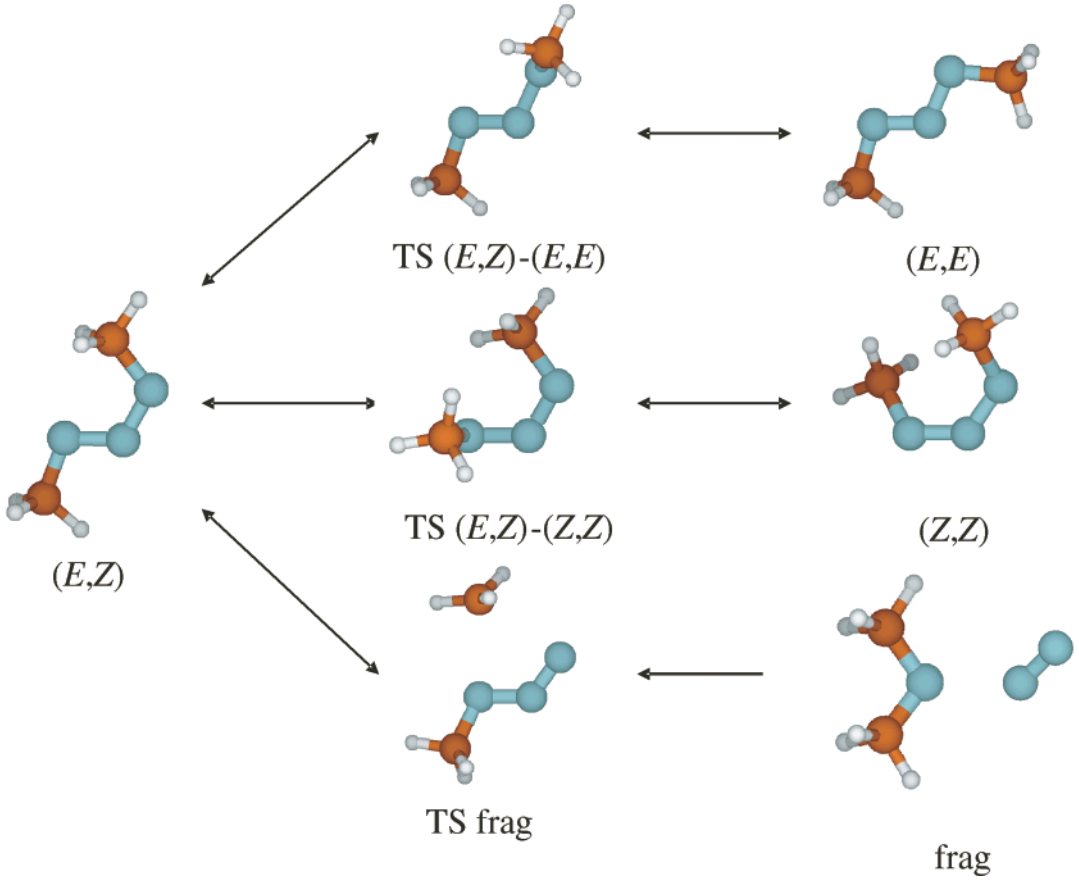


© 2007 NRC Canada

Table 1. Relative energy (kJ mol^{-1}) comparison of the three conformers of MeN_3Me^-, the interconversion and methyl transfer transition states, and products, with respect to the lowest energy conformer (*E*,*Z*).

	Relative energy (kJ mol^{-1})					
Level of theory	(*E*,*E*)	(*Z*,*Z*)	MTS	(*E*,*Z*) → (*E*,*E*) TS	(*E*,*Z*) → (*Z*,*Z*) TS	NMe_2^- + N_2
HF/6–31G(d)	11.9	85.2	353.5	123.4	125.5	–144.7
HF/6–31+G(d)	6.1	88.1	348.4	115.6	127.0	–151.4
MP2/6–31G(d)	20.0	82.8	251.8	146.6	132.5	–92.4
MP2/6–31+G(d)	10.9	75.8	194.9	134.7	134.3	–99.3

Fig. 4. The structures on the reaction pathways of dimethyltriazenide rearrangement and fragmentation.



For 3-methyl attack, the dimethyltriazenide ion formed in the product complex depends on the isomer of 1,3,3-trimethyltriazene and which one of the two 3-methyl groups is attacked. The sp methyl attack of (*Z*)-1,3,3-trimethyltriazene results in the formation of (*E*,*Z*)-1,3-dimethyltriazenide ion, whereas the ap methyl attack results in (*Z*,*Z*)-1,3-dimethyltriazenide ion. Attack of (*E*)-1,3,3-trimethyltriazene at the sp methyl results in (*E*,*E*)-1,3-dimethyltriazenide ion, whereas attack at the ap methyl results in (*E*,*Z*)-1,3-dimethyltriazenide ion formation. Of the three distinct dimethytriazenide ions (Fig. 4), the (*E*,*Z*)-dimethyltriazenide ion was found to be more stable than the (*E*,*E*) and (*Z*,*Z*) conformers (Table 1), with the (*Z*,*Z*) isomer being especially unstable because of the steric collision of the methyl groups forcing a non-planar C_2 arrangement. Comparison to methyltriazenide ion reveals that the barrier to fragmentation via a methyl shift is nearly identical. However, the (*E*,*Z*) to (*E*,*E*) rotational barrier is, for the most part, slightly lower, and the (*E*,*Z*) to (*Z*,*Z*) barrier is higher. This trend was also revealed for the comparison between triazenide and methyltriazenide.

The relevant geometrical parameters are given in Tables S7-S10 of the Supplementary Data.[2] At most levels of theory, reactions involving fluoride were exothermic, whereas those involving chloride, bromide, and iodide were progressively more endothermic (Tables 2 and S11–S14). We were able to note some general trends for all of the S_N2 reactions. The (*Z*) barriers are generally lower than the (*E*) barriers, except for the 3 ap attack. For the (*Z*) forms, the barrier increases from 1-attack to 3 sp to 3 ap. For 1-attack of fluoride, the barrier for 1,3,3-trimethyltriazene is lower than that of 1-methyltriazene and 1,3-dimethyltriazene. For 3 ap attack, the barriers are higher than that of the less-substituted 3-methyltriazene (ap), 1,3-dimethyltriazene (ap),

© 2007 NRC Canada

Table 2. Relative energy comparison (MP2/6–31+G*, kJ mol^{-1}), with respect to the separated reactants of each reaction, of the 1,3,3-trimethyltriazene S_N2 reaction pathways.

	Relative energy (kJ mol^{-1})							
	(*Z*)-				(*E*)-			
Level of theory	RC	TS	PC	SP	RC	TS	PC	SP
F^-, 1-attack	–92.0	22.1	–188.0	–119.3	–43.2	77.0	–128.3	–59.5
F^-, 3 sp attack	–92.0	32.4	–63.3	–20.0	–82.2	76.8	3.4	50.7
F^-, 3 ap attack	–84.7	72.0	10.3	55.8	–82.2	63.3	–4.6	39.8
Cl^-, 1-attack	–55.9	78.7	–80.9	–9.0	–20.1	137.7	–21.1	50.8
Cl^-, 3 sp attack	–55.9	105.8	51.8	90.3	–50.6	152.6	109.5	161.0
Cl^-, 3 ap attack	–52.7	154.1	116.4	166.0	–50.6	144.3	102.0	150.0
Br^-, 1-attack	–58.8	79.3	–49.7	30.4	–43.1	140.3	10.1	90.2
Br^-, 3 sp attack	–58.8	105.8	72.8	129.6	–53.8	154.3	130.2	200.4
Br^-, 3 ap attack	–56.1	157.9	139.4	205.4	–53.8	147.8	125.3	189.4
I^-, 1-attack	–44.9	100.5	–17.9	66.3	–44.9	100.5	–17.9	66.3
I^-, 3 sp attack	–44.9	138.7	121.4	176.5	–40.2	187.4	175.3	236.2
I^-, 3 ap attack	–42.8	193.9	185.6	241.3	–40.2	182.8	170.0	225.3

and 3,3-dimethyltriazene. The poor stability of the product (*Z*,*Z*)-dimethyltriazenide ion accounts for trends involving ap attack on the (Z) form. For the fluoride ion, with the (*E*) form of 1,3,3-dimethyltriazene, the barrier increases from 3 ap to 3 sp to 1-attack, whereas for the other halogens, the barrier increases from 1 attack to 3 ap to 3 sp. For the fluoride ion attacking the sp position, no trend is noted upon comparison with the less-substituted triazenes, whereas for the other halogens, the barriers are mostly lower than that of 3-methyl- (10), 1,3-dimethyl-, and 3,3-dimethyltriazene (11).

To summarize, the reaction pathways of (*E*)- and (*Z*)-1,3,3-dimethyltriazene with the halides are endothermic, with the exception of the fluoride reaction. The endothermicity increases with the size of the halide anion. The (*E*) barriers are usually higher than the (*Z*) barriers. The barriers of 1 attack decrease upon increasing methyl substitution. Because the S_N2 barriers are usually lower for 1 attack, and because of the high rearrangement and fragmentation barriers in the dimethyltriazenide ion resulting from 3 attack, the 1 attack is expected to be the dominant mode of action of triazene-based drugs.

Acknowledgements

The authors wish to thank the Department of Astronomy and Physics, Saint Mary's University (SMU) for providing access to Cygnus, a Sun Enterprise 4500. The authors also wish to thank the Atlantic Computational Excellence Network (ACEnet) for access to the SGI computers located at Memorial University (Herzberg; a SGI Onyx 3400, and Verdandi, Skuld, and Urdur; SGI Altix 350 clusters). CCP acknowledges the past support of the Natural Science and Engineering Research Council of Canada (NSERC). KGD would like to acknowledge the continuing support of the Faculty of Graduate Studies and Research (FGSR), SMU. TGE would like to acknowledge the support of the Student Employment Experience Program, SMU (Fall 2003 – Winter 2004). CCP also thanks Keith Vaughan for originally suggesting the study of S_N2 reactions of substituted triazenes.

References

1. K. Vaughan. The Chemistry of antitumor agents. Blackie, Glasgow. 1990. Chapter 5. pp.159–186.
2. S.K. Carter and M.A. Friedman. Eur. J. Cancer. **8**, 85, (1972).
3. J.R.P. Godin, K. Vaughan, and K. W. Renton. Can. J. Physiol. Pharmacol. **59**, 1234 (1981).
4. D.A. Clarke, R.K. Barclay, C.C. Stock, and R.S. Rondesvedt. Proc. Soc. Exp. Bio. Med. **90**, 484 (1955).
5. E. Carvalho, A.P. Francisco, J. Iley, and E. Rose. Bioorg. Med. Chem. **8**, 1719 (2000) and references therein.
6. T.A. Connors, P.M. Goddard, K. Merai, W.C.J. Ross, and D.E.V. Wilman. Biochem. Pharmacol. **25**, 241 (1976).
7. M. Julliard and G. Vernin. Ind. Eng. Chem. Prod. Res. Rev. **20**, 287 (1981).
8. K. Vaughan and M.F.G. Stevens. Chem. Soc. Rev. **7**, 377 (1978).
9. C.C. Pye, K. Vaughan and J.F. Glister. Can. J. Chem. **80**, 447 (2002).
10. K.G. Doucet, C.C. Pye, and T.G. Enright. J. Mol. Struct. THEOCHEM. **802**, 21 (2006).
11. K.G. Doucet, C.C. Pye, and T.G. Enright. J. Mol. Struct. THEOCHEM. **821**, 166–170 (2007).
12. M.J. Frisch, G.W. Trucks, H.B. Schlegel, G.E. Scuseria, M.A. Robb, J.R. Cheeseman, V.G. Zakrzewski, J.A. Montgomery, Jr., R.E. Stratmann, J.C. Burant, S. Dapprich, J.M. Millam, A.D. Daniels, K.N. Kudin, M.C. Strain, O. Farkas, J. Tomasi, V. Barone, M. Cossi, R. Cammi, B. Mennucci, C. Pomelli, C. Adamo, S. Clifford, J. Ochterski, G.A. Petersson, P.Y. Ayala, Q. Cui, K. Morokuma, D.K. Malick, A.D. Rabuck, K. Raghavachari, J.B. Foresman, J. Cioslowski, J.V. Ortiz, A.G. Baboul, B.B. Stefanov, G. Liu, A. Liashenko, P. Piskorz, I. Komaromi, R. Gomperts, R.L. Martin, D.J. Fox, T. Keith, M.A. Al-Laham, C.Y. Peng, A. Nanayakkara, M. Challacombe, P.M.W. Gill, B. Johnson, W. Chen, M.W. Wong, J.L. Andres, C. Gonzalez, M. Head-Gordon, E.S. Replogle, and J.A. Pople. Gaussian 98 [computer program], Revision A.9. Gaussian Inc., Pittsburgh, PA. 1998.
13. M.J. Frisch, G.W. Trucks, H.B. Schlegel, G.E. Scuseria, M.A. Robb, J.R. Cheeseman, J.A. Montgomery, Jr., T. Vreven, K.N. Kudin, J.C. Burant, J.M. Millam, S.S. Iyengar, J. Tomasi, V. Barone, B. Mennucci, M. Cossi, G. Scalmani, N. Rega,

© 2007 NRC Canada

G.A. Petersson, H. Nakatsuji, M. Hada, M. Ehara, K. Toyota, R. Fukuda, J. Hasegawa, M. Ishida, T. Nakajima, Y. Honda, O. Kitao, H. Nakai, M. Klene, X. Li, J.E. Knox, H.P. Hratchian, J.B. Cross, C. Adamo, J. Jaramillo, R. Gomperts, R.E. Stratmann, O. Yazyev, A.J. Austin, R. Cammi, C. Pomelli, J.W. Ochterski, P.Y. Ayala, K. Morokuma, G.A. Voth, P. Salvador, J.J. Dannenberg, V.G. Zakrzewski, S. Dapprich, A.D. Daniels, M.C. Strain, O. Farkas, D.K. Malick, A.D. Rabuck, K. Raghavachari, J.B. Foresman, J.V. Ortiz, Q. Cui, A.G. Baboul, S. Clifford, J. Cioslowski, B.B. Stefanov, G. Liu, A. Liashenko, P. Piskorz, I. Komaromi, R. L. Martin, D.J. Fox, T. Keith, M.A. Al-Laham, C.Y. Peng, A. Nanayakkara, M. Challacombe, P.M.W. Gill, B. Johnson, W. Chen, M.W. Wong, C. Gonzalez, and J.A. Pople. Gaussian 03 [computer program], Revision B.05. Gaussian, Inc., Pittsburgh, PA. 2003.

14. A.P Scott and L. Radom. J. Phys. Chem. **100**, 16502 (1996).
15. C.C. Pye. Int. J. Quant. Chem. **76**, 62 (2000).
16. S. Huzinaga, J. Andzelm, M. Klobukoski, E. Radio-Andzelm, Y. Sakei, H. Tatewaki. Gaussian basis sets for molecular calculations. Elsevier: Amsterdam. 1984.

© 2007 NRC Canada

Glycoluril-derived crown clips as new ditopic receptors

Mohammad Rahimizadeh, E. Rezaei Seresht, Mehdi Bakavoli, and Mehdi Pordel

Abstract: Several new ditopic receptors have been synthesized from 4,4′-bis(methoxyphenyl)glycoluril (**1**). The first receptor site is a cleft composed of two fused 2-imidazolone rings, which are flanked by two aromatic side walls, and the second site is a crown ether moiety.

Key words: receptors, crown compounds, glycoluril, molecular clips.

Résumé : On a effectué la synthèse de plusieurs nouveaux récepteurs ditopiques au départ de la 4,4′-bis(méthoxyphényl)glycoluril (**1**). Le premier site récepteur est une fente formée par deux noyaux 2-imidazole condensés flanqués de deux murs latéraux aromatiques alors que le second site récepteur est un éther couronne.

Mots-clés : récepteurs, composés couronnes, glycoluril, pinces moléculaires.

[Traduit par la Rédaction]

Introduction

Receptors in living organisms play fundamental roles in the growth, nutrition, and differentiation of animal cells (1). Artificial receptors are capable of mimicking this function, which can lead to a better understanding of the natural processes and additionally to the development of new artificial systems for use in drug delivery, catalysis, and so forth (2).

Diphenylglycoluril-based clip molecules have been prepared and extensively studied in the Nolte group over the past decade (3). These molecules possess a well-defined cavity that allows the binding of different phenolic guests via a combination of several non-covalent interactions (H-bonding, π–π stacking, and the cavity effect) (3). The introduction of crown ether chains and alkyl tails to these receptors can lead to a new generation of the so-called amphiphilic basket receptors, which are also able to bind alkaline metal ions and aggregate in water into well-defined nanostructures (4, 5). Here, we describe the synthesis of new diphenylglycoluril-based ditopic receptors, bearing crown ether units, with potential ability to bind both neutral aromatic guests and alkaline metal ions, simultaneously.

Results and discussion

We have utilized the commercially available 4,4-dimethoxybenzil (**7**) as a potentially interesting candidate for the synthesis of more engineered clips, since the ring-activating *p*-methoxy group on the phenyl nucleus could allow the possibility of electrophilic aromatic substitution ortho- to it. Alternatively, the methoxy group could be demethylated to give the more-reactive hydroxy group that can start up a variety of methods for further structural elaboration and derivatization. Therefore, 4,4-bis(methoxyphenyl)glycoluril (**1**) was prepared quantitatively from compound **7** and urea in trifluoroacetic acid and toluene by azeotropic distillation according to a published method (Scheme 1) (6). The molecular clips **3a**–**3c** were subsequently synthesized from **1** by means of an amido alkylation reaction in the presence of potassium hydroxide in DMSO (Scheme 1). Notably, the clip-like structures of these molecules can be easily deduced from the X-ray structure of **3a** (6). Therein, the *o*-xylene rings define a tapered cavity, and the two fused five-membered rings of the glycoluril form a shallow floor, which is electron-rich with two hydrogen-bond-acceptor sites. ^{1}H NMR studies were the first to reveal that the molecular clips, with their pre-organized clefts, are excellent receptors for neutral aromatic guests, particularly dihydroxybenzenes (7–11). For example, upon binding of resorcinol, the guest simultaneously forms two hydrogen bonds to the π orbitals of the carbonyl groups of the clip. The binding strength of this type of guests within the molecular clips can span a wide range of values ($K_{association}$ = 0–10^5 (mol/L)$^{-1}$), which vary with simple modification in either host or guest molecule. Compounds **2b** and **2c** are more susceptible to nucleophilic attack by **1** than **2a**. So, the reaction time was changed from 2 h for **2a** to 4 h for **2b** and **2c**. The side wall **2a** is commercially available, and the other side walls (**2b** and **2c**) were prepared via chloromethylation of *o*-xylene and 1,2,3,4-tetramethylbenzene, recpectively. For the demethylation of the methoxy groups of the clips **3a**–**3c**, pyridine hydrochloride was used as a demethylating agent and as a result, compounds **4a**–**4c** were produced in yields higher than 65%. Then, the hydroxy-functionalized clips **4a**–**4c** were reacted with ditosylates **6a**–**6c** in acetonitrile with K_2CO_3 as a base to yield **5a**–**5i** (Scheme 2). The structures of compounds **5a**–**5i** were confirmed from their spectral and analytical data. For example, in the ^{1}H NMR spectrum of

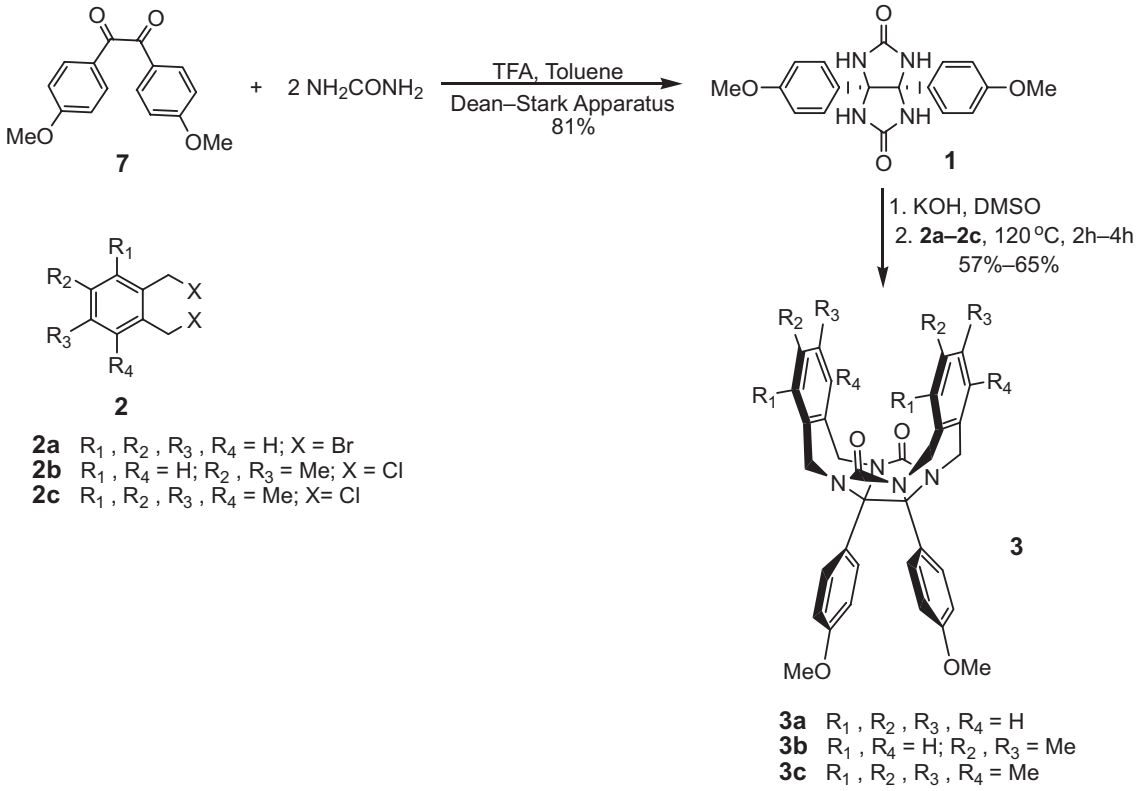
Received 10 April 2007. Accepted 24 August 2007. Published on the NRC Research Press Web site at canjchem.nrc.ca on 6 October 2007.

M. Rahimizadeh, E.R. Seresht, M. Bakavoli,[1] and Mehdi Pordel. Department of Chemistry, School of Sciences, Ferdowsi University, Mashhad 91375-1436, Iran.

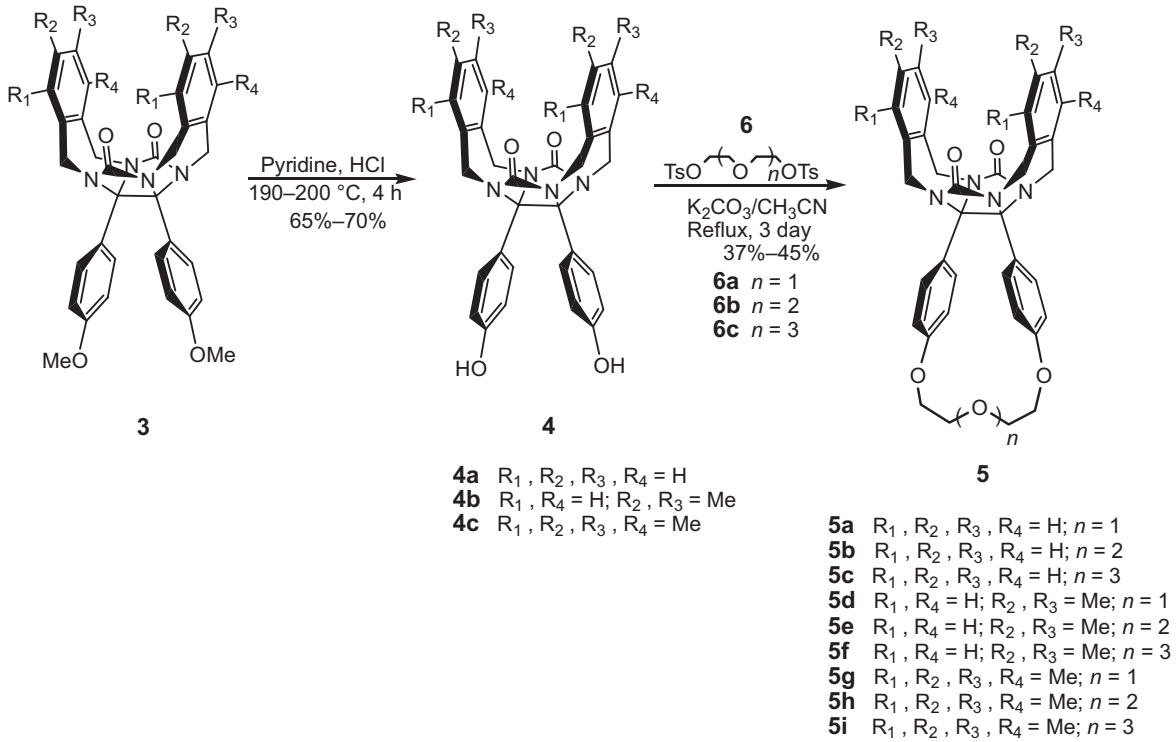
[1]Corresponding author (e-mail: mbakavoli@yahoo.com).

 doi:10.1139/V07-115 © 2007 NRC Canada

Scheme 1.



Scheme 2.



5g, an AB system (3.97 and 5.17 ppm) with geminal coupling (J = 16 Hz) indicates the non-equivalent methylene protons of the clip moiety. The methyl groups on aromatic side walls appeared as two sharp singlets at δ 2.16 and 2.46 ppm, the protons of para-disubstituted aromatic rings as two doublets at δ 6.61 and 6.93 ppm (J = 9 Hz), and the methylene protons in polyether moiety as two triplets at δ 3.67 and 4.28 ppm (J = 4 Hz).

© 2007 NRC Canada

Conclusion

In summary, several new glycoluril-based receptors with crown ether moieties have been synthesized and characterized. These ditopic receptors are good candidates to bind with dihydroxybenzene derivatives as well as alkaline metal ions, simultaneously. We expect that the binding strength of dihydroxybenzenes with the cleft will be influenced by steric hindrance on side-wall rings. So, the repulsive van der Waals interactions between methyl groups in **3b** and **3c** can alter the cleft shape and hence causes an appreciable change in the binding strengths. On the other hand, it seems viable that compounds **5a**–**5i** are able to show allosteric behavior, as the binding of alkaline metal ions with the crown ether moiety may have influence on the binding of dihydroxybenzenes in the cleft. These studies are currently in progress in our laboratory.

Experimental

Toluene was distilled from sodium benzophenone ketyl. MeCN was distilled from $CaCl_2$. CH_2Cl_2 and MeOH were distilled from CaH_2. Silica gel 60 (0.040–0.063 mm, Merck) was used for column chromatography. 4,4′-Dimethoxybenzil (**7**) and 1,2-bis(bromomethyl)benzene (**2a**) were purchased from Merck company. 1,2,3,4-Tetramethylbenzene was purchased from Aldrich company. 1,2-Bis(chloromethyl)-4,5-dimethylbenzene (**2b**) (12), pyridine hydrochloride (13), and oligoethylene glycol ditosylates (**6a**–**6c**) (14) were prepared according to the literature. Melting points were recorded on an Electrothermal type 9100 melting-point apparatus and are uncorrected. The IR spectra were obtained on a 4300 Shimadzu spectrometer and only noteworthy absorptions are listed. The ^{1}H NMR (100 MHz) spectra were recorded on a Bruker AC 100 spectrometer. Chemical shifts are reported in ppm downfield from TMS as internal standard; coupling constants *J* are given in Hertz. The mass spectra were scanned on a Varian Mat. CH-7 at 70 eV. Elemental analysis was performed on a Thermo Finnigan Flash EA microanalyzer.

1,2-Bis(chloromethyl)-3,4,5,6-tetramethylbenzene (2c)

The title compound was prepared similar to **2b** with slight modification as follows: a mixture of 1,2,3,4-tetramethylbenzene (26.8 g, 0.2 mol), paraformaldehyde (18 g, 0.6 mol) and concd. HCl (125 mL) was refluxed with stirring for 10 h. The reaction mixture was cooled, and the precipitated solid was filtered, washed with water (2 × 50 mL) and cold hexane (30 mL), and dried in vacuo.

Yield: 27.7 g (60%); white needles; mp 140–142 °C. IR (KBr): 2913, 1439, 1270, 685 cm^{-1}. ^{1}H NMR ($CDCl_3$) δ: 2.25 (s, 6 H, 2 × CH_3), 2.36 (s, 6 H, 2 × CH_3), 4.80 (s, 4 H, 2×CH_2). EI-MS *m*/*z* (%): 231 (M^+). Anal. calcd. for $C_{12}H_{16}Cl_2$: C, 89.94; H, 10.06. Found: C, 89.76; H, 10.26.

*13b,13c-Di(4-methoxyphenyl)-5,7,12,13b,13c,14-hexahydro-5a,6a,12a,13a-tetraaza-benzo[5,6]azuleno[2,1,8-*ija*]benzo[*f*]azulene-6,13-dione (3a)*

This compound was synthesized according to a literature procedure (6). Mp > 300 °C. ^{1}H NMR ($CDCl_3$) δ: 3.70 (s, 6 H, 2 × OCH_3), 4.15 (d, *J* = 16 Hz, 4 H, 4 × *CH*H), 4.76 (d, *J* = 16 Hz, 4 H, 4 × *CH*H), 6.67 (d, *J* = 8 Hz, 4 H, Ar–H), 6.97–7.30 (m, 12 H, Ar–H).

13b,13c-Di(4-methoxyphenyl)-2,3,9,10-tetramethyl-5,7,12,13b,13c,14-hexahydro-5a,6a,12a,13a-tetra-aza-benzo[5,6]azuleno[2,1,8-ija]benzo[f]azulene-6,13-dione (3b)

4,4-Bis(methoxyphenyl)glycoluril (**1**) (2.48 g, 7 mmol) and freshly ground potassium hydroxide (4.0 g, 70 mmol) in DMSO (50 mL) were heated to 120 °C with vigorous stirring for 30 min. Then, 1,2-bis(chloromethyl)-4,5-dimethylbenzene (**2b**) (3.04 g, 15.0 mmol) was added in one portion, and stirring was continued at this temperature for 4 h. On cooling, the reaction mixture was added to water (500 mL) and stirred for 30 min. The resulting light-brown precipitate was collected by filtration, washed with water (3 × 400 mL) and acetone (3 × 100 mL), and dried in vacuo.

Yield: 2.66 g (62%); mp > 300 °C. IR (KBr): 2963, 1709, 1611, 1512, 1458, 1253 cm^{-1}. ^{1}H NMR ($CDCl_3$) δ: 2.12 (s, 12 H, 4 × CH_3), 3.70 (s, 6 H, 2 × OCH_3), 4.10 (d, *J* = 16 Hz, 4 H, 4 × *CH*H), 4.71 (d, *J* = 16 Hz, 4 H, 4 × *CH*H), 6.65 (d, *J* = 8 Hz, 4 H, Ar–H), 6.98 (d, *J* = 8 Hz, 4 H, Ar–H), 7.04 (s, 4 H, Ar–H). EI-MS *m*/*z* (%): 614 (M^+). Anal. calcd. for $C_{38}H_{38}N_4O_4$: C, 74.25; H, 6.23; N, 9.11. Found: C, 74.34; H, 6.48; N, 9.02.

*13b,13c-Di(4-methoxyphenyl)-1,2,3,4,8,9,10,11-octa-methyl-5,7,12,13b,13c,14-hexahydro-5a,6a,12a,13a-tetraazabenzo[5,6]azuleno[2,1,8-*ija*]benzo[*f*]azulene-6,13-dion (3c)*

The title compound was prepared as described for **3b** using 3.46 g (15 mmol) of compound **2c** and 2.48 g (7 mmol) of compound **1**. Yield: 2.67 g (57%); mp > 300 °C. IR (KBr): 2912, 1703, 1610, 1512, 1460, 1253 cm^{-1}. ^{1}H NMR ($CDCl_3$) δ: 2.15 (s, 12 H, 4 × CH_3), 2.43 (s, 12 H, 4 × CH_3), 3.67 (s, 6 H, 2 × OCH_3), 3.85 (d, *J* = 16 Hz, 4 H, 4 × *CH*H), 5.12 (d, *J* = 16 Hz, 4 H, 4 × *CH*H), 6.62 (d, *J* = 8 Hz, 4 H, Ar–H), 7.02 (d, *J* = 8 Hz, 4 H, Ar–H). EI-MS *m*/*z* (%): 670 (M^+). Anal. calcd. for $C_{42}H_{46}N_4O_4$: C, 75.20; H, 6.91; N, 8.35. Found: C, 74.98; H, 6.86; N, 8.12.

Synthesis of hydroxy-funtionalized clips 4a–4c

General procedure

Compound **3** (2.5 mmol) was added to a flask containing pyridine hydrochloride (11.5 g, 0.1 mol), and the mixture was heated at 190–200 °C for 4 h. The hot brown syrup was poured into aq. HCl (5%, 50 mL), and the precipitated solid was filtered, washed with water (3 × 50 mL) and $CHCl_3$ (2 × 25 mL), and dried in vacuo at 80 °C to give compound **4**.

*13b,13c-Di(4-hydroxyphenyl)-5,7,12,13b,13c,14-hexahydro-5a,6a,12a,13a-tetraaza-benzo[5,6]azuleno[2,1,8-*ija*]benzo[*f*]azulene-6,13-dione (4a)*

Yield: 0.93 g (70%); mp > 300 °C. IR (KBr): 3356 (br), 1682, 1614, 1516, 1464, 1277 cm^{-1}. ^{1}H NMR (DMSO-d_6) δ: 4.08 (d, *J* = 16 Hz, 4 H, 4 × *CH*H), 4.60 (d, *J* = 16 Hz, 4 H, 4 × *CH*H), 6.58 (d, *J* = 8 Hz, 4 H, Ar–H), 6.83 (d, *J* = 8 Hz, 4 H, Ar–H), 6.97–7.30 (m, 8 H, Ar–H), 9.49 (s, 2 H, 2 × OH). EI-MS *m*/*z* (%): 530 (M^+). Anal. calcd. for $C_{32}H_{26}N_4O_4$: C, 72.44; H, 4.94; N, 10.56. Found: C, 72.60; H, 5.12; N, 10.38.

© 2007 NRC Canada

13b,13c-Di(4-hydroxyphenyl)-2,3,9,10-tetramethyl-5,7,12,13b,13c,14-hexahydro-5a,6a,12a,13a-tetra-aza-benzo[5,6]azuleno[2,1,8-ija]benzo[f]azulene-6,13-dione (4b)

Yield: 0.98 g (67%); mp > 300 °C. IR (KBr): 3374 (br), 1691, 1615, 1515, 1464, 1279 cm^{-1}. ^1H NMR (DMSO-d_6) δ: 2.09 (s, 12 H, 4 × CH_3), 3.99 (d, *J* = 16 Hz, 4 H, 4 × *CH*H), 4.52 (d, *J* = 16 Hz, 4 H, 4 × *CH*H), 6.56 (d, *J* = 8 Hz, 4 H, Ar–H), 6.81 (d, *J* = 8 Hz, 4 H, Ar–H), 6.94 (s, 4 H, Ar–H), 9.47 (s, 2 H, 2 × OH). EI-MS *m/z* (%): 586 (M^+). Anal. calcd. for $C_{36}H_{34}N_4O_4$: C, 73.70; H, 5.84; N, 9.55. Found: C, 73.95; H, 6.02; N, 9.73.

13b,13c-Di(4-hydroxyphenyl)-1,2,3,4,8,9,10,11-octamethyl-5,7,12,13b,13c,14-hexahydro-5a,6a, 12a,13a-tetraaza-benzo[5,6]azuleno[2,1,8-ija] benzo[f]azulene-6,13-dione (4c)

Yield: 1.04 g (65%); mp > 300 °C. IR (KBr): 3381 (br), 1685, 1614, 1515, 1470, 1278 cm^{-1}. ^1H NMR (DMSO-d_6) δ: 2.07 (s, 12 H, 4 × CH_3), 2.34 (s, 12 H, 4 × CH_3), 3.73 (d, *J* = 16 Hz, 4 H, 4 × *CH*H), 4.94 (d, *J* = 16 Hz, 4 H, 4 × *CH*H), 6.55 (d, *J* = 8 Hz, 4 H, Ar–H), 6.90 (d, *J* = 8 Hz, 4 H, Ar–H), 9.42 (s, 2 H, 2 × OH). EI-MS *m/z* (%): 642 (M^+). Anal. calcd. for $C_{40}H_{42}N_4O_4$: C, 74.74; H, 6.59; N, 8.72. Found: C, 74.48; H, 6.82; N, 8.55.

Synthesis of crown clips 5a–5i

General procedure

Ditosylate **6** (1.5 mmol) was added in small portions during a period of 12 h to the refluxing mixture of **4** (1.5 mmol) and K_2CO_3 (0.83 g, 6 mmol) in dry MeCN (60 mL). The reflux was continued for 3 days. Then, the solvent was evaporated in vacuo, and the light-brown solid was partitioned between aq. NaOH (5%, 75 mL) and CH_2Cl_2 (75 mL). The organic layer was washed with water (75 mL), dried (Na_2SO_4), and evaporated to dryness. After column chromatography (eluent: CH_2Cl_2 – MeOH, 100:3, *v/v*), compound **5** was obtained as white powder.

Crown clip 5a

The title compound was obtained according to the general procedure, starting with **4a** and **6a**.

Yield: 0.39 g (44%); mp > 300 °C. IR (KBr): 2917, 2849, 1703, 1509, 1455, 1233 cm^{-1}. ^1H NMR ($CDCl_3$) δ: 3.68 (t, *J* = 6 Hz, 4 H, CH_2OCH_2), 4.19–4.34 (m, 8 H, 4 × *CH*H, 2 × $ArOCH_2$), 4.81 (d, *J* = 16 Hz, 4 H, 4 × *CH*H), 6.66 (d, *J* = 8 Hz, 4 H, Ar–H), 6.95–7.30 (m, 12 H, Ar–H). EI-MS *m/z* (%): 600 (M^+). Anal. calcd. for $C_{36}H_{32}N_4O_5$: C, 71.99; H, 5.37; N, 9.33. Found: C, 72.10; H, 5.42; N, 9.38.

Crown clip 5b

The title compound was obtained according to the general procedure, starting with **4a** and **6b**.

Yield: 0.40 g (42%); mp > 300 °C. IR (KBr): 2925, 2854, 1706, 1512, 1454, 1256 cm^{-1}. ^1H NMR ($CDCl_3$) δ: 3.65–3.85 (m, 8 H, OCH_2CH_2O, 2 × OCH_2), 4.05–4.30 (m, 8 H, 4 × *CH*H, 2 × $ArOCH_2$), 4.78 6.91–7.30 (m, 12 H, Ar–H). EI-MS *m/z* (%): 644 (M^+). Anal. calcd. for $C_{38}H_{36}N_4O_6$: C, 70.79; H, 5.63; N, 8.69. Found: C, 70.51; H, 5.53; N, 8.83.

Crown clip 5c

The title compound was obtained according to the general procedure, starting with **4a** and **6c**.

Yield: 0.39 g (38%); mp > 300 °C. IR (KBr): 2917, 2852, 1709, 1610, 1457, 1254 cm^{-1}. ^1H NMR ($CDCl_3$) δ: 3.68 (s, 8 H, 2 × OCH_2CH_2O), 3.80 (t, *J* = 5 Hz, 4 H, 2 × OCH_2), 4.02 (t, *J* = 5 Hz, 4 H, 2 × $ArOCH_2$), 4.18 (d, *J* = 16 Hz, 4 H, 4 × *CH*H), 4.77 (d, *J* = 16 Hz, 4 H, 4 × *CH*H), 6.66 (d, *J* = 8 Hz, 4 H, Ar–H), 6.93–7.30 (m, 12 H, Ar–H). EI-MS *m/z* (%): 688 (M^+). Anal. calcd. for $C_{40}H_{40}N_4O_7$: C, 69.75; H, 5.85; N, 8.13. Found: C, 69.98; H, 5.91; N, 8.18.

Crown clip 5d

The title compound was obtained according to the general procedure, starting with **4b** and **6a**.

Yield: 0.44 g (45%); mp > 300 °C. IR (KBr): 2922, 1706, 1608, 1508, 1455, 1236 cm^{-1}. ^1H NMR ($CDCl_3$) δ: 2.10 (s, 12 H, 4 × CH_3), 3.63 (t, *J* = 4 Hz, 4 H, CH_2OCH_2), 4.08–4.25 (m, 8 H, 4 × *CH*H, 2 × $ArOCH_2$), 4.71 (d, *J* = 16 Hz, 4 H, 4 × *CH*H), 6.60 (d, *J* = 9 Hz, 4 H, Ar–H), 6.84 (d, *J* = 9 Hz, 4 H, Ar–H), 6.99 (s, 4 H, Ar–H). EI-MS *m/z* (%): 656 (M^+). Anal. calcd. for $C_{40}H_{40}N_4O_5$: C, 73.15; H, 6.14; N, 8.53. Found: C, 73.40; H, 6.22; N, 8.41.

Crown clip 5e

The title compound was obtained according to the general procedure, starting with **4b** and **6b**.

Yield: 0.44 g (42%); mp > 300 °C. IR (KBr): 2920, 1708, 1610, 1509, 1457, 1253 cm^{-1}. ^1H NMR ($CDCl_3$) δ: 2.13 (s, 12 H, 4 × CH_3), 3.65–3.84 (m, 8 H, OCH_2CH_2O, 2 × OCH_2), 4.90–4.22 (m, 8 H, 4 × *CH*H, 2 × $ArOCH_2$), 4.72 (d, *J* = 16 Hz, 4 H, 4 × *CH*H), 6.63 (d, *J* = 8 Hz, 4 H, Ar–H), 6.92 (d, *J* = 8 Hz, 4 H, Ar–H), 7.02 (s, 4 H, Ar–H). EI-MS *m/z* (%): 700 (M^+). Anal. calcd. for $C_{42}H_{44}N_4O_6$: C, 71.98; H, 6.33; N, 7.99. Found: C, 71.82; H, 6.37; N, 8.06.

Crown clip 5f

The title compound was obtained according to the general procedure, starting with **4b** and **6c**.

Yield: 0.43 g (39%); mp > 300 °C. IR (KBr): 2917, 1714, 1609, 1509, 1452, 1251 cm^{-1}. ^1H NMR ($CDCl_3$) δ: 2.12 (s, 12H, 4 × CH_3), 3.68–3.82 (m, 12 H, $OCH_2CH_2OCH_2CH_2O$, 2 × OCH_2), 3.98–4.20 (m, 8 H, 4 × *CH*H, 2 × $ArOCH_2$), 4.72 (d, *J* = 16 Hz, 4 H, 4 × *CH*H), 6.65 (d, *J* = 8 Hz, 4 H, Ar–H), 6.94 (d, *J* = 8 Hz, 4 H, Ar–H), 7.01 (s, 4 H, Ar–H). EI-MS *m/z* (%): 744 (M^+). Anal. calcd. for $C_{44}H_{48}N_4O_7$: C, 70.95; H, 6.49; N, 7.52. Found: C, 71.12; H, 6.52; N, 7.36.

Crown clip 5g

The title compound was obtained according to the general procedure, starting with **4c** and **6a**.

Yield: 0.46 g (43%); mp > 300 °C. IR (KBr): 2925, 1705, 1508, 1458, 1427, 1227 cm^{-1}. ^1H NMR ($CDCl_3$) δ: 2.16 (s, 12 H, 4 × CH_3), 2.46 (s, 12 H, 4 × CH_3), 3.67 (t, *J* = 4 Hz, 4 H, CH_2OCH_2), 3.97 (d, *J* = 16 Hz, 4 H, 4 × *CH*H), 4.28 (t, *J* = 4 Hz, 4 H, 2 × $ArOCH_2$), 5.17 (d, *J* = 16 Hz, 4 H, 4 × *CH*H), 6.61 (d, *J* = 9 Hz, 4 H, Ar–H), 6.93 (d, *J* = 8 Hz, 4 H, Ar–H). EI-MS *m/z* (%): 712 (M^+). Anal. calcd. for $C_{44}H_{48}N_4O_5$: C, 74.13; H, 6.79; N, 7.86. Found: C, 74.36; H, 6.87; N, 7.76.

Crown clip 5h

The title compound was obtained according to the general procedure, starting with **4c** and **6b**.

© 2007 NRC Canada

Yield: 0.44 g (39%); mp > 300 °C. IR (KBr): 2917, 1714, 1509, 1453, 1421, 1252 cm^{-1}. ^1H NMR ($CDCl_3$) δ: 2.16 (s, 12 H, 4 × CH_3), 2.43 (s, 12 H, 4 × CH_3), 3.60–3.75 (m, 8 H, OCH_2CH_2O, 2 × OCH_2), 3.88–4.15 (m, 8 H, 4 × *CH*H, 2 × $ArOCH_2$), 5.14 (d, *J* = 16 Hz, 4 H, 4 × *CH*H), 6.60 (d, *J* = 8 Hz, 4 H, Ar–H), 6.95 (d, *J* = 8 Hz, 4 H, Ar–H). EI-MS *m*/*z* (%): 756 (M^+). Anal. calcd. for $C_{46}H_{52}N_4O_6$: C, 72.99; H, 6.92; N, 7.40. Found: C, 72.81; H, 6.97; N, 7.26.

Crown clip 5i

The title compound was obtained according to the general procedure, starting with **4c** and **6c**.

Yield: 0.44 g (37%); mp > 300 °C. IR (KBr): 2914, 1705, 1509, 1458, 1427, 1253 cm^{-1}. ^1H NMR ($CDCl_3$) δ: 2.15 (s, 12 H, 4 × CH_3), 2.43 (s, 12 H, 4 × CH_3), 3.66–4.10 (m, 16 H, $OCH_2CH_2OCH_2CH_2O$, 2 × OCH_2, 4 × *CH*H), 5.16 (d, *J* = 16 Hz, 4 H, 4 × *CH*H), 6.61 (d, *J* = 8 Hz, 4 H, Ar–H), 6.95 (d, *J* = 8 Hz, 4 H, Ar–H). EI-MS *m*/*z* (%): 800 (M^+). Anal. calcd. for $C_{48}H_{56}N_4O_7$: C, 71.98; H, 7.05; N, 6.99. Found: C, 71.85; H, 7.08; N, 6.87.

References

1. J.L. Goldstein, R.G.W. Anderson, and M.S. Brown. Nature (London), **279**, 679 (1979).
2. J.I. Kikuchi and Y. Murakami. J. Incl. Phenom. Mol. Rec. Chem. **32**, 209 (1998).
3. A.E. Rowan, J.A.A.W. Elemans, and R.J.M. Nolte. Acc. Chem. Res. **32**, 995 (1999).
4. A.P.H.J. Schenning, B. de Bruin, M.C. Feiters, and R.J.M. Nolte. Angew. Chem., Int. Ed. Engl. **33**, 1662 (1994).
5. A.P.H.J. Schenning, B. Escuder, J.L.M. van Nunen, B. de Bruin, D.W.P.M. Löwik, A.E. Rowan, S.J. Van der Gaast, M.C. Feiters, and R.J.M. Nolte. J. Org. Chem. **66**, 1538 (2001).
6. B.S. Creaven, J.F. Gallagher, J.P. McDonagh, J. McGinley, B.A. Murray, and G.S. Whelan. Tetrahedron, **60**, 137 (2004).
7. R.P. Sijbesma, A.P.M. Kentgens, R.J.M. Nolte. J. Org. Chem. **56**, 3199 (1991).
8. R.P. Sijbesma, A.P.M. Kentgens, E.T.G. Lutz, J.H. van der Maas, and R.J.M. Nolte. J. Am. Chem. Soc. **115**, 8999 (1993).
9. J.N.H. Reek, R.P. Sijbesma, and R.J.M. Nolte. *In* Computational approaches in supramolecular chemistry. *Edited by* G. Wipff. Kluwer, Dordrecht. 1994. Vol. 426.
10. J.N.H. Reek, A. H. Priem, H. Engelkamp, A.E. Rowan, J.A.A.W. Elemans, and R.J.M. Nolte. J. Am. Chem. Soc. **119**, 9956 (1997).
11. G.T.W. Gieling, H.W. Scheeren, R. Israel, and R.J.M. Nolte. Chem. Commun. 241 (1996).
12. I. Shahak and E.D.J. Bergmann. J. Chem. Soc. C, 1005 (1966).
13. L. Pignataro, M. Benaglia, R. Annunziata, M. Cinquini, and F. Cozzi. J. Org. Chem. **71**, 1458 (2006).
14. M. Ouchi, Y. Inoue, T. Kanzaki, and T. Hakushi. J. Org. Chem. **49**, 1408 (1984).

© 2007 NRC Canada

Cross-conjugated *Z*- and *E*-3-ferrocenylmethylidene-4-methyl-2-phenylpenta-1,4-dienes — Synthesis and some chemical properties

Juan Manuel Martínez Mendoza, Lena Ruíz Ramírez, Ruben Alfredo Toscano, Simon Hernández Ortega, Cecilio Alvarez Toledano, Marcos Flores Alamo, and Elena I. Klimova

Abstract: Dehydration of (*Z*)- and (*E*)-4-ferrocenyl-3-isopropenyl-2-phenylbut-3-en-2-ols and *Z*-3-ferrocenylmethylidene-4-methyl-2-phenylpentane-2,4-diol affords (*Z*)- and (*E*)-3-ferrocenylethylidene-4-methyl-2-phenylpenta-1,4-dienes with a system of three cross-conjugated double bonds. One of the methylidene groups of the trienes obtained is smoothly protonated under the action of tetrafluoroboric acid etherate to yield (*Z*)- and (*E*)-3-ferrocenyl-2-isopropenyl-1-methyl-1-phenylallyl tetrafluoroborates. The cross-conjugated trienes undergo cationic cycloaddition to these allylic cations as well as proton-induced cyclodimerization resulting in 7-ferrocenyl-4-ferrocenylmethylidene-1,3-dimethyl-5-phenyl-8-(1-phenylethylidene)bicyclo[3.3.1]non-2-ene and isomeric 1,5-diferrocenyl-2,6-diisopropenyl-3,7-diphenylocta-1,3,6-trienes.

Key words: cross-conjugated trienes, ferrocenylallylic cations, cyclodimerization, cycloaddition, ferrocene.

Résumé : La déshydratation des (*Z*)- et (*E*)-4-ferrocényl-3-isopropényl-2-phénylbut-3-én-2-ols et du *Z*-3-ferrocényl-méthylidène-4-méthyl-2-phénylpentane-2,4-diol conduit aux (*Z*)- et (*E*)-3-ferrocényléthylidène-4-méthyl-2-phénylpenta-1,4-diènes qui comportent un système à trois doubles liaisons à conjugaison croisée. Sous l'action de l'éthérate de l'acide tétrafluoroborique, il se produit une protonation facile d'un des groupes méthylènes des triènes qui ont été obtenus avec production de tétrafluoroborates de (*Z*)- et (*E*)-4-3errocényl-2-isopropényl-1-méthyl-1-phénylallyle. Les triènes à conjugaison croisée conduisent à une cycloaddition cationique de ces cations allyliques ainsi qu'une cyclodimérisation induite par les protons qui conduit à la formation du 7-ferrocényl-4-ferrocénylméthylidène-1,3-diméthyl-5-phényl-8-(1-phényléthylidène)bicyclo[3.3.1]non-2-ène ainsi qu'aux 1,5-diferrocényl-2,6-diisopropényl-3,7-diphénylocta-1,3,6-triènes isomères.

Mots-clés : triènes à conjugaison croisée, cations ferrocénylallyliques, cyclodimérisation, cycloaddition, ferrocène.

[Traduit par la Rédaction]

Introduction

Recently, the interest in the chemistry of ferrocenes has increased because of their possible practical applications. Data on the industrial use of the ferrocene derivatives, available from the patent literature (1, 2), reflect mainly their employment in military-industrial establishment, rocket technologies, and medicine. Publications demonstrating the use of ferrocene derivatives in nonlinear optics devices, chemistry of polymeric materials, biology, and synthetic organic chemistry (asymmetric synthesis) has appeared since 1994 (3–7).

The ferrocene molecule itself is an energy-rich structure. Therefore, studies on compounds comprising other energy-rich fragments, such as ene, diene, and polyene chains, fused carbo- and hetero-cyclic systems, in addition to the ferrocene moiety, are of special interest.

Investigations into ferrocene-containing polyene compounds aim at the studies of strain energy, optical properties of ferrocenylpolyenes, mechanisms of highly selective reactions involved in the in vitro and in vivo syntheses of various aliphatic, carbocyclic, and heterocyclic compounds, and their potential use as molecular building blocks and in the realm of supramolecular chemistry as redox-switching receptors. The most-studied compounds of this type are represented by linear ferrocenylalkenes and alka-1,3-dienes (8–12).

The following approaches are employed for the synthesis of ferrocenylalka-1,3-dienes and exocyclic ferrocenylalka-1,2,3-trienes with a terminal methylidene group: dehydration

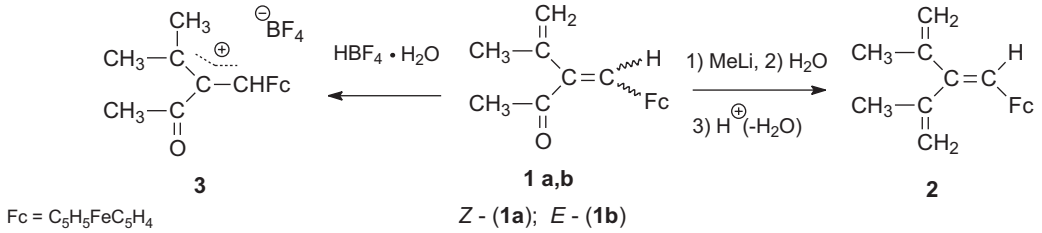
Received 21 February 2007. Accepted 09 July 2007. Published on the NRC Research Press Web site at canjchem.nrc.ca on 11 October 2007.

J.M.M. Mendoza, L.R. Ramírez, M.F. Alamo, and E.I. Klimova.[1] Facultad de Química, Universidad Nacional Autónoma de México, Cd. Universitaria, Coyoacán, C.P. 04510, México D.F., México.
R.A. Toscano, S.H. Ortega, and C.A. Toledano. Instituto de Química, Universidad Nacional Autónoma de México, Cd. Universitaria, Coyoacán, C.P. 04510, México D.F., México.

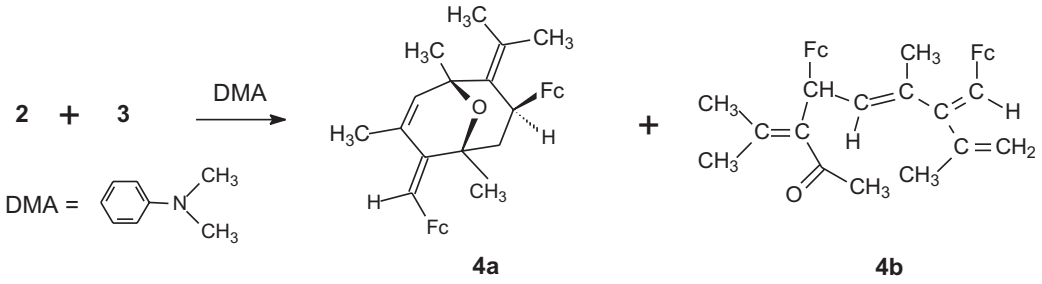
[1]Corresponding author: (e-mail: klimova@servidor.unam.mx).

 doi:10.1139/V07-105 © 2007 NRC Canada

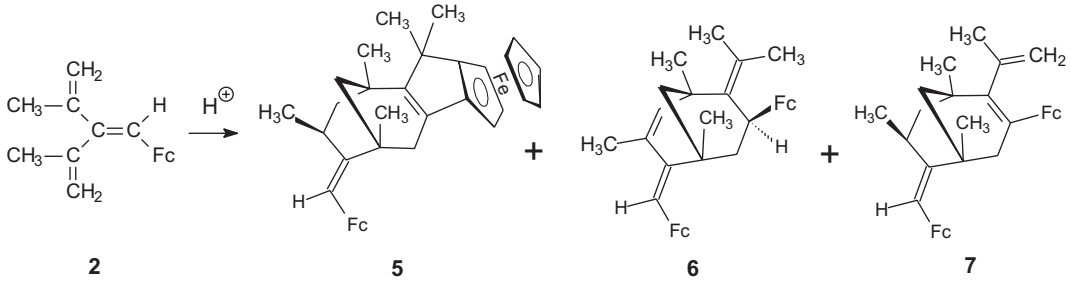
Scheme 1.



Scheme 2.



Scheme 3.

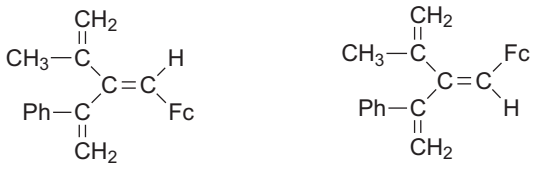


of ferrocenyl(methyl)allylic alcohols (13–15), deprotonation of ferrocenyl(methyl)allyl cations (13–18), and the Wittig reaction (19). Diferrocenyl-, aryl- and alkylferrocenyl-, aryl-, and alkyldiferrocenylbuta-1,3-dienes and 1,3-bis(ferrocenylmethylidene)-2-methylidenecycloalkanes have been synthesized (20, 21), and their highly diastereoselective thermally induced and acid-catalyzed cyclodimerization (13–22) and cationic cycloaddition (15, 19–22) have been studied. The reaction products comprised ferrocenyl-substituted six-membered carbocycles or carbocycles fused to other carbo- or hetero-cyclic systems. Some of them possessed high biological activities (17). Experimental evidence of the stepwise non-synchronous mechanism of acid-catalyzed cyclodimerization has been obtained (22), which is of theoretical significance.

With relation to synthetic and theoretical organic chemistry and the chemistry of high-molecular-mass compounds, it was of interest to inquire into the question of a feasibility of synthesizing the simplest representatives of linear cross-conjugated ferrocenyl-substituted trienes and to study their properties.

Previously, we have reported the synthesis of isomeric (*Z*)- and (*E*)-2-acetyl-1-ferrocenyl-3-methylbuta-1,3-dienes (**1a**, **1b**) (23) and 3-ferrocenylmethylidene-2,4-dimethylpenta-1,4-diene (**2**) (24), a new type of cationic cycloaddition of the triene **2** to a cation (**3**) and acid-catalyzed cyclodimerization of the triene **2** resulting in polycyclic structures

Scheme 4.



of the type (**4**–**7**) (Schemes 1–3). Naturally, it was suggested that the formation of the cyclodimers **4**–**7** is a characteristic feature of cross-conjugated heterotrienes of the type **1a**, **1b**, and triene **2**.

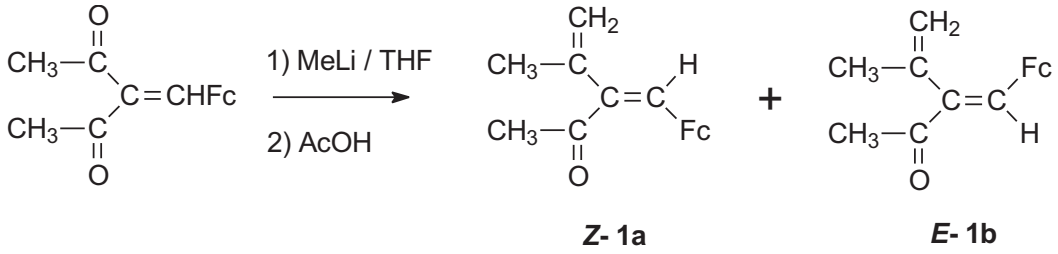
In continuation of our previous studies, we synthesized isomeric (*Z*)- and (*E*)-3-ferrocenylmethylidene-4-methyl-2-phenylpenta-1,4-dienes (**8a**, **8b**) (Scheme 4) as the new representatives of the cross-conjugated linear trienes and studied some of their chemical properties.

Results and discussion

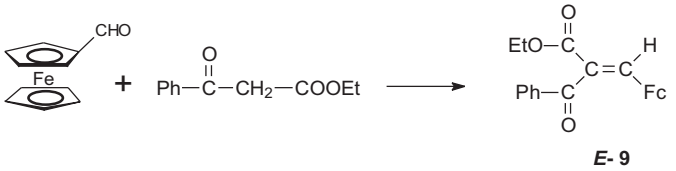
(*Z*)- and (*E*)-2-Acetyl-1-ferrocenyl-3-methylbuta-1,3-dienes (**1a** and **1b**) and ethyl 2-benzoyl-ferrocenylacrylate (**9**) (Schemes 5 and 6) served as the starting compounds for the synthesis of the target trienes (**8a**) and (**8b**).

© 2007 NRC Canada

Scheme 5.



Scheme 6.



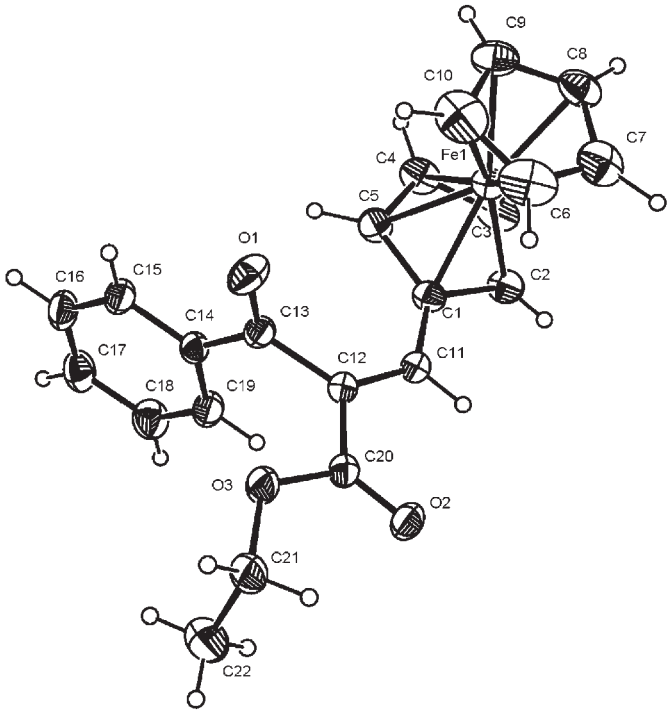
Compound **9** was obtained in high yield as a single isomer. The spatial structure of compound **9** was established on the basis of the X-ray diffraction analysis of a single crystal of compound **9** prepared by crystallization from dichloromethane (Table 1). The general view of the molecule **9** is shown in Fig. 1, and no special comments are needed. The X-ray results indicate that compound **9** has an (*E*)-configuration. (*Z*)-2-Acetyl-1-ferrocenyl-3-methylbuta-1,3-diene (**1a**) was found to react with PhLi to yield a mixture of 1,2- (**10a**) and 1,4-addition products (**11a** and **11b**) in a ~1:1 ratio, whereas the (*E*)-isomeric diene **1b** affords the (*E*)-isomeric alcohol (**10b**) (Scheme 7).

Compounds **10a** and **11** were separated by column chromatography on alumina. According to the data from ^{1}H and ^{13}C NMR spectra, the ferrocenyl ketone **11** is formed as a ~2:1 mixture of two diastereomers. They were separated by TLC on SiO_2; the structure of the major diastereomer **11a** was established by X-ray diffraction analysis on the single crystal grown by crystallization from chloroform. The general view of the molecule **11a** is shown in Fig 2, and its principal geometric parameters are presented in Table 1 without special comments. The results obtained suggest that **11a** is (*S,S*)-4-ferrocenyl-3-isopropenyl-4-phenylbutan-2-one (eclipsed conformation), and compound **11b** has apparently (*S,R*)-configuration.

The structures of compounds **10a** and **10b** were additionally confirmed by the data from ^{1}H and ^{13}C NMR and by formation of a Diels–Alder adduct (**12**) with *N*-phenylazodicarboximide (Scheme 8). According to the ^{1}H NMR spectra of compound **12**, it was formed as a single diastereomer, which suggests the stereospecificity of the process. Ethyl 2-benzoyl-3-ferrocenylacrylate (**9**) reacts with MeLi like acetylbutadiene (**1a**) to give a diol (**13**) and a hydroxy ketone (**14**) in a ~2:1 ratio (^{1}H NMR data) (Scheme 9); the latter being a ~5:1 mixture of two diastereomers, **14a** and **14b**.

These compounds were separated by column chromatography on Al_2O_3 and characterized by the data from mass spectrometry, elemental analysis, and ^{1}H and ^{13}C NMR spectroscopy. The structure of the diol **13**, including its (*Z*)-configuration, was established by X-ray diffraction analysis of a single crystal grown by crystallization from chloroform.

Fig. 1. Molecular structure of **9**.



The general view of compound **13** is shown in Fig. 3, and its geometric parameters (25) are given in Table 1.

Our attempts to establish configurations of the diastereomeric hydroxy ketones **14a** and **14b** failed.

We have found that all alcohols obtained (**10a**, **10b**, **13**, **14a**, and **14b**) underwent smooth dehydration when treated with $POCl_3$ in pyridine at 20 °C. The alcohols **10a**, **10b**, and **13** afforded mixtures of isomeric (*Z*)- and (*E*)-3-ferrocenylethylidene-4-methyl-2-phenylpenta-1,4-dienes (**8a** and **8b**) (Scheme 10).

Dehydration of the hydroxy ketones **14a** (or **14b**) did not affect the chiral centers to yield compounds **15a** (or **15b**), respectively, as single diastereomeric forms (Scheme 11).

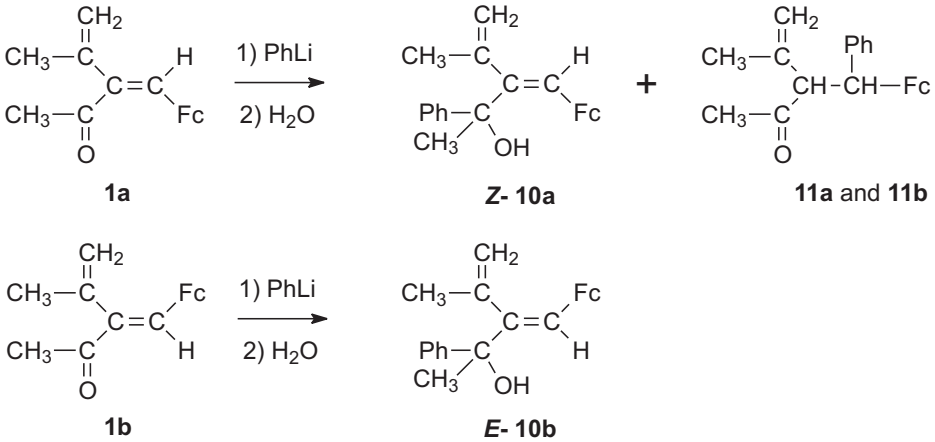
The structures of these enones were confirmed by the data from mass spectrometry, elemental analysis, and ^{1}H and ^{13}C

© 2007 NRC Canada

Table 1. Selected bond lengths and bond angles for compounds **6**, **9**, **11a**, and **13**.

Selected bond lengths	*r* (Å)	Selected bond angles	ω (°)
6			
C(1)—C(9)	1.534(6)	C(1)–C(9)–C(5)	112.7(4)
C(5)—C(9)	1.520(6)	C(8)–C(1)–C(9)	109.1(4)
C(4)—C(12)	1.341(6)	C(9)–C(1)–C(2)	105.4(4)
C(1)—C(8)	1.552(6)	C(9)–C(5)–C(4)	107.9(4)
C(7)—C(8)	1.534(6)	C(1)–C(8)–C(7)	115.3(4)
C(5)—C(6)	1.566(6)	C(1)–C(2)–C(3)	125.0(4)
C(5)—C(4)	1.539(6)	C(35)–C(34)–C(36)	111.4(4)
C(3)—C(4)	1.485(6)	C(3)–C(4)–C(5)	116.1(4)
C(1)—C(2)	1.505(6)	C(4)–C(5)–C(6)	109.4(4)
9			
C(1)—C(11)	1.459(3)	C(1)–C(11)–C(12)	129.0(2)
C(11)—C(12)	1.341(3)	C(11)–C(12)–C(20)	118.0(2)
C(12)—C(13)	1.509(3)	C(11)–C(12)–C(13)	124.3(2)
C(13)—O(1)	1.214(3)	C(20)–C(12)–C(13)	117.71(19)
C(12)—C(20)	1.483(3)	C(1)–C(11)–H(11)	115.5
C(20)—O(2)	1.201(3)	C(12)–C(13)–O(1)	119.2(2)
C(20)—O(3)	1.341(3)	C(12)–C(20)–O(2)	125.4(2)
11a			
C(1)—C(11)	1.513(3)	C(1)–C(11)–C(12)	112.65(17)
C(11)—C(12)	1.517(3)	C(12)–C(11)–C(20)	109.18(16)
C(11)—C(20)	1.557(3)	C(11)–C(20)–C(19)	109.76(17)
C(19)—O(1)	1.204(2)	C(19)–C(20)–C(21)	109.08(17)
C(19)—C(20)	1.513(3)	C(23)–C(21)–C(22)	121.6(2)
C(20)—C(21)	1.512(3)	C(23)–C(21)–C(20)	117.9(2)
C(21)—C(23)	1.389(3)	C(20)–C(19)–O(1)	121.8(2)
13			
C(1)—C(2)	1.526(4)	C(1)–C(2)–O(1)	103.7(2)
C(2)—C(3)	1.538(4)	C(1)–C(2)–C(3)	114.4(2)
C(3)—C(4)	1.539(4)	C(4)–C(3)–C(7)	122.3(3)
C(2)—O(1)	1.447(3)	C(2)–C(3)–C(7)	119.1(3)
C(3)—C(7)	1.341(3)	C(18)–C(4)–C(3)	111.5(2)
C(4)—O(2)	1.453(3)	C(5)–C(4)–O(2)	106.2(2)
C(7)—C(8)	1.463(4)	C(18)–C(4)–O(2)	106.6(2)

Scheme 7.



NMR spectroscopy (see Experimental Section); however, we could not establish their configurations.

Dehydration of the alcohols **10a**, **10b**, and **13** under the action of boiling acetic acid afforded only one geometrical isomer, viz., (*E*)-3-ferrocenylethylidene-4-methyl-2-phenylpenta-1,4-diene **8b** (Scheme 12).

In our opinion, the change in the initial (*Z*)- or (*E*)-configuration of the tertiary alcohols (see Schemes 8 and 10) in the

© 2007 NRC Canada

Fig. 2. Molecular structure of **11a**.

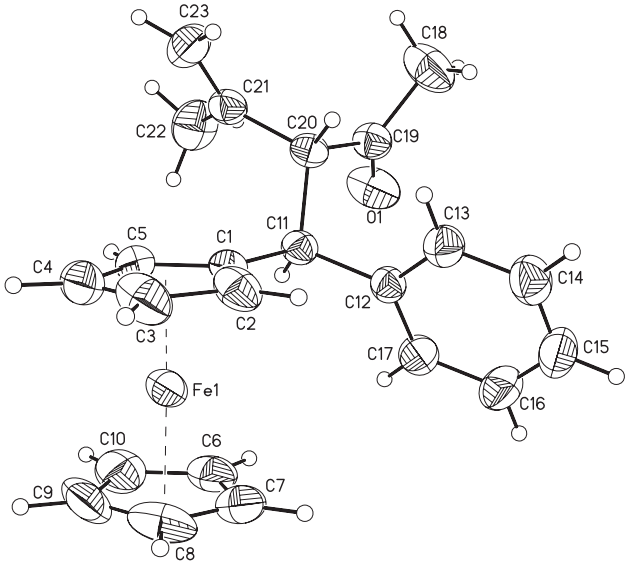
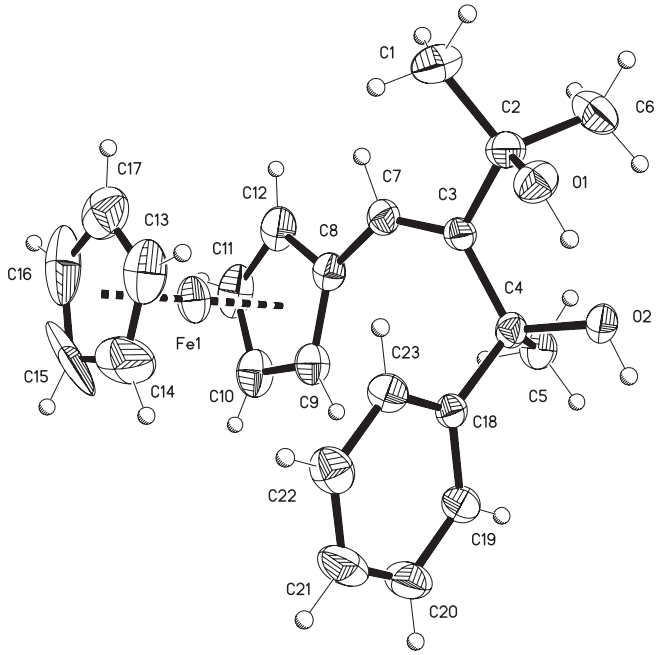
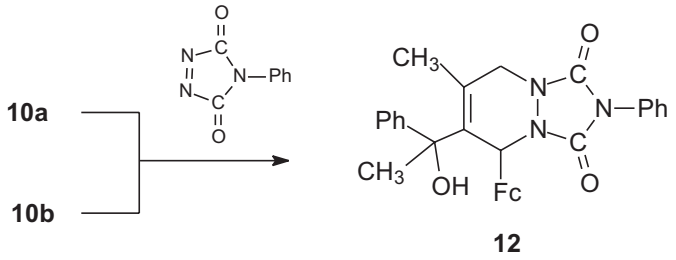


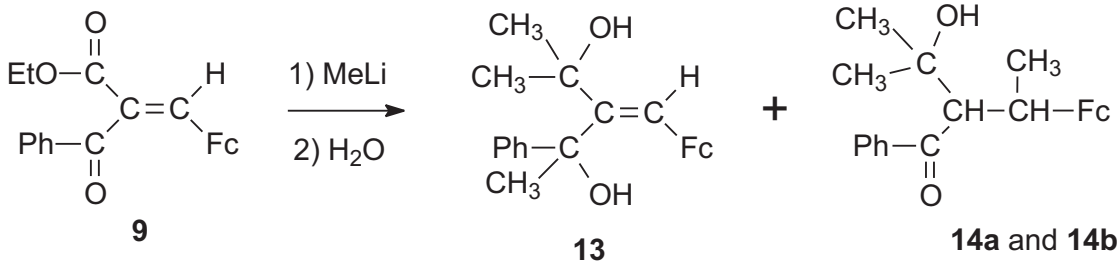
Fig. 3. Molecular structure of **13**.



Scheme 8.



Scheme 9.



dehydration into (*E*)- and (*Z*)-trienes, respectively, results upon the rotation about the sesquialteral C(1)–C(2) bonds in the transient tetrafluoroborates of the ferrocenyl(methyl)phenylallylic cations (**16a**) and (**16b**) despite the fairly high energetic barrier (26–29) (Scheme 13).

This suggestion has been confirmed in the studies of the chemical behavior of tetrafluoroborates of the allylic cations **16a** and **16b** obtained upon action of tetrafluoroboric acid etherate on the trienes **8a** and **8b** (Scheme 14).

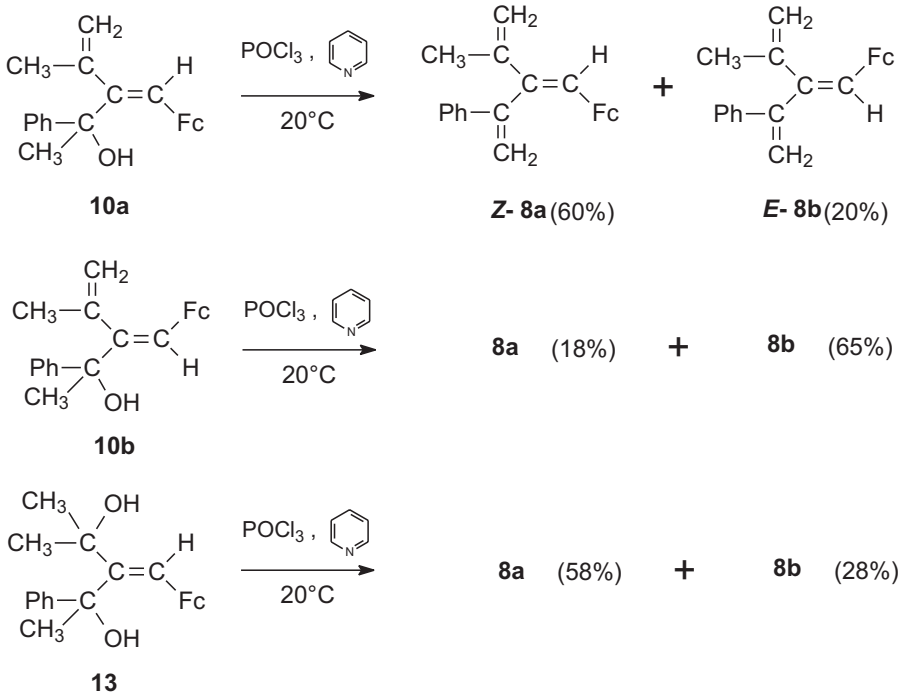
Treatment of the trienes **8a** and **8b** with HBF_4 – Et_2O results in crystalline salts **16a** and **16b** because of the protonation of only one CH_2=C group, namely, that bearing the phenyl substituent, and the formation of the most-stable phenylallylic cations. The ^{1}H NMR spectra of the cations **16a** and **16b** contain multiplets for the protons of the methyl groups of the CH_3–C=CH_2 fragments with a characteristic allylic coupling constant and the corresponding multiplets for the protons of the =CH_2 groups alongside low-field singlets for the protons of the methyl groups of the Ph–C–CH_3 fragments, which supports their structures.

In solutions (CD_2Cl_2), the salts **16a** and **16b** undergo gradual isomerization to form mixtures of two isomers (**16a** $\rightleftarrows$ **16b** and **16b** $\rightleftarrows$ **16a**) in variable proportions depending on the time of the experiment, judging from the ^{1}H NMR data.

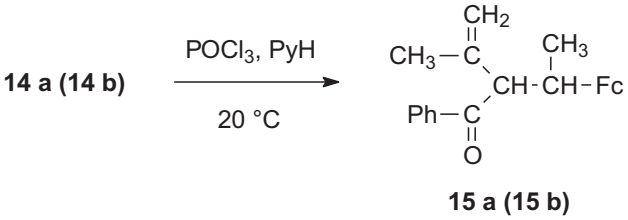
Deprotonation of the solid tetrafluoroborates **16a** and **16b** under the action of *N,N*-dimethylaniline resulted in virtually pure original trienes **8a** and **8b**, respectively. Treatment of

© 2007 NRC Canada

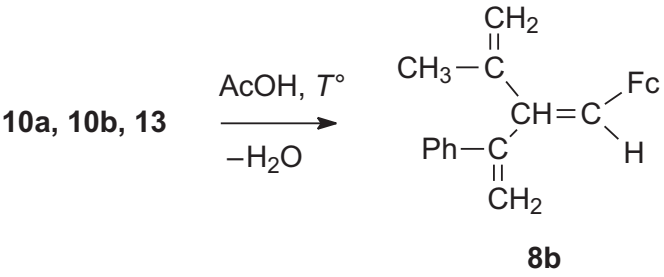
Scheme 10.



Scheme 11.



Scheme 12.



solutions of the salts **16a** and **16b** in CH_2Cl_2 with *N,N*-dimethylaniline at 20 °C for prolonged periods (1–2 h) afforded mixtures of the isomeric trienes **8a** and **8b** with (*E*)-isomer **8b** predominating.

The trienes **8a** and **8b** are orange powders; they undergo oxidation and polymerization upon storage under ordinary conditions. In boiling benzene, they form [4+2]-cycloadducts with *N*-phenylmaleimide (Scheme 15).

The adduct (**17**) was isolated as a ~3:1 mixture of *exo*-**17a** and *endo*-**17b** isomers (^{1}H NMR data), which were separated by TLC on silica gel. Their structures were confirmed by the data from ^{1}H and ^{13}C NMR spectra, and assignment to the *exo*- and *endo*-isomers was made based on the previously established criteria (13, 14, 23). Assigining the adduct **17a** to the *exo*-series resulted from the fact that the signals for all the protons of the C_5H_4 moiety of the ferrocene unit appeared in a lower field of the ^{1}H NMR spectrum than those of the unsubstituted cyclopentadienyl ring. For the isomer **17b**, the multiplet for two protons of the C_5H_4 moiety (δ = 4.10) occurred in a higher field than the singlet for the protons of the C_5H_5 group (δ 4.18), which is typical of *endo*-adducts of ferrocenyl-substituted 1,3-dienes. The spectra of the adducts **17a** and **17b** contained signals for the isopropenyl groups with characteristic multiplicities of the $-CH_3$ and $=CH_2$ groups.

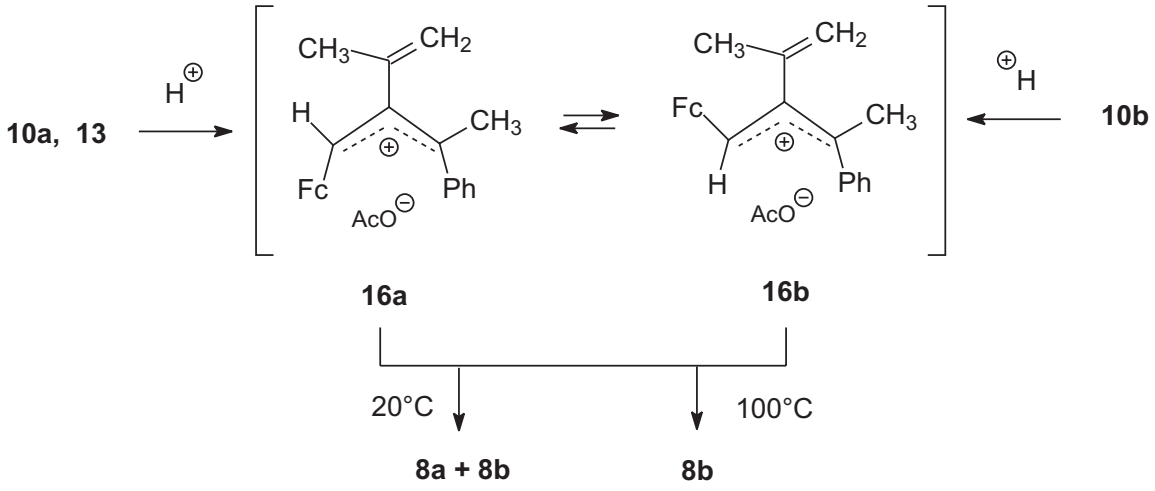
Boiling of the trienes **8a** and **8b** in a 10:1 mixture of acetic and trifluoroacetic acids afforded dimerization products with linear (**18a**–**18c**) and cyclic (**19**) structures (Scheme 16).

The linear dimer **18** was obtained as a ~3:2:1 mixture of three isomers (^{1}H NMR data), which were separated by TLC on SiO_2 and characterized by mass and ^{1}H and ^{13}C NMR spectra and data from elemental analysis, but their spatial structures have yet to be elucidated.

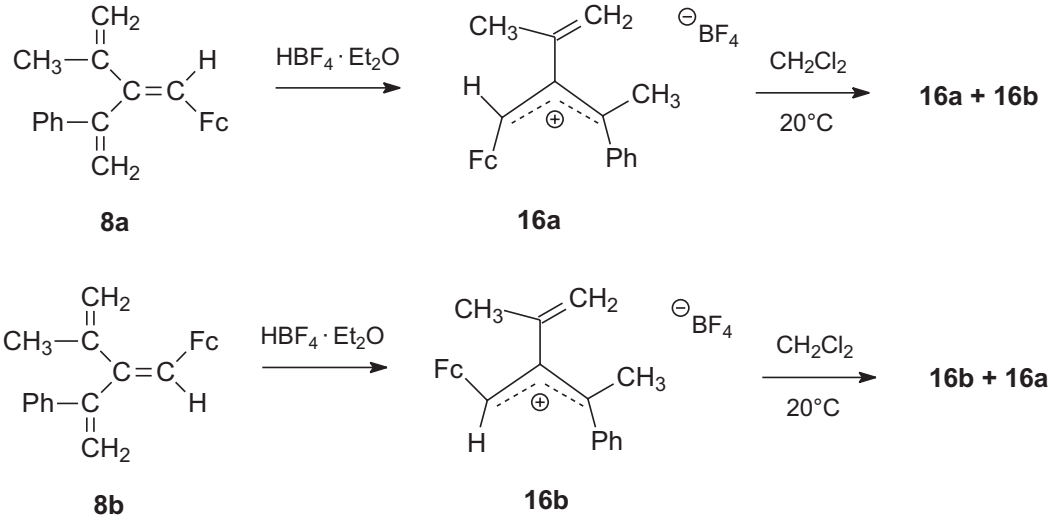
The cyclodimer **19** was isolated as a single diastereomer (yield: ~20%). The ^{1}H NMR spectrum of this compound contained three singlets for the methyl groups, two singlets for the olefinic protons, signals for the protons of two ferrocenyl and two phenyl fragments, a doublet of doublets and a singlet for the protons of two mtethylene groups, and a doublet of doublets of a methine proton. The ^{13}C NMR spectrum contained signals for the carbon atoms of two ferrocene units, three methyl, two methylene, and one methine groups, eight carbon atoms bearing no protons, and two olefinic carbon atoms. The spectroscopic data confirm unequivocally

© 2007 NRC Canada

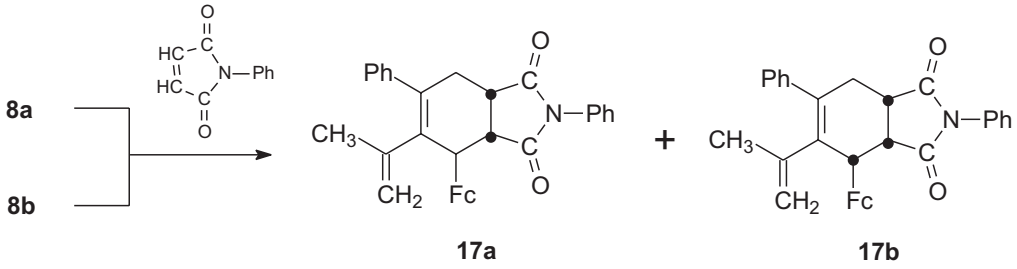
Scheme 13.



Scheme 14.



Scheme 15.



the cyclic structure of compound **19** analogous to that of compound **6**.

The structure of the cyclodimer **6** has been elucidated recently. According to the data from X-ray analysis of a single crystal prepared by crystallization from ethanol, the cyclodimer **6** is 7-ferrocenyl-4-ferrocenylmethylidene-8-isopropylidene-1,3,5-trimethylbicyclo[3.3.1]non-2-ene with a system of two fused six-membered rings (Fig. 4).

The main geometric parameters of this compound are listed in Table 1. The values of the C–C and C=C bond lengths in the carbocyclic fragments as well as of the Fe–C and C–C bond lengths and the geometric parameters of the ferrocene sandwiches are similar to the standard ones.

The compounds **18a**–**18c** and **19** were obtained from the reactions of the trienes **8a** and **8b** with the tetrafluoroborates **16a** and **16b** (Scheme 17).

© 2007 NRC Canada

Scheme 16.

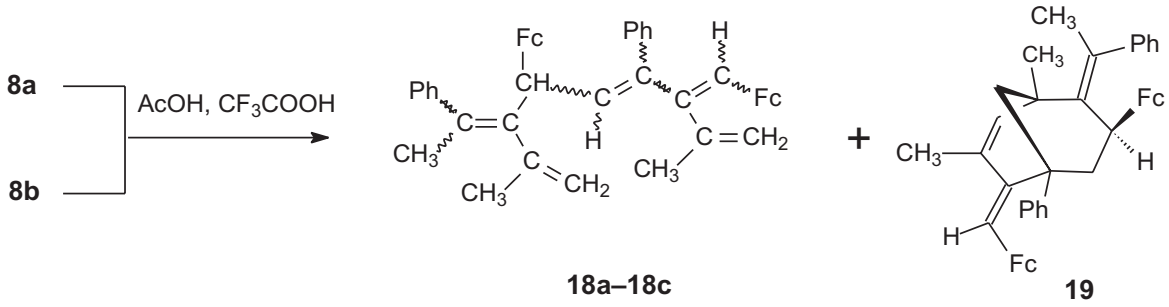
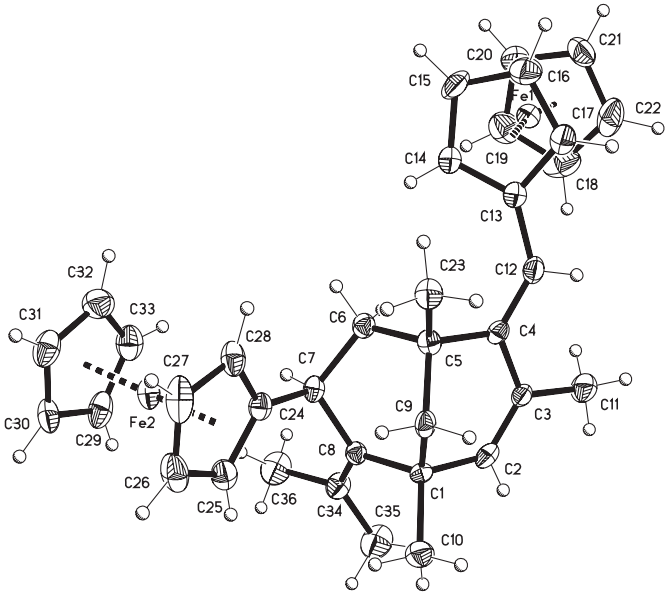


Fig. 4. Molecular structure of **6**.



Scheme 17.



The formation of compounds **18** and **19** seems to result from intramolecular transformation of an intermediate dimeric linear allylic cations (**20**) and (**21**) according to Scheme 18.

Deprotonation of the linear cation **20** under the action of *N,N*-dimethylaniline results in linear dimers **18a**–**18c**, while deprotonation of a bicyclic carbocation existing in equilibrium with the former cation yields the product **19**.

The stereospecific character of the formation of the cyclodimer **19** can apparently be rationalized by configurational features of the intermediate dimeric allylic cation **20** where the carbenium center and the carbon atom of the $=CH_2$ group, on one hand, and the terminal methylidene fragment and the carbon atom of the isopropenyl group, on the other hand, are spatially proximal to enable intramolecular double alkylation. In our opinion, studies of the effects of diverse factors on the features of dimerization of linear cross-conjugated trienes deserve undoubtedly detailed investigations aimed at revealing hitherto unknown processes of intermolecular interactions.

Experimental

The ^1H and ^{13}C NMR spectra were recorded on a Unity Inova Varian spectrometer (300 and 75 MHz, respectively) for solutions in $CDCl_3$ with Me_4Si as the internal standard. The mass spectra were obtained on a Varian MAT CH-6 instrument (EI MS, 70 eV). The ^1H NMR spectra of the tetrafluoroborates **16a** and **16b** were recorded for solution in CD_2Cl_2. An Elemental Analysis system (GmbH) was used for elemental analyses. IR spectra were obtained for KBr pellets on a PerkinElmer FTIR Spectrophotometer model 1605. Chromatographic separations were carried out on columns with alumina (Brockmann activity III).

The following reagents were purchased from Aldrich: ferrocenecarbaldehyde, 99%; pentane-2,4-dione, 99%; ethyl benzoylacetate, tech., 90%; methyllithium, 1.6 mol/L solution in diethyl ether; phenyllithium, 1.9 mol/L solution in cyclohexane–ether; acetic acid, glacial, 99.99%; *N,N*-dimethylaniline, 99%; *N*-phenylmaleimide, 97%; 4-phenyl-1,2,4-triazoline-3,5-dione, 98%; and pyridine, 99%. Tetrafluoroboric acid etherate, 50%–52%, was purchased from Alfa Aesar.

(*Z*)- and (*E*)-2-Acetyl-1-ferrocenyl-3-methyl-1,3-butadienes (1a) and (1b)

These compounds were prepared by reaction of 3-(ferrocenylmethylidene)pentane-2,4-dione (23) with methyllithium in tetrahydrofuran.

(*Z*)-2-Acetyl-1-ferrocenyl-3-methyl-1,3-butadiene (1a)

Yield: 70%; orange crystals, mp 58–60 °C (mp 58 –60 °C (23)). MS *m/z*: 294 [M].

(E)-2-Acetyl-1-ferrocenyl-3-methylbuta-1,3-diene (1b)

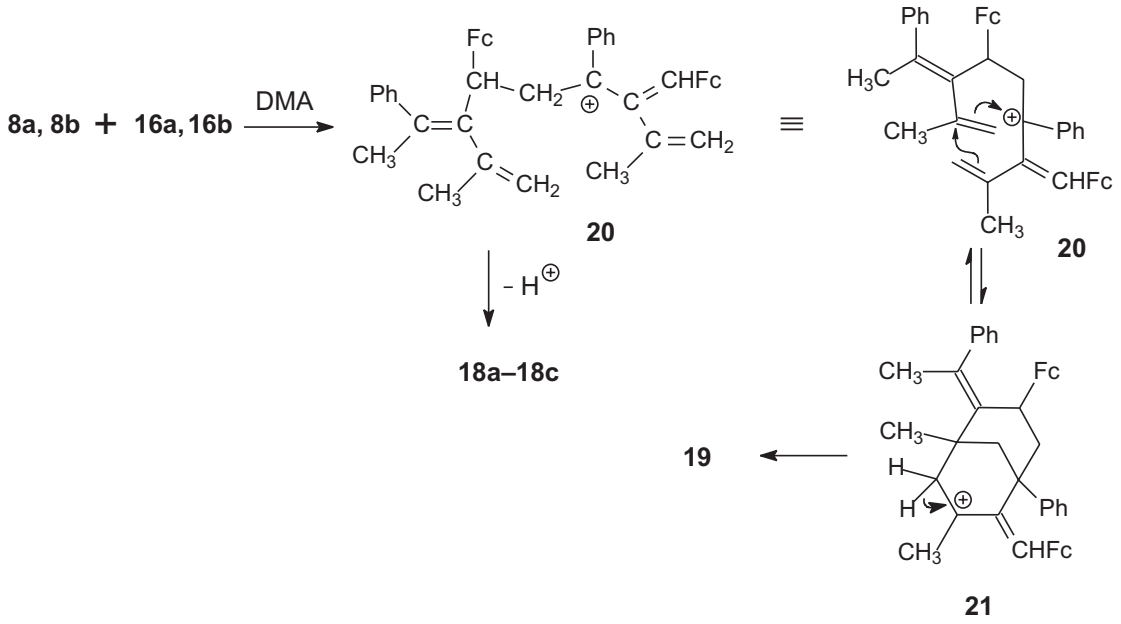
Yield: 76%; red crystals, mp 84–85 °C (mp 84–85 °C (23)). MS *m/z*: 294 [M].

Cyclomerization of 3-ferrocenylmethylidene-2,4-dimethylpenta-1,4-diene (2)

Compound **6** was obtained by dimerization of 3-ferrocenylmethylidene-2,4-dimethylpenta-1,4-diene (**2**) according to the known procedure (23, 24). The reaction products were separated by preparative TLC on silica gel (hexane). The physical and ^1H NMR spectroscopic charac-

© 2007 NRC Canada

Scheme 18.



teristics of compound **6** were in accord with the literature data (24).

7-Ferrocenyl-4-ferrocenylmethylidene-8-isopropylidene-1,3,5-trimethylbicyclo[3.3.1]non-2-ene (6)

Yield: 10%; orange crystals, mp 204–205 °C (mp 204–205 °C (24)). MS *m/z*: 584 $[M]^+$.

(*E*)-Ethyl 2-(ferrocenylmethylidene)benzoylacetate (9)

A mixture of FcCHO (4.3 g, 0.02 mol), ethyl benzoylacetate (3 mL), piperidine (1 mL), and pyridine (1 mL) in dry benzene (100 mL) was refluxed for 10 h. The reaction mixture was washed with 5% HCl to remove the amines, and the organic layer was concentrated to dryness. Diethyl ether (100 mL) was added to the residue, and the precipitate was filtered off and dried on a filter to give (*E*)-ethyl 2-(ferrocenylmethylidene)benzoylacetate **9**: yield 6.01 g (81%), dark red crystals, mp 157–158 °C. IR (KBr, cm^{-1}): 818, 845, 1102, 1478, 1663, 1690, 1850, 1716, 3030. ^{1}H NMR (30 MHz, $CDCl_3$) δ: 1.14 (3H, t, *J* = 7.2 Hz, CH_3), 4.14 (5H, s, C_5H_5), 4.18 (2H, q, *J* = 7.2 Hz, CH_2), 4.27 (2H, m, C_5H_4), 4.31 (2H, m, C_5H_4), 7.45–7.62 (3H, m, C_6H_5), 7.78 (1H, s, CH=), 7.96 (2H, m, C_6H_5). ^{13}C NMR (75 MHz, $CDCl_3$) δ: 14.02 (CH_3), 61.01 (CH_2), 70.92, 71.75 (C_5H_4), 69.75 (C_5H_5), 76.69 (C_{ipso}Fc), 128.69, 129.10, 133.66 (C_6H_5), 143.94 (CH=), 126.42, 136.55 (2C), 165.16, 195.90 (2 C=O). MS *m/z*: 388 $[M]^+$. Anal. calcd. for $C_{22}H_{20}FeO_3$: C 68.08, H 5.18, Fe 14.39; found: C 68.18, H 5.21, Fe 14.27.

The reactions of the dienes (1a) and (1b) with phenyllithium

A solution of PhLi (1.9 mol/L solution in cyclohexane – diethyl ether, 15 mL) was added to a stirred solution of compound **1a** (1.47 g, 5 mmol) in dry benzene (100 mL); the mixture was stirred for additional 30 min at 20 °C, and the excess of phenyllithium was quenched by addition of water (50 mL). The organic layer was separated, washed with water (2 × 20 mL), and dried (Na_2SO_4). The solvent was removed in vacuo, and the residue was chromatographed on Al_2O_3 (hexane–ether, 2:1) to give 0.74 g (40%) of the alcohol **10a** ((*Z*)-isomer) and 0.72 g (39%) of the ketone **11a** and **11b** (~2:1). The compounds **11a** and **11b** were separated by preparative TLC on silica gel (hexane).

(Z)-4-Ferrocenyl-3-isopropenyl-2-phenyl-3-buten-2-ol (10a)

Yield: 40%; yellow crystals, mp 142–143 °C. IR (KBr, cm^{-1}): 820, 851, 1002, 1100, 1467, 1643, 1667, 1845, 3030, 3340. ^{1}H NMR (300 MHz, $CDCl_3$) δ: 1.67 (3H, dd, *J* = 1.2 and 1.5 Hz, CH_3), 1.84 (3H, s, CH_3), 2.50 (1H, bs, OH), 4.06 (5H, s, C_5H_5), 4.10 (2H, m, C_5H_4), 4.21 (2H, m, C_5H_4), 4.54 (1H, dd, *J* = 1.2 and 2.4 Hz, CH_2=), 4.92 (1H, dd, *J* = 1.5, 2.4 Hz, CH_2=), 6.28 (1H, s, CH=), 7.28–7.45 (5H, m, C_6H_5). MS *m/z*: 372 $[M]^+$. Anal. calcd. for $C_{23}H_{24}FeO$: C 74.20, H 6.50, Fe 15.00; found: C 74.38, H 6.66, Fe 14.79.

4-Ferrocenyl-3-isopropenyl-4-phenyl-2-butanon (11a)

Yield: 20%; orange crystals, mp 178–179 °C. IR (KBr, cm^{-1}): 821, 834, 1025, 1103, 1473, 1640, 1658, 1708, 1912, 3030. ^{1}H NMR (300 MHz, $CDCl_3$) δ: 1.60 (3H, dd, *J* = 0.9 and 1.5 Hz, CH_3), 1.88 (3H, s, CH_3), 3.72 (1H, d, *J* = 11.7 Hz, CH), 3.76 (5H, s, C_5H_5), 3.97 (1H, m, C_5H_4), 4.02 (1H, d, *J* = 11.7 Hz, CH), 4.04 (1H, m, C_5H_4), 4.07 (2H, m, C_5H_4), 4.88 (1H, bs, CH_2=), 4.90 (1H, dd, *J* = 0.9 and 1.8 Hz, CH_2=), 7.20 (1H, m, C_6H_5), 7.32–7.40 (4H, m, C_6H_5). MS *m/z*: 372 $[M]^+$. Anal. calcd. for $C_{23}H_{24}FeO$: C 74.20, H 6.50, Fe 15.00; found: C 74.09, H 6.59, Fe 15.11.

4-Ferrocenyl-3-isopropenyl-4-phenyl-2-butanon (11b)

Yield: 12%; orange crystals, mp 184–186 °C. IR (KBr, cm^{-1}): 820, 832, 1009, 1102, 1469, 1648, 1662, 1716, 1926, 3024. ^{1}H NMR (300 MHZ, $CDCl_3$) δ: 1.67 (3H, dd, *J* = 1.2 and 1.5 Hz, CH_3), 1.96 (3H, s, CH_3), 3.83 (1H, d, *J* = 11.1 Hz, CH), 3.98 (5H, s, C_5H_5), 4.03 (2H, m, C_5H_4), 4.09 (1H, d, *J* = 11.1 Hz, CH), 4.13 (2H, m, C_5H_4), 4.67 (1H, bs,

© 2007 NRC Canada

CH_2=), 4.75 (1H, dd, J = 1.2 and 2.1 Hz, CH_2=), 7.28–7.54 (5H, m, C_6H_5). MS m/z: 372 $[M]^+$. Anal. calcd. for $C_{23}H_{24}FeO$: C 74.20, H 6.50, Fe 15.00; found: C 74.31, H 6.35, Fe 15.18.

(E)-4-Ferrocenyl-3-isopropenyl-2-phenyl-3-buten-2-ol (10b)

Analogously, the reaction of the diene **1b** (1.47 g, 5 mmol) with PhLi gave 1.34 g of the alcohol ***(E)*-10b**. Yield: 72%; orange powder, mp 174–175 °C. IR (KBr, cm^{-1}): 818, 850, 1012, 1109, 1446, 1648, 1671, 1845, 3032, 3345. ^1H NMR (300 MHz, $CDCl_3$) δ: 1.60 (3H, dd, J = 0.9 and 1.2 Hz, CH_3), 1.75 (3H, s, CH_3), 2.44 (1H, bs, OH), 4.10 (5H, s, C_5H_5), 4.18 (2H, m, C_5H_4), 4.45 (2H, m, C_5H_4), 4.65 (1H, dd, J = 0.9, 2.1 Hz, CH_2=), 5.09 (1H, dd, J = 1.2 and 2.1 Hz, CH_2=), 6.31 (1H, s, CH=), 7.32–7.61 (5H, m, C_6H_5). MS m/z: 372 $[M]^+$. Anal. calcd for $C_{23}H_{24}FeO$: C 74.20, H 6.50, Fe 15.00; found: C 74.17, H 6.37, Fe 15.19.

Condensation of the hydroxydienes (10a) and (10b) with 4-phenyl-1,2,4-triazoline-3,5-dione

4-Phenyl-1,2,4-triazoline-3,5-dione (0.2 g, 1.22 mmol) was added portionwise to a stirred solution of the diene **10a** (or **10b**) (0.37 g, 1 mmol) in benzene (30 mL) at 0–5 °C as the solution discolored. Stirring was continued for an additional 1 h, and the solvent was evaporated. Column chromatography of the residue on Al_2O_3 (hexane–dichloromethane, 2:1) gave the adduct **12**.

N-Phenyl-3-ferrocenyl-5-methyl-4-(1-phenyl-1-hydroxyethyl)-1,2,3,6-tetrahydropyridazine-1,2-dicarboximide (12)

Yield: 0.40 g (from **10a**) (73%), 0.44 g (from **10b**); yellow crystals, mp 223–225 °C. ^1H NMR (300 MHz, $CDCl_3$) δ: 1.26 (3H, bs, CH_3), 1.67 (3H, s, CH_3), 2.19 (1H, s, OH), 4.01 (1H, d, J = 16.5 Hz, CH_2), 4.16 (1H, d, J = 16.5 Hz, CH_2), 4.25 (5H, s, C_5H_5), 4.21 (2H, m, C_5H_4), 4.27 (1H, m, C_5H_4), 4.44 (1H, m, C_5H_4), 6.28 (1H, s, CH), 7.28–7.63 (10H, m, 2 C_6H_5). ^{13}C NMR (75 MHz, $CDCl_3$) δ: 18.09, 27.21 (2 CH_3), 48.41 (CH_2), 50.56 (CH), 65.88, 67.09, 68.15, 69.96 (C_5H_4), 69.12 (C_5H_5), 90.72 (C_{ipso}Fc), 125.50, 125.78, 127.79, 128.07, 128.67, 129.23 (2 C_6H_5), 75.20, 122.58, 131.60, 139.90, 146.91 (5 C), 148.78, 152.91 (2 C=O). MS m/z: 548 $[M]^+$. Anal. calcd. for $C_{31}H_{29}FeN_3O_3$: C 68.02, H 5.34, Fe 10.20, N 7.67; found: C 67.87, H 5.38, Fe 10.32, N 7.71.

The reactions of the *E*-ethyl 2-(ferrocenylmethylidene)benzoylacetate (9) with methyllithium

A solution of MeLi (1.6 mol/L solution in diethyl ether, 20 mL) was added to a stirred solution of compound **9** (1.94 g, 5 mmol) in dry benzene (100 mL); the mixture was stirred for additional 30 min at 20 °C, and the excess of methyllithium was quenched by addition of water (50 mL). The organic layer was separated, washed with water (2 × 20 mL), and dried (Na_2SO_4). The solvent was removed in vacuo, and the residue was chromatographed on Al_2O_3 (hexane–ether, 2:1) to give 0.95 g (50%) of the alcohol **13** ((*Z*)-isomer) and 0.48 g (25%) of the ketone **14a** and **14b** (~5:1), mp 113–114 °C. The compounds **14a** and **14b** were separated by preparative TLC on silica gel (hexane).

(Z)-4-Ferrocenylmethylidene-4-methyl-2-phenylpentan-2,4-diol (13)

Yield: 50%; yellow crystals, mp 142–143 °C. IR (KBr, cm^{-1}): 764, 858, 1006, 1101, 1460, 1642, 1670, 1859, 3030, 3343–3408. ^1H NMR (300 MHz, $CDCl_3$) δ: 1.65 (3H, s, CH_3), 1.67 (3H, s, CH_3), 1.73 (3H, s, CH_3), 3.42 (1H, bs, OH), 4.04 (5H, s, C_5H_5), 3.45 (1H, m, C_5H_4), 3.88 (1H, m, C_5H_4), 4.06 (1H, m, C_5H_4), 4.10 (1H, m, C_5H_4), 4.13 (1H, bs, OH), 6.45 (1H, s, CH=), 7.27–7.55 (5H, m, C_6H_5). ^{13}C NMR (75 MHz, $CDCl_3$) δ: 29.67, 31.85, 32.63 (3 CH_3), 67.90, 67.99, 69.25, 70.94 (C_5H_4), 68.97 (C_5H_5), 76.78, 79.21 (2 C–OH), 82.86 (C_{ipso}Fc), 123.02 (CH=), 126.13, 127.28, 128.37 (C_6H_5), 148.40, 148.67 (2 C). MS m/z: 390 $[M]^+$. Anal. calcd. for $C_{23}H_{24}FeO$: C 70.77, H 6.72, Fe 14.32; found: C 70.59, H 6.86, Fe 14.47.

3-Benzoyl-4-ferrocenyl-2-methyl-2-pentanol (14a)

Yield: 17%; orange crystals, mp 121–122 °C. IR (KBr, cm^{-1}): 764, 849, 1005, 1103, 1468, 1649, 1668, 1710, 1929, 3034, 3358. ^1H NMR (300 MHz, $CDCl_3$) δ: 1.20 (3H, s, CH_3), 1.36 (3H, s, CH_3), 1.42 (3H, d, J = 7.2 Hz, CH_3), 3.30 (1H, m, J = 3.9 and 7.2 Hz, CH), 3.52 (1H, d, J = 3.9 Hz, CH), 3.91 (1H, br s, OH), 4.09 (5H, s, C_5H_5), 3.66 (1H, m, C_5H_4), 3.82 (1H, m, C_5H_4), 4.05 (1H, m, C_5H_4), 4.17 (1H, m, C_5H_4), 7.23–7.60 (5H, m, C_6H_5). ^{13}C NMR (75 MHz, $CDCl_3$) δ: 16.97, 28.07, 30.19 (3 CH_3), 33.29, 60.80 (2 CH), 66.97, 67.21, 67.65, 67.81 (C_5H_4), 68.84 (C_5H_5), 72.95 (C–OH), 95.31 (C_{ipso}Fc), 128.09, 128.60, 132.99 (C_6H_5), 138.56 (C_{ipso}), 206.43 (C=O). MS m/z: 390 $[M]^+$. Anal. calcd. for $C_{23}H_{24}FeO$: C 70.77, H 6.72, Fe 14.32; found: C 70.63, H 6.81, Fe 14.41.

3-Benzoyl-4-ferrocenyl-2-methyl-2-pentanol (14b)

Yield: 6%; orange crystals, mp 136–137 °C. IR (KBr, cm^{-1}): 763, 853, 1004, 1107, 1478, 1656, 1668, 1715, 1932, 3033, 3367. ^1H NMR (300 MHz, $CDCl_3$) δ: 1.23 (3H, s, CH_3), 1.30 (3H, s, CH_3), 1.40 (3H, d, J = 6.9 Hz, CH_3), 3.28 (1H, m, CH), 3.46 (1H, d, J = 5.4 Hz, CH), 3.90 (1H, br s, OH), 4.04 (5H, s, C_5H_5), 3.70 (1H, m, C_5H_4), 3.79 (1H, m, C_5H_4), 3.87 (1H, m, C_5H_4), 3.96 (1H, m, C_5H_4), 7.30–7.64 (5H, m, C_6H_5). ^{13}C NMR (75 MHz, $CDCl_3$) δ: 18.02, 29.01, 30.05 (3 CH_3), 34.52, 60.05 (2 CH), 67.40, 67.51, 67.90, 68.65 (C_5H_4), 68.75 (C_5H_5), 72.30 (C–OH), 95.30 (C_{ipso}Fc), 128.25, 128.47, 128.55 (C_6H_5), 133.25 (C_{ipso}), 204.05 (C=O). MS m/z: 390 $[M]^+$. Anal. calcd. for $C_{23}H_{24}FeO$: C 70.77, H 6.72, Fe 14.32; found: C 70.85, H 6.61, Fe 14.52.

Dehydration of the alcohols (10a), (10b), (13), (14a), and (14b) with $POCl_3$–PyH

The alcohols **10a**, **10b**, **13**, **14a**, or **14b** (0.01 mol) was added to a mixture of dry pyridine (100 mL) and $POCl_3$ (1.0 mL) and stirred at 30–40 °C for 3 h (TLC control). The reaction mixture was treated with water (100 mL) and benzene (100 mL); the organic layer was separated, washed with water (3 × 50 mL), and concentrated in vacuo. The residue was chromatographed on a column with Al_2O_3 in hexane to yield trienes **8a** and **8b** and dienes **15a** and **15b**.

(Z)- and (E)-3-Ferrocenylmethylidene-4-methyl-2-phenyl-1,4-pentadienes (8a) and (8b) from the alcohol (10a)

Yield: 80% (~3:1); orange powder, mp 61–64 °C.

© 2007 NRC Canada

(Z)-3-Ferrocenylmethylidene-4-methyl-2-phenyl-1,4-pentadiene (8a)

Yield: 54%; orange powder, mp 68–69 °C. IR (KBr, cm^{-1}): 817, 820, 841, 1005, 1100, 1475, 1642, 1661, 1698, 1927, 3032. ^1H NMR (300 MHz, $CDCl_3$) δ: 2.09 (3H, dd, J = 0.6 and 1.2 Hz, CH_3), 4.00 (5H, s, C_5H_5), 4.13 (2H, m, C_5H_4), 4.35 (2H, m, C_5H_4), 4.94 (1H, m, J = 0.6 and 1.5 Hz, CH_2=), 4.97 (1H, m, J = 1.2 and 1.5 Hz, CH_2=), 5.13 (1H, d, J = 1.8 Hz, CH_2=), 5.86 (1H, d, J = 1.8 Hz, CH_2=), 6.46 (1H, s, CH=), 7.24–7.56 (5H, m, C_6H_5). ^{13}C NMR (75 MHz, $CDCl_3$) δ: 20.87 (CH_3), 68.99, 69.70 (C_5H_4), 69.04 (C_5H_5), 81.32 (C_{ipso}Fc), 114.85, 114.90 (2 CH_2=), 125.11 (CH=), 126.11, 127.67,128.42 (C_6H_5), 139.06, 139.14, 143.21, 146.48(4C). MS m/z: 354 $[M]^+$. Anal. calcd. for $C_{23}H_{22}Fe$: C 77.97, H 6.26, Fe 15.77; found: C 78.10, H 6.19, Fe 15.81.

(E)-3-Ferrocenylmethylidene-4-methyl-2-phenyl-1,4-pentadiene (8b)

Yield: 14%; orange powder, mp 74–75 °C. IR (KBr, cm^{-1}): 818, 822, 841, 1003, 1102, 1473, 1645, 1660, 1687, 1924, 3034. ^1H NMR (300 MHz, $CDCl_3$) δ: 2.00 (3H, dd, J = 0.9 and 1.5 Hz, CH_3), 4.08 (5H, s, C_5H_5), 4.19 (2H, m, C_5H_4), 4.41 (2H, m, C_5H_4), 4.97 (1H, dd, J = 1.5 and 2.4 Hz, CH_2=), 5.12 (1H, dd, J = 0.3 and 1.8 Hz, CH_2=), 5.23 (1H, m, J = 0.9 and 2.4 Hz, CH_2=), 5.31 (1H, dd, J = 0.3 and 1.8 Hz, CH_2=), 5.91 (1H, s, CH=), 7.28–7.38 (5H, m, C_6H_5). ^{13}C NMR (75 MHz, $CDCl_3$) δ: 20.42 (CH_3), 68.96, 69.35 (C_5H_4), 69.02 (C_5H_5), 81.39 (C_{ipso}Fc), 114.40, 116.20 (2 CH_2=), 127.15 (CH=), 127.43, 127.93,128.87 (C_6H_5), 141.09, 142.10, 143.83, 150.11(4 C). MS m/z: 354 $[M]^+$. Anal. calcd. for $C_{23}H_{22}Fe$: C 77.97, H 6.26, Fe 15.77; found: C 77.84, H 6.32, Fe 15.58.

(Z)- and (E)-3-Ferrocenylmethylidene-4-methyl-2-phenyl-1,4-pentadienes 8a and 8b from the alcohol (10b)

Yield: 83% (~1:3.6); orange powder, mp 62–65 °C.

(Z)- and (E)-3-Ferrocenylmethylidene-4-methyl-2-phenyl-1,4-pentadienes (8a) and (8b) from the diol (13)

Yield: 86% (~2:1); orange powder, mp 62–64 °C.

3-Benzoyl-4-ferrocenyl-2-methyl-1-pentene (15a)

Yield: 74%; orange powder, mp 133–134 °C. IR (KBr, cm^{-1}): 820, 838, 1001, 1100, 1470, 1653, 1661, 1727, 1920, 3030. ^1H NMR (300 MHz, $CDCl_3$) δ: 1.34 (3H, d, J = 7.2 Hz, CH_3), 1.74 (3H, dd, J = 0.9 and 1.2 Hz, CH_3), 3.33 (1H, m, J = 7.2, 10.5 Hz, CH), 4.12 (5H, s, C_5H_5), 3.88 (1H, m, C_5H_4), 3.98 (1H, m, C_5H_4), 4.00 (1H, m, C_5H_4), 4.15 (1H, m, C_5H_4), 3.94 (1H, d, J = 10.5 Hz, CH), 4.94 (2H, m, CH_2=), 7.29–7.74 (5H, m, C_6H_5). MS m/z: 372 $[M]^+$. Anal. calcd. for $C_{23}H_{24}FeO$: C 74.20, H 6.50, Fe 15.00; found: C 74.12, H 6.31, Fe 15.15.

3-Benzoyl-4-ferrocenyl-2-methyl-1-pentene (15b)

Yield: 71%; orange powder, mp 126–127 °C. IR (KBr, cm^{-1}): 819, 840, 1004, 1103, 1468, 1652, 1660, 1728, 1921, 3028. ^1H NMR (300 MHz, $CDCl_3$) δ: 1.26 (3H, d, J = 6.9 Hz, CH_3), 2.04 (3H, dd, J = 0.9 and 1.2 Hz, CH_3), 2.96 (1H, m, CH), 3.73 (1H, d, J = 9.9 Hz, CH), 4.04 (5H, s, C_5H_5), 3.96 (1H, m, C_5H_4), 4.06 (1H, m, C_5H_4), 4.10 (1H, m, C_5H_4), 4.14 (1H, m, C_5H_4), 5.02 (2H, m, CH_2=), 7.39–7.93 (5H, m, C_6H_5). MS m/z: 372 $[M]^+$. Anal. calcd. for $C_{23}H_{24}FeO$: C 74.20, H 6.50, Fe 15.00; found: C 74.11, H 6.63, Fe 14.89.

Dehydration of the alcohols (10a), (10b), and (13) with AcOH

A solution of the alcohols **10a**, **10b**, or **13** (5 mmol) in benzene (50 mL) and AcOH (20 mL) was stirred at 20 °C for 5 h. Then, water (50 mL) was added; the organic layer was separated, washed with 5% $NaHCO_3$, and concentrated. The residue was chromatographed on Al_2O_3 (hexane) to give the triene **8b**.

(E)-3-Ferrocenylmethylidene-4-methyl-2-phenyl-1,4-pentadienes (8b)

Yield: 74%–82%; orange powder, mp 74–75 °C.

(Z)- and (E)-3-Ferrocenyl-2-isopropenyl-1-methyl-1-phenylallylium tetrafluoroborates (16a and 16b)

These compounds were prepared by the addition of tetrafluoroboric acid etherate to a solution of the triene **8a** or **8b** in dry diethyl ether. The crystalline residues that precipitated were filtered off, washed with dry diethyl ether, and dried in vacuo. The yields of the salts were quantitative. All operations with solid salts were carried out in an atmosphere of dry nitrogen.

Compound (16a)

Yield: 91%; black crystals, mp 219–221 °C. ^1H NMR (300 MHz, CD_2CI_2) δ: 2.23 (3H, s, CH_3), 2.26 (3H, s, CH_3), 4.65 (5H, s, C_5H_5), 4.75 (2H, m, C_5H_4), 5.09 (2H, m, C_5H_4), 5.94 (1H, br s, CH_2=), 6.07 (1H, br s, CH_2=), 7.15–7.56 (5H, m, C_6H_5), 8.34 (1H, s, CHFc). MS m/z: 442 $[M]^+$. Anal. calcd. for $C_{23}H_{23}BF_4Fe$: C 62.49, H 5.24, F 17.19, Fe 12.63; found: C 62.34, H 5.31, F 17.27, Fe 12.56.

Compound (16b)

Yield: 94%; black crystals, mp 226–228 °C. ^1H NMR (300 MHz, CD_2CI_2) δ: 1.93 (3H, s, CH_3), 1.96 (3H, s, CH_3), 4.39 (5H, s, C_5H_5), 4.60 (2H, m, C_5H_4), 4.88 (1H, m, C_5H_4), 5.33 (1H, m, C_5H_4), 5.52 (1H, br s, CH_2=), 5.70 (1H, br s, CH_2=), 7.17–7.48 (5H, m, C_6H_5), 8.20 (1H, s, CHFc). MS m/z: 442 $[M]^+$. Anal. calcd. for $C_{23}H_{23}BF_4Fe$: C 62.49, H 5.24, F 17.19, Fe 12.63; found: C 62.63, H 5.13, F 17.02, Fe 12.88.

Isomerization of the tetrafluoroborates (16a) and (16b)

A solution of the salt **16a** or **16b** (0.44 g, 1 mmol) in dry CD_2CI_2 (10 mL) was kept at room temperature for 4. The ^1H NMR spectrum of the solutions contains signals for two products: **16a** and **16b** (~1:2).

The reaction of the tetrafluoroborates (16a) and (16b) with N,N-dimethylaniline

N,N-Dimethylaniline (1.5 mL) was added with stirring to a tetrafluoroborate **16a** or **16b** (0.88 g, 2 mmol). The nearly black solution gradually turns orange in ~20 min. The reaction products were extracted with benzene (3 × 30 mL); the combined extract was washed with water (20 mL), 5% HCl (2 × 20 mL), and water (20 mL); the organic layer was dried with $CaCl_2$; and the solvent was distilled off. The residue

© 2007 NRC Canada

was chromatographed on a column with Al_2O_3 (hexane). A fraction of pure triene **8a** or **8b** were isolated.

Triene (8a) (from the salt 16a)
Yield: 84%; mp 68–69 °C.

Triene (8b) (from the salt 16b)
Yield: 88%; mp 74–75 °C.

Condensation of the trienes (8a) and (8b) with *N*-phenylmaleimide

A solution of the triene **8a** (or **8b**) (0.35 g, 1 mmol) and *N*-phenylmaleimide (0.2 g, 1.24 mmol) in toluene (50 mL) was refluxed for 3 h and concentrated. The residue was chromatographed on Al_2O_3 (hexane – dichloromethane, 3:1) to give 0.37 g (70%) (from **8a**) or 0.40 g (75%) (from **8b**) of the adducts **17** as a mixture of two isomers **17a** and **17b** (~3:1, NMR data), yellow crystals, mp 188–200 °C. The isomers were separated by preparative TLC on Al_2O_3 (hexane–benzene, 1:1).

Endo-adduct (17a)
Yield: 50%; yellow powder, mp 208–209 °C. IR (KBr, cm^{-1}): 770, 826, 1002, 1035, 1102, 1157, 1186, 1385, 1436, 1498, 1629, 1685, 1711, 1776, 2872, 2937, 3081. ^{1}H NMR (300 MHz, $CDCl_3$) δ: 1.64 (3H, m, J = 0.9 Hz, CH_3), 2.86 (1H, dd, J = 6.0 and 12.0 Hz, CH_2), 3.18 (1H, dd, J = 7.8 and 12.0 Hz, CH_2), 3.41 (1H, m, CH), 3.74 (1H, dd, J = 1.5 and 9.0 Hz, CH), 4.18 (5H, s, C_5H_5), 4.10 (2H, m, C_5H_4), 4.27 (2H, m, C_5H_4), 4.25 (1H, d, J = 1.5 Hz, CHFc), 4.93 (1H, m, J = 0.9 Hz, CH_2=), 5.00 (1H, m, CH_2=), 7.02–7.05 (2H, m, C_6H_5), 7.12–7.49 (8H, m, C_6H_5). MS *m*/*z*: 527 $[M]^+$. Anal. calcd. for $C_{33}H_{29}FeNO_2$: C 75.15, H 5.54, Fe 10.59, N 2.65; found: C 74.91, H 5.63, Fe 10.69, N 2.59.

Exo-adduct (17b)
Yield: 15%; yellow powder, mp 201–202 °C. IR (KBr, cm^{-1}): 767, 821, 1001, 1027, 1102, 1148, 1186, 1387, 1435, 1501, 1630, 1685, 1714, 1766, 2875, 2939, 3080. ^{1}H NMR (300 MHz, $CDCl_3$) δ: 1.88 (3H, m, J = 1.2 Hz, CH_3), 2.75 (1H, dd, J = 9.6 and 15.3 Hz, CH_2), 3.07 (1H, dd, J = 8.1 and 15.3 Hz, CH_2), 3.24 (1H, m, CH), 3.37 (1H, dd, J = 5.4 and 9.6 Hz, CH), 4.04 (5H, s, C_5H_5), 4.11 (2H, m, C_5H_4), 4.14 (1H, m, C_5H_4), 4.27 (1H, m, C_5H_4), 4.47 (1H, d, J = 5.4 Hz, CHFc), 5.01 (1H, m, J = 1.2 Hz, CH_2=), 5.10 (1H, m, CH_2=), 7.09–7.13 (2H, m, C_6H_5), 7.23–7.46 (8H, m, C_6H_5). ^{13}C NMR (75 MHz, $CDCl_3$) δ: 22.86 (CH_3), 28.57 (CH_2), 39.79, 42.21, 48.06 (3 CH), 67.07, 68.58 (C_5H_4), 69.21 (C_5H_5), 83.55 (C_{ipso}Fc), 117.29 (CH_2=), 126.70, 126.87, 127.66, 128.11, 128.49, 128.94 (2 C_6H_5), 131.71, 134.86, 140.39, 142.95, 144.54(5 C), 177.42, 178.53 (2 C=O). MS *m*/*z*: 527 $[M]^+$. Anal. calcd. for $C_{33}H_{29}FeNO_2$: C 75.15, H 5.54, Fe 10.59, N 2.65; found: C 75.29, H 5.43, Fe 10.42, N 2.71.

Dimerization of (*Z*)- and (*E*)-3-Ferrocenylmethylidene-4-methyl-2-phenyl-1,4-pentadienes (8a) and (8b)

A solution of the triene **8a** (or **8b**) (0.70 g, 2 mmol) in glacial acetic acid (50 mL) and CF_3COOH (5 mL) was refluxed for 4 h, cooled to ambient temperature, and diluted with water (100 mL). The reaction products were extracted with benzene (3 × 50 mL), 5% aq. $NaHCO_3$, and water and dried with Na_2OS_4. The solvent was distilled off, and the residue was subjected to preparative TLC on silica gel (hexane) to yield 6-ferrocenyl-3-ferrocenylmethylidene-7-isopropylidene-2-methyl-4,8-diphenyl-nona-1,4,7-trienes **18a**–**18c** and 7-ferrocenyl-4-ferrocenylmethylidene-8-(1-phenylethylidene)-1,3-dimethyl-5-phenyl-bicyclo[3.3.1]non-2-ene **19**.

6-Ferrocenyl-3-ferrocenylmethylidene-7-isopropylidene-2-methyl-4,8-diphenyl-nona-1,4,7-triene (18a)
Yield: 34%; R_f = 0.63, orange powder, mp 164–165 °C. IR (KBr, cm^{-1}): 820, 998, 1007, 1105, 1134, 1179, 1379, 1451, 1518, 1641, 1676, 1684, 2879, 2923, 3078. ^{1}H NMR (300 MHz, $CDCl_3$) δ: 1.74 (3H, br s, CH_3), 1.90 (3H, s, CH_3), 2.07 (3H, m, J = 0.6 and 0.9 Hz, CH_3), 3.69 (5H, s, C_5H_5), 4.02 (5H, s, C_5H_5), 4.01 (1H, m, C_5H_4), 4.15 (2H, m, C_5H_4), 4.37 (2H, m, C_5H_4), 4.48 (1H, d, J = 10.8 Hz, CHFc), 4.57 (2H, m, C_5H_4), 4.70 (1H, m, C_5H_4), 4.83 (1H, m, CH_2=), 4.93 (1H, m, CH_2=), 4.98 (1H, m, CH_2=), 5.28 (1H, m, CH_2=), 5.49 (1H, s, CH=), 5.86 (1H, d, J = 10.8 Hz, CH=), 6.88 (2H, m, C_6H_5), 7.14–7.51 (8H, m, C_6H_5). ^{13}C NMR (75 MHz, $CDCl_3$) δ: 21.95, 23. 34, 32,52 (3 CH_3), 41.74 (CH), 66.63, 66.81, 67.01, 67.23, 67.49, 67.89, 68.48, 69.34 (2 C_5H_4), 68.62, 69.17 (2 C_5H_5), 83.25, 90.34 (2 C_{ipso}Fc), 117.43, 118.21 (2 CH_2=), 124.31, 130.10 (2 CH=), 126.79, 126.99, 127.45, 128.32, 128.47, 128.98 (2 C_6H_5), 125.83, 131.87, 132.29, 134,09, 134.73, 139.91, 140.95, 143.54 (8C). MS *m*/*z*: 708 $[M]^+$. Anal. calcd. for $C_{46}H_{44}Fe_2$: C 77.97, H 6.26, Fe 15.77; found: C 78.12, H 6.18, Fe 15.81.

6-Ferrocenyl-3-ferrocenylmethylidene-7-isopropylidene-2-methyl-4,8-diphenyl-nona-1,4,7-triene (18b)
Yield: 21%; R_f = 0.57, orange powder, mp 171–172 °C. IR (KBr, cm^{-1}): 818, 1001, 1006, 1101, 1140, 1182, 1383, 1448, 1521, 1640, 1660, 1681, 2882, 2936, 3085. ^{1}H NMR (300 MHz, $CDCl_3$) δ: 1.63 (3H, m, J = 0.9 Hz, CH_3), 1.82 (3H, s, CH_3), 2.12 (3H, m, CH_3), 3.74 (5H, s, C_5H_5), 4.05 (5H, s, C_5H_5), 3.95 (2H, m, C_5H_4), 4.08 (1H, m, C_5H_4), 4.12 (1H, m, C_5H_4), 4.20 (2H, m, C_5H_4), 4.35 (2H, m, C_5H_4), 4.42 (1H, d, J = 10.5 Hz, CHFc), 4.72 (1H, m, CH_2=), 5.14 (1H, m, CH_2=), 5.32 (1H, m, CH_2=), 5.57 (1H, s, CH=), 5.86 (1H, m, CH_2=), 6.05 (1H, d, J = 10.5 Hz, CH=), 7.12–7.61 (10H, m, 2 C_6H_5). ^{13}C NMR (75 MHz, $CDCl_3$) δ: 21.76, 23. 44, 32.36 (3 CH_3), 41.85 (CH), 66.58, 66.63, 67.19, 67.34, 67.09, 67.57, 68.29, 69.07 (2 C_5H_4), 68.60, 69.23 (2 C_5H_5), 83.28, 90.37 (2 C_{ipso}Fc), 117.31, 118.28 (2 CH_2=), 124.48, 130.15 (2 CH=), 126.83, 127.03, 127.34, 128.49, 128.53, 128.74 (2 C_6H_5), 125.57, 130.48, 132.13, 134,03, 134.58, 139.84, 140.66, 143.32 (8 C). MS *m*/*z*: 708 $[M]^+$. Anal. calcd. for $C_{46}H_{44}Fe_2$: C 77.97, H 6.26, Fe 15.77; found: C 77.85, H 6.29, Fe 15.66.

6-Ferrocenyl-3-ferrocenylmethylidene-7-isopropylidene-2-methyl-4,8-diphenyl-nona-1,4,7-triene (18c)
Yield: 9%; R_f = 0.49, orange powder, mp 158–159 °C. IR (KBr, cm^{-1}): 822, 1003, 1011, 1101, 1131, 1181, 1390, 1447, 1527, 1643, 1661, 1678, 2881, 2926, 3071. ^{1}H NMR (300 MHz, $CDCl_3$) δ: 1.86 (3H, br s, CH_3), 1.92 (3H, m, CH_3), 2.06 (3H, s, CH_3), 4.03 (5H, s, C_5H_5), 4.11 (5H, s,

© 2007 NRC Canada

Table 2. Crystal data, data collection, and refinement parameters for compounds **6**, **9**, **11a**, and **13**.

Crystal	**6**	**9**	**11a**	**13**
Empirical formula	$C_{36}H_{40}Fe_2$	$C_{22}H_{20}FeO_3$	$C_{23}H_{24}FeO$	$C_{23}H_{26}FeO_2$
Formula mass	584.38	388.23	372.27	390.29
Color, habit	Orange prism	Dark red prism	Yellow prism	Orange prism
Crystal dimensions (mm)	0.346 × 0.064 × 0.048	0.60 × 0.50 × 0.35	0.30 × 0.16 × 0.13	0.392 × 0.174 × 0.062
Crystal system	Monoclinic	Monoclinic	Monoclinic	Monoclinic
Space group	$P2_1/c$	$P2_1/n$	$P2_1/n$	$P2_1/n$
Z	4	4	4	4
a (Å)	14.3336(12)	9.539(2)	7.6853(4)	13.3329(10)
b (Å)	13.7797(11)	17.236(4)	14.0988(8)	8.7769(6)
c (Å)	15.9865(13)	11.120(2)	17.177(1)	17.2372(13)
α (°)	90	90	90	90
β (°)	114.784(2)	93.816(14)	93.750(1)	98.362(2)
γ (°)	90	90	90	90
Collection ranges	$-17 \le h \le 17$; $-16 \le k \le 16$; $-19 \le l \le 19$	$-1 \le h \le 11$; $-1 \le k \le 21$; $-13 \le l \le 13$	$-9 \le h \le 9$; $-16 \le k \le 16$; $-20 \le l \le 20$	$-16 \le h \le 13$; $-10 \le k \le 10$; $-20 \le l \le 20$
Temperature (K)	298(2)	298(2)	291(2)	298(2)
Volume (Å^3)	2866.7(4)	1824.2(7)	1857.3(2)	1994.2(2)
$D_{calcd.}$ (Mg m^{-3})	1.354	1.413	1.331	1.300
Radiation	Mo Kα (λ = 0.71073 Å)	Mo Kα (λ = 0.71073 Å)	Mo Kα (λ = 0.71073 Å)	Mo Kα (λ = 0.71073 Å)
Absorption coeff.(μ) (mm^{-1})	1.035	0.845	0.819	0.769
F(000)	1232	808	784	824
θ range for data collection (°)	2.04–25.06	2.18–26.00	1.87–25.00	1.81 – 25.35
Observed reflections	23021	4540	14976	11909
Independent reflections	5054 (R_{int} = 0.0836)	3578 (R_{int} = 0.0444)	3267 (R_{int} = 0.0442)	3646 (R_{int} = 0.0562)
Data/restraints/parameters	5054/0/348	3578/0/201	3267/0/228	3646/0/287
Maximum shift/error	0.000	0.000	0.000	0.001
Goodness-of-fit on F^2	1.095	1.051	0.909	0.893
Final R indices [$I > \sigma(I)$]	R_1 = 0.0721, wR_2 = 0.1424	R_1 = 0.0434, wR_2 = 0.1338	R_1 = 0.0374, wR_2 = 0.0809	R_1 = 0.0497, wR_2 = 0.0768
R indices (all data)	R_1 = 0.1042, wR_2 = 0.1554	R_1 = 0.0513, wR_2 = 0.1370	R_1 = 0.0499, wR_2 = 0.0840	R_1 = 0.0876, wR_2 = 0.0864

C_5H_5), 3.96–4.20 (8H, m, 2 C_5H_4), 4.55 (1H, d, J = 11.1 Hz, CHFc), 4.87 (1H, m, CH_2=), 5.00 (1H, m, CH_2=), 5.02 (1H, m, CH_2=), 5.35 (1H, m, CH_2=), 5.52 (1H, s, CH=), 5.91 (1H, d, J = 11.1 Hz, CH=), 7.15–7.43 (10H, m, 2 C_6H_5). ^{13}C NMR (75 MHz, $CDCl_3$) δ: 21.85, 23. 37, 32,53 (3 CH_3), 41.91 (CH), 66.84, 66.92, 67.26, 67.49, 67.12, 67.64, 68.49, 69.16 (2 C_5H_4), 68.71, 69.32 (2 C_5H_5), 83.34, 90.43 (2 C_{ipso}Fc), 117.43, 118.32 (2 CH_2=), 122.57, 129.87 (2 CH=), 125.29, 126.37, 127.02, 128.31, 128.58, 128.63 (2 C_6H_5), 124.16, 129.11, 130.88, 132.41, 134.42, 139.76, 140.52, 143.64 (8 C). MS m/z: 708 [M]$^+$. Anal. calcd. for $C_{46}H_{44}Fe_2$: C 77.97, H 6.26, Fe 15.77; found: C 77.79, H 6.37, Fe 15.95.

7-Ferrocenyl-4-ferrocenylmethylidene-8-(1-phenylethylidene)-1,3-dimethyl-5-phenyl-bicyclo[3.3.1]non-2-ene (19)

Yield: 14%; R_f = 0.71, yellow powder, mp 182–183 °C. IR (KBr, cm^{-1}): 769, 1001, 1010, 1108, 1125, 1179, 1392, 1442, 1531, 1640, 1654, 1660, 2877, 2929, 3070. ^{1}H NMR (300 MHz, $CDCl_3$) δ: 1.51 (3H, s, CH_3), 1.81 (3H, d, J = 1.2 Hz, CH_3), 1.92 (3H, s, CH_3), 2.35 (1H, dd, J = 5.7 and 13.2 Hz, CH_2), 2.54 (2H, s, CH_2), 2.73 (1H, dd, J = 3.6 and 13.2 Hz, CH_2), 3.95 (1H, dd, J = 3.6 and 5.7 Hz, CH), 4.14 (5H, s, C_5H_5), 4.23 (5H, s, C_5H_5), 4.13 (2H, m, C_5H_4), 4.18 (2H, m, C_5H_4), 4.21 (2H, m, C_5H_4), 4.31 (1H, m, C_5H_4), 4.49 (1H, m, C_5H_4), 6.12 (1H, q, J = 1.2 Hz, CH=), 6.29 (1H, s, CH=), 7.08–7.63 (10H, m, 2 C_6H_5). ^{13}C NMR (75 MHz, $CDCl_3$) δ: 23.05, 26. 14, 29.32 (3 CH_3), 39.18, 40.14 (2 CH_2), 43.18 (CH), 43.56, 52.08 (2C), 68.63, 68.79, 69.52, 69.70 (2 C_5H_4), 68.84, 69.61 (2 C_5H_5), 79.24, 83.41 (2 C_{ipso}Fc), 119.23, 126.63 (2 CH=), 127.24, 127.43, 127.64, 127.83, 127.95, 128.56 (2 C_6H_5), 121.94, 129.18, 133.07, 142.10, 143.48, 144.21 (6C). MS m/z: 708 [M]$^+$. Anal. calcd. for $C_{46}H_{44}Fe_2$: C 77.97, H 6.26, Fe 15.77; found: C 77.90, H 6.31, Fe 15.85.

Condensation of the tetrafluoroborates (16a) and (16b) with the trienes (8a) and (8b)

The triene **8a** (or **8b**) (0.35 g, 1 mmol) was added to a solution of the tetrafluoroborate **16a** (or **16b**) (0.49g, 1.1 mmol) in dichloromethane (60 mL), and the mixture was stirred at 20 °C for 1 h. *N*,*N*-Dimethylaniline (0.6 mL) was then added, and stirring was continued for 30 min. The reaction mixture was washed with water, 5% HCl, and water and dried with $CaCl_2$. The solvent was removed in vacuo, and the reaction products were separated by TLC on SiO_2 (hex-

© 2007 NRC Canada

ane). The following compounds were obtained: compounds **18a**–**18c** (42%, ~3:2:1), compound **19** (28%), and polymeric products.

Compound (18a)
Yield: 21%; R_f = 0.63, orange powder, mp 163–165 °C.

Compound (18b)
Yield: 14%; R_f = 0.57, orange powder, mp 171–172 °C.

Compound (18c)
Yield: 9%; R_f = 0.49, orange powder, mp 158–159 °C.

Compound (19)
Yield: 28%; R_f = 0.71, yellow powder, mp 182–183 °C.

X-ray crystallographic studies

The unit-cell parameters and the X-ray diffraction intensities were recorded on a Bruker Smart Apex CCD area detector/ω diffractometer (compounds **6**, **11a**, and **13**) and on a Siemens P4 diffractometer (compound **9**). The principal geometrical parameters of the molecules **6, 9, 11a**, and **13** are listed in Table 1. The crystallographic data, the parameters of the X-ray diffraction experiment, and refinements are listed in Table 2. The structure of compounds **6, 9, 11a**, and **13** were solved by the direct method [SHELXS-97, (30)] and refined using full-matrix least-squares on F^2.[2]

Acknowledgements

This work was supported by the grant DGAPA–UNAM (Mexico, grant IN 207606). Thanks are due to E.A. Vazquez Lopez, R.I. Del Villar Morales, M. Gutierrez Franco, and G.A. Duarte Lisi for their technical assistance.

References

1. E.G. Perevalova, M.D. Reshetova, and K.I. Grandberg. Methods of Organometallic chemistry: organoiron compounds. Ferrocene. Nauka: Moscow. 1983. [In Russian].
2. A. Togni and T. Hayashi. Ferrocenes. VCH, Weinheim. 1995.
3. Ch. Ganter and T. Wagner. Chem. Ber. **128**, 1157 (1995).
4. M.E. Kuehne and V.K. Bandarage. J. Org. Chem. **61**, 1175 (1996).
5. R. Bosque, C. Lopez, J. Sales, and X. Solans. J. Organomet. Chem. **483**, 61 (1994).
6. A. Togni and R.L. Halterman. Metallocenes. Wiley-VCH, Weinheim, Germany. 1998.
7. R.W. Heo, F.B. Sonoza, and T.R. Lee. J. Am. Chem. Soc. **120**, 1621 (1998).
8. E. Stankovic, S. Toma, R.V. Boxel, I. Asselberghs, and A. Persoons. J. Organomet. Chem. **637–639**, 426 (2001).
9. L.M. Tolbert, X. Zhao, Y. Ding, and L.A. Bottomley. J. Am. Chem. Soc. **117**, 12891 (1995).
10. B. Bildstein, W. Skibar, M. Schweiger, H. Kapacka, and K. Wurst. J. Organomet. Chem. **622**, 135 (2001).
11. A.E. Kaifer and S. Mendoza. Comprehensive supramolecular chrmistry I. *Edited by* G.W. Gokel. Pergamon, Oxford. 1996.
12. A. Peruga, J.A. Mata, D. Sainz, and E. Periz. J. Organomet. Chem. **637–639**, 191 (2001).
13. A.N. Pushin, E.I. Klimova, and V.A. Sazonova. Russ. J. Gen. Chem. **59**, 1102 (1989).
14. E.G. Perevalova, E.I. Klimova, V.V. Kruchkova, and A.N. Pushin. Russ. J. Gen. Chem. **59**, 873 (1989).
15. V.N. Postnov, E.I. Klimova, A.N. Pushin, and N.N. Meleshonkova. Metalloorg. Khim. **4**, 116 (1991).
16. E.I. Klimova, A.N. Pushin, and V.A. Sazonova. J. Organomet. Chem. **270**, 319 (1984).
17. E.I. Klimova, L. Ruiz Ramirez, M. Martinez Garcia, P. G. Espinosa, and N.N. Meleshonkova. Russ. Chem. Bull. **45**, 2743 (1996).
18. E.I. Klimova, M. Martínez García, T. Klimova, C.T. Alvarez, R.A. Toscano, and L. Ruiz Ramirez. J. Organomet. Chem. **598**, 254 (2000).
19. I.D. Mendez, T. Klimova, E. Klimova; S.O. Hernandez, F.J. Perez, and M.G. Martinez. J. Organomet.Chem. **689**, 2503 (2004).
20. E.I. Klimova, T.B. Klimova, M. Martínez García, and L. Ruíz Ramírez. J. Organomet. Chem. **579**, 30 (1999).
21 E.I. Klimova, T.B. Klimova, M. Martínez García, and L. Ruíz Ramírez. Mendeleev Commun. 233 (1998).
22. E.I. Klimova, M. Martínez García, T. Klimova, and J.M. Mendez Stivalet. J. Organomet. Chem. **602**, 105 (2000).
23. E.I. Klimova, T. Klimova, J.M. Mendez Stivalet, C.T. Alvarez, R.A. Toscano, S.O. Hernandez, L. Ruíz Ramírez, L.V. Bakinovscky, and M.G. Martínez. Eur. J. Org. Chem. 1714 (2004).
24. E.I. Klimova, T.B. Klimova, J.M. Mendez Stivalet, R.A. Toscano, C.T. Alvarez, and M. Martínez García. J. Organomet. Chem. **689**, 3232 (2004).
25. L.E. Sutton (*Editor*). Tables of interatomic distances and configuration in molecules and ions. The Royal Chemical Society, London. 1965.
26. G.A. Olah and R.J. Spear. J. Am. Chem. Soc. **97**, 1539 (1975).
27. W.G. Young, S.U. Sharman, and S. Winstein. J. Am. Chem. Soc. **82**, 1376 (1960).
28. M.J.A. Habib, J. Park, and W.E. Watts. J. Chem. Soc. C, 2556 (1970).
29. G.A. Olah and M. Mayer. J. Am. Chem. Soc. **98**, 7333 (1976).
30. G.M. Sheldrick. SHELXL-97 [computer program]. Program for the Refinement of Crystal Structures. University of Göttingen, Germany. 1994.

[2] Supplementary data for this article are available on the journal Web site (canjchem.nrc.ca) or may be purchased from the Depository of Unpublished Data, Document Delivery, CISTI, National Research Council Canada, Ottawa, ON K1A 0R6, Canada. DUD 5210. For more information on obtaining material, refer to cisti-icist.nrc-cnrc.gc.ca/irm/unpub_e.shtml. CCDC 272999 for compound **6**, 273000 for compound **9**, 273001 for compound **11a**, and 273002 for compound **13** contain the crystallographic data for this manuscript. These data can be obtained, free of charge, via www.ccdc.cam.ac.uk/conts/retrieving.html (or from the Cambridge Crystallographic Data Centre, 12 Union Road, Cambridge CB2 1EZ, UK; fax +44 1223 336033; or deposit@ccdc.cam.ac.uk).

© 2007 NRC Canada

Coriolis coupling effects on energy transfer: classical-trajectories analysis for CO_2 + Ar collisions

E. Borges and J.P. Braga

Abstract: Energy transfer on CO_2 + Ar collisions is studied by performing classical-trajectories simulations in a non-rigid potential-energy surface. Partition of molecular kinetic energy into vibration, rotation, and Coriolis coupling is made in a Cartesian coordinates system, coupled to vibrational normal modes. Initial atomic translational energies are selected from a range of 0.004–0.4 au, and initial molecular rotational states are fixed at rotational quantum numbers *j*, equal to 1, 20, 40, and 60. Effects of these different initial conditions are investigated, and the Coriolis influence on the energy transferred is analyzed.

Key words: Coriolis coupling, energy, classical trajectories.

Résumé : On a étudié le transfert d'énergie lors de collisions de CO_2 + Ar en faisant appel à des simulations de trajectoires classiques dans une surface d'énergie potentielle non rigide. On a effectué la partition de l'énergie cinétique moléculaire en vibration, en rotation et en couplage de Coriolis dans un système de coordonnées cartésiennes couplé aux modes vibrationnels normaux. On a choisi les énergies de translation atomique initiales dans les valeurs allant de 0,004 à 0,4 au et on a fixé les états rotationnels moléculaires initiaux aux nombres quantiques rotationnels, j, 1, 20, 40 et 60. On a étudié les effets de ces conditions initiales diverses et on a analysé l'influence de Coriolis sur l'énergie qui est transférée.

Mots-clés : couplage de Coriolis, énergie, trajectoires classiques.

[Traduit par la Rédaction]

Introduction

Experimental and theoretical investigations about the rovibrational interaction in excited polyatomic molecules indicate that Coriolis coupling can account, in some cases, for more than 20% of the overall anharmonic correction for several medium-size molecules (1). In a dynamical process, the Coriolis coupling affects the intramolecular energy transfer, which cannot be characterized as vibrational or rotational energy.

For example, as discussed in ref. 2, close degenerate rovibrational levels of vibrationally excited polyatomic molecules were separated by Coriolis interactions during state-to-state energy transfer processes. A discrepancy between rotational energy transferred and collisional relaxation rates was attributed to the increase of vibrational energy transfer, caused by the Coriolis coupling. This effect is also responsible for the combination bands involving stretching and out-of-plane bending as discussed in ref. 3, in which a theoretical model was proposed to describe the interactions between (1,0,0) and (0,0,1) states of H_2O molecules. Therefore, the Coriolis coupling plays an important role in the energy transfer involving polyatomic molecules (4–6), and its quantification is essential for a complete energetic description of collisional processes. At the same time, particular attention has been devoted to interactions of CO_2 with rare-gas atoms. Several experimental and theoretical studies describing energetic effects and formation of CO_2–Ar clusters have been investigated in detail (7–10). However, there is no information about the Coriolis coupling effect in CO_2–Ar energetics. In a recent work, the Coriolis coupling influence on the rotational and vibrational energy transfer in H_2O + Ar collisions (11) was described by using a classical trajectory approach. The method proposed in ref. 11 is used in the present work to analyze effects of different rotational states and atomic translational energies on the energy transfer because of CO_2 + Ar collisions. The molecular kinetic energy is partitioned into vibrational, rotational, and Coriolis components. The relative importance of the Coriolis coupling is analyzed in the present study.

Received 3 April 2007. Accepted 22 August 2007. Published on the NRC Research Press Web site at canjchem.nrc.ca on 17 October 2007.

E. Borges and J.P. Braga.[1] Departamento de Química, ICEx Universidade Federal de Minas Gerais, Belo Horizonte 31270–901, MG, Brasil.

[1]Corresponding author (e-mail: jpbraga@ufmg.br).

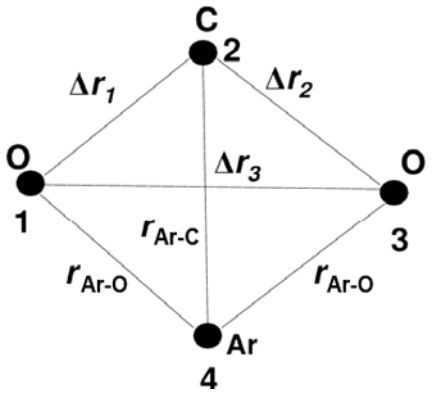
Computational method

Potential-energy surface

A fourth-order anharmonic potential surface, based on spectroscopic data, is used to describe the CO_2 molecule,

 doi:10.1139/V07-113 © 2007 NRC Canada

Fig. 1. Internuclear coordinates in the CO_2–Ar collision system.



$$[1]\quad V_{(\Delta r_1,\Delta r_2,\Delta r_3)} = f_{11}(\Delta r_1^2 + \Delta r_2^2) + f_{12}\Delta r_1\Delta r_2 + f_{\alpha\alpha}\Delta r_3^2 + f_{111}(\Delta r_1^3 + \Delta r_2^3) + f_{112}(\Delta r_1^2\Delta r_2 + \Delta r_1\Delta r_2^2) + f_{1\alpha\alpha}(\Delta r_1 + \Delta r_2)\Delta r_3^2 + f_{1111}(\Delta r_1^4 + \Delta r_2^4) + f_{1112}(\Delta r_1^3\Delta r_2 + \Delta r_1\Delta r_2^3) + f_{1122}\Delta r_1^2\Delta r_2^2 + f_{11\alpha\alpha}(\Delta r_1^2 + \Delta r_2^2)\Delta r_3^2 + f_{12\alpha\alpha}\Delta r_1\Delta r_2\Delta r_3^2 + f_{\alpha\alpha\alpha\alpha}\Delta r_3^4$$

The force constants are f_{11} = 0.5148, f_{12} = 0.0814, $f_{\alpha\alpha}$ = 0.0901, f_{111} = −0.6498, f_{112} = −0.0515, $f_{1\alpha\alpha}$ = −0.0747, f_{1111} = −0.4652, f_{1112} = −0.0429, f_{1122} = −0.1066, $f_{1\alpha\alpha 2}$ = 0.5139, $f_{11\alpha\alpha}$ = 0.2281, and $f_{\alpha\alpha\alpha\alpha}$ = −0.014; unit is au (12). Also, the internal coordinates Δr_1, Δr_2, and Δr_3 are generated in atomic units (au). Interactions between CO_2 and Ar are described by a Buckingham-form pair potential (13), which is written as

$$[2]\quad V_{\text{pair}} = \frac{6\varepsilon e^{\lambda(1-r/r_m)}}{\lambda - 6} - \frac{\lambda\varepsilon}{\lambda - 6}\left(\frac{r_m}{r}\right)^6$$

The pairwise potential parameters are $\varepsilon = 0.34 \times 10^{-3}$ au, r_m = 7.20 au, and λ = 1.70 for Ar–C; and $\varepsilon = 0.29 \times 10^{-3}$ au, r_m = 6.80 au, and λ = 1.50 for Ar–O in which ε and r_m are the potential's well depth and equilibrium distances, respectively. Figure 1 shows the internuclear coordinates used in the potential-energy surface for the CO_2–Ar system.

Initial conditions

Cartesian coordinates, coupled to vibrational normal modes, are used. The transformation between vibrational normal modes and Cartesian coordinates can be obtained by the matrix equation proposed by Crawford and Fletcher (14, 15)

$$[3]\quad \Delta u = M^{\frac{1}{2}}\tilde{B}G^{-1}LQ$$

in which Δu represents the displacements Cartesian coordinates, Q represents the normal coordinates, and M is a diagonal matrix that contains the mass factor of each particle. The vibrational matrices L, B, and G are related to molecular masses and geometries (16). Defining $m_T = m_C$ (carbon mass) + m_O (oxygen mass), fixing the molecule on the z axis, and using eq. [3], the molecule-fixed Cartesian coordinates for the CO_2 molecule are obtained as

$$[4]\quad z_1 = -\frac{1}{\sqrt{2m_O}}Q_1 - \sqrt{\frac{m_C}{2m_O m_T}}Q_3 + z_{1e}$$

$$z_2 = \sqrt{\frac{2m_O}{m_C m_T}}Q_3$$

$$z_3 = \frac{1}{\sqrt{2m_O}}Q_1 - \sqrt{\frac{m_C}{2m_O m_T}}Q_3 - z_{3e}$$

$$y_1 = -\sqrt{\frac{m_C}{2m_O m_T}}Q_{2a}$$

$$y_2 = \sqrt{\frac{2m_O}{m_C m_T}}Q_{2a}$$

$$y_3 = -\sqrt{\frac{m_C}{2m_O m_T}}Q_{2a}$$

$$x_1 = -\sqrt{\frac{m_C}{2m_O m_T}}Q_{2b}$$

$$x_2 = \sqrt{\frac{2m_O}{m_C m_T}}Q_{2b}$$

$$x_3 = -\sqrt{\frac{m_C}{2m_O m_T}}Q_{2b}$$

in which $z_{1e} = z_{3e}$ = 4.14 au are the equilibrium coordinates and Q_1, Q_{2a}, Q_{2b}, and Q_3 are the symmetrical, bending, and unsymmetrical normal modes (the bending mode, Q_2, is degenerate in two components Q_{2a} and Q_{2b}), respectively. If Ev_i is the spectroscopic vibrational energy, the normal coordinates are generated as

$$[5]\quad Q_i(t) = (2Ev_i/\lambda_i)^{1/2}\cos(\lambda^{1/2}{}_i + \sigma_i) \qquad i = 1,\ 2a,\ 2b,\ 3$$

in which $\lambda_i = 4\pi^2\upsilon_i^2$; υ_i are the vibrational frequencies, σ_i are arbitrary phase factors, $0 \le \sigma_i \le 2\pi$, which are randomly selected from $\sigma_i = 2\pi\xi_i$. The random numbers ξ_i are uniformly distributed between 0 and 1. If r_{kl} is the distance between the nuclei k and l, the potential energy surface can be described in relation to internuclear distances, $R_{kl} = [(x_k - x_1)^2 + (y_k - y_1)^2 + (z_k - z_1)^2]^{1/2}$. Defining b as the impact parameter selected from $b = b_{max}\,\xi_b{}^{1/2}$ and choosing r_{max} large enough to make the atom–molecule interaction negligible, the atomic position can be generated as

$$[6]\quad x_{Ar} = 0$$

$$y_{Ar} = b$$

$$z_{Ar} = -(r^2{}_{max} - b^2)^{1/2}$$

In this study, b_{max} = 9.45 au and r_{max} = 18.90 au. The molecular kinetic energy is $E_{kin} = E_{vib} + E_{rot} + E_{Cor}$ in which E_{vib},

© 2007 NRC Canada

E_{rot}, and E_{Cor} are the vibrational, rotational, and Coriolis terms, respectively. These components are defined in Cartesian coordinates as

$$[7] \qquad E_{\text{vib}} = \frac{1}{2}\sum_{1}^{3}(p_{ix}^2 + p_{iy}^2 + p_{iz}^2)$$

$$[8] \qquad E_{\text{rot}} = \frac{1}{2}\sum_{1}^{3}\begin{bmatrix} m_i\omega_x^2(z_i + y_i)^2 + m_i\omega_y^2(z_i + x_i)^2 + m_i\omega_z^2(x_i + y_i)^2 \\ -2m_i(\omega_x\omega_z x_i z_i + \omega_x\omega_x x_i y_i + \omega_x\omega_x y_i z_i) \end{bmatrix}$$

$$[9] \qquad E_{\text{Cor}} = \omega_x\sum_{1}^{3}[m_i(\Delta y_i\dot{z}_i - \dot{y}_i\Delta z_i)] + \omega_y\sum_{1}^{3}[m_i(\Delta z_i\dot{x}_i - \dot{z}_i\Delta x_i)] + \omega_z\sum_{1}^{3}\sum_{1}^{3}[m_i(\Delta x_i\dot{y}_i - \dot{x}_i\Delta y_i)]$$

in which p_{ix}, p_{iy}, and p_{iz} are the linear moments and ω_x, ω_y, and ω_z are the angular velocities. The symbol delta represents the possible displacements from the equilibrium position for each coordinate. The linear moments can be calculated by the temporal derivative of the kinetic energy in Cartesian coordinates, i.e,

$$[10] \qquad p_{z_i} = \sum_{i=1}^{3} m_i\dot{z}_i + \omega_x\sum_{i=1}^{3} m_i\Delta z_i - \omega_y\sum_{i=1}^{3} m_i\Delta x_i$$

$$p_{y_i} = \sum_{i=1}^{3} m_i\dot{y}_i - \omega_x\sum_{i=1}^{3} m_i\Delta z_i + \omega_z\sum_{i=1}^{3} m_i\Delta x_i$$

$$p_{x_i} = \sum_{i=1}^{3} m_i\dot{x}_i + \omega_x\sum_{i=1}^{3} m_i\Delta z_i - \omega_z\sum_{i=1}^{3} m_i\Delta y_i$$

By using the relations in eq. [4], the linear momenta can be rewritten as

$$[11] \qquad p_{z_1} = -\frac{m_{\text{O}}}{(2m_{\text{O}})^{1/2}}\dot{Q}_1 - \left(\frac{m_{\text{O}}m_{\text{C}}}{2m_{\text{T}}}\right)^{1/2}\dot{Q}_3 - \omega_y\left(\frac{m_{\text{O}}m_{\text{C}}}{2m_{\text{T}}}\right)^{1/2}Q_{2\text{a}} - \omega_x\left(\frac{m_{\text{O}}m_{\text{C}}}{2m_{\text{T}}}\right)^{1/2}Q_{2\text{b}}$$

$$p_{z_2} = \left(\frac{2m_{\text{O}}m_{\text{C}}}{m_{\text{T}}}\right)^{1/2}\dot{Q}_3 - \omega_y\left(\frac{2m_{\text{O}}m_{\text{C}}}{2m_{\text{T}}}\right)^{1/2}Q_{2\text{a}} - \omega_x\left(\frac{2m_{\text{O}}m_{\text{C}}}{m_{\text{T}}}\right)^{1/2}Q_{2\text{b}}$$

$$p_{z_3} = \frac{m_{\text{O}}}{(2m_{\text{O}})^{1/2}}\dot{Q}_1 - \left(\frac{m_{\text{O}}m_{\text{C}}}{2m_{\text{T}}}\right)^{1/2}\dot{Q}_3 - \omega_y\left(\frac{m_{\text{O}}m_{\text{C}}}{2m_{\text{T}}}\right)^{1/2}Q_{2\text{a}} + \omega_x\left(\frac{m_{\text{O}}m_{\text{C}}}{2m_{\text{T}}}\right)^{1/2}Q_{2\text{b}}$$

$$p_{y_1} = -\left(\frac{m_{\text{O}}m_{\text{C}}}{2m_{\text{T}}}\right)^{1/2}\dot{Q}_{2\text{b}} - \omega_x\frac{m_{\text{O}}}{(2m_{\text{O}})^{1/2}}\dot{Q}_1 - \omega_x\left(\frac{m_{\text{O}}m_{\text{C}}}{m_{\text{T}}}\right)^{1/2}Q_3$$

$$p_{y_2} = \left(\frac{2m_{\text{O}}m_{\text{C}}}{m_{\text{T}}}\right)^{1/2}\dot{Q}_{2\text{b}} + \omega_x\left(\frac{2m_{\text{O}}m_{\text{C}}}{m_{\text{T}}}\right)^{1/2}Q_3$$

$$p_{y_3} = -\left(\frac{m_{\text{O}}m_{\text{C}}}{2m_{\text{T}}}\right)^{1/2}\dot{Q}_{2\text{b}} + \omega_x\frac{m_{\text{O}}}{(2m_{\text{O}})^{1/2}}Q_1 - \omega_x\left(\frac{m_{\text{O}}m_{\text{C}}}{2m_{\text{T}}}\right)^{1/2}Q_3$$

$$p_{x_1} = -\left(\frac{m_{\text{O}}m_{\text{C}}}{2m_{\text{T}}}\right)^{1/2}\dot{Q}_{2\text{a}} + \omega_y\frac{m_{\text{O}}}{(2m_{\text{O}})^{1/2}}Q_1 + \omega_y\left(\frac{m_{\text{O}}m_{\text{C}}}{2m_{\text{T}}}\right)^{1/2}Q_3$$

$$p_{x_2} = \left(\frac{2m_{\text{O}}m_{\text{C}}}{m_{\text{T}}}\right)^{1/2}\dot{Q}_{2\text{a}} - \omega_y\left(\frac{2m_{\text{O}}m_{\text{C}}}{m_{\text{T}}}\right)^{1/2}Q_3$$

$$p_{x_3} = -\left(\frac{m_{\text{O}}m_{\text{C}}}{2m_{\text{T}}}\right)^{1/2}\dot{Q}_{2\text{a}} - \omega_y\frac{m_{\text{O}}}{(2m_{\text{O}})^{1/2}}Q_1 + \omega_y\left(\frac{m_{\text{O}}m_{\text{C}}}{2m_{\text{T}}}\right)^{1/2}Q_3$$

© 2007 NRC Canada

in which

$$[12]\quad \dot{Q}_1 = P_1 = (2Ev_i - \lambda_1 Q_1^2)^{1/2}$$

$$\dot{Q}_{2a} = P_{2a} - \omega_y Q_3 + \omega_z Q_{2b} = (2Ev_{2a} - \lambda_2 Q_{2a}^2)^{1/2} - \omega_y Q_3$$

$$\dot{Q}_{2b} = P_{2b} - \omega_x Q_3 - \omega_z Q_{2a} = (2Ev_{2b} - \lambda_2 Q_{2b}^2)^{1/2} - \omega_x Q_3$$

$$\dot{Q}_3 = P_3 - \omega_x Q_{2b} + \omega_y Q_{2a} = (2Ev_3 - \lambda_2 Q_3^2)^{1/2} - \omega_x Q_{2b} + \omega_x Q_{2a}$$

are the momenta conjugate to the normal modes.

The molecular kinetic energy can also be written as

$$[13]\quad 2E_{kin} = I_{xx}\omega_x^2 + I_{yy}\omega_y^2 - 2I_{xy}\omega_x\omega_y + \dot{Q}_1^2 + \dot{Q}_{2a}^2 + \dot{Q}_{2b}^2 + \dot{Q}_3^2 + 2\omega_x(Q_{2a}\dot{Q}_3 - Q_3\dot{Q}_{2a}) + 2\omega_y(Q_3\dot{Q}_{2b} - Q_{2b}\dot{Q}_3)$$

in which I_{xx}, I_{yy}, and I_{xy} are the moments of inertia. The center of mass of the system atom–molecule does not move with the time in the space-fixed system, and the molecular translational energy is zero. The atom moves toward the molecule with velocity equal to

$$[14]\quad V_{Ar} = \left(\frac{m_T}{m_T + m_{Ar}}\right) V_R$$

in which V_R is the relative velocity between the atom and the molecule, obtained from the initial collisional energy.

Final conditions

The molecule-fixed coordinates are randomly transformed to space-fixed coordinates, i.e., laboratory referential, through Euler's angles and for a given potential surface configuration, initial coordinates, and linear moments, the Hamilton's equations are integrated. A Runge–Kutta algorithm of fifth and sixth order was used as numerical integrator of the classical coupled equations of motion. All the trajectories were checked to produce relative errors of 10^{-4}% in the energy conservation during the integration. Final conditions are established by the final coordinates and linear moments after removing the center of mass motion (17), and final energies are calculated as in eqs. [7–9] in the molecule-fixed coordinates. For each set of 2000 trajectories, the average energy transferred was computed. This number of trajectories is sufficient to produce converged results to the energy transfer, i.e., the average energy transferred after 2000 trajectories or 2500 trajectories gives identical results within six significant figures.

Results and discussion

The transformation between Cartesian and normal coordinates described in eq. [3] is valid in the harmonic limit and can provide reliable results if the total molecular energy is not too large (18). By taking the higher molecular energetic states used in this work, together with eqs. [4] and [5], one obtains the correspondent Cartesian-coordinates values. The harmonic contribution can be obtained from these values and represents about 95.0% of the total intramolecular potential along the trajectories performed. Therefore, the partition of the internal energy into vibrational, rotational, and Coriolis, as in eq. [12], gives reliable results. Also, the present results can provide insights into the rovibrational coupling and rotational contribution to the molecular activation of CO_2 molecules by Ar. Atomic translational energies used in this work were taken from a range of 0.004–0.4 au. Values of molecular initial rotational states were fixed at rotational quantum numbers j, equal to 1, 20, 40, and 60. Initial vibrational levels were fixed in the ground vibrational state, i.e., vibrational quantum numbers n_1, n_{2a}, n_{2b}, and n_3 were equal to zero.

Time evolution of vibrational, rotational, and Coriolis molecular components, as a function of different rotational states, is simulated for the isolated molecule, without collision with the Ar atom, as shown in Fig. 2. Coriolis and rotational components are strongly mixed in low rotational states, $j = 1$. For rotational states corresponding to $j = 20$ and $j = 40$, Coriolis and rotational components are decoupled, and the increase in rotational activation energy is greater than Coriolis activation. Rotational and vibrational components are coupled for $j = 60$.

Atomic translational energy transferred into vibrational, rotational, and Coriolis molecular components are presented in Fig. 3. For all initial conditions used, the process was characterized by molecular activation. In some cases, vibrational and rotational deactivations are observed, although the overall effect was a molecular activation. This effect was attributed to high Coriolis activation, which is greater than total rovibrational deactivation in these cases. Results for the energy transfer, by fixing the initial vibrational energies in the ground state and initial rotational energies corresponding to $j = 1$ and $j = 20$, are presented in Figs. 3*a* and 3*b*. There are two regimes, which characterize the effect of atomic collisional energies on the vibrational, rotational, and Coriolis components during the CO_2 + Ar process:

(*i*) Collisional energy equal to 0.004–0.04 au, $j = 1$, and $j = 20$. Molecular activation is effective, since both rotational and Coriolis activation exceed the vibrational deactivation. Coriolis activation is greater than rotational activation, and T–C (translation to Coriolis), T–R (translation to rotation), V–R (vibration to rotation), and V–C (vibration to Coriolis) are the observed channels of energy transfer.

(*ii*) Collisional energy in the range of 0.08–0.4 au, $j = 1$, and $j = 20$. Coriolis, rotational, and vibrational activa-

© 2007 NRC Canada

Fig. 2. Time evolution of the intramolecular energies for the molecule isolated. Vibrational states, n_1, n_{2a}, n_{2b}, and n_3 are equal to zero; and rotational states, j, are in the range of 1–60. (a) j = 1, (b) j = 20, (c) j = 40, and (d) j = 60.

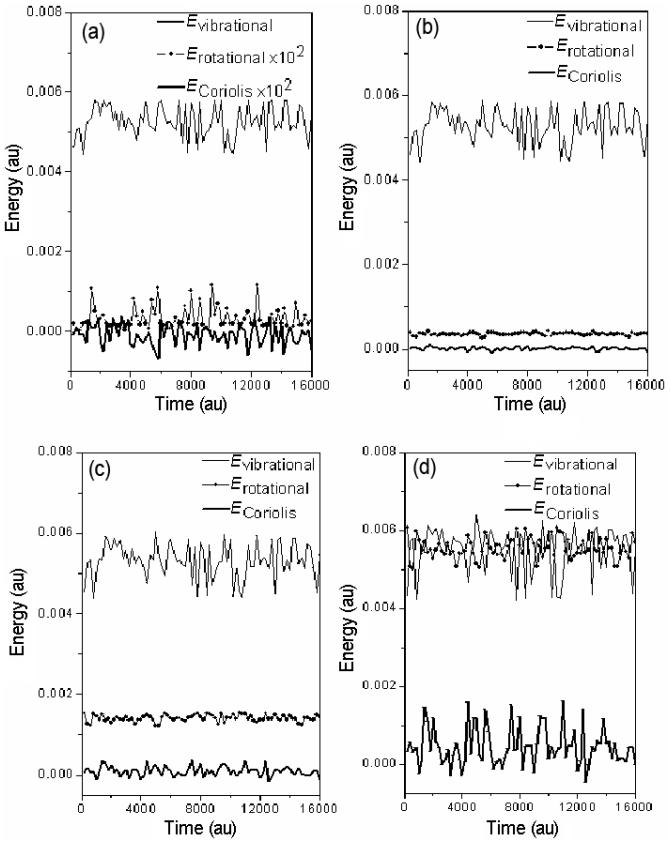
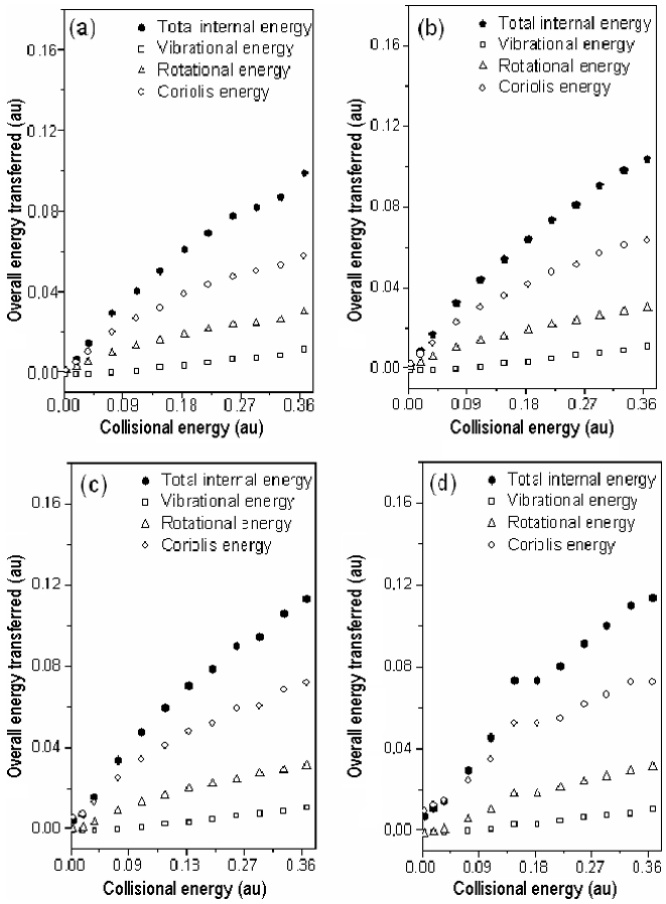


Fig. 3. Overall energy transferred for the CO_2 + Ar collisions. Vibrational states, n_1, n_{2a}, n_{2b}, and n_3 are equal to zero; and rotational states, j, are in the range of 1–60. (a) j = 1, (b) j = 20, (c) j = 40, and (d) j = 60.



tion is observed in this case. The main processes are T–C, T–R, and T–V (translation to vibration). The Coriolis activation is greater than rotational and vibrational activation. The sudden limit, in which the collision time decreases with the increasing of collisional energy, is reached.

Results obtained for vibrational energies in the ground state, for different collisional energies and rotational energies corresponding to j = 40 and j = 60 are presented in Figs. 3c and 3d. The following regimes characterize the influence of collisional energies on intramolecular energy transfer:

(*i*) Collisional energy equal to 0.004 au, and j = 40. Vibrational and rotational deactivations are observed. The vibrational deactivation is greater than rotational deactivation. However, the Coriolis activation exceeds the deactivations, and a molecular activation is reached. Therefore, one can observe the following processes as the dominant ones: T–V, V–C, and R–C (rotation to Coriolis). These results indicate that the molecular rotational energy decreases after the collision, even for j = 40, and this fact can be partially attributed to rotational energy flux to the Coriolis coupling.

(*ii*) Collisional energy equal to 0.02–0.08 au, and j = 40. Vibrational deactivation is present, but rotational and Coriolis activations are present. As a global process, molecular activation is observed. The dominant channels are T–V, V–C, and V–R.

(*iii*) Collisional energy in the range of 0.16–0.40 au, and j = 40. Vibrational, rotational, and Coriolis activation are obtained together with the processes T–V, V–C, and V–R.

(*iv*) Collisional energy equal to 0.004 and 0.02 au, and j = 60. Vibrational and rotational deactivations are obtained. For the collision energy equal to 0.004 au, the rotational deactivation is greater than vibrational deactivation. Again, molecular activation is observed because of Coriolis activation. These regimes are characterized by the channels T–V, V–C, and R–C.

(*v*) Collisional energy of 0.04 au, and j = 60. Vibrational deactivation, rotational and Coriolis activation take place together with global molecular activation. The main processes are T–V, V–C, and V–R.

(*vi*) Collisional energy in the range of 0.08–0.4 au, and j = 60. Vibrational, rotational, and Coriolis activation are observed, and the main energy channels are T–V, V–C, and V–R. The sudden limit is reached.

The results presented here for the energy transferred are in agreement with previous works concerning this system (17). On the other hand, our results show the fundamental role played by the Coriolis coupling in the energetics of the

© 2007 NRC Canada

CO_2 + Ar system. The characterization of energy-transfer channels can be totally different if this coupling is not considered. For example, in ref. 17, it was proposed that most of translational energy absorbed by the molecule during the CO_2 + Ar collision was stored in the vibrational modes. After the collision, this stored energy will flow back to the atomic translational energy. However, our results suggest that the Coriolis coupling is the main drain of vibrational energy for low energetic states.

Another different point between this work and ref. 17 is the independence of the mechanism T–V with respect to the initial rotational states of the molecule, as discussed in ref. 17. However, if the Coriolis coupling is considered, the mechanism T–V is influenced by the initial rotational states, as presented in Fig. 3 and discussed before. The Coriolis component acts as an intermediate channel to the energy flux among the intramolecular components of the kinetic energy. A similar result has been also observed for the H_2O + Ar system (11), and the Coriolis coupling seems to be general and important for different noble gas atom – triatomic systems. Therefore, essential subtleties of energy-transfer processes can be missed if a rigid approximation is used. The active degrees of freedom in this analysis are the vibrational and rotational components, since translational motions are removed when the process is finished. In the initial conditions, the molecule was fixed on the z axis, but in the final conditions, the three components of the angular momentum are present. Therefore, the expression for the rovibrational coupling is

$$[15] \quad E_{\mathrm{Cor}} = 2\omega_x(Q_{2a}\dot{Q}_3 - \dot{Q}_3\dot{Q}_{2a}) + 2\omega_y(Q_3\dot{Q}_{2b} - Q_{2b}\dot{Q}_3) + 2\omega_z(Q_{2a}\dot{Q}_{2b} - Q_{2b}\dot{Q}_{2a})$$

Analysis of Coriolis coupling can be inferred from eq. [15]. Since $\dot{Q}_1$ does not contain terms in angular velocities, as written in eq. [12], one may conclude that $\dot{Q}_1$ is not important for the Coriolis coupling. This is in fact the case, as eq. [15] implies. Although one might expect that Coriolis coupling will be more effective for higher vibrational or rotational states, this assumption is clearly invalid if the Q_1 mode is excited for the CO_2 molecule. Coupling between vibrational and rotational degrees of freedom is caused by the asymmetric and bending normal modes.

Conclusion

The classical-trajectory approach has been used to analyze the Coriolis coupling on the rotational and vibrational energy transfer for CO_2 + Ar collisions. The molecular kinetic energy was partitioned in vibrational, rotational, and Coriolis components by using a Cartesian coordinates system coupled to vibrational normal modes. Collisional energies selected from a range of 0.004–0.4 au and initial rotational states corresponding to quantum numbers j in the range 1–60 were used as initial conditions. Molecular activation takes place for all energetic states analyzed. However, different intramolecular energies channels are observed. In some cases, molecular activation was observed even with vibrational and rotational deactivation, and this was attributed to Coriolis activation.

The Coriolis and rotational components are superimposed at low rotational states. For low collisional energies, the Coriolis coupling is the main drain of vibrational energy, and molecular activation becomes more important for higher collisional energies. The Coriolis activation is greater than rotational activation for all energies studied. As a general conclusion, the Coriolis coupling plays a fundamental role on the vibrational and rotational energy transfer mechanisms and should be quantified in a complete classical dynamics simulation for the CO_2–Ar system.

Acknowledgements

This work was supported by Conselho Nacional de Desenvolvimento Científico e Tecnológico (CNPq) and Fundação de amparo à pesquisa do estado de Minas Gerais (FAPEMIG).

References

1. P. Carbonniere and V. Barone. Chem. Phys. Lett. **392**, 365 (2004).
2. O.L. Polyansky, N.F. Zobov, S.Viti, J.Tennyson, P.F. Bernath, and L.Wallace. J. Mol. Spec. **186**, 422 (1997).
3. V.I. Starikov. J. Mol. Struct. **384**, 73 (1996).
4. J.G. Haub, B.J. Orr. J. Chem. Phys. **86**, 3380 (1987).
5. C.P. Bewick, J.F. Martins, and B.J. Orr. J. Chem. Phys. **93**, 8643 (1990).
6. R. Parson. J. Chem. Phys. **92**, 304 (1990).
7. J.C. Belchior, J.P. Braga, and N.H.T. Lemes. Can. J. Chem. **79**, 211 (2001).
8. J.C. Belchior, N.H.T. Lemes, and J.P. Braga. Phys. Chem. Chem. Phys., **1**, 23 (1999).
9. M. Boyukata, E. Borges, J.P.Braga, and J.C.Belchior. Can. J. Chem. **85**, 47 (2007).
10. J.Thiévin, Y. Cadudal, R. Georges, and A.A. Vigasin, J. Mol. Spect. **240**, 141 (2006).
11. E. Borges, G.G. Ferreira, J.P. Braga, and J.C. Belchior. Int. J. Quantum. Chem. **106**, 2643 (2006).
12. M.A. Pariseau, I. Suzuki, and J. Overend. J. Chem. Phys. **42**, 2335 (1965).
13. M.B. Sevryuk nand G.D. Billing. Chem. Phys. **185**, 199 (1994).
14. B.L Crawford and W.H. Fletcher. J. Chem. Phys. **20**, 141 (1950).
15. E. Borges, J.P. Braga, and J.C. Belchior. Quim. Nova, **30**, 497 (2007).
16. E.B. Wilson, J.C. Decius, and P.C. Cross. Molecular vibrations: the theory of infrared and raman vibrational spectra. McGraw-Hill Book Company, New York. 1955.
17. H.H. Suzukawa and M. Wolfsberg. J. Chem. Phys. **68**, 455 (1978).
18. T. Yan and W.L. Hase. J. Phys. Chem. A, **105**, 2617 (2001).

© 2007 NRC Canada

Ceric-sulfate-catalyzed synthesis of 14-aryl- or 14-alkyl-14*H*-dibenzo[*aj*]xanthene under conventional heating and microwave irradiation

Nagarajan Panneer Selvam, Gnanamani Shanthi, and Paramasivan T. Perumal

Abstract: A simple and facile procedure for the synthesis of 14-aryl- or 14-alkyl-14*H*-dibenzo[*aj*]xanthenes is described. The procedure takes place by the one-pot condensation of 2-naphthol with aldehydes in the presence of anhydrous ceric sulfate as the catalyst under solvent-free conventional heating and microwave irradiation.

Key words: xanthene, one-pot condensation, aldehyde, 2-naphthol, ceric sulfate, solvent-free, microwave irradiation.

Résumé : On a mis au point une méthode simple et efficace d'effectuer la synthèse de 14-aryl- ou 14-alkyl-14*H*-dibenzo[*aj*]xanthènes qui implique une réaction de condensation monotope du 2-naphtol avec des aldéhydes en présence de sulfate cérique anhydre agissant comme catalyseur, en l'absence de solvant et faisant appel à des chauffages conventionnels ou des irradiations de microondes.

Mots-clés : xanthène, condensation monotope, aldéhyde, 2-naphtol, sulfate cérique, sans solvant, irradiation de microondes.

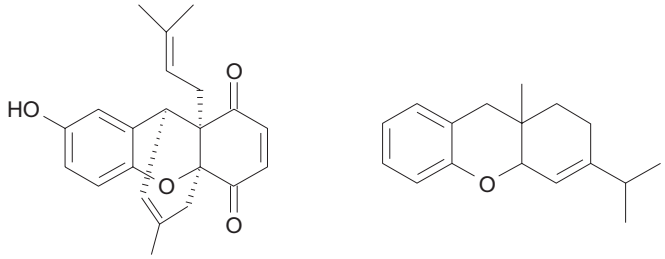
[Traduit par la Rédaction]

Introduction

Recently, much attention has been focused on the synthesis of aryl-14*H*-dibenzo[*aj*]xanthenes because of their significant biological activities as antibacterials (1), antivirals (2), anti-inflammatory agents (3), in photodynamic therapy (4), and for their role as antagonists of the paralyzing action of zoxazolamine (5). Xanthene-based compounds have also been investigated for agricultural bactericide activity, and some other benzoxanthenes find applications in industries, such as dyes in laser technology (6) and fluorescent materials for visualization of biomolecules (7). A number of xanthene-based skeletons are also available from natural sources; for example, tetrahydroxanthene **1**, ehretianone **2** (Fig. 1), and santalin pigments have been isolated from a number of plant species (8).

Various procedures have been reported for the synthesis of xanthene derivatives, including the reaction of aryloxy magnesium halides with triethyl orthoformate (9), cyclodehydration (10), trapping of benzynes by phenols (11), intramolecular phenyl carbonyl coupling reaction of benzaldehyde and acetophenones (12), cyclization of polycyclic aryl triflate esters (13), and cyclocondensation between 2-hydroxy aromatic aldehydes and 2-tetralones (14). Additionally, 14*H*-dibenzoxanthenes and its analogues are prepared by the reaction of 2-naphthol with 2-naphthol-1-methanol (15), formamide (16), carbon monoxide (17), and aldehyde acetals (18). Khosropour et al. (19) reported the synthesis of alkyl-14*H*-dibenzo[*aj*]xanthenes from aldehydes, β-naphthol, and *p*-toluenesulfonic acid in 1,2-dichloroethane as solvent and under solvent-free condition. The reaction required extended time as long as 2.5–24 h, and yields of some of the products were not satisfactory. Hence, practical methods of obtaining benzoxanthenes are of great interest in the lead optimization process of drug discovery.

Fig. 1. Examples of xanthene derivatives.



1 **2**

To avoid these limitations, we have started the search for a new catalyst with high catalytic activity and non-hazardous method with shorter reaction time involving simple work-up procedure. Recent literature has shown considerable interest in the use of Ce(IV) reagents, especially cerium(IV) ammonium nitrate (CAN) (20), in the construction of carbon–carbon and carbon–heteroatom bonds. The use of Ce(IV) sulfate (21) as Lewis acid catalyst is very scarce.

As part of our research program directed towards the development of highly expedient methods and the syntheses of diverse heterocyclic compounds of biological significance (22), we herein disclose a new, convenient, and one-pot synthesis of aryl-14*H*-dibenzo[*aj*]xanthene and alkyl-14*H*-

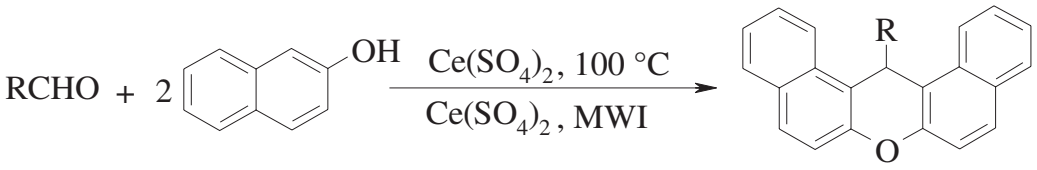
Received 21 June 2007. Accepted 20 August 2007. Published on the NRC Research Press Web site at canjchem.nrc.ca on 17 October 2007.

N.P. Selvam, G. Shanthi, and P.T. Perumal.[1] Organic Chemistry Division, Central Leather Research Institute, Chennai 600 020, India.

[1]Corresponding author (e-mail: ptperumal@gmail.com).

 doi:10.1139/V07-116 © 2007 NRC Canada

Scheme 1. Synthesis of 14*H*-dibenzoxanthene.



Scheme 2. Synthesis of acetamidophenol.

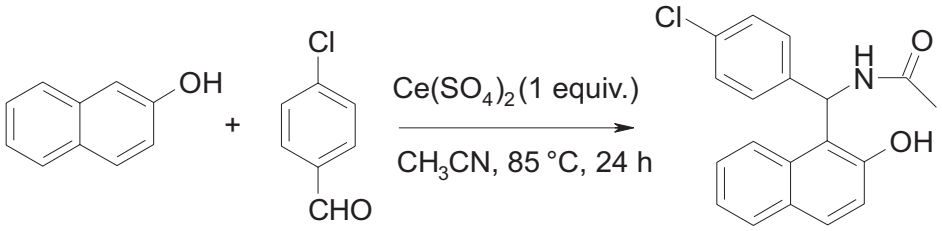


Table 1. Screening of various solvents.

Entry	Solvent	Time (h)	Yield (%)[a]
1	Dichloroethane	4	70
2	Toluene	4	72
3	Acetonitrile	24	5
4	Methanol	8	75
5	1,4-Dioxane	4	80
6	Neat	2	85

Note: Reactions were carried out in 2 mmol scale.
[a]Isolated yields.

Table 2. Optimization of the reaction conditions.

Entry	Catalyst (equiv.)	Time (h)	Yields (%)[a]
1	1	2	85
2	0.5	2	88
3	0.4	2	90
4	0.3	2	94
5	0.2	2	94
6	0.1	2	88

Note: Reactions were carried out in 2 mmol scale.
[a]Isolated yields.

dibenzo[*aj*]xanthene from aldehydes and β-naphthol catalyzed by $Ce(SO_4)_2$ under solvent-free conventional and microwave conditions in excellent yields (Scheme 1).

Results and discussion

This work is an extension of our previous results describing the synthesis of acetamidophenols (23) by Ritter-type reaction from 2-naphthol and araldehydes in acetonitrile in the presence of anhyd. $Ce(SO_4)_2$, where acetonitrile is involved in the reaction sequence as a nucleophile (Scheme 2).

In an initial endeavor, we carried out the reaction of 2-naphthol with 4-chlorobenzaldehyde in the presence of one equiv. of the catalyst under different reaction conditions using various solvents (Table 1). Excellent results were obtained when the reaction was carried out neat. Similarly, the mole ratio of $Ce(SO_4)_2$ was studied, and the results are listed in Table 2. It was found that the amount of $Ce(SO_4)_2$ affects the yield of the product, with 20 mol% of $Ce(SO_4)_2$ being optimum (Scheme 3).

The substrate scope of the reaction under the optimized conditions was investigated, and the results were summarized in Table 3. The reaction was amenable to a wide variety of substituents on araldehydes. The nature of functional groups on the aromatic ring of the aldehyde exerted a strong influence on the reaction time. An increase in the reaction rate was observed with aryl aldehydes bearing electron-withdrawing group.

The reaction with pyrazolyl aldehyde afforded new pyrazolyl xanthene in good yield (Scheme 4). The structure of the product **3** was confirmed by single crystal X-ray analysis (Fig. 2) and spectral data.[2]

Encouraged by these results, we extended our protocol by using substituted phenols (e.g., 4-methoxyphenol, 4-chlorophenol, 3-nitrophenol, and 1-naphthol) instead of 2-naphthol. The reactions were very sluggish, and no product formation was observed.

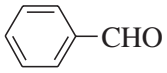
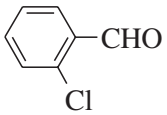
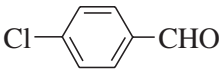
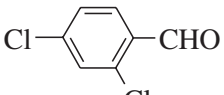
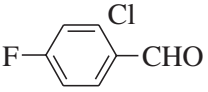
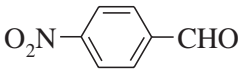
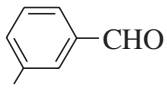
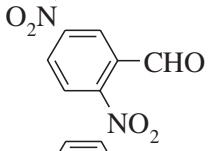
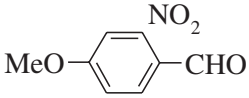
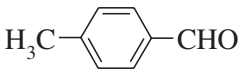
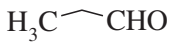
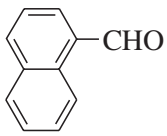
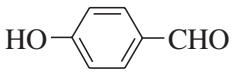
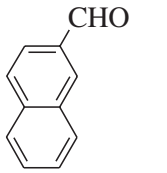
Conclusion

In summary, we have developed a convenient and efficient method for the synthesis of aryl- or alkyl-14*H*-dibenzo[*aj*]xanthenes, via three-component reaction offering various advantages, such as shorter reaction time, milder condition, high yield, general applicability, and the use of inexpensive and commercially available cerium(IV)sulfate.

[2] Supplementary data for this article are available on the journal Web site (canjchem.nrc.ca) or may be purchased from the Depository of Unpublished Data, Document Delivery, CISTI, National Research Council Canada, Ottawa, ON K1A 0S2, Canada. DUD 5223. For more information on obtaining material, refer to cisti-icist.nrc-cnrc.gc.ca/irm/unpub_e.shtml. CCDC 654516 contains the crystallographic data for this manuscript. These data can be obtained, free of charge, via www.ccdc.cam.ac.uk/conts/retrieving.html (Or from the Cambridge Crystallographic Data Centre, 12 Union Road, Cambridge CB2 1EZ, UK; fax +44 1223 336033; or deposit@ccdc.cam.ac.uk).

© 2007 NRC Canada

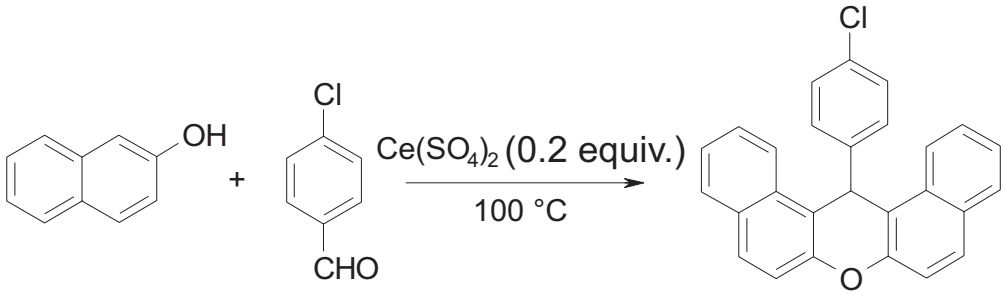
Table 3. Syntheses of various substituted 14-aryl- and 14-alkyl-14*H*-dibenzo[*aj*]xanthenes.

Entry	Aldehyde	Method A		Method B		Mp [°C]
		Time [h]	Yield [%][a]	Time [min]	Yield [%][a]	
1		2.0	92	2.0	94	183–185 (19)
2		1.5	90	2.0	93	212–214 (19)
3		2.0	94	2.0	95	286–289 (19)
4		2.0	86	2.0	90	252–254 (24*a*)
5		2.0	85	2.0	88	237–239 (19)
6		1.5	93	1.5	94	306–308 (19)
7		2.0	96	2.0	95	210–211 (19)
8		1.5	88	2.0	90	290–291 (24*b*)
9		2.5	84	2.0	88	202–204 (19)
10		2.0	78	2.0	80	224–227 (19)
11		2.5	80	2.0	84	148–151 (19)
12		2.5	86	3.5	90	202–204
13		5.0	65	8.0	70	200–202
14		2.5	92	3.0	94	198–200

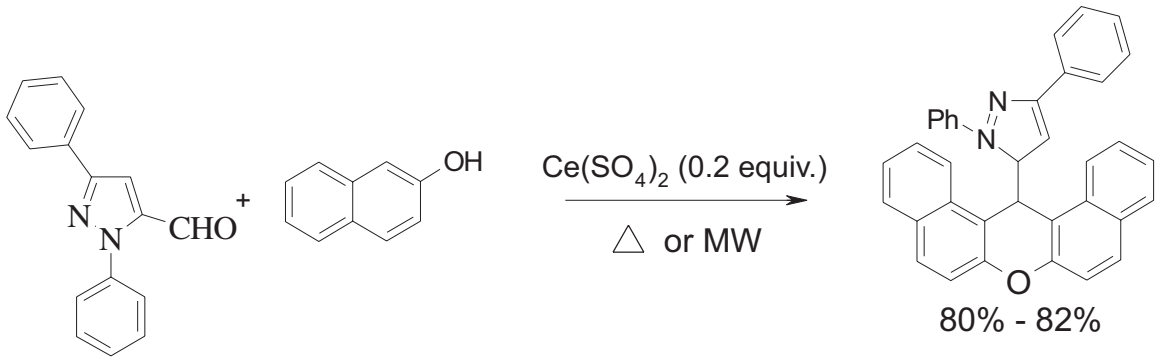
[a]Isolated yields and all products were characterized by comparison of their NMR, IR, mass, and physical data with those of authentic samples.

© 2007 NRC Canada

Scheme 3. Synthesis of 14-(4-chloro-phenyl)-14*H*-dibenzo[*aj*]xanthene.

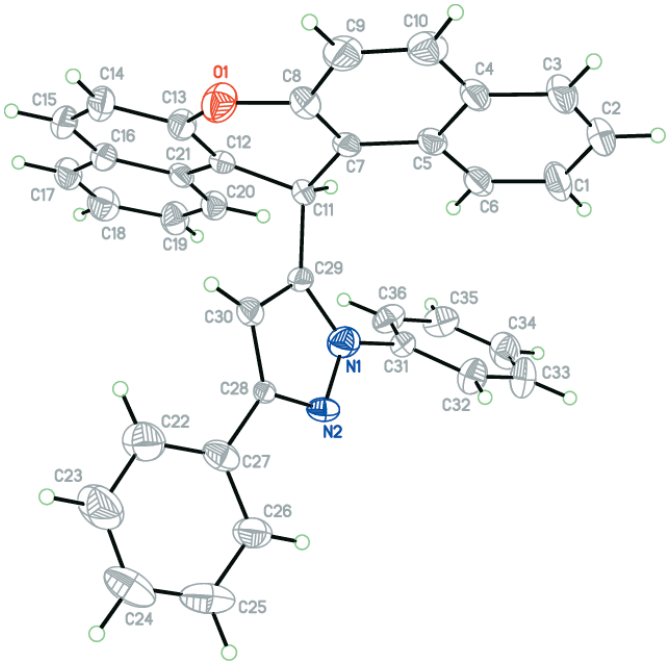


Scheme 4. Synthesis of pyrazolyl xanthene.



3

Fig. 2. ORTEP diagram of compound **3**.



Experimental

Materials and general

Glassware were hot-air oven-dried prior to use. Cerium(IV) sulfate and 4-methoxy phenol were purchased from Lancaster Research Chemicals. All other reagents were purchased from S.D. Fine-Chem. Limited and used as received. Acetonitrile was distilled from CaH_2 under nitrogen and stored over 4 Å molecular sieves. DMSO-d_6 was purchased from Aldrich. Melting points were determined in open capillary tubes and are uncorrected. IR measurements were carried out using KBr pellets in PerkinElmer Spectrometer RXI–FTIR. ^{1}H NMR and ^{13}C NMR spectra were recorded in JEOL 500 MHz high-resolution NMR spectrometer with TMS as an internal standard. Mass spectra were obtained using JEOL DX–303 in EI ionization mode at 70 eV. TLC was performed on precoated Polygram SIL G/UV$_{254}$ sheets.

Typical experimental procedure for the synthesis of aryl-14*H*-dibenzo[*aj*]xanthenes

Method A

A mixture of the aldehyde (2 mmol), 2-naphthol (4 mmol), and anhyd. ceric sulfate (0.4 mmol) was stirred at 100 °C for the appropriate time as mentioned in Table 3. Completion of the reaction was confirmed by TLC. The reaction mixture was extracted with dichloromethane (3 × 15 mL), ceric sulfate was filtered off, and the filtrate was concentrated under reduced pressure. The solid obtained was recrystallized from ethyl alcohol.

Method B

A mixture of the aldehyde (2 mmol), 2-naphthol (4 mmol), and anhyd. ceric sulfate (0.4 mmol) was inserted in a microwave oven (BPL BMG 800 TS model) on a silica gel solid support and irradiated at 300 W for the appropriate time as mentioned in Table 3. Completion of the reaction was confirmed by TLC. The reaction mixture was extracted with dichloromethane (3 × 15 mL), ceric sulfate was filtered

© 2007 NRC Canada

off, and the filtrate was concentrated under reduced pressure. The solid obtained was recrystallized from ethyl alcohol.

14-Phenyl-14*H*-dibenzo[*aj*]xanthene (Table 3, entry 1)

White solid, mp 183–185 °C (lit. value 185 °C) (19). IR (KBr) ν_{max} cm^{-1}: 3021, 1623, 1592, 1402, 1250, 805. ^1H NMR (500 MHz, $CDCl_3$) δ: 6.55 (s, 1H), 7.03 (t, 1H, *J* = 7.6 Hz), 7.17 (t, 2H, *J* = 7.6 Hz), 7.42 (t, 2H, *J* = 6.9 Hz), 7.52 (d, 2H, *J* = 9.2 Hz), 7.58 (m, 4H), 7.79 (d, 2H, *J* = 9.15 Hz), 7.83 (d, 2H, *J* = 7.65 Hz), 8.42 (d, 2H, *J* = 9.15 Hz). ^{13}C NMR (125 MHz, $CDCl_3$) δ: 38.2, 117.4, 118.2, 122.8, 124.4, 126.53, 126.9, 128.4, 128.6, 128.9, 129.0, 131.2, 131.6, 145.2, 148.8. MS *m*/*z*: 358 (M^+).

14-(2-Chlorophenyl)-14*H*-dibenzo[*aj*]xanthene (Table 3, entry 2)

White solid, mp 212–214 °C (lit. value 215 °C) (19). IR (KBr) ν_{max} cm^{-1}: 3026, 1601, 1583, 1422, 1249, 820. ^1H NMR (500 MHz, $CDCl_3$) δ: 6.79 (s, 1H), 6.88 (p, 2H, *J* = 8.4 Hz), 7.25 (d, 1H, *J* = 7.6 Hz), 7.38 (d, 1H, *J* = 7.6 Hz), 7.42 (t, 2H, *J* = 7.6 Hz), 7.48 (d, 2H, *J* = 8.4 Hz), 7.61 (t, 2H, *J* = 8.4 Hz), 7.78 (d, 2H, *J* = 8.4 Hz), 7.81 (d, 2H, *J* = 8.4 Hz), 8.73 (d, 2H, *J* = 8.4 Hz). ^{13}C NMR (125 MHz, $CDCl_3$) δ: 34.7, 118.1, 118.2, 123.6, 124.5, 127.0, 127.9, 128.0, 128.8, 129.2, 129.7, 130.2, 130.9, 131.9, 131.9, 143.7. MS *m*/*z*: 393 (M + 1).

14-(4-Chlorophenyl)-14*H*-dibenzo[*aj*]xanthene (Table 3, entry 3)

White solid, mp 286–289 °C (lit. value 289 °C) (19). IR (KBr) ν_{max} cm^{-1}: 2925, 1590, 1484, 1242, 1083, 807. ^1H NMR (500 MHz, $CDCl_3$) δ: 6.71 (s, 1H), 7.16 (d, 2H, *J* = 7.6 Hz), 7.4 (t, 4H, *J* = 7.6 Hz), 7.51 (d, 2H, *J* = 8.4 Hz), 7.60 (m, 4H), 7.89 (d, 4H, *J* = 7.6 Hz), 8.62 (d, 2H, *J* = 7.6 Hz). ^{13}C NMR (125 MHz, $CDCl_3$) δ: 39.9, 117.5, 118.2, 123.8, 125.1, 127.6, 128.9, 129.2, 129.8, 130.2, 131.2, 131.3, 131.4, 145.0, 148.5. MS *m*/*z*: 393 (M + 1).

14-(2,4-Dichlorophenyl)-14*H*-dibenzo[*aj*]xanthene (Table 3, entry 4)

White solid, mp 252–254 °C (lit. value 253–255 °C) (24*a*). FTIR (KBr) ν_{max} cm^{-1}: 3059, 1620, 1590, 1465, 1247, 806. ^1H NMR (500 MHz, $CDCl_3$) δ: 6.74 (s, 1H), 6.87 (d, 1H, *J* = 8.45 Hz), 7.26 (m, 2H), 7.42 (m, 4H), 7.60 (t, 2H, *J* = 6.9 Hz), 7.78 (d, 2H, *J* = 9.2 Hz), 7.81 (d, 2H, *J* = 8.4 Hz), 8.63 (d, 2H, *J* = 8.4 Hz). ^{13}C NMR (125 MHz, $CDCl_3$) δ: 34.3, 117.5, 118.2, 123.2, 124.6, 127.1, 128.5, 128.8, 129.2, 129.4, 130.7, 130.9, 131.7, 132.8, 132.9, 142.3, 148.9. MS *m*/*z*: 428 (M + 2).

14-(4-Fluorophenyl)-14*H*-dibenzo[*aj*]xanthene (Table 3, entry 5)

Brown solid, mp 237–239 °C (lit. value 239 °C) (19). IR (KBr) ν_{max} cm^{-1}: 3068, 1623, 1592, 1242, 959, 744. ^1H NMR (500 MHz, $CDCl_3$) δ: 6.47 (s, 1H), 6.80 (t, 2H, *J* = 9.15 Hz), 7.40 (t, 2H, *J* = 7.65 Hz), 7.45 (m, 4H), 7.57 (t, 2H, *J* = 7.65 Hz), 7.78 (d, 2H, *J* = 9.15 Hz), 7.82 (d, 2H, *J* = 7.6 Hz), 8.32 (d, 2H, *J* = 8.4 Hz). ^{13}C NMR (125 MHz, $CDCl_3$) δ: 37.3, 115.3, 115.5, 117.2, 118.1, 122.6, 124.4, 126.9, 128.9, 129.1, 129.7, 129.7, 131.1, 131.4, 140.9, 148., 160.2, 162.08. MS *m*/*z*: 377.1 (M + 1).

14-(4-Nitrophenyl)-14*H*-dibenzo[*aj*]xanthene (Table 3, entry 6)

Pink-brown solid, mp 306–308 °C (lit. value 310 °C) (19). IR (KBr) ν_{max} cm^{-1}: 2930, 1594, 1517, 1343, 1241, 828. ^1H NMR (500 MHz, $CDCl_3$) δ: 6.93 (s, 1H), 7.50 (m, 2H), 7.67 (m, 4H), 8.03 (m, 8H), 8.71 (d, 2H, *J* = 8.4 Hz). ^{13}C NMR (125 MHz, $CDCl_3$) δ: 36.4, 116.2, 117.7, 123.1, 123.6, 124.7, 127.2, 128.7, 129.6, 130.7, 130.8, 145.9, 148.1, 152.6. MS *m*/*z*: 403 (M^+).

14-(3-Nitrophenyl)-14*H*-dibenzo[*aj*]xanthene (Table 3, entry 7)

Yellow solid, mp 210–211 °C (lit. value 211 °C) (19). IR (KBr) ν_{max} cm^{-1}: 3077, 1592, 1527, 1347, 1250, 810. ^1H NMR (500 MHz, $CDCl_3$) δ: 6.55 (s, 1H), 7.23 (t, 1H, *J* = 7.65 Hz), 7.41 (t, 2H, *J* = 6.9 Hz), 7.49 (d, 2H, *J* = 8.4 Hz), 7.59 (t, 2H, *J* = 7.6 Hz), 7.79 (m, 6H), 8.27 (d, 2H, *J* = 8.4 Hz), 8.41 (s, 1H). ^{13}C NMR (125 MHz, $CDCl_3$) δ: 37.8, 115.9, 118.2, 121.8, 122.1, 122.8, 124.7, 127.3, 129.2, 129.6, 129.7, 131.1, 134.4, 147.0, 148.3, 148.8. MS *m*/*z*: 403 (M^+).

14-(2-Nitrophenyl)-14*H*-dibenzo[*aj*]xanthene (Table 3, entry 8)

Yellow solid, mp 290–291 °C (lit. value 293 °C) (24*b*). IR (KBr) ν_{max} cm^{-1}: 2921, 1581, 1350, 1241, 809. ^1H NMR (500 MHz, $CDCl_3$) δ: 7.02 (t, 1H, *J* = 7.6 Hz), 7.18 (t, 1H, *J* = 7.65 Hz) 7.41 (t, 2H, *J* = 6.85 Hz), 7.47 (t, 3H, *J* = 8.4 Hz), 7.54 (s, 1H), 7.58 (t, 2H, *J* = 7.6 Hz), 7.78 (t, 5H, *J* = 7.65 Hz), 8.51 (d, 2H, *J* = 8.4 Hz). ^{13}C NMR (125 MHz, $CDCl_3$) δ: 32.6, 117.6, 118.1, 122.7, 124.8, 125.0, 127.4, 127.7, 128.8, 129.5, 131.0, 131.8, 132.3, 134.2, 140.9, 147.1, 149.5. MS *m*/*z*: 404.69 (M + 1).

14-(4-Methoxyphenyl)-14*H*-dibenzo[*aj*]xanthene (Table 3, entry 9)

Yellow solid, mp 202–204 °C (lit. value 204 °C) (19). IR (KBr) ν_{max} cm^{-1}: 2922, 1592, 1510, 1030, 810. ^1H NMR (500 MHz, $CDCl_3$) δ: 3.60 (s, 3H), 6.44 (s, 1H), 6.66 (d, 2H, *J* = 8.4 Hz), 7.39 (m, 4H), 7.47 (d, 2H, *J* = 8.4 Hz), 7.56 (t, 2H, *J* = 8.4 Hz), 7.77(d, 2H, *J* = 9.15 Hz), 7.81 (d, 2H, *J* = 8.4 Hz), 8.37 (d, 2H, *J* = 8.4 Hz). ^{13}C NMR (125 MHz, $CDCl_3$) δ: 37.18, 55.1, 113.9, 117.6, 118.1, 122.8, 124.3, 126.9, 128.8, 128.9, 129.2, 131.1, 131.5, 137.5, 148.7, 157.9. MS *m*/*z*: 389.8 (M + 1).

14-(4-Methylphenyl)-14*H*-dibenzo[*aj*]xanthene (Table 3, entry 10)

Light-brown solid, mp 224–227 °C (lit. value 229 °C) (19). IR (KBr) ν_{max} cm^{-1}: 2925, 1590, 1520, 1250, 810. ^1H NMR (500 MHz, $CDCl_3$) δ: 2.13 (s, 3H), 6.46 (s, 1H), 6.96 (d, 2H, *J* = 7.65 Hz), 7.42 (t, 4H, *J* = 7.6 Hz), 7.49 (d, 2H, *J* = 9.2 Hz), 7.57 (t, 2H, *J* = 8.4 Hz), 7.78 (d, 2H, *J* = 9.2 Hz), 7.82 (d, 2H, *J* = 7.6 Hz), 8.40 (d, 2H, *J* = 8.4 Hz). ^{13}C NMR (125 MHz, $CDCl_3$) δ: 21.0, 37.7, 109.6, 117.5, 118.1, 122.8, 124.3, 126.8, 128.2, 128.9, 129.2, 131.1, 131.5, 136.0, 142.2, 148.8. MS *m*/*z*: 373 (M + 1).

© 2007 NRC Canada

14-Ethyl-14*H*-dibenzo[*aj*]xanthene (Table 3, entry 11)

White solid, mp 148–151 °C (lit. value 152 °C) (19). IR (KBr) ν_{max} cm^{-1}: 3062, 2926, 1623, 1588, 1049, 1395. ^1H NMR (500 MHz, $CDCl_3$) δ: 0.55 (t, 3H, *J* = 7.65 Hz), 2.10 (p, 2H, *J* = 4.6 Hz), 5.58 (t, 1H, *J* = 3.8 Hz), 7.37 (d, 2H, *J* = 8.4 Hz), 7.44 (t, 2H, *J* = 6.9 Hz), 7.60 (t, 2H, *J* = 7.65 Hz), 7.77 (d, 2H, *J* = 8.4 Hz), 7.87 (d, 2H, *J* = 8.4 Hz), 8.25 (d, 2H, *J* = 8.4 Hz). ^{13}C NMR (125 MHz, $CDCl_3$) δ: 9.1, 28.4, 31.7, 116.0, 117.6, 122.6, 124.2, 126.7, 128.3, 128.9, 131.1, 131.6, 150.2. MS *m*/*z*: 311 (M + 1).

14-Naphthalen-1-yl-14*H*-dibenzo[*aj*]xanthene (Table 3, entry 12)

White solid, mp 202–204 °C. IR (KBr) ν_{max} cm^{-1}: 3049, 1590, 1397, 1245, 806. ^1H NMR (500 MHz, $CDCl_3$) δ: 7.11 (s, 1H), 7.20 (t, 1H, *J* = 7.7 Hz), 7.29 (t, 2H, *J* = 6.7 Hz), 7.36 (t, 2H, *J* = 8.4 Hz), 7.48 (m, 4H), 7.69 (d, 1H, *J* = 6.9 Hz), 7.75 (m, 6H), 8.46 (d, 2H, *J* = 8.4 Hz), 9.14 (d, 1H, *J* = 9.2 Hz). ^{13}C NMR (125 MHz, $CDCl_3$) δ: 34.53, 118.28, 118.47, 122.77, 123.51, 123.53, 125.28, 125.95, 126.56, 126.73, 127.61, 128.78, 128.94, 129.40, 129.66, 130.14, 131.12, 132.08, 133.91, 142.61, 148.68. EI-MS *m*/*z*: 410 (M + 2); Anal. calcd. for $C_{31}H_{20}O$: C, 91.15; H, 4.93. Found: C, 91.08; H, 4.94.

4-(14*H*-Dibenzo[*aj*]xanthen-14-yl)-phenol (Table 3, entry 13)

White solid, mp 200–204 °C. IR (KBr) ν_{max} cm^{-1}: 3373, 1593, 1511, 1243, 815, 744. ^1H NMR (500 MHz, $CDCl_3$) δ: 4.78 (s (br), 1H), 6.42 (s, 1H), 6.56 (d, 2H, *J* = 8.4 Hz), 7.35 (d, 2H, *J* = 8.4 Hz), 7.39 (t, 2H, *J* = 6.9 Hz), 7.46 (d, 2H, *J* = 9.2 Hz), 7.56 (t, 2H, *J* = 7.6 Hz), 7.77 (d, 2H, *J* = 8.4 Hz), 7.81 (d, 2H, *J* = 7.7 Hz), 8.35 (d, 2H, *J* = 8.4 Hz). ^{13}C NMR (125 MHz, $CDCl_3$) δ: 37.17, 115.37, 117.55, 118.08, 122.74, 124.32, 126.85, 128.83, 128.89, 129.45, 131.12, 131.44, 137.56, 148.72, 153.90. EI-MS *m*/*z*: 375 (M + 1). Anal. calcd. for $C_{27}H_{18}O_2$: C, 86.61; H, 4.85. Found: C, 86.45; H, 4.86.

14-Naphthalen-2-yl-14*H*-dibenzo[*aj*]xanthene (Table 3, entry 14)

Pale-yellow solid, mp 198–200 °C. IR (KBr) ν_{max} cm^{-1}: 3052, 1594, 1430, 1250, 813, 742. ^1H NMR (500 MHz, $CDCl_3$) δ: 6.67 (s, 1H), 7.31 (t, 1H, *J* = 7.7 Hz), 7.37 (m, 3H), 7.54 (d, 2H, *J* = 9.2 Hz), 7.58 (m, 5H), 7.81 (m, 5H), 8.09 (s, 1H), 8.51 (d, 2H, *J* = 8.4 Hz). ^{13}C NMR (125 MHz, $CDCl_3$) δ: 38.42, 117.12, 118.14, 122.82, 124.38, 125.70, 126.09, 126.67, 126.95, 127.55, 127.98, 128.64, 128.94, 129.13, 131.20, 131.61, 132.18, 133.23, 133.91, 142.44, 148.85. EI-MS *m*/*z*: 410 (M + 2). Anal. calcd. for $C_{31}H_{20}O$: C, 91.15; H, 4.93. Found: C, 90.98; H, 4.94.

3-(14*H*-Dibenzo[*aj*]xanthen-14-yl)-1,4-diphenyl-1H-pyrazole (3)

White solid, mp 234–236 °C. IR (KBr) ν_{max} cm^{-1}: 3057, 1594, 1502, 1401, 1243, 742, 688. ^1H NMR (500 MHz, $CDCl_3$) δ: 6.53 (s, 1H), 7.14 (t, 1H, *J* = 7.7 Hz), 7.29 (t, 2H, *J* = 8.4 Hz), 7.35 (d, 2H, *J* = 8.4 Hz), 7.40 (m, 6H), 7.51 (m, 5H), 7.75 (d, 2H, *J* = 9.2 Hz), 7.83 (m, 3H), 8.13 (d, 2H, *J* = 8.4 Hz). ^{13}C NMR (125 MHz, $CDCl_3$) δ: 27.87, 117.67, 118.08, 119.02, 122.83, 124.37, 126.23, 126.34, 126.64, 126.98, 128.41, 128.46, 128.75, 128.80, 129.25, 129.98, 131.02, 134.15, 139.73, 149.17, 151.47. EI-MS *m*/*z*: 501 (M + 1). Anal. calcd. for $C_{36}H_{24}N_2O$: C, 86.38; H, 4.83; N, 5.60. Found: C, 86.50; H, 4.84; N, 5.58.

Acknowledgments

One of the authors, N.P., thanks the Council of Scientific and Industrial Research, New Delhi, India, for the research fellowship.

References

1. T. Hideo. JP 56 005 480. 1981.
2. J.P. Poupelin, G. Saint-Rut, O. Foussard-Blanpin, G. Narcisse, G. Uchida-Ernouf, and R. Lacroix. Eur. J. Med. Chem. **13**, 67 (1978).
3. R.W. Lambert, J.A. Martin, J.H.K.E.B. Merrett, and G.J. Thomas. WO 9 706 178, 1997.
4. (*a*) R.M. Ion. Prog. Catal. **2**, 55 (1997); (*b*) R.M. Ion, D. Frackowiak, A. Planner, and K. Wiktroowicz. Acta. Biochim. Pol. **45**, 833 (1998).
5. (*a*) G. Saint-Ruf and H.T. Hieu. Bull. Chim. Ther. **7**, 83 (1972); (*b*) G. Saint-Ruf, H.T. Hieu, and J.P. Poupelin. Naturwissenschaften, **62**, 584 (1975).
6. S.M. Mechen, S.C. Benson, J.Y.L. Lam, W. Zhen, D. Sun, B.B. Rosenblum, S.H. Khan, and M. Taing. US Patent 6 583 168, 2003.
7. C.G. Knight and T. Stephens. Biochem. J. **258**, 683 (1989).
8. (*a*) O. Sirkeeioglu, N. Talinli, and A. Akar. J. Chem. Res. Synop. 502 (1995); (*b*) M. Ahmad, T.A. King, Do-K. Ko, B.H. Cha, and J. Lee. J. Phys. D: Appl. Phys. **35**, 1473 (2002).
9. (*a*) G. Casiraghi, G. Casnati, and M. Cornia. Tetrahedron Lett. **14**, 679 (1973); (*b*) G. Casiraghi, G. Casnati, M. Catellini, and M. Cornia. Synthesis, 564 (1974).
10. (*a*) A. Bekaert, J. Andrieux, and M. Plat. Tetrahedron Lett. **33**, 2805 (1992); (*b*) R.J. Sarma and J.B Baruah. Dyes Pigm. **64**, 91 (2005).
11. (*a*) D.W. Knight and P.B. Little. Synlett. 1141 (1998); (*b*) D.W. Knight and P.B. Little. J. Chem. Soc., Perkin Trans. I. **15**, 1771 (2001).
12. C.-W. Kuo and J.-M. Fang. Synth. Commun. **31**, 877. (2001).
13. J.-Q. Wang and R.G. Harvey. Tetrahedron, **58**, 5927 (2002).
14. A. Jha and J. Beal. Tetrahedron Lett. **45**, 8999 (2004).
15. R.N. Sen and N. Sarkar. J. Am. Chem. Soc. **47**, 1079 (1925).
16. P. Papini and R. Cimmarusti. Gazz. Chim. Ital. **77**, 142 (1947).
17. K. Ota and T. Kito. Bull. Chem. Soc. Jpn. **49**, 1167 (1976).
18. J.A. Van Allan, D.D. Giannini, and T.H. Whitesides. J. Org. Chem. **47**, 820 (1982).
19. A.R. Khosropour, M.M. Khodaei, and H. Oghannian. Synlett. 955 (2005).
20. (*a*) J.R. Hewe, K.-L. Chen, and S. Anahan. J. Chem. Soc., Chem. Commun. 1425 (1994); (*b*) M.V.R. Reddy, B. Malhotra, and Y.D. Vanker. Tetrahedron Lett. **36**, 486 (1995); (*c*) E. Manzo, G. Barone, E. Bedini, A. Iadonisi, L. Mangoni, and M. Parrilli. Tetrahedron, **58**, 129 (2002); (*d*) P. Goswami and P. Chowdhury. New J. Chem. **24**, 955 (2000); (*e*) X.-F. Zeng, S.-J. Ji, and S.-Y. Wang. Tetrahedron, **61**, 10235 (2005); (*f*) G. Savitha and P.T. Perumal. Tetrahedron Lett. **47**, 3589 (2006).
21. (*a*) M.E. Armenta-Armenta and A.F. Diaz. Environ. Sci. Technol. **39**, 5872 (2005); (*b*) X.-C. Guo and Q.-Y. Chen. J. Fluorine Chem. **88**, 63 (1998); (*c*) H. Yan and N. Toshima. Synthetic Metals, **69**, 151 (1995); (*d*) J.A. Posten, Jr., R.V.

© 2007 NRC Canada

Siriwardane, E.P. Fisher, and A.L. Miltz. Appl. Surf. Sci. **214**, 83 (2003).

22. (*a*) G. Sivaprasad, P.T. Perumal, V.R. Prabavathy, and N. Mathivanan. Bioorg. Med. Chem. Lett. **16**, 6302 (2006); (*b*) K. Sujatha, P. Shanmugam, P. T. Perumal, D. Muralidharan, and M. Rajendran. Bioorg. Med. Chem. Lett. **16**, 4893 (2006); (*c*) R. Sridhar, P.T. Perumal, S. Etti, G. Shanmugam, M.N. Ponnuswamy, V.R. Prabavathy, and N. Mathivanan. Bioorg. Med. Chem. Lett. **14**, 6035 (2004); (*d*) C.J. Magesh, S.V. Makesh, and P.T. Perumal. Bioorg. Med. Chem. Lett. **14**, 2035 (2004).
23. N. Panneer Selvam, and P.T. Perumal. Tetrahedron Lett. **47**, 7481 (2006).
24. (*a*) L. Nagarapu, S. Kanveri, V. Mahankhali, and S. Apuri. J. Mol. Catal. A: Chem. **266**, 104 (2007); (*b*) B. Rajitha, B.S. Kumar, Y.T. Reddy, P.N. Reddy, and N. Sreenivasulu. Tetrahedron Lett. **46**, 8691 (2005).

© 2007 NRC Canada

On the origin of some cubebene derivatives — Diels–Alder adducts and the diene structures of solidago compounds

Christopher K. Jankowski, André Pelletier, Eduardo Diaz T., Jacqueline M.R. Belanger, Jocelyn J.R. Paré, Andre Aumelas, Thierry Besson, Maria de Fatima Pereira, and Laurent Mauclaire

Abstract: Two reactions, HCl addition and the thermal and (or) microwave assisted Diels–Alder condensation, were performed on α-cubebene (**1**), a vinylcyclopropane-containing tricyclic sesquiterpene. The diene structures originating from these reactions and from subsequent rearrangements of **1** were identified. The stereochemistry of the resulting adducts was established using mostly 2D high-resolution NMR.

Key words: cubebene, tricyclic terpenes from Solidago Canadensis L, Diels–Alder microwave condensation on vinylcyclopropane system.

Résumé : Le α-cubébène (**1**), un sesquiterpène qui contient une unité vinylcyclopropane, a été soumis à une réaction d'addition de HCl et une de condensation de Diels–Alder thermique à l'aide de microondes. On a identifié les structures diéniques qui trouvent leur origine dans ces réactions et dans les réarrangements subséquents du composé **1**. On a déterminé la stéréochimie des adduits qui en résultent en se basant principalement sur la RMN bidimensionnelle à haute résolution.

Mots-clés : cubébène, terpènes tricycliques provenant de *Solidago Canadensis* L., condensation de Diels–Alder à l'aide de microondes sur un système vinylcyclopropane.

[Traduit par la Rédaction]

Introduction

Cyclopropane-containing terpenes are present in many botanical extracts (1). The complex relation between the biological origin of this strained cyclopropane system and its facile rearrangement in vitro complicates the exact structural identification. The cyclopropane system is even more susceptible to rearrangement when in proximity to a double bond, as this often induces diene character (2). If the interactive method of extraction, such as microwave-assisted extraction, is used, the likelihood of such reactions increases yet again (3).

We were interested in elaborating our hypotheses on the possible origin of α-cubebene (**1**), a popular vinylcyclopropane-containing tricyclic sesquiterpene present in several plant extracts (in particular, Solidago Canadensis L) (4). In previous papers, we have already reported on its microwave-induced rearrangement (3).

Our current hypothesis should take into account the predominantly photochemical (hν) mode of these transformations on the plant level, the symmetry-allowed processes relating various diene structures, and their stereochemistry.

For such a system one can consider various possibilities, including a Cope rearrangement (5), a relatively easy vinylcyclopropane-cyclopentene rearrangement (5), and exo–endo double bond isomerization. Finally, the entire system manifests several possible sigmatropic shifts with and without respect to Woodward–Hoffmann formalism because of uncertainty as to the concerted character of these transformations (7). The following hypothesis towards a possible retro-synthesis of **1** can then be elaborated as per Scheme 1.

Scheme 1 suggests that germacrene D (**4**) can be a precursor of tricyclic unsaturated sesquiterpenes such as cubebenes **2**, **5,** etc. It is worth noting that **4** is a naturally abundant

Received 20 June 2007. Accepted 22 August 2007. Published on the NRC Research Press Web site at canjchem.nrc.ca on 17 October 2007.

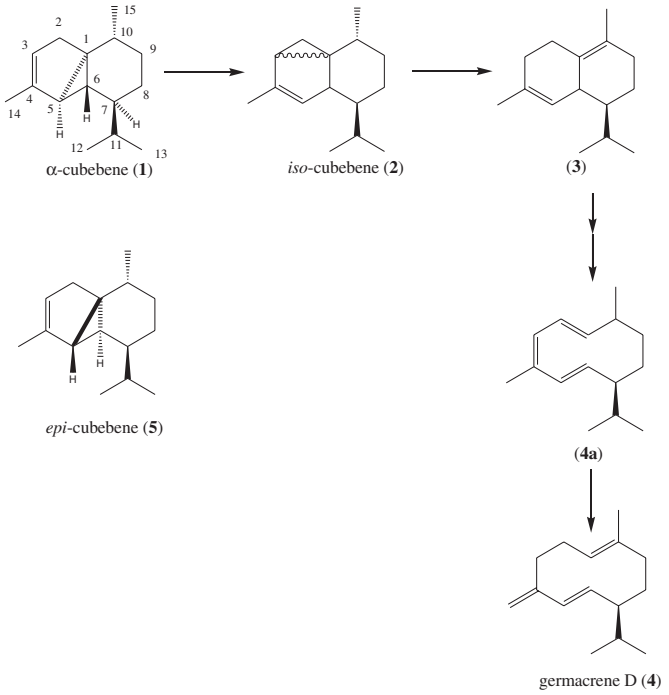
Dedicated to the memory of Professor Wilfried A. König.

C.K. Jankowski,[1,3] A. Pelletier, and A. Aumelas.[2] Département de chimie et biochimie, Université de Moncton, Moncton, NB E1A 3E9, Canada.
E. Diaz T. Instituto de Quimica, Universidad Nacional Autonoma de Mexico, 04150 Mexico, DF, Mexico.
J.M.R. Belanger, and J.J.R. Paré. Environment Canada, ETC, MAP Division, River Road, Ottawa, ON K1A 0H3, Canada.
T. Besson, and M. de Fatima Pereira. Laboratoire de biotechnologies et chimie bioorganique, FRE CNRS 2766, Université de La Rochelle, 17042 La Rochelle, France.
L. Mauclaire. CE de Saclay, DRECAM, SCM, bat 125,CE de Saclay, bp 2, 91191 Gif-sur-Yvette, France.

[1]Corresponding author (e-mail: jankowc@umoncton.ca).
[2]Present address: CBS, INSERM, Faculté de Pharmacie, Université de Montpellier 2, 28 rue des Novacelles,33 Montpellier, France.
[3]Secondary address: CE de Saclay, DRECAM, SCM, bat 125,CE de Saclay, bp 2, 91191 Gif-sur-Yvette, France.

 doi:10.1139/V07-112 © 2007 NRC Canada

Scheme 1. Possible retro synthetic pathway for the biogenesis of α-cubebene **1**.

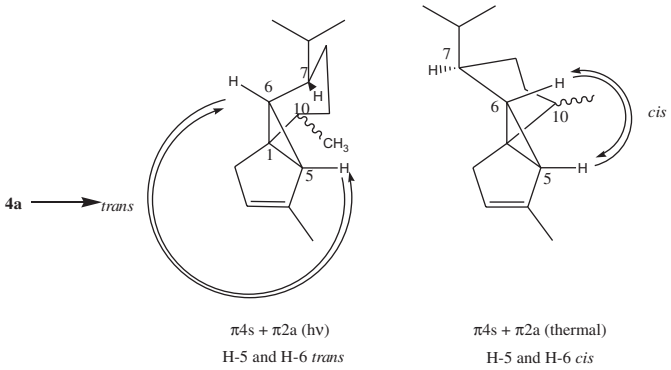


monocyclic sesquiterpene triene, and that like **1**, it has four unsaturations (cycle and three double bonds). It is often present together with natural α-cubebene (**1**) and *epi*-α-cubebene (**5**) as a potential precursor to both. As a part of this transformation it is assumed that **4** enters the isomerization of the double bond from exo to endo position, followed by the shift of the remaining double bond to a more stable conjugated position. One can assume that the rearrangement will then be reduced to a hexatriene-bicyclo[3.1.0]hexene transformation. The bio-originated product will have a geometry conforming to the photochemical pathways of π4s + π2a (Scheme 2) (7, 8) (or of its optical isomer, or both).

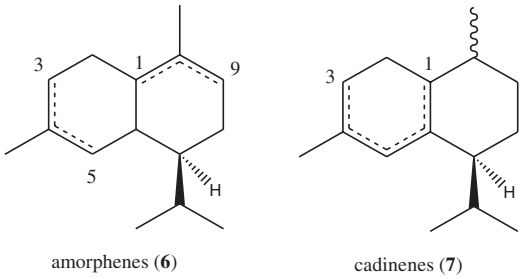
According to Scheme 2, the stereochemistry at the C-10 center is lost because of the non-regioselective H-shift at this carbon. The only remaining stereocenter, C-7 involved, has its isopropyl group β-oriented and is thus a valuable reference point to follow the stereochemistry of these compounds. The value of this hypothesis is reinforced by König transformation (9, 10) of the germacrene D (**4**) into the series of amorphanes (**6**) and closely related cadinenes (**7**) (Scheme 3).

To have the cubebene geometry conform to Scheme 3, H-5 and H-6 should be trans (this is true for both cubebenes and *epi*-cubebenes); as well, H-7 must be trans to H-6 to maintain the voluminous isopropyl group in the equatorial position (Scheme 4). The concerted character of such a photocyclisation, which was suggested by Padwa et al. (11), was subsequently challenged by Seeley (12). If this second hypothesis is retained, steric hindrance should be a driving force of the stereochemistry final product. The isopropyl group should remain in the equatorial position, and the C_1–C_5 bond should be formed through a less hindered pathway.

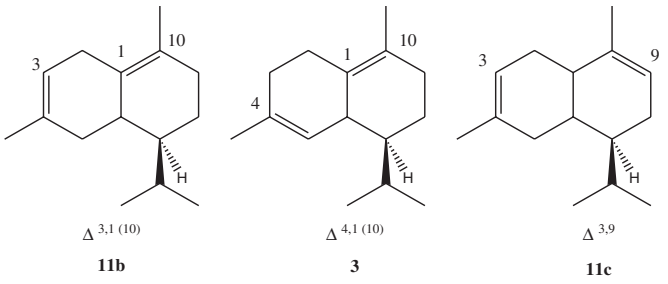
Scheme 2. Differences between thermal or photochemical ring closure leading to **1**.



Scheme 3. Skeleton structures of the amorphenes **6** and cadinenes **7** families.



Scheme 4. The dienes possibly coming from the cyclopropane ring opening of α-cubebene **1** and capable of forming the dichlorinated product **13**.



In such a manner, the hypothesis of formation of cubebene from germacrene D (**4**) via the photochemical pathway in plant could be advanced. Many uncertain points remain open. For example, the second vinylcyclopropane *iso*-cubebene **2** structure could undergo rearrangements leading to more strained structures prior to allowing the formation of either of the two cubebenes by thermal (13) or microwave-assisted conditions (14). Many of the compounds presented in Schemes 1–3 displayed the diene structures. It seems necessary then to show that the dienes are effectively present in these pathways. The best way to confirm this point is to perform two reactions: (*i*) in particular the Diels–Alder addition, enabling the trapping of the diene isomeric structure and the addition of HCl to the double bond and (*ii*) following the opening of the cyclopropane toward olefin, the second addition of HCl (with or without its previous rearrangement because of the carbocation formation).

© 2007 NRC Canada

Results and discussion

Diels–Alder reaction on α-cubebene (1)

As a first step of this study, we performed molecular modelling of many of the dienes discussed here (Scheme 5). The dienes were limited here to those able to produce the homoannular *s-cis*-1,3-diene conformation from the cubebene structure. It is also observed that the cubebenes with the cyclopropane in the C1-C3 position are less stable than those having the cyclopropane in the C1-C5 position. A similar conclusion could be drawn for the monocyclic trienes presented in Scheme 1: the starting triene structure can undergo either the 1,5 sigmatropic shift or the less favoured 1,3 shift; however, germacrene D (**4**) remains among the most stable triene substrates. The most interesting six diene structures **8a**–**8f** were those that originated from the cyclopropane-bearing ring of **1** but were also 1,3-homoannular dienes with their natural s-cis conformation. Incidentally, the molecular modelling of these six diene structures shows that the diene, cadinene-3,5-diene (**8b**), is the most stable of this group of six homoannular dienes.

We chose maleic anhydride as a dienophile because of its proven dienophile character, its solubility, and its easy focalisation under microwave heating. Two different modes of Diels–Alder reaction were performed: thermal and microwave-assisted (MAP and in vessel) (14), and the reactions were monitored using GC-MS, GC, and TLC.

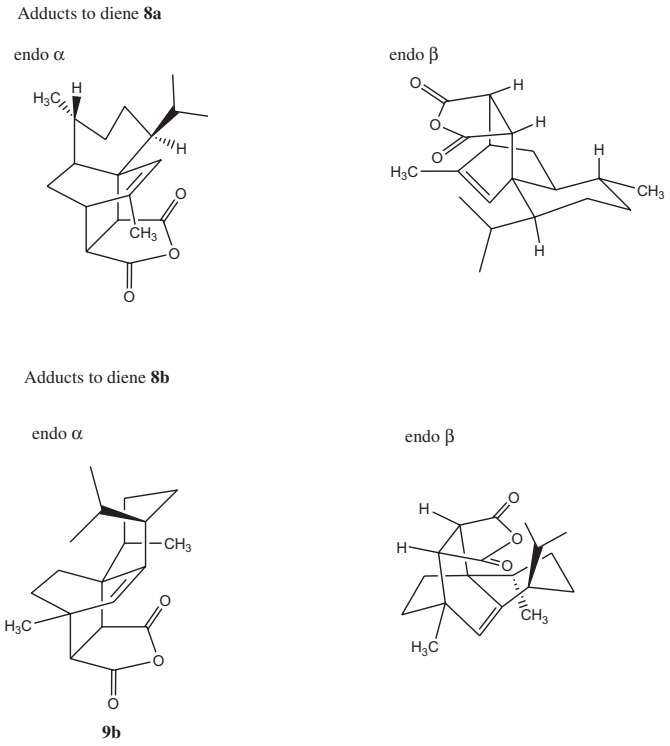
GC-MS revealed the presence of the Diels–Alder adduct at *m/z* 302, which was obtained by heating substrates at a 1:1 molar ratio in toluene, for variable amounts of time, or by microwave. The yield was optimized at 12% in the thermal reaction; it was up to 23% with microwave heating but only 15% using MAP method (15).

The careful chromatographic isolation of this adduct enabled us to further identify its structure as being **9**, essentially from the 2D NMR evidence. The final adduct structure relative configuration at asymmetric carbons, discussed as being a result of two diastereo differentiating approaches (endo, exo) from two possible sides of the molecule of cubebene **1**, was established from the NOESY experiments performed (Fig. 1). The problem of the structure of the starting diene was again examined at this point.

All six isomeric diene structures **8a**–**8f** (Scheme 5) are *s-cis* homoannular dienes. The most distinctive spectral characteristic of the adducts obtained from these dienes was predicted to be the number of vinylic proton signals and the methyl-15 being attached to sp^2 or to sp^3 carbon C-4. The presence of the signal at 5.73 ppm (doublet 2Hz) for one proton in its 500 MHz spectrum eliminates two of these structures from consideration; the methyl-15 singlet signal was then observed and identified as being attached to the sp^3 quaternary carbon at 1.286 ppm. The isopropyl signal displayed the large non-equivalence of its two methyls (0.90 and 0.75 ppm doublets), indicating the steric hindrance in this crowded structure (16).

These results lead to the conclusion that the adduct structure fitted best the structure of diene **8b** (Scheme 6). Further analyses were then performed, taking into consideration four structures — two possibilities of approaches (resulting in Diels–Alder adducts endo or exo) of the dienophile to diene **8b** — from the alpha or beta side of **1**, with the isopropyl

Scheme 5. Structures of the four most likely adducts, as supported by preliminary results.



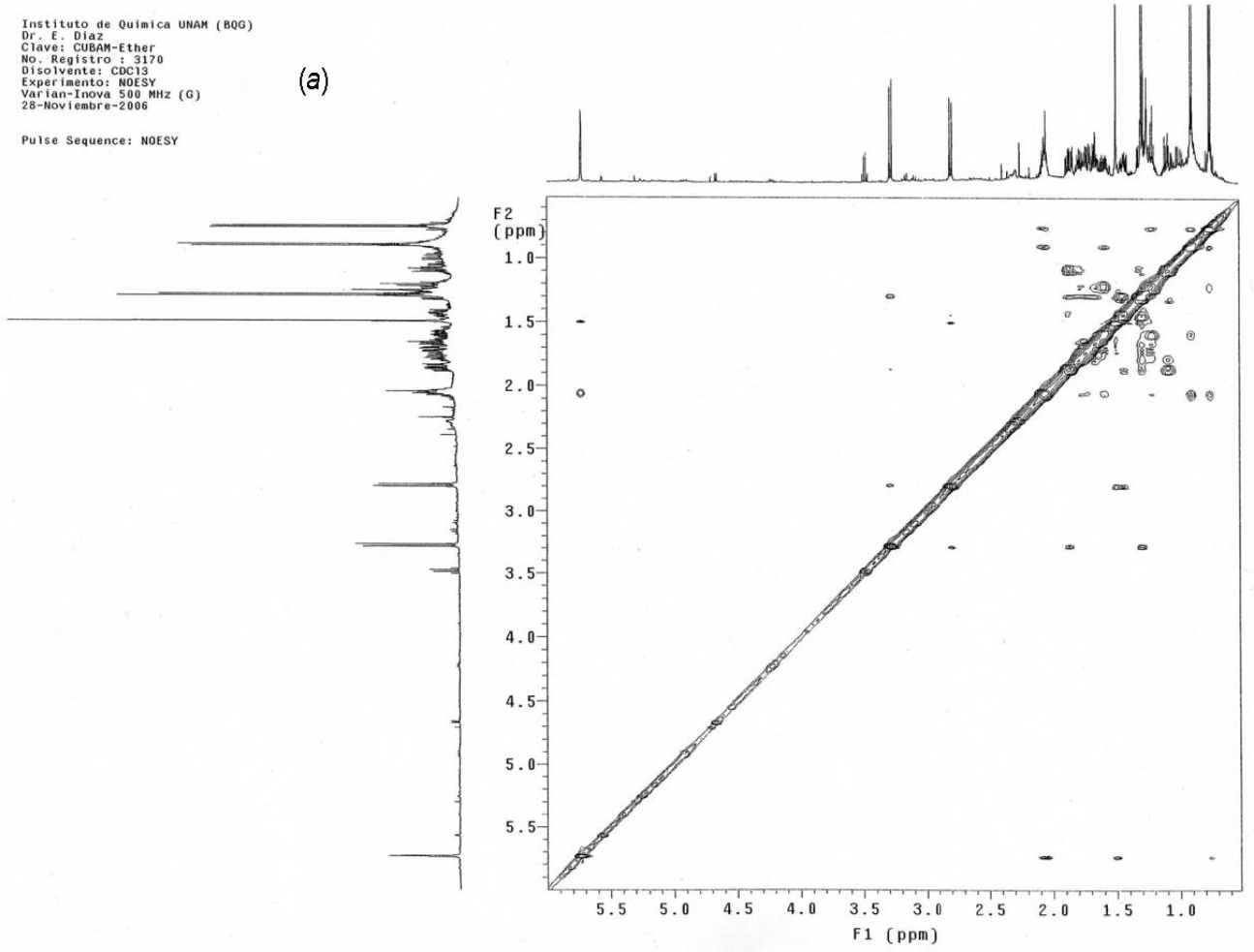
beta orientation in this natural product serving as a reference to the identification of these sides of the molecule.

Molecular modelling indicates that the endo adducts obtained from α (opposite to the isopropyl side of **1**) are more stable than their corresponding exo adducts. The approach from the same side of the isopropyl (β) but according to the endo preference also gives a relatively stable adduct isomer (Scheme 4). The calculated energies of four isomeric structures resulting from the diene **8b** (endo or exo complexes) indicated that for diene **8b**, the adduct endo alpha displayed 55.77 kcal/mol (1 cal = 4.184 J), compared with the second endo beta of 56.53 kcal/mol and to two exo resulting complexes at α 61.29 kcal/mol and β at 58.28 kcal/mol. This difference is also an indication that the presence of a bulky isopropyl group played a direct role in this addition. The reciprocal trans orientation of methyl C-14 and the isopropyl groups should be maintained in this adduct structure and the *endo*-α adduct will, however, have both substituents in equatorial positions. The same analysis was performed for the diene **8a**, which does not lead to the obtained adduct **9**.

To complete the analysis, high-resolution 2D proton NMR experiments were performed. The NOE experiments enabled us to distinguish between these adducts, in particular between endo-α and endo-β, by evaluating the distance between the maleic methine protons and CH_3-4, for example, as well as the vinyl proton and three methyls (C-14 and two from the isopropyl group). The complete analysis of H-1 and C-13 is summarized in Table 1. The key element to support the proposed structure was the clean AB pattern for both methines belonging to the maleic anhydride moiety of adduct. The signals at 3.25 and 2.77 ppm (d, J = 9 Hz) show the lack of any additional couplings, which eliminated struc-

© 2007 NRC Canada

Fig. 1. NMR of adduct **9b** NOESY. (*a*) Upper run: 500 MHz ^{1}H spectrum. Lower run: NOESY within 0–6 ppm range. (*b*) Scheme of NOE interactions.

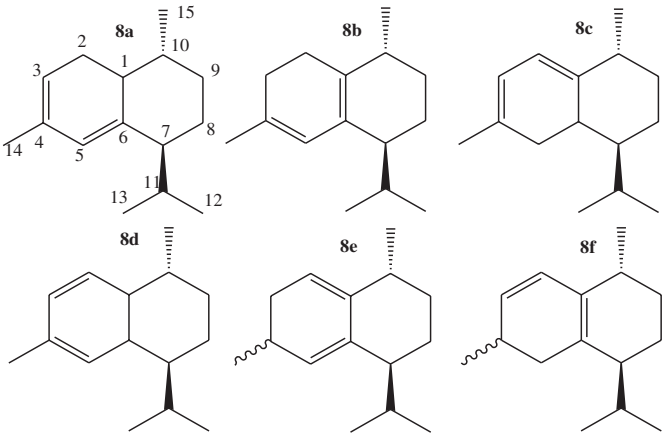


tures of adducts originating from dienes **a**, **d**, **e**, and **f**. The one vinylic proton at 5.73 ppm (d, J = 2 Hz) finally eliminates the structure of adduct arising from diene **8c**. (Fig. 1)

It is worth noting that the cubebene **1** vinylcyclopropane system should undergo a 1,3-sigmatropic shift to form diene **8a** instead of the usually more favoured 1,5-sigmatropic shift that would form diene **8b**. Conversely, assuming that the α-cubebene **1** is first isomerized via the vinylcyclopropane–cyclopentene rearrangement pathway (Scheme 5) to the isomeric cubebene **2** also with the vinylcyclopropane to form the 1,4-diene **8b**, it should undergo 1,3-sigmatropic migration but also a more complex two-step H-migration to

© 2007 NRC Canada

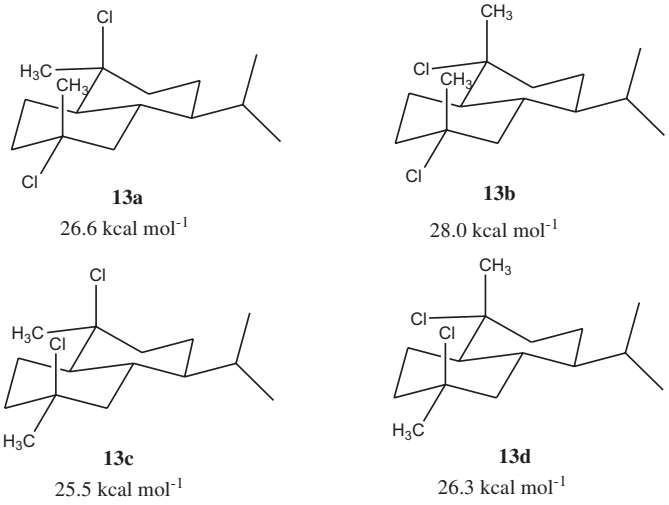
Table 1. Some of the possible dienes resulting from the opening of the cyclopropane and its subsequent rearrangement. These particular dienes are capable of forming Diels–Alder adducts. The table shows energies computed from Hyperchem™ and general information pertinent to each structure that will help identify the adduct formed (1 cal = 4.184 J).



Diene	Position of the double bond	Hybridization of C-15 following adduct formation	Number of vinyl protons in adduct	ΔE (kcal mol^{-1})[a]
8a	3,5	sp^2	1	4.23 (H-1,β), 2.66 (H-1,α)
8b	1,4	sp^3	1	0.00
8c	1,3	sp^3	2	7.11
8d	2,4	sp^2	1	7.09 (cis), 6.59 (trans)
8e	1,5	sp^3	0	2.23 (CH_3-4,β), –1.49 (CH_3-4,α)
8f	2,6	sp^3	1	0.72 (CH_3-4,β), 0.3 (CH_3-4,α)

[a]Referred to the most stable diene structure **8b**.

Scheme 6. The four stereoisomers of the dihydrochlorinated products **13** and their energies. (1 cal = 4.184 J).



finally achieve the 3,5-diene. Incidentally, the cubebenes **1** and **5** have been found to be more stable than the *iso*-cubebene (**2**) by up to 5 kcal mol^{-1}.

The syntheses of the identical adduct by both thermal and microwave-assisted methods were observed. The difference between endo-β and endo-α approaches to the 1,4-diene (**8b**) is the presence of the bulky isopropyl group, which cannot share space with the relatively large maleic anhydride bridge. The β equatorial orientation of this isopropyl is also an important internal reference point to the identification of the stereochemistry of the entire adduct (absolute configuration **7*S***, **10*R***). The isopropyl-bearing ring of the diene remains, then, the stereo template to follow the regio and stereo specificity of the addition. The final stereochemistry of the adduct **9** can then be proposed as in Scheme 5 and Fig. 1, leading to the structure obtained in agreement to the diene behaviour, following the predictions of both Hirsch (7) and Padwa et al. (11), as far as absolute configuration is concerned. The appealing attempt of the separation of diene **8b** as a result of cubebene **1** rearrangement through heating or MAP modes, as in König's case (9, 10), was unsuccessful, and led instead to a mixture of olefinic compounds. It seems, then, that the maleic anhydride dienophile can be considered as an efficient and specific quencher of this diene among some other dienes.

HCl addition to cubebene (1)

The second attempted reaction was the addition of HCl in methanol solution of α-cubebene (**1**) at 0–5 °C. This was expected to produce the additional evidence for the diene structure discussed in the previous sections through, first, the Markovnikov addition to the 3,4-double bond of the α-cubebene (**1**) followed by an acid-catalyzed rearrangement of its cyclopropane moiety, rearranged through the carbocation pathway (these two reactions could take place in the opposite order). If the elucidation of the addition outcome in the first step is easy, the cyclopropane rearrangement is difficult to predict, especially for the terpenes. The bicyclo[3,1,0]hexene frame could undergo many types of rearrangement under acidic conditions, leading also to the opening of cyclopropane and the formation of dienes. The

© 2007 NRC Canada

presence of several potential tertiary carbocations bears witness to this difficulty.

When cubebene (**1**) was treated with a dry HCl saturated methanol solution at 0–5 °C, the major product (25% of yield) displayed the addition of two HCl molecules, as indicated by mass spectrometry. Unambiguous identification of the adduct stereochemistry is, therefore, the best proof of diene structure for **3**.

In the abundant literature on the subject of diene sesquiterpenes, some structures are of particular interest: those of dienes **11**, **9**, **10**, and **12**, the last one characterized by König et al. (9, 10). These dienes, however, were isolated from two completely different Solidago species; although in terpene chemistry the isomerization and rearrangement of the skeleton is relatively frequent, this does not lead to well-defined diene adducts. Diels–Alder reactions on these dienes were not attempted by König, but in 1998 he attempted to isomerize the diene with pTsOH and obtained another stable isomer. Incidentally, four structures with the best fit for the HCl addition product are described in the next section of this paper.

König's heating of this diene revealed an easy shift of the double bond of the structure, with three other dienes being obtained through this isomerization. The production of the Diels–Alder adduct in the case of α-cubebene (**1**) used in this study is thus a chemically formal proof of trapping of the double bond in the 1,3-conjugated *s-cis* homoannular position; however, this diene is isomeric to the one described by König (9, 10).

The NMR spectra (1D and 2D) of the dihydrochloro-cubebene adduct product showed that the adduct should have two *trans*-fused rings and that both methyls (C-14 and C-15) are equatorial (meaning that both chlorine atoms were axial, thus confirming the Markovnikov rules). It is generally accepted that in methyl derivatives of cyclohexane, as well as in a terpene field, the equatorial methyl-13 signal displays a chemical shift at 35–37 ppm, at ca. 10 ppm lower field than the axial one (20–23 ppm). The chemical shift in the 1D C^{13} NMR spectrum of compound **13c** shows two methyl signals, identified with help of DEPT experiments as being methyl-5 at 37.8 ppm and methyl-10 at 34.9 ppm. Because of the chemical shift, we can conclude that both methyls are in equatorial positions (17, 18). The 600 MHz spectra (Table 2) and Fig. 2) enabled us to establish the structure of the dichloro derivative as being **13c**, with two chlorine atoms placed on carbons 10 and 4, respectively. Further study of the dihydrochloro adducts **13** was performed with help of molecular modelling of eight possible structures for these dichloro adducts: four in *trans*-fused and four in *cis*-fused decalins. The most stable structures in the two series were those with the quaternary carbons bearing Cl and CH_3 groups (C-4 and C-10) and where both methyls were equatorial **13c**. It is necessary to point out that the presence of the CH_3 and Cl on the same carbon will always lead to one axial substituent contributing to the creation of two gauche interactions (19). When we consider the addition of the first HCl to the molecule under the two-step addition scheme, the original α-cubebene (**1**) double bond position responds well to the dichloro derivative structure. Under the same hypothesis, the second double bond can originate in either of two essentially similar structures: with the double bond in the 1,10/1,14 position or in position 9,10/1,14 where it is unrelated to the cyclopropane moiety.

Table 2. NMR data for adduct **9b** ($CDCl_3$) ^1H and ^{13}C.

C No.	δ C	δ H
1	36.5q	—
2	34.0	1.86(ax), 1.09(eq)
3	34.6	1.44(eq), 1.31(ax)
4	29.7q	—
5	128.78	5.73 (d, *J* = 2.0 Hz)
6	147.0q	—
7	45.0	2.06
8	22.3	1.22(eq), 1.58(ax)
9	29.0	1.66(eq), 1.69(ax)
10	38.2	1.82
11	28.0	2.05
12	20.8	0.90
	(a)	
13	17.0	0.75
14	16.9	1.30
15	22.85	1.50
Maleic anhydride moiety		
1a	47.0	3.78 (d, *J* = 9 Hz)
4a	50.9	2.79 (d, *J* = 9 Hz)
Cla-CO	172.18	
C4a-CO	171.7	

Note: ax = axial, eq = equatorial, q = non-protonated carbon, d = doublet.

A second hypothesis of formation of the dichloro derivative could also be advanced. The acid catalysis of the cubebene **1** leads to diene **3**, already observed by König et al. (9, 10), which undergo double Markovnikov addition of HCl. Note that this second one-step route leads to the addition of protons from HCl to the carbons C-5 and C-1, instead of to C-3 and C-1 as in the first route. To clarify this point, deuteration with dry DCl in deuterated methanol was attempted. The reaction enabled us to establish the position of deuteration at C-1, C-9, C-3, and C-5. There are then four endocyclic unconjugated dienes with double bonds at -4,9 (**9**), -10,4 (**3**), -3,1, and -3,9, which can produce the Markovnikov's dihydrochloro adduct corresponding to the one identified in this work. The presence of exocyclic double bond dienes was turned down because of the absence of exocyclic methylene signals in the NMR proton spectra of this series. The fact that many amorphenes were identified in some extracts can be asserted by the deuteration (9, 20).

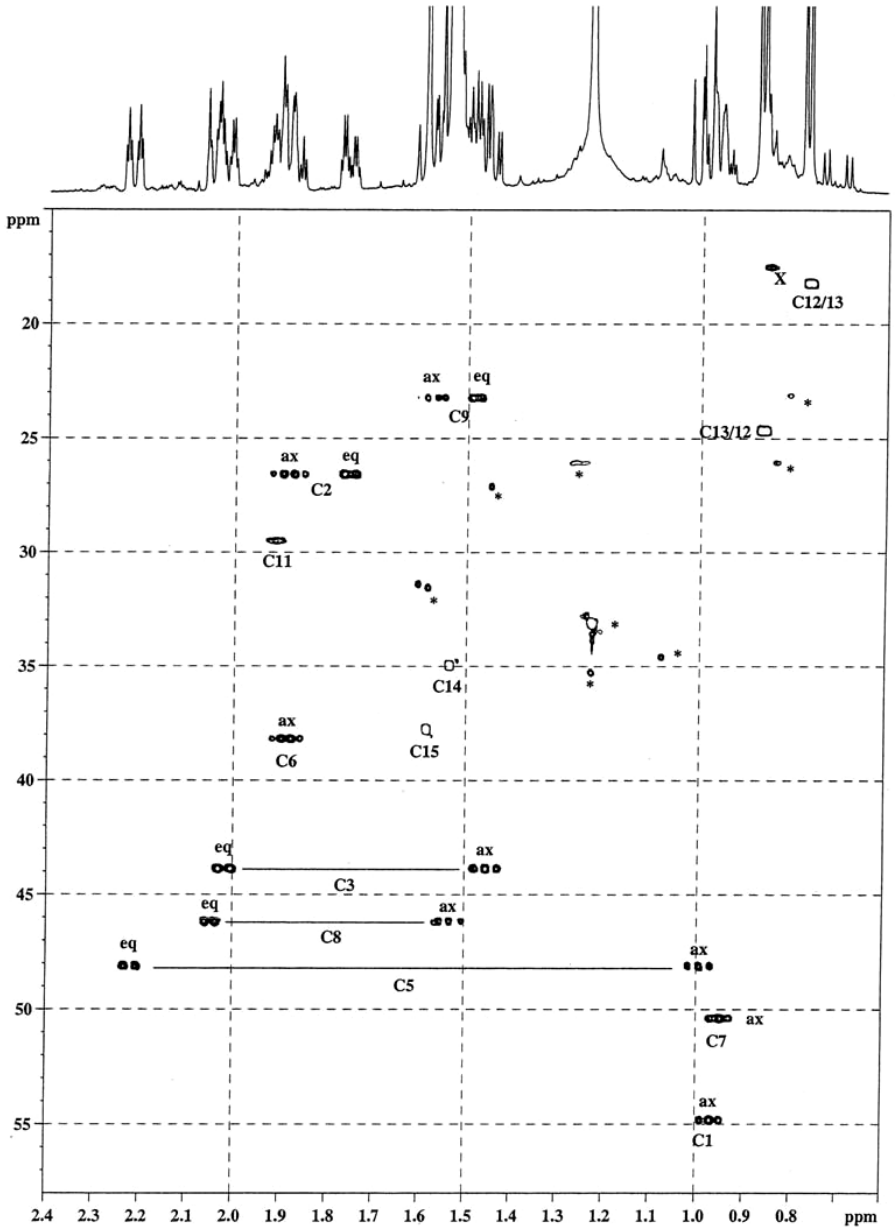
Because of the identification of reduced intensity of proton chemical shifts corresponding to the H-3, H-5, and H-9 in HSQC experiments on the DCl adduct, we concluded that the diene structures were one or many of the followings **3**, **11a**–**11c**.

Conclusion

The Diels–Alder adduct stereochemistry identification is an interesting attempt to show the corresponding isomeric diene presence within the very complex scheme for cubebene isomerization. The diene structure is then deduced from the adduct structural features. The stereochemistry of this adduct was established in a satisfactory manner con-

© 2007 NRC Canada

Fig. 2. NMR of dichloro derivative **13c** HSQC (600 MHz).



forming to the cycloaddition rules: the dienophile comes from the less hindered side of the diene to form the adduct. These results are reinforced by the molecular modelling calculations.

It is then assumed that the hydrochlorination of **1** proceeded via the formation of the protonated species, which is rearranged to the more stable of two possible carbocations leading to the Markovnikov addition as a final result.

Unfortunately, there are at least four possible diene structures that fit the HCl addition to the double bond: both vinylic carbons have the same substitution level but not the same access to the double bond for the bulky Cl^- ion.

More interestingly, to give such a dichloro adduct, the diene should have its double bond placed in, for example, -3,4 and -1,10 positions. This means that no single one of these dienes is able to produce the Diels–Alder addition described in this study. König's heating experiments revealed an easy shift of the double bond of the diene structure. The production of the Diels–Alder adduct in the case of α-cubebene (**1**) used in this study is thus a chemically formal proof of the quenching of the double bond in the 1,3-conjugated *s-cis* homo annular position; however, this diene is isomeric to the one described by König (9, 10).

The isomerization of the vinylcyclopropane to cyclopentene and the shift of the original double bond of cubebene both took place. In such a manner, the easy epimerisation of cubebene under microwave conditions is justified.

Once the dienes have been obtained, they can be further rearranged into those that are Diels–Alder precursors. In this respect, this diene is more stable since it is homonuclear and 1,3-conjugated and has natural *s-cis* conformation. For this purpose, the formal identification of the Diels–Alder adduct with maleic anhydride is very symptomatic. Both reactions,

© 2007 NRC Canada

Table 3. NMR data for dichloro derivative **13c** ($CDCl_3$) H-1 and C-13.

C No.	δ C	δ H
1	55.0	0.97(ax)
2	26.5	1.74(eq), 1.87(ax)
3	43.6	1.44(ax), 2.03(eq)
4	74.8(q)	—
5	48.1	0.99(ax), 2.23(eq)
6	38.2	1.87(ax)
7	50.3	0.945(ax)
8	46.2	1.53(eq), 2.06(ax)
9	23.2	1.49(eq), 1.575(ax)
10	78.0(q)	—
11	29.5	1.92
Methyls		
12	18.7	0.76[a]
13	24.8	0.88[a]
14	34.9	1.53
15	37.8	1.58(s)

Note: q = non-protonated carbon, s = singlet, ax = axial, eq = equatorial.
[a]Assignment can be inversed.

Diels–Alder and the addition of HCl, proceeded by several stepwise mechanisms. In such a manner, the respecting or not of the Woodward–Hoffmann formalism for the Diels–Alder adduct stereochemistry should then be considered as accidental.

Incidentally, the structure of the dihydrochloro adduct **13c** (Tables 3 and 4) is different than those described by, for example Burk (21) and Piers (22); as well, it has a different isopropyl orientation. X-ray analysis of the equivalent dihydrohalo structures also displays such a differently oriented isopropyl (23).

It is thus concluded that the cubebenes **1** and **3** with their original cyclopropyl–vinyl system can isomerize to many dienes: to 1,3- conjugated or to several deconjugated ones. The first is able to produce the Diels–Alder adduct and the second system produces the addition of two HCl.

When considering the -1,2 and -1,10 double bond containing intermediates, it is also possible to assume that their spontaneous reaction should go in the direction of the cubenol, leaving the hydroxyl group on the angular C-1 position (3) as observed in our previous paper when reacting **1** with methanol/HCl (3, 24).

The results of this deuterium labelling should be interpreted cautiously because of the sigmatropic shifts possible in this system and because of, as usual, the partial and relatively low yield of this reaction.

Experimental

General

All chemicals, solvents, chromatographic materials, and deuterated solvents were purchased from Sigma-Aldrich Chemicals (USA). The cubebene sample was obtained from Solidago Canadensis L as described in ref. 3 and the pure samples of compound **1** were also purchased from Sigma-Aldrich Chemicals.

Table 4. NMR of partial deuteration experiment in **13c** synthesis.

Double bond position	D position in ^{1}H NMR	Proton suppression
-4,9 **11a**	d5, d9	0.99(H-5ax), 1.575(H-9ax)
–10,4 **3**	d1, d5	0.97(H-1), 0.99(H-5ax)
–3,10 **11b**	d1, d3	0.97(H-1), 1.44(H-3ax)
–3,9 **11c**	d3, d9	1.44(H-3ax), 1.575(H-9ax)

NMR spectroscopy

NMR 1D experiments were performed using a Varian Inova spectrometer at 500 MHz for proton and 125 MHz for carbon-13 and a Bruker AMX at 600 MHz for proton and 125 MHz for carbon-13, respectively. In all cases the samples recorded at 295 K were prepared in $CDCl_3$ (dimethylsulfoxide-d_6) ca. 10% solution at 25 °C; chemical shifts were referred to the TMS or referenced to a residual signal of chloroform at 7.24 ppm. Selected 2D experiments were run using a standard Varian package of Inova programs for COSY and NOESY. For HSQC experiments, the Inova program for short range coupling (less than 140 Hz for 1*J* Hz) was used. The long range proton–carbon experiments (HMBC) were recorded with a Varian Inova pulse program, optimized for long range couplings (3*J* C, H 9.0 Hz). A DQF-COSY spectrum (25) was collected on a 800 × 1024 data matrix and the TOCSY spectrum was collected with a mixing time of 80 ms (26). In all experiments the carrier frequency was set at the centre of the spectrum. The (^{1}H,^{13}C) HSQC (27) experiments were recorded with a delay of 3.5 ms (1*J* CH = 143 Hz) and the (^{1}H,^{13}C) HSQC-TOCSY experiment with a mixing time for proton–proton transfer of 80 ms to identify the network of one-bond and several proton–carbon connectivities, respectively. All data were processed with the XWINNMR software and one zero filling and π/3 phase shifted sine bell window function were applied in both dimensions before Fourier transform.

All NMR high resolution 1D and 2D detailed experiments data could also be transmitted to the interested persons from the corresponding author (CKJ, U de Moncton, Canada).

Mass spectroscopy

Mass spectra of all products were recorded on Agilent 6890 with mass selective detector (model 5973) (U de Moncton, Moncton, New Brunswick), the column used was a HP5-MS (30 m, 0.25 μm), the GC-MS EI and CI (NH_3) experiments on Riber 1030 GC-MS (U de Paris, Paris, France), and ESI-PI on a Micromass Quatro II (U de Paris, Paris, France), as well on an Agilent 19091S-436 with packed column HP5-MS (0.25 mm, 60 m, 0.25 μm) (Environment Canada, Ottawa, Canada). The GC-MS was used as the control of the progress of purification of chromatographic fractions for adduct **9b** and for the dichloro derivative **13c**. The mass spectroscopy was also used to determine the deuteration level of this last compound in a series of experiments as described in the following.

Molecular modelling

All molecular modelling results performed on HyperChem 6.02 on dienes and adducts are available on request from the corresponding author (CKJ, U de Moncton, Canada).

© 2007 NRC Canada

Microwaves

Microwave experiments were carried out at atmospheric pressure using a focused microwave reactor (CEM Discover™) (28) or MAP technology (14, 15). The instrument consists of a continuous focused microwave power output from 0 to 300W. Reactions were performed in a glass vessel equipped with a condenser; it is also possible to work under dry atmosphere, in vacuo, or under pressure (0–20 torr, tubes of 10 mL, sealed with a septum) (1 torr = 133.322 4 Pa). The temperature content of a vessel is monitored using a calibrated IR sensor mounted under the vessel. All experiments were performed using stirring option whereby the contents of a vessel are stirred by means of a rotating plate located below the floor of the microwave cavity and a Teflon-coated magnetic stir bar in the vessel. In all experiments a power of 300 W was selected and the reflux temperature was reached with a ramp of about 1 min. The time of the reaction does not include the ramp period.

Synthesis

*(4,10a-dimethyl-7b-*iso*-propyl-decaline-5ene)1a,4a-maleic acid anhydride (9b)*

Diels–Alder condensation of **1** with maleic anhydride (thermal reaction). Cubebene (**1**) (100 mg, ca. 0.5 mmol) and maleic anhydride (40 mg, 0.45 mmol, less than equimolar ratio) were dissolved in anhydrous toluene and heated in the stainless vessel for 24 h at 130 °C. Two consecutive flash column chromatography separations on silica gel column of adduct **9b** were then performed on the oily residue under TLC (hexane/ether 9:1, R_f = 0.7) and GC-MS controls (using mass chromatogram at *m/z* 302). The yield of pure adduct **9b** was 12% (16–18 mg) with an optical rotation of α_{25} = +38° (ethanol). MS eight main ions in **9b**, EI-spectrum *m/z* (I%): 302 (12, M^+), 274 (72), 259 (16), 231 (56), 203 (100), 185 (17), 164 (82), 145 (39).

Diels–Alder condensation of **1** with maleic anhydride (microwave reaction). Yield of **9b** 15%–23%. Conditions: CEM Discover™ 300 W at the reflux temperature of toluene for 5–30 min.

*4β,10β-dichloro-4α,10α-dimethyl-7β-*iso*-propyl-*trans*-decalin (13c)*

Addition of HCl to **1** at 0–5 °C. To a solution of α-cubebene (**1**) (90 mg, 0.5 mmol) in methanol (20 mL) (the equal volume of dry methanol saturated with hydrochloric acid (g) was added). The reaction mixture was left at 0–5 °C for 24 h then cautiously evaporated in vacuo. The resulting product **13c** (14 mg), mp 104–107 °C, TLC: petroleum ether, R_f = 0.4, isolated by column then by preparative TLC chromatographies on silica gel, yield 25%. In this separation, 31 mg of starting compound **1** and three unidentified compounds were separated. MS: For the compound **13c** CI-MS (NH_3) mass spectra revealed the presence of *m/z* 294 (100, NH_4^+), 277 (3, MH^+) 276 (2). The ESI spectrum confirmed double chlorination at *m/z* 277 (55, MH^+) and 279 (35, MH^+).

Addition of DCl to **1** was performed in a similar mode (also see ref. 3).

Synthesis by microwave-assisted addition of HCl

A solution of α-cubebene (100 mg, 0.5 mmol) in methanol (12.5 mL) (saturated with hydrochloric acid) was irradiated at 25 W with a ramp period of 1 min until reflux was reached. Heating of the solution was then maintained for 30 min, and after cooling the solvent was removed in vacuo. The various products observed by TLC analysis were then separated by column chromatography (petroleum ether) and analyzed as in previous procedure. Yield of **13c** 15%.

Acknowledgments

We would like to thank A. Savoie (U de Moncton) for helpful discussion and his involvement in the primary stage of this study, S. Arseneau (U de Moncton) for some molecular modelling and energy computing calculations and C. Fajolles (CEA) for precious graphical assistance. One of the authors (TB) thanks CEM Corp. for multiform support and technical assistance. The generous financial support of Environment Canada through Youth Horizons Fellowship was greatly appreciated.

References

1. (*a*) Y.H. Kuo, C.H. Chen, S.C. Chien, and Y.L. Lin. J. Nat. Prod. **65**, 25 (2002); (*b*) E. Ormeno, C. Fernandez, and J.P. Mevy. Phytochemistry, **68**, 840 (2007); (*c*) S. Arctander. Perfume and flavor materials of natural origin. *Edited by* S. Arctander. Elizabeth, New Jersey. 1960. pp. 281–285.
2. (*a*) I. Guterman, M. Shalit, N. Menda, D. Piestun, M. Dafny-Yelin, G. Shalev, E. Bar, O. Davydov, M. Ovadis, M. Emanuel, J. Wang, Z. Adam, E. Pichersky, E. Lewinsohn, D. Zamir, A. Vainstein, and D Weiss. Plant Cell, **14**, 2325 (2002); (*b*) D. Kalemba, J. Gora, A. Kurowski, and T. Majda. Zesz. Nauk. Politech. Lodz. Chem. Spozw. **47**, 92 (1990); (*c*) O.P. Vig. Indian J. Chem. Sect. B, **17**; 352 (1979); (*d*) V.H. Kaapadia, B.A. Nagasampagi, V.G. Naik, and S. Deve. Tetrahedron, **21**, 607 (1965); (*e*) N.H. Andersen. Phytochemistry, **16**, 1731 (1977); (*f*) L.A. Burk and M.D. Soffer. Tetrahedron, **32**, 2083 (1976); (*g*) V. Herout and F. Santavy. Coll. Czech. Chem. Comm. **19**, 118 (1959); (*h*) B.A. Nagasampagi, L. Yankov, and S. Deve. Tetrahedron Lett. 1913 (1968); (*i*) D.W. Connell, R.F. Hildebrand, and M.D. Suderland. Tetrahedron Lett. 519 (1968); (*j*) V. Sykora, V. Herout, and F. Sorm. Coll. Czech. Chem. Comm. **21**, 2181 (1958).
3. C.K. Jankowski, A. Savoie, D. Lesage, J.R.J.P. Paré, J.M.R. Belanger, M. de Fatima Pereira, V. Thiery, T. Besson, O. Maciejak, F. Toma, L. Mauclaire, and Xiangjun Liao. J. Mex. Chem Soc. **50**, 90 (2006).
4. (*a*) A.A. Kasali, O. Ekundayo, C. Paul, and W.A. König. Phytochemistry, **59**, 805 (2002); (*b*) N. Bulow and W.A. König. Phytochemistry, **55**, 141 (2000).
5. I. Fleming. Frontier orbitals in organic chemistry. J. Wiley, New York. 1976. pp. 42–45, 73–132.
6. J.E. Baldwin. Chem. Rev. **103**, 1197 (2003).
7. J.A. Hirsch. Concepts in theoretical organic chemistry. Allyn and Bacon, Boston, Mass. 1974. Chap. 3. pp. 77–78.
8. H.R. Sonawane, N.S. Bellur, D.G.T. Kulkarni, and J.R. Ahuja. Synlett, **12**, 875 (1993).
9. S. Melching, N. Bulow, K. Wihstutz, S. Jung, and W.A. König. Phytochemistry, **44**, 1291 (1997).
10. A.M. Adio, C. Paul, H. Tesso, P. Kloth, and W.A. König. Tetrahedron: Asymmetry, **15**, 1631 (2004).
11. (*a*) A. Padwa, S.K. Bur, and H.J. Zhang. J. Org. Chem. **70**, 6833 (2005); (*b*) A. Padwa and S. Clough. J. Am. Chem. Soc. **92**, 5803 (1970).

© 2007 NRC Canada

12. D.A. Seeley. J. Am. Chem. Soc. **94**, 4378 (1972).
13. J. Saltiel, D.F. Sears, Y.P. Sun, and J.O. Choi. J. Am. Chem. Soc. **114**, 3607 (1992).
14. J.R.J. Paré and J.M.R. Belanger. Microwave assisted process (MAP™): Principles and applications. *In* Instrumental methods in food analysis. *Edited by* J.R.J. Paré and J.M.R. Belanger. Elsevier Science, Amsterdam, The Netherlands. 1997. Chap. 10. pp. 395–420.
15. (*a*) H.E. Zimmerman and G.A. Epling. J Am. Chem. Soc. **94**, 7806 (1972); (*b*) W.G. Darben, G. Loder, and J. Ipastski. Top. Curr. Chem. **54**, 23 (1975).
16. (*a*) D.J. Collins, J.J. Hobbs, and S. Sternhell. Aust. J. Chem. **16**, 1030 (1963); (*b*) E.B. Whipple. J. Chem. Phys. **35**, 1039 (1961).
17. N.S. Bhacca and D.H.Williams. Application of NMR spectroscopy in organic chemistry. Holden Day, San Francisco, Calif. 1964. p. 108.
18. E. Breitmaier and W. Voelter. C-13 NMR spectroscopy. Methods and application. Chemie Verlag, Weinheim, Germany. 1974. p. 123.
19. E.L. Eliel and S.H. Wilen. Stereochemistry of organic compounds. Wiley-Interscience, London, UK. 2004. pp. 227–229.
20. S. Picaud, L. Olofsson, M. Brodelius, and P.E. Brodelius. Arch. Biochem. Biophys. **436**, 215 (2005).
21. (*a*) L.A Burk and M.D. Soffer. Tetrahedron Lett. **46**, 4367 (1971); (*b*) A. Tanaka, H. Uda, and A. Yoshikoi. J. Chem. Soc. Chem. Commun. **6**, 308 (1969).
22. E. Piers and W.M. Phillips-Johnson. Can. J. Chem. **53**, 1281 (1975).
23. (*a*) M.D. Soffer and G.E. Gunay. Tetrahedron. Lett. **19**, 1355 (1965); (*b*) F. Hanic. Chem. Listy, **52,** 165 (1958); (*c*) F. Gantis. Kristallografiya, **3**, 277 (1958).
24. A. Furstner and P. Hannen. Chem. Eur. J. **12**, 3006 (2006).
25. M. Rance, O.W. Sorensen, G. Bodenhausen, G. Wagner, R.R. Ernst, and K.Wuthrich. Biochem. Biophys. Res. Commun. **117**, 479 (1983).
26. M. Rance. J. Magn. Reson. **74**, 557 (1987).
27. G. Bodenhausen and D.J. Ruben. Chem. Phys. Lett. **69**, 185 (1980).
28. (*a*) Microwaves in organic synthesis. *Edited by* A. Loupy. Wiley-VCH Verlag, Weinheim, Germany. 2006; (*b*) J.D. Fergusson. Mol. Diversity, **7**, 280 (2003).

© 2007 NRC Canada

Homoallylic ketones and pyrroles by way of copper-catalyzed cascade additions of alkyl-substituted vinyl Grignard reagents to esters

Aurélie A. Dörr and William D. Lubell

Abstract: Exploring the scope of the copper-catalyzed cascade addition of vinyl Grignard reagents to carboxylic esters, a set of substituted homoallylic ketones (γ,δ-unsaturated ketones) have been synthesized in 11%–94% yields from treatment of methyl 4-methoxybenzoate and methyl *N*-Boc-β-alaninate with different methyl-, dimethyl-, and phenyl-substituted vinyl Grignard reagents in the presence of catalytic amounts of CuCN in THF. The respective 2,4-di-, 2,3,5-tri-, and 2,3,4,5-tetrasubstituted pyrroles were obtained in 47%–93% yields from the homoallylic ketones by a sequence featuring ozonolysis followed by Paal–Knorr condensation with ammonium formate.

Key words: copper-catalyzed cascade addition, homoallylic ketone, alkyl-substituted vinyl Grignard reagents, ozonolysis, pyrrole, γ,δ-unsaturated ketone.

Résumé : En étudiant l'étendue de la réaction d'addition en cascade de réactifs de Grignard vinyliques sur des esters carboxyliques catalysée par des sels de cuivre, une série de cétones homoallyliques (cétones γ,δ-insaturées) substituées a été synthétisée avec des rendements de 11%–94% à partir du 4-méthoxybenzoate de méthyle et du *N*-Boc-β-alaninate de méthyle avec différents réactifs de Grignard vinyliques substitués par des groupements méthyle, diméthyle et phényle, dans le THF. Des pyrroles 2,4-di, 2,3,5-tri et 2,3,4,5-tétrasubstitués ont été obtenus avec des rendements de 47%–93% à partir des cétones homoallyliques suite à une séquence réactionnelle incluant une ozonolyse suivie d'une condensation de Paal–Knorr avec de l'ammonium formate.

Mots-clés : addition en cascade catalysée au cuivre, cétone homoallylique, réactif de Grignard vinylique substitués, ozonolyse, pyrrole, cétone γ,δ-insaturée.

[Traduit par la Rédaction]

Introduction

The γ,δ-unsaturated carbonyl unit is a structural component of natural products (1) and an important intermediate in the synthesis of terpenoids (2) and heterocycles such as pyrroles (3), dihydropyrroles (3*a*, 4), pyridines (5), and isoquinolines (5*a*). Moreover, homoallylic ketones (γ,δ-unsaturated ketones) are particularly useful as precursors to 1,4-diketone intermediates for the preparation of cyclopentanones (6), pyrroles (7), furans (7*h*–7*k*, 8), thiophenes (7*j*–7*k*), and pyridazines (7*k*, 9).

In light of their broad utility for making compounds of biological and technological importance, the synthesis of γ,δ-unsaturated carbonyl compounds has attracted considerable interest. Among the methods for synthesizing γ,δ-unsaturated systems (10–14), a notable one of choice has been the 1,4-addition of suitably substituted alkenyl metallic reagents to an α,β-unsaturated carbonyl compound. For example, conjugate additions to α,β-unsaturated ketones of alkenyl Grignard reagents in the presence (15*a*–15*h*) and absence (15*i*–15*k*) of catalytic copper salts, as well as the 1,4-additions of alkenyl copper (16–19) and boron (20) reagents, have all been used to make homoallylic ketones. Alternative methods for making γ,δ-unsaturated carbonyl units include the direct insertion of aroyl cyanides (21*a*) and aldehydes (21*b*, 21*c*) to zirconacyclopentenes, the allylation of silyl enol ethers (22), and various allylations of unsaturated compounds under ruthenium (23), palladium (24), copper (25) and nickel (26) catalysis. The Claisen–Cope (1*m*, 27) and Carrol (28) rearrangements (29) and the Wittig (30) methodology have also found utility in the construction of γ,δ-unsaturated carbonyl compounds.

Homoallylic ketones have been obtained by the reaction of excess vinylmagnesium halide onto various carboxylic acid derivatives, including carboxylic acids (31*a*–31*c*), esters (31*b*, 32), acid anhydrides (31*b*), and acid halides (33). Low yields and the competitive formation of side products, such as tertiary alcohols and alkenyl ketones, have limited the utility of this methodology (31*b*–31*c*, 33). Copper salts have been utilized to enhance product formation in these cascade addition processes. For example, CuCl was added to the cascade reaction of excess vinylmagnesium chloride to fatty carboxylic acids and esters to produce mixtures of 1,6-diones and homoallylic ketones in 6%–47% yields (32). Significantly improved yields of homoallylic ketone were

Received 9 April 2007. Accepted 20 August 2007. Published on the NRC Research Press Web site at canjchem.nrc.ca on 25 October 2007.

A.A. Dörr and W.D. Lubell. Département de Chimie, Université de Montréal, C.P. 6128. Succursale Centre-Ville, Montréal, QC H3C 3J7, Canada.

[1]Corresponding author (e-mail: lubell@chimie.umontreal.ca).

 doi:10.1139/V07-114 © 2007 NRC Canada

achieved in the cascade reaction of excess vinylmagnesium bromide to methyl esters by employing catalytic amounts of $Cu(OAc)_2$ or CuCN (34). This version of the copper-catalyzed cascade addition proved effective for the synthesis of the parent but-4-en-1-ones using a variety of methyl carboxylates, including aromatic and aliphatic esters as well as N-protected α-, β-, and γ-amino esters.

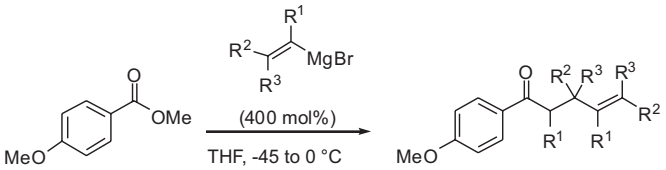
Mixtures of homoallylic ketone and tertiary alcohol were also isolated from cascade reactions using α-methyl-, β-methyl-, and β,β-dimethyl substituted vinylmagnesium halides in additions to carboxylic acids, esters, and acid anhydrides (35, 36) in the absence of copper. For example, the treatment of methyl *p*-toluate with isopropenyl- and prop-1-enyl-magnesium bromides gave, respectively, 2,4-dimethyl-1-(*p*-tolyl)pent-4-en-1-one and 3-methyl-1-(*p*-tolyl)hex-4-en-1-one in 65% and 54% yields, along with 7%–11% of the corresponding tertiary alcohol resulting from two sequential 1,2-addition reactions of the alkenyl Grignard reagent onto the ester carbonyl (35). On the other hand, treatment of ethyl benzoate with 2-methylprop-1-enyl-magnesium bromide was reported to produce exclusively the tertiary alcohol 2,6-dimethyl-4-phenyl-heptadi-2,5-en-4-ol in 70% yield (36).

In considering these issues (35–36), and the success of the copper-catalyzed cascade addition of vinyl Grignard reagent to esters for preparing the parent but-4-en-1-ones (34), the reactions of esters with various alkenyl Grignard reagents and CuCN have now been investigated to provide substituted homoallylic ketones. The scope of this reaction has been examined by employing a diverse set of methyl-, dimethyl-, and phenyl-substituted vinyl Grignard reagents on two substrates: methyl 4-methoxybenzoate and methyl *N*-Boc-β-alaninate. Furthermore, the corresponding homoallylic ketones **2**–**8**, which were obtained in 11%–94% yields, were subsequently used to provide a diverse set of substituted pyrroles **9**–**13** in 47%–93% yields by a route featuring ozonolysis of the olefin to provide 1,4-dione and 4-oxo aldehyde intermediates for Paal–Knorr condensations with ammonium formate.

Results and discussion

Methyl 4-methoxybenzoate and *N*-Boc-β-alanine methyl ester were treated with a set of commercially available α- and β-methyl and di-methyl substituted Grignard reagents, as well as α- and β-phenylvinyl Grignard reagents that were freshly prepared in-house. We first examined the cascade addition of 400 mol% of α- and β-methyl and dimethyl-substituted Grignard reagents to methyl 4-methoxybenzoate in the absence of copper salts (Scheme 1). Homoallylic ketones **3a** and **4a** were obtained in 80% and 36% yields from employing as Grignard reagent, respectively, 1-propenylmagnesium bromide and 2-methyl-1-propenylmagnesium bromide. Only starting methyl ester was, however, recovered from the reactions using isopropenylmagnesium bromide and 1-methyl-1-propenyl-magnesium bromide as Grignard reagent. The Cu-catalyzed cascade additions of substituted vinyl Grignard reagents were then performed using three types of conditions (Scheme 2). Condition A (Table 1) featured premixing Grignard reagent (400 mol%) and a catalytic amount of CuCN (30%–40 mol%) in THF at −45 °C for 10 min before treatment with a solution of the ester. Condition B (Table 1) employed more CuCN (60 mol%) and a longer premixing time (2 h) with the Grignard reagent (400 mol%) in THF at –45 °C before treatment with a solution of the ester. Condition C was identical to condition B except for the use of more Grignard reagent (500 mol%).

Scheme 1. Cascade addition in the absence of copper salts.



	R^1	R^2	R^3	(%)[a]
3a	H	Me	H	80
4a	H	Me	Me	36
5a	Me	H	H	SM
6a	Me	Me	H	SM

[a] Isolated yield

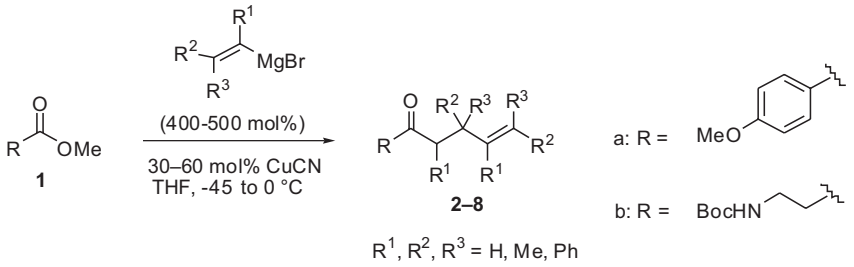
Substituted homoallylic ketones **3**–**8** were usually obtained in relatively higher yields (Table 1, 11%–94%) using Condition B vs. Condition A (Table 1, 9%–88% yields). This improvement was more evident in the synthesis of homoallylic ketones from methyl 4-methoxybenzoate rather than from *N*-Boc-β-alaninate, which seemed less sensitive to the change. For example, the yields of homoallylic ketone **4a** possessing a quaternary gem-dimethyl carbon were improved from 66% to 75% yield using Condition B (Table 1, entry 3); however, in the case of the *N*-Boc-β-alaninate-derived counterpart **4b**, they dropped from 25% to 20% (Table 1, entry 10).

Some changes were observed using Condition C vs. Condition B in the synthesis of homoallylic ketones from *N*-Boc-β-alaninate. This amelioration was particularly evident for the synthesis of homoallylic ketones **5b** and **7b**, respectively, from using isopropenylmagnesium bromide and 2-phenylvinylmagnesium bromide; the yields were improved from 38% to 63%, respectively, and from 11% to 78% (Table 1, entries 11 and 13). On the other hand, a minor 3%–5% improvement in yield was observed in the synthesis of homoallylic ketones **3b** and **6b** using 500 mol% of 1-propenylmagnesium bromide or 1-methyl-1-propenyl-magnesiumbromide, respectively, (Table 1, entries 9 and 12), and no amelioration was observed in the case of the synthesis of homoallylic ketones **4b** and **8b** from 2-methyl-1-propenylmagnesium bromide and 1-phenylvinylmagnesium bromide, respectively (Table 1, entries 10 and 14).

Olefins **3a**, **3b**, and **7b** were isolated as mixtures of double bond isomers from reactions employing the β-methyl- and β-phenyl-substituted vinyl Grignard reagents, 1-propenylmagnesium bromide and 2-phenylvinylmagnesium bromide. On the other hand, (4*Z*)-1-(4-methoxyphenyl)-3,5-diphenylpent-4-en-1-one (**7a**) was isolated in 61% yield as a single isomer. The ratios of *E*/*Z* isomers **3a**, **3b**, and **7b** were measured by integration of the olefinic protons in their respective ^{1}H NMR spectra as well as by LC-MS analysis in the case of **3a**. The *E* and *Z* geometry was assigned on the basis of the characteristic coupling constants of the vinylic protons (Table 1). Homoallylic ketones **3a** and **3b** were observed to contain predominantly the *Z*-isomer (*E*/*Z* 35:65

© 2007 NRC Canada

Scheme 2. Synthesis of homoallylic ketones **2–8** by copper-catalyzed cascade addition.



and 29:71), and low selectivity was observed for olefin **7b** (*E*/*Z* 60:40). The influence of the reaction conditions on the stereoselectivity of the olefin has yet to be investigated, however the geometry of the double bond in the final product does not reflect the geometry of the starting Grignard reagent. For example, when employing an isomeric mixture of *E*- and *Z*-2-phenylvinylmagnesium bromide, only *E*-isomer **7a** (Table 1, entry 6) was isolated from 4-methoxybenzoate and a nearly equal ratio of two isomers **7b** (Table 1, entry 13) was obtained from *N*-Boc-β-alanine methyl ester.

Mixtures of isomers were also isolated from the reactions using 1-methyl-1-propenylmagnesium bromide. Homoallylic ketone **6a** was isolated as a mixture of three isomers, which were observed to exist in a 7.1:1.6:1.3 ratio, by LC-MS analysis of three peaks possessing the same molecular weight, and in an 8.4:0.9:0.7 ratio, as esteemed by integration of the sets of aromatic doublets in the ^{1}H NMR spectrum. Homoallylic ketone **6b** was isolated as a mixture of two isomers that were inseparable by analytical LC-MS and measured as an 8.5:1.5 ratio by integration of the vinyl protons in the ^{1}H NMR spectrum. Homoallylic ketones **6a** and **6b** may exist as mixtures of syn and anti diastereomers as well as cis and trans olefins, however their assignment could not be made because of difficulties in separating pure isomers; instead, the mixtures were used directly for pyrrole synthesis as described below.

The ability to use mixtures of substituted vinyl organometallic reagents in multi-component reactions would provide novel access to a greater diversity of γ,δ-unsaturated ketones. The cascade addition of two different Grignard reagents was thus explored by adding vinylmagnesium bromide and isopropenylmagnesium bromide to 4-methoxybenzoate (Scheme 3, Table 2). In certain cases, the desired 4-methyl homoallylic ketone **14a**, resulting from the 1,2-addition of vinylmagnesium bromide to the ester followed by the 1,4-addition of isopropenylmagnesium bromide to the enone intermediate, was obtained as the major product, albeit in low yield. Homoallylic ketone **14a** was contaminated with 2,4-dimethyl homoallylic ketone **5a** and the parent homoallylic ketone **2a** resulting from 1,2- and 1,4-additions of only isopropenylmagnesium bromide or vinylmagnesium bromide, respectively. Four conditions were explored to optimize the production of 4-methyl product **14a**. The resultant crude product was then purified by column chromatography to give an inseparable mixture of homoallylic ketones **14a**, **5a**, and **2a**. The product ratio was determined by LC-MS analysis of the purified mixture of homoallylic ketones. Initially, relatively equal amounts of the Grignard reagents were premixed for 10 min at −45 °C with CuCN (30 mol%) before the addition of the ester to produce a 4.6:2.8:2.6 ratio of **14a/5a/2a** (Table 2, entry 1). Then varying amounts of the isopropenylmagnesium bromide and CuCN were premixed in THF for 2 h at −45 °C, prior to the addition of the vinylmagnesium bromide (100 mol%) and methyl ester (Table 2, entries 2–3). When 300 and 100 mol% of the methyl-substituted vinyl Grignard reagent were, respectively, premixed with 60 and 100 mol% of copper salt, homoallylic ketones **14a/5a/2a** were obtained in ratios of 4.1:4.4:1.6 (Table 2, entry 2) and 4.1:3.7:2.2 (Table 2, entry 3). To date, our best results were obtained by premixing isopropenylmagnesium bromide (110 mol%) with 60 mol% of CuCN prior to the addition of ester and vinylmagnesium bromide (100 mol%), which provided ketones **14a/5a/2a** in a 5.6:0.6:3.8 ratio (Table 2, entry 4). A sample of 4-methyl ketone **14a** was finally isolated by HPLC purification for characterization purposes.

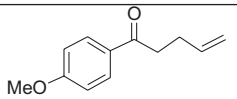
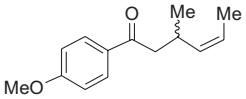
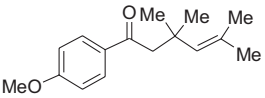
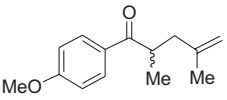
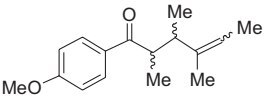
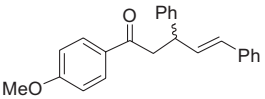
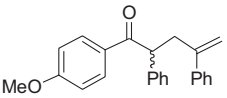
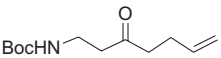
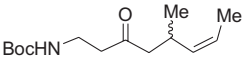
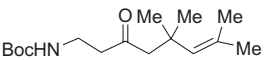
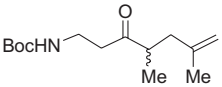
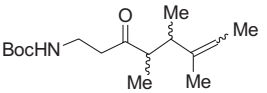
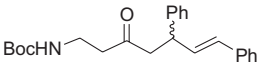
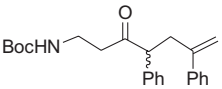
Pyrrole synthesis was next performed using the γ,δ-unsaturated ketones (Scheme 4). Previously, a library of 1,2,5-trisubstituted pyrroles was synthesized from homoallylic ketones that were obtained from the cascade reaction of vinyl Grignard reagent by an approach featuring olefin oxidation using the Tsuji–Wacker reaction and subsequent Paal–Knorr condensation on the resulting 1,4-diones with different amines (7*a*). With substituted homoallylic ketones **3** and **5–8** now in hand, we explored a similar olefin oxidation/Paal–Knorr strategy to prepare 2,4-di-, 2,3,5-tri-, and 2,3,4,5-tetra-substituted pyrroles **9–13** (Fig. 1). For the oxidation of homoallylic ketones **3** and **5–8**, ozonolysis in MeOH/CH_2Cl_2 at –78 °C, followed by treatment with Me_2S and freeze-drying gave crude 1,4-dicarbonyl compounds that were typically of sufficient purity for the subsequent condensation step. The Paal–Knorr reaction was accomplished by treatment of the crude 1,4-dicarbonyl compounds with ammonium formate. In the synthesis of pyrroles **10**, **11b**, **12**, and **13**, the ozonolysis product was condensed with ammonium formate in the presence of NaOAc/HOAc (100 mol% *w*/*w*) in acetonitrile at 65 °C to give the desired targets in 47%–93% yields from the corresponding homoallylic ketone (7*a*). Alternatively, substituted pyrroles **9** and **11a** were best obtained in 59%–70% yields by treating the ozonolysis product with ammonium formate and KOAc in a AcOH/CH_3CN/H_2O mixture (1:1:1) at 80 °C.

Conclusion

The scope of the copper-catalyzed cascade addition of vinylmagnesium bromide to carboxylic esters for the synthesis of homoallylic ketones has been expanded by the em-

© 2007 NRC Canada

Table 1. Reaction conditions and yields for the synthesis of homoallylic ketones **2**–**8**.

Entry	R^1	R^2	R^3	Product		Reaction conditions	Isolated yield (%)	*J* Hz *E* / *Z*	Isomeric ratio LC-MS (^{1}H NMR)	(t_R) [a]	Ref
1	H	H	H		**2a**	A B	70 69	—	—	—	31*a*,*c* 37
2	H	Me	H		**3a**	A B	88 94	N.d. /1.56, 10.01	35:65 (35:65 E/Z)	30.31, 29.82	—
3	H	Me	Me		**4a**	A B	66 75	—	—	—	—
4	Me	H	H		**5a**	A B	46 81	—	100 (> 99:1)	—	—
5	Me	Me	H		**6a**	A B	9 24 (33)[b]	N.d.	71:16:13 (84:9:7)	33.45, 32.63, 32.28	—
6	H	Ph	H		**7a**	A B	6[1] 28 (73)[b]	5.63, 15.90	100 (> 99:1 E/Z)	—	—
7	Ph	H	H		**8a**	A B	24 (49)[b] 50	—	100 (> 99:1)	—	—
8	H	H	H		**2b**	A	94	—	—	—	7*a*
9	H	Me	H		**3b**	A B C	55 71 74	N.d. / 1.65, 9.62	N.d. (29:71 E/Z)	27.51	—
10	H	Me	Me		**4b**	A B C	25 20 21	—	—	—	—
11	Me	H	H		**5b**	A B C	44 38 63	—	100 (> 99:1)	—	—
12	Me	Me	H		**6b**	A B C	15 (26)[b] 21 (34)[b] 26 (49)[b]	N.d.	N.d. (85:15)	30.93	—
13	H	Ph	Ph		**7b**	A B C	22 (31)[b] 11 78	6.21, 15.90 / 10.95, 11.47	N.d. (60:40 E/Z)	31.56	—
14	Ph	H	H		**8b**	A B C	22 41 38	—	100 (> 99:1)	—	—

Note: N.d. indicates Not determined.
[a]Retention time in minutes.
[b]Yields based on recovered starting methyl ester.

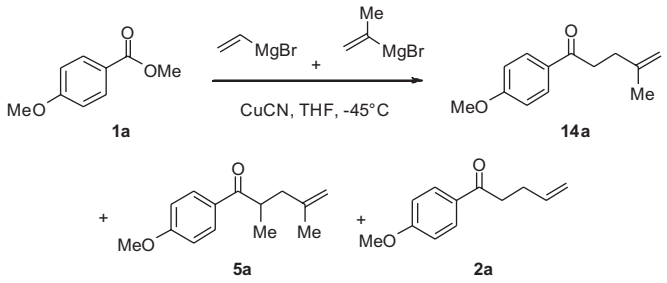
© 2007 NRC Canada

Table 2. Conditions for the addition of two different Grignard reagents to methyl *p*-methoxybenzoate.

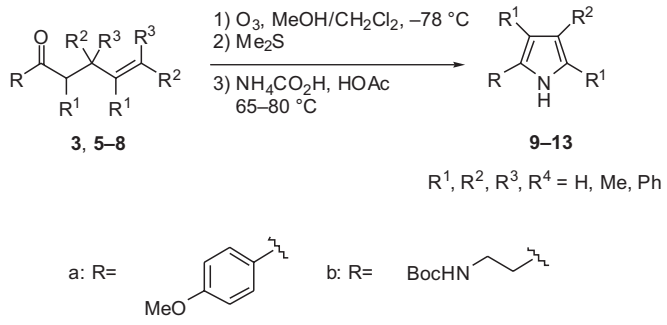
Entry	Reaction conditions	CuCN (mol%)	Vinylmagnesium bromide (mol%)	Isopropenylmagnesium bromide (mol%)	Premixed time	Ratio **14a/5a/2a**[a]	Yield of **14a** (%)
1	D	30	100	120	10 min	4.6:2.8:2.6	15 (17)[b]
2	E	60	100	300	2 h	4.0:4.4:1.6	30
3	F	100	100	100	2 h	4.1:3.7:2.2	13 (16)[b]
4	G	60	100	110	1 h	5.6:0.6:3.8	17 (27)[b]

[a]Determined by LC-MS analysis of the isolated mixture.
[b]Yields based on recovered starting methyl ester.

Scheme 3. Addition of two different Grignard reagents to methyl *p*-methoxybenzoate.



Scheme 4. Synthesis of 2,4-di-, 2,3,5-tri-, and 2,3,4,5-tetra-substituted pyrroles **9–13**.



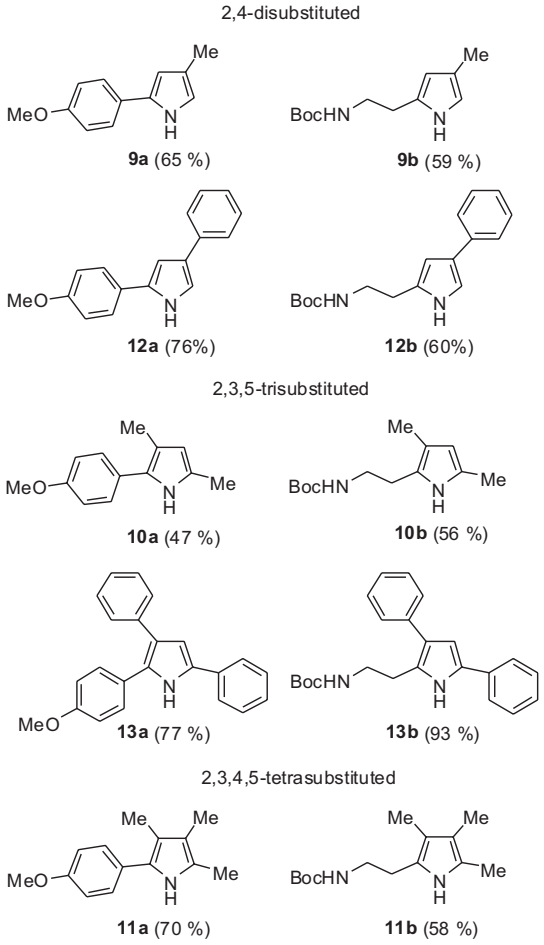
ployment of substituted vinyl Grignard reagents. Substituted γ,δ-unsaturated ketones were synthesized in 11%–94% yields on respective treatments of methyl 4-methoxybenzoate and methyl *N*-Boc-β-alaninate with methyl-, dimethyl-, and phenyl-substituted vinyl Grignard reagents in the presence of catalytic CuCN in THF. A series of diverse substituted pyrroles were then prepared in two steps from the substituted γ,δ-unsaturated ketones, by employing an olefin ozonolysis/Paal–Knorr condensation procedure. 2,4-Di-, 2,3,5-tri-, and 2,3,4,5-tetra-substituted pyrroles **9–13** were synthesized in 47%–93% overall yields from their respective homoallylic ketones. Moreover, a cursory investigation of the addition of a combination of isopropenyl- and vinylmagnesium bromides onto methyl 4-methoxybenzoate demonstrated that two different vinyl Grignard reagents may be used in this cascade reaction to broaden the diversity of homoallylic ketone products.

Experimental

General

For reactions performed under anhydrous conditions, glassware was flame-dried, and the reaction was performed

Fig. 1. Yields of polysubstituted pyrroles **9–13** (see ref. 38 for **12a**).



under a positive pressure of argon using anhydrous solvents that were transferred by syringe. Anhydrous solvents (THF, CH_3CN, MeOH) were dried by passage through solvent filtration systems (GlassContour, Irvine, California). Final reaction mixture solutions were dried over $MgSO_4$. Chromatography was on a 230–400 mesh silica gel, and TLC was on aluminium-backed silica plates. Mass spectrometry data were obtained at the Université de Montréal Mass Spectrometry facility. The ratios of isomers of homoallylic ketones **3–8** were determined by analytical LC-MS (Prevail column from Alltech, Inc, 4.6 × 250 mm, 5 μm, C_{18}) with a flow rate of 0.5 mL/min using CH_3CN (0.1% TFA)/H_2O (0.1% TFA) from 20:80 to 80:20 in 45 min. The retention times (t_R) are reported in minutes. The product ratios of homoallylic ketones **14a/5a/2a** were deter-

© 2007 NRC Canada

mined by analytical LC-MS (Gemini from Phenomenex Inc., 4.6 × 50 mm, 5 μm, C_{18}) with a flow rate of 0.5 mL/min using CH_3CN (0.1% TFA)/H_2O (0.1% TFA) from 20:80 to 80:20 in 14 min. ^1H NMR spectra were measured in $CDCl_3$ or acetone-d_6 at 400 and 300 MHz and referenced to $CDCl_3$ (7.26 ppm) or acetone-d_6 (2.05). ^{13}C NMR were measured in $CDCl_3$ at 100 and 75 MHz and referenced to $CDCl_3$ (77.0 ppm) or acetone-d_6 (29.92). Methyl 4-methoxybenzoate **1a** was purchased from Sigma-Aldrich and *N*-Boc-β-alanine methyl ester **1b** was prepared from β-alanine by Boc-protection (di-*tert*butyl dicarbonate/Na_2CO_3 in dioxane/H_2O) followed by esterification using acetyl chloride in MeOH (7*a*). Except for α- and β-phenylvinyl Grignard reagents, which were freshly prepared in-house before use, Grignard reagents and copper (I) cyanide (99%) were all purchased from Sigma-Aldrich and used as received. The chemical shifts for the carbons and the protons of the minor isomers are respectively reported in parentheses and in brackets.

N-(Boc)-β-alanine methyl ester (1b)

A stirred suspension of β-alanine (26.7 g, 300 mmol) in dry MeOH (100 mL) was added dropwise to a premixed solution of acetyl chloride (27.7 mL, 400 mmol) in dry MeOH (100 mL, and the components were premixed at 5 °C and stirred in an ice bath for 30 min) at 8–10 °C. After 3 h the ice bath was removed and stirring was continued overnight. The solution was poured into Et_2O (600 mL) and cooled for 2 h. The precipitate was collected and the mother liquor was evaporated to a residue that yielded more product after addition of MeOH (50 mL) and Et_2O (70 mL). β-Alaninate methyl ester hydrochloride (33.5 g, 240 mmol) was dissolved in dioxane/H_2O (2:1, 260 mL) and treated with solid Na_2CO_3 (27.6 g, 260 mmol), cooled to 0 °C, treated with $(Boc)_2O$ (57.6 g, 260 mmol), stirred at room temperature (RT) overnight and evaporated to a residue, which was taken up in Et_2O. Water was added to the residue and the aqueous phase was extracted with Et_2O. The organic phases were combined and washed with water, dried ($MgSO_4$), filtered and evaporated to give a pale yellow gum (47.9 g, 98%). ^1H NMR (300 MHz, $CDCl_3$) δ: 1.41 (s, 9H), 2.50 (t, J = 6.1 Hz, 2H), 3.31–3.42 (m, 2H), 3.67 (s, 3H), 5.05 (br s, 1H). ^{13}C NMR (75 MHz, $CDCl_3$) δ: 173.0, 155.9, 79.4, 51.8, 36.1, 34.5, 28.4. HRMS *m*/*z* 226.1052 [M + Na, calcd. for $[C_9H_{17}NO_4Na]$: 226.1050].

Condition A for the synthesis of homoallylic ketone

A flask containing CuCN (30–40 mol%) was flame-dried and filled with dry THF (2.0 mL per 1.0 mmol of CuCN). The suspension was cooled to −45 °C under argon atmosphere and treated via syringe with the vinyl Grignard reagent (400 mol%). The slurry was stirred for 10 min and then treated dropwise with a solution of ester (100 mol%) in dry THF (2.0 mL per 1.0 mmol of ester). The resultant mixture was stirred for 1 h at −45 °C. The cold bath was removed and replaced with an ice bath and the reaction mixture was allowed to stir and warm slowly to RT overnight. The reaction mixture was quenched by treatment with NaH_2PO_4 solution (200% *v*/*v* based on total reaction volume; 1 mol/L aqueous) at 0 °C. After vigorous shaking, the layers were separated, and the aqueous phase was extracted with Et_2O (2 ×). The combined organic extracts were washed with saturated $NaHCO_3$ solution and brine, dried ($MgSO_4$), filtered, and evaporated to give the homoallylic ketone. The crude product was then purified as specified.

Condition B for the synthesis of homoallylic ketone

A solution of Grignard reagent (400 mol%) in THF was added to a flame-dried flask containing CuCN (60 mol%) at −45 °C under argon atmosphere. The slurry was stirred for 2 h and then treated dropwise with a solution of ester (100 mol%) in dry THF (2.0 mL per 1.0 mmol of ester). The resultant mixture was stirred for 1 h at −45 °C and treated as described in Condition A. The crude product was then purified as specified.

Condition C for the synthesis of homoallylic ketone

A solution of Grignard reagent (500 mol%) in THF was employed as described for Condition B.

1-(4-Methoxy-phenyl)-pent-4-en-1-one (2a)

According to procedure A, the treatment of methyl 4-methoxybenzoate (2.0 g, 12 mmol) with vinylmagnesium bromide (1.3 mol/L in THF, 37.0 mL, 3.41 mmol) in the presence of CuCN (321 mg, 3.61 mmol) gave a crude oil that was purified using column chromatography (10% ethyl acetate in hexane) to give homoallylic ketone **2a** (1.6 g, 70%) as a pale yellow oil. TLC R_f 0.36 (10:90 EtOAc/Hexane). ^1H NMR (300 MHz, $CDCl_3$) δ: 2.49 (q, J = 6.74 Hz, 2H), 3.04 (t, J = 7.44 Hz, 2H), 3.88 (s, 3H), 4.97–5.14 (m, 2H), 5.84–6.00 (m, 1H), 6.90–7.00 (m, 2H), 7.91–8.00 (m, 2H). ^{13}C NMR (75 MHz, $CDCl_3$) δ: 198.2, 163.5, 137.6, 130.4, 130.1, 115.3, 113.8, 55.6, 37.5, 28.5. HRMS *m*/*z* 191.1073 [M + H^+, calcd. for $[C_{12}H_{15}O_2]^+$: 191.1066].

1-(4-Methoxy-phenyl)-3-methyl-hex-4-en-1-one (3a)

According to procedure B, the treatment of methyl 4-methoxybenzoate (332 mg, 2.00 mmol) with 1-propenylmagnesium bromide (0.5 mol/L in THF, 16 mL, 8.0 mmol) in the presence of CuCN (107 mg, 1.20 mmol) gave a crude oil that was purified using column chromatography (10% ethyl ether in hexane) to give homoallylic ketone **3a** (411 mg, 94%) as a pale yellow oil. TLC R_f 0.27 (10:90 Et_2O/Hexane). LC-MS and ^1H NMR analysis showed a 6.5:3.5 mixture of 2 isomers. ^1H NMR (300 MHz, $CDCl_3$) δ: 1.00–1.03 (2d partially overlapped, J = 6.39, 6.67 Hz, 3H), 1.56–1.67 (dd partially overlapped with m, J = 1.61, 6.70, 3H), 2.75–3.00 (m, 2.2 H), 3.11–3.28 (m, 0.8H), 5.19–5.30 (m, 0.8H), 5.32–5.47 (m, 1.2H), 6.91–7.00 (m, 2H), 7.91–8.00 (m, 2H). ^{13}C NMR (75 MHz, $CDCl_3$) δ: (198.4) 198.4, 163.4, (136.1) 135.6, 130.6, 130.5, (123.6) 123.3, 113.8, 55.6, 45.7 (45.6), (33.2) 28.5, 21.2 (20.6), (18.1) 13.1. HRMS *m*/*z* 219.1378 [M + H^+, calcd. for $[C_{14}H_{19}O_2]^+$: 219.1380].

1-(4-Methoxy-phenyl)-3,3,5-trimethyl-hex-4-en-1-one (4a)

According to procedure B, the treatment of methyl 4-methoxybenzoate (332 mg, 2.00 mmol) with 2-methyl-1-propenylmagnesium bromide (0.5 mol/L in THF, 16 mL, 8.0 mmol) in the presence of CuCN (107 mg, 1.20 mmol) gave a crude oil that was purified using column chromatog-

© 2007 NRC Canada

raphy (10% ethyl ether in hexane) to give homoallylic ketone **4a** (369 mg, 75%) as a yellow oil. TLC R_f 0.33 (10:90 Et_2O/Hexane). ^1H NMR (300 MHz, $CDCl_3$) δ: 1.25 (s, 6H), 1.63 (d, J = 1.24 Hz, 3H), 1.69 (d, J = 1.15 Hz, 3H), 3.00 (s, 2H), 3.85 (s, 3H), 5.21–5.28 (m, 1H), 6.87–6.96 (m, 2H), 7.87–8.00 (m, 2H). ^{13}C NMR (75 MHz, $CDCl_3$) δ: 198.5, 163.2, 133.4, 131.6, 130.8, 130.6, 113.5, 55.5, 49.8, 35.4, 29.6 (2C), 28.2, 19.1. HRMS *m/z* 247.1692 [M + H^+, calcd. for $[C_{16}H_{23}O_2]^+$: 247.1693].

1-(4-Methoxy-phenyl)-2,4-dimethyl-pent-4-en-1-one (5a)

According to procedure B, the treatment of methyl 4-methoxybenzoate (332 mg, 2.00 mmol) with isopropenylmagnesium bromide (0.5 mol/L in THF, 16 mL, 8.0 mmol) in the presence of CuCN (107 mg, 1.20 mmol) gave a crude oil that was purified using column chromatography (10% ethyl ether in hexane) to give homoallylic ketone **5a** (354 mg, 81%) as a colorless oil. TLC R_f 0.32 (10:90 Et_2O/Hexane). ^1H NMR (300 MHz, $CDCl_3$) δ: 1.18 (d, J = 6.87 Hz, 3H), 1.75 (s, 3H), 2.11 (dd, J = 7.69, 14.46 Hz, 1H), 2.54 (dd, J = 6.33, 14.43 Hz, 1H), 3.57–3.71 (m, 1H), 3.88 (s, 3H), 4.69 (s, 1H), 4.76 (s, 1H), 6.89–7.03 (m, 2H), 7.89–8.05 (m, 2H). ^{13}C NMR (75 MHz, $CDCl_3$) δ: 202.5, 163.5, 143.4, 130.7, 129.5, 113.9, 112.1, 55.6, 41.6, 38.3, 22.8, 17.5. HRMS *m/z* 219.1383 [M + H^+, calcd. for $[C_{14}H_{19}O_2]^+$: 219.1380].

1-(4-Methoxy-phenyl)-2,3,4-trimethyl-hex-4-en-1-one (6a)

According to procedure B, the treatment of methyl 4-methoxybenzoate (332 mg, 2.00 mmol) with 1-methyl-1-propenylmagnesium bromide (0.5 mol/L in THF, 16 mL, 8.0 mmol) in the presence of CuCN (107 mg, 1.20 mmol) gave a crude oil that was purified using column chromatography (5% ethyl ether in hexane) to give homoallylic ketone **6a** [116 mg, 24% (33% based on recovered starting material)] as a pale orange oil. TLC R_f 0.32 (10:90 Et_2O/Hexane). ^1H NMR (300 MHz, $CDCl_3$) measurement of aromatic signals showed a 8.4:0.9:0.7 mixture of 3 isomers, δ: 0.89–0.92 (m, 2.5H), 0.99–1.08 (m, 3H) [1.18–1.23 (m, 0.5H)], 1.55–1.70 (m, 6H), 3.02–3.55 (m, 1.8H) [2.45–2.72 (m, 0.1H), 4.25–4.44 (m, 0.1H)], 3.89 (s, 2.5H) [3.87 (s, 0.5H)], 5.30–5.43 (m, 0.8H) [5.00–5.30 (m, 0.1H) 5.50–5.65 (m, 0.1H)], 6.90–7.00 (m, 2H), [7.82–7.89 (m, 0.15H), 7.92–7.99 (m, 0.15H)] 8.00–8.08 (m, 1.7H). ^{13}C NMR (75 MHz, $CDCl_3$) δ: 203.9, 163.6, 137.3, 130.9 (130.8), (132.2) 130.6 (130.4), 121.4 (120.7), 113.9 (113.8) (113.6), 55.6, 43.2 (43.4), 36.9 (35.6), 18.5 (18.6), 17.7 (17.5), 17.1 (16.1), 13.3. HRMS *m/z* 247.1698 [M + H^+, calcd. for $[C_{16}H_{23}O_2]^+$: 247.1693].

1-(4-Methoxy-phenyl)-3,5-diphenyl-pent-4-en-1-one (7a)

According to procedure A, the treatment of methyl 4-methoxybenzoate (166 mg, 1.00 mmol) with β-phenylvinylmagnesium bromide (0.5 mol/L in THF, 8 mL, 4 mmol) in the presence of CuCN (36 mg, 0.40 mmol) gave a crude mixture that was triturated in Et_2O/Hexane (1:1) to give homoallylic ketone **7a** (209 mg, 61%) as a white crystaline solid, mp 107–110 °C. TLC R_f 0.21 (20:80 Et_2O/Hexanes). ^1H NMR (400 MHz, $CDCl_3$) δ: 3.40–3.53 (dd, J = 6.70, 16.35 Hz, 1H) partially overlapped with (dd, J = 7.39, 16.35 Hz, 1H), 3.88 (s, 3H), 4.30–4.40 (m, 1H), 6.39 (d, J = 15.90 Hz, 1H), 6.45 (dd, J = 5.63, 15.99 Hz, 1H), 6.93–7.01 (m, 2H), 7.16–7.38 (m, 10H), 7.93–8.02 (m, 2H). ^{13}C NMR (75 MHz, $CDCl_3$) δ: 196.8, 163.6, 143.6, 137.4, 132.9, 130.5, 130.4, 130.1, 128.8, 128.6, 127.9, 127.3, 126.7, 126.4, 113.9, 55.6, 44.3, 44,2. HRMS *m/z* 365.1510 [M + Na, calcd. for $[C_{24}H_{22}O_2Na]$: 365.1512].

1-(4-Methoxy-phenyl)-2,4-diphenyl-pent-4-en-1-one (8a)

According to procedure B, the treatment of methyl 4-methoxybenzoate (332 mg, 2.00 mmol) with α-phenylvinylmagnesium bromide (0.5 mol/L in THF, 16 mL, 8.0 mmol) in the presence of CuCN (107 mg, 1.20 mmol) gave a crude oil that was purified using column chromatography (10% ethyl acetate in hexane) to give homoallylic ketone **8a** (343 mg, 50%) as an orange oil. TLC R_f 0.47 (20:80 EtOAc/Hexane). ^1H NMR (400 MHz, $CDCl_3$) δ: 2.97 (ddd, J = 0.82, 6.97, 14.65 Hz, 1H), 3.52 (ddd, J = 0.87, 7.32, 14.62 Hz, 1H), 3.81 (s, 3H), 4.67 (t, J = 7.16 Hz, 1H), 4.93 (d, J = 1.21 Hz, 1H), 5.19 (d, J = 1.25 Hz, 1H), 6.80–6.86 (m, 2H), 7.17–7.41 (m, 10H), 7.82–7.88 (m, 2H). ^{13}C NMR (100 MHz, $CDCl_3$) δ: 197.5, 162.9, 145.4, 140.5, 139.2, 130.6, 129.3, 128.4, 128.0, 127.8, 127.1, 126.6, 126.0, 114.4, 113.2, 55.0, 51.0, 39.2. HRMS *m/z* 343.1693 [M + H^+, calcd. for $[C_{24}H_{23}O_2]^+$: 343.1688].

***tert*-Butyl-3-oxo-hept-6-enylcarbamate (2b)**

Prepared according to procedure A. NMR data was consistent with the literature (7*a*).

***tert*-Butyl-5-methyl-3-oxo-oct-6-enylcarbamate (3b)**

According to procedure C, the treatment of β-alanine methyl ester (203 mg, 1.00 mmol) with 1-propenylmagnesium bromide (0.5 mol/L in THF, 10 mL, 5.0 mmol) in the presence of CuCN (54 mg, 0.60 mmol) gave a crude oil that was purified using column chromatography (20% ethyl acetate in hexane) to give homoallylic ketone **3b** (189 mg, 74%) as a pale yellow oil. TLC R_f 0.35 (20:80 EtAc/Hexane). ^1H NMR (300 MHz, $CDCl_3$) measurement of olefinic signals showed a 7.1:2.9 mixture of 2 isomers, δ: 0.92–1.00 (2d partially overlapped, J = 6.68, 6.70 Hz, 3H), 1.42 (s, 9H), 1.61 (dd, J = 1.74, 6.81, 3H), 2.35 (d, J = 7.09 Hz, 2H), 2.61 (t, J = 5.65 Hz, 2H), 2.95–3.11 (m, 1H), 3.32 (q, J = 5.89 Hz, 2H), 4.99 (br s, 1H), 5.14 (tq, J = 1.65, 9.62 Hz, 1H), 5.22–5.44 (m, 1H). ^{13}C NMR (75 MHz, $CDCl_3$) δ: 210.1, 156.0, (135.4) 135.0, (124.1) 123.7, 79.3, 50.4, 43.4, 35.2 (33.0), 28.5, 28.1, 21.1 (20.7), (18.0) 13.0. HRMS *m/z* 278.1724 [M + Na, calcd. for $[C_{14}H_{25}NO_3Na]$: 278.1727].

***tert*-Butyl-5,5,7-trimethyl-3-oxo-oct-6-enylcarbamate (4b)**

According to procedure A, the treatment of β-alanine methyl ester (246 mg, 1.21 mmol) with 2-methyl-1-propenylmagnesium bromide (0.5 mol/L in THF, 9.70 mL, 4.84 mmol) in the presence of CuCN (43 mg, 0.48 mmol) gave a crude oil that was purified using column chromatography (15% ethyl acetate in hexane) to give homoallylic ketone **4b** (86 mg, 25%) as a pale orange oil. TLC R_f 0.40 (20:80 EtOAc/Hexane). ^1H NMR (300 MHz, $CDCl_3$) δ: 1.17 (s, 6H), 1.42 (s, 9H), 1.68 (d, J = 1.24 Hz, 3H), 1.71 (d, J = 1.15 Hz, 3H), 2.49 (s, 2H), 2.60 (t, J = 5.60, 2H), 3.30 (q, J = 5.80 Hz, 2H), 5.02 (br s, 1H), 5.12–5.15 (m, 1H). ^{13}C NMR (75 MHz, $CDCl_3$) δ: 210.4, 156.0, 132.5, 131.7, 79.2, 55.2, 44.5, 35.2, 35.2, 29.6, 28.5 (2C), 28.1, 19.1. HRMS

© 2007 NRC Canada

m/*z* 306.2039 [M + Na, calcd. for [$C_{16}H_{29}NO_3Na$]: 306.2040].

***tert*-Butyl-4,6-dimethyl-3-oxo-hept-6-enylcarbamate (5b)**

According to procedure C, the treatment of β-alanine methyl ester (203 mg, 1.00 mmol) with isopropenylmagnesium bromide (0.5 mol/L in THF, 10 mL, 5.0 mmol) in the presence of CuCN (54 mg, 0.60 mmol) gave a crude oil that was purified using column chromatography (10% ethyl acetate in hexane) to give homoallylic ketone **5b** (160 mg, 63%) as a colorless oil. TLC R_f 0.35 (20:80 EtOAc/Hexane). ^{1}H NMR (300 MHz, $CDCl_3$) δ: 1.06 (d, *J* = 6.94 Hz, 3H), 1.42 (s, 9H), 1.77 (s, 3H), 2.00 (dd, *J* = 7.52, 14.22 Hz, 1H), 2.37 (dd, *J* = 7.10, 14.20 Hz, 1H), 2.60–2.77 (m, 3H), 3.35 (q, *J* = 5.91 Hz, 2H), 4.66 (s, 1H), 4.77 (s, 1H), 5.00 (br s, 1H). ^{13}C NMR (75 MHz, $CDCl_3$) δ: 214.0, 156.0, 142.9, 112.6, 79.3, 44.6, 41.1, 40.9, 35.3, 28.5, 22.4, 16.3. HRMS *m*/z 278.1724 [M + Na, calcd. for [$C_{14}H_{25}NO_3Na$]: 278.1727].

***tert*-Butyl-4,5,6-trimethyl-3-oxo-oct-6-enylcarbamate (6b)**

According to procedure C, the treatment of β-alanine methyl ester (203 mg, 2.00 mmol) with 1-methyl-1-propenylmagnesium bromide (0.5 mol/L in THF, 10 mL, 5.0 mmol) in the presence of CuCN (54 mg, 0.60 mmol) gave a crude oil that was purified using column chromatography (10% ethyl acetate in hexane) to give homoallylic ketone **6b** [74 mg, 26% (49% based on recovered starting material)] as a pale orange oil. TLC R_f 0.38 (10:90 EtOAc/Hexane). ^{1}H NMR (300 MHz, $CDCl_3$) measurement of olefinic signals showed a 8.5:1.5 mixture of 2 isomers, δ: 0.87 (d, *J* = 6.76 Hz, 2.6 H) [0.97, (d, *J* = 7.12 Hz, 0.4H)], 0.91 (d, *J* = 6.93 Hz, 2.6H) [1.06 (d, *J* = 6.82 Hz, 0.4H)], 1.42 (s, 9H), 1.50–1.57 (m, 3H), 1.57–1.64 (m, 3H), 2.40–2.97 (m, 4H), 3.20–3.40 ((q, *J* = 5.87 Hz) partially overlapped with [q, *J* = 5.75 Hz], 2H), 4.90–5.11 (br s, 1H), [5.11–5.20 (m, 0.1H)] 5.24–5.35 (m, 0.9H). ^{13}C NMR (75 MHz, $CDCl_3$) δ: 215.3, 156.1, 136.7, 121.5, 79.3, 50.1 (49.4), 42.3, (36.7) 36.4, 35.3, 28.5, (18.9) 18.2, 17.4 (16.6), 15.7 (15.0), 13.2 (13.1). HRMS *m*/*z* 306.2040 [M + Na, calcd. for [$C_{16}H_{29}NO_3Na$]: 306.2040].

***tert*-Butyl-5,7-diphenyl-3-oxo-hept-6-enylcarbamate (7b)**

According to procedure C, the treatment of β-alanine methyl ester (406 mg, 2.00 mmol) with β-phenylvinylmagnesium bromide (0.5 mol/L in THF, 20 mL, 10 mmol) in the presence of CuCN (107 mg, 1.20 mmol) gave a crude mixture that was purified using column chromatography (20% ethyl acetate in hexane) to give homoallylic ketone **7b** (590 mg, 78%) as a pale yellow oil. TLC R_f 0.30 (20:80 EtOAc/Hexane). ^{1}H NMR (300 MHz, $CDCl_3$) measurement of olefinic signals showed a 3:2 mixture of 2 isomers, δ: 1.38–1.50 (s partially overlapped with s, 9H), 2.35–2.70 (m, 2H), 2.77 (dd, *J* = 7.56, 15.62 Hz, 0.5H), 2.87 (dd, *J* = 6.95, 15.59 Hz, 0.5H), 2.94 (d, *J* = 7.33 Hz, 1H), 3.20–3.35 (m partially overlapped with m, 2H), 4.09 (q, *J* = 6.93 Hz, 0.5H), 4.35–4.48 (m, 0.5H), 4.91 (br d, *J* = 5.95 Hz, 1H), 5.83 (t, *J* = 10.95 Hz, 0.5H), 6.32 (dd, *J* = 6.21, 15.89 Hz, 0.5H), 6.40 (d, *J* = 15.93 Hz, 0.5H), 6.54 (d, *J* = 11.47 Hz, 0.5H), 7.15–7.40 (m, 10H). ^{13}C NMR (75 MHz, $CDCl_3$) δ: 208.7, 156.0, 143.6, 142.8, 137.1, 136.9, 133.6, 132.3, 130.2, 129.9, 129.0, 128.9, 128.7, 128.6, 128.4, 127.7, 127.5, 127.3, 127.2, 126.9, 126.8, 126.4, 79.4, 79.4, 50.6, 48.9, 44.1, 43.6, 43.3, 39.7, 35.1, 35.1, 28.5, 28.5. HRMS *m*/*z* 402.2040 [M + Na, calcd. for [$C_{24}H_{29}NO_3Na$]: 402.2042].

***tert*-Butyl-4,6-diphenyl-3-oxo-hept-6-enylcarbamate (8b)**

According to procedure B, the treatment of β-alanine methyl ester (406 mg, 2.00 mmol) with α-phenylvinylmagnesium bromide (0.5 mol/L in THF, 16 mL, 8.0 mmol) in the presence of CuCN (107 mg, 1.20 mmol) gave a crude oil that was purified using column chromatography (10% ethyl acetate in hexane) to give homoallylic ketone **8b** (309 mg, 41%) as a sticky orange oil. TLC R_f 0.35 (20:80 EtOAc/Hexane). ^{1}H NMR (300 MHz, $CDCl_3$) δ: 1.42 (s, 9H), 2.40–2.65 (m, 2H), 2.86 (dd, *J* = 6.98, 14.32 Hz, 1H), 3.20–3.32 (m, 2H), 3.40 (dd, *J* = 7.02, 14.25 Hz, 1H), 3.78 (t, *J* = 7.29 Hz, 1H), 4.28 (br s, 1H), 4.95 (d, *J* = 1.09 Hz, 1H), 5.20 (d, *J* = 1.17 Hz, 1H), 7.11–7.17 (m, 2H), 7.25–7.42 (m, 8H). ^{13}C NMR (75 MHz, $CDCl_3$) δ: 156.1, 145.8, 140.6, 138.2, 129.0, 128.6, 128.4, 127.8, 127.6, 126.5, 115.0, 79.3, 57.3, 42.2, 38.3, 38.1, 35.3, 28.5. HRMS *m*/*z* 402.2043 [M + Na, calcd. for [$C_{24}H_{29}NO_3Na$]: 402.2040].

Condition D for the synthesis of homoallylic ketone with two different Grignard reagents

A solution of vinylmagnesium bromide (0.8 mol/L in THF, 1.25 mL, 1.00 mmol) and isopropenylmagnesium bromide (0.5 mol/L in THF, 2.40 mL, 1.20 mmol) was added to a flame-dried flask containing CuCN (27 mg, 0.30 mmol) at –45 °C under argon atmosphere. The slurry was stirred for 10 min and then treated dropwise with a solution of ester (166 mg, 1.00 mmol) in dry THF (2 mL). The resultant mixture was stirred for 1 h at –45 °C and treated as described in Condition A. The crude product was then purified using column chromatography (10% ethyl acetate in hexane) to give 98 mg of a mixture of **14a/5a/2a** in a ratio of 4.6:2.8:2.6 as determined by LC-MS analysis.

Condition E for the synthesis of homoallylic ketone with two different Grignard reagents

A solution of isopropenylmagnesium bromide (0.5 mol/L in THF, 6.00 mL, 3.00 mmol) was added to a flame-dried flask containing a suspension of CuCN (54 mg, 0.60 mmol) at –45 °C under argon atmosphere. The slurry was stirred for 2 h and then treated dropwise with a solution of vinylmagnesium bromide (1 mol/L in THF, 1.00 mL, 1.00 mmol) and ester (166 mg, 1.00 mmol) in dry THF (2 mL). The resultant mixture was stirred for 1 h at –45 °C and treated as described in Condition A. The crude product was then purified using column chromatography (10% ethyl acetate in hexane) to give 170 mg of a mixture of **14a/5a/2a** in a ratio of 4.1:4.4:1.6 as determined by LC-MS analysis.

Condition F for the synthesis of homoallylic ketone with two different Grignard reagents

The reaction was performed as described for condition E with isopropenylmagnesium bromide (0.5 mol/L in THF, 2.00 mL, 1.00 mmol), CuCN (90 mg, 1.0 mmol), vinylmagnesium bromide (1 mol/L in THF, 1.00 mL, 1.00 mmol), and ester (166 mg, 1.00 mmol) in dry THF (2 mL) to give

© 2007 NRC Canada

98 mg of a mixture of **14a/5a/2a** in a ratio of 4.1:3.7:2.2 as determined by LC-MS analysis.

Condition G for the synthesis of homoallylic ketone with two different Grignard reagents

A solution of isopropenylmagnesium bromide (0.5 mol/L in THF, 2.20 mL, 1.10 mmol) was added to a flame-dried flask containing CuCN (54 mg, 0.60 mmol) at −45 °C under argon atmosphere. The slurry was stirred for 1 h and then treated dropwise with a solution of ester (166 mg, 1.00 mmol) in dry THF (2 mL) and vinylmagnesium bromide (1 mol/L in THF, 1.00 mL, 1.00 mmol). The resultant mixture was stirred for 10 min at −45 °C and treated as described in Condition A. The crude product was then purified using column chromatography (10% ethyl acetate in hexane) to give 123 mg of a mixture of **14a/5a/2a** in a ratio of 5.6:0.6:3.8 as determined by LC-MS analysis.

1-(4-Methoxy-phenyl)-3-methyl-hex-4-en-1-one (14a)

A sample of **14a** was obtained by HPLC purification performed on a reverse-phase Prevail column from Alltech Inc. (22 × 250 mm, 5 μm, C_{18}) with a flow rate of 10 mL/min using CH_3CN (0.1% TFA)/H_2O (0.1% TFA) from 40:60 to 80:20 in 50 min. ^{1}H NMR (400 MHz, $CDCl_3$) δ: 1.80 (s, 3H), 2.45 (t, J = 7.68 Hz, 2H), 3.08 (t, J = 7.70 Hz, 2H), 3.88 (s, 3H), 4.73 (s, 1H), 4.77 (s, 1H), 6.90–7.00 (m, 2H), 7.90–8.00 (m, 2H). ^{13}C NMR (75 MHz, $CDCl_3$) δ: 198.5, 163.5, 145.0, 130.7, 130.5, 113.9, 110.2, 55.6, 36.6, 32.2, 22.9. HRMS m/z 205.1223 [M + H^+, calcd. for $[C_{13}H_{17}O_2]^+$: 205.1221].

General procedure H: pyrrole synthesis

A solution of homoallylic ketone (100 mol%) in CH_2Cl_2/MeOH (1:5, 13.5 mL per 1.00 mmol of homoallylic ketone) was treated with ozone bubbles at –78 °C until a blue color persisted, purged with a stream of argon bubbles, treated with dimethyl sulphide (500 mol%), and stirred overnight, after which time the bath temperature had warmed to RT. Removal of the volatiles by rotary evaporation gave crude 1,4-dicarbonyl product, which was taken up into a solution of AcOH/H_2O/MeCN (1:1:1, 10 mL per 1.0 mmol of homoallylic ketone) and treated with ammonium formate (500 mol%) and KOAc (6 000 mol%). The mixture was heated at 80 °C until complete consumption of starting material was observed by TLC. After cooling to RT, the reaction mixture was partitioned between an organic phase of Et_2O/CH_2Cl_2 (2:1) and Na_2CO_3 solution (5% aq.). The layers were separated, and the aqueous phase was extracted twice with Et_2O/CH_2Cl_2 (2:1). The combined organic phases were washed with pH 6.8 phosphate buffer and dried ($MgSO_4$). Volatiles were removed by successive rotary evaporation and lyophilization to give the crude pyrrole product, which was purified as specified.

General procedure I — pyrrole synthesis

As described in general procedure H, crude 1,4-dicarbonyl product was produced by ozonolysis of the homoallylic ketone (100 mol%). It was then taken up into a solution of acetonitrile (12.5 mL per 1.00 mmol of homoallylic ketone) containing ammonium formate (500 mol%) and NaOAc/AcOH (100 mol% *w*/*w*, prepared by mixing equimolar quantities of NaOAc and HOAc). The mixture was heated at 65 °C until complete consumption of the starting material was observed by TLC. After cooling to RT, the reaction mixture was partitioned between Et_2O/CH_2Cl_2 (2:1) and pH 6.8 sodium phosphate buffer. The layers were separated, and the organic phase was washed with pH 6.8 sodium phosphate buffer. The aqueous phase was extracted twice with Et_2O/CH_2Cl_2 (2:1), and the combined organic phases were dried ($MgSO_4$). Volatiles were removed by successive rotary evaporation and lyophilization to give crude pyrrole product, which was purified as specified.

2-(4-Methoxy-phenyl)-4-methyl-1*H*-pyrrole (9a)

Prepared from homoallylic ketone **3a** (30 mg, 0.14 mmol) according to procedure H to yield crude product (19.4 mg), which was purified using column chromatography (20% ethyl acetate in hexane) to give pyrrole **9a** (17 mg, 65%) as a mauve gum. TLC R_f 0.40 (20:80 EtOAc/Hexane). ^{1}H NMR (300 MHz, $CDCl_3$) δ: 2.16 (s, 3H), 3.83 (s, 3H), 6.26 (s, 1H), 6.59 (s, 1H), 6.85–6.95 (m, 2H), 7.33–7.42 (m, 2H), 8.08 (br s, 1H). ^{13}C NMR (75 MHz, $CDCl_3$) δ: 158.2, 132.2, 126.2, 125.2, 120.6, 116.1, 114.4, 106.6, 55.4, 12.1. HRMS m/z 188.1070 [M + H^+, calcd. for $[C_{12}H_{14}NO]^+$: 188.1065].

2-(4-Methoxy-phenyl)-3,5-dimethyl-1*H*-pyrrole (10a)

Prepared from homoallylic ketone **5a** (55.4 mg, 0.250 mmol) according to procedure I to yield crude product (43.5 mg) that was purified using column chromatography (15% ethyl acetate in hexane) to give pyrrole **10a** (24 mg, 47%) as a deep purple gum. TLC R_f 0.43 (20:80 EtOAc/Hexane). ^{1}H NMR (300 MHz, $CDCl_3$) δ: 2.20 (s, 3H), 2.29 (s, 3H), 3.82 (s, 3H), 5.82 (d, J = 2.60 Hz, 1H), 6.90–7.00 (m, 2H), 7.28–7.36 (m, 2H), 7.75 (br s, 1H). ^{13}C NMR (75 MHz, $CDCl_3$) δ: 157.8, 127.6, 127.0, 126.9, 126.8, 115.4, 114.2, 109.9, 55.4, 13.1, 12.4. HRMS m/z 202.1226 [M + H^+, calcd. for $[C_{13}H_{16}NO]^+$: 202.1217].

2-(4-Methoxy-phenyl)-3,4,5-trimethyl-1*H*-pyrrole (11a)

Prepared from homoallylic ketone **6a** (23 mg, 0.090 mmol) according to procedure H to yield crude product (19.2 mg) that was purified using column chromatography (20% ethyl acetate in hexane) to give pyrrole **11a** (14 mg, 70%) as a purple gum. TLC R_f 0.49 (20:80 EtOAc/Hexane). ^{1}H NMR (400 MHz, $CDCl_3$) δ: 1.99 (s, 3H), 2.13, (s, 3H), 2.23 (s, 3H), 3.84 (s, 3H), 6.90–6.97 (m, 2H), 7.28–7.36 (m, 2H), 7.60 (br s, 1H). ^{13}C NMR (400 MHz, $CDCl_3$) δ: 157.9, 127.8, 127.4, 126.6, 115.6, 114.8, 114.2, 114.0, 55.4, 11.3, 10.4, 9.3.

2-(4-Methoxy-phenyl)-4-phenyl-1*H*-pyrrole (12a)

Prepared from homoallylic ketone **7a** (50.8 mg, 0.150 mmol) according to procedure I (ozonolyzis carried out in CH_2Cl_2) to yield crude product that was purified using column chromatography (20% ethyl acetate in hexane) to give pyrrole **12a** (28.3 mg, 76%) as a blue gum. TLC R_f 0.30 (20:80 EtOAc/Hexane). ^{1}H NMR (400 MHz, $CDCl_3$) δ: 3.82 (s, 3H), 5.95 (s. 0.5H), 6.60 (d, J = 2.72 Hz, 1H), 6.85–6.93 (m, 2H), 7.11–7.40 (m, 10H), 8.00 (br s, 1H). HRMS m/z 250.1222 [M + H^+, calcd. for $[C_{17}H_{16}NO]^+$: 250.1226].

© 2007 NRC Canada

2-(4-Methoxy-phenyl)-3,5-diphenyl-1*H*-pyrrole (13a)

Prepared from homoallylic ketone **8a** (81 mg, 0.24 mmol) according to procedure I to yield crude product (70.7 mg) that was purified using column chromatography (15% ethyl acetate in hexane) to give pyrrole **13a** (59.5 mg, 77%) as a beige powder. TLC R_f 0.40 (20:80 EtOAc/Hexane). ^{1}H NMR (300 MHz, $CDCl_3$) δ: 3.84 (s, 3H), 6.71 (br s, 1H), 6.83–6.94 (m, 2H), 7.13–7.65 (m, 12H), 8.39 (br s, 1H). ^{13}C NMR (100 MHz, $CDCl_3$) δ: 158.9, 136.6, 129.1, 128.4, 128.4, 126.5, 125.9, 123.8, 123.1, 114.3, 108.4, 55.4. HRMS *m/z* 326.1539 [M + H^+, calcd. for $[C_{23}H_{20}NO]^+$: 326.1530].

***tert*-Butyl-[2-(4-methyl-1*H*-pyrrol-2-yl)]ethylcarbamate (9b)**

Prepared from homoallylic ketone **3b** (32.5 mg, 0.120 mmol) according to procedure H to yield crude product (24.3 mg) that was purified using column chromatography (20% ethyl acetate in hexane) to give pyrrole **9b** (16 mg, 59%) as a brown gum. TLC R_f 0.20 (20:80 EtOAc/Hexane). ^{1}H NMR (300 MHz, acetone-d_6) δ: 1.38 (s, 9H), 1.98 (s, 3H), 2.68 (t, J = 7.43 Hz, 2H), 3.15–3.31 (m, 2H), 5.66 (s, 1H), 5.87 (br s, 1H), 6.36 (s, 1H), 9.42 (br s, 1H). ^{13}C NMR (75 MHz, acetone-d_6) δ: 156.8, 130.0, 118.3, 115.0, 107.8, 78.4, 41.5, 28.6, 12.1. HRMS *m/z* 247.1417 [M + Na^+, calcd. for $[C_{12}H_{20}N_2O_2Na]$: 247.1414].

***tert*-Butyl-[2-(3,5-dimethyl-1*H*-pyrrol-2-yl)]ethylcarbamate (10b)**

Prepared from homoallylic ketone **5b** (70 mg, 0.27 mmol) according to procedure I to yield crude product (63.8 mg) that was purified using column chromatography (20% ethyl acetate in hexane) to give pyrrole **10b** (36.3 mg, 56%) as a brown gum. TLC R_f 0.22 (20:80 EtOAc/Hexane). ^{1}H NMR (300 MHz, acetone-d_6) δ: 1.39 (s, 9H), 1.90 (s, 3H), 2.10 (s, 3H), 2.62 (t, J = 7.43 Hz, 2H), 3.11–3.21 (m, 2H), 5.46 (s, 1H), 5.96 (br s, 1H), 9.17 (br s, 1H). ^{13}C NMR (75 MHz, acetone-d_6) δ: 156.6, 125.5, 124.1, 114.6, 108.2, 78.4, 41.6, 28.6, 27.2, 12.9, 11.1. HRMS *m/z* 239.1766 [M + H^+, calcd. for $[C_{13}H_{23}N_2O_2]^+$: 239.1754].

***tert*-Butyl-[2-(3,4,5-trimethyl-1*H*-pyrrol-2-yl)]ethylcarbamate (11b)**

Prepared from homoallylic ketone **6b** (42.7 mg, 0.150 mmol) according to procedure I to yield crude product (29.1 mg) that was purified using column chromatography (20% ethyl acetate in hexane) to give pyrrole **11b** (22 mg, 58%) as a brown gum. TLC R_f 0.24 (20:80 EtOAc/Hexane). ^{1}H NMR (400 MHz, $CDCl_3$) δ: 1.45 (s, 9H), 1.92 (s, 3H), 1.93 (s, 3H), 2.14 (s, 3H), 2.71 (t, J = 6.61 Hz, 2H), 3.23–3.36 (m, 2H), 4.66 (br s, 1H), 7.66 (br s, 1H). ^{13}C NMR (75 MHz, $CDCl_3$) δ: 156.3, 122.1, 121.8, 114.9, 113.9, 79.5, 40.6, 28.5, 26.9, 11.1, 9.3, 9.2. HRMS *m/z* 253.1910 [M + H^+, calcd. for $[C_{14}H_{25}N_2O_2]^+$: 253.1909].

***tert*-Butyl-[2-(4-phenyl-1*H*-pyrrol-2-yl)]ethylcarbamate (12b)**

Prepared from homoallylic ketone **7b** (140 mg, 0.370 mmol) according to procedure I to yield crude product that was purified using column chromatography (20%–30% ethyl acetate in hexane) to give pyrrole **12b** (63.4 mg, 60%) as a pink foam. TLC R_f 0.08 (20:80 EtOAc/Hexane). ^{1}H NMR (400 MHz, $CDCl_3$) δ: 1.35 (s, 9H), 2.70–2.83 (m, 2H), 3.31–3.46 (m, 2H), 4.84 (br s, 1H), 5. 88 (s. 0.5H), 6.11 (d, J = 2.52 Hz, 1H), 7.05–7.27 (m, 8H), 8.48 (br s, 1H). HRMS *m/z* 287.1754 [M + H^+, calcd. for $[C_{17}H_{23}N_2O_2]^+$: 287.1759].

***tert*-Butyl-[2-(3,5-diphenyl-1*H*-pyrrol-2-yl)]ethylcarbamate (13b)**

Prepared from homoallylic ketone **8b** (91.8 mg, 0.242 mmol) according to procedure I to yield crude product (86.2 mg) that was purified using column chromatography (15% ethyl acetate in hexane) to give pyrrole **13b** (81.1 mg, 93%) as a beige powder. TLC R_f 0.26 (20:80 EtOAc/Hexane). ^{1}H NMR (300 MHz, $CDCl_3$) δ: 1.44 (s, 9H), 3.07 (t, J = 6.22 Hz, 2H), 3.43–3.60 (m, 2H), 4.84 (br s, 1H), 6.65 (d, J = 2.65 Hz, 1H), 7.15–7.65 (m, 10H), 9.51 (br s, 1H). ^{13}C NMR (100 MHz, $CDCl_3$) δ: 156.9, 136.9, 132.7, 131.0, 128.9, 128.8, 128.6, 127.9, 126.6, 125.9, 125.6, 123.6, 106.3, 80.1, 39.6, 28.5, 28.3. HRMS *m/z* 385.1886 [M + Na^+, calcd. for $[C_{23}H_{26}N_2O_2Na]$: 385.1880].

Acknowledgement

This research was supported by the Natural Sciences and Engineering Research Council (NSERC) of Canada as well as the Fond Québecois de Recherche sur la Nature et les Technologies (FQRNT) of Québec. We thank the Université de Montréal Mass Spectroscopy facility for mass spectral analyses.

References

1. (*a*) Y. Li, J.-P. Feng, W.-H. Wang, J. Chen, and X.-P. Cao. J. Org. Chem. **72**, 2344 (2007); (*b*) H.-J. Zhang, C. Ma, N.V. Hung, N.M. Cuong, G.T. Tan, B.D. Santarsiero, A.D. Mesecar, D.D. Soejarto, J.M. Pezzuto, and H.H.S. Fong. J. Med. Chem. **49**, 693 (2006); (*c*) U. Albrecht, M. Lalk, and P. Langer. Bioorg. Med. Chem. **13**, 1531 (2005); (*d*) A. Bhatt, C.B.W. Stark, B.M. Harvey, A.R. Gallimore, Y.A. Demydchuk, J.B. Spencer, J. Staunton, and P.F. Leadlay. Angew. Chem. Int. Ed. **44**, 7075 (2005); (*e*) C. Campagnuolo, E. Fattorusso, A. Romano, O. Taglialatela-Scafati, N. Basilico, S. Parapini, and D. Taramelli. Eur. J. Org. Chem. 5077 (2005); (*f*) A.V. Baranovskii, R.P. Litvinovskaya, and V.A. Khripach. Russ. J. Org. Chem. **40**, 1608 (2004); (*g*) A.A. Cossé, R.J. Bartelt, and B.W. Zilkowski. J. Nat. Prod. **65**, 1156 (2002); (*h*) T. Agatsuma, H. Ogawa, K. Akasaka, A. Asai, Y. Yamashita, T. Mizukami, S. Akinaga, Y. Saitoh. Bioorg. Med. Chem. **10**, 3445 (2002); (*i*) A. Rueda, E. Zubía, M.J. Ortega, J.J. Salvá. J. Nat. Prod. **64**, 401 (2001); (*j*) Y. Yang, K. Kinoshita, K. Koyama, K. Takahashi, T. Tai, Y. Nunoura, and K.J. Watanabe. J. Nat. Prod. **62**, 1672 (1999); (*k*) P. Rüngeler, V. Castro, G. Mora, N. Gören, W. Vichnewski, H.L. Pahl, I. Merfort, and T.J. Schmidt. Bioorg. Med. Chem. **7**, 2343 (1999); (*l*) K. Pari, P.J. Rao, B. Subrahmanyam, J.N. Rasthogi, and C. Devakumar. Phytochemistry, **49**, 1385 (1998); (*m*) T. Masso, A. Portella, and E. Rus. Perfum. Flavor. **15**, 42 (1990); (*n*) I. Yamamoto, S. Tanaka, T. Fujimoto, and K. Ohta. J. Org. Chem. **54**, 747 (1989); (*o*) A. Evidente. J. Nat. Prod. **50**, 173 (1987); (*p*) J.E. Hochlowski, and D.J. Faulkner. J. Org. Chem. **49**, 3838 (1984); (*q*) M. Johnston, R. Raines, M. Chang, N. Esaki, K. Soda, and C. Walsh. Biochemistry, **20**, 4325 (1981); (*r*) Atta-ur-Rahman. *In* Natural product chemistry. *Edited by* Atta-ur-Rahman. Springler-Verlag, Berlin, Germany. 1986. p. 330; (*s*)

© 2007 NRC Canada

R.R. Schmidt. *In* Natural product chemistry. *Edited by* Atta-ur-Rahman. Springler-Verlag, Berlin, Germany. 1986. p. 383.

2. C.H. Heathcock, S. Graham, M.C. Pirrung, F. Plavac, and C.T. White. *In* The total synthesis of natural products. Vol. 5. *Edited by* J. ApSimon. Wiley, New York. 1983. Chap. 2.
3. (*a*) M. Yoshida, M. Kitamura, and K. Narasaka. Bull. Chem. Soc. Jpn. **76**, 2003 (2003); (*b*) H. Tsuitsui, M. Kitamura, and K. Narasaka. Bull. Chem. Soc. Jpn. **75**, 1451 (2002); (*c*) H. Tsuitsui and K. Narasaka. Chem Lett. 45 (1999).
4. (*a*) M. Kitamura, Y. Mori, and K. Narasaka. Tetrahedron Lett. **46**, 2373 (2005); (*b*) M. Yoshida, M. Kitamura, and K. Narasaka. Chem Lett. 144 (2002); (*c*) Y. Koganemaru, M. Kitamura, and K. Narasaka. Chem Lett. 784 (2002); (*d*) K. Uchiyama, Y. Hayashi, and K. Narasaka. Chem Lett. 1261 (1998); (*e*) T. Mikami and K. Narasaka. Chem Lett. 338 (2000).
5. (*a*) H. Tsuitsui and K. Narasaka. Chem. Lett. 526 (2001); (*b*) M. Tingoli, M. Tiecco, L. Testaferri, R. Andrenacci, and R. Balducci. J. Org. Chem. **58**, 6097 (1993); (*c*) T. Hosokawa, N. Shimo, K. Maeda, A. Sonoda, and S.-I. Murahashi. Tetrahedron Lett. **17**, 383 (1976).
6. R.A. Ellison. Synthesis, 397 (1973).
7. (*a*) K.A. Hansford, V. Zanzavora, A. Dörr, and W.D. Lubell. J. Comb. Chem. **6**, 893 (2004); (*b*) K.A. Hansford, S.A.P. Guarin, W.G. Skene, W.D. Lubell. J. Org. Chem. **70**, 7996 (2005); (*c*) B. Jolicoeur and W.D. Lubell. Org. Lett. **8**, 6107 (2006); (*d*) R. Dhawan, and B.A. Arndtsen. J. Am. Chem. Soc. **126**, 468 (2004); (*e*) B.K. Banik, S. Samajdar, and I. Banik. J. Org. Chem. **69**, 213 (2004); (*f*) R.U. Braun, K. Zeitler, and T.J. Muller. J. Org. Lett. **3**, 3297 (2001); (*g*) E. Baltazzi and L.I. Krimen. Chem. Rev. **63**, 511 (1963); (*h*) H. Chochois, M. Sauthier, E. Maerten, Y. Castaner, and A. Mortreux. Tetrahedron, **62**, 11740 (2006); (*i*) G. Minetto, L.F. Raveglia, and M. Taddei. Org. Lett. **6**, 389 (2004); (*j*) D.S. Mortensen, A.L. Rodriguez, K.E. Carlson, J. Sun, B.S. Katzenellenbogen, and J.A. Katzenellenbogen. J. Med. Chem. **44**, 3838 (2001); (*k*) S, Raghavan, and K. Anuradha. Synlett, **5**, 711 (2003).
8. (*a*) H.S.P. Rao and S. Jothilingam. J. Org. Chem. **68**, 5392 (2003); (*b*) B.W. Greatrex, M.C. Kimber, D.K. Taylor, and E.R.T. Tiekink. J. Org. Chem. **68**, 4239 (2003); (*c*) W.C. Christopfel, and L.L. Miller. J. Org. Chem. **51**, 4169 (1986); (*d*) P. Bosshard and C.H. Eugster. Adv. Heterocycl. Chem. **7**, 377 (1966).
9. A. Dörr and W.D. Lubell. Biopolymers (Peptide Science), **88**, 290 (2007).
10. (*a*) A.R. Katritzky, M.V. Voronkov, and D. Toader. J. Org. Chem. **63**, 9987 (1998); (*b*) A.R. Katritzky, and D. Toader. J. Am. Chem. Soc. **119**, 9321 (1997).
11. S. Takano, S. Tomita, M. Takahashi, and K. Ogasawara. Chem. Lett. 1569 (1987).
12. T. Fujiwara, T. Iwasaki, and T. Takeda. Chem. Lett. 1321 (1993).
13. D.V. Avilov, M.G. Malusare, E. Arslancan, and D.C. Dittmer. Org. Lett. **6**, 2225 (2004).
14. D. Imao, A. Itoi, A. Yamasaki, M. Shirakura, R. Ohtoshi, K. Ogata, Y. Ohmori, T. Ohta, Y. Ito. J. Org. Chem. **72**, 1652 (2007).
15. (*a*) S.M. Allin, J.S. Khera, C.I. Thomas, J. Witherington, K. Doyle, M.R.J. Elsegood, and M. Edgar. Tetrahedron Lett. **47**, 1961 (2006); (*b*) D. Giomi, M. Piacenti, and A. Brandi. Eur. J. Org. Chem. 4649 (2005); (*c*) K. Totani, T. Nagatsuka, K.-I. Takao, S. Ohba, and K.-I. Tadano. Org. Lett. **1**, 1447 (1999); (*d*) Y. Han and V.J. Hruby. Tetrahedron Lett. **38**, 7317 (1997); (*e*) K.-H.A. Ahn, B.R. Klassen, and S.J. Lippard. Organometallics, **9**, 3178 (1990); (*f*) T.R. Hoye, A.S. Magee, and R.E. Rosen. J. Org. Chem. **49**, 3224 (1984); (*g*) H. Mori and R. Ohuchi. Chem. Pharm. Bull. **23**, 980 (1975); (*h*) H. Mori and R. Ohuchi. Chem. Pharm. Bull. **23**, 559 (1975); (*i*) G.L. Larson, I. Montes de López-Cepero, and L.E. Torres. Tetrahedron Lett. **25**, 1673 (1984); (*j*) S, Watanabe, K. Suga, and T. Fujita. Isr. J. Chem. **11**, 71 (1973); (*k*) G. Cahiez, P. Venegas, C.E. Tucker, T.N. Majid, and P. Knochel. J. Chem. Soc. Chem. Commun. 1406 (1992).
16. (*a*) F. Näf and P. Degen. Helv. Chim. Acta, **54**, 1939 (1971); (*b*) R.E. Ireland and P. Wipf. J. Org. Chem. **55**, 1425 (1990).
17. J. Hooz and R.B. Layton. Can. J. Chem. **48**, 1626 (1970).
18. (*a*) W.X. Zheng and X. Huang. Synthesis, 2497 (2002); (*b*) A. El-Batta, T.R. Hage, S. Ploktin, and M. Bergdahl. Org. Lett. **6**, 107 (2004).
19. A. Barbero, F.J. Pulido, J.A. Rincó, P. Cuadrado, D. Galisteo, and H. Martínez-Garciá. Angew. Chem. Int. Ed. **40**, 2101 (2001).
20. (*a*) S. Hara, S. Hyuga, M. Aoyama, M. Sato, and A. Suzuki. Tetrahedron Lett. **31**, 247 (1990); (*b*) E. Takada, S. Hara, and A. Suzuki. Tetrahedron Lett. **34**, 7067 (1993); (*c*) S. Hara, S. Ishimura, and A. Suzuki. Synlett, 993 (1996); (*d*) Y. Satoh, H. Serizawa, S. Hara, and A. Suzuki. J. Am. Chem. Soc. **107**, 5225 (1985); (*e*) P. Jacob and H.C. Brown. J. Am. Chem. Soc. **98**, 7832 (1976).
21. (*a*) S. Zhou, B. Yan, and Y. Liu. J. Org. Chem. **70**, 4006 (2005); (*b*) C. Zhao, J. Yan, and Z. Xi. J. Org. Chem. **68**, 4355 (2003); (*c*) C. Zhao, T. Yu, and Z. Xi. Chem. Commun. (Cambridge), 142 (2002).
22. (*a*) T. Mukaiyama, H. Nagaoka, M. Ohshima, and M. Murakami. Chem. Lett. 1009 (1986); (*b*) K. Kudo, K. Saigo, Y. Hashimoto, H. Houchigai, and M. Hasegawa. Tetrahedron Lett. **32**, 4311 (1991); (*c*) K. Kudo, Y. Hashimoto, H. Houchigai, M. Hasegawa, and K. Saigo. Bull. Chem. Soc. Jpn. **66**, 848 (1993); (*d*) T. Ishihara, T. Shinozaki, and M. Kuroboshi. Chem. Lett. 1369 (1989).
23. (*a*) B.M. Trost, J.A. Martinez, R.J. Kulawiec, and A.F. Indolese. J. Am. Chem. Soc. **115**, 10402 (1993); (*b*) S. Dérien and P.H. Dixneuf. J. Chem. Soc. Chem. Commun. 2551 (1994).
24. (*a*) A.R. Katritzky, Z. Huang, and Y. Fang. J. Org. Chem. **64**, 7625 (1999); (*b*) L. Zhao and X. Lu. Org. Lett. **4**, 3903 (2002); (*c*) Z. Wang and X. Lu. Chem. Commun. (Cambridge), 535 (1996); (*d*) Z. Wang and X. Lu. J. Org. Chem. **61**, 2254 (1996); (*e*) J. Tsuji, I. Miniami, and I. Shimizu. Chem. Lett. 1325 (1983).
25. M. Yasuda, S. Tsuji, Y. Shigeyoshi, and A. Baba. J. Am. Chem. Soc. **124**, 7440 (2002).
26. S. Condon-Gueugnot, D. Dupré, J.-Y. Nédélec, and J. Périchon. Synthesis, 1457 (1997).
27. (*a*) G. Saucy and R. Marbet. Helv. Chim. Acta, **50**, 2091 (1967); (*b*) M. Koreeda and J.I. Luengo. J. Am. Chem. Soc. **107**, 5572 (1985); (*c*) M. Morita, S. Sakaguchi, and Y. Ishii. J. Org. Chem. **71**, 6285 (2006); (*d*) T. Higashino, S. Sakaguchi, and Y. Ishii. Org. Lett. **2**, 4193 (2000); (*e*) G. Nordmann and S.L. Buchwald. J. Am. Chem. Soc. **125**, 4978 (2003); (*f*) H. Tamio, Y. Akihiro, and I. Yoshihiko. Synth. Commun. **19**, 2109 (1989); (*g*) G. Büchi and D.E. Vogel. J. Org. Chem. **50**, 4664 (1985); (*h*) R.M. Roberts and R.G. Landolt. J. Am. Chem. Soc. **87**, 2281 (1965); (*i*) T. Masso, A. Portella, and E. Rus. Perfum. Flavor. **15**, 39 (1990); (*j*) W. Giersch and I. Farris. Helv. Chim. Acta, **87**, 1601 (2004); (*k*) S.-I. Murahashi, Y. Makabe, and K. Kunita. J. Org. Chem. **53**, 4489 (1988).
28. (*a*) W. Kimmel and A.C. Cope. J. Am. Chem. Soc. **65**, 1992 (1943); (*b*) M.F. Carroll. J. Chem. Soc. 704 (1940); (*c*) J.

© 2007 NRC Canada

Tsuji, I. Minami, and I. Shimizu. Chem. Lett. 1721 (1984); (*d*) E.C. Burger and J.A. Tunge. Org. Lett. **6**, 2603, 2004).
29. J. Nowicki. Molecules, **2000**, 1420 (2000).
30. (*a*) T. Nishiyama, J.F. Woodhall, E.N. Lawson, and W. Kitching. J. Org. Chem. **54**, 2183 (1989); (*b*) C.A. Cornish and S. Warren. J. Chem. Soc. Perkin Trans. 1, 2585 (1985); (*c*) C.A. Cornish and S. Warren. Tetrahedron. Lett. **25**, 2603 (1983); (*d*) T.H. Kim and S. Isoe. J. Chem. Soc. Chem. Commun. 730 (1983).
31. (*a*) K. Suga, S. Watanabe, Y. Yamaguchi, and M. Tohyama. Synthesis, 189 (1970); (*b*) K. Suga, S. Watanabe, T. Fujita, and Y. Takahashi. Aust. J. Chem. **26**, 2123 (1973); (*c*) S. Watanabe, K. Suga, and Y. Yamaguchi. J. Appl. Chem. Biotechnol. **22**, 43 (1972).
32. S. Watanabe, K. Suga, T. Fujita, and I. Takahashi. Can. J. Chem. **50**, 2786 (1972).
33. K. Suga, T. Fujita, S. Watanabe, and Y. Takahashi. Synthesis, 133 (1974).
34. K.A. Hansford, J. Dettwiler, and W.D. Lubell. Org. Lett. **5**, 4887 (2003).
35. S. Watanabe, K. Suga, T. Fujita, and N. Saito. Aust. J. Chem. **30**, 427 (1977).
36. N. Boccara and P. Maitte. Bull. Soc. Chim. Fr. **4**, 1448 (1972).
37. (*a*) H. Ikeda, T. Minegishi, T. Miyashi, P.S. Lakkaraju, R.R. Sauers, and H.D. Roth. J. Phys. Chem. B, **109**, 2504 (2005); (*b*) E.N. Marvell and T.H.-C. Li. J. Am. Chem. Soc. **100**, 883 (1978); (*c*) J.M. Watson, J.L. Irvine, and R.M. Roberts. J. Am. Chem. Soc. **95**, 3348 (1973).
38. (*a*) W. Zhao and E.M. Carreira. Chem. Eur. J. **12**, 7254 (2006); (*b*) M.J. Hall, S.O. McDonnell, J. Killoran, and D.F. O'Shea. J. Org. Chem. **70**, 5571 (2005).

© 2007 NRC Canada

Cytotoxic rotenoloids from the stems of *Derris trifoliata*

Sarot Cheenpracha, Chatchanok Karalai, Chanita Ponglimanont, and Kan Chantrapromma

Abstract: A new rotenoloid, designated 7a-*O*-methylelliptonol, was isolated from hexane and CH_2Cl_2 extracts from the stems of *Derris trifoliata* together with ten known compounds. Their structures were determined by spectroscopic methods, mainly 1D and 2D NMR. The cytotoxicity of all compounds was also evaluated against human cancer cell lines.

Key words: Derris trifoliata, Leguminosae, 7a-*O*-methylelliptonol, cytotoxicity, rotenoloids.

Résumé : À partir des produits extraits des tiges de *Derris trifoliata* à l'aide d'hexane et de dichlorométhane, on a isolé un nouvel roténoloïde dénommé 7a-méthylelliptonol aux côtés de dix autres composés connus. Leurs structures ont été déterminées par des méthodes spectroscopiques, particulièrement de RMN mono- et bidimensionnelles. On a aussi évalué la cytotoxicité de chacun des produits vis-à-vis de familles de cellules cancéreuses humaines.

Mots-clés : Derris trifoliata, légumineuse, 7a-méthylelliptonol, cytotoxicité, roténoloïdes.

[Traduit par la Rédaction]

Introduction

Derris trifoliata Lour. is a mangrove plant in the Leguminosae family (1, 2), distributed throughout the tropical regions of Asia and East Africa, and is widely used in cattle and sheep dips for the control of ticks and other ectoparasites. It is currently used in horticulture against aphids, caterpillars, sawflies, wasps, raspberry beetles, and red spiders (3). Previous chemical investigations of the leaves and stems have resulted in flavonoid glycosides (4) and rotenoids (5), whereas unusual rotenoloids (6, 7) were isolated from the roots and seeds of *D. trifoliata*. The inhibitory effect of several rotenoids, such as deguelin and α-toxicarol, on mouse skin tumor promotion in an in vivo test and on an invasion of human fibrosarcoma HT1080 cells through Matrigel-coat filters has been reported (5, 8). In this present study, we report the structural elucidation of a new rotenoloid, 7a-*O*-methylelliptonol (**1**), together with ten known compounds (**2**–**11**) from the stems of *D. trifoliata* as well as their cytotoxicity against KB, BC, and NCI-H187 cell lines.

Received 10 July 2007. Accepted 16 September 2007. Published on the NRC Research Press Web site at canjchem.ca on 19 October 2007.

S. Cheenpracha, C. Karalai,[1] and C. Ponglimanont. Department of Chemistry, Faculty of Science, Prince of Songkla University, Hat-Yai, Songkhla 90112, Thailand.
K. Chantrapromma. Research Unit of Natural Products Utilization, School of Science, Walailak University, Thasala, Nakhon Si Thammarat 80160, Thailand.

[1]Corresponding author (e-mail: chatchanok.k@psu.ac.th or chatchanok_k@yahoo.com).

Results and discussion

The hexane and CH_2Cl_2 extracts of the stems of *D. trifoliata* were subjected to column chromatography to give a new compound **1** together with ten known compounds (**2**–**11**) shown in Fig. 1. Their structures were elucidated using 1D and 2D NMR spectroscopic data and compared with those reported in the literature.

Compound **1** was obtained as a pale yellow viscous oil with a molecular formula $C_{21}H_{20}O_6$ determined by ESI-TOFMS ($[M + H]^+$ *m/z* 369.1345, calcd. 369.1338). The IR spectrum (1673 cm^{-1}) suggested the presence of a conjugated carbonyl system. UV absorptions at λ_{max} 205, 236, 257, 281, and 293 nm were characteristic of a benzofuran chromophore (9, 10). The ^{13}C NMR spectral data (Table 1) showed a total of 21 carbons with one carbonyl carbon at δ 204.4. The assignments of all carbons were achieved by ^{13}C NMR, DEPT, HMQC, and HMBC experiments. The carbon chemical shift values suggested an oxymethylene carbon (δ 63.5) and two aromatic rings with 12 aromatic carbons identified as four methines (δ 100.9, 112.8, 106.7, 126.5), eight quarternary carbons of which 5 were oxygenated (δ 143.0, 149.1, 149.2, 152.7, 158.8), and 3 non-oxygenated (δ 110.5, 117.9, 125.6). Moreover, the ^1H NMR spectral data of **1** (Table 1) displayed signals corresponding to three singlet signals of methoxyl groups at δ 3.60, 3.81, and 4.18, methylene protons at δ 2.15–2.23 (2H, m, H-6a), oxymethylene protons at δ 4.18–4.21 (2H, m, H-6), a methine proton at δ 4.69 (1H, dd, *J* = 5.7, 4.5 Hz, H-12a), two singlet signals of aromatic protons at δ 6.39 (1H, s, H-1) and 6.42 (1H, s, H-4) and two ortho-coupled doublets centered at δ 7.23 (1H, dd, *J* = 8.7, 0.6 Hz, H-10) and 7.46 (1H, d, *J* = 8.7 Hz, H-11). These ^1H and ^{13}C NMR data were similar to those of 7a-*O*-methyldeguelol (**2**) (6), except for the presence of a 1,2-disubstituted furan moiety at δ 7.01 (1H, dd, *J* = 2.4, 0.6 Hz,

 doi:10.1139/V07-120 © 2007 NRC Canada

Fig. 1. Structures of isolated compounds from the stems of *D. trifoliata*.

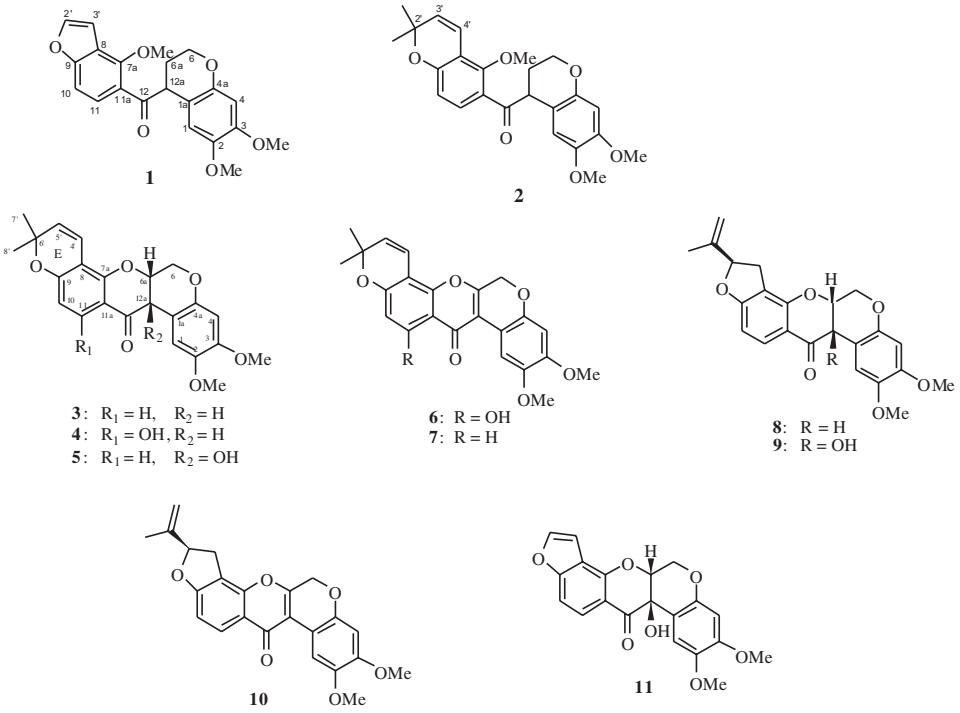


Table 1. ^{1}H and ^{13}C NMR spectral data of compounds **1** and **2** in $CDCl_3$ (300 and 125 MHz).

	1			2	
C/H	δ_C	δ_H (mult, *J* in Hz)	HMBC ($^{1}H \rightarrow {}^{13}C$)	δ_C	δ_H (mult, *J* in Hz)
1	112.8	6.39 (s)	1a, 3, 4, 4a, 12a	112.7	6.40 (s)
1a	110.5			110.0	
2	149.1			149.0	
3	143.0			142.9	
4	100.9	6.42 (s)	1a, 2, 3	100.9	6.40 (s)
4a	149.2			149.1	
6	63.5	4.18–4.21 (m)	4a, 6a, 12a	63.5	4.17–4.21 (m)
6a	25.3	2.15–2.23 (m)	1a, 6, 12, 12a	25.3	2.21–2.23 (m)
7a	152.7			155.5	
8	117.9			114.9	
9	158.8			157.4	
10	106.7	7.23 (dd, 8.7, 0.6)	7a, 8, 9, 11a	112.8	6.62 (d, 8.4)
11	126.5	7.46 (d, 8.7)	7a, 9, 12	130.9	7.35 (d, 8.4)
11a	125.6			125.2	
12	204.4			202.7	
12a	45.8	4.69 (dd, 5.7, 4.5)	1, 1a, 2, 4a, 6a, 12	44.6	4.61 (dd, 6.0, 4.2)
2′	144.9	7.63 (d, 2.4)	8, 9	76.9	
3′	105.5	7.01 (dd, 2.4, 0.6)	2′, 7a, 8, 9	130.6	5.71 (d, 9.9)
4′				116.4	6.62 (d, 9.9)
2′-Me_2				28.0	1.46 (s)
				28.0	1.45 (s)
2-OMe[a]	56.2	3.81 (s)	2	55.8	3.81 (s)
3-OMe[a]	56.8	3.60 (s)	3	56.2	3.64 (s)
7a-OMe	60.5	4.18 (s)	7a	63.5	3.80 (s)

[a]May be interchangeable.

© 2007 NRC Canada

H-3′) and 7.63 (1H, d, J = 2.4 Hz, H-2′) instead of a 2,2-dimethylchromene moiety [δ 5.71 (1H, J = 9.9 Hz, H-3′), 6.62 (1H, J = 9.9 Hz, H-4′), 1.45 and 1.46 (each 3H, s, 2′-Me_2)] of **2**. In the HMBC spectrum, correlations of H-2′ with carbons at δ 158.8 (C-9) and 117.9 (C-8) and of H-3′ with δ 158.8 (C-9), 152.7 (C-7a) and 117.9 (C-8) indicated the location of the furan ring at C-8 and C-9. A methine proton H-11 showed correlations with carbons at δ 204.4 (C-12), 158.8 (C-9), and 152.7 (C-7a); a methine H-12a with δ 204.4 (C-12), 149.2 (C-4a), 149.1 (C-2), 112.8 (C-1), 110.5 (C-1a), and 25.3 (C-6a); two methylenes 2H-6a with δ 204.4 (C-12), 110.5 (C-1a), 63.5 (C-6), and 45.8 (C-12a); and methoxyl protons at δ 4.18 with δ 152.7 (C-7a). Thus, the attachment of a carbonyl group at C-12 and a methoxyl group at C-7a could be assigned. The absolute configuration at C-12a of 7a-*O*-methyldeguelol (**2**) ($[\alpha]^{28}_D$ –18.2°) has been suggested by Yenesew et al. (6, 7). Compound **1** is levorotatory ($[\alpha]^{28}_D$ –17.4°), thus most likely has the same configuration at C-12a as **2**. However, the absolute configuration at C-12a in **1** remains to be determined. Therefore, the structure of the new compound **1** was elucidated as 7a-*O*-methylelliptonol.

The remaining compounds were characterized as 7a-*O*-methyldeguelol (**2**) (6), deguelin (**3**) (11), α-toxicarol (**4**) (11), tephrosin (**5**) (11), 6a,12a-dehydro-α-toxicarol (**6**) (11), 6a,12a-dehydrodeguelin (**7**) (11), rotenone (**8**) (12), 12a-hydroxyrotenone (**9**) (13), 6a,12a-dehydrorotenone (**10**) (12), and 12a-hydroxyelliptone (**11**) (10) by the analysis of 1D and 2D NMR, mass information, and comparison with their reported physical and spectroscopic data. In addition, compounds **6**, **9**, and **10** were reported for the first time as metabolites of *D. trifoliata*.

As summarized in Table 2, compounds **1**, **3**, **4**, **8**, and **9** exhibited significant cytotoxic effects against KB, BC, and NCI-H187 cell lines with ED_{50} values in the general range of 0.05 nM to 4.1 μM, whereas compounds **2**, **7**, and **10** were found to be selectively active against NCI-H187 cell lines. It should be noted that the rotenoids (**3**, **4**, **8**, **9**, and **11**) with sp^3 hybridization at C-6a and C-12a exhibited strong activity against KB and BC cell lines, whereas the rotenoids (**6**, **7**, and **10**) with olefinic carbons at C-6a and C-12a showed no activity at all. The most interesting finding is the extraordinarily potent anticancer activity against NCI-H187 cell lines (IC_{50} = 0.05 nM) of compound **8**, which showed a much higher effect than ellipticine (IC_{50} = 2.44 μM). The result of the present study indicates that rotenone (**8**) could be a potent candidate as a phytotherapeutic lung cancer inhibitor.

Table 2. Cytotoxic activities of compounds **1**–**11**.

	Cell lines (μM)		
Compounds	KB	BC	NCI-H187
1	4.1	3.8	3.0
2	30.5	13.9	4.1
3	1.8	1.5	0.1
4	1.7	0.2	0.2
6	>100	>100	>100
7	>100	>100	3.1
8	1.7	0.2	0.05[a]
9	1.6	0.1	0.05
10	>100	>100	3.3
11	2.4	10.1	0.3

Note: Key to cell lines used: KB = oral human epidermoid carcinoma; BC = human breast cancer cells; NCI-H187 = human small cells lung cancer. Compound 5 was not determined because of decomposition.
[a]Results are expressed as ED_{50} values in nM.

Experimental section

General experimental procedures

Melting points were determined on an Electrothermal melting point apparatus. The optical rotation $[\alpha]_D$ values were determined with a JASCO P-1020 polarimeter. UV spectra were measured with a Specord S 100 (Analytikjena). The IR spectra were measured with a PerkinElmer FTS FT-IR spectrophotometer. The ^1H and ^{13}C NMR spectra were recorded using a 500 MHz Varian Unity Inova and a 300 MHz Bruker FT-NMR Ultra Shield™ spectrometers. Chemical shifts are recorded in part per million (δ) in $CDCl_3$, acetone-d_6 or CD_3OD with tetramethylsilane (TMS) as an internal reference. The ESI-TOFMS were obtained from a Micromass LCT mass spectrometer. Quick column chromatography (QCC) and column chromatography (CC) were carried out on silica gel 60 F_{254} (Merck) and silica gel 100 (Merck), respectively. Precoated plates of silica gel 60 F_{254} and reversed-phase (RP-18 F_{254S}) were used for analytical purposes.

Plant material

The stems of *D. trifoliata* were collected in April 2002 at the Mangrove Research Station in Nakhon Si Thammarat Province, Thailand. The plant material was identified by Prof. Puangpen Sirirugsa and a voucher specimen (No. SC02) has been deposited in the Herbarium of the Department of Biology, Faculty of Science, Prince of Songkla University, Songkhla, Thailand.

Extraction and Isolation

Ground-dried stems of *D. trifoliata* (16.2 kg) were successively immersed at room temperature in hexane, CH_2Cl_2, and MeOH (each 2 × 10 L, 5 days). After evaporation, the viscous crude hexane (73.4 g), CH_2Cl_2 (118.1 g), and MeOH (350.5 g) extracts were obtained. A portion of crude hexane extract (21.7 g) was subjected to QCC and eluted with gradient elution of hexane, EtOAc, and MeOH which afforded ten fractions (A1–A10). Fraction A7 (0.94 g) was purified by CC and prep. TLC with EtOAc/hexane (1:3 *v*/*v*) to give **2** (16.6 mg), **3** (12.7 mg), **4** (5.0 mg), and **8** (8.2 mg). Fraction A8 (0.47 g) was further separated by CC (EtOAc/hexane, 1:3 *v*/*v*) followed by reversed-phase prep. TLC (MeOH/H_2O, 1:3 *v*/*v*) to afford **1** (55.5 mg), **5** (2.5 mg), **9** (9.7 mg), and **11** (16.7 mg). The crude CH_2Cl_2 extract (118.1 g) was fractionated by QCC over silica gel using gradient elution of hexane/EtOAc and EtOAc/MeOH. The eluate was combined on the basis of TLC analysis to give five fractions (B1–B5). Fraction B2 (6.82 g) was separated by CC with EtOAc/hexane (1:4 *v*/*v*), followed by prep. TLC with EtOAc/hexane (1:4 *v*/*v*) to afford **6** (17.2 mg). Fraction B4 (31.35 g) was purified by QCC with hexane and increasing polarity with EtOAc and MeOH to give five subfractions (B4a–B4e). Sub-

© 2007 NRC Canada

fraction B4c (4.96 g) was further separated by CC with CH_2Cl_2, followed by reversed-phase prep. TLC ($MeOH/H_2O$, 7:3 *v*/*v*) to yield **7** (2.2 mg) and **10** (101.1 mg).

7a-*O*-Methylelliptonol ((2,3-dimethoxy-chroman-12a-yl)-(7a-methoxy-benzofuran-11a-yl)-methanone)

Yellow viscous oil. $[\alpha]^{28}_D$ –17.4° (c 0.16, MeOH). UV (MeOH) nm (log ε): 205 (4.47), 236 (4.50), 257 (3.90), 281 (3.76), and 293 (3.78). IR (neat, cm^{-1}) δ: 2956, 1673, 1515. ^1H and ^{13}C NMR: Table 1. ESI-TOFMS $[M + H]^+$ *m*/*z* 369.1345; calcd. for $C_{21}H_{21}O_6$: 369.1338.

Cytotoxicity Assay

The cytotoxic assay employed the colorimetric method (14). Ellipticine, the reference substance, exhibited activity toward KB, BC, and NCI-H187 cell lines with ED_{50} ranges of 1.22–2.44 μM.

Acknowledgments

We thank the Center for Innovation in Chemistry: Postgraduate Education and Research Program in Chemistry, funded by the Royal Thai Government; Graduate School and Natural Products from Mangrove Plants and Synthetic Materials Research Unit (NSU), Prince of Songkla University; and the Biodiversity Research and Training Program (BRT) for financial support. The bioassays research facility of BIOTEC is also gratefully acknowledged for bioactivity tests.

References

1. S. Aksornkoae, G.S. Maxwell, S. Havanond, and S. Panichsuko. Plants in mangroves. Chalongrat Publisher, Bangkok, Thailand. 1992. p. 67.
2. N. Bamroongrugsa and Songklanakarin. J. Sci. Technol. **21**, 377 (1999).
3. R. Cremlyn. Pesticides: Preparation and mode of action. John Wiley and Sons, New York. 1978. p. 41.
4. A.G.R. Nair and T.R. Seetharaman. J. Nat. Prod. **49**, 710 (1986).
5. C. Ito, M. Itoigawa, N. Kojima, H.T.W. Tan, J. Takayasu, H. Tokuda, H. Nishino, and H. Furukawa. Planta Med. **70**, 8 (2004).
6. A. Yenesew, E.K. Mushibe, M. Induli, S. Derese, J.O. Midiwo, J.M. Kabaru, M. Heydenreich, A. Koch, and M.G. Peter. Phytochemistry, **66**, 653 (2005).
7. A. Yenesew, J.T. Kiplagat, S. Derese, J.O. Midiwo, J.M. Kabaru, M. Heydenreich, and M.G. Peter. Phytochemistry, **67**, 988 (2006).
8. H. Matsuda, K. Yoshida, K. Miyagawa, Y. Asao, S. Takayama, S. Nakashima, F. Xu, and M. Yoshikawa. Bioorg. Med. Chem. **15**, 1539 (2007).
9. S. Cheenpracha, R. Srisuwan, C. Karalai, C. Ponglimanont, S. Chantrapromma, K. Chantrapromma, H.-K. Fun, S. Anjum, and Atta-ur-Rahman. Tetrahedron, **61**, 8656 (2005).
10. N. Thasana, M. Chuankamnerdkarn, and S. Ruchirawat. Heterocycles, **55**, 1121 (2001).
11. C.C. Andrei, P.C. Vieira, J.B. Fernandes, M.F. Das, G.F. Da Silva, and E.R. Fo. Phytochemistry, **46**, 1081 (1997).
12. D.G. Carlson, D. Weisleder, and W.H. Tallent. Tetrahedron, **29**, 2731 (1973).
13. A.F. Magalhaes, A.M.G. Azevedo Tozzi, B.H.L. Noronha Sales, and E.G. Magalhaes. Phytochemistry, **42**, 1459 (1996).
14. P. Skehan, R. Storeng, D. Scudiero, A. Monks, J. McMahon, D. Vistica, J.T. Warren, H. Bokesch, S. Kenney, and R.M. Boyd. J. Nat. Cancer Inst. **82**, 1107 (1990).

© 2007 NRC Canada

A pentacene intermediate via formal intramolecular photoredox of a 6,13-pentacenequinone in aqueous solution

Yunyan Hou and Peter Wan

Abstract: The formal intramolecular photoredox reaction (or tandem phototautomerizations) of aromatic ketones in aqueous solution discovered in our laboratory has been extended to a number of acenequinones. In particular, we were interested in whether the photoredox reaction could be applied to 2-(hydroxymethyl)-6,13-pentacenequinone (**4**), which would result in 2-formyl-6,13-dihydroxypentacene (**10**) and hence offer a photochemical method for synthesizing a pentacene derivative. Whereas a number of acenequinones displayed a range of photoredox reactivity, photolysis of **4** in acidic aqueous solution (pH < 3) resulted in a clean intramolecular photoredox reaction, via an enol intermediate, to give **10** (green compound; $\Phi \sim 0.2$ at pH 1), which was too reactive for isolation or trapping by standard ArOH trapping agents such as acetic anhydride. These reactions may be viewed as a one-way photochemical intramolecular "redox switch" from quinone to hydroquinone with concurrent oxidation of an attached hydroxymethyl (alcohol) moiety. Without the attached alcohol moiety, these acenequinones are photostable in aqueous solution. The trend in observed relative reactivity may be partially rationalized by examining changes in molecular orbital coefficients observed in the calculated HOMOs and LUMOs (at the AM1 level).

Key words: pentacene, acenequinones, photoredox, enol, acid catalysis.

Résumé : La réaction photoredox intramoléculaire formelle (ou phototautomérisations en tandem) de cétones aromatiques en solution qui a été découverte dans notre laboratoire a été étendue à un certain nombre d'acènequinones. En particulier, nous étions intéressés à déterminer si la réaction photoredox pouvait être appliquée à la 2-(hydroxyméthyl)6,13-pentacènequinone (**4**) qui conduirait à la formation du 2-formyl-6,13-dihydroxypentacène (**10**) et qui offrirait une méthode de synthèse de dérivés pentacènes. Alors qu'un bon nombre d'acènequinones présentent des activités photoredox diverses, la photolyse du composé **4** dans une solution aqueuse acide (pH inférieur à 3) donne lieu à une réaction photoredox intramoléculaire propre, par le biais d'un intermédiaire énolique, et elle conduit à la formation du produit **10** (un composé vert; Φ approximatif de 0,2, à un pH de 1) qui est trop réactif pour être isolé ou piégé par les agents habituels de piégeage des ArOH, tel l'anhydride acétique. On peut donc considérer que ces réactions sont des "interrupteurs redox" à sens unique pour les réactions photochimiques intramoléculaires et qu'elles permettent le passage d'une quinone à une hydroquinone avec l'oxydation concurrente de la portion alcoolique, hydroxyméthyle, qui y est attachée. En l'absence de la portion alcoolique qui y est attachée, ces acènequinones sont photostables en solution aqueuse. La tendance qui a été observée pour la réactivité relative peut être partiellement rationalisée par un examen des changements dans les coefficients des orbitales moléculaires qui ont été observées dans les hautes élevées et basses vacantes, au niveau AM1.

Mots-clés : pentacène, acènequinones, photoredox, énol, catalyse acide.

[Traduit par la Rédaction]

Introduction

Pentacene is a promising candidate for application as a novel organic semiconductor (1). However, it is sensitive to both oxygen and light and has low solubility. To overcome these disadvantages, considerable efforts have been directed at synthesizing new pentacene derivatives (2). Among them, pentacenequinone derivatives have been employed as synthetic precusors because of their stability and ready accessibility. Recently, photochemical methods based on extrusion of molecular fragments for the synthesis of pentacenes have also been reported (3, 4).

Our group reported some time ago that 2-(hydroxymethyl)-9,10-anthraquinone (**1**) undergoes a very efficient new type of intramolecular photoredox reaction (or equivalently viewed as proceeding via tandem phototautomerizations) in neutral aqueous solution to give 2-formyl-9,10-dihydroxyanthracene (**2**) ($\Phi \sim 0.8$) (5). This reaction was ob-

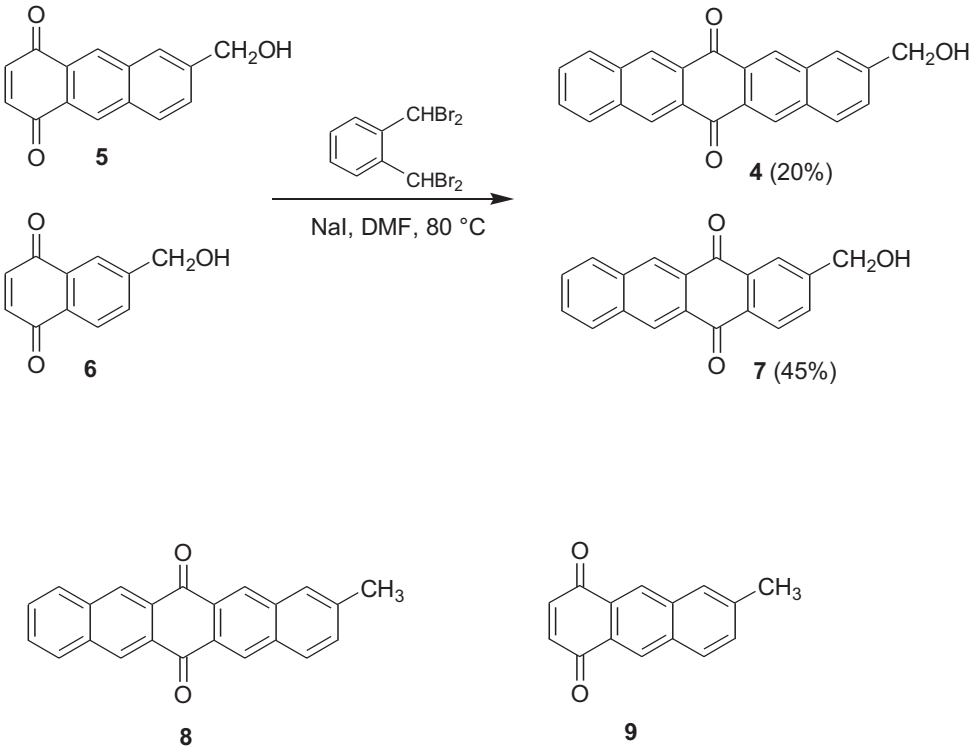
Received 22 June 2007. Accepted 27 August 2007. Published on the NRC Research Press Web site at canjchem.nrc.ca on 19 October 2007.

Y. Hou and P. Wan.[1] Department of Chemistry, Box 3065, University of Victoria, Victoria, BC V8W 3V6, Canada.

[1]Corresponding author (e-mail: pwan@uvic.ca).

 doi:10.1139/V07-117 © 2007 NRC Canada

Scheme 1.



served only in protic solvents, with highest quantum yields in water. The mechanism is unimolecular in substrate but is catalyzed (mediated) by water. In the presence of oxygen, dihydroxyanthracene **2** is quantitatively converted to 2-formylanthraquinone (**3**) (eq. [1]) (5). We have also discovered that simple benzophenones can react via this pathway; thus, 3-(hydroxymethyl)benzophenone undergoes the same photoredox reaction (via T_1) but requires pH < 3 (6). These reactions are termed photoredox because of the fact that a formal transfer of electrons through the meta positions of the benzene ring is required. Based on these findings, we anticipated that 2-(hydroxymethyl)-6,13-pentacenequinone (**4**) might undergo the photoredox reaction as well, which would give rise to a corresponding dihydroxypentacene derivative. Herein, we report a new photochemical method involving an intramolecular redox process to prepare a pentacene intermediate from **4** and associated photochemistry for related acenequinones.

Results and discussion

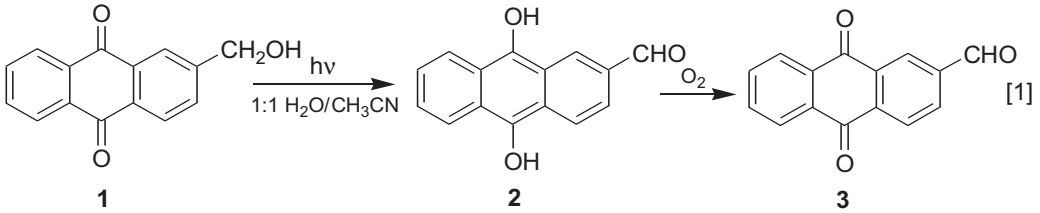
Materials

The potential photoredox chemistry of pentacenequinone **4** and associated acenequinones **5**–**7** (chosen based on their relative ease of synthesis) was explored in this work. Acenequinones **4** and **7** were readily prepared via the condensation (in situ Diels–Alder) of the corresponding acenequinones **5** and **6**, respectively, with α,α,α′,α′-tetrabromo-*o*-xylene (Scheme 1). Acenequinones **5** and **6** are known compounds and were prepared by following or adapting the corresponding literature methods (7, 8). 2-Methyl-6,13-pentacenequinone (**8**) was also studied to test the requirement of a hydroxymethyl (alcohol) moiety in the anticipated photoredox chemistry. It was made using the same reaction shown in Scheme 1, starting with 6-methyl-1,4-anthraquinone (**9**).

UV–vis studies

As shown for the reaction of **1** (5), UV–vis studies were particularly informative of reaction because the photochemical transformation (eq. [1]) involves a substantial change in chromophore, going from an aromatic ketone/quinone to a dihydroxy-substituted polycyclic aromatic compound (anthracene). In the case of **1**, the initial photochemical product **2** is coloured (orange). We anticipated similar UV–vis changes on the photoredox reaction of **4**–**7**. UV–vis studies of **4** (10^{-6} to $10^{-}5$ mol/L, solvent: 1:3 H_2O/CH_3CN, pH 1 and 7 (water portion), argon purged, 350 nm lamps, 3.0 mL quartz cuvette) were carried out initially. No changes were observed in neat CH_3CN or in H_2O/CH_3CN (water at pH 7),

[1]



[1]

© 2007 NRC Canada

Fig. 1. UV–vis traces observed on photolysis of pentacenequinone **4** (1:3 H_2O/CH_3CN, pH 1, λ_{ex} 350 nm, argon purged). Photolysis times were 10–20 s except for the final trace (2 min). New absorption bands at 318, 473, and 657 nm are consistent with the formation of dihydroxypentacene **10** (Inset: expansion of the long wavelength region).

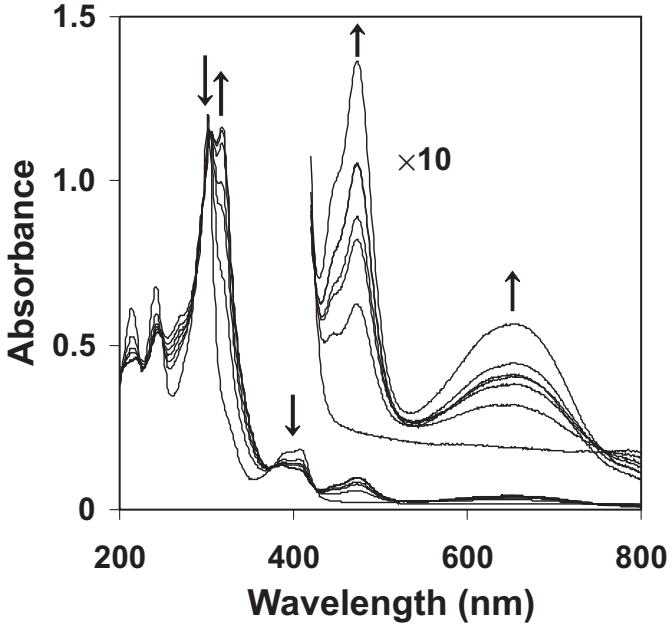
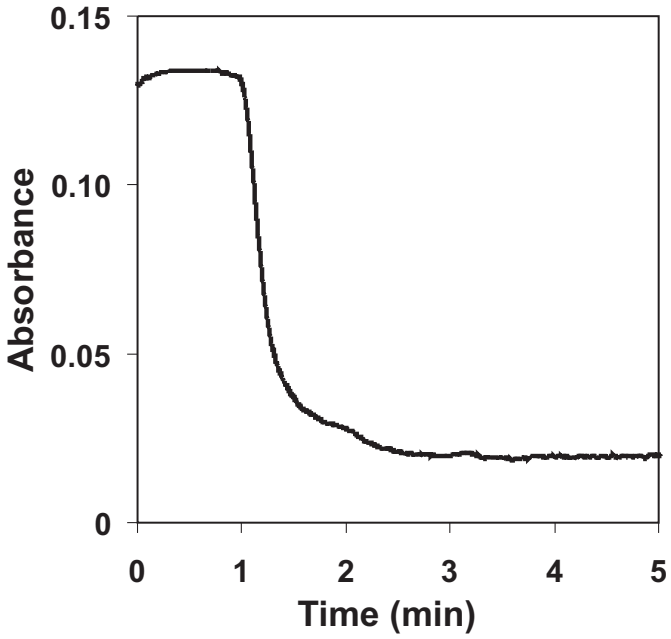


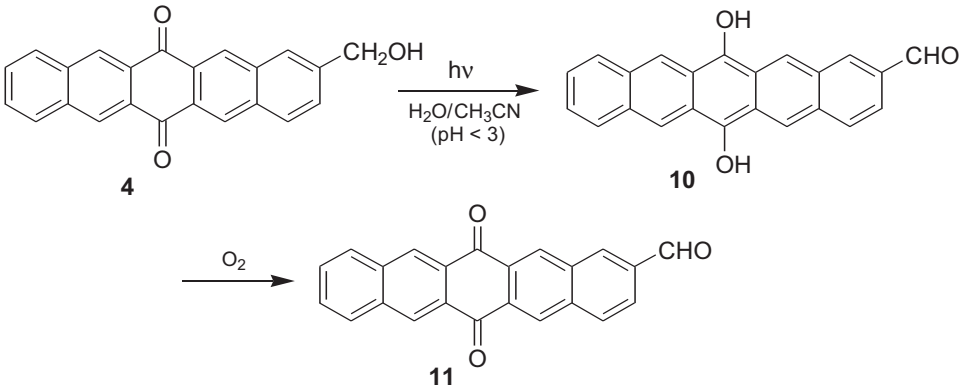
Fig. 2. Decay of photogenerated dihydroxypentacene **10** (from pentacenequinone **4** in 1:3 H_2O/CH_3CN, pH 1) on exposure to air upon opening cuvette (absorbance monitored at 473 nm).



but dramatic changes were observed in H_2O/CH_3CN at pH 1 (Fig. 1). Photolysis at this pH resulted in the formation of an intense new absorption band at 318 nm and two additional (less intense) visible bands at 473 and 657 nm, the latter being a very broad band covering 550–780 nm. Based on what is known for **1** shown in eq. [1], the same reaction for **4** would give rise to 6,13-dihydroxypentacene **10** (eq. [2]). Pentacenes are known to absorb strongly in the visible region, with the longest wavelength band in the 500–700 nm, depending on substituents (2*a*, 4). The broad absorption at 657 nm is consistent with the formation of a pentacene. These new absorption bands disappeared within 1 min of opening the cuvette to air or oxygen (Fig. 2) and within 1 h when the cuvette was unopened and sealed. The resulting UV–vis spectrum was identical to an authentic sample of pentacenequinone aldehyde **11**, which has a UV–vis spectrum similar to that of **4**. This is consistent with a highly reactive dihydroxypentacene derivative that is readily air-oxidized to give **11**. Notably, **8**, although structurally very similar to **4**, did not show reaction under the stated conditions.

The effect of pH on the relative quantum efficiency of the photoredox reaction of **4** was examined next. As noted for pH 7, no reaction was observed. Using the UV–vis method, the relative quantum efficiency for the formation of **10** was followed at different pH values (1:3 H_2O/CH_3CN, the pH of the water portion varied). The results show that the photoredox efficiency strongly depends on the pH of the solution (Fig. 3). The photoredox reaction was not observable above pH 3 and reaches maximum efficiency at about pH ≅ 0, although higher acidities were not employed in this study.

Whereas UV–vis studies of **5** (pH 1 and 7) gave only small incremental changes even on prolonged photolysis, indicative of a much less reactive chromophore, the same studies of **6** (pH 7) gave rise to two new strongly absorbing bands at 268 and 392 nm, which were assignable to dihydroxynaphthalene **12** (Fig. 4 and Scheme 2). For this compound, acid was not required for the efficient photoredox reaction, akin to what was observed for **4**. In-



[2]

© 2007 NRC Canada

Fig. 3. Effect of pH on the efficiency of photoredox reaction of pentacenequinone **4** monitored at 318 nm (formation of dihydroxypentacene **10**; λ_{ex} 350 nm; 1:3 H_2O/CH_3CN (pH 1), argon purged). ΔA is the difference in the absorbance before and after irradiation.

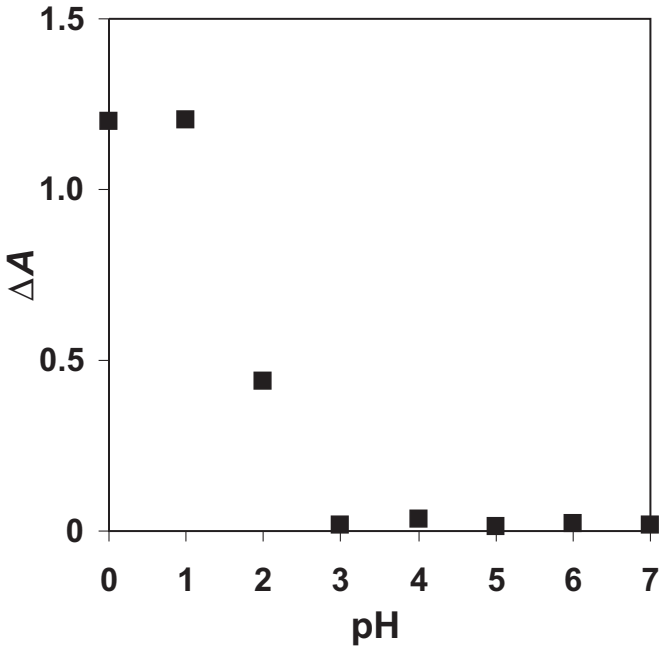
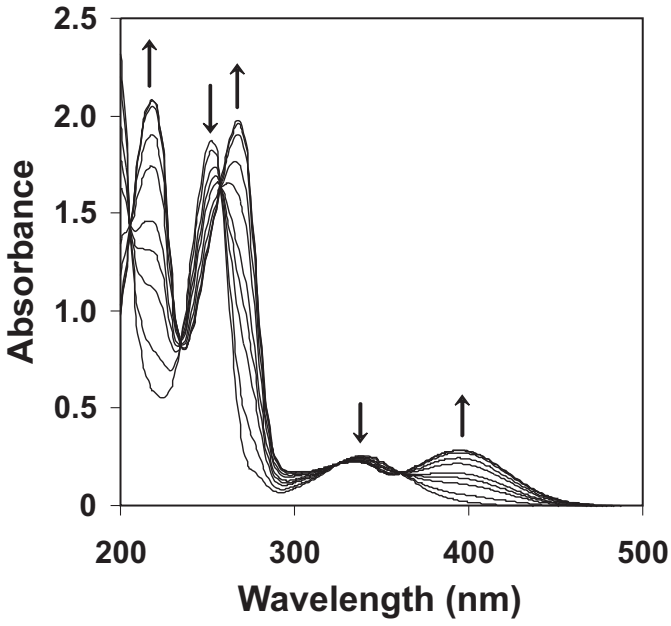
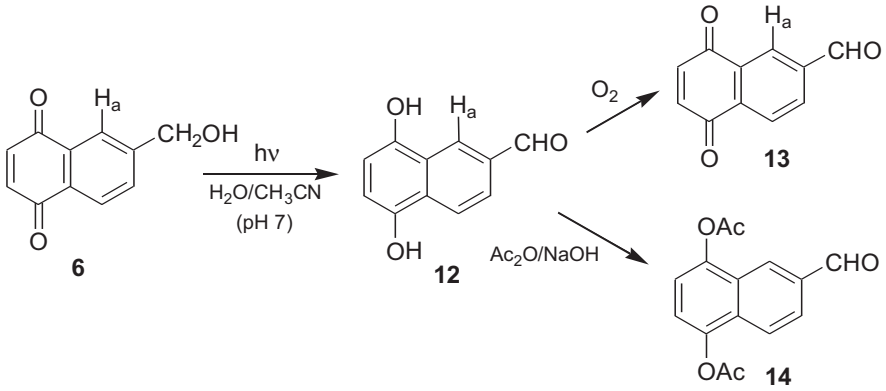


Fig. 4. UV–vis traces observed on photolysis of naphthoquinone **6** (1:1 H_2O/CH_3CN, pH 7, λ_{ex} 350 nm, argon purged). Photolysis times were 2–20 s. Growth of absorption bands at 268 and 392 nm is consistent with the formation of dihydroxynaphthalene **12**.



Scheme 2.



deed, the use of acid did not result in any enhancement of the photoredox reaction. Photolysis in neat CH_3CN gave no observable changes. The photoredox product in this case (dihydroxynaphthalene **12**) was more stable in air or oxygen, as the coloured intermediate remained unchanged for at least 1 day in the sealed cuvette. Shown in Fig. 5 are solutions of photolyzed acenequinones **1**, **4**, and **6** illustrating the varied colours observable in this family of photoredox reactions in aqueous solution. Finally, UV–vis studies of **7** gave no observable changes in the UV–vis spectrum (pH 1 or 7) with prolonged times, indicative of an essentially unreactive acenequinone.

Product studies

Semi-preparative photolyses were carried out to confirm the reactivity of the compounds (based on the previously mentioned UV–vis studies) and to isolate, characterize, and in some cases trap initial photoproducts. Acenequinones **4**–**8** were photolyzed (10^{-5} to 10^{-3} mol/L, λ_{ex} 350 nm, argon purged) in H_2O/CH_3CN (various pH values) as well as in neat CH_3CN. Semi-preparative photolysis of **4** (pale yellow) in 1:3 H_2O/CH_3CN (pH 1) gave a green to dark green solution depending on irradiation time, indicative of photoredox chemistry. When left standing in the photolysis tube after irradiation with no precautions to prevent entry of air, the colour changed to a pale yellow within 1 h, indicative of a reactive initial photoproduct. When the photolyzed solution was exposed to air after photolysis (pouring the solution into a flask exposed to air), the green colour disappeared immediately. In view of the reactive nature of the initially formed photoproduct, no attempts were made to isolate it in these runs. Instead, the solutions were exposed to air after photolysis and extracted with CH_2Cl_2. Work-up using this method gave exclusively 2-formyl-6,13-pentacenequinone

© 2007 NRC Canada

Fig. 5. Dramatic differences in observed colours in the photolysis of **6** (pH 7), **1** (pH 7), and **4** (pH 1) (L to R) in 1:1 H_2O/CH_3CN (λ_{ex} 350 nm, 15 min, argon purged). In sealed vessels, the colour remained unchanged for at least a day for **6** and **1** and a few hours for **4**.



(**11**) (yields 20%–70% by NMR, depending on photolysis time). No reaction was observed when photoyzed in pH 7 or in neat CH_3CN, consistent with the UV–vis studies reported earlier. In addition, no reactions were observed without photolysis (in the presence or absence of oxygen).

Attempts were made to characterize the initially formed (green) dihydroxypentacene intermediate **10**. Initial experiments were carried out by photolyzing samples of **4** in an NMR tube so the formation of **10** could be observed directly by NMR without work-up or exposure to air. However, because of the very low solubility of **4** in aq. CH_3CN, these photolyses proved to be impractical. Attempts were also made to trap **10** using acetic anhydride (as the ester) and methyl iodide (as the methyl ether) in situ, but in all experiments attempted, only **11** was isolated, consistent with the highly reactive nature of the initially formed product **10**.

Photolysis of the closely related methylpentacenequinone **8** under similar conditions as for **4** or even on extended photolysis did not give any reaction. The photolyzed solution did not develop any colour and upon work-up, the starting material was recovered unchanged. Thus, the photoredox reaction requires an α-hydroxy moiety at the carbon directly attached to the aromatic ring for the reaction to proceed. As the chromophores (and structures) of **4** and **8** are otherwise identical, it would appear that the mechanism allows any formed intermediates — up to a critical product forming step — to return (deactivate) efficiently to starting material.

Photolysis of **6** (1:1 H_2O/CH_3CN, pH 7) resulted in a yellow solution that slowly (several days) faded when left in the vessel and turned to pale yellow within a few hours when exposed to air. On work-up in air, naphthoquinone aldehyde **13** was formed exclusively (30%–60%, depending on photolysis time). To provide further evidence for the reaction scheme shown in Scheme 2, trapping of **12** was attempted. Thus, after photolysis under an argon purge, sufficient solid NaOH was added to the photolysate to basicify the solution. This resulted in the solution turning from yellow to red, consistent with formation of a naphtholate chromophore (via deprotonation of **12**). Excess Ac_2O was then added under argon, which quenched the red colour. Upon work-up, the only product isolable was diacetoxyanthracene aldehyde **14** thus confirming the reaction sequence shown in Scheme 2.

As further evidence for the formation of **12** as the primary photochemical product from **6**, photolyses were also carried out in NMR tubes (10^{-3} mol/L, 1:9 D_2O/CD_3CN, pD 7, λ_{ex} 350 nm, argon purged, 10 min). Photolysis gave a dark yellow solution with a reduction of the signals at δ 4.80 (s) and 8.07 (s) assigned to the methylene and aromatic H_a protons of **6**, respectively, (Scheme 2), with concomitant growth of the aldehyde (CHO; δ 10.07) and H_a (δ 8.70) protons assignable to the initial photoredox product **12**. Based on NMR integration, the yield of **12** was estimated to be about 14%. Upon introduction of oxygen via a syringe needle, the dark yellow colour was bleached. In the NMR, the peaks assignable to **12** disappeared. In particular, a new aldehyde peak at δ 10.13 and an aromatic singlet (H_a) at δ 8.55 are assignable to oxidized product **13**.

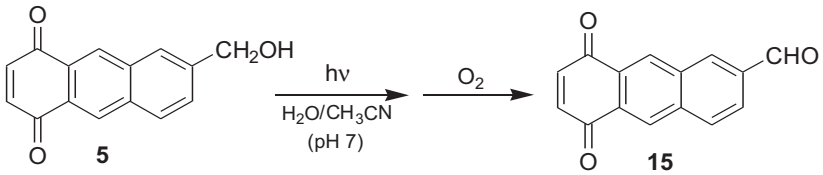
Using the photoredox reaction reported for **1** as a secondary actinometer (Φ = 0.8, pH 2), we estimated a quantum yield of photoredox for **4** (1:3 H_2O/CH_3CN, pH 1) and **6** (1:1 H_2O/CH_3CN, pH 7) to be about 0.2 and 0.4, respectively. Although these compounds are not as reactive as the parent anthraquinone system **1**, they nevertheless have substantial quantum yields of reaction at a suitable pH.

Although acenequinone **5** also underwent the photoredox reaction, it exhibited low reactivity in neutral or acidic solution. This compound required photolysis times that were about an order of magnitude longer for similar conversion. Because of its much lower reactivity, no attempts were made to characterize the initially formed photoredox product and only the final air-oxidized product **15** was isolated (eq. [3]). No reaction was observed without irradiation (in the presence or absence of oxygen). Of all the acenequinones studied in this work, compound **7** proved to be the only one that was photochemically inert. Thus, photolysis of this compound (pH 1, 7) gave no reaction and the compound could be recovered unchanged. Initially we were puzzled by this result although one could imagine a number of photophysical reasons to explain the lack of reaction. However, the lack of reactivity of this compound as well as the reactivity of the other systems can be partly rationalized by resorting to an examination of HOMO and LUMO characteristics (vide infra).

Reaction mechanisms

We believe that the observed formal intramolecular photoredox reactions of the present acenequinones, includ-

[3]

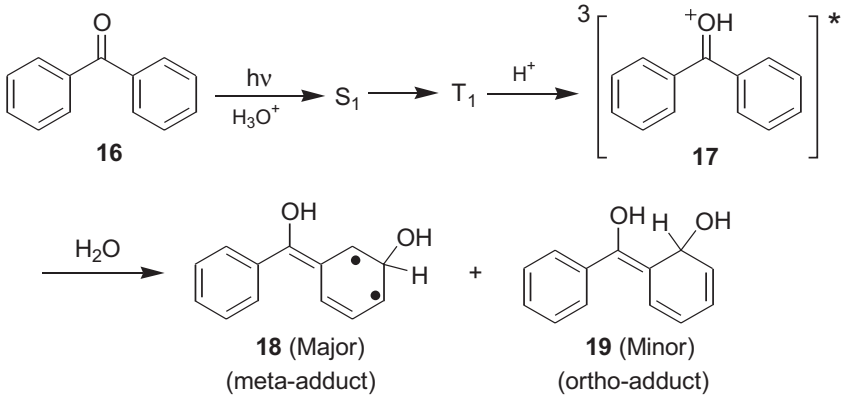


© 2007 NRC Canada

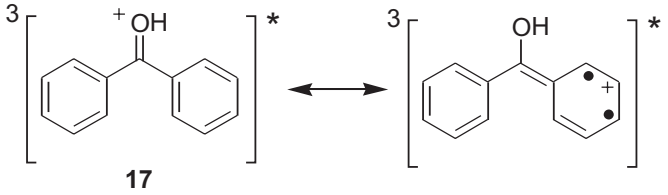
ing the "parent" anthraquinone (5) and "simple" benzophenone (6) systems, are closely related to the acid-catalyzed photohydration of benzophenone (**16**) reported by Wirz and co-workers (9) (eq. [4]). They discovered that the protonation (at the carbonyl) of triplet benzophenone **16** results in an overall *photohydration* reaction, to give water-adducts **18** and **19** with a preference for **18**, i.e., hydration at the meta position (eq. [4]). This reaction was unexpected and has missed detection in the past because of the instability of the hydration products (**18** and **19**), which readily revert back to **16**. Wirz and co-workers (9) assigned a pK_a of –0.4 for the protonated triplet excited state. The mechanism (9) of photohydration presumably involves initiation protonation of the carbonyl oxygen of triplet excited benzophenone **16**, to generate an excited triplet state conjugate acid **17** that has its positive charge significantly delocalized to the ortho and meta positions of the benzene ring (e.g., as shown in eq. [5]), as would be anticipated based on the Zimmerman "ortho–meta" effect for benzene ring site activation in photochemical reactions (10, 11). Attack by water at these sites of positive charge would lead to the observed hydration products, which upon deactivation to their ground states would not be expected to be long-lived and readily return to benzophenone (**16**) by dehydration (with re-aromatization). Although the above acid-catalyzed photohydration of benzophenone reported by Wirz and co-workers (9) gave no isolable *stable* product, it seemed reasonable to assume that the protonation of triplet excited benzophenone (**16**) and aromatic ketones and related compounds, such as acenequinones, might lead to other types of acid-catalyzed chemistry, a prime example of which was the photoredox reaction of benzophenone **20** to give **21** in acidic aqueous solution reported by us (6) (eq. [6]).]

In view of this background and the fact that acenequinones also tend to react via T_1 with photochemical behaviour (12) that is closely allied to what is known for benzophenones, we propose that the mechanism of photoredox reaction of the acenequinones reported in this work also start with a T_1 reactive state that is sufficiently basic to be protonated at pH 7 or at pH < 3, depending on the substrate. Intramolecular photoredox reaction requires protonation of the ketone (by acid or by water) and deprotonation of the C-H proton at the CH_2OH moiety. This is a unique mechanism in photochemistry in that two very different types of excited state proton transfers are required (simultaneously or sequentially). A working mechanism is shown for pentacenequinone **4** (Scheme 3). Although not shown explicitly, all excited states shown in this mechanism are triplets. Compound **4** requires acid for the photoredox pathway to be observed. Thus, excited state protonation gives rise to an excited triplet state conjugate acid **22a,b** that is sufficiently reactive for the subsequent deprotonation of the C-H proton in the CH_2OH moiety, this being the product forming step. That is, both the triplet excited state and the protonated triplet **22a,b** can return to starting material without going on to product. Deprotonation of the C-H proton in CH_2OH seems reasonable if the positive charge is strongly delocalized to the ring position with the CH_2OH group, acidifying the C-H proton. Such a step would give the double enol **23**, which is assumed to be initially generated in its

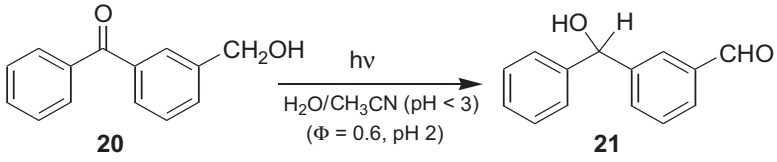
[4]



[5]

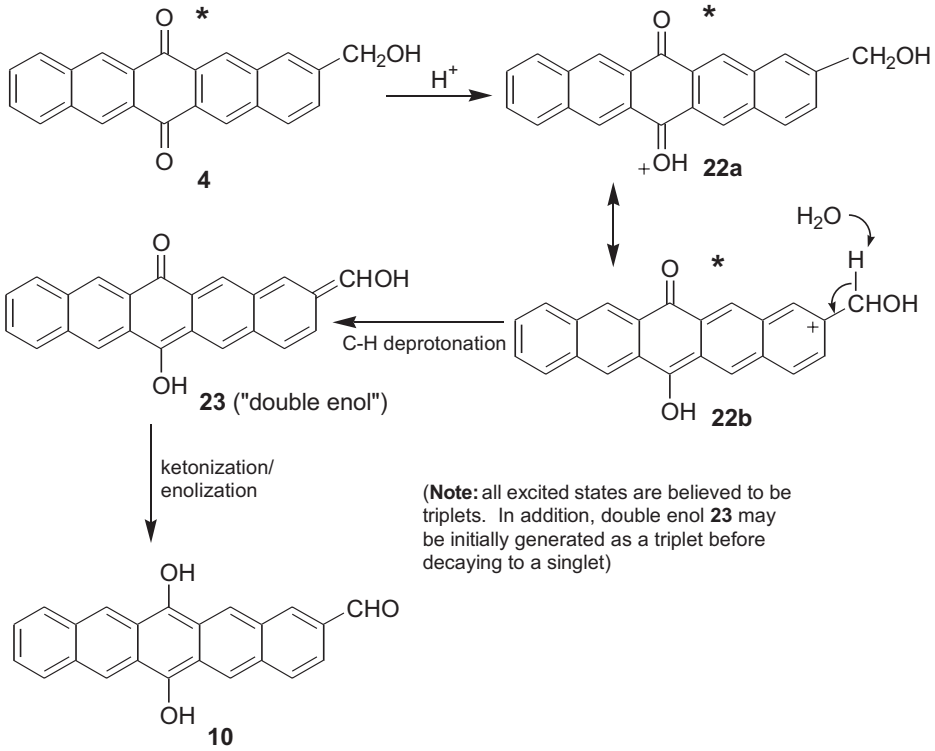


[6]



© 2007 NRC Canada

Scheme 3.



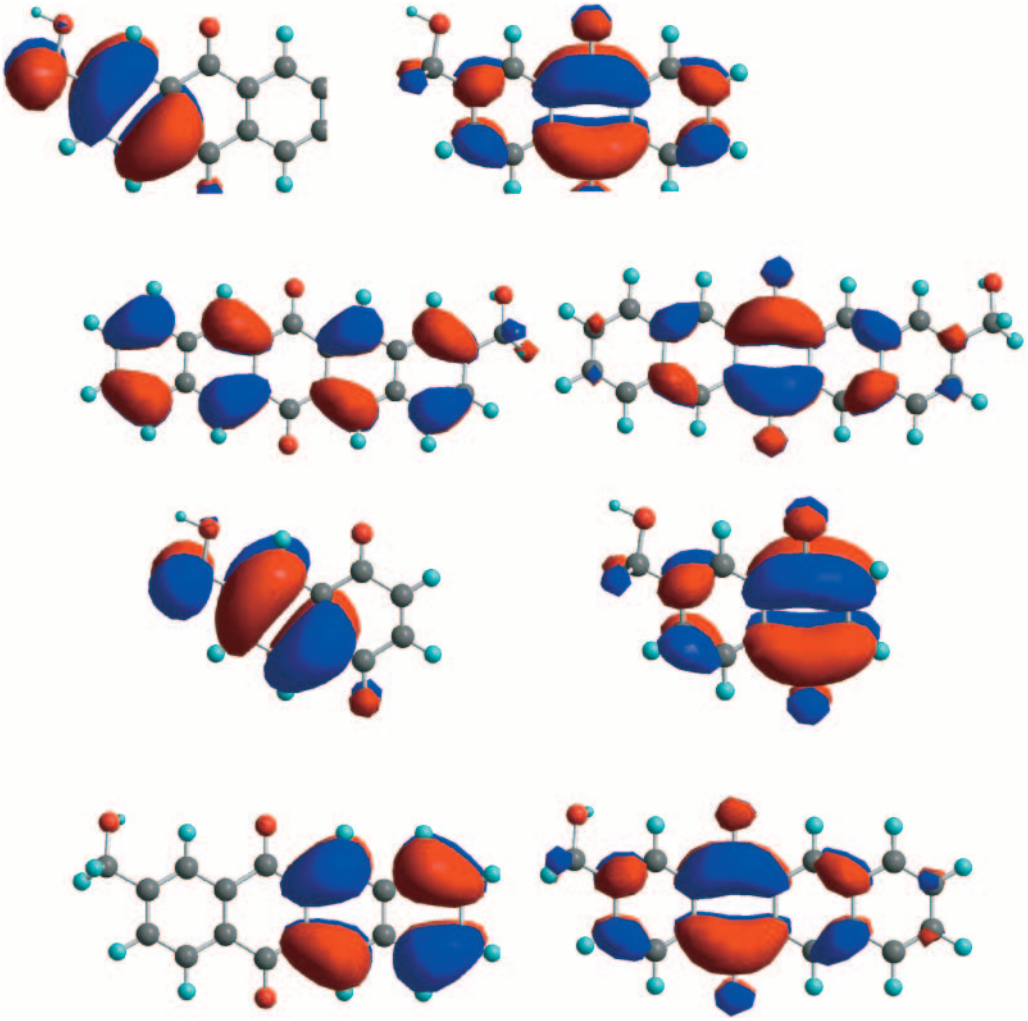
triplet excited state but subsequently deactivates to its ground state singlet. This is followed by ketonization–enolization (tandem tautomerization), which would give the formal redox product **10**. It is also possible that water could attack the positive charge on the ring (of **22b**) resulting in a photohydration reaction like that reported for benzophenone in acid (9). The extent of this pathway is unknown for these compounds.

The overall reaction requires the formal movement of π electrons from one end (CH_2OH) of the molecule to the other (C=O) (Scheme 3). That this can occur for such a large π system as a naphthalene ring in pentacenequinone **4** was unexpected. Since **4** absorbs into the visible (up to 450 nm), the photochemical transformation is a way of storing solar energy in the form of the high energy species dihydroxypentacene **10**, which is a compound capable of reducing other molecules such as molecular oxygen. Conceivably, other uses may be possible.

Although Wirz and co-workers (9) did not explicitly offer an explanation as to why the carbonyl oxygen of benzophenone (**16**) in T_1 becomes much more basic, one can envisage that in aqueous solution the T_1 state may have substantial charge transfer character (as opposed to its known diradical character in typical organic solvents). Such a highly polarized excited state enables the photohydration (9) and the intramolecular photoredox reactions to proceed. Moreover, water is also an essential medium to mediate proton transfer reactions that are required in the reaction mechanism. We have carried out calculations of HOMOs and LUMOs (Chem 3D, AM1) for all of the compounds studied in this work in an attempt to predict the migration of charge on excitation. We assume that a simple picture of the excited state can be obtained by the promotion of an electron from the HOMO to the LUMO without regard to spin multiplicity. For all the reactive acenequinones (**1**, **4**, **5**, and **6**), examination of HOMO and LUMO coefficients (some of which are shown in Fig. 6) show that there is significant to substantial migration of charge from at least the ring with CH_2OH substituent to the carbonyl and to the other ring(s) in the compound. This charge transfer (migration) would make the carbonyl oxygen more basic. On trapping of this charge transfer state with a proton (protonation of the carbonyl oxygen), one can assume that some of the residual positive charge (sites of electron deficiency) will be localized on the ring with the CH_2OH substituent, making the CH proton on the CH_2OH more acidic. At this level of calculation, there is also evidence to suggest that the C–H bond (of the CH_2OH) moiety also donates electron density for compounds **1**, **4**, and **6**, but less so for **4**. This would have the added effect of making this proton even more acidic. Indeed, **1** and **6** were the most reactive compounds (at pH 7). For pentacenequinone **4**, the HOMO and LUMO characteristics are not as optimal; for this compound, reaction was only observable below pH 3. The presence of the OH group is also particularly crucial, because it provides a further inductive acidifying effect and also makes the whole group readily oxidizable (to the aldehyde). For the unreactive compound **7** (Fig. 6), the same calculations show that the charge transfer is in the *opposite direction*, that is, from the rings without the CH_2OH group (the "naphthalene" ring) to the carbonyl and to the ring containing the CH_2OH group. Although this charge transfer will still make the carbonyl oxygen more basic in the excited state and hence undergo protonation, one would not anticipate the same reactivity of the CH_2OH group, since the ring in which it is attached is now more electron-rich than in the ground state. Indeed, this compound

© 2007 NRC Canada

Fig. 6. Calculated (Chem 3D, AM1) HOMOs (left) and LUMOs (right) for acenequinones (top to bottom) **1** (reactive), **4** (reactive), **6** (reactive), and **7** (unreactive).



proved to be photochemically inert! Thus, simple semi-empirical MO calculations at the AM1 level are useful for the prediction of qualitative reactivity patterns for these compounds.

Experimental section

Instrumentation

NMR spectra were recorded on a Bruker 300 or 500 MHz for ^{1}H and 75 or 125 MHz for ^{13}C. IR spectra were recorded on a PerkinElmer 283 instrument. UV–vis spectra were measured on a Cary 1 instrument. Mass spectra were obtained on a Kratos Concept H instrument.

Materials

All solvents were best reagent grade, except CH_3CN that was HPLC grade. Deuterated solvents $CDCl_3$, $(CD_3)_2CO$, DMSO-d_6 were purchased from the Cambridge Isotope Laboratory (99.9% D). All synthetic precursors used below were purchased from Sigma-Aldrich and used as received.

6-(Hydroxymethyl)-1,4-anthraquinone (5)

This compound was made according to the published procedure (7) with 45% overall yield (mp 180–182 °C, lit. value (7) 178 to 179 °C). IR (KBr, cm^{-1}) 3498, 1670, 1650. ^{1}H NMR (300 MHz, $CDCl_3$) δ: 8.59 (s, 2H), 8.05 (d, 1H, J = 8.8 Hz), 8.03 (s, 1H), 7.68 (d, 1H, J = 8.8 Hz), 7.05 (s, 2H), 4.92 (s, 2H). ^{13}C NMR (DMSO- d_6, 75 MHz) δ: 184.4, 184.3, 144.6, 134.0, 139.9, 134.3, 133.4, 130.0, 128.8, 128.2, 127.9, 127.7 (2C), 126.3, 62.7. EIMS *m*/*z* 238 (M^+, 100), 221 (10).

2-(Hydroxymethyl)-6,13-pentacenequinone (4)

A mixture of **5** (0.43 g, 1.8 mmol), α,α,α′,α′-tetrabromo-o-xylene (1.14 g, 2.7 mmol), and NaI (2.70 g, 18 mmol) were heated in 5 mL DMF for 3 h at 80 °C to give a dark brown mixture. After cooling, 50 mL of cold water was added followed by the addition of 10 mL of 10% $NaHSO_3$ dropwise until the dark brown colour was bleached. The mixture was extracted with 3 × 25 mL CH_2Cl_2 and dried over anhydr. $MgSO_4$. Removal of the solvent gave a brown solid, which upon separation by column chromatography (silica gel; CH_2Cl_2 and ethyl acetate as eluents) gave 0.13 g of **4** (21%, yellow powder), mp (decomp) 286 °C. IR (KBr, cm^{-1}) 3403,

© 2007 NRC Canada

1691, 1676. ^{1}H NMR (DMSO-d_6, 500 MHz) δ: 8.95 (s, 1H), 8.94 (s, 1H), 8.93 (s, 1H), 8.89 (s, 1H), 8.38–8.33 (m, 2H), 8.31 (d, 1H, J = 8.5 Hz), 8.23 (s, 1H), 7.84–7.79 (m, 2H), 7.75 (d, 1H, J = 8.5 Hz), 5.54 (t, OH, J = 5.6 Hz), 4.75 (d, 2H, J = 5.6 Hz). ^{13}C NMR (DMSO-d_6, 125 MHz) δ: 182.2, 182.1, 144.7, 134.8 (2C), 134.74, 134.72, 133.9, 130.4, 130.3, 130.1 (2C), 129.9 (2C), 129.8 (2C), 129.1 (2C), 129.0, 128.9, 128.8, 126.2, 62.7. EI MS m/z 338 (M^+, 100), 321 (5). HRMS calcd. for $C_{23}H_{14}O3$ 338.0943; found 338.0928.

2-Methyl-6,13-pentacenequinone (8)

Following the method described for the synthesis of **4**, use of 6-methyl-1,4-anthraquinone (**9**, from ref. 7) (0.12 g, 0.54 mmol), α,α,α′,α′-tetrabromo-o-xylene (0.32 g, 0.81 mmol), NaI (0.81 g, 5.4 mmol) gave 60 mg (35%, yellow powder), mp (decomp) 307 °C. IR (KBr, cm^{-1}) 1676, 1615. ^{1}H NMR ($CDCl_3$, 500 MHz) δ: 8.92 (s, 2H), 8.89 (s, 1H), 8.83 (s, 1H), 8.13–8.09 (m, 2H), 8.01 (d, 1H, J = 8.4 Hz), 7.87 (s, 1H), 7.71–7.67 (m, 2H), 7.53 (d, 1H, J = 8.4 Hz), 2.58 (s, 3H). ^{13}C ($CDCl_3$, 125 MHz) δ: 183.4, 183.3, 140.2, 135.8 (2C), 135.52, 135.49, 133.8, 132.1, 130.98, 130.94, 130.3 (2C), 130.2, 130.1, 129.96, 129.94, 129.8, 129.6 (2C), 129.3 (2C), 22.2. EIMS m/z 322 (M^+, 100). HRMS calcd. for $C_{23}H_{14}O2$ 322.0994; found 322.0993.

6-(Hydroxymethyl)-1,4-naphthoquinone (6)

This compound was synthesized according to the published procedure (8), except for the last hydrolysis step involving 6-(bromomethyl)-1,4-naphthoquinone, in which 1.5 equiv. of silver trifluoacetate was used instead of 5 equiv. of $CaCO_3$. Upon column chromatography (silica gel; CH_2Cl_2), 0.2 g (70%, yellow powder) was obtained, mp 80–82 °C, lit. value (8) 81 to 82 °C. IR (KBr, cm^{-1}) 3447, 1662, 1598. ^{1}H NMR (300 MHz, $CDCl_3$) δ: 8.07 (d, 1H, J = 8.1 Hz), 8.05 (s, 1H), 7.76 (d, 1H, J = 8.1 Hz), 6.96 (s, 2H), 4.85 (s, 2H). ^{13}C (75 MHz, $CDCl_3$) δ: 185.3, 185.1, 147.7, 139.0, 138.8, 132.2, 131.9, 131.3, 127.1, 124.4, 64.5. EIMS m/z 188 (M^+, 100), 160 (90).

2-(Hydroxymethyl)-5,12-naphthacenequinone (7)

A mixture **6** (0.22 g, 1.2 mmol), NaI (1.76 g, 11.7 mmol), and α,α,α′,α′-tetrabromo-*o*-xylene (0.74 g, 1.76 mmol) in 4 mL DMF was heated to 80 °C overnight. After work-up and purification (as described for **4**), 0.29 g (85%) of a yellow powder was obtained, mp (decomp) 190 °C. IR (KBr, cm^{-1}) 3327, 1675, 1603. ^{1}H NMR (300 MHz, $CDCl_3$) δ: 8.84 (s, 2H), 8.40 (d, 1H, J = 8.1 Hz), 8.38 (s, 1H), 8.13–8.05 (m, 2H), 7.83 (d, 1H, J = 8.1 Hz), 7.73–7.64 (m, 2H), 4.91 (s, 2H). ^{13}C NMR (DMSO-d_6, 75 MHz) δ: 182.2, 181.9, 149.8, 134.5 (2C), 133.7, 132.5, 131.9, 130.0 (2C), 129.6 (2C), 129.3, 128.9, 128.8 (2C), 127.0, 124.1, 62.2. EIMS m/z 288 (M^+, 100), 259 (50). HRMS calcd. for $C_{19}H_{12}O3$ 288.0786; found 288.0792.

General photolysis procedure

Preparative photolyses were carried out using a Rayonet RPR 100 photochemical reactor using 350 nm lamps, a water-cooled cold finger, and 100 mL quartz tubes. Solutions (10^{-4} mol/L in substrate) were purged with argon for 15 min prior to photolysis and kept under a stream of argon during irradiation. Unless otherwise noted, all the photolyses were worked up in the presence of air. Photolyzed solutions were extracted with CH_2Cl_2. Upon solvent evaporation, the material was analyzed initially by NMR for product identification and determination of conversions and yields. Subsequently, separation and purification of products were achieved using prep. TLC (silica gel, CH_2Cl_2).

Photolysis of 2-(hydroxymethyl)-6,13-pentacenequinone (4)

Compound **4** (3 mg in 75 mL of CH_3CN and 25 mL of H_2O, pH 1) was irradiated (16 lamps) for 1 min to give 18% yield of **11** (2-formyl-6,13-pentacenequinone), which was subsequently isolated in pure form. IR (KBr, cm^{-1}) 1698, 1675. ^{1}H NMR (300 MHz, $CDCl_3$) δ: 10.2 (s, 1H), 9.10 (s, 1H), 8.97 (s, 1H), 8.95 (s, 2H), 8.93 (d, 1H, J = 8.6 Hz), 8.58 (s, 1H), 8.23 (d, 1H, J = 8.6 Hz), 8.19–8.05 (m, 2H), 7.78–7.64 (m, 2H). EIMS m/z 336 (M^+, 100), 307 (10). HRMS calcd. for $C_{23}H_{12}O3$ 336.0786; found 336.0787.

Photolysis of 2-methylpentacenequinone (8)

Photolysis of **8** as for **4** gave no reaction. The NMR of the isolated material was identical to that of the starting material.

Photolysis of 6-(hydroxymethyl)-1,4-naphthoquinone (6)

Photolysis of **6** (5 mg in 50 mL of CH_3CN and 50 mL of H_2O, pH 7; 4 lamps, 1 min) gave **13** (6-formyl-1,4-naphthoquinone, 44% yield by NMR), which was subsequently isolated. IR (KBr, cm^{-1}) 1697, 1664, 1597. ^{1}H NMR (300 MHz, $CDCl_3$) δ: 10.17 (s, 1H), 8.57 (s, 1H), 8.25 (s, 2H), 7.07 (s, 2H). ^{13}C NMR (CD_3Cl, 75 MHz) δ: 190.8, 184.4, 184.1, 139.9, 139.2, 139.1, 135.4, 133.4, 132.8, 128.7, 127.6. EIMS m/z 186 (M^+, 100), 157 (40). HRMS calcd. for $C_{11}H_6O3$ 186.0317; found 186.0322.

Photolysis of **6** was also carried out in which the initially formed photoredox product **12** was trapped with Ac_2O to give **14** as follows (all carried out under argon): A solution of **6** (10 mg in 50 mL of CH_3CN and 50 mL of H_2O, pH 7) irradiated for 5 min. Upon photolysis, sufficient solid NaOH was added to turn the yellow brown solution to red. This was followed by the addition of 1 mL of Ac_2O, which turned the solution to a brown colour. After work-up in air, the crude material was characterized with ^{1}H NMR, which was consistent with 50% conversion to **14** (6-formyl-1,4-diacetoxynaphthalene). Further separation and purification was achieved by prep. TLC (silica gel, CH_2Cl_2). IR (KBr, cm^{-1}) 1754, 1699. ^{1}H NMR (300 MHz, $CDCl_3$) δ: 10.15 (s, 1H), 8.38 (s, 1H), 7.99 (s, 2H), 7.39 (dd, 2H, J = 8.1 Hz, J = 8.1 Hz,), 2.50 (s, 3H), 2.47 (s, 3H). ^{13}C NMR ($CDCl_3$, 75 MHz) δ: 191.9, 169.4 (2C), 145.5, 144.4, 134.8, 130.5, 127.9, 127.4, 124.3, 123.2, 121.4, 119.3, 21.4, 21.2. EIMS m/z 272 (M^+, 5), 230 (15), 188 (100), 43 (40). HRMS calcd. for $C_{15}H_{12}O5$ 272.0685; found 272.0687.

Photolysis of 6-(hydroxymethyl)-1,4-anthraquinone (5)

A solution of **5** (3 mg in 50 mL of CH_3CN and 50 mL of H_2O, pH 7, 16 lamps) was irradiated for 1 min, which gave an aldehyde product in less than 2% conversion. Upon photolysis for 30 min, 30% conversion to 6-formyl-1,4-

© 2007 NRC Canada

anthraquinone (**15**) could be achieved. IR (KBr, cm^{-1}) 1706, 1668, 1589. ^1H NMR ($CDCl_3$, 300 MHz) δ: 10.22 (s, 1H), 8.78 (s, 1H), 8.67 (s, 1H), 8.54 (s, 1H), 8.16 (dd, 2H, J = 8.1 Hz), 7.11 (s, 2H). ^{13}C NMR ($CDCl_3$, 75 MHz) δ: 191.5, 184.5, 184.3, 140.3 (2C), 137.9, 136.7, 135.7, 134.5, 131.5, 130.6, 130.3, 129.5, 128.8, 126.5. EIMS m/z 236 (M^+, 100), 207 (20). HRMS calcd. for $C_{15}H_8O3$ 236.0473; found 236.0466.

Comparison of colours observed in the photolysis of 1, 4, and 6

Solutions of **1** (5 mg, 1:1 H_2O/CH_3CN, pH 7), **4** (5 mg, 1:3 H_2O/CH_3CN, pH 1), and **6** (5 mg, 1:1 H_2O/CH_3CN, pH 7) were prepared in 100 mL Pyrex volumetric flasks. After purging with a stream of argon, the flasks were irradiated at 350 nm (16 lamps) for 15 min to develop the colours observed in Fig. 5.

Acknowledgments

We acknowledge financial support from the Natural Sciences and Engineering Research Council (NSERC) of Canada and the University of Victoria.

References

1. F. Würthner. Angew. Chem. Int. Ed. **40**, 1037 (2001).
2. (*a*) J. Jiang, B.R. Kaafarani, and D.C. Neckers. J. Org. Chem. **71**, 2155 (2006); (*b*) C.R. Swartz, S.R. Parkin, J.E. Bullock, J.E. Anthony, A.C. Mayer, and G.G. Malliaras. Org. Lett. **7**, 3163 (2005); (*c*) E.J. Hwang, Y.E. Kim, C.J. Lee, and J.W. Park. Thin Solid Films, **499**, 185 (2006); (*d*) K. Kobayashi, R. Shimaoka, M. Kawahata, M. Yamanaka, and K. Yamaguchi. Org. Lett. **8**, 2385 (2006); (*e*) S.H. Chan, H.K. Lee, Y.M. Wang, N.Y. Fu, X.M. Chen, Z.W. Cai, and H.N.C. Wong. Chem. Commun. (Cambridge, U.K.), 66 (2005); (*f*) J.E. Anthony. Chem. Rev. **106**, 5028 (2006).
3. K.P. Weidkamp, A. Afzali, R.M. Tromp, and R.J. Hamers. J. Am. Chem. Soc. **126**, 12740 (2004).
4. H. Yamada, Y. Yamashita, M. Kikuchi, H. Watanabe, T. Okujima, H. Uno, T. Ogawa, K. Ohara, and N. Ono. Chem. Eur. J. **11**, 6212 (2005).
5. M. Lukeman, M. Xu, and P. Wan. Chem. Commun. (Cambridge), 136 (2002).
6. D. Mitchell, M. Lukeman, D. Lehnherr, and P. Wan. Org. Lett. **7**, 3387 (2005).
7. D.H. Hua, K. Lou, J. Havens, E.M. Perchellet, Y. Wang, J.P. Perchellet, and T. Iwamoto. Tetrahedron, **60**, 10155 (2004).
8. E. Torres, C.A. Panetta, N.E. Heimer, B.J. Clark, and C.L. Hussey. J. Org. Chem. **56**, 3737 (1991).
9. M. Ramseier, P. Senn, and J. Wirz. J. Phys. Chem. A, **107**, 3305 (2003).
10. H.E. Zimmerman. J. Am. Chem. Soc. **117**, 8988 (1995).
11. H.E. Zimmerman. J. Phys. Chem. A, **102**, 5616 (1998).
12. H. Görner. Photochem. Photobiol. **77**, 171 (2003).

© 2007 NRC Canada

(*R*)-1-Phenylethylamine as chiral auxiliary in the diastereoselective synthesis of tetrahydro-β-carboline derivatives

Aleksandra Siwicka, Krystyna Wojtasiewicz, Andrzej Leniewski, Jan K. Maurin, Anna Zawadzka, and Zbigniew Czarnocki

Abstract: Modified sodium borohydrides were used in the reduction of the imine moiety in compounds containing the (*R*)-1-arylethylamine motif as a chiral auxiliary. Diastereomeric products were formed with moderate to good stereoselectivity and were effectively separated by column chromatography.

Key words: asymmetric synthesis, indole alkaloids, hydrogen bond.

Résumé : On a utilisé des borohydrures de sodium modifiés pour effectuer la réduction de la portion imine de composés contenant un motif (*R*)-aryléthylamine comme auxiliaire chiral. Il y a formation de produits diastéréomères avec des stéréosélectivités allant de modérées à bonnes et il est possible de les séparer d'une façon efficace par chromatographie sur colonne.

Mots-clés : synthèse asymétrique, alcaloïdes de l'indole, liaison hydrogène.

[Traduit par la Rédaction]

Introduction

Both enantiomers of 1-phenylethylamine (α-methylbenzylamine, α-PEA **3**) remain as attractive chirality sources in various asymmetric transformations. Their use as resolving agents, chiral ligands in catalytic processes, and synthetic chiral auxiliaries in stereodifferentiating reactions of prochiral substrates have been the subject of in-depth reviews (1, 2).

More recently, an interesting example of the use of α-PEA **3** in an asymmetric Strecker reaction leading to enantiomerically enriched 1-amino-*cis*-3-azabicyclo[4.4.0]decan-2,4-diones has been reported (3). In this process, which is called a second-generation asymmetric synthesis, trimethylsilyl cyanide was the reagent allowing a stereoselective cyanide-ion addition to the prochiral precursor derived from α-PEA and cyclohexanone derivative. In another application, **3** was used as the chiral auxiliary in the preparation of enantiopure conformationally constrained Gly-(*s-cis*)-Pro Turn Mimetic (4). The reaction of the prochiral imine moiety in α-PEA derivatives gave an access to a variety of chiral, nonracemic aliphatic amines (5). Conveniently, these processes can be performed as one-pot procedures. The use of α-PEA, even in the industrial scale, was proven possible, as illustrated by the development and the scale-up of the endothelin antagonists synthesis (6). The process involves the preparation of a racemic intermediate followed by an efficient dynamic resolution with a chiral amine.

In the field of the stereoselective synthesis of pharmacologically relevant compounds, we presented recently the application of α-PEA in the preparation of enantiomerically pure lortalamine analogues (7) and (*R*)-(–)-mianserin (8) compounds that are well-known antidepressants. The Bischler–Napieralski cyclization followed by diastereoselective reduction of the imine bond were the key steps in the enantiodivergent synthesis of both enantiomers of *N*-acetylcalycotomine (9) that was carried out in our laboratory (10). Encouraged by the positive results of using α-PEA in the stereoselective formation of isoquinoline alkaloids, we decided to extend this procedure to tetrahydro-β-carboline analogues.

Received 25 April 2007. Accepted 02 September 2007. Published on the NRC Research Press Web site at canjchem.nrc.ca on 25 October 2007.

A. Siwicka, K. Wojtasiewicz, A. Leniewski, A. Zawadzka, and Z. Czarnocki.[1] Faculty of Chemistry, Warsaw University, Pasteura 1, 02-093 Warsaw, Poland.
J.K. Maurin. National Institute of Public Health, Chełmska 30/34, 00-750 Warsaw, Poland; Institute of Atomic Energy, 05-400 Otwock-Świerk, Poland.

[1]Corresponding author (email: czarnoz@chem.uw.edu.pl)

Results and discussion

The synthetic sequence started with the reaction of tryptamine **1** with diethyl oxalate followed by the treatment with (*R*)-1-phenylethylamine to afford the diamide **5** almost quantitatively (Scheme 1).

After careful optimization, we found that the subsequent Bischler–Napieralski cyclization gave best results when performed in refluxing dichloromethane with $POCl_3$.

Since all attempts to isolate and characterize the resulting imine **7** were unsuccessful because of its instability as a free base, we decided to subject its hydrochloride salt to a metal hydride reduction. Thus, upon treatment with sodium borohydride in EtOH, a pair of diastereomeric amines **9a** and **9b** was formed in 62:38 ratio, respectively, based upon

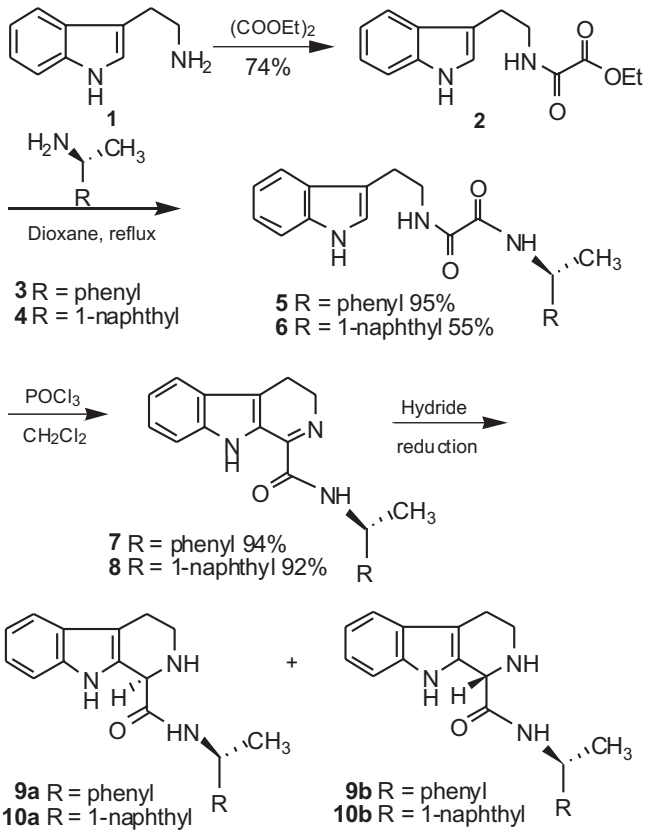
 doi:10.1139/V07-118 © 2007 NRC Canada

Table 1. Diastereomeric output for the reduction of **7** with various borohydrides.

Entry	Reducing reagent	Yield of **9**[a]	Ratio of **9a**:**9b**[b]
1	$NaBH_4$	81	62:38
2	$NaBH(CH_3COO)_3$	88	75:25
3	$NaBH[(CH_3)_2CHCOO]_3$	84	66:34
4	$NaBH[(CH_3)_3CCOO]_3$	89	78:22

[a]Isolated yield (%) of both **9a** and **9b**.
[b]Estimated from ^{1}H NMR on the crude reaction mixture.

Scheme 1. Reaction sequence leading to diastereoselective synthesis of tetrahydro-β-carboline derivatives (**9a**, **9b**, **10a**, and **10b**).



^{1}H NMR spectrum of the crude reaction mixture. The ratio of **9a** and **9b** was not affected neither by a prolonged contact with strongly basic solution of the reducing agent nor by solvent variations; these observations ruled out the possibility of an asymmetric transformation caused by a base-catalyzed epimerization at C-1 atom.

Therefore, it seemed reasonable to assume that both diastereomers **9a** and **9b** were formed in unequal amounts because of the chiral induction during a kinetically governed hydride approach to the substrate **7**. The prochiral imine moiety can be regarded as a planar structure resembling a carbonyl group, and the reduction process can be rationalized using the Cram or Felkin stereochemical models (11). Accordingly, the increase of steric demands in the nucleophile and (or) the imine molecules might have a positive effect on the chirality transfer.

Since it is well-known that sodium borohydride, modified with controlled amounts of simple carboxylic acids, forms reducing agents of enhanced selectivity (12), we applied such combined reagents to C=N bond reduction in **7**. Disappointingly, the diastereoselectivity was not improved significantly when hydrides such as $NaBH(AcO)_3$, $NaBH(i\text{-}PrCOO)_3$, and $NaBH(t\text{-}BuCOO)_3$ were applied.

Fortunately, the mixture of isomers could be effectively separated by column chromatography, affording pure and stable compounds **9a** and **9b**. The configuration at C-1 stereogenic centre in compound **9a** was assigned as (*R*) by the chemical transformation of **9a** into (*1R*)-1-(hydroxymethyl)-2-acetyl-1,2,3,4-tetrahydro-β-carboline of known absolute configuration by the method developed earlier in our laboratory (13). Full details for this procedure will be published in due course.

Seeking further improvement in the stereoselectivity, we decided to apply the same synthetic sequence using (*R*)-(+)-1-(1-naphthyl)ethylamine (**4**), another well-known and effective chiral inductor (7), as a chiral auxiliary. Thus, compound **8** was prepared in a good yield from tryptamine **1** and was consecutively subjected to a series of reactions affording easily separable diastereomers **10a** and **10b**. The results were summarized in Tables 1 and 2.

In contrast to previous results, the increase of steric parameters neither in the reducing agent molecule nor in the imine-containing target derivative **8** did not give a significant improvement of the stereochemical outcome. In a search for a feasible explanation of the previous observations, we investigated the problem using quantum chemical methods. Despite considerable efforts, it was impossible to obtain good quality monocrystals of imine **7**, and therefore we performed a molecular modelling to find its optimal geometry. The procedure consisted of consecutive molecular- mechanic search through a conformational space and ab initio calculations used for conformers to optimize their geometries and to find the corresponding energies (14).[2] The two low-energy conformers **7a** and **7b** are shown in Fig. 1, where **7a** has the lowest total electron energy. Noticeably, in both conformers **7a** and **7b**, a strong hydrogen bond between the amide carbonyl group and the indole NH define the shape of the reacting part of the molecule. As a consequence, the chiral fragment derived from the 1-phenylethylamine was di-

[2]We used a Spartan'04 for Windows software for both tasks; a conformational search using MMFF94 force field and a Monte Carlo algorithm was performed. Two different low-energy conformers were selected for further ab initio optimization. A restricted Hartree–Fock method with the standard 6-31G** basis set was then applied. These calculations showed that the conformational energy ΔE between **7a** and **7b** was 2.383 kcal/mol.

© 2007 NRC Canada

Table 2. Diastereomeric output for the reduction of **8** with various borohydrides.

Entry	Reducing reagent	Yield of **10**[a]	Ratio of **10a**:**10b**[b]
1	$NaBH_4$	91	66:34
2	$NaBH(CH_3COO)_3$	86	76:24
3	$NaBH[(CH_3)_2CHCOO]_3$	93	64:36
4	$NaBH[(CH_3)_3CCOO]_3$	86	83:17

[a]Isolated yield (%) of both **10a** and **10b**.
[b]Estimated from ^{1}H NMR on the crude reaction mixture.

Fig. 1. The structure of conformers **7a** and **7b**.

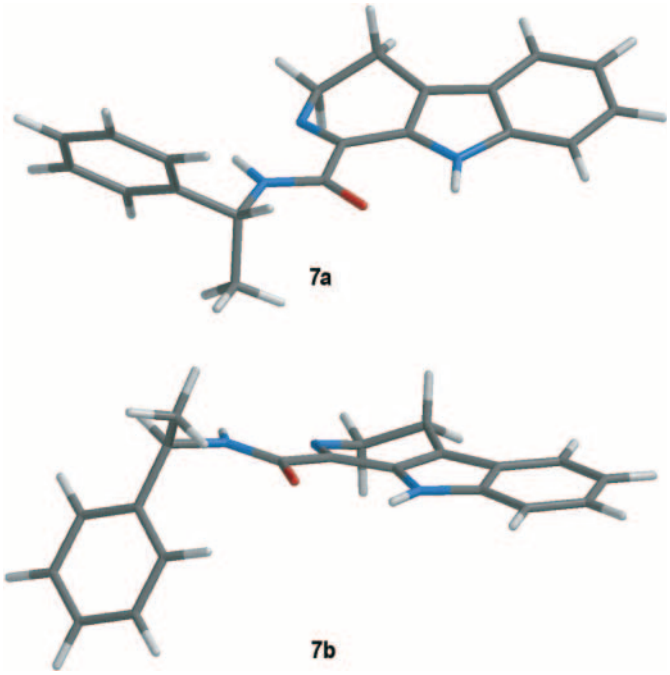
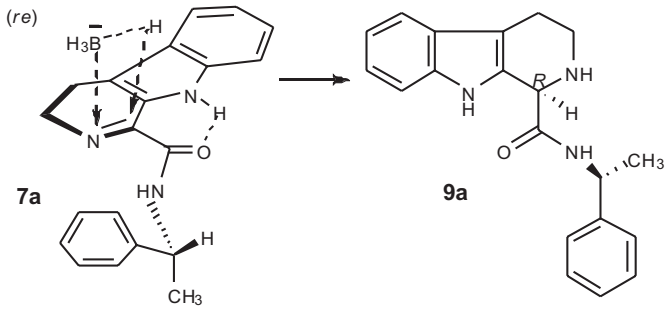


Fig. 2. Stereochemical model for the reduction of **7a**.



rected apart from the imine area (consult also Fig. 2), thus lowering its ability to the chirality induction. Apparently, such a disfavored interaction was not present in the isoquinoline analogue of imine **7**, thus allowing us to observe much better diastereoselectivity (10).

When a Felkin–Evans trajectory (15) for an early transition state was applied to conformer **7a** (Fig. 2), two major conclusions can be drawn from this consideration. First, the model correctly predicts diastereomer **9a** as the major product of the reduction process. Second, the bulkiest substituent of the chiral auxiliary (phenyl or naphthyl ring) is located in the most-remote part of the molecule and is guided in the opposite direction to the incoming nucleophile. This model accounts convincingly for both the relatively low level of diastereodifferentiation during the addition step and for only a small improvement after the replacement of the phenyl in compound **7** by the naphthyl moiety in compound **8**.

Conclusion

In the presented approach, we demonstrated the possibility to extend our earlier findings concerning the diastereoselective preparation of tetrahydroisoquinoline derivatives using enantiopure (*R*)-1-arylethylamines onto β-carboline analogues.

Despite moderate selectivity, the described method might be an attractive alternative to the existing procedures (16, 17, 18) because of the relatively high chemical yields and facile chromatographic separation of diastereomers, which then may be subjected to further transformations leading to the pure enantiomers of 1-substitued-tetrahydro-β-carboline derivatives. The work in this area is in progress.

Experimental

(1*R*)-*N*-[(1*R*)-1-phenylethyl]-2,3,4,9-tetrahydro-1*H*-β-carboline-1-carboxamide 9a and (1*S*)-*N*-[(1*R*)-1-phenylethyl]-2,3,4,9-tetrahydro-1*H*-β-carboline-1-carboxamide 9b

In a typical experiment (see Table 1, entry 4), a sample of compound **5** (335 mg, 1 mmol) was refluxed in methylene chloride (15 mL) with $POCl_3$ (0.5 mL, 5.5 mmol) for 2 h. After that time, the volatiles were evaporated, and dry MeOH (10 mL) was slowly introduced. The mixture was evaporated into dryness, and the procedure was repeated twice followed by the evaporation with a fresh portion of xylene (20 mL) to remove traces of methanol. The residue was then dissolved in dioxane (20 mL), and a freshly prepared modified borohydride solution was introduced at 10 °C. The borohydride was prepared by stirring $NaBH_4$ (180 mg, 4 mmol) with pivaloyl acid (1.11 g, 12 mmol) in dry THF (10 mL) for 3 h. The resultant solution was stirred for 1 h at 10 °C and was poured onto 5% aq. NaOH (50 mL). The mixture was then extracted with methylene chloride (3 × 20 mL). After drying and evaporation, the residue was subjected to column chromatography on silica gel

© 2007 NRC Canada

using ethyl formate as eluent to afford pure diastereomers **9a** and **9b** (R_f values are 0.45 and 0.49, respectively).

Selected data for compound **9a**: brown foam (194 mg, 61%). $[\alpha]_D^{23}$ +55.2 (*c* 0.5, $CHCl_3$). ^{1}H NMR δ_H: 8.85 (1H, br s, H-9), 7.96 (1H, br d, *J* = 7 Hz, $NHCHCH_3$), 7.47 (1H, d, *J* = 8 Hz, H-8), 7.38 (1H, br t, *J* = 2 Hz, H-2) 7.31 (1H, d, *J* = 8 Hz, H-5), 7.27–7.24 (3H, m, H_{arom}), 7.21–7.18 (2H, m, H_{arom}), 7.14 (1H, td, *J* = 7.5 Hz, *J* = 1 Hz, H-6), 7.07 (1H, m, H-7), 5.09 (1H, qt, *J* = 7.5 Hz, H-1′), 4.62 (1H, s, H-1), 3.26 (1H, dt, *J* = 13 Hz, *J* = 5 Hz, H-3), 2.97 (1H, m, H-3), 2.77 (1H, dt, *J* = 15.5 Hz, *J* = 5 Hz, H-4), 2.72–2.66 (1H, m, H-4), 1.54 (3H, d, *J* = 7 Hz, H-2′). ^{13}C NMR δ_C: 170.6, 143.0, 136.0, 129.6, 128.7, 127.2, 126.8, 125.8, 121.8, 119.2, 118.0, 111.2, 109.2, 54.7, 48.4, 42.0, 22.5, 22.2. ESI-MS *m*/*z* (%): 320 (100%, M + H^+). HR-MS (ES(+)): $[M + H]^+$ calcd. for $C_{20}H_{22}N_3O$: 320.1763; found: 320.1776.

Selected data for compound **9b**: (48 mg, 15%). ^{1}H NMR δ_H: 8.92 (1H, br s, H-9), 7.96 (1H, br d, *J* = 6.5 Hz, $NHCHCH_3$), 7.57 (1H, d, *J* = 8 Hz, H-8), 7.48 (1H, br t, *J* = 9 Hz, H-2), 7.38–7.33 (5H, m, H_{arom}), 7.20 (1H, m, H_{arom}), 7.16 (1H, m, H-6), 7.08 (1H, m, H-7), 5.06 (1H, qt, *J* = 7.5 Hz, H-1′), 4.56 (1H, s, H-1), 3.25 (1H, m, H-3), 3.05 (1H, m, H-3), 2.79 (1H, m, H-4), 2.71 (1H, m, H-4), 1.45 (3H, d, *J* = 6.5 Hz, H-2′). ^{13}C NMR δ_C: 170.5, 143.1, 136.0, 129.8, 128.7, 127.4, 126.8, 126.1, 121.8, 119.2, 118.0, 111.2, 109.1, 57.7, 48.6, 41.9, 22.4, 22.0. HR-MS (ES(+)): $[M + H]^+$ calcd. for $C_{20}H_{22}N_3O$: 320.1763; found: 320.1769.

Acknowledgments

The support from grant PBZ-KBN-126/T09/13 is gratefully acknowledged.

References

1. E. Juaristi, J.L. Leon-Romo, A. Reyes, and J. Escalante. Tetrahedron: Asymmetry, **10**, 2441 (1999).
2. E. Juaristi, J. Escalante, J.L. Leon-Romo, and A. Reyes. Tetrahedron: Asymmetry, **9**, 715 (1998).
3. P. Bisel, K.P. Fondekar, F.J. Volk, and A.W. Frahm. Tetrahedron, **60**, 10541 (2004).
4. F.M. Cordero, F. Pisaneschi, K.M. Batista, S. Valenza, F. Machetti, and A. Brandi. J. Org. Chem. **70**, 856 (2005).
5. G.V. Grishina, E.R. Luk'yaenko, and A.A. Borisenko. Russ. J. Org. Chem. **41**, 807 (2005).
6. C.P. Ascroft, S. Challenger, D. Cifford, A.M. Derrick, Y. Hajikarimian, K. Slucock, T.V. Silk, N.M. Thomson, and J.R. Williams. Org. Process Res. Dev. **9**, 663 (2005).
7. J. Biała, Z. Czarnocki, and J.K. Maurin. Tetrahedron: Asymmetry, **13**, 1021 (2002).
8. J. Pawłowska, Z. Czarnocki, K. Wojtasiewicz, and J.K. Maurin. Tetrahedron: Asymmetry, **14**, 3335 (2003).
9. Z. Czarnocki, D.B. MacLean, and W.A. Szarek Can. J. Chem. **64**, 2205 (1986).
10. M. Ziółkowski, Z. Czarnocki, A. Leniewski, and J. K. Maurin. Tetrahedron: Asymmetry, **10**, 3371 (1999).
11. E.L. Eliel, and S.H. Wilen. Stereochemistry of organic compounds. John Wiley & Sons. New York. 1994.
12. M. Periasamy, and P. Thirumalaikumar. J. Organomet. Chem. **609**, 137 (2000).
13. Z. Araźny, Z. Czarnocki, K. Wojtasiewicz, and J.K. Maurin. Tetrahedron: Asymmetry, **11**, 2793 (2000).
14. Spartan'04 [computer program]. Wavefunction Inc., Irvine, California, USA, 2005.
15. N. Giubellina, W. Aelterman, and N. De Kimpe. Pure Appl. Chem. **75**, 1433 (2003).
16. P. Roszkowski, K. Wojtasiewicz, A. Leniewski, J.K. Maurin, T. Lis, and Z. Czarnocki. J. Mol. Catal. A: Chem. **232**, 143 (2005).
17. U. Rinner, T. Hudlicky, H. Gordon, and G.R. Pettit. Angew. Chem., Int. Ed. **43**, 5342 (2004).
18. T. Morimoto, N. Suzuki, and K. Achiwa. Heterocycles, **63**, 2097 (2004).

© 2007 NRC Canada

A mild and efficient synthesis of chloroesters by the cleavage of cyclic and acyclic ethers using $Bi(NO_3)_3 \cdot 5H_2O$ as a catalyst under solvent-free conditions

V. Suresh, N. Suryakiran, and Y. Venkateswarlu

Abstract: A facile, efficient synthesis of chloroesters is described. The reaction of cyclic and acyclic ethers with acid chlorides in the presence of catalytic amounts of $Bi(NO_3)_3 \cdot 5H_2O$ under solvent-free conditions yielded the corresponding chloroesters. Also, the catalyst can be recovered conveniently and reused efficiently for at least six times.

Key words: Bismuth(III) nitrate pentahydrate, cyclic and acyclic ethers, chloroesters.

Résumé : On décrit une méthode simple et efficace de synthèse des chloroesters. La réaction d'éthers cycliques et acycliques avec des chlorures d'acides, en présence de quantités catalytiques de $Bi(NO_3)_2 \cdot 5H_2O$ et dans des conditions sans solvant, fournit les chloroesters correspondants. De plus, il est possible de récupérer facilement le catalyseur et de le réutiliser d'une façon efficace au moins six fois.

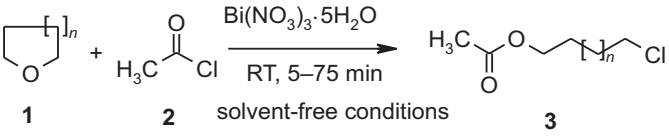
Mots-clés: pentahydrate du nitrate de bismuth(III), éthers cycliques et acycliques, chloroesters.

[Traduit par la Rédaction]

Introduction

The cleavage of cyclic and acyclic ethers with acid chlorides, leading to the synthesis of the corresponding chloroesters, is a versatile organic transformation, as they are important and key constituents in organic synthesis, particularly in the synthesis of natural products (1). Transformation of cyclic ethers into haloesters is a direct and straightforward method for producing bifunctional synthetic intermediates and also an important method for the removal of ethereal protecting groups (2). In organic synthesis, hydroxyl groups are protected as aliphatic, benzylic, and allylic ethers (3), which can subsequently be cleaved for further transformations (4–7). The cleavage of ethers with acyl chlorides has been reported using Lewis acids, such as SmI_2 (8), $ZnCl_2$ (9), $FeCl_3$ (10), I_2 (11), $MoCl_5$ (12), $PdCl_2(PPh_3)_2$ (13), $CoCl_2$ (3), and very recently $InBr_3$ (14). However, using strongly acidic conditions frequently leads to the formation of undesirable side products, which in turn decrease the purity and yields of the desired products. Most of the reported methods have one or other limitations, such as long reaction time, unavailability of the catalyst, difficulties in handling, and tedious workup procedures with unsatisfactory yields. Thus, a mild, efficient catalyst for the cleavage of cyclic and acyclic ethers with acid chlorides is highly desirable. In view of the merits in catalytic processes, we are interested in the development of inexpensive, mild, and non-polluting reagent for the acid-chloride-directed cleavage of cyclic and acyclic ethers.

Scheme 1.



Organic reactions using mild and water-tolerant catalysts received much attention in recent years, as they can be handled conveniently, and the products can be easily recovered from the reaction mixture, thus making the experimental procedure simple and eco-friendly. Among Lewis acid catalysts, the bismuth(III) nitrate pentahydrate is relatively non-toxic, inexpensive, stable in atmospheric conditions, and used in various organic transformations (15). Also, to the best of our knowledge, there is no report on the use of $Bi(NO_3)_3 \cdot 5H_2O$ for the cleavage of cyclic and acyclic ethers with acid chlorides. Recently, we reported $Bi(NO_3)_3 \cdot 5H_2O$ as a mild and efficient Lewis acid catalyst for *N-tert*-butoxycarbonylation of amines (16). In continuation of our work on catalytic application of metal nitrate salts in the multi-step synthesis of natural products in our laboratory, we have observed that $Bi(NO_3)_3 \cdot 5H_2O$ can be utilized efficiently for the cleavage of cyclic and acyclic ethers with different acid chlorides into the corresponding chloroesters under solvent-free conditions.

Results and discussion

In this report (Scheme 1), we describe an efficient and facile method for the synthesis of chloroesters. This method

Received 31 May 2007. Accepted 20 October 2007. Published on the NRC Research Press Web site at canjchem.nrc.ca on 9 November 2007.

V. Suresh, N. Suryakiran, and Y. Venkateswarlu.[1] Organic Chemistry Division I, Indian Institute of Chemical Technology, Hyderabad 500 007, India.

[1]Corresponding author (e-mail address: luchem@iict.res.in).

 doi:10.1139/V07-126 © 2007 NRC Canada

Scheme 2. Plausible mechanism.

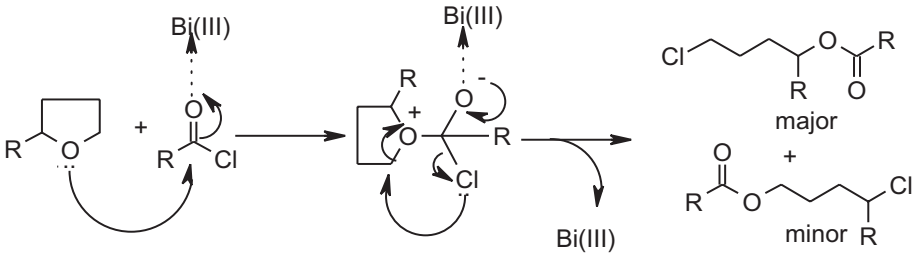


Table 1. Comparison of various catalysts on the reaction of tetrahydrofuran with acetyl chloride at room temperature under solvent-free conditions.

Entry	Catalyst [mol%]	Time (min)	Yield (%)
1	$Bi(NO_3)_3{\cdot}5H_2O$ [50]	10	96
2	$Bi(NO_3)_3{\cdot}5H_2O$ [10]	10	95
3	$Bi(NO_3)_3{\cdot}5H_2O$ [5]	10	95
4	CAN [5]	90	85
5	$Zr(NO_3)_2{\cdot}xH_2O$ [5]	40	80
6	$La(NO_3)_3{\cdot}6H_2O$ [5]	30	90
7	$Bi(OTf)_3$ [5]	60	90
8	$BiCl_3$ [5]	120	90
9	$ZnCl_2$ [5]	60	95
10	I_2 [5]	120	91
11	Zn [5]	180	87
12	Graphite [5]	360	90
13	$InBr_3$ [5]	180	89
14	HNO_3	60	50

does not need expensive reagents or special care to exclude the moisture from the reaction medium. All the reactions proceeded efficiently and smoothly at room temperature, and the products were obtained in excellent yields (Table 1). Furthermore, the reaction conditions are very mild. Bismuth(III) nitrate pentahydrate is highly oxophilic and forms labile bond with carbonyl oxygen to initiate the formation of C–O bond with cyclic and acyclic ethers (Scheme 2). We first examined the reaction of tetrahydrofuran **1** with acetyl chloride **2** under solvent-free conditions to give the corresponding chloroesters **3** in 95% yield (Table 2, entry 2). To compare the catalytic activity of the bismuth(III) nitrate pentahydrate, we carried out the reaction in different Lewis acid catalysts, such as $Bi(OTf)_3$, $BiCl_3$, $La(NO_3)_3{\cdot}6H_2O$, CAN, $ZrO(NO_3)_2{\cdot}xH_2O$, and other reported catalysts. However, bismuth(III) nitrate pentahydrate was found to be the most effective in terms of reaction time as well as yields of the product (Table 1). This success of the reaction encouraged us to carry out the reaction on various cyclic and acyclic ethers with different acid chlorides in the presence of 5mol% of $Bi(NO_3)_3{\cdot}5H_2O$. The ring cleavage of tetrahydropyran is considerably slower than that of tetrahydrofuran at room temperature with low yields (55%). Using slightly elevated temperature (50 °C), the reaction is completed in 1 h with 90% yield (Table 2, entries 7–9). In the case of asymmetrical ethers, the cleavage took place selectively at the unsubstituted side of ether (Table 2, entries 10 and 13). However, in the presence of cyclic and acyclic ethers in the same substrate, formation of products (chloroesters) was observed only with acyclic part of the substrate (Table 2, entries 17 and 18).

Further, we have studied the reusability of the catalyst without any modification of the reaction conditions. After completion of the reaction, ethyl acetate (10 mL) was added; the catalyst was recovered by filtration and reused without loss of its activity for six runs (Table 3). The organic layer was concentrated under reduced pressure to get the crude product. From the foregoing results, it is evident that $Bi(NO_3)_3{\cdot}5H_2O$ is an efficient and reusable catalyst for the synthesis of chloroesters under solvent-free conditions.

Conclusion

In conclusion, we described an efficient and facile synthesis of chloroesters in the presence of catalytic amount of $Bi(NO_3)_3{\cdot}5H_2O$ under solvent-free conditions. The advantages of the method are reduced reaction time, inexpensive catalyst, and simple experimental and work up procedure with high yields of products. This makes it a useful addition to the existing methodologies.

Experimental

Typical experimental procedure for preparation of chloroesters

To a mixture of cyclic/acyclic ether (10 mmol) and acid chloride (10 mmol), was added $Bi(NO_3)_3{\cdot}5H_2O$ (5 mol%) at 0–5 °C followed by stirring at room temperature for an appropriate time (Table 2). After completion of the reaction as monitored by TLC, ethyl acetate (10 mL) was added, and the catalyst was recovered by filtration. The solvent ethyl acetate was washed with water, brine, dried over anhyd. sodium sulphate, and removed under reduced pressure to give a crude product, which was purified on a silica-gel column to yield the pure products. The products were characterized by spectral and analytical data or by comparison with authentic samples.

Table 2. Entry 4

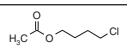
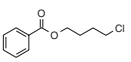
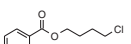
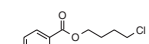
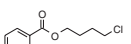
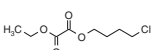
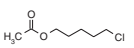
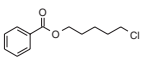
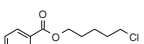
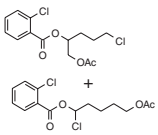
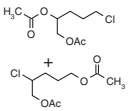
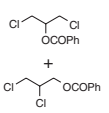
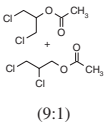
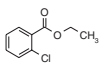
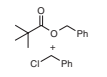
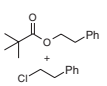
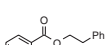
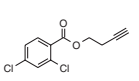
^{1}H NMR ($CDCl_3$, 300 MHz) δ: 1.99 (m, 4H), 3.6 (m, 2H), 4.4 (m, 2H), 7.28 (dd, J = 7.4 and 1.5Hz, 1H), 7.5 (d, J = 1.5 Hz, 1H), 7.8 (d, J = 7.4 Hz, 1H). EI-MS: 281 (M^+). Anal. calcd. for $C_{11}H_{11}Cl_3O_2$: C, 47.14; H, 3.92; Cl, 38.03. Found: C, 46.92; H, 3.94; Cl, 37.77.

Entry 5

^{1}H NMR ($CDCl_3$, 200 MHz) δ: 1.97 (m, 4H), 3.60 (m, 2H), 4.40 (m, 2H), 7.31 (m, 1H), 8.13 (dd, J = 8.1 and

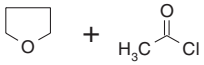
© 2007 NRC Canada

Table 2. $Bi(NO_3)_3 \cdot 5H_2O$-catalyzed cleavage of cyclic and acyclic ethers by acid chlorides under solvent-free conditions.

Entry	Ether	Acid chloride	Product[a]	Temp., Time (min)	Yield (%)[b]
1				RT, 10	96
2				RT, 10	96
3				RT, 15	90
4				RT, 15	87
5				RT, 15	92
6				RT, 10	98
7				50 °C, 60	90
8				50 °C, 75	90
9				50 °C, 60	90
10			 (9:1)	RT, 10	85
11			 (9:1)	RT, 15	70
12			 (7:3)	RT, 5	90
13			 (9:1)	RT, 5	85
14				RT, 30	85
15				RT, 10	90
16				RT, 10	91
17				RT, 25	85
18				RT, 30	80

[a] The structures of the products were established from their spectral data (IR, ^{1}H NMR, EI-MS).
[b] Isolated yields obtained after column chromatography.

Table 3. Synthesis of chloroesters using $Bi(NO_3)_3 \cdot 5H_2O$ as an efficient and reusable catalyst.

Entry	Substrates	Time (min)	Yield (%)
1		10	96
2	2nd run	10	95
3	3rd run	10	96
4	4th run	10	96
5	5th run	10	95
6	6th run	10	95

1.5 Hz, 1H,), 8.51 (dd, J = 8.1 and 1.5 Hz, 1H). EI-MS: 248 (M^+). Anal. calcd. for $C_{10}H_{11}Cl_2NO_2$: C, 48.38; H, 4.43; Cl, 28.62; N, 5.64. Found: C, 48.41; H, 4.47; Cl, 28.58; N, 5.65.

Entry 6

^{1}H NMR ($CDCl_3$, 200 MHz) δ: 1.39 (t, J = 6.90 Hz, 3H), 1.90 (m, 4H), 3.58 (m, 2H), 4.31 (m, 4H). EI-MS: 208 (M^+). Anal. calcd. for $C_8H_{13}ClO_4$: C, 46.15; H, 6.49; Cl, 17.06. Found: C, 46.05; H, 6.28; Cl, 16.99.

Entry 10a

^{1}H NMR ($CDCl_3$, 200 MHz) δ: 1.66 (m, 2H), 1.79 (m, 2H), 2.00 (s, 3H), 3.41 (m, 2H), 4.29 (d, 2H, J = 3.5 Hz), 4.79 (m, 1H), 7.47 (m, 2H), 7.73 (m, 1H), 7.6 (m, 1H). EI-MS: 275 (M^+). Anal. calcd. for $C_{13}H_{16}Cl_2O_2$: C, 56.72; H, 5.81; Cl, 25.81. Found: C, 56.74; H, 5.86; Cl, 25.77.

Entry 10b

^{1}H NMR ($CDCl_3$, 200 MHz) δ: 1.72 (m, 4H), 2.02, (s, 3H), 2.15 (m, 2H), 4.00 (m, 2H), 6.67 (m, 1H), 7.50 (m, 2H), 7.61 (m, 1H), 7.87 (m, 1H). EI-MS: 275 (M^+). Anal. calcd. for $C_{13}H_{16}Cl_2O_2$: C, 56.72; H, 5.81; Cl, 25.81. Found: C, 56.75; H, 5.84; Cl, 25.75.

Entry 17

^{1}H NMR ($CDCl_3$, 300 MHz) δ: 3.03 (t, J = 6.79 Hz, 2H), 4.49 (t, J = 7.5 Hz, 2H), 7.23 (m, 8H), 7.7 (d, 1H, J = 1.5 Hz). EI-MS: 260 (M^+). Anal. calcd. for $C_{15}H_{13}ClO_2$: C, 69.23; H, 4.99; Cl, 13.65. Found: C, 69.10; H, 5.03; Cl, 13.60.

Entry 18

^{1}H NMR ($CDCl_3$, 300 MHz) δ: 1.97 (m, 1H), 2.64 (m, 2H), 4.41 (t, J = 6.79 Hz, 2H,), 7.3 (m, 1H), 7.47 (s, 1H), 7.81 (d, 2H, J = 7.5 Hz). EI-MS: 243 (M^+). Anal. calcd. for $C_{11}H_8Cl_2O_2$: C, 54.32; H, 3.29; Cl, 29.21. Found: C, 54.35; H, 3.32; Cl, 29.17.

Acknowledgements

The authors are thankful to CSIR, UGC, and MoES, New Delhi for financial assistance and to Dr J.S. Yadav, Director, IICT for his constant encouragement.

© 2007 NRC Canada

References

1. (*a*) M.V. Bhatt and S.U. Kulkarni. Synthesis, 249 (1983); (*b*) A. Maercker. Angew. Chem., Int. Ed. Engl. **26**, 972 (1987).
2. T.W. Greene and P.G.M. Wuts. Protective groups in organic synthesis. 3rd ed. Wiley, New York. 1999. Vol. 23.
3. J. Iqbal and R.R. Srivastava. Tetrahedron, **47**, 3155 (1991); and references cited therein.
4. R. Amouroux and S. Ejjiyar. Tetrahedron Lett. **32**, 3059 (1991).
5. J. Nystrom, T.D. McCanna, P. Helquist, and R. Amouroux. Synthesis, 56, (1988).
6. Y. Guindon, M. Therien, Y. Girard, and C. Yoakim. J. Org. Chem. **52**, 1680 (1987).
7. Y. Guindon and P.C. Anderson. Tetrahedron Lett. **28**, 2485 (1987).
8. D.W. Kwon and Y.H. Kim. J. Org. Chem. **67**, 9488 (2002).
9. J.B. Cloke and F.J. Pilgrim. J. Am. Chem. Soc. **61**, 2667 (1939).
10. B. Ganem and V.R. Small Jr. J. Org. Chem. **39**, 3728 (1974).
11. J.S. Yadav, B.V.S. Reddy, P.M.K. Reddy, and M.K. Gupta, Tetrahedron Lett. **46**, 8493 (2005).
12. Q. Guo, T. Miyaji, G. Gao, R. Hara, and T. Takahashi. Chem. Commun. 1018 (2001).
13. I. Pri-Bar and J.K. Stille. J. Org. Chem. **47**, 1215 (1982).
14. J.S. Yadav, B.V. Subba Reddy, Murli K. Reddy, Uttam Desh, and M.K. Guptha. J. Mol. Cat. Sec. A Chem. **271**, 266 (2007).
15. (*a*) N.M. Leonard, L.C. Wieland, and R.S. Mohan. Tetrahedron, **58**, 8373 (2002); (*b*) L.C. Wieland, H.M. Zerth, and R.S. Mohan. Tetrahedron Lett. **43**, 4597 (2002); (*c*) S. Samajdar, F.F. Becker, and B.K. Bnik. Tetrahedron Lett. **41**, 8017 (2000); (*d*) B.A. Nattier, K.J. Eash, and R.S. Mohan. Synthesis, 1010 (2001); (*e*) I.M. Baltork, M.M. Khodaei, and K. Nikoofar. Tetrahedron Lett. **44**, 591 (2003); (*f*) V.M. Alexander, A.C. Khandekar, and S.D. Samant. Synlett, 1895 (2003); (*g*) N. Srivastava and B.K. Banik. J. Org. Chem. **68**, 2109 (2003); (*h*)V.M. Alexander, R.P. Bhat and S.D. Samant. Tetrahedron Lett. **46**, 6957 (2005).
16. N. Suryakiran, P. Prabhakar, T. Srikanth Reddy, M. Srinivasulu, N. Raghvendhra Swamy, and Y. Venkateswarlu. J. Mol. Cat. A Chem. **264,** 40 (2006).

© 2007 NRC Canada

Microwave-assisted one-pot synthesis of some new furo[2,3-*b*]quinolines using potassium carbonate under solvent-free conditions

M. Raghavendra, Halehatty S. Bhojya Naik, and Bailure S. Sherigara

Abstract: A rapid, solvent-free microwave-assisted method has been developed for the synthesis of novel furoquinolines. The title compounds were achieved by the reaction between corresponding 2-hydroxy-3-formyl-quinolines (**1a**–**1c**) with chloroacetamide, ethylchloroacetate, and phenacylbromide in specially designed microwave (MW) oven for organic synthesis in unsealed borosil vessel in presence of potassium carbonate. In this method, isolation is accomplished by just treating the reaction mixture with water, and products were obtained in high yield. Hence, this method was found to be very effective and ecofriendly. The structure of the newly synthesized compounds has been evaluated on the basis of analytical, IR, ^{1}H NMR, and mass spectral data.

Key words: furoquinoline, microwave irradiation, potassium carbonate, solvent-free conditions.

Résumé : On a mis au point une méthode rapide, sans solvant et assistée par les microondes pour la synthèse de nouvelles furoquinoléines. Les synthèses des composés mentionnés dans le titre ont été réalisées en faisant réagir les 2-hydroxy-3-formylquinoléines correspondantes (**1a**–**1c**) avec du chloroacétamide, du chloroacétate d'éthyle et du bromure de phénacylel, en présence de carbonate de potassium, dans un four à microondes spécialement conçu pour les synthèses organiques dans un contenant en borosil non scellé. Dans cette méthode, on isole les produits par un simple traitement du mélange réactionnel avec de l'eau et les rendements en produits obtenus sont élevés. On a donc trouvé que cette méthode est très efficace et écologiquement acceptable. Les structures des nouveaux composés synthétisés ont été déterminées sur la base d'analyses et de données de spectrométrie IR, RMN du ^{1}H et de masse.

Mots-clés : furoquinoléine, irradiation par microondes, carbonate de potassium, conditions sans solvant.

[Traduit par la Rédaction]

Introduction

Synthetic organic reactions performed under non-traditional conditions are gaining popularity, primarily to circumvent growing environmental concerns (1). Microwave-assisted heating is an invaluable synthesis technology, since it often dramatically reduces reaction times, typically from days or hours, minutes, or even seconds. It can also provide pure products in quantitative yields. Solvent-free reaction techniques are successfully coupled with microwave (MW) to avoid the use of low boiling point solvents, which may sometimes lead to explosions. Additionally, the use of poisonous and expensive solvents can also be avoided to make manipulations of the reactions much easier. The use of microwave for the synthesis of organic compounds under solvent-free conditions proved to be an efficient and safe technique, as it requires shorter reaction times, gives higher yield, and the reactions are easily carried out compared with conventional heating methods (2–3). In addition, the limitations of the microwave-assisted reactions in solvents, namely, the development of high pressure and the need for specialized sealed vessels, are circumvented via the solid-catalyst strategy, which enables organic reactions to occur rapidly at atmospheric pressures and scale up the reactions on a preparative scale (4).

Furo[2,3-*b*]quinoline derivatives constitute an important group of bioactive natural products, such as dictamnine, acrophylline, confusameline, skimmianine, kokusaginine, and aplopine (5–10). They were found to possess a wide-range of biological properties, such as anti-allergic (5), anti-inflammatory (6), cytotoxic (7), antiplatelet aggregation (8–9), and the voltage-gated potassium channel blocking activities (10). Due to their biological importance, several methods have been reported for the synthesis of furoquinoline derivatives (11–15). However, those methods involve multisteps, are time-consuming, produce low yield, and more importantly, the use of more solvents makes those methods less economic. So, there is still need for developing simple, efficient and eco-friendly methods.

Hence, in continuation of our studies on microwave-assisted organic synthesis of linearly condensed quinolines (16–19), by adopting green chemistry, we wish to report microwave-assisted novel synthesis of furo[2,3-*b*]quinoline derivatives using solid base catalyst under solvent-free microwave-irradiation conditions.

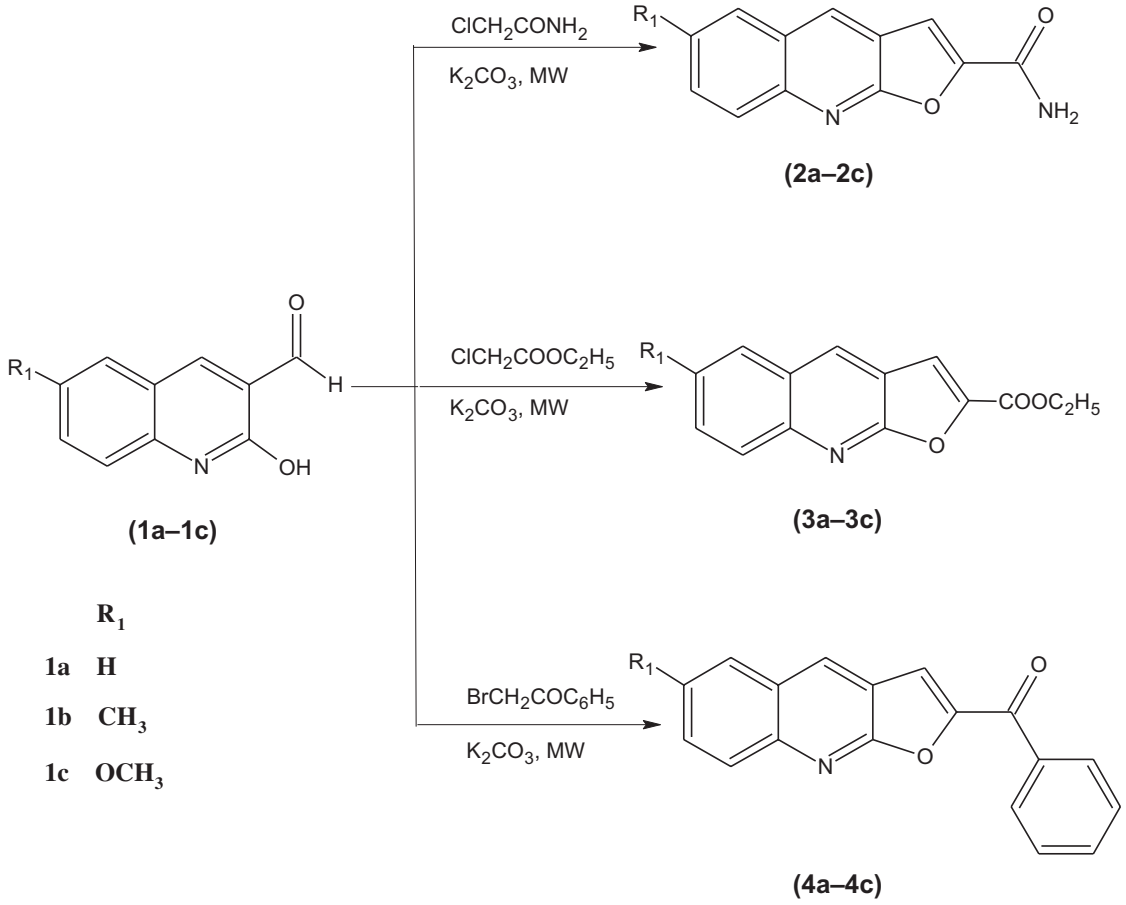
Received 5 April 2007. Accepted 4 September 2007. Published on the NRC Research Press Web site at canjchem.nrc.ca on 9 November 2007.

M. Raghavendra, H.S.B. Naik,[1] and B.S. Sherigara. Department of P G Studies and Research in Industrial Chemistry, School of Chemical Sciences, Kuvempu University, Shankaraghatta, Karnataka, India.

[1]Corresponding author (e-mail: hsb_naik@rediffmail.com).

 doi:10.1139/V07-124 © 2007 NRC Canada

Scheme 1.



Results and discussion

2-Hydoxy-3-formyl quinolines (**1a**–**1c**), were found to be the excellent starting materials for the synthesis of novel furoquinoline derivatives. The starting compounds were prepared according to the literature method (20). In the present study, the cyclization of (**1a**–**1c**) with phenacylbromide, chloroacetamide, and ethylchloroacetate under microwave irradiation in one pot furnished the title compounds (**2a**–**2c**), (**3a**–**3c**), and (**4a**–**4c**) in good yields (Scheme 1).

The reaction proceeds through the nucleophilic substitution of a halogen. Then, the carbanion intermediate results after treatment by a base, which adds on the aldehydic carbon atom with simultaneous elimination of water, resulting in the formation of the cyclized products (21) (Scheme 1). The temperature was measured by introducing the thermometer inside the reaction mixture just at the end of the reaction, and the temperature was found to be 130–135 °C. To see whether these conditions work under non-microwave experiment, reactions were carried out in a pre-heated oil bath. It has been found that although the reaction did take place, the yield was quite low. The acceleration of reactions by microwave exposure results from material–wave interactions leading to thermal effects (which may be easily estimated by temperature measurements) and specific (non-purely thermal) effects. Clearly, a combination of these two contributions can be responsible for the observed effects.

Thermal effects (dielectric heating) can result from dipolar polarization as a consequence of dipole–dipole interactions between polar molecules and the electromagnetic field. They originate in the dissipation of energy into heat as an outcome of agitation and intermolecular friction of molecules when dipoles change their mutual orientation at each alternation of the electric field at a very high frequency.

This energy dissipation in the core of materials allows a much more regular repartition in temperature when compared with classical heating. Classical thermal phenomena (conduction, convention, radiation, and so forth) only play a secondary role in the a posteriori equilibration of temperature, and as a result of this, the rate of the reaction increases in MW method.

The IR absorption bands observed in the region 3000–3200 cm^{-1}, due to tautomeric form of –NH and –OH stretching frequency, and in ^1H NMR spectrum, a broad singlet due to –NH at δ 11.0 and a singlet at δ 10.5 due to –CHO group found in the starting compound (**1a**–**1c**) were absent in the final compounds.

The IR spectra of **3a** exhibited the typical ester carbonyl group absorption at 1680 cm^{-1}. The ^1H NMR (DMSO-d_6) spectrum of the compound (**3a**) displayed a triplet at δ 1.39 (3H), a quartet at 4.38 (CH_2) characteristic of an ethyl group, singlet at 8.56 (C_3–H), and singlet at δ 8.22 (C_4–H). The aromatic proton signals appeared between 7.35–8.10 ppm, indicating that the reactive partner was attached to

© 2007 NRC Canada

the quinoline moiety. The structure of **3a** was further confirmed by the appearance of the molecular-ion peak at *m*/*z* 241 (M^+).

Material and methods

Melting points were determined in open capillaries and are uncorrected. The FTIR spectra were recorded on NICOLETAVATAR 360-FTIR instrument by using KBr pellets. The ^{1}H NMR were recorded on a BRUKER AMX-400 spectrometer operating at 400 MHz and mass spectra on AGILENT LC-MSD-TRAP-XCT mass spectrometer. Elemental analyses were done on Vario EL CHNOS elemental analyzer. Focused microwave irradiations were performed with specially designed microwave oven (Biotage, Emrys Optimizer operating at 300 W) for organic synthesis.

Experimental

General microwave procedure for the synthesis of furo[2,3-*b*]quinolines

A mixture of **1a** (1.730 g, 10 mmol), phenacylbromide (1.990 g, 10 mmol), and anhyd. potassium carbonate (1.380 g, 20 mmol) was ground for uniform mixing. The mixture was then subjected to microwave irradiation in a microwave oven for 12 min at an interval of 1 min at 160 W to complete the reaction (TLC). The reaction mixture was then poured into water, stirred, and the solid obtained was filtered and dried. The crude product was recrystallized from aq. DMF to give 2.322 g (85%) of **4a**. All other compounds were prepared in a similar way with 85%–90% yield.

Physical and spectral data of the products

Furo[2,3-b]quinoline-2-carboxamide (2a)

Recrystallized from aq. DMF. Yield: 85% (MW). Mp: 226–228 °C. IR (KBr) cm^{-1}: 3330, 3145 ($CONH_2$). ^{1}H NMR (400 MHz, DMSO-d_6): 7.50 (2H, bs, –$CONH_2$), 8.55 (s, C_3–H), 8.20 (s, C_4–H), 7.33–8.12 (m, 4H, Ar–H). MS *m*/*z*: 212 (M^+). Anal. calcd. for $C_{12}H_8N_2O_2$: C, 67.92; H, 3.77; N, 13.20. Found: C, 67.90; H, 3.79; N, 13.22

6-Methylfuro[2,3-b]quinoline-2-carboxamide (2b)

Recrystallized from aq. DMF. Yield: 86% (MW). Mp: 237–239 °C. IR (KBr) cm^{-1}: 3340, 3155 ($CONH_2$). ^{1}H NMR (400 MHz, DMSO-d_6): 2.11 (s, 3H, –CH_3), 7.53 (2H, bs, –$CONH_2$), 8.53 (s, C_3–H), 8.24 (s, C_4–H), 7.30–8.14 (m, 3H, Ar–H). MS *m*/*z*: 226 (M^+). Anal. calcd. for $C_{13}H_{10}N_2O_2$: C, 69.02; H, 4.42; N, 12.38. Found: C, 69.04; H, 4.47; N, 12.34.

6-Methoxyfuro[2,3-b]quinoline-2-carboxamide (2c)

Recrystallized from aq. DMF. Yield: 90% (MW). Mp: 250–252 °C. IR (KBr) cm^{-1}: 3350, 3150 ($CONH_2$). ^{1}H NMR (400 MHz, DMSO-d_6): 3.90 (3H, s, Ar–OCH_3), 7.54 (2H, bs, –$CONH_2$), 8.50 (s, C_3–H), 8.18 (s, C_4–H), 7.25–8.12 (m, 3H, Ar–H). MS *m*/*z*: 242 (M^+). Anal. calcd. for $C_{13}H_8N_2O_3$: C, 64.46; H, 4.13; N, 11.57. Found: C, 64.42; H, 4.16; N, 11.54.

Ethyl furo[2,3-b]quinoline-2-carboxylate (3a)

Recrystallized from aq. DMF. Yield: 86% (MW). Mp: 251–253 °C. IR (KBr) cm^{-1}: 1680. ^{1}H NMR (400 MHz, DMSO-d_6): 1.39 (t, 3H, –CH_3), 4.38 (q, 2H, –OCH_2), 8.56 (s, C_3–H), 8.22 (s, C_4–H), 7.35–8.10 (m, 4H, Ar–H). MS *m*/*z*: 241 (M^+). Anal. calcd. for $C_{14}H_{11}NO_3$: C, 69.70; H, 4.56; N, 5.80. Found: C, 69.74; H, 4.52; N, 5.84.

Ethyl 6-methylfuro[2,3-b]quinoline-2-carboxylate (3b)

Recrystallized from aq. DMF. Yield: 88% (MW). Mp: 245–247 °C. IR (KBr) cm^{-1}: 1675 cm^{-1}. ^{1}H NMR (400 MHz, DMSO-d_6): 2.16 (s, 3H, –CH_3), 1.39 (t, 3H, –CH_3), 4.38 (q, 2H, –OCH_2), 8.57 (s, C_3–H), 8.24 (s, C_4–H), 7.40–8.13 (m, 3H, Ar–H). MS *m*/*z*: 255 (M^+). Anal. calcd. for $C_{15}H_{13}NO_3$: C, 70.58; H, 5.09; N, 5.49. Found: C, 70.53; H, 5.06; N, 5.42

Ethyl 6-methoxyfuro[2,3-b]quinoline-2-carboxylate (3c)

Recrystallized from aq. DMF. Yield: 87% (MW). Mp: 220–222 °C. IR (KBr) cm^{-1}: 1670. ^{1}H NMR (400 MHz, DMSO-d_6): 3.95 (3H, s, Ar–OCH_3), 1.39 (t, 3H, –CH_3), 4.38 (q, 2H, –OCH_2), 8.58 (s, C_3–H), 8.28 (s, C_4–H), 7.37–8.12 (m, 3H, Ar–H). MS *m*/*z*: 255 (M^+). Anal. calcd. for $C_{15}H_{13}NO_3$: C, 66.42; H, 4.79; N, 5.16. Found: C, 66.46; H, 4.83; N, 5.19.

Furo[2,3-b]quinolin-2-yl(phenyl)methanone (4a)

Recrystallized from aq. DMF. Yield: 89% (MW). Mp: 236–237 °C. IR (KBr) cm^{-1}: 1660. ^{1}H NMR (400 MHz, DMSO-d_6): 8.60 (s, C_3–H), 8.21 (s, C_4–H), 7.49–8.18 (9H, m, Ar–H). MS *m*/*z*: 273 (M^+). Anal. calcd. for $C_{18}H_{11}NO_2$: C, 79.12; H, 4.03; N, 5.12. Found: C, 79.16; H, 4.06; N, 5.00.

(6-Methylfuro[2,3-b]quinolin-2-yl)(phenyl)methanone (4b)

Recrystallized from aq. DMF. Yield: 90% (MW). Mp: 247–249 °C. IR (KBr) cm^{-1}: 1670 cm^{-1}. ^{1}H NMR (400 MHz, DMSO-d_6): 2.26 (s, 3H, –CH_3), 8.58 (s, C_3–H), 8.24 (s, C_4–H), 7.45–8.13 (8H, m, Ar–H). MS *m*/*z*: 287 (M^+). Anal. calcd. for $C_{19}H_{13}NO_2$: C, 79.44; H, 4.52; N, 4.87. Found: C, 79.47; H, 4.56; N, 4.83.

(6-Methoxyfuro[2,3-b]quinolin-2-yl)(phenyl)methanone (4c)

Recrystallized from aq. DMF. Yield: 86% (MW). Mp: 260–262 °C. IR (KBr) cm^{-1}: 1665. ^{1}H NMR (400 MHz, DMSO-d_6) 4.10 (3H, s, Ar–OCH_3), 8.56 (s, C_3–H), 8.28 (s, C_4–H), 7.43–8.11 (8H, m, Ar–H). MS *m*/*z*: 303 (M^+). Anal. calcd. for $C_{19}H_{13}NO_3$: C, 75.24; H, 4.29; N, 4.62. Found: C, 75.20; H, 4.24; N, 4.64.

Conclusion

In conclusion, a simple microwave-assisted method has been developed for the synthesis of furo[2,3-*b*]quinolines under solvent-free conditions in presence of K_2CO_3. This microwave-irradiation method is superior from the view of the yield, reaction time, and facial workup compared with the conventional (thermal) method.

© 2007 NRC Canada

Acknowledgement

Authors are thankful to the Director, Sophosticated Instrumentation Facility Center, Indian Institute of Science (IISc), Bangalore, for the spectral data.

References

1. (*a*) U.R. Pillai, E. Ahle-Demessie, and R.S. Varma. J. Mater. Chem. **12**, 3199 (2002); (*b*) A Oussaid, L.N. Thach, and A. Loupy. Tetrahedron Lett. **38**, 2451 (1997).
2. A. Loupy (*Editor*). Microwaves in organic synthesis. Wiley-VCH Verlag Gmbh & Co. KGaA, Weinheim, Germany. 2002.
3. B.L. Hayes. Microwave synthesis: chemistry at the speed of light. CEM Publishing, Matthews, NC. 2002.
4. (*a*) D. Vilemin and A.B. Alloum. Synth. Commun. **21**, 63 (1991); (*b*) J.M. Lerstif, L. Toupet, S. Sinbandhit, F. Tonnard, J. Bazureau, and P.J. Hamelin. Tetrahedron, **53**, 6351 (1997).
5. A.C. Huang, T.P. Lin, S.C. Kuo, and J.P. Wang. J. Nat. Prod. **58**, 117 (1995).
6. C.P. Chang, T.P. Lin, J.P. Wang, and S.C. Kuo. Chin. Pharm. J. **53**, 239 (2001).
7. W.N. Setzer, M.C. Setzer, J.M. Schmidt, D.M. Moriarity, B. Vogler, S. Reeb, A. M. Holmes, and W.A. Haber. Planta Med. **66**, 493 (2000).
8. K.S. Chen, Y.L. Chang, C.H. Teng, C.F. Chen, and Y.C. Wu. Planta Med. **66**, 80 (2000).
9. I.S. Chen, H.F. Chen, M.J. Cheng, Y.L. Chang, C.M. Teng, I. Tsutomu, J.J. Chen, and I.L. Tsai. J. Nat. Prod. **64**,1143 (2001).
10. I. Butenschon, K. Moller, and W. Hansel. J. Med. Chem. **44**, 1249 (2001).
11. J.A. Diment, E. Ritchie, and W.C. Taylor. Aust. J. Chem. **22**, 1797 (1969).
12. T. Sekiba. Bull. Chem. Soc. Jpn. **46**, 577 (1973).
13. R.G. Cooke and H.F. Haynes. Aust. J. Chem. **11**, 221 (1958).
14. T. Sato and M. Ohta. Bull. Chem. Soc. Jpn. **31**, 161 (1958).
15. (*a*) N.S. Narasimhan, M.V. Paradkar, and R.H. Alurkar. Tetrahedron, **27**, 351. (1971); (*b*) N. S. Narasimhan, R. S. Mali. Tetrahedron, **30**, 4153 (1974).
16. B.P. Nandeshwarappa, D.B. Arun Kumar, H.S. Bhojya Naik, V.P. Vaidya, and K.M. Mahadevan. J. Sulfur Chem. **2**6 373 (2005).
17. B.P. Nandeshwarappa, D.B. Arun Kumar, M.N. Kumaraswamy, Y.S. Ravi Kumar, H.S. Bhojya Naik, and K.M. Mahadevan. Phosphorous, Sulfur Silicon Relat. Elem. **181**, 1545 (2006).
18. M. Raghavendra, H.S. Bhojya Naik, and B.S. Sherigara. J. Sulfur Chem. **27**, 347 (2006).
19. H.S. Bhojya Naik, M.S. Ramesh, B.V. Swetha, and T.R. Roopa. Phosphorous, Sulfur Silicon Relat. Elem. **181**, 533 (2006).
20. O. Meth-Cohn, B. Narine, and B. Tarnowski. J. Chem. Soc., Perkin Trans. 1, 1520 (1981).
21. K. Yoshizawa, S. Toyota, F. Toda, and I. Csoregh. Green Chem. **5**, 353 (2003).

© 2007 NRC Canada

Molecular studies of the initiation and termination steps of the anionic polymerization of P=C bonds

Bronwyn H. Gillon, Kevin J.T. Noonan, Bastian Feldscher, Jennifer M. Wissenz, Zhi Ming Kam, Tom Hsieh, Justin J. Kingsley, Joshua I. Bates, and Derek P. Gates

Abstract: The initiation and termination steps of the anionic polymerization of P=C bonds have been modeled. The initiation step was investigated through the stoichiometric reaction of MesP=CPh_2 (**1**) with RLi (R = Me or *n*-Bu). In each case, the addition was highly regioselective with the formal attack of R^- at phosphorus to give the carbanion Li[Mes(R)P–CPh_2] (**3a**, R = Me; **3b**, R = *n*-Bu). To simulate the termination step in the anionic polymerization of **1**, carbanions **3a** and **3b** were quenched in situ with various electrophiles. Through these reactions, several new tertiary phosphines have been prepared, namely, Mes(Me)P–CPh_2H (**4a**), Mes(*n*-Bu)P-CPh_2H (**4b**), Mes(Me)P–CPh_2Me (**6a**), Mes(Me)P–CPh_2–$P(NEt_2)_2$ (**7a**), Mes(Me)P–CPh_2–$SiMe_2H$ (**8a**), and Mes(Me)P–CPh_2–$SiMe_3$ (**9a**). In addition, compounds **4a**, **7a**, **8a**, and **9a** were characterized by X-ray crystallography. Most of the metrical parameters are typical of tertiary phosphines; however, the P–CPh_2H bonds were elongated in all cases reflecting the considerable steric bulk surrounding this bond. Unexpectedly, an unusually large ^{31}P–^{31}P coupling constant ($^2J_{PP}$ > 200 Hz) was observed for **7a** both in solution and the solid state. This observation may be rationalized by a through space P···P interaction. This rationale is further supported by the short P···P distance [P(1)—P(2) = 2.966(1) Å; cf. $\Sigma\, r_{vdw}$ = 3.7 Å] and a small P–C–P bond angle for **7a** [P(1)–C(11)–P(1) = 99.17(9)°].

Key words: phosphaalkenes, phosphorus polymers, phosphines, anionic polymerization.

Résumé : On a développé un modèle pour les étapes d'initiation et de terminaison de la polymérisation anionique des liaisons P=C. On a étudié l'étape d'initiation par le biais de la réaction stoechiométrique du MesP=CPh_2 (**1**) avec du RLi (R = Me ou Bu). Dans chacun des cas, l'addition est très régiosélective avec une attaque formelle du R^- sur le phosphore pour conduire à la formation du carbanion Li[Mes(R)P–CPh_2] (**3a**, R = Me; **3b**, R = Bu). Dans le but de simuler l'étape de terminaison de la polymérisation du composé **1**, les carbanions **3a** et **3b** ont été piégés in situ avec divers électrophiles. Par le biais de ces réactions, on a obtenu plusieurs nouvelles phosphines tertiaires, soit: Mes(Me)P–CPh_2H (**4a**); Mes(Bu)P–CPh_2H (**4b**); Mes(Me)P–CPh_2Me (**6a**); Mes(Me)P–CPh_2–$P(NEt_2)$ (**7a**); Mes(Me)P–CPh_2–$SiMe_2H$ (**8a**) et Mes(Me)P–CPh_2–$SiMe_3$ (**9a**). De plus, on a caractérisé les composés **4a**, **7a**, **8a** et **9a** par diffraction des rayons X. La plupart des paramètres métriques sont typiques des phosphines tertiaires; toutefois, dans tous les cas, les liaisons P–CPh_2H sont allongées et cette caractéristique reflète l'encombrement stérique important aux abords de cette liaison. D'une façon inattendue, on a observé une constante de couplage ^{31}P–^{31}P exceptionnellement élevée ($^2J_{PP}$ > 200 Hz) avec le composé **7a**, tant à l'état solide qu'en solution. On peut rationaliser cette observation à l'aide d'une interaction P···P à travers l'espace. Ce raisonnement est supporté par la courte distance P···P [P(1)—P(2) = 2,966(1) Å; cf. $\Sigma\, r_{vdw}$ = 3,7 Å] et un faible angle P–C–P pour le composé **7a** [P(1)–C(11)–P(1) = 99,17(9)°].

Mots-clés : phosphaalcènes, polymères du phosphore, phosphines, polymérisation anionique.

[Traduit par la Rédaction]

Introduction

Phosphaalkenes, compounds with genuine (2p–3p) π bonds, are an intriguing class of low-coordinate phosphorus species. Although the first stable derivatives were reported in the late 1970s, interest in phosphaalkenes continues to grow because of their parallelism to the chemistry of C=C bonds and their potential applications (1–3). For example, compounds with P=C bonds are being explored as ligands in transition-metal-catalyzed reactions (4–7) and in polymer science (8–13).

Recently, we reported the polymerization of phosphaalkene **1** to afford poly(methylenephosphine) **2**, a new functional phosphine polymer with alternating phosphorus and carbon atoms in the main chain (see Scheme 1) (12). Our initial studies suggested that the polymerization of **1** required high temperatures (>150 °C), long reaction times, and high concentrations, even in the presence of radical or anionic initiators. We subsequently showed that short-chain oligomers could be obtained when **1** is treated with anionic

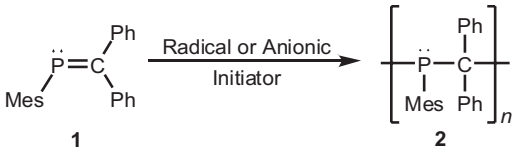
Received 23 July 2007. Accepted 12 September 2007. Published on the NRC Research Press Web site at canjchem.nrc.ca on 22 November 2007.

B.H. Gillon, K.J.T. Noonan, B. Feldscher, J.M. Wissenz, Z.M. Kam, T. Hsieh, J.J. Kingsley, J.I. Bates, and D.P. Gates.[1] Department of Chemistry, University of British Columbia, 2036 Main Mall, Vancouver, BC V6T 1Z1, Canada.

[1]Corresponding author (e-mail: dgates@chem.ubc.ca).

 doi:10.1139/V07-121 © 2007 NRC Canada

Scheme 1.



initiators (i.e., MeLi) in THF solution at ambient temperature (14). This solution oligomerization has now been extended to the living anionic polymerization of monomer **1** to afford homopolymer **2** and block copolymers with controllable architectures (11). To further develop the living anionic polymerization of P=C bonds and to prepare end-functionalized polymers, it is necessary to fully understand the mechanism of anionic chain growth for **1**.

To our knowledge, there is little previous work on the reaction of P=C bonds with typical anionic initiators. Of particular relevance to our studies is the synthesis of phosphine oxide **5a** from phosphaalkene **1** (15) (see Scheme 2). Specifically, treating **1** with MeLi followed by MeOH and air oxidation afforded **5a**. Both the carbanion (**3a**) and the phosphine (**4a**) were the proposed intermediates in this reaction. In a separate study, the addition of MeLi to $RP{=}C(SiMe_3)_2$ (R = Mes, *t*-Bu) afforded $Li[MeRPC(SiMe_3)_2]$, which was characterized spectroscopically (16–18). In several other studies, the addition of alkyllithium reagents across the P=C bond in phosphinines and triphosphafulvenes similarly afforded only the P-alkyl products (19). These regioselective additions are consistent with the predicted polarity of the P=C bond, based on the electronegativities of phosphorus (δ+) and carbon (δ–). Interestingly, alkyllithium reagents can also react with phosphaalkenes with preservation of the P=C bond (20).

In this paper, we disclose our molecular-model studies of the initiation and termination steps of the anionic polymerization of **1**. Two initiators were chosen for the present studies: MeLi and *n*-BuLi. Although *n*-BuLi is a better initiator for the anionic polymerization of **1** (11, 12), MeLi is optimal in molecular-model studies, since the small Me substituent is more likely to afford crystalline products. The new compounds obtained may be utilized as molecular models for the development of the coordination chemistry of polymer **2**. Moreover, the development of methods to end-functionalize poly(methylenephosphine)s will afford telechelic polymers, which may function as precursors to novel block copolymers.

Results and discussion

The phosphaalkene **1** was prepared according to literature methods (21, 22). A pale-yellow solution of **1** in THF was treated with a slight excess of alkyllithium at low temperatures, resulting in an immediate color change to deep red. Analysis of the reaction mixture using $^{31}P\{^1H\}$ NMR spectroscopy confirmed the complete conversion of **1** to the carbanion **3a** (δ = −44.3) or to **3b** (δ = –31.1). These intermediates are believed to be related to the active species in the anionic polymerization of **1**.

Carbanion **3a** was quenched by addition of water or methanol to afford model compound **4a** ($\delta_{^{31}P}$ = –24.0). Additionally, $^{13}C\{^1H\}$, ^1H NMR spectroscopy, and low resolution EI-MS (M^+, m/z = 332) were consistent with the proposed structure. The ^1H NMR spectrum of **4a** shows a notably downfield doublet resonance at δ = 4.87 ($^2J_{HP}$ = 5 Hz), which is assigned to the benzylic proton. Importantly, a doublet resonance is observed in the alkyl region (δ = 1.31, $^2J_{HP}$ = 6 Hz), which is attributed to the $P\text{-}CH_3$ protons. Clearly, addition of the methyl anion occurs regioselectively at the phosphorus atom of the P=C bond. Also found in the alkyl region are sharp singlets at 2.52 and 2.21 ppm that are assigned to the ortho- and para-methyl protons of the mesityl group, respectively.

Clear, colorless crystals suitable for X-ray diffraction were obtained from the slow evaporation of a concentrated solution of **4a** in hexanes. The molecular structure and the crystallographic data appear in Fig. 1, Table 1, and the Supplementary data.[2] The molecular structure provides insight into the steric nature of the substituents around the P atom. Importantly, the cone angle of the model compound **4a** was estimated to be roughly 140°, which is comparable to that of triphenylphosphine (145°) (23).[3] The P—C bond lengths (Å) fall into the typical range for P—C single bonds [P(1)—C(1) = 1.852(1), P(1)—C(10) = 1.840(2), P(1)—C(11) = 1.882(1)] (24). Presumably, steric repulsion is responsible for the slight elongation of P(1)—C(11). For comparison, related P—C bonds where the carbon atom has two aryl substituents (i.e., $RArP\text{–}CHPh_2$) are ~1.90 Å in length (25, 26).

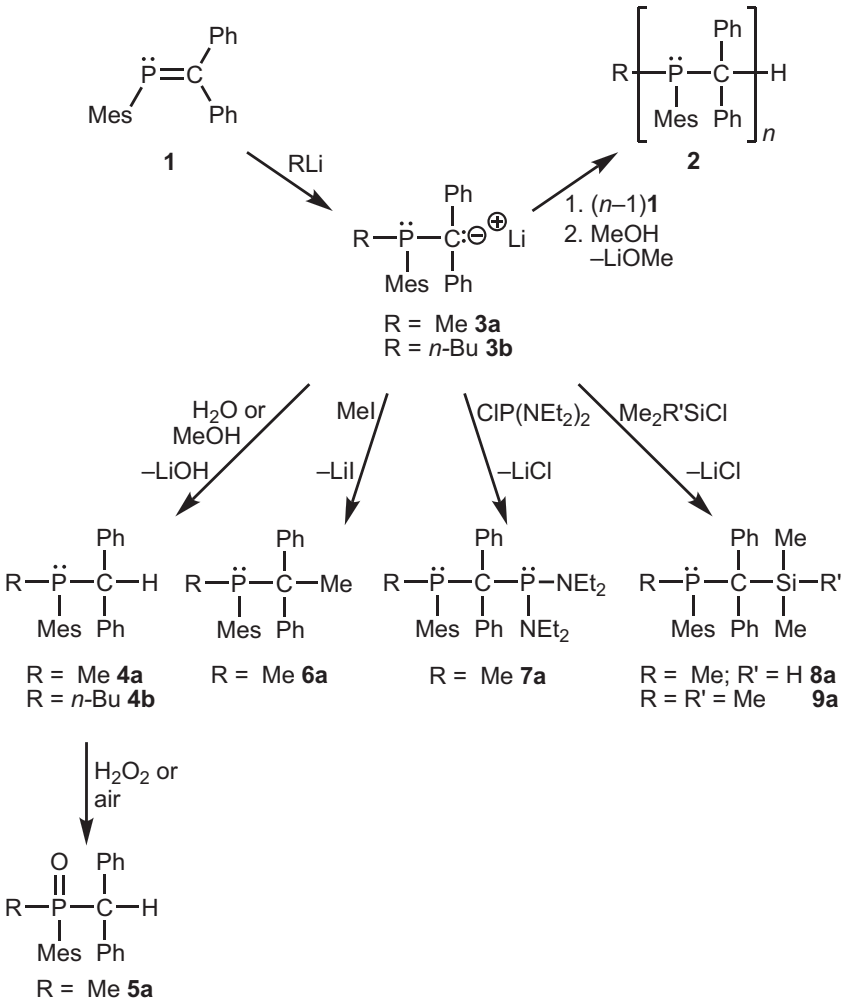
Using *n*-BuLi as the initiator for **1**, the related compound **4b**, was prepared by terminating carbanion **3b** with water. Again, the reaction was quantitative as suggested by $^{31}P\{^1H\}$ NMR spectroscopy (δ = –12.4). Upon workup, analytically pure **4b** was isolated in good yield (85%) as a yellow oil. Akin to the Me-initiated **4a**, the ^1H NMR spectrum of *n*-Bu-initiated **4b** showed a characteristic doublet resonance at 4.91 ppm ($^2J_{HP}$ = 5 Hz), which is assigned to the benzylic proton. A sharp singlet at 2.20 ppm is assigned to the para-methyl mesityl protons. In contrast to the sharp signals observed for **4a**, the ortho-methyl mesityl protons in **4b** exhibit a broad signal centred at 2.56 ppm. The broadening may be a consequence of restricted rotation about the P—C (ipso-mesityl) bond. Additionally, there is considerable broadening of the resonance assigned to the ortho-methyl mesityl carbon (δ = 23.8) in the $^{13}C\{^1H\}$ NMR spectrum. Another interesting feature in the ^1H NMR spectrum of **4b** is

[2] Supplementary data for this article are available on the journal Web site (canjchem.nrc.ca) or may be purchased from the Depository of Unpublished Data, Document Delivery, CISTI, National Research Council Canada, Ottawa, ON K1A 0R6, Canada. DUD 5227. For more information on obtaining material, refer to cisti-icist.nrc-cnrc.gc.ca/irm/unpub_e.shtml. CCDC 655085 (**4a**), 655086 (**7a**), 655087 (**8a**), and 655088 (**9a**) contain the crystallographic data for this manuscript. These data can be obtained, free of charge, via www.ccdc.cam.ac.uk/conts/retrieving.html (or from the Cambridge Crystallographic Data Centre, 12 Union Road, Cambridge CB2 1EZ, UK; fax +44 1223 336033; or deposit@ccdc.cam.ac.uk).

[3] The ligand cone angle θ was estimated according to Tolman's method for an unsymmetrical phosphine ($PR_1R_2R_3$) ligand. The cone angle is the apex angle of a cylindrical cone centrally positioned 2.28 Å away from the P. The edges of the cylindrical cone encompassed the van der Waals radii of the outermost atoms on each substituent on P. Using X-ray crystallographic data for **4a**, θ was estimated to be ~140°.

© 2007 NRC Canada

Scheme 2. Initiation of **1** with alkyllithium reagents and subsequent termination with electrophiles.



the diastereotopic protons adjacent to the stereogenic phosphorus atom. In particular, they give rise to two sets of multiplets (δ = 2.02 and 1.55). Assignments were made with the help of ^{1}H–^{1}H COSY, HMQC, and HMBC experiments.

To model the end-functionalization of polymer **2**, we investigated the termination of the methyl-initiated species **3a** with different electrophiles. These end-functionalized products are envisaged as model systems for the heretofore-unknown telechelic polymers.

To obtain Me-terminated **6a**, carbanion **3a** was quenched with neat methyl iodide, affording an orange solution ($\delta_{^{31}P}$ = –13.5). Model compound **6a** was characterized by ^{1}H, ^{13}C{^{1}H}, and ^{31}P NMR spectroscopy and low resolution EI-MS (M^+, *m/z* = 346). Although analytically pure material could not be isolated, analysis by NMR spectroscopy suggests 95% or higher purity. As with butyl-initiated **4b**, the signal assigned to the ortho-methyl mesityl protons in the ^{1}H NMR spectrum (δ = 1.87) is broad. Two doublets are observed in the alkyl region (1.70 ppm, $^2J_{PH}$ = 13 Hz; 1.39 ppm, $^3J_{PH}$ = 7 Hz). The resonance with the larger P–H coupling constant is assigned to the P-CH_3 group whilst the other signal is attributed to the quenching methyl group.

Phosphine end-functionalized **7a** was prepared by quenching **3a** with a solution of $ClP(NEt_2)_2$ (1.1 equiv.) in THF. The crude diphosphine was purified by washing the solid with cold hexanes (–78 °C). As expected, the ^{31}P{^{1}H} NMR spectrum of the product showed that the phosphorus atoms are inequivalent and are observed as two doublets (P2: δ = 105.3, P1: δ = –9.4; $^2J_{pp}$ = 205 Hz). The observed coupling constant is considerably larger than in a related asymmetric diphosphine [$Ph_2PCH_2P(NC_4H_4)_2$, $^2J_{PP}$ = 147 Hz] (27) and suggests some direct P–P interaction. In contrast to the broadened signals observed in **4b** and **6a**, the ortho-methyl mesityl groups in **7a** are inequivalent in both the ^{1}H and ^{13}C{^{1}H} NMR spectra. Presumably, this results from restricted rotation due to the increased steric bulk in **7a**.

X-ray-quality crystals of **7a** were grown from toluene. Crystallographic data are shown in Fig. 2, Table 1, and the Supplementary data.[2] Interestingly, the P(1)–C(11)–P(2) bond angle (99.17(9)°) is more acute than a typical sp^3-hybridized C atom. This small bond angle, combined with the short P···P distance [P(1)—P(2) = 2.966(1) Å, cf. Σ r_{vdw} = 3.7 Å], may account for the large coupling constant ($^2J_{PP}$) observed in solution. To confirm that the structure observed in solution is the same as that in the solid state, a solid-state ^{31}P NMR spectrum was recorded, which revealed a similarly large coupling constant ($^2J_{PP}$ = 255 Hz). Surprisingly, both nitrogen atoms are planar with the sum of the bond angles at nitrogen totaling 360°. Likely, the planarity is due to donation of nitrogen electron density into P(2), and this notion is

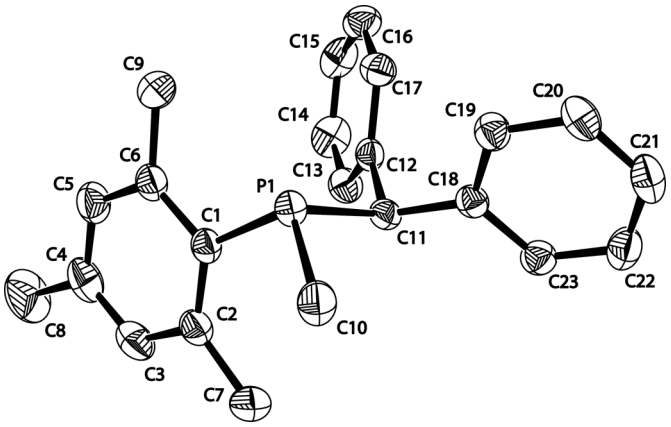
© 2007 NRC Canada

Table 1. X-ray crystallographic data of **4a**, **7a**, **8a**, and **9a**.

Crystal	**4a**	**7a**	**8a**	**9a**
Formula	$C_{23}H_{25}P$	$C_{31}H_{44}N_2P_2$	$C_{25}H_{31}PSi$	$C_{26}H_{33}PSi$
Formula weight	332.40	506.62	390.56	404.58
Crystal system	monoclinic	monoclinic	monoclinic	triclinic
Space group	$P2_1/c$	$P2_1/n$	$C2/c$	$P\bar{1}$
Color	colorless	colorless	colorless	colorless
a (Å)	18.867(2)	9.528(5)	20.677(5)	9.165(5)
b (Å)	6.1290(5)	15.614(5)	8.955(5)	10.757(5)
c (Å)	16.618(2)	18.935(5)	23.987(5)	12.689(5)
α (°)	90	90	90	79.511(5)
β (°)	92.401(3)	94.828(5)	101.555(5)	71.398(5)
γ (°)	90	90	90	75.169(5)
V (Å^3)	1919.9(3)	2807.0(19)	4351(3)	1143.3(9)
Z	4	4	8	2
T (K)	173(2)	173(2)	173(2)	173(2)
μ(Mo Kα) (cm^{-1})	1.44	1.77	1.89	1.82
Crystal size (mm)	0.2 × 0.2 × 0.1	1.4 × 0.6 × 0.4	1.4 × 1.2 × 1.0	1.0 × 1.0 × 0.5
$D_{calcd.}$ (g cm^{-3})	1.150	1.199	1.192	1.175
2θ(max) (°)	56.02	56.04	56.36	55.66
No. of reflections	26221	27995	54740	27579
No. of unique data	4580	6560	5281	5333
R_{int}	0.040	0.050	0.033	0.024
Reflections/parameters ratio	20.82	12.84	14.35	13.85
R_1, wR_2 [$I > 2\sigma(I)$][a]	0.0388, 0.0925	0.0418, 0.0944	0.0350, 0.0883	0.0306, 0.0820
R_1, wR_2 (all data)[a]	0.0662, 0.1015	0.0787, 0.1149	0.0446, 0.0950	0.0354, 0.0862
GOF	1.053	1.017	1.029	1.054

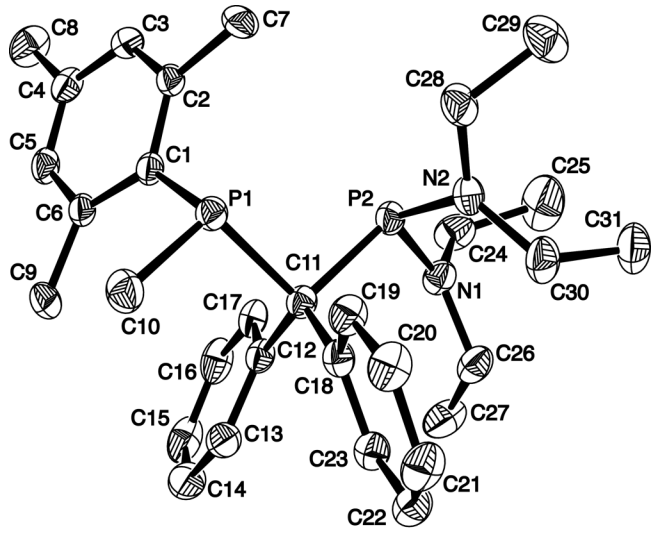
[a] $R_1 = \Sigma|(|F_o| - |F_c|)|/\Sigma|F_o|$. $wR_2 = [\Sigma(F_o^2 - F_c^2)^2/\Sigma w(F_o^2)^2]^{1/2}$.

Fig. 1. Molecular structure of **4a** (50% probability ellipsoids). Hydrogen atoms are omitted for clarity. Selected bond lengths (Å): P(1)—C(1) = 1.852(1); P(1)—C(10) = 1.840(2); P(1)—C(11) = 1.882(1). Selected bond angles (°): C(10)–P(1)–C(1) = 107.34(7); C(10)–P(1)–C(11) = 100.51(7); C(1)–P(1)–C(11) = 100.18(6).



reinforced by the short P—N distances; P(2)—N(1) = 1.678(2) and P(2)—N(2) = 1.689(2) Å (28). In related bis(amino)phosphines, the P—N bonds are often shortened to 1.6–1.7 Å, which is accompanied by planarity at the nitrogen (29–32). Also, addition of the functional end-group lengthens the backbone P—C bonds to beyond typical single bonds [P(1)—C(11) = 1.942(2) and P(2)—C(11) = 1.951(2) Å] (28).

Fig. 2. Molecular structure of **7a** (50% probability ellipsoids). Hydrogen atoms are omitted for clarity. Selected bond lengths (Å): P(1)—C(1) = 1.851(2); P(1)—C(10) = 1.843(2); P(1)—C(11) = 1.942(2); P(2)—C(11) = 1.951(2); P(2)—N(1) = 1.678(2); P(2)—N(2) = 1.689(2); P(1)···P(2) = 2.966(1). Selected bond angles (°): C(1)–P(1)–C(10) = 105.1(1); C(1)–P(1)–C(11) = 110.05(9); C(10)–P(1)–C(11) = 101.5(1); P(1)–C(11)–P(2) = 99.17(9); C(11)–P(2)–N(1) = 103.87(8); C(11)–P(2)–N(2) = 105.97(9); N(1)–P(2)–N(2) = 107.80(9); Σ angles about N(1) atom = 359.7(3)°; Σ angles about N(2) atom = 359.4(3)°.



© 2007 NRC Canada

Addition of Me_2HSiCl or Me_3SiCl to carbanion **3a** produced silane end-functionalized **8a** and **9a**, respectively. These compounds formed quantitatively from **3a** according to the ^{31}P NMR spectra of the reaction mixtures (**8a**: δ = –23.9, **9a**: δ = –25.4); however, their high solubility resulted in low isolated yields of pure product after recrystallization (**8a**: 50%, **9a**: 14%). Analogous to that mentioned previously for **7a**, the ^1H NMR signals for the ortho-methyl protons of the mesityl group were inequivalent, and two broad signals were observed (**8a**: δ = 3.1 and 1.1, **9a**: δ = 2.8 and 0.9). Importantly, for **8a**, a singlet resonance is observed at 4.58 ppm, which is assigned to the Si–H proton. Although the methyl protons of the $SiMe_3$ moiety are equivalent in **9a**, the methyl protons of the $SiMe_2H$ moiety are inequivalent in **8a**. In particular, the $SiHMe_2$ group in **8a** shows two sets of doublets at 0.10 ppm ($^3J_{HH}$ = 3 Hz) and 0.05 ppm ($^3J_{HH}$ = 3 Hz). Both **8a** and **9a** were also characterized by low resolution EI-MS (M^+: m/z = 390 for **8a** and 404 for **9a**), elemental analysis (**8a** only), and X-ray crystallography.

Crystals of **8a** and **9a** were obtained from hexanes. The molecular structures and important lengths and angles are given in Figs. 3 and 4, and additional data is provided in Table 1 and the Supplementary data.[2] As with the other model compounds, **4a** and **7a**, the P—CPh_2H bond lengths [**8a**: P(1)—C(11) = 1.902(1), **9a**: P(1)—C(1) = 1.920(1) Å] are significantly longer than the two other P—C bonds [avg. for **8a** and **9a** = 1.835(5) Å]. Similar to that discussed previously, this elongation may be attributed to steric congestion. The small size of the $SiMe_2H$ moiety compared with the $SiMe_3$ moiety is reflected by the smaller P–C–Si bond angles in **8a** [**8a**: P(1)–C(11)–Si(1) = 106.57(6)°, **9a**: P(1)–C(1)–Si(1) = 111.52(6)°]. Remarkably, these angles are much larger than the the analogous angle in diphosphine **7a** [P(1)–C(11)–P(2) = 99.17(9)°] in which we speculate there is a weak P···P interaction.

Summary

In closing, the initiation and termination steps in the anionic polymerization of P=C bonds have been modeled. The initiation step was investigated through the stoichiometric reaction of MesP=CPh_2 (**1**) with RLi (R = Me or *n*-Bu). In all cases, the addition was highly regioselective with the formal attack of R^- at phosphorus to give the carbanion Li[Mes(R)P–CPh_2] (**3a/3b**). To simulate the termination step in the anionic polymerization of **1**, carbanions **3a** and **3b** were quenched in situ with electrophiles such as a proton (from H_2O or MeOH), a methyl cation (from MeI), a phosphenium moiety (from $ClP(NEt_2)_2$), or a silylium moiety (from Me_2HSiCl or Me_3SiCl). In this way, five new tertiary phosphines and one diphosphine were accessed and will function as models for poly(methylenephosphine)s. Four of these molecules were characterized crystallographically.

In future, we will extend this chemistry to the polymer **2** with the goal of preparing end-functional telechelic polymers that can be employed in the synthesis of novel block copolymers. In addition, these new compounds will be used to prepare molecular complexes that will serve as models for macromolecular coordination complexes of poly(methylenephosphine)s.

Fig. 3. Molecular structure of **8a** (50% probability ellipsoids). Hydrogen atoms are omitted for clarity except for H(1). Selected bond lengths (Å): P(1)—C(1) = 1.834(2); P(1)—C(10) = 1.824(2); P(1)—C(11) = 1.902(1); Si(1)—C(11) = 1.910(2); Si(1)—C(24) = 1.855(2); Si(1)—C(25) = 1.849(2); Si(1)—H(1) = 1.36(2). Selected bond angles (°): C(1)–P(1)–C(10) = 107.39(7); C(1)–P(1)–C(11) = 106.61(6); C(10)–P(1)–C(11) = 102.33(7); P(1)–C(11)–Si(1) = 106.57(6).

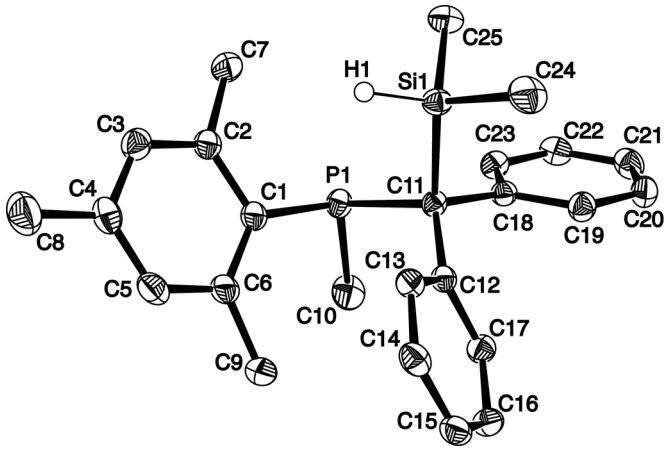
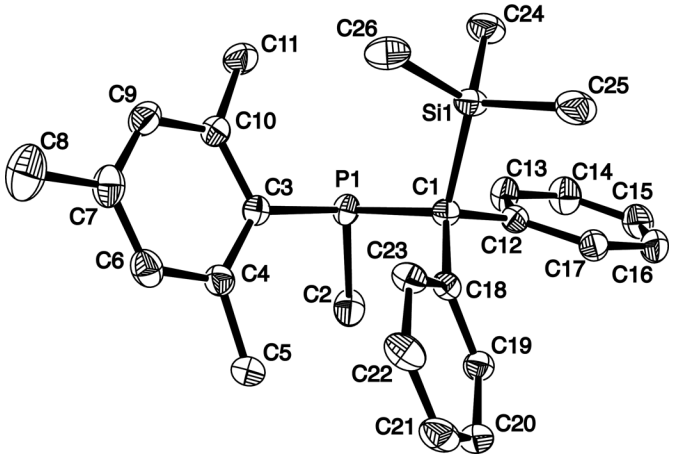


Fig. 4. Molecular structure of **9a** (50% probability ellipsoids). Hydrogen atoms are omitted for clarity. Selected bond lengths (Å): P(1)—C(1) = 1.920(1); P(1)—C(2) = 1.839(2); P(1)—C(3) = 1.844(1); C(1)—Si(1) = 1.944(1). Selected bond angles (°): C(1)–P(1)–C(2) = 101.38(6); C(2)–P(1)–C(3) 106.97(7); C(1)–P(1)–C(3) = 107.53(5); P(1)–C(1)–Si(1) = 111.52(6).



Experimental

Materials and general procedure

All manipulations of oxygen- and (or) moisture-sensitive compounds were performed under a nitrogen atmosphere using standard Schlenk and (or) glovebox techniques. Hexanes, diethyl ether, and dichloromethane were deoxygenated with nitrogen and dried by passing through a column containing activated alumina. THF was freshly distilled from sodium/benzophenone ketyl. Distilled water and methanol were degassed prior to use. $CDCl_3$ was distilled from P_2O_5 and degassed. CD_2Cl_2 and C_6D_6 were purchased from Cambridge Isotope Laboratories and were dried over molecular

© 2007 NRC Canada

sieves (3 Å). PCl_3, $HNEt_2$, MeI, MeLi (1.6 mol/L in Et_2O), and *n*-BuLi (1.6 mol/L in hexanes) were purchased from Aldrich and used as received. Alkyllithium reagents were titrated prior to use. Me_2SiHCl and Me_3SiCl were distilled over CaH_2 and degassed prior to use. $MesP{=}CPh_2$, **1**, was prepared following literature procedures (21, 22). $ClP(NEt_2)_2$ was prepared from an adaptation of a literature method (33). A solution of $HNEt_2$ (190 mL, 1.84 mol) and CH_2Cl_2 (300 mL) was added slowly to a cooled (–78 °C) solution of PCl_3 (40 mL, 0.46 mol) in CH_2Cl_2 (250 mL). The reaction mixture was slowly warmed to room temperature and stirred for 1 h, and the solvent was removed in vacuo. The resulting solid was extracted with hexanes (3 × 150 mL) and filtered. Hexanes was removed in vacuo. The resulting oil was distilled under vacuum, yielding a colorless liquid (89 g, 92%). $^{31}P\{^1H\}$ NMR (C_6D_6, 121.5 MHz): δ = 154.8. ^1H NMR (C_6D_6, 300 MHz): δ = 2.9–3.1 (m, 8H, CH_2); 0.94 (t, 12H, $^3J_{HH}$ = 7 Hz, CH_3).

^{31}P, ^1H, and $^{13}C\{^1H\}$ NMR spectra were recorded on Bruker AV300 or AV400 spectrometers at room temperature. Solid-state NMR experiments were performed on a Bruker Avance DSX400 spectrometer operating at frequencies of 400.13 MHz and 161.98 MHz for ^1H and ^{31}P respectively, using a Bruker triple resonance 4mm MAS probe. Chemical shifts for ^{31}P NMR spectra are reported relative to H_3PO_4 as an external standard (85% in H_2O, δ = 0). Chemical shifts for $^{13}C\{^1H\}$ NMR spectra are reported relative to CD_2Cl_2 (δ = 54.0) or $CDCl_3$ (δ = 77.2). Chemical shifts for ^1H NMR spectra are reported relative to residual $CHDCl_2$ (δ = 5.32) or $CHCl_3$ (δ = 7.27) or C_6HD_5 (δ = 7.16). Mass spectra were recorded on a Kratos MS 50 instrument. Elemental analyses were performed by Mr. Minaz Lakha in the Departmental Microanalysis Facility.

Preparation of Mes(Me)P–CPh_2Li (3a)

Typical procedure

To a cooled (–78 °C) solution of phosphaalkene **1** (2.06 g, 6.5 mmol) in THF or Et_2O (~150 mL) was slowly added MeLi in Et_2O (5.2 mL, 1.5 mol/L, 7.8 mmol). Upon addition, there was an immediate color change from yellow to dark red. The cooled solution was stirred for 1 h and then warmed to room temperature where it was stirred for an additional 1 h. The concentration for use in subsequent steps was 0.043 mol/L (see preparation of **4a**). $^{31}P\{^1H\}$ NMR spectroscopy of an aliquot removed from the reaction mixture showed a single signal (δ = −42.0 in THF, −44.3 in Et_2O).

Preparation of Mes(*n*-Bu)P–CPh_2Li (3b)

To a stirred yellow solution of **1** (0.64 g, 2.0 mmol) in Et_2O (~30 mL) at –78 °C, a solution of *n*-BuLi in hexanes (3.0 mL, 1.4 mol/L, 4.2 mmol) was added rapidly. The mixture turned bright orange upon addition and was stirred at –78 °C for 30 min. Subsequently, the solution was warmed to room temperature where it was stirred for an additional 1 h. Over this time, the solution turned from bright orange to red. The reaction was monitored by $^{31}P\{^1H\}$ NMR spectroscopy, affording a single signal for **3b** (δ = –31.1). This solution was used in the preparation of **4b**.

Preparation of Mes(Me)P–CPh_2H (4a)

To a stirred red solution of **3a** in THF (150 mL, 0.043 mol/L, 6.4 mmol) was added degassed MeOH (0.4 mL). From the resultant colorless solution, THF was removed in vacuo, affording a white solid residue. The soluble fraction was extracted into hexanes (3 × 50 mL), and the resultant solution was evaporated to dryness, affording a yellow oil. The oil was dissolved in minimal hexanes at reflux (~5 mL). The solution was slowly cooled to room temperature to afford colorless crystals suitable for X-ray diffraction.

Yield: 0.50 g (24%). $^{31}P\{^1H\}$ NMR (CD_2Cl_2, 121.5 MHz): δ = –24.0 (s). ^1H NMR (CD_2Cl_2, 300 MHz): δ = 7.58 – 7.10 (m, 10H, Ph–*H*), 6.77 (s, 2H, *m*-Mes–*H*), 4.87 (d, $^2J_{HP}$ = 5 Hz, 1H, CPh_2H), 2.52 (s, 6H, *o*-Mes–CH_3), 2.21 (s, 3H, *p*-Mes–CH_3), 1.31 (d, $^2J_{HP}$ = 6 Hz, 3H, P–CH_3). $^{13}C\{^1H\}$ NMR (CD_2Cl_2, 75.5 MHz) (unassigned): δ = 146.0 (d, J_{CP} = 15 Hz), 144.3, 144.1, 144.0, 143.8 (4 × s or 2 × d), 140.4 (s), 131.4–127.4 (m), 52.8 (d, $^1J_{CP}$ = 16 Hz), 24.6, 24.4 (2 × s or 1 × d), 10.8 (d, $^1J_{CP}$ = 18 Hz, P–CH_3). MS (EI, 70 eV) *m*/*z* (%): 332 (28) [M^+], 167 (100) [$CHPh_2^+$], 165 (44) [M^+ – $CHPh_2$], 119 (12) [Mes^+].

Preparation of Mes(*n*-Bu)P–CPh_2H (4b)

To a stirred solution of carbanion **3b** in Et_2O (2.0 mmol) was added dropwise degassed H_2O until the reaction mixture turned pale yellow (several drops). The mixture was then dried with $MgSO_4$, filtered, and the soluble fraction was extracted with Et_2O (2 × 10 mL). The solvent was removed in vacuo at 60 °C to afford pure **4b** as a pale yellow oil.

Yield: 0.65 g (85 %). ^{31}P NMR (CD_2Cl_2, 121.5 MHz): δ = –12.4 (s). ^1H NMR (CD_2Cl_2, 400 MHz) (assignments made with the aid of a COSY experiment): δ = 7.57 (d, $^3J_{HH}$ = 8 Hz, 2H, Ph–*H*), 7.36 (m, 4H, Ph–*H*), 7.24 (m, 1H, Ph–*H*), 7.15 (m, 2H, Ph–*H*), 7.06 (m, 1H, Ph–*H*), 6.77 (br s, 2H, *m*-Mes–*H*), 4.91 (d, $^2J_{PH}$ = 5 Hz, 1H, CPh_2H), 2.56 (br s, 6H, *o*-Mes–CH_3), 2.20 (s, 3H, *p*-Mes–CH_3), 2.02 (m, 1H, P–C*H*H), 1.55 (m, 1H, P–C*H*H), 1.22 (m, 2H, $CH_2CH_2CH_3$), 1.08 (m, 2H, PCH_2CH_2), 0.74 (t, $^3J_{HH}$ = 7 Hz, 3H, CH_2CH_3). $^{13}C\{^1H\}$ NMR (CD_2Cl_2, 100.6 MHz) (assignments made with the aid of HMQC/HMBC experiments): δ = 143.6 (d, $^2J_{CP}$ = 12 Hz, *i*-Ph–*C*), 143.4 (d, $^2J_{CP}$ = 13 Hz, *i*-Ph–*C*), 139.5 (s, *p*-Mes–*C*), 130.2 (br, *m*-Mes–*C*), 129.7 (d, $^1J_{CP}$ = 26 Hz, *i*-Mes–*C*), 129.5 (d, $^3J_{CP}$ = 9 Hz, *o*-Ph–*C*), 129.1 (s, *o*-Mes–*C*), 128.9 (d, $^3J_{CP}$ = 9 Hz, *o*-Ph–*C*), 128.6 (s, *p*-Ph–*C*), 127.1 (d, $^4J_{CP}$ = 2 Hz, *m*-Ph–*C*), 126.5 (d, $^4J_{CP}$ = 2 Hz, *m*-Ph–*C*), 51.6 (d, $^1J_{CP}$ = 16 Hz, *C*HPh_2), 30.2 (d, $^2J_{CP}$ = 20 Hz, P–CH_2CH_2), 25.5 (d, $^1J_{CP}$ = 16 Hz, P–*C*H_2), 24.7 (d, $^3J_{CP}$ = 13 Hz, $CH_2CH_2CH_3$), 23.8 (v br, *o*-Mes–*C*H_3), 21.2 (s, *p*-Mes–*C*H_3), 14.1 (s, CH_2CH_3). MS (EI, 70 eV) *m*/*z* (%): 374 (29) [M^+], 167 (100) [CPh_2H^+], 151 (24) [$PMes^+$]. Found (calcd.) (%): C, 83.81 (83.39); H, 8.55 (8.34).

Synthesis of Mes(Me)P–CPh_2Me (6a)

MeI (1.6 mL, 26 mmol) was added dropwise to a solution of **3a** in Et_2O (160 mL, 0.16 mol/L, 26 mmol). The solution was stirred for 30 min over which time its color changed from red to orange. The solvent was removed in vacuo, the soluble fraction was extracted with hexanes, and evaporated

© 2007 NRC Canada

to dryness. The product was purified by sublimation (140 °C, 0.1 mmHg).

Yield = 5.7 g (64 %). ^{31}P NMR ($CDCl_3$, 121.5 MHz): δ = –13.5 (s). ^{1}H NMR ($CDCl_3$, 300 MHz): δ = 7.47 (m, 2H, Ph–*H*), 7.21 (m, 6H, Ph–*H*), 7.01 (m, 2H, Ph–*H*), 6.74 (s, 2H, Mes–*H*), 2.23 (s, 3H, *p*-Mes–CH_3), 1.87 (br, 6H, *o*-Mes–CH_3), 1.70 (d, $^2J_{PH}$ = 13 Hz, 3H, P–CH_3), 1.39 (d, $^3J_{PH}$ = 7 Hz, 3H, CPh_2CH_3). ^{13}C{^{1}H} NMR ($CDCl_3$, 75.5 MHz,) (unassigned): δ = 148.3 (d, J_{CP} = 14 Hz), 146.3 (d, J_{CP} = 16 Hz), 144.7 (s), 138.8 (s), 129.9 (s), 128.7–127.4 (m), 125.8 (s), 125.4 (s), 49.1 (d, J_{CP} = 24 Hz), 28.8 (d, J_{CP} = 15 Hz), 23.5 (d, J_{CP} = 18 Hz), 20.8 (s), 9.0 (d, $^1J_{CP}$ = 21 Hz, P–CH_3). MS (EI, 70 eV) *m*/*z* (%): 346 (7) [M^+], 181 (100) [M^+ – P(Mes)(CH_3)], 165 (16) [M^+ – $CPh_2(CH_3)$], 119 (5) [Mes^+].

Preparation of Mes(Me)P–CPh_2–$P(NEt_2)_2$ (7a)

To a cooled (0 °C) solution of **3a** in THF (20 mL, 0.32 mol/L, 6.4 mmol) was slowly added a solution of $ClP(NEt_2)_2$ (1.50 g, 7.1 mmol) in THF (20 mL). An aliquot was removed from the yellow reaction mixture for ^{31}P NMR spectroscopic analysis. After evaporation of the volatiles in vacuo, the soluble fraction was extracted into toluene (30 mL). Removal of the toluene in vacuo afforded the crude product, which was washed with hexanes at –78 °C two times. Crystals suitable for X-ray diffraction were obtained from slow evaporation of a saturated toluene solution.

Yield: 1.73 g (54%). ^{31}P NMR ($CDCl_3$, 121.5 MHz): δ = 105.3 (d, $^2J_{PP}$ = 205 Hz, *P*N_2), –9.4 (d, $^2J_{PP}$ = 205 Hz, *P*Mes). ^{31}P MAS NMR (8.5 kHz, recycle delay of 20 s, 162.0 MHz): δ = 108.3 (d, $^2J_{PP}$ = 255 Hz, *P*N_2), –7.9 (d, $^2J_{PP}$ = 255 Hz, *P*Mes). ^{1}H NMR ($CDCl_3$, 400 MHz) δ = 7.79 (br, 2H, Ph–*H*), 7.43 (br, 2H, Ph–*H*), 7.28–7.14 (m, 6H, Ph–*H*), 6.90 (br, 1H, *m*-Mes–*H*), 6.55 (br, 1H, *m*-Mes–*H*), 3.01–2.52 (m, 11H, NCH_2 and *o*-Mes–CH_3), 2.25 (s, 3H, *p*-Mes–CH_3), 1.38 (d, $^2J_{PH}$ = 9 Hz, 3H, P–CH_3), 0.97 (m, 9H, NCH_2CH_3 and *o*-Mes–CH_3), 0.84 (t, 6H, $^3J_{HH}$ = 7 Hz, NCH_2CH_3). ^{13}C{^{1}H} NMR ($CDCl_3$, 100.6 MHz) (assignments made with the aid of HMQC/HMBC experiments): δ = 147.7 (s, *o*-Mes–*C*), 141.3 (br, Ar–*C*), 141.0 (t, J_{PC} = 5 Hz, Ar–*C*), 138.6 (s, *p*-Mes–*C*), 131.9–127.6 (m, Ar–*C*), 126.9 (s, Ar–*C*), 126.4 (s, Ar–*C*), 124.8 (d, J_{PC} = 4 Hz, Ar–*C*), 63.9 (dd, $^1J_{PC}$ = 46 and 34 Hz, P–*C*Ph_2–P), 44.5 (d, $^2J_{PC}$ = 21 Hz, N–*C*H_2), 44.0 (d, $^2J_{PC}$ = 20 Hz, N–*C*H_2), 26.2 (br s, *o*-Mes–*C*H_3), 21.6 (br s, *o*-Mes–*C*H_3), 21.0 (s, *p*-Mes–*C*H_3), 14.5 (d, $^3J_{PC}$ = 3 Hz, NCH_2CH_3), 14.0 (d, $^3J_{PC}$ = 5 Hz, NCH_2CH_3), 9.7 (t, $^1J_{PC}$ = 22 Hz, P–*C*H_3).

Preparation of Mes(Me)P–CPh_2–$SiMe_2H$ (8a)

To the red solution of **3a** (40 mL, 0.079 mol/L, 3.2 mmol) in THF (40 mL), neat Me_2HSiCl (0.5 mL, 4.6 mmol) was added. An immediate color change to yellow was observed. The solvent was removed in vacuo, and the residue was dissolved in hexanes (3 × 5 mL). Following solvent evaporation, the crude product was recrystallized from a minimal amount of hot hexanes in an inert atmosphere to afford large colorless crystals.

Yield: 0.62 g (50%). ^{31}P NMR (C_6D_6, 121.5 MHz): δ = –23.9 (s). ^{1}H NMR (C_6D_6, 300 MHz): δ = 7.70 (br s, 2H, Ph), 7.3–6.5 (m, 10H, Ph and *m*-Mes–*H*), 4.58 (br s, 1H, Si–*H*), 3.1 (br s, 3H, *o*-Mes–CH_3), 2.18 (s, 3H, *p*-Mes–CH_3), 1.45 (d, $^2J_{PH}$ = 8 Hz, 3H, P–CH_3), 1.1 (br s, 3H, *o*-Mes–CH_3), 0.10 (d, $^3J_{HH}$ = 3 Hz, 3H, Si–CH_3), 0.05 (d, $^3J_{HH}$ = 3 Hz, 3H, Si–CH_3). ^{13}C{^{1}H} NMR (CD_2Cl_2, 75.5 MHz) (assignments made with the aid of HMQC/HMBC experiments): δ = 147.6 (s, Mes–*C*), 147.3 (s, Mes–*C*), 142.5 (s, Mes–*C*), 142.1 (d, $^1J_{PC}$ = 7 Hz, *i*-Mes–*C*), 139.5 (s, Mes–*C*), 131–128 (m, Ph–*C*), 125.7 (s, Ph–*C*), 45.7 (d, $^1J_{PC}$ = 45 Hz, P*C*Ph_2), 21.2 (s, *p*-Mes–*C*H_3), 7.81 (d, $^1J_{PC}$ = 23 Hz, P*C*H_3), –3.96 (d, $^3J_{PC}$ = 5 Hz, Si*C*H_3), –5.66 (d, $^3J_{PC}$ = 6 Hz, Si*C*H_3). MS (EI, 70 eV) *m*/*z* (%): 390 (38) [M^+], 375 (17) [M^+ – CH_3], 332 (45) [M^+ – $SiMe_2$], 223 (69) [M^+ – PMesMe], 167 (100) [CPh_2^+]. Found (calcd.) (%): C, 77.20 (76.88); H, 7.64 (8.00).

Preparation of Mes(Me)P–CPh_2–$SiMe_3$ (9a)

To the red solution of **3a** in Et_2O (22 mL, 0.14 mol/L, 3.2 mmol), neat Me_3SiCl (0.4 mL, 3.2 mmol) was added. An immediate color change to yellow was observed accompanied by the formation of a white precipitate. The solution was filtered, the solvent was removed in vacuo, and the soluble fraction was extracted into Et_2O (3 × 15 mL). The Et_2O was removed in vacuo. The crude product was dissolved in a minimal amount of hexanes, and slow evaporation afforded colorless crystals suitable for X-ray crystallography.

Yield = 0.18 g (14%). ^{31}P NMR ($CDCl_3$, 121.5 MHz): δ = –25.4 (s). ^{1}H NMR ($CDCl_3$, 300 MHz): δ = 7.6 (br s, 2H, Ph), 7.3–7.1 (m, 8H, Ph), 6.8 (br s, 2H, *m*-Mes–*H*), 2.8 (br s, *o*-Mes–CH_3), 2.22 (s, 3H, *p*-Mes–CH_3), 1.33 (d, $^2J_{PH}$ = 8 Hz, 3H, P–CH_3), 0.9 (br s, 3H, *o*-Mes–CH_3), –0.02 (s, 9H, $Si(CH_3)_3$). MS (EI, 70 eV) *m*/*z* (%): 404 (100) [M^+], 389 (26) [M^+ – CH_3], 331 (44) [M^+ – $SiMe_3$], 167 (39) [M^+ – CPh_2SiMe_3], 73 (34) [M^+ – MesMePCPh_2].

X-ray crystallography

Crystal data and refinement parameters are listed in Table 1. Additional data are available in the Supplementary data.[2] All single crystals were immersed in oil and mounted on a glass fiber. Data for **4a** were collected on a Bruker X8 APEX diffractometer with graphite-monochromated Mo Kα radiation. Data for **7a**, **8a**, and **9a** were collected on a Bruker X8 APEX II diffractometer. Data were collected and integrated using the Bruker SAINT software package (34). All structures were solved by direct methods and subsequent Fourier difference techniques and were refined anisotropically for all non-hydrogen atoms. Hydrogen atoms were included in idealized positions and refined isotropically except in **4a** where they were not refined. All data sets were corrected for Lorentz and polarization effects. All calculations were performed using the SHELXTL crystallographic software package from Bruker-AXS (35).

Compounds **4a**, **8a**, and **9a** did not show any crystallographic complexity. Compound **7a** was a split crystal, and cell_now (within SAINT) was used to determine that the second domain was rotated from the first domain by 4.4°. Only the first domain was integrated because there was little or no overlap between the two lattices. One of the ethyl groups was disordered at C(28) and C(29). The disorder at carbon was modeled by including two additional carbon at-

© 2007 NRC Canada

oms [C(28b) and C(29b)] and refining their respective populations [occupancy: 0.78(2) and 0.22(2)].

Acknowledgement

This work was supported by the Natural Sciences and Engineering Research Council (NSERC) of Canada. The Canada Foundation for Innovation (CFI) and The British Columbia Knowledge Development Fund (BCKDF) are gratefully acknowledged for infrastructure support. The authors wish to thank to Dr. Brian O. Patrick for assistance with X-ray crystallography and Dr. Richard Darton and Professor Colin Fyfe for acquiring the solid-state NMR spectrum of **7a**.

References

1. K.B. Dillon, F. Mathey, and J.F. Nixon. Phosphorus: the carbon copy. Wiley, West Sussex, England. 1998.
2. F. Mathey. Angew. Chem., Int. Ed. **42**, 1578 (2003).
3. R. Appel. *In* Multiple bonds and low coordination in phosphorus chemistry. *Edited by* M. Regitz and O.J. Scherer. Thieme, Stuttgart. 1990. Chap. D4.
4. P. Le Floch. Coord. Chem. Rev. **250**, 627 (2006).
5. M. Freytag, S. Ito, and M. Yoshifuji. Chem. Asian J. **1**, 693 (2006).
6. B. Deschamps, X. Le Goff, L. Ricard, and P. Le Floch. Heteroat. Chem. **18**, 363 (2007).
7. L. Weber. Angew. Chem., Int. Ed. **41**, 563 (2002).
8. T. Baumgartner and R. Réau. Chem. Rev. **106**, 4681 (2006).
9. V.A. Wright, B.O. Patrick, C. Schneider, and D.P. Gates. J. Am. Chem. Soc. **128**, 8836 (2006).
10. V.A. Wright and D.P. Gates. Angew. Chem., Int. Ed. **41**, 2389 (2002).
11. K.J.T. Noonan and D.P. Gates. Angew. Chem., Int. Ed. **45**, 7271 (2006).
12. C.-W. Tsang, M. Yam, and D.P. Gates. J. Am. Chem. Soc. **125**, 1480 (2003).
13. C.-W. Tsang, B. Baharloo, D. Riendl, M. Yam, and D.P. Gates. Angew. Chem., Int. Ed. **43**, 5682 (2004).
14. B.H. Gillon and D.P. Gates. Chem. Commun. 1868 (2004).
15. T.A. van der Knaap and F. Bickelhaupt. Tetrahedron Lett. **23**, 2037 (1982).
16. B.-L. Li and R.H. Neilson. Inorg. Chem. **23**, 3665 (1984).
17. Z.-M. Xie, P. Wisian-Neilson, and R.H. Neilson. Organometallics, **4**, 339 (1985).
18. R. Appel, C. Casser, and F. Knoch. Chem. Ber. **119**, 2609 (1986).
19. For examples, see: (*a*) S. Ito, H. Miyake, M. Yoshifuji, T. Höltzl, and T. Veszprémi. Chem. Eur. J. **11**, 5960 (2005); (*b*) S. Ito, H. Miyake, H. Sugiyama, and M. Yoshifuji. Tetrahedron Lett. **45**, 7019 (2004); (*c*) A. Moores, L. Ricard, and P. Le Floch. Angew. Chem., Int. Ed. **42**, 4940 (2003); (*d*) G. Märkl and A. Merz. Tetrahedron Lett. **32**, 3611 (1968); (*e*) G. Märkl, F. Lieb, and A. Merz. Angew. Chem., Int. Ed. **6**, 87 (1967).
20. For examples, see: (*a*) S. Ito, M. Freytag, and M. Yoshifuji. Dalton Trans. 710 (2006); (*b*) S. Ito, K. Toyota, and M. Yoshifuji. Chem. Commun. 1637 (1997); (*c*) M. Yoshifuji, H. Kawanami, Y. Kawai, K. Toyota, M. Yasunami, T. Niitsu, and N. Inamoto. Chem. Lett. 1053 (1992); (*d*) S. J. Goede, and F. Bickelhaupt. Chem. Ber. **124**, 2677 (1991).
21. G. Becker, W. Uhl, and H.-J. Wessely. Z. Anorg. Allg. Chem. **479**, 41, (1981).
22. M. Yam, J.H. Chong, C.W. Tsang, B.O. Patrick, A.E. Lam, and D.P. Gates. Inorg. Chem. **45**, 5225 (2006).
23. For details of the Tolman method, see: C.A. Tolman. Chem. Rev. **77**, 313 (1977).
24. CRC handbook of chemistry and physics. 84th ed. CRC Press, Boca Raton, Florida. 2003.
25. P. Maire, S. Deblon, F. Breher, J. Geier, C. Böhler, H. Rüegger, H. Schönberg, and H. Grützmacher. Chem. Eur. J. **10**, 4198 (2004).
26. B. Manz, and G. Maas. J. Chem. Soc., Chem. Commun. 25 (1995).
27. A.D. Burrows, M.F. Mahon, S.P. Nolan, and M. Varrone. Inorg. Chem. **42**, 7227 (2003).
28. L. Pauling. The nature of the chemical bond and the structure of molecules and crystals: an introduction to modern structural chemistry. 3rd ed. Cornell University Press, New York. (1960).
29. P.W. Dyer, J. Fawcett, M.J. Hanton, R.D.W. Kemmitt, R. Padda, and N. Singh. Dalton Trans. 104 (2003).
30. F. Dahan, P.W. Dyer, M.J. Hanton, M. Jones, D.M.P. Mingos, A.J.P. White, D.J. Williams, and A.M. Williamson. Eur. J. Inorg. Chem. 732 (2002).
31. I. Shevchenko, V. Andrushko, E. Lork, and G.V. Röschenthaler. Eur. J. Inorg. Chem. 2985 (2002).
32. S.A. Reiter, S.D. Nogai, and H. Schmidbaur. Dalton Trans. 247 (2005).
33. P.G. Chantrell, C.A. Pearce, C.R. Torer, and R.J. Twaits. J. Appl. Chem. **14**, 563 (1964).
34. SAINT V [computer program]. 7.03A ed. Bruker AXS Inc., Madison, Wisconsin. 1997–2003.
35. SHELXTL V [computer program]. 5.1 ed. Bruker AXS Inc., Madison, Wisconsin. 1997.

© 2007 NRC Canada

Structural finding of *R/S*-3,4-dihydro-2,2-dimethyl-6-halo-4-(substituted phenylaminocarbonylamino)-2*H*-1-benzopyrans as selective pancreatic β-cells $K_{ATP\text{-}p\beta}$ channel openers

Sk. Mahasin Alam, Soma Samanta, Amit Kumar Halder, Soumya Basu, and Tarun Jha

Abstract: *R*/*S*-3,4-Dihydro-2,2-dimethyl-6-halo-4-(substituted phenylaminocarbonyl-amino)-2*H*-1-benzopyrans are pancreatic β-cells potassium ($K_{ATP\text{-}p\beta}$) channel openers with inhibitory effect on insulin secretion. To find the more active and effective benzopyrans as selective potassium ($K_{ATP\text{-}p\beta}$) channel openers towards the pancreatic tissues, quantitative structure–activity relationships (QSAR) study was performed using E-state and R-state indices along with Wang–Ford charges, *n*-octanol/water partition coefficient, molar refractivity, and indicator parameters. QSAR models were developed by statistical techniques, e.g., multiple linear regression (MLR), principle component regression analysis (PCRA), and partial least squares (PLS) analysis. The generated equations were validated by the leave-one-out cross-validation method. The models show the importance of ETSA indices of atom numbers 16, 17, 18, 19, 21 as well as 22. The positive coefficient of S_{16}, S_{17}, S_{18}, S_{19}, S_{21}, and S_{22} indicate that with the increase of the value of E-state indices, desired activity decreases. RTSA index is also important for the biological activity, and the atom numbers 16, 17, 18, 19, 20 and 22 are involved in van der Waals interactions. RTSA index also possesses negative impact on the inhibition of residual insulin secretion. Wang–Ford charges of some particular atoms are also important for the inhibition. Increase of *n*-octanol/water partition coefficients of compounds inhibit insulin secretion, and the presence of chlorine atom at *m*- and *p*- positions of the phenyl ring B is necessary for the inhibition of residual insulin secretion.

Key words: benzopyran derivatives, potassium channel openers, PCRA, PLS, QSAR.

Résumé : Les *R*/*S*-3,4-dihydro-2,2-diméthyl-6-halogéno-4-(phénylaminocarbonylamino substitué)-2*H*-1-benzopyranes provoquent l'ouverture des canaux du potassium des cellules β du pancréas ($K_{ATP\text{-}p\beta}$) et de ce fait conduisent à une inhibition de la sécrétion de l'insuline. Dans le but de trouver des benzopyranes plus actifs et plus efficaces pour l'ouverture des canaux du potassium des cellules β du pancréas ($K_{ATP\text{-}p\beta}$) vis-à-vis des tissus du pancréas, on a réalisé une étude « QSAR » en utilisant des indices des états E et R ainsi que les charges de Wang-Ford, le coefficient de partage *n*-octanol/eau, la réfractivité molaire et les paramètres indicateurs. On a développé les modèles « QSAR » à l'aide de techniques statistiques, soit la régression linéaire multiple (RLM), l'analyse de la régression du composant principal (ARCP) et l'analyse des moindres carrés partiels (MCP). On a validé les équations générées par la méthode de validation croisée où on ne tient pas compte d'une valeur. Les modèles mettent en évidence l'importance des indices « ETSA » des numéros atomiques 16, 17, 18, 19, 21 ainsi que 22. Le coefficient positif de S_{16}, S_{17}, S_{18}, S_{19}, S_{21}, et S_{22} indique que l'augmentation de la valeur des indices de l'état E est accompagnée d'une diminution de l'activité recherchée. L'indice « RTSA » est aussi important pour l'activité biologique et les numéros 16, 17, 18, 19, 20 et 22 sont impliqués dans les interactions de van der Waals. L'indice « RSTA » possède aussi un impact négatif sur l'inhibition de la sécrétion résiduelle de l'insuline. Les charges de Wang-Ford de certains atomes sont aussi importants pour l'inhibition. L'augmentation des coefficients de partage *n*-octanol/eau des composés inhibe la sécrétion de l'insuline et la présence d'atomes de chlore dans les positions *m*- et *p*- du noyau aromatique B est nécessaire pour l'inhibition de la sécrétion résiduelle de l'insuline.

Mots-clés : dérivés benzopyrane, ouverture des canaux du potassium, ARCP, MCP, « QSAR ».

[Traduit par la Rédaction]

Received 18 July 2007. Accepted 11 October 2007. Published on the NRC Research Press Web site at canjchem.nrc.ca on 22 November 2007.

S.M. Alam, S. Samanta, A.K. Halder, S. Basu, and T. Jha.[1] Medicinal and Pharmaceutical Chemistry, Department of Pharmaceutical Technology, P.O. Box 17020, Jadavpur University, Kolkata 700 032, India.

[1]Corresponding author (e-mail: tjupharm@yahoo.com).

 doi:10.1139/V07-127 © 2007 NRC Canada

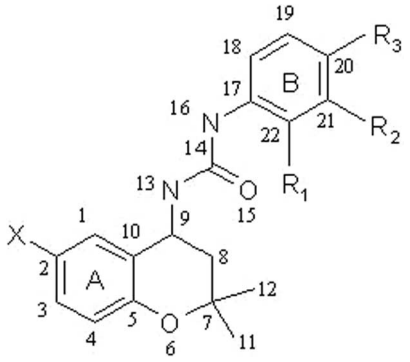
Introduction

Potassium channels are ion channels. The specificity of ion channels depends on the selectivity towards a specific inorganic ion and these are gated by the specific stimulus. Depending on the stimulus, these may be of voltage gated, mechanically gated or ligand gated. The ligand is either a neurotransmitter or a nucleotide (1). Potassium (K^+) channels have an entrance pore of about 0.4 nm (which is the size of dehydrated potassium ion) (2). When K^+ channels are opened, the cell hyperpolarizes i.e., inhibited. K^+ channel blocking, on the other hand, leads to the depolarization. K^+ channels are mainly of four types i.e., voltage gated (delayed rectifier K_V, rapid delayed rectifier or K_{VR}, slow delayed rectifier or K_{VS}, transient outward current or K_A, inward rectifier or K_{IR}), calcium activated (high conductance BK_{Ca}, intermediate conductance IK_{Ca}, small conductance SK_{Ca}), receptor coupled (muscarinic activated K_m) and ATP sensitive K^+ channels (K_{ATP}) (3). From the clinical point of view, K_{ATP} are of particular interest. These were first found in heart (3), now known to be present in wide varieties of tissues including the secretary cells, e.g., insulin secreting pancreas β cells ($K_{ATP\text{-}p\beta}$), neurons, skeletal and smooth muscles. With an increase in the cellular ATP levels, these channels are blocked and the membrane potential decreases. When the [ATP]:[ADP] ratio falls, potassium efflux is increased and the hyperpolarization of the cell occurs which prevents the voltage operated Ca^{2+} channel from opening (4). The structure of the K_{ATP} channel is a subunit organization consisting of an inward rectifier channel K_{ir} (either K_{ir} 6.1 or K_{ir} 6.2) with sulfonylurea receptors (SUR) subunit. The combination of K_{ir} and SUR constitute a pore-forming octameric complex. SUR is a member of ABC transporter protein and is a transmembrane protein containing 15 transmembrane sequences and two large cytosolic loops. SUR receptors have two isoforms, SUR1 (high affinity) and SUR2 (SUR2A and SUR2B – both low affinity). SUR1/K_{ir} 6.2 constitute the neuronal and the pancreatic β cells, SUR2A/K_{ir} 6.2 are present in the cardiac K_{ATP} channels and SUR2B/K_{ir} 6.1 or 6.2 constitute the vascular smooth muscle K_{ATP} channels (5).

Because K_{ATP} channel activation leads to the hyperpolarization of cells, it results in different physiological responses like smooth muscle relaxation, vasodilatation, insulin release inhibition, shortening of cardiac action potential. Thus, potassium (K_{ATP}) channel openers (PCOs), which antagonize the action of ATP, can be used in several disorders like hyperglycemia, hypertension, angina pectoris, asthma etc. Nicorandil (the drug which combines the action of K_{ATP} channel opening and nitrovasodilatory effects) is used in angina pectoris and hypertension. Cromokalim and its active isomer lemakalim are also used in hypertension (6). Minoxidil and diazoxide are used in the treatment of severe hypertension and in alopecia (7). Some benzopyran derivatives are now being used in the treatment of asthma. *R*/*S*-3,4-dihydro-2,2-dimethyl-6-halo-4-(substituted phenylaminocarbonylamino)-2*H*-1-benzopyrans are a new series of potassium ($K_{ATP\text{-}p\beta}$) channel openers selective towards pancreatic β cells (8).

To find the structural requirements for the more active and selective pancreatic β-cells potassium ($K_{ATP\text{-}p\beta}$) channel openers, quantitative structure-activity relationships (QSAR) study was performed on *R*/*S*-3,4-dihydro-2,2-dimethyl-6-halo-4-(substituted phenylamino-carbonylamino)-2*H*-1-benzopyrans as a part of our composite program of rational drug design (9–18). The general structure of these compounds is shown in Fig. 1.

Fig. 1. General structure of *R*/*S*-3,4-dihydro-2,2-dimethyl-6-halo-4-(substituted phenylaminocarbonylamino)-2*H*-1-benzopyrans with arbitrary numbering.



Three statistical analyses, e.g., multiple linear regression analysis (MLR), principle component regression analysis (PCRA) and partial least square (PLS) were used in the QSAR study to find out the structural requirement of this series of compounds.

Materials and methods

Dataset and parameters

The percentage of residual insulin secretion (PRIS) data of *R*/*S*-3,4-dihydro-2,2-dimethyl-6-halo-4-(substituted phenylaminocarbonylamino)-2*H*-1-benzopyrans was collected from the published work of Sebille et al. (8). PRIS is the measure of the percentage of insulin release from pancreatic islets isolated from adult fed Wistar rats. PRIS was converted to the logarithmic scale. The logarithm of the percentage of residual insulin secretion (Log PRIS) was used as the response variable in the present study and shown in Table 1. For the measurement of insulin secretion, isolated pancreatic islets from rats were used (8). Insulin release was measured radio-immunologically and expressed in terms of the percentage of residual insulin secretion (PRIS).

Topological indices like ETSA and RTSA indices (19–22) as well as Wang–Ford charges (q_x), n-octanol/water partition coefficient (log *P*), molar refractivity (MR) and indicator parameters are used as the predictor variables. ETSA and RTSA indices were calculated using the computer program "Mouse" (23). In the program, molecular connection table in a specified format is given along with the intrinsic state values of different atoms as inputs. Common atoms of molecule were numbered consecutively keeping the serial number same in all molecules. Wang–Ford charges, n-octanol/water partition coefficient (Log *P*) and molar refractivity (MR) were calculated using *Chem* 3D *Pro* package (24). Wang–Ford charges (q_x) were calculated from the energy minimized geometry. The energy minimization was done by using RHF (restricted Hartree-Fock: closed shell) wave function. Log *P* and MR were calculated based on Ghose and Crippen's fragmentation method. Indicator parameters were also used to find the role of the specific substituent(s)

© 2007 NRC Canada

Table 1. Percentage of residual insulin secretion data of *R/S*-3,4-dihydro-2,2-dimethyl-6- halo-4-(substituted phenylaminocarbonylamino)-2*H*-1-benzopyrans.

Cpd No.	X	R_1	R_2	R_3	PRIS[a]	Log PRIS
1	F	H	H	H	83.8±3.5	1.923
2	Cl	H	H	H	87.7±3.5	1.943
3	Br	H	H	H	75.9±4.0	1.880
4	F	OCH_3	H	H	88.4±4.8	1.946
5	Cl	OCH_3	H	H	94.6±3.7	1.976
6	Br	OCH_3	H	H	72.8±5.5	1.862
7	F	H	OCH_3	H	66.6±3.3	1.823
8	Cl	H	OCH_3	H	84.0±4.8	1.924
9	Br	H	OCH_3	H	73.5±4.0	1.866
10	F	H	H	OCH_3	89.0±3.9	1.949
11	Cl	H	H	OCH_3	79.3±4.6	1.899
12	Br	H	H	OCH_3	79.2±3.7	1.899
13	F	CH_3	H	H	79.0±3.3	1.898
14	Cl	CH_3	H	H	85.0±3.1	1.929
15	Br	CH_3	H	H	79.5±3.5	1.900
16	F	H	CH_3	H	75.2±2.7	1.876
17	Cl	H	CH_3	H	65.8±4.4	1.818
18	Br	H	CH_3	H	63.4±3.1	1.802
19	F	H	H	CH_3	70.6±3.8	1.849
20	Cl	H	H	CH_3	69.5±3.4	1.842
21	Br	H	H	CH_3	72.9±4.0	1.863
22	F	Cl	H	H	51.4±3.1	1.711
23	Cl	Cl	H	H	40.3±1.5	1.605
24	Br	Cl	H	H	41.8±3.5	1.621
25	F	H	Cl	H	28.0±1.5	1.447
26	Cl	H	Cl	H	25.0±1.3	1.398
27	Br	H	Cl	H	28.6±1.7	1.456
28	F	H	H	Cl	22.8±1.2	1.358
29	Cl	H	H	Cl	34.6±1.9	1.539
30	Br	H	H	Cl	25.7±1.5	1.410

[a]PRIS indicates percentage of residual insulin secretion (mean ± SEM).

at the specific position(s) towards the biological activity. I_ClR_2 and I_ClR_3 indicate the presence or the absence of chlorine atom at R_2 and R_3 positions respectively in the general structure.

Statistical analysis

Three statistical methods i.e., MLR, PCRA, and PLS were employed to develop QSAR models and briefly described in the following sections.

Multiple linear regressions (MLR)

The correlation analysis was carried out on the data set containing the response variable and all descriptors. Intercorrelated parameters were removed. All possible combinations of parameters were considered for the multiple regression analysis (25). Statistical qualities of MLR equations were judged by parameters like correlation coefficient (R), adjusted R^2 (R^2_a), variance ratio (F), probability factor related to F-ratio (p), and standard error of estimate (s).

Principle component regression analysis (PCRA)

In PCRA, the factor scores are used as the independent variables. Factor scores were obtained from factor analysis after *VARIMAX* rotation (26–29). The factor analysis was carried out on the data matrix containing all the independent variables. Regression analysis was performed using factor scores as the predictor variables. The factor loadings of all the variables are shown in Table 2.

Partial least square (PLS)

In PLS, the latent variables or components were determined which are linear combinations of the original variables (30). To avoid over fitting, the number of components were selected by the cross-validation method. The predicted variables were selected on the basis of the standardized regression coefficients. Variables with smaller standardized coefficients were removed from PLS regression. The PLS regression model was developed using variables with the larger standardized coefficients.

Validation of QSAR models

The predictive powers of MLR, PCRA and PLS models were validated by Leave-One-Out (LOO) cross-validation method. The predicted residual sum of square (*PRESS*), total sum of squares (*SSY*), cross-validated R^2 (R^2_{cv}), standard deviation error of prediction (*SDEP*) and Standard error of

© 2007 NRC Canada

Table 2. Factor loadings of variables after *VARIMAX* rotation.

Variables	*F*1	*F*2	*F*3	*F*4	*F*5	*F*6	*F*7	*F*8	*F*9	Communality
Log PRIS	0.041	0.387	0.369	–0.178	0.083	0.107	0.776	–0.081	–0.133	0.965
S_1	**–0.992**	0.068	–0.034	0.029	–0.014	–0.028	0.027	0.038	–0.012	0.993
S_2	**–0.991**	0.072	–0.045	0.024	–0.014	–0.030	0.010	0.041	–0.014	0.992
S_3	**–0.991**	0.071	–0.040	0.026	–0.014	–0.028	0.019	0.040	–0.014	0.993
S_4	**–0.992**	0.065	–0.026	0.034	–0.013	–0.027	0.040	0.035	–0.010	0.994
S_5	**–0.991**	0.038	–0.001	0.054	–0.011	–0.029	0.077	0.021	0.003	0.994
S_6	**–0.972**	0.097	0.029	0.024	0.031	–0.064	–0.025	–0.005	–0.002	0.961
S_7	**–0.976**	–0.037	0.048	0.108	–0.007	–0.036	0.150	–0.011	0.038	0.994
S_8	**–0.983**	–0.007	0.041	0.092	–0.007	–0.031	0.133	–0.002	0.023	0.995
S_9	**–0.984**	–0.008	0.033	0.093	–0.003	–0.033	0.118	0.002	0.025	0.994
S_{10}	**–0.992**	0.047	–0.011	0.049	–0.012	–0.028	0.060	0.026	–0.000	0.994
S_{11}	**–0.982**	0.028	0.049	0.074	–0.010	–0.021	0.155	0.003	0.013	0.997
S_{12}	**–0.982**	0.028	0.049	0.074	–0.010	–0.021	0.155	0.003	0.013	0.997
S_{13}	**–0.969**	0.071	0.094	0.065	–0.012	0.004	0.196	0.004	–0.000	0.996
S_{14}	**–0.870**	–0.115	0.222	0.227	0.031	–0.016	0.336	–0.071	0.077	0.996
S_{15}	–0.504	0.601	0.045	–0.326	–0.100	0.155	0.118	0.127	–0.207	0.830
S_{16}	**–0.725**	0.048	0.368	0.123	–0.025	0.072	0.475	–0.084	0.041	0.919
S_{17}	–0.423	–0.255	0.484	0.385	0.077	0.035	0.516	–0.166	0.137	0.946
S_{18}	–0.463	–0.158	0.268	0.230	–0.127	0.081	**0.742**	–0.077	0.086	0.950
S_{19}	–0.152	–0.266	–0.053	–0.190	–0.185	0.005	**0.852**	–0.014	0.021	0.893
S_{20}	–0.009	0.081	0.048	–0.163	**–0.902**	–0.072	0.346	0.036	–0.017	0.975
S_{21}	–0.171	–0.113	0.171	–0.551	0.422	0.182	0.399	–0.309	0.286	0.922
S_{22}	0.057	–0.050	0.106	**0.884**	0.299	–0.096	0.142	0.013	0.002	0.917
R_1	**0.990**	–0.024	0.049	–0.017	0.024	0.027	0.015	–0.030	0.001	0.986
R_2	**0.988**	–0.053	0.049	–0.012	0.022	0.024	0.016	–0.040	0.006	0.985
R_3	**0.989**	–0.037	0.049	–0.015	0.024	0.027	0.016	–0.035	0.002	0.985
R_4	**0.990**	–0.007	0.050	–0.018	0.027	0.028	0.016	–0.025	–0.004	0.986
R_5	**0.991**	0.015	0.055	–0.008	0.033	0.025	0.019	–0.015	–0.000	0.989
R_6	**0.989**	–0.046	0.066	0.029	0.035	0.008	0.031	–0.036	0.030	0.989
R_7	**0.990**	0.045	0.067	0.019	0.046	0.014	0.027	–0.002	0.012	0.990
R_8	**0.978**	0.147	0.052	–0.040	0.033	0.040	0.011	0.034	–0.030	0.988
R_9	**0.988**	0.084	0.056	–0.008	0.031	0.026	0.017	0.028	–0.001	0.989
R_{10}	**0.992**	0.004	0.057	–0.010	0.025	0.023	0.012	–0.017	0.002	0.989
R_{11}	**0.955**	0.229	0.050	–0.071	0.045	0.056	0.003	0.047	–0.069	0.984
R_{12}	**0.955**	0.232	0.046	–0.069	0.046	0.053	0.004	0.047	–0.069	0.984
R_{13}	**0.944**	0.249	0.056	–0.003	0.013	0.025	0.003	0.167	0.007	0.986
R_{14}	0.391	–0.015	0.027	–0.249	0.204	0.073	0.113	**–0.783**	–0.204	0.930
R_{15}	**0.884**	0.131	0.100	0.232	0.063	–0.058	0.036	0.232	0.131	0.941
R_{16}	0.617	**0.712**	0.049	–0.090	0.002	0.048	0.027	0.202	–0.002	0.942
R_{17}	0.398	**0.825**	0.006	–0.290	–0.021	0.046	0.044	0.042	0.004	0.930
R_{18}	0.090	–0.061	0.010	–0.181	0.154	0.230	–0.047	0.168	**0.734**	0.690
R_{19}	0.214	0.503	0.137	0.129	0.617	0.273	–0.067	0.203	–0.346	0.954
R_{20}	0.077	0.296	0.108	–0.149	**–0.874**	–0.025	0.077	0.117	–0.148	0.934
R_{21}	–0.005	0.072	0.122	–0.607	0.590	0.100	0.074	–0.249	0.237	0.869
R_{22}	0.067	0.056	–0.036	**0.872**	0.311	–0.156	–0.012	0.122	–0.115	0.918
q_1	**–0.944**	–0.062	–0.095	0.026	0.163	–0.063	0.081	0.103	–0.037	0.953
q_2	**0.977**	–0.058	0.069	0.004	–0.034	0.043	–0.030	–0.061	0.019	0.971
q_3	**–0.982**	0.074	–0.044	–0.020	0.022	–0.032	0.019	0.061	–0.016	0.978
q_4	**0.975**	–0.035	–0.021	0.116	–0.078	0.005	–0.034	–0.082	–0.002	0.980
q_5	**–0.877**	–0.182	0.223	–0.032	0.236	0.088	0.126	0.173	–0.028	0.963

© 2007 NRC Canada

Table 2. (*concluded*).

Variables	*F*1	*F*2	*F*3	*F*4	*F*5	*F*6	*F*7	*F*8	*F*9	Communality
q_6	0.065	0.227	**–0.908**	–0.016	–0.048	–0.050	–0.221	–0.093	0.053	0.946
q_7	0.231	–0.171	**0.870**	0.236	–0.111	0.079	0.099	0.018	–0.057	0.926
q_8	–0.246	0.111	**–0.808**	0.180	0.029	–0.424	0.075	–0.032	–0.054	0.948
q_9	0.545	–0.205	–0.128	–0.666	0.235	0.313	0.061	0.091	0.019	0.964
q_{10}	0.167	0.469	0.219	0.338	–0.553	–0.128	–0.193	–0.222	0.042	0.820
q_{11}	0.055	0.061	–0.608	**–0.705**	0.114	–0.064	0.179	0.003	0.066	0.927
q_{12}	0.029	0.143	**0.883**	0.070	–0.013	0.090	0.069	–0.108	0.077	0.837
q_{13}	–0.422	0.335	0.210	0.679	–0.174	0.193	–0.131	–0.057	0.031	0.885
q_{14}	0.166	**–0.871**	0.033	–0.041	0.225	–0.128	0.179	–0.162	0.156	0.938
q_{15}	–0.155	**0.736**	–0.518	0.086	–0.164	–0.170	–0.144	0.029	–0.075	0.925
q_{16}	–0.113	**0.751**	–0.169	0.408	–0.099	–0.273	–0.051	0.117	–0.209	0.917
q_{17}	0.087	**–0.878**	0.076	–0.376	–0.013	–0.006	–0.073	0.119	–0.097	0.955
q_{18}	–0.009	**0.803**	–0.002	0.020	0.014	0.528	0.111	–0.112	0.149	0.972
q_{19}	–0.105	–0.363	–0.192	0.155	0.039	**–0.867**	–0.174	–0.030	0.002	0.987
q_{20}	0.096	0.036	0.236	–0.009	0.289	**0.911**	0.056	0.049	0.005	0.986
q_{21}	–0.062	–0.023	–0.198	0.193	–0.002	**–0.810**	–0.042	0.233	–0.418	0.969
q_{22}	–0.066	**0.777**	–0.155	–0.008	–0.173	0.237	–0.001	–0.294	0.401	0.965
Log *P*	**–0.717**	–0.539	–0.209	–0.009	–0.138	–0.036	–0.146	0.001	0.102	0.903
MR	**–0.853**	0.275	–0.111	–0.076	0.081	0.088	–0.085	0.173	–0.196	0.911
Dipole	0.025	0.607	–0.344	–0.332	0.283	–0.002	–0.369	–0.080	–0.222	0.868
I_ClR_2	0.024	–0.079	–0.450	0.467	–0.440	0.420	–0.387	0.132	0.108	0.976
I_ClR_3	–0.033	–0.183	0.092	0.072	0.443	–0.419	–0.633	–0.188	0.199	0.895
Variance	0.488	0.109	0.072	0.075	0.056	0.057	0.055	0.021	0.022	0.950

Note: Factor loadings > 0.7 are shown in boldface.

PRESS (S_{PRESS}) were considered for the validation of QSAR models.

Results and discussion

The results of three statistical methods used to develop the QSAR models were discussed below under three different sections. For all statistical methods, the logarithm of the percentage of residual insulin secretion (log PRIS) was used as the response variable and shown in Table 1. The ETSA indices, RTSA indices and Wang–Ford charges of the selected atoms, n-octanol/water partition coefficients (log *P*) and indicator variables were used as the predictor variables to develop the QSAR models.

Multiple Linear Regressions (MLR)

Multiple Linear Regression analysis was performed to develop the QSAR models. Intercorrelated parameters were removed based on the correlation analysis. All the possible combinations of parameters were considered for the development of QSAR equations. Among all generated models four models are considered as better models based on the statistical qualities. Parameters selected for MLR models are listed in Table 3. Correlation matrix among the response variable and the selected parameters are shown in Table 4.

Combination of ETSA indices and log *P* yields the following equation:

$$\text{Log PRIS} = -4.676\ (\pm 0.575) + 2.134\ (\pm 0.233)\ S_{16} + 0.921\ (\pm 0.156)\ S_{19} + 0.067\ (\pm 0.020)\ S21 - 0.378\ (\pm 0.026)\log P \quad [1]$$

$n = 30$, $R = 0.968$, $R^2 = 0.937$,

$R^2_a = 0.927$, $F(4,25) = 92.851$, $p < 0.00001$,

s = 0.052, $SSY = 1.088$, $PRESS = 0.101$,

$R^2_{cv} = 0.907$, $SDEP = 0.058$, $S_{PRESS} = 0.064$.

where n is the number of data point. S_{16}, S_{19}, and S_{21} are the E-state indices of atoms 16, 19, and 21. Log *P* is the n-octanol/water partition coefficient of compounds in logarithmic scale. R, R^2_a, F, p, s, $PRESS$, SSY, R^2_{cv}, $SDEP$, S_{PRESS} are correlation coefficient, adjusted R^2, variance ratio, probability factor related to F-ratio and standard error of estimate, predicted residual sum of square, total sum of squares, cross-validated R^2, standard deviation error of prediction, and standard error of PRESS. The values mentioned in parentheses are the 95% confidence intervals of the regression coefficients. All regression coefficients are significant at 95% level as supported by their *t*- and *p*-values (shown in Table 5). The calculated values according to eq. [1] are listed in Table 6. Equation [1] explains 92.7% and predicts 90.7% of variances of the activity. The positive coefficient of S_{16}, S_{19} and S_{21} indicate the negative contribution of these indices towards the inhibition of insulin secretion. The negative coefficient of log *P* indicates that with the increase in

© 2007 NRC Canada

Table 3. ETSA indices, RTSA index, Wang–Ford charges of selected atoms, partition coefficient, and indicator variables.

Compound No.	S_{16}[a]	S_{17}[a]	S_{18}[a]	S_{19}[a]	S_{21}[a]	R_{20}[b]	q_{18}[c]	q_{19}[c]	q_{20}[c]	log P[d]	I_ClR_2[e]	I_ClR_3[e]
1	2.777	0.705	1.806	1.845	1.845	4.662	–0.248	–0.030	–0.168	2.990	0	0
2	2.838	0.753	1.845	1.877	1.877	4.630	–0.239	–0.033	–0.172	3.390	0	0
3	2.859	0.770	1.859	1.888	1.888	4.609	–0.242	–0.037	–0.162	3.660	0	0
4	2.772	0.564	1.750	1.806	1.762	4.892	–0.039	–0.207	–0.069	2.870	0	0
5	2.832	0.612	1.789	1.838	1.794	4.861	–0.057	–0.194	–0.072	3.270	0	0
6	2.854	0.629	1.802	1.849	1.805	4.839	–0.076	–0.180	–0.084	3.540	0	0
7	2.772	0.614	1.767	1.788	0.651	5.130	–0.249	0.010	–0.314	2.870	0	0
8	2.833	0.662	1.806	1.820	0.683	5.098	–0.232	–0.001	–0.306	3.270	0	0
9	2.854	0.679	1.820	1.832	0.694	5.085	–0.241	0.003	–0.309	3.540	0	0
10	2.773	0.643	1.750	1.762	1.762	3.054	–0.109	–0.234	0.280	2.870	0	0
11	2.834	0.691	1.789	1.794	1.794	3.022	–0.100	–0.241	0.284	3.270	0	0
12	2.855	0.708	1.802	1.805	1.805	3.001	–0.098	–0.240	0.282	3.540	0	0
13	2.845	0.751	1.844	1.866	1.928	4.692	–0.287	–0.309	0.348	3.480	0	0
14	2.906	0.799	1.882	1.898	1.960	4.661	–0.163	–0.087	–0.143	3.880	0	0
15	2.927	0.816	1.896	1.909	1.972	4.340	–0.170	–0.082	–0.146	4.150	0	0
16	2.818	0.721	1.827	1.882	1.063	4.764	–0.258	–0.021	–0.204	3.480	0	0
17	2.879	0.769	1.866	1.914	1.095	4.733	–0.254	–0.024	–0.204	3.880	0	0
18	2.900	0.786	1.880	1.925	1.106	4.711	–0.254	–0.024	–0.204	4.150	0	0
19	2.804	0.713	1.843	1.928	1.928	2.300	–0.250	–0.052	–0.047	3.480	0	0
20	2.865	0.761	1.882	1.960	1.960	2.269	–0.246	–0.050	–0.056	3.880	0	0
21	2.886	0.777	1.896	1.972	1.972	2.247	–0.287	0.001	–0.073	4.150	0	0
22	2.713	0.517	1.712	1.981	1.694	4.689	–0.298	–0.010	–0.222	3.550	0	0
23	2.774	0.565	1.750	1.813	1.726	4.658	–0.308	–0.009	–0.214	3.950	0	0
24	2.795	0.582	1.764	1.825	1.737	4.637	–0.339	0.010	–0.234	4.220	0	0
25	2.733	0.589	1.743	1.750	0.535	4.759	–0.202	–0.104	–0.053	3.550	1	0
26	2.794	0.637	1.782	1.782	0.567	4.736	–0.176	–0.108	–0.017	3.950	1	0
27	2.816	0.654	1.795	1.793	0.579	4.706	–0.187	–0.113	–0.047	4.220	1	0
28	2.746	0.628	1.712	1.694	0.694	2.288	–0.324	0.142	–0.277	3.550	0	1
29	2.806	0.676	1.750	1.726	1.726	2.257	–0.299	0.066	–0.264	3.950	0	1
30	2.828	0.693	1.764	1.737	1.737	2.235	–0.319	0.141	–0.282	4.220	0	1

[a] S_{16}, S_{17}, S_{18}, S_{19}, and S_{21} indicate ETSA indices of atom numbers 16, 17, 18, 19, and 21, respectively.
[b] R_{20} indicates RSTA index of atom number 20.
[c] q_{18}, q_{19}, and q_{20} indicate Wang–Ford charges of atom numbers 18, 19, and 20, respectively.
[d] log P indicates the partition coefficient.
[e] I_ClR_2 and I_ClR_3 indicate presence or absence of chlorine atom at meta- and para- position of phenyl ring B.

the value of log P the inhibition of residual insulin secretion increases.

An attempt was also made to develop another model using combination of RTSA index of the atom 20 (R_{20}) containing the substitution R_3 with eq. [1] which yields the following equation:

[2] Log PRIS = – 4.540 (±0.536) + 2.092 (±0.217) S_{16} + 0.811 (±0.153) S_{19} + 0.090 (±0.021) S_{21} + 0.022 (±0.010) R_{20} – 0.361 (±0.025) log P

n = 30, R = 0.974, R^2 = 0.948, R^2_a = 0.937, $F(5,24)$ = 87.602 $p < 0.00001$, s = 0.049, SSY = 1.088, $PRESS$ = 0.090, R^2_{cv} = 0.917, $SDEP$ = 0.055, S_{PRESS} = 0.061.

The values mentioned in parentheses are the 95% confidence intervals of the regression coefficients. All regression coefficients are significant at 95% level as supported by their t- and p-values (shown in Table 5). Equation [2] explains 93.7% and predicts 91.7% of variances of the activity. The calculated values according to eq. [2] are presented in Table 6. R_{20} is the RTSA index of the atom 20. The positive coefficient of R_{20} indicates the negative contribution of R_{20} towards the inhibition of the residual insulin secretion.

Another model was developed using ESTA index, Wang–Ford charges, partition coefficient and the indicator parameter and is given below:

[3] Log PRIS = – 1.039 (±0.343) + 1.895 (±0.214) S_{18} – 1.101 (±0.200) q_{19} – 0.367 (±0.108) q_{20} – 0.192 (±0.031) log P – 0.273 (±0.037) I_ClR_2

n = 30, R = 0.969, R^2 = 0.939, R^2_a = 0.927, $F(5,24)$ = 74.399, $p < 0.00001$, s = 0.052, SSY = 1.088, $PRESS$ = 0.118, R^2_{cv} = 0.892, $SDEP$ = 0.063, S_{PRESS} = 0.070.

The values mentioned in parentheses are the 95% confidence intervals of the regression coefficients. All regression

© 2007 NRC Canada

Table 4. Correlation matrix among response variable, ETSA indices, RTSA index, partition coefficient, and indicator variables used in MLR equations.

	Log PRIS	S_{16}	S_{17}	S_{18}	S_{19}	S_{21}	R_{20}	q_{18}	q_{19}	q_{20}	log P	I_ClR_2	I_ClR_3
Log PRIS	1.000	0.444	0.381	0.522	0.535	0.486	0.217	0.437	–0.477	0.273	–0.496	–0.595	–0.592
S_{16}		1.000	0.844	0.884	0.467	0.299	–0.025	0.148	–0.120	0.075	0.428	–0.273	–0.193
S_{17}			1.000	0.900	0.453	0.284	–0.208	–0.080	0.004	0.116	0.313	–0.239	–0.071
S_{18}				1.000	0.699	0.293	0.019	0.012	–0.098	0.070	0.320	–0.203	–0.399
S_{19}					1.000	0.405	0.123	–0.103	–0.056	–0.031	0.197	–0.306	–0.562
S_{21}						1.000	–0.340	0.129	–0.268	0.330	0.016	–0.584	–0.059
R_{20}							1.000	0.184	–0.209	–0.217	–0.197	0.205	–0.577
q_{18}								1.000	–0.757	0.513	–0.435	0.122	–0.388
q_{19}									1.000	–0.863	0.382	–0.127	0.568
q_{20}										1.000	–0.238	0.122	–0.313
log P											1.000	0.228	0.228
I_ClR_2												1.000	–0.111
I_ClR_3													1.000

Table 5. t and p values of eqs. [1–5].

Equation No.	Intercept/parameters	t value	p value
[1]	Intercept	–8.131	0.000
	S_{16}	9.153	0.000
	S_{19}	5.889	0.000
	S_{21}	3.303	0.003
	log P	–14.512	0.000
[2]	Intercept	–8.469	0.000
	S_{16}	9.651	0.000
	S_{19}	5.308	0.000
	S_{21}	4.212	0.000
	R_{20}	2.267	0.033
	log P	–14.301	0.000
[3]	Intercept	–3.032	0.006
	S_{18}	8.852	0.000
	q_{19}	–5.49	0.000
	q_{20}	–3.384	0.002
	log P	–6.137	0.000
	I_ClR_2	–7.448	0.000
[4]	Intercept	21.124	0.000
	S_{17}	6.541	0.000
	q_{18}	4.427	0.000
	log P	–4.809	0.000
	I_ClR_2	–11.066	0.000
	I_ClR_3	–10.240	0.000
[5]	Intercept	171.974	0.000
	f2	7.868	0.000
	f3	7.271	0.000
	f4	–5.682	0.000
	f6	2.289	0.032
	f7	12.413	0.000
	f9	3.409	0.002

coefficients are significant at 95% level as supported by their t- and p-values (shown in Table 5). Equation [3] explains 92.7% and predicts 89.2% of variances of the activity. The calculated values according to the eq. [3] are given in Table 7. S_{18} is ETSA index of the atom number 18; q_{19} and q_{20} are the Wang-ford charges of atom numbers 19 and 20 respectively. The positive coefficient of S_{18} suggests that with the increase in the value of S_{18} the inhibition of residual insulin secretion decreases. The negative coefficients of q_{19} and q_{20} indicate that the higher negative charges on atoms 19 and 20 are more detrimental for the inhibition of residual insulin secretion. The presence of chlorine atom at R_2 position of the general structure is favorable for the inhibition of residual insulin secretion as suggested by the negative coefficient of I_ClR_2.

Two indicator parameters were used with ETSA index of atom number 17 (S_{17}) as well as Wang–Ford charge of the atom number 18 (q_{18}) and log P to generate a fruitful QSAR model. These yield the eq. [4] as follows:

[4] Log PRIS = 1.864 (±0.088) + 0.783 (±0.120) S_{17} + 0.523 (±0.118) q_{18} – 0.123 (±0.026) log P – 0.343 (±0.031) I_ClR_2 – 0.306 (±0.030) I_ClR_3

n = 30, R = 0.978, R^2 = 0.957, R^2_a = 0.948,

$F(5,24)$ = 107.42, p < 0.00001, s = 0.044,

SSY = 1.088, $PRESS$ = 0.086, R^2_{cv} = 0.921,

$SDEP$ = 0.054, S_{PRESS} = 0.060.

Equation [4] explains 94.8% and predicts 92.1% of variances of the activity. The calculated values according to eq. [4] are presented in Table 7. The values mentioned in parentheses are the 95% confidence intervals of the regression coefficients. All regression coefficients are significant at 95% level as supported by their t- and p-values (shown in Table 5). The positive coefficient of S_{17} suggests that the higher value of S_{17} is unfavorable for the inhibition of the residual insulin secretion. The positive coefficient of q_{18} indicates that the higher negative charge on the atom 18 is

© 2007 NRC Canada

Table 6. Observed (Obs.), calculated (Calc.), residual (Res.), predicted residual (Pres.), and LOO-predicted (Pred.) activities of eqs. [1] and [2].

		Eq. [1]				Eq. [2]			
Compound	Obs.	Calc.	Res.	Pres.	Pred.	Calc.	Res.	Pres.	Pred.
1	1.923	1.944	–0.020	–0.024	1.947	1.955	–0.032	–0.038	1.961
2	1.943	1.954	–0.011	–0.012	1.955	1.967	–0.024	–0.026	1.969
3	1.880	1.908	–0.028	–0.029	1.910	1.923	–0.042	–0.046	1.926
4	1.946	1.937	0.010	0.012	1.935	1.954	–0.008	–0.010	1.956
5	1.976	1.945	0.031	0.033	1.943	1.964	0.012	0.014	1.962
6	1.862	1.901	–0.039	–0.042	1.904	1.922	–0.059	–0.066	1.928
7	1.823	1.845	–0.022	–0.029	1.852	1.845	–0.022	–0.029	1.852
8	1.924	1.856	0.068	0.083	1.841	1.857	0.068	0.082	1.842
9	1.866	1.811	0.056	0.067	1.799	1.814	0.053	0.063	1.803
10	1.949	1.898	0.051	0.064	1.886	1.880	0.069	0.090	1.860
11	1.899	1.909	–0.010	–0.011	1.910	1.891	0.008	0.009	1.890
12	1.899	1.863	0.036	0.040	1.859	1.847	0.052	0.059	1.840
13	1.898	1.928	–0.031	–0.033	1.931	1.946	–0.048	–0.053	1.951
14	1.929	1.939	–0.010	–0.011	1.940	1.957	–0.028	–0.033	1.962
15	1.900	1.893	0.008	0.009	1.891	1.907	–0.006	–0.008	1.908
16	1.876	1.827	0.049	0.054	1.822	1.826	0.050	0.055	1.821
17	1.818	1.838	–0.020	–0.023	1.841	1.838	–0.020	–0.023	1.841
18	1.802	1.792	0.010	0.013	1.789	1.794	0.008	0.010	1.792
19	1.849	1.898	–0.049	–0.056	1.905	1.857	–0.008	–0.011	1.860
20	1.842	1.909	–0.067	–0.076	1.918	1.869	–0.027	–0.036	1.878
21	1.863	1.863	–0.001	–0.001	1.863	1.825	0.037	0.053	1.810
22	1.711	1.710	0.001	0.001	1.710	1.717	–0.006	–0.014	1.724
23	1.605	1.537	0.068	0.081	1.524	1.566	0.039	0.051	1.554
24	1.621	1.491	0.130	0.160	1.461	1.523	0.099	0.135	1.486
25	1.447	1.462	–0.015	–0.019	1.466	1.469	–0.022	–0.027	1.475
26	1.398	1.473	–0.075	–0.090	1.488	1.480	–0.082	–0.099	1.497
27	1.456	1.429	0.027	0.035	1.422	1.438	0.018	0.023	1.433
28	1.358	1.449	–0.091	–0.115	1.473	1.410	–0.052	–0.078	1.436
29	1.539	1.525	0.014	0.018	1.521	1.509	0.030	0.040	1.499
30	1.410	1.481	–0.071	–0.096	1.506	1.467	–0.057	–0.079	1.489

conducive for the inhibition. The negative coefficient of I_ClR_3 indicates that chlorine atom at para position of phenyl ring B is required for the inhibition of the residual insulin secretion. Equation [4] is the best MLR models amongst all developed MLR models.

Principle Component Regression Analysis (PCRA)

When factor scores were used as the independent parameters in multiple linear regressions, the following equation was obtained:

[5] Log PRIS = 1.774 (±0.010) + 0.083 (±0.010) f2 + 0.076 (±0.010) f3 – 0.060 (±0.010) f4 + 0.024 (±0.010) f6 + 0.130 (±0.010) f7 + 0.036 (±0.010) f9

$n = 30$, $R = 0.966$, $R^2 = 0.933$, $R^2_a = 0.915$, $F(6,23) = 53.000$, $p < 0.00001$ $s = 0.057$, SSY = 1.088, $PRESS = 0.119$, $R^2_{cv} = 0.891$, $SDEP = 0.063$, $S_{PRESS} = 0.072$.

Equation [5] explains 91.5% and predicts 89.1% of the variances of the activity. The calculated values of log PRIS according to eq. [5] are listed in Table 8. The values mentioned in parentheses are the 95% confidence intervals of the regression coefficients. All regression coefficients are significant at 95% level as supported by their *t*- and *p*-values (shown in Table 5). Any one factor contains the information for different descriptors. In eq. [5], the factor scores are used instead of the original variables. As the factor score contains information for the different descriptors, the loss of information is thus avoided. From the factor scores used, the significance of the original variable for the activity can be obtained. The factor score 2 indicates the importance of the RTSA indices of the atom numbers 16, 17, Wang–Ford charge of the atom numbers 14, 15, 16, 17, 18, and 22. The factor score 3 indicates the importance of Wang–Ford charge of the atom numbers 6, 7, 8 and 12. The factor score 4 indicates the importance of the ETSA index of the atom number 22, the RTSA index of the atom number 22 and Wang–Ford charge of the atom number 11. The factor score 6 indicates the importance of Wang–Ford charge of the atom numbers 19, 20, and 21. The factor score 7 indicates the importance of the ETSA index of the atom numbers 18 and 19. The factor score 9 indicates the importance of the RTSA index of

© 2007 NRC Canada

Table 7. Observed (Obs.), calculated (Calc.), residual (Res.), predicted residual (Pres.), and LOO-predicted (Pred.) activities of eqs. [3] and [4].

		Eq. [3]				Eq. [4]			
Compound	Obs.	Calc.	Res.	Pres.	Pred.	Calc.	Res.	Pres.	Pred.
1	1.923	1.906	0.018	0.022	1.902	1.919	0.004	0.005	1.918
2	1.943	1.908	0.036	0.040	1.903	1.912	0.031	0.034	1.909
3	1.880	1.883	–0.003	–0.003	1.883	1.891	–0.011	–0.012	1.892
4	1.946	1.981	–0.035	–0.048	1.994	1.933	0.014	0.019	1.927
5	1.976	1.965	0.011	0.013	1.962	1.912	0.064	0.081	1.895
6	1.862	1.927	–0.065	–0.080	1.942	1.882	–0.020	–0.025	1.887
7	1.823	1.864	–0.041	–0.054	1.878	1.862	–0.039	–0.049	1.873
8	1.924	1.871	0.054	0.062	1.862	1.859	0.065	0.070	1.854
9	1.866	1.842	0.024	0.027	1.839	1.835	0.031	0.033	1.833
10	1.949	1.883	0.067	0.096	1.854	1.958	–0.009	–0.010	1.960
11	1.899	1.886	0.013	0.017	1.883	1.951	–0.052	–0.059	1.958
12	1.899	1.859	0.040	0.051	1.847	1.932	–0.034	–0.039	1.937
13	1.898	2.002	–0.104	–0.142	2.040	1.875	0.023	0.027	1.871
14	1.929	1.933	–0.003	–0.004	1.933	1.928	0.002	0.002	1.928
15	1.900	1.903	–0.003	–0.003	1.904	1.904	–0.004	–0.005	1.905
16	1.876	1.855	0.021	0.023	1.853	1.866	0.010	0.011	1.865
17	1.818	1.855	–0.037	–0.041	1.859	1.857	–0.039	–0.042	1.860
18	1.802	1.830	–0.028	–0.032	1.835	1.837	–0.035	–0.040	1.842
19	1.849	1.862	–0.013	–0.015	1.860	1.864	–0.015	–0.016	1.865
20	1.842	1.860	–0.018	–0.021	1.863	1.855	–0.013	–0.014	1.856
21	1.863	1.785	0.078	0.101	1.762	1.813	0.050	0.058	1.805
22	1.711	1.618	0.093	0.113	1.598	1.677	0.034	0.048	1.663
23	1.605	1.609	–0.004	–0.005	1.610	1.660	–0.055	–0.076	1.681
24	1.621	1.570	0.051	0.066	1.555	1.624	–0.003	–0.004	1.626
25	1.447	1.445	0.002	0.003	1.444	1.441	0.006	0.010	1.437
26	1.398	1.434	–0.036	–0.054	1.452	1.443	–0.045	–0.068	1.466
27	1.456	1.423	0.033	0.053	1.404	1.417	0.039	0.061	1.395
28	1.358	1.471	–0.112	–0.167	1.525	1.445	–0.087	–0.139	1.496
29	1.539	1.545	–0.006	–0.007	1.546	1.446	0.093	0.140	1.399
30	1.410	1.444	–0.034	–0.046	1.456	1.416	–0.006	–0.009	1.419

the atom number 18. The factor loadings of variables are shown in Table 2. All coefficients of parameters and intercepts in these equations are significant at more than 95% level as supported by their *t*- and *p*- values. *t*- and *p*- values of eqs. [1]–[5] are shown in Table 5.

Partial Least Squares (PLS)

The number of the optimum components (latent variables) was found to be 2 to obtain the final equation and optimization was done by cross-validation method. Based on standard regression coefficients, the following variables were selected for the final equation.

$$\text{[6]}\quad \text{Log PRIS} = -5.292 + 0.495\,S_{16} + 0.256\,S_{17} + 0.578\,S_{18} + 0.464\,S_{19} + 0.060\,S_{21} + 0.355\,R_{16} + 0.322\,R_{17} + 0.170\,R_{19} - 1.876\,q_6 - 0.101\log P - 0.133\,I_\mathrm{ClR}_2 - 0.14672\,I_\mathrm{ClR}_3$$

$n = 30$, $R = 0.972$, $R^2 = 0.944$, $R^2_a = 0.904$, $R^2_{cv} = 0.910$, $F = 229.19$, $p < 0.0001$, $s = 0.060$, SSY = 1.088, PRESS = 0.098, SDEP = 0.057, $S_{PRESS} = 0.076$.

Equation [6] explains 90.4% and predicts 91.0% of variances of the activity. The positive coefficient of S_{16}, S_{17}, S_{18}, S_{19}, S_{21}, R_{16}, R_{17}, and R_{19} indicate that the higher values of these parameters are detrimental for the inhibition of the residual insulin secretion. The negative coefficient of q_6 suggests that the higher negative charge on the atom number 6 is detrimental for the inhibition. The negative coefficient of log *P* indicates that with the increase in the value of log *P* the inhibition of the residual insulin secretion increases.

All models are validated by the leave one out (LOO) cross-validation method. The observed (Obs), calculated (Calc), residual (Res), predicted residual (Pres) and LOO-predicted (Pred) activities of eqs. [1]–[6] are shown in Tables 6, 7, and 8.

Conclusion

The results of QSAR analysis show the importance of ETSA indices of the atom numbers 16, 17, 18, 19, and 21. ETSA index of atom 22 is also important as observed in eq. [5]. As ETSA indices contain the electronic information,

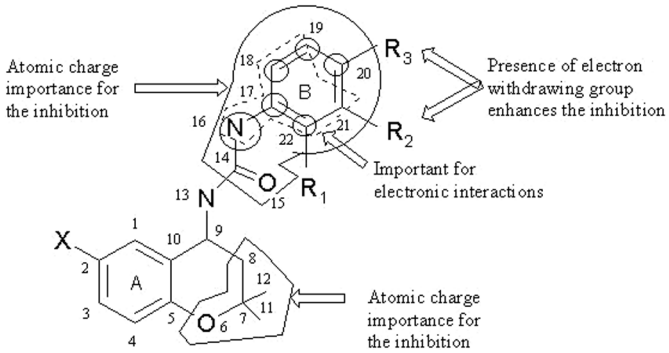
© 2007 NRC Canada

Table 8. Observed (Obs.), calculated (Calc.), residual (Res.), predicted residual (Pres.), and LOO-predicted (Pred.) activities of eqs. [5] and [6].

		Eq. [5]				Eq. [6]			
Compound	Obs.	Calc.	Res.	Pres.	Pred.	Calc.	Res.	Pres.	Pred.
1	1.923	1.888	0.036	0.040	1.884	1.887	0.036	0.043	1.880
2	1.943	1.902	0.041	0.047	1.896	1.883	0.060	0.068	1.875
3	1.880	1.865	0.015	0.017	1.863	1.843	0.037	0.043	1.837
4	1.946	1.927	0.019	0.026	1.920	1.945	0.001	0.004	1.942
5	1.976	1.939	0.036	0.053	1.923	1.943	0.033	0.043	1.933
6	1.862	1.899	–0.037	–0.053	1.915	1.913	–0.051	–0.058	1.920
7	1.823	1.844	–0.021	–0.023	1.847	1.853	–0.030	–0.031	1.854
8	1.924	1.847	0.077	0.087	1.837	1.842	0.082	0.099	1.825
9	1.866	1.824	0.043	0.081	1.785	1.863	0.003	0.010	1.856
10	1.949	1.930	0.020	0.026	1.923	1.935	0.014	0.025	1.924
11	1.899	1.937	–0.038	–0.049	1.949	1.925	–0.026	–0.030	1.929
12	1.899	1.912	–0.013	–0.018	1.917	1.902	–0.003	–0.003	1.902
13	1.898	1.794	0.104	0.228	1.669	1.963	–0.065	–0.076	1.974
14	1.929	1.961	–0.031	–0.036	1.965	1.917	0.012	0.015	1.914
15	1.900	1.935	–0.035	–0.039	1.940	1.892	0.008	0.011	1.889
16	1.876	1.857	0.019	0.021	1.855	1.848	0.028	0.033	1.843
17	1.818	1.859	–0.041	–0.046	1.864	1.834	–0.016	–0.017	1.835
18	1.802	1.836	–0.033	–0.037	1.839	1.805	–0.003	–0.004	1.806
19	1.849	1.891	–0.042	–0.054	1.903	1.898	–0.049	–0.052	1.901
20	1.842	1.894	–0.052	–0.069	1.911	1.884	–0.042	–0.048	1.890
21	1.863	1.866	–0.003	–0.004	1.867	1.858	0.005	0.005	1.858
22	1.711	1.711	–0.000	–0.000	1.711	1.712	–0.001	–0.005	1.716
23	1.605	1.627	–0.022	–0.029	1.635	1.602	0.003	–0.004	1.609
24	1.621	1.594	0.027	0.038	1.583	1.594	0.027	0.025	1.596
25	1.447	1.383	0.064	0.094	1.353	1.416	0.031	0.039	1.408
26	1.398	1.454	–0.057	–0.105	1.503	1.490	–0.092	–0.121	1.519
27	1.456	1.383	0.073	0.108	1.349	1.380	0.076	0.094	1.362
28	1.358	1.462	–0.104	–0.132	1.490	1.448	–0.090	–0.134	1.492
29	1.539	1.504	0.035	0.041	1.498	1.469	0.070	0.095	1.444
30	1.410	1.490	–0.080	–0.106	1.516	1.468	–0.058	–0.088	1.498

these atoms may involve in the electronic interaction of compounds with receptors for inhibition of residual insulin secretion. The results also show the importance of RTSA indices of the atom numbers 16, 17, 18, and 20. R-state indices of atoms 19 and 22 are also important from the point of eq. [5]. Since the R-state index of an atom encodes the dispersive/van der Waals interactions with the active sites, the atom numbers 16, 17, 18, 19, 20, and 22 may be involved in the dispersive/van der Waals interactions with the receptor for the inhibition. Wang–Ford charge of the atom numbers 19 and 20 are important for the inhibition of residual insulin secretion. Similarly Wang–Ford charges of atoms 6, 7, 8, 11, 12, 14, 15, 16, 17, 18, 21, and 22 are important from eq. [5]. The results showed that the hydrophobicity of compounds (log *P*) is also important for the inhibition of residual insulin secretion. The results also show the importance of two indicator variables. The presence of chlorine atoms at m- and p- position of phenyl ring B is required for the inhibition of the residual insulin secretion. Among all generated MLR equations, eq. [4] is the best model with higher statistical qualities. The statistical qualities of the best MLR equation, PCRA and PLS equations are comparable with each other except the *F*-ratio PLS equation (*F*=229.19). All the models (MLR, PCRA, and PLS) show the importance of atom numbers 16, 17, 18, 19, and 20 for the inhibition of residual insulin secretion. Both the MLR and PLS models show the importance of two indicator parameters (*I*_ClR_2 and *I*_ClR_3) and log *P* for the inhibition. Both the PCRA and PLS models show the importance of atom number 6 and 21 for the inhibition of residual insulin secretion. Atoms and substituents important for the inhibition are shown in Fig. 2.

Fig. 2. Important atoms and substituents for the inhibition of insulin secretion. Atoms bounded by circles are important for van dispersive/dar Waals interactions.



© 2007 NRC Canada

Acknowledgement

The authors are grateful to University Grants Commission (UGC), New Delhi and All India Council for Technical Education (AICTE), New Delhi for awarding research projects. One of the authors, S.S. is grateful UGC for awarding a Senior Research Fellowship (SRF). Authors are also thankful to the authority of Jadavpur University for their help and encouragement.

References

1. B. Alberts, A. Johnson, J. Lewis, M. Raff, K. Roberts, and P. Walter. Molecular Biology of the Cell. 4th ed. Garland Science, NY. 2002. p. 632.
2. T. Nogrady. Medicinal chemistry: A biochemical approach,. 2nd ed. Oxford University Press, NY. 2004. pp. 344–345.
3. D.J. Triggle. *In* Textbook of drug design and discovery. 3rd ed. *Edited by* P. Krogsgaard-Larsen, T. Liljefors, and U. Madsen. Taylor & Francis, NY. 2002. pp. 187–200.
4. J.R. Fozard and P.W. Manley. Prog. Respir. Res. **31**, 77 (2001).
5. M. Schwanstecher, C. Sieverding, H. Dorschner, I. Gross, L. Aguilar-Bryan, C. Schwanstecher, and J. Bryan. EMBO J. **17**, 5529 (1998).
6. H.P. Rang, M.M. Dale, J.M. Ritter, and P.K. Moore. Pharmacology. 5th ed. Churchill Livingstone, Edinburgh, Scotland. 2003. p. 294.
7. K. Lawson. Pharmacol. Ther. **70**, 39 (1996).
8. S. Sebille, D. Gall, P. de Tullio, X. Florence, P. Lebrun, and B. Pirotte. J. Med. Chem. **49**, 4690 (2006).
9. S. Samanta, B. Debnath, S. Gayen, B. Ghosh, K. Srikanth, and T. Jha. Farmaco, **60**, 818 (2005).
10. B. Debnath, S. Gayen, S. Samanta, A. Basu, B. Ghosh, and T. Jha. Ind. J. Chem. A **45A**, 93 (2006).
11. A. Basu, S. Gayen, S. Samanta, P. Panda, K. Srikanth, and T. Jha. Can. J. Chem. **84**, 458 (2006).
12. S. Samanta, Sk.M. Alam, P. Panda, and T. Jha. Internet Electron J. Mol. Des. **6**, 503 (2006).
13. S. Samanta, B. Debnath, A. Basu, S. Gayen, K. Srikanth, and T. Jha. Eur. J. Med. Chem. **41**, 1190 (2006).
14. T. Jha, B. Debnath, S. Samanta, and A. U. De. Internet. Electron. J. Mol. Des. **2**, 539 (2003) [online]. Available from http://www.biochempress.com.
15. S. Gayen, B. Debnath, and T. Jha. Internet Electron. J. Mol. Des. **3**, 771 (2004) [online]. Available from http://www.biochempress.com.
16. S. Gayen, B. Debnath, A. Basu, S. Samanta, B. Ghosh, S.K. Naskar, and T. Jha. Internet Electron. J. Mol. Des. **4**, 210 (2005) [online]. Available from http://www.biochempress.com.
17. B. Debnath, S. Samanta, S. Gayen, A. Basu, B. Ghosh, and T. Jha. Internet Electron. J. Mol. Des. **4**, 393 (2005) [online]. Available from http://www.biochempress.com.
18. S. Gayen, B. Debnath, S. Samanta, B. Ghosh, A. Basu, and T. Jha. Internet Electron. J. Mol. Des. **4**, 556 (2005) [online]. Available from http://www.biochempress.com.
19. H. Hall, B. Mohney, and L. B. Kier. Quant. Struct.-Act. Relat. **10**, 43 (1991).
20. C. de Gregorio, L.B. Kier, and L.H. Hall. J. Comput. Aid. Mol. Des. **12**, 557 (1998).
21. R. Carrasco, J.A. Padron, and J. Galvez. J. Pharm. Pharmaceut. Sci. **7**, 19 (2004).
22. O. Ivanciuc. Topological indices. *In* Handbook of chemoinformatics. *Edited by* J. Gasteiger. Wiley-VCH, Weinheim, Germany. 2003. pp. 981–1003.
23. Mouse: A computer program developed by S.K. Naskar of the Department of Computer Science and Engineering, Jadavpur University, Kolkata, India, and B. Debnath for the calculation of the ETSA Index [computer program].
24. Chem 3D Pro Version 5.0 and Chem Draw Ultra Version 5.0 are programs CambridgeSoft Corporation, Cambridge, MA [computer program].
25. G.W. Snedecor and W.G. Cochran. Statistical methods. 6th ed. Oxford & IBH. New Delhi, India. 1967. pp. 381–418.
26. R. Franke. Theoretical drug design methods. Elsevier. Amsterdam. 1984. p 184–195.
27. J.T. Leonard and K. Roy. Bioorg. Med. Chem. Lett. **16**, 4467 (2006).
28. J.T. Leonard and K. Roy. Bioorg. Med. Chem. **14**, 1039 (2006).
29. K. Roy, I. Sanyal, and P. P. Roy. SAR QSAR Environ. Res. **17**, 563 (2006).
30. S. Wold and L. Eriksson. *In* Chemometric methods in molecular design. *Edited by* H. Van de Waterbeemd. Wiley-VCH, Weinheim, Germany. 1995. pp. 312–317.

© 2007 NRC Canada

Rotating ring-disk voltammetric investigations on the degradation rate of the nickel(III)-glycylglycyl-L-histidine complex

María V. Alipázaga, Denise Lowinsohn, Mauro Bertotti, and Nina Coichev

Abstract: The voltammetric behavior of the Ni(II)/glycylglycyl-L-histidine complex and the degradation of the electrogenerated Ni(III) species were investigated by cyclic voltammetry. Results of electrochemical and spectrophotometric experiments indicated some differences in the nature and reactivity of Ni(III) complexes formed by two independent routes, i.e., anodic oxidation of Ni(II) and homogeneous oxidation by an autocatalytic reaction in a medium containing oxygen and S(IV) (H_2SO_3, HSO_3^-, and SO_3^{2-}). The Ni(III) species formed electrochemically reacts in a fast chemical process (EC mechanism) and the observed rate constant of the degradation (k = 0.17 s^{-1}) was determined by a rotating ring-disk electrode technique measuring kinetic collection efficiency values as a function of the rotation rate.

Key words: nickel, glycylglycyl-L-histidine, sulfite, degradation reaction, rotating ring-disk voltammetry.

Résumé : Faisant appel à des méthodes de voltampérométrie cyclique, on a étudié le comportement voltampérométrique du complexe Ni(II)/glycylgly-L-cylhistidine et la dégradation des espèces Ni(III) électrogénérées. Les résultats des expériences électrochimiques et spectrophotométriques indiquent qu'il existe de légères différences dans la nature et la réactivité des complexes de Ni(III) qui se forment par deux voies réactionnelles indépendantes, soit l'oxydation anodique du Ni(II) et l'oxydation homogène par une réaction autocatalytique dans un milieu contenant de l'oxygène et des espèces à base de S(IV), telles H_2SO_3, HSO_3^- et SO_3^{2-}. Les espèces de Ni(III) qui se forment d'une façon électrochimique réagissent par un processus chimique rapide (mécanisme EC) et on a déterminé la constante de vitesse observée pour la dégradation (k = 0,17 s^{-1}) par la technique de l'électrode à disque tournant en mesurant les valeurs de l'efficacité de la collection cinétique en fonction de la vitesse de rotation.

Mots-clés: nickel, glycylglycyl-L-histidine, sulfite, réaction de dégradation, voltampérométrie à disque tournant.

[Traduit par la Rédaction]

Introduction

Nickel compounds are well established as human carcinogens (1). As nickel(II) aqua cation is physiologically redox inactive, its toxicity in vivo is inferred to involve activation by coordination with peptides and proteins in which the N-terminus, N-deprotonated amides, histidine imidazoles, and cysteine thiolates provide the principal ligand groups (2). Metallopeptides, of the general form Ni^{II}(Xaa-Xaa-His) (where Xaa is any amino acid), simple or when appended to proteins or other agents, have previously been shown to mediate oxidative protein cross-linking (3) and cleavage of DNA (4–7) and proteins (8) in the presence of $KHSO_5$, magnesium monoperoxyphthalate, or S(IV) (H_2SO_3, HSO_3^-, and SO_3^{2-}).

In suitable experimental conditions, the oxidation of some divalent transition metal ions is accelerated in the presence of S(IV) and dissolved oxygen (9–15). In the case of Ni(II), several works have been reported in the literature (11, 13, 16–19). Currently, increasing interest in the formation of Ni(III) peptide complexes has been noticed because of the probable participation of these species in DNA damage processes (7).

In our previous work (7), DNA strand breaks and oxidation of 2′-deoxyguanosine were observed in air saturated solutions containing micromolar concentrations of Ni^{II}GGH complex (GGH = glycylglycyl-L-histidine) and S(IV). This study showed that the extent of DNA damage depends on the ratio of both Ni^{II}GGH and S(IV) concentration and the ionic strength. It was also demonstrated that Ni^{II}GGH reacts rapidly with S(IV) in air saturated solution to produce Ni^{III}GGH. A mechanism was proposed where, in a first step, Ni^{III} oxidizes SO_3^{2-} to $SO_3^{\bullet-}$, which then reacts with dissolved oxygen to produce $SO_5^{\bullet-}$, initiating radical chain reactions.

As transition metal ions in the trivalent state can be conveniently generated by both chemical and electrochemical procedures, investigations on the nature and reactivity of Ni(III) peptide compounds constitute a topic of relevance. In the present work, a complementary study was carried out to better understand the stability of Ni^{III}GGH in aqueous solution.

Cyclic voltammetric measurements provide a simple diagnostic method for the preliminary study of homogeneous re-

Received 14 September 2007. Accepted 19 October 2007. Published on the NRC Research Press Web site at canjchem.nrc.ca on 22 November 2007.

M.V. Alipázaga, D. Lowinsohn, M. Bertotti, and N. Coichev.[1] Instituto de Química, Universidade de São Paulo, CP 26077, CEP 05513–970 São Paulo, Brazil.

[1]Corresponding author (e-mail: ncoichev@iq.usp.br).

 doi:10.1139/V07-128 © 2007 NRC Canada

actions coupled to redox processes. Quantitative information can be gained by performing the experiments in conditions where the mass transfer coefficient of the reactant or intermediate is experimentally varied relative to the inherent rate of the chemical reaction. A typical approach employed in studying coupled chemical reactions is based on the use of rotating ring-disk electrode voltammetry (RRDE). RRDE experiments allow the rate of mass transfer to be adjusted to a value comparable to the rate of the chemical reaction, and the limiting current is analyzed using appropriate kinetic equations to determine the rate constant of the homogeneous reaction. Hence in the present work, efforts to fully characterize the electrochemical behavior of the $Ni^{II}GGH$ species and to determine the rate constant of the degradation process, probably involving the reaction between anodically generated Ni(III) complex and the ligand, are shown. In addition, the formation of the Ni(III) complex was also verified by spectrophotometric techniques.

Experimental

Reagents

All reagents were of analytical grade (Merck or Sigma-Aldrich) and were used as received. Solutions were prepared by using deionized water purified with a Milli-Q Plus Water system (Millipore). A S(IV) solution was prepared daily with the $Na_2S_2O_5$ reagent.

In the experiments fresh $Ni^{II}GGH$ solutions were used, which were prepared by dissolving GGH peptide in water (pH = 7.0) followed by the addition of a Ni(II) solution (solutions were prepared to have a 10% excess of peptide to restrain any $Ni(OH)_2$ precipitation). The final pH was adjusted with 0.1 mol/L NaOH or 0.1 mol/L $HClO_4$ solutions. No buffer was used since some anions (such as carbonate and phosphate) may displace de peptide ligand.

In some experiments, the ionic strength *I* was adjusted in 0.05 mol/L with $NaClO_4$.

In all experiments, air saturated solutions were employed for which the oxygen concentration can be considered to be 0.25 mmol/L (20). A pHmeter Metrohm model 713 with a glass electrode (filled with satd. NaCl) was used in the pH measurements. Measurements were performed at 25.0 °C.

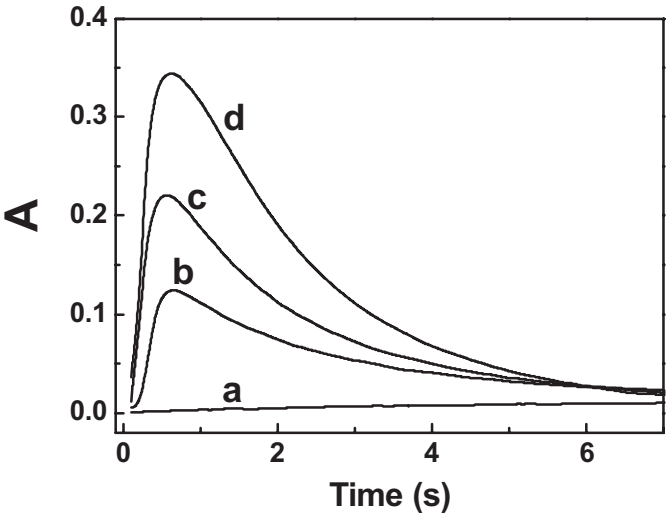
Spectrophotometric measurements

In these experiments, an equal volume of S(IV) solution was mixed with the metal ion complex solution. UV–vis spectra of the $Ni^{II}GGH$ complex were obtained using a HP8453A diode array spectrophotometer, which was coupled to a Pro-K 2000 stopped-flow mixing accessory (Applied Photophysics) to collect kinetic information on the decomposition of the Ni(III) species upon addition of S(IV). Measurements were performed at 25.0 °C. In general, all kinetics traces were recorded at least 3–5 times. The final concentrations after the mixture are indicated in Fig. 1.

Electrochemical measurements

Rotating ring-disk electrochemical experiments were carried out using an analytical rotator (AFMSRX) connected to an AFCBP1 bipotentiostat (Pine Instrument Company) with data acquisition software made available by the manufacturer (ASWCV2, PineChem). Current potential curves were typically recorded at a 20 mV s^{-1} potential scan rate. The glassy carbon – glassy carbon ring-disk electrodes (AFMT29) had the following dimensions: disk radius 0.5613 cm, inner radius of the ring 0.6248 cm, and outer radius of the ring 0.7925 cm. The electrodes were polished using 0.3 μm alumina before use. A platinum wire and a Ag/AgCl (satd. NaCl) were used as counter and reference electrodes, respectively. During rotating ring-disk electrode (RRDE) experiments, the disk electrode potential was scanned between the limits 0.2 and 1.0 V, the ring being maintained at 0.1 V to collect the material generated at the disk. A 0.05 mol/L $NaClO_4$ solution (pH = 7.0) was used as supporting electrolyte. After the electrochemical generation of $Ni^{III}GGH$, the pH was about the same.

Fig. 1. Absorbance due to $Ni^{III}GGH$ formation after addition of S(IV) to a $Ni^{II}GGH$ solution. [$Ni^{II}GGH$] = 200 μmol L^{-1}, pH = 7.0, I = 0.05 mol L^{-1} ($NaClO_4$), T = 25.0 °C. [S(IV)]: (a) 0, (b) 25, (c) 50, and (d) 100 μmol L^{-1}.



Results and discussion

Spectrophotometric studies

Ni(II) can form square planar complexes with GGH by coordination of the terminal amine group, two deprotonated amide nitrogens, and the imidazole-N3 of the histidine residue (21). In addition, potentiometric studies (22) have shown that $Ni^{II}(H_{-2}GGH)^-$, containing two deprotonated amide nitrogens, is the major species present in solution at pH higher than 6.4. In the present work, $Ni^{II}GGH$ represents all species present in solution and $Ni^{II}(H_{-2}GGH)^-$ refers to the complex with the peptide ligand with two deprotonated nitrogens coordinated to the nickel ion.

Our detailed previous work showed that $Ni^{II}GGH$ is rapidly oxidized to $Ni^{III}GGH$ in the presence of S(IV) in air saturated solution (7). Figure 1 shows the absorbance changes at 340 nm (maximum absorption peak for the Ni(III) complex) obtained after the addition of S(IV) to a $Ni^{II}GGH$ solution. A short induction period can be observed especially at lower S(IV) concentrations, its extension depending on the S(IV) concentration and traces of $Ni^{III}GGH$ initially present. After the induction period, the absorbance reaches a maximum value within 0.6 s as a result of a very efficient and

© 2007 NRC Canada

fast formation of $Ni^{III}GGH$. The amount of generated $Ni^{III}GGH$ is a function of added S(IV) when both the metal complex and oxygen are in large excess.

Reactions 1 to 9 represent the main steps involving the oxidation of $Ni^{II}GGH$ in the presence of S(IV) and oxygen (7).

Initiation

[1] $Ni^{II}GGH + O_2 \rightarrow Ni^{III}GGH + O_2^{-}$

Autocatalytic process

[2] $HSO^{-}_3 \rightleftharpoons SO^{2-}_3 + H^+ \quad pK_a = 7.2$

[3] $Ni^{III}GGH + SO^{2-}_3 \rightarrow Ni^{II}GGH + SO^{\bullet -}_3$

[4] $SO^{\bullet -}_3 + O_2 \rightarrow SO^{\bullet -}_5$

[5] $Ni^{II}GGH + SO^{\bullet -}_5 \rightarrow Ni^{III}GGH + SO^{2-}_5$

[6] $SO^{2-}_3 + O_2 \rightarrow SO^{2-}_5$

[7] $HSO^{-}_5 \rightleftharpoons SO^{2-}_5 + H^+ \quad pK_a = 9.4$

[8] $Ni^{II}GGH + HSO^{-}_5 \rightarrow Ni^{III}GGH + SO^{\bullet -}_4 + OH^-$

[9] $Ni^{II}GGH + SO^{\bullet -}_4 \rightarrow Ni^{III}GGH + SO^{2-}_4$

In this autocatalytic process, some Ni(III) is necessary to initiate the reactions. This species might be produced at trace levels by the spontaneous oxidation of $Ni^{II}GGH$ by dissolved oxygen (eq. [1]). $Ni^{III}GGH$ then reacts with SO^{2-}_3 to form the $SO^{\bullet -}_3$ radical (eq. [3]), and the further reaction with O_2 gives $SO^{\bullet -}_5$ (eq. [4]). In an autocatalytic process, $Ni^{II}GGH$ (in large excess, 2.0×10^{-4} mol/L) is oxidized to $Ni^{III}GGH$ by $SO^{\bullet -}_5$ (eq. [5]). HSO^{-}_5 and $SO^{\bullet -}_4$ can also oxidize $Ni^{II}GGH$ in subsequent steps (eqs. [6–9]). The $Ni^{III}GGH$ generated species can be also reduced by SO^{2-}_3 (eq. [3]), continuing the chain reaction. This redox cycling will depend on the critical balance between oxygen and sulfite concentrations, which will controll the overall reaction (S(IV) oxidation to S(VI) and concurrent oxygen consumption).

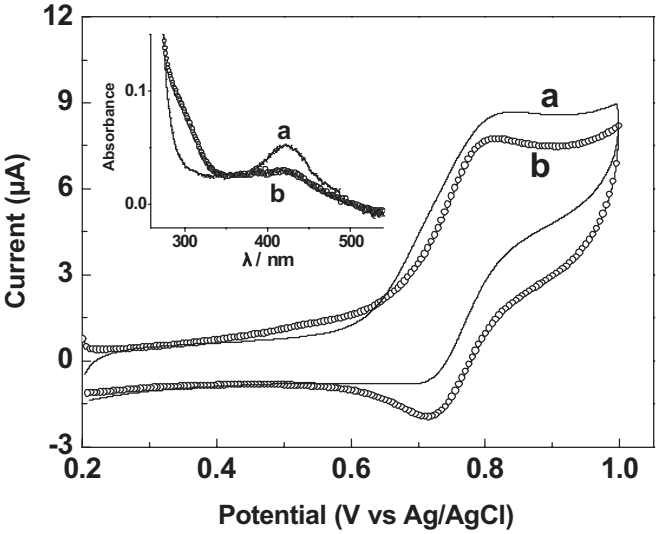
The $SO^{\bullet -}_3$ radical formation in this reaction has also been confirmed by previous EPR spin trapping studies (7) using DMPO (5,5-dimethyl-1-pyrroline-*N*-oxide). The possible involvement of $HO^{\bullet}$ in the mechanism was ruled out since the characteristic spectrum of the DMPO/$HO^{\bullet}$ adduct was not observed.

On the other hand, another interesting issue that can be observed in Fig. 1 is based on the decrease of the absorbance after less than 1 s. This process is associated with the decomposition of the Ni(III) species, which may involve a back-reaction to the Ni(II) complex (eq. [3], if S(IV) is in excess and in conditions of lack of oxygen) and oxidation of the ligand as it will be further discussed.

Voltammetric studies

To evaluate the relative stability of the Ni(III) complex produced on the surface of a glassy carbon electrode, some preliminary experiments were carried out using cyclic voltammetry at quiescent conditions. The voltammetric profile shown in Fig. 2, curve a, indicates the irreversibility of the electrodic process that presents an anodic peak, E_{pa}, at around 0.8 V vs. Ag/AgCl probably related to the oxidation of $[Ni^{II}(H_{-2}GGH)]^-$ (eq. [10]), the predominant species at pH 7. A $E_{1/2}$ of 0.96 V vs. NHE was found, similar to that previously reported in the literature (23). The absence of the corresponding cathodic peak can be a consequence of the degradation of the electrochemically generated $Ni^{III}GGH$ species at the timescale of the experiment.

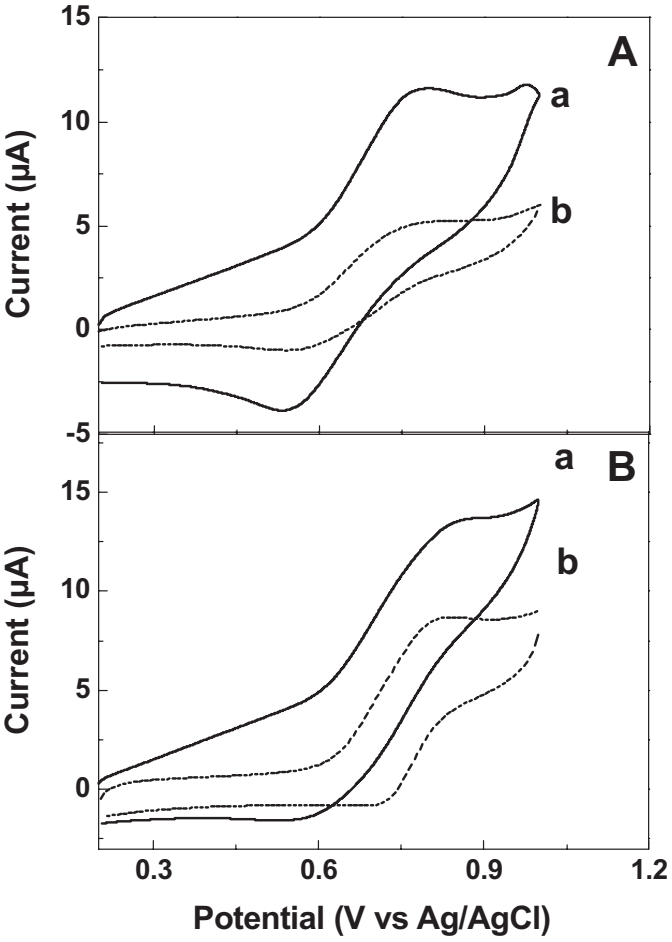
Fig. 2. Voltammograms recorded at the disk electrode in an air saturated solution containing 0.2 mmol L^{-1} $Ni^{II}GGH$ and 0.05 mol L^{-1} $NaClO_4$ (pH = 7.0) (a) before and (b) after addition of 0.2 mmol L^{-1} S(IV) (final concentration in solution). v = 20 mV s^{-1}, T = 25.0 °C. Inset shows the respective UV–vis spectra.



With the addition of S(IV) to an air saturated solution containing $Ni^{II}GGH$, a fast reaction occurs with the formation of $Ni^{III}GGH$, followed by its decomposition as discussed earlier (Fig. 1). Hence, curve b in Fig. 2 corresponds to the voltammogram of a solution containing the degradation product (some Ni(II) complex with the oxidized ligand) of the chemically generated $Ni^{III}GGH$ species and the remaining $Ni^{II}GGH$, which was present in large excess. Some differences are promptly noticed, the most relevant one being the appearance of a small cathodic wave at 0.72 V. This result may indicate that the anodic oxidation of these different Ni(II) complexes follows different pathways, one of the Ni(III) species being further reduced in the reverse potential sweep. The existence of a different Ni(II) species in solution, upon addition of S(IV), can be verified by analyzing the spectra shown in the inset of Fig. 2, obtained in the same conditions. After $Ni^{III}GGH$ decomposition, only the band at 420 nm (due to $Ni^{II}GGH$) and a new band and shoulder around 305 nm were observed in the final spectrum. The band at 305 nm may be evidence of the formation of a new species resulting from the process involving oxidative decarboxylation of ligand, according to the literature (eqs. [14–16]) (24). Thus, the chemical formation and further degradation of the $Ni^{III}GGH$ species yield a solution with different composition, probably containing the oxidized

© 2007 NRC Canada

Fig. 3. Voltammograms recorded at the disk electrode in an air saturated solution containing 0.2 mmol L^{-1} $Ni^{II}GGH$ and 0.05 mol L^{-1} $NaClO_4$ (pH = 7.0) at different scan rates (a) 100 mV s^{-1} and (b) 20 mV s^{-1} and at different temperatures (A) 7 °C and (B) 24 °C.



ligand, if a comparison is made with the initial solution containing Ni(II) and the ligand.

To clearly demonstrate the existence of a chemical step following the anodic process, voltammetry was also performed at different scan rates and temperature conditions. Accordingly, Fig. 3 shows in a convincing way that by performing the electrochemical experiment at low temperature (7 °C) and in a relatively short time window (100 mV s^{-1}), a cathodic response is noticed in the reverse potential sweep, whereas a similar process is absent at the other experimental conditions. These results support the conclusion on the existence of a coupled chemical reaction following the anodic oxidation of the Ni(III) complex (eq. [11]).

Figure 4 shows voltammograms obtained with the RRDE at different rotation rate values in a solution containing $Ni^{II}GGH$. The anodic wave and the concurrent cathodic step are one-electron processes represented by eqs. [10] and [12].

[10] $[Ni^{II}(H_{-2}GGH)]^- \rightarrow [Ni^{III}(H_{-2}GGH)] + e^-$

(at the disk)

Fig. 4. Current responses in RRDE experiments from a solution containing 0.2 mmol L^{-1} $Ni^{II}GGH$ and 0.05 mol L^{-1} $NaClO_4$ (pH = 7.0) at various rotation rates: (a) 100, (b) 900, and (c) 1600 rpm. Scan rate = 20 mV s^{-1}, E_{ring} = 0.1 V, T = 25 °C.

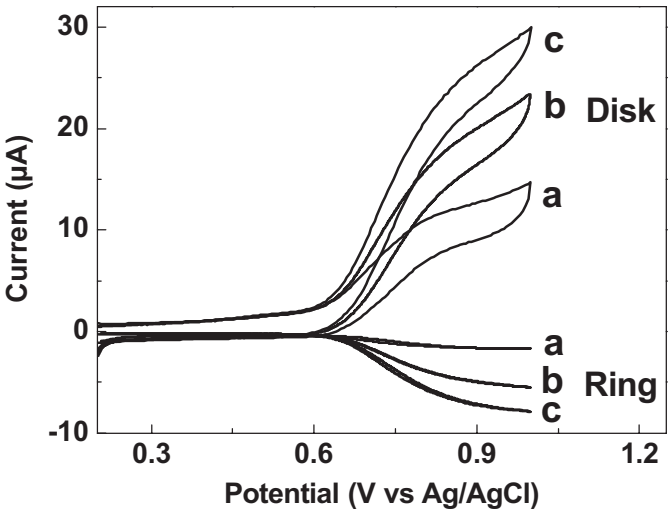


Table 1. N_k as a function of ω N_k was calculated as the ratio between limiting currents measured at the ring and the disk

ω/rpm	100	400	900	1600	2500
N_k	0.12	0.22	0.25	0.27	0.28

[11] $[Ni^{III}(H_{-2}GGH)] \rightarrow$ products

[12] $[Ni^{III}(H_{-2}GGH)] + e^- \rightarrow [Ni^{II}(H_{-2}GGH)]^-$

(at the ring)

The collection efficiency (N), defined as the ratio of the limiting current values measured at the ring and the disk electrodes, indicates the amount of material electrogenerated at the disk that reaches the ring. Typical N values for $Fe(CN)_6^{3-}$ (an electroactive species whose cathodic reduction leads to the stable $Fe(CN)_6^{4-}$ anion) are close to 0.37; it is necessary to point out that in the $Fe(CN)_6^{3-}/Fe(CN)_6^{4-}$ system, no subsequent chemical reaction occurs after the generation of $Fe(CN)_6^{4-}$.

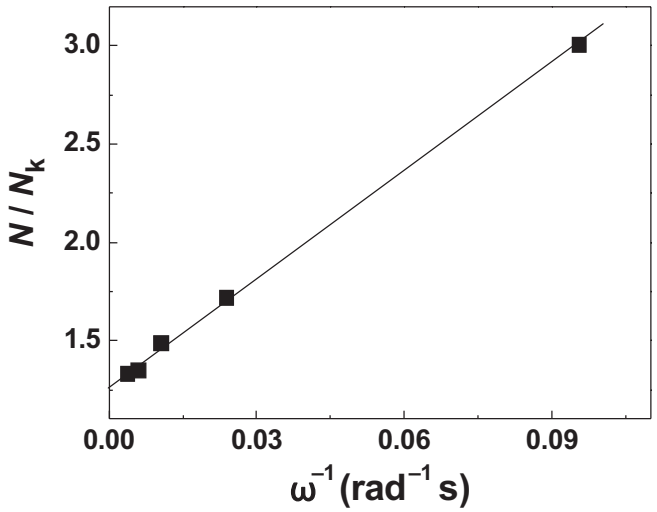
Since the transit time between the disk and the ring is dependent on the rotation rate, a more noticeable signal at the ring is observed at the higher rotation rate (1600 rpm) because at this experimental condition the decomposition reaction (eq. [11]) takes place to a less significant extent. Kinetic collection efficiency values (N_k) at various rotation rates are shown in Table 1 and corroborate these conclusions because the likelihood of detecting a short-lived intermediate is increased at short time windows. The determination of the rate constant associated with the coupled chemical reaction (eq. [11]) was based on the N/N_k vs. $1/\omega$ plot that would give a straight line according to the following equation

[13] $N/N_k = 1 + 1.28(\nu/D)^{1/3}(k/\omega)$

where N was calculated as 0.37, N_k is the kinetic collection efficiency, D is the diffusion coefficient of the electroactive

© 2007 NRC Canada

Fig. 5. Dependence of N/N_k (where N is collection efficiency measured for ferrocyanide and N_k is the collection efficiency measured for $Ni^{II}GGH$) on the reciprocal of the rotation rate for data in the 0.2 mmol L^{-1} $Ni^{II}GGH$ and 0.05 mol L^{-1} $NaClO_4$ (pH = 7.0), T = 25 °C.



species (calculated as 1.80×10^{-6} cm^2 s^{-1} by using data from the limiting current values in steady-state hydrodynamic voltammetric experiments), ν is the solution viscosity, and k is the rate constant. By using the slope of the straight line shown in Fig. 5, k was found to be 0.17 s^{-1}.

The decomposition process of $Ni^{III}GGH$ may involve highly reactive species (eqs. [14–16]) (24) as proposed in studies on the oxidation of $Ni^{II}GGH$ by oxygen (in the absence of S(IV)). In this mechanism, after $Ni^{III}GGH$ formation the carboxylate group of the peptide might donate an electron to that transiently formed Ni^{III} species, resulting a carboxyl radical, which could undergo rapid decarboxylation. The loss of CO_2 to form a His Cα-centered free radical (eq. [14]), which would be highly reactive with oxygen, is followed by superoxide formation (eq. [15]) and subsequent $N^{II}GGH'$ generation (eq. [16]) (where $Ni^{II}GGH'$ is Ni^{II}Gly-Gly-α-hydroxy-D,L-histamine).

[14] $Ni^{III}GGH \rightarrow Ni^{II}GGH^{\cdot} + CO_2$

[15] $Ni^{II}GGH^{\cdot} + O_2 \rightarrow Ni^{II}GGH\text{-}O_2^{\cdot}$

[16] $Ni^{II}GGH\text{-}O_2^{\cdot} \xrightarrow{H_2O} Ni^{II}GGH'$

Further evidence of the formation of a highly reactive nickel superoxide complex during the $Ni^{III}GGH$ decomposition comes from our previous EPR spin trapping studies (7). A solution containing only $Ni^{II}GGH$ and DMPO (in absence of S(IV)) generated the characteristic spectrum of DMPOX (5,5-dimethyl-pyrrolidone-(2)-oxy-(1)) (25). The formation of DMPOX is indirect evidence for peroxy radical ($ROO^{\cdot}$) generation, which is trapped by DMPO. Therefore, an intermediate radical, such as $Ni^{II}GGH\text{-}O_2^{\cdot}$ (eq. [15]), is likely to be the species capable of oxidizing DMPO (1.87 V vs. NHE) (26) to DMPOX.

Conclusions

Cyclic voltammetry and rotating ring-disk electrode voltammetry provided qualitative and quantitative information on the reaction involving the electrogenerated transient Ni(III) and the ligand GGH. However, the combination of spectrophotometry (7), EPR spin trapping (7), electrochemical techniques, and the available literature (eq. [14–16]) (24) still does not allow a definitive assignment of the many species involved in the autocatalytic process of $Ni^{II}GGH$ oxidation in the presence of S(IV) and dissolved oxygen and the further decomposition step. The system is complex and the results can only explain in part the observed spectra and voltammetric changes.

Acknowledgments

We gratefully acknowledge the financial support from Fundação de Amparo à Pesquisa do Estado de São Paulo (FAPESP) and Conselho Nacional de Pesquisa e Desenvolvimento Tecnológico (CNPq) (Brazilian Agencies).

References

1. International Agency for Research on Cancer. IARC Monographs on the evaluation of carcinogenic risk to humans. Vol. 49. Chromium, Nickel and Welding, Lyon, France. 1990.
2. B. Sarkar. *In* Coordination chemistry. *Edited by* J.P. Laurent. Vol. 21, Pergamon, Oxford, UK. 1981.
3. K.C. Brown, S.H. Yang, and T. Kodadek. Biochemistry, **34**, 4733 (1995).
4. J.G. Muller, R.P. Hickerson, R.J. Perez, and C.J. Burrows. J. Am. Chem. Soc. **119**, 1501 (1997).
5. Q. Liang, D.C. Ananias, and E.C. Long. J. Am. Chem. Soc. **120**, 248 (1998).
6. X. Huang, M.E. Pieczko, and E.C. Long. Biochemistry, **38**, 2160 (1999).
7. M.V. Alipázaga, R.G.M. Moreno, E. Linares, M.H.G. Medeiros, and N. Coichev. Dalton Trans. **23**, 3738 (2005).
8. B. Cuenoud, T.M. Tarasow, and A. Schepartz. Tetrahedron Lett. **33**, 895 (1992).
9. N. Coichev and R. van Eldik. Inorg. Chem. **30**, 2375 (1991).
10. N. Coichev, R. van Eldik, and D.A. Franz. J. Chem. Educ. **71**, 767 (1994).
11. D.E. Linn, M.J. Dragan, and D.E. Miller. Inorg. Chem. **29**, 4356 (1990).
12. H.R. Pezza and N. Coichev. J. Coord. Chem. **47**, 107 (1999).
13. M.V. Alipázaga, D. Lowinsohn, M. Bertotti, and N. Coichev. Dalton Trans. **2**, 267 (2004).
14. M.V. Alipázaga, R.G.M. Moreno, and N. Coichev. Dalton Trans. **13**, 2036 (2004).
15. M.V. Alipázaga and N. Coichev. Anal. Lett. **36**, 2255 (2003).
16. H.D. Moya, E.A. Neves, and N. Coichev. J. Chem. Educ. **76**, 930 (1999).
17. D.E. Linn, S.D. Rumage, and J.L. Grutsch. Int. J. Chem. Kinet. **25**, 489 (1993).
18. H.R. Pezza, R.L. Bonifácio, and N. Coichev. J. Chem. Res-M. 1520 (1999).
19. L.B. Carvalho, M.V. Alipazaga, D. Lowinsohn, M. Bertotti, and N. Coichev. J. Braz. Chem. Soc. **17**, 1400 (2006).
20. C. Brandt and R. Van Eldik. Chem Rev. **95**, 119 (1995).
21. N. Camerman, A. Camerman, and B. Sarkar. Can. J. Chem. **54**, 1309 (1976).

© 2007 NRC Canada

22. R.W. Hay, M.M. Hassan, and Ch. You-Quan. J. Inorg. Biochem. **52**, 17 (1993).
23. F.P. Bossu and D.W. Margerum. Inorg. Chem. **16**, 1210 (1977).
24. W. Bal, M.I. Djuran, D.W. Margerum Jr., E.T. Gray, M.A. Mazid, R.T. Tom, E. Nieboer, and P.J. Sadler. J. Chem. Soc. Chem. Commun. 1889 (1994).
25. G.M. Rosen and E.J. Rauckman. Mol. Pharmacol. **17**, 233 (1980).
26. R. Radi, J.S. Beckman, K.M. Bush, B.A. Freeman. J. Biol. Chem. **266**, 4244 (1991).

© 2007 NRC Canada

Reactions of aniline in acetic acid solutions containing cyanuric chloride and hydrogen chloride acceptors

Kirill A. Kolmakov

Abstract: Two reaction pathways in acetic acid solution containing cyanuric chloride, aniline, and some hydrogen chloride acceptors (triethylamine, sodium acetate, pyridine) were studied. Both aryl amination and acylation can be performed with high yields under proper reaction conditions. Contrary to the only known literature report on the reactions between carbonic acids and cyanuric chloride in the presence of a hydrogen chloride acceptor (triethylamine), it was established that acid chlorides are not formed. A scheme involving the replacement of chlorine atoms by acetate ion in the initial stage was proposed for the acylation of aniline promoted by cyanuric chloride.

Key words: acetic acid, acylation, aniline, cyanuric chloride, aryl amination.

Résumé : On a étudié deux voies réactionnelles pour les réactions de l'aniline dans des solutions d'acide acétique contenant du chlorure cyanurique et des accepteurs du chlorure d'hydrogène, tels la triéthylamine, l'acétate de sodium et la pyridine. En choisissant les conditions expérimentales appropriées, on peut réaliser aussi bien les réactions d'amination aromatique que celles d'acylation, avec de bons rendements. Contrairement à ce qui a été rapporté dans la seule publication connue sur les réactions entre les acides carboniques et le chlorure cyanurique en présence d'un accepteur de chlorure d'hydrogène (triéthylamine), on a démontré qu'il n'y a pas de formation de chlorures d'acide. On propose un schéma impliquant le remplacement des atomes de chlore par l'ion acétate dans l'étape initiale de la réaction d'acylation de l'aniline catalysée par le chlorure cyanurique.

Mots-clés : acide acétique, acylation, aniline, chlorure cyanurique, amination aromatique.

[Traduit par la Rédaction]

Introduction

Acetic acid as solvent has a unique combination of valuable qualities, the most important of which are environmental compatibility, low toxicity, low flammability, and the possibility to recycle. All these are complemented by miscibility with water and most organic solvents, high polarity, and high boiling point. At the same time, its application in preparative organic chemistry is narrow. The reactions of cyanuric chloride (2,4,6-trichloro-1,3,5-triazine (**1**, Scheme 1)) with aniline and with acetic acid, respectively, have been known for more than 60 years (1), while the interactions between *all three* still have not been studied. In our most recent research, we devised an efficient and "green" synthetic approach to aryl amination of cyanuric chloride with various aromatic amines using acetic acid as solvent (2). No attempts to perform amination (or other type of nucleophilic substitution) in acetic acid medium had been reported previously. We found that mono- and di-arylamino derivatives (**2a**, **2b**) are formed smoothly at ambient temperature in the absence of hydrogen chloride acceptors, while conventional procedures utilize bases (1). The final third stage of substitution in **1**, a typically difficult transformation to achieve with aromatic amines, is complete after 30 min heating at 118 °C in acetic acid (2). One needs to know why acetic acid is superior to conventional polar organic solvents in the aryl amination of **1** and why acylation, as an expected side reaction, is eliminated. Apart from acid–base interaction between aniline and acetic acid, it is well known that carbonic acids can act as acylating agents, especially at elevated temperatures (3). One could expect that **1**, with the reactive C-Cl function, may interact with acetic acid and thus promote acylation of aniline. The formation of acetyl chloride and cyanuric acid (Scheme 1, **3a**), as a result of cyanuric chloride dechlorination (solvilysis) in boiling acetic acid, was mentioned in the literature (1*a*, 1*d*). Further, in 1981 Lahoti and Wagle (4) suggested cyanuric chloride as a reagent for preparation of acid chlorides, amides, and esters. The authors claimed that when **1** was treated with a carbonic acid and triethylamine (1 equiv. each) in acetone, the corresponding acid chloride was readily formed. We decided to check whether the recipe (4) worked for acetic acid as substrate. If it did, acetyl chloride could form in the process of aryl amination. This extremely reactive acylating agent definitely would compete with **1** in reaction with aniline. In the context of further utilization of acetic acid for nucleophilic substitution reactions in preparative organic chemistry, we decided to explore the two alternative reaction pathways

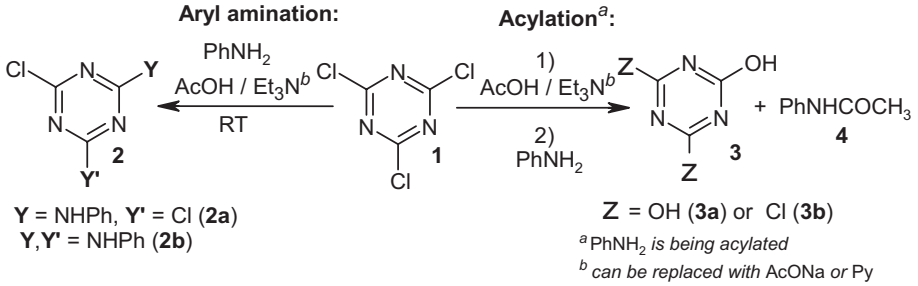
Received 16 July, 2007. Accepted 20 October 2007. Published on the NRC Research Press Web site at canjchem.nrc.ca on 22 November 2007.

K.A. Kolmakov.[1] Department of Chemistry, University of Toronto, Toronto, ON M5S 3H6, Canada.

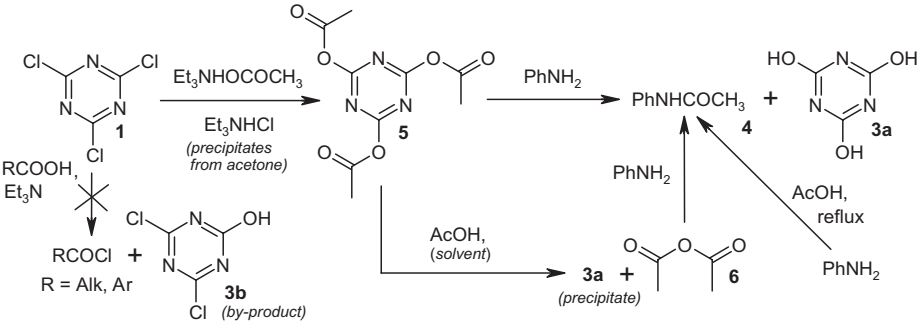
[1]Contact (e-mail: kkolmako@chem.utoronto.ca).

 doi:10.1139/V07-129 © 2007 NRC Canada

Scheme 1.



Scheme 2.



(aryl amination of **1** and acylation of aniline) in an acetic acid – cyanuric chloride – triethylamine – aniline system with acetic acid as solvent. Even though the two reaction pathways in the system seem to be obvious and involve simple and readily available reagents, no comparative studies have been published. The influence of hydrogen chloride acceptors, especially homogeneous (e.g., triethylamine, pyridine, sodium acetate) acceptors, must be deciding and should also be studied.

Results and discussion

In our initial experiments on acylation assisted by cyanuric chloride, we attempted to follow the recipe suggested by Lahoti and Wagle (4) with acetic acid as a substrate and acetone as solvent. According to the authors, insoluble 4,6-dichloro-[1,3,5]triazin-2-ol (Schemes 1 and 2, **3b**) was formed as a by-product, while acid chlorides were isolated in good and moderate yields by simple evaporation of filtrates that also contained Et_3N.

Regarding the isolation protocol, we considered it unlikely that acid chlorides and a tertiary amine could exist unreacted in the same solution (quarternary ammonium salt has to be formed (3*d*). Note that by-product **3b** is rather acidic (pK = 3.2 (2*d*)) and also would have reacted. When we added Et_3N to an acetone solution containing acetic acid and cyanuric chloride in molar ratio 1:1:1, a precipitate did form, as described, but turned out to be triethylamine hydrochloride ($Et_3N \times HCl$) rather than **3b**. The salt was identified by means of ^1H NMR, mass-spectrometry, and by melting point.

We took two other substrates, i.e., 4-nitrobenzoic and trichloroacetic acids (mentioned in (4) among illustrative examples) and obtained exactly the same salt ($Et_3N \times HCl$) as a by-product. Importantly, acid chlorides were not detected in the reaction mixtures (see Experimental section).

Regarding the reaction scheme in general, we would like to emphasize that 1 equiv. of chlorine (one chlorine atom) goes to form triethylamine hydrochloride, as we established. Logically, acid chlorides cannot be the major reaction products. All of this makes the formation of acid chlorides, as described in the above mentioned paper (4), very doubtful. Further tests showed that amides, namely acetanilide (Scheme 2, **4**), were formed (together with other products including aryl amination products **2a** and **2b**) when aniline (1 equiv.) was added to the reaction mixtures. However, amides proved to be problematic to isolate from reaction mixtures without using preparative chromatography, and we focused on experiments in acetic acid medium. The interaction between carbonic acids and **1** can be illustrated by Scheme 2. It explains the formation of triethylamine hydrochloride. The key point is that in acetic acid – cyanuric chloride – triethylamine system, the only possible nucleophile is acetate ion. Acetate replaces the chlorine atom in the course of aromatic nucleophilic substitution. Chlorine is a leaving group, while 4,6-dichloro-[1,3,5]triazin-2-ol acetate (acetate of compound **3b**) or 1,3,5-triazine-2,4,6-triol acetate (**5**) (when 1 or 3 equiv. of Et_3N is added, respectively) are the products. The presence of **5** in the reaction mixtures was detected by mass spectrometry. Importantly, we established that the reaction does not proceed in the absence of Et_3N. Cyanuric chloride is stable in acetic acid at room temperature; the ^1H NMR or ^{13}C NMR spectra of **1** in CD_3COOD solution are invariant over 2 days. Equilibrium is only shifted when an acetic acid solution of cyanuric chloride is heated to boil so that acetyl chloride distills off. Another way to shift the equilibrium is the introduction of Et_3N (or other HCl acceptors). In this case triethylamine hydrochloride is formed, which binds HCl. In the final stage of the re-

© 2007 NRC Canada

action sequence, 4,6-dichloro-[1,3,5]triazin-2-yl group has to be the leaving group, because the acidity of 4,6-dichloro-[1,3,5]triazin-2-ol **3b** is higher (pK = 3.2 (1*d*)) than that of aliphatic carbonic acids or benzoic acid. As a result, target amides are formed, and compound **3b** is washed off by basic solutions. Cyanuric acid (**3a**), with pK value about 4.7, is acidic enough to be the leaving group. We would prefer to consider the formation of amides promoted by cyanuric chloride as a case of activated ester method (see Scheme 2), which has a wide application in organic (mostly peptide) synthesis (5). The method involves the conversion of acids to esters with hydroxy compounds whose anions are good leaving groups (4-nitrophenol, 1-hydroxybenzitriazole, and many others). The esters then react with amines or amino acids to furnish amides.

To embark on experiments with acetic acid as solvent, we first combined aniline, cyanuric chloride, and Et_3N in the molar ratio 1:1:1 (1 equiv. each). Triethylamine, a strong base, was neutralized with acetic acid, and the mixture was cooled to ambient temperature before being added to the solution of cyanuric chloride. Aniline was also neutralized with acetic acid beforehand (see experimental details later). We tried different sequences of the reagent addition. When aniline (1 equiv.) was added immediately or even 3 h after Et_3N (1 equiv.), aryl amination proved to be the predominant reaction. Only trace amounts of acetanilide **4** were detected. Further experiments showed that the course of the reaction could be changed when no less than 3 eqiuv. of Et_3N was added to the reaction mixture. To completely eliminate the aryl amination, the acetic acid solution of cyanuric chloride and Et_3N must be left for a long time (10–12 h) before the addition of aniline. Aniline was taken in excess (~4 equiv.) to provide maximum yield. Extraction of the reaction mixture with benzene and subsequent treatment with dilute hydrochloric acid and alkali gave a chromatographically pure sample of **4** (the purity and identity was checked by means of ^{1}H NMR and HPLC). The isolated yield was 77%, assuming all three chlorine atoms of **1** reacted. The yield of **4** is slightly higher (81%) when Et_3N is replaced by sodium acetate and is considerably lower (56%) when pyridine is used instead.

The analysis of an acetic acid solution containing cyanuric chloride and Et_3N (in the form of its acetate) revealed some interesting facts. First, a precipitate of cyanuric acid **3a** was formed. It was identified by mass spectroscopy and elemental analysis; the isolated yield was about 72%. Further, triethylamine hydrochloride was isolated with 92% yield from the liquid phase upon diluting with hexane. The formation of this salt confirms the proposed reaction scenario (Scheme 2). Regarding the reactivity of cyanuric chloride in general, our results are consistent with some of the previously reported data, showing that selective substitution of one chlorine atom in cyanuric chloride is often problematic (1*d*). To explain the formation of cyanuric acid (**3a**), one should keep in mind that acetic acid is a protonic solvent. Such solvents must cause solvolysis of the "active ester" **5**. We observed a rapid formation of **3a** when water was added to the solutions of **1** and Et_3N in acetone or acetic acid. In dry acetic acid medium, the only possible solvolysis product was acetic anhydride (Scheme 2, **6**), whose presence in the reaction mixture was confirmed by means of mass spectrometry and ^{1}H NMR. No trace of acetyl chloride was detected. We may assume that the formation of insoluble cyanuric acid **3a** could be an additional driving force of the solvolysis, which leads to the formation of acetic anhydride. Finally, we found it possible to perform acylation of aniline with acetic acid as a "green reaction" simply by heating aniline in a large volume (~ 80 mol excess) of acetic acid under reflux (~1 h) in the absence of catalysts or dehydrating agents, as recommended in (3*a*).

Meanwhile, no trace of **4** was detected when 3 equiv. of all three reagents were mixed simultaneously. Thus, when aniline (3 equiv.) was added to the reaction mixture immediately after Et_3N (3 equiv.), aryl amination prevailed and a precipitate was formed (see Experimental section). The major product (92%, according to HPLC) was 6-chloro-*N*,*N*′-diphenyl-[1,3,5]triazine-2,4-diamine (Scheme 1, di-substituted product **2a**). Up to 66% of this compound was isolated by simple filtration of the reaction mixture after 6 h exposure at ambient temperature. Et_3N can be replaced by sodium acetate or pyridine with the same result. An excellent yield (96%, isolated) of di-substituted product was achieved when water was added to the reaction mixture (together with the reagents), which precipitated the reaction product. To obtain pure mono-substituted product **2b** in the reaction with 1 equiv. of aniline, the temperature should be maintained at about 15 °C and water should also be added. Otherwise, substantial amounts of di-substituted product **2a** are formed.

All these experiments demonstrate that acetate ion, as a weaker nucleophile, fails to compete with aniline in the reaction with cyanuric chloride in acetic acid solutions. It was established in the late 1940s that salts and acids are dissociated to a very little extent (6) in acetic acid medium, in contrast to water solutions. Thus, acetates are barely dissociated in anhydrous acetic acid, and consequently the effective concentration (activity) of the nucleophile is very low. Note that neat acetic acid exists in the form of dimers with strong intramolecular hydrogen bonds and, as acid, dissociates weakly (6).

Conclusions

Two reactions of aniline in acetic acid solutions containing cyanuric chloride and hydrogen chloride acceptors have been established, not considering the acid–base interaction between aniline and acetic acid. Either transformation, aryl amination or acylation, can be performed smoothly and with high yields under proper reaction conditions. The results show that acetic acid can be used as solvent for aryl amination of cyaniric chloride **1** and most probably other heterocyclic halides with no risk of acylation. This is due to the lower nucleophilicity of the acetate ion and a weak dissociation of acetates in anhydrous acetic acid medium. The presence of HCl acceptors (triethylamine, pyridine, sodium acetate) does not influence the aryl amination, which predominates in acetic acid solution. Mono- or di-phenylamino-1,3,5-triazine derivatives (**2a** and **2b**) were obtained in good and excellent yields when acetic acid solutions of cyanuric chloride, aromatic amines (1 or 2 equiv.), and an acetate (1 or 2 equiv., respectively) were combined simultaneously at ambient temperature. On the other hand, a clean procedure

© 2007 NRC Canada

for the preparation of acetanilide **4** promoted by cyanuric chloride has been developed. It is very likely to be applicable to other acids and amines. To achieve acylation, it is first necessary to complete the reaction between cyanuric chloride and 3 equiv. of triethylammonium acetate, which causes the replacement of all three chlorine atoms; sodium or pyridinium acetates can also be used. For acylation, acetic acid has to be dry, while aryl amination is not impeded by the addition of water. Acetyl chloride is never formed in the course of the reaction between cyanuric chloride and acetic acid in the presence of triethylammonium acetate in acetone or acetic acid solutions. In acetic acid solution containing cyanuric chloride and triethylammonium (or sodium) acetate, cyanuric acid **3a** and acetic anhydride **6** are formed as solvolysis products. Acetic anhydride is the actual acylating agent in the subsequent reaction with aniline.

Experimental section

General

All chemicals were purchased from Sigma-Aldrich Chemical Company and used as received. Progress of the reactions was monitored by HPLC or TLC on silica gel SIL G/UV 254 plates and chloroform/acetone (10:1) as mobile phase. HPLC was performed using a 5500 Varian Vista chromatograph equipped with Waters Symmetry C-18 reverse-phase column (4.6/150 mm, 5 μ particle size, methanol/water (80:20 vol.) as mobile phase). Mass spectra were recorded on Micromass 70S-250 sector mass spectrometer; NMR spectra on a Varian spectrometer at 300 MHz (^{1}H) and 75 MHz (^{13}C). Acetic acid (Sigma-Aldrich, 99.7%, ACS reagent grade) was freshly distilled and subjected to fractional crystallization under inert atmosphere. Triethylamine and pyridine were distilled over KOH and dried over CaH_2. Sodium acetate (anhydrous) was dried at 150 °C under vacuum. All the experiments on acylation and aryl amination were carried out under inert atmosphere, unless otherwise noted.

Aryl amination of cyanuric chloride

*Preparation of 6-chloro-*N,N′*-diphenyl-[1,3,5]triazine-2,4-diamine (di-substituted derivative 2b)*

Method A (in glacial acetic acid medium)

Triethylamine (3.6 mL, 0.025 mol) and aniline (1.95 g, 0.021 mol) were added dropwise upon cooling (t < 35 °C) to 30 mL of acetic acid and the solution was combined with **1** (1.84 g, 0.01 mol) dissolved in 30 mL of AcOH. After 6 h a precipitate was filtered, washed with boiling water (20 mL × 2) to neutral pH, and dried to furnish 1.96 g (66%) of **2b**.

Method B (in the presence of water and with sodium acetate as HCl acceptor)

A solution of **1** (1.84 g, 0.01 mol) in 30 mL of AcOH was combined with a solution of aniline (1.95 g, 0.021 mol) and CH_3COONa (2.0 g, 0.025 mol) in the mixture of AcOH (10 mL) and H_2O (10 mL) at RT without protection from air and then left for 4 h. The precipitate was treated as described above to furnish 2.85 g (96%) of compound **2b**. Melting point (192–194 °C) and spectroscopic data agreed with previoulsy reported data (1*e*).

Preparation of 4,6-dichloro-[1,3,5]triazin-2-yl-phenylamine (mono-substituted derivative 2a)

To a stirred solution of **1** (9.2 g, 0.05 mol) in 150 mL of acetic acid 4.65 g (0.05 mol, 1 equiv.) of aniline and 7.2 mL (0.05 mol, 1 equiv.) of Et_3N in a mixture of 20 mL of AcOH and 80 mL of H_2O was added dropwise within 15 min at 15–17 °C upon cooling with ice water (not letting AcOH to freeze). In the open air, the reaction mixture was left for 1 h at this temperature and then diluted with 1 L of brine. The solid was collected, dried, and recrystallized from 330 mL of heptane (insoluble impurities were filtered off the hot solution) to afford 7.47 g (62%) of pure (HPLC, NMR) compound **2a**, whose melting point (136 to 137 °C) and spectroscopic data was in accordance with that previously reported (1*d*).

Acylation of aniline

Acylation promoted by cyanuric chloride

Et_3N (0.60 mL, 4 mmol) was added dropwise to 5 mL of AcOH, the mixture cooled to RT, combined with a solution of **1** (0.184 g, 1 mmol) in 5 mL of AcOH and left overnight. Aniline (0.370 g, 4 mmol) in 3 mL of AcOH was added and left for 6 h upon stirring. The mixture was diluted with 30 mL of water containing 10 g of NH_4Cl and extracted with benzene (3 × 10 mL). The extract was consequently washed with 10 mL of 0.5 mol/L HCl and 10 mL of 0.5 mol/L NaOH, dried over $MgSO_4$, and evaporated under reduced pressure to furnish 312 mg (77%) of chromatographically pure (~99%, according to HPLC) acetanilide **4**, whose melting point (113 to 114 °C) and ^{1}H NMR agreed well with the literature data (7).

Acylation of aniline with acetic acid as solvent

Aniline (0.93 g, 0.01 mol) was refluxed in 50 mL of glacial acetic acid for 2 h, the solvent evaporated under vacuum, the residue washed with 0.1 N HCl (20 mL), then H_2O (3 × 10 mL) to neutral pH and dried to furnish 1.11g (82%) of pure acetanilide.

Identification of by-products

Triethylamine hydrochloride

Colorless needles, mp 251–253 °C (lit. value 254–260 °C, Merk Index Vol. 13, p. 9740). ^{1}H NMR (300 MHz, D_2O) δ: 1.10 (t, 3H, Et), 3.02 (m, 2H, Et), 4.67 (br. s, H_2O + H^+). HRMS (EI, 70 eV) calcd. for $C_6H_{15}N$ (M^+ – HCl): 101.1204; found: 101.1204.

Cyanuric acid (3a)

Colorless solid, does not have a clear melting point (1*a*). MS (EI, 70 eV) *m*/*z*: 129 (M^+, 100), 86 (M^+ – NHCO, 25), 70 (M^+ – NHCO – O, 20), 58 (NHCONH, 10). HRMS (EI, 70 eV) calcd. for $C_3H_3N_3O_3$: 129.0174; found: 129.0176.

Acetic anhydride (6)

Isolated by fractional distillation of the reaction mixtures under reduced pressure (dry argon atmosphere was maintained), bp 80–83 °C/100mm. ^{1}H NMR (300MHz, $CDCl_3$) showed the characteristic signal of acetyl group protons in Ac_2O at 2.22 ppm (acetyl group protons in AcOH and AcCl

© 2007 NRC Canada

resonated at 2.09 and 2.62 ppm respectively). MS (EI, 70 eV) *m*/*z*: 101 (M^+, 100), 43 (CH_3CO^+, 40).

Acid chlorides

Careful fractional distillation of the reaction mixtures in inert atmosphere did not lead to isolation of the chlorides, as claimed in (4). Because of the extremely high reactivity, no "direct" methods for chromatographic detection of acid chlorides are known. Derivatization, which is normally used in the preparation step of chromatographic analysis (8), fails to distinguish chlorides from anhydrides or other acylating agents. While working with acetic, 4-nitrobenzoic, and trichloroacetic acids as substrates, ^{13}C NMR spectroscopic study of the reaction mixtures showed that they contain several components, including unreacted cyanuric chloride **1**. We compared ^{13}C NMR spectra of authentic samples of 4-nitrobenzoyl chloride, acetyl chloride, and trichloroacetyl chloride with that of reaction mixtures but did not observe the characteristic signals of "acid chloride" carbonyl groups. Mass spectrometric analysis did not reveal any peaks that could be attributed to the acid chlorides either.

Acknowledgement

The author thanks The University of Toronto Chemistry Department (Canada) for fellowship support and is also grateful to Dr. Maxim Karpov (St. Petersburg State University, Russia) for good advice.

References

1. For the reactions and properties of cynauric chloride and cyanuric acid, see: (*a*) E.M. Smolin and L. Rapoport. *In* The chemistry of heterocyclic compounds. Interscience Publishers, NY. 1959. p. 53; (*b*) J.T. Thurston, J.R. Dudley, D.W. Kaiser, I. Hechenbleikner, F.C. Schaefer, and D. Holm-Hansen. J. Am. Chem. Soc. **73**, 2981 (1951); (*c*) W.M. Pearlman and C.K. Banks. J. Am. Chem. Soc. **70**, 3726 (1948); (*d*) S. Horrobin. J. Chem. Soc. Chem. Commun. 4130 (1963); (*e*) K. Tagaki, T. Hattori, H. Kunisada, and Y. Yuki. J. Polym. Sci., Part A: Polym. Chem. **38**, 4385 (2000).
2. For an efficient "green" approach to aryl amination of cyanuric chloride using acetic acid as solvent, see: K.A. Kolmakov. J. Heterocycl. Chem. In press.
3. For the acylation of amines in acetic acid medium, see: (*a*) K.V. Krishna Mohan, N. Narender, and S.J. Kulkarni. Green Chem. **8**, 368 (2006); (*b*) V.G. Shabalin, M.M. Chemeris, and V.V. Kon'shin. Izv. Vyssh. Uchebn. Zaved. Lesn. Zh. **1**, 81 (2004); (*c*) L.M. Litvinenko, D.M. Aleksandrova, and S.F. Prokopovich. Ukr. Khim. Zh. **27**, 494 (1961); (*d*) for the interaction between acid chlorides and triethylamine see: J. Kajima Mulengi, O. Bensaid, and S. Bensalem. J. Soc. Alger. Chim. **6**, 207 (1996).
4. Cyanuric chloride, a reagent for the preparation of acid chlorides, amides, and esters, see: R.J. Lahoti and D.R. Wagle. Indian J. Chem. Sect. B, **20**, 852 (1981).
5. Activated ester method in peptide synthesis, see: N.L. Benoiton. Chemistry of peptide synthesis. CRC Press. 2005. p. 36.
6. Acetic acid solutions of electrolytes, see: S. Bruckenstein and I.M. Kolthoff. J. Am. Chem. Soc. **78**, 2974 (1956) and the refs. cited therein.
7. E. Kolehmainen, K. Laihia, R. Kauppinen, D. Rasola, and A. Puchala. J. Phys. Org. Chem. **8**, 577 (1995).
8. For chromatographic analysis of acid chlorides and anhydrides see: (*a*) J.M. Bissinger, K.T. Rullo, T.J. Stoklosa, C.M. Shearer, and N.J. De Angelis. J. Chromatogr. **268**, 102 (1983); (*b*) P. Maki-Arvela, E. Paatero, and T. Salmi. J. Chem. Technol. Biotechnol. **61**, 1 (1994).

© 2007 NRC Canada

Primary ion fluence dependence in time-of-flight SIMS of a self-assembled monolayer of octadecylphosphonic acid molecules on mica discussion of static limit[1]

M. Nieradko, N.W. Ghonaim, L. Xi, H.Y. Nie, J. Francis, O. Grizzi, K. Yeung, and W.M. Lau

Abstract: By using a self-assembled monolayer of octadecylphosphonic acid molecules, $CH_3(CH_2)_{17}PO(OH)_2$, on mica as a model of the "soft" materials, such as self-assembled monolayers (SAMs) and multilayers in many biological systems as well as artificially engineered molecular electronic systems, we have examined the effects of primary ion fluence on time-of-flight secondary ion mass spectrometry (TOF-SIMS) of the technologically important model. Our measurements clearly show that although the intensity per unit primary ion fluence of most atomic ions and many small fragment ions do not vary by more than 10% for the fluence range of 10^{10}–10^{13} cm^{-2}, the intensity of the parent molecular ion can drop by two orders of magnitude in this fluence range. While the changes are different for the primary ion beams of Bi_3^+ (25 keV, 45°), Bi^+ (25 keV, 45°), and Ar^+ (8 keV, 45°), they are all substantial, with the damage cross section induced by the Bi_3^+ beam being the largest (6 000 $Å^2$). Since different secondary ions have quite different intensity changes, the analytical results derived from TOF-SIMS can vary significantly by the time and duration of the measurements in the TOF-SIMS experiment. Therefore, our results suggest that for TOF-SIMS of molecular layers such as SAMs, the primary ion fluence condition should be recorded and reported. In general, the validity of the static condition becomes questionable when the cumulative primary ion fluence exceeds 1×10^{11} cm^{-2}.

Key words: SIMS, static SIMS, TOF-SIMS, soft materials, self-assembled monolayer, bilayer, surface of biological materials.

Résumé : En prenant une monocouche autoassemblée de molécules d'acide octadécylphosphonique, $CH_3(CH_2)_{17}PO(OH)_2$, sur du mica comme modèle des matériaux souples, tels les monocouches autoassemblées (MAA) et les multicouches qu'on retrouve dans plusieurs systèmes biologiques ainsi que les systèmes électroniques moléculaires mis en place artificiellement, on a examiné les effets de la fluence ionique primaire sur la spectrométrie de masse de l'ion secondaire en temps de vol (SMIS-TDV) du modèle technologiquement important. Nos mesures montrent clairement que, même si l'intensité par unité de fluence de l'ion primaire de la plupart des ions atomiques et que plusieurs petits ions fragments ne varient pas plus de 10% pour la plage de fluence allant de 10^{10} à 10^{13} cm^{-2}, l'intensité de l'ion moléculaire parent peut diminuer par deux ordres de grandeur dans cette plage de fluence. Même si les changements diffèrent avec les divers faisceaux des ions primaires du Bi_3^+ (25 keV, 45°), Bi^+ (25 keV, 45°) et Ar^+ (8 keV, 45°), ils sont toutefois toujours importants et la section droite du dommage induit par le faisceau de Bi_3^+ est le plus important (6 000 $Å^2$). En se basant sur le fait que les changements dans les intensités varient d'une façon importante avec la nature des ions secondaires, les résultats analytiques obtenus à l'aide de la spectrométrie de masse de l'ion secondaire en temps de vol peuvent donc varier d'une façon significative avec le temps et la durée des mesures faites de cette façon. Les résultats obtenus suggèrent donc que pour les SMIS-TDV de couches moléculaires telles que les monocouches autoassemblées, la condition primaire de fluence ionique devrait être enregistrée et rapportée. En général, la validation de la condition statique peut être remise en question quand la fluence cumulative de l'ion primaire dépasse 1×10^{11} cm^{-2}.

Received 14 June 2007. Accepted 24 September 2007. Published on the NRC Research Press Web site at canjchem.nrc.ca on 22 November 2007.

M. Nieradko, N.W. Ghonaim,[2] L. Xi, H.Y. Nie, J. Francis, and W.M. Lau.[3] Surface Science Western, University of Western Ontario, London, ON N6A 5B7, Canada.
K. Yeung.[2] Department of Chemistry, University of Western Ontario, London, ON N6A 5B7, Canada.
O. Grizzi. Centro Atomico Bariloche, CNEA, Instituto Balseiro, UNC & CONICET, Bustillo 9500, 8400 Bariloche, RN, Argentina

[1]This article is part of a Special Issue dedicated to Professor G. Michael Bancroft.
[2]Present address: Department of Biochemistry, University of Western Ontario, London, ON N6A 5B7, Canada.
[3]Corresponding author (e-mail: llau22@uwo.ca).

 doi:10.1139/V07-123 © 2007 NRC Canada

Mots-clés : spectrométrie de masse de l'ion secondaire (SMIS), SMIS statique, spectrométrie de masse de l'ion secondaire en temps de vol (SMIS-TDV), matériaux mous, monocouche autoassemblée, bicouche, surface de matériaux biologiques.

[Traduit par la Rédaction]

Introduction

The surface analytical technique of static secondary ion mass spectrometry (static SIMS), as a means of nondestructive characterization, is now widely used for many surface science applications (1). One emerging field of applications bearing particular importance is the analysis of "soft" molecular layers in both molecular electronics and biological systems, soft materials that include submonolayers of adsorbed organic molecules, self-assembled monolayers (SAM), bi-layer and multi-layer lipid molecules, cell membranes, and surfaces of other biological systems (2–9). They are soft because the intermolecular bonding is commonly van der Waals in nature. In these studies the characterization often requires the detection and imaging of the parent and fragment ions of a constituent with a concentration much less than a monolayer. SIMS, in conjunction with the time-of-flight (TOF) technique, is indispensable because of its rather unique capability in detecting such a trace surface concentration. This detection sensitivity allows the completion of an analysis with a very low primary ion irradiation fluence so that in the course of the analysis only very few of the surface atoms and (or) molecules are struck by a primary ion. As such, when they are probed, all the atoms and (or) molecules are likely in their original condition because all prior probing events are too far away to affect them. Under this "static" condition the SIMS signals can be used to deduce the very original nature of the surface. The accomplishment of this measurement outcome is attractive to most studies, including studies of molecular layers in molecular electronics and biological systems. However, the soft nature of these molecular layers makes them susceptible to changes induced by ion bombardment; hence, further clarification of the static condition in this context is required.

By definition, the maximum primary ion fluence below which the static condition is valid really depends on the radial range of the surface interactions induced by the arrival impact of a specific primary ion on a specific surface. Hence, the static condition itself is by no means "static", and it is more difficult to satisfy when the surface is soft and more susceptible to ion-induced changes. In fact, in the early development of static SIMS most specimens of interest were stable inorganic materials with surfaces relatively immune to ion-induced changes. The radial range is often correlated to the collision cross-section, which is typically about 10^{-14} cm^2 for most ion bombardment at the keV range for many metals, semiconductors, and dielectrics (10–12). For an analysis of this type, the static condition can be quite forgiving and is often specified with a primary ion fluence lower than 1×10^{13} cm^{-2}. In 1991 and 1992, Legett and Vickerman measured (13–14) the primary ion fluence dependence of secondary ion signals from polymers poly(ethylene terephthalate), poly(tetrafluoroethylene), poly(vinyl chloride), and poly(methyl methacrylate) and showed the damage of the original nature of the polymer caused by both ion bombardment and ion neutralization. In 1995, Delcorte et al. (15) cautioned any casual claim of nondestructive measurements and insightfully proclaimed that there is no real "static" condition, and one should always be careful about bombardment-induced effects during any ion beam analysis. In 1996, Gilmore and Seah (16) carefully examined the static SIMS condition for polymers such as poly(ethyleneterephthalate) and poly(tetrafluoroethylene) with 4 keV argon and xenon primary ions and made the practical recommendation that for the analysis of polymers, the primary ion fluence limit for maintaining the static condition should not be higher than 1×10^{12} cm^{-2}. Since then, most studies of soft materials have indeed adopted this recommendation.

Because primary ion bombardment effects on soft molecular layers have not yet been studied thoroughly, we have begun to study the effects of primary ion fluence in TOF-SIMS and TOF ion scattering spectroscopy (ISS) for the soft molecular layers in the molecular electronics and biological systems in our own on-going research. In this article, we report on some of our results collected from the special specimens of octadecylphosphonic acid, $CH_3(CH_2)_{17}PO(OH)_2$, on mica in the form of a self-assembled monolayer (referred to as OPA/mica, with the molecule referred to as OPA-H). These specimens were used to model the silane-based and phosphyl-based molecular layers in molecular electronics and cell membranes. They were also chosen because our research group had already acquired some prior knowledge on their formation mechanism and technical skills on the use of TOF-SIMS and atomic force microscopy (17, 18).

The article will focus on the exemplification of the sensitive TOF-SIMS changes in the fluence regimes of 10^{11} to 10^{13} cm^{-2}, with some data points collected below 10^{11} cm^{-2} whenever the data collection is practical. Since the Bi_3^+ ion beam is one of the primary ion beams of choice in the recent research of soft molecular layers, most of the results shown in this article were collected with it. To illustrate some of our ideas on the possible ion–surface interactions causing the observed sensitivity of primary ion fluence, we will also show some TOF-SIMS results of Bi^+ and Ar^+ on OPA/mica and of Bi_3^+ on alkyl-thiols/Au(111).[4] In addition, we will briefly correlate these results with those from our scanning probe microscopic studies of the ion–surface interactions on these molecular layers (19).

Results and discussion

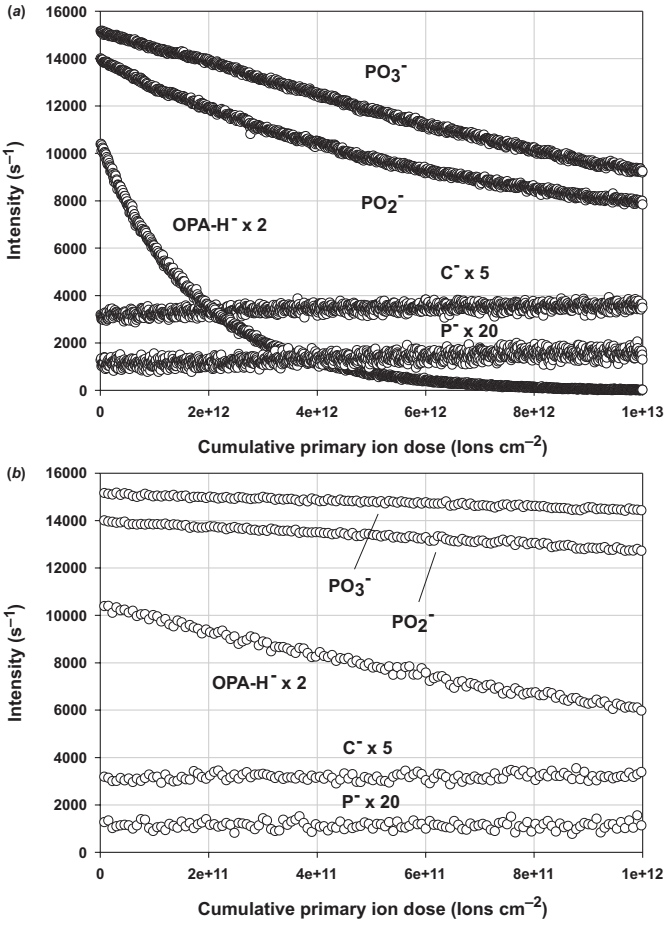
Primary ion fluence dependence of negative secondary ions from OPA/mica with Bi_3^+

As expected, the secondary parent ion intensity critically depends on the primary ion fluence for the model molecular layer sample of OPA/mica in the entire primary ion fluence

[4] N. Ghonaim. Manuscript in preparation.

© 2007 NRC Canada

Fig. 1. Relative TOF-SIMS negative secondary ion intensities as a function of primary ion fluence for OPA on mica using a Bi_3^+ ion beam within a cumulative primary ion fluence of (*a*) 10^{13} cm^{-2} and (*b*) 10^{12} cm^{-2}.



range from about 1×10^{10} to 1×10^{13} cm^{-2}. Negative secondary ion intensities are shown in this example because the negative secondary ion yield is much higher than the positive ion counterpart. The comparison between negative and positive secondary ions can be found later in the paper. From Figs. 1*a* and 1*b*, one sees that the parent molecular ion (OPA-H$^-$) drops exponentially, with a decrease in intensity of two orders of magnitude when the cumulative primary ion fluence increases from 1×10^{10} to 1×10^{13} cm^{-2}. Similarly, the characteristic phosphate fragments PO_3^- and PO_2^- decrease in intensity immediately as well, but these changes are much less marked within 1×10^{12} cm^{-2}. The measured changes are definitely not caused by any system error because the negative fragment ion intensity of elemental carbon (C$^-$) and phosphorus (P$^-$) change very little in the same cumulative primary ion fluence range. Conceivably the bombardment leads to bond breakage in the adsorbed molecules causing a drop in the concentration of the virgin molecules. The bond breakage, on the other hand, increases the number of carbon atoms having dangling bonds, which may lead to the observed increase in the C$^-$ intensity. As revealed in the following sections, the C$^-$ intensity for TOF-SIMS with Bi^+ and Ar^+ and that of C^+ for Bi_3^+ also increase with increasing cumulative primary ion fluence. All these observations, together with the observations that the parent ion intensities in all these bombardment conditions consistently decrease exponentially with the cumulative primary ion fluence, converge to the inference that the primary ion bombardments in all these cases are causing a very significant damage to the adsorbed molecules. To further support the results shown by the plots of the primary ion fluence dependence of the selective ions in Fig. 1, we show the negative ion mass spectra of OPA/mica at a cumulative primary ion fluence of 1×10^{11} cm^{-2} (Fig. 2*a*) and 1×10^{13} cm^{-2} (Fig. 2*b*) and those of a bare mica at a cumulative primary ion fluence of 1×10^{13} cm^{-2} (Fig. 2*c*). Once again, the parent molecular ion intensity in Fig. 2*a* drops rapidly in Fig. 2*b* and is obviously absent in Fig. 2*c*. In Fig. 2*b*, some fragments derived from the bombardment damage of OPA, such as PO_2^- and PO_3^-, are seen; once again, they are absent in Fig. 2*c*. A comparison of Figs. 2*a* and 2*b* also shows that the intensity drop for the OPA parent molecular ion is much more significant than those of the PO_2^- and PO_3^- fragment ions. While no signals from the mica substrate are seen in Fig. 2*a*, they appear in Fig. 2*b*. However, this does not necessarily mean that a large fraction of the OPA coverage has been completely removed, because the PO_2^- and PO_3^- signals are still strong in Fig. 2*b* and a careful examination of the intensity of P$^-$ (see also Fig. 1*b*) shows little change up to a primary ion fluence of 1×10^{13} cm^{-2}.

In principle, the observed exponential decrease of the parent molecular secondary ion intensity is a convoluted effect of damage and removal of the OPA molecule, together with the possible change in ion yield. However, OPA removal due to sputtering or desorption should not be an important attribute in the low primary ion fluence range of the present work. For example, if a removal yield of 10 molecules per primary ion is assumed, the decrease in OPA surface density should still be less than 10% for a primary ion fluence of 1×10^{13} cm^{-2}. There are further experimental observations supporting the insignificance of OPA removal. First, the P$^-$ intensity does not change significantly at the primary ion fluence of 1×10^{13} cm^{-2}, as shown in Fig. 1. If removal of OPA is important, one would expect a significant drop in the P$^-$ intensity. Second, an atomic force microscopic analysis of the sample after receiving a primary ion fluence of 1×10^{13} cm^{-2} shows no void in the self-assembled monolayer. Regarding the ion yield factor, subsequent sections of this article show that similar exponential decreases of the parent molecular ion intensity are evident for positive ion measurements with Bi_3^+ and negative ion measurements with Ar^+ and Bi^+. This indicates that the observed exponential decreases of the parent molecular ion intensity in all these cases are mainly due to the damage of the parent molecules induced by the primary ion bombardment.

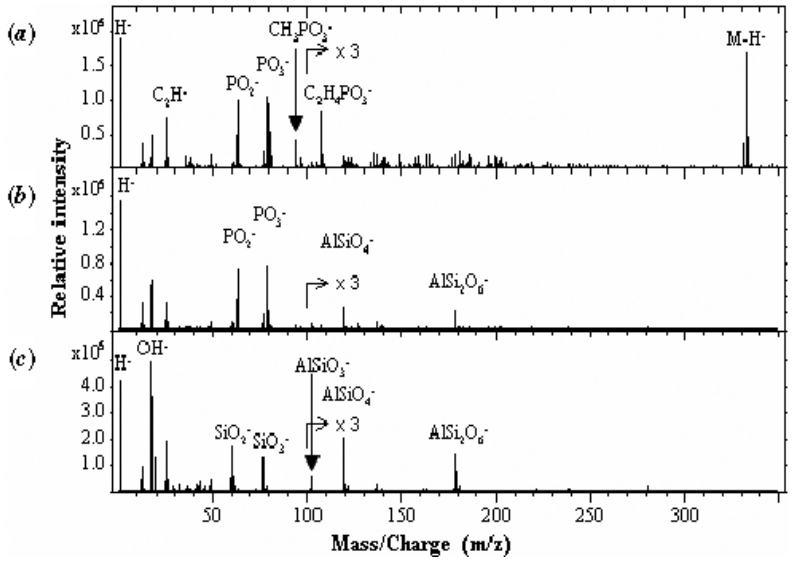
To further analyze the observed secondary parent ion intensity changes as a function of primary ion fluence, we assume that the observed exponential drop of the parent molecular ions is due to the damage of the parent molecule, OPA-H, by the primary ion bombardment. Taking this assumption, we adopt the following common description with the concept of damage cross-section (1),

$$[1] \qquad I_t(\phi) = I_o \exp(-\sigma\phi)$$

where I_o and I_t are the respective secondary parent ion intensities at the beginning of the measurements and at time t, ϕ is

© 2007 NRC Canada

Fig. 2. TOF-SIMS negative secondary ion mass spectra for OPA on mica using a Bi_3^+ ion beam within a cumulative primary ion fluence of (*a*) 1×10^{11} cm^{-2} and (*b*) 1×10^{13} cm^{-2}. The spectrum from bare mica with a cumulative primary ion fluence of 1×10^{13} cm^{-2} is included in (*c*).



the cumulative primary ion fluence after time *t*, and σ is the damage cross-section for the parent molecule. It turns out that the damage cross-section of the parent OPA-H$^-$ molecule by Bi_3^+ at 25 keV and at an incident angle of 45° is about 6×10^{-13} cm^2 (or 6 000 Å^2). This is consistent with the work by Galera et al. (20) on the Langmuir–Blodgett monolayer of arachidic acid on gold with 2 keV Cs^+ and an ion incident angle of 20°. The damage cross-section in this previous case is ~1×10^{-13} cm^2. In comparison, Benninghoven and Sichtermann (11) reported significantly smaller damage cross-sections (from 1 to 7×10^{-14} cm^2) for various parentlike ions from a sample of leucine (with 2.25 keV Ar^+ as the primary ion). We speculate that the relative large damage cross-sections for molecular layers such as self-assembled monolayers and Langmuir–Blodgett films may arise from the agility of the damaged molecules and their diffusion inevitably extends the radial range of molecular damage.

With the estimated damage cross-section value of 6×10^{-13} cm^2 and eq. [1], we can further calculate the primary ion fluence limit for the static condition by adopting the Gilmore and Seah recommendation of setting the fluence limit by allowing not more than a 10% change in the secondary ion intensity. The result in this case is 2×10^{11} cm^{-2}, which is significantly lower than the prevalent assumption of a fluence limit of 1×10^{12} cm^{-2} for the static condition. If this prevalent fluence limit assumption were adopted in the study of OPA/mica under the same analysis condition in this work, the maximum secondary ion intensity change in the fluence range of 1×10^{12} cm^{-2} is 39%. Obviously, the claim of the static condition is invalid.

What are the practical scientific implications of erroneously going beyond the primary ion fluence limit of the static condition? The immediate implication is that any measurements of the surface density of a molecule with a large damage cross-section will become rather arbitrary when the measurements only claim the validity of the static condition without specifying the actual cumulative primary ion fluence for the measurements. In addition, rectifying this error by resorting to calculations of relative intensities with one molecular species as an internal reference may not work because the damage cross-sections are likely molecule and (or) fragment dependent, even for the same primary ion bombardment conditions. For example, the data in Fig. 1 clearly show that the damage cross-section for OPA-H$^-$ is higher than PO_3^- and PO_2^-. Hence, we advocate that in TOF-SIMS studies of soft molecular layers, one should mind the effects of primary ion fluence. With our estimated primary ion fluence limit of 2×10^{11} cm^{-2} for OPA/mica with 25 keV Bi_3^+, we recommend that the static condition should be set to 1×10^{11} cm^{-2} for TOF-SIMS studies of soft molecular layers. However, we prefer to recommend that a thorough check of the primary ion fluence dependence is the best remedy for reducing any measurement errors induced by the dependence of primary ion fluence.

Primary ion fluence dependence of positive secondary ions from OPA/mica with Bi_3^+

Under Bi_3^+ bombardment, the detection of negative secondary ions commonly gives more intense signals than that of positive secondary ions from an oxide matrix. For the sake of completeness of illustrating the primary ion fluence dependence in this work, we show the secondary ion intensities of OPA+H$^+$ and C$^+$ as a function of primary ion fluence in Figs. 3*a* and 3*b*. Although the signal-to-noise statistics displayed in Fig. 3 are far from ideal, the data do show clearly that while the intensity of C$^+$ increases slowly, the parent molecular ion intensity drops rapidly. When we fit the data for OPA+H$^+$ using eq. [1], we obtain a damage cross-section of ~ 5×10^{-13} cm^{-2}. Because the signal-to-noise level of this set of data is poor, we do not speculate on any difference in damage cross-section or damage mechanism between the negative secondary ion detection and the positive ion detection.

© 2007 NRC Canada

Fig. 3. Relative TOF-SIMS positive secondary ion intensities as a function of primary ion fluence for OPA on mica using a Bi_3^+ ion beam within a cumulative primary ion fluence of (*a*) 10^{13} cm^{-2} and (*b*) 10^{12} cm^{-2}.

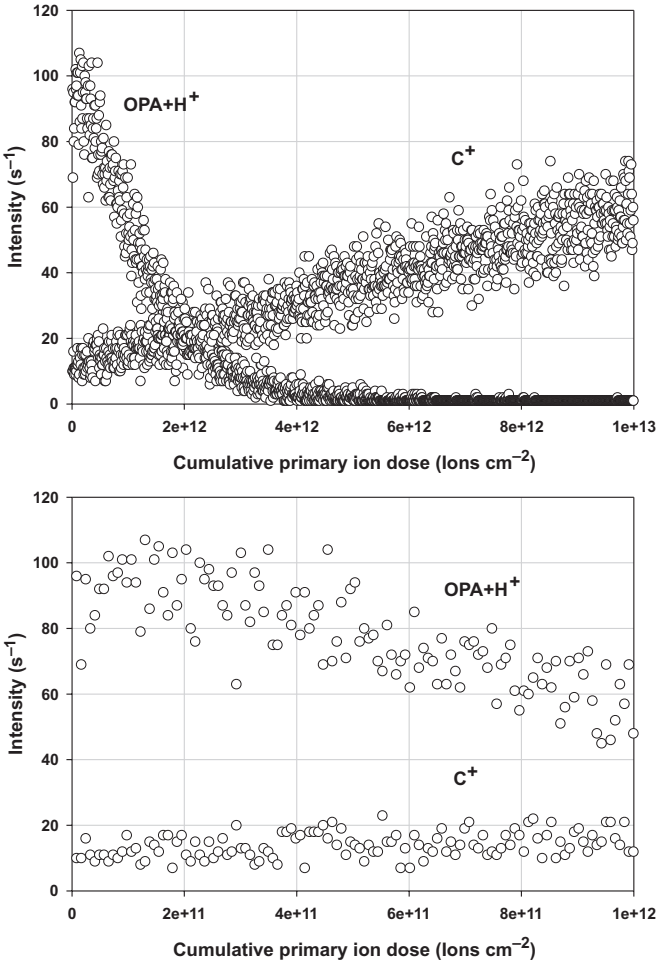
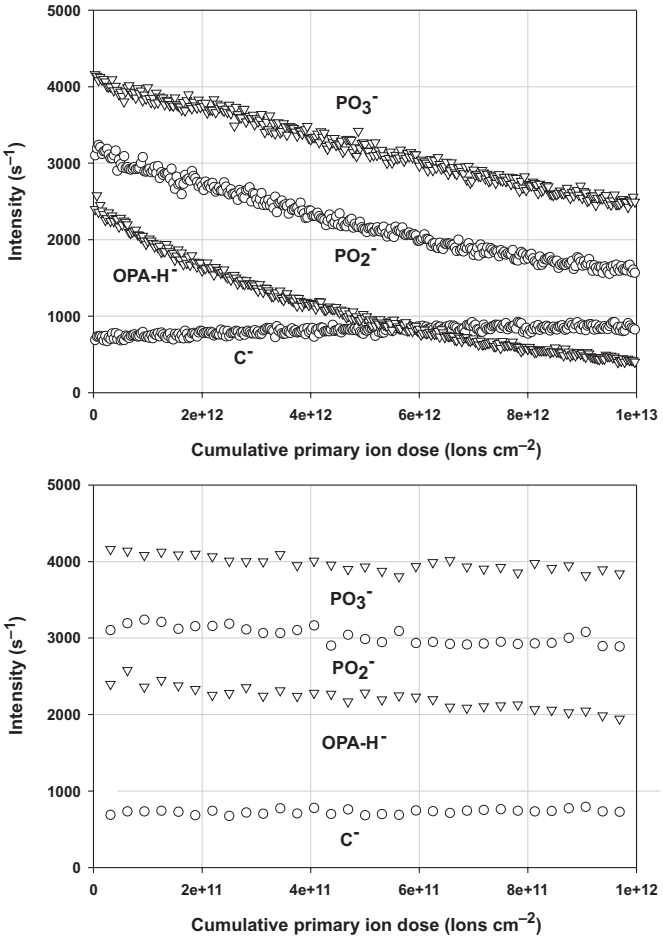


Fig. 4. Relative TOF-SIMS negative secondary ion intensities as a function of primary ion fluence for OPA on mica using a Bi^+ ion beam within a cumulative primary ion fluence of (*a*) 10^{13} cm^{-2} and (*b*) 10^{12} cm^{-2}.



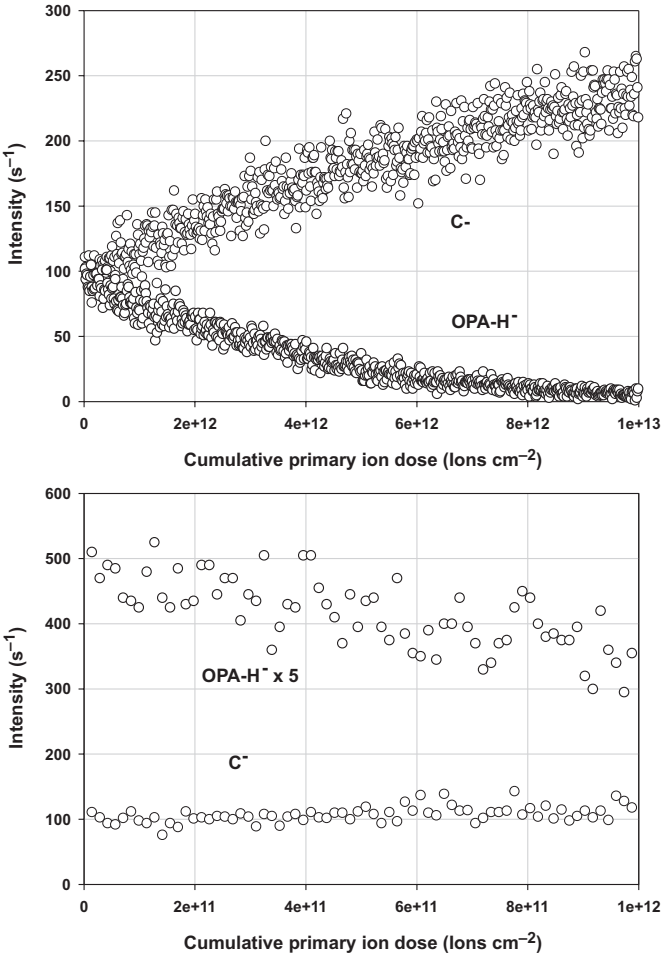
Comparison of the results from OPA/mica with Bi_3^+ with those with Bi^+ and Ar^+

Our preliminary results from bombardment of the OPA/mica by a 25 keV Bi^+ source shows similar dependencies on primary ion fluence for OPA-H$^-$ and C$^-$ as well as the characteristic phosphate headgroups PO_3^- and PO_2^-, as shown in Figs. 4*a* and 4*b*. The intensity of the carbon fragment ion slowly increases throughout the experiment while the intensity of the parent molecular ion drops exponentially. As expected, the Bi_3^+ ion beam outperforms the Bi^+ ion beam in producing characteristic secondary ion intensities in the same fluence range because of the nature of cluster ion bombardment (2). Fitting of the Bi^+ OPA-H$^-$ profile with eq. [1] gives a damage cross-section of 2×10^{-13} cm^2. For comparison purposes, bombardment of the OPA/mica by an 8 keV Ar^+ source is shown in Figs. 5*a* and 5*b*. The molecular ion is only weakly detected compared with using either of the bismuth ion sources. As a result, each point of the profile is summed over five scans to give a less noisy appearance. Fitting of the Ar^+ OPA-H$^-$ profile with eq. [1] gives a damage cross-section of 3×10^{-13} cm^2. The smaller damage cross-section of OPA-H$^-$ using the Bi^+ source compared with the Bi_3^+ source is expected, as discussed in the literature with various studies of thin organic layers under cluster ion bombardment (3, 5). The kinetic energy of the Bi^+ source is 25 keV while that of the Bi_3^+ source is ~8 keV per atom. Therefore the Bi^+ source will penetrate deeper into the specimen while producing less damage in the near-surface plane compared with each atom of the Bi_3^+ source.

With the readily available TRIM/SRIM codes for studying molecular dynamics in the collision cascades, we use a hypothetical sample of 2 nm polyethylene on alumina to cross-check the effects of primary ion bombardment for Bi^+ (25 keV, 45°), Bi^+(8 keV, 45°), and Ar^+ (8 keV, 45°). The calculations give the 3-dimensional ion, recoil, and vacancy distribution statistics, and have been prevalently used in the interpretation of SIMS results (2, 5). In the present work, we find that Ar^+ at 8 keV produces 3 to 4 carbon vacancies and 10 hydrogen vacancies per Ar^+ in the polymer layer, which is about two times less than Bi^+ at 25 keV. However, the lateral range of the vacancy distribution in the polymer layer in both cases is about the same. This may be the reason the damage cross-section of Ar^+ at 8 keV is close to that of Bi^+ at 25 keV. Although the TRIM calculations do not take into

© 2007 NRC Canada

Fig. 5. Relative TOF-SIMS negative secondary ion intensities as a function of primary ion fluence for OPA on mica using an Ar^+ ion beam within a cumulative primary ion fluence of (*a*) 10^{13} cm^{-2} and (*b*) 10^{12} cm^{-2}.



account many-body interactions and likely over-simplify the collision cascade activities induced by cluster ion bombardment, we find that three Bi^+ ions at 8 keV produce at least two times more hydrogen and carbon vacancies in the top polymer layer than 1 Bi^+ at 25 keV. Our experimental results show that the damage cross-section of Bi_3^+ at 25 keV is indeed larger than that of Bi^+ at 25 keV.

Comparison of the SIMS results from OPA/mica with those from alkyl-thiols/Au(111)

In our on-going research on TOF-SIMS and TOF-ISS of soft molecular layers, we have used the OPA/mica model to represent the silane and phosphyl self-assembled monolayer families and the alkyl-thiol/Au(111) model to represent the thiol self-assembled monolayer family. Briefly, the TOF-SIMS of the alkyl-thiol/Au(111) model is also sensitively dependent on the primary ion fluence, and the primary ion fluence limit for the static condition is also much lower than 1×10^{12} cm^{-2}. Hence, the extent of molecular damage is not fundamentally different from the OPA/mica model. In fact, our TOF-ISS studies of the alkyl-thiol/Au(111) model, which detect neutral recoil emission as well as ion emission from the surface, have also independently confirmed that primary ion fluence causing damage to 10% of surface molecules is below 1×10^{12} cm^{-2}, even for 4 keV Ar^+ (20° incidence).[5] Although the TOF-SIMS of the OPA/mica and the alkyl-thiol/Au(111) model are both influenced by molecular damage, the overall primary ion fluence dependence of the alkyl-thiol/Au(111) model is different from that of the OPA/mica model. For example, while the SIMS signals of the large molecular ions from OPA/mica generally drop exponentially, those from thiols/Au do not change monotonically. In other words, those from thiols/Au are quite complicated. The difference arises from the fact that during TOF-SIMS with a reactive primary ion such as bismuth, cesium, or oxygen, the primary ion bombardment does not only cause molecular damage but also affects the relative ion yields of some ions. By examining the intensity changes of all secondary ions (or the lack of changes) in the OPA/mica model with Bi_3^+ (both negative secondary ions and positive secondary ions), Bi^+ (negative secondary ions), and Ar^+ (negative secondary ions), we have not observed any obvious ion yield changes induced by the accumulation of primary ion fluence. In comparison, the ion yield changes are very obvious in the alkyl-thiols/Au model. The detailed description of the results collected from the alkyl-thiol/Au(111) model will be given elsewhere.[4]

Complementary results from scanning probe microscopy of relevant model specimens

In the present study of the OPA/mica model, we have used atomic force microscopy to verify the presence of a "complete" monolayer of OPA molecules on a freshly cleaved flat mica surface. In this context, complete means no observation of any detectable voids in the layer. After the TOF-SIMS experiments, we used AFM to track the molecular damage inferred from the TOF-SIMS data. Interestingly, no clear evidence of void formation has been detected. The fact that the molecular damage inferred from TOF-SIMS is not accompanied by sputter removal or desorption of the molecules is further confirmed by the observation of a constant P^- intensity for a primary ion fluence up to 1×10^{13} cm^{-2} in the Bi_3^+ experiment, which has the highest damage cross-section. As mentioned earlier in this article, we speculate that the "molecular damage" inferred from the changes of parent molecular ion intensity may be the combined effect of the fragmentation of some parent molecules being influenced by a primary ion arrival and the diffusion of the altered molecules. Drastic removal of the parent or altered molecules from the surface are not necessary conditions for the observed primary ion fluence dependence of secondary ion intensity. If so, AFM cannot detect the surface chemistry changes induced by the primary ion fluence.

We want to note in this discussion that in our recent examination of short-chain alkyl-thiols on Au(111), we have observed from scanning tunneling microscopy that while the original surface lattice of short-chain alkyl-thiols (C_2H_5S or C_3H_7S) on Au(111) is ordered, a seemingly armless ion bombardment with a low fluence of 10 eV H^+ can cause some drastic changes on the ordering of the surface lattice

[5] O. Grizzi. Manuscript in preparation.

© 2007 NRC Canada

and clear evidence of bombardment-induced diffusion of molecules can be recorded (19). This set of new results supports our speculation of a "fragmentation + diffusion" mechanism causing our observed sensitive primary ion fluence on TOF-SIMS analysis of a soft molecular layer.

Conclusion

The primary ion fluence effects on the TOF-SIMS data from an octadecylphosphonic acid (OPA) self-assembled monolayer (SAM) on freshly cleaved mica (muscovite) have been studied with Bi_3^+, Bi^+, and Ar^+ primary ion beams. The parent molecular secondary ions in all change rather drastically as a function of primary fluence below 1×10^{11} to 1×10^{13} cm^{-2}. Fitting of the OPA-H^- data (Bi_3^+ ion beam, 25 keV, 45° incident angle) to a single exponential function gives a damage cross-section of 6×10^{-13} cm^2 (6 000 $Å^2$) for the parent molecular ion. A similar damage cross-section of the parent molecular ion is observed during the collection of positive secondary ions. The static limit for TOF-SIMS of OPA/mica with Bi_3^+ is estimated to be 2×10^{11} cm^{-2}, which is significantly lower than the prevalent static limit of 1×10^{12} cm^{-2} in TOF-SIMS. In comparison to Bi_3^+ (25 keV, 45°), Bi^+ (25 keV, 45°), and Ar^+ (8 keV, 45°) have OPA-H^- damage cross sections of 2×10^{-13} cm^2 and 3×10^{-13} cm^2, respectively. With these data, we recommend that it is safer to set the static condition to 1×10^{11} cm^{-2} for TOF-SIMS of soft molecular layers. Ideally, the primary ion fluence condition and the secondary ion changes as a function of primary ion fluence should be measured and reported.

Experimental

Sample preparation

Crystalline octadecylphosphonic acid (OPA), $CH_3(CH_2)_{17}PO(OH)_2$, was obtained from Alfa Aesar (Ward Hill, Massachusetts). The sample preparation was performed according to the procedure of Nie et al. (16). An OPA SAM of approximately 100% coverage was prepared by spin-coating a 2 mmol/L solution of OPA in trichloroethylene onto freshly cleaved muscovite mica at 5 000 rpm. This coating was then dried with nitrogen to remove any weakly adsorbed molecules or other loose contaminants. The mica was 1 cm x 1 cm in size. Four regions were etched onto this coated mica, one for each TOF-SIMS time profile performed. A second bare piece of muscovite mica was also cleaved for comparison purposes in the TOF-SIMS studies.

AFM measurements

Topography measurements were performed using a PSIA XE-100 microscope. The sample surface was scanned in noncontact, low-voltage mode with a scan area of 1 μm × 1 μm. The low voltage mode was used to observe fine surface features that were present in SAMs

TOF-SIMS measurements

An ION-TOF (Gmbh) TOF-SIMS IV single-stage reflectron instrument with 10 kV post acceleration was used to study the OPA SAMs prepared on the mica substrate. A pulsed, low-energy electron flood gun was used to neutralize sample charging. All measurements were performed at room temperature. The raw data was analyzed using the IonSpec program. All intensities were normalized against the total intensity of each particular spectrum. The lack of detectable damage arising from the low energy electron irradiation during the measurements was confirmed by the fact that no change was observed after the TOF-SIMS measurement was paused, by blanking the primary ion beam without stopping the low energy electron irradiation.

Negative secondary ion OPA on mica time profile with Bi_3^+ source

Negative secondary ion measurements were performed using a (10 kHz) pulsed 25 keV Bi_3^+ primary ion beam at an incidence angle of 45°. The primary ion beam with a pulsed current of 0.12 pA was focused and rastered onto a 128 × 128 μm^2 area, delivering a cumulative ion dose of 1 x 10^{13} ions cm^{-2}.

Negative secondary ion OPA on mica time profile with Bi^+ source

Negative secondary ion measurements were performed using a (10 kHz) pulsed 25 keV Bi^+ primary ion beam at an incidence angle of 45°. The primary ion beam with a pulsed current of 0.5 pA was focused and rastered onto a 128 × 128 μm^2 area, delivering a cumulative ion dose of 1×10^{13} ions cm^{-2}.

Positive secondary ion OPA on mica time profile with Bi_3^+ source

Positive secondary ion measurements were performed under these same conditions and an identical cumulative ion dose. The primary ion beam pulsed current was 0.13 pA.

Positive secondary ion mica time profile with Bi_3^+ source

Positive secondary ion measurements were performed under these same conditions and an identical cumulative ion dose. The primary ion beam pulsed current was 0.13 pA

Negative secondary ion OPA on mica time profile with Ar^+ source

Negative secondary ion measurements were performed using a (10 kHz) pulsed 8 keV Ar^+ primary ion beam at an incidence angle of 45°. The primary ion beam with a pulsed current of 0.182 pA was focused and rastered onto a 256 × 256 μm^2 area, delivering a cumulative ion dose of 1×10^{13} ions cm^{-2}.

Acknowledgement

This work was partially supported by the Natural Sciences and Engineering Research Council of Canada (NSERC) Discovery Grant (Grant No. 327221 06), the NSERC CIAM Grant, Surface Science Western (SSW), and the Faculty of Science of the University of Western Ontario. SSW was founded in 1981 at the University of Western Ontario by several visionary leaders including Professor Mike Bancroft who was its founding director. All authors are grateful to Professor Bancroft for his initiation of the research center and his scientific advice for SSW from 1981 to the present.

© 2007 NRC Canada

References

1. J.C. Vickerman and D. Briggs. TOF-SIMS: Surface analysis by mass spectrometry. IM Publications, Chichester, UK. 2001.
2. S.C.C. Wong, N.P. Lockyer, and J.C. Vickerman. Surf. Interface Anal. **37**, 721 (2005).
3. Y.-P. Kim, M.-Y. Hong, J.M. Kim, E.K. Oh, H. Kyong-Shon, D.W. Moon, H.-S. Kim, and T.G. Lee. Anal. Chem. **79**, 1377 (2007).
4. P.L. Clode, R.A. Stern, and A.T. Marshall. Microsc. Res. Tech. **70**, 220 (2007).
5. D. Debois, A. Brunelle, and O. Laprévote. Int. J. Mass Spectrom. **260**, 115 (2007).
6. Z. Pernber, K. Richter, J.-E. Mansson, and H. Nygren. Biochim. Biophys. Acta, **1771**, 202 (2007).
7. L.G. Wu, X.C. Lu, K.S. Kulp, M.G. Knize, E.S.F. Berman, E.J. Nelson, J.S. Felton, and K.J.J. Wu. Int. J. Mass Spectrom. **260**, 137 (2007).
8. K. Börner, P. Malmberg, J.-E. Månsson, and H. Nygren. Int. J. Mass Spectrom. **260**, 128 (2007).
9. A.M. Piwowar and J.A. Garrdella, Jr. Anal. Chem. **79**, 4126 (2007).
10. A. Benninghoven, D. Jaspers, and W. Sichtermann. Appl. Phys. **11**, 35 (1976).
11. A. Benninghoven and W. Sichtermann. Int. J. Mass Spectrom. Ion Phys. **40**, 177 (1981).
12. W. Lange, M. Jirikowsky, and A. Benninghoven. Surf. Sci. **136**, 419 (1984).
13. G.J. Leggett and J.C. Vickerman. Anal. Chem. **63**, 561 (1991).
14. G.J. Leggett and J.C. Vickerman. Appl. Surf. Sci. **55**, 105 (1992).
15. A. Delcorte, L.T. Weng, and P. Bertrand. Nucl. Instrum. Methods Phys. Res. B, **100**, 213 (1995).
16. I.S. Gilmore and M.P. Seah. Surf. Interface Anal. **24**, 746 (1996).
17. J.T. Francis, H.-Y. Nie, N.S. McIntyre, and D. Briggs. Langmuir, **22**, 9244 (2006).
18. H.-Y. Nie, M.J. Walzak, and N.S. McIntyre. J. Phys. Chem. B, **110**, 21101 (2006).
19. L. Xi, W.M. Lau, and O. Grizzi. Appl. Surf. Sci. In press.
20. R. Galera, J. Blais, and G. Bolbach. Int. J. Mass Spectrom. Ion Proc. **107**, 531 (1991).

© 2007 NRC Canada

Accurate UV–visible spectral analysis of thiomolybdates

R. Stephen Reid, Rhett J. Clark, and Emmanuel K. Quagraine

Abstract: The UV–visible spectra of various thiomolybdates have been studied. Cross-contamination during synthesis and extensive overlap in the spectra have hindered the UV–vis characterization to date. We report the use of multivariate curve fitting for the accurate quantification of the composition of thiomolybdate mixtures as well as the molar absorptivities at key wavelengths of the spectrum of each pure thiomolybdate. The synthesis and isolation of all four thiomolybdates by a common synthetic route using $(NH_4)_2S$ is also reported. This is the first time that monothiomolybdate has been isolated from aqueous solution.

Key words: Thiomolybdates, UV–visible spectroscopy, speciation, curve fitting.

Résumé : On a déterminé les spectres UV–visible de divers thiomolybdates. Des contaminations croisées au cours des synthèses et des recouvrements dans les spectres avaient toujours empêché leur caractérisation jusqu'à maintenant. On a fait appel à une méthode d'ajustement de courbe à plusieurs variables pour faire une quantification précise de la composition de mélanges de thiomolybdates et pour déterminer les absorptivités molaires à des longueurs d'onde clés des spectres de chacun des thiomolybdates purs. On rapporte aussi la synthèse et l'isolement de chacun des quatre thiomolybdates par une voie de synthèse commune à l'aide de $(NH_4)_2S$. C'est la première fois que le monothiomolybdate a pu être isolé à partir d'une solution aqueuse.

Mots-clés : thiomolybdates, spectroscopie UV–visible, spéciation, ajustement de courbe.

[Traduit par la Rédaction]

Introduction

Thiomolybdates (MoS_xO_{4-x}), herein called TM*x* where *x* represents the number of S ligands, are known to cause copper deficiency in ruminants (1). For an overview of TM chemistry, see the review by Laurie (2). TM interconversions are relatively slow processes (minutes to hours), and the determination of these rate constants is paramount to modeling the actions of copper in the rumen. The work reported here forms part of an ongoing study toward this goal (3, 4).

TM4 and, likely, TM3 are the primary copper antagonists, while TM2 and TM1 are probably not responsible (5). However, because of the sequential nature of TM formation, the synthesis of pure (>99.5%) TM compounds is difficult. A reliable means for determining the composition (±0.1%) of all TMs in a mixture is crucial for quantitative study.

TMs are formed by successive substitution of O with S ligands (Scheme 1). The synthesis is well-known in general terms and has been performed for some time (6), with the exception of TM1, which is said to be difficult to isolate (6–8). Previously, the synthesis required H_2S gas, which is toxic and harmful to the environment. However, since H_2S has a pKa1 of 7 and a pKa2 of about 17 (9), and TM synthesis is performed at pH values ranging from 10 to 13, HS^- is certainly the dominant sulfide species and probably the nucleophilic species involved in the reaction. This was first proposed by Harmer and Sykes (6).

Scheme 1.

$$TM_{x-1} \underset{OH^-}{\overset{HS^-}{\rightleftharpoons}} TM_x \underset{OH^-}{\overset{HS^-}{\rightleftharpoons}} TM_{x+1}$$

To synthesize a pure TM, the reaction conditions must be such that reaction is stopped when the desired TM is at a maximum. To favor further substitution of S, one can increase the S:Mo ratio, decrease the pH, increase the temperature, and increase the reaction time. To synthesize TM1, TM2, and TM3, careful adjustment of the parameters is necessary, and even then, it is extremely difficult to avoid cross-contamination with other TMs. An effective means of characterizing the TM purity and composition is therefore required.

Pure TM4 synthesis, on the other hand, is very easy because the reaction is simply forced to proceed completely, avoiding cross-contamination. Manipulation of the synthesis by increasing reaction times and using greater S:Mo ratios did not effect the UV–vis spectrum. This indicated that TM4 was already being obtained at 100% purity.

TM purity has been obtained by a variety of techniques and reported in the literature. One common method used is elemental analysis (6, 10, 11). However, a positive result with elemental analysis must be backed up by another method because an equimolar mixture of the two surrounding TMs gives the same theoretical values as the pure de-

Received 06 July 2007. Accepted 24 September 2007. Published on the NRC Research Press Web site at canjchem.nrc.ca on 30 November 2007.

R.S. Reid,[1] R.J. Clark, and E.K. Quagraine. Department of Chemistry, University of Saskatchewan, Saskatoon, SK S7N 5C9, Canada.

[1]Corresponding author (email: steve.reid@usask.ca).

 doi:10.1139/V07-122 © 2007 NRC Canada

sired TM. Also, the differences typically determined between theoretical and experimental percentages of Mo and S are insufficient for accurately determining purity.

^{95}Mo NMR has shown some promise for determining TM purity. Each TM gives a single, sharp peak, well-resolved from the others (12). Despite the nucleus's significant quadrupole moment, the electronic environment around Mo in all four thiomolybdates is apparently sufficiently symmetric to result in minimal quadrupolar broadening. ^{95}Mo, however, has a natural abundance of 15.72% and is a low-sensitivity nucleus resulting in a poor signal-to-noise ratio. To get a reasonable spectrum for quantitative analysis, high concentrations (~0.1 mol/L) and long acquisition times (>10 min) are needed. Contributions of other TMs, up to about 5%, may go undetected. TMs are also rather unstable in water with decreased stability with decreased number of S atoms. These long acquisition times mean that hydrolysis will occur before the spectrum is obtained.

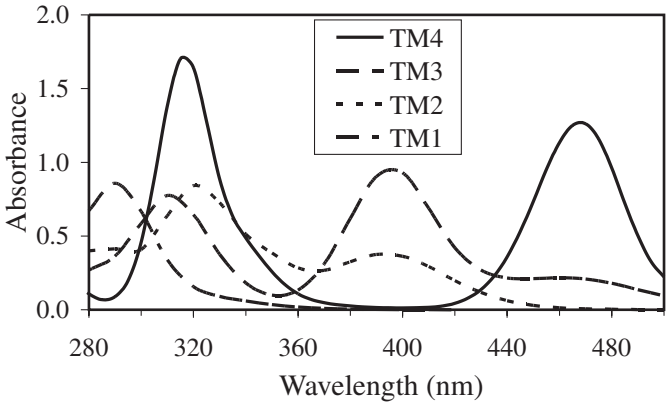
Ogra et al. used fast atom bombardment mass spectrometry (FAB-MS) to identify the presence and molecular mass of the TM of interest (13). However, attempts in our group to quantify purity using FAB and electrospray (ES)-MS were ineffective because of a large degree of fragmentation (12). This is partly due to degradation and hydrolysis of the samples at the high temperatures that were incurred. ES-MS also caused a loss of S during the analysis and may have even reacted with the less-stable TMs (TM1 and TM2) to form increased amounts of TM3 or TM4.

All TMs give characteristic UV–vis spectra (Fig. 1), making this technique useful for speciation. It has been used extensively for this purpose (6, 10, 14, 15). The strongly overlapping absorbances, however, make it difficult to identify molar-absorptivity constants because purity cannot be readily determined by inspection. Originally, elemental analysis was used to confirm a pure compound, and then the UV–vis spectrum was taken and used to directly measure absorptivity constants, which were subsequently used as a reference for purity. The uncertainty of the purity of the original compound makes the resultant absorptivities suspicious.

Some workers have used single-wavelength measurements, selecting a wavelength where there are only two absorbing species, particularly when performing kinetic studies (6, 16). The assumption made in such an approach is that contributions of all other TMs in the sample to the spectrum are negligible. The quantities of the absorbing species are determined by a simple fit. This method relies on the quality of the absorptivity constants available as the composition is directly related to it. It also requires that the assumed species make up 100% of all absorbing TM species present. This is rarely the case. Thus, it can be concluded that the monitoring of a single wavelength is insufficient for quantitative determinations.

TM1 has proven to be difficult to synthesize in pure form. The only reported isolation of TM1 was the potassium salt using methanol at –15 °C for 24 h with a yield of 10% (17). Otherwise, its presence has been inferred using UV–vis spectroscopy during TM formation (18). Supposed characteristic λ_{max} and ε (molar absorptivities) have also been inferred during reaction in solution (15) but again do not account for contamination.

Fig. 1. Simulated UV–vis spectra of 10^{-4} mol/L solutions of TM1, TM2, and TM3. The TM4 spectrum is of an actual synthesized sample.



The entire TM2 spectrum is overlapped by TM3, a common contaminant when synthesizing TM2. This makes ε determination via standard Beer's Law curve highly suspected. The corresponding elemental analysis seen in the literature for TM2 also leaves doubt that the original sample was pure (10).

Because mutual TM contamination is so common, an effective method for determining accurate concentrations of individual TMs in mixed-TM samples is necessary. Preliminary results obtained by analyzing data at six wavelengths using Microsoft Excel® readily displayed discrepancies with literature results obtained from univariate analysis. This demonstrates the need for a more-robust mode of analysis.

Multivariate curve fitting provides simultaneous determination of large numbers of parameters; in this case, these parameters are molar absorptivities of all TMs present at each wavelength selected as well as the fractional composition of all species present in a given sample. This method has a number of advantages over univariate analyses. First, it eliminates the need for selecting an appropriate single wavelength. Second, absorbance errors will be averaged out over data at all wavelengths and will not directly affect any single result. It also removes the linear dependence amongst the parameters. Overall, multi-wavelength analysis is more-robust, and the determination of purity simultaneously with absorptivities improves the accuracy of both values. For an overview of mathematical modeling, see the text by Gershenfeld (19).

This paper describes the synthesis of TMs using $(NH_4)_2S$ solution as a reagent. Curve-fitting techniques are then used to determine both the absorptivities for each TM and the composition of TM mixtures in aqueous solutions. This work differs from others in the literature in that there are no assumptions made as to the initial purity of the synthesized samples. TM1 is also isolated for the first time.

Experimental

All chemicals used were reagent-grade and used without purification. Sodium molybdate ($Na_2MoO_4 \cdot H_2O$, 99.5%–103%), cesium chloride (CsCl), aq. ammonia solution (28%–30%), and anhyd. diethylether were obtained from BDH (Toronto, Canada). Ammonium sulfide (minimum

© 2007 NRC Canada

20% $(NH_4)_2S$) and Sephadex® G-25 were obtained from Sigma (St. Louis, USA.). Anhyd. ethanol was purchased from Commercial Alcohols Inc. (Brampton, Canada). The thiomolybdates; mono-, $Cs_2MoO_3S{\cdot}1/2H_2O$; di-, $(NH_4)_2MoO_2S_2{\cdot}2H_2O$; tri-, Cs_2MoOS_3; and tetra-, $(NH_4)_2MoS_4$; were synthesized as described in this paper. H_2O was millipore-grade and was deoxygenated with argon before use.

TM absorptivities

UV–vis spectra were taken on a Beckman 640 diode array spectrometer with single beam using a 1 cm quartz cuvette. Spectra were typically taken over a range of 275 to 500 nm. When measuring TM0-contaminated TM1 samples for the purpose of determining molar absorptivities, a range of 200 to 500 nm was used.

The pure salts of TM0 and TM4 were dissolved in water, and the UV–vis absorbances were measured. Absorptivities were determined from the slope of the Beer's Law plots at the desired wavelengths. TM1 and TM3 were synthesized to contain contamination from only TM0 and TM4, respectively. All TMs were added to clean, dry volumetric flasks. Measurements were taken immediately after dilution to avoid hydrolysis.

Preliminary studies showed that TM1, the least stable TM in solution, underwent minimal hydrolysis in the first three minutes, TM2 was stable for about 10 min with TM3 and TM4 showing increasing stability. Errors due to hydrolysis are expected to be minimal for TM1 and negligible for all other TMs.

The absorptivities of these TMs were then determined by curve fitting using Origin7 and the principle that absorbances are additive (see eq. [1]). TM2 was synthesized and characterized in the same fashion.

$$[1] \qquad A = \sum_{i=0}^{4} \alpha_i \varepsilon_i c_i$$

The subscript i represents the TMs (0–4), α is the fraction of a given TM, and ε is the molar absorptivity at a given wavelenth. A and c are the absorbance and concentration, respectively.

Test solutions containing all TMs were made by dissolving TMs of known composition in water with varying concentrations and measuring their UV–vis absorbance. For hydrolysis experiments, a single TM of known purity was dissolved in water and made to volume. In this case, the solution was left in the cuvette to hydrolyze and the UV–vis spectra were taken at regular time intervals. Typically, 5 min intervals were used, but in the case of TM3, hydrolysis was sufficiently slow that 10 min intervals were used. For TM4, 30 min intervals were used.

Synthesis

For TM1, TM3, and TM4, the presence of air was not found to have an effect during synthesis, and so no precautions were taken. TM2, however, was synthesized under inert atmosphere, as discoloration due to oxidation occurred quickly in air. All TMs were stored under Argon.

TM1 $(Cs)_2MoO_3S{\cdot}1/2H_2O$

$Na_2MoO_4{\cdot}H_2O$ (1.0 g, 4.13 mmol) was dissolved in a solution of water (1.2 mL) and 8 mL of aq. ammonia (28%–30%) and placed in an ice bath to reduce the temperature to ~5 °C. 2 mL of $(NH_4)_2S$ solution (20%) was also cooled in an ice bath and was added to the molybdate solution. The reaction mixture (~pH 13) was mixed and allowed to stand for 10 min before a CsCl solution (2.8 g, 16.63 mmol in 2 mL of water) was added. The reaction mixture was added to a previously cooled mixture of 15 mL diethyl ether and 5 mL ethanol, shaken, and left to stand to precipitate for about 15 min. A fine yellow precipitate (1.39 g, 75% yield) formed. This precipitate was filtered and washed three times with 10 mL of ethanol then twice with 10 mL of diethyl ether. The pale yellow, crystalline $Cs_2MoO_3S{\cdot}1/2H_2O$ was dried and stored under an inert atmosphere. The level of hydration was determined by X-ray crystallography (20).

TM2 $(NH_4)_2MoO_2S_2{\cdot}2H_2O$

$Na_2MoO_4{\cdot}H_2O$ (1.0 g, 4.13 mmol) was dissolved in 1.2 mL of water and 5 mL of aq. ammonia (28%–30%) and cooled in an ice bath. 4.8 mL of cold $(NH_4)_2S$ solution (20%) was added, mixed, and allowed to react in an ice bath for 10 min. Precipitation occurred by adding 20 mL of a cold 1:1 ethanol/ether mixture, followed by 20 mL of ether, and then 12 mL of ethanol. The mixture was allowed to stand for another 15 min before the fluffy yellow-orange precipitate was filtered out. This precipitate easily browned in air, so precipitation was performed in a filter flask attached to a Schlenk line with thorough washing with ethanol then ether. The dried TM2 was quickly transferred to a storage vial and stored under inert atmosphere. The product was amorphous, making X-ray crystallography ineffective. A ^1H NMR standard-additions experiment was used to determine the stoichiometry of hydration.

TM3 Cs_2MoOS_3

$Na_2MoO_4{\cdot}H_2O$ (0.5 g, 2.07 mmol) was dissolved in 1 mL of water and 1 ml of aq. ammonia (28%–30%). To this was added 5 mL of $(NH_4)_2S$ solution (20%). To avoid precipitation of $(NH_4)_2MoO_2S_2{\cdot}2H_2O$ before the addition of CsCl, neither solution was precooled, and the mixture was mixed with gentle swirling. The mixture was then allowed to stand at room temperature for 8 min before a CsCl solution (1.4 g in 2 mL of water) was added. Deep-orange precipitate formed immediately, and 10 mL of 1:1 ethanol/ether was added to improve the yield (71%). The product was washed with 10 mL of cold water, twice with 10 mL of ethanol and twice with 10 mL of diethyl ether, dried, and stored under inert atmosphere. The addition of non-polar solvents to the filtrate caused the product that was dissolved by water to precipitate. This product is of higher purity as determined by techniques described elsewhere in this paper. The product was then filtered, washed with ethanol and ether, and stored under inert atmosphere.

TM4 $(NH_4)_2MoS_4$

$Na_2MoO_4{\cdot}H_2O$ (1.0 g, 4.13 mmol) was dissolved in 2 mL of water, and to it was added 15 mL of $(NH_4)_2S$ solution (20%). The contents (~pH 10) were stoppered, shaken, and allowed to stand in a 35 °C water bath. After about 3 h, dark

© 2007 NRC Canada

Table 1. Molar absorptivities of the TMs at λ_{max} from this work and selected references for comparison.

	This work			Erickson 2000 (15)			Muller 1969 (21)	
	λ_{max}	ε	±	λ_{max}	ε	±	λ_{max}	ε
TM0	207	10 100	200				208	8400
							231	2800
TM1	290	8600	50	290	7390		288	8000
				314	2900		314	3000
TM2	286	4300	50	290	3940	40	288	3000
	321	8470	60	322	6740	60	318	6000
	395	3790	30	394	3230	50	394	3000
TM3	312	7330	40	312	7500	40	313	6600
	396	9550	80	396	9030	80	392	8700
	461	1860	20	462	2080	10	465	2300
TM4	317	17 300	300	318	16 480	190	317	18 000
	468	12 800	200	468	11 870	150	467	13 000

Note: λ_{max} is in nm, and ε is in $Lmol^{-1}cm^{-1}$; ± in this work is the standard deviation from the experimental values, ± in reference 14 is the standard deviation of the slope of absorbance vs. concentration curves.

green rod-like crystals began to form, but the mixture was allowed to stand for at least 4 h to ensure completeness of reaction. 10 mL of a cold mixture of 1:1 ethanol/ether was added, shaken vigorously, and left in an ice bath for 30 min to improve the yield (79%). The precipitate consisted of fine dark-red crystals with a green shimmer as well as the rod-like crystals that had formed previously. The product was filtered and washed with 10 mL of cold water, 10 mL of 1:1 ethanol/ether, and 10 mL of ether before storing under inert atmosphere. As with TM3, a second precipitate formed in the filtrate. This was filtered and washed with 10 mL of 1:1 ethanol/ether and twice with 10 mL of ether to obtain a red scaly precipitate (22% yield). This product was also dried and stored under inert atmosphere.

Results and discussion

UV–vis characterization

The inevitability of mutual contamination of TM samples makes it necessary to have an effective means of analyzing the composition of the sample. UV–vis spectroscopy is a useful technique for analyzing TMs, but it is limited by the great deal of overlap in the TM spectra. It also typifies the limitations of assuming that a synthesized TM is pure when measuring its spectrum.

To use UV–vis effectively for speciation, the molar absorptivities of each pure species must be determined despite the inevitable contamination of all real samples. The Origin7 software contains a curve-fitting routine that was used to find these constants. The molar absorptivities at λ_{max} of the pure TMs as determined by fitting are shown in Table 1, along with selected literature values for comparison. Errors for TM1, TM2, and TM3 are in terms of standard deviation of the measured and fitted absorbances. For TM0 and TM4 where ε values were determined by Beer's Law plots, errors are standard deviation of the slope. Solution concentrations are assumed to be exact.

The use of curve-fitting techniques allows for the simultaneous fitting of multiple variables. The software iterates all parameters beginning at preset values. Iterations stop when the overall error, the difference between actual and fitted values, is minimized. Also, to reduce the error, a minimum of ten solutions of the same composition but differing concentrations were fit.

Curve fitting was done by fitting the absorbances at a subset of selected wavelengths. The wavelengths included all λ_{max} as well as a few other chosen wavelengths that would help to characterize all of the peaks such that all peaks were represented by at least three wavelengths. If too many points are selected, there is no further improvement of the results. If there are too few points selected, there may be more combinations of absorptivities possible to fit the data, especially when there are multiple TMs overlapping. In all, 13 wavelengths were selected.

When fitting UV–vis data of the TM solutions, there are two sets of unknowns, the absorptivities of each pure TM at the selected wavelengths and the composition of the real (impure) TM sample. These unknowns cannot be fit simultaneously, and so each set was fit separately.

The absorptivities were fit using eq. [2].

$$[2] \qquad A_\lambda = \left(\sum_{i=0}^{4} \alpha_{i\text{“}x\text{”}} \varepsilon_{i\lambda} \right) c_{\text{“}x\text{”}} / \mathrm{Fm}_{\text{“}x\text{”}}$$

A_λ is the absorbance at wavelength λ, $\alpha_{i\text{“}x\text{”}}$ is the fraction of a given TM in the impure "TM*x*" sample, *c* is the g/L concentration of the impure TM sample, Fm is the average formula mass of the sample, and $\varepsilon_{x\lambda}$ is the molar absorptivity of TM*x* at wavelength λ.

Absorbance values are the dependent variables, and each array consists of absorbances at an individual wavelength in-

© 2007 NRC Canada

curred by all solutions. The concentrations of the solutions are the independent variables, and the absorptivities are the parameters to be fitted. The absorptivities of any known TMs and the fractional TM composition are input as constants.

The fractional TM composition is set at an estimated value based on inspection of the UV–vis spectrum of the sample. The formula mass is then calculated from the formula mass of each TM component and the fraction present in the sample. However, it must be noted that the counter ion of each TM is dependent on which TM was the target of the synthesis. For example, when synthesizing TM3, the target would be $Cs_2MoO_3S \cdot 1/2H_2O$, and so any TM4 that forms would be Cs_2MoS_4 as opposed to the ammonium salt that would be produced by TM4 synthesis. If the contaminating TM was accompanied by a different counter ion, the FM would not be determinable prior to the fit. Figure 2*a* illustrates the quality of fit for absorptivity determination. Some wavelengths have been removed for clarity.

Attempts to determine all TM absorptivities simultaneously failed because of the large number of variables and the great dependency of the variables on each other. Each TM was therefore characterized individually. TM0 and TM4, which were available in pure form, were measured directly, and their absorptivities were determined via Beer's Law curves.

TM4 is the final product in the series to be formed. The ability to synthesize it in pure form facilitated the characterization of the other TMs. We are certain of the purity of TM4 because the reaction could be driven to completion by increasing the S:Mo ratio, a more acidic pH, and a longer reaction time. It was found that attempts to force the reaction further, i.e., even greater S:Mo ratios, resulted in no changes to the product, indicating that only TM4 was present.

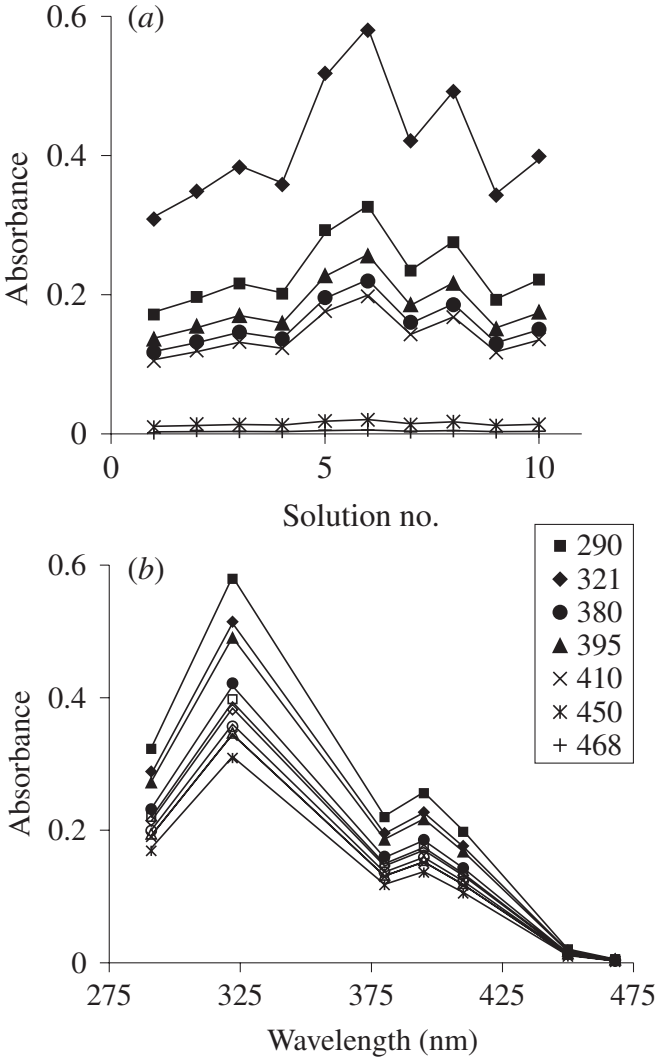
Further evidence of TM4 purity can be seen in the UV–vis spectrum. It contains no evidence of a peak around 395 nm. This would be indicative of TM3, the primary contaminant. Also, when mixtures of synthesized TMs were measured, there were no irregularities observed between theoretical and actual values. Misidentified TM4 purity would have become evident at this point.

Each subsequent TM was carefully synthesized to contain contamination only by already characterized TMs. For example, synthesized "TM3" contained TM4 but no TM2, while "TM1" contained only TM0 as a contaminant. Initially, the identities of the contaminants were determined by qualitative inspection of the UV–vis spectra.

The TM3 or TM1 absorptivities were thus the only unknowns. This reduced the number of variables and improved the quality of fit. It should be noted that, initially, all TMs were included to establish those that weren't present. Once all absorptivities were known, fitting was again repeated with all TMs included to ensure the results.

The second fitting stage involved finding the composition of a given impure sample. The absorbance is still the dependent variable, but the array consists of the absorbance values of all selected wavelengths for one solution. The independent variables are now the TM absorptivities from the fit in step 1. The solution concentrations and average formula mass are input as constants, and the α values are the parameters to be determined. Figure 2*b* shows the quality of fit when determining the TM composition. Again, some wavelengths were removed for clarity.

Fig 2. (*a*) Origin7 fit to find molar absorptivities. (*b*) Origin7 fit to find TM composition in impure sample. The data points are the selected wavelengths used in this study; the solid lines represent the fit. Each curve was obtained by measuring solutions of varying concentration but constant composition. The legend values are in nm.



With the TM fractions determined, the average formula mass was recalculated based on the new results, and the composition was reacquired. This process was repeated until the parameters no longer changed. The compositional data were then input into the first-fitting program to recalculate the absorptivities, which were subsequently used to redetermine the composition. This process was repeated until convergence was achieved.

There are some significant discrepancies between absorptivities achieved in this work compared with other works. This is due to the characterization methods in conjunction with potentially impure samples that are assumed to be pure. By determining the composition concomitantly with the absorptivities, all values are more reliable and not dependent on the purity of the synthesized sample.

© 2007 NRC Canada

In the case of TM1, the absorptivity obtained in this work at 290 nm is greater than the absorptivities obtained from other works. Because TM1 was difficult to synthesize, this value was previously obtained by monitoring its formation in solution. During formation, there is no point at which only TM1 is present because of the rapid formation of TM1 and TM2. It is likely that TM2 will begin to form before conversion to TM1 is complete. The presence of TM2 accounts for the second small peak that was often recorded as belonging to TM1 (6, 15, 18). Being able to synthesize and isolate the TM1 salt was paramount to being able to characterize TM1 and subsequently TM2. This will also improve our ability to study TM kinetics in the future.

TM2 was difficult to synthesize in pure form. It was also very difficult to identify contamination by inspecting the UV–vis spectrum. The presence of TM1 is completely overlapped by the TM2 peak at 286 nm. Contamination by TM3 would produce an increase in the peak at 321 nm. Even though TM3 absorbs around 461 nm, the absorbance is weak, and so small amount of TM3 may go unnoticed in the TM2 spectrum. It also may be possible to have some contribution of TM0 in the sample, which does not absorb in the studied region, and would reduce the overall absorbance.

The TM3 spectrum gives away the fewest clues about contamination. One method of attempting to quantify purity was to find a characteristic peak ratio between the peaks at 396 and 461 nm (11). There has been very little agreement on this value in the literature (7, 8, 11). However, the presence of TM2 will decrease both absorbances by a similar amount, since the difference in absorptivities between the TMs at both wavelengths is similar. This method still carries the assumption of purity.

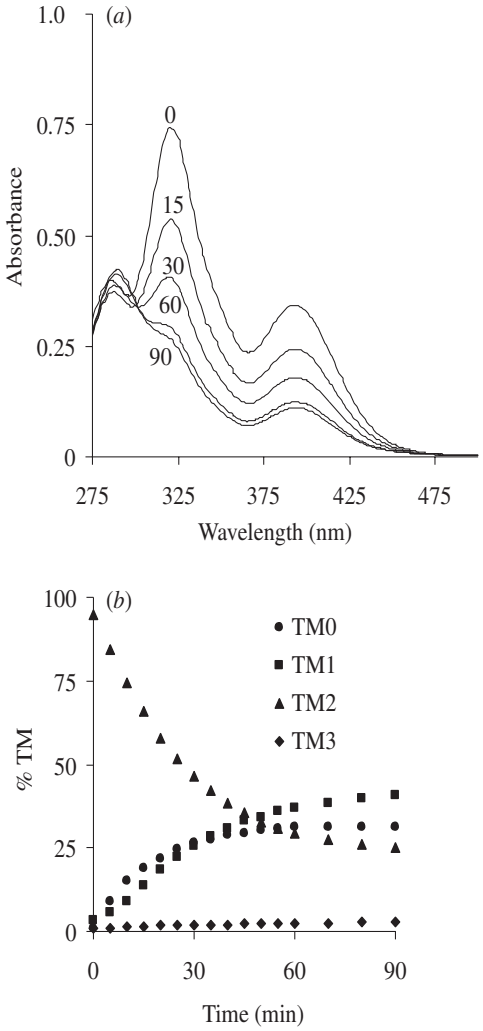
Qualitatively, one can identify the primary contaminant in synthesized "TM3". Around 461 nm, TM3 has a plateau. The formation of a discernable peak is due to TM4. If TM2 is the primary contaminant, a shoulder should appear at 286 nm. This may be difficult to observe if there is only a small amount of TM2 present. Curve fitting is a reliable way of quantifying TM impurities in TM3.

The primary difference between this method of characterization and others is that purity and absorptivities are determined simultaneously. Direct measurement of absorptivities may result in very good precision, but the accuracy is intimately dependant on the initial purity of the sample. By fitting both absorptivity and composition together, the error in one is not compounded in the determination of the other. This method also utilizes the mass of the sample and accounts for the actual formula mass and not that of the target species. This minimizes errors incurred by assuming molar concentrations.

The ultimate goal of this work is to be able to find TM concentrations in a mixture. Equation [2] was used to determine the percentage of each TM in the solution at that time. All TMs were included in the equation. Because only one solution is being fit at a time, the error in the fit is expected to be greater than is achieved from fitting multiple data sets at once. This error is much more sensitive to the quality of the original solution. However, the results over time are expected to be consistent.

Figure 3*a* shows UV–vis spectra of a "TM2" sample in water as hydrolysis occurs. For clarity, some spectra in the series have been removed. Figure 3*b* shows the percentage of each TM present during each measurement. This task was performed with all different TMs as the starting material with the same success (data not shown). These percentages can be easily converted to TM concentrations for kinetic analysis.

Fig 3. (*a*) UV–vis spectra of a TM2 solution sample hydrolyzing with time. The numbers represent the incubation time in minutes. (*b*) Composition data obtained from Origin7 fit of UV–vis spectra in Fig. 3*a*.



The increase in absorbance at 461 nm indicates the formation of TM3 as is confirmed during fitting. This is significant because it shows that hydrolysis is not a unidirectional process. This phenomenon has implications with the kinetic treatment of the data. This will be discussed in future publications.

The rise in the peak at 286 nm is accompanied by a slight bathochromic shift, indicating an increase in TM1. TM1 absorbs more strongly than TM2 at this wavelength, resulting in an overall increase in absorbance. The strong decrease in absorbance at 321 and 396 nm indicates the loss of TM2. TM1 absorbs very weakly in these regions, and TM3 is being formed in very small quantities.

After about 90 min, there is very little change in the UV–vis spectrum. Because the reaction is occurring in a sealed

© 2007 NRC Canada

cuvette, sulfide cannot be released to the atmosphere and thus remains in the space above the solution. Equilibrium is attained between the sulfide in gas phase and liquid phase, and so the TM composition stabilizes. No TM4 is formed in this experiment, as expected.

These observations are mirrored in the fitting results shown in Fig. 3*b*. A good quality of fit was maintained throughout the analysis. The percentage TM curves also appear to have very little scatter, indicating that the fitting is sensitive to small changes in concentration.

The ability to determine TM concentrations accurately provides the basis for being able to accurately calculate TM formation and hydrolysis rate constants toward the ultimate goal of modeling rumen copper. These results are currently being pursued and will be reported at a later date.

Conclusion

Multi-wavelength curve fitting has been used to accurately characterize the UV–vis spectra of the TMs as well as to quantify TM mixtures. Effective characterization is a crucial step toward measuring the kinetics of TM interconversions and their relevance to Cu antagonism, which in turn is necessary for our final goal of modeling Cu–ligand speciation in the bovine rumen. Synthesis and isolation of all TMs are also reported using a common synthetic route using $(NH_4)_2S$ as a sulfide source. TM1 was isolated in solid form for the first time from aqueous solution.

Acknowledgement

This research was funded by the Agriculture Development Fund of Saskatchewan and the University of Saskatchewan.

References

1. E.J. Underwood and N.F. Suttle. The mineral nutrition of livestock. 3rd ed. CAB International Publishing. New York, New York. 1999.
2. S.H. Laurie. Eur. J. Inorg. Chem. 2443 (2000).
3. R.S. Reid and M.A. Attaelmannan. J. Inorg. Biochem. **69**, 59 (1998).
4. M.A. Attaelmannan and R.S. Reid. J. Inorg. Biochem. **64**, 215 (1996).
5. N.F. Suttle. Annu. Rev. Nutr. **11**, 121 (1991).
6. M.A. Harmer and A.G. Sykes. Inorg. Chem. **19**, 2881 (1980).
7. A. Muller, E. Diemann, R. Jostes, and H. Bogge. Angew. Chem., Int. Ed. Engl. **20**, 934 (1981).
8. N.J. Clarke and S.H. Laurie. J. Inorg. Biochem. **12**, 37 (1980).
9. S. Licht, F. Forouzan, and K. Longo. Anal. Chem. **82**, 1356 (1990).
10. N.J. Clarke, S.H. Laurie, M.J. Blandamer, J. Burgess, and A. Hakin. Inorg. Chim. Acta **130**, 79 (1987).
11. J.W. McDonald, G.D. Friesen, L.D. Rosenhein, and W. E. Newton. Inorg. Chim. Acta **72**, 205 (1983).
12. E.K. Quagraine. Chemistry. University of Saskatchewan, Saskatoon. 2000.
13. Y. Ogra, Y. Komada, and K. T. Suzuki. J. Inorg. Biochem. **75**, 199 (1999).
14. E.K. Quagraine and R.S. Reid. J. Inorg. Biochem. **85**, 53 (2001).
15. B.E. Erickson and G.R. Helz. Geochim. Cosmochim. Acta **64**, 1149 (2000).
16. J.E. Brule, Y.T. Hayden, K.P. Callahan, and J.O. Edwards. Gazetta Chimica Italiana, **118**, 93 (1988).
17. A. Muller, H. Dornfeld, H. Schulze, and R. C. Sharma. Z. Anorg. Allg. Chem. **468**, 193 (1980).
18. P.J. Aymonino, A.C. Ranada, and A. Muller. Z. Anorg. Allg. Chem. **371**, 295 (1969).
19. N. Gershenfeld. The nature of mathematical modeling. Cambridge University Press. Cambridge, UK. 1999.
20. D.M. Thome. Chemistry. University of Saskatchewan, Saskatoon. 2001.
21. A. Muller, E. Diemann, and U. Heidborn. Z. Anorg. Allg. Chem. **371**, 136 (1969).

© 2007 NRC Canada